MALAYSIAN JOURNAL OF ANALYTICAL SCIENCES

*Published by The Malaysian Analytical Sciences Society*

ISSN
1394 - 2506

# Vol 21 No 1 (2017)

# Vol 21 No 2 (2017)

# Vol 21 No 3 (2017)

# Vol 21 No 4 (2017)

# Vol 21 No 5 (2017)

# Vol 21 No 6 (2017)

# 2017

**Malaysian Journal of Analytical Sciences Vol 21 No 1 2017**

Articles 12-30 are selected papers from the "The 28th Symposium of Malaysian Chemical Engineers (SOMChE 2015), 'Towards Net Carbon Neutrality', 21 - 22 October 2015, Palm Garden Hotel, IOI Resort, Putrajaya; organised by Department of Chemical & Process Engineering, UKM & Fuel Cell Institute, UKM."

Guest Editor: Edy Herianto Majlan.

**Page**

1. A SCREEN-PRINTED COPPER ION SENSOR WITH PHOTOCURABLE POLY(N-BUTYL ACRYLATE) MEMBRANE BASED ON IONOPHORE O-XYLYLENE BIS(N,N-DIISOBUTYLDITHIOCARBAMATE) 1
(Sensor Ion Kuprum Bercetak Skrin Berasaskan Ionofor O-Xililen Bis(N,N-Diisobutil-ditiokarbamat) Dalam Membran Terawatfoto Poli(n-butil akrilat))
*Kook Shih Ying and Lee Yook Heng*

2. $MgCl_2$ AS EFFICIENT AND INEXPENSIVE CATALYST FOR THE SYNTHESIS OF 1,4-DIHYDROPYRIDINE DERIVATIVES 13
($MgCl_2$ Sebagai Pemangkin Cekap dan Murah untuk Sintesis Terbitan 1,4-Dihidropiridina)
*Siti Nur Aqlili Riana Mohd Asseri, Sian Hui Tan, Wan Nurul Khursyiah Wan Mohamad, Seng Chee Poh, Poh Wai Chia, Su-Yin Kan, Tse Seng Chuah*

3. DEEP EUTECTIC SOLVENT AS A MEDIA IN SWELLING AND DISSOLUTION OF OIL PALM TRUNK 20
(Pelarut Eutektik Sebagai Media dalam Pembengkakan dan Pelarutan Batang Kelapa Sawit)
*Emilia Abdulmalek, Syarilaida Zulkefli, Mohd. Basyaruddin Abdul Rahman*

4. A SINGLE HPLC METHOD FOR SEPARATION OF OLIGOSTILBENES FROM DIFFERENT DIPTEROCARPACEAE EXTRACTS 27
(Kaedah KCPT untuk Pemisahan Oligostilbene dari Ekstrak Dipterocarpaceae yang Berbeza)
*Erni Muis, Rohaity Ramli, Nurhuda Manshoor*

5. PRELIMINARY STUDY ON PRODUCTION OF MONOACYLGLYCEROL AND DIACYLGLYCEROL OF VIRGIN COCONUT OIL VIA ENZYMATIC GLYCEROLYSIS USING LIPASE *Candida antarctica* (Novozyme 435) 37
(Kajian Awal Penghasilan Monoasilgliserol dan Diasilgliserol Minyak Kelapa Dara Melalui Gliserolisis Berenzim Menggunakan Lipase *Candida antarctica* (Novozyme 435))
*Darfizzi Derawi, Nurin Afiqah Zairul Azman, Mohd Fadlly Jumadi*

6. MOLLUSCICIDAL ACTIVITY OF *Entada rheedii* STEM BARK METHANOLIC EXTRACT AGAINST PADDY PEST *Pomacea canaliculata* (GOLDEN APPLE SNAIL) 46
(Aktiviti Moluskisida oleh Ekstrak Metanol Kulit Batang *Entada rheedii* Terhadap Perosak Padi *Pomacea canaliculata* (Siput Gondang Emas))
*Nur Suraya Abdullah, Noorshilawati Abdul Aziz, Rosminah Mailon*

7. THE COMMON PITFALL OF USING ENRICHMENT FACTOR IN ASSESSING SOIL HEAVY METAL POLLUTION 52
(Kepincangan Penggunaan Faktor Pengkayaan dalam Menilai Pencemaran Logam Berat di dalam Tanah)
*Seng-Chee Poh and Norhayati Mohd Tahir*

8. SYNTHESIS AND STRUCTURAL CHARACTERIZATION OF N-BROMOBENZOYL-N'-(1,10-PHENANTHROLIN-5-YL)THIOUREA DERIVATIVES 60
(Sintesis dan Penentuan Struktur Ligan Terbitan N-Bromobenzoil-N'-(1,10-Fenantrolin-5-il)tiourea)
*Rosidah Shardin, Siew San Tan, Mohammad B. Kassim*

9. SOLIDIFIED FLOATING ORGANIC DROP MICROEXTRACTION–ELECTROTHERMAL ATOMIC ABSORPTION SPECTROMETRY FOR THE DETERMINATION OF TRACE AMOUNTS OF LEAD IN WATER SAMPLES 72
(Pengekstrakan Mikro Pemejalan Titisan Organik Terapung-Spektrometri Serapan Atom Elektrotermal bagi Penentuan Jumlah Surih Plumbum di dalam Sampel Air)
*Arnon Thongsaw, Ratana Sananmuang, Gareth M. Ross, Wipharat Chuachuad Chaiyasith*

10. GROWTH EVALUATION OF MICROALGAE ISOLATED FROM PALM OIL MILL EFFLUENT IN SYNTHETIC MEDIA 82
(Penilaian Pertumbuhan Mikroalga Yang Telah Dipencil Dari Effluen Kilang Minyak Sawit Dalam Media Sintetik)
*Sharifah Najiha Badar, Zahira Yaakob, Sharifah Najiha Timmiati*

11. DETERMINATION OF CAFFEINE IN SURFACE WATER USING SOLID PHASE EXTRACTION AND HIGH PERFOMANCE LIQUID CHROMATOGRAPHY 95
(Penentuan Kafien di Permukaan Air Mengunakan Pengekstrakan Fasa Pepejal dan Kromatografi Cecair Prestasi Tinggi)
*Fouad Fadhil Al-Qaim, Siti Hasmah Jusof, Md Pauzi Abdullah, Zainab Haider Mussa, Nurfaizah Abu Tahrim, Wan Mohd Afiq Wan Mohd Khalik, Mohamed Rozali Othman*

12. SCREENING OF TROPICAL NATIVE AQUATIC PLANTS FOR POLISHING PULP AND PAPER MILL FINAL EFFLUENT 105
(Saringan Tumbuhan Akuatik Asli Tropika untuk Rawatan Penambahbaikan Sisa Pulpa dan Kertas)
*Jamilah Ahmad, Siti Rozaimah Sheikh Abdullah, Hassimi Abu Hassan, Reehan Adne Abdul Rahman, Mushrifah Idris*

13. CHARACTERIZATION STUDIES OF SODIUM ALGINATE/SULFONATED GRAPHENE OXIDE BASED POLYMER ELECTROLYTE MEMBRANE FOR DIRECT METHANOL FUEL CELL 113
(Kajian Pencirian Bagi Membran Elektrolit Polimer Berasaskan Sodium Alginat/Sulfonat Grafin Oksida untuk Sel Bahan Api Metanol Langsung)
*Norazuwana Shaari and Siti Kartom Kamarudin*

14. ROLE OF ACTIVE CHROMIUM SPECIES ON DIFFERENT SUPPORT FOR DEHYDROGENATION OF PROPANE 119
(Peranan Spesies Kromium Aktif pada Penyokong yang Berbeza dalam Tindak balas Penyahhidrogenan Gas Propana)
*Wan Nor Roslam Wan Isahak, Zatil Amali Che Ramli, Ibdal Satar, Mohamed Wahab Mohamed Hisham, Mohd Ambar Yarmo*

15. COMPARISON STUDY BETWEEN EXTRUSION AND INJECTION MOLDING ON CELLULAR STRUCTURE OF PP/PS/PMMA TERNARY BLEND FOAM 127
(Kajian Perbandingan di antara Kaedah Proses Penyemperitan dan Proses Pengacuan Suntikan ke atas Struktur Sel PP/PS/PMMA Campuran Pertigaan Busar Polimer)
*Rahida Wati Sharudin and Masahiro Ohshima*

16. SYNTHESIS AND CHARACTERIZATION OF HYDROXYAPATITE NANOPARTICLE 136

(Sintesis dan Pencirian Nanozarah Hidrosiapatit)
*Sahlil Miraz Mohamed Rafie and Darman Nordin*

17. IRON AND MANGANESE REMOVAL BY NANOFILTRATION AND ULTRAFILTRATION MEMBRANES: INFLUENCE OF pH ADJUSTMENT 149
(Penyingkiran Besi dan Mangan oleh Membran Penurasan-Nano dan Penurasan-Ultra: Pengaruh Pelarasan pH)
*Norherdawati Kasim, Abdul Wahab Mohammad, Siti Rozaimah Sheikh Abdullah*

18. CHARACTERIZATION OF ACTIVATED CARBON USING CHEMICAL ACTIVATION VIA MICROWAVE ULTRASONIC SYSTEM 159
(Pencirian Karbon Teraktif Menggunakan Sistem Pengaktifan Kimia Melalui Ketuhar Gelombang Ultrasonik)
*Norakmalah Mohd Zawawi, Fazlena Hamzah, Mahanim Sarif, Shareena Fairuz Abdul Manaf, Ani Idris*

19. $CeO_2$-$TiO_2$ FOR PHOTOREDUCTION OF $CO_2$ TO METHANOL UNDER VISIBLE LIGHT: EFFECT OF CERIA LOADING 166
($CeO_2$-$TiO_2$ untuk Penurunan $CO_2$ kepada Metanol di bawah Radiasi Cahaya Nampak:Kesan Pemuatan Ceria)
*Hamidah Abdullah, Nur Aminatulmimi Ismail, Zahira Yaakob, Maksudur R. Khan, Syarifah Abd Rahim*

20. EFFECT OF CALCINATION TEMPERATURE ON ZnO/$TIO_2$ COMPOSITE IN PHOTOCATALYTIC TREATMENT OF PHENOL UNDER VISIBLE LIGHT 173
(Kesan Pengkalsinan Suhu ke atas Komposit ZnO/$TiO_2$ untuk Menyingkirkan Fenol Melalui Fotopemangkin di bawah Cahaya Nampak)
*Nur Syazrin Amalina Abdullah, Sufian So'aib, Jaganatthan Krishnan*

21. TREATMENT OF METHYLENE BLUE IN WASTEWATER USING *Scirpus grossus* 182
(Rawatan Metilena Biru dalam Air Sisa Menggunakan *Scirpus grossus*)
*Enas Abdulqader, Siti Rozaimah Abdullah, Hassimi Abu Hasan, Reehan Adre Ab. Rahim, Mushrifah Idris*

22. CHEMICAL AND PHYSICAL CHARACTERIZATION OF OIL PALM EMPTY FRUIT BUNCH 188
(Pencirian Kimia dan Fizikal Bagi Tandan Kosong Buah Kelapa Sawit)
*Nurul Suraya Rosli, Shuhaida Harun, Jamaliah Md Jahim*

23. PALM KERNEL SHELL-DERIVED BIOCHAR AND CATALYST FOR BIODIESEL PRODUCTION 197
(Biochar dan Pemangkin Berasaskan Tempurung Kelapa Sawit untuk Penghasilan Biodiesel)
*Dayang Nuradila, Wan Azlina Wan Ab Karim Ghani, Azil Bahari Alias*

24. PREDICTION OF INDUSTRIAL CATALYSTS DEACTIVATION RATE USING FIRST PRINCIPLE MODEL AND OPERATING DATA 204
(Ramalan Kadar Penyahaktifan Mangkin Industri Menggunakan Model Prinsip Pertama dan Data Operasi)
*Abbas Azarpour and Sharifah Rafidah Wan Alwi*

25. THE EFFECT OF GLUCOSE ADDITION IN ACETONE-BUTANOL-ETHANOL FERMENTATION FROM PALM OIL MILL EFFLUENT BY *Clostridium acetobutylicum* NCIMB 619 213
(Kesan Penambahan Glukosa dalam Fermentasi Aseton-Butanol-Etanol daripada Efluen Kilang Kelapa Sawit oleh *Clostridium acetobutylicum* NCIMB 619)
*Azima Syafaini Japar, Mohd. Sobri Takriff, Jamaliah Md. Jahim, Abdul Amir Hassan Kadhum*

26. POLYETHERSULFONE/PLURONIC F127 BLENDED NANOFILTRATION MEMBRANES FOR XYLITOL PURIFICATION 221
(Membran Penurasan-Nano Campuran Polietersulfon/Pluronik F127 untuk Penulinan Xilitol)
*Khalefa A. Faneer, Rosiah Rohani, Abdul Wahab Mohammad*

27. SEED CULTURE CONDITIONS FOR HIGH YIELD OF CELLULOLYTIC ENZYMES PRODUCTION FROM *Pycnoporus sanguineus* 231
(Keadaan Kultur Benih untuk Penghasilan Enzim Selulolitik daripada *Pycnoporus sanguineus*)
*Rafidah Jalil, Mohd Sahaid Kalil, Norliza Abdul Rahman, Aidil Abdul Hamid, Mohd Farid Ahmad*

28. CRUDE PALM OIL BIODIESEL BY TRANSESTERIFICATION PROCESS USING CHOLINE HYDROXIDE CATALYST 240
(Biodiesel Minyak Sawit Mentah Melalui Proses Transesterifikasi Menggunakan Mangkin Kolin Hidroksida)
*Renita Manurung, Nadya G. Bestari, Dania K. Syabri*

29. SYNTHESIS, CHARACTERIZATION AND CATALYTIC PERFORMANCE OF CERIA-SUPPORTED COBALT CATALYST FOR METHANE DRY REFORMING TO SYNGAS 248
(Sintesis, Pencirian dan Prestasi Mangkin Kobalt Sokongan Ceria untuk Penghasilan Semula Metana Kontang Kepada Gas Sintesis)
*Bamidele V. Ayodele, Mohd Nasir Nor Shahirah, Maksudur R. Khan, Chin Kui Cheng*

30. EFFECTS OF AGITATION CONDITIONS ON BACTERIAL CELLULOSE PRODUCTION BY *Acetobacter xylinum 0416* IN FERMENTATION OF MATURED COCONUT WATER MEDIUM 261
(Kesan Goncangan ke atas Penghasilan Selulosa Bakteria oleh *Acetobacter xylinum 0416* Melalui Fermentasi Air Kelapa Tua)
*Faezah Esa, Norliza Abd. Rahman, Mohd Sahaid Kalil, Siti Masrinda Tasirin*

*Malaysian Journal of Analytical Sciences, Vol 21 No 1 (2017): 1 - 12*
*DOI: http://dx.doi.org/10.17576/mjas-2017-2101-01*

MALAYSIAN JOURNAL OF ANALYTICAL SCIENCES
*Published by The Malaysian Analytical Sciences Society*
ISSN 1394 - 2506

# A SCREEN-PRINTED COPPER ION SENSOR WITH PHOTOCURABLE POLY(N-BUTYL ACRYLATE) MEMBRANE BASED ON IONOPHORE O-XYLYLENE BIS(N,N-DIISOBUTYLDITHIOCARBAMATE)

## (Sensor Ion Kuprum Bercetak Skrin Berasaskan Ionofor O-Xililen Bis(N,N-Diisobutil-ditiokarbamat) Dalam Membran Terawatfoto Poli(n-butil akrilat))

Kook Shih Ying and Lee Yook Heng*

*School of Chemical Sciences and Food Technology, Faculty of Science and Technology, Universiti Kebangsaan Malaysia, 43600 UKM Bangi, Selangor, Malaysia*

**Corresponding author: leeyookheng@yahoo.co.uk*

Received: 6 September 2016; Accepted: 22 November 2016

**Abstract**

A screen-printed copper ion sensor with photocurable poly(n-butyl acrylate) (pBA) membrane based on ionophore o-xylylene bis(N,N-diisobutyldithiocarbamate) (o-xc) was successfully fabricated. Poly(2-hydroxylethyl methacrylate) (pHEMA)-modified Ag/AgCl screen-printed electrode was used in the development of the sensor and the sensor was characterized by potentiometric method. Optimization of pBA membrane for the electrode was carried out by varying the compositions of sodium tetrakis[3,5-bis(trifluoromethyl)phenyl]borate (NaTFPB) and o-xc to determine the best analytical performance. The addition of NaTFPB and the increment of its ratio relative to o-xc showed super-Nernstian, small linear range, and high detection limit. For sensor fabricated based on o-xc without the addition of NaTFPB, the sensor showed Nernstian response. The best optimized sensor showed Nernstian slope with 31.29 mV/decade over a wide linear range of $1.0 \times 10^{-2} - 1.0 \times 10^{-6}$ M and low detection limit of $1.89 \times 10^{-7}$ M. The sensitivity of this sensor was also improved over the other copper ion sensors fabricated by similar photocuring technique. In addition, based on the separate solution method (SSM), this sensor exhibited good selectivity towards copper ion with low logarithm selectivity coefficient value for monovalent and divalent cations namely $K^+$, $Na^+$, $Ca^{2+}$, $Mg^{2+}$, $Ni^{2+}$ and $Co^{2+}$.

**Keywords:** screen-printed copper ion sensor, photocurable poly(n-butyl acrylate) membrane, ionophore o-xylylene bis(N,N-diisobutyldithiocarbamate), potentiometry

**Abstrak**

Sensor ion kuprum bercetak skrin yang berasaskan kepada ionofor o-xililen bis(N,N-diisobutilditiokarbamat) (o-xc) dalam membran terawatfoto poli(butil-akrilat) (pBA) telah dibangunkan. Sensor ion elektrod bercetak skrin Ag/AgCl terubahsuai poli(2-hidroksiletil metakrilat) (pHEMA) telah digunakan dalam pembangunan sensor dan pencirian sensor telah dijalankan melalui kaedah potensiometri. Pengoptimunan komposisi membran sensor ion pada elektrod telah dijalankan untuk menentukan prestasi analisis yang terbaik dengan mengubah komposisi sodium tetrakis[3,5-bis(trifluorometil)fenil]borat (NaTFPB) dan o-xc. Penambahan NaTFPB dan peningkatan nisbahnya terhadap o-xc dalam membran menunjukkan super-Nernstian, julat linear yang pendek dan had pengesanan yang tinggi. Sensor ion yang direka bentuk dengan menggunakan o-xc tanpa penambahan NaTFPB menunjukkan rangsangan Nernstian. Sensor ion yang terbaik menunjukkan kecerunan Nernstian iaitu 31.29mV/dekad, julat linear dari $1.0 \times 10^{-2} - 1.0 \times 10^{-6}$ M dan had pengesanan terendah $1.89 \times 10^{-7}$ M. Kepekaan sensor yang telah dibangunkan juga adalah lebih baik berbanding dengan sensor-sensor ion kuprum lain yang telah direka bentuk melalui kaedah rawatan foto yang sama. Nilai pekali keselektifan potensiometri ditentukan dengan kaedah larutan berasingan (SSM). Sensor tersebut juga memberikan keselektifan yang baik terhadap kation pengganggu dengan menunjukkan nilai pekali logaritma keselektifan yang rendah bagi kation monovalen dan divalen seperti $K^+$, $Na^+$,$Ca^{2+}$, $Mg^{2+}$, $Ni^{2+}$ dan $Co^{2+}$.

**Kata kunci**: sensor ion kuprum bercetak skrin, membran terawatfoto poli(n-butil akrilat), ionofor o-xililen bis(N,N-diisobutilditiokarbamat); potensiometri

## Introduction

Copper is one of the most widely spread heavy metals in the environment. It is extensively used for industrial, agricultural, and domestic purposes due to its high electrical conductivity, chemical stability, and potential to form alloy with other metals [1]. Copper is also an essential trace element to human health and involves in electron transfer process of various biological system [1,2]. However, copper as one of the heavy metal ions is considered toxic to many living organisms due to its non-biodegradable behavior [3]. Long term exposure to copper will cause irritation of the nose, mouth, eyes, headache, and stomach problems [4]. Intentionally high uptake of copper may exhibit toxicity and pose a threat to human health by causing Alzheimer's disease, Wilson's disease, hypoglycemia, liver and kidney damage, and gastrointestinal problem as the tolerance limit of copper in human body is 2 mg per day [5,6]. In addition, copper can act as a potential endocrine disrupter by modulating the estrogenic activity of endogenous hormones. By replacing zinc atom from the zinc fingers of estrogen receptor with copper, the binding of the receptor with DNA hormone responsive elements in the cell nucleus is prevented [7]. Therefore, in view of the widespread use of copper, its occurrence in the environment, and its adverse effects, its determination is important and highlights are needed for an efficient method of copper detection.

Application of ion sensor for the determination of metal ions has been widely developed because of its high selectivity, low detection limit, low cost analysis, require no sample pretreatment, and sensitive to electronics [8-10]. Among the ion sensors types, potentiometric detection method is the simplest method that offers various advantages such as fast and easy preparation procedures, simple instrumentation, fast response time, wide linear range, and may also suitable for online analysis [6,11]. The common ion sensor construction is normally based on polymeric membrane consisting the immobilized sensing material [12]. Hence, in the fabrication of an ion sensor, the ionophore as the electroactive and sensing material, should exhibits stronger affinity for a particular metal ion [13]. The copper ionophore o-xc used is shown in Figure 1.

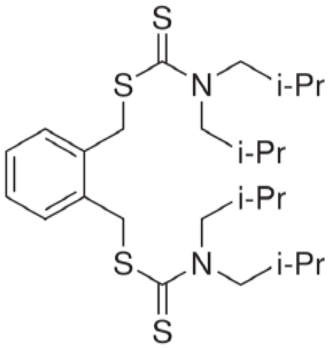



Figure 1. Structure of ionophore *o*-xylylene bis(N,N-diisobutyldithiocarbamate) (o-xc)

O-xc compound is a good ionophore as it shows a very good selectivity towards copper ion in copper ion sensors as reported by Kamata et al. [14], Woznica et al. [15], Birinci et al. [16], and Kisiel et al. [17]. O-xc is a non-cyclic compound, which consists of dithiocarbamate functional group. The sulfur atoms from the dithiocarbamate group pose σ orbital donor and n-back donation characteristic [18-19]. Thus, the sulfur atoms act as the active sites and able to coordinate with copper (II) ion to form a chelate with a four member ring [20].

Besides that, it is also crucial to select the right immobilization matrix for ionophore immobilization due to the nature of the ionophore. The selection will be affected by the types of immobilized matrix, and thus affect the performance of the sensor [21]. Most of the reported copper ion sensors utilized poly(vinyl chloride) (PVC)

membrane as polymer matrix because of its relatively low cost, high tensile strength, chemical inertness, and plasticizer compatibility [22-24]. A conventional copper ion sensor based on ionophore o-xc with PVC membrane was developed by Kamata et al. [14]. This sensor showed a Nernstian slope of 29 mV/decade within the linear range from $1.0 \times 10^{-6}$ to $1.0 \times 10^{-1}$ M, the detection limit of $1.4 \times 10^{-7}$ M and good selectivity over a wide variety of interference cations including alkali, alkaline earth, transition, and heavy metal ions. Another copper ion sensor with the same membrane components but used different conductive material, graphite, epoxy, and hardener mixture as the solid contact for the ion selective electrode reported by Birinci et al [16]. The sensor displayed a Nernstian response of 31.3 mV/decade over a linear range, $1.0 \times 10^{-6}$ to $1.0 \times 10^{-1}$ M, the detection limit of $4.9 \times 10^{-7}$ M and selective towards copper ions over common interference cations. PVC membrane is a hard polymer. A plasticizer is always needed to obtain a soft and elastic property for an optimum response. Therefore, both reported copper ion sensor used plasticizing solvent mediator, o-nitrophenyl octyl ether, in the membrane preparation in order to be functional as a copper ion sensor. However, plasticizer incorporation resulted in weakening the mechanical strength and adhesion of the polymer on the surface of electrode. Consequently, the polymer membrane tends to be peeled off easily from the transducer and causes a major shift of sensor response [25-27].

Alternatively, plasticizer-free acrylate polymer has become a choice of membrane material in this work. This polymer has various advantages. For instance, it is self-plasticizing, so it does not need any kind of external plasticizer. Acrylate polymer is also photocurable and can be formed by photopolymerization on an electrode surface [28-29]. Compared with PVC membrane deposition method such as solvent casting which needs at least one day of solvent evaporation [16], this photopolymerization method is fast and simple [28]. Moreover, this polymer also has lower glass transition temperature value, $T_g$, enable an excellent adhesion on solid surfaces. Therefore, it is suitable for application in solid state ion sensor [29]. Woznica et al. [15] have reported a solid-state copper ion sensor based ionophore o-xc with photocurable pBA membrane onto the surface of conducting layer, poly(3-octylthiophene-2,5-diyl) (POT) modified ion selective electrode. Without the addition of plasticizer, this sensor demonstrated a good selectivity towards various interference cations. However, lower Nernstian slope was observed with 26.3 mV/decade in the range of $1.0 \times 10^{-6}$ to $1.0 \times 10^{-1}$M with detection limit of $1.0 \times 10^{-6.3}$ M. A drop casting application for ionophore immobilization and entrapment method within pBA membrane in this sensor fabrication is said to be less efficient because this method causes an insufficient amount of ionophore o-xc presence in the membrane. Therefore, a more efficient immobilization method is also needed to render an improved performance of a sensor.

Furthermore, concerning solid state ion selective electrode coupled with potentiometric detection, screen-printed electrode represents a high interest when considering the technological aspects that offer low cost and simplicity of manufacturing, mass production, and long term stability [30,31]. High sensitivity, low detection limit, and no requirement of large volume of sample also other important advantages using screen-printed electrode [32]. Previously reported copper ion sensors based ionophore o-xc with PVC or pBA membranes are non-screen-printed solid-state sensors [15-17]. Therefore, the intention of this study is to explore a screen-printed copper ion sensor based ionophore o-xc with photocurable pBA membrane. Instead of drop cast immobilization method, the ionophore o-xc was immobilized within the pBA membrane during the photopolymerization. The optimization of the composition of the ion selective pBA membrane for preparing the best copper ion sensor was also detailed.

## Materials and Methods

### Reagents and chemicals

Chemicals used in this study included n-butyl acrylate (nBA), 2,2-dimethoxy-2-phenylacetophenone (DMPP), 1,6-hexanediol diacrylate (HDDA), 2-hydroxylethyl metacrylate (HEMA) from Sigma Aldrich; sodium tetrakis [3,5-bis(trifluoromethyl) phenyl] borate (NaTFPB), *o*-xylylene bis(N,N-diisobutyldithiocarbamate) (o-xc) from Fluka; copper (II) chloride dihydrate from S&M, sodium chloride from SYSTERM, potassium chloride from Sigma Aldrich, calcium chloride from HMBG, cobalt chloride hexahydrate from AJAX, and magnesium chloride and nickel chloride hexahydrate from Fluka. All chemicals are analytical grade and used as obtained. Deionized water was used for the standard solution preparation.

**Apparatus**

The electrochemical measurements were performed using an Orion Ion meter. A double junction Ag/AgCl was used as the reference electrode. The reference electrode was filled with 0.1 M Tris HCl buffer at pH 7.00 saturated with AgCl as internal reference solution and 0.1M lithium acetate as gel bridge electrolyte. The working electrode was an Ag/AgCl screen-printed electrode (Scrint Print Sdn. Bhd., Malaysia). An ultraviolet (UV) exposure unit (R.S.Ltd) installed with four light tubes transmitting UV light at the wavelength of 350 nm was used for photopolymerization of pBA membrane.

**Preparation of poly(2-hydroxylethyl methacrylate) (pHEMA) as inner layer**

A mixture of 913 µL HEMA monomers and 15.68 mg of photoinitiator, DMPP was drop-coated onto the Ag/AgCl screen printed electrode. The electrode was then placed in the UV-exposure unit for photopolymerization process. Before the irradiation of UV, the unit was purged with nitrogen gas for 2 minutes and then irradiated for 3 minutes under constant flow of nitrogen gas. The polymer film formed was then hydrated with 0.1 M of copper (II) chloride dihydrate solution for 30 minutes to form the inner layer of the sensor. This photocuring method was similar to the method reported by Lee & Hall [28] with minor modification.

**Preparation of ion selective poly(n-butyl acrylate) pBA membrane**

A mixture of nBA monomers, cross linker HDDA, photoinitiator DMPP, and required amounts of lipophilic salt, NaTFPB and ionophore o-xc was prepared as shown in Table 1. The mixture was then deposited on the top of the hydrated pHEMA inner layer and then photocured in a UV- exposure unit under a nitrogen gas atmosphere for 8 minutes to form the self-plasticizing and ion selective pBA membrane. The procedures to fabricate copper ion sensor with pHEMA-pBA membrane and the design of pHEMA modified-Ag/AgCl screen printed electrode with pBA membrane are shown in Figure 2 and Figure 3 which reported by Alva [33] with minor modification.

Table 1. Composition of ion selective pBA membrane

| Sensor No. | nBA (wt%) | HDDA (wt%) | DMPP (wt%) | o-xc (wt%) | NaTFPB (mol%) |
|---|---|---|---|---|---|
| 1 | 96.64 | 0.10 | 0.97 | 0.97 | 80.00 |
| 2 | 96.96 | 0.10 | 0.97 | 0.97 | 60.00 |
| 3 | 97.28 | 0.10 | 0.97 | 0.97 | 40.00 |
| 4 | 97.45 | 0.10 | 0.97 | 0.97 | 30.00 |
| 5 | 97.61 | 0.10 | 0.98 | 0.98 | 20.00 |
| 6 | 97.92 | 0.10 | 0.98 | 0.98 | 1.00 |
| 7 | 97.04 | 0.10 | 0.98 | 0.98 | - |
| 8 | 97.47 | 0.10 | 0.97 | 1.46 | - |
| 9 | 96.99 | 0.10 | 0.97 | 1.94 | - |
| 10 | 96.06 | 0.10 | 0.96 | 2.88 | - |

**Procedure to evaluate the copper ion sensor responses**

A complete electrochemical cell was setup which consisted of reference electrode and copper ion sensor. Both reference electrode and copper sensor were connected to an Orion ion meter and the potential differences or electromotive force (EMF) in mV unit were recorded when a stable reading was reached. Copper ion sensor with varying composition of pBA membrane was measured with the standard solution of copper (II) chloride dihydrate in the range of $10^{-1}$M to $10^{-8}$M. The graph of EMF versus logarithm of copper (II) chloride dihydrate concentration was plotted and the slope of the graph was determined [34].

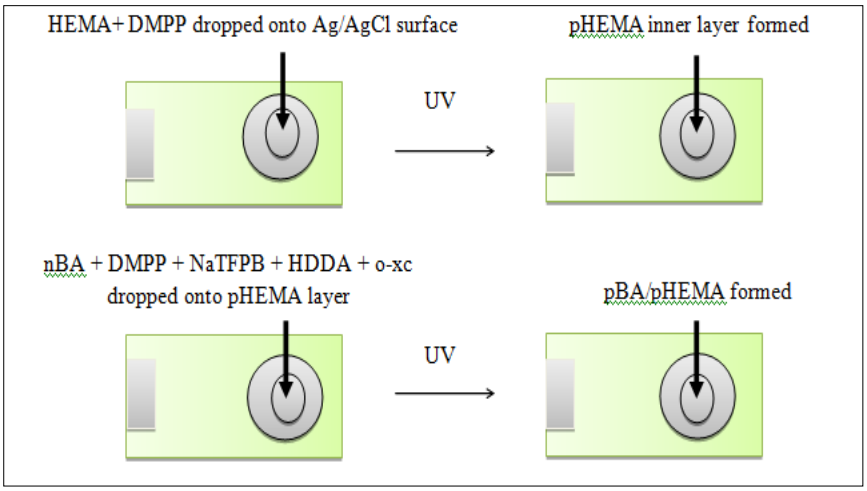



Figure 2. Steps to fabricate Ag/AgCl screen-printed copper ion sensor with pHEMA-pBA membrane

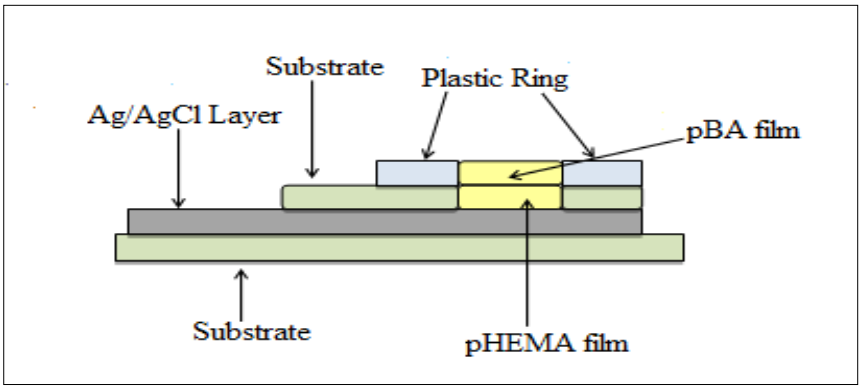



Figure 3. The design of Ag/AgCl screen printed electrode with pBA-pHEMA membrane

The selectivity behavior of the ion sensor is usually described in terms of selectivity coefficient. The selectivity coefficient of the proposed electrode was determined by separate solution method (SSM) with reference to Nicolsky-Eisenmann equation [35]. An amount of 0.01 M of interference ions NaCl, KCl, $CaCl_2$, $CoCl_2$, $MgCl_2$ and $NiCl_2$ were prepared and the potential differences were measured to evaluate the selectivity of the copper ion sensor. The measurements were done in triplicate for each interference ions and the average value was taken to determine the logarithm selectivity coefficient of the sensor.

## Results and Discussion

### Effect of lipophilic salt NaTFPB on copper ion sensor response

The presence of anionic sites has been known to be beneficial to cation selective sensor especially those sensors with neutral ionophore. It can increase the anionic property of the ion selectivity membrane by reducing the surface resistance, attracting more cations to the membrane surface, and enhancing the cation exchange process at the membrane-solution interface [36,37]. The lipophilic salt used in this study was NaTFPB as showed in Figure 4. The anionic site was created by NaTFPB in this work after entrapped together with ionophore into the membrane phase. Therefore, it is vital in determining the exact composition of lipophilic salt NaTFPB and ionophore o-xc inside the membrane as these two components will affect the sensitivity and selectivity of the ion sensor significantly [36].

Seven batches of copper ion sensor with different amounts of NaTFPB were fabricated to evaluate their performances.

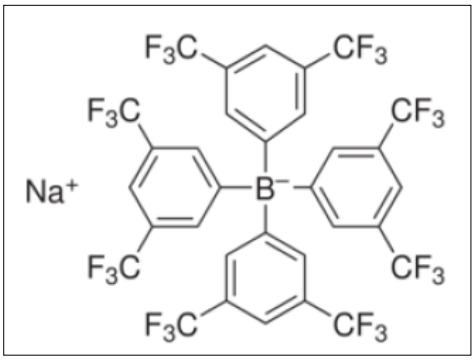



Figure 4. NaTFPB molecule with negatively charged B

Nernstian response is revealed when calibration graph of potential differences versus logarithm of ion activity is linear with a slope of 29.58 mV/decade for every 10 increment of divalent ion concentration at 298.15 K [38]. According to Figure 5 and Table 2, Sensor 1 to Sensor 5 with 80 mol%, 60 mol%, 40 mol%, 30 mol% and 20 mol% of NaTFPB showed super-Nernstian response while Sensor 6 and Sensor 7 with 1 mol% and 0 mol% of NaTFPB showed Nernstian response.

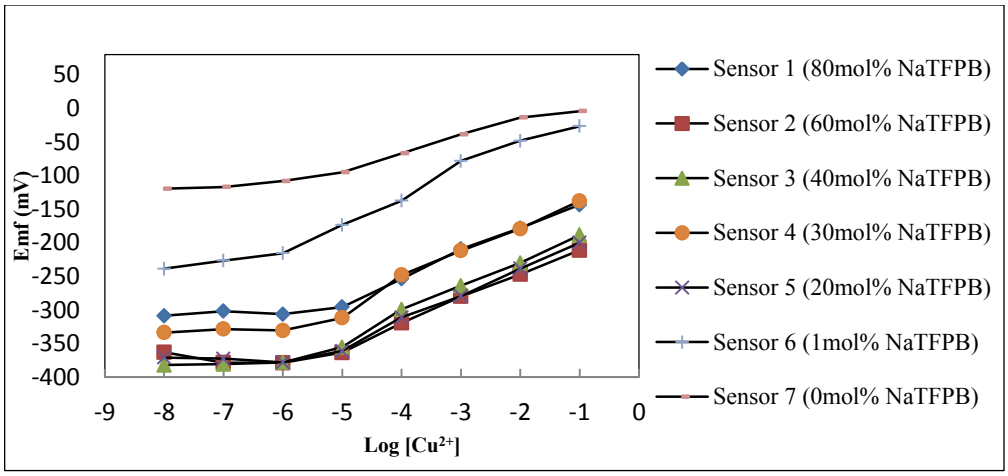



Figure 5. Potentiometric response of copper ion sensors based on 1 wt% of ionophore o-xc and different amounts of NaTFPB lipophilic salts.

NaTFPB lipophilic salt is known to reduce the membrane resistance and increase the anion site. With the aim of anion sites, the ion-transport process from aqueous phase to organic phase (pBA membrane) becomes faster because it induces the efficiency of cations attraction to the membrane surface [26]. Nevertheless, excessive amount of NaTFPB may cause the pBA membrane to become over polar and negatively charged. This will lead to a fast influx of copper (II) ions into the pBA membrane and a depletion zone of the copper (II) ions from the Nernst diffusion layer can be occurred. Therefore, a super-Nernstian response was observed in Sensor 1 to Sensor 5 [39].

Table 2. Performance of copper ion sensors based on 1 wt% ionophore o-xc and different amounts of NaTFPB lipophilic salts

| Sensor No. | Slope (mV/decade) | Linear Range (M) | Detection Limit (M) | ($R^2$) |
|---|---|---|---|---|
| 1 | 37.24 | $10^{-1} – 10^{-4}$ | $1.00 \times 10^{-5}$ | 0.999 |
| 2 | 37.06 | $10^{-1} – 10^{-4}$ | $8.70 \times 10^{-6}$ | 0.998 |
| 3 | 36.59 | $10^{-1} – 10^{-4}$ | $3.39 \times 10^{-6}$ | 0.998 |
| 4 | 36.32 | $10^{-1} – 10^{-4}$ | $1.83 \times 10^{-6}$ | 0.998 |
| 5 | 35.55 | $10^{-1} – 10^{-4}$ | $1.62 \times 10^{-6}$ | 0.997 |
| 6 | 28.71 | $10^{-1} – 10^{-4}$ | $1.23 \times 10^{-6}$ | 0.999 |
| 7 | 27.20 | $10^{-2} – 10^{-5}$ | $1.19 \times 10^{-6}$ | 0.999 |

Furthermore, *o*-xc is a neutral molecule, the non-symmetry arrangement of the dithiocarbamate group induces a polarity within the ionophore because the structure of ionophore o-xc consisted of two dithiocarbamate functional group at the ortho position of the benzene ring. Hence, with the addition of NaTFPB anionic salt, it further increases the polarity and negative charge of the pBA membrane and a super-Nernstian response is expected. Therefore, a super-Nernstian response was observed in Sensor 1 to Sensor 5 [39]. Super-Nernstian behavior is undesirable because such response is unstable and irreproducible. Excessive of NaTFPB will also lead to a loss of sensor selectivity towards copper (II) ions. Hence, when lower amounts of NaTFPB were used, e.g. 1 mol% and 0 mol% as in Sensor 6 and Sensor 7 in the pBA membrane, Nernstian response was observed due to lower ionic behavior. The low or non-requirement of the lipophilic anion such as TFPB in this sensor membrane for optimum response also indicated that the membrane itself might contain certain amount of anionic charge intrinsically.

In terms of detection limit, ion sensors which consisted of NaTFPB in the pBA membrane showed a higher detection limit. With the high polarity and anionic effect of the pBA membrane, an excessive influx of copper (II) ion from sample into the membrane induced and this cannot be balanced out by the ion exchange process of inner electrolyte at the membrane-inner electrolyte phase. Thus, the two sides of membrane are failed in achieving a thermodynamic equilibrium and higher detection limit was obtained. This is also parallel to previous study by Mi et al. [40] who reported that if the membrane is not at a steady stage, a higher influx of ion will lead to a higher detection limit.

Given that the pBA membrane without the addition of NaTFPB showed a better potentiometric response and the lowest detection limit, membrane composition of Sensor 7 was chosen for further optimization.

**Effect of ionophore o-xc on copper ion sensor response**

Figure 6 presents the calibration curves of four copper ion sensors with different amounts of ionophore o-xc. Their performances were evaluated and tabulated in Table 3.

According to Table 3, all four copper ion sensors showed Nernstian responses and explained a good response towards the sensitivity. The increment amount of ionophore o-xc also improved the performances of the copper ion sensor. This is because the polarity within the pBA membrane depends on the ionophore o-xc. Hence, higher amount of ionophore o-xc accelerates the ion transfer process from aqueous phase to pBA membrane phase. Besides, the movement of copper (II) ion through the pBA membrane is based on 'ion-jumping' or 'hopping' mechanism which mean passing an ion 'bucket' from one carrier to the other until it reaches the surface of Ag/AgCl electrode [41]. Therefore, with the higher amount of ionophore o-xc within the pBA membrane, the ion-transport process within the pBA membrane becomes better and faster. Thus, Sensor 10 with the highest amount of ionophore o-xc showed the best response.

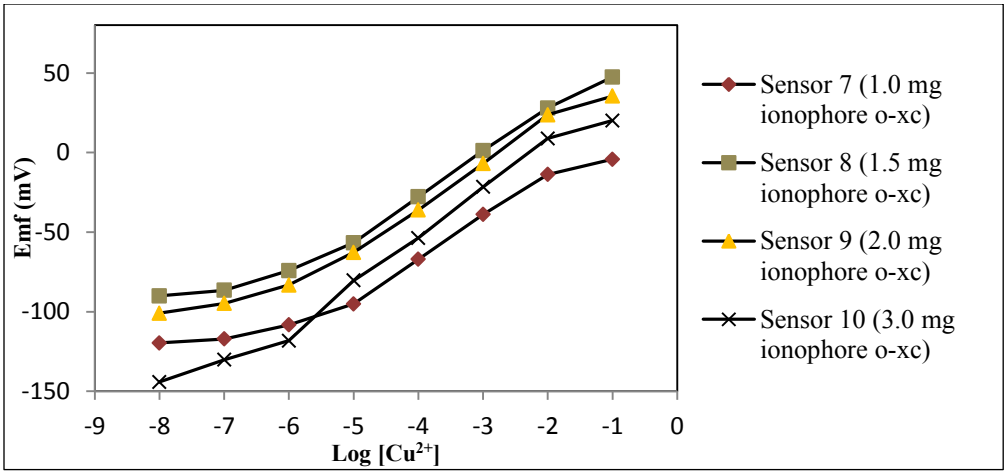



Figure 6. Potentiometric response of copper ion sensors based on 0 wt% of NaTFPB and different amounts of ionophore o-xc

Table 3. Performance of copper ion sensors based on 0 wt% of NaTFPB and different amounts of ionophore o-xc

| Sensor No. | Slope (mV/decade) | Linear Range (M) | Detection Limit (M) | ($R^2$) |
|---|---|---|---|---|
| 7 | 27.20 | $10^{-2} – 10^{-5}$ | $1.19 \times 10^{-6}$ | 0.999 |
| 8 | 28.31 | $10^{-2} – 10^{-5}$ | $8.49 \times 10^{-7}$ | 0.999 |
| 9 | 28.84 | $10^{-2} – 10^{-5}$ | $5.17 \times 10^{-7}$ | 0.999 |
| 10 | 31.29 | $10^{-2} – 10^{-6}$ | $1.89 \times 10^{-7}$ | 0.999 |

Sensor 10 showed the lowest detection limit of $1.89 \times 10^{-7}$ M and wider linear range, $10^{-2}$ - $10^{-6}$ M. This is due to a high amount of ionophore o-xc inside the pBA membrane. Higher amount of ionophore allowed more complexation to occur between copper (II) ion and ionophore o-xc. Thus more influx of copper (II) ion into the membrane was expected. The pBA membrane thus saturated with the copper (II) ion and this stabilized the copper (II) ion concentration at the interface of membrane-inner electrolyte. As a result, the sensitivity of the sensor towards copper (II) ion was increased and a wider linear range was obtained. A wider linear range subsequently lowers the detection limit [42].

**Selectivity on copper ion sensor**

Interference study was carried out for the best four copper ion sensors; Sensor 7 to Sensor 10 by the separate solution method (SSM). This selectivity method was used when the ion sensor showed Nernstian response within a linear range. In the SSM, the emf of an electrochemical cell between a reference electrode and the ion sensor was measured with each of the two separate solutions, namely one of the solution containing the ion analyte A with selected concentration. Meanwhile the other solution contained the interference ion B with the same concentration. If the measured values are $E_A$ and $E_B$, the logarithm selectivity coefficient can be calculated from the Nicolsky-Eisenman equation as shown in equation 1 below:

$$\log K_{A,B}^{pot} = \frac{(E_B - E_A)Z_A F}{2.303RT} + \left(1 - \frac{Z_A}{Z_B}\right)\log a_a \quad (1)$$

where R is the gas constant, T is the temperature in Kelvin unit, F is the Faraday constant, E is the potential difference of ion in mV, Z is the ion charge, A is the main ion, copper (II) ion in this work, B is the interference ion, and $a_a$ is concentration of 0.01 M used in this work.

From Table 4, it was found that the higher the amount of ionophore o-xc, the lower the value of logarithm selectivity coefficient was obtained. According to Alva [33], the lower the value of logarithm $K_{A,B}^{pot}$, the more selective the ion sensor. Selectivity of the membrane pBA was affected by the tendency of ionophore in forming a stable complex with the analyte ion and the selectivity coefficient can be also be explained and determined by the following equation 2:

$$K_{ij}^{pot} = \frac{\Sigma_n K_{j,n}}{\Sigma_n K_{i,n}} = \frac{\Sigma_n \beta_{js,n}^{w} k_{js,n} ({}^{c_s}/_{k_s})^n}{\Sigma_n \beta_{is,n}^{w} k_{is,n} ({}^{c_s}/_{k_s})^n} \quad (2)$$

where j is the interference ion and i is the main ion. $\beta_{js,n}^{w}$ and $\beta_{is,n}^{w}$ are complex stability constant, $k_{js,n}$ and $k_{is,n}$ is distribution constant, $k_s$ is distribution of free ligand constant, and $c_s$ is concentration of ligand S (ionophore). Selectivity is influenced by the saturation of ionophore o-xc-copper (II) complex within the pBA membrane. Hence, copper ion sensor with the highest amount of ionophore o-xc showed the lowest value of logarithm selectivity coefficient due to formation of more complexes. Besides, high distribution of ionophore o-xc-copper (II) complex could also prevent the influx of interference ion into the membrane; thus, further increase the selectivity of the copper ion sensor [42].

Table 4. Logarithm selectivity coefficient $Log(K_{Cu^{2+},M^{n+}}^{pot})$ for four ion sensors with different amounts of ionophore o-xc

| Sensor No. | Interference Ions | | | | | |
|---|---|---|---|---|---|---|
| | $K^+$ | $Na^+$ | $Mg^{2+}$ | $Ni^{2+}$ | $Co^{2+}$ | $Ca^{2+}$ |
| 7 | 0.44± 0.18 | 0.58±0.09 | -1.53±0.19 | -1.18±0.05 | -1.11±0.06 | -1.15±0.44 |
| 8 | -0.13±0.10 | -0.01±0.10 | -2.27±0.05 | -2.13±0.07 | -2.07±0.11 | -2.15±0.07 |
| 9 | -0.45±0.05 | -0.40±0.03 | -2.62±0.10 | -2.40±0.09 | -2.35±0.06 | -2.40±0.08 |
| 10 | -1.49±0.10 | -1.41±0.15 | -3.30±0.07 | -3.09±0.02 | -3.05±0.05 | -3.12±0.06 |

Among the four copper ion sensors, Sensor 10 showed the best selectivity towards copper (II) ion with the lowest logarithm selectivity coefficient for all the interference cations. From the four divalent interference cations, cobalt ion gave higher logarithm selectivity coefficient. This might be related to the radius of the interference cations [43] as cobalt (II) ion has a similar ionic radius with copper (II) ion. However, the logarithm selectivity coefficient of the ion sensor towards cobalt (II) ion was -3.05±0.05, which showed that interference effect from cobalt ion was insignificant. Monovalent interference cation such as potassium and sodium gave higher logarithm selectivity coefficient. Such larger value is aroused from the $(1 - \frac{2}{Z_B})$ in the Nicolsky-Eisenman equation. Hence, the smaller the charge of the interference ion, $Z_B$, the larger the value of logarithm selectivity coefficient [1]. Furthermore, potassium and sodium ions have larger ionic radius and different chemical properties from copper (II) ion as potassium and sodium ions belong to alkali metal ion whereas copper (II) ion is a heavy metal ion, the disturbance produced by these two ions is negligible. Therefore, the above results demonstrated that Sensor 10 showed a good selectivity towards copper (II) ion.

**Comparison with previous studies**

The performances of the screen-printed copper ion sensor in this work were compared with the previously reported copper ion sensor based ionophore o-xc (Table 5).

Table 5. Comparison between screen-printed copper ion sensor and reported potentiometric copper ion sensors with ionophore *o*-xylylene bis(N,N-diisobutyldithiocarbamate)

| **Ionophore Immobilization Matrix** | **Linear Range (M)** | **Detection Limit (M)** | **Slope (mV/decade)** | **$\mathbf{Log(K^{pot}_{Cu^{2+},M^{n+}})}$** | **Ref.** |
|---|---|---|---|---|---|
| Poly(n-butyl acrylate)-photocured membrane, non-plasticised | $1.0\times10^{-6}$ - $1.0\times10^{-2}$ | $1.89\times10^{-7}$ | 31.29 | $K^+$(-1.49), $Na^+$(-1.41), $Mg^{2+}$(-3.30), $Ca^{2+}$(-3.12), $Ni^{2+}$(3.09), $Co^{2+}$(-3.05) | This work |
| Poly(n-butyl acrylate) (drop cast membrane) | $1.0\times10^{-6}$ - $1.0\times10^{-1}$ | $1.00\times10^{-6.3}$ | 26.30 | $K^+$(-1.60), $Na^+$(-2.4), $Ca^{2+}$(-4.00), $Ni^{2+}$(-3.70) | [15] |
| Poly(lauryl acrylate-hexyl acrylate) | $1.0\times10^{-6}$ - $1.0\times10^{-2}$ | $1.00\times10^{-6.5}$ | 27.20 | $Na^+$(-1.8), $Mg^{2+}$(-6.1), $Ni^{2+}$(-5.7) | [17] |
| Poly(vinyl chloride)-Plasticised | $1.0\times10^{-6}$ - $1.0\times10^{-1}$ | $4.90\times10^{-7}$ | 31.30 | $K^+$(-2.42), $Na^+$(-4.71), $Ca^{2+}$(-3.50), $Ni^{2+}$(-2.30) | [16] |
| Poly(vinyl chloride) - Plasticised | $1.0\times10^{-6}$ - $1.0\times10^{-1}$ | $1.40\times10^{-7}$ | 29.0 | $K^+$(-2.35), $Na^+$(-2.65), $Mg^{2+}$(-3.60), $Ca^{2+}$(-3.60), $Ni^{2+}$(-3.20), $Co^{2+}$(-4.00) | [14] |

This copper ion sensor showed comparable selectivity with the reported copper ion sensors. When compared with previously reported solid stated copper ion sensor with acrylate membrane, this copper ion sensor gives a better performance in terms of sensitivity with higher Nernstian slope (31.29 mV/decade) and lower detection limit.

## Conclusion

A screen-printed copper ion sensor with photocurable pBA non-plasticised membrane based on ionophore o-xc via direct ionophore entrapment method had been fabricated and demonstrated good analytical performances. Besides, it is also shown that the composition of ionophore o-xc and anionic site (TFPB) within the pBA membrane has a strong influence on the response of the copper ion sensor. The introduction of NaTFPB inside the pBA membrane did not give good response whereas the membrane without the addition of NaTFPB showed a better performance. The membrane bearing the composition (w/w %) of 96.06:0.10:0.96:2.88 (nBA:HDDA:DMPP:o-xc) gives the best analytical performances. The sensitivity, detection limit and selectivity of the Cu(II) ion sensor obtained were comparable or slightly better than other reported copper ion sensors.

## Acknowledgement

We acknowledged the research fund from Ministry of Higher Education for PRGS grant (PRGS/1/2015/SG01/UKM/02/1) and Universiti Kebangsaan Malaysia via the Research Grant (DPP-2016-064).

## References

1. Kopylovich, M. N., Mahmudov, K. T. and Pombeiro, A. J. L. (2011). Poly(vinyl) chloride membrane copper-selective electrode based on 1-phenyl-2-(2-hydroxyphenylhydrazo) butane-1,3-dione. *Journal of Harzardous Materials*, 186: 1154 – 1162.
2. Chen, J., Li, Y. K. L, Zhong, W., Wang, H., Wu, Z., Yi, P. and Jiang, J. (2016). Cyclam-functionalized carbon dots sensor for sensitive and selective detection of copper (II) ion and sulfide anion in aqueous media and its imaging in live cells. *Sensors and Actuators B*, 224: 298 – 306.
3. Rajagopalan, V., Boussaad, S. and Tao, N. J. (2003). Detection of heavy metal ions based on quantum point contacts. *Nano Letters*, 3: 851 – 855.

4. Ghaedi, M., Tashkhourian, J., Montazerozohori, M., Nejati Biyareh, M. and Sadeghian, B. (2014). Highly selective and Sensitive determination of copper ion based on two novel optical sensors. *Arabian Journal of Chemistry*: 1 – 8.
5. Tang, L., Li, F., Liu, M. and Nandhakumar, R. (2011). Single sensor for two metal ions: Colorimetric recognition of $Cu^{2+}$ and fluorescent recognition of $Hg^{2+}$. *Spectrochimica Acta Part A*, 78: 1168 – 1172.
6. Chandra, S., Tomar, P. K., Kumar, A., Malik, A. and Singh, A. (2013). Fabrication of copper-selective PVC membrane electrode based on newly synthesized copper complex of Schiff base as carrier. *Journal of Saudi Chemical Society*, 1–7.
7. Georgescu, B., Georgescu, C., Daraban, S., Bouaru, A. and Pascalau, S. (2011). Heavy metals acting as endocrine disrupters. *Scientific Papers: Animal Science and Biotechnologies*, 44: 89 – 93.
8. Jasinski, A., Guzinski, M., Lisak, G., Bobacka, J. and Bochenska, M. (2015). Solid-contact lead(II) ion-selective electrodes for potentiometric determination of lead(II) in presence of high concentrations of Na(I), Cu(II), Cd(II), Zn(II), Ca(II) and Mg(II). *Sensors and Actuators B*, 218: 25 – 30.
9. Singh, A. K., Mehtab, S and Jain, A. K. (2006). Selective electrochemical sensor for copper (II) ion based on chelating ionophores. *Analytica Chimica Acta*, 575: 25 – 31.
10. Uygun, Z. O. and Ertugrul, U. H. D. (2014). A short footnote: Circuit design for faradaic impedimetric sensors and biosensors. *Sensors and Actuators B*, 202: 448 – 453.
11. Santini, A. O., Pezza, H. R. and Pezza, L. (2007). Development of a potentiometric mefenamate ion sensor for the determination of mefenamic acid in pharmaceuticals and human blood serum. *Sensors and Actuators B*, 128: 117 – 123.
12. Galovic, O., Samardzic, M. and Sak-bosnar, M. (2015). A new microsensor for the determination of anionic surfactants in commercial products. *International Journal of Electrochemical Science*, 10: 5176 – 5193.
13. Jain, A. K., Gupta, V. K., Singh, L. P. and Raisoni, J. R. (2005). Chelating ionophore based membrane sensors for copper (II) ions. *Talanta*, 66: 1355 – 1361.
14. Kamata, S., Murata, H., Kubo, Y. and Bhale, A. (1989). Copper (II)-selective membrane electrodes based on o-xylylene bis(dithiocarbamates) as neutral carriers. *Analyst*, 114: 1029 – 1031.
15. Woznica, E., Mieczkowski, J. and Michalska, A. (2011). Electrochemical evidences and consequences of significant differences in ions diffusion rate in polyacrylate-based ion-selective membranes. *Analyst*, 136: 4787 – 4793.
16. Birinci, A., Eren, H., Coldur, F., Coskun, E. and Andac, M. (2016). Rapid determination of trace level copper in tea infusion samples by solid contact ion selective electrode. *Journal of Food and Drug Analysis*: 1 – 8.
17. Kisiel, A., Woznica, E., Wojciechowski, M., Bulska, E., Maksymiuk, K. and Michalska, A. (2015). Potentiometric layered membranes. *Sensors and Actuators B*, 207: 995 – 1003.
18. Baba, I. (2006). Sebatian ditiokarbamat: penyumbang kemajuan kimia tak organik. Universiti Kebangsaan Malaysia, Bangi, Malaysia.
19. Layla, J. N. A. and Maher, A. M. (2013). Synthesis and characterization of some metal (II) complexes of dithiocarbamate. *Tikrit Journal of Pure Science*, 3: 115 – 121.
20. Joanna, S. L. and Marek, T. (1990). Flow-Injection Extraction-Spectrophotometric Copper with Dithiocarbamates, *Analytical Sciences,* 6: 415 – 419.
21. Ulianas, A., Lee, Y. H., Ahmad, M., Lau, H., Ishak, Z. and Tan, L. L. (2014). A regenerable screen-printed DNA biosensor based on acrylic microsphere – gold nanoparticle composite for genetically modified soybean determination. *Sensors and Actuators B,* 190: 694 – 701.
22. Peper, S., Ceresa, A., Qin, Y. and Bakker, E. (2003). Plasticizer-free microspheres for ionophore-based sensing and extraction based on a methyl methacrylate-decyl methacrylate copolymer matrix. *Analytical Chimica Acta*, 500: 127 – 136.
23. Aksuner, N., Henden, E., Yilmaz, I. and Cukurovali, A. (2012). A novel optical chemical sensor for the determination of nickel (II) based on fluorescence quenching of newly synthesized thiazolo-triazol derivative and application to real samples. *Sensors and Actuators B*, 166-167: 269 – 274.
24. Ngarisan, N. I., Ngah, C. W. Z., Ahmad, C. W. M. and Kuswandi, B. (2014). Optimization of polymer inclusion membranes (PIMs) preparation for immobilization of Chrome Azurol S for optical sensing of aluminum (III). *Sensors and Actuators B*, 203: 465 – 470.
25. Puig-Lleixa, C., Jimenez, C., Fabregas, E. and Bartroli, J. (1998). Potentiometric pH sensors based on urethane-acrylate photocurable polymer membranes. *Sensors and Actuators B*, 49: 211 – 217.

26. Yew, P. L. and Lee, Y. H. (2014). A reflectometric ion sensor for potassium based on acrylic microspheres. *Sensors and Actuators B*, 191: 719 – 726.
27. Yang, X., Hibbert, D. B. and Alexander, P. W. (1998). Flow injection potentiometry by poly (vinyl chloride)-membrane electrodes with substituted azacrown ionophores for the determination of lead (II) and mercury (II) ions. *Analytical Chimica Acta,* 372: 387 – 398.
28. Lee, Y. H. and Hall, E. A. H. (2001). Assessing a photocured self-plasticised acrylic membrane recipe for $Na^+$ and $K^+$ ion selective electrodes. *Analytical Chimica Acta*, 443: 25 – 40.
29. Alva, S., Lee, Y. H., and Ahmad, M. (2005). A new lithium ion selective sensors based on self plasticising acrylic films and disposable screen printed electrode. *Asian Conference on Sensors and the International Conference on New Techniques in Pharmaceutical and Biomedical Research – Proceedings*: 48 – 51.
30. Ogonczyk, D., Tymecki, L., Wyzkiewicz, I., Koncki, R. and Glab, S. (2005). Screen-printed disposable urease-based biosensors for inhibitive detection of heavy metal ions. *Sensors and Actuators B*, 106: 450 – 454.
31. Renedo, O. D., Alonso-Lomillo, M. A., and Martinez, M. J. A. (2007). Recent developments in the field of screen-printed electrodes and their related applications. *Talanta*, 73: 202 – 219.
32. Miscoria, S. A., Jacq, C., Maeder, T. and Martin, N. R. (2014). Screen-printed electrodes for electroanalytical sensing, of chromium VI in strong acid media. *Sensors and Actuators B*, 195: 294 –302.
33. Alva, S. (2008). Pembinaan sensor ion dan biosensor potentiometri pepejal berasaskan elektrod bercetak skrin dan filem fotopolimer metakrilik-akrilik. Thesis PhD. Universiti Kebangsaan Malaysia. Bangi. Malaysia.
34. Jumal, J., Yamin, B. M., Ahmad, M. and Lee, Y. H. (2012). Mercury ion-selective electrode with self-plasticizing poly (n–buthylacrylate) membrane based on 1, 2 -bis-(n'–benzoylthioureido) cyclohexane as ionophore. *APCBEE Procedia*, 3: 116 – 123.
35. Umezawa, Y., Bühlmann, P., Umezawa, K., Tohda, K. and Amemiya, S. (2000). Potentiometric Selectivity Coefficients of Ion-Selective Electrodes. Part I. Inorganic Cations (Technical Report). *Pure and Applied Chemistry*, 72: 1851 – 2082.
36. Lee, Y. H. and Hall, E. A. H. (1996). Methacrylate-acrylate based polymers of low plasticiser content for potassium ion-selctive membranes, *Analytical Chimica Acta*, 324: 47 – 56.
37. Rezvani, I. S. A., Darroudi, A., Arbab, Z. M. H., Zohuri, G. and Ashraf, N. (2013). Ion imprinted polymer based potentiometric sensor for the trace determination of Cadmium (II) ions. *Arabian Journal of Chemistry*: 1 – 6.
38. Buck, R. P. and Lindneri, E. R. N. (1994). Recommendations for nomenclature of ion-selective electrodes. *Pure and Applied Chemistry*, 66: 2527 – 2536.
39. Mittal, S. K., Sharma, H. K., Kumar, A. S. K. (2004). Samarium (III) selective membrane sensor based on tin(IV) boratophosphate. *Sensors*, 4: 125 – 135.
40. Mi, Y., Mathison, S., Goines, R., Logue, A. and Bakker, E. (1999). Detection limit of polymeric membrane potentiometric ion sensors: How can we go down to trace levels? *Analytical Chimica Acta*, 397: 103 – 111.
41. Lee, Y. H., Toth, K. and Hall, E. A. H. (2004). Ion-transport and diffusion coefficients of non-plasticized methacrylic-acrylic ion-selective membranes. *Talanta*, 63: 73 – 87.
42. Ulianas, A. (2007). Kesan perubahan komposisi membran dan elektrolit dalaman terhadap rangsangan sensor ion kalium. Thesis Master. Universiti Kebangsaan Malaysia. Bangi. Malaysia.
43. Gupta, K. C. and Arc, M. J. D. (2000). Performance evaluation of copper ion selective electrode based on cyanocopolymers. *Sensors & Actuators B. Chemical*, 62: 6 – 11.

*Malaysian Journal of Analytical Sciences, Vol 21 No 1 (2017): 13 - 19*
*DOI: http://dx.doi.org/10.17576/mjas-2017-2101-02*

MALAYSIAN JOURNAL OF ANALYTICAL SCIENCES
*Published by The Malaysian Analytical Sciences Society*
ISSN 1394 - 2506

# $MgCl_2$ AS EFFICIENT AND INEXPENSIVE CATALYST FOR THE SYNTHESIS OF 1,4-DIHYDROPYRIDINE DERIVATIVES

## ($MgCl_2$ Sebagai Pemangkin Cekap dan Murah untuk Sintesis Terbitan 1,4-Dihidropiridina)

Siti Nur Aqlili Riana Mohd Asseri[1], Sian Hui Tan[1], Wan Nurul Khursyiah Wan Mohamad[1], Seng Chee Poh[1], Poh Wai Chia[1,2]*, Su-Yin Kan[3], Tse Seng Chuah[4]

[1]*School of Marine Science and Environment*
[2]*Institute Marine Biotechnology*
*Universiti Malaysia Terengganu, 21030 Kuala Terengganu, Terengganu, Malaysia*
[3]*Faculty of Health Sciences,*
*Universiti Sultan Zainal Abidin, 21300 Kuala Terengganu, Terengganu, Malaysia*
[4]*School of Food Science and Technology,*
*Universiti Malaysia Terengganu, 21030 Kuala Terengganu, Terengganu, Malaysia*

**Corresponding author: pohwai@umt.edu.my*

Received: 17 August 2016; Accepted: 25 October 2016

**Abstract**

The synthesis of 1,4-dihydropyridine (1,4-DHP) derivatives in the presence of alkaline earth metal chlorides was reported. Specifically, the $MgCl_2$ catalyzed the synthesis of 1,4-DHP derivatives in good yields, ranging from 69 – 87%. The $Mg^{2+}$ serves as the Lewis acid catalyst in the formation of 1,4-DHP and the proposed mechanism of the formation of 1,4-DHP was elaborated in this manuscript. There are many advantages employing $MgCl_2$ as a catalyst in this study, including inexpensive, ubiquitous availability of this metal, simple filtration protocol, which has spark considerable interest in the use of this catalyst in promoting organic reactions.

**Keywords**: alkaline earth metal, magnesium chloride; 1,4-dihydropyridine

**Abstrak**

Sintesis terbitan 1,4-dihidropiridina (1,4-DHP) dalam kehadiran logam alkali bumi dibincangkan dalam artikel ini. Secara khususnya, sintesis terbitan 1,4-DHP melalui pemangkin $MgCl_2$ memberi peratusan hasil yang baik, dalam lingkungan 69 –87%. Ion $Mg^{2+}$ bertindak sebagai pemangkin asid Lewis dalam pembentukan 1,4-DHP dan cadangan mekanisma terhadap pembentukan 1,4-DHP telah dihuraikan dalam manuskrip ini. Terdapat banyak kelebihan menggunakan $MgCl_2$ sebagai pemangkin dalam kajian ini, termasuk kos yang murah, ketersediaan logam ini, protokol pengekstrakan yang mudah, yang mana ini telah mencetuskan minat yang besar dalam penggunaan pemangkin ini dalam pelbagai tindak balas organik.

**Kata kunci**: logam alkali bumi, magnesium klorida, 1,4-dihydropiridin

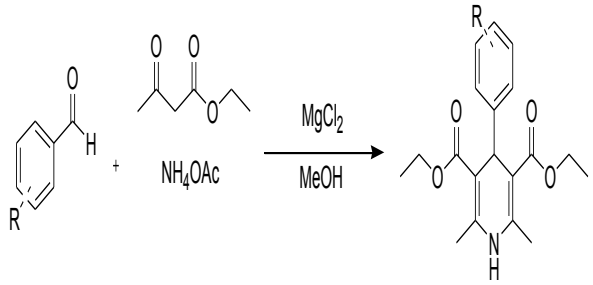
## Introduction

1,4-dihydropyrdines (1,4-DHPs) are important classes of pharmaceutical compounds that are usually prescribed clinically for the treatment of cardiovascular diseases, such as heart failure, angina pectoris and hypertension [1]. In the pharmaceutical pipeline today, there are more than twelve 1,4-DHPs drug candidates commercially available in the global market, such as the nifedipine [2], felodipine [3], nicardipine [4] and etc., which were used to treat cardiovascular diseases.

Due to the attractiveness of the 1,4-DHPs in pharmaceutical application, various synthetic approaches to produce 1,4-DHP derivatives have been reported, such as the use microwave irradiation [5], solar thermal energy [6], ultrasound irradiation [7], ionic liquids [8], and $AlCl_3$ as Lewis catalyst [9]. In spite of the above efforts to improve further on the 1,4-DHPs reactions, a number of drawbacks have been identified such as unsatisfactory yields, high reaction temperatures and long reaction hours [10].

Recently, there are a number of literatures reported on the use of alkaline earth metals for organic transformations. For instance, $MgCl_2$ has been successfully employed for the aldol synthesis of α-dimethylsilylesters [11]. An improved method on the Biginelli reaction by using alkaline earth metal chlorides such as $MgCl_2$, $CaCl_2$, $BaCl_2$ and $SrCl_2$ as homogenous catalysts in the presence of acetic acid as solvent had been reported [12]. The synthesis of dihydropyridine, acridine and xanthene derivatives with $Ca(OTf)_2$ in the presence of $Bu_4NPF_6$ as additive and water as solvent has also been disclosed recently [13]. The alkaline earth metals are the most abundant elements encountered in our daily lives in which most of it can be found buried in the earth crust and in the ocean [14]. On green chemistry perspective, the use of alkaline earth metals in organic reactions are favorable due to the fact that, metals such as calcium and magnesium are ubiquitously available in nature compared to other transition and lanthanide elements [15]. However, only limited organic reactions which employ alkaline earth metals as catalysts were reported as their applications are not being fully explored [16].

In the course of our research to synthesize bioactive heterocyclic compounds, herein we report the synthesis of 1,4-DHP derivatives catalyzed by $MgCl_2$ from the starting materials benzaldehydes, ethyl acetoacetate and ammonium acetate (as shown in Scheme 1). The advantages of this protocol include the exclusion of additional additive, for example $Bu_4NPF_6$ and the reaction could be accomplished within four hours. The synthesized products were obtained in good yield as described in this paper.




Scheme 1. The $MgCl_2$ catalyzed the synthesis of 1,4-DHP derivatives

## Materials and Methods

All the chemicals and solvents used without further purification in this study are supplied by Merck, Acros organic and HmbG® chemicals. These include benzaldehyde, 4-fluorobenzaldehyde, 4-chlorobenzaldehyde, 4-nitrobenzaldehyde, 4-bromobenzaldehyde, ethylacetoacetate, ammonium acetate, methanol, ethyl acetate, n-hexane and silica gel 60 (0.063-0.200mm). The FT-IR spectra were recorded on Perkin Elmer 100 FT-IR spectrometer, in spectral range of 4000 – 400 $cm^{-1}$. $^1H$ and $^{13}C$-NMR spectra were recorded using Bruker Avance III 400 spectrometer, with deuterated chloroform as solvent at room temperature at 400 MHz. GC-MS analyses were performed using Shimadzu QP2010SE.

**Synthesis of the 1,4-DHP derivatives**

To a mixture of benzaldehyde derivatives (1.47 mmol), ammonium acetate (1.47 mmol), and ethyl acetoacetate (1.47 mmol) in methanol (3 ml), $MgCl_2$ was added (0.15 mmol) and the mixture were heated under reflux for four hours. After the completion of the reaction, the solvent was evaporated under reduced pressure to obtain the crude product. The crude product was then purified over silica gel column chromatography (hexane: ethyl acetate = 7:3, v/v) to give the title compounds **1a-1k**.

## Results and Discussion

The optimized condition was determined using a model reaction that consisted of benzaldehyde, ethyl acetoacetate and ammonium acetate. The model reaction was first conducted without adding any catalysts, recorded only 30% yield after the reaction was heated under reflux for four hours in methanol. The use of catalytic amount of $MgCl_2$ greatly enhanced the yield of the desired product and the best yield was recorded with the use of 5 mmol of $MgCl_2$ which afforded 87% yield of the desired product. Next, the study of using various alkaline earth metals in different solvents was evaluated. Based on the optimization study (Table 1), the maximum yield of **1a** was recorded when the reaction was heated under reflux for four hours in the presence of 5 mmol of $MgCl_2$ as catalyst in MeOH.

Table 1. Synthesis of **1a** under different solvents and alkaline earth metals.

| Entry | Solvent | $MgCl_2$ Time/ Yield (%) | $CaCl_2$ Time/ Yield (%) | $SrCl_2$ Time/ Yield (%) | $BaCl_2$ Time/ Yield (%) |
|---|---|---|---|---|---|
| 1 | MeOH | 4h/ 87 | 4h/ 75 | 4h/ 79 | 4h/ 82 |
| 2 | AcOH | 4h/ 37 | 4h/ 33 | 4h/ 32 | 4h/ 35 |
| 3 | THF | 4h/ 70 | 4h/ 65 | 3h/ 72 | 4h/ 67 |
| 4 | DMSO | 5h/ 82 | 4h/ 80 | 4h/ 76 | 5h/ 78 |

The improved protocol was employed to synthesize different substituted 1,4-DHP derivatives by using a variety of benzaldehydes. As shown in Table 2, all the reactions proceeded smoothly in the presence of $MgCl_2$ and the desired products were isolated in moderate to good yields, ranging from 69 – 87%. The electronic effect of different substituted groups on benzaldehydes was also evaluated. Specifically, the benzaldehydes bearing the electron-withdrawing group gave a higher yield compared to benzaldehydes bearing electron-donating group (Table 2, 1b -1j vs 1k). This result was in agreement with a previous study on the synthesis of the 1,4-DHP derivatives using ultrasound method [17]. Among the investigated electron-withdrawing substituents, the *para*- position gave a higher yield compared to *ortho*- and *meta*- position (Table 2, 1b -1e vs 1f-1j). In the previous study, the side products (Figure 1) were usually yielded along with the desired products [17]. Gratifyingly, under this improved protocol which utilized $MgCl_2$ as catalyst, only one 1,4-DHP derivative was isolated for each reaction, with no side products isolated during the purification process in the column chromatography.

Table 2. The isolated yields and melting point obtained for compounds 1a – 1k

| Product | R | Time (h) | Isolated Yield (%) | M. P ($^oC$) | |
|---|---|---|---|---|---|
| | | | | Observed | Reported |
| 1a | Ph- | 4 | 87 | 155.7 | 158 – 160 [18] |
| 1b | 4-$NO_2$ | 4 | 83 | 130.3 | - |
| 1c | 4-Br | 4 | 80 | 168.1 | 165 – 167 [19] |
| 1d | 4-F | 4 | 81 | 157.9 | 155 – 157 [20] |
| 1e | 4-Cl | 4 | 80 | 147.9 | 147 – 148 [21] |
| 1f | 2-Cl | 4 | 73 | 121.3 | 122 – 123 [22] |
| 1g | 2-F | 4 | 72 | 150.5 | 148 – 152 [23] |
| 1h | 2-Br | 4 | 70 | 142.7 | 140 – 141 [19] |
| 1i | 3-F | 4 | 72 | 103.7 | 102 – 104 [24] |
| 1j | 3-Br | 4 | 71 | 125.7 | 115 – 117 [24]<br>126 – 127 [19] |
| 1k | 4-$CH(CH_3)_2$ | 4 | 69 | 95.7 | 97 [25] |

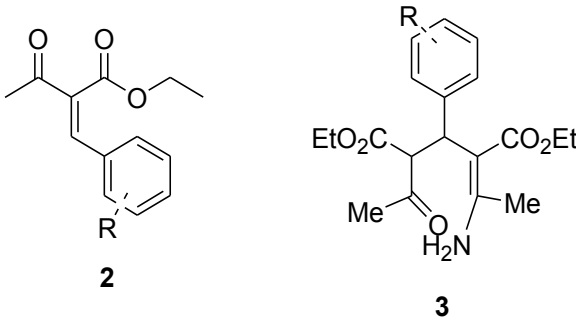
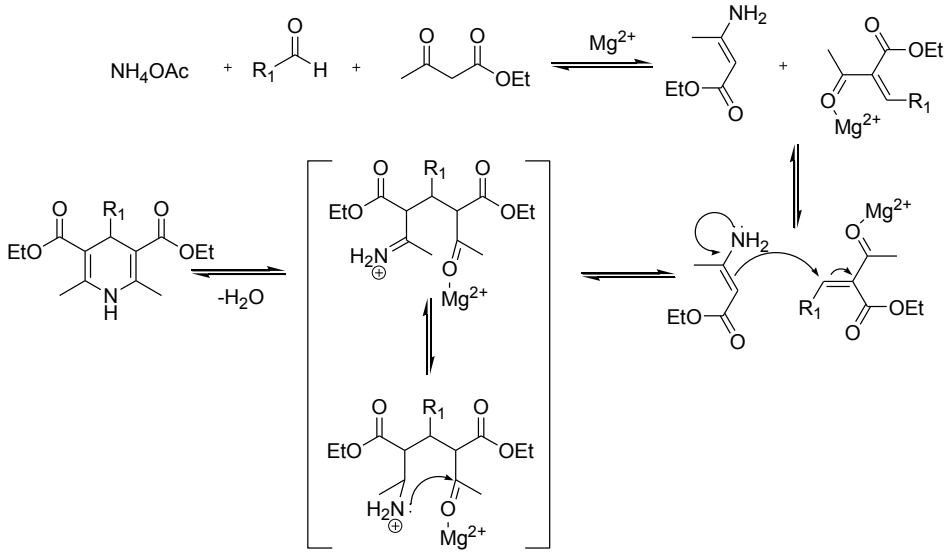



Figure 1. The side products, 2 and 3 were reported to be produced from the Hantzsch 1,4-dihydropyridine synthesis [17]

The proposed mechanism for the formation of 1,4-DHP catalyzed by $MgCl_2$ was elaborated in Scheme 2. Firstly, one equivalent of ethyl acetoacetate reacted with benzaldehyde to form the knoevenagel adduct and one equivalent of ammonium acetate reacted with ethyl acetoacetate to form ester enamine. Subsequently, the Michael-type addition and condensation occurred to yield 1,4-DHP derivative as the final product. The $Mg^{2+}$ serves as the Lewis acid catalyst in the formation of 1,4-DHP derivatives.




Scheme 2. The proposed mechanism for the formation of 1,4-DHP derivatives catalyzed by $MgCl_2$

**Physical and spectral data**

The spectroscopic data of the synthesized compounds **1a – 1k** is as follows:

**2,6-dimethyl-4-phenyl-1,4-dihydropyridine-3,5-dicarboxylic diethyl ester (1a)**

M.p: 98.4 $^{o}$C; IR (cm-1): v(N-H) 3343.60, v(C-H)sp$^2$ 3088.64, v(CH)sp$^3$ 2982.34, v(C=O) 1687.24, v(C=C) 1651.62, v(C-N) 1373.70; $^{1}$H- NMR (ppm): (t, 6H, CH3) 1.149, (s, 6H, CH3) 2.266, (m, 4H, CH2) 4.018, (s, 1H, CH) 4.917, (s, 1H, NH) 5.463, (t,2H, CH ) 7.150, (m, 1H, CH) 7.047, ( d, 2H, CH) 7.21; $^{13}$C- NMR (ppm): 19.2, 14.8,30.2, 130.8, 60.8, 128.2, 128.6, 126.2, 100.4, 165.4, 143.6. GC-MS: m/z 329 $[M+H]^+$.

**2,6-dimethyl-4-(4nitro-phenyl)-1,4- dihydropyridine-3,5-dicarboxylic diethyl ester (1c)**
M.p: 130.3 $^{o}$C; IR (cm-1): v(N-H) 3345.61, v(C-H)sp$^2$ 3091.14, v(C-H)sp$^3$ 2987.30, v(C=O) 1689.11, v(C=C) 1648.32, v(C-N) 1373.61; $^{1}$H- NMR (ppm): (t, 6H, CH3) 1.215, (s, 6H, CH3) 2.294, (m, 4H, CH2) 4.086, (s, 1H, CH) 4.951, (s, 1H, NH) 6.125, (d,2H, CH ) 7.324, (d, 2H, CH) 7.165; $^{13}$C- NMR (ppm): 18.9, 13.6, 30.8, 130.5, 60.6, 148.2, 123.7, 145.7, 100.8, 165.8, 142.7. GC-MS: m/z 375 $[M+H]^+$.

**2,6-dimethyl-4-(4-bromo-phenyl)-1,4-dihydropyridine-3,5-dicarboxylic diethyl ester (1c)**
M.p: 168.1 $^{o}$C; IR (cm-1): v(N-H) 3343.10, v(C-H)sp$^2$ 3078.12, v(C-H)sp$^3$ 2983.14, v(C=O) 1689.20, v(C=C) 1654.22, v(C-N) 1371.21; $^{1}$H- NMR (ppm): (t, 6H, CH3) 1.215, (s, 6H, CH3) 2.331, (m, 4H, CH2) 4.087, (s, 1H, CH) 4.962, (s, 1H, NH) 5.576, (d,2H, CH ) 6.876, (d, 2H, CH) 7.247; $^{13}$C- NMR (ppm): 18.4, 13.8, 59.9, 30.2, 130.6, 131.8, 120.2, 136.2, 100.6, 165.4, 142.2. GC-MS: m/z 407 $[M+H]^+$.

**2,6-dimethyl-4-(4-fluoro-phenyl)-1,4-dihydropyridine-3,5-dicarboxylic diethyl ester (1d)**
M.p: 157.9 $^{o}$C; IR (cm-1): v(N-H) 3346.12, v(C-H)sp$^2$ 3087.22, v(C-H)sp$^3$ 2984.32, v(C=O) 1688.34, v(C=C) 1653.12, v(C-N) 1374.20; $^{1}$H- NMR (ppm): (t, 6H, CH3) 1.231, (s, 6H, CH3) 2.325, (m, 4H, CH2) 4.070, (s, 1H, CH) 4.962, (s, 1H, NH) 5.648, (d, 2H, CH ) 6.879, (d, 2H, CH) 7.277; $^{13}$C- NMR (ppm): 18.9, 13.8, 30.8, 130.8, 60.3, 133.6, 159.4, 115.4, 100.7, 165.2, 142.8. GC-MS: m/z 347 $[M+H]^+$.

**2,6-dimethyl-4-(4-chloro-phenyl)-1,4-dihydropyridine-3,5-dicarboxylic diethyl ester (1e)**
M.p: 177.7 $^{o}$C; IR (cm-1): v(N-H) 3338.60, v(C-H)sp$^2$ 3087.23, v(C-H) sp$^3$ 2982.10, v(C=O) 1689.10, v(C=C) 1652.24, v(C-N) 1373.12; $^{1}$H- NMR (ppm): (t, 6H, CH3) 1.244, (s, 6H, CH3) 2.336, (m, 4H, CH2) 4.100, (s, 1H, CH) 4.962, (s, 1H, NH) 5.671, (d,2H, CH ) 7.104, (d, 2H, CH) 7.238; $^{13}$C- NMR (ppm): 18.7, δ14.2, 30.6, 130.6, 59.6, 130.5, 128.2,135.4, 100.8, 165.5, 143.2. GC-MS: m/z 363 $[M+H]^+$.

**2,6-dimethyl-4-(2-chloro-phenyl)-1,4-dihydropyridine-3,5-dicarboxylic diethyl ester (1f)**
M.p: 145.6 $^{o}$C; IR (cm-1): v(N-H) 3338.54, v(C-H)sp$^2$ 3089.10, v(C-H) sp$^3$ 2982.27, v(C=O) 1689.37, v(C=C) 1653.24, v(C-N) 1373.23; $^{1}$H- NMR (ppm): (t, 6H, CH3) 1.224, (s, 6H, CH3) 2.340, (m, 4H, CH2) 4.118, (s, 1H, CH) 4.996, (s, 1H, NH) 5.579, (d,1H, CH ) 7.075, (t, 1H, CH) 7.164, (t,1H, CH ) 6.940, (d, 1H, CH) 6.983; $^{13}$C-NMR (ppm): 18.1, 13.4, 20.5, 130.6, 59.8, 134.5, 100.3, 136.2, 126.4, 126.8, 128.3, 165.8, 142.2. GC-MS: m/z 363 $[M+H]^+$.

**2,6-dimethyl-4-(2-fluoro-phenyl)-1,4-dihydropyridine-3,5-dicarboxylic diethyl ester (1g)**
M.p: 150.4 $^{o}$C; IR (cm-1): v(N-H) 3337.18, v(C-H)sp$^2$ 3089.22, v(C-H) sp$^3$ 2985.16, v(C=O) 1687.46, v(C=C) 1653.17, v(C-N) 1372.54; $^{1}$H- NMR (ppm): (t, 6H, CH3) 1.224, (s, 6H, CH3) 2.337, (m, 4H, CH2) 4.100, (s, 1H, CH) 4.996, (s, 1H, NH) 5.630, (d,1H, CH ) 6.951, (t, 1H, CH) 6.816, (t,1H, CH ) 7.164, (d, 1H, CH) 7.074; $^{13}$C-NMR (ppm): 18.5, 13.6, 19.7, 130.6, 59.9, 124.5, 100.5, 115.2, 127.4, 123.9, 162.8, 165.2, 142.4. GC-MS: m/z 347 $[M+H]^+$.

**2,6-dimethyl-4-(2-bromo-phenyl)-1,4-dihydropyridine-3,5-dicarboxylic diethyl ester (1h)**
M.p: 145.7 $^{o}$C; IR (cm-1): v(N-H) 3337.37, v(C-H)sp$^2$ 3086.93, v(C-H) sp$^3$ 2983.33, v(C=O) 1688.76, v(C=C) 1653.70, v(C-N) 1372.14; $^{1}$H- NMR (ppm): (t, 6H, CH3) 1.150, (s, 6H, CH3) 2.267, (m, 4H, CH2) 4.031, (s, 1H, CH) 5.663, (s, 1H, NH) 5.774, (d,1H, CH ) 7.179, (t, 1H, CH) 6.864, (t,1H, CH ) 6.893, (d, 1H, CH) 7.205; $^{13}$C-NMR (ppm): 18.7, 13.7, 23.1, 131.6, 59.8, 134.5, 100.8, 131.2, 127.7, 123.7, 126.8, 165.3, 142.8. GC-MS: m/z 407 $[M+H]^+$.

**2,6-dimethyl-4-(3-fluoro-phenyl)-1,4-dihydropyridine-3,5-dicarboxylic diethyl ester (1i)**
M.p: 151.8 $^{o}$C; IR (cm-1): v(N-H) 3337.97, v(C-H)sp$^2$ 3089.24, v(C-H) sp$^3$ 2983.45, v(C=O) 1689.35, v(C=C) 1653.66, v(C-N) 1372.72; $^{1}$H- NMR (ppm): (t, 6H, CH3) 1.200, (s, 6H, CH3) 2.291, (m, 4H, CH2) 4.107, (s, 1H, CH) 5.360, (s, 1H, NH) 5.672, (s,1H, CH ) 6.788, (d, 1H, CH) 6.779, (t,1H, CH ) 7.124, (d, 1H, CH) 6.833; $^{13}$C-NMR (ppm): 18.4, 13.2, 30.2, 130.5, 59.3, 139.4, 124.8, 113.0, 118.0, 162.0, 100.8, 165.4, 142.8. GC-MS: m/z 347 $[M+H]^+$.

**2,6-dimethyl-4-(3-bromo-phenyl)-1,4-dihydropyridine-3,5-dicarboxylic diethyl ester (1j)**
M.p: 140.1 $^oC$; IR (cm-1): v(N-H) 3339.61, v(C-H)sp² 3088.24, v(C-H) sp³ 2982.14, v(C=O) 1689.15, v(C=C) 1652.26, v(C-N) 1373.10; $^1H$- NMR (ppm): (t, 6H, CH3) 1.303, (s, 6H, CH3) 2.328, (m, 4H, CH2) 4.190, (s, 1H, CH) 4.438, (s, 1H, NH) 5.762, (s,1H, CH ) 7.233, (d, 1H, CH) 7.249, (t,1H, CH ) 7.037, (d, 1H, CH) 7.012; $^{13}C$-NMR (ppm): 18.7, 13.3, 29.5, 132.6, 59.8, 139.7, 130.7, 123.5, 128.6, 129.0, 100.4, 165.6, 142.8. GC-MS: m/z 407 $[M+H]^+$.

**4-(4-isopropyl-phenyl)-2,6-dimethyl-1,4-dihydro-pyridine-3,5-dicarboxylic acid diethyl ester (1k)**
M.p: 95.7 $^oC$; IR (cm-1): v(N-H) 3337.33, v(C-H)sp² 3090.62, v(C-H) sp³ 2869.61, v(C=O) 1692.76, v(C=C) 1655.24, v(C-N) 1370.93, v(C-O) 1211.51; $^1H$- NMR (ppm): (t, 6H, CH3) 1.207, (d, 6H, $CH_3$) 1.248, (s, 6H, $CH_3$) 2.316, (m, 1H, CH) 2.824, (m, 4H, $CH_2$) 4.090, (s, 1H, CH) 4.961, (s, 1H, NH) 5.732, (d, 2H, Ar-H) 7.046, (d, 2H, Ar-H) 7.178; $^{13}C$- NMR (ppm): 19.6, 14.3, 33.6, 127.8, 59.7, 143.8, 125.9, 146.3, 39.1, 23.9, 104.3, 167.8, 145.1. GC-MS: m/z 371 $[M+H]^+$.

There are many advantages of using of $MgCl_2$ in the Hantzsch dihydropyridine synthesis, including the simple separation process, mildness of this technique, no side products and good yields. The alkaline earth metals are inexpensive, especially $MgCl_2$ which can be found ubiquitously buried in the earth's crust. Although various literatures have been generated with respect to the synthesis of 1,4-DHP derivatives, most of these methods relied on the use of expensive chemicals, toxic chemicals or harsh condition.

## Conclusion

A simple, mild and high yielding protocol for the synthesis of 1,4-DHP derivatives catalyzed by $MgCl_2$, an alkaline earth metal has successfully developed. The mildness of this technique, experimental simplicity and the inexpensive of this catalyst have rendered this protocol an attractive way for the synthesis of 1,4-DHP derivatives. Furthermore, this heterogeneous catalyst can be easily removed with simple filtration technique. Further application using alkaline earth metals in other organic reactions are continuously been explored in our laboratory.

## Acknowledgement

This research was funded by the Fundamental Research Grant Scheme (FRGS), grant number 59292.

## References

1. Stone, P. H., Antman, E. M., Muller, J. E. and Braunwald, E. (1980). Calcium channel blocking agents in the treatment of cardiovascular disorders. Part II: Hemodynamic effects and clinical applications. *Annals of Internal Medicine*, 93(6): 886 – 904.
2. Shan, R., Velazquez, C. and Knaus, E. (2004). Syntheses, calcium channel agonist-antagonist modulation activities, and nitric oxide release studies of nitrooxyalkyl 1,4-dihydro-2,6-dimethyl-3-nitro-4-(2,1,3-benzoxadiazol-4-yl) pyridine-5-carboxylate racemates, enantiomers, and diastereomers. *Journal of Medicinal Chemistry*, 47(1): 254 – 261.
3. Visentin, S., Rolando. B., Stilo. A. D., Frutterro, R., Novara, M., Carbone, E., Roussel, C., Vanthuyne, N. and Gasco, A. (2004). New 1,4-dihydropyridines endowed with NO-donor and calcium channel agonist properties. *Journal of Medicinal Chemistry*, 47(10): 2688 – 2693.
4. Eharkar, P. S., Desai, B., Gaveria, H., Varu, B., Loriya, R., Naliapara, Y., Shah, A. and Kulkarni, V. M. (2002). Three-dimensional quantitative structure-activity relationship of 1,4-dihydropyridines as antitubercular agents. *Journal of Medicinal Chemistry*, 45(22): 4858 – 4867.
5. Anniyappan, M., Muralidharan, D. and Perumal, P. T. (2002). Synthesis of Hantzsch 1,4- dihydropyridines under microwave irradiation. *Synthetic Communications,* 32(4): 659 – 663.
6. Mekheimer, R. A., Hameed, A. A. and Sadek, K. U. (2008). Solar thermochemical reactions: four-component synthesis of polyhydroquinoline derivatives induced by solar thermal energy. *Green Chemistry*, 10(5): 592 – 593.
7. Shaabani, A., Rezayan, A. H., Rahmati, A. and Sharifi, M. (2006). Ultrasound-accelerated synthesis of 1,4-dihydropyridines in an ionic liquid. *Monatshefte fur Chemie,* 137(1): 77 – 81.

8. Legeay, J., Eyndeb, J.J.V. and Bazureau, J. P. (2005). Ionic liquid phase technology supported the three component synthesis of Hantzsch 1,4-dihydropyridines and Biginelli 3,4-dihydropyrimidin-2(1*H*)-ones under microwave dielectric heating. *Tetrahedron*, 61(52): 12386 – 12397.
9. Sharma, S. D., Hazarika, P. and Konwar, D. (2008). A simple, green and one-pot four component synthesis of 1,4-dihydropyridines and their aromatization. *Catalysis Communications*, 9(5): 709 – 714.
10. Maheswara, M., Siddaiah, V., Rao, Y. K., Yew-Min, T. and Sridhar, C. (2006). A simple and efficient one-pot synthesis of 1,4-dihydropyridine using heterogenous catalyst under solvent-free conditions. *Journal of Molecular Catalysis A: Chemical*, 260(1): 179 – 180.
11. Miura, K., Nakagawa, T. and Hosomi, A. (2015). Metal chloride-promoted aldol reaction of α-dimethylsilylesters with aldehydes, ketones, and α-enones. *Synlett*, 12: 1917 – 1921.
12. Shahnaz, K., Majid, M. H., Minou, K., Farahnaz, K. B. and Zohreh, D. (2008). A very high yielding and facile alkaline earth metals homogeneous catalysis of Biginelli reaction: An improved protocol. *Green Chemistry*, 1(2): 133 – 139.
13. Yaragorla, S., Singh, G. and Pareek, A. (2015). Alkaline earth metal catalyzed, one-pot, multi-component approach for the synthesis of dihydropyridine, acridine and xanthene derivatives in water. *Indian Journal of Chemistry*, 54: 1321 – 1326.
14. Cotton, F. A., Wilkinson, G. and Gaus, O. L. (1995). *Basic Inorganic Chemistry*. J. Wiley & Sons. New York.
15. Kobayashi, S. and Yamashita, Y. (2011). Alkaline earth metal catalysts for asymmetric reactions. *Accounts of Chemical Research*, 44(1): 58 – 71.
16. Alexander, J. S. and Ruhlandt-Senge, K. (2002). Not just heavy "Grignards": Recent advances in the organometallic chemistry of the alkaline earth metals calcium, strontium and barium. *European Journal of Inorganic Chemistry*, 11: 2761 – 2774.
17. Wang, S-X., Li, Z-L., Zhang J-C. and Li J-T. (2008). The solvent-free synthesis of 1,4-dihydropyridines under ultrasound irradiation without catalyst. *Ultrasonics Sonochemistry*, 15(5): 667 – 680.
18. Reddy, B. Palakshi., Rajesh, K. and Vijayakumar, V. (2011). Ionic Liquid [EMIM]OAc under ultrasonic irradiation towards Synthesis of 1,4-DHP's. *Journal of the Chinese Chemical Society*, 58(3): 384 – 388.
19. Zolfigol, M. A., Salehi, P. and Safaiee, M. (2006). An efficient and eco-friendly procedure for the synthesis of Hantzsch ethyl 1,4-dihydro-2,6-dimethylpyridine-3,5-dicarboxylates under mild and green conditions. *Letters in Organic Chemistry*, 3(2): 153 – 156.
20. Kuraitheerthakumaran, A., Pazhamalai, S. and Gopalakrishnan, M. (2011). An efficient and solvent-free one-pot synthesis of 1,4-dihydropyridines under microwave irradiation. *Chinese Chemical Letters*, 22(10): 1199 – 1202.
21. Yadav, D. K., Patel, R., Srivastava,V. P., Watal, G. and Yadav, L. D. S. (2011). LiBr as an efficient catalyst for one-pot synthesis of Hantzsch 1,4-dihydropyridines under mild conditions. *Chinese Journal of Chemistry*, 29(1): 118 – 122.
22. Osnaya, R., Arroyo, G., Parada, L., Delgado, F., Trujillo, J., Salmón, M. and Miranda R. (2003). Biginelli vs Hantzsch esters study under infrared radiation and solventless conditions. *Arkivoc*, 11: 112 – 117.
23. Bridgwood, K. L., Veitch, G. E. and Ley, S. V. (2008). Magnesium nitride as a convenient source of ammonia: Preparation of dihydropyridines. *Organic Letters*, 10(16): 3627 – 3629.
24. Chang, C-C., Cao, S., Kang, S., Kai, L., Tian, X., Pandey, P., Dunne, S. F., Luan, C-H., Surmeier, D. J. and Silverman, R. B. (2010). Antagonism of 4-substituted 1,4-dihydropyridine-3,5-dicarboxylates toward voltage-dependent L-type $Ca^{2+}$ channels Ca V 1.3 and Ca V 1.2. *Bioorganic & Medicinal Chemistry*, 18(9): 3147 – 3158.
25. Sabitha, G., Arundhati, K., Sudhakar, K., Sastry, B. S. and Yadav, J. S. (2009). $CeCl_3 \cdot 7H_2O$-catalyzed one-pot synthesis of Hantzsch 1,4-dihydropyridines at room temperature. *Synthetic Communications*, 39(16): 2843 – 2851.

*Malaysian Journal of Analytical Sciences, Vol 21 No 1 (2017): 20 - 26*
*DOI: http://dx.doi.org/10.17576/mjas-2017-2101-03*

MALAYSIAN JOURNAL OF ANALYTICAL SCIENCES
*Published by The Malaysian Analytical Sciences Society*
ISSN 1394 - 2506

# DEEP EUTECTIC SOLVENT AS A MEDIA IN SWELLING AND DISSOLUTION OF OIL PALM TRUNK

## (Pelarut Eutektik Sebagai Media dalam Pembengkakan dan Pelarutan Batang Kelapa Sawit)

Emilia Abdulmalek[1,2]*, Syarilaida Zulkefli[1], Mohd. Basyaruddin Abdul Rahman[1,2]

[1]*Department of Chemistry, Faculty of Science*
[2]*Enzyme and Microbial Technology Research, Faculty of Biotechnology and Biomolecular Science*
*Universiti Putra Malaysia, 43400 UPM Serdang, Selangor, Malaysia*

**Corresponding author: emilia@upm.edu.my*

Received: 17 August 2015; Accepted: 9 November 2016

**Abstract**

Pre-treatment is a crucial step in biomass processing prior to the hydrolysis or fermentation to bioethanol. Herein, the potential of deep eutectic solvent (DES) in the pretreatment of oil palm biomass were described. The mechanism of swelling and dissolution of oil palm trunk (OPT) was studied under optical microscopy. The OPT fibres were stirred and heated at 100 °C in choline chloride:glycerol (ChCl:Gly), choline chloride:ethylene glycol (ChCl:EG), ethylammonium chloride:glycerol (EAC:Gly) and ethylammonium chloride:ethylene glycol (EAC:EG) with 1:2 molar ratio each. All DESs tested had showed homogenous swelling and disintegration of small fragments interaction mode with OPT. There were more small fragments observed in EAC-based DES compared to ChCl-based DES. This finding supports the result for the percentage of dissolution where OPT in EAC-based DES recorded higher dissolution with 55% and 50% in EAC:EG and EAC:Gly respectively whereas ChCl-based DES recorded only 33% and 29% in ChCl:EG and ChCl:Gly, respectively. In ChCl-based DESs the fragmentations were accompanied by large unswollen section of fibres. The formation of small fragments indicates that the fibres experienced a fast dissolution. Therefore, the EAC-based DESs proved to be a better swelling and dissolution media for oil palm biomass pretreatment compared to ChCl-based DES.

**Keywords:** deep eutectic solvent, oil palm biomass, dissolution, swelling, pre-treatment

**Abstrak**

Pra-rawat adalah satu langkah dalam pemprosesan biomas sebelum hidrolisis atau fermentasi kepada bioetanol. Disini, potensi pelarut eutektik (DES) dalam pra-rawat biomas kelapa sawit telah diterangkan. Mekanisma pembengkakan dan pemelarutan batang kelapa sawit (OPT) telah dikaji dengan mikroskop optik. Fiber OPT telah dikacau dan dipanaskan pada suhu 100 ºC dalam kolin klorida:gliserol (ChCl:Gly), kolin klorida:etilin glikol (ChCl:EG), etilammonium klorida: gliserol (EAC:Gly) dan etilammonium klorida: etilin glikol (EAC:EG) dengan kadar molar 1:2 setiap satu. Semua DES yang dikaji telah menunjukkan mod interaksi pembengkakan secara setara dan pecahan fragmen kecil dengan OPT. Lebih banyak fragmen kecil dapat dilihat dalam DES berasaskan EAC berbanding dengan DES berasaskan ChCl. Ini disokong oleh peratusan pelarutan dimana OPT dalam DES berasaskan EAC menunjukkan keputusan lebih tinggi dengan masing – masing 55% dan 50% dalam EAC:EG and EAC:Gly sementara DES berasaskan ChCl hanya menunjukkan masing – masing 33% dan 29% dalam ChCl:EG dan ChCl:Gly. Bagi DES berasaskan ChCl, fragmentasi adalah disertai dengan kehadiran fiber besar yang tiada pembengkakan. Pembentukkan fragmen kecil menunjukkan bahawa fiber mengalami pelarutan yang cepat. Oleh itu, DES berasaskan EAC terbukti lebih baik sebagai media pembengkakan dan pelarutan bagi OPT berbanding DES berasaskan ChCl.

**Kata kunci**: pelarut eutektik, biomas kelapa sawit, pelarutan, pembengkakan, prarawat

## Introduction

Deep eutectic solvent (DES) is a new class of solvent that emerged from ionic liquid (IL) family which is formed by the combination of ammonium salt and a hydrogen bond donor [1]. The two components that have a high melting point each, for example choline chloride (302 °C) and urea (133 °C), exhibit a freezing point depression of 12 °C, making it a liquid as a mixture at room temperature [2]. Various combinations of DES have been studied by changing the ammonium salt and the hydrogen bond donor. Examples of hydrogen bond donors used are alcohols, amides, carboxylic acids and amines [3]. Not only can the component be varied, the molar ratio of each component can also be varied. This widens the type of DES that can be formed. There are many advantages of DES including their biodegradability, thermal stability, low melting point and the fact that they are highly cost-efficient [1]. DES is easily prepared by simple mixing of the two selected substances, ammonium salt (e.g. choline chloride) and a hydrogen bond donor (e.g. glycerol), at 80 °C [4].

DES has shown considerably high potential in biocatalysis reactions such as hydrolysis, transesterification, and esterification. It was reported that choline chloride: glycerol (ChCl:Gly) as a co-solvent of aqueous reactions can enhance the reaction up to 20-fold [5]. The use of 10% (v/v) of ChCl:Gly as the reaction medium for the hydrolysis of *p*-nitrophenyl acetate led to a 3-fold increase for pig liver esterase (PLE) and *Rhizopusoryzae esterase* (ROE) [5]. The properties and performance of DES in biocatalysis has led to our interest in exploring its utilization in dissolving high crystalline compounds such as lignocellulosic biomass in view of progressing with the enzymatic hydrolysis of the treated biomass.

Pre-treatment of biomass is crucial in order to break down the highly crystalline cellulose. The process will ease the access of cellulase to the amorphous cellulose, where this can enhance the conversion of monosaccharides (e.g. glucose). Francisco et al. [6] explored the application of the novel DES solvent system on lignocellulosic biomass. They reported that the solubility of lignin increased by the addition of lactic acid in DES, while cellulose gave negative results. However, a malic acid-proline series enhanced the dissolution of starch and cellulose. This report proved that the DES system or low transition temperature mixtures (LTTMs) can dissolve some of the lignin, although the screened mixtures gave low solubility for cellulose and starch.

Observation of the swelling and dissolution of fibre in certain solvents is one of the methods used to characterise the quality of solvents in terms of its ability to dissolve and swell the fibres. Many studies have been carried out for the dissolution of cellulose and wood fibre in various types of solvents such as NaOH [7], *N*-methylmorpholine-*N*-oxide (NMMO) [8], lithium chloride/urea/water [9] and ionic liquids [10-13]. The swelling process of cellulosic materials can improve the reactivity and accessibility of the cellulose. This phenomenon can be used to introduce activation of the substrate [14]. Five different modes were proposed for wood and cotton fibre dissolution as a function of solvent quality by using an NMMO-water system with or without additives [8].

Similar interactions were observed by using NaOH-water and ionic liquids for various types of plant fibres and cellulosic materials. Cuissinat and Navard [8] had classified dissolution of wood and fibre into 5 different classes according to its degree of swelling or dissolution. The modes include fast dissolution by disintegration into fragments (Mode 1), swelling by ballooning with dissolution (Mode 2), swelling by ballooning without dissolution (Mode 3), homogenous swelling (Mode 4) and no swelling and no dissolution (Mode 5). In view of the advantages of DES over ionic liquid, an investigation of DES as a medium for biomass pre-treatment was conducted. This report is one of the earliest works on utilising DES for dissolving and pre-treatment of raw oil palm biomass. The properties of oil palm biomass fibre after pre-treament with DES were observed through optical microscopy.

## Materials and Methods

### Preparation of OPT fibre

OPT fibre was obtained from Biomass Technology Center (BTC) of Malaysian Palm Oil Board (MPOB). By using a thermo chemical refiner, the fibre was cleaned, shredded and refined into loose fibrous material. Prior to usage, the fibre was sieved to size 250 μm and dried to constant weight.

**Preparation of deep eutectic solvent**

DESs of 1:2 molar ratio (Table 1) were prepared by stirring the two components, ammonium salt and hydrogen bond donor (e.g.: 0.1 mol for ChCl and 0.2 mol for Gly), at a temperature of 80 °C. The mixture was stirred until a homogenous and colourless liquid was obtained [1].

Table 1. DESs used in the study

| DES | Ammonium Salt | Hydrogen Bond Donor |
|---|---|---|
| ChCl:Gly | Choline chloride | Glycerol |
| ChCl:EG | Choline chloride | Ethylene glycol |
| EAC:Gly | Ethylammonium chloride | Glycerol |
| EAC:EG | Ethylammonium chloride | Ethylene glycol |

**Dissolution of oil palm biomass**

The samples were prepared by adding 0.5 g of fibre (250 µm) into 9.5 g of DES in a screw capped vial. All mixtures were incubated in an oil bath at 100 °C with vigorous stirring. After 24 hours of incubation, a small amount of dissolution mixture was taken from each sample for observation. The swelling and dissolution mechanism was observed using an optical microscope with a Metallux 3 (Leitz) [(Nikon DS-Fil-42)]. A small portion of the dissolution mixture was placed on a glass plate and viewed at 20 times magnification.

**Percentage dissolution of oil palm trunk**

5% of fibre (250 µm) in DES was prepared by adding 0.5 g fibre in 9.5 g of DES. The mixture was incubated in oil bath at 100 °C with vigorous stirring. All dissolutions were carried out for 48 hours. After 48 hours, the mixture was centrifuged and filtered using crucible glass to separate the undissolved fibre. The filtration was washed with distilled water and dried in an oven at 50 °C overnight. Filtered sample was then cooled in desiccator and weighed to a constant weight. The percentage of fibre dissolved was calculated using equation 1:

$$\text{Fiber dissolved (\%)} = \frac{w_i - w_f}{w_i} \times 100 \quad (1)$$

where $w_i$ is the weight of initial fibre and $w_f$ is the weight of residue recovered.

## Results and Discussion

OPT was pre-treated in four different DESs (Table 1) in order to observe the type of interaction when the ammonium salt or hydrogen bond donor is varied. All data was taken within 24 hours for observation under optical microscopy. Figure 1 shows the shape of fibre observed in ChCl:Gly, ChCl:EG, EAC:Gly and EAC:EG after 24 hours of heating and stirring. Based on our observations, all DESs exhibited homogenous swelling and disintegration of small fragments for OPT fibres.

Homogenous swelling occurs when the solvent only swell the fibres and this does not lead to any dissolution of the fibres in the media. This type of interaction will make the fibre stay in the swollen state and thus leads to bad solvation for wood fibre as the swelling occurs very slowly. Cuissinat and Navard [8] suggested that in this type of behaviour, the solvent penetrates the fibre matrix at its loose regions such as pores and less dense disordered point, without making contact to the general part of the fibre. Unfortunately, this mode of interaction will not affect the cellulose crystal in dissolution or reformation to amorphous cellulose.

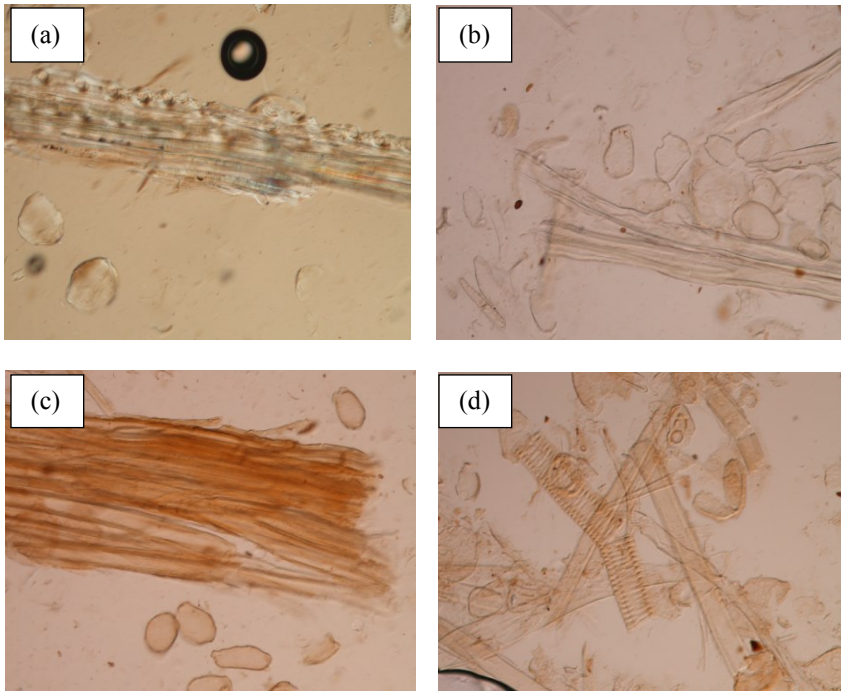



Figure 1. OPT in (a) ChCl:Gly, (b) ChCl:EG, (c) EAC:Gly and (d) EAC:EG after 24 hours at 100 °C

Disintegration of small fragments of the fibres was another type of interaction observed in the sampling. This indicates fast dissolution where the fibres were broken over all their length, giving large rod-like pieces [8]. These small fragments will then easily dissolve in the media. Based on our data, this interaction is rather low in ChCl-based DES but more frequent in EAC:Gly and EAC:EG (Figure 2). The presence of more small fragments in EAC-based DES media showed that the solvent can provide good dissolution and thus indicates that they are better solvent compared to ChCl:Gly and ChCl:EG (Figure 3).

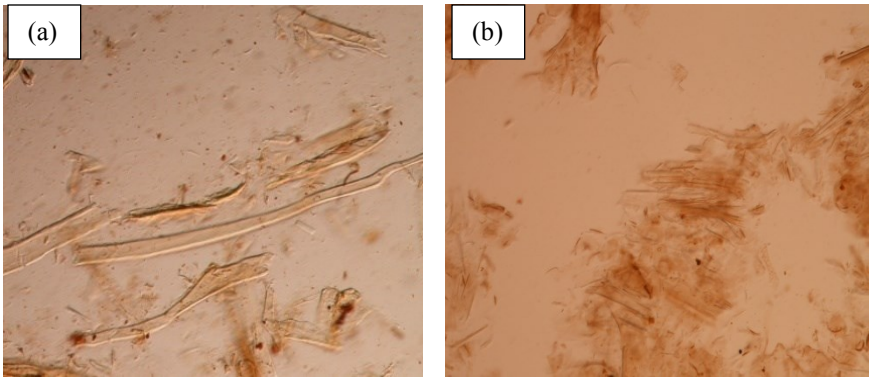



Figure 2. Fibre treated at t = 20 hours in (a) EAC:Gly and (b) EAC:EG. Small fragments were generated mainly by agitation provided

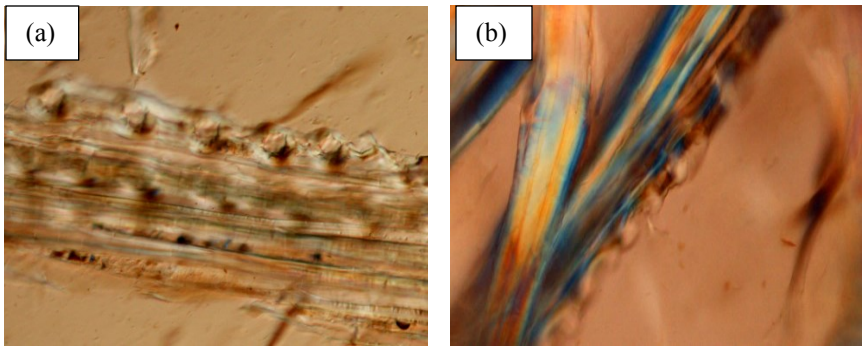
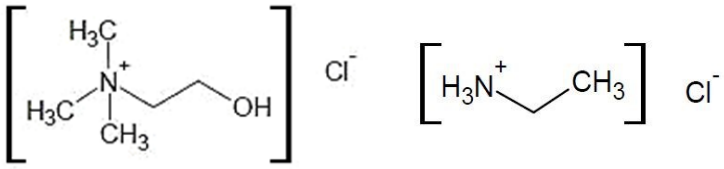



Figure 3. OPT fibre in (a) ChCl:Gly and (b) ChCl:EG at t = 24 hours

In addition, the dissolution of OPT in each solvent were calculated. ChCl-based DES showed lower percentage of solubility than EAC-based DES (Table 2). This result clearly supports the earlier findings that EAC-based DES has higher capability in terms of dissolution of oil palm biomass. Figure 4 shows the chemical structure for ChCl and EAC. EAC has simpler structure compared to ChCl where EAC has only one alkyl chain. ChCl has three methyl groups attached to the nitrogen atom. Thus, ChCl only has one H that can make hydrogen bond with cellulose. EAC salt has 3H and ethyl chain attached to the nitrogen atom. This may help EAC-based DES to dissolve lignocellulosic materials better than ChCl-based DES.

Table 2. Percentage of dissolution for OPT in DESs after 48 hrs of pre-treatment.

| **Solvent** | **Solubility (wt %)** |
|---|---|
| ChCl:Gly | 33.27 |
| ChCl:EG | 29.13 |
| EAC:Gly | 50.77 |
| EAC:EG | 55.60 |




(a) Choline chloride (b) Ethylammonium chloride

Figure 4. Chemical structure of (a) choline chloride and (b) ethylammonium chloride

There are several other solvents that have been tested for mechanism of swelling and dissolution on wood fibres and cellulose derivatives. The solvents are *N*-methylmorpholine-*N*-oxide (NMMO), sodium hydroxide (NaOH) and ionic liquids (ILs). NMMO and NaOH are well known as conventional cellulose solvents. NMMO with small percentage of water (17% and 35%) and NaOH showed excellent quality for wood and cellulose solvents [8]. Nitrocellulose in NMMO-water (17% and 35%) showed small fragmentation where the solvents give strong penetration and thus dissolves nitrocellulose in the media (Mode 1) [10].

ILs have been studied in order to offer alternative solvents for cellulose. The quality of ILs for wood and cellulose fibres can range from Mode 1 to Mode 4. 1-n-butyl-3-methylimidazolium chloride, $C_4$mimCl showed the best media for cotton and wood fibre with disintegration of small fragments and dissolves in $C_4$mimCl (Mode 1) [15]. 1-ethyl-3-methylimidazolium chloride, EmimCl and 1-butyl-3-methylimidazolium chloride, BmimCl shows swelling by ballooning with dissolution occurred for cellulose fibre (Mode 2) [16]. Whereas for OPT, OPF and EFB fibres, both ILs exhibited homogenous swelling without dissolution. In this paper, we carried out the swelling and dissolution of OPT in DESs with aim to provide alternative solvent for wood and cellulose fibres. Based on our findings, DESs exhibited type of mechanism in Mode 1-4.

Although ILs and DESs have similarity in terms of quality, DESs have advantage in terms of solvent properties. ILs are hazardous due to the halide anions and very poor biodegradability. It requires high purity since small amount of impurity can affect its physical properties. The synthesis of ILs can't be described as an environmental friendly process since it requires large amount of salts and solvents in order to achieve complete anion exchange [17]. In contrast to ILs, DESs are cheaper, easier to synthesize and biodegradable [1]. Drawbacks of ILs lead DESs to be the alternative solvent for ILs and other conventional cellulose solvents.

Swelling and dissolution of wood fibre in DESs can be the easiest and fastest method in determining quality of solvents based on the modes introduced by Cuissinat and Navard [8], using simple instrument (optical microscopy) with low cost and less toxic solvent (DESs).

## Conclusion

DESs were prepared and their effectiveness as pre-treatment media for oil palm biomass was studied under optical microscopy. DESs showed their potential as pre-treatment media for lignocellulosic biomass although currently its effectiveness has not surpassed some ILs. Based on our findings, DESs can provide homogeneous swelling and disintegration of small fragments for OPT fibres. The EAC-based DES showed better interaction than ChCl-based DES for dissolution of oil palm biomass. Currently, we are looking at the enzymatic hydrolysis of the DES pre-treated oil palm biomass and preparing other DESs for the pre-treatment.

## Acknowledgement

Authors would like to acknowledge the financial support given by the Graduate Research Fellowship (GRF), Universiti Putra Malaysia for this project.

## References

1. Gorke, J. T., Srienc, F. and Kazlauskas, R. J. (2008). Hydrolase-catalyzed biotransformations in deep eutectic solvents. *Chemical Communication*, 10: 1235 – 1237.
2. Abbott, A. P., Boothby, D., Capper, G., Davies, D. L. and Rasheed, R. K. (2004). Deep eutectic solvents formed between choline chloride and carboxylic acid: versatile alternatives to ionic liquids. *Journal of American Chemical Society,* 126: 9142 – 9147.
3. Nkuku, C. A. and LeSuer, R. J. (2007). Electrochemistry in deep eutectic solvents. *Journal of Physical Chemistry B*, 111(46), 13271 – 13277.
4. Zhao, H., Baker, G. A. and Holmes, S. (2011). New eutectic ionic liquids for lipase activation and enzymatic preparation of biodiesel. *Organic & Biomolecular Chemistry*, 9(6): 1908 – 1916.
5. Lindberg, D., Revenga, M. and Widersten, M. (2010). Deep eutectic solvents (DESs) are viable cosolvents for enzyme-catalyzed epoxide hydrolysis. *Journal of Biotechnology,* 147: 169 – 171.
6. Francisco, M., Bruinhorst, A. and Kroon, M. C. (2012). New natural and renewable low transition temperature mixtures (LTTMs): screening as solvents for lignocellulosic biomass processing. *Green Chemistry*, 14 (8): 2153 – 2157.
7. Moigne, N. and Navard, P. (2010). Dissolution mechanism of wood cellulose fibres in NaOH/water. *Cellulose,* 17(1): 31 – 45.
8. Cuissinat, C. and Navard, P. (2006) Swelling and dissolution of cellulose part I: Free floating cotton and wood fibres in *N*-Methylmorpholine-*N*-oxide-water mixtures. *Macromolecular Symposium*, 244: 1 – 18.

9. Tatárová, I., Manian, A. P., Široká, B. and Bechtold, T. (2010). Nonalkali swelling solutions for regenerated cellulose. *Cellulose,* 17(5), 913 – 922.
10. Cuissinat, C., Navard, P. and Heinze, T. (2008). Swelling and dissolution of cellulose, Part V: Cellulose derivatives fibres in aqueous systems and ionic liquid. *Cellulose*, 15(1): 75 – 80.
11. Swatlotski, R. P., Spear, S. K., Holbrey, J. D. and Rogers, R. D. (2002). Dissolution of cellulose with ionic liquids. *Journal of American Chemical Society*, 124(18): 4974 – 4975.
12. Vancov, T., Alston, A-S., Brown, T. and McIntosh, S. (2012). Use of ionic liquid in converting lignocellulosic material to biofuels. *Renewable Energy,* 45: 1 – 6.
13. Zhu, S., Wu, Y., Chen, Q., Yu, Z., Wang, C., Jin, S., Ding, Y. and Wu, G. (2006). Dissolution of cellulose with ionic liquids and its application:a mini review. *Green Chemistry,* 8(4), 325 – 327.
14. Kunze, J. and Fink, H. P. (2005). Structural changes and activation of cellulose by caustic soda solution with urea. *Macromolecular Symposium,* 223: 175 – 187.
15. Cuissinat, C., Navard, P. and Heinze, T. (2008). Swelling and dissolution of cellulose. Part IV: Free floating cotton and wood fibres in ionic liquids. *Carbohydrate Polymers,* 72(4): 590 – 596.
16. Abdul Rahman, M. B., Ishak, Z. I., Abdullah, D. K., Aziz, A. A., Basri, M. and Salleh, A.B. (2012). Swelling and dissolution of oil palm biomass in ionic liquids. *Journal of Oil Palm Research,* 24: 1267 –1276.
17. Zhang, Q., Vigier, K. D. O., Royer, S. and Jerome, F. (2012). Deep eutectic solvents: Syntheses, properties and applications. *Chemical Society Reviews,* 41(21): 7108 – 7146.

*Malaysian Journal of Analytical Sciences, Vol 21 No 1 (2017): 27 - 36*
*DOI: http://dx.doi.org/10.17576/mjas-2017-2101-04*

MALAYSIAN JOURNAL OF ANALYTICAL SCIENCES
*Published by The Malaysian Analytical Sciences Society*
ISSN 1394 - 2506

# A SINGLE HPLC METHOD FOR SEPARATION OF OLIGOSTILBENES FROM DIFFERENT DIPTEROCARPACEAE EXTRACTS

## (Kaedah KCPT untuk Pemisahan Oligostilbene dari Ekstrak Dipterocarpaceae yang Berbeza)

Erni Muis[1], Rohaity Ramli[1,2], Nurhuda Manshoor[1,2]*

[1]*Faculty of Pharmacy*
[2]*Atta-ur-Rahman Institute for Natural Products Discovery*
*Universiti Teknologi MARA Selangor, Puncak Alam Campus, 43200 Puncak Alam, Selangor, Malaysia*

**Corresponding author: nurhuda15@salam.uitm.edu.my*

Received: 3 October 2016; Accepted: 24 November 2016

**Abstract**

One standard chromatographic conditions of HPLC was developed for different Dipterocarpaceae plant extracts. The purpose of this study is to achieve an optimized chromatographic method that is able to produce a reasonably good separation and resolution of oligostilbenes in plant crude extracts. For this purpose, five model samples of Dipterocarpaceae extracts, *Shorea parvifolia, Shorea ovalis, Dipterocarpus crinitus, Dipterocarpus gracilis* and *Hopea* spp. were used. The parameters, which include types of chromatographic solvents, types of mobile phase elution, solvent composition and the injection volumes, were modified. The results showed that the optimum chromatographic conditions were achieved when a gradient elution was adopted, with the solvent composition of $H_2O$: ACN from 95:5 to 25:75 in 20 minutes. The injection volume of 5 µL is best for a 1 mg/ml sample concentration. The temperature was maintained at 35 °C and the flow rate was at 1.0 ml/min. Some compromises were taken into account such as having less accurate method if compared with a single method developed for single extract or sample. The method showed positive results when tested on 10 extracts of the same family from different plant parts and localities.

**Keywords**: dipterocarpaceae, *Shorea* spp., *Dipterocarpus* spp., chromatography, high performance liquid chromatography

**Abstrak**

Satu kaedah piawai untuk keadaan kromatografi KCPT telah dibina untuk ekstrak dari tumbuhan Dipterocarpaceae yang berlainan. Tujuan kajian ini ialah untuk mencapai satu kaedah kromatografi optimum yang dapat menghasilkan pemisahan komponen oligostilbene dari ekstrak tumbuhan dengan resolusi yang baik. Untuk tujuan ini, lima sampel ekstrak tumbuhan Dipterocarpaceae, *Shorea parvifolia, Shorea ovalis, Dipterocarpus crinitus, Dipterocarpus gracilis* dan *Hopea* spp. telah digunakan sebagai model. Parameter yang merangkumi jenis pelarut, jenis aliran fasa bergerak, komposisi pelarut dan isipadu suntikan sampel telah diubahsuai. Keputusan menunjukkan kaedah kromatografi yang sesuai berjaya dicapai apabila aliran bercerun digunakan dengan komposisi pelarut $H_2O$: ACN dari 95:5 kepada 25:75 di dalam masa 20 minit. Isipadu suntikan 5 µL adalah sesuai untuk larutan sampel berkepekatan 1 mg/ml. Suhu turus ditetapkan pada 35 °C dan kadar aliran fasa bergerak adalah pada 1.0 ml/min. Walaubagaimanapun, resolusi setiap kromatogram tidak sebaik dan sejitu apabila kaedah berlainan dibangunkan untuk setiap sampel secara individu. Kaedah ini telah telah menunjukkan keputusan yang positif apabila diuji ke atas sepuluh ekstrak lain dari famili tumbuhan yang sama. Sampel ujian tersebut adalah dari bahagian tumbuhan yang berlainan dan dari kawasan pensampelan yang berbeza.

**Kata kunci:** dipterocarpaceae, *Shorea* spp., *Dipterocarpus* spp., kromatografi, kromatografi cecair prestasi tinggi

## Introduction

Dipterocarpaceae family produces a high diversity of oligostilbene structures, ranging from dimeric to octameric stilbenes. Oligostilbenes are the most phytochemical components that were studied on this family due to their abundance in the plants which can be isolated from their leaves, bark, wood, heartwood and seeds. Oligostilbenes have attracted a major attention due to the bioactivities of crude extracts, fractions, as well as the isolated pure compounds including anti-inflammatory, cytotoxicity, antimicrobial and antioxidant activities [1-3]. As the isolation and characterization techniques for plant compounds developed, investigations of oligostilbenes became more abundant and more new compounds from various families were characterized. In our previous report, we have isolated 5 new oligostilbenes from *Neobalanocarpus heimii* [4].

Chromatographic technique is now being used beyond its original purpose, which is to separate and purify a mixture of compounds. It is also used to identify and quantify the individual components of mixtures in the phytochemical and analytical chemistry [5]. High performance liquid chromatography (HPLC) analysis plays a major role in phytochemical analysis including identification of crude plant extracts [6]. Method development for HPLC requires decisions regarding the choice of column, mobile phase, detectors, and method quantitation [7]. Optimization of HPLC conditions and other important perspectives during method development are conducted to provide a simple, precise, rapid and accurate analysis of plants.

The obvious challenge in chromatographic profiling of plant extracts is repetitive method development works whenever working with new samples. Usually, the chromatographic method differs for every sample. Thus, chromatographic method is developed for one particular sample only at one time. This leads to the increase consumption of money and time. We were suggesting a dereplication strategy to identify compounds as early as in a crude mixture in order to work faster [8,9].

The aim of analysis of each HPLC method may vary for each developmental area. In phytochemical studies, HPLC are frequently applied for quantitative and qualitative analysis of organic compounds in natural plant extracts, such as and alkaloids from *Nicotiana spp.*[10]. In a different field, a number of HPLC methods have been developed for the quantification of samples such as sildenafil in human plasma [11], acetazolamide, furosemide and phenytoin in suspensions [12].

Phytochemical studies of Dipterocarpaceae by using HPLC are conducted to determine the composition of the plant such as resveratrol dimer O-glucosides with enantiomeric aglycones [13], bergenin phenylpropanoates [14], oligostilbenoids and 3-ethyl-4-phenyl-3,4-dihydroisocoumarins [15].

In this study, one standard method of chromatographic conditions of HPLC is developed to analyze different samples of Dipterocarpaceae extracts. Optimization of developing method involves the changing of solvent conditions and injection volume only. Conditions, such as column temperature and types of solvents were selected based on the previous study [4], flow rate was calculated based on Van Deemter equation for mobile phase velocity, and the wavelengths were measured prior to the experiments.

## Materials and Methods

### Materials and reagents

The model samples, *Shorea parvifolia, Shorea ovalis, Dipterocarpus crinitus, Dipterocarpus gracilis* and *Hopea* spp. are available at Atta-ur-Rahman Institute for Natural Product Discovery repository. The test samples were collected from Malaysian National Parks, mainly in the area of Selai and Kuala Kerian. Organic solvents used for extraction were of analytical grade. Acetonitrile used for HPLC analyses were of chromatographic grade from RCI Labscan. Ultrapure water (18 MΩ $cm^{-1}$) was obtained from PURELAB® Option water purification system (ELGA).

### Instrumentation

The HPLC system is a Dionex Ultimate 3000 from Thermoscientific. The system is equipped with an ultra-pressure pump, a degasser, an auto sampler and a diode array detector (DAD). The chromatographic profiles and the integrated data were recorded using Chromeleon Chromatography software. The separations were achieved through a Phenomenex® Luna 5 µm C18 column (150 X 4.6 mm) equipped with a guard column of similar chemistry.

**Extraction of samples**
An amount 1 g of each sample was extracted in 10 ml of acetone. Extraction was carried out by maceration under sonication. For each sample, the extraction process was repeated 3 times. The extracts were filtered and reduced under vacuum. The samples were transferred into vials and dried over nitrogen gas.

**Sample preparation for HPLC analysis**
The samples were prepared by dissolving the extracts in acetonitrile to the concentration of 1000 ppm according to the weight. Then, the samples were filtered through 0.45 µm membrane filter into HPLC vials.

**HPLC analysis**
The HPLC analyses for Dipterocarpaceae crude extracts were established at the wavelengths of 215 nm, 254 nm and 283 nm. The column temperature was maintained at 35 °C, and the flow-rate was set at 1 ml/min. The injection volumes were 5 and 10 µl for each analysis. The mobile phase were acetonitrile: water (ACN:$H_2O$) at different compositions, for both isocratic and gradient elution mode.

The system was purged prior to initiation of analysis to ensure the line tubes are free from air bubbles. The column was conditioned for 30 minutes and the baseline was monitored for irregularities. The sample injections were performed automatically by an auto sampler. The column was flushed with 95% acetonitrile for 5 minute after each chromatographic run, followed by a 5-minute post-run at solvent composition of the next injection.

**Method development and validation**
A method development was initiated by a full-range gradient of ACN:$H_2O$ (5:90 to 95:5), enables the elution of all compounds in sample ranging from polar to non-polar compounds. By keeping the initial solvent composition of ACN:$H_2O$ at 5:90, the water component was gradually reduced at the end of chromatographic run, until the retention time of the last peak achieve maximum chromatographic run, and/or an isocratic gradient is achieved. The run-time was adjusted to accommodate the retention time of all compounds in the samples. Each chromatogram was analyzed and the best solvent composition was decided. The analyses were continued by keeping the end solvent composition of selected condition, while gradually increasing acetonitrile percentage in the initial composition. Using this strategy, the solvent compositions were adjusted until an isocratic gradient was achieved. An optimum condition was selected for the best separation of all model samples. The system is also enable to create a curve gradient (Figure 1), which were also tested for all samples. The injection volumes were also tested.

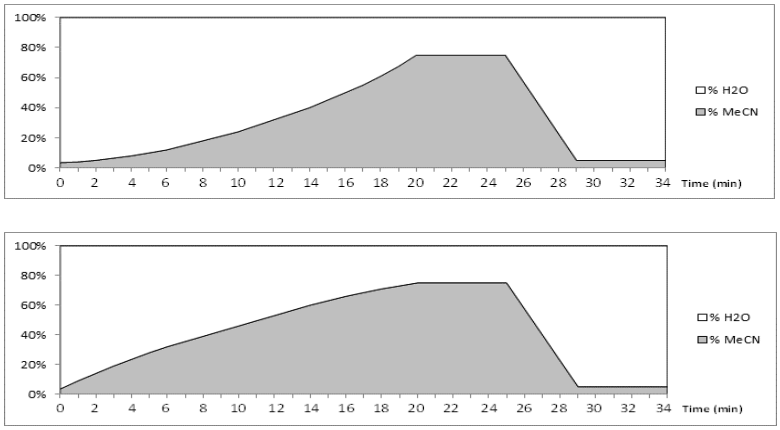



Figure 1. Curve gradient elution; concave (top) and convex (bottom) gradient elution, The graph represent the percentage of water and acetonitrile

## Results and Discussion

### Chromatographic conditions for model sample

All model samples had undergone a full-range gradient method to obtain the overall performance of their chromatographic profiles. The full-range gradient method is also a standard gradient elution scouting run to determine the best elution mode to be chosen in this study. Dolan [16] had suggested that the scouting run can be a guide tool to determine the best elution mode for a specific sample, column and eluent system. The chromatographic profiles samples using the full-range gradient method show that the samples occupied more than 40% of the separation space (Figure 2). This indicates that the separation should be done by the gradient elution.

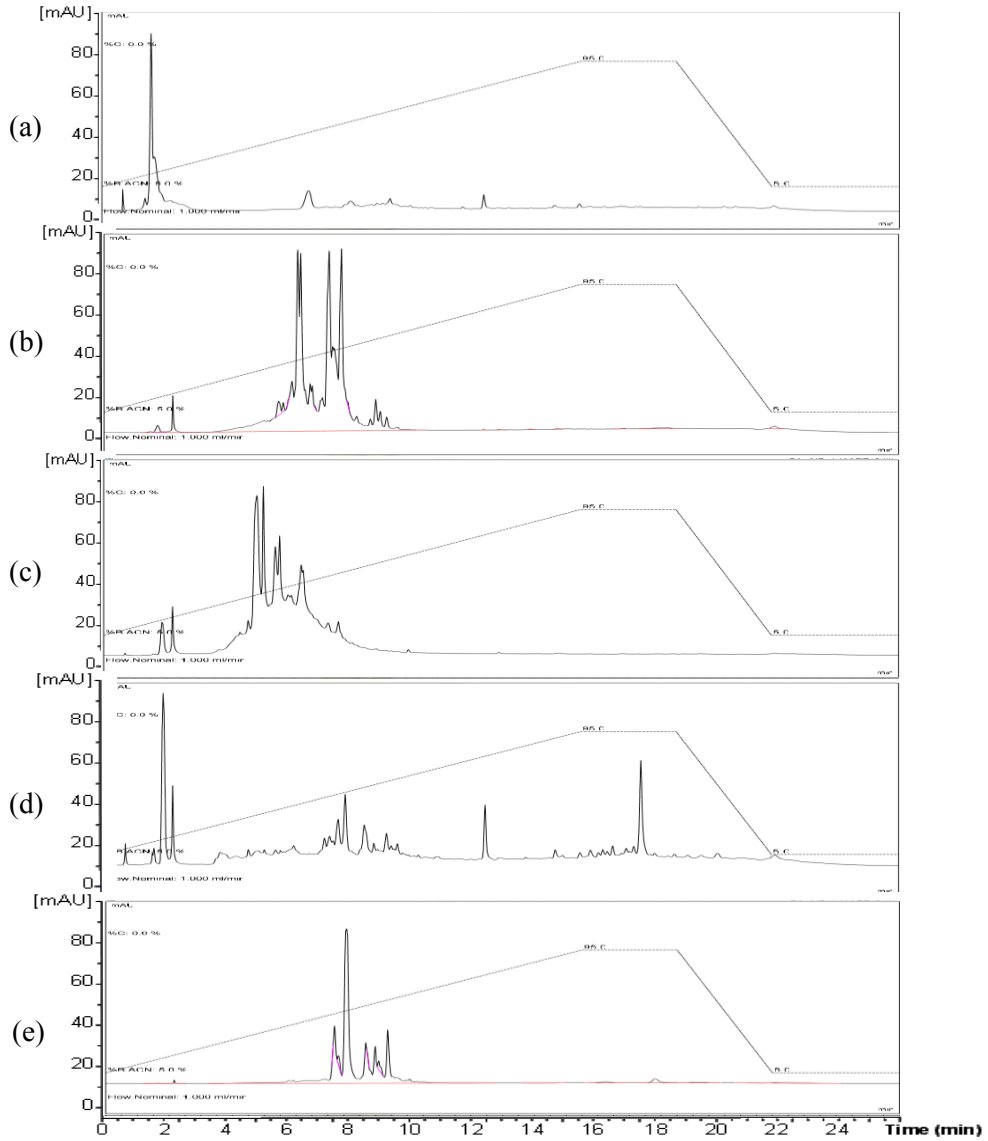



Figure 2. Chromatogram profiles of model samples using full-range gradient method of ACN:$H_2O$ (5:95 to 95:5 in 15 minutes); (a) *Shorea parvifolia*, (b) *Shorea ovalis*, (c) *Dipterocarpus crinitus*, (d) *Dipterocarpus gracilis*, and (e) *Hopea* spp

From the initial analysis of the chromatographic profile, we have decided to increase the chromatographic run from 15 to 20 minutes to accommodate the wide range of retention time for compounds in *Dipterocarpus gracilis.* The analyses were continued by changing the solvent composition of the initial and the end of a chromatographic run. All chromatographic profiles were analyzed and after some adjustment and modification, an isocratic mode of ACN:$H_2O$ (5:95 to 75:25 in 20 minutes) was considered performing a reasonably good separation for all samples. Figure 3 shows the chromatographic profiles of all model samples using the selected chromatographic conditions.

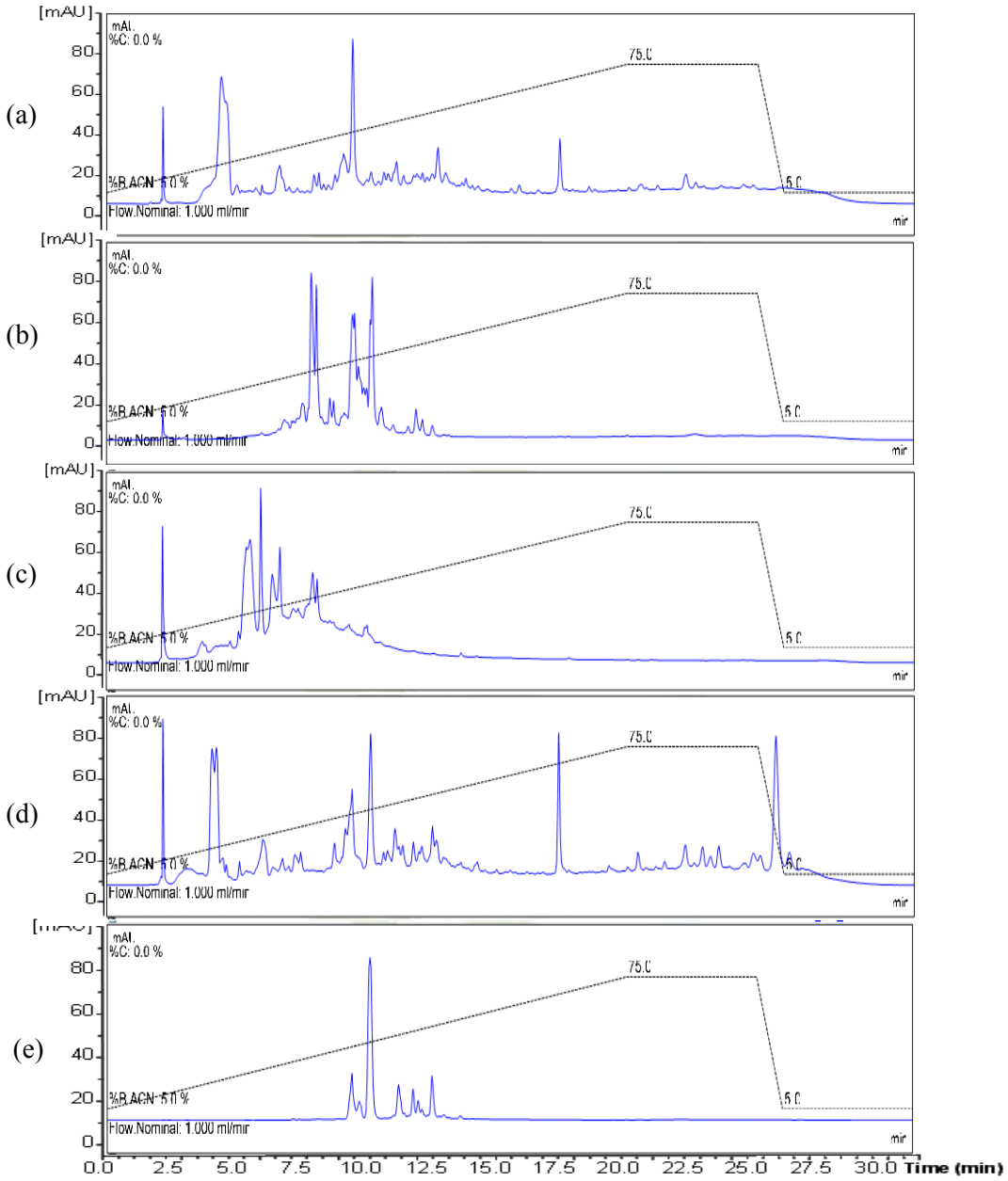



Figure 3. Chromatographic profiles of model samples using an isocratic mode of ACN:$H_2O$ (5:95 to 75:25 in 20 minutes); (a) *Shorea parvifolia,* (b) *Shorea ovalis,* (c) *Dipterocarpus crinitus,* (d) *Dipterocarpus gracilis,* and (e) *Hopea* spp

**Curved gradient method**

Basically, there are two types of curved gradient method; concave and convex gradients. These methods were tested to discover any improvements on the separation of samples. In a reverse phase chromatography, concave and convex gradients were used for analyzing multi-component samples which require the extra resolution either at the beginning or at the end of the gradient. The elution rate was maintained at $H_2O$:ACN (95:5 to 25:75 in 20 minutes) for both gradient method. The results, however, did not show any improvement in the resolution and failed to achieve optimal separation of model samples. Thus, it was not considered for further optimization of the chromatographic conditions for the model samples.

**Injection volume**

Injection volume is considered as one of the parameter that can be modified to achieve optimized method development for better separation of all samples. In this study, the gradient elution was fixed to be $H_2O$:ACN (95:5 to 25:75) and the run time was set up to be 20 minutes. The chromatograms showed that the injection volume had the significant effect on the chromatographic resolution. The shapes of peaks were improved, thus producing a better resolution. Previous studies [17,18] also showed that with the increase of injection volume, the resolution of separated compounds would be decreased. In this study, the injection volume of 5 µl per injection of samples is considered to be the best compromise.

**Method validation on test samples**

Ten plant samples were chosen to be tested with the optimized chromatographic conditions to ensure the reproducibility of the developed method. The tested samples are from the same family as the model samples but different parts of the plant that were studied. The tested samples were taken from the wood of the buttress and each species were from two places in Malaysia (Selai and Kuala Kerian). *Shorea parvifolia, Shorea leprosula, Shorea ovalis, Dipterocarpus crinitus* and *Hopea* spp. were chosen to test the method. Figures 4(a-e) show the chromatographic profiles of all tested samples.

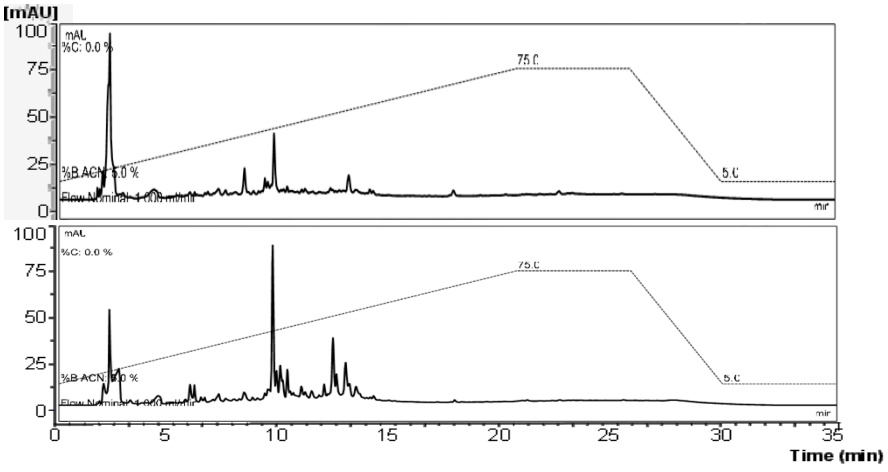



Figure 4(a). Chromatographic profiles of test samples using an isocratic mode of ACN:$H_2O$ (5:90 to 75:25 in 20 minutes) of *Shorea parvifolias.* The top chromatogram is for sample from Selai and the bottom is sample from Kuala Kerian

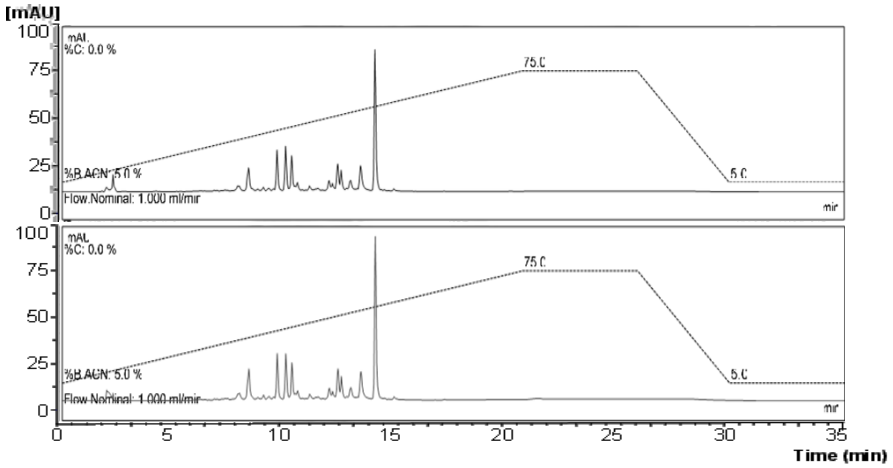



Figure 4(b). Chromatographic profiles of test samples using an isocratic mode of ACN:$H_2O$ (5:90 to 75:25 in 20 minutes) of *Shorea leprosula.* The top chromatogram is for sample from Selai and the bottom is sample from Kuala Kerian

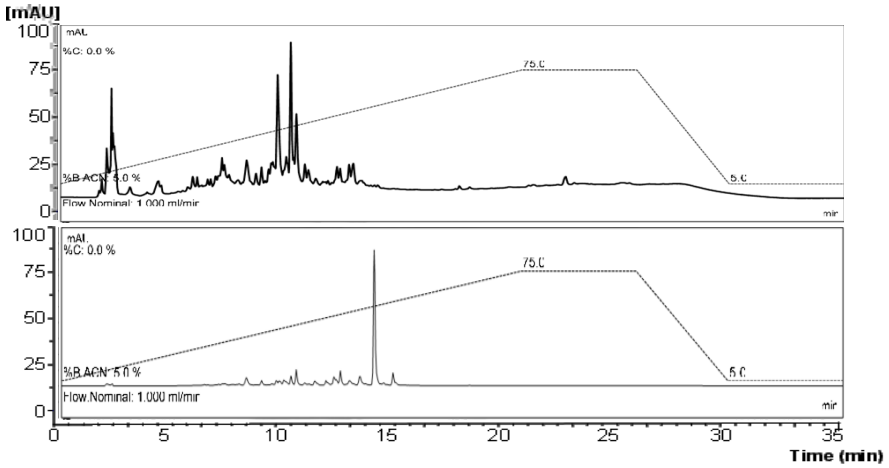



Figure 4(c). Chromatographic profiles of test samples using an isocratic mode of ACN:$H_2O$ (5:90 to 75:25 in 20 minutes) of *Shorea ovalis.* The top chromatogram is for sample from Selai and the bottom is sample from Kuala Kerian

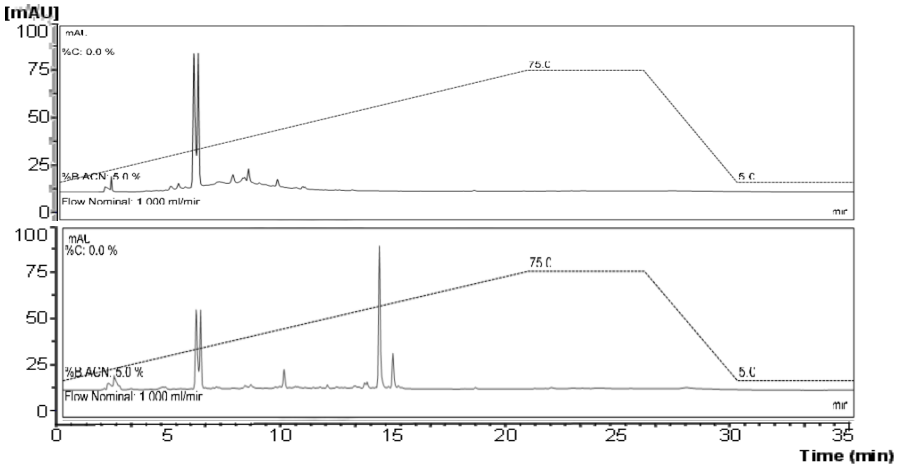



Figure 4(d). Chromatographic profiles of test samples using an isocratic mode of ACN:$H_2O$ (5:90 to 75:25 in 20 minutes) of *Dipterocarpus crinitus.* The top chromatogram is for sample from Selai and the bottom is sample from Kuala Kerian

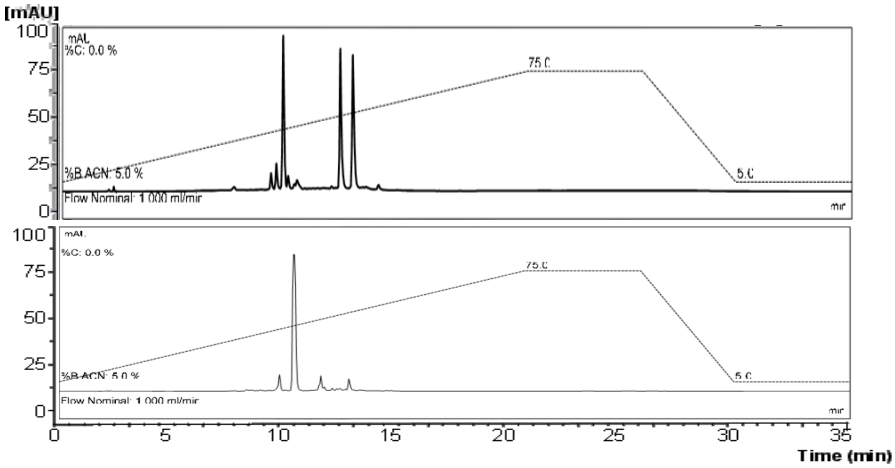



Figure 4(e): Chromatographic profiles of test samples using an isocratic mode of ACN:$H_2O$ (5:90 to 75:25 in 20 minutes) of *Hopea* spp. The top chromatogram is for sample from Selai and the bottom is sample from Kuala Kerian

The optimum chromatographic profiles for Dipterocarpaceae plant extracts were achieved by a gradient elution of water-acetonitrile from 95:5 to 25:75 in 20 minutes. A smaller injection volume is more favourable for a better resolution, in this case is 5 µL per injection. This standard method can reduce the overall assay development time for analysis of similar samples and provide essential information regarding the effects of chromatographic parameters on the separation. A longer gradient time will increase the retention of compounds in the column. Thus, the elution is slower and overlapping peaks for early-eluting compounds can be avoided. Nonetheless, longer gradient time up to a limit will cause overlapping peaks to the late-eluting compounds. Since the compounds were retained longer in the column, there is a chance that peaks will not eluted during the fixed run time and may be missing from the analyzed samples.

Though the tested samples can be separated by using the optimized method, it is best to individually alter the chromatographic conditions. This is to ensure better separation and resolution of samples and as well as a more accurate method can be achieved.

## Conclusion

The results show that a single chromatographic method for analyses of different plant samples is possible. A gradient elution method using water-acetonitrile (from 95:5 to 25:75) and injection volume of 5 µL was the chosen and optimized method. The run time was extended to 20 minutes to give sufficient time for the compounds to be eluted from the column and to avoid peak overlapping. Other parameters, the column temperature (35 °C) and the flow rate (1.0 ml/min) were kept constant.

As far as phytochemical studies are concerned, the ability of such a method to separate a set of plants samples using only one chromatographic condition provides a useful tool for more efficient natural compounds isolation. This eliminates the dependence on reproducing precise chromatographic data for every single plant sample, which has significantly influenced the energy and time consumptions. The strategy of having a single method for chromatographic condition can increase the productivity of phytochemical analysis of plant extracts, and avoid the replication of developing chromatographic conditions unnecessarily.

## Acknowledgement

The members of this project would like to thank Atta-ur-Rahman Institute for Natural Products Discovery, Research Management Institute (RMI), UiTM for supporting this project by providing laboratory space and administrative assistance. We are also grateful to The Ministry of Education (MOE) for the research funding under the Fundamental Research Grant Scheme (FRGS). We also want to thank Puan Marina Ismail, Akademi Pengajian Bahasa, UiTM for proofreading the manuscript.

## References

1. Ito, T. (2011). Structures of oligostilbenoids in dipterocarpaceaeous plants and their biological activities. *Yakugaku Zasshi,* 131(1): 93 – 100.
2. Ito, T., Akao, Y., Tanaka, T., Iinuma, M. and Nozawa, Y. (2002). Vaticanol C, a novel resveratrol tetramer, inhibits cell growth through induction of apoptosis in colon cancer cell lines. *Biological and Pharmaceutical Bulletin*, 25(1): 147 – 148.
3. Zuraida, W., Ahmat, N., Hazana, N. and Ainaa, N. (2011). The evaluation of antioxidant, antibacterial and structure identification activity of trimer resveratrol from Malaysia's Dipterocarpaceae. *Australian Journal of Basic and Applied Scienc,e* 5(5): 926 – 929.
4. Bayach, I., Manshoor, N., Sancho-Garcia, J. C., Choudhary, M. I., Trouillas, P., Weber, J. F. F. (2015). Oligostilbenoids from the heartwood of *N. heimii* and insights in their biogenesis. *Chemistry - An Asian Journal,* 10: 198 – 211.
5. Boligon, A. A. and Athayde, M. L. (2014). Importance of HPLC in analysis of plants extracts. *Austin Chromatography*, 1(3): 2 – 3.
6. Bucar, F., Wube, A. and Schmid, M. (2013). Natural product isolation–how to get from biological material to pure compounds. *Natural Product Reports,* 30(4): 525 – 545.
7. Prathap, B., Dey, A., Srinivasarao, G. H., Johnson, P. and Arthanariswaran, P. A. (2013). Review-importance of RP-HPLC in analytical method development. *International Journal of Novel Trends in Pharmaceutical Sciences,* 3: 15 – 23.
8. Manshoor, N. and Weber, J. F. F. (2015) Mass spectrometric analysis for discrimination of Diastereoisomers. *Mass Spectrometry Letters,* 6(4): 99 – 104.
9. Manshoor, N. and Weber J. F. F. (2015) Mass fragmentation patterns as fingerprints for positive identification of polyphenolic compounds in a crude extract. *Mass Spectrometry Letters,* 6(4): 105 –111.
10. Moghbel, N., Ryu, B. and Steadman, K. J. (2015). A reversed-phase PLC-UV method developed and validated for simultaneous quantification of six alkaloids from *Nicotiana* spp. *Journal of Chromatography B,* 997: 142 – 145.

11. Al-Hroub, H., Alkhawaja, B., Alkhawaja, E. and Arafat, T. (2015). Sensitive and rapid HPLC-UV method with back-extraction step for the determination of sildenafil in human plasma. *Journal of Chromatography B,* 1009: 1 – 6.
12. Sila-on, W., Na-Ranong, S., Rakrod, S., Ornlaor, S. and Joungmunkong, Z. (2015). Development and validation of RP-HPLC method for determination of acetazolamide, furosemide and phenytoin extemporaneous suspensions. *Asian Journal of Pharmaceutical Sciences,* 11: 138 – 139.
13. Ito, T., Nishiya, K., Oyama, M., Tanaka, T., Murata, J., Darnaedi, D. and Iinuma, M. (2013). Novel isolation of resveratrol dimer O-glucosides with enantiomeric aglycones from the leaves of *Shorea cordifolia*. *Phytochemistry Letters,* 6(4): 667 – 670.
14. Ito, T., Hara, Y., Oyama, M., Tanaka, T., Murata, J., Darnaedi, D. and Iinuma, M. (2012). Occurrence of bergenin phenylpropanoates in *Vatica bantamensis*. *Phytochemistry Letters,* 5(4): 743 – 746.
15. Morikawa, T., Chaipech, S., Matsuda, H., Hamao, M., Umeda, Y., Sato, H. and Pongpiriyadacha, Y. (2012). Antidiabetogenic oligostilbenoids and 3-ethyl-4-phenyl-3, 4-dihydroisocoumarins from the bark of *Shorea roxburghii*. *Bioorganic & Medicinal Chemistry*, 20(2): 832 – 840.
16. Dolan, J. W. (2000). Starting out right, Part VI-the scouting gradient alternative. *LC GC Europe,* 13(6): 388 – 395.
17. Eisenbeiss, F., Ehlerding, S., Wehrli, A. and Huber, J. F. K. (1985). Optimization of throughput in preparative column liquid chromatography by column overloading and partial fractionation of the effluent. *Chromatographia,* 20(11): 145 – 145.
18. Ren, D. B., Yang, Z. H., Liang, Y. Z., Fan, W. and Ding, Q. (2013). Effects of injection volume on chromatographic features and resolution in the process of counter-current chromatography. *Journal of Chromatography A,* 1277: 7 – 14.

*Malaysian Journal of Analytical Sciences, Vol 21 No 1 (2017): 37 - 45*
*DOI: http://dx.doi.org/10.17576/mjas-2017-2101-05*

MALAYSIAN JOURNAL OF ANALYTICAL SCIENCES
*Published by The Malaysian Analytical Sciences Society*
ISSN 1394 - 2506

# PRELIMINARY STUDY ON PRODUCTION OF MONOACYLGLYCEROL AND DIACYLGLYCEROL OF VIRGIN COCONUT OIL VIA ENZYMATIC GLYCEROLYSIS USING LIPASE *Candida antarctica* (Novozyme 435)

## (Kajian Awal Penghasilan Monoasilgliserol dan Diasilgliserol Minyak Kelapa Dara Melalui Gliserolisis Berenzim Menggunakan Lipase *Candida antarctica* (Novozyme 435))

Darfizzi Derawi[1]*, Nurin Afiqah Zairul Azman[1], Mohd Fadlly Jumadi[2]

[1] *School of Chemical Sciences and Food Technology, Faculty of Science and Technology, Universiti Kebangsaan Malaysia, 43600 UKM Bangi, Selangor, Malaysia*
[2] *Sime Darby Research Sdn. Bhd., 42690 Carey Island, Selangor, Malaysia*

**Corresponding author: darfizzi@ukm.edu.my*

Received: 29 January 2016; Accepted: 22 November 2016

**Abstract**

Virgin coconut oil (VCO) consists mainly of saturated medium chain fatty acids which are 48.8% lauric acid (C12:0) and 20.0% myristic acid (C14:0). Both medium chain fatty acids are essential in increasing metabolism and possess antibacterial properties. These fatty acids of VCO are in the form of triacylglycerols (TAGs). Hence, VCO has to be converted into a simpler form such as mono- and diacylglycerols (MAGs and DAGs) in order to increase its antibacterial functionality in metabolism. In this paper, VCO was chemically modified via enzymatic glycerolysis reaction conducted at a molar ratio of 1:1 (VCO:glycerol) and catalysed by lipase enzyme, *Candida antarctica* (Novozyme 435). The reaction was carried out in an incubator shaker at 50 °C and 250 rpm of reaction speed. Reaction parameters were reaction time (24 and 48 hours) and enzyme concentrations (3, 5 and 10%). The product comprises of 3.3% MAG, 3.6% DAG and 93.1% TAG has been obtained by preliminary optimum reaction condition at temperature of 50 °C with 5 %wt of enzyme concentration at 24 hours of reaction time. Chemical analysis techniques used were thin layer chromatography (TLC), fourier transformation infrared (FT-IR) spectroscopy and gas chromatography (GC). Products are potentially to be used as food emulsifier, pharmaceutical binders, antibacterial products as well as food additives.

**Keywords**: virgin coconut oil, glycerolysis, lipase enzyme, monoacylglycerol, diacylglycerol

**Abstrak**

Kandungan utama minyak kelapa dara (VCO) adalah asid lemak tepu berantai sederhana dengan 48.8% adalah asid laurik (C12:0) dan 20.0% asid miristik (C14:0). Asid lemak dengan rantaian sederhana adalah penting dalam meingkatkan kadar metabolisma dan mempunyai ciri-ciri anti-bakteria. Asid lemak dalam VCO adalah dalam bentuk triasilgliserol (TAG). Oleh itu, VCO perlu ditukarkan kepada bentuk yang lebih ringkas seperti mono dan diasilgliserol (MAG dan DAG) untuk meningkatkan fungsi anti-bakteria dalam metabolisma. Dalam kajian ini, VCO diubahsuai secara kimia melalui tindak balas gliserolisis berenzim yang dijalankan pada nisbah molar 1:1 (VCO:gliserol) dengan enzim lipase *Candida antarctica* (Novozyme 435) sebagai pemangkin. Tindak balas ini telah dijalankan dalam inkubator bergetar pada suhu 50 °C dengan kelajuan 250 rpm. Parameter tindak balas yang dilakukan adalah masa tindak balas (24 dan 48 jam) dan kepekatan enzim (3, 5 dan 10%). Hasil tindak balas terdiri daripada 3.3% MAG, 3.6% DAG dan 93.1% TAG telah diperolehi dengan kondisi tindak balas optimum awal pada suhu tindak balas 50 $^{o}$C dengan kepekatan enzim 5 %wt pada 24 jam tindak balas. Teknik analisis kimia yang digunakan adalah kromatografi lapisan nipis (TLC), spektroskopi transformasi fourier inframerah (FT-IR) dan kromatografi gas (GC). Produk berpotensi untuk digunakan sebagai pengemulsi makanan, pengikat dalam farmaseutikal, produk anti-bakteria dan bahan tambah dalam makanan.

**Kata kunci**: minyak kelapa dara, gliserolisis, enzim lipase, monoasilgliserol, diasilgliserol

## Introduction

Monoacylglycerol and diacylglycerol are chemical compounds which having one or two acyl groups attached to the glycerol backbone. A mixture of monoacylglyceol (MAG) and diacylglycerol (DAG) are commercially manufactured via glycerolysis reaction, in which fats and oils reacted with gycerol and undergo a transesterification reaction. MAG and DAG have both hydrophilic and hydrophobic portions which make them known as nonionic molecules. The molecular structure of MAG contains two free hydroxyl groups while DAG has one [1]. These molecules show excellent emulsifying properties due to their characteristics, and thus, being widely applied in the food, cosmetics, pharmaceuticals and chemical industries. Figure 1 shows the chemical structure of MAG and DAG.

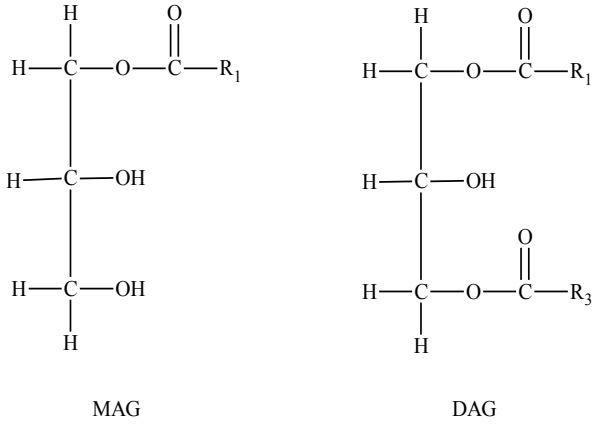



Figure 1. General chemical structure of MAG and DAG

Commercially, MAGs are used as binders in tablets and as emollients for transdermal slow-release drugs in the pharmaceutical industry. Furthermore, they are used as the most common food emulsifiers i.e. bakery products, margarines, dairy products, confectionery and sauces in the food industry. In cosmetics, they are often used as texturizing agents and for improving the consistency of creams and lotions [2]. In addition, MAGs are used in plastic production, textile processing and oil formulation for different types of machinery due to their excellent lubricating and plasticizing properties [3].

Meanwhile, DAGs are used as additives or carriers in the food, medicinal and cosmetic industry. A published literature proposed mechanisms for dietary DAG as it exhibits anti-obesity activity and can prevent postprandial hypertriacylglycerolemia in experimental animals and humans [4]. DAG oil has plentiful applications in edible products such as cooking oil, frying oil, salad oil and dressing, mayonnaise, shortening, margarine, chocolate and ice cream [5].

A previous work has attempted to manufacture MAGs and DAGs on an industrial scale by continuous chemical glycerolysis of fats and oils at high temperature (220 – 250 °C) employing inorganic alkaline catalysts under nitrogen gas atmosphere [6]. Unfortunately, the products suffered a few discrepancies with several disadvantages in the process itself [7]. The products were unattractively dark-coloured and have a burnt taste due to the high reaction temperature involved. Nonetheless, the chemical catalysis process was energy intensive, thus low yields were produced (30 – 40%) which acquired product purification by molecular distillation [8].

The use of enzymes as catalyst to modify the structure and composition of oils and fats has recently gained considerable attention, resulting in important advances in this specific field of biotransformation. Recently, enzymatic reactions have been considered as an alternative for chemical methods in large-scale productions [9]. Lipases are enzymes that hydrolyze fatty acids from lipid species such as triacylglycerols. Lipases catalyze the whole range of ester exchange reactions (alcoholysis, acidolysis, esterification, glycerolysis) and hydrolysis. The mild reaction condition and high purity MAG are the desirable advantages of enzymatic processes compared to chemical methods [10]. In parallel to green chemistry concept, enzyme reactions require less solvent which generated cleaner products. Figure 2 shows the X-ray structure of *Candida antarctica* lipase A. The enzyme is classified as hydrolase [11].

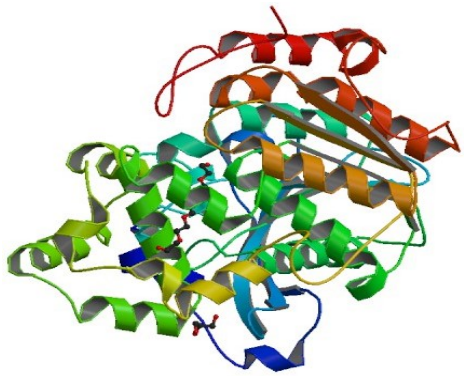


Figure 2. X-ray structure of *Candida antarctica lipase A*

Virgin coconut oil (VCO) is obtained from the fresh and mature kernel of the coconut (*Cocos nucifera* L.) through mechanical and natural means. The selection methods could involve heat provided that it does not lead to alteration or transformation of the oil. Approximately 60% of the total oil of coconut oil being medium chain triglycerides (MCTs) and thus it is considered as a natural source of MCTs. The term MCT refers to triacylglycerol which is composed of a glycerol backbone and three saturated fatty acids with chain length of 6 – 12 carbons. MCTs have been reported to be beneficial to human health. MCTs are mainly used as a nutritional supplement for patients suffering from absorbtion disability caused by intestinal resection and also as a component of infant feeding formulas [12]. A study had reported that MCTs have beneficial effects on weight control and glucose, as well as lipid metabolism [13]. Compared with other triglycerides that mainly contain saturated long chain fatty acids, MCTs have a lower melting point, smaller molecular size, lower solidification temperature and lower energy density. These distinct chemical properties affect the ways in which MCTs are absorbed and metabolized [14].

This preliminary study on enzymatic glycerolysis of VCO using a commercial immobilized *Candida antarctica* lipase (Novozyme 435) was performed to evaluate potential chemical modification method to produce MAGs and DAGs for various applications.

## Materials and Methods

### Materials

Virgin coconut oil (produced by Country Farm Sdn. Bhd.) was directly purchased from a local market and used without any pre-treatments. Lipase *Candida antarctica* (Novozyme 435) were purchased from Sigma-Aldrich and glycerol (99.5%) were obtained from Systerm.

### Physicochemicals analysis of VCO

#### *Saponification value (SV)*

Saponification values (SV) were determined using the International Union of Pure and Applied Chemistry (IUPAC) method II.D.2 [15]. In a reflux condenser, 2.0 g of oil samples were added with Ethanolic KOH 0.5 N and boiled for

60 minutes. The mixtures were cooled and subsequently titrated with 0.5 N HCl until the pink colour disappear and changed to colourless. All SV determinations were carried out in triplicates.

***Iodine value (IV)***

The determination of iodine value (IV) of oil was carried out according to the IUPAC method II.D.7 [15]. A reaction was held in the dark between 0.5 g of oil samples with the Wij's solution for 1 hour. The mixture was consequently titrated with sodium thiosulphate solution. IV values were determined in triplicates and expressed as gram of iodine absorbed by 100 g of the fats (g $I_2$/ 100 g).

***Free fatty acids value (FFA)***

Free fatty acid (FFA) value was ascertained using the IUPAC method II.D.1 [15]. An amount 5.0 g of oil samples were added with 50 mL of neutralized diethyl ether: ethanol (1:1; v/v) and 1 – 2 mL of phenolphthalein indicator. The mixture was heated on a hot plate with controlled temperature around 40 °C. It was then titrated with a standard NaOH until a constant pink colour was obtained. All FFA value determinations were conducted in triplicates and expressed as mg of KOH required to neutralize the free fatty acids in 1 g of VCO (mg KOH/g oil).

***Peroxide value (PV)***

The determination of Peroxide Value (PV) was carried out according to AOCS Cd 8b-90 [16]. An amount 5.0 g of samples were added with 30 mL of mixture of acetic acid and chloroform in a conical flask and mixed well. Then, 0.5 mL of concentrated potassium iodide (KI) was pipetted into the mixture and the flask was manually shaken for a minute. After shaking, 30 mL of distilled water and few drops of starch were added and the mixture was titrated gradually with 0.01 N sodium thiosulphate until the blue colour has disappeared.

***Moisture content***

Determination of moisture content was based on the AOAC method [17] with slight alteration. Sample was weighed and heated at 105 °C in a crucible for at least 7 hours and then, cooled to room temperature. The crucible was re-weighed with the sample inside until constant readings were gathered. Moisture content was calculated based on weight difference obtained.

**Fatty acids methyl ester (FAME) analysis**

Exactly 0.2 ml oil samples were prepared by dissolving in hexane and later added with 0.2 mL of 1 M sodium methoxide. The mixture was vortexed and FAME solution in the upper layer was collected for GC-FID analysis. The analysis of FAME was conducted with Shimadzu GC-17A gas chromatography equipped with a flame ionization detector (FID). BPX-70 column was used in this experiment (0.25 mm internal diameter, 30 m length and 0.25 µm film thickness). The column was initially set at 100 $^{o}$C and held for 3 minutes, then increased to 245 $^{o}$C and held for another 10 min at a rate of 4 $^{o}$C/min. The temperature of injector and detector port were 250 °C and 280 °C respectively. Helium gas with purity level 99.99% is used as carrier gas.

**Enzymatic glycerolysis reaction**

Glycerolysis reaction was modified based on a research conducted by Pinyahpong et al. [18]. The molar ratio used for VCO:glycerol was 1:1. An approximately 2.8% (w/v) of distilled water was added based on the volume of oil used and 3 %wt of lipase enzyme was added based on the weight of glycerol. The reaction was carried out at 50 $^{o}$C in a shaking incubator with 250 rpm for 24 hours.

After 24 hours, the reaction stopped and the enzyme was then separated from the mixture using filter paper in a present of vacuum condition. The filtrate was placed into a separating funnel and followed by 50 mL of chloroform, 50 mL of ethanol and 30 mL of diethyl ether were added to separate excess glycerol. The mixture was then washed with 100 mL of sodium chloride (4 times) and 100 ml of sodium hydroxide (4 times). This is to remove the free fatty acids from the glycerolysis reaction. Finally, the product was obtained after using rotary evaporator. This paper will discuss some factors that affected lipase-catalysed glycerolysis such as time of reaction (24 hours and 48 hours) and enzyme concentration used; 3%, 5% and 10% of glycerol (w/w).

**Chemical compositions analysis**

Product identification was analysed using Thin Layer Chromatography (TLC). An aliquots of the reaction mixtures were applied on a silica gel 60 plate (Merck) in developing solvent mixture of n-hexane:diethyl ether:acetic acid (70:30:1; v/v). The spots of each product were visualized by immersing the plate in $KmNO_4$ solution.

The composition of products were analysed by using gas chromatography (Shimadzu GC-17A) fitted with a capillary column (DB-5ht, 30 m × 0.320 mm, 0.25 μm thickness) and equipped with a flame ionization detector (FID). The separation of compounds was performed using the following oven temperature profile: initial temperature 80 $^{o}$C, programmed to 350 $^{o}$C at 10 $^{o}$C/min, and final temperature held for 10 min. The sample was prepared by adding 0.03 mL of sample in 1 mL of ethyl acetate in a vial. Only 0.1 μL of the prepared sample was injected into GC.

The functional groups analysis of product was determined using FT-IR spectroscopy. In this study, FT-IR with the model of Perkin Elmer Spectrum BX was used. The sample was smeared thinly on the NaCl plate and FT-IR spectrum was recorded.

## Results and Discussion

**Physicochemicals properties of VCO**

The results obtained were within accepted levels according to Asian Pacific Coconut Community (APCC) specifications [19] as shown in Table 1. The molecular mass determined for VCO is 651.57 g/mol. VCO was converted to fatty acids methyl ester (FAME) and its composition was determined by using gas chromatography. A standards of FAME was calibrated and established for each peak of compound prior sample analysis. The chromatogram of methyl esters of VCO is shown in Figure 3.

Table 1. Physicochemical Properties of VCO

| Tests | Value | APCC Standard |
|---|---|---|
| Saponification Value (mg KOH / g) | 258.30 | 250 – 260 |
| Free Faty Acids (mg KOH / g) | 0.225 | 0.5 max |
| Iodine Value (g $I_2$ / 100 g) | 4.13 | 4.1 – 11.0 |
| Peroxide Value (meq / kg) | 0.2 | 3.0 mas |
| Moisture Content (% weight) | 0.11 | 0.1 – 0.5 |

Retention time is the time taken by certain compounds to move along the column towards the detector. This period depends on the boiling point of each compound. Compounds with higher boiling points have longer retention period. In general, the boiling point of the compound was influenced by several molecular factors such as the number of carbon (carbon chain length) and the number of double bonds that exist in the compound. The number of carbon is in conjunction with the molecular weight of these compounds. Heavier molecules (high molecular weight) have higher boiling points. This caused the molecule to be less volatile and therefore will be detected slower, thus prolonged its detention time. Similarly, compounds with more double bonds have longer period of detention [20].

The peaks composition of product were compared with the retention times of calibrated methyl esters standards as followed, mehyl caprilate (3.375 min); methyl caprate (5.581 min); methyl laurate (9.071 min); methyl myristate (12.913 min); methyl palmitate (16.708 min); methyl stearate (20.283 min); methyl oleate (20.853 min) and methyl linolate (22.022 min). From the observation on the GC result, methyl caprylate that has 6 carbons had the shortest retention time and was detected the earliest. Methyl stearate has 18 carbons which produced longer detention period. Meanwhile, methyl stearate, oleate and linolate have the same carbon number of 18. However, linolate has 2 double bonds and thus, produced the longest detention period.

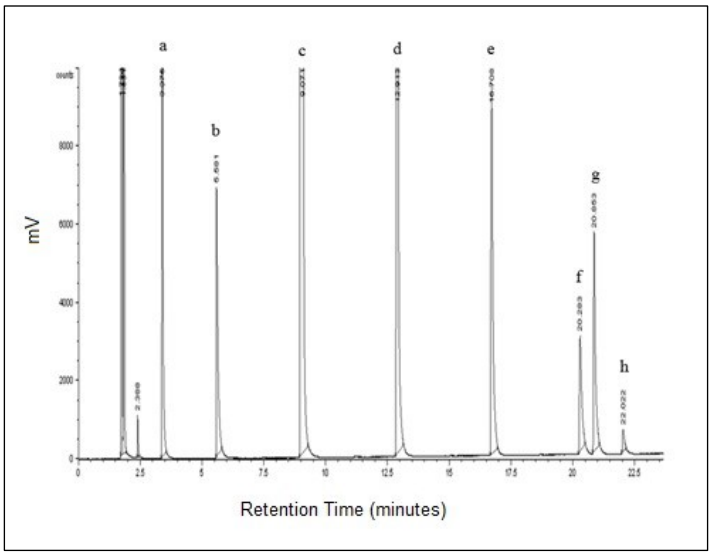



Figure 3. GC chromatogram of VCO (a: methyl caprilate, b: methyl caprate, c: methyl laurate, d: methyl myristate, e: methyl palmitate, f: methyl stearate, g: methyl oleate, h: methyl linolate)

The carbon chain composition of VCO was tabulated in Table 2 and compared to APCC standard [19]. The results showed that VCO sample consists of caprylic (C8:0), capric (C10:0), lauric (C12:0), myristic (C14:0), palmitic (C16:0), stearic (C18:0), oleic (C18:1) and linoleic (C18:2). It was found that VCO contains high saturated fatty acids (SFA) which was 93.9% and low unsaturated fatty acids which was 6.0%. These findings were in agreement with Mansor et al [12].

Table 2. Fatty acids composition of VCO

| Fatty Acid Composition | Percentage (%) | APCC Standard (%) |
|---|---|---|
| Caprylic acid | 6.3 | 4.6 – 10.0 |
| Capric acid | 5.4 | 5.0 – 8.0 |
| Lauric acid | 48.8 | 45.1 – 53.2 |
| Myristic acid | 20.0 | 16.8 – 21.0 |
| Palmitic acid | 9.8 | 7.5 – 10.2 |
| Stearic acid | 3.6 | 2.0 – 4.0 |
| Oleic acid | 5.4 | 5.0 – 10.0 |
| Linoleic acid | 0.6 | 1.0 – 2.5 |

**Product compositions**

TLC was used to validate the products after the reaction. Based on the results, TLC plate confirmed the product formation. MAG (i) was detected first, followed by 1,2-DAG (ii), 1,3-DAG (iii) and TAG (iv) respectively (Figure 4). The components were detected based on their polarity. No fatty acids were detected on the TLC plate.

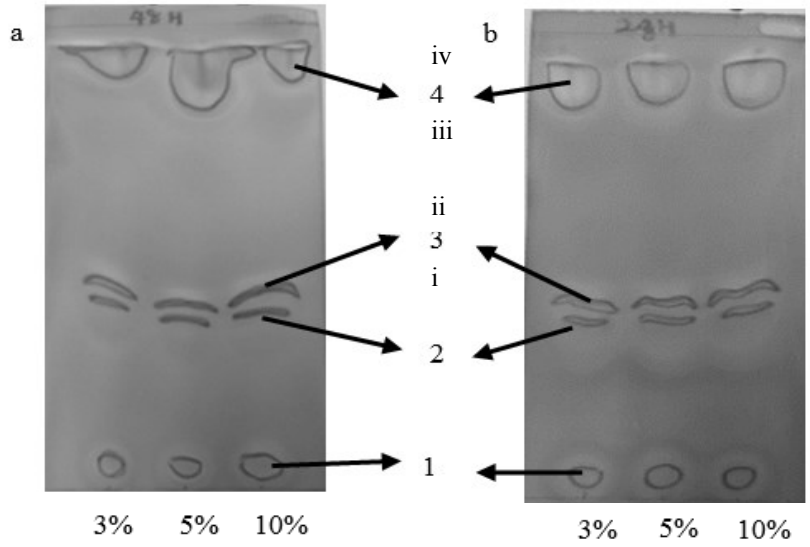



Figure 4. TLC plate of glycerolysis reaction (a: Reaction time for 48 hours; b: Reaction time for 24 hours)

In this study, glycerolysis between VCO and glycerol (molar ratio 1:1) with 3, 5 and 10 %wt of ezyme concentration at 50 $^{o}$C for 24 and 48 hours were investigated. The results showed that 3 %wt of enzyme at 24 hours of reaction gave 1.4% MAG, 2.2% DAG and 96.4% of unreacted TAG. It was observed that 5% of enzyme at 24 hours of reaction yielded increment on MAG and DAG contents. However, there were no increment observed for conversion of MAG and DAG if increase the enzyme concentration to 10 %wt. The reaction was continued with pro-long the reaction time. It was reported that no significant increment of MAG and DAG content for 48 hours at any enzyme concentrations. The percentage of conversions are still low and not fully optimized. But, this findings proved that the conversion of VCO in TAG form into simpler compounds (MAG and DAG) is possible to be done through enzymatic glicerolysis with further investigations. Some parameters have to optimized and different types of lipase enzymes have to be considered for this reaction. In order to push forward the reaction, selected factors that may favour the reaction have been studied such as time of reaction (RT) and percentage of enzyme concentrations. Based on the results (Table 3), glycerolysis with 5 % of enzyme loading and 24 hours of reaction time gave the highest composition of MAG and DAG.

Table 3. Compositions of products

| **Enzyme Concentration (%)** | **Reaction Time (hours)** | **Product Compositions (%)** | | |
|---|---|---|---|---|
| | | **MAG** | **DAG** | **TAG** |
| 3 | 24 | 1.4 | 2.2 | 96.4 |
| 5 | 24 | 3.3 | 3.6 | 93.1 |
| 10 | 24 | 1.5 | 3.2 | 95.3 |
| 3 | 48 | 0.5 | 1.5 | 98.0 |
| 5 | 48 | 0.6 | 1.2 | 98.2 |
| 10 | 48 | 1.6 | 2.4 | 96.0 |

## Conclusion

Preliminary findings conclude that glycerolysis reaction of VCO as the starting material was successfully performed. The optimum condition for the reaction was 5% enzyme loading at 50 °C for 24 hours of reaction time. Based on GC analysis results, the product comprises 3.3% MAG, 3.6% DAG and 93.1% TAG. The product identification was further confirmed through TLC plate analysis technique.

## Acknowledgement

Authors would like to acknowledge Universiti Kebangsaan Malaysia and Ministry of Higher Education for the research facilities and financial support provided through research grant no. FRGS/2/2014/ST01/UKM/02/2.

## References

1. Chen, B., McClements, D. J. and Decker, E. A. (2014). Impact of diacylglycerol and monoacylglycerol on the physical andchemical properties of stripped soybean oil. *Food Chemistry*, 142: 365 – 372.
2. Al-Darmaki, N., Lu, T., Al-Duri, B., Harris, J. B., Favre, T. L. F., Bhaggan, K. and Santos, R. C. D. (2011). Solubility measurements and analysis of binary, ternary and quaternary systems of palm olein, squalene and oleic acid in supercritical carbon dioxide. *Separation and Purification Technology*, 83: 189 – 195.
3. Pyo, Y. G., Hong, S. I., Kim, Y., Kim, B. H. and Kim, I. H. (2012). Synthesis of monoacylglycerol containing pinolenic acid via stepwise esterification using a cold active lipase. *Biotechnology Progress*, 28(5): 1218 – 1224.
4. Kielczynski, P., Szalewski, M., Balcerzak, A., Malanowski, A., Siegoczynski, R. M. and Ptasznik, S. (2012). Investigation of high-pressure phase transitions in DAG (diacylglycerol) oil using the Bleustein–Gulyaev ultrasonic wave method. *Food Research International*, 49: 60 – 64.
5. Reyes, G., Yasunaga, K., Rothenstein, E., Karmally, W., Ramakrishnan, R. and Holleran, S. (2008). Effects of a 1,3-diacylglycerol oil-enriched diet on postprandial lipemia in people with insulin resistance. *Journal of Lipid Research*, 49: 670 – 678.
6. Sonntag (1982). Glycerolysis of fats and methyl esters – status. *Journal of the American Oil Chemists' Society*, 59(10): 795 – 802.
7. Bornscheuer, U. T. (1995). Lipase-catalyzed Syntheses of Monoacylglycerols. *Enzyme and Microbial Technology*, 17: 578 – 586.
8. Ferreira-Dias, S., Correia, A. C., Baptista, F. O. and Fonseca, M. M. R. (2001). Contribution of response surface design to the development of glycerolysis systems catalyzed by commercial immobilized lipases. *Journal of Molecular Catalysis B: Enzymatic*, 11: 699 – 711.
9. Zhu, Q., Li, T., Wang, Y., Yang, B. and Ma, Y. (2011). A two-stage enzymatic process for synthesis of extremely pure high oleic glycerol monooleate. *Enzyme and Microbial Technology*, 48: 143 – 147.
10. Gunstone, F. D. (1999). Enzymes as biocatalysts in the modification of natural lipids. *Journal of the Science of Food and Agriculture*, 79(12): 1535 – 1549.
11. Brandt, A. M., Li, X. G., Nymalm-Rejstrom, Y., Airenne, T., Kanerva, L. T. and Salminen, T. A (2009). The X-ray Structure of *Candida antarctica* Lipase A. *RCSB Protein Data Bank* (PDB).
12. Mansor, T. S. T., Che, Man, Y. B., Shuhaimi, M., Abdul, Afiq, M. J. and Ku, Nurul, F. K. M. (2012). Physicochemical properties of virgin coconut oil extracted from different processing methods. *International Food Research*, 19(3): 837 – 845.
13. Marten, B., Pfeuffer, M. and Schrezenmeir, J. (2006). Medium-chain triglyceride (review). *International Dairy Journal*, 16: 1374 – 1382.
14. International Union of Pure and Applied Chemistry (IUPAC) (1979). Standard Methods for the Analysis of Oils, Fats and Derivatives. 6th edition. Oxford: Pergamon Press.
15. Nandi, S., Gangopadhyay, S. and Ghosh, S. (2005). Production of medium chain glycerides from coconut and palm kernel fatty acid distillates by lipasecatalyzed reaction. *Enzyme and Microbial Technology*, 36: 725 – 728.
16. PORIM (1995) PORIM test method. Malaysia: Palm Oil Research Institute of Malaysia.
17. AOAC Official Methods Of Analysis (1997). Association of Official Analytical Chemists. 17th edition. Washington DC.
18. Pinyahpong, P, Sriburi, P and Phutrakul, S. (2012). Synthesis of monoacylglycerol from glycerolysis of crude glycerol with coconut oil catalyzed by *Carica papaya* lipase. *International Journal of Chemical, Molecular, Nuclear, Materials and Metallurgical Engineering*, 6 (10): 926 – 931.

19. Asian and Pacific Coconut Community (2003). Internet: standard for virgin coconut oil. Downloaded from http://www.apccsec.org/standards.htm/ [Date access 15/1/2015].
20. Littlewood, A. B. (1970). Gas chromatography: Principles, techniques and applications. New York: Academic Press.

*Malaysian Journal of Analytical Sciences, Vol 21 No 1 (2017): 46 - 51*
*DOI: http://dx.doi.org/10.17576/mjas-2017-2101-06*

MALAYSIAN JOURNAL OF ANALYTICAL SCIENCES
*Published by The Malaysian Analytical Sciences Society*
ISSN 1394 - 2506

# MOLLUSCICIDAL ACTIVITY OF *Entada rheedii* STEM BARK METHANOLIC EXTRACT AGAINST PADDY PEST *Pomacea canaliculata* (GOLDEN APPLE SNAIL)

## (Aktiviti Moluskisida oleh Ekstrak Metanol Kulit Batang *Entada rheedii* Terhadap Perosak Padi *Pomacea canaliculata* (Siput Gondang Emas))

Nur Suraya Abdullah*, Noorshilawati Abdul Aziz, Rosminah Mailon

*Faculty of Plantation and Agrotechnology,*
*Universiti Teknologi MARA Pahang, 26400 Bandar Tun Abdul Razak, Jengka, Pahang, Malaysia*

**Corresponding author: nsa@pahang.uitm.edu.my*

Received: 5 August 2016; Accepted: 30 November 2016

**Abstract**

The study was conducted to evaluate the molluscicidal activity of *E. rheedii* methanol bark extract against *P. canaliculata* and to screen for phytochemical compounds of *E. rheedii* bark extracts. The golden apple snails with size range of 20 – 40 mm were treated with four different concentrations of *E. rheedii* (1000, 5000, 10000 and 20000 ppm) and paddy-field water mix with 50% methanol serving as the control treatment. The molluscicidal effects of the extract were evaluated after 24, 48 and 72 hours. The results of the study showed that high treatment concentrations (10000 and 20000 ppm) recorded the highest mortality rate (100%) while low concentrations (1000 ppm) showed the lowest mortality rate (27%). However, no mortality was recorded in the control treatment. The molluscicides activity with $LC_{50}$ is 1,611 ppm and $LC_{90}$ is 4,266 ppm and could be attributed to the presence of saponin in the bark extracts. *E. rheedii* bark extract provides a great potential for developing green pesticides to control *P. canaliculata*. Nevertheless, further research is needed to determine its biochemical mechanism.

**Keywords**: golden apple snail, *Entada rheedii*, molluscicidal activity, phytochemical content

**Abstrak**

Kajian ini dijalankan untuk menilai aktiviti moluskisida oleh ekstrak metanol kulit kayu *E. rheedii* terhadap *P. canaliculata* dan untuk menyaring sebatian fitokimia yang terkandung di dalam ekstrak kulit kayu *E. rheedii.* Siput gondang emas bersaiz antara 20 – 40 mm telah dirawat dengan empat kepekatan *E. rheedii* yang berbeza (1000, 5000, 10000 dan 20000 ppm) dan campuran air sawah padi dengan 50% metanol menjadi rawatan kawalan. Kesan moluskisida oleh ekstrak dinilai selepas 24, 48 dan 72 jam. Keputusan kajian menunjukkan bahawa kepekatan rawatan tinggi (10000 dan 20000 ppm) mencatatkan kadar kematian tertinggi (100%) manakala kepekatan yang rendah (1000 ppm) menunjukkan kadar kematian yang paling rendah (27%). Walau bagaimanapun, tiada kematian direkodkan dalam rawatan kawalan. Aktiviti moluskisida dengan $LC_{50}$ adalah 1611 ppm dan $LC_{90}$ adalah 4266 ppm boleh dikaitkan dengan kehadiran saponin dalam ekstrak kulit kayu. Ekstrak kulit kayu *E. rheedii* mempunyai potensi yang besar dalam membangunkan racun perosak yang selamat terhadap alam sekitar untuk mengawal *P. canaliculata.* Walau bagaimanapun, penyelidikan lanjut perlu dilakukan untuk menentukan mekanisme biokimianya.

**Kata kunci**: siput gondang emas, *Entada rheedi*i, aktiviti moluskisida, kandungan fitokimia

## Introduction

The golden apple snail, *Pomacea canaliculata* (*P. canaliculata*) is native to South America [1] and has been introduced from Argentina to Taiwan in the 1980's for the purpose of food commercialization. Nevertheless, due to the low response of consumers towards snails as food, it has affected the marketing and farming activities of golden apple snail and caused producers to close their farms. Hence, it was contributed to the establishment and distribution of the snail populations that became a major invasive rice pest in South-East Asia [2]. In Malaysia, *P. canaliculata* was first found in abandoned mines; Puchong, Selangor in 1991 [3] and then was introduced in Keningau, Sabah in 1992. Then, it was spread throughout Peninsular Malaysia and caused extensive damage to paddy field areas in the Northern parts of Malaysia especially in the state of Perlis and Kedah. The problem became more serious due to the climatic change, which influences the rapid distribution and spread of snails throughout irrigation areas [4].

*P. canaliculata* was known as the most destructive invasive species that attacked and destroyed the young stems and paddy leaves. It has been reported that the snails could eat about 7-24 rice seedlings per day. Although farmers can control the snail populations in their paddy field plots through the application of various types of chemical fertilizers, but the problem is ever increasing because of the continuous supply and snail distribution through the water irrigation system [4]. Many approaches including chemical, mechanical or biological methods have been applied to control the widespread of golden apple snails in the field plantation area but the practice may have positive and negative impacts to humans, the environment and the ecosystem. Previous studies reported that the usage of chemical fertilizers such as metaldehyde and niclosamide can cause water pollution and thus affect the ecosystem or water sources [5]. The uses of mechanical techniques such as rice-duck mutualism [2] and attractant bite using jackfruit, papaya, spinach, cassava leaves and banana leaves are also effective. Badrulhadza and Yahya [6] found that snails are more attracted to jackfruit and papayas, thus this method is also important as it could contribute to the integrated management of golden apple snails in field plantation areas. Besides that, the application of biological control and pesticides derived from extracts of seed, leaves, fruit or other plant parts also give significant impacts in the management of the snails. Leaves extracts of *Solanum* species [7], *Barringtonia racemosa* L. kernel extract [5], and extracts of *Agave filifera*, *Ammi majua* and *Canna indica* leaves and flowers [8] have been reported as effective in controlling snails in their plantation areas. The effectiveness of the plant extracts in controlling snails may be due to the presence of bio-active compounds such as saponins, flavanoids, and terpenoids that react with pest body system.

*Entada rheedii* (*E. rheedii*) Spreng or known as African Dream Herb is a woody climber of the legume family. This plant is found in Africa and South-East Asia [9,10]. Some chemical contents of *E. rheedii* are antigenic acids, fatty acids, entadamide A, B, and C, phaseoloidine, echynosystic type sapogenin, saponin, saponin III, triglycerides, triterpenes and triterpenoids can be found in all parts of *E. rheedii.* Saponins and heterosides can be found in the bark and seed parts. Besides that, *E. rheedii* gives antitumor effects and is toxic to molluscs. This may be due to the presence of saponin that could break the red blood cells and disrupt the haemolysis system in molluscs [11]. Hence, the present study was carried out to evaluate the potential use of *E. rheedii* stem bark extracts on *P. canaliculata.* The information generated from this research could be beneficial for further studies on the specific compounds that lead to the mortality of *P. canaliculata.*

## Materials and Methods

### Plant material

The selection of *E. rheedii* as tested plant in this study was based on the presence of phytochemical constituents such as saponin, which reportedly could lower the surface tension of water and restrict the breathing process of *P. canaliculata*. The plant species *E. rheedii* was collected from Kota Bharu, Kelantan. The effectiveness of the stem bark extract against *P. canaliculata* was assessed to determine the toxicity effects.

### Preparation of *Entada rheedii* stem bark extracts

About 500 mg of *E. rheedii* stem bark was grounded into fine powder and then macerated with 2.3 L of methanol (MeOH) in a 3000-mL beaker at room temperature for 24 hours. The extract was filtered with filter paper, and then concentrated to dryness under reduced pressure in a rotary evaporator. The crude extract was stored in a labelled specimen jar.

**Preparation of treatment concentrations**
Four treatment concentrations consisting of 1000, 5000, 10000 and 20000 ppm were prepared from the crude extract of *E. rheedii* using methanol 50% (v/v) to determine the lethal death at 50% ($LD_{50}$) and lethal death at 90% ($LD_{90}$) values. Paddy-field water with 50% methanol served as the control treatment.

**Sampling of tested golden apple snail**
The golden apple snails with size range of 20 – 40 mm were collected from Pahang Tua Paddy Field in the Integrated Agriculture Development Area (IADA) Pekan, Pahang. The shell height was used for size determination in order to get a uniform size for the toxicity test in laboratory conditions [12]. Tested snails were acclimatized in the laboratory in four different plastic aquariums and fed with papaya leaves for seven days.

**Molluscicidal activity**
The molluscicidal activity was performed using the methods described by Reish and Oshida [13] with some modifications. Each treatment was triplicated. Paddy-field water with pH 6.78 taken from the location of the collected snails was filled in four plastic containers to a depth of seven centimetres measured from the bottom of the container. Ten test snails were placed in the plastic containers and were then covered with netting cloth to prevent them from crawling out during experiments. The test snails were allowed to move freely for about 30 minutes and 100 ml of the treatment concentration were then poured into plastic containers. The mortality of the golden apple snails was assessed every 24 hours of exposure for 3 days. The death of the snails and the toxicity effects were determined by mucus secretion through the operculum gap [5] and the lack of mobility or if the body is retracted well into or hanging out of the shell [14].

**Phytochemical screening**
Phytochemical screening was performed using the methods described by Rauf et al. [15] to determine the presence of glycoside, alkaloids, saponins, tannins, flavanoids and terpenoids.

**Test for glycosides**
The extract was hydrolyzed with hydrochloric acid (HCl) and neutralized with sodium hydroxide (NaOH) solution. A few drops of Fehling's A and B solutions were added and the formation of a red precipitate indicates the presence of glycoside compounds.

**Test for alkaloids**
An amount 0.2g of extract was added with 2% $H_2SO_4$ and warmed for two minutes. The solution was filtered and then added with few drops of Dragendorff's reagent. The appearance of orange red precipitation indicates the presence of alkaloids.

**Test for saponins**
An amount 0.2g of extract was added with 5ml distilled water and heated to boiling point. The appearance of creamy mist with small bubbles indicates the presence of saponins.

**Test for tannins**
A small amount of extract was mixed with distilled water, heated to boiling point on water bath and then filtered. A few drops of ferric chloride were added and the appearance of a dark green colour indicates the presence of tannins.

**Test for flavonoids**
An amount 0.2g of extract was dissolved in diluted NaOH, and added with few drops of HCl. The turn of a yellowish colour to colourless indicated the presence of flavanoids.

**Test for terpenoids**
An amount 0.2g of extract was mixed with 2 mL of chloroform ($CHCl_3$) then 3 mL of concentrated $H_2SO_4$ was added to form a layer. The layer with reddish brown colour shows the presence of terpenoids in extract.

**Statistical analysis**

The mean and standard errors were analyzed using analysis of variance (ANOVA) and Least Significant Difference (LSD) for pairwise comparison to determine the significant differences among each treatment. The concentration that could kill 50% ($LC_{50}$) and 90% ($LC_{90}$) of tested snails were determined from Finney's Table [16].

## Results and Discussion

**Mortality of *P.canaliculata* against *E.rheedii stem* bark methanolic extracts**

The results of the study revealed that no mortality was found in the control treatment of the tested *P. canaliculata* after 72 hours of exposure. (Figure 1). The 100% mortality rate of *P. canaliculata* was observed in 20, 000 ppm MeOH extracts after 48 hours exposure to such conditions. A 100% mortality rate was also recorded in high concentrations of 10, 000 and 20, 000 ppm respectively after 72 hours exposure (Table 1). The response of the snails to the treatments was determined through mucus production (Figure 2). Brain et al. [17] stated that *P. canaliculata* response to the pesticides through secretion of mucus by means to reduce their contact to the molluscicides. In addition, the presence of saponins cause toxicity to snails and affect cell membrane and lower the surface tension.

Table 1. Response of *P. canaliculata* against different concentrations of *E. rheedii* stem bark methanolic extract after 24, 48 and 72 hours

| Treatment Concentration (ppm) | Percentage of Mortality (%) | | |
|---|---|---|---|
| | 24 hours | 48 hours | 72 hours |
| 0(Control) | 0 | 0 | 0 |
| 1000 | 7 | 17 | 27 |
| 5000 | 27 | 87 | 93 |
| 10000 | 40 | 97 | 100 |
| 20000 | 47 | 100 | 100 |

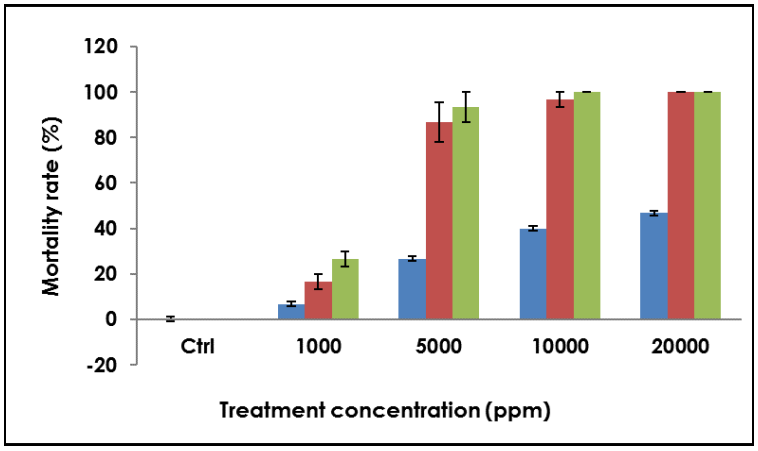



Figure 1. Mortality rate of *P. canaliculata* in control treatment and different concentrations of MeOH

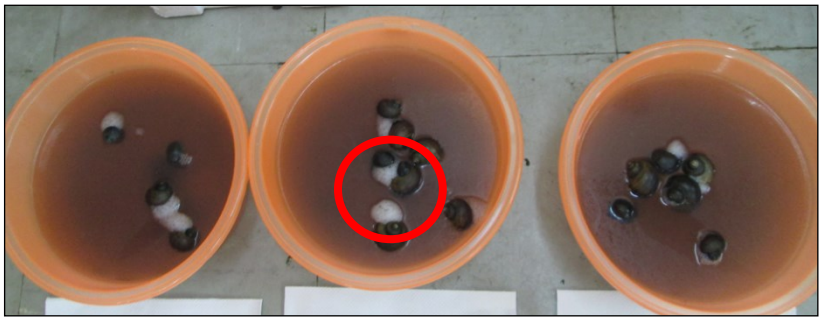


Figure 2. Mucus secretions in *P. canaliculata* during application of *E. rheedii* stem barks extract treatments

Phytochemical screening test (Table 2) showed the presence of bioactive compounds such as alkaloids, flavanoids, glycosides, saponins, tannins and terpenoids in the bark extract of *E. rheedii*. Previous studies reported that flavanoids and saponins both could block the process of breathing probably due to diffusion of oxygen through the gills of the golden apple snails which is then obstructed by the secretion of mucus [5]. Several plants with molluscicidal activity had been identified such as *Chenopodium ambrosioides* and *Ruta chalepensis* with secondary metabolites of flavanoids, triterpenes, saponins, and alkaloids [18]. Based on the probit analysis of $LD_{50}$ and $LD_{90}$, in order to control 50% and 90% of the golden apple snail population, about 1611 ppm and 4266 ppm of *E. rheedii* bark crude extract concentration could be applied respectively.

Table 2. Phytochemical screening test of *E. rheedii* stem bark extract

| **Phytochemical Content** | **Presence of Bioactives Compound in Methanolic Extract** |
|---|---|
| Alkaloids | - |
| Flavonoids | + |
| Glycosides | + |
| Saponins | + |
| Tannins | + |
| Terpenoids | + |

## Conclusion

The results of the study revealed that high concentrations of methanolic bark extracts of *E. rheedii* (10000 ppm and 20000 ppm) are able to kill 100% of tested *P. canaliculata* after 72 hours exposure. Phytochemical screening test also showed the presence of bioactive compounds such as saponins, tannins and terpenoids in the bark extract, which demonstrated the potential use of *E. rheedii* as a new source of green pesticides in controlling the population of golden apple snail in paddy field plantation areas. In addition, it is suggested to test the effectiveness of *E. rheedii* bark extract against juvenile stages of the golden apple snail. However, further studies are needed to develop its potential as green molluscicides.

## Acknowledgement

The authors acknowledge the Ministry of Higher Education (MOHE) for provided financial support through Fundamental Research Grant Scheme (FRGS/1/2016/WAB01/UITM/03/2), Integrated Agriculture Development Area (IADA) and Universiti Teknologi MARA Pahang for provided materials and facility throughout this research

**References**


1. Shengzhang, D. Guowan, Z., Xiaoping, Y. and Changhuan, F. (2012). Biological control of golden apple snail, *Pomacea canaliculata* by Chinese soft shelled turtle, *Pelodiscus sinensis* in the wild rice, *Zizania latifolia* field. *Journal of Scientia Agricola*, 69(2):142 – 146.
2. Kaiming, L., Jia-en, Z., Li, F., Benliang, Z., Mingzhu, L., Prem, P. and Ying, O. (2013). The biological control of *Pomacea canaliculata* population by rice-duck mutualism in paddy fields. *Biological Science and Technology*, 23(6): 674 – 690.
3. Yahaya, H., Saad, A., Azmi, M., Muhamad Hisham, M. N., Nordin, M. and Fakrulabadi, S. (2010). Manual Teknologi Pengurusan Siput Gondang Emas. Malaysian Agriculture Research and Development Institute (MARDI). pp 54.
4. Noor Hasyierah M.S., Dachyar, A., Mohamed Zulkali, M.D., Nilawati, P. and Rohaina, N. (2012). Distribution and management of *Pomacea canaliculata* in the northern region of Malaysia: Mini Review. *APCBEE Procedia,* 2: 129 – 134.
5. Musman, M. (2010). Toxicity of *Barringtonia racemosa* (L.) kernel extract on *Pomacea canaliculata* (Ampullariidae). *Tropical Life Sciences Research,* 21(2): 41 – 50.
6. Badrulhadza, A. and Mohd Hafizi, Y. (2014). Kawalan siput gondang di sawah menggunakan umpan penarik. *Jurnal Teknologi,* 70(6): 9 – 12.
7. Gehad, T. E., Rawia, A. Z. and Eman, T. E. (2009). Molluscicidal activity of some *Solanum* species extracts against the snail *Biomphalaria alexandrina*. *Journal of Parasitology Research,* 2009: 1 – 5.
8. Rawi, S. M., Al-Hazmi, M. and Seif Al Nassr, F. (2011). Comparative study of the molluscicidal activity of some plant extracts on the snail vector of *Schistosoma mansoni, Biomphalaria alexandrina*. *International Journal of Zoological Research,* 7(2): 169 – 189.
9. Nzowa, L. K., Barboni, L., Teponno, R. B., Ricciutelli, M., Lupidi, G., Quassinti, L., Bramucci, M., and Tapondjou, L. A. (2009). Rheediinosides A and B, two antiproliferative and antioxidant triterpene saponins from *Entada rheedii. Phytochemistry,* 71 (2-3): 254 – 261.
10. Abu Sufian, M., Shafaat-Al-Mehedi, M., Mohammad, A. R. and Mohammad, R. H. (2015). Biological Investigation of *Entada rheedii* Spreng, and Isolation of Entadamide A from its seed. *International Research Journal of Pharmacy,* 6(7):411 – 414.
11. Ong, H.C. (2004). Tumbuhan liar: Khasiat ubatan & kegunaan lain. *Utusan Publications*, pp 241.
12. Massaguni, R. and Md Latip, S. N. H. (2012). Neem crude extract as potential biopesticide for controlling golden apple snail, pomacea canaliculata, pesticides-advances in chemical and botanical pesticides, Soundararajan, R. P. (Ed.), InTech Publisher.
13. Reish, D. L. and Oshida, P. S. (1987). Manual of methods in aquatic environment research. Part 10: Shorterm static bioassay. FAO Fisheries Technical Paper 247. *Food and Agriculture Organization of the United Nations.* pp 81.
14. Massaguni, R. and Md Latip, S. N. H. (2015). Assessment the molluscicidal properties of azadirachtin against golden apple snail (*Pomacea canaliculata*). *Malaysian Journal of Analytical Sciences,* 19(4): 781 – 789.
15. Rauf, A., Qaisar, M., Uddin, G., Akhtar, S. and Muhammad, N. (2012). Preliminary phytochemical screening and antioxidant profile of *Euphorbia prostrate. Middle-East Journal of Medicinal Plants Research,* 1(1): 9 – 13.
16. Finney, D.J. (1971). Probit analysis, 3rd edition. Cambridge University Press. pp 333.
17. Brain, K. R., Hadgraft, J., and Al-Shatalebi, M. (1990). Membrane modification in activity of plant molluscicides. *Planta Medica*, 56: 663 – 664.
18. Hmamouch, M., Lahlon, M., and Agonum, A. (2000). Molluscicidal activity of some Moroccan Medicinal Plants. *Fitoterapia*, 71: 308 – 314.

*Malaysian Journal of Analytical Sciences, Vol 21 No 1 (2017): 52 - 59*
*DOI: http://dx.doi.org/10.17576/mjas-2017-2101-07*

MALAYSIAN JOURNAL OF ANALYTICAL SCIENCES
*Published by The Malaysian Analytical Sciences Society*
ISSN 1394 - 2506

# THE COMMON PITFALL OF USING ENRICHMENT FACTOR IN ASSESSING SOIL HEAVY METAL POLLUTION

## (Kepincangan Penggunaan Faktor Pengkayaan dalam Menilai Pencemaran Logam Berat di dalam Tanah)

Seng-Chee Poh* and Norhayati Mohd Tahir

*School of Marine and Environmental Sciences,*
*Universiti Malaysia Terengganu, 21030 Kuala Terengganu, Terengganu, Malaysia*

**Corresponding author: poh@umt.edu.my*

Received: 5 November 2016; Accepted: 8 December 2016

**Abstract**

A soil pollution assessment of heavy metal Zn, Cu, Cr, Cd, Ni and Pb was carried out in Kuala Terengganu, Malaysia. A total of 245 surface soil samples were sampled and have been subjected to a total digestion and analyzed by inductive couple plasma-optical emission spectrometry (ICP-OES). The contamination of the soils was assessed on the basis of enrichment factors (EFs). Large discrepancies in results of enrichment factor associated with the choices of reference elements in the EFs' calculation have been observed. Our study show that the choice of four commonly-used reference elements (Al, Fe, Ca and Mn) in enrichment calculation could easily alter the enrichment factor values of element of interest by more than 4-folds although the results were supposed to be similar regardless of which reference elements being used. This could lead to serious misinterpretation of soil quality assessment result.

**Keywords**: soil quality assessment, Malaysia soil, elemental analysis, acid digestion

**Abstrak**

Satu penilaian pencemaran logam berat Zn, Cu, Cr, Cd, Ni dan Pb dalam tanah telah dijalankan di Kuala Terengganu, Malaysia. Sebanyak 245 sampel tanah telah diambil, diproses berdasarkan kaedah penghadaman asid dan kepekatan logam berat telah dianalisa dengan menggunakan spektrofotometer pancaran plasma gandingan aruhan (ICP-OES). Pencemaran tanah telah dinilai menggunakan pendekatan faktor pengkayaan. Kajian ini menunjukan nilai-nilai faktor pengkayaan boleh berbeza dengan ketara apabila pengiraan faktor pengkayaan dirujukkan kepada elemen rujukan yang berbeza. Kajian kami mendapati nilai-nilai faktor pengkayaan boleh berbeza sebanyak empat kali ganda apabila pengiraan faktor pengkayaan merujuk kepada Al, Fe, Ca dan Mn dan perbezaan nilai-nilai faktor pengkayaan boleh membawa wujudnya kesilapan dalam mentafsir kualiti tanah yang dikaji.

**Kata kunci**: kajian kualiti tanah, tanah Malaysia, analisa unsur, penghadaman asid

## Introduction

Heavy metals like Cd, Pb, Zn, Cu, Cr and Ni in soil have received wide attention due to their potential toxic impact on the environment if present in excessive concentrations. It is critically important to carry out soil quality monitoring program on a regular basis, particularly in urban watershed to support sustainable planning and development for better livelihood. There are three common approaches of assessing soil quality: (1) take measurements periodically over the time to monitor changes or trends in soil quality; (2) compare measured values to a standard or reference soil condition (i.e. Netherlands' Dutch Target, Australia's Soil Investigation Level,

USEPA Ecological Screening Levels, British Soil Guideline and Japanese Environmental Quality Standards). The former method is commonly used by stakeholders to identify areas where problems occur, to identify areas of special interest, or to compare fields under different management systems over time and latter generally adopted by law enforcement authorities for soil pollution control and mitigation. Finally, the third approach is based on calculation of enrichment factors (EFs) to evaluate anthropogenic influences on soil quality.

Enrichment factor is an index used as a proxy to assess the heavy metals contamination level in soil by estimating the differential of heavy metal concentrations against uncontaminated background or reference levels [1,2]. An enrichment factor can be defined as in equation 1:

$$\mathrm{EF}_i = \frac{(\mathrm{y/x})_{\mathrm{sample}}}{(\mathrm{y/x})_{\mathrm{background}}} \quad (2)$$

where, $y$ is concentration of target metal, $x$ is concentration of reference element or normalizer in soil and in background or baseline reference material. In soil quality study, the interpretation of enrichment factor is based on the deviation of the ratio between a metal of interest and a reference element that exhibit conservative and immobile behavior in environment in a sample to the equivalent ratio in a reference material from unity (Efs = 1). Enrichment factor equal to one is generally taken to mean that there has been no net gain or loss of a metal in the sampled soil respective to the reference material. Enrichment factor ratio should increase (Efs > 1) if there has been a net gain of metal concentration due to extra input (e.g. anthropogenic sources), and a net loss of metal concentration in the system (e.g. due to weathering, biological assimilation) should decrease the ratio value (Efs < 1).

Enrichment factor is practice widely in environmental studies. Nevertheless, the assumption of enrichment factor as pollution detection tool inherits many theoretical shortcomings [3,4]. The work done by Reimann and de Caritat [3,4] concluded that EFs calculation is strongly influenced by the natural variable composition of the reference material, biogeochemical processes and physico-chemical alteration of elements in crust materials. The authors regarded using EFs to interpret pollution event in any environmental sudies as doubtful. The primary objective of this study is to determine the metal concentrations in soil of Kuala Terengganu. Fortuitously, this study will allow to test the reliability of enrichment factor as a pollution proxy for soil quality assessment.

## Materials and Methods

### Soil sampling

The soil quality assessment was carried out in Kuala Terengganu district, Malaysia (5.33°N, 103.1°E, Figure 1). Sampling of soil had been accomplished on 245 cells of 1 km x 1 km square grid using the topographic maps. About 1 kg of soil sample was collected from the first 10-15cm of the upper soil horizon using a plastic spade at each grid. The collected samples were air-dried, ground, and passed through sieve of a 0.6 mm mesh size for subsequent acid digestion.

### Soil digestion and chemical analysis

All soil digestion and element analysis was performed in analytical chemistry laboratory of Universiti Malaysia Terengganu (UMT). All apparatus used in this experiment were acid-cleaned with 10% $HNO_3$. The soil digestion procedure for heavy metal analysis was carried out using USEPA method 3052. In general, an acid mixture of $HNO_3$:HCl:HF (9:4:1) ml ratio was added to 0.5 g of soil sample inside a Teflon vessel. Later, digestions of soils were performed in a microwave-heated oven (Ethos Plus Milestone, USA) at 210 °C for 20 minutes. After digestion, small amount of saturated $H_3BO_3$ acid was added into solution to neutralize remaining active HF in solution. The digested solution then makes up to 25 ml of final volume with ultrapure deionized water. A complete digested soil sample will normally yield a clear solution. Quality control and quality assurance also carried out by using two standard reference materials *SRM-2709* and *SRM-2711* obtained from the National Institute of Standards and Technology (NIST, USA). The SRMs were subjected to similar sample treatment procedures as described above. All samples and SRMs were analyzed for Al, Fe, Mn, Ca, Zn, Cu, Cr, Cd, Ni and Pb by inductive couple plasma optical emission spectrometer (Varian Vista Pro, Australia). SRMs recovery result shows that the analytical accuracy for all measured metals in SRM (n = 12) was within 5-15% error for all metals, expect for Cr which was 10-25% error.

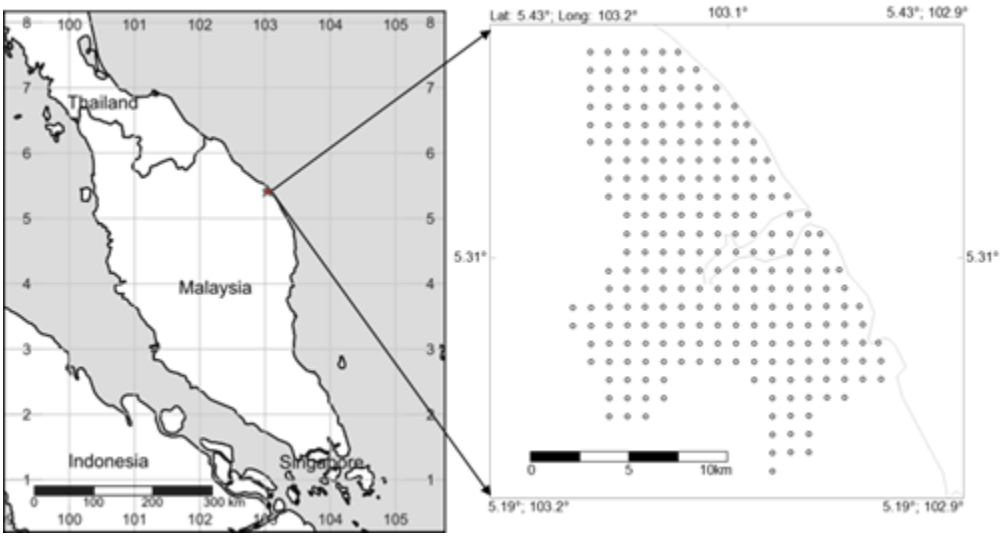



Figure 1. The sampling site in Kuala Terengganu district

**Enrichment factor calculation and geochemical mapping**

The calculation of a normalized enrichment factor for a given metal for this study is represented by equation 1. Where, $EF_i$ is the enrichment factor of target metal *i*, $(y/x)_{sample}$ is the target metal to reference (conservative) element' ratio in the samples of interest; while $(y/x)_{background}$ is the target metal to reference metal ratio in world soil baseline reference taken from Ure and Berrow [5].

## Results and Discussion

**Heavy metals concentration in Kuala Terengganu soil**

The concentration range of metals in Kuala Terengganu soils and their mean values are given in Table 1. The mean concentration values of all metals, except Cd in surface soil of Kuala Terengganu were lower than those reported in worldwide average values [5].

Level of Al (0.45%), Ca (0.14%), Mn (82.9 mg/kg) in the soil samples studied was found much lower (10 fold) than those reported by Ure and Berrow [5] for world average values 6.65%, 1.96% and 760 mg/kg, respectively. The studied soil samples were relatively poor in Fe, Cu, Cr, Zn and Ni. The mean values of these metals were lower than those reported by Zarcinas et al. [7] for Malaysian agricultural soils (Table 2) and for world average value [5]. Level of Pb (23.6 mg/kg) detected in the soil samples were similar to those found in Zarcinas et al. [7] (26.4 mg/kg) and worldwide average value (29.2 mg/kg). Conversely, the content of Cd in studied soil ranged between 0.38 and 6.78 mg/kg with the median concentration of 1.28 mg/kg and was found to be two times greater than the mean concentration of world average (0.62 mg/kg).

The *Baging, Rhutapai, Rusila* and *Rudua* soil series associated to BRIS (Beach Ridges Interspersed with Swales) were reported as dominant soils in these areas [6]. The low heavy metal concentrations in Kuala Terengganu soil indicates the sampled soils are mainly originated from highly weathered BRIS soils. The decreasing order of concentration on the different metals Fe>Al>Ca>Mn>Zn>Pb>Cr>Cu>Ni>Cd reflects their abundance in BRIS soil are associated with low cation exchange capacity, low organic matter content, and excessively-drained sandy soil properties promote leaching losses.

Table 1. The range, median, mean of selected metals in surface soil of Kuala Terengganu (in mg $kg^{-1}$, n=245)

| Metal | Range | Median | Mean | Worldwide Average [5] |
|---|---|---|---|---|
| Al* | 0.14-1.44 | 0.42 | 0.45 | 6.65 |
| Fe* | 0.22-7.70 | 1.54 | 1.57 | 3.20 |
| Mn | 2.53-356 | 51.3 | 82.9 | 760 |
| Ca* | 0.01-1.17 | 0.08 | 0.14 | 1.96 |
| Zn | 4.61-204 | 31.4 | 38.3 | 59.8 |
| Cu | 0.82-148 | 9.39 | 10.9 | 25.8 |
| Cr | 3.05-50.1 | 21.6 | 20.5 | 84.0 |
| Cd | 0.38-6.78 | 1.21 | 1.28 | 0.62 |
| Ni | 1.91-16.7 | 7.18 | 7.02 | 33.7 |
| Pb | 2.54-160 | 21.9 | 23.6 | 29.2 |

*values reported in weight percent, wt.%

**Soil pollution assessment of heavy metals using enrichment factor**

To allow quantitative comparisons between degrees of metals enrichment in the soil pollution assessment, Sutherland [8] and Loska et al [9] had distinguished five contamination categories of the enrichment factor. An EF < 2 is deficiency of minimal enrichment, suggestive of no or minimal pollution; EF 2 - 5 is moderate enrichment; EF 5 - 20 is significant enrichment; EF 20 - 40 is very high enrichment and EF > 40 is extremely high enrichment, indicating an extreme pollution signal. Several elements are utilized as normalizer in enrichment factor, in particular element that have been associated with rock-forming minerals (see summary in Table 2).

Table 2. Selection and justification of reference element for enrichment factor calculation in relation to assess anthropogenic impact

| Normalizer | Justification | Reference |
|---|---|---|
| Al | Al has no significant anthropogenic input compared to the large of geogenic element; Ion potential of Al is close to target elements, reduce variation in comparison | [10] |
| Mn | Mn is one of largest components of soil | [11] |
| Fe | Fe is abundant in soils; considered to be free from anthropogenic contribution | [1, 12] |
| Ca | Ca is one of the main components of the Earth's Crust, concentration in soil is connected with the matrix, lower mining interference factor (MIF) compared to Al and Zr | [9] |
| Zr | Zr has no significant anthropogenic source and resides primarily in the weathering-resistant heavy mineral Zircon | [13] |
| Sc | Sc is stable to supergene processes associated with oxidation and chemical weathering | [14] |
| Sr | Sr is one of the main components of the Earth's Crust, concentration in soil is connected with the matrix | [15] |
| Ti | Ti is a common rock-forming element and very resistant to weathering in the soil. | [16] |

The scatter plot in Figure 2 illustrates a comparison study of selected elements EF against different normalizers (Fe, Al, Ca and Mn) and the obtained results showed that EF values of metal were different corresponding to the

normalizers used. For better interpretation, four different colour lines representing the contamination categories scale suggested by Sutherland [8] and Loska et al. [9] were plotted (Figure 2). For example, if a sample fall within green and yellow line, then the sample was classified as being moderate enriched (EF = 2-5). If it falls between the yellow and orange line, then the sample was classified as significant enrichment (EF = 5-20). If a sample surpassed the orange line but was within the red line, then the sample was classified as being very highly enriched (EF = 20-40). Samples with the enrichment factor greater than 40 that were found to have surpassed the red line were classified as samples with severe pollution. If samples fall below green line (EF < 2), then samples were classified as depletion to minimal enrichment suggestive of no or minimal pollution.

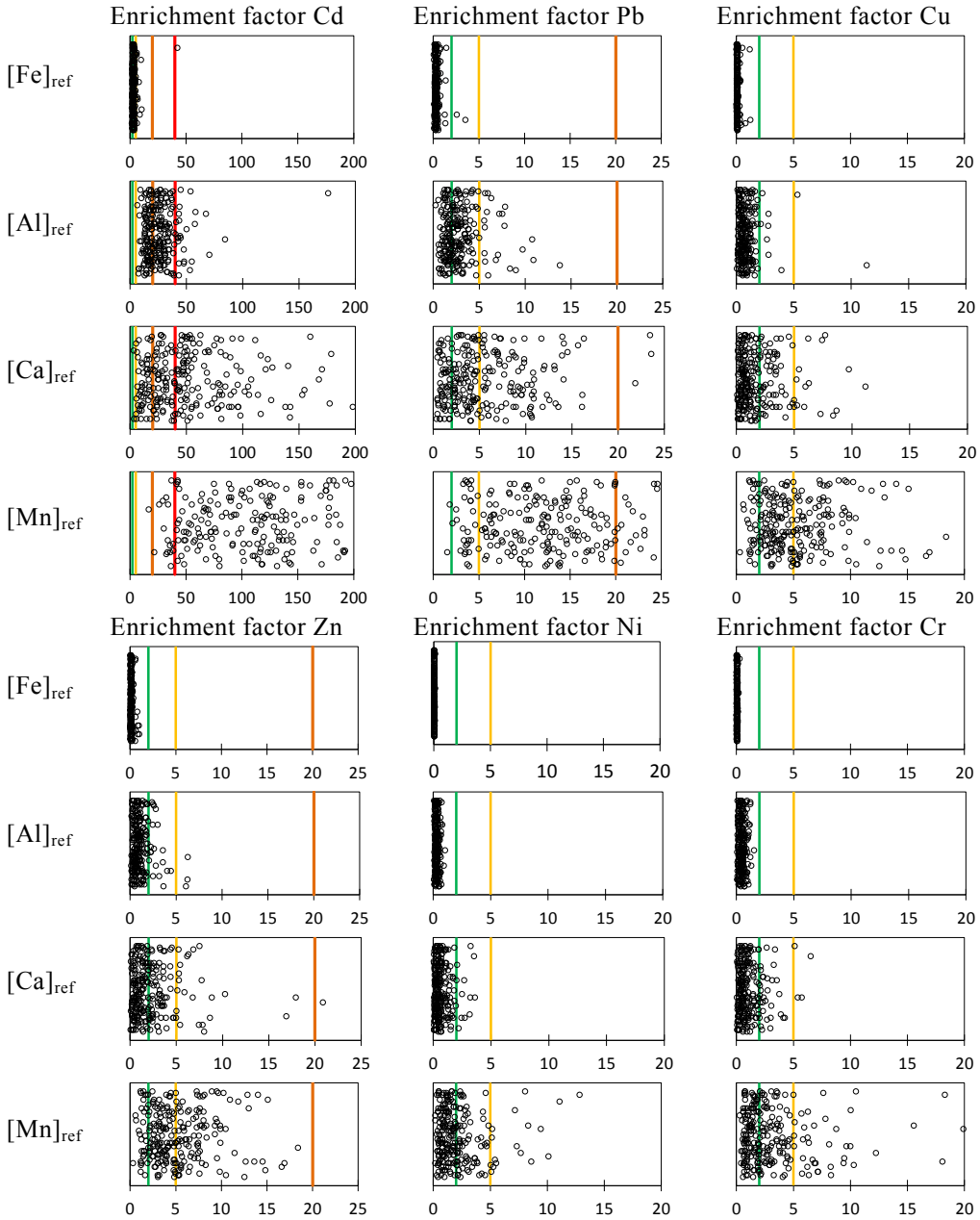



Figure 2. Comparison of enrichment factor for target metals using different notmaliser; green, yellow, orange and red colour lines representing contamination categoresis scale proposed by Loska et al. [9] and Sutherland [8]

Theoretically, the selection of reference element used in EFs calculation should hardly be affected by weathering processes and should show little variability of occurrence [3]. If different reference elements are selected to calculate EFs, they should all show similar pollution signals regardless of which normalizers were being used. In this study, however, all four sets of EFs calculation (refer Figure 2) bear no relationship to each other.

Figure 2 show EFs values for all metals derived from all four normalizers differ in the range from 1 to 4-folds. EFs derived from Ca and Mn normalizer generally had overestimated amount compared to Al and Fe. We found that 93% and 6% of the Cd samples were classified as extremely high polluted and very high polluted respectively when Mn was used as reference element. These outcomes are very different to the other reference elements, in particular to Fe normalizer. For Fe reference-EFs, 95% of Cd samples were classified as moderate enriched or lower. Al and Ca normalizer also produced a wide range of EFs for Cd samples and these values ranged between Fe and Mn references derived EFs. These discrepancies reflect that EFs do not provide a simple technique to differentiate particular suite of metals was whether of anthropogenic origin or vice versa.

The color contour maps of Pb concentration and EFs in Figure 3 were created using the inverse distance weighting (IDW) spatial interpolation technique in ESRI ArcMap 9.2. In Figure 3, the Pb hotspots in Kuala Terengganu soils are marked in red colors. The Pb concentration for Kuala Terengganu soils were also compared to Dutch environmental pollutant reference values, also known as "Dutch target" used in environmental remediation, investigation and cleanup purposes. For Kuala Terengganu, three out of 245 samples had exceeded the Dutch recommendation value of 85 mg/kg. The spatial variations for each metal for Kuala Terengganu soil in this study can be found in Poh [17].

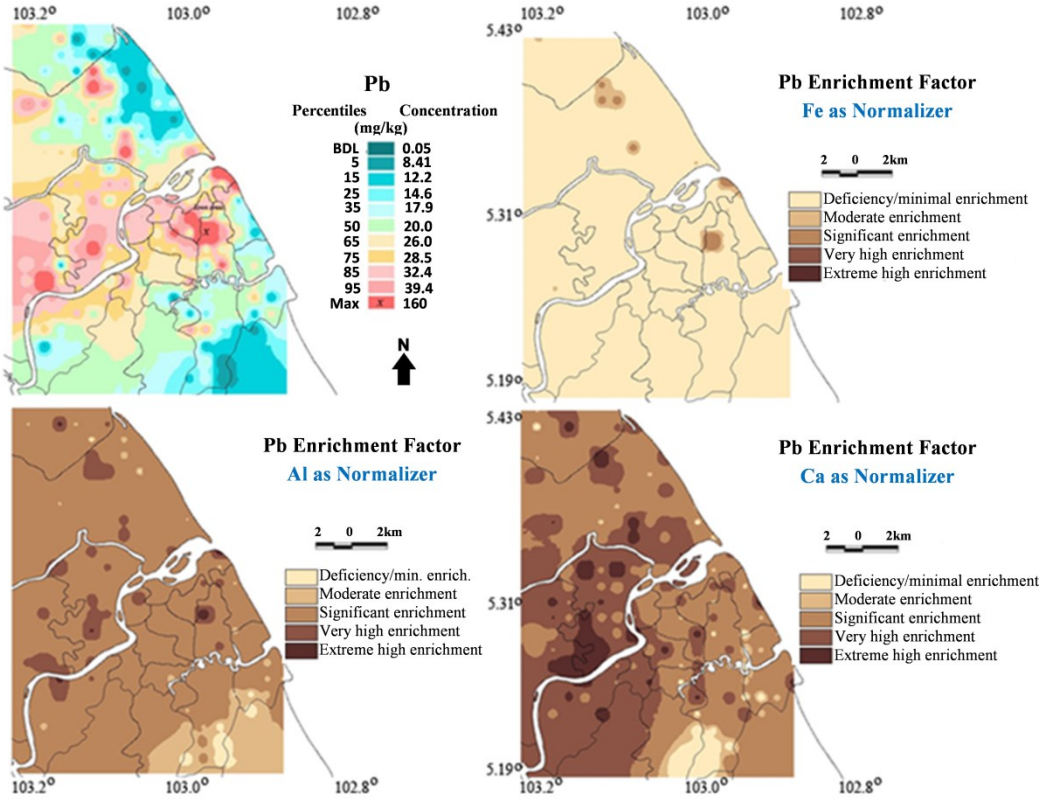



Figure 3. Comparison of the calculated EFs for Pb in Kuala Terengganu soils

Three striking features of the EFs pattern of Pb are evident in Figure 3. First, the EFs for Pb show great spatial variation compared to Pb distribution pattern in Kuala Terengganu soil. Second, this variation is multidimensional; that is three different set of reference element show mainly independent of EFs variation. For example, when EFs was calculated relative to the Pb/Al ratio, the pattern of high Pb enrichment was recorded at the same areas in the Pb concentration map. However, when the EFs Pb/Fe ratio distribution was compared to Pb concentration map, it turns out, several high enrichment values near the central part of the map disappeared. Furthermore, when EFs Pb/Ca ratio distribution was compared, the high anomaly near to river mouth was no longer present in the map. Meanwhile, an unexpected extremely high EFs had appeared scattered in the central part of the map. Third, these EFs patterns have a pervasive missed-interpretation of pollution signal. In this case, EFs Pb/Al ratio distribution showed 50% of Kuala Terengganu soils were significantly enriched by Pb but EFs Pb/Fe ratio distribution, on the other hand illustrated that 99% of areas were still less contaminated by Pb. The results could overestimate, underestimate, or simply incorrectly estimate the environmental pollution.

The potential sources of errors for EFs technique mentioned above can be explained in a number of ways. First, a huge natural variation in concentration of the different elements in reference materials (i.e. continental crust value, world soil average) exist and using single mean value from a skewed distribution dataset (i.e. Ure and Berrow [5]) does not permit a reasonable EFs assessment. Ure and Berrow [5] reported Pb concentration in world soil is ranges from 1 – 888 mg/kg with average value of 29.2 mg/kg, obviously the given mean value does not reflect the true average Pb concentration for world average soil. This is one of a very good example to show that using the mean world soil value as a proxy of "natural background values" in enrichment factor inherent a serious flaw to estimate pollution signal in environment.

Second, an inhomogeneous distribution of reference elements in the study area could also lead to misinterpretation in EFs. Overestimation of EFs occurs when the chosen reference elements (normalizer) showed a natural spatial variation that was as large as, or larger than, that of the target metal of interest [4]. In this study, we used quartile coefficient of dispersion (cqv) statistical analysis to compare the dispersion of the maximum concentration differences between Pb and other reference elements. The calculated cqv for Ca, Fe and Al against Pb was 2.2, 1.1 and 0.7 respectively, indicated that the natural spatial variation of Ca was found 2 times greater than Pb. We found that the large dispersion of Ca concentration has attributed greater EFs value of Pb in Kuala Terengganu and the Pb/Ca ratio EFs was found greater than Pb/Al and Pb/Fe ratio EFs by order of two magnitudes (Figure 3).

The large discrepancies in EFs value could be due to two other factors: (i) the differential solubility of refractory minerals in acid digestion protocols as well as grain size fractionation effect resulted different concentration of metal elements in Earth materials and; (ii) the significance of biogeochemical and weathering processes that control element concentration in Earth surface are not considered in EFs assessment on pollution studies. Reimann and de Caritat [3,4] and Desaules [18] have provide a detailed explanation and references in conceptual shortcomings of EFs in environmental studies.

## Conclusion

Our work demonstrated that application of enrichment factor in the assessment of soil pollution level in Kuala Terengganu inherent a major weakness. One unanticipated finding was that the choice of four commonly-used reference elements (Al, Fe, Ca and Mn) for enrichment calculation could easily alter the enrichment factor values of Pb by more than 4-folds although the results were supposed to be similar regardless of which reference elements being used. This bias can be attributed to the absent of a reliable "natural background value" or references. Another shortcoming of EFs approach in assessing the level of anthropogenic sources to environment is EFs did not take into account the natural variation of element concentration in environmental samples in relation to biogeochemical and localized lithogenic processes as mentioned in Reimann and de Caritat [3,4] and Desaules [18]. Therefore, application of enrichment factor as a way to fingerprint the anthropogenic source of heavy metals in soils requires extra caution in future study.

## Acknowledgements

This work was supported by the Universiti Malaysia Terengganu. We especially thank Foo Toon Fong and Mohd Rafie Rosly for assistance with soil sampling.

**References**


1. Dragović, S., N. Mihailović, and B. Gajić (2008). Heavy metals in soils: Distribution, relationship with soil characteristics and radionuclides and multivariate assessment of contamination sources. *Chemosphere*, 72(3): 491 – 495.
2. Luo, X.-S., S. Yu, Y.-G. Zhu, and X.-D. Li (2012). Trace metal contamination in urban soils of China. *Science of The Total Environment*, 421–422:17 – 30.
3. Reimann, C. and Caritat, P. D. (2000). Intrinsic flaws of element enrichment factors (EFs) in environmental geochemistry. *Environmental Science & Technology*, 34(24):5084 – 5091.
4. Reimann, C. and Caritat, P. D. (2005). Distinguishing between natural and anthropogenic sources for elements in the environment: Regional geochemical surveys versus enrichment factors. *Science of The Total Environment*, 337(1–3): 91 – 107.
5. Ure, A. M. and Berrow, M. L. (1982). The elemental constituents of soils, in environmental chemistry: Volume *2*, H.J.M. Bowen, Editor. The Royal Society of Chemistry: pp. 94 – 204.
6. Biot, Y. Z. and Razak, A. H. (1982). Semi-detailed soil survey report of the Terengganu river basin. Department of Agriculture, Malaysia.
7. Zarcinas, B. A., Ishak, C. F., McLaughlin, M. J. and Cozens, G. (2004). Heavy metals in soils and crops in Southeast Asia. *Environmental Geochemistry and Health*, 26(4): 343 – 357.
8. Sutherland, A. R. (2000). Bed sediment-associated trace metals in an urban stream, Oahu, Hawaii. *Environmental Geology*, 39(6): 611 – 627.
9. Loska, K., D. Wiechuła, and Korus, I. (2004). Metal contamination of farming soils affected by industry. *Environment International*, 30(2): 159 – 165.
10. Bourennane, H., Douay, F., Sterckeman, T., Villanneau, E., Ciesielski, H., King, D. and Baize, D. (2010). Mapping of anthropogenic trace elements inputs in agricultural topsoil from Northern France using enrichment factors. *Geoderma*, 157(3–4): 165 – 174.
11. Chen, H., Teng, Y., Lu, S., Wang, Y. and Wang, J. (2015). Contamination features and health risk of soil heavy metals in China. *Science of The Total Environment*, 512–513: 143 – 153.
12. Ye, C., Li, S., Zhang, Y. and Zhang, Q. (2011). Assessing soil heavy metal pollution in the water-level-fluctuation zone of the Three Gorges Reservoir, China. *Journal of Hazardous Materials*, 191(1–3): 366 –372.
13. Schulin, R., Curchod, F., Mondeshka, M., Daskalova, A. and Keller, A. (2007). Heavy metal contamination along a soil transect in the vicinity of the iron smelter of Kremikovtzi (Bulgaria). *Geoderma*, 140(1–2): 52 – 61.
14. Qin, F., Ji, H., Li, Q., Guo, X., Tang, L. and Feng, J. (2014). Evaluation of trace elements and identification of pollution sources in particle size fractions of soil from iron ore areas along the Chao River. *Journal of Geochemical Exploration*, 138: 33 – 49.
15. Krishna, A. K. and Govil, P. K. (2008). Assessment of heavy metal contamination in soils around Manali industrial area, Chennai, Southern India. *Environmental Geology*, 54(7): 1465 – 1472.
16. Szolnoki, Z., Farsang, A., and Puskás, I. (2013). Cumulative impacts of human activities on urban garden soils: Origin and accumulation of metals. *Environmental Pollution*, 177: 106 – 115.
17. Poh, S. C. (2008). Distribution and source apportionment of elements in urban soil of Kuala Terengganu, Malaysia, Thesis Universiti Malaysia Terengganu, Malaysia.
18. Desaules, A., (2012). Critical evaluation of soil contamination assessment methods for trace metals. *Science of The Total Environment*, 426: 120 – 131.

*Malaysian Journal of Analytical Sciences, Vol 21 No 1 (2017): 60 - 71*
*DOI: http://dx.doi.org/10.17576/mjas-2017-2101-08*

MALAYSIAN JOURNAL OF ANALYTICAL SCIENCES
*Published by The Malaysian Analytical Sciences Society*
ISSN 1394 - 2506

# SYNTHESIS AND STRUCTURAL CHARACTERIZATION OF *N*-BROMOBENZOYL-*N*'-(1,10-PHENANTHROLIN-5-YL)THIOUREA DERIVATIVES

## (Sintesis dan Penentuan Struktur Ligan Terbitan *N*-Bromobenzoil-*N*'-(1,10-Fenantrolin-5-il) tiourea)

Rosidah Shardin[1], Siew San Tan[1], Mohammad B. Kassim[1,2]*

[1]*School of Chemical Sciences and Food Technology, Faculty of Science and Technology*
[2]*Fuel Cell Institute*
*Universiti Kebangsaan Malaysia, 43600 UKM Bangi, Selangor, Malaysia*

**Corresponding author: mb_kassim@ukm.edu.my*

Received: 28 September 2016; Accepted: 8 December 2016

**Abstract**

Derivatives of *N*-bromobenzoyl-*N*'-(1,10-phenanthrolin-5-yl)thiourea were successfully synthesized from the reaction of 1,10-phenanthroline with *x*-bromobenzoylisothiocyanate (*x* = *ortho*, *meta* and *para*) to give phen-*o*-BrBT, phen-*m*-BrBT and phen-*p*-BrBT, respectively. The molecular structures of the derivatives compounds were elucidated based on the crystal structure of *N*-bromobenzoyl-*N*'-(1,10-phenanthrolin-5-yl)thiourea, CHNS elemental analysis, mass spectrometry, spectroscopic data (infrared, ultraviolet-visible, nuclear magnetic resonance and luminescence) and cyclic voltammetry.The mass spectrum show similar *m/z* values at 460.9 and 260.0, which represent the molecular ions for $[(\text{phen-}x\text{-BrBT})\text{-Na}]^+$ and $[\text{BrBT}]^+$, respectively. The presence of a $\nu$(NH) (3389-3599 $cm^{-1}$) and the disappearance of $\nu(NH_2)$ bands from 1,10-phenanthroline-5-amine indicate the formation of the *N*-bromobenzoyl-*N*'-(1,10-phenanthrolin-5-yl)thiourea. Attachment of a Br atom to the benzoyl moiety reduced the stretching frequency of C=O group by >20 $cm^{-1}$ compared with phen-BT ligand. The compounds exhibit two $\pi\rightarrow\pi^*$ bands at 231 and 269-270 nm for the phenanthroline and benzoyl moieties, respectively. The resonance for N-H proton appeared at $\delta$ = 11.53-12.49 ppm. In addition, $^{13}C$ resonance signals for C=S and C=O groups were recorded at around 182 and 167.39-169.08 ppm, respectively. The synthesis and effect of a Br substitution on the structural and luminescence properties of *N*-bromobenzoyl-*N*'-(1,10-phenanthrolin-5-yl)thiourea derivatives are presented and discussed in this study.

**Keywords**: benzoylthiourea, 1,10-phenanthroline, thiocyanate, infrared, luminescence

**Abstrak**

Terbitan *N*-bromobenzoil-*N*'-(1,10-fenantrolin-5-il)tiourea telah disintesis melalui tindak balas di antara 1,10-fenantrolina dengan *x*-bromobenzoilisotiosianat (*x* = *orto*, *meta* and *para*) masing-masing menghasilkan sebatian phen-*o*-BrBT, phen-*m*-BrBT dan phen-*p*-BrBT. Struktur sebatian ditentukan berdasarkan struktur kristal *N*-benzoil-*N*'-(1,10-fenantrolin-5-il)tiourea, analisis unsur CHNS, spektrometri jisim, data spektroskopi (inframerah, ultralembayung-boleh nampak, pendarcahaya dan resonans magnetik nuklear) dan voltammetri kitaran. Spektrum jisim bagi ketiga-tiga sebatian ini menunjukkan nilai *m/z* yang sama pada 460.9 dan 260.0 masing-masing mewakili ion molekul $[(\text{phen-}x\text{-BrBT})\text{-Na}]^+$ dan $[\text{BrBT}]^+$. Kemunculan isyarat $\nu$(NH) pada 3389-3599 $cm^{-1}$ dan kehilangan frekuensi regangan $\nu(NH_2)$ bagi sebatian 1,10-fenantrolin-5-amina menunjukkan pembentukan molekul *N*-bromobenzoil-*N*'-(1,10-fenantrolin-5-il)tiourea. Kehadiran atom bromo pada gelang benzoil telah merendahkan frekuensi regangan $\nu$(CO) sebanyak >20 $cm^{-1}$ berbanding *N*-bromobenzoil-*N*'-(1,10-fenantrolin-5-il)tiourea. Spektrum elektronik sebatian memapar dua jalur serapan bagi peralihan $\pi\rightarrow\pi^*$ pada 231 dan 269-270 nm masing-masing berpunca daripada moieti fenantrolina dan benzoil. Isyarat resonan $^1H$ (N-H) hadir pada $\delta$ = 11.53-12.49 ppm manakala, isyarat $^{13}C$ bagi kumpulan berfungsi utama C=S dan C=O telah dikenal pasti masing-masing pada 182 dan 167.39-169.08 ppm. Sintesis dan kesan

kehadiran Br pada posisi *orto*, *meta* dan *para* terhadap struktur serta sifat pendarcahaya sebatian dilapor dan dibincang di dalam kajian ini.

**Kata kunci:** benzoilthiourea, 1,10-fenantrolina, tiosianat, inframerah, pendarcahaya

## Introduction

Polypyridine compounds such as 1,10-phenanthroline (phen) are one of the most widely used chelating ligands in modern coordination chemistry [1,2]. The shape of the phen favors the formation of metal complexes via chelation and hence, phen and its derivatives are widely used ligands in metal complexes. The metal complexes of phen derivatives have many applications in various fields such as molecular catalysis, solar energy conversion, herbicides and nucleic acid probes. Besides, metal-phen compound has also been used in the development of luminescence-based sensors for pH, anions and cations [3].

Thiourea compounds are essential as building blocks in the synthesis of heterocyclic compounds [4]. Substituted thioureas have gained great attention in the preparation of wide variety of biologically active compounds [5,6]. Thioureas are also an important class of organic compounds, which showed high biological activity, used as corrosion inhibitors and antioxidant, and were also widely used as polymer components [7]. The synthesis of thiourea derivatives can be easily done with a good yield [8]. One of the thiourea derivatives that have gained a lot of attention is benzoylthiourea, which has shown a wide range of biological activities including antiviral [9], antibacterial [10,11], antifungal [12], herbicidal [13] and acting as chelating agents [14,15].

Phenanthroline derivatives and bromobenzoylthiourea compounds are widely used chelating agents in the coordination chemistry [1,4]. This study attempts to combine both classes of the compounds to form a multi-dentate benzoylthiourea ligand that contains both moieties. Subsequently, this new multi-dentate chelating ligand can be used to form stable complexes with metal ions. The derivatives of *N*-bromobenzoyl-*N*'-(1,10-phenanthrolin-5-yl)thiourea compounds are expected to be a more effective class of the organic compounds to coordinate with metal ions due to the presence of lone pair electrons on nitrogen, sulphur and oxygen atoms. In addition, the $\pi$-electron cloud in the phen and benzoylthiourea moieties will also add to the stability of the coordination complexes through delocalization of electrons across the coordination sphere.

In this paper, we present the synthetic method, structural and electronic properties of *N*-bromobenzoyl-*N*'-(1,10-phenanthrolin-5-yl)thiourea derivatives. In addition we also discussed the effects of the Br substitution on the structural and luminescence properties of the compounds.

## Materials and Methods

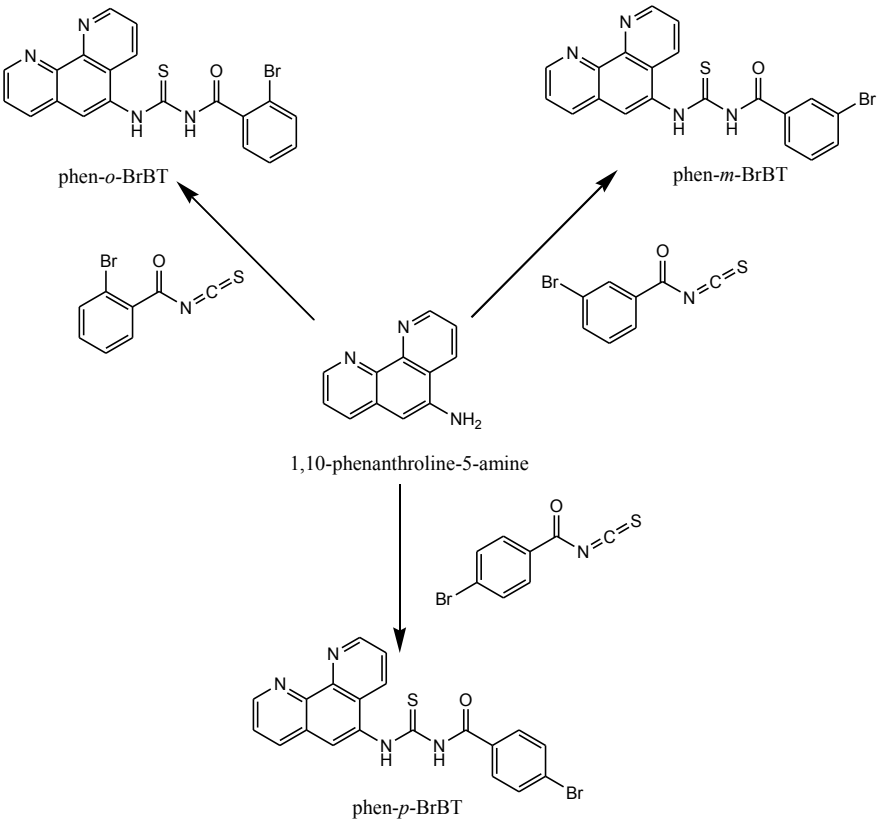
### Chemicals and instrumentation

Benzoyl chloride, 1,10-phenanthroline-5-amine, *o*-bromobenzoyl chloride, *m*-bromobenzoyl chloride and *p*-bromobenzoyl chloride were purchased from Fluka (Malaysia). All solvents were of reagent grade quality and were obtained from commercial suppliers and used without further purification.

Melting points were determined on an Electrothermal 9100. Elemental (C, H, N and S) analyses were performed on Leco 932 analyzer. The mass spectra were recorded on a Bruker micrOTOF-Q 86 spectrometer equipped with an electrospray ionization (ESI) module. The source temperature was maintained at 180 ˚C at an approximately 0.4 bar pressure. Infrared measurements of the complexes were recorded by using Agilent Cary 630 spectrophotometer in the range of 4000-400 $cm^{-1}$ in the ATR Diamond mode, whereas the UV-Vis absorption spectra were obtained by using a 1 cm path length quartz cell on a Perkin-Elmer Lambda 35 spectrometer. The $^{1}H$ NMR and $^{13}C$ NMR spectra were collected on a ECP 400 (Delta-NMR) spectrophotometer as deuterated DMSO solution. The chemical shifts were scaled to parts per million (ppm) with reference to TMS. The electrochemical measurements were carried out with a Voltalab PGZ402, AmetekVersastat 4 system. Steady state emission spectra were recorded on an Edinburgh FLS920 time resolved fluorescence spectrometer at 298 K in $CH_3CN$, using 1 cm path length quartz cell.

**Synthesis of *N*-(x-bromobenzoyl)-*N*'-(1,10-phenanthrolin-5-yl)thiourea**

Firstly, *ortho*-, *meta*- and *para*-bromobenzoyl chloride derivatives (1.5 mmol) were reacted with ammonium thiocyanate (1.15 mmol) in acetone (30 ml) to give the corresponding bromobenzoylisothiocyanate derivatives followed by a condensation with 1,10-phenanthroline-5-amine in ethanol (20 ml) to give *o*-bromobenzoyl-(1,10-phenanthrolin-5-yl)thiourea [phen-*o*-BrBT], *m*-bromobenzoyl-(1,10-phenanthrolin-5-yl)thiourea [phen-*m*-BrBT] and *p*-bromobenzoyl-(1,10-phenanthrolin-5-yl)thiourea [phen-*p*-BrBT] compounds, respectively (Scheme 1). The reaction mixtures were left to stir for 5 hours at 80˚C. The products were collected as yellow precipitates and the solvents were removed under reduced pressure. The precipitates were then rinsed with cold acetone to give the desired products. Recrystallization in a suitable solvent gave a pure yellowish crystalline product.




Scheme 1. Schematic diagram for the synthesis of *N*-(*x*-bromobenzoyl)-*N*'-(1,10-phenanthrolin-5-yl)thiourea derivatives from *x*-bromobenzoylisothiocyanate and 1,10-phenanthroline-5-amine

## Results and Discussion

The phen-BT, phen-*o*-BrBT, phen-*m*-BrBT and phen-*p*-BrBT compounds were characterized on the basis of the mass spectrometry, CHNS elemental analysis and the spectroscopic data from infrared, ultraviolet-visible, nuclear magnetic resonance ($^{1}$H and $^{13}$C) spectroscopy. Besides, the cyclic voltammetry and luminescence properties of these compounds also were recorded to provide more information on the electronic states and structures. Overall, the reactions gave a reasonable to good yield (58-68%) as summarized in Table 1.

Table 1. The yield and melting point of *N*-(bromobenzoyl)-*N*'-(1,10-phenanthrolin-5-yl)thiourea derivatives

| Compound | Yield (%) | Melting point (°C) |
|---|---|---|
| phen-BT | 65.0 | - |
| phen-*o*-BrBT | 63.5 | 197.5 – 198.3 |
| phen-*m*-BrBT | 57.9 | 146.3 – 151.3 |
| phen-*p*-BrBT | 68.0 | 175.2 – 176.5 |

**Elemental analysis of C, H, N and S**

There was some deviation from the theoretical value for C, H, N and S contents in the phen-BT, phen-*o*-BrBT, phen-*m*-BrBT and phen-*p*-BrBT compounds. These differences are within the experimental errors and may be due to a contamination from the recrystallization solvent and atmospheric water. This is not uncommon as the solvent is quite polar and the compound contains Br atom that can also induce polarity in the molecule. We proposed a new chemical formula for each compound taking into consideration that the samples might be contaminated as shown in Table 2. The calculation revealed that the highest deviation (0.86) was for carbon content in the phen-*p*-BrBT sample.

Table 2. The elemental CHNS contents in phen-BT, phen-*o*-BrBT, phen-*m*-BrBT and phen-*p*-BrBT and the proposed new chemical formula to account for an acetone and water content

| Compound | Experiment (theory), % | | | | Proposed Chemical Formula | Largest Deviation (Element) |
|---|---|---|---|---|---|---|
| | C | H | N | S | | |
| phen-BT | 66.61 (67.02) | 4.83 (3.94) | 15.78 (15.63) | 8.73 (8.95) | $C_{20}H_{14}N_4OS \cdot 0.2H_2O \cdot 0.15C_3H_6O$ | 0.67 (H) |
| phen-*o*-BrBT | 53.54 (54.93) | 4.47 (3.00) | 11.72 (12.81) | 7.22 (7.33) | $C_{20}H_{13}BrN_4OS \cdot 1.1H2O \cdot 0.55 C_3H_6O$ | 0.66 (H) |
| phen-*m*-BrBT | 53.59 (54.93) | 4.12 (3.00) | 12.03 (12.81) | 7.17 (7.33) | $C_{20}H_{13}BrN_4OS \cdot 0.95H_2O \cdot 0.4C_3H_6O$ | 0.47 (H) |
| phen-*p*-BrBT | 56.55 (54.93) | 4.05 (3.00) | 12.14 (12.81) | 7.37 (7.33) | $C_{20}H_{13}BrN_4OS \cdot 0.9C_3H_6O$ | 0.86 (C) |

**Mass spectrometry**

The electron impact mass-spectrum of a representative compound namely phen-*p*-BrBT (Figure 1) shows the corresponding *m/z* value of the parent molecule with one mole of associated sodium ion, [phen-*x*-BrBT)-Na]$^+$ at 460.9 (459.0 *theory*). A fragmentation with *m/z* value corresponding to [BrBT]$^+$ was observed at 260.0 (258.9 *theory*). Similarly, the mass spectrum and the fragmentation masses of other derivatives agreed with the structures as shown in Figure 1.

**X-ray crystal structures**

The structure of *N*-(benzoyl)-*N*'-(1,10-phenanthrolin-5-yl)thiourea [phen-BT] [16] (Figure 2) was used as a reference to provide additional information in the determination of the molecular structure of the bromo-substituted analogues.

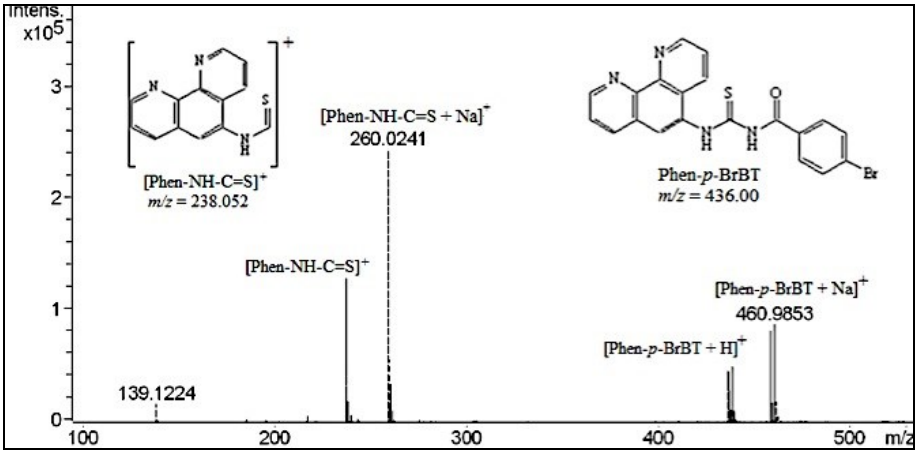



Figure 1. The mass-spectrum showing the molecular ion of phen-*p*-BrBT and its fragmentations as a representative compound.

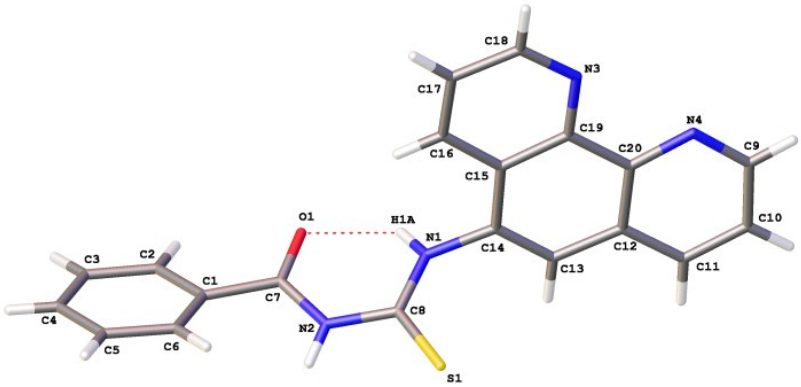



Figure 2. The molecular structure of the phen-BT with a dashed line indicates the intramolecular hydrogen bond that forms a pseudo-six membered ring

In the structure of phen-BT, the benzoyl and 1,10-phenanthroline moieties were attached to the terminal nitrogen atoms of the thiourea moiety at *cisoid* and *transoid* position relative to the thiono N2—C8 and N1—C8 bonds. The phenyl and phenanthroline rings are twisted relative to the central thiourea fragment with dihedral angles of 29.46(12)˚ and 74.06(8)˚, respectively. The phenyl and phenanthroline rings are almost perpendicular to each other with dihedral angle of 83.15(10)˚.

The S1—C8 and O1—C7 in the compound showed a typical double bond character with bond lengths of 1.651(2) and 1.222(3) Å respectively, and are comparable to other thiourea derivatives [17,18]. All C-N bonds (N2—C7, N2—C8, N1—C8 and N2—C14) in the thiourea fragments were in the range of 1.431(3) to 1.329(3) Å, which are an intermediate distance between those expected for single and double CN bonds (1.47 and 1.27 Å, respectively). Among these CN bonds, we noticed that N2—C14 was the longest bond, which indicated a $C_{sp}^{2}$-$N_{sp}^{2}$ single bond while N1—C8 bond was the shortest bond with more double bond character.

In the crystal structure of phen-BT compound, there was an intramolecular hydrogen bond, N1—H1A···O1 resulting in the formation of a pseudo six-membered ring (N1/H1A/O1/C7/N2/C8) in the molecule. The present of the

intramolecular hydrogen bond may contributed to the shift in the infrared signal of the C=O group and to a lesser extend to the $^{1}H$ and $^{13}C$ signals of the compounds since the spectrum were collected in a solution phase.

**Infrared spectra**

The infrared spectrum of phen-BT is shown in Figure 3 and the characteristic functional groups are listed in Table 3. Generally, the IR spectrum of 1,10-phenanthroline moiety shows strong bands in the 1400-1650 $cm^{-1}$ regions [19]. A band at around 1420 $cm^{-1}$ exhibits the stretching frequency of $\nu(C\text{-}N_{phen})$, which indicates a highly delocalized electronic distribution in the thiourea moiety.

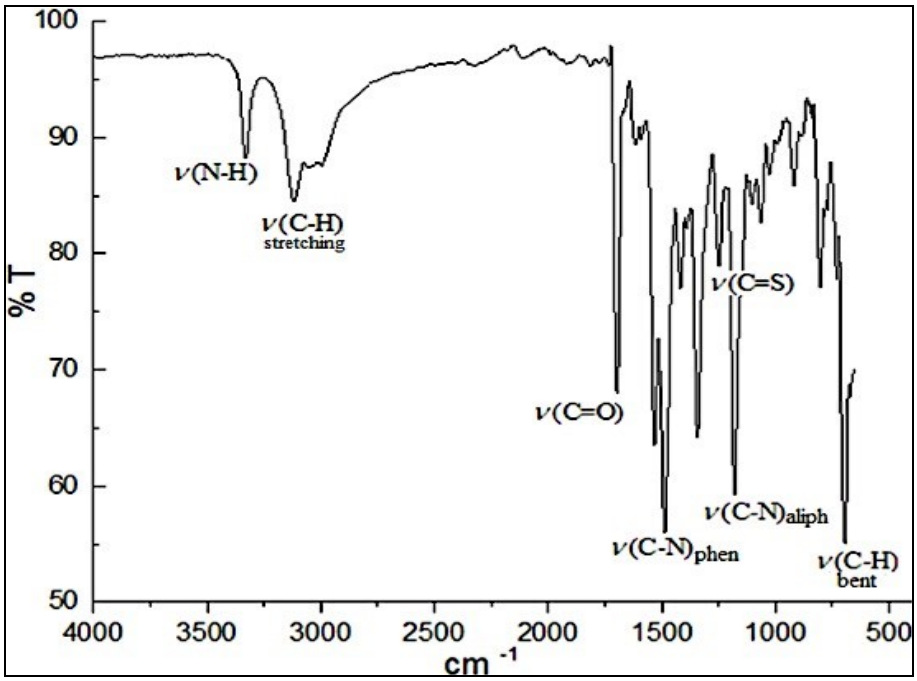



Figure 3. The infrared spectrum of phen-BT

Table 3. The stretching frequencies of characteristic functional groups for phen-BT, phen-*o*-BrBT, phen-*m*-BrBT and phen-*p*-BrBT compounds

| Compound | IR spectrum ($cm^{-1}$) | | | |
|---|---|---|---|---|
| | $\nu$(NH) | $\nu(C\text{-}N_{phen})$ | $\nu$(C=O) | $\nu$(C=S) |
| phen-BT | 3332 | 1420 | 1700 | 1254 |
| phen-*o*-BrBT | 3513 | 1422 | 1672 | 1258 |
| phen-*m*-BrBT | 3513 | 1422 | 1673 | 1251 |
| phen-*p*-BrBT | 3596 | 1420 | 1676 | 1259 |

It is important to note the disappearance of $\nu(NH_2)$ stretching frequency of the amine group and the appearance of $\nu$(NH) stretching band at 3332, 3513, 3513 and 3596 $cm^{-1}$ in the spectra of phen-BT, phen-*o*-BrBT, phen-*m*-BrBT and phen-*p*-BrBT, respectively. The later band is an important indicator for the formation of the *N*-bromobenzoyl-*N*'-(1,10-phenanthrolin-5-yl)thiourea molecules. In addition, bands at 3521-3599 $cm^{-1}$ regions indicate the asymmetric and symmetric vibrations frequencies for (N-H) of the secondary thioamide group.

A strong band at 1672-1700 $cm^{-1}$ was ascribed to the stretching vibration of the C=O group. The frequency for the C=O band decreases by >20 $cm^{-1}$ due to a more delocalised electronic distribution across the structural geometry and the presence of an intramolecular hydrogen bonding between the O atom of the C=O group with N-H as suggested by the X-ray crystal structure [20]. Furthermore, the presence of bromo atom as an electron-withdrawing group at the benzoyl moiety has weakened the C=O bond. Halogen atom with high electronegativity such as bromine is capable of reducing the electron density of the benzene ring and hence, has indirectly affected the neighbouring C=O group.

**Ultraviolet-visible spectra**

The UV absorption spectra of the phen-BT, phen-*o*-BrBT, phen-*m*-BrBT and phen-*p*-BrBT compounds are shown in Figure 4 and the data is collected in Table 4. The ligands display two strong absorption bands in the ultra-violent region with absorption maxima at 231 (ε= 54,795-61,870 $Lmol^{-1}cm^{-1}$) and 269-270 nm (ε= 36,711-57,513 $Lmol^{-1}cm^{-1}$) that can be attributed to the π→π* ligand-centred (LC) transitions.

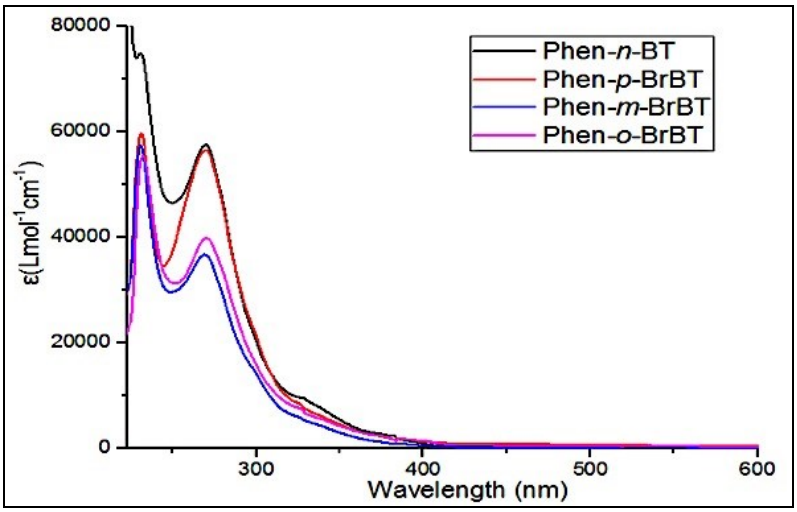



Figure 4. The electronic absorption spectra of *N*-bromobenzoyl-*N*'-(1,10-phenanthrolin-5-yl)thiourea derivatives in acetonitrile

The intensity of phen-*p*-BrBT absorption band appears the highest compared to phen-*m*-BrBT and phen-*o*-BrBT. In addition, there is no significant change in the energy of the electronic absorption bands compared with the substituted phen-BT. However, the bromo-substituent in the phen-*o*-BrBT molecule has a restricted structural conformation and appeared to impede the electron transfer slightly for the higher energy transitions.

Table 4. Molar absorptivity and $\lambda_{max}$ of phen-BT, phen-*o*-BrBT, phen-*m*-BrBT and phen-*p*-BrBT compounds

| **Compound** | **UV-Vis ($CH_2Cl_2$)** |
|---|---|
| | **λ(nm) / ε($Lmol^{-1}cm^{-1}$)** |
| phen-BT | 270 (57,513), 231 (61,870) |
| phen-*o*-BrBT | 269 (39,828), 231 (54,795) |
| phen-*m*-BrBT | 269 (36,711), 231 (57,405) |
| phen-*p*-BrBT | 270 (56,517) , 231 (59,724) |

**Nuclear magnetic resonance spectroscopy**

The structures of all compounds with the atomic numbering scheme are shown in Figure 5. The data are compiled in Table 5 and Table 6, respectively. In accordance with the IR spectra, the chemical shift of $H(N_1)$ were observed at 12.36, 12.49 and 12.53 ppm for phen-*o*-BrBT, phen-*m*-BrBT and phen-*p*-BrBT, respectively. The signal for the amine proton $\delta H(N_1)$ appears as the most deshielded proton signals since the proton was influenced by two electronegative groups (C=O and C=S) in the proximate distances. The signals of $\delta H(N_2)$ were slightly shielded and were observed in the downfield region at 12.26, 12.01 and 11.97 ppm for phen-*o*-BrBT, phen-*m*-BrBT and phen-*p*-BrBT, respectively. The signals for the phenanthroline protons were observed in the downfield region at δ=7.46-9.15 ppm.

Table 5. The $^1$H NMR signals of the *N*-(bromobenzoyl)-*N*'-(1,10-phenanthrolin-5-yl)thiourea derivatives

| **Proton** | **δ, ppm (coupling patterns, *J-coupling*, proton)** | | | |
|---|---|---|---|---|
| | **Phen-BT** | **Phen-*o*-BrBT** | **Phen-*m*-BrBT** | **Phen-*p*-BrBT** |
| HNa | 12.63 (s,H) | 12.36 (s, H) | 12.49 (s,1H) | 12.53 (s,1H) |
| HNb | 11.88 (s,1H) | 12.26 (s,1H) | 12.49 (s,1H) | 12.53 (s,1H) |
| H9, H16 | 12.53 (s,1H) | 9.14 (m, $J_1$=3.9 Hz, $J_2$=1.6 Hz,2H) | 9.13 (t, J= 4.2 Hz,2H) | 9.13 (t, $J_1$= 4.9 Hz,2H) |
| H12 | 8.20 (s,1H) | 8.18 (s,1H) | 8.25 (s,1H) | 8.16 (s,1H) |
| H10, H15 | 8.08 (m, $J_1$= 7.6 Hz, 2H) | 7.83 (m, $J_1$= 19.9 Hz, $J_2$= 4.1 Hz, 2H) | 7.82 (m, $J_1$= 8.4, $J_2$= 4.3 Hz, 2H) | 7.99 (m, $J_1$= 8.1 Hz, 2H) |
| H11, H14 | 8.52 (dd, $J_1$= 18.7 Hz, $J_2$= 8.2 Hz, 2H) | 8.55 (dd, $J_1$= 8.1 Hz, $J_2$= 1.5 Hz, 1H)<br>8.43 (dd, J1= 8.2 Hz, J2= 1.3 Hz, 1H) | 8.54 (d, $J_1$= 8.1 Hz,1H)<br>8.49 (d, $J_1$= 8.4 Hz,1H) | 8.53 (d, J= 8.1 Hz,1H)<br>8.48 (d, J1= 8.4 Hz,1H) |
| Phenyl ring (H2,H3,H4,H5,H6) | 7.87-7.78 (m, 2H)/$\delta_{H2\&H6}$<br>7.70(t, $J_1$= 7.3 Hz, 1H)/$\delta_{H4}$<br>7.59 (t, $J_1$= 7.7 Hz, 2H)/$\delta_{H3\&H5}$ | 7.76 (d, J1=8.1 Hz, 1H)/$\delta_{H2}$<br>7.71 (d, J1= 6.2 Hz, 1H)/$\delta_{H6}$<br>7.58-7.45 (m, 2H)/$\delta_{H4\&H5}$ | 8.16 (s,1H)/$\delta_{H2}$<br>8.16 (s,1H)/$\delta_{H2}$<br>7.54 (t, $J_1$= 7.9Hz, 1H)/$\delta_{H5}$<br>7.88 (d, $J_1$= 8.1 Hz, 1H) $\delta_{H4}$ | 7.85-7.77 (m,4H)/$\delta_{H2,H3,H5\&H6}$ |

s: singlet; d: doublet; t: triplet; m: multiplet

Table 6. The $^{13}$C NMR signals of the *N*-(bromobenzoyl)-*N*'-(1,10-phenanthrolin-5-yl)thiourea derivatives

| **Carbon** | **δ, ppm** | | | |
|---|---|---|---|---|
| | **Phen-BT** | **Phen-*o*-BrBT** | **Phen-*m*-BrBT** | **Phen-*p*-BrBT** |
| C=S | 182.49 | 182.04 | 182.39 | 182.43 |
| C=O | 168.75 | 169.08 | 167.39 | 167.98 |
| C9, C16 | 132.97 | 146.42 | 146.38 | 146.45 |
| | 132.69 | 145.43 | 145.36 | 145.43 |

Table 6 (cont'd). The $^{13}$C NMR signals of the *N*-(bromobenzoyl)-*N*'-(1,10-phenanthrolin-5-yl)thiourea derivatives

| Carbon | δ, ppm | | | |
|---|---|---|---|---|
| | **Phen-BT** | **Phen-*o*-BrBT** | **Phen-*m*-BrBT** | **Phen-*p*-BrBT** |
| C10, C15 | 125.37 | 128.34 | 128.46 | 125.43 |
| | | 128.18 | 128.33 | 126.23 |
| C11 | 137.37 | 133.68 | 136.27 | 132.60 |
| C12 | 126.32 | 129.86 | 125.46 | 127.72 |
| C14 | 128.39 | 133.24 | 132.67 | 131.46 |
| C17, C20 | 150.54 | 150.90 | 150.87 | 150.88 |
| | 150.48 | 150.66 | 150.66 | 150.66 |
| C18, C19 | 129.33 | 132.76 | 126.24 | 128.32 |
| | 128.99 | 132.46 | | |
| C1, C13 | 133.85 | 137.12 | 125.05 | 132.08 |
| | 133.71 | 136.95 | 133.77 | 132.00 |
| C2 | 124.01 | 126.23 | 124.22 | 123.84 |
| C3 | 124.29 | 125.57 | 136.97 | 124.19 |
| C4 | 123.77 | 125.57 | 123.86 | 133.75 |
| C5 | 124.29 | 123.88 | 131.23 | 123.19 |
| C6 | 124.01 | 119.44 | 122.07 | 123.84 |

As for the $^{13}$C NMR spectra, the most downfield signals were attributed to the resonances of C=S and C=O groups. The carbon atoms of the thiocarbonyl group appeared at 182.04, 182.39 and 182.04 ppm for phen-*o*-BrBT, phen-*m*-BrBT and phen-*p*-BrBT, respectively. The results revealed that the C=S signal was shifted downfield compared to that of C=O (167.39-169.08 ppm), which is partly due to the resonance effects of the CO and -NH- groups. These features and chemical shifts of the $^{1}$H and $^{13}$C NMR spectra are in agreement with the crystal structure of phen-BT as depicted in Figure 5.

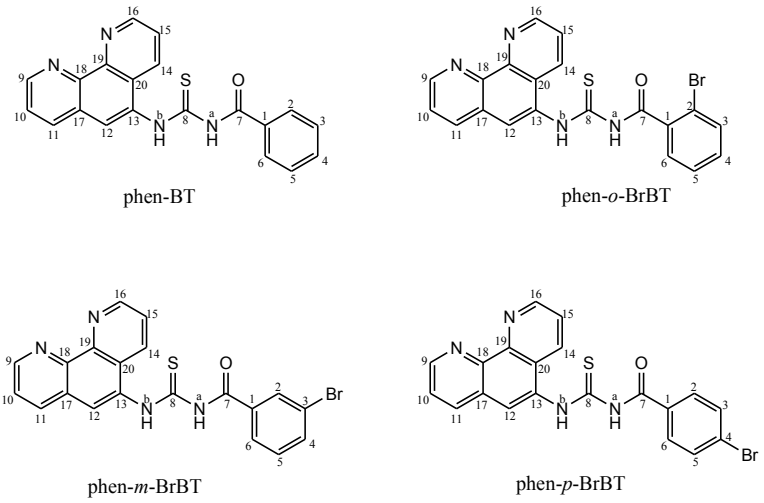



Figure 5. The structure of *N*-(bromobenzoyl)-*N*'-(1,10-phenanthrolin-5-yl)thiourea derivatives with the atomic numbering scheme for NMR structure elucidation

**Cyclic voltammetry**

Cyclic voltammetry is an important technique in electrochemistry analysis because it provides useful information on electron transfer process. The electrochemical cell consist of three electrodes - a platinum disk working electrode (2 mm, diameter), $Ag/Ag^+$ reference electrode (0.01 M $AgNO_3$; 0.1 M tetrabutylammonium perchlorate in $CH_2Cl_2$) and a platinum counter electrode. The potentials (1 mM) were recorded in $CH_2Cl_2$ with 0.1 M $[(n\text{-}C_4H_9)_4N]PF_6$. All compounds exhibit an irreversible oxidation and reduction redox couples. The redox potentials are listed in Table 7.

Table 7. The redox potentials for oxidation and reduction processes of phen-BT, phen-*o*-BrBT, phen-*m*-BrBT and phen-*p*-BrBT

| Compound | Irreversible processes | |
|---|---|---|
| | $E_p^{ox}$ | $E_p^{red}$ |
| Phen-BT | +1.68 | -1.43 |
| Phen-*o*-BrBT | +1.70 | -1.50 |
| Phen-*m*-BrBT | +1.42 | -1.60 |
| Phen-*p*-BrBT | +1.60 | -1.21 |

All derivatives showed irreversible redox potentials at (1.42 – 1.70) V and –(1.21 – 1.60) V for oxidation and reduction processes, respectively. Bromine atom has an overall destabilizing influence on the phenyl ring with the *o*- and *p*-bromo substituents exert higher stabilization to the phenyl ring. Thus, phen-*m*-BrBT was relatively easier to be oxidized compared with the phen-*o*-BrBT and phen-*p*-BrBT derivatives. Likewise, phen-*o*-BrBT and phen-*p*-BrBT derivatives would be much easier to be reduced, i.e. accept electron. However, only phen-*p*-BrBT derivative behaves as expected. Other factors such as solvent interactions might influence the redox behaviours of the molecules.

**Luminescence properties**

The concentration of the compounds is 9 x $10^{-6}$ mol $dm^{-3}$ and the luminescence quantum yields were calculated by using 2-aminopyridine ligand as a standard with $\phi_{std}$= 0.37 in $CH_3CH_2OH$ [19]. Figure 6 shows the emission spectra of the compounds. The excitation wavelength ($\lambda_{ex}$) for each sample was selected according to their absorption wavelength ($\lambda_{max}$) and listed in Table 8. Phen-*m*-BrBT, shows a relatively high fluorescence quantum yield ($\phi_s$ = 5.40 x $10^{-2}$ s) compared with that of *para* and *ortho* substituted analogues.

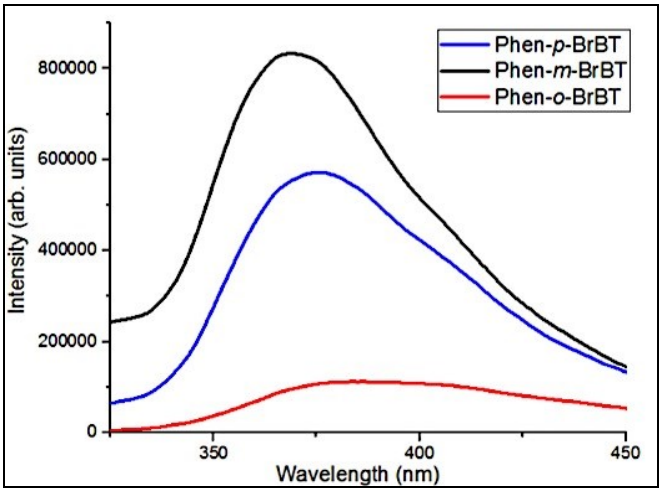



Figure 6. The steady-state fluorescence spectra of Br-substituted Phen-BT compounds measured in $CH_2Cl_2$

Table 8. The emission spectra, $\lambda_{em}$ of phen-BT, phen-*o*-BrBT, phen-*m*-BrBT and phen-*p*-BrBT compounds

| **Ligands** | $\lambda_{ex}$ **(nm)** | $\lambda_{em}$ **(nm)** | **Quantum Yield,** $\varphi_s$ **in** $CH_2Cl_2$ |
|---|---|---|---|
| Phen-BT | 270 | 365 | $7.27 \times 10^{-2}$ |
| Phen-*o*-BrBT | 269 | 379 | $5.61 \times 10^{-3}$ |
| Phen-*m*-BrBT | 269 | 369 | $5.40 \times 10^{-2}$ |
| Phen-*p*-BrBT | 270 | 375 | $2.29 \times 10^{-2}$ |

## Conclusion

The phen-*o*-BrBT, phen-*m*-BrBTand phen-*p*-BrBT compounds were successfully synthesized and characterized by analytical and spectroscopic techniques. The molecular structural properties are in agreement with the previously reported phen-BT crystal structure. The bromo atom at the *orto*, *meta* and *para* positions of the phenyl ring in the benzoyl moiety has weakened the C=O bond by reducing the electron density of the phenyl ring. In addition, the luminescence quantum yield appears to the affected by the Br substituent with the phen-*m*-BrBT derivative showing the highest quantum yield.

## Acknowledgements

This work has been partly supported by the Ministry of Science Technology and Innovation under the Science Fund scheme (06-01-02-SF1001) and Ministry of Higher Education with *MyMaster* support for RS and an exploratory research grant (ERGS/1/2013/TK07/UKM/02/2).

## References

1. Sammes, P. G and Yahioglu, G. (1994). 1,10-phenanthroline: a versatile ligand. *Journal of Chemical Society Reviews,* 23: 327 – 334.
2. Shen. Y. and Sullivan, B. P. (1995). A versatile preparative route to 5-substituted-1,10-phenanthroline ligands via 1,10-phenanthroline 5,6-epoxide. *Inorganic Chemistry*, 34: 6235 – 6236.
3. Ramírez-Silva, M. T., Gómez-Hernández, M., de Lourdes Pacheco-Hernández, M., Rojas-Hernández, A. and Galicia, L. (2004). Spectroscopy study of 5-amino-1, 10-phenanthroline. *Spectrochimica Acta Part A: Molecular and Biomolecular Spectroscopy*, 60(4): 781 – 789.
4. Kodomari, M., Suzuki, M., Tanigawa, K. and Aoyama, T. (2005). A convenient and efficient method for the synthesis of mono- and *N*,*N*-disubstituted thioureas. *Tetrahedron Letters*, 46: 5841 – 5843.
5. Alkherraz, A. M, Lusta, Z. I. and Zubi, A. E. (2014). Synthesis and use of thiourea derivative(1-phenyl-3-benzoyl-2-thiourea) for extraction of cadmium ion. *International Journal of Chemical, Materials Science and Engineering,* 8(2): 15 – 17.
6. Ren, J. S., Diprose, J., Warren, J., Esnouf, R. M., Bird, L. E., Ikemizu, S., Slater, M., Milton, J., Balzarini, J., Stuart, D. L., and Stammers, D. K. (2000). Phenylethylthiazolythiourea (PETT) non-nucleoside inhibitors of HIV-1 and HIV-2 reverse transcriptases. Structural and biochemical analyses. *Journal of Biological Chemistry,* 275(8): 5633 – 5639.
7. Katritzky, A. R., Li, J. and Gordeev, M. F. (1993). New synthetic routes to furans and dihydrofurans from 1-propargylbenzotriazole. *Journal of Organic Chemistry,* 58(11): 3038 – 3041.
8. Koch, K. R. (2001). New chemistry with old ligands: *N*-alkyl- and *N*,*N*-dialkyl-*N*'-acyl(aroyl)thioureas in co-ordination, analytical and process chemistry of the platinum group metals. *Coordination Chemistry Reviews*, 216: 473 – 488.
9. Sun, C. W. and Zhang, X. D. (2007). Synthesis and crystal structure of S-(+)-*N*'-tertbutylaminocarbonyl-*N*-[3-methyl-2-(4-chlorophenyl)butyryl]thiourea. *Chinese Journal of Structural Chemistry,* 26(2): 153 – 156.
10. Saeed. A. Khera, A. Abbas. N. Latif, M. Sajid, I. and Florke, U. (2010). Synthesis, characterization, crystal structures, and antibacterial activity of some new 1-(3,4,5-trimethoxybenzoyl)-3-arylthioureas. *Turkish Journal of Chemistry*, 34(3): 335 – 345.

11. Saeed, S., Rashid, N., Ali, M. and Hussain, R. (2010). Synthesis, characterization and antibacterial activity of nickel(III) and copper(II) complexes of N-(alkyl(aryl)carbamothioyl)-4-nitrobenzamide. *European Journal of Chemistry*, 1(3): 200 – 205.
12. Eweis, M., Elkholy, S. S. and Elsabee, M. Z. (2006). Antifungal efficacy of chitosan and its thiourea derivatives upon the growth of some sugar-beet pathogens. *International Journal of Biological Macromolecules*, 38(1): 1 – 8.
13. Soung, M. G., Park, K. Y., Song, J. H. and Sung, N. D. (2008). Herbicidal activity and molecular similarity of 1-(4-chloro-2-fluoro-5-propargyloxyphenyl)-3-thiourea derivatives. *Journal of the Korean Society for Applied Biological Chemistry*, 51(3): 219 – 222.
14. Das, D. K. and Fres. J. (1984). N-α-(5-bromopyridyl)-*N*'-benzoyl thiourea (BrPBT) as a new chelating agent for the spectrophotometric determination of rhodium(III). *Fresenius Journal of Analytical Chemistry*, 318(8): 612.
15. Shome, S. C. Mazumdar, M., and Haldar, P. K. (1980). *N*-Alpha-pyridyl-*N*'-benzoylthiourea as a chelating agent for the determination of iridium. *Journal of the Indian Chemical Society*, 57(2): 139 – 141.
16. Mat Rashid, F. L., Lee, Y. H., Daran, J. C. and Kassim, M. B. (2011). *N*-Benzoyl-*N*'-(1,10-phenanthrolin-5-yl)thiourea dichloromethane hemisolvate monohydrate. *Acta Crystallographica,* E67: 1397 – 1398.
17. Al-abbasi, A. A., Tan, S. S. and Kassim, M. B. (2010). 1-benzoyl-3-(4-hydroxyphenyl)thiourea. *Acta Crystallographica,* E66: 3181 – 3190.
18. Tan, S. S., Al-abbasi, A. A., Mohamed Tahir, M. I. and Kassim, M. B. (2014). Synthesis, structure and spectroscopic properties of cobalt(III) complexes with 1-benzoyl-(3,3-disubstituted)thiourea. *Polyhedron*, 68: 287 – 294.
19. Shahroosvand, H., Abbasi, P. Notash, B. and Najafi, L. (2013). Separation of functionalized 5,6-disubstituted-1,10-phenanthroline for dye-sensitized solar cell applications. *Journal of Chemistry,* 2013: 1 – 8.
20. Allen, F. H., Kennard, O., Waston, D. G., Barmmer, L., Orpen, A. G. and Taylor, R. (1987). Tables of bond lengths determined by X-ray and neutron diffraction. Part 1. Bond lengths in organic compounds. *Journal of Chemical Society Perkin Transactions,* 2: 1 – 19.

*Malaysian Journal of Analytical Sciences, Vol 21 No 1 (2017): 72 - 81*
*DOI: http://dx.doi.org/10.17576/mjas-2017-2101-09*

MALAYSIAN JOURNAL OF ANALYTICAL SCIENCES
*Published by The Malaysian Analytical Sciences Society*
ISSN 1394 - 2506

# SOLIDIFIED FLOATING ORGANIC DROP MICROEXTRACTION–ELECTROTHERMAL ATOMIC ABSORPTION SPECTROMETRY FOR THE DETERMINATION OF TRACE AMOUNTS OF LEAD IN WATER SAMPLES

## (Pengekstrakan Mikro Pemejalan Titisan Organik Terapung-Spektrometri Serapan Atom Elektrotermal bagi Penentuan Jumlah Surih Plumbum di dalam Sampel Air)

Arnon Thongsaw, Ratana Sananmuang, Gareth M. Ross, Wipharat Chuachuad Chaiyasith*

*Department of Chemistry,*
*Research Center for Academic Excellence in Petroleum, Petrochemical and Advanced Materials,*
*Faculty of Science,*
*Naresuan University, Phitsanulok, Thailand 65000*

**Corresponding author: wipharatc@nu.ac.th*

Received: 14 September 2016; Accepted: 6 December 2016

**Abstract**

Solidified floating organic drop microextraction (SFODME) was utilized as a separation or pre-concentration step prior to electrothermal atomic absorption spectrometric (ETAAS) determination of ultra-trace amounts of lead. The method was based on the formation of an extractable complex between Pb(II) and 1-(2-pyridylazo)-2-naphathol (PAN) as a chelating agent. The main parameters affecting the performance of SFODME, namely, type and volume of organic solvent, pH, concentration of the chelating agent, extraction time, stirring rate, extraction temperature, disperser solvent, ionic strength, and interference effect were investigated and optimized. Under optimized experimental conditions a pre-concentration factor of 22.03 and a detection limit of 0.064 μg $L^{-1}$ for the pre-concentration from 13.0 mL water sample was achieved. The relative standard deviation of the measurements in the range of 1.3 – 2.5% (n = 6). The proposed method was assessed through the analysis of certified reference water and recovery experiment with satisfactory results.

**Keywords:** solidified floating organic drop microextraction, lead, electrothermal atomic absorption spectrometry, water samples

**Abstract**

Pengekstrakan mikro pemejalan titisan organik terapung (SFODME) digunakan sebagai langkah pemisahan atau pemekatan sebelum penentuan jumlah surih plumbum ditentukan menngunakan spektrometri serapan atom elektrotermal (ETAAS). Kaedah ini berasaskan kepada pembentukkan kompleks yang boleh diekstrak di antara Pb(II) dan 1-(2p-piridilazo)-2-naphol (PAN) sebagai agen pengkelat. Parameter utama yang memberi kesan kepada prestasi SFODME iaitu jenis dan isipadu pelarut organik, pH, kepekatan agen pengkelat, masa pengekstrakan, kesan pengacauan, suhu pengesktrakan, pelarut serakan, kekuatan ionik dan kesan gangguan telah dikaji dan dioptimumkan. Keadaan optimum bagi eksperimen diperolehi dengan faktor pemekatan pada 22.03 dan had pengesanan dicapai pada 0.064 μg $L^{-1}$ bagi pemekatan 13.0 mL sampel air. Pengukuran sisihan piawai relatif berada pada julat 1.3 – 2.5% (n = 6). Kaedah yang dicadangkan juga dinilai melalui analisis sampel air rujukan yang disahkan dan ujian perolehan semula yang mencapai keputusan memuaskan.

**Kata kunci:** pengekstrakan mikro pemejalan titisan organik terapung, plumbum, spektrometri serapan atom elektrotermal, sampel air

## Introduction

Nowadays, increasing global environmental pollution is great concern. Heavy metals belong to a class of pollutants that can produce undesirable effects, even if they are present in minuscule amounts. Among the different heavy metals, lead is one of the most common and most toxic pollutants released into the environment from various industrial activities [1]. The accumulation of heavy metals in adults, is associated with heart disease, cancer, and may cause many serious disorders like anemia, kidney diseases, nervous disorder, and even death [2].

The important sources of lead are industrial processes such as smelting of lead, recycling of lead batteries, manufacturing of lead paints, etc. [3], and automobile exhausts. Water quality has become an issue of vital importance as it is an essential resource that is threatened by pollution. Maximum allowable limit of total Pb in drinking water considered safe by the United States Environmental Protection Agency (EPA) and Ministry of public health, Thailand is 10 μg $L^{-1}$ [4]. The tap water intended for human consumption is controlled regularly for an extensive array of potential contaminants by certified authorities.

Modern instrumental methods including spectrometry, namely, inductively coupled plasma mass spectrometry, inductively coupled plasma atomic emission spectrometry, and atomic absorption spectrometry, etc. [5-7] have been used for the determination of traces of metal ions in various media. However, because of the low concentration of Pb and the complexity of the environmental samples, direct analysis using the instruments is often impeded by matrix interferences. Several methods have been proposed for separation and pre-concentration of trace Pb, such as, liquid-liquid extraction (LLE) [8, 9], solid-phase extraction (SPE) [10-12], coprecipitation [13], cloud point extraction (CPE) [14, 15], and ion exchange [16]. Although these are the most commonly used sample pre-treatment methods, they have some drawbacks such as large consumption of reagents, low enrichment factors, multistage operation, and lengthy separation.

The miniaturized pre-concentration method based on LLE including, single drop microextraction (SDME) [17], hollow fiber liquid phase microextraction (HF-LPME) [18], homogeneous liquid-liquid extraction [19], and dispersive liquid-liquid microextraction (DLLME) [20, 21]. Solidified floating organic drop microextraction (SFODME) was introduced as one of these by Khalili Zanjini et al. [22]. In this method, a small volume of an organic solvent with a melting point near room temperature (in the range of 10-30 °C), which is immiscible with water, is delivered to the surface of an aqueous sample containing the analytes. When the equilibrium is reached, the sample vial is placed in an ice bath to solidify the microdrop which is easily removed and allowed to melt for the quantification of analytes [23].

In the present work, trace analysis of lead was developed based on SFODME technique and determination by electrothermal atomic absorption spectrometry (ETASS). 1-(2-pyridylazo)-2-naphthol (PAN), a chelating reagent widely used for many metals and that permits the pre-concentration of trace metals from solution [24], is used to extract Pb into the organic phase. This method was applied for the determination of lead in mineral bottled and tap water samples.

## Materials and Methods

### Instrumentation

The experiments were performed with a Varian Model SpectrAA 220Z atomic absorption spectrometer equipped with Zeeman background correction. A lead hollow cathode lamp was used as the radiation source. The analytical wavelength (283.3 nm), spectral bandwidth (0.5 nm) and lamp current (10.0 mA) were used as recommended by manufacturer. The graphite furnace temperature program was optimized and are showed in Table 1. The pH measurements were carried out with a Metrohm pH meter model 827 pH lab equipped with a combined glass electrode.

### Reagents and solutions

All reagents used in this study were of analytical grade. The stock solution of Pb(II) was obtained from AVS Titrinorm (VWR inter-national, Belgium). Working standard solutions were prepared daily by appropriate dilution from the stock solution with deionized water. The stock solutions of the chelating agent, 1-(2-pyridylazo)-2-

naphthol; PAN, (Acros organics, USA) were prepared by dissolving appropriate amounts in ethanol (ITALMAR, Thailand). The extraction solvent, 1-undecanol, was purchased from Merck, Germany. Buffer solutions of ammonium acetate (pH 4, 0.2 mol $L^{-1}$), phosphate (pH 7.0, 0.2 mol $L^{-1}$), and ammonium chloride (pH 9, 0.2 mol $L^{-1}$) were used to adjust the pH in the range of 2.0-12.0. The laboratory glassware was kept overnight in a 10% $HNO_3$ solution. The glassware was washed with deionized water and dried prior to use.

Table 1. Temperature program of ETAAS for determination of Pb

| Step | Temperature (°C) | Time (s) | Argon flow rate (L/min) |
|---|---|---|---|
| 1 | 95 | 15.0 | 0.3 |
| 2 | 120 | 5.0 | 0.3 |
| 3 | 400 | 14.0 | 0.3 |
| 4 | 2100 | 2.9 | 0 |
| 5 | 2100 | 2.0 | 0.3 |

**Extraction procedure**
An amount of 13 mL aliquot, either 15 μg $L^{-1}$ standard or water sample, was placed in a 15-mL screw cap glass vial with flat bottom containing a magnetic stirrer bar. The pH of the solution was adjusted to 6 using phosphate buffer and 0.5 mL of a solution of PAN chelating agent (3.0 mmol $L^{-1}$) was added. After the solution was mixed thoroughly, 90 μL of 1-undecanol was spiked into the stirring solution and was mixed for 20 min at 625 rpm, after that, the vial was cooled in an ice bath. The solidified drop of 1-undecanol was obtained rapidly. The solidified solvent was transferred into a vial and where it melted immediately. Therefore, the extract was diluted with ethanol (500 μL) and Pb(II) concentration was determined by electrothermal atomic absorption spectrometer.

**Water samples**
In order to validate the method, various water samples, including tap and mineral bottled water (Phitsanulok, Thailand) were selected. A water samples were filtered through a 0.45 μm Whatman filter membrane to remove any suspended material prior to the analysis.

## Results and Discussion

**Optimization of extraction conditions**
In order to obtain high pre-concentration factor (PF) [25] and good extraction recovery (ER), the effect of different parameters that affect extraction conditions such as type and volume of extraction solvent, pH, amount of chelating agent, stirring rate, extraction time and extraction temperature were optimized.

**Effect of type and volume of the extraction solvent**
To obtain optimal results, an appropriate extraction solvent must be chosen. It should have low volatility, density lower than water, low toxicity, and a melting point near room temperature (10 – 30 °C). In this paper, 1-undecanol (m.p. 13–15 °C) and 1-dodecanol (m.p. 22–24 °C), were used for the initial investigation. When the extraction was done, the analytical absorbances were about 0.071 and 0.034, respectively. Therefore, 1-undecanol was selected as the extraction solvent for further experiment in this study.

To evaluate the effect of the extraction solvent volume, different volumes of 1-undecanol were added in the range of 20 – 150 μL. The results of this experiment are shown in Figure 1. It can be seen that relative absorbance increased with increasing 1-undecanol volume in the range of 20 – 90 μL, and then decreased with further volume increases. Therefore, 90 μL was chosen as the optimum volume of the extraction solvent for further experiments. After the extraction procedure, the obtained of PF was 22.03.

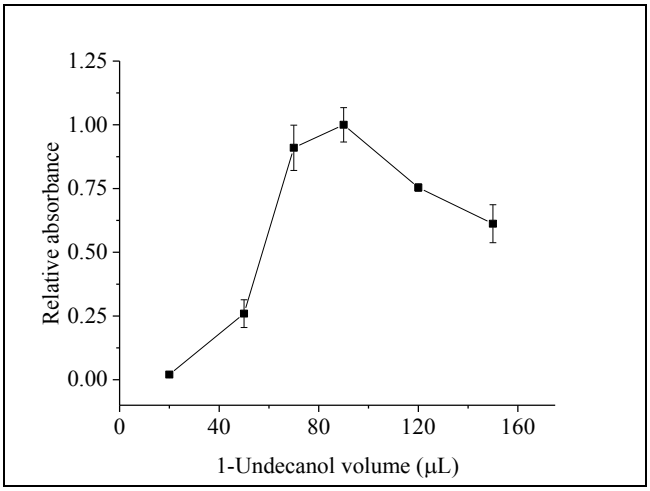



Figure 1. Effect of 1-undecanol volume on the extraction efficiency of lead. Utilized conditions: concentration of Pb(II), 15 μg $L^{-1}$; aqueous volume, 13 mL; pH 6; chelating agent, PAN, 3.0 mmol $L^{-1}$, 0.5 mL; extraction time, 3 min; stirring rate, 625 rpm; room temperature

**Effect of the sample pH**

The pH of the sample has an effect on metal complex formation. Furthermore, pH also has influences toward the extraction efficiency of Pb(II). Therefore, the effect of pH on the procedure was investigated in the range of 3.0-12.0. As shown in Figure 2, an absorbance maximum was observed pH equal to 9.0. Accordingly, a pH 9, obtained with ammonium chloride buffer, was selected for the optimization studies and real sample analysis.

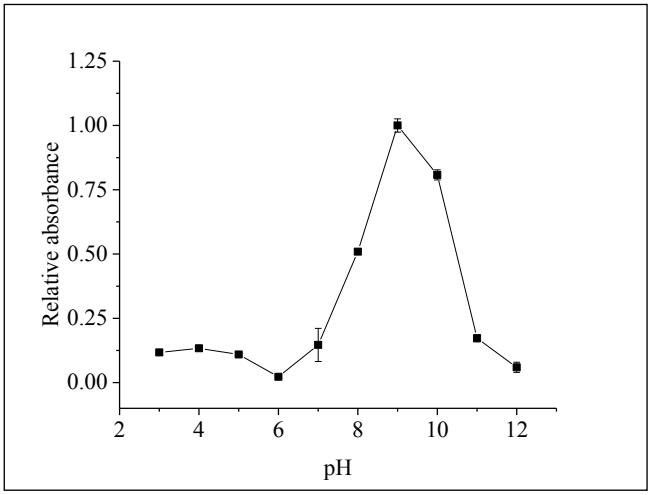



Figure 2. Effect of pH on the extraction efficiency of lead. Conditions are the same as in Figure 1 except pH, and 1-undecanol volume, 90 μL

**Effect of the PAN concentration**

The effect of PAN concentration, as chelating reagent, on the extraction efficiency was studied using various amounts of ligand ranging from 0.1 to 10.0 mmol $L^{-1}$ (equal 0.0038 to 0.38 mmol $L^{-1}$ in final volume of sample, 13

mL). The absorbance was stable when the concentration of ligand was higher than 3.0 mmol $L^{-1}$, indicating the complete complexation. Therefore, 3.0 mmol $L^{-1}$ (equal 0.115 mmol $L^{-1}$ in final solution) was chosen as the optimum concentration for the lead extraction.

**Extraction time**

Another important factor that affects the extraction is the extraction time, because of the mass transfer phenomena governing the extraction efficiency of the analyte in SFODME. The effect of the extraction time was studied by varying it in the range of 10 – 120 min under constant experimental conditions. The results are shown in Figure 3. It was found that with increasing extraction time, up to 40 min, the analytical signal increased, and remained constant at a longer extraction times. Thus, 40-min extraction was chosen as the optimum extraction time.

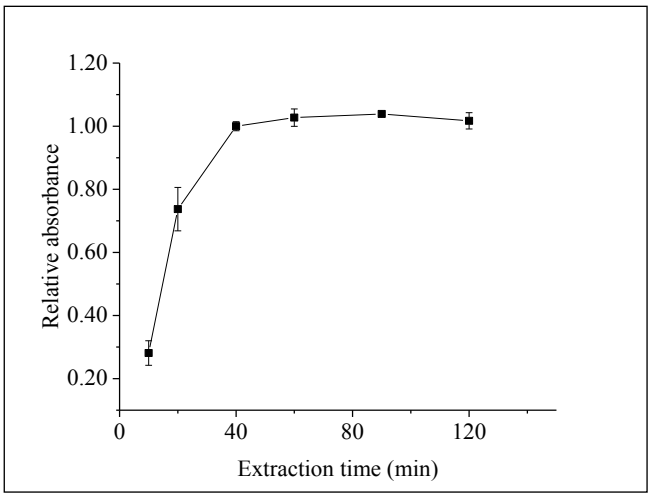



Figure 3. Effect of extraction time on the extraction efficiency of lead. Conditions are the same as in Figure 2 except extraction time. Performed at pH 9

**Stirring rate**

To enhance the extraction efficiency, sample stirring during the extraction procedure was applied. Based on the film theory of convective-diffusive mass transfer, increasing the stirring rate can decreased the thickness of the dilution film in the aqueous phase, so the mass-transfer will be increased. The effect of stirring rate on extraction efficiency was studied in the range of 100 – 1,200 rpm. The experimental results show that the analytical signal increases rapidly with increasing stirring rate from 375 to 750 rpm, and then remains constant upon further increases up to 1200 rpm. Therefore, a stirring rate of 750 rpm was employed for analysis.

**Extraction temperature**

Temperature affects the solubility of the organic solvent in water as well as the emulsification and therefore influences the extraction efficiency. This effect was performed by varying the extraction temperature between 20 °C and 80 °C. The results in Figure 4 showed that the relative absorbance increases with increasing extraction temperature up to 50 °C. At temperatures higher than 50 °C, 1-undecanol was slightly dissolved into the aqueous sample, affecting the analytical signal. Consequently, the extraction temperature at 50 °C was chosen for further study.

**Effect of salts**

The influence of ionic strength on the SFODME method was investigated by adding various amounts of sodium chloride (NaCl) and potassium chloride (KCl) in the range 0 – 5.0% (m/v) to the sample. The obtained results indicate that increasing the salt concentration from 0% to 5.0% does not significantly increase the extraction efficiency. Therefore, salts were not added to the aqueous samples studied in this work.

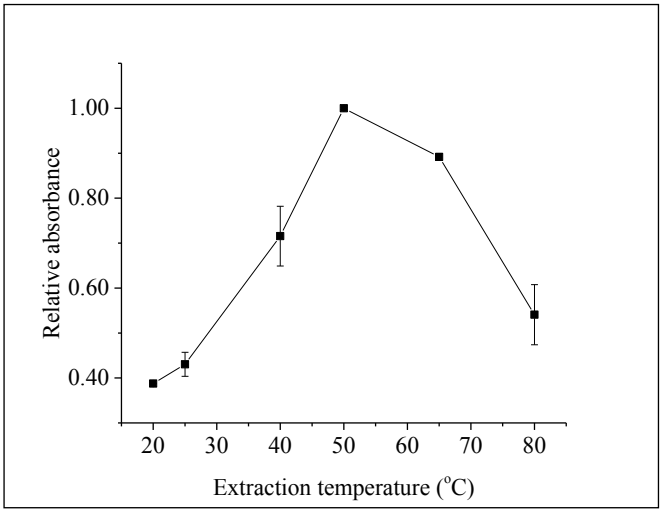



Figure 4. Effect of extraction temperature on the extraction efficiency of lead. Conditions are the same as in Figure 3 except extraction temperature. Performed with extraction time of 40 min

A summary of optimal conditions obtained for the SFODME method for pre-concentration and determination of lead is illustrated in Table 2.

Table 2. Optimal conditions for SFODME of lead ions

| **Optimal Conditions for SFODME of Pb(II)** | |
|---|---|
| Extraction solvent | 1-undecanol |
| Diluent | ethanol |
| pH | 9 |
| PAN concentration (mmol $L^{-1}$) | 3.0 |
| Extraction time (min) | 40 |
| Stirring rate (rpm) | 750 |
| Sample volume (mL) | 13 |
| Extraction phase volume (mL) | 0.090 |
| Extraction temperature (˚C) | 50 |

**Interference study**

The selectivity of the proposed method in the extraction and determination of the analyte was investigated as well. In these experiments, solutions of 10 μg $L^{-1}$ of Pb(II) containing interfering ions were treated using the optimized procedure. The tolerance limit was set as the amount of ion required to cause an error of ±5% in the determination of lead. The maximum tolerance limits of the investigated cations and anions are given in Table 3. The extraction by SFODME method is based on the fact that the target ions can form hydrophobic metal–PAN complex and them can be extracted to the extraction solvent (1-undecanol). Nonetheless, the tolerance limits of $Mg^{2+}$ and $Fe^{3+}$ were not as high as other ions, the concentration of $Mg^{2+}$ and $Fe^{3+}$ were at trace levels in several water samples. Therefore, these results indicate that the developed method can be applied to analysis of Pb in various water samples.

Table 3. Tolerance limits of interfering ions in the determination of 10 μg $L^{-1}$ Pb(II)

| Ions | Interfering Ratio (ion/Pb) | Pb(II) Recovery (% ± SD) |
|---|---|---|
| $Na^+$ | 1000 | 103.0 ± 0.1 |
| $K^+$ | 1000 | 94.9 ± 0.2 |
| $Cd^{2+}$ | 100 | 94.2 ± 0.3 |
| $Cr^{3+}$ | 1000 | 97.9 ± 0.1 |
| $As^{3+}$ | 100 | 92.4 ± 0.1 |
| $NO_3^-$ | 100 | 101.8 ± 0.1 |
| $SO_4^{2-}$ | 100 | 100.5 ± 0.2 |
| $PO_4^{3-}$ | 100 | 102.5 ± 0.1 |

**Analytical performance**

The analytical characteristics such as the linear range, precision, detection limit, and pre-concentration factor were obtained by processing standard solution of Pb. The calibration curve was obtained using the optimized conditions for the SFODME procedure followed by lead concentration determination by ETAAS. Linearity was obtained with lead concentration in the range up to 30.0 μg $L^{-1}$. The regression equation for lead determination is express as below

$$A = 0.0131C + 0.0100 \quad (1)$$

where A is the absorbance and C is the lead concentration in solution (μg $L^{-1}$). The correlation coefficient of the calibration curve equation was higher than 0.99. The pre-concentration factor was calculated as the ratio of the volume of the sample prior pre-concentration divided by the volume after pre-concentration. It was found to have a value of 22.03. The LOD and LOQ defined as $3S_b/m$ and $10S_b/m$ (where $S_b$ is standard deviation of the blank and $m$ is the slope of the calibration graph) were found to be 0.064 and 0.214 μg/L, respectively. The relative standard deviation (%RSD) for 6 replicate determinations at 15 μg $L^{-1}$ of Pb(II) is ±2.5%.

**Sample analysis**

To examine the reliability of this procedure, the method was applied for the determination of lead in mineral bottled and tap water samples. The accuracy of the proposed method was verified by spiking experiments at two concentration levels. As tabulated in Table 4, the recoveries of the added lead were always higher than 91%. To verify the accuracy of the proposed procedure, the method was used for the determination of lead in a sample of NRC-CNRC, National Research Council of Canada (SLRS-4). The results of this test are presented in Table 4, good agreement between the determined and certified values was obtained. Furthermore, these results indicate that the matrices of the mineral bottled and tap water samples had little effect on the SFODME–ETAAS method for the determination of lead. Comparison of pre-concentration techniques used for lead determination with ETAAS was showed in Table 5.

Table 4. Determination of lead(II) in several water samples. (n=2)

| Sample | Certified (μg $L^{-1}$) | Added (μg $L^{-1}$) | Found (μg $L^{-1}$) | Recovery (%) |
|---|---|---|---|---|
| SLRS-4 (River water) | 0.086 ± 0.007 | - | 0.090 ± 0.019 | 105.0 ± 1.9 |
| Drinking water1 | | 0.0 | 0.7 ± 0.2 | - |
| | | 5.0 | 5.6 ± 0.1 | 97.0 ± 0.1 |
| | | 15.0 | 15.3 ± 0.1 | 97.6 ± 2.5 |

Table 4 (cont'd). Determination of lead(II) in several water samples. (n=2)

| Sample | Certified (µg $L^{-1}$) | Added (µg $L^{-1}$) | Found (µg $L^{-1}$) | Recovery (%) |
|---|---|---|---|---|
| Drinking water 2 | | 0.0 | ND* | - |
| | | 5.0 | 4.7 ± 0.1 | 94.8 ± 1.3 |
| | | 15.0 | 15.3 ± 0.2 | 102.1 ± 1.9 |
| Drinking water 3 | | 0.0 | ND* | - |
| | | 5.0 | 5.2 ± 0.3 | 103.7 ± 1.3 |
| | | 15.0 | 12.4 ± 0.2 | 82.7 ± 5.7 |
| Drinking water 4 | | 0.0 | 1.56 ± 0.3 | - |
| | | 5.0 | 6.8 ± 0.2 | 105.9 ± 1.9 |
| | | 15.0 | 16.9 ± 0.3 | 102.2 ± 3.6 |
| Drinking water 5 | | 0.0 | 1.8 ± 0.1 | - |
| | | 5.0 | 6.8 ± 0.1 | 101.0 ± 1.4 |
| | | 15.0 | 15.2 ± 0.2 | 89.4 ± 2.5 |
| Tap water 1 | | 0.0 | ND* | - |
| | | 10.0 | 10.2 ± 0.2 | 101.1 ± 2.3 |
| | | 20.0 | 21.5 ± 0.5 | 107.4 ± 2.4 |
| Tap water 2 | | 0.0 | 1.9 ± 0.1 | - |
| | | 10.0 | 12.0 ± 0.4 | 100.6 ± 1.9 |
| | | 20.0 | 21.6 ± 0.4 | 98.1 ± 4.4 |
| Tap water 3 | | 0.0 | 2.9 ± 0.2 | - |
| | | 10.0 | 12.0 ± 0.4 | 91.5 ± 1.9 |
| | | 20.0 | 21.6 ± 0.4 | 93.6 ± 4.0 |
| Tap water 4 | | 0.0 | 0.3 ± 0.1 | - |
| | | 10.0 | 10.5 ± 0.1 | 102.5 ± 1.2 |
| | | 20.0 | 20.2 ± 0.4 | 99.6 ± 1.8 |
| Tap water 5 | | 0.0 | 1.3 ± 0.3 | - |
| | | 10.0 | 12.0 ± 0.2 | 107.1 ± 0.9 |
| | | 20.0 | 21.0 ± 0.2 | 98.8 ± 1.7 |

*N.D.: Not detected

Table 5. Comparison of pre-concentration techniques used for lead determination with ETAAS

| Analytical Technique | Chelating Reagent | Sample Volume (mL) | Linear Range (µg $L^{-1}$) | LOD (µg $L^{-1}$) | %RSD | PF | Reference |
|---|---|---|---|---|---|---|---|
| Batch-CPE | 5-Br-PADAP | 10.0 | Up to 30.0 | 0.08 | 2.8 | 50 | [26] |
| Batch-DLLME | DDTP | 5.0 | 0.05 – 1.0 | 0.02 | 2.5 | 150 | [27] |
| On-line-SPE | PSTH-cpg | 3.3 | 0.1 – 10.0 | 0.012 | 3.2 | 20.5 | [12] |
| SFODME | PAN | 13.0 | 0.0 – 30.0 | 0.064 | 2.48 | 22.03 | This work |

PF: pre-concentration factor

## Conclusion

It has been shown that solidified floating organic drop microextraction (SFODME) combined with ETAAS, can be used for the separation or pre-concentration of ultra-trace amount of lead in mineral bottled and tap water samples. A comparison of the represented method with the other liquid–liquid microextraction methods using different detection techniques for lead extraction and determination was successfully identified. It can be seen that the working range of SFODME-ETAAS is wider than that of the other reported methods. The main advantages of this methodology are simplicity, low cost, high enrichment factor, rejection of matrix constituents, and minimum use of organic solvents. Additional studies are in progress to evaluate the parameters of the SFODME method for pre-concentration and determination of other metals using various ligands and complexing agents in different matrices.

## Acknowledgements

The authors acknowledge the financial support from Science Achievement Scholarship of Thailand and Research Center for Academic Excellence in Petroleum, Petrochemical and Advanced Materials, Faculty of science, Naresuan University, Thailand. We are grateful to Dr. Filip Kielar for his kind assistance on English editing.

## References

1. Yurtsever, M. and Şengil, İ. A. (2009). Biosorption of Pb(II) ions by modified quebracho tannin resin. *Journal of Hazardous Materials*, 163: 58 – 64.
2. Afridi, H. I., Kazi, T. G., Kazi, G. H., Jamali, M. K. and Shar, G. Q. (2006). Essential trace and toxic element distribution in the scalp hair of Pakistani myocardial infarction patients and controls. *Biological Trace Element Research*, 113: 19 – 34.
3. Jusko, T. A., Henderson Jr, C. R., Lanphear, B. P., Cory-Slechta, D. A., Parsons, P. J. and Canfield, R. L. (2008). Blood lead concentrations < 10μg/dL and child intelligence at 6 years of age. *Environmental Health Perspectives*,116: 243 – 248.
4. Drinking water contaminants: Standards and Regulations, EPA (2016). Access online from http://water.epa.gov/drink/contaminants /index.cfm). Accessed date 06.09.16.
5. Jitaru, P. and Adams, F. C. (2004). Speciation analysis of mercury by solid-phase microextraction and multi-capillary gas chromatography hyphenated to inductively coupled plasma–time-of-flight-mass spectrometry. *Journal of Chromatography A*, 1055: 197 – 207.
6. Oleszczuk, N., Castro, J. T., da Silva, M. M., Maria das Graças, A. K., Welz, B., and Vale, M. G. R. (2007). Method development for the determination of manganese, cobalt and copper in green coffee comparing direct solid sampling electrothermal atomic absorption spectrometry and inductively coupled plasma optical emission spectrometry. *Talanta*, 73: 862 – 869.
7. Mierzwa, J., Sun, Y. C., and Yang, M. H. (1997). Determination of Co and Ni in soils and river sediments by electrothermal atomic absorption spectrometry with slurry sampling. *Analytica Chimica Acta*, 355: 277 – 282.
8. Wang, J. and Hansen, E. H. (2002). FI/SI on-line solvent extraction/back extraction pre-concentration coupled to direct injection nebulization inductively coupled plasma mass spectrometry for determination of copper and lead. *Journal of Analytical Atomic Spectrometry*, 17: 1284 – 1289.
9. Ndung'u, K., Franks, R. P., Bruland, K. W., and Flegal, A. R. (2003). Organic complexation and total dissolved trace metal analysis in estuarine waters: comparison of solvent-extraction graphite furnace atomic absorption spectrometric and chelating resin flow injection inductively coupled plasma-mass spectrometric analysis. *Analytica Chimica Acta*, 481: 127 – 138.
10. Ghaedi, M., Montazerozohori, M. and Soylak, M. (2007). Solid phase extraction method for selective determination of Pb(II) in water samples using 4-(4-methoxybenzylidenimine) thiophenole. *Journal of Hazardous Materials*, 142: 368 – 373.
11. Dadfarnia, S., Talebi, M., Shabani, A. M. H. and Beni, Z. (2007). Determination of lead and cadmium in different samples by flow injection atomic absorption spectrometry incorporating a microcolumn of immobilized ammonium pyrrolidine dithiocarbamate on microcrystalline naphthalene. *Croatian Chemica Acta*, 80: 17 – 23.
12. Alonso, E. V., Cordero, M. S., De Torres, A. G. and Pavón, J. C. (2006). Lead ultra-trace on-line preconcentration and determination using selective solid phase extraction and electrothermal atomic absorption spectrometry: applications in seawaters and biological samples. *Analytical and Bioanalytical Chemistry*, 385: 1178 – 1185.

13. Peker, D. S. K., Turkoglu, O. and Soylak, M. (2007). Dysprosium (III) hydroxide coprecipitation system for the separation and preconcentration of heavy metal contents of table salts and natural waters. *Journal of Hazardous Materials*, 143: 555 – 560.
14. Luconi, M. O., Silva, M. F., Olsina, R. A. and Fernández, L. P. (2000). Cloud point extraction of lead in saliva via use of nonionic PONPE 7.5 without added chelating agents. *Talanta*, 51: 123 – 129.
15. Chen, J., Xiao, S., Wu, X., Fang, K., and Liu, W. (2005). Determination of lead in water samples by graphite furnace atomic absorption spectrometry after cloud point extraction. *Talanta*, 67: 992 – 996.
16. Purohit, R., and Devi, S. (1992). Determination of trace amounts of lead by chelating ion exchange and on-line preconcentration in flow-injection atomic absorption spectrometry. *Analytica Chimica Acta*, 259: 53 – 60.
17. Liang, P., Liu, R. and Cao, J. (2008). Single drop microextraction combined with graphite furnace atomic absorption spectrometry for determination of lead in biological samples. *Microchimica Acta*, 160: 135 – 139.
18. Rasmussen, K. E. and Pedersen-Bjergaard, S. (2004). Developments in hollow fibre-based, liquid-phase microextraction. *TrAC Trends in Analytical Chemistry*, 23: 1 – 10.
19. Farajzadeh, M. A., Bahram, M., Zorita, S., and Mehr, B. G. (2009). Optimization and application of homogeneous liquid–liquid extraction in preconcentration of copper (II) in a ternary solvent system. *Journal of Hazardous Materials*, 161: 1535 - 1543.
20. Kozani, R. R., Assadi, Y., Shemirani, F., Hosseini, M. R. M., and Jamali, M. R. (2007). Part-per-trillion determination of chlorobenzenes in water using dispersive liquid–liquid microextraction combined gas chromatography–electron capture detection. *Talanta*, 72: 387 – 393.
21. Jain, R. and Singh, R. (2016). Applications of dispersive liquid–liquid micro-extraction in forensic toxicology. *TrAC Trends in Analytical Chemistry*, 75: 227 – 237.
22. Zanjani, M. R. K., Yamini, Y., Shariati, S. and Jönsson, J. Å. (2007). A new liquid-phase microextraction method based on solidification of floating organic drop. *Analytica Chimica Acta*, 585: 286 – 293.
23. Dadfarnia, S. and Shabani, A. M. H. (2010). Recent development in liquid phase microextraction for determination of trace level concentration of metals – A review. *Analytica Chimica Acta*, 658: 107 – 119.
24. Zhu, X., Zhu, X. and Wang, B. (2006). Determination of trace cadmium in water samples by graphite furnace atomic absorption spectrometry after cloud point extraction. *Microchimica Acta*, 154: 95 – 100.
25. Moghadam, M. R., Dadfarnia, S. and Shabani, A. M. H. (2011). Speciation and determination of ultra-trace amounts of chromium by solidified floating organic drop microextraction (SFODME) and graphite furnace atomic absorption spectrometry. *Journal of Hazardous Materials*, 186: 169 – 174.
26. Chen, J., Xiao, S., Wu, X., Fang, K. and Liu, W. (2005). Determination of lead in water samples by graphite furnace atomic absorption spectrometry after cloud point extraction. *Talanta*, 67: 992 – 996.
27. Naseri, M. T., Hosseini, M. R. M., Assadi, Y. and Kiani, A. (2008). Rapid determination of lead in water samples by dispersive liquid–liquid microextraction coupled with electrothermal atomic absorption spectrometry. *Talanta*, 75: 56 – 62.

*Malaysian Journal of Analytical Sciences, Vol 21 No 1 (2017): 82 - 94*
*DOI: http://dx.doi.org/10.17576/mjas-2017-2101-10*

MALAYSIAN JOURNAL OF ANALYTICAL SCIENCES
*Published by The Malaysian Analytical Sciences Society*
ISSN 1394 - 2506

# GROWTH EVALUATION OF MICROALGAE ISOLATED FROM PALM OIL MILL EFFLUENT IN SYNTHETIC MEDIA

## (Penilaian Pertumbuhan Mikroalga Yang Telah Dipencil Dari Effluen Kilang Minyak Sawit Dalam Media Sintetik)

Sharifah Najiha Badar[1]*, Zahira Yaakob[1], Sharifah Najiha Timmiati[2]

[1]*Department of Chemical and Process Engineering, Faculty of Engineering and Built Environment*
[2]*Fuel Cell Institute*
*Universiti Kebangsaan Malaysia, 43600 UKM Bangi, Selangor, Malaysia*

**Corresponding author: najihabadar@gmail.com*

Received: 1 June 2016; Accepted: 8 December 2016

**Abstract**

Discharging waste without removing harmful compounds can lead to serious environmental and health issues. Despite of the high content of pollutants, wastewater environment can become an ideal condition for the growth of several microorganisms. Some species of microalgae have been found living in palm oil mill effluent (POME), making it suitable to be used in biological treatment. However, the ability of microalgae to grow and its composition characteristics in synthetic media are unknown. Therefore, this study evaluated the growth characteristics and biochemical productivity of *Chlorella sorokiniana* UKM3, *Coelastrella sp.* UKM4 and *Chlorella sp.* UMACC324, which had been previously isolated from POME. Bold's Basal Media (BBM) was used as the medium for cultivation. The experimental works were performed in a lab-scale photobioreactor at room temperature under continuous illumination for 14 days. From this study, *Coelastrella sp.* UKM4 showed the highest value of growth rates (0.52±0.03 $d^{-1}$), biomass productivity (0.07±0.02 $g.L^{-1}.d^{-1}$), lipid content (66.42±2.87 $mg.L^{-1}$, 7.26%) and lipid productivity (452.42 $mg.L^{-1}.d^{-1}$), whereas the highest chlorophyll content was observed in *Chlorella sorokiniana* UKM3 (26.84±1.76 $mg.L^{-1}$).

**Keywords**: microalgae, growth, biomass, chlorophyll content, lipid content

**Abstrak**

Pembuangan sisa yang tidak dirawat terlebih dahulu boleh menyebabkan isu yang serius terhadap alam sekitar dan kesihatan. Walaupun kandungan bahan pencemar adalah tinggi, air sisa boleh menjadi habitat yang ideal bagi pertumbuhan sesetengah spesis mikroorganisma. Beberapa spesies mikroalga telah dijumpai hidup dalam effluen kilang minyak sawit (POME). Ini menjadikan spesis mikroalga tersebut sesuai digunakan dalam proses rawatan sisa secara biologikal. Walau bagaimanapun, keupayaan mikroalga untuk bertumbuh dan ciri-ciri komposisinya didalam media sintetik adalah tidak diketahui. Oleh itu, kajian ini dijalankan untuk menilai ciri-ciri pertumbuhan dan produktiviti biokimia bagi *Chlorella sorokiniana* UKM3, *Coelastrella sp.* UKM4 dan *Chlorella sp.* UMACC324, yang sebelum ini telah dipencil dari POME. Media Bold's Basal (BBM) telah digunakan sebagai medium pertumbuhan. Kajian ini telah dilakukan dalam fotobioreaktor berskala-makmal pada suhu bilik dan dibawah pencahayaan yang berterusan selama 14 hari. Daripada hasil kajian ini, *Coelastrella sp.* UKM4 telah menunjukkan nilai yang tertinggi dalam kadar pertumbuhan (0.52±0.03 $hari^{-1}$), produktiviti biojisim (0.07±0.02 $g.L^{-1}$ $hari^{-1}$), kandungan lipid (66.42±2.87 $mg.L^{-1}$, 7.26%) dan produktiviti lipid (452.42 $mg.L^{-1}.hari^{-1}$). Kandungan klorofil yang paling tinggi pula dapat dilihat pada *Chlorella sorokiniana* UKM3 (26.84±1.76 $mg.L^{-1}$).

**Kata kunci:** mikroalga, pertumbuhan, biojisim, kandungan klorofil, kandungan lipid

## Introduction

Algae represent diverse groups of photosynthetic organisms with various sizes and shapes. There are two major types of algae, (a) Microalgae: unicellular and microscopic form of algae with the size of 3-10 μm, and (b) macroalgae (giant kelps or seaweeds): multicellular organisms and the most complex form of algae with the size reaching up to 70 m long [1,2]. These primitive chlorophyll-containing organisms are unique and can be found in various habitats on earth where light is available with little moisture, even in unusual and extreme conditions. Interestingly, algae have different ecological roles, where some algae are attached to other aquatic plants or submerged rocks, while others are found floating in the water. All aquatic animals are dependent directly or indirectly on algae since algae act as the base of the food chain, converting several nutrients into organic matter and oxygenating the water. For instance, aquatic life such as fishes depends on the number of algae. There would be no fish if there are no algae in the lake. Furthermore, the growth of algae is heavily influenced by a number of environmental factors, such as the amount of light penetrating the water, nutrients concentrations, temperature, parasitic relationships (bacteria or fungi), and also salinity of the medium growth [3–7].

On top of that, algae are able to manufacture their own food through photosynthesis like any other terrestrial plants. However, algae lack complex tissues and organs, such as stems and roots, which characterise the complex green plants [8]. These simple structures give them the ability to grow rapidly, doubling their growth within a short period of time. Other than that, algae are efficient in capturing solar energy and utilising carbon dioxide ($CO_2$) from their surrounding compared to trees and other green plants [1,9,10]. $CO_2$ plays an important role in microalgae cellular activities. In fact, approximately 50% of carbon is present in microalgae biomass and this carbon is obtained from the utilisation of $CO_2$ [8]. Furthermore, important biochemical, such as polyunsaturated fatty acids, pigments, lipids, proteins, carbohydrates, and vitamins, can be extracted from algae to be used in the production of high-value products such as fertilisers, cosmetics, and drugs [11–15]. Moreover, several different systems are available to grow algae in industrial sectors, namely open ponds, covered ponds, raceways, and engineered systems (photobioreactors) [13,16]. The comparisons of open and closed systems [17,18] are shown in Table 1.

Table 1. Comparisons of open and closed systems

| | **Open Systems** | **Closed Systems** |
|---|---|---|
| Contamination | High risk | Low risk |
| $CO_2$ | High $CO_2$ losses | Lower $CO_2$ losses |
| Evaporation | High evaporation losses | Low evaporation losses |
| Light | Poor light penetration | Excellent light used |
| Scale up | Easy to scale up | Difficult to scale up |
| Process | Difficult to control the process | Easy to control the process |
| Biomass | Low biomass productivity | High biomass productivity |
| Area | Required large area | Low area requirement |
| Harvesting | High cost | Relatively low cost |
| Investment | Low cost | High cost |
| Operation | Low cost | High cost |

As the world energy demand still depends heavily on fossil fuels, the global oil reserves would eventually become exhausted. The escalating price of oil also has caused dilemma among industrial activities, transportation sectors, and residential needs [19]. Furthermore, the search for suitable biomass from available food crops for biofuel production has indeed generated a lot of controversies. The use of agricultural land solely for biofuels production causes limited land available for food production. Thus, food supply becomes limited and eventually sparks hunger issues, food arguments, and sustainability issues. However, the ability of algae to have high productivities, grow

easily in the brackish or marine environment, does not need agricultural land and does not compete with edible oil crops makes it suitable to be the new source of biofuels. The land quality and soil fertility is not an issue in cultivating algae because algae grow in water, not soil [20]. Microalgae lipid in the form of triacylglycerides (TAGs) can be transformed into biofuel products, such as methyl ester, biodiesel, and gasoline substitute. Seaweeds biomass also has been considered as a new source of biofuels in the form of biomethane and bioethanol [21,22].

The release of untreated wastewater into the water bodies and high concentration of greenhouse gases in the atmosphere have caused climate change, threatened the global environment, and sparked health issues. Various methods (physical, chemical and biological) have been applied and compared to treat the wastes produced. Previous studies have asserted that the most effective and environmental friendly method is by using the biological approach. Biological treatments rely on microorganisms, such as bacteria, to break down organic wastes by using cellular processes. Apart from using bacteria, microalgae are one of the options to be used in biological treatment. The use of microalgae for the removal of pollutants and $CO_2$ in the wastewater is known as phycoremediation [23–25].

In Malaysia, the increasing demand for palm oil has directly increased the amount of palm oil wastes, such as empty fruit bunches (EFB), palm oil mill effluent (POME), and fibres. POME is a viscous and acidic brown liquid that releases highly unpleasant odour. It is the most expensive and difficult waste to manage compared to the rest. Typically, POME contains high concentration of total solids, organic and inorganic matters, oil, and also heavy metals. The high amount of organic matter causes high level of chemical oxygen demand (COD) and biochemical oxygen demand (BOD). However, some species of microalgae have been found living in the POME environment despite of the high content of pollutants. These microalgae use the organic matter in POME as nutrient for growth. The ability of microalgae to adapt and assimilate nutrient, as well as grow successfully in POME have made them suitable to be used in wastewater treatment. According to Ding et al. [25], POME-isolated microalgae, namely *Chlamydomonas sp.* UKM6 was able to reduce 29.1% of COD, 73% of total nitrogen content, and 63.5% of total phosphorus content in wastewater. Meanwhile, Tamil Selvam et al. [26] reported that *Characium sp.* isolated from POME was able to reduce 88.6% of total nitrogen content and 98% of phosphorus content in anaerobic POME. Besides functioning as nutrient removal, the biomass produced from microalgae in wastewater treatment can be used to produce multiple useable products [27–30].

Although these microalgae are able to thrive in POME, the adaptation ability of each microalga is varied from one species to another. Different environment or growth conditions can affect the ability of microalgae to grow and produce biomass. Thus, the main focus of this research is to determine the capability of POME-isolated microalgae to grow in synthetic media, as well as to compare their potential in producing biomass and biochemical products.

## Materials and Methods

### Algae strain

Three species of microalgae, namely *Chlorella sorokiniana* UKM3, *Coelastrella sp.* UKM4, and *Chlorella sp.* UMACC324 were obtained from Algae Culture Room, Faculty of Engineering and Built Environment, University Kebangsaan Malaysia (UKM), Bangi, Selangor, Malaysia. All the species were previously isolated from palm oil mill effluent.

### Preparation of media

Bold's Basal Media (BBM) is a freshwater algae medium that has been used to grow a variety of algal cultures. It was prepared by adding and mixing ten different components. BBM stock solutions (per litre) contain 25 g sodium nitrate ($NaNO_3$); 2.5 g calcium chloride dehydrate, ($CaCl_2.2H_2O$); 7.5 g magnesium sulfate heptahydrate ($MgSO_4.7H_2O$); 7.5 g potassium phosphate ($K_2HPO_4$); 17.5 g monopotassium phosphate ($KH_2PO_4$); 2.5 g sodium chloride (NaCl); 11.42 g boric acid ($H_3BO_3$); Alkaline EDTA solution containing 50 g ethylenediaminetetraacetic acid (EDTA); and 31 g potassium hydroxide (KOH); Acidified iron solution containing 4.98 g iron (II) sulfate heptahydrate ($FeSO_4.7H_2O$); and 1 ml concentrated sulfuric acid ($H_2SO_4$); Trace Metal solution containing 8.82 g zinc sulfate heptahydrate ($ZnSO_4.7H_2O$); 1.44 g manganese (II) chloride tetrahydrate ($MnCl_2.4H_2O$); 0.71 g molybdenum trioxide ($MoO_3$); 1.57 g copper (II) sulfate pentahydrate ($CuSO_4.5H_2O$); and 0.49 g cobalt (II) Nitrate Hexahydrate ($Co(NO_3)_2.6H_2O$) [31,32].

**Preparation of inoculums**

The POME-isolated microalgae stock cultures (10% v/v) were grown in Erlenmeyer flask (250 ml) containing 100 ml of synthetic media. Erlenmeyer flask opening was closed with sterile non-absorbance cotton wool. The culture was then incubated at constant room temperature (25±1 $^{o}$C), shaken at 100 rpm using an orbital shaker with 24 hours illuminations. After 10 days, the cultures were ready to be used as inoculums when the OD reading reached 1.0 at a wavelength of 750nm. Sub-culturing the microalgae culture has to be done every month in order to ensure the viability of the culture.

**Experimental procedure**

The experimental vessels were made by converting 1 litre Erlenmeyer flasks into lab-scale photobioreactors. Microalgae cultures were sparged with ambient air that was supplied by the gas compressor. The opening flasks were closed using silicone stopper. The air was introduced into all the flasks through sterilised silicon tube at 0.5 vvm (gas volume flow per unit of liquid volume per minute), constantly. Cool white fluorescent lamps were uniformly aligned behind the photobioreactors. These artificial lights were continuously supplied at an intensity of 54 µmol $m^{-2}$ $s^{-1}$. All sets of experiments were undertaken at room temperature (25±1 $^{o}$C) in batch mode and each experimental condition was conducted in duplicate. The pH of growth medium was not maintained throughout the experiment period. The samples were taken every 24 hours for 14 days. Figure 1 illustrates the experimental set up of the three strains of POME-isolated microalgae.

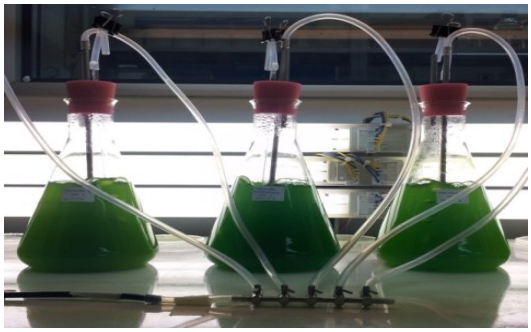


Figure 1. Experimental set-up

**Optical density (OD)**

The optical densities of growing cultures were measured by using portable spectrophotometer (HACH DR 2800, USA) at a wavelength of 750 nm [33,34]. The specific growth rate, $\mu$ ($day^{-1}$) of microalgae was calculated by using Equation (1) below:

$$\mu = \frac{\ln x_2 - \ln x_1}{t_2 - t_1} \quad (1)$$

where, $x_1$ and $x_2$ represent OD readings at 750 nm, while $t_1$ and $t_2$ are the time interval [35,36].

The maximum specific growth rate, $\mu_{max}$ ($day^{-1}$) was determined by using Logistic equation based on the optical density results. The rate of microalgae growth ($dx/dt$) is shown below [37,38].

$$\frac{dX}{dt} = \mu_{max} \left(1 - \frac{X}{X_{max}}\right) X \quad (2)$$

At the beginning of growth where $t = t_o$, the microalgae concentration was given by the initial concentration value ($X = X_o$). After integration, Equation (2) becomes:

$$X = \frac{X_o\, X_{max}\, e^{\mu_{max} t}}{X_{max} - X_o + X_o e^{\mu_{max} t}} \quad (3)$$

where, $X$ is the concentration of microalgae, $X_o$ is the initial concentration of microalgae, $X_{max}$ *is* the maximum value of the microalgae concentration, and $t$ is the time during cultivation. The calculations were carried out using MATLAB R2013a programme.

**Cell dry weight (CDW)**

The microalgae biomass was determined based on cell dry weight method. The microalgae samples were taken and filtered using vacuum filter accompanied with Whatman GF/C filter paper (1.2 µm pore sizes). Then, these filter papers were allowed to be dried in the oven (DHG 9146-A, China) overnight at 105°C until a constant weight was achieved. The cell weight was measured using an analytical balance (XB 220A, Switzerland) and calculated using Equation (4). Besides, the biomass productivity of microalgae was calculated using Equation (5) below [11].

$$\text{Cell dry weight, } (g.L^{-1}) = \frac{X_f - X_o}{V} \quad (4)$$

$$\text{Biomass productivity } (g.L^{-1}.d^{-1}) = \frac{\Delta X}{\Delta t} = \frac{(X_t - X_o)}{(t - t_o)} \quad (5)$$

where, $X_o$ is initial weight of filter paper (g), $X_f$ is filter paper weight after filtration (g), $V$ is the volume of microalga culture (L), while $X_t$ and $X_o$ are dry weights ($g.L^{-1}$) at time $t$ and $t_o$ respectively.

The efficiency of $CO_2$ fixation was calculated in terms of $CO_2$ consumed by microalgae. The $CO_2$ consumption rate was calculated by using Equation (6). It was derived from the typical molecular formula of microalgae biomass, $CO_{0.48}H_{1.83}N_{0.11}P_{0.01}$ [39,40].

$$CO_2 \text{ consumption rate, } P_{CO2} \ (g\ CO_2.L^{-1}d^{-1}) = 1.88 \text{ x biomass productivity} \quad (6)$$

**Chlorophyll content**

The cultures were harvested and centrifuged at 5000 rpm for 10 minutes. The supernatant was discarded. Furthermore, in order to extract the pigments, the collected samples were re-suspended with 90% methanol until the biomass appeared colourless. The cell debris was then removed via centrifugation. The absorbance of the extracted solvent was measured against a blank solvent at the given wavelengths using a portable spectrophotometer (HACH DR 2800, USA). The chlorophyll content was estimated using the following equations [41].

$$\text{Chlorophyll } a\ (mg.L^{-1}) = (16.5 \times A_{665}) - (8.3 \times A_{650}) \quad (7)$$

$$\text{Chlorophyll } b\ (mg.L^{-1}) = (33.8 \times A_{650}) - (12.5 \times A_{665}) \quad (8)$$

$$\text{Chlorophyll } a{+}b\ (mg.L^{-1}) = (4.0 \times A_{665}) + (25.2 \times A_{650}) \quad (9)$$

**Lipid content**

The cultures were collected via centrifugation at 5000 rpm for 10 minutes. The supernatant was discarded. The lipid in microalgae cells was extracted using Folch method [42]. The collected cells after centrifugation were mixed with chloroform-methanol (2:1 v/v) and sonicated. An amount of 0.9% sodium chloride (NaCl) was added to the mixture and left overnight. Next, the lower phase was collected and allowed to evaporate to remove the organic solvent. Moreover, sulfuric acid was added to the samples and incubated in boiling water for 10 minutes. Then, 5 ml of sulfophospho-vanillin [43] was added and the samples were measured at 520nm. The lipid standard curve was established by using cholesterol. The values of lipid content (%) and productivity were calculated using the equations below [11].

$$\text{Lipid content } (\%) = \frac{W_2}{W_1} \times 100\% \quad (10)$$

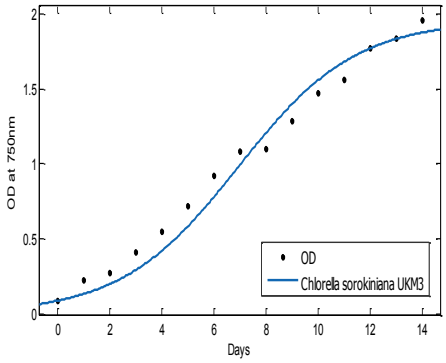
$$\text{Lipid productivity, } Y\ (mg.L^{-1}day^{-1}) = \frac{L \times \Delta W_1}{\Delta t} \quad (11)$$

where, $W_1$ is total biomass produced in day (mg.L$^{-1}$), $W_2$ is total lipid content (mg.L$^{-1}$), $L$ is lipid content (%), $\Delta t$ is duration of cultivation (day) and $\Delta W_1$ is variation of biomass concentration (mg.L$^{-1}$).

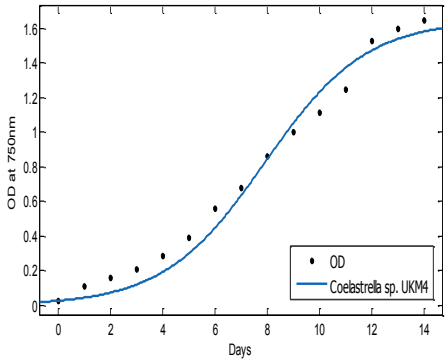
## Results and Discussion

### Microalgae growth evaluation

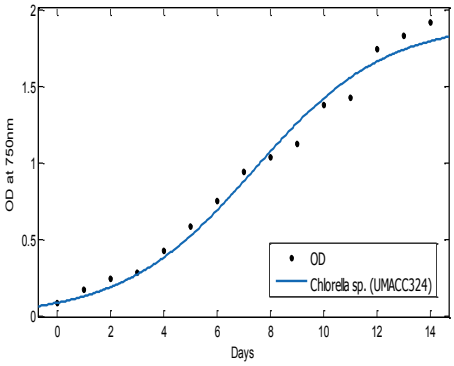
Synthetic media are artificial and simplified media that are designed to provide nutrients for growth of freshwater algae, as well as for maintaining algal strains. In microbial cell suspensions, cell turbidity can be determined easily by using the optical density method [44]. However, inaccuracies can occur due to the existence of pigments (chlorophyll *a* and *b*) content. Thus, the suitable wavelength that minimises the pigment absorbance should be carefully selected. For algal suspensions, the error can be minimised by measuring the cell density at a wavelength beyond the range of chlorophyll contents, such as at 750 nm. In this experiment, all three isolated microalgae were cultured in batch mode for 14 days without any optimisation factor that might affect the growth and biochemical composition. The results indicated that each species showed similar trends and adhered to the standard growth curve for microalgae. The algal growth curves based on OD 750nm are shown in Figure 2. All the microalgae underwent lag, exponential, and stationary phases when growing in synthetic media. Based on the graph, the lag phase of all the species was consistent from day 0 to day 4, followed by exponential phase (day 4 to day 10), and stationary phase (day 10 to day 14). However, the decline (death) phase was not achieved by day 14. The initial pH of BBM medium was around 6.9 to 7.1 and this value was observed to increase (up to pH 8.0) as the culture grew. The rise of pH levels is a good indicator as it shows that the microalgae are indeed growing in the culture medium. According to Borowitzka [45] and Goldman et al. [46], the pH value usually increases due to the photosynthetic activity of microalgae.




(a) *Chlorella sorokiniana* UKM3




(b) *Coelastrella sp.* UKM4




(c) *Chlorella sp.* UMACC324

Figure 2. Growth curves of POME-isolated microalgae at $OD_{750nm}$

According to Dailey and Reish [47], some algae species grow by increasing their cell number (cell division), rather than in size. The rate of cell division was varied according to the species and their living conditions. The increasing of algal biomass over a period of time is known as the new production or growth rate. Specific growth rate refers to the cell regeneration, which is the way of how fast the cells are dividing in a culture. Most of microalgae growth process can be explained by using the Logistic model. It is a common model of population growth with sigmoid profiles independent of substrate concentration [37]. The growth rates of each microalga species were calculated based on Equations (1) and (3). The results for growth rates are shown in Table 2.

Table 2. Growth rates of POME-isolated microalgae in synthetic media

| **Microalgae sp.** | **Specific Growth Rate, μ ($d^{-1}$)** | **Maximum Specific Growth Rate, $\mu_{max}$ ($d^{-1}$)** | **Logistic Equation** |
|---|---|---|---|
| *Chlorella sorokiniana* UKM3 | 0.20 ± 0.05 | 0.44 ± 0.02 | $X = \frac{0.17\, e^{0.44t}}{1.87 + 0.09e^{0.44t}}$ |
| *Coelastrella sp.* UKM4 | 0.22 ± 0.03 | 0.52 ± 0.03 | $X = \frac{0.05\, e^{0.52t}}{1.62 + 0.03e^{0.52t}}$ |
| *Chlorella sp.* UMACC324 | 0.19 ± 0.04 | 0.41 ± 0.01 | $X = \frac{0.18\, e^{0.41t}}{1.83 + 0.09e^{0.41t}}$ |

The growth rate of microalgae can be altered by optimising and modifying the growth conditions. Besides that, the increase of inoculum density also can affect the algal growth. A study conducted by Griffith and Harrison et al. [48] stated that the growth rate, μ, decreased when the concentrations of inoculum increased. Thus, in this study, only one inoculum density at OD reading of 1.0 was used in all runs. Based on the results shown in Table 2, *Coelastrella sp.* UKM4 achieved the highest growth rate, followed by *Chlorella sorokiniana* UKM3 and *Chlorella sp.* UMACC324. In addition, Tamil Selvam [49] discovered that the specific growth rate for *Chlorella sorokiniana* in BBM medium was 0.18±0.01 $d^{-1}$. This value is slightly lower than the result obtained in this study, whereby μ attained by *Chlorella sorokiniana* UKM3 was 0.20±0.05 $d^{-1}$. Meanwhile, according to Vello et al. [50], the specific growth rates for *Chlorella sp.* UMACC322 and UMACC325 were 0.49±0.02 $d^{-1}$ and 0.51±0.1 $d^{-1}$, respectively. The values are higher compared to the growth rate displayed by the *Chlorella* strain in this study. The variation of algal growth rates usually related to the growth conditions and algal requirements [5–7].

Moreover, primary productivity was obtained by measuring the increase in biomass over a period of time. Productivity or called yield in mass algal culture differs from standing crop biomass. A standing crop can be described as the total dried biomass of the living organisms present in a given environment. The total biomass of standing crop may be high, but the productivity would be low. Occasionally, low biomass content shows high productivity and specific growth rates, or possibly the other way around. Maximum yield or productivity is usually obtained at intermediate densities and growth rates, while maximum growth rates usually occur at lower density. High densities cause slower growth rates due to several limiting factors, which alter the biochemical aspect within the cells. Besides, algal biomass would continue to increase until a factor limits its generation [51]. The shadowing effect also can cause a decrease in specific growth rates but higher biomass concentrations can be achieved. Furthermore, in a condition where light or nutrients are limited, low biomass concentration and high specific growth rates are expected to occur in the cultivation systems [52–54].

In this experiment, *Coelastrella* strain attained higher biomass productivity (0.07±0.02 $g.L^{-1}.d^{-1}$) in comparison to *Chlorella sorokiniana* and *Chlorella sp*. The productivity results are comparable with the microalgae growth rate. The higher productivity and growth rate achieved by *Coelastrella sp.* UKM4 showed that this microalga has the potential to be cultivated in a large-scale production to generate biomass for fertilisers, animal feed, and other

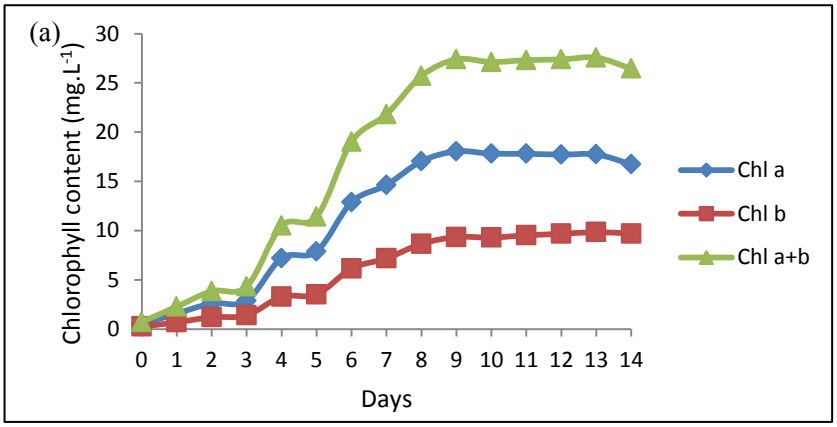
products. However, Minhat et al. [55] reported that the biomass concentration of *Chlorella sorokiniana* UKM3 in BBM was 2.52 $g.L^{-1}$, which is higher than the result obtained in this study. The results of biomass concentration, productivity, and $CO_2$ consumption rates are presented in Table 3. The consumption of $CO_2$ is related directly to the biomass production. As the biomass increases, the consumption rate also increases. Therefore, *Coelastrella sp*. has the potential to be used in carbon sequestration process compared to other strains.

Table 3. Biomass concentration, productivity, and $CO_2$ consumption rates of POME-isolated microalgae

| **Microalgae sp.** | **Biomass Concentration ($g.L^{-1}$)** | **Biomass Productivity ($g.L^{-1}.d^{-1}$)** | **$CO_2$ Consumption Rate ($g\ CO_2.L^{-1}d^{-1}$)** |
|---|---|---|---|
| *Chlorella sorokiniana* UKM3 | 0.86 | 0.06 ± 0.02 | 0.11 ± 0.03 |
| *Coelastrella sp.* UKM4 | 0.95 | 0.07 ± 0.02 | 0.13 ± 0.04 |
| *Chlorella sp.* UMACC324 | 0.78 | 0.05 ± 0.01 | 0.09 ± 0.01 |

**Biochemical content evaluation**

Pigmentation and storage product are important criteria in the classification of algae. Different groups of algae exhibit various colours due to the differences found in pigmentation. All the microalgae species used in this study are members of the division *Chlorophyta* or green algae. The pigments of green algae are chlorophyll *a* and *b*, whereas their accessory pigments are carotenoids and xanthophylls. Chlorophyll (green pigment) is an extremely important biomolecule for photosynthesis and growth. Furthermore, microalgae with high pigment content have the potential to be used as sources of dyes [6,7]. In this experiment, microalgae were treated using methanol to extract the chlorophyll content. Figure 3 illustrates the amount of chlorophyll content in each species. Based on the graphs, *Chlorella sorokiniana* UKM3 showed the highest chlorophyll content (Chl *a*+*b*) which is 26.84±1.76 $mg.L^{-1}$ at day 13. This value is higher compared to the result obtained by Tamil Selvam [49], which is 12.24±0.48 $mg.L^{-1}$. As for *Coelastrella sp*. UKM4, the chlorophyll content was the highest (26.47±6.14 $mg.L^{-1}$) at day 10, while *Chlorella sp.* UMACC324 was at day 13 (26.21±0.49 $mg.L^{-1}$). The chlorophyll content for all the species began to increase drastically from day 3 until day 8 before reaching stationary state. After day 11, the chlorophyll content in *Coelastrella sp.* showed a reduction (19.63 $mg.L^{-1}$). The reduction of chlorophyll content is directly related to the reduction of photosynthesis activity [56]. Besides, both *Chlorella* strains showed better performance in terms of chlorophyll availability compared to *Coelastrella sp.* at the end of cultivation. Although the microalgae used in this study are from the same division, the chlorophyll content presented in each species differed slightly. However, the amounts have been comparable with each other.



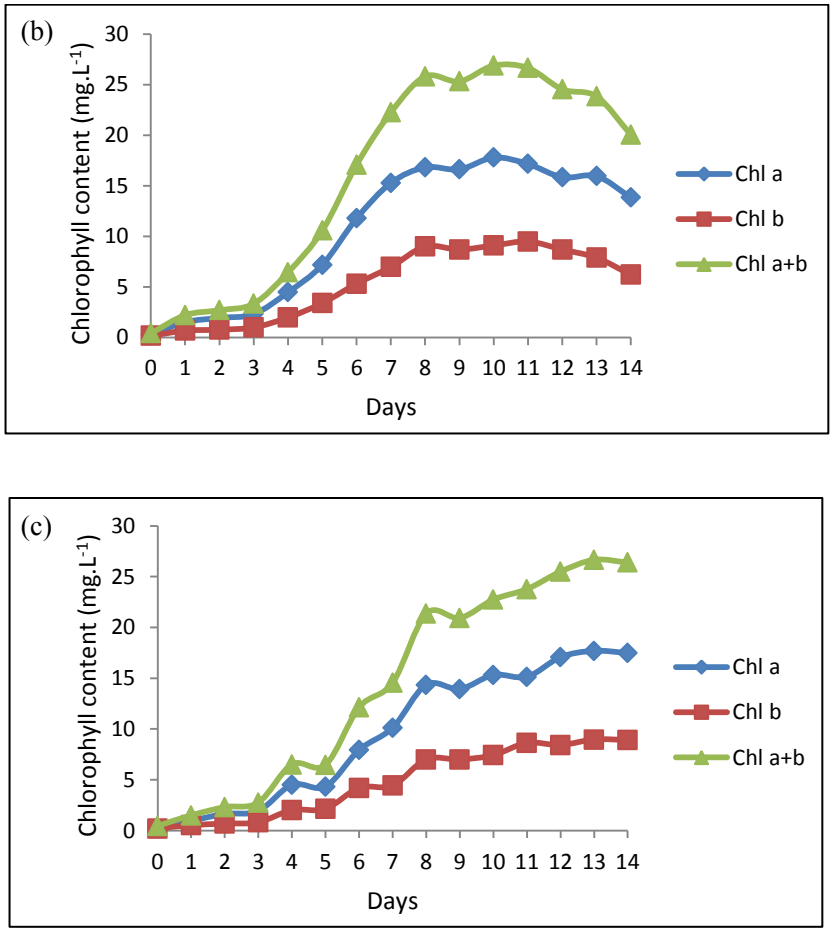



Figure 3. Chlorophyll content in POME-isolated microalgae (a) *Chlorella sorokiniana* UKM3, (b) *Coelastrella sp.* UKM4 and (c) *Chlorella sp.* UMACC324

Algae store their lipids in various ways; depending on the species, growth conditions and also the growth stage when microalgae are harvested. When algal cells are actively growing, the major lipids found within the cells are in the form of glycolipids and phospholipids. The overall lipid profile changes when algae enter a less active growth phase or encounter environmental stress. Algae will slow down their rate of proliferation and start to store Triacylglycerides (TAGs) as the dominant lipid in cell vacuoles [19, 57-59]. In this experiment, microalgae lipids were extracted by employing the Folch method and then estimated using the sulfophospho-vanillin (SPV) method. Furthermore, the lipid content was calculated by using the cholesterol standard curve. Figure 4 shows the lipid content ($mg.L^{-1}$) for each microalga, while Table 4 presents the percentages of lipid content and lipid productivity.

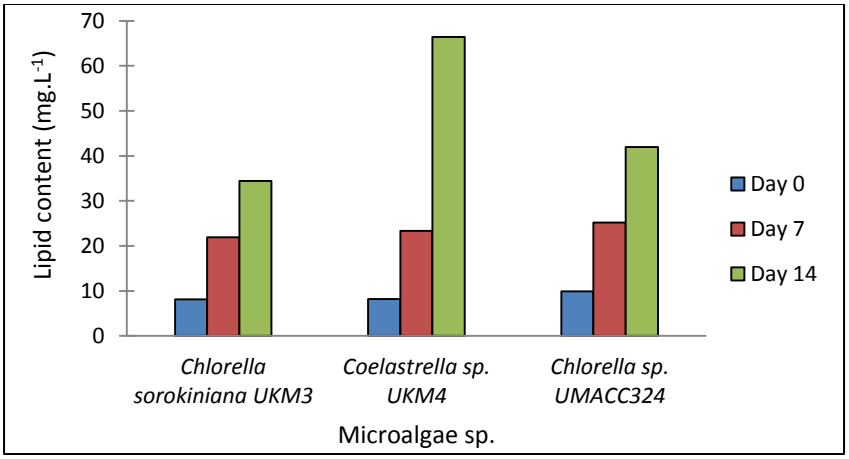



Figure 4. Lipid content ($mg.L^{-1}$) of POME-isolated microalgae

Table 4. Lipid content (%) and lipid productivity of microalgae in synthetic media

| **Microalgae sp.** | **Lipid Content (%)** | **Lipid Productivity ($mg.L^{-1}.d^{-1}$)** |
|---|---|---|
| *Chlorella sorokiniana* UKM3 | 4.65 | 221.03 |
| *Coelastrella sp.* UKM4 | 7.26 | 452.42 |
| *Chlorella sp.* UMACC324 | 6.68 | 269.74 |

Figure 4 depicts that the lipid content of microalgae increased as the culture grew from day 0 (lag phase) to day 14 (stationary phase). At the end of this experiment (day 14), the highest lipid content was recorded in *Coelastrella sp.* UKM4 (66.42±2.87 $mg.L^{-1}$), followed by *Chlorella sp.* UMACC324 (41.94±1.73 $mg.L^{-1}$) and *Chlorella sorokiniana* UKM3 (34.43±1.38 $mg.L^{-1}$). Although *Chlorella sorokiniana* UKM3 produced high biomass concentration compared to *Chlorella sp.* UMACC324, the values of lipid content and productivity had been the lowest. However, Tamil Selvam [49] reported that *Chlorella sorokiniana* attained 72.14±2.01 $mg.L^{-1}$ of lipid content, which is higher than the result obtained in this study. According to Sarmidi [60], the variation of lipid content in microalgae cultured in batch mode is directly related to the culture age, as well as nutrient depletion.

## Conclusion

This study examined the growth rates and biochemical compositions of POME-isolated microalgae when cultured in synthetic media. *Coelastrella sp.* UKM4 showed better performance in terms of growth rates, biomass concentration and lipid content. However, *Chlorella sorokiniana* UKM3 exhibited the highest chlorophyll content compared to other species. The studies pertaining to the microalgae growth are definitely useful and offer important data for cell growth optimisation process, besides understanding their adaptability in different growth conditions. The biochemical products generated by microalgae are also economically useful in various industries for a wide range of purposes. Microalgae species with high growth rate and biochemical content have the potential to be used in the production of biofuels, dyes, and other high valuable products. Therefore, future work is required to fully characterise the microalgae compositions in order to predict its potential for the future development of algae-based industries.

## Acknowledgement

The authors would like to thank and acknowledge Grant KK-2014-014 from Universiti Kebangsaan Malaysia (UKM) in providing the financial support for this project.

**References**

1. Hillison, C. I. (1977). Seaweeds, A color-coded, illustrated guide to common marine plants of east coast of the United States. Keystone Books. The Pennsylvania State University Press: pp. 1 – 5.
2. Garson, J. (1989). Marine natural products. *Natural Product Reports*, 6: 143 – 170.
3. Hoffmann, L. (1989). Algae of terrestrial habitats. *The Botanical Review,* 55: 77 – 105.
4. Satpati G. G., Barman, N., Chakraborty, T. and Pal, R. (2011). Unusual habitat of algae. *Journal of Algal Biomass Utilization*, 2(4): 50 – 52.
5. Black, J. G. (2008). Microbiology. Seventh ed. International Student Version. John Wiley & Sons (Asia) Pte. Ltd.
6. Campbell, N. A. and Reece, J. B. (2005). Biology. Seventh Ed. Pearson Education. San Francisco: Inc. Benjamin Cummings.
7. Talaro, K. P. (2009). Foundations in microbiology. Basic Principle, Sixth Ed. New York: McGraw-Hill: pp. 809.
8. Barsanti, L. and Gualtieri, P. (2006). Algae biotechnology. In: Algae: Anatomy, biochemistry, and biotechnology CRC Press Taylor and Francis Group, Boca Raton: pp. 324 – 359.
9. Cheng, J., Huang, Y., Feng, J., Sun, J., Zhou, J. and Cen, K. (2013). Improving $CO_2$ fixation efficiency by optimizing *Chlorella* PY-ZUI culture conditions in sequential bioreactors. *Bioresource Technol*ogy, 144: 321 – 327.
10. Anjos, M., Fernandes, B. D., Vicente, A. A., Teixeira, J. A. and Dragone, G. (2013). Optimization of $CO_2$ biomitigation by *Chlorella vulgaris*. *Bioresource Technology,* 139: 149 – 154.
11. Hakalin, N. L. S., Paz, A. P., Aranda, D. A. G. and Moraes, L. M. P. (2014). Enhancement of cell growth and lipid content of a freshwater microalgae *Scenedesmus sp.* by optimizing nitrogen, phosphorus and vitamin concentrations for biodiesel production. *Natural Sci*ences, 6: 1044 – 1054.
12. Pulz, O. and Gross, W. (2004). Valuable products from biotechnology of microalgae. *Applied Microbiology and Biotechnology,* 65(6): 635 – 648.
13. Chisti, Y. (2007). Biodiesel from microalgae. *Biotechnology Advances,* 25(3): 294 – 306.
14. Spolaore, P., Joannis-Cassan, C., Duran, E. and Isambert, A. (2006). Commercial applications of microalgae. *Journal of Bioscience and Bioengineering*, 101: 87 – 96.
15. Iriani, D., Suriyaphan, O. and Chaiyanate, N. (2011). Effect of iron concentration on growth, protein content and total phenolic content of *Chlorella sp.* cultured in basal medium. *Sains Malaysiana*, 40(4): 353 – 358.
16. Grima, E. M., Fernandez, F. G. A., Camacho, F. G. and Chisti, Y. (1999). Photobioreactors: Light regime, mass transfer and scaleup. *Journal of Biotechnol*ogy, 70: 231 – 247.
17. Pulz, O. (2001). Photobioreactors: Production systems for phototrophic microorganisms. *Applied Microbiology and Biotechnology*, 57: 287 – 293.
18. Grobbelaar, J. U. (2000). Physiological and technological considerations for optimising mass algal cultures. *Journal of Applied Physiology*, 12: 201 – 206.
19. Oncel, S. S. (2013). Microalgae for macroenergy world. *Renewable and Sustainable Energy Reviews*, 26: 241 – 264.
20. FAO, Food & Agriculture Organization of United Nation. (2009). Algae based biofuels: A review of challenges and opportunities for developing countries: pp. 1 – 60.
21. Hughes, A. D., Kelly, M. S., Black, K. D. and Stanley, M. S. (2012). Biogas from macroalgae: Is it time to revisit the idea? *Biotechnology for Biofuels,* 5: 1 – 7.
22. Stanley, M. S. and Day, J. G. (2014). Algal bioenergy. In: John Wiley & Sons, Ltd: Chichester: pp. 1 – 10.
23. Sydney, E. B., Strum, W., de Carvalho, J. C., Thomaz-Soccol, V., Larroche, C., Pandey, A. and Soccol, C. R. (2010). Potential carbon dioxide fixation by industrially important microalgae. Bioresource Technology, 101: 5892 – 5896.
24. Bilanovic, D., Andargatchew, A., Kroeger, T. and Shelef, G. (2009). Freshwater and marine microalgae sequestering of $CO_2$ at different C and N concentrations - response surface methodology analysis. *Energy Conversion and Management,* 50: 262 – 267.
25. Ding, G. T., Yaakob, Z., Takriff, M. S., Salihon, J. and Abd Rahaman, M. S. (2016). Biomass production and nutrient removal by a newly-isolated microalgal strain *Chlamydomonas sp.* in palm oil mill effluent (POME). *International Journal of Hydrogen Energy*, 41: 4888 – 4895.

26. Tamil Selvam, T. B., Renganathan, R. and Takriff, M.S. (2015). Nutrient removal of POME using POME isolated microalgae strain, *Characium sp. Advanced Materials Research*, 1113: 364 – 369.
27. Basiron, Y. (2007). Palm oil production through sustainable plantations. *European Journal of Lipid Science and Technology*, 109: 289 – 295.
28. Bhatia, S., Othman, Z. and Ahmad, A. L. (2007). Pretreatment of palm oil mill effluent (POME) using *Moringa oleifera* seeds as natural coagulant. *Journal of Hazardous Materials*, 145 (1-2): 120 – 126.
29. Putri, E. V., Md. Din, M. F., Ahmed, Z., Jamaluddin, H. and Chelliapan, S. (2011). Investigation of microalgae for high lipid content using palm oil mill effluent (POME) as carbon source. *International Conference on Environment and Industrial Innovation*, 12: 85 – 89.
30. Zainal, A., Yaakob, Z., Takriff, M. S., Rajkumar, R. and Abdul Ghani, J. (2012). Phycoremediation in anaerobically digested palm oil mill effluent using cyanobacterium, *Spirulina platensis*. *Journal of Biobased Materials and Bioenergy,* 6: 1– 6.
31. Bold, H. C. (1949). The morphology of *Chlamydomonas chlamydogama sp. nov. Bulletin of the Torrey Botanical Club*, 76: 101 – 108.
32. Bischoff, H. W. and Bold, H. C. (1963). Phycological studies IV. Some soil algae from enchanted rock and related algal species. University of Texas, Austin, 6318: pp. 1 – 95.
33. Griffiths, M. J., Garcin, C., Van Hille, R. P. and Harrison, S. T. (2011). Interference by pigment in the estimation of microalgal biomass concentration by optical density. *Journal of Microbiological Methods*, 85(2): 119 – 123.
34. Lizzul, A. M., Hellier, P., Purton, S., Baganz, F., Lamommatos, N. and Campos, L. (2014). Combined remediation and lipid production using *Chlorella Sorokiniana* grown on wastewater and exhaust gases. *Bioresource Technol*ogy, 151: 12 – 18.
35. Pirt, S. J. (1975). Principles of microbe and cell cultivation. Blackwell Scientific Publications, Oxford: pp. 274.
36. Lee, J. B. and Kim, B. Y. (2002). Growth characteristics of five microalgal species isolated from Jeju Island and four Microalgal stock strains in hatchery. *Algae*, 17(2): 117 – 125.
37. Rao, C. S., Sathish, T., Brahamaiah, P., Kumar, T. P. and Prakasham, R. S. (2009). Development of a Mathematical Model for *Bacillus Circulans* Growth and Alkaline Protease Production Kinetics. *Journal of Chemical Technology and Biotechnol*ogy, 84: 302 – 307.
38. Yang, J. S., Rasa, E., Tantayotai, P., Scow, K. M., Yuan, H. L. and Hristova, K. R. (2011). Mathematical model of *Chlorella minutissima* UTEX2341 growth and lipid production under photoheterotrophic fermentation conditions. *Bioresource Technol*ogy, 102(3): 3077 – 3082.
39. Ho, S., Chen, W. and Chang, J. (2010). *Scenedesmus obliquus* CNW-Nas a potential candidate for $CO_2$ mitigation and biodiesel production. *Bioresource Technology,* 101: 8725 – 8730.
40. Chisti, Y. (2008). Biodiesel from microalgae beats bioethanol. *Trends Biotechnology,* 26(3): 126 – 131.
41. Richmond, A. (2004). Handbook of Microalgae Culture, Biotechnology and Applied Phycology, Blackwell Science Ltd.
42. Folch, J., Lees, M. and Stanley, G. H. S. (1957). A simple method for the isolation and purification of total lipids from animal tissues. *Journal of Biological Chemistry*, 226: 497 – 509.
43. Frings, C. S. and Dunn, R. T. (1970). A colorimetric method for determination of total serum lipid based on the sulfophospho-vanillin reaction. *American Journal of Clinical Pathology*, 53: 89 – 91
44. Rocha, J. M., Garcia, J. E. and Henriques, M. H. (2003). Growth aspects of the marine microalgae *Nannochloropsis gaditana*. *Biomolecular Engineering*, 20:237 – 242.
45. Borowitzka, M. A. (1998). Limits to growth in wastewater treatment with algae. Wong Y. S. and Tam N. F. Y., Editors. Springer Verlag: pp. 203 – 226.
46. Goldman, J. C., Azov, Y., Riley, C. B. and Dennett, M. R. (1982). The effect of pH in intensive cultures. i. biomass regulation. *Journal of Experimental Marine Biology and Ecology*, 57: 1 – 13.
47. Dailey, M. D. and Reish, D. J. (1993). Ecology of the Southern California bight: A synthesis and interpretation. University of California Press. *Science*: pp. 926.
48. Griffith, M. J. and Harrison, S. T. L. (2009). Lipid productivity as a key characteristic of choosing algal species for biodiesel production. *Journal of Applied Phycology*, 21: 493 – 507.
49. Tamil Selvam, T. B. (2015). penyingkiran nutrien dari POME dengan menggunakan mikroalga dan sianobakteria yang dipencil dari POME serta potensi biojisim yang diperolehi. Tesis Sarjana, Fakulti Kejuruteraan dan Alam Bina. Universiti Kebangsaan Malaysia.

50. Vello, V., Phang, S. M., Chu, W. L., Majid, N. A., Lim, P. E. and Loh, S. K. (2013). Lipid productivity and fatty acid composition-selection of *Chlorella* strains isolated from Malaysia for biodiesel production. *Journal of Applied Phycology*: 26(3), 1399 – 1413.
51. Lembi, C. A. and Waaland, J. R. (1988). Algae and Human Affairs. Cambridge University Press: pp. 590.
52. Gitelson, A., Qiuang, H. and Richmond, A. (1996). Photic volume in photoreactors supporting ultrahigh population densities of the photoautotroph *Spirulina Platensis. Applied and Environmental Microbiology,* 62: 1570 – 1573.
53. Vonshak, A., Abeliovich, A., Boussiba, S. and Richmond, A. (1982). Production of *Spirulina* biomass: Effect of environmental factors and population density. *Biomass*, 2: 175 – 185.
54. Reichert, C. C., Reinehr, C. O. and Costa, J. A. V. (2006). Semicontinuous cultivation of the cyanobacterium *Spirulina platensis* in a closed photobioreactor. *Brazilian Journal of Chemical Engineering*, 23(1): 23 – 28.
55. Minhat, Z., Abd Rahaman, M. S., Takriff, M. S. dan Tan Kofli, N. (2016). Differentiation of biomass composition between isolated and commercial strains of microalgae. *Journal of Engineering Science and Technology*, 11(5): 737 – 744.
56. Mata, T. M., Martins, A. A. and Caetano, N. S. (2010). Microalgae for biodiesel production and other applications: A review. *Renewable and Sustainable Energy Reviews*, 14(1): 217 – 232.
57. Khan, S. A., Rashmi, Husain, M. Z., Prasad, S. and Benerjee, U. C. (2009). Prospects of biodiesel production from microalgae in India. *Renewable and Sustainable Energy Review*, 13: 2361 – 2372.
58. Murphy, D. J. (2005). Plant lipids: Biology, utilisation and manipulation. Oxford, UK: Blackwell Publishing Ltd.
59. Kropat, J., Tottey, S., Birkenhirl, R. P., Depege, N., Huijser, P. and Merchant, S. (2005). Regulator of nutritional copper signalling in *Chlamydomonas* in an SBP domain protein that recognize the GTAC core of copper response element. *Proceedings of the National Academy of Sciences,* 102: 18730 – 18735.
60. Sarmidi, A. (2009). Review of biofuel oil and gas production processes from microalgae. *Energy Conversion and Management*, 50: 1834 – 1840.

*Malaysian Journal of Analytical Sciences, Vol 21 No 1 (2017): 95 - 104*
*DOI: http://dx.doi.org/10.17576/mjas-2017-2101-11*

MALAYSIAN JOURNAL OF ANALYTICAL SCIENCES
*Published by The Malaysian Analytical Sciences Society*
ISSN 1394 - 2506

# DETERMINATION OF CAFFEINE IN SURFACE WATER USING SOLID PHASE EXTRACTION AND HIGH PERFOMANCE LIQUID CHROMATOGRAPHY

## (Penentuan Kafien di Permukaan Air Mengunakan Pengekstrakan Fasa Pepejal dan Kromatografi Cecair Prestasi Tinggi)

Fouad Fadhil Al-Qaim[1,2]*, Siti Hasmah Jusof[l], Md Pauzi Abdullah[1,3], Zainab Haider Mussa[1], Nurfaizah Abu Tahrim[1], Wan Mohd Afiq Wan Mohd Khalik[1], Mohamed Rozali Othman[1,3]

[1]*School of Chemical Sciences and Food Technology, Faculty of Science and Technology, Universiti Kebangsaan Malaysia, 43600 UKM Bangi, Selangor, Malaysia*
[2]*Chemistry Department, Faculty of Sciences for Women, Babylon University, P.O. Box 4, Hilla, Iraq*
[3]*Centre for Water Research and Analysis (ALIR), Faculty of Science and Technology, Universiti Kebangsaan Malaysia, 43600 UKM Bangi, Selangor, Malaysia*

**Corresponding author: fouadalkaim@yahoo.com*

Received: 9 April 2016; Accepted: 8 October 2016

**Abstract**

A new analytical method development based on solid phase extraction (SPE) combined with high performance liquid chromatography (HPLC) was carried out. The optimum working conditions were obtained based on selection of 250 mL sample loading, 0.25 µL methanol as reconstitution solvent, 100% methanol as mobile phase and 270 nm as the optimum wavelength. Good linearity was obtained in the range of 0.015 – 400 mg/L and the regression coefficient, $R^2$, was 0.995. Limit of detection and quantification were calculated at LOD = 0.06 µg/L and LOQ = 0.2 µg/L respectively. Repeatability and robustness has showed good performance with low relative standard deviation less than 3.29% and 3.50% respectively. Time-of-flight mass spectrometry (TOF/MS) instrument was used to confirm that caffeine is definitely present in surface water with level of concentration ranged from 31.7 to 50.1 µg/L. All results were analyzed statistically using one-way ANOVA, Tukey with interval confidence 95% and P-value 0.05.

**Keywords:** caffeine, stimulant, emerging pollutant, water quality, time of flight/mass spectrometry

**Abstrak**

Pembangunan kaedah analisis baru berasaskan pengekstrakan fasa pepejal bersama kromatografi cecair prestasi tinggi (KPCT) telah dijalankan. Kaedah optimum diperolehi berdasarkan tetapan iaitu 250 mL muatan sampel, 0.25 µL metanol sebagai pelarut, 100% methanol sebagai fasa bergerak dan 270 nm panjang gelombang yang optimum. Nilai kelinearan baik diperolehi pada julat kepekatan 0.015 – 400 mg/L dan nilai pekali regresi, $R^2$ ialah 0.995. Had pengesanan dan kuantifikasi dihitung masing – masing pada LOD = 0.06 µg/L and LOQ = 0.2 µg/L. Kebolehulangan dan keteguhan kaedah menunjukkan prestasi baik dengan nilai sisihan piawai relatif yang rendah iaitu masing – masing kurang daripada 3.29% dan 3.50%. Spektrometri jisim masa penerbangan (TOF/MS) digunakan untuk mengesahkan kehadiran kafein di permukaan air dengan aras kepekatan antara julat 31.7 hingga 50.1 µg/L. Keputusan dianalisa mengunakan pendekatan statistik seperti ANOVA satu hala, Tukey dengan aras keyakinan 95% and nilai p 0.05.

**Kata kunci:** kafein, perangsang, pencemar baru, kualiti air, spektrometri jisim/masa penerbangan

## Introduction

Caffeine (1,3,7-trimethyxanthine) is a chemical substance widely used in foods, beverages and drugs materials. Caffeine content in chocolate usually ranges between 5 and 35 mg/oz while in medicine tablet such as Anacin and Excedrin within the range of 30 - 200 mg concentration per tablet [1]. In human body, only 0.5 - 10% of caffeine was required for energy metabolism and the remaining will be excreted [2]. The occurrence of caffeine residue in aquatic environment is related to its presence in food and beverage waste, clinical waste, agricultural and poultry industry either through direct wastewater discharges or disposal of effluent water treatment plants (WWTPs) [3-5]. In groundwater environment, the septic system failure could be the main source of pollution with pharmaceuticals [6]. The residue of caffeine in surface water usually traced at low level concentrations within the range of ng/L to µg/L [7,8]. Nevertheless, it is still threatening to aquatic ecosystem especially living organism likes coral, which is highly sensitive to caffeine [9]. Moreover, this chemical substance posing high solubility and slow rate of degradation, lead to be more persistent in aquatic environments [10]. However, Al-Qaim et al. reported that caffeine can be removed by electrochemical degradation using graphite-poly vinyl chloride as anode as well its by-products which are formed during treatment process [11].

The target drug residues normally occur at low (ng/L to µg/L) levels so the pre-concentration is required to increase the detection limit of caffeine. Solid-phase extraction (SPE) is one of the method which is usually chosen [12,13]. A part from this, solid-phase microextraction (SPME) [14,15] or liquid-phase microextraction [16] have also been developed for this purpose.

Analysis of caffeine residue in natural waters have been carried in many countries by using various instruments mainly by liquid chromatography [3,5,17] and gas chromatography [7,18,19]. However, information of caffeine residue present in Malaysian environment is still limited and unclear. To best of our knowledge, the study on the occurrence of caffeine residue in surface water of Malaysian aquatic environment has not been reported except one study [17] which was conducted by our team. Thus, this study was aimed to extend the optimize work on method development of caffeine residue in water samples and to evaluate the developed method to the analysis of real samples.

## Materials and Methods

Analytical grade standard of caffeine was purchased from Sigma Aldrich (USA). HPLC-grade solvents namely methanol and methyl tert-butyl ether were purchased from Merck (Germany) and J.T. Baker (USA). Solid phase extraction cartridges, Oasis HLB 3 mL were purchased from Waters (USA). Membrane glass microfiber filters with diameter 47 mm were purchased from Whatman (UK). Deionized water was obtained by using a Mili-Q Easypure Rodi, Barnstead (USA) instrument.

Caffeine stock solutions were prepared in methanol at 1000 mg/L level concentrations and stored at −18 °C. Primary mixture stock solutions were then subsequently diluted for optimization study. A series of stepwise dilution solutions (0.015 – 400 mg/L, n=11) were used for the construction of external calibration curves in order to determine the unknown concentration of caffeine. Repeatability test was performed at three concentration levels (50, 100 and 200 mg/L). Limit of detection and quantification of caffeine were obtained based on 3:1 and 10:1 signal to noise ratios respectively. Robustness was performed based on injection volume at three different values (20, 21 and 22 µL).

### Method extraction

In general, the method extraction was reported somewhere with a little modification [17], solid phase cartridge initially was conditioned with 2 mL methyl tert-butyl ether (MTBE), 2 mL methanol (MeOH) and 2 mL deionized water. Then required water samples were loaded continuously into the cartridge at flow rate 9.0 mL/min. Cartridge was then washed with 2 mL of deionized water before left for dryness approximately half an hour. After that, cartridge was eluted with 5 mL MTBE, 2 mL acetone-MeOH (21-9; v/v), and 3 mL acetone-MeOH (9-21; v/v). Extracted sample was placed under nitrogen stream to complete dryness prior to reconstitute with required volume of methanol.

**HPLC-UV analysis**
High performance liquid chromatography (HPLC PERKIN ELMER 785A) with Chromolith® Performance RP-18e (4.6 x 10 mm, 5 µm) column equipped with UV/Vis as detector was used in this study. The optimization work was divided into two portions namely extraction (SPE) and chromatographic performance (HPLC). During the extraction process, effect of changes on variables namely sample volume and re-constitute sample volume were investigated. Meanwhile HPLC performance was tested on optimum condition for variable mobile phase and wavelength. 20 µL was injected as a final volume of sample using HPLC. Each sample was injected at least three times to ensure the precision and for other statistical analysis.

**TOF/MS analysis**
Mass spectrometry was performed on ESI-TOF instrument (micrOTOF-Q, Bruker /Germany). The results were obtained with the following settings: MS capillary voltages, 4000/3500 (PI/NI); drying–gas flow rate, 8.0 L/min; drying gas temperature, 190 $^{0}$C; and nebulizer pressure, 4.0 bar. One adduct ion, namely $[M+H]^{+}$ was observed for ESI (+) analysis in PI mode. Caffeine was acquired using an independent reference spray via the LockSpray interference to ensure accuracy and reproducibility. A mixture of sodium hydroxide and formic acid (FA) was used as the lock mass m/z 90.9766 to 974.8132. The accurate mass was calculated using software Daltonics DataAnalysis incorporated in the instrument.

**Statistical analysis**
The statistical analysis of variance (one-way ANOVA) was achieved for sample volume, reconstitute volume, wavelength and mobile phase by using Minitab Version 17, Tukey with P = 0.05 and 95% as interval confidence.

**Sample collection**
Surface water samples were collected from Alur Ilmu, the storm water channel in Universiti Kebangsaan Malaysia. This channel was connected to the downstream of Langat River. Five stations were chosen during the period of study in November 2014. Samples were collected once from each sampling point. The coordinates for these sampling sites are listed in Table 1. Water sample was collected by using 1 litre glass bottle, capped and transferred directly to laboratory for further analysis.

Table 1. Description of sampling location

| Station | Longitude | Latitude | Remark |
|---|---|---|---|
| S1 | 02°55.336N | 101°47.280E | Upstream, nearby faculty cafeteria |
| S2 | 02°55.393N | 101°47.304E | Drainage after faculty cafeteria |
| S3 | 02°55.534N | 101°47.264E | Drainage before student centre cafeteria |
| S4 | 02°55.579N | 101°47.234E | Drainage after student centre cafeteria |
| S5 | 02°55.727N | 101°47.063E | Downstream, nearby university mosque |

## Results and Discussion

**Effect of sample volume and reconstitution volume on recovery**
This method was compared with other previous methods in terms of mobile phase and retention time. Alvi and Muhammad reported that they used a very complicated mobile phase (15 mM potassium phosphate (pH 3.5) and acetonitrile (83:17, v/v). The drawback of using buffer solution is to clog the column with the salt of buffer if there is no enough washing. Our study also compared with other previous reported work in terms of solvent consumption [20]. Chowdhury et al., reported that caffeine was separated after 20 min run at 1.0 mL which means each run could consume 20 mL [21], compared to our study, only 1.0 mL was consumed at 0.3 mL/min for each run.

The volume of sample was spiked at 100 µg/L of caffeine and three sample volumes (100, 250 and 500 mL) were tested. Sample with volume 250 mL indicated the highest recovery compared to 100 and 500 mL samples (Figure

1a). The recovery of caffeine was the lowest when 500 mL was used. This result is related to the unsuitability of using large volume of sample with the size of the cartridge (3cc). The volume 100 mL gives high recovery (84.57%) but still less than the recovery obtained by 250 mL (87.53%). However, 250 mL was selected to the next experiments for further considerations.

Figure 1b shows that three different volumes of methanol (0.25, 0.50 and 1.00 mL) were tested as reconstitution solvent after solid phase extraction loading. Highest recovery was obtained at 79.12% by using 0.25 mL of methanol as reconstitute solvent. Other volumes gave recovery at 72.03% (1 mL MeOH) and 71.66% (0.5 mL MeOH) which were not significantly different, more explanations in the next section. From these results, 0.25 mL reconstitute volume was selected for further experiments.

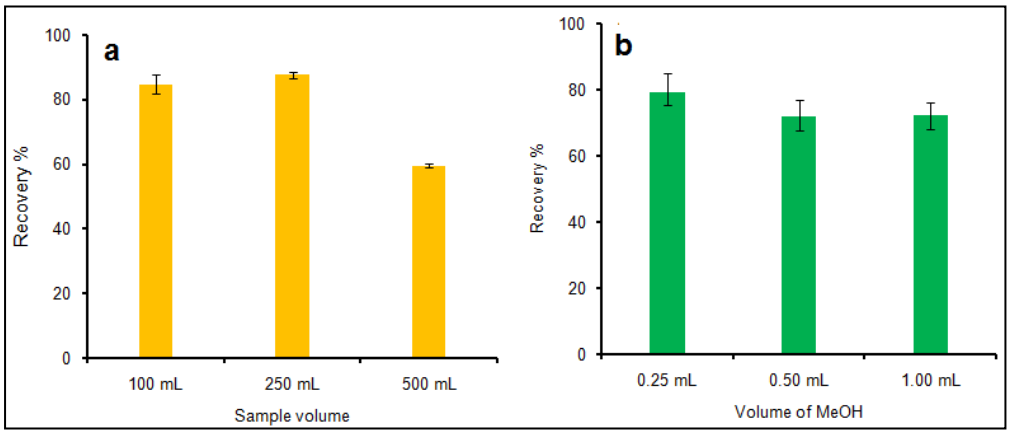



Figure 1. Effect of (a) sample volume, and (b) volume of solvent on the recovery of caffeine

**Effect of mobile phase and wavelength**

In this study, the isocratic elution program was used for seven mobile phases (100% MeOH (S1), DIW:MeOH (20:80) (S2), DIW:MeOH (40:60) (S3), DIW:MeOH (60:40) (S4), DIW:MeOH (80:20) (S5), 100% DIW (S6), ACN:MeOH (40:60) (S7)) as presented in Figure 2. Four mobile phases were presented because the others exhibited very low signal or not detected so they were excluded from the graph. However, the mobile phase chosen for analytical method validation was 100% MeOH, presented a mobile phase holdup time of 0.652 min and good separation as shown in Table 2.

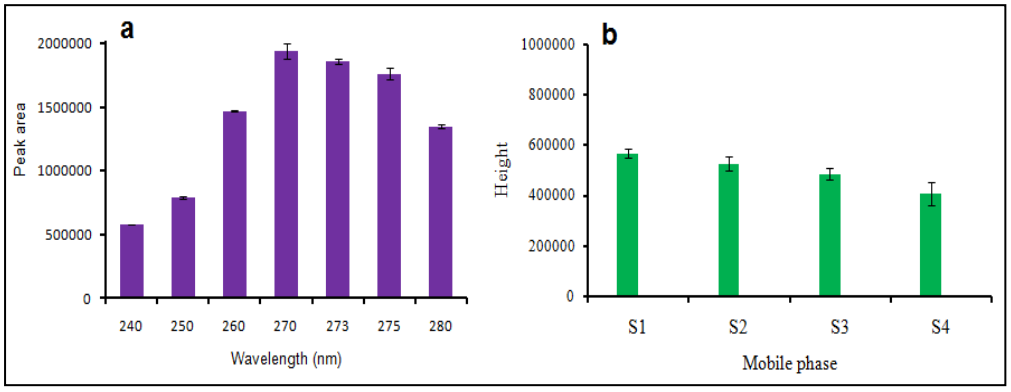



Figure 2. Effect of (a) wavelength, and (b) mobile phase on the sensitivity of caffeine analysis

Mobile phase ACN:MeOH (40:60) (S7) exhibited very low peak signal (peak area 8743 and peak height 2469) which means an additional of acetonitrile reduce the efficiency of elution for caffeine (data not shown). In case of mobile phase (100% DIW) no peak was obtained, may be this was attributed to the very low polarity of this mobile phases to be suitable for elution of caffeine. Consequently, the mobile phases DIW:MeOH (20:80) (S2), DIW:MeOH (40:60) (S3), DIW:MeOH (60:40) (S4) produced less peak height sequentially. From these results, increasing the amount of water in the mobile phase has led to low peak height and broad peak which are not good in terms of separation using high performance liquid chromatography.

Wavelength was another parameter considered in this study using HPLC instrument equipped with ultra-violet (UV) detector. Optimization of wavelength is very important because the targeted compound has optimum absorbance on its own wavelength. The optimum of chromatographic signal response was obtained at 270 nm. At this wavelength, caffeine signal response was obtained with maximum peak area which was observed at 1940353.25 µV/s.

Wavelength was optimised at 240, 250, 260, 270, 273, 275 and 280 nm. At 270 nm, the concentration of caffeine was the highest compared to the rest of the wavelengths. The peak area of caffeine was influenced by the wavelength but the retention time and the shape were not influenced. Wavelength was not responsible for elution of caffeine from column, but it only affected the absorbance. However, a significant difference was observed at all the wavelengths except at 270, 273 and 275 nm.

**Method performance**

Analytical performances namely linearity, repeatability, robustness, detection limit and quantification limit were tested and presented in Table 2 and 3, respectively. Good linearity was obtained by plotting external calibration of a series of caffeine standard solution (n = 11). Regression equation was expressed as $y = 13273x + 46610$ with regression coefficient $R^2 = 0.995$. Repeatability of the developed method was tested using intra and inter-day precision at 3 level concentrations (50, 100, 200 mg/L). Analysis of results indicated that repeatability of developed method was precise with RSD value < 3.29%, which explained good routine work. Limit of detection and quantification were calculated at LOD = 0.066 µg/L and LOQ = 0.20 µg/L respectively. Robustness test was performed on volume injection and flow rate of mobile phase. The results showed that the method is robust. Relative standard deviation for both effect of volume injection and flow rate ranged from 3.50% to 1.95% respectively.

Table 2. Precision of SPE method on caffeine analysis

| **Concentration (mg/L)** | **Intra-day (n = 9)** | | **Inter-day (n = 18)** | |
|---|---|---|---|---|
| | **Concentration ± SD** | **Rt ± SD** | **Peak Area ± SD** | **Rt ± SD** |
| 50 | 50.36 ± 0.115 | 0.652 ± 0.002 | 49.84 ± 0.224 | 0.652 ± 0.001 |
| 100 | 99.5 ± 7.662 | 0.652 ± 0.001 | 100.5 ± 0.603 | 0.654 ± 0.002 |
| 200 | 198.74 ± 2.027 | 0.652 ± 0.001 | 192.05 ± 1.108 | 0.652 ± 0.001 |

Table 3. Robustness test on HPLC performance for caffeine analysis (n = 3)

| **Variable** | **Level** | **Peak Area ± SD** | **Rt ± SD** |
|---|---|---|---|
| Volume injection (µL) | 20 | 50.9 ± 0.186 | 0.652 ± 0.001 |
| | 21 | 53.8 ± 0.078 | 0.651 ± 0 |
| | 22 | 55.22 ± 0.138 | 0.652 ± 0 |
| Flow rate of mobile phase (mL/min) | 0.30 | 52.45 ± 0.488 | 0.651 ± 0.001 |
| | 0.31 | 51.02 ± 0.209 | 0.632 ± 0 |
| | 0.32 | 48.34 ± 0.247 | 0.615 ± 0.001 |

**Statistical analysis**

The most significant results were obtained with volume of MeOH as reconstitute solvent, volume of sample, mobile phase composition and wavelength of caffeine absorbance. The significance value in terms of P-value was 0.000 in all cases which means high significant results were obtained. In case of volume used for MeOH, three volumes (0.25, 0.50 and 1.00 mL) were tested by one-way ANOVA. An amount 0.50 and 1.00 mL volumes were shared with same letter B means it was not significant but both volumes were significantly different from 0.25 mL volume.

Table 4. Statistical analysis of variance for the different independent factors using Tukey method and 95% confidence, P value less than 0.05.

| **Volume of MeOH as Reconstitute Solvent** | | | | | | | | | | | | |
|---|---|---|---|---|---|---|---|---|---|---|---|---|
| **Factor Value** | **N** | **Mean or Recovery** | | | | | **Grouping** | | | | | |
| 0.25 | 3 | 79.073 | A | | | | | | | | | |
| 0.50 | 3 | 71.660 | | B | | | | | | | | |
| 1.00 | 3 | 71.337 | | B | | | | | | | | |
| **Sample Volume** | | | | | | | | | | | | |
| **Factor Value** | **N** | **Mean of Recovery** | | | | | **Grouping** | | | | | |
| 250 | 3 | 87.53 | A | | | | | | | | | |
| 100 | 3 | 84.57 | | B | | | | | | | | |
| 500 | 3 | 59.50 | | | C | | | | | | | |
| **Mobile Phase Composition** | | | | | | | | | | | | |
| **Factor Symbol** | **N** | **Mean of Peak Area** | | | | | **Grouping** | | | | | |
| S1 | 4 | 565263 | A | | | | | | | | | |
| S2 | 4 | 526415 | A | B | | | | | | | | |
| S3 | 4 | 484833 | | B | | | | | | | | |
| S4 | 4 | 406861 | | | C | | | | | | | |
| S7 | 2 | 2469 | | | | D | | | | | | |
| S5 | 4 | 462 | | | | D | | | | | | |
| **Wavelength of Caffeine** | | | | | | | | | | | | |
| **Factor Value** | **N** | **Mean of Peak Area** | | | | | **Grouping** | | | | | |
| 270 | 4 | 1940353 | A | | | | | | | | | |
| 273 | 4 | 1863330 | | B | | | | | | | | |
| 275 | 4 | 1764819 | | | C | | | | | | | |
| 260 | 4 | 1470816 | | | | D | | | | | | |
| 280 | 4 | 1348010 | | | | | E | | | | | |
| 250 | 4 | 791823 | | | | | | F | | | | |
| 240 | 4 | 580249 | | | | | | | | | G | |

Sample volume was statistically tested and exhibited very high significant difference in terms of peak area. The sample volumes (100, 250 and 500 mL) were totally statistically different as shown in Table 4. Sample volume (100 mL) was selected as the best sample volume because of its highest recovery. Mobile phase composition was also investigated statistically. However, mobile phase S1 and S2 were not differed significantly since both of them were

represented by letter A. Furthermore, the mobile phases S2 and S3, and S5 and S7 were not differed significantly. Mobile phase S4 was only significantly different from other mobile phases. Based on all these results, Methanol, S1, was selected as the best solvent because it produced sharp peak and well separated. Finally, seven mobile phases were tested to investigate the significance. All wavelengths were significantly different (all different letters) as shown in Table 4. The wavelength 270 nm was selected as the best wavelength based on its peak height.

**Analysis of real samples**

Analysis of caffeine residue in surface water was successfully carried out. Level of concentration was recorded within the range of 31.7 to 50.1 µg/L. The highest concentration was 50.1 µg/L recorded at S5 drainage nearby UKM's mosque (downstream) and the lowest concentration was 31.7 µg/L which was S1 nearby cafeteria (upstream). The concentration of caffeine at other stations were recorded 34.7 µg/L (S2) after cafeteria, 43.1 µg/L (S3) and 44.6 µg/L (S4). The results suggested that flushing from upstream to downstream as well as the discharge of water mixed with the tea beverages as the major factors for contribution the occurrence of caffeine in surface water. The increasing of caffeine gradually from S1 to S5 was not surprising because the number of sources increased as well in the same line. Finally, the site S5 was considered as the meeting point for all these sources thus it exhibited the highest concentration of caffeine. All results were tested statistically and showed a significant different among all sites as shown in Figure 3. The chromatogram peak of caffeine residue detected in water samples is presented in Figure 4.

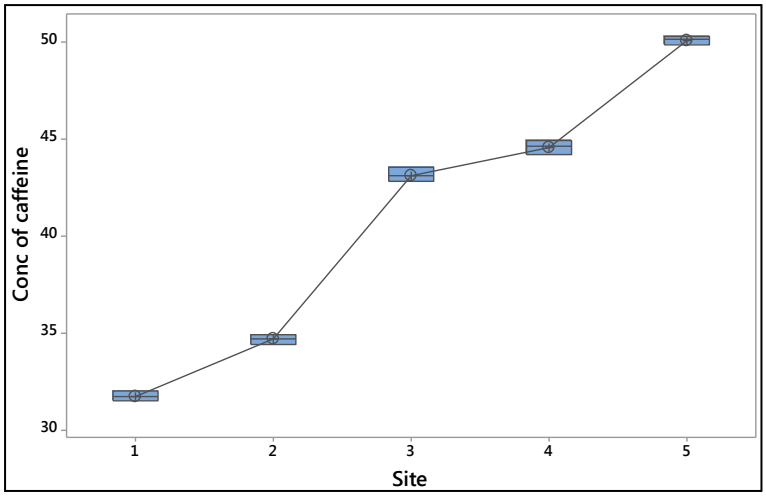



Figure 3. Box plot of the concentration of caffeine against sampling sites at 95% confidence interval and P-value 0.05

**TOF screening and confirmation**

For selection of the MS ionization mode, a standard solution of caffeine in 1:9 MeOH-$H_2O$ was separated and analyzed by LC-TOF/MS. The MS was tuned for $[M+H]^+$ ions in the ESI (+) ionization mode and for $[M-H]^-$ ions in the ESI (−) modes. The positive ionization mode was preferred for caffeine. Caffeine was not detected in the negative ionization mode. TOF/MS was selected as a better solution to confirm that caffeine was present in surface water (one sample was selected). The *m/z* of the caffeine was extracted from the total ionic chromatogram (TIC) in positive ionization mode as proton adduct $[M+H]^+$ with 0.2 ppm mass error through Bruker Daltonics DataAnalysis software as shown in Figure 5. To increase the selectivity of TOF measurements, a narrow accurate mass interval was used to reconstruct the chromatographic traces. Extracted ion chromatogram (EIC) was typically extracted using Bruker Daltonic software with 20 mDa mass window for caffeine in water sample.

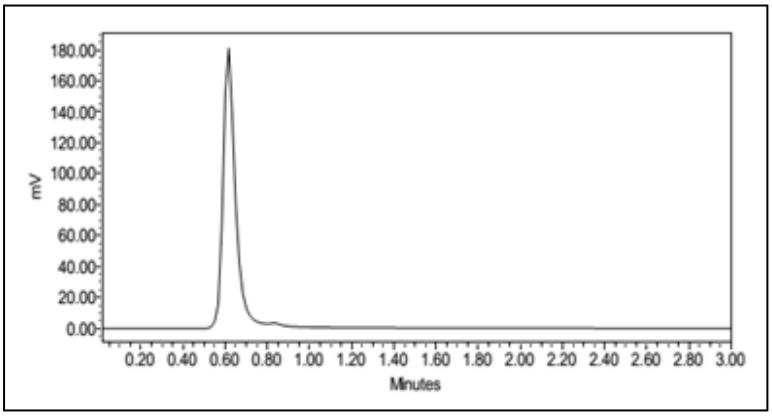



Figure 4. Signal response of caffeine residue traced in surface water by HPLC

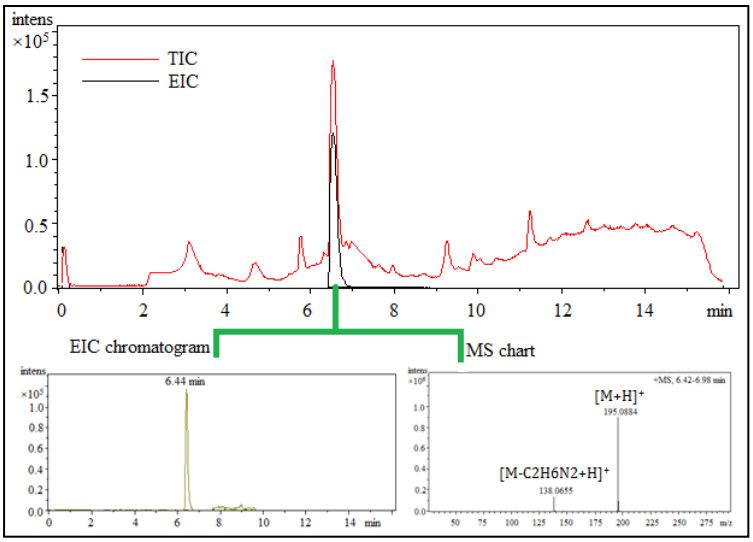



Figure 5. Confirmation profile for caffeine in surface water using LC-TOF/MS

## Conclusion

The optimization results showed that the HPLC developed method presented here can be considered reliable for the determination of caffeine residue in surface water. Good validation results were obtained in terms of linearity, precision, sensitivity and robustness on method extraction and HPLC performances. An application of the developed method on real samples showed that the occurrence of caffeine residue could reach to µg/L level of concentrations.

## Acknowledgement

This study has been funded by Research University Grants UKM-DLP-2012-024, UKM-AP-2011-21, BKP-FST-K001671 and FRGS-1-2013-ST01-UKM-01-1. Authors are thankful to ALIR staff for facilities assistance during research activities.

**References**

1. Ferreira, A. P., de Lourdes, C. and da Cunha, N. (2005). Anthropic pollution in aquatic environment: Development of a caffeine indicator. *International Journal of Environmental Health Research,* 15: 303 – 311.
2. Buerge, I. J., Poiger, T., Müller, M. D. and Buser, H. R. (2003). Caffeine, an anthropogenic marker for wastewater contamination of surface waters. *Environmental Science & Technology,* 37: 691 – 700.
3. Gardinali, P. R. and Zhao, X. (2002). Trace determination of caffeine in surface water samples by liquid chromatography–atmospheric pressure chemical ionization–mass spectrometry (LC–APCI–MS). *Environment International*, 28: 521 – 528.
4. Barrett, M. H., Hiscock, K. M., Pedley, S., Lerner, D. N., Tellam, J. H. and French, M. J. (1999). Marker species for identifying urban groundwater recharge sources: a review and case study in Nottingham, UK. *Water Research,* 33: 3083 – 3097.
5. Chen, Z., Pavelic, P., Dillon, P. and Naidu, R. (2002). Determination of caffeine as a tracer of sewage effluent in natural waters by on-line solid-phase extraction and liquid chromatography with diode-array detection. *Water Research,* 36: 4830 – 4838.
6. Seiler, R. L., Zaugg, S. D., Thomas, J. M. and Howcroft, D. L. (1999). Caffeine and pharmaceuticals as indicators of waste water contamination in wells. *Groundwater,* 37: 405 – 410.
7. Lacina, P., Mravcová, L. and Vávrová, M. (2013). Application of comprehensive two-dimensional gas chromatography with mass spectrometric detection for the analysis of selected drug residues in wastewater and surface water. *Journal of Environmental Sciences,* 25: 204 – 212.
8. Al-Qaim, F. F., Abdullah, M. P., Othman, M. R., Mussa, Z. H., Zakaria, Z., Latip, J. and Afiq, W. M. (2015). Investigation of the environmental transport of human pharmaceuticals to surface water: A case study of persistence of pharmaceuticals in effluent of sewage treatment plants and hospitals in Malaysia. *Journal of the Brazilian Chemical Society,* 26: 1124 – 1135.
9. Mompelat, S., Le Bo, B. and Thomas, O. (2009). Occurrence and fate of pharmaceutical products and by-products, from resource to drinking water. *Environment International,* 35: 803 – 814.
10. Gibson, A. M., Morgan, R. M., MacDonald, N. and Nikitin, A. G. (2012). Possible effects of the presence of common household chemicals in the environment: the growth of an aquatic bacterial species on high concentrations of caffeine. *Journal of Biotech Research,* 4: 72 – 79.
11. Al-Qaim, F. F., Mussa, Z. H., Othman, M. R. and Abdullah, M. P. (2015). Removal of caffeine from aqueous solution by indirect electrochemical oxidation using a graphite-PVC composite electrode: A role of hypochlorite ion as an oxidising agent. *Journal of Hazardous Materials*, 300: 387 – 397.
12. Al-Qaim, F. F., Abdullah, M. P. and Othman, M. R. (2012). Analysis of different therapeutic classes using liquid chromatography-mass spectrometry in the aquatic environment: A review. *International Journal of Pharmacy and Pharmaceutical Sciences*, 4: 3 – 11.
13. Mohamed, F. F., Abdullah, M. P., Othman, M. R. and Zakeria, Z. B. (2012). SPE-LC-Mass spectrometry analysis for basic pharmaceuticals with different therapeutic classes in aquatic environment. *Journal of Applied Sciences Research*, 8: 2124 – 2132.
14. Moeder, M., Schrader, S., Winkler, M. and Popp, P. (2000). Solid-phase microextraction–gas chromatography–mass spectrometry of biologically active substances in water samples. *Journal of Chromatography A*, 873: 95 – 106.
15. Werres, F., Stien, J., Balsaa, P., Schneider, A., Winterhalter, P. and Overath, H. (2000). Automatisierte Bestimmung polarer Arzneimittelrückstände in Wässern mittels Festphasenmikroextraktion (SPME) und Derivatisierung. *Vom Wasser*, 94: 135 – 147.
16. Rasmussen, K. E. and Pedersen-Bjergaard, S. (2004). Developments in hollow fibre-based, liquid-phase microextraction. *TrAC Trends in Analytical Chemistry*, 23: 1 – 10.
17. Al-Qaim, F. F., Abdullah, M. P., Othman, M. R., Latip, J. and Zakaria, Z. (2014). Multi-residue analytical methodology-based liquid chromatography-time-of-flight-mass spectrometry for the analysis of pharmaceutical residues in surface water and effluents from sewage treatment plants and hospitals. *Journal of Chromatography A,* 1345: 139 – 153.
18. Verenitch, S. S., Lowe, C. J. and Mazumder, A. (2006). Determination of acidic drugs and caffeine in municipal wastewaters and receiving waters by gas chromatography–ion trap tandem mass spectrometry. *Journal of Chromatography A,* 1116: 193 – 203.

19. Gomes, P. C. L., Barnes, B. B., Santos-Neto, A. J., Lancas, F. M. and Snow, N. H. (2013). Determination of steroids, caffeine and methylparaben in water using solid phase microextraction-comprehensive two-dimensional gas chromatography–time of flight mass spectrometry. *Journal of Chromatography A,* 1299: 126 – 130.
20. Alvi, S. N., and Muhammad M. H. (2011). Validated HPLC method for determination of caffeine level in human plasma using synthetic plasma: Application to bioavailability studies. *Journal of Chromatographic Science,* 49: 292 – 296.
21. Chowdhury, S. R., Maleque, M., and Shihan, M. H. (2012). Development and validation of a simple RP-HPLC method for determination of caffeine in pharmaceutical dosage forms. *Asian Journal of Pharmaceutical Analysis*, *2*: 1 – 4.

*Malaysian Journal of Analytical Sciences, Vol 21 No 1 (2017): 105 - 112*
*DOI: http://dx.doi.org/10.17576/mjas-2017-2101-12*

MALAYSIAN JOURNAL OF ANALYTICAL SCIENCES
*Published by The Malaysian Analytical Sciences Society*
ISSN 1394 - 2506

# SCREENING OF TROPICAL NATIVE AQUATIC PLANTS FOR POLISHING PULP AND PAPER MILL FINAL EFFLUENT

## (Saringan Tumbuhan Akuatik Tropika Tempatan untuk Rawatan Penyudahan Sisa Pulpa dan Kertas)

Jamilah Ahmad[1], Siti Rozaimah Sheikh Abdullah[1]*, Hassimi Abu Hassan[1], Reehan Adne Abdul Rahman[1], Mushrifah Idris[2]

[1]*Department of Chemical and Process Engineering, Faculty of Engineering and Built Environment*
[2]*Tasik Chini Research Centre, Faculty of Science and Technology*
*Universiti Kebangsaan Malaysia, 43600 UKM Bangi, Selangor, Malaysia*

**Corresponding author: rozaimah@ukm.edu.my*

Received: 21 October 2015; Accepted: 14 June 2016

**Abstract**

Pulp and paper mill industry is one of the biggest water users that produce wastewater containing dye and various toxic compounds. The study was conducted to screen for potential tropical native aquatic plants, which can be used in phytoremediation mainly for the removal of colour and chemical oxygen demand (COD) from pulp and paper mill effluent. Three selected tropical native aquatic plants, *Scirpus grossus, Azola pinnata* and *Salvinia molesta* were planted in a greenhouse at UKM for screening test. Real final effluent from a pulp and paper mill in Pahang was characterized and contained 181 PtCo for colour and 72.4 mg/L COD at pH 8.1. This wastewater was exposed to weed plant, *Scirpus grossus* and floating plants, *Azola pinnata* and *Salvinia molesta.* The final effluent was analysed after 28$^{th}$ day of exposure. The percentage of colour removal for the three tropical native plants *Scirpus grossus, Azola pinnata* and *Salvinia molesta* were 50.28%, 43.09% and 49.72% respectively. While for COD removal, all the three plants successfully removed 100% COD. From the result, the best tropical native aquatic plant to remove colour and COD for pulp and paper mill effluent is *Scirpus grossus.*

**Keywords**: biological treatment, phytoremediation, effluent, colour, chemical oxygen demand

**Abstrak**

Industri kilang kertas adalah salah satu pengguna air yang terbanyak dan menghasilkan air sisa yang mengandungi pewarna dan pelbagai sebatian toksik. Kajian ini dijalankan untuk menyaring bagi tumbuhan tropika asli yang berpotensi untuk proses fitoremediasi dalam penyingkiran warna dan permintaan oksigen kimia (COD) daripada sisa air kilang pulpa dan kertas. Tiga jenis tumbuhan tropika asli telah dipilih iaitu *Scirpus grossus, Azola pinnata* dan *Salvinia molesta* ditanam dalam rumah tumbuhan di UKM untuk ujian saringan. Efluen sebenar dari sebuah kilang pulpa dan kertas di Pahang telah dicirikan dan mengandungi 181 PtCo untuk warna dan 72.4 mg/L untuk COD pada pH 8.1. Air sisa ini telah didedahkan kepada tumbuhan rumpai iaitu *Scirpus grossus* dan tumbuhan terapung *Azola pinnata* dan *Salvinia molesta*. Efluen ini dianalisis selepas diuji/didedahkan sehingga hari ke-28. Penyingkiran warna untuk tiga tumbuhan asli yang dipilih iaitu *Scirpus grossus, Azola pinnata* dan *Salvinia molesta* adalah masing-masing sebanyak 50.28%, 43,09% dan 49,72%. Manakala bagi penyingkiran COD bagi *Scirpus grossus, Azola pinnata* dan *Salvina Natans* ialah 100% penyingkiran. Daripada keputusan itu, tumbuhan tropika asli yang terbaik untuk menyingkirkan warna dan COD dari effluen kilang pulpa dan kertas adalah *Scirpus grossus*.

**Kata kunci:** rawatan biologi, fitoremediasi, efluen, warna, permintaan oksigen kimia

## Introduction

In Malaysia, there have been more than one billion capacities of pulp and paper. According to Roda and Rathi [1], Malaysia has 67 of pulp and paper mill industries that produce papers from pulp or recycled paper. These industries produce about 76 to 228 $m^3$ of water per tonne. Pulp and paper mill industries are also known as the sixth industry contributing pollution to environment [2-3]. Pollutants released from pulp and paper mill effluent into environment cause numerous problems and physiological impairment. Due to high organic pollutants in the pulp and paper mill effluent will affect aquatic communities [10].

The problems associated with pulp and paper mill effluents are pH, colour, and high levels of Biochemical Oxygen Demand (BOD), Chemical Oxygen Demand (COD), Suspended Solid (SS) and Absorbable Organic Halides (AOX). Paper manufacturing process releases chlorinated substances in the effluent as the major contaminants formed [4-7]. Pulp and paper mill wastewater is a concern for the environment due to its after effects. Some researchers [8-10] more focused on environmental friendly technologies for treatment of wastewater. They use biological approach for the removal of contaminants from the effluent. The biological treatment processes are able to reduce colour, COD, BOD and toxic low molecular weight chlorinated lignin derivatives.

Last few decades, there has been an increase in improving the ability of plants to remove environmental pollutants. Genes from microbes and plants are being used successfully to enhance the ability of plants to tolerate, remove and degrade pollutants [11]. Therefore, phytoremediation on a basis of plant is suitable for biological treatment for pulp and paper mill effluent. Phytoremediation uses plants to treat contaminated effluent. This technology has been extensively reviewed through literature studies [12-19]. Phytoremediation takes advantage of the natural ability of plants to extract chemicals from water, soil and air using energy from sunlight. Some advantages and disadvantages are listed in Table 1. Its primary advantage is that it is approximately 10 times less expensive than conventional strategies [20]. Other advantages of phytoremediation over the engineering or bioremediation methods include the possibility of a useful product such as wood, pulp or bioenergy [21]. Plants act as soil stabilizer, minimizing the amount of contaminated dust that could leave the site and enter the surrounding neighbourhoods [11].

Table 1. Advantages and disadvantages of phytoremediation

| Advantages | Disadvantages |
|---|---|
| Less costly than mechanical methods | Limited to shallow contaminants |
| Passive, solar driven | Phytotoxicity of contaminants |
| High public acceptance | Slower than mechanical methods |
| Retains topsoil | Unknown effects of biodegradation products |
| Less secondary waste generation | Potential of contaminants to enter the food chain. |

Phytoremediation in pulp and paper mill effluent treatment may take one of several forms: phytoextraction, rhizofiltration, phytostabilization, and phytovolatilization. Phytoextraction refers to process in which plants are used to concentrate metals from the soil into the roots and shoots the plant; rhizofiltration is the use of plant roots to absorb, concentrate or precipitate contaminants from effluents. Phytostabilization is the uptake and release into atmosphere of volatile materials such as mercury [22].

The aim of this study is to screen for potential tropical native aquatic plants, which can be used in phytoremediation mainly for polishing of colour and COD from pulp and paper mill final effluent.

## Materials and Methods

### Plant propagation

The selected plant, *Scirpus grossus* were planted in a greenhouse at UKM for preliminary studies and as a stock for further studies in phytotoxicity. The plant sources were taken from Tasik Chini, Pahang. The tenure of *Scirpus*

*grosuss* is between 8 – 10 weeks. Upon reaching maturity, this plant was taken for preliminary test. For *Azola pinnata* and *Salvinia molesta*, they were grown in greenhouse. Figure 1 (a) shows the samplings of *Scirpus grossus* taken at Tasik Chini, (b) matured *Scirpus grossus* planted at greenhouse, (c) *Salvinia molesta* and (d) *Azola pinnata* in greenhouse, Universiti Kebangsaan Malaysia.

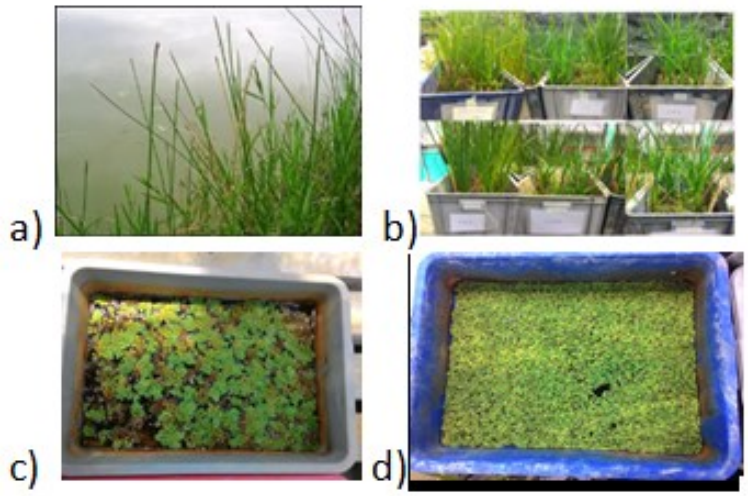



Figure 1. (a) *Scirpus grossus* at Tasik Chini, (b) matured *Scirpus grossus* at greenhouse, c) *Salvinia molesta*, (d) *Azola pinnata* at greenhouse

**Experimental set – up for preliminary test**

The preliminary test was conducted batch wise in crates of 10 L. Real final effluents from a pulp and paper mill industry in Pahang acted as a contaminant. All crates for *Scirpus grossus* filled with 5 kg of sands and 2 L of wastewater except for control contaminant (CC) filled with only tap water. All crates would be topped up with tap water by 1 L for every 2 days. The schematic diagram for experimented sets of *Scirpus grossus* is shown in Figure 2. There were four crates containing eight plants in each crate labelled as CC, R1, R2 and R3. The *Scirpus grossus* planted in two rows.

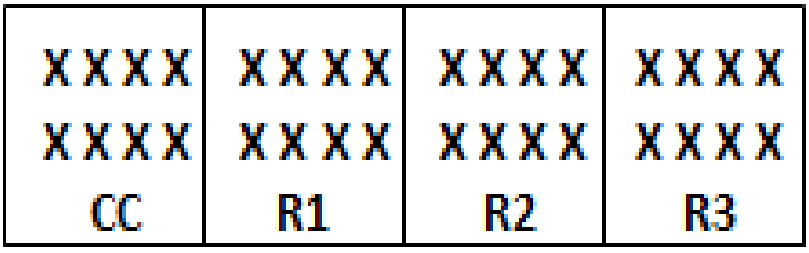



Figure 2. Schematic diagram of sets of *Scirpus grossus* in preliminary test

Floating plants of *Salvinia molesta* and *Azola pinnata* were prepared in three crates for each plant as shown in Figure 3 and Figure 4, respectively. Crate for control contaminant for *Salvinia molesta* and *Azola pinnata* labelled as SC and AC respectively containing 2 L of tap water. Crates for sample (S1/A1 & S2/A2) contained 2 L of wastewater. The crates were filled with 300g of the floating plants.

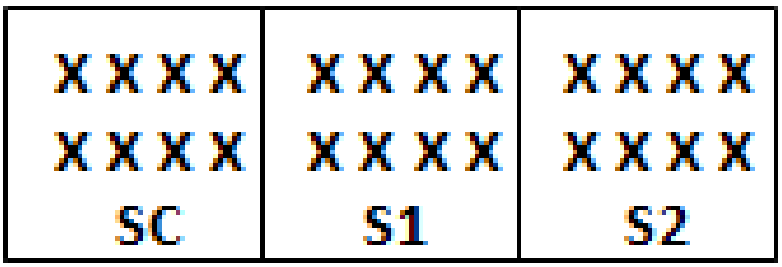



Figure 3. Schematic diagram of sets of *Salvinia molesta* in preliminary test

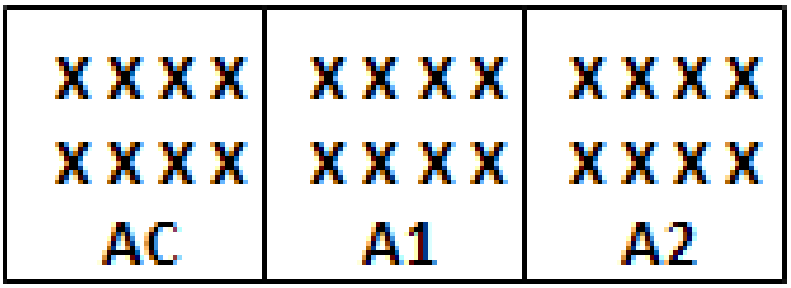



Figure 4. Schematic diagram of sets of *Azola pinnata* in preliminary test

After 28th day exposure, liquid sample from each crate were collected for determining the colour and COD.

## Results and Discussion

**Physical plant growth observation**

The observation on the physical appearance of *Scirpus grossus, Salvinia molesta* and *Azola pinnata* during the preliminary test when exposed to real wastewater was summarized in Table 2.

Table 2. Observation and physical appearance of *Scirpus grossus, Salvinia molesta* and *Azola pinnata* on day 0 compared to day 28

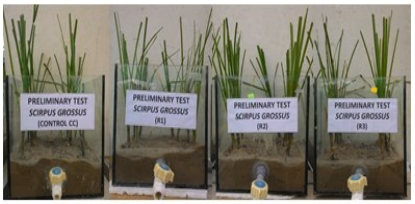
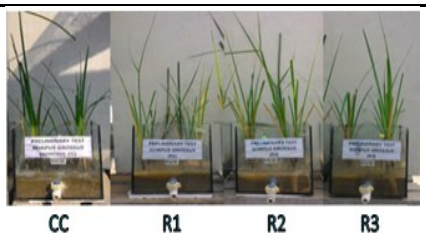
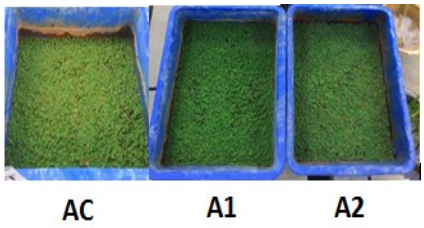
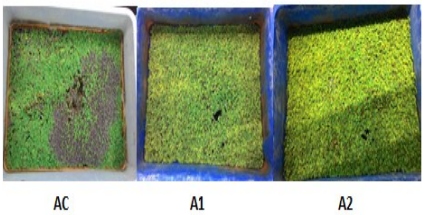
| Day of Exposure | Physical Appearance of Plants |
|---|---|
| | *Scirpus grossus* |
| Day 0 |  CC R1 R2 R3 |

Table 2 (cont'd). Observation and physical appearance of *Scirpus grossus, Salvinia molesta* and *Azola pinnata* on day 0 compared to day 28

| **Day of Exposure** | **Physical Appearance of Plants** |
|---|---|
| Day 28 |   |
| | *Salvinia molesta* |
| Day 0 |   |
| Day 28 |   |
| | *Azola pinnata* |
| Day 0 |   |
| Day 28 |   |

From the observation, the *Scirpus grossus* still survived until day 28. Nevertheless, there were also withered plants during the preliminary test. For *Scirpus grossus,* it started withered on day 7 compared to the control contaminant (CC) started on day 10. After day 28; the leaves grew in almost 20 cm higher than before, showing that after exposure, the *Scirpus grossus* can still survive and grow. *Salvinia molesta* and *Azola pinnata* withered starting on day 14 for both floating plants. The control crate withered faster than the contaminant crate. However, both floating plants can survive until day 28.

**Removal of colour and COD**

The characterization results of wastewater before and after exposure for all plants were summarized in Table 3. From the observation, colour and COD decreased from day 3. From Table 3, COD was totally removed by all plants. In addition, 50.28%, 49.72% and 43.09% of colour were removed by *Scirpus grossus, Salvinia molesta* and *Azola pinnata* respectively.

Table 3. Characterization of wastewater after exposure

| **Types of plants/characteristic** | | **Colour (PtCo)** | **COD (mg/L)** |
|---|---|---|---|
| *Scirpus grossus* | Average | 90 | 0 |
| | Percentage (%) | 50.28 | 100 |
| *Salvinia molesta* | Average | 91 | 0 |
| | Percentage (%) | 49.72 | 100 |
| *Azola pinnata* | Average | 103 | 0 |
| | Percentage (%) | 43.09 | 100 |
| Wastewater | | 181 | 72.4 |

Figure 5 shows the percentage removal of colour and COD. Hence, from this study, the most suitable tropical native plant used in colour and COD removal is *Scirpus grossus.*

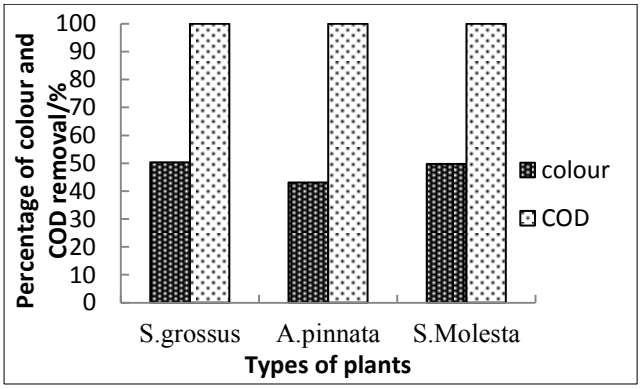



Figure 5. Removal of colour and COD by three plants *Scirpus grossus, Salvinia molesta* and *Azola pinnata*

## Conclusion

The results showed that between the three plants, *Scirpus grossus, Salvinia molesta* and *Azola pinnata* are able to remove colour and COD from real pulp and paper mill final effluent. Nevertheless, *Scirpus grossus* is the best tropical native plant for colour and COD removal through phytoremediation. Hence, *Scirpus grossus* is recommended for treatment wastewater pulp and paper mill.

**Acknowledgement**

The authors would like to thank to Faculty of Engineering and Built Environment and Tasik Chini Research Centre, Universiti Kebangsaan Malaysia (UKM) and Ministry of Higher Education, Malaysia for granting this project under DIP-2014-020.

## References

1. Roda, J. M. and Rathi, S. (2006). Malaysia report: Feeding China's expending demand for wood pulp. Centre For International Forestry Research. Jakarta, Indonesia.
2. Ali, M. and Sreekrishnan, T. R. (2001). Aquatic toxicity from pulp and paper mill effluent: A review. *Advances in Environment Research,* 5: 175 – 196.
3. Meagher, R. B. and Heaton, A. C. P. (2005). Strategies for the engineered phytoremediation of toxic element pollution: Mercury and arsenic. *Journal of Industrial Microbiology and Biotechnology,* 32: 502 – 513.
4. Chaudhary S, Rohella R, Manthan M. and Sahoo N (2002). Decolorization of craft paper mill effluent by white rot fungi. *Journal of Microbiology*, 38: 221 – 224.
5. Hossain, M. S. K, Das, M. and Ibrahim, S. H. (2001). Aerobic studies on pollution abatement of sulfite pulp bleaching effluent using Phanerochaete chrysosporium (MTCC-787). *Journal of Industrial Pollution Control*, 17: 191 – 200.
6. Jayaramraja, P. R, Anthony T, Rajendran R. and Rajkumar K (2001). Decolourisation of paper mill effluent by *Aspergillus fumigatus* in bioreactor. *Pollution Research*, 20: 309 – 312.
7. Pokhrel D. and Viraraghavan T. (2004) Treatment of pulp and paper mill wastewater – A review. *Science of Total Environment*, 333: 37 – 58.
8. Barton, D. A, Lee, J. W, Bukley, D. B. and Jett, S. W. (1996). Biotreatment of kraft mill condensate for reuse. *Proceeding Tappi Minimum Effluent Mills Symposium*, GA Atlanta, USA.
9. Nagarathamma R, Bajpai P, Bajpai PK (1999) studies on decolourisation, decolourisation, degradation and detoxification of chlorinated lignin compunds in kraft bleaching effluents by Ceriporiopsis subvermispora. *Process Biochemistry,* 34: 939 – 948.
10. Purnima, D. and Kumar, V. (2014). Biological approach for the treatment of pulp and paper effluent in sequence batch reactor. *Journal of Bioremediation & Biodegradation*, 5 (3): 1 – 10.
11. Doty, S. L. (2008). Enhancing phytoremediation through the use of transgenics and endophytes. *New Phytologist*, 179: 318 – 333.
12. Schnoor, J. L, Licht, L. A, McCutcheon, S. C., Wolfe, N. L. and Carreira, L. H. (1995). Phytoremediation of contaminated soils and sediments. *Environmental Science and Technology*, 29: 318 – 323.
13. Salt, D.E., Smith, R. D., Raskin, I. (1998). Phytoremediation. *Annual Review of Plant Physiology and Plant Molecular Biology,* 49: 643 – 668.
14. Meagher, R. B. (2000). Phytoremediation of toxic elemental and organic pollutants. *Current Opinion in Plant Biology,* 3: 153 – 162.
15. Dietz, A. and Schnoor, J. L. (2001). Advance in phytoremediation. *Environmental Health Perspectives,* 109: 163 – 168.
16. McCutcheon, S. C. and Schnoor, J. L. (2003). Phytoremediation: transformation and control of contaminants. New Jersey, NJ, USA: John Wiley & Sons, Inc.
17. Newman, L.A. and Reynolds, C. M. (2004). Phytodegradation of organic compounds. *Current Opinion in Biotechnology*,15: 225 – 230.
18. Suresh, B. and Ravishankar, G. A. (2004). Phytoremediation – A novel and promising approach for environmental clean – up. *Critical Reviews in Biotechnology,* 24: 97 – 12.
19. Pilon-Smith, E. A. H. and Freeman, J. L. (2006). Environmental cleanup using plants: Biotechnological advances and ecological consideration. *Frontiers in Ecology and The Environment*, 4: 203 – 210.

20. Chappel, J. (1998). Phytoremediation of TCE in groundwater using populus. US Environmental Protection Agency.
21. Stanton, B, Eaton J, Johnson J, Rice D, Schuette B, Moser B. 2002. Hybrid popular in the pacific Northwest. *Journal of Forestry,* 100: 28 – 33.
22. Yan-de, J., Zhen-li, H. E. and Xiao-e, Y. (2007). Role of soil rhizobacteria in phytoremediation of heavy metal contaminated soils. *Journal of Zhejiang University Science B,* 8(3):192 – 207.

*Malaysian Journal of Analytical Sciences, Vol 21 No 1 (2017): 113 - 118*
*DOI: http://dx.doi.org/10.17576/mjas-2017-2101-13*

MALAYSIAN JOURNAL OF ANALYTICAL SCIENCES
*Published by The Malaysian Analytical Sciences Society*
ISSN 1394 - 2506

# CHARACTERIZATION STUDIES OF SODIUM ALGINATE/SULFONATED GRAPHENE OXIDE BASED POLYMER ELECTROLYTE MEMBRANE FOR DIRECT METHANOL FUEL CELL

## (Kajian Pencirian Bagi Membran Elektrolit Polimer Berasaskan Sodium Alginat/Sulfonat Grafin Oksida untuk Sel Bahan Api Metanol Langsung)

Norazuwana Shaari[1]* and Siti Kartom Kamarudin[2]

[1]*Fuel Cell Institute*
[2]*Department of Chemical and Process Engineering, Faculty of Engineering and Built Environment*
*Universiti Kebangsaan Malaysia, 43600 UKM Bangi, Selangor, Malaysia*

**Corresponding author: ctie@ukm.edu.my*

Received: 21 October 2015; Accepted: 14 June 2016

**Abstract**

This work used blending and casting method to synthesis sodium alginate/sulfonated-GO (SA/SGO) polymer electrolyte membrane for direct methanol fuel cell (DMFC). The composition of sulfonated-GO in the membrane is varied from 0 wt% to 1 wt%. The functional groups in the membrane were confirmed by Fourier Transform Infrared analysis. The water uptake capacity of the membrane as observed was reduced with addition of sulfonated-GO as filler in the membrane. Thus, the proposed membrane has good potential to be an alternative membrane in DMFC application.

**Keywords**: fuel cell, graphene oxide, alginate, direct methanol fuel cell

**Abstrak**

Kerja ini menggunakan kaedah pemutus dan pengadunan untuk sintesis polimer membran elektrolit sodium alginat/ sulfonat-GO (SA/SGO) untuk aplikasi sel bahan api metanol langsung (DMFC). Komposisi sulfonat-GO dalam membran diubah daripada 0% berat kepada 1% berat. Kumpulan berfungsi dalam membran telah disahkan oleh analisis Infra merah transformasi Fourier. Kapasiti pengambilan air oleh membran seperti yang diperhatikan telah berkurangan dengan penambahan sulfonat-GO sebagai pengisi dalam membran. Oleh itu, membran yang dicadangkan mempunyai potensi yang baik untuk menjadi membran alternatif dalam aplikasi DMFC.

**Kata kunci:** sel bahan api, grafin oksida, alginat, sel bahan api metanol langsung

## Introduction

The advantages of DMFC as green technology exclusively in portable application tools such as laptop, camera and etc., has been attracted many researchers to explore their enhancement. With very less pollutant emission at the end process, low temperature works condition, compact design, and high power density is the enforcement of their commercialization today [1]. However, there are several things that hindered this commercialization process. The DMFC issues is relate to the low power density, sluggish in kinetic reaction of methanol oxidation, methanol crossover phenomena that leads to the mixed potential and fuel wasting in cathode side and also the very expensive of Nafion membrane that was used as main polymer electrolyte membrane in almost Fuel Cell types systems including DMFC [2].

Nafion is not well known as polymer electrolyte membrane due to its specialty in high proton conductivity, high mechanical strength, and strong chemical stability and well perform in fuel cell performance. It can be said that until now Nafion is the most ideal polymer electrolyte membrane candidate. But, the awareness of fuel cell researchers was increasing nowadays on the bad side of Nafion membrane especially their harmful material used in Nafion, fluorine, and high methanol crossover as well [3]. Thus, many efforts on finding new material for suited as polymer electrolyte membrane function to replace Nafion membrane. The environmental friendly, low cost, and low methanol crossover material seems the most needed characteristics to improved Nafion drawbacks. Alginate is the biopolymer who have that characteristics as it was selected in many applications such medical, packaging, also fuel cell as main polymer matrix membrane [4].

Alginate is a prominent water-soluble polysaccharide found in brown seaweed consisting of (1-4)-linked β-D-mannuronic acid (M) and α-L-gluronic acid (G) units. It has very high water absorption as can absorb 200-300 times its own weight in water. Alginate is able to be invented into a variety forms such as film, microspheres and fibers because of their reversible solubility [5]. However, the application of alginate is limited owing to several weaknesses that high water solubility and low mechanical strength [6]. Its hydrophilicity can be the major problem in DMFC performance because over water uptake in polymer electrolyte membrane will leads to the high swelling ratio thus burst the membrane during working process. Other than that sodium alginate membrane easy to dissolve in wet condition thus lowered its mechanical stability [7].

Inorganic filler such as CNT, zeolite, silica and graphene oxide is the common used to reduce hydrophilic characteristics of polymer. Nowadays, the graphene based material seems conquer the various function including as a filler in membrane [8]. Sulfonated Graphene Oxide is the product of graphene oxide modification process which has many attractive properties. The capability of SGO to be inorganic filler was recognized due to the presence of sulfonic acid group ($SO_3H^-$) on graphene oxide sheets which can contribute in good hydrogen bonding formation with other polymers. The formation of strong hydrogen bonding between SGO and Sodium Alginate polymer matrix can decreased the hydrophilicity and water uptake capacity due to the 'blocking effect' function of SGO [9]. Based on our research, there is no bio-composite Sodium Alginate/sulfonated-GO has been produced yet for DMFC application. Therefore, this research will combine the advantages of Sodium Alginate and sulfonated -GO to form a bio-membrane that have high durability which reduced their water uptake capacity to avoid swelling problem. Effect of sulfonated-GO addition and their interaction were studied using physical observation, Fourier Transform Infrared (FTIR) analysis and water uptake performance test.

## Materials and Methods

### Materials

TIMREX PG25 graphene oxide was purchased from TIMCAL Ltd. Methanol ($CH_3OH$,99.7%). Sodium alginate, hydrogen peroxide aqueous solution ($H_2O_2$, 35%), sulfanilic acid, and sodium nitrite solution were obtained from Sigma Aldrich. These chemicals were used as received without further purification. Deionized (DI) water through a Millipore system (Milli-Q) was used in all experiments.

### Preparation of sulfonated graphene oxide

Graphene oxide by 50 mg added to 8 ml of 0.06 M sulfanilic acid solution at a temperature of 70 °C. With continuous stirring, 2 ml of sodium nitrite solution is added dropwise to the mixture and let stand for 12 hours at a constant temperature of 70 °C. After reaction occurs, the mixture was washed and collected by centrifuge. Then, collected sulfonated-GO is washed for several times more with water until reaching pH 7. The washed SGO solution was dried and SGO powder was obtained.

### Preparation of sulfonated-GO based sodium alginate bio-composite films

Sodium alginate was dissolved in deionized water 1 % (w/v) to obtain a solution of alginate. The various weight percentage of sulfonated-GO (0.2 wt% - 1.0 wt%) was added into Sodium alginate solution to produce a SA/SGO composite film. The mixture must be stirred continuously for 30 minutes with a magnetic stirrer. Heterogeneous solution was transferred to a glass substrate, left at room temperature for 72 hours for thin film formation process. A

series of bio-composite film were coded as SA, SA/SGO-1, SA/SGO-2, SA/SGO-3, SA/SGO-4, SA/SGO-5 according to the different wt% of sulfonated-GO loading.

**Characterization**

The functional groups of Al/SGO with were confirmed by Fourier transform infrared spectroscopy (FTIR). Thirty-two scans were accumulated for FTIR characterization with a resolution of 4 $cm^{-1}$ for each spectrum.

**Performance test (water uptake)**

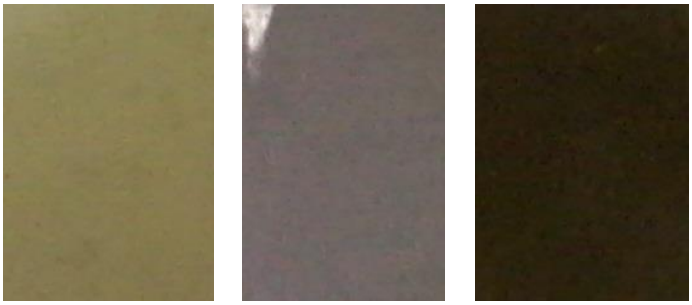
Changes in weight and length (or thickness) of wet and dry membranes will be able to determine the rate of water absorption and swelling ratio of the membrane. The membrane was soaked in water for 24 hours at room temperature. In the wet condition, the weight of membrane was recorded which the liquid droplets on the membrane surface was removed. Earlier moist membrane was dried under vacuum pressure at temperature 100 ˚C for 1 hour. Weight of the membrane in the dry state was also recorded. Using equations (1), water uptake (WU%) can be determined.

$$WU\% = \frac{mass_{wet} - mass_{dry}}{mass_{dry}} \times 100 \quad (1)$$

## Results and Discussion

**Physical observation**

Polymer electrolyte based Sodium alginate thin film with different weight percentage of sulfonated-GO was observed physically and the Figure of each membrane thin film is presented in Figure 1. The colours of membranes become dark when concentration of sulfonated-GO was increased. However, the films were still flexible and homogeneous.



0.6 wt % SGO 0.8 wt% SGO 1.0 wt% SGO

Figure 1. Physical observation sodium alginate membrane with different wt. % of sulfonated-GO

**Fourier transform infrared spectroscopy**

The interactions between sodium alginate and sulfonated-GO were investigated by FTIR analysis. The FTIR spectrum for sodium alginate and SA/SGO membrane were presented in transmittance bands as shown in Figure 2. The FTIR spectrum of SA was compared with previous work and it seems similar. There are four major spectrum belongs to SA which at 3347 $cm^{-1}$, 1600 $cm^{-1}$, 1414 $cm^{-1}$ and 1030 $cm^{-1}$ and its attributed to OH stretching vibration, $COO^-$ stretching vibration of carboxylate salt group, and stretching vibration of C-O-C groups, respectively [10]. The dominant spectrum of GO was emerged at 3401 $cm^{-1}$ for OH group stretching vibration, 1624 $cm^{-1}$ for C=C stretching vibration and 1043 $cm^{-1}$ assigned to C-O groups vibration. All the spectrum of Sodium Alginate and Graphene Oxide was seen exist in the SA/SGO membrane composite. In addition, the membrane composite also has new spectra instead of SA and GO dominant spectrum which appear at around 1024 $cm^{-1}$, 1080 $cm^{-1}$ and 1280 $cm^{-1}$

which attributed to the S–O symmetrical, asymmetric stretching vibration (O=S=O), and sulfonic acid groups bands ($-SO_3H$), respectively.

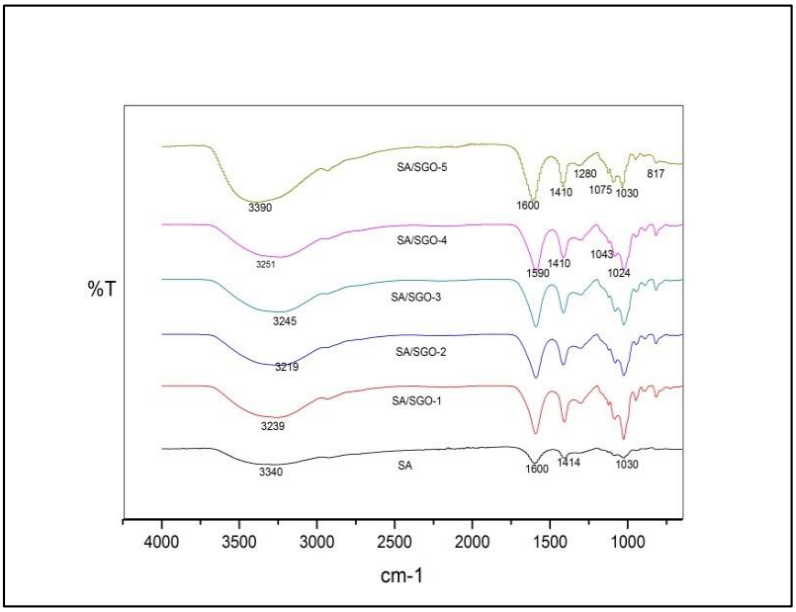



Figure 2. FTIR spectra of Sodium Alginate and various wt. % of sulfonated-GO in sodium alginate membrane

The broadening happened for OH group spectrum at 3347 $cm^{-1}$ it was shifted to the smaller wavelength of 3239 $cm^{-1}$ which is signal that existing of hydrogen bonding interaction between SA and sulfonated-GO [11]. Other than that, the spectrum of SA at 1414 $cm^{-1}$ was also somewhat shifted to the 1410 $cm^{-1}$ wavelength. This spectrum shifting occurred regarding to the existence of hydrogen bonding formation attributed to the interaction of hydroxyl groups in Alginate and polar groups in Sulfonated-GO [9]. This interaction is important factor for increase the mechanical stability of Sodium Alginate which can form and interactive 'blocking effect' especially for water solubility reduction.

**Performance test (water uptake)**

As mentioned above, the performance of polymer electrolyte membrane will be degrading if the amount of water absorbed is over the optimum range. The overloading of water leading to the swelling problem thus membrane will be ruptured. However, the water presence is still important for hydronium ion sources in proton transfer. Thus, the water uptake test is important to ensure that the polymer electrolyte membrane absorbed water in ideal range. Figure 3 are present the result of water uptake of SA-SGO membrane with variation of sulfonated-GO wt%. As presented, the pristine sodium alginate membrane has very high water uptake capacity (180%), which is contra to SA-SGO membrane that have lower water uptake capacity with different content of sulfonated-GO in the membrane. The increasing amount of sulfonated-GO has reduced water uptake due to the blocking ability as filler in the membrane [11]. Higher sulfonated-GO content brings to higher barrier for water absorption of the membrane. The hydrogen bonding existed between sulfonated-GO filler and sodium alginate polymer has strengthened the interfacial adhesion of the membrane composite thus reduce the water uptake capacity. The stronger interfacial adhesion, the lesser the gap size between filler and polymer which the gap is the space for water molecules pass through the membrane [9].

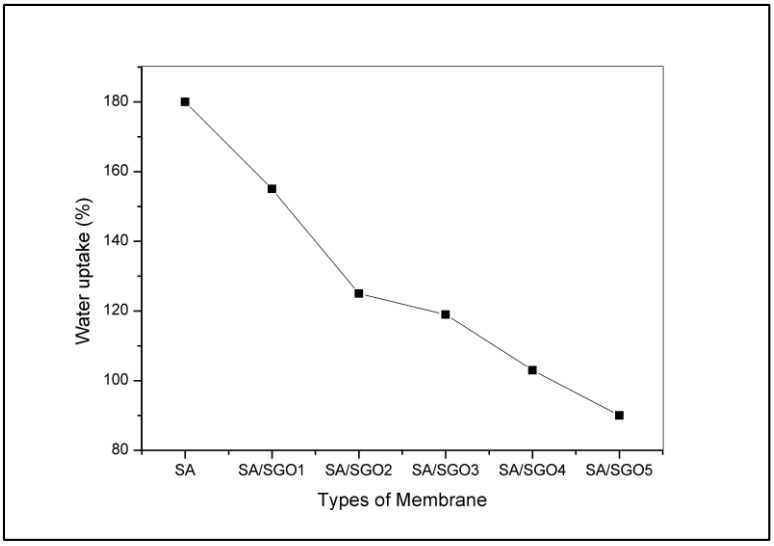



Figure 3. Water uptake of Sodium Alginate and SA/SGO membrane

## Conclusion

The FTIR analysis has confirmed that there is interaction between sodium alginate biopolymer and sulfonated-GO due to the presence of primary spectrum of sodium alginate and GO in the bio-composite. The hydrogen bonding interaction between SA and sulfonated-GO possibly increase the interfacial adhesion between SA and sulfonated-GO consequently enhance the mechanical stability of the bio-composite. The results showed that the existence of sulfonated-GO as filler in sodium alginate biopolymer has reduced the water solubility of the polymer. The lowest water uptake for bio-composite membrane is 90% (SA/SGO-5) with half reduction compared to pure sodium alginate. The present SA/SGO membrane suggested to be further explored in terms of morphology, structure and other performance such proton conductivity and methanol permeability. The excellent water uptake test is the good indicator that this membrane can perform well in DMFC application. The combination between Sodium Alginate polymer and sulfonated-GO seems match to each other with good interaction occur. The major drawback of Nafion also can be solved by using cheaper Sodium Alginate polymer. Thus, the findings in this study can be part of enforcement of DMFC application commercialization in future.

## Acknowledgements

The authors gratefully acknowledge the financial support given for this work by the Universiti Kebangsaan Malaysia (UKM) under GUP-2013-031 and Ministry of Education FRGS/2/2013/TK06/UKM/01/1.

## References

1. Kamaruddin, M. Z. F., Kamarudin, S. K., Daud, W. R. W. and Masdar, M. S. (2013). An overview of fuel management in direct methanol fuel cells. *Renewable and Sustainable Energy Reviews*, 24: 557 -565.
2. Ahmad, H., Kamarudin, S.K., Hasran, U.A., Daud W.R.W. (2010). A Novel Hybrid Nafion-Pbi-Zp Membrane For Direct Methanol Fuel. *International Journal of Hydrogen Energy* , 36: 14668-14677.
3. Shaari, N. and Kamarudin, S. K. (2015). Chitosan and alginate types of bio-membrane in fuel cell application: An overview. *Journal of Power Sources*, 289: 71 - 80.
4. Pasini Cabello, S. D., Mollá, S., Ochoa, N. A., Marchese, J., Giménez, E. and Compañ, V. (2014). New bio-polymeric membranes composed of alginate-carrageenan to be applied as polymer electrolyte membranes for DMFC. *Journal of Power Sources*, 265: 345 - 355.
5. Jost, V., Kobsik, K., Schmid, M. and Noller, K. (2014). Influence of plasticiser on the barrier, mechanical and grease resistance properties of alginate cast films. *Carbohydrate Polymers*, 110: 309 -319.
6. Li, J., He, J., Huang, Y., Li, D. and Chen, X. (2015). Improving surface and mechanical properties of alginate films by using ethanol as a co-solvent during external gelation. *Carbohydrate Polymers*,123: 208 - 216.

7. Tavassoli-Kafrani, E., Shekarchizadeh, H. and Masoudpour-Behabadi, M. (2016). Development of edible films and coatings from alginates and carrageenans. *Carbohydrate Polymers,* 137: 360 - 374.
8. Yuan, T., Pu, L., Huang, Q., Zhang, H., Li, X. and Yang, H. (2014). An effective methanol-blocking membrane modified with graphene oxide nanosheets for passive direct methanol fuel cells. *Electrochimica Acta,* 117: 393 - 397.
9. Jiang, Z., Zhao, X. and Manthiram, A. (2013). Sulfonated poly(ether ether ketone) membranes with sulfonated graphene oxide fillers for direct methanol fuel cells. *International Journal of Hydrogen Energy,* 38(14): 5875 - 5884.
10. Ionita, M., Pandele, M. A. and Iovu, H. (2013). Sodium alginate/graphene oxide composite films with enhanced thermal and mechanical properties. *Carbohydrate Polymers,* 94(1): 339 - 344.
11. Heo, Y., Im, H. & Kim, J. (2013). The effect of sulfonated graphene oxide on sulfonated poly (ether ether ketone) membrane for direct methanol fuel cells. *Journal of Membrane Science,* 425 – 426: 11 -22.

*Malaysian Journal of Analytical Sciences, Vol 21 No 1 (2017): 119 - 126*
*DOI: http://dx.doi.org/10.17576/mjas-2017-2101-14*

MALAYSIAN JOURNAL OF ANALYTICAL SCIENCES
*Published by The Malaysian Analytical Sciences Society*
ISSN 1394 - 2506

# ROLE OF ACTIVE CHROMIUM SPECIES ON DIFFERENT SUPPORT FOR DEHYDROGENATION OF PROPANE

## (Peranan Spesies Kromium Aktif pada Penyokong yang Berbeza dalam Tindak balas Penyahhidrogenan Gas Propana)

Wan Nor Roslam Wan Isahak[1,2]*, Zatil Amali Che Ramli[2], Ibdal Satar[2], Mohamed Wahab Mohamed Hisham[3], Mohd Ambar Yarmo[3]

[1]*Department of Chemical and Process Engineering, Faculty of Engineering and Built Environment*
[2]*Fuel Cell Institute*
[3]*School of Chemical Sciences and Food Technology, Faculty of Science and Technology*
*Universiti Kebangsaan Malaysia, 43600 UKM Bangi, Selangor, Malaysia*

**Corresponding author: wannorroslam@ukm.edu.my*

Received: 21 October 2015; Accepted: 14 June 2016

**Abstract**

Dehydrogenation of propane (DHP) was studied over a series of $Cr_2O_3$–$Al_2O_3$ and $Cr_2O_3$-$SiO_2$ catalysts, prepared by incipient wetness impregnation and sol gel (SG) method, respectively, to gain a better understanding of the nature and distribution of chromium (Cr) species and their catalytic function. To this end, the catalysts were characterized by $N_2$-physisorption and X-ray diffraction (XRD). $N_2$-physisorption analysis of $Cr_2O_3$-$SiO_2$ showed the relatively higher surface area of 391.1 $m^2$/g, compared with $Cr_2O_3$-$Al_2O_3$ of 224.3 $m^2$/g. The combination method of sol gel and sonothermal also produced smaller particles size of catalyst with higher microporosity of 23.5% and smaller pores size of 6 nm. The good surface properties of $Cr_2O_3$-$SiO_2$ enabled the high conversion of propane of 55% at 550 °C. At higher temperature of 600 °C, the Cr species might be reduced into lower oxidation state and inhibit the catalytic behavior to produce hydrogen.

**Keywords**: chromium (II) oxide, thermodynamic consideration, sonothermal, catalytic behavior, hydrogen energy

**Abstrak**

Tindak balas penyah-hidrogenan gas propana (DPP) telah dikaji menggunakan beberapa siri mangkin $Cr_2O_3$–$Al_2O_3$ dan $Cr_2O_3$-$SiO_2$ yang dihasilkan melalui kaedah impregnasi basah dan sol gel (SG) method, untuk memahami sifat dan serakan spesies logam Cr dan fungsi pemangkinannya. Dalam kajian ini, mangkin diciri menggunakan kaedah jerapan gas $N_2$ dan pembelauan sinar X (XRD). Analisis jerapan $N_2$ bagi mangkin $Cr_2O_3$-$SiO_2$ menunjukkan ia mempunyai luas permukaan yang paling tinggi sebanyak 391.1 $m^2$/g, berbanding mangkin $Cr_2O_3$-$Al_2O_3$ sebanyak 224.3 $m^2$/g. Kombinasi kaedah sol gel (SG) dan sonotermal menghasilkan mangkin yang bersaiz lebih kecil dengan keporosan mikro sebanyak 23.5% dan saiz liang sebanyak 6 nm. Ciri-ciri permukaan yang baik ditunjukkan oleh mangkin $Cr_2O_3$-$SiO_2$ menyumbang kepada aktiviti tindak balas yang baik dengan peratus penukaran propana yang tinggi sebanyak 55% pada suhu 550 °C. Pada suhu tindak balas 600 °C pula, spesies logam Cr boleh terturun kepada keadaan pengoksidaan yang lebih rendah dan merencat tindak balas pemangkin bagi menghasilkan gas hidrogen sebagai produk utama.

**Kata kunci:** kromium (II) oksida, pendekatan termodinamik, sonotermal, sifat pemangkinan, tenaga hidrogen

## Introduction

Propane is produced as a by-product of two other processes, natural gas processing and petroleum refining. The processing of natural gas involves removal of butane, propane, and large amounts of ethane from the raw gas, in order to prevent condensation of these volatiles in natural gas pipelines. Commonly, the dehydrogenation of propane can produce propene and hydrogen as a greener and future fuel sources and carried higher energy [1]. The reaction conditions play a major role to direct the reaction route and selected products. It is possible to produce hydrogen by catalytic dehydrogenation of propane, according to the following reaction (equation 1 and 2):

$$C_3H_8 \rightarrow C_3H_6 + H_2 \qquad \Delta H^o = 124\ kJ.mol^{-1} \tag{1}$$

$$C_3H_8\ (g) \rightarrow C\ (s) + C_2H_6\ (g) + H_2\ (g) \qquad \Delta H^o = 19.1\ kJ.mol^{-1} \tag{2}$$

However, this reaction cannot be carried out easily due to its strong endothermicity ($\Delta H^o_r = 124\ kJ.mol^{-1}$). Sattler et al. [2] were reviewed various type of catalytic dehydrogenation of light alkanes into other products namely methane, hydrogen, ethane and other series of alkenes. Several type of catalyst have been studied by researchers such as platinum-based, gallium oxide-based and vanadium oxide-based catalysts. In other work, Lee et al. [3] was reported the Sn addition to the $Pt_{0.5}/\theta\text{-}Al_2O_3$ catalyst can decreased the cracking products of $C_1$-$C_3$ and increase the stability and olefin selectivity.

This paper was focused on the hydrogen formation by catalytic dehydrogenation of propane. The effect of chromium species was also studied. The pure hydrogen can be produced from this reaction.

## Materials and Methods

### Thermodynamic consideration

The catalyst selection was performed using a simple thermodynamic approach based on thermodynamic data. Several pyrolysis routes have been selected to study the possibility. For example, the propane gas can be pyrolyzed into methane and hydrogen. There was some possible route for propane dehydrogenation reaction (equation 3 - 5).

$$C_3H_8 \rightarrow C_3H_6 + H_2 \tag{3}$$

$$C_3H_8 \rightarrow 2C + CH_4 + 2H_2 \tag{4}$$

$$C_3H_8 \rightarrow 3C + 4H_2 \tag{5}$$

### Synthesis of catalyst

The catalyst $15\%Cr_2O_3/\gamma\text{-}Al_2O_3$ was synthesized by using the wet impregnation method. 3.95g of $Cr(NO_2)_3{\cdot}9H_2O$ was dissolved in 10 ml of distilled water. Then, 8.5g of $\gamma\text{-}Al_2O_3$ was added into the solution and stir for 1 hour. The mixed sample was introduced to ultrasonicator for 10 minutes. The sample was dried at 110 °C and calcine at 400 °C for 3 hours before the catalyst is ready to test in reaction.

The $15\%Cr_2O_3/SiO_2$-sol gel (SG) was prepared by sol gel method by mixing the tetraethyl orthosilicate (TEOS) and ethanol with molar ratio of 1:1 to obtain a sol gel precursor solution. Then, several amount of $Cr(NO_2)_3{\cdot}9H_2O$ was dissolved in distilled water followed by some nitric acid addition. Both mixtures were stirred by vigorous magnetic stirring separately at room temperature until the pH 2 was observed. The solution was lifted for 24 hours until gelation is complete. The samples were dried at 110 °C and calcined at 400 °C for 3 hours before ready for use.

### Characterization of catalyst

Nitrogen adsorption at 77K (liquid nitrogen) was conducted using a Micromeritics ASAP 2010 instrument to obtain the adsorption isotherm of each sample. The Brunauer-Emmett-Teller (BET) surface area, micropore volume and micropore area were calculated from the isotherms. Before analysis was conducted, the samples were degassed at 350 °C for 6 hours. The crystallinity analyses of the samples were performed using a Bruker DB-Advance X-ray Diffractometer (XRD), Germany. The analyses were performed with 1-g samples, employing Cu Kα radiation at 2θ ranging from 10° to 80°.

**Propane pyrolysis reaction**

The propane pyrolysis was conducted using fluidized bed reactor under propane gas flows at ranging of 30 – 70 mL/min. The output gas was analyzed using GC-FID.

## Results and Discussion

**Thermodynamic consideration**

There were several possible reactions might be occurred during the pyrolysis of propane as showed in Table 1. The reactions 3 to 5 (R1-R5) are very favorable at low temperature. However, the possible R1 and R2 is need high temperature to occur (more than 972 k). Theoretically, R3 to R5 can occur at relatively low ranging temperature of 180 – 402 K. However, the presence of energy barrier or high activation energy during the reaction contributed the sum of error around 30 kJ/mol$^{-1}$ or 500 K. It was noted that the tendency to produce carbon during propane pyrolysis is high in the present of metal oxide catalyst [4,5].

Table 1. Thermodynamics data of possible reactions for propane pyrolysis

| Reaction Involved | ΔH (Kj·Mol$^{-1}$) | ΔS (J·Mol$^{-1}$·K$^{-1}$) | ΔG (Kj·Mol$^{-1}$) | T (K) | Reaction Possibility |
|---|---|---|---|---|---|
| $C_3H_6$ (g) → $C_3H_6$ (g) + $H_2$ (g) **R1** | 124.2 | 127.8 | 0 | 972 | Favourable at high temperature |
| $C_3H_8$ (g) → $C_2H_2$ (g) + $CH_4$ (g) + $H_2$ (g) **R2** | -197.7 | -153.8 | -5 | 1253 | Favourable at very high temperature |
| $C_3H_8$ (g) → C (s) + $C_2H_6$ (g) + $H_2$ (g) **R3** | 19.1 | 84.7 | -5 | 285 | Favourable |
| $C_3H_8$ (g) → 2C (s) + $CH_4$ (g) + 2$H_2$ (g) **R4** | 29.0 | 189.3 | -5 | 180 | Favourable |
| $C_3H_8$ (g) → 3C (s) + 4$H_2$ (g) **R5** | 103.8 | 270.9 | -5 | 402 | Favourable |

**Catalysts surface properties**

Figure 1 showed the adsorption-desorption isotherm of the fresh support and modified catalyst. The fresh $SiO_2$ (Figure 1 (a)) and $Al_2O_3$ (Figure 1 (b)) showed the adsorption isotherms type II and IV, respectively. However, the dispersion of $Cr_2O_3$ on $SiO_2$ (in Figure 1 (c)) was changed the adsorption isotherm into type I. Type I isotherms are observed for the adsorption of gases on microporous solids whose pore sizes are not much larger than the molecular diameter of the adsorbate. This property can bring forward the solid-gases reaction which is most of the reaction occurs in pores and surfaces [6]. On the other hand, the $Cr_2O_3/SiO_2$ catalyst (Figure 1 (d)) showed the hysteresis type IV represented to slit-shaped pores with uniform in size [7]. This type of hysteresis can maximize the reactant adsorption during reaction and desorbed the products easily. Table 2 showed the better surface properties of $Cr_2O_3/SiO_2$ with higher surface area and microporosity of 391.1 m$^2$/g and 23.5%, respectively. The higher surface area with maximum metal oxide dispersion would lead the higher active sites and subsequently contribute to good catalytic activity.

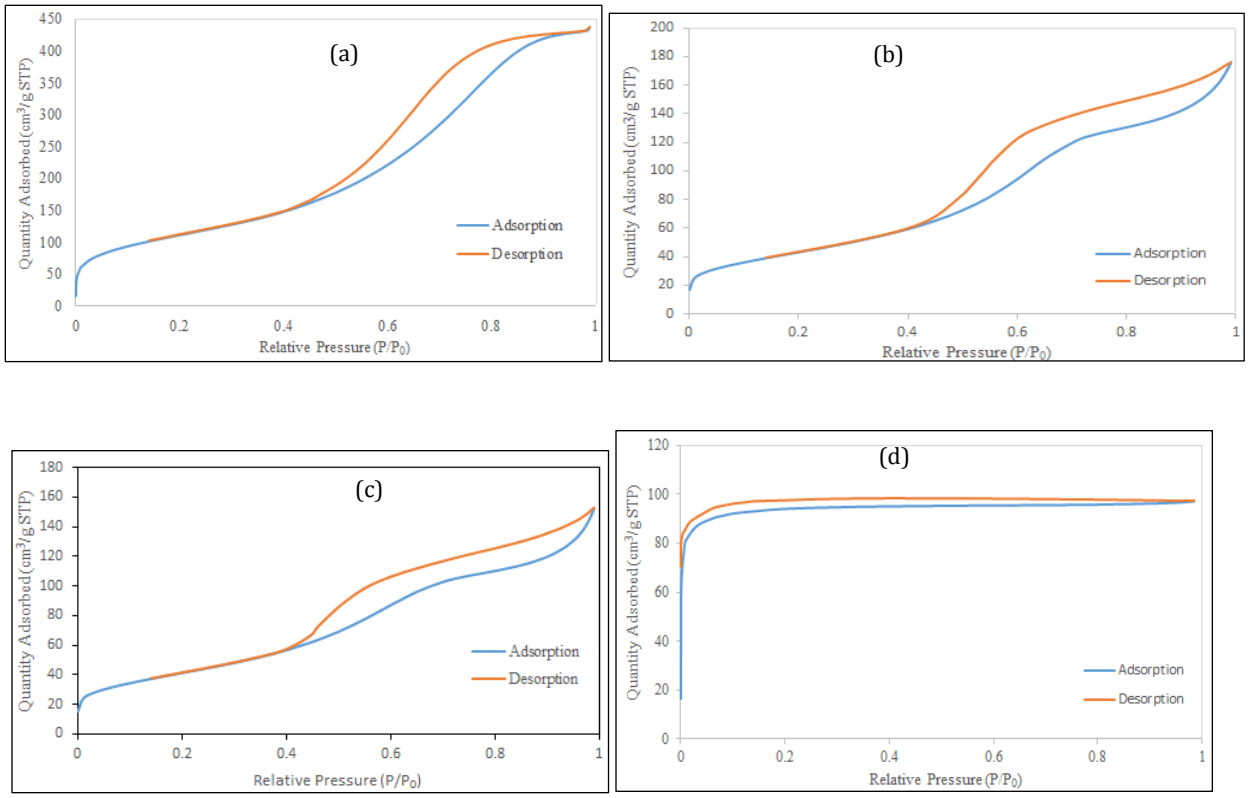



Figure 1. The isotherms of a) $SiO_2$, b) $Al_2O_3$, c) $Cr_2O_3$-$Al_2O_3$ and d) $Cr_2O_3$-$SiO_2$ SG

Table 2. The physical properties of catalysts

| Selected Catalysts | Microporosity (%) | Pores Size (nm) | Surface area ($m^2/g$) |
|---|---|---|---|
| $SiO_2$ | 4.8 | 6.83 | 391.1 |
| $Al_2O_3$ | 1.3 | 6.85 | 154.4 |
| $Cr_2O_3$-$Al_2O_3$ | 1.4 | 6.02 | 308.8 |
| $Cr_2O_3$-$SiO_2$ | 23.5 | 6.19 | 224.3 |

**Crystallinity of catalyst**

XRD analyses were performed for the $Cr_2O_3/Al_2O_3$, $Cr_2O_3/SiO_2$, $SiO_2$ and $Al_2O_3$ as a support. Figure 2 (a) and 2 (b) showed the XRD patterns for semicrystalline $SiO_2$ and crystalline $Al_2O_3$, respectively. Figure 2(c) showed the low intensity of $Cr_2O_3$ phase which detected at 34.8° and 54.4° with rhombohedral lattice system and the diffraction data match very well with JCPDS card of $Cr_2O_3$ (JCPDS 70-3765). No $CrO_2$ phase was detected in this catalyst. The $Cr_2O_3/SiO_2$ catalyst (Figure 2 (d)) showed three phases of $Cr_2O_3$ at 32.6°, 34.7° and 54.3° with rhombohedral lattice system. The single phase of $CrO_2$ was detected at 64.1° with orthorhombic lattice system and the diffraction data match very well with the JCPDS card of $CrO_2$ (JCPDS 75-7969). The high oxygen level of $CrO_2$ phase can accelerate the propane cracking into hydrogen, propene, methane and carbon deposition [8]. After reaction, the graphite phase was detected in the catalyst due to carbon deposition as one of the product of the reaction at relatively high temperature. Besides, the Cr(IV) was fully reduced into Cr(III) due to high temperature reaction of 600 °C.

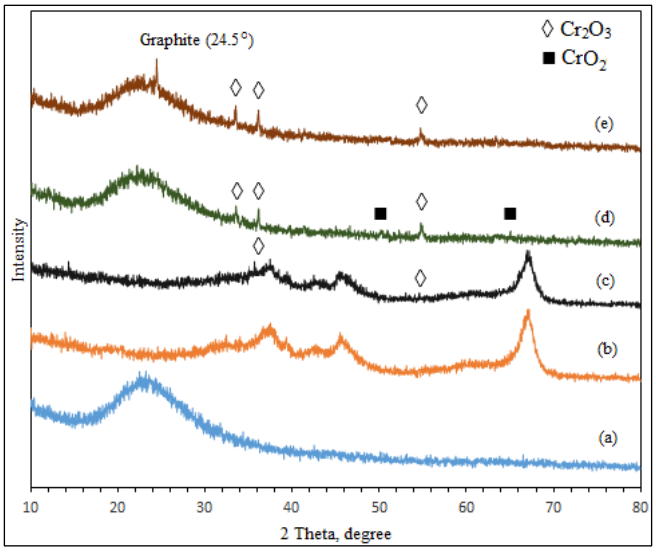



Figure 2. XRD diffractogram of (a) fresh $SiO_2$, (b) fresh $Al_2O_3$, (c) 15%$Cr_2O_3/Al_2O_3$, (d) 15%$Cr_2O_3/SiO_2$ and (e) 15%$Cr_2O_3/SiO_2$ after reaction

**Catalytic performances**

The pyrolysis reaction of propane gas was studied based on several parameters such as the effect of reaction temperature, reactant flowrate, reaction time and catalysts type. This reaction was performed in the range of temperature of 450 – 600 °C. The range was selected by calculation of thermodynamic data which was favorable to occur. Figure 3 showed the effect of reaction temperature on propane pyrolysis into hydrogen and other hydrocarbon or carbon due to highly dispersion of Cr species on $SiO_2$ surfaces. However, at 600 °C, the propane conversion was relatively decreases due to $Cr_2O_3$ fully converted to $CrO_2$ which decrease the catalyst activity of dehydration reaction with $C_3H_6$ and $H_2$ are dominant products. Figure 4 showed the effect of residence time to propane conversion. The residence time is depended to the flowrate of the reactant which reacted to the catalyst. In this reaction, it was noted that higher residence time of 30 seconds gave the longer time for reaction to be occurred and achieved the completion.

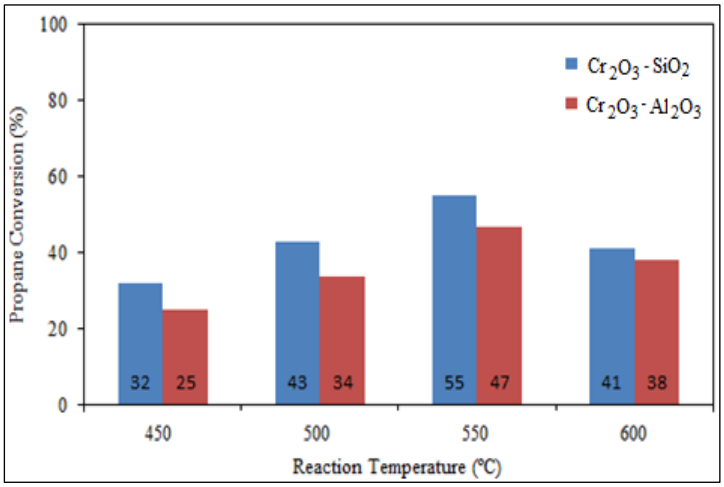



Figure 3. Effect of reaction temperature of (a) $Cr_2O_3/SiO_2$ SG and (b) $Cr_2O_3/Al_2O_3$ (Reaction carried out at flowrate of 60 mL/min)

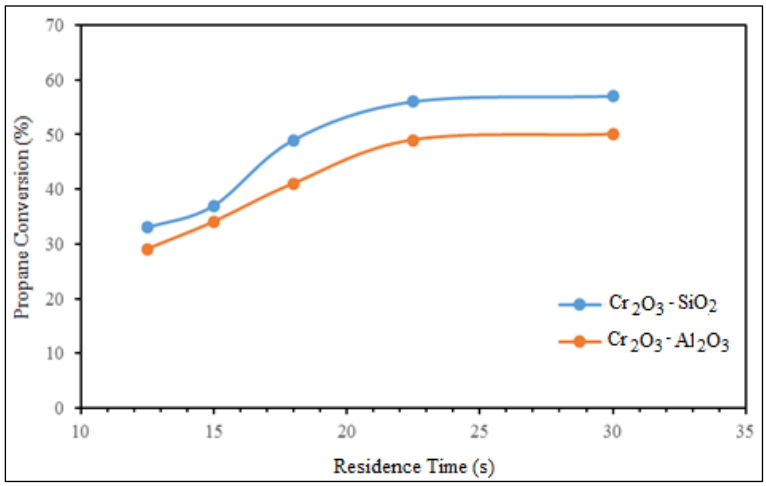



Figure 4. Effect of residence time of the reaction on $H_2$ production for (a) $Cr_2O_3$-$Al_2O_3$ and (b) $Cr_2O_3$-$SiO_2$ SG (Reaction carried out at 550 °C)

In Figure 5, at different reaction temperature, the $Cr_2O_3$-$SiO_2$ SG showed a series of products. At 550 °C, the hydrogen is a major product followed by carbon deposition and $C_3H_6$ formation. However, at 600 °C, the propene is significantly increased. It was noted that the high energy supply can bring forward the reaction route which produced hydrogen and propene as major products [3].

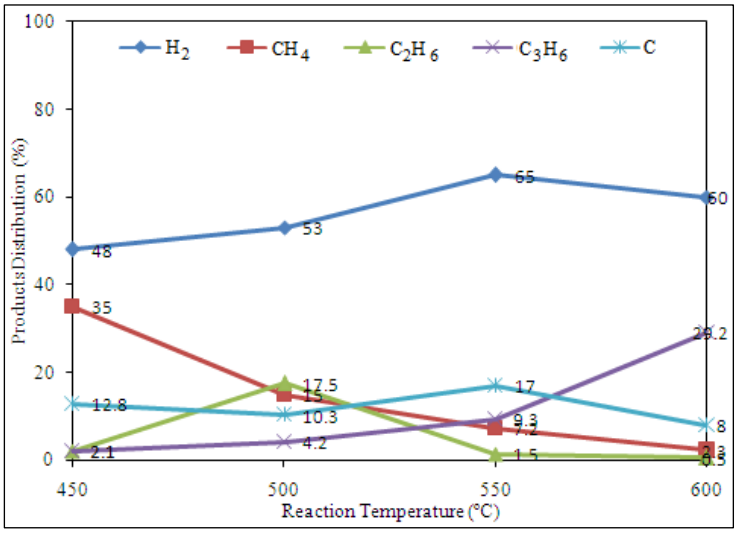
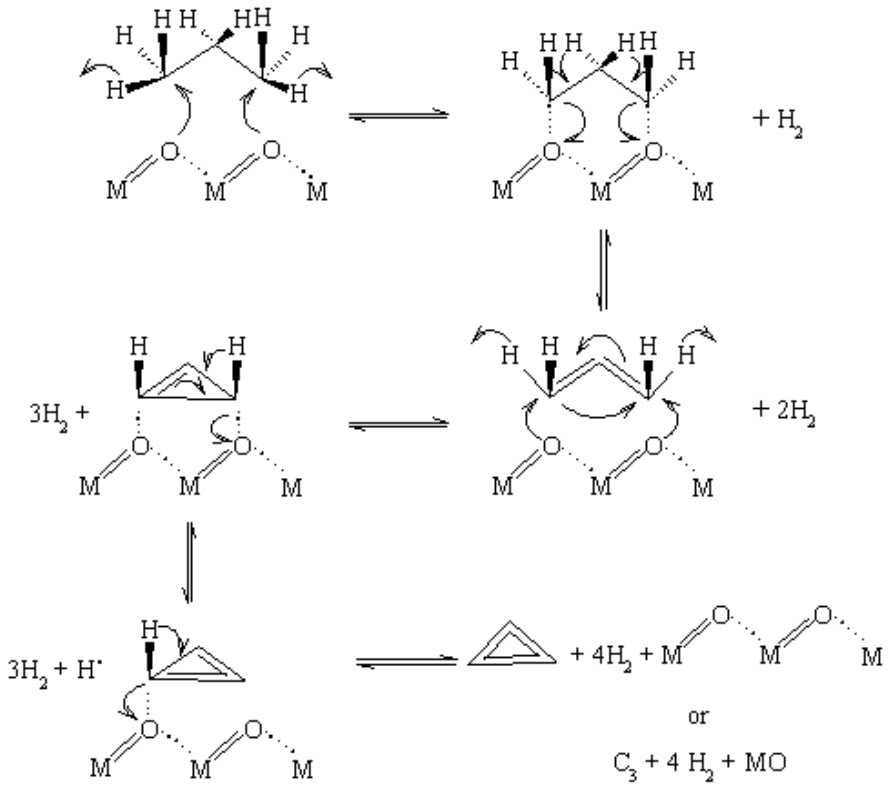



Figure 5. The products distribution from propane pyrolysis using $Cr_2O_3$-$SiO_2$ SG at optimum condition (Reaction was carried out at flowrate of 60 mL/min)

**Proposed mechanism**

Thermodynamics theory approach can be used for evaluation the potential of metal oxide (MO) as catalyst in propane pyrolysis process. Theoretically, the breaking of hydrogen chain from carbon can easier occur if the formation of the new bond between MO and carbon is stronger. The bond between the carbon and MO known as

physical interaction (van der wall bond), where the interaction is weak, but due to the effects of temperature, the heavier atoms (i.e., carbon and MO) tends easier to form a slightly stronger bonds than lighter atoms (i.e., hydrogen), consequently, the hydrogen bonds in the carbon is easier to break at lower temperatures. Thus, the catalyst material is expected to help increase the rate of hydrogen production and reduces the reaction temperature. The reaction mechanism between the MO with propane can be described in several possible routes as showed in Scheme 1.




Scheme 1. Proposed mechanism of propane dehydrogenation over metal oxide catalyst

A thermodynamic calculation to illustrate that the mechanism (1) may only occur at high temperatures (≈ 400 K) due to the entropy of the reaction is very high [9,10] . This due to the process of acquiring C is through the chain termination mechanism of double or triple bonds of C. In this case, all of the hydrogen atom consist of propane has been transformed into four moles of $H_2$ molecules and created a very stable double or triple bond of carbon which required a relatively high energy to dissociate. However, this mechanism just a form that is closest to clarify the possibility of the mechanism due to this mechanism is very complex which involves the variety of free radicals [11].

## Conclusion

Hydrogen as a green fuel was successfully produce by dehydrogenation of propane in the presence of Cr-based catalyst. Thermodynamic calculation showed the feasibility of propane pysolysis into several products such as hydrogen, methane, propene and carbon depends on the reaction temperature. The $Cr_2O_3/SiO_2$ catalyst showed the better surface properties with high surface area of 393.1 $m^2/g$, microporosity of 23.5% and slit-shaped micropores. These properties were contributed to the higher propane conversion of due to high catalytic and gas adsorption ability. At 550 °C, the hydrogen, $C_3H_6$ and carbon were dominant products with 55% of propane conversion. However, in long period, the high carbon deposition can deactivate the catalyst by covering the pores and surface and reduce the selectivity to hydrogen as a major product.

**Acknowledgement**

The authors wish to thank Universiti Kebangsaan Malaysia (UKM) for funding this project under research grant, DIP-2016-010, FRGS/1/2015/SG01/UKM/02/2 and DPP-FKAB-2015 and the Centre of Research and Innovation Management (CRIM) UKM for the use of the instruments.

**References**

1. Caspary, K. J., Gehrke, H., Heinritz-Adrian, M. and Schwefer, M. (2008). Handbook of heterogeneous catalysis. Chapter 14: Dehydrogenation of alkanes. John Wiley & Sons.
2. Sattler, J. J. H. B., Ruiz-Martinez, J., Santillan-Jimenez, E. and Weckhuysen, B. M. (2014). Catalytic dehydrogenation of light alkanes on metals and metal oxides. *Chemical Reviews,* 114 (20): 10613 –10653.
3. Lee, M-H., Nagaraja, B. M., Lee, K. Y. and Jung, K. D. (2014). Dehydrogenation of alkane to light olefin over $PtSn/Al_2O_3$ catalyst: Effects of Sn loading. *Catalysis Today,* 232: 53 – 62.
4. Wagman, D. D., Evans, W. H., Parker, V. B., Schumm, R. H., Halow, I., Bailey, S. M., Churney, K. L. and Nutall, R. L. (1989). The NBS tables of chemical thermodynamic properties selected values for inorganic and C1 and C2 organic substance in SI units. *Journal of Physical Chemistry Reference Data,* 11 (2): 1807.
5. Isahak, W. N. R. W., Ramli, Z. A. C., Ismail, M. W., Ismail, K., Yusop, R. M., Hisham, M. W. M. and Yarmo, M. A. (2013). Adsorption–desorption of $CO_2$ on different type of copper oxides surfaces: Physical and chemical attractions studies. *Journal of $CO_2$ Utilization,* 2: 8 – 15.
6. Brunauer, S., Emmett, P. H. and Teller, E. (1938). Adsorption of gasses in multimolecular layers. *Journal of the American Chemical Society,* 60: 309 – 316.
7. Rouquerol, J., Avnir, D., Fairbridge, C. W., Everett, D. H., Haynes, J. H., Pernicone, N., Ramsay, J. D. F., Sing, K. S. W. and Unger, K. K. (1994). IUPAC Recommendations for the characterization of porous solids. *Pure and Applied Chemistry,* 66: 1739 – 1758.
8. Kumar, M. S., Hammer, N., Rønning, M., Holmen, A., Chena, D., Walmsley, J. C. and Øye, G. (2009). The nature of active chromium species in Cr-catalysts for dehydrogenation of propane: New insights by a comprehensive spectroscopic study. *Journal of Catalysis,* 261 (1): 116 – 128.
9. Karapet'yants, M. K. and Karapet'yants, M. L. (1970). Thermodynamic constants of inorganic and organic compounds. Ann Arbor-Humphrey Science Publishers.
10. Zeng, G., Tian, Y. and Li, Y. (2010). Thermodynamic analysis of hydrogen production for fuel cell via oxidative steam reforming of propane. *International Journal of Hydrogen Energy,* 35 (13): 6726 –6737.
11. Albright, L. F., Crynes, B. L. and Corcoran, W. H. (1983). Pyrolysis: Theory and industrial practice New York: Academic Press.

*Malaysian Journal of Analytical Sciences, Vol 21 No 1 (2017): 127 - 135*
*DOI: http://dx.doi.org/10.17576/mjas-2017-2101-15*

MALAYSIAN JOURNAL OF ANALYTICAL SCIENCES
*Published by The Malaysian Analytical Sciences Society*
ISSN 1394 - 2506

# COMPARISON STUDY BETWEEN EXTRUSION AND INJECTION MOLDING ON CELLULAR STRUCTURE OF PP/PS/PMMA TERNARY BLEND FOAM

## (Kajian Perbandingan di antara Kaedah Proses Penyemperitan dan Proses Pengacuan Suntikan ke atas Struktur Sel PP/PS/PMMA Campuran Pertigaan Busar Polimer)

Rahida Wati Sharudin[1,3]* and Masahiro Ohshima[2]

[1]*Faculty of Chemical Engineering,*
*Universiti Teknologi MARA, 40450 Shah Alam, Selangor, Malaysia*
[2]*Department of Chemical Engineering,*
*Kyoto University, Kyoto 615-8510, Japan*
[3]*Institute for Infrastructure Engineering & Sustainable Management (IIESM), Faculty of Civil Engineering,*
*Universiti Teknologi MARA, 40450 Shah Alam, Malaysia*

**Corresponding author: rahida@salam.uitm.edu.my*

Received: 21 October 2015; Accepted: 14 June 2016

**Abstract**

The effect of blending method on the blend morphology as well as cellular structure of Polypropylene (PP)/Polystyrene (PS)/ Polymethyl methacrylate (PMMA) ternary polymer blend was investigated. The blending method highly influenced the dispersion and size of dispersed domain where the injection molding method was successfully reduced the size of dispersed domain from 10 µm by extrusion further down to 1 µm in average diameter. The batch pressure quenched foaming of the ternary blend prepared by extrusion and injection molding with supercritical carbon dioxide ($CO_2$) was conducted in the temperature range of 130 to 160°C to observe the controllability of bubble location and size in two different ternary blend systems. The experimental results showed that method of sample preparation is one of the important factors in controlling the cellular structure of ternary blend foam besides interfacial tension, foaming temperature, and viscoelasticity.

**Keywords:** polymer blend, extrusion, injection molding, cellular structure, foam

**Abstrak**

Kesan kaedah pencampuran pada morfologi dan juga struktur sel Polipropena (PP)/Polisterina (PS)/ Polimetil metaakrilat (PMMA) campuran pertigaan polimer telah dikaji. Kaedah pencampuran sangat mempengaruhi penyebaran dan saiz domain di mana kaedah pengacuan suntikan telah berjaya mengurangkan saiz domain dari 10 µm oleh kaedah penyemperitan kepada serendah 1 µm diameter purata. Proses pelepasan tekanan secara mendadak dengan karbon dioksida genting lampau ($CO_2$) telah dijalankan bagi penghasilan sampel busar daripada gabungan pertigaan polimer dalam lingkungan suhu 60-130°C untuk melihat kebolehkawalan lokasi gelembung dan saiz. Keputusan eksperimen menunjukkan bahawa kaedah penyediaan sampel, tegangan antara permukaan dua polimer, suhu pembentukan busar dan likat-kenyal adalah faktor penting untuk mengawal struktur sel dalam sistem gabungan pertigaan polimer.

**Kata kunci:** percampuran polimer, penyemperitan, pengacuan suntikan, struktur sel, busar

## Introduction

Polymer blends received many attentions due to the increasing application of plastic industry especially in automobile, packing, and many potential applications. Recently, much attention has been directed to ternary polymer blend [1]. Prior to develop a new material based on multi-component polymer, understanding and controlling the phase morphology are the primary interest. This is because the morphology is directly influenced the mechanical performance in polymer blend [2]. These final properties of polymer blend can be controlled by considering polymer molecular structure, composition, molecular weight [3], and method of blend preparation [4]. According to Guo et al. [5], in ternary polymer system, one of the minor components formed an encapsulating layer around domains of other minor components (encapsulation-type morphology) as shown in Figure 1. Whereas in other systems the two minor components formed independent phases (separation-type morphology).

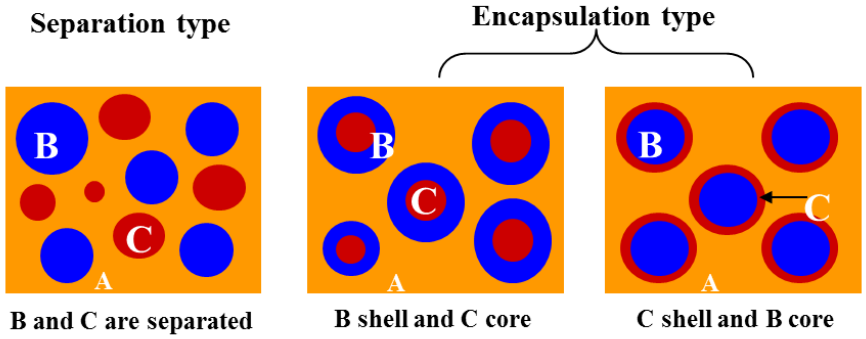



Figure 1. Three possible morphologies of ternary polymer blend, (A: matrix, B and C: dispersed phase)

They claimed that these ternary blend systems can also be predicted by calculating the Gibbs free energy or interfacial energy shown in the following equations [5]:

$$\left(\sum A_i \gamma_{ij}\right)_{B+C} = (4\pi)^{1/3}\left[n_B^{1/3} x^{2/3} \gamma_{AB} + n_C^{1/3} \gamma_{AC}\right](3V_C)^{2/3} \quad (1)$$

$$\left(\sum A_i \gamma_{ij}\right)_{B/C} = (4\pi)^{1/3}\left[n_B^{1/3} (1+x)^{2/3} \gamma_{AB} + n_C^{1/3} \gamma_{BC}\right](3V_C)^{2/3} \quad (2)$$

$$\left(\sum A_i \gamma_{ij}\right)_{C/B} = (4\pi)^{1/3}\left[n_B^{1/3} x^{2/3} \gamma_{BC} + n_C^{1/3} (1+x)^{2/3} \gamma_{AC}\right](3V_C)^{2/3} \quad (3)$$

where $A$ is interfacial area, $\gamma_{ij}$ is interfacial tension between component $i$ and $j$, $V$ is the volume of particle and $x = V_B/V_C$, $n_B$ and $n_C$ are numbers of particles of B and C phases in the system. The values of $\Sigma A\gamma_{ij}$ are compared for the three structures and the equilibrium phase structure of the system is predicted by considering the lowest free energy needed for creating the morphology.

In recent years, there are relatively few studies done on multicomponent blend foaming have been reported. In spite of the fact that the understanding on phase morphology of multicomponent blend is less understood, lack attention is given to ternary polymer blend foaming study. As in binary polymer blend foaming, the concept of creating a microcellular/ nanocellular foam based on solubility and diffusivity of $CO_2$ is also can be applied in ternary polymer blend foaming. By exploiting ternary polymer blend morphology as a template for foaming and by differentiating the solubility of foaming agent as well as the elasticity of the domain to be foamed from the domains to be kept solid state, the bubble location and size could be controlled in the targeting domains [6] as illustrated in Figure 2.

However, the cellular structure is determined not only by the morphology and physical properties of polymers such as viscosity, solubility and diffusivity of the physical foaming agent in the polymers, but also by the size of dispersed domain. Several studies showed that size of dispersed domain was successfully reduced by improving compatibility between polymers [7-10], adding third immiscible component to binary polymer blend [11] and preparing blend sample via injection molding [12].

The work described here is a follow-up to our previous study on PP/PS/PMMA ternary blend foaming [6]. In the current study, the effect of dispersed domain's size on cellular structure of ternary polymer blend was investigated. We compare the cellular structure of PP/PS/PMMA blend foams prepared by two different blending methods namely extrusion and injection molding. A series of pressure quench foaming experiments have been conducted to evaluate the role of blending method effects on size of dispersed domain and foaming behaviour of ternary polymer blend.

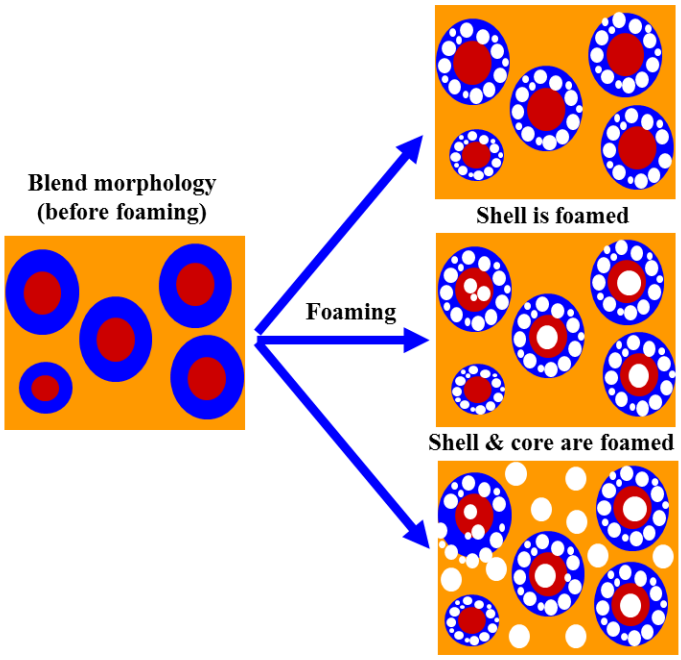



Figure 2. Possible cellular structures of ternary polymer blend foam

## Materials and Methods

### Materials

Polypropylene (PP, Mw= 410,000) and Polycarbonate (PC, Mw= 22,000) were supplied by Mitsubishi Chemical. Polystyrene (PS, Mw= 192,000) and Poly (methyl-methacrylate) (PMMA, Mw= 120,000) were obtained from Aldrich Chemical Co. All polymers were used as received.

### Sample preparation

Blend samples were mixed and compounded via injection molding at 260 °C for PP/PS/PMMA (80/10/10) and 280 °C for PC/PS/PMMA (80/10/10) blend samples. The morphology of the sheet was investigated via SEM (Tiny-SEM, Technex Lab Co. LTD., Tokyo, Japan).

### Batch physical foaming process

The injection molded PP/PS/PMMA ternary blend samples were placed in a high-pressure vessel. The pressure vessel was pressurized by $CO_2$ and was rapidly heated to the desired saturation temperature. After a given time of saturation (about 6 hours), the $CO_2$ in the pressure vessel was quickly released at a rate of 10 MPa/s to nucleate bubble in the polymer. The foamed blends were taken out for further analyses mainly by SEM.

**SEM analysis**

Blend as well as foam samples were cryo-fractured by nitrogen gas and were then gold coated prior been analyzed via SEM (Tiny- SEM, Technex Co. Ltd., Japan).

## Results and Discussion

**Blend morphology characterization**

In our previous study [6], the SEM micrographs of the obtained PP/PS/PMMA blends before acid acetic and cyclohexane treatments clearly showed the sea and island morphology where PP as a sea while PS/PMMA minor phases existed in the form of a dispersed spherical particles at approximately 10 μm in average diameter. It was also observed that some particles were detached while preparing the sample for microscopy analysis, and this resulted in voids in the matrix. According to Reignier et. al [13], there are three possible phase structures could be obtained for ternary blend system which are:

(i) the PMMA phase is encapsulated by the PS phase (PS/PMMA);
(ii) the PS phase is encapsulated by the PMMA phase (PMMA/PS); and
(iii) the PS and PMMA phases form separate phases (PS+PMMA).

For the purpose of identifying type of morphology in PP/PS/PMMA blend, the solvent etching was conducted. It was found that PMMA is encapsulated by PS where PMMA was selectively removed by acetic acid and PS by cyclohexane. The predicted morphologies by interfacial free energy model corroborated the morphologies experimentally as shown in Table 1. The most stable morphology is represented by the lowest value of surface energy of Gibbs energy of mixing [14].

Figure 3 shows the SEM micrographs of blend morphologies of the samples before and after solvent etching prepared by injection molding. The SEM results show that injection molded of PP/PS/PMMA blend gave elongated domain. The increasing shear flow gave increasing elongation until it reached a critical shear rate at which elongated domains dispersed into finer domain. Our results also show that injection molding was successfully reduced the size of dispersed domain while the morphology remained the same. This indicates that sample with a large number of finely dispersed domain could be achieved by injection molding. According to Zhong et al. [15], smaller dispersed domain can be achieved due to large force acting on the dispersed domains induced by high injection flow rate causes the particles became more deformed and were easier to break up.

Table 1. Predicted equilibrium morphology for PP/PS/PMMA ternary blends by Gibbs free energy or interfacial free energy

| Type of morphology | $\Sigma A\gamma_{ij}$ (dyne cm) |
|---|---|
| B+C | 40.1 N |
| B/C | 32.6 N |
| C/B | 42.0 N |

PP matrix (PP: A, PS: B, PMMA: C)

**Foaming behavior of PP/PS/PMMA (80/10/10) ternary blend system prepared by extruder and injection molding**

In our previous paper [6], we have reported that the pressure quench foaming result demonstrated an interesting phenomenon where a unique cell structure of PS/PMMA dispersed domain was kept their spherical shape and been encapsulated by large void space at foaming temperature range of 130 to 155 ºC. From the observation, we claimed that large bubbles were originated from the interface between PP matrix and PMMA/PS core-shell domain, and small bubbles were from PP matrix. For all foaming temperature studied, it was observed that controllability of bubble nucleation and location in PP/PS/PMMA blend was restricted by high interfacial tension between PP matrix

and PMMA/PS core-shell domain. High value of the interfacial tension between two polymers generally provides a channel for $CO_2$ diffusion. As a result, the nucleation of bubble is limited only in amorphous PP matrix and at the interface between PP matrix and PMMA/PS core-shell domain.

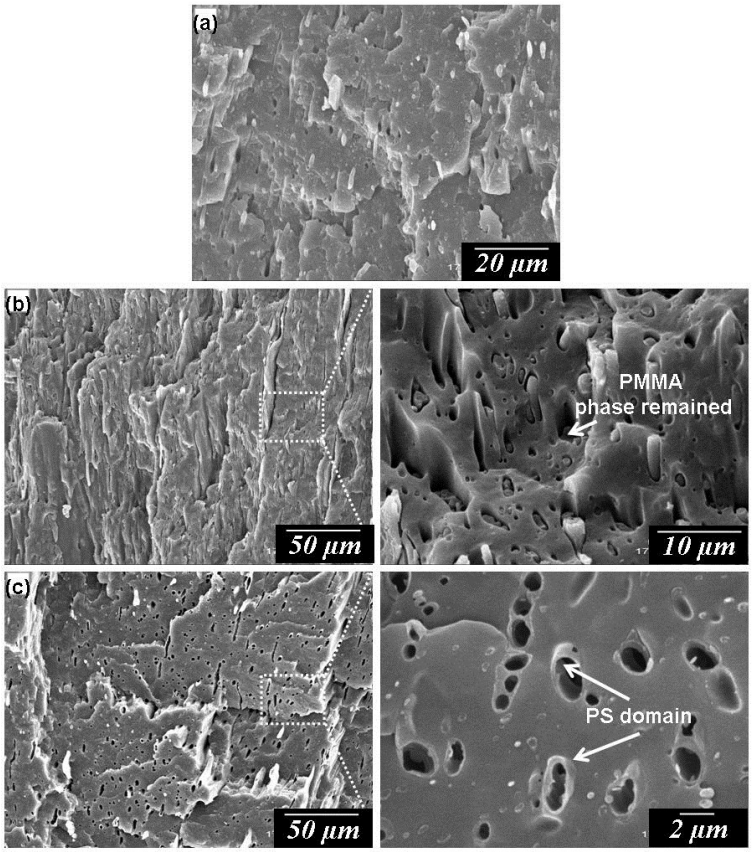



Figure 3. PP/PS/PMMA (80/10/10) ternary blend prepared by injection molding. (a) As-prepared; (b) After cyclohexane etching; and (c) After acetic acid etching.

By using the same concept of preparing microcellular/nanocellular foam as in our previous study, new approach is introduced in order to control the bubble nucleation at polymer interface. It is believed that smaller size of dispersed domain probably could reduce the loss of $CO_2$ via diffusion, and thus enhances bubble nucleation. We use the approach of preparing blend sample via injection molding to obtain smaller dispersed domain as compared to extruded blend sample. As reported by Son et al. [12] injection condition affects domain size where high injection flow rate and low injection temperature could successfully reduce the domain size of dispersed phase.

The observed encapsulation-type morphology of PP/PS/PMMA (80/10/10) blend was utilized as template for foaming. Batch foaming was then performed on the injection molded sample in the temperature range of 130 to 160 ºC while the saturation pressure and depressurization rate were kept constant. Figure 4 shows the cell structure of the blend sample corresponding to the SEM image shown in Figure 3. At 130 ºC sample was partly foamed. From the observation, the bubble was originated from amorphous PP while PMMA/PS domains remained as particles. At 150 ºC, fine well-distributed cell was obtained. An increased of domain distribution as well as the decreased of average domain size leads to a small cell size and high cell density. Figure 4c clearly shown the PMMA/PS domains

were adhered to the PP cell wall. Overall, blend sample prepared by injection molding which has smaller domain size leads to a cell size decrease and cell density increase.

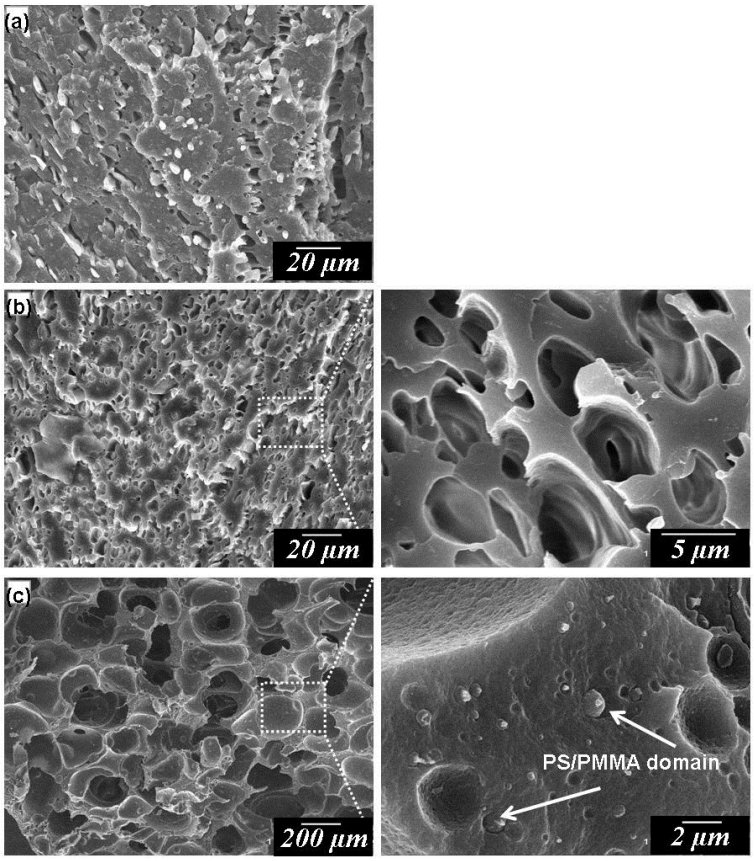



Figure 4. Cell structures of PP/PS/PMMA (80/10/10) foams prepared by injection molding at various foaming temperatures: (a) 130 ºC; (b) 150 ºC; and (c) 160 ºC

Figure 5 compares the graphs of the cell size distribution of PP/PS/PMMA (80/10/10) blend foams prepared by different methods; extrusion and injection molding. The uniformity of cell size was increased in sample prepared by injection molding. The cell size of the extrusion blend foam shows a broad distribution with cell size in a range of 4 to 45 μm. On the other hand, the cell size distribution of the injection molding blend foam becomes narrower than that of extrusion blend foam, and they are in range from 1 to 12 μm. Reducing size of dispersed domain showed a beneficial effect on the cellular structure of the investigated blend in terms of cell size and cell uniformity.

**Blend morphology and foaming behaviour of PC/PS/PMMA (80/10/10) ternary blend system prepared by injection molding**

PC/PS/PMMA (80/10/10) blend was prepared via injection molding to further investigate the effect of dispersed domain size on the cell structure. Blend morphology of sample was first examined to identify the type of morphology. Droplet-type morphology or so called sea-island morphology with nano-sized PS core and PMMA shell was obtained due to incompatibility between those polymers as depicted in Figure 6.

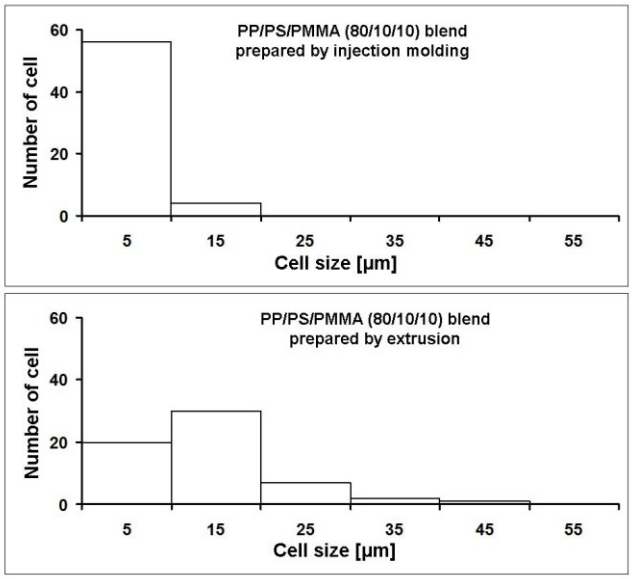



Figure 5. Cell size distribution of PP/PS/PMMA (80/10/10) blend foams at 150 ºC

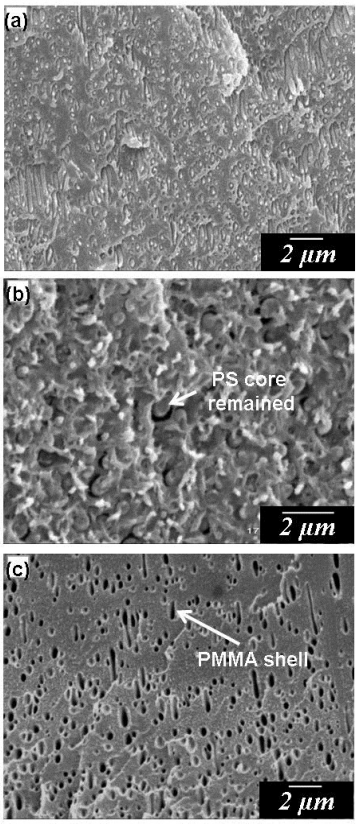



Figure 6. PC/PS/PMMA (80/10/10) ternary blend prepared by injection molding. (a) As-prepared; (b) After acetic acid etching; and (c) After cyclohexane etching

Under similar foaming conditions, PC/PS/PMMA blend foam was prepared. Figure 7a shows that sample could be foamed slightly at 130 ºC. As the foaming temperature increased to 150 ºC, bimodal cell structure was formed (Figure 7b). Enlarge image of Figure 7b shows that PS/PMMA domain remained as its original shape. When the blend sample was foamed at 160 ºC, the foam exhibited a small cell size and low cell density. This might due to the increase in $CO_2$ diffusivity with the increase of the foaming temperature. By comparison of cell structures of PP/PS/PMMA (80/10/10) blend samples prepared by extrusion and injection molding, it can be observed that the decreased in dispersed domain size is not only decreased the cell size, but it also reduced the $CO_2$ diffusion into the polymer interface. Hence, the cell properties of ternary polymer blend could be improved by preparing the sample via injection molding.

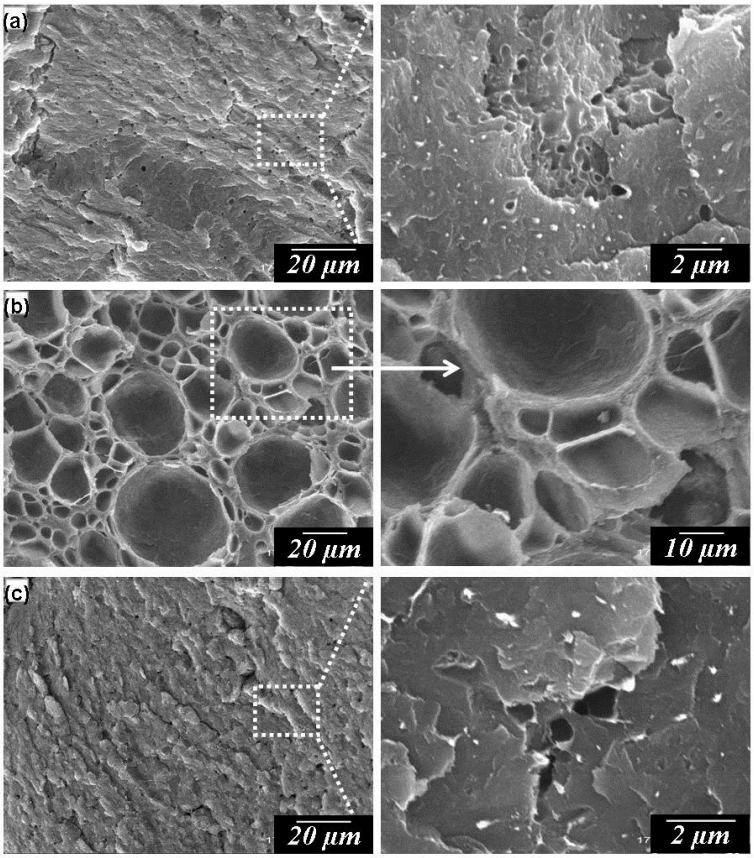



Figure 7. Cell structures of PC/PS/PMMA (80/10/10) foams prepared by injection molding at various foaming temperatures (a) 130 ºC, (b) 150 ºC and (c) 160 ºC

## Conclusion

The effect of blending method on the dispersed domain size and cellular structure of ternary blend was studied. The approach of preparing blend sample via injection molding has been introduced to control the dispersed domain size of the polymer blend. For the injection molded PP/PS/PMMA blend, an incredible drop of dispersed domain size was observed compared to extruded PP/PS/PMMA blend from approximately 10 µm in average diameter to almost 1 µm. Accordingly, reducing dispersed domain size was found beneficial effect on the cellular structure of the blend. Cell density and uniformity of PP/PS/PMMA blend can be enhanced with the reduction of dispersed domain size, which impedes $CO_2$ loss via diffusion through polymer interface.

**Acknowledgement**

The authors would like to thank the Research Management Institute (RMI), Universiti Teknologi MARA (UiTM) for the financial support of the project under the Research Acculturation Grant Scheme (RAGS) (600-RMI/RAGS5/3 (68/2013)). In addition, Material Processing Engineering Laboratory of Kyoto University is also acknowledged for providing material and technical support.

**References**

1. Hsu, W.P. (2007). A closed-loop behavior of ternary polymer blends composed of three miscible binaries. *Thermochimica Acta*, 454: 50 – 56.
2. Tseng, F. P., Lin, J. J., Tseng, C. R. and Chang, F. C. (2001). Poly(oxypropylene)-amide grafted polypropylene as novel compatibilizer for PP and PA6 blends. *Polymer*, 42: 713 – 725.
3. Radusch, H. J., Dosher, P. and Lause, G. (2005). Phase behaviour and mechanical properties of heterophasic polypropylene-ethylene/ propylene copolymers systems. *Polymer,* 50: 279 – 285.
4. Li, X., Han, Y. and An, L. (2003). Surface morphology control of immiscible polymer-blend thin films. *Polymer*, 44: 8155 – 8165.
5. Guo, H. F., Packirisamy, S., Gvozdic, N. V. and Meier D. J. (1997). Prediction and manipulation of the phase morphologies of multiphase polymer blends: 1. Ternary systems. *Polymer*, 38: 785 – 794.
6. Sharudin, R.W., Alwi, H. and Ohshima, M. (2013). PP/PS/PMMA ternary blend foaming using supercritical $co_2$. *Advanced Materials Research*, 701: 17 – 22.
7. Gnatowski, A. and Koszkul, J. (2005). Investigations of the influence of compatibilizer and filler type on the properties of chosen polymer blends. *Journal of Materials Processing Technology,* 162 – 163: 52 – 58.
8. Kim, J. K., Yi, D. K., Jeon, H. K. and Park, C. E. (1999). Effect of the functional group inhomogeneity of an in situ reactive compatibilizer on the morphology and rheological properties of immiscible polymer blends. *Polymer,* 40: 2737 – 2743.
9. Zhai, W., Wang, H., Yu, J., Dong, J. and He, J. (2008). Foaming behaviour of polypropylene/ polystyrene blends enhanced by improved interfacial compatibility. *Journal of Polymer Science Part B: Polymer Physics*, 4 6: 1641 – 1651.
10. Zhang, Q., Yang, H. and Fu, Q. (2004). Compatibilization of immiscible poly(propylene)/polystyrene blends using clay. *Polymer*, 45 : 1913 – 1922.
11. Elias, L., Fenouillot, F., Majeste, J. C. and Cassagnau, P. H. (2007). Morphology and rheology of immiscible polymer blends filled with silica nanoparticles. *Polymer*, 48: 6029 – 6040.
12. Son, Y., Ahn, K. H. and Char, K. (2011). Effects of processing conditions and reactive compatibilizers on the morphology of injection molded poly(phenylene oxide)/Nylon 6 Blends. *Polymer Engineering and Sciences,* 40 : 1385 – 1394.
13. Reignier, J., Favis, B. D. and Heuzey, M-C. (2003). Factors influencing encapsulation behavior in composite droplet-type polymer blends. *Polymer,* 44(1): 49 – 59.
14. Valera, T. S., Morita, A. T. and Demarquette, N. R. (2006). Study of morphologies of PMMA/PP/PS ternary blends. *Macromolecules*, 39(7): 2663 – 2675.
15. Zhong, G. J. and Li, Z. M. (2005). Injection molding-induced morphology of thermoplastic polymer blends. *Polymer Engineering and Sciences*, 45(12): 1655 – 1665.

*Malaysian Journal of Analytical Sciences, Vol 21 No 1 (2017): 136 - 148*
*DOI: http://dx.doi.org/10.17576/mjas-2017-2101-16*

MALAYSIAN JOURNAL OF ANALYTICAL SCIENCES
*Published by The Malaysian Analytical Sciences Society*
ISSN 1394 - 2506

# SYNTHESIS AND CHARACTERIZATION OF HYDROXYAPATITE NANOPARTICLE

## (Sintesis dan Pencirian Nanozarah Hidrosiapatit)

Sahlil Miraz Mohamed Rafie* and Darman Nordin

*Department of Chemical and Process Engineering,*
*Faculty of Engineering and Built Environment,*
*Universiti Kebangsaan Malaysia, 43600 UKM Bangi, Selangor, Malaysia*

**Corresponding author: sahlilmiraz.rafie@gmail.com*

Received: 21 October 2015; Accepted: 14 June 2016

**Abstract**

In this research, hydroxyapatite (HA) nano-size powder was synthesized using wet chemical precipitation technique under atmospheric pressure where calcium hydroxide ($Ca(OH)_2$) and ortho-phosphoric acid ($H_3PO_4$) were used as precursors. Distilled water was used as a diluting media for the reaction and sodium hydroxide (NaOH) was used to control the initial pH. The initial pH values, reaction temperature and calcined temperature play an important role in the morphology on HA as well as the phase formation and degree of crystallinity. Nano HA powder has been studied at different initial pH value which is between 9.00 to 11.00, reaction temperature from 80 °C to 100 °C and calcined temperature at 700 °C to 800 °C. The optimum initial pH value was found at pH 10.00, reaction temperature at 100 °C and calcined temperature was at 800 °C. The crystallographic properties were evaluated by X-ray diffraction (XRD), Fourier Transform Infrared (FTIR) and Field Emission Scanning Microscope (FESEM). The Design Expert version 9.0.2 with statistical and graphical analysis of the result, by using analysis of variance (ANOVA) was applied to optimize variable in the process of synthesis of HA. Based on analysis of variance (ANOVA) that has been perform, calcined temperature was to be influential variables on mass of HA with value of probability less than 0.05.

**Keywords**: hydroxyapatite, chemical precipitation, crystallinity, morphology, optimization

**Abstrak**

Dalam kajian ini, nanozarah hidroksiapatit (HA) dihasilkan melalui kaedah pemendakan di bawah tekanan atmosfera di mana kalsium hidroksida ($Ca(OH)_2$) dan asid orto fosforik ($H_3PO_4$) merupakan larutan asas bagi penyediaan HA. Air suling digunakan sebagai agen pelarut dalam menyediakan larutan asas bagi proses pemendakan ini. Larutan natrium hidroksida di gunakan bagi mengawal nilai pH. Nilai pH, suhu tindak balas dan suhu relau merupakan faktor penting dalam pencirian dan penghabluran nanozarah HA. Nanozarah HA disediakan pada nilai pH antara 9.00 hingga 11.00, suhu tindak balas 80 °C hingga 100 °C dan suhu relau pada 700 °C hingga 800 °C. Pencirian nanozarah HA di uji menggunakan X-ray Difractometer (XRD), Inframerah Transformasi Fourier (FTIR), dan Mikroskop Pengimbas Pancaran Medan (FESEM). Perisian Design-Expert 9.0.2 digunakan untuk menganalisis data dan pengoptimuman penghasilan mendakan HA. Berdasarkan analisis varian (ANOVA) yang dilakukan, suhu relau merupakan pemboleh ubah yang mempengaruhi berat HA dengan nilai kemungkinan kurang dari 0.05.

**Kata kunci:** hikdroksiapatit, mendakan bahan kimia, penghabluran, pencirian, pengoptimuman

## Introduction

Tissue disease and defect, and bone disease are serious health condition that can affect the life for those who suffer on it. Since last four decades, various revolution has been introduced in order to make improvement of the uses of

ceramic. This improvement is about special design ceramic for repair and reconstruction of diseased or damaged parts of the body. Ceramic used in this field is called bioceramic. Two alternative ways to replace tissue are transplantation and implantation. The advantages of bioceramic offer over transplant are availability, reproducibility and reliability. Bioceramic can be classified into two group which are bioinert (ceramic that have no influent on surrounding living tissue) and bioactive ceramic (capable of bonding with living tissue as example calcium phosphate (HA) and certain compositions of glasses. Over past few decade, synthetic hydroxyapatite (HA) has been recognize as important bone substitute materials in orthopedics and dentistry due to its biological similarity to the mineral phase of human bones [1]

Due to excellent biocompatibility and tissue bio-activity properties, hydroxyapatite (HA) which is inorganic bioceramic also known as calcium phosphate ceramic that being main inorganic composition of natural bone has been extensively investigated for medical application. Because of this reason, many techniques have been developed for synthesis of HA such as mechanochemical synthesis, combustion preparation, wet chemical deposition, electrochemical deposition, sol-gel method, hydrothermal synthesis and many more [2].

From the previous researcher, HA was successfully used in separation of protein enzymes, nucleic acid, virus and other biological molecules. HA act as a prototype for bones and teeth with proven compability, HA also widely used in medical implants [3].

The size of morphology of HA used in bone is nano-sized needle-like crystals. HA can be used in various form of shape including powders, granules, dense and porous block. There is a need to characterize the HA powder depending on desired application. Using wet synthesis technique, various parameters can be controlled such as purity, crystallinity, and morphology because different morphologies will be used in different application for example small spherical particle used in thermal spray coating while needle-shape or rod-shape used in bone repair composite material [4].

Recently, nano HA get attention from the researcher because nano HA play an important role in various biomedical application due to its unique function properties of high surface area volume ratio where its structure is ultra fine similar to natural bone. There are few method to synthesis nano HA such as chemical precipitation, spray drying, sol-gel and more. In natural bone and teeth, the nanoparticle sized of HA crystal is embedded in the collagen matrix with average length of 50nm. In fact, collagen is act as template in the controlled biomineralization process [5].

## Materials and Methods

### Precipitation

In order to obtain nano-HA by precipitation method, calcium hydroxide and ortho-phosphoric acid was used as initial precursor. The experimental involve additional of desired amount of 0.67 M of ortho-phosphoric acid (Merck, 85%) to desired amount of 1 M calcium hydroxide (Merck). The chemical equation involve is:

$$10Ca(OH)_2 + 6H_3PO_4 \longrightarrow Ca_{10}(PO_4)_6(OH)_2 + H_2O \quad (1)$$

### Characterization

The crystal phase and degree of crystallinity were characterized using X-ray diffraction (XRD, D8-Advance, Bruker company, Germany) with Cu Kα radiation (λ=0.15408). The XRD data were collected at room temperature over 2θ range of 20 – 55°. Chemical characterization of nano HA was performed using Fourier Transform Infrared spectroscopy (FTIR, Thermo Scientific, Nicolet 6700) The morphology and size distribution of synthesized nano HA were investigated by using Field Emission Scanning Microscope (FESEM, Zeiss SUPRA 55VP).

### Statistical analysis using Design of Experiment

Response surface methodology (RSM) with central composite design (CCD) was employed to investigate the effect of synthesis parameter process of HA response to mass of HA obtained. Three independent parameters namely, reaction temperature, pH value and calcined temperature at three different levels each, were employed. The parameters chosen and the levels were based on previous study [6,7,8] and suitability with the condition of the product, hydroxyapatite. The experimental plan was designed and the results obtained were analyzed according to

Design Expert version 9.0.2 software to build and evaluate models as well as to plot the three-dimensional response surface curves. The experiments is run in random in order to minimize the effects of unexpected variability in the observe responses due to irrelevant factors.

## Results and Discussion

### XRD and FTIR study on nano HA: Effect of pH variation

The effect of initial pH value was observed by variety the initial pH in range 9.00 until 11.00 at different reaction temperature which are at 80 until 100 °C and calcined temperature at 700 °C. In Figure 1 it can be seen that different pH value will affect the peak and crystallinity in XRD pattern. The variation of initial pH value give effect for the peak of XRD pattern where from the result it can be observe the pH 10.00 is most suitable value for synthesis HA where at pH 10.00, only peak for pure HA can be trace. In Figure 2 and Figure 3 show the peak for XRD for pH variation at reaction temperature 90 °C and 100 °C.

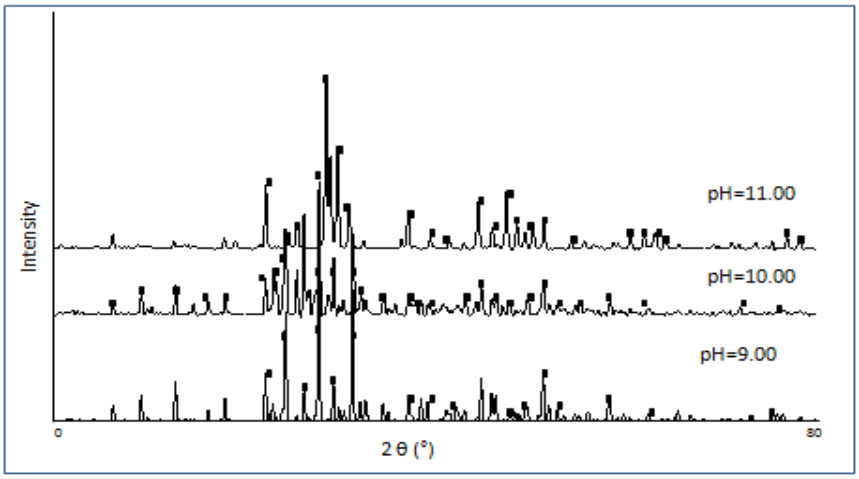



Figure 1. XRD pattern for pH variation at reaction temperature 80 °C and calcined temperature 700 °C

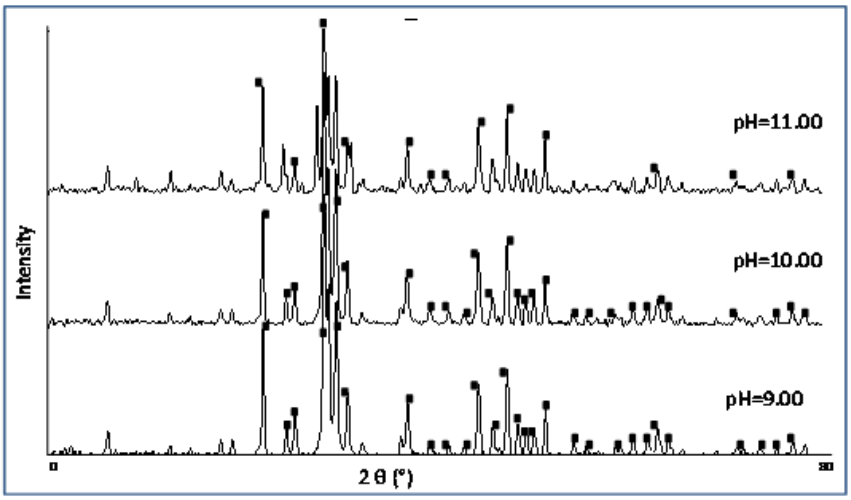



Figure 2. XRD pattern for pH variation at reaction temperature 90 °C and calcined temperature 700 °C.

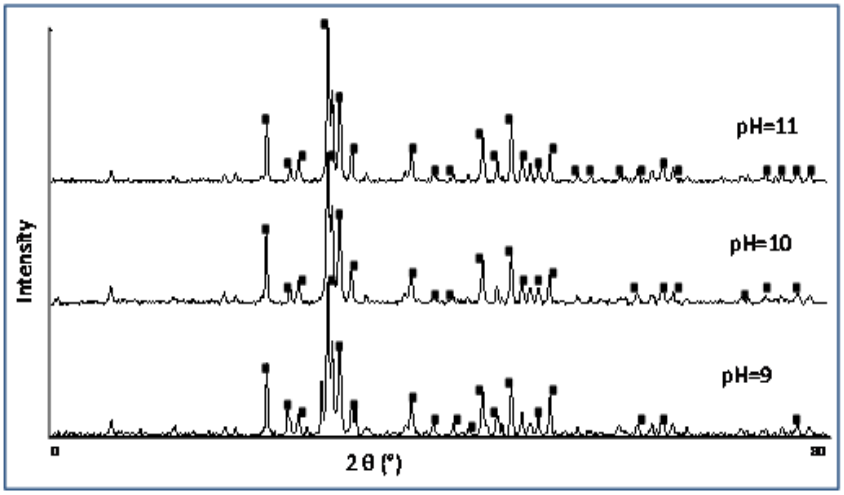



Figure 3. XRD pattern for pH variation at reaction temperature 100 °C and calcined temperature 700 °C.

For FTIR spectra it can be observe in Figure 4 all sample have similar pattern where the sharp band at 1414 $cm^{-1}$. The band 3571 $cm^{-1}$ is attributed to the bending of hydroxyl group ($OH^-$) and the band at 631 $cm^{-1}$ is related to bending vibration of hydroxyl group. Characteristic of HA are found at 1457 $cm^{-1}$, 1414 $cm^{-1}$ and 1416 $cm^{-1}$ which are represent carbonate ($CO_3^{2}$) group.

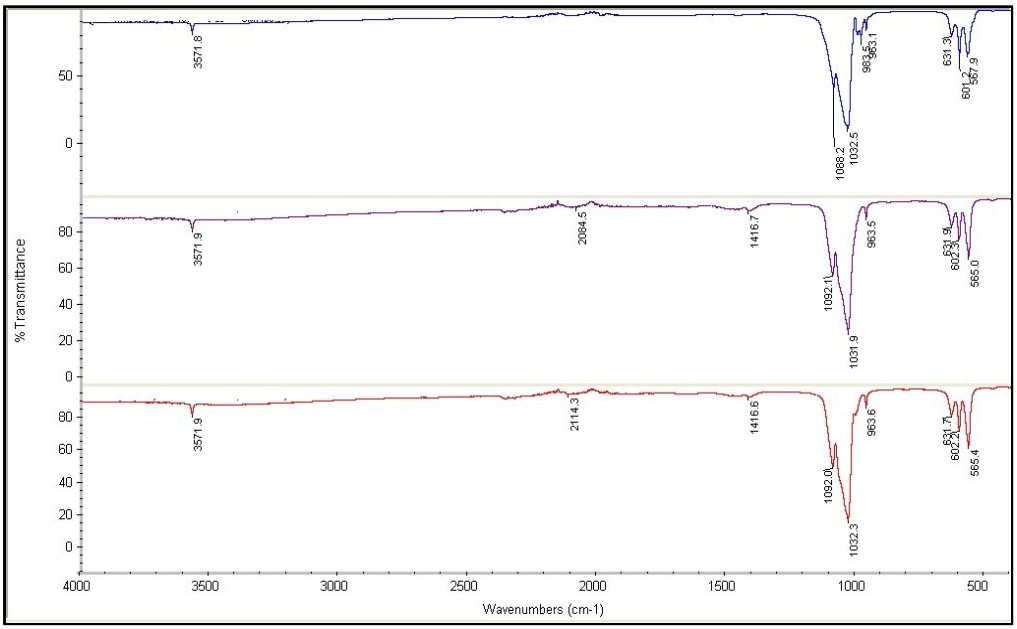



Figure 4. FT-IR spectra of nano HA at reaction temperature 80 °C and calcined temperature 700 °C

**Effect of reaction temperature**

The reaction temperature for stirring also play an important role that can affect the morphology of HA. The reaction temperature was varied from 80 °C to 100 °C. Temperature usually influenced the crystal phase and degree of crystallinity where during the crystallization process the reaction temperature was dependent factor on the morphology. Crystallinity is referring to the arrangement of the atom or molecules in periodic order. Depend on a certain condition, the shape of a crystal was determined by kinetics compared to thermodynamics. The kinetic of crystal face can be influenced by external factor as example supersaturation temperature and mixing [6]. All the diffraction pattern revealed peak of HA. The sharpness of the diffraction peak increase as the reaction temperature increase. Increase in sharpness of diffraction peak show increasing in crystallinity of the HA form [7].

Figure 5 shows the XRD pattern for synthesis of HA are different at different reaction temperature. The pH value was varied between 9.00 until 11.00 and the calcined temperature was varied from 700 °C and 800 °C. From the peak pattern, it shows as the reaction temperature increase, the peak become sharper and narrow that show the increase in crystallinity of the HA. It shows that the sample at highest reaction temperature which is at 100 °C have better crystallinity of HA compared to sample at 80 °C and 90 °C.

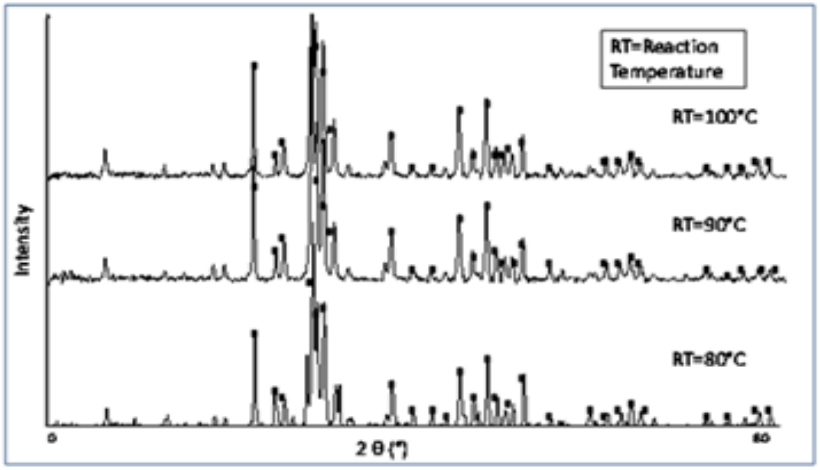



Figure 5. XRD pattern for reaction temperature variation at pH 9.00 and calcined temperature 700 °C

Figure 6 shows the FTIR spectra of HA at different reaction temperature. It can be observed that all the spectra have almost same peak where $PO^{4-}$ was obtained at 565, 602 and 1032 $cm^{-1}$ and $CO^{3-}$ was appear at 963 and 1416. There are two shoulder peak at 631 and 3571 which are typically stretching vibration and bending mode of HA.

**Effect of Calcined temperature**

Other than initial pH value and reaction temperature, calcined temperature also play an important factor in the synthesis of HA. From the previous researcher, increase in calcined temperature will increase the crystallinity as peak become narrow and sharp moving where the temperature was varied from 100 to 800 °C [8]. It has been proven as the peak of diffraction become narrow and sharp as the calcined temperature increase from 700°C to 800 °C.

The temperature for calcined was set at 700 and 800 °C at different pH value which are 9, 10 and 11 where for reaction temperature was varied from 80, 90 and 100 °C. From Figure 7 it can be observed the crystallinity of HA is increase when the temperature increase. For temperature calcined at 700 °C, the peak is lower compared to HA that calcined at 800 °C. It shows that calcined temperature also be the factor of preparing the HA.

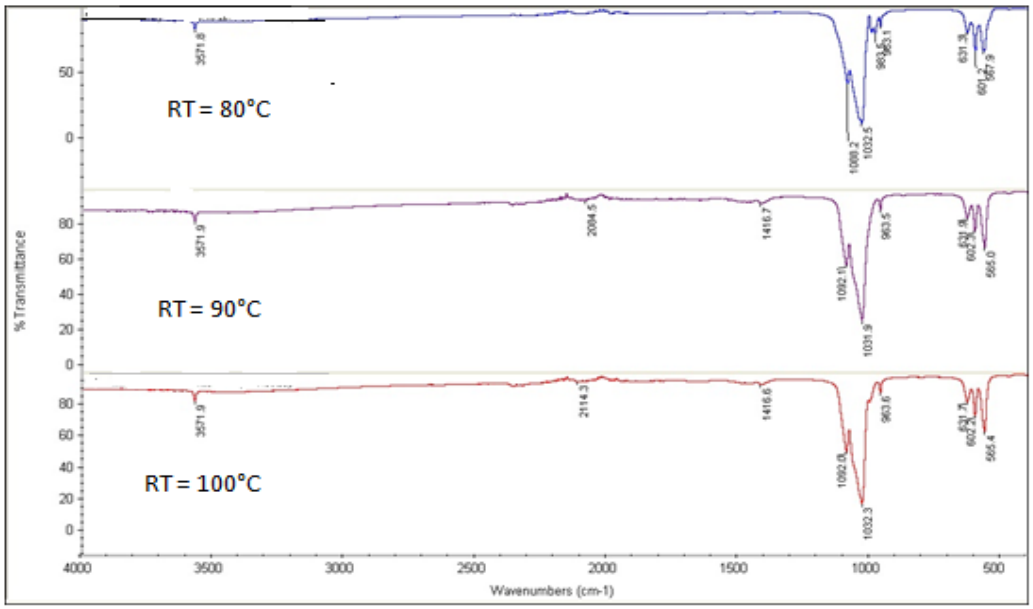



Figure 6. FT-IR spectra of nano HA at pH value 9.00 and calcined temperature 700 °C

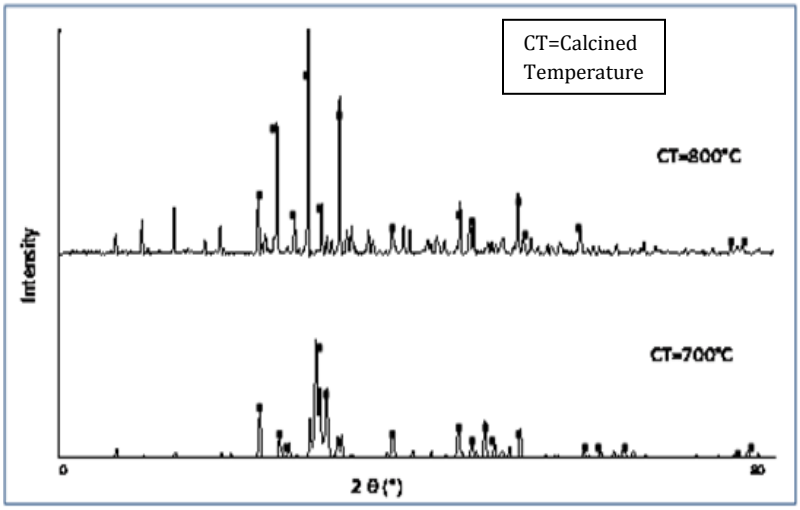



Figure 7. XRD pattern for calcined temperature variation at pH 9.00 and reaction temperature 80 °C

FTIR patterns was presented in Figure 8 The spectra possess an $OH^{1-}$ group in the region of 3571 $cm^{-1}$ and $PO_4^{3-}$ lies in region 1080 $cm^{-1}$. So, from this analysis, the detection of HA in all sample are confirmed. The peak at 700 °C are sharper compare to 800 °C. A weak band of $CO_3$ was detect at few sample in region 1416 $cm^{-1}$ and $H_2O$ also be detecting at band 1852 $cm^{-1}$. As the temperature increase the peaks are going to be weak which is in agreement with published data. The characteristic band of inorganic carbonate ion suggest that carbon gets dissolve in organic from atmosphere instead of dissolve in HA crystal [8].

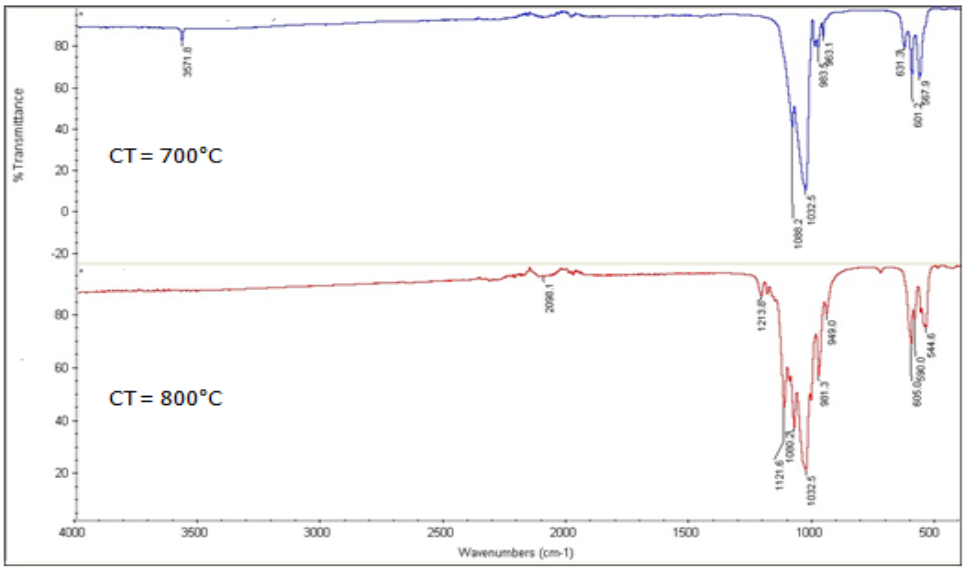



Figure 8. FT-IR spectra of nano HA at pH 9.00 and reaction temperature 80 °C

**The morphology of hydroxyapatite crystal: Effect of initial pH value**

From the FESEM analysis of HA particle that shown in Figure 9 and Figure 10 below show that initial pH value play an important role in morphology controlling HA particle. The HA that synthesis at pH 9.00 have sphere - like nano particle where the size of the particle about 209.9 nm. For nano particle HA at pH 10, the particle look like needle with average size 42.43 nm. For the research conduct by Abidi and Murtaza [8], at pH 10.00 and 11.00, the HA is sphere-like nano particle with narrow distribution range and good dispersibility at pH 10.00 where at pH 8.00, the shape of HA is needle-like.

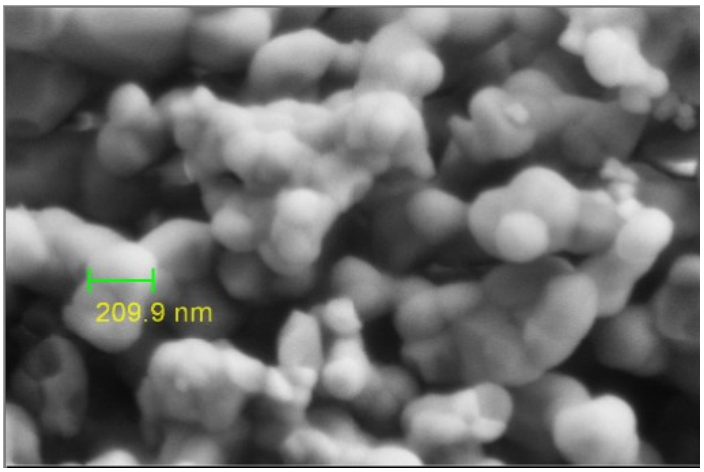



Figure 9. FESEM image for HA at pH 9.00

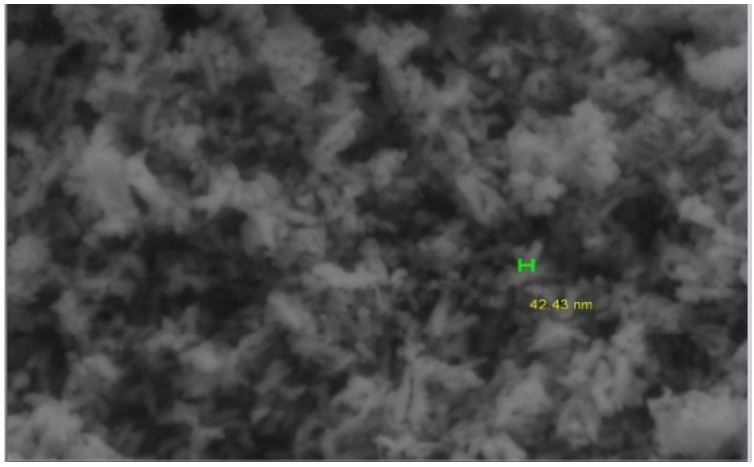



Figure 10. FESEM image for HA at pH 10.00

**Effect of reaction temperature**

The reaction temperature is an important factor in synthesis HA where it can affect the morphology of HA. Nanoparticle of HA can be exhibit in various morphologies which are needle-like and spherical-like, both shape is common and suitable used in many type of technologies application. The natural bone is composed of needle-like nanoparticle and because of that the synthesis of nanoparticle HA in needle-like shape is timely needed requirement [8]. In Figure 11 and Figure 12, the shape of the crystal is different where nanoparticle HA that prepare at temperature 80 °C has almost needle-like shape with 42.43 nm size where at reaction temperature 100°C it clearly shows the shape of the crystal is needle-like with size of the particle 58.06 nm. It shows that the temperature is an important role in morphology of HA.

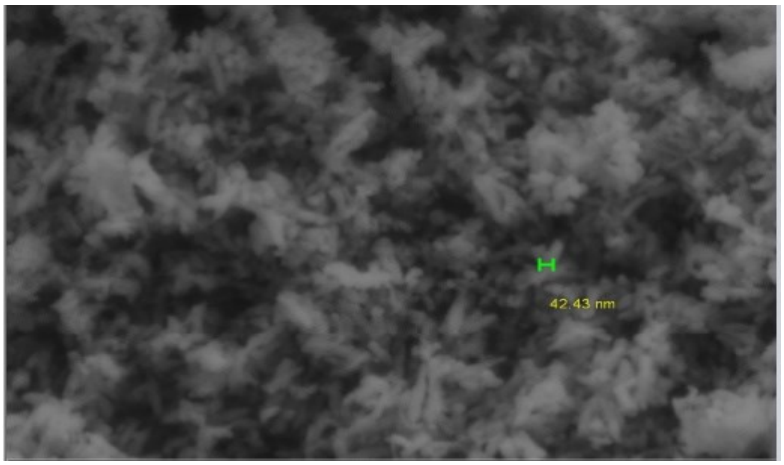



Figure 11. FESEM image for HA at reaction temperature 80 °C

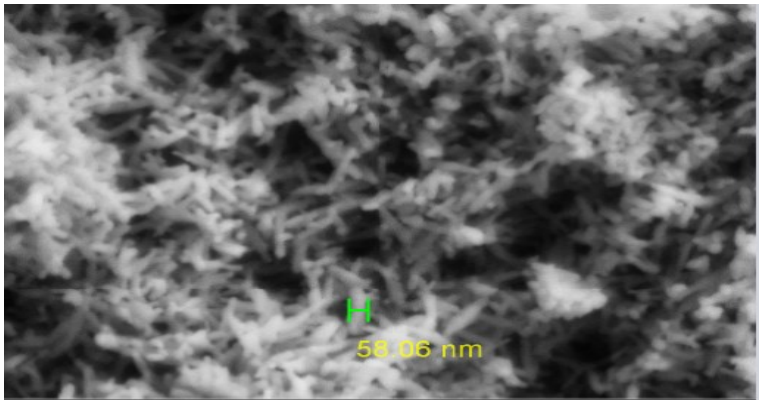



Figure 12. FESEM image for HA at reaction temperature 100 °C

**Effect of calcined temperature**

FESEM observation was performed to record the image of nanoparticle HA at calcined temperature 700 °C and 800°C. It is well known that spherical powder has better rheological properties compared to irregular powder and lead to produce better coating for hip implant. In order to produce high quality of powder for hip implant it's very important to control granule spherical morphology. It has been demonstrated by increase temperature cause HA precipitate size increase [8]. In Figure 13 and Figure 14, it can be observed that nanoparticle HA will give different shape when calcined at different temperature. At 700°C, the nanoparticle HA is needle-like shape with particle size 82.63 nm where at 800°C is spherical-like shape with particle size 227.8 nm These two shape is most popular in medical application. Different synthesis condition is performing according to the application.

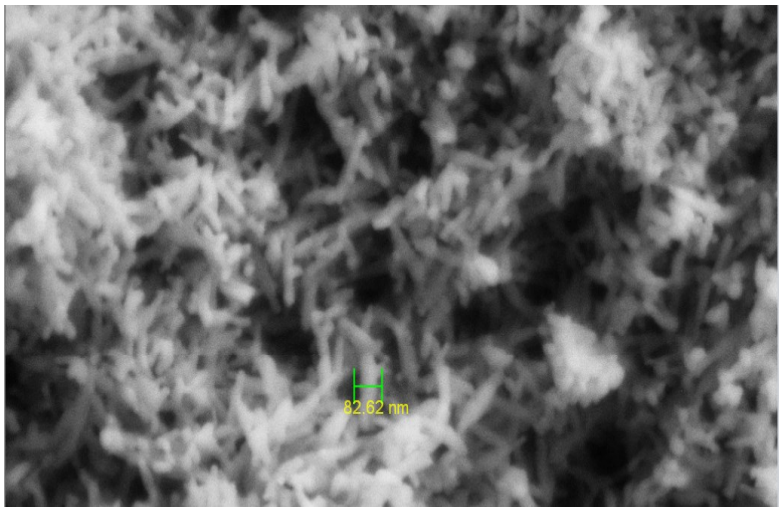



Figure 13. FESEM image for HA at calcined temperature 700 °C

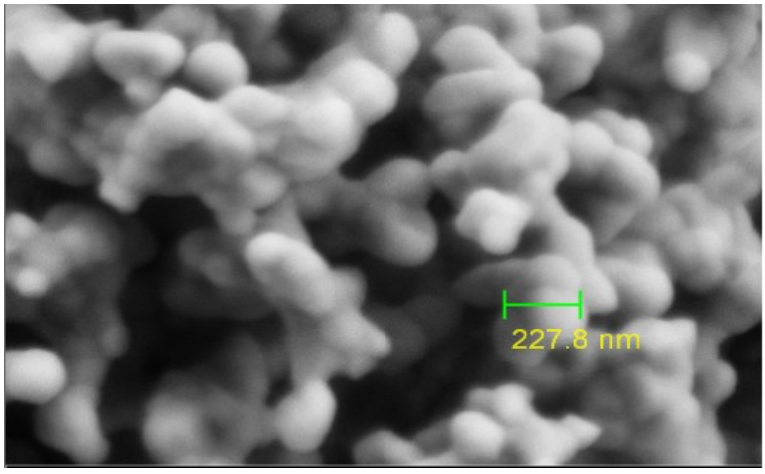



Figure 14. FESEM image for HA at calcined temperature 800 °C

**Design of Experiment (DOE): Statistical analysis**

For the three examined factors the CCD model efficiently designed a second order response to fit the surface. According to the design, the mass of synthesis HA was determined at different combination of parameters in order to evaluate the combined effect of these factors. The model used in this analysis was quadratic model. The degree of significance of each factor is represented in the table by its p-value. When a factor has a p-value of less than 0.05 ($P < 0.05$), it indicates model terms are significant with a confidence level of 0.95 [9]. The test result for Analysis of Variance (ANOVA) test for RSM parameter was shown in Table 1. From the table, F-value for model is 4.18 with p-value less than 0.05 which indicate model term are significant under selected condition. In this case, parameter C which is calcined temperature is a significant model term with p-value 0.0017.

Table 1. ANOVA for RSM parameter

| Source | Sum of Squares | df | Mean Square | F Value | p-value (Prob > F) |
|---|---|---|---|---|---|
| Model | 38.52 | 9 | 4.28 | 4.18 | 0.0363 |
| A (reaction temperature) | 0.67 | 1 | 0.67 | 0.65 | 0.4465 |
| B (pH) | 0.10 | 1 | 0.10 | 0.10 | 0.7592 |
| C (Calcined temperature) | 24.90 | 1 | 24.90 | 24.33 | 0.0017 |
| AB | 9.800E-003 | 1 | 9.800E-003 | 9.575E-003 | 0.9248 |
| AC | 0.22 | 1 | 0.22 | 0.21 | 0.6586 |
| BC | 0.54 | 1 | 0.54 | 0.53 | 0.4909 |
| $A^2$ | 0.56 | 1 | 0.56 | 0.54 | 0.4847 |
| $B^2$ | 1.53 | 1 | 1.53 | 1.50 | 0.2609 |
| $C^2$ | 1.96 | 1 | 1.96 | 1.92 | 0.2086 |

ANOVA result for response parameter are shown in Table 2 . The value of $R^2$ provide a measure how much variation in the observed response value can be explained by the experimental factor and their interaction. The value of $R^2$ is always between 0 to 1. The closer $R^2$ value to 1, the stronger the model is and better it predict the response [9]. The value for $R^2$ for this test is 0.843.

Table 2. ANOVA result for response parameter

| **Std. Dev.** | **1.01** | **$R^2$** | **0.843** |
|---|---|---|---|
| Mean | 7.61 | Adj $R^2$ | 0.641 |
| C.V. % | 13.30 | Pred $R^2$ | -0.337 |
| PRESS | 61.08 | Adeq Precision | 6.686 |

Response surface methodology is use to trace the efficiently for the optimum value of the significant variable. In this research the focus in this study to optimize the parameter used which are reaction temperature, pH value and calcined temperature respect to mass of HA formed from synthesis process. In Figure 15, it shows the optimum pH value which is at pH 9.00 and the reaction temperature is at 90 °C.

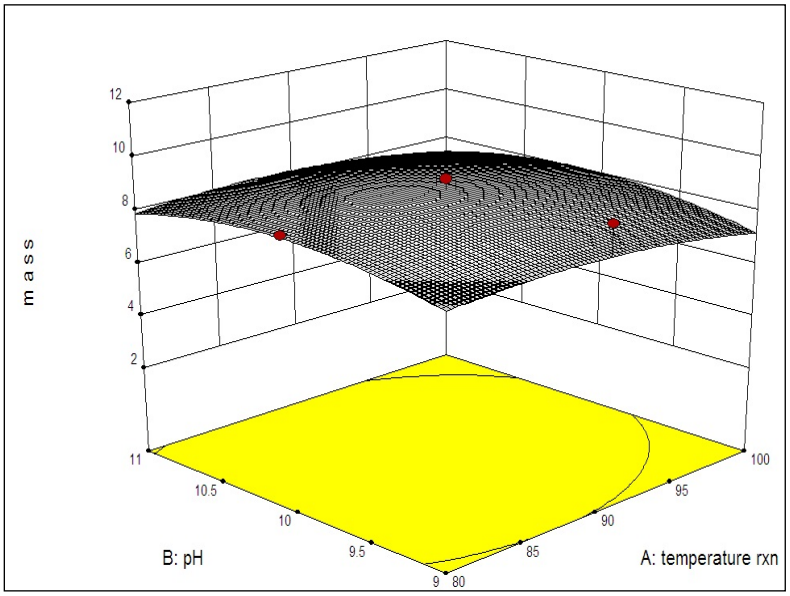



Figure 15. Response surface plot for combined variable pH value and temperature reaction

Table 3 shows the result for experimental and predicted mass of nanoparticle HA based on ANOVA. The predicted mass of HA differ from experimental result where the highest mass was predicted at 90 °C, pH 10.00 and 700 °C which is 9.54 g. Equation below is the linear corelation related the variables that influence the mass of HA formed from synthesis process

$$\text{Mass} = 8.82 - 0.26.A + 0.10.B - 1.58.C + 0.0135\ A.B - 0.16\ A.C + 0.26\ B.C - 0.46\ A^2 - 0.76\ B^2 - 0.86\ C^2 \quad (2)$$

A positive sign in the equation above represent a synergetic effect of the variable and negative sign represnet an antagoniistic effect of the variable.

Table 3. Result for experimental and predicted mass of HA

| Run | Factor 1 A: Reaction T (°C) | Factor 2 B: pH | Factor 3 C: Calcined T(°C) | Experimental Mass (g) | Predicted Mass (g) |
|---|---|---|---|---|---|
| 1 | 90 | 10.00 | 800 | 6.12 | 6.39 |
| 2 | 80 | 9.00 | 700 | 8.00 | 8.62 |
| 3 | 90 | 11.00 | 700 | 6.42 | 8.17 |
| 4 | 80 | 10.00 | 700 | 8.72 | 8.63 |
| 5 | 100 | 10.00 | 700 | 7.42 | 8.11 |
| 6 | 90 | 9.00 | 700 | 9.12 | 7.97 |
| 7 | 90 | 10.00 | 700 | 9.22 | 9.54 |
| 8 | 90 | 10.00 | 700 | 9.22 | 8.82 |
| 9 | 100 | 11.00 | 800 | 5.92 | 5.15 |
| 10 | 100 | 9.00 | 700 | 8.42 | 8.36 |
| 11 | 80 | 9.00 | 800 | 5.12 | 5.27 |
| 12 | 100 | 11.00 | 700 | 8.42 | 8.12 |
| 13 | 100 | 9.00 | 800 | 3.92 | 4.36 |
| 14 | 80 | 11.00 | 700 | 8.82 | 8.23 |
| 15 | 80 | 11.00 | 800 | 6.02 | 5.93 |
| 16 | 90 | 10.00 | 700 | 9.22 | 9.54 |
| 17 | 90 | 10 | 700 | 9.22 | 8.82 |

## Conclusion

The study of three tested parameters which are reaction temperature, pH value and calcined temperature were investigate and it show these parameters have significant effect on mass of HA formed, the characteristic and the morphology of the nanoparticle that synthesis using wet chemical precipitation method. Wet chemical precipitation method was used due to its reproducibility, simplicity and economical. The analysis of XRD, FTIR and FESEM show that all sample are in nanoparticle size. From the XRD pattern, the highest crystallinity occurs at condition reaction temperature 100 °C, pH value 10.00 and calcined temperature 800 °C. The spectra of FTIR show all the sample contain HA and from the image FESEM, nanoparticle HA formed from this research is needle-like and spherical-like with the range particle size between 40 to 200 nm. Optimization of parameters in synthesis of nanoparticle HA was determined using Design expert version 9.0.2. Based on analysis of variance (ANOVA) that has been perform, calcined temperature was to be influential variables on mass of HA with value of probability less than 0.05.

## Acknowledgement

The author would like to acknowledge Universiti Kebangsaan Malaysia (DIP-2014-014 and IP-2014-018) for supporting this research project.

## References

1. Eshtiagh-Hosseini, H., Housaindokht, M. R. and Chahkandi, M. (2007). Effects of parameters of sol–gel process on the phase evolution of sol–gel-derived hydroxyapatite. *Materials Chemistry and Physics*, 106(2): 310 – 316.
2. Feng, W., Mu-Sen, L., Yu-Peng, L. and Yong-Xin, Q. (2005). A simple sol–gel technique for preparing hydroxyapatite nanopowders. *Materials Letters*, 59(8): 916 – 919.

3. Yin, G., Liu, Z., Zhan, J., Ding, F. and Yuan, N. (2002). Impacts of the surface charge property on protein adsorption on hydroxyapatite. *Chemical Engineering Journal*, 87(2): 181 – 186.
4. Kramer, E., Podurgiel, J. and Wei, M. (2014). Control of hydroxyapatite nanoparticle morphology using wet synthesis techniques: Reactant addition rate effects. *Materials Letters*, 131: 145 – 147.
5. Mostafa, A. A., Oudadesse, H., Mohamed, M. B., Foad, E. S., Le Gal, Y. and Cathelineau, G. (2009). Convenient approach of nanohydroxyapatite polymeric matrix composites. *Chemical Engineering Journal*, 153(1): 187 – 192.
6. Wang, P., Li, C., Gong, H., Jiang, X., Wang, H. and Li, K. (2010). Effects of synthesis conditions on the morphology of hydroxyapatite nanoparticles produced by wet chemical process. *Powder Technology*, 203(2): 315 – 321.
7. Wijesinghe, W. P. S. L., Mantilaka, M. M. M. G. P. G., Premalal, E. V. A., Herath, H. M. T. U., Mahalingam, S., Edirisinghe, M., Rajapakse, R. P. V. J. and Rajapakse, R. M. G. (2014). Facile synthesis of both needle-like and spherical hydroxyapatite nanoparticles: Effect of synthetic temperature and calcination on morphology, crystallite size and crystallinity. *Materials Science and Engineering*: C, 42: 83 – 90.
8. Abidi, S. S. A. and Murtaza, Q. (2014). Synthesis and characterization of nano-hydroxyapatite powder using wet chemical precipitation reaction. *Journal of Materials Science & Technology*, 30(4): 307 –310.
9. Stanić, V., Dimitrijević, S., Antonović, D. G., Jokić, B. M., Zec, S. P., Tanasković, S. T. and Raičević, S. (2014). Synthesis of fluorine substituted hydroxyapatite nanopowders and application of the central composite design for determination of its antimicrobial effects. *Applied Surface Science*, 290: 346 – 352.

*Malaysian Journal of Analytical Sciences, Vol 21 No 1 (2017): 149 - 158*
*DOI: http://dx.doi.org/10.17576/mjas-2017-2101-17*

**MALAYSIAN JOURNAL OF ANALYTICAL SCIENCES**
***Published by The Malaysian Analytical Sciences Society***
**ISSN 1394 - 2506**

# IRON AND MANGANESE REMOVAL BY NANOFILTRATION AND ULTRAFILTRATION MEMBRANES: INFLUENCE OF pH ADJUSTMENT

## (Penyingkiran Besi dan Mangan oleh Membran Penurasan-Nano dan Penurasan-Ultra: Pengaruh Pelarasan pH)

Norherdawati Kasim [1,3]*, Abdul Wahab Mohammad [1,2], Siti Rozaimah Sheikh Abdullah[1]

[1]*Department of Chemical and Process Engineering, Faculty of Engineering and Built Environment*
[2]*Research Centre for Sustainable Process Technology (CESPRO), Faculty of Engineering and Built Environment*
*Universiti Kebangsaan Malaysia, 43600 UKM Bangi, Selangor, Malaysia*
[3]*Department of Chemistry, Centre for Defence Foundation Studies,*
*National Defence University of Malaysia, Kem Sg. Besi, 57000 Kuala Lumpur, Malaysia*

**Corresponding author: herdawati@upnm.edu.my*

Received: 21 October 2015; Accepted: 14 June 2016

**Abstract**

Iron and manganese present naturally in groundwater. Both metallic ions at excessive amounts normally contribute to rusty taste and reddish color to the water. Membrane technology may improve the conventional groundwater treatment method which commonly requires a large area and a lot of manpower. The present experimental work focused on membrane filtration of iron and manganese in order to study the influence of pH adjustment to the prepared artificial groundwater based on the permeate quality and membrane performances. In this study, two commercially available polyamide nanofiltration and ultrafiltration membranes (PA-NF, PA-UF) were tested to examine their capabilities in treating groundwater for drinking water resources. In order to achieve WHO drinking water standard, permeate quality of the artificial groundwater is considered satisfy if concentration of iron and manganese has reached 0.3 and 0.1 mg/L, respectively. Experimental results showed that pH at a range of 3-11 have significantly improved membrane performance in terms of their rejection. Rejection of iron at a feed concentration of 100 mg/L increased as pH of the feed solution increased for all tested membranes. However, the manganese rejection with a feed concentration at 50 mg/L showed various pattern of performance for each membrane. The pH of feed solution played an important role in changing the membrane surface properties and also, the characteristic of solute. This concludes that solute-membrane interaction mechanism has improved the performance of the tested membranes.

**Keywords**: iron rejection, manganese rejection, artificial groundwater, pH adjustment, drinking water

**Abstrak**

Besi dan mangan wujud semulajadi di dalam air bawah tanah. Kedua-dua ion logam ini pada jumlah yang berlebihan menyumbang kepada rasa berkarat dan warna yang kemerahan pada air. Kajian ini memberi tumpuan kepada penurasan logam besi dan mangan oleh membran dengan tujuan untuk mengkaji kesan pelarasan pH terhadap air bawah tanah buatan berdasarkan kepada kualiti telapan dan prestasi membran. Dalam ujikaji ini, dua membran poliamida penurasan-nano dan penurasan-ultra (PA-NF, PA-UF) yang boleh didapati secara komersial telah diuji untuk mengkaji keupayaan dalam merawat air bawah tanah sebagai sumber air minuman. Untuk mencapai piawaian WHO bagi air minuman, kualiti telapan air bawah tanah buatan dianggap memuaskan jika kepekatan besi dan mangan masing-masing mencapai 0.3 dan 0.1 mg/L. Keputusan ujikaji menunjukkan bahawa pH di antara julat 3-11 dengan ketaranya telah menambahbaik prestasi membran dari segi penyingkiran. Penyingkiran besi pada kepekatan suapan 100 mg/L telah meningkat apabila pH suapan meningkat untuk semua membran yang diuji. Walau bagaimanapun, penyingkaran mangan dengan kepekatan suapan pada 50 mg/L menunjukkan kepelbagaian corak prestasi bagi setiap membran. pH larutan suapan memainkan peranan penting dalam mengubah sifat-sifat permukaan membran

dan juga sifat bahan terlarut. Kesimpulannya, mekanisme interaksi bahan terlarut-membran telah meningkatkan prestasi membran yang diuji.

**Kata kunci:** penyingkiran besi, penyingkiran mangan, air bawah tanah, pelarasan pH, air minuman

## Introduction

Most of countries around the world rely on surface water for their daily needs including for drinking water sources. This is because surface water can be easily found over the land surface either in rivers, ponds, lakes, swamps or other fresh (not salty) sources. However, this natural water resource is more easily contaminated and contains most bacteria and other microorganism. Along with surface water, groundwater resources play a vital role in the production of clean and adequate drinking water supply all around the world. In countries such as Germany, Canada and the United States of America, nearly 70% of drinking water originates from groundwater [1]. The quality of groundwater is much better than surface water as soils, sands or rocks underneath the ground have become the filtration layers. It has been reported that most of groundwater consists some metal such as iron and manganese which naturally leach from many types of rocks and soils [2]. Iron (Fe) and manganese (Mn) are common metallic elements that exist together naturally especially in deeper wells [3]. Both are commonly found in water and are essential elements required in small amounts by all living organisms. Presence of excess amount of Fe and Mn resulted in metallic taste of water, slightly reddish colored water and rusty-brown stains of products like paper, cloths, and plastics [4]. World Health Organization (WHO) suggested that Fe and Mn concentrations in drinking water should be less than 0.3 mg/L and 0.1 mg/L, respectively [5].

The natural occurrence of Fe and Mn in groundwater usually with very little or without existence of oxygen, typically in deeper wells, in areas where groundwater flow is slow, and also in areas where groundwater flows through soils rich in organic matter. Fe and Mn usually present in natural groundwater in their most soluble form as divalent ions, $Fe^{2+}$ and $Mn^{2+}$. In soluble form they are colorless in groundwater but when exposed to air, they get oxidized then turn to insoluble form of $Fe^{3+}$ and $Mn^{4+}$, respectively and leave the water with brown-red color. Several techniques have been applied to remove these metals from groundwater including ion-exchange and water softening, adsorption by activated carbon, aeration and filtration, biosorption, ionic liquid extraction, and so forth [6–10]. Recently, the application of membrane technology including nanofiltration (NF) in water treatment for producing drinking water resources has been increased rapidly. NF technology is able to overcome operational problems that used to associate with conventional technique. In addition, other advantages of NF membranes are high retention of divalent ions at lower operating pressure and higher flux with lower energy consumption.

Numerous studies have been reported in investigating the ability of membrane filtration in water treatment [11–13]. However, only a limited number of studies have examined the removal of Fe and Mn in groundwater by using NF membranes [14]. Therefore, this study was conducted with the aim to investigate the influence of operating variables on the retention of Fe and Mn in groundwater using NF membranes. Along with this membrane, the treatment was also conducted by UF membrane in order to compare their performances. In this work, Fe and Mn removal were investigated using polyamide NF and UF membrane assigned as PA-NF and PA-UF, respectively. The main objective of this study is to investigate the influence of feed solution pH on the prepared synthetic groundwater, quality of permeate samples and performance of the membranes. Further analysis according to surface morphology images was measured by field emission scanning electron microscopy (FESEM) to further understand the rejection mechanisms involved.

## Materials and Methods

### Chemicals and membranes

All of purchased chemicals were analytical grade with high purity and no further purification required before used. Ferrous chloride tetrahydrate ($FeCl_2.4H_2O$) was procured from HmbG® Chemicals and manganese chloride tetrahydrate ($MnCl_2.4H_2O$) was obtained from Bendosen Laboratory Chemicals. In the preparation of synthetic groundwater, both chemicals were used by dissolving them in ultra-pure water with conductivity less than 1µS/cm as a single component for filtration experiment. The feed solution with individual metal of Fe and Mn were provided at initial concentration of 100 mg Fe/L and 50 mg Mn/L, respectively. The synthetic groundwater was freshly prepared a day before filtration experiment and kept in a cold room. This procedure was conducted to avoid

the divalent ions from being oxidized. Ferrous iron reagent powder (HACH Permachem®, USA) was used for determination of the remaining $Fe^{2+}$ ion in permeate from each filtration. Manganese reagent set (HACH Permachem®, USA) consisting of buffer powder citrate type for Mn and sodium periodate were used for detection of $Mn^{2+}$ in permeate samples. Individual salt solutions of sodium chloride, sodium sulphate and calcium chloride (NaCl, $Na_2SO_4$ and $CaCl_2$) were freshly prepared using NaCl (Merck, Germany), $Na_2SO_4$ and $CaCl_2$ (Sigma, USA). Low concentration of hydrochloric acid (HCl) and sodium hydroxide (NaOH) were used for pH adjustment on the feed solution.

Two different type of membranes were employed in order to investigate their performances for groundwater treatment, specifically for Fe and Mn removal. Both NF and UF membranes were supplied by Sterlitech Corp., USA. The polyamide (PA) flat sheet NF and UF membranes denoted as PA-NF and PA-UF, respectively were soaked overnight prior to use. The specification of the selected membranes is provided in Table 1.

Table 1. Specification of membranes

| **Parameter** | **PA-NF** | **PA-UF** |
|---|---|---|
| Manufacturer | Koch | Osmonics |
| [a]MWCO (Da) | 200 | 1000 |
| [a]pH range at 25°C | 4-10 | 2-11 |
| [b]Contact angle (°) | 44 ± 2.5 | 66 ± 2.5 |

[a] – data provided by manufacturer, [b] – data obtained from contact angle measurement at ambient temperature, MWCO – molecular weight cut off

**Experimental set-up**

A bench-scale dead-end stirred cell procured from Sterlitech Corporation, WA (Model HP4750) that houses a 49 mm diameter flat sheet membrane with effective area of 14.6 $cm^2$ was used for filtration experiment. The filtration set-up comprises of a nitrogen gas tank, 2000 mL reservoir tank, 300 mL stainless steel stirred cell and a precision balance (Sartorious AG, Germany, Model AX6202) connected to a data acquisition personal computer. Filtration experiments by the selected membranes were conducted for 1 to 3 hour and permeate sample was collected for further water quality analysis. The remaining $Fe^{2+}$ and $Mn^{2+}$ ions in permeate was measured by using spectrophotometer (HACH, Model DR3900).

Filtration experiments were performed to investigate the ability of applied membranes based on permeability, flux and rejection using ultra pure water and samples of synthetic groundwater. All membranes were soaked in ultra-pure water for overnight prior to use. This step was purposely to remove preservatives, and the soaking step also considered as a wetting process for the membrane. Then, compaction of membrane was conducted for 30 to 45 minutes by pressurizing the stirred cell with nitrogen gas at 5 bar without stirring. After compaction, the pure water permeability test was conducted. For determination of flux and rejection, a volume of 250 mL of feed solution was placed into the stirred cell and filtered for permeate sample collection.

Pure water flux was calculated by the following Eq. 1 where, $J_w$ is pure water flux ($L \cdot h^{-1} \cdot m^{-2}$), $Q$ is amount of water collected (L) for $\Delta t$ (h) which is time duration using a membrane coupon with area $A$ ($m^2$).

$$J_w = \frac{Q}{A \Delta t} \quad (1)$$

The flux of sample of feed solution was measured by the following Eq. 2 where $J$ is the sample flux ($L \cdot h^{-1} \cdot m^{-2} \cdot bar^{-1}$), as a function of permeability, $L_p$ ($L \cdot h^{-1} \cdot m^{-2} \cdot bar^{-1}$) and applied transmembrane pressure, $\Delta P$ (bar) taking the osmotic pressure difference between feed and permeate, $\Delta \pi$ (bar) into account.

$$J = L_p\,(\Delta P - \Delta\pi) \tag{2}$$

The rejection of sample of feed solution and the removal efficiency of NF and UF membranes during the filtration was measured by Eq. 3, where $R_o$ is the observed rejection and $C_p$ and $C_f$ are the concentration of permeate and feed, respectively.

$$R_o = \left(1 - \frac{C_p}{C_f}\right) \times 100\% \tag{3}$$

**Characterization of membrane**

The detail protocol for determination of characteristics of the selected commercial membranes was described in earlier publication [15]. In that publication TFC-SR3 and GHSP were referred to the PA-NF and PA-UF membrane, respectively. The hydrophilicity of membrane surface was analyzed by contact angle measurements using a static sessile drop method by goniometer contact angle (Ramé-Hart, Model 290, Netcong, USA). The analysis was conducted by using ultra-pure water dropped on top of a clean membrane surface with three series of measurement at three different spots. Images of the top surface and cross-sectional morphologies of membranes were provided by field emission scanning electron microscopy (FESEM) (Zeiss SUPRA 55VP Oberkochen, Germany). The instrument was equipped with an energy dispersive X-ray (EDX) analysis system to identify foulants that have been filtered by the membranes. The membrane pure water permeability, $L_p$ was determined by measurement of water flux at operating pressure ranged of 1 to 5 bar using ultra-pure water at conductivity less than 1 µS/cm and conducted at room temperature. Membranes were immersed in ultra-pure water and kept for overnight before compaction at 5 bar for 30 to 45 min prior to use.

**Iron and manganese ion analysis**

Permeate samples of Fe and Mn were analyzed using spectrophotometer (HACH, USA, Model DR3900). The collected permeate after filtration process was checked for water quality analysis in identifying the best operating variables to meet the drinking water standards. Physico-chemical parameters were measured to investigate the efficiency of membranes. Conductivity, pH and TDS were measured using pH/EC/TDS benchtop meter (HANNA, UK, Model HI-2550), whereas turbidity were analyzed by using turbidimeter (HACH, USA, Model 2100AN). Color, Fe and Mn in permeate were detected by using spectrophotometer (HACH, Model DR3900). All parameters were analyzed according to the APHA standard methods.

## Results and Discussion

**Surface characteristic of NF and UF membranes: Water flux**

Three different coupons of PA-NF and PA-UF were used for measurement of water fluxes. The average volumetric water flux at applied pressure of 5.0 bar for PA-NF membrane was found 10.75 ± 0.5 L $m^{-2}$ $h^{-1}$. The result obtained was lesser than the PA-UF membrane flux at 15.85 ± 0.5 L $m^{-2}$ $h^{-1}$. From the observed results, these indicated that all coupons of PA-NF and PA-UF membranes conducted for this objective have permeability of 2.15 ± 0.5 L $m^{-2}$ $h^{-1}$ $bar^{-1}$ and 3.17 ± 0.5 L $m^{-2}$ $h^{-1}$ $bar^{-1}$, respectively. These results showed that the separation layer of PA-UF membrane was more permeable to water in comparison to PA-NF. Data obtained from manufacturer had reported that the molecular weight cut off for PA-NF and PA-UF were 200 and 1000 Da, respectively. Therefore, results of water flux were congruent with the specification of PA-NF and PA-UF membranes. Data of water fluxes is presented in Table 2 for comparison.

**Hydrophilicity**

The hydrophilicity of membranes was measured by static sessile drop method. The contact angle between pure water droplet and the clean surface of membrane is a measurement of wettability of membranes. The higher value of contact angle indicates that the membrane is more hydrophobic. Three series of measurement at three different spots of clean membranes were conducted a day after the samples were kept overnight in a desiccator. The average contact angles of three clean membrane coupons for each PA-NF and PA-UF was found at 44° ± 2.5 and 66° ± 2.5, respectively. Results showed that PA-NF is more hydrophilic than PA-UF membrane. The findings of contact angle

of the selected NF and UF membranes in this study revealed that both membranes were suitable for further application in treating groundwater. However, the potential of both membranes in rejecting contaminants and meeting the drinking water standard should be the main priority.

Table 2. Water permeability test of NF and UF membranes

| **Parameter** | **PA-NF** | **PA-UF** |
|---|---|---|
| Average volumetric water flux ($L \cdot m^{-2} \cdot h^{-1}$) | 10.75 ± 0.5 | 15.85 ± 0.5 |
| Membrane permeability ($L \cdot m^{-2} \cdot h^{-1} \cdot bar^{-1}$) | 2.15 ± 0.5 | 3.17± 0.5 |

**Effect of pH on solute and membrane**

The prepared synthetic groundwater containing of $Fe^{2+}$ and $Mn^{2+}$ ions was added with low concentration (0.1 M) of hydrochloric acid (HCl) or sodium hydroxide (NaOH) in order to adjust the pH of feed solution in the range of pH 3 to 11. Fig. 1 represents the physical observation on the feed solution of synthetic groundwater at pH 9 prepared for filtration experiment. This result is used to further show that there was color changed in the feed solution as the solute has transformed from lower to higher oxidation state.

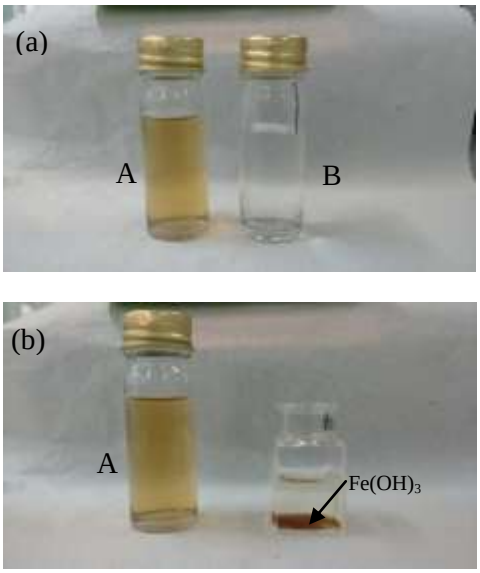



Figure 1. Physical properties of 100 mg Fe/L (a) at feed pH 9.3 (sample A), pH 6.5 (sample B) and (b) when $Fe(OH)_3$ formed as flocs

Insoluble trivalent ferric ions, $Fe^{3+}$ or known as iron solid commonly occur as colourful bright reddish-yellow to yellowish-brown stains as in sample A in Fig. 1(a). When sample A was exposed to air at ambient temperature for about 10 to 20 minutes, precipitate of iron hydroxide ($Fe(OH)_3$) was settled down at the bottom of cell as shown in Fig. 1(b). The initial pH of $FeCl_2$ and $MnCl_2$ feed solution right after preparation of the synthetic groundwater was found at 6.0 ± 0.5. At this condition, both divalent metal ions were soluble in water, with the prepared synthetic groundwater samples consist of either $Fe^{2+}$ or $Mn^{2+}$ ions were colourless as sample B in Figure 1(a). By increasing the pH, the soluble divalent ions were slowly oxidized to become insoluble and stable ions as the following Eq. 4 and Eq. 5;

$$Fe^{2+} + 3H_2O \rightarrow Fe(OH)_3 + 3H^+ + e^- \quad (4)$$

$$Mn^{2+} + 2H_2O \rightarrow MnO_2 + 4H^+ + 2e^- \quad (5)$$

The stability of $Fe^{2+}$ ions depend not only on pH but also on the activity of electrons. The occurrence and behaviour of $Mn^{2+}$ ions is not similar to Fe. It was found that $Fe^{2+}$ is more easily and rapidly oxidized than $Mn^{2+}$. Precipitation of $Fe(OH)_3$ and $MnO_2$ was due to the feed solution having bigger size of particles formed once the pH feed solution has increased. Therefore, size exclusion was expected to be the domain rejection mechanism for feed solution at higher pH and membrane performance has been significantly influenced by the feed pH adjustment.

**Permeate quality**

Fig. 2(a) presents the permeate concentrations measured after filtration experiments using feed solution with 100 mg Fe/L at adjustment of pH in the range of pH 3 to 11. Results show that at these pH range, the concentration of metallic ions detected in permeate decreased with increasing pH. For Fe removal by PA-NF membrane at pH 9 and 11, permeate concentration measured were well below than the acceptable limit for drinking water standard set by WHO which were 0.08 and 0.12 mg Fe/L, respectively. Whereas by using PA-UF membrane, results showed that the permeate quality (0.12, 0.07 and 0.13 mg Fe/L) was satisfied when feed solution used were at pH 7, 9 and 11. These results indicated that Fe rejection was succesful at pH 9 and above. It was found that poor rejection of Fe by both NF and UF membranes when feed solution pH was adjusted below 7. Thus, results proved that pH has importantly impacted Fe removal as also reported by other scholars [16]. The feed pH may change the nature of the membrane surface charge and pore size, as well as the dissolved metal species and therefore can affect the membrane separation efficiency [17]. Between pH 3 and 7, almost all Fe present as soluble $Fe^{2+}$. Higher than pH 8, Fe is predominantly present as insoluble $Fe^{3+}$ and easily precipitate as $Fe(OH)_3$ on the surface of membrane. Therefore, Fe removal at this point were mainly by size exclusion (seiving effect).

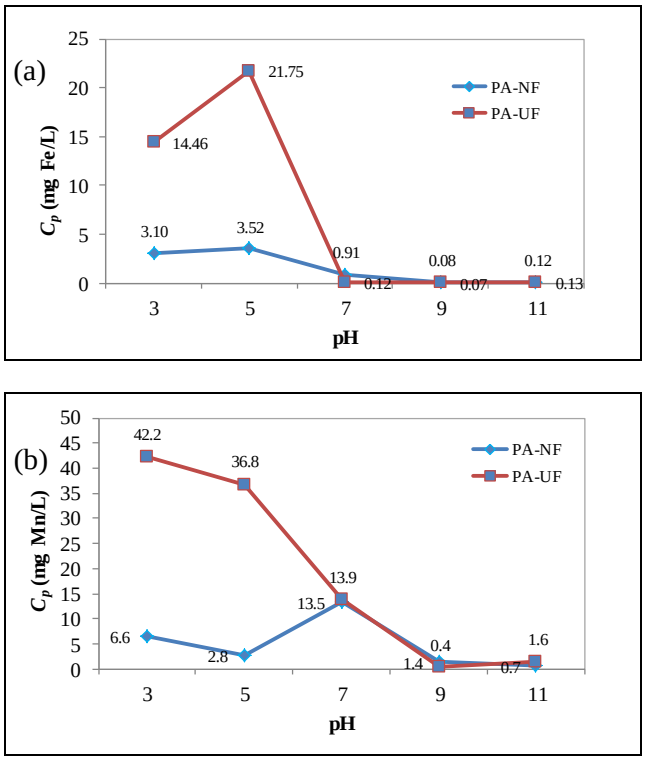



Figure 2. Effect of pH on permeate concentration for filtration of (a) Fe and (b) Mn from synthetic groundwater

For Mn removal with feed concentration at 50 mg Mn/L, it was found that the best quality of permeate achieved when using feed solution at pH 9 with detected permeate concentration at 0.4 mg Mn/L as shown in Fig. 2(b). This value was achieved by filtration using PA-NF membrane. However, it was considered as unsatisfied as for drinking water since the acceptable value should be at least 0.1 mg Mn/L. Poor quality of permeate at below than pH 9 especially by PA-UF membrane probably attributed by the effect of concentration polarization. The occurence and behavior of Mn is not similar to Fe, as $Fe^{2+}$ ions were easily and rapidly oxidized than $Mn^{2+}$ ions. At higher than pH 9, Mn is slowly exist as stable $Mn^{4+}$ and insoluble as $MnO_2$ which then precipitate on the surface of membrane or blocked in the pores. At this point, Mn removal could be attributed solely by size exclusion. Between pH 3 and 7, Mn exist as soluble $Mn^{2+}$ and thus, easily permeate and pass through membrane pores. As a result, poor rejection occured especially at pH 3 with high value of permeate concentration at 42.2 mg Mn/L was detected. In acidic feed solution, membrane pores could be expanded. At this point, PA-NF was reported to be positively charged. Low retention at pH 3 explained that solute-membrane interaction is the main mechanism and dominated by the nature of membrane pores.

**Rejection**

Fig. 3 presents the effect of feed pH on Fe and Mn rejection by using PA-NF and PA-UF membrane. In general, as the pH increased from 3 to 11, the rejection of these metallic ions inreased. This can be mainly caused by the solute-membrane charges interaction. It is obviously showed that rejection of Fe at various feed pH were higher than Mn. Lower rejection of Mn could be attributed solely to the electrostactic effect interaction between membrane material and $Mn^{2+}$ ions [18]. The isoelectric point (IEP) of PA-NF is in the range of 6 to 8 as reported by De Munari et al. [19]. This membrane is characterized as an amphoteric membrane whereby it is positively charged in solution less than pH 6 and negatively charged in solution more than pH 8. Between pH 3 and 5, the membrane is positively charged and lower Fe rejection could be due to dissolved $Fe^{2+}$ were easily permeate the membrane pores. Thus, charge repulsion and size exclusion are less important at this feed pH range. At pH 7, high Fe rejection mainly because of electrostatic interaction between the membrane and the ions was zero. Therefore, the ions did not easily permeate through the membrane and contribute to higher rejection of Fe at IEP of membrane.

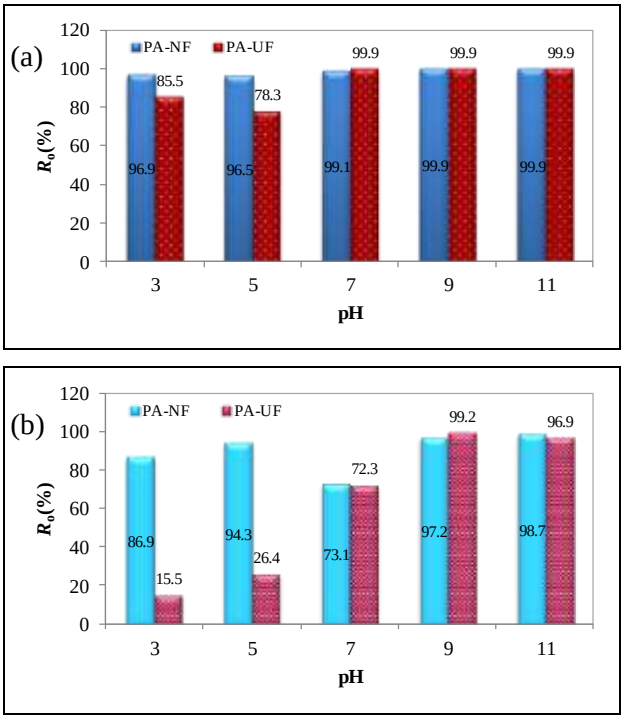



Figure 3. Rejection of (a) Fe and (b) at various feed pH by using 100 mg Fe/L and 50 mg Mn/L, 5 bar, 25 °C with 500 rpm stirring rate

The pH of feed solution may change the nature of the membrane surface charge and pore size, as well as that of dissolved metal species and therefore can affect the membrane separation efficiency. PA-NF membrane has reached higher rejection rate for both metals in comparison with PA-UF as depicted in Fig. 3(a) and 3(b), respectively. Similar findings for Fe removal has previously been reported by Jusoh et al. [7] and De Munari et al. [19]. Regarding to $Mn^{2+}$ ions, De Munari and Schafer [14] reported that PA-NF membrane has achieved more than 95% of rejection at pH 7. In Fig. 3(b), Mn rejection at pH 7 has inreased very well to >70% from 26% rejection at pH 5. At pH 9, higher Mn rejection was achieved to more than 95% and mainly because of changes of solute charges to a stable form which easily removed by membrane as further explained in the earlier section. The good rejection at this condition was mainly contributed by solute-membrane charge interactions. The charge of solute influenced the extent of rejection by NF membranes though the precise mechanism of rejection will depend upon the particular membrane in use [20].

**Surface morphology analysis**

An image of fouled PA-NF membranes for filtration of single metal component in synthetic groundwater at pH 9 is presented in Fig. 4. From visual observation, brownish cake layer become visible on top surface of membrane $(PA\text{-}NF)_A$, resulted from Fe removal. Whereas, blackish cake layer formed on the surface of membrane $(PA\text{-}NF)_B$ after filtration with synthetic groundwater solution with Mn ions. The cake layer formed mainly because of precipitation of $Fe(OH)_3$ and $MnO_2$ as explained in the earlier section. Bordoloi et al. [21] reported that the SEM image with EDS analysis of arsenic (As) and iron (Fe) removal from groundwater by oxidation-coagulation at optimized pH revealed that the sorption of As onto the poorly crystalline precipitate of $Fe(OH)_3$ and existence of a small amount of $MnO_2$. The FESEM images of the precipitate obtained in the presence of Fe and Mn for filtration by both PA-NF and PA-UF membranes at adjusted pH of feed solutions are depicted in Figure 5. The precipitates of $Fe(OH)_3$ on PA-NF and PA-UF membranes are presented by Fig. 5(a) and 5(c), respectively. Whereas, Fig. 5(b) and 5(d) indicate the precipitate of $MnO_2$ on the PA-NF and PA-UF membranes with aggregated large regularly shaped particles suggestive of stable crystallinity of precipitate. In comparison to $Fe(OH)_3$, $MnO_2$ was found more stable especially at pH higher than 8.

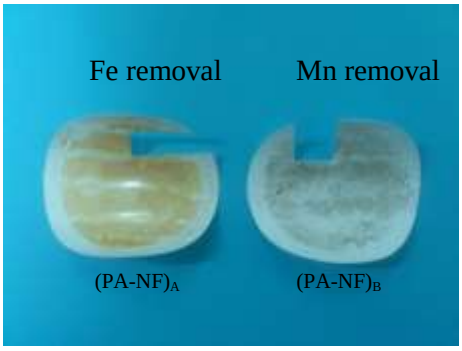



Figure 4. Visualization on physical quality of fouled PA-NF membranes for filtration at 5 bar and pH 9

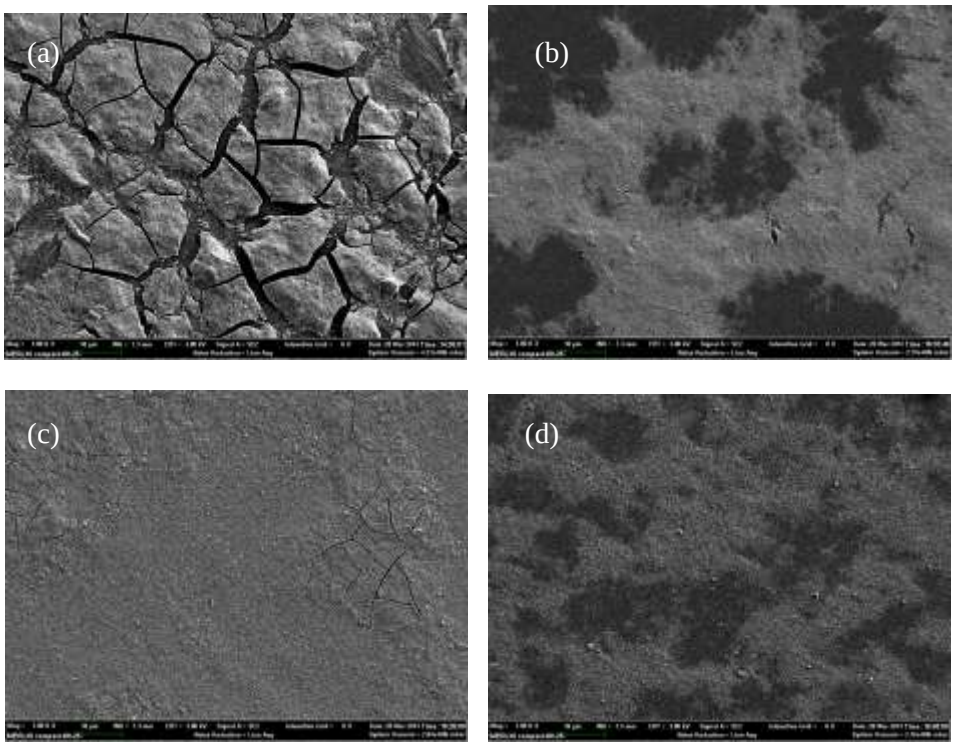



Figure 5. FESEM image of (a) $Fe(OH)_3$ (b) $MnO_2$ on PA-NF, and (c) $Fe(OH)_3$ (d) $MnO_2$ on PA-UF membranes

## Conclusion

The solute-membrane interaction during removal of iron and manganese from synthetic groundwater were investigated in this study. The rejection mechanism of both metallic ions by using PA-NF and PA-UF membranes were also identified and evaluated in this work. The main focus for this paper was to inspect the effect of adjustment on the initial pH of feed solution mainly on the rejection behaviour, permeate quality towards meeting the drinking water standard and also changes on solubility of solute in feed solution. The efficiencies of these membranes were assessed based on permeability, water flux and rejection capabilities at 5 bar and pH of feed solution (pH 3 - 11). The rejection for metallic ions ($Fe^{2+}$ and $Mn^{2+}$) in artificial groundwater using these membranes were significantly influenced by the adjustment of pH. Particularly, rejections of both metals by PA-NF were found higher than PA-UF for all cases. In addition, results proved that PA-NF membrane had efficiently rejected $Fe^{2+}$ and $Mn^{2+}$ ions to the allowable value for drinking water based on WHO standards. Excellent separation performance of PA-NF membrane was mainly due to its effective separation layer of membrane structure.

The significant contribution of solute-membrane charge interactions was determined and influenced by the initial pH of feed solution. It was observed that an increase of pH determined a higher efficiency of Fe and Mn rejections by PA-NF membrane. Higher pH of the feed solution contributed to transformation of soluble divalent $Fe^{2+}$ and $Mn^{2+}$ ions to insoluble $Fe^{3+}$ and $Mn^{4+}$ ions which were more stable and easily precipitated on membrane surfaces. The increase of feed solution pH has decreased the solubility of the divalent metallic ions ($Fe^{2+}$ and $Mn^{2+}$). Therefore, flocculation of metallic ions in the feed solution as the pH increased has resulted to higher rejection of the metal components from the synthetic groundwater. In conclusion, all findings in this study contributed to possibility of developing the membrane technology for Malaysia's groundwater treatment specifically in the removal of Fe and Mn for clean and safe drinking water resources.

**Acknowledgement**

The authors would like to thank Universiti Kebangsaan Malaysia by the grant ICONIC-2013-002 for financial supports. Additionally, the first author is gratefully wished special thanks to the Ministry of Higher Education Malaysia and also the National Defence University of Malaysia for funding the scholarship.

**References**

1. Filip, Z. and Demnerova, K. (2009). Survival in groundwater and FT-IR characterization of some pathogenic and indicator bacteria. *Threats to Global Water Security*: 117 – 122.
2. Stewardship, W., Series, I. (2007). Iron & manganese in groundwater, Br. Columbia Groundwater Association.
3. Ahmad, M. (2012). Iron and manganese removal from groundwater, Thesis University of Oslo.
4. Marchovecchio, R. H., Botte, J. E. and Freiji, S. E (2011). Heavy metals, major metals, trace elements, in: Handbook Water Analysis, CRC Press.
5. World Health Organization, WHO. (2008). Guidelines for drinking-water quality, in: Recomendations, Volume1, 3rd edition, World Health Organization, Geneva: pp. 390 – 399.
6. Chaturvedi, S. and Dave, P. N. (2012). Removal of iron for safe drinking water. *Desalination*, 303: 1–11.
7. Jusoh, A., Cheng, W. H., Low, W. M., Nora'aini, A. and Megat Mohd Noor, M. J. (2005). Study on the removal of iron and manganese in groundwater by granular activated carbon. *Desalination*, 182: 347 –353.
8. Ellis, D., Bouchard, C. and Lantagne, G. (2000) Removal of iron and manganese from groundwater by oxidation and microfiltration. *Desalination*, 130: 255 – 264.
9. Abdul Kadir, A., Othman, N. B. and Azmi, N. M (2012). Potential of using Rosa Centifolia to remove iron and manganese in groundwater treatment. *International Journal of Sustainable Construction Engineering Technology*, 3: 70 – 82.
10. Hussin, N. H., Yusoff, I., Alias, Y., Mohamad S., Rahim, N.Y. and Ashraf, M. A. (2013). Ionic liquid as a medium to remove iron and other metal ions: A case study of the North Kelantan Aquifer, Malaysia. *Environmental Earth Science*, 71: 2105 – 2113.
11. Choo, K.-H., Lee, H and Choi., S.-J. (2005). Iron and manganese removal and membrane fouling during UF in conjunction with prechlorination for drinking water treatment. *Journal of Membrane Science*, 267: 18 – 26.
12. Potgieter, J. H., Mccrindle R. I., Sihlali, Z., Schwarzer R. and Basson, N. (2005). Removal of iron and manganese from water a high organic carbon loading part I : The effect of various coagulants. *Water, Air Soil Pollution*, 162: 49 – 59.
13. Lin, J. L., Huang, C., Pan, J. R. and Wang, Y. S. (2013). Fouling mitigation of a dead-end microfiltration by mixing-enhanced preoxidation for Fe and Mn removal from groundwater. *Colloids Surfaces A Physicochemical and Engineering Aspects*, 419: 87 – 93.
14. De Munari, A. and Schäfer, A. I. (2010). Impact of speciation on removal of manganese and organic matter by nanofiltration. *Journal of Water Supply Research and Technology Aqua*, 59 : 152 – 163.
15. Kasim, N., Mohammad, A.W. and Abdullah, S. R. S. (2015). Characterization of hydrophilic nanofiltration and ultrafiltration membranes for groundwater treatment as potable water resources. *Desalination and Water Treatment*, 57(17): 7711 – 7720.
16. Bordoloi, S., Nath, M. and Dutta, R. K. (2013). pH-conditioning for simultaneous removal of arsenic and iron ions from groundwater. *Process Safety and Environmental Protection*, 91: 405 – 414.
17. Al-Rashdi, B. A. M., Johnson, D. J. and Hilal, N. (2013). Removal of heavy metal ions by nanofiltration. *Desalination*, 315: 2 – 17.
18. Kabsch-Korbutowicz, M. and Winnicki, T. (1996). Application of modified polysulfone membranes to the treatment of water solutions containing humic substances and metal ions. *Desalination*, 105: 41 – 49.
19. De Munari, A., Semiao, A. J. C. and Antizar-Ladislao, B. (2013). Retention of pesticide endosulfan by nanofiltration: Influence of organic matter-pesticide complexation and solute-membrane interactions. *Water Research*, 47: 3484 – 3496.
20. Waite, T. D. (2005). Chemical speciation effects in nanofiltration separation, in: T.D. Schäfer, Andrea I., Fane, A.G., Waite (Ed.), Nanofiltration-principles Application. Elsevier B.V.: pp. 148 – 168.
21. Bordoloi, S., Nath, S. K., Gogoi, S. and Dutta, R. K. (2013). Arsenic and iron removal from groundwater by oxidation-coagulation at optimized pH: Laboratory and field studies. *Journal of Hazardous Materials*, 260: 618 – 626.

*Malaysian Journal of Analytical Sciences, Vol 21 No 1 (2017): 159 - 165*
*DOI: http://dx.doi.org/10.17576/mjas-2017-2101-18*

MALAYSIAN JOURNAL OF ANALYTICAL SCIENCES
*Published by The Malaysian Analytical Sciences Society*
ISSN 1394 - 2506

# CHARACTERIZATION OF ACTIVATED CARBON USING CHEMICAL ACTIVATION VIA MICROWAVE ULTRASONIC SYSTEM

## (Pencirian Karbon Teraktif Menggunakan Sistem Pengaktifan Kimia Melalui Ketuhar Gelombang Ultrasonik)

Norakmalah Mohd Zawawi[1], Fazlena Hamzah[1]*, Mahanim Sarif[2], Shareena Fairuz Abdul Manaf[1], Ani Idris[3]

[1]*Biocatalysis & Biobased Material Research Group, Green Technology and Sustainable Development Research Community, Faculty of Chemical Engineering, Universiti Teknologi MARA, 40450 Shah Alam, Selangor, Malaysia*
[2]*Wood Chemistry and Protection Program, Forest Product Division, Forest Research Institute Malaysia (FRIM),52109 Kepong, Malaysia*
[3]*Faculty of Chemical Engineering, Universiti Teknologi Malaysia, 81310 Skudai, Johor, Malaysia*

**Corresponding author: fazlena@salam.uitm.edu.my*

Received: 21 October 2015; Accepted: 14 June 2016

**Abstract**

Higher adsorption capacities of activated carbon (AC) can be evaluate according to pore volume, porosity and surface area. AC with higher pore volume, porosity and surface area desired in the present study in order to enhance the properties of AC supercapacitor. Thus, the present studies focus on the chemical activation process to increase the characterization of AC. The study was using bamboo waste as a precursor and the activation process was conducted using microwave ultrasonic system. The chemical agent used during the process was KOH and $H_2SO_4$. Microwave activation was conducted at intensity 100 W and 300 W for 30 min and sonication frequency was constantly set at 200 Hz for 60 min. The sample was carbonized at temperature of 400 ºC and 800 ºC using furnace for 2 hours. Then, AC was characterized for surface area using BET analysis and functioning group using FTIR analysis. The results shown the carboxyl, aliphatic, aromatic and phenolic hydroxyl group are present on raw bamboo while new functional group such as alkyl halide and some of some weak bands appeared which analogous with out of plane bending mode of the C-H or O-H group occur for AC. Active surface area and total pore volume of AC supercapacitor in 5M of concentration for $H_2SO_4$ and KOH corresponded to 1167 $m^2/g$, 0.724 $cm^3/g$, 740.10 $m^2/g$, 0.462 $cm^3/g$, respectively.

**Keywords**: supercapacitor, microwave-ultrasonic, activation, chemical, carbonization

**Abstrak**

Kapasiti penjerapan yang tinggi pada karbon teraktif boleh dinilai mengikut isipadu liang, keliangan dan luas permukaan. Keaktifan karbon dengan isi padu liang yang tinggi, tahap keliangan yang besar dan luas permukaan yang tinggi amat dikehendaki di dalam kajian ini bagi meningkatkan sifat-sifat keaktifan karbon superkapasitor. Oleh itu, kajian ini memberi tumpuan kepada proses pengaktifan kimia untuk meningkatkan pencirian yang diperlukan dalam karbon aktif. Kajian ini telah menggunakan sisa buluh sebagai pelopor dan proses pengaktifan telah dijalankan menggunakan sistem ultrasonik-gelombang mikro. Agen kimia yang digunakan semasa proses pengaktifan adalah KOH dan $H_2SO_4$. Pengaktifan gelombang ketuhar telah digunakan pada intensiti 100 W dan 300 W selama 30 min dan kekerapan sonikasi telah ditetapkan pada 200 Hz selama 60 min. Sampel telah dikarbonisasi pada suhu 400 ºC dan 800 ºC mengunakan relau selama 2 jam. Kemudian, karbon aktif dikelaskan bagi mendapatkan luas permukaan dengan menggunakan analisis BET dan kumpulan berfungsi pula menggunakan analisis FTIR. Keputusan menunjukkan karboksil aliphatik, aromatik dan kumpulan fenolik hidrosil hadir pada bahan asas buluh manakala kumpulan berfungsi baharu seperti alkil halida dan beberapa kumpulan yang lemah muncul dimana serupa dengan lenturan mod bagi C-H atau O-H yang terhasil pada karbon aktif. Kawasan permukaan yang aktif dan jumlah isipadu liang

karbon aktif superkasitor pada kepekatan 5M untuk $H_2SO_4$ and KOH sepadan mengikut aturan 1167 $m^2/g$, 0.724 $cm^3/g$, 740.10 $m^2/g$, 0.462 $cm^3/g$.

**Kata kunci:** superkapasitor, gelombang mikro-ultrasonik, pengaktifan, bahan kimia, karbonisasi

## Introduction

Activated carbon (AC) is widely use as catalyst, catalyst support and adsorbent for the removal of pollutant order from liquid to gases and for purification or recovery of chemicals [1]. A wide range of carbonaceous materials such as agricultural wastes or industrial wastes, coconut shell, coal and wood can be used as activated carbon precursor. In industrial practice, coal and coconut shell are two major sources for the production of activated carbon [2]. Bamboo, one of the lignocellulosic resources is a potential precursor for activated carbon due to its flexible, efficient and economical materials [3]. Bamboo has a high volatile matter and low of ash content that required in AC processing with high adsorption capacities are related to property of pore volume, porosity and surface area. Current approach in AC processing gave AC with a small of surface area, limited power intensity and energy capacity and low of porosity [4]. In order to overcome these problems, chemical activation and microwave ultrasonic activation has been introduced to enlarge the surface area, extensive the power intensity and energy capacity and enhance the porosity of AC.

Activated carbon works by the process of adsorption. Adsorption is a process when one material adheres to the surface of another material by means of physical or chemical attraction between the materials. There are two processes involves in development the formation of AC which are activation and carbonization processes. In activation, there are two types of method in order to produce activated carbon from carbonaceous material which is chemical and physical method. Physical activation procedure required two step of process which are carbonization and followed by activation using steam, oxygen or carbon dioxide as an activation agent while chemical activation procedure involves a single stage by using chemical as activating agent such as zinc chloride, potassium hydroxide, phosphoric acid and others [5]. Chemical procedure takes a few of advantage than physical method which has higher carbon yield and better developed of pore structure [6].

Thus, in the present study, bamboo was prepared for AC by using different of chemical activation agent which is KOH and $H_2SO_4$ under microwave ultrasonic radiation for activation process and continues with a single step of carbonization process at different temperature. The aim of this study is to characterize the characteristics of bamboo properties as activated carbon with chemical activation in microwave-ultrasonic activation.

## Materials and Methods

### Materials

The chemicals used in this study are sulphuric acid ($H_2SO_4$) and potassium hydroxide (KOH) purchased from R&M Chemical, Inc. Both chemicals were analytical grade.

### Preparation of activated carbon

The precursor for activated carbon was residual bamboo obtained from Forest Research Institute Malaysia (FRIM). A total 50 g of dry bamboo was placed into crucible and the chemical agent, KOH or $H_2SO_4$ was added into the sample with ratio 1:1. Then, the sample undergoes microwave activation with different energy power for 2 hr. Activate sample was cooled and washed with distilled water until pH 6 to 7. The sample was dried in oven at 110 ºC for 24 hours and stored in desiccator before undergoes carbonization process. Next, the sample was carbonized in the Vermont Furnace (Carbolite, Keison) under the flow of 150 $cm^3$/min nitrogen for 2 hours. After carbonization process, the activated carbon was cooled to ambient temperature for further analysis. Parameter used in the present study is stated in Table 1.

Table 1. Parameter used in Microwave-ultrasonic system with chemical agent

| Sample | Experiment Procedure | Chemical Activating Agent |
|---|---|---|
| AC_OH_8 | Ultrasonic-MW (300W)-Carbonize (800°C) | Base - KOH |
| AC_OH_4 | Ultrasonic-MW (300W)-Carbonize (400°C) | Base - KOH |
| AC_H_8 | Ultrasonic-MW (300W)-Carbonize (800°C) | Acid - $H_2SO_4$ |
| AC_H_4 | Ultrasonic-MW (300W)-Carbonize (400°C) | Acid - $H_2SO_4$ |
| AC_K_8 | Ultrasonic-MW (100W)-Carbonize (800°C) | Base - KOH |
| AC_K_4 | Ultrasonic-MW (100W)-Carbonize (400°C) | Base - KOH |
| AC_SO_8 | Ultrasonic-MW (100W)-Carbonize (800°C) | Acid - $H_2SO_4$ |
| AC_SO_4 | Ultrasonic-MW (100W)-Carbonize (400°C) | Acid - $H_2SO_4$ |

**Proximate analysis of precursor**

The raw material sample was characterized for proximate analysis by using American Society for Testing and Materials standard in order to determine the moisture content of bamboo (ASTM D 2867-99), the presence of volatile matter (ASTM D 5832-98), the ashes content (ASTM D 2866-94) and the amount of fixed carbon and waxes composition [7].

**Characterization of activated carbon**

Brunauer, Emmett, Teller (BET) test (Xyracorp, Autosorb-1, Malaysia) was used in order to determine the specific surface area of a variety materials by the BET Nitrogen adsorption technique. The adsorption process handled in 1 hour by using quick single point and multipoint particular BET surface area determinations.

Field Emission Scanning Electron Microscope (FESEM) was carried out using Carl Zeiss, Supra 40VP, Germany in conducive to examine the morphology of the sample and to analyze the composition, distribution and phase structure of residual bamboo. The sample must be electrically connected to the sample holder in order to prevent charging and distortion of the image.

Fourier Transform Infrared Spectroscopy (FTIR) (Perkin Elmer, Spectrum One-FTIR, USA) was performed in order to identify chemical bonds in a molecule by producing an infrared absorption spectrum for functional group classification. FTIR creates the absorbance spectra representing the unique chemical bonds and the molecular structure of the sample material. FTIR spectra were recorded between 4000 and 500 $cm^{-1}$ by using AVATAR 360 Spectrophotometer.

## Results and Discussion

**Determination of surface area and pore size**

Table 2 shows the total of active surface area and total pore volume analyzed using nitrogen adsorption/desorption. The acquired results determined the surface of the chemical activation with base, KOH consist a greater surface area as well as pore volume as compared with chemical activation using acid activating agent, $H_2SO_4$. The carbonization of bamboo at 800 ºC gave a higher active surface area then carbonization at 400 ºC. The highest of active surface area obtained was 1162.73 $m^2/g$ with total pore value 0.7237 $cm^3/g$ using 300W of MW-ultrasonic radiation power. The active surface area obtain from the study was compare with previous research on AC derived from different agricultural waste and tabulated in Table 3. The result indicated that present study gave highest $V_{mic}$ and active surface area is at the power with another AC using KOH as activating agent. This comparison showed bamboo is one of the efficient and effective precursor in produce a high of $V_{mic}$ carbon.

Table 2. Chemical properties of produced activated carbon

| Experiment | Active Surface Area ($m^2/g$) | Total Pore Volume ($cm^3/g$) |
|---|---|---|
| AC_OH_8 | 1162.73 | 0.7237 |
| AC_OH_4 | 2.8791 | 0.0024 |
| AC_H_8 | 740.09 | 0.4019 |
| AC_H_4 | 478.14 | 0.2262 |
| AC_K_8 | 24.6062 | 0.0172 |
| AC_K_4 | 1.8299 | 00063 |
| AC_SO_8 | - | 0.0066 |
| AC_SO_4 | 4.7868 | 0.0078 |

Table 3. Pore structure from other agricultural wastes by MW with KOH activation

| Precursor | Power (W) | $S_{BET}$ ($m^2/g$) | $V_{mic}$ ($cm^3/g$) | Ref |
|---|---|---|---|---|
| Bamboo | 300 | 1162.73 | 0.7237 | This work |
| Oil palm fiber | 600 | 1223.00 | 0.4200 | [8] |
| Coconut husk | 600 | 1356.30 | 0.3920 | [9] |
| Pineapple | 600 | 1006.00 | 0.2800 | [10] |
| *Siris* seed pods | 620 | 1824.80 | 0.6450 | [11] |

**Proximate analysis**

Table 4 show the properties of raw bamboo precursor. Before undergoes the proximate analysis, raw bamboo has been dried into oven for 30 min (BamP) and 15 min (BamPr) of temperature in order to remove impurities and water content. From the results, it showed that BamP consist of low moisture content when compared to BamPr. For volatile and ash content, sample BamP gave a higher value which is 45.320% and 1.98% while BamPr sample obtain 40.178% of volatile content and 1.5% of ash content. For fixed carbon content BamPr sample have 58.322% whereas BamP consist of 52.7% of fixed carbon. High ash content is undesired in AC processing because it represents amount of inorganic material from the precursor activation and a numerous treatment needed to be take place [12].

Table 4. Proximate of raw bamboo precursor

| Experiment | Moisture Content (%) | Volatile Content (%) | Ash Content (%) | Fixed Carbon (%) |
|---|---|---|---|---|
| BamP | 13.300 | 45.320 | 1.98 | 52.7 |
| BamPr | 14.356 | 40.178 | 1.5 | 58.322 |

**Elemental analysis (CHNS-O analysis)**

Table 5 summarizes the results of elemental analysis which gave the percentage of carbon, hydrogen, nitrogen and sulphur present in the sample. The result indicated that the largest elements inside activated carbon are oxygen and carbon. With increment of activation temperature, there was decreasing in carbon content which probably due to the discharge of volatiles [13]. In chemical activation of acid activating agent, $H_2SO_4$ the activation process has

provoked a progress of discharge oxygen with notable loss at 800 ºC. Discharge of oxygen happened because element of oxygen intimate the fraction of oxygen content was not located around the pore entry of activated carbon [14]. High of moisture and volatile content also give a higher value for oxygen element. On the contrary, there was a decreasing of carbon content in a higher temperature. Besides that, there was a reduction of hydrogen element at a temperature 800 ºC. The percentages of carbon significantly high at temperature 400 ºC with radiation power 300 W and 100 W based on different type of activating agent. The precursor of carbon could barely be heated without impregnation of activation agent, demonstrating that activation agent acted as the fundamental MW absorber at the primary stage. With the evolution of pore structure, the AC itself could acquire MW energy [15]. At low microwave energy, the pore structure was not satisfactorily created which improved with the expanding of microwave power. Nevertheless, at tremendous radiation power, absorbed MW energy eclipse at some of power so that the overfull energy keep create a small feature of carbon burnt and the structure was destroyed [16].

Table 5. Result of elemental analysis

| Experiment | Carbon (%) | Hydrogen (%) | Nitrogen (%) | Sulphur (%) | Oxygen (%) |
|---|---|---|---|---|---|
| AC_OH_4 | 30.3338 | 2.5647 | 0.4022 | 0.0000 | 66.6993 |
| AC_H_4 | 37.5033 | 0.8403 | 0.2574 | 0.0386 | 61.3604 |
| AC_OH_8 | 20.5301 | 1.8585 | 1.1981 | 0.0000 | 76.4133 |
| AC_H_8 | 14.0534 | 0.1058 | 0.399 | 0.0167 | 85.4251 |
| AC_K_4 | 28.5147 | 2.4452 | 0.380 | 0.0130 | 68.6471 |
| AC_SO_4 | 26.2542 | 1.8933 | 0.149 | 0.0000 | 71.7035 |
| AC_K_8 | 21.4699 | 0.6440 | 0.412 | 0.0471 | 77.4270 |
| AC_SO_8 | 20.7577 | 0.7182 | 0.466 | 0.0000 | 78.0581 |

**FTIR analysis**

The prepared activated carbon was analyzed for functional group using FTIR shown a following bands: 3308.78 $cm^{-1}$ was attributed to O-H vibration in hydroxyl groups. The location of hydrogen bonded OH groups usually at range 3200 – 3750 $cm^{-1}$ for alcohol and phenol which involve in hydrogen bonding may be due to adsorbed water [17], C=C stretching vibration of aromatic rings at 1599.98 $cm^{-1}$, the relatively intense band at 1031.89 $cm^{-1}$ can be assigned to alcohol or phenol groups of R-OH, 1234.05 $cm^{-1}$ with absence of C=O stretching from the esters (C-O) of strong intensity absorptions. Figure 1 shown band at range 756 – 540 $cm^{-1}$ with 667.07 $cm^{-1}$ is (C-O-H) twist abroad with strong aliphatic, 1350.48 $cm^{-1}$ of amines compound occurs which correlated out of plane bending absorption, alkanes (C-H $CH_2$) found at range of 1457.03 $cm^{-1}$ bending absorption of methylene groups and 1784.93 $cm^{-1}$ denotes C=O stretching from ketones (C=OR), aldehyde (C=OH) and carboxylic acid (COOH). Some weak bands also appeared in the range of 600 – 900 $cm^{-1}$ which associated with out-of-plane bending mode of (C-H) and O-H group. Heating at a high of temperature make some of peaks disappear in AC_K_8 and AC_H_8. The main surface functional groups present on the activated carbon of bamboo are lactones, ketones, carboxylic anhydrides, quinine structure and aromatic ring [18].

**Activated carbon morphology**

Figure 2 indicates the FESEM images of the raw bamboo and derived AC. There was no pore development on the precursor of raw bamboo residual and the structure of the surface is rough and uneven. From Figure 1a, many large pores shape and size were clearly found on the AC surface after the activation process of MW-ultrasonic and chemical activation. The well-developed pores had led to the large surface area and porous structure of the activated carbon had shown in Figure 1c and 1d. It can be seen that there was a significant difference between sample from KOH and $H_2SO_4$ surface texture. Pore development was caused by the breakdown of some material in the precursor due to thermal expansion during the activation step [19]. The reaction rate between the activating agent which is KOH and carbon also increase when the precursor is subjected to high activation temperature, thus leading to the formation of well-developed pores [20].

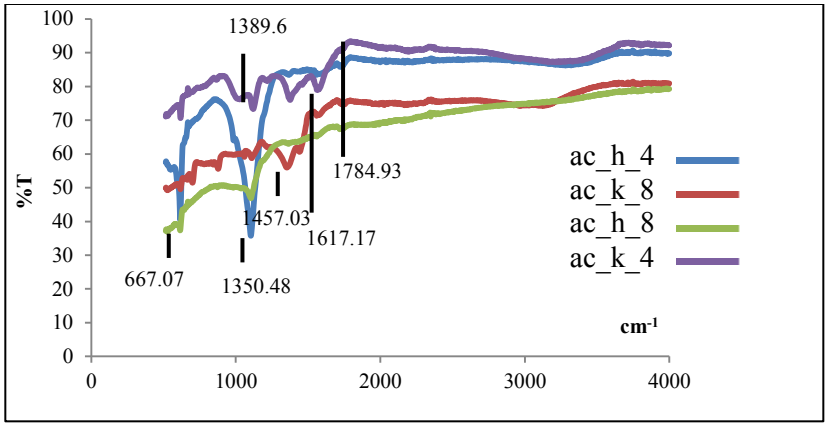



Figure 1. FTIR Spectra of activated carbon

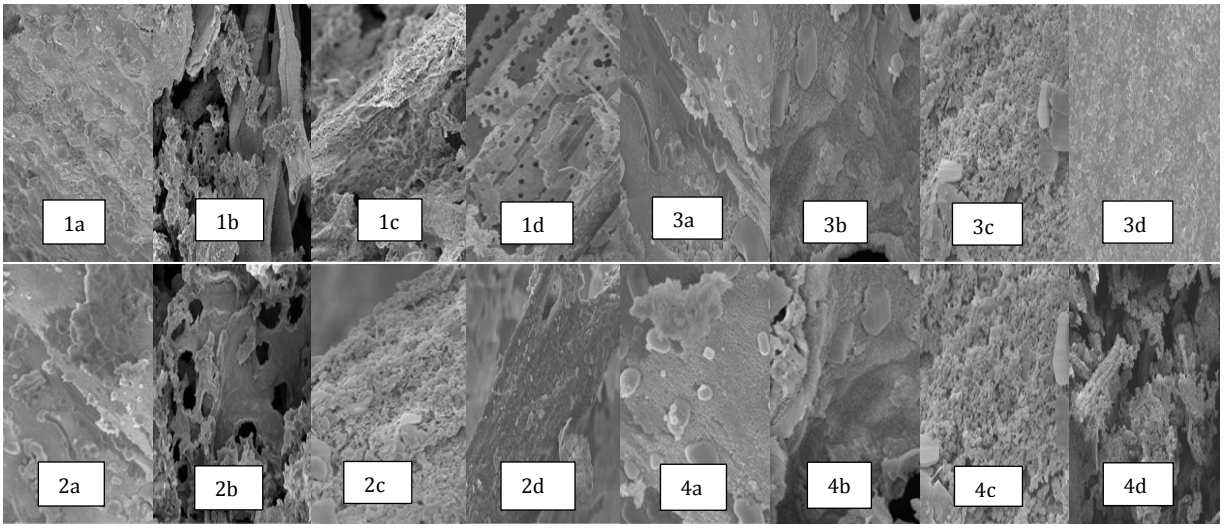



Figure 2. FESEM Mag. 1.00K and 5.00K (1a & 2a) AC_H_4a; (1b & 2b) AC_H_4b; (1c & 2c) AC_K_4; (1d & 2d) AC_OH_4; Mag. 1.00K and 5.00K (3a & 4a) AC_H_8a; (3b & 4b) AC_H_8b; (3c & 4c) AC_K_8; (3d & 4d) AC_OH_8

## Conclusion

The present investigation showed that bamboo is a promising precursor to be used in the preparation of activated carbon. In the view of experiment results, the best activated carbon properties of the sample prepared from the bamboo raw material by a one-step chemical activation with base activating agent, KOH with MW-ultrasonic radiation power 300 W were obtained at the carbonization temperature of 800 ºC with the highest of surface area, 1162.73 $m^2/g$. The active surface area of the bamboo activated carbon derived in this work was considered relatively high besides being mesopores. The result proved that the potentially of MW-ultrasonic activation was rapid, efficient and feasible as a viable activation method.

## Acknowledgement

The present research was made possible through a Research Acculturation Colloborative Effort (RACE) by Universiti Teknologi MARA (600-RMI/RACE 16/6/2 (9/2012)) and also facilities and constant encouragement from Faculty of Chemical Engineering, Universiti Teknologi MARA is gratefully acknowledged.

**References**

1. Chen, D., Zhou, J. and Zhang, Q. (2014). Effects of heating rate on slow pyrolysis behavior, kinetic parameters and products properties of moso bamboo. *Bioresource Technology*, 169 (9): 313 – 319.
2. Liu, Q.-S., Zheng, T., Wang, P. and Guo, L. (2010). Preparation and characterization of activated carbon from bamboo by microwave-induced phosphoric acid activation. *Industrial Crops and Products*, 31(2): 233 – 238.
3. Wang, R., Amano, Y. and Machida, M. (2013). Surface properties and water vapor adsorption–desorption characteristics of bamboo-based activated carbon. *Journal of Analytical and Applied Pyrolysis*, 104: 667 – 674.
4. Lee, Y. J., Kim, G.-P., Bang, Y., Yi, J., Seo, J. G. and Song, I. K. (2014). Activated carbon aerogel containing graphene as electrode material for supercapacitor. *Materials Research Bulletin*, 50: 240 –245.
5. Iqbaldin, M. N. M., Khudzir, I., Azlan, M. I. M., Zaidi, A. G., Surani, B. and Zubri, Z. (2013). Properties of Coconut Shell Activated Carbon. *Journal of Tropical Forest Science*, 25 (4): 497 – 503.
6. Dabrowski, A., Podkościelny, P., Hubicki, Z. and Barczak, M. (2005). Adsorption of phenolic compounds by activated carbon- a critical review. *Chemosphere*, 58 (8) :1049 – 1070.
7. Gonzalez, P. G. and Pliego-Cuervo, Y. B. (2013). Physicochemical and microtextural characterization of activated carbons produced from water steam activation of three bamboo species. *Journal of Analytical and Applied Pyrolysis*, 99: 32 – 39.
8. Foo, K.Y. and Hameed, B. H. (2012) Adsorption characteristics of industrial solid waste derived activated carbon prepared by microwave heating for methylene blue. *Fuel Processing Technology*, 99 –103.
9. Foo, K. Y. and Hameed, B. H. (2012). Coconut husk derived activated carbon via microwave induced activation: effects of activation agents, preparation parameters, and adsorption performance. *Chemical Engineering Journal*, 184: 57 – 65.
10. Foo, K. Y. and Hameed, B. H. (2012). Porous structure and adsorptive properties of pineapple based activated carbons prepared via microwave assisted KOH and $K_2CO_3$ activation. *Microporous and Mesoporous Materials*, 148: 191 – 195.
11. Ahmed, M. J. and Theydan, S. K. (2013). Microporous activated carbon from Siris seed pods by microwave-induced KOH activation for metronidazole adsorption. *Journal of Analytical and Applied Pyrolysis*, 99: 101 – 109.
12. Koplan, S., Okun, D. T., Hillman, J. A., Lane, C. R., Pearson, D. R. and Aranoff, S. L. (2006). Certain activated carbon from China. U.S International Trade Commission. Washington.
13. Ma, X., Yang, H., Yu, L., Chen, Y. and Li, Y. (2014). Preparation, surface and pore structure of high surface area activated carbon fibers from bamboo by steam activation. *Materials*, 7(6): 4431 – 4441.
14. Paiva, M. C. R., Bernardo, C. A. and Nardin, M. (2000). Mechanical, surface and interfacial characteristic of pitch and PAN-carbon fibres. *Carbon*, 38: 1323 – 1327.
15. Wang, T. H., Tan, S. X. and Liang, C. H. (2009). Preparation and characterization of activated carbon from wood via microwave-induced $ZnCl_2$ activation. *Carbon*, 47: 1880 – 1883.
16. Deng, H., Li, G., Yang, H., Tang, J. and Tang, J. (2010). Preparation of activated carbons from cotton stalk by microwave assisted KOH and $K_2CO_3$ activation. *Chemical Engineering Journal*, 163 (3): 373 – 381.
17. Ahmad, A. A. and Hameed, B. H. (2009). Reduction of COD and color of dyeing effluent from a cotton textile mill by adsorption onto bamboo-based activated carbon. *Journal of Hazardous Materials*, 172 (2-3): 1538 – 1543.
18. Ahmad, M. A., Ahmad Puad, N. A. and Bello, O. S. (2014). Kinetic, equilibrium and thermodynamic studies of synthetic dye removal using pomegranate peel activated carbon prepared by microwave-induced KOH activation. *Water Resources and Industry*, 6: 18 – 35.
19. Nazri, I., Ahmad, Z. A., Ahmad, M. A., Ahmad, N. and Sulaiman, S. K. (2010). Optimization of process variables for malachite green dye removal using rubber seed coat based activated carbon. *International Journal of Engineering and Technology,* 11: 305 – 311.
20. Sun, Y. and Webley, P. A. (2010). Preparation of activated carbons from corncob with large specific surface area by a variety of chemical activators and their application in gas storage. *Chemical Engineering Journal,* 162: 883 – 892.

*Malaysian Journal of Analytical Sciences, Vol 21 No 1 (2017): 166 - 172*
*DOI: http://dx.doi.org/10.17576/mjas-2017-2101-19*

MALAYSIAN JOURNAL OF ANALYTICAL SCIENCES
*Published by The Malaysian Analytical Sciences Society*
ISSN 1394 - 2506

# $CeO_2$-$TiO_2$ FOR PHOTOREDUCTION OF $CO_2$ TO METHANOL UNDER VISIBLE LIGHT: EFFECT OF CERIA LOADING

## ($CeO_2$-$TiO_2$ untuk Penurunan $CO_2$ kepada Metanol di bawah Radiasi Cahaya Nampak:Kesan Pemuatan Ceria)

Hamidah Abdullah[1,2]*, Nur Aminatulmimi Ismail[1], Zahira Yaakob[2], Maksudur R. Khan[1], Syarifah Abd Rahim[1]

[1]*Faculty of Chemical and Natural Resources Engineering, Universiti Malaysia Pahang, 26300, Kuantan, Pahang, Malaysia*
[2] *Department of Chemical and Process Engineering, Faculty of Engineering and Built Environment, Universiti Kebangsaan Malaysia, 43600 UKM Bangi, Selangor, Malaysia*

**Corresponding author: hamidah@ump.edu.my*

Received: 21 October 2015; Accepted: 14 June 2016

**Abstract**

A visible light-driven photocatalyst, $CeO_2$-$TiO_2$ catalyst with different ceria loading was synthesized by impregnation method between $TiO_2$ powder and cerium oxide nanoparticles slurry. The prepared catalyst samples were characterized by X-ray diffraction (XRD), surface area analysis, UV-vis absorption spectroscopy and photoluminescence spectroscopy (PL). The band gap of $CeO_2$-$TiO_2$ catalyst was found to be 2.15 – 2.4 eV. The band gap reduction clearly indicated the successful loading of $CeO_2$ on $TiO_2$. The photocatalytic activity was determined by measuring the photoreduction of $CO_2$ to methanol in aqueous solution under visible light. The effect of cerium loading in the range of 1 to 5 wt% on the photocatalytic activity was studied and 2 wt% $CeO_2$-$TiO_2$ was found to exhibit the maximum photoactivity of 18.6 µmol/g.catalyst after 6 hours irradiation. Results showed that the prepared photocatalyst is visible light active and may be used as effective catalyst in photoreduction of $CO_2$ to methanol.

**Keywords**: metal oxide, photocatalyst, band gap, nanoparticles

**Abstrak**

Fotomangkin yang boleh diaplikasi di bawah radiasi cahaya nampak iaitu mangkin $CeO_2$-$TiO_2$ yang berbeza muatan ceria telah disintesis dengan kaedah impregnasi serbuk titanium dioksida dengan mendakan partikel nano cerium dioksida. Ciri mangkin yang dihasilkan dikaji dengan menggunakan pembelauan sinar-X (XRD), analisis luas permukaan, UV-Vis spektrofotometer dan spektroskopi fotoluminesen (PL). Jurang tenaga mangkin $CeO_2$-$TiO_2$ adalah di antara 2.15 eV hingga 2.4 eV. Pengurangan jurang tenaga jelas menunjukkan pemuatan $CeO_2$ ke atas $TiO_2$ telah berjaya. Aktiviti fotopemangkinan ditentukan melalui tindak balas penurunan gas karbon dioksida ($CO_2$) di dalam larutan akueus kepada metanol dan dijalankan di bawah radiasi cahaya nampak. Kesan pemuatan 1 hingga 5 peratus berat cerium ke atas $TiO_2$ terhadap aktiviti fotopemangkinan telah dikaji dan $CeO_2$-$TiO_2$ dengan 2 peratus berat cerium didapati menunjukkan fotosensitiviti maksimum iaitu penghasilan 18.6 µmol/g.mangkin selepas 6 jam radiasi. Hasil kajian menunjukkan bahawa fotomangkin yang dihasilkan adalah aktif di bawah cahaya nampak dan dijangka efektif untuk penurunan $CO_2$ kepada metanol.

**Kata kunci:** logam oksida, fotomangkin, jurang tenaga, partikel nano

## Introduction

The photocatalytic reduction of carbon dioxide ($CO_2$) to fuel has been reported as an alternative way to tackle the global warming and shortage of fuels problem. Among the semiconductor photocatalysts that have been studied, titania dioxide ($TiO_2$) has been considered the most promising photocatalyst due to its non-toxic, low cost, and photostable [1]. One of the drawbacks of the existing semiconductor typically $TiO_2$ is that it has a wide band gap. This limits its catalytic activity under the visible light. In such cases, the photogenerated electron hole pair's recombination is fast, resulting less electron hole pairs availability that that can be utilized for $CO_2$ reduction. Several strategies have been reported by modifying the structure of $TiO_2$ to enhance its photoactivity under visible light and lower the recombination rate of photogenerated electron hole pairs. Among modifications made was doping rare earth element with the $TiO_2$. This study has demonstrated that the modified $TiO_2$ catalysts enhance the photocatalytic ability as to compare to $TiO_2$. Some examples are clearly shown in the researches of others; degradation of organic compounds such as Eu-$TiO_2$ for Rhodamine B (RB) degradation [2], La-$TiO_2$, Pr-$TiO_2$, Nd-$TiO_2$ for reduction of hexavalent chromium and degradation of methylene blue [3] and La-$TiO_2$ and Ce-$TiO_2$ for degradation of methylene blue [4].

Ceria was chosen by many researchers among the rare earth elements because it is one of the four most abundant rare earth elements. It appearances that composites of ceria-titania have shown remarkable photocatalytic activity under visible light irradiation for water splitting and degradation of organic compounds due to its capability in adsorbing visible light and inhibit the photogenerated electron hole pairs recombination [5]. To the best of our knowledge, there are a few reports on ceria-titania for $CO_2$ photoreduction. Recently, Xiong et al. and Matejova et al. studied the $CeO_2$-$TiO_2$ catalyst activity for photocatalytic conversion of $CO_2$ to liquid products (methanol and formaldehyde) and to gaseous products ($CH_4$ and CO), respectively [6,7]. However, the study was limited under UV light irradiation study only. Our previous study reported that $CeO_2$-$TiO_2$ showed a higher methanol yield than $TiO_2$ catalyst for $CO_2$ photocatalytic reduction under visible light irradiation [8]. This paper represents the extension of previous study by study the effect of ceria amount loading on characterization and $CO_2$ photocatalytic reduction to methanol under visible light irradiation.

## Materials and Methods

### Catalyst preparation

The $CeO_2$-$TiO_2$ powder was prepared based on our previous work [8]. In brief, firstly, $CeO_2$ nanoparticle slurry was prepared by dissolved required amount of (Ce $(NO_3)_3.6H_2O$) in 20% ethanol solution at 50 °C and subsequently, 3M ($NH_4OH$) was added under stirring. The process was completed when the reaction slurry color turned from colorless to light yellow. Then, 5 g of $TiO_2$ powder was added to the $CeO_2$ slurry and stirred for 5 hours. The slurry was filtered, dried at 100 °C overnight and calcined at 500 °C for 4 hours. The catalyst was prepared in 1 wt%, 2 wt% and 5 wt% of ceria loading.

### Catalyst characterization

The crystalline structure and phase purity of the catalysts were determined by X-ray diffraction (XRD) analysis using Bruker D8 Focus Advance powder diffractometer with a Cu Kα radiation of wavelength 0.15406 nm, scanned from 10 to 80° with 0.025° step size. The surface area and pore parameters of the samples was determined by nitrogen adsorption–desorption analysis at 77 K using a Micrometrics ASAP 2010, using the Brunauer- Emmet- Teller and Barrett- Joyner- Halenda (BET/ BJH) method over the pressure range $P/P_o$= 0.02 - 1.0. The diffuse reflectance spectra of the catalyst samples over a range of 200 – 800 nm were recorded by a UV-vis-NIR spectrophotometer. The photoluminescence spectra were measured by Edinburgh FS920 photoluminescence spectroscopy, using Xenon Lamp (450W) as the excitation source and 300 nm as the excitation wavelength over a range of 330 to 600 nm.

### Photocatalytic activity

The photoreduction of $CO_2$ was performed according to the procedure reported in our previous study [8]. In brief, 0.3 g catalyst powder was dispersed in the $CO_2$ aqueous solution. The $CO_2$ aqueous solution was prepared by bubbling 0.4 $L.min^{-1}$ of $CO_2$ for 30 minutes into 300 ml of 0.1 M NaOH solution in the reactor consists of 500 ml Pyrex glass reactor equipped with a quartz trap with 220 mm length which is irradiated using artificial visible light produced by a 500 W Xenon lamp (Jiquang, Shanghai) with a wavelength range of 300 to 800 nm. Then, the reaction was started by switching on the light. 5 ml of the suspension were withdrawn from the reactor at every 1hour interval of reaction for 6 hours of irradiation period, while the gas products were collected using gas bags. The liquid and gas products were analyzed using Agilent Gas Chromatography (GC) with a flame ionization detector (FID) and thermal conductivity detector (TCD), respectively. Analytical results indicated that the methanol is the main product in liquid sample and no products were detected in the gaseous samples.

## Results and Discussion

### XRD analysis

The crystal phase identification and crystallite size estimation were usually checked by XRD**.** Figure 1 shows the XRD patterns of the as-synthesized $CeO_2$-$TiO_2$ with different cerium loading. It can be seen that the peaks at 2θ

values of 25.17°, 37.60°, 47.76°, 54.01° and 62.60° which are indexed to the (101), (004), (200), (105) and (204) planes of the anatase phase of $TiO_2$ (JCPDS: 21-1272) appeared for all samples. It is noteworthy that no cerium oxide peaks could be observed in the XRD spectra for samples with 1 wt% ceria loading. This might be due to all the ceria ions were incorporated into the structures of titania or the size of the particles which are too small that cannot be detected by XRD. On the other hand, the small peak of cerium oxide was seen to appear in the spectra for 2 wt% loading and the peaks was clearly seen for 5 wt% loading. The crystallite sizes of anatase of samples were calculated using Scherrer's equation according to (101) peak. The values are 9.9 nm, 9.8 nm and 9.2 nm for $CeO_2$-$TiO_2$ samples of 1 wt%, 2 wt% and 5 wt% ceria loading on $TiO_2$, respectively. The crystalline size of the anatase phase formed decreased with the content of Ce oxide doped, which indicates that the Ce species inhibit the growth of anatase $TiO_2$ crystallite and it agrees well with the literature report [9].

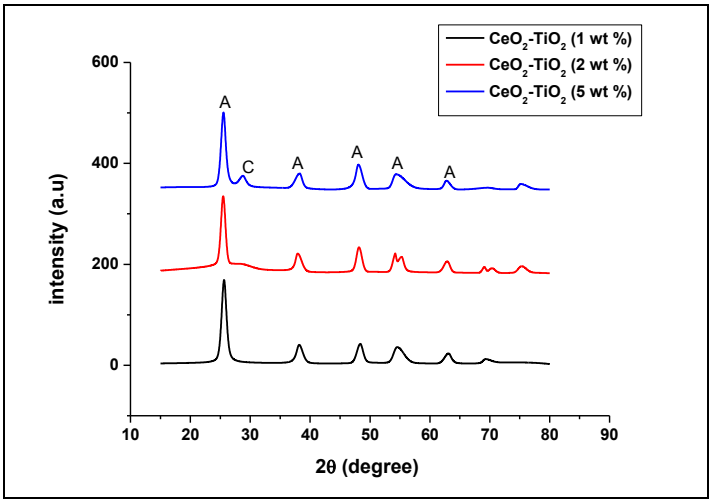



Figure 1. X-ray diffraction patterns of all photocatalysts (*A=anatase phase, C=Cerianite phase)

**BET/BJH Analysis**

Figure 2 shows the pore size distribution curves of all photocatalysts. The pore diameter was ranged from 8 – 15 nm indicating that the pores are mainly mesoporous in nature. The textural properties of the catalysts are summarized in Table 1, which shows that the surface area and pore volume changes was insignificantly with ceria loading of 1 wt% and 2 wt% but drastically decreases with 5 wt%. It was previously reported that the specific surface area and the pore volume of catalyst prepared by the impregnation method decrease with increasing metal loading [10].

Table 1. BET/BJH analysis of all photocatalyst

| Sample | Surface area ($m^2/g$) | Pore volume ($cm^3/g$) | Mean pore size (nm) |
|---|---|---|---|
| $CeO_2$-$TiO_2$ (1 wt%) | 105.4 | 0.37 | 12 |
| $CeO_2$-$TiO_2$ (2 wt%) | 104.9 | 0.40 | 15 |
| $CeO_2$-$TiO_2$ (5 wt%) | 63.9 | 0.16 | 8 |

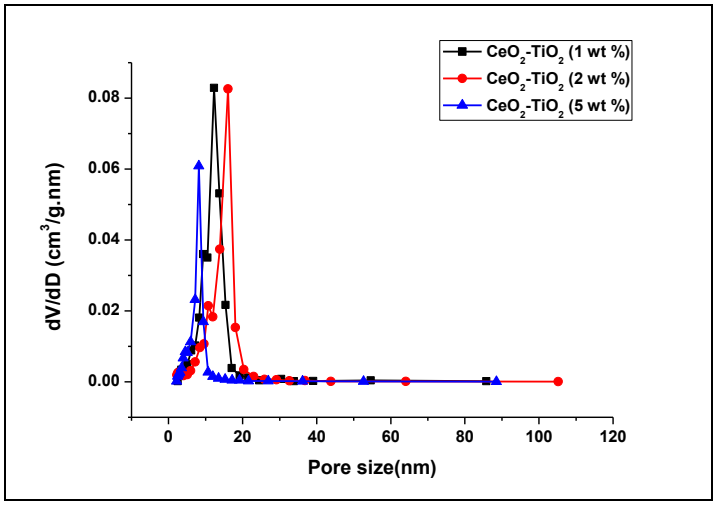



Figure 2. Pore size distribution of all photocatalysts

**UV-Vis-NIR analysis**

UV-Vis-NIR spectra of $CeO_2$-$TiO_2$ with different ceria loading are presented in Figure 3(a) to explore the influence of the ceria addition amount on the optical property of $TiO_2$. From the Figure 3(a), a slight shift to the visible light region occurred as the amount of ceria was increased corresponds to a band gap of 2.4, 2.2 eV, and 2.15 eV for 1 wt%, 2 wt% and 5 wt% ceria loading on $TiO_2$, respectively as shown in Figure 3(b). This indicates that the $CeO_2$-$TiO_2$ absorbs well in the visible light region due to presence of ceria. This is due to the charge transfer from impurity level to the conduction band. The impurity is caused by some of $Ce^{3+}/Ce^{4+}$ sites have been replaced by $Ti^{4+}$ ions [11]. The absorption increases with the increasing of ceria content since the color of $CeO_2$-$TiO_2$ changes from pale yellow to yellow from the observation in the catalyst preparation.

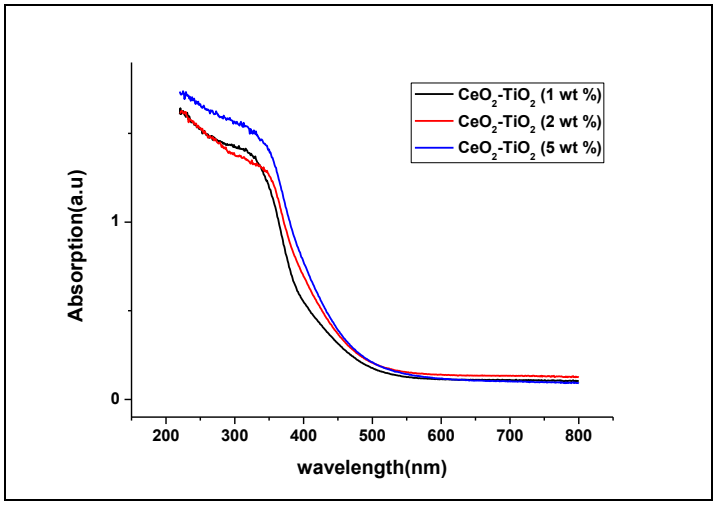



Figure 3(a). UV-vis NIR spectra of all photocatalysts

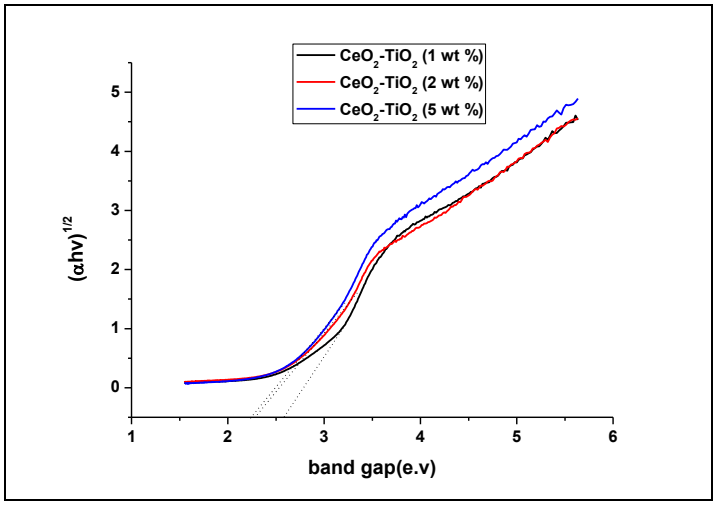



Figure 3(b). The optical absorption edges of all photocatalysts

**Photoluminescence analysis**

The photoluminescence spectra are useful to understand the surface process in which photogenerated electron-holes take part in photocatalysis. The existence of photoluminescence can be attributed to the recombination of excited electron-hole pairs. In Figure 4, there are two obvious PL peaks at 420 nm which attributed to the band-edge free exciton luminescence while the peak at 470 nm indicates the bound exciton luminescence [12]. The peaks positions for all samples are basically the same. However, the intensity of PL spectra is different. It shows that the intensity is decrease, indicating the lower rate of recombination of electron-hole pairs with increasing ceria loading. This is due to the possibility of $Ce^{3+}$ ions existence in $CeO_2$-$TiO_2$ that could interact with holes and inhibit the recombination of photogenerated electron-holes [6].

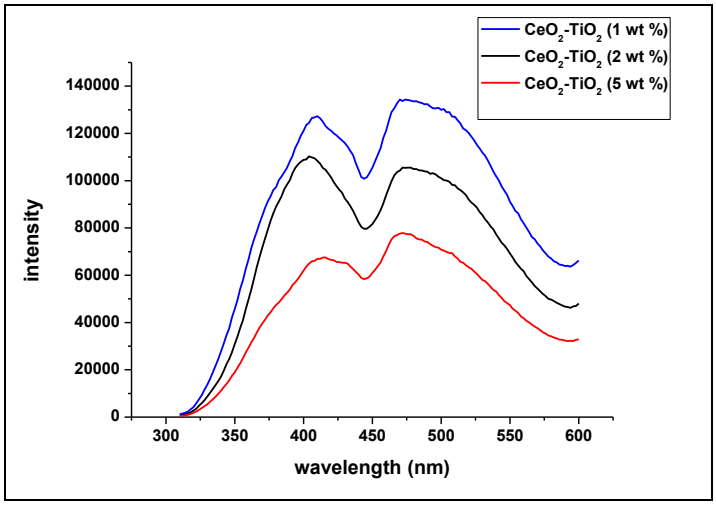



Figure 4. Photoluminescence Spectra of all photocatalysts

**Photocatalytic activity**

Methanol was determined in liquid phase while there were no products in gas phase. Other products such as formic acid and formaldehyde could also be formed [13], but they were undetectable. The methanol is possibly produced by the reduction of $CO_2$ and carbonate ($CO_2$ dissolve in water and form carbonate in water) as in Equation (1)-(3).

$$CO_2 + 6H^+ + 6e^- \longrightarrow CH_3OH + H_2O \quad (1)$$

$$H_2CO_3 + 6H^+ + 6e^- \longrightarrow CH_3OH + 2H_2O \quad (2)$$

$$CO_3^{2-} + 8H^+ + 6e^- \longrightarrow CH_3OH + 2H_2O \quad (3)$$

Figure 5 shows the yield of methanol formation by $CO_2$ photocatalytic reduction as functions of the irradiation time for $CeO_2$-$TiO_2$ with 1 wt%, 2 wt% and 5 wt% ceria loading. It can be seen that the yield of methanol increased with the irradiation time for all photocatalysts. The methanol yield increased with increasing ceria loading from 1 wt% to 2 wt%. This may be due to the extend response range into visible light region with increase the ceria loading, thus more photo energy could be absorbed by catalyst thus generate more electron-hole pairs. Moreover, the decreasing of electron hole recombination rate with increasing ceria loading also contributes in enhancing the methanol yield.

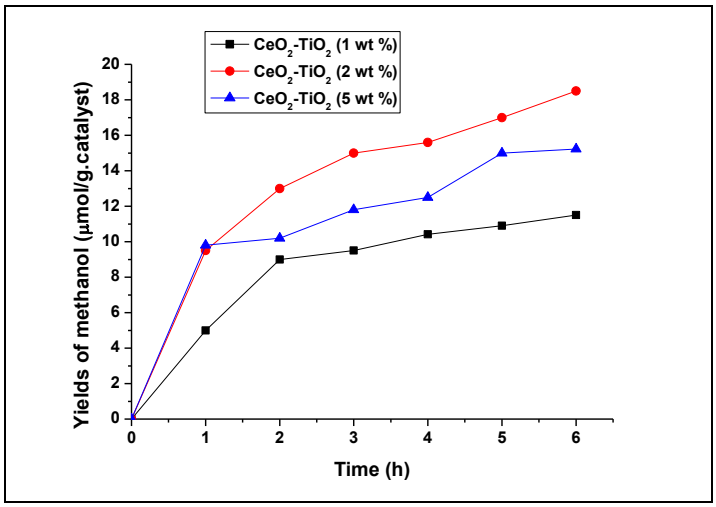



Figure 5. Yields of methanol as functions of irradiation time over all photocatalysts.

However, the methanol yield decreased after loading with 5 wt% ceria although the band gap and electron hole recombination rate decrease indicating that there is an optimum amount cerium loading for $CeO_2$-$TiO_2$. Moreover, the decreasing of specific surface area of 5 wt% $CeO_2$-$TiO_2$ catalyst also the factor that causes the decreasing in methanol yield since less reactant could be adsorbed onto the catalyst surface. The mechanism explanation of the decreasing of methanol yield could be described as follows: $TiO_2$ can adsorb carbonate species efficiently [14]. Then, $CeO_2$ which dispersed on the $TiO_2$ surface can absorb visible light and transfer the excited electrons to $TiO_2$ so that the carbonate species on the $TiO_2$ surface can be reduced to methanol. The coverage of $TiO_2$ surface by $CeO_2$ is optimum at 2 wt%, thus enough uncovered surface of $TiO_2$ for carbonate species adsorption. However, more $CeO_2$ has covered the surface of $TiO_2$ when the ceria loading increases to 5 wt%, resulted less surface of $TiO_2$ is in contact with carbonate species. Therefore, the photocatalytic activity decreases due to lowering of the available surface area even though the absorption of light by $CeO_2$ increases.

## Conclusion

The series of $CeO_2$-$TiO_2$ nano photocatalysts with different ceria loading were synthesized and characterized. The characterization results show that crystallite size, the surface area, the band gap and the electron hole recombination rate decreased as the ceria loading increased. The best ceria loading percentage to obtain optimum methanol yield in $CO_2$ phocatalytic reduction under visible light irradiation is 2 wt%.

## Acknowledgement

The authors would like to extend their deepest appreciate on to the Ministry of Education (MOE), Universiti Kebangsaan Malaysia and Universiti Malaysia Pahang for financial support of this research under RAGS (RDU131418) and FRGS (RDU120112).

## References

1. Corma, A., and Garcia, H. (2013). Photocatalytic reduction of $CO_2$ for fuel production: Possibilities and challenges. *Journal of Catalysis,* 308: 168 – 175.
2. Zhang, Y., Zhang, H., Xu, Y., and Wang, Y. (2003). Europium doped nanocrystalline titanium dioxide: preparation, phase transformation and photocatalytic properties. *Journal of Materials Chemistry,* 13: 2261.
3. Parida, K. M. and Sahu, N. (2008). Visible light induced photocatalytic activity of rare earth titania nano-composites. *Journal of Molecular Catalysis A: Chemistry:* 287: 151 – 158.
4. Shi, H., Zhang, T., An, T., Li, B. and Wang, X. (2012). Enhancement of photocatalytic activity of nano-scale $TiO_2$ particles co-doped by rare earth elements and heteropolyacids. *Journal of Colloid Interface Science,* 380: 121 – 127.
5. Aman, N., Satapathy P. K., Mishra, T., Mahato, M., and Das, N. N. (2012). Synthesis and photocatalytic activity of mesoporous cerium doped $TiO_2$ as visible light sensitive photocatalyst. *Materials Research Bulletin,* 47: 179 – 183.
6. Matejova, L., Koci, K., Reli, M., Capek, L., Hospodkova, A., Peikertova, P., Matej, Z., Obalova, L., Wach, A., Kustrowski, P. and Kotarba, A. (2014). Preparation, characterization and photocatalytic properties of cerium doped $TiO_2$: On the effect of Ce loading on the photocatalytic reduction of carbon dioxide. *Applied Catalysis B: Environmental,* 152: 172 – 183.
7. Xiong, Z., Zhao, Y., Zhang, J. and Zheng, C. (2014). Efficient photocatalytic reduction of $CO_2$ into liquid products over cerium doped titania nanoparticles synthesized by a sol–gel auto-ignited method. *Fuel Processing Technology,* 135: 6 – 13.
8. Abdullah, H., Khan, M. R., Pudukudy, M., Yaakob, Z. and Ismail, N. M. (2015). $CeO_2$-$TiO_2$ as a visible light active catalyst for the photoreduction of $CO_2$ to methanol. *Journal of Rare Earths,* 33: 1155 – 1161.
9. Liu, Z., Guo, B., Hong, L. and Jiang, H. (2005). Preparation and characterization of cerium oxide doped $TiO_2$ nanoparticles. *Journal of Physics and Chemistry of Solids*, 66: 161 – 167.
10. Ioanna, G., Christina, F., Christos, K. and Soghomon, B. (2006). Molecular structure and catalytic activity of $V_2O_5/TiO_2$ catalysts for the SCR of NO by $NH_3$: In situ Raman spectra in the presence of $O_2$, $NH_3$, NO, $H_2$, $H_2O$, and $SO_2$. *Journal of Catalysis*. 239: 1 – 12.
11. Xu, A. W., Gao, Y. and Liu, H. Q. (2002). The preparation, characterization, and their photocatalytic activities of rare-earth-doped $TiO_2$ nanoparticles. *Journal of Catalysis,* 207: 151 – 157.
12. Wu, J., Liu, Q., Gao, P. and Zhu, Z. (2011). Influence of praseodymium and nitrogen co-doping on the photocatalytic activity of $TiO_2$. *Materials Research Bulletin,* 46: 1997 – 2003.
13. Tahir, M. and Amin, N. S. (2013). Advances in visible light responsive titanium oxide-based photocatalysts for $CO_2$ conversion to hydrocarbon fuels. *Energy Conversion Management,* 76: 194 – 214.
14. Inoue, T., Fujishima, A., Konishi, S. and Honda, K. (1979). Photoelectrocatalytic reduction of carbon dioxide in aqueous suspensions of semiconductor powders. *Nature,* 277: 637 – 638.

*Malaysian Journal of Analytical Sciences, Vol 21 No 1 (2017): 173 - 181*
*DOI: http://dx.doi.org/10.17576/mjas-2017-2101-20*

MALAYSIAN JOURNAL OF ANALYTICAL SCIENCES
*Published by The Malaysian Analytical Sciences Society*
ISSN 1394 - 2506

# EFFECT OF CALCINATION TEMPERATURE ON ZnO/TIO$_2$ COMPOSITE IN PHOTOCATALYTIC TREATMENT OF PHENOL UNDER VISIBLE LIGHT

## (Kesan Pengkalsinan Suhu ke atas Komposit ZnO/TiO$_2$ untuk Menyingkirkan Fenol Melalui Fotopemangkin di bawah Cahaya Nampak)

Nur Syazrin Amalina Abdullah*, Sufian So'aib, Jaganatthan Krishnan

*Faculty of Chemical Engineering,*
*Universiti Teknologi Mara, 40450 Shah Alam, Selangor, Malaysia*

**Corresponding author: syaz_pingu@yahoo.com*

Received: 21 October 2015; Accepted: 14 June 2016

**Abstract**

Composite catalyst ZnO/TiO$_2$ of molar ratio 0.75% was synthesized via sol gel method. The effect of preparation method on the crystal morphology was investigated. The catalyst particles were calcinated at 500 $^{o}$C,550 $^{o}$C and 600 °C for 3 hours. The XRD results revealed that calcination temperature controls the crystalline phase in terms of homogeneity and surface area of catalyst produced. The particle size was found to increase with calcination temperature suggesting the effect of different calcination temperatures on catalytic activity for complete degradation of phenol. The result found that ZnO/TiO$_2$ catalyst calcinated at 600 $^{o}$C resulted in 70% phenol degradation within five hours of irradiation time under visible light. The kinetic behavior of phenol degradation was found to fit with pseudo first order Langmuir-Hinshelwood kinetic model.

**Keywords**: sol gel, ZnO/TiO$_2$ catalyst, photocatalytic degradation, visible light, kinetic

**Abstrak**

Pemangkin komposit ZnO/TiO$_2$ dengan 0.75% nisbah molar telah di sintesis melalui kaedah sol gel. Kesan kaedah penyediaan pada morfologi kristal itu telah di selidiki. Zarah-zarah pemangkin telah dikalsinkan pada suhu 500 $^{o}$C, 550 $^{o}$C dan 600 $^{o}$C selama 3 jam. Keputusan XRD menunjukkan suhu pengkalsinan mengawal fasa kristal dari segi kesamaan dan kawasan permukaan pemangkin dihasilkan. Saiz zarah didapati meningkat sejajar dengan peningkatan suhu pengkalsinan mencadangkan kesan suhu pengkalsinan yang berbeza pada aktiviti pemangkin untuk penyingkiran penuh fenol. Keputusan mendapati pemangkin ZnO/TiO$_2$ yang dikalsinkan pada 600 $^{o}$C boleh menyebabkan 70% fenol terdegradasi bagi tempoh lima jam masa penyinaran di bawah cahaya nampak. Kelakuan kinetik degradasi fenol didapati sesuai dengan pseudo peringkat pertama model kinetik Langmuir - Hinshelwood.

**Kata kunci:** sol gel, mangkin ZnO/TiO$_2$, degradasi fotomangkin, cahaya nampak, kinetik

## Introduction

Phenol if present even in lower concentrations causes water pollution in terms of reduction in taste and strong odor. The toxicity imparted by phenol is mainly sourced from industrial wastewater especially petrochemical industries. To date, promising treatment using Advanced Oxidation Process (AOPs) which relies on highly reactive chemical compound such as hydroxyl radical (OH) are gaining favorable in water remediation [1]. The main reason for this immense attraction is because the process is capable to bring complete removal of pollutant by converting broad of them to water and carbon dioxide. Among various AOPs process, the photocatalytic oxidation methods appear to be most effective for the treatment of wastewater contaminated with phenolic compound as this process offer lower

cost compared to other AOPs treatments. In addition, other major advantages of photocatalytic treatment include ambient operating conditions and complete destruction of water pollutants without generation of secondary pollutants. Titanium dioxide ($TiO_2$) has been subject of the most work in photocatalytic treatment applications due to its high activity, relative chemical stability, inertia to corrosion, reducing cost and environment friendly. Nonetheless, photooxidation by $TiO_2$ photocatalytic alone relies on ultraviolet light which only makes up to 5% of solar light.

To address this, coupling two or more semiconductors that able to undergo photo-excitation under much broader visible light spectrum seem to provide a novel approach to achieve a higher efficient charge separation and enhances interfacial charge [2]. Specifically, absorption of $TiO_2$ can be extended to visible range [3] when coupling with other semiconductor or doping with non-metal or metal ion such as B, C, N, $Fe^{3+}$ and $Zn^{2+}$ [4] or metal oxides such as ZnO and MgO. Previous works reported that ZnO appeared as promising photocatalyst and alternative to $TiO_2$ since its photo degradation mechanism was identical to $TiO_2$. Furthermore, ZnO is known to have wider direct gap as well as higher solar reception and utilization efficiency for organic pollutant degradation [5]. In short, the doping energy level that is forming between ZnO-$TiO_2$ can generate more photon utilization and consequently, a higher photocatalytic activity will be attained. Therefore, it is highly advantageous to develop $TiO_2$-ZnO based photocatalyst to enhanced activities under visible light. At present, a number of synthetic methods have been used to synthesize the nanostructures of catalyst. Sol gel technique is common and convenient approach to obtain products of controlled shape and size at high purity and low cost [6]. Others advantages are low processing temperature, which resulting uniform nanostructures for easier control of the kinetics of the chemical reaction.

In this work, the photocatalytic degradation of phenol was carried using doped $TiO_2$ with ZnO operating under visible light. The photocatalytic activity of ZnO/$TiO_2$ was optimized by applying optimum calcination temperature during catalyst synthesis. This was followed by characterization using Scanning Electron Microscopy (SEM) and X-ray Diffraction (XRD) technique.

## Materials and Methods

### Synthesizing $TiO_2$/ZnO composite catalysts via sol gel method

The zinc and titanium precursor solutions were prepared separately. $TiO_2$ precursor sol was prepared by mixing 30 mL of tetraisopropyl titanate with 100 mL ethanol absolute forming solution A. The solution was stirred for half an hour. In order to obtain ZnO precursor sol, 0.04g of zinc acetate and 90 mL deionized water were mixed with 10 mL acetic acid to form solution B. The solution was then stir until zinc acetate completely dissolved. The starting materials ratio was equal to ZnO/$TiO_2$ (molar ratio) of 0.75% dopant concentration. Then, solution B was added drop by drop into solution A under vigorous stirring for 2 hours in order to increase the solubility. The mixed sol was aged for 24 hours at room temperature until forming gel. The product dried in an oven at 100 °C for about 24 hours in order to evaporate the solvent and to remove the organic residuals. The crystal form of sample was then ground using mortar and pestle before calcinate for 3 hours with the heating rate of 3C$^o$/minutes at three different calcination temperatures of 500, 550 and 600 $^o$C.

### Photocatalytic activity

The photocatalytic activity of the synthesized composite catalyst was tested with phenol as a model pollutant at atmospheric pressure and room temperature. A 100 ml of phenol solution with initial concentration of 10 ppm was mixed with 0.1 g of the ZnO/$TiO_2$ catalyst in the photoreactor. The catalysts were suspended in an aqueous solution of phenol in 100 ml beaker. The suspension was illuminated by a 25 Watt Fluorescent lamp in a closed box. Prior to irradiation, the suspension was magnetically stirred in dark for 30 minutes to attain the adsorption-desorption equilibrium between the catalyst and the solution and 2 ml of sample was taken out and analyzed. In order to maximize the energy exchange between the source of irradiation and reaction mixture, the lamp has been placed in the centre of the reactor with distance of 6 cm from phenol solution [7]. After 30 minutes' irradiation, 2 ml sample was taken out and centrifuge for 10 minute at 10000 rpm to separate catalyst and phenol solution. Next, 1 ml of supernatant was mixed with Folin reagent and finally analyst by UV-visible spectrophotometers at 750 nm. Consequently, the procedure was repeated after every 30 minutes until complete 5 hours reaction of lamp illumination. The experiments were repeated for different calcination temperature. Then, the photodegradation efficiency can be calculated from the equation 1:

$$\eta = \frac{[(c_o - c_t)]}{c_o} \; x \; 100\% \quad (1)$$

where η is define as phenol degradation rate efficiency, $C_o$ is define as concentration of phenol at initial time (before illuminate) and $C_t$ is concentration of phenol at specific time.

**Kinetic studies of photocatalytic degradation of phenol on ZnO/$TiO_2$**

Langmuir-Hinshelwood (L-H) model was used to describe kinetics of photocatalytic degradation of ZnO/$TiO_2$. It has been widely used for phenol catalytic reaction rate equations in liquid-phase photocatalysis for a surface-catalyzed reaction. When the concentrations of water and oxygen remain constant, the equation model can be presented as follows to determine the reaction rate:

$$r = -\frac{dC}{dt} = \frac{kK_{LH}C}{1+K_{LH}C} \quad (2)$$

where r is the reaction rate (mg $m^{-3}$ $min^{-1}$), C is the initial concentration (mg $m^{-3}$), K is the reaction rate constant (mg $m^{-3}$ $min^{-1}$) and $K_{LH}$ is the Langmuir adsorption constant ($m^3$ $min^{-1}$) related to the limiting rate of reaction at maximum coverage for the experimental conditions.

The reaction rate is dependent on the experimental conditions (experimental setup design, irradiation conditions, and inlet concentration) and also on the competitive mechanisms of photochemical reactions, and adsorption. At low concentrations of phenols, $K_{LH}C$ ($K_{LH}Ceq << 1$) is negligible and equation (2) becomes a pseudo-first-order rate expression (3), as denoted below:

$$r = -\frac{dC}{dt} = k_{LH}K_L C_{eq} = k_{app}C_{eq} \quad (3)$$

Integrating equation (3)

$$\ln\frac{C_{eq}}{C} = k_{app}t + \text{constant} \quad (4)$$

Equations (2) – (3) account for the adsorption of the reactant (phenols) only but do not consider the adsorption on catalyst of any intermediates or products formed during the course of the degradation reaction. When the adsorption is relatively low or when initial concentration of pollutants is very low, the reaction can be simplified to pseudo-first-order kinetics. A plot of − ln(C/*C*o) versus reaction time *t* yields a straight line, and the slope is the apparent rate constant *(*k).

$$\ln\frac{C}{C_o} = -kt \quad (5)$$

**Characterization**

The synthesized catalysts are characterized by XRD and SEM studies for their structural and morphological characteristics respectively. Structure and phase composition are determined by X-ray diffraction (XRD) and Cu Ka radiation (l = 1.5418 A˚) at 20 kV and the diffraction angle being in the range of $10^o$–$80^o$.The crystallite size of the samples were then calculate using Scherrer's equation (6).

$$D = \frac{k\lambda}{\beta\cos\theta} \quad (6)$$

where θ is the diffraction angle, λ is the X-ray wavelength (0.154059 nm), β is the full width at half maximum (FWHM) of the diffraction, D is the crystallite size and k is a constant (shape factor, about 0.9).

While, the morphology was characterized by a high-resolution scanning electron microscopy, SEM at an accelerating voltage of 50 kV.

## Results and Discussion

### Effect of calcination temperature

A comparative study was conducted to describe the effect of calcination temperature on the efficiency of synthesized ZnO/$TiO_2$. The rates of phenol degradation with respect to different calcination temperature are shown on Figure 1. The result shows the phenol was degraded up to 70% at calcination temperature of 600 $^oC$, (Figure 1 (a)) compared to 36% at 550 $^oC$ (Figure 1(b)) and 40% at 500 $^oC$ (Figure 1(c)). Complete removal only took 120 minutes' reaction at optimum 600 $^oC$ calcination temperature. The degradation rate of phenol turned drastically low after 120 minutes. This phenomenon may explain the presence of inhibition occurred on the surface of Zn-$TiO_2$ catalyst. Other than that, it is believed photo-corrosion effect adsorption on the surface of catalyst during photocatalytic reaction contributed to low degradation rate [8]. Furthermore, the lower photocatalytic activity of phenol possibly can be explained by the less photo-generated electron and holes participated in reaction [9]. Consequently, reducing the availability of surface actives site for reaction to take place. On other words, more recombination occurred at the interface due to less electrons and hole scavengers present in lower heat treatment of synthesized composite catalyst. In addition, higher aggregation shown Figure 4(a) lead to lower reaction rates since it possessed smaller surface area.

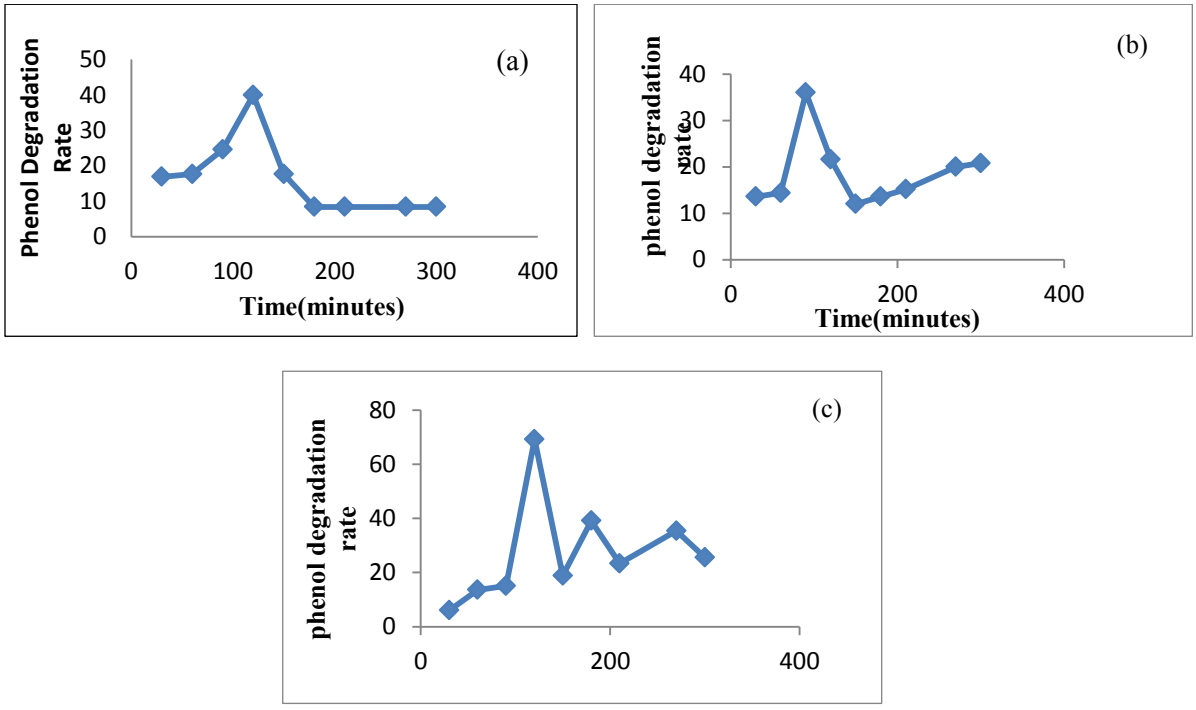



Figure 1. Phenol degradation profile by composite catalyst calcinated at different temperature: (a)500 $^oC$, (b)550 $^oC$ and (c) 600 $^oC$

These experimental results indicate that ZnO/$TiO_2$ synthesized at 600 $^oC$ works more effectively corresponding to the maximum formation of hydroxyl radical on the ZnO/$TiO_2$ surface resulting in the destruction of the target pollutant [10]. Morever, maximum phenol degradation achieved at this temperature was contributed by the formation of higher anatase phase which consequently enhances the crytallization of the phase [11]. Another reason, this can be due to the enhancement of the reaction rate took place between the organic molecules and the hydroxyl

radicals and due to the increasing collision frequency of molecules to make ZnO and $TiO_2$ highly reactive under light excitation.

Apparently, effective degradation rate in all samples suggested $TiO_2$ doping with ZnO resulted narrow band gap. Therefore, it can be deduced doping $TiO_2$ with some metal oxide such ZnO appears to be the most promising to enhance photocatalytic activity under visible light. It is therefore reasonable to conclude photocatalytic activity of $ZnO/TiO_2$ was remarkably improved by applying higher calcination temperature. Carina et al. [12] demonstrated doping $TiO_2$ with ZnO optimized photocatalytic activity of Rhodamine under visible light. The presence of ZnO precursor boosts the vacant hydroxyl radicals for oxidation of dye. In addition, to wider light adsorption spectrum to visible light, ZnO also provides large surface to volume ratio to maximize surface contact with the pollutant. Another study by Janitabar et al. [13] made point that longer wavelength than catalyst band gap was needed in order to excite the surface thus increasing rate of degradation against pollution. These studies highlighted the influence of ZnO application as doping material and light on efficiency of reaction rate.

**Kinetic studies of photocatalytic degradation of phenol on $ZnO/TiO_2$**

Kinetic of photocatalytic obeyed first order reaction since apparent constant increased with temperature. This illustration can be explained by considering Langmuir-Hinshelwood model. The relationship between ln C/Co versus time, t was shown in Figure 2. The values of $k_{app}$ represented by slope of graph can be obtained directly from linear curve in the plot. Value of rate constant shown in Figure 2 of photocatalytic degradation is influenced by calcination temperature. The lower reaction rate is probably due to impenetrability of the suspension and dissipation of light by catalyst particles [14]. However, the values obtained are still within the range of the previous studies (0.001-0.5).

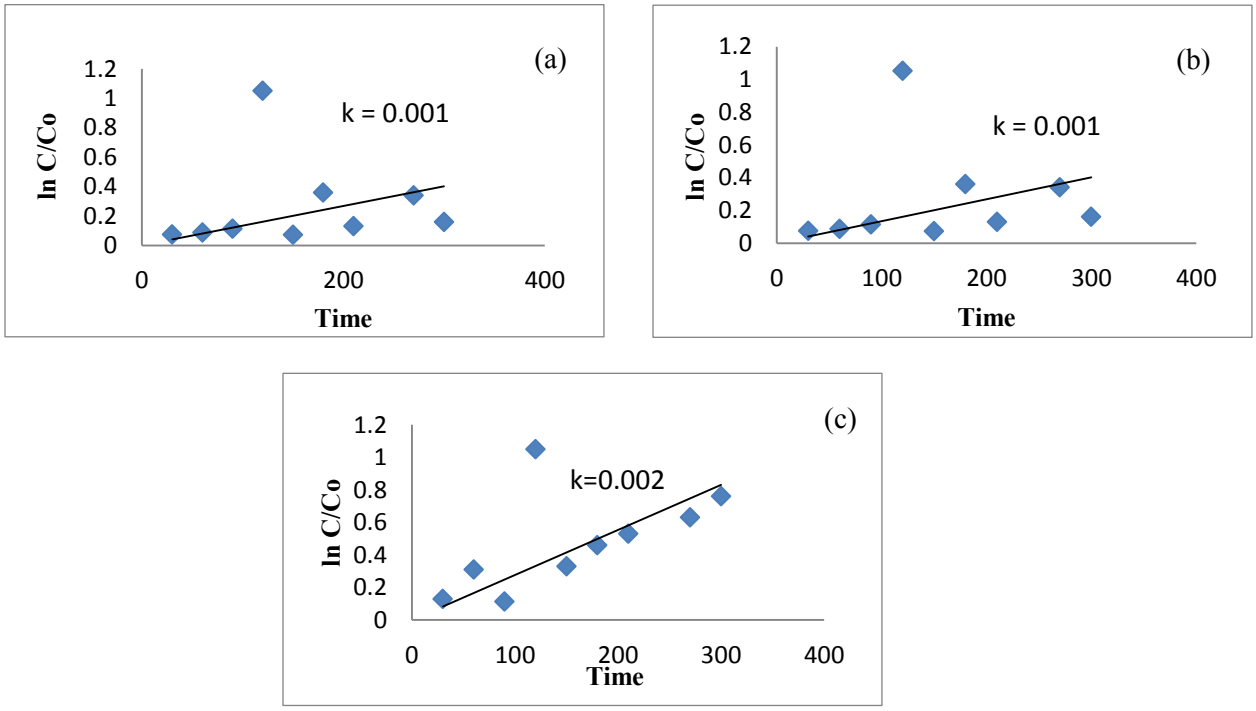



Figure 2. Pseudo first order kinetic plot by composite catalyst calcinate at different temperature: (a) 500 °C, (b) 550 °C and (c) 600 °C

**X-ray diffractometer analysis**

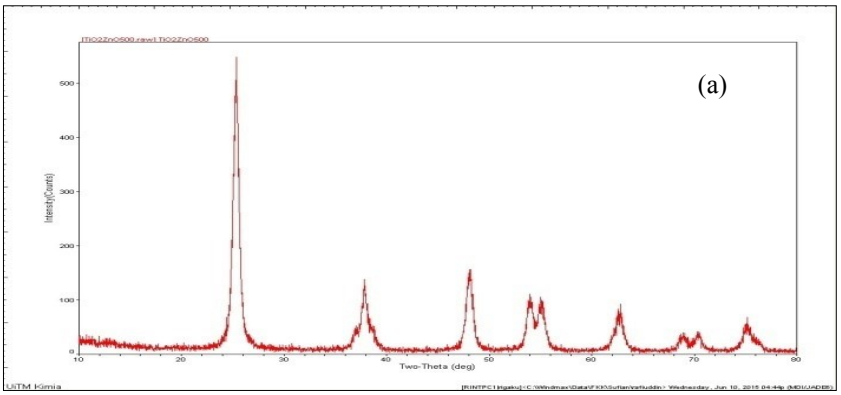
X-ray diffractometer (XRD) pattern was used in the determination of phase structure of photocatalyst calcinated at various temperatures. Based on the standard card of #JCPDS 84-1286 [15], for the sharp diffraction peaks located at $2\theta$ = 25.0°, 37.2°,38.4°, 39.1°, 48.2°, 54.0°, 55.3° and 63.4°, can be attributed to the (101), (004), (112), (200), (105), (211), (118), and (220) planes, respectively. All samples posses' almost similar diffraction peaks (Figure 3) which suggested only anatase phase present in the structure without any detectable ZnO related peaks. Rajesh et al proposed that photocatalytic activity of $TiO_2$ can be enhanced with the presence of anatase phase for degradation of dyes and organic contaminant in water as compared to rutile phase [16]. Dorian et al found that influencing factor such as higher number of surface hydroxyl group adsorbed on the anatase phase and slower charge carrier recombination contributed to higher rate of photocatalytic degradation of many pollutant [17].

Furthermore, no trace of wurtzite could be detected in the XRD pattern. This probably due to small dopant concentration of ZnO used in this study which is only 0.75%. This finding is in agreement with the reported studies where disappearances of ZnO peaks is attributed to the very small of crystallite size [3]. Figure 3(a) illustrates the highest intensity at 600$^o$C and sharpen peaks indicate at higher calcination temperature up to 600 $^o$C promotes higher crystallinity of catalyst forming. The average of crystallize size of the powder were then calculated using Scherrer equation and tabulated in Table 1.

Table 1. Different crystallize size with respect to various calcination temperature

| Sample | Crystalline size, D (nm) |
|---|---|
| ZnO/$TiO_2$-500$^o$C | 8.76 |
| ZnO/$TiO_2$-550$^o$C | 17.59 |
| ZnO/$TiO_2$-600$^o$C | 29.24 |

An increase in the width of diffraction indicates a decrease in size of crystallite. As seen from Figure 3 where the line width of diffraction peak at different temperature changes considerably. The variation could be due to formation of anatase phase as crystallize size also increasing.



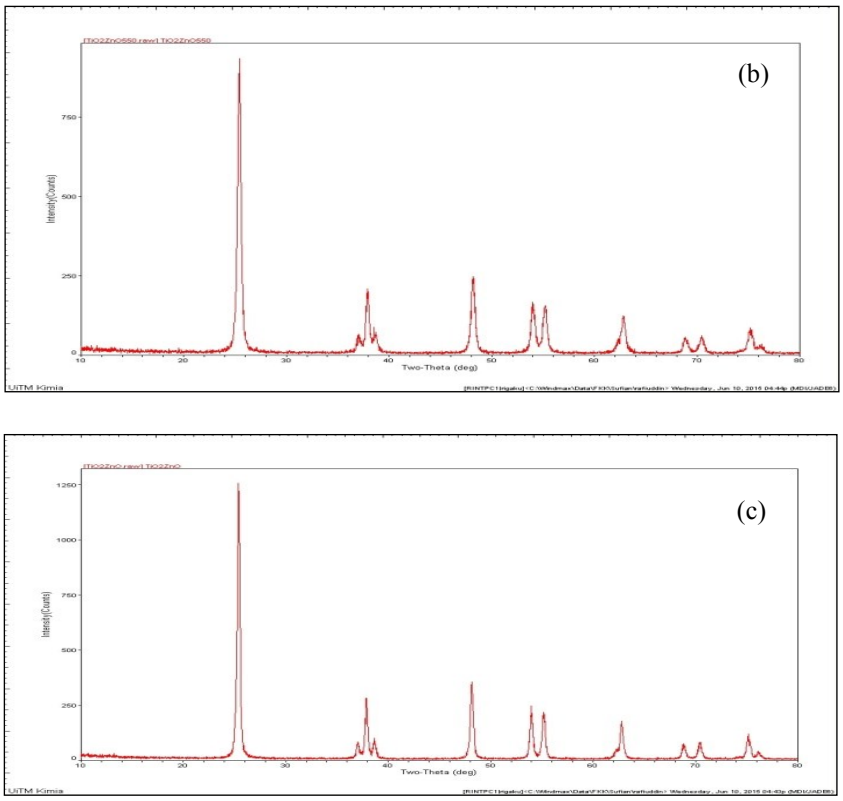



Figure 3. XRD analysis for ZnO-$TiO_2$ calcinated at different temperature: (a) ZnO/$TiO_2$-500 $^oC$, (b) ZnO/$TiO_2$-550 $^oC$, (c) ZnO/$TiO_2$-600 $^oC$

**Scanning electron microscopy analysis**

The morphology of ZnO/$TiO_2$ at different calcination temperature was characterized using Scanning Electron Microscopy (SEM). Based on observation, all prepared samples were found agglomerated and the particles were an irregular in size and shape. According to measurement, all sample as shown in Figure 4 having size of particles not more than 30 µm. Besides, the presence of small particles estimated to be less than 10 µm in diameter widely distributed within the samples were also observed.

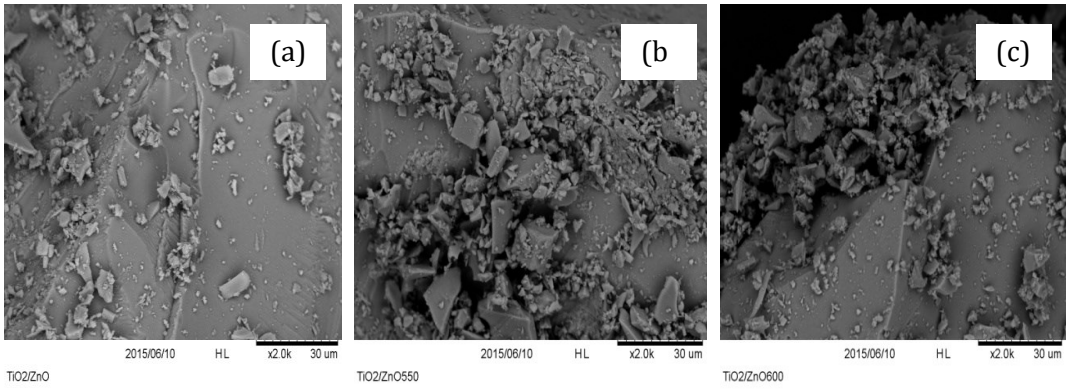



Figure 4. SEM analysis for ZnO-$TiO_2$ calcinated at different temperature:(a) ZnO/$TiO_2$ 500 $^oC$, (b) ZnO/$TiO_2$-550 $^oC$ and (c) ZnO/$TiO_2$ 600 $^oC$

In agreement with the result obtained from XRD, it seems that $TiO_2$ is major component whereby ZnO were widely dispersed. It can be noticed that there was coagulation of particles in Figure 4(a) compared to the result in figure 4(b) where flocculation reduced specific surface area of synthesized catalyst. While, less aggregation on the surface ZnO/$TiO_2$ observed from figure 4(c) suggests more prolonged lifetime of excited state which leads to more effective reaction rate. Therefore, it can be deduced that the smaller particles would give higher surface area which is favorable for higher photocatalytic activity. This is likely due to many factors such as time taken for complete stirring of catalyst suspension, rate of stirring as well as temperature used during calcination [18] step potentially induced the formation of particle size.

## Conclusion

The photocatalytic efficiency was evaluated using phenol solution as a model pollutant. The maximum efficiency of photodegradation rate of phenol was achieved at calcination temperature of 600 $^oC$. The crystalline size showed an increasing trend with respect to higher calcination temperature. The rate constant also increased with increasing calcination temperature. The adsorption kinetics was found to follow pseudo-first-order kinetics.

## Acknowledgement

Authors would like to thank Research Management Centre (RMC), Universiti Teknologi MARA (UiTM) and Ministry of Higher Education Malaysia for funding through RAGS GRANT: 600-RMI/RAGS 5/3 (73 /2013).

## References

1. Pera-Titus, M., Garcıa-Molina, V., Baños, M. A., Giménez, J. and Esplugas, S. (2004). Degradation of chlorophenols by means of advanced oxidation processes: a general review. *Applied Catalysis B: Environmental*, 47(4): 219 – 256.
2. Annadurai, G., Ling, L. Y. and Lee, J. (2007). Biodegradation of phenol by Pseudomonas pictorum on immobilized with chitin. *African Journal of Biotechnology*, 6(3): 296 – 303.
3. Zou, X., Dong, X., Wang, L., Ma, H., Zhang, X. and Zhang, X. (2014). Preparation of Ni doped ZnO-$TiO_2$ composites and their enhanced photocatalytic activity. *International Journal of Photoenergy*, 2014: 1 – 8.
4. Dey, S. and Mukherjee, S. (2010). Performance and kinetic evaluation of phenol biodegradation by mixed microbial culture in a batch reactor. *International Journal of Water Resources and Environmental Engineering*, 3(2): 40 – 49.
5. Busca, G., Berardinelli, S., Resini, C. and Arrighi, L. (2008). Technologies for the removal of phenol from fluid streams: A short review of recent developments. *Journal of Hazardous Materials*, 160(2), 265 – 288.
6. Udom, I., Myers, P. D., Ram, M. K., Hepp, A. F., Archibong, E., Stefanakos, E. K. and Goswami, D. Y. (2014). Optimization of photocatalytic degradation of phenol using simple photocatalytic reactor. *American Journal of Analytical Chemistry*, 5(11): 743 – 750.
7. Sikirman, A., Krishnan, J., Jai, J. and Faraziehan, S. (2014). Preparation, characterization and effectivity of N, Fe-$TiO_2$ as a visible light active photocatalyst. *Advanced Materials Research,* 894: 245 – 249.
8. Feng, C., Li, G., Ren, P., Wang, Y., Huang, X. and Li, D. (2014). Effect of photo-corrosion of $Ag_2CO_3$ on visible light photocatalytic activity of two kinds of $Ag_2CO_3$/$TiO_2$ prepared from different precursors. *Applied Catalysis B: Environmental*, 158: 224 – 232.
9. Wang, Z-P., Xu, J., Cai, W-M., Zhou, B-X., He, Z-G., Cai, C-G. and Hong, X-T. (2005). Visible light induced photodegradation of organic pollutants on nitrogen and fluorine co-doped $TiO_2$ photocatalyst. *Journal of Environmental Sciences*, 17(1): 76 – 80.
10. Yu, J., Yu, H., Cheng, B., Zhou, M. and Zhao, X. (2006). Enhanced photocatalytic activity of $TiO_2$ powder (P25) by hydrothermal treatment. *Journal of Molecular Catalysis A: Chemical*, 253(1): 112 –118.
11. Yu, J. G., Yu, H. G., Cheng, B., Zhao, X. J., Yu, J. C.and Ho, W. K. (2003). The effect of calcination temperature on the surface microstructure and photocatalytic activity of $TiO_2$ thin films prepared by liquid phase deposition. *The Journal of Physical Chemistry B*, 107(50): 13871 – 13879.
12. Pei, C. C. and Leung, W. W. F. (2013). Photocatalytic degradation of Rhodamine B by $TiO_2$/ZnO nanofibers under visible-light irradiation. *Separation and Purification Technology*, 114: 108 – 116.

13. Janitabar Darzi, S. and Movahedi, M. (2014). Visible light photodegradation of phenol using nanoscale $TiO_2$ and ZnO impregnated with merbromin dye: A mechanistic investigation. *Iranian Journal of Chemistry and Chemical Engineering*, 33(2): 55 – 64.
14. Abramović, B. F., Anderluh, V. B., Topalov, A. S. and Gaál, F. F. (2004). Kinetics of photocatalytic removal of 2-amino-5-chloropyridine from water. *Acta Periodica Technologica*, 35: 79 – 86.
15. Joint Committee on Powder Diffraction Standards. Powder Diffraction File, Card No.21-1272. Swarthmore, PA.
16. Tayade, R. J., Surolia, P. K., Kulkarni, R. G. and Jasra, R. V. (2007). Photocatalytic degradation of dyes and organic contaminants in water using nanocrystalline anatase and rutile $TiO_2$. *Science and Technology of Advanced Materials*, 8(6): 455 – 462.
17. Hanaor, D. A. and Sorrell, C. C. (2011). Review of the anatase to rutile phase transformation. *Journal of Materials Science*, 46(4): 855 – 874.
18. Amrollahi, R., Hamdy, M. S. and Mul, G. (2014). Understanding promotion of photocatalytic activity of $TiO_2$ by Au nanoparticles. *Journal of Catalysis*, 319: 194 – 199.

*Malaysian Journal of Analytical Sciences, Vol 21 No 1 (2017): 182 - 187*
*DOI: http://dx.doi.org/10.17576/mjas-2017-2101-21*

MALAYSIAN JOURNAL OF ANALYTICAL SCIENCES
*Published by The Malaysian Analytical Sciences Society*
ISSN 1394 - 2506

# TREATMENT OF METHYLENE BLUE IN WASTEWATER USING *Scirpus grossus*

## (Rawatan Metilena Biru dalam Air Sisa Menggunakan *Scirpus grossus*)

Enas Abdulqader Saeed Almaamary[1], Siti Rozaimah Sheikh Abdullah[1]*, Hassimi Abu Hasan[1], Reehan Adne Ab. Rahim[1], Mushrifah Idris[2]

[1]*Department of Chemical and Process Engineering, Faculty of Engineering and Built Environment*
[2]*Tasik Chini Research Center, Faculty of Science and Technology*
*Universiti Kebangsaan Malaysia, 43600 UKM Bangi, Selangor, Malaysia*

**Corresponding author: rozaimah@ukm.edu.my*

Received: 21 October 2015; Accepted: 14 June 2016

**Abstract**

Phytoremediation is an emerging technology that should be considered for the remediation of contaminated sites because of its aesthetic advantages and long-term applicability. The possibility of *Scirpus grossus* for degradation of a basic dye, methylene blue (MB) was investigated. The effect of the operational parameter of different dye concentrations (0, 200, 400, 600, 800 and 1000 mg/L) was determined, and the water quality parameters namely pH, dissolved oxygen (DO), biochemical oxygen demand (BOD), chemical oxygen demand (COD) and total organic carbon (TOC) were monitored. The UV-Visible absorption confirmed the degradation of MB within 72 days. The removal efficiency of methylene blue dye from synthetic wastewater was determined to be in the range of 86 – 38% for all treatments at different concentrations (200 – 1000 mg/L) respectively. Furthermore, the highest removals for BOD, COD in 400 mg/L and TOC in 200 mg/L MB were 69, 58 and 63% respectively.

**Keywords:** phytoremediation, *Scirpus grossus*, methylene blue, decolourisation, water quality

**Abstrak**

Fitopemulihan merupakan teknologi baru yang perlu dipertimbangkan untuk pemulihan tapak tercemar kerana kelebihan estetik dan kebolehgunaan bagi jangka panjang. Kemungkinan *Scirpus grossus* untuk degradasi pewarna asas, metilena biru (MB) telah dikaji. Kesan parameter operasiiaitu kepekatan pewarna yang berbeza (0, 200, 400, 600, 800 dan 1000 mg/L) ditentukan dan parameter kualiti air iaitu pH, oksigen terlarut (DO), permintaan oksigen biokimia (BOD), permintaan oksigen kimia (COD) dan jumlah karbon organic (TOC) dipantau. Penyerapan UV cahaya nampak mengesahkan degradasi MB dalam masa 72 hari. Kecekapan penyingkiran pewarna metilena biru daripada air sisa sintetik telah ditentukan dalam lingkungan 38 – 86% untuk semua rawatan dalam kepekatan yang berbeza (200 – 1000 mg/L) masing-masing. Tambahan pula, penyingkiran tertinggi bagi BOD, COD dalam 400 mg/L dan TOC dalam 200 mg/L MB masing-masing adalah 69, 58 dan 63%.

**Kata kunci:** pemulihan-fito, Scirpus grossus, metilena biru, penyahwarnaan warna, kualiti air

## Introduction

Major progress in textile industry has caused serious environmental problems, since the textile industries use dyes to colour their products and, as a result, generate a considerable amount of coloured effluents causing water pollution. These dyes can be mutagenic, carcinogenic and can impart toxicity to aquatic life [1]. Discharge of dye-bearing wastewater poses a severe problem. In textile industries, about 10 – 15% of the dye gets lost in the effluent during the dyeing process [2]. Effluents containing dye produce wastewaters having a high chemical oxygen demand

(COD), biological oxygen demand (BOD), and other toxic chemical compounds [3]. The values of COD, BOD and TOC in textile effluents are 276 – 1379, 99 – 350 and 74 – 530 mg/L, respectively [4]. Various techniques like adsorption, coagulation, ozonation, and electrolysis are used for the purification and decolourization of dyeing wastewater [5]. Due to low biodegradability of dyes, a conventional treatment process such as the physical-chemical method is not very effective. Moreover, all these methods have different colour removal capabilities, incur high costs, and have low efficiency [6].

In recent years, microorganisms have been reported for degradation of textile dyes [7–10]. The knowledge that plants can also be used to clean up contaminated soil has opened up new avenues of research, and has provided a basis for the present-day use of constructed wetlands for treating municipal and industrial waste streams. In this study, constructed wetland systems (CWs) employing horizontal subsurface flow were set up in a greenhouse, with and without *Scirpus grossus.* We aim to study the role of a native Malaysian plant, *Scirpus grossus* (*S. grossus*), in a subsurface batch system to remove textile dyes containing methylene blue dye (MB) at different concentrations (200, 400, 600, 800 and 1000 mg/L) from synthetic wastewater. *S. grossus* is an aquatic species with a high growth rate, and has the ability to degrade contaminants, giving an insight into the involvement of bacteria and the prediction of metabolic pathways behind the degradation of the dye. This technology has received attention lately as an innovative and cost-effective alternative to the more established treatment methods used at hazardous waste sites [11]. Thus, the phytoremediation potential of the plant for the synthetic dye of MB was evaluated.

## Materials and Methods

### Plant source of *Scirpus grossus*

*S. grossus* was collected from a freshwater lake, Tasik Chini in Pahang, Malaysia for propagation for one month until the first generation was produced.

### Concentration and analysis of dye in synthetic wastewater

This experiment was conducted in a greenhouse at Universiti Kebangsaan Malaysia (UKM), under subsurface batch system (SSF) using *S. grossus* plants on various dye concentrations for 72 days. 33 aquarium glasses were used in this study, 15 aquaria containing synthetic wastewater contaminated with MB, and each concentration with three replicates (R1, R2, R3). There were another three aquaria-containing MB-contaminated wastewaters, only without plants as contaminant controls (CC1, CC2, CC3) for each concentration of MB. The last three acquiria acted as plant controls (PC1, PC2, PC3), as illustrated in Figure 1a.

Each aquarium was layered from top to bottom with 8 cm of gravel with a size of Φ10–20 mm, 3 cm of gravel with a size of Φ 1–5 mm and 10 cm of sieved fine sand of Φ 2 mm (Figure 1b). Each aquarium was filled with 7 L of synthetic wastewater prepared by mixing tap water with MB (R&M Chemicals Marketing, UK) at different concentrations (200, 400, 600, 800 and 1000 mg/L). An aliquot of 10 mL of decolourised solution of the dye was centrifuged at 4000 rpm for 10 min to remove all particulate matter using Eppendorf Centrifuge (AG 22331 Hamburg, Germany), and then the absorbance of the solution was measured at 665 nm wavelength using UV/vis spectrophotometer (DR 3900 HACH). The decolourisation percentage for the respective dyes was calculated using equation 1 based on initial and final absorbance:

$$\text{Decolorization (\%)} = \frac{(\text{Initial absorbance at 0 h}) - (\text{Observed absorbance at t})}{(\text{Initial absorbance at 0 h})} \quad (1)$$

### Monitoring and analysis of operational parameters

The operational parameters were determined during 72 days of exposure with sampling performed on days 0, 7, 14, 28, 42 and 72. The parameters of pH temperature (T, $^{\circ}$C), dissolved oxygen (DO, mg/L) and oxidation reduction potential (ORP, mV) were recorded to observe the physicochemical changes in water using a Metrohan multi-probe of (Model 877, Swiss) for the pH, ORP and temperature measurements. For dissolved oxygen, the YSI sensor (Model 550A, USA) was used.

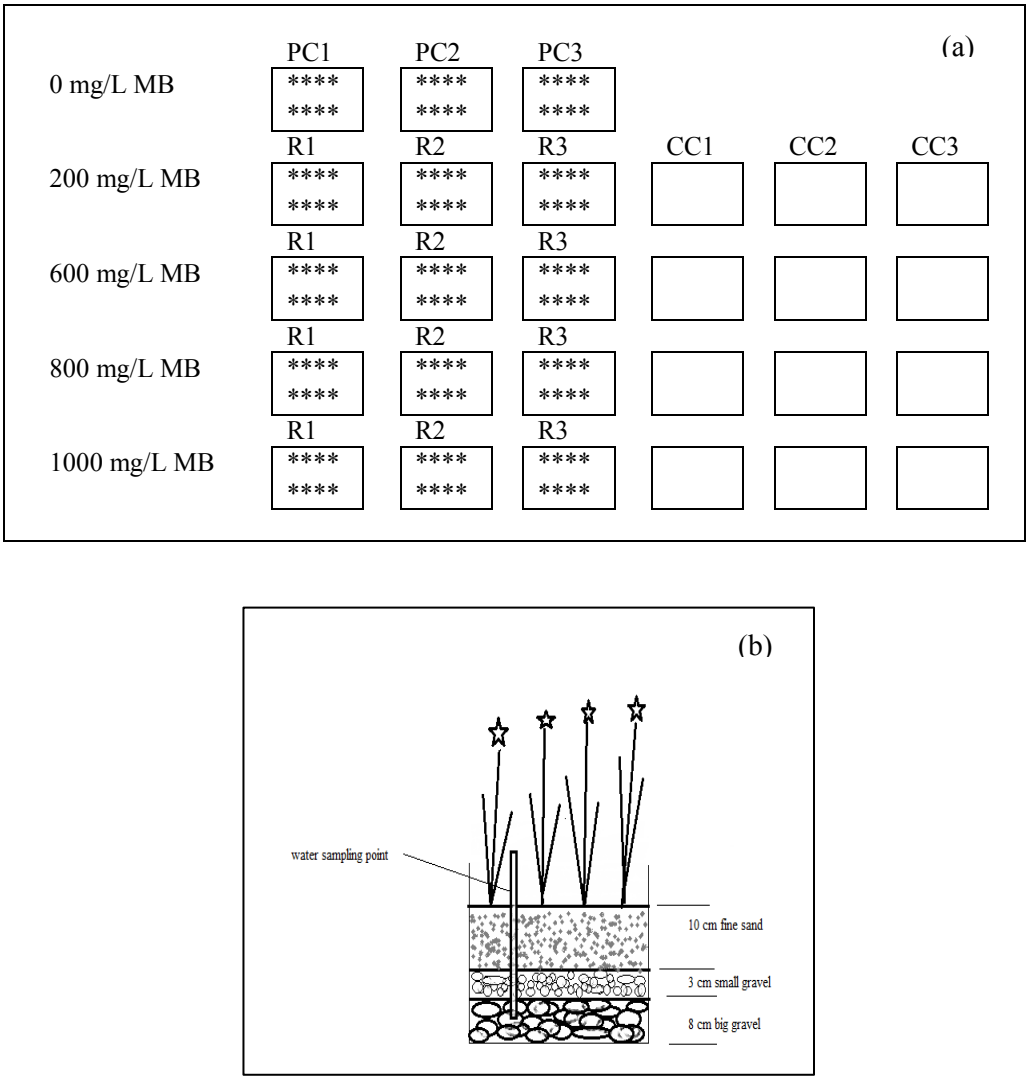



Figure 1. (a) Experimental set-up of the phytotoxicity experment, (b) Schematic diagram of an aquarium for the phytotoxicity test

**Analysis of water quality parameters (BOD, COD, TOC)**

BOD, COD and TOC of the MB contaminated water were determined. The COD and TOC values were determined using a spectrophotometer (DR3900 HACH, Germany). The BOD value was determined by measuring the dissolved oxygen levels in the sample before and after incubation for five days, according to Winkler's iodometric method [3]. BOD was calculated using equation 2 as follows:

$$\mathrm{BOD}\left(\frac{\mathrm{mg}}{\mathrm{L}}\right) = \frac{D_0 - D_5}{P} \quad (2)$$

where $D_0$ is define as initial DO concentration in the sample, $D_5$ is DO concentration after five days and $P$ is decimal volumetric fraction of sample used.

## Results and Discussion

### Variation of operational parameters for different dye concentrations

The physical parameters (i.e. T, pH, DO and ORP) were recorded throughout the phytotoxicity test, as shown in Table 1. For treatment with plants and without plants at different concentrations of MB dye (200, 400, 600, 800 and 1000 mg/L), the range of temperature with plants was between 28.3 – 29 $^{o}$C, while the temperature without a plant was 29 $^{o}$C. The pH ranged between 8.2 – 8.6 in the aquarium with plants; for the aquarium without plants, the pH ranged between 9 – 10, with increasing pH during the treatment of 72 days. With regard to DO, the average value range between 4.3 – 4.7 mg/L in the aquarium with plants, indicating that the organism used oxygen for MB degradation. The average value of DO in the aquarium without plants was between 2.7 – 3.4 mg/L. The ORP range value was between -201till -139 mV for the aquarium with plants, while the values of ORP in the aquarium without plants was -184 till -172 mV, with the reading increasing with time. The negative values of ORP throughout the MB dye treatment show that the condition was under anaerobic conditions [12]. However, for the aquaria with plants, the conditons were less anaerobic and became more aerobic with treatment duration.

Table 1. Average operational parameters in phytotoxicity test with and without *Scirpus grossus* in MB contaminant

| **Parameters** | **With *Scirpus grossus*** | **Without *Scirpus grossus*** |
|---|---|---|
| Temperature ($^{o}$C) | 28.4 ± 0.4 | 29 ±0.3 |
| pH | 8.2 ± 0.4 | 9.4 ± 0.6 |
| DO (mg/L) | 4.5 ± 0.2 | 3.2 ± 0.4 |
| ORP (mV) | -171 ± -24 | -180 ± -8 |

### Decolourisation of MB dye by *S. grossus*

In the screening experiments, the decolourisation of MB by *S.grossus* at different dye concentrations showed different decolourisation patterns. The decolourisations of 86, 52, 47, 34 and 38% were observed for 200, 400, 600, 800 and 1000 mg/L respectively, at the end of 72 day exposure. The maximum decolourisation occurred at 200 mg/L (86%); whereas the minimum decolourisation was obtained for 800 mg/L (34%). The increasing MB concentration caused decreasing percentages of MB decolourisation values monitored throughout 72 days (Figure 2), indicating some toxicity effects on the plants. The low percentage of decolourisation at higher concentrations of dye was due to the inhibitory effects of the dye transformation process (Figure 2). As for the comparison with the control aquaria without plants, the decolourisations of MB were only 31% (200 mg/L), 15% (400 mg/L), 19% (600 mg/L), 2% (800 mg/L) and 19% (1000 mg/L). These results confirm the ability of *S. grossus* plants to decolourise MB dye. In previous studies, 98% MB was removed using *Limna minor* after six days [13], while a removal effiency of 65.7–89.30% was obtained by [14] through an adsorption process using *peat* with MB concentration of 19–134 mg/, which is comparable with our results.

### Monitoring of BOD, COD and TOC

BOD, COD and TOC are widely used methods to determine organic matter in wastewater [15]. The BOD, COD and TOC values of synthetic wastewater for different dye concentrations were found to decrease in the test samples treated with *S. grossus* for 72 days, as depicted in Figure 3. The highest efficiency removal of BOD was 69% for 400 mg/L dye concentration; while the lowest was 21% for 800 mg/L. The BOD removals were 46, 25 and 37% for 200, 600 and 1000 mg/L respectively. Similarly, the highest efficiency removal of COD was 58% for 400 mg/L and the lowest was 21 % for 800 mg/L, while the COD removals were 40, 30 and 26 mg/L for 200, 600 and 1000 mg/L respectively. As for the TOC, the highest removal was 63% for 200 mg/L while the lowest was 26% for 1000 mg/L. 49, 36 and 39% were obtained for 400, 600 and 800 mg/L respectively. The results obtained for BOD, COD and TOC removal indicated that *S. grossus* has the ability to decolourise MB in contaminated water.

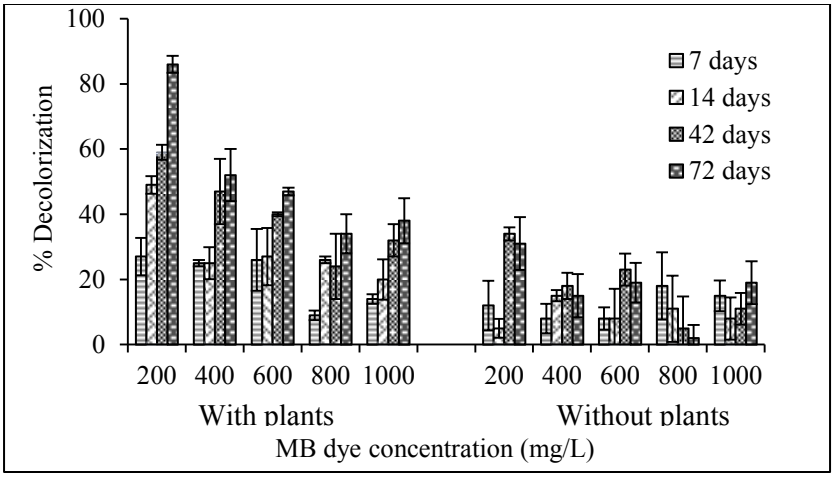



Figure 2. Effect of increasing concentrations of MB (200, 400, 600, 800 and 1000 mg/L) on the percentage of decolourisation monitored at 7, 14, 42 and 72 days with and without *S. grossus*

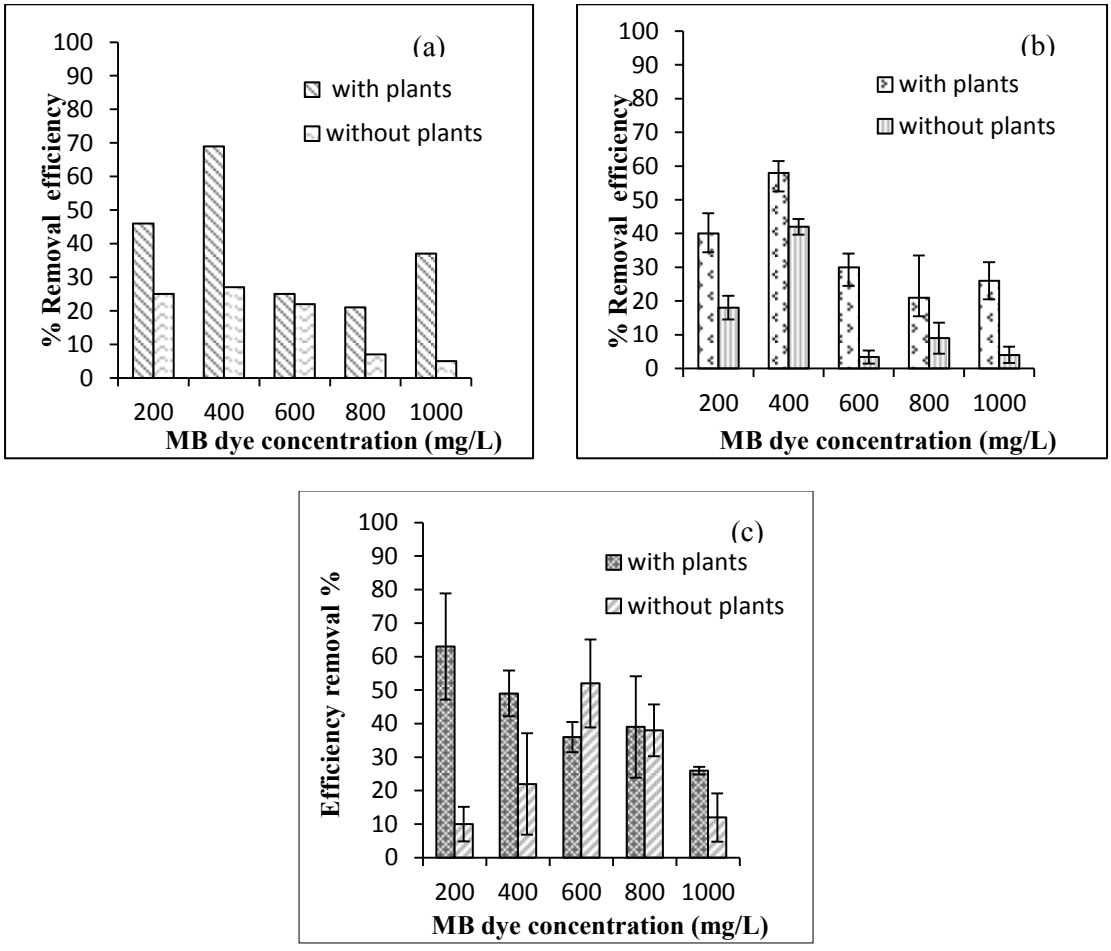



Figure 3. Removal percentages of (a) BOD, (b) COD and (c) TOC for different concentrations of MB dye

## Conclusion

We have demonstrated the ability of S. *grossus* to decolourise MB dye at different concentrations (200, 400, 600, 800 and 1000 mg/L) after 72 days in a subsurface batch system. Based on the results, the highest dye removal of 86% and 38% was obtained for MB dye concentrations of 200 and 1000 mg/L respectively. Compared to the results obtained from the aquarium without plants, the dye removals were only 31% and 2% at MB dye concentrations of 200 and 800 mg/L respectively. These results give evidence that *S. grossus* was able to remove dye from wastewater.

## Acknowledgements

We would like to thank Tasik Chini Research Centre, Universiti Kebangsaan Malaysia (UKM) and Ministry of Higher Education, Malaysia for granting this project through GUP-2015-022 and AP-2015-013.

## References

1. Kadirvelu, K., Kavipriya, M., Karthika, C., Radhika, M., Vennilamani, N. and Pattabhi, S. (2003). Utilization of various agricultural wastes for activated carbon preparation and application for the removal of dyes and metal ions from aqueous solutions. *Bioresource Technology,* 87(1): 129 – 132.
2. Kabra, A. N., Khandare, R. V, Waghmode, T. R. and Govindwar, S. P. (2012). Phytoremediation of textile effluent and mixture of structurally different dyes by Glandularia pulchella (Sweet) Tronc. *Chemosphere,* 87(3): 265 – 272.
3. Kagalkar, A. N., Jagtap, U. B., Jadhav, J. P., Govindwar, S. P. and Bapat, V. (2010). Studies on phytoremediation potentiality of Typhonium flagelliforme for the degradation of Brilliant Blue R. *Planta,* 232(1): 271 – 285.
4. Bulc, T. G. and Ojstrsek, A. (2008). The use of constructed wetland for dye-rich textile wastewater treatment. *Journal of Hazardous Materials*, 155(1–2): 76 – 82.
5. Khataee, A. R., Movafeghi, A., Torbati, S., Salehi Lisar, S. Y. and Zarei, M. (2012). Phytoremediation potential of duckweed (Lemna minor L.) in degradation of C.I. Acid Blue 92: artificial neural network modeling. *Ecotoxicology and Environmental Safety*, 80: 291 – 298.
6. Aubert, S. and Schwitzguébel, J. P. (2004). Screening of plant species for the phytotreatment of wastewater containing sulphonated anthraquinones. *Water Research*, 38(16): 3569 – 3575.
7. Kalme, S. D., Parshetti, G. K., Jadhav, S. U. and Govindwar, S. P. (2007). Biodegradation of benzidine based dye Direct Blue-6 by Pseudomonas desmolyticum NCIM 2112. *Bioresource Technology,* 98(7): 1405 – 1410.
8. Khandare, R. V, Kabra, A. N., Tamboli, D. P. and Govindwar, S. P. (2011). The role of Aster amellus Linn. in the degradation of a sulfonated azo dye Remazol Red: a phytoremediation strategy. *Chemosphere*, 82(8): 1147 – 1154.
9. Kalyani, D. C., Telke, A. A., Dhanve, R. S. and Jadhav, J. P. (2009). Ecofriendly biodegradation and detoxification of Reactive Red 2 textile dye by newly isolated Pseudomonas sp. SUK1. *Journal of Hazardous Materials*, 163(2–3): 735 – 742.
10. Shedbalkar, U., Dhanve, R. and Jadhav, J. (2008). Biodegradation of triphenylmethane dye cotton blue by Penicillium ochrochloron MTCC 517. *Journal of Hazardous Materials*, 157(2–3): 472 – 479.
11. Patil, A. V. and Jadhav, J. P. (2013). Evaluation of phytoremediation potential of Tagetes patula L. for the degradation of textile dye Reactive Blue 160 and assessment of the toxicity of degraded metabolites by cytogenotoxicity. *Chemosphere*, 92(2): 225 – 232.
12. Carliell, C. M., Barclay, S. J. Naidoo, N. Buckley, C.A., Mulholland, D. A. and Senior, E. (1994). Anaerobic decolourisation of reactive dyes in conventional sewage treatment processes. *Water* SA, 20: 341 – 344.
13. Reema R. M., Saravanan P., Dharmendira K. M. and Renganathan, S. (2011). Accumulation of methylene blue dye by growing Lemna minor. *Separation Science and Technology*, 46: 1052 – 1058.
14. Suteu, D. Zaharia, C. Muresan, A. Muresan, R. and Popescu, A. (2009). Using of industrial waste materials for textile wastewater treatment. *Environmental Engineering and Management Journal*, 8(5): 1097 – 1102.
15. Mohan, S., V. Rao, N. C. and Karthikeyan, J. (2002). Adsorptive removal of direct azo dye from aqueous phase onto coal based sorbents: A kinetic and mechanistic study. *Journal of Hazardous Materials*, 90(2): 189 – 204.

*Malaysian Journal of Analytical Sciences, Vol 21 No 1 (2017): 188 - 196*
*DOI: http://dx.doi.org/10.17576/mjas-2017-2101-22*

MALAYSIAN JOURNAL OF ANALYTICAL SCIENCES
*Published by The Malaysian Analytical Sciences Society*
ISSN 1394 - 2506

# CHEMICAL AND PHYSICAL CHARACTERIZATION OF OIL PALM EMPTY FRUIT BUNCH

## (Pencirian Kimia dan Fizikal Bagi Tandan Kosong Buah Kelapa Sawit)

Nurul Suraya Rosli[1], Shuhaida Harun[1,2]*, Jamaliah Md Jahim[1,2], Rizafizah Othaman[3]

[1]*Department of Chemical and Process Engineering, Faculty of Engineering and Built Environment*
[2]*Research Centre for Sustainable Process Technology (CESPRO), Faculty of Engineering and Built Environment*
[3]*School of Chemical Sciences and Food Technology, Faculty of Science and Technology*
*Universiti Kebangsaan Malaysia, 43600 UKM Bangi, Selangor, Malaysia*

**Corresponding author: harun.shuhaida@ukm.edu.my*

Received: 21 October 2015; Accepted: 14 June 2016

**Abstract**

The interest in Oil Palm Empty Fruit Bunch (OPEFB) as a promising feedstock for bioconversion into value added products is growing fast, thus a thorough analysis of its component becomes necessary. In this study, the biomass chemical composition and physical feature of OPEFB was analysed to explore and understand the potential of OPEFB as bioconversion feedstock. National Renewable Energy Laboratory (NREL) standard protocols were used to characterize and determine the chemical composition of OPEFB. Through this protocol, the structural and non-structural constituents and their compositions were determined based on unextracted and extracted native OPEFB. Structural constituents include the carbohydrate, such as the glucan, xylan and arabinan, and lignin accounted for 31.2%, 18.7%, 2.7%, and 27.7%, while the non-structural constituents mainly refer to ash and extractives accounted for 0.10% and 11.87%. In addition, Fourier Transform Infrared Spectroscopy (FTIR) and X-Ray Diffraction (XRD) analysis were also used to further characterize the chemical structure of OPEFB. The FTIR spectral peaks representing the functional groups cellulose, hemicellulose and lignin were observed. Through XRD analysis, the crystallinity index of native OPEFB fiber was calculated around 40%, while it was 37% for the powder form OPEFB. Nevertheless, the physical feature or surface morphology of the OPEFB fiber has been study by using Scanning Electron Microscopy (SEM). It shows a rigid strand's surface and the presence of silica bodies which commonly found in woody plant.

**Keywords**: lignocellulose, composition, morphology, spectroscopy, crystallinity

**Abstrak**

Minat terhadap tandan kosong buah kelapa sawit (OPEFB) sebagai bahan mentah secara penukaran bio telah menjanjikan hasil produk tambah nilai yang berkembang pesat, oleh itu suatu analisis yang menyeluruh komponennya menjadi keperluan. Dalam kajian ini, komposisi kimia biomas dan ciri-ciri fizikal OPEFB dianalisis untuk meneroka dan memahami potensi OPEFB sebagai bahan mentah untuk penukaran bio. Protokol piawai *National Renewable Energy Laboratory* (NREL) telah digunakan untuk mencirikan dan menentukan komposisi kimia OPEFB. Melalui protokol ini, juzuk struktur atau bukan struktur dan komposisi mereka telah ditentukan. Juzuk struktur termasuk karbohidrat, seperti glukan, xilan dan arabinan dan lignin menyumbang kepada 31.2%, 18.7%, 2.7%, dan 27.7%, manakala juzuk bukan struktur terutamanya merujuk kepada abu dan ekstraktif menyumbang kepada 0.10% and 11.87%. Di samping itu, analisis Spektroskopi Inframerah Transformasi Fourier (FTIR) dan belauan sinar-X (XRD) juga digunakan untuk mencirikan lagi struktur kimia OPEFB. Puncak spektrum FTIR yang mewakili kumpulan berfungsi daripada selulosa, hemiselulosa dan lignin telah diperhatikan. Melalui analisis XRD, indeks penghabluran gentian OPEFB asli dikira sekitar 40%, manakala ia adalah 37% untuk OPEFB berbentuk serbuk. Walau bagaimanapun, ciri atau permukaan fizikal morfologi serat OPEFB asli yang telah dikaji dengan menggunakan Mikroskopi Imbasan Elektron (SEM). Ia menunjukkan permukaan helaian yang tegar dan kehadiran badan-badan silika yang biasa ditemui dalam tumbuhan berkayu.

**Kata kunci:** lignoselulosa, komposisi, morfologi, spektroskopi, penghabluran

## Introduction

In the recent year, there are more than 5 000 000 hectares' oil palm are cultivated in Malaysia, making the country world's largest exporter of palm oil. As one of the leading producer and exporters of palm oil products, the palm oil industry in Malaysia collectively generate massive amount of oil palm lignocellulosic biomass waste, with oil palm empty fruit bunch (OPEFB) accounting about 16 million tons per year [1].

The OPEFB have traditionally been burnt in incinerator of palm oil mill and their ash recycled into the plantation as fertilizer. However, due to the environmental problem, the incineration of OPEFB has been discouraged [2]. In order to protect the environment and to ensure the sustainability of the oil palm industry, the lignocellulosic biomass waste must be fully exploited.

The building block of native OPEFB fiber is made up from a complex matrix of three main polymers which are cellulose, hemicellulose and lignin. It composed approximately around 44.2% cellulose, 33.5% hemicellulose and 20.4% of the lignin [3]. It also reported that OPEFB is composed 32.9% glucan, 22.4% xylan and 1.4% arabinan [4]. The lignocellulosic material from OPEFB has been considered as a very good source of fermentable sugar for conversion into value added products [5-7]. Cellulose and hemicellulose can be hydrolysed chemically by acid or enzymatically into glucose and a variety of pentose and hexose sugars, which can then be fermented to produce bioethanol.

The investigation on the potential utilization of OPEFB fiber as renewable bioresource require a comprehensive chemical and physical characterization of the biomass. Therefore, the objectives of this study were to examine the surface morphology of OPEFB and quantity of major and minor component of native OPEFB fiber with the aim to utilize them as raw material for biorefinery.

## Materials and Methods

### Raw material

The OPEFB used in this study was collected from Seri Ulu Langat's Palm Oil Milling Factory, Dengkil Selangor with initial moisture content of 55%. The OPEFB was then sun-dried for 72 hours until the moisture content reached less than 10%, and then grounded into approximately 2 mm particle size using a mill (Fritsch GmBH, Germany). The grounded OPEFB were packed in a sealed bag and stored at - 40˚C.

### Compositional analysis

The chemical analysis of native OPEFB fiber was carried out using National Renewable Energy Laboratory (NREL) standard biomass analytical procedure with 3 replication. Moisture content analysis was carried out using moisture analyser (Denver Instrument, Germany), while the ash analysis was conducted using a furnace at 575 ˚C for 24 hours [9].

### Extractive analysis

The total extractive determination was carried out with water for 8 hours followed with the 95% ethanol for 8 hours in a soxhlet extractor. The ethanol soluble material and water soluble material such as non-structural sugar, nitrogenous compound, inorganic compound and waxes were removed during the two-stage extraction process [10]. Non-structural materials must be removed from the biomass prior to analysis to prevent the inteferences.

### Carbohydrates and lignin analysis

The extractive-free sample were hydrolyzed using sequential acid hydrolysis procedure utilizing 72% sulphuric acid at 30 ˚C for an hour and followed by 4% sulphuric acid at 121˚C for an hour [11] [12]. The hydrolyzate was filtered and analyzed for monosaccharides using high performance liquid chromatography (HPLC) (Dionex Ultimate 3000, Thermo Scientific, USA) equipped with refractive index detector (RI) and Rezex Phenomex Monosaccharide column (RPM). The hydrolyzate samples and standards were analyzed at 60 ˚C with the flowrate of 0.6 ml/min and

20 µL injection volume [13]. Post-hydrolysis analyses of the liquid sample from water extraction were also done to quantify the oligomeric sugar. The insoluble portion filtered from the acid hydrolysis process were dried for overnight in a desiccator and were regard as acid insoluble lignin. The filtrate will then quantified spectrophotometrically at 320 nm using 1 cm pathlength cuvette for acid soluble lignin.

**Morphology study**
Scanning electron microscopy (SEM) analysis was conducted to view the surface structure of native OPEFB fiber. The freeze-dried sample was prepared by sputter-coated with gold prior to imaging with SEM with magnification power of 100 to 2000x.

**Spectroscopy characterization**
Fourier Transform Infrared spectroscopy (FTIR) analysis was performed to detect the functional groups presence in the cellulose, hemicellulose and lignin portion of the native OPEFB fiber. FTIR spectra were obtained using a KBr disc containing grounded sample. The sample were scan from 4000 to 400 $cm^{-1}$ with resolution of 4 $cm^{-1}$.

**Crystallinity study**
The crystallinity of cellulose in the native OPEFB were studied using X-ray diffraction (XRD) profile. The sample were scanned over scattering angle (2θ) from 10˚ to 50˚. The crystallinity index (CrI) of the sample was estimated by using equation (1) as follows [14]:

$$CrI = \left[\frac{I_{002} - I_{am}}{I_{002}}\right] x\ 100 \quad (1)$$

where, $I_{002}$ is the highest peak intensity of crystalline fractions and $I_{am}$ define as the low intensity peak at the amorphous region.

## Results and Discussion

**Compositional analysis**
The purpose of this part of the paper was to study the composition of native OPEFB fiber for utilizing them as raw material for production of value-added product. The composition of native OPEFB fiber were analyzed for structural carbohydrates, lignin, ash and extractives content. The compositional analyses of native OPEFB fiber were made based native-overall unextracted OPEFB, extractive-free OPEFB, and corrected native-whole OPEFB as presented in Table 1. These results were expressed as the percentage of the oven-dried, native whole unextracted OPEFB.

Since woody lignocellulosic biomass, such as OPEFB contain high amount of extractives which influence the compositional analyses of structural and non-structural constituents, the native-whole unextracted and solvent-extracted OPEFB were both analysed for the purposes comparing the composition of major constituents, determining the extractable non-structural constituents in the OPEFB, and finally making the appropriate corrections in the composition of particular constituents [15]. Characterization of native-whole unextracted OPEFB only, can be considered inaccurate because the hydrophobic extractives such as oil and waxes inhibit the penetration of sulphuric acid into the biomass causing incomplete hydrolysis thus affecting the analyses for structural carbohydrates [10]. While expressing the result in extractive free basis, also does not allow direct comparison between compositions of the extracted and unextracted materials, since removal of the extractives changes the composition of the constituents in the biomass [8]. Thus, in this study the identified constituents in the extractives were used to correct and convert the composition of the extractives-free OPEFB, from native-whole unextracted basis to the corrected native-whole OPEFB basis.

The structural carbohydrates are the major constituents that made-up structure of lignocellulosic biomass of OPEFB, varied from 57.9% in the native-whole unextracted OPEFB to 51.5% in the extractive-free OPEFB. This yielded about 6.4% reduction in the structural carbohydrates after the extraction which mainly composed of glucan and xylan with a small amount of arabinan. The compositions of these carbohydrate constituents between the native-whole unextracted and the extractive-free OPEFB differed respectively from 35.0% to 30.9% for glucan, from 20.3% to 18.2% for xylan and from 3.10% to 2.46% for arabinan. The arabinan has shown the largest composition difference, with a 21% reduction, and followed by glucan and xylan with 11% and 10% reduction

respectively. The removal of extractive also reduced the lignin content from 34.9% in the native-whole unextracted OPEFB to 27.5% in the extractive-free OPEFB. This shows that the extractives contained approximately around 21% of lignin, while the other 79% was still intact in the extractive-free OPEFB fiber. High lignin content in native-whole unextracted OPEFB was due to the presence of extractives which resulted in falsely high lignin values when unhydrolyzed carbohydrates condense with acid insoluble lignin.

Table 1. Composition of native-whole unextracted, extractive-free and corrected native-whole of OPEFB fiber

| **Constituents** | **Composition of OPEFB (results expressed as a percentage of the oven-dried, native-whole unextracted OPEFB)** | | |
|---|---|---|---|
| | **Native-whole Unextracted OPEFB** | **Extractive-free OPEFB** | **Corrected Native-whole OPEFB** |
| 1. Structural Constituent | | | |
| Structural carbohydrates | 57.9 ±2.46 | 51.5 ±1.40 | 52.6 ±1.40 |
| *Glucan* | 34.6 ±2.39 | 30.9 ±1.40 | 31.2 ±1.35 |
| *Xylan* | 20.3 ±0.05 | 18.2 ±0.40 | 18.7 ±0.39 |
| *Arabinan* | 3.10 ±0.02 | 2.46 ±0.05 | 2.7 ±0.06 |
| Total Lignin | 35.0 ±2.18 | 27.7 ±0.68 | 27.7 ±0.68 |
| Acid Insoluble Lignin | 28.00±1.94 | 22.07±0.69 | 22.07±0.69 |
| Acid Soluble Lignin | 7.07±0.74 | 5.65±0.04 | 5.65±0.04 |
| 2. Non-structural Constituent | | | |
| Ash | 0.40 ±0.01 | 0.10 ±0.01 | 0.10 ±0.01 |
| Total Extractives | NR | 12.9 ±2.25 | 11.87 ±2.25 |
| Identified Water Extractives | NR | 1.06±0.09 | 0.06±0.07 |
| *Glucose Oligo* | NR | 0.24±0.03 | NR |
| *Xylose Oligo* | NR | 0.43±0.03 | NR |
| *Arabinose Oligo* | NR | 0.25±0.01 | NR |
| *Sucrose* | NR | 0.06±0.07 | 0.06±0.07 |
| *Glucose* | NR | 0.02±0.01 | NR |
| *Xylose* | NR | 0.07±0.004 | NR |
| Ethanol Extractives | NR | 2.32±0.17 | 2.32±0.17 |
| Other Extractives | NR | 9.49±2.75 | 9.49±2.75 |
| 3. Moisture content | 9.51±1.46 | 9.51±1.46 | 9.51±1.46 |
| Total Composition | 102.81 | 101.71 | 101.78 |

All values are mean of duplicate ± standard deviation, NR= Not Relevant

In the non-structural constituent, the ash was greatly affected by the extraction process. The ash content decreased from 0.4% in the native-whole unextracted OPEFB to 0.1% in the extractive-free OPEFB. This indicates that the extractive-free OPEFB contained approximately only 25% of the ash content with the remaining 75% have been solubilize during the two-stage extraction process. The number of extractives for extractive-free OPEFB basis were accounted around 12.9% which made up of water and ethanol soluble constituents and other extractives. The other extractives composition maybe contains acetyl group, protein content, soluble ash, soluble lignin and many unidentified constituents. As reported in Table 1 the highest compositional content for corrected native-whole

OPEFB, was for the glucan component followed by xylan and arabinan with 31.2%, 18.7% and 2.7%. The amount of structural carbohydrate of corrected native-whole OPEFB were slightly higher than extractive-free OPEFB because the measured soluble sugar except sucrose in the extractives of the extractive-free OPEFB basis, have been used to correct the compositions of structural carbohydrate. These reduce the number of extractives for corrected native-whole OPEFB to 11.87% which is 92% of the total extractives from extractives–free OPEFB basis. The amount accounted for extractives in corrected native-whole OPEFB in this study is still high since many of its constituents such as soluble ash and lignin have not been measured properly. The lignin content of OPEFB fiber in this study is considered high as its make up more than half of the carbohydrates composition and hence the pretreatment step must be applied to the OPEFB to overcome the recalcitrance nature of this biomass for further used as the source of fermentable sugar. The lignin level was also comparable to the lignin content of hardwood. The composition of structural and non-structural constituents of corrected native-whole OPEFB fiber in this work was comparable to the previous studies as shows in Table 2.

Table 2. Composition of extractive-free OPEFB fiber from previous works

| **Constituents** | **This Study** | **Hassan et al. [1]** |
|---|---|---|
| *Structural Constituent* | | |
| Glucan | 31.2 ±1.35 | 36.1 ±4.80 |
| Xylan | 18.7 ±0.39 | 22.4 ±2.17 |
| Arabinan | 2.7 ±0.06 | NA |
| Lignin | 27.7 ±0.68 | 26.5 ±2.91 |
| *Non-structural Constituent* | | |
| Ash | 0.10 ±0.01 | 2.93 ±0.27 |
| Extractives | 11.87 ±2.25 | 12.74 ±0.96 |

NA= Not Available

**Morphology analysis**

Figure 1a and b illustrate the SEM images for the surface structure of native OPEFB fiber with different magnification. The native OPEFB fiber had a rigid surface with a layer of matrix material like lignin or waxes that covered the whole surface of the fiber. This layer might be the protective layer present in most plants to prevent water loss. The cell walls of this biomass are thicker than the hardwood which result in high coarseness and rigidity index as reported by previous studies [16].

Moreover, there are great numbers of silica bodies found embedded on the surface of the fiber strands as highlighted in the Figure 1a and b. The silica bodies are attach to circular craters which are spread uniformly over the strand's surface. In addition to cellulose, hemicellulose and lignin, OPEFB is also rich in inorganic elements such as silica and metal ions [17]. The main constituents present in the silica bodies are silicon and oxygen as reported by the previous works [18]. Silica bodies are the most often mineral found on the surface of woody plants, formed by the invasion and hardening of soil minerals into sedimentary cavities between and within cell wall during plant growth [19]. The surface recalcitrance of the native OPEFB fiber serves as a major physical barrier for enzymatic hydrolysis process due to the difficulty in penetrating the surface to access the cellulose and hemicellulose for sugar production.

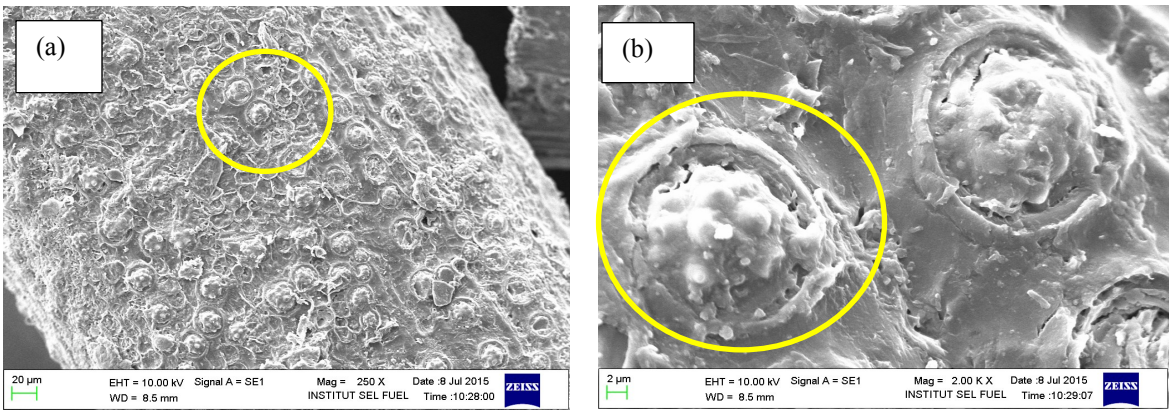



Figure 1. SEM images (a) and (b) of native OPEFB fiber at different magnification (200x; 2000x)

**Spectroscopy analysis**

FTIR spectroscopy was used to investigate the functional group presence in the native OPEFB fiber. Figure 2 shows the FTIR spectra of native OPEFB fiber. A strong and broad absorption was observed at a wavenumber of 3355 $cm^{-1}$ which is related to the stretching of H-bonded in hydroxyl group of cellulose, respectively [20]. The other prominent one around wavenumber of 2900 $cm^{-1}$ is due to the C-H stretching of $CH_2$ from the $CH_2$-OH group in cellulose [21]. In addition, the area of 1800 to 600 $cm^{-1}$ is called the fingerprint area of spectra which has many sharp and well defined absorption bands due to the various functional groups presence in each component of OPEFB. The distinctive bands in the fingerprint region and the components to which these peaks are shown in Table 3.

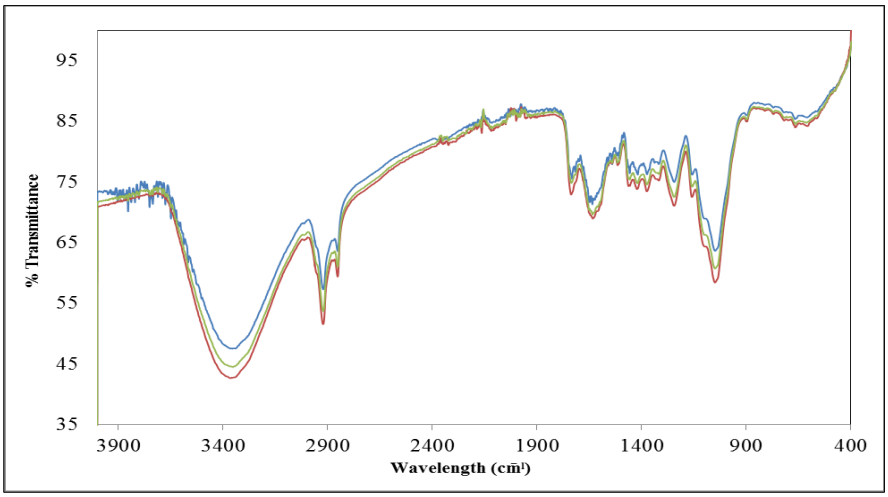



Figure 2. FTIR spectra of native OPEFB

The peak at around wavenumber of 1733$cm^{-1}$ can be seen from the spectra, which occur due to the C=O stretching of the acetyl and uronic ester groups of the hemicellulose ester. The peak also represents the carbonyl ester linkages of the carboxylic groups of ferulic and p-coumaric monomeric lignin [22]. The peak at 1635 $cm^{-1}$ was correspond to the bending vibration of the hydroxyl groups of cellulose. Sun and Cheng also reported that the band around 1600 $cm^{-1}$ was probably due to the bending mode of water, since hemicelluloses have strong affinity for water [23]. The

absorption band 1244 and 1541 $cm^{-1}$ are arise mostly from aromatic ring of lignin, while the band around 1635, 1375, 1049 and 667 $cm^{-1}$ are mainly due to carbohydrates and have no significant contribution from the lignin [24].

Table 3. FTIR wavenumber characterization of native OPEFB [20-27]

| **Wavenumber ($cm^{-1}$)** | **Compound** |
|---|---|
| 3355 | O-H stretching |
| 2850-2920 | C-H stretching in methyl and methylene group |
| 1733 | C=O stretching in unconjugated ketones, carbonyl and in ester groups |
| 1635 | O-H bending |
| 1541 | C=C stretching from aromatic ring of lignin |
| 1375 | C-H bending in cellulose and hemicellulose |
| 1244 | C-O-C stretching of aryl-alkyl ether |
| 1049 | Aromatic C-H in plane deformation-O deformation in primary alcohol |
| 667 | C-O out of plane bending mode |

**Crystallinity analysis**

The degree of cellulose crystallinity is a major factor in investigating the potential of OPEFB as the feedstock for bioconversion due to its effects on the enzymatic hydrolysis process as low crystallinity of cellulose increase the efficiency of cellulose hydrolysis by cellulase. Figure 3 shows the X-ray diffractogram of native OPEFB fiber and powder resulted from grinding process with particle size measured as less 250 µm.

By comparing with the cellulose standard available in the database of XRD system, two main peaks were observed from the XRD patterns at 2θ = 22.5 and 2θ = 16 representing peak $I_{002}$ and $I_{011}$, respectively. As in figure 3, peak $I_{011}$ for both samples are corresponding to the amorphous region of hemicellulose and lignin while peaks $I_{002}$ represent the crystalline region of cellulose [22]. The crystallinity index of native OPEFB fibers were calculated as 40%, while for the powder form of OPEFB fiber with particle size less than 250µm was 37%. Slight decrease in the crystallinity shows that smaller particle size cause decrease in the cellulose crystallinity of the fiber as reported by Sun & Cheng [23]. The X-ray diffractogram of the fiber and powder form of native OPEFB were also found to be comparable with the X-ray diffractogram of SigmaCell cellulose type 20 from the previous work [1].

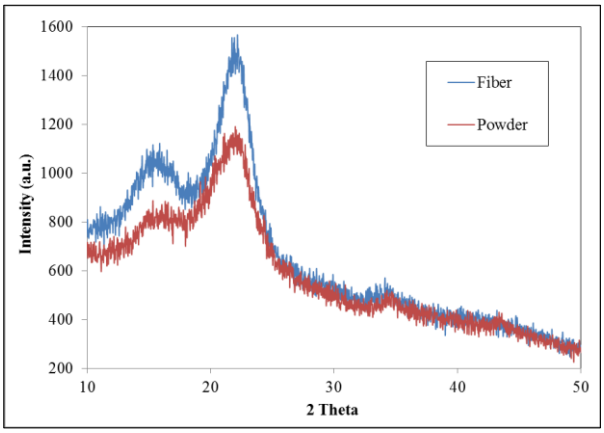


Figure 3. X-ray diffractogram of fiber and powder form of native OPEFB

## Conclusion

In the present study, it was found that the OPEFB fiber were made up of 31.4% of glucan, 18.6% xylan and 2.7% arabinan with the lignin accounted around 23,9%. As for non-structural constituents of OPEFB fiber, the ash and extractive content was around 0.1% and 8.18%. The morphological study by SEM shows the surface structure of OPEFB fiber is mainly consist of silica bodies. Spectroscopic analysis by FTIR shows a comparable result indicated the presence of the cellulose, hemicellulose and lignin in the fiber. While XRD analysis indicated the crystalline nature of cellulose in the native OPEFB fiber through the (200) peak at 2θ=22.5. OPEFB fiber has the potential as the low-cost feedstock for bioconversion as it contains the polymer of carbohydrates such as cellulose and hemicellulose but due to the surface morphology, crystallinity nature of its element, and the present of lignin, the process required a preliminary pretreatment step to optimize the production of fermentable sugar.

## Acknowledgement

The authors would like to acknowledge Ministry of Education Malaysia and Universiti Kebangsaan Malaysia for the financial and technical support of this research under grant LRGS/2013/UKM-UKM/PT/01.

## References

1. Hassan, O., Tang, P. L., Maskat, M. Y., Md. Illias, R., Badri, K., Jahim, J. and Mahadi, N. M. (2013). Optimization of pretreatments for the hydrolysis of oil palm empty fruit bunch fiber (EFBF) using enzyme mixtures. *Biomass and Bioenergy,* 56: 137 – 146.
2. Rahman, S. H., Choudhury, J. P., Ahmad, A. I. and Kamaruddin, A. H. (2007). Optimization studies on acid hydrolysis of oil palm empty fruit bunch fiber for production of xylose. *Bioresource Technology,* 98: 554 – 559.
3. Astimar, A. A., Husin, M. and Anis, M. (2002). Preparation of cellulose from oil palm empty fruit bunches via ethanol digestion: Effect of acid and alkali catalyst. *Journal of Oil Palm Research,* 14: 9 – 14.
4. Ming, J. L., Ming, W. L., Gunawan, C. and Dale, B. (2010). Ammonia fiber expansion (AFEX) pretreatment, enzymatic hydrolysis, and fermentation on empty palm fruit bunch fiber (EFBF) for cellulosic ethanol production. *Applied Biochemical Biotechnology,* 162: 1847 –1857.
5. Hamzah, F., Idris, A. and Tan, K. S. (2011). Preliminary study on enzymatic hydrolysis of treated oil palm (Elaeis) empty fruit bunches fibre (EFB) by using combination of cellulase and beta-1,4 glucosidase. *Biomass and Bioenergy,* 35: 1055 – 1059.
6. Shuit, S. H., Tan, K. T., Lee, K. T. and Kamaruddin, A. H. (2009). Oil palm biomass as a sustainable energy source: A Malaysian case study. *Energy,* 34(9): 1225 – 1235.
7. Sulaiman, M. A., Abdullah, N., Gerhauser, H. and Shariff, A. (2011). An outlook of Malaysian energy, oil palm industry and its utilization of wastes as useful resource. *Biomass Bioenergy,* 35: 3775 – 3786.
8. Hames, B. R., Scarlata, C., Sluiter, A., Sluiter, J. and Templeton, D. (2008). Preparation of sample for compositional analysis: Laboratory analytical procedures *(LAP).* Colorado, United State: National Renewable Energy Laboratory.
9. Sluiter, A., Hames, B., Ruiz, R., Scarlata, C., Sluiter, J. and Templeton, D. (2005). Determine of ash in biomass: Laboratory analytical procedures *(LAP).* Colorado, United States: National Renewable Energy Laboratory.
10. Sluiter, A., Ruiz, R., Scarlata, C., Sluiter, J. and Templeton, D. (2008). Determination of extractives in biomass. Golden, Colorado: National Renewable Energy Laboratory.
11. Sluiter, A., Hames, B., Ruiz, R., Scarlata, C., Sluiter, J., Templeton, D. and Crocker, D. (2008). Determination of structural carbohydrates and lignin in biomass. Golden Colorado: National Renewable Energy Laboratory.
12. Sluiter, J. B., Ruiz, R. O., Scarlata, C. J., Sluiter, A. D. and Templeton, D. W. (2010). Compositional analysis of lignocellulosic feedstock: Review and description of methods. *Journal of Agricultural Food Chemistry,* 58(16): 9043 – 9053.
13. Abdul, P. M., Harun, S., Md. Jahim, J., Markom, M. and Hassan, O. (2011). Effect of column's temperature and evaluation of RID and ELSD as a suitable ion exchange HPLC detection method of simple sugars. *Journal of Science and Technology,* 49(58): 599 – 604.
14. Segal, L., Creely, J. J., Martin, A. E. and Conrad, C. M. (1959). An empirical method for estimating the degree

of crystallinity of native cellulose using the X-ray diffractometer. *Textile Research Journal,* 29(10): 786 – 794.

15. Thammasouk, K., Tandjo, D. and Penner, M. H. (1997). Influence of Extractives on the Analysis of Herbaceous Biomass. *Journal of Agricultural and Food Chemistry,* 45(2): 437 – 443.
16. Law, K. N. and Jiang, X. (2001). Comparative papermaking properties of oil-palm empty fruit bunch. *Tappi Journal,* 84: 1 – 13.
17. Law, K. N., Daud, W. W. and Ghazali, A. (2007). Morphology and chemical nature of fiber strands of oil palm empty fruit bunch (OPEFB). *Bioresources,* 2: 351 – 362.
18. Lins, U., Barros, C. F., Da Cunha, M. and Miguens, F. C. (2002). Structure, morphology and composition of silicon biocomposites in the palm tree *Syagrus coronata* (Mart.) Becc. *Protoplasma,* 220: 89 – 96.
19. Yoon, C. J. and Kim, K. W. (2008). Anatomical descriptions of silicified woods from madagascar and indonesia by scanning electron microscopy. *Micron,* 39(7): 815 – 831.
20. Khalil, H. S., Ismail, H., Rozman, H. D. and Ahmad, M. N. (2001). The effect of acetylation on interfacial shear strength between plant fibres and various matrices. *European Polymer Journal,* 37(5): 1037 – 1045.
21. Xiao, X., Bian, J., Li, M. F., Xu, H., Xiao, B. and Sun, R. C. (2014). Enhanced enzymatic hydrolysis of bamboo (*Dendrocalamus gigantus munro*) culm by hydrothermal pretreatment. *Bioresource Technology,* 159: 41 – 47.
22. Nazir, M. S., Wahjoedi, B. A., Yussof, A. W. and Abdullah, M. A. (2013). Eco-friendly extraction and characterization from oil palm empty fruit bunch. *BioResources,* 8(2): 2161 – 2172.
23. Sun, Y. and Cheng, J. (2002). Hydrolysis of lignocellulosic materials for ethanol production: A review. *Bioresource Technology,* 83: 1 – 11.
24. Ching, Y. C. and Ng, T. S. (2014). Effect of preparation conditions on cellulose from oil palm empty fruit bunch fiber. *Bioresource Technology,* 9(4): 6373 – 6385.
25. Nomanbhay, S. M., Hussain, R. and Palanisamy, K. (2013). Microwave-assisted alkaline pretreatment and microwave assisted enzymatic saccharification of oil palm empty fruit bunch fiber for enhanced fermentable sugar yield. *Journal of Sustainable Bioenergy System,* 3: 7 – 17.
26. Pandey, K. K. (1999). A study of chemical of soft and hardwood and wood polymers by FTIR spectroscopy. *Journal of Applied Polymer,* 71: 1969 – 1975.
27. Kargarzadeh, H., Ahmad, I., Abdullah, I., Dufresne, A., Zainudin, S. and Sheltami, R. (2012). Effects of hydrolysis conditions on the morphology, crystallinity, and thermal stability of cellulose nanocrystals extracted from kenaf bast fibers. *Cellulose,* 19(3): 855 – 866.

*Malaysian Journal of Analytical Sciences, Vol 21 No 1 (2017): 197 - 203*
*DOI: http://dx.doi.org/10.17576/mjas-2017-2101-23*

MALAYSIAN JOURNAL OF ANALYTICAL SCIENCES
*Published by The Malaysian Analytical Sciences Society*
ISSN 1394 - 2506

# PALM KERNEL SHELL-DERIVED BIOCHAR AND CATALYST FOR BIODIESEL PRODUCTION

## (Biochar dan Pemangkin Berasaskan Tempurung Kelapa Sawit untuk Penghasilan Biodiesel)

Dayang Nuradila[1], Wan Azlina Wan Ab Karim Ghani[1]*, Azil Bahari Alias[2]

*[1]Department of Chemical and Environmental Engineering, Faculty of Engineering, Universiti Putra Malaysia, 43400 UPM Serdang, Selangor, Malaysia*
*[2]Faculty of Chemical Engineering, Universiti Teknologi MARA,40450 Shah Alam, Selangor, Malaysia*

**Corresponding author: wanazlina@upm.edu.my*

Received: 21 October 2015; Accepted: 14 June 2016

**Abstract**

A promising catalyst based on a biomass pyrolysis by-product, biochar, has been developed to produce biodiesel. A carbon-based solid acid catalysts were prepared by sulfonating pyrolysis char with concentrated sulfuric acids. The catalysts were characterized using thermogravimetric analyses (TGA), scanning electron microscope (SEM), Fourier transform infrared spectroscopy (FTIR) and surface area analyzer. Prepared catalysts were studied for their ability to catalyze transesterification of vegetable oils. The catalyst sulfonated with the concentrated sulfuric acid demonstrated considerable conversion in free fatty acid esterification. Further investigation of the catalyst was conducted to determine the effect of sulfonation time (1 and 3 hours) and surface area on the transesterification reactions. The surface area of the biochar was increased by chemical treatment using 10M potassium hydroxide through porosity development. Results showed the catalyst with the highest surface area and acid density to have the highest catalytic activity to produce biodiesel from canola oil in the presence of methanol as the reagent. The effects of alcohol to oil (A:O) molar ratio, reaction time and catalyst loading on the esterification reaction catalyzed by the sulfonated biochar were also investigated. Results revealed that more than 90% biodiesel yield was achieved at 15 wt% of catalyst amount, methanol to oil molar ratio was 9:1 and the agitation rate was 700 rpm. As a conclusion, the prepared biochar-based catalyst has a tremendous potential to be used in a process converting a high Free Fatty Acids (FFA) feedstock to biodiesel.

**Keywords:** transesterification, vegetable oil, palm kernel shell, biochar-based catalyst

**Abstrak**

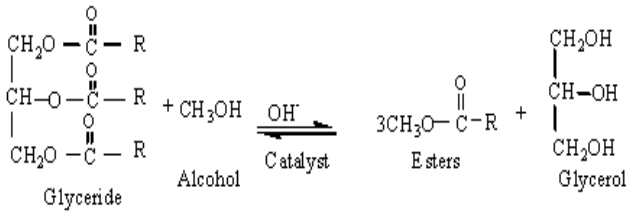
Pemangkin yang berasaskan pirolisis biomass produk sampingan, biochar, telah dibangunkan untuk penghasilan biodiesel. Pemangkin asid pepejal berasaskan karbon telah dihasilkan daripada sulfonasi pirolisis char dengan asid sulfurik pekat. Pemangkin telah dicirikan menggunakan analisis termogravimetri (TGA), mikroskop imbasan elektron (SEM), spektroskopi infra merah transformasi Fourier (FTIR) dan penganalisa luas permukaan. Pemangkin yang tersedia telah dikaji keupayaannya untuk menjadi pemangkin transesterifikasi minyak sayur-sayuran. Pemangkin sulfonat dengan asid sulfurik pekat menunjukkan penukaran ini boleh dipertimbangkan dalam pengesteran asid lemak bebas. Kajian lanjut terhadap pemangkin telah dijalankan untuk menentukan kesan masa sulfonasi (1 dan 3 jam) dan luas permukaan pada tindak balas transesterifikasi. Luas permukaan biochar telah meningkat melalui rawatan kimia menggunakan 10M kalium hidroksida melalui pembangunan liang. Hasil kajian telah menunjukkan pemangkin dengan luas permukaan dan ketumpatan asid yang paling tinggi mempunyai aktiviti pemangkinan tertinggi bagi pengeluaran biodiesel daripada minyak kanola dengan kehadiran metanol sebagai reagen. Nisbah molar kesan alkohol kepada minyak (A:O), masa tindak balas dan muatan pemangkin keatas tindak balas pengesteran yang dimangkinkan oleh biochar sulfonat turut disiasat. Hasil kajian menunjukkan bahawa lebih daripada 90% hasil biodiesel telah dicapai pada 15 wt% daripada jumlah pemangkin, nisbah molar metanol kepada minyak adalah 9:1 dan kadar pergolakan adalah 700 rpm.

Kesimpulannya, pemangkin berasaskan biochar yang dihasilkan mempunyai potensi yang amat besar untuk digunakan dalam proses penukaran bahan mentah asid lemak bebas tinggi (FFA) kepada biodiesel.

**Kata kunci:** transeterifikasi, minyak sayuran, tempurung kelapa sawit, pemangkin berasaskan biochar

## Introduction

Increasing environmental problems, global fuel consumptions and strike increase in fossil fuel price has led to production of renewable fuels such as biodiesel. Biodiesel, consisting of methyl esters of long chain fatty acids has become very attractive as a biofuel due to its environmental benefits, renewable and less polluting alternatives. Biodiesel can be produced from straight vegetable oil, animal oil/fats, tallow and waste cooking oil. The largest possible source of suitable oil comes from oil crops such as rapeseed, palm or soybean. Biodiesel has a higher flash point than fossil diesel and so is safer in the event of a crash. The biodiesel yields are estimated 90% to 40% more energy than the energy invested in producing it [1]. Biodiesel can be produced by the transesterification of vegetable oils with alcohol which involved the reaction of a triglyceride (fat/oil) with an alcohol to form esters and glycerol in the presence of a catalyst. The economy of the process depends on the type and quantity of catalyst used among other factors. Transesterification of vegetable oil as shown in Scheme 1.




Scheme 1. Transesterification of vegetable oil

The reaction between the fat or oil and the alcohol is a reversible reaction and so the alcohol must be added in excess to drive the reaction towards the right and ensure complete conversion. The catalyst can be homogeneous or heterogeneous depending on whether it is in the same or different phase with reactants; oil and alcohols [2]. Homogeneous basic catalyst such as potassium hydroxide (KOH) is widely used in industrial processes. However, drawbacks such as difficulties in the recovery of the catalyst and the formation of abundant wastewater in the neutralizing and separating processes are the major disadvantages in alkali-catalyzed transesterification processes [3]. Therefore, heterogeneous catalyst is recommended due to easier operational processes, higher activity and selectivity and longer catalyst lifetimes [3]. Recently, sulfonated carbon precursors derived from the partial carbonization of sugar, starch, or cellulose for catalyzing the production of biodiesel is of great interest. Biochar as carbon based precursor is well established in recent literatures [4,5]. In this study, low cost and renewable carbon-based precursor (biochar) is investigated as a solid acid catalyst for the transesterification process of mixture of canola oil for biodiesel production. Surface chemistry and physical and structural changes biochar –based catalyst was also using Fourier Transform Infrared (FTIR) spectroscopy, Scanning Electron Microscopy (SEM), Bruner-Emmet-Teller (BET) surface area composition of methyl esters produced using Gas Chromatography-Mass Spectrometry (GC-MS) analysis.

## Materials and Methods

### Catalyst preparation

Palm kernel shells (PKS) biochar was used as carbon precursor. The as-received biochar was ground and sieved between 300 – 500 μm and then dried in an oven at 110 °C for 2 hours. The carbonized biochar mixed and stirred with 0.1 $molL^{-1}$ HCl for 1 hour. The activated biochar samples were then sulfonated using sulfuric acid for 15 hours at 150 °C and ambient pressure [6]. Subsequently, the sulfonated biochar was washed with excessive distilled water and dried in an oven at 110 °C overnight.

**Characterization study**

The BET surface area of the prepared catalyst was measured with surface area analyzer (Quantachrome AS1Win). Morphological study was carried out with a scanning electron microscopy (SEM) (HITACHI model, S-3400N, Japan). A Perkin-Elmer pyris diamond thermogravimetry (TG/DTG) was used for TGA. The presence of functional group on the surface of the PKS biochar and catalyst (after the sulfonation process) was analyzed by using Fourier Transform Infrared (FTIR) spectroscopy (model Perkin-Elmer 100 series, USA at the frequency ranges of 600 $cm^{-1}$ to 4000 $cm^{-1}$. Composition of the methyl ester was analyzed with gas chromatography-mass spectrometry (GC-MS) (QP2010 Plus SHIMADZU).

**Transesterification procedures**

Transesterification was carried out in a 250 ml 3 neck round bottom flask equipped with a reflux condenser and a magnetic stirrer. PKS-based biochar was used as catalyst with the amount varied from 5 to 15wt% and the methanol ratio was kept constant 9:1. Catalysts were first suspended in a methanol at 65 °C under vigorous mixing for 2 hours. Later, the catalyst was separated by centrifuge, and the reaction mixture was loaded into rotary evaporator to remove excess methanol. Methyl-ester phase was then obtained in a separating funnel. The obtained methyl ester was then washed and dried in the oven. Products in the biodiesel consist of methyl esters, monoglycerides, diglycerides and triglycerides. Composition of the methyl ester was analyzed using GC method. The experiments were repeated for other parameters includes molar ratio alcohol to oil (3:1, 6:1 and 9:1), catalyst loading (5 wt%, 10 wt% and 15 wt%) and agitation rate (350 rpm, 700 rpm and 1100 rpm).

## Results and Discussion

**Catalyst characterizations**

The measured BET surface areas are shown in Table 1. There was pronounced increases in micro pore surface area when the raw biochar was activated and treated with strong sulfuric acid. This is likely due to the nature of the biochar substrate, which were all forms of woody biomass. Visual observation of the catalyst samples via SEM was performed to gain insight into catalyst morphology and pores size. As shown in Fig. 1(a) and (b), the catalyst samples have a highly irregular, convoluted fibrous surface structure, with little regular texturing. The structure of the biochar had a highly complex network of pores, channels and otherwise fibrous ridged surfaces, as opposed to the planar structure of sugar-derived biochar.

Table 1. BET Surface area of raw biochar and biochar-based catalyzed

| Sample | BET surface area ($m^2/g$) |
|---|---|
| Biochar | 0.02 |
| Biochar-based catalyst | 290.44 |

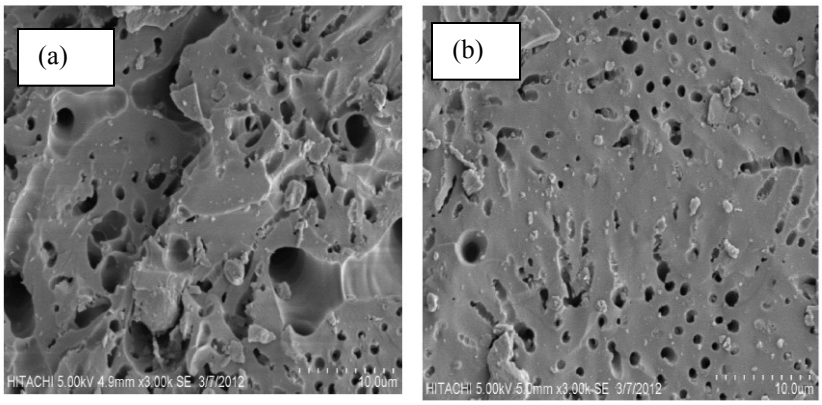



Figure 1. SEM images of (a) PKS biochar and (b) PKS-biochar based catalyst

Fig. 2 compares surface functional groups between raw biochar and biochar based catalyst. The IR spectrum of raw biochar shows a peak 724 $cm^{-1}$ and 830 $cm^{-1}$ for sulfonated char attributed to the ring C-H bonds of aromatic and heteroatomic compounds 11. In addition, peaks attributable to aromatic ring modes can be found at peaks 1498 $cm^{-1}$ for PKS biochar and 1495 and 1577 $cm^{-1}$ for sulfonated biochar. Peaks attributable to C-O-C asymmetric stretching are presented in both PKS biochar at 1170 $cm^{-1}$, and sulfonated biochar at 1119 and 1158 $cm^{-1}$.

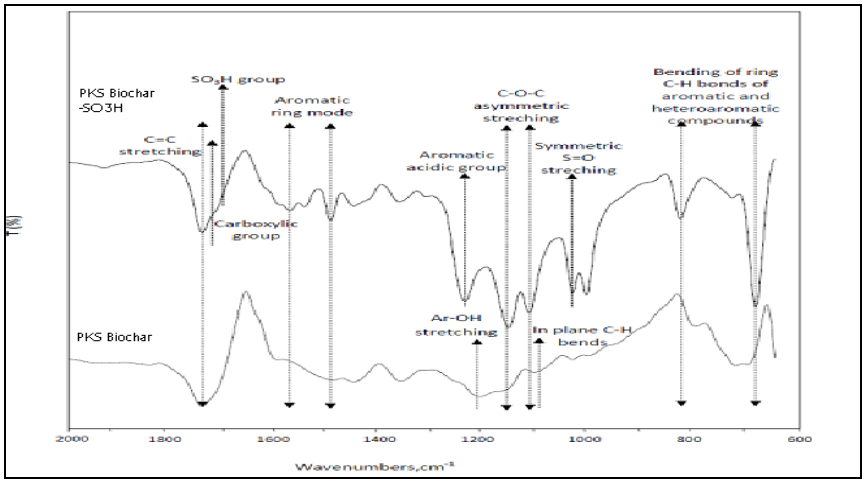



Figure 2. FTIR for PKS biochar before and after sulfonation

The PKS biochar also has peaks at 1107 $cm^{-1}$ which corresponding to in-plane C-H bends while at 1214 $cm^{-1}$ attributable to Ar-OH stretching. At peak 1745 $cm^{-1}$, both samples attributable to C=C stretching. The peaks attributed to aromatic acidic groups and carboxylic groups can be found at spectrum 1242 and 1730 $cm^{-1}$ for sulfonated char. Besides, the spectrum for sulfonated biochar exhibits a peak at 1035 $cm^{-1}$ which can be attributed to the symmetric S=O stretching and a peak at 1710 $cm^{-1}$ attributable to the presence of $SO_3H$ groups thereby confirming the incorporation of sulfonic groups onto the carbon matrix.

Fig. 3(a) and (b) shows TGA patterns for raw biochar and biochar based catalyst. The results indicated that the raw biochar has two distinctive peaks at 100 °C and 600 °C which corresponds to moisture content and lignin content respectively. While for sulfonated PKS biochar (catalyst demonstrated that desorption was occurring at 350 °C. The event can be attributed to desorption from a weak Brønsted acid site, which corresponds to the presence of COOH−groups as determined by FTIR. The event correlates with the sulfonic groups observed in the FTIR spectra for each catalyst. The TGA results were also analyzed to determine the approximate distribution of the type of acid sites.

**Effect of reaction conditions**

The effect of catalysts amount on the methyl ester content in the transesterification are showed in Fig. 4. The results showed that the use of 15wt% catalyst s, oil to molar ratio (9:1) and reaction times 3 hrs gave more than 90% methyl ester yield. However, when reducing the catalyst amount to 5 wt%, the methyl ester content decreased remarkably to below than 30%. This could be due to the fact that greater catalyst had increased the catalyst activity or transesterification due to high acidity [7]. This was verified with results shown in FTIR (see Fig. 2). Furthermore, as shown in Fig. 5 methyl ester yield about 90% after 2 hours reaction and there was no significant increase when the reaction time was prolonged. This is in accordance with which indicates that the reaction is completed [7].

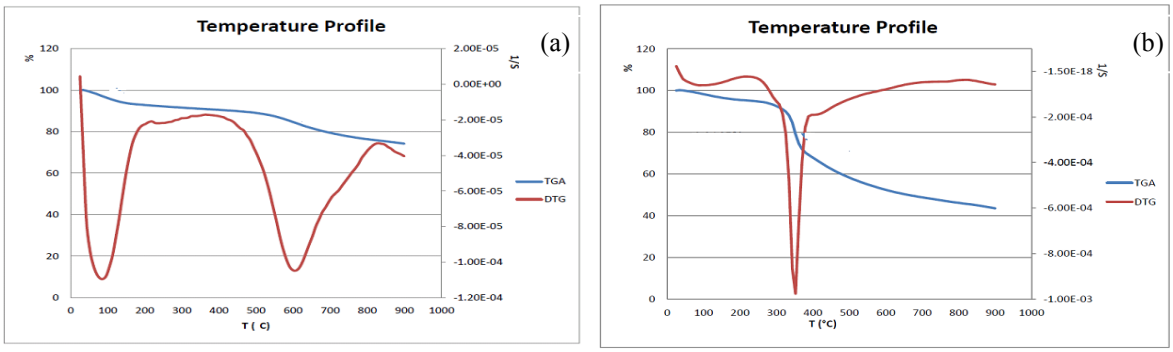



Figure 3. TGA patterns for (a) raw biochar and (b) biochar-based catalyst

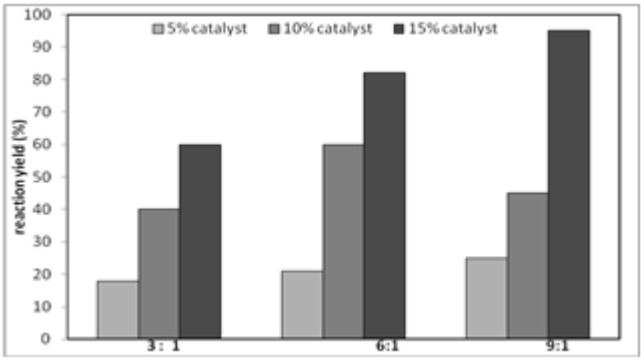



Figure 4. Reaction yields of methyl ester (ME) for various oil to methanol ratio and catalyst loading at constant speed ( 350 rpm)

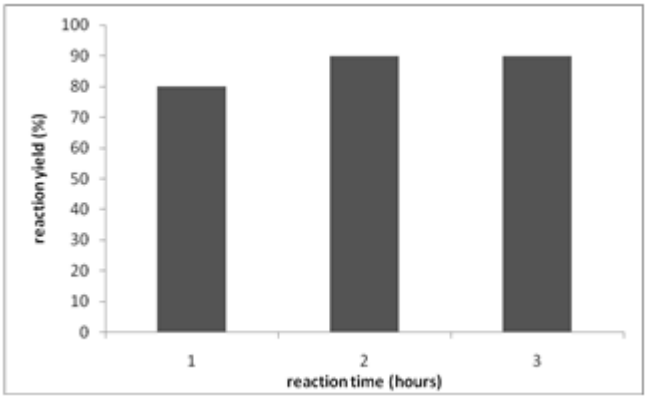



Figure 5. Reaction yields of methyl ester (ME) for different reaction time

Table 3 summarizes the chemical composition of the synthesized biodiesel of canola oil obtained in this study. It was observed that the fatty acid found in the biodiesel sample range from C6 until C22 FAME. The methyl ester compounds found in the sample are derived from the usage of methanol in the transesterification reaction. The main FAME in the biodiesel sample were oleic acid (C18:1), palmitic acid (C16:0), stearic acid (C18:0) and linolenic

acid (C18:3) The cetane number (quality of the diesel fuel) of biodiesel depends on the distribution of fatty acid in the original oil or fat from which it was produced. The major factor affecting FAME yields was the plant itself and variation will occur depending on climate and processing methods [8].

Table 3. Composition of FAME in canola oil biodiesel sample

| Peak | Retention Time (min) | Identity | % Area | Acid |
|---|---|---|---|---|
| 1 | 9.325 | C10 | 0.4492 | Decanoic acid (capric) |
| 2 | 12.019 | C12 | 7.9655 | Dodecanoic acid (lauric) |
| 3 | 12.868 | C22 | 0.0472 | Docosanoic acid (behenic) |
| 4 | 13.190 | C6 | 0.0838 | 2,4-hexadienedioic acid (sorbic) |
| 5 | 16.300 | C20 | 0.0657 | 11,14,17 eicosatrienoic acid (linolenic) |
| 6 | 16.341 | C18 | 0.1645 | 9-octadecenoic acid (oleic) |
| 7 | 16.533 | C16 | 6.7855 | Hexadecanoic acid (palmitic) |
| 8 | 16.689 | C10 | 1.9735 | Benzenepropanoic acid |
| 9 | 17.527 | C13 | 0.0624 | Tridecanoic acid |
| 10 | 18.258 | C18 | 78.049 | 9-octadecenoic acid (oleic) |
| 11 | 18.410 | C18 | 0.9745 | 9,12,15-octadecatrienoic acid (linolenic) |
| 12 | 18.475 | C18 | 2.7400 | Octadecanoic acid (stearic) |
| 13 | 20.056 | C20 | 0.4923 | cis-11-eicosenoic acid |
| 14 | 21.883 | C11 | 0.1460 | Undecanoic acid |

## Conclusion

Transesterification of vegetable oil was studied using biochar-derived catalyst to produce biodiesel with high methyl ester content under different conditions. It was found that biochar-based catalyst was successfully produced through sulfonation with sulfuric acid. The optimum conditions (with 90% conversion) for this reaction is suggested at 15wt% catalyst loading, oil to molar ratio (9:1) and 2 hrs reaction time and at moderate temperature 65°C. Thus, it proved that sulfonated PKS biochar shows considerable potential for use as a catalyst in biodiesel production.

## Acknowledgement

Authors would like to acknowledge the financial support from Ministry of Education (MOE), Malaysia via FRGS grant (Program code: FRGS/1/2014/TK05/UPM/02/8).

## References

1. Di Serio, M., Tesser, R., Pengmei, L. and Santacesaria, E. (2008). Heterogeneous catalysts for biodiesel production. *Energy & Fuels*, 22(1): 207 – 217.
2. Ejikeme, P. M., Anyaogu, I. D., Ejikeme, C. L., Nwafor, N. P., Egbuonu, C. A. C., Ukogu, K. and Ibemesi, J. A. (2010). Catalysis in biodiesel production by transesterification processes-An insight. *Journal of Chemistry*, 7(4): 1120 – 1132.
3. Hara, M. (2009). Environmentally benign production of biodiesel using heterogeneous catalysts. *ChemSusChem*, *2*(2): 129 – 135.
4. Rebitanim, N. Z., Ghani, W. A. W. A. K., Rebitanim, N. A. and Salleh, M. A. M. (2013). Potential applications of wastes from energy generation particularly biochar in Malaysia. *Renewable and Sustainable Energy Reviews*, 21: 694 – 702.
5. Mahmoud, D. K., Salleh, M. A. M. and Karim, W. A. (2012). Characterization and evaluation of agricultural solid wastes as adsorbents: A review. *Journal of Purity, Utility Reaction and Environment* 1(9): 451 – 459.

6. Srilatha, K., Issariyakul, T., Lingaiah, N., Sai Prasad, P. S., Kozinski, J. and Dalai, A. K. (2010). Efficient esterification and transesterification of used cooking oil using 12-tungstophosphoric acid (TPA)/$Nb_2O_5$ Catalyst. *Energy & Fuels*, 24(9): 4748 – 4755.
7. Lien, Y. S., Hsieh, L. S. and Wu, J. C. (2010). Biodiesel synthesis by simultaneous esterification and transesterification using oleophilic acid catalyst. *Industrial & Engineering Chemistry Research*, 49(5): 2118 – 2121.
8. Bamgboye, A. I. and Hansen, A. C. (2008). Prediction of cetane number of biodiesel fuel from the fatty acid methyl ester (FAME) composition. *International Agrophysics*, 22(1): 21 – 29.

*Malaysian Journal of Analytical Sciences, Vol 21 No 1 (2017): 204 - 212*
*DOI: http://dx.doi.org/10.17576/mjas-2017-2101-24*

MALAYSIAN JOURNAL OF ANALYTICAL SCIENCES
*Published by The Malaysian Analytical Sciences Society*
ISSN 1394 - 2506

# PREDICTION OF INDUSTRIAL CATALYSTS DEACTIVATION RATE USING FIRST PRINCIPLE MODEL AND OPERATING DATA

## (Ramalan Kadar Penyahaktifan Mangkin Industri Menggunakan Model Prinsip Pertama dan Data Operasi)

Abbas Azarpour[1]* and Sharifah Rafidah Wan Alwi[2]

[1]*Chemical Engineering Department,*
*University Teknologi Petronas, 32610 Bandar Seri Iskandar, Perak, Malaysia*
[2]*Process Systems Engineering Center (PROSPECT),*
*Research Institute for Sustainable Environment, Faculty of Chemical Engineering,*
*Universiti Teknologi Malaysia, 81310 UTM Sekudai, Johor, Malaysia*

**Corresponding author: abbas.azarpour@utp.edu.my*

Received: 21 October 2015; Accepted: 14 June 2016

**Abstract**

Catalyst deactivation is the loss of catalytic activity and /or selectivity over the course of time. Catalyst deactivation is a considerable and enduring problem in the operation of industrial catalytic processes. It is very costly in terms of catalyst replacement and process shutdown. The deactivation phenomenon not only affects the final product quality but also negatively influences the efficiency of the downstream processes. Therefore, a practical method which can accurately predict the deactivation rate can be a quite advantage to the industrial processes. In this paper, the deactivation rate of the industrial catalyst is predicted using operating data and catalyst specifications. The first principle model (FPM) is employed to predict the catalysts deactivation rate. The devised model is implemented into an industrial catalyst, which is palladium supported on carbon (Pd/C) utilized for the purification process of terephthalic acid, to show its applicability. The whole programs to obtain the rate of catalyst deactivation have been coded into Matlab R2013a environment. The model validated against industrial data. For the proposed catalyst, the catalyst sintering order is calculated with less that 3 percent error, and the pre-exponential values and the activation energy for the deactivation were calculated 0.00092 $h^{-1}$ and 5279 J $mol^{-1}$. Moreover, the catalyst is deactivated after around 360 days of operation. The methods, which are devised in this study, can be applied to any industrial catalyst to calculate the rate of deactivation.

**Keywords**: catalyst, deactivation rate, first principle model, sintering

**Abstrak**

Penyahaktifan mangkin adalah kehilangan aktiviti mangkin dan / atau kepilihan mangkin yang berkadaran dengan masa. Penyahaktifan mangkin adalah masalah besar yang sering berlaku dalam proses pemangkinan di industri. Ini kerana penggantian mangkin memakan kos yang tinggi dan boleh menyebabkan penutupan proses. Fenomena penyahaktifan tidak hanya memberi kesan kepada kualiti akhir produk tetapi juga mempengaruhi kecekapan proses hiliran. Oleh itu, satu kaedah praktikal yang mampu meramal dengan tepat kadar penyahaktifan boleh menjadi satu kelebihan untuk proses industri. Dalam penyelidikan ini, kadar penyahaktifan pemangkin industri diramalkan menggunakan operasi data dan spesifikasi mangkin. Model prinsip pertama (FPM) digunakan untuk meramalkan kadar penyahaktifan mangkin itu. Model yang dihasilkan ini digunakan sebagai mangkin di industri, iaitu palladium disokong pada karbon (Pd/C) digunakan untuk proses penulenan asid tereftalik, untuk membuktikan keterterapannya. Keseluruhan pengaturcaraan untuk mendapatkan kadar penyahaktifan mangkin telah dikodkan ke dalam perisian Matlab R2013a. Model ini telah disahkan terhadap data industri. Bagi mangkin yang dicadangkan, urutan pensinteran mangkin dikira dengan ralat kurang daripada 3 peratus, dan nilai pra-eksponen serta tenaga pengaktifan untuk penyahaktifan

yang dikira adalan 0.00092 $h^{-1}$ and 5279 J $mol^{-1}$. Selain itu, mangkin telah dinyahaktif selepas sekitar 360 hari operasi. Kaedah-kaedah yang direka dalam kajian ini boleh diaplikasikan untuk segala jenis mangkin industri bagi mengira kadar penyahaktifan.

**Kata kunci:** mangkin, kadar penyahaktifan, prinsip model pertama, pensinteran

## Introduction

Catalyst deactivation, the loss over time of catalytic activity or selectivity, is a considerable economical concern in the operation of industrial catalytic processes. Catalyst deactivation is referred to the interaction between the impurities and the catalyst in the process which the catalyst is utilized. Any physical or chemical interaction that declines the catalyst activity or selectivity is categorized as catalyst deactivation phenomena. Deactivation results in a shortened lifetime of the catalyst, and the replacement of the deactivated catalyst with a fresh one is required to maintain the product quality and the efficiency of the catalytic process. Deactivation of the industrial catalyst can vary from several seconds to several months. Shorter catalyst lifetime has a significantly adverse influence on the process economics. Therefore, to increase the catalyst lifetime can be considered as a great success in a catalytic process [1].

Catalyst deactivation is significantly related to the catalyst application and scientifically it has numerous challenges. Figure 1 displays the deactivation time for some processes in the refining and petrochemical industries. The deactivation time refers to the time after which a catalyst has lost so much of its initial activity that it must be replaced or regenerated. Regeneration is usually possible, but there is a limit. At the end of the cycle life the catalyst is recycled or, when this is more economical, disposed. It is clear that disposal should be postponed as long as possible and that recycling is becoming more and more important. In accordance to Figure 1, the deactivation time fluctuates prominently for the different processes. Depending on the process used the catalyst cycle life may vary from a few seconds, as in fluid catalytic cracking (FCC), to several years, as in for instance ammonia synthesis. Deactivation of a hydrodesulphurisation (HDS) catalyst is much slower, depending on the feed, in the order of months or a year [2].

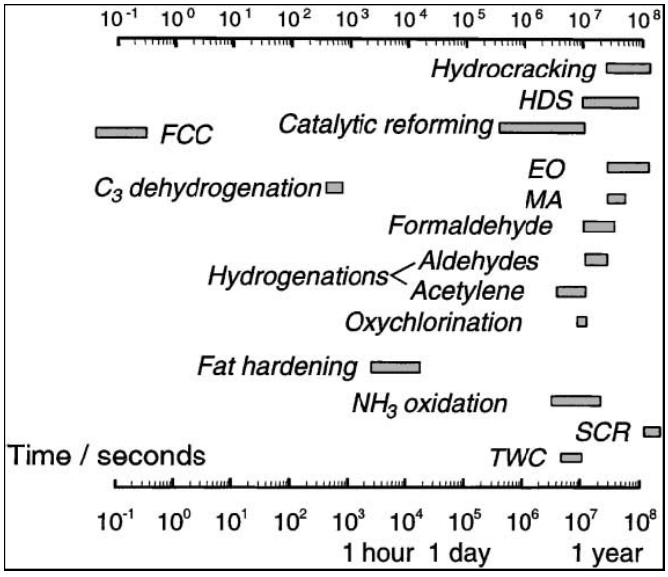



Figure 1. Time scale of deactivation of different catalytic processes

Modeling and simulation is an effective tool to analyse the process engineering systems. It is employed to improve the process efficiency and predict the process performance under different operating conditions. The accuracy of

the modeling effort is strongly related to the parameters involved into the developed model. The two most important parameters which are very influential on the model outputs precision are the rate of reactions and deactivation rate [3, 4]. The latter is considered when the catalytic process suffers from the deactivation phenomenon. Note that most of the industrial catalytic processes deal with the deactivation of the catalyst. Thus, to employ a suitable method which is able to accurately predict the rate of deactivation can improve the accuracy of the mathematical model considered for the catalytic process.

The reasons for catalyst deactivation can be divided into five categories as poisoning, fouling, sintering, mechanical deactivation through attrition or erosion, and corrosion/leaching by the reaction mixture [2, 5]. Therefore, the cause of the catalyst deactivation might originate from different reasons. Moreover, any catalysts depending on the type of process might encounter different mechanisms through the way of deactivation. Thus, to devise a model which ignores the complicated mechanisms of the deactivation and can be employed for the prediction of any catalysts utilized in the catalytic processes is a real and great advantage to the area of the modeling of such processes [6, 7].

Thermally induced catalyst deactivation is a major concern in high temperature catalytic processes. Thermal deactivation might take place due to different reasons. They might be loss of catalytic surface area, loss of support area, reactions/transformations of catalytic phases to non-catalytic phases, and loss of active material. The first two reasons are usually considered as sintering. Sintering phenomenon usually occurs at high temperature reactions, and its rates rely on temperature, reaction atmosphere, and catalyst formulation. Sintering is one of the significant reasons for the deactivation of supported metals catalysts. These precious metal catalysts are widely employed in the industries of petrochemicals, refineries, polymer, chemicals, and pharmaceuticals [8].

There are many studies carried out on the catalytic systems for the derivation of catalyst deactivation rate. Pellegrini et al. [9] did an extensive study on the several aged 0.5 wt.% palladium supported on carbon (Pd/C) catalysts taken from different purified terephthalic acid (PTA) production plants. The results verified that all catalysts experienced Pd sintering regardless of the nature and amount of contaminants. Li et al. [10] studied the positive effect of silica on the stability and activity of Ni/alumina catalyst. The results revealed that the addition of silica efficiently restricted the hydration of alumina support, and inhibited the deactivation of Ni/alumina catalyst. Salmi et al. [11] devised a model and applied it to a batch-wise hydrogenation of sitosterol to sitostanol on a platinum catalyst in the presence of a sulphurous poison. The model was able to determine the behaviour of the system based on the adsorption-reaction-poisoning idea. Sørensen [12] developed a methodology to estimate the deactivation models for industrial catalysts. The model employed the movement of the determined axial temperature profile to obtain the information on the deactivating phenomena. In this model, the temperature profile change determines the deactivation trend. The goal is to cover the calculated progress of the temperature profile through the reactor and deactivation models, estimating the deactivation model by means of non-linear least square. Keyvanloo et al. [13] investigated the impacts of carbon monoxide and hydrogen partial pressures on the deactivation by carbon of a CoPt/AlSi Fischer-Tropsch catalyst.

The objective of this paper is to predict the deactivation rate of industrial catalysts encountering sintering phenomenon utilizing first principle model and the process data. The operating data including the catalytic process information and catalyst specifications are used to devise the relevant model. In the developed model, the operational variables are incorporated into the model, and the catalyst deactivation rate is calculated considering the effects of the variables simultaneously.

Purified terephthalic acid (PTA) is the ninth largest industrial chemical, which is utilized as a raw material for the production of polyester, especially polyethylene terephthalate. Terephthalic acid (TA) is produced via the transition metal-catalyzed oxidation of p-xylene (PX) in acetic acid (AA), which is one of the largest industrial-scale applications of homogeneous catalysis. Co, Mn, and Br are the components of the catalyst [14]. Following reaction shows the PX oxidation:

$$H_3C - C_6H_4 - CH_3 \xrightarrow{Air/(Co-Mn-Br)} HOOC - C_6H_4 - COOH \quad (1)$$

The crude terephthalic acid (CTA) produced from PX oxidation consists of 4-carboxybenzaldehyde (4-CBA), which results in the discoloration of CTA. The purification of CTA is carried out in a fixed-bed reactor (FBR) contained Pd/C catalyst through the hydrogenation of 4-CBA to para-toluic acid (pta) in the water. The hydropurification reaction can be summarized as follows [9]:

$$OHC - C_6H_4 - COOH \xrightarrow{H_2/(Pd/C)} H_3C - C_6H_4 - COOH \quad (2)$$

Pd/C catalyst bears sintering of Pd particles, which is an inevitable reason for the catalyst deactivation. Sintering phenomenon is one the most commonly reasons for the industrial catalysts deactivation [9].

## Materials and Methods

In order to devise the model, the data of the catalyst and operation are required. The following sections deal with the data acquisition of industrial Pd/C catalyst and the hydropurification process.

### Materials: Catalyst and characterization

Samples of deactivated 0.5 wt. % Pd/C catalyst were gathered from different PTA production plants. Inductively coupled plasma (ICP), x-ray powder diffraction (XRPD), extended x-ray absorption fine structure (EXFAS) spectroscopy, transmission electron microscopy (TEM), energy dispersive spectroscopy (EDS), CO chemisorption, and catalyst activity methods were carried out to analyse the deactivation phenomenon of Pd/C catalyst [9].

### Pd surface area

The Pd surface area considerably decreases when the temperature increases. Industrial 0.5 wt. % Pd/C catalyst was used for the Pd surface area measurement. A chemisorption stoichiometry of Pd/CO equal to 2 and a surface Pd atomic density of $1.27 \times 10^{19}$ atoms/m$^2$ were taken into account to estimate the Pd surface area [15].

### Powder analysis

The PTA powder analysis was done in the industrial plant. Samples of the PTA powder were taken at the end of the dryer at certain times of the daily operation. The samples were analysed using the HPLC machine [16].

### Operating data

The operating data including the hydropurification system and the catalyst specifications are required. The operating data can usually be found in the process flow diagram, and the catalyst specifications are included into the operating manual.

### Methods

In this section, the methodology employed for the perdition of the deactivation rate is explained. Figure 2 shows the methodology used for this study.

The operating data including the catalyst specifications are used to calculate the deactivation rate parameter using the following mass balance for the different components, which their values are analysed for each particular-time:

$$C_{i,in} - C_{i,out} + (r_k)\,\rho_B\,\tau\,a(t)\,\eta_k = 0 \quad (3)$$

where $C$ is the component concentration, $r$ is the rate of reaction, $\rho_B$ is the bulk density, $\tau$ is the residence time of the component, $a$ is the deactivation rate parameter, and $\eta$ is the effectiveness factor. For the hydrogenation of 4-CBA, three reactions are considered as depicted in Figure 3 [17].

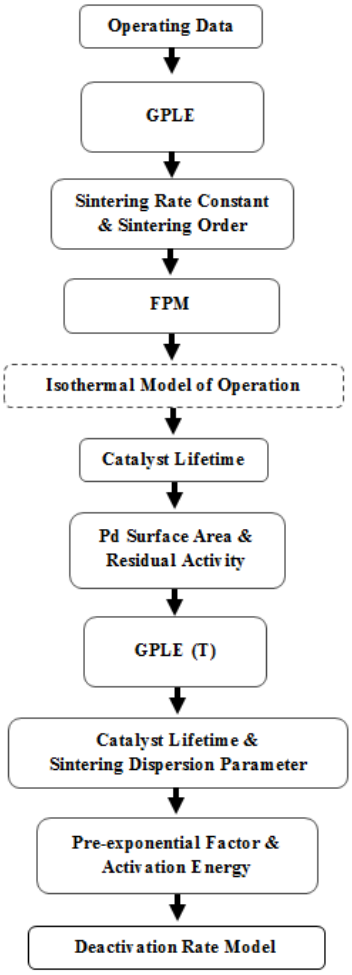



Figure 2. Flowchart for methodology

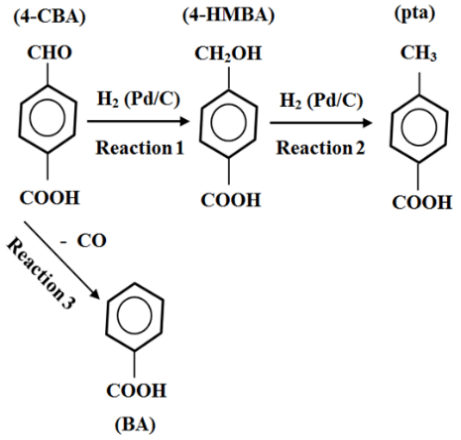



Figure 3. Hydrogenation reactions of 4-CBA

The calculated parameter is incorporated into the general power law expression (GPLE), which is usually used for the presentation of sintering phenomenon for the catalyst. The following equation shows the GPLE [5]:

$$-r_d = -\frac{da}{dt} = k_d a^m = k_{do} exp\left(\frac{-E_d}{R}\left(\frac{1}{T}-\frac{1}{T_R}\right)\right)\left(\frac{S}{S_o}-\frac{S_{eq}}{S_o}\right)^m \quad (4)$$

where $k_{do}$ is the pre-exponential factor; $a$ is the metallic sintering dispersion parameter; $m$ is the sintering order; $k_d$ is the sintering rate constant; $S$ is the active surface of the catalyst; $S_o$ is the initial active surface of the catalyst; $E_d$ is the activation energy; $T_R$ is the reference temperature; and the ratio of $S_{eq}$ to $S_o$ is the residual active surface of the catalyst.

The calculated sintering rate constant and sintering order via writing a code into Matlab2013a environment using nonlinear technique are emerged into a simple deactivation rate model. The preliminary simple model is incorporated into first principle model (FPM) consisting of mass balances of the catalytic process at isothermal condition to predict the catalyst lifetime.

Then, the measured Pd surface area and the residual activity of the catalyst, which is different for different types of catalyst, are incorporated into GPLE to finally derive the catalyst lifetime and sintering dispersion parameter under different operating conditions. Using the obtained values, the pre-exponential factor and activation energy for deactivation are computed, which results in the derivation of the catalyst deactivation rate model.

The whole program was coded into Matlab 2013a environment. First, the partial differential equations were transformed into ordinary differential equation using backward difference method. The resulted equations were solved using *ode45* and *optimset* commands with the tolerance less than $10^{-8}$.

## Results and Discussion

The experimental and modeling results are analysed in this section. To implement the devised strategy, the data of the operation and catalyst are required. The study on the deactivated industrial Pd/C catalyst reveals that the most part of Pd particles are segregated. Moreover, Pd/C catalyst is aged owing to the sintering of Pd and the reduction of Pd active surface area [9]. Figure 4 shows a deactivated Pd/C catalyst. Regarding the measurement of Pd surface area, Pd/C catalyst was thermally treated at different temperatures up to 800 °C. The results showed that Pd experiences the sintering phenomenon. The relation between Pd surface area with the temperature can be found in Pernicone et al. [15]. Regarding the residual activity of the aged catalyst, Table 1 signifies the values of residual activity for different samples of Pd/C catalyst taken from different PTA production plants [9].

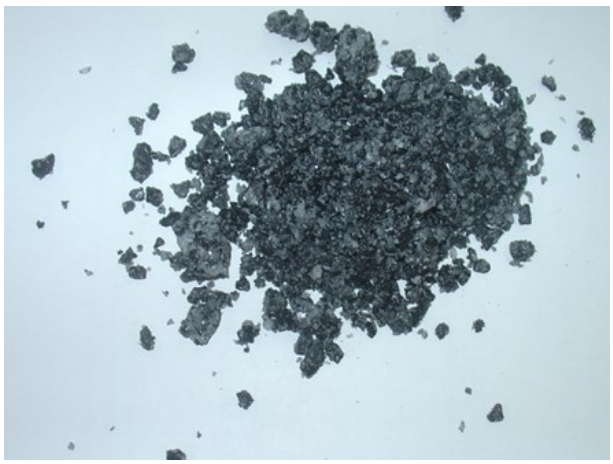


Figure 4. Deactivated Pd/C catalyst taken from the bottom of the reactor

Table 1. Residual activity of different Pd/C catalysts

| Catalyst Sample | Residual Activity (-) |
|---|---|
| A | 0.11 |
| B | 0.09 |
| C | 0.1 |

In this study, the average residual activity was considered as 0.1. PTA powder analysis was done in the PTA plant laboratory, and the results were reported at Azarpour et al. [18]. The operating data and the Pd/C catalyst specifications are shown in Table 2 [16].

Table 2. Operating data of the hydropurification process and Pd/C catalyst specifications

| Item | Value |
|---|---|
| Pressure (barg) | 73.5 |
| Temperature (°C) | 285 |
| Feed flowrate (t $h^{-1}$) | 196 |
| Hydrogen flowrate (kg $h^{-1}$) | 13.2 |
| TA concentration (wt.%) | 23 |
| Catalyst bed length (m) | 7.4 |
| Catalyst bed diameter (m) | 2.8 |
| Particle diameter (mm) | 3.53 |
| Bulk density (kg $m^{-3}$) | 475 |
| Bed void fraction (-) | 0.44 |
| Particle porosity (-) | 0.61 |

Table 3 includes the modeling outputs for different sintering orders along with the model error values. The pre-exponential values and the activation energy for the deactivation were calculated 0.00092 $h^{-1}$ and 5279 J $mol^{-1}$. Table 4 incorporates the trend of the catalyst deactivation through the operation days. It implies that the catalyst is totally deactivated after 360 days of operation. More information on the modeling and the derivation of the deactivation rate of Pd/C catalyst are available in the published papers [19, 20].

Table 3. Sintering order values and the relevant percent relative errors

| Sintering Order | Percent Relative Error (%) |
|---|---|
| 1 | 12.9 |
| 1.4 | 8.3 |
| 1.8 | 3.7 |
| 1.9 | 3.0 |
| 2.0 | 2.6 |
| 2.1 | 2.4 |
| 2.2 | 2.6 |
| 2.6 | 6.1 |
| 3.0 | 9.9 |

Table 4. Pd/C catalyst deactivation trend over the days of operation

| Operation Days | Deactivation Trend (%) |
|---|---|
| 30 | 17 |
| 60 | 27 |
| 90 | 37 |
| 120 | 46 |
| 150 | 55 |
| 180 | 64 |
| 210 | 73 |
| 240 | 82 |
| 270 | 90 |
| 300 | 95 |
| 330 | 98 |
| 360 | 100 |

## Conclusion

A methodology to derive the deactivation rate of the industrial catalysts was given. It is used for the catalysts encountering sintering phenomenon, which is one of the commonest reasons for the industrial catalysts deactivation. The model considers the operating data, catalyst specifications, functionality of catalyst surface area on temperature, and residual activity to structure the model. The study was applied to the industrial Pd/C catalyst, which is used for the hydropurification process in PTA production plant. The model validated against industrial data. For the proposed catalyst, the catalyst sintering order is calculated with less that 3 percent error, and the pre-exponential values and the activation energy for the deactivation were calculated 0.00092 $h^{-1}$ and 5279 J $mol^{-1}$. Moreover, the catalyst is deactivated after around 360 days of operation. The model can be used for the industrial catalysts suffering from sintering phenomenon.

## References

1. Argyle, M. D. and Bartholomew, C. H. (2015). Heterogeneous catalyst deactivation and regeneration: A review. *Catalysts*, 5: 145 - 269.
2. Moulijn, J. A., Van Diepen, A. and Kapteijn, F. (2001). Catalyst deactivation: Is it predictable?: What to do? *Applied Catalysis A: General*, 212: 3 - 16.
3. Markos, J., Brunovska, A. and Ilavsky, J. (1987). Modelling of catalytic reactors with catalyst deactivation: Iv. Parameter estimation of the rate equations of heterogeneous catalyst deactivation. *Chemical Papers*, 41: 375.
4. Roininen, J. and Alopaeus, V. (2008). Modeling of catalyst activity profiles in fixed-bed reactors with a moment transformation method. *Industrial & Engineering Chemistry Research*, 47: 8192 - 8196.
5. Bartholomew, C. H. (2001). Mechanisms of catalyst deactivation. *Applied Catalysis A: General*, 212: 17 - 60.
6. Chang, J.-S. and Hung, B.-C. (2002). Optimization of batch polymerization reactors using neural-network rate-function models. *Industrial & Engineering Chemistry Research*, 41: 2716 - 2727.
7. Zahedi, G., Elkamel, A., Lohi, A., Jahanmiri, A. and Rahimpor, M. (2005). Hybrid artificial neural network—first principle model formulation for the unsteady state simulation and analysis of a packed bed reactor for $CO_2$ hydrogenation to methanol. *Chemical Engineering Journal*, 115: 113 - 120.
8. Bartholomew, C. H. (1994). Sintering kinetics of supported metals: perspectives from a generalized power law approach. *Studies in Surface Science and Catalysis*, 88: 1 - 18.

9. Pellegrini, R., Agostini, G., Groppo, E., Piovano, A., Leofanti, G. and Lamberti, C. (2011). 0.5 Wt.% Pd/C catalyst for purification of terephthalic acid: irreversible deactivation in industrial plants. *Journal of Catalysis*, 280: 150 - 160.
10. Li, H., Zhao, Y., Gao, C., Wang, Y., Sun, Z. and Liang, X. (2012). Study on seactivation of $Ni/Al_2O_3$ Catalyst for liquid phase hydrogenation of crude 1, 4-butanediol aqueous solution. *Chemical Engineering Journal*, 181: 501 - 507.
11. Salmi, T., Murzin, D.Y., Wärnå, J., Mäki-Arvela, P. and Martin, G. (2013). Integrated modelling of reaction and catalyst deactivation kinetics—hydrogenation of sitosterol to sitostanol over a palladium catalyst. *Chemical Engineering Science*, 104: 156 - 165.
12. Sørensen, M. D. P. (2014). Deactivation models by fitting the progression of temperature profiles–coking model for the MTG process in adiabatic reactors. *Chemical Engineering Science*, 106: 126 - 135.
13. Keyvanloo, K., Fisher, M. J., Hecker, W. C., Lancee, R. J., Jacobs, G. and Bartholomew, C.H. (2015). Kinetics of deactivation by carbon of a cobalt fischer–tropsch catalyst: Effects of CO and $H_2$ partial pressures. *Journal of Catalysis*, 327: 33 - 47.
14. Partenheimer, W. (1995). Methodology and scope of metal/bromide autoxidation of hydrocarbons. *Catalysis Today*, 23: 69 - 158.
15. Pernicone, N., Cerboni, M., Prelazzi, G., Pinna, F. and Fagherazzi, G. (1998). An investigation on Pd/C industrial catalysts for the purification of terephthalic acid. *Catalysis Today*, 44: 129 - 135.
16. STPC (2010). Operating manual of Pta/Pet production plant. (Shahid Tondgooyan Petrochemical Company (Iran)).
17. Zhou, J.-H., Shen, G.-Z., Zhu, J. and Yuan, W.-K. (2006). Terephthalic acid hydropurification over Pd/C catalyst. *Studies in Surface Science and Catalysis*: 293 - 296.
18. Azarpour, A., Alwi, S. R. W., Zahedi, G., Madooli, M. and Millar, G. J. (2015). Catalytic activity evaluation of industrial Pd/C catalyst via gray-box dynamic modeling and simulation of hydropurification reactor. *Applied Catalysis A: General*, 489: 262 - 271.
19. Azarpour, A., Nejad G. B. T., Wan Alwi, S.R., Abdul Manan, Z. and Madooli Behbehani, M. (2015). Prediction of Pd/C catalyst deactivation rate and assessment of optimal operating conditions of industrial hydropurification process. *Industrial & Engineering Chemistry Research*, 54: 7067 - 7082.
20. Azarpour, A. and Zahedi, G. (2012). Performance analysis of crude terephthalic acid hydropurification in an industrial trickle-bed reactor experiencing catalyst deactivation. *Chemical Engineering Journal*, 209: 180 - 194.

*Malaysian Journal of Analytical Sciences, Vol 21 No 1 (2017): 213 - 220*
*DOI: http://dx.doi.org/10.17576/mjas-2017-2101-25*

**MALAYSIAN JOURNAL OF ANALYTICAL SCIENCES**
***Published by The Malaysian Analytical Sciences Society***
**ISSN 1394 - 2506**

# THE EFFECT OF GLUCOSE ADDITION IN ACETONE-BUTANOL-ETHANOL FERMENTATION FROM PALM OIL MILL EFFLUENT BY *Clostridium Acetobutylicum* NCIMB 619

## (Kesan Penambahan Glukosa dalam Fermentasi Aseton-Butanol-Etanol daripada Efluen Kilang Kelapa Sawit oleh *Clostridium Acetobutylicum* NCIMB 619)

Azima Syafaini Japar[1]*, Mohd. Sobri Takriff[2], Jamaliah Md. Jahim[1], Abdul Amir Hassan Kadhum[1]

[1]*Department of Chemical and Process Engineering*
[2] *Research Center for Sustainable Process Technology*
*Faculty of Engineering and Built Environment,*
*Universiti Kebangsaan Malaysia, 43600, UKM Bangi, Selangor, Malaysia*

**Corresponding author: azima.syafaini@siswa.ukm.edu.my*

Received: 21 October 2015; Accepted: 14 June 2016

**Abstract**

This study investigates the production of acetone, butanol and ethanol (ABE) in sterilized sludge of palm oil mill effluent (POME) with the addition of glucose by *Clostridium acetobutylicum* NCIMB 619. Glucose concentrations of 5 g/L, 10 g/L and 15 g/L were used with volume percentage of 3% (v/v) and 5% (v/v) for each concentration. The highest ABE production of 9.89 g/L was observed with the addition of 10 g/L glucose with volume percentage of 5% (v/v) compared to 0.49 g/L in the control batch, with highest ABE productivity and yield, $Y_{P/S}$ of 0.14 g/L/h and 1.36 g ABE/g substrate, respectively. Providing culture with 15 g/L glucose with volume percentage of 5% (v/v) was found to reduce the ABE production with lower productivity and ABE yield. The lower production at higher sugar level might be due to sugar inhibition that occurred during the process.

**Keywords**: acetone-butanol-ethanol fermentation, palm oil mill effluent, *Clostridium acetobutylicum*, glucose addition

**Abstrak**

Kajian ini dilakukan bagi menentukan kesan penamabahan glukosa terhadap penghasilan aseton, butanol dan etanol (ABE) di dalam medium mendakan efluen kilang kelapa sawit (POME) steril oleh *Clostridium acetobutylicum* NCIMB 619. Kepekatan glukosa yang digunakan adalah 5 g/L, 10 g/L dan 15 g/L dengan peratus isipadu sebanyak 3% (v/v) dan 5% (v/v) bagi setiap kepekatan. Penghasilan ABE yang paling tinggi iaitu sebanyak 9.89 g/L diperoleh pada penambahan 10 g/L glukosa dengan peratus isipadu 5% (v/v) berbanding 0.49 g/L ABE yang diperoleh di dalam medium kawalan. Produktiviti dan hasil ABE yang diperoleh juga adalah yang tertinggi iaitu masing-masing sebanyak 0.14 g/L/j dan 1.36 g ABE/g substrat. Penambahan 15 g/L glukosa dengan peratus isipadu sebanyak 5% (v/v) didapati mengurangkan penghasilan ABE dengan produktiviti dan hasil ABE yang paling rendah disebabkan oleh perencatan gula yang berlaku semasa proses fermentasi.

**Kata kunci**: fermentasi aseton-butanol-etanol, efluen kilang kelapa sawit, *clostridium acetobutylicum*, penambahan glukosa

## Introduction

The biological production of Acetone-Butanol-Ethanol (ABE) via fermentation have started during the First World War declined 1960s due to introduction of chemical process and higher cost of raw materials [1]. The interest in ABE fermentation was once again increases due to the rapid depletion of petroleum resources, fluctuating fuel price

as well as increase in public awareness on effects of toxic and greenhouse gases produced from fossil fuel combustion [2,3]. All these factors sparked in the attention of alternative fuels namely acetone, butanol and ethanol production through bioprocesses.

The most challenging aspects in ABE fermentation are to make the process economically feasible with zero competition with food crops to obtain raw material resources [4]. One of the solutions is to utilize industrial waste such as palm oil mill effluent (POME) that is readily available in Malaysia and able to reduce the cost of raw material. POME is an industrial waste that comes under the group of lignocellulose biomass consisting of various suspended components including cell wall, organelle and fiber, carbohydrate components which covered hemicellulose and simple sugar, nitrogenous compound including protein and amino acid and free organic acids and all these features make POME as a potential substrate for ABE fermentation [5-7].

POME characteristics as shown in Table 1 depend on the quality of raw material and method of oil processing in palm oil mill [8]. More than 50% of water used in crude oil production eventually ended up as POME [9,10]. POME was generated from three unit processes in a palm oil mill namely sterilization of fresh palm fruit (FFB) (38%), clarification process of extracted crude oil (6%) and hydro cyclone separation (4%) [11]. Based on previous studies, ABE fermentation using POME as media can produce total solvent between 0.30 and 2.66 g/L [7,12-15].

Several studies have reported that limited glucose content in the substrate produced higher amount of organic acids compared to ABE [1]. The cell metabolic shifting to ABE production will not occur if the glucose concentration in the substrate less than 7 g/L [16,17]. Other studies also reported that fermentation with limited presence of glucose resulting in the insufficient of final product of acids to achieve the desired amount of ABE [18-20]. Therefore, the objective of this study was to investigate the effect of glucose addition in ABE production via fermentation using sterilized POME sludge by *C. acetobutylicum* NCIMB 619.

Table 1. Characteristics of palm oil mill effluent (POME) [21]

| **Parameter** | **Average** | **Range** |
|---|---|---|
| pH | 4.2 | 3.4 - 5.2 |
| Biological oxygen demand (BOD) (g/L) | 25000 | 10250 - 43750 |
| Chemical oxygen demand (COD) (g/L) | 51000 | 15000 - 100000 |
| Total solid (g/L) | 40000 | 11500 - 79000 |
| Suspended solid (g/L) | 18000 | 5000 - 54000 |
| Volatile solid (g/L) | 34000 | 9000 - 72000 |
| Oil and grease (g/L) | 6000 | 130 - 18000 |
| Ammoniacal nitrogen (g/L) | 35 | 4 - 80 |
| Total nitrogen (g/L) | 750 | 180 - 1400 |

## Materials and Methods

### Organism, maintenance and inoculum preparation

*C. acetobutylicum* NCIMB 619 was obtained from NCIMB Ltd (Aberdeen, UK) and the laboratory stocks were routinely maintained as spore suspensions in sterile deoxygenated Reinforced Clostridial Medium (RCM) at 37 $^{o}$C. Raw POME obtained from Sime Darby's East Palm Oil Mill in Carey Island was centrifuged at 2000 rpm for 5 minutes to separate the supernatant and the sludge. Sterilization of the sludge was conducted using autoclave at 121 $^{o}$C for 15 minutes.

### Fermentation process and analysis

The fermentation process was carried out anaerobically in 250 mL conical flask at 37 $^{o}$C for 72 hours with working volume of 170 mL without agitation and no pH correction was made. Glucose concentration of 5 g/L (POME5),

10 g/L (POME10) and 15 g/L (POME15) were used with volume percentage of 3% (v/v) and 5% (v/v) for each concentration. The glucose was added into sterilized POME sludge and deoxygenated using purified nitrogen gas for 15 minutes to achieve the anaerobic condition. Samples for analysis of pH, cell concentration, reducing sugar and solvents production were taken at regular interval. The pH values were determined using pH meter, while cell concentration and reducing sugar in the samples were determined by volatile suspended solid (VSS) and Miller methods [22], respectively. The concentrations of acetone, butanol, ethanol and organic acids were measured by gas chromatography (Eppendorf, German) that is equipped with flame ionization detector (FID) with initial operating temperature of 40$^{o}$C for 8 minutes and then increased to 130 $^{o}$C at the rate of 4 $^{o}$C/minute for 2 minutes. The temperature of injector and detector was operated at 250 $^{o}$C with helium as the carrier gas.

**Liquid-liquid extraction**

Liquid-liquid extraction was conducted to recover ABE from the fermentation broth before the samples were injected into gas chromatography. Oleyl alcohol was used as solvent which has been reported as a potential separation solvent for ABE [23]. Oleyl alcohol was added into the sample in centrifuge tube at the ratio of 1:1 (oleyl alcohol-sample). The solution was then mixed using vortex mixer at 1600 rpm for 1 minute in order to increase the interaction between oleyl alcohol and the sample. To complete the phase separation, the solution was centrifuged at 2000 rpm for 5 minutes. Assuming the organic and aqueous phase were separated completely, all samples were diluted with 99.5% dichloromethane (DCM) at the ratio of 0.5:1 (DCM:sample). Samples from both phases were mixed by vortex mixer at 1600 rpm for 1 minute to ensure the interaction between samples and DCM occurred effectively. A complete mixing will produce two layers of liquid due to the different density. The bottom layer was taken and filtered using 0.2 µm nylon syringe filter before being transferred to sealed GC vial tubes for further analysis.

## Results and Discussion

**ABE production with the addition of 3% (v/v) glucose**

The summary of total ABE and organic acids production is presented in Table 2 and Figure 1 with ethanol as the major product. It also shows that the production of ABE increased as the glucose concentration increased where in the control batch, only 0.49 g/L ABE produced with a yield, $Y_{P/S}$ of 0.04 g ABE/g substrate and productivity of 0.007 g/L/h. POME15 produced the highest amount of ABE which is 3.44 g/L with the production of acetic acid and butyric acid of 123.9 g/L and 1.17 g/L, respectively. POME5 produced the lowest amount of ABE (2.84 g/L) and produced the highest amount of organic acids which is 165.7 g/L with 163.4 g/L of acetic acid and 0.34 g/L of butyric acid. All three medium produced a high concentration of acetic acid. ABE production was related to the activity of proteolysis enzyme that could affect the degradation of enzymes activity that involved in ABE fermentation [24]. The activity of proteolysis enzyme also might degrade the activity of tiolase enzyme that can change acetyl-CoA to acetoacetyl-CoA in the culture which is important in the production of acetone and butanol [25].

Table 2. Summary of ABE fermentation performance with the addition of 3% (v/v) glucose

| Parameter | Glucose Concentration | | |
|---|---|---|---|
| | 5 g/L | 10 g/L | 15 g/L |
| Initial pH | 4.26 | 4.27 | 4.30 |
| Max. cell concentration (g/L) | 63.5 | 59.0 | 58.0 |
| Total ABE (g/L) | 2.84 | 3.30 | 3.44 |
| A:B:E ratio | 0.2:0.6:9.2 | 0.3:0.7:9 | 0.3:0.9:8.8 |
| Total organic acids (g/L) | 165.7 | 106.0 | 125.1 |
| $Y_{P/S}$ (g ABE/g substrate) | 0.57 | 0.81 | 0.82 |
| $Y_{X/S}$ (g cell/g substrate) | 0.71 | 0.98 | 0.71 |
| Productivity (g/L/h) | 0.04 | 0.05 | 0.05 |

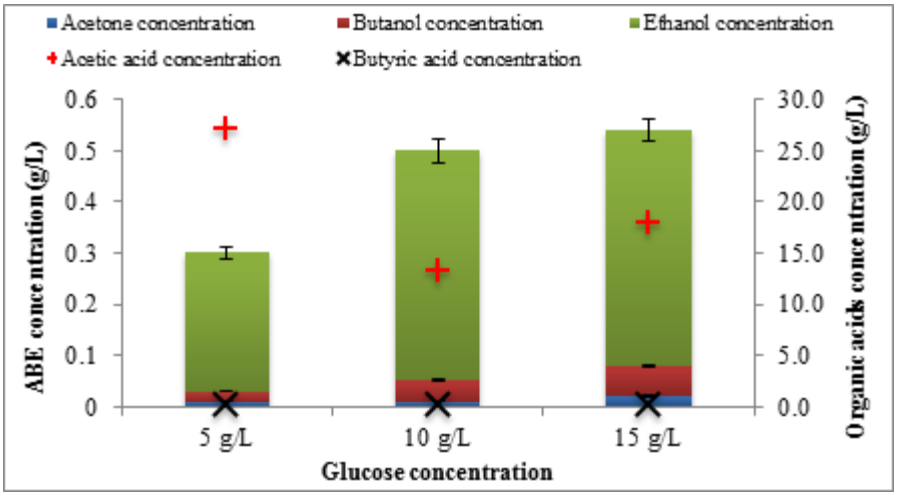



Figure 1. Maximum concentration of ABE and organic acids with the addition of 3% (v/v) glucose

**ABE production with the addition of 5% (v/v) glucose**

Total production of ABE and organic acids with the addition of 5% (v/v) glucose was summarized in Table 3 and Figure 2 with ethanol as the major product. For POME5 and POME10, the maximum ABE concentration of 0.50 g/L and 0.52 g/L, respectively was collected after 48 hours of fermentation while for POME10, maximum ABE concentration of 1.95 g/L was obtained after 72 hours of fermentation. POME5 produced 30.6% and 86.7% more acetone compared to POME15 and POME10.

Other than that, POME5 also produced 0.60 g/L butanol which is two folds higher compared to POME15 that only produced 0.26 g/L and 45.8% more butanol than that in POME10. At the same time, POME10 produced the highest concentration of ethanol which is 9.44 g/L while POME5 and POME15 produced 2.87 g/L and 1.88 g/L ethanol, respectively. Total ABE of 9.89 g/L produced in POME10 was the highest with total organic acids of 40.05 g/L. POME15 produced the lowest concentration of ABE (2.82 g/L) with organic acids concentration of 6.83 g/L.

Table 3. Summary of ABE fermentation performance with the addition of 5% (v/v) glucose

| **Parameter** | **Glucose Concentration** | | |
|---|---|---|---|
| | **5 g/L** | **10 g/L** | **15 g/L** |
| Initial pH | 4.30 | 4.48 | 4.31 |
| Max. cell concentration (g/L) | 63.5 | 59.0 | 62.3 |
| Total ABE (g/L) | 4.45 | 9.89 | 2.82 |
| A:B:E ratio | 2.2:1.3:6.5 | 0.13:0.33:9.5 | 2.4:0.9:6.7 |
| Total organic acids (g/L) | 0.14 | 40.05 | 6.83 |
| $Y_{P/S}$ (g ABE/g substrate) | 0.62 | 1.36 | 0.28 |
| $Y_{X/S}$ (g cell/g substrate) | 0.84 | 0.76 | 1.63 |
| Productivity (g/L/h) | 0.06 | 0.14 | 0.04 |

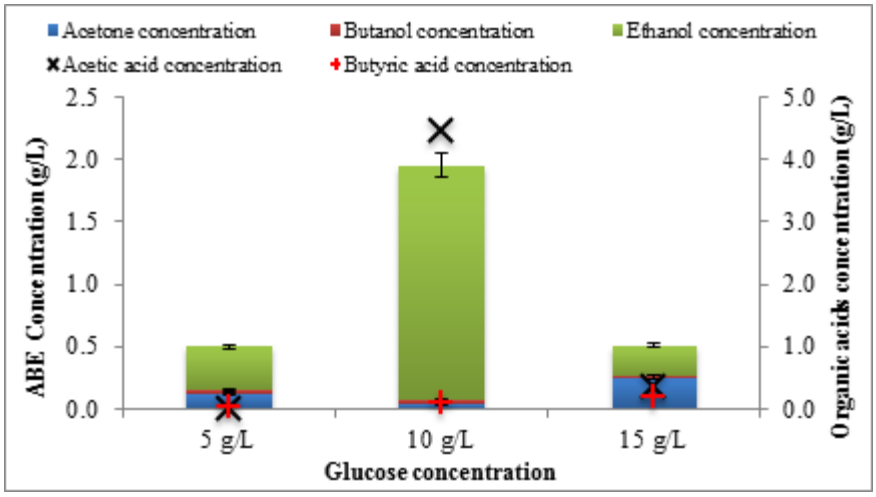



Figure 2. Maximum concentration of ABE and organic acids with the addition of 5% (v/v) glucose

**Comparison of ABE fermentation performance with the addition of 3% (v/v) and 5% (v/v) glucose**

Based on Figure 3, it was found that with the addition of 3% (v/v) glucose, enhanced the ABE production where in control batch, only 0.49 g/L ABE was produced with yield, $Y_{P/S}$ of 0.04 g ABE/g substrate and productivity of 0.007 g/L/h (Data was not shown). POME5 produced 2.84 g/L ABE with yield, $Y_{P/S}$ of 0.57 g ABE/g substrate. POME10 and POME15 produced 3.30 g/L ABE with yield, $Y_{P/S}$ of 0.81 g ABE/g substrate and 3.44 g/L ABE with yield, $Y_{P/S}$ of 0.82 g ABE/g substrate, respectively.

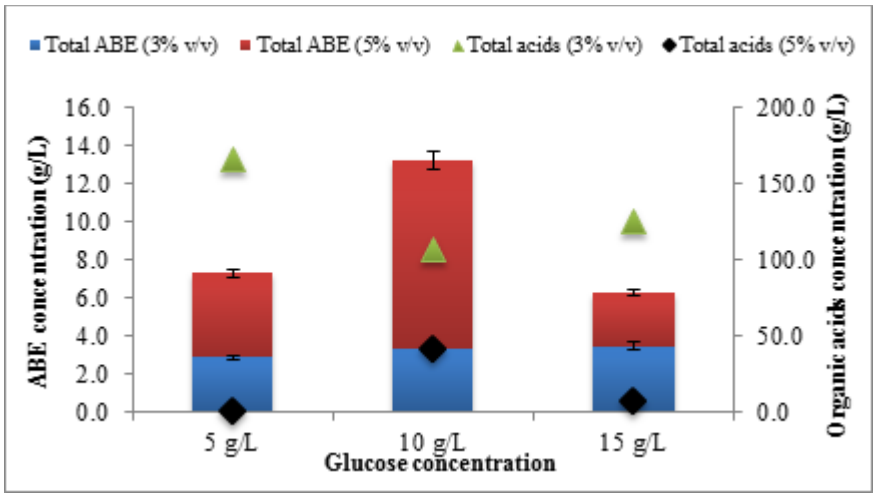



Figure 3. Comparison of ABE performances with the addition of glucose

However, ABE production was decreased at 15 g/L glucose with the addition of 5% (v/v) where high level of sugar in the medium was found to inhibit the production of ABE [26]. ABE fermentation using a high carbon source concentration may be controlled by the mass transfer rate, where high concentration carbon source could increase the viscosity of the culture and reduced the rate of mass transfer altogether [27].

Other than that, POME10 produced the highest ABE concentration which is 9.89 g/L with yield, $Y_{P/S}$ of 1.36 g ABE/g substrate while POME5 and POME15 produced 4.45 g/L and 2.82 g/L ABE, respectively where POME15 produced the lowest yield, $Y_{P/S}$ of 0.28 g ABE/g substrate. It was also found that the addition of 3% (v/v) glucose produced the highest amount of organic acids that might be due to the acid crash that occurred when the un-dissociated acids in the culture was more than 57-60 mmol/L [28]. Furthermore, the results obtained from this study are comparable to previous reports as shown in Table 4.

Table 4. Comparison of ABE fermentation performances

| **Species** | **Substrate** | **Glucose Content (g/L)** | **ABE Concentration (g/L)** | **Yield, $Y_{P/S}$ (g ABE/g substrate)** | **Productivity (g/L/h)** | **Reference** |
|---|---|---|---|---|---|---|
| *C. acetobutylicum* NCIMB 619 | Raw POME | 3.40 | 2.05 | 0.90 | 0.04 | [15] |
| *C. beijerinckii* BA101 | Treated corn fiber | 23.60 | 9.30 | nd. | nd. | [29] |
| *C. acetobutylicum* ATCC 824 | Spoilage date palm | 36.20 | 10.42 | nd. | 0.14 | [30] |
| *C. beijerinckii* ATCC 55025 | Wheat bran | 21.30 | 11.80 | 0.32 | 0.16 | [31] |
| *C. acetobutylicum* NCIMB 619 | Sterilized POME | 15.82 | 9.89 | 1.36 | 0.14 | This study |

*nd. – not determine

## Conclusion

The addition of glucose in sterilized POME media was found to increase the ABE production. Based on the results of this study, the production of ABE and organic acids is higher as the glucose concentration increasing using 3% (v/v). However, for the glucose addition of 5% (v/v), the high level of sugar present in the culture was found to inhibit the ABE production. Glucose concentration of 10 g/L produced the highest concentration of ABE (9.89 g/L) with product yield, $Y_{P/S}$ of 1.36 g ABE/g substrate while glucose concentration of 15 g/L produced the lowest concentration of ABE and product yield, $Y_{P/S}$ with 2.82 g/L and 0.28 g ABE/g substrate, respectively.

## Acknowledgment

The authors wish to thank Yayasan Sime Darby for funding the research through a grant number PKT6/2012.

## References

1. Jones, D. T. and Woods, D. R. (1986). Acetone-butanol fermentation revisited. *Microbiology and Molecular Biology Reviews*, 50 (4): 484 – 524.
2. Wyman, C. E. (2007). What is (and is not) vital to advancing cellulosic ethanol. *Trends Biotechnology*, 25: 153 – 157.
3. Lynd, L. R., Laser, M. S., Bransby, D., Dale, B. E., Davison, B. and Hamilton, R. (2008). How biotech can transform biofuels. *Nature Biotechnology*, 26: 169 – 172.
4. Rajeev, K. S., Lalitha, D. G., Kuniparambil, R., Deepthy, A. and Ashok, P. (2011). Butanol fuel from biomass: revisiting ABE fermentation. Biofuels: Alternative feedstocks and conversion processes: pp. 571 – 586.
5. Ugoji, E. (1997). Anaerobic digestion of palm oil mill effluent and its utilization as fertilizer for environmental protection. *Renewable Energy*, 10: 291 – 294.
6. Somrutai, W., Takagi, M. and Yoshida, T. (1996). Acetone-butanol fermentation by *Clostridium aurantibutyricum* ATCC 17777 from a model medium for palm oil mill effluent. *Journal of Fermentation and Bioengineering*, 81: 543 – 547.

7. Kalil, M. S., Pang, W. K., Wan Yusoff, W. M., Sadazo, Y. and Abdul Rahman, R. (2003). Direct fermentation of palm oil mill effluent to acetone-butanol-ethanol by solvent producing Clostridia. *Pakistan Journal of Biological Sciences*, 6: 1273 – 1275.
8. Parveen, F. R., Rajeev, P. S., Hakimi Ibrahim, M. and Esa, N. (2010). Review of current palm oil mill effluent (POME) treatment methods: Vermicomposting as a sustainable practice. *World Applied Sciences Journal*, 10 (10): 1190 – 1201.
9. Ma, A. N. (1999). Treatment of palm oil mill effluent. In. Oil palm and the environment: A Malaysian perspective. Kuala Lumpur: Malaysia Oil Palm Grower's Council: 113 – 126.
10. Ahmad, A. L., Ismail, S. and Bhatia, S. (2003). Water recycling from palm oil mill effluent (POME) using membrane technology. *Desalination*, 157: 87 – 95.
11. Sethupathi, S. (2004). Removal of residues oil from palm oil mill effluent (POME) using chitosan, Thesis Universiti Sains Malaysia.
12. Azima, S. J., Mohd Sobri, T., Jamaliah, M. J. and Abd Amir, H. K. (2014). The potential of supernatant and sludge of POME in ABE fermentation by *Clostridium acetobutylicum*. *Australian Journal of Basic and Applied Sciences* 8(19): 44 – 46.
13. Japar, A.S., Takriff, M. S., Jahim, J. M. and Kadhum, A. A. H. (2013). Acetone-butanol-ethanol fermentation from palm oil mill effluent using *Clostridium acetobutylicum*. *Developments in Sustainable Chemical and Bioprocess*. New York: Springer Science & Business Media: pp. 35 – 41.
14. Yusof, S. J. H. M. (2010). Fermentasi aseton-butanol-etanol (ABE) dan perolehan ABE daripada kaldu fermentasi. Thesis Master. Universiti Kebangsaan Malaysia.
15. Masngut, N. (2007). Aplikasi reaktor aliran berayun bagi penghasilan aseton-butanol-etanol oleh *Clostridium acetobutylicum* NCIMB 13357. Thesis Master. Universiti Kebangsaan Malaysia.
16. Long, S., Jones, D. T. and Woods, D. R. (1984). The relationship between sporulation and solvent production in *Clostridium acetobutylicum* P262. *Biotechnology Letters*, 6: 529 – 534.
17. Monot, F., Engasser, J. M. and Petitdemange, H. (1983). Regulation of acetone butanol production in batch and continuous cultures of *Clostridium acetobutylicum*. *Biotechnology Symposium*, 13: 207 – 216.
18. Bahl, H., Andersch, W., Braun, K. and Gottschalk, G. (1982). Effect of pH and butyrate concentration on the production of acetone and butanol by *Clostridium acetobutylicum* grown in continuous culture. *European Journal of Applied Microbiology and Biotechnology*, 14: 17 – 20.
19. Haggstrom, L. and Enfors, S. O. (1982). Continuous production of butanol with immobilized cells of *Clostridium acetobutylicum*. *Applied Biochemistry and Biotechnology*, 7: 35 – 37.
20. Rogers, P. (1984). Genetics and biochemistry of Clostridium relevant to development of fermentation processes. *Applied Microbiology*, 31: 1 – 60.
21. Malaysian Palm Oil Board, MPOB. (2012). Oil palm and the environment. www.mpob.com.my/en/palm-info/environment/520-achievements [20 Mac 2013].
22. Miller, G. L. (1959). Use of dinitrosalicylic acid reagent for determination of reducing sugar. *Analytical Chemistry* 31: 426 – 429.
23. Boudreau, T. M. and Gordon, A. H. (2006). Improved ethanol-water separation using fatty acids. *Process Biochemistry*, 41: 980 – 983.
24. Yaacob, N. S. (2003). Performance of solvent (acetone-butanol-ethanol) fermentation by *Clostridium saccharobutylicum* strain P262 and NCIMB 8052 using free and immobilized cells system. Thesis Master. Universiti Putra Malaysia.
25. Lee, S. Y., Park, J. H., Jang, S. H., Nielsen, L. K., Kim, J. and Jung, K. S. (2008). Fermentative butanol production by clostridia. *Biotechnology and Bioengineering*, 101 (2): 209 – 228.
26. Qureshi, N., Cotta, M. A. and Saha, B. C. (2013). Bioconversion of barley straw and corn stover to butanol (a biofuel) in integrated fermentation and simultaneous product recovery bioreactors. *Food and Bioproducts Processing*, 92(3): 298 – 308.
27. Madihah, M. S., Sahaid, K. M., Suraini, A. A. and Karim, M. I. A. (2001). Direct fermentation of gelatinized sago starch to acetone-butanol-ethanol by *Clostridium acetobutylicum. World Journal of Microbiology & Biotechnology*, 17: 567 – 576.
28. Gao, K and Rehmann, L. (2014). ABE fermentation from enzymatic hydrolysate of NAOH-pretreated corncobs. *Biomass and Bioenergy*, 66: 110 – 115.

29. Qureshi, N., Saha, B. C., Hector, R. E. and Cotta, M. A. (2008). Removal of fermentation inhibitors from alkaline peroxide pretreated and enzymatically hydrolyzed wheat straw: Production of butanol from hydrolysate using *Clostridium beijerinckii* in batch reactors. *Biomass and Bioenergy,* 32: 1353 –1358.
30. Abd-Alla, M. H and El-Enany, A. E. (2012). Production of acetone-butanol-ethanol from spoilage date palm (*Phoenix dactylifera* L.) fruits by mixed culture of *Clostridium acetobutylicum* and *Bacillus subtilis. Biomass and Bioenergy,* 42: 172 – 178.
31. Liu, Z., Ying, Y., Li., F., Ma, C. and Xu, P. (2010). Butanol production by *Clostridium beijerinckii* ATCC 55025 from wheat bran. *Journal of Industrial Microbiology & Biotechnology*, 37 (5): 495 – 501.

*Malaysian Journal of Analytical Sciences, Vol 21 No 1 (2017): 221 - 230*
*DOI: http://dx.doi.org/10.17576/mjas-2017-2101-26*

MALAYSIAN JOURNAL OF ANALYTICAL SCIENCES
*Published by The Malaysian Analytical Sciences Society*
ISSN 1394 - 2506

# POLYETHERSULFONE/PLURONIC F127 BLENDED NANOFILTRATION MEMBRANES FOR XYLITOL PURIFICATION

## (Membran Penurasan-Nano Campuran Polietersulfon/Pluronik F127 untuk Penulinan Xilitol)

Khalefa A. Faneer[1,2], Rosiah Rohani[1]*, Abdul Wahab Mohammad[1]

[1]*Department of Chemical and Process Engineering, Faculty of Engineering and Built Environment, Universiti Kebangsaan Malaysia, 43600 UKM Bangi, Selangor, Malaysia*
[2]*Department of Environment Engineering, High Institute for Comprehensive Professions, Bent Baya, Wadi Al-Ajal, Libya.*

**Corresponding author: rosiah@ukm.edu.my*

Received: 21 October 2015; Accepted: 14 June 2016

**Abstract**

Obtaining high purity of xylitol is a stone corner in medicine industries. Many conventional techniques (crystallization and adsorption) were used for xylitol purification from fermentation media. Recently, membrane technology received a great attention due to its high performance in xylitol purification. Among renowned copolymers used for polymer blending to produce membranes, pluronic is receiving much attention due to its strong hydrophilic characteristic and could work as pore former and surface modifier. Polyethersulfone (PES) polymer has been reportedly used for polymer blending as it possesses mechanical and chemical stabilities. Therefore, this work demonstrates the preparation of nanofiltration (NF) membrane using: (1) PES and (2) PES blended with 1.71% and 5% of Pluronic (F127), via phase inversion method. All fabricated membranes were subjected to investigations such as contact angle for hydrophilicity and water and solution flux for membrane performance. The findings showed increasing in water flux from 24.6 L/m$^2$.h to 70.2 L/m$^2$.h as 5% of Pluronic added. Further, the hydrophilicity improved from 80.1 ± 1.93$^o$ to 72 ±0.3$^o$ and 67.6 ± 0.72$^o$ when 1.71 and 5% of Pluronic F127 added respectively. Therefore, the addition of Pluronic f127 has a great impact on PES membrane for xylitol permeation.

**Keywords**: polyethersulfone, pluronic F127, xylitol, NF membrane, purification

**Abstrak**

Memperoleh ketulenan yang tinggi bagi xilitol merupakan salah satu batu loncatan di dalam industri perubatan. Terdapat banyak teknik konvensional (penghabluran dan penjerapan) yang telah digunakan untuk penulenan xilitol daripada media penapaian. Baru-baru ini, teknologi membran banyak menarik perhatian dengan prestasinya yang bagus dalam penulenan xilitol. Antara kopolimer yang sering digunakan untuk campuran polimer dalam penghasilan membran adalah pluronik yang telah menerima perhatian kerana sifat hidrofiliknya dan boleh membantu dalam pembentukan liang serta pengubahsuai permukaan membran. Polimer polietersulfon (PES) telah dilaporkan digunakan untuk polimer campuran kerana ia mempunyai kestabilan mekanikal dan kimia. Oleh itu, kerja ini menunjukkan penyediaan membran penurasan-nano (NF) menggunakan: (1) PES dan (2) PES dicampur dengan 1.71% dan 5% Pluronik (f127), melalui kaedah fasa songsangan. Kesemua membran yang dihasilkan dicirikan menggunakan sudut sentuhan untuk sifat hidrofilik dan fluks air serta larutan bagi prestasi membran. Hasil kajian menunjukkan peningkatan dalam fluks air daripada 24.6 L/m$^2$.h kepada 70.2 L/m$^2$.h apabila 5% Pluronik F127 ditambah. Selanjutnya, sifat hidrofilik membran bertambah baik iaitu daripada 80.1 ± 1.93$^o$ kepada 72 ± 0.3$^o$ dan 67.6 ± 0.72$^o$ apabila 1.71 dan 5% Pluronik F127 ditambah. Didapati penambahan Pluronik F127 memberi kesan yang besar ke atas membran PES untuk penyerapan xilitol.

**Kata kunci:** polietersulfon, pluronik F127, xylitol, membran NF, penulenan

## Introduction

Xylitol is classified as a non-cariogenic, beside as a sweetener, it becomes valuable for those who suffer caries and diabetic [1]. This non-cariogenic property makes xylitol an important product in cosmetic, pharmaceutical and food industries [2]. The upstream processing of xylitol production can be achieved by chemical and biotechnological methods [3, 4], while the downstream xylitol purification can be accomplished by crystallization, adsorption and membrane technology [2, 5]. Nanofiltration (NF) membrane has been targeted to be used by many researchers due to its molecular weight cut-off (MWCO) ranges from 200 – 2000 g/mol [6] that will be suitable to purify xylitol (152.15 g/mol) [1, 5]. To fabricate this NF membrane, polyethersulfone (PES) was reportedly used due to its advantages such as easy to synthesize, high chemical resistance and vast pH tolerance [7, 8]. Further, PES arise an outstanding oxidative stability [9]. However, the most imperfection of using PES is the lack of hydrophilicity of this polymer, which could leads to fast membrane fouling [10]. This drawback can be minimized by blending hydrophilic copolymer to PES membrane matrix such as polyvinyl pyrrolidone (PVP), polyethylene glycol (PEG) and Pluronic. Among these copolymers, Pluronic F127 was considered as a good pore forming agent and surface modifier because of its chemical stability [11, 12].

In recent years, poly (propylene oxide) (PPO) Pluronic triblock copolymers of poly (ethylene oxide) and (PEO) have worked as dual functions as pore former and surface modifier in membrane fabrication [13]. The Pluronic additive (PEO–PPO–PEO) segregated during phase inversion process to the polymer/water interface because of the low interfacial energy between the water and hydrophilic segment, as the water-insoluble, hydrophobic segment of the copolymer promptly anchored in the polymer matrix. [14]. The possible reason is that Pluronic f127 is perfect surfactant, as the surface chemistry of Pluronic F127/PES blend membrane might be reconstructed to reduce the interfacial free energy [15]. PEO chain introduced to the membrane matrix as hydrophilic part where works as adsorption resistant (antifouling) of the molecules as well as hydrophilicity enhancer. i.e. surface modifier. Meanwhile PPO segments represented the hydrophobic units of Pluronic copolymers and distributed closer to the centre of membrane pores [10, 16, 17]. Overall, there are two main processes (presented in Figure 1) lead to formation of PES/ Pluronic F127 via: (1) Aggregation of hydrophilic units which were responsible of surface modifier, and (2) Micellization of hydrophobic units that form the membrane pores.

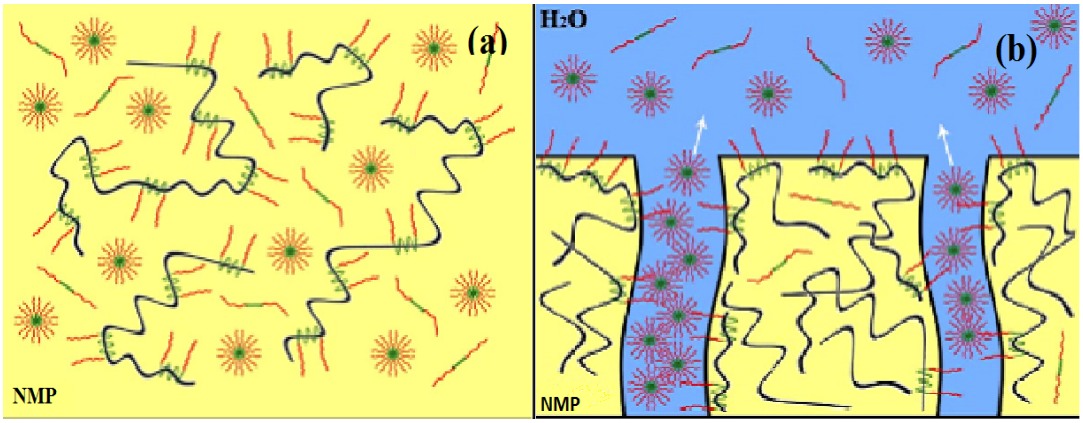



Figure1. Dual function of Pluronic F127 in the membrane formation process via: (a) blending of polymer with Pluronic F127 in a homogeneous dope solution, (b) immersing the membrane in a water bath to form the surface structure and pores in membrane [16].

In most NF membranes synthesis reported, the fabrication via phase inversion process was repeatedly found in the literature due to its simplicity for certain input parameters e.g. using water as the non-solvent [7, 18]. The incorporation of pluronic at a specific ratio to the main polymer was reported [10, 11, 15] where the main polymer became the backbone of the membrane structure and pluronic acted as the co-polymer. It was also reported on the addition of different additives composition depending on their screening work or optimization conducted, e.g.

Zhang et al. [15] used 20 to 100% of pluronic, the 20% was the best composition for dyes rejection. Chao et al. [13] studied the effect of 1 to 9% of pluronic on membrane morphology and found that the water flux increased as well as pores and porosity. Ng et al. [19] found that 1.71 % of polyvinyl alcohol (PVA) is a significant composition to achieve high salt rejection, while Loh et al. [14] investigated systematically the effect of adding 5, 10 and 15% of pluronic on pore forming of PES membrane and it was found that the best composition is at 10% as it achieved the highest pure water flux. On the other side, different composition of additives added to the solution could give a significant impact on the mechanical properties of the synthesized membrane as reported by Ng et al. [19]. Based on the studies, two different composition of Pluronic F127 at 1.71 and 5% are considered for the fabrication of the membrane using PES and the flux/ rejection of xylitol separation difference is measure.

Thus the aim of this study was to fabricate NF membranes from pure PES and PES blended with Pluronic F127 in 1.71 and 5 % as reported in [14, 19] via phase inversion method. Next these membranes were characterized to investigate the pure water flux (PWF), contact angle, separation performance of xylitol mixture solution and the rejection test of xylitol mixture solution.

## Materials and Methods

### Materials

Polyethersulfone (PES) granule, (Good fellow) as the membrane main polymer. Pluronic F127 (Nanoamor) has been used as the copolymer. N-methyl-2-pyrrolidone (NMP) with analytical purity 99.7% (Fluka, Germany) was used as solvent and distilled water was used as non-solvent. Xylitol, xylose and arabinose powder of 99% (Acros Organic) were used as received.

### Membrane preparation

The three NF membranes were fabricated via phase inversion under different preparation parameters as tabulated in Table 1. Initially, PES granules were dried at 60 °C for 72 hours to remove moisture. Each doped solution was stirred for 4 hours to make a homogenous solution. Next, to avoid pinholes and highlights on the membranes, the homogeneous solution was left for 24 hours to release air bubble. Then, the casting machine Elcometer 4340 Automatic Film Applicator with the speed at 76 mm/s was used to cast the membranes. A suitable amount of suspension was poured on a glass sheet and cast by casting knife set at 200 µm at room temperature. Finally, the fabricated membranes were left for 30 s for evaporation before submerged in deionized water for 2 hours for solvent exchange purposes. The synthesized membranes were stored in distilled water at ambient temperature prior to use.

Table 1. Polymer doped solution composition and parameters

| PES (wt. %) | Pluronic f127 (wt. %) | NMP (wt. %) | Temperature ($^{o}$C) | Stirring speed (rpm) |
|---|---|---|---|---|
| 18 | - | 82 | 60 | 450 |
| 18 | 1.71 | 82 | 60 | 450 |
| 18 | 5 | 82 | 60 | 450 |

### Membrane characterization: Contact angle

The contact angle was used to find out the changes in the hydrophilicity to figure out the hydrophilicity of PES and PES/Pluronic F127 membranes. All membranes were dried at room temperature for 48 hours followed by measuring the contact angle using the contact angle goniometer (Rame-Hart model 200) equipped with DROPimage Software with an accuracy of 60.10 °. The conditions used to measure the contact angle were under deionized water and air at (25 – 28 °C).

**Pure water flux (PWF)**

Dead-end permeation cell (Sterlitech HP4750, Sterlitech Corporation, USA) was used to evaluate the pure water flux (PWF) of the membranes. The schematic diagram of the dead-end cell is illustrated in Figure 2. The filtration was performed at three different pressures (4, 6 and 8 bar). The PWF was calculated using equation (1):

$$J = \frac{\mathrm{V}}{\mathrm{A}*\mathrm{t}} \quad (1)$$

As J is PWF (L/m$^2$.h), A is the effective membrane area (14.6 cm$^2$), V is the permeate volume (L) and t is sampling time (h). To minimize experimental errors, 3 to 5 samples were collected and then the average value of Flux was reported.

**Permeate flux performance**

The permeate flux performance was conducted using the dead-end cell (Figure 2) at 4 bar with using xylitol mixture solution (xylitol, xylose, and arabinose) and calculated using equation (1). The concentrations of the components in the xylitol mixture are tabulated in Table 2 and the composition is based on the real xylitol fermentation broth as reported by [2].

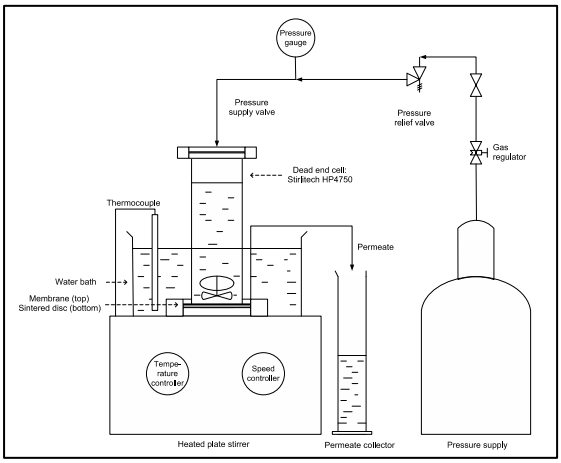



Figure 2. Schematic diagram of the dead end permeation cell [20]

Table 2. Xylitol mixture compositions

| Component | Concentration (g/L) |
|---|---|
| xylitol | 2 |
| xylose | 0.15 |
| arabinose | 0.3 |

**Rejection test**

The xylitol mixed solution rejection was evaluated on the batch type filtration by using dead-end cell. 300 ml of xylitol mixed solution was poured into this cell. The test was conducted at 4 bars. Equation (2) was used to calculate rejection:

$$\mathrm{R}\ \% = (1 - \frac{Cp}{\mathrm{Cf}})*100 \quad (2)$$

where R is the rejection, $C_p$ is the permeate concentration and $C_f$ is the feed concentration.

The standard calibration curve was plotted to calculate $C_p$. High performance liquid chromatography (HPLC) (Ultimate 3000, Thermo scientific, USA) coupled with refractive index detector (RID) was used to obtain the solute concentrations under these conditions: Column type: RPM (Rezex, dimension: 300 x 7.8 mm, USA), mobile phase: DI water, detector: Refractive Index (RI) (Refractomax 520, ERC, USA), flow rate: 0.6 min/ml and Temperature: 60 $^oC$.

## Results and Discussion

### Membrane characterization: contact angle

As clearly seen in Table 3, the pure PES membrane has the highest contact angle at 80.1 ± 1.93$^o$. However, when Pluronic F127 at 1.71% and 5% were incorporated with the PES membrane, the contact angle has dropped to 72 ±0.3$^o$ and 67.6 ± 0.72$^o$, respectively. These results indicated that there was an essential surface modification happened at the membrane upon the copolymer incorporation [16, 21]. Lower contact angle represented higher hydrophilicity. Vatanpour et al. [22] explained that when hydrophilic additives were added to the main polymer during the phase inversion process, the hydrophilic additives migrates spontaneously to the membrane/water interface in order to minimize the interface energy and thus resulted in lower contact angle value.

Table 3. Contact angle of all membranes measured at 25 $^oC$

| Membrane Type | Contact Angle ($^o$) |
|---|---|
| PES | 80.1 ± 1.93 |
| PES/Pluronic 1.71% | 72 ± 0.3 |
| PES/Pluronic 5% | 67.6 ± 0.72 |

It is also possible that the porous structure on the outer membrane surface is the reason in the contact angle variation, not only influenced by polymer/copolymer interaction during the synthesis [11]. It is believed that by enhancing hydrophilicity of the membrane will result in a better membrane resistance to fouling [23]. Fouling can be occurred due to solution molecules adhesion during the filtration process, which can be considered as a major drawback in membrane application.

### Pure water flux

All pure and Pluronic incorporated PES membranes were initially wetted and further subjected to compaction at 12 bars for 30 min until the PWF have achieved steady state. The PWF of pure and blended PES membranes have varied greatly with the addition of different compositions of the copolymer (Pluronic f127). As shown in Figure 3, the water flux of PES membrane was 24.6 L/m$^2$.h at 4 bars, while for PES/Pluronic F127 at 1.71 and 5% membranes increased to 63.8 and 70.2 L/m$^2$.h respectively. This variation might happens due to the change in the hydrophilicity [10] (as discussed in previous section). Vatsha et al. [21] reported that when additive of PVP at 2–10% was added to neat PES membrane, the water flux increased with regards to the improvement in the membrane hydrophilicity, as well as the enlargement of membrane pores after additive addition.

### Permeate flux

The permeate flux was carried out at 4 bars with the volume capacity of 300 mL of xylitol mixture solution to evaluate the flux rate profile for PES membranes incorporated with F127 at 1.71 and 5% in comparison to the pure PES membrane. The concentration of the simulated xylitol mixed solution used in this study exactly followed the work reported by Mussatto [2], which have used real fermentation broth solution to purify xylitol from sugarcane bagasse. Figure 4 showed the improvement of membrane separation after adding 1.71% and 5% of pluronic F127. The permeate flux of xylitol mixture was about 27 L/m$^2$.h for pure PES membrane while PES/Pluronic F127 of 1.71 and 5% membranes could achieved 2-3 times higher fluxes, around 50 and 82 L/m$^2$.h respectively. Zhao et al. [16] reported that the increase of permeate flux of PES/pluronic membrane compared with pure PES membrane was

considerably acceptable due to the adjustment/enlargement of PES/Pluronic membrane pore size comparing to PES membrane. These results is also comparable to the work by Susanto et al. [11].

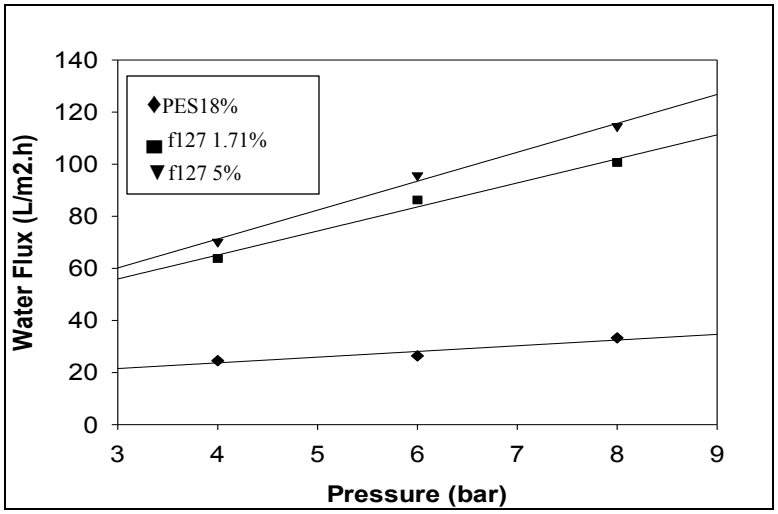



Figure 3. The pure water flux of neat PES and PES/Pluronic F127 (1.71% and 5%) at Temperature: 25 $^{o}$C

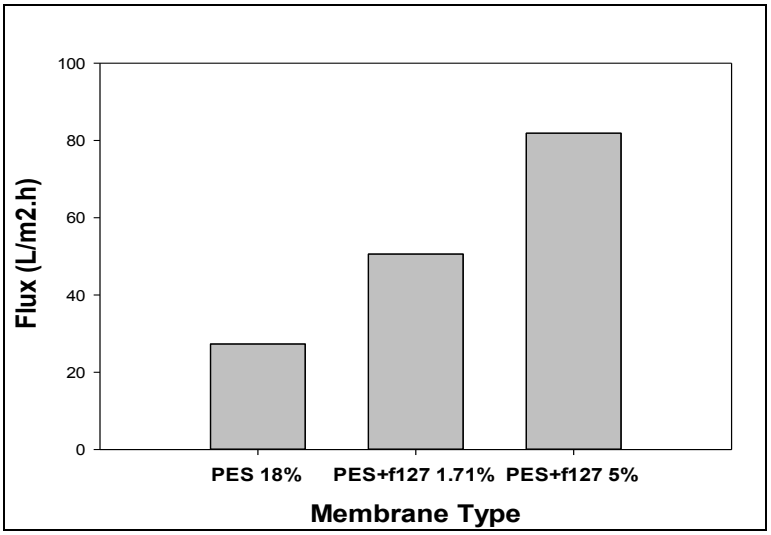



Figure 4. The separation performance of PES and PES/Pluronic membranes. (Stirring speed: 450 rpm, Temperature: 25 °C, Pressure: 4 bar).

However, PES/Pluronic membrane at 5% showed higher normalized fluxes with time compared to pure PES and PES/Pluronic 1.71% membranes as shown in Figure 5. The flux dropped dramatically at the initial run due to the adsorption and/or deposition of xylitol solution droplets on the membrane surface especially in the first few minutes of operation by the permeate flow. Subsequently, PES/Pluronic 1.71% membrane achieved slightly higher than neat PES membrane. The permeate fluxes have enhanced because of Pluronic presence, the higher the pluronic composition, the better flux observed for the synthesized membrane. It can be obviously seen that fouling has occurred in PES membrane even at the starting time due to the membrane property, which is less hydrophilic (80 °)

than the PES/pluronic membrane. This result is agreed by Zhao et al. [16] where PES controlled membrane had a remarkably lower flux recovery ratio (FRR) comparing to PES/Pluronic F127 and the FRR value indicates that the higher FRR value for the membrane, the better antifouling and hydrophilicity properties its possess. The xylitol normalized flux was increased in PES/pluronic membranes due to the function of pluronic as pore forming agent. The flux declined over the filtration time is possibly because of the deposition of sugar molecules on the membrane surface to create concentration polarization/ fouling.

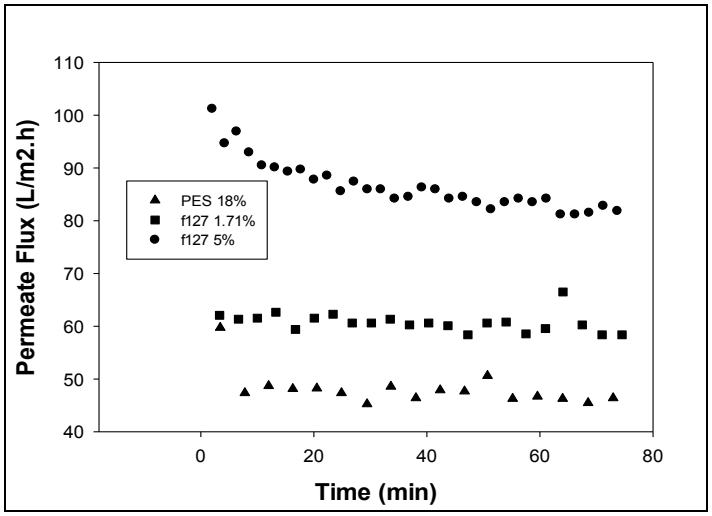



Figure 5. The normalized flux vs time of PES and PES/Pluronic membranes. (Stirring speed: 450 rpm, Temperature: 25 $^{o}$C)

From the analytical side, addition of pluronic to the dope solution during the synthesis process may have affected on the membrane structure, the hydrophilicity of PES was enhanced; this is because of pluronic hydrophilic character [11]. Thus, the fouling phenomenon was mitigated due to the improvement of hydrophilicity. Zhang et al. [15] observed that when pluronic was added to PES membrane, the hydrophilicity improved positively from 68.4° ± 3° to 43.3° ± 2° as pluronic composition increased from 20 to 100% (polymer weight ratios of $W_{f127}$ /$W_{PES}$ are varying in casting solutions ).

**Rejection test**

The rejection test was performed to study the capability of PES and PES/Pluronic F127 membranes at 1.71 and 5% to purify xylitol. It was performed under constant pressure at 4 bars by using xylitol mixture solution. Basically, the calibration curve for three components (xylitol, xylose, and arabinose) was plotted and presented in Figure 6. The calibration curve is required to calculate the permeate concentration, where the equations on the Figure 6 were used for that purposes. Based on the permeate concentration calculated, equation (2) was used to compute the rejection for single PES membrane and for the 1.71 and 5% PES/ Pluronic F127 membranes. $R^2$ value (linearity) was super high (≥ 0.96) for all plots. This indicates the reliability of the calibration curves to be used to measure the xylitol rejection later.

Table 4 illustrated the rejection results of PES and PES membranes incorporated with 1.71 and 5% pluronic. It is clearly marked that PES/Pluronic 5% membrane had the highest rejection 88.1% compared to 1.71% PES/ pluronic F127 membrane at 80.6% and the pure PES membrane rejection was 87.9%. Chao et al. [13] reported that the effects of pluronic composition (1,3,5,7 and 9%) on the PES membrane has increased the BSA rejection from about 70% to around 80% (about 10% difference), and doubled the water flux from 210 to 380 L/$m^2$.h, respectively. Their results are highly corresponded with these findings when 1.71 and 5% of pluronic F127 were added to PES membrane. Similar results were also reported by Susanto et al. [11] upon conducting the comparison study among

PVP, PEG and pluronic with PES. They found that the rejection has declined from 87% (PES membrane) to 72% (PES/ pluronic 10% membrane). This shows that with addition of small amount of pluronic F127 to PES membrane, the xylitol rejection rate slightly decreased compared with PES membrane. Whereas, when pluronic composition increases, the rejection slightly increases and relatively better than single PES membrane. It is suggested that PPO units effectively work as pore forming agent due to its hydrophobic character. Moreover, the micellization process is responsible in forming the membrane pores and thus the pore diameter of PES/ Pluronic F127 membrane enlarges. The proposed mechanism is that, during the solvent exchange process, the micelles of Pluronic F127 trap in the skin layer. The interaction between PES and Pluronic F127 micelles lose the skin layer of the shaped membranes. Upon extraction of the hydrophilic Pluronic F127 micelles from the membranes via non-solvent during phase inversion, the regions left in the membranes control the pore size of it. Therefore, the pore radius of the skin layer is strongly affected by the size of Pluronic f127 micelles, which establishes an indirect judgment for pore structure changes, as observed in this work. In addition to that, Kochkodan et al. [24] found that the significant pore enlargement in the membrane surface leads to an increase in the water flux and loss in rejection of bovine serum albumin (BSA).

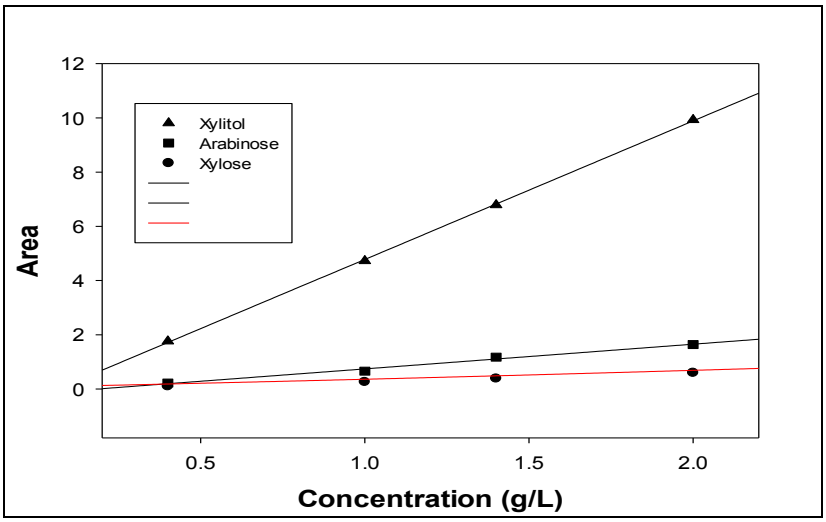



Figure 6. The calibration curve of xylitol, xylose, and arabinose

Table 4. The xylitol, arabinose and xylose rejection of all membranes (T : 25 $^{o}$C, Stirring speed : 450 rpm, P: 4 bar)

| Membrane Type | Xylitol Rejection | Arabinose Rejection | Xylose Rejection |
|---|---|---|---|
| PES | 87.9 | 82.7 | 74.7 |
| PES/Pluronic 5% | 88.1 | 82.3 | 76 |
| PES/Pluronic 1.71% | 80.6 | 76.3 | 66.7 |

## Conclusion

The hydrophilic copolymer of Pluronic F127 at two different compositions was successfully incorporated to PES membrane as pore forming agent and surface modifier. This PES blended with Pluronic F127 membranes at 1.71 and 5% were compared with pure PES membrane. All membranes were fabricated via phase inversion method to purify the desirable xylitol from simulated biomass fermentation broth. The PWF and permeate flux increased to 2-3 times in presence of Pluronic F127 due to the enlargement of pore diameters and modification of the membrane

surface by pluronic presence. Whereas, the rejection slightly decreased at the lower amount of pluronic (1.71%) used which due to PPO role of forming the membrane pores. Characterization for the contact angle of the membranes found that the hydrophilicity improved because of the presence of hydrophilic PEO unite properties in pluronic F127. Both hydrophilic PEO segments and hydrophobic PPO units respectively work as surface modifier and pore former in pluronic.

**Acknowledgement**

The authors gratefully acknowledge the LRGS Project Future Biorefineries (LRGS/2013/UKM_UKM/PT/03) and Fundamental Research Grant Scheme (FRGS/2/2013/TK05/UKM/02/4) by Ministry of Science, Technology and Innovation (MOSTI) and Geran Galakan Penyelidikan Muda (GGPM-074-2013) by UKM for providing financial support for this research project.

**References**

1. da Silva, S. S. and Chandel, A. K. (2012). d-Xylitol: Fermentative product, application and commercialization. Springer.
2. Mussatto, S. I., Santos, J. C., Ricardo Filho, W. C. and Silva, S. S. (2006). A study on the recovery of xylitol by batch adsorption and crystallization from fermented sugarcane bagasse hydrolysate. *Journal of Chemical Technology and Biotechnology*, 81(11): 1840 – 1845.
3. Rafiqul, I. S. M. and Mimi Sakinah, A. M. (2012). A perspective bioproduction of xylitol by enzyme technology and future prospects. *International Food Research Journal*, 19(2): 405 – 408.
4. Martinez, E. A., e Silva, J. B. D. A., Giulietti, M. and Solenzal, A. I. N. (2007). Downstream process for xylitol produced from fermented hydrolysate. *Enzyme and Microbial Technology*, 40(5): 1193 – 1198.
5. Affleck, R. P. (2000). Recovery of xylitol from fermentation of model hemicellulose hydrolysates using membrane technology. Virginia Polytechnic Institute and State University.
6. Bolong, N., Saad, I., Ismail, A. F., Salim, M. R., Rana, D. and Matsuura, T. (2011). Charge property modeling of nanofiltration hollow fiber membranes. *International Journal of Simulation: Systems, Science and Technology*, 12(3): 12 – 16.
7. Li, J. F., Xu, Z. L., Yang, H., Yu, L. Y.and Liu, M. (2009). Effect of $TiO_2$ nanoparticles on the surface morphology and performance of microporous PES membrane. *Applied Surface Science*, 255(9), 4725 –4732.
8. Zhao, W., Huang, J., Fang, B., Nie, S., Yi, N., Su, B., Li, H. and Zhao, C. (2011). Modification of polyethersulfone membrane by blending semi-interpenetrating network polymeric nanoparticles. *Journal of Membrane Science*, 369(1): 258 – 266.
9. Su, B., Zhao, C. and Sun, S. (2011). Polyethersulfone hollow fiber membranes for hemodialysis. INTECH Open Access Publisher.
10. Wang, Y. Q., Su, Y. L., Ma, X. L., Sun, Q. and Jiang, Z. Y. (2006). Pluronic polymers and polyethersulfone blend membranes with improved fouling-resistant ability and ultrafiltration performance. *Journal of Membrane Science*, 283(1): 440 – 447.
11. Susanto, H. and Ulbricht, M. (2009). Characteristics, performance and stability of polyethersulfone ultrafiltration membranes prepared by phase separation method using different macromolecular additives. *Journal of Membrane Science*, 327(1): 125 – 135.
12. Susanto, H., Buchori, L., Sumardiono, S., Fajar, B., Istirokhatun, T. and Widiasa, I. N. (2009). Ultrafiltration as pretreatment of reverse osmosis: Low fouling ultrafiltration membrane prepared from polyethersulfone–amphiphilic block copolymer blend. *Reaktor*, 12(4): 203 – 210.
13. Liu, C., Yun, Y., Wu, N., Hua, Y. and Li, C. (2013). Effects of amphiphilic additive Pluronic F127 on performance of poly (ether sulfone) ultrafiltration membrane. *Desalination and Water Treatment*, 51(19-21): 3776 – 3785.
14. Loh, C. H., Wang, R., Shi, L. and Fane, A. G. (2011). Fabrication of high performance polyethersulfone UF hollow fiber membranes using amphiphilic Pluronic block copolymers as pore-forming additives. *Journal of Membrane Science*, 380(1): 114 – 123.
15. Zhang, Y., Su, Y., Chen, W., Peng, J., Dong, Y. and Jiang, Z. (2011). A feasible post-treatment of drying and rewetting for preparation of high-flux Pluronic F127/polyethersulfone nanofiltration membranes. *Industrial & Engineering Chemistry Research*, 50(8): 4678 – 4685.

16. Zhao, W., Su, Y., Li, C., Shi, Q., Ning, X. and Jiang, Z. (2008). Fabrication of antifouling polyethersulfone ultrafiltration membranes using Pluronic F127 as both surface modifier and pore-forming agent. *Journal of Membrane Science*, 318(1): 405 – 412.
17. Wang, Y. Q., Su, Y. L., Sun, Q., Ma, X. L. and Jiang, Z. Y. (2006). Generation of anti-biofouling ultrafiltration membrane surface by blending novel branched amphiphilic polymers with polyethersulfone. *Journal of Membrane Science*, 286(1): 228 – 236.
18. Lalia, B. S., Kochkodan, V., Hashaikeh, R. and Hilal, N. (2013). A review on membrane fabrication: Structure, properties and performance relationship. *Desalination*, 326: 77 – 95.
19. Ng, L. Y., Leo, C. P. and Mohammad, A. W. (2011). Optimizing the incorporation of silica nanoparticles in polysulfone/poly (vinyl alcohol) membranes with response surface methodology. *Journal of Applied Polymer Science*, 121(3): 1804 – 1814.
20. Rohani, R., Hyland, M. and Patterson, D. (2011). A refined one-filtration method for aqueous based nanofiltration and ultrafiltration membrane molecular weight cut-off determination using polyethylene glycols. *Journal of Membrane Science*, 382(1): 278 – 290.
21. Vatsha, B., Ngila, J. C. and Moutloali, R. M. (2014). Preparation of antifouling polyvinylpyrrolidone (PVP 40K) modified polyethersulfone (PES) ultrafiltration (UF) membrane for water purification. *Physics and Chemistry of the Earth, Parts A/B/C*, 67: 125 – 131.
22. Vatanpour, V., Madaeni, S. S., Moradian, R., Zinadini, S. and Astinchap, B. (2011). Fabrication and characterization of novel antifouling nanofiltration membrane prepared from oxidized multiwalled carbon nanotube/polyethersulfone nanocomposite. *Journal of Membrane Science*, 375(1): 284 – 294.
23. Mulder, J. (2012). Basic principles of membrane technology. Springer Science & Business Media.
24. Kochkodan, V., Johnson, D. J., and Hilal, N. (2014). Polymeric membranes: Surface modification for minimizing (bio) colloidal fouling. *Advances in Colloid and Interface Science*, 206: 116 – 140.

*Malaysian Journal of Analytical Sciences, Vol 21 No 1 (2017): 231 - 239*
*DOI: http://dx.doi.org/10.17576/mjas-2017-2101-27*

MALAYSIAN JOURNAL OF ANALYTICAL SCIENCES
*Published by The Malaysian Analytical Sciences Society*
ISSN 1394 - 2506

# SEED CULTURE CONDITIONS FOR HIGH YIELD OF CELLULOLYTIC ENZYMES PRODUCTION FROM *Pycnoporus sanguineus*

## (Keadaan Kultur Benih untuk Penghasilan Enzim Selulolitik daripada *Pycnoporus sanguineus*)

Rafidah Jalil[1], Mohd Sahaid Kalil[1]*, Norliza Abdul Rahman[1], Aidil Abdul Hamid[2], Mohd Farid Ahmad[3]

[1]*Department of Chemical & Process Engineering, Faculty of Engineering & Built Environment*
[2]*School of Bioscience and Biotechnology, Faculty of Science & Technology*
*Universiti Kebangsaan Malaysia, 43600 UKM Bangi, Selangor, Malaysia*
[3]*Forest Research Institute Malaysia (FRIM), 52109 Kepong, Selangor, Malaysia*

**Corresponding author: sahaid@ukm.edu.my*

Received: 21 October 2015; Accepted: 14 June 2016

**Abstract**

Low yields and productivity in fermentation industry usually due to poor quality of seed culture (inoculum). As the first stage in the fermentation process, inoculum consistency in terms of size and quality is clearly important for high yield of enzymes production. Selection of microorganism also plays an important role in improving the productivity. Fungi type of white rot basidiomycetes species is a well-known cellulolytic enzymes producer and capable to degrade many types of lignocellulosic biomass. Cellulolytic enzymes produced from white rot fungi, *Pycnoporus sanguineus* (PS) were investigated. The PS cultured on different agar media and parameter conditions of seed culture preparation in liquid medium broth were compared. Seed culture conditions of PS were influenced by many factors such as type of medium used for fungal growth, temperature, incubation time in liquid medium and subculture time on agar medium. PS was full-grown on potato dextrose agar (PDA) on day 5 compared to malt extract agar (MEA) on day 7. Seed culture conditions was determined using standard liquid medium, potato dextrose broth (PDB) at constant temperature (30 °C), agitation speed (150 rpm) and pH (4.8) for duration of seven days using two different subculture of PS that were grown for five and seven days. It was found that the five days' subculture of PS shown 3.93% higher cell dry weight of fungal biomass (3.44 g/L on day 5) and higher cellulolytic enzymes activity; 95.49% (FPase), 3.14% (CMCase), 7.71% (exoglucanases) and 14.93% (xylanases). Maximum cellulolytic enzymes were found after 48 hours' incubation with filter paper activity (FPase) of 1.79 U/mL, carboxymethyl cellulase activity (CMCase) of 3.36 U/mL, exoglucanase activity (Avicelase) of 0.59 U/mL and xylanase enzymes activity of 0.66 U/mL. Reducing sugars concentration decreased from day 1 to 7 due to consumption of sugars for fungal growth. Seed culture conditions were strongly influenced by subculture and incubation time in liquid medium to produce high yield of cellulolytic enzymes from PS.

**Keywords**: white rot fungi, *Pycnoporus sanguineus*, seed culture, cellulolytic enzymes, fermentation

**Abstrak**

Hasil dan produktiviti yang rendah dalam industri fermentasi biasanya disebabkan oleh kultur benih (inokulum) yang kurang berkualiti. Pada peringkat pertama proses fermentasi, konsistensi inokulum dari segi saiz dan kualiti sangat penting bagi pengeluaran enzim yang tinggi. Pemilihan mikroorganisma juga memainkan peranan penting dalam meningkatkan produktiviti. Jenis kulat pereput putih dari spesies basidiomycetes sangat terkenal sebagai pengeluar enzim selulolitik dan ia mampu untuk mengurai pelbagai jenis bahan lignoselulosa. Dalam kajian ini, enzim selulolitik dihasilkan daripada kulat pereput putih, *Pycnoporus sanguineus* (PS) yang dihidupkan di atas agar dan perbandingan parameter berbeza penyediaan kultur benih dalam medium cecair dikaji. Kultur benih PS dipengaruhi oleh pelbagai faktor seperti jenis medium yang digunakan untuk pertumbuhan kulat, suhu, masa pengeraman di atas medium agar dan di dalam medium cecair. Pertumbuhan maksimum PS di atas agar kentang dekstrosa (PDA) dicapai pada hari ke-lima berbanding dengan agar ekstrak malt (MEA) pada hari ke-tujuh. Kultur benih ditentukan dengan menggunakan medium piawai iaitu medium kentang dekstrosa (PDB) pada suhu malar (30 °C),

kelajuan pengadukan (150 rpm) dan pH (4.8) untuk tempoh masa tujuh hari menggunakan dua kultur PS berbeza yang dieram selama lima dan tujuh hari. Didapati bahawa kultur PS 5 hari menunjukkan berat kering sel kulat yang lebih tinggi iaitu 3.93% (3.44 g/L pada hari ke-lima) dan aktiviti enzim selulolitik lebih tinggi; 95.49% (FPase), 3.14% (CMCase), 7.71% (ekoglukanase) and 14.93% (xilanase). Pengeluaran enzim selulolitik maksimum diperolehi selepas 48 jam pengeraman dengan aktiviti kertas turas (FPase) 1.79 U/mL, aktiviti karboksimetil selulase (CMCase) 3.36 U/mL, aktiviti eksoglukanase (Avicelase) 0.59 U/mL dan aktiviti enzim xilanase 0.66 U/mL. Selain itu, kepekatan gula penurun berkurang dari hari 1-7 disebabkan oleh penggunaan gula untuk pertumbuhan kulat. Ini menunjukkan bahawa keadaan inokulum dipengaruhi oleh jenis kultur dan masa pengeraman dalam medium cecair untuk pengeluaran hasil enzim selulolitik yang tinggi dari PS.

**Kata kunci:** kulat pereput putih, *Pycnoporus sanguineus*, kultur benih, enzim selulolitik, penapaian

## Introduction

Cellulolytic enzymes productions have been studied extensively throughout the world. These enzymes produced using microorganisms either bacteria or fungi. Commercially, fungi types from *Trichoderma* species have been used for production of cellulase [1]. Today, studies have been carried out to discover other potential of fungi that can produce high cellulolytic enzymes. These enzymes responsible to convert cellulose into glucose; fermentable sugars that will be used in fermentation industry to produce biofuel and value added products. Cellulolytic enzymes consist of complete cellulase system that classified into three major classes; endoglucanases, exoglucanases and β-glucosidases [2]. All enzymes have their specific roles; endoglucanases act randomly on soluble and insoluble cellulose chains, exoglucanases release the cellobiose from the reducing and non-reducing ends of cellulose chains and β-glucosidases release glucose from cellobiose release by exoglucanases [3].

*Pycnoporus sanguineus* (PS) is one of basidiomycetes species of white rot fungi also known as wood decaying fungi that has highly potential for lignocellulolytic enzymes production. It could degrade the lignocellulosic component of cellulose, hemicellulose and lignin. It acts as a biological pre-treatment as well as to produce value added products [4]. PS has a promising capacity with multi applications, so that it can be a feedstock bio refinery sector as well as for enzymes industry [5]. PS is also a good and thermostable cellulase producer that can maintain more than 90% of activities above temperature of 90 $^{\circ}$C [6]. It can grow at moderately high temperature (37 $^{\circ}$C) [1]. This fungus was applied in agro-industrial waste because of their good results in many applications [7].

In fermentation industry, there are a few stages involved in enzymes production starting from subculture of microorganism on agar medium followed by seed culture or inoculum preparation before proceed for the production culture of enzymes production. Efficient enzymes will be the main catalyst for fermentable sugar production in fermentation industry. Since degradation process of lignocellulosic biomass using enzymes is slow and less economical, new methods have been explored to enhance the fermentable sugars for high yield production [8]. One of the factors is during seed culture or inoculum preparation stage that will be the key for the enhancement of product yield. The critical step for enzymes production is seed culture stage and the selection of its correct conditions will influence the yield of cellulolytic enzymes produced. There are many factors influenced the seed culture conditions such as type of medium used for fungal growth, temperature, pH, incubation time in liquid medium and subculture time on medium agar. Production of enzymes using PS at temperature ranging from 30 to 40 $^{0}$C can maintained its activity up to 85% and the optimum pH is 5 [1]. pH of medium is important since it plays an important role in fungal growth by inducing its morphological structural and enzymes secretion [7].

The aimed of this study is to determine the seed culture conditions of PS as inoculum to produce cellulolytic enzymes. Identification of maximum cellulolytic enzymes activities was carried out using different subcultures of PS to determine the effect of subculture incubation time on product yields.

## Materials and Methods

### Fungal strain

White rot fungi PS was obtained from the Wood Mycology Laboratory, Forest Research Institute Malaysia. It was collected from a dead tree in the FRIM Campus. In the laboratory, the fungus was firstly grown on Petri dish containing two different agar media namely, Malt extract agar (MEA)(12.75 g/L maltose, 2.75 g/L dextrin, 2.35 g/L

glycerol, 0.78 g/L peptone and 15.0 g/L agar) and Potato dextrose agar (PDA)(4 g/L potato starch, 20 g/L dextrose and 15 g/L agar) to determine the mycelia growth diameter at temperature of 30 °C for seven days.

**Seed culture condition**

For the seed culture preparations, 1 $cm^3$ mycelia disc cut of PS using sterilized cork borer from the petri dish were inoculated into seven shake flasks containing 100 mL of PDB. The experimental works were carried out in triplicates. The liquid medium used for seed culture preparation in this experiments consist of 4 g/L potato and 20 g/L dextrose, with pH of medium is 4.8. The seed culture was incubated at temperature of 30 °C and was shaken at 150 rpm [9]. The sampling of seed culture broth was carried out every day. The flask containing mycelia of fungi was filtered using filter paper to determine the cell dry weight of fungal biomass. The fungal biomass was oven dried at 60 °C in an oven for 24 hours until reached a constant weight. The filtrate collected known as supernatant was further analyzed for its reducing sugars content and cellulolytic enzymes activities.

**Reducing sugars and enzymatic assays**

Reducing sugars and enzymatic assays were assayed from the supernatant collected from the filtration of seed culture. Reducing sugars released were assayed based on the method described by Miller [10]. 1 mL of sample of supernatant was mixed with 3 mL DNS reagent and boiled for 5 minutes in a water bath. After cooled down, 20 mL of distilled water was added to reaction mixture and the sample was analyzed using UV-Vis spectrophotometer at 540 nm to obtain the absorbance value. The reducing sugar released was calculated based on the standard curves.

Cellulase and xylanase activities were assayed based on the method described by Ghose [11] and Ghose & Bisaria [12], respectively. The activities were measured based on the concentration of reducing sugar released. For cellulase enzymes activities, reaction mixture consists of 0.5 mL substrate solution and 0.5 ml sample. For substrate solution, it consists of 1% of Carboxymethyl cellulose (CMCase assay) and 1% of avicel (Avicelase assay) in 0.05 M sodium citrate buffer. The reaction mixtures were incubated for 30 minutes at temperature of 50 °C. An amount 3 mL of DNS reagent was then added into the mixture and boiled for five minutes before being analyzed using spectrophotometer to determine the absorbance value. For filter paper activity (FPase), the reaction mixture consists of 1 mL 0.05 M sodium citrate buffer, Whatman filter paper (No. 1) strip measuring 1 cm x 6 cm. and 0.5 mL sample. The reaction mixtures were incubated for one hour at 50 °C. For xylanase enzyme activities, similar method as the CMCase was carried out to determine cellulase activities but only 1% xylan was used in 0.05 M sodium citrate buffer as substrate solutions. Enzymes activities for cellulase and xylanase enzymes were measured using standard curve of glucose and xylose respectively.

## Results and Discussion

**Effect of different agar media on growth of *Pycnoporus sanguineus***

The growth diameter of PS was studied using different agar media namely; MEA and PDA. It was found that the PS grew faster on PDA compared to MEA as shown in Figure 1. The fungal growth rate on PDA and MEA recorded were 1.27 cm/day and 0.93 cm/day, respectively.

These results could suggest that the fast growth rate of PS on PDA was probably influenced by the present of dextrose in the agar medium. The present observations are in the agreement with a previous report, where dextrose has been proven to be the best carbon source for fungal growth during incubation time compared to maltose [13]. Instead of using PDA as medium for fungal growth, lignocellulosic biomass has been added in medium as substrate for fungal growth. Rice husk as substrate in agar medium can increase the growth rate (1.24 cm/day) of PS at growth conditions of 28 °C for seven days [14]. As compared to this study, using PDA alone and by increasing the incubation temperature (30 °C) can increase the growth rate up to 1.27 cm/day for five days.

**Effect of different subculture of pycnoporus sanguineus on cell dry weight (CDW) of fungal biomass**

The growth rate of PS was also influenced by the conditions of seed culture. In this study, the PS was grown at two different conditions on agar plate known as subculture five days (Sc PS-5) and subculture seven days (Sc PS-7). It was found that the seed culture using Sc PS-5 produced higher CDW of the fungal biomass 3.44 g/L compared to Sc PS-7 (3.31 g/L) at day five of incubation time (Figure 2). It shows that 3.93% decreased of CDW when the Sc PS-7 was applied for seed culture production. However, the mycelia growth based on CDW of fungal biomass did not

have direct correlation with production of cellulolytic enzymes [14]. It has been proven in this study for Sc PS-5. When CDW was 3.44 g/L at day 5, the CMCase was 3.36 U/mL. While at day 2, CDW was only 1.88 g/L with highest activity of CMCase (2.44 U/mL).

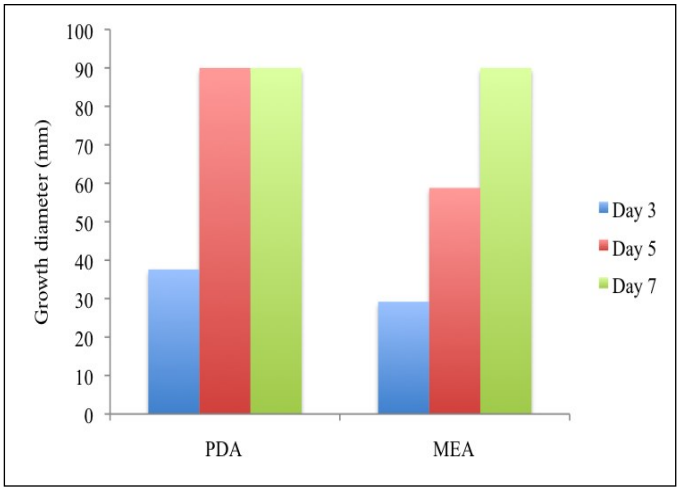



Figure 1. Growth of *Pycnoporus sanguineus* on MEA and PDA

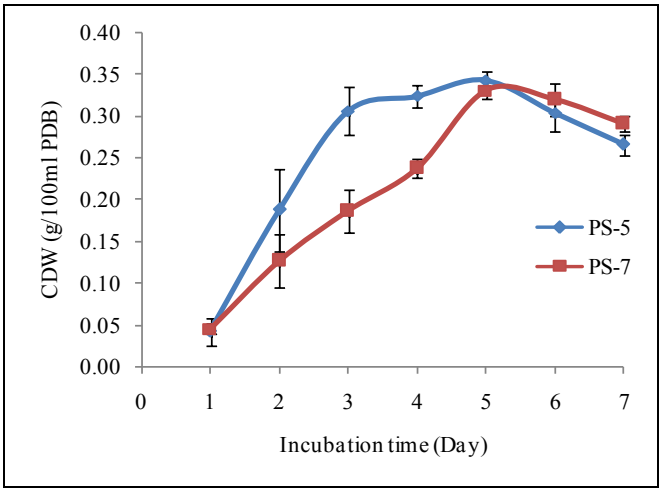



Figure 2. Cell dry weight (CDW) of *Pycnoporus sanguineus*

**Reducing sugars assay of *Pycnoporus sanguineus***

Reducing sugars (RS) for both subcultures of PS decreased from day 1 to day 7 of incubation time as shown in Figure 3. This is due to the glucose consumption during fungal growth and the initial glucose present in the liquid medium was utilized for fungal growth [15]. Sc PS-7 consumed more glucose (17.75 mg/mL) as compared to Sc PS-5 (16.80 mg/mL) for its growth. It is because older cultures need more nutrients to maintain its further growth.

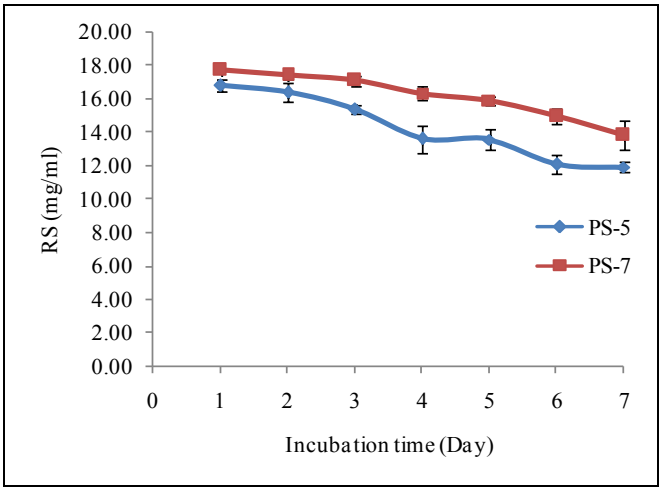



Figure 3. Reducing sugars (RS) of *Pycnoporus sanguineus*

**Cellulolytic enzymes activities of *Pycnoporus sanguineus* for different incubation time of subcultures**

***Filter paper assay activities (FPase)***

FPase is a total cellulase activities resulting from the combination of different cellulase enzymes in the culture filtrate [2]. Figure 4 shows the comparison of filter paper activities of PS. It is found that the maximum FPase activity obtained using Sc PS-5 was 1.79 U/mL after 48 hours' incubation time. As compared to other *Pycnoporus* species; *Pycnoporus coccineus* produced 0.93 U/mL of FPase after incubated for three days [16].

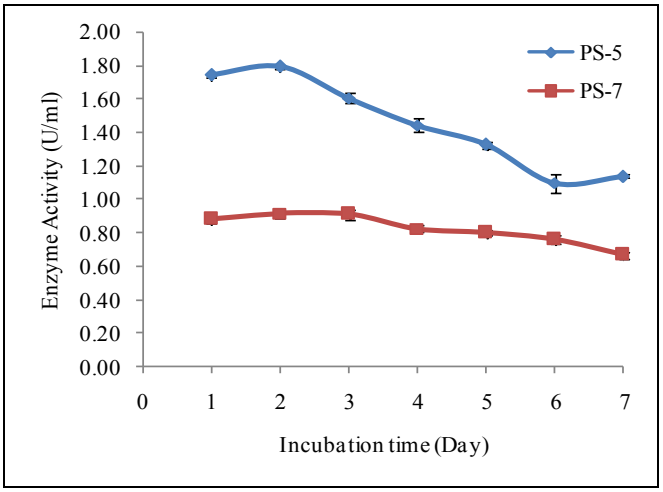



Figure 4. FPase of *Pycnoporus sanguineus*

***Carboxymethyl cellulase @ Endoglucanase enzymes activities (CMCase)***

CMCase enzymes activities for both subcultures have been analyzed and compared as shown in Figure 5. It is found that maximum CMCase activity was 3.36 U/ml after 48 hours' incubation time using Sc PS-5. Previous research reported that PS produced maximum CMCase activity level (1.43 U/mg on 8$^{th}$ day) at pH 5.0 and decreasing or

increasing the pH value will decrease the activity level [1]. For *Pycnoporus coccineus*, it produced 0.95 U/ml of CMCase after incubated for three days [16].

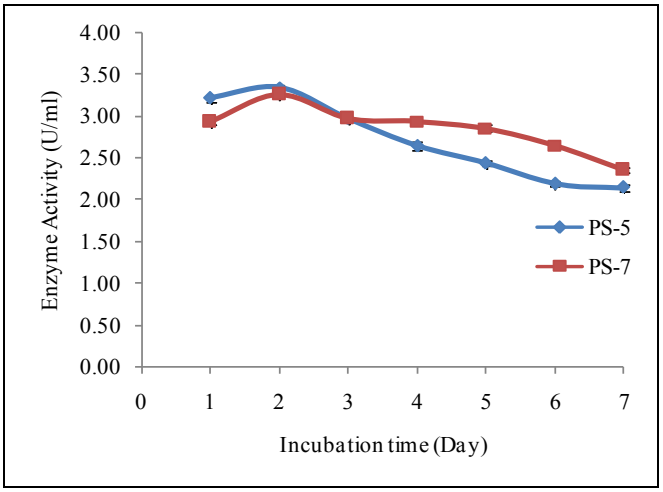



Figure 5. CMCase of *Pycnoporus sanguineus*

***Avicelase @ Exoglucanases activities***

Exoglucanase known also as avicelase enzyme activity was measured using microcrystalline cellulose (Avicel) as the substrate. The activities for avicelase enzymes were compared and shown in Figure 6. It is found that the maximum Avicelase activity (0.59 U/ml) was obtained after 48 hours' incubation time using Sc PS-5. As compared to Sc PS-7, it shows very small significant different with 6.78% of activities decreased. Previous research reported that 0.30 U/mg of Avicelase produced from PS after 8$^{th}$ day [1].

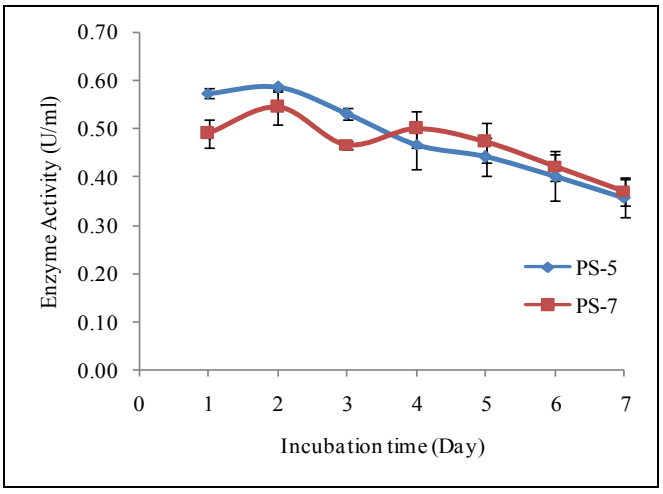



Figure 6. Avicelase of *Pycnoporus sanguineus*

***Xylanase enzymes activities***

Maximum xylanase enzymes activities for Sc PS-5 (0.66 U/mL) were higher than Sc PS-7 (0.57 U/mL) after 48 hours' incubation time (Figure 7). Previous research reported that *Aspergillus niger* was produced 0.71 U/mL of xylanase activities after 30 hours' incubation times [17].

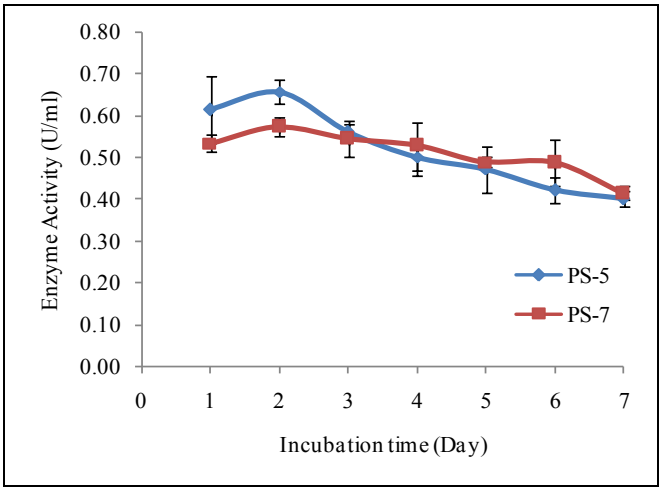



Figure 7. Xylanase of *Pycnoporus sanguineus*

**Comparison of seed culture conditions using different subculture of *Pycnoporus sanguineus***

Based on the findings, comparisons between both subcultures were analyzed. It was found that the seed culture condition to produce cellulolytic enzymes was obtained using Sc PS-5 on agar medium followed by 48 hours' incubation time during seed culture or inoculum preparation. These findings were achieved at constant temperature of 30 $^{\circ}$C, agitation speed of 150 rpm and pH of 4.8 using 1 cm$^3$ of mycelia disc as fungal inoculum source. Table 1 below shows the summary of cellulolytic enzymes produce at 48 hours' incubation time using both subcultures.

Table 1. Comparison of *Pycnoporus sanguineus* cellulolytic enzymes activity at 48 hours' incubation times

| **Enzyme** | **Sc PS-5** | **Sc PS-7** |
|---|---|---|
| FPase (U/mL) | 1.79 | 0.92 |
| CMCase (U/mL) | 3.36 | 3.25 |
| Avicelase (U/mL) | 0.59 | 0.55 |
| Xylanase (U/mL) | 0.66 | 0.57 |

From Table 1, it shows that all the cellulolytic enzymes activity was higher using Sc PS-5 compared to Sc PS-7. This seed culture conditions can be used as a base-line study for enzymes production from PS. Besides, it can reduce the culture times from seven to five days as commonly applied by other researchers [5,4,18].

## Conclusion

The seed culture conditions of PS to produce enzymes was obtained using Sc PS-5 with the highest cellulase; FPase (1.79 U/mL), CMCase (3.36 U/mL), Avicelase (0.59 U/mL) and xylanase enzymes activities (0.66 U/mL) after 48 hours' incubation time. Results obtained at the constant pH medium (pH 4.8), temperature (30 $^{\circ}$C), agitation speed (150 rpm), and mycelium disc size (1 $cm^3$). These findings help to reduce the inoculum preparation time.

## Acknowledgement

The authors gratefully acknowledge the Hadiah Latihan Persekutuan (HLP) from Jabatan Perkhidmatan Awam (JPA) of Malaysia, the Research University (RU) Grant provided by University Kebangsaan Malaysia (UKM) (FRGS/2/2013/TK05/UKM/02/1 & UKM-GUP-2013-037) and Forest Research Institute Malaysia (FRIM) to support this research work.

## References

1. Quiroz-Castaneda, R. E., Balcazar-Lopez, E., Dantan-Gonzalez, E., Martinez, A., Folch-Mallol, J. and Martinez -Anaya, C. (2009). Characterization of cellulolytic activities of *Bjerkandera adusta* and *Pycnoporus sanguineus* on Solid Wheat Straw Medium. *Electronic Journal of Biotechnology,* 12(4): 1 – 8.
2. Praveen, K., Usha, K.Y., Shanthi, B., Ramanjaneyulu, G., Naveen, M. and Reddy B. R. (2012). Production of cellulolytic enzymes by a mushroom – stereum ostrea. *International Journal of Research in Biochemistry and Biophysics*, 2(1):1 – 4.
3. Namita, B., Rupinder, T., Raman, S. and Sanjeev, K. S. (2012). Production of cellulases from Aspergillus niger NS-2 in solid state fermentation on agricultural and kitchen waste residues. *Waste Management*, 32: 1341 – 1346.
4. Teoh, Y. P., Mashitah, M. D. and Salmiah, U. (2011). Media selection for mycelia growth, antifungal activity against wood-degrading fungi and GC-MS study by *Pycnoporus sanguineus*. *Bioresources*, 6(3): 2719 – 2731.
5. Pooja, S., Othman, S., Rokiah, H., Leh, C. P. and Rajeev, P. S. (2012). Biodegradation study of *Pycnoporus san guineus* and its effect on structural and chemical features on oil palm biomass chips. *Lignocellulose,* 1(3):210 – 227.
6. Gutierrez-Soto, G., Medina-Gonzalez, G. E., Gracia-Zambrano, E. A., Trevino-Ramirez, J. E. and Hernandez-Luna, C. E. (2015). Selection and characterization of a native *Pycnoporus sanguineus* as a lignocellulolytic extract producer from submerged cultures of various agroindustrial wastes. *BioResources,* 10(2):3564 – 3576.
7. Onofre, S. B., Santos, Z. P. Q., Kagimura, F. Y. and Mattiello, S. P. (2015). Cellulases produced by the endo-phytic fungus *Pycnoporus sanguineus* (L.) Murrill. *African Journal of Agricultural Research,* 10(13):1557 – 1564.
8. Ibrahim, C.O. (2007). Development of applications of industrial enzymes from Malaysian indigenous microbial sources. *Bioresource Technology,* 99: 4572 – 4582.
9. Shobana, P. and Maheswari, N. U. (2013). Production of cellulase from *Aspergillus fumigatus* under submerged and solid state fermentation using agricultural waste. *International Journal of Advances in Pharmacy, Biology and Chemistry*, 2(4): 595 – 599.
10. Miller, G. L. (1959). Use of dinitrosalicylic acid reagent for determination of reducing sugar. *Analytical Chemistry*, 13(6): 426 – 428.
11. Ghose, T. K. (1987). Measurement of cellulase activities. *Pure & Applied Chemistry*, 59:257 – 268.
12. Ghose, T. K. and Bisaria, V. S. (1987). Measurement of hemicellulase activities Part 1: Xylanases. *Pure & Applied Chemistry*, 59(12): 1739 – 1752.
13. Manjunathan, J. and Kaviyarasan, V. (2010). Studies on the growth requirements of *Lentinus tuberregium* (Fr.) and edible mushroom. *Middle East Journal Science Research*, 5(2): 81 – 85.
14. Quiroz-Castaneda, R. E., Perez-Mejia, N., Martinez-Anaya, C., Acosta-Urdapilleta, L. and Folch-Mallol, J. (2010). Evaluation of different lignocellulosic substrates for the production of cellulases and xylanases by the basidiomycete fungi *Bjerkandera adusta* and *Pycnoporus sanguineus*. *Biodegradation*, Springer Science Business Media.
15. Potumarthi, R., Baadhe, R. R., Nayak, P. and Jetty, A. (2013). Simultaneous pretreatment and saccharification of rice husk by *Phanerochete chrysosporium* for improved production of reducing sugars. *Bioresource Techno-logy*, 128: 113 – 117.

16. Tomoko, S., Hajime, S., Mitsuro, I., Muneyoshi, Y., Yuko, O., Kazuhiro, M., Tsutomu, I., Kengo, M. and Masanobu, N. (2012). Screening of lignocellulolytic enzyme producers: enzyme system from Aspergillus tubingensis for hydrolysis of sugi pulp. *Bulletin of FFPRI*, 11(2): 57 – 63.
17. Cunha, F. M., Esperanca, M. N., Z angirolami, T. C., Badino, A.C. and Farinas, C. S. (2012). Sequential solid-state and submerged cultivation of aspergillus niger on sugarcane bagasse for the production of cellulase. *Bioresource Technology* 112: 270 – 274.
18. Vijya, C.and Reddy, R. M. (2012). Bio-delignification ability of locally available edible mushrooms for the biological treatment of crop residues. *Indian Journal of Biotechnology*, 11:191 – 196.

*Malaysian Journal of Analytical Sciences, Vol 21 No 1 (2017): 240 - 247*
*DOI: http://dx.doi.org/10.17576/mjas-2017-2101-28*

MALAYSIAN JOURNAL OF ANALYTICAL SCIENCES
*Published by The Malaysian Analytical Sciences Society*
ISSN 1394 - 2506

# CRUDE PALM OIL BIODIESEL BY TRANSESTERIFICATION PROCESS USING CHOLINE HYDROXIDE CATALYST

## (Biodiesel Minyak Sawit Mentah Melalui Proses Transesterifikasi Menggunakan Mangkin Kolin Hidroksida)

Renita Manurung*, Nadya G. Bestari, Dania K. Syabri

*Department of Chemical Engineering, Faculty of Engineering,*
*Universitas Sumatera Utara, 20155 Medan, Sumatera, Indonesia*

**Corresponding author: renitachem@yahoo.com*

Received: 21 October 2015; Accepted: 14 June 2016

**Abstract**

Biodiesel is generally made by transesterification using alkaline catalyst. Choice of catalyst used greatly affects the biodiesel produced. Choline Hydroxide (ChOH) catalyst is a basic ionic liquid having excellent catalytic reactions in the synthesis of palm biodiesel from Crude Palm Oil (CPO). This catalyst is able to produce biodiesel without soap formation which at the end of the reaction, three layers formed. They are biodiesel, the catalyst itself and glycerol. This makes it easy to separate biodiesel from the by product. Several other important variables in addition to the choice of catalyst and is catalyst dosage, molar ratio of ethanol to CPO and reaction time. The highest yield of biodiesel produced is 99.84% with molar ratio of ethanol to CPO is 9:1, reaction time is 90 minutes, 5.5% catalyst (w/w) at 70 °C and 400 rpm stirring speed. The most influential variable is catalyst dosages that give the significant difference yield of biodiesel produced. It evidenced by more dosages of catalyst used will provide a higher yield of biodiesel.

**Keywords**: choline hydroxide, crude palm oil, ethanol, ionic liquid, palm biodiesel

**Abstrak**

Biodiesel umumnya dihasilkan secara transesterifikasi menggunakan mangkin beralkali. Pilihan mangkin yang digunakan sangat mempengaruhi biodiesel yang dihasilkan. Kolin hidroksida (ChOH) adalah cairan ionik bes yang memiliki tindak balas pemangkinan yang sangat baik dalam sintesis biodiesel sawit dari minyak sawit mentah (CPO). Mangkin ini mampu menghasilkan biodiesel tanpa pembentukan sabun di mana pada akhir tindak balas membentuk tiga lapisan. Lapisan tersebut adalah biodiesel, mangkin itu sendiri dan gliserol. Hal ini memudahkan pemisahan biodiesel dari produk sampingan tersebut. Beberapa pemboleh ubah penting selain pilihan mangkin adalah dos mangkin, nisbah molar etanol terhadap CPO dan masa tindak balas. Hasil tertinggi dari biodiesel adalah 99.84% dengan nisbah molar etanol terhadap CPO adalah 9:1, masa tindak balas 90 minit, 5.5% mangkin (w/w) pada 70 °C dan kelajuan putaran 400 rpm. Pemboleh ubah yang paling berpengaruh adalah dos mangkin yang memberikan perbezaan hasil yang signifikan terhadap biodiesel yang dihasilkan. Ini membuktikan dengan semakin banyak dos mangkin yang digunakan akan memberikan hasil biodiesel yang lebih tinggi.

**Kata kunci:** kolin hidroksida, minyak sawit mentah, etanol, cecair ionik, biodiesel sawit

## Introduction

Biodiesel, an alternative diesel fuel, is made from renewable biological sources such as vegetable oils and animal fats. It is biodegradable and nontoxic, has low emission profiles and so is environmentally beneficial [1]. According to the statistics, 70% of manufacturing cost in producing biodiesel is contributed by feedstock [2]. Indonesia has a

big potential for producing biodiesel because the developments in Indonesia's Crude Palm Oil (CPO) production is increasing every year.

Biodiesel is mostly produced by a transesterification reaction, from oil with an alcohol and the presence of a catalyst to generate mono-alkyl esters and glycerol, which are then separated and purified [3]. Alcohols such as methanol and ethanol are the most commonly used. The yield of biodiesel using ethanol as alcohol reactant and ChOH catalyst is higher than using methanol as alcohol reactant [4]. In addition, ethanol can be produced from renewable agricultural resources [5]. So the use of ethyl esters is more environmentally friendly than the use of methyl ester.

Ionic liquids have been successfully used as a catalyst to catalyze transesterification reaction towards biodiesel production with good performance, higher conversion and selective production of biodiesel and glycerol conversion [6]. Ionic liquids are organic salts with a low melting point and very low vapor pressure [7]. Choline hydroxide (ChOH) catalyst exhibited better catalytic activity compared with other basic ionic liquid catalysts [8]. Ionic liquid-based catalyst choline does not cause the formation of soap. Reaction conditions such as temperature, time, molar ratio and dose of catalyst are optimized to obtain highest conversion in producing biodiesel [9]. The structure ChOH shows the presence of ion $OH^-$ in Figure 1.

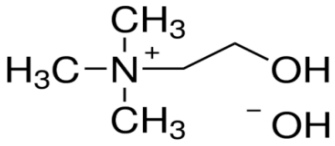


Figure 1. The ionization structure of choline hydroxide

**Materials and Methods**

The raw materials used are crude palm oil (CPO) obtained from PT Perkebunan Nusantara IV (PTPN IV). Alcohol used is ethanol ($C_2H_5OH$) and choline hydroxide (ChOH) was used as catalyst. Transesterification reaction is carried out by the stirring speed 400 rpm and a constant temperature of 70°C with process variables as follows: 1) dose of catalyst, 2) the molar ratio of ethanol:CPO and 3) reaction time.

CPO with a certain amount of weight is weighed and followed by the preparation of ethanol and a catalyst ChOH. CPO and ethanol were mixed at a specific molar ratio in a flask equipped with reflux condenser, thermometer and stirrer. Afterwards, ChOH was added and the mixture was stirred and heated using a hot plate till a constant temperature was reached. After that, the mixture was separated using a separator funnel until 2-3 layers were formed, then washed until the washed water is clear. Analysis can be performed after the ethyl ester prepared.

Factors that influence the reaction such as catalyst dosage, molar ratio of ethanol toward CPO and reaction time were analyzed systematically with the response surface methodology (RSM) with a central composite design (CCD). Level code and the combination of research can be seen in Table 1 and Table 2, respectively. Design equation models offered during the three factors which are as follows [10].

$$Y = \beta_1 + \beta_2\chi_1 + \beta_3\chi_2 + \beta_4\chi_3 + \beta_5\chi_1\chi_2 + \beta_6\chi_2\chi_3 + \beta_7\chi_1\chi_3 + \beta_8\chi_1^2 + \beta_9\chi_2^2 + \beta_{10}\chi_3^2 + \varepsilon \quad (1)$$

Table 1. Level code on experimental design

| Variables | Code | Levels | | | | |
|---|---|---|---|---|---|---|
| | | **-1.673** | **-1** | **0** | **1** | **1.673** |
| Catalyst Dosage (w/w) | $X_1$ | 2.5 | 3 | 4 | 5 | 5.5 |
| Molar Ratio Ethanol:CPO | $X_2$ | 4:1 | 6:1 | 9:1 | 12:1 | 14:1 |
| Reaction Time (min) | $X_3$ | 40 | 60 | 90 | 120 | 140 |

Table 2. Central Composite Design for Three Variables

| No | Dose of Catalyst (w/w) | Molar Ratio Ethanol:CPO | Reaction Time (minute) |
|---|---|---|---|
| 1 | -1 | -1 | -1 |
| 2 | -1 | 1 | 1 |
| 3 | 1 | -1 | 1 |
| 4 | 1 | 1 | -1 |
| 5 | 0 | 0 | 0 |
| 6 | -1 | -1 | 1 |
| 7 | -1 | 1 | -1 |
| 8 | 1 | -1 | -1 |
| 9 | 1 | 1 | 1 |
| 10 | 0 | 0 | 0 |
| 11 | -1.673 | 0 | 0 |
| 12 | 1.673 | 0 | 0 |
| 13 | 0 | -1.673 | 0 |
| 14 | 0 | 1.673 | 0 |
| 15 | 0 | 0 | -1.673 |
| 16 | 0 | 0 | 1.673 |
| 17 | 0 | 0 | 0 |

## Results and Discussion

**Free fatty acid (FFA) and water content**

Analysis free fatty acids and moisture have been done to raw materials CPO. Comparative analysis of the levels of free fatty acids for CPO against palm oil degummed (DPO) can be seen in Figure 2.

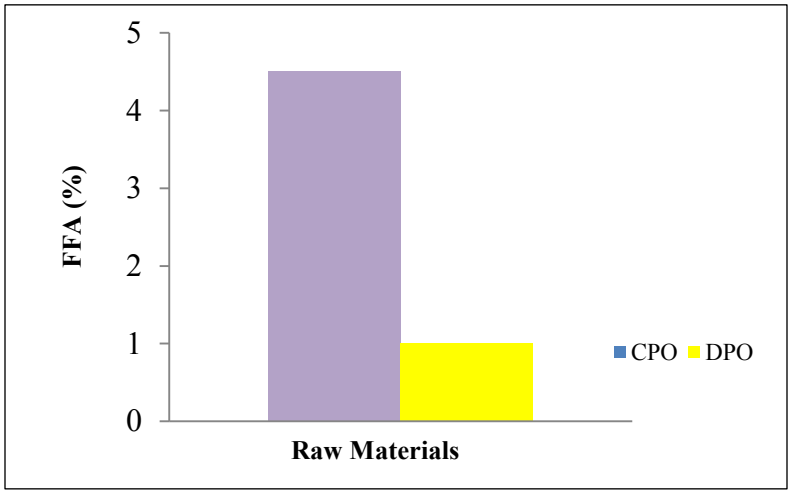



Figure 2. Free fatty acid level

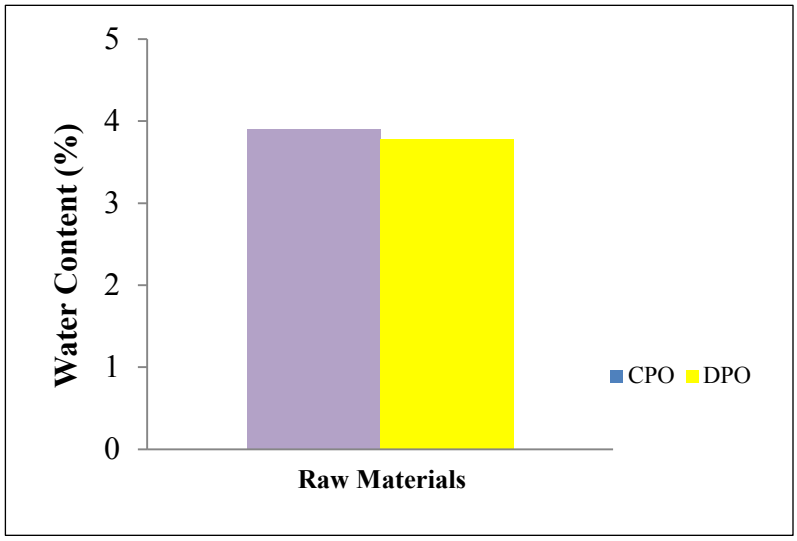



Figure 3. Water content

Low water content can generate higher products conversion. In addition to FFA and water, CPO also contain gum that can interfere the performance of the catalyst, therefore CPO needs to be degummed.

**CPO as the raw material**

Preliminary research has been done on CPO and DPO as basic of raw material selection. With the same reaction conditions, % yield of the ethyl ester of CPO and DPO can be seen as shown in Figure 4.

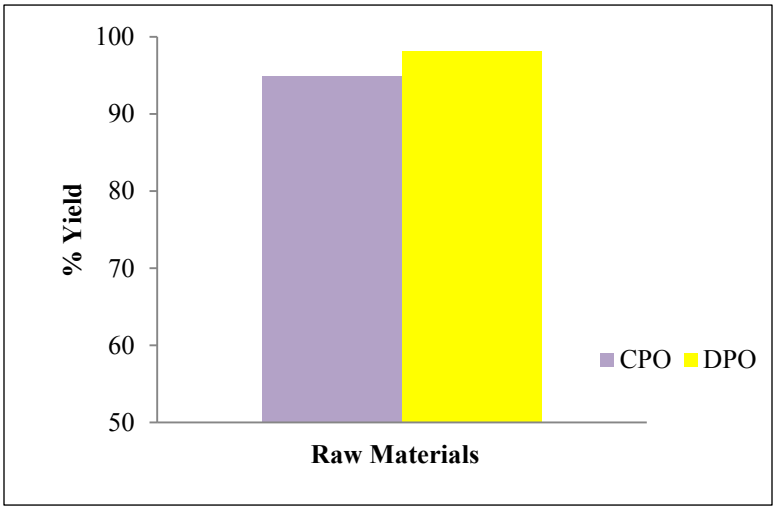



Figure 4. Percentage yield ethyl ester of CPO and DPO

Figure 4 shows the percentage yield of ethyl ester of CPO and DPO with reaction temperature at 70 °C and a stirring speed 400 rpm. Catalyst dosage used was 4% (w/w), molar ratio of ethanol against the raw material is 9:1

and reaction time is 90 minutes. Percentage yield of DPO is 98.17 and 94.92 for CPO. Based on the data above, the raw materials are selected in this study is the CPO as percentage yield obtained from the experiment is not too far difference from DPO. With the high FFA and high water content of CPO, the ionic liquid ChOH able to catalyze the transesterification reaction very well, with percentage yield of ethyl ester is 94.92%.

Manufacturing biodiesel from CPO, as raw materials without pre-treatment is able to lower production costs. The cost of raw materials contributes about 70% of the total cost of production. Pre-treatment CPO make the preparation of raw material more complex, so the cost of it as raw material higher than no pre-treatment CPO. Therefore, using CPO as raw material for biodiesel production was instrumental in lowering the total cost of production so that the price of biodiesel can be predicted cheaper.

**Effect of process variables toward percentage yield**

Following the experimental results data in a central composite design and the combination of the research can be seen in Table 3.

Table 3. Yield ethyl ester in central composite design

| No | Dose of Catalyst (w/w) | Molar Ratio Ethanol:CPO | Reaction Time (minute) | % Yield |
|---|---|---|---|---|
| 1 | -1 | -1 | -1 | 63.578 |
| 2 | -1 | 1 | 1 | 95.318 |
| 3 | 1 | -1 | 1 | 97.930 |
| 4 | 1 | 1 | -1 | 97.070 |
| 5 | 0 | 0 | 0 | 98.174 |
| 6 | -1 | -1 | 1 | 60.500 |
| 7 | -1 | 1 | -1 | 97.569 |
| 8 | 1 | -1 | -1 | 97.002 |
| 9 | 1 | 1 | 1 | 97.538 |
| 10 | 0 | 0 | 0 | 98.174 |
| 11 | -1.673 | 0 | 0 | 61.296 |
| 12 | 1.673 | 0 | 0 | 99.845 |
| 13 | 0 | -1.673 | 0 | 99.505 |
| 14 | 0 | 1.673 | 0 | 98.907 |
| 15 | 0 | 0 | -1.673 | 96.653 |
| 16 | 0 | 0 | 1.673 | 65.870 |
| 17 | 0 | 0 | 0 | 98.174 |

Experimental data were analyzed using STATISTICA program, to get the parameters from the model that will provide the estimation of influence of variables against ethyl ester percentage yield. Statistical analysis to determine the significant influence of variables is shown in Table 4.

Table 4. Regression coefficients

| Model Parameter | Parameter Estimate | Standard Error | Computed T-Value | *P*-Value |
|---|---|---|---|---|
| Intercept | 97.617 | 5.188 | 18.813 | $2.35 \times 10^{-7}$ |
| $X_1$ | 20.863 | 5.148 | 4.052 | 0.004 |
| $X_2$ | -13.147 | 6.377 | -2.061 | 0.078 |
| $X_3$ | 9.957 | 4.943 | 2.014 | 0.083 |
| $X_1^2$ | 2.459 | 5.408 | 0.454 | 0.662 |
| $X_2^2$ | -8.149 | 4.943 | -1.648 | 0.143 |
| $X_3^2$ | -10.460 | 5.408 | -1.934 | 0.094 |
| $X_1X_2$ | -17.282 | 6.435 | -2.685 | 0.031 |
| $X_1X_3$ | 1.681 | 6.435 | 0.261 | 0.801 |
| $X_2X_3$ | 0.091 | 6.435 | 0.014 | 0.989 |

Based on the Table 4, the most significant parameter is the dose of the catalyst and combination of catalyst dosage and molar ratio ethanol to CPO. Since p-value is 0.05, the other parameter is considering as insignificant. Polynomial equation is expressed as equation 2 below.

$$Y_{yield} = 976179 + 208637X_1 - 131470X_2 + 24599X_1^2 - 172828X_1X_2 \quad (2)$$

The experimental data are shown in graphical form contour plot that showing the relationship the two variables against percentage yield (see Figure 5, 6 and 7). Figure 5 shows the relationship between the dose of the catalyst and the molar ratio of ethanol to CPO against percentage yield of ethyl esters. Based on the graph, it shows that the effect is given by catalyst dosage to the percentage yield of ethyl esters greater than molar ratio. The greater dose of the catalyst makes the process of converting oil into ethyl ester higher. Low doses of catalysts can also produce biodiesel with high yields but is followed by the amount of the molar ratio of ethanol: CPO. The use of catalysts with high enough doses followed by the high molar ratio of ethanol to CPO can raise percentage yield of ethyl ester.

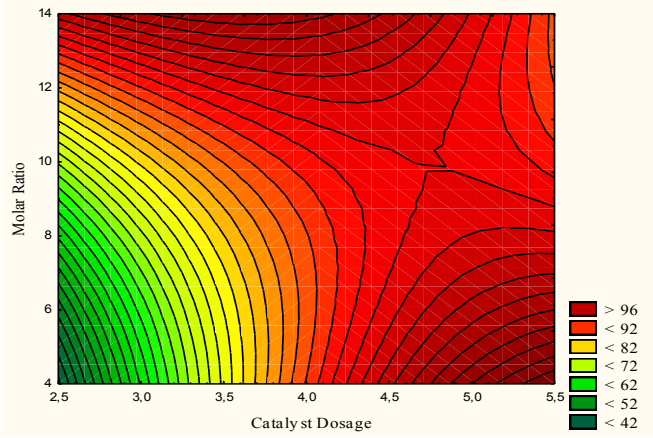



Figure 5. Contour plot of catalyst dosage and molar ratio ethanol: CPO against percentage yield

Figure 6 shows the relationship between the dose of the catalyst and reaction time against percentage yield. In this figure, it can be seen that the use of catalysts ChOH with high enough doses, the conversion of triglycerides into biodiesel is also high, but must be followed by the optimal reaction time. If the transesterification reaction time is too long exceeding the optimum time, the conversion of the resulting biodiesel can be low. For a short time, the biodiesel produced is high enough so that the use of catalysts ChOH is very advantageous in biodiesel transesterification reaction. The catalyst dosage and reaction time effect on yield greatly significant.

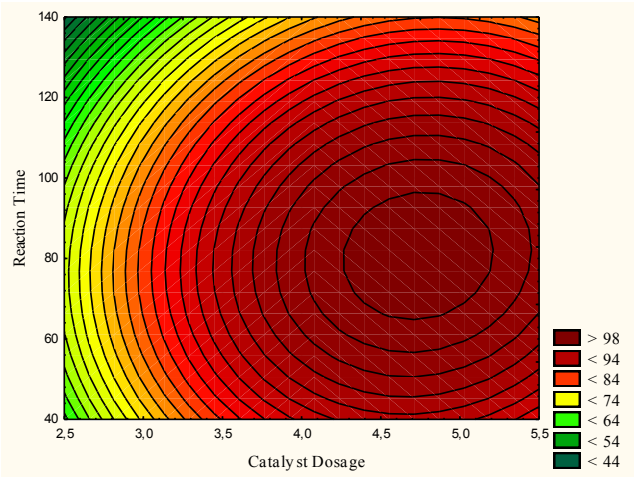



Figure 6. Contour plot of catalyst dosage and reaction time against percentage yield

Figure 7 shows the relationship between the molar ratio of ethanol: CPO and reaction time against percentage yield of ethyl ester. From this contour plot, it can be seen that the high molar ratio of ethanol to CPO, can produce biodiesel with a high percentage yield. As for the reaction time, on the contrary, the long reaction times, can cause biodiesel produced is low. Transesterification short reaction time is sufficient to produce the high percentage yield of ethyl ester. Effect of reaction time on biodiesel is more dominant than the molar ratio of ethanol to CPO.

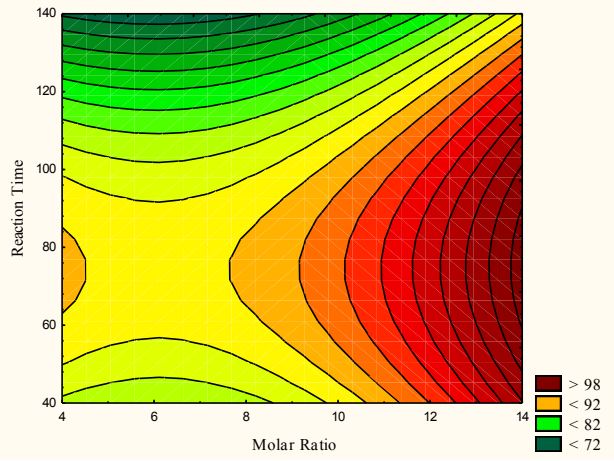



Figure 7. Contour plot of molar ratio ethanol: CPO and reaction time against percentage yield

## Conclusion

CPO as feedstock in biodiesel production without going through the pre-treatment can produce good enough yields of biodiesel using a basic catalyst ionic liquid choline hydroxide (ChOH). Ethanol has great potential in biodiesel production as a reactant alcohol because it is renewable and included in agricultural cycle. The optimum point in biodiesel production is 99.84% at 70 °C with a molar ratio of ethanol against crude palm oil was 9:1, the catalyst dosage 5.5% (w/w) and the reaction time is 90 minutes. The variables that most influence are the catalyst dosage followed by reaction time and the molar ratio. The lower of catalyst dosage and more doses of catalyst and molar ratio of ethanol: CPO will produce higher percentage yield.

## Acknowledgement

The facilities supports from Chemical Process Laboratory, Department of Chemical Engineering, Faculty of Engineering, University of Sumatera Utara, North Sumatera, Medan 20155, Indonesia.

## References

1. Ma, F. and Hanna, M. A. (1999). Biodiesel production: A review. *Bioresource Technology*, 70(1): 1 – 15.
2. Izah, S. C. and Ohimain, E. I. (2013). The challenge of biodiesel production from oil palm feedstock in Nigeria. *Greener Journal of Biological Sciences*, 3(1): 1 – 12.
3. Taufiq-Yap, Y. H., Abdullah, N. F. and Basri, M. (2011). Biodiesel production via transesterification of Palm oil using $NaOH/Al_2O_3$ catalysts. *Sains Malaysiana*, 40(6): 587 – 594.
4. Manurung, R., Dania K. S. and Nadya G. B. (2015). Methyl ester as biodiesel from crude palm oil (CPO) using choline hydroxide catalyst. Proceeding of the 22nd Regional Symposium on Chemical Engineering, Malaysia.
5. Suppalakpanya, K., Ratanawilai, S., Nikhom, R. and Tongurai, C. (2011). Production of ethyl ester from crude palm oil by two-step reaction using continuous microwave system. *Sonklanakarin Journal of Science and Technology*, 33(1): 79 – 86.
6. Ishak, Z. I., Sairi, N. A., Alias, Y., Aroua, M. K. T and Yusoff, R. (2014). Ionic liquids as green catalysts for transesterification reactions to produce biodiesel and glycerol carbonate – a review. *Processing Technology*.
7. Van Doorslaer, C., Wahlen, J., Mertens, P., Binnemans, K. and De Vos, D. (2010). Immobilization of molecular catalysts in supported ionic liquid phases. *Dalton Transactions*, 39(36): 8377 – 8390.
8. Fan, M., Huang, J., Yang, J. and Zhang, P. (2013). Biodiesel production by transesterification catalyzed by an efficient choline ionic liquid catalyst. *Applied Energy*, 108: 333 – 339.
9. Reddy, E. R., Sharma, M., Chaudhary, J. P., Bosamiya, H. and Meena, R. (2014). One-pot synthesis of biodiesel from high fatty acid *Jatropha curcas* oil using bio-based basic ionic liquid as a catalyst. *Current Science*, 106(10): 1394 – 1400.
10. Manurung, R. (2005). Optimasi dan kinetika transesterifikasi minyak sawit menjadi etil ester. *Thesis Magister Teknik Kimia*, 24: pp. 30 – 34.

*Malaysian Journal of Analytical Sciences, Vol 21 No 1 (2017): 248 - 260*
*DOI: http://dx.doi.org/10.17576/mjas-2017-2101-29*

MALAYSIAN JOURNAL OF ANALYTICAL SCIENCES
*Published by The Malaysian Analytical Sciences Society*
ISSN 1394 - 2506

# SYNTHESIS, CHARACTERIZATION AND CATALYTIC PERFORMANCE OF CERIA-SUPPORTED COBALT CATALYST FOR METHANE DRY REFORMING TO SYNGAS

## (Sintesis, Pencirian dan Prestasi Mangkin Kobalt Sokongan Ceria untuk Penghasilan Semula Metana Kontang Kepada Gas Sintesis)

Bamidele V. Ayodele[1,2], Mohd Nasir Nor Shahirah[1,2] , Maksudur R. Khan[1], Chin Kui Cheng[1,2]*

[1]*Faculty of Chemical & Natural Resources Engineering*
[2]*Centre of Excellence for Advanced Research in Fluid Flow (CARIFF)*
*Universiti Malaysia Pahang, Lebuhraya Tun Razak, 26300 Gambang Kuantan, Malaysia*

**Corresponding author: chinkui@ump.edu.my*

Received: 21 October 2015; Accepted: 14 June 2016

**Abstract**

In this study the synthesis, characterization and catalytic performance of $CeO_2$ (Ceria) supported Co catalyst was investigated. First, the ceria was synthesized by direct thermal decomposition of $Ce(NO_3)_3.6H_2O$ and subsequently impregnated with 20 wt.% Co using aqueous solution of $Co(NO_3)_2.6H_2O$ as a precursor. The synthesized catalyst was characterized using TGA, $N_2$-adsorption-desorption, X-ray Diffractometry (XRD), Field Emission Scanning Electron Microscope (FESEM-EDX), and Fourier Transformation Infrared (FTIR). The catalytic property of the ceria-supported cobalt catalyst was tested in methane dry reforming using a stainless steel fixed bed reactor. The dry reforming reaction was performed at the temperature range of 923-1023 K under a controlled atmospheric pressure and constant gas hourly space velocity (GHSV) of 30000 $h^{-1}$. The effects of reactant ($CH_4$ and $CO_2$) feed ratio was investigated on reactants conversion, product yields, and selectivity. The ceria-supported cobalt catalyst recorded highest catalytic activity at a $CH_4$: $CO_2$ ratio of 0.9 and temperature of 1023 K. The highest values of 79.5% and 87.6% were recorded for the $CH_4$ and $CO_2$ conversions respectively. Furthermore, highest yields of 41.98% and 39.76%, as well as selectivity of 19.56% and 20.72%, were obtained for $H_2$ and CO respectively. Syngas ratio of 0.90 was obtained from the dry reforming of methane, making it suitable as feedstock for Fischer-Tropsch synthesis (FTS).

**Keywords:** ceria, cobalt, Fischer-Trosch synthesis, methane dry reforming, syngas

**Abstrak**

Dalam kajian ini, sintesis, pencirian berserta prestasi tindakbalas pemangkin $Co/CeO_2$ telah dijalankan. Terdahulu, ceria disintesis daripada penguraian terma secara langsung ke atas $Ce(NO_3)_3.6H_2O$, diikuti oleh formulasi dengan 20% logam Co menggunakan larutan akueus $Co(NO_3)_2.6H_2O$ sebagai pelopor. Mangkin yang diperolehi dicirikan dengan menggunakan kaedah TGA, $N_2$-penjerapan penyaherapan, pembelauan sinar X (XRD), Mikroskop Pengimbas Elektron Pancaran Medan – Sinar-X Serakan Tenagan (FESEM-EDX) dan Inframerah Tranformasi Fourier (FTIR). Prestasi pemangkin $Co/CeO_2$ telah diuji untuk tindakbalas penghasilan metana kontang di dalam reaktor keluli tahan karat. Tindakbalas kimia tersebut telah dijalankan pada suhu berjulat daripada 923-1023 K, tekanan 1 atm serta GHSV bersamaan 30000 $h^{-1}$. Kesan nisbah reaktan ($CH_4$ and $CO_2$) terhadap penukaran reaktan serta hasil dan pemilihan produk telah disiasat. Mangkin $Co/CeO_2$ mencatatkan aktiviti pemangkin paling tinggi pada nisbah $CH_4/CO_2$ bersamaan 0.9 dan suhu 1023 K. Penukaran $CH_4$ and $CO_2$ mencatatkan nilai tertinggi bersamaan 79.5% dan 87.6%. Tambahan pula, hasil tertinggi bersamaan 37.6% dan 40% berserta sifat pemilihan bersamaan 19.56% dan 20.72% untuk $H_2$ dan CO telah direkodkan. Nisbah gas sintesis bersamaan 0.9 telah diperolehi daripada penghasilan semula metana kontang bersesuaian untuk tindakbalas sintesis Fischer-Trosch.

**Kata kunci:** ceria, kobalt, sintesis Fischer-Tropsch, penghasilan semula metana, gas sintesis

## Introduction

The utilization of energy derived from fossil sources as transportation fuel has been one of the major concerns of researchers in the past five decades [1,2]. This is due to the emissions of greenhouse gases such as $CO_2$ into the biosphere during the combustion of these fuels [3,4]. Several reports have shown that these greenhouse gases are the main causes of global warming through "greenhouse effect" [5–7]. Efforts of researchers have been concentrated on how to mitigate the emissions of these greenhouse gases [3,8,9]. Methane ($CH_4$) is one of the key components of greenhouse gases as well as a major source of fossil fuel [10]. It is inexpensive and abundance in nature, hence a good building block for $C_1$ chemistry [11]. One way to mitigate the emissions of the greenhouse gases, as well as increasing energy output via dry reforming process [9].

Dry reforming of methane depicted in Equation (1) has received wide research attention due to its advantage to utilize both $CO_2$ and $CH_4$, the two principal components of greenhouse gases for production of synthesis gas (a mixture of $H_2$ and CO) [12–14]. This syngas can be used as chemical intermediates for the production of synthetic fuel via Fischer-Tropsch synthesis (FTS) [15,16].

$$CO_2 + CH_4 \rightarrow H_2 + CO \qquad \Delta H_{1023K} = 261\text{kJ}mol^{-1} \tag{1}$$

Dry reforming of methane as a highly endothermic process is majorly constraint with catalyst deactivation from sintering and carbon deposition [17,18]. There have been concerted efforts by researchers in the field of catalysis in designing and developing catalysts with high activity and stability to overcome challenges of sintering and carbon depositions [19,20].

Up to date, the activity and stability of supported metal-based catalysts such as Pt, Pd, Ru, Rh, Ir, Ni and Co, have been investigated for dry reforming of methane [21]. Reports have shown that supported noble metals catalysts such as Pt, Pd, Ru, Rh, and Ir are very active and highly stable during dry reforming of methane [22–24]. However, these noble-metal catalysts are not readily available and very expensive [25]. Hence, the application of these noble metals to catalyze dry reforming of methane will not be economical in the event of scale up. Supported Ni-based catalysts have high activity and are inexpensive [26]. Nevertheless, the usage of Ni-based catalysts in dry reforming of methane has been constraint by their susceptibility to catalyst deactivation via sintering and carbon depositions [27]. Supported Co-catalyst which is less expensive compared to noble-metal catalysts has been reported as a good alternative to Ni-based catalysts in terms of stability [28].

In addition to using good metal-based catalysts, its play a significant role in enhancing the thermal stability of catalysts during dry reforming of methane [29]. Reports have shown that efficient dispersion of active metals on supports such as $SiO_2$, $\alpha$-$Al_2O_3$ $CeO_2$, $La_2O_3$ and $ZrO_2$ to a large extent affect the pore morphology, confinement and chemical effect of the catalysts [30]; [14]. This will invariably retard coke formation as well as reduce the tendency of the active metal to sinter. The use of ceria ($CeO_2$)-supported Co catalyst has been extensively studied for ethanol steam reforming [31–33]. However, there are limited studies on the dry reforming of methane over ceria supported Co catalyst [34, 35].

This present study focuses on the synthesis, characterization and catalytic performance of ceria supported Co catalyst for dry reforming of methane. The ceria support was prepared by thermal decomposition of cerium (III) nitrate hexahydrate and subsequently used for the synthesis of the $Co/CeO_2$ catalyst via wet impregnation method [36].

## Materials and Methods

### Catalyst synthesis

The schematic diagram depicting the steps involved in the catalyst synthesis is shown in Figure 1. First, the ceria support used for the catalyst synthesis was prepared by thermal decomposition of $Ce(NO_3)_3.6H_2O$ (99.99% trace metal basis, Sigma-Aldrich) at 773 K for 2 hours to obtained $CeO_2$ powder [36,37]. The $CeO_2$ powder was

subsequently impregnated with aqueous solution of $Co(NO_3)_2.6H_2O$ (20 wt% Co loading) by wet impregnation method and then stirred continuously for 3 hours at room temperature. Thereafter, the mixture containing the catalyst precursor and the support was dried at 393 K for 24 hours and then calcinate at 873 K for 5 hours.

**Catalyst characterization**

The physicochemical properties of the fresh 20 wt% $Co/CeO_2$ catalyst were determined by temperature programmed calcination using thermogravimetric analyzer (TA instrument, Q 500). The catalyst sample was heated from 298 to 1173 K at heating rates of 10, 15 and 20 K/min. The specific surface area, pore volume and average pore diameter of the catalyst were measured by $N_2$ adsorption-desorption isotherm at 77 K using Thermo Scientific Surfer Analyzer. Prior to the $N_2$ adsorption-desorption experiment, the catalyst was degassed at 573 K for 3 hours. Phase identification, as well as the crystallinity of the 20 wt% $Co/CeO_2$ catalyst, was determined by Rigaku X-ray powder diffraction analysis (XRD) (Miniflex II) with Cu Kα (45kV, 0.154 nm) radiation.

The morphology and elemental composition of the catalyst sample were carried out using JEOL FESEM (JSM-7800F) equipped with EDX. Temperature-programmed reduction (TPR) of the fresh catalyst was performed in a fixed bed reactor. The catalyst weighing 200 mg was heated from 373 – 1073 K in a flow of 60 ml/min of $H_2/N_2$ (1:5). The amount of hydrogen consumed was measured using gas chromatography (GC) equipped with thermal conductivity detector (TCD). The GC consists of two packed columns namely Supelco Molecular Sieve 13x (10 ft × 1/8 in OD × 2 mm ID, 60/80 mesh, Stainless Steel) and Agilent Hayesep DB (30 ft × 1/8 in OD × 2 mm ID, 100/120 mesh, Stainless Steel). Helium gas with flow rate of 20 ml $min^{-1}$ was used as the carrier at operating column temperature of 393 K.

The nature of chemical bond of the catalyst was measured using Perkin Elmer Fourier transform infrared (FTIR) (Nicolet iS-50) spectrometer. The sample was analysed using an attenuated total reflectance (ATR) method within 4000-400 $cm^{-1}$.

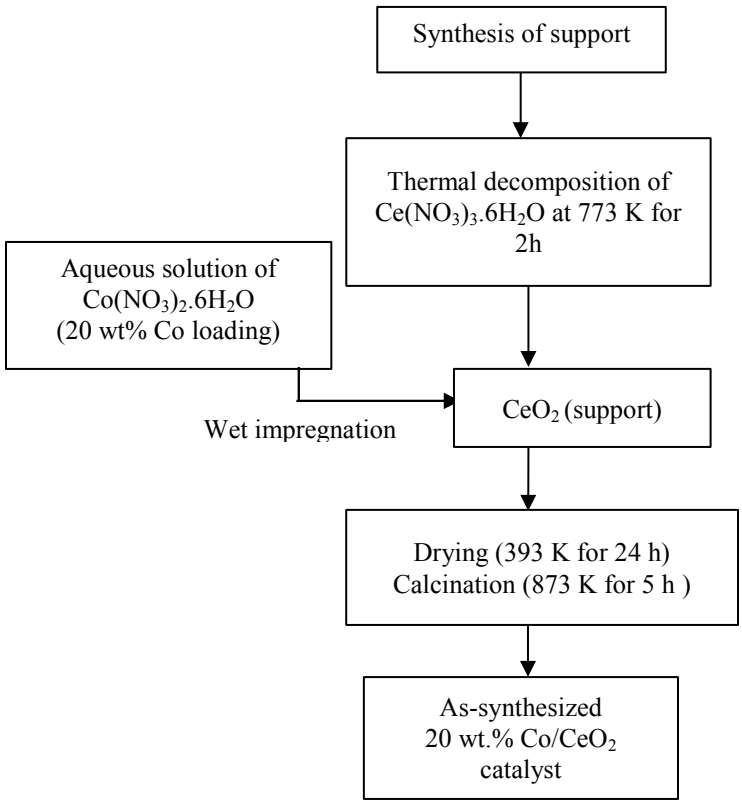



Figure 1. Schematic diagram of steps involved in the synthesis of the 20 wt% $Co/CeO_2$ catalyst

**Catalyst activity test**

The catalyst activity test was performed in a stainless steel fixed bed reactor under controlled atmospheric pressure. The stainless steel tubular reactor was loaded with 200 mg catalyst sample supported with quartz wool. The fixed bed reactor was positioned in a furnace equipped with a Type-K thermocouple to monitor the temperature of the catalytic bed. Prior to the commencement of the activity test, the catalyst was reduced *in situ* in a flow of 60 ml/min of $H_2/N_2$ (1:5) at 873 K for 1 h. The flow of the reactant gases ($CH_4$ and $CO_2$) into the reactor was monitored using Alicat digital mass flow controller. The dry reforming of methane was performed at varying feed ratios ranged 0.1-1.0 and reaction temperature ranged 923 – 1023 K. The compositions of the reactant gases as well as the products ($H_2$ and CO) were monitored using GC-TCD. The activity of the catalyst was measured based on the conversions of the reactants, the yield, and selectivity of the products formed as shown in equations (2) – (7).

$$CH_4 \text{ conversion } (\%) = \frac{F_{CH_{4in}} - F_{CH_{4out}}}{F_{CH_{4in}}} \times 100 \quad (2)$$

$$CO_2 \text{ conversion } (\%) = \frac{F_{CO_{2in}} - F_{CO_{2out}}}{F_{CO_{2in}}} \times 100 \quad (3)$$

$$H_2 \text{ yield} = \frac{F_{H_{2out}}}{2 \times F_{CH_{4in}}} \times 100 \quad (4)$$

$$CO \text{ yield} = \frac{F_{CO_{out}}}{F_{CH_{4in}} + F_{CO_{2in}}} \times 100 \quad (5)$$

$$H_2 \text{ Selectivity} = \frac{F_{H_{2out}}}{F_{H_{2out}} + F_{CH_{4out}} + F_{CO_{2out}} + F_{CO}} \times 100 \quad (6)$$

$$CO \text{ Selectivity} = \frac{F_{H_{2out}}}{F_{CH_{4out}} + F_{CO_{2out}} + F_{COout}} \times 100 \quad (7)$$

$F_{CO_{2in}}$, = inlet molar flow of $CO_2$; $F_{CO_{2out}}$ = outlet molar flow of $CO_2$; $F_{CH_{4in}}$, = inlet molar flow of $CH_4$; $F_{CH_{4out}}$ = outlet molar flow of $CH_4$; $F_{H_{2out}}$, = outlet molar flow of $H_2$; $F_{COout}$ = outlet molar flow of CO.

## Results and Discussion

**Catalyst characterization**

The temperature programmed calcination of the fresh catalyst is shown in Figure 2. Four distinct peaks (I to IV) can be identified from the TGA curve. Peaks I-III can be attributed to sequential loss of physical and hydrated water while peak IV depicts decomposition of the cobalt nitrate to obtain $Co_3O_4$. This trend is consistent with the findings of [38] in their study on dry reforming of methane over alumina supported cobalt catalyst.

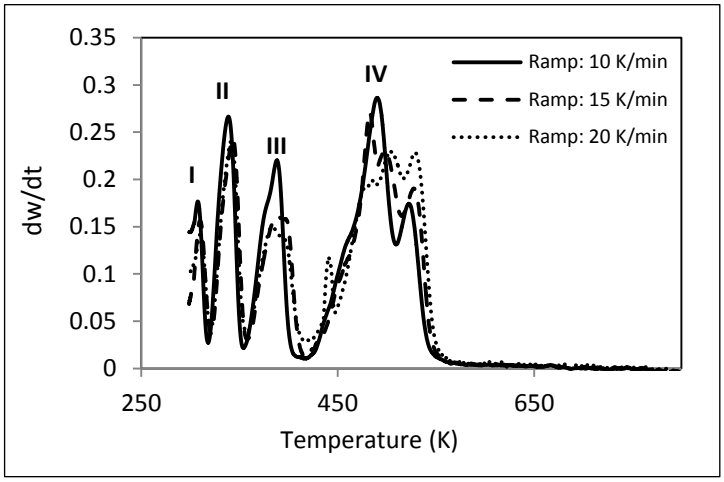



Figure 2. Temperature Programmed Calcination of the 20 wt% $Co/CeO_2$ catalyst

The determination of the mesoporous structure and specific surface of the 20 wt% $Co/CeO_2$ catalyst from $N_2$ adsorption-desorption isotherm is depicted in Figure 3. The $Co/CeO_2$ catalyst isotherm has a characteristic of Type IV isotherm curve with H3 hysteresis loop. Since the relative pressure (P/P°) is > 0.55, the catalyst exhibited uniform mesoporous structure with capillary condensation. The BET specific area of the catalyst was estimated from the sorptomatic data processing software as 39.89 $m^2g^{-1}$ while the pore volume and average pore diameter obtained from Barrett, Joyner, and Hallenda (BJH) method were estimated to be 0.0141 $cm^3g^{-1}$, and 1.16 nm respectively.

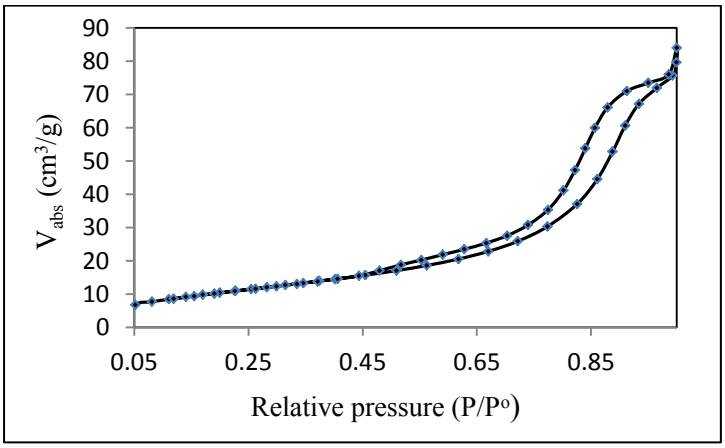



Figure 3. $N_2$ adsorption-desorption isotherm of the 20 wt% $Co/CeO_2$ catalyst

The XRD pattern of the catalyst sample is depicted in Figure 4. Distinct peaks of $CeO_2$ and $Co_3O_4$ crystals can be seen at 2θ = 29.4°, 38.4°, 48.7°, 57.9° and 2θ = 31.3°, 44.5°, 59.7°, 65.1°, 67.7°, 77.1° respectively. The diffraction peaks obtained for $CeO_2$ can be assigned to the crystalline phase of (111), (220), (311), (220) and (422) which represent faced-centre cubic structure [39].

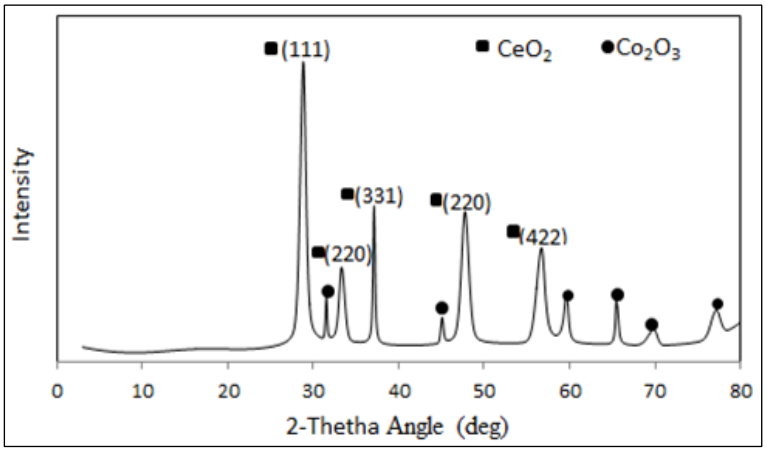



Figure 4. XRD pattern of the 20 wt% $Co/CeO_2$ catalyst

The FESEM micrograph and EDX dot mapping showing the morphology and the elemental composition of the 20 wt% $Co/CeO_2$ catalyst are depicted in Figures 5-7 respectively. The FESEM micrograph (Figure 5) shows the

irregularity and the agglomeration of the catalyst particle sizes. While the EDX dot mapping (Figure 6) confirms the presence of Co, Ce and O as stimulated during the synthesis of the catalyst. The elemental compositions of the catalysts obtained from the EDX dot mapping (Figure 7) corresponds to the stimulated amount used for the catalysts synthesis.

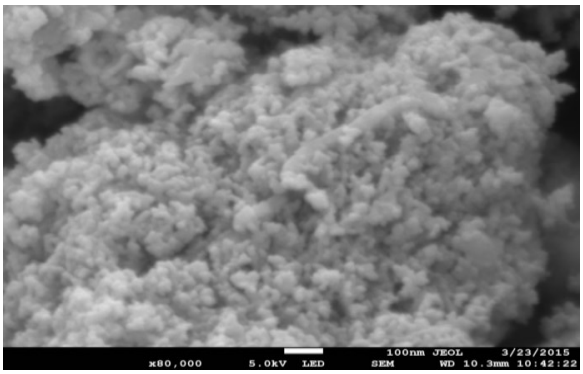



Figure 5. The FESEM micrograph of the 20 wt% $Co/CeO_2$ catalyst

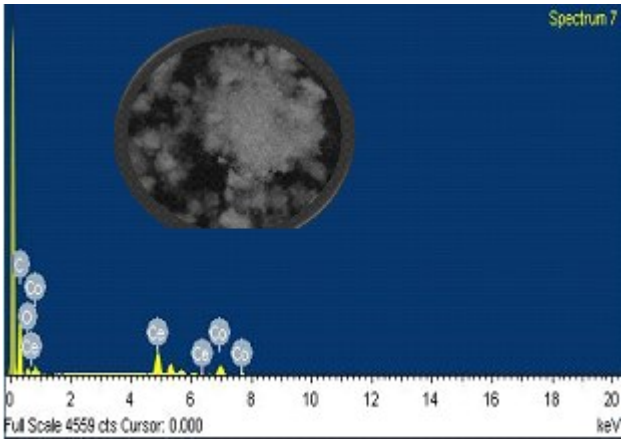



Figure 6. The EDX dot mapping of the 20 wt% $Co/CeO_2$ catalyst

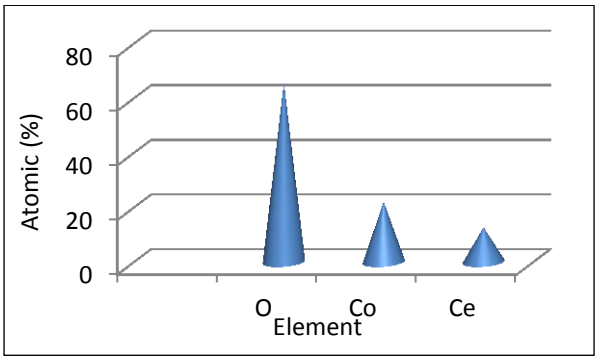



Figure 7. The elemental composition of the 20 wt% $Co/CeO_2$ catalyst obtained from EDX-mapping

In order to check the reducibility of the catalyst in a flow of $H_2$, the catalyst was subjected to $H_2$-TPR. Significantly, two peaks centralized at a temperature of 423, and 673 K can be identified from the $H_2$-TPR profile. The peaks could be attributed to the sequential reduction of $Co_3O_4$ to Co crystallite represented in equation 8. The peak at 423 K could be attributed to the reduction of $Co_3O_4$ which has a weak interaction with the support to CoO. The peak at 577K with a stronger interaction can be attributed to the reduction of CoO to Co [40].

$$Co_3O_4 \rightarrow CoO \rightarrow Co \quad (8)$$

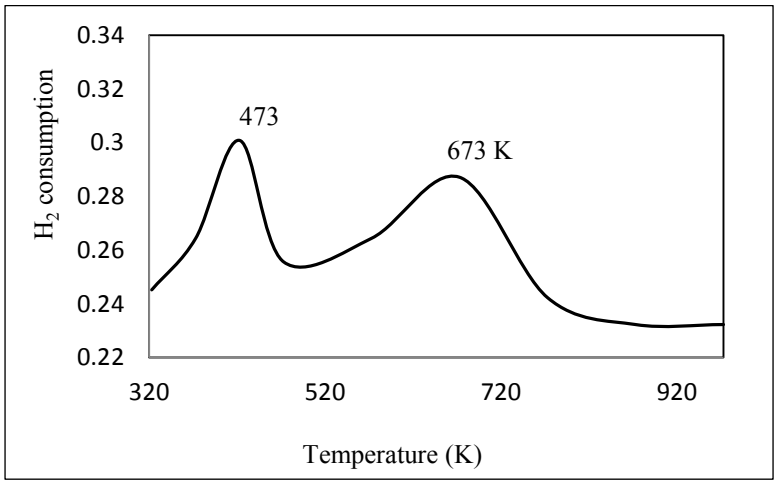



Figure 8. $H_2$-TRP profile of the 20 wt% $Co/CeO_2$ catalyst

The FTIR spectra of the catalyst are shown in Figure 9. The spectra band can be identified at 3400, 1670, 667 and 567 $cm^{-1}$ respectively. The bands at 3400 and 1670 $cm^{-1}$ can be attributed to $OH^-$ which is due to water moisture and COO from dissolved atmospheric $CO_2$. The band obtained at 1670 and 667 $cm^{-1}$ can be attributed to stretching metal oxides (M-O) bond from Co-O and Ce-O respectively.

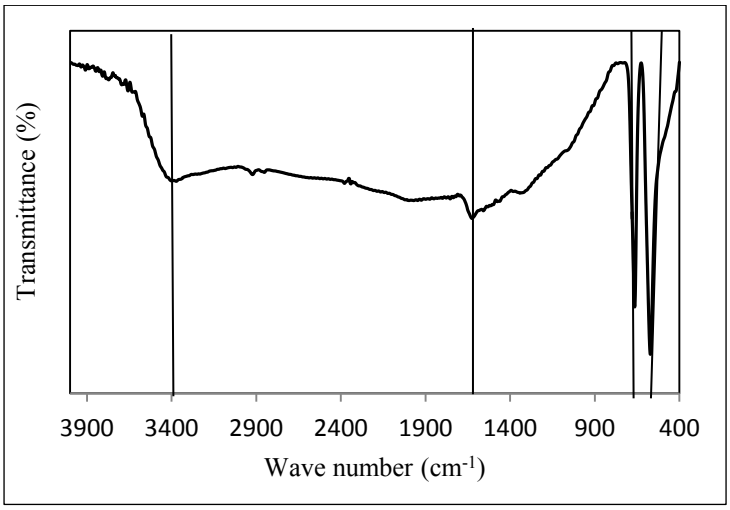



Figure 9. FTIR spectra of the 20 wt% $Co/CeO_2$ catalyst

**Catalyst activity**

The performance of the ceria supported Co catalyst was measured from the conversions of the reactant gas to syngas, the yields of the syngas produced as well as the products selectivity. The effects of feed ratios (0.1-1.0) and temperature (923 – 1023K) were investigated on the catalyst activity in terms of conversions, yields, and selectivity in methane dry reforming process. The conversions of $CH_4$ and $CO_2$ depicted in Figures 10 and 11 increases with feed ratio and temperature signifying the temperature dependent nature of the dry reforming reaction. The conversion of $CH_4$ increases from 43.2% to a maximum value of 79.5%. Similarly, conversion of $CO_2$ increases from 17.8% to 87.6%. The catalyst shows higher activity towards $CO_2$ conversion compared to $CH_4$. This could be as a result of reversed water gas shift reaction shown in equation 9 [41].

$$CO_2 + H_2 \rightarrow H_2O + CO \quad \Delta H_{298} = 41\text{kJmol}^{-1} \tag{9}$$

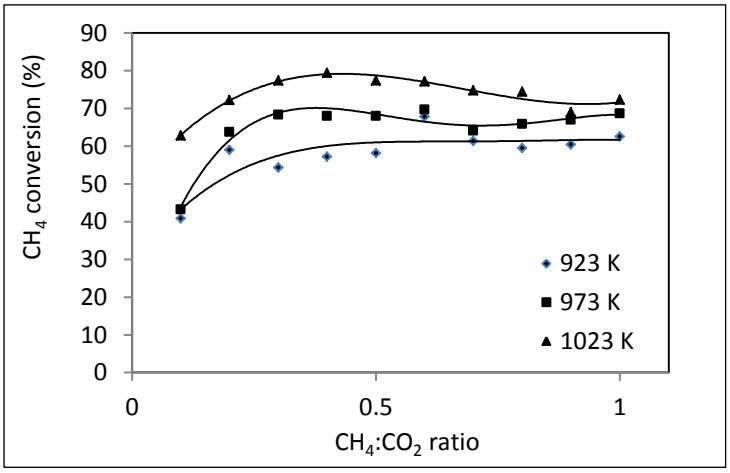



Figure 10. Effect of feed ratio and temperature on conversion of $CH_4$ over 20 wt% $Co/CeO_2$ catalyst

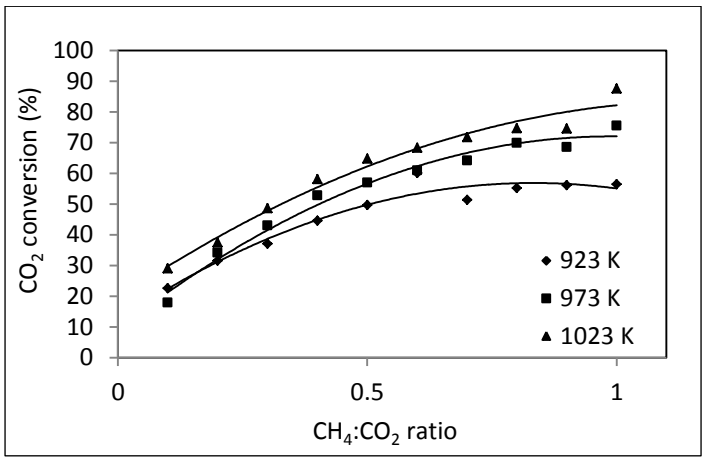



Figure 11. Effect of feed ratio and temperature on conversion of $CO_2$ over 20 wt% $Co/CeO_2$ catalyst.

The catalytic performances of the 20 wt% $Co/CeO_2$ catalyst in term of products (CO and $H_2$) yields are depicted in Figures 12 and 13, respectively. It is noteworthy that both $H_2$ and CO yields increase with feed ratios and temperature. The yield of $H_2$ increases from 1.69% to reach a maximum value of 41.98%. While the yield of CO increases from 6.56% to the maximum value of 39.76%. A similar observation has been reported by Sajjidi et al. [42] for dry reforming of methane over $Ni–Co/Al_2O_3–ZrO_2$ nanocatalyst. The highest yield of 42% and 58% were obtained for $H_2$ and CO respectively. In the present study, at the highest yield of $H_2$ and CO, syngas ratio of 1.05 was obtained. This makes the syngas produced from the dry reforming of methane over the 20 wt% $Co/CeO_2$ catalyst suitable as a chemical intermediate to produce oxygenated fuel via FTS. Apparently, the catalyst shows a higher activity towards $H_2$ yield compared to CO yield. The observation could be attributed to temperature dependent nature of $CH_4$ decomposition. The decomposition of $CH_4$ increases with temperature leading to an increase in the formation of $H_2$ [43].

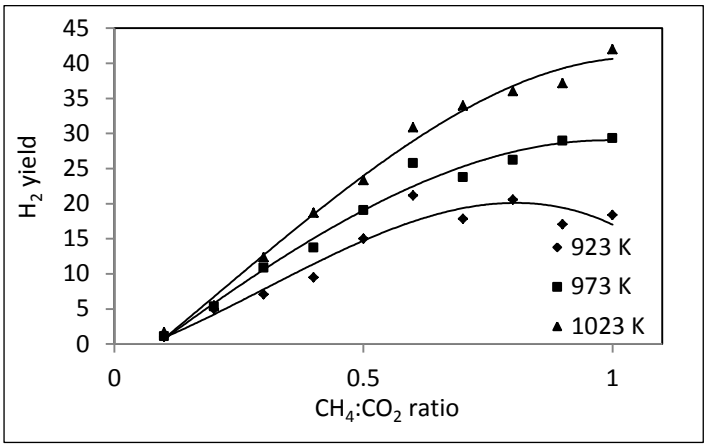



Figure 12. Effect of feed ratio and temperature on the yield of $H_2$ over 20 wt% $Co/CeO_2$ catalyst

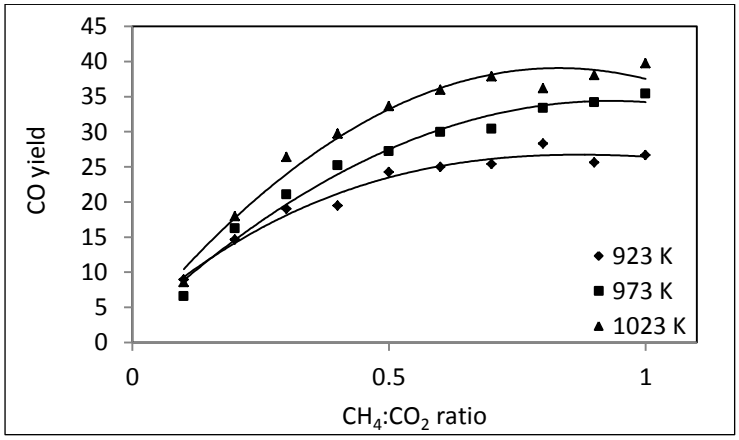



Figure 13. Effect of feed ratio and temperature on the yield of CO over 20 wt% $Co/CeO_2$ catalyst

The selectivity of the 20 wt% $Co/CeO_2$ catalyst towards $H_2$ and CO production is shown Figures 14 and 15, respectively. The $H_2$ and CO selectivity significantly increase with feed ratio and temperature from 1.16% and 8.56% to reach a maximum value of 19.56% and 20.72% respectively. This observation is consistent with the findings of Zheng et al. [44] who employed $Co/\gamma\text{-}Al_2O_3$ for dry reforming of methane to syngas. The authors,

however, obtain a higher selectivity of 95% and 85% for $H_2$ and CO. The difference in result could be linked to high surface area $\gamma$-$Al_2O_3$ used as support compared to Ceria as well as the difference in experimental conditions.

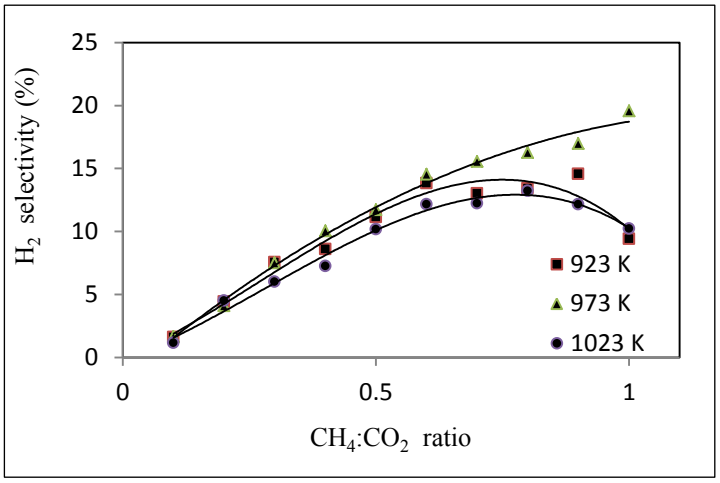



Figure 14. Effect of feed ratio and temperature on the selectivity of $H_2$ over 20 wt% $Co/CeO_2$ catalyst

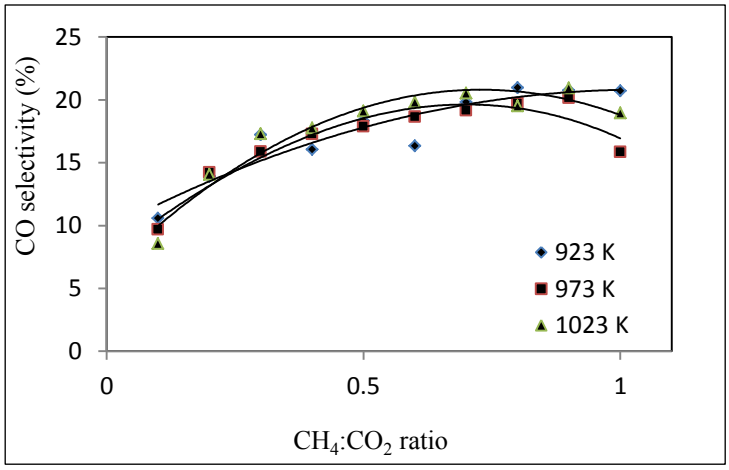



Figure 15. Effect of feed ratio and temperature on the selectivity of CO over 20 wt% $Co/CeO_2$ catalyst

## Conclusion

In this study, we have reported the synthesis, characterization and catalytic performance of ceria supported Co catalyst. The catalyst was synthesized by wet impregnation method and characterized by different physicochemical properties using techniques such as TGA, $N_2$-adsorption-desorption, XRD, FESEM-EDX, and FTIR. The catalytic performance of the as-synthesized catalyst was tested in dry reforming of methane for the production of syngas. The catalyst shows good performance towards reactant conversion, products yield, and selectivity. Syngas ratio of 0.9 was produced from the dry reforming of methane over the ceria supported catalyst, making the process suitable for the production of feedstock for FTS process.

**Acknowledgement**

The authors would like to acknowledge the research fund RDU130501 granted by the Ministry of Science, Technology and Innovation Malaysia (MOSTI) and the DSS scholarship granted to Bamidele V. Ayodele by Universiti Malaysia Pahang.

**References**

1. Guo, S., Shao, L., Chen, H., Li, Z., Liu, J. B., Xu, F. X., Li, J. S., Han, M. Y., Meng, J., Chen, Z. M. and Li, S. C. (2007). Inventory and input–output analysis of $CO_2$ emissions by fossil fuel consumption in Beijing. *Ecological Informatics*, 12: 93 – 100.
2. Shearer, C., Bistline, J., Inman, M. and Davis, S. J. (2014). The effect of natural gas supply on US renewable energy and $CO_2$ emissions. *Enviromental Research Letters*, 9(9): 1 - 12.
3. Clarke, L., Kyle, P., Wise, M., Calvin, K., Edmonds, J., Kim, S., Placet, M. and Smith, S. (2008). $CO_2$ Emissions mitigation and technological advance : An updated analysis of advanced technology scenarios *PNNL Report Pacific Northwest National Laboratory, Richmond*.
4. Ang, C. T., Morad, N., Ismail, M. T. and Ismail, N. (2013). Projection of carbon dioxide emissions by energy consumption and transportation in Malaysia: A time series approach. *Journal of Energy Technologies and Policy*, 3: 1 - 10.
5. Korre A, Nie Z. and Durucan S. (2010). Life cycle modelling of fossil fuel power generation with post-combustion $CO_2$ capture. *International Journal of Greenhouse Gas Control* , 4: 289 – 300.
6. Samimi, A. and Zarinabadi S. (2012). Reduction of greenhouse gases emission and effect on environment. *Journal of American Science,* 8: 1011 - 1015.
7. Mathiesen, B. V., Lund, H. and Karlsson K.. (2011). 100% Renewable energy systems, climate mitigation and economic growth. *Applied Energy*, 88: 488 – 501.
8. Ross, J. R. H. (2015). Natural gas reforming and $CO_2$ mitigation. *Catalysis Today*, 100: 151 –158.
9. Braga, T. P., Santos, R. C., Sales, B. M., da Silva, B. R., Pinheiro, A. N., Leite, E. R. and Valentini A. (2014). $CO_2$ mitigation by carbon nanotube formation during dry reforming of methane analyzed by factorial design combined with response surface methodology. *Chinese Journal of Catalysis*, 35: 514 –523.
10. Aasberg-Petersen, K., Dybkjær, I., Ovesen, C. V., Schjødt, N. C., Sehested, J. and Thomsen, S. G. (2011). Natural gas to synthesis gas - catalysts and catalytic processes. *Journal of Natural Gas Science and Engineering,* 3: 423 – 459.
11. Verykios, X. E. (2003). Catalytic dry reforming of natural gas for the production of chemicals and hydrogen. *International Journal of Hydrogen Energy*, 28: 1045 – 1063.
12. Sharifi, M., Haghighi, M., Rahmani, F. and Karimipour, S. (2014). Syngas production via dry reforming of $CH_4$ over Co- and Cu-promoted $Ni/Al_2O_3–ZrO_2$ nanocatalysts synthesized via sequential impregnation and sol–gel methods. *Journal of Natural Gas Science and Engineering,*21: 993 – 1004.
13. Ba, K, Oszk, A., Kecsk, T. and Erd A. (2014). Dry reforming of $CH_4$ on Rh doped Co $/Al_2O_3$ catalysts *Catalysis Today,* 228: 123 - 130.
14. Ayodele, B. V., Khan, M. R, Lam, S. S. and Cheng, C. K. (2016). Production of CO-rich hydrogen from methane dry reforming over lanthania-supported cobalt catalyst: Kinetic and mechanistic studies. *International Journal of Hydrogen Energy*, 41: 4603 - 4615.
15. Khodakov, A. Y, Chu, W. and Fongarland, P. (2007). Advances in the development of novel cobalt Fischer − Tropsch Catalysts for Synthesis of Long-Chain Hydrocarbons and Clean Fuels. *Chemical Reviews*, 107(5): 1692 - 1744.
16. Yao, Y., Liu, X., Hildebrandt, D. and Glasser D. (2011). Fischer-Tropsch synthesis using $H_2/CO/CO_2$ syngas mixtures over an iron catalyst. *Industrial Engineering Chemical Research,* 50: 11002 –11012.
17. Lee, J. H., You, Y. W., Ahn, H. C., Hong, J. S., Kim, S. B., Chang, T. S. and Suh, J. K. (2014). The deactivation study of Co–Ru–Zr catalyst depending on supports in the dry reforming of carbon dioxide. *Journal of Industrial and Engineering Chemistry*, 20: 284 – 289.
18. Ruckenstein, E. and Wang, H. Y. (2002). Carbon deposition and catalytic deactivation during $CO_2$ reforming of $CH_4$ over $Co/\gamma\text{-}Al_2O_3$ catalysts. *Journal of Catalysis*, 205: 289 – 293.
19. Zhang, J., Wang, H. and Dalai A. (2007). Development of stable bimetallic catalysts for carbon dioxide reforming of methane. *Journal of Catalysis*, 249: 300 – 310.

20. Corthals, S., Witvrouwen, T., Jacobs, P. and Sels B. (2011). Development of dry reforming catalysts at elevated pressure: D-optimal vs. full factorial design. *Catalysis Today*, 159: 12 – 24.
21. Li, D., Nakagawa, Y. and Tomishige K. (2011). Methane reforming to synthesis gas over Ni catalysts modified with noble metals. *Applied Catalysis A General*, 408: 1 – 24.
22. Özkara-Aydınoğlu, Ş. and Aksoylu, A. E. (2010). $CO_2$ reforming of methane over Pt–Ni/$Al_2O_3$ catalysts: Effects of catalyst composition, and water and oxygen addition to the feed. *International Journal of Hydrogen Energy*, 36: 2950 –2959.
23. Wisniewski, M., Boréave, A. and Gélin P. (2005). Catalytic $CO_2$ reforming of methane over Ir/$Ce_{0.9}Gd_{0.1}O_{2-x}$. *Catal Communications*, 6: 596 – 600.
24. Kim, S., Qadir, K., Jin, S., Reddy, A. S., Seo, B., Mun, B. S., Joo, S. H. and Park, J. Y. (2012). Trend of catalytic activity of CO oxidation on Rh and Ru nanoparticles: Role of surface oxide. *Catalysis Today*, 185:131 – 137.
25. Budiman, A.W., Song, S-H., Chang, T-S., Shin, C-H. and Choi M-J. (2012). Dry reforming of methane over cobalt catalysts: A literature review of catalyst development. *Catal Surveys from Asia*, 16: 183 –197.
26. Hadian, N., Rezaei, M., Mosayebi, Z. and Meshkani, F. (2012). $CO_2$ reforming of methane over nickel catalysts supported on nanocrystalline $MgAl_2O_4$ with high surface area. *Journal of Natural Gas Chemistry,* 21: 200 – 206.
27. Sehested, J. (2005). Four challenges for nickel steam-reforming catalysts. *Catalysis Today*, 111: 103 –110.
28. Oliveira, H., Franceschinib, D. and Passos F. (2014). Cobalt catalyst characterization for methane decomposition and carbon nanotube growth. *Journal of Brazilian Chemical Society*, 25: 2339 – 2349.
29. Frontera, P, Macario, A., Aloise, A., Antonucci, P. L., Giordano, G. and Nagy, J. B. (2013). Effect of support surface on methane dry-reforming catalyst preparation. *Catalysis Today*, 218: 18 – 29.
30. Shi, L., Yang, G., Tao, K., Yoneyama, Y., Tan, Y. and Tsubaki N. (2013). An introduction of $CO_2$ conversion by dry reforming with methane and new route of low-temperature methanol synthesis. *Account of Chemical Research*, 46: 1838 – 1847.
31. Zhang, B., Cai, W., Li, Y., Xu, Y. and Shen W. (2008). Hydrogen production by steam reforming of ethanol over an Ir/$CeO_2$ catalyst: Reaction mechanism and stability of the catalyst. *International Journal of Hydrogen Energy*, 33: 4377 – 4386.
32. Zhang, B., Tang, X., Li, Y., Cai, W., Xu, Y. and Shen, W. (2006). Steam reforming of bio-ethanol for the production of hydrogen over ceria-supported Co, Ir and Ni catalysts. *Catalysis Communications*, 7: 367 – 372.
33. da Silva, A. M., de Souza, K. R., Mattos, L. V., Jacobs, G., Davis, B. H. and Noronha, F. B. (2011). The effect of support reducibility on the stability of Co/$CeO_2$ for the oxidative steam reforming of ethanol. *Catalysis Today*, 164: 234 – 239.
34. Luisetto, I, Tuti, S. and Di Bartolomeo E. (2012). Co and Ni supported on $CeO_2$ as selective bimetallic catalyst for dry reforming of methane. *International Journal of Hydrogen Energy*, 37: 15992 – 15999.
35. Abasaeed, A. E, Al-fatesh, A. S, Naeem, M. A, Ibrahim, A. A. and Fakeeha, A. H. (2015). Catalytic performance of $CeO_2$ and $ZrO_2$ supported Co catalysts for hydrogen production via dry reforming of methane. *International Journal of Hydrogen Energy*, 6818 – 6826.
36. Ayodele, B. V., Hossain, M. A., Chong, S. L, Soh, J. C, Abdullah, S., Khan, M. R. and Cheng, C. K. (2016). Non-isothermal kinetics and mechanistic study of thermal decomposition of light rare earth metal nitrate hydrates using thermogravimetric analysis. *Journal of Thermal Analysis and Calorimetry,* 125(1): 423 - 435.
37. Lee, S. S, Zhu, H., Contreras, E. Q, Prakash, A., Puppala, H. L. and Colvin, V. L. (2012). High temperature decomposition of cerium precursors to form ceria nanocrystal libraries for biological applications. *Chemistry Materials,* 24: 424 – 432.
38. Foo, S. Y. (2012). Oxidative dry reforming of methane over alumina-supported Co-Ni catalyst systems. Doctor of Philosophy Thesis, University of New South Wale, Australia.
39. Wang, H, Liu, Y., Wang, L. and Qin, Y. N. (2008). Study on the carbon deposition in steam reforming of ethanol over Co/$CeO_2$ catalyst. *Chemical Engineering Journal*, 145: 25 – 31.
40. Zeng, S., Fu, Xiaojuan Z., Tiezhuang W. and Xiaoman S. H. (2014). Influence of Fe doping on structure and water oxidation activity of nanocast $Co_3O_4$. *Fuel Process Technology*, 114: 4 – 10.
41. Zeng, S., Zhang, X. Fu, X. Zhang, L. Su, H. and Pan, H. (2012). Co/$Ce_xZr_{1-x}O_2$ solid-solution catalysts with cubic fluorite structure for carbon dioxide reforming of methane. *Applied Catalysis B, Environmen*tal, 136: 308 – 316.

42. Sajjadi, S. M, Haghighi, M. and Rahmani, F. (2014). Dry reforming of greenhouse gases $CH_4/CO_2$ over MgO-promoted Ni-Co/$Al_2O_3$-$ZrO_2$ nanocatalyst: Effect of MgO addition via sol-gel method on catalytic properties and hydrogen yield. *Journal of Sol-Gel Science Technology*, 70(1): 111 –124.
43. San-José-Alonso, D., Juan-Juan, J., Illán-Gómez, M. J. and Román-Martínez, M. C. (2009). Ni, Co and bimetallic Ni-Co catalysts for the dry reforming of methane. *Applied Catalysis A General*, 371: 54 – 59.
44. Zeng, S., Zhang, L., Zhang, X., Wang, Y., Pan, H. and Su, H. (2012). Modification effect of natural mixed rare earths on Co/γ-$Al_2O_3$ catalysts for $CH_4/CO_2$ reforming to synthesis gas. *International Journal of Hydrogen Energy,* 37: 9994 – 10001.

*Malaysian Journal of Analytical Sciences, Vol 21 No 1 (2017): 261 - 266*
*DOI: http://dx.doi.org/10.17576/mjas-2017-2101-30*

MALAYSIAN JOURNAL OF ANALYTICAL SCIENCES
*Published by The Malaysian Analytical Sciences Society*
ISSN 1394 - 2506

# EFFECTS OF AGITATION CONDITIONS ON BACTERIAL CELLULOSE PRODUCTION BY *Acetobacter xylinum 0416* IN FERMENTATION OF MATURED COCONUT WATER MEDIUM

## (Kesan Goncangan ke atas Penghasilan Selulosa Bakteria oleh *Acetobacter xylinum 0416* Melalui Fermentasi Air Kelapa Tua)

Faezah Esa, Norliza Abd. Rahman*, Mohd Sahaid Kalil, Siti Masrinda Tasirin

*Department of Chemical and Process Engineering,*
*Faculty of Engineering and Built Environment,*
*University of Malaysia, 43600 UKM Bangi, Selangor, Malaysia*

**Corresponding author: norlizajkkp@ukm.edu.my*

Received: 21 October 2015; Accepted: 14 June 2016

**Abstract**

Bacterial cellulose (BC), a pure form of three-dimensional biopolymer is gaining extensive interest due to its unique physical and mechanical properties. The effects of different agitation conditions on BC synthesis by *Acetobacter xylinum 0416* have been compared. Fermentations were carried out at 150 and 200 rpm using rotatory incubator shaker and rotatory shaker in a constant temperature room of 30 ºC. Matured coconut water was used as a sustainable medium due to its low cost and availability. The medium was adjusted to pH 4.5 or pH 5.5 and BC pellets were collected after 7 days of fermentation. The constant temperature room appeared to has fluctuate degree of heat during fermentation up to 37 °C and suppressed the BC production. In rotatory incubator shaker, the BC produced have insignificant different in comparison to pH and rotation speed. These results indicate that matured coconut water has potential as the carbon source for BC synthesis and optimization of fermentation temperature is important to produce enormous yield of BC.

**Keywords:** bacterial cellulose, matured coconut water, fermentation, agitation speed

**Abstrak**

Selulosa bakteria (SB) iaitu sejenis tiga-dimensi biopolimer sedang mendapat tumpuan yang meluas disebabkan oleh sifat fizikal dan mekanikalnya yang unik. Kesan goncangan yang berbeza terhadap sintesis SB oleh bakteria *Acetobacter xylinum 0416* telah dibandingkan. Proses fermentasi telah dilakukan pada kelajuan 150 rpm dan 200 rpm menggunakan inkubator penggoncang berputar yang tertutup dan inkubator penggoncang berputar terbuka yang terletak di dalam bilik malar pada suhu tetap 30 °C. Air kelapa tua digunakan sebagai medium mapan kerana mudah diperoleh pada kos yang rendah. Media ini dilaraskan pada pH 4.5 atau pH 5.5 dan pelet BS dikumpulkan selepas 7 hari fermentasi. Suhu bilik malar didapati berubah-ubah sepanjang fermentasi sehingga meningkat kepada 37 °C dan membantutkan penghasilan SB. Melalui penggunaan inkubator penggoncang berputar yang tertutup, SB yang terhasil mempunyai perbezaan kuantiti yang tidak signifikan dari segi pH dan kelajuan goncangan. Keputusan ini menunjukkan air kelapa tua mempunyai potensi sebagai sumber karbon bagi sintesis SB dan pengoptimuman suhu fermentasi adalah penting untuk menghasilkan SB yang banyak.

**Kata kunci**: bakteria selulosa, air kelapa tua, fermentasi, kelajuan goncangan.

## Introduction

Cellulose is the most abundant biological polymer on earth, mainly synthesized on the plasma membrane of plants and assemble within the cell wall. It plays an important role in sustaining the integrity of this structure. Cellulose exhibited high stiffness, strength and high thermal stability. Concerning on its properties and enormous quantity available in nature, plant cellulose has been used in numerous purposes by man. However, plant cellulose has many impurities such as hemicellulose and lignin which require harsh treatment for removal [1]. Indeed, this development regrettably had created great problems to biosphere ecology particularly deforestation issue.

To overcome these problems, the use of bacterial cellulose (BC) has been suggested as a better choice in replacing plant cellulose. BC is synthesized extracellular by some bacteria especially by acetic acid bacteria [2]. Even though, BC has similar chemical formula with plant cellulose, its fibrils formation is chemically pure and possess superior physiochemical properties that plant cellulose cannot provide. This cellulosic microfibrils become a promising biomaterial in various fields including biomedical [3], food [4,5,6] and electronic [7,8]. Most *Acetobacter xylinum* strains produce high level of cellulose under static condition. However, development of large scale BC production by improving its fermentation system is important for cellulose production.

Coconut palm is the fourth important industrial crop planted in Malaysia after palm oil, rubber and paddy [9]. Food and Agriculture Organization of The United Nations Statistics Division [10] has state Malaysia had produced an average of 646932 tonnes of coconuts in 2013. Some coconut products traded in the world markets are coconut oil, copra, desiccated coconut and coir. In the meantime, matured coconut water become a common waste product from this process. The matured coconut water which is available in plenty amount and contains various essential contents [11] that support the growth of bacteria is suitable as an economical culture medium.

Thus, the objective of this study is to investigate the best conditions for cellulose growth from *Acetobacter xylinum 0416* in an economic cost using matured coconut water as culture medium. The effect of three factors that are pH of the growth medium, rotation speed and incubation condition on the amount of cellulose produced were determined.

## Materials and Methods

### Bacterial strain

*Acetobacter xylinum 0416* used in this study was supplied by The Malaysian Agricultural Research and Development Institute. The strain was sub-cultured in matured coconut water medium contains the following constituents per liter: D-glucose 80 g, ammonium sulphate 5g, 10% of inoculum and acetic acid glacial. All media were autoclaved at 120 °C for 15 minutes. The working culture were prepared at 30 °C for 3 days before used.

### Fermentation medium

For fermentation, medium, matured coconut water residues were collected from copra dealer and been adjusted with glacial acetic acid to 4.5 or 5.5. The culture medium was sterilized by autoclave at 120 °C for 15 min.

### BC synthesis

Bacteria were fermented in matured coconut water culture medium of different pH and different rotation speed, 150 rpm and 200 rpm for BC production (Table 1). Two types of fermentation condition were compared: 1. Fermented in rotatory incubator shaker; 2. Fermented by rotatory shaker that has been placed in a constant temperature room of 30 ºC (Controlled room) (Figure 1). The fermentation process was carried out at 30 °C for 7 days using experimental design shown in Table 1.



Figure 1. a) Rotatory incubator shaker; b) Rotatory shaker

Table 1. Experimental design of process variables.

| No. | Incubation Types | Rotation Speed (rpm) | Initial pH |
|---|---|---|---|
| 1 | Incubator | 150 | 4.5 |
| 2 | | | 5.5 |
| 3 | | 200 | 4.5 |
| 4 | | | 5.5 |
| 5 | Controlled room | 150 | 4.5 |
| 6 | | | 5.5 |
| 7 | | 200 | 4.5 |
| 8 | | | 5.5 |

At the end of fermentation, pH changes were measured using pH meter. The BC samples, harvested in both culture medium, were rinsed with water and subsequently treated with 0.1M NaOH solution for 20 minutes at 100 °C and thoroughly washed with water until total neutralization.

**Dry weight of BC**

To determine the dry weight of BC, the purified samples were dried at 45 °C until reaching constant weight and kept for further characterization.

## Results and Discussion

In coconut water medium, acetic acid was used to bring down the pH as it had a better effect on *Acetobacter xylinum 0416* growth compared to other acids [12]. The acetic acid was broken down to carbon dioxide and water which allow more energy generated by bacteria. Thus, leading to more efficient utilization of sugars for cellulose synthesis [13].

After 7 days of fermentation, the final pH of each samples was measured. Most the highest yield for *Acetobacter xylinum 0416* strains were achieved after seven days of incubation [14,15]. Figure 2 represents reductions of pH from their initial values. Both pH of culture in fermented in rotatory incubator shaker decreased to less than pH 3.7 while fermentation in controlled room have pH reduction in a range of 4.08 to 4.38. This analysis suggests that culture in incubator have better carbon consumption for growth than culture in controlled room.

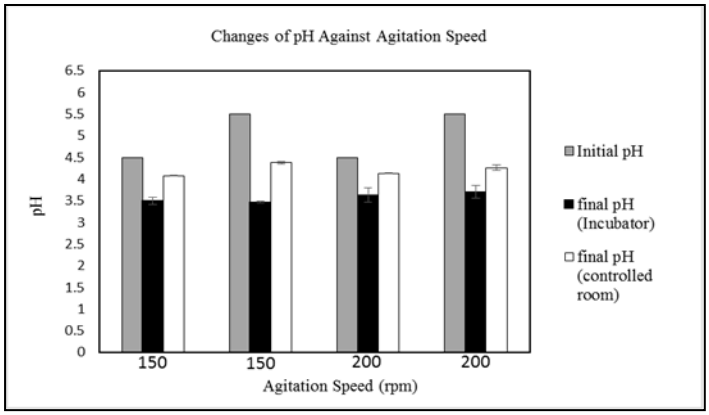



Figure 2. pH changes on various agitation speed and incubation types

Comparison on BC structure (Figure 3) and yield of both fermentation conditions were made. BC commonly produced in the form of gelatinous pellicle through static condition. However, some strains of cellulose-producing bacteria could produce sphere-like cellulose under agitated process while other strains were unable to exhibit this capability even under the same condition. The formation of this sphere-like shape might result from the shear force produced during agitation cultivation that cause intertwine of cellulose ribbon. In this study, *Acetobacter xylinum 0416* was unable to produce sphere-like cellulose. The cellulose had irregular shape which appear in chunk and aggregate form. This finding suggesting that the structure of cellulose is not universally produce by *Acetobacter xylinum 0416* strains [16].

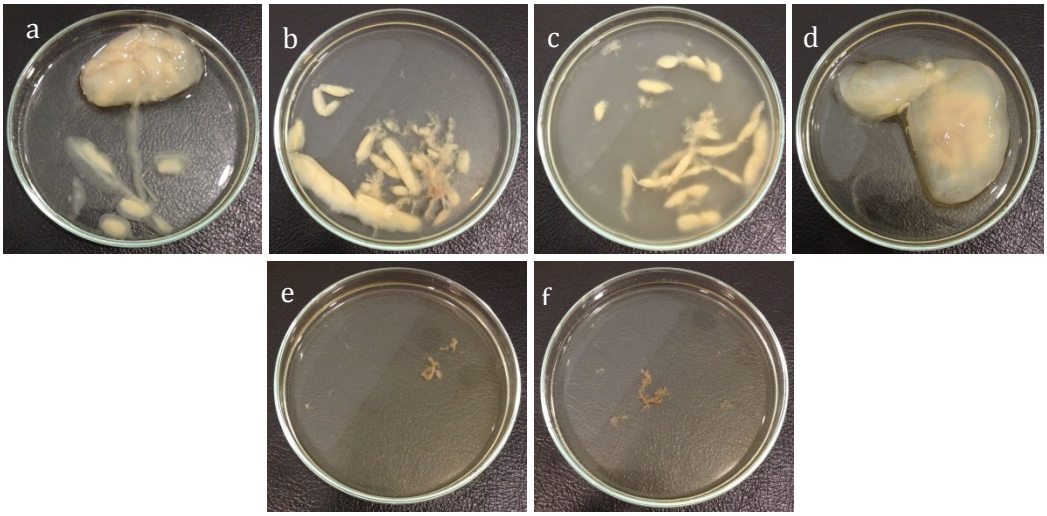



Figure 3. Fermentation of culture medium at rotation speed of (a-b) 150 rpm in incubator shaker, (c-d) 200 rpm in incubator shaker and (e-f) 150 and 200 rpm in controlled room

There was no BC formation at pH 4.5 and pH 5.5 after 7 days fermentation in controlled room. The culture was unable to produce any BC even though the growth of bacteria did occur (reduction of pH). This might result from unstable temperature of controlled room during this fermentation process where the temperature kept fluctuate up to 37 °C.

Some factors can cause temperature fluctuation was often opening of controlled room as it was free access to anyone. When the door was open, more heat and humidity to be released and it will take longer time to reach its normal temperature. Besides that, when the machines in the room were turned on, the internal heat sources released cause disturbance to the constant temperature. Hence, the heat must be compensated with a proper cooling system.

Table 2 summarized the dry weight of cellulose produced by *Acetobacter xylinum 0416* under different rotational speeds, initial pH, and incubation condition. Based on this data, an increase in the biomass yield in increasing cultivation rotational speed might due to improved aeration. Moreover, these results proposed that there was no relationship between cellulose yield and BC sizes for this strain.

Table 2. Bacterial production on various types of incubation, agitation speed and pH

| No. | Incubation Types | Rotational speed (rpm) | Initial pH | Dry Weight (g) |
|---|---|---|---|---|
| 1. | Incubator | 150 | 4.5 | 0.047 |
| 2. | | | 5.5 | 0.035 |
| 3. | | 200 | 4.5 | 0.098 |
| 4. | | | 5.5 | 0.137 |
| 5. | Controlled room | 150 | 4.5 | 0 |
| 6. | | | 5.5 | 0 |
| 7. | | 200 | 4.5 | 0 |
| 8. | | | 5.5 | 0 |

## Conclusion

Matured coconut water has potential as an economic medium which can serve as carbon substrates for BC production. Choosing the right incubation process is important to maximize the yield of BC synthesis. Besides that, more study should be done on different rotational speed to have high yield in short duration of fermentation.

## References

1. Ummartyotin, S. and Manuspiya H. (2015). A critical review on cellulose: From fundamental to an approach on sensor technology, *Renewable and Sustainable Energy Reviews,* 41: 402 – 412.
2. Sengun, I. Y. and Karabiyikli, S. (2011). Importance of acetic acid bacteria in food industry. *Food Control,* 5: 647 – 656.
3. Wu, J., Zheng, Y., Song, W., Luan, J., Wen, X., Wu, Z., Chen, X., Wang, Q. and Guo. S. (2014). In situ synthesis of silver-nanoparticles/bacterial cellulose composites for slow-released antimicrobial wound dressing. *Carbohydrate Polymer,* 102: 762 – 771.
4. Pérez, C. D., De'Nobili, M. D., Rizzo, S. A., Gerschenson, L. N., Descalzo, A. M. and Rojas, A. M. (2013). High methoxyl pectin–methyl cellulose films with antioxidant activity at a functional food interface. *Journal of Food Engineering,* 116: 162 – 169.
5. Lin, S. B., Chen, L. C. and Chen, H. H. (2011). Physical characteristics of surimi and bacterial cellulose composite gel. *Journal of Food Process Engineering,* 34: 1363 – 1379.
6. Shi, Z., Zhang, Y., Phillips, G. O. and Yang, G. (2014). Utilization of bacterial cellulose in food. *Food Hydrocolloids,* 35: 539 – 545.
7. Zhou, T., Chen, D., Jiu, J., Nge, T. T., Sugahara, T., Nagao, S., Koga, H. and Nogi. M. (2013). Electrically conductive bacterial cellulose composite membranes produced by the incorporation of graphite nanoplatelets in pristine bacterial cellulose membranes. *Polymer Letters*, 7(9): 756 – 766.

8. Gadim, T. D. O., Figueiredo, A. G. P. R., Rosero-Navarro, N. C., Vilela, C., Gamelas, J. A. F., Barros-Timmons, A., Neto, C. P., Silvestre, A. J. D., Freire, C. S. R. and Figueiredo, F. M. L. (2014). Nanostructured bacterial cellulose–poly(4-styrene sulfonic acid) composite membranes with high storage modulus and protonic conductivity. *ACS Applied Material Interfaces,* 6(10): 7864 – 7875.
9. Sivapragasam A. (2008). Coconut in Malaysia – Current development and potential for re-vitalization. 2nd International Plantation Industry Conference and Exhibition (IPICEX2008).
10. Food and Agriculture Organization of The United Nations Statistics Division (2015). Access from http://faostat3.fao.org/compare/E [28 July 2015].
11. Prades, A., Dornier, M., Diop, N. and Pain, J. P. (2011). Coconut water uses, composition and properties: A review. *Fruits*, 67 (2):87 – 107.
12. Jagannath, A., Kalaiselvan, A., Manjunatha, S. S., Raju, P. S. and Bawa, A. S. (2008). The effect of pH, sucrose and ammonium sulphate concentrations on the production of bacterial cellulose (Nata-de-coco) by *Acetobacter xylinum*. *World Journal of Microbiology and Biotechnology,* 24: 2593 – 2599.
13. Vandamme E. J., de Baets, S., Vanbaelen, A., Joris, K. and de Wulf, P. (1998). Improved production of bacterial cellulose and its application potential. *Polymer Degradation and Stability,* 59: 93 – 99.
14. Cavka, A., Guo, X., Tang, S. Winestrand, S., Jonsson, L. J. and Hong, F. (2013). Production of bacterial cellulose and enzyme from waste fiber sludge. *Biotechnology for Biofuels*. 6: 25 – 35.
15. Huang, C., Yang, X. Y., Xiong, L., Guo, H. J., Luo, J., Wang, B., Zhang, H. R., Lin, X. Q. and Chen, X. D. (2013). Evaluating the possibility of using acetone-butanol-ethanol (ABE) fermentation wastewater for bacterial cellulose production by Gluconacetobacter xylinus. *Letters in Applied Microbiology,* 60(5): 491 – 496.
16. Hu, Y. and Catchmark, J. M. (2010). Formation and characterization of spherelike bacterial cellulose particles produced by *Acetobacter xylinum JCM 9730* strain. *Biomacromolecules,* 11:1727 – 1734.

**Malaysian Journal of Analytical Sciences Vol 21 No 2 2017**

Articles 10-19 are selected papers from the "National Congress on Membrane Technology (NATCOM 2016), 'Membranes Technology for Efficient Separation and Energy Generation', 24 - 25 August 2016, Pulai Spring Resort, Johor Bahru; organised by Advanced Membrane Technology Research Centre, Universiti Teknologi Malaysia, Malaysia."

Guest Editor: Lau Woei Jye

Articles 20-26 are selected papers from the "The 28th Symposium of Malaysian Chemical Engineers (SOMChE 2015), 'Towards Net Carbon Neutrality', 21 - 22 October 2015, Palm Garden Hotel, IOI Resort, Putrajaya; organised by Department of Chemical & Process Engineering, UKM & Fuel Cell Institute, UKM."

Guest Editor: Edy Herianto Majlan.


| | | **Page** |
|---|---|---|
| 1. | A REVIEW OF EXPLOSIVE RESIDUE DETECTION FROM FORENSIC CHEMISTRY PERSPECTIVE<br>(Satu Ulasan Pengesanan Residu Letupan dari Sudut Pandangan Kimia Forensik)<br>*Mohamad Afiq Mohamed Huri, Umi Kalthom Ahmad, Roliana Ibrahim, Mustafa Omar* | 267 |
| 2. | GLUCOSE PRODUCTION FROM STEAM-ALKALI-CHEMICAL PRE-TREATED OIL PALM TRUNK BIOMASS VIA ENZYMATIC SACCHARIFICATION PROCESS<br>(Penghasilan Glukosa dari Pra-Rawatan Wap-Kimia-Alkali Biomas Batang Kelapa Sawit Melalui Proses Sakarifikasi Enzim)<br>*Nurul Wahidah Mazlan, Long Wee Lai, Nur Akmal Suliman, Marini Ibrahim, Rahmad Mohd Taib, Rozila Alias* | 283 |
| 3. | THE CHEMICAL CONSTITUENTS FROM YOUNG TUBERS of *Hydnophytum formicarum*<br>(Juzuk Kimia Daripada Tuber Muda *Hydnophytum formicarum*)<br>*Nur Shafiqa Abdullah, Wan Yaacob Wan Ahmad, Noor Aziiraa Sabri* | 291 |
| 4. | ISOLATION OF FOUR STEROIDS FROM THE LEAVES OF FERN *Adiantum latifolium* Lam<br>(Pengasingan Empat Steroid Daripada Daun Paku Pakis *Adiantum latifolium* Lam)<br>*Andi Rifki Rosandy, Nurnida Mohd. Kamal, Noraini Talip, Rozida Khalid, Muntaz Abu Bakar* | 298 |
| 5. | THE CHEMICAL CONSTITUENTS FROM THE FRUITS OF *Johannesteijsmannia altifrons* AND ANTIBACTERIAL ACTIVITY<br>(Komposisi Kimia Daripada Buah *Johannesteijsmannia altifrons* dan Aktiviti Antibakteria)<br>*Noor Aziiraa Sabri, Wan Yaacob Wan Ahmad, Nur Shafiqa Abdullah, Nazlina Ibrahim* | 304 |
| 6. | GEOCHEMISTRY AND CLAY MINERALS OF SURFACE SEDIMENTS OF SOUTHWESTERN JOHOR, MALAYSIA<br>(Geokimia dan Mineral-mineral Liat Enapan Permukaan di Barat Daya Johor, Malaysia)<br>*Hasrizal Shaari, Noor Azhar Mohd Shazili, Lina Idayu Abdullah, Nor Antonina Abdullah, Mohd Lokman Husain, Norhayati Md. Tahir* | 312 |
| 7. | THE SYNTHESIS OF ZINC OXIDE/CARBON SPHERES NANOCOMPOSITES AND FIELD ELECTRON EMISSION PROPERTIES<br>(Sintesis Nanokomposit Zink Oksida/Sfera Karbon dan Sifat Pemancaran Elektron Medan)<br>*Suriani Abu Bakar, Suhufa Alfarisa, Azmi Mohamed, Norhayati Hashim* | 323 |

8. ISOTHERMAL MODELLING BASED EXPERIMENTAL STUDY OF DISSOLVED HYDROGEN SULFIDE ADSORPTION FROM WASTE WATER USING EGGSHELL BASED ACTIVATED CARBON 334
(Model Isoterma Berdasarkan Kajian Penjerapan Hidrogen Sulfida Terlarut daripada Air Sisa Menggunakan Karbon yang Diaktifkan Berasaskan Kulit Telur)
*Omar Abed Habeeb, Ramesh Kanthasamy, Gomaa Abdelgawad Mohammed Ali, Rosli Mohd. Yunus*

9. A COMPARATIVE STUDY ON THE INHIBITORY ACTION OF SOME GREEN INHIBITORS ON THE CORROSION OF MILD STEEL IN HYDROCHLORIC ACID MEDIUM 346
(Kajian Perbandingan Tindakan Rencatan oleh Perencat Hijau ke atas Pengaratan Keluli Lembut di dalam Medium Asid Hidroklorik)
*Moorthy Shyamala and Arthanas Arulanantham*

10. MORPHOLOGICAL PROPERTIES OF POLY(VINYLIDENE FLUORIDE-CO-TETRAFLUOROETHYLENE MEMBRANE: EFFECT OF SOLVENTS AND POLYMER CONCENTRATIONS 356
(Sifat-Sifat Morfologi Membran Kepingan Rata Poli(Vinilidena Fluorida-Ko Tetrafluoridaetilena): Kesan Pelarut dan Kepekatan Polimer)
*Amira Mohd Nasib, Irfan Hatim, Nora Jullok, Hameed R. Alamery*

11. PREPARATION AND CHARACTERIZATION OF DIFFERENT LOADING OF ZINC OXIDE ON ACTIVATED CARBON NANOFIBERS 365
(Penyediaan dan Pencirian Gentian-Nano Karbon Teraktif Pada Kepekatan Zink Oksida Yang Berbeza)
*Faten Ermala Che Othman, Norhaniza Yusof, Amirul Afiat Raffi, Hasrinah Hasbullah, Farhana Aziz, Wan Norharyati Wan Salleh, Ahmad Fauzi Ismail*

12. SURFACE MODIFICATION OF PSF/$TIO_2$ MEMBRANES USING SILANE COUPLING AGENTS AND DC PLASMA TECHNIQUE 372
(Modifikasi Permukaan Membran PSF/$TiO_2$ Menggunakan Ejen Gandingan Silana dan Teknik Plasma DC)
*Soraya Ruangdit, Thawat Chittrakarn, Sudkhet Anuchit, Chalad Yuenyao*

13. FABRICATION OF PES/MnO MIXED MATRIX MEMBRANES FOR CADMIUM REMOVAL 381
(Pembuatan PES/MnO Membran Campuran Matrik dalam Penyingkiran Kadmium)
*Soon Onn Lai, Kok Chung Chong, Zhi Wei Kerk, Boon Seng Ooi,Woei Jye Lau*

14. A FABRICATION OF A LOW–COST ZEOLITE BASED CERAMIC MEMBRANE VIA PHASE INVERSION AND SINTERING TECHNIQUE 391
(Fabrikasi Membran Seramik Kos Rendah Berasaskan Zeolit Melalui Kaedah Penyongsangan Fasa dan Sinteran)
*Mohd Ridhwan Adam, Mohd Hafiz Dzarfan Othman, Mohd Hafiz Puteh, Mohammad Arif Budiman Pauzan, Mukhlis A Rahman, Juhana Jaafar*

15. THE EFFECT OF NOVEL MULTIWALLED CARBON NANOTUBE-TITANIA NANOTUBE HYBRID IN POLYAMIDE ACTIVE LAYER TOWARDS WATER PERMEABILITY AND HIGH SODIUM CHLORIDE REJECTION PERFORMANCE OF NANOFILTRATION MEMBRANE DESALINATION 402
(Kesan Novel Hibrid Karbon Tiub Nano Pelbagai Dinding-Titania Tiub Nano dalam Lapisan Aktif Poliamida Terhadap Prestasi Kebolehtelapan Air dan Penyingkiran Natrium Klorida yang Tinggi Bagi Membran Penapisan Nano Pengenyahmasin)
*Ihsan Wan Azelee, Pei Sean Goh, Woei Jye Lau, Ahmad Fauzi Ismail, Masood Rezaei Dasht Arzhandi, Kar Chun Wong, Mahesan Naidu Subramaniam*

16. THE INFLUENCE OF CARBONIZATION TEMPERATURE ON THE DEVELOPMENT OF CARBON MEMBRANE WITH SUPERIOR $CO_2/CH_4$ SEPARATION PERFORMANCE 409
(Pengaruh Suhu Karbonisasi Kepada Pembangunan Membran Karbon Dengan Kesan Pemisahan Gas $CO_2/CH_4$ Yang Cemerlang)
*Norazlianie Sazali,Wan Norharyati Wan Salleh, Mohamad Azuwa Mohamed, Nor Hafiza Ismail, Norafiqah Rosman, Farhana Aziz, Ahmad Fauzi Ismail*

17. REMOVAL AND RECOVERY OF CHROMIUM (IV) ION VIA TRI-N-OCTYL METHYLAMMONIUMCHLORIDE-KEROSENE POLYPROPYLENE SUPPORTED LIQUID MEMBRANE 416
(Penyingkiran dan Pemulihan Semula Kromium (IV) melalui Membran Cecair Berpenyokong Tri-n-oktil metilammoniumklorida-kerosin-polipropilena)
*Raja Norimie Raja Sulaiman and Norasikin Othman*

18. THE MORPHOLOGICAL PROPERTIES STUDY OF PHOTOCATALYTIC $TIO_2$/PVDF DUAL LAYER HOLLOW FIBER MEMBRANE FOR ENDOCRINE DISRUPTING COMPOUNDS DEGRADATION 426
(Kajian Sifat Morfologi Membran Fotopemangkin Gentian Berongga Dwi Lapisan $TiO_2$/PVDF untuk Penguraian Sebatian Pengganggu Endokrin)
*Roziana Kamaludin, Mohd Hafiz Dzarfan Othman,Siti Hamimah Sheikh Abdul Kadir, Mukhlis A Rahman, Juhana Jaafar*

19. METHANOL PERMEABILITY AND PROPERTIES OF POLYMER ELECTROLYTE MEMBRANE BASED ON GRAPHENE OXIDE- SULFONATED (POLYETHER ETHER) KETONE 435
(Kebolehtelapan Metanol dan Sifat-Sifat Membran Polimer Elektrolit Berasaskan Grafin Oksida-Polieter Eter Keton Tersulfon)
*Nuor Sariyan Suhaimin, Madzlan Aziz, Juhana Jaafar*

20. RADIOTRACER APPLICATION IN MALAYSIA: RESIDENCE TIME DISTRIBUTION STUDY 445
(Aplikasi Teknologi Penyurih di Malaysia: Kajian Taburan Masa Mastautin)
*Noraishah Othman, Nor Pa'iza Mohamed Hassan, Roslan Yahya, Mior Ahmad Khusaini Adnan, Mohd Rabaie Shari, Hearie Hassan, Airwan Affendy Mahmood*

21. RESPONSE SURFACE METHODOLOGY ON WAX DEPOSIT OPTIMIZATION 452
(Pengoptimuman Lilin Mendap Menggunakan Kaedah Gerak Balas Permukaan)
*Norida Ridzuan, Zulkefli Yaacob, Fatmawati Adam*

22. ISOLATION, PURIFICATION AND IDENTIFICATION OF MICROALGAE FROM COAL-FIRED POWER PLANT ENVIRONMENT 460
(Pemencilan, Penulenan dan Identifikasi Mikroalga daripada Persekitaran Loji Janakuasa Arang Batu)
*Muhammad Nazry Chik, Liyana Yahya, Kamrul Fakir Kamarudin, Ding Gong Tao, Mohd Sobri Takriff*

23. EFFECT OF MASS LOADING AND MICROWAVE ABSORBER APPLICATION METHOD ON THE PRODUCT FROM MICROWAVE ASSISTED PYROLYSIS OF PALM OIL MILL EFFLUENT 470
(Kesan Beban Jisim dan Aplikasi Kaedah Penyerap Gelombang Mikro Kepada Produk Terhasil daripada Sisa Buangan Kilang Kelapa Sawit Melalui Proses Pirolisis Bantuan Gelombang Mikro)
*Zakiuddin Januri, Siti Shawalliah Idris, Hafifah Amirah Akhawan, Norazah Abd. Rahman, Sharmeela Matali, Shareena Fairuz Abd Manaf*

24. MOLECULAR WEIGHT CUT-OFF DETERMINATION OF PRESSURE FILTRATION MEMBRANES VIA COLORIMETRIC DETECTION METHOD 484
(Penentuan Berat Sekatan Molekul Bagi Membran Penurasan TekananMelalui Kaedah Pengesanan Kolorimetri)

*Izzati Izni Yusoff, Rosiah Rohani, Abdul Wahab Mohammad*

25. PALM OIL-BASED PRECURSORS FOR DEVELOPMENT OF POLYMERIC DELIVERY SYSTEM 496
(Pelopor Berasaskan Minyak Sawit untuk Pembangunan Sistem Penyampai Polimer)
*Rida Tajau, Rosiah Rohani, Wan Nor Roslam Wan Isahak, Mek Zah Salleh*

26. CHARACTERIZATION OF SODIUM SILICATE DERIVED FROM SUGARCANE BAGASSE ASH 512
(Pencirian Natrium Silikat yang Dihasilkan daripada Abu Hampas Tebu)
*Norsuraya Sahiron, Norhasyimi Rahmat, Fazlena Hamzah*

*Malaysian Journal of Analytical Sciences, Vol 21 No 2 (2017): 267 - 282*
*DOI: https://doi.org/10.17576/mjas-2017-2102-01*

MALAYSIAN JOURNAL OF ANALYTICAL SCIENCES
*Published by The Malaysian Analytical Sciences Society*
ISSN 1394 - 2506

# A REVIEW OF EXPLOSIVE RESIDUE DETECTION FROM FORENSIC CHEMISTRY PERSPECTIVE

## (Satu Ulasan Pengesanan Residu Letupan dari Sudut Pandangan Kimia Forensik)

Mohamad Afiq Mohamed Huri[1]*, Umi Kalthom Ahmad[1], Roliana Ibrahim[2], Mustafa Omar[3]

[1]*Department of Chemistry, Faculty of Science*
[2]*Information System Department, Faculty of Computing*
*Universiti Teknologi Malaysia, 81310 UTM Johor Bahru, Johor, Malaysia*
[3]*Science & Technology Research Institute of Defense (STRIDE),*
*48100 Batu Arang, Selangor, Malaysia*

**Corresponding author: afiqhuri91@gmail.com*

Received: 10 August 2016; Accepted: 19 January 2017

**Abstract**

The growing threat of terrorism activities has caused an urgent need of improved forensic explosive analysis. Complex matrices, limited samples, and ambiguous interpretations serve as challenges for a forensic chemist in order to link the evidence to the perpetrator of the crime. This review focuses on three aspects namely screening techniques, extraction techniques, and instrumental techniques. For the screening techniques, this review focuses on fast detection based on chemical respond for pre- and post-explosion residues. Different types of extraction methods including swabbing technique, solid phase extraction, and solid phase microextraction were discussed. Instrumental techniques covered in this review included gas chromatography, high performance liquid chromatography, ion chromatography and capillary electrophoresis.

**Keywords**: explosive residue, forensic chemistry, screening techniques, extraction techniques, instrumental techniques

**Abstrak**

Peningkatan ancaman aktiviti keganasan telah membawa kesedaran akan perlunya penambahbaikan dalam analisis forensik. Matriks sampel yang kompleks, sampel terhad dan penafsiran yang tidak jelas menjadi satu cabaran dalam bidang kimia forensik untuk mengaitkan antara bahan bukti dan pelaku jenayah. Ulasan ini akan memberi tumpuan kepada tiga bahagian iaitu teknik saringan, teknik pengekstrakan dan teknik instrumen. Untuk kaedah saringan, kajian ini akan memberi tumpuan kepada pengesanan pantas residu letupan berdasarkan tindak balas kimia untuk sebelum dan selepas letupan. Pelbagai jenis kaedah pengekstrakan dibincangkan termasuk teknik sapuan, pengekstrakan fasa pepejal, dan pengekstrakan fasa pepejal mikro. Teknik peralatan yang akan dibincangkan dalam ulasan ini pula melibatkan kromatografi gas, kromatografi cecair berprestasi tinggi, kromatografi ion dan elektroforesis rerambut.

**Kata kunci**: residu letupan, kimia forensik, teknik saringan, teknik pengekstrakan, teknik instrumentasi

## Introduction

Terrorism is often portrayed as unlawful acts of violence, disregarding the safety of civilians with intent to create fear for their senseless ideology [1]. Terrorism brings harm not only to structural or physical injury, but the victims will sustain the damage from the aspect of psychological, economic and social damage [2]. Based on Global Terrorism Database (GTD) from the year 2000 until 2010, 57% of terrorism method (Figure 1) used by terrorists is

from bombing terrorism [3]. The distribution comprises of armed assault (31%), hostage taking (9%) and, unknown (2%), unarmed assault (1%) and hijacking (<1%).

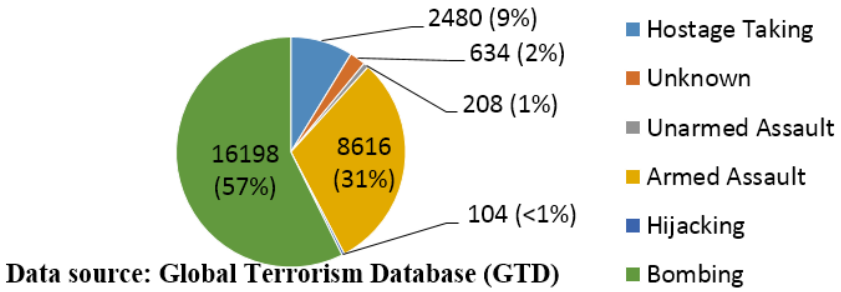



Figure 1. Distribution of terrorism method used by terrorist (2000 – 2010)

Bombing served as the preferred method of terrorism and this callous act of terrorism often happens in public spaces and cost innocent lives to be taken in their target [4-6]. Yavuz et al. [7] in their study on the terrorist bombing in Istanbul reported that 85% of deaths occurred at public spaces such as in the street, school, post-office, hotel lobby, university or campus and many others that involved non-combatant civilians. According to Bosnar et al. [8], suicidal deaths involving explosives have always been connected to terrorism instead of the unusual method of committing suicide.

The expanding threat, unlawful behavior and illicit activities utilizing energetic explosive materials for criminal and terrorism activities have urged the need for a reliable, rapid but also an accurate investigation technique for analyzing crucial puzzles left at the scene of the crime. Analysis of explosive residues become more difficult since the residues of origin material from post-blast samples are usually trapped and fused into surrounding. To identify unknown explosive samples, it demands a competency technique to determine an extensive number of organic and inorganic explosive material. It is of great importance for the explosive and their post-blast residues analysis to assist forensic scientist in determining the origin of explosive material used in the bombing and eventually help the law enforcement in narrowing down the investigation. Therefore, the review emphasizes on steps to track traces of evidence, method of extraction and the use of analytical instrumentation for explosive residue analysis.

**Sample collection**

The forensic scientist needs to analyze and gather information on the physical evidence collected to link the crime scene with the crime perpetrator. The results of laboratory analysis are important to deter terrorist activities and to reduce the occurrences of crime [9-12]. There are many challenges faced by investigating officers and forensic scientist before the results can be taken to court for the prosecution [13].

Numerous studies were reported regarding explosive by performing fields experiments to investigate the properties of explosive, pattern of post-blast sample distribution, or potential source of evidence. Chemical explosive is classified as low or high explosives according to their rates of decomposition [14]. Varga and Ubrich studied the chemical properties of high explosive dynamite via gas chromatography with electron capture detector (GC-ECD) and ion chromatography (IC), by using solid phase extraction (SPE) as the extraction method [15]. Their study revealed that other than dinitrotoluene (DNT) and ethylene glycol dinitrate (EGDN), inorganic components of post-explosion products ($Na^+$, $NH_4^+$, and $NO_3^-$) were also found in dynamite post-blast residues.

The knowledge on explosive residue distribution is important for comparison analysis with real samples. Various approaches were made on the study of explosive residues distribution by using trays [16, 17] or witness plates [18-20] placed at different distances from the epicenter of the explosion. The impact from the detonation process resulting in the fragment or residue from the explosive device will be ejected outward from the epicenter of the

explosion. However, almost all studies showed no clear relationship between the amount of explosive detected with the distance from the detonation or amount of explosive used for the detonation process [21, 22]. Many factors contribute to this lack of correlation between the explosive residues distribution with the amount of explosive detected from post-blast explosive residues including efficiency of the detonation, non-homogenous fragment residual dispersal, and influence of wind direction during detonation process.

Determining potential source of evidence is a very crucial step to track traces the explosive residues. Numerous efforts have been made by researchers to study on variety possible source of evidence so that it can become references for the future cases. These sources can exist in the form of solid [23] or porous material [24]. Since the bombing terrorism cases always involve human either as the perpetrator or as the casualty, human skin and hair having a potential of becoming a reliable source for retrieving explosive residues [25-28]. Clothes also have a potential becoming a positive source of evidence since clothes are always intact with the human body [29]. Considering bombing incident also happens in open areas, the possibilities of explosive residues seeping into the ground and making the soil become a potential source to track the explosive residues [30, 31]. Since the properties of water as a universal solvent to contain explosive residues, numerous studies were also done to detect the explosive in water [32-34].

Numerous challenges are often confronted during the process of collecting and analyzing the physical evidence. At the crime scene explosion, the evidence tends to blend into the background thus making the collection process difficult. The fraction, residue or unexploded material that usually blend with surrounding include soil, water, rubble, debris, fabric or any physical material involved in the explosion and the amount of material remains from the devices were usually of limited quantity [33, 35-37]. Shankill Road explosion incident in 1993 is an example when the evidence were mixed with 15 tons of rubble and needed painstaking examination before the remains of the explosive device were discovered among the rubbles [35]. The perpetrator in this incident used short relay electronic explosive device using high explosive as the main component.

Massive explosions usually leave traces when compared to small explosions. Because of that reason, it is not extraordinary if only a small fraction of the samples remains after detonation and combustion processes. For example, the Bali bombing on 12 October 2002 involved three explosions at three different places with different explosion damage [4]. The first explosion took place at Paddy's Bar before the second and the largest explosion exploded a moment later outside the Sari nightclub. Approximately 45 seconds after the blast at Sari nightclub, a third bomb exploded 10 km away near to the United States and Australian Consulates. Compared to the second and largest explosion that used vehicle-borne improvised explosive device (VBIED), the third and the smallest explosion outside the consulate provided more promising physical evidence as compared to the other two explosions.

The blast location or center of the blast must be discovered and approached with extreme steps of precaution. If any portion of the device is visible to the naked eyes during approaching the seat of the explosion most likely to contain, it must be packaged and labeled because it will make an excellent source of recovering of explosive residue. In Boston marathon bombing in 2013, the remaining pieces from a pressure cooker bomb were successfully discovered at the scene of explosion [38]. The explosion killed three peoples and injured more than 200 people.

Post blast samples collected are often placed in a sealed container, with the appropriate size. Soil or soft material in the form of powder can be stored in ziplock plastic bags. Metal, debris or any sharp object should be wrapped with protective material to prevent the samples from piercing the container. Other good sources of explosive residues are soil or any solid object that could be penetrated such as wood, insulation, plastics and metals [9]. Physical evidence that is attached to the victims or deceases must be taken into account and recovered in steps and precautions. In the Bali bombing of 2005, the bearing and electrical connectors were recovered from wounded victims and TNT explosive compound was successfully identified [39].

**Screening: On-site detection of explosive devices and residues**

Screening test for explosive trace residues in a post-blast forensic investigation is one of the important strategies for the on-site detection of explosives [40, 41]. The sensing methodology of optical and non-optical methods has been

widely applied by law enforcement and transportation security [42-46]. Trained canine team, metal detector, X-ray imaging, ion mobility spectrometry, and portable gas chromatography mass spectrometry (GC-MS) are among the examples of non-optical sensing methods. Spot test kit and thin layer chromatography are examples of preliminary colour tests often employed in laboratory screening of explosive residues.

Trained canine team, is a common and effective method for detection of explosives by training the dog to identify the explosives through vapour sniffing [9]. This approach is still widely practiced in airports or in crime scenes to locate evidence or any prohibited items including drugs and explosives. The abilities between humans and dogs were differentiated by the effectiveness of the olfactory system of the dog that can sniff the vapour much better when compared to human [47, 48]. However, the disadvantages of the canine teams are high maintenance, tendency for environmental distraction, physiological boredom and only the trainer can handle the sniffer dog limit the method for every operation [11].

X-ray imaging are widely used in security post, airports or border control to detect any prohibited items from passing the security line [49-51]. The recent system of the dual-view system is replacing a single view system which allows the image to be viewed at 360° and in pseudo-colors [49]. However, it has some weaknesses because the x-ray cannot penetrate high-density material such as a machine. Various items jumbled in the baggage, including organic materials, bottles, battery, electronic device together with cables and wire, increases the complexity of the image thus causing the possibilities of overlooking the existence of the explosive device.

Numerous reports were made on the development of spectroscopic sensors for detection of explosives [11, 52-55]. The principle of spectroscopy is the interaction between matter and the electromagnetic radiation, whereby samples from the explosive vapour are drawn from the surface or air into the drift region [56]. The ionized samples are then separated through the electric field, according to the mobility of ions or mass to charge ratio before being detected by the spectrometer detector. A few separation techniques combined with mass spectrometry have been developed for real-time detection of explosives (Table 1). Ion mobility spectrometry (IMS) [57] is an example of spectroscopic method that has been used on the field for detection of explosives [58-61]. The method has high selectivity and sensitivities, but until now, numerous efforts were made for miniaturization of the instruments and each instrument itself is very expensive.

Table 1. Example of explosive detection via spectrometry method

| Spectrometry Method | Explosive Analytes | Detection Limit | References |
|---|---|---|---|
| AFT-MS | PETN[1], tetryl, RDX[2], NG[3] | 10 ppq | [62] |
| DBDI-MS | RDX, TNT[4], PETN | 0.01-0.1 ng | [59] |
| ESI-IMS | TNT, 2,4-DNT[5], 2-ADNT[6], 4-NT[7], TNB[8], RDX, HMX[9], EGDN[10], NG | 0.015-0.190 ppm | [60] |
| NCD-IMS | RDX,TNT, PETN | 0.07-0.3 ng | [61] |

[1]PETN: pentaerythritol tetranitrate
[2]RDX: cyclo-1,3,5-trimethylene-2,4,6-trinitramine
[3]NG: nitroglycerin
[4]TNT: trinitrotoluene
[5]2,4-DNT: 2,4-dinitrotoluene
[6]2-ADNT: 2-amino-4,6-dinitrotoluene
[7]4-NT: 4-nitrotoluene
[8]TNB: trinitrobenzene
[9]HMX: cyclo-tetramethylene-tetranitramine
[10]EGDN: dinitro-ethyleneglycol

Most portable kits utilized classical screening tests based on optical and colorimetric analyzes. They are usually high in portability, low in price, and provide rapid and reliable explosives detection. Fisco, in 1975 developed a portable thin layer chromatography (TLC) analysis for the detection of explosives [44]. The kit requires 20-30 minutes for the TLC development prior to visualization using portable UV lamp at 254 nm. Longer analysis time,

the need to prepare various amounts of chemical reagent in the developer chamber, and low portability were major weaknesses of this method. Another approach for detection of explosive is from colorimetric reaction via spot test analysis named as ELIT [40], *Detection Kit Detex* [43], and *FORANEX* [63] spot test kit were among the rapid and reliable colorimetric analytical methods for detection of explosives. However, the techniques needed subsequent instrumental analysis in order to confirm the presence of certain components of the explosive. Recent advanced techniques utilized the capabilities of hexaazamacrocycle-capped [64]. Mohan and Chand reported on the rapid colour formation from red to blue with a detection limit at femtomolar ($10^{-15}$ mol/dm$^3$) concentration level. Table 2 shows the specific chemical reagents for the detection of certain explosives based on their respective color formation.

Table 2. Reference reagents for detection of explosive via colorimetric reaction [4, 37, 43, 63, 65]

| Reagent | Composition | Explosive Analytes | Color Formation |
|---|---|---|---|
| Griess reagents | alphanaphtylamine and sulfanilic in acetic acid with zinc dust as reducing agent | RDX, PETN, Nitrate ion | Pink color |
| Nessler reagent | potassium iodide and mercury (II) chloride in deionized water | TNT, Ammonium ion | Red-orange color |
| Chloride reagent | concentrated silver nitrate in deionized water | Chloride ion | White precipitate |
| Sulfate reagent | 10% barium chloride in deionized water | Sulfate ion | White precipitate |
| Perchlorate reagent | 0.3% methylene blue in deionized water | Perchlorate ion | Purple color |
| Peroxides reagent | diphenylamine in concentrated sulphuric acid | Peroxides | Dark blue color |

**Sample extraction**

Detection of explosive residues after a bombing incident is possible because not all the explosive materials are consumed during an explosion. Furthermore, characteristic by-products may be formed by the chemical reactions that take place during an explosion. Several methods of extraction techniques were employed to extract the explosive from the matrices, including swabbing technique solid phase extraction (SPE) and solid phase microextraction (SPME) [19, 25, 66]. The method of extraction is crucial to collect the analytes of interest effectively. Furthermore, a variety of the physical evidence will be recovered at the crime scene including soil, water, hair or debris need to be analyzed afterwards [24, 28, 33].

The swabbing technique is commonly used for collecting residues from solid surfaces such as metal, plastics, human skin, and cloth. The efficiency of swabbing technique not only depends on the area being swabbed but also other factors such as the type of solvent used, interval of time between explosion and analysis and the nature of the target sample [19, 26, 67, 68]. Song et al. in their study reported that polyester swabs were superior compared to the cotton swabs [68]. Their studies also indicated that dry swabbing was not an efficient technique as compared to wet swabbing. Wipes using alcohol was also found as a compromising solvent for its efficiency to transfer most of the target analyte from the surfaces to the polyester swab. However, the porosity, thickness and the nature of the surfaces may also reduce the effectiveness of swabbing technique [29].

The most challenging extraction process comes from matrices such as sand and soil. These matrices are found with many interferences from the surrounding such as fertilizers or waste product from home cleaning appliances that may be dissipated into the ground. Sample control from surrounding areas around the crime scene with the same physical properties of the soil at the seat of blast must be collected and taken to the laboratory before being analyzed

and compared with the questioned soil to remove the possibilities of background interferences. Most reported studies used EPA Method 8330 or a modified version of the EPA method to extract the target analytes from the soil [69, 70]. Halasz et al. [71] conducted their study on detection of explosives and degradation products in soil environment. Acetonitrile was used as the solvent to extract the analytes of interest. The sample was subjected to a sonication process for 18 hours prior to analysis by using HPLC-UV at 254 nm. Their study also revealed that from the training sites and former explosives manufacturing plants, the explosives compounds can be transferred from ground surfaces to groundwater and plant tissues.

Solid phase extraction (SPE) is a popular method for removing impurities and pre-concentration of target analytes [72]. This method mainly consists of four steps; conditioning, loading, washing and elution process. Warren et al. [73] applied a combined swab and SPE in their sample preparation. The sample was swabbed with a wetted ethanol cotton swab before the extract was passed through a Chromosorb-104 adsorbent column (washed with one-time acetone and three times of ethyl acetate). The loading sample was washed with ethanol/water fraction (50:50) for the collection of inorganic compound and the adsorbent was further washed using methyl tert-butyl ether/pentane before ethyl acetate fraction was used to elute the organic compound. The percentage recoveries of the selected inorganic ions (sodium, ammonium, potassium, magnesium, calcium, fluoride, chloride, nitrite, bromide, chlorate, nitrate, phosphate, sulphate, perchlorate, glucose, fructose and sucrose) were varied from 45.9% to 96.8%. However, it showed low percentage recoveries of selected organic explosive (nitroglycerin (NG), 2,4-dinitrotoluence (2,4-DNT), 2,6-dinitrotoluene (2,6-DNT), 3,4-dinitrotoluene (3,4-DNT), 2,4,6-trinitrotoluene (TNT), PETN and RDX) from 31.4% to 56%. Ahmad et al. [16] applied the SPE method on the post-blast water samples. For the optimization process, five nitro explosive compounds namely as HMX, 2,4-DNT, RDX, TNT and PETN was selected and undergoes pre-concentration process via SPE before being analyzed by using micellar electrokinetic chromatography (MEKC) and GC-ECD. They used LiChrolut EN SPE cartridges as their SPE adsorbent and used 10 mL of methanol followed by 20 mL distilled water for the conditioning process. The samples (200 mL) were allowed to pass through the SPE cartridge at the flow rate of 3 mL/min before the analytes were collected with three portions of 3 mL acetonitrile. From the optimization process, the SPE pre-concentration technique had succeeded to lower the detection limit by more than 1000 times and gave a good percentage recovery (>87%). From the post-blast water sampling, both RDX and PETN were detected in the range of 0.05 – 0.17 ppm and 0.0124 – 0.039 ppm respectively.

Solid phase microextraction (SPME) is an innovative approach of green technology to reduce the amount of solvent use for the extraction process, cutting the cost and chemical exposure to the human body [66]. Several factors affecting extraction process included the type of fiber use, nature of target analytes, the complexity of the matrices, temperature and desorption times. A study of solid phase microextraction combined with GC-ECD has been made on organic explosive samples [74]. Four types of fiber namely, polydimethylsiloxane (PDMS), polydimethylsiloxane/divinylbenzene (PDMS/DVB), Carboxen$^{TM}$/ polydimethylsiloxane (CAR/PDMS), and polyacrylate were used to study the relationship between the water solubility and the fibers. PDMS/DVB fiber with 30 minutes stirring showed a better result as compared to other fibers. Another study by Ahmad and Heng [75] demonstrated the effect of salting out procedure with 10% NaCl gave the best extraction of their target analytes of 2,6-dinitrotoluene (2,6-DNT), trinitrotoluene (TNT) and pentaerythritol tetranitrate (PETN).

**Instrumental techniques**

Instrumentation plays an important role in the detection of target compounds from various matrices. They are often combined with specific detectors for sensitive and selected detection of the explosive target compounds (Figure 2).

An extensive review on instrumental techniques for the detection of explosive was reported by Kolla [76]. The review covers the instrumental techniques pertaining to organic and inorganic analytes. However, the review was limited to gas chromatography (GC), high performance liquid chromatography (HPLC), capillary electrophoresis (CE), and ion chromatography (IC) analysis of explosive residues up to 1994. For chromatographic separation, a survey was done on articles searched using the keywords of *explosive* and selected instruments, GC, HPLC, IC and CE (Figure 3). Analysis of explosive using GC appeared to be the most popular followed by HPLC, IC and CE. The interest of explosive study had significantly increased between 2003 to 2005, but display a decreasing trend from 2005 to 2007 before showing an increasing pattern from 2008 to 2015 (Figure 3). This trend was obtained

following media reports of series bombing terrorism attacks such as Bali Bombing (2002), Delhi Bombing 2008, Mumbai Bombing (2008) Jakarta Bombing (2009), Moscow Bombing (2010), Norways Attack (2011) and Boston Marathon Bombings (2013).

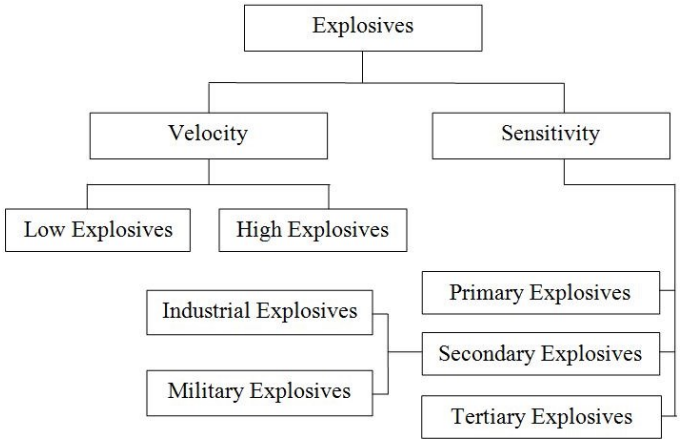



Figure 2. Classification of chemical explosives [14]

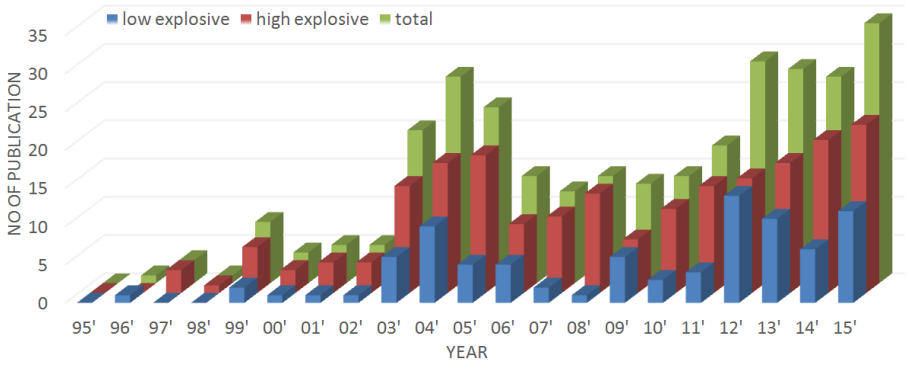



Figure 3. Distribution of journal publications on selected instrumentation based on SCOPUS database from year 2000 – 2015

**Gas chromatography**

Gas chromatography (GC) is frequently used for the identification of organic explosive compounds since the technique has high selectivity and sensitivity towards organic constituent analysis. However, the GC instruments prohibit non-volatile, mixture water samples and sparked samples to prevent the column from bearing the damage. Because of that, extra precaution on sample preparation is needed for every process. The detectors used combined with GC are electron capture detection (ECD) [30,74,77], thermal energy analyzer (TEA) [78,79], mass spectrometry (MS) [71, 80, 81], and tandem mass spectrometry (MS/MS) [82, 83]. Although ECD is less selective than TEA or MS, it is a sensitive means of detecting nitroaromatic base explosives [55]. ECD devices operate by passing a beam of electrons between two electrodes. When a sample elutes from the GC column, organic nitrate groups and the other electronegative moieties 'capture' these electrons, interrupting the current and thereby producing a signal. Varga and Ulbrich [15] successfully extracted TNT and PETN by using water as the medium of extraction and subsequent separation by using GC-ECD. However, nitrate ester based explosive compound such as ethylene glycol dinitrate (EGDN) and nitroglycerin (NG) were difficult to extract using water due to their hydrolysis

process. Ahmad et al. [27] had succeeded in detecting both PETN and RDX from the C4 explosive residues on hair samples by using GC-ECD. Three hair samples were located at 2.5 m, 5.0 m, and 7.5 m from the point of the blast. Their studies concluded that the human head hair has the potential to become a reliable source for explosive residues to be deposited and the concentration of residue deposited on the hair decreased with distance.

Gas chromatography-tandem mass spectrometry (GC-MS/MS) has become an alternative to gas chromatography-mass spectrometry (GC/MS). GC/MS/MS is an analytical tool of choice as the technique is more superior on the selectivity and sensitivity besides its powerful capabilities for detecting compounds in complex matrices. Perr et al. [82] have developed a GC/MS/MS method by using positive chemical ionization (GC/PCI/MS/MS) approach to analyze organic high explosives of nitrobenzene, 2-nitrotoluene, 3-nitroltoluene, 4-nitrotoluene, 1,3-dinitrobenzene, 2,6-dinitrotoluene, 2,4-dinitrotoluene, 1,3,5-trinitrobenzene, 2,4,6-trinitrotoluene, RDX, 4-amino-2,6 dinitrotoluene, 2-amino-4,6-dinitrotoluene, tetryl and HMX with low LOD (0.0006- 0.0414 ng/mL). This method successfully reduced sample preparation steps as the samples can be analyzed without any sample pre-concentration as well as reducing sample loss or sample contamination.

**High performance liquid chromatography**

High performance liquid chromatography is commonly used to detect the organic explosive compounds that are non-volatile. HPLC is often used as the instrument for analysis of explosives as it is amenable for the analysis compounds that have low volatility, high sensitive to heat and high molecular weight [55]. This will overcome the problem of detection of explosives that are thermally unstable and resulting in decomposition products in the vapors [76]. The common detector for HPLC is ultraviolet detector (HPLC-UV). The wide range of HPLC detection between 190-800 nm provides an excellent range of separation. Miller et al. [24] employed HPLC-UV for the identification of explosives from porous materials. By changing the temperature and methanol-water mobile phase ratio in HPLC system, separation of RDX, TNT and PETN was successfully achieved within 20 minutes. At a temperature of 30°C and methanol-water mixture of 50:50 was found as the optimum condition for the isocratic separation of target analytes. There was another study applying HPLC-UV for the analysis of organic high explosive on the analysis of nitroglycerin (NG) in post-blast samples [84]. By using reversed-phase C18 column employing acetonitrile-water (60:40) mixture and UV wavelength detection at 210 nm, the LOD of NG detection was obtained at very low concentration (20 ng).

Ultra-high performance liquid chromatography (UHPLC) has recently been a favorite among the researchers because of its effectiveness for compound separation. Makarov et al. used UHPLC equipped with photodiode array detector to study the hydrolysis kinetics of 2,4,6,8,10,12-hexanitro-2,4,6,8,10,12 hexaazaisowurtzitane (CL-20), octahydro-1,3,5,7-tetranitro-1,3,5,7-tetrazocine (HMX), and hexahydro-1,3,5- trinitro-1,3,5-triazine (RDX) [85]. By using liophilic salts (KPF6) as mobile-phase additives, the study obtained a good range detection limit of CL-20, HMX and RDX at range of 0.04-0.05 mg/L. UHPLC, when combined with mass spectrometry (MS) or tandem mass spectrometry (MS/MS), makes the instrument a powerful tool regarding selectivity and sensitivity. Schramm et al. [86] developed a hyphenated method of ultra-high performance liquid chromatography-atmospheric pressure chemical ionization-tandem mass spectrometry (UHPLC-APCI-MS/MS). Fifteen nitro explosives were successfully detected at very low concentration (0.3-0.5 ppb) and their degradation products in environmental water samples.

**Ion chromatography**

Ion chromatography (IC) method was used to separate inorganic anions and cations found in post blast residues from homemade inorganic explosives as one of the types that was frequently used in terrorism attacks. Johns et al. [18] conducted an analysis of inorganic explosives on pipe bomb and soil samples via IC using suppressed IC on a Dionex column with potassium hydroxide as eluent for anions. For cations analysis, a Dionex SCS 1 column was employed using oxalic acid/acetonitrile as eluent for detection. Both anions ($Cl^-$, $ClO_4^-$, $ClO_3^-$, $NO_3^-$ and $SO_4^{2-}$) and cations ($NH_4^+$, $Na^+$ and $K^+$) were successfully separated and detected.

Simultaneous determination of inorganic ions is very important to meet the need of real field determination. However, in most cases, anions and cations are usually determined separately using different separation systems with different types of columns and conditions. Meng et al. [87] developed a non-suppressed ion chromatographic method by connecting anion and cation exchange columns directly in series for the separation and determination of

five inorganic anions ($Cl^-$, $NO_2^-$, $NO_3^-$, $SO_4^{2-}$, and $ClO_3^-$) and three cations ($NH_4^+$, $K^+$, and $Na^+$) simultaneously in explosive residues. The method was successfully applied to the analysis of the inorganic explosive residues samples from the explosion site with satisfactory results.

**Capillary electrophoresis**

In the explosive analysis, capillary electrophoresis (CE) serves as a complimentary technique to ion chromatography (IC) in the analysis of inorganic low explosives residues. CE components require narrow-bore capillary, a controllable high voltage power supply, two electrode, two buffer reservoirs and a detector. In CE, the targeted analytes elute from one end of the capillary under the influence of electric field and the analytes are separated according to ionic mobility. The requirement of sample site is low and can be applied to both anions and cations. It gives shorter time of analysis but sacrificing the separation of analytes [88].

Hopper et al. [89] conducted simultaneous separation of anions and cations to analyze a variety of low explosives in post-blast residues. Both anions ($Cl^-$, $NO_2^-$, $NO_3^-$, $SO_4^{2-}$, $ClO_4^-$, $SCN^-$, $ClO_3^-$, and $OCN^-$) and cations ($NH_4^+$, $K^+$, $Na^+$, $Ca^{2+,}$ and $Mg^{2+}$) were successfully separated under 7 minutes. The major disadvantages of CE over IC are poor reproducibility and sensitivity. It gave lower sensitivity because of the low amount of analytes that could be injected resulting in tiny peak volumes [90]. Ahmad et al. [91] have developed a CE method by using 25 mM 2,6-pyridinedicarboxylic acid (PDC) as a background electrolyte (BGE) and the addition of 0.5 mM cetyltrimethylammonium hydroxide (CTAH) to reverse the direction of electroosmotic flow (EOF). This method was successfully used to determine four anions ($Cl^-$, $NO_3^{2-}$ and $SO_4^{2-}$, and $SCN^-$) and three cations ($Ca^{2+}$, $Fe^{2+,}$ and $Fe^{3+}$) simultaneously under 7 minutes at pH 4.7. This method was also successfully applied to the analysis of post-blast explosive residues of black powder and ammonium nitrate-fuel oil (ANFO).

**Other techniques**

There are other instrumental techniques, most of which were upgraded version of the conventional instrumental techniques for the analysis of explosive. Infrared spectroscopy was developed for detection of explosive in 1960. Pristera et al. [92] successfully compiled 68 infrared spectrograms including high explosive compound and other ingredients of explosive by using conventional dispersive IR spectroscopic method. Fourier transform infrared spectroscopy (FTIR) was discovered at the end of 1970. However, the application of FTIR on the explosive analysis began in 1990 with the analysis of HMX explosive compound [93]. Compared to conventional IR, FTIR gave more benefits in terms of speed of analysis and sensitivity. Primera-Pedrozo et al. [94] developed an advanced technique for qualitative and quantitative analysis of explosives on metallic surfaces using fibre optic coupled reflection/absorption infrared spectroscopy (RAIRS). Their study revealed low detection limit of 2,6-DNT (200 $ng/cm^3$), TNT (160 $ng/cm^3$), PETN (200 $ng/cm^3$), HMX (400 $ng/cm^3$), and Tetryl (200 $ng/cm^3$). However, the study was only limited to highly reflective metallic surfaces.

X-ray powder diffraction (XRD) and X-ray fluorescence (XRF) are non-destructive methods for the composition analysis of the crystalline materials. Both of the methods are different but complementary to each other whereby XRD is used to analyze the phases or compounds meanwhile XRF is utilized for the analysis of the elemental composition of the crystalline material [95, 96]. The analysis of explosive using XRD begun in 1947 with 18 organic explosives were chosen to study their X-ray diffraction pattern [97]. O'Flynn et al. [98] developed a pixellated X-ray diffraction (PixD) system by combining both angular and energy dispersive X-ray diffraction into one system. By integrating principal component and discrimination analysis into the PixD system, a model was developed which can be used to identify explosive and inert samples.

There are many difficulties involved in the identification of materials and devices after an explosion. Thus, a wide range of analytical techniques or instrumentations are currently available and applicable for analysis of explosive residues. The choices of method used are dependent upon the type of sample collected and the types of analytes to be examined and studied. Table 3 shows some of the survey of explosive residue analysis with various instrumentation technique and types of explosive samples.

Table 3. Survey of explosive residue analysis

| Analytes | Sample | Instrument | References |
|---|---|---|---|
| Urea nitrate (UN) | Post-blast debris | Gas chromatography mass spectrometry (GC/MS) | [99] |
| NB, 2-NT, 3-NT, 4-NT, 1,3-DNB, 2,6-DNT, 2,4-DNT, 3,4-DNT, 1,3,5-TNB, 2,4,6-TNT, AMDNT, Tetryl, HMX | - | Gas chromatography positive chemical ionization and tandem mass (GC/PCI/MS/MS) spectrometry | [82] |
| NG, 2,6-DNT, 2,4-DNT, TNT, PETN | Soil | Solvating gas chromatography with thermal energy analyzer (SGC/TEA) | [78] |
| TNT , DNT | TNT, dynamite | Gas chromatography with electron captured detector (GC/ECD) and Ion chromatography (IC) | [15] |
| PETN, RDX, TNT | Hair | Gas chromatography with electron captured detector (GC/ECD) | [28] |
| RDX, PETN | Semtex plastic explosive | Fourier transform-infrared spectroscopy (FTIR) | [14] |
| C-4, TNT, PETN | Improvised explosive devices (IED) | Fourier transform-infrared spectroscopy (FTIR) | [100] |
| HMX, RDX, TNT, DNT, PETN | Soil | High performance liquid chromatography (HPLC) | [101] |
| HMTD, TATP | Peroxide explosive | High Performance liquid chromatography-atmospheric Pressure chemical ionization-tandem mass spectrometry (HPLC-APCI-MS/MS) | [102] |
| HMX, RDX, TNB, DNB, NB, TNT, Tetryl, 2,4-DNT, 2,6-DNT, 2-NT, 4-NT, 3-NT, NG, PETN | Plastic explosive | Capillary electrophoresis (CE) | [103] |
| $NH_4^{+}$, $K^+$, $Na^+$ $Ca^{2+}$, $Mg^{2+}$, $HS^-$, $Cl^-$, $NO_2^-$, $NO_3^-$, $SO_4^{2-}$, $ClO_4^-$, $SCN^-$, $ClO_3^-$, $OCN^-$ | Pyrodex® RS,black powder, and smokeless powders. | Capillary electrophoresis (CE) | [89] |
| $Cl^-$, $NO_2^-$, $HSO_4^-$, $NO_3^-$, $ClO_3^-$, benzoate, $HS_2O_3^-$ | Black powder | Ion chromatography/mass spectrometry (IC/MS) | [104] |

Table 3 (cont'd). Survey of explosive residue analysis

| Analytes | Sample | Instrument | References |
|---|---|---|---|
| $Cl^-$, $NO_2^-$, $NO_3^-$ , $SO_4^{2-}$, $SCN^-$ | Soil | Ion chromatography (IC) | [69] |
| RDX | - | X-ray powder diffraction (XRD) | [105] |
| Lead and mercury | Detonator | X-ray fluorescence (XRF) | [106] |
| RDX, TNT, 4-AMDNT, TNB, DNB, 2,6-DNT, 2-NT, 4-NT, Tetryl, HMX, NB | Soil | Micellar electrokinetic capillary chromatography (MEKC) and high performance liquid chromatography (HPLC) | [107] |
| Arsine compound ,TNT | gas shells | Micellar electrokinetic capillary chromatography (MEKC) and high performance liquid chromatography (HPLC) | [108] |
| TNT, RDX, PETN | - | Ion mobility spectrometry (IMS) | [61] |
| TNT, 2,4-DNT, 2-ADNT, 4-NT, HMX, EGDN,NG | | explosives using electrospray ionization/ion mobility spectrometry (ESI-IMS) | [60] |

## Conclusion

The screening process from the usage of trained canine team to portable detection instrument either as sensors or a portable kit as an improvement on classical biological olfactory system shows the capabilities of new technology to be directly applied in fieldwork. Extraction process has evolved from year to year towards a green technology and has demonstrated a significant impact on the total cost, time consumption and decreased amount on chemical usage. Combined with the right instrumentation, research study allowed the constituent or element of interest to be analyzed with high selectivity and sensitivity. Simultaneous detection of anions and cations in inorganic explosive showed promise for the reduction of analysis time and chemical consumption. Developments of SPME techniques has become a trending method when compared to the conventional liquid extraction that consumed more chemicals and cause risk to researcher's health. The development of an explosive database in the future will become a great tool for researcher reference for lab-to-lab comparison.

Much research work can be improved in order to cope with the advancement in terrorism. For the sake of global security, other than enhancement of law enforcement and military strength, attention should be paid to the importance of research and development on the analysis of scientific evidence, particularly on explosive residue analysis.

## Acknowledgement

Thanks are due to the Department of Chemistry, Faculty of Science, Universiti Teknologi Malaysia, Johor, for research facilities as well as to Malaysian Ministry of Higher Education (MOHE) for financial assistance through FRGS grant no R.J130000.7826.4F200 (4F200). Collaboration assistance from Science & Technology Research Institute of Defense (STRIDE) is also greatly acknowledged.

## References

1. Leistedt, S. J. (2013). Behavioural aspects of terrorism. *Forensic Science International*. 228(1–3): 21 – 27.
2. Miguel, E. and Roland, G. (2011). The long-run impact of bombing Vietnam. *Journal of Development Economics*, 96(1): 1 – 15.
3. Global Terrorism Database (2015) Available from: http://www.start.umd.edu/gtd [Date access 20 June 2015].
4. Royds, D., Lewis, S. W. and Taylor, A. M. (2005). A case study in forensic chemistry: The Bali bombings. *Talanta*, 67(2): 262 – 268.

5. Landman, A., Teich, J. M., Pruitt, P., Moore, S. E., Theriault, J., Dorisca, E., Harris, S., Crim, H., Lurie, N. and Goralnick, E. (2015). The Boston marathon bombings mass casualty incident: One emergency department's information systems challenges and opportunities. *Annals Emergency Medicine*, 66(1): 51 – 59.
6. Hicks, M. H., Dardagan, H., Bagnall, P. M., Spagat, M., and Sloboda, J. A. (2011). Casualties in civilians and coalition soldiers from suicide bombings in Iraq, 2003 – 2010: A descriptive study. *Lancet*, 378(9794): 906 – 914.
7. Yavuz, M. S., Asirdizer, M., Cetin, G., Yavuz, M. F. Cansunar, F. N. and Kolusayin, R. O. (2004). Deaths due to terrorist bombings in Istanbul (Turkey). *Journal Clinical Forensic Medicine*, 11(6): 308 – 315.
8. Bosnar, A., Stemberga, V., Coklo, M., Grgurevic, E., Zamolo, G., Cucic, T. and di Nunno, N. (2006). War and suicidal deaths by explosives in southwestern Croatia. *Archives of Medical Research*, 37(3): 392 – 394.
9. Yinon, J. and Zitrin, S. (1981). The analysis of explosives. 1st ed. England: Pergamon press. pp. 59 –118.
10. Lahoda, K. G., Collin, O. L., Mathis, J. A., LeClair, H. E., Wise, S. H. and McCord, B. R. (2008). A survey of background levels of explosives and related compounds in the environment. *Journal of Forensic Sciences*, 53(4): 802 – 806.
11. Singh, S. (2007). Sensors – An effective approach for the detection of explosives. *Journal of Hazardous Materials*, 144(1–2): 15 – 28.
12. Yinon, J. and Zitrin, S. (1996). Modern methods and applications in analysis of explosives. 1st ed. England: John Wiley & Sons. pp. 2 – 213.
13. Adams, D. E., Mabry, J. P., McCoy, M. R. and Lord, W. D. (2013). Challenges for forensic science: New demands in todays world. *Australian Journal of Forensic Sciences*, 45(4): 347 – 355.
14. Akhavan, J. (1991). Analysis of high-explosive samples by fourier transform raman spectroscopy. *Spectrochimica Acta Part A: Molecular Spectroscopy*. 47(9–10): 1247 – 1250.
15. Varga, R. and Ulbrich, P. (2004). Some experience with trace analysis of post-explosion residues. *Academic and Applied Research in Public Management Science*. 3(4): 633 – 646.
16. Ahmad, U. K., Rajendran, S., Ling L. W. and Hooi, Y. C. Hooi, (2008). Forensic analysis of high explosives residues in post-blast water samples employing solid phase extraction for analyte pro-concentration. *Malaysian Journal of Analytical Sciences,* 12(2): 367 – 374.
17. Taylor, S., Hewitt, A., Lever, J., Hayes, C., Perovich, L., Thorne, P. and Daghlian, C. (2004). TNT particle size distributions from detonated 155-mm howitzer rounds. *Chemosphere*, 55(3): 357 – 367.
18. Johns, C., Shellie, R. A., Potter, O. G., O'Reilly, J. W., Hutchinson, J. P., Guijt, R. M., Breadmore, M. C., Hilder, E. F., Dicinoski, G. W. and Haddad, P. R. (2008). Identification of homemade inorganic explosives by ion chromatographic analysis of post-blast residues. *Journal of Chromatography A*, 1182(2): 205 –214.
19. Thompson, R. Q., Fetterolf, D. D., Miller, M. L. and Mothershead R. F. (1999). Aqueous recovery from cotton swabs of organic explosives residue followed by solid phase extraction. *Journal of Forensic Sciences*, 44(4): 795 – 804.
20. Hutchinson, J. P., Evenhuis, C. J., Johns, C., Kazarian, A. A., Breadmore, M. C., Macka, M., Hilder, E. F. and Haddad, P. R. (2007). Identification of inorganic improvised explosive devices by analysis of postblast residues using portable capillary electrophoresis instrumentation and indirect photometric detection with a light-emitting diode. *Analytical Chemistry*, 79(18): 7005 – 7013.
21. Borusiewicz, R., Zadora, G. and Zieba-Palus, J. (2013). Chemical analysis of post explosion samples obtained as a result of model field experiments. *Talanta*, 116: 630 – 636.
22. Abdul-Karim, N., Blackman, C. S., Gill, P. P., Wingstedt, E. M. M. and Reif, B. A. F. (2014). Post-blast explosive residue-a review of formation and dispersion theories and experimental research. *RSC Advances*, 4(97): 54354 – 54371.
23. Song-im, N., Benson, S. and Lennard, C. (2013). Stability of explosive residues in methanol/water extracts, on alcohol wipes and on a glass surface. *Forensic Science International*. 226(1–3): 244 – 253.
24. Miller, C. J., Elias, G., Schmitt, N. S. and Rae, C. (2010). Identification of explosives from porous materials: Applications using reverse phase high performance liquid chromatography and gas chromatography. *Sensing and Imaging: An International Journal*, 11(2): 61 – 75.
25. Ahmad, U. K., Rajendran, S. and Hassan, S. A. (2008). Forensic analysis of explosive residues from hand swabs. *Malaysian Journal of Analytical Sciences*, 12(1): 213 – 226.
26. Twibell, J. D., Turner, S. L., Smalldon, K. W. and Higgs, D. G. (1984). The persistence of military explosives on hands. *Journal of Forensic Sciences*, 29(1): 284 – 290.

27. Ahmad, U. K., Bakar, N. H. A. and Abdullah, S. A. A. S. (2012). Analysis of C4 explosive residues on post blast hair samples. *Jurnal Teknologi*, 57(1): 163 – 171.
28. Oxley, J. C., Smith, J. L., Bernier, E., Moran, J. S. and Luongo, J. (2009). Hair as forensic evidence of explosive handling. *Propellants, Explosives, Pyrotechnics*. 34(4): 307 – 314.
29. Huri, M. A. M. and Ahmad, U. K. (2014). Forensic analysis of high explosive residues from selected cloth. *Malaysian Journal of Analytical Sciences*, 18(1): 68 – 77.
30. Walsh, M. E. (2001). Determination of nitroaromatic, nitramine, and nitrate ester explosives in soil by gas chromatography and an electron capture detector. *Talanta*, 54(3): 427 – 438.
31. Bausinger, T., Dehner, U. and Preub, J. (2004). Determination of mono-, di- and trinitronaphthalenes in soil samples contaminated by explosives. *Chemosphere*, 57(8): 821 – 829.
32. Babaee, S. and Beiraghi, A. (2010). Micellar extraction and high performance liquid chromatography-ultra violet determination of some explosives in water samples. *Analytica Chimica Acta*, 662(1): 9 – 13.
33. Kamyshny, A., Magdassi, S., Avissar, Y. and Almog, J. (2003). Water-soaked evidence: Detectability of explosive traces after immersion in water. *Journal of Forensic Sciences*, 48(2): 312 –317.
34. Monteil-Rivera, F., Beaulieu, C. Deschamps, S. Paquet, L. and Hawari, J. (2004). Determination of explosives in environmental water samples by solid-phase microextraction–liquid chromatography. *Journal of Chromatography A*. 1048(2): 213 – 221.
35. McCorkell, W. J. and Griffin, R. M. (1998). An overview of the scientific examinations performed after an explosion on the Shankill road. *Science and Justice*, 38(2): 75 –79.
36. Hawthorne, S. B., Lagadec, A. J. M., Kalderis, D., Lilke, A. V. and Miller, D. J. (2000). Pilot-scale destruction of TNT, RDX, and HMX on contaminated soils using subcritical water. *Environmental Science and Technology*, 34(15): 3224 – 3228.
37. Hoffman, C. M. and Byall, E. B. (1974). Identification of explosive residues in bomb scene investigations. *Journal of Forensic Sciences*, 19(1): 54 – 63.
38. Sara, M. and Ellen. O. L. (2015). Timeline of Boston marathon bombing events. Available from: http://www.boston.com/news/local/massachusetts/2015/01/05/timeline-boston-marathon-bombing-eve nts/qiYJmANm6DYxqsusVq66yK/story.html. [Date access 25 November 2015].
39. Oam, D. R. (2013). A ten year retrospective of the bombing campaign in Indonesia by terrorists, 2002–2006. *Australian Journal of Forensic Sciences*, 45(2): 123 – 146.
40. Reynolds, J., Nunes, P. Whipple, R. and Alcaraz, A. (2006). On-site analysis of explosives in various matrices. *NATO Security through Science Series C: Environmental Security*. Springer: pp. 27 – 32.
41. Yinon, J. (2002). Field detection and monitoring of explosives. *TrAC Trends in Analytical Chemistry*. 21(4): 292 – 301.
42. Germain, M. E. and Knapp, M. J. (2009). Optical explosives detection: From color changes to fluorescence turn-on. *Chemical Society Reviews*, 38(9): 2543 – 2555.
43. Stancl, M. and Kyncl, M. (2008). Some detection procedures for liquid explosives, in Detection of liquid explosives and flammable agents in connection with terrorism, H. Schubert and A. Kuznetsov, Editors, Springer Netherlands. pp. 79 – 96.
44. Fisco, W. (1975). A portable explosives identification kit for field use. *Journal of Forensic Science,* 20(1): 141 – 148.
45. Johns, S. H., Wist, A. A., and Najam, A. R. (1979). Spot tests: A color chart reference for forensic chemists. *Journal of Forensic Sciences*, 24(3): 631 – 649.
46. Nambayah, M. and Quickenden, T. I. (2004). A quantitative assessment of chemical techniques for detecting traces of explosives at counter-terrorist portals. *Talanta*, 63(2): 461 – 467.
47. Furton, K. G. and Myers, L. J. (2001). The scientific foundation and efficacy of the use of canines as chemical detectors for explosives. *Talanta*, 54(3): 487 – 500.
48. Quignon, P., Kirkness, E., Cadieu, E., Touleimat, N., Guyon, R., Renier, C., Hitte, C., Andre, C., Fraser, C., and Galibert, F. (2003). Comparison of the canine and human olfactory receptor gene repertoires. *Genome Biology*, 4(12): R80.
49. Wetter, O. E. (2013). Imaging in airport security: Past, present, future, and the link to forensic and clinical radiology. *International Journal of Industrial Ergonomics*, 1(4): 152 – 160.
50. Wells, K. and Bradley, D. A. (2012). A review of X-ray explosives detection techniques for checked baggage. *Applied Radiation and Isotopes*, 70(8): 1729 – 1746.

51. Michel, S., Mendes, M., de Ruiter, J. C., Koomen, G. C. M. and Schwaninger, A. (2014). Increasing X-ray image interpretation competency of cargo security screeners. International *Journal of Industrial Ergonomics*, 44(4): 551 – 560.
52. Moore, D. S. (2007). Recent advances in trace explosives detection instrumentation. *Sensing and Imaging: An International Journal*, 8(1): 9 – 38.
53. Yinon, K. (2007). Counterterrorist detection techniques of explosives.1st ed. Uk: Elsevier: pp. 1 – 440.
54. Caygill, J. S., Davis, F. and Higson, S. P. J. (2012). Current trends in explosive detection techniques. *Talanta*, 88: 14 – 29.
55. Mäkinen, M., Nousiainen, M. and Sillanpää, M. (2011). Ion spectrometric detection technologies for ultra-traces of explosives: A review. *Mass Spectrometry Reviews,* 30(5): 940 – 973.
56. Ewing, R. G., Waltman, M. J., Atkinson, D. A., Grate, J. W., and Hotchkiss, P. J. (2013). The vapor pressures of explosives. *TrAC Trends in Analytical Chemistry*, 42(1): 35 – 48.
57. Ewing, R. G., Atkinson, D. A., Eiceman, G. A. and Ewing, G. J. (2001). A critical review of ion mobility spectrometry for the detection of explosives and explosive related compounds. *Talanta*, 54(3): 515 – 529.
58. Voyksner, R. D. and Yinon, J. (1986). Trace analysis of explosives by thermospray high-performance liquid chromatography – mass spectrometry. *Journal of Chromatography A*, 354: 393 – 405.
59. Na, N., C. Zhang, M. Zhao, S. Zhang, C. Yang, X. Fang, and X. Zhang, (2007). Direct detection of explosives on solid surfaces by mass spectrometry with an ambient ion source based on dielectric barrier discharge. *Journal of Mass Spectrometry*, 42(8): 1079 – 1085.
60. Reid A. G., Klasmeier, J. and Hill Jr, H. H. (2000). Analysis of explosives using electrospray ionization/ion mobility spectrometry (ESI/IMS). *Talanta*. 50(6): 1291 – 1298.
61. Khayamian, T., Tabrizchi, M. and Jafari, M. T. (2003). Analysis of 2,4,6-trinitrotoluene, pentaerythritol tetranitrate and cyclo-1,3,5-trimethylene-2,4,6-trinitramine using negative corona discharge ion mobility spectrometry. *Talanta*, 59(2): 327 – 333.
62. Ewing, R. G., Clowers, B. H. and Atkinson, D. A. (2013). Direct real-time detection of vapors from explosive compounds. *Analytical Chemistry*, 85(22): 10977 – 10983.
63. Ruslan, N. N. (2009). A spot test kit for the field detection of selected explosives, Universiti Teknologi Malaysia. Thesis Bachelor of Science (Industrial Chemistry).
64. Mohan, M. and Chand, D. K. (2014). Visual colorimetric detection of TNT and 2,4-DNT using as-prepared hexaazamacrocycle-capped gold nanoparticles. *Analytical Methods*, 6(1): 276 – 281.
65. Feigl, F. and Anger, V.(1972). Spot tests in inorganic analysis: Elsevier Publishing Company.
66. Furton, K.G., Almirall, J. R., Bi, M., Wang, J. and Wu, L. (2000). Application of solid-phase microextraction to the recovery of explosives and ignitable liquid residues from forensic specimens. *Journal of Chromatography A*, 885(1-2): 419 – 432.
67. DeTata, D. A., Collins, P. A., and McKinley, A. J. (2013). A comparison of common swabbing materials for the recovery of organic and inorganic explosive residues. *Journal of Forensic Sciences*. 58(3): 757 – 763.
68. Song-im, N., Benson, S. and Lennard, C. (2012). Evaluation of different sampling media for their potential use as a combined swab for the collection of both organic and inorganic explosive residues. *Forensic Science International*, 222(1-3): 102 – 110.
69. Ahmad, U. K., Tze, O. S., Ghazali, M. F., Hooi, Y. C., and Abdullah, M. K. (2011). Analysis of anionic post-blast residues of low explosives from soil samples of forensic interest. *Malaysian Journal of Analytical Sciences*. 15(2): 213 – 226.
70. Williford, C.W. and Mark, B. R. (1999). Extraction of tnt from aggregate soil fractions. *Journal of Hazardous Materials*, 66(1-2): 1 – 13.
71. Halasz, A., Groom, C., Zhou, E., Paquet, L., Beaulieu, C., Deschamps, S., Corriveau, A., Thiboutot, S., Ampleman, G., Dubois, C. and Hawari, J. (2002). Detection of explosives and their degradation products in soil environments. *Journal of Chromatography A*, 963(1): 411 – 418.
72. Abd-Talib, N., Mohd-Setapar, S. H. and Khamis, A. K. (2014). The benefits and limitations of methods development in solid phase extraction: Mini review. *Jurnal Teknologi (Sciences and Engineering),* 69(4): 69 – 72.
73. Warren, D., Hiley, R. W., Phillips, S. A. and Ritchie, K. (1999). Novel technique for the combined recovery, extraction and clean-up of forensic organic and inorganic trace explosives samples. *Science and Justice*. 39(1): 11 – 18.

74. Calderara, S., Gardebas, D. and Martinez, F. (2003). Solid phase micro extraction coupled with on-column GC/ECD for the post-blast analysis of organic explosives. *Forensic Science International*, 137(1): 6 – 12.
75. Ahmad, U. K. and Heng, K. K. (2007). Solid phase microextraction-gas chromatography for the analysis of explosives in post blast water samples. *Jurnal Teknologi*, 46: 59 – 74.
76. Kolla, P. (1994). Gas-chromatography, liquid-chromatography and ion chromatography adapted to the trace analysis of explosives. *Journal of Chromatography A*, 674(1-2): 309 – 318.
77. Pan, X., Zhang, B. and Cobb, G. P. (2005). Extraction and analysis of trace amounts of cyclonite (RDX) and its nitroso-metabolites in animal liver tissue using gas chromatography with electron capture detection (GC-ECD). *Talanta*, 67(4): 816 – 823.
78. Bowerbank, C. R., Smith, P. A., Fetterolf, D. D. and Lee, M. L. (2000). Solvating gas chromatography with chemiluminescence detection of nitroglycerine and other explosives. *Journal of Chromatography A*. 902(2): 413 – 419.
79. Jiménez, A. M. and Navas, M. J. (2004). Chemiluminescence detection systems for the analysis of explosives. *Journal of Hazardous Materials*, 106(1): 1 – 8.
80. Chakrabortty, A., Bagchi, S. and Chandra L. S. (2015). Studies of fire debris from bomb blasts using ion chromatography, gas chromatography–mass spectrometry and fluorescence measurements – evidence of ammonium nitrate, wax-based explosives and identification of a biomarker. *Australian Journal of Forensic Sciences*, 47(1): 83 – 94.
81. Fan, W. and Almirall, J. (2014). High-efficiency headspace sampling of volatile organic compounds in explosives using capillary microextraction of volatiles (CMV) coupled to gas chromatography-mass spectrometry (GC-MS) microextraction techniques. *Analytical and Bioanalytical Chemistry*, 406(8): 2189 – 2195.
82. Perr, J. M., Furton, K. G., and Almirall, J. R. (2005). Gas chromatography positive chemical ionization and tandem mass spectrometry for the analysis of organic high explosives. *Talanta*, 67(2): 430 – 436.
83. Kozole, J., Levine, L. A., Tomlinson-Phillips, J. and Stairs, J. R. (2015). Gas phase ion chemistry of an ion mobility spectrometry based explosive trace detector elucidated by tandem mass spectrometry. *Talanta*, 140: 10 – 19.
84. Ahmad, U. K., Harun S. N., and Hooi, Y. C. (2011). Forensic analysis of nitroglycerin in post blast samples. *3rd International Conferences and Workshops on Basic and Applied Sciences*: pp. 1 – 7.
85. Makarov, A., LoBrutto, R., Christodoulatos, C. and Jerkovich, A. (2009). The use of ultra high-performance liquid chromatography for studying hydrolysis kinetics of CL-20 and related energetic compounds. *Journal of Hazardous Materials*, 162(2-3): 1034 – 1040.
86. Schramm, S., Léonço, D., Hubert, C., Tabet, J.-C., and Bridoux, M. (2015). Development and validation of an isotope dilution ultra-high performance liquid chromatography tandem mass spectrometry method for the reliable quantification of 1,3,5-triamino-2,4,6-trinitrobenzene (TATB) and 14 other explosives and their degradation products in environmental water samples. *Talanta*, 143: 271 – 278.
87. Meng, H. B., Wang, T. R., Guo, B. Y., Hashi, Y., Guo, C. X. and Lin, J. M. (2008). Simultaneous determination of inorganic anions and cations in explosive residues by ion chromatography. *Talanta*, 76(2): 241 – 245.
88. Hargadon, K. A. and McCord, B. R. (1992). Explosive residue analysis by capillary electrophoresis and ion chromatography. *Journal of Chromatography A*, 602(1–2): 241 – 247.
89. Hopper, K. G., LeClair, H. and McCord, B. R. (2005). A novel method for analysis of explosives residue by simultaneous detection of anions and cations via capillary zone electrophoresis. *Talanta*, 67(2): 304 – 312.
90. Cruces-Blanco, C., Gamiz-Gracia, L. and Garcia-Campana, A. M. (2007). Applications of capillary electrophoresis in forensic analytical chemistry. *TrAC Trends in Analytical Chemistry*. 26(3): 215 – 226.
91. Ahmad, U. K., Jamari, N. L. and Nagayah, S. (2012). Simultaneous determination of inorganic ions in post-blast residues using capillary electropheresis. *Malaysian Journal of Analytical Sciences*. 12(1): 25 – 31.
92. Pristera, F., Halik, M., Castelli, A. and Fredericks, W. (1960). Analysis of explosives using infrared spectroscopy. *Analytical Chemistry*, 32(4): 495 – 508.
93. Achuthan, C. P. and Jose, C. I. (1990). Studies on octahydro-1,3,5,7-tetranitro-1,3,5,7-tetrazocine (HMX) polymorphism. *Propellants, Explosives, Pyrotechnics*. 15(6): 271 – 275.

94. Primera-Pedrozo, O. M., Soto-Feliciano, Y. M., Pacheco-Londoño, L. C. and Hernández-Rivera, S. P. (2009). Detection of high explosives using reflection absorption infrared spectroscopy with fiber coupled grazing angle probe/FTIR. *Sensing and Imaging: An International Journal,* 10(1-2): 1 – 13.
95. Mantler, M. and Schreiner, M. (2011). X-ray analysis of objects of art and archaeology. *Journal of Radioanalytical and Nuclear Chemistry,* 247(3): 635 – 644.
96. Sánchez Ramos, S., Bosch Reig, F., Gimeno Adelantado, J., Yusá Marco, D. and Doménech Carbó, A. (2014). Application of XRF, XRD, thermal analysis, and voltammetric techniques to the study of ancient ceramics. *Analytical and Bioanalytical Chemistry*, 373(8): 893 – 900.
97. Soldate, A. M. and Noyes, R. M. (1947). X-ray diffraction patterns for the identification of crystalline constituents of explosives. *Industrial and Engineering Chemistry*, 19(7): 442 – 444.
98. O'Flynn, D., Reid, C. B., Christodoulou, C., Wilson, M. D., Veale, M. C., Seller, P., Hills, D. Desai, H., Wong, B. and Speller, R. (2013). Explosive detection using pixellated X-ray diffraction (PixD). *Journal of Instrumentation*, 8(3): 1 – 15.
99. Almog, J., Espino, D., Tamiri, T. and Sonenfeld, D. (2013). Trace analysis of urea nitrate in post-blast debris by GC/MS. *Forensic Science International*, 224(1–3): 80 – 83.
100. Banas, K., Banas, A., Moser, H. O., Bahou, M., Li, W., Yang, P., Cholewa, M. and Lim, S. K. (2010). Multivariate analysis techniques in the forensics investigation of the postblast residues by means of fourier transform-infrared spectroscopy. *Analytical Chemistry*, 82(7): 3038 – 3044.
101. Paull, B., C. Roux, M. Dawson, and P. Doble, (2004). Rapid screening of selected organic explosives by high performance liquid chromatography using reversed-phase monolithic columns. *Journal of Forensic Sciences*, 49(6): 1181 – 1186.
102. Xu, X., Van De Craats, A. M., Kok, E. M. and De Bruyn, P. C. A. M. (2004). Trace analysis of peroxide explosives by high performance liquid chromatography-atmospheric pressure chemical ionization-tandem mass spectrometry (HPLC-APCI-MS/MS) for forensic applications. *Journal of Forensic Sciences*, 49(6): 1230 – 1236.
103. Oehrle, S. A., (1996). Analysis of nitramine and nitroaromatic explosives by capillary electrophoresis. *Journal of Chromatography A*, 745(1-2): 233 – 237.
104. Lang, G.-H. L. and Boyle, K. M. (2009). The analysis of black powder substitutes containing ascorbic acid by ion chromatography/mass spectrometry. *Journal of Forensic Sciences*, 54(6): 1315 – 1322.
105. Sun, J., Shu, X., Liu, Y., Zhang, H., Liu, X., Jiang, Y., Kang, B., Xue, C. and Song, G. (2011). Investigation on the thermal expansion and theoretical density of 1,3,5-trinitro-1,3,5-triazacyclohexane. *Propellants, Explosives, Pyrotechnics*, 36(4): 341 – 346.
106. Koudryashov, V. I., Serebryakov, A. S. and Smirnov, V. V. (2006). Investigation of possibility to detect the detonators of the explosive devices by means of EC XRF approach, in detection and disposal of improvised explosives, Schubert, H. and Kuznetsov, A. Editors, *Springer Netherlands*: pp. 223 – 226.
107. Kleiböhmer, W., K. Cammann, J. Robert, and Mussenbrock, E. (1993). Determination of explosives residues in soils by micellar electrokinetic capillary chromatography and high-performance liquid chromatography: A comparative study. *Journal of Chromatography A*, 638(2): 349 – 356.
108. Smedts, B. R., Baeyens, W. and De Bisschop, H. C. (2003). Separation of arsines and trinitrotoluene by reversed phase high performance liquid chromatography and micellar electrokinetic capillary chromatography. *Analytica Chimica Acta*, 495(1-2): 239 – 247.

*Malaysian Journal of Analytical Sciences, Vol 21 No 2 (2017): 283 - 290*
*DOI: https://doi.org/10.17576/mjas-2017-2102-02*

MALAYSIAN JOURNAL OF ANALYTICAL SCIENCES
*Published by The Malaysian Analytical Sciences Society*
ISSN 1394 - 2506

# GLUCOSE PRODUCTION FROM STEAM-ALKALI-CHEMICAL PRE-TREATED OIL PALM TRUNK BIOMASS VIA ENZYMATIC SACCHARIFICATION PROCESS

## (Penghasilan Glukosa dari Pra-Rawatan Wap-Kimia-Alkali Biomas Batang Kelapa Sawit Melalui Proses Sakarifikasi Enzim)

Nurul Wahidah Mazlan, Long Wee Lai*, Nur Akmal Suliman, Marini Ibrahim, Rahmad Mohd Taib, Rozila Alias

*Department of Science and Biotechnology,*
*Faculty of Engineering and Life Sciences,*
*Universiti Selangor, Jalan Timur Tambahan, 45600 Bestari Jaya, Selangor, Malaysia*

**Corresponding author: zki@unisel.edu.my*

Received: 7 June 2016; Accepted: 1 February 2017

**Abstract**

This study proposed lignocellulosic oil palm trunk (OPT) biomass can be used as alternative substrate for glucose emanation *via* enzymatic saccharification route. The OPT biomass was pre-treated using steam-alkali-chemical (SAC) method prior to enzymatic saccharification process for glucose formation. Three basic physiochemical parameters such as enzyme concentration (20 – 100 FPU.mL$^{-1}$), pH (4.0 – 8.0) and reaction temperature (30 – 60 °C) were intensively studied. Results revealed that all parameters gave significant effect on glucose production. By setting the enzyme hydrolysis conditions at pre-determined parameters points, i.e. enzyme concentration, 60 FPU.mL$^{-1}$; pH, 6.0 and reaction temperature, 50 °C, respectively; 4.27 g.L$^{-1}$ of glucose was attained at 72 hours hydrolysis. There is 4.49-fold of glucose increment in SAC-treated OPT substrate compared to untreated ones. This research also indicates enzyme digestibility can be enhanced by using treated OPT as substrate.

**Keywords:** oil palm trunk biomass, steam-alkali-chemical pre-treatment, enzymatic saccharification, cellulase enzyme

**Abstrak**

Kajian ini mencadangkan lignoselulosa biomas batang kelapa sawit (OPT) boleh digunakan sebagai alternatif substrat bagi penghasilan glukosa melalui kaedah enzim sakarifikasi. Biomas OPT terlebih dahulu dirawat dengan wap-kimia-alkali (SAC) sebelum proses sakarifikasi enzimatik bagi pembentukan glukosa. Tiga fizikokimia parameter asas seperti kepekatan enzim (20 – 100 FPU.mL$^{-1}$), pH (4.0 – 8.0) dan suhu tindak-balas (30 – 60 °C) telah dikaji secara intensif. Hasil kajian menunjukkan bahawa semua parameter memberi kesan ke atas pengeluaran glukosa. Dengan menetapkan syarat enzim hidrolisis pada parameter yang telah ditentukan, iaitu masing-masing; kepekatan enzim, 60 FPU.mL$^{-1}$; pH, 6.0 dan suhu tindak-balas, 50 °C; 4.27 g.L$^{-1}$ glukosa telah dicapai pada 72 jam hidrolisis. Glukosa meningkat sebanyak 4.49 kali ganda dalam SAC-rawatan OPT substrat berbanding yang tidak dirawat. Kajian ini juga membuktikan penghadaman enzim boleh dipertingkatkan dengan menggunakan OPT terawat sebagai substrat.

**Kata kunci:** biomas batang kelapa sawit, pra-rawatan wap-kimia-alkali, sakarifikasi enzimatik, enzim selulase

## Introduction

Glucose is one of the most important monosaccharide with the chemical formula of $C_6H_{12}O_6$ and a molar mass of 180.16 g.mol$^{-1}$. It is the simplest form of sugar and serves as a main carbon source to living organisms including animals, human, plants and microbes for energy and metabolic requirement. Recently, glucose is produced from

lignocellulosic biomass waste such as sugarcane bagasse [1], corn stover [2] and oil palm [3]. This is because lignocellulosic biomass waste contains a higher amount of cellulose and hemicellulose which are able to be converted into sugars (mainly glucose). The produced glucose can be used as a cheaper alternative to feedstock for industrial applications particularly in fermentation industry. Usually, cellulase enzyme is required and employed to achieve the convertible goal. The efficiency of enzyme conversion towards its substrate depends on the enzymatic saccharification system. This means that the system has to provide optimal conditions for enzyme to digest its substrate in order for maximum product formation to occur. In line with this, fundamental physiochemical parameters such as enzyme concentration, pH and reaction temperature must be well manipulated [4].

However, the native behavior of recalcitrant lignocellulosic biomass makes the enzyme hydrolysis more challenging. In order to maximize sugar formation from lignocellulosic substrate, pretreatment on lignocellulosic biomass is inevitable. Apparent objectives of the pretreatment are i) to alter the structure of lignocellulose so as to make cellulose more accessible to cellulase and ii) to shatter the lignin seal and disrupt the crystalline structure of cellulose [5]. Therefore, the pretreatment step is crucial as it can maximize cellulose recovery from lignocellulosic substrate into usable form. Previous study has shown that microwave-alkali (Mw-A) pretreatment is capable of reducing lignin in small quantity. In contrast, steam-alkali-chemical (SAC) which is a double-step pretreatment method has proven to be more efficient in terms of lignin removal. According to Lai et al. [6], a significant decrease in the amount of lignin i.e. 87.07% was seen when using SAC method; whereas reduction of lignin using Mw-A pretreatment method was recorded to be only 15.33%. Lignin removal is essential since the presence of lignin will act as a shield that prevents cellulose from being hydrolyzed by cellulolytic enzymes. Thus, the double-step pretreatment (i.e. SAC method) was selected and used to pre-treat the OPT substrate in this study.

Currently, Malaysia is recognized as the world's second largest palm oil producers after Indonesia [7]. The oil palm biomass waste has amounted to 59 million tons annually which include (dry weight): oil palm empty fruit brunches (OPEFB), oil palm frond (OPF) and oil palm trunk (OPT), respectively. To eliminate bulk oil palm biomass in a more economic way; one of the method is to convert the oil palm biomass into fermentable sugars. The formed sugars (mainly glucose) can be utilized as carbon feedstock by microbes to produce the desired fermentative products such as organic acids, bio-ethanol and so on. The present study has chosen oil palm trunk (OPT) biomass as the substrate candidate. This is due to limited research data that focused on oil palm trunk studies compared to other parts of oil palm such as oil palm frond, oil palm empty fruit bunch and palm kernel shell. [8]. In order to maximize lignin removal and cellulose recovery, steam-alkali-chemical (SAC) pre-treatment method is used to accomplish the objectives. There are three important parameters to be considered for glucose conversion under enzymatic saccharification process, namely: enzyme concentration, pH and reaction temperature and all was investigated thoroughly. Apart from that, the findings of this research can provide complementary research data to oil palm study.

## Materials and Methods

### Raw materials

The pulverized oil palm trunk (OPT) biomass was provided by Concept Renewable Energy Sdn. Bhd., Malaysia. It was sieved to a particle size of less than 1.0 mm and dried at 45 °C for 3 days [7].The OPT samples were kept in 4 °C chiller prior to pre-treatment and enzymatic hydrolysis.

### Chemical reagents and enzymes

The chemicals used in the experiment were of analytical grade with highest purity, i.e. 96 – 99% and purchased from Merck (M) Sdn. Bhd. namely: sodium hydroxide (NaOH), acetic acid ($CH_3COOH$), potassium sodium tartrate ($KNaC_4H_4O_6{\cdot}4H_2O$), sodium metabisulfite ($Na_2S_2O_5$), phenol ($C_6H_6O$), sodium azide ($NaN_3$) and 3,5-dinitrosalicylic acids. The household bleach (sodium hypochlorite solution, 5.75% active chlorine) was bought from Tesco hypermarket. Meanwhile, the cellulase enzyme produced from *Trichodermareesei*, citric acid monohydrate ($C_6H_{10}O_8$) and trisodium citrate dehydrate ($C_6H_9Na_3O_9$) were obtained from Sigma-Aldrich (M) Sdn. Bhd.

### Steam-alkali-chemical (SAC) pre-treatment method

Ten grams of oil palm trunk (OPT) sample was soaked in a beaker containing 200 mL of 2.5 M NaOH solution for 1 hour. The mixture was brought to autoclave at temperature, 121 °C; reaction time, 20 min and pressure, 1.224 kg-

force.cm$^{-2}$, respectively [6]. Upon completion, the aqueous NaOH solution was discarded and the OPT slurry was washed with tap water (4 x 1000 mL) followed by distilled water (4 x 1000 mL). The steam alkaline slurry was then added with 200 mL of NaClO. The pH of the mixture was adjusted to acidic condition at pH 3.5 using $CH_3COOH$ [9]. The acid solution was then filtered-off and washed again with tap water (4 x 1000 mL) followed by distilled water (4 x 1000 mL). The SAC treated oil palm trunk sample was freeze-dried and kept at 4 °C for enzymatic saccharification reaction. The content of the chemical constituents such as cellulose, hemicellulose, lignin and extractives of raw and treated OPT substrate is presented in Table 1.

Table 1. Chemical composition of raw and treated oil palm trunk biomass (g per 100 g biomass)

| Pretreatment | (g per 100 g biomass) | | | |
|---|---|---|---|---|
| Type | Cellulose | Hemicellulose | Lignin | Extractives |
| Raw[7] | 50.78 ± 1.05 | 30.36 ± 1.10 | 17.87 ± 1.68 | 0.99 ± 1.73 |
| Mw-A[7] | 71.88 ± 2.55 | 11.77 ± 2.30 | 15.13 ± 0.40 | 1.22 ± 0.16 |
| SAC[9] | 42.70 ± 0.57 | 52.80 ± 1.36 | 1.90 ± 0.04 | 2.60 ± 0.76 |

All measurements were duplicated and fall within the relative percentage difference below 5% [10].
Mw-A: Microwave-alkali, SAC: Steam-alkali-chemical

**Cellulase enzyme activity**

The cellulase enzyme activity was measured according to Ghose's protocol [11]. One unit of filter paper unit (FPU) was defined as the amount of enzyme which produced 2.0 mg of glucose from 50 mg of filter paper at temperature, 50 °C; pH, 4.8 and reaction time, 60 min, respectively. The cellulase activity obtained from this assay was 104.42 FPU.ml$^{-1}$.

**Enzymatic hydrolysis and glucose analysis**

The enzymatic saccharification reaction was performed in a glass jar and the reaction temperature was manipulated using water bath. 1 % (w/v) of SAC-treated OPT was discharged into a glass jar containing 20 mL of 50 mM sodium citrate buffer and 100 µL of 2 % of $NaN_3$. In the enzymatic hydrolysis study, physiochemical parameters such as enzyme concentration (20 – 100 FPU.mL$^{-1}$), pH (4.0 – 8.0) and reaction temperature (30 – 60 °C) were tested using one-a-time variable method. For instance, when enzyme concentration analysis was carried out, both pH and temperature were set to 4.8 and 50 °C, respectively. The pre-set constant values were set according to the manufacturer's recommendation [12]. Once the optimal conditions such as enzyme concentration, pH and temperature were pre-determined; these selected conditions were used to re-run the enzymatic saccharification on untreated and SAC-treated OPT.

For all enzymatic study, exactly 200 µL of enzyme hydrolysate was withdrawn and deposited into microtube at specific intervals. The sample was mixed with DNS reagent (ratio of sample and DNS = 1:1), heated and agitated at 100 °C and 400 rpm, respectively for 15 min on a thermoblock. The brown color solution was used to determine glucose concentration at 540 nm using spectrophotometer (Thermo, Genesys 20). The reducing sugars derived from enzyme hydrolysis were considered as glucose equivalent [13]. All hydrolysis experiment was performed in triplicate and error was within ± 5% [14].

## Results and Discussion

**Effect of different enzyme concentration on glucose production**

In this study, cellulase concentrations (20 – 100 FPU.mL$^{-1}$) were tested at fixed pH, 4.8; reaction temperature, 50 °C and substrate mass, 1% (w/v), respectively. Figure 1 illustrates the 72 hours' time profile of glucose formation derived from saccharification process.

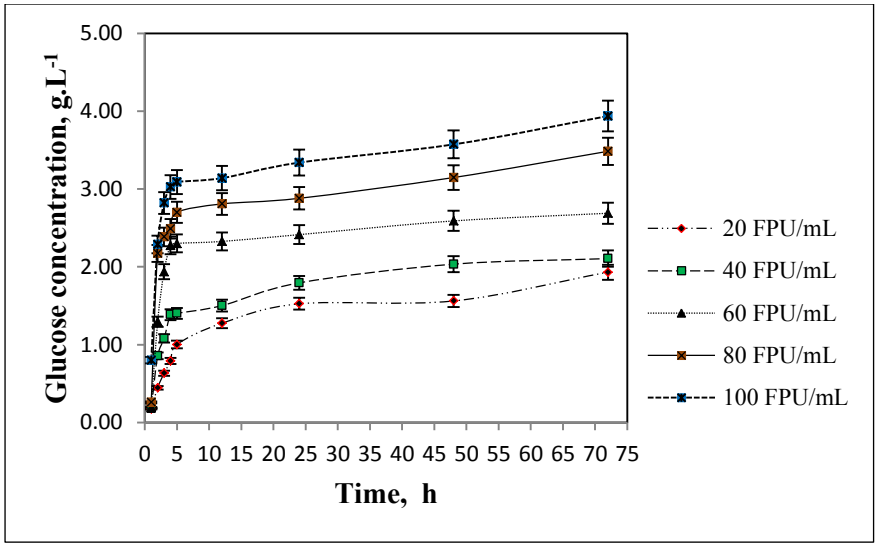



Figure 1. Effect of different enzyme concentration (20 – 100 FPU/mL) on glucose production

After the 72 hours enzyme saccharification, a glucose concentration of 1.93 $g.L^{-1}$ was recorded at 20 $FPU.mL^{-1}$ enzyme concentrations. When the enzyme amount increases from 40 – 100 FPU/mL, glucose concentration also increased to 2.11 – 3.94 $g.L^{-1}$ with an increment value of 9.32 – 104.15%. This indicates that formation of glucose amount in the present study could be enhanced by supplying a higher dose of cellulase enzyme. When more cellulase is supplied, there will be extra active sites available for substrate (present study: substrate is SAC-treated OPT). Hence, it will be easier for substrate to bind to the enzymes' active sites to form enzyme-substrate complex. This will eventually accelerate the enzymatic reaction and thus more glucose is released.

Although, the maximum glucose concentration was attained at 100 $FPU.mL^{-1}$; 60 $FPU.mL^{-1}$ of cellulase concentration was selected for the subsequent enzymatic study. This is because the cellulase enzyme cannot be recycled and a higher dose of enzyme usage will contribute to higher operation cost. Moreover, previous studies which demonstrated the usage of cellulase enzyme in enzymatic saccharification on lignocellulosic biomass for glucose production, utilized enzyme concentrations within the range of 20 – 60 $FPU.mL^{-1}$ [15-17]. Based on these views, enzyme concentration at 60 $FPU.mL^{-1}$ was selected and used for the next experiment.

**Effect of different pH on glucose production**

In this investigation, different pH values (pH 4.0 – 8.0) were tested on pre-selected enzyme concentration (60 $FPU.mL^{-1}$), reaction temperature (50 °C) and 1% (w/v) of SAC-treated OPT substrate for glucose production. Figure 2 depicts glucose concentration increased from strong to weak acidic condition (pH 4.0 – 6.0), i.e. 1.27 to 4.03 $g.L^{-1}$. There is about 3.17-fold of glucose increment when compared to pH 6.0 and pH 4.0. On the other hand, at neutral and weak alkaline pH conditions (i.e. pH 7.0 and pH 8.0), the glucose concentration slightly declined compared to pH 6.0, *viz.*10.92 – 11.66 % or equivalent to 3.56 and 3.59 $g.L^{-1}$, respectively. In general, the ionic group of enzyme reacts well within suitable pH ranges either in acidic or alkaline conditions. The variation of pH causes modification on enzymes' ionic groups and its three-dimensional structure [18]. The changing of enzyme structure or shape makes substrate unfit to enzymes' active sites and thus reduces the chances of enzyme-substrate complex formation. This can directly impede the rate of enzymatic reaction.

Current study revealed that cellulase enzyme is active in weak acidic and weak alkaline pH range (pH 6.0 – 8.0). The stronger acidic pH conditions (< pH 6.0) did not favour the cellulase hydrolysis. This is the reason for getting lower glucose content at pH 4.0 – 5.0 compared to pH 6.0 – 8.0. It is obvious that the optimal pH point is pH 6.0 and it was chosen for subsequent study.

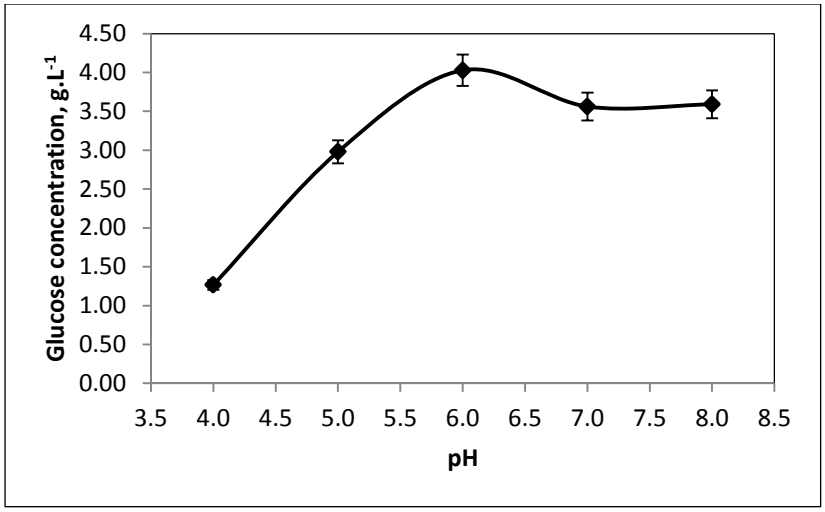



Figure 2. Effect of different pH (4.0 – 8.0) on glucose production

**Effect of different temperature on glucose production**

The range of temperatures, 30 to 60 °C was tested for glucose production by using 1% (w/v) of SAC-treated OPT sample. Other parameters such as enzyme concentration and pH were pre-set according to previous studies, i.e. 60 $FPU.mL^{-1}$ and pH 6.0, respectively.

Figure 3 demonstrates the glucose production from cellulase-SAC OPT hydrolysis at different temperature points. It is observed that glucose amount increased from 2.01 to 3.68 $g.L^{-1}$ when reaction temperatures rise from 30 to 50 °C. The total increment is up to 83.08%. The possible explanation is that the enzyme-catalysed reaction like most chemical reactions; proceeds at a faster velocity when temperature is increased. The temperature rise during enzymatic saccharification process imparts more kinetic energy to reactant molecules, resulting in more productive collision per unit time [19]. Consequently, more glucose is released when the system temperature was boosted from 30 to 50 °C.

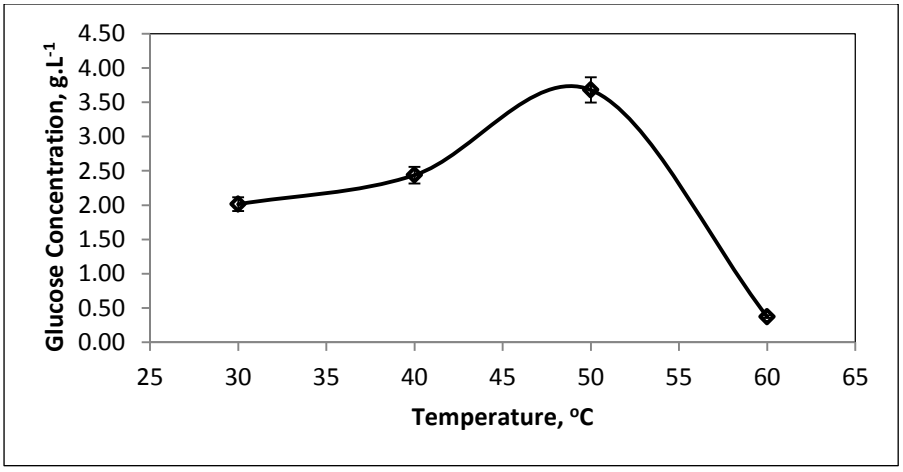



Figure 3. Effect of different temperature (30 – 60 °C) for glucose production

On the other hand, only 0.37 $g.L^{-1}$ of glucose concentration was obtained at 60 °C. This is in line with the fact that enzyme molecules possess delicate structure. The disruption of enzyme tertiary structure can occur when enzyme is exposed to temperature beyond its optimal point (present study; temperature optimal point = 50 °C). Similar phenomenon is observed in hydrolysis of cellulase-Mw-A treated OPEFB substrate where cellulase displayed deactivation when the reaction temperature is beyond 50 °C [20]. As shown in Figure 3, enzyme is considered to be partially denatured as it lose its catalytic power when temperature > 50 °C. This explains why reaction temperature of 60 °C gained less glucose amount compared to reaction temperature of 30 and 40 °C, respectively. Based on Figure 3, the optimal hydrolysis temperature point is 50 °C and it was selected for subsequent enzymatic experiment.

**Comparison of untreated and SAC-treated OPT under pre-determined enzymatic conditions**

The comparison of untreated and SAC-treated OPT sample was performed under pre-determined enzymatic conditions where enzyme concentration, pH and reaction temperature were set to 60 $FPU.mL^{-1}$, 6.0 and 50 °C, respectively. The amount of both substrates used in this study was 1% (w/v). After the 72 hours enzyme hydrolysis, up to 4.27 $g.L^{-1}$ glucose concentration was obtained in SAC-treated OPT; whereas the untreated OPT sample only produced 0.95 $g.L^{-1}$ of glucose (as shown in Figure 4). The glucose increased 4.49-fold when using the SAC-treated OPT biomass as a substrate.

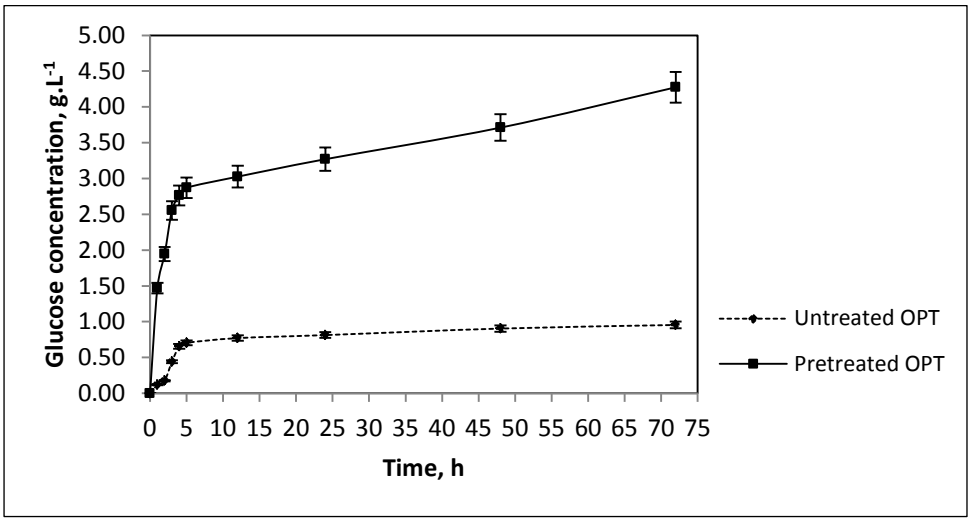



Figure 4. Glucose production for untreated and SAC-treated OPT under pre-selected enzyme hydrolysis conditions

The SAC pre-treatment process has enhanced the enzyme digestibility towards its substrate. This is attributed to disruption of encrusted lignocellulosic OPT structure by loosening the complex linkage among the cellulose, hemicellulose and lignin. Hence, more amorphous cellulose is released and readily available for cellulase enzyme. Binod et al. stated that treated lignocellulosic biomass contain more amorphous cellulose whereas untreated biomass contain more crystalline cellulose and the former is easily digested by cellulose [21]. In short, SAC pre-treatment process can effectively enhance the enzymatic saccharification rate in this study.

A recent report revealed that 72 hours enzymatic hydrolysis on SAC treated oil palm trunk biomass produced 16.59 $g.L^{-1}$ of glucose [9]. In contrast, the present study which had used a single enzyme (cellulase) to accomplish the hydrolysis process only produced 4.27 $g.L^{-1}$ of glucose at 72 hours. The main reason for the significant difference (glucose concentration) between these works is the use of an additional enzyme, i.e. addition of β-glucosidase in hydrolysis reaction. The existence of β-glucosidase not only improves enzymatic hydrolysis performance but also expedites the enzymatic saccharification rate. Therefore, more glucose is formed in the former study. However,

when using two enzymes in hydrolysis reaction, the glucose production cost will dramatically increase. Moreover, the cellulolytic enzymes cannot be recycled. Since one of the objective is to reduce the operational cost, this study only employed cellulase enzyme in the saccharification reaction for glucose production.

In another study, Hamzah et al. had conducted 24 hours' enzyme hydrolysis on Mw-A treated OPEFB [20]. The glucose amount of 0.49 $g.L^{-1}$ and 0.72 $g.L^{-1}$ were recorded for single enzyme (cellulase) and two enzymes (cellulase + β-glucosidase), respectively. Comparatively, 3.27 $g.L^{-1}$ amount of glucose was formed at 24 hours (see Fig. 4); which is 4.51 to 6.67-fold higher than previous study. This explains that SAC-treated substrate with its lower lignin content has more advantage compared to Mw-A treated substrate. The double-step pre-treatment outperformed single-step pretreatment in lignin removal. Lignin behaves like a protected shield and avoids cellulose from being hydrolyzed by cellulase. Through harsher pre-treatment method (like SAC conditions), lignin is removed effortlessly and more amorphous cellulose is exposed. Consequently, enzyme digestibility towards SAC OPT substrate is enhanced and resulted in more glucose formation.

## Conclusion

Three physiochemical parameters namely: enzyme concentration, pH and reaction temperature were tested in this investigation. Results divulged that optimal conditions for enzyme hydrolysis on steam-alkali-chemical (SAC) treated OPT were 100 $FPU.mL^{-1}$ of enzyme concentration, pH 6.0 and reaction temperature at 50 °C, respectively. However, 60 $FPU.mL^{-1}$ of cellulase was chosen in the subsequent enzymatic study as to reduce the operational cost for glucose production. A 4.49-fold of glucose increment was attained in enzymatic saccharification on SAC-treated OPT compared to untreated ones. In conclusion, SAC pretreatment can be potentially scaled up for industrial applications. The study also suggested that oil palm trunk biomass can be a cheaper alternative of substrate for high value added products such as glucose.

## Acknowledgement

The authors would like to thank to Concept Energy Resources (M), Sdn. Bhd. and Faculty of Engineering and Life Sciences, Universiti Selangor for providing the oil palm trunk sample, facilities and chemical reagents, respectively during this investigation.

## References

1. Liu, Y-Y., Xu, J-L., Zhang, Y., Liang, C-Y., He, M-C., Yuan, Z-H. and Xie, J. (2016). Reinforced alkali-pretreatment for enhancing enzymatic hydrolysis of sugarcane bagasse. *Fuel Processing Technology*, 143: 1 – 6.
2. Pang, F., Xue, S., Yu, S., Zhang, C., Li, B. and Kang, Y. (2013). Effects of combination of steam explosion and microwave irradiation (Se–Mi) pretreatment on enzymatic hydrolysis, sugar yields and structural properties of corn stover. *Industrial Crops Production*, 42: 402 – 408.
3. Noparat, P., Prasertsan, P., O-Thong, S. and Pan, X. (2015). Dilute acid pretreatment of oil palm trunk biomass at high temperature for enzymatic hydrolysis. *Energy Procedia*, 79: 924 – 929.
4. Lai, L. W., Teo, C. L, Wahidin, S. and Annuar, M. S. M. (2014). Determination of enzyme kinetic parameters on sago starch hydrolysis by linearized graphical methods. *Malaysian Journal of Analytical Sciences,* 18(3): 527 – 533.
5. Ewanick, B. R. (2012). Hydrothermal pretreatment of lignocellulosic biomass, in: Keith, W. (eds.), Bioalcohol production: Biochemical conversion of lignocellulosic biomass, Woodhead, Washington. pp. 1 – 23.
6. Lai, L. W., Teo, C. L. and Idris, A. (2013). Different pretreatment methods to evaluate lignin content in oil palm trunk. *Proceeding of International Conference on Industrial Engineering and Management Science*, *Shanghai (China)*. DEStech Publication Inc., Lancaster. pp. 156 – 162.
7. Lai, L-W. and Idris, A. (2013). Disruption of oil palm trunks and fronds by microwave-alkali pretreatment. *Bioresources*, 8(2): 2792 – 2804.
8. Yuanisa, A, Ulum, K. and Wardani, A. K. (2015). Pretreatment of oil palm trunk lignocellulose as first step to produce second generation of bioethanol: A review. *Jurnal Pangan Agroindustri*, 3(4): 1620 – 1626.
9. Lai, L. W. and Idris, A. (2016). Comparison of steam-alkali-chemical and microwave-alkali pretreatment for enhancing the enzymatic saccharification of oil palm trunk. *Renewable Energy*, 99: 738 – 746.

10. van Soest, P. J., Robertson, J. B. and Lewis, B. A. (1991). Methods for dietary fiber, neutral detergent fiber, and nonstarch polysaccharides in relation to animal nutrition. *Journal of Dairy Science*, 74: 3583 –3597.
11. Ghose, T. K. (1987). Measurement of cellulase activities. *Pure Applied Chemistry*, 59(2): 257 – 268.
12. NOVO-NORDISK. (1999). PRODUCT SHEET OF CELLUCLAST 1.5 L. B153I-GB. PP.1 – 3.
13. Lai, L. W., Yahya, S. S. M., Nor, N. M. and Sulong, M. R. (2016). Enzymatic saccharification on ammonia pretreated oil palm trunk biomass for glucose production: an optimization using response surface methodology. *Malaysian Journal of Analytical Sciences*, 20(1): 21 – 30.
14. Wee, L. L., Annuar, M. S. M., Ibrahim, S. and Chisti, Y. (2011). Enzyme-mediated production of sugars from sago starch: Statistical process optimization. *Chemical Engineering Communications*, 198(11): 1339 – 1353.
15. Ruiz, H. A., Vicente, A. A. and Teixeira, J. A. (2012). Kinetic modeling of enzymatic saccharification using wheat straw pretreated under autohydrolysis and organosolv process. *Industrial Crops Productions*, 26(1): 100 – 107.
16. Zhang, Z., O'Haraa, I. M. and Dohertyb, W. O. S. (2013). Effects of pH on pretreatment of sugarcane bagasse using aqueous imidazolium ionic liquids. *Green Chemistry*, 15(2): 431 – 438.
17. Tan, H. T., Lee, K. T. and Mohamed, A. R. (2011). Pretreatment of lignocellulosic palm biomass using a solvent–ionic liquid [BMIM]Cl for glucose recovery: an optimization study using response surface methodology. *Carbohydrate Polymers*, 83(4): 1862 – 1868.
18. Shuler, M. L. and Kargi, F. (1992). Bioprocess Engineering: Basic Concepts, 2nd ed., Prentice Hall, New Jersey. pp. 57 – 104.
19. Segel, I. H. (1976). Biochemical calculations: How to solve mathematic problem in general biochemistry, 2nd ed., John Wiley and Sons, United State. pp. 208 – 323.
20. Hamzah, F., Idris, A. and Tan, K. S. (2011). Preliminary study on enzymatic hydrolysis of treated oil palm empty fruits bunches (EFB) fibre by using combination of cellulase and β-1,4-glucosidase. *Biomass Bioenergy,* 35(3): 1055 – 1059.
21. Binod, P., Satyanagalakshmi, K., Sindhu, R., Janu, K. U., Sukumaran, R. K. and Pandey, A. (2012). Short duration microwave assisted pretreatment enhances the enzymatic saccharification and fermentable sugar yield from sugarcane bagasse. *Renewable Energy*, 37(1): 109 – 116.

*Malaysian Journal of Analytical Sciences, Vol 21 No 2 (2017): 291 - 297*
*DOI: https://doi.org/10.17576/mjas-2017-2102-03*

MALAYSIAN JOURNAL OF ANALYTICAL SCIENCES
*Published by The Malaysian Analytical Sciences Society*
ISSN 1394 - 2506

# THE CHEMICAL CONSTITUENTS FROM YOUNG TUBERS of *Hydnophytum formicarum*

## (Juzuk Kimia Daripada Tuber Muda *Hydnophytum formicarum*)

Nur Shafiqa Abdullah, Wan Yaacob Wan Ahmad*, Noor Aziiraa Sabri

*School of Chemical Sciences and Food Technology,*
*Faculty of Science and Technology*
*Universiti Kebangsaan Malaysia, 43600 UKM Bangi, Selangor, Malaysia*

**Corresponding author: wanyaa@ukm.edu.my*

Received: 6 December 2016; Accepted: 16 January 2017

**Abstract**

The fine powders of young tubers of *Hydnophytum formicarum* was extracted by Soxhlet methanol extraction for 18 hours in three days continuously. The filtrate then was evaporated by rotary evaporator until it became concentrated solution. The fractionation and purification of the extract by vacuum liquid chromatography and radial chromatography has led to the discovery of four compounds namely sinapinic acid, β-sitosterol acetate, β-sitosterol and stigmasterol. Structures of the compounds were established by interpreting mass spectral data, $^{1}$H and $^{13}$C-APT NMR, Infrared and by comparison with literature data.

**Keywords**: *Hydnophytum formicarum*, sinapinic acid, β-sitosterol acetate, β-sitosterol, stigmasterol

**Abstrak**

Serbuk halus tuber muda *Hydnophytum formicarum* telah diekstrak melalui pengekstrakan Soxhlet selama 18 jam dalam tiga hari secara berturutan. Hasil penurasan kemudian telah disejat menggunakan penyejat berputar sehingga menjadi larutan yang likat. Pemfraksian dan penulenan ekstrak menggunakan kromatografi cecair vakum dan kromatografi radial membawa kepada penemuan empat sebatian yang bernama asid sinapinik, β-sitosterol asetat, β-sitosterol dan stigmasterol. Struktur sebatian ini telah ditentukan dengan mentafsirkan data spektrum jisim, RMN $^{1}$H dan $^{13}$C-APT, Inframerah serta secara membandingkannya dengan data kepustakaan.

**Kata kunci:** *Hydnophytum formicarum*, asid sinapinik, β-sitosterol asetat, β-sitosterol, stigmasterol

## Introduction

Rubiaceae is the largest plant family containing 10,700 species and 637 genera that consists mainly of tropical woody plants with great pharmacological potential [1]. The previous phytochemical study of all Rubiaceae species, published from 1990 to 2014, stated that the most common secondary metabolites of this family were iridoids, anthraquinones, triterpenes and indole alkaloids as well as other varying alkaloid subclasses [2]. One of the species, *Hydnophytum formicarum* or ant plant, is a tuberous ephyphytic of medicinal plant known in Malaysia as Raja Satong or Kepala Beruk or Sarang Semut. It is commonly found in Southeast Asia (Malaysia and Indonesia), Papua New Guinea and Pacific Islands [3].

The objectives of this study are to isolate compounds from the young tubers of *Hydnophytum formicarum* by extraction and fractionation using several chromatographic techniques as well as to elucidate structures of pure

compounds. Traditionally, the decoction of *Hydnophytum formicarum* tubers was used as a drink for liver and intestinal complaints. Soxhlet extraction with methanol was employed in this study in view of the use of the tubers by local people for medicinal purposes by boiling in water . Moreover, more constituents can be extracted by Soxhlet compared to maceration. Darwis et al. reported flavonoid, phenolic, aldehydes, ketones, terpenoids and tannin in the ethanol *Hydnophytum formicarum* extract [4]. Previous studies reported several compounds from *Hydnophytum formicarum* such as β-sitosterol [5], 7,3′,5′-trihydroxyflavanone [6], stigmasterol, protocatechualdehyde, butin, butein, and isoliquiritigenin [3]. Figure 1 below shows a young tuber of *Hydnophytum formicarum*. The tubers of *Hydnophytum formicarum* have been scientifically proven to contain bioactive constituents such as antioxidant and antimicrobial [3] and antiproliferative [7].



Figure 1. Young tuber of *Hydnophytum formicarum*

## Materials and Methods

### General

The $^{1}H$ and $^{13}C$-APT NMR spectra were recorded with Avance III 700 MHz Bruker in $CDCl_3$ with the chemical shifts, δ, in ppm and the values of coupling constants, *J*, in Hz. LC-MSToF spectra were taken on the Dionex/Bruker Micro ToFQ and FTIR spectra were recorded on the Perkin-Elmer Spectrum 400 FT-IR/FT-NIR.

### Plant material

Young tubers of *Hydnophytum formicarum* were bought in April 2015 from a seller at Kampung Lak Lok, Jertih, Besut, Terengganu. A voucher specimen (UKMB 40312) was deposited at the Herbarium of Universiti Kebangsaan Malaysia Bangi (UKMB).

### Extraction and isolation

The air-dried young tubers of *Hydnophytum formicarum* were cut into small pieces and ground into fine powder by using grinding machine. The powder (1.04 kg) was then extracted with methanol by using Soxhlet for 6 hours in three days to give 15.0 g (1.44 %) of dark-brown extract after solvent removal by rotary evaporator. The extract was subjected to vacuum liquid chromatography (VLC) by using silica gel 7747 (Merck) eluted with increasing polarity of *n*-hexane and ethyl acetate. The eluents were combined based on their silica gel thin layer chromatography (TLC) (Merck 5554) profile to give seven fractions (A-G). Fraction A and B was washed with *n*-hexane to give stigmasterol (37.0 mg) and β-sitosterol (22.0 mg). Fraction E (0.84 g) was further purified by column chromatography (CC) using *n*-hexane-ethyl acetate (7:3) to yield six fractions (E1-E6). The E6 was pure to give sinapinic acid (29.0 mg). Fraction C (1.2 g) was further purified by radial chromatography (RC) using *n*-hexane-ethyl acetate (7:3) to produce β-sitosterol acetate (23.7 mg).

## Results and Discussion

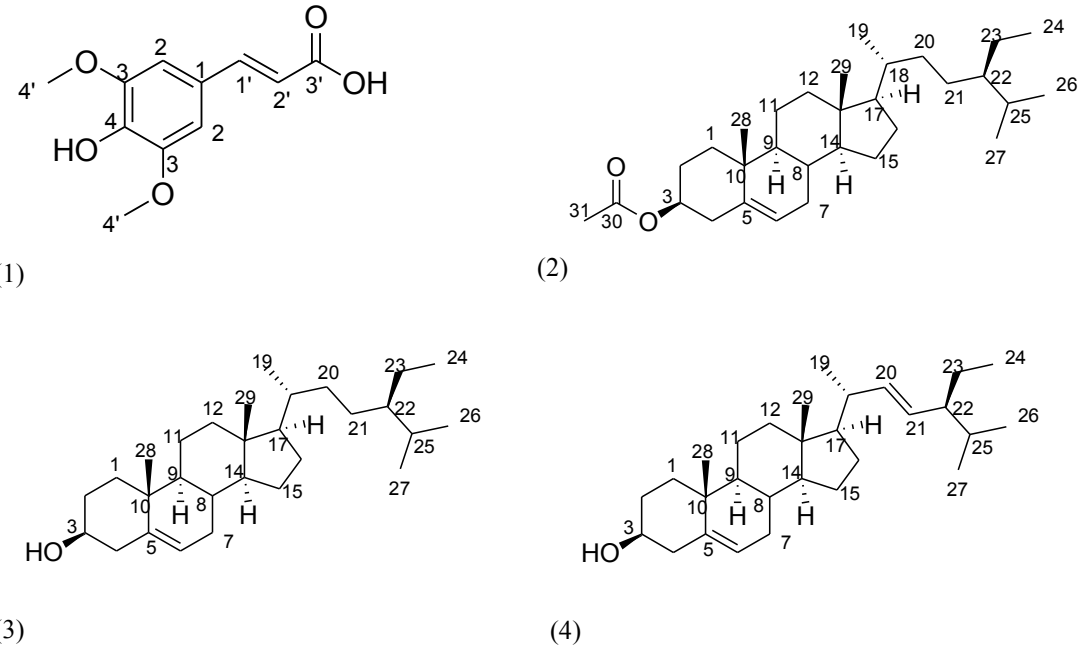
### Characterization study

Sinapinic acid (29.0 mg): white powder; Rf = 0.70 (*n*-hexane-ethyl acetate, 7:3); ESI-MS (m/z): 247.2077 $[M+Na]^+$, $C_{11}H_{12}O_5$; FTIR (ATR) $cm^{-1}$: 3412 (O-H), 2916 and 2849 ($Csp^3$-H), 1711 (C=O carboxylic acid), 1268 and 1158 (C-O), 1463-1632 (C-C aromatic), 718-1032 ($Csp^2$-H).

β-Sitosterol acetate (23.7 mg): white needles; Rf = 0.81 (*n*-hexane-ethyl acetate, 7:3); ESI-MS (m/z): 479.3404 $[M+Na]^+$, $C_{31}H_{52}O_2$; FTIR (ATR) $cm^{-1}$: 2928 and 2868 (C*sp*$^3$-H), 1674 (C=O), 1458, 1378 (C*sp*$^3$-H).

β-Sitosterol (22.0 mg): white needles; Rf = 0.94 (*n*-hexane-ethyl acetate, 8:2); ESI-MS (m/z): 437.6012 $[M+Na]^+$, $C_{29}H_{50}O$; FTIR (ATR) $cm^{-1}$: 3374 (O-H), 2933 and 2866 (C*sp*$^3$-H), 1052 (C-O), 801 (O-H), 1463 and 1378 (C*sp*$^3$-H), 801-957 (C*sp*$^2$-H).

Stigmasterol (37.0 mg): white needles; Rf = 0.90 (*n*-hexane-ethyl acetate, 9:1); ESI-MS (m/z): 435.4306 $[M+Na]^+$, $C_{29}H_{48}O$; FTIR (ATR) $cm^{-1}$: 3330 (O-H), 2931 and 2869 (C*sp*$^3$-H), 1052 (C-O), 800 (O-H), 1644 (C=C), 1463, 1376 (C*sp*$^3$-H).



(1) (2)

(3) (4)

Figure 2. Molecular structures of sinapinic acid (1), β-sitosterol acetate (2), β-sitosterol (3) and stigmasterol (4)

Table 1. $^1$H and $^{13}$C-APT NMR (700 MHz, $CDCl_3$) spectral data of sinapinic acid and literature

| No. | Sinapinic acid | | Sinapinic acid* | |
|---|---|---|---|---|
| | **$\delta_C$** | **$\delta_H$ (ΣH, *m*, *J*)** | **$\delta_C$** | **$\delta_H$ (ΣH, *m*, *J*)** |
| 1 | 139.9 | | 139.2 | |
| 2 | 106.0 | 7.04 (2H, *s*) | 106.6 | 7.01 (2H, *s*) |
| 3 | 148.3 | | 148.4 | |
| 4 | 145.6 | | 146.0 | |
| 1′ | 115.6 | 6.29 (1H, *d*, *J* = 15.9 Hz) | 116.1 | 6.39 (1H, *d*, *J* = 15.8 Hz) |
| 2′ | 127.0 | 7.61 (1H, *d*, *J* = 15.9 Hz) | 126.0 | 7.58 (1H, *d*, *J* = 15.9 Hz) |
| 3′ | 167.4 | | 167.9 | |
| 4′ | 56.0 | 3.93 (6H, *s*) | 56.5 | 3.91 (6H, *s*) |

Source: *[8]

Comparison of $^{1}H$ and $^{13}C$-APT NMR spectral data of sinapinic acid (Table 1) with those literature data confirmed that both are of the same compound [8]. The ESI-MS gave molecular ion at m/z 247.2077 $[M+Na]^+$, which corresponded to the molecular formula $C_{11}H_{12}O_5$. Sinapinic acid and its ester had been isolated from Rubiaceae family such as *Gardenia jasminoides* [12] and *Mussaenda incana* [13] supports its existence in *Hydnophytum formicarum*.

Similarity of $^{1}H$ and $^{13}C$-APT NMR spectral data of β-sitosterol acetate (Table 2) with those of Gohari et al. and Ran et al. confirmed that they are of the same structure. The ESI-MS showed molecular ion at m/z 479.3404 $[M+Na]^+$, which is in accordance with the molecular formula $C_{31}H_{50}O_2$. To the best of our knowledge, this is the first time β-sitosterol acetate has been isolated from *Hydnophytum formicarum*, and this sterol has never been reported before from any other genus of Rubiaceae.

The NMR spectral data ($^{1}H$ and $^{13}C$-APT) of β-sitosterol and stigmasterol (Table 3) in agreement with those of literature data [11]. The ESI-MS exhibited respective molecular ions at m/z 437.6012 $[M+Na]^+$ and 435.4306 $[M+Na]^+$, which matched the molecular formulas of $C_{29}H_{50}O$ (β-sitosterol) and $C_{29}H_{48}O$ (stigmasterol). Besides frequent identification of these sterols as common compounds in many plants species, they are also found in the Rubiaceae family such as *Fadogia homblei* [14] and *Rudgea jasminoides* [15].

Table 2. $^{1}H$ and $^{13}C$-APT NMR (700 MHz, $CDCl_3$) spectral data of β-sitosterol acetate and literature

| **No.** | **β-Sitosterol acetate** | | **β-Sitosterol acetate** | |
|---|---|---|---|---|
| | **$\delta_C$** | **$\delta_H$ (Σ**H, ***m***, ***J*** **Hz)** | **$\delta_C$*** | **$\delta_H$ (Σ**H, ***m***, ***J*** **Hz)**** |
| 1 | 36.3 | | 37.0 | |
| 2 | 27.5 | | 27.8 | |
| 3 | 72.0 | 4.67 (1H, *m*) | 73.9 | 4.55 (1H, *m*) |
| 4 | 38.9 | | 38.1 | |
| 5 | 138.4 | | 138.2 | |
| 6 | 123.9 | 5.15 (1H, *d*, *J* = 4.5) | 122.5 | 5.37 (1H, *d*, *J* = 4.2) |
| 7 | 32.2 | | 32.0 | |
| 8 | 31.5 | | 31.9 | |
| 9 | 50.3 | | 50.1 | |
| 10 | 36.3 | | 36.6 | |
| 11 | 21.2 | | 21.0 | |
| 12 | 39.8 | | 39.6 | |
| 13 | 42.6 | | 42.2 | |
| 14 | 56.2 | | 56.8 | |
| 15 | 24.4 | | 24.4 | |
| 16 | 28.4 | | 28.8 | |
| 17 | 56.1 | | 56.0 | |
| 18 | 40.4 | | 40.4 | |
| 19 | 21.5 | 0.91 (3H, *d*, *J* = 6.5) | 21.5 | 0.91 (3H, *d*, *J* = 5.0) |
| 20 | 34.2 | | 34.0 | |
| 21 | 26.2 | | 26.1 | |
| 22 | 51.2 | | 51.2 | |
| 23 | 25.4 | | 25.4 | |

Table 2 (cont'd). $^{1}H$ and $^{13}C$-APT NMR (700 MHz, $CDCl_3$) spectral data of β-sitosterol acetate and literature

| No. | β-Sitosterol acetate | | β-Sitosterol acetate | |
|---|---|---|---|---|
| | $\delta_C$ | $\delta_H$ (ΣH, *m*, *J* Hz) | $\delta_C$* | $\delta_H$ (ΣH, *m*, *J* Hz)** |
| 24 | 12.2 | | 12.2 | |
| 25 | 30.0 | | 31.8 | |
| 26 | 19.2 | 0.85 (3H, *d*, *J* = 7.0) | 19.0 | 0.83 (3H, *d*, *J* = 6.7) |
| 27 | 21.2 | | 21.2 | |
| 28 | 19.3 | | 19.3 | |
| 29 | 12.1 | 1.83 (3H, *s*) | 12.0 | 1.00 (3H, *s*) |
| 30 | 172.0 | | 170.2 | |
| 31 | 21.2 | 2.03 (3H, *s*) | 21.4 | 2.03 (3H, *s*) |

Source: *[9] and **[10]

Table 3. $^{1}H$ and $^{13}C$-APT NMR (700 MHz, $CDCl_3$) spectral data of stigmasterol and β-sitosterol and literature

| No. | Stigmasterol | | Stigmasterol* | | β-Sitosterol | | β-Sitosterol* | |
|---|---|---|---|---|---|---|---|---|
| | $\delta_C$ | $\delta_H$ (ΣH, *m*, *J* Hz) | $\delta_C$ | $\delta_H$ (ΣH, *m*, *J* Hz) | $\delta_C$ | $\delta_H$ (ΣH, *m*, *J* Hz) | $\delta_C$ | $\delta_H$ (ΣH, *m*, *J* Hz) |
| 1 | 37.4 | | 37.6 | | 37.3 | | 37.5 | |
| 2 | 32.0 | | 32.1 | | 32.0 | | 31.9 | |
| 3 | 71.9 | 3.52 (1H, *m*) | 72.1 | 3.52 (1H, *m*) | 71.9 | 3.52 (1H, *m*) | 72.0 | 3.53 (1H,*tdd*, *J* = 4.5, 4.2, 3.8) |
| 4 | 42.4 | | 42.4 | | 42.4 | | 42.5 | |
| 5 | 140.9 | | 141.1 | | 140.8 | | 140.9 | |
| 6 | 121.8 | 5.34 (1H, *t*, *J* = 2.6) | 121.8 | 5.34 (1H, t, *J* = 2.1) | 121.8 | 5.34 (1H, *t*, *J* = 2.4) | 121.9 | 5.36 (1H, *t*, *J* = 6.4) |
| 7 | 32.0 | | 31.8 | | 32.0 | | 32.1 | |
| 8 | 32.0 | | 31.8 | | 32.0 | | 32.1 | |
| 9 | 50.2 | | 50.2 | | 50.2 | | 50.3 | |
| 10 | 36.6 | | 36.6 | | 36.2 | | 36.7 | |
| 11 | 21.2 | | 21.5 | | 21.1 | | 21.3 | |
| 12 | 39.9 | | 39.9 | | 39.8 | | 39.9 | |
| 13 | 42.4 | | 42.4 | | 42.4 | | 42.6 | |
| 14 | 56.9 | | 56.8 | | 56.8 | | 56.9 | |
| 15 | 24.4 | | 24.4 | | 26.1 | | 26.3 | |
| 16 | 29.3 | | 29.3 | | 28.3 | | 28.5 | |
| 17 | 56.2 | | 56.2 | | 56.1 | | 56.3 | |
| 18 | 40.6 | | 40.6 | | 36.2 | | 36.3 | |
| 19 | 21.2 | 0.84 (3H, *d*, *J* = 4.1) | 21.7 | 1.13 (3H, *d*, *J* = 6.8) | 19.1 | 0.91 (3H, *d*, *J* = 5.0) | 19.2 | 0.93 (3H, *d*, *J* = 6.5) |
| 20 | 138.4 | 5.02 (1H, *dd*, *J* = 15.2, 8.7) | 138.7 | 5.05 (1H, *m*) | 34.0 | | 34.2 | |

Table 3 (cont'd). $^{1}H$ and $^{13}C$-APT NMR (700 MHz, $CDCl_3$) spectral data of stigmasterol and β-sitosterol and literature

| No. | Stigmasterol | | Stigmasterol* | | β-Sitosterol | | β-Sitosterol* | |
|---|---|---|---|---|---|---|---|---|
| | $\delta_C$ | $\delta_H$ (ΣH, *m*, *J* Hz) | $\delta_C$ | $\delta_H$ (ΣH, *m*, *J* Hz) | $\delta_C$ | $\delta_H$ (ΣH, *m*, *J* Hz) | $\delta_C$ | $\delta_H$ (ΣH, *m*, *J* Hz) |
| 21 | 129.4 | 5.15 (1H, *dd*, *J* = 15.2, 8.7) | 139.6 | 5.01 (1H, *m*) | 26.1 | | 26.3 | |
| 22 | 45.9 | | 46.1 | | 45.9 | | 46.1 | |
| 23 | 25.5 | | 25.4 | | 23.1 | | 23.3 | |
| 24 | 12.1 | 0.86 (3H, *t*, *J* = 7.1) | 12.1 | 0.82 (3H, *t*, *J* = 6.7) | 12.0 | 0.84 (3H, *t*, *J* = 7.2) | 12.2 | 0.84 (3H, *t*, *J* = 7.2) |
| 25 | 29.3 | | 29.6 | | 29.2 | | 29.4 | |
| 26 | 19.9 | 0.85 (3H, *d*, *J* = 6.7) | 20.2 | 0.80 (3H, *d*, *J* = 6.6) | 19.8 | 0.83 (3H, *d*, *J* = 6.7) | 20.1 | 0.83 (3H, *d*, *J* = 6.4) |
| 27 | 19.9 | 0.82 (3H, *d*, *J* = 6.7) | 19.8 | 0.89 (3H, *d*, *J* = 6.6) | 19.9 | 0.81 (3H, *d*, *J* = 6.7) | 19.6 | 0.81 (3H, *d*, *J* = 6.4) |
| 28 | 18.8 | 0.69 (3H, *s*) | 18.9 | 0.89 (3H, *s*) | 19.1 | 0.67 (3H, *s*) | 19.0 | 0.68 (3H, s) |
| 29 | 12.0 | 1.01 (3H, *s*) | 12.2 | 1.22 (3H, *s*) | 12.0 | 1.00 (3H, *s*) | 12.0 | 1.01 (3H, s) |

Source: *[11]

## Conclusion

Chromatographic separation of Soxhlet methanol extract of *Hydnophytum formicarum* young tubers yielded four compounds namely sinapinic acid, β-sitosterol acetate, β-sitosterol and stigmasterol. Sinapinic acid and β-sitosterol acetate can be used to evaluate their biological activities such as antimicrobial, antioxidant, anti-cancer and anti-inflammatory properties.

## Acknowledgement

We would like to thank the Ministry of Education, Malaysia and Univeristi Kebangsaan Malaysia (UKM) for financial support under the DLP-2013-018 grant. Special thanks to School of Chemical Sciences and Food Technology, Faculty of Science and Technology, UKM and Centre for Research and Innovation Management (CRIM) UKM for the technical support on NMR, LC-MSToF and FTIR instrumentation.

## References

1. Ahmad, R., Mahbob, E. N. M., Noor, Z. M., Ismail, N. H., Lajis, N. H. and Shaari K. (2010). Evaluation of antioxidant potential of medicinal plants from Malaysian Rubiaceae (subfamily rubioideae). *African Journal of Biotechnology*, 9(46): 7948 – 7954.
2. Martins, D. and Nunez, C.V. (2015). Secondary metabolites from Rubiaceae species. *Molecules*, 20(7): 13422 – 13495.
3. Prachayasittikul, S., Buraparuangsang, P., Worachartcheewan, A., Isarankura-Na-Ayudhya, C., Ruchirawat, S. and Prachayasittikul, V. (2008). Antimicrobial and antioxidative activities of bioactive constituents from *Hydnophytum formicarum* Jack. *Molecules* 13(4): 904 – 921.
4. Darwis, D., Hertiani, T. and Samito, E. (2014). The effects of *Hydnophytum formicarum* ethanolic extract toward lymphocyte, vero and T47d cells proliferation in vitro. *Journal of Applied Pharmaceutical Science*, 4(6): 103 – 109.
5. Prachayasittikul, S., Pingaew, R., Yamkamon, V., Worachartcheewan, A., Wanwimolruk, S., Ruchirawat, S. and Prachayasittikul, V. (2012). Chemical constituents and antioxidant activity of *Hydnophytum formicarum* Jack. *International Journal of Pharmacology,* 8(5): 440 – 444.

6. Abdullah, H., Pihie, A. H. L., Hohmann, J. and Molnar, J. (2010). A natural compound from *Hydnophytum formicarum* induces apoptosis of MCF-7 cells via up-regulation of Bax. *Cancer Cell International,* 10: 1 – 6.
7. Ueda, J., U., Tezuka, Y., Banskota, A.H., Le Tran, Q., Kim, Q., Harimaya, Y., Saiki, I. and Kadota, S. (2002). Antiproliferative activity of Vietnamese medicinal plants. *Biological and Pharmaceutical Bulletin*, 25(6): 753 – 760.
8. Cai, R., Arntfield, S. D. and Charlton, J. L. (1999). Structural changes of sinapinic acid and sinapine bisulfate during autoclaving with respect to the development of colored substances. *Journal of the American Oil Chemist's Society* 76: 433 – 441.
9. Gohari, A. R., Saeidnia, S., Malmir, M., Yazdanpanah, M. and Ajani, Y. (2011). Sterols and flavonoids of Lomatopodium staurophyllum. *Journal of Medicinal Plants*, 10(39): 43 – 48.
10. Ran, T., Cheng, Z.W. & Zhen, W.K. (2013). Antibacterial/antifungal activity and synergistic interactions between polyprenols and other lipids isolated from *Ginkgo Biloba* leaves. *Molecules* 18: 2166 – 2182.
11. Chaturvedula, V. S. P. and Prakash, I. (2012). Isolation of stigmasterol and β-sitosterol from the dichloromethane extract of *Rubus suavissimus*. *International Current Pharmaceutical Journal,* 1(9): 239 – 242.
12. Nishizawa, M., Izuhara, R., Kaneko, K. and Fujimoto, Y. (1987). 3-Caffeoyl-4-sinapoylquinic acid, a novel lipoxygenase inhibitor from *Gardeniae fructus*. *Chemical and Pharmaceutical Bulletin,* 35: 2133 – 2135.
13. Dinda, B., Debnath, S. and Majumder, S. (2005). Chemical constituents of *Mussaenda incana*. *Indian Journal of Chemistry*, 44(11): 2362 – 2365.
14. Mohammed, A. M. A., Coombes, P. H., Crouch, N. R. and Mulholland D. A. (2013). Chemical constituents from *Fadogia homblei* de wild (Rubiaceae). *International Letters of Chemistry, Physics and Astronomy,* 9(2): 116 – 124.
15. Lopes, M. N. L., Mazza, F. C., Maria, C. M., Young, M. C. M and Bolzani, V.S. (1999). Complete assignments of $^{1}H$ and $^{13}C$-NMR Spectra of the 3,4-seco-triterpene canaric acid isolated from *Rudgea jasminoides*. *Journal of Brazilian Chemical Society* (10)3: 237 – 240.

*Malaysian Journal of Analytical Sciences, Vol 21 No 2 (2017): 298 - 303*
*DOI: https://doi.org/10.17576/mjas-2017-2102-04*

MALAYSIAN JOURNAL OF ANALYTICAL SCIENCES
*Published by The Malaysian Analytical Sciences Society*
ISSN 1394 - 2506

# ISOLATION OF FOUR STEROIDS FROM THE LEAVES OF FERN *Adiantum latifolium* Lam

## (Pengasingan Empat Steroid Daripada Daun Paku Pakis *Adiantum latifolium* Lam)

Andi Rifki Rosandy[1], Nurnida Mohd. Kamal[2], Noraini Talip[2], Rozida Khalid[1], Muntaz Abu Bakar[1]*

[1]*School of Chemical Sciences and Food Technology, Faculty of Science and Technology*
[2]*School of Environmental and Natural Resources Sciences, Faculty of Science and Technology*
*Universiti Kebangsaan Malaysia, 43650 UKM Bangi, Selangor, Malaysia*

**Corresponding author: muntaz@ukm.edu.my*

Received: 1 August 2016; Accepted: 27 February 2017

**Abstract**

Isolation of compounds from methanol extract from the leaves of *Adiantum latifolium* Lam. had been conducted by using radial chromatography and thin layer chromatography (TLC) techniques. Their structures were elucidated by ultraviolet-visible (UV), infrared (IR), nuclear magnetic resonance (NMR) and mass spectroscopy (MS) and by comparison with the previous literatures. Four steroids compound were isolated namely the Stigmast-4-en-3-one (**1**), Stigmasta-4,22-dien-3-on (**2**), Stigmasterol (**3**) and *β*-Sitosterol (**4**).

**Keywords:** *Adiantum latifolium*, adiantaceae, steroid

**Abstrak**

Pengasingan sebatian daripada ekstrak metanol daripada daun *Adiantum latifolium* Lam. telah dilakukan dengan menggunakan teknik kromatografi pepejal dan teknik kromatografi lapisan nipis (TLC). Struktur semua sebatian dicirikan dengan menggunakan ultra lembayung (UV), inframerah (IR), resonans magnet nukleus (NMR) dan spektroskopi jisim (MS), dan secara perbandingan dengan data kepustakaan. Empat sebatian steroid telah diasingkan iaitu, Stigmasta-4-en-3-on (**1**), Stigmasta-4,22-dien-3-on (**2**), Stigmasterol (**3**) and *β*-Sitosterol (**4**).

**Kata kunci:** *Adiantum latifolium*, adiantaceae, steroid

## Introduction

*Adiantum* is a genus belonging to the Adiantaceae family that consists of nearly 150 species and are widely distributed all over the world [1]. This species is indigenous to the central of America and northern South America and known as the common weed species in plantation [2]. It was introduced into Malaysia and became naturalized especially in palm plantation as weed. *Adiantum* is known in different names between countries. In some countries, this species is known as Maidenhair fern (English), Hansraj (India) and Tie Xian Jue Shu (China). Traditionally, most of the *Adiantum* species are used for treatments of chest complaints, cough, increase of lactation, colds, aid-kidney function, antiphrastic and to treat dandruff [3]. In Chinese medicinal practice, they also use *Adiantum* species to cure human and animal diseases including relief of internal heat or fever, enhancement of urination, removal of urinary calculus, relief of cough, cure of diarrhea and bleeding stoppage [4]. Concerning the phytochemical studies, most of *Adiantum* species have produced sterols [5, 6], any classes of flavonoid triterpenoids [7, 8, 9] and any classes of triterpenoids [10]. According to Nonato et al., *Adiantum latifolium* Lam can be used to

treat anxiolytic and analgesic [11]. So far, the chemical structures from *Adiantum latifolium* Lam have not reported. The main objective of this paper is to describe the isolation and structure characterization from the frond part of *Adiantum latifolium* Lam.

## Materials and Methods

### Plant materials

In July 2014, the leaves part of *Adiantum latifolium* Lam were collected from Tasik Chini Research Center, Pahang, Malaysia. Herbarium specimen of NMK091 was deposited at the Universiti Kebangsaan Malaysia Herbarium (UKMB).

### Extraction and isolation

Dried ground of the leaves of *Adiantum latifolium* Lam (120 g) was macerated with methanol at room temperature. The filtrate was concentrated using a rotary evaporator to yield a dark green extract (4 g, 4%). A 3-g portion of the extract was fractionated by using radial chromatography (RC) with 4 mm thickness silica gel on a round glass plate eluted with increasing polarity of *n*-hexane-EtOAc. The eluents that showed the same profile on thin layer chromatography (TLC) chromatogram were combined to give three fractions (I-III). Purification of fraction I (600 mg) was carried out using RC with a silica gel plate of 1 mm thickness eluted with 95:5 *n*-hexane-EtOAc in 5% polarity increment to yield compounds **1** (3 mg). Purification of fraction II (410 mg) was conducted, utilizing another RC with silica gel plate of 1 mm thickness. Elution with 9:1 *n*-hexane-EtOAc produced compound **2** (5 mg) and **3** (20 mg). Purification of fraction III (430 mg) was then performed using RC with the silica gel plate of 1 mm. Elution with 7:2:1 *n*-hexane-EtOAc-$CHCl_3$ resulted in compound **4** (8 mg).

### Compound identification

Structure elucidation of pure compound was determined based on the spectral data recorded on Shimadzu UV-260 spectrophotometer, Frontier Perkin-Elmer FTIR/NIR spectrophotometer and Bruker NMR 700 MHz Cryo-Probe instrument that included 1-D and 2-D NMR. Mass of compounds was recorded by using LCMS-Ultra Performance Liquid Chromatography (UPLC), Brand Waters. The isolation was then carried out by radial chromatography using round glass plates of the Merck Kieselgel 60 PF254 (art. no. 7749) and the profile was analyzed using smaller pieces from aluminum sheets of 20 x 20 cm of the Merck TLC silica gel 60 F254 of 0.25 mm thickness (art. no. 5554) and then detected under UV light (254 nm) or by a $CeSO_4$ spraying reagent test.

## Results and Discussion

### Stigmast-4-en-3-one (1)

White crystal; m.p: 82-84$^o$C. ESI-MS *m/z* 413 $[M+H]^+$ (calc. for $C_{29}H_{49}O$). UV (MeOH) $\lambda_{max}$: 241 nm. IR $v_{max}$ (ATR) $cm^{-1}$: 2926-2868 (C$sp^3$-H), 1708 (-C=O), 1678-1414 (-C=C-), 1243-1125 (C-O), 969 (-$CH_3$). $^1$H-NMR (700 MHz, $CDCl_3$) and $^{13}$C-NMR (175 MHz, $CDCl_3$) are tabulated in Table 1.

### Stigmasta-4, 22-dien-3-on (2)

Colorless crystal; m.p: 80-82$^o$C. ESI-MS *m/z* 411.3627 $[M+H]^+$ (calcd for $C_{29}H_{47}O$). IR $v_{max}$ (ATR) $cm^{-1}$: 2929-2867 (C$sp^3$-H), 1708 (-C=O), 1453 (-C=C-), 1376-1307 (-C-O), 958-907 (-$CH_3$). $^1$H-NMR (700 MHz, $CDCl_3$) and $^{13}$C-NMR (175 MHz, $CDCl_3$) are tabulated in Table 1.

### Stigmasterol (3)

Colorless crystal; m.p: 168–170$^o$C. ESI-MS *m/z* 413 $[M+H]^+$ (calcd for $C_{29}H_{49}O$). IR $v_{max}$ (ATR) $cm^{-1}$: 3423 (*br*-OH), 2936 (C$sp^3$-H), 1642-1449 (C=C), 1112 (C-OH), 910 (-$CH_3$). $^1$H-NMR (700 MHz, $CDCl_3$) and $^{13}$C-NMR (175 MHz, $CDCl_3$) is tabulated in Table 1.

### *β*-Sitosterol (4)

Colorless crystal; m.p: 144–146$^o$C. ESI-MS *m/z* 415 $[M+H]^+$ (calcd for $C_{29}H_{51}O$). IR $v_{max}$ (ATR) $cm^{-1}$: 3346 (*br*-OH), 2987-2831 (C$sp^3$-H), 1449 (-C=C-), 1022 (C-OH), 910 (-$CH_3$). $^1$H-NMR (700 MHz, $CDCl_3$) and $^{13}$C-NMR (175 MHz, $CDCl_3$) is tabulated in Table 1.

Table 1. NMR data (APT and $^{1}$H NMR) of compound **1-4**

| No | APT (ppm) | | | | $^{1}$H (*mult.*, *J* in Hz, ΣH)) | | | |
|---|---|---|---|---|---|---|---|---|
| | **1** | **2** | **3** | **4** | **1** | **2** | **3** | **4** |
| 1 | 35.7 | 35.7 | 37.2 | 37.2 | | | | |
| 2 | 33.9 | 33.8 | 32.0 | 32.0 | | | | |
| 3 | 199.7 | 199.7 | 71.8 | 71.8 | - | - | 3.51 (*m*; 1H) | 3.51 (*m*; 1H) |
| 4 | 123.7 | 123.7 | 42.2 | 42.2 | 5.74 (*s*;1H) | 5.74 (*s*; 1H) | | |
| 5 | 171.8 | 171.8 | 140.7 | 140.7 | - | - | - | - |
| 6 | 33.0 | 33.0 | 121.7 | 121.7 | | | 5.34 (*t*, *J*=5.4; 1H) | |
| 7 | 32.0 | 32.0 | 31.6 | 31.6 | | | | |
| 8 | 36.1 | 35.6 | 31.9 | 31.9 | | | | |
| 9 | 53.8 | 55.9 | 50.1 | 50.1 | | | | |
| 10 | 38.6 | 38.6 | 36.5 | 36.5 | - | - | - | - |
| 11 | 21.0 | 21.0 | 21.0 | 21.0 | | | | |
| 12 | 39.6 | 39.6 | 39.7 | 39.7 | | | | |
| 13 | 42.3 | 42.4 | 42.3 | 42.3 | - | - | - | - |
| 14 | 55.9 | 53.8 | 56.7 | 56.7 | | | | |
| 15 | 24.2 | 24.2 | 26.0 | 26.0 | | | | |
| 16 | 28.8 | 28.9 | 28.9 | 28.9 | | | | |
| 17 | 56.0 | 56.0 | 56.0 | 56.0 | | | | |
| 18 | 12.0 | 11.9 | 11.8 | 11.8 | 0.72 (*s*; 3H) | 0.75 (*s*; 3H) | 0.68 (*s*; 3H) | 0.73 (*s*; 3H) |
| 19 | 17.4 | 17.4 | 19.0 | 19.0 | 1.19 (*s*; 3H) | 1.20 (*s*; 3H) | 0.99 (*s*; 3H) | 1.18 (*s*; 3H) |
| 20 | 36.1 | 40.5 | 40.5 | 40.5 | | | | |
| 21 | 21.2 | 21.2 | 18.7 | 18.7 | 0.93 (*d*, *J*= 6.6; 3H) | 1.03 (*d*, *J*= 6.6; 3H) | 0.91 (*d*, *J*=6.3; 3H) | 1.02 (*d*, *J*=7.5; 3H) |
| 22 | 34.0 | 138.1 | 138.3 | 33.95 | | 5.15 (*dd*, $J_1$ = 15.1, $J_2$ = 8.7; 1H) | 4.99 (*dd*, $J_1$= 9.0, $J_2$= 15.5; 1H) 1H | |
| 23 | 26.1 | 129.4 | 129.2 | 26.10 | | 5.04 (*dd*, $J_1$ =15.1, $J_2$ = 8.7; 1H) | 5.14 (*dd*, $J_1$= 9.0, $J_2$= 15.5; 1H) | |
| 24 | 51.2 | 51.2 | 51.2 | 51.2 | | | | |
| 25 | 29.1 | 32.0 | 29.1 | 29.1 | | | | |
| 26 | 19.8 | 19.0 | 19.8 | 19.8 | 0.84 (*d*, *J*= 6.8; 3H) | 0.86 (*d*, *J*= 6.4; 3H) | 0.81 d (*d*, *J*= 6.5; 3H) | 0.80 (*d*, *J*=6.0; 3H) |
| 27 | 19.0 | 21.1 | 19.4 | 19.4 | 0.82 (*d*, *J*= 6.8; 3H) | 0.86 (*d*, *J*= 6.4; 3H) | 0.76 (*d*, *J*= 6.5; 3H) | 0.85 (*d*, *J*=6.0; 3H) |
| 28 | 23.0 | 25.4 | 23.0 | 23.0 | | | | |
| 29 | 11.9 | 12.0 | 11.9 | 11.9 | 0.85 (*t*, *J* =7.2; 3H) | 0.82 (*t*, *J*= 7.3; 3H) | 0.84 t (*t*, *J*= 3.3; 3H) | 0.81 (*m*; 3H) |

*APT (experiment for $^{13}$C NMR).

Four steroid compounds were successfully isolated from the methanol extract of the frond part of *A. latifolium*. The known compounds were elucidated based on the FTIR, MS and NMR ($^1$H and $^{13}$C) techniques and by comparison of physical and spectroscopic data with values found in the literature. Table 1 displays $^1$H and $^{13}$C NMR data of the isolated compounds. Stigmast-4-en-3-one (**1**) was isolated as a white amorphous. FT-IR (ATR) $v_{max}$ cm$^{-1}$: 2926-2868 (cyclic aliphatic), 1731 (-C=O) and 1647-1459 (-C=C-). The mass spectrum showed a molecular ion peak ESI-MS $[M]^+$ at *m/z* 412 which was analyzed for the molecular formula $C_{29}H_{48}O$. The $^{13}$C-NMR data showed the presence of 29 carbon signals representing six methyl carbons at $\delta_C$ of 11.9, 12.0, 17.4, 19.0, 19.8 and 21.2 ppm; eleven methylene carbons at $\delta_C$ of 35.7, 33.9, 33.0, 32.0, 21.0, 39.6, 24.2, 28.8, 34.0, 26.1 and 23.0 ppm; eight methine carbons at $\delta_C$ of 123.7, 36.1, 53.8, 55.9, 56.0, 36.1, 51.2 and 29.1 ppm; and four quaternary carbons at $\delta_C$ of 199.7, 171.8, 38.6, and 42.3 ppm. Based on the data, compound 1 can be assigned as a cyclic aliphatic triterpenoid where a double bond is formed between C-4 and C-5, while carbonyl is formed at C-3. Meanwhile, a total of 46 protons appeared in the $^1$H-NMR spectrum as shown in Table 1. Two singlet methyls bound directly to the rings, $\delta_H$ 0.75 (H-18) and 1.20 (H-19). Three doublet methyls at $\delta_H$ 1.03 (H-21), 0.86 (H-26) and 0.86 (H-27), and one triplet methyl at $\delta_H$ 0.82 (H-29) are located at the side chain outside the rings of the main skeleton. The occurrence of one highly-deshielded proton at $\delta_H$ 5.74 (H-4) indicated the presence of one pair of double bond. The typical signal for the olefinic H-6 of the steroidal skeleton was evident from a proton at $\delta_C$ 5.74, integrating for one-proton.

Stigmasta-4,22-dien-3-on (**2**) is a white amorphous with m.p. 80-82 °C. Its IR spectrum showed $v_{max}$ absorption peaks at 2929-2867 (C$sp^3$-H), 1708 (-C=O), 1453 (-C=C-), 1376-1307 (-C-O) and 958-907 (-$CH_3$). Compound **2** gave positive responses to the Liebermann-Burchard spray reagent, which indicated the presence of a triterpenoid nucleus**.** This assumption was reinforced by the $^{13}$C-NMR data that indicated the presence of 29 carbons as tabulated in Table 1 which included three olefinic carbon signals at $\delta_C$ 123.7 (C-4), 138.1 (C-22) and 129.4 (C-23) and one carbonyl at δc 199.7 (C-3). The $^1$H-NMR spectra showed the presence of 46 protons. Compound **2** had very similar NMR data with those of compound **1** except for the presence of two olefinic protons instead of two methylenes. Two olefinic protons were determined to be H-22 and H-23 based on its HMBC spectrum. Consequently, a molecular ion peak $[M + H]^+$ at *m/z* 411 was exhibited in its mass spectrum data, which gave a possible molecular formula of $C_{29}H_{47}O$. The combined spectral data of $^{13}$C NMR suggested that the triterpenoid was stigmasta-4.22-dien-3-on, which was further supported by comparison with the literature as tabulated in Table 1.

Stigmasterol (**3**) was obtained as colourless needle crystals. The mass spectral data indicated the molecular formula of this compound to be $C_{29}H_{48}O$ with *m/z* of 412. The FTIR spectral data showed a broad absorbance peak at 3423 cm$^{-1}$, illustrating the stretching vibration of O-H bond, and the peak at 1112 cm$^{-1}$ indicated the vibration band of C-O bend. The peak of C$sp^3$-H stretch appeared at 2936 cm$^{-1}$. An absorbance peak of symmetrical C=C stretching at 1642 cm$^{-1}$ indicated the existence of olefinic group in this compound. The $^1$H NMR experiment of (**3**) displays information of the presence of two singlet methyls bound directly to the rings, $\delta_H$ 0.68 (H-18) and 0.99 (H-19). Three doublet methyls at $\delta_H$ 0.91 (H-21), 0.81 (H-26) and 0.79 (H-27), and one triplet methyl at $\delta_H$ 0.84 (H-29) are located at the side chain outside the rings of the main skeleton. A proton at $\delta_H$ 3.51 (H-3) is attached to the oxygen-binding carbon (C-3). The occurrence of three highly-deshielded protons at $\delta_H$ 5.34 (H-6), 4.99 (H-22), and 5.14 (H-23) indicated the presence of two pairs of double bond. The typical signal for the olefinic H-6 of the steroidal skeleton was evident from a proton at $\delta_C$5.34 integrating for one-proton. The other olefinic protons, H-22 and H-23, are neighbours and are in *trans* position as indicated by their large coupling constants (*J*=15.2). The APT experiment showed that this compound contained 29 carbons consisting of 6 methyls, 9 methylenes, 11 methines, and 3 quarternary carbons. A methine carbon at $\delta_C$ 71.5 (C-3) indicated a carbon attached to an oxygen atom (oxymethine) which revealed the existence of a hydroxyl group. The presence of two double bonds in the molecule was confirmed by two pairs of highly deshielded carbons at $\delta_C$ 140.7 (C-5), 121.7 (C-6), 138.3 (C-22), and 129.2 (C-23). The DBE (Double Bond Equivalent) value is six, which means that this compound is a tetracyclic compound containing two double bonds. Therefore, compound **3** is identified as stigmasterol.

*β*-Sitosterol (**4**) was obtained in the form of colorless needle crystals. The mass spectrum showed a molecular ion peak EI-MS $[M+H]^+$ at *m/z* 212 which was analyzed for the molecular formula $C_{29}H_{51}O$. Compound **4** also identified as steroid with a DBE value of five, one for a double bond and the other three as a tetracyclic chain. The differences between compound **3** and **4** lay on C-22 and C-23, where compound **4** had a double bond (Figure 1).

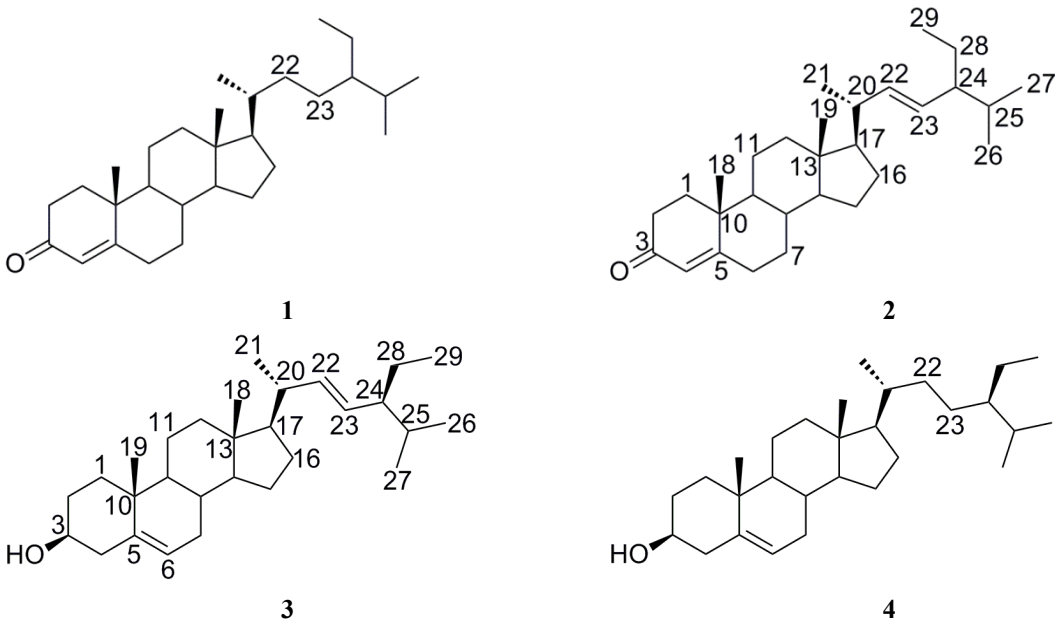



Figure 1. Chemical structures of **1**, **2**, **3** and **4**

## Conclusion

Four steroids namely Stigmast-4-en-3-one (**1**), stigmasta-4,22-dien-3-on (**2**), Stigmasterol (**3**) and *β*-Sitosterol (**4)** were successfully isolated from the leaves of *Adiantum latifolium* Lam. This is the first reported phytochemical study from this plant.

## Acknowledgement

We would like to thank the School of Environmental and Natural Resources Science and the School of Chemical Science and Food Technology, Faculty of Science and Technology, Universiti Kebangsaan Malaysia (UKM); for providing research facilities and also would also like to express our gratitude to the Ministry of Higher Education Malaysia and UKM for the financial support through research grants of Regenerations of co-dominant plant family in Tasik Chini (DPP-2015-144), FRGS-1-2014-SG01-UKM-02-5 and Indonesia Endowment Fund for Education (LPDP).

## References

1. Boonkerd, T. and Pollawatn, R. (2011). *Adiantum capillus*-junonis Rupr.: An additional species of *Adiantum* L. (Pteridaceae) for Thailand. *Science Asia,* 37: 370 – 372.
2. Piggott, A. G. (1988). Ferns of Malaysia in colour. Malaysia, Kuala Lumpur, Tropical Press. pp 420 –421.
3. Rajurkar, N. S. and Gaikwad, K. (2012). Evaluation of phytochemicals, antioxidant activity and elemental content of *Adiantum capillus veneris* leaves. *Journal of Chemical and Pharmaceutical Research,* 4(1): 365 – 374.
4. Pan, C., Chen, Y. G., Ma, X. Y., Jiang, J. H., He, F. and Zhang, Y. (2011). Phytochemical constituents and pharmacological activities of plants from the genus *Adiantum*: A review. *Tropical Journal of Pharmaceutical Research,* 10(5): 681 – 692.
5. Guarrera, P. M., Lucchese, F. and Medori, S. (2008). Ethnophytotherapeutical research in high molise region (Central-Southern Italy). *Journal of Ethnobiology and Ethnomedicine*, 4: 1 – 11.
6. Marino, A., Elberti, M. G. and Cataldo, A. (1989). Phytochemical investigations of *Adiantum capillus-veneris*. *Journal of Biological Research Bollettino Della Societaltaliana Di Biologia Sperimentale*. 65: 461 – 463.

7. Imperato, F. (1982). Kaempferol 3-sulphate in the fern *Adiantum capillus-verenis*. *Phytochemistry*, 21: 2158 – 2159.
8. Imperato, F. (1982). A new acylated flavonol glucoside from the fern *Adiantum capillus-verenis* L. *Journal of Chemistry and Industry*, 16: 604.
9. Pourmorad, F., Hosseinimehr, S. J. and Shahablmajd, N. (2006). Antioxidant activity, phenol and flavonoid contents of some selected Iranian medicinal plants. *African Journal of Biotechnology*, 5: 1142 – 1145.
10. Abdel-Halim, O. B., Ibraheim, Z. Z. and Shiojima, K. (2002). Oleanane triterpenes from *Adiantum capillus-verenis* growing in Egypt. *Alexandria Journal of Pharmaceutical Sciences*, 16: 87 – 92.
11. Nonato, F. R., Noguiera, T. M., Barros, T. A., Lucchese, A. M., Oliviera, C. E., Santos, R. R., Soares, M. B. and Villarreal, C. F. (2011). Antinociceptive and anti-inflammatory activities of *Adiantum latifolium* Lam.: evidence for a role of IL-1β inhibition. *Journal of Ethnopharcological,* 136(3): 518 –524.

*Malaysian Journal of Analytical Sciences, Vol 21 No 2 (2017): 304 - 311*
*DOI: https://doi.org/10.17576/mjas-2017-2102-05*

MALAYSIAN JOURNAL OF ANALYTICAL SCIENCES
*Published by The Malaysian Analytical Sciences Society*
ISSN 1394 - 2506

# THE CHEMICAL CONSTITUENTS FROM THE FRUITS OF *Johannesteijsmannia altifrons* AND ANTIBACTERIAL ACTIVITY

## (Komposisi Kimia Daripada Buah *Johannesteijsmannia altifrons* dan Aktiviti Antibakteria)

Noor Aziiraa Sabri[1], Wan Yaacob Wan Ahmad[1]*, Nur Shafiqa Abdullah[1], Nazlina Ibrahim[2]

[1]*School of Chemical Sciences and Food Technology, Faculty of Science and Technology*
[2]*School of Biosciences and Biotechnology,Faculty of Science and Technology*
*Universiti Kebangsaan Malaysia, 43600 UKM Bangi, Selangor, Malaysia*

**Corresponding author: wanyaa@ukm.edu.my*

Received: 10 October 2016; Accepted: 16 January 2017

**Abstract**

Isolation on the hexane extract of the fruits of *Johannesteijsmannia altifrons* by vacuum liquid and radial chromatography yielded three known compounds namely β-sitosterol, γ-taraxasterol and stigmasterol. Their structures were determined using one-dimensional and two-dimensional nuclear magnetic resonance spectroscopy, fourier transform infra-red spectroscopy and mass spectrometry. All the isolated compounds were tested for their antibacterial activity using disc diffusion and minimum inhibitory concentration (MIC). All three compounds showed weak and moderate activities against all nine tested bacteria. This is the first report on the isolation of compounds from this species and on the antibacterial activity of γ-taraxasterol.

**Keywords**: *Johannesteijsmannia altifrons*, β-sitosterol, γ-taraxasterol, stigmasterol, antibacterial

**Abstrak**

Pemencilan ke atas ekstrak heksana bagi buah *Johannesteijsmannia altifrons* dengan kromatografi cecair vakum dan radial menghasilkan tiga sebatian yang pernah ditemui bernama β-sitosterol, γ-taraksasterol dan stigmasterol. Strukturnya ditentukan dengan spektroskopi resonans magnet nukleus satu-dimensi dan dua-dimensi, spektroskopi infra-merah transformasi Fourier dan spektrosmetri jisim. Kesemua sebatian yang dipencilkan diuji aktiviti bakterianya dengan kaedah peresapan cakera dan kepekatan perencatan minimum (KPM). Kesemua tiga sebatian menunjukkan aktiviti yang lemah dan sederhana terhadap kesemua sembilan bakteria yang diuji. Ini merupakan laporan pertama mengenai pemencilan sebatian daripada spesies ini dan mengenai aktiviti antibakteria bagi γ-taraksasterol.

**Kata kunci**: *Johannesteijsmannia altifrons*, β-sitosterol, γ-taraksasterol, stigmasterol, antibakteria

## Introduction

*Johannesteijsmannia* belonging to the Arecaceae family contains four species which are *J. altifrons, J. lanceolata, J. magnifica* and *J. perakensis. Johannesteijsmannia altifrons* which is also known as "Daun Sang" (Malay) and Joey Palm (English) commonly found in Kelantan, Perak, Terengganu, Pahang, Johor and Kedah [1]. No chemical constituents have ever been isolated or characterized from *Johannesteijsmannia altifrons*. The family of Arecaceae has been reported to contain flavonoids [2], alkaloids [3], terpenoids, steroids, fatty acids and tannins [4].Thus, conducting a phytochemical study on *Johannesteijsmannia altifrons* is vital to further enrich our knowledge on the species. In this study, the hexane extract from fruits of *Johannesteijsmannia altifrons* was purified and led to the discovery of known β-sitosterol, γ-taraxasterol and stigmasterol. Previously, Singh and Ghanapriya [5] reported β-sitosterol and stigmasterol inhibited at low levels (1+) against *Staphylococcus aureus*, *Bacillus subtilis* and

*Escherichia coli*. According to previous study by Manriquez et al. [6], both β - sitosterol and stigmasterol gives MIC value at 16.5 µg/mL against Staphylococcus aureus. Previous study discovered no inhibition of β-sitosterol and stigmasterol reported on *Escherichia coli, Bacillus subtilis* and *Salmonella thyphimurium* [6]. There are three types of extracts in this study which are hexane, chloroform and methanol but hexane extract was chosen to be purified further. This is because compounds from hexane extract are easily separated and purified compared to the other two extracts.

## Materials and Methods

### General

Different spectroscopic methods were used to elucidate the structures of β-sitosterol, γ-taraxasterol and stigmasterol including ultraviolet–visible spectroscopy, mass spectroscopy, fourier transform infra-red spectroscopy, one-dimensional, two-dimensional and carbon-13 nuclear magnetic resonance spectroscopy. The one-dimensional, two-dimensional and carbon-13 nuclear magnetic resonance spectroscopy spectra were recorded using Avance III 600 MHz Bruker. Deuterated chloroform ($CDCl_3$) was used as the NMR solvent with the chemical shifts, $\delta_H$, in ppm and the values of coupling constants, *J*, in Hz. Mass spectra were recorded by using the LC-mass spectrometry (LC-MS) on the Dionex/Bruker Micro ToFQ. The infra-red spectra were recorded on the Perkin-Elmer Spectrum 400 and the UV-VIS spectra were obtained in chloroform using UV-2400PC. Vacuum liquid chromatography (VLC) was prepared by using silica gel of Merck 7747. For radial chromatography (RC), silica gel with $PF_{254}$ containing gypsum (Merck 7749) was used. Thin layer chromatography (TLC) was performed on commercially pre-coated aluminum silica gel 60 $F_{254}$ of Merck 5554.

### Plant materials

The fruits of *Johannesteijsmannia altifrons* were collected at Pelagat Forest Reserve, Besut, Terengganu in February 2015. A voucher specimen (UKMB 40309) was deposited at the Herbarium of Universiti Kebangsaan Malaysia, Bangi (UKMB).

### Extraction and isolation

The air-dried, fruits of *Johannesteijsmannia altifrons* (786 g) were extracted for 3 days in methanol at room temperature, followed by filtration to give methanol solution. They were then extracted with *n*-hexane three times, combined and rotary evaporated to afford 4.42 g (0.56%) of greenish brown fruit *n*-hexane extract. The extract was fractionated by VLC, eluted with increasing polarity of *n*-hexane-ethyl acetate to collect the less polar and more polar fractions. The fractions were combined based on their silica gel TLC profiles. The VLC gave 16 fractions ($F_1$- $F_{16}$). Since fractions $F_4$ to $F_7$ have similar components, they were combined and further fractionated using RC to produce four combined fractions ($F_{41}$-$F_{44}$). The third fraction ($F_{43}$) contained β-sitosterol (32 mg). Then, fractions $F_9$-$F_{12}$ were combined and purified by RC to yield 7 combined fractions ($F_{91}$-$F_{97}$); fractions $F_{94}$ and $F_{96}$ contained γ-taraxasterol (25 mg) and stigmasterol (0.55 g), respectively.

### Bioassay

The pure compounds were assayed for antibacterial activity by using two methods which are disc diffusion and minimum inhibitory concentration (MIC) as described by Mamman et al. [7], Mukhtar and Ghori [8], and Yap et al. [9] with some modification, against nine bacteria; *Staphylococcus aureus,* Methicillin-resistant *Staphylococcus aureus (MRSA), Bacillus subtilis*, *Bacillus thruriengiensis*, *Escherichia coli*, *Salmonella thyphimurium, Serratia marcescens, Vibrio fluvialis* and *Vibrio cholera*. The pure compounds were prepared at 30 µg/mL in DMSO.

### Disc diffusion

Disc diffusion method for antibacterial testing was carried out to determine antibacterial activity of the pure compounds. The nine bacteria were spread on the Mueller-Hinton agar surface by using a sterile swab and the plates were dried for 15 minutes. Then, 100 µL of each dilution of the pure compounds was impregnated into sterile, blank disc of 6 mm in diameter and placed on the Mueller-Hinton agar surface. The positive control used was chloramphenicol 30 µg/disc which is a standard commercial antibiotic. The negative control used was DMSO (100%). The plates were then incubated at 37 $^oC$ for 24 hours. After the incubation, the plates were examined for inhibition zone and the results were recorded. The diameter of inhibition zones were measured in millimeter (mm).The test was repeated three times to ensure reliability.

**Minimum inhibition concentration**

Minimum Inhibition Concentration (MIC) was carried out to determine the lowest concentration of the compounds that could inhibit the visible growth of tested bacteria by using 96 microwell plate. An amount 100 µL of pure compounds undergo dilutions from 30 to 0.117 µg/mL. 50 µL of nine bacteria were added into wells containing compounds. The 96 microwell plate was incubated at 37 $^{o}$C for 24 hours. The positive and negative controls used were 100 µL of respective chloramphenicol antibiotic and DMSO. Then, 50 µL of 3-[4,5-dimethylthiazol-2-yl]-2,5-diphenyltetrazolium bromide (MTT) was added to each single well and the plate was incubated at 37 $^{o}$C for 2 hour. The colour development was observed and the results were recorded. The test was repeated three times to ensure reliability.

## Results and Discussion

The ESI-MS gave molecular ion at $[M+Na]^+$ m/z 437.3381 which β-Sitosterol appeared as colourless needles. The ESI-MS gave molecular ion at $[M+Na]^+$ m/z 437.3381 which corresponded to the molecular formula $C_{29}H_{50}O$ (414.3862 + 22.9898 = 437.3759; Δ 0.40513). The IR spectrum showed absorption peaks at 3385 cm$^{-1}$ which is characteristic of O-H stretching, peaks at 2936 and 2868 cm$^{-1}$ due to aliphatic or C-H stretching ($CH_3$). Other absorption frequencies include peak at 1708 cm$^{-1}$ due to absorption of C=C stretching. The $^1$H NMR spectrum of β-sitosterol showed a multiplet signal at $\delta_H$ 3.53 (H-3), indicates the presence of a hydroxyl methine proton. The occurrence of a highly-deshielded signal at $\delta_H$ 5.36 (H-6) indicates the presence of a vinylic proton. On the other hand, a singlet signal at $\delta_H$ 1.02 indicates a methyl group at H-29. Two doublet signals at $\delta_H$ 0.86 and 0.91 are due to the two non-equivalent methyls at H-26 and H-27 of an isopropyl group. The $^{13}$C NMR spectrum showed that β-sitosterol contains 29 different carbon atoms consisting of six methyls, 11 methylenes, nine methines, and three quaternary carbons. Signal of methine carbon at $\delta_C$ 71.8 ppm indicates a carbon attached to an oxygen atom which showed the existence of a hydroxyl group at C-3. Two highly deshielded signals at $\delta_C$ 140.8 and 121.7 ppm, which are assigned to C-5 and C-6 indicates there is one carbon double bond in the molecule. According to the available data as well as comparison with the literature [10], the compound is confirmed to be β-sitosterol.

γ-Taraxasterol was obtained as colourless needle crystal. The ESI-MS showed a molecular ion peak at $[M+Na]^+$ m/z 449.2842 which corresponded to the molecular formula $C_{30}H_{50}O$ (426.3862 + 22.9898 = 449.3759; Δ 0.09176). The IR spectrum displayed a broad absorbance peak at 3385 cm$^{-1}$ which characteristic of O-H stretching. Absorptions at 2927 and 2871 cm$^{-1}$ represent the C$sp^3$-H stretching. The $^1$H NMR spectrum showed signal of a proton at $\delta_H$ 3.51 (H-3) is attached to the oxygen-binding carbon (C-3). This is deshielded proton which is hydroxyl methine proton. Seven singlet methyls at signals $\delta_H$ 1.61 (H-23), 1.10 (H-24), 0.82 (H-25), 0.81 (H-26), 1.29 (H-27), 0.80 (H-28) and 1.05 (H-30) indicating that they are attached to quaternary carbons and bound directly to the ring system. There is only one highly deshielded proton at $\delta_H$ 5.37 (H-21) indicating the olefinic proton that attaches to a double bond carbon (C-21). The $^{13}$C NMR spectrum showed γ-taraxasterol is formed by 30 carbon atoms consisting of eight methyls, nine methylenes, seven methines, and six quarternary carbons. A methine carbon at $\delta_C$ 80.7 indicates a carbon attached to an oxygen atom which showed the existence of a hydroxyl group at C-3. There are two highly deshielded olefinic carbon signals at $\delta_C$ 141.0 (C-20) and 121.7 (C-21) suggests that there is one double bond contained in the molecule. Through comparison of the observed data with literature [11], the compound is identified as γ-taraxasterol.

Stigmasterol was isolated as colourless needles. The ESI-MS gave molecular ion at $[M+Na]^+$ *m/z* 435.3279 which corresponded to the molecular formula $C_{29}H_{48}O$ (412.3705 + 22.9898 = 435.3603; Δ 0.0324). The IR spectrum displayed stretching band for O-H at 3354 cm$^{-1}$. Peaks at 2934 and 2866 cm$^{-1}$ indicate the presence of aliphatic or C-H stretching ($CH_3$). A band at 1667 cm$^{-1}$ appears due to the existence of olefinic group in this compound. The $^1$H NMR spectrum displayed signals for six methyls. Two singlet methyls at signals $\delta_H$ 0.69 (H-18) and 1.02 (H-19) indicating that they are bound directly to the ring system. Three doublet methyls at $\delta_H$ 0.93 (H-21), 0.84 (H-26) and 0.7 (H-27), and one *triplet* methyl at $\delta_H$ 0.83 (H-29) are located at the side chain outside the rings of the main skeleton. Hydroxyl methine proton appeared at $\delta_H$ 3.54 (H-3) which attached to the oxygen-binding carbon (C-3). Three highly-deshielded protons presence at $\delta_H$ 5.36, 5.03, and 5.09 due to the presence of two pairs of double bond which assigned at H-6, H-22 and H-23. The $^{13}$C NMR spectrum showed stigmasterol contained 29 carbon atoms consisting of six methyls, nine methylenes, 11 methines, and three quaternary carbons. Signal at $\delta_C$ 71.8 indicates a

methine carbon attached to an oxygen atom which showed the existence of a hydroxyl group at C-3. There are four olefinic carbon signals that appear downfield and highly deshielded at $\delta_C$ 140.8 (C-5), 121.7 (C-6), 138.3 (C-22) and 129.3 (C-23) suggests that there are two double bonds in the molecule. Based on the discussion above and data comparison with literature [10], the compound is identified as stigmasterol. The spectra of β-sitosterol, γ-taraxasterol and stigmasterol are shown in Figures 1, 2 and 3, respectively.

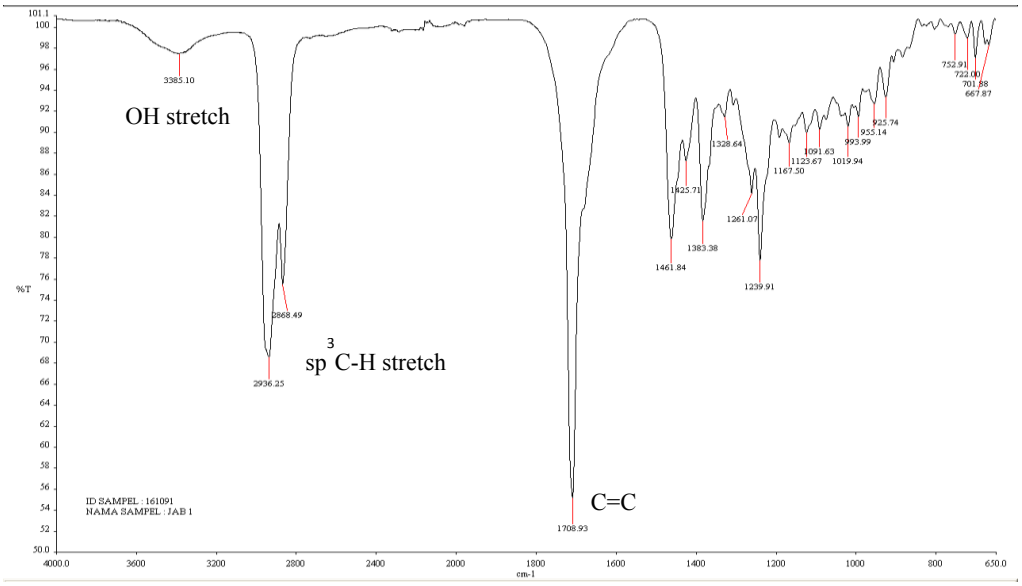



Figure 1. The infra-red spectrum of β-sitosterol

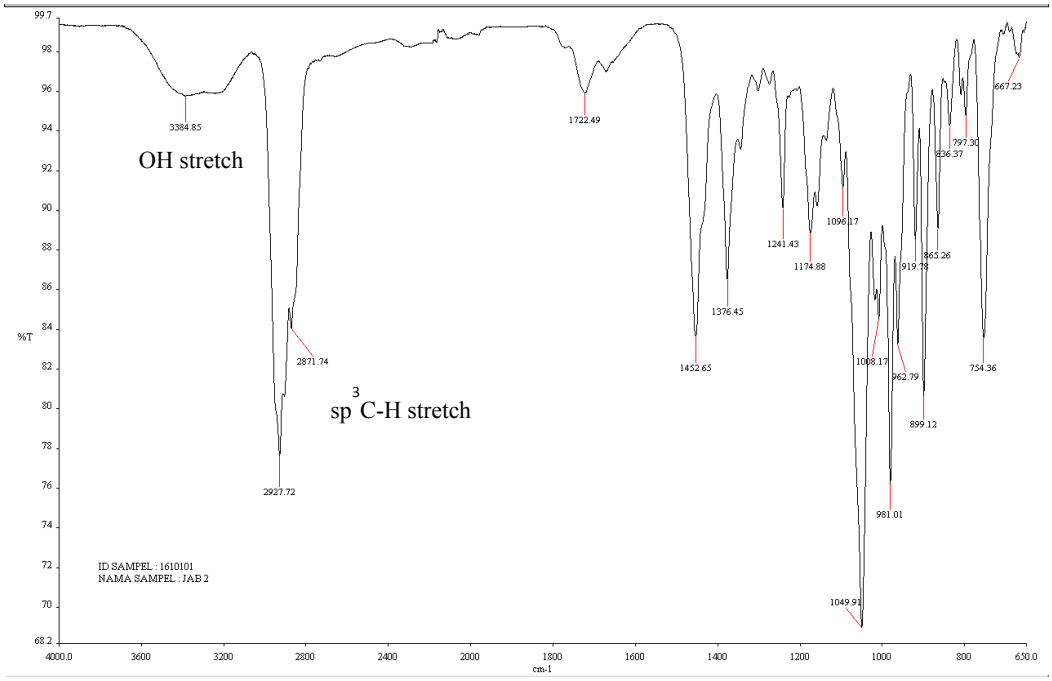



Figure 2. The infra-red spectrum of γ-taraxasterol

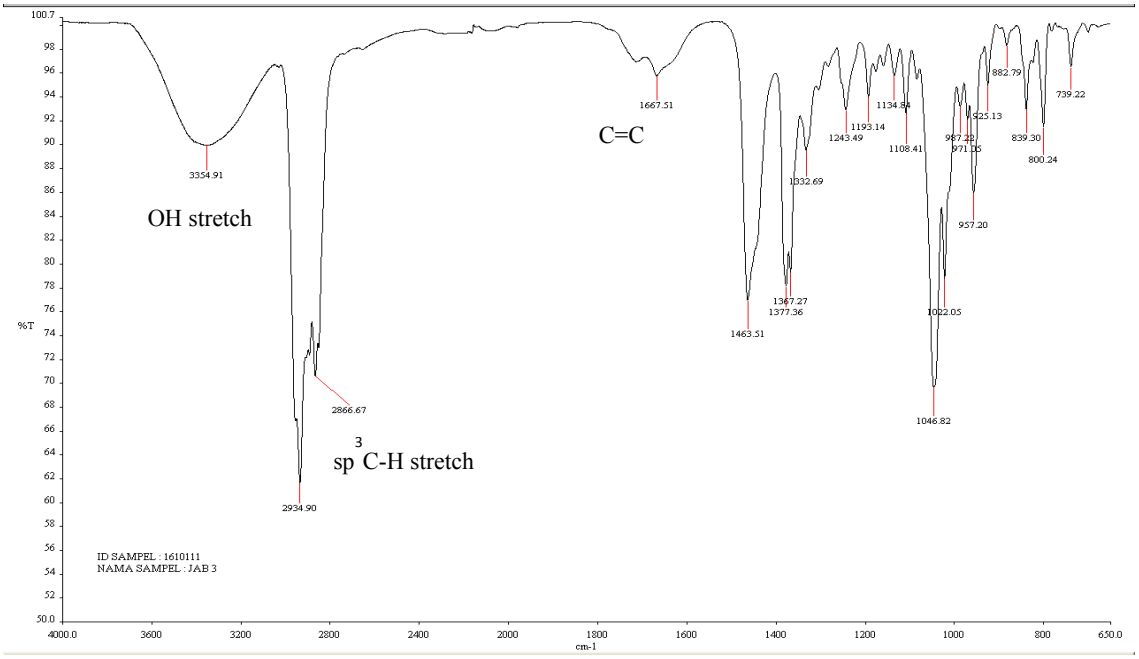
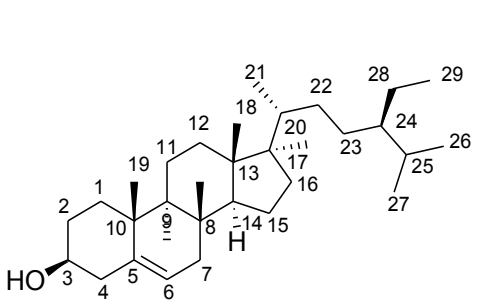
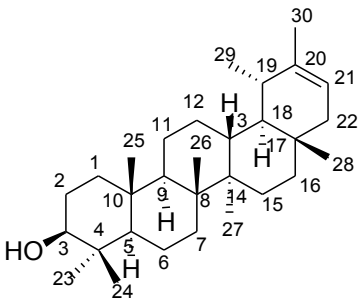


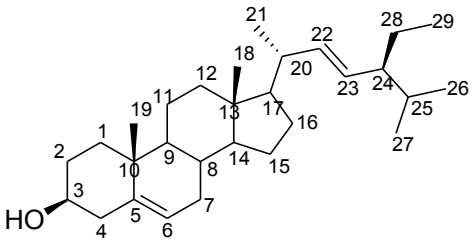

Figure 3. The infra-red spectrum of stigmasterol



β-Sitosterol



γ-Taraxasterol



Stigmasterol

Figure 4. Structures of the pure compounds

**Antibacterial activity**

The pure compounds isolated from the fruits of *Johannesteijsmannia altifrons* were tested for antibacterial activity. In disc diffusion method, β-sitosterol showed low inhibition which is 7.0 ± 0.00 mm against *Vibrio fluvialis*, MRSA and *Bacillus subtilis* whereas γ-taraxasterol and stigmasterol exhibited moderate activities against *Escherichia coli*, *Serratia marcescens*, *MRSA* and *Bacillus subtilis*. Based on the results, it was observed that β-sitosterol has inhibition against one gram negative bacteria and two gram positive bacteria. This may probably due to the morphological differences between gram negative and gram positive bacteria in terms of their cell wall composition. The gram positive bacteria only have an outer peptidoglycan which is not effective permeability barrier compared to gram negative bacteria that have both outer membrane and peptidoglycan. This makes the gram negative bacteria cell wall impermeable to most of the drugs [12]. For stigmasterol, the inhibition occurs at low level (1+) against *Staphylococcus aureus*, *Bacillus subtilis* and *Escherichia coli* which is similar as reported by Singh dan Ghanapriya [5]. Besides, γ-taraxasterol showed moderate (2+) inhibition against *Serratia marcescens* and *Bacillus subtilis.* Kanamysin and vancomysin used as positive controls and the results showed all compounds have lower inhibitory activity against all tested bacteria compared to the antibiotics. DMSO as negative control did not show any antibacterial activity against tested bacteria. The inhibitory zone values for all compounds are shown in Table 1.

Table 1. Antibacterial activity of the pure compounds in disc diffusion method

| **Pure Compounds** | **β-Sitosterol** | **γ-Taraxasterol** | **Stigmasterol** | **Kanamysin (K)*/ Vancomysin (V)**** |
|---|---|---|---|---|
| | **Inhibitory Zone (mm)** | | | |
| *Escherichia coli* * | - | 7.0 ± 0.53 | 7.0 ± 0.00 | 20 ± 1.00 (K) |
| *Vibrio fluvialis* * | 7.0 ± 0.00 | 7.0 ± 0.00 | 7.0 ± 0.00 | 35 ± 1.04 (K) |
| *Salmonella thyphimurium* * | - | 7.0 ± 0.00 | 7.0 ± 0.00 | 26 ± 0.00 (K) |
| *Vibrio cholera* * | - | - | - | 10 ± 0.00 (K) |
| *Serratia marcescens* * | - | 11.0 ± 0.00 | 11.0 ± 0.00 | 23 ± 1.52 (K) |
| Methicillin-resistant *Staphylococcus aureus (MRSA)* ** | 7.0 ± 0.00 | 7.0 ± 0.00 | 8.0 ± 0.5 | 20 ± 0.00 (V) |
| *Bacillus thruriengiensis* ** | - | - | - | 22 ± 0.00 (V) |
| *Bacillus subtilis* ** | 7.0 ± 0.00 | 10.0 ± 0.5 | 7.0 ± 0.00 | 28 ± 0.00 (V) |
| *Staphylococcus aureus* ** | - | 7.0 ± 0.53 | 7.0 ± 0.00 | 25 ± 0.00 (V) |

Mean measurement: SD (n = 3), * Gram negative, ** Gram positive

In minimum inhibition concentration (MIC) method, all compounds gave value of 7.5 µg/mL against *Staphylococcus aureus*, *Escherichia coli*, *Vibrio cholera*, *Serratia marcescens*, *Bacillus thruriengiensis* and *Bacillus subtilis* whereas previous report showed both β-sitosterol and stigmasterol have higher MIC value of 16.5 µg/mL and no inhibition against *Escherichia coli* and *Bacillus subtilis*. No explanation can be given on the difference. First report on antibacterial activity of γ-taraxasterol provides new knowledge for the compound. The MIC values are shown in Table 2.

Table 2. Antibacterial activity of the pure compounds in minimum inhibitory concentration (MIC) method

| **Pure compounds** | **β-Sitosterol** | **γ-Taraxasterol** | **Stigmasterol** |
|---|---|---|---|
| | **MIC (µg/mL)** | | |
| *Escherichia coli* | 7.5 | 7.5 | 7.5 |
| *Vibrio fluvialis* | 30 | 30 | 30 |
| *Salmonella thyphimurium* | 15 | 15 | 15 |
| *Vibrio cholera* | 7.5 | 7.5 | 7.5 |
| *Serratia marcescens* | 7.5 | 7.5 | 7.5 |
| Methicillin-resistant *Staphylococcus aureus (MRSA)* | 15 | 15 | 30 |
| *Bacillus thruriengiensis* | 7.5 | 7.5 | 7.5 |
| *Bacillus subtilis* | 7.5 | 7.5 | 7.5 |
| *Staphylococcus aureus* | 7.5 | 7.5 | 7.5 |

## Conclusion

The investigation on the chemical constituents from fruits of *Johannesteijsmannia altifrons* resulted in the isolation of three known compounds which are β-sitosterol, γ-taraxasterol and stigmasterol. In disc diffusion method, the isolated compounds showed no inhibition against *Vibrio cholera* and *Bacillus thruriengiensis*, and weak or moderate activities against other seven bacteria. In MIC method, the lowest and highest MIC values were at respective 7.5 and 30 µg/mL. All the compounds have been reported for the first time from this plant.

## Acknowledgment

Authors would like to thank the Ministry of Education, Malaysia and Universiti Kebangsaan Malaysia (UKM) for the financial support under DLP-2013-018 grant and "Program Pelajar Cemerlang (PPC)" scholarship under Public Service Department, Malaysia. Special thanks to School of Chemical Sciences and Food Technology, Faculty of Science and Technology, UKM and Centre for Research and Innovation Management (CRIM) UKM for technical support on NMR, LC-MSToF, UV and FTIR instrumentation.

## References

1. Dransfield, J. (1972). The genus *Johannesteijsmannia* H. E. Moore Jr. *The Gardens Bulletin Singapore*, 26: 63–83.
2. Muhaisen, H. (2002). Flavonoids from the base leaves of *Caryota urens* (Palmae). *American Scientific Publishers*, 6(11): 1225 – 1229.
3. Dyana, J. P. and Kanchana, G. (2012). Preliminary phytochemical screening of *Cocos nucifera* L. flowers. *International Journal of Current Pharmaceutical Research*, 4(3): 3 – 4.
4. Benmehdi, H., Hasnaoui, O., Benali, O. and Salhi, F. (2012). Phytochemical investigation of leaves and fruits extracts of *Chamaerops humilis* L. *Journal of Material and Environmental Science*, 3(2): 320 – 237.
5. Singh, S. and Ghanapriya, N. (2014). Chemical constituents and antibacterial activity of *Phaleria macrocarpa*. *International Journal of Pharmaceutical Sciences and Research*, 5(8): 3157 – 3162.
6. Manríquez-Torres, J. J., Zúñiga-estrada, A., González-ledesma, M. and Torres-valencia, J. M. (2007). The antibacterial metabolites and proacacipetalin from *Acacia cochliacantha. Journal of the Mexican Chemical Society*, 51(4): 228 – 231.
7. Mamman, P. H., Mshelia, W. P., Susbatrus, S. C. and Sambo, K. W. (1989). Antibacterial effects of crude extract of *Azadirachta indica* against *Escherichia coli, Salmonella* 142 spp and *Staphylococcus aureus*. *International Journal of Medicine and Medical Sciences*, 5(1): 14 – 18.
8. Mukhtar, S. and Ghori, I. (2012). Antibacterial activity of aqueous and ethanolic extracts of garlic, cinnamon and turmeric against *Escherichia coli* ATCC 25922 and *Bacillus subtilis* DSM 3256. *International Journal of Applied Biology and Pharmaceutical Technology*, 3(2): 131 – 136.

9. Yap, P. S. X., Chong Y. T. E., Wong, Y. Y., Lim, X. Y., Ang J. H., Goh, H. S. L., Lai, M. X. S, Mai, C. W., Buru, S. A., Pichika, M. R. and Lim, S. H. E. (2013). Antibacterial and antifungal testing of the different extracts of *Dillenia obovata* (blume) Hoogl. *World Journal of Pharmacy and Pharmaceutical Sciences*, 2(5): 3946 – 3962.
10. Chaturvedula, V. S. P. and Prakash, I. (2012). Isolation of Stigmasterol and β-Sitosterol from the dichloromethane extract of *Rubus suavissimus*. *International Current Pharmaceutical Journal*, 1(9): 239 – 242.
11. Yekta, M. M., Hamid, S. and Alavi, R. (2008). New triterpenoids from *Peucedanum ruthenicum*. *Iranian Journal of Pharmaceutical Sciences*, 4(4): 289 – 294.
12. Ghansar, N. H., Bhopale, S. U. and Prabhune, V. S. (2012). *In vitro* studies of antimicrobial properties of extracts from Unani medicinal plants. *International Journal of Pharmaceutical Bio Sciences*, 3(1): 240 – 249.

*Malaysian Journal of Analytical Sciences, Vol 21 No 2 (2017): 312 - 322*
*DOI: https://doi.org/10.17576/mjas-2017-2102-06*

MALAYSIAN JOURNAL OF ANALYTICAL SCIENCES
*Published by The Malaysian Analytical Sciences Society*
ISSN 1394 - 2506

# GEOCHEMISTRY AND CLAY MINERALS OF SURFACE SEDIMENTS OF SOUTHWESTERN JOHOR, MALAYSIA

## (Geokimia dan Mineral-mineral Liat Enapan Permukaan di Barat Daya Johor, Malaysia)

Hasrizal Shaari[1,2]*, Noor Azhar Mohd Shazili[2], Lina Idayu Abdullah[1], Nor Antonina Abdullah[1], Mohd Lokman Husain[1], Norhayati Md. Tahir[1]

[1]*School of Marine and Environmental Science*
[2]*Institute of Oceanography and Environment*
*Universiti Malaysia Terengganu, 21030 Kuala Terengganu, Terengganu, Malaysia*

**Corresponding author: riz@umt.edu.my*

Received: 19 December 2016; Accepted: 18 February 2017

**Abstract**

Surface sediments from tropical coastal settings of Southwestern Johor, Malaysia, were analyzed for grain size, major element content and clay minerals using particle size analyzer, scanning electron microscope-energy dispersive spectrometer (SEM-EDS) and X-ray Diffractometer (XRD). This work is aimed at investigating the geochemical composition of surface sediments and possible anthropogenic inputs from urban settlements. Sediment texture was found to be clayey with an average of 45.15%. The abundance of major elements in decreasing order is $SiO_2$ > $Al_2O_3$ > $K_2O$ ≥ $ClO_2$ ≥ $Na_2O$ > MgO > MnO > ZnO. The dominance of $SiO_2$ appears to be linked with the draining of Sungai Pulai to the study area. The concentration of ZnO registered a hundred times higher than the average natural level of zinc in the earth's crust. Higher levels of Zn might be derived from the combination of anthropogenic input and natural geochemical processes. Mineral abundance follows the order of quartz > kaolinite > muscovite > smectite > calcite> illite. Smectite was detected in the upper river sediment, but was not present in the estuarine sediment. This is likely due to the accumulation and intensity of weathering products. The dominance of quartz in the coastal sediments is due to the intense weathering process.

**Keywords:** tropical, sediments, elements, clay minerals, Malaysia

**Abstrak**

Sedimen permukaan dari pesisiran pantai tropika di Barat Daya Johor, Malaysia, telah dianalisis untuk saiz butiran, kandungan unsur utama dan mineral liat dengan menggunakan penganalisa saiz partikal, imbasan elektron mikroskop-spektrometer serakan tenaga (SEM-EDS) and pembelauan sinaran-X (XRD). Kajian ini bertujuan untuk mengkaji komposisi geokimia enapan permukaan dan input antropogenik yang mungkin hadir dari penempatan bandar. Tekstur enapan adalah terdiri daripada liat dengan purata pecahan saiz liat sebanyak 45.15%. Kelimpahan elemen utama secara tertib menurun adalah seperti berikut $SiO_2$ > $Al_2O_3$ > $K_2O$ ≥ $ClO_2$ ≥ $Na_2O$ > MgO > MnO > ZnO. Dominasi $SiO_2$ membayangkan terdapat perkaitan dengan aliran Sungai Pulai ke kawasan kajian. Kepekatan ZnO direkodkan beratus kali lebih tinggi daripada tahap semula jadi purata zink di dalam kerak bumi. Tahap Zn yang lebih tinggi mungkin diperolehi daripada gabungan input antropogenik dan proses geokimia semula jadi. Kelimpahan mineral mengikuti urutan berikut kuarza> kaolinit> muskovit> smektit> kalsit> ilit. Smektit dikesan pada enapan di bahagian hulu sungai namun tiada di dalam enapan muara. Keadaan ini mungkin disebabkan oleh pengumpulan dan keamatan produk luluhawa. Dominasi kuarza di dalam sedimen pantai adalah disebabkan oleh proses luluhawa.

**Kata kunci:** tropika, enapan, elemen-elemen, mineral liat, Malaysia

## Introduction

Southwestern Johor has a unique environment due to the combination of different ecosystems (i.e. river, mangrove, estuary and beaches) and rapid development zone (i.e. Tanjung Pelepas Port, industrial area, oil terminal and urbanization). A report by ASEAN/US CRMP [1] stated that ~ 80% of Johor land is formed by sedimentary, metasedimentary and igneous rocks of pre-quaternary while the remaining 20% is covered by unconsolidated to semi consolidated quaternary sediments. Rapid development in this area over the past two decades might have caused changes in elemental composition. Thus, there is a possibility that the sediment deposits in coastal areas of Southwestern Johor are derived from natural and/ or anthropogenic sources. In certain conditions, the elements in surface sediment are governed by their concentration, relative proportions from various sources, components and forcing mechanisms. Some reports indicated the significant role of grain size sediments in controlling the element's content in coastal area [2-4], and the enrichment of elements in fine-grained sediments is attributed to their adsorption capabilities and low contents of quartz [5]. Based on the previous reports, we consequently presume that the relationship between elements and grain size can be applied as the environmental indicator in the coastal area of Southwestern Johor. Recently, several environmental studies have been conducted in the coastal area of Southwestern Johor [6-10]. However, there have been no reports that focus on the distribution of sediment mineral contents and geochemical composition in surface sediment. Thus, this paper presented and discussed the abundance and distribution of major elements and clay minerals composition in surface sediment of the Southwestern Johor.

## Materials and Methods

### Sample collection and preservation

Table 1 shows the coordinates of sampling points in the study area. The surface sediment samples were collected from 20 stations at different ecosystems of the coastal area of Southwestern Johor (Figure 1) using the ponar grab. The samples were then put in labelled plastic bags and brought back to the laboratory for further analysis.

Table 1. Latitude and longitude of the sampling points in the study area

| Station | Latitude | Longitude |
|---|---|---|
| 1 | 01°19.647' N | 103°26.180' E |
| 2 | 01°19.419' N | 103°25.792' E |
| 3 | 01°19.943' N | 103°26.352' E |
| 4 | 01°20.206' N | 103°25.108' E |
| 5 | 01°18.383' N | 103°25.222' E |
| 6 | 01°18.895' N | 103°26.259' E |
| 7 | 01°20.169' N | 103°25.517' E |
| 8 | 01°20.040' N | 103°25.320' E |
| 9 | 01°19.175' N | 103°32.482' E |
| 10 | 01°21.758' N | 103°32.206' E |
| 11 | 01°23.966' N | 103°32.146' E |
| 12 | 01°26.492' N | 103°29.655' E |
| 13 | 01°27.457' N | 103°33.188' E |
| 14 | 01°22.604' N | 103°38.342' E |
| 15 | 01°23.208' N | 103°38.743' E |
| 16 | 01°20.636' N | 103°34.372' E |
| 17 | 01°16.260' N | 103°30.960' E |
| 18 | 01°15.608' N | 103°30.531' E |
| 19 | 01°17.040' N | 103°28.734' E |
| 20 | 01°16.980' N | 103°30.600' E |

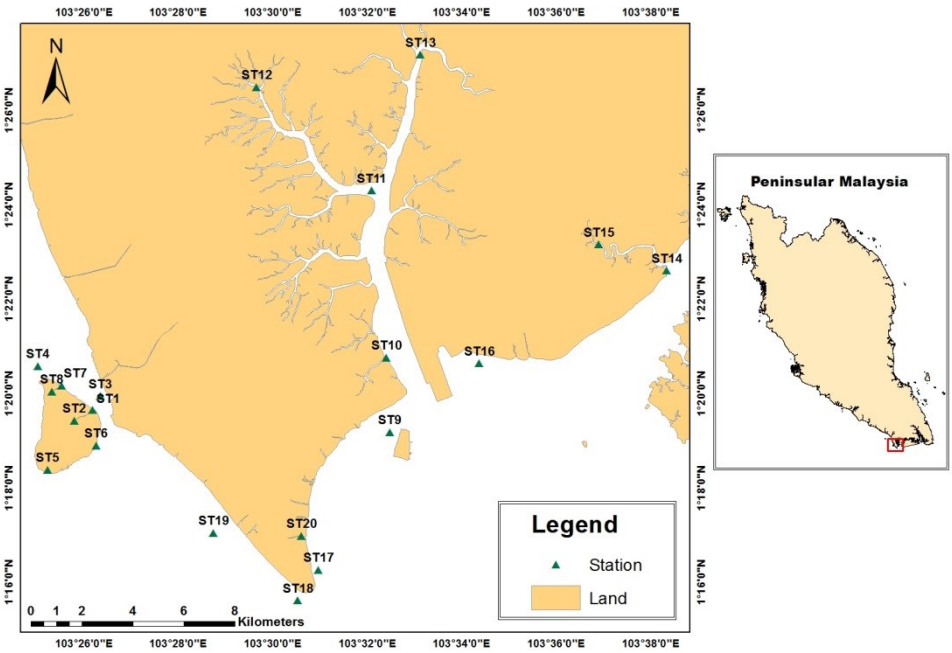



Figure 1. Location of sampling stations in the study area

**Analytical techniques**

Approximately 5g of sediment samples were used in determining particle size. Homogenized samples were treated with 10ml calgon solution overnight and injected into the particle size analyzer MALVERN Mastersizer 2000. All data collected were subjected to statistical analysis using moment statistical method. The relative proportion of sand, silt and clay were determined using the textural triangle proposed by USDA [11]. The major oxide elements in sediment were analyzed by using scanning electron microscope-energy dispersive spectrometer (SEM-EDS). The samples were placed on the stub using double sided tape and coated with gold by Auto Fine Coater JFC 1600. The selected major oxide elements ($SiO_2$, $Al_2O_3$, $Na_2O$, MgO, CaO, $K_2O$, MnO, ZnO) were observed by using SEM model 6360 LA JOEL. Sediment samples for clay mineral analysis were dried in the oven (< 50 °C) and powdered using pestle mortar. The type of clay minerals present in the samples was analyzed using X-ray Diffractometer (XRD). The sample was placed on a glass slide and scanned for certain degrees using radiation of Cu-Kα equipped with automatic divergent tilt. The Joint Committee on Powder Diffraction Standards (JCPDS) was used as a reference. Peaks produced from X-Ray Diffractogram enabled the determination of d-spacing which associated with the types of mineral.

## Results and Discussion

Table 2 shows the percentage of sand, silt, clay and the textural class of sediments in the study area. The distribution patterns of sand, silt and clay are shown in Figure 2, 3 and 4, respectively. Most of the sediments in the study area can be classified as cohesive sediments where the size of sediments is less than 125 μm in diameter and large surface area in relation to its mass. The high percentage of clay particles with the value > 50% was recorded at ST1, ST2, ST3, ST4, ST7, ST11, ST13 and ST17. The high percentage of sand with the value > 50% was found at ST6, ST10, ST12, ST15, ST16 and ST18. Only ST5 registered silt content more than 50%.

Table 2. Percentage of sand, silt and clay and textural classes of sediments in the study area

| Station | Sand (%) | Silt (%) | Clay (%) | Textural class |
|---|---|---|---|---|
| 1 | 22.73 | 10.69 | 66.56 | Clay |
| 2 | 27.83 | 8.16 | 63.98 | Clay |
| 3 | 34.92 | 7.91 | 57.83 | Clay |
| 4 | 37.98 | 6.50 | 55.52 | Clay |
| 5 | 36.14 | 55.86 | 8.01 | Silt loam |
| 6 | 54.09 | 6.91 | 39.02 | Sandy clay |
| 7 | 32.07 | 7.90 | 60 | Clay |
| 8 | 49.4 | 6.53 | 44.08 | Sandy clay |
| 9 | 42.14 | 7.42 | 48.98 | Sandy clay |
| 10 | 73.88 | 24.50 | 23.66 | Sandy clay loam |
| 11 | 21.81 | 15.40 | 62.8 | Clay |
| 12 | 61.1 | 4.15 | 37.74 | Sandy clay loam |
| 13 | 21.09 | 15.83 | 63.09 | Clay |
| 14 | 44.26 | 6.91 | 48.86 | Clay |
| 15 | 51.02 | 5.89 | 43.1 | Sandy clay |
| 16 | 63.47 | 7.87 | 28.67 | Sandy clay loam |
| 17 | 36.9 | 8.01 | 55.1 | Clay |
| 18 | 79.86 | 4.24 | 15.9 | Sandy Loam |
| 19 | 48.52 | 5.94 | 45.55 | Sandy clay |
| 20 | 37.22 | 8.63 | 54.18 | Clay |

The relative proportion of textural classes of sediment was based on the percentage of sand, silt and clay (Table 2). Generally, the southwestern coastal area of Johor is dominated with clay (ST1, ST2, ST3, ST4, ST7, ST11, ST13, ST14, ST17 and ST20), sandy clay (ST6, ST8, ST9, ST15 and ST19), sandy clay loam (ST10, ST12 and ST16), sandy loam (ST18) and silt loam (ST5). Coarse sediment is dominant in two areas namely Tanjung Pelepas Port (ST10 and ST16), and the coastal area between south Pulau Kukup (ST 5) and Tanjung Piai National Park (ST18). The prevalence of coarse sediment in Tanjung Pelepas Port might be due to the wave action created by shipping activities and the deepening process of the port through dredging activities. Both processes will destabilize the composition of sediment in the port area and it will be much easier for them to be transported out in any condition involving increasing water forces. Meanwhile, finer sediment tends to accumulate in the upstream of Sungai Pulai (ST11 and ST13), northern part of Pulau Kukup (ST1, ST3 and ST7) and in front of Tanjung Piai town (ST19 and ST20). We assume that the accumulation of finer sediment had occurred due to the low energy environment. This will offer a suitable condition for the deposition of fine-grain sediment in those three areas compared to Tanjung Pelapas Port and the coastal area between south Pulau Kukup and Tanjung Piai National Park. Consequently, it is hypothesized that the different distribution pattern of sand, silt, clay and textural classes of sediment are relatively due to the different forces of water energy in this environment.

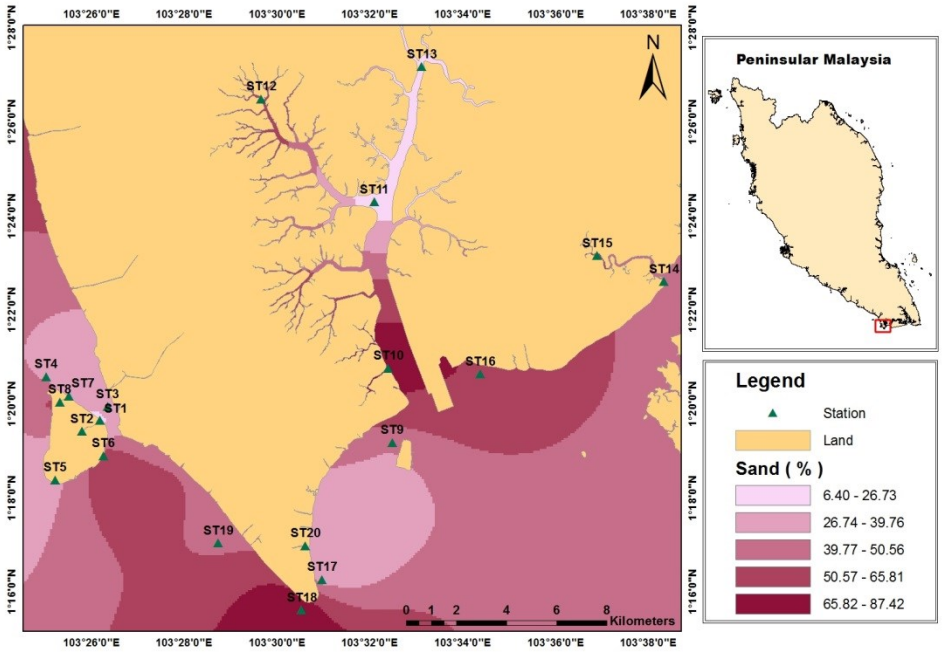



Figure 2. Distribution patterns of sand in the study area

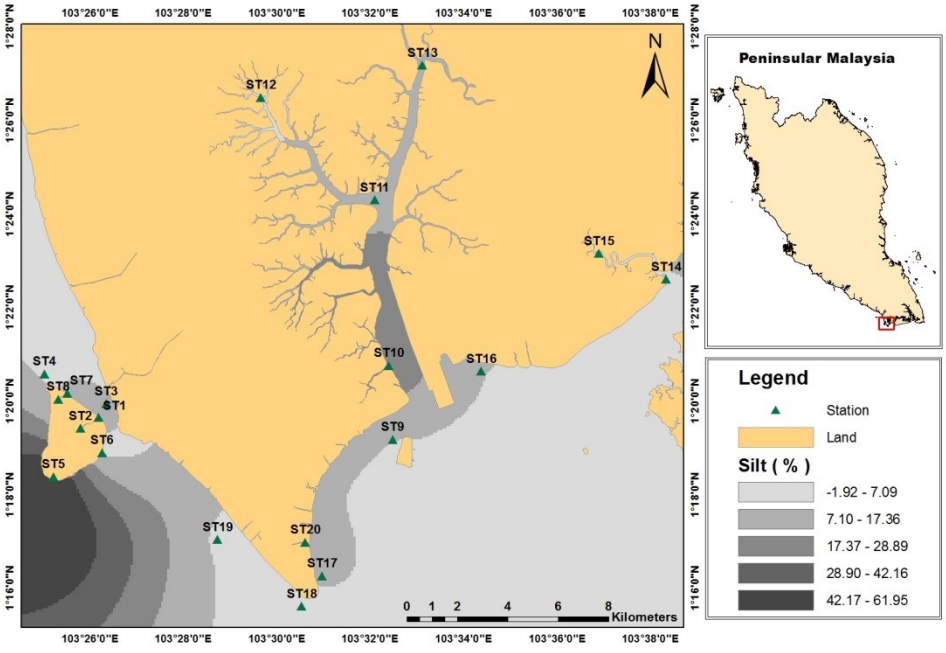



Figure 3. Distribution patterns of silt in the study area

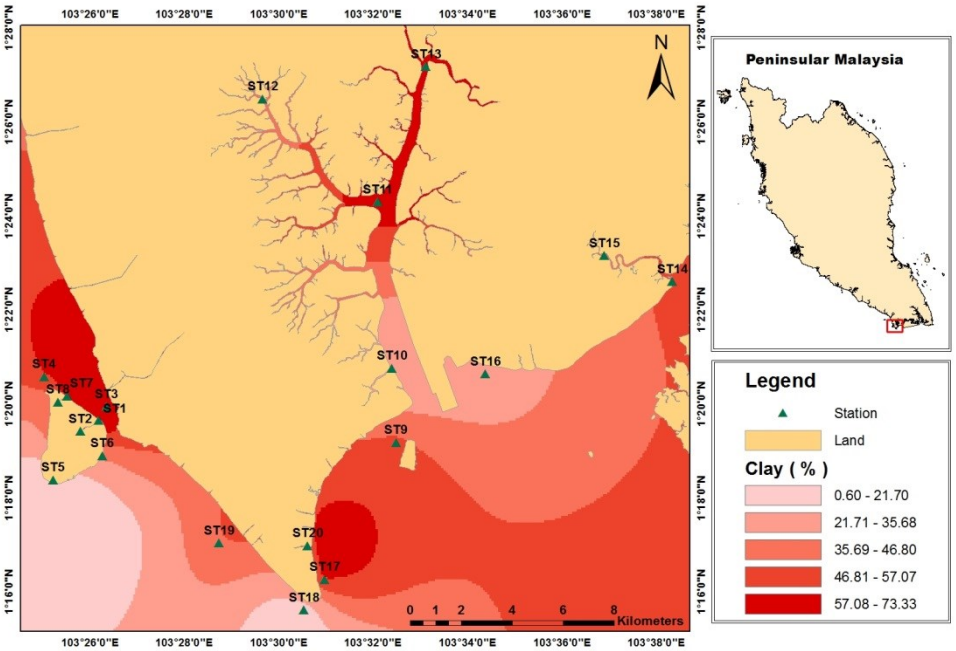



Figure 4. Distribution patterns of % clay in the study area

**Element oxides**

Table 3 shows the percentage of element oxides in the study area. The dominant element oxides found in the study area are $SiO_2$ (59.62%) followed by $Al_2O_3$ (12.49%). The rest of the element oxides such as $K_2O$, $ClO_2$, $MgO_2$, $MnO_2$ and $ZnO_2$ are present in trace amounts. The dominance of $SiO_2$ indicates that the area is highly siliceous [12]. The higher percentages of $SiO_2$ are found at ST6 (75.43%) and ST5 (72.47%), which show that these stations are most siliceous compared to the other of stations. The dominance of quartz might be due to the weathering product of granite, which is the dominant rock discovered in southern Peninsular Malaysia [13]. It is assumed that the quartz becomes the most resistant mineral in the coastal area of Southwestern Johor due to high temperatures and annual rainfall of tropical climatic conditions thus leading to the presence of high $SiO_2$ content.

The second most abundant element oxide is $Al_2O_3$ (corundrum) formed from igneous rock. The high content of this element at ST12 might be due to high-energy of water in upstream that erodes, transports and deposits sediments into the mangrove area. Wayne et al. [14] suggest that $Al_2O_3$ in certain environments are strongly influenced by aeolian input driven by wind activity and higher energy transport. The formation of corundum also occurs during hydrothermal alteration of volcanic and ultramafic rocks, under regional metamorphism of alumina-rich clays and bauxites, and in alkaline magmas that are alumina-supersaturated and silica-undersaturated [15].

The other oxide elements present in surface sediments of the study area were $K_2O$ (2.19%), $ClO_2$ (2.12%), $Na_2O$ (2.11%) and MgO (1.90%). $K_2O$ is a major element oxide present in trace amounts in the study area. This might be due to the sediment deposits originating from the dissolution of K-feldspar and mica [16]. Manganese oxide is a minor component of sediment with a value below 0.5% of dry weight and exists in the sediment as carbonate phase and oxi-hydroxide phase. The average content of MnO in the study area was 0.96 %. This value is about one-fold lower than $K_2O$, $ClO_2$, $Na_2O$ and MgO.

Table 3. Percentage of element oxides in sediments of the study area

| Station | $SiO_2$ | $Al_2O_3$ | $K_2O$ | $ClO_2$ | $Na_2O$ | MgO | MnO | ZnO |
|---|---|---|---|---|---|---|---|---|
| 1 | 55.16 | 8.64 | 1.67 | 2.64 | 1.15 | 1.2 | 0.9 | 1.43 |
| 2 | 56.26 | 9.63 | 1.62 | 2.7 | 5.2 | 1.02 | 0.84 | 0.6 |
| 3 | 57.18 | 8.91 | 3.14 | 1.65 | 1.25 | 1.14 | 1.23 | 0.37 |
| 4 | 59.27 | 9.23 | 3.22 | 2.07 | 1.64 | 1.26 | 0.64 | 0.54 |
| 5 | 72.47 | 8.71 | 2.51 | 2.72 | 7.31 | 1.43 | 0.4 | 1.07 |
| 6 | 75.43 | 19.51 | 1.74 | 1.67 | 4.12 | 2.46 | 0.87 | 0.51 |
| 7 | 59.22 | 9.31 | 1.84 | 1.86 | 4.32 | 2.44 | 0.98 | 0.42 |
| 8 | 60.43 | 20.45 | 1.67 | 1.48 | 1.7 | 2.51 | 1.15 | 0.79 |
| 9 | 55.82 | 9.01 | 1.79 | 1.94 | 1.4 | 2.34 | 1.43 | 0.61 |
| 10 | 61.24 | 9.94 | 1.83 | 1.87 | 1.89 | 1.35 | 0.86 | 0.55 |
| 11 | 55.47 | 18.6 | 2.65 | 3.02 | 2.03 | 1.48 | 0.84 | 0.58 |
| 12 | 58.87 | 24.86 | 2.74 | 2.69 | 1.46 | 1.64 | 0.89 | 0.57 |
| 13 | 57.24 | 22.63 | 3.1 | 2.51 | 0.83 | 2.12 | 0.82 | 0.59 |
| 14 | 53.14 | 16.71 | 1.49 | 2.64 | 1.45 | 2.21 | 0.74 | 0.5 |
| 15 | 60.4 | 16.04 | 1.69 | 1.95 | 0.69 | 2.46 | 1.19 | 1.13 |
| 16 | 62.04 | 8.73 | 2.47 | 1.92 | 1.79 | 2.01 | 0.79 | 0.50 |
| 17 | 57.3 | 8.31 | 2.91 | 1.11 | 0.61 | 2.35 | 1.29 | 1.35 |
| 18 | 57.84 | 5.04 | 2.46 | 2.38 | 1.64 | 2.45 | 1.83 | 0.99 |
| 19 | 60.15 | 10.3 | 1.57 | 2.26 | 1.43 | 2.37 | 0.63 | 0.82 |
| 20 | 53.72 | 8.33 | 1.86 | 1.43 | 1.65 | 2.11 | 0.76 | 0.46 |
| Average | 59.62 | 12.49 | 2.19 | 2.12 | 2.11 | 1.90 | 0.96 | 0.70 |
| SD (±) | 5.48 | 5.68 | 0.58 | 0.51 | 1.70 | 0.53 | 0.32 | 0.32 |

The lowest abundant element oxide in this environment is ZnO. However, the content of this element oxide is relatively higher compared to the earth's crustal values. The concentration of ZnO (~ 0.7%) registered a hundred times higher value than the average natural zinc in the earth's crust (70 ppm). In the manufacturing industry, ZnO is widely used as an additive in numerous materials and products including rubbers, plastics, ceramics, glass, cement and lubricants [17]. Thus, it is plausible that the anthropogenic input might be mixed with the natural zinc-origin products, causing an enrichment of ZnO in this environment.

SEM imagery and major element peaks clearly show the differences in grain particle shapes and element contents between downstream (Figure 5a) and upstream (Figure 5b) areas. Downstream sediments are characterized with sorted and more rounded angularity grain, higher content of silicon and aluminum. On the other hand, the upstream sediment recorded was poorly sorted and angular type of grain. There is a possibility that high-energy water especially during monsoon season sorted and smoothed the edges of grain particle in the transportation process of sediment from upstream to downstream.

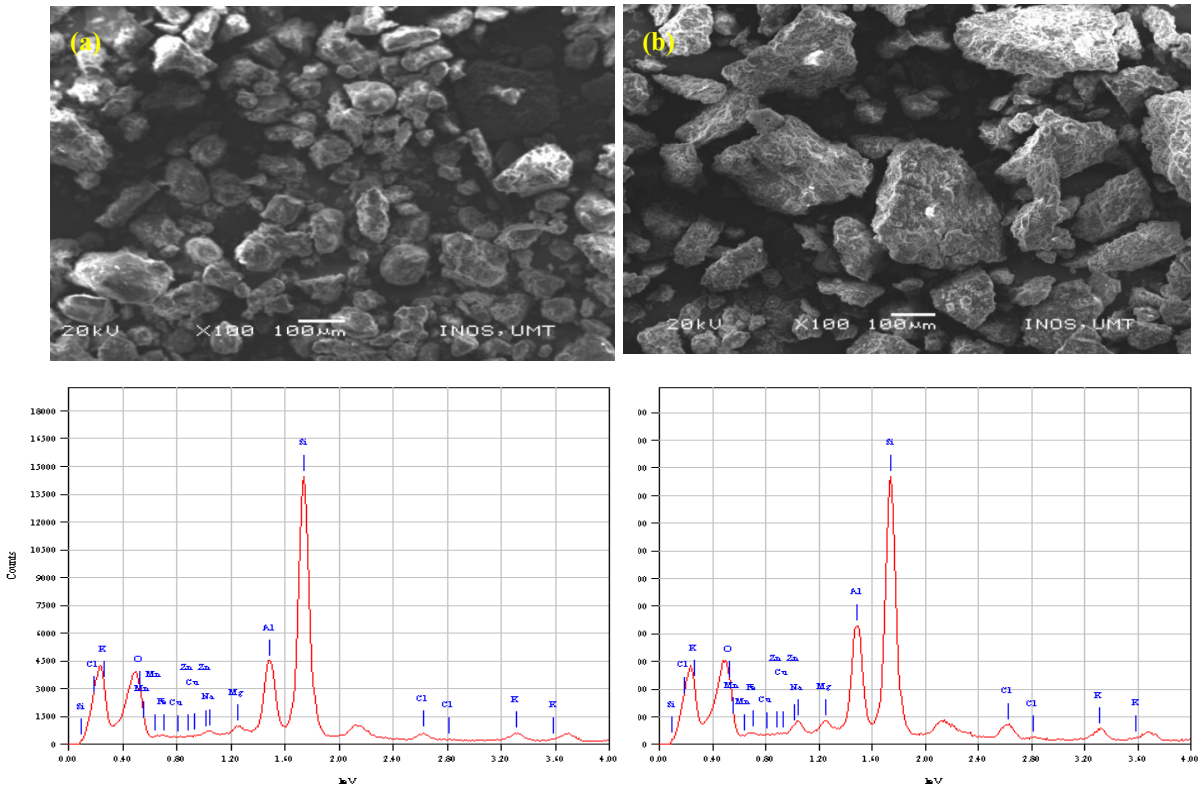



Figure 5. An example of SEM-EDS imagery and major element peaks of (a) downstream and (b) upstream area

**Clay minerals**

Table 4 shows the clay minerals present in the study area. Quartz (Figure 6a) is the dominant mineral found in most of the stations (ST1, ST2, ST3, ST8, ST10, ST11, ST12, ST14, ST15, ST19 and ST20) and frequent at ST4, ST6, ST7, ST13, ST16, and ST17, while few at ST5, ST9 and ST18. The second most abundant clay mineral is kaolinite (Figure 6b) which is dominant at ST1 and ST13. Kaolinite is present at station ST3 and ST6, in moderate amounts whereas exists in small amounts at other remaining station. Hurst [18] proposed that the distribution of kaolinite is often associated with the exfoliation and change in content of mica minerals in sediments. This might be due to the influence of weathering. Pehlivanoglou et al. [4] suggested that low distribution of kaolinite was due to unfavorable climatic conditions as well as physicochemical factors including sediment origin, rapid transportation and deposition process at the sampling station. Presence of kaolinite as a dominant clay mineral indicated maturity of the sediments and the weathering stage. The predominance of kaolinite indicated humid periods that lead to intensive leaching and chemical weathering [19].

The third abundant mineral in the surface sediment is muscovite (Figure 6c). This clay mineral is present at ST10 and ST11 in moderate amount, while ST1, ST8, ST12 and ST13 show the presence of muscovite in small amounts. High content of muscovite can be found at Sungai Pulai (ST10 and ST11), respectively. According to Rothwell [20], muscovite was the second most stable primary mineral after quartz. Muscovite is usually found in coarse-grained igneous rock and intermediate metamorphic rock [21]. The existence of this clay mineral in the sediments indicated that the sediments are still young [22].

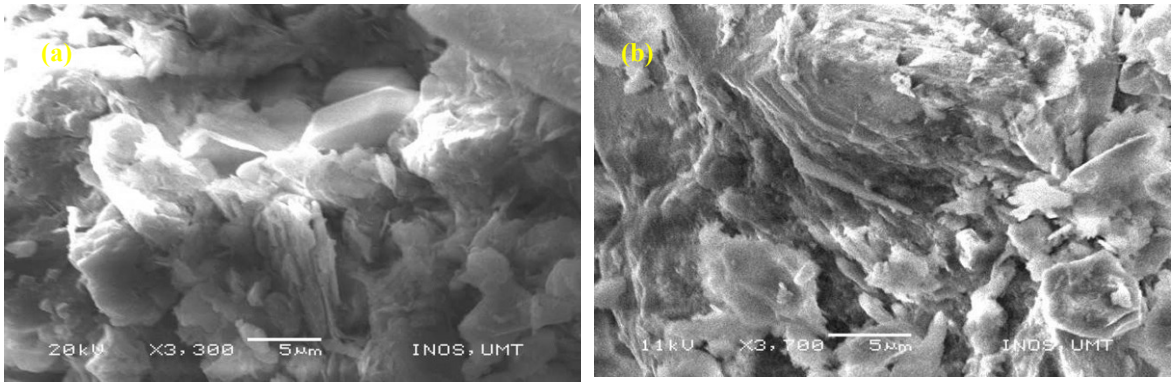
Only four stations had shown the presence of illite with ST13 showing moderate amounts while ST8, ST15 and ST20 show small amounts of illite. On the other hand, ST15 is the only station showing moderate content of smectite in the study area. The presence of smectite in small amounts at ST1, ST2 and ST13 might be influenced by

the accumulation and intensity of weathering products. El-Attar et al. [23] found that smectite exists on the surface layer of sediment by the mixing of aeolian inputs from the plateau.

Table 4. The presence of clay minerals in sediments of the study area

| Station | Clay Minerals | | | | | |
|---|---|---|---|---|---|---|
| | Quartz | Calcite | Smectite | Illite | Kaolinite | Muscovite |
| 1 | +++ | + | + | - | +++ | + |
| 2 | +++ | - | + | - | + | - |
| 3 | +++ | - | - | - | ++ | - |
| 4 | ++ | - | - | - | + | - |
| 5 | + | - | - | - | + | - |
| 6 | ++ | - | - | - | ++ | - |
| 7 | ++ | - | - | - | + | - |
| 8 | +++ | - | - | + | + | + |
| 9 | + | - | - | - | + | - |
| 10 | +++ | - | - | - | ++ | ++ |
| 11 | +++ | - | - | - | + | ++ |
| 12 | +++ | - | - | - | + | + |
| 13 | ++ | + | + | ++ | +++ | + |
| 14 | +++ | + | - | - | + | - |
| 15 | +++ | - | ++ | + | + | - |
| 16 | ++ | - | - | - | + | - |
| 17 | ++ | - | - | - | + | - |
| 18 | + | - | - | - | + | - |
| 19 | +++ | - | - | - | + | - |
| 20 | +++ | - | - | + | + | - |

+++ Mineral present in large amount (dominant)
++ Mineral present in moderate amount (frequent)
+ Mineral present in small amount (few)
- Mineral not present



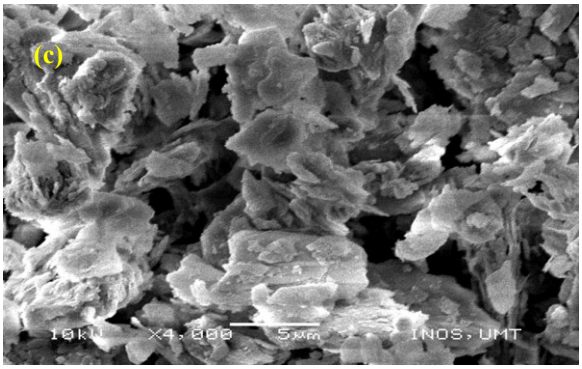



Figure 6. Morphological features of clay minerals found in the study area (a) quartz (b) kaolinite and (c) muscovite

## Conclusion

The mean concentrations of studied element oxides in decreasing order is as follows $SiO_2 > Al_2O_3 > K_2O \geq ClO_2 \geq Na_2O > MgO > MnO > ZnO$. The presence of quartz as the dominant mineral in this tropical environment is consistent with $SiO_2$ as the most abundant major element oxide. The abundance of kaolinite compared to other clay minerals indicated the advance-weathering stage and reflection of granite as the major rock type in the area. The higher level of ZnO as compared to the earth's crustal value is associated with the combination of anthropogenic input, and natural geological and geochemical processes. The change in grain surface morphology and sorting from the upstream to the downstream show the intensity of sediment transport processes.

## Acknowledgement

This research was funded by the Ministry of Science, Technology and Innovation through e-science grants no 04-01-12-SF0113. The authors wish to express their gratitude to the staff of Oceanography Laboratory, School of Marine and Environmental Science and Institute of Oceanography and Environment (INOS) for their assistance and hospitality throughout the sampling and analytical period.

## References

1. Association of Southeast Asian National United States Coastal Resources Management Project (ASEAN/US CRMP). (1991). The coastal environmental profile of South Johore, Malaysia. ICLARM Technical Report 24: 1 – 65.
2. Abdullah, N. A., Shazili, N. A. M., Yaacob, R. and Kamaruzzaman, Y. (2014). Grain size and metallic trace element contents in sediments of Kemaman Coast, Terengganu, Malaysia, South China Sea. *Journal of Earth Science and Engineering*, 4: 80 – 87.
3. Kamaruzzaman, Y., Mohd Yusuf, N., Shazili N. A. M. and Saad, S. (2011). Heavy metal concentration in the surface sediment of Tanjung Lumpur mangrove forest, Kuantan, Malaysia. *Sains Malaysiana*, 40(2): 89 – 92.
4. Pehlivanoglou, K., Trontsios, G. and Tsirambides, A. (2004). Grain size distribution, clay mineralogy and chemistry of bottom sediments from the outer Thermaikos Gulf, Aegean Sea, Greece. *Mediterranean Marine Science*, 5 (1): 43 – 53.
5. Zhou, D., Yuan-Bo, L. and Cheng-Kui, Z. (1994). Oceanology of China Seas. Springer-Science and Business Media, Dorrecht.
6. Yusoff, A. H., Zulkifli, S. Z., Ismail, A. and Mohamed, C. A. R. (2015). Vertical trend of trace metals deposition in sediment core off Tanjung Pelepas Harbour, Malaysia. *Procedia Environmental Sciences*, 30: 211 – 216.
7. Zulkifli, S. Z., Mohamat-Yusuff, F., Ismail, A., Aziz, A. Sabuti, A. A. and Mohamed, C. A. R. (2015). Status of heavy metals in surface sediments of the western part of the Johor Straits using a sediment quality guideline. *World Journal of Fish and Marine Sciences*, 7 (3): 214 – 220.

8. Guan, W. S., Ghaffar, M. A., Ali, M. M. and Cob, Z. C. (2014). The Polychaeta (Annelida) communities of the Merambong and Tanjung Adang Shoals, Malaysia, and its relationship with the environmental variables. *Malayan Nature Journal*, 66: 168 – 183.
9. Sabri, S., Said, M. I. M., Azman, S., Muda, K., Kassim, M. A. M. and Salmiati (2012). Copper in water, sediment and *Strombus Canarium* at South Western Coast of Peninsular Malaysia. *International Journal of Environmental Science and Development*, 3(3): 217 – 219.
10. Azlan, N. I. and Othman, R. (2009). Monitoring of mangrove area using remote sensing toward shoreline protection. *GIS Ostrava*, 1: 25 – 28.
11. US Department of Agriculture (USDA). (1987). Agricultural resources: Cropland, water and conservation situation and outlook report. AR-Econ. Res. Serv. Washington, D.C.: pp. 439.
12. Abdullah, N. A., Yaakob, R., Ahmad, S., Chung, M. K. and So, A. N. (2007). Major elements and oxides of the South China Sea surface sediments off Johor Coasts. *Journal of Sustainability Science and Management*, 2(1): 79 – 85.
13. Abad, S. N. A. K. S., Mohamad, E. T. and Komoo, I. (2014). Dominant weathering profiles of granite in Southern Peninsular Malaysia**.** *Engineering Geology*, 183: 208 – 215.
14. Wayne, D. R, Fesha, I. G., Shaw, J. N., Wood, C. W., Feng, Y., Norfleet, M. L. and Van Santen. E. (2002). Land use effects on soil quality parameters for identical soil taxa. *In* Van Santen, E. (ed.) *Southern Conservation Tillage Conference for Sustainable Agriculture,* Auburn, Alabama. 24-26 June 2002. Alabama Agricultural Experiment Station and Auburn University: pp. 233 – 238.
15. Wenk, H-R. and Bulakh, A. (2004). Minerals their constitution and origin. Cambridge University Press. pp. 635.
16. Eberl, D. D. (1993). Three zones for illite formation during burial diagenesis and metamorphism. *Clays & Clay Minerals*, 41: 26 – 37.
17. Battez, H. A., Gonzalez, R., Viesca, J., Fernandez, J., Diazfernandez, J., MacHado, A., Chou, R. and Riba, J. (2008). CuO, $ZrO_2$ and ZnO nanoparticles as antiwear additive in oil lubricants. *Wear*, 265 (3–4): 422 – 428.
18. Hurst, A. (1999). Textural and geochemical micro-analysis in the interpretation of clay mineral characteristics: Lessons from sandstone hydrocarbon reservoirs. *Clay Minerals*, 34(1):137 – 149.
19. Singer, A. (1984). The paleoclimatic interpretation of clay minerals in sediments - A review. *Earth-Science Review*, 21: 251 – 293.
20. Rothwell, R. G. (1989). Minerals and mineraloids in marine sediments: An optical guide. Elsevier Applied Science, London: pp. 279.
21. Fanning D.S., Keramidas, V.Z and El-Desoky, M.A. (1989). In: Minerals in soil environments, 2nd Edition: pp. 551 – 634.
22. Tribble, J. S. and Wilkens, R. H. (1999). Mineralogy and microfabric of sediment from the Western Mediterranean *Sea*. *Proceedings of the Ocean Drilling Program, Scientific Results*, 161: 99 – 110.
23. El-Attar, H. A., Jackson, M. L. and Volk, V.V. (1972). Fluorine loss from silicates on ignition. *American Mineralogist*, 57: 246 – 452.

*Malaysian Journal of Analytical Sciences, Vol 21 No 2 (2017): 323 - 333*
*DOI: https://doi.org/10.17576/mjas-2017-2102-07*

MALAYSIAN JOURNAL OF ANALYTICAL SCIENCES
*Published by The Malaysian Analytical Sciences Society*
ISSN 1394 - 2506

# THE SYNTHESIS OF ZINC OXIDE/CARBON SPHERES NANOCOMPOSITES AND FIELD ELECTRON EMISSION PROPERTIES

## (Sintesis Nanokomposit Zink Oksida/Sfera Karbon dan Sifat Pemancaran Elektron Medan)

Suriani Abu Bakar[1,2]*, Suhufa Alfarisa[1,2,3], Azmi Mohamed[1,4], Norhayati Hashim[1,4]

[1]*Nanotechnology Research Centre, Faculty of Science and Mathematics*
[2]*Department of Physics, Faculty of Science and Mathematics*
*Universiti Pendidikan Sultan Idris, 35900 Tanjung Malim, Perak, Malaysia*
[3]*Department of Physics, Faculty of Mathematics and Natural Science,*
*Universitas PGRI Palembang, Jl. Jend Ahmad Yani 9/10 Ulu, Palembang 30251, South Sumatera, Indonesia*
[4]*Department of Chemistry, Faculty of Science and Mathematics,*
*Universiti Pendidikan Sultan Idris, 35900 Tanjung Malim, Perak, Malaysia*

**Corresponding author: absuriani@yahoo.com*

Received: 19 November 2016; Accepted: 6 March 2017

**Abstract**

Zinc oxide (ZnO)/carbon spheres (CS) nanocomposites were successfully synthesised using waste engine oil as precursor for the CS production. ZnO nanorods were grown using sol-gel immersion method with MgZnO as the seeded catalyst and thermal chemical vapour deposition was used to synthesise CS. Different configurations of ZnO/CS structures were prepared i.e. CS-coated ZnO and ZnO-coated CS. The structures of composite samples were analysed using field emission scanning electron microscopy (FESEM), Energy-Dispersive X-ray (EDX), micro-Raman and X-ray Diffraction Spectroscopy (XRD). FESEM observations revealed the structural changes of pristine ZnO and CS in composite structures. The as-present of ZnO or CS was believed to affect the subsequent growth of another structure. Field electron emission (FEE) properties of both nanocomposites were also investigated. It was found that ZnO-coated CS sample has better FEE properties with lower turn-on (3.48 $V\mu m^{-1}$) and threshold field (6.35 $V\mu m^{-1}$) obtained at current density of 0.1 and 1 $\mu Acm^{-2}$, respectively. This study highlighted that nanocomposites of ZnO and CS have successfully enhanced the field emission performances of materials compared with pristine ZnO or CS due to the structural changes of material emitter.

**Keywords:** zinc oxide, carbon spheres, waste engine oil, field electron emission

**Abstrak**

Nanokomposit zink oksida (ZnO)/sfera karbon (SK) telah berjaya disintesis menggunakan minyak enjin terpakai sebagai pelopor untuk penghasilan SK. Nanorod ZnO telah ditumbuhkan menggunakan kaedah rendaman sol-gel dengan MgZnO sebagai pemangkin berbenih dan pemendapan wap kimia terma telah digunakan untuk mensintesis SK. Konfigurasi yang berlainan bagi struktur ZnO/SK telah disediakan iaitu SK bersalut ZnO dan ZnO bersalut SK. Struktur sampel komposit dianalisis menggunakan *Mikroskop* Imbasan *Elektron* Pancaran *Medan* (FESEM), penyerakan tenaga sinar-X (EDX), spektroskopi mikro-Raman dan pembelauan sinar-X (XRD). Pemerhatian FESEM menunjukkan perubahan struktur ZnO dan CS tulen dalam struktur komposit. ZnO atau CS sedia ada dipercayai memberi kesan kepada pertumbuhan seterusnya struktur lain. Sifat pemancaran elektron medan (PEM) bagi kedua-dua nanokomposit juga turut dikaji. Kajian mendapati bahawa sampel ZnO bersalut SK mempunyai ciri-ciri PEM yang lebih baik dengan nilai medan permulaan (3.48 $V\mu m^{-1}$) dan ambang (6.35 $V\mu m^{-1}$) yang lebih rendah diperolehi pada ketumpatan arus 0.1 dan 1 $\mu Acm^{-2}$. Kajian ini menekankan nanokomposit ZnO dan SK telah berjaya meningkatkan prestasi pemancaran medan bahan berbanding dengan ZnO atau CS tulen disebabkan oleh perubahan struktur bahan pemancar.

**Kata kunci:** zink oksida, sfera karbon, minyak enjin terpakai, pemancaran elektron medan

## Introduction

Field emission is a quantum process of electron emission from a material where the electrons in Fermi level tunnel the energy barrier to vacuum level under high applied electric field [1]. Emission characteristics of a material are based on the Fowler-Nordheim (F-N) theory as followed in Eq. 1 [2]:

$$J = \frac{A(\beta E)^2}{\varphi} exp\left(\frac{B\varphi^{3/2}}{\beta E}\right) \quad (1)$$

The current emission density (J) at applied electric field (E) can be calculated from the above equation. A and B are constants of 1.54 x $10^{-6}$ $AV^{-2}eV$ and 6.83 x $10^{9}$ $eV^{-3/2}Vm^{-1}$, respectively. Field enhancement factor of emitter (β) is an important FEE characteristic and can be calculated from the slope of ln ($J/E^2$) vs 1/E curve using the equation $\beta = -B\varphi^{3/2}/slope$. A typical benchmark that have been reported in the literature for FEE characterization comparison are the turn-on and threshold field, maximum current obtained (before the destruction of the emitter) as well as emission stability. Turn-on field for FEE is the field required to emit current density which is greater than the electrical noise-floor [3]. There is no agreement on the value of current density to be specified and the definition of turn-on and threshold field, it is determined by the group research themselves. For example, Ghosh et al. [4, 5] and Srivastava et al. [6] defined turn-on and threshold field to be the field required by the film to produce current density of 10 $\mu Acm^{-2}$ and 1 $mAcm^{-2}$ respectively. While Bonard and co-worker [90] specified the current density of 10 $\mu Acm^{-2}$ and 10 $mAcm^{-2}$ respectively. Since there is no specific definition of both turn-on and threshold field and as current density does not increase linearly with applied field, the result cannot be accurately compared. The comparisons between the results were only a rough estimation to claim that theirs is better than others. In this study, they are defined as the current density at applied field of 0.1 and 1 $\mu Acm^{-2}$, respectively for turn-on and threshold field.

To increase the FEE performance of the materials, it can be composited to further enhance the electron emission performance of those nanocomposites. Take carbon material such as carbon nanotubes (CNTs) as example, in view of its potential application as good electron emitters, however it can be easily degraded and damaged by the following factors [7-10], therefore the improvement of the FEE can be achieved by fabricating CNTs and zinc-oxide (ZnO) as nanocomposites [11-13]. The order of the configuration of CNTs/ZnO composites is the crucial component that lead to the enhancement of field emission ability, where it frequently occurs that the materials fabricated at the top is more likely to help the FEE performances. ZnO/CNTs nanocomposites structure have been reported to improve the FEE performance of material [1, 11-14]. In our recently published work [11], the investigation was done on the composite configuration to enhance the FEE performance by using two different configurations of ZnO/vertically aligned CNTs (VACNTs) where the order of the nanocomposites plays an important role in improving the FEE properties of pristine VACNTs.

The work revealed that the VACNTs-coated ZnO nanocomposites configuration showed a lower turn-on and threshold field at only 0.49 and 1.41 $V\mu m^{-1}$ as compared to the ZnO-coated VACNTs of 1.60 (turn-on) and 2.03 (threshold field) $V\mu m^{-1}$ respectively. The presence of different ZnO nanostructures including nanorods, nanoflowers and nanorods-nanoflakes for ZnO-coated CNTs configuration were seen to play significant role towards enhancing FEE performances [13]. Among the ZnO nanostructured used the growth of CNTs on ZnO nanoflower demonstrated the highest FEE performance of 0.8 $V\mu m^{-1}$ at 1 $uAcm^{-2}$ of turn-on field. ZnO is a semiconducting material with wide direct band gap (3.37 eV), large binding energy of 60 meV and and work function of 5.3 eV [1]. It has been applied in many electronic devices due to its unique and versatile properties [15-17]. ZnO nanostructures also showed promising application in field emission devices due to its high mechanical strength, chemical stability and good optical properties [18, 19]. On the other hand, carbon materials are well known as a conducting material which is good for electron emission application. One type of carbon materials namely carbon spheres (CS) has been reported to have a comparable field emission properties as compared to other materials [20].

Here we presented the composite structures of ZnO/CS and their FEE properties. To the best of our knowledge, this is the first report on the FEE of the CS synthesised from waste engine oil (WEO) with two different configurations of nanocomposite; CS-coated aligned ZnO nanorod and ZnO nanorod-coated CS sample. Recently, we reported the use of WEO for the production of another carbon material namely CNTs [21] and amorphous Al-Cu alloy nanowires decorated with CS [22]. The use of waste [23-27] and natural precursors [28-36] to produce carbon materials may not only be beneficial for nanotechnology research field but also preserve the environmental sustainability at the same time. The CS were synthesised using thermal chemical vapour deposition (TCVD) method while the ZnO were synthesised using the sol-gel method. The structural and field emission properties of ZnO/CS nanocomposites samples were then systematically investigated.

## Materials and Methods

The production of ZnO/CS was performed in two different synthesis processes which were (i) the synthesis of ZnO nanorods using sol-gel immersion process and (ii) the synthesis of CS via thermal chemical vapour deposition (TCVD) method. Two different configurations were prepared as illustrated in Figure 1. For the CS-coated ZnO sample, ZnO nanorods were initially grown followed by the synthesis of CS and vice versa for the ZnO-coated CS sample.

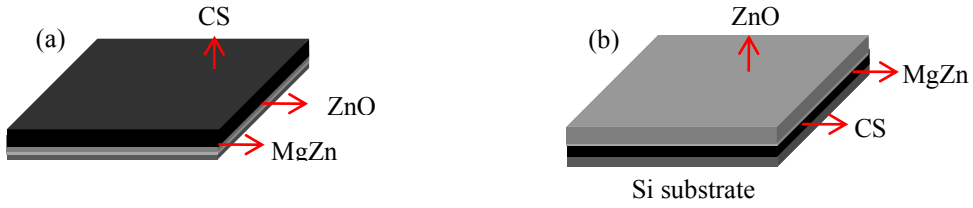



Figure 1. Different configurations of composite materials (a) CS-coated ZnO and (b) ZnO-coated CS

The synthesis procedures of CS from WEO precursor was similar to previous report [21, 22]. However, different synthesis parameters were used. An amount 3 ml of WEO mixed with 5.33 wt% ferrocene catalyst was heated at 450 °C in precursor zone and deposited onto Si substrate in 800 °C synthesis furnace. The synthesis process was carried out for 30 min under Ar gas flow at the rate of 0.25 $Lmin^{-1}$. Meanwhile, the synthesis of ZnO nanorods was adopted from [37]. MgZnO was initially deposited as the seeded catalyst. Collected samples were characterized using field emission scanning electron microscopy (FESEM-Hitachi SU8020), energy-dispersive X-ray (EDX), micro-Raman spectroscopy (Horiba Jobin Yvon-DU420A-OE-325) and X-ray diffraction (XRD) instrument (Bruker AXS D9). Field emission properties of the samples were measured using FEE equipment (Hewlett-Packard 34401A multimeter) at emission area of 0.1 $cm^2$ and distance between two electrodes was 100 µm.

## Results and Discussion

Figure 2(a) – (f) present the FESEM images of the prepared ZnO nanorods, CS and their nanocomposites with different configurations. It was observed in Figure 2 (a) that the ZnO nanorods were vertically aligned with length up to 1.6 µm. Wide diameter distribution of the rods in the range of 42.8 – 285.7 nm were measured. This was due to the non-unifom MgZnO particles size as the template for the ZnO nanorods growth. The growth of ZnO nanorods was also believed occurred on the collection of agglomerated MgZnO particles. High density of CS was obtained with diameter of the spheres were ranged from 0.17 to 2.57 µm as seen in Figure 2(b). The morphology of CS was modified after grown on ZnO nanorods as seen in Figure 2(c) and (d). Most of the spheres were decorated with short tube-like particles and grains which seemed to grow covering the CS. This was believed due to the adsorption of ZnO particles on the surface of CS which further become the catalyst for the secondary growth of short tube-like carbon structure. Somehow, the perfectly round shape of CS was still observed with diameter range from 1.1 to 2.7 µm.

Figure 2(e) and (f) show the FESEM observation of ZnO-coated CS sample. High density and uniformly grown ZnO nanorods on CS were observed. Slightly different to the pristine aligned ZnO nanorods, flower-like ZnO

nanostructures consisted of many hexagonal rods were also produced on the top of ZnO nanorods. The diameter of the rods was observed to be between 31.3 to 187.5 nm, in the smaller range as compared to pristine ZnO. This indicated the important presence of CS as the nucleation site for the growth of ZnO nanostructures. MgZnO particles were believed to be well deposited with uniform size on the CS, thus produced a better growth of ZnO nanostructures. Only small amount of CS was still observed as seen in the inset of Figure 2(f). The perfect alignment of ZnO nanorods cannot be observed due to the spherical shape of CS template. ZnO nanorods were initially grown on the uneven surface of MgZnO-coated CS template. Once the saturated condition was achieved, nucleation of aligned ZnO nanorods got slower. There was no more space for the growth of nanorods on the MgZnO-coated CS template, hence the ZnO particles started to nuclei on the top of the rods. Then, the aggregated ZnO particles formed the flower-like structure as can be observed in Figure 2(e)-(f).

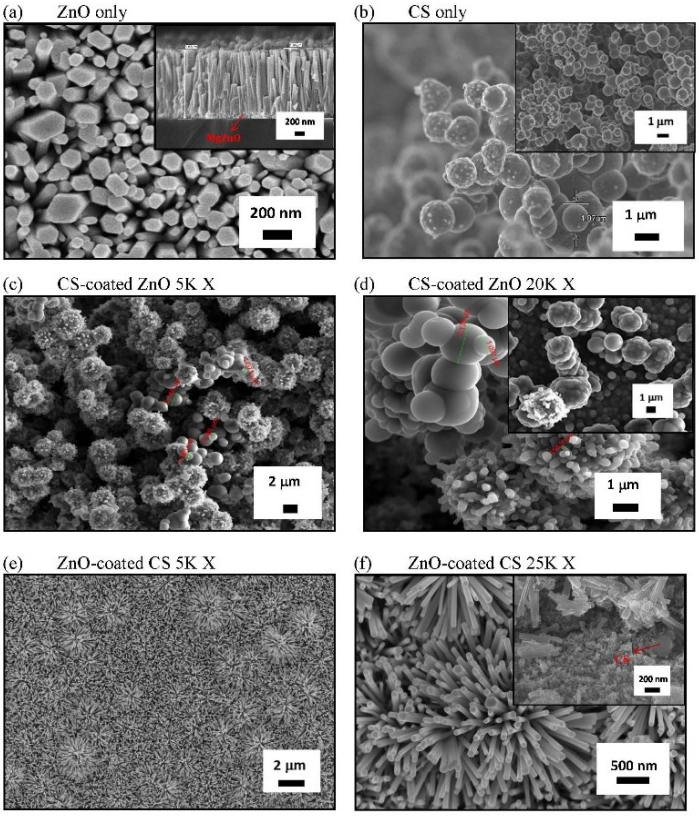



Figure 2. FESEM images of (a) ZnO nanorods, (b) CS, (c-d) CS-coated ZnO and (e-f) ZnO-coated CS nanocomposites

EDX analysis was performed to investigate the elemental compositions of the composite materials. Figure 3 show the EDX spectrum of both ZnO-coated CS and CS-coated ZnO samples. Carbon, oxygen, and Zn elements were detected from overall structure. The Si peaks was believed to come from the substrate used. The average atomic of zinc and oxygen was found to be 1:1 which indicated a good stoichiometric ratio of ZnO. Moreover, low amount of Mg element can be detected in this sample. The concentration of Zn atoms decreased in the CS-coated ZnO sample. This was in line with FESEM observation where during the synthesis of CS at high temperature of 800°C, the ZnO nanorods were fully etched and turned to be ZnO flakes structure. In the meantime, Zn and oxygen atoms were also suspected to be adsorbed on the surface of CS.

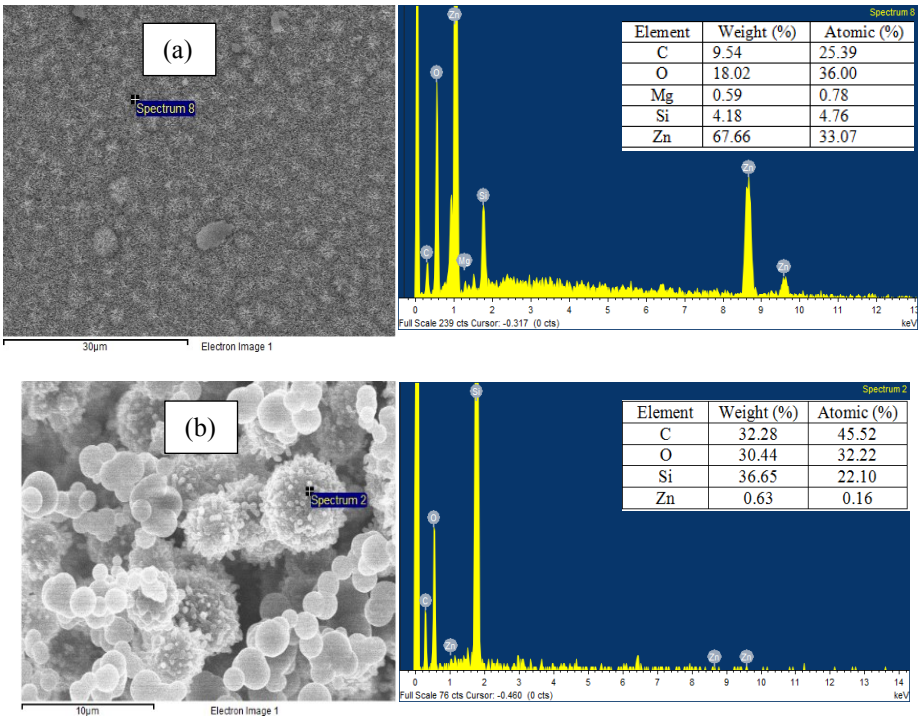



Figure 3. EDX analysis showing elemental compositions of ZnO/CS nanocomposites (a) ZnO-coated CS and (b) CS-coated ZnO

Micro-Raman spectra of the as-prepared samples are presented in Figure 4. The micro-Raman spectrum of pristine CS shows the *D* (disorder) and *G* (graphitic) band at 1357.70 and 1598.2 $cm^{-1}$, respectively with the intensity ratio of *D* and *G* band ($I_D/I_G$) ratio was found to be 0.79. Micro-Raman spectrum of ZnO nanorods only shows one typical ZnO characteristics at 438.18 $cm^{-1}$ attributed to the $E_2$ (high) modes. It also confirmed wurtzite hexagonal phase of ZnO nanorods. Peak at 303.76 $cm^{-1}$ was derived from the use of Si as the substrate. Micro-Raman spectra of ZnO/CS nanocomposites present both characteristic peaks of materials. ZnO-coated CS remained show the wurtzite hexagonal phase of ZnO characteristic at 438.18 $cm^{-1}$ which presented by a clear $E_2$ (high) mode.

Only CS characteristics can be observed from the Raman spectrum of CS-coated ZnO sample. However, micro-Raman spectrum at lower shift range Figure 4(b) showed a sharp low intense peak at 444.13 $cm^{-1}$ which corresponded to Raman active mode of wurtzite ZnO structure ($E_2$ high). This mode was shifted to a higher number. It might due to the increase of the stress or defect in the ZnO crystal [38]. Moreover, $I_D/I_G$ ratio of the CS increased to be 0.91 (ZnO-coated CS) and 0.88 (CS-coated ZnO) after being composited with ZnO. These indicated the lower crystallinity of CS in both composite structures as compared to the pristine CS. The reasonable explanation to these occurrences was due to the changes of CS structure after being combined with ZnO. In case of ZnO-coated CS sample, annealing process of MgZnO thin layer and ZnO nanorods alter the structure of CS where it introduced more defect of C–C bonding in the spheres. The highest ratio of 0.91 was obtained from this structure. In addition, for the growth of CS on ZnO nanostructures, defect-induced from the bonding of carbon from CS and oxygen from the ZnO nanostructures was responsible to the higher defect of CS [13].

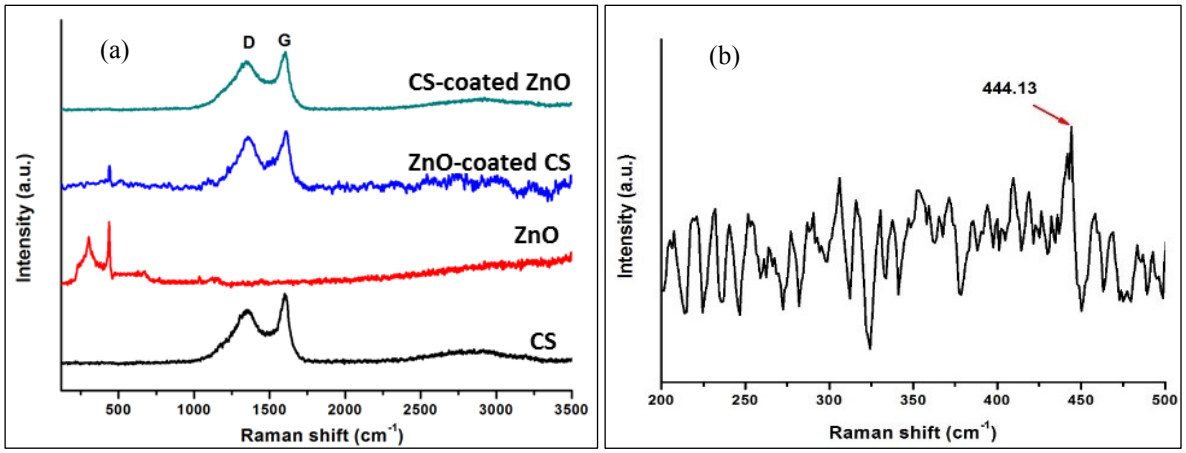



Figure 4. (a) Micro-Raman spectra of ZnO/CS nanostructures and (b) Raman profile at lower wavenumber of CS-coated ZnO structure shows the shift of $E_2$ high mode due to the compressive stress

Typical XRD patterns of ZnO/CS nanostructures are presented in Figure 5. Both samples show the characteristic peaks of ZnO and carbon. Similar to the pristine ZnO nanorods, the most intense peak was observed at ~34° along the (002) orientation [19]. ZnO-coated CS sample presents a broad and low intense peak at 43.40° which attributed to carbon phase from CS. Another ZnO peak was shown by a low intense peak at 47.49° along the (102) orientation. Diffraction peaks of ZnO in CS-coated ZnO sample are located at 2θ of 34.49, 36.15, 47.60 and 56.20° which are in good agreement with the standard of hexagonal ZnO crystal (PDF-01-080-0075). Meanwhile, carbon phase at 44.67 and 52.3° are well matched with the standard of cubic carbon crystal (PDF-01-080-0017) with the lattice parameter of 3.539 Å.

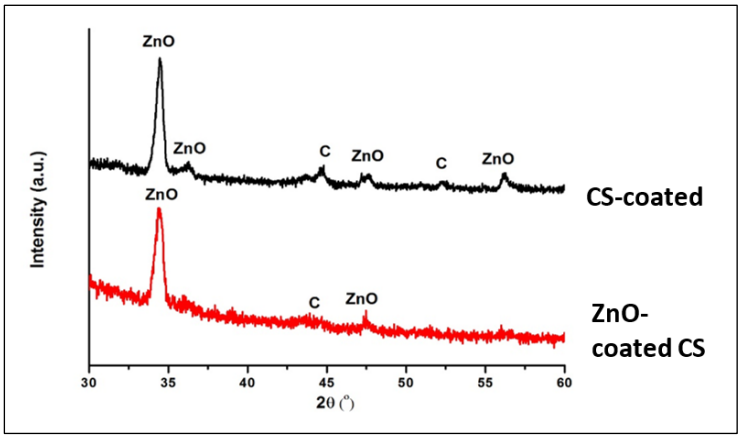



Figure 5. XRD patterns of CS/ZnO nanostructures composites

Figures 6 and 7 present the J-E and F-N plot of different ZnO and ZnO/CS nanocomposites materials. The measurements were taken at fixed electrodes separation of 100 µm and applied voltage was increased from 0 to 1000 V. Table 1 presents the summary of FEE characteristics of the as-prepared samples. Several repeated measurements have been conducted on the CS sample, but the current emission was still not observed. Due to its spherical structure, CS are less suitable to be applied as electron emitter. ZnO nanorods possessed moderate turn on

and threshold fields at 5.65 and 7.34 V/µm, respectively with maximum current density of 3.46 µA/cm$^2$. Composite structures of ZnO/CS successfully enhanced the FEE properties. Turn on and threshold values of CS-coated ZnO sample were founded to be at 6.83 and 7.88 V/µm and maximum current density of 2.51 µA/cm$^2$. Modification of CS structure with the presence of short tube-like carbon structure which covered the CS was believed promoted a better emission site as compared to pristine CS. Interestingly, ZnO-coated CS structure where the ZnO nanostructures were grown on CS as the template exhibited an obvious decrement in the turn on value to be as low as 3.48 V/µm and the threshold field was also decreased to be 6.35 V/µm. This structure presented a better FEE performance compared with the pristine ZnO nanorods as well as CS-coated ZnO composite structure. In addition, highest $\beta$ value up to 5485 and maximum current density of 3.78 µA/cm$^2$ were obtained. Higher conductivity of CS compared to ZnO nanorods promoted a better electron transfer from the CS through ZnO nanorods structures to the vacuum level at high applied voltage. Moreover, the high aspect ratio of ZnO nanostructures with a good crystallinity and uniform rods diameter were also responsible for the high $\beta$ value of ZnO-coated CS composite material [6].

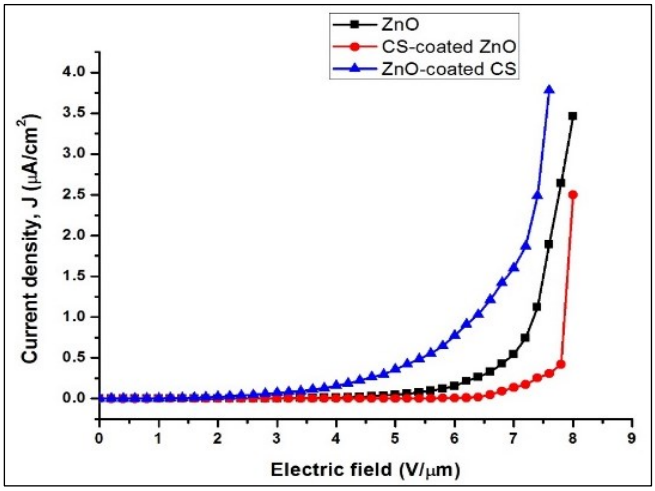



Figure 6. The J-E curves of the ZnO and ZnO/CS nanocomposites materials

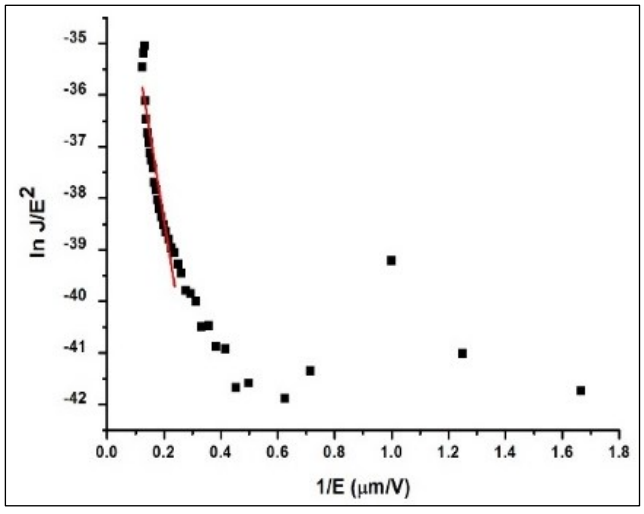



Figure 7. F-N plots of ZnO and ZnO/CS nanocomposites materials (a) ZnO, (b) CS-coated ZnO and (c) ZnO-coated CS

Table 1. FEE characteristics of CS, ZnO nanorods and their composite materials

| Sample | Turn on Field at 0.1 µA (V/µm) | Threshold Field at 1 µA (V/µm) | *J* Max (µA/cm$^2$) | $\beta$ |
|---|---|---|---|---|
| ZnO | 5.65 | 7.34 | 3.46 | 2452 |
| ZnO-coated CS | 3.48 | 6.35 | 3.78 | 5879 |
| CS-coated ZnO | 6.83 | 7.88 | 2.51 | 755 |

To study the emission current stability, a constant electric field was applied to the ZnO nanorods and ZnO/CS nanocomposites materials for one hour duration time. The current vs time graphs for both samples are presented in Figure 8 and the detail of their current emission fluctuation order is given in Table 2. The current emission of ZnO nanorods was moderately stable since frequent fluctuations to a high current value were observed. This was due to the wide diameter range of ZnO nanorods. Smaller diameter rods proportional with the length and rods spacing is preferable for a better FEE performance. Although ZnO nanorods current emission was less stable, the emission of ZnO nanorods was found to be higher in the order of $10^{-6}$ A than the CNTs which was in the order of $10^{-7}$ A [11]. ZnO nanomaterials have negative electron affinity [18] which can support the current emission due to their ability to emit electrons to the vacuum with little energy loss.

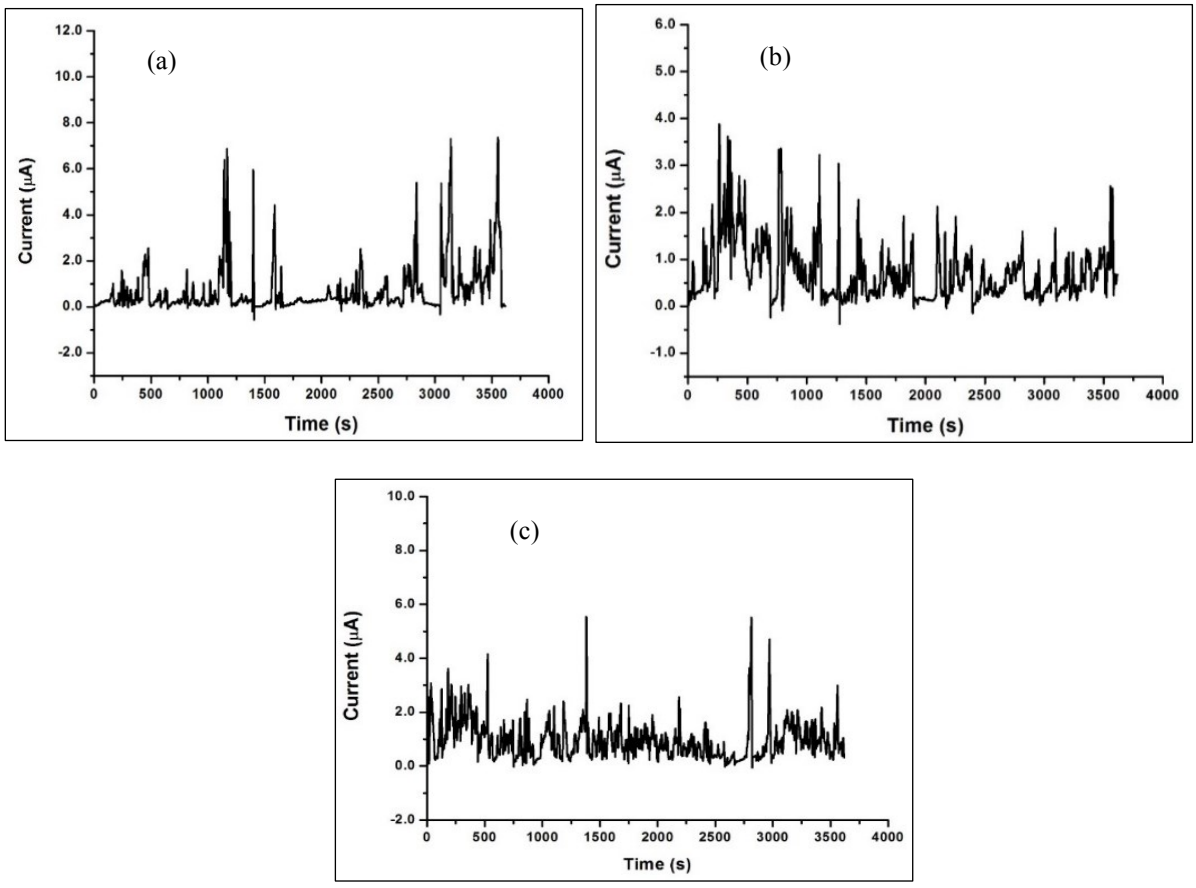



Figure 8. Current stability measurement of (a) ZnO and (b)-(c) ZnO/CS nanostructures composites

Table 2. Current emission fluctuation order of carbon material, ZnO nanorods and their composite structures

| Sample | Current Fluctuation Order (Ampere) |
|---|---|
| ZnO | $10^{-8} – 10^{-6}$ |
| ZnO-coated CS | $10^{-9} – 10^{-6}$ |
| CS-coated ZnO | $10^{-7} – 10^{-6}$ |

The growth of ZnO nanorods on CS sample gave better emission stability as compared to pristine ZnO and CS-coated ZnO samples. This was believed due to the presence of as-grown CS and high uniformity with smaller ZnO nanorods, flower-like ZnO nanostructures size which is more favourable for electron emission application. High conductivity of carbon materials promoted better electrons transfer and led to the enhancement of field emission. Moreover, the carbon materials acted as the additional catalyst which improved the uniformity and crystal quality of ZnO nanostructures.

## Conclusion

ZnO/CS nanocomposites were successfully synthesised using the combination of sol-gel immersion and TCVD method. Waste material precursor namely WEO was used to produce CS in this study. The structure of ZnO and CS were modified after being composited. In case of CS-coated ZnO, the structural change of CS was believed due to the adsorption of ZnO particles on the surface of CS. Meanwhile, the as-presence of CS in ZnO-coated CS sample has promoted a better growth ZnO nanostructure. This structure also presented the best FEE performances with the lowest turn on (3.48 V/μm) and threshold field (6.35 V/μm) as well as highest maximum current density (3.78 $\mu A/cm^2$) and field enhancement factor up to 5879 with better emission current stability. The presence of conductive carbon material which is CS promoted the well electron transfer from the CS through the ZnO nanostructures to vacuum level at high electric field. A better structure of ZnO nanorods with uniform diameter size was also responsible to the better FEE properties of this nanocomposites structure. It can be concluded that the ZnO-coated CS nanocomposites has great future applications in field emission devices such as flat panel displays and flat lamps.

## Acknowledgement

The authors are thankful to Fundamental Research Grant Scheme (Grant code: 2015-0154-102-02) and UPSI for financial and technical supports of this work.

## References

1. Patra, R., Ghosh, S., Sharma, H. and Vankar V. D. (2013). High stability field emission from zinc oxide coated multiwalled carbon nanotube films. *Advanced Materials Letters*, 4 (11): 849 – 855.
2. Fowler, R. H. and Nordheim, L. (1928). Electron emission in intense electric fields. *Proceedings of the Royal Society of London. Series A*, 119 (781): 173 – 18.
3. Leong, J. G. S. (2008). Controlled growth of uniform diameter multiwall carbon nanotube arrays via chemical vapor deposition for application in field emission devices. Master Thesis Northeastern University, Boston, Massachusetts, USA.
4. Ghosh, P., Subramanian, M., Afre, R. A., Zamri, M., Soga, T., Jimbo, T., Filip, V. and Tanemura, M. (2009). Growth of Y-junction bamboo-shaped CNx Nanotubes on GaAs substrate using single feedstock. *Applied Surface Science,* 255(8): 4611 – 4615.
5. Ghosh, P., Zamri, M., Subramanian, M., Soga, T., Jimbo, T., Katoh, R. and Tanemura, M. (2008). Bamboo-shaped aligned CNx nanotubes synthesized using single feedstock at different temperature and study of their field electron emission. *Journal of Physics D: Applied Physics*, 41 (15): 155405 – 155412.
6. Srivastava, S. K., Vankar, V. D., Sridhar Rao, D. V. and Kumar, V. (2006). Enhanced field emission characteristics of nitrogen-doped carbon nanotube films grown by microwave plasma enhanced chemical vapor deposition process. *Thin Solid Films,* 515: 1851 – 1856.

7. Hu, H., Zhang, D., Liu, Y., Yu, W. and Guo, T. (2015). Highly enhanced field emission from CuO nanowire arrays by coating of carbon nanotube network films. *Vacuum*, 115: 70 – 74.
8. Yan, X., Tay, B. K. and Miele, P. (2008). Field emission from ordered carbon nanotube-ZnO heterojunction arrays. *Carbon*, 46: 753 – 758.
9. Cai, D. and Liu, L. (2013). The screening effects of carbon nanotube arrays and its field emission optimum density. *AIP Advances*, 3 (12): 122103.
10. Heo, Y. W., Tien, L. C., Kwon, Y., Norton, D. P., Pearton, S. J., Kang, B. S. and Ren, F. (2004). Depletion-mode ZnO nanowire field-effect transistor. *Applied Physics Letters*, 85 (12): 2274 – 2276.
11. Suriani, A. B., Dalila, A. R., Mohamed, A., Mamat, M. H., Malek, M. F., Soga, T. and Tanemura, M. (2016). Fabrication of vertically aligned carbon nanotubes–zinc oxide nanocomposites and their field electron emission enhancement. *Materials Design*, 90: 185 – 195.
12. Suriani, A. B., Safitri, R. N., Mohamed, A., Alfarisa, S., Isa, I. M., Kamari, A., Hashim, N., Ahmad, M. K., Malek, M. F. and Rusop M. (2015). Enhanced field electron emission of flower-like zinc oxide on zinc oxide nanorods grown on carbon nanotubes. *Materials Letters*, 149: 66 – 69.
13. Suriani, A. B., Safitri, R. N., Mohamed, A., Alfarisa, S., Malek, M. F., Mamat, M. H. and Ahmad M. K. (2016). Synthesis and field electron emission properties of waste cooking palm oil-based carbon nanotubes coated on different zinc oxide nanostructures. *Journal of Alloys and Compounds*, 656: 368 –377.
14. Dutta, M. and Basak, D. (2019). Multiwalled carbon nanotubes/ZnO nanowires composite structure with enhanced ultraviolet emission and faster ultraviolet response. *Chemical Physics Letters*, 480(4-6): 253 –257.
15. Flickyngerová, S., Tvarožek, V. and Gašpierik, P. (2010). Zinc oxide - A unique material for advanced photovoltaic solar cells. *Journal of Electrical Engineering*, 61(5): 291 – 295.
16. Nohavica, D. and Gladkov. P. (2010). ZnO nanoparticles and their applications-new achievements. *Proceedings of the 2nd International Conference on Nanotechnology*, 10: 12 – 14.
17. Vaseem, M., Umar, A. and Hahn, Y. B. (2010). ZnO nanoparticles: Growth, properties, and applications. *American Scientific Publishers*, New York: pp. 1 – 36.
18. Jin, H., Li, Y., Li, J. and Gu, C. (2009). Field emission from ZnO nanostructures with different morphologies. *Microelectronic Engineering,* 86 (4): 1159 – 1161.
19. Mamat, M. H., Khusaimi, Z., Zahidi, M. M., Suriani, A. B., Siran, Y. M., Rejab, S. A. M., Asis, A. J., Tahiruddin, S., Abdullah, S. and Rusop M. (2011). Controllable growth of vertically aligned aluminum-doped zinc oxide nanorod arrays by sonicated sol–gel immersion method depending on precursor solution. *Japanese Journal of Applied Physics,* 50: 1 – 6.
20. Banerjee, D., Sen, D. and Chattopadhyay, K. K. (2013). Simple chemical synthesis of porous carbon spheres and its improved field emission by water vapor adsorption. *Microporous and Mesoporous Materials*, 171: 201 – 207.
21. Suriani, A. B., Alfarisa, S., Mohamed, A., Isa, I. M., Kamari. A., Hashim, N., Mamat, M. H., Mohamed, A. R. and M. Rusop, M. (2015). Quasi-aligned carbon nanotubes synthesised from waste engine oil. *Materials Letters*, 139: 220 – 223.
22. Suriani, A. B., Alfarisa, S., Mohamed, A., Kamari. A., Hashim, N., Isa, I. M., Mamat, M. H., Malek, M. F. and Ahmad, M. K. (2015). Amorphous Al–Cu alloy nanowires decorated with carbon spheres synthesised from waste engine oil. *Journal of Alloys and Compounds*, 642: 111 – 116.
23. Suriani, A. B., Nor, R. M. and Rusop, M. (2010). Vertically aligned carbon nanotubes synthesized from waste cooking palm oil. *Journal Ceramic Society Japan*, 118: 963 – 968.
24. Suriani, A. B., Dalila, A. R., Mohamed, A., Mamat, M. H., Salina, M., Rosmi M. S., Rosly, J., Nor, R. M. and Rusop, M. (2013), Vertically aligned carbon nanotubes synthesized from waste chicken fat. *Materials Letters*, 101: 61 – 64.
25. Suriani, A. B., Dalila, A. R., Mohamed, A., Isa, I. M., Kamari, A., Hashim, N., Soga, T. and Tanemura, M. (2015). Synthesis of carbon nanofibres from waste chicken fat for field electron emission applications. *Materials Research Bulletin*, 70: 524 – 529.
26. Suriani, A. B., Norhafizah, J., Mohammed, A., Mamat, M. H., Malek, M. F. and Ahmad, M. K. (2016). Scaled-up prototype of carbon nanotube production system utilizing waste cooking palm oil precursor and its nanocomposite application as supercapacitor electrodes. *Journal of Materials Science: Materials in Electronics*, 27(11): 11599 – 11605.

27. Suriani, A. B., Dalila, A. R., Mohamed, A., Soga, T. and Tanemura, M. (2015). Synthesis, structural, and field electron emission properties of quasi-aligned carbon nanotubes from gutter oil. *Materials Chemistry and Physics*, 165: 1 – 7.
28. Azmina, M. S., Suriani, A. B., Falina, A. N., Salina, M. and Rusop, M. (2012). Temperature effects on the production of carbon nanotubes from palm oil by thermal chemical vapor deposition method. *Advanced Materials Research*, 364: 359 – 362.
29. Azmina, M. S., Suriani, A. B., Falina, A. N., Salina, M., Rosly, J. and Rusop, M. (2012). Preparation of palm oil based carbon nanotubes at various ferrocene concentration. *Advanced Materials Research*, 364: 408 – 441.
30. Shamsudin, M. S., Suriani, A. B., Abdullah, S., Yahya, S. Y. S. and Rusop, M. (2013). Impact of thermal annealing under nitrogen ambient on structural, micro-raman, and thermogravimetric analyses of camphoric-CNT. *Journal of Spectroscopy*, 2013: 1 – 7.
31. Azmina, M. S., Suriani, A. B., Salina, M., Azira, A. A., Dalila, A. R., Asli, N. A., Rosly, J., Nor, R. M. and Rusop, M. (2012). Variety of bio-hydrocarbon precursors for the synthesis of carbon nanotubes. *Nano Hybrids*, 2: 43 – 63.
32. Zobir, S. A. M., Bakar, S. A., Abdullah, S., Zainal, Z., Sarijo, S. H. and Rusop, M. (2012). Raman spectroscopic study of carbon nanotubes prepared using Fe/ZnO-palm olein-chemical vapour deposition. *Journal of Nanomaterials*, 2012: 1 – 6.
33. Asli, N. A., Shamsudin, M. S., Suriani, A. B., Rusop, M. and Abdullah, S. (2013). Effect of the ratio of catalyst to carbon source on the growth of vertically aligned carbon nanotubes on nanostructured porous silicon templates. *International Journal of Industrial Chemistry*, 4(23): 1 – 7.
34. Asli, N. A., Shamsudin, M. S., Falina, A. N., Azmina, M. S., Suriani, A. B., Rusop, M. and Abdullah, S. (2013). Field electron emission properties of vertically aligned carbon nanotubes deposited on a nanostructured porous silicon template: the hidden role of the hydrocarbon/catalyst ratio. *Microelectronic Engineering*, 108: 86 – 92.
35. Suriani, A. B., Azira, A. A., Nik, S. F., Nor R. M. and Rusop, M. (2009). Synthesis of vertically aligned carbon nanotubes using natural palm oil as carbon precursor. *Materials Letters*, 63(30): 2704 – 2706.
36. Shamsudin, M. S., Achoi, M. F., Asiah, M. N., Ismail, L. N., Suriani, A. B., Abdullah, S., Yahya, S. Y. S. and Rusop, M. (2012). Synthesis and nucleation-growth mechanism of almost catalyst-free carbon nanotubes grown from Fe-filled sphere-like graphene-shell surface. *Journal of Nanostructure in Chemistry*, 3(13): 1 – 12.
37. Salina, M., Ahmad, R., Suriani, A. B. and Rusop, M. (2012). Bandgap alteration of transparent zinc oxide thin film with Mg dopant. *Transactions on Electrical and Electronic Materials*, 13(2): 64 – 68.
38. Wu, X., Wei, Z., Zhang, L., Wang, X., Yang, H. and Jiang, J. (2014). Optical and magnetic properties of Fe doped ZnO nanoparticles obtained by hydrothermal synthesis. *Journal of Nanomaterials*, 2014: 1 – 6.

*Malaysian Journal of Analytical Sciences, Vol 21 No 2 (2017): 334 - 345*
*DOI: https://doi.org/10.17576/mjas-2017-2102-08*

MALAYSIAN JOURNAL OF ANALYTICAL SCIENCES
*Published by The Malaysian Analytical Sciences Society*
ISSN 1394 - 2506

# ISOTHERMAL MODELLING BASED EXPERIMENTAL STUDY OF DISSOLVED HYDROGEN SULFIDE ADSORPTION FROM WASTE WATER USING EGGSHELL BASED ACTIVATED CARBON

## (Model Isoterma Berdasarkan Kajian Penjerapan Hidrogen Sulfida Terlarut daripada Air Sisa Menggunakan Karbon yang Diaktifkan Berasaskan Kulit Telur)

Omar Abed Habeeb[1], Ramesh Kanthasamy[1]*, Gomaa Abdelgawad Mohammed Ali[2,3], Rosli Mohd. Yunus[1]

[1]*Faculty of Chemical Engineering & Natural Resources Engineering*
[2]*Faculty of Industrial Sciences and Technology*
*Universiti Malaysia Pahang, Gambang, 26300 Kuantan, Pahang, Malaysia*
[3]*Chemistry Department, Faculty of Science,*
*Al–Azhar University, Assiut, 71524, Egypt*

**Corresponding author: ramesh@ump.edu.my*

Received: 8 June 2016; Accepted: 19 January 2017

**Abstract**

This paper reports on the experimental work using batch process conducted to determine the adsorption capacity of dissolved hydrogen sulfide in the synthetic wastewater onto the activated carbon which is derived from the eggshell. Fourier Transform Infrared Spectroscopy (FTIR), Energy-Dispersive X-ray Spectroscopy (EDX), Scanning Electron Microscopy (SEM), and particle size distribution have been used to characterize the prepared material. The raw materials of chicken eggshell are adopted to retrieve the carbon content which is then activated using KOH as the activation agent. The examined concentration of dissolved hydrogen sulfide is ranging from 100 to 500 ppm. The maximum adsorption capacity of the dissolved $H_2S$ onto the activated carbon is 289.3 mg/g and the equilibrium time is 6 hours. The examined pH value in this study is ranging from 4.5 to 5.5. The two well-known equilibrium adsorption isotherm models, i.e. the Langmuir and the Freundlich models, are employed. It is found that the adsorption isotherm capacity agrees very well to the Freundlich isotherm model. This paper attempts to show the difficulties of converting $CaCO_3$ to carbon due to the fact that the raw material contains higher calcium (Ca) content instead of carbon. It is concluded that the carbon derived from the chickens' eggshells is very beneficial for treatment of dissolved $H_2S$ in waste water.

**Keywords**: adsorption, hydrogen sulfide, chicken eggshells, activated carbon, isotherm

**Abstrak**

Kajian ini melaporkan mengenai kerja eksperimen menggunakan proses kelompok yang dijalankan untuk menentukan kapasiti penjerapan hidrogen sulfida terlarut dalam air sisa sintetik ke dalam karbon yang diaktifkan dihasilkan daripada kulit telur. Spektroskopi Inframerah Fourier (FTIR), Spektroskopi X-ray Tenaga Serakan (EDX), Mikroskop Imbasan Elektron (SEM), dan taburan saiz zarah telah digunakan untuk mencirikan bahan yang disediakan. Kulit telur ayam sebagai bahan mentah telah digunakan untuk mendapatkan semula kandungan karbon yang kemudiannya diaktifkan dengan menggunakan KOH sebagai agen pengaktifan. Julat kepekatan hidrogen sulfida yang diperiksa adalah di antara 100 hingga 500 ppm. Kapasiti penjerapan maksimum $H_2S$ terlarut ke dalam karbon diaktifkan adalah 289.3 mg/g dan masa keseimbangan selama 6 jam. Julat nilai pH yang diperiksa dalam kajian ini di antara 4.5 hingga 5.5. Kedua-dua model penjerapan isoterma keseimbangan terkenal seperti model Freundlich dan Langmuir telah dilaksanakan. Kapasiti penjerapan isoterma didapati selari dengan model isoterma Langmuir. Kajian ini cuba menunjukkan kesukaran untuk menukar $CaCO_3$ kepada karbon disebabkan oleh bahan mentah

mengandungi kandungan kalsium (Ca) yang tinggi dan bukannya karbon. Ini dapat disimpulkan bahawa karbon yang diperolehi daripada kulit telur ayam adalah sangat bermanfaat untuk rawatan $H_2S$ terlarut dalam air sisa.

**Kata Kunci**: penjerapan, hidrogen sulfida, kulit telur ayam, karbon diaktifkan, isoterma

## Introduction

Hydrogen sulfide ($H_2S$) is a very toxic, corrosive and flammable gas. It is a colorless gas, best known for its strong smell, much like the strong nauseating smell of rotten eggs. The $H_2S$ is volatile in water and soluble in some polar organic solvents [1]. It is also a reducing agent and oxidizes easily when the conditions are right and corrodes metals and even concrete. For example, $H_2S$ will oxidize gradually to elemental sulfur and over time oxidize to sulfuric acid and eventually damage the sewer [2]. Under specific conditions such as at a low concentration (1.36 mg/L) pH between 3 to 5 and immersion time of more than two hours, $H_2S$ has been found to have an inhibiting effect on iron corrosion [3, 4]. Moreover, $H_2S$ is also a harmful and putrid gaseous compound. It can create health problems, like coma, irritated eyes, and respiratory system irritation. Furthermore, the human nose can detect $H_2S$ at concentrations as low as 0.5 part-per-billion-volume (ppbv) [5]. Therefore, excess exposure to $H_2S$ can cause both chronic and acute ramifications [6]. Surprisingly, the allowable limit of $H_2S$ in drinking water is not specified by the World Health Organization (WHO) [7]. Most of the sulfide found in water may be expected to exist as molecular $H_2S$ at pH less than 4 [8]. Bisulfide and sulfide ions can be found when $H_2S$ is dissolved in water as per the following reaction:

$$H_2S_{(g)} \leftrightarrow H_2S_{(aq)} \quad (1)$$

$$H_2S_{(aq)} \leftrightarrow H^+ + HS^- \quad (2)$$

$$HS^- \leftrightarrow H^+ + S^{2-} \quad (3)$$

Reaction 2 (reverse direction) occurs at pH <4.5 [9] and reaction 3 (forward direction) happens at pH ≥ 9 [10]. In a natural environment, acid rain is precipitated through the oxidation of $H_2S$ to sulfuric acid. $H_2S$ dissolves easily in water (4-6 g/L) and it is poisonous to almost all types of life forms [11]. Owing to the above reasons, various agencies have been consistently developing solutions to remove $H_2S$. It could be removed in three different ways such as adsorption, oxidation, and scrubbing. Recently, there is a renewed interest in using adsorption process as an effective method to remove the pollutant e.g. $H_2S$ from wastewater. Adsorption is a physio-chemical technique, involving mass transfer between the liquid and the solid phase [12]. A considerable amount of literatures detailing on the removal of $H_2S$ have been published [13-15]. These studies have reported that the adsorption rate of $H_2S$ is affected by many factors such as surface area of adsorbent, pore size, moisture content, pH, and surface chemistry (oxygen containing functionalities). The experimental and simulation study detailing on $H_2S$ adsorption on impregnated activated carbon under an anaerobic condition has been carried out by Xiao et al. [13]. They have applied a sodium carbonate impregnated activated carbon as the adsorbent for low concentration $H_2S$ in nitrogen under the anaerobic condition in a fixed bed [13]. Moreover, sludge-derived $H_2S$ adsorbents have received considerable attentions from the galvanizing industry [14].

Other study has been conducted by Guo et al. [15], whereby they have studied activated carbons derived from oil-palm shell as an adsorption of $H_2S$ [15]. In addition, study on ferric and alum water treatment residuals has been conducted by Wang and Pei [16]. Possible materials to be used as adsorbents of $H_2S$ such as Fine Rubber Particle Media (FRPM) and crushed oyster shell have been tested by Wang [17] and Asaoka [18], respectively. Recently, the low-cost carbon-based materials such as agricultural wastes have been used as pollutant adsorbent such as rice husks [19], banana and orange peels [20], coconut shell [21], macadamia nut shells [22], fibers of oil palm empty fruit bunches [23], rice straw [24]. Several studies have documented that activated carbon has been widely used as an adsorbent for achieving high water purification. So far, very little attention has been paid to remove $H_2S$ from wastewater in liquid phase.

Therefore, this paper addresses on the use of eggshells as the source of activated carbon to adsorb dissolved $H_2S$ as liquid form out of wastewaters. It is important to note that eggshells are abundant and environmental friendly [25]. In this paper, our objective is to assess the effectiveness of activated carbon derived from eggshell waste as an adsorbent of dissolved $H_2S$ from waste water. Also, we aim to characterize this adsorbent and find the suitable isotherm adsorption model to be fitted with this adsorption process.

## Materials and Methods

### Preparation of activated carbon

In this study, the activated carbon derived from eggshells has been used as an adsorbent of $H_2S$ appeared in the petroleum refinery synthetic waste water. Firstly, the eggshells (around 100 pieces) were collected from restaurants around Kajang, Selangor, Malaysia. A sample of the eggshells was then carefully rinsed several times with deionized water and acidic solvent to remove impurities and pollutants. After that, the sample was gradually dried under 105 °C for eight hours. Then the dried eggshell was grinded into powder form. The powder (10 g) was placed in a furnace and gradually heated up to 700 °C [26], at constant heating rate of 10 °C/min with nitrogen ($N_2$) flow rate of 150 mL/min. Then the result product was soaked in concentrated solution of KOH for 24 hours. After that, it is filtered and dried under 105℃. Finally, the activation process is done in a horizontal tubular furnace at temperature of 750℃, which is subjected to constant heating rate of 10℃/min with $N_2$ flow rate of 150 mL/min. The prepared material was coded as ACES.

### Characterization of activated carbon

In this study, the pH value of the carbon surface was measured by taking a sample of 0.4 g of dry carbon powder added to 20 mL of water and the suspension was stirred overnight to reach equilibrium. Then, the pH value of the suspension was measured. Moreover, the surface morphology of the sample was examined using a Scanning Electron Microscope (SEM). Elemental analysis on the chemical composition of the sample was conducted using the energy-dispersive X-ray spectroscopy (EDX). The particle size distribution was also measured. The Fourier Transform Infrared Spectroscopy (FTIR) analysis has been used for the examination of functional groups on the surface of adsorbent.

### Hydrogen sulfide solution

In this study, the synthetic waste water was prepared according to the procedure reported by Asaoka et al. [18]. A portion of $Na_2S.9H_2O$ was dissolved in 500 mL solution of 0.01 M KCl purged with $N_2$ gas. Thereafter, the pH of the solution was adjusted to 4.5 – 5.5 using 0.2 M HCl [18]. The concentration of dissolved $H_2S$ in water is 4 – 6 g/L [11]. All forms of $H_2S$ are harmful to organisms, and they can exist in a solution in three forms, i.e. hydrogen sulfide ($H_2S$), bisulfide ($HS^-$) and sulfide ($S^{2-}$) [27].

### Batch equilibrium studies

The adsorption capacity of the ACES has been carefully studied by examining its ability in removing $H_2S$ from synthetic wastewater. The pollutant concentration was initially measured. The pH of the solution was controlled to 4.5 – 5.5 using NaOH and HCl. The experiments of the adsorption process of $H_2S$ were conducted using a batch mode process. For each experiment, the adsorption was carried out using 0.1 g of adsorbent after degassing at 105℃ for 24 hours in the oven. The solution was rotated at 160 rpm with an electric shaker for 9 hours to test their adsorption capacities. Upon the filtration of the suspensions, the initial and final concentration were measured. The adsorption capacity of the pollutants was calculated using equation 4 below:

$$q_e = \frac{(C_0 - C_e)V}{m} \tag{4}$$

where $V$ is the solution volume ($L$), $m$ is the adsorbent amount ($g$), $C_o$ and $C_e$ are the initial and final concentrations of the pollutants, and ($q_e$) is adsorption capacity in mg/g. All adsorption experiments were repeated and the maximum deviation was within 5%. All the measurements were done at fume hood as $H_2S$ is a very dangerous gas. The adsorbent sample yield can be calculated using the following equation 5 below:

$$Yield(\%) = \frac{W_c}{W_o} \times 100\% \tag{5}$$

where $W_c$ and $W_o$ are the dry weight of the final sample ($g$) and the dry weight of precursor ($g$), respectively. The equilibrium data were then fitted using the adsorption isotherm models, namely the Langmuir and the Freundlich models.

**Adsorption isotherm models**

The adsorption isotherm models explained the connection between the amounts of adsorbate adsorbed per unit mass of adsorbent (equilibrium adsorption capacity, $q_e$) at constant temperature and adsorbate's concentration at equilibrium conditions ($C_e$). Langmuir and Freundlich models are considered the well-known equilibrium adsorption isotherm models, and they were employed in the current study. Langmuir isotherm assumes monolayer adsorption onto a surface containing a finite number of adsorption sites of uniform strategies of adsorption with no transmigration of adsorbate in the plane of surface [28]. The linear form of Langmuir's isotherm model is given by the following equation 6 below:

$$\frac{C_e}{q_e} = \frac{1}{Q_{max}\, K_l} + \left(\frac{1}{Q_{max}}\right) C_e \tag{6}$$

where $C_e$ is the equilibrium concentration of the adsorbate ($H_2S$) (mg/L), $q_e$ is the amount of adsorbate adsorbed per unit mass of adsorbent (mg/g), and parameters such as $Q_{max}$ and $b$ are Langmuir constants related to monolayer adsorption capacity and affinity of adsorbent towards adsorbate, respectively. The essential characteristics of the Langmuir isotherm can be expressed in terms of a dimensionless equilibrium parameter ($R_L$), which is defined by:

$$R_L = \frac{1}{1+bC_0} \tag{7}$$

where $C_o$ is the $H_2S$ initial concentration (in mg/L). The value of $R_L$ indicates the type of the isotherm to be either unfavorable, linear, favorable, or irreversible as reported in Table 1.

Table 1. The range values of $R_L$

| **Value of $R_L$** | **Type of isotherm** |
|---|---|
| $R_L > 1$ | Unfavorable |
| $R_L = 1$ | Linear |
| $0 < R_L < 1$ | Favorable |
| $R_L = 0$ | Irreversible |

The Freundlich isotherm is another adsorption isotherm model which assumes heterogeneous surface energies, in which the energy term in Langmuir equation varies as a function of the surface coverage [29]. The correlation coefficients ($R^2$) is used to judge the applicability of an isotherm model. The well-known logarithmic form of the Freundlich model is given by the following equation 8 below:

$$\log q_e = \log K_F + \frac{1}{n} \log C_e \tag{8}$$

where $q_e$ is the adsorption capacity at equilibrium (mg/g), $C_e$ is the equilibrium concentration of the adsorbate ($H_2S$) and $K_F$ and n are Freundlich constants.

**Adsorption kinetic models**

Normally, the pseudo-first-order, pseudo-second-order and other kinetic models are used to simulate adsorption kinetics and determine the reaction rates. The mathematical relations of pseudo-first-order and pseudo-second-order are as given in equations 9 and 10, respectively [30,31]:

$$\log(q_e - q_t) = \log q_e - \frac{k_1}{2.303}\, t \tag{9}$$

$$\frac{1}{q_t} = \frac{1}{k_2 q_e^2} + \frac{1}{q_e}\, t \tag{10}$$

where $q_e$ and $q_t$ are the $H_2S$ adsorbed (mg/g) at equilibrium and at time t (h), respectively. $k_1$ ($h^{-1}$) and $k_2$ (g/mg h) are the rate constants for pseudo-first-order and pseudo-second-order, respectively.

## Results and Discussion

### Textural characterization of prepared activated carbon

Table 2 shows the composition of eggshell after the carbonization process. As seen, the prepared materials showed a high of carbon and oxygen of 30.36% and 50.27%, respectively. Indicating the carbon structure of the prepared material. Calcium is lower as compared to carbon and oxygen, which is could be attributed to remaining component of eggshells. Furthermore, the morphology of the adsorbent surface was tested using SEM, it is interesting to find that the extural structure of the ACES particles has porous structure with fine pores and cracks as shown in Figure 1. The porous materials is preferable for the adsorption processes as it will discussed in the coming sections.

Table 2. The elemental composition of ACES

| Element | Weight % | Weight Error (±) |
|---|---|---|
| Carbon (C) | 30.36 | 0.47 |
| Oxygen (O) | 50.27 | 0.86 |
| Molybdenum (Mo) | 6.16 | 0.31 |
| Calcium (Ca) | 12.48 | 0.31 |
| Potassium (K) | 0.40 | 0.07 |
| Magnesium (Mg) | 0.33 | 0.07 |
| Total | 100.00 | |

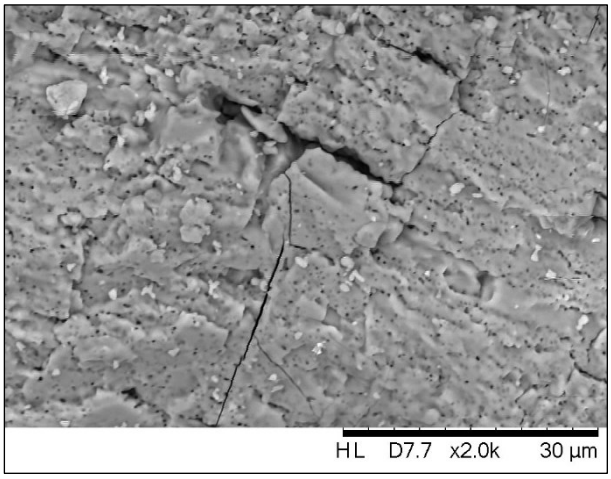



Figure 1. SEM image of ACES

Figure 2 shows the particle size distribution of adsorbent and Figure 3 shows another analytical test which is reporting on the FTIR structure of ACES particle. From Figure 3, it is obvious that the FTIR spectrum of ACES reveals three peaks. Each peak represents different functional group which might play an important role in the adsorption process. This corresponds to the presence of OH (hydroxyl), C=C (alkynes), and C–O (anhydrides) derivatives. Therefore, these surface functional groups could enhance the adsorption capacity of acidic pollutant (dissolved $H_2S$) in the waste water. Apart from that, at lower pH, the $H^+$ component which is high in concentration

may increase the positively charged $CaOH^{2+}$. It has been indicated that some reactions might occur during the adsorption process on the surface of adsorbent. Hence, reaction outlined in equation (11) might happen due to the oxygen content supporting the carbonization process of raw material. However, the dissociation of calcium oxide in water outlined in equation (12) forms calcium hydroxide ($Ca(OH)_2$) on the surface of ACES adsorbent which might help the adsorbent to attract via active site the acidic pollutant such as $H_2S$. Moreover, in equation (13) the $OH^-$ from $Ca(OH)_2$ reacts with $H_2S$ to form $Ca(HS)_2$ which is then converted to element sulfur as demonstrated in equation (14).

$$CaCO_3 \rightarrow CaO + CO_2 \quad (11)$$
$$CaO + H_2O \rightarrow Ca(OH)_2 \quad (12)$$
$$Ca(OH)_2 + H_2S \rightarrow Ca(HS)_2 + 2H_2O \quad (13)$$
$$Ca(HS)_2 + O_2 \rightarrow Ca(OH)_2 + 2S \quad (14)$$

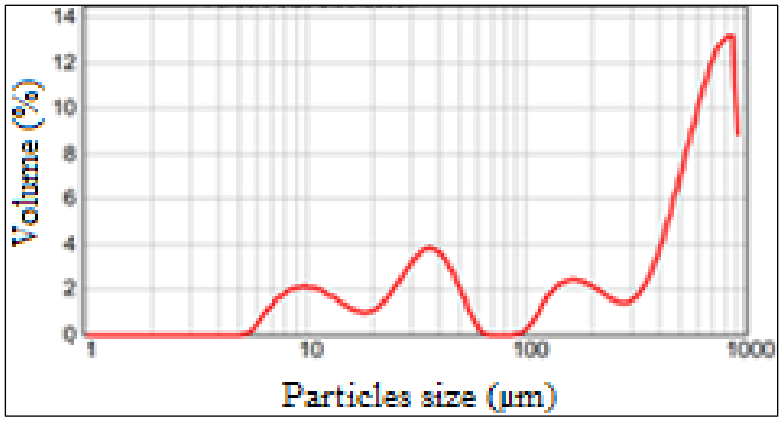



Figure 2. The particle size activated carbon derived from eggshell

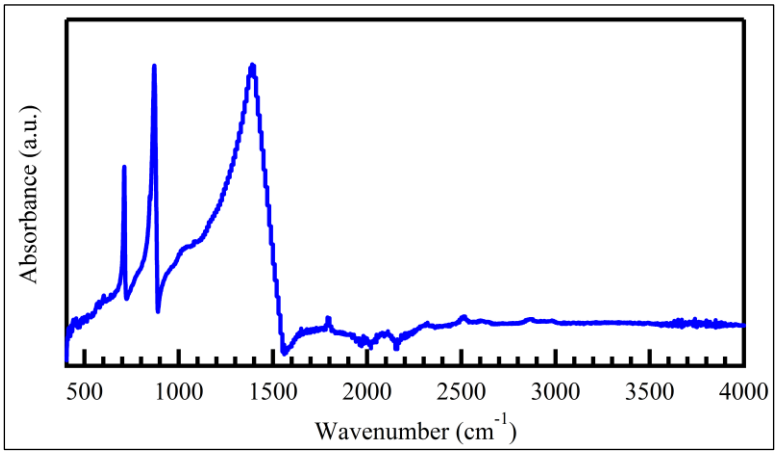



Figure 3. FTIR spectra of the ACES

**Effect of contact time and initial hydrogen sulfide concentration on adsorption equilibrium**

A series of contact time experiments for $H_2S$ have been carried out at different initial concentrations (100 – 500 mg/L) and at temperature of 30 ˚C. Figure 4 shows that the equilibrium time of 6 hours is required for $H_2S$ removal with the higher range of initial concentration (300 – 500 mg/L). However, with lower initial concentrations range (100 – 200 mg/L), a equilibrium time of 5 hours is required. As can be clearly seen from Figure 4, the amount of adsorbed $H_2S$ onto the modified adsorbent (ACES) increases with time and it reaches an asymptote as time progresses. The results reveals that the $H_2S$ adsorption rate is high at the initial stage of the contact period, and it becomes slower thereafter. This phenomenon happens due to the activity of functional group on the surface of adsorbent. It has been noted that vacant surface sites are vastly available for adsorption during the initial stage. However, as time elapses, it is difficult to occupy the remaining vacant surface sites due to the repulsive forces between the solute molecules on the solid and bulk phases. The results of this study indicate that the initial concentration has an important role in the adsorption capacity. Similarly, Choo et al. has found that higher concentration yields enhanced driving force along the pores, resulting in higher adsorption capacity [32]. However, Xiao et al. have shown that the effect of concentration is lower [13]. The contact time affects the adsorption capacity as well. From the current study, the effects of driving force and mass transfer are minimal in the dynamic adsorption. Moreover, it is limited by the rate of molecular diffusion into deeper pores and the adsorption process. The percentage of removal of $H_2S$ is 43%, which is calculated using equation 15 below:

$$Removal\ (\%) = \frac{C_0 - C_e}{C_0} \times 100 \tag{15}$$

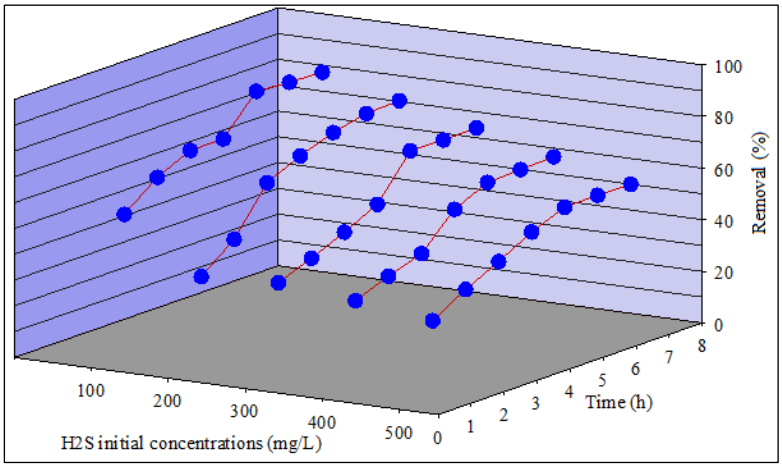



Figure 4. Effect of agitation time on $H_2S$ adsorption onto ACES at various initial concentrations (100 – 500 mg/L)

**Adsorption isotherms**

The adsorption isotherm demonstrates the adsorption process when it reaches an equilibrium state. It reveals on how the adsorption molecules are distributed between the solid phase and the liquid phase. The analysis of the isotherm data, which is performed by fitting the data on different isotherm models, is an important step to find the suitable model that can be used for design purposes [33]. Basically, adsorption isotherm is important to describe how solutes interact with adsorbents, and is critical in optimizing the use of adsorbents. $R^2$ value is used to identify the appropriate model of the adsorption process. Figure 5 shows the Langmuir isotherm model, where $1/q_e$ changes linearly with $1/C_e$, at a slope of $1/Q_o b$. The Langmuir constants $b$ and $Q_o$ are shown in Table 3. $R^2$ is 0.9849, indicating that the fitting error is quite high compare with Freundlich isotherm model. To support that, the essential characteristics of the Langmuir isotherm can be expressed in terms of a dimensionless equilibrium parameter ($R_L$),

and the value of $R_L$ is 0.069. Indeed, this indicates that the Langmuir isotherm is favorable for the adsorption of $H_2S$ by the ACES under the working conditions considered in this study.

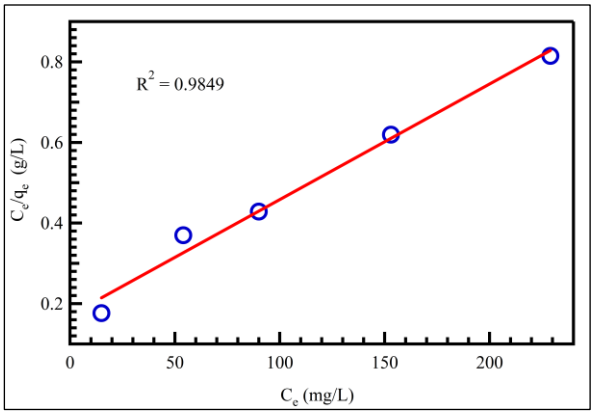



Figure 5. Langmuir adsorption isotherm of $H_2S$ adsorption onto ACES

Table 3. Parameters of Langmuir and Freundlich adsorption isotherm models of $H_2S$ adsorption onto ACES

| **Langmuir** | | | **Freundlich** | | |
|---|---|---|---|---|---|
| $Q_{max}$ (mg/g) | $K_L$ (L/mg) | $R^2$ | $K_F$ (mg/g (L/mg)$^{1/n}$) | 1/n | $R^2$ |
| 289.3 | 0.02704 | 0.9849 | 25.16 | 0.452 | 0.9874 |

According to Freundlich isotherm plot (log $q_e$ vs. log $C_e$), 1/$n$ of 0.452 could be obtained from the slope the straight line gives as shown in Figure 6, showing that the adsorption of $H_2S$ on the ACES is favorable. Accordingly, the Freundlich constants $K_F$ and $n$ are reported in Table 3. $R^2$ is 0.9874, indicating that the fitting error is lower than that of the Langmuir model. Table 4 compares the adsorption capacities of various adsorbents. It is interesting to see that the ACES has the highest adsorption capacity as compared to other adsorbents reported in the literature.

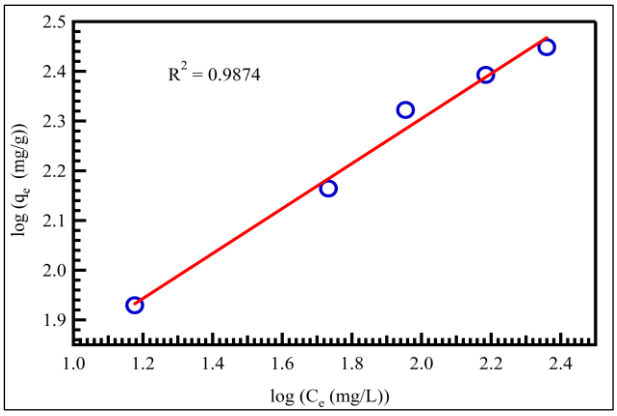



Figure 6. Freundlich adsorption isotherm of $H_2S$ adsorption onto ACES

Table 4. Comparison of maximum monolayer adsorption capacity of dissolved $H_2S$ on various adsorbents

| **Adsorbent** | **Adsorbate** | **Adsorption Capacity (mg/g)** | **References** |
|---|---|---|---|
| Carbon derived from eggshells | $H_2S$ | 289.3 | This work |
| IAC under anaerobic conditions | $H_2S$ | 9.4 | [34] |
| Fine rubber particle media | $H_2S$ | 0.12 | [17] |
| Crushed oyster shell | $H_2S$ | 12 | [18] |
| Red mud | $H_2S$ | 17 | [35] |
| Carbonated steel slag | $H_2S$ | 7.5 | [36] |
| Activated carbon from sawdust pellets | $H_2S$ | 6.2 | [37] |

**Adsorption kinetics**

The relation between $\log(q_e-q_t)$ and time showed straight lines as displayed in Figure 7a for the pseudo-first-order kinetic model. $R^2$ and $k_1$ values are listed in Table 5. On the other hand, linear relationships were obtained by plotting $t/q_t$ versus t (Figure 7b) for the pseudo-second-order kinetic model. Moreover, the $q_e$ and $k_2$ were determined from the slope and the intercept of the plot and listed in Table 5.

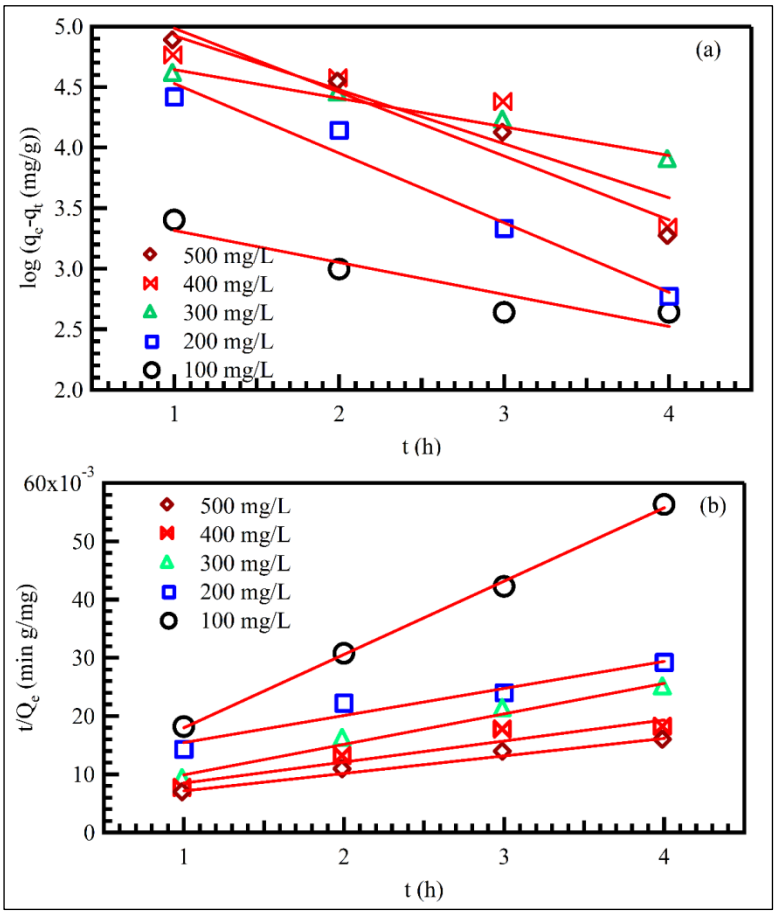



Figure 7. Pseudo-first-order (a) and pseudo-second-order (b) models of $H_2S$ adsorption onto ACES

Table 5. Pseudo-first-order and pseudo-second-order kinetic models' parameters for adsorption of $H_2S$ onto ACES

| Kinetic Model | Parameter | Initial $H_2S$ Concentration (mg/L) | | | | |
|---|---|---|---|---|---|---|
| | | 100 | 200 | 300 | 400 | 500 |
| Pseudo-first-order kinetic model | $K_1$ (1/h) | 0.264 | 0.574 | 0.236 | 0.445 | 0.527 |
| | $R^2$ | 0.884 | 0.970 | 0.820 | 0.950 | 0.970 |
| Pseudo-second-order kinetic model | $K_2$ (g/mg h) | 0.024 | 0.002 | 0.005 | 0.002 | 0.002 |
| | $R^2$ | 0.998 | 0.943 | 0.981 | 0.907 | 0.980 |

This procedure is more likely to predict the behavior over the whole range of adsorption. It shows a good agreement between the experimental and the calculated $q_e$ values (Table 5). It is found that, the correlation coefficients for the second-order kinetic model were higher than those for the pseudo-first-order model, indicating the applicability of the second-order kinetic model to describe the adsorption process of $H_2S$ onto the prepared ACES $R^2$ values obtained are shown in Table 5 and they are low compared to those obtained from pseudo-second-order. Table 5 lists the calculated parameters and it is found that the adsorption of $H_2S$ on ACES could be best described by the second-order kinetic model.

## Conclusion

The activated carbons have been prepared and analyzed to characterize their physical and chemical properties. The resulting solid samples have been used in the adsorption process of dissolved hydrogen sulfide from aqueous solution. From the current study, the activated carbon derived from the eggshell has the maximum adsorption capacity of 289.3 mg/g which is the highest amongst the other adsorbents reported earlier. The result indicate also that the initial concentration has an important role in the adsorption capacity. The adsorption isotherm fit very well to the well-known Freundlich isotherm model. In addition, the process followed the pseudo-second-order kinetic model. Thus, it can be concluded that eggshell is a very useful green and economic adsorbent due to its good accessibility and absence of any toxic and hazardous elements. Therefore, it is a very suitable candidate for removing $H_2S$ from wastewater.

## Acknowledgement

This work has been funded by Universiti Malaysia Pahang, Faculty of Chemical and Natural Resources Engineering, through a local research grant scheme (ERGS) No. RDU130618.

## References

1. Patnaik, P. (2013). Handbook of inorganic chemicals. McGraw-Hill, New York.
2. Vollertsen, J., Nielsen, A. H., Jensen, H. S., Wium-Andersen, T. and Hvitved-Jacobsen, T. (2008). Corrosion of concrete sewers – the kinetics of hydrogen sulfide oxidation. *Science of The Total Environment*, 394(1): 162 – 170.
3. Agrahari, G. K., Rawat, A., Verma, N. and Bhattacharya, P. K. (2013). Removal of dissolved $H_2S$ from wastewater using hollow fiber membrane contactor: Experimental and mathematical analysis. *Desalination*, 314: 34 – 42.
4. Ma, H., Cheng, X., Li, G., Chen, S., Quan, Z., Zhao, S. and Niu, L. (2000). The influence of hydrogen sulfide on corrosion of iron under different conditions. *Corrosion Science*, 42(10): 1669 – 1683.
5. Skrtic, L. (2006). Hydrogen sulfide, oil and gas, and people's health. Thesis Master, Universiti of California.
6. Lambert, T. W., Goodwin, V. M., Stefani, D. and Strosher, L. (2006). Hydrogen sulfide ($H_2S$) and sour gas effects on the eye. A historical perspective. *Science of The Total Environment*, 367(1): 1 – 22.
7. World Health Organization (2008). Guidelines for drinking-water quality: incorporating first and second addenda. WHO Press: pp. 185.
8. Hughes, M. N., Centelles, M. N. and Moore, K. P. (2009). Making and working with hydrogen sulfide: the chemistry and generation of hydrogen sulfide in vitro and its measurement in vivo: a review. *Free Radical Biology and Medicine*, 47(10): 1346 – 1353.

9. Kularatne, K. I. A., Dissanayake, D. P. and Mahanama, K. R. R. (2003). Contribution of dissolved sulfates and sulfites in hydrogen sulfide emission from stagnant water bodies in Sri Lanka. *Chemosphere*, 52(5): 901 – 907.
10. Yongsiri, C., Vollertsen, J. and Hvitved-Jacobsen, T. (2004). Effect of temperature on air-water transfer of hydrogen sulfide. *Journal of Environmental Engineering*, 130(1): 104 – 109.
11. Heinonen, A. (2012). Adsorption of hydrogen sulfide by modified cellulose nano/microcrystals. Master Thesis, Lappeenranta University of Technology.
12. Wesley Jr, E. W. (1980). Principles of water quality management. CBI Publishing Company Inc, Boston, USA.
13. Xiao, Y., Wang, S., Wu, D. and Yuan, Q. (2008). Experimental and simulation study of hydrogen sulfide adsorption on impregnated activated carbon under anaerobic conditions. *Journal of Hazardous Materials*, 153(3): 1193 – 1200.
14. Yuan, W. and Bandosz, T. J. (2007). Removal of hydrogen sulfide from biogas on sludge-derived adsorbents. *Fuel,* 86(17): 2736 – 2746.
15. Guo, J., Luo, Y., Lua, A. C., Chi, R. A., Chen, Y. L., Bao, X. T. and Xiang, S. X. (2007). Adsorption of hydrogen sulphide ($H_2S$) by activated carbons derived from oil-palm shell. *Carbon*, 45(2): 330 – 336.
16. Wang, C. and Pei, Y. (2012). The removal of hydrogen sulfide in solution by ferric and alum water treatment residuals. *Chemosphere*, 88(10): 1178 – 1183.
17. Wang, N., Park, J. and Ellis, T. G. (2013). The mechanism of hydrogen sulfide adsorption on fine rubber particle media (FRPM). *Journal of Hazardous Materials*, 260: 921 – 928.
18. Asaoka, S., Yamamoto, T., Kondo, S. dan Hayakawa, S. (2009). Removal of hydrogen sulfide using crushed oyster shell from pore water to remediate organically enriched coastal marine sediments. *Bioresource Technology*, 100(18): 4127 – 4132.
19. Poulton, S. W., Krom, M. D., Van Rijn, J. and Raiswell, R. (2002). The use of hydrous iron (III) oxides for the removal of hydrogen sulphide in aqueous systems. *Water Research*, 36(4): 825 – 834.
20. Haddadian, Z., Shavandi, M. A., Abidin, Z. Z., Fakhru'l-Razi, A. and Ismail, M. H. S. (2013). Removal methyl orange from aqueous solutions using dragon fruit (Hylocereusundatus) foliage. *Chemical Science Transactions*, 2(3): 900 – 910.
21. Yang, K., Peng, J., Srinivasakannan, C., Zhang, L., Xia, H. and Duan, X. (2010). Preparation of high surface area activated carbon from coconut shells using microwave heating. *Bioresource Technology*, 101(15): 6163 – 6169.
22. Martins, A. C., Pezoti, O., Cazetta, A. L., Bedin, K. C., Yamazaki, D. A., Bandoch, G. F., Asefa, T., Visentainer, J. V. and Almeida, V. C. (2015). Removal of tetracycline by NaOH-activated carbon produced from macadamia nut shells: kinetic and equilibrium studies. *Chemical Engineering Journal*, 260: 291 – 299.
23. Farma, R., Deraman, M., Awitdrus, A., Talib, I. A., Taer, E., Basri, N. H., Manjunatha, J. G., Ishak, M. M., Dollah, B. N. M. and Hashmi, S. A. (2013). Preparation of highly porous binderless activated carbon electrodes from fibres of oil palm empty fruit bunches for application in supercapacitors. *Bioresource Technology*, 132: 254 – 261.
24. Gao, P., Liu, Z. H., Xue, G., Han, B. and Zhou, M. H. (2011). Preparation and characterization of activated carbon produced from rice straw by $(NH_4)_2HPO_4$ activation. *Bioresource Technology*, 102(3): 3645 – 3648.
25. Pundir, C. S., Bhambi, M. and Chauhan, N. S. (2009). Chemical activation of egg shell membrane for covalent immobilization of enzymes and its evaluation as inert support in urinary oxalate determination. *Talanta*, 77(5): 1688 – 1693.
26. Giraldo, L. and Moreno-Piraján, J. C. (2014). Study of adsorption of phenol on activated carbons obtained from eggshells. *Journal of Analytical and Applied Pyrolysis*, 106: 41 – 47.
27. Silva, P. R., Ponte, H. A., Ponte, M. J. J. S. and Kaminari, N. M. S. (2011). Development of a new electrochemical methodology at carbon steel/Na2S system for corrosion monitoring in oil refineries. *Journal of Applied Electrochemistry*, 41(3): 317 – 320.
28. Weber, T. W. and Chakravorti, R. K. (1974). Pore and solid diffusion models for fixed-bed adsorbers. *AIChE Journal*, 20(2): 228 – 238.
29. Weber, W. J. (1972). Physicochemical processes for water quality control. Wiley Interscience, New York: pp. 640.
30. Abdel Ghafar, H. H., Ali, G. A. M., Fouad, O. A. and Makhlouf, S. A. (2015). Enhancement of adsorption efficiency of methylene blue on $Co_3O_4/SiO_2$ nanocomposite. *Desalination and Water Treatment*, 53(11), 2980 – 2989.

31. Agarwal, S., Sadegh, H., Monajjemi, M., Hamdy, A. S., Ali, G. A. M., Memar, A. O., Shahryarighoshekandi, R., Tyagi, I. and Gupta, V. K. (2016). Efficient removal of toxic bromothymol blue and methylene blue from wastewater by polyvinyl alcohol. *Journal of Molecular Liquids*, 218: 191 – 197.
32. Choo, H. S., Lau, L. C., Mohamed, A. R. and Lee, K. T. (2013). Hydrogen sulfide adsorption by alka-line impregnated coconut shell activated carbon. *Journal of Engineering Science and Technology*, 8: 741 – 753.
33. El-Geundi, M. S. (1991). Homogeneous surface diffusion model for the adsorption of basic dyestuffs onto natural clay in batch adsorbers. *Adsorption Science & Technology*, 8(4): 217 – 225.
34. Xiao, Y., Wang, S., Wu, D. and Yuan, Q. (2008). Catalytic oxidation of hydrogen sulfide over unmodified and impregnated activated carbon. *Separation and Purification Technology*, 59(3): 326 – 332.
35. Sahu, R. C., Patel, R., and Ray, B. C. (2011). Removal of hydrogen sulfide using red mud at ambient conditions. *Fuel Processing Technology*, 92(8): 1587 – 1592.
36. Asaoka, S., Okamura, H., Morisawa, R., Murakami, H., Fukushi, K., Okajima, T., Katayama, M., Inada, Y., Yogi, C. and Ohta, T. (2013). Removal of hydrogen sulfide using carbonated steel slag. *Chemical Engineering Journal*, 228: 843–849.
37. Kazmierczak-Razna, J., Gralak-Podemska, B., Nowicki, P. and Pietrzak, R. (2015). The use of microwave radiation for obtaining activated carbons from sawdust and their potential application in removal of $NO_2$ and $H_2S$. *Chemical Engineering Journal*, 269: 352 – 358.

*Malaysian Journal of Analytical Sciences, Vol 21 No 2 (2017): 346 - 355*
*DOI: https://doi.org/10.17576/mjas-2017-2102-09*

**MALAYSIAN JOURNAL OF ANALYTICAL SCIENCES**
***Published by The Malaysian Analytical Sciences Society***
**ISSN 1394 - 2506**

# A COMPARATIVE STUDY ON THE INHIBITORY ACTION OF SOME GREEN INHIBITORS ON THE CORROSION OF MILD STEEL IN HYDROCHLORIC ACID MEDIUM

## (Kajian Perbandingan Tindakan Rencatan oleh Perencat Hijau ke atas Pengaratan Keluli Lembut di dalam Medium Asid Hidroklorik)

Moorthy Shyamala[1]* and Arthanas Arulanantham[2]

[1]*Department of Chemistry,*
*Government College of Technology, Coimbatore-641013, Tamil Nadu, India*
[2]*Department of Chemistry,*
*S.N.S College of Technology, Coimbatore-641013, Tamil Nadu, India*

**Corresponding author: shyamphd@yahoo.com*

Received: 24 February 2015; Accepted: 9 February 2017

**Abstract**

The inhibitive action of the extracts of three green inhibitors namely *Adathoda vasica, Eclipta alba and Centella asiatica* were investigated. Polarization method indicates that the plant extracts are under mixed control i.e promoting retardation of both anodic and cathodic reactions. The impedance method reveals that charge-transfer process controls the corrosion of mild steel. The plant-extracts obeys Langmuir adsorption isotherm. Kinetics and reason for the corrosion inhibition or the nature of adsorption is clearly shown. Physisorption mechanism has been proposed for the inhibition action of these plant extracts. The protective film formed on the surface was confirmed by Scanning Electron Microscopy (SEM). From hydrogen permeation method, all the plant extracts were able to reduce the permeation current. Results obtained in all the methods are very much in good agreement with increasing inhibition efficiency in the order: *Eclipta alba* > *Adathoda vasica* > *Centella asiatica*. Among the three plant extracts studied, the maximum inhibition efficiency was found in *Eclipta alba* which showed 99.6% inhibition efficiency at 8.0 % v/v concentration of the extract.

**Keywords**: mild steel, corrosion inhibition, plant-extracts, hydrochloric acid, physisorption

**Abstrak**

Tindakan perencatan oleh tiga ekstrak perencat hijau iaitu *Adathoda vasica, Eclipta alba dan Centella asiatica* telah dikaji. Kaedah polarisasi menunjukkan bahawa ekstrak tumbuhan di bawah kawalan campuran akan menghasilkan tindak balas perencatan bagi kedua–dua anod dan katod. Kaedah galangan mendedahkan bahawa proses pemindahan cas mengawal kakisan terhadap keluli lembut. Bahan ekstrak tumbuhan mematuhi penjerapan isoterma Langmuir. Kinetik dan sebab bagi perencatan kakisan atau sifat penjerapan jelas dapat ditunjukkan. Tindakan perencatan dari ekstrak tumbuhan adalah dicadangkan sebagai mekanisma serapan fizikal. Filem pelindung yang terbentuk di permukaan telah disahkan melalui mikroskopi elektron pengimbasan (SEM). Melalui kaedah penyerapan hidrogen, semua ekstrak tumbuhan dikenalpasti dapat mengurangkan penelapan arus. Keputusan yang diperolehi dalam semua kaedah amat bersetuju dengan peningkatan kecekapan rencatan adalah mengikut tertib iaitu *Eclipta alba* > *Adathoda vasica* > *Centella asiatica*. Di antara ketiga–tiga ekstrak tumbuhan yang dikaji, kecekapan rencatan maksimum diperolehi dari *Eclipta alba* iaitu 99.6% pada 8.0% v/v kepekatan ekstrak.

**Kata kunci**: keluli lembut, perencat kakisan, ekstrak tumbuhan, asid hidroklorik, serapan fizikal

## Introduction

Mild steel are widely used in boilers, motor car bodies, machines, gears, pipes, tanks and in most of the chemical industries. Hydrochloric acid and sulphuric acids are the medium generally used for pickling mild steel. About 90% of pickling problems can be solved by introducing appropriate pickling inhibitor to the medium. The recent and growing trend is using plant extracts as corrosion inhibitor on mild steel in acid medium due to their biodegradability, ecofriendliness, less toxicity, cost effectiveness, easy availability, environmentally safe, soluble and highly stable nature in acidic solutions. Owing to strict environmental legislation, emphasis is being focused on development of naturally occurring substances as corrosion inhibitors. Recently, many plant extracts have been reported to be very effective corrosion inhibitors for the protection of mild steel in acidic media [1 – 4]. In this study, the inhibition effect of the extracts of three green inhibitors namely *Adathoda vasica (Adathodai), Eclipta alba (Karisilankani) and Centella asiatica (Vallarai)* on the corrosion of mild steel in 1N hydrochloric acid was investigated using electrochemical and non-electrochemical methods.

## Materials and Methods

### Preparation of mild steel specimen

Mild steel strips were mechanically cut into strips of size 4.5 cm × 2 cm × 0.2 cm containing the composition of 0.14% C, 0.35% Mn, 0.17% Si, 0.025% S, 0.03% P and the remainder is Fe and provided with a hole of uniform diameter to facilitate suspension of the strips in the test solution for weight loss method. For electrochemical studies, mild steel strips of the same composition but with an exposed area of $1cm^2$ were used. Mild steel strips were mechanically polished with emery papers of 1/0 to 4/0 grades and subsequently degreased with trichloroethylene or acetone and finally with de-ionized water and stored in the desiccator. Accurate weight of the samples was taken using electronic balance.

### Preparation of the green inhibitors

The leaves of the *Adathoda vasica*, *Eclipta alba* and *Centella asiatica* were taken and cut into small pieces and they were dried in an air oven at 80 ºC for 2 hours and ground well into powder. An amount 10g of the sample was refluxed in 100 mL of distilled water for 1 hours. The refluxed solution was then filtered carefully and the filtrate volume was made up to 100 mL using double distilled water which is the stock solution and the concentration of the stock solution is expressed in terms of % (v/v). From the stock solution, 2% - 10% concentration of the extracts was prepared using 1N hydrochloric acid.

### Weight loss method

The pretreated specimens' initial weights were noted and were immersed in the experimental solution (in triplicate) with the help of glass hooks at 30 °C for a period of 3 hours. The experimental solution used was 1N HCl in the absence and presence of various concentrations of the plant extracts. After three hours, the specimens were taken out, washed thoroughly with distilled water, dried completely and their final weights were noted. From the initial and final weights of the specimen, the loss in weight was calculated and tabulated. From the weight loss, the corrosion rate (mmpy), inhibition efficiency (%) and surface coverage (θ) of plant extracts was calculated using the equation 1 – 3 as shown below:

$$\text{Corrosion rate (mmpy)} = KW / ATD \quad (1)$$

where $K = 8.76 \times 10^4$ (constant), W= weight loss in g, A=area in sq.cm, T= Time in hours and D=density in gm/ cu.cm (7.86).

$$\text{Inhibition efficiency (\%)} = (CR_B - CR_I) / CR_B \times 100 \quad (2)$$

$$\text{Surface coverage } (\theta) = CR_B - CR_I \ / CR_B \quad (3)$$

where $CR_B$ and $CR_I$ are Corrosion rates in the absence and presence of the inhibitors.

**Potentiodynamic polarization method**

Potentiodynamic polarization measurements were carried out using electrochemical analyzer. The polarization measurements were made to evaluate the corrosion current, corrosion potential and tafel slopes. Experiments were carried out in a conventional three-electrode cell assembly with a time interval of 10 – 15 minutes was given for each experiment to attain the steady state open circuit potential. The polarization was carried from a cathodic potential of – 800mV (vs SCE) to an anodic potential of – 200 mV (Vs SCE) at a sweep rate of 1 mV per second. The inhibitor efficiency was calculated using equation 4 below:

$$IE\ (\%) = \frac{I_{Corr} - I^*_{Corr}}{I_{Corr}} \times 100 \quad (4)$$

where $I_{corr}$ and $I^*_{corr}$ are corrosion current in the absence and presence of inhibitors.

**Electrochemical impedance method**

The electrochemical AC-impedance measurements were also performed using electrochemical analyzer. A sine wave with amplitude of 10 mV was superimposed on the steady open circuit potential. The real part (Z') and the imaginary part (Z") were measured at various frequencies in the range of 100 KHz to 10 MHz. A plot of Z' vs Z" was made. From the plot, the charge transfer resistance ($R_t$) was calculated and the double layer capacitance was then calculated using the equation 5 below:

$$C_{dl} = \frac{1}{2\pi} f_{max}\ R_t \quad (5)$$

The experiments were carried out in the absence and presence of different concentrations of inhibitors. The percentage of inhibition efficiency was calculated using the equation 6 below:

$$IE\ (\%) = \frac{R_t^* - R_t}{R_t^*} \times 100 \quad (6)$$

where $R_t^*$ and $R_t$ are the charge transfer resistance in the presence and absence of inhibitors.

**Hydrogen permeation method**

The permeation current was measured using hydrogen permeation apparatus in 1N HCl medium in the absence and presence of optimum concentration of extracts.

**Surface examination studies**

Surface examination of mild steel specimens in the absence and presence of the optimum concentration of the extracts immersed for 3 hours at 30 $^oC$ were studied with the magnification of 1000X specimens. The protective film formed on the surface of the mild steel was confirmed by scanning electron microscopy (SEM) studies.

## Results and Discussion

**Weight loss studies**

The various corrosion parameters were obtained from weight loss method in1N hydrochloric acid in the absence and presence of various concentrations of the plant extracts ranging from 2% to 10% v/v are listed in Table 1.

It was found that the optimum concentration for *Adathoda vasica* was found to be 6% v/v with maximum inhibition efficiency of 99.0%, *Eclipta alba* at 8% v/v with maximum inhibition efficiency of 99.6% and *Centella asiatica* at 10% v/v with maximum inhibition efficiency of 85.3% for a period of 3 hours of immersion time. This result indicated that the plant extracts could act as good corrosion inhibitors.

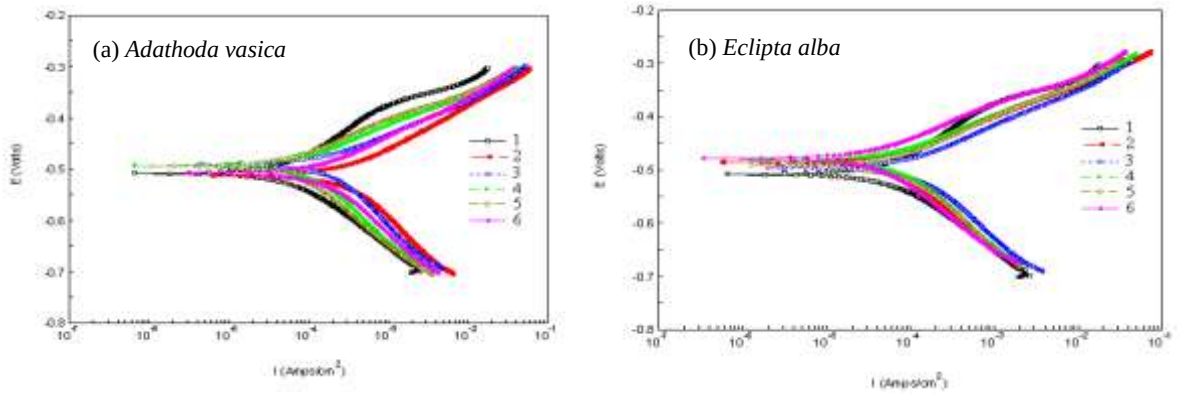
Table 1. Corrosion parameters obtained from weight loss measurements for mild steel in 1N HCl with various concentrations of the plant extracts

| Name of the Plant Extract | Conc. of Extract (% in v/v) | Corrosion Rate (mmpy) | Inhibition Efficiency (%) | Surface Coverage (θ) |
|---|---|---|---|---|
| *Adathoda vasica* | Blank | 30.67 | - | - |
| | 6.0 | 0.30 | 99.0 | 0.990* |
| | 8.0 | 0.35 | 98.8 | 0.988 |
| | 10.0 | 0.58 | 98.1 | 0.981 |
| *Eclipta alba* | 6.0 | 0.98 | 96.8 | 0.968 |
| | 8.0 | 0.12 | 99.6 | 0.996* |
| | 10.0 | 0.12 | 99.6 | 0.996 |
| *Centella asiatica* | 6.0 | 8.55 | 72.1 | 0.721 |
| | 8.0 | 6.56 | 78.6 | 0.786 |
| | 10.0 | 4.50 | 85.3 | 0.853* |

**Maximum inhibition efficiency*

**Potentiodynamic polarization studies**

Potentiodynamic polarization studies as shown in Figures 1a – 1c revealed that the extracts act through mixed mode of inhibition as the polarization curves have not shifted towards more positive potential or more negative potential but has shifted towards less negative potential and lower current density values upon the addition of extract. It was observed that with increase in concentration of the plant extract from 2% to 10%, the maximum inhibition efficiency of 99.2% was observed for *Adathoda vasica* at an optimum concentration of 6% v/v, for *Eclipta alba* extract with 99.7% at 8% v/v and *Centella asiatica* with 85.7% at 10% v/v of the extract (Table 2).



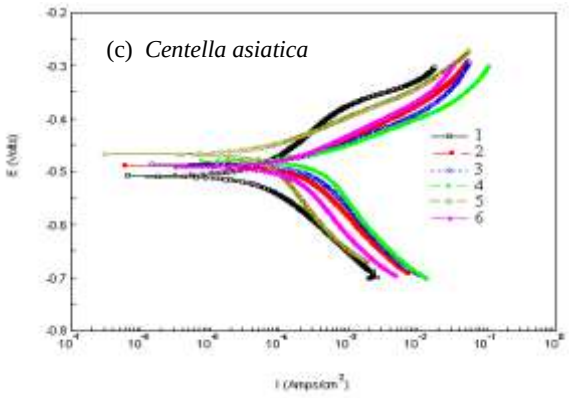



Figure 1. Potentiodynamic polarization curves for mild steel in 1N HCl solution in the absence and presence of various concentrations of the plant extracts (a) *Adathoda vasica, (b) Eclipta alba and (c) Centella asiatica* (Note legend information: 1 – blank, 2 – 2.0% v/v, 3 – 4.0% v/v, 4 – 6.0% v/v, 5 – 8.0% v/v and 6 – 10.0% v/v)

Table 2. Potentiodynamic polarization parameters for mild steel in 1N HCl at 30 $^{o}$C containing various concentrations of the plant extracts

| **Name of the Plant Extract** | **Conc. of Extract (% in v/v)** | **$E_{corr}$ (V)** | **$I_{corr}$ (mA/cm$^2$)** | **Tafel Slope mV/decade** | | **Inhibition Efficiency (%)** |
|---|---|---|---|---|---|---|
| | | | | **$b_a$** | **$b_c$** | |
| Blank | - | -0.510 | 3.57 | 78 | 122 | - |
| *Adathoda vasica* | 6.0 | -0.493 | 0.02 | 74 | 120 | 99.2 |
| *Eclipta alba* | 8.0 | -0.496 | 0.01 | 74 | 122 | 99.7 |
| *Centella asiatica* | 10.0 | -0.492 | 0.51 | 76 | 124 | 85.7 |

**Electrochemical impedance studies**

Impedance measurements were studied to evaluate the charge transfer resistance ($R_t$) and double layer capacitance ($C_{dl}$) as shown in Table 3 and through these parameters the inhibition efficiency was calculated. From Figure 2, the obtained Impedance diagrams are almost in a semi-circular appearance, indicating that the charge - transfer process mainly controls the corrosion of mild steel. Deviations of perfect circular shape are often referred to the frequency dispersion of interfacial impedance. In fact, in the presence of the plant extracts the values of $R_t$ has enhanced and the values of double layer capacitance are also brought down to the maximum extent. The decrease in $C_{dl}$ shows that the adsorption of the inhibitors takes place on the metal surface in acidic solution. A good agreement is observed between the results of weight loss method and electrochemical methods (Potentiodynamic Polarization method and Impedance method) in the order: *Eclipta alba > Adathoda vasica > Centella asiatica.*

Table 3. Impedance parameters for the corrosion of mild steel in 1N HCl in the absence and presence of various concentrations of the plant extracts at 30 °C

| Name of the Plant Extract | Conc. of Extract (% in v/v) | $R_t$ ($\Omega$ cm$^2$) | $C_{dl}$ ($\mu$F/cm$^2$) | Inhibition Efficiency (%) |
|---|---|---|---|---|
| Blank | - | 7.58 | 285.34 | |
| *Adathoda vasica* | 6.0 | 285.23 | 7.65 | 97.3 |
| *Eclipta alba* | 8.0 | 358.80 | 6.00 | 97.9 |
| *Centella asiatica* | 10.0 | 54.32 | 39.88 | 86.0 |

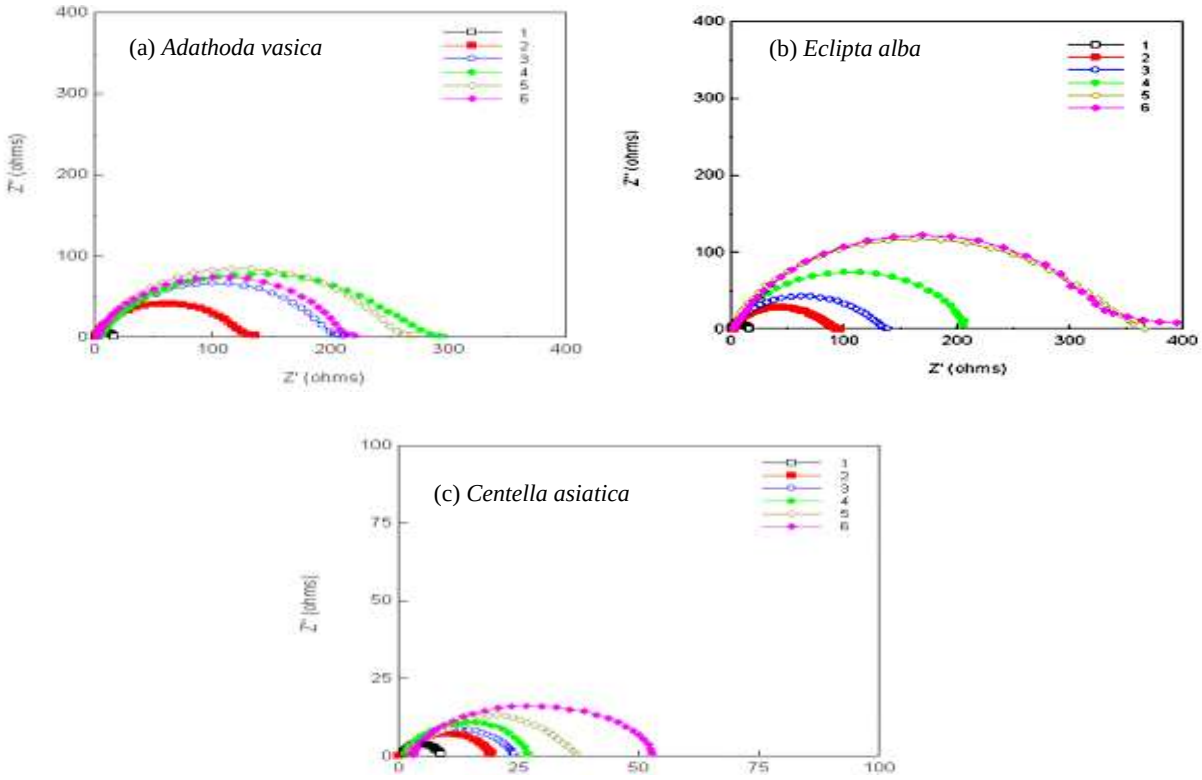



Figure 2. Impedance diagrams for mild steel in 1N HCl solution in the absence and presence of various concentrations of the plant extract: (a) *Adathoda vasica*, (b) *Eclipta alba* and (c) *Centella asiatica*. (Note legend information: 1 – blank, 2 – 2.0% v/v, 3 – 4.0% v/v, 4 – 6.0% v/v, 5 – 8.0% v/v and 6 – 10.0% v/v)

**Kinetics and reason for the corrosion inhibition**

The major phytochemical constituents present in *Adathoda vasica* are the alkaloids namely vasicine and vasicinone (Figure 3), in *Centella asiatica* is asiaticoside, a triterpene glycoside (Figure 4), and in *Eclipta alba* are wedelolactone, β-sitosterol, stigmasterol (Figure 5a – 5c) and also an alkaloid namely ecliptine [5, 6]. Inspection of the chemical structures of the phytochemical constituents reveals that the compounds can adsorb on the metal surface via the lone pair of electrons present on their oxygen atoms and make a barrier for charge and mass transfer leading to decrease the interaction of the metal with the corrosive environment. As a result, the corrosion rate of the

metal was decreased**.** The formation of film layer essentially blocks discharge of $H^+$ and dissolution of metal ions. Due to electrostatic interaction, the protonated constituent's molecules are adsorbed (physisorption) and high inhibition is expected [1]. Acid pickling inhibitors containing organic N, S and OH groups behave similarly to inhibit corrosion [7 – 10].

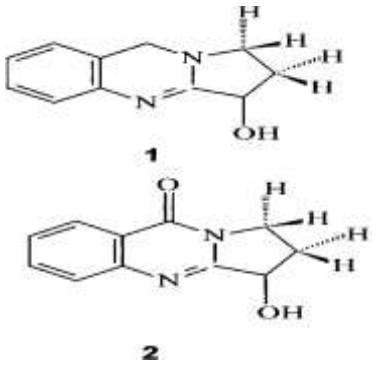


Figure 3. Chemical structure of (1) vasicine and (2) vasicinone

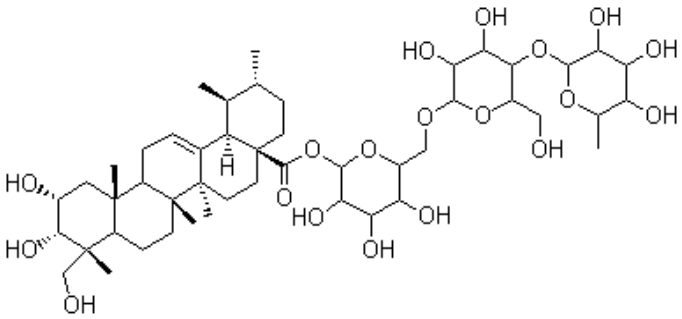
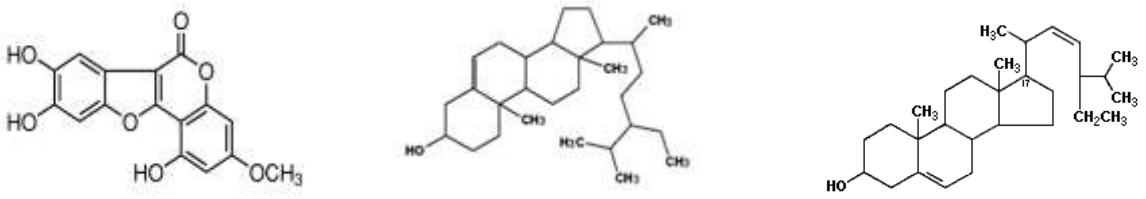


Figure 4. Chemical structure of asiaticoside



(a) (b) (c)

Figure 5. Chemical structure of (a) wedelolactone, (b) β-sitosterol and (c) stigmasterol

The adsorption of different concentrations of *Adathoda vasica*, *Eclipta alba* and *Centella asiatica* extracts on the surface of mild steel in 1N hydrochloric acid followed Langmuir adsorption isotherm as shown in Figure 6.

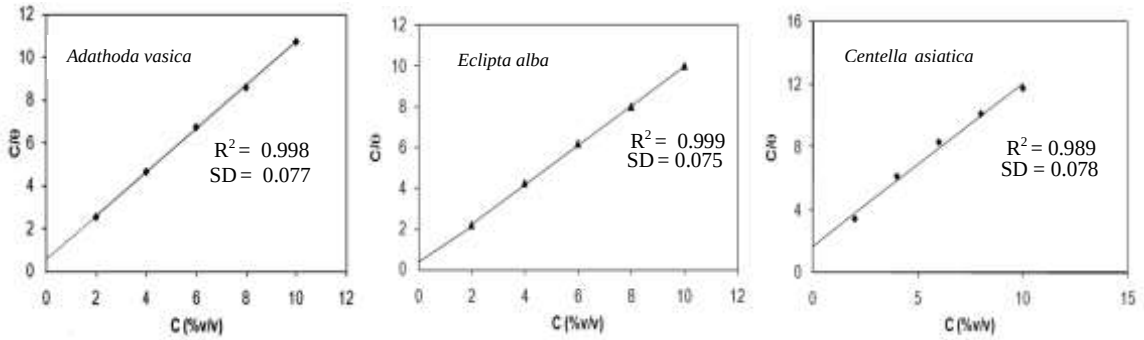



Figure 6. Langmuir adsorption isotherm plot for the adsorption of different concentrations of the green inhibitors on the surface of mild steel in 1N HCl solution

**Surface examination studies**

From the SEM images it shows the presence of a protective film over the surface of the mild steel in the presence of the inhibitors and the protective film is uniform in the order: *Eclipta alba* > *Adathoda vasica* > *Centella asiatica.* The SEM morphology of the adsorbed protective film on the mild steel surface has confirmed the high performance of inhibitive effect of the plant extracts as shown in Figures 7a to 7d, respectively.

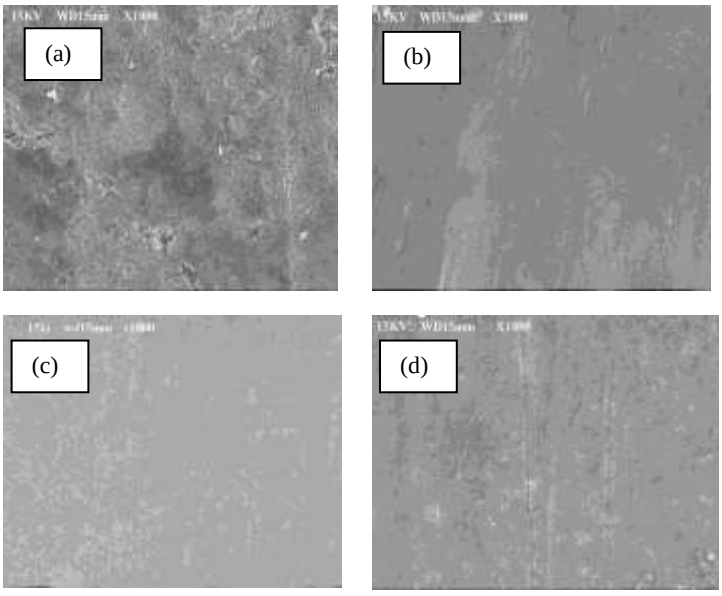



Figure 7. Mild steel immersed in 1N HCl solution (a) blank, (b) with optimum concentration (6% v/v) of *Adathoda vasica*, (c) optimum concentration (8% v/v) of *Eclipta alba* and optimum concentration (10% v/v) of *Centella asiatica*

From the hydrogen permeation studies on mild steel in 1N HCl in the absence and presence of inhibitors, it was observed that all the prepared extracts were able to reduce the permeation current compared to the control because

those inhibitors, which reduce the permeation current are good at inhibiting the entry of hydrogen into the metal concerned. The decrease in the permeation current follows the order: *Eclipta alba* > *Adathoda vasica* > *Centella asiatica.* Permeation current *vs*. time curves for mild steel in 1N HCl in the absence and presence of inhibitors are shown in Figure 8 and their corresponding permeation are given in Table 5.

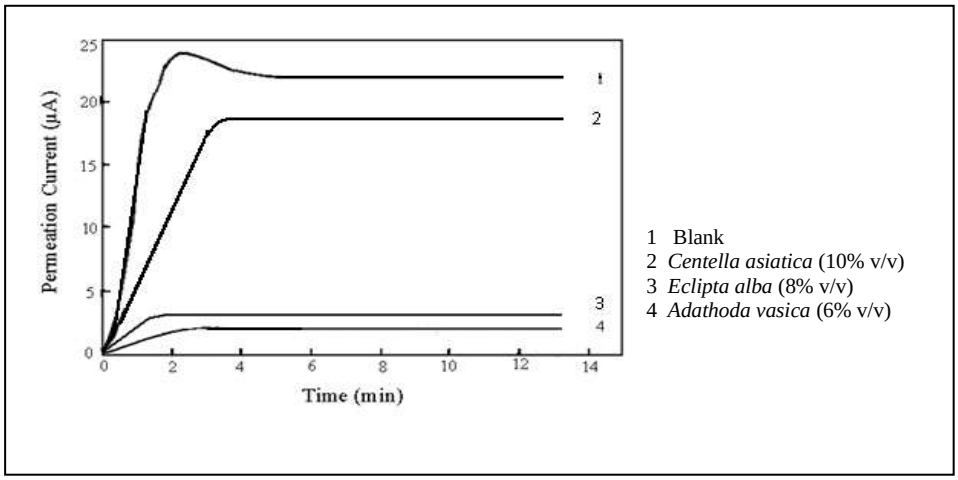



Figure 8. Hydrogen permeation current *vs.* time plots for mild steel in 1N HCl solution in the absence and presence of an optimum concentration of the plant extracts

Table 5. Hydrogen permeation current parameters in the absence and presence of inhibitors

| **Inhibitor** | **Conc. of the Extract (% in v/v)** | **Permeation Current (μA)** | **Reduction in Permeation Current (%)** |
|---|---|---|---|
| Blank | - | 23.0 | - |
| *Centella asiatica* | 10.0 | 19.4 | 15.65 |
| *Eclipta alba* | 8.0 | 2.2 | 90.43 |
| *Adathoda vasica* | 6.0 | 3.1 | 86.52 |

## Conclusion

Green inhibitors namely *Adathoda vasica*, *Eclipta alba* and *Centella asiatica* were proved to be good and efficient inhibitors for corrosion of mild steel in 1N hydrochloric acid. Potentiodynamic polarization studies revealed that the extracts act through mixed mode of inhibition. The impedance studies revealed that charge-transfer process mainly controls the corrosion of mild steel. The mechanism involved is the phytochemical constituents in the plant extracts have adsorbed on the metal surface forming a protective thin film layer preventing the discharge of $H^+$ ions and dissolution of metal ions and has prevented the small corrosion on the surface of the metal. The adsorption followed Langmuir adsorption isotherm. The SEM morphology confirmed the high performance of inhibitive effect of the green inhibitors. Results obtained in weight loss method were very much in good agreement with the electrochemical methods and hydrogen permeation method in the order: *Eclipta alba* > *Adathoda vasica* > *Centella asiatica* and among the three plant extracts studied, the maximum inhibition efficiency was found in *Eclipta alba* which showed 99.6% inhibition efficiency at 8.0% v/v concentration of the extract.

**References**

1. Muthukrishnan, P., Saravana Kumar, K., Jeyaprabha, B. and Prakash, P. (2014). Anticorrosive activity of *Kigelia pinnata* leaves extract on mild steel in acidic media. *Metallurgical and Materials Transactions A*, 45: 4510 – 4524.
2. Nazeer, A. A., Shalabi, K. and Fouda, A. S. (2015). Corrosion inhibition of carbon steel by Roselle extract in hydrochloric acid solution: Electrochemical and surface study. *Research on Chemical Intermediates*, 41(7): 4833 – 4850.
3. Gülşen, A. (2012). Corrosion inhibition of mild steel by Laurus nobilis leaves extract as green inhibitor. *Research on Chemical Intermediates*, 38(7): 1311 – 1321.
4. Shalabi, K., Fouda, A. S., Elewady, G. Y. and El-Askalany, A. (2014). Adsorption and inhibitive properties of *Phoenix dactylifera* L. extract as a green inhibitor for aluminum and aluminum-silicon alloy in HCl. *Protection of Metals and Physical Chemistry of Surfaces*, 50(3): 420 – 431.
5. Herb Information (2015). Access from www.himalayahealthcare.com/herbfinder.
6. Bhargava, K. K. (1970). Himalaya herbal monograph. *Indian Journal of Chemistry*, 8: 664.
7. Anupama, K. K. and Abraham, J. (2013). Electroanalytical studies on the corrosion inhibition behavior of guava (*Psidium guajava*) leaves extract on mild steel in hydrochloric acid. *Research on Chemical Intermediates*, 39(9): 4067 – 4080.
8. Al-Otaibia, M. S., Al-Mayoufa, Khana, M., Mousaa, A. A., Al-Mazroab, S. A and Alkhathlana, H. Z. (2014). Corrosion inhibitory action of some plant extracts on the corrosion of mild steel in acidic media, *Arabian Journal of Chemistry*, 7(3): 340 – 346.
9. Benali, O., Selles, C. and Salghi, R. (2014). Inhibition of acid corrosion of mild steel by *Anacyclus pyrethrum* L. extracts. *Research on Chemical Intermediates*, 40(1): 259 – 268.
10. Patel, N. S., Jauhariand, S., Mehta, G. N., Al-Deyab, S. S., Warad, I., and Hammouti, B. (2013). Mild steel corrosion inhibition by various plant extracts in 0.5 M sulphuric acid. *International Journal of Electrochemical Science*, 8: 2635 – 2655.

*Malaysian Journal of Analytical Sciences, Vol 21 No 2 (2017): 356 - 364*
*DOI: https://doi.org/10.17576/mjas-2017-2102-10*

MALAYSIAN JOURNAL OF ANALYTICAL SCIENCES
*Published by The Malaysian Analytical Sciences Society*
ISSN 1394 - 2506

# MORPHOLOGICAL PROPERTIES OF POLY(VINYLIDENE FLUORIDE-CO-TETRAFLUOROETHYLENE MEMBRANE): EFFECT OF SOLVENTS AND POLYMER CONCENTRATIONS

## (Sifat–Sifat Morfologi Membran Kepingan Rata Poli(Vinilidena Fluorida-Ko Tetrafluoridaetilena): Kesan Pelarut dan Kepekatan Polimer)

Amira Mohd Nasib*, Irfan Hatim, Nora Jullok, Hameed R. Alamery

*School of Bioprocess Engineering,*
*Universiti Malaysia Perlis, 02600 Arau, Perlis, Malaysia*

**Corresponding author: amira.m.nasib@gmail.com*

Received: 26 August 2016; Accepted: 8 January 2017

**Abstract**

Poly(vinylidene fluoride-co-tetrafluoroethylene) (PVDF-co-PTFE) flat sheet membranes were prepared via phase inversion process by means of immersion precipitation. The effects on the microstructure of prepared membranes by using different solvents and the effect of polymer solution composition (polymer concentration) on the membrane morphologies and the membrane porosity were studied. Three different solvents were employed, which were, N,N-dimethylacetamide (DMAc), N-methyl-2-pyrrolidone (NMP) and N,N-dimethylformamide (DMF). Different polymer concentrations were used; 20 wt.%, 25 wt.% and 30 wt.%. Brookfield viscometer was used to measure the viscosity for each polymer solution before the membrane was casting. The morphological study for the cross-sectional area of PVDF-co-PTFE membrane was carried out by using scanning electron microscope (SEM). The membrane porosity was determined by using the weight difference and density resulted from the immersing of dry membrane into octanol for 15 seconds. The results showed that the polymer concentration was a particularly important parameter. At different polymer concentration, the precipitant plays an important role and finally influence the prepared membrane microstructure. At higher concentration of PVDF-co-PTFE polymer, the prepared membrane possessed a sponge-like membrane structures, whereas at lower concentration, a finger-like structure was obtained. It was also found that, the membrane porosity decreases with the increasing of polymer concentration. The effect of different solvent reflected to different morphologies of the prepared flat sheet membranes. Prepared membrane with more sponge-like structure indicated a weak dissolution solvent was used. Hence, a small amount of water needed to induce precipitation and reduced the precipitation rate.

**Keywords**: PVDF-co-PTFE polymer, phase inversion, polymer concentration, membrane morphology

**Abstrak**

Membran kepingan rata poli (vinilidena fluorida-ko-tetrafluoridaetilena) (PVDF-ko-PTFE) telah disediakan dengan kaedah fasa penyongsangan menggunakan fasa pemisah bukan pelarut teraruh (FPBT). Kesan ke atas mikrostruktur membran tersedia dengan menggunakan pelarut yang berbeza dan kesan komposisi larutan penuangan (kepekatan polimer) ke atas morfologi membran dan keliangan membran telah dikaji. Tiga pelarut yang berbeza digunakan ialah N,N-dimetilasetamida (DMAs), N-metil-2-pirolidon (NMP) dan N,N-dimetilformamida (DMF). Kepekatan polimer yang berbeza akan digunakan, iaitu pada 20 wt.%, 25 wt.% dan 30 wt.%. Brookfield viskometer digunakan untuk mengukur kelikatan lasrutan polimer sebelum membran diacukan. Kajian morfologi bagi kawasan keratan rentas membran PVDF-co-PTFE telah dijalankan dengan menggunakan mikroskop elektron pengimbas (SEM). Analisis keputusan keliangan ditentukan dengan perendaman membran kering di dalam oktanol selama 15 saat. Keputusan menunjukkan bahawa kepekatan polimer adalah parameter penting. Pada kepekatan polimer yang berbeza, bahan pemendak memainkan peranan yang penting dan akhirnya mempengaruhi mikrostruktur membran tersedia. Pada kepekatan polimer PVDF-ko-PTFE yang lebih tinggi, membran tersedia memiliki struktur membran seperti span,

sedangkan pada kepekatan yang lebih rendah, struktur seperti-jejari telah diperolehi. Ia juga mendapati bahawa, keliangan membran menurun dengan peningkatan kepekatan polimer. Penggunaan pelarut yang berbeza terkesan kepada berlainan morfologi membran kepingan rata yang tersedia. Membran tersedia dengan struktur seperti span menunjukkan pelarut pelarutan lemah telah digunakan. Oleh itu, jumlah air yang sedikit diperlukan untuk mendorong mendakan dan mengurangkan kadar mendakan.

**Kata kunci**: PVDF-ko-PTFE polimer, fasa pemisah, kepekatan polimer, morfologi membran

## Introduction

The first commercial membrane was invented via phase inversion method by Loeb and Sourirajan in early 1960's [1]. Phase inversion is a demixing process whereby the initially homogenous polymer solution changed from a liquid to a solid state in a controlled manner. The process can be achieve in different ways, which are (a) non-solvent induced phase separation (NIPS) or known as immersion precipitation; (b) thermally induced phase separation (TIPS); and (c) vapour induced phase separation (VIPS). It is reported that among these techniques, NIPS is the most popular method for the membrane fabrication because it allows the preparation of many membrane morphologies [2, 3]. However, different variable of phase inversion parameters applied will give different morphological properties of the prepared membranes, and consequently on their properties [4]. These include the composition of polymer solution (polymer concentration, solvent, co-solvent, additives and their respective concentration) [5], the types of support materials (polymer, glass, metal, nonwovens, etc.) [6], the thickness of the casted polymer films [7], the temperature and evaporation time before immersion [8], as well as the temperature and composition of the coagulation bath [9]. Therefore, the preparation of membrane will exhibit different properties of the membranes and it is necessary to understand the factors contribute to the changes of membrane properties [10].

The membranes can be made from inorganic material and/or organic material. Fluoropolymers such as poly(vinylidene fluoride) (PVDF) is among attractive organic material that been used for commercial membrane fabrication. Usually, fluoropolymers possess a high thermal stability, chemical resistance and lower surface tension due to low polarizability and strong electronegativity of the fluorine atom, its small van Der Waals radius and the strong C-F bond [11-13]. The application fields of PVDF membrane had been reported by many researchers which include the application in pharmaceutical industry for removal of endotoxins from pharmaceutical grade-water system; application in membrane distillation for reverse osmosis pre-treatment for brackish water and seawater [14], application in waste water treatment for textile dye removal [15, 16], recovery of ethanol [17], application as a separator in lithium-ion rechargeable batteries [7], and absorption of $CO_2$ [18]. Despite the advantages of PVDF membrane mentioned in the previous work, there still a room for improvement to enhanced the hydrophobicity and mechanical properties of the prepared membrane [19, 20]. Poly(vinylidene fluoride-co-tetrafluoroethylene) (PVDF-co-PTFE) is a PVDF copolymer. The increase in the fluorine content results to more hydrophobic material than PVDF due to the incorporation of an amorphous phase of tetrafluoroethylene (TFE) into the main vinylidenefluoride (VDF) constituent blocks. The contact angle of PVDF membrane is around 70 to 80° can be increased up to 100° by using PVDF-co-PTFE polymer. In addition, Feng et al. (2004) in their study of preparation and properties of microporous membrane from PVDF-co-PTFE for membrane distillation reported that the addition of TFE in PVDF gave a superior mechanical strength compared to PVDF [21].

In this work, three different solvents (N,N-dimethylacetamide, N-methyl-2-pyrrolidone and N,N-dimethyl-foemamide) at different PVDF-co-PTFE polymer concentration (20 wt.%, 25 wt.% and 30 wt.%) was used to explore the effect on the prepared membrane properties. The polymer solution viscosity was measured by using Brookfield viscometer. Meanwhile, the morphologies of prepared membranes were characterized by using scanning electron microscope (SEM), whereas the membrane volume porosity was determined by gravimetric method.

## Materials and Methods

### Materials

Poly (vinylidene fluoride-co-tetrafluoroethylene) (PVDF-co-PTFE) was obtained from Arkema Pte Ltd, Singapore. Three solvents were used namely N,N-dimethylacetamide (DMAc), N-methyl-2-pyrrolidone (NMP) and N,N-dimethylfoemamide (DMF). DMAc (≥ 99.0% purity) was purchased from Merck Millipore Corporation, NMP (≥

99.5% purity) from Sigma Aldrichand DMF (≥ 95.0% purity) from Fisher Scientific. All solvents were used as a solvent without any purification.

**Polymer solution preparation**

PVDF-co-PTFE powder and its solvent (DMAc, NMP and DMF) were dissolved in a sealed conical flask under continuous rotation for 2 hours using an overhead stirrer. The rotation speed was constant at 200 rpm. Throughout the stirring process, the temperature of the mixture was maintained at 50 °C. A homogenous polymer solution was then degassed in an oven with a temperature of 45 to 50 °C for 24 hours [22].

**Phase inversion method**

The non-solvent induced phase separation (NIPS) was choosen to cast a flat sheet membrane. A PVDF-co-PTFE solution was casted onto a glass plate using a hand-casting knife with a knife gap set at 400±10 μm and followed by exposed to the surrounding air for 30 seconds. The cast film together with the glass plate was immersed into a coagulation bath immediately for 24 hours after the evaporation period come to an end. The coagulation bath medium consists of purely distilled water. Finally, the solidified membrane was taken out from the coagulation bath and dried at room temperature for 24 hours [22].

**Characterization of prepared membrane**

The polymer solution viscosity was measured by a Brookfield Dial Reading Viscometer (RVT Model) using a cylindrical sample container. The result of all measurement was taken from the mean of at least three single measurement at room temperature. Meanwhile, the prepared membrane surface and the cross section morphological studies was carried out by using a scanning electron microscope (SEM) model JSM 6260 LE JEOL. The pore sizes was observed through the SEM images and measured by using SEMAFORE software. Whereas, the porosity of the prepared membrane was analysed by using an octanol test. The membrane porosity, ω was defined as the volume of the membrane pores divided by the total volume of the porous membrane [21]. The sample was immersed into octanol for 15 seconds to improve the hydrophilicity. The sample was immersed into distilled water for 2 min before being dried using a filter paper. Mass of samples before and after soaked in both octanol and distilled water were recorded. Equation (1) was used to calculate the membrane porosity.

$$\omega = \frac{m_n/\rho_n}{m_n/_{p_n} + {}^{m_p}/_{\rho_p}} \quad (1)$$

where ω is the porosity of the membrane, $m_p$ is the mass of dry membrane (g), $m_n$ is the mass of absorbed octanol (g), $\rho_p$ is the density of the membrane (g/cm$^3$), and $\rho_n$ is the density of octanol (g/cm$^3$). This method is used to estimate the porosity by determined the weight of liquid contained in the membrane pores.

## Results and Discussion

**Effect of different solvent in polymer solution**

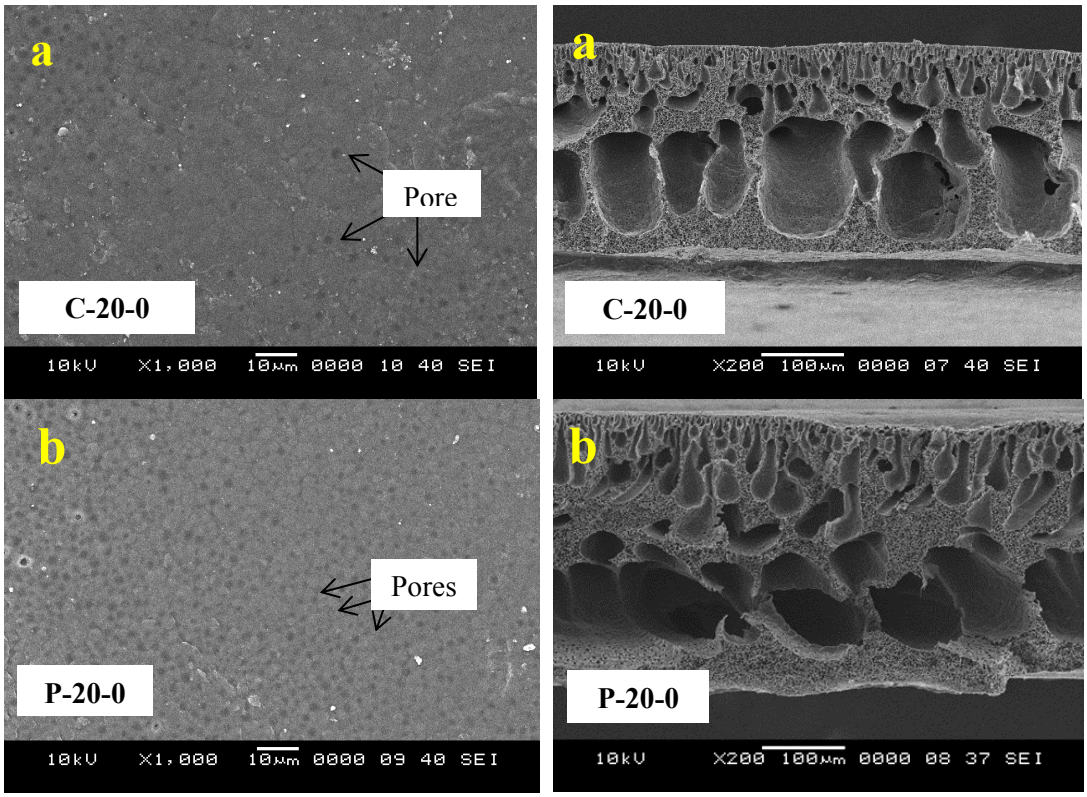
Three different solvents, DMAc, NMP and DMF were used to study the effect on the prepared membrane properties. The preparation of polymer solution was by adding 20 wt.% of PVDF-co-PTFE into 80 wt.% of solvent. Table 1 lists the formulation used to prepare the polymer membranes and the polymer solution viscosity reading.

Table 1. Fabrication conditions of flat sheet PVDF-co-PTFE membrane

| Membrane Code | Polymer Solution Composition | | Viscosity (cp) |
|---|---|---|---|
| | PVDF-co-PTFE (wt.%) | Solvent | |
| C-20-0 | 20 | 80 wt.% DMAc | 750 |
| P-20-0 | 20 | 80 wt.% NMP | 1000 |
| F-20-0 | 20 | 80 wt.% DMF | 2100 |

The viscosity of the polymer solution was an important parameter, which used to determine the inter-diffusion rate of solvent and non-solvent during the immersion precipitation process. Therefore, it affected the kinetics of the phase inversion throughout the membrane formation. As shown in Table 1, the viscosity of 20 wt.% PVDF-co-PTFE prepared with different solvents were found to be highest by using DMF and followed by NMP and DMAc respectively. According to Gracia-Fernandez, increasing of polymer solution viscosity reduced the coagulation rate of the polymer solution [23]. Hence, lower in coagulation rate hindered the formation of finger-like structure or even macro-voids.

Figure 1 shows the micrographs of the surface and cross sections of the flat sheet membranes. As can be seen from the figure, the cross sectional area of C-20-0, P-20-0 and F-20-0 membranes exhibited inhomogeneous structures due to the presence of large voids and cavities with different size and shape beneath the skin. It is observed that the number and size of interconnected macrovoids for the membrane casting with DMAc solvent was larger than the membrane casting with NMP and DMF solvents. This structure indicated a fast precipitation rate during the immersion process. Meanwhile, the least macrovoids formation can be seen from F-20-0 micrograph. The membrane microstructure exhibited a mixture of finger-like and a sponge-like structure throughout the membrane cross section. The elimination of macro-voids from the cross section structure along with the highest reading of polymer solution viscosity agree with each other. Similar result was obtained by Peng et al. where increasing the polymer solution viscosity was the main approach to suppress the macro-voids from the prepared membrane cross section [24].



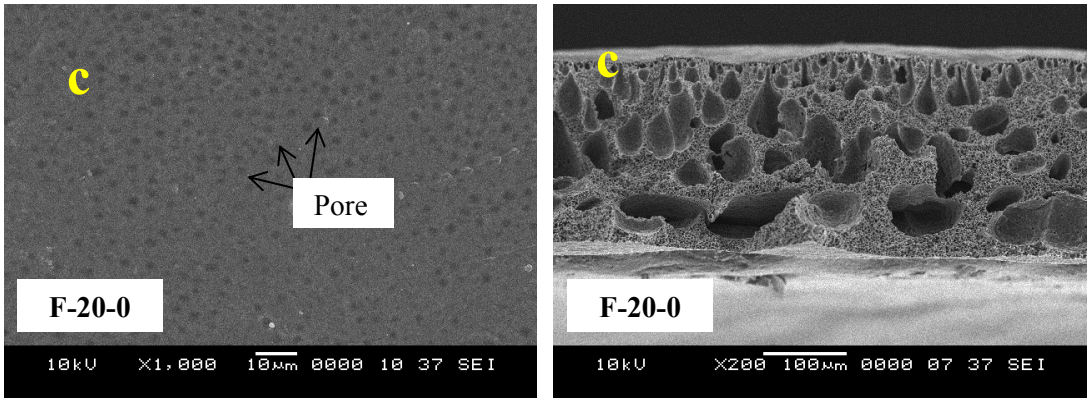



Figure 1. SEM micrographs of flat sheet membranes surface and cross sectional area prepared by using 20 wt.% PVDF-co-PTFE with different solvent; (a) DMAc, (b) NMP and (c) DMF

Table 2. Membrane pore size and porosity with different solvents

| Membrane Code | Solvent | Pore Size (µm) | | Porosity, ε (%) |
|---|---|---|---|---|
| | | Minimum | Maximum | |
| C-20-0 | DMAc | 4.3 ± 1.7 | 115.0 ± 35.1 | 47.6 |
| P-20-0 | NMP | 4.0 ± 1.6 | 153.8 ± 34.7 | 53.7 |
| F-20-0 | DMF | 4.3 ± 1.9 | 76.9 ± 20.6 | 35.8 |

It has been generally accepted that the morphology of prepared membrane affected by the precipitation rate which will then influences the membrane properties [19]. Table 2 represents the membrane properties of PVDF-co-PTFE membranes casted with different solvents in terms of pore sizes and porosity measured by using SEMAFORE software. It can be seen that the smallest pore size was contributed by F-20-0, followed by C-20-0 and P-20-0 respectively. The membrane used NMP as solvent obtained the maximum pore size of 153.8 µm, larger than those other membranes. The membrane prepared by NMP showed the highest porosity value which was 53.7%, which can be related to the pore sizes. This findings agreed with the research conducted by Li et al. in investigation of mixed solvents effect on the membrane performance [25]. Therefore, the growing of membrane macrovoids leads to higher porosity.

**Effect of polymer concentration**

Three different polymer concentrations were used (20 wt.%, 25 wt.% and 30 wt.%) to study their effects on the prepared flat sheet membrane. Table 3 summarizes the fabrication conditions of flat sheet PVDF-co-PTFE membrane along with their polymer solution viscosities. NMP was chosen to be a constant solvent for all three different polymer concentrations. Increasing the polymer concentration from 20 wt.% to 30 wt.% caused a greatly increasing of polymer solution viscosity from 1000 cp to 16500 cp.

Polymer concentration in polymer solution plays an important part in determining the membrane properties. Figure 2 represents the SEM micrographs of PVDF-co-PTFE flat sheet membrane using different polymer concentrations. It can be obviously seen that the increasing of polymer concentration in the casting solution changed the pore morphologies from large macrovoids to thin finger-like voids with combination of sponge-like elements. The number and size of maximum cavities were reduced with increasing of polymer concentration from 20 to 30 wt. %. The maximum cavities size was reduced from 153.8 µm at 20 wt.% to 46.2 µm at 30 wt. % of polymer concentration.

Table 3. Fabrication conditions of flat sheet PVDF-co-PTFE membrane

| Membrane Code | Polymer Solution Composition | | Viscosity (cp) |
|---|---|---|---|
| | PVDF-co-PTFE (wt.%) | Solvent | |
| P-20-0 | 20 | 80 wt.% NMP | 1000 |
| P-25-0 | 25 | 75 wt.% NMP | 3800 |
| P-30-0 | 30 | 70 wt.% NMP | 16500 |

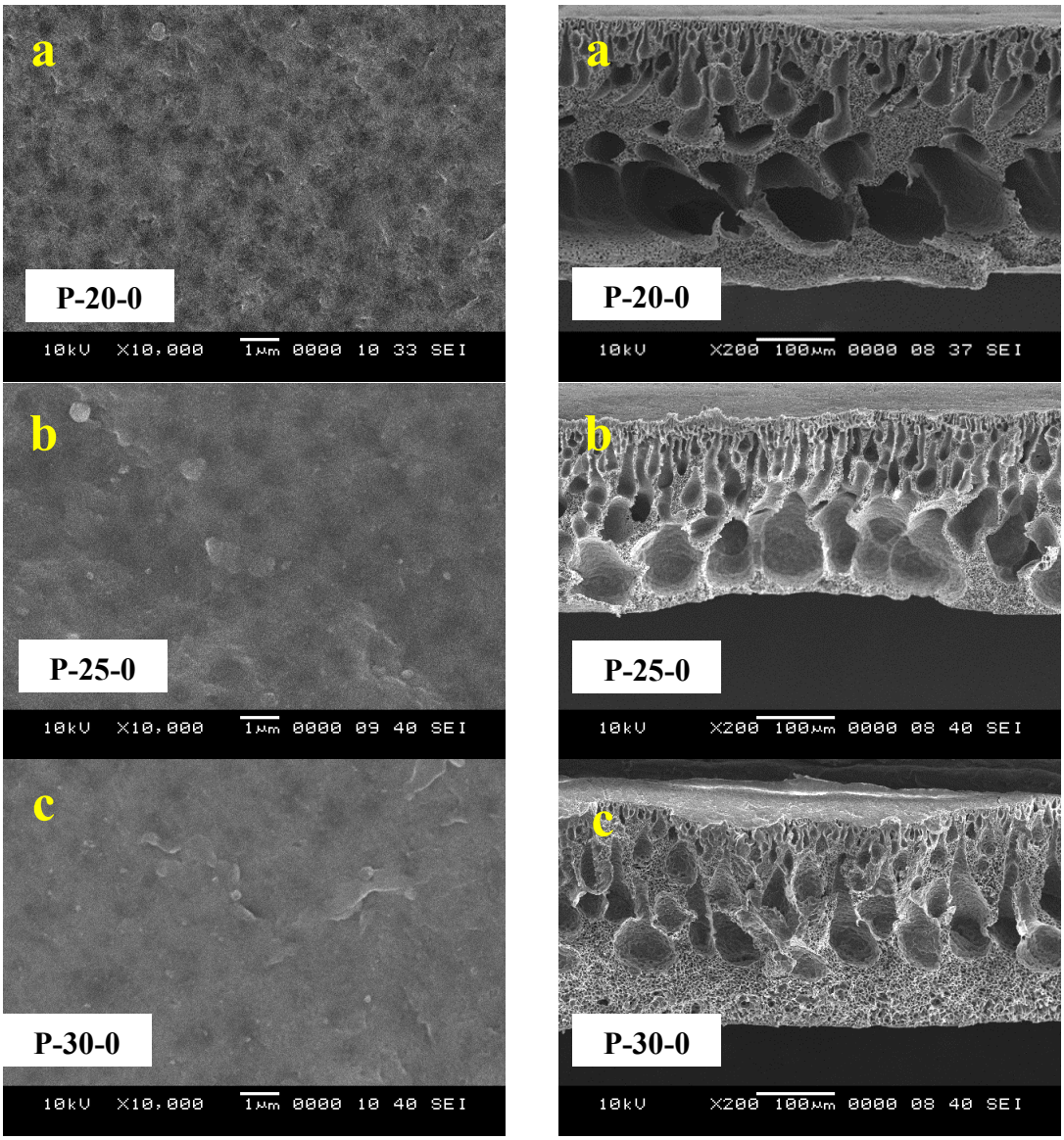



Figure 2. SEM micrographs of flat sheet membranes surface and cross sectional area using different polymer concentrations by using NMP as a solvent. (a) 20 wt.%, (b) 25 wt.% and (c) 30 wt.%

Increasing the polymer concentration resulted in higher polymer concentrations at the polymer/non-solvent interface prior the immersion in the non-solvent coagulation bath. This implied the volume fraction of polymer increases. Therefore, diffusion rate of solvent and non-solvent was slowed down, thus resulted in delay demixing. Consequently, the membrane morphology changes from macrovoids to a more spongy structure [3]. A similar result also found by Hołda et al. in the study of polysulfone concentration effects on the nanofiltration membranes. As the polysulfone concentration increased, the number of macrovoids decreases and their shape changes from a finger-like to pear-like structure [26]. The findings were also agreed in another research conducted by Marbelia et al. [8]. Formation of smaller pores as increasing of polymer concentration was due to the delayed liquid-liquid demixing between the solvent and non-solvent [8].

Figure 3 shows the effect of polymer concentration on porosity. The average porosity of membrane decreases with the increased of the polymer concentration. The increasing of polymer concentration in the polymer solution resulted in higher polymer concentration at the non-solvent interface. This implied that the volume fraction of polymer increased and consequently lower porosity was obtained [3].

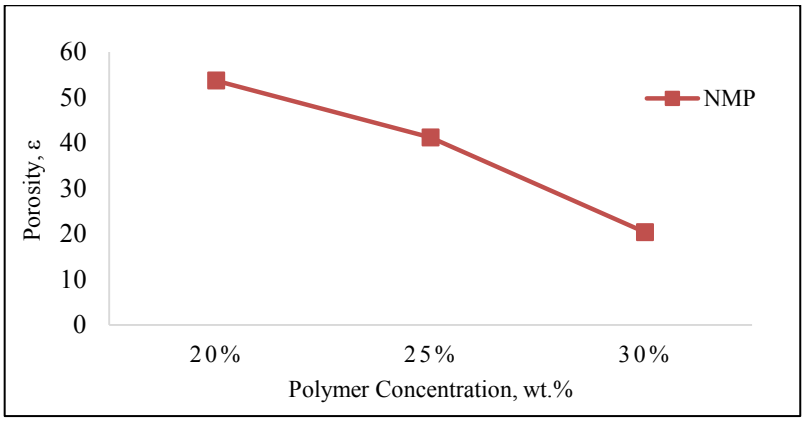



Figure 3. Effect of polymer concentration on PVDF-co-PTFE membrane porosity

## Conclusion

The PVDF-co-PTFE membranes were prepared by using phase inversion by means NIPS method. The membrane morphology, porosity and pore size obtained was greatly depends on the experimental parameters such as the selection of solvent and the concentration of polymer used. The results reveals that the types of solvents used in the casting solution considerably affected the membrane properties. From SEM micrographs, higher number of finger-like macrovoids formed when DMAC was used instead of DMF due to the rate of precipitation of polymer solution using DMAc is faster due to lower viscosity. On the other hand, sponge-like structure with lower porosity can be observed by using DMF as a solvent. With increasing polymer concentration lead to increasing in polymer solution viscosity, hence the precipitation rate becomes slower. The structure of the prepared membranes changes remarkably from finger-like macrovoids to sponge-like as the polymer concentration increased. In addition, the number of macrovoids also decreased. The alteration of the pore structure resulted in decreasing of pore sizes and consequently, the membrane porosity was reduced.

## Acknowledgement

This work was financially supported by research grant from Malaysia government.

## References

1. Liu, F., Hashim, N. A., Liu, Y., Abed, M. M. and Li, K. (2011). Progress in the production and modification of PVDF membranes. *Journal of Membrane Science*, 375(1): 1 - 27.

2. Mulder, J. (2012). Basic principles of membrane technology. Springer Science & Business Media.
3. Guillen, G. R., Pan, Y., Li, M. and Hoek, E. M. (2011). Preparation and characterization of membranes formed by nonsolvent induced phase separation: A review. *Industrial & Engineering Chemistry Research*, 50(7): 3798 - 3817.
4. Khayet, M. and Matsuura, T. (2011). Membrane distillation: Principles and applications. Elsevier, Amsterdam.
5. See-Toh, Y. H., Ferreira, F. C. and Livingston, A. G. (2007). The influence of membrane formation parameters on the functional performance of organic solvent nanofiltration membranes. *Journal of Membrane Science*, 299(1): 236 - 250.
6. Gevers, L. E., Aldea, S., Vankelecom, I. F. and Jacobs, P. A. (2006). Optimisation of a lab-scale method for preparation of composite membranes with a filled dense top-layer. *Journal of Membrane Science*, 281(1): 741 - 746.
7. Ji, G.-L., Zhu, B.-K., Cui, Z.-Y., Zhang, C.-F. and Xu, Y.-Y. (2007). PVDF porous matrix with controlled microstructure prepared by TIPS process as polymer electrolyte for lithium ion battery. *Polymer*, 48(21): 6415 - 6425.
8. Marbelia, L., M. R. Bilad, A. Piassecka, P.S. Jishna, P.V. Naik & I.F. Vankelecom, (2016). Study of PVDF asymmetric membranes in a high-throughput membrane bioreactor (HT-MBR): Influence of phase inversion parameters and filtration performance. *Separation and Purification Technology*, 162: 6 - 13.
9. Ahmad, A., Ramli, W., Fernando, W. and Daud, W. R. W. (2012). Effect of ethanol concentration in water coagulation bath on pore geometry of PVDF membrane for membrane gas absorption application in $CO_2$ removal. *Separation and Purification Technology*, 88: 11 - 18.
10. Buonomenna, M., Macchi, P., Davoli, M. and Drioli, E. (2007). Poly (vinylidene fluoride) membranes by phase inversion: the role the casting and coagulation conditions play in their morphology, crystalline structure and properties. *European Polymer Journal*, 43(4): 1557 - 1572.
11. Souzy, R. and Ameduri, B. (2005). Functional fluoropolymers for fuel cell membranes. *Progress in Polymer Science*, 30(6): 644 - 687.
12. Drobny, J. G. (2008). Technology of fluoropolymers. CRC Press, Florida.
13. Cui, Z., Drioli E. and Lee, Y. M. (2014). Recent progress in fluoropolymers for membranes. *Progress in Polymer Science*, 39(1): 164 - 198.
14. Alkhudhiri, A., Darwish, N. and Hilal, N. (2012). Membrane distillation: A comprehensive review. *Desalination*, 287: 2 - 18.
15. Kang, G.-D. and Cao, Y.-M. (2014). Application and modification of poly (vinylidene fluoride)(PVDF) membranes – A review. *Journal of Membrane Science*, 463: 145 - 165.
16. Deowan, S. A., Galiano, F., Hoinkis, J., Johnson, D., Altinkaya, S. A., Gabriele, B., Hilal, N., Drioli, E. and Figoli, A. (2016). Novel low-fouling membrane bioreactor (MBR) for industrial wastewater treatment. *Journal of Membrane Science*, 510: 524 - 532.
17. Zhan, X., Li, J., Huang, J.and Chen, C. (2010). Enhanced pervaporation performance of multi-layer PDMS/PVDF composite membrane for ethanol recovery from aqueous solution. *Applied Biochemistry and Biotechnology*, 160(2): 632 - 642.
18. Mansourizadeh, A., Ismail, A. F., Abdullah, M. S. and Ng, B. C. (2010). Preparation of polyvinylidene fluoride hollow fiber membranes for $CO_2$ absorption using phase-inversion promoter additives. *Journal of Membrane Science*, 355(1): 200 - 207.
19. Wang, J., Zheng, L., Wu, Z., Zhang, Y. and Zhang, X. (2016). Fabrication of hydrophobic flat sheet and hollow fiber membranes from PVDF and PVDF-CTFE for membrane distillation. *Journal of Membrane Science*, 497: 183 - 193.
20. Ameduri, B. (2009). From vinylidene fluoride (VDF) to the applications of VDF-containing polymers and copolymers: Recent developments and future trends. *Chemical Reviews*, 109(12): 6632 - 6686.
21. Feng, C., Shi, B., Li, G. and Wu, Y. (2004). Preparation and properties of microporous membrane from poly (vinylidene fluoride-co-tetrafluoroethylene)(F2.4) for membrane distillation. *Journal of Membrane Science*, 237(1): 15 - 24.
22. Ooi, B., Yatim, N., Ahmad, A. and Lai, S. (2012). Preparation of polyvinylidene fluoride membrane via dual coagulation bath system and its wettability study. *Journal of Applied Polymer Science*, 124(S1): 225 - 232

23. García-Fernández, L., García-Payo, M. and Khayet, M. (2014). Effects of mixed solvents on the structural morphology and membrane distillation performance of PVDF-HFP hollow fiber membranes. *Journal of Membrane Science*, 468: 324 - 338.
24. Peng, N., Chung, T.-S. and Wang, K. Y. (2008). Macrovoid evolution and critical factors to form macrovoid-free hollow fiber membranes. *Journal of Membrane Science*, 318(1): 363 - 372.
25. Li, Q., Xu, Z. L. and Yu, L.Y. (2010). Effects of mixed solvents and PVDF types on performances of PVDF microporous membranes. *Journal of Applied Polymer Science*, 115(4): 2277 - 2287.
26. Hołda, A. K., Aernouts, B., Saeys W. and Vankelecom, I. F. (2013). Study of polymer concentration and evaporation time as phase inversion parameters for polysulfone-based SRNF membranes. *Journal of Membrane Science*, 442: 196 - 205.

*Malaysian Journal of Analytical Sciences, Vol 21 No 2 (2017): 365 - 371*
*DOI: https://doi.org/10.17576/mjas-2017-2102-11*

MALAYSIAN JOURNAL OF ANALYTICAL SCIENCES
*Published by The Malaysian Analytical Sciences Society*
ISSN 1394 - 2506

# PREPARATION AND CHARACTERIZATION OF DIFFERENT LOADING OF ZINC OXIDE ON ACTIVATED CARBON NANOFIBERS

## (Penyediaan dan Pencirian Gentian-Nano Karbon Teraktif Pada Kepekatan Zink Oksida Yang Berbeza)

Faten Ermala Che Othman, Norhaniza Yusof*, Amirul Afiat Raffi, Hasrinah Hasbullah, Farhana Aziz, Wan Norharyati Wan Salleh, Ahmad Fauzi Ismail

*Advanced Membrane Technology Research Centre,*
*Faculty of Chemical & Energy Engineering,*
*Universiti Teknologi Malaysia, 81310 Skudai, Johor Bahru, Malaysia*

**Corresponding author: norhaniza@petroleum.utm.my*

Received: 26 August 2016; Accepted: 8 January 2017

**Abstract**

The study deals on the modified PAN-based activated carbon nanofibers (ACNFs) embedded with different amount of zinc oxides (ZnO) (0, 5, 10, and 15% relative to PAN wt.) to be used as adsorbents for natural gas adsorption. The nanofibers (NFs) were successfully fabricated via electrospinning process at optimize parameters. The resultant NFs underwent three steps of pyrolysis process which are stabilization, carbonization and activation at optimum parameters. The morphological structure and diameter of pure and modified ACNFs were characterized using SEM while the existences of chemical bonds were analyzed by FTIR analysis. XRD analysis was done to identify the crystallinity of the ACNFs. BET method was used to identify the specific surface area (SSA) and nitrogen adsorption isotherm of the samples. The results showed that the SSA of ACNF5 (163.04 $m^2/g$) is significantly higher compared to the pristine and other modified ACNFs, nevertheless the obtained results is much lower compared to average theoretical value. SEM micrograph depicted that all ACNF samples possessed average diameter of 300 – 500 nm with smooth and aligned structure. The presence of white spots as ZnO alongside the NFs has been confirmed with FTIR and XRD analysis. From these findings, it is believed that ACNFs/ZnO will become a new adsorbent with great potential for gas adsorption and storage in the near future applications.

**Keywords**: activated carbon nanofibers, zinc oxide, polyacrylonitrile, specific surface area

**Abstrak**

Kajian ini membincangkan tentang gentian-nano karbon teraktif (ACNFs) terubah suai berasaskan polimer PAN yang digabungkan dengan kandungan zink oksida (ZnO) yang berbeza (0, 5, 10, dan 15% berdasarkan berat PAN) untuk digunakan sebagai penjerap dalam penjerapan gas asli. Gentian-nano (NFs) telah berjaya direka melalui proses putaran elektro menggunakan parameter-paramter optimum daripada kajian terdahulu. Kemudian, NFs yang terbentuk akan melalui tiga peringkat proses pirolisis iaitu penstabilan, karbonisasi, dan pengaktifan menggunakan parameter optimum daripada kajian terdahulu. Struktur morfologi dan diameter ACNFs tulen dan yang telah diubahsuai dengan ZnO telah dicirikan menggunakan SEM manakala kewujudan ikatan kimia telah dianalisis menggunakan FTIR. Selain itu, untuk mengenalpasti penghabluran ACNFs yang terhasil, analisis yang dikenali sebagai XRD telah dijalankan. Kaedah BET pula dijalankan untuk mengenal pasti luas permukaan tertentu (SSA) dan isoterma penjerapan nitrogen. Hasil kajian menunjukkan bahawa SSA sampel ACNF5 (163,04 $m^2/g$) adalah lebih tinggi berbanding dengan ACNFs tulen atau ACNFs yang telah diubahsuai yang lain..Walau bagaimanapun, keputusan yang diperoleh menunjukkan SSA yang jauh lebih rendah berbanding dengan nilai teori purata. Melalui SEM mikrograf, semua sampel ACNFs yang dihasilkan melalui kajian ini memiliki diameter purata dari 300 hingga 500 nm dengan struktur licin dan sejajar. Kehadiran bintik putih sebagai ZnO telah disahkan melalui analisis FTIR dan XRD.

Penemuan ini membuktikan bahawa ACNFs/ZnO akan menjadi penjerap baru yang mempunyai potensi besar dalam aplikasi penjerapan dan penyimpanan gas pada masa hadapan.

**Kata kunci:** gentian karbon teraktif, zink oksida, poliakrilonitril, luas permukaan spesifik

## Introduction

Activated carbon (AC) has been widely utilized as adsorbent in various applications in recent years included in water or gas adsorption due to their porous structure, high specific area, and cost-friendly [1]. Currently, AC can be developed by using various types of precursors such as pitch, lignin, polymers, and also synthetic precursor, however polyacrylonitrile (PAN)-based adsorbents have become an attractive alternative as PAN precursor could produce high carbon yield up to 56% as compared to the other precursors [2]. However, a new enhanced material known as activated carbon nanofibers (ACNFs) with highly microporous structure with finer structure and greater specific surface area [3] have been developed in order to overcome the disadvantages of AC that possessed low SSA and limited the gas adsorption capabilities. Ascribed by its low resistance to bulk flow, high adsorption-desorption kinetics, heat stability, and high strength; PAN-based ACNFs have received major attention from researcher all over the globe and were studied for their potential as excellent gas adsorbents [4].

Nanofibers (NFs) can be fabricated by various techniques included template synthesis, phase separation, electrospinning, and self-assembly [5]. Out of those available techniques, electrospinning seems to produce NFs with smaller diameter with uniform distribution structures. Moreover, electrospinning offers more advantages than other techniques such as versatility, efficiency, and feasibility in large quantities production. Recently, in order to improvised the NFs structures, the electrospun NFs were subjected to activation process to create new macropores and micropores structures, with smaller fiber diameter and greater SSA. Furthermore, incorporation of additives such as metal oxide into the NFs was proven can enhance the structure of the NFs. Metal oxide nanoparticles such as magnesium oxide (MgO), manganese dioxide ($MnO_2$), zinc oxide (ZnO), and nickel oxide (NiO) have been profound to be as excellent candidate that could enhance the physicochemical properties of PAN-based ACNFs due to their catalytic effects [6]. These nanoparticles themselves are high in SSA and the addition of right amount of these nanoparticles into the NFs solution are believed could improve their structure as well as adsorption capabilities.

In this study, the ACNFs embedded with ZnO were produced through suitable electrospinning and activation method under optimum parameters obtained from previous studies [7]. The objective of this present study is to prepare the ACNFs incorporated with ZnO and to study their microstructural properties and surface area for suitable gas adsorbent materials.

## Materials and Methods

### Nanofibers fabrication

The polymer polyacrynitrile (PAN) and solvent N, N-dimethylformamide (DMF) were purchased from Sigma-Aldrich while zinc oxide (ZnO) powder was purchased from Alfa Aesar. Homogenous DMF solutions of PAN containing 0, 5, 10, and 15% (relative to PAN wt.) of ZnO were stirred gently for 24 hours at room temperature. The nanofibers (NFs) were prepared by using a lab-scale electrospinning machine NFOM1000-1503 supplied from Nfiber at optimum voltage of 12.4kV, the distance between the needle tip to collector of 20 cm, and flow rate of 1 ml/hour. The resultant NFs with 0, 5, 10, and 15% of ZnO were denoted as NF0, NF5, NF10, and NF15, respectively.

### Activation of nanofibers

The resultant NFs were underwent three stages of pyrolysis process. Start with stabilization with pure air until the temperature of 275 $^{\circ}$C, followed by carbonization under inert air condition until 600 $^{\circ}$C, and finally activation with activating gas such as carbon dioxide until 800 $^{\circ}$C, in order to improve the porous structure of the NFs and directly increasing the specific surface area with 30 minutes of resting time for each stage. After activation, the NFs were known as activated carbon nanofibers (ACNFs). In this study, ACNFs with 0, 5, 10, and 15% of ZnO were denoted as ACNF0, ACNF5, ACNF10, and ACNF15, individually.

**Characterization**

In order to better understanding of the PAN-based ACNF/ZnO produced, there are several characterization analyses have been conducted. The morphology and diameter of the NFs have been characterized using field emission scanning electron microscopy (FESEM) while the elemental analysis and chemical studies of the NFs were analyzed by using X-ray diffraction (XRD) analysis and Frontier Transform Infrared (FTIR) analysis, respectively. Moreover, Brunauer–Emmett–Teller (BET) analysis was used in order to study specific surface area and pore size distribution of all the resultant NFs. The surface area and microspore analysis of NFs and ACNFs were investigated using nitrogen gas ($N_2$) adsorption isotherm at 77 K (ASAP2020, Micromeritics, USA).

## Results and Discussion

**Morphological studies of nanofibers**

Figure 1 shows the SEM images of PAN-based ACNF/ZnO with different loading of ZnO prior activation. It can be seen that the all NFs possessed smooth, straight, and aligned structure with several white spots attached alongside the fibers (Figure 1b, c, d) that represent the existence of ZnO. The fibers diameter was varied in all concentrations. From the figure, it obviously can be seen that the pristine NFs possessed the largest fiber diameter as compared to NFs embedded with ZnO. It was found that addition of ZnO has reduced the diameter of the NFs up to 45%, with average diameter of NF0 is 576.8 ± 55.91 nm and was reduced to 325 ± 43.1 nm in all modified NFs (NFs embedded with ZnO).

After activation, the NFs were transformed into activated carbon nanofibers (ACNFs) and the SEM photographs of all pristine and modified ACNFs are shown in Figure 2. It can be seen that the ACNFs possessed rougher, irregular, and undulated structure compared to NFs prior activation. The average diameter of the all NFs also decreased up to 40% from 450 nm to 270 nm due to the removal of PAN and other molecules during the heat treatment resulting in weight loss and NFs' diameter reduction [8, 9]. As shown in Figure 2(b), ACNF5 possessed the finest fiber structure with well-dispersed and a few agglomeration of ZnO alongside/inside the ACNFs as compared to the others.

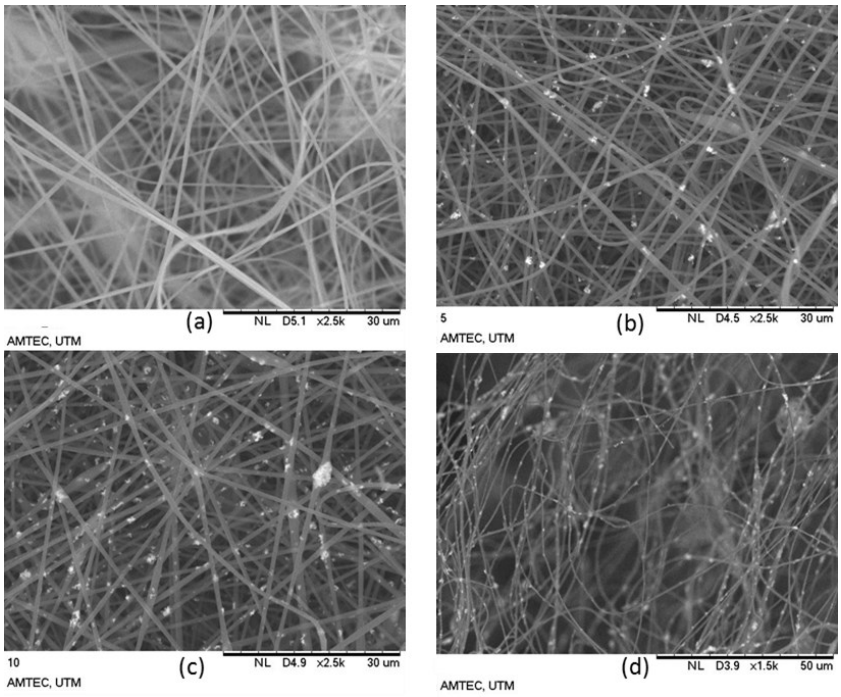



Figure 1. SEM micrograph of nanofibers with different loading of zinc oxide prior activation (a) NF0, (b) NF5, (c) NF10 at 2500x magnification and (d) NF15 at 1500x magnification

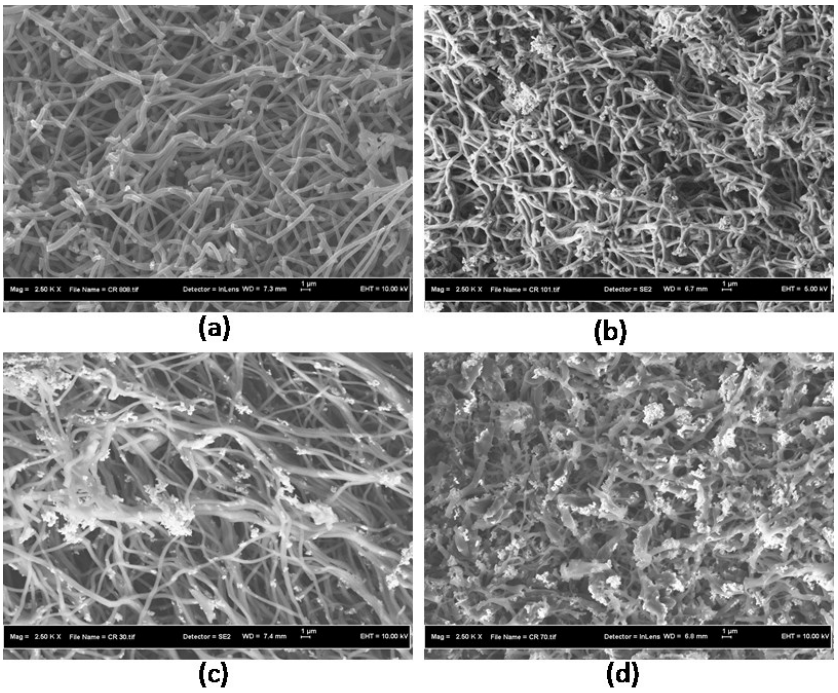



Figure 2. SEM micrograph of nanofibers with different loading of zinc oxide after activation (a) ACNF0, (b) ACNF5, (c) ACNF10, and (d) ACNF15 at 2500x magnification

Although this result counterback the result of previous research conducted by Dadvar et al. [6], as they said the increasing the amount of metal oxide loaded, the smaller the diameter of the NFs; this study has concluded that NFs were only affected by the amount of metal oxide, which is up to its maximum loading depends on the type of the metal oxide used in order to produce NFs with better structure. This phenomenon is believed could start as early as during the dope preparation and fiber preparation stages as the amount and types of the metal oxide used can affect the viscoelasticity of the solution and varies the ejection time of jet to arrive at the collector and these behaviors are believed to give impact to the diameter of the NFs [10].

**Chemical bond studies**

Figure 3 shows the FTIR spectra for NFs embedded with 0 and 5% of ZnO prior and after activation. As can be seen, there are various peaks appeared in the NFs prior activation (Figure 3a) and some of the peaks were removed after activation due to heat treatment (Figure 3b), and it is believed only carbon and hydrogen peaks were left. Theoretically, numerous new transition structures were formed during pyrolysis. As can be seen in Figure 3(a), there are five major peaks can be detected in both NF0 and NF5 that represent different vibrations existed in the NFs prior activation. However, there is one high peak was detected at wavenumber 445.7 $cm^{-1}$ in NF5 that represents Zn-O vibrations [11, 12]. Nevertheless, the appearance of unknown peak around wavenumber 400 – 700 $cm^{-1}$ in Figure 3 is believed due to the existence of other vibrations that overlapped at the same wavenumber range such as C-C, C-N, and C-O. After activation, there are only three major peaks were detected at 1285.5, 1433.1, and 1581.7 $cm^{-1}$ represent C=O, C-H, and C=C vibrations, respectively [13].

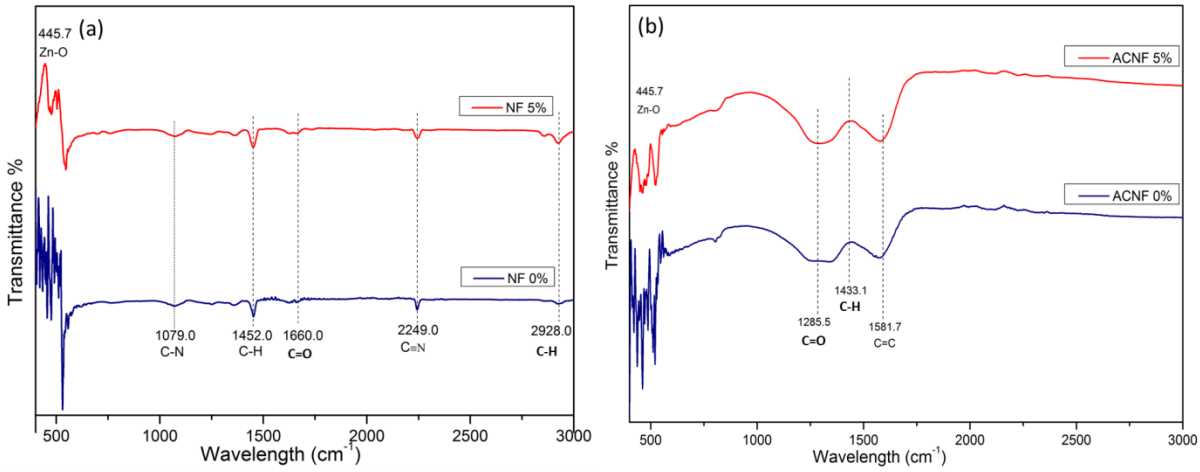



Figure 3. FTIR spectra of NF0 and NF5 (a) prior activation and (b) after activation

**Elemental analysis**

The crystallographical behaviors of both NF0 and NF5 prior and after activation have been analyzed by using X-ray diffraction analysis as shown in Figure 4. It can be seen that prior activation, the structure of the NFs is amorphous and after activation, the structure become more crystalline. As shown in Figure 4(a), the obvious peak detected at 16.7$^{o}$ in NF0 represents the polymer PAN peak [12] while the other two sharp peaks that only appeared in NF5 at 31.85 and 36.3$^{o}$ represents the ZnO peaks. However, in Figure 4(b), the polymer peak changed to carbon peak after activation and it was detected at 13.2$^{o}$ [13]. As detected in Figure 4(a), the same ZnO peaks were also observed in ACNF5 with addition of two other ZnO peaks at 34.6 and 47.55$^{o}$ [14 – 16]. It is believed these two peaks already appeared in the NF5; however it cannot be seen due to amorphous structure of the NFs.

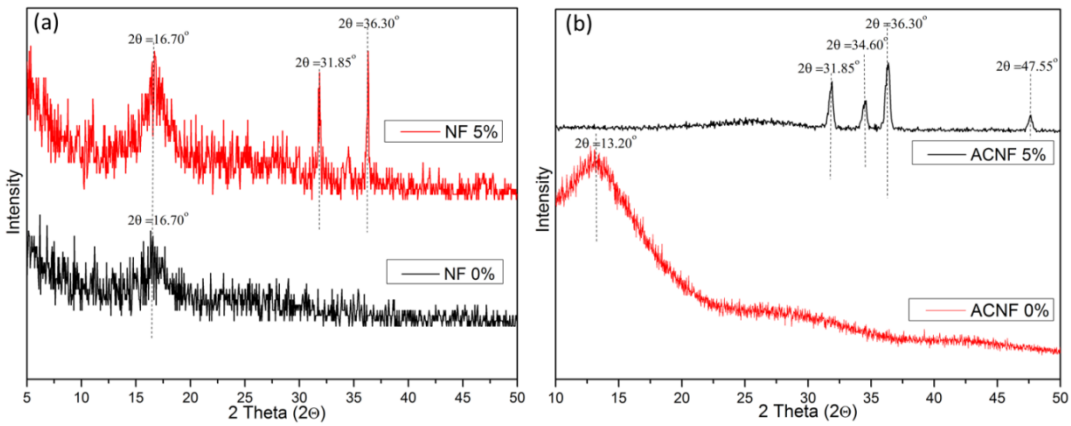



Figure 4. X-ray diffractogram of NF0 and NF5 (a) prior activation and (b) after activation

**BET surface area**

Brunauer–Emmett–Teller (BET) analysis was used to determine the specific surface area (SSA) of all resultant NFs as depicted in Table 1. Prior activation, the addition of low or high concentration of ZnO bring no effect to the enhancement of SSA of the NFs (see data in Table 1), in contrast it shows pristine NFs possessed the largest SSA.

However, after heat treatment was conducted to the NFs, there is significant increment in SSA of NFs especially for ACNF5 that possessed total SSA of 163.04 $m^2/g$. The result obtained was comparable to the previous study conducted by Kahjwal and friends (2016) [16] as they obtained BET results of 137 $m^2/g$ after the calcination of NFs embedded with ZnO at 700 $^oC$.

However, the addition of 10 and 15% of ZnO into the NFs showed no significant increment in SSA even after activation as compared to the ACNFs with 5% ZnO. This phenomenon occurred due to the higher amount of ZnO (more than 5%) could probably inhibited the catalytic effect of the ZnO that increasing the diameter of the resultant NFs and it also believed the fiber distribution became broader. As the diameter increases, the SSA are believed to reduce and it is important to note that the right amount of ZnO are the main concern in order to produce NFs with smaller diameter and high SSA. Higher specific surface area is believed could increase the adsorption performance due to increasing adsorption active sites [17].

Table 1. Comparison of specific surface area of nanofibers embedded with different concentration of ZnO prior and after activation

| Sample | Prior activation ($m^2/g$) | After activation ($m^2/g$) |
|---|---|---|
| NF0 | 9.1300 | 3.9446 |
| NF5 | 8.9070 | 163.0416 |
| NF10 | 5.3658 | 29.1523 |
| NF15 | 7.4454 | 24.9459 |

## Conclusion

Thorough chemical, physical and thermal characterizations that have been employed in this study, the effects of incorporating ZnO in PAN-based NFs have been investigated. Composite ACNF/ZnO after heat treatment possessed average diameter of 270 nm and SSA obtained ranging from 3.9446 to 163.0416 $m^2/g$. By using various type of characterization techniques like FE-SEM, BET, XRD, and FTIR, have provided better understanding on morphological and structural properties of PAN-based ACNFs embedded with various concentration of ZnO.

## Acknowledgement

The authors would like to acknowledge the financial support from the Malaysian Ministry Education and Universiti Teknologi Malaysia under GUP grant (Q.J130000.2542.05H46 and Q.J130000.2546.12H54) and Higher Institution Centre of Excellent (HiCoE) grant. One of the authors would also like to acknowledge the technical and management support from Research Management Centre (RMC), Universiti Teknologi Malaysia.

## References

1. Diez, N., Díaz, P., Álvarez, P., González, Z., Granda, M., Blanco, C., Santamaría, R. and Menéndez, R. (2014). Activated carbon fibers prepared directly from stabilized fibers for use as electrodes in supercapacitors. *Materials Letters*, 136: 214 – 217.
2. Liu, H. Q. and Hsieh, Y. L. (2002). Ultrafine fibrous cellulose membranes from electrospinning of cellulose acetate. *Journal of Polymer Science B: Polymer Physics*, 40: 2119 – 2129.
3. Alcañiz-Monge, J., Lozano-Castelló, D., Cazorla-Amorós, D. and Linares-Solano, A. (2009). Fundamentals of methane adsorption in microporous carbons. *Microporous and Mesoporous Materials*, 124(1-3): 110 – 116.
4. Díez, N., Alvarez, P., Granda, M., Blanco, C., Santamaria, R. and Menéndez, R. (2015). A novel approach for the production of chemically activated carbon fibers. *Chemical Engineering Journal*, 260: 463 – 468.
5. Kumar, P. R., Khan, N., Vivekanandhan, S., Satyanarayana, N., Mohanty, A. K., and Misra, M. (2012). Nanofibers: Effective generation by electrospinning and their applications. *Journal of Nanoscience and Nanotechnology*, 12: 1 – 25.

6. Dadvar, S., Tavanai, H. and Morshed, M. (2012). Effect of embedding MgO and $Al_2O_3$ nanoparticles in the precursor on the pore characteristics of PAN based activated carbon nanofibers. *Journal of Analytical and Applied Pyrolysis*, 98: 98 – 105.
7. Bhardwaj, N. and Kundu, S. C. (2010). Electrospinning: A fascinating fiber fabrication technique. *Biotechnology Advances*, 28: 325 – 347.
8. Venugopal, J., Zhang, Y. Z. and Ramakrishna, S. (2004). Electrospun nanofibres: biomedical applications. *Proceedings of the Institution of Mechanical Engineers, Part N: Journal of Nanomaterials, Nanoengineering and Nanosystems*, 218(1): 35 – 45.
9. Khalil, K. A., Sherif, E. M., Nabawy, A. M., Abdo, H. S., Marzouk, W. W. and Alharbi, H. F. (2016). Titanium carbide nanofibers-reinforced aluminium compacts, a new strategy to enhance mechanical properties. *Materials*, 9(5): 399 – 413.
10. Haroosh, H. J., Dong, Y., Chaudhary, D. S., Ingram, G. D. and Yusa, S. I. (2013). Electrospun PLA/PCL composites embedded with unmodified and 3-aminopropyltriethoxysilane (ASP) modified halleysite nanotubes (HNT). *Applied Physics A: Materials Science and Processing*, 110(2): 433 – 442.
11. Harish, K. and Renu, R. (2013). Structural and optical characterization of ZnO nanoparticles synthesized by microemulsion route. *International Letters of Chemistry, Physical and Astronomy*, 19: 26 – 36.
12. Sun, M., Lan, B., Lin, T., Cheng, G., Ye, F., Yu, L., Cheng, X. and Zheng, X. (2013). Controlled synthesis of nanostructured manganese oxide: crystalline evolution and catalytic activities. *CrystEngComm*, 15(35): 7010 – 7018.
13. Yusof, N. and Ismail, A. F. (2012). Post spinning and pyrolysis processes of polyacrylonitrile (PAN)-based carbon fiber and activated carbon fiber: A review. *Journal of Analytical and Applied Pyrolysis*, 93: 1 – 13.
14. Babu, K. S., Reddy, A. R., Sujatha, C., Reddy, K. V. and Mallika, A. N. (2013). Synthesis and optical characterization of porous ZnO. *Journal of Advanced Ceramics*, 2(3): 260 – 265.
15. Cipriani, E., Zanetti, M., Bracco, P., Brunella, V., Luda, M. P. and Costa, L. (2015) Crosslinking and carbonization processes in PAN films and nanofibers. *Polymer Degradation and Stability*, 123: 178 –188.
16. Kanjwal, M. A., Barakat, N. A., Sheikh, F. A., Park, D. K. and Kim, H. Y. (2010). Physicochemical characterizations of electrospun ($ZnO$-$GeO_2$) nanofibers and their optical properties. *Journal of Materials Science,* 45(14): 3833 – 3840.
17. Im, J. S., Park, S. J., Kim, T. J., Kim, Y. H. and Lee, Y. S. (2009). The study of controlling pore size on electrospun carbon nanofibers for hydrogen adsorption. *Journal of Colloid and Interface Science*, 318 (1): 42 – 49.

*Malaysian Journal of Analytical Sciences, Vol 21 No 2 (2017): 372 - 380*
*DOI: https://doi.org/10.17576/mjas-2017-2102-12*

MALAYSIAN JOURNAL OF ANALYTICAL SCIENCES
*Published by The Malaysian Analytical Sciences Society*
ISSN 1394 - 2506

# SURFACE MODIFICATION OF PSF/$TIO_2$ MEMBRANES USING SILANE COUPLING AGENTS AND DC PLASMA TECHNIQUE

## (Modifikasi Permukaan Membran PSF/$TiO_2$ Menggunakan Ejen Gandingan Silana dan Teknik Plasma DC)

Soraya Ruangdit[1], Thawat Chittrakarn[1]*, Sudkhet Anuchit[1], Yutthana Tirawanichakul[1], Chalad Yuenyao[2]

*[1]Membrane Science and Technology Research Center, Department of Physics, Faculty of Science, Prince of Songkla University, Hat Yai, Songkhla 90112, Thailand*
*[2]Department of Physics, Faculty of Science and Technology, Phetchabun Rajabhat University, 83 M.11 St.Saraburi-Lom Sak, Muang, Phetchabun 67000, Thailand*

**Corresponding author: tawat.c@psu.ac.th*

Received: 26 August 2016; Accepted: 8 January 2017

**Abstract**

Preparation and surface modification of PSF/$TiO_2$ membranes by DC Ar-plasma were conducted to improve membrane hydrophilicity and gas permeation efficiency. Using $TiO_2$ as a photocatalyst, photocatalysis could be induced upon the plasma exposure. Radicals from this process led to an increase in the membrane hydrophilicity. In order to improve the dispersion quality of $TiO_2$ in an organic membrane, methyltrimethoxysilane (TMMS) or ethyltrimethoxysilane (TEMS) was utilized as coupling agents to modify the $TiO_2$ surface prior to blending. The coupling agents caused organic silane bonds on the $TiO_2$ surface leading to a better dispersion of nanoparticle on the membrane matrix. The incorporation of modified-$TiO_2$ tended to decrease membrane water contact angles (WCA) to the lowest value when compared with PSF membranes with unmodified $TiO_2$ and neat PSF membranes. Results also showed that TMMS could produce better outcomes compared to TEMS. It was found that the modified-$TiO_2$ could decrease the WCA. More importantly, pressure normalized flux of $CO_2$ and $CH_4$ gases of PSF/modified-$TiO_2$ membrane was found to increase with slightly decrease in the selectivity of $CO_2/CH_4$.

**Keywords**: silane coupling agent, surface modification, gas separation membrane, low pressure DC-plasma, polysulfone

**Abstrak**

Penyediaan dan modifikasi permukaan membran PSF/$TiO_2$ oleh DC Ar-plasma telah dijalankan untuk meningkatkan kehidrofilikan membran dan kecekapan penyerapan gas. Menggunakan $TiO_2$ sebagai foto-pemangkin, fotopemangkinan dapat didorong apabila terdedah kepada plasma. Radikal daripada proses ini membawa kepada peningkatan dalam kehidrofilikan membran. Untuk meningkatkan kualiti penyebaran $TiO_2$ dalam membran organik, metiltrimetoksisilana (TMMS) atau etiltrimetoksisilana (TEMS) telah digunakan sebagai agen gandingan untuk mengubah suai permukaan $TiO_2$ sebelum campuran. Ejen-ejen gandingan menyebabkan ikatan silana organik di permukaan $TiO_2$ yang membawa kepada penyebaran nanopartikel yang lebih baik pada matriks membran. Penggabungan $TiO_2$ yang diubahsuai cenderung untuk mengurangkan sudut sentuhan air membran (WCA) kepada nilai yang paling rendah berbanding membran PSF dengan $TiO_2$ yang tidak diubahsuai dan membran PSF kawalan. Keputusan juga menunjukkan bahawa TMMS boleh menghasilkan hasil yang lebih baik berbanding PPSMI. Ia telah mendapati bahawa $TiO_2$ yang diubahsuai boleh mengurangkan WCA. Lebih penting lagi, tekanan fluks normal gas $CO_2$ dan $CH_4$ daripada membran PSF/$TiO_2$ yang diubahsuai didapati meningkat dengan sedikit penurunan kepilihan $CO_2/CH_4$.

**Kata kunci:** ejen gandingan silana, modifikasi permukaan, membran pemisahan gas, tekanan rendah dc-plasma, polisulfon

## Introduction

Membrane technology is currently widely used in many industrial sectors and one of its important applications is for gas separation process. As $CO_2$ gas is the main causes of greenhouse effect that leads to global warming, many attempts were made to develop an ideal membrane for $CO_2$ adsorption and separation [1]. Polysulfone (PSF) is one of the high potential and widely used polymers because it has many advantages such as excellent stability and resistivity to high temperature and acid-base environments and easy to be used for membrane making [2, 3]. However, PSF is hydrophobic in nature [4]. For the PSF membranes to be used in the $CO_2/CH_4$ gas separation, the hydrophilicity of the membrane surface needs to be improved. This improvement is quite important due to the differences of the quadrupole moments of these two gases [5].

Konruang et al. [5] discussed differences of several gases that have small molecules and very little differences in size. Besides, electronic properties, polarizability and quadrupole moment, which we can be used for the extract gas, were also discussed. Table 1 shows the structure, polarizability and quadrupole moment of $CO_2$ and $CH_4$ gases [6]. Considering electronic properties of $CO_2$ and $CH_4$ gases, we can see that membrane surfaces, which have a higher polarity can absorb a higher polarizability and quadrupole moment gas more than of lower polarizability and quadrupole moment gas. Therefore, hydrophilic properties represent the polarity of membrane surfaces, which is the cause for $CO_2$ to permeate more through such a membrane than $CH_4$. The quadrupole moment affects the gas permeation through the membranes. For hydrophilic polymeric membranes, the permeability of $CO_2$, which has a quadrupole moment and polarizability of about $13.4 \times 10^{-40}$ $Cm^2$ and $2.93\times 10^{-40}$ $J^{-1}C^2m^2$, respectively, is higher than of $CH_4$, which has a quadrupole moment and polarizability of about zero and $2.89\ 10^{-40}$ $J^{-1}C^2m^2$, respectively [6]. Therefore, research and development are required to improve the hydrophilicity of membranes. [5].

Table 1. Structure, physical and electronic properties of gas molecules [6]

| **Molecule** | **Structure** | **Polarizability** ($10^{-40}$ **$J^{-1}$ $C^2$ $m^2$**) | **Quadrupole moment** ($10^{-40}$ **C $m^2$**) |
|---|---|---|---|
| $CO_2$ | Linear | 2.93 | 13.4 |
| $CH_4$ | Tetrahedral | 2.89 | 0 |

Titanium dioxide ($TiO_2$) can improve the hydrophilicity of membranes because of its photocatalytic property [7, 8]. Typically, electrons in the valence band of a photocatalytic material will jump to the conduction band when they are stimulated by a photon. The holes are created in the valence band and the electron from the donor molecule can move to this hole. At the same time, an electron from the valence band can be transferred to the acceptor [9, 10]. For this reason, the photo catalyst can take the interaction with the molecules at the material surface. Additionally, the stimulation of $TiO_2$ at the membrane surface can decrease the surface roughness and eventually, lead to the decrease in membrane contact angle [11].

However, the minimum energy for the stimulation of $TiO_2$ has to be equal with the band energy gap that is about 3.2 eV [12, 13]. Unlike PSF, $TiO_2$ is an inorganic material and the dispersion of $TiO_2$ particles in the PSF matrix is quite low. Madaeni et al. [14] studied the increase of $TiO_2$ loading in polyethersulfone (PES) support. Here, an increase in the $TiO_2$ content of the polydimethylsiloxane (PDMS) matrix lead to an increase in the self-condensation, polarity, and polar groups. Nevertheless, the $CO_2$ permeability in that work is reported to decrease. Chen and Yakovlev [15] studied the modification of $TiO_2$ nanoparticles by the interaction with organic silane. They found the creation of Si-O-Ti bonds and organic groups after $TiO_2$ was modified by 3-aminopropyltrimethoxysilane (APTES) and phenyltrimethoxysilane (PTMS).

This current work studied the modification of PSF membranes using dry/wet phase inversion method. $TiO_2$ nanoparticles were modified by silane-coupling agents, including trimethoxymethylsilane (TMMS) and triethoxymethylsilane (TEMS). The modified $TiO_2$ was then incorporated into the PSF membrane matrix to increase its hydrophilic properties and the permeance of $CO_2$. In order to further enhance the gas separation properties, the

obtained membranes were treated by DC Ar-plasma and then the permeance of the hydrophilicity of plasma treated membranes was studied.

## Materials and Methods

Pellets of PSF (UDEL P-1700) were supplied by Solvay (China). Polymer solvents included N,N-dimethylacetamide (DMAc) and tetrahydrofuran (THF) was purchased from Sigma-Aldrich (Singapore) and ACI Lab-scan (Australia), respectively. Titanium dioxide ($TiO_2$; 32 nm APS powder MW. 79.90) nanoparticles, methyltrimethoxysilane (TMMS) and ethyltrimethoxysilane (TEMS) were supplied by Alfa Aesar (China). The TMMS and TEMS were used as silane coupling agent while $TiO_2$ was used as an inorganic additive. Ethanol (EtOH) and methanol (MeOH) were supplied by J.T. Baker. All chemicals and materials were used as received.

In order to modify the surface of $TiO_2$ nanoparticles by a silane coupling agent, 1 g of $TiO_2$ was dispersed in 100 ml of RO water under vigorous stirring. The obtained solution was sonicated for 10 min before the addition of the silane coupling agent with a concentration of 12.5 wt.%. The reflux process was taking place for 5 hours at a temperature of 80 $^oC$. The as-modified $TiO_2$ was alternately cleaned by RO water and EtOH and collected by centrifugation at 10,000 rpm twice. The collected $TiO_2$ was then dried at 100 $^oC$ for 24 hours before use.

In the first step of membrane preparation, PSF pellets were dried at 80 $^oC$ for 24 hours to remove moisture. The dry/wet phase inversion method was used for membrane preparation in this research. Four types of membranes were prepared. They are pure PSF, PSF/$TiO_2$, PSF/($TiO_2$-TMMS) and PSF/($TiO_2$-TEMS) membranes. The PSF/($TiO_2$-TMMS) and PSF/($TiO_2$-TEMS) ones were PSF membranes incorporated with $TiO_2$ and further modified by TMMS and TEMS agent. The membrane designations before and after plasma treatment are shown in Table 2.

Table 2. Designation of the samples

| Sample | Plasma Treated | Untreated |
|---|---|---|
| PSF | A1 | B1 |
| PSF/$TiO_2$ | A2 | B2 |
| PSF/($TiO_2$-TEMS) | A3 | B3 |
| PSF/($TiO_2$-TMMS) | A4 | B4 |

During membrane preparations, PSF, DMAc, THF and $TiO_2$ (or $TiO_2$-TMMS or $TiO_2$-TEMS) were blended at a weight ratio of 22.5:38.25:38.25:1.0, respectively, at 50 – 60 $^oC$ for 24 hours. The completely dissolved solution was then cast on a smooth and clear glass plate with a wetting thickness of about 150 µm. The cast membrane was freely placed in ambient air (evaporation time, ET) for 90 and 120 s before immersed in RO-water for 15 min followed by in MeOH solution for another 2.5 hours. Subsequently, the membrane was dried under ambient conditions for 24 hours. Finally, the membrane was dried in an electric oven at 70 $^oC$ for 12 hours before usage.

The optimized membrane surface was further modified by DC glow discharge plasma generated from Ar gas. The membrane sample was placed on the anode electrode as shown in Figure 1. The inter-electrode gap was controlled at about 3 cm. Before Ar gas was fed into the plasma chamber, gas pressure in the chamber was controlled at $5.90\times10^{-2}$ mbar. Afterwards, Ar gas was fed into the chamber through a needle valve until the pressure reached $2.00\times10^{-1}$ mbar. The pressure was constant throughout the plasma treatment. Discharge power and treatment time were 20 W and 4 min, respectively.

After plasma treatment, membrane hydrophilicity was determined by measurements of water contact angle (WCA) at different ageing times. The spread tendency of a liquid that drops on a smooth surface of a solid. To measure the WCA, the contact angle measuring instrument (Model OCA 15 EC, Data Physics Instruments GmbH, Germany) was used. Membrane samples for WCA measurements were cut into rectangular shape with a dimension of 3 mm in width and 10 mm in length. The membrane was fixed on a clear and smooth glass slide. Liquid was dropped on the

membrane surface and the measured WCA was analyzed by using SCA software. The WCA was measured for at least three times per sample and the average was presented in Table 3. Fourier transform infra-red (FTIR) spectroscope was used to analyze the functional groups on the modified membrane surface. The distribution of $TiO_2$ particles in the membrane matrix was analyzed through the micrograph of the scanning electron microscope (SEM) while the skin layer thickness was measured by SEM micrograph combined with the computer software, Carnoy versions 2.0®. Atomic force microscope (AFM) was utilized to analyze the roughness of membrane surfaces. The separation properties of all resultant membranes were evaluated through gas permeation measurement.

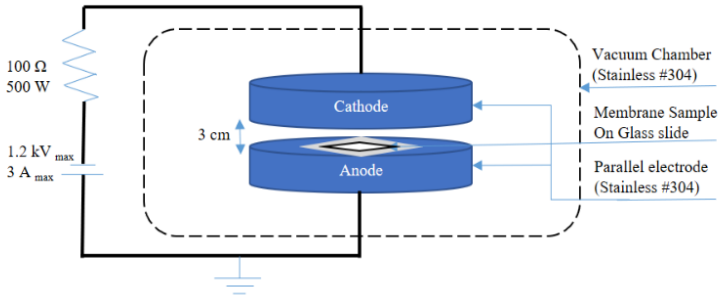



Figure 1. Schematic diagram of the membrane sample placed on the anode electrode in the DC plasma system used in this work.

Table 3. Water contact angle of membrane samples prepared at different conditions

| Samples | Water contact angle (θ) | |
|---|---|---|
| | Evaporation Time (ET) 90 s | Evaporation Time (ET) 120 s |
| B1 | 83.30 ± 5.19 | 83.80 ± 6.22 |
| B2 | 92.36 ± 2.09 | 81.89 ± 0.43 |
| B3 | 81.84 ± 2.30 | 89.86 ± 1.82 |
| B4 | 72.95 ± 1.83 | 70.07 ± 5.90 |

## Results and Discussion

### Water contact angle

As shown in Table 3, contact angles of membranes prepared at ET of 90 s, it was found that WCA of B2 increased to 92.36° whereas the WCA of B4 and B3 decreased to 72.95° and 81.84°, respectively. For membranes prepared at ET of 120 s, the highest WCA value was measured on the surface of B3 whereas the lowest WCA appeared on the surface of B4. WCA of B4 was 13° lower than of the pure B1 membrane. This indicated that modified $TiO_2$ by TMMS gave membranes with higher hydrophilic than by TEMS.

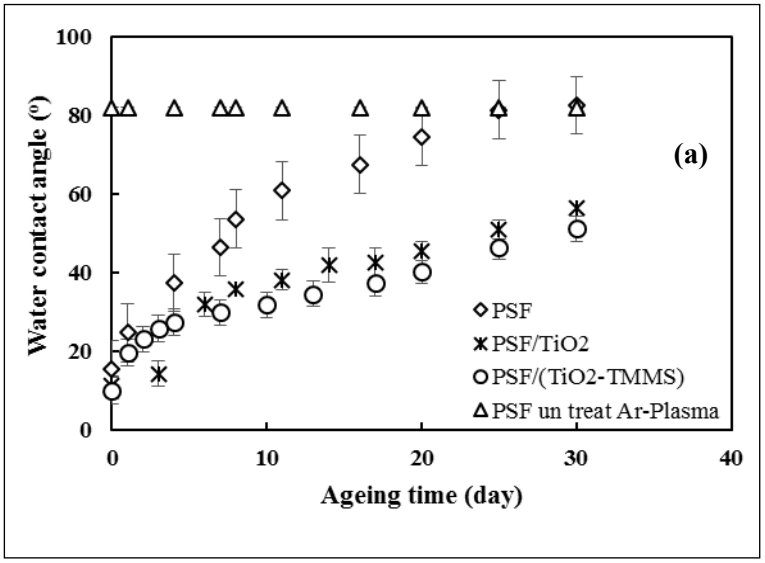
Table 4 shows the WCA of Ar-plasma treated membrane surfaces. It can be seen that WCA of PSF membranes that were plasma treated with a discharge power and exposure time of 20 W and 4 min, respectively, decreased clearly. From Table 4, WCA of A4 membrane prepared at ET of 90 and 120 s decreased about 60°. The lowest WCA (9.96 ± 5.32°) appeared on the surface of A4 membrane prepared at ET of 120 s. This phenomenon showed that TMMS affected the dispersion of $TiO_2$ in the matrix of PSF membranes. Furthermore, the photocatalytic property of $TiO_2$ in PSF membranes was stimulated by plasma radiation leading to an increase in hydrophilicity. TMMS showed an increase silane bonds on $TiO_2$ surface which enable it to improve functional groups of organic compounds capture, as explained by Zhao et al. [16].

Table 4. Water contact angle of Ar-plasma treated (20 W, 4 min) membranes

| Sample | Contact angle (θ) | |
|---|---|---|
| | Evaporation Time (ET) 90 s | Evaporation Time (ET) 120 s |
| A1 | 17.06 ± 2.35 | 15.34 ± 1.35 |
| A2 | 17.36 ± 2.51 | 11.11 ± 2.45 |
| A4 | 12.58 ± 3.57 | 9.96 ± 2.32 |

When the surface of $TiO_2$ was improved with TMMS, $TiO_2$ exhibited properties of organic material and was well dispersed in an organic membrane. Typically, $TiO_2$ showed the photocatalytic properties after it was activated by plasma. These phenomena represent the increase of hydrophilic properties. Similar to Hashimato et al. [11] suggestion, $TiO_2$ excited by ultraviolet (UV) light revealed hydrophilic properties. Besides, $TiO_2$ can induce the dissociation of water without the use of external voltage. Therefore, $TiO_2$ induced the surface of a membrane to be more hydrophilic. The glow discharge plasma consisted of several elements and a frequency range of UV. UV light encourages its photocatalytic properties. In this work, the permanency of hydrophilicity of plasma treated membrane was evaluated. We found that in the ageing time of 30 days, WCA of plasma treated membrane surface gradually retrieved to the WCA of pure and untreated PSF membrane. The WCA of pure and plasma treated membrane recovered faster when compared with A2 and A4 membranes. Importantly, the lowest recovery of WCA appeared on the surface of A4.

Figure 2 shows that the WCA of plasma treated PSF membranes was increased with ageing time. Using B1 as a reference, the WCA of A1 increased faster when compared with that of A2 and A4 membranes. However, WCA of A1 and became close to B1 membrane in the storage time of 25 days. The recovery rate of WCA in A2 was similar to the result obtained from A4 membrane. For A2 membranes prepared with ET of 120 s, WCA increased to 56.25 ± 1.96° after being stored at room temperature for 25 days, while the A4 at the same ageing time showed about 51.24 ± 1.47°. It was clear that WCA at ageing time of 30 days of A4 recovered slower than that of A2 membranes. Additionally, for the membrane prepared with ET 90 s, WCA of A2 and A4 membrane were about 70.33 ± 1.24° and 58.35 ± 1.64°, respectively. It was confirmed that modified $TiO_2$ can prolong the hydrophilicity of the plasma treated PSF membranes. Due to the fact that hydrophilicity of the membrane surface easily causes contamination by airborne smirch in ambient condition. This explained the temporary water-like property [6].



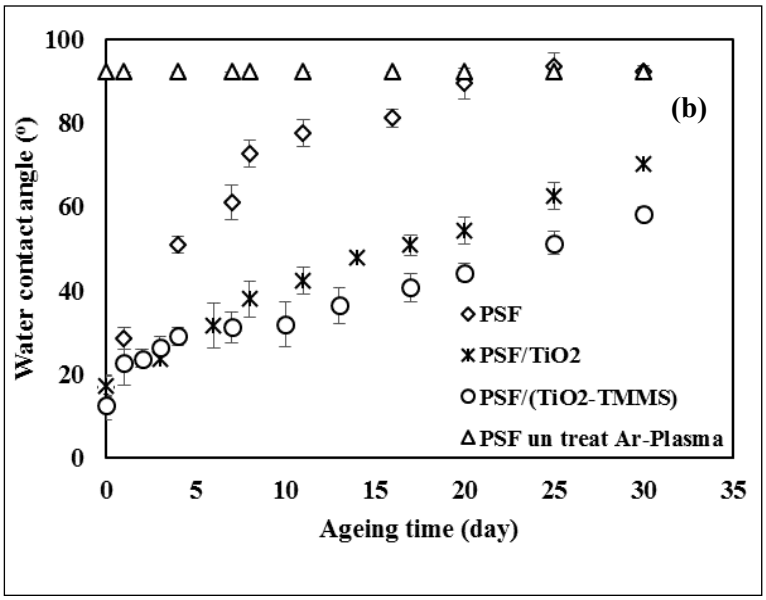



Figure 2. Variation of WCA with a storage time of 30 days of untreated and Ar-plasma treated membranes prepared at ET 120 s (a) and 90 s (b). PSF: A1, PSF/TiO2: A2, PSF/(TiO2-TMMS): A4 and PSF untreated Ar-Plasma: B1.

**Fourier transform infra-red spectroscopy**

Since PSF membranes are organic materials whereas $TiO_2$ is an inorganic material, the agglomeration of $TiO_2$ generally take place when it is blended in PSF membranes. To improve this problem, the modification of $TiO_2$ surfaces by a silane coupling agent was conducted. The objective of this modification was to introduce the organic functional group on the surface of $TiO_2$ nanoparticles. Introduction of organic groups on the surface of $TiO_2$ affected the dispersion of them in the polymer matrix. Figure 3 shows the FTIR spectrum of B2 and B4 membranes. It is shown that the Ti-O-Si bonds [17] appeared in a wavenumber range of 910 – 960 $cm^{-1}$. In the B4 system more Ti-O-Si bonds were created than in the B2 system. The number of Ti-O-Si bonds creations lead to an increase of the compatibility of the modified $TiO_2$ with the matrix of PSF membranes.

**Scanning electron microscope results**

Figure 4 shows an SEM micrograph at a magnification of 5,000x of a membrane cross section and Figure 4(a) shows the thick and dense selective layer and a large number of pores in the sub-structure of B1. The agglomeration and dispersion of $TiO_2$ particles in the membrane structure can be observed through the SEM micrograph. From Figure 4(a) and 4(b), the thicknesses of the skin layer membranes are 0.9 and 0.1 µm, respectively. $TiO_2$ was dispersed less in the PSF matrix compared to the modified ones with TMMS. This shows the enhancement of Ti-O-Si bonds in B4 membranes within 0.3 µm membrane thickness. The selective or skin layer of both B2 and B4 was thinner than of the B1 membrane. Additionally, the wall of pore of B2 and B4 membranes were thicker than of the B1 membrane. The variation of skin layer thickness affected the gas permeation rate of prepared membranes. According to these reasons, the plasma treated membrane showed greater gas permeation rate in A4 membrane compared to that of A1 and A2 membranes.

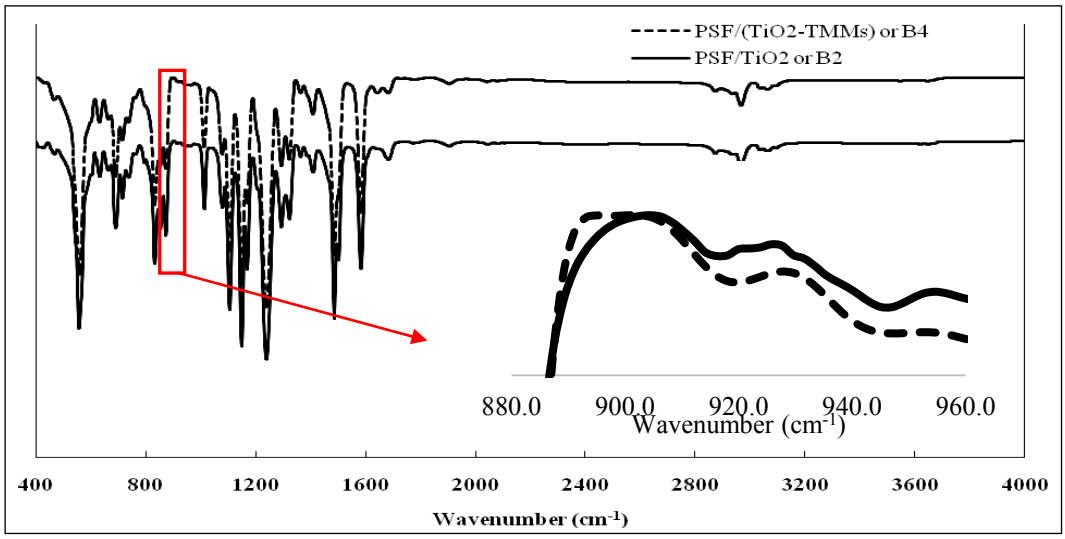



Figure 3. FTIR spectrum of B2 and B4 membranes.

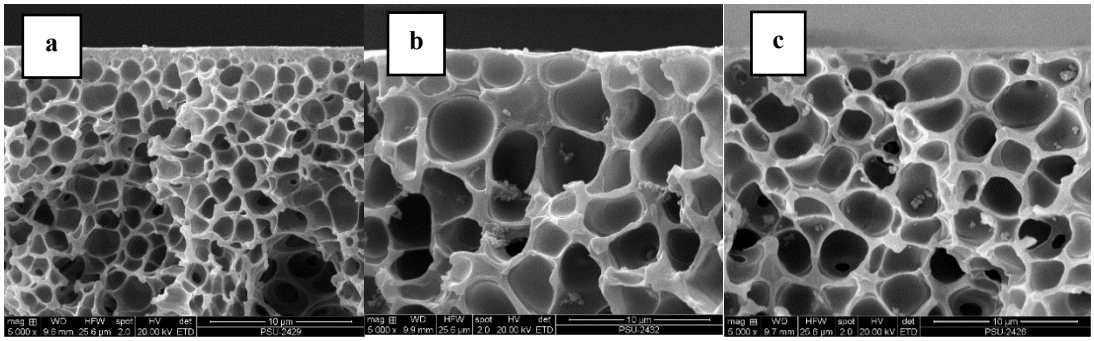
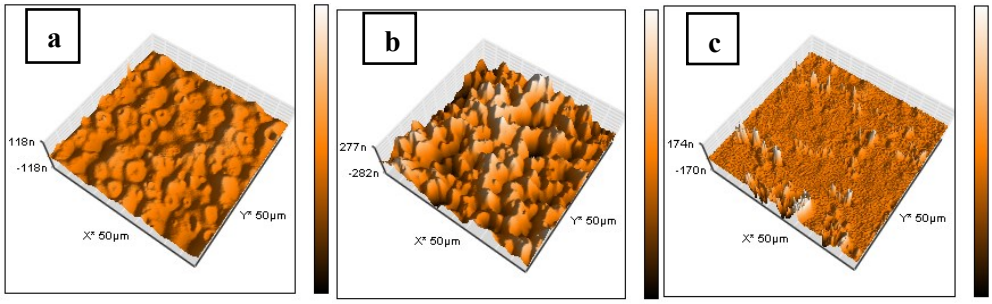



Figure 4. SEM micrographs (5,000x) of B1 (a), B2 (b) and B4 (c) membranes prepared with ET of 120 s

**Atomic force microscope**

Figure 5(a) to (c) show the surface morphology of B1, B2, and A4 membranes. An area of 50×50 $\mu m^2$ was scanned. It was shown that the highest roughness appeared on the surface of the B2 membrane prepared with ET of 120 s, whereas for plasma treated PSF/($TiO_2$-TMMS), A4 membranes, the lowest roughness appeared when compared with B2 membranes. AFM results, when PSF was adulterated by $TiO_2$ it creates more roughness on the membrane surface as shown in Figure 5b (roughness at nanometer scale). After plasma treatment, the membrane surface was reduced in its roughness, as shown in Figure 5c. It should be emphasized that the smoother surface does not reflect more hydrophilicity upon the decrease nanoscale roughness, which then reduces the probability of the lotus effect occurrence. This finding is useful and can be explored further.




Rms 11.359 nm Rms 92.013 nm Rms 29.875 nm

Figure 5. AFM micrographs of B1 (a), B2 (b), and A4(c) membranes after plasma treatment

**Gas permeation testing**

The maximum permeance of $CO_2$ was about 80.81±0.09 GPU measured with the A4 membrane, which was prepared with ET of 120 s. This result corresponded to the aim of this study. The $CO_2$ permeance of A4 membranes is higher than of A1 and A2 membranes prepared with the same ET. From Table 5, it can be seen that the $CO_2$ permeance of A1 and A2 membranes were about 18.36 ± 0.07 and 17.46 ± 0.05 GPU, respectively. Similarly, the permeance of $CH_4$ increased from 3.29 ± 0.05 to 18.59 ± 0.07 GPU for A1 and A4 membranes, respectively. In addition to the gas permeance, the maximum $CO_2/CH_4$ selectivity was about 6.84 ± 0.01 for A2 membranes prepared with ET of 120 s. It was shown that the selectivity of gas inversely varied with the gas permeance. Consequently, the minimum ideal $CO_2/CH_4$ selectivity of about 4.34 ± 0.01 determined for the A4 membranes because these membranes showed the maximum gas permeation. To enhance both the permeance and the selectivity of gases, further studies should be conducted with new aspects such as facilitated transport and refined mixed matrix membranes to be considered.

Table 5. Permeance (P/L) and ideal $CO_2/CH_4$ selectivity of plasma treated membranes (ET 120 s)

| Sample, ET 120 s | P/L (GPU) | | Selectivity of $CO_2/CH_4$ |
|---|---|---|---|
| | $CO_2$ | $CH_4$ | |
| A1 | 18.36(±0.07) | 3.29(±0.05) | 5.58(±0.02) |
| A2 | 17.46(±0.05) | 2.55(±0.02) | 6.84(±0.01) |
| A4 | 80.81(±0.09) | 18.59(±0.07) | 4.35(±0.01) |

## Conclusion

In summary, preparation of flat sheet asymmetric PSF membranes by incorporation with the modified $TiO_2$ at evaporation time (ET) of 90 and 120 s was conducted. PSF/($TiO_2$-TMMS) membrane prepared with ET at 120 s showed better results for $CO_2$ permeation by 340% and 363% compared with the PSF and PSF/$TiO_2$ membranes, respectively. Surface modification by DC Ar-plasma at indicated conditions showed improvement of membrane surface hydrophilicity. The maximum increase of the hydrophilic properties belonged to the plasma treated PSF/($TiO_2$-TMMS) membrane preparing with ET at 120 s. The plasma treatment decreased WCA by 85.78% in PSF/($TiO_2$-TMMS) membrane. Additionally, the permeance of the hydrophilic property created from Ar-plasma treatment for PSF/($TiO_2$-TMMS) membranes was reported to improve. The hydrophilic property could sustain for over 30 days. The study of chemical change through the FTIR spectrum found an increase of Ti-O-Si bonds in the wavenumber range of 910-960 $cm^{-1}$. This confirmed the bonding of $TiO_2$ with TMMS coupling agent and lead to the enhancement of dispersion of modified $TiO_2$ in the PSF membranes. The dispersion of $TiO_2$ was also confirmed

by SEM micrographs. This study also found that $TiO_2$ modified with TMMS leading to the enhancement of their hydrophilicity, although a slight decrease in $CO_2/CH_4$ selectivity was evidenced.

**Acknowledgement**

Special thanks to Wanichapichart, P. and Durrast, H., Prince of Songkla University (PSU) for their kind editing. Financial support from the National Talented Scholarship in Science Project is also acknowledged. The authors would like to thank to the Membrane Science and Technology Research Center (MSTRC) and Physics Department, PSU for providing the infrastructure needed.

**References**

1. Yuenyao, C., Tirawanichakul, Y. and Chittrakarn, T. (2015). Asymmetric polysulfone gas separation membranes treated by low pressure DC glow discharge plasmas. *Journal of Applied Polymer Science*, 132(24): 42116 – 42126.
2. Zhang, Y. and Liu, P. (2015). Polysulfone (PSF) composite membrane with micro-reaction locations (MRLs) made by doping sulfated $TiO_2$ deposited on $SiO_2$ nanotubes (STSNs) for cleaning waste water. *Journal of Membrane Science,* 493: 275 – 284.
3. Xueli, G., Haizeng, W., Jian, W., Xing, H. and Congjie, G. (2013). Surface-modified PSF UF membrane by UV-assisted graft polymerization of capsaicin derivative moiety for fouling and bacterial resistance. *Journal of Membrane Science,* 445: 146 – 155.
4. Yang, Y., Zhang, H., Wang, P., Zheng, Q. and Li, J. (2007). The influence of nano-sized $TiO_2$ fillers on the morphologies and properties of PSF UF membrane. *Journal of Membrane Science,* 288: 231 – 238.
5. Konruang, S., Sirijarukul, S., Wanichapichart, P., Yu, L. and Chittrakarn, T. (2015). Ultraviolet-ray treatment of polysulfone membranes on the $O_2/N_2$ and $CO_2/CH_4$ separation performance. *Journal of Applied Polymer Science*, 132(25): 42074 – 42082.
6. Bae, Y.-S. and Lee, C.-H. (2005). Sorption kinetics of eight gases on a carbon molecular sieve at elevated pressure. *Journal of Carbon*, 43: 95 – 107.
7. Huang, S.-Y., Ganesan, P. and Popov, B. N. (2010). Electrocatalytic activity and stability of niobium-doped titanium oxide supported platinum catalyst for polymer electrolyte membrane fuel cells. *Journal of Applied Catalysis B: Environmental,* 96: 224 – 231.
8. Albiter, E., Valenzuela, M. A., Alfaro, S., Valverde-Aguilar, G. and Martínez-Pallares, F. M. (2015). Photocatalytic deposition of Ag nanoparticles on $TiO_2$: Metal precursor effect on the structural and photoactivity properties. *Journal of Saudi Chemical Society,* 19: 563 – 573.
9. Djurišic, A. B., Leung, Y. H. and Ching Ng, A. M. (2014). Strategies for improving the efficiency of semiconductor metal oxide photocatalysis. *Journal of Royal Society of Chemistry,* 1: 400 – 410.
10. Monllor-Satoca, D., Gómez, R., González-Hidalgo, M. and Salvador, P. (2007). The ''Direct–Indirect'' model: An alternative kinetic approach in heterogeneous photocatalysis based on the degree of interaction of dissolved pollutant species with the semiconductor surface. *Journal of Catalysis Today,* 129: 247 – 255.
11. Hashimoto, K., Irie, H. and Fujishima, A. (2005). $TiO_2$ photocatalysis: A historical overview and future prospects. *Japanese Journal of Applied Physics*, 44(12): 8269 – 8285.
12. Khatun, N., Rini, E. G., Shirage, P., Rajput, P., Jha, S. N. and Sen, S. (2016). Effect of lattice distortion on band gap decrement due to vanadium substitution in $TiO_2$ nanoparticles. *Journal of Materials Science in Semiconductor Processing,* 50: 7 – 13.
13. Liu, H., Lv, T. and Zhu, Z. (2016). Direct band gap narrowing of $TiO_2/MoO_3$ heterostructure composites for enhanced solar-driven photocatalytic activity. *Journal of Solar Energy Materials & Solar Cells,* 153: 1 – 8.
14. Madaeni, S. S., Badieh, M., Vatanpour, V. and Ghaemi, N. (2012). Effect of titanium dioxide nanoparticles on polydimethylsiloxane/polyethersulfone composite membranes for gas separation. *Journal of Polymer Engineering and Science*, 56: 2664 – 2674.
15. Chen, Q. and Yakovlev, N. L. (2010). Adsorption and interaction of organic silanes on $TiO_2$ nanoparticles. *Journal of Applied Surface Science*, 257: 1395 – 1400.
16. Zhao, J., Milanova, M., Marijn, M.C.G. and Dutschk, V. (2012). Surface modification of $TiO_2$ nanoparticles with silane coupling agents. *Journal of Colloids and Surfaces A*, 413: 273 – 279.
17. Li, Z., Hou, B., Xu, D., Sun, Y., Hu, W. and Deng, F. (2005). Comparative study of sol–gel-hydrothermal and sol–gel synthesis of titania–silica composite nanoparticles. *Journal of Solid State Chemistry,* 178: 1395 – 1405.

*Malaysian Journal of Analytical Sciences, Vol 21 No 2 (2017): 381 - 390*
*DOI: https://doi.org/10.17576/mjas-2017-2102-13*

MALAYSIAN JOURNAL OF ANALYTICAL SCIENCES
*Published by The Malaysian Analytical Sciences Society*
ISSN 1394 - 2506

# FABRICATION OF PES/MnO MIXED MATRIX MEMBRANES FOR CADMIUM REMOVAL

## (Pembuatan PES/MnO Membran Campuran Matrik dalam Penyingkiran Kadmium)

Soon Onn Lai[1], Kok Chung Chong[1], Zhi Wei Kerk[1], Boon Seng Ooi[2]*,Woei Jye Lau[3]

[1]*Lee Kong Chian Faculty of Engineering and Science,*
*Universiti Tunku Abdul Rahman, Jalan Sungai Long, Bandar Sungai Long, 43300 Kajang, Malaysia*
[2]*School of Chemical Engineering, Engineering Campus,*
*University Sains Malaysia, Seri Ampangan, 14300 Nibong Tebal, Pulau Pinang, Malaysia.*
[3]*Advanced Membrane Technology Research Centre (AMTEC),*
*Universiti Teknologi Malaysia, 81310 Skudai, Johor, Malaysia*

**Corresponding author: chobs@usm.my*

Received: 26 August 2016; Accepted: 8 January 2017

**Abstract**

With increasing industrial activities around the globe, water source had been severely polluted by various heavy metal substances that lead to adverse effect not only to the environment but also to human being. The content of heavy metal in wastewater especially cadmium was increasing in the recent years and can be attributed to the strong demand of cadmium in the battery and electroplating industry. In this study, the potential of novel nanocomposite mixed matrix membrane incorporated with manganese oxide ($MnO_2$) nanoparticle for cadmium removal was investigated. The membranes were fabricated using polyethersulfone (PES) by phase inversion technique with different manganese oxide nanoparticle loading. Prior to performance evaluation, the membranes were characterized by their structural morphology, surface chemistry and cadmium adsorption capability. The results suggested that PES membrane incorporated with 2.0 ratio of $MnO_2$/PES exhibited the best result in both cadmium adsorption (51.7 mg/g) and water permeability (1462 L/m$^2$.h.bar). This indicated the prospect of this membrane to be applied in wastewater treatment industry.

**Keywords**: mixed matrix membrane, polyethersulfone, cadmium, wastewater

**Abstrak**

Sumber air di seluruh dunia telah teruk tercemar dengan pelbagai bahan logam berat yang akan memberi kesan buruk kepada alam sekitar dan manusia. Pencemaran air ini adalah akibat daripada aktiviti-aktiviti perindustrian yang semakin pesat di dunia kita. Kandungan logam berat dalam air sisa terutamanya kadmium semakin meningkat dalam beberapa tahun ini disebabkan oleh permintaan kadmium yang tinggi terutamanya dalam industri bateri dan elektropenyaduran. Dalam kajian ini, potensi membran campuran matrik yang baharu dengan mangan oksida ($MnO_2$) dikajikan dalam sistem turas aliran lintang untuk penyingkiran kadmium. Membran ini dibuat daripada polietersulfona (PES) dengan teknik fasa berbalik dengan pelbagai berat zarah nano mangan oksida. Sebelum kajian dijalankan, membran dicirikan dengan kajian struktur dan permukaan morfologi, keliangan, sudut kenalan permukaan, kajian pembenaman $MnO_2$ dan kajian penjerapan kadmium. Hasil kerja kajian ini mencadangkan bahawa membran PES dengan nisbah 2.0 $MnO_2$ menunjukkan keputusan yang memberangsangkan dalam penjerapan kadmium (51.7 mg/g) dan fluks air tulen yang paling tinggi (1,462 L/m$^2$.h.bar). Keputusan kajian ini telah menunjukkan membran mempunyai potensi yang besar digunakan dalam industri rawatan air sisa.

**Kata kunci:** membran matriks campuran, polietersulfon, kadmium, air sisa

## Introduction

Since the industrial revolution in the human history, the environmental pollution by heavy metals has become more severe, leading to the catastrophic environmental and health problems. Cadmium (Cd) is a commonly used heavy metal in the industry, particularly in the battery, electroplating and pigment [1]. Nevertheless, Cd is a carcinogen to living organisms, where the presence of it will pose threat to the aquatic system and human health. Owing to strong industrial growth and increasing demand of Cd around the world, the wastewater containing Cd had increased drastically in the recent years [2].

Many wastewater treatment technologies had been developed for heavy metal removal. These include precipitation, ion exchange and solvent extraction. Although these methods are widely used in the industrial application, they possess disadvantages such as high capital cost, discharges of toxics solvent, disposal of sludge, and etc. [3]. One of the alternative methods to overcome these issues is membrane technology.

Membrane technology had been developed rapidly in the past two decades due to the advances in the membrane fabrication and characterization techniques. Several membrane separation techniques had been used in the seawater desalination and wastewater treatment, namely, reverse osmosis (RO), nanofiltration (NF) and ultrafiltration (UF) [4, 5]. Despite the successful application of membrane technology in the wastewater industry, the membrane performance as a function of filtration time is still a main concern as membrane is prone to fouling, especially in the treatment of wastewater containing heavy metals [6]. In this work, the potential of novel mixed matrix membrane embedded with manganese oxide ($MnO_2$) nanoparticles was evaluated for Cd removal. The membrane fabrication and characterization techniques, adsorption behavior and separation efficiency were investigated by performing static adsorption and cross flow filtration experiment under various experimental conditions.

## Materials and Methods

### Materials

The main polymeric material used for the membrane fabrication was polyethersulfone (Radel A300 PES) with a molecular weight of 58,000 g/mol purchased from Amoco Chemicals. Polyvinylpyrrolidone (PVP) and N-methylpyrrolidinone (NMP) obtained from Merck were used as additives and solvent, respectively. Ethanol and potassium permanganate were supplied by KLH Chemicals and used for nanoparticle synthesis. Cadmium chloride purchased from R & M Chemicals was used to prepare feed solution.

### Synthesis of manganese oxide particles

The synthesis method adopted in this study was similar to the literature reported by Subramanian et al. [7]. Potassium permanganate was first dissolved in distilled water followed by the addition of ethanol. The mixture was stirred until brownish black precipitate of manganese oxide was formed. The precipitate was filtered by Whitman filter paper and cleaned with distilled water to remove the unwanted impurities. Subsequently, the precipitate was dried in a vacuum oven at 60 $^{o}$C for 24 hours to remove the moisture content before use.

### Membrane preparation

The membrane fabrication technique employed in this study was phase inversion technique which has been discussed elsewhere in details [8]. A pre-determined amount of PES and additive ($MnO_2$ and PVP) were weighed and added to NMP solvent. The solution was stirred for 4 hours by magnetic stirrer followed by sonication at 60 $^{o}$C for 24 hours to produce homogenous dope solution. The viscosity of the dope solution was recorded by digital viscometer (98965-40, Cole-Parmer) to investigate the effect of the ratio of $MnO_2$ and PES.

In the flat sheet membrane fabrication, the dope solution was cast evenly onto a flat glass plate. A casting glass rod was used to cast the solution into a film with a thickness of 230 – 250 μm. The casted film was then immersed into distilled water at room temperature to induce phase inversion. The formed membrane was immersed in water for 3 days in order to removal residual trace of solvent. Finally, the membrane was dried in a vacuum oven at 60 $^{o}$C for 24 hours to completely remove the moisture content. Table 1 lists the composition of dope solution used in this study for membrane fabrication.

Table 1. Composition of dope solution

| Membrane | $MnO_2$/PES Ratio | PES (wt.%) | PVP (wt.%) | NMP (wt.%) | $MnO_2$ (wt.%) | Viscosity (Cp) |
|---|---|---|---|---|---|---|
| PES | 0 | 15.00 | 1.50 | 83.50 | - | 200 |
| $MnO_2$/PES-0.5 | 0.5 | 13.95 | 1.40 | 77.67 | 6.98 | 1,800 |
| $MnO_2$/PES-1.0 | 1.0 | 13.04 | 1.30 | 72.60 | 13.04 | 2,000 |
| $MnO_2$/PES-1.5 | 1.5 | 12.24 | 1.22 | 68.18 | 18.36 | 9,450 |
| $MnO_2$/PES-2.0 | 2.0 | 11.54 | 1.15 | 64.23 | 23.08 | 12,450 |
| $MnO_2$/PES-2.2 | 2.2 | 11.28 | 1.13 | 62.78 | 24.81 | 13,250 |

**Characterization**

The structure of the $MnO_2$ was identified by transmission electron microscopy (TEM). The $MnO_2$ sample was first reduced for 30 min by inducing hydrogen to remove any carbon deposit, and then carefully transferred to a porous carbon film supported on a metal grid at scale bar of 20 to 50 nm. The sample was then examined with an accelerating voltage at 400 KeV to obtain the electron micrographs.

Fourier transform infrared–attenuated total reflectance (FTIR–ATR) (Perkin Elmer) was used to investigate the functional group of $MnO_2$ before and after the cadmium adsorption test. Additionally, the functional groups of $MnO_2$ particles in the PES membranes were also identified by FTIR-ATR.

The membrane surface and cross sectional morphologies were examined using scanning electron microscope (SEM) (Hitachi TM3000). The samples were cryogenically fractured liquid nitrogen into a small strip. The membranes were then coated with a thin layer of platinum by sputter machine before SEM analysis.

Both membrane surface roughness and pore size of the flat sheet membranes were structurally characterized using atomic force microscopy (AFM) (Seiko SPA-300HV). The membrane samples were first washed using ethanol to remove any trace residual. The samples were cut into square pieces with area of approximately 1.0 $cm^2$ and attached to the sample holder in the scanner tube. The AFM images were obtained with tapping mode with a scanning size of 5 μm × 5 μm.

The contact angle of the flat sheet membrane was measured by sessile drop technique using contact angle goniometer (DataPhysics, OCA15Plus). Distilled water droplet was placed on 10 to 20 regions on the membrane surface and average contact angle was reported.

Membrane porosity was calculated by the gravitational method as explained in the literature [9]. The weight of the membrane samples were first weighted as dry weight and then immersed into water for 24 hours. The weight of the wetter membrane was measured as wet weight and the porosity ($P_r$) was determined using Equation 1.

$$P_r = \frac{W_w - W_d}{d_w \times s \times l} \quad (1)$$

where $W_w$ is the weight of wet membrane (g), $W_d$ is the weight of dry membrane (g), $s$ is the surface area of membrane ($cm^2$), $l$ is the thickness of wet membrane (cm) and $d_w$ is the density of water at room temperature.

**Experimental work**

The adsorption test of cadmium using the fabricated membrane was studied using batch adsorption technique. The Cd solution was prepared by dissolving cadmium chloride ($CdCl_2$) in distilled water. The batch adsorption was carried out in a 15 mL sample tube with 10 mL of Cd solution with a concentration of 30 ppm and membrane with mass of 0.01 g, and pH value remained as constant at 9. The sample tube was placed in incubation shaker at 250 rpm, 25 $^oC$ for 48 hours. Additionally, the effect of pH value on the Cd adsorption was investigated by mixing the

membrane with 10 mL of 100 ppm Cd solution at different pH values. The concentration of Cd residual was analyzed using inductively coupled plasma-optical emission spectrometry (ICP-OES). The analysis was repeated three times to yield average result. The equilibrium adsorption capacity ($q_e$) of the membrane was determined using Equation 2 [10].

$$q_e = \frac{(C_i - C_e)V}{M_m} \quad (2)$$

where $c_i$ (mg/g) is the initial Cd solution concentration, $c_e$ (mg/g) is the equilibrium Cd solution concentration, $v$ is the volume of Cd solution ($l$) and $M_m$ is the mass of the dry membrane which is added into the solution (g).

The Cd removal was also conducted by the cross flow filtration system as illustrated in Figure 1. Flat sheet membrane with an area of 14.5 $cm^2$ was installed in the membrane module. The feed stream consisting of Cd solution with a concentration of 100 ppm was pumped into the membrane module at 0.1 bar. The quality of permeate was determined at every 30 min interval by ICP-OES. The pure water flux is then determined by Equation 3 [10].

$$J_w = \frac{Q}{A\Delta t \Delta p} \quad (3)$$

where $J_w$ is pure water flux (l/$m^2$.h), $Q$ is the volume of permeate (l), $A$ is the effective membrane area ($m^2$), $\Delta t$ is the sampling time (h) and $\Delta p$ is the transmembrane pressure difference.

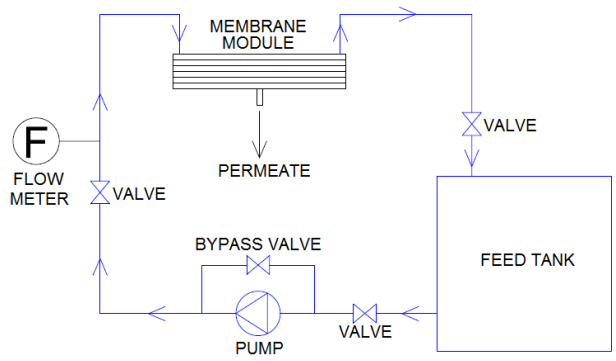


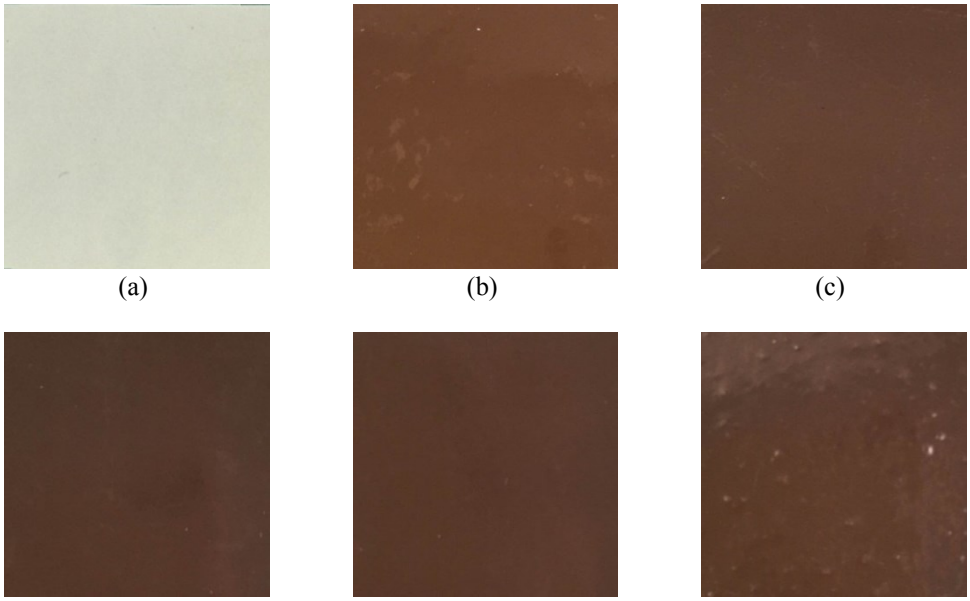

Figure 1. Schematic diagram of cross flow filtration system

## Results and Discussion

### Characterization of $MnO_2$ nanoparticles and PES/$MnO_2$ MMMs

Figure 2 shows the images of six different membranes used in the experiment. It was observed that the color of membrane turned brownish when $MnO_2$ was added to PES. The color became darker with higher dosage of $MnO_2$. The results were consistent with the original colour of $MnO_2$.

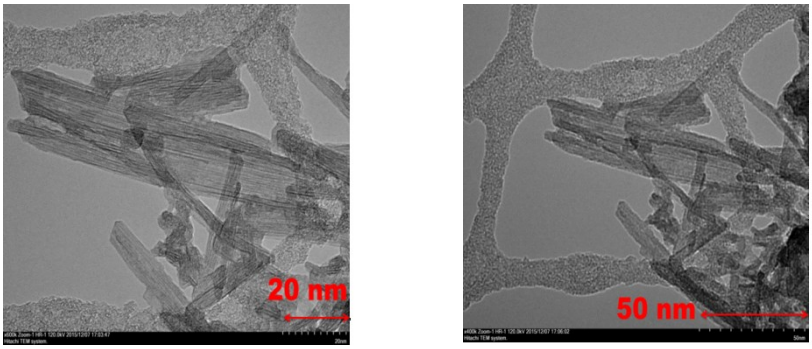
Figure 3 shows the TEM images of the synthesized $MnO_2$. The $MnO_2$ structure appeared to be rod-like structure with a dimension of 125 ± 30 nm. Such structure was achieved when the product of $MnO_2$ was formed as a result of addition of ethanol to aqueous solution of potassium permanganate ($KMnO_4$).



(a) (b) (c)

(d) (e) (f)

Figure 2. Images of six different membranes used (a) PES, (b) $MnO_2$/PES-0.5, (c) $MnO_2$/PES-1.0, (d) $MnO_2$/PES-1.5, (e) $MnO_2$/PES-2.0 and (f) $MnO_2$/PES-2.2




(a) (b)

Figure 3. TEM images of manufactured $MnO_2$ at different scale bars, (a) 20 nm and (b) 50 nm

Figure 4 depicts the FTIR spectra of $MnO_2$ particles and the membrane embedded with and without $MnO_2$. It is found that a sequence of adsorption bands for the $MnO_2$ was appeared at 3394.8, 1542.5 and 1412.2 $cm^{-1}$. Strong adsorption peak observed at 3394.8 $cm^{-1}$ was assigned to -OH stretching vibration because large amount of hydroxyl groups presented in $MnO_2$. The band at region of 1542.5 $cm^{-1}$ might be attributed to asymmetric N-O stretching vibration. On the other hand, the band at region of 1412.23 $cm^{-1}$ might be resulted by C-C stretching vibration.

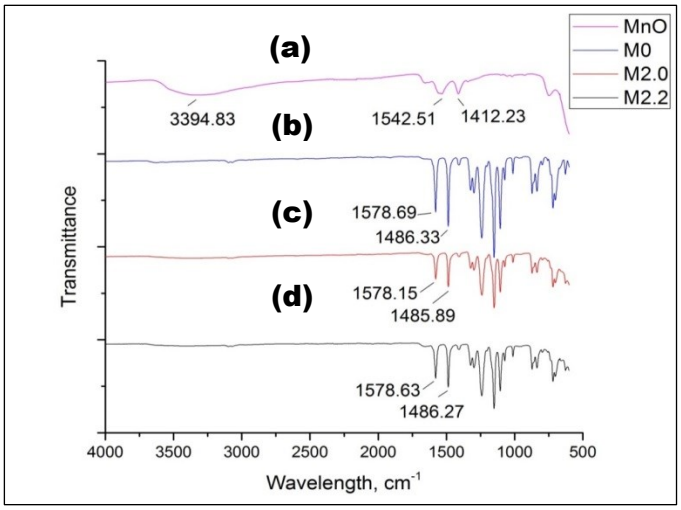



Figure 4. FTIR spectrums of (a) $MnO_2$ particles, (b) PES, (c) $MnO_2$/PES-2.0 and (d) $MnO_2$/PES-2.2

Table 2 summarizes the contact angle when water droplet placed onto the surface of six different membranes. It could be observed that the contact angle decreased significantly from 63.73° for the neat membrane to 18.13° for the $MnO_2$/PES-2.2 membrane. This indicated significant improvement in membrane surface hydrophilicity. Such improvement resulted from embedding $MnO_2$ particles in the PES membrane was most probably due to the presence of large amount of hydroxyl groups in $MnO_2$, which could be proved by FTIR result. A membrane with improved surface hydrophilicity generally would ameliorate membrane water permeability as shown in Table 2. It could also be noticed that the overall porosity values of all membranes were high (76 – 94.8%) (Table 2). This could be caused by low concentration of polymer used as well as addition of PVP (which acted as pore forming agent) in the casting solution. Moreover, the porosity appeared to increase from 76.81% in neat PES membrane to 94.81% in the $MnO_2$/PES-2.2 membrane. This was due to the addition of $MnO_2$, which was super-hydrophilic in nature as evidenced by the results of FTIR and contact angle.

Table 2. Pure water permeability, contact angle and overall porosity of various membranes

| **Membrane** | **PWF ($L/m^2h$)** | **Contact Angle (°)** | **Overall Porosity (%)** |
|---|---|---|---|
| PES | 22.74 (±0.39) | 63.73 (±2.96) | 76.81 (±0.65) |
| $MnO_2$/PES-0.5 | 234.93 (±1.68) | 46.89 (±4.45) | 77.11 (±-0.13) |
| $MnO_2$/PES-1.0 | 248.84 (±1.56) | 37.68 (±6.18) | 77.73 (±0.21) |
| $MnO_2$/PES-1.5 | 508.77 (±1.68) | 32.94 (±8.52) | 81.31 (±0.44) |
| $MnO_2$/PES-2.0 | 1461.99 (±3.93) | 20.82 (±4.52) | 85.89 (±0.36) |
| $MnO_2$/PES-2.2 | 1288.36 (±12.33) | 18.13 (±7.57) | 94.81 (±0.28) |

Figure 5 shows the AFM surface images of all the membrane samples provided in atomic-level resolution. *Ra* value is known as roughness value. It increased drastically from 17.34 nm in the neat membrane (M0) to >58 nm in the $MnO_2$/PES-2.0 membrane when the weight ratio of $MnO_2$/PES was increased from zero to 2.0. This could be resulted by the distribution of $MnO_2$ embedded in the membranes. A membrane with higher roughness value indicates better filtration performance. Hence, the M2.0 membrane was shown to have the best filtration performance compared with the M2.2 membrane.

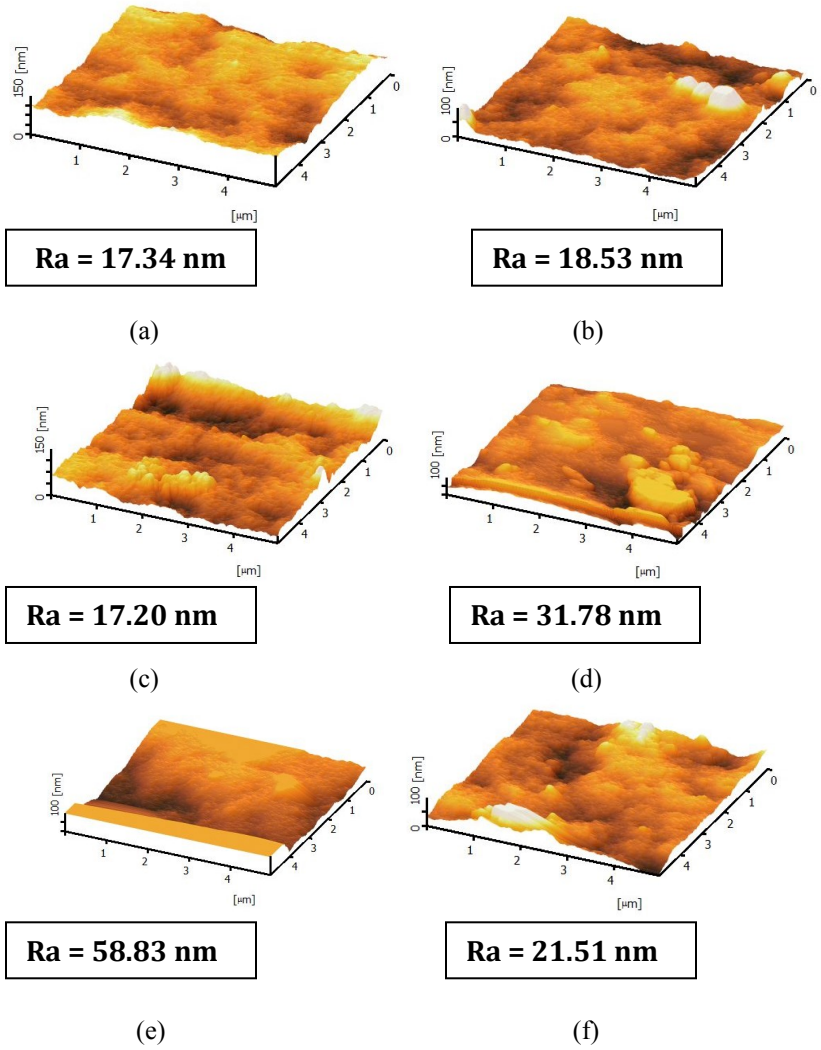



Figure 5. AFM images of various membranes with different $MnO_2$/PES ratios, (a) PES, (b) $MnO_2$/PES-0.5, (c) $MnO_2$/PES-1.0,(d) $MnO_2$/PES-1.5, (e) $MnO_2$/PES-2.0 and (f) $MnO_2$/PES-2.2

**Cadmium adsorption studies: Effect of adsorbent dosage and initial concentration (isotherm analysis)**

Both the effects of adsorbent dosage and initial concentration were studied at 25 $^{o}$C and pH = 9 by differing the Cd initial concentration of 10, 30, 50 and 100 ppm for various membranes with different PES/$MnO_2$ ratios. Neat membrane was not tested for this experiment because it had no adsorption capacity of Cd due to the absence of $MnO_2$ particles. Figure 6 shows that when the $MnO_2$/PES ratio increased, the Cd adsorption capacity increased accordingly. The maximum Cd adsorption capacity for $MnO_2$/PES-0.5, $MnO_2$/PES-1.0, $MnO_2$/PES-1.5, $MnO_2$/PES-2.0 and $MnO_2$/PES-2.2 were found to be 31.63, 35.29, 45.89, 51.71 and 49.82 mg/g, respectively. The enhancing adsorption capacity of prepared membranes was clearly attributed to the increasing dosage of $MnO_2$ adsorbents for Cd adsorption. In addition, the positive relationship between initial Cd concentration and Cd adsorption capacity was also obviously observed in Figure 6.

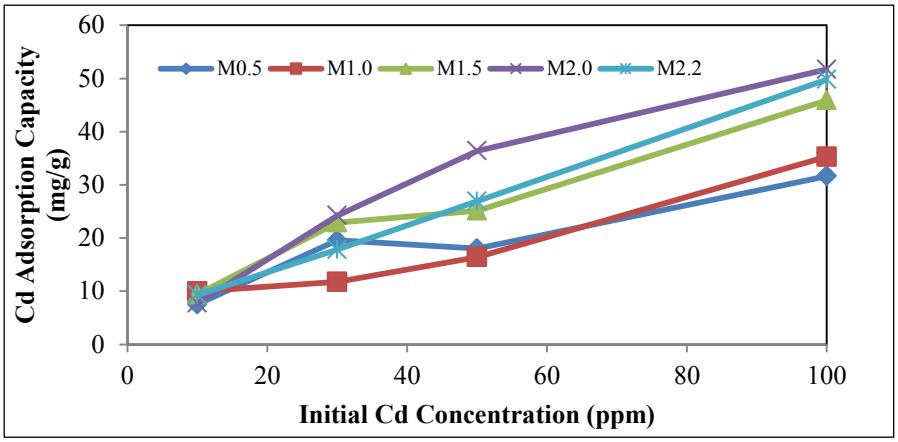



Figure 6. Adsorption isotherm of Cd using membranes with different $MnO_2$/PES ratios. (Operating Conditions: pH = 9, membrane dose = 1g/L, temperature = 25 $^oC$, contact time = 48 hours)

**Effect of pH**

The pH value is deemed to be a pivotal parameter in controlling Cd removal efficiency because of the strong aggressive bond between hydrogen ions and heavy metal ions in allocation of sites for adsorption. Figure 7 shows the removal efficiency of Cd under different pH values (i.e. pH 3, 5, 7, 9 and 11) during the adsorption studies. From the experiment, $MnO_2$/PES-2.0 membrane was chosen to be used because of its highest adsorption capacity among other membranes. As can be seen, better Cd removal efficiency was found to be in alkaline solution. The optimum Cd removal was observed between pH 9 to pH 11 for the $MnO_2$/PES-2.0 membrane attributed to the increase in the electrostatic attraction between the positively charge $Cd^{2+}$ ions and the negative charged binding sites of the functional group present on the cell surface which is similar to the reported by Al-Homaidan et al. and Adhiya et al [11, 12].

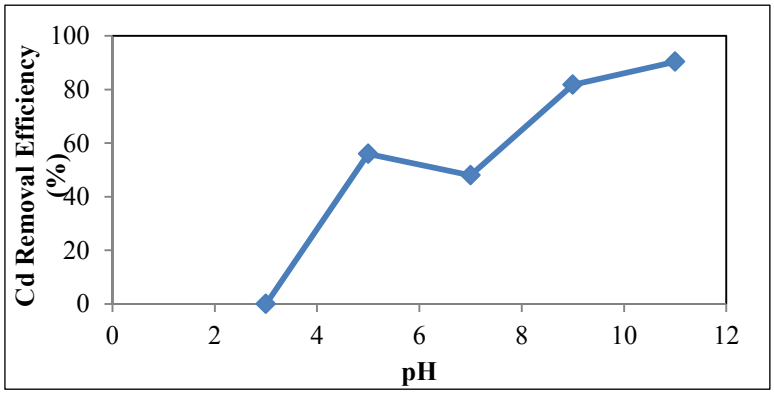



Figure 7. Effect of initial pH value on Cd removal by $MnO_2$/PES-2.0 (Operating Conditions: initial Cd concentration = 30 mg/L, membrane dose = 1g/L, temperature = 25$^oC$, contact time = 48 hours)

**Effect of contact time**

Effect of contact time (5, 10, 20, 30, 60, 120, 240, 360, 480 and 720 min) was investigated for the $MnO_2$/PES-2.0 membrane at initial Cd concentration of 30ppm. Figure 8 shows that Cd was more rapidly removed at the starting,

while the removal rate slowed down as the time passed. The higher rate of Cd removal initially might be due to larger surface area of the membrane embedded with $MnO_2$ for Cd adsorption. As time passed, the availability of surface area would become smaller, and hence the rate of Cd removal slowed down. The adsorption equilibrium was reached after 480 min.

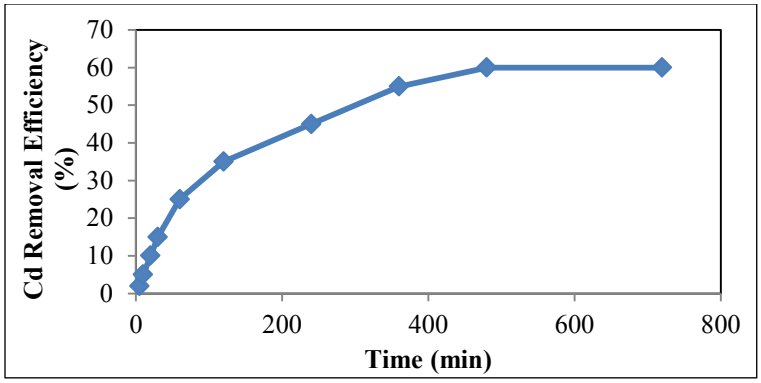



Figure 8. Effect of contact time on Cd removal by $MnO_2$/PES-2.0 (Operating Conditions: initial Cd concentration = 30 mg/L, membrane dose = 1g/L, temperature = 25 $^oC$, pH = 9)

**Continuous filtration**

The performance of optimum membrane, which was PES/ $MnO_2$-2.0 membrane, for Cd removal in the dead-end filtration process is depicted in Figure 9. According to the result, $MnO_2$/PES-2.0 membrane was capable of maintaining the Cd concentration below the maximum contamination level (MCL) of 10 ppb as stated by World Health Organization (WHO) for approximately 4000 $cm^3$ of permeate.

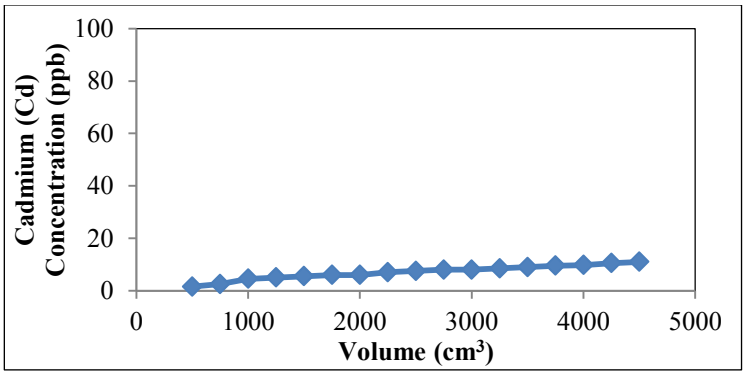



Figure 9. Adsorption of Cd from aqueous solution using $MnO_2$/PES-2.0 membrane (Operating conditions: initial Cd concentration = 100 ppb, pH = 9, temperature = 25 $^oC$, pressure = 5 bar)

## Conclusion

In this study, the $MnO_2$/PES mixed matrix membranes with different $MnO_2$ additives were successfully fabricated in laboratory scale. The fabricated membrane was characterized to understand the effect of the additives on the membrane morphology. The addition of $MnO_2$ in the membrane showed the increment of the surface roughness and better porosity. The $MnO_2$/PES membranes were found to have the highest Cd removal efficiency between pH 9 and 11 attributed to the electrostatic attraction between the positively charge $Cd^{2+}$ ions and the negative charged binding

sites of the functional group which lead to the possible application of Cd removal at broad pH range from pH 4 to 11. The filtration results showed that the $MnO_2$/PES-2.0 membrane was capable of producing permeate of good quality with Cd concentration below 10 ppb (the MCL set by WHO). This proved that the $MnO_2$/PES-2.0 membrane was very effective in removing Cd from aqueous solutions. In summary, the PES/$MnO_2$-2.0 membrane shows a great potential to be applied Cd removal from various wastewater treatment industry.

**References**


1. Mehdi, G. and Hamid, R. M. (2015). Enhancing performance of hybrid liquid membrane process supported by porous anionic exchange membranes for removal of cadmium from wastewater. *Chemical Engineering Journal*, 264(1): 241 – 250.
2. Tingting, D., Liangrong, Y., Menghao, Z., Zhini, L., Xitong, S., Jiemiao, Y. and Huizhou L. (2015). Removal of cadmium (II) from wastewater with gas-assisted magnetic separation. *Chemical Engineering Journal*, 280(1): 426 – 432.
3. Yilmaz, Y. (2016). Removal of heavy metals in wastewater by using zeolite nano-particles impregnated polysulfonemembranes. *Journal of Hazardous Materials*, 309(1): 53 – 64.
4. Chong, K. C., Lai, S. O., Lee, K. M., Lau, W. J., Ismail, A. F. and Ooi, B. S. (2014). Characteristic and performance of polyvinylidene fluoride membranes blended with different polymeric additives in direct contact membrane distillation. *Desalination and Water Treatment*, 2014 (1): 1 – 9.
5. Mocha, N. M., Lau, W. J., Ng, B. C., Ismail, A. F. and Veerasamy, D. (2015). Preparation and characterization of PVDF membranes incorporated with different additives for dyeing solution treatment using membrane distillation. *Desalination and Water Treatment*, 56(1): 1999 – 2012.
6. Bourawi, M., Ding, Z. and Khayet, M. (2006). A framework for better understanding membrane distillation process. *Journal of Membrane Science*, 285(1): 4 – 29.
7. Subramanian, V., Zhu, H. and Wei, B. (2008). Alcohol-assisted room temperature synthesis of different nanostructured manganese oxides and their pseudocapacitance properties in neutral electrolyte. *Chemical Physics Letters*, 453(4-6): 242 – 249.
8. Ahmad, A. L., Ideris, N., Ooi, B. S., Low S. C. and Ismail, A. (2012). Synthesis of polyvinlidene fluoride (PVDF) membranes for protein binding: Effect of casting thickness. *Journal of Applied Polymer Science*, 128(5): 3438 – 3445.
9. Chong, K .C., Lai, S. O., Lau, W. J. and Ooi, B.S. (2014). Preparation, characterization and performance of polyvinylidene fluoride membrane for sodium chloride rejection in direct contact membrane distillation. *Materials Research Innovation*, 18(S6): 359 – 363.
10. Jamshidi Gohari, R., Halakoo, E., Nazri, N., Lau, W. J, Matsuura, T. and Ismail, A. (2014). Improving performance and antifouling capability of PES UF membranes via blending with highly hydrophilic hydrous manganese dioxide nanoparticles. *Desalination*, 335(1): 87 – 95.
11. Al-Homaidan A., Jamila A. A., Al-Hazzani A. A., Al-Ghanayem A., Alabbad A. F. (2015). Adsorptive removal of cadmium ions by *Spirulina platensis* dry biomass. *Saudi Journal of Biological Sciences*, 22: 795 – 800.
12. Adhiya J., Xiaohua C., Richard T. S., Samuel J. T. (2002). Binding of aqueous cadmium by the lyophilized biomass of *Chlamydomonas reinhardtii*. *Colloids and Surfaces*, 210: 1 – 11.

*Malaysian Journal of Analytical Sciences, Vol 21 No 2 (2017): 391 - 401*
*DOI: https://doi.org/10.17576/mjas-2017-2102-14*

MALAYSIAN JOURNAL OF ANALYTICAL SCIENCES
*Published by The Malaysian Analytical Sciences Society*
ISSN 1394 - 2506

# A FABRICATION OF A LOW–COST ZEOLITE BASED CERAMIC MEMBRANE VIA PHASE INVERSION AND SINTERING TECHNIQUE

## (Fabrikasi Membran Seramik Kos Rendah Berasaskan Zeolit Melalui Kaedah Penyongsangan Fasa dan Sinteran)

Mohd Ridhwan Adam[1], Mohd Hafiz Dzarfan Othman[1]*, Mohd Hafiz Puteh[2], Mohammad Arif Budiman Pauzan[1], Mukhlis A Rahman[1], Juhana Jaafar[1]

[1]*Advanced Membrane Technology Research Centre (AMTEC), Faculty of Chemical and Energy Engineering*
[2]*Faculty of Civil Engineering*
*Universiti Teknologi Malaysia, 81310 UTM, Skudai, Johor, Malaysia.*

**Corresponding author: hafiz@petroleum.utm.my*

Received: 26 August 2016; Accepted: 8 January 2017

**Abstract**

The usage of ceramic membranes is gaining enormous attention due to their higher selectivity, permeation rate, and chemical and thermal stability as compared to the polymeric membrane. Owing to the fact of these superior properties, the search of a low-cost ceramic membrane is still in demand. To date, the fabrication of ceramic membrane using natural zeolite as the membrane ceramic loading has yet to be explored. Thus, this study aims to develop natural zeolite (Clinoptilolite) as the ceramic source in the fabrication of low-cost hollow fibre ceramic membrane (HFCM) via phase inversion and sintering techniques. Several fabrication parameters were also studied namely air gap distance, bore fluid flow rate and sintering temperature throughout this research. The best ceramic membrane was fabricated using 5 cm air – gap distance, 13 mL $min^{-1}$ of bore fluid flow rate and 1000 °C of sintering temperature. The acceptable strength and morphological behaviour of finger-like and sponge-like voids were found to be an advantageous characteristic of the fabricated membrane. The cheap and yet abundant raw ceramic material as well as low sintering temperature are eventually reduced the cost of membrane production.

**Keywords**: natural zeolite, ceramic membrane, phase inversion, sintering

**Abstrak**

Penggunaan membran seramik semakin mendapat perhatian ramai berasaskan sifat pemilihan yang tinggi, kadar keserapan, dan daya ketahanan yang tinggi terhadap suhu dan bahan kimia berbanding dengan membran polimer. Berdasarkan fakta tentang sifat-sifat yang hebat ini, maka pencarian terhadap membran seramik kos rendah masih lagi menjadi permintaan. Sehingga kini, fabrikasi membran seramik menggunakan zeolit semulajadi sebagai bahan seramik masih belum dikaji. Justeru itu, kajian ini memfokuskan kepada pembangunan zeolit semulajadi (Clinoptilolite) sebagai bahan sumber seramik dalam fabrikasi membran seramik gentian berongga (HFCM) berkos rendah melalui kaedah penyongsangan fasa dan sinteran. Beberapa parameter fabrikasi telah dikaji iaitu jarak ruang udara, kadar aliran cecair penebuk dan suhu sinteran. Membran seramik terbaik telah diperoleh menggunakan jarak ruang udara sebanyak 5 cm, kadar aliran cecair penebuk iaitu 13 mL $min^{-1}$ dan 1000 °C bagi suhu sinteran. Nilai kekuatan dan sifat morfologi yang memuaskan bagi stuktur span dan jejari dikenal pasti menjadi ciri - ciri kelebihan bagi membran yang difabrikasi. Harga yang murah dan sumber asli bahan seramik yang banyak serta suhu sinteran yang rendah justeru mengurangkan kos penghasilan membran ini.

**Kata kunci:** zeolit semulajadi, membran seramik, penyongsangan fasa, sinteran

## Introduction

In recent years, the development in hollow fibre membrane contactors has gained an enormous attention for the elimination of various volatile contaminants including ammonia [1]. A membrane contactor is a system that attains gas/liquid and liquid/liquid mass transfer without the dispersal of one phase within another. Usually, most of the hollow fibres used are commonly has microporous and hydrophobic properties. In the case of the gas/liquid separation, the penetration of aqueous solution into gas-filled pores is avoided since the hydrophobic properties of the membrane hindered the penetration of this high surface tension materials. Hence, the volatile compound will volatilize from the feed, diffuse through the gas-filled membrane pores, and then be removed by a sweep gas, sucked up by a vacuum or reacted with a stripping solution [2].

Hollow fibre membrane contactors have shown to be useful for eradicating low-concentration solutes from wastewater and they may verify to be a smart substitute for the present work. Hollow fibre membrane contactors, usually in a shell and tube configuration, offer many benefits over traditional contact operations. Membrane contactors provide a large and stable interfacial area. Two fluids flowing across the hollow fibre allow mass transfer to occur between the fluids. The hydrophobic microporous membrane provides the transfer area and restricts the permeation of water. The transfer takes place at the pore opening, inside the pore, or at the pore exit.

Currently, most of the commercially available and commonly used hollow fibre membranes are made from polymeric materials such as polyethylene, polypropylene, polyimide, etc., For instance, for gases in water, polypropylene (PP), polytetrafluoroethylene (PTFE), and polyvinylidene fluoride (PVDF) are normally used as hydrophobic polymers [3,4]. Most of these polymeric hollow fibres are vulnerable to chemical and thermal stresses, resulting in morphological changes and membrane swelling. These changes have weakening effects towards the membrane performance [5,6,7]. Therefore, polymeric membranes are limitedly applicable in mild operating conditions, namely low temperature and low acidity or alkalinity.

As a solution into this matter, a new approach has been developed in the invention of hollow fibre ceramic membranes (HFCM). Owing to the fact that their better thermal stability chemical resistance, ceramic membranes are superior over polymeric membranes in harsher environment. Numbers of studies have shown the achievement in the preparation of hollow fibre membranes of the ceramic materials such as aluminium oxide ($Al_2O_3$), $SrCe_{0.95}Yb_{0.05}O_{3-}\alpha$ (SCYb), $Ba_{0.5}Sr_{0.5}Co_{0.8}Fe_{0.2}O_{3-\delta}$ (BSCF), $La_{1-x}Sr_xCo_{1-y}Fe_{3-\alpha}$ (LSCF), etc. [8,9]. However, the production of a low cost ceramic membrane is still in search. Thus, zeolite is known to have a potential in producing a cheaper but effective HFCM.

Natural zeolites are raw materials can be found abundantly across the globe, and have been shown to possess interesting ceramic properties especially through high temperature (~1150 °C) phase transformations [10]. Natural zeolites are the principal inorganic cation exchangers that possesses high selectivity, ion exchange capacity and compatibility towards the natural environment. Currently, various different types of this mineral have been discovered. The most abundant natural zeolite that occurs in relatively large minerable sedimentary deposits in satisfactorily high purity in many parts across the globe is known as clinoptilolite [11].

The ion-exchange features of the zeolite minerals were first discovered in 1858 [12]. Clinoptilolite is also known to be as one of the ion exchanger with a high affinity for ammonium ion. Clinoptilolite possesses significant macroporosity since it shows a classical alumina silicate like structure. In nature, the cations present on clinoptilolite are sodium, potassium and calcium. The selectivity order of natural zeolite among cations shows that ammonium ion is one of the highest selected cations toward zeolite. Therefore, it is strongly believed that natural zeolite has an ability in the removal of ammonia from the solution concerning adsorption and ion exchange feature.

This work aims towards the development of low cost ceramic membrane in liquid-liquid membrane contactor system. It is known that most of the ceramic-typed membranes are made of metal oxides, which are normally hydrophilic in nature. This is due to the presence of hydroxyl ($OH^-$) groups on the surface. This property avoids them to be applicable in some applications which necessitate only hydrophobic membranes, such as non-polar solvent extraction, membrane contactor, vapour permeation and water ozonation [13]. However, the hydrophobicity properties of ceramic membranes can be enhanced by surface modification. More than a few types of surface

modifying agents can be used such as fluoroalkylsilanes (FAS), polydimethylsiloxane (PDMS), alcohol, chloroalkylsilanes, etc. [14]. Thus, the fabrication of zeolite-based HFCM for the liquid-liquid membrane contactor system is highly aimed to be realized. Consequently, the removal of ammonia in wastewater via ceramic membrane contactor system can be done.

## Materials and Methods

### Raw materials

The fine zeolite powder was prepared by grinding and sieving the zeolite stone purchased from Indonesia prior to the experiment. Polyethersulfone (PESf, Radel A300, Ameco Performance, USA), Arlacel P135 gel (CRODA), and N-methyl-pyrrolidone (NMP, QRëC™) were used as polymer binder, dispersant and solvent, respectively. The suspension composition (ceramic powder weight ratio of 35 wt.%) and the hollow fibre ceramic membrane (HFCM) fabrication parameters namely air-gap distance and bore fluid flow rate are listed in Table 1 and Table 2, respectively.

Table 1. The composition of zeolite based hollow fibre ceramic membrane

| Composition | Zeolite (g) | Arlacel P135 (g) | PESf (g) | NMP (g) |
|---|---|---|---|---|
| 35 wt.% | 35 | 1 | 5 | 59 |

Table 2. Zeolite based hollow fibre ceramic membrane spinning parameters used

| Fibre | Bore Fluid Flow Rate (mL/Min) | Air Gap (Cm) |
|---|---|---|
| 1 | 10 | 3 |
| 2 | 10 | 5 |
| 3 | 10 | 7 |
| 4 | 7 | 5 |
| 5 | 10 | 5 |
| 6 | 13 | 5 |

### Preparation of spinning suspension

The low-cost zeolite based hollow fibre ceramic membrane was prepared by immersion-induced phase inversion and sintering technique. Firstly, Arlacel P135 was dissolved in NMP solvent at vigorous stirring. After a homogeneous solution was formed, the pre-dried zeolite powder (the weight ratio specified in Table 1) was slowly added and projected into the ball milling process using NQM-2 planetary ball mill. After 48 hours of milling, PESf of desired weight was added into the dope and further milled for another 48 hours. The resulting suspension was degassed for 30 minutes at room temperature to eliminate the air bubbles.

### Fabrication of zeolite based hollow fibre ceramic membrane

After the degassing process, the spinning suspension was inserted into a syringe pump and extruded through a tube-in-orifice spinneret with internal diameter of 0.5 mm and external diameter of 2.8 mm. Tap water was used as the internal coagulant or also known as bore fluid solution. The fibre membrane precursor passed through a certain air-gap distance were immersed in a water coagulant (external coagulant) bath for 24 hours (Figure 1) to let the phase inversion process to be completed. Afterwards, the membrane precursors were dried at room temperature. Finally, the hollow fibre ceramic membrane precursors were calcined in air for 4 hours at various sintering temperatures in the range of 950 - 1050 °C by using a tubular furnace (XL - 1700). About 5 – 8 of membrane precursors were placed into the alumina boat and subjected into the furnace for stipulated time. The temperature was increased from room temperature to 600 °C at a rate of 2 °C $min^{-1}$ and held for 2 hours, then to target temperature at a rate of 5 °C

$min^{-1}$ and held for 4 hours. The temperature was later cooled down at a rate of of 5 °C $min^{-1}$ to room temperature. In this process, the polymer binder was burned off leaving only ceramic material in the HFCM.

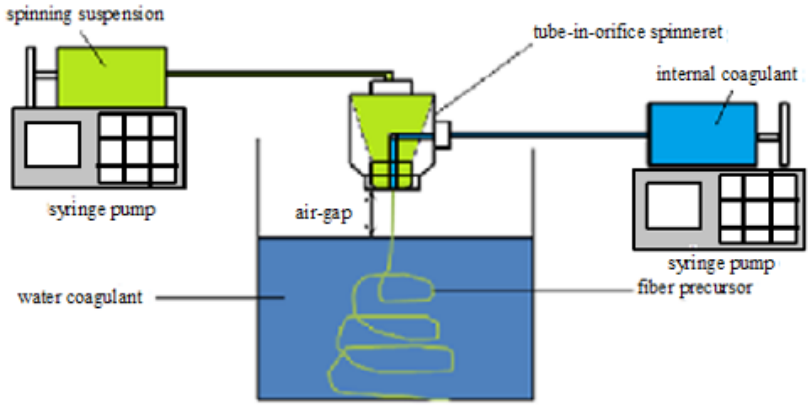



Figure 1. The schematic diagram of the phase inversion process set up for the fabrication of hollow fibre ceramic membrane

**Characterization**

The viscosity of the spinning suspension was measured instantly prior to the spinning process using viscometer (BROOK FIELD) at shear rate range between 1 $s^{-1}$ and 100 $s^{-1}$ at room temperature. The morphologies of the HFCM for all parameters studied were analyzed using scanning electron microscopy (SEM, Hitachi Model TM 3000) at different magnifications. Prior to the SEM analysis, the samples were gold coated under vacuum for 3 minutes. The morphological behavior as well as the wall thickness were examined through this analysis. In addition, the three-point bending tests were done in order to measure the mechanical strength of the zeolite HFCM using INSTRON 3342. The HFCMs about 5 cm in length were tested in three – point bending instrument and at least a triple set of test were done for each parameter studied. The mechanical strength (σF) was calculated using Equation (1) as follow [15];

$$\sigma F = \frac{8FLD_o}{\pi(D_o^4 - D_i^4)} \quad (1)$$

where F is the maximum load at which the fracture occurred while L, $D_o$, and $D_i$ are the length of span (43 mm), the outer diameter, and the inner diameter of the hollow fibres, respectively.

## Results and Discussion

**Rheology of ceramic suspension**

In this study, the presence of ceramic (35 wt.%) loading has affected the viscosity of the suspension. The viscosity of the ceramic suspension at shear rate of 1 – 100 $s^{-1}$ is shown in Figure 2. The rheological profile of this ceramic suspension containing Zeolite/NMP/Arlacel/PESf is found to conform the non-Newtonian behavior that has been previously reported by Kingsbury and Li [16]. The viscosity of Zeolite/NMP/Arlacel/PESf suspension was determined at a shear rate of 30 $s^{-1}$. The viscosity of this suspension was found to be 1.0308 Pa.s. From the SEM analysis, all HFCMs spun at this ceramic loading show the formation of the finger-like voids. According to Kingsbury and Li, the formation of finger-like structure is mainly dominated by the viscosity of the ceramic suspension [16]. A finger-like formation occurred when less viscous fluid (non-solvent) comes into contact with high viscous fluid (ceramic suspension) [17]. In addition, they have investigated that the critical viscosity value for their ceramic is 12.1 Pa.s at the shear rate of 30 $s^{-1}$. This value has been established as the threshold value for the formation of finger-like void in the membrane morphology. In other words, if the viscosity value obtained was beyond above this critical viscosity value, the formation of finger-like void is unfavorably to occur. In this study, the viscosity of the 35 wt.% ceramic loading suspension is far lesser than the critical viscosity value. Thus, the

formation of finger-like void is most likely to be attain. This theory is positively supported by the SEM analysis results which shown the presence of finger-like structure in most of the fabricated HFCMs.

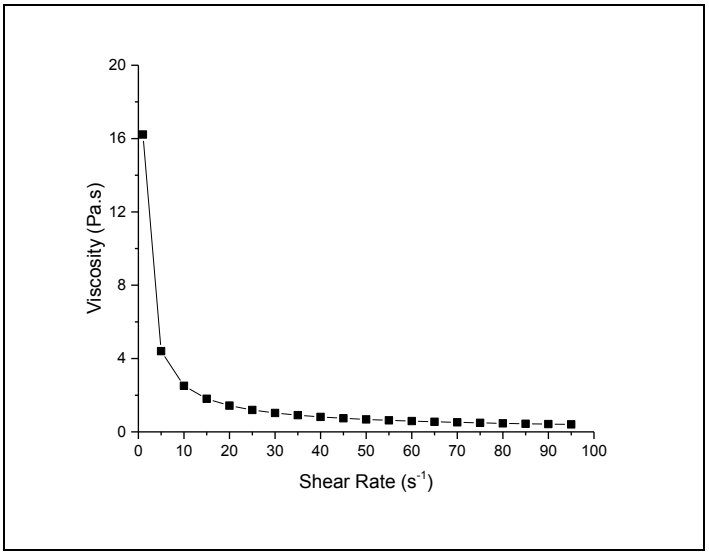



Figure 2. The rheological profile of ceramic suspension containing Zeolite/NMP/Arlacel/PESf with 35 wt. % of zeolite content

**Effect of air-gap distance**

The effect of air-gap distance on the structural behavior of zeolite based HFCM was studied at three different air-gap distances at a constant bore fluid flow rate of 10 mL $min^{-1}$. The obtained HFCM precursors were first sintered at 1000 °C prior to the morphological analysis through SEM. The SEM images of these HFCMs were depicted in Figure 3.

From Figure 3, it can be clearly seen that all three HFCMs showed the formation of finger-like void and sponge-like structures in all membranes. The finger-like void is significantly observed and obtained as the air-gap distance increased. The voids were elongated from the inner part towards the outer of the fibre as the air-gap distance enhanced. The best finger-like void was obtained by the air-gap of 5 cm (Figure 3b) since it gives the higher value in mechanical strength (Figure 4). In addition, the elongation of finger-like structure was not significantly enhanced as the air-gap increased from 5 to 7 cm. Furthermore, the formation of finger-like void were in good agreement with the viscosity analysis findings. According to Kingsbury and Li, the presence of water moisture in the air has encouraged a minor combination between non-solvent and solvent and thus amplified the viscosity at the outer surface. This phenomenon thus stifled the formation of outer finger-like void and preferred the formation of inner finger-like structure. In addition, 5 cm was selected as the best air-gap distance due to its mechanical strength (Figure 4). The lower value of mechanical strength possessed by air-gap 7 cm (Figure 3c) is due to the significant distortion suffered by the inner structure of the membrane. Similar phenomenon has been reported in Li et al. study [18].

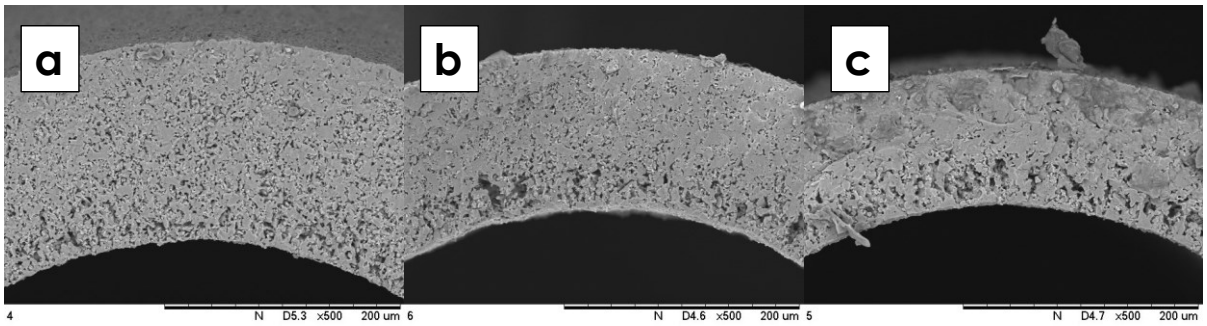



Figure 3. Cross-sectional SEM images of the zeolite based HFCMs spun at different air-gap distance: (a) fibre 1, 3 cm; (b) fibre 2, 5 cm; and (c) fibre 3, 7 cm, at a fixed bore fluid flow rate of 10 mL $min^{-1}$ and 35 wt.% of ceramic loading, respectively

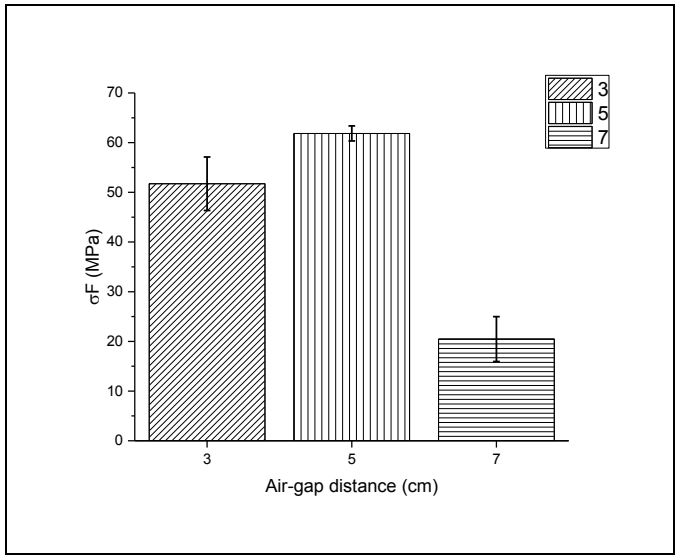



Figure 4. Flexural strength of the zeolite based HFCMs spun at different air-gap distance: (a) fibre 1, 3 cm; (b) fibre 2, 5 cm; and (c) fibre 3, 7 cm, respectively

**Effect of bore fluid flow rate**

The morphological behavior of zeolite based HFCM spun at different bore fluid flow rate were depicted in Figure 5. The studied bore fluid flow rate in this study namely 7 mL $min^{-1}$, 10 mL $min^{-1}$, and 13 mL $min^{-1}$, at a static air-gap distance of 5 cm and ceramic loading of 35 wt.% of zeolite. From the figure, it can be seen that the alteration of bore fluid flow rate has significantly change the morphologies of the HFCMs produced. The low flow rates (7 mL $min^{-1}$and 10 mL $min^{-1}$) is found to distort the bore shape formation of the fibre. However, the regular formation of the outer contours of the fibre was obtained by all fibres spun at different bore fluid flow rate without any distortion. The deformation of inner shape of the fibre can be clearly seen when the fibres spun at low bore fluid flow rates (7 mL $min^{-1}$and 10 mL $min^{-1}$), while a completely circular shape was obtained by the bore fluid of 13 mL $min^{-1}$.

The shrinkage of the HFCM was always obtained in the phase inversion process. This is due to the rate of solvent (NMP) diffusion from the suspension is always faster than the rate of diffusion of water into the suspension [19]. The shrinkage of the fibre was also attributed to the inward radial force which eventually resulted in the deformation of the inner shape of the fibre. There are two main reasons attributed into this phenomenon namely hydrodynamic

force and solidification rate. A low bore fluid flow rate (7 mL $min^{-1}$and 10 mL $min^{-1}$) could not generate a sufficient hydrodynamic force (outward) against the ceramic suspension which in turn resulting in the distortion of the bore shape.

The low bore fluid flow rates also produced a slow solidification rate. The slow solidification rate attributed to the incomplete solidification of polymer in the inner surface of the fibre which in turn is not durable enough to resist the inward radial force and thus distorted the formation of the circular contour of the fibre. The flow rate of 13 mL $min^{-1}$ is found to be the best bore fluid flow rate in order to produce the perfect circular shape of the inner contour of the zeolite based HFCM.

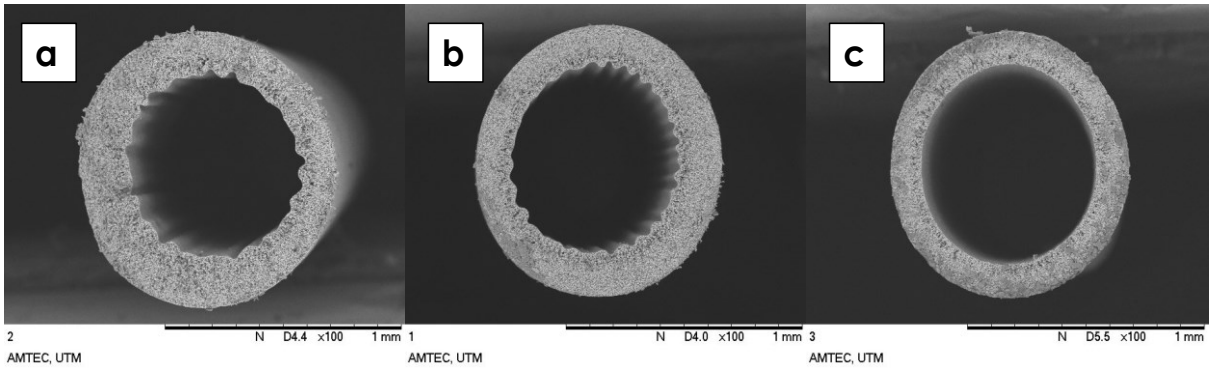



Figure 5. SEM images of the zeolite based HFCMs spun at different bore fluid flow rate: (a) fibre 4, 7 mL $min^{-1}$; (b) fibre 5, 10 mL $min^{-1}$; and (c) fibre 6, 13 mL $min^{-1}$, at a fixed 35 wt.% of ceramic loading and air-gap distance of 5 cm, respectively

**Effect of sintering temperature on zeolite based HFCM properties: Sintering shrinkage**

The zeolite based HFCM precursors were subjected into air calcination in order to remove the polymer binder and only ceramic would remain in the fibre. The sintering profile of the zeolite based HFCM is depicted in Figure 6. At first stage of the calcination, all polymer binders were eliminated at 600 °C. The grain growth of the ceramic particles is occurred at targeted sintering temperature (950 °C – 1100 °C). Figure 7 shows the cross-sectional images of the zeolite based HFCMs before and after calcination at varying sintering temperatures. From the images, it can be clearly seen that the fibre has shrunk when sintered as compared to the fibre precursor. The shrinkage of the fibre is further incremented as the temperature increased.

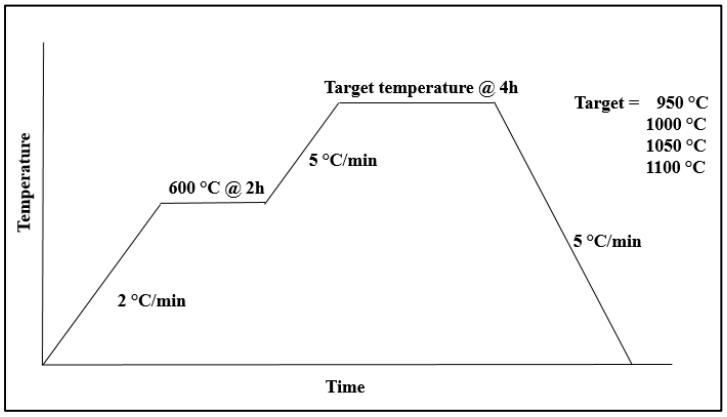



Figure 6. Sintering profile of the zeolite based HFCM

The radial shrinkage of the zeolite based HFCMs increased from 22% to 37% as the sintering temperature increased from 950 °C to 1100 °C. The increment in the shrinkage value suggested that the formation of sintering neck caused by the diffusion of the particles in the fibre [18]. Further enhance in sintering temperature has led to the destruction of the fibre due to the melting of the ceramic.

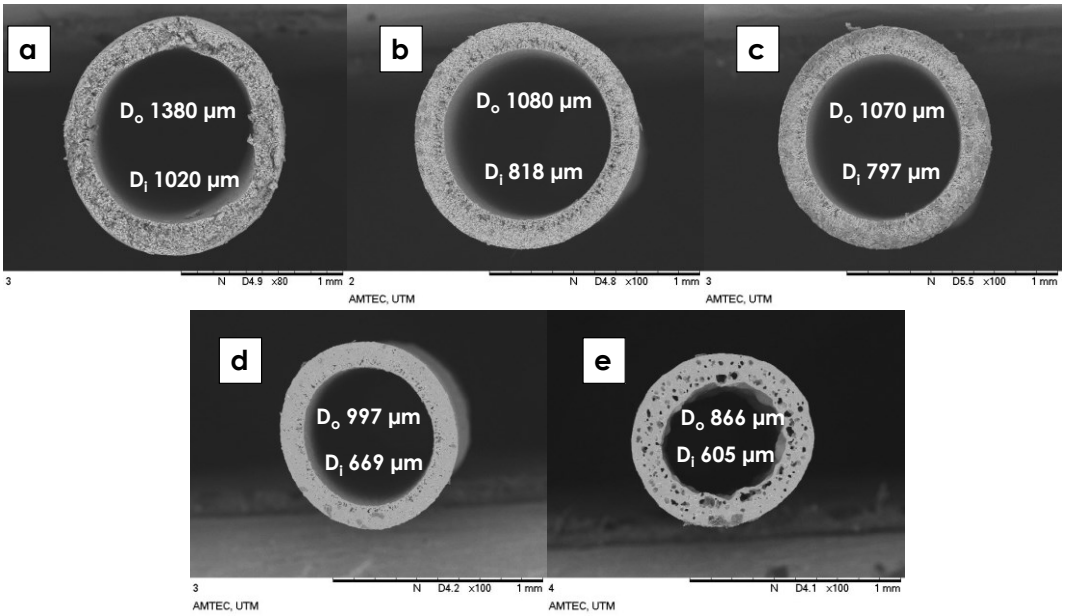



Figure 7. Cross-sectional SEM images of the zeolite based HFCMs (fibre 6) before (a) and after calcination at different sintering temperatures: (b) 950 °C; (c) 1000 °C; (d) 1050 °C; and (e) 1100 °C, fabricated at a fixed air-gap distance of 5 cm, bore fluid flow rate of 13 mL $min^{-1}$, and ceramic loading of 35 wt.% of zeolite, respectively.

**SEM microstructure of zeolite based HFCM**

Figure 8 depicts the microstructure of the cross-sectional zeolite based HFCMs before and after the sintering process has taken place at different temperature. The images of these membranes were taken at the magnification of 500 x in order to see the porous microstructure of the membranes.

From the images, it can be clearly seen that the sintering temperature had significantly affect the microstructure porosity of the inner and outer parts of the membranes. Before the sintering process has done, the particles of the ceramic altogether with the binder were freely distributed throughout the membrane and loosely packed in the membrane. As the sintering process has taken place, the polymer has been eliminated and left only the ceramic in the membrane. During this process, the grain growth of the particles occurred and the membrane is shrunk and densified. The formation of finger-like void is also significantly enhanced as the sintering temperature increased from 950 °C to 1000 °C. Similarly, Wang et al. [20] reported the densification of β-sialon ceramics at a temperature of 1650 °C, for the highest mechanical strength for the ceramic.

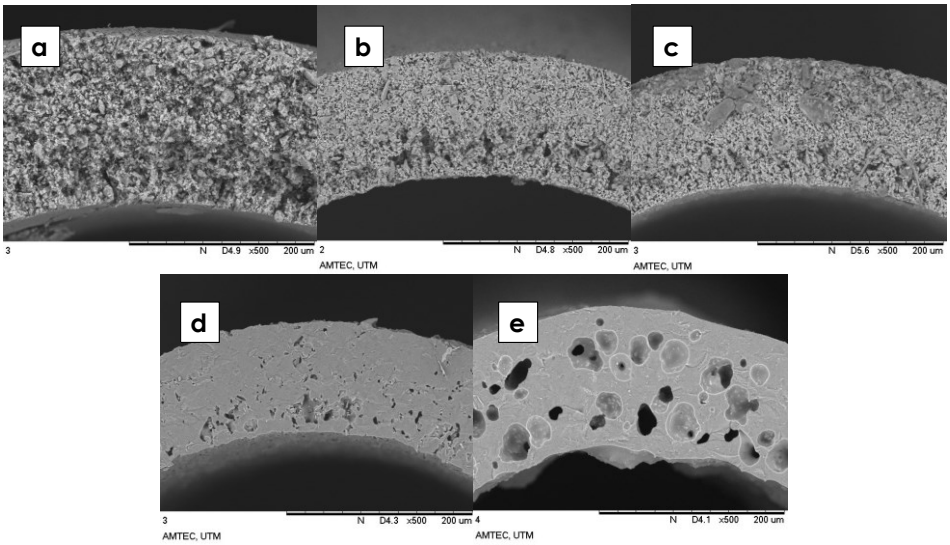



Figure 8. Cross-sectional SEM images (magnification 500x) of the zeolite based HFCMs (fibre 6) before (a) and after calcination at different sintering temperatures: (b) 950 °C; (c) 1000 °C; (d) 1050 °C; and (e) 1100 °C, respectively

As the temperature further increased to 1050 °C, the ceramic particle became densified both in inner and outer parts of the membrane. The destruction in finger-like voids and the formation of macro voids were significantly increased. At 1100 °C, the membrane became completely dense and compacted accompanied with the presence of macro voids all over the structure. At this stage, the ceramic material is approaching its melting point. The formation of macro voids could be attributed by the space left by the particles when it starts to closely packed to one another. The closed-up images of the particles is shown in Figure 9 where the images were taken at 3000 x magnification. Therefore, the best sintering temperature for the fabrication of zeolite based HFCM is 1000 °C. Although the most densified membrane could give the highest mechanical strength, but it is unfavorably desired since it will eventually give a lower permeation and flux.

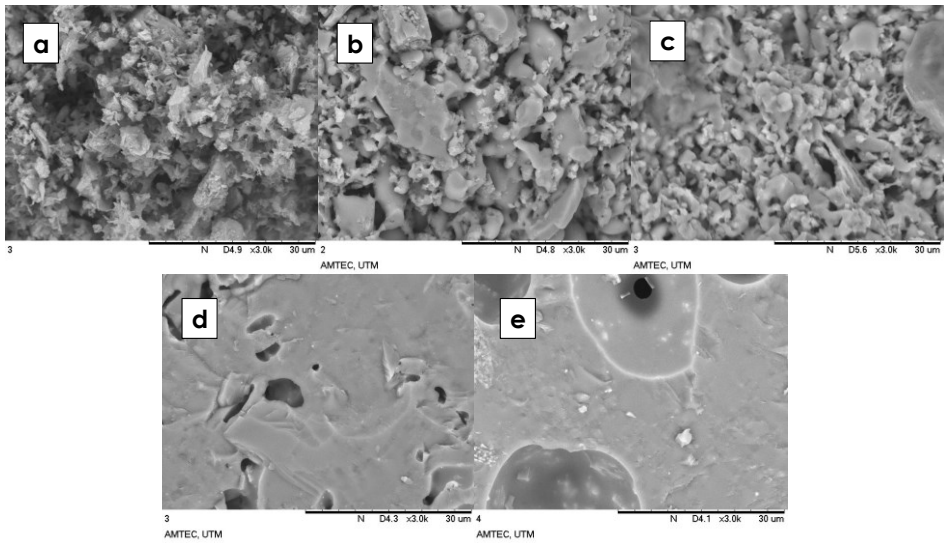



Figure 9. SEM images (magnification 3000x) of the cross-sectional zeolite based HFCMs (fibre 6) before (a) and after calcination at different sintering temperatures: (b) 950 °C; (c) 1000 °C; (d) 1050 °C; and (e) 1100

## Conclusion

A low-cost zeolite based hollow fibre ceramic membrane was successfully fabricated using phase inversion and sintering techniques. The best fabrication parameters were 5 cm air-gap distance, 13 mL $min^{-1}$ of bore fluid flow rate and sintering temperature of 1000 °C. The acceptable strength and morphological behavior of finger-like and sponge-like voids were found to be an advantageous characteristic of the fabricated membrane. Its pleasant structure with a separation layer from either inner and outer surface may be beneficial for applications in separation and filtration of volatile compounds such as ammonia in liquid-liquid membrane contactor system.

## Acknowledgement

This research is fully supported by HICoE grant, R.J090301.7846.4J194. The authors fully acknowledged Ministry of Higher Education (MOHE) and Universiti Teknologi Malaysia (UTM) for the approved fund which makes this important research viable and effective.

## References

1. Ozturk, I., Altinbas, M., Koyuncu, I., Arikan, O. and Yangin, C. G. (2003). Advanced physico-chemical treatment experiences on young municipal landfill leachates. *Waste Management*, 23: 441 – 446.
2. Gabelman, A. and Hwang, S. (1999). Hollow fiber membrane contactors, *Journal of Membrane Science*, 159: 61 – 67.
3. Keshavarz, P., Ayatollahi, S. and Fathikalajahi, J. (2008). Mathematical modelling of gas-liquid membrane contactors using random distribution of fibres. *Journal of Membrane Science*, 325: 98 – 108.
4. Tan, X., Tan, S. P., Teo, W. K. and Li, K. (2006). Polyvinylidenefluoride (PVDF) hollow fibre membranes for ammonia removal from water. *Journal of Membrane Science*, 271: 59 – 68.
5. Barbe, A. M., Hogan, P. A. and Johnson, R. A. (2000). Surface morphology changes during initial usage of hydrophobic, microporous polypropylene membranes. *Journal of Membrane Science*, 172: 149 –156.
6. Wang, R., Li, D. F., Zhou, C., Liu, M. and Liang, D. T. (2004). Impact of DEA solutions with and without $CO_2$ loading on porous polypropylene membranes intended for use as contactors. *Journal of Membrane Science*, 229: 147 – 157.
7. Dindore, V. Y., Brilman, D. W. F., Feron, P. H. M. and Versteeg, G. F. (2004). $CO_2$ absorption at elevated pressures using a hollow fiber membrane contactor. *Journal of Membrane Science*, 235: 99 – 109.
8. Liu, S., Tan, X., Li, K. and Hughes, R. (2001). Preparation and characterisation of $SrCe_{0.95}Yb_{0.05}O_{2.975}$ hollow fibre membranes. *Journal of Membrane Science*, 193: 249 – 260.
9. Liu, S., Li, K. and Hughes, R. (2003). Preparation of porous aluminium oxide ($Al_2O_3$) hollow fibre membranes by a combined phase-inversion and sintering method. *Ceramic International*, 29: 875 –881.
10. Velez, M. H., Herrera, O. R., Martin, A. A., Rodriguez, A. J. and Malherbe, R. R. (1995). New materials obtained from high temperature phase transformation of natural zeolites. *Journal of Material Science Letter*, 14: 1653 – 1656.
11. Mumpton, F. A. (1978). Natural zeolites: A new industrial mineral commodity, in: L.B. Sand, F.A. Mumpton (Eds.), Natural Zeolites, Occurrence, Properties, Use. Pergamon Press, New York: pp. 285 –302.
12. Li, J. L. and Chen, B. H. (2005). Review of $CO_2$ absorption using chemical solvents in hollow fibre membrane contactors. *Separation and Purification Technology,* 41: 109 – 122.
13. Alami Younssi, S., Iraqi, A., Rafiq, M., Persin, M., Larbot, A. and Sarrazin, J. (2003). γ alumina membranes grafting by organosilanes and its application to the separation of solvent mixtures by pervaporation. *Separation and Purification Technology*, 32: 175 – 179.
14. Krajewski, S. R., Kujawski, W., Dijoux, F., Picard, C. and Larbot, A. (2004). Grafting of $ZrO_2$ powder and $ZrO_2$ membrane by fluoroalkylsilanes. *Colloids and Surface A*, 243: 43 – 47.
15. Othman, M. H. D., Wu , Z., Droushiotis, N., Doraswami, U., Kelsall, G. and Li, K. (2010). Single-step fabrication and characterisations of electrolyte / anode dual – layer hollow fibres for microtubular solid oxide fuel cells. *Journal of Membrane Science*, 351: 196 – 204.
16. Kingsbury, B. F. K. and Li, K. (2009). A morphological study of ceramic hollow fibre membranes. *Journal of Membrane Science*, 328: 134 – 140.
17. Nitman, J., Daccord, G. and Stanley, H. E. (1985). Fractal growth of viscous fingers: Quantitative characterization of a fluid instability phenomenon. *Nature,* 314: 141 – 144.

18. Li, L., Chen, M., Dong, Y., Dong, X., Cerneaux, S., Hampshire, S., Cao, J., Zhu, L., Zhu, Z. and Liu, J. (2016). A low-cost alumina-mullite composite hollow fiber ceramic membrane fabricated via phase-inversion and sintering method. *Journal of the European Ceramic Society*, 36: 2057 – 2066.
19. Bonyadi, S., Chung, T. S. and Krantz W. B. (2007). Investigation of corrugation phenomenon in the inner contour of hollow fibre during the non-solvent induced phase-separation process. *Journal of Membrane Science*, 299: 200 – 210.
20. Wang, J. W., Li, L., Zhang, J. W., Xu, X. and Chen, C. S. (2016). β-Sialon ceramic hollow fiber membranes with high strength and low thermal conductivity for membrane distillation. *Journal of the European Ceramic Society,* 36: 59 – 65.

*Malaysian Journal of Analytical Sciences, Vol 21 No 2 (2017): 402 - 408*
*DOI: https://doi.org/10.17576/mjas-2017-2102-15*

MALAYSIAN JOURNAL OF ANALYTICAL SCIENCES
*Published by The Malaysian Analytical Sciences Society*
ISSN 1394 - 2506

# THE EFFECT OF NOVEL MULTIWALLED CARBON NANOTUBE-TITANIA NANOTUBE HYBRID IN POLYAMIDE ACTIVE LAYER TOWARDS WATER PERMEABILITY AND HIGH SODIUM CHLORIDE REJECTION PERFORMANCE OF NANOFILTRATION MEMBRANE DESALINATION

## (Kesan Hibrid Karbon Tiub Nano Pelbagai Dinding-Titania Tiub Nano Novel dalam Lapisan Aktif Poliamida Terhadap Prestasi Kebolehtelapan Air dan Penyingkiran Natrium Klorida yang Tinggi Bagi Membran Penapisan Nano Pengenyahmasin)

Ihsan Wan Azelee, Pei Sean Goh*, Woei Jye Lau, Ahmad Fauzi Ismail, Masood Rezaei Dasht Arzhandi, Kar Chun Wong, Mahesan Naidu Subramaniam

*Advanced Membrane Technology Research Centre (AMTEC), Universiti Teknologi Malaysia, 81310 Skudai, Johor, Malaysia*

**Corresponding author: peisean@petroleum.utm.my*

Received: 26 August 2016; Accepted: 8 January 2017

**Abstract**

In this study, thin film nanocomposite (TFN) membranes were prepared by incorporating multi-walled carbon nanotube-titania nanotube (MWCNT-TNT) hybrid into the polyamide layer via interfacial polymerization on the surface of PS35 commercial substrate. The study showed that in the neat thin film composite (TFC), the presence of PIP in polyamide layer increased the water permeability (from 0.54 to 2.25 L/m$^2$ h bar) but decreased the NaCl rejection (from 86.48 to 47.45%). Interestingly, the presence of MWCNT-TNT in MPD-PIP polyamide layer increased the NaCl rejection by 38.68% (47.45 to 86.13%) while giving a significant water permeability performance at 0.86 L/m$^2$ h bar. The incorporation of acid treated MWCNT-TNT has improved the water permeability from 0.86 to 0.89 L/m$^2$ h bar while decreasing the NaCl rejection from 86.13 to 77.51%. Further investigation of MWCNT-TNT loading at pH 2 revealed that the increase of its loading in polyamide layer decreased both water permeability and NaCl rejection performance of the membrane. Overall, it can be concluded that the addition of an appropriate loading of surface modified MWCNT-TNT into the polyamide layer can remarkably improve the performance of conventional TFC membranes for desalination applications. In addition, incorporating PIP in the polyamide layer reduces the capability of the membrane on NaCl rejection.

**Keywords**: water desalination, thin film nanocomposite membrane, MWCNT-TNT hybrid

**Abstrak**

Dalam kajian ini, filem nipis komposit nano (TFN) membran telah disediakan dengan menggabungkan karbon tiub nano pelbagai dinding-titania tiub nano (MWCNT-TNT) ke dalam lapisan poliamida melalui pempolimeran antara muka di permukaan substrat PS35 membran komersial. Kajian ini menunjukkan bahawa tanpa MWCNT-TNT, kehadiran PIP dalam lapisan poliamida meningkatkan kebolehtelapan air (daripada 0.54 kepada 2.25 L/m$^2$ h bar) tetapi mengurangkan penyingkiran NaCl (daripada 86.48 kepada 47.45%). Menariknya, kehadiran MWCNT-TNT dalam lapisan poliamida MPD-PIP meningkatkan penyingkiran NaCl pada 38.68% (47.45 kepada 86.13%) sambil memberi prestasi kebolehtelapan air yang besar pada 0.86 L/m$^2$ h bar. Penggabungan MWCNT-TNT ygng dirawat asid telah meningkat kebolehtelapan air dari 0.86 to 0.89 L/m$^2$ h bar namun mengurangkan penyingkiran NaCl (daripada 86.13 kepada 77.51%). Siasatan lanjut terhadap muatan MWCNT-TNT pada pH 2 mendedahkan bahawa peningkatan muatannya dalam lapisan poliamida menurun kedua-dua prestasi membran terhadap kebolehtelapan air dan penyingkiran NaCl. Secara keseluruhan, dapat disimpulkan bahawa penambahan muatan dan pH yang

sesuai bagi MWCNT-TNT ke dalam lapisan poliamida dapat meningkatkan lagi prestasi membran TFC konvensional untuk aplikasi pengenyahmasin. Di samping itu, menggabungkan PIP dalam lapisan poliamida mengurangkan keupayaan membran terhadap penyingkiran NaCl.

**Kata kunci:** pengenyahmasin air, membran filem nipis komposit nano, hibrid MWCNT-TNT

## Introduction

Nanofiltration (NF) which lies between ultrafiltration (UF) and reverse osmosis (RO) is a separation technique used in desalination process mostly to reject multivalent ions rather than monovalent ions. NF shows some advantages over RO such as greater water permeability and lower operating pressure [1]. The thin film composite (TFC) NF membrane is normally fabricated through interfacial polymerization (IP) process of two immiscible phases in the formation of thin and dense polyamide layer. Nowadays, TFC NF membrane has also been widely applied for water purification, wastewater treatment, food processing and bio-separation [2].

Recently, many efforts have been made to tailor the structural properties of polyamide-based TFC membrane to improve the separation performance of the membrane. The introduction of polymeric nanocomposites either by mixed matrix membrane or incorporated in polyamide layer of the membrane have gained interest of many researchers. Various nanomaterials such as silica, zeolite, graphite, metal oxide nanomaterials and carbon nanotubes (CNTs) have been introduced for membrane application due to their unique features including the ability to promote high permeability and decreased in fouling resistance [3]. Evidently, each nano-materials have their own unique properties, but a single material is unlikely to simultaneously offer several if not all, of these beneficial features for membrane fabrication. This has led to recent developments and application of hybrid nanomaterials capable of synergistically contributing the advantages of their individual components and thereby reducing their shortcoming [4].

The present work aims to evaluate the feasibility of using multi-walled carbon nanotubes-titania (MWCNT-TNT) hybrid as nanofillers of thin film nanocomposite (TFN) membrane. Even though many works on inorganic nanoscale particles have been studied, however, there is still no exploration on hybrid nanomaterials for water desalination membrane. In this study, a hybrid of MWCNT-TNT will be incorporated into the polyamide layer of TFN membrane to harness the unique characteristic of both MWCNTs and TNTs. The TFN membrane will be evaluated in term of their water permeability and NaCl rejection performance.

## Materials and Methods

### Materials

Commercial ultrafiltration (UF) membrane obtained from Sterlitech was used for membrane substrate. 1,3,5-benzenetricarboxylic acid chloride (TMC, Acros Organic) in n-hexane (Fisher Chemical), 1,3-phenylenediamine (MPD, Merck) and piperazine (PIP, Merck) in RO water were used in TFC membrane fabrication for PA layer. Titanium dioxide nanoparticles ($TiO_2$, Degussa P25 Evonik), multi-walled carbon nanotube (MWCNT, Aldrich), hydrochloric acid (HCl, Merck), sulfuric acid ($H_2SO_4$, Merck 95 – 97%), nitric acid ($HNO_3$, Merck 65%) and sodium hydroxide (NaOH, Merck) and sodium hydroxide (NaOH, Merck) were used to synthesize hybrid MWCNT-TNT. Sodium chloride (NaCl, Merck) was used in salt water preparation.

### Synthesis of MWCNT-TNT hybrid

MWCNT-TNT hybrid was synthesized by oxidization and hydrothermal method. Firstly, 1g of MWCNTs was acid refluxed in $H_2SO_4$:$HNO_3$ (each 3 M, 3:1, v/v) (250 ml) at 80 °C for 24 hours. The solution was filtered and washed to get pH neutral before oven-dried. 3 g of oxidized MWCNTs and $TiO_2$ (1:5) was undergone the hydrothermal process for 24 hours at 120 °C in 10M NaOH (100 ml). The MWCNT-TNT was washed until pH lower than 9 and was treated with HCl solution (0.1M) to obtain pH 3 – 4. The final product was washed to pH neutral and dried in an oven at 60 °C. To prepare the acid treated filler (a-MWCNT-TNT), the prepared MWCNT-TNT was treated with hydrochloric acid (HCl). Briefly, a 0.2g of MWCNT-TNT was added into a solution of pH 2 containing 0.05 HCl solution and was shake for 24 hours. All the solution were prepared with a specific gravity of 0.03M NaCl solutions as buffer solution. The precipitate of a-MWCNT-TNT was filtered and dried in the oven at 60 °C [5].

**Synthesis of polyamide layer**

Two types of polyamide layer were formed by (i) MPD (1.5wt) / TMC (0.05wt) which indicated as TFC A and (ii) MPD (1.13wt)-PIP (0.37wt) / TMC (0.05wt) indicated as TFC B. The polyamide layer for thin film composite (TFC) membrane was introduced via interfacial polymerization (IP) process on the surface of PS35 substrate membrane. The PS35 substrate was kept in RO water for at least 24 hours prior to interfacial polymerization (IP) process. Briefly, the MPD or MPD-PIP, was dissolved in RO water and the solution was covered by tissue paper to prevent from light oxidation [6]. In separated solution, TMC was dissolved in n-hexane. All the solutions were stirred at a minimum of 3 hours prior to use. To begin IP process, 40 ml of MPD aqueous solution (0.8 g MPD in 40 ml RO water) was poured and fully covered the PS35 substrate surface which was held horizontally for 1 min. The excess MPD solution and residual droplets were gently removed by using a soft rubber roller. Then, 40 ml of TMC solution (0.04 g TMC in 40 ml n-hexane) was also poured and fully covered on the substrate and was drained off after 50 s. The synthesized TFC membrane was dried for 1 min at ambient condition and 5 min later in the oven at 65 $^{o}$C. Finally, the TFC membrane was cooled for 1 min at ambient condition before continued to be rinsed with water and stored in RO water container [7]. The membrane (mentioned as MWCNT-TNT/TFC) were fabricated similarly to TFC membrane, except that during the interfacial polymerization, the MWCNT-TNT (0.05 wt.% or 0.1 wt.%) was dispersed and sonicated for 30 min in organic solution of TMC in n-hexane and was reacted with MPD or MPD-PIP immobilized on PS35 substrate commercial membrane

**Characterization of MWCNT-TNT, TFC and TFN membranes**

The crystal configuration of MWCNT-TNT hybrid was analyzed by X-ray diffraction (XRD) analysis. The tabular morphology of MWCNT-TNT hybrid was observed by transmission electron microscopy (TEM, HT 7700, Hitachi). The Zeta potential analysis (Malvern Zetasizer, Nano ZS) was utilized to determine the charge of the MWCNT-TNT and fabricated membrane. The hydrophilicity of membranes was measured by contact angle goniometer (OCA 15Pro, Dataphysics).

**Performance study of TFC and TFN membranes**

Pure water permeability and salt rejection performance by RO water and standard aqueous solution of NaCl (2000ppm) were conducted using dead end RO cell at an applied pressure of 15 bar. All permeation experiments were performed using circular membranes with an effective area of 14.6 cm$^2$. The membrane water permeability was evaluated by dividing the water flux value (Eq. 1) with operating pressure (15 bar).

$$J = \frac{V}{A \times t} \tag{1}$$

where $V$ is the permeate volume (L), $A$ is the membrane active area (m$^2$) and $t$ is the experiment time (h) to obtain $V$. The salt rejection was calculated based on following Equation 2:

$$R(\%) = \left(1 - \frac{C_p}{C_f}\right) \times 100 \tag{2}$$

where $C_p$ and $C_f$ are the concentration (ppm) of the permeate and feed solution, respectively.

## Results and Discussion

**XRD analysis**

The XRD analysis of MWCNT-TNT hybrid, MWCNTs and TNTs are represented in Figure 1. The self-synthesized TNTs sample shows an intense peak at 2-theta values of 10.48$^{o}$, 24.76 $^{o}$ and 48.58 $^{o}$. These patterns correspond to the crystal structure of TNTs. The peaks at a 2-theta values of 25.78 $^{o}$ and 43.13 $^{o}$ in XRD pattern of MWCNTs correspond to the cylindrical concentric tubular structure of MWCNTs and the sp$^3$ hybridization of the carbon atom. The characterization peak of MWCNTs at 25.78$^{o}$ can also be observed clearly in the formation peak at 26.18$^{o}$ in the patterns of MWCNT-TNT hybrid, which suggested the successful formation of MWCNT-TNTs [8]. Meanwhile, an intense peak at 2-theta values of 24.98$^{o}$, 26.18$^{o}$ and 48.72 $^{o}$ for MWCNT-TNT hybrid samples supported the

formation of TNTs nanotubes. The diffraction peak 10.48° and 11.1° showed by TNTs and MWCNT-TNT hybrid, respectively, a notable feature of the tubular structure of $TiO_2$ nanomaterials [8].

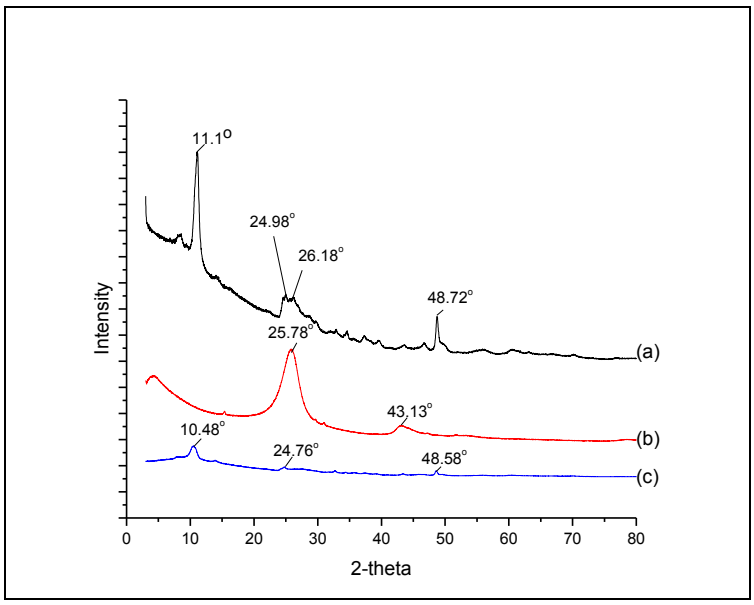



Figure 1. XRD patterns of (a) self-synthesized MWCNT-TNT hybrid, (b) commercial MWCNTs and (c) self-synthesized TNT

**TEM analysis**

TEM images (Figure 2) clearly demonstrate the tubular structure of MWCNT-TNT hybrid which depicted the open end of MWCNTs in the MWCNT-TNT hybrid. The MWCNT have the outer diameter in the range of 16 –20 nm while 71 – 141 nm for TNT, as indicated by TEM image. In addition, there were no $TiO_2$ nanoparticles (NPs) observed in TEM image of MWCNT-TNT hybrid, confirming that $TiO_2$ NPs was completely converted into TNTs after the hydrothermal treatment. These findings are consistent with the XRD results. Liu et al. [8],who applied the same hydrothermal method for the synthesized of MWCNT-TNT hybrid indicated the homogeneous mixture of nanotube was difficult to be achieved through the simple mechanical mixing.

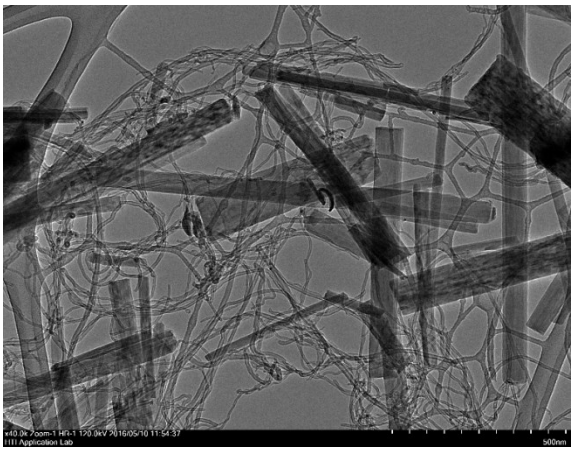


Figure 2. TEM image (magnification: 40K) of MWCNT-TNT hybrid

**Membrane performance**

Water permeability and NaCl rejection were evaluated for the membrane performance to determine the effect of the addition of MWCNT-TNT hybrid as nanofiller in polyamide layer of composite membrane. It was observed (Figure 3) that the water permeability of TFC membrane was increased from 0.54 to 2.25 L/m$^2$ h bar when piperazine as a co-monomer was used in polyamide selective layer (TFC B). The transport property that includes flux and rejection of nanofiltration membranes were greatly influenced by monomer type during polyamide layer formation which in accordance with that reported Saha and Joshi [9]. It was also believed that the addition of piperazine into PA layer will disturb the restricted chain flexibility of MPD-TMC PA, resulting in high water permeability in TFC B [9].

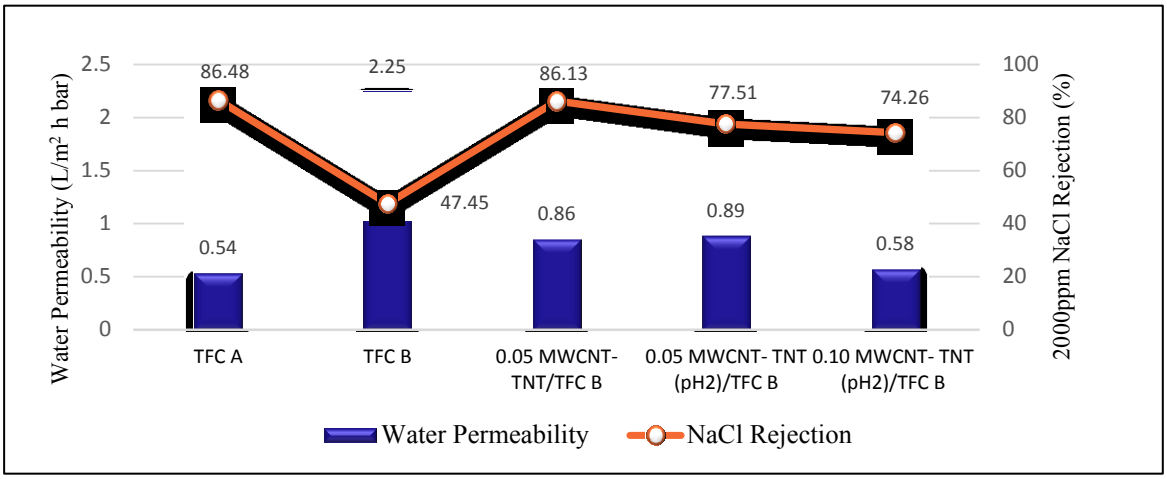



Figure 3. Water permeability and NaCl separation of thin film composite membranes (TFC) of TFC A [MPD (1.5wt) / TMC (0.05wt)] and TFC B [MPD (1.13wt)-PIP (0.37wt) / TMC (0.05wt)]. (Test conditions: 15 bar, 25 $^o$C, 2000 ppm NaCl aqueous solution)

However, the sharp increase in water permeability deteriorating the NaCl rejection from 86.48% to 47.45%. This observation is in agreement with that of reported by Wu et al. [1] where PIP was used as co-monomer. Uniquely, by incorporating the MWCNT-TNT hybrid in TFC B, the NaCl rejection increased from 47.45% to 86.13%, while the water permeability was higher compared to TFC A. The existence of hydrogen on MWCNT-TNT can enhance the hydrogen bonding formation in PA layer which in turn decreased the pore sizes in PA layer while later contributed to low water permeability and increase NaCl rejection [9]. Moreover, the successful synthesis of MWCNT-TNT as confirmed by XRD and TEM provides unique properties for the membrane which offers pore channels and high hydrophilicity of hybrid to increase water permeability while reject certain dissolved ions [10], [11]. Meanwhile, when the MWCNT-TNT was treated with acid (a-MWCNT-TNT) and was incorporated into the polyamide layer of TFC B, the water permeability was increased as indicated by decreasing contact angle from 72.92 to 61.71$^o$ of the membrane as shown in Table 1.

However, a-MWCNT-TNT/TFC B showed a slightly decreased in NaCl rejection. The polymer links formed from PIP and TMC, which occurs faster in polyamide layer of TFC B might compete with the bonding between a-MWCNT-TNT with the free –COCl groups of TMC [1]. Hence, contributed to the decreased in surface negative charge of the membrane as provided by the positive value of zeta potential (Table 1). The further increased of a-MWCNT-TNT in polyamide layer of TFC B deteriorated NaCl rejection of membrane performance. It is possibly due to the tendency of NaCl molecules to pass through some voids between a-MWCNT-TNT and polyamide at high loading of the hybrid nanotube [11]. Moreover, higher a-MWCNT-TNT loading (0.10 MWCNT-TNT) led to ineffectiveness on water permeability, which likely suggests the formation of thicker polyamide rejection layer under this a-MWCNT-TNT loading condition [12, 13].

Table 1. The properties of MWCNT-TNT hybrid and TFC/TFN membranes prepared in this work

| MWCNT-TNT / Membrane | Contact Angle ($^o$) | Surface Zeta Potential (mV) |
|---|---|---|
| MWCNT-TNT | - | -8.95 |
| a-MWCNT-TNT | - | 26.6 |
| TFC A | 90.22 ± 2.81 | - |
| TFC B | 52.66 ± 3.39 | -14.1 |
| 0.05 MWCNT-TNT/TFC B | 72.92 ± 3.56 | -10.6 |
| 0.05 a-MWCNT-TNT/TFC B | 61.71 ± 2.21 | 17.2 |
| 0.10 a-MWCNT-TNT/TFC B | 75.77 ± 2.97 | 14.3 |

## Conclusion

Novel TFN membranes for nanofiltration were fabricated by incorporating MWCNT-TNT hybrid. The MWCNT-TNT hybrid was successfully synthesized, which was confirmed by XRD and TEM analysis. The mixed cross-linking of MPD-PIP diamine monomer during interfacial polymerization in polyamide layer decreased the rejection of NaCl to an average of 39%. The unique properties of MWCNT-TNT hybrid such as tubular structure have improved the membrane performance in terms of water permeability and NaCl rejection. The acid treatment of MWCNT-TNT with HCl possibly provided external Cl group which help on PA layer formation. However, it might compete with the fast reaction of PIP monomer which decrease the negative charge of the membrane and decreased the salt rejection. Worth noting that the higher loading of a-MWCNT-TNT in MPD-PIP polyamide layer decreased both water permeability and NaCl rejection of membrane performance due to the dense PA layer formation.

## Acknowledgement

The authors would like to acknowledge the financial supports provided by Ministry of Higher Education (FRGS Grant: 4F306 and HiCOE Grant: 4J196) and Universiti Teknologi Malaysia for Research University Grant: 02G43. Author, Ihsan Wan Azelee thanks the sponsorship given by Ministry of Higher Education under MyBrain15 (MyPhD) scheme during his Ph.D. studies.

## References

1. Wu, D., Yu, S., Lawless, D. and Feng, X. (2015). Thin film composite nanofiltration membranes fabricated from polymeric amine polyethylenimine imbedded with monomeric amine piperazine for enhanced salt separations. *Reactive and Functional Polymers*, 86: 168 – 1835.
2. Lau, W. J., Ismail, A. F., Goh, P. S., Hilal, N. and Ooi, B. S. (2014). Characterization methods of thin film composite nanofiltration membranes. *Separation and Purification Reviews*, 44 (2): 135 – 156.
3. Vatanpour, V., Esmaeili, M. and Farahani, M. H. D. A. (2014). Fouling reduction and retention increment of polyethersulfone nanofiltration membranes embedded by amine-functionalized multi-walled carbon nanotubes. *Journal of Membrane Science*, 466: 70 – 81.
4. Natarajan, T. S., Lee, J. Y., Bajaj, H. C., Jo, W.-K. and Tayade, R. J. (2016). Synthesis of multiwall carbon nanotubes/$TiO_2$ nanotube composites with enhanced photocatalytic decomposition efficiency. *Catalysis Today*, 282: 13 – 23.
5. Mudunkotuwa, I. A. and Grassian, V. H. (2010). Citric acid adsorption on $TiO_2$ nanoparticles in aqueous suspensions at acidic and circumneutral pH : Surface coverage , surface speciation , and its impact on nanoparticle - nanoparticle interactions. *Jounal of American Chemical Society*, 132: 14986 – 14994.
6. Lind, M. L., Suk, D. E., Nguyen, T. V. and Hoek, E. M. V. (2010). Tailoring the structure of thin film nanocomposite membranes to achieve seawater RO membrane performance. *Environmental Science and Technology*, 44 (21): 8230 – 8235.
7. Xie, W., Geise, G. M., Freeman, B. D., Lee, H. S., Byun, G. and McGrath, J. E. (2012). Polyamide interfacial composite membranes prepared from m-phenylene diamine, trimesoyl chloride and a new disulfonated diamine. *Journal of Membrane Science*, 403 – 404: 152 – 161.

8. Liu, X., Yan, R., Zhang, J., Zhu, J. and Wong, D. K. Y. (2015). Evaluation of a carbon nanotube-titanate nanotube nanocomposite as an electrochemical biosensor scaffold. *Biosensors and Bioelectronics*, 66: 208 – 215.
9. Saha, N. K. and Joshi, S. V. (2009). Performance evaluation of thin film composite polyamide nanofiltration membrane with variation in monomer type. *Journal of Membrane Science*, 342 (1–2): 60 – 69.
10. Daer, S., Kharraz, J., Giwa, A. and Hasan, S. W. (2015). Recent applications of nanomaterials in water desalination: A critical review and future opportunities. *Desalination*, 367: 37 – 48.
11. Zhang, L., Shi, G.-Z., Qiu, S., Cheng, L.-H. and Chen, H.-L. (2011). Preparation of high-flux thin film nanocomposite reverse osmosis membranes by incorporating functionalized multi-walled carbon nanotubes. *Desalination and Water Treatment*, 34(1–3): 19 – 24.
12. Ma, N., Wei, J., Liao, R. and Tang, C. Y. (2012). Zeolite-polyamide thin film nanocomposite membranes: Towards enhanced performance for forward osmosis. *Journal of Membrane Science*, 405 – 406: 149 – 157.
13. Wan Azelee, I., Goh, P. S., Lau, W. J., Ng, B. C. and Ismail, A. F. (2016). Development of thin film nanocomposite embedded with graphene oxide for $MgSO_4$ removal. *Journal of Engineerning Science and Technology*, 11(7): 974 – 986.

*Malaysian Journal of Analytical Sciences, Vol 21 No 2 (2017): 409 - 415*
*DOI: https://doi.org/10.17576/mjas-2017-2102-16*

MALAYSIAN JOURNAL OF ANALYTICAL SCIENCES
*Published by The Malaysian Analytical Sciences Society*
ISSN 1394 - 2506

# THE INFLUENCE OF CARBONIZATION TEMPERATURE ON THE DEVELOPMENT OF CARBON MEMBRANE WITH SUPERIOR $CO_2/CH_4$ SEPARATION PERFORMANCE

## (Pengaruh Suhu Karbonisasi Kepada Pembangunan Membran Karbon Dengan Kesan Pemisahan Gas $CO_2/CH_4$ Yang Cemerlang)

Norazlianie Sazali[1,2],Wan Norharyati Wan Salleh[1,2]*, Mohamad Azuwa Mohamed[1,2], Nor Hafiza Ismail[1,2], Norafiqah Rosman[1,2], Farhana Aziz[1,2], Ahmad Fauzi Ismail[1,2]

[1]*Advanced Membrane Technology Research Centre (AMTEC)*
[2]*Faculty of Chemical and Energy Engineering (FCEE)*
*Universiti Teknologi Malaysia, 81310 Skudai, Johor Darul Takzim, Malaysia.*

**Corresponding author: hayati@petroleum.utm.my*

Received: 26 August 2016; Accepted: 8 January 2017

**Abstract**

In this study, P84-based carbon tubular membranes were fabricated and characterized in terms of their structural morphology and gas permeation properties, by using Scanning Electron Microscopy (SEM) and pure gas permeation system, respectively. The polymer tubular membranes were then carbonized under nitrogen atmosphere at different carbonization temperatures of 600, 700, 800 and 900 °C, with heating rate of 3°C/min and thermal soak time of 30 minutes. The manipulation of carbonization temperatures was required to see if it could enhance the permeation properties as desired. Pure gas permeation tests were performed using $CO_2$ and $CH_4$ gases. The $CO_2/CH_4$ selectivity was found increasing as the carbonization temperature was increased from 600 to 800 °C. The carbon membrane carbonized at 800°C showed the most promising result for $CO_2/CH_4$ selectivity, rendering 69.48 and $CO_2$ permeance of 206.1 GPU.

**Keywords**: carbonization temperature, tubular support, P84 copolyimide, carbon membrane, gas separation

**Abstrak**

Dalam kajian ini, membran tiub karbon berasaskan P84 telah direka dan dicirikan dari segi morfologi dan penyerapan gas dengan menggunakan mikroskopi elektoron pengimbasan (SEM), dan sistem penyerapan gas tulen. Membran polimer tiub kemudian dikarbonisasi dalam kawalan gas nitrogen pada suhu karbonisasi berbeza iaitu 600, 700, 800 dan 900 °C dengan kadar pemanasan 3 °C/min dan kawalan haba selama 30 minit. Pengubahsuaian syarat karbonisasi diperlukan untuk mempertingkatkan ciri – ciri penyerapan gas. Ujian penyerapan gas tulen telah dilakukan dengan menggunakan gas $CO_2$ dan gas $CH_4$. Keterpilihan gas $CO_2/CH_4$ telah meningkat apabila suhu karbonisasi meningkat daripada 600 ke 800°C. Daripada kajian ini, membran karbon yang dikarbonisasi pada suhu 800 °C menunjukkan bacaan yang paling tinggi dengan nilai keterpilihan $CO_2$ /$CH_4$ sebanyak 69.48 dan nilai kebolehtelapan $CO_2$ ialah 206.1 GPU.

**Kata kunci:** suhu karbonisasi, sokongan tubul, P84 kopolimid, membran karbon, pemisahan gas

## Introduction

Membrane technology has gained interest as fluids separation media. Membrane is semi permeable barrier that allows only specific molecules to pass through, while discriminating others. Since there is no occurrence of phase

change during the separation [1], membranes technology offers minimal energy requirement [2]. Moreover, the membrane technology incorporating an efficient and straightforward separation approach with no moving parts makes it as preferable process. The membrane technology has shown a great industrial potential in seawater desalination, water filtration, wastewater treatment, dialysis and gas separation. Since the past decades, the depletion of natural gas quality, where the presence of impurities is prominent, has encouraged researches on membrane technology to focus on natural gas purification [3, 4]. There are several well-established processes such as adsorption, chemical absorption and cryogenic distillation which have been implemented in the purification process. These conventional processes, however, are known to suffer from high energy requirement, toxic refrigerant, unit corrosion, expensive maintenance and high operation cost. Membrane for gas separation offers a lot of advantages including space efficiency, requiring no complicated integration into the power plant, no regeneration, and chemical are not needed [5].

However, there is a trade-off suffered by polymeric membrane; which highly permeable membranes commonly accompanied by poor gas pair selectivity and vice versa [6, 7]. Since then, researches has highlights numerous strategies to overcome the limitation. Among them, new class of membrane known as carbon membrane was discovered. Carbon membrane is resulted from carbonized formed of polymeric precursor. During carbonization, polymeric precursor began to decompose, causing the functional group presence to breakage and form amorphous material. The resulted amorphous material having bimodal pore distribution having better thermal stability, chemically resistant towards various concentrations of acid, hot organic solvent and alkaline solution compared to their polymeric counterpart [8-9]. The gas separation performance of carbon membrane has been highlighted over the years. Owing to their bimodal pore distribution, carbon membrane performed well above the Robeson Upperbound. However, due to the fragility of carbon membrane structure, good handling is needed to avoid structural collapse [10]. To overcome the limitation, fabricating carbon membrane on ceramic substrate is among preferable approach [11]. In this study, supported carbon membrane was prepared via dip-coating method due to its straightforwardness approach and cost-effective [12, 13].

Since development of tubular supported carbon membrane is a relatively new approach, it is important to identify the most ideal carbonization temperature that could result in high performance carbon membrane. Therefore, this study aims to develop tubular supported carbon membrane for $CO_2/CH_4$ separation using different carbonization temperatures.

## Materials and Methods

A commercially available polyimide-type polymer was chosen as a precursor, which is a thermally stable co-polyimide BTDA-TDI/MDI (P84), procured from Sigma Aldrich (CAS#: 58698-66-1). The measured density of P84 was about 1.31g/cm$^3$ with glass transition temperature ($T_g$) of 315 $^oC$ [14]. N-Methyl-2-Pyrrolidone (NMP) was used as solvent; which is a strong, aprotic solvent with high solvency and low volatility, purchased from Merck (Germany). Porous tubular ceramic was purchased from Shanghai Gongtao Ceramics Co. Ltd. The dimension of the porous tubular ceramic was about 8 cm in length, 13 mm in outer diameter and 10 mm in inner diameter. The porosity of the support was 40 – 50% with an average pore size of 0.2 μm.

To begin, P84 was dissolved in NMP, stirred using mechanical stirrer and sonicated to remove trapped bubbles from the solution. The tubular support was immersed into the polymeric solution for 15 minutes and the process was repeated three times. The supported membrane was dried at temperature of 80 °C for 24 hours, followed by immersion in methanol for 2 hours. The sample was then placed in oven at temperature of 100 °C for 2 hours to remove the methanol prior to carbonization. Subsequently, the supported membrane was placed at the center of the Carbolite horizontal tubular furnace to undergo carbonization process. Heat treatment was performed at 300 °C for 30 minutes, followed by carbonization at temperatures of 600 °C, 700 °C, 800 °C and 900 °C, with heating rate of 3 °C /min under nitrogen gas (200 mL/min) as illustrated in Figure 1. The nomenclature of the resultant carbon tubular membrane was given in the form of CM-Carbonization Temperature and the resultant carbon membranes was given in the form (CM-Carbonization Temperature); denoted as CM-600, CM-700, CM-800, CM-900. All samples were cooled naturally at room temperature under air atmosphere after completing each heating cycle.

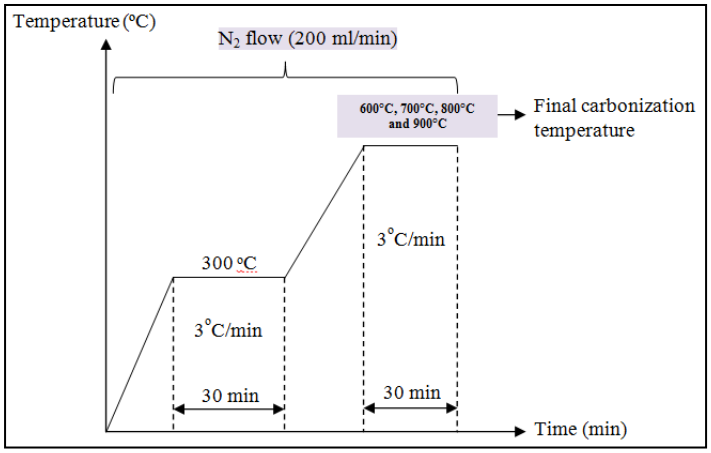



Figure 1. Heat treatment profile

The morphological structures of the P84-based membranes were viewed via scanning electron microscopy (SEM) model JEOL JSM-5610LV. In this study, free-standing carbon membrane in the form of flat sheet (without tubular support) was prepared for characterization purposes. The membrane was fabricated under the same condition as supported carbon membrane. A small piece of the tested membranes was cut and conditioned in liquid nitrogen to prepare an unreformed structure, which was then mounted on sample stubs. The sample was then coated with gold by sputter coating under vacuum. The performance of the carbon membrane was indicated by the gas permeance and gas selectivity. The carbon tubular membranes were tested using in-house gas permeation system. The system consists of flexible hose, permeation cell, valve, pressure regulator and soap bubble meter, which was fabricated to measure the pure gas permeation rate for tubular supported membranes. The 8 cm carbon tubular membrane was placed inside tubular stainless steel module, which was 14 cm in length. The membrane was fitted with rubber O-rings to allow the membrane to be housed in the module without leakages.

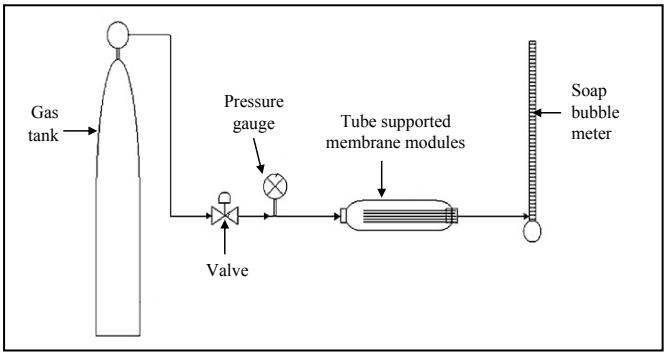



Figure 2. Gas permeation system [15]

Figure 2 shows the gas permeation system reported by a previous study [9]. Pure $CO_2$ (0.33nm) and $CH_4$ (0.38 nm) gases were fed separately into the module at a trans membrane pressure of 8 bars. The permeance, *P/l* (GPU) and selectivity, α of the membranes were calculated using the following equations:

Permeance, *P:*

$$(P/l)_i = \frac{Q_i}{\Delta p.A} = \frac{Q}{\pi D l \Delta P} \quad (1)$$

Selectivity, α:

$$\alpha_{A/B} = \frac{P_A}{P_B} = \frac{(P/l)_A}{(P/l)_B} \quad (2)$$

where *P/l* is the permeance of the membrane, *Qi* is the volumetric flow rate of gas *i* at standard temperature and pressure ($cm^3$ (STP/s), *p* is the pressure difference between the feed side and the permeation side of the membrane (cmHg), *A* is the membrane surface area ($cm^2$), *D* is an outer diameter of the membrane (cm), and *l* is an effective length of the membrane (cm).

The volumetric flow rate of gas permeate was measured by using the soap bubble flow meter. Similar gas permeation system had also been used in the previous study [13]. The feed pressure of 8 bars was applied throughout the experiment. This permeation test was repeated for at least three membrane samples.

## Results and Discussion

Scanning Electron Microscopy (SEM) was used to characterize the morphological structure of P84-based polymeric and carbon membranes prepared under different carbonization temperature. Figure 3(a) shows the cross section microphotographs of the P84-based polymeric membrane, while Figure 3(b) to 3(e) show the cross section microphotographs of P84-based carbon membranes prepared at 600, 700, 800 and 900 °C. It was observed that all P84 membranes tested under different carbonization temperature had porous structure. Compared between P84-based polymeric membrane and P84-based carbon membrane under different carbonization temperature, it was clearly seen that P84-based carbon membranes with high carbonization temperature had higher density, compactness structure and less thickness, as shown in Figures 3(b) to 3(e), than P84-based polymeric membranes, as shown in Figure 3(a). It was found that the formed polymer chains had increased the packing density of the membranes, and some of the pores had become narrow due to the densification of carbon structure. Similar findings had also been reported elsewhere [16]. As the final carbonization temperature was increased, the gas passed through the membrane structure according to their kinetic diameter. Thus, the increment of carbonization final temperature produced a carbon membrane with a higher permeability and selectivity.

As can be seen in Figures 3(b) to 3(e), the structure of the prepared membrane experienced increasing density when temperature was increased from CM-600 to CM-800. On the other hand, the morphological structure for CM 900 resulted in low packing density, as higher temperatures caused the pores to shrink and finally disappeared. At 700 to 800 °C, the pores started to enlarge up; however when the temperature reached around 1000 °C, the pores of the carbonized material were mainly closed [17].

The permeance and selectivity of the membranes were then measured using gas permeation test apparatus at room temperature (Table 1). From the gas permeation test, the performance of the P84-based tube supported carbon membrane was characterized by two important factors, which are permeance and selectivity. As shown by the gas permeation test results, the carbon membranes had presented an excellent performance compared to the polymeric membranes. In addition, the increment in smaller molecule permeance was more prominent compared to larger molecules, resulting in higher gas pair selectivity, according to the increment of carbonization temperature. Carbon membranes contain constrictions in its structure which are closer to molecular dimensions of gas molecules compared to polymeric membranes. The pore system generally consisted of extensive openings with narrow constrictions. The separation was caused by the passage of smaller gas molecules through the pores, while the larger gas molecules were blocked, as well as due to the transport mechanism. Thus, it exhibited high selectivity for the smaller gas molecules, which were $CO_2$. These findings are in agreement with the work done by Ismail and David [18]. For both precursor and carbon membranes, the best performance of the membranes was obtained at the pressure of 8 bars. This result could be endorsed to the combination of low porosity and the kinetic diameter of the

gases, which could result to the pore blocking and resistance of gas transport at higher feed pressure. Similar results were also reported by Hosseini and Chung [19].

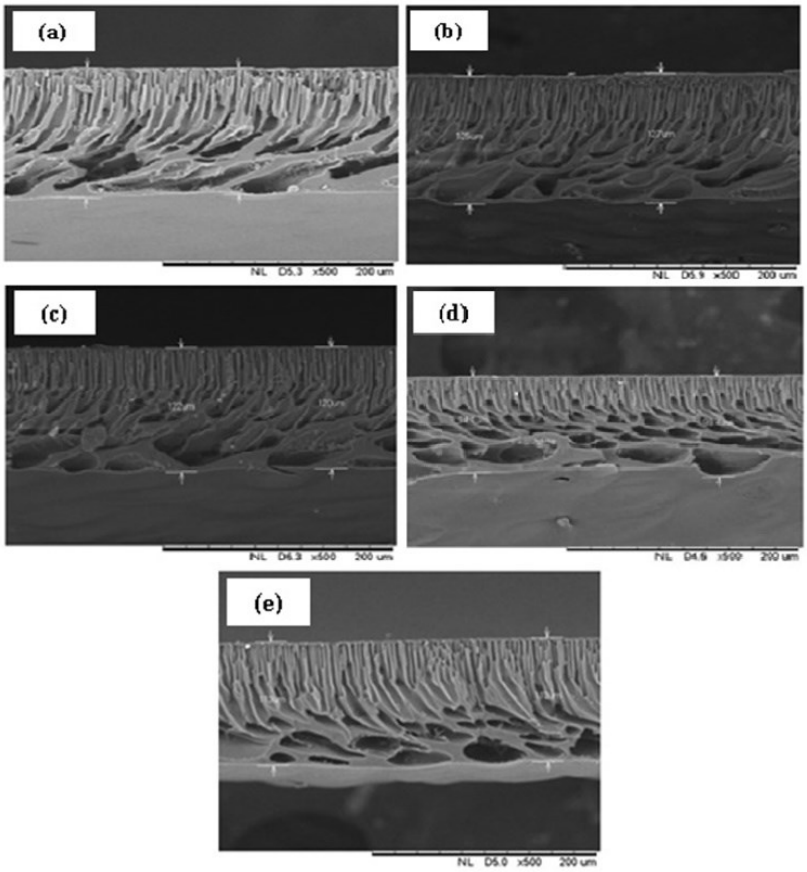



Figure 3. SEM images for (a) P84 Polymeric, (b) CM-600, (c) CM-700, (d) CM-800, and (e) CM-900

In general, low carbonization temperature would produce membrane with poor performances due to poor structural arrangements. On the other hand, at excessive high carbonization temperature, the structural of the carbon membrane would collapse and result in highly dense membrane. Accordingly, the permeability of two pure gases with different molecular sizes; $CO_2$ (3.30Å), and $CH_4$ (3.80Å), through the resulting carbon membranes were measured. The gas permeance of the prepared carbon membranes was found following the order of $CO_2 > CH_4$, according to their kinetic diameters. Consequently, the gas permeance was hindered while possessing poor gas pair selectivity. In addition, the micropores within the carbon membrane allowed smaller molecules (kinetic diameter of $CO_2$ is 3.3Å) to permeate easily across the membrane, while discriminating larger molecule (kinetic diameter of $CH_4$ is 3.8Å), or better known as molecular sieving effect. The molecular sieving effect, commonly reported as separation mechanism in carbon membrane, resulted from the breakage of benzene ring and other functional group, and created bimodal rigid pore distribution. Hence, the resulting membrane showed high $CO_2$permeance and $CO_2$/ $CH_4$ selectivity. The permeability of $CO_2$, and $CH_4$ gases increased due to increase of carbonization temperature from 600 to 800 °C.

Table 2. Gas Permeance and Selectivity of polymeric and carbon membranes.

| Sample | Permeance (GPU) | | Selectivity |
|---|---|---|---|
| | $CO_2$ | $CH_4$ | $\alpha_{CO2/CH4}$ |
| P84 Polymeric | 1.21 | 0.46 | 2.63 |
| CM-600 | 7.42 | 1.12 | 6.63 |
| CM-700 | 122.81 | 2.86 | 42.94 |
| CM-800 | 205.67 | 2.96 | 69.48 |
| CM-900 | 175.39 | 2.90 | 60.48 |

However, the gas permeance decreased when 900 °C of carbonization temperature was applied. This indicates that pores and carbon structure of the carbon membrane became rigid and compact; and some of the pores might change into closed pores during the carbonization. This phenomenon is often related to structure compaction and entanglement of polymer chain when polymer composition exceeds the ideal temperature. Consequently, poor structural arrangements induced higher mass transport resistance and hindered the permeation of all tested gases. In addition, significant reduction of $CO_2$ permeance compared to $CH_4$ further suggested severe structural arrangement for at macroscopic level at 900 °C carbonization temperature, leading to lesser $CO_2/CH_4$ selectivity.

Further carbonization temperature caused the pores to shrink and finally disappear. This pattern is in agreement with the fact that at high temperature, carbonized membranes will possess a microporous structure that is capable to recognize different kinetic diameter of gases, which then will increase the selectivity. Similar findings were also reported by Salleh and Ismail [16]. The increasing trend suggested that the micropores formation and the carbon structure of the carbon membrane became rigid and compact; and some of the pores might change into closed pores during the carbonization process. In general, high carbonization temperature will induce higher porosity. Polyimides are known to exhibit high permselectivity for various gas pairs; especially for $CO_2/CH_4$, and high chemical resistance, thermal stability and mechanical strength. Many researchers reported that P84 polyimide as one of the best materials for membrane-based $CO_2/CH_4$ separation, due to its attractive combination of gas permselectivity and permeability [20] .

## Conclusion

The gas permeation properties of prepared tubular supported carbon membrane are highly dependent on carbonization temperatures. Results in this study revealed that the ideal $CO_2/CH_4$ selectivity of 69.48 with $CO_2$ permeance of 206.10 GPU can be obtained by using carbon membranes at temperature of 800 °C. The study also shows that tubular supports possess higher membrane area per unit module volume, which results in high permeance.

## Acknowledgement

The authors gratefully acknowledge the financial support from Ministry of Higher Education and Universiti Teknologi Malaysia (UTM) under Higher Institution Centre of Excellence Scheme (Project Number: R.J090301.7846.4J188) and research University Grant Scheme (Project Number: Q.J130000.25546.12H76; Q.J130000.2642.10J79). The authors would also like to acknowledge technical and management support from Research Management Centre (RMC), Universiti Teknologi Malaysia

## References

1. Favre, E. (2010). Polymeric membranes for gas separation, in comprehensive membrane science and engineering, E. Drioli and L. Giorno (Editors). Elsevier: Oxford: pp. 155 - 212.
2. Lie, J. A. and Hägg, M.-B. (2006). Carbon membranes from cellulose: Synthesis, performance and regeneration. *Journal of Membrane Science*, 284: 79 - 86.
3. Adewole, J. K., Ahmad, A. L., Ismail, S. and Leo, C. P. (2013). Current challenges in membrane separation of $CO_2$ from natural gas: A review. *International Journal of Greenhouse Gas Control,* 17: 46 - 65.

4. Md Nordin, N. A. H., Racha, S. M., Matsuura, T., Misdan, N., Sani, N. A. A., Ismail, A. F. and Mustafa, A. (2015). Facile modification of ZIF-8 mixed matrix membrane for $CO_2/CH_4$ separation: Synthesis and preparation. *RSC Advances*, 5: 43110 - 43120.
5. Salleh, W. N. W., Ismail, A. F., Matsuura, T. and Abdullah, M. S. (2011). Precursor selection and process conditions in the preparation of carbon membrane for gas separation: A review. *Separation & Purification Reviews,* 40: 261 - 311.
6. Robeson, L. M. (1991). Correlation of separation factor versus permeability for polymeric membranes. *Journal of Membrane Science*, 62: 165 - 185.
7. Reuse, E. (2016). Polymeric membranes for gas separation, in reference module in materials science and materials engineering. Elsevier.
8. Gilron, J. and Soffer, A. (2002). Knudsen diffusion in microporous carbon membranes with molecular sieving character. *Journal of Membrane Science*, 209: 339 - 352.
9. Sazali, N., Salleh, W. N. W., Nordin, M., Hadi, N. A., Harun, Z. and Ismail, A. F. (2015). Matrimid-based carbon tubular membranes: The effect of the polymer composition. *Journal of Applied Polymer Science,* 132: 42394 - 42400.
10. Saufi, S. M. and Ismail, A. F. (2004). Fabrication of carbon membranes for gas separation - A review. *Carbon*, 42: 241 - 259.
11. Briceño, K., Montané, D., Garcia-Valls, R., Iulianelli, A. and Basile, A. (2012). Fabrication variables affecting the structure and properties of supported carbon molecular sieve membranes for hydrogen separation. *Journal of Membrane Science*, 415 – 416: 288 - 297.
12. Kargari, A., Shamsabadi, A. A. and Babaheidari, M. B. (2014). Influence of coating conditions on the $H_2$ separation performance from $H_2/CH_4$ gas mixtures by the PDMS/PEI composite membrane. *International Journal of Hydrogen Energy*, 39: 6588 - 6597.
13. Sazali, N., Salleh, W. N. W., Nordin, N. A. H. M. and Ismail, A. F. (2015) Matrimid-based carbon tubular membrane: Effect of carbonization environment. *Journal of Industrial and Engineering Chemistry*, 32: 167 - 171.
14. Lua, A. C. and Shen, Y. (2013). Preparation and characterization of asymmetric membranes based on nonsolvent/NMP/P84 for gas separation. *Journal of Membrane Science*, 429: 155 - 167.
15. Basu, A., Akhtar, J., Rahman, M. H. and Islam, M. R. (2004). A review of separation of gases using membrane systems. *Petroleum Science and Technology*, 22:1343 - 1368.
16. Salleh, W. N. W. and Ismail, A. F. (2012). Fabrication and characterization of PEI/PVP-based carbon hollow fiber membranes for $CO_2/CH_4$ and $CO_2/N_2$ separation. *AIChE Journal,* 58: 3167 - 3175.
17. Fuertes, A. B., Nevskaia, D. M. and Centeno, T. A. (1999). Carbon composite membranes from Matrimid® and Kapton® polyimides for gas separation. *Microporous and Mesoporous Materials,* 33: 115 - 125.
18. Ismail, A. F. and David, L. I. B. (2001). A review on the latest development of carbon membranes for gas separation. *Journal of Membrane Science*, 193: 1 - 18.
19. Hosseini, S. S., Peng, N., and Chung, T. S. (2010). Gas separation membranes developed through integration of polymer blending and dual-layer hollow fiber spinning process for hydrogen and natural gas enrichments. *Journal of Membrane Science*, 349: 156 - 166.
20. Barsema, J. N., Klijnstra, S. D., Balster, J. H., van der Vegt, N. F., Koops, G. H. and Wessling, M. (2004). Intermediate polymer to carbon gas separation membranes based on Matrimid PI. *Journal of Membrane Science*, 238: 93 - 102.

*Malaysian Journal of Analytical Sciences, Vol 21 No 2 (2017): 416 - 425*
*DOI: https://doi.org/10.17576/mjas-2017-2102-17*

MALAYSIAN JOURNAL OF ANALYTICAL SCIENCES
*Published by The Malaysian Analytical Sciences Society*
ISSN 1394 - 2506

# REMOVAL AND RECOVERY OF CHROMIUM(VI) ION VIA TRI-N-OCTYL METHYLAMMONIUM CHLORIDE-KEROSENE POLYPROPYLENE SUPPORTED LIQUID MEMBRANE

## (Penyingkiran dan Pemulihan Semula Kromium(VI) melalui Membran Cecair Berpenyokong Tri-n-oktil metilammonium klorida-kerosin-polipropilena)

Raja Norimie Raja Sulaiman[1] and Norasikin Othman[1, 2]*

[1]*Faculty of Chemical and Energy Engineering*
[2]*Centre of Lipids Engineering and Applied Research (CLEAR),*
*Ibnu Sina Institute of Scientific and Industrial Research (IBNU SINA-ISIR)*
*Universiti Teknologi Malaysia, 81310 UTM Johor Bahru, Johor, Malaysia*

**Corresponding author: norasikin@cheme.utm.my*

Received: 26 August 2016; Accepted: 8 January 2017

**Abstract**

The presence of chromium in the natural water can be toxic to aquatic organism and is one of the major environmental problems. Therefore, the removal and recovery of chromium from industrial wastewater is very crucial to accomplish the standard discharge concentration limit. Supported liquid membrane is one of the processes which combines the extraction and recovery process in one single stage. This paper presents an experimental study on the removal and recovery of chromium ions from acidic aqueous solutions through a flat-sheet supported liquid membrane (FSSLM) system. Through this system, chromium ions were transported from feed phase into stripping phase via Tri-n-octyl-methylammoniumchloride (TOMAC)-kerosene-polypropylene supported liquid membrane (SLM). The liquid membrane phase was prepared by dissolving the corresponding volume of the carrier, TOMAC in organic diluent of kerosene. The stripping agent used was sodium hydroxide (NaOH) solution whereas the membrane support used was commercial Accurel polypropylene membrane with good features of 100 µm thickness, porosity of 72% and effective pore size of 0.10 µm. The chromium ion concentration in the feed and stripping phases as a function of time was analysed using an atomic absorption spectrometry (AAS). The effects of different operational variables such as TOMAC concentration in the membrane phase, NaOH concentration in the stripping phase and pH of the aqueous feed phase were investigated. The result demonstrated that about 90 and 98% of 150 ppm of chromium was removed and recovered, respectively at favorable condition of 1.0 M TOMAC, 0.5 M NaOH and pH 2 of the feed phase.

**Keywords**: supported liquid membrane, chromium, removal, recovery, acidic aqueous solution

**Abstrak**

Kehadiran kromium di dalam sumber air semula jadi adalah toksik kepada organisma akuatik dan salah satu masalah utama alam sekitar. Oleh itu, penyingkiran dan pemulihan semula kromium daripada air sisa industri adalah sangat perlu untuk memenuhi had kepekatan piawaian pelepasan. Membran cecair berpenyokong adalah salah satu proses yang menggabungkan penyingkiran dan pemulihan semula dalam satu peringkat proses. Kertas kerja ini membentangkan satu kajian eksperimen tentang penyingkiran dan pemulihan semula ion kromium dari larutan berasid melalui sistem helaian rata membran cecair berpenyokong (FSSLM). Melalui sistem ini, ion kromium dibawa dari fasa suapan ke fasa pelucutan melalui Tri-n-oktil-metilammonium klorida (TOMAC)–kerosin-polipropilena membran cecair berpenyokong (SLM). Fasa cecair membran telah disediakan dengan melarutkan sejumlah pembawa, TOMAC dalam pelarut organik kerosin. Ejen pelucutan yang digunakan adalah larutan sodium hidroksida (NaOH) manakala membran sokongan yang digunakan ialah Accurel polipropilena membran komersial yang mempunyai ciri-ciri yang baik dengan ketebalan 100µm, keliangan 72% dan saiz liang 0.10 µm. Kepekatan ion kromium dalam

fasa suapan dan fasa pelucutan terhadap fungsi masa dianalisis menggunakan spektrometri penyerapan atom (AAS). Kesan pembolehubah operasi yang berbeza seperti kepekatan TOMAC dalam fasa membran, kepekatan NaOH dalam fasa pelucutan dan pH fasa suapan telah dikaji. Keputusan menunjukkan bahawa sekitar 90 dan 98% daripada 150 ppm kromium telah disingkirkan dan dipulihkan semula pada 1.0 M TOMAC, 0.5 M NaOH dan pH 2 fasa luaran.

**Kata kunci:** membran cecair berpenyokong, kromium, penyingkiran, pemulihan semula, larutan berasid

## Introduction

Electroplating waste containing hazardous heavy metal of chromium is an environmental concern especially to the natural water system. Normally industrial electroplating waste contain both hexavalent and trivalent forms of chromium. According to Malaysia's environmental law, the standard discharge regulation of industrial effluent containing hexavalent and trivalent chromium is 0.05 and 1.0 ppm respectively [1]. Chromium(VI) is one of the most dangerous carcinogenic and mutagenic heavy metals as it is toxic for humans, animals, plants and microorganisms [2]. If these wastes are directly discharged into the natural water system, they will undoubtedly cause a lot of environmental problems. Thus, the removal and recovery of chromium is very crucial to bring down the concentration of such hazardous metal ions below the discharge standards. Hexavalent chromium is not precipitated as an insoluble hydroxide. Therefore hexavalent chromium need to be reduced to the trivalent state. The common reducing agent used include sulfur dioxide or bisulphite addition at low pH of 2 to 3. However this process suffers from high cost of sodium bisulphite. The use of inexpensive reducing agents such as ferrous sulphate significantly increase the volume of hydroxide sludge [3]. Besides, the solvent extraction method involves large amount of chemical consumption whereas electrodialysis provides high cost of operation [4, 5].

In order to overcome this problem, many researchers found that liquid membrane extraction technology has a great potential and has been reported as an advanced technique for separating solutes. Liquid membrane technology has attracted much interest for its potential impact in the fields of separation processes because the main advantage of liquid membrane configuration treatment is a single step process, in which removal and recovery processes occur simultaneously [6, 7]. This technique also provides high efficiency in separation and selectivity toward the desired solute as reported by Harrudin et al. [8]. Liquid membrane technologies have been commonly used to separate and recover many types of metals from diluted solutions. There are three types of liquid membrane technology namely bulk liquid membrane, emulsion liquid membrane and supported liquid membrane. Liquid membrane systems in which solvents containing carriers are placed in a porous support material are called supported liquid membrane (SLM). Supported liquid membrane has been extensively used for the recovery of organic matter, heavy metals and precious metals. The main advantages of SLM are the small amounts of organic phase and extractant used, one-step mass transfer, the possibility of achieving high separation factors, concentration of extracted compound during separation, and low separation costs [9, 10].

Carrier is one of the important components in the liquid membrane formulation. Carriers can be categorized as acidic, basic and solvating. For acidic type carrier, the metal extraction based on the cationic exchange reaction. The acidic carriers which are normally used for the extraction of various metal cations including chelating ( 5,8-diethyl-7-hydroxy- dodecan-6-oxime (LIX63), 2-hydroxy-5-nonylacetophenone oxime (LIX841) and etc) and phosphorus derivative (di-2-ethylhexyl phosphoric acid (D2EHPA), di-2,4,4-trimethylpentylmonothio phosphinic acid (Cyanex 302), di-2,4,4-trimethylpentyl phosphinic acid (Cyanex 272) and etc). On the other hand the basic type carrier tend to perform the extraction of anionic metal complexes through an anionic exchange reaction. Several basic carriers used for metal extraction are Trioctylamine (TOA), Tridodecylamine (TDA), Tri-octylmethylammonium chloride (TOMAC) and so forth. In order to achieve this exchange, the amine must be first converted to the amine salt to provide the anion to exchange with the metal species [11]. Besides, the solvating carrier are weakly basic in nature and thus they extract either neutral metal complexes or acids and suitable to extract the alkaline earth metals [12].

In this present work, Tri-n-octyl- methylammoniumchloride (TOMAC) is employed for the removal and recovery of chromium ion using supported liquid membrane process. To the best of our knowledge, the chromium compounds will release the anion complexes into the water. Hence, the best carrier for these anion complexes is the basic type carrier. Furthermore, TOMAC no need to be protonated because this compound in ionic complexes. Previously, TOMAC also have been reported as a good basic carrier for various anion complexes extraction with higher

efficiency [13]. The important parameters influencing the removal and recovery efficiency such as carrier and stripping agent concentration, and pH of the feed phase were investigated.

## Materials and Methods

### Materials

Potassium dichromate, $K_2Cr_2O_7$ as a feed solution was purchased from Sigma Aldrich. Tri-n-octyl methyl ammonium chloride (TOMAC) as a carrier and kerosene as diluent was procured from Fluka and Merck, respectively. The structure of TOMAC is illustrated in Figure 1. Sodium hydroxide, NaOH as a stripping agent was supplied from Qrec. All chemicals are analytical grade and were used without further purification as received. Stock Cr (VI) solutions were prepared by dissolving $K_2Cr_2O_7$ in distilled water. Polypropylene membrane of 100 µm thickness, 72% porosity and an effective pore size of 0.1 µm was obtained from Accurel Membrana was used as membrane support for the liquid membrane in supported liquid membrane process.

### Preparation of liquid membranes and rig set-up

The organic liquid membrane was prepared by dissolving a specified volume of TOMAC in the kerosene. Then, the polymeric hydrophobic microporous polypropylene membrane was impregnated with the liquid membrane for 24 h. After impregnation, the membrane support was let to drip for a few seconds and the excess liquid membrane was wiped from the membrane surface using the filter paper. The cleaning procedure was done gently in order to ensure that there is no liquid membrane was removed from the membrane pores. Then, the membrane was applied between the feed and strip cells as demonstrated in Figure 2. About 400 ml of feed and strip solutions were added into cell 1 and cell 2, respectively. The initial concentration of chromium in the feed phase was 150 ppm. NaOH solution was used as a stripping phase. The samples were taken from the feed and strip phase for each 30 minute and were analysed using Atomic Absorption Spectrometry (AAS) in order to observe the changes in the chromium concentration. The pH of feed phase and stripping phase was measured using a Metler Toledo pH meter. The new membrane support was used for each experiment. All experiment was carried out at ambient temperature (25±1 ºC).

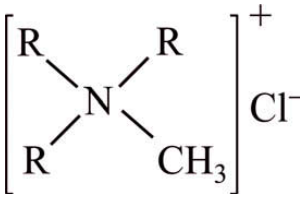



Figure 1. Structure of tri-n-octyl methyl ammonium chloride (TOMAC); R= $C_8H_{17}$

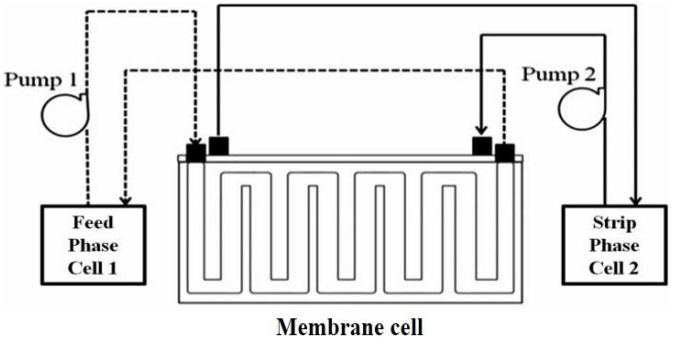



Figure 2. Schematic diagram of supported liquid membrane process [8]

**Determination of removal and recovery performance**

The determination of the removal and recovery percentages of chromium ion through SLM process were calculated using the following equations as below:

$$\text{Removal (\%)} = \frac{[Cr]_{f_o} - [Cr]_{f_t}}{[Cr]_{f_o}} \text{ x } 100\% \quad (1)$$

$$\text{Recovery (\%)} = \frac{[Cr]_s}{[Cr]_{f_o}} \text{ x } 100\% \quad (2)$$

where $[Cr]_{f_o}$ represents initial concentration of chromium in the feed phase; $[Cr]_{f_t}$ represents final concentration of chromium in the feed phase and $[Cr]_s$ represents a concentration of chromium in the strip phase.

**Determination of permeability value**

Membrane permeability is the ability of a membrane to allow the desired solute to pass through it. Permeability, p ($cms^{-1}$) of the chromium ions transferred from the feed phase to the strip phase can be determined by Equation (3) and (4) below:

$$\text{Permeability, } p = \frac{dC}{C} \cdot \frac{1}{dt} \cdot \frac{V}{A} \quad (3)$$

By integration Equation (3), Equation (4) was obtained,

$$\ln \frac{C}{C_{fi}} = - p \left(\frac{A}{V}\right) . t \quad (4)$$

where $C_{fi}$ is the initial concentration of metal ion in the feed phase, $c$ is the concentration of metal ion at given time, $p$ is permeability value ($cms^{-1}$), A is the effective area of membrane ($cm^2$), $v$ is the volume of aqueous feed phase ($cm^3$) and t is the time (s).

## Results and Discussion

**Mechanism of chromium ions transport across supported liquid membrane**

All stable complexes of hexavalent chromium are anionic species which exist in different forms in the aqueous phase depending on the pH. Under alkaline or neutral condition, chromium predominantly exist as chromate ions ($CrO_4^{2-}$) whereas at slightly acidic condition, hydrochromate ions ($HCrO_4^-$) take place as the dominant species. At very low pH and high total chromium (VI) concentration, the dichromate ion ($Cr_2O_7^{2-}$) predominates [14]. In that case, in this study, chromium ions exist as hydrochromate ions ($HCrO_4^-$) in the feed phase at low initial concentration of Cr (VI) solutions. The mechanism of removal and recovery on the chromium ion is shown in Figure 3. In SLM transport process, the diffusion of chromium ions takes place via the following steps:

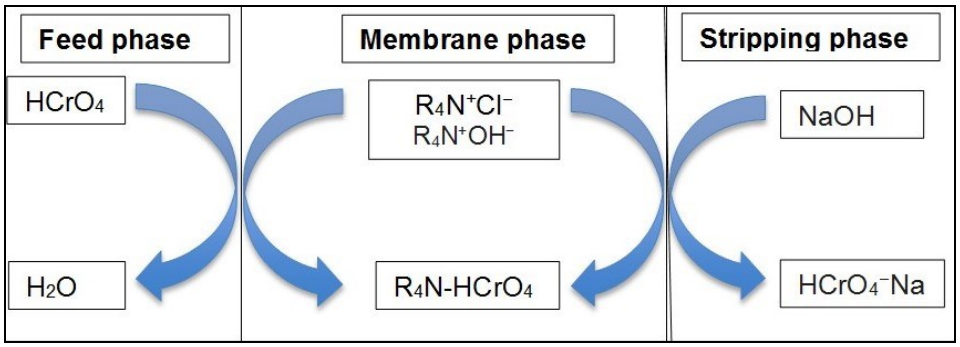



Figure 3. Removal and recovery mechanism of chromium ion by TOMAC

a) The carrier, TOMAC in the membrane phase react with the stripping agent, NaOH at the membrane-internal interface as represented in Equation (5) below:

$$[R_4N^+Cl^-]_{org} + [NaOH]_{aq} \longleftrightarrow [R_4N\text{-}OH]_{org} + [Cl^-]_{aq} + [Na^+]_{aq} \quad (5)$$

b) There are two types of carrier exists in the membrane phase which are $[R_4N^+Cl^-]$ and $[R_4N^+OH^-]$. Therefore, at the feed-membrane interface, hydrochromate ions chemically react with both types of carrier as shown in Equation (6) and (7) below:

$$[HCrO_4^-]_{aq} + [R_4N^+Cl^-]_{org} \longleftrightarrow [R_4N\text{-}HCrO_4]_{org} + [Cl^-]_{aq} \quad (6)$$
$$[HCrO_4^-]_{aq} + [R_4N^+OH^-]_{org} \longleftrightarrow [R_4N\text{-}HCrO_4]_{org} + [OH^-]_{aq} \quad (7)$$

c) The formation of $R_4N\text{-}HCrO_4$ complex diffuse across the membrane phase from feed-membrane interface to the membrane-internal interface reversibly, where the stripping reaction take place with stripping agent, NaOH as shown in Equation (8). The created complex $HCrO_4Na$ is insoluble in the membrane phase and will not diffuse back to the feed phase.

$$[R_4N\text{-}HCrO_4]_{org} + [NaOH]_{aq} \quad [HCrO_4Na]_{org} + [R_4N\text{-}OH]_{aq} \quad (8)$$

**Effect pH of feed phase**

One of the important variables for the removal and recovery performance of Cr(VI) in the supported liquid membrane process is pH of the feed solution. Basically, the stable anion complexes of chromium exist in different form depending on the pH. Figure 4(a) illustrates the effect of various pH on the removal of Cr(VI). The pH was adjusted using sulphuric acid and sodium hydroxide solution for acidic and basic range, respectively. On the other hand, the calculated permeability value at different pH is tabulated in Table 1. Based on the result obtained, the highest removal percentage was observed at pH 2 (89%) with the highest permeability value of 5.91 x $10^{-2}$ $cms^{-1}$. Further increase pH value up to 3, the removal percentage was slightly reduced to 80% with the permeability value of 4.32 x $10^{-2}$ $cms^{-1}$. In fact, at pH 2 and 3 which are acidic medium, hydrochromate ions ($HCrO_4^-$) are more predominant, thus showing the efficiency of TOMAC to chemically react with this type of anions. However, pH 2 which is more acidic, can induce higher ions dissociation from the chromium complexes. This condition will produce more hydrochromate ions in the feed phase and increases the rate formation of the solute-carrier complexes. In that case more chromium ions can be transported through the membrane, thus enhancing the permeation rate. Furthermore, the higher proton concentration also can act as a driving force to encourage the permeation of the chromium ions through the membrane. This is strongly supported by Raut et al. [15] who reported that the acidic feed solution give the high permeability values for strontium transport due to the tendency of ionic complexes formation. Under neutral condition (pH 7), the removal percentage was also high which is 87% with permeability value of 5.83 x $10^{-2}$ $cms^{-1}$. At this stage, chromium predominantly exist as chromate ions ($CrO_4^{2-}$). This anion species requires two carrier for the complexation [16]. So this condition greatly enhances the permeation of chromium ions through the membrane.

At the recovery stage as shown in Figure 4 (b), the percentage of chromium recovery gradually decreased from 98 to 56% upon increasing the pH value from 2 to 7. At acidic range, the difference in the proton concentration gradient between the feed and receiving phases is the driving force for the transportation of chromium ion into the stripping phase. In contrast, at the neutral condition, the presence of ($CrO_4^{2-}$) ions react slowly with TOMAC in the membrane phase with 1:2 mole ratio of Cr: TOMAC as shown through equation (9) below, thus causing the recovery rate to be reduced. Hence, the optimum pH for removal and recovery of chromium achieved at pH 2.

$$CrO_4^{2-} + [R_4N^+Cl^-]_{org} \quad [R_4N\text{-}CrO_4\text{-}NR_4]_{org} + [Cl^-]_{aq} \quad (9)$$

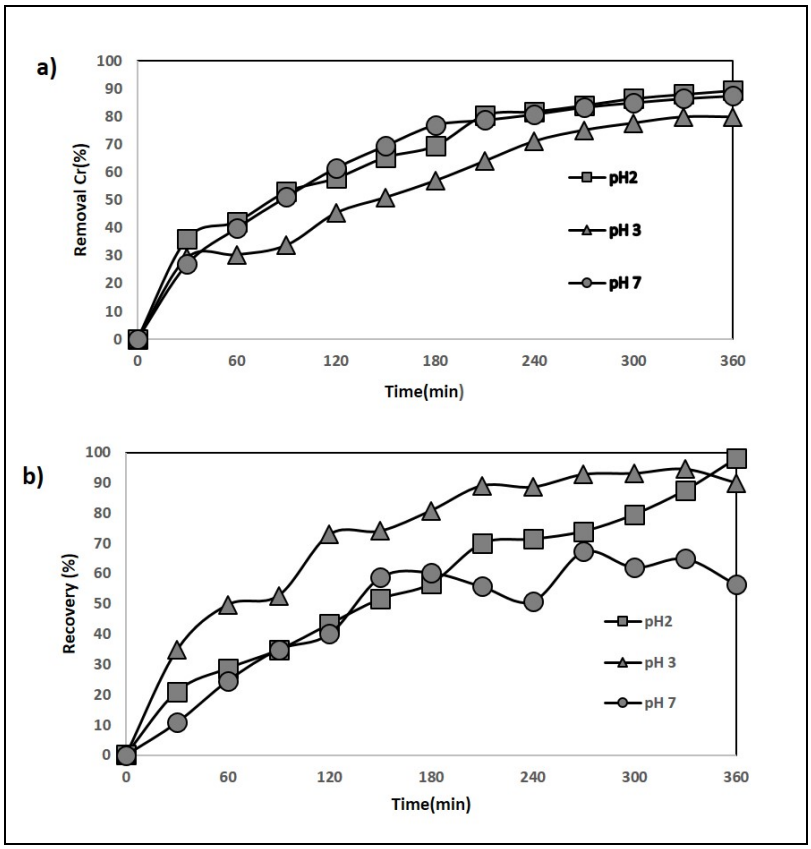



Figure 4. (a) Effect pH of feed phase on the removal of chromium ion (Experimental condition: Feed phase= 150 ppm, TOMAC = 1.0M; NaOH =1.0M, flow rate = 100 ml/min) and (b) Effect pH of feed phase on the recovery of chromium ion (Experimental condition: Feed phase = 150 ppm, TOMAC =1.0M, NaOH = 1.0M, flow rate = 100 ml/min)

Table 1. Permeability coefficient value as a function of pH of feed phase

| Effect pH of Feed Phase | Permeability Value ($P \times 10^{-2}$ , $cms^{-1}$) |
|---|---|
| 2 | 5.91 |
| 3 | 4.32 |
| 7 | 5.83 |

**Effect of carrier concentration**

Figure 5(a) presents the effect of carrier concentration on the removal of chromium ion by varying the TOMAC concentration from 0.5 to 1.5 M. The permeability value as a function of carrier concentration is also shown in Table 2. Basically, the carrier in the liquid membrane phase plays a significant role through complexation with the chromium ions in the feed-membrane interface which reversibly transport them to the internal phase. The results show that the removal percentage of chromium ions increased from 13 to 89% and reached a plateau within 360 min of extraction upon increasing TOMAC concentration from 0.5 to 1.5 M, respectively. Besides, the permeability value also increased from $0.53 \times 10^{-2}$ $cms^{-1}$ to $5.91 \times 10^{-2}$ $cms^{-1}$ with increasing carrier concentration from 0.5 to

1.0 M, respectively. At 0.5 M, the carrier concentration is inadequate to aid the mass transfer of chromium ion through SLM process. Therefore more chromium anion accumulate in the feed-membrane interface without being transported. So this condition increased the mass transport resistance and leads to the low permeation of chromium ions through the membrane phase. In contrast, at higher carrier concentration, there are more available carriers for the formation of solute-carrier complexes, hence enhancing the removal efficiency.

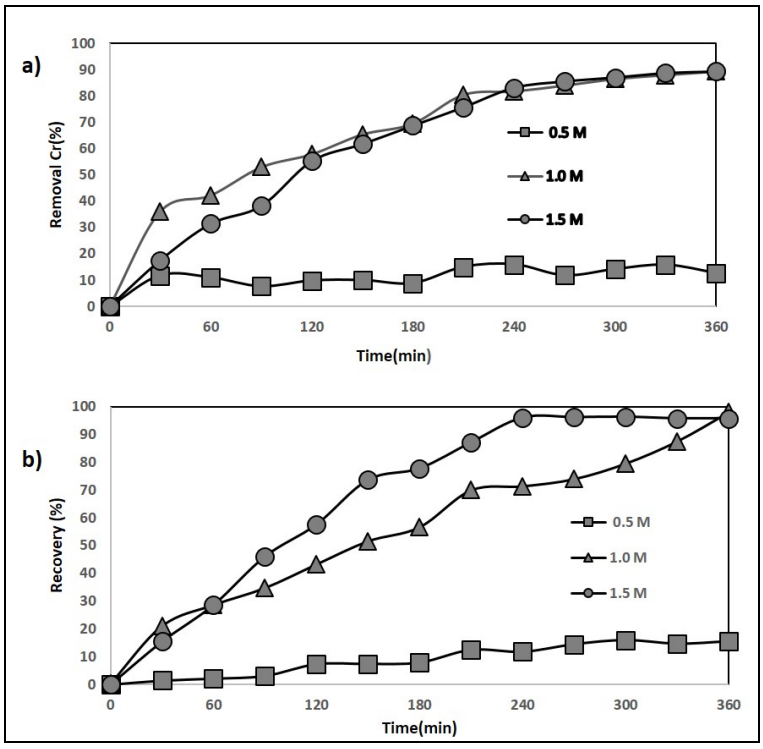



Figure 5. (a) Effect of TOMAC concentration on the removal of chromium ion (Experimental condition: Feed phase = 150 ppm (pH: 2), NaOH = 1.0M, flow rate = 100ml/min) and (b) Effect of TOMAC concentration on the recovery of chromium (Experimental condition: Feed phase = 150 ppm (pH: 2), NaOH = 1.0M, flow rate = 100 ml/min)

Based on the result obtained, 1.0 M TOMAC is adequate for the chromium ion transportation in SLM process with the highest permeability value of 5.91 x $10^{-2}$ $cms^{-1}$. This is strongly supported by Nayl and Aly [17] who reported that 1.0 mol TOMAC required 1.0 mol Cr during the reaction of extraction occur in the membrane phase. Further increase of carrier concentration only cause the excess carrier in the membrane phase which thereby affecting the removal efficiency. This is also in agreement with Kumar et al. [18] who claimed that above the optimal value, the solute transportation decreased because of the extra resistance offered by the excess carrier molecules in the membrane phase. As can be seen, beyond 1.0 M, the permeability value also decreased to 5.74 x $10^{-2}$ $cms^{-1}$. This is due to the viscosity effect caused by the excess carrier concentration which resists the transportation of the chromium ions through the membrane phase. This result is in line with Bey et al. [19] who reported that at certain values of carrier concentrations, the viscosity of the organic phase increases, thus slowing the organic complex diffusion through the pores.

On the other hand, Figure 5(b) displays the recovery result of the Cr(VI) extraction for various carrier concentration from 0.5 to 1.5 M. The maximum recovery was achieved at 1.0 M TOMAC (98%) followed by 1.5 M (96%) and 0.5 M (16%). It indicates that simultaneous extraction and stripping occurred completely during the process. This

means the carrier concentration increased proportionally with the recovery percentage of chromium ion in the stripping phase. The higher carrier concentration means higher opportunity of chromium-carrier complexes to be stripped by stripping agent at the membrane-internal interface, hence leading to the higher recovery percentage. According to Equation (6) and (7), 1 mol of Cr ion needs 1 mol of TOMAC for the complexation, thus 1.0 M TOMAC was enough for the next experiment.

Table 2. Permeability coefficient value as a function of carrier concentration

| Effect of TOMAC Concentration (M) | Permeability Value ($P \times 10^{-2}$, $cms^{-1}$) |
|---|---|
| 0.5 | 0.53 |
| 1.0 | 5.91 |
| 1.5 | 5.74 |

**Effect of stripping agent concentration**

A stripping agent in the receiving phase plays an important role in order to completely strip the solute ion at the membrane-internal interface. Therefore an appropriate stripping agent which can chemically complex with the desired solute ion is necessary to successfully recover the targeted solute. Figure 6(a) depicts the relationship between NaOH concentration and the removal percentage of chromium ions. The permeability result is also presented in Table 3. Based on the result obtained, as increasing NaOH concentration from 0.5 to 1.5 M, the removal efficiency of chromium linearly increased from 80 to 89% and reached plateau. The permeability value also increased proportionally with stripping agent concentration from $4.06 \times 10^{-2}$ $cms^{-1}$ to $5.91 \times 10^{-2}$ $cms^{-1}$ at 0.5 M and 1.0 M, respectively. This can be attributed to the insufficient stripping agent at 0.5 M to strip the chromium ions into the stripping phase. Therefore, more available of chromium-TOMAC complexes are trapped and accumulated in the membrane-strip interface without being stripped which tends to block the transportation of the other complexes through the membrane.

As can be observed, the permeability value at this time is the lowest, which indicates that very low permeation occurred because the membrane phase is clogged with these complexes. Further increase up to 1.0 M NaOH, the highest permeability reached up to $5.91 \times 10^{-2}$ $cms^{-1}$. At this state, more available NaOH appeared in the membrane-strip interface, thereby enhancing the transportation of more chromium ions through the membrane phase. This is in line with Alguacil et al. [20] who reported that the overall permeation coefficient of Cr(VI) increases with the concentration of stripping agent. However, beyond 1.0 M, the permeability value slightly decreased to $5.11 \times 10^{-2}$ $cms^{-1}$. Based on the transport mechanism shown in Figure 3, the counter transport also occurred where the $OH^-$ ion from stripping phase also acts as a driving force by complexation with the carrier in the membrane- strip interface to aid the permeation of chromium ions through SLM process. Therefore at excess NaOH concentration, the driving force from the stripping phase only become saturated. At this condition, the number of chromium ion which permeate through the membrane phase seems to reduce as about 100% of chromium ions were already transported to the stripping phase at 1.0 M NaOH. Besides, a higher concentration of NaOH will lead to the higher ionic strength which thereby causing the inefficiency of the recovery process.

Venkatesan and Palanivelu [21] also reported that the degree of extraction remains constant afterwards as the stripping agent concentration achieved the maximum rate. This is due to the saturation of the driving force for diffusion through the SLM owing to an increase of metal complexes concentration at the membrane-internal interface. So, 0.5 M NaOH concentration is adequate for the chromium extraction. Besides, Figure 6(b) shows the recovery result at 0.5 M NaOH concentration is higher than 1.0 M. This means that the stripping reaction occurs very fast at the membrane-internal interface. Thus 0.5 M of NaOH concentration is adequate in achieve a high recovery rate of chromium.

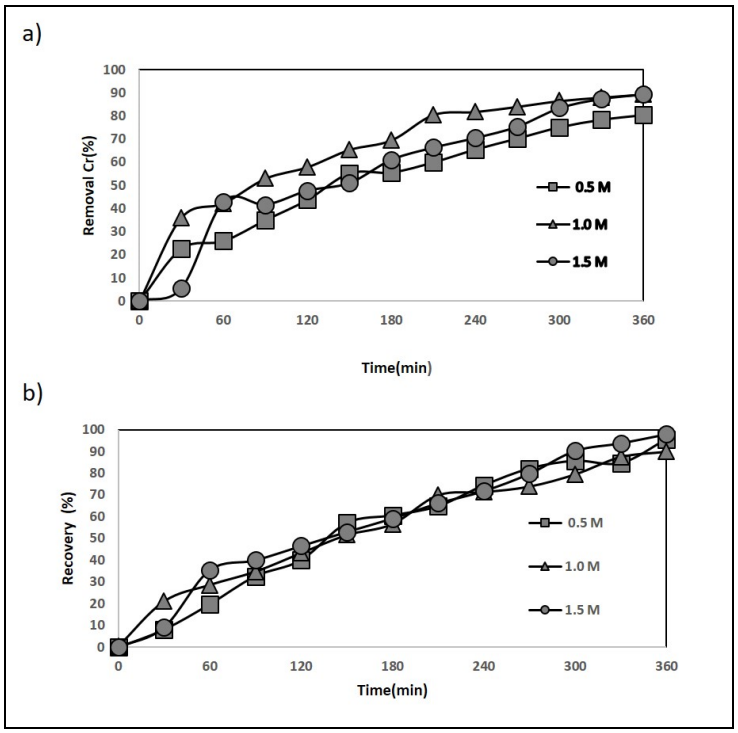



Figure 6. (a) Effect of NaOH concentration on the removal of chromium ion (Experimental condition: Feed phase = 150 ppm (pH: 2), TOMAC = 1.0M, flow rate = 100 ml/min) and (b) Effect of NaOH concentration on the recovery of chromium ion (Experimental condition: Feed phase = 150 ppm (pH: 2), TOMAC = 1.0M, flow rate = 100)

Table 3. Permeability coefficient value as a function of stripping agent concentration

| **Effect of NaOH Concentration (M)** | **Permeability Value ($P \times 10^{-2}$ , $cms^{-1}$)** |
|---|---|
| 0.5 | 4.06 |
| 1.0 | 5.91 |
| 1.5 | 5.11 |

## Conclusion

In conclusion, the extraction of Cr(VI) was successfully performed in SLM process using TOMAC as a carrier and NaOH as a stripping agent. TOMAC and NaOH can act as an excellent carrier and stripping agent for the removal and recovery of chromium ion. At pH 2 of feed phase with 1.0 M TOMAC and 0.5 M NaOH, about 90 and 98% of chromium can be successfully removed and recovered, respectively using a supported liquid membrane process.

## Acknowledgement

The authors would like to acknowledge the Ministry of Higher Education (MOHE) and Universiti Teknologi Malaysia (Research Grant GUP: Q.J130000.2546.14H21) for financial support in making this research possible.

## References

1. Malaysia Environmental Quality Report (Industrial Effluent) Regulations (2009). Malaysian Department of Environment, P.U. (A) 434.

2. Cavaco, S. A., Fernandes, S., Margarida, M. and Ferreira, M. (2007). Removal of chromium from electroplating industry effluents by ion exchange resins. *Journal of Hazardous Materials*, 144: 634 – 638.
3. Unnithan, M. R. and Anirudhan, T. S. (2001). The kinetics and thermodynamics of sorption of chromium (VI) onto the iron(III) complex of a carboxylated polyacrylamide-grafted sawdust. *Industrial & Engineering Chemistry Research*, 40(12): 2693 – 2701.
4. Kul, M. and Oskay, K. O. (2015). Separation and recovery of valuable metals from real mix electroplating wastewater by solvent extraction. *Hydrometallurgy*, 155: 153 – 160.
5. Sadyrbaeva, T. Z. (2016). Removal of chromium (VI) from aqueous solutions using a novel hybrid liquid membrane-electrodialysis process. *Chemical Engineering and Processing,* 99: 183 – 191.
6. Othman, N., Harrudin, N., Idris, A., Ooi, Z. Y., Fatiha, N. and Sulaiman, R. N. R. (2016). Fabrication of polypropylene membrane via thermally induced phase separation as a support matrix of tridodecylamine supported liquid membrane for Red 3BS dye removal. *Desalination and Water Treatment*, 57: 12287 – 12301.
7. Noah, N. F. M., Othman, N. and Jusoh, N. (2016). Highly selective transport of palladium from electroplating wastewater using emulsion liquid membrane process. *Journal of the Taiwan Institute of Chemical Engineers*, 64: 134 – 141.
8. Harrudin, N., Othman, N., Sin, A. L. E. and Sulaiman, R. N. R. (2015). Selective removal and recovery of Black B reactive dye from simulated textile wastewater using the supported liquid membrane process. *Environmental Technology*, 36(3): 271 – 280.
9. Harruddin, N., Othman, N., Idris, A., Ooi, Z. Y. and Goto, M. (2014). Supported liquid membrane extraction of reactive dye using fabricated polypropylene membrane. *Journal of Chemical Engineering of Japan*, 47(10): 761 – 769.
10. Ruhela, R., Panja, S., Sharma, J. N., Tomar, B. S., Tripathi, S. C., Hubli, R. C. and Suri, A. K. (2012). Facilitated transport of Pd(II) through a supported liquid membrane (SLM) containing N, N, N, N-tetra-(2 ethylhexyl) thiodiglycolamide T (2EH) TDGA: A novel carrier. *Journal of Hazardous Materials*, 229 – 230: 66 – 71.
11. Agreda, D. D., Garcia-Diaz, I., Lopez, F. A. and Alguacil, F. J. (2011). Supported liquid membranes technologies in metals removal from liquid effluents. *Revision Metal*, 47 (2):146 – 168.
12. Parhi, P. K. (2013). Supported liquid membrane principle and its practices: A short review. *Journal of Chemistry*: 1 – 11.
13. Goyal, R. K., Jayakumar, N. S. and Hashim, M. A. (2011). Chromium removal by emulsion liquid membrane using $[BMIM]^{+}[NTf2]^{-}$ as stabilizer and TOMAC as extractant. *Desalination*, 278: 50 – 56.
14. Eyupoglu, V., Surucu, A. and Kunduracioglu, A. (2015). Synergistic extraction of Cr(VI) from Ni(II) and Co(II) by flat sheet supported liquid membranes using TIOA and TBP as carriers. *Polish Journal of Chemical Technology*, 17(2): 34 – 42.
15. Raut, D. R., Mohapatra, P. K. and Manchanda, V. K. (2012). A highly efficient supported liquid membrane system for selective strontium separation leading to radioactive waste remediation. *Journal of Membrane Science*, 390 – 391: 76 – 83.
16. Björkegren, S. (2012). A study of the heavy metal extraction process using emulsion liquid membranes. Master Thesis. Chalmers University of Technology, Sweden.
17. Nayl, A. A. and Aly, H. F. (2015). Solvent extraction of V(V) and Cr(III) from acidic leach liquors of ilmenite using Aliquat 336. *Transactions of Nonferrous Metals Society of China*, 25: 4183 − 4191.
18. Kumar, A., Manna, M. S., Ghoshal, A. K. and Saha, P. (2016). Study of the supported liquid membrane for the estimation of the synergistic effects of influential parameters on its stability *Journal of Environmental Chemical Engineerin*g, 4: 943 – 949.
19. Bey, S., Criscuoli, A., Simone, S., Figoli, A., Benamor, M. and Drioli, E. (2011). Hydrophilic PEEK-WC hollow fibre membrane contactors for chromium (VI) removal. *Desalinatio*n, 283: 16 – 24.
20. Alguacil, F. G., Diaz, I. G. and Lopez, F. (2013). Transport of Cr (VI) using an advanced membrane technology and ($PJMTH^{+}NO^{3-}$) ionic liquid derived from amine Primene JMT as green chemicals. *Desalination and Water Treatment*, 51: 7201 – 7207.
21. Venkateswaran, P. and Palanivelu, K. (2005). Studies on recovery of hexavalent chromium from plating wastewater by supported liquid membrane using tri-n-butyl phosphate as carrier. *Hydrometallurgy*, 78:107 – 115.

*Malaysian Journal of Analytical Sciences, Vol 21 No 2 (2017): 426 - 434*
*DOI: https://doi.org/10.17576/mjas-2017-2102-18*

MALAYSIAN JOURNAL OF ANALYTICAL SCIENCES
*Published by The Malaysian Analytical Sciences Society*
ISSN 1394 - 2506

# THE MORPHOLOGICAL PROPERTIES STUDY OF PHOTOCATALYTIC $TIO_2$/PVDF DUAL LAYER HOLLOW FIBER MEMBRANE FOR ENDOCRINE DISRUPTING COMPOUNDS DEGRADATION

## (Kajian Sifat Morfologi Membran Fotopemangkin Gentian Berongga Dwi Lapisan $TiO_2$/PVDF untuk Penguraian Sebatian Pengganggu Endokrin)

Roziana Kamaludin[1], Mohd Hafiz Dzarfan Othman[1]*,Siti Hamimah Sheikh Abdul Kadir[2], Mukhlis A Rahman[1], Juhana Jaafar[1]

[1]*Advanced Membrane Technology Research Centre (AMTEC), Universiti Teknologi Malaysia, 81310 Skudai, Johor, Malaysia*
[2]*Institute of Medical Molecular Biotechnology, Faculty of Medicine, Sungai Buloh Campus, Universiti Teknologi MARA, Jalan Hospital, 47000, Sungai Buloh, Selangor, Malaysia*

**Corresponding author: hafiz@petroleum.utm.my*

Received: 26 August 2016; Accepted: 8 January 2017

**Abstract**

Various Endocrine Disrupting Compounds (EDCs) either natural or synthetics have been identified including bisphenol A (BPA), dioxin, polychlorinated biphenyls, and dichlorodiphenyltrichloroethane (DDT). These compounds which present widely in the product of solvent industry, agricultural, pharmaceuticals and household convenience may directly or indirectly interrupt the normal function of endocrine system. Recently, the EDCs threats to human health have led to the increasing demand of clean water sources which excites a challenge for the contaminants removal processes. Conventional treatment methods may not completely remove the contaminants, meanwhile advanced oxidation process (AOPs) especially photocatalysis have been proven efficient in removing the contaminants. Even though photocatalysis is efficient in suspension of either nano- or microscale, the immobilizing $TiO_2$ in the membrane matrix for catalyst separation purposes have decreased the adsorption of organic substances on the $TiO_2$ surface with potential loss of $TiO_2$ during long-time usage. This lead to the emerging in the exploration and fabrication of dual layer hollow fiber (DLHF) membrane for better performance of immobilized $TiO_2$. Therefore, we exploit this fact to investigate the incorporation of photocatalysis into dual-layer hollow fiber membrane which are believed may improve the photocatalytic degradation and separation efficiency. The FESEM results showed that both layers are compatible with each other and there are no delamination found between layers. The presence of outer layer does not influence the surface roughness; however improve the hydrophilicity and membrane strength. Altogether, photocatalytic dual layer hollow fiber (DLHF) membrane was successfully fabricated using co-extrusion technique.

**Keywords:** dual layer, hollow fiber, $TiO_2$, photocatalytic

**Abstrak**

Pelbagai sebatian pengganggu endokrin sama ada semula jadi atau buatan telah dikenalpasti termasuk bisphenol A (BPA), dioxin, polychlorinated biphenyls, dan dichlorodiphenyltrichloroethane (DDT). Sebatian ini yang wujud secara meluas di dalam produk industri pelarut, pertanian, farmaseutikal, dan keperluan rumah mampu menggangu secara lansung atau tidak langsung fungsi normal sistem endokrin. Baru-baru ini, ancaman sebatian pengganggu endokrin kepada kesihatan manusia telah membawa kepada peningkatan permintaan sumber air bersih yang merangsang satu cabaran bagi proses penyingkiran bahan pencemaran.. Kaedah rawatan konvensional mungkin tidak membuang bahan pencemaran dengan sepenuhnya, tetapi proses pengoksidaan maju (AOP) terutama fotopemangkinan telah terbukti berkesan dalam menyingkirkan bahan pencemaran. Walaupun fotopemangkinan cekap dalam skala nano atau skala hablur pemangkin, immobilisasi $TiO_2$ ke dalam matriks membran untuk

tujuan pemisahan pemangkin telah mengurangkan penyerapan bahan pencemar di permukaan $TiO_2$ dengan potensi kerugian $TiO_2$ untuk penggunaan yang lama. Ini membawa kepada penerokaan dan fabrikasi dwi lapisan gentian berongga (DLHF) membran untuk prestasi immobilisasi $TiO_2$ yang lebih baik. Oleh itu, kami mengeksploitasi fakta ini untuk menyiasat penubuhan fotopemangkinan ke dalam dwi-lapisan membran gentian berongga yang dipercayai boleh meningkatkan kecekapan fotopemangkin dalam proses degradasi dan pemisahan bahan pencemar. Keputusan FESEM menunjukkan bahawa kedua-dua lapisan serasi dengan satu sama lain dan tidak ada delaminasi di antara dua lapisan. Kehadiran lapisan luar tidak mempengaruhi kekasaran permukaan; bagaimanapun meningkatkan sifat hidrofilik dan membran kekuatan. Secara keseluruhan, dwi lapisan membran gentian berongga telah berjaya direka menggunakan teknik penyemperitan bersama.

**Kata kunci:** dwi lapisan, gentian berongga, $TiO_2$, fotopemangkin

## Introduction

Endocrine system plays a vital role in the in the regulation of hormone and body homeostasis, hence slight interruption in their normal behavior by exogenous chemicals may ruin the entire system [1]. Therefore, endocrine disrupting compounds (EDCs) can be defined as exogenous chemicals that may directly or indirectly interrupt the normal function of endocrine system functions [2]. These contaminants either natural or synthetics [3] are detectable in the product of industry, agricultural, pharmaceuticals and household convenience [4]. Various EDCs have been identified including bisphenol A (BPA) [5], dioxin, polychlorinated biphenyls, dichlorodiphenyltrichloroethane (DDT) [6] and many more. Since decades ago, the presence of EDCs in household water has become major concerns among public. In addition, some EDCs including BPA have long half-lives as they are designed to improve the product usage however, they are not easily biodegradables, thus turn out to pose a threat to wildlife and humans [7]. These threats have led to the increasing demand of clean water sources which excites a challenge for the contaminants removal processes. Conventional treatment methods such as membrane filtration, adsorption and bioreactor based membrane and bioreactors may not completely remove the contaminants, meanwhile advance treatment options, including ultraviolet (UV) irradiation, hybrid system and advanced oxidation process (AOPs) have been proven efficient in removing the contaminants. Advanced oxidation processes, photocatalysis can be widely defined as photochemical reaction accelerated by the presence of a catalyst [8]. In particular, photocatalysis have been used for such significant applications such as production of renewable fuels, disinfection of water and air, mineralization of organic contaminants, and synthesis of organic compounds [2]. Heterogeneous photocatalysis accelerated by semi-conductor metal oxides is a fast-growing field and identified as a promising tool for water treatment [9] where organic contaminants are shown to be degraded up to 90% under suspension of semi-conductor photocatalytic operation [10].

Several semiconductors such as Titanium Oxide ($TiO_2$), Zinc Oxide (ZnO), Ferric Oxide ($Fe_2O_3$), Cadmium Sulfide (CdS), and Zinc Sulfide (ZnS) can act as photocatalysts [11], however among many candidates; $TiO_2$ is the most suitable material use at present due to its impressive photoactivity [12]. More significantly, $TiO_2$ exhibit strong oxidizing ability and high stability properties in addition to the lowest cost of operation [13]. Even though photocatalysis is efficient in suspension of either nano- or microscale $TiO_2$ catalyst particles in a photocatalytic reaction, the separation of the $TiO_2$ particles is a major problem that always limits the application of these photocatalytic processes for treating the contaminants. Immobilizing $TiO_2$ in the membrane matrix is thought to solve the separation problem; however this method decreased the adsorption of organic substances on the $TiO_2$ surface with potential loss of $TiO_2$ during long-time usage [14]. This lead to the emerging in the exploration and fabrication of dual layer hollow fiber (DLHF) membrane for better performance of immobilized $TiO_2$.

A series of studies have revealed the use of polymeric dual-layer hollow fiber membranes for various applications, such as gas separation [15], forward osmosis (FO) [16], protein and liquid separation [17] as well as nanofiltration (NF) [18]. Compared to the single layer hollow fiber (SLHF) membrane, dual layer hollow fiber membrane are much more attractive because it significantly saves materials cost, less complex post treatment process and better membrane performance. Recently, polyvinylidene fluoride (PVDF) has been widely used as both outer and inner layer membrane material as they are recognized to have excellent resistance to corrosive chemicals, powerful mechanical strength, good thermal stability and ease of processing ability with common organic solvents [19]. Meanwhile the incorporation of an additive into polymer membrane is shown to increase the membrane pore size and porosity [20]. In this regard, the outer layer of dual layer hollow fiber membrane immobilized with $TiO_2$ will

provide reaction site for the photocatalytic degradation in the presence of UV light, while the inner membrane layer will act as separation layer. Therefore, the photocatalytic degradation process may be performed in a system in which reaction and separation processes occur simultaneous. In addition, high $TiO_2$ is expected to speed up the processes.

To date, no studies have been reported on the degradation of EDCs by photocatalytic dual-layer hollow fibre membrane reactions. Hence, the present study is conducted to investigate the incorporation of $TiO_2$ photocatalysis into dual-layer hollow fiber membrane to improve the photocatalytic degradation efficiency.

## Materials and Methods

The fabrications of dual layer hollow fiber membranes consist of polymer dope preparation and dry-wet spinning method, followed by qualitative and quantitative examination of the membrane morphology and properties.

### Materials

Polyvinylidene fluoride (PVDF, Kynar 760 Series-powder, Solvay Specialty Polymers France) was used as polymer based without purification. A titanium dioxide ($TiO_2$ P25) nanoparticle was supply by Evonik GmbH, Germany. Polyethelene Glycole (PEG) 6000 was purchased from FLUKA. Dimethylacetamide (DMAC, QReC) was used as solvent to dissolve polymer without further purification.

### Preparation of dope solution

PVDF, PEG and $TiO_2$ were dried in a 50 $^{\circ}$C vacuum oven for 24 hours to remove moisture prior to dope preparation. The, PEG/$TiO_2$ and DMAc at desired amount were added in Scott bottle with an overhead stirrer. After the PEG/$TiO_2$ mixture became a homogeneous solution, the desired amounts of PVDF were added to the solution. The detailed compositions of the polymer dope solutions and spinning condition are shown in Table 1. The viscosity of the polymer dope solutions were measured using viscometer.

Table 1. Dope composition and spinning conditions of the hollow fiber membranes.

| | **Dual layer (DL)** | **Single Layer (SL)** |
|---|---|---|
| Outer dope composition (wt.%) | PVDF/$TiO_2$/DMAc (15/3/82) | - |
| Outer dope flow rate (ml/min) | 2 | - |
| Inner dope composition (wt.%) | PVDF/PEG/DMAc (18/5/77) | PVDF/$TiO_2$/DMAc (15/3/82) |
| Inner dope flow rate (ml/min) | 8 | 8 |
| Bore fluid | Distilled water | Distilled water |
| Bore fluid flow rate (ml/min) | 8 | 8 |
| Air gap (cm) | 10 | 10 |
| Take up speed (Hertz) | 1.3 | 1.3 |
| Spinneret dimension (mm) | 0.8/1.2/2.6/3.0/3.5 | 0.8/1.2/2.6 |

Then, the dope solutions were cooled down to room temperature, followed by degassed using ultrasonic bath system at ambient temperature overnight prior to spinning. Both SLHF and DLHF membranes were fabricated using dry/wet phase inversion spinning technique (Figure 1).

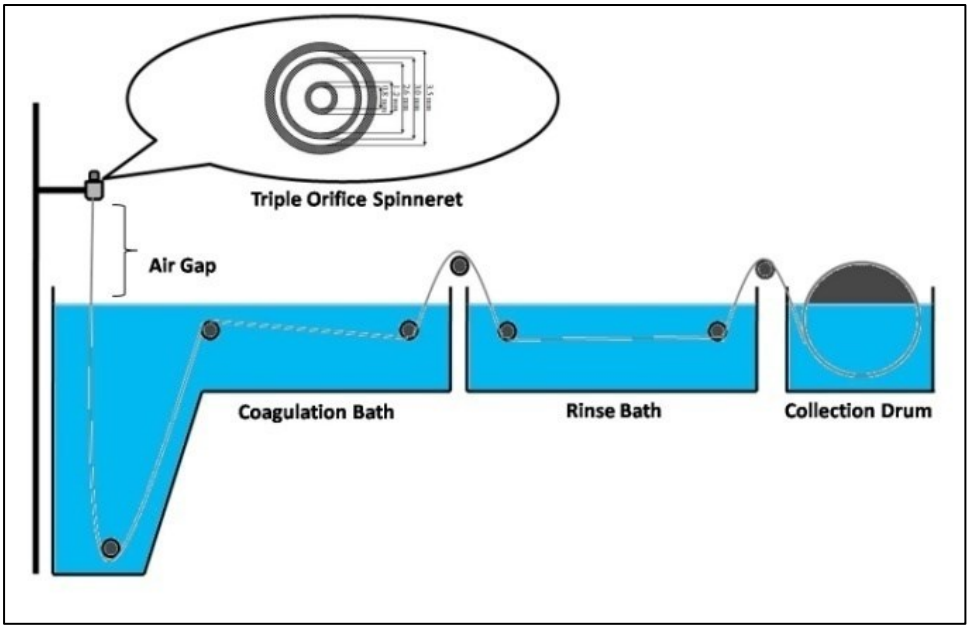



Figure 1. Dual layer hollow fiber spinning method

The dope solution was transferred into dope reservoir syringe pump followed by the dope extrusion using a triple orifice spinneret. Prior to drying, the as-spun membrane fibers were immersed into water bath for 1 day to remove residual solvent. Then, 50 pieces of 30 cm length of as-spun fiber segments were put together to form a bundle. Four to six bundles were sent to post treatment in one batch using ethanol: water, 50:50 wt.% for 1 hour followed by 100% of ethanol for another 1 hour in order to improve the membrane wet ability and pore collapse. Finally, the fibers bundles were dried at room temperature for 3 days.

**Characterization of the dual layer hollow fiber membrane**

The morphological nature of both DLHF and SLHF were explored qualitatively with the help of Field Emission Scanning Electron Microscopy (FESEM; Model: SU2080, Hitachi). The $TiO_2$ nanoparticle distribution on top surface of the tested composite membrane was investigated using the line scan of spectrum of Energy Dispersion of X-ray (EDX; Model: X-MaxN 51-XMX1011, Oxford Instrument). Prior to positioned on a metal holder, both DLHF and SLHF were immersed in liquid nitrogen for 1 min and then fractured into short samples to expose their cross sectional characteristics. The samples then were sputter coated with gold under vacuum approximately for 3 min. The cross section and surface DLHF and SLHF were examined at various magnifications. The distribution of $TiO_2$ nanoparticles on both DLHF and SLHF membrane surface were scan randomly by EDX.

The membrane surface roughness was determined using Atomic Force Microscopy (AFM; Model: SE-100, Park System). DLHF and SLHF samples were cut into pieces of 3 cm by 5 cm and areas of 20 µm x 20 µm of sample were scanned by tapping mode.

Contact angle measurements were conducted using the contact angle goniometer (Model: OCA 15EC, Dataphysic). 2µL of deionized water as contact liquid was dropped on the fiber surface and the measurements were obtained at different points of each sample.

The measurement of tensile strength of the hollow fibers was established by LRX, LLYOD test machine. At least six fibres with 50 mm length were tested with a load cell of 2.5 kN, at a constant elongation velocity of 10 mm/m at room temperature and the average data were taken for each sample. Tensile strength were determined by using the following equation (1) (IPC-TM-650):

$$\text{Tensile strength (Pa)} = \frac{\text{Load at break(N)}}{\text{Cross sectional area (m}^2\text{)}} \quad (1)$$

The membrane porosity, ε was measured using dry-wet weight method. The membrane was soaked in pure water for 3 hours, and then was weighed after absorption of the pure water. The membrane then was dried by filter paper before weighed again to obtain their dry weight. The porosity of membrane was calculated by using the following equation (2):

$$\varepsilon = \frac{w1-w2}{V\rho w} \times 100\% \quad (2)$$

where ε is the porosity of the membrane (%), *w1* is the mass of the wet membrane, *w2* is the mass of the dry membrane, *V* is the volume of the membrane and *ρw* is the density of water (1.0 g/cm$^3$).

## Results and Discussion

Figure 2 shows representative FESEM images of the dual layer and single layer $TiO_2$/PVDF hollow fiber membrane. As shown in the Figure 2 (a2), the finger like structure developed at the outer and inner layer, whereas the sponge like structure developed at the intermediate layer. Porous structure was achieved with the addition of the pore former, PEG 6000 into the DLHF inner layer dope solution. As shown in the Figure 2 (a2), the resultant DLHF have large macrovoids and porous inner layer membrane. This finding is in an agreement with previously reported study where they reported the formation of a macrovoids and a large area of sponge-like structure in their membrane [21]. Both layers are compatible with each other and there are no delamination and interfacial resistance when PVDF was used for both inner and outer layer dopes.

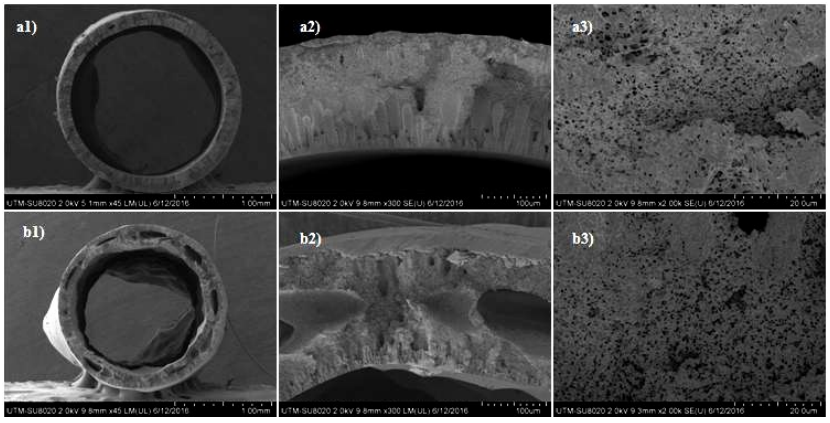



Figure 2. Cross-sectional and partial cross section FE-SEM images of the dual layer and single layer $TiO_2$/PVDF hollow fiber membrane for (a) DLHF and (b) SLHF

It is expected that the mutual diffusion of polymers was established between the inner and outer layers, thus two distinct layers cannot be observed. Hence, the estimation of outer layer thickness of DLHF membranes was performed by the distribution of $TiO_2$ nanoparticles in the outer layer as shown in the Figure 3 (a4). EDX analysis show that there is less diffusion of $TiO_2$ particles into the inner layer of DLHF membrane as compared to SLHF membrane. It is believed that the particles might have distributed evenly over the DLHF outer membrane surface. Even though SLHF showed higher $TiO_2$ loading, the $TiO_2$ nanoparticles are entrapped in the membrane matrix. Therefore, they might not be fully utilized for their photocatalytic properties due to the limit penetration of the light source through thick membrane layer. Hence, higher $TiO_2$ loading in SLHF are wasted as compared to the lower $TiO_2$ loading on the membrane surface of DLHF.

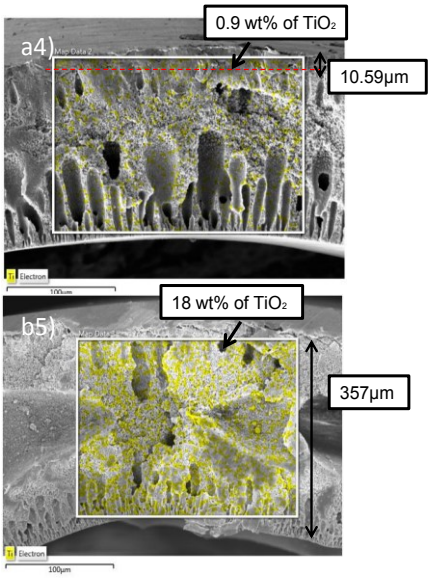



Figure 3. The EDX mapping of TiO2 distribution in DLHF (a4) and SLHF (b5) membrane layer

Figure 4 present the FESEM images of the outer surface of the DLHF and SLHF membranes. As can be seen, the $TiO_2$ nanoparticles were uniformly distributed on both configurations of the membrane surfaces. The surface of both membranes is composed of a microporous structure with relatively large pores as determined by AFM analysis.

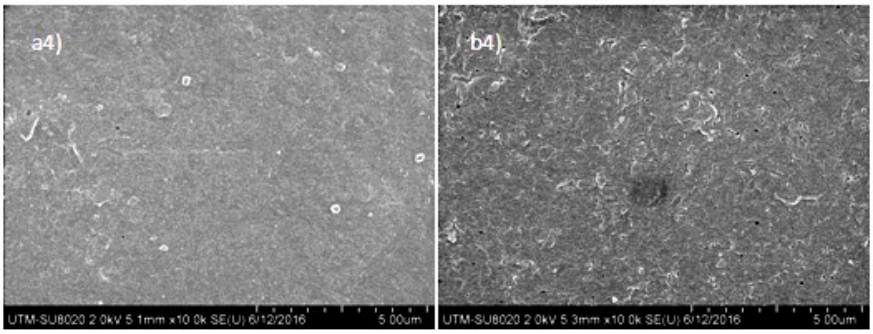



Figure 4. Surface FE-SEM images of the dual layer and single layer TiO2/PVDF hollow fiber membrane for (a) DLHF and (b) SLHF

Figure 5 shows the three dimensional AFM images and surface roughness (Ra) of the DLHF and SLHF $TiO_2$/PVDF membranes. The AFM images clearly show that the membrane surface roughness of both configurations has no significant difference because the $TiO_2$ particles loading in the dope solutions are equal. The surface roughness was strongly dependent on the $TiO_2$ loading and distribution of $TiO_2$ on the membrane surface. The Ra value of DLHF and SLHF membranes were 41.550 and 40.934 nm, respectively.

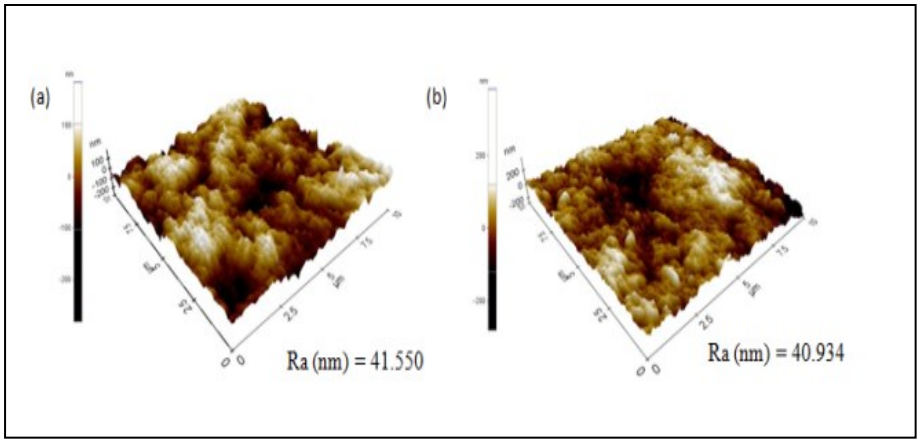



Figure 5. Surface roughness image of outer surface of (a) DLHF and (b) SHLF TiO2 /PVDF hollow fiber membranes

Table 2 summarizes the results of the tensile strength, elongation at break, contact angle, pure water flux, rejection, porosity and pore size of the membranes of both configurations. The tensile strength and elongation at break of the DLHF membranes was higher than SLHF membranes. This is because the presence of the outer layer of DLHF membranes has strengthened its structure. DLHF is more hydrophilic than SLHF. It could be observed from contact angle analysis as listed in Table 2. This finding is accordingly with the findings reported by Dzinun et al. [22]. The presence of hydrophilic nature of $TiO_2$ particle at the outer layer of the DLHF membranes has successfully improved the hydrophilicity of the membrane, which higher affinity towards water is better for water-related separation process. In addition, uniform distribution of $TiO_2$ particles at the outer layer surface will improved photocatalytic reaction site too. Therefore, the degradation and separation of EDCs are promisingly efficient.

Table 2. Performance of hollow fiber membranes with different configuration

| **Configuration** | **Tensile Strength (Mpa)** | **Elongation at Break (%)** | **Contact Angle (°)** | **Porosity** |
|---|---|---|---|---|
| Dual Layer Hallow Fiber (DLHF) | 15.87 ± 0.52 | 90.33 ± 13.81 | 64.60 | 2.081 ± 1.009 |
| Single Layer Hallow Fiber (SLHF) | 11.14 ± 0.35 | 59.95 ± 2.21 | 79.32 | 1.509 ± 0.262 |

## Conclusion

Dual layer hollow fiber membranes have successfully fabricated by single step co-extrusion techniques. The obtained dual layer hollow fiber membranes consists of sandwich-like structure where finger-like voids formed from the inner and the outer surface of membrane and separated by sponge-like structure at the middle of the membranes cross-section. The incorporation of $TiO_2$ nanoparticles into the outer membrane layers has increased their hydrophilicity, thus suggesting that the photocatalytic DLHF membranes also have a good separation potential in water-related processes. It is interesting to note that the co-extrusion technique is capable to produce a DLHF membrane with uniformly distributed high loading of $TiO_2$ particles at the outer layer surface which might highly efficient for photocatalytic degradation of EDCs. However, the investigation of photocatalytic reactions are needed in the future works to justify their degradation capability.

**Acknowledgement**

The authors gratefully acknowledge financial support from the Ministry of Education Malaysia under the Higher Institution Centre of Excellence Scheme (Project Number: R.J090301.7846.4J193). The authors would also like to thanks Research Management Centre, Universiti Teknologi Malaysia for the technical support.

**References**

1. Schmidler, C. (2015). Endocrine System Glands and Hormones. Access online http://www.healthpages.org/ anatomyfunction/endocrine system-gland/
2. Chang, H-S., Choo, K-H., Lee B-W. and Choi, S-J. (2009). The methods of identification, analysis, and removal of endocrine disrupting compounds (EDCs) in water. *Journal of Hazardous Materials* 172: 1 –12.
3. Filali-Meknassi, Y., Tyagi, R. D., Surampalli, R. Y., Barata, C. and Riva, M. C. (2004). Endocrine disrupting compounds in wastewater, sludge treatment processes and receiving waters: Overview. *Practical Periodical Hazard, Toxic, and Radioactive Waste Management*, 8: 1 – 18.
4. Kralchevska, R. P., Milanova, M. M., Hristova, I. L. and Todorovsky, D. S. (2013). Some endocrine disrupting compounds in the environment and possibilities for their removal / degradation. *Bulgarian Chemical Communications*, 45, 2: 131 – 143.
5. Pan, B., Lin, D., Mashayekhi, H. and Xing, B. (2008). Adsorption and hysteresis of bisphenol A and 17α-ethinyl estradiol on carbon nanomaterials. *Environmental Science & Technology*, 42(15): 5480 –5485.
6. Grasselli, F., Baratta, L., Baioni, L., Bussolati, S., Ramonib, R., Grolli, S. and Basini, G. (2010). Bisphenol A disrupts granulosa cell function. *Domestic Animal Endocrinology*, 39: 34 – 39.
7. Rubin, B. S. (2011). Bisphenol A: An endocrine disruptor with widespread exposure and multiple effects. *Journal of Steroid Biochemistry and Molecular Biology*, 127(1-2): 27 – 34.
8. Stahlhut, R. W., Welshons, W. V. and Swan, S. H. (2009). Bisphenol A data in NHANES suggest longer than expected half-life, substantial non-food exposure, or both. *Environmental Health Perspective*, 117: 784 – 789.
9. Kondarides, D. I. (2010). Photocatalysis. Catalysis. Encyclopedia of life support systems (EOLSS), developed under the auspices of the UNESCO. EOLSS Publishers, Paris.
10. Dalrymple, O. K., Yeh, D. H. and Trotz, M. A. (2007). Removing pharmaceuticals and endocrine-disrupting compounds from wastewater by photocatalysis. *Journal of Chemical Technology and Biotechnology*, 82: 121 – 134.
11. Xin, Y., Gao, M. Wang, Y. and Ma, D. (2014). Photoelectrocatalytic degradation of 4-nonylphenol in water with $WO_3/TiO_2$ nanotube array photoelectrodes. *Chemical Engineering Journal*, 242: 162 – 169.
12. Umar, M. and Aziz, H. A. (2013). Photocatalytic degradation of organic pollutants in water. INTECH Open Access Publisher: pp. 195 – 208.
13. Hashimoto, K., Irie, H. and Fujishima, A. (2005). $TiO_2$ photocatalysis: A historical overview and future prospects. *Japanese Journal of Applied Physics*, 44(12): 8269 – 8285.
14. Rao, K. V. S., Subrahmanyam, M. and Boule, P. (2004). Immobilized $TiO_2$ photocatalyst during long-term use: decrease of its activity. *Applied Catalysis B: Environmental*, 49(4): 239 – 249.
15. Peng, N., Chung, T.-S., Chng, M. L. and Aw, W. (2010). Evolution of ultra-thin dense-selective layer from single-layer to dual-layer hollow fibers using novel Extem® polyetherimide for gas separation. *Journal of Membrane Science*, 360: 48 – 57.
16. Yang, Q., Wang, K. Y. and Chung, T.-S. (2009). Dual-layer hollow fibers with enhanced flux as novel forward osmosis membranes for water production. *Environmental Science and Technology,,* 43: 2800 – 2805.
17. Ong, Y. K. and Chung, T. (2012). High performance dual-layer hollow fiber fabricated via novel immiscibility induced phase separation (I2PS) process for dehydration of ethanol. *Journal of Membrane Science,* 421–422: 271 – 282.
18. Sun, S. P. Wang, K.Y. Peng, N. Hatton, T. A. and Chung, T.-S. (2010). Novel polyamideimide/ cellulose acetate dual-layer hollow fiber membranes for nanofiltration. *Journal of Membrane Science*, 363: 232 –242.
19. Lee, J., Park, B., Kim, J. and Park, B. S. (2015). Effect of PVP, lithium chloride, and glycerol additives on PVDF dual-layer hollow fiber membranes fabricated using simultaneous spinning of TIPS and NIPS. *Macromolecular Research*, 23(3): 291 – 299.
20. Khayet, M., Mengual, J., I. and Matsuura, T. (2005). Porous hydrophobic/hydrophilic composite membranes application in desalination using direct contact membrane distillation. *Journal of Membrane Science,* 252(1): 101 – 113.

21. Setiawan, L., Wang, R., Shi, L., Li, K. and Fane, A. G. (2012). Novel dual-layer hollow fiber membranes applied for forward osmosis process. *Journal of Membrane Science*, 421 – 422: 238 – 246.
22. Dzinun, H., Othman, M. H. D., Ismail, A. F., Puteh, M. H., Rahman, M. A. and Jaafar, J. (2015). Fabrication of dual layer hollow fibre membranes for photocatalytic degradation of organic pollutants. *International Journal of Chemical Engineering and Applications*, 6(4): 289 – 292.

*Malaysian Journal of Analytical Sciences, Vol 21 No 2 (2017): 435 - 444*
*DOI: https://doi.org/10.17576/mjas-2017-2102-19*

MALAYSIAN JOURNAL OF ANALYTICAL SCIENCES
*Published by The Malaysian Analytical Sciences Society*
ISSN 1394 - 2506

# METHANOL PERMEABILITY AND PROPERTIES OF POLYMER ELECTROLYTE MEMBRANE BASED ON GRAPHENE OXIDE-SULFONATED (POLYETHER ETHER) KETONE

## (Kebolehtelapan Metanol dan Sifat-Sifat Membran Polimer Elektrolit Berasaskan Grafin Oksida-Polieter Eter Keton Tersulfon)

Nuor Sariyan Suhaimin[1], Madzlan Aziz[1,2]*, Juhana Jaafar[2]

[1]*Chemistry Department, Faculty of Science*
[2]*Advanced Membrane Technology Research Centre*
*Universiti Teknologi Malaysia, 81310 Skudai, Johor, Malaysia*

**Corresponding author: madzlan@utm.my*

Received: 26 August 2016; Accepted: 8 January 2017

**Abstract**

Graphene oxide sulfonated polyether ether ketone (GO-SPEEK) is a promising proton exchange membrane (PEM) to replace the commercial PEM in Direct Methanol Fuel Cell (DMFC) application. The GO films were prepared from natural graphite flakes by the modified Hummer's Method. The structure and physicochemical characterization techniques were applied to impart insight into the specific structure, element composition as well as the functional groups by using Attenuated Total Reflection infrared spectroscopy (ATR), X-Ray diffraction (XRD), and Raman Spectroscopy. The incorporation of graphene oxide in SPEEK not only improved membrane behaviors of PEM in terms of ion exchange capacity (1.231 mequiv.g$^{-1}$), water uptake (53.45%) and proton conductivity (0.0537), but also positively blocking of methanol molecules passing through membrane, thus making them appealing as proton exchange membranes (PEMs).

**Keywords**: graphene oxide, sulfonated polyether ether ketone, proton exchange membrane, X-ray diffraction

**Abstrak**

Grafin oksida sulfona polieter eter keton (GO-SPEEK) merupakan proton pertukaran membran (PEM) yang menjanjikan pengantian PEM komersial dalam aplikasi sel bahan api metanol langsung (DMFC). Filem GO dihasilkan daripada grafit semulajadi menggunakan kaedah Hummer diubahsuai. Teknik – teknik pencirian struktur fizikal dan kimia telah digunakan untuk mendapatkan maklumat tentang struktur spesifik, komposisi elemen dan juga kumpulan berfungsi dengan menggunakan ATR spektroskopi inframerah, pembelauan sinar-X (XRD), dan spektroskopi Raman. Penambahan grafin oksida kedalam sulfona poli (eter eter keton) bukan sahaja meningkatkan prestasi PEM dari aspek kapasiti pertukaran ion (1.231 mequiv.g$^{-1}$), pengambilan air (53.45%) dan kekonduksian proton (0.0537), tetapi juga mampu untuk menahan molekul metanol dari merentasi membran, sekaligus menjadikannya sangat sesuai sebagai PEM.

**Kata kunci:** grafin oksida, polieter eter keton tersulfon, proton pertukaran membran, pembelauan sinar-X

## Introduction

Fuel cells are electrochemical devices that manage to directly convert chemical energy into electrical energy. Thus, it offers a promising alternative to conventional fossil fuel systems, due to their high efficiency, environmental

friendly and flexible application. Among them, proton exchange membrane fuel cell (PEMFC) has been gaining much attention due to its low system complexity, with high power density.

The proton exchange membrane (PEM), a thin membrane plays a crucial role in the performance of PEMFC as it is the heart of the PEMFC system enables fuel cells to conduct its electron by attracting the protons, and enabling them to diffuse through the layer, while maintaining their proton state. One of the most common and commercially available PEMs is the Dupont's Nafion® due to their high proton conductivity and chemical stability. However, the performance efficiency and application has been greatly hindered by several challenges such as high cost, methanol crossover and loss of conductivity above 80 °C in DMFC [1].

To overcome these issues, many studies have been conducted to develop affordable PEM with low methanol permeability for DMFC applications [2 – 4]. Sulfonated poly (ether ether ketone)(SPEEK), the most influential sulfonated aromatic polymer, is widely considered as a promising polymer electrolyte for proton exchange membrane fuel cells (PEMFC) as it offers adequate proton conductivity with low cost of production [5].

## Materials and Methods

The materials used in the experiments were included of commercial graphite powder (60–85%) supplied by Superior Graphite Co. while hydrochloric acid (HCl, 37%), sodium hydroxide (NaOH), sodium nitrate ($NaNO_3$) and sulfuric acid ($H_2SO_4$, 95 – 97%) were from Merck. Potassium permanganate ($KMnO_4$, 99%) was purchased from Bendosen. Hydrogen peroxide ($H_2O_2$, 35%). All materials were used as received. Distilled water was used throughout this study.

### Preparation of graphene oxide films

In order to prepare graphene oxide (GO), natural graphite powders and $NaNO_3$ are added slowly into the concentrated $H_2SO_4$ in ice bath with constant stirring for 45 min. Then, $KMnO_4$ (6 g) is added slowly to the solution and ensured the mixture temperature not exceeding 5 °C. The mixture then kept stirred for 1 hour before removing the ice bath. At intermediate temperature stage (35 – 37 °C) the mixture was stirred for 1 hour until it became pasty brownish. The reaction was continued with addition of distilled water (115 mL) resulting in sudden increases of temperature which was maintained at 90 °C for 15 min. Finally, the oxidation reaction was terminated by the addition of distilled water (350 mL) and $H_2O_2$ (30%, 10 mL). The mixture then left overnight with agitation to ensure its homogeneity followed by washing with HCl for several times. After that, the yield will be washed with distilled water several times and sonicated for 30 min in order to obtain the GO solution. The dry form of GO was obtained after drying for 24 hours in the oven [6, 7].

### Preparation of SPEEK and GO-SPEEK

For preparation of proton exchange membrane (PEM), 10 wt.% of SPEEK solution was prepared by dissolving SPEEK in DMSO. An amount 0.1 g of GO were added into DMSO and stirred for 3 hours to produce homogeneous solution. This solution then added into SPEEK solution, and the mixture was vigorously stirred for 24 hours at room temperature in order to produce homogeneous solution. The mixture then heated to 100 °C to evaporate the DMSO solvent. This preparation method was known as solution intercalation method. The solution then was cast on a glass plate with casting knife to form a solution film. The resultant film then dried in oven for 24 hours at 70 °C. The membrane was further dried for 6 hours at 100 °C to completely remove residual solvent. Finally, the membrane was treated with 1 M sulfuric acid solution for 24 hours at room temperature and subsequently rinsed with water several times in order to remove the remaining acid [8].

### Characterization of GO and hybrid nanomaterial

In order to characterize GO and PEM, the samples were examined by Perkin Elmer Spectrum One ATR in the mid IR region. The morphology of samples was determined by Field-Emission Scanning Electron Microscope (FESEM) model Hitachi SU8020. All X-ray diffraction (XRD) spectra of GO and PEM were scanned by Bruker Advance D8 Siemens 500 diffractometer, using Cu Kα radiation ($\lambda$ = 0.15418 nm, 40 kV, 40 mA). The scanning rate is 1 s with interval of 0.05°, 2θ range of 20° – 80° in the ambient temperature. Raman spectra were recorded from 200 to 2000 $cm^{-1}$ on a Reninshaw Via-Reflex Concoal Raman Microprobe of England using a 532 nm excitation.

Liquid uptake measurement is a technique to study the swelling behavior of SPEEK and GO-SPEEK membrane. The membranes will be dried in oven at 60 °C for 48 hours. The films will be initially weighted before soaking in deionized water for overnight at room temperature, and then will be blotted dry with adsorbent paper to remove any surface moisture. It then will be reweighted. The water uptake will be calculated as follows (equation 1):

$$\text{Water Uptake} = (W_w - W_d)/ W_d \times 100 \quad (1)$$

where $W_w$ and $W_d$ are the weights of the wet membrane and the dry membrane, respectively.

The proton conductivity was measured by impedance spectroscopy over a frequency range of 1 Hz to 107 Hz with 50 mV to 500 mV oscillating voltage, using solatron 1260 gain phase analyzer. The ion exchange capacity (IEC) of the membranes was measured with the titration technique. GO-SPEEK and Nafion were soaked in a large volume of 0.1 mol $L^{-1}$ HCl solution, washed with distilled water to remove excess HCl and then immersed in 1 M sodium chloride (NaCl) aqueous solution to release protons from the membrane. The released $H^+$ was back titrated with a 0.01 M sodium hydroxide (NaOH) aqueous solution using phenolphthalein as an indicator. The IEC value (in meq.$g^{-1}$), which is defined as milli equivalents (meq.) of sulfonic groups per gram of dried sample is obtained from the following equation 2:

$$IEC = V_{NaOH} \times C_{NaOH}/W_{dry} \quad (2)$$

where $V_{NaOH}$ is the volume of NaOH consumed, $C_{NaOH}$ is the concentration of NaOH and $W_{dry}$ is the weight of the dry membrane (g) [9].

The methanol permeability of membrane was measured using permeation cell composed of two reservoirs, each with a capacity of 50 ml. Before the test, the membranes were prehydrated for at least 24 hours. Each reservoir was separated by membrane. One reservoir was filled with a 1 M methanol solution, and deionized water was placed in the other reservoir. Both compartments were stirred continuously with a magnetic stirrer during the permeability experiment. The methanol permeability was found using this equation 3:

$$C_B(t) = A/V_B \times (DK/L)\, C_A (t - t_o) \quad (3)$$

where $C_A$ and $C_B$ are the concentrations of methanol in the donor and receptor reservoirs. A and L are the diffusion area and thickness of the membrane, respectively. The product of D and K is the methanol permeability ($cm^2s^{-1}$).

## Results and Discussion

### Attenuated total reflection infrared spectrometer

The availability of functional groups in GO and the chemical interactions between the functional groups of GO and SPEEK were examined by ATR spectroscopy. Figure 1 depicted the spectra of GO and GO-SPEEK. The spectrum of GO illustrates a strong and broad absorption in the range of 3700 – 2000 $cm^{-1}$ can be assigned to the stretching vibrations of structural OH groups and physisorbed water molecules. The band at 1716.8 $cm^{-1}$ can be ascribed to the C=O stretching vibration of COOH groups, and the absorptions arising from the O-H bending vibration, epoxide groups and skeletal ring vibrations are observed at 1619.08 $cm^{-1}$. The peaks at 1389.89 $cm^{-1}$ represent the O-H deformation vibration of COOH groups and can be used to evaluate the amount of COOH groups. The appearance of absorption at 1233.6 $cm^{-1}$ is related to phenolic groups. The 1044.72 $cm^{-1}$ is assigned to C-O-C stretching vibrations which confirm the presence of epoxide group in GO layers. For GO-SPEEK spectra, the presence of sulfonic acid group in SPEEK was confirmed by the strong characteristic peaks at 1219.72, 1081.93 and 1024.82 $cm^{-1}$, were assigned to the symmetric and asymmetric O=S=O stretching vibrations, as their intensities with respect to the backbone carbonyl (C=O) band at 1641.32 $cm^{-1}$.The broad peak appearing at 3412 $cm^{-1}$ assigned to O-H vibration double confirmed the presence of sulfonic acid groups in SPEEK samples, which interacting with molecular water [10].

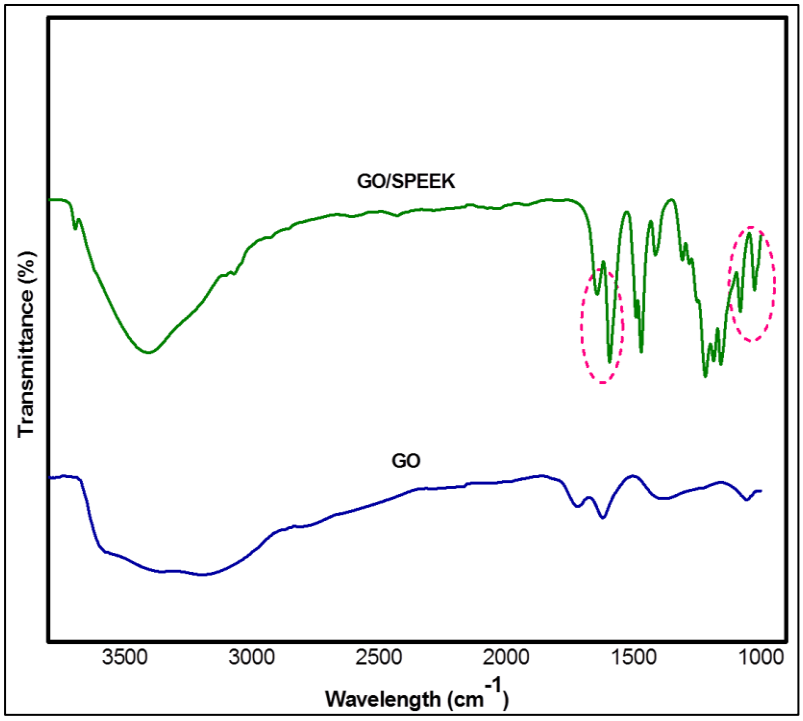



Figure 1. ATR spectra of GO and GO-SPEEK

**Raman spectroscopy**

Typical Raman spectra of pristine graphite, GO and GO-SPEEK obtained at an excitation wavelength of 532 nm are shown in Figure 2. Graphite shows a single sharp peak G band at ~1581 $cm^{-1}$, which corresponds to the vibration of $sp^2$ network, and low intensity of D band indicates defects existed in the graphite edges at 1354 $cm^{-1}$. In Raman spectra, the oxidation of graphite can be manifested by the changes in the relative intensity of two main D and G peaks. In comparison with graphite, GO exhibits a broader and blue-shifted G band at around 1580 $cm^{-1}$ with an intense D band at 1350 $cm^{-1}$ which is consistent with literature reported values [11–14]. During oxidation, the intensity of the D bands increase significantly, suggesting increased disorder and symmetry breaking in the graphitic layers due to attachment of hydroxyl and epoxide groups on the carbon basal plane. After incorporation GO into SPEEK, the D and G band for GO can't be observed as the spectra present at 1152.32 assigned to O=S=O vibration for $SO_3H$ group.

**Field emission scanning electron microscopy (FESEM)**

Field emission scanning electron microscopy (FESEM) images of GO, SPEEK and GO-SPEEK are shown in Figure 3. It can be observed (Figure 3a) that after oxidation, the GO shows an agglomeration of the exfoliated flakes. Moreover, there is some wrinkles and folding on the surfaces and edges indicating that the graphitic domain was decorated with oxygen-containing functional groups. Besides, the morphological features of the membranes show the microscale images of the cross-sectional area of SPEEK and GO-SPEEK (Figure 3b and 3c) with sponge-like structures. The various sizes of GO particles are visible in the GO-SPEEK membrane. These fillers are uniformly distributed throughout the matrix due to the interfacial interaction, which is attributed between the sulfonic group of SPEEK and the oxygenated group of GO through hydrogen bonding.

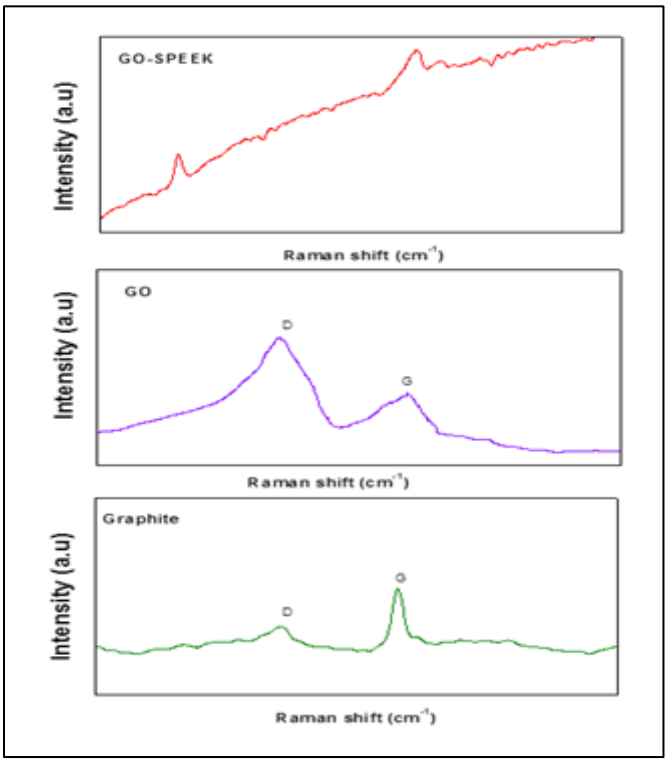



Figure 2. Raman spectra for graphite, GO and GO-SPEEK

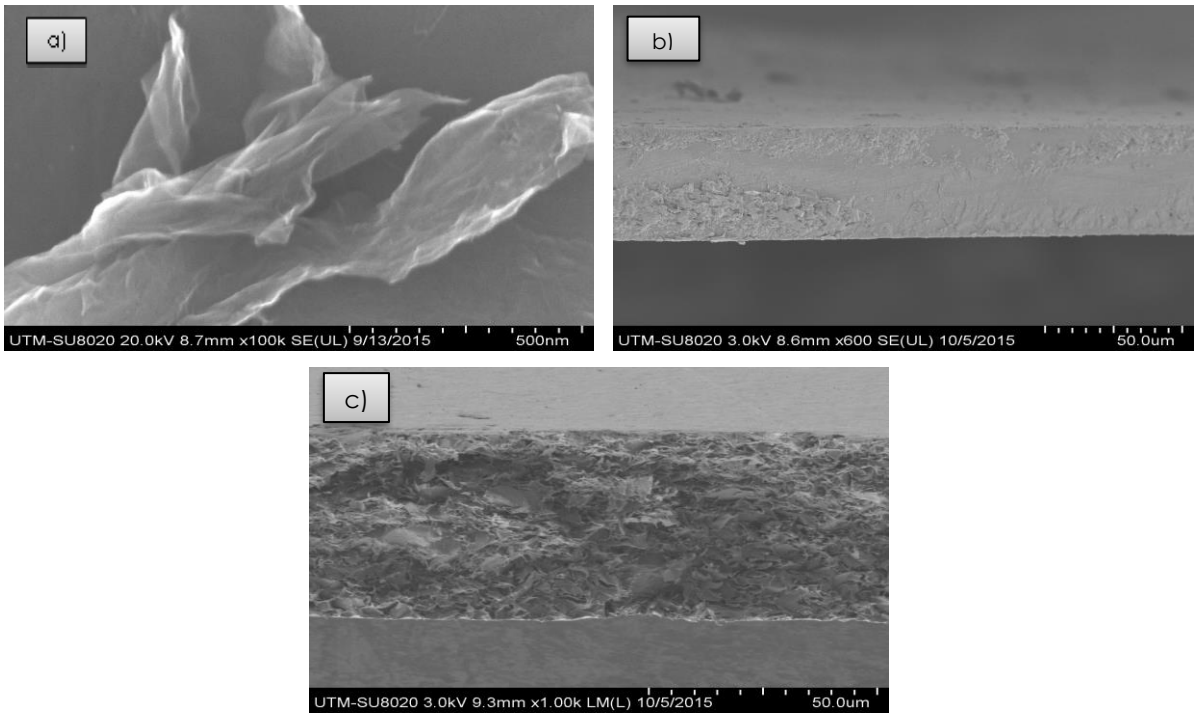



Figure 3. FESEM image of (a) GO, (b) SPEEK, and (c) GO-SPEEK

**X-ray diffraction**

Figure 4 illustrates XRD of graphite, GO, SPEEK and GO-SPEEK. This method can be used to confirm exfoliation process occurred in the pristine graphite during the oxidation process. The pattern of the raw graphite shows a very strong (002) peak at 2θ = 26.35° for a typical graphitic structure with layer spacing of 0.338 nm, indicates highly ordered crystal structure. However, after undergoing oxidation, it is obviously that the characteristic of graphitic peak completely disappears and in the meantime a new diffraction peak of (002) appearing at about 2θ = 11.04° with layer spacing 0.801 nm which indicating the layer distance was higher than the graphite. This happens due to the oxygen functional groups attached to both side of graphene sheets and the increasing atomic scale roughness to the graphene sheets. Therefore, it can be concluded that the expandable graphite was successfully oxidized. In the meanwhile for SPEEK, it was found that it gives a broad signal around the reflections which indicated it exists as fully amorphous structure. Generally, PEEK commonly considered as semi-crystallinity polymer, and that was confirmed by the appearance of a sharp crystalline peak of the range of 20 – 30° [15,16]. However, the crystallinity has been effectively decreased after the process of sulfonation. The XRD pattern of pristine SPEEK shows a broad peak overlay with the range of 13 – 25°, which indicates the lower crystallinity of SPEEK. The incorporated GO sheets are completely covered by the SPEEK polymers; therefore, there are no significant peaks observed for the fillers in the GO-SPEEK composites which indicate crystalline GO nanosized breaks and diffuse inside SPEEK polymer chains thus produce particulate nanocomposites membranes.

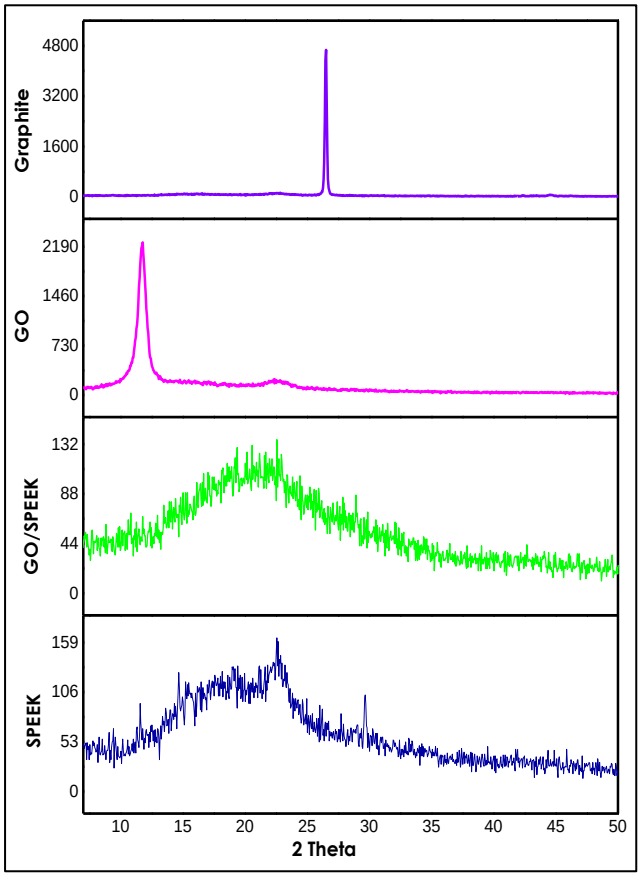



Figure 4. X-ray spectra for graphite, GO, SPEEK and GO-SPEEK

**Water uptake and swelling behaviour**

Water plays a crucial role in proton exchange membranes and influence proton transport across their membranes as proton could transport along with hydrogen-bonded ionic pathway and cationic mixtures such as $H_3O^+$, $H_5O_2^+$ and $H_9O_4^+$ in the water [17]. In order for membranes to have high proton conductivity and low resistance, it is desired for them to have a high water uptake capacity. Low amount of water uptake would reduce proton transport, while too much water uptake leads to excessive swelling hence loss of the dimensional stability. Figure 5 shows the percentage of water uptake for Nafion® 112, SPEEK and GO-SPEEK at varying temperature. The similar trend shows for the all samples which are the water uptake increase with the increasing temperature. Higher of temperature would introduce more movement of polymer chains as a result lead to more free volume for water absorption [9]. Plain SPEEK gives a higher water uptake percentage rather than commercial membrane, Nafion. However the plain SPEEK exhibits higher swelling percentage compared to commercial Nafion as depicted in Figure 6. This shortcoming improved when GO is introduced into the SPEEK. In line to the plain SPEEK, the composite membranes shows an increase in water uptake, even substantially enhanced two times higher than commercial membrane. This may result from the formation of hydrophilic channel within -OH on the GO edge and $–SO_3H$ groups in SPEEK which could lead decreasing of an average inter-chain distance of SPEEK. In contrast to plain SPEEK, GO-SPEEK gives a higher water uptake however surprisingly it gives lower swelling percentage compared to commercial PEM.

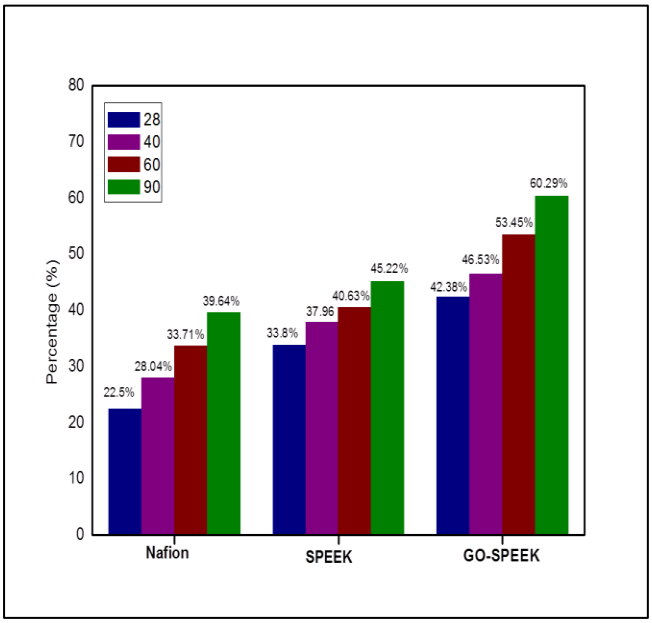



Figure 5. Percentage of water uptake for Nafion, SPEEK and GO-SPEEK at varying temperature

Table 1 depicts the value obtained for IEC and proton conductivity for Nafion, plain SPEEK and GO-SPEEK. Ion-exchange capacity (IEC) is an important property for membranes intended to be used as PEMs. Membranes with high IECs is expected to transport protons effectively through the available conducting ionic sites by proton hopping mechanism[18]. Sulfonic acid based PEMs, with high acidity and high ionization power, are one of the best choices in this area. It is observed that GO-SPEEK was the most acidic membrane as it exhibited the highest IEC compared to other membrane. This is in agreement with water uptake results.

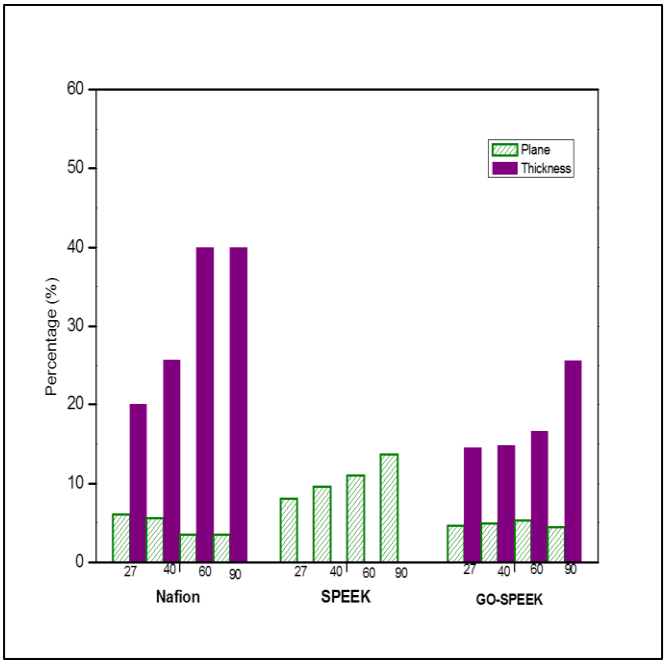



Figure 6. Percentage of swelling for Nafion, SPEEK and GO-SPEEK at varying temperature

Table 1. IEC, methanol permeability and proton conductivity (σ) of the Nafion, plain SPEEK and GO-SPEEK membranes at 85 °C

| **Sample** | **IEC (mequiv.g$^{-1}$)** | **Methanol Permeability (x 10$^{6}$ cm$^{2}$s$^{-1}$)** | **Proton Conductivity (Scm$^{-1}$)** |
|---|---|---|---|
| Nafion® 112 | 0.895 | 1.59 | 0.0612 |
| SPEEK | 0.982 | 0.97 | 0.0382 |
| GO-SPEEK | 1.231 | 0.36 | 0.0537 |

Proton conductivity is a crucial parameter to determine the fuel cell performance l. As shown in Table 1, the proton conductivity of GO-SPEEK membrane a bit lowered rather than the commercial Nafion® 112, however it still higher than 1 x $10^{-2}$ $Scm^{-1}$ which regarded as the lowest value of practical interest for PEM in fuel cells [19, 20] Proton conductivity relies on various factors, such as water uptake, IEC and the microstructure of the membrane [21]. Based on the structure, it could be understandable that by incorporating GO, it introduces inter-connected proton transfers channel [22], which able to facilitate proton transfer through the membrane. Hence this composite membrane exhibits higher proton conductivity compared to blank SPEEK. In addition, the proton transport in membranes requires well-connected channels formed by ion clusters of hydrophilic sulfonic acid groups. Hence, the content and the diameter of the connected channels gives remarkable effect on the proton transport rate in the membrane. The formation of isolated ionic cluster in the continuous hydrophobic phase occurred when the density of sulfonic acid groups low. The ionic clusters might be blocked from the GO with low proton conductivity although the water uptake and IEC increased in GO-SPEEK.

Membranes for practical usage of PEMs in DMFC were required to possess high conductivity and low methanol permeability. The methanol permeability of GO-SPEEK, blank SPEEK, and Nafion® 112 are shown in Table 1. It can be seen that the methanol permeability of SPEEK and GO-SPEEK are much lower than commercial membrane.

These results could be explained by their microstructure. Nafion® 112 membrane creates a simple hydrophobicity-hydrophilicity separation because of high hydrophobicity of the perfluorinated backbone and high hydrophilicity of the attached sulfonic acid groups. These well-connected hydrophilic domains act as substance movement channels, which not restricted to only proton and water, but also smaller polar molecules such as methanol could get through these channels. This circumstance results to high value of methanol permeability. In contrast, the SPEEK has smaller hydrophobicity and hydrophilicity differences compared to commercial membrane. Thus less constructed separation into hydrophobic and hydrophilic domains yields to lower methanol permeability than Nafion [23 – 25]. When the GO incorporated into SPEEK, it functions as barrier to connect the hydrophilic channels. GO block the polar molecules, methanol from easily passing through the membrane. This phenomenon is called "blocking effect". Besides, the interfacial interaction between GO and SPEEK polymer also contributes to the decreasing of it as GO and SPEEK interaction restricts the formation of broad hydrophilic channel requires by methanol transportation [26].

## Conclusion

Composite membrane based on GO-SPEEK had been successfully prepared. Physical and chemical properties were investigated. The performances of the composite membranes such as water uptake, dimensional stability, IEC, methanol permeability and proton conductivity were investigated. Though the capacity of water uptake were greatly improved with the introduction of GO into SPEEK, but it still able to reduce swelling ratio. The proton conductivities of GO-SPEEK slightly decrease compared to commercial membrane, Nafion®112. These results indicate that GO-SPEEK membranes possessed as promising PEM in fuel cell.

## Acknowledgement

The author wish to acknowledge funding from the Ministry of Higher Education (MOHE) for Fundamental Research Grant Scheme (FRGS) (vote no: R.J130000.7826.4F798), the Physic Laboratory of the Faculty of Science and Material Laboratory of The Faculty of Mechanical Engineering, Universiti Teknologi Malaysia for assistance given.

## References

1. Sharaf, O. Z. and Orhan, M. F. (2014). An overview of fuel cell technology: Fundamentals and applications. *Renewable and Sustainable Energy Reviews*, 32 (1): 810 – 853.
2. Lucia, U. (2014). Overview on fuel cells. *Renewable and Sustainable Energy Reviews*, 30(1): 164 –169.
3. Norddin, M. N. A. M., Ismail, A. F., Rana, D., Matsuura, T., Mustafa, A. and Tabe-Mohammadi, A. (2008). Characterization and performance of proton exchange membranes for direct methanol fuel cell: Blending of sulfonated poly(ether ether ketone) with charged surface modifying macromolecule. *Journal of Membrane Science*, 323(2): 404 – 413.
4. Tripathi, B. P. and Shahi, V. K. (2011). Organic–inorganic nanocomposite polymer electrolyte membranes for fuel cell applications. *Progress in Polymer Science (Oxford)*, 36(7): 945 – 979.
5. Jaafar, J., Ismail, A. F. and Matsuura, T. (2009). Preparation and barrier properties of SPEEK/Cloisite 15A®/TAP nanocomposite membrane for DMFC application. *Journal of Membrane Science*, 345 (1-2): 119 – 127.
6. Chakraborty, S., Guo, W. H., Hauge, R. H. and Billups, W. E. (2008). Reductive alkylation of muorinated graphite. *Chemistry of Materials*, 20(9): 3134 – 3136.
7. Hummers, W. S. and Offeman, R. E. (1958). Preparation of graphitic oxide. *Journal of the American Chemical Society*, 80 (6):1339 – 1339.
8. Jaafar, J., Ismail, A. F. and Matsuura, T. (2012). Effect of dispersion state of Cloisite15A on the performance of SPEEK/Cloisite15A nanocomposite membrane for DMFC application. *Journal of Applied Polymer Science*, 124 (2): 969 – 977.
9. Park, C. H., Lee, C. H., Guiver, M. D. and Lee, Y. M. (2011). Sulfonated hydrocarbon membranes for medium-temperature and low-humidity proton exchange membrane fuel cells (PEMFCs). *Progress in Polymer Science (Oxford)*, 36 (11): 1443 – 1498.
10. Kudin, K. N., Ozbas, B., Schniepp, H. C., Prud'homme, R. K., Aksay, I. A. and Car, R. (2008). Raman spectra of graphite oxide and functionalized graphene sheets. *Nano Letters*, 8(1): 36 – 41.

11. Ferrari, A. C., Meyer, J. C., Scardaci, V., Casiraghi, C., Lazzeri, M. and Mauri F. (2006). Raman spectrum of graphene and graphene layers. *Physical Review Letters*, 97 (18): 74 – 81.
12. Childres, I., Jauregui, L., Park, W., Cao, H. and Chen, Y. (2013). Raman spectroscopy of graphene and related materials. *New Developments in Photon and Materials Research*, 16 (2): 1 – 20.
13. Tuinstra, F. and Koenig, L. (1970). Raman spectrum of graphite. *The Journal of Chemical Physics*, 53 (1): 1126 – 1130.
14. Ferrari, A.C. and Basko, D. M. (2013). Raman spectroscopy as a versatile tool for studying the properties of graphene. *Nature Nanotechnology*, 8(4): 235 – 246.
15. Mecheri, B., D'Epifanio, A., Traversa, E. and Licoccia S. (2008). Sulfonated polyether ether ketone and hydrated tin oxide proton conducting composites for direct methanol fuel cell applications. *Journal of Power Sources*, 178(2): 554 – 560.
16. Krishnan, P., Park, J. S. and Kim, C. S. (2006). Preparation of proton-conducting sulfonated poly(ether ether ketone)/boron phosphate composite membranes by an in situ sol-gel process. *Journal of Membrane Science*, 279 (6): 220 – 229.
17. Fu, T., Cui, Z., Zhong, S., Shi, Y., Zhao, C. and Zhang, G. (2008). Sulfonated poly(ether ether ketone)/clay-$SO_3H$ hybrid proton exchange membranes for direct methanol fuel cells. *Journal of Power Sources*, 185(5): 32 – 39.
18. Hasani-sadrabadi, M. M., Emami, S. H. and Ghaffarian, R. (2008). Nanocomposite membranes made from sulfonated poly (ether ether ketone) and montmorillonite clay for fuel cell applications. *Energy & Fuels*, 22(4): 2539 – 2542.
19. Peighambardoust, S. J., Rowshanzamir, S. and Amjadi, M. (2010). Review of the proton exchange membranes for fuel cell applications. *International Journal of Hydrogen Energy*, 35(17): 9349 – 9384.
20. Barbir, F. (2006). PEM fuel cells. *Fuel Cell Technology*, 2(1): 27 – 51.
21. Eisenberg A. (1970). Clustering of ions in organic polymers. A theoretical approach. *Mucromolecules*, 3(2): 147 – 154.
22. He, Y., Tong, C., Geng, L. and Liu, L. (2014). Enhanced performance of the sulfonated polyimide proton exchange membranes by graphene oxide: Size effect of graphene oxide. *Journal of Membrane Science*, 458(2): 36 – 46.
23. Jiang, Z., Zhao, X. and Manthiram, A. (2013). Sulfonated poly(ether ether ketone) membranes with sulfonated graphene oxide fillers for direct methanol fuel cells. *International Journal of Hydrogen Energy*, 38 (14): 5875 – 5884.
24. Li, L., Zhang, J. and Wang Y. (2003). Sulfonated poly(ether ether ketone) membranes for direct methanol fuel cell. *Journal of Membrane Science*, 226(3): 159 – 167.
25. Li, X., Liu, C., Lu, H., Zhao, C., Wang, Z. and Xing, W. (2005). Preparation and characterization of sulfonated poly(ether ether ketone ketone) proton exchange membranes for fuel cell application. *Journal of Membrane Science*, 255(1-2):149 – 155.
26. Heo, Y., Im, H. and Kim, J. (2013). The effect of sulfonated graphene oxide on sulfonated poly (ether ether ketone) membrane for direct methanol fuel cells. *Journal of Membrane Science*, 425(1): 11 – 22.

*Malaysian Journal of Analytical Sciences, Vol 21 No 2 (2017): 445 - 451*
*DOI: https://doi.org/10.17576/mjas-2017-2102-20*

MALAYSIAN JOURNAL OF ANALYTICAL SCIENCES
*Published by The Malaysian Analytical Sciences Society*
ISSN 1394 - 2506

# RADIOTRACER APPLICATION IN MALAYSIA: RESIDENCE TIME DISTRIBUTION STUDY

## (Aplikasi Teknologi Penyurih di Malaysia: Kajian Taburan Masa Mastautin)

Noraishah Othman*, Nor Pa'iza Mohamed Hassan, Roslan Yahya, Mior Ahmad Khusaini Adnan, Mohd Rabaie Shari, Hearie Hassan, Airwan Affendy Mahmood

*Plant Assessment Technology, Industrial Technology Division*
*Malaysian Nuclear Agency, 43000 Bangi, Selangor, Malaysia*

**Corresponding author: noraishah@nm.gov.my*

Received: 21 October 2015; Accepted: 14 June 2016

**Abstract**

The residence time distribution (RTD) study at power generation plant was successfully carried out using radiotracer technology. In this study, $Tc^{99m}$ was used as the source of radioactive whereas NaI(Tl) detector was the scintillant detector. Previous study only concentrated on getting the flow rate from two successive peaks without producing any mathematical model. Thus, the hydrodynamics behaviour of the liquid inside the plant was weakly described. In this study, axial dispersed plug flow model is the best RTD model due to minimal value of sum of square which is $0.261 \times 10^{-5}$ compare to other RTD models recommended by International Atomic Energy Agency (IAEA).

**Keywords**: residence time distribution, radiotracer technology, RTD models, sum of square

**Abstrak**

Kajian taburan masa mastautin (RTD) telah berjaya dilakukan di loji janakuasa elektrik menggunakan teknologi penyurih. Untuk kajian ini, $Tc^{99m}$ telah digunakan sebagai penyurih radioaktif manakala pengesan NaI digunakan sebagai pengesan sintilasi. Kajian terdahulu hanya memberi maklumat berkaitan pengukuran kadar alir yang terhasil daripada dua puncak turutan yang terhasil tanpa membuat laporan berkaitan permodelan RTD. Oleh itu, kelakuan hidrodinamik bendalir di dalam loji tidak dapat dijelaskan dengan baik. Untuk kajian ini, model aliran palam taburan aksial merupakan model terbaik RTD berbanding model yang dicadangkan oleh IAEA kerana nilai jumlah kuasa dua terhasil yang rendah iaitu $0.261 \times 10^{-5}$.

**Kata kunci:** taburan masa mastautin, teknologi penyurih, permodelan RTD, jumlah kuasa dua

## Introduction

Radiotracers are widely used for the measurement of the flow rate of liquids, gases and solids in many industrial systems. An investigation of many major industrial applications including fluidized beds, sugar crystallizers, trickle bed reactors, cement rotary kiln, wastewater treatment unit and also inter-well communications in oil fields can be performed by the injection of a radiotracer at the inlet of the system and monitoring the radiotracer at the outlet. The output data can be treated and analyzed to investigate the behavior of the system or hydrodynamics of the fluid inside the plant. Moreover, radioisotope-based technology continues to play a rapidly growing role in assisting industry to enhance their production efficiency and also for optimization [1]. Radiotracer technology has proved itself as a sensitive tool for investigating and solving plant process problems namely process malfunctions and anomalies as well as mechanical damages. Radiotracer techniques have many advantages such as high detection

sensitivity, in-situ detection, and availability of a wide range of compatible radiotracers for different phases, rapid response, reliability and accuracy of results [2].

The residence time distribution (RTD) of a reactor is a characteristic of the flow pattern that occurs in the chemical reactor, being one of the most informative characterizations of the reactor [3]. The principle of a tracer experiment consists of a common impulse-response method: injection of a tracer at the inlet of a system and recording the concentration–time curve at the outlet of the system. RTD is obtained after the preliminary treatment of radiotracer data, including background correction, correction, radioactive decay correction, starting point correction, filtering, and data extrapolation and area-normalization as described by Kasban et al. [4]. RTD, which was first developed by Danckwerts [5] has been utilized by many researchers to diagnose the possible system malfunctions such as bypassing, leakage, blockage, channelling, fouling and backmixing as well as helping in estimating the quality of mixing. It also depends on the flow hydrodynamics and the reactor geometry and has influence on the reactor for chemical performances such as conversion and yield. The method gives information on the measured system by evaluating concentration of a tracer compound, which is added as a stimulus at the system inlet.

Moreover, mathematical model should be obtained for hydrodynamics study so that the behaviour of the fluid in the plant or reactor can be understood well. Extensive radiotracer experiments have been carried out successfully in various industries, which indicate the survival and reliability of radiotracers in hostile environments. The next case studies will be describing the successful application of radiotracer technology in industries worldwide. Sugiharto et al. [6] determined the RTD and the system flow rate in a 24 in. multiphase flow hydrocarbon transmission pipeline containing approximately 95% water, 3% crude oil, 2% gas and negligible solid material. Nevertheless, the types of radiotracer sources used in this experiment were different; I-13 and Na-24 were used independently for the measurement of the RTD in hydrocarbons and water, respectively. In this instance, the tanks in series model best described the RTD of the system. The authors also discovered that the water moved faster than the hydrocarbon even though the density of the water is higher. This might be because water is more dominant in the transmission line and because the movement of the crude oil is slowed by friction with gas at the top layer and friction at the water–crude oil interface. Behin and Aghajari [7] studied the RTD measurement in a pilot-scale oil–water separator operated by Drood oil of the Iranian Offshore Oil Company (IOOC) located in Kharg Island using 5mCi I-131 as sodium iodide and 4mCi of I-131 as iodobenzene for the aqueous and organic phase, respectively. The separation of the crude oil and water mixtures is an important process in the oil and chemical industries. The researchers reported that the experimental results were in a good agreement using the model of perfect mixing tanks in series (with a dead zone) to describe the liquid behavior. The models obtained in these two case studies were both tanks in series models. It can therefore be concluded that tanks in series models suited the multiphase flow profile.

In addition, each case study developed a mathematical model that fitted the experimental results satisfactorily although the chosen models varied between applications. Pant et al. [8] conducted an RTD study in a pilot and an industrialized fluid catalytic cracking unit (FCCU) using an intrinsic tracer. The identified tracers were lanthanum-140 and sodium-24 and were obtained from the catalyst sample. The tracers were characterized using neutron activation analysis to investigate the degree of axial mixing and radial distribution in the riser section of the FCCUs and to determine the residence time distribution of the catalyst. The axial dispersion model (ADM) was used to represent the actual RTD obtained from the radiotracer experiments. According to Pant et al. [8], the ADM is the best model to describe material flow in a tabular reactor, such as FCCU, because this model can describe one-dimensional convection and dispersion in a pipe. Radiotracer techniques are extensively used for measurement of process parameters such as mean residence time (MRT), residence time distribution (RTD), flow rate, material inventory in full-scale industrial reactors, high detection sensitivity, physico-chemical compatibility, in-situ detection, limited memory effect and use in hostile industrial environment [1, 2]. In this study, RTD was fruitfully conducted using radiotracer approach in one of the biggest Power Station in Malaysia.

## Materials and Methods

About 10ml of eluted Tc-99m from $^{99}Mo/^{99m}Tc$ generator was engaged as radiotracer in this study. According to IAEA 2008 [1], the injected activity of $Tc^{99m}$ is ≈ 37 GBq is used for water tracing in surface bodies (rivers, sea) for dispersion of effluent studies (outfalls) and dispersion coefficient measurements. Nevertheless, in this study about 10.6Bq was employed. The experiment was carried out by injection of $Tc^{99m}$ into 2.1m diameter underground

Calvert pipeline. The temperature of operating liquid is about 39-40$^{o}$C along the 580m pipeline. The injection point was chosen at the outlet of the condenser and the detection point was at the effluent of pipe which was about 580m away from the injection point. This location showed that the tracer was mixing homogenously with the liquid since according to IAEA practice, the shortest perfect mixing is about 100 inner diameter length [1, 2]. The scintillation detector, NaI was used to detect the presence of the emitted radiotracer for RTD study. Fig. 1 shows the schematic diagram of the buried pipelines. The influent and the effluents are coming from and to the sea respectively.

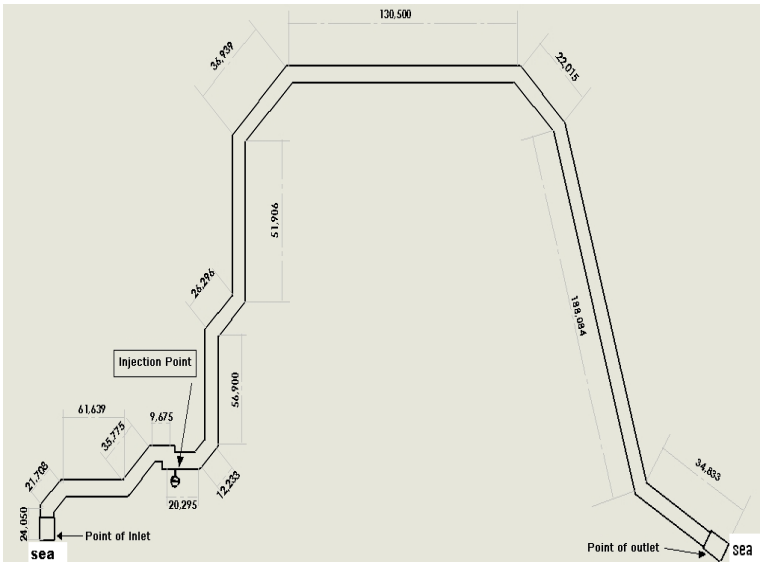



Figure 1. Schematic diagram of buried pipeline

**Results and Discussion**

Figure 2 shows the results of radioactive monitoring in which the gamma rays are detected in count per seconds (cps) from $Tc^{99m}$ and received by scintillation detector. The sampling time was set until the reading from data acquisition system (DAS) showed the background level. The experimental data obtained has statistical fluctuations which need to be treated prior RTD determination. The data has to undergo background correction, radioactive decay correction, starting point correction, filtration and data extrapolation prior RTD modelling.

Residence Time Distribution (RTD) is a fundamental parameter in reactor design which can give information on how long the substrate has been in the reactor and the RTD analysis can help characterizing the extent of their deviation from ideal behavior. The E(t) function is the RTD where E(t) dt is the fraction of the flow, measured at the exit, that is in the system between times t and (t +dt):

$$E(t) = \frac{C(t)}{\int_0^\infty C\,(t)dt} \quad (1)$$

where C(t) is the concentration of radiotracer monitored by NaI scintillation detectors in counts per second (cps) as numerator and denominator is the area under the curve of plotted C(t).

Figure 3 displays the RTD response after application of Equation (1). It shows the tall, sharp and narrow peak of RTD curve or well-defined Gaussian curve which indicates homogenous mixing of radiotracer in the system. The data is continuous RTD curves which represent the relation between radiation intensity versus time. In this study, RTD modelling was performed using International Atomic Energy Agency (IAEA) RTD software. The six recommended RTD models by IAEA are the axial dispersed plug flow model, the axial dispersed plug flow with exchange model, the perfect mixers in series model, the perfect mixers in series with exchange model, the perfect mixers in parallel model and the perfect mixers with recycle model. Details of each model can be obtained from the

IAEA [1, 2]. Mathematical RTD models can provide theoretical information as well as the hydrodynamic behaviour of the reactor.

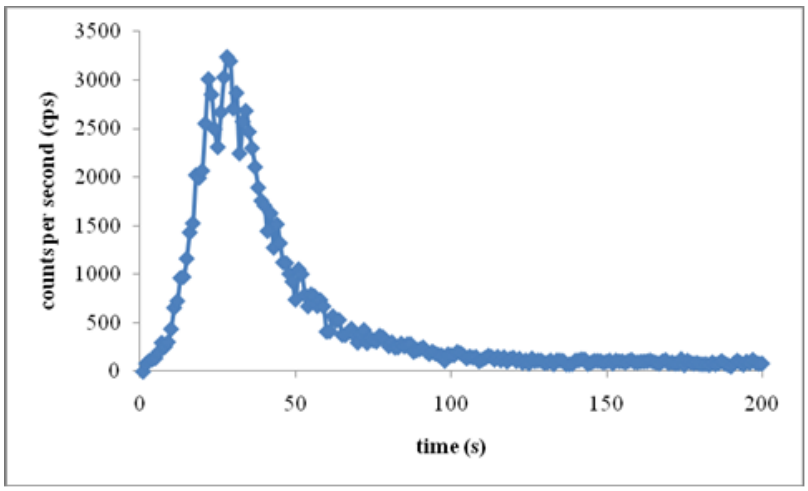



Figure 2. Detection of emitted gamma rays from $Tc^{99m}$

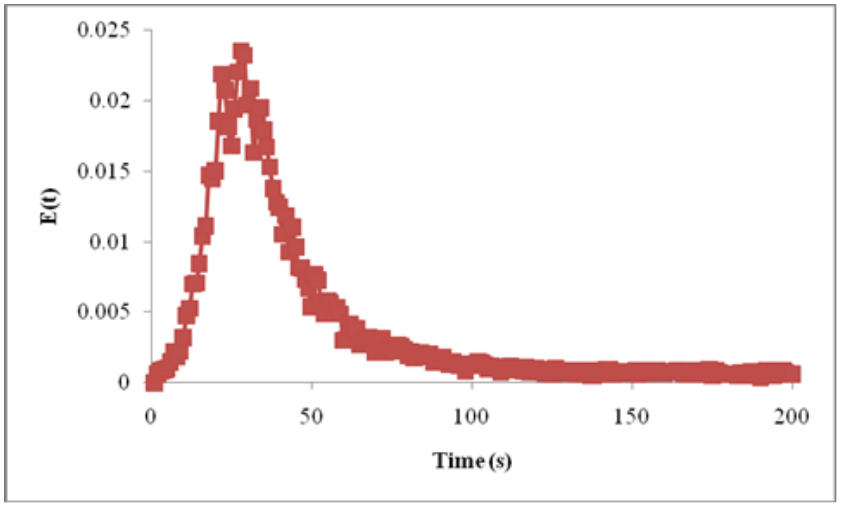



Figure 3. RTD profile of monitored tracer

The radiotracer experiments showed that only three models successfully fitted the experimental data. These RTD models are the axial dispersed plug flow model, the axial dispersed plug flow with exchange model and the perfect mixers in series model as shown in Figures 4, 5 and 6, respectively. The success of the models are due to the fact that the flow that passing through in the pipeline is behaving as plug flow which represents axial dispersion plug flow model. The unsuccessful fitted RTD model was the perfect mixers with recycle model, the perfect mixers in parallel model and the perfect mixers in series with exchange model. The failure of curve fitting from these models due to the absence of perfect mixer in the actual plant. The best fit is chosen based upon the minimum value of sum of square, which is the difference between the experimental data and the model [1, 6].

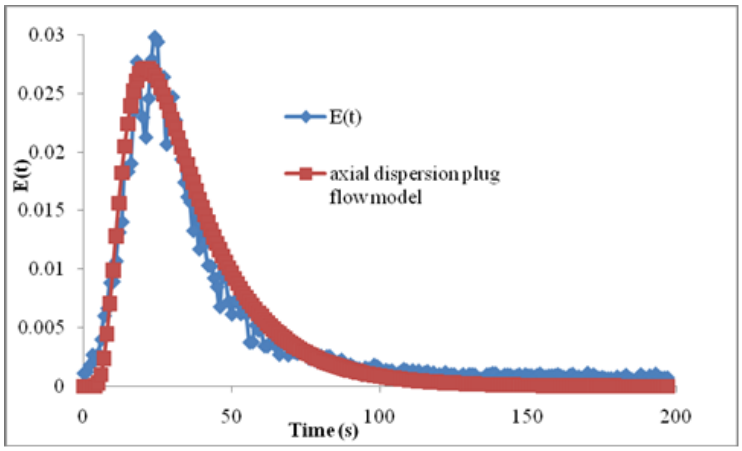



Figure 4. Axial dispersion plug flow model

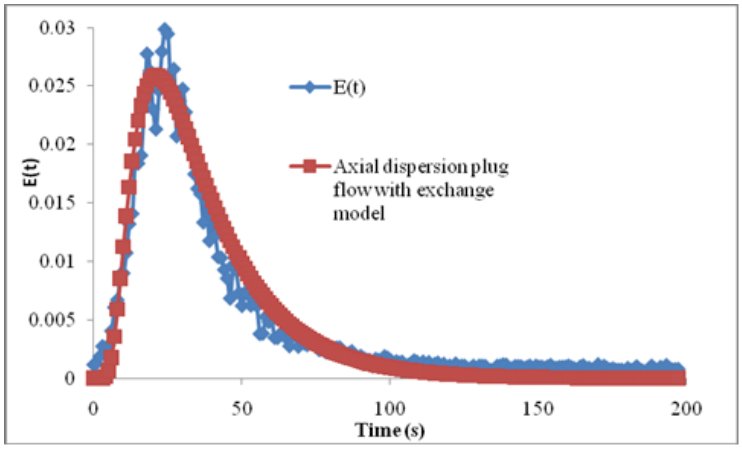



Figure 5. Axial dispersion plug flow with exchange model

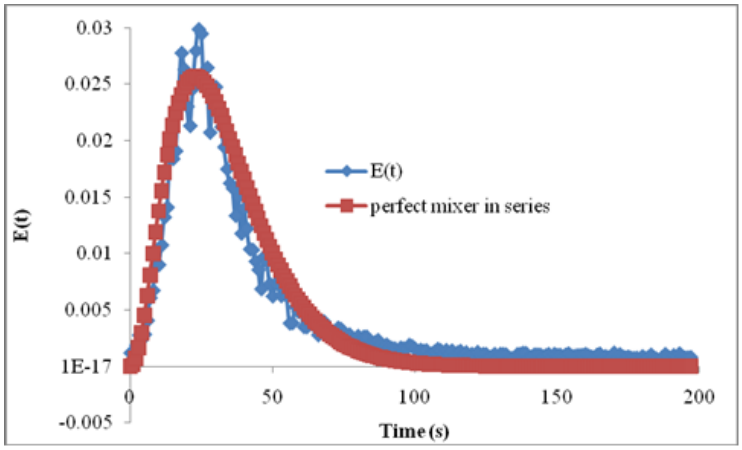



Figure 6. Perfect mixer in series model

The axially dispersed plug flow model is widely used in practice. This flow is the superimposition of convection which is the bulk movement of the fluid as a plug and some amount of dispersion. This model is a proper approximation also for quite a variety of quasi one-dimensional situations such as river flow, underground water flow as well as packed columns and has two parameters which are non-dimensional Péclet number, Pe and τ. The curves get sharper and sharper when Pe is increased. They always have one single peak and the peak height and tail length are correlated (tail is short when peak is sharp and vice versa). It is often necessary to characterize convection as related to velocities and flow rates which is the behavior of plug flow [1, 2].

Furthermore, the sum of the squares of the differences between the model and the data are minimized and fulfilled using the following equation [6]:

$$Sum\ of\ Square\ (SSE) = [\frac{1}{N_T}\int_0^\infty [E_{exp}(\theta) - E_m\ (\theta, N)]^2\ d\theta]^{1/2} = Minimum \quad (2)$$

where $N_T$ is the number of data points, $E_{exp}(\theta)$ is the experimentally measured curve, and $E_m(\theta, N)$ is the simulated model. Table 1 shows the results of optimized parameters for successful RTD model. Only three RTD models have successfully fitted the experimental curve. These model are axial dispersed plug flow model, axial dispersed plug flow with exchange model followed by the perfect mixers in series model.

Table 1. Optimized parameters for each model

| **Models** | **τ** | **Pe** | **N** | **J** | **Sum of square (SSE)** | **Rank** |
|---|---|---|---|---|---|---|
| Axial dispersion plug flow model | 0.36 | 0.53 | 1.0 | *na* | 0.261 x $10^{-5}$ | 1 |
| Axial dispersion plug flow with exchange model | 0.30 | 0.47 | 1.0 | 1.0 | 0.305 x $10^{-5}$ | 2 |
| Perfect mixer in series model | 0.33 | *na* | *na* | 0.33 | 0.348 x $10^{-5}$ | 3 |

Where τ is the mean residence time or the total volume of the system divided by the flow rate,
Pe is Péclet number,
J is number of tank,
N is a mass transfer coefficient;
*na* – not applicable.

According to Table 1, both the axial dispersed plug flow model and the axial dispersed plug flow with exchange model can be considered as the best fit followed by the perfect mixers in series model. The axial dispersed plug flow model is best described the experimental RTD curve because the sum of square (SSE) is minimum which is 0.261 x $10^{-5}$ compare to perfect mixer in series, which is 0.348 x $10^{-5}$. Additionally, the axial dispersed plug flow model is more applicable to flows in long pipes and the axial dispersed plug flow with exchange model indicates that there is effective mixing because the value of N is equal to 1 [1, 2]. Besides, the lowest value of Pe shows that dispersion operation is more dominant than convection, and thus, there is plug flow.

## Conclusion

The present work describes the radioactive experiments using radiotracer technology to study the (RTD). A field study was carried out as a case study and the best RTD models were precisely identified. The axial dispersed plug flow model, the axial dispersed plug flow with exchange model and the perfect mixers in series model are the RTD models which inflexibly fitted the experimental RTD well whereas axial dispersed plug flow model described best RTD model due to minimal value of sum of square.

**Acknowledgement**

All authors acknowledge the Plant Assessment Technology team which made an outstanding effort for accomplishment of this project. They also thank the Director of BKT, NM for the financial support.

**References**

1. IAEA (2008). Residence time distribution method for industrial and environmental applications. Training course series 931, Vienna, Austria.
2. IAEA-TECDOC-1262 (2001). Radiotracer technology as applied to industry.Vienna, Austria.
3. Arratia, P. E., Lacombe, J. P., Shinbrot, T. and Muzzio, F. J. (2004). Segregated regions in continuous laminar stirred tank reactors. *Chemical Engineering Science*, 59:1481 – 1490.
4. Kasban, H., Zahran, O., Arafa, H., El-Kordy, M., Elaraby, S. M. S. and Abd El-Samie, F. E. (2010). Laboratory experiments and modeling for industrial radiotracer applications. *Applied Radiation and Isotopes*, 68: 1049 – 1056.
5. Danckwerts, P. V. (1953). Continuous flow systems and distribution of residence times. *Chemical Engineering and Science*, 2: 1 – 13.
6. Sugiharto, S., Suud, Z., Kurniadi, R., Wibisono, W. and Abidin, Z. (2009). Radiotracer method for residence time distribution study in multiphase flow system. *Applied Radiation and Isotopes,* 67: 1445 –1448.
7. Behin, J. and Aghajari, M. (2008). Influence of water level on oil–water separation by residence time distribution curves investigations. *Separation and Purification Technology*, 64: 48 – 55.
8. Pant, H. J., Sharma, V. K., Nair, A. G. C., Tomar, B. S., Nathaniel, T. N., Reddy, A. V. R. and Singh, G.(2009). Application of 140-La and 24Na as intrinsic radiotracers for investigating catalyst dynamics in FCCUs. *Applied Radiation and Isotopes,* 67: 1591 – 1599.

*Malaysian Journal of Analytical Sciences, Vol 21 No 2 (2017): 452 - 459*
*DOI: https://doi.org/10.17576/mjas-2017-2102-21*

MALAYSIAN JOURNAL OF ANALYTICAL SCIENCES
*Published by The Malaysian Analytical Sciences Society*
ISSN 1394 - 2506

# RESPONSE SURFACE METHODOLOGY ON WAX DEPOSIT OPTIMIZATION

## (Pengoptimuman Lilin Mendap Menggunakan Kaedah Gerak Balas Permukaan)

Norida Ridzuan*, Zulkefli Yaacob, Fatmawati Adam

*Faculty of Chemical Engineering & Natural Resources,*
*Universiti Malaysia Pahang, 26300 Gambang, Pahang, Malaysia*

**Corresponding author: norida@ump.edu.my*

Received: 21 October 2015; Accepted: 14 June 2016

**Abstract**

In this study, the application of response surface method design based on rotatable central composite design (CCD) was used to optimize wax deposit using Design Expert 7.1.6 software. The process consisted of 13 experiments involving eight factorial points and five replications at the center point. The influence of operating parameters on the weight of wax deposit was investigated using cold finger apparatus. The experimental result indicated that the amount of wax deposit was significant due to factors of cold finger temperature and experimental duration. The wax deposit amount decreased significantly with the decrease of experimental duration when the cold finger temperature increased to 25 °C. The minimum value of 0.0042 g of wax deposit was obtained at the optimized conditions of 1.5 hours and 25 °C, respectively.

**Keywords**: cold finger method, crude oil, optimization

**Abstrak**

Dalam kajian ini, penggunaan kaedah gerak balas permukaan berdasarkan reka bentuk komposit berpusat berputar (CCD) digunakan bagi mengoptimumkan lilin mendap menggunakan perisian Design Expert 7.1.6. Proses ini terdiri daripada 13 eksperimen yang melibatkan lapan titik faktorial dan lima ulangan di titik pusat. Pengaruh parameter operasi terhadap berat lilin mendap telah dikaji dengan menggunakan radas jejari sejuk. Hasil eksperimen menunjukkan bahawa jumlah lilin mendap dipengaruhi oleh faktor suhu jejari sejuk serta tempoh eksperimen. Jumlah lilin mendap akan berkurang sekiranya tempoh eksperimen dikurangkan berserta peningkatan suhu jejari sejuk kepada 25 °C. Nilai minimum 0.0042g lilin mendap telah diperolehi pada keadaan yang optimum iaitu pada 1.5 jam dan 25 °C .

**Kata kunci:** kaedah jejari sejuk, minyak mentah, pengoptimuman

## Introduction

The major problem faced by the petroleum industry especially in flow assurance is the deposition of wax from crude oil at the tubing, pipeline, and surface flow line [1–3]. The formation of solid wax may lead to increased pumping power, decreased flow rate or even total blockage of line, with loss of production and capital investment [4]. Waxes are solids essentially made of mixtures of long chains, either normal or branched alkane compound formed when the temperature of crude oil falls below the wax appearance temperature (WAT) [5].

Normal conditions for reservoir temperature and pressures are within the range of 70 to 150 °C and 8,000 –15,000 psi, respectively [3, 6], while ocean floor temperature is around 4 °C [3]. When crude oil is transported from reservoir to pipeline, the crude oil temperature decreases below its wax appearance temperature (WAT) due to heat

lost to surroundings [3, 7]. At ambient condition, for carbon atom chains less than four atoms (C1 to C4), it will show a gaseous state. Meanwhile, in the range of carbon atoms from C5 to C16, it turns to liquid and for carbon atoms more that C17, it forms solid [8]. Flow assurance is expected to lead to losses of billions of dollars yearly worldwide [9]. Many remediation techniques to encounter deposition problem have been employed, including removal and prevention approaches such as chemical, mechanical and thermal methods [5, 10 – 12]. To avoid wax deposition problems, the understanding of physicochemical characteristics of wax phase is needed [13].

The deposition of wax from crude oil is influenced by several factors, such as wax content and composition, flow rate, temperature difference between oil and pipe surface, and cooling rate along the pipeline [9]. Kelechukwu et al. [14, 15] claimed that the most common factor for wax deposition is the decrease of crude oil temperature. Many researchers have investigated the factor that gives the best influence on wax deposition. Shear and temperature effects have been observed by Jennings and Weispfennig toward wax deposition [16, 17]. They found an increase in shear increased wax inhibition; however, for the temperature effect, the inhibition result contradicted with the shear effect.

Previously, the optimum combination of operating conditions for minimum wax deposition has been studied by implementing one-factor-at-a-time technique (OFAT). However, this technique cannot examine the interactions of the factors considered. Therefore, to determine the impact of two or more factors on a response, Design Expert (DO) software was introduced. DO is a statistical software package that is specifically designed to perform the design of experiment (DOE). An experiment is a series of tests, called runs, in which changes are made in the input variables in order to identify the reasons for changes in the output response [18 – 20]. This software is able to offer comparative tests, screening, characterization, optimization, robust parameter design, mixture designs and combined designs. It also manages to come up with a systematic plan for the minimum number experiments to avoid time consumption [18, 19].

To optimize a response (output variable) that is influenced by several independent variables (input variables), response surface methodology (RSM) was introduced. RSM is a collection of mathematical and statistical techniques for building an empirical model. A group of researcher has investigated the factor that gives the best influence on wax deposition. For example, Valenijad et al. [21] have studied the experimental factors that affect crude oil wax deposition problem using Taguchi method. These factors include inlet crude oil temperature, temperature difference between the oil and pipe wall, flow rate of crude oil, wax content and time. However, there are limited studies on optimization that have been performed to optimize the process parameters for wax deposition by using response surface methodology and central composite design.

The present study focused on the development of a mathematical model for wax deposit prediction to describe the effects and the relationships between the process variables to obtain minimum yield of wax deposit formation using CCD**.**

## Materials and Methods

### Materials

Poly(ethylene-co-vinyl acetate) (EVA), n-heptane (purity 99.5%), and petroleum ether were obtained from Sigma-Aldrich. The raw crude oil sample was kindly supplied by PETRONAS Refinery from Kerteh, Terengganu, Malaysia. The characteristics of the crude oil sample are listed in Table 1.

### Cold finger experimental set up

The rate of wax deposition of crude oil was evaluated using cold finger apparatus as shown in Figure 1. This apparatus is suitable for understanding the temperature correlation between bulk crude oil and the wall that is exposed to the temperature below WAT [17, 22, 23]. To run the experiment, a stainless steel jar was filled with 300 mL of crude oil sample. The crude oil needs to be conditioned above WAT for the purpose of thermal treatment for 1 hour in order to solubilize any precipitated wax. The experiments were carried out for 2 hours and the temperature of the crude oil sample needed to be maintained at 50 °C. The total amount of inhibitor used for each experiment was about 10 mL. The experiments were repeated three times to obtain precise data. The deposit was then scrapped

off from the finger, weighed, and saved for potential analysis. Visual observation of the wax was made for determining the physical characteristics.

Table 1. Summary of the list of equipment used for physical analysis

| Equipment | Usage |
|---|---|
| Differential scanning calorimeter (DSC) | To determine the wax appearance temperature (WAT) of the crude oil sample. |
| Cloud point and pour point apparatus, model Koehler | To determine the pour point of the crude sample. |
| Brookfield rotational digital, model DV-III (spindle No. 31) | To determine the rheology behavior of the crude oil sample. |
| Gas pycnometer, model Micromeritics AccuPyc II 1340 | To measure the density of the crude oil sample. |
| Acetone precipitation technique (Modified UOP method 46-64) | Extraction of wax crystal from the crude oil sample. |

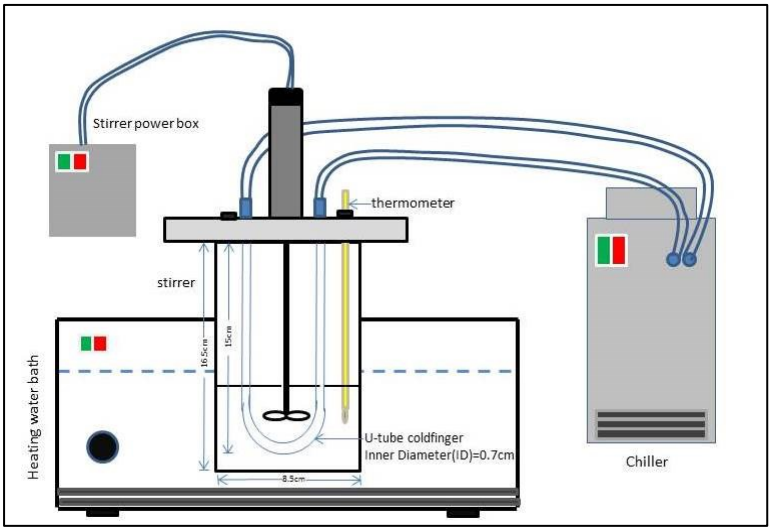



Figure 1. Cold finger apparatus set up

**Experimental design**

A standard RSM design called central composite design (CCD) was applied to study the wax deposit variables. The two independent variables studied were the cold finger temperature (A) and experimental duration (B) that were coded at five levels. Details of the lower limit and upper limit are shown in Table 2. The CCD includes eight factorial points and five replications at the center point, in which a total of 13 experimental runs were employed to fit a second-order polynomial model using Design Expert (State-Ease, USA) version 7.1.6. The inhibitor concentration and speed of rotation were set for 5000ppm and 0 rpm respectively for each run.

Table 2. Five-level two-factor central composite design condition variables

| Independent Variables | Code Symbol | Coded Level | | | | |
|---|---|---|---|---|---|---|
| | | -α | -1 | 0 | 1 | + α |
| Cold finger temperature (°C) | A | 5 | 10 | 15 | 20 | 25 |
| Experimental duration (h) | B | 1 | 1.5 | 2 | 2.5 | 3 |

## Results and Discussion

CCD was employed in this study to optimize wax formation. The experimental work was done using cold finger test. The influence of cold finger temperature (A) and experimental duration (B) on the amount of wax deposit was investigated. An actual experimental model as shown in Table 3 was developed to predict the optimum condition for wax formation in order to minimize the expression of wax deposit. Figure 2 displays the experimental and predicted data from the polynomial relationship for each response. This model indicates a good model and shows a satisfactory correlation between the experimental and predicted values because the clusters of experimental and predicted values for the amount of wax deposit amount are close to the diagonal line in the parity plot (Figure 2). ANOVA test was carried out to prove the significance of each variable in the model. Table 4 shows ANOVA results. The final equation in terms of coded factors for the second-order polynomial is presented by Equation (1).

$$\text{Ln (wax deposit+0.02), g} = -0.19 + 0.15\,B - 1.03\,A - (7.338E-03)\,AB + 0.033\,B^2 - 0.35\,A^2 \quad (1)$$

Table 3. Central composite design matrix for the experimental design and corresponding results

| Std | Factor * | | Wax Deposit (g) | | | |
|---|---|---|---|---|---|---|
| | A | B | Experimental | Experimental | Predicted | Predicted |
| | Uncoded (Coded) | Uncoded (Coded) | Value[a] (X),g | Value[b] (X') | Value[b] (Y') | Value [b] (Y),g |
| 1 | 1.5(−1) | 10(−1) | 1.5 | 0.42 | 0.366 | 1.33 |
| 2 | 2.5(1) | 10(−1) | 2.25 | 0.82 | 0.666 | 1.95 |
| 3 | 1.5(−1) | 20(1) | 0.2 | -1.51 | -1.694 | 0.15 |
| 4 | 2.5(1) | 20(1) | 0.3 | -1.14 | -1.394 | 0.23 |
| 5 | 1(−2) | 15(0) | 0.65 | -0.40 | -0.814 | 0.55 |
| 6 | 3(2) | 15(0) | 1.1 | 0.11 | -0.214 | 1.17 |
| 7 | 2(0) | 5(−2) | 1.5 | 0.42 | 1.546 | 1.58 |
| 8 | 2(0) | 25(2) | 0 | -3.91 | -2.574 | 0.01 |
| 9 | 2(0) | 15(0) | 0.75 | -0.26 | -0.514 | 0.81 |
| 10 | 2(0) | 15(0) | 0.75 | -0.26 | -0.514 | 0.81 |
| 11 | 2(0) | 15(0) | 0.75 | -0.26 | -0.514 | 0.81 |
| 12 | 2(0) | 15(0) | 0.75 | -0.26 | -0.514 | 0.81 |
| 13 | 2(0) | 15(0) | 0.75 | -0.26 | -0.514 | 0.81 |

A: Experimental duration, h, B: Cold Finger temperature, °C

[a]Experiment values of wax deposit

[b]Wax deposit that has been transformed according to the requirement of the statistical analysis.

*Constant variables: 5000 ppm and 0 rpm

$$X' = \text{Ln}(\text{wax deposit} + 0.02)$$

$$Y', (g) = -0.19 + 0.15B - 1.03A - (7.338E-03)BA + 0.033B^2 - 0.35A^2$$

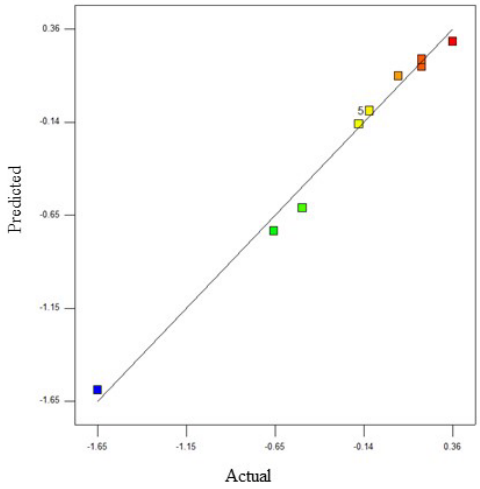



Figure 2. The comparison of predicted and experimental values for wax deposit amount using CCD

The fitness of the model is expressed by the $R^2$ value, which is 0.9886, indicating that 98.86% of the variability in the response can be explained by the model. Meanwhile, the coefficient of determination (adjusted $R^2$) was calculated and determined as 0.9805, indicating that only 1.95% of the total variation were not included in the model. This value indicates a good agreement between the observed and the predicted values of wax deposit formation. Therefore, the regression model was applied to calculate the predicted values and the usefulness of the model as shown in Table 3, where the predicted values are closely matched with the experimental values after the transformation. In other words, the model obtained is applicable to predict the optimum conditions that will minimize the expression of wax deposit.

Table 4 shows the results for ANOVA. The significant terms are corresponded to A, B and $B^2$. This result reveals that cold finger temperature (B) gave the most significant effect to the expression of wax deposit ($P < 0.0001$) compare to experimental duration (A) factor. However, this significant effect could also be easily observed from Figure 3, where the highest cold finger temperature reduced the expression of wax deposit amount, and in contrast, lower temperature enhanced the formation of wax deposit.

Table 4. Analysis of variance (ANOVA) for the response of wax deposit using CCD

| Source | Sum of Squares | DF | Mean Square | F Value | p-value Prob > F |
|---|---|---|---|---|---|
| Model | 16.19 | 5 | 3.24 | 121.77 | < 0.0001 |
| A - Experimental duration | 0.27 | 1 | 0.27 | 10.11 | 0.0155 |
| B - Cold finger temperature | 12.62 | 1 | 12.62 | 474.51 | < 0.0001 |
| AB | $2.15 \times 10^{-4}$ | 1 | $2.15 \times 10^{-4}$ | $8.10 \times 10^{-3}$ | 0.9308 |
| $A^2$ | $2.60 \times 10^{-2}$ | 1 | $2.60 \times 10^{-2}$ | 0.97 | 0.3585 |
| $B^2$ | 2.86 | 1 | 2.86 | 107.44 | < 0.0001 |
| Residual | 0.19 | 7 | $2.70 \times 10^{-2}$ | | |
| Lack of Fit | 0.19 | 3 | 0.062 | | |
| Pure Error | 0 | 4 | 0 | | |
| Cor Total | 16.38 | 12 | | | |

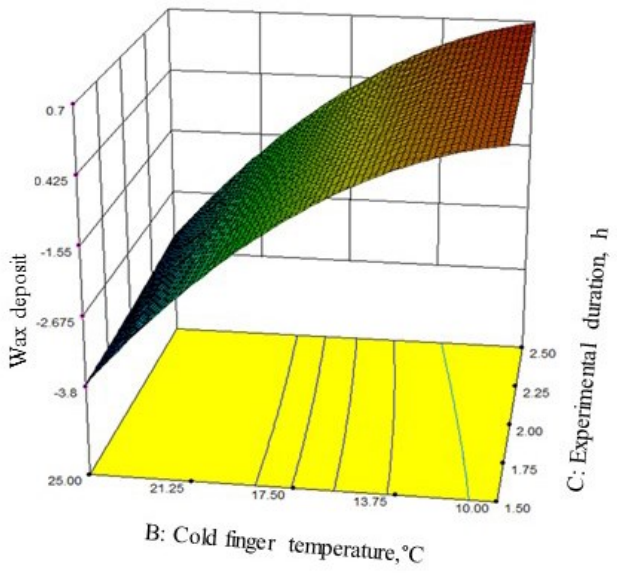



Figure 3. The comparison of predicted and experimental values of wax deposit amount using CCD

For model validation, 10 additional experiments were conducted by varying the experimental duration and cold finger temperature within the factor limit. The model validation of experimental and predicted data is shown in Table 5. The percentage between experimental and predicted values based on the model was found less than 10%. It can be seen that the validation correlation between the experimental and predicted values of wax deposit is in the form of a satisfactory correlation. For example, the actual experimental validation of 0.73 g of wax deposit was obtained at 1.5 hours and 15 °C. Meanwhile, the predicted values of wax deposit at the same condition was 0.72 g. Hence, the model for wax study can be considered to be valid.

**Optimization studies**

The optimization was performed to minimize the amount of wax deposited on the cold finger by using the selected range of variables after investigating the effect of experimental duration (A) and cold finger temperature (B), in which contour plots and response surface plot were produced according to the model (Equation (1)) as shown in Figure 3.

The response surface plot shows the optimum predicted wax amount for minimum wax formation. By applying the desirability function method in RSM, 9 solutions were obtained for the optimum covering criteria with the desirability value close to 1. In this case, the first solution was selected as a good desirability for a minimum amount of wax deposit with the desirability equal to 0.992. At this point, weight deposit is 0.0042 g at 1.5 hours experimental duration and 25 °C cold finger temperature, respectively. Table 6 shows the summary of the optimized wax deposit condition compared to the original value. It was found that after the optimization, the minimum value of 0.0042 g was achieved. It shows that 150-fold decrement of wax formation expression was achieved compared to prior the optimization.

Table 5. Model validation experiments and predicted data

| No of Experiments | Factors* A | Factors* B | Experimental Value[a] (X), g | Experimental Value[b] (X') | Predicted Value[b] (Y') | Predicted Value[b] (Y), g |
|---|---|---|---|---|---|---|
| 1 | 1.7 | 10 | 1.4 | 0.35 | 0.41 | 1.48 |
| 2 | 2 | 17 | 0.58 | -0.51 | -0.64 | 0.51 |
| 3 | 1.5 | 15 | 0.73 | -0.29 | -0.30 | 0.72* |
| 4 | 2.3 | 12 | 1.45 | 0.39 | 0.42 | 1.50 |
| 5 | 3 | 20 | 0.4 | -0.87 | -1.12 | 0.31 |
| 6 | 1.5 | 18 | 0.43 | -0.80 | -1.03 | 0.34 |
| 7 | 2.4 | 14 | 1.16 | 0.17 | 0.16 | 1.15 |
| 8 | 2.8 | 20 | 0.31 | -1.11 | -1.22 | 0.27 |
| 9 | 2 | 14 | 0.99 | 0.01 | 0.01 | 0.99 |
| 10 | 2 | 7 | 1.61 | 0.49 | 0.55 | 1.72 |

A: Experimental duration, h and B: Cold Finger Temperature, °C
[a]Experimental values of wax deposit
[b]Wax deposit that has been transformed according to the requirement of the statistical analysis
$X' = \mathrm{Ln}(\text{wax deposit} + 0.02)$
$Y', (g) = -0.19 + 0.15B - 1.03A\ (7.338E-03)BA + 0.033B^2 - 0.35A^2$
*An example of satisfactory correlation between the experimental and predicted

Table 6. Summary of the optimized wax deposit condition

| Factor | Optimum Condition | Original Condition | Experimental Optimum Value[a], G | Experimental Original Value[b], G [24] |
|---|---|---|---|---|
| A - Experimental duration (h) | 0 | 0 | 0.0042 | 0.7500 |
| B - Cold finger temperature (°C) | 25 | 15 | | |
| C - Speed of rotation (rpm) | 1.5 | 2 | | |
| D - Inhibitor concentration (ppm) | 5000 | 5000 | | |

[a]Optimum condition and optimum values obtained from RSM result
[b]Original condition and the best experimental values obtained from FFD result [24]

## Conclusion

The optimization for the condition of wax deposit formation was achieved using response surface methodology. The optimized conditions were obtained at 1.5 hours and 25 °C. The minimum value achieved after the optimization was 0.0042 g, which is 150-fold decrement of wax formation expression compared to prior the optimization.

## Acknowledgement

The authors would like to express high appreciation to Universiti Malaysia Pahang and the Ministry of Education (MOE), Malaysia, through the Research Acculturation Grant Scheme (RAGS-RDU 121414) for having this research project to be successfully conducted.

**References**


1. Adewusi, V. (1997). Prediction of wax deposition potential of hydrocarbon systems from viscosity-pressure correlations. *Fuel*, 76: 1079 – 1083.
2. Alben, K. (2002). Design, analyze, and optimize with Design-Expert. *Analytical Chemistry*, 74: 222 –223.
3. Alghanduri, L. M., Elgarni, M. M., Daridon, J.L., and Coutinho, J. A. P. (2010). Characterization of Libyan waxy crude oils. *Energy & Fuels*, 24: 3101 – 3107.
4. Azevedo, L.F.A., and Teixeira, A. M. (2003). A critical review of the modeling of wax deposition mechanisms. *Petroleum Science and Technology*, 21: 393 – 408.
5. Benallal, A., Maurel, P., Agassant, J. F., Darbouret, M., Avril, G. and Pueriere, E. (2008). Wax deposition in pipelines: Flow-loop experiments and investigations on a novel ppproach. *In Proceeding of SPE Annual Technical Conference and Exhibition*: pp. 1 – 17.
6. Huang, Z. (2011). Application of the fundamentals of heat and mass transfer to the investigation of wax depo sition in subsea pipelines.Ph.D Thesis. University of Michingan,USA.
7. Huang, Z., Lu, Y., Hoffmann, R. and Fogler, H. S. (2011). The effect of operating temperatures on wax deposition. *Energy & Fuels*, 25: 5180 – 5188.
8. Jennings, D. W., and Breitigam, J. (2010). Paraffin inhibitor formulations for different application environments: From heated injection in the desert to extreme cold arctic temperatures. *Energy & Fuels*, 24: 2337 – 2349.
9. Jennings, D. W. and Weispfennig, K. (2005). Effects of shear and temperature on wax deposition: Coldfinger investigation with a Gulf of Mexico crude oil. *Energy & Fuels*, 19:1376 – 1386.
10. Jennings, D. W., and Weispfennig, K. (2006). Effect of shear on the performance of paraffin inhibitors: Cold finger investigation with Gulf of Mexico crude oils. *Energy & Fuels*, 20: 2457 – 2464.
11. Kelechukwu, E., Said Al-Salim, H. S., and Yassin, A. A. M. (2010). Influencing factors governing paraffin wax deposition during crude production. *International Journal of the Physical Sciences*, 5: 2351 – 2362.
12. Kelland, M. A. (2014). Production Chemicals for the oil and gas industry. Second Edition. CRC Press.
13. Lashkarbolooki, M., Esmaeilzadeh, F. and Mowla, D. (2011). Mitigation of wax deposition by wax-crystal modifier for Kermanshah crude oil. *Journal of Dispersion Science and Technology*, 32: 975 –985.
14. Lashkarbolooki, M., Seyfaee, A., Esmaeilzadeh, F. and Mowla, D. (2010). Experimental investigation of wax deposition in Kermanshah crude oil through a monitored flow loop apparatus. *Energy & Fuels*, 24: 1234 – 1241.
15. Lazić, Ž. R. (2004). Design of experiments in chemical engineering: A practical guide. John Wiley & Sons.
16. Lee, H.V. and Taufiq-yap, Y. H. (2015). Optimization study of binary metal oxides catalyzed transesterification system for biodiesel production. *Process Safety and Environmental Protection*, 94: 430 – 440.
17. Mahto, V., Verma, D., Kumar, A. and Sharma, V. P. (2014). Wax deposition in flow lines under dynamic conditions. *Petroleum Science and Technology*, 32: 1996 – 2003.
18. Misra, S., Baruah, S. and Singh, K. (1995). Paraffin problems in crude oil production and transportation: A review. *SPE Production & Facilitie*s, 10: 50 – 54.
19. Kelechukwu, E. M., Said Al-Salim, H., and Saadi, A. 2013. Prediction of wax deposition problems of hydro-carbon production system. *Journal Petroleum Science and Engineering*, 108: 128 – 136.
20. Dos Santos, J. D. S. T., Fernandes, A. C. and Giulietti, M. (2004). Study of the paraffin deposit formation using the cold finger methodology for Brazilian crude oils. *Journal Petroleum Science and Engineering*, 45: 47 – 60.
21. Towler, B. F., Jaripatke, O., and Mokhatab, S. 2011. Experimental investigations of the mitigation of paraffin wax deposition in crude oil using chemical additives. *Petroleum Science and Technology*, 29: 468 – 483.
22. Valinejad, R. and Nazar, A. R. S. (2013). An experimental design approach for investigating the effects of operating factors on the wax deposition in pipelines. *Fuel*, 106: 843 – 850.
23. Wei, B. (2015). Recent advances on mitigating wax problem using polymeric wax crystal modifier. *Journal of Petroleum Exploration and Production Technology*, 5: 391 – 401.
24. Ridzuan, N., Yaacob, Z. and Adam, F. (2016). Screening of factor influencing wax deposition using full factorial experimental design. *Petroleum Science and Technology*, 34: 84 – 90.

*Malaysian Journal of Analytical Sciences, Vol 21 No 2 (2017): 460 - 469*
*DOI: https://doi.org/10.17576/mjas-2017-2102-22*

MALAYSIAN JOURNAL OF ANALYTICAL SCIENCES
*Published by The Malaysian Analytical Sciences Society*
ISSN 1394 - 2506

# ISOLATION, PURIFICATION AND IDENTIFICATION OF MICROALGAE FROM COAL-FIRED POWER PLANT ENVIRONMENT

## (Pemencilan, Penulenan dan Identifikasi Mikroalga daripada Persekitaran Loji Janakuasa Arang Batu)

Muhammad Nazry Chik[1], Liyana Yahya[1], Kamrul Fakir Kamarudin[2], Ding Gong Tao[2], Mohd Sobri Takriff[2]*

[1]*Emission and Waste Management Technology Group,*
*TNB Research Sdn Bhd, No 1, Lorong Air Hitam, Kawasan Institusi Penyelidikan, 43000 Kajang, Selangor, Malaysia*
[2]*Department of Chemical and Process Engineering, Faculty of Engineering and Built Environment,*
*Universiti Kebangsaan Malaysia, 43600 UKM Bangi, Selangor, Malaysia*

**Corresponding author: sobritakriff@ukm.edu.my*

Received: 21 October 2015; Accepted: 14 June 2016

**Abstract**

Carbon capture and storage (CCS) through biological approach has attracted much attention as global warming and climate change issue becomes a worldwide agenda. Energy production industry from coal in Malaysia produced 50.661 million metric tons of carbon dioxide in 2012, and the trend showed it will keep increasing year by year. CCS through biological approach can be done by microalgae which are versatile microorganism which perform photosynthesis process that can store $CO_2$ in the biomass form. In this study, microalgae strains were isolated from the native environment nearby a coal-fired power plant, where samples were collected in different canal in which pre-treated flue gases are discharged. The microalgae strains were identified by both morphological and molecular approaches. Result from 18s rRNA gene sequencing showed that the isolated strains is *Chlorella* sp. with similarity 99% with *Chlorella* sp. SAG 211-18. The identified strains of microalgae then cultivated with three concentration of $CO_2$ (ambient air, 1% and 5%) and the growth rate showed 0.4017 $day^{-1}$, 0.5752 $day^{-1}$ and 0.4427 $day^{-1}$ respectively. Different concentration of $CO_2$ (ambient air, 1% and 5%) showed that the isolated strains yielded 1.005$gL^{-1}$, 1.101$gL^{-1}$ and 1.035$gL^{-1}$ respectively. This study also showed that with different concentration of $CO_2$, the sequestration rate is ranging from 1% to 4.3%.

**Keywords**: microalgae, isolation, purification, DNA sequencing

**Abstrak**

Pemerangkapan dan penyimpanan karbon (CCS) melalui pendekatan biologi telah menarik minat pengkaji disebabkan masalah pemanasan dan perubahan iklim global. Pada tahun 2012 sahaja, Malaysia telah menghasilkan 50.661 juta ton metrik karbon dioksida hasil daripada penghasilan tenaga yang bersumberkan arang batu, dan tahun demi tahun penghasilan karbon dioksida dijangkakan akan terus meningkat. Pemerangkapan dan penyimpanan karbon melalui pendekatan biologi boleh dilakukan oleh mikroalga yang merupakan mikroorganisma unggul di mana ianya berupaya menjalankan proses fotosintesis dalam menukarkan karbon dioksida ke dalam bentuk biojisim. Dalam kajian ini, mikroalga dipencilkan daripada habitat asal yang merupakan terusan bagi air penyejuk untuk stesen janakuasa arang batu. Mikroalga yang diperoleh, dikenalpasti menggunakan kaedah pengecaman secara morfologi dan molekul. Hasil keputusan pengenal pastian molekul menggunakan kaedah penjujukan genom 18s rRNA mendapati, mikroalga yang berjaya dipencilkan adalah *Chlorella* sp. yang mempunyai persamaan sehingga 99% dengan *Chlorella* sp. SAG 211-18. Mikroalga yang telah menjalani proses identifikasi kemudiannya dikultur menggunakan 3 kepekatan karbon dioksida yang berbeza ($CO_2$ pada udara persekitaran, $CO_2$ 1% dan $CO_2$ 5%) dan hasil menunjukkan kadar pertumbuhan masing-masing adalah 0.4017 $hari^{-1}$, 0.5752 $hari^{-1}$, dan 0.4427 $hari^{-1}$. Pada kepekatan $CO_2$ yang berbeza ($CO_2$ pada udara persekitaran, $CO_2$ 1% dan $CO_2$ 5%), hasil biojisim yang terkumpul daripada pengkulturan mikroalga masing-masing

adalah 1.005gL$^{-1}$, 1.101gL$^{-1}$ dan 1.035gL$^{-1}$. Kajian juga menunjukkan pada kepekatan $CO_2$ yang berbeza, kadar pemerangkapan karbon dioksida adalah pada kadar 1% sehingga 4.3%.

**Kata kunci:** mikroalga, pemencilan, penulenan, penjujukan DNA

## Introduction

Studies on microalgae mostly ranging around the ability of biomass accumulation for food additive, colouring and high value product such as anti-oxidant. This research field has been widely explore in the previous decade and the exploration on other branches of microalgae utilization has taken place recently due to environmental concern especially regarding to global warming due to the rising of carbon dioxide produce by human activities [1 – 4]. Microalgae are a robust microorganism which can survive and thrive in different mode; photo-autotrophic, mixotrophic, heterotrophic and some mixture of complex metabolism to survive in harsh culture condition [5 – 8]. The ability of microalgae to conduct photo-autotrophic showed that microalgae has the potential to be applied in the process of carbon capture and storage (CCS) [9].

As the world progress and develop in becoming more advanced society, the energy demands around the world keep increasing year by year. Energy is a vital factor for progress to the advanced society since large scale activities such as urbanization, industrial activities; plantation, mining and livestock farming are becoming into commercial scale and subsequently demand higher energy input. Most of the world energy demand is supplied by fossil fuels burning power plants, which are using different sources of fossil fuel such as coal, natural gases, and petroleum based product [10, 11]. According to a report from Suruhanjaya Tenaga Malaysia, there are 4 main sources of fossil fuels are used as primary energy supply in Malaysia. The sources are crude oil, petroleum product, natural gas and, coal and coke [12]. All this generates $CO_2$, carbon monoxide and methane which is the main contributor to the global warming effect since these gases trap the heat and has increased the world temperature in the range of 1° to 2° C over the past decade. The only renewable source of energy used by Malaysia from 1978 until 2010 was hydropower energy. However since the year 2011, biodiesel, biomass, biogas and solar has contribute small portion of energy supply which around 115, 183, 4, 11 ktoe respectively for year 2012 [12].

Before the pre-industrial era, the $CO_2$ concentration in the air was recorded below 300 ppm. Since then, the concentration of $CO_2$ has steeply increased and has causing the rise of global temperature. According to the report from Mauna Loa Observatory (NOAA-ESRL), the atmospheric $CO_2$ concentration on June 2015 was recorded around 402.8 ppm [13]. Compare to the previous years of June 2014 and 2013, the concentration of $CO_2$ was recorded at 401.15 ppm 398.58 ppm. The effect of higher $CO_2$ concentration has been affecting the human life since breaking hot temperature during the summer season has been recorded around the world [14]. The effect of global warming has also affecting Malaysia; where for the past two years Malaysia had experienced hot temperature well above the normal average temperature.

Tenaga Nasional Berhad (TNB) is the largest utilities company in Malaysia and supplies most of the electricity to Malaysian Peninsular and State of Sabah through the Malaysian National Grid. The main energy source for electricity power generation for TNB is coal and coke which is relatively cost effective, coupling with state of the art technology in reducing $CO_2$ emission with collaboration with Alstom S. A. from France [15]. However, the emission of $CO_2$ is still an '*Achilles Heels*' for this system and thus, new approach has been embarked to counter and reduce more on $CO_2$ emission. The available solution is though CCS using microalgae [16, 17]. Thus, this paper reports on the works and progress of isolation of microalgae in the native environment near to the coal-fired power plant [18]. This works covers the isolation, morphological and molecular identification of isolated microalgae.

## Materials and Methods

### Isolation of microalgae

Samples were collected from the canal of cooling water from Stesen Janakuasa Sultan Azlan Shah, Manjung Perak, west coast of Malaysian Peninsular, 4° 9' 31.158" S latitude and 100° 38' 30.3396" E longitude. The power plant uses coal as the fuel and is among the major power generation plant in Malaysia, having installed capacity of 3 units of 700 MW. The canals form a discharge point of sea water used in the steam cooling process in the upstream. Besides steam cooling, the sea water also was used as jet water spray as to discard debris, being injected with hypochlorite as

disinfectant and also sprayed as part flue gas desulphurisation process before finally aerated (air bubbled) in the canals before being discharged to the open sea. Thus, any microalgae species that are available from the sea water intake shall experience varying degrees of hydrodynamic stresses, disinfection and temperature difference based on the process described above, and thus any ones which found dominant in the canals shall be the ones who are robust enough to survive further in bioreactors performing carbon biofixation exposed to actual power plant's flue gas. Collections of samples were conducted during the noon time where the suspected source areas of microalgae were exposed to sunlight at the maximum light density. The light intensity during the afternoon period can reach as high as 60,000 Lux during the sunny day. Microalgae which survived in photo-autotrophic mode tend to float on the surface area to capture energy from the sun for photosynthesis process.

The samples from the source were added with F/2 Medium, TNBR medium and Bold Basal's Medium (BBM) respectively with ratio of 1:1 (volume/volume) to promote growth of microalgae available in the targeted samples. The samples were maintained in 50 mL centrifuge tube, at room temperature at 28 °C and kept with continuous light exposure at 12,000 lux by 50 W fluorescent daylight type lamps. The samples were monitored daily to determined suitable medium for isolation as well as the growth curves of microalgae.

The samples were maintained and observed under microscope (Cole-Parmer, USA) for isolation and morphological screening purpose. Microscope used is equipped with light chamber, measuring grid embedded with the software provided by Motic Image Plus 2.0 and image capturing camera. Observation of microalgae growth in the liquid medium was continued with plating method by using the respective medium with 1.25% agar plate. In the parallel of liquid medium and 1.25% agar cultivation, the growth of microalgae were measured by biomass accumulation, cell density and amounts of colonies on the plate respectively.

**Cultivation**

Samples of microalgae which has been promoted by F/2 medium, TNBR medium and BBM medium were observed and screened morphologically and has been done by comparing to the online catalogue provided by University of Texas, The Culture Collection of Algae at Goettingen University (international acronym SAG). Morphological identification was done by determining the characteristic of isolated microalgae; size, availability of membrane wall and flagella, and the shape of chloroplast.

After growth of microalgae were observed, cultures of microalgae were transferred into 250 mL Duran Schott Bottle with F/2 medium, TNBR medium and BBM medium respectively with 10 percent of inoculums from the source of microalgae. To promote more growth, cultured microalgae were sparged with air to avoid settling as well as providing the $CO_2$ from ambient air. Cultivation of microalgae was then continued until single/pure strain achieved in the culture system. Single/Pure strains of microalgae was achieved by continuous plating using F/2, TNBR, and BBM Medium agar. The pure strains were then re-cultivated into F/2 medium and TNBR medium liquid solution for inoculum preparation as well as for the molecular identification purpose. Microalgae biomass were collected daily to plot the growth curve of microalgae and calculate the specific growth rate ($\mu_{max}$). The $\mu_{max}$ value was determined by using the MathLab 9.0 version software with application of Logistic Modelling. Generally the growth curve of microalgae is in the sigmoid shape and previous studies has successfully fit the original data with the Logistic Model [19, 20, 21]. Thus, in this study, Logistic Model was used to fit the data and determined the value of $\mu_{max}$. The $\mu_{max}$ values were calculated using Equation 1 below:

$$X = \frac{XoXmax \cdot e^{\mu_{max}t}}{Xmax - Xo + Xoe^{\mu_{max}t}} \quad (1)$$

where X is the value of predicted biomass achieved by the Logistic Model, $X_0$ is the initial biomass achieved during the experimental set up, and $X_{max}$ is the maximum biomass achieved while t is the time take during the experiment.

**Molecular identification**

Single/Pure strain of microalgae achieved in isolation process was used in molecular identification. Wet biomass of microalgae were collected and genomic DNA was extracted from it by using liquid nitrogen. Liquid nitrogen is a good agent for extraction due to the low temperature properties which it has boiling point at -196 °C and this will freeze and

crystalize the microalgae cells in the biomass instantly. Wet biomasses from cultivated microalgae were soaked into liquid nitrogen and homogenized with mortar and pestle for initial steps in breaking the cell wall of microalgae in order to extract the genomic DNA (gDNA). Next steps in achieving gDNA, extraction kit from Promega containing nuclei lysis solution, protein precipitation solution, isopropanol, ethanol and RNase solution was used according to manual from the manufacturer. Biomass achieved was then extracted using plant extraction kit by Promega Wizard Genomic DNA Purification Kit [22]. 18s rRNA genes Polymeric Chain Reaction (PCR) amplified using forward (50 TACTGTGAAACTGCGAATGGCTC 30) and reverse (50 TGATCCTTCCGCAGGTTCACCTA 30) primer was used in this process [23, 24]. The primer was design by FirstBase Sdn Bhd. Purified and single cultured microalgae from the coal-fired power plant were further identified using molecular identification.

PCR products were sequenced by Life Technologies (China). The sequenced products were compared with NCBI data bank using the BLAST Program. (NCBI BLAST, USA). Top ten similar results were achieved and compared for the similarity in the percentage value.

**Carbon dioxide sequestration**

Single/Pure strain of microalgae were then cultivated in 2L Schott Duran Bottle with 3 outlets on the top of the cap; 1) used for $CO_2$ sparging inlet point, 2) used for $CO_2$ sampling outlet, 3) used for secondary outlet as shown in Figure 1. Different $CO_2$ concentration at ambient air condition, 1% $CO_2$ and 5% $CO_2$ were tested to determine the preliminary result for $CO_2$ sequestration rate. $CO_2$ analyzer (Quantek, Model902D) was used in this run where infra-red sensor read the $CO_2$ concentration continuously. Continuous data were collected using data logger.

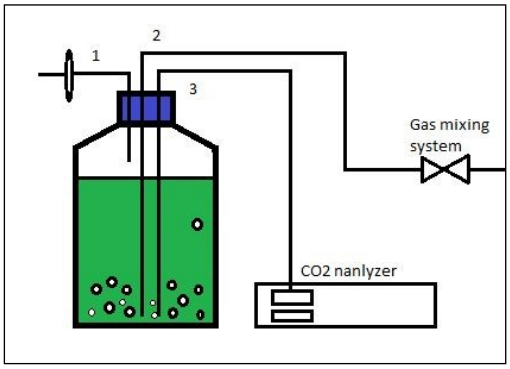



Figure 1. Schematic of cultivation in 2L Schott Duran for $CO_2$ sequestration experiments; 1) air outlet, 2) gas mixing system inlet and 3) $CO_2$ analyzer outlet

## Results and Discussion

**Isolation of microalgae**

The samples that were collected have a pH ranging around 7.0 to 8.5. This alkalinity can be explained due to the sample of the water; usage water containing isolated microalgae source was used as a cooling water for the coal-fired power plant which ash from the burning coal contribute to this phenomena [25, 26].

Isolation process of microalgae with both liquid medium and 1.25% agar plate showed that microalgae only survived in the F/2 Medium and TNBR medium. Isolation using BBM in liquid medium and agar plate showed lower growth in liquid medium cultivation, while in agar plate there was no colony detected. This can be explained due to higher salinity of F/2 medium and TNBR medium which both used artificial seawater as a component of the medium, while BBM has much lower salinity [27]. Microalgae which has been collected from the source has been exposed and acclimatized to the higher salinity environment for long period of time. From this finding, it can be determined that F/2 medium and TNBR medium is the most suitable medium compare to BBM. Thus, only F/2 medium and TNBR medium was chosen for the next experiment on purification and identification process. Besides sea water as the main

factor for higher salinity, higher alkalinity of the water at the source of isolation place was effected by the ash produced by the coal-fired power plant. Result also showed that at pH more than 7, isolated microalgae start to pick up the higher phase of growth.

**Cultivation and morphological identification of microalgae**

Isolated and purified microalgae were cultivated in F/2 medium and TNBR medium. Growth profiles of the microalgae were determined by biomass accumulation in both F/2 and TNBR medium. Figure 2 showed the growth curve of isolated microalgae in TNBR medium (ambient air, 1% and 5% $CO_2$) and Figure 3 showed the growth curve of isolated in F/2 medium (ambient air and 5% $CO_2$). From the growth profile, the specific maximum growth rate ($\mu_{max}$) of each cultivation was determined by using MathLab 9.0 version software. Logistic model was used for the curve fitting in for the microalgae growth curve. Population and productivity of microalgae has been widely using Logistic Model for curve fitting since the Logistic equation often represent growth data better than the exponential one [21]. The value of $\mu_{max}$ was calculated according to the Equation 1.

Result of $\mu_{max}$ showed that TNBR medium promote better growth by producing higher $\mu_{max}$ value compare to F/2 medium. By using TNBR medium the value of $\mu_{max}$ achieved were 0.4046 $day^{-1}$, 0.4288 $day^{-1}$ and 0.4908 $day^{-1}$ for ambient air, 1 % $CO_2$ and 5% $CO_2$ respectively. Result of $\mu_{max}$ from F/2 medium achieved were 0.2784 $day^{-1}$ and 0.3937$day^{-1}$ for ambient air and 5% $CO_2$ respectively. Higher value of $\mu_{max}$ achieved by TNBR medium cultivated microalgae was due to high nutrients content compare to the F/2 medium. TNBR medium used in this experiment is an optimized medium from F/2 medium.

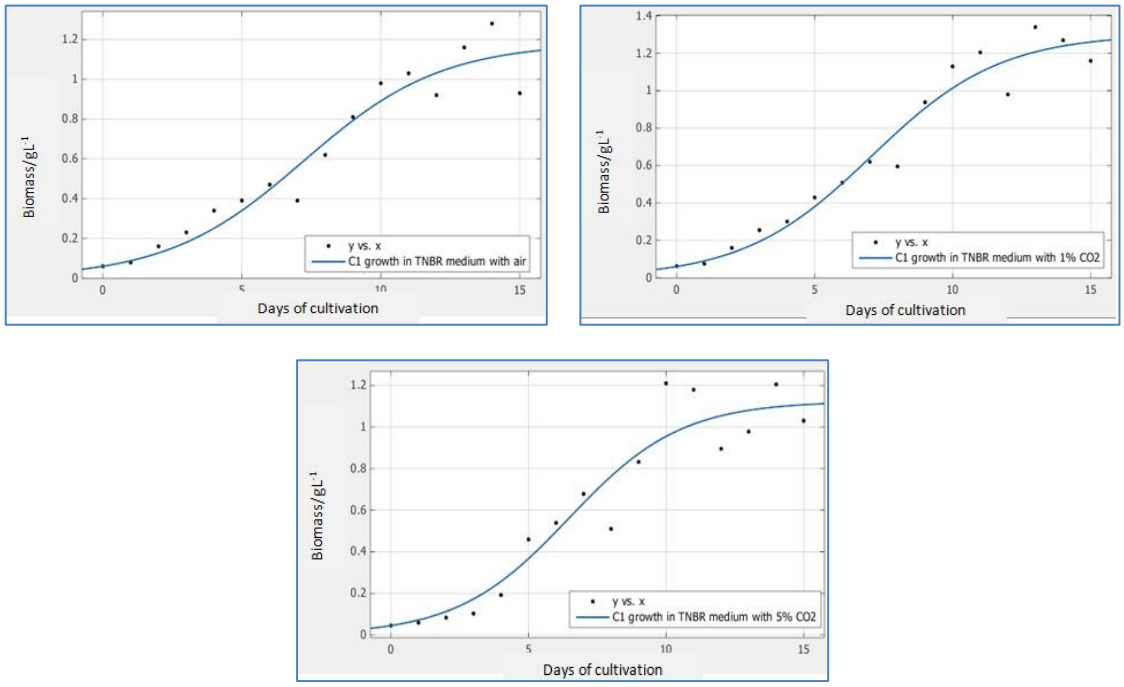



Figure 2. Growth curve of isolated *Chlorella* sp. with TNBR medium at ambient air, 1%and 5% $CO_2$

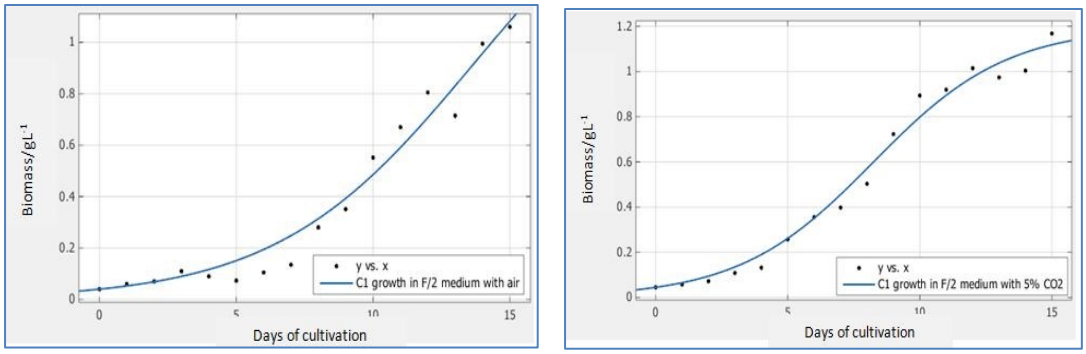



Figure 3. Growth curve of Chlorella sp. with F/2 medium at ambient air, and 5% $CO_2$

Morphological identification was conducted by characterization of microalgae. Under microscopic observation, the size of the purified microalgae is ranging around 4.24 ~10 µm with the area around 56.48 $\mu m^2$. The visible characteristic that can be observed was round shape with transparent outer membrane. All the purified microalgae showed round or ellipsoidal shape with a thin layer of membrane without any extension of flagella. The purified microalgae also have gridle shape of chloroplast. The chloroplast occupies most of periphery except for the cell ends. It also has the tendency to clump together into big colonies with a slow movement [28]. By assessment of all the morphological characteristic of the isolated microalgae, the suspected species was *Chlorella* sp. Figure 4 shows the morphological view under 400x magnifications with comparison from *Chlorella* sp. from UTEX (1000x magnification). Microalgae *Chlorella* species is blue-green algae which is belongs to phylum chlorophyta division. Most of Chlorella species survived and cultivated in freshwater conditions. However, several reports and studies on isolation showed the versatility and the availability of *Chlorella* species to adapt and survive in marine environment [29, 30]. Other result from NCBI also showed that several microalgae which were isolated from South China Sea were confirmed to be *Chlorella* species. Thus, it make the morphological identification of this experiment valid to be *Chlorella* sp. Further identification was confirmed with molecular identification with genes sequencing.

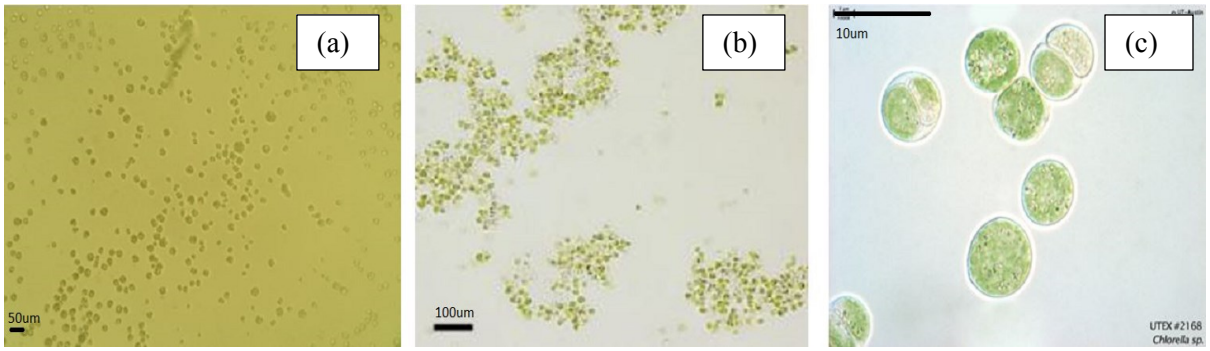



Figure 4. Morphological observation of (1)isolated microalgae (40x magnification) with comparison from (2) Imase et al. and (3) *Chlorella* sp. of UTEX (1000x magnification) [31]

**Molecular identification of microalgae**

Extraction and Purification of gDNA was conducted with a procedure suggested by the manual form the manufacturer (Promega) as mention in methodology section. Extracted gDNA then amplified using PCR with 18s rRNA primer before it is sequenced. Figure 5 showed that PCR product were run into gel for confirmations before the PCR product undergoes sequencing process.

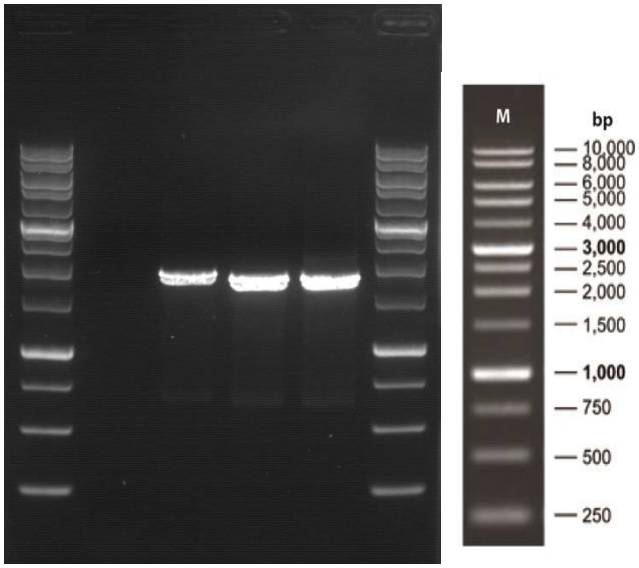



Figure 5. Result of PCR gel run on the ladder. Negative (-) was the PCR non-template control (water only), and positive (+) is positive control using DNA extracted from human blood sample as a template

PCR product which has been successfully sequenced has the size of 1792bp. Full sequenced by 18s rRNA gave full sequenced of the isolated microalgae. Full sequenced obtained from sequencing process was blast into the NCBI BLAST software to compare the obtained result with the gene bank for the identification purpose. Top ten hits blast result were observed and showed in the Figure 6 in the form of phylogenetic tree where most of the result showed the similarity to the isolated microalgae from the coal-fired power plant. Result from the list of showed seven out of ten confirm up to 99% that an isolated, purified and sequenced microalgae is *Chlorella* sp. Thus, from molecular result plus with similar characteristic by morphological identification, it was confirm that isolated microalgae were *Chlorella* sp.

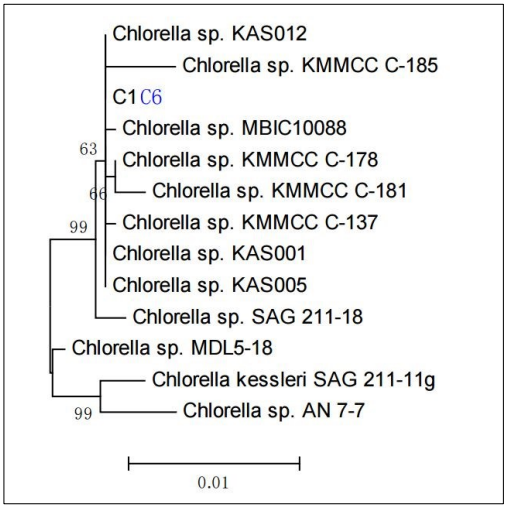



Figure 6. Top ten of phylogenetic tree of isolated microalgae; *Chlorella* sp. from NCBI genes bank database

Among the similar result from the phylogenetic tree, *Chlorella* sp. SAG 211-18 showed similarity almost to 99%. According to the data base from the Experimental Phycology and Culture Collection of Algae at the University of Goettingen (EPSAG), this microalgae which was formally called as *Chlorella sorokiniana* was isolated from Sweden. The source of the microalgae was from freshwater habitat which is surrounded by the Baltic Sea. Similar to the isolated microalgae in this study, the species was exposed to harsh environment surrounding of coal-fired power plant and closed proximity to the marine environment.

**$CO_2$ sequestration**

Isolated native microalgae were tested for its capability in performing carbon capture and storage (CCS) by sequestration of $CO_2$. Result from the $\mu_{max}$ value, showed that TNBR medium gave better result in the growth profile of microalgae. Thus in the $CO_2$ sequestration test, TNBR medium was used as the main medium for microalgae cultivation. $CO_2$ was supplied by mixing the 95% purity of $CO_2$ with compress air. At 1% and 5 % concentration, $CO_2$ were fixed for the run and the percentage was set using volume/volume ratio (v/v).Results of $CO_2$ sequestration by isolated *Chlorella* sp. are shown in Figure 7a and 7b. Result from 1% and 5% of $CO_2$ input showed that isolated *Chlorella* sp. manage to sequester $CO_2$ up to 4.3% and 4.5% respectively. Comparison with previous result showed that marine *Chlorella* sp. showed lower $CO_2$ sequestration uptake compare to the *Chlorella* sp. which has been reported previously which is ranging from the 15% to 30% ability to absorb the CO2 into the biomass form [18, 32]. Higher uptake $CO_2$ can be achieved in optimization of higher $CO_2$ input and aeration rate.

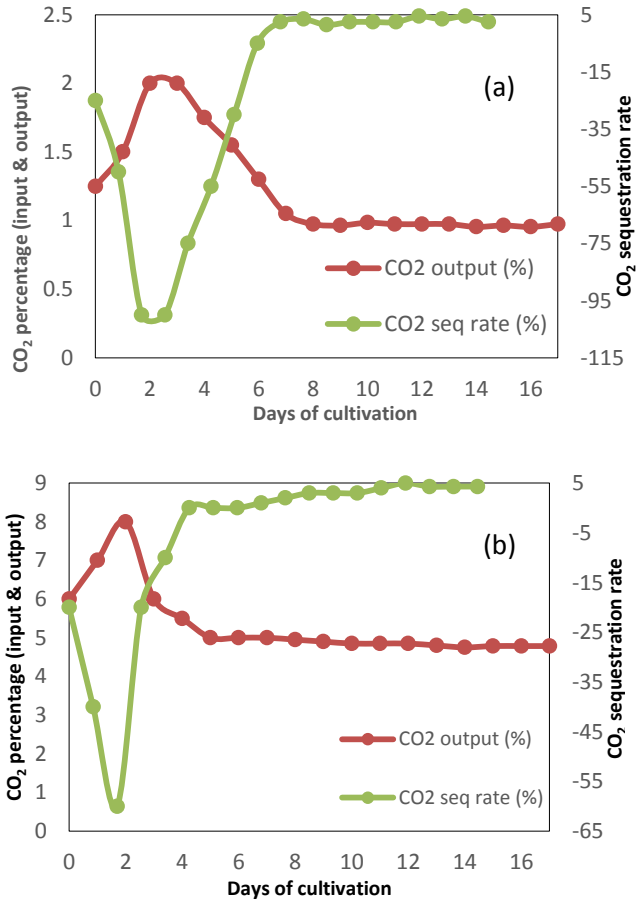



Figure 7. Result of *Chlorella* sp. in performing $CO_2$ sequestration at a) 1% $CO_2$ concentration and b) 5% $CO_2$ concentrations, repectively

However, higher accumulation of $CO_2$ in the first phase of algae culturing has produce a spike in the beginning of 5 to 7 days of cultivation periods. These phenomena can be explained by the lag phase of microalgae which has lower growth at the initial stage. Higher accumulation at the initial stage can be reduced with better inoculation process which is inoculums at the exponential phase are used for every single run. Acclimatization of microalgae to higher $CO_2$ concentration will also contribute to higher sequestration rate and reduce the accumulation of $CO_2$ in the initial phase.

The spike reduction with time of cultivation has shown that microalgae has the potential that can be tapped to produced biomass even with higher $CO_2$ concentration compare to the ambient air and this biomass later can be utilized in other product that can contribute to more capital as the world moving forward for the generating waste from the wealth. Thus, the isolated *Chlorella* sp. showed significant result in CCS by converting the $CO_2$ supplied into the biomass form.

## Conclusion

Chlorella sp. has been isolated from the native environment of Stesen Janakuasa Sultan Azlan Shah. Through morphological and molecular identification it has been confirmed that isolated strain is Chlorella sp. which has similar sequenced to *Chlorella sorokinia* from SAG 211-18. Isolated *Chlorella* sp. also showed that for higher growth it more favor the TNBR medium by achieving higher μmax value compare to the F/2 medium. At higher $CO_2$ percentage, isolated Chlorella sp. showed that it has potential in reducing the $CO_2$ while still survive and accumulate the biomass. Therefore, isolated Chlorella sp. can be used and explored more on its $CO_2$ tolerance at higher $CO_2$ concentration and can be utilized to biofixation of $CO_2$ from coal-fired power plant, which contributes to a reduction in global warming.

## Acknowledgement

The authors would like to acknowledge and thank TNB Research Technical Board Committee for approving a seed fund no. TNBR/SF0157/2014 and UKM in supporting the research financially and educationally between 2014 and 2015. Also appreciating the Management of TNB Janamanjung Sdn. Bhd. for their co-operation and support.

## References

1. Certik, M. and Shimizu S. (1999). Biosynthesis and regulation of microbial polyunsaturated fatty acid production. *Journal of Bioscience and Bioengineering*, 87(1): 1 - 14.
2. Hama, S. and Kondo, A. (2012). Enzymatic biodiesel production: An overview of potential feedstocks and process development. *Bioresource Technology*, 135: 386 - 395.
3. Fujii, K. (2012). Process integration of supercritical carbon dioxide extraction and acid treatment for astaxanthin extraction from a vegetative microalga. *Food Bioproducts Processing*, 90(4): 762 - 766.
4. Kao, C.Y., Chiu, S. Y., Huang, T. T., Dai, L., Wang, G. H, Tseng, C. P., Chen, C. H. and Lin, C. S. (2012). A mutant strain of microalga Chlorella sp. for the carbon dioxide capture from biogas. *Biomass and Bioenergy*, 36: 132 - 140.
5. Liang, Y., Sarkany, N. and Cui, Y. (2009). Biomass and lipid productivities of Chlorella vulgaris under autotrophic, heterotrophic and mixotrophic growth conditions. *Biotechnology Letters,* 31(7): 1043 -1049.
6. Perez-Garcia O, Escalante F. M. E., De-Bashan L. E. and Bashan Y. (2011). Heterotrophic cultures of microalgae: Metabolism and potential products. *Water Research,* 45: 11 - 36.
7. EL-Sheekh, M. M., Bedaiwy, M. Y., Osman M. E. and Ismail, M. M. (2012). Mixotrophic and heterotrophic growth of some microalgae using extract of fungal-treated wheat bran. *International Journal of Recycling Organic Waste in Agriculture*, 1(1): 1 - 9.
8. Wensel, P., Helms, G., Hiscox, B., Bavis, W. C., Kirchoff, H., Bule, M., Yu, L. and Chen S. (2014). Isolation, characterization, and validation of oleaginous, multi-trophic, and haloalkaline-tolerant microalgae for two-stage cultivation. *Algal Research*, 4: 2 - 11.
9. Pires, J. C. M., Alvim-Ferraz, M. C. M., Martins, F. G. and Simões M. (2012). Carbon dioxide capture from flue gases using microalgae: Engineering aspects and biorefinery concept. *Renewable and Sustainable Energy Reviews*, 16(5): 3043 - 3053.

10. Radmann, E. M., Camerini, F. V., Santos, T. D. and Costa, J. A. V. (2011). Isolation and application of $SO_X$ and $NO_X$ resistant microalgae in biofixation of $CO_2$ from thermoelectricity plants. *Energy Conversion Management*, 52(10): 3132 - 3136.
11. de Morais M. G. and Costa J. A. V. (2007). Isolation and selection of microalgae from coal fired thermoelectric power plant for biofixation of carbon dioxide. *Energy Conversion Management*, 48(7): 2169 - 2173.
12. Malaysia Energy Information Hub (2013). Primary Energy Supply (Ktoe). Putrajaya, Malaysia.
13. $CO_2$now.org. Earth's $CO_2$ home page. Access from http://co2now.org/.
14. Tans P., Keeling R. (2015). Global Greenhouse Gas Reference Network. Mauna Loa http://www.esrl.noaa.gov/gmd/ccgg/trends/. Accessed online [July 13, 2015].
15. Alstom S. A. (2013). Case Study: Steam Product Solutions. Manjung Unit 4 - Malaysia. Ultra-Supercritical Coal-Fired Power Plant. Baden, Switzerland.
16. Jansson, C. and Northen, T. (2010). Calcifying cyanobacteria — the potential of biomineralization for carbon capture and storage. *Current Opinion Biotechnology*, 21(3): 365 - 371.
17. Skjånes, K., Lindblad, P. and Muller J. (2007). Bio$CO_2$ - a multidisciplinary, biological approach using solar energy to capture $CO_2$ while producing $H_2$ and high value products. *Biomolecular Engineering*, 24(4): 405 - 413.
18. Ramanan, R., Kannan, K., Deshkar, A., Yadav, R. and Chakrabarti T. (2010). Enhanced algal $CO_{(2)}$ sequestration through calcite deposition by Chlorella sp. and Spirulina platensis in a mini-raceway pond. *Bioresource Technology*, 101(8): 2616 - 2622.
19. Zhao, L., Chen, Y. and Schaffner, D. W. (2001). Comparison of logistic regression and linear regression in modeling percentage data. *Applied and Environmental Microbiology*, 67(5): 2129 - 2135.
20. Kargi, F. (2009). Re-interpretation of the logistic equation for batch microbial growth in relation to Monod kinetics. *Letters in Applied Microbiology*, 48(4): 398 - 401.
21. Xu, Y. and Boeing, W. J. (2014). Modeling maximum lipid productivity of microalgae: Review and next step. *Renewable and Sustainable Energy Reviews*, 32: 29 - 39.
22. Promega (2010). Wizard Genomic DNA Purification Kit Quick Protocol, FB022. 2010: 1123 - 1126.
23. Simon, N., Campbell, L., Ornolfsdottir, E., Groben, R., Guillou, L., Lange, M. and Medlin, L. K. (2000). Oligonucleotide probes for the identification of three algal groups by dot blot and fluorescent whole-cell hybridization. *Journal of Eukaryotic Microbiology*, 47(1):76 - 84.
24. Krienitz, L., Ustinova, I., Friedl, T. and Huss V. A. R. (2001). Traditional generic concepts versus 18S rRNA gene phylogeny in the green algal family Selenastraceae (*Chlorophyceae, Chlorophyta*). *Journal of Phycology*, 37(5): 852 - 865.
25. Heischkamp, E., Varlik, M., Korkmaz, Ö., Oeljeklaus, G. and Görner K. (2011). Analysis of operating conditions of a flue gas scrubbing process for $CO_2$ separation in a coal-fired power plant. *Energy Procedia*, 4:1377 - 1384.
26. Ma, S., Chen, G., Guo, M., Zhao, L., Han, T., Zhu, S. (2014). Path analysis on $CO_2$ resource utilization based on carbon capture using ammonia method in coal-fired power Plants. *Renewable and Sustainable Energy Reviews*, 37: 687 - 697.
27. Shen, Q. H., Gong, Y. P., Fang, W. Z., Bi, Z. C., Cheng, L. H., Xu, X. H. and Chen, H. L. (2015). Saline wastewater treatment by *Chlorella vulgaris* with simultaneous algal lipid accumulation triggered by nitrate deficiency. *Bioresource Technology*, 193: 68 - 75.
28. Gerken, H. G., Donohoe, B. Knoshaug, E. P. (2013). Enzymatic cell wall degradation of *Chlorella vulgaris* and other microalgae for biofuels production. *Planta*, 237(1): 239 - 253.
29. Nurachman, Z., Hartini, H., Rahmaniyah, W. R., Kurnia, D., Hidayat, R., Prijamboedi, B., Suendo, V., Ratnaningsih, E., Panggabean, L. M. G. and Nurbaiti, S. (2015). Tropical marine *Chlorella* sp. PP1 as a source of photosynthetic pigments for dye-sensitized solar cells. *Algal Research*, 10: 25 - 32.
30. Mathimani, T., Uma, L. and Prabaharan D. (2015). Homogeneous acid catalysed transesterification of marine microalga *Chlorella* sp. BDUG 91771 lipid – An efficient biodiesel yield and its characterization. *Renewable Energy*, 81: 523 - 533.
31. Imase, M., Watanabe, K., Aoyagi, H. and Tanaka, H. (2008). Construction of an artificial symbiotic community using a Chlorella-symbiont association as a model. *FEMS Microbiology Ecology,* 63(3): 273 - 282.
32. Borkenstein, C. G., Knoblechner, J., Frühwirth, H. and Schagerl M. (2011). Cultivation of Chlorella emersonii with flue gas derived from a cement plant. *Journal of Applied Phycology*, 23(1): 131 - 135.

*Malaysian Journal of Analytical Sciences, Vol 21 No 2 (2017): 470 - 483*
*DOI: https://doi.org/10.17576/mjas-2017-2102-23*

MALAYSIAN JOURNAL OF ANALYTICAL SCIENCES
*Published by The Malaysian Analytical Sciences Society*
ISSN 1394 - 2506

# EFFECT OF MASS LOADING AND MICROWAVE ABSORBER APPLICATION METHOD ON THE PRODUCT FROM MICROWAVE ASSISTED PYROLYSIS OF PALM OIL MILL EFFLUENT

## (Kesan Beban Jisim dan Aplikasi Kaedah Penyerap Gelombang Mikro Kepada Produk Terhasil daripada Sisa Buangan Kilang Kelapa Sawit Melalui Proses Pirolisis Bantuan Gelombang Mikro)

Zakiuddin Januri[1], Siti Shawalliah Idris[1, 2]*, Hafifah Amirah Akhawan[1], Norazah Abd. Rahman[1, 2, 3], Sharmeela Matali[1, 2], Shareena Fairuz Abd Manaf[1, 2]

[1]*Faculty of Chemical Engineering*
[2]*CoRe of Green Technology & Sustainable Development*
[3]*CoRe of Frontier Materials & Industry Application*
*Universiti Teknologi MARA, 40450 Shah Alam, Selangor Darul Ehsan, Malaysia*

**Corresponding author: shawal075@salam.uitm.edu.my*

Received: 21 October 2015; Accepted: 14 June 2016

**Abstract**

Approximately, about 50 million tons of Palm Oil Mill Effluent (POME) is produced every year, however, discharge of POME to open water source will cause negative impact to environment. High production of POME makes it impossible to dispose at the disposal company, therefore, *in-situ* treatment has been developed. Current disposal method implemented by palm oil industries is through biodegradable pond. This method is applied due to high water content in POME about 90% of water. Microwave assisted pyrolysis would be an alternative method to deal with the POME since not only can disposed but also can convert to valuable material such as solid char and pyrolytic oil. In this paper, effect of mass loading of POME at a range of 100 to 500 grams with additional activated carbon (AC) was studied. Microwave power level, radiation time and mixing ratio of AC were set constant at 1000 W, 30 minutes and 5%, respectively. Product yields of solid and liquid were analyzed for the best process performance. Solid char obtained has a potential to be utilized as solid fuel since its energy content was >20 MJ/kg and has high carbon content at >80%. Meanwhile, about 20% of chemical content in the pyrolytic oil has the carbon number in the range of $C_1$ to $C_{10}$.

**Keywords**: mass loading, microwave absorber, microwave-assisted pyrolysis, palm oil mill effluent

**Abstrak**

Dianggarkan lebih kurang 50 juta ton Sisa Buangan Kilang Kelapa Sawit (POME) dihasilkan setiap tahun. Pembuangan POME ke sumber air semulajadi seperti sungai akan menyebabkan impak negatif kepada alam sekitar. Penghasilan POME yang tinggi menyebabkan ianya mustahil untuk dilupuskan oleh syarikat pelupusan, oleh yang demikian, rawatan *in-situ* dibangunkan. Cara pelupusan terkini oleh industri kelapa sawit adalah melalui kaedah kolam bio-degradasi. Kaedah ini diaplikasikan berikutan kandungan air yang tinggi di dalam POME iaitu lebih kurang 90% daripada isi kandungannya. Oleh yang demikian, kaedah menambahbaik pirolisis bantuan gelombang mikro (MAP) digunakan dan sekaligus POME dapat dilupuskan dan menukar hasil yang bermanfaat seperti arang pepejal and minyak pirolisis. Di dalam kajian ini, kesan berat kandungan POME di dalam anggaran 100 g ke 500 g dengan penambahan karbon aktif diberi tumpuan. Kadar kekuatan gelombang mikro, masa radiasi dan nisbah pencampuran karbon aktif masing – masing dimalarkan pada kadar 1000 W, 30 minit dan 5%. Penghasilan produk arang pepejal dan minyak pirolitik dianalisis untuk menentukan kadar terbaik penghasilannya. Arang pepejal yang terhasil mempunyai potensi sebagai sumber tenaga dan mempunyai kapasiti tenaga sekurang-kurangnya >20 MJ/kg dan mengandungi kandungan

karbon >8%. Sementara itu, lebih kurang 20% kandungan bahan kimia di dalam minyak pirolitik terdiri daripada karbon nombor pada kadar $C_1$ to $C_{10}$.

**Kata kunci:** beban jisim, penyerap ketuhar gelombang mikro, pirolisis bantuan gelombang mikro, air sisa kilang saw

## Introduction

In general, agriculture is one of the industries that generates large amount of harmful wastes or effluents. Example of effluent produced from agriculture industry is palm oil mill effluent (POME). According to Aziz and Mun, the palm oil industry has generated the highest percentage of effluent as compared to the other agriculture industries [1]. Due to this problem, most of the palm oil mills applied the cheapest alternatives by discharging POME on the land or releasing it into the river. Consequently, this action will cause negative impacts to human health, aquatic life, environment and ecological system such as clogging and water logging of the soil, kills the vegetation on contact, water depletion and aquatic pollution if not treated properly [2]. There are several methods that have been applied in palm oil industry to treat POME such as aerobic, anaerobic, digestion, biodegradation, gasification and ponding treatment [3]. However, there are drawbacks from these methods, which can reduce the efficiency of POME treatment. Lorestani et al., stated that ponding treatment provides longer retention time for the POME to be degraded, low treatment efficiency, large requirement of land, large amount of methane being released and large amount of sludge production [4]. Therefore, there is a potential method as an alternative treatment of POME through microwave pyrolysis. According to Khalid et al. and Salema et al., various studies about microwave heating on POME have been performed by researchers nowadays [5, 6]. Microwave pyrolysis can convert POME into three different useful products which are solid-char, liquid and gas. Moreover, microwave pyrolysis provides more advantages compared to the other methods such as shorter exposure time for POME to be degraded and can break down polycyclic aromatic hydrocarbon into low hydrocarbon chain. In addition, microwave pyrolysis is more economical and convenient since it can be operated *in-situ* [7]. Therefore, the aim for this study is to investigate the feasibility of converting POME into valuable materials such as solid char and pyrolytic oil through microwave assisted pyrolysis process.

About 2.5 tons of palm oil mill effluent (POME) was generated for every ton of palm oil produced. According to Lorestani et al., it was stated that the huge contribution of POME was generated from the combination of wastewater from three main sources which are sterilization, clarification and hydrocyclone processes [4]. POME can be considered as the most harmful waste to human health and environment. POME has high organic load and concentrated colloidal slurry of 95 - 96% of water, 0.6 - 0.7% of oil and 4 - 5% of fine cellulose material [8]. According to Lorestani et al., it was stated that POME contains various suspended materials including short fibers, cell wall, organelles, nitrogenous materials ranging from proteins to amino acids, carbohydrates that ranging from hemicelluloses to a simple sugar, free organic acids and some mineral constituents [4]. Moreover, liquid effluent from palm oil mill includes dissolved constituents such as high concentration of carbohydrates, protein, minerals, nitrogenous compounds and lipids which can be converted into useful materials using specific process. Other than that, POME has a bad odor and thick brownish liquid that contains high solids, oil and grease, high content of chemical oxygen demand (COD) and biochemical oxygen demand (BOD) [2]. It is proven that POME is harmful to human health, aquatic life and environment not only because it contains so much pollutants but the dark brown color itself can impart some negative effect. Therefore, it is necessary to treat the POME before being discharged to the environment.

There are numerous treatments of POME that proposed by several researchers. POME can be treated by conventional method or biological method. However, limited studies on microwave pyrolysis are available particularly relating to treatment of POME. The list of methods and its details are presented in Table 1. As can be seen, the existing methods available had not focused on upgrading the wastes to valuable materials. Thus, microwave assisted pyrolysis technique deems feasible for the recovery of POME to produce valuable materials such as bio-char and pyrolytic oil.

Table 1. List of palm oil mill effluent treatment methods

| Treatment | Details | References |
|---|---|---|
| Anaerobic digestion | • Breakdown the biodegradable material without the presence of oxygen<br>• Produce methane, carbon dioxide and fertilizers | [4, 8, 9] |
| Adsorption by Fungi | • To remove the impurities and colour from the POME.<br>• This treatment takes time as it needs to nurture the fungi. | [10] |
| Aerobic biological | • Degradation of organic material with the presence of oxygen.<br>• Decrease carbon content and inorganic nitrogen.<br>• Can change the pH from acidic to alkali. | [11, 12] |
| Facultative pond | • The effluent is discharged to the pond and let it degrades by itself.<br>• It takes longer retention time. | [13, 16] |
| Membrane | • Separate organic material effectively | [14, 17] |

Pyrolysis is a heating process of materials without the presence of oxygen. Generally, conventional pyrolysis transfers the heat from outer surface to the center of the material by external heating which includes conduction, convection and radiation [18]. In conventional heating, material is heated volumetrically by heating energy is dissipated through the material from the surface by means of convection, conduction and radiation [19]. In comparison to conventional pyrolysis, microwave pyrolysis technique uses microwave radiation in order to generate heat. As the microwave radiation is penetrated into the material, it causes the electromagnetic energy to be converted into thermal energy. Microwave consists of electric and magnetic field which perpendicular to each other and will cause rotation or collision of the molecules. By referring to the microwave frequency, the molecular dipole inside the material will rapidly rotate about 2450 million times per second and causing frictions that convert the electromagnetic energy into heat [20]. In addition, microwave radiation will penetrate into the material and heat the absorber first [21]. Material that can absorb microwave radiation is called as dielectric [22]. The examples of materials that influence the dielectric properties are water and salt. Therefore, microwave heating is most efficient on the material that contain high amount of dielectric molecules. Since, POME has high moisture content, microwave-assisted pyrolysis is very suitable for treating POME. Additional of microwave absorber material such as activated carbon can enhance microwave assisted pyrolysis process. There are several methods of application of microwave absorber in the microwave assisted pyrolysis process. Microwave absorber could be mixed homogeneously with sample [23] or it can be in separate crucible [21]. Both of these methods could give different effects on the product yields. In this study, both methods were applied in order to study the effect of mass loading toward the method of application of microwave absorber.

## Materials and Methods

### Experimental setup

In this study, the untreated POME was used as a sample for microwave pyrolysis process. The untreated POME sample was collected from the final discharge point in FELDA Serting, Negeri Sembilan before it was channeled to the treatment pond. The samples were prepared in three conditions namely a sample without the presence of activated carbon, a sample mixed homogeneously with activated carbon and a sample with the presence of activated carbon in crucible as stated in Figure 1. Each condition has 5 different mass loading which are 100, 200, 300, 400 and 500g of POME. Activated carbon used in this study was obtained from Sigma-Aldrich. About constant 5% wt/wt of activated carbon was used in this study. Therefore, the mass loadings used in this experiment and the weight percentage of activated carbon used in this study are stated in Table 2. Wet POME sample that had been prepared was placed in a quartz reactor.

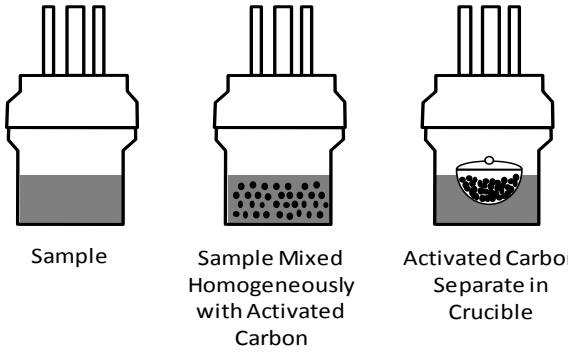



Figure 1. Method application of activated carbon in reactor

Table 2. Mass loading and activated carbon ratio

| Mass of POME Sample (g) | Weight of Activated Carbon (g) |
|---|---|
| 100 | 5 |
| 200 | 10 |
| 300 | 15 |
| 400 | 20 |
| 500 | 25 |

Then, the reactor was placed into the microwave chamber with a lid having three openings, each for inert gas input, thermocouple and gas exit, respectively. The quartz reactor was purged for duration of 20 minutes with nitrogen gas (99.9%) at a flow rate of 250 mL/min in order to remove any remaining oxygen. However, the flow rate of nitrogen gas was kept constant at 150 mL/min during the process[26]. POME sample was run with the different conditions and mass loadings in order to obtain an optimum mass that can produce highest yields of solid and liquid product. The microwave power input and radiation time were kept constant at 1000 W and 30 minutes, respectively.

**Analytical methods**

The liquid product was condensed in the condenser and collected in the liquid sample holder. After that, the liquid product was washed with hexane and then analyzed with the analytical method. For solid product (char), it is collected once the experiment was completed and analyzed after being cooled down at room temperature. Figure 2 shows the schematic diagram for the microwave pyrolysis system. Solid product which is the solid char obtained was analyzed for its physical properties through proximate, ultimate and calorific analyses was conducted by using thermogravimetric analysis (TGA/ SDTA851) manufactured by Mettler, elemental analyzer (Thermo Finnigan Flashed 1112) and bomb calorimeter (Ika-works C5000 Control Germany D79019), respectively. Meanwhile, pyrolytic oil extracted from the liquid product was analyzed using gas chromatography mass spectrometer (GCMS) model GC Varian 450-GC. Helium was used as a carrier gas at a flow rate of 1 mL/min. Non-polar capillary column was selected for detection of C and H atoms or C-C bonds. Oven temperature initially was set at 100 °C and then it is kept constant for 2 minutes at a heating rate of 5 °C/min. After that, it was increased to 200 °C at a heating rate of 10 °C/min. Then, it was followed by heating to 260 °C at a heating rate of 4 °C/min. Temperature was maintained at 260 °C for 15 minutes. For chromatography, injection temperature was set at 270 °C. Chemical compound in the liquid oil was traced and identified at the setting of mass per ion, M/Z = 30 – 500. Split ratio was set at 1:10.

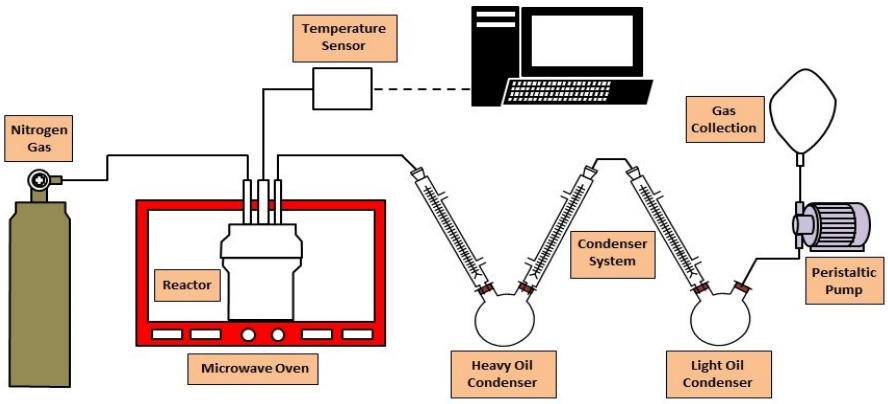



Figure 2. Schematic diagram for microwave pyrolysis system [26]

## Results and Discussion

### Raw material characterization

In general, the characteristic of raw material can be classified into two types which are physical and chemical properties. Physical properties of POME obtained from proximate analysis using Thermogravimetric Analyzer (TGA) Mettler Toledo TGA/SDTA 851 and followed the standard of ASTM D7582-12. Figure 3 shows that water content in dried POME start to vaporize at temperature 40 °C to 136 °C.

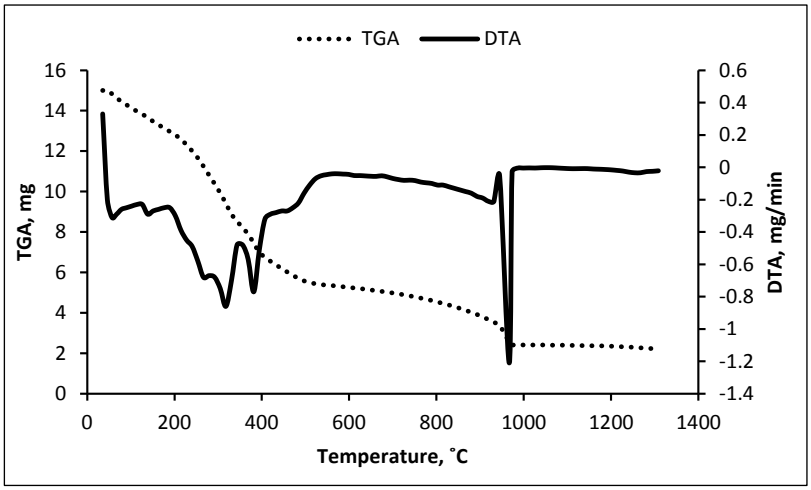



Figure 3. Thermal degradation of proximate analysis of raw material

All volatile matter inside POME starts to degrade at temperature 139 °C to 939 °C before it is released to surrounding. The optimum temperature for degradation of POME is known to be at the temperature of 320.13 °C where all longer hydrocarbons are converted into lower hydrocarbons. Other than that, thermal degradation of proximate analysis of raw material also provides value for moisture content, volatile combustible matter, fixed carbon and ash. Fixed carbon is a combustible residue after volatile matter was removed and ash is a weight of residue after combustion in an open crucible. All the values obtained from proximate analysis are important for raw material characterization. Therefore, the characterization of POME is stated in the Table 3. Chemical properties of palm oil mill effluent (POME) can be obtained from ultimate analysis, energy content and fusing point of ash. Since

POME is in the form of liquid, the physical properties of this raw material can only be analyzed by observation of specific weight such as volume.

Table 3. Characterization of raw palm oil mill effluent (POME)

| Characteristic | % |
|---|---|
| Moisture content | 14.4 |
| Volatile combustible matter | 13.7 |
| Fixed carbon | 71 |
| Fixed ash content | 0.9 |

Ultimate analysis is used to determine the percent of C, H, N, S, O and ash. The percent of C, H, N, S, O and ash obtained is important in order to identify chemical formula which then can be used in various chemical and biological reactions. However, for this analysis, the chemical composition of POME is obtained from literature. According to Khairuddin et al., the chemical formula for POME is $C_{25}H_5N_5SO_{59}$ [24]. Table 4 shows the percent C, H, N, S and O of POME obtained from the literature. Energy content is a potentially critical element in combustion. For this study, the energy content of POME is obtained from the literature. In a study by Januri et al., energy content in POME can be considered as high which is 16.16 MJ/kg [25]. Since the energy content inside POME is high, it has a potential to be used in future as fuel and the source of energy.

Table 4. Ultimate analysis for raw palm oil mill effluent (POME)

| Element | C (%) | H (%) | N (%) | S (%) | O (%) |
|---|---|---|---|---|---|
| As Received | 26.57 | 4.97 | 5.66 | 1.05 | 61.78 |
| Dry basis | 31.04 | 3.92 | 6.61 | 1.23 | 56.15 |
| Dry Ash free basis | 31.37 | 5.87 | 6.68 | 1.24 | 54.84 |

**Product yield**

Generally, the pattern of product yield formed from microwave pyrolysis of POME for solid are showed an increment with the increased of mass loadings as shown in Figure 4. However, the conversion of POME into solid char show a divergent pattern as shown in Table 5 as the mass loading increased, the conversion dropped from ~98 to ~61%. This is due to the condition where water is the dominant inside the POME was activated, self-propagated and vaporized during the pyrolysis but it limited the pyrolysis process condition, which reduced the conversion of solid char. Process of releasing the water content from the POME took place and decreased the pyrolysis reaction. No conversion of solid char was observed for all samples with non-microwave absorber indicating the sample was not fully pyrolyzed even though high conversion was achieved. Meanwhile, sample with microwave absorber regardless it is mixed homogeneously or in separate crucible, solid char was formed at low mass loading below 200 g with yield and conversion for both mixed homogeneously and in separate crucible were ~1.5% yields; ~98.5% conversion and ~3.3% yields; 96.7% conversion, respectively. Addition of microwave absorber has increased the reaction temperature and consequently increased the product yields [27]. Solid char was formed with aid of microwave absorber during microwave assisted pyrolysis process. Indeed the introduction of microwave absorber via separate crucible has increased yields of solid char formed. Microwave absorber bed in separate crucible improved the microwave irradiation towards the absorbance properties of POME [21]. Low conversion of solid char was observed at high mass loading at range 300 to 500 g. This was due to the depth of penetration of microwave radiation through the sample. The depth of penetration of microwave energy into the sample is measurement to determine how much the completion of pyrolysis.

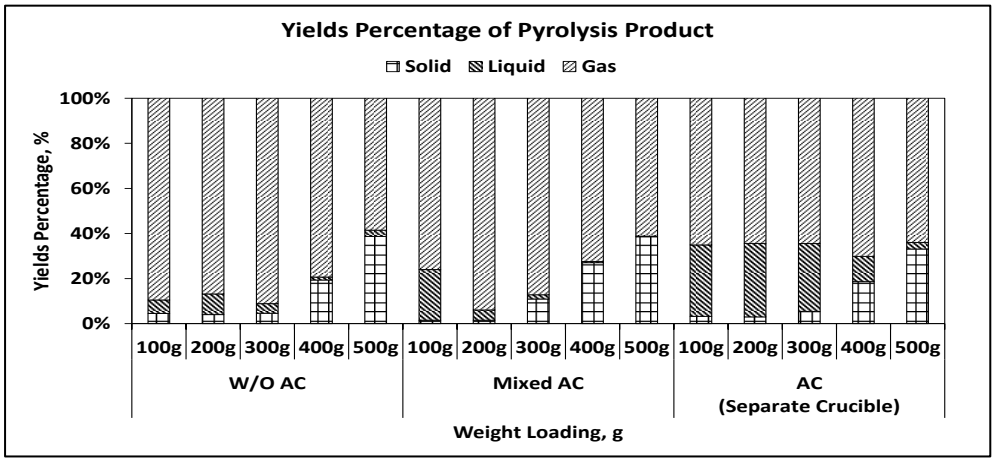



Figure 4. Yield percentage of product distribution

Table 5. Conversion of POME into solid char

| Conditions | Mass Loading (G) | Solid Yields (%) | Conversion (%) | Visual Result |
|---|---|---|---|---|
| No activated carbon | 100 | 4.50 | 96.00 | Semi coke |
| | 200 | 4.05 | 95.95 | Dried sample |
| | 300 | 4.67 | 95.33 | Dried sample |
| | 400 | 19.40 | 80.60 | Undried sample |
| | 500 | 38.70 | 61.30 | Undried sample |
| With activated carbon (mix homogeneously) | 100 | 1.50 | 98.50 | Char |
| | 200 | 1.50 | 98.50 | Char |
| | 300 | 10.97 | 89.03 | Semi coke |
| | 400 | 27.03 | 72.98 | Undried sample |
| | 500 | 38.54 | 61.46 | Undried sample |
| With activated carbon (separate crucible) | 100 | 3.30 | 96.70 | Char |
| | 200 | 3.05 | 96.95 | Char |
| | 300 | 5.47 | 94.53 | Semi coke |
| | 400 | 18.60 | 81.40 | Dried sample |
| | 500 | 33.08 | 66.92 | Dried sample |

The practical reason for determining the depth of penetration is to ensure efficient heating of the materials throughout its interior. If the frequencies are higher, the microwave radiation might get absorbed on the surface of the materials, and will penetrate only a short distance [28]. High volume of sample might affect the depth of penetration of microwave radiation. Thus, the presence of activated carbon with high dielectric properties enhanced the depth of penetration of microwave radiation and heated the materials uniformly. It has been stated by R. Meredith (1998), dielectric constant plays an important role in the power penetration [29].

In comparison, yield of liquid product decreased when the mass loading increased as shown in Figure 4. Liquid product yield consists of two components, which are pyrolytic oil and water in the form of aqueous that had been vaporized during the microwave assisted pyrolysis process. This is due to the effectiveness of pyrolysis condition of POME, which is the mass loading to the microwave irradiation. Through observation of Figure 5, yields of liquid product increased with two different methods application of activated carbon as microwave absorber applied. Thus, pyrolytic thermal cracking could be achieved with the application of microwave absorber during microwave assisted pyrolysis process [30]. Consequently it would increase yields of liquid product with the addition of microwave absorber into raw material [27, 31]. Activated carbon in separate crucible produced more yields of liquid product and furthermore, the percentage of pyrolytic oil separated from yields of liquid product was also higher compared to pyrolytic oil gain from the process which sample has been mixed homogeneously with activated carbon. It could be said that, microwave assisted pyrolysis process achieved highest reaction temperature from the heating of activated in separate crucible which promoted high hydrocarbon breakdown of POME and produced more pyrolytic oil. Similar trend was observed from other researcher by formed the microwave absorbent bed in the microwave assisted pyrolysis reactor that increased the pyrolytic oil yield [32]. Increase in the mass loading has reduced the pyrolytic oil yields in the yields of liquid product due to the incomplete pyrolysis reached. Hence, sample that has mass loading more than 300 g in average cannot obtain fully pyrolyzed condition successfully, indicating by the low conversion percentage of solid char, low solid char yields and low pyrolytic oil yields. This can be concluded that 300 g sample with the presence of microwave absorber can be the maximum mass loading to pyrolyze POME and separated microwave absorbent during microwave assisted pyrolysis process will be the best applicable method for microwave absorbent application in the process.

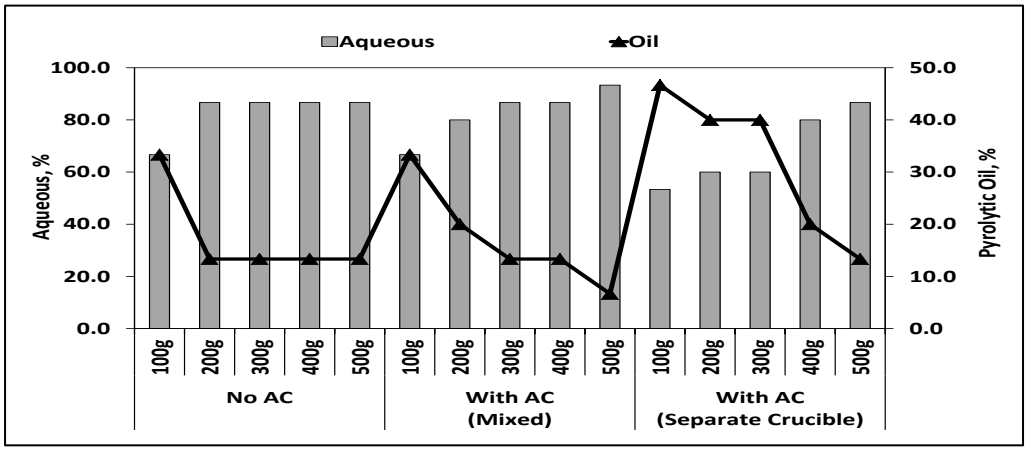



Figure 5. Aqueous –pyrolytic oil percentage extracted from liquid yields

**Solid product analysis**

Solid char was analyzed for it physical properties by proximate and ultimate analysis. From the proximate analysis data obtained from Table 6, microwave assisted pyrolysis released the volatile matter out from the raw POME thus it promoted the formation of solid at low mass loading at 100 g. Indeed almost complete pyrolysis was achieved by POME using this method. Lack of dielectric constant properties in raw POME has reduced the potential of microwave assisted pyrolysis.

With the improvised microwave assisted pyrolysis method by the addition of the microwave absorber such as activated carbon, has increased the total dielectric constant of the sample thus enhanced the pyrolysis process through higher temperature [33-35]. It was observed that the addition of microwave absorber (AC), for both mixed homogeneously and in separate crucible has increased the efficiency of pyrolysis through the effectiveness of microwave radiation absorbed and activated more molecule to generate more heat energy at high mass loading such as 200 g and 300 g for the method of mixed AC homogeneously and in separate crucible respectively. By releasing

the higher amount of volatile matter from raw POME during pyrolysis process, it elevated the fixed carbon content in the solid char derived and it is consistent with the findings reported by other researchers on char derived from microwave assisted pyrolysis process [28, 36, 37]. Meanwhile, other research was found on pyrolysis of POME for bio-char, it resulted moisture content and ash content that were consistent with the char obtained [38]. On the other hand, high fixed carbon content in the solid char indicated high percentage of carbon element in the solid char, as can be seen in the ultimate analysis result in Table 6.

Table 6. Proximate and ultimate analysis of solid product of microwave assisted pyrolysis of POME

| Conditions | Sample (g) | Proximate Analysis | | | | *Ultimate Analysis | | | | | | |
|---|---|---|---|---|---|---|---|---|---|---|---|---|
| | | %M | %VM | %FC | %A | C | H | N | S | **O | H/C | O/C |
| No activated carbon | 100 | 6.46 | 2.93 | 64.2 | 26.41 | 52.05 | 10.22 | 0.00 | 0.00 | 37.73 | 0.20 | 0.91 |
| | 200 | 0.43 | 30.97 | 31.03 | 37.57 | 46.30 | 11.16 | 0.00 | 0.00 | 42.54 | 0.24 | 0.93 |
| | 300 | 2.31 | 40.5 | 35.76 | 21.43 | 48.85 | 9.47 | 0.00 | 0.00 | 41.68 | 0.19 | 0.92 |
| | 400 | 3.94 | 70.64 | 19.95 | 5.47 | 39.96 | 10.85 | 0.00 | 0.00 | 49.20 | 0.27 | 1.34 |
| | 500 | 25.7 | 60.2 | 12.7 | 1.4 | 56.01 | 17.76 | 0.00 | 0.00 | 26.22 | 0.32 | 1.10 |
| With activated carbon (mix homogeneously) | 100 | 3.1 | 5.21 | 68.89 | 22.8 | 34.66 | 1.90 | 0.00 | 0.00 | 63.44 | 0.05 | 1.95 |
| | 200 | 2.8 | 11.6 | 59.62 | 25.98 | 31.30 | 2.05 | 0.00 | 0.00 | 66.65 | 0.07 | 2.25 |
| | 300 | 7.6 | 21.76 | 33.44 | 37.2 | 42.36 | 4.44 | 0.00 | 0.00 | 53.20 | 0.10 | 1.58 |
| | 400 | 5.2 | 61.8 | 25.06 | 7.94 | 34.29 | 5.28 | 0.00 | 0.00 | 60.43 | 0.15 | 1.94 |
| | 500 | 18.9 | 70.5 | 6.32 | 4.28 | 37.05 | 5.09 | 0.00 | 0.00 | 57.86 | 0.14 | 2.23 |
| With activated carbon (separate crucible) | 100 | 0.87 | 1.6 | 51.93 | 45.6 | 73.59 | 13.63 | 11.89 | 0.00 | 0.89 | 0.19 | 0.03 |
| | 200 | 1.87 | 8.72 | 52.01 | 37.4 | 81.67 | 6.63 | 7.45 | 0.00 | 4.25 | 0.08 | 0.09 |
| | 300 | 4.6 | 11.6 | 48.7 | 35.1 | 73.52 | 9.66 | 6.14 | 0.00 | 10.68 | 0.13 | 0.25 |
| | 400 | 4.12 | 54.7 | 32.28 | 8.9 | 49.15 | 7.89 | 4.12 | 0.00 | 38.85 | 0.16 | 0.89 |
| | 500 | 12.6 | 49.6 | 30.82 | 6.98 | 40.16 | 9.53 | 2.49 | 0.00 | 47.83 | 0.24 | 1.58 |

*Dry ash free basis
** Calculated by difference

Elemental content obtained from this analysis is then compared to the coal since coal is used as a solid fuel. According to Jing-biao et al., the percentage of C, H, N, S and O of *Baotou* bituminous coal are 70.18, 4.64, 1.5, 0.44 and 11.36%, respectively [39]. It was observed that carbon content in the microwave assisted pyrolysis process with the microwave absorber in separate crucible has high carbon content as compared to the one the mixed homogeneously. In comparison to the percentage of C, H, N S, O of coal, the solid char obtained from microwave assisted pyrolysis process with microwave absorber in separate crucible had almost identical elemental properties. The O/C ratio of the char obtained from microwave assisted pyrolysis process in separate crucible has low value as compared to other process. Solid char obtained has low H/C and O/C atomic ratio which indicates high carbon content and low hydrogen and oxygen content indicating the presence of low hydrocarbon compound in the solid char. The energy content is determined in order to identify the feasibility of utilizing solid product from pyrolysis of POME as alternative fuel in future. Figure 6 shows the gross calorific value of solid product from microwave pyrolysis of POME. It was observed that gross calorific value for both the chars obtained in the absence and the presence of microwave absorber in the condition of mixed homogeneously were kept increasing at range 100 g to 300 g except for the solid char obtained from process that microwave absorber in separate crucible. Its energy content decreased when mass loading increased to 300 g. In addition, sample having mass loading of 400 and 500 g for all methods/arrangements are known to be zero since the samples were in un-dried condition. Incomplete pyrolysis condition was found in this mass loading.

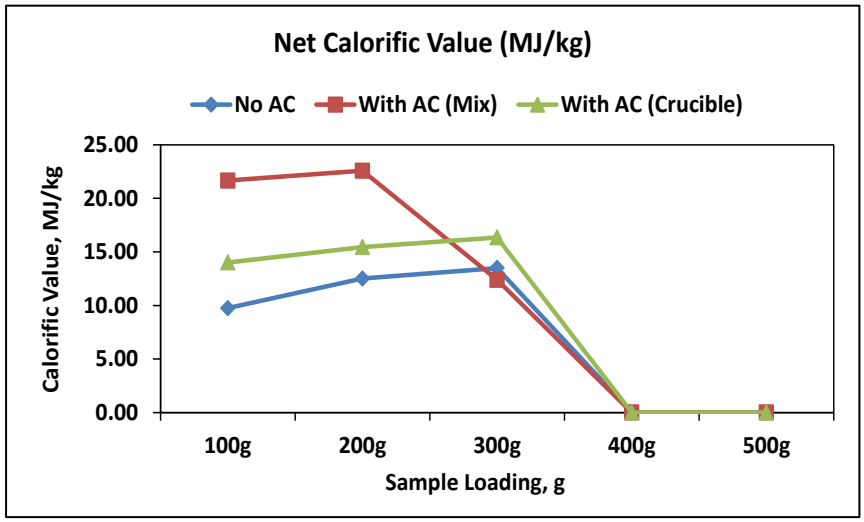



Figure 6. Net calorific value of solid product of POME

It is proven that solid product of microwave pyrolysis of POME that has high energy content which is more than 15000 J/g can be used as an alternative fuels in future. According to Thangalazhy-Gopakumar, solid char obtained from pyrolysis of POME was around 12.8 ± 0.2 MJ/kg [38]. It is consisted with the energy content obtained from microwave assisted pyrolysis of POME without the presence of microwave absorber. Energy content slightly increased from when it was pyrolysis with the aid of microwave absorber during the microwave pyrolysis process in separate crucible. The presence of microwave absorber increased the reaction temperature and consequently increased the fixed carbon content and elevated the energy content. However, solid char obtained from microwave assisted pyrolysis with the mixed homogeneously with activated carbon has higher energy content from the rest. Activated carbon itself has a quite high of energy content thus it increased the energy content of solid char obtained. Table 7 shows the gross and net calorific value of microwave pyrolysis of POME. The equation used to calculate net calorific value is shown in Equation 1.

$$\text{Net calorific value, kJ/kg} = \text{Gross calorific value} - 24.44(9\%\ \text{H} + \%\text{M}) \quad (1)$$

**Pyrolytic oil analysis**

Pyrolytic oil extracted from liquid product was analyzed for its chemical content by using gas chromatography mass spectrometer (GCMS). Pyrolysis oil extracted from the liquid product contain valuable hydrocarbon that can be potential to recover either in single component or as the oil. Through the observation in Figure 7, it was found that low chain ester such as 1,2-benzenedicarboxylic acid diisooctyl ester, 2-propenoic acid, 2-methyl dodecyl ester, and 9,12-octadecadienoic acid (Z,Z)- phenylmethyl ester was recovered in the pyrolytic oil at low mass loading. It was consistent with research on the pyrolytic oil from sewage sludge by other researchers [40, 41]. Meanwhile the nitrogenated compound was highly observed in the pyrolytic oil from microwave assisted pyrolysis of POME without microwave absorber. Nitrogenated compounds were not favorable for fuels; however, their presence can be reduced by changing the operating parameters [38].

Table 7. Gross and net calorific value of solid product of POME

| Conditions | Sample (g) | Gross Calorific Value (MJ/kg) | Net Calorific Value (MJ/kg) |
|---|---|---|---|
| No activated carbon | 100 | 11.415 | 9.75 |
| | 200 | 14.042 | 12.51 |
| | 300 | 15.137 | 13.49 |
| | 400 | n.d* | n.d* |
| | 500 | n.d* | n.d* |
| With activated carbon (mix homogeneously) | 100 | 22.049 | 21.66 |
| | 200 | 22.965 | 22.58 |
| | 300 | 13.125 | 12.40 |
| | 400 | n.d* | n.d* |
| | 500 | n.d* | n.d* |
| With activated carbon (separate crucible) | 100 | 15.645 | 14.02 |
| | 200 | 16.383 | 15.45 |
| | 300 | 17.743 | 16.35 |
| | 400 | n.d* | n.d* |
| | 500 | n.d* | n.d* |

* Not Detected

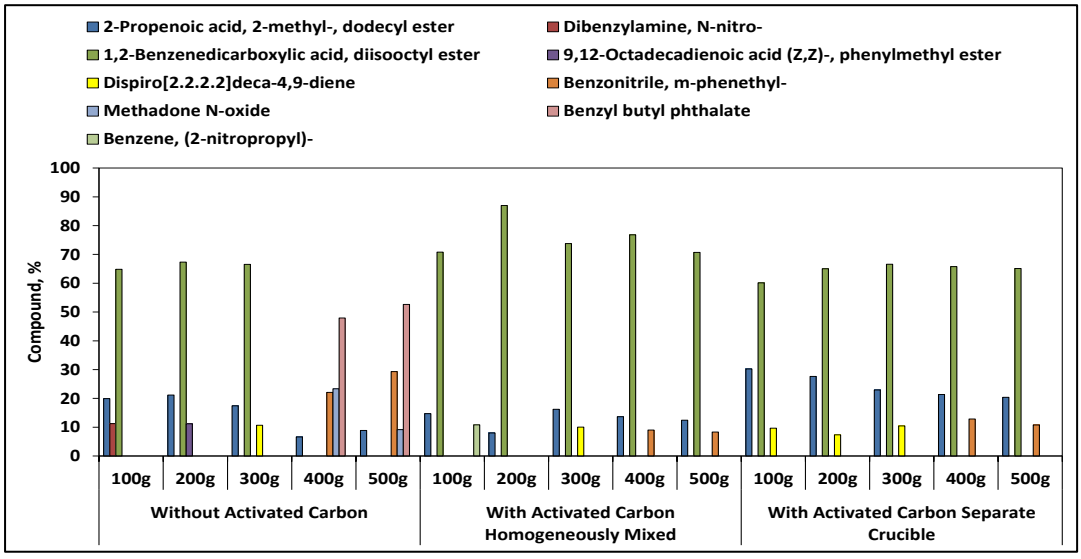



Figure 7. Chemical compound percentage from total ion chromatogram of pyrolytic oil

Thus, pyrolytic oil for both process mixed microwave absorber homogeneously and in separate crucible, eliminated and breakdown the nitrogenated compound into other low hydrocarbon compound. Moreover, low hydrocarbon chain compound production was elevated in the process with microwave absorber in separate crucible as shown in

Figure 8. Radiation temperature increased rapidly during the course of pyrolysis when microwave absorber in separate crucible was used. The introduction of microwave absorber added further reaction by increasing the radiation temperature and enhancing the hydrocarbon cracking with the dehydrogenation process through the Diels-Alder reaction [42]. With the increased of low hydrocarbon chain in the pyrolytic oil, it would increase the potential of pyrolytic oil to become fuel.

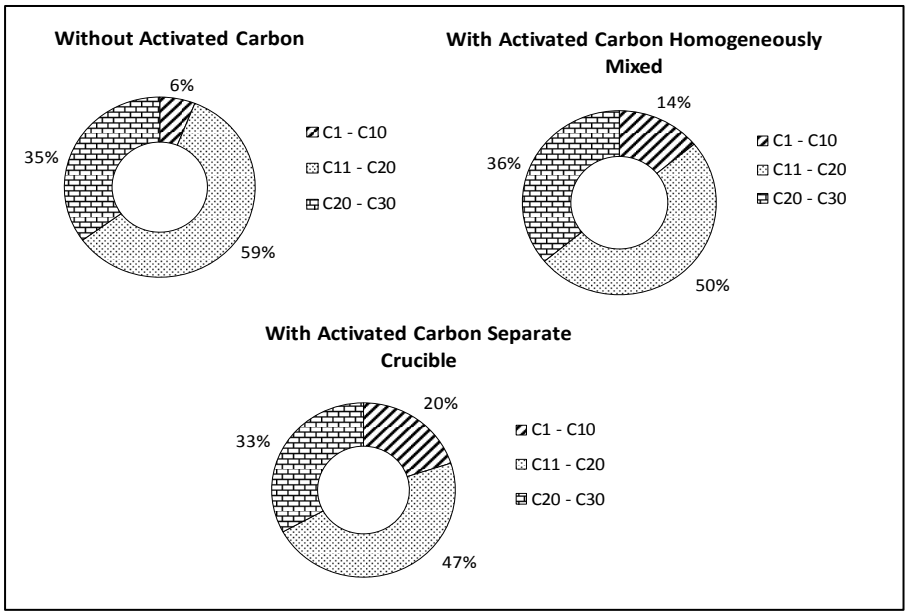



Figure 8. Proportion of chemical compound in pyrolytic oil according to carbon number

## Conclusion

In conclusions, this research has been carried out in order to study the effect of different sample mass loading and method application of activated carbon as microwave absorbent to the product yield of microwave-assisted pyrolysis of palm oil mill effluent (POME). POME cannot be fully pyrolyzed using domestic modified microwave oven with the highest microwave power level and longest radiation time. With the presence of activated carbon either by mixed it homogeneously or in the separate crucible, pyrolysis of POME can be improved. Solid product obtained from this study has high energy and oil extracted from liquid product condensed contain some chemical that has tendency to be an alternative fuel in future. Therefore, microwave-assisted pyrolysis treatment of POME is an alternative way to reduce the waste, hence preventing negative impacts to human and environment such as disease and pollution. These advantages have proven that microwave-assisted pyrolysis technique is able to transform waste into wealth in future.

## Acknowledgement

This work was financially supported by Excellence Research Grant (600-RMI/DANA 5/3/RIF) with the experimental equipment and facility provided by Research Management Institute, Universiti Teknologi MARA (UiTM) and Faculty of Chemical Engineering, UiTM.

## References

1. Aziz, N. A. and Mun, D. L. K. (2012). Malaysia's biomass potential. Access online http://www.besustainablemagazine.com/cms2/malaysias-biomass-potential/.
2. Rupani, P. F., Singh, R. P., Ibrahim, M. H. and Esa, N. (2010). Review of current palm oil mill effluent (POME) treatment methods: vermicomposting as a sustainable practice. *World Applied Sciences Journal*, 11(1): 70 – 81.

3. Iwuagwu, J. O. and Ugwuanyi, J. O. (2014). Treatment and valorization of palm oil mill effluent through production of food grade yeast biomass. *Journal of Waste Management*, 2014: 1 - 9.
4. Lorestani, A. (2006). Biological treatment of palm oil mill effluent (POME) using an up-flow anaerobic sludge fixed film (UASFF) bioreactor. Thesis Doctor of Philosophy, Universiti Teknologi Malaysia.
5. Khalid, K., Soon, E. M. L. and Chow, K. F. (1998). Microwave drying of palm oil mill effluent. *Pertanika Journal of Science & Technology*, 6(2): 121 – 130.
6. Salema, A. A. and Ani, F. N. (2010). Microwave pyrolysis of oil palm fibres. *Jurnal Mekanikal*, 30: 77 – 86.
7. Faris, N. A. F. A. (2014). Effect of power level on product yield for microwave pyrolysis of palm oil mill effluent (POME). Thesis Bachelor Chemical Engineering, Chemical Engineering Faculty, Universiti Teknologi MARA.
8. Ling, Y. L. (2007). Treatability of palm oil mill effluent (POME) using black liquor in an anaerobic treatment process. Thesis Doctoral of Philosophy, Universiti Sains Malaysia.
9. Borja, R., Banks, C. J., Martin, A. and Khalfaoui, B. (1995). Anaerobic digestion of palm oil mill effluent and condensation water waste: an overall kinetic model for methane production and substrate utilization. *Bioprocess Engineering*, 13(2): 87 – 95.
10. Neoh, C. H., Yahya, A., Adnan, R., Majid, Z. A. and Ibrahim, Z. (2013). Optimization of decolorization of palm oil mill effluent (POME) by growing cultures of *Aspergillus fumigatus* using response surface methodology. *Environmental Science and Pollution Research*, 20(5): 2912 – 2923.
11. Oswal, N., Sarma, P. M., Zinjarde, S. S. and Pant, A. (2002). Palm oil mill effluent treatment by a tropical marine yeast. *Bioresource Technology*, 85(1): 35 – 37.
12. Agamuthu, P., Tan, E. L. and Shaiful, A. A. A. (1986). Effect of aeration and soil inoculum on the composition of palm oil mill effluent (POME). *Agricultural Wastes*, 15(2): 121 – 132.
13. Teng, T. T., Wong, Y. S., Ong, S. A., Norhashimah, M. and Rafatullah, M. (2013). Start-up operation of anaerobic degradation process for palm oil mill effluent in anaerobic bench scale reactor (ABSR). *Procedia Environmental Sciences*, 18: 442 – 450.
14. Abdurahman, N., Azhari, N. and Rosli, Y. (2013). The performance evaluation of anaerobic methods for palm oil mill effluent (POME) treatment: A review. INTECH Open Access Publisher.
15. Chin, K. K., Lee, S. W. and Mohammad, H. H. (1996). A study of palm oil mill effluent treatment using a pond system. *Water Science and Technology*, 34(11): 119 – 123.
16. Chooi, C. (1984). Ponding system for palm oil mill effluent treatment. *Proceeding on Workshop of Palm Oil Mill Effluent Technology*: pp. 53 – 63.
17. Fakhru'l-Razi, A. and Noor, M. J. M. M. (1999). Treatment of palm oil mill effluent (POME) with the membrane anaerobic system (MAS). *Water Science and Technology*, 39(10-11): 159 – 163.
18. Mushtaq, F., Mat, R. and Ani, F. N. (2014). A review on microwave assisted pyrolysis of coal and biomass for fuel production. *Renewable and Sustainable Energy Reviews*, 39: 555 – 574.
19. Appleton, T. J., Colder, R. I., Kingman, S. W., Lowndes, I. S. and Read, A. G. (2005). Microwave technology for energy-efficient processing of waste. *Applied Energy*, 81(1): 85 – 113.
20. Calabrò, E. and Magazù, S. (2012). Comparison between conventional convective heating and microwave heating: an FTIR spectroscopy study of the effects of microwave oven cooking of bovine breast meat. *Journal of Electromagnetic Analysis and Applications*, 4(11): 433 – 449.
21. Ismail, K., Ishak, M. A. M., Ab Ghani, Z., Abdullah, M. F., Safian, M. T. U., Idris, S. S., Tahiruddin, S., Yunus, M. F. M. and Hakimi, N. I. N. M. (2013). Microwave-assisted pyrolysis of palm kernel shell: Optimization using response surface methodology (RSM). *Renewable Energy*, 55: 357 – 365.
22. Fernández, F., Arenillas, A., and Menéndez, J. Á. (2011). Microwave heating applied to pyrolysis, advances in induction and microwave heating of mineral and organic materials, Stanisław Grundas (Ed.). INTECH Open Access Publisher.
23. Wang, L., Lei, H., Ren, S., Bu, Q., Liang, J., Wei, Y., Liu, Y., Lee, G. S. J., Chen, S., Tang, J. and Zhang, Q. (2012). Aromatics and phenols from catalytic pyrolysis of Douglas fir pellets in microwave with ZSM-5 as a catalyst. *Journal of Analytical and Applied Pyrolysis*, 98: 194 – 200.
24. Khairuddin, M. N., Sulaiman, A., Syahlan, S., Zulkefli, F., Bula, J., Wan Abdul Rahman, W. M. N., Kassim, J., Md Isa, I. and Mat Tahir, M. R. (2013). Analysis and management of methane emissions from dumping pond: A cases study at Felda Jengka 8 palm oil mill. *Proceeding KONAKA*: pp. 35 – 41.

25. Januri, Z., Rahman, N. A., Idris, S. S., Matali, S., Manaf, S. F. A., Faris, N. A. F. A. and Rosland, N. (2014). Effect of activated carbon as microwave absorbance on the yields of microwave assisted pyrolysis of palm oil mill effluent. *3rd IET International Conference on Clean Energy and Technology*: pp. 1 - 9.
26. Januri, Z., Rahman, N. B. A., Idris, S. S., Matali, S., Manaf, A. and Fairuz, S. (2014). Yields performance of automotive paint sludge via microwave assisted pyrolysis. In Applied Mechanics and Materials. Trans Tech Publications: pp. 191 – 195.
27. Zuo, W., Tian, Y. and Ren, N. (2011). The important role of microwave receptors in bio-fuel production by microwave-induced pyrolysis of sewage sludge. *Waste Management*, 31(6): 1321 – 1326.
28. Salema, A. A., Yeow, Y. K., Ishaque, K., Ani, F. N., Afzal, M. T. and Hassan, A. (2013). Dielectric properties and microwave heating of oil palm biomass and biochar. *Industrial Crops and Products*, 50: 366 – 374.
29. Meredith, R. (1998). Engineer's Handbook of Industrial Microwave Heating. London: The Institution of Electrical Engineers.
30. Lam, S. S., Russell, A. D., Lee, C. L. and Chase, H. A. (2012). Microwave-heated pyrolysis of waste automotive engine oil: Influence of operation parameters on the yield, composition, and fuel properties of pyrolysis oil. *Fuel*, 92(1): 327 – 339.
31. Chemat, F. and Poux, M. (2001). Microwave assisted pyrolysis of urea supported on graphite under solvent-free conditions. *Tetrahedron Letters*, 42(22): 3693 – 3695.
32. Xie, Q., Peng, P., Liu, S., Min, M., Cheng, Y., Wan, Y., Li, Y., Lin, X., Liu, Y., Chen, P. and Ruan, R. (2014). Fast microwave-assisted catalytic pyrolysis of sewage sludge for bio-oil production. *Bioresource Technology*, 172: 162 – 168.
33. Dai, Q., Jiang, X., Wang, F., Chi, Y. and Yan, J. (2013). PCDD/Fs in wet sewage sludge pyrolysis using conventional and microwave heating. *Journal of Analytical and Applied Pyrolysis*, 104: 280 – 286.
34. Jiang, J. and Ma, X. (2011). Experimental research of microwave pyrolysis about paper mill sludge. *Applied Thermal Engineering*, 31(17): 3897 – 3903.
35. Menéndez, J. A., Domınguez, A., Inguanzo, M. and Pis, J. J. (2004). Microwave pyrolysis of sewage sludge: analysis of the gas fraction. *Journal of Analytical and Applied Pyrolysis*, 71(2): 657 – 667.\
36. Wang, X. H., Chen, H. P., Ding, X. J., Yang, H. P., Zhang, S. H. and Shen, Y. Q. (2009). Properties of gas and char from microwave pyrolysis of pine sawdust. *BioResources*, 4(3): 946 – 959.
37. Menendez, J. A., Inguanzo, M. and Pis, J. J. (2002). Microwave-induced pyrolysis of sewage sludge. *Water Research*, 36(13): 3261 – 3264.
38. Thangalazhy-Gopakumar, S., Al-Nadheri, W. M. A., Jegarajan, D., Sahu, J. N., Mubarak, N. M. and Nizamuddin, S. (2015). Utilization of palm oil sludge through pyrolysis for bio-oil and bio-char production. *Bioresource Technology*, 178: 65 – 69.
39. Jing-Biao, Y. and Ning-Sheng, C. (2006). A TG-FTIR study on catalytic pyrolysis of coal. *Journal of Fuel Chemistry and Technology*, 34(6): 650 – 654.
40. Domí, A., Menendez, J. A., Inguanzo, M., Bernad, P. L. and Pis, J. J. (2003). Gas chromatographic–mass spectrometric study of the oil fractions produced by microwave-assisted pyrolysis of different sewage sludges. *Journal of Chromatography A*, 1012(2): 193 – 206.
41. Xiong, S., Zhuo, J., Zhang, B. and Yao, Q. (2013). Effect of moisture content on the characterization of products from the pyrolysis of sewage sludge. *Journal of Analytical and Applied Pyrolysis*, 104: 632 –639.
42. Bolotov, V. A., Udalov, E. I., Parmon, V. N., Tanashev, Y. Y. and Chernouso, Y. D. (2012). Pyrolysis of heavy hydrocarbons under microwave heating of catalysts and adsorbents. *Journal of Microwave Power and Electromagnetic Energy*, 46(1): 39 – 46.

*Malaysian Journal of Analytical Sciences, Vol 21 No 2 (2017): 484 - 495*
*DOI: https://doi.org/10.17576/mjas-2017-2102-24*

MALAYSIAN JOURNAL OF ANALYTICAL SCIENCES
*Published by The Malaysian Analytical Sciences Society*
ISSN 1394 - 2506

# MOLECULAR WEIGHT CUT-OFF DETERMINATION OF PRESSURE FILTRATION MEMBRANES VIA COLORIMETRIC DETECTION METHOD

## (Penentuan Berat Sekatan Molekul Bagi Membran Penurasan TekananMelalui Kaedah Pengesanan Kolorimetri)

Izzati Izni Yusoff, Rosiah Rohani*, Abdul Wahab Mohammad

*Department of Chemical and Process Engineering,*
*Faculty of Engineering and Built Environment,*
*Universiti Kebangsaan Malaysia, 43600 UKM Bangi, Selangor, Malaysia*

**Corresponding author: rosiah@ukm.edu.my*

Received: 21 October 2015; Accepted: 14 June 2016

**Abstract**

Molecular weight cut-off (MWCO) of commercial and in-house fabricated membranes is obtained at 90% rejection of various types of solutes with different molecular weights (MWs). PEG quantification methods have been favorably employed to determine membranes' MWCO. Most of the quantification methods utilizing high-end equipment using high performance liquid chromatography (HPLC) and low-end colorimetric method. HPLC method requires an established chromatographic technique using specific diluents, columns and detectors while the most referred colorimetric method requires a few processing steps with concentration up to 7.5 ppm by using UV spectrophotometer. In this work, a newly modified colorimetric method was established to conduct a simple measurement for a membrane's MWCO. The newly modified method has an excellent linearity for the calibration curves which $R^2$ values are closed to 1 with concentration of up to 150 ppm. A MWCO determination test conducted using different commercial membranes for confirming this newly modified method found that similar MWCO values were obtained as given by the membrane' manufacturers. In conclusion, this newly modified method is simpler than the formerly used colorimetric method, reliable and applicable for determining the MWCO of membranes ranging from UF to NF at a higher range of PEG concentrations (>150 ppm).

**Keywords:** molecular weight cut-off, polyethylene glycol, spectrophotometric, colorimetric, membrane

**Abstrak**

Berat sekatan molekul (MWCO) bagi membran komersial dan yang dihasilkan sendiri diperolehi pada 90% penolakan pelbagai jenis bahan larut dengan berat molekul yang berbeza (MWs). Kaedah kuantifikasi menggunakan PEG adalah yang paling digemari digunakan bagi menentukan MWCO daripada membran yang di sintesis. Kebanyakan kaedah menggunakan peralatan atasan seperti kromatografi cecair berprestasi tinggi (HPLC) dan kaedah bawahan seperti kaedah kolorimetri. Kaedah HPLC memerlukan teknik kromatografi yang tertubuh menggunakan bahan pencair, tiang dan pengesan tertentu manakala kaedah kolorimetri memerlukan beberapa langkah pemprosesan dengan kepekatan hanya dalam julat sehingga 7.5 ppm menggunakan spektrofotometer UV. Oleh yang demikian dalam kajian ini, satu kaedah kolorimetri baru yang diubahsuai telah ditubuhkan untuk mengukur MWCO membran. Kaedah ini mempunyai kelinearan yang sangat baik, di mana nilai $R^2$ menghampiri 1 dengan kepekatan sehingga 150 ppm. Ujian penentuan MWCO dijalankan menggunakan beberapa membran komersial yang berbeza untuk mengesahkan kaedah baru diubahsuai ini didapati bahawa nilai MWCO yang sama telah diperolehi bagi membran, seperti yang diberikan oleh pengeluar membran. Kesimpulannya, kaedah yang baru diubahsuai ini adalah lebih mudah daripada kaedah kalorimetri yang dahulunya digunakan, boleh dipercayai dan diguna pakai bagi menentukan MWCO daripada membran NF sehingga membran UF malah pada julat kepekatan PEG yang lebih tinggi.

**Kata kunci:** berat sekatan molekul, polietilena glikol, spektrofotometer, kolorimetri, membran

## Introduction

Membrane-based technologies are the leading technology for all kinds of separation techniques due to its intrinsic characteristics such as operational simplicity, environmental impact, high selectivity and permeability in transport of specific components [1]. A membrane is an interphase between two adjacent phases acting as a selective barrier, regulating the transport of substances between the two compartments for separating feed species such as mixture of liquid, gas and colloidal particle [2, 3]. Membranes with good resistant and selectivity are necessary to ensure efficient separation process and very important for the industrial sector to obtain high purity products. Selectivity is dependent on the pore size of the membranes [4]. Furthermore, one of the major factor in obtaining an effective separation is by determining relative size of solute molecule to pass through the membrane pores [5]. Thus, the pore sizes of the membrane and its distribution play a crucial role in determining the efficiency of filtration [6, 7].

Membrane pore sizes could be determined by several analytical methods. Solute rejection method, bubble point method, soluble probe method, liquid replacement and visual observation techniques (e.g., atomic force microscopy and scanning electron microscopy) are the methods commonly employed to measure the pore sizes of membranes [8 - 10]. Each of these methods has its own advantages and limitations. Some of the techniques outlined might not be useful in the determination of pore size of membranes in term of their molecular weight cut-off (MWCO) since they cannot predict the membranes' sieving effects based on the removal of particles and solutes through the membranes under actual operating conditions and transport mechanism [10, 11].

Among the outlined methods, the solute rejection method is an effective technique to investigate the separation characteristics of various solutes by membranes because it measures solute rejection using actual filtration experiments with non-ionic solutes of a known molecular weight (MW) such as polyethylene glycol (PEG), oligostyrenes, alkanes and dextrans[10]. A membrane's MWCO is a representation of membrane selectivity for solute molecules of different MW, where the MW value is obtained from the solute molecule that gives a 90% rejection when a range of different MW solutes are filtered in the targeted solvent [12, 13]. PEGs have been widely used for the determination of the nominal MWCO because of their colloidal properties, which gives low-fouling levels [11]. There are various detection methods for PEG but most of the methods utilizing high-end equipment such as high performance liquid chromatography (HPLC) and low-end colorimetric method. HPLC method requires an established chromatographic technique using specific diluents, columns and detectors while colorimetric method requires a number of processing steps to dilute PEG based on the formation of a complex with barium chloride and iodine solution until a very low concentration of up to 7.5 ppm using UV spectrophotometer [14]. Since most reliable PEG detection techniques require the use of sophisticated instruments (which some instrument may not be available in many laboratories) and apply complex protocols, the colorimetric detection method have attracted considerable attentions in PEG detection applications with regard to their simplicity and versatility [15].

MWCO determination by colorimetric method was first used by [16] and has been extensively used thereafter by many research groups worldwide for quantifying the MWCO of their fabricated membranes [3, 5, 17-19]. However, there is no work ever reported to date, on the verification of the method with any types of commercial membranes of known MWCO to confirm its accuracy. Furthermore, the MWCO of the reported synthesized membranes were only in the ultrafiltration (UF) ranges. For instance, [16] reported the MWCO of the synthesized membrane from cellulose acetate butyrate was around 15,000 g/mol upon using PEGs in range of 1,000 to 20,000 g/mol to determine the MWCO value. In different occasions, [3] and [17] have used PEGs with MW of up to 35,000 and 65,000 g/mol, respectively, for the MWCO determination and the reported MWCO was also in UF ranges. So far, the method has never been reported for determining the MWCO of nanofiltration (NF) range membranes other than UF only. NF membrane is one type of pressure filtration membrane, situated between reverse osmosis (RO) and UF. NF typically represents filtration and rejection of solutes with sizes in the region of 200 – 2,000 g/mol [20] while UF represents solutes greater than 2,000 g/mol. Thus, this colorimetric method for PEG detection in the NF to UF membrane MWCO application has become the basis to be focused in this study.

Next, one of the identified drawback of this colorimetric method for MWCO determination is that it uses very low solute concentrations [16]. This is because at high concentration of PEG, the solute solution tends to precipitate. Thus, the reaction for this method is dependent on the concentration of the solution used [21]. However, low concentration of solute rejection may affect the membrane solute retention, in which consequently caused inaccurate MWCO reading. The concentration influenced the dipole moment interaction, which in turn affected the solute rejection [20]. Therefore, high concentration of feed solution is required to be used when performing the pressured membrane filtration in order to obtain a more accurate permeate concentration prediction [22]. Therefore in this study, a simple yet sensitive and detectable PEG of various MW ranges (600 – 20,000 g/mol) at different concentration ranges from low (0 ppm) and high (150 ppm) was established for a simple and reliable MWCO determination method in comparison to the previous method reported by [16]. This newly modified method is further tested using various commercial membranes of NF and UF for method verification to confirm the feasibility of the modified colorimetric method for determining MWCO of the membranes.

## Materials and Methods

### Materials

Barium chloride, hydrochloric acid, potassium iodide and iodine were supplied by Friendemann Schmidt from Chemolab Supplies. PEG with nominal MW (g/mol) of 600 (PEG600), 1,000 (PEG1000), 3,000 (PEG3000), 6,000 (PEG6000), 10,000 (PEG10000) and 20,000 (PEG20000) were from Sigma Aldrich supplied by Chemolab Supplies. Table 1 showed the properties of the PEGs involved. All chemicals were used as received.

Table 1. Various PEG properties differentiated by their MW

| PEG MW | Appearance | $M_n$ (g/mol) | Hydroxyl Value |
|---|---|---|---|
| PEG600 | Clear viscous colourless liquid | 590 – 610 | 176 – 200 |
| PEG1000 | White waxy solid | 950 – 1,050 | 105 – 120 |
| PEG3000 | White flakes | 2,700 – 3,300 | 34 – 42 |
| PEG6000 | White flakes | 5,500 – 6,500 | 16 – 20 |
| PEG10000 | White flakes | 9,000 – 12,500 | 9 – 12 |
| PEG20000 | White flakes | 16,000 – 28,000 | 4 – 7 |

A range of commercial membranes with different nominal MWCO from 200 to 20,000 g/mol (produced by different manufacturers) that were used in this work are tabulated in Table 2 below.

Table 2. List of commercial membranes with their nominal MWCO and manufacturer

| Membranes | Nominal MWCO Given by Manufacturer (g/mol) | Manufacturer |
|---|---|---|
| NF™ | 200 – 300 | Dow Filmtec™ |
| NF2 | 200 – 400 | Amfor Inc. |
| NF270 | 400 | Dow Filmtec™ |
| PES3 | 3,000 | Amfor Inc. |
| TF(GM) | 4,000 | GE Osmonics |
| PES10 | 10,000 | Amfor Inc. |
| PS20 | 20,000 | Amfor Inc. |

**Reagents and PEG preparation**

There were two types of reagents used for the determination of PEG, namely iodine solution (Reagent 1) and barium chloride solution (Reagent 2). Reagent 1 was prepared by dissolving 1.27 g iodine crystal in 100 mL of 2% (w/v) solution. It was further diluted for 10 times prior to use. Reagent 2 was prepared by dissolving 5 g of barium chloride in 100 mL of 1 M hydrochloride acid to form a 5% (w/v) solution [16]. 150 ppm PEG solutions (PEG600, PEG1000, PEG3000, PEG6000, PEG10000 and PEG20000) were prepared by dissolving 0.15 g of PEG in 1 L ultrapure water (Arium® Pro, Sartorius Malaysia Sdn Bhd, Malaysia). The solution was then being sonicated by using Analog Ultrasonic Cleaner (WUC-A03H, Daihan Scientific).

To plot PEGs standard curve, a series of concentration were prepared in range 2.5 - 7.5 ppm for Sabde et al. method while 10 – 150 ppm for the newly modified method (proposed in this work). Blank for both methods were prepared by using ultrapure water and were also added with reagent 1 and 2 as samples while blank used for spectrophotometer (Genesys 10UV, Thermo Electron Corporation, USA) was ultrapure water without addition of any reagents.

**Newly modified PEG method**

In initial MWCO determination method using PEG, the basis of the work was based on the method reported by [16], which applies the reaction of barium and iodide with PEG to form two complexes. Whereas this newly modified method is based on the formation of a single complex between PEG and iodine only. The comparison of both methods is presented in Table 3. In the newly modified method, the concentration range is increased to 150 ppm from 7.5 ppm in Sabde et al. method. The PEG sample volume used for the test was only 0.3 mL instead of 4 mL as compared to the previous method. Furthermore, only 1 reagent was used in the newly modified method than the other method, which used 2 reagents. However, the reaction time to dissolve the PEG in the reagent was double to stabilize the reaction.

Table 3. Comparison between the newly modified method and the method used by Sabde et al.

| Conditions | Sabde et al. Method | Newly Modified Method |
|---|---|---|
| Reagent 1 (mL) | 1 | 3 |
| Reagent 2 (mL) | 1 | None |
| Samples volume (mL) | 4 | 0.3 |
| Concentration range (ppm) | 0 - 7.5 | 0 - 150 |
| Reaction Time (min) | 15 | 30 |
| Spectrophotometer wavelength (nm) | 535 | 535 |
| PEG MW range (g/mol) | 600 – 20,000 | 600 – 20,000 |

In preparation to plot PEGs standard curve according to [16], 4 mL of PEG solution with different concentration were prepared in range 0 – 7.5 ppm. Then, 1 mL of each Reagent 1 and 2 were added. After 15 minutes, absorbance values were taken by using a spectrophotometer 535 nm against the blank reagent.

Meanwhile the standard curve plots for the newly modified method required the use of 0.3 mL of PEG solution in water with different concentration in the range of 0 – 150 ppm. Then, 3 mL of Reagent 1 was added. After 30 min, absorbance values were taken by using a spectrophotometer at the same wavelength with the previous method.

**Methods accuracy test**

In order to test the accuracy for both methods presented and reported by Sabde et al. [16] and the newly modified method (refer Table 4), three PEG sample solutions were used to calculate their concentration by using dilution equation ($M_1V_1 = M_2V_2$) from the initial PEG concentration of 150 ppm. These solutions were prepared for every MW of PEGs used (from PEG600 to PEG20000). The solutions were then being tested using both methods. Table 4

show the three solutions that were used in this test. The accuracy test is considered as successful when the final concentration values of the PEG solution calculated from dilution equation is the same or very near with the concentration values obtained from the standard curve plotted.

Table 4. Sample solutions used for methods accuracy test

| Volume of initial PEG solution (mL) | Volume of ultrapure water added into the solution (mL) | Final concentration of PEG solution calculated (ppm) |
|---|---|---|
| 0.2 | 14.8 | 5.3 |
| 0.6 | 14.4 | 16.0 |
| 1.0 | 14.0 | 26.7 |

Note: The PEG sample tested was from PEG600 to PEG20000

**Membrane filtration**

MWCO values of various commercial NF and UF membranes were given by the manufacturers (refer Table 2) are to be confirmed by using the newly modified method in comparison to Sabde et al. method. To determine this, solute rejections (SR) of the membranes were evaluated with various MW PEG solutions from 600 to 20,000 g/mol with concentration of 150 ppm at 30 bar by using a dead-end filtration cell (HP4750, Sterlitech Corporation, USA) [12]. The typical representation of the feed, permeate and retentate of the filtration solution through the membrane is shown in Figure 1. The membrane SR is defined by using Eq. (1) where, $C_f$ and $C_p$ are the PEG concentrations in the feed and permeate solution, respectively. The concentration of PEG was determined based on its absorbance mode in UV-spectrophotometer at wavelength 535 nm.

$$SR = \left(1 - \frac{C_p}{C_f}\right) \times 100 \quad (1)$$

Water flux of membrane with an active surface area of 14.6 $cm^2$ (which was compacted at 30 bar for 30 min) was determined by using Eq. (2) where J is the permeate flux (L./$m^2$.h), V is volume of permeate (L), A is effective membrane area ($m^2$) and t is operating time (h).

$$J = \frac{V}{A \times t} \quad (2)$$

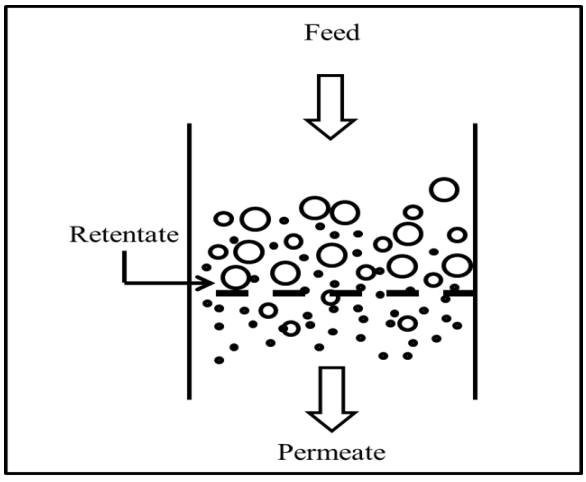



Figure 1. Schematic representation of membrane filtration system design by dead-end filtration cell

## Results and Discussion

### Newly modified PEG methods for MWCO determination

The standard calibration curves plot for the newly modified method in comparison to the method used by Sabde et al. [16] are shown in Figure 2 and the summary of the linear equations from the plot is presented in Table 5. Note that Sabde et al. [16] did not present their calibration curve plot in their report, thus re-plotting is required for a fair comparison for both methods.

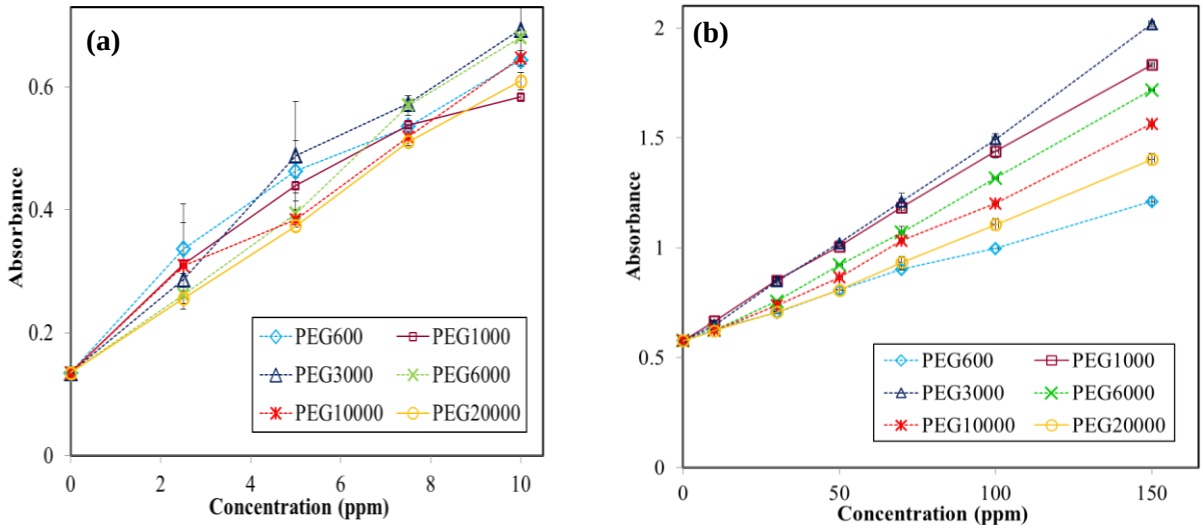



Figure 2. Standard curve of PEG for both methods with uses of PEG from MW 600 to 20,000 g/mol, a) Sabde et al. method and b) newly modified method

As shown in Figure 2 (a) and 2 (b), both methods gave a linear response to PEG at certain concentration for certain MW PEG. However, the curves for Sabde et al. method for different MW PEGs were only slightly differ to each other causes overlapping between the curves probably due to the low concentration of each of the PEGs solution used. On the other hand, the standard curves of the newly modified method showed linear curves without overlapping with one another probably because higher concentrations of solutions were used. These distinguished each curve of different PEGs MW. The curves are expected to be separated from one another for different PEGs MW since they have a different value of hydroxyl value for each of the PEGs (refer Table 1). PEG600 have the highest hydroxyl value as compared to other PEGs while PEG20000 has the lowest value. This hydroxyl value of PEG influences the absorbance reading in UV-spectrophotometer, where high MW of PEG will give low absorbance reading since their hydroxyl values are low and vice versa. The method used by Sabde et al. [16] did not show that they have this characteristic since all the standard curves plotted have overlapped to each other. This happened probably because of the reactivity of halogen group ($Cl^-$ from barium chloride) in Sabde et al. method was lower than the iodide ion ($I^-$) used in newly modified method. The reactivity in halogen group is in the following order (I > Br > Cl > F) [23, 24], where $Cl^-$ is confirmed to have a low reactivity than $I^-$ in their group. Thus, it is difficult for the $Cl^-$ to completely substitute the hydroxyl group in PEG. As a result, almost the same absorbance values for PEGs were obtained even at different MW and were used to plot the standard curve at the y-axis (refer Figure 2).

Moreover, the method used by Sabde et al. [16] obtained in this work possessed linear plots for concentration from 0 to 10 ppm only for PEG600 to PEG20000. At higher concentration (above 10 ppm), the complex tends to precipitate causing non-linear plots if the data is included. Although we found that 10 ppm is the highest

concentration to get a plot with $R^2$ of above 0.9 than 7.5 ppm as reported, this concentration is way too low compared to the newly modified method that can reach 150 ppm or may be more. Initially, this colorimetric method has been successfully used by few researchers in biological fields for many years [25]. For example, it was used for detecting PEG and PEGylated molecules in biological samples like protein [26], enzyme [13] and genes [21]. Shaffer and Critchfield on year 1947 was the first to develop this most commonly cited method for quantification of PEG molecules based on the formation of insoluble complexes between PEG and heteropoly inorganic acids (phosphomolybdic and silicotungstic acid) in the presence of barium chloride. The precipitate was then collected and washed for several times prior to testing it with iodine in order to detect the PEG [25]. Perhaps, this was the main reason for the employment of barium chloride for the quantification of PEG/PEGylated molecules in biological samples and this has answered the importance of the precipitation to occur in the method reported by Shaffer and Critchfield [25]. However, in the application of membrane technology especially for MWCO determination, it was found that precipitation of PEG is an undesirable step and must be avoided since it could interfere during the reading of absorbance values by using UV spectrophotometer. The presence of precipitate causes spectral interferences due to the colloidal particles spread in the solution [27, 28]. Therefore, in order to have an accurate absorbance reading, appropriate dilutions of the samples are necessarily required to make sure their concentrations are below 7.5 ppm before the addition of the two reagents (barium chloride and iodine) into the samples to avoid precipitation from occurs.

Table 5. Equation of standard curve and $R^2$ values for Sabde et al. method and newly modified method

| PEG MW (g/mol) | Sabde et al. Method | | Newly Modified Method | |
|---|---|---|---|---|
| | **Linear Equation** | **$R^2$ Value** | **Linear Equation** | **$R^2$ value** |
| PEG600 | y = 0.0546x + 0.135 | 0.9431 | y = 0.0043x + 0.578 | 0.9959 |
| PEG1000 | y = 0.0506x + 0.135 | 0.9319 | y = 0.0085x + 0.578 | 0.9991 |
| PEG3000 | y = 0.0588x + 0.135 | 0.9779 | y = 0.0094x + 0.578 | 0.9977 |
| PEG6000 | y = 0.0551x + 0.135 | 0.9955 | y = 0.0074x + 0.578 | 0.9952 |
| PEG10000 | y = 0.0517x + 0.135 | 0.9863 | y = 0.0064x + 0.578 | 0.9954 |
| PEG20000 | y = 0.0484x + 0.135 | 0.9982 | y = 0.0053x + 0.578 | 0.9937 |

Based on the results shown in Figure 2(b) and Table 5, the newly modified method gave linear relationship from 0 to 150 ppm for PEG600 to PEG20000 with $R^2$ values nearly 1. Please note that this newly modified method is solely depended on complex formation between PEG and iodine only. The reaction is called halogenation where hydroxyl group in PEG will be substituted by iodide ion [24]. In this reaction, there is no precipitation produced and observed since there is no involvement of metal ions like barium ion that can form precipitate. The main advantage of this method is that there is no precipitate formed even at concentration up to 400 ppm. Furthermore, this newly modified method only used 0.3 mL of the collected samples, is tenth times much lower than Sabde et al. method which required as much as 4 mL samples during PEGs detection. There are membranes which requires 1 hour only to collect 1 mL permeate, thus this newly modified method could reduce the time required for permeate collection.

Since there was no reaction mechanism so far reported for both methods, the mechanisms are proposed in Figure 3 based on the findings obtained in this work. Both methods use Lewis acid-Lewis base reaction as basis, where halogen (Cl or/and I) acts as the electrophilic species (Lewis acid) while electron-rich organic compound (PEG) as the nucleophilic species (Lewis base) [24]. As for the former method by Sabde et al. [16], the mechanism is as shown in Figure 3 (Reaction 1). Firstly, hydroxyl group (OH) at both end of PEG is substituted with chloride ion ($Cl^-$) (upon addition of barium chloride solution into PEG solution), left barium ion ($Ba^{2+}$) on its own. $Ba^{2+}$ thereafter forms ionic bonding with iodide ion ($I^-$) after the addition of iodine solution into the mixture. This bonding tends to precipitate at concentration 10 ppm. In contrast, hydroxyl group of PEG is substituted directly by $I^-$ upon the addition of iodine solution into PEG solution as illustrated in Figure 3 (Reaction 2) for the newly modified method. No precipitation is produced in Reaction 2 as found in Reaction 1.

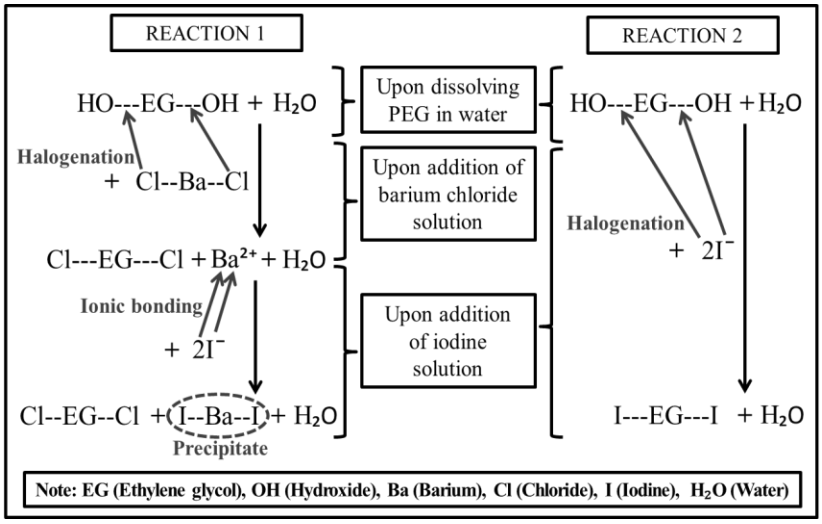



Figure 3. Proposed reaction mechanism for MWCO determination methods

**Methods accuracy test**

Three types of PEG with different MW were used for this accuracy test which is PEG with lowest (PEG600), middle (PEG6000) and highest (PEG20000) MW. A set of samples solution were prepared from these three PEGs to examine the accuracy of both compared methods. The test was repeated for three times to determine the standard deviation and further minimizing the error.

From the results showed in Table 6, both methods gave accurate values (calculated and actual) for the concentration of the samples solution. There was no dilution needed during the accuracy test for the newly modified method. However, the former method required some dilutions to be done especially for PEG6000 and PEG20000 (refer Table 6). The concentrations of the solutions were 16.0 and 26.7 ppm, respectively. At this concentration, precipitation tends to occur since their concentrations are above 10 ppm. Therefore, dilution must be conducted during using the former method to determine the concentration of the solutions. Luckily, the dilution work that has been conducted to eliminate precipitation is easily done since their final concentration is known. However, if this former method is applied for quantifying the MWCO of a membrane from pressure filtration, it will be very difficult to identify the dilution factor to bring the solution's concentration at below 10 ppm since the permeate concentration is unknown. Thus, this test can be showed as a proof that the newly modified method is easier, more reliable and accurate to be used in determining MWCO of various filtration membranes specifically for NF and UF than the former method reported by Sabde et al. [16].

**Commercial membranes solute filtration test**

Commercial NF and UF membranes were used in solute filtration test for the MWCO study. NF and NF270 membranes were kindly donated by Dow Chemical Company. TF(GM) membranes and NF2, PES3, PES10, and PS20 were purchased from GE Osmonics and Amfor Inc. respectively (refer Table 2 for details). MWCO of all membranes were determined by using PEG with MW ranges from 600 to 20,000 g/mol. The solute MW ranges was divided into two categories: (i) NF range for MWCO below 2,000 g/mol, and (ii) UF range for MWCO above 2,000 g/mol. Table 7 and Figure 4 show the results of the fluxes and MWCO for all the NF and UF membranes tested by both methods. It was found that the fluxes for the membranes in water were higher than in the PEG solutions, as expected. This is because the solutes in the solution hinder the permeation of water thus reducing the flux. The PEGs used for the flux in PEGs are from PEG600 to PEG20000. This flux value was averaged out from the flux obtained at each PEG solutions used. The higher the MW of PEG used, the lower the flux recorded.

Table 6. Comparison between calculated and actual concentration of unknown samples

| **PEG MW (g/mol)** | **Sabde et al. Method** | | | **Newly Modified Method** | | |
|---|---|---|---|---|---|---|
| | **600** | **6000** | **20000** | **600** | **6000** | **20000** |
| Dilution factor | No | 0.25 | 0.25 | No | No | No |
| Absorbance value | | | | | | |
| Run 1 | 0.427 | 0.362 | 0.469 | 0.601 | 0.697 | 0.721 |
| Run 2 | 0.427 | 0.361 | 0.466 | 0.601 | 0.697 | 0.721 |
| Run 3 | 0.426 | 0.362 | 0.464 | 0.601 | 0.696 | 0.721 |
| Values by standard curve (ppm) | | | | | | |
| Run 1 | 5.3 | 16.5 | 27.6 | 5.3 | 16.0 | 26.7 |
| Run 2 | 5.3 | 16.4 | 27.4 | 5.3 | 16.0 | 26.7 |
| Run 3 | 5.3 | 16.5 | 27.2 | 5.3 | 16.0 | 26.7 |
| Values by calculation (ppm) | 5.3 | 16.0 | 26.7 | 5.3 | 16.0 | 26.7 |
| Standard deviation | ±0 | ±0.058 | ±0.2 | ±0 | ±0 | ±0 |

Table 7. Membrane separation properties (flux and MWCO) of the different commercial membranes obtained from dead-end filtration test

| **Membrane** | **Pure Water Flux ($L/m^2.h$)** | **PEGs Flux ($L/m^2.h$)** | **Sabde et al. Method** | | **Newly Modified Method** | | **Nominal MWCO by Manufacturer (g/mol)** |
|---|---|---|---|---|---|---|---|
| | | | **MWCO** | **% Error** | **MWCO** | **% Error** | |
| NF$^{TM}$ | 175.2 | 163.7±2.95 | 550 | +83.3 | 550 | +83.3 | 200 – 300 |
| NF2 | 174.8 | 109.6±1.16 | 500 | +25.0 | 500 | +25.0 | 200 – 400 |
| NF270 | 389.2 | 194.3±4.92 | 530 | +32.5 | 530 | +32.5 | 400 |
| PES3 | 175 | 164.4±2.45 | 3250 | +8.3 | 2980 | -0.7 | 3000 |
| TF(GM) | 258 | 244.9±1.01 | 4600 | +15.0 | 3990 | -0.3 | 4000 |
| PES10 | 150 | 129.3±0.65 | 2600 | -74.0 | 10000 | 0 | 10000 |
| PS20 | 280 | 205.5±0.78 | 8600 | -57.0 | 19850 | -0.8 | 20000 |

In terms of the MWCO values, the newly modified method gave the most accurate values for the UF membranes as given by the manufacturers. For example, PES10 has the same value as given while PES3, TG(GM) and PS20 values were found to be <1% difference than the given values indicating the accuracy of the newly modified method. However, the MWCO values of the UF membranes determined by Sabde et al. method was different from the nominal MWCO given by the manufacturer. There are up to 74% difference in the calculated values. Of all the tested UF membranes, PES10 and PS20 have the farthest difference compared to others. This difference might be due to the dilution factor, which is required during the determination. The bigger the concentration of the PEG, the tendency for precipitation to occur is higher. Therefore, the detection of the absorbance values in spectrophotometer became imprecise.

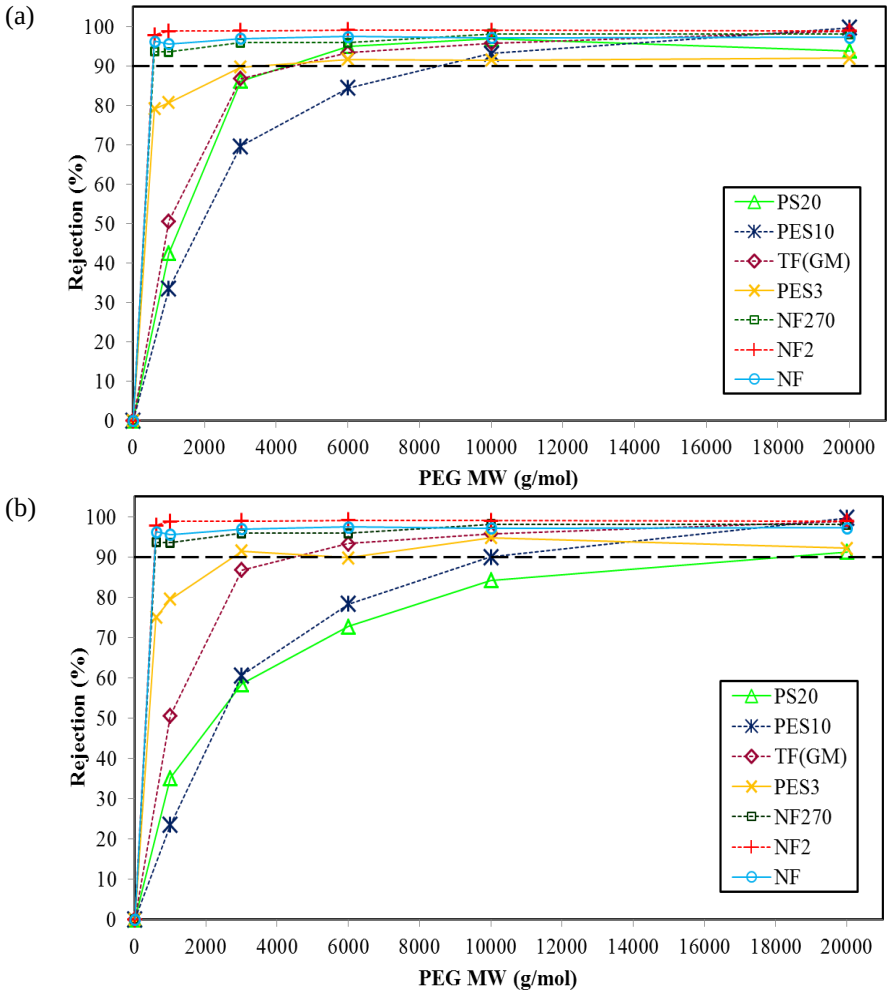



Figure 4. MWCO curve for commercial membranes using the PEG as solute filtration following both methods, (a) Sabde et al. and (b) newly modified method

Meanwhile the difference in MWCO values for NF membranes (for both method) were unavoided due to the lowest MW of PEG is 600 g/mol only while the membranes' MWCO were given in the range of 200 to 400 g/mol. NF270 and NF2 have the closest MWCO values while NF™ has the farthest values. Since the current method could not apply PEG 200 and 400 yet, optimization of the method is still on going to include this PEG in the range. NF membrane's MWCO at 500<MWCO<2000 g/mol is expected to give accurate values as found in UF ranges. Similar research work was reported to confirm the developed MWCO method [12, 29, 30]. The difference in the MWCO of the membrane in comparison to the values provided by the manufacturers was discussed in details. For example, [12] have found a single run of pressure filtration with a mixture of PEGs in aqueous solution to determine MWCO of membranes. However, the method used to determine the MWCO have utilized a high-end equipment of HPLC coupled with ELSD detector though using PEGs as the solutes. Other work has also used gas chromatography (GC) with specific column to determine the styrene derivatives [10], alkanes detected in HPLC [30]. Based on this comparison study, the newly modified method is confirmed can accurately determine the MWCO in the range of 500 to 20,000 g/mol, which indicates the reliability of this method to substitute the method currently referred to [16].

## Conclusion

A simple yet sensitive MWCO detection method was modified and developed from the commonly referred method in order to accurately determine PEG concentration in solute retention. The accuracy of this method is confirmed based on the filtration test using a range of commercial membranes. The MWCO values were found to be closed to the values given by the manufacturer. Since the accuracy of this method was verified and confirmed, this newly modified method could be used for determining membranes MWCO of either commercial or synthesized ones. High concentration of PEGs solution could be detected without the need for dilution since appropriate single reagent was used, thus no precipitation is presence as supported by the proposed reaction mechanism. This method can accurately determine the membrane MWCO (g/mol) in the range of 500<MWCO<20,000 as confirmed in this work.

## Acknowledgment

The authors would like to acknowledge the financial support of the Fundamental Research Grant Scheme (FRGS/2/2013/TK05/UKM/02/4), GUP-2016-086 (UKM), Department of Chemical and Process Engineering, Universiti Kebangsaan Malaysia and MyMaster by MOSTI for the MSc scholarship.

## References

1. Alam, J., Dass, L. A., Alhoshan, M. S., Mostafa Ghasemi and Mohammad, A. W. (2011). Development of polyaniline-modified polysulfone nanocomposite membrane. *Applied Water Science*, 2(1): 37 - 46.
2. Zhao, Q., Quanfu, A. F., Ji, Y., Qian, J. and Gao, C. (2011). Polyelectrolyte complex membranes for pervaporation, nanofiltration and fuel cell applications. *Journal of Membrane Science*, 379(1-2): 19 - 45.
3. Prafulla, G. B., Sapkal, V. S. and Sapkal, R. S. (2012). The optimization and production polyethersulfone ultrafiltration flat sheet membranes using lithium chloride as additives. *International Journal of Engineering Research and Development* 1(12): 65 - 68.
4. Uludag, H., Paul, D.V. and Patrick, A. T. (2000). Technology of mammalian cell encapsulation. *Advanced Drug Delivery Reviews*, 42: 29 - 64.
5. Derakhsheshpoor, R., Homayoonfal, M., Akbari, A. and Mehrnia, M. R. (2013). Amoxicillin separation from pharmaceutical wastewater by high permeability polysulfone nanofiltration membrane. *Journal of Environmental Health Science and Engineering*, 11(1): 9 - 19.
6. Idris, A. and Zain, N. M. (2006). Effect of heat treatment on the performance and structural details of polyethersulfone ultrafiltration membranes. *Jurnal Teknologi*, 44: 27 - 40.
7. Kim, K. J., Fanen, A. G., Ben Aimb, R., Liub, M. G., Jonsson, G., Tessaro, C. I. C., Broekd, A. P. and Bargemand, D. (1994). A comparative study of techniques used for porous membrane characterization: Pore characterization. *Journal of Membrane Science*, 87: 35 - 46.
8. Nakao, S.-I. (1994). Review: Determination of pore size distribution 3. Filtration membranes. *Journal of Membrane Science*, 96: 131 - 165.
9. Changzsheng, Z., Xuesong, Z. and Yilun, Y. (2000). Determination of pore size and pore size distribution on the surface of hollow-fiber filtration membranes: A review of methods. *Desalination*, 129: 107 - 123.
10. Kang, E., Lee, Y., Chon, K. and Cho, J. (2014). Effects of hydrodynamic conditions (diffusion vs. convection) and solution chemistry on effective molecular weight cut-off of negatively charged nanofiltration membranes. *Desalination*, 352: 136 - 141.
11. Hassan, A. R. and Ismail, A. F. (2004). Characterization of nanofiltration membranes by the solute transport method: some practical aspects in determining of mean pore size and pore size distributions. *Regional Symposium on Membrane Science and Technology*. Puteri Pan Pacific Hotel, Johor Bharu, Malaysia: pp. 1 - 13.
12. Rohani, R., Hyland, M. and Patterson, D. (2011). A refined one-filtration method for aqueous based nanofiltration and ultrafiltration membrane molecular weight cut-off determination using polyethylene glycols. *Journal of Membrane Science*, 382(1-2): 278 - 290.
13. Felo, M. and DeFrees, S. (2012). Nucleotide Sugar Purification using membranes in google patent. Novo Nordisk A/S, Bagsvaerd (DK): United States. 27.
14. Cheng, T. L., Chuang, K. H., Chen, B. M. and Roffler, S. R. (2012). Analytical measurement of PEGylated molecules. *Bioconjugate Chemistry*, 23(5): 881 - 899.
15. Kolate, A., Baradia, D., Patil, S., Vhora, I., Kore, G. and Misra, A. (2014). PEG - A versatile conjugating ligand for drugs and drug delivery systems. *Journal of Control Release*, 192: 67 - 81.

16. Sabde, A. D., Trivedi, M. K., Ramachandhran, V., Hanra, M. S. and Misra, B. M. (1997). Casting and characterization of cellulose acetate butyrate based UF membranes. *Desalination*, 114: 223 - 232.
17. Idris, A., Mat Zain, N. and Noordin, M. Y. (2007). Synthesis, characterization and performance of asymmetric polyethersulfone (PES) ultrafiltration membranes with polyethylene glycol of different molecular weights as additives. *Desalination*, 207(1-3): 324 - 339.
18. Padaki, M., Isloor, A. M. and Wanichapichart, P. (2011). Polysulfone/N-phthaloylchitosan novel composite membranes for salt rejection application. *Desalination*, 279(1-3): 409 - 414.
19. Prafulla, G. B., Sapkal, R. S. and Sapkal, V. S. (2008). Influence of ethanol concentration on the performance of polyethersulfone ultrafiltration membranes. *International Journal of ChemTech Research*, 4(4): 1518 - 1521.
20. Shirley, J., Mandale, S. and Kochkodan, V. (2014). Influence of solute concentration and dipole moment on the rejection of uncharged molecules with nanofiltration. *Desalination*, 344: 116 - 122.
21. Fella, C. (2008). Dynamic and effective gene vectors via ph-sensitive peg-shielding. Thesis Doctor of Philosophy. Faculty of Chemistry and Pharmacy, Ludwig Maximilian University of Munich, Miltenberg.
22. Christopher, B., Drewes, J. E., Pei, X. and Gary, A. (2004). Factors affecting the rejection of organic solutes during NF/RO treatment - A literature review. *Water Research*, 38: 2795 - 2809
23. Bernadisiute, U., Antanelis, T., Vareikis, A. and Makuska, R. (2008). Iodination of poly(ethylene glycol) by a mixture of triphenyl phosphite and iodomethane. *Chemija*, 19(2): 43 - 49.
24. Moulay, S. (2013). Molecular iodine/polymer complexes. *Journal of Polymer Engineering*, 33(5): 389 - 443.
25. Shaffer, C. B. and Critchfield, F. H. (1947). Solid polyethylene glycols (carbowax compounds) quantitative determination in biological materials. *Analytical Chemistry*, 19(1): 32 - 35.
26. Barker, T. H., Klinger, M. M., Feldman, D. S., Fuller, G. M. and Hagood, J. S. (2001). Spectrophotometric analysis for determining the average number of poly(ethylene) glycol molecules on PEGylated proteins utilizing a protein digestion step. *Analytical Biochemistry*, 290(2): 382 - 385.
27. Lozzi, I., Pucci, A., Pantani, O. L., D'Acqui, L. P. and Calamai, L. (2008). Interferences of suspended clay fraction in protein quantitation by several determination methods. *Analytical Biochemistry*, 376: 108 - 114.
28. Wuelfing, W. P., Kosuda, K., Templeton, A. C., Harman, A., Mowery, M. D. and Reed, R. A. (2006). Polysorbate 80 UV/vis spectral and chromatographic characteristics – defining boundary conditions for use of the surfactant in dissolution analysis. *Journal of Pharmaceutical and Biomedical Analysis*, 41: 774 - 782.
29. Tam, C. M. and Tremblay, A. Y. (1991). Membrane pore characterization-comparison between single and multicomponent solute probe techniques. *Journal of Membrane Science*, 57: 271 - 287.
30. Rissler, K. (1996). High-performance liquid chromatography and detection of polyethers and their mono(carboxy)alkyl and -arylalkyl substituted derivatives. *Journal of Chromatography A*, 742: 1 - 54.

*Malaysian Journal of Analytical Sciences, Vol 21 No 2 (2017): 496 - 511*
*DOI: https://doi.org/10.17576/mjas-2017-2102-25*

MALAYSIAN JOURNAL OF ANALYTICAL SCIENCES
*Published by The Malaysian Analytical Sciences Society*
ISSN 1394 - 2506

# PALM OIL-BASED PRECURSORS FOR DEVELOPMENT OF POLYMERIC DELIVERY SYSTEM

## (Pelopor Berasaskan Minyak Sawit untuk Pembangunan Sistem Penyampai Polimer)

Rida Tajau[1,2], Rosiah Rohani[1]*, Wan Nor Roslam Wan Isahak[1], Mek Zah Salleh[2]

[1]*Department of Chemical and Process Engineering, Faculty of Engineering and Built Environment, Universiti Kebangsaan Malaysia, 43600 UKM Bangi, Selangor, Malaysia*
[2]*Radiation Processing Technology Division, Malaysia Nuclear Agency, 43000 Kajang, Selangor, Malaysia*

**Corresponding author: rosiah@ukm.edu.my*

Received: 21 October 2015; Accepted: 14 June 2016

**Abstract**

The use of precursors from natural based polymers offer a more biocompatible and biodegradable properties in producing polymer drug vehicle compared to drug vehicles made from synthetic polymer precursors, which normally found in high molecular weight (MW). High MW polymer will lead to immunologic inflammatory responses due to their lower biodegradability and higher cytotoxicity compared to low MW that could give smaller particle size, higher solubility, higher release efficiency, non-immunogenic, better biodegradability and lower cytotoxicity. Therefore, this study is aimed to produce valuable precursors, particularly to produce epoxidized palm olein (EPOo) and diol, to be used in the development of a new polymeric drug vehicle with low MW. An EPOo was synthesized via *in-situ* epoxidizing of palm olein (POo) with peracid and sulfuric acid ($H_2SO_4$) catalyst. Meanwhile the diol was synthesized using hydroxylation of palm oil-based oleic acid via esterification of oleic acid (OA) with glycerol and 4-dodecylbenzyl sulfonic acid catalyst (DBSA). It was found that both palm oil-based precursors have been successfully synthesized from natural resources of palm oil. Physico-chemical properties of the synthesized precursors showed that the EPOo and the diol possess average molecular weight (MW) between 900-1500 g/mol and hydroxyl functionality between 2 and 3, based on the presence of hydroxyl (O-H) group functionality, showed in the Infra-red (IR) spectra in the range of 3200-3600 $cm^{-1}$. These low MW palm oil based-precursors have potential uses for the design and development of new properties of polymeric drug vehicle such as acrylated palm olein (APOo) and polyol polyester, which will produce particle size in the range of 100 - 200 nm or smaller with high efficiency drug loading and controlled release profiles.

**Keywords**: drug delivery system, palm oil, polymeric nanoparticle

**Abstrak**

Penggunaan pelopor dari polimer semulajadi bagi menghasilkan penyampai ubat polimer mempunyai kelebihan tertentu iaitu ianya bersifat bioserasi dan biodegradasi berbanding sistem penyampai ubat yang dibuat daripada pelopor polimer sintetik, kebiasaannya mempunyai berat molekul (MW) yang tinggi. Polimer dengan MW yang tinggi boleh menyebabkan gerak balas keradangan keimunan akibat kurang keterbiodegradasikan dan kesitotoksikan yang tinggi dibandingkan MW yang rendah yang boleh menghasilkan partikel bersaiz lebih kecil, keterlarutan dan kecekapan perlepasan yang tinggi, tidak imunogen, terbiodegradasi dengan lebih baik dan sitotoksiti yang rendah. Oleh itu, kajian ini bertujuan menghasilkan pelopor yang bersifat istimewa, terutamanya minyak sawit olein terepoksida (EPOo) dan diol yang digunakan dalam membangunkan sistem penyampaian ubat dengan MW yang rendah. EPOo telah disintesis menggunakan pengepoksidaan *in-situ* minyak sawit olein (POo) dengan perasid dan pemangkin asid sulfurik ($H_2SO_4$). Sementara itu, diol disintesis menggunakan penghidroksilan minyak sawit oleik menggunakan pengesteran asid oleik (OA) dengan gliserol dan pemangkin asid sulfonik 4-dodesilbenzil (DBSA). Hasil penemuan mendapati kedua-dua pelopor yang berasaskan minyak sawit ini telah berjaya disintesis daripada sumber semulajadi minyak sawit. Sifat fisiko-kimia pelopor yang telah disintesis menunjukkan EPOo dan diol mempunyai berat

molekul (MW) antara 900-1500 g/mol dan bilangan hidroksil antara 2 dan 3, berdasarkan kehadiran kumpulan berfungsi hidroksil (O-H), yang ditunjukkan dalam spektra Infra-merah (IR) dalam julat 3200-3600 $cm^{-1}$. Pelopor berasaskan minyak sawit yang mempunyai berat molekul yang rendah berpotensi untuk direkabentuk bagi membangunkan sistem penyampai ubat polimer yang bersifat baru seperti minyak sawit olein terakrilat (APOo) dan poliol poliester, yang menghasilkan partikel bersaiz 100-200 nm atau lebih kecil dengan kecekapan pemuatan ubat dan profil perlepasan terkawal yang tinggi.

**Kata kunci:** sistem penyampai ubat, minyak sawit, nanopartikel polimer

## Introduction

Polymers are amongst the most extensively explored and widely use materials as drug vehicles for localized and sustained delivery of drug (medication) to a patient [1, 2]. There are different types of drug vehicles such as macromolecular carriers (macromolecular prodrugs, protein-macromolecule conjugates and gene medicines complexed with macromolecular carriers), particulate carriers (micro/nanoparticles, liposomes, dendrimers, lipoproteins, nanotubes, micro/nanospheres and micro/nanoemulsions) and cellular carriers (leucocytes, platelets, erythrocytes, nanoerythrocytes, hepatocytes, and fibroblast) [3-5].

Natural polymers are currently gaining a lot of research interest due to their advantages such as utilizing environmental friendly materials and involving low energy process which is way better than the synthetic polymers produced via chemical synthesis. The trend of using palm oil based materials for the development of polymeric drug vehicles is growing due to the natural polymer's biocompatibility compared to the petrochemical-based polymers [6-11]. In addition, the synthetic polymers commonly use chemicals that emits greenhouse gases (GHGs), utilizes high energy during the products preparation and processing and most importantly generates toxic by-products [12]. Thus, the use of renewable feed stock resources such as from palm oil products is receiving numerous interest compared to petrochemical-based products.

In this study, new precursors namely epoxidized palm olein (EPOo) and diol were developed from the palm oil product of palm olein (POo) and oleic acid (OA) for the EPOo and diol, respectively. The chemical reaction of epoxidation and esterification processes were applied in developing a non-toxic and cleaner reaction of the palm oil based-precursors. Epoxidation process is performed using *in-situ* generated peroxyacetic acid due to several advantages, such as minimum amounts of reactants are needed to prepare the epoxidising reagent and safer preparation and handling, compare using the preformed peroxyacid that had handling problems since the concentrated peroxyacid is unstable and explosive [13]. Besides, the peroxyacetic was selected due to its easy availability, low production cost and stability at high temperatures, compare to the peroxybenzoic acid, peroxyformic acid, peroxyfluoroacetic acid, *m*–chloroperoxybenzoic acid and *m*–nitroperoxybenzoic acid [13-14].

Esterification process is performed with an oleic acid and a 4-dodecylbenzyl sulfonic acid (DBSA) for the diol production, in the absence of solvent. The DBSA was selected because is more efficient catalyst in water where it can act as emulsifier and catalyst compared to other catalysts such as hydrochloric acid, sulphuric acid, phosphoric acid ($H_3PO_4$ and *p*-toluenesulfonic acid [15-17]. Besides, the esterification process with the DBSA catalyst is considerable as green process, cheap and high product yields [17].

In this work, the study included synthesizing and characterizing of the synthesized precursors. The EPOo and diol produced from the palm oil product are expected to exhibit promising physicochemical properties and have great potential for application in development of new polymeric drug vehicles.

## Materials and Methods

In both preparations of the EPOo and diol, the experimental set-up used in this work was reported and referred in our previous work [18, 19]. The set-up consists of reaction flask, mechanical stirrer, thermometer, reflux condenser and oil batch.

### Preparation of epoxidized palm olein based precursors

A food grade palm olein (POo) (FFM Marketing Sdn. Bhd) was used as a feedstock to produce the EPOo while other chemicals in this preparation were purchased from Systerm Chem Ar. Initially the POo was vacuum distilled

prior to use. Then the POo (1.62 mol) underwent in-situ epoxidizing in the per-acid solution to form the EPOo at the temperature between 60 – 65 $^{o}$C for 2.5 hours [14, 20]. The per-acid solution consisted of a glacial acetic acid (4 mol), a hydrogen peroxide (8.24 mol) and a sulphuric acid (1%). The chemicals were purchased from Systerm Chem Ar., Merck and HmBG Chemical, respectively. After the epoxidation reaction was completed, the EPOo was immediately transferred from the reaction flask to 2 L glass beaker. Next, the EPOo was washed with distilled water and vacuum distilled. The summary of the overall EPOo synthesis process is presented in Figure 1 below.

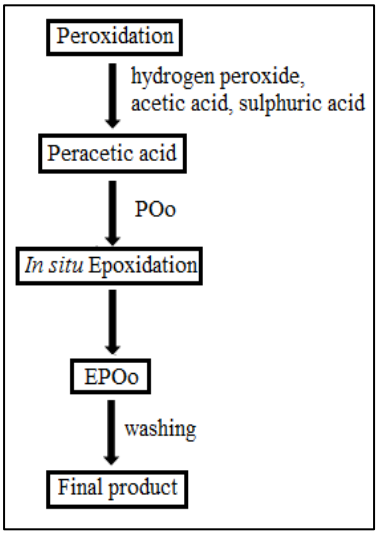



Figure 1. The synthesis routes of the EPOo

**Preparation of diol as palm oil based precursors**
On another occasion, oleic acid (OA) (R&M Chemicals) was vacuum distilled for 3 hours before vacuum recrystallized in acetonitrile. After recrystallization, the OA (1.2 mol) was esterified with glycerol (2.4 mol) and 4-dodecylbenzyl sulfonic acid (DBSA) (0.15 mol) to produce diol at the temperature below 120 $^{o}$C for three hours [15]. The chemicals were purchased from R&M, Systerm Chem Ar. and Fluka, respectively. Next, the synthesized diol was immersed in a mixture solution consist of ethanol (5%) and natrium chloride (5%) for 24 hours before vacuum distilled and collected for characterization.

The yield of the reaction for the EPOo and the diol was calculated using Equation (1).

$$\% \text{ Reaction yield} = \left[\frac{\text{Final yield (g)}}{\text{reactant(g)}}\right] \times 100 \quad (1)$$

**Characterization of the precursor's physicochemical properties: Oxirane oxygen content (OOC)**
The OOC test was performed following the standard method of AOCS method Cd 9-57, 1963 [21].

$$\% \text{ OOC} = \frac{(1.6 \times \text{N} \times \text{v})}{\text{w}} \quad (2)$$

where N is normality of hydrogen bromide (HBr), while v is volume of HBr in mL and w is weight of resin in gram.

**Acid value**
The acid value (AV) was calculated according to the test method is technically equivalent to ASTM D974 [22]:

$$AV=\frac{(5.61 \times v)}{w} \quad (3)$$

where 5.61 is a concentration conversion coefficient (a number of mg KOH corresponding to 1 mL of 0.1 N KOH), v is volume of 0.1 N KOH and w is weight of resin in gram.

**Saponification value**
The saponification value (SV) was calculated according to the test method ASTM D 1962-67 [23].

$$SV=\frac{[56.1\ (B-S) \times N]}{w} \quad (4)$$

where B is volume of 0.5 N HCl required by Blank, S is volume of 0.5 N HCl required by Sample, N is concentration value of HCl = 0.5 N and w is weight of resin in gram.

**Iodine value**
The iodine value (IV) was calculated according to the Hanus method as described in the AOCS (Cd 1-25) [24].

$$IV=\frac{[(B-S)\times N \times 0.127\ X\ 100]}{w} \quad (5)$$

where B is volume of 0.1 N sodium thiosulfate required by Blank, S is volume of 0.1 N sodium thiosulfate required by Sample, N is concentration value of sodium thiosulfate = 0.1 N and w is weight of resin in gram.

**Ester value**
Ester Value (EV) is defined as the mg of KOH required to react with ester content (glycerin or glycerol) after saponification one gram of fat. EV was determined by the equation described in literatures [25-27], where the EV is defined as the difference between the saponification value and acid value:

$$EV = SV - AV \quad (6)$$

where SV is saponification value and AV is acid value of sample.

**Percentage of ester**
Percentage of ester was calculated from ester value and molecular weight by the Equation (7) described by Lubrizol [27]:

$$\%\ Ester = \frac{[(EV)(MW\ ester)]}{10 \times 56.1} \quad (7)$$

where EV is ester value of sample and the value calculated following Equation (6) and MW is molecular weight of ester = 126.11 g/mol.

**Hydroxyl value**
The OHV was calculated according to the test method ASTM D4274-99 Method C [28].

$$OHV=\frac{(B-S)\times 28.05}{w} + AV \quad (8)$$

where B is volume of 0.5 N ethanolic potassium hydroxide required by Blank, S is volume of 0.5 N ethanolic potassium hydroxide required by sample, w is weight of resin in gram and AV is acid value of sample.

**Hydroxyl number functionality**
The hydroxyl number functionality (OHf) was determined by the equation described by Ionescu [29] and used known hydroxyl value and molecular weight of sample:

$$\mathrm{OHf} = \frac{\mathrm{OHV} \times \mathrm{MW}}{56100} \tag{9}$$

where OHV is hydroxyl value of sample and MW is average molecular weight of sample.

**Dynamic viscosity**
The dynamic viscosities of the products in liquid form were measured using Brookfield viscometer (Model RV: DVII + Pro) at 25 °C [30]. The spindle plate with grade 40 and CPE-44PY cup were selected for measuring viscosity.

**Average molecular weight**
The average molecular weight of sample was determined by the equation described by Xu et al. [31] by using known saponification value (SV) and acid value (AV) of sample.

$$\text{Average Molecular Weight} = \frac{168300}{\mathrm{SV\text{-}AV}} \tag{10}$$

where SV is saponification value and the value was obtained using method (iii) and calculated following Equation (4) and AV is acid value and the value was obtained using method (ii) and calculated using Equation (3).

**Fourier transform infrared spectroscopy**
The infrared (IR) spectroscopy of the samples was performed using diamond attenuated total reflectance (DATR) technique. The infrared spectrums of the samples were recorded in the range of 4000 $cm^{-1}$ to 650 $cm^{-1}$ by spectrum 400, FT-IR/FTNIR spectrometer (Perkin Elmer, UK).

**Thermogravimetric analysis**
Thermogravimetric analysis (TGA) was performed using the TGA-SDTA 851e Mettler Toledo instrument (USA). Samples were analyzed in temperature range from 27 °C to 800 °C, heating rate of 10 °C/min.

**Differential scanning calorimetry**
Differential scanning calorimetry (DSC) was carried out using the DSC 822, Mettler Toledo instrument (USA). Samples were scanned at 5 °C/min at first heating cycle from -100 °C to 200 °C and followed by the cooling cycle from 200 °C to -100 °C.

## Results and Discussion

**Physico-chemical properties of the palm oil based precursors**
Table 1 showed the physico-chemical properties of the palm oil-based precursors. The values in Table 1 were obtained using Equation (2) to (8). The acid value of POo and OA was 0.56% and increased to 8.09% and 67.32% after conversion to EPOo and diol, respectively. The iodine value of POo and OA were 61.47 mg KOH/g oil and 83.91 mg KOH/g oil which is almost similar to the work reported by Ramli et al. [32] at 61.67 mg KOH/g oil and Derawi et al. [8, 14] at 62 mg KOH/ g oil, but slightly higher to the work reported by Ramli et al. [33] at 78.2 mg KOH/g oil for the IV value of high-oleic acid palm oil. The POo was found to have a complete epoxidization to EPOo based on the reduction of the iodine value of POo from 61.47 to 0 mg KOH/g oil (Table 1), which corresponds to the complete conversion of the POo carbon double bond (C=C) to the epoxide (oxirane) ring of EPOo and similar to the reported previous study by Derawi et al. at IV 61.67 drops to 3.30 to 0.51 [14]. Due to this reason, the oxirane oxygen content (OOC) of the EPOo have increased to 3.33% compared to the POo OOC value of 0.04% only in the beginning of the reaction (Table 1). This OOC EPOo result is similar to the previous study

reported by Giita Silverajah et al. (3.23%) [34]. Meanwhile the saponification value of POo to EPOo was slightly reduced, 196.21 and 192.50 mg KOH/g oil, respectively. Further similarity was the slight reduction of ester value and ester percentage, which were recorded for the POo and EPOo (refer Table 1). This corresponds to the minor modification on triglyceride structure of POo by introducing epoxide ring to the POo's for producing of new triglyceride structure of EPOo [14, 35].

Table 1. Physico-chemical properties of the new precursors

| **Conducted Test** | **Raw Material 1: Poo** | **Precursor 1: Epoo** | **Raw Material 2: OA** | **Precursor 2: Diol** |
|---|---|---|---|---|
| Acid value (%) | 0.56 | 8.09 | 0.56 | 67.32 |
| Iodine value (mg KOH/ g oil) | 61.47 | 0 | 83.91 | - |
| Oxirane oxygen content (%) | 0.04 | 3.33 | - | - |
| Saponification value (mg KOH/g oil) | 196.21 | 192.50 | 188.80 | 132.58 |
| Hydroxyl value (mg KOH/ g oil) | - | - | 231.07 | 114.53 |
| Ester value (mg KOH/ g oil) | 195.65 | 184.41 | 188.24 | 65.26 |
| Ester (%) | 43.98 | 41.45 | 42.32 | 14.67 |
| Viscosity (centipoise, cP) | 73.10 | 382.60 | 32.90 | 328.30 |

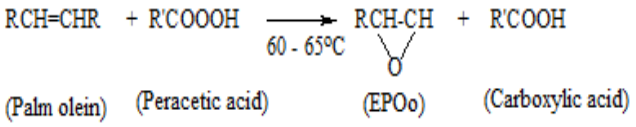
On the other hand, the saponification value of OA was decreased from 188.80% to 132.58% (Table 1) after the diol formation. This corresponds to the conversion of the carboxylic of OA to diol's ester, which was supported by the decrease in the ester value (or ester) of OA from 188.24 (or 42.32%) to 65.26 (or 14.67%) of diol, as well as the decrease of the hydroxyl value of OA to diol from 231.07 to 114.53, respectively (Table 1). The dynamic viscosity of POo and OA have increased drastically in EPOo and diol form, which showed initial confirmation of the formation of the new targeted precursors of EPOo and diol (Table 1). This result will be further confirmed by the analytical measurement presented in the following sections.

**The EPOo and Diol precursors' reaction mechanism**

The reaction mechanism for EPOo precursor formation is essential to be identified in order to understand the in situ epoxidation of POo with peracetic acid. In this study, POo was preferable as raw material due to its valuable physicochemical properties that consist of monounsaturated triacylglycerol (TAG), POP (42.8%), and diunsaturated TAG, POO (35.7%), where this TAG structures can be chemically or enzymatically modified to produce new green materials for utilization in industrial and pharmaceutical products applications [8-10, 14]. Furthermore, POo is derived from natural friendly source (a liquid fraction of palm oil), it's cheaper compare to petrochemical-based products and more importantly, POo is the largest renewable resources in Malaysia [8].

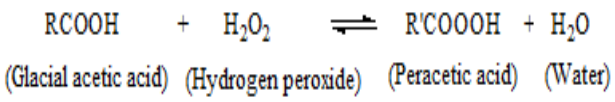
Moreover, the conventional chemical treatment method is the most widely used process of epoxidation compare to such as enzymes, metal catalysts and acid ion exchange resin methods [14, 36]. This chemical treatment method is also known as an efficient method for functionalization reactive group onto unsaturation sites (carbon double bonds) in organic compounds and resulted valuable properties of epoxides [14, 36, 37].

In this work, an established method called conventional chemical treatment by Ahmad et al. [20] is used and referred for the production of the EPOo where an alkene (POo) is reacted with peracetic acid [38-39] refer to reaction scheme (11). This epoxidation is known as an acid-catalyzed reaction [36]. The yield of reaction obtained using this method is 84.52%.




(11)

The peracetic acid solution was prepared from the glacial acetic acid (RCOOH) as an oxygen carrier and the hydrogen peroxide ($H_2O_2$) as an oxygen donor in the presence of catalytic inorganic sulphuric acid ($H_2SO_4$). The reaction mechanism of the peracetic acid formation is presented in scheme (12).




(12)

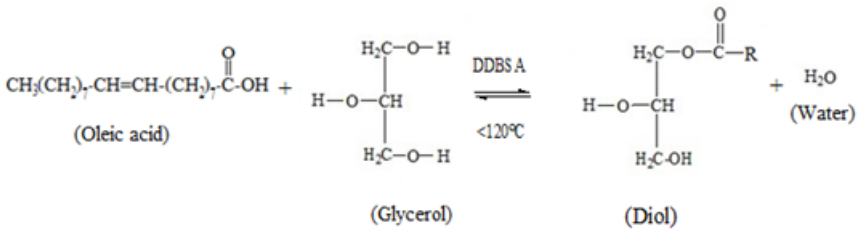
Acetic acid was found to be widely used as an oxygen carrier in the epoxidation process besides the formic acid [36]. The reaction conversion was found to be above 80% by using acetic acid, and also the higher conversion is still depends on the synthesis parameter such as temperature, reactants molar ratio, catalyst and mixing speed. In this work, the percentage of the relative conversion of the POo to EPOo, (conversion from double bonds to epoxide ring), by in situ epoxidation for 2.5 hours of reaction time is 89.04 ± 10.56 %. The theoretical value of the OOC is 3.74% [14] while the value obtained in this work is 3.33%. The OOC value was found to be different from the theoretical value probably due to the difference in the epoxidation parameters and reagent composition such as stirring speed, temperature, reaction time, type of reactants and reactants molar ratio [14, 36-37].

The catalytic inorganic of sulphuric acid have been chosen in this system because it was found to be more efficient in producing a high conversion of double bonds to epoxide ring when compared to other inorganic catalyst such as hydrochloric acid (HCI), nitric acid ($HNO_3$) and phosphoric acid ($H_3PO_4$) [36, 40]. Derawi and Salimon [14] worked on the epoxidation of POo using the performic acid reaction system [14]. They found that the conversion of epoxidation is 96.5% with a reaction yield of 91.3% for 2.5 hours of reaction time. However, this epoxidation process is considered as expensive compared to using the acetic acid because formic acid is more expensive than acetic acid [14].

However the purification method that we currently used in this work would require attentive washing and transferring in the recovery of the precursors in a way to obtain higher (maximum) yield as reported by other researchers [14, 36].

The average MW of the POo and EPOo were 860.21 and 912.64 g/mol, respectively, which were determined by titration method utilizing saponification value (an analytical method for measuring molecular weight of triglycerides in oils) and calculated using Equation (10).

We used acid-catalyzed homogeneous esterification reaction for diol production, in the absence of solvent [15-16, 18, 39]. In this study, OA was preferable as raw material due to its valuable chemical structure that consist of a carboxyl site and a carbon-carbon double bond at the ninth position, refer to scheme (13), which is reactive and can be further modified into high value-added products [16, 40-41], as well as its a plant or bio-based oil [an 18-carbon (C18) monounsaturated fatty acid] [16, 41]. This reaction system was conducted at temperature in the range of 115-118 $^{o}$C, in the presence of 3A molecular sieve as drying agent. The yield of reaction obtained was 72.65 % for 3 hours reaction time [refer Eq. (13)].




(13)

In this work, we used 4-dodecylbenzyl sulfonic acid (DBSA) as additive to homogenize the reaction system due to the reactants of OA and glycerol is not miscible. The DBSA was selected because it can act as emulsifier and catalyst (or known as a surfactant-type catalyst) compared to other surfactants such as cetyltrimethyl ammonium bromide (CTAB), tetradecyl trimethyl ammonium *bromide* (TTAB) and Esterquat [15-17]. In addition, DBSA is more efficient catalyst in water than other Bronsted acids such as HCl, $H_2SO_4$, $H_3PO_4$ and *p*-toluenesulfonic acid (PTSA). DBSA works well for dehydration reactions such as the esterification, etherification, thioetherification, and dithioacetalization in water, hence, gaining maximum yield of reaction (approximately 96%) [17]. This process was compared with the previous study by Kolvari et al. [17], where they conducted the condensation process of benzil (PhCOCOPh) and 1,2- diaminobenzene in $H_2O$ solvent at room temperature for 2 hours by using of 10% of the DBSA and resulted the reaction yield about a 96%. The results showed that the DBSA catalyst play important role to catalyze the reactions to obtain a high yield product above a 70% for at least a 3 hours reaction time. Besides, these reaction systems is considerable as green process, non-toxic, high product yields and cheap. However, the purification method of diol need carefully washing and transferred to gain maximum yield of reaction.

The average molecular weight of diol is expected in the range of 800 – 1000 g/mol [15] or less than 1500 g/mol [18], determined by GPC. The theoretical value of the average molecular weight of oleic acid is 282.47 g/mol. Further analysis of diol for chemical structure determination using nuclear magnetic resonance (NMR) spectroscopy, gas chromatograph (GC) or gas chromatograph-mass spectrometer (GC-MS) methods will be reported in future publications to identify the possibility of nearby functional group (neighbouring group participation) involvement in the reactions, especially the carbon double bond [39].

**FTIR analysis for EPOo and Diol precursors**

Figure 2 showed the spectra of the POo and EPOo in transmittance mode. The presence of epoxy group absorption in the EPOo at 834 $cm^{-1}$ corresponds to the formation of the epoxy ring in the EPOo molecular structure. In the previous study by few researchers [14, 19, 34, 42], the FTIR absorption of oxirane was identified at around 834 to 893 $cm^{-1}$. The absorption value was found to be slightly different for each of the researchers probably due to the difference in the synthesis parameters such as reactants, catalyst, temperature and mixing speed [14, 19, 34, 42]. In spite of that, the presence of the epoxy (oxirane) group in Figure 2 is strongly indicated that the EPOo was successfully synthesized via in-situ epoxidation of the POo from palm oil based.

Figure 3 showed the FTIR spectra of the OA and the diol. The O-H absorption was in the range of 3200 – 3600 $cm^{-1}$ corresponded to the hydroxyl group of the diol (broad). The hydroxyl value of the diol produced in this work was 114.53 (refer Table 1), which might represent at least two hydroxyl functionality in the diol, refer to scheme (13) and calculated according to Equation (9), which resulted approximately 2.78 of the hydroxyl number functionality. The average MW of the diol was taken as 1361 g/mol [18]. Five bands for the C-O absorptions in the range of 1000 – 1305 $cm^{-1}$ appeared in the spectra at 1010, 1038, 1124, 1182, 1304 $cm^{-1}$, which correspond to the ester functional group [16, 18]. Furthermore the carbonyl functional group (C=O) peak at 1716 $cm^{-1}$ has become shorter after the esterification due to diol formation and this has further confirmed the diol formation.

Based on the FTIR spectral analyses (refer Figure 2 and 3), the formation of EPOo and diol from POo and OA, respectively, are established. Numerous advantageous such as green renewable resources, cheaper and non-toxic were offered for utilizing a natural polymer as the raw material in designing polymeric drug vehicles [12]. Further

analysis on the thermal properties of the precursors are required to identify and understand their degradation and thermal transition properties which are the important aspect in the design and development of polymeric drug vehicles.

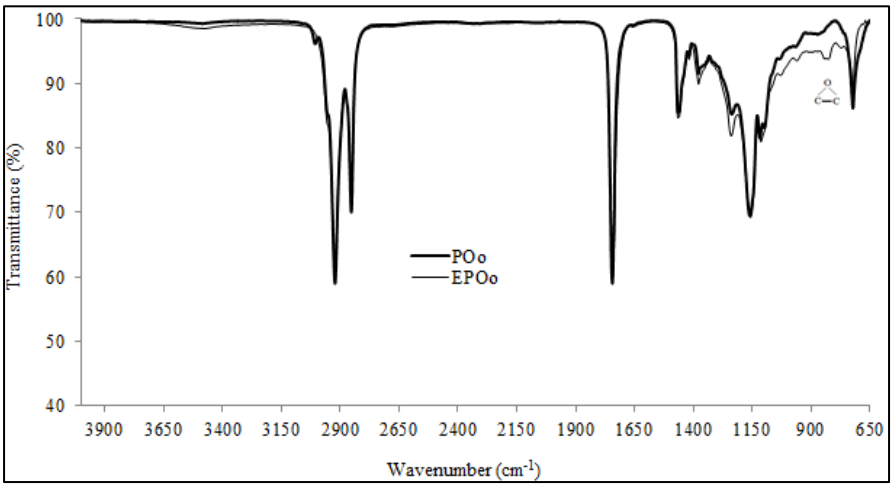



Figure 2. FTIR spectra of EPO in comparison to POo

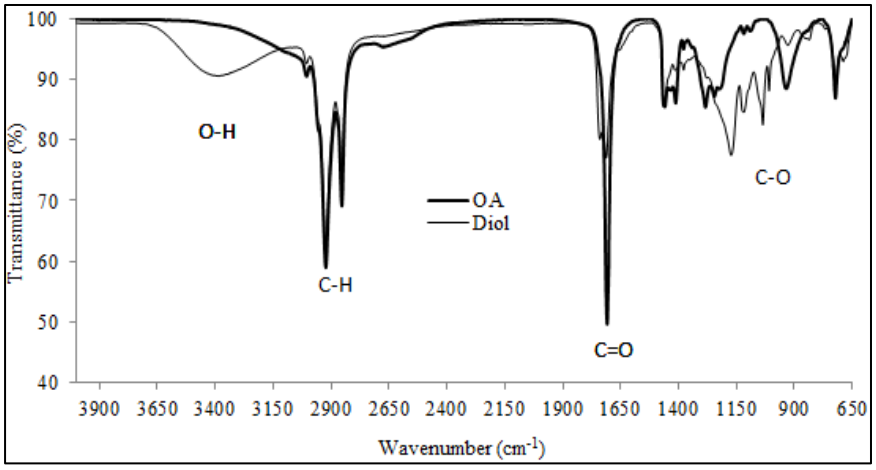



Figure 3. FTIR spectra of diol in comparison to OA

**Thermal analysis for EPOo and Diol precursors**

Figure 4 and 5 showed the thermal degradation (measured by TGA) and the corresponding derivative (DTG) thermograms of the POo and the EPOo, respectively. TGA thermogram curves of the POo and EPOo showed a single stage decomposition, for POo started at temperature 283 $^{o}$C to 479 $^{o}$C and for EPOo started at temperature 275 $^{o}$C to 523 $^{o}$C. Approximately about ~2% weight loss at the temperature of up to 300 $^{o}$C was observed, which was attributed to the loss of moisture content (Figure 5). The POo showed a degradation peak at the maximum temperature ($T_{max}$) of 440 $^{o}$C and the POo was fully degraded at higher temperature, 479 $^{o}$C. Meanwhile, the EPOo showed a slightly lower degradation peak at $T_{max}$ 407 $^{o}$C than the POo and the precursor was fully degraded at a higher temperature of 523 $^{o}$C, which is similar to the work reported by Tee et al. at 409 $^{o}$C [43] and Giita Silverajah

et al. at 405.1 $^{o}$C, respectively [34] for the peak degradation and was fully degraded at 491 °C and 504.3 °C for the EPO, respectively [34, 43]. The presence of oxirane ring have made the EPOo to have a slightly low thermal resistance compared to POo due to the plasticization effect (soft segment) of epoxide [34, 44] thus having a lower degradation peak (407 $^{o}$C) than the POo (at 440 $^{o}$C).

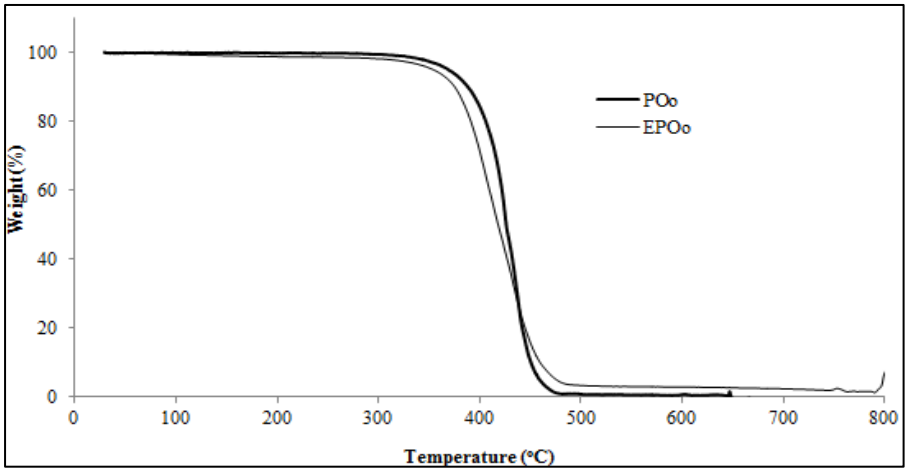



Figure 4. TGA thermograms of POo and EPOo

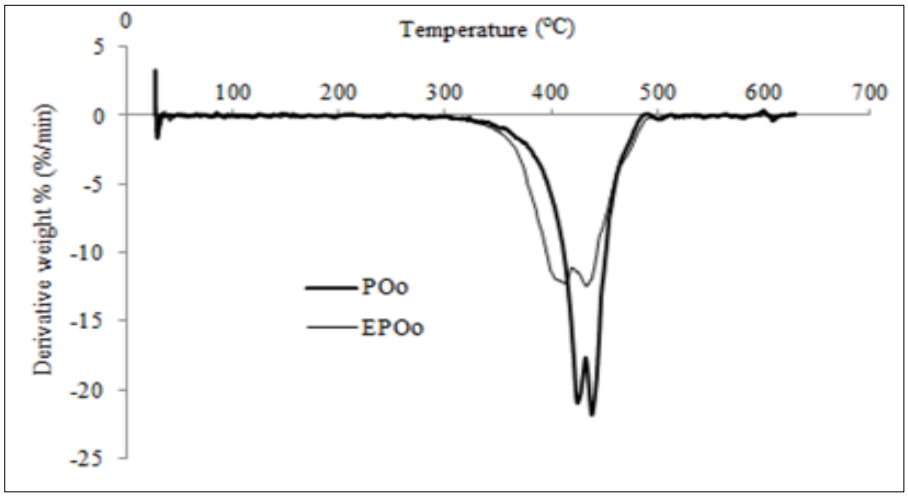



Figure 5. DTG thermograms of POo and EPOo

Figure 6 showed the DSC thermogram of the POo and the EPOo measured for the heating and cooling cycle (first heating cycle) from temperature -100 to 200 $^{o}$C. The DSC thermograms of POo and EPOo showed a single melting temperature ($T_m$) peak at 5 $^{o}$C and 15 $^{o}$C, respectively, almost in the range of the $T_m$ study reported by [34, 45-46]. The similarity on the $T_m$ for the palm olein is at 4.74 $^{o}$C, 6.94 $^{o}$C, 9 $^{o}$C and 17.79 $^{o}$C, as reported by Abdulkarim and Ghazali [45] and Zhang et al. [46], respectively. For the $T_m$ EPO is shifted to 24.46 °C and 37.69 °C, which is reported by Giita Silverajah [34].

Meanwhile three crystallization temperature ($T_c$) of POo were observed at $T_{max}$ -58 °C (in the range of -64 to -55 °C), -25 °C (in the range of -31 to -19 °C) and -3 °C (in the range of -7 to -1 °C), of which the different finding was reported by Zhang et al. approximately at −9.30 °C, 1.39 °C and 14.36 °C [46]. The EPOo thermogram also showed three $T_c$ peaks at $T_{max}$ -1 °C (in the range of -4 to 2 °C), 5 °C (between 2 – 8 °C) and 26 °C (in the range of 20 to 29 °C) when the sample is being cooled (Figure 6). This result is similar to the study reported by Tan and Chow where one of the EPO $T_c$ is at -0.97 °C, which is in the range of temperatures between $T_g$ and $T_m$ when the sample is being cooled [47].

The glass transition temperature ($T_g$) of EPOo was found approximately at $T_{max}$ -7 °C, occurred in the range of -16 to 2 °C (Figure 6). The $T_g$ of EPOo was found to be different from the finding reported by Tan and Chow at -18 °C [47] due to the difference composition of the palm oil been used such as from the palm oil by Tan and Chow and from the palm olein in our study. The $T_g$ of the POo could not be observed in the DSC thermogram (Figure 6), which is might due to the weak transition of $T_g$ especially for crystalline and low amorphous materials [47].

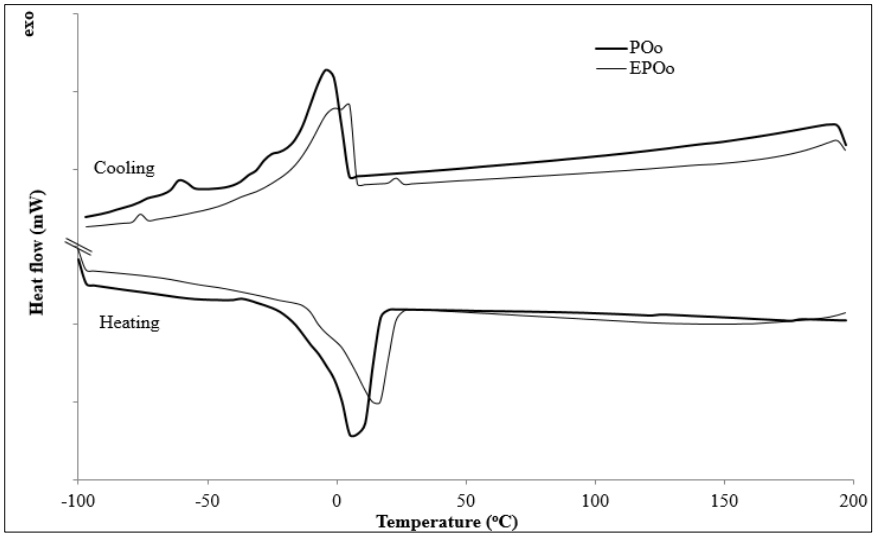



Figure 6. DSC thermograms of POo and EPOo

The TGA and DTG thermograms of the oleic acid and the diol are presented in the respective Figure 7 and 8. The thermogram patterns of both showed low thermal resistance of diol where the decomposition for OA started at temperature 180 °C to 438 °C. Meanwhile, the decomposition of diol started at temperature 108 °C to 516 °C. TGA curves of oleic acid and diol (Figure 7) showed two and three stages decomposition, respectively. In the oleic acid thermogram, the first stage represented the major degradation of the OA at $T_{max}$ 291 °C (in the range of 124 to 323 °C). This might be attributed to the loss of fatty acid in oleic acid, a carboxylic acid, which is about ~88 % from the total weight loss. The second stage occurred at $T_{max}$ 347 °C (in the range of 325 to 411 °C), which probably due to the total weight loss of carbon double bonds (C=C) and hydrocarbon (C-H) of about ~8 %. The OA was found to completely degrade at 438 °C.

Meanwhile the first stage degradation in the diol thermogram showed a slower decomposition process (than the OA) which is about ~14 % of the total weight loss at $T_{max}$ 125 °C (in the range of 79 to 200 °C). This might be attributed to the decomposition of hydroxyl group (O-H), which was produced from the hydroperoxide group (-OOH) (formed from oxidation of oil) and was found to be unstable at above 100 °C [48]. The decomposition of the hydroperoxide involved cleavage of the O-O bond in the hydroperoxide hence produced hydroxy-radical [48]. Based on this justification, the first stage decomposition temperature in the diol was strongly attributed to degradation of hydroxyl group.

In the second stage degradation, the major degradation of diol was recorded at $T_{max}$ 362 $^{o}$C (in the range of 204 to 426 $^{o}$C), which consist of about ~76 % of the major total weight loss. This involved bond cleavage on the carboxyl site which later produced ester group in the formation of ester radical. Thus, it can be concluded that this second stage decomposition pattern was possibly attributed to the degradation of the ester group (C-O) (Figure 7 and 8). The third stage degradation is about ~4 % weight loss at $T_{max}$ 492 $^{o}$C (in the range of 457 to 516 $^{o}$C), which might be attributed to bond cleavage of carbon double bond (C=C) and hydrocarbon (C-H) sides and further heating at 516 $^{o}$C showed a complete degradation of diol.

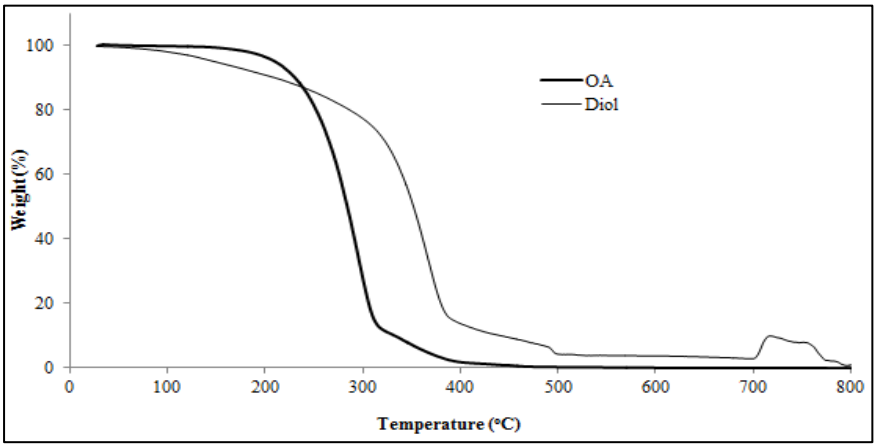



Figure 7. TGA thermograms of OA and diol

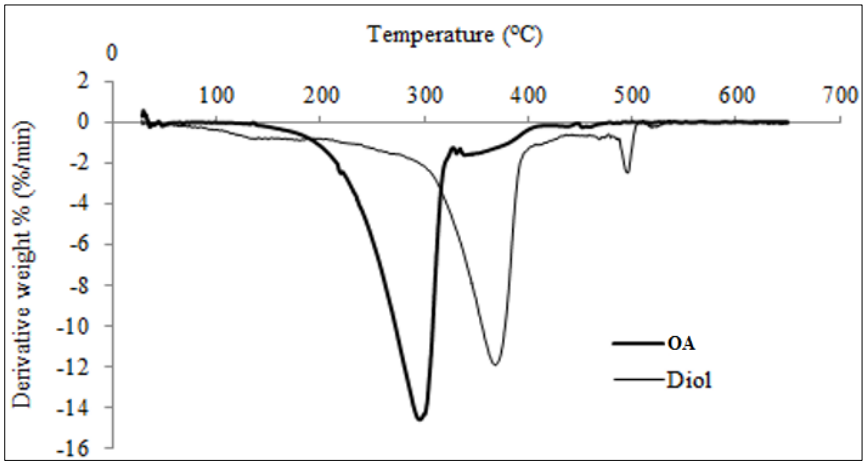



Figure 8. DTG thermograms of OA and diol

Figure 9 shows the DSC thermograms of the oleic acid and the diol. Two melting peaks of oleic acid were indicated at $T_{max}$ -25 $^{o}$C (in the range of -31 to -13 $^{o}$C) and 10 $^{o}$C (in the range of 2 $^{o}$C to 23 $^{o}$C) and also two $T_c$ peaks of oleic acid were occurred at $T_{max}$ -27 $^{o}$C (in the range of -31 to -22 $^{o}$C) and -5 $^{o}$C (in the range of -10 to -1 $^{o}$C) (Figure 9). The oxidative of oleic acid was associated with the thermal decomposition (Figure 7 and Figure 8) which was started from 124 $^{o}$C to $T_{max}$ at 151 $^{o}$C (in the range of 124 to 173 $^{o}$C), as shown in Figure 9.

Four peaks of the diol $T_m$ occurred at $T_{max}$ -40 $^oC$, -27 $^oC$, -4 $^oC$ (in the range of -49 to 5 $^oC$) and 133 $^oC$ (in the range of 112 to 142 $^oC$), as shown in Figure 9. The diol thermogram also showed one $T_c$ peak occurred at $T_{max}$ -21.81 $^oC$ (in the range of -36 to -13 $^oC$). The $T_g$ oleic acid is detectable at 2.18 $^oC$ (in the range of -0.67 $^oC$ to 5.18 $^oC$), as shown in the DSC thermogram. The $T_g$ of the diol was observed at $T_{max}$ -57 $^oC$ and -12.59 $^oC$ (Figure 9), which showed that the diol contains soft and hard segment of molecules structure where the $T_g$ peaks occurred in the range of $T_m$ and $T_c$ temperatures [16, 41]. Besides, the diol $T_g$ results is near to the range of the study reported by Mohd Mustafa et al. at -33.87 ºC, -18.29 ºC and -15.28 ºC [49]. The study reported the palm oleic acid based alkyd resins were prepared from oleic acid and glycerol with the presence of phthalic anhydride using the one step fatty acid process technique for two hours [49]. The similarity between these studies is the process systems are conducted in the absence of solvent.

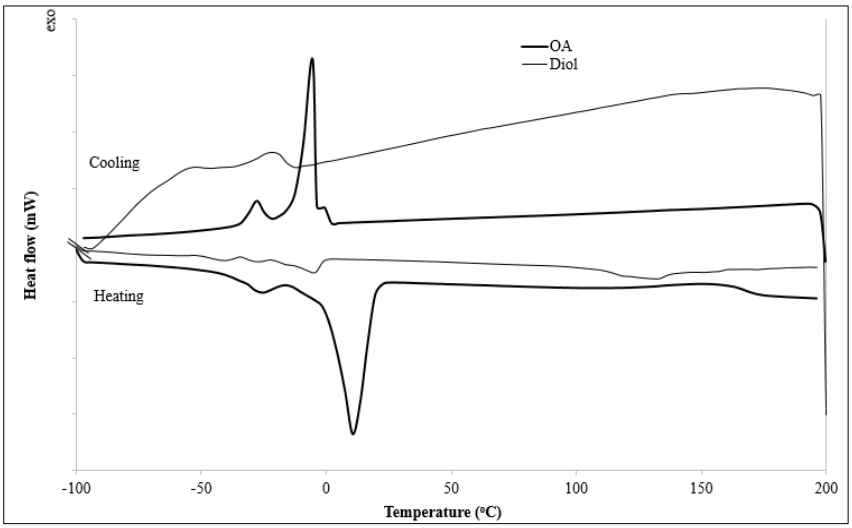



Figure 9. DSC thermograms of OA and diol

The thermal properties of the precursors in comparison to their raw materials found in this study (measured from the TGA, DTG and DSC analyses) are consistent and in line with the chemical properties obtained from the FTIR spectral analysis in Figure 2 and 3, such as the appearance of the functional groups of epoxy (oxirane) in the EPOo and hydroxyl and ester in the diol. This thermal property provided the overview of the degradation mechanisms and thermal transition ($T_g$, $T_c$ and $T_m$) of EPOo and diol. The thermal properties will be useful in elucidating the degradation and thermal behavior in designing and developing the future polymeric drug delivery vehicles.

## Conclusion

The synthesis of palm oil-based precursors namely EPOo and diol via in-situ epoxidation and esterification techniques using the respective POo and OA were successfully conducted. The procedures offer several advantages including cheap, cleaner reactions and high yields as confirmed by the proposed mechanism. The precursors exhibited promising physicochemical and thermal properties that could be used in designing new polymers such as acrylated palm oil (APOo) and polyol polyester for application in drug delivery system. These new precursors can be further investigated to be used in designing new concepts of biomaterial to create smart polymeric drug vehicle due to their soft, flexible and thermal resistance properties as confirmed by the FTIR, TGA, DTG and DSC analyses.

## Acknowledgement

The authors gratefully acknowledge Malaysia Nuclear Agency for materials and instruments support (NM-R&D-15-01), the Division of Radiation Processing Technology, the Radiation Curing and Synthesis Group and Universiti Kebangsaan Malaysia for providing the research grant of GUP/086/2016.

**References**


1. Liechty, W. B., Kryscio, D. R., Slaughter, B. V. and Peppas, N. A. (2010). Polymers for drug delivery systems. *Annual Review Chemical and Biomolecular Engineering,* 1: 149 – 173.
2. Vilara, G., Tulla-Puche, J. and Albericio, F. (2012). Polymers and drug delivery systems. *Current Drug Delivery,* 9(4): 1 - 24.
3. Saurabh, K. V., Rani, S., Rani, S. and Kesari, A. (2013). Drug targeting by erythrocytes: A carrier system. *Scholars Academic Journal of Pharmacy,* 2(2): 144 – 156.
4. Srikanth, K., Rama Mohan Gupta, V., Manvi, S. R. and Devanna, N. (2012). Particulate carrier systems – a review. *International Research Journal of Pharmacy,* 3(11): 22 – 26.
5. Takakura, Y. and Hashida, M. (1996). Macromolecular carrier systems for targeted drug delivery: Pharmacokinetic considerations on biodistribution. *Pharmaceutical Research,* 13(6): 820 – 831.
6. Abdelwahab, S. I., Sheikh, B. Y., Elhassan Taha, M. M., Chee, W. H., Abdullah, R., Yagoub, U., El-Sunousi, R. and Eid, E. E. (2013). Thymoquinone-loaded nanostructured lipid carriers: preparation, gastroprotection, in vitro toxicity, and pharmacokinetic properties after extravascular administration. *International Journal of Nanomedicine,* 8: 2163 – 2172.
7. Baharu, M. N., Kadhum, A. A. H., Al-Amiery, A. A., and Mohamad, A. B. (2015). Synthesis and characterization of polyesters derived from glycerol, azelaic acid, and succinic acid. *Green Chemistry Letters and Reviews,* 8(1): 31 - 38.
8. Derawi, D., Abdullah, B. M., Huri, H. Z., Yusop, R. M., Salimon, J., Hairunisa, N. and Salih, N. (2014). Palm olein as renewable raw materials for industrial and pharmaceutical products applications: chemical characterization and physicochemical properties studies. *Advances in Materials Science and Engineering,* 2014:1 - 5.
9. Tajau, R., Mohd Dahlan, K. Z., Mahmood, M. H., Wan Yunus, W. M. Z., Ismail, M., Salleh, M. and Muhammad Faisal, S. (2012). Acrylated vegetable oil nanoparticle as a carrier and controlled release of the anticancer drug-thymoquinone. *International Conference on Enabling Science and Nanotechnology 2012* (ESciNano 2012), Persada Johor International Convention Center, Johor Bahru, Malaysia.
10. Tajau, R., Wan Yunus, W. M. Z., Mohd Dahlan, K. Z., Mahmood, M. H., Hashim, K., Ismail, M., Salleh, M. Z. and Che Ismail, R. (2013b). Radiation-induced formation of acrylated palm oil nanoparticle using pluronic f-127 microemulsion system. *Pertanika Journal of Science and Technology,* 21 (21): 135 – 142.
11. Zainol, S., Basri, M., Basri, H., Shamsuddin, A. F., Abdul-Gani, S. S., Abedi Karjiban, R. and Abdul-Malek, E. (2012). Formulation Optimization of a palm-based nanoemulsion system containing levodopa. *International Journal of Molecular Sciences,* 13: 13049 - 13064.
12. Vroman, I. and Tighzert, L. (2009). Biodegradable polymers. *Materials,* 2: 307 - 344.
13. Goud, V. V., Dinda, S., Patwardhan, A. V. and Pradhan, N. C. (2010). Epoxidation of Jatropha (Jatropha curcas) oil by peroxyacids. *Asian-Pacific Journal of Chemical Engineering*, 5: 346 – 354.
14. Derawi, D. and Salimon, J. (2010). Optimization on epoxidation of palm olein by using performic acid. *E-Journal of Chemistry*, 7(4): 1440 - 1448.
15. Mahmood, M. H., Tajau, R., Salleh, M. Z. and Che Ismail, R. (2011). Malaysia Patent No. MY-142814-A: Method for manufacturing palm oil based hydroxyl containing products for use in making polyurethane materials.
16. Rihayat, T. and Suryani. (2010). Synthesis and properties of biobased polyurethane/montmorillonite nanocomposites. *World Academy of Science, Engineering and Technology,* 4(5): 714 - 718.
17. Kolvari, E., Zolfigol, M. A. and Peiravi, M. (2012). Green synthesis of quinoxaline derivatives using pdodecylbenzensulfonic acid as a surfactant-type Bronsted acid catalyst in water. *Green Chemistry Letters and Reviews,* 5(2): 155 - 159.
18. Tajau, R., Mahmood, M. H., Salleh, M. Z., Che Ismail, R., Abang Othman, A. M., Abdul Rahman, F. and Mohd Dahlan, K. Z. (2008). Synthesis and characterization of a highly-functional polyol-polyurethane based palm oil for photo-curable resin. *The Nuclear Malaysia R&D Seminar 2008*, Selangor, Malaysia.
19. Tajau, R., Mahmood, M. H., Salleh, M. Z., Mohd Dahlan, K. Z., Che Ismail, R., Muhammad Faisal, S. and Sheikh Abdul Rahman, S. M. Z. (2013a). Production of uv-curable palm oil resins/oligomers using laboratory scale and pilot scale systems. *Sains Malaysiana*, 42(44): 459 - 467.

20. Ahmad, S., Rafie, A. and Ismail, Z. (1987). PORIM Report PO (125a) 87: Epoxidized palm oil and palm stearin as plasticizer/stabilizer. Selangor, Malaysia: Palm Oil Research Institute of Malaysia (PORIM).
21. Bolley, D. S., Gall, R. J., Goldsmith, W. F., Maerker, G., Pohle, W. D., Sobatzki, R. J., Walker, R.O. and Barlow, D. O. (1964). Report of the epoxidized oils subcommittee on oxirane oxygen. *Journal of the American Oil Chemists Society,* 41(1): 86 - 87.
22. ASTM. (2011). D974: Standard test method for acid and base number by color-indicator titration. West Conshohocken, Pennsylvania, Unites State of America: ASTM International.
23. ASTM. (1979). D 1962-67: Test for saponification value of drying oils, fats and polymerized fatty acids. Annual Book of American Society for Testing and Material (ASTM) Standards. 29: 259 - 261.
24. AOCS. (1988). Cd 1-25: Iodine Value of Fats and Oils Wijs Method. The American Oil Chemists' Society (AOCS) Official Method.
25. Beare-Rogers, J., Dieffenbacher, A., and Holm, J. V. (2001). International Union of Pure And Applied Chemistry (IUPAC) joint committee of International Union of Nutritional Sciences and Iupac Commission on Food: Lexicon of lipid nutrition. *Pure Applied Chemistry,* 73(4): 685 - 744.
26. Codex, F. C. (1972). Food Chemicals Codex Second Edition. United State of America: National Academic of Sciences, Washington.
27. Lubrizol. (2015). Lubrizol test procedure. TP-TM-006C: Determination of saponification value: pp. 1 - 2.
28. ASTM. (2000). D 4274 – 99: Standard test methods for testing polyurethane raw materials: Determination of hydroxyl numbers of polyols. Annual Book of ASTM Standards.
29. Ionescu, M. (2005). Chemistry and technology of polyols for polyurethanes. Rapra Technology Limited. Shropshire, United Kingdom.
30. Brookfield. (2015). Operating instructions (Manual No. M/03-165-C0508W) for Brookfield Digital Viscometer Model DV-II. Brookfield Engineering Laboratories Inc. Stoughton, Massachusetts, U.S.A.
31. Xu, H., Miao, X. and Wu, Q. (2006). High quality biodiesel production from a microalga Chlorella protothecoides by heterotropic growth in fermenters. *Journal of Biotechnology,* 126: 499 - 507.
32. Ramli, M. R., Siew, W. L. and Cheah, K. Y. (2009). Production of high oleic palm oils on a pilot scale. *Journal of the American Oil Chemists' Society,* 86(8): 587 - 594.
33. Ramli, M. R., Siew, W. L. and Cheah, K. Y. (2008). Properties of high-oleic palm oils derived by fractional crystallization. *Journal of Food Science,* 73(3): 140 - 145.
34. Giita Silverajah, V. S., Ibrahim, N. A., Zainuddin, N., Wan Yunus, W. M. Z., and Abu Hassan, H. (2012). Mechanical, thermal and morphological properties of poly(lactic acid)/epoxidized palm olein blend. *Molecules,* 17: 11729 - 11747.
35. Derawi, D. and Salimon, J. (2013). Palm olein polyols production by batch and continuous hydrolysis. *Sains Malaysiana*, 42(8): 1121 – 1129.
36. Saurabh, T., Patnaik, M., Bhagt, S. L. and Renge, V. C. (2011). Epoxidation of vegetable oils: A review. *International Journal of Advanced Engineering Technology,* 2(4): 491 - 501.
37. Saurabh, T., Patnaik, M., Bhagat, S. L. and Renge, V. C. (2012). Studies on synthesis of biobased epoxide using cottonseed oil. *International Journal of Advanced Engineering Research and Studies,* 1(2): 279 - 284.
38. Bartlett, P. D. (1950). Recent work on the mechanisms of peroxide reactions. *Record of Chemical Progress*, 11: 47 – 51.
39. Scrimgeour, C. (2005). Chemistry of fatty acids. 6th Edition. John Wiley & Sons. Inc., Publishers, Scotlands.
40. Salimon, J., Abdullah, B., M., Yusop, R. M. and Salih, N. (2014). Synthesis, reactivity and application studies for different biolubricants. *Chemistry Central Journal,* 8(1): 1 -11.
41. Lligadas, G., Ronda, J. C. and Cádiz, M. G. V. (2010). Oleic and undecylenic acids as renewable feedstocks in the synthesis of polyols and polyurethanes. *Polymers,* 2: 440 - 453.
42. Czub, P. and Franek, I. (2013). Epoxy resins modified with palm oil derivatives - preparation and properties. *Polimery,* 58(2): 135 - 139.
43. Tee, Y. B., Talib, R. A., Abdan, K., Chin, N. L., Basha, R. K. and Md Yunos, K. F. (2016). Comparative study of chemical, mechanical, thermal and barrier properties of poly(lactic acid) plasticized with epoxidized soybean oil and epoxidized palm oil. *BioResource,* 11(1): 1518 - 1540.
44. Giita Silverajah, V. S., Ibrahim, N. A., Wan Yunus, W. M. Z., Abu Hassan, H. and Chieng, B. W. (2012). A comparative study on the mechanical, thermal and morphological characterization of poly(lactic acid)/epoxidized palm oil blend. *International Journal of Molecular Sciences,* 13: 5878 -5898.

45. Abdulkarim, S. M., and Ghazali, H. M. (2007). Comparison of melting behaviors of edible oils using conventional and hyper differential scanning calorimetric scan rates. *ASEAN Food Journal,* 14(1): 25 -35.
46. Zhang, X., Li, L., Xie, H., Liang, Z., Su, J., Liu, G. and Li, B. (2013). Comparative analysis of thermal behavior, isothermal crystallization kinetics and polymorphism of palm oil fractions. *Molecules,* 18: 1036 - 1052.
47. Tan, S. G. and Chow, W. S. (2010). Thermal properties of anhydride-cured bio-based epoxy blends. *Journal of Thermal Analysis and Calorimetry*, 101: 1051 - 1058.
48. Mahungu, S. M., Hansen, S. L. and Artz, W. E. (1998). Volatile compounds in heated oleic acid-esterified propoxylated glycerol. *Journal of the American Oil Chemists' Society,* 75(6): 683 - 690.
49. Mohd Mustafa, S. F., Gan, S. N. and Yahya, R. (2013). Synthesis and characterization of novel alkyds derived from palm oil based polyester resin. *Asian Journal of Chemistry*, 25(15): 8737 - 8740.

*Malaysian Journal of Analytical Sciences, Vol 21 No 2 (2017): 512 - 517*
*DOI: https://doi.org/10.17576/mjas-2017-2102-26*

MALAYSIAN JOURNAL OF ANALYTICAL SCIENCES
*Published by The Malaysian Analytical Sciences Society*
ISSN 1394 - 2506

# CHARACTERIZATION OF SODIUM SILICATE DERIVED FROM SUGARCANE BAGASSE ASH

## (Pencirian Natrium Silikat yang Dihasilkan daripada Abu Hampas Tebu)

Norsuraya Sahiron, Norhasyimi Rahmat, Fazlena Hamzah*

*Faculty of Chemical Engineering*
*Universiti Teknologi MARA, 40450 Shah Alam, Selangor, Malaysia*

**Corresponding author: fazlena@salam.uitm.edu.my*

Received: 21 October 2015; Accepted: 14 June 2016

**Abstract**

This study explores the potential of sugarcane bagasse ash (SCBA) as a precursor in the extraction of sodium silicate. SCBA was obtained from sugarcane bagasse, residual waste from sugar industries. In the present study, sugarcane bagasse (SCB) was burnt with different temperatures 600 °C, 800 °C and 1000 °C for 2 hours and 4 hours and then the ash washed using hydrochloric acid (HCl) to remove metallic ions and impurities. The ash was characterized using X-ray Fluorescence (XRF). The result indicated that SCBA at 1000 °C for 4 hours using acid washing method gave the highest composition of silica which is 88.13%. Then, the ash with the highest silica composition was extracted using 3M of sodium hydroxide (NaOH) solution. During the process NaOH will bind with silicate to form sodium silicate ($Na_2SiO_2$) and water ($H_2O$). The formation of sodium silicate was characterized and compare with commercial sodium silicate using Fourier Transform Infrared Spectroscopy.

**Keywords**: sodium silicate, sugarcane bagasse ash, waste renewable

**Abstrak**

Kajian ini meneroka potensi abu hampas tebu (SCBA) sebagai pelopor dalam pengekstrakan natrium silikat. Abu hampas tebu ini telah diperolehi daripada industri gula. Dalam kajian ini, hampas tebu (SCB) dibakar dengan suhu yang berbeza iaitu pada suhu 600 °C, 800 °C dan 1000 °C selama 2 jam dan 4 jam dan kemudian abu dicampur dengan asid hidroklorik (HCl) dan ditapis untuk mengeluarkan ion logam dan kekotoran. Abu di analisis menggunakan pendarfluor Sinar-X (XRF). Hasilnya menunjukkan bahawa abu hampas tebu (SCBA) pada 1000 °C selama 4 jam dengan menggunakan kaedah basuhan asid memberikan komposisi silika tertinggi iaitu 88.13%. Kemudian, abu dengan komposisi silika yang paling tinggi akan diekstrak menggunakan 3M natrium hidroksida (NaOH). Semasa proses, NaOH akan bergabung dengan silikat untuk membentuk natrium silikat ($Na_2SiO_2$) dan air ($H_2O$). Pembentukan natrium silika dianalisis dan bandingkan dengan silika natrium yang digunakan dipasaran menggunakan Spektroskopi Inframerah Transformasi Fourier.

**Kata kunci**: natrium silikat, hampas tebu, sisa diperbaharui

## Introduction

Sugarcane or *Saccharum officinarum L*. is a perennial grass that thrives in hot and humid locations. It is originated in Papua, New Guinea and spread throughout Southeast Asia, India, the Mediterranean, Caribbean, Hawaii and the southern United States. According to Jorina [1], the structures of sugarcane comprised of stalks, leaves and a root system. The stalk contains the juice which used to make sugar and is broken up in segments called joints. The length and diameter of the joints and stalk vary by sugarcane species. Each joint has a node and an inter node and the leaves are attached to the node. The root system at the base of the plant anchors the grass to the soil and adsorb

in water and nutrients from the ground. When the top part of the sugarcane is cut, the roots remain intact, the plant will regrow from where it was cut. It can take about six to 24 months for the plant to grow to maturity [1]. Sugarcane is harvested when it reaches maturity and during the dry season of the particular sugar cane plantation. The sugarcane juice extract from the stalk is highly valued and is the source of 70 percent of the world's sugar and has the highest number of calories per unit area of any plant [1]. The sugars derived from sugarcane are commonly used in syrups, juices, and molasses. After juice was extract from stalks, the waste left is called sugarcane bagasse (SCB). The main constituents of SCB include cellulose, hemicellulose, ash and wax [2].

In Malaysia, large region of northern area is devoted to sugarcane plantation, which produces more than 700000 tonnes of sugarcane. This waste from sugarcane was abundance in Malaysia and usually used as a primary fuel source and additive in construction industries [3]. Normally for every metric ton of sugarcane production, 270 kg bagasse is generated. Approximately 50% amount of this waste generally will be reused for energy and bioethanol application, while the remaining 50% will be stockpiled or burnt that could pose environmental problem [4]. From biomass viewpoint, sugarcane plantation produces not only granulated sugar, but also bagasse, cane tops and dry leaves that potentially could be converted into useful energy and chemical feedstock. SCB itself contributes to the main biomass wastes, which represents 30 – 40% wastes from sugar production. Wide array of initiatives has been taken by researchers and scientist to utilize the SCB waste, one of which is sugarcane bagasse ash as the supplementary material in cement construction [5]. Several studies have investigated bagasse ash potential applications such as producing silica gel as adsorbent, raw material for ceramic, cements and concrete additives, catalyst, cosmetics, paint and coating, etc. based on its characteristics. SCB is a potential feedstock that can be convert to sugarcane bagasse ash (SCBA) by pyrolysis process which also known to be a renewable resource for silica content.

In local plantation it was a valuable by products that often uses as a primary fuel source to supply all the energy needs to power the plants. Burning bagasse as an energy source yields its ash, considered as a waste causing disposal problems. Therefore, this study will show that burning sugarcane bagasse will produce a valuable product through extraction process which is sodium silicate. Sodium silicate has been diligently produced from utilizing waste from sugar industry, SCBA. Currently in market, sodium silicate was synthesized by petroleum derivatives which are identified to be toxic and environmentally unfriendly. Moreover, the processing is very costly, in which total cost of raw material passes through different cycles of process is estimated to be expensive. Unlike the production of sodium silicate from SCBA, a green and economical approach has been developed to convert the SCB to ash through burning in laboratory furnace. It is then extracted and treated by simplified chemical methods to produce high purity of sodium silicate, and the cost involved is very minimal. The SCBA is preferable as a source for silicate production since it is renewable, available in Malaysia, cheap, natural, less toxic and high silica content. So, this seems to open a wide possibility of developing the silica precursor from SCBA. In order to achieve the goal of the study, the waste material which is Sugarcane bagasse was utilize as a source of silica and determine the potential of SCB as a source of silicate. However, this ash have a potential to be reused in other application due to it silica composition. According to Worthanakul et al., on the study of Characterization for Post-treatment Effect of Bagasse Ash for Silica Extraction, the silica content in SCBA might range from 60% to 89 %. The silica contents of bagasse and its ash vary depending on the type of soil, environment and harvesting period and process [6].

This study helps to determine the effect of varying parameters of temperature, curing time and acid washing method on the composition of silica present in the SCBA. Sodium silicate produced from this project can be utilized and applied in different applications i.e. detergent auxiliaries, adhesive use, concrete and cement treatment, as agent for drilling fluids, silica source for synthesis of mesoporous materials [7].

## Materials and Methods

### Materials

Silicate Supernatant Extraction was carried out using SCBA in order to extract silica for the further study. This study focus on the performance of thermochemical treatment to extract maximum amount of silica and also the performance of that sodium silicate as a silica source. Sugarcane bagasse were collected from juice processes industry (small industry). The bagasse was cut to ensure complete burning. Then SCB were pyrolysis in the laboratory furnace (CARBOLITE RHF 16-8 Chamber Furnace) at different heating temperature which is 600 °C,

800 °C and 1000 °C, respectively for 2 hours and 4 hours. The collected bagasse ash will be grinded and sieved to homogenize sample.

**Analysis of chemical composition in sugarcane bagasses ash**
The binder was used to compress SCBA into solid form (coin shape), by using hand compression at 40 psi. After that, the sample in solid form were put in X-ray Fluorescence (XRF) sample case and arranged in the prescribed positions in the machine, then the sample case was located in analysis hole and the result of the chemical composition of each sample was displayed after 1 minute on a monitor of a computer interfaced with the machine. Then, the ash with the highest silica composition was proceed with acid washing and silica extraction method.

**Acid washing to remove the impurities**
The process started with 5 gram of SCBA was dispersed into 50 mL of 1 M Hydrochloric solution (HCl), the suspension is then stirred for 2 hours at room temperature. The suspension obtain was filtered by Whatman No. 41 ashless filter paper and the solid residue was washed with 30 mL of distilled water to remove metallic ions completely. The washings are collected and dried for 24 hours at 60 °C for further process.

**Silica supernatant extraction**
Treatment with alkali is very effective in altering the chemical and physical structure and to remove metal impurities. The SCBA residue was dispersed in 50 ml of 3M of Sodium Hydroxide solution. The mixture was boiled for 4 hours at $80^{O}$C, vigorous stirred and reaction time was varied during this process to produce sodium silicate solution. The suspension was then filtered through an ashless Whatman No 41 in order to remove carbon residue. The filtrate solution obtain was characterized for determination of sodium silicate.

**Fourier transform infrared spectroscopy analysis**
Fourier transform infrared spectroscopy (FTIR Perkin Elmer, USA) was used to analyze the functional group of the sample. As the sample used was in liquid form, then the dropper was used to spread liquid sample over the plate and the sample was scan to identify specific functional group presence. Absorption bands were used to confirm the identity of a pure compound or to detect the presence of specific impurities.

## Results and Discussion

**Sugarcane bagasses ash**
The SCBA obtained from pyrolysis process in the laboratory furnace (CARBOLITE RHF 16-8 Chamber Furnace) at different heating temperature was shown in Figure 1.



600 °C 800 °C 1000 °C

Figure 1. Observation of SCBA colour at different temperature

The ashes obtained at 600 °C were dark in colour indicating the presence of unburnt carbon, while the ones heated at 800 °C and 1000 °C were slightly milky white and as temperature increases the amount of ash produced decreases

because they will be less carbon deposits. SCBA obtain after burning in laboratory furnace and have been analyze using X-ray fluorescent (XRF) analysis, the result was tabulated in Table 1.

Table 1. Compositions of silica in SCBA at different temperature and time

| Temperature (°C) | Composition of Silica in SCBA (wt. %) | | | |
|---|---|---|---|---|
| | Without Acid Washing | | After Acid Washing | |
| | 2 Hours | 4 Hours | 2 Hours | 4 Hours |
| 600 | 37.76 | 40.25 | 74.14 | 76.83 |
| 800 | 42.47 | 43.62 | 82.78 | 83.18 |
| 1000 | 52.39 | 53.05 | 86.72 | 88.13 |

**Effect of temperature and time on the silica composition**

The effect of times and temperature on the composition of silica present in the SCBA is shown in Table 1. Based on the overall analysis result without acid washing, 4 hours burning time were gave higher silica composition than 2 hours burning time. At temperature 600 °C without acid washing method, silica composition at 4 hour is 40.25% compare to 2 hours burning time which is only 37.76% of silica content. There are about 2.49% different of silica composition. While at temperature 800 °C the amount of silica was observed between 2 hours and 4 hours burning time are 42.47% and 43.62%, respectively which gave the different about 1.15%. Finally, at temperature 1000 °C, the composition of silica present at 2 hours and 4 hour are 52.39% and 53.05% respectively. So, the different is only 0.66%. Therefore, 1000 °C at 4 hours burning time without acid washing method give the highest silica composition which is 53.05%. But, there are does not much differences in composition between the 2 and 4 hour burning times.

**Effect of acid washing method on the silica composition**

The silica composition of SCBA which undergoes acid washing method at 600 °C, 800 °C and 1000 °C reveal that 4 hours burning time produce more silica amount compared to 2 hours burning time. Even there is a little difference in composition but both 2 and 4 hours burning time give the higher amount of silica content. By referring to the Table 1, amount of silica composition at 600 °C, 800 °C and 1000 °C at 2 hours are 74.14%, 82.78% and 86.72%, respectively. While quantities of silica observed at 600 °C, 800 °C and 1000 °C at 4 hours are 76.83%, 83.18% and 88.13% respectively. The pattern of the silica composition exists in the three different temperature was slightly increase from temperature 600 °C to 1000 °C. This is because at the higher burning temperature can improve the amount of silica present but the temperature must not exceed the silica melting point which is 1600 °C. Hence, from the Table 1, temperature at 1000 °C with 4 hours burning time with undergoes acid washing method give the highest silica composition which is 88.13%. Therefore, time and temperature are the most important parameter in order to achieve highest silica composition. Thus, suitable combination of time and temperature would help to improve the silica composition present.

As in the result, the composition of silica using acid washing method is higher than without using acid washing method for all samples, this is because the acid washing method helps to remove the impurities from the sugarcane bagasse ash. From the three temperature, 600 °C, 800 °C and 1000 °C, the composition of silica at 800 °C burning for 4 hours and undergoes acid washing was give highest composition which is 88.13%. The result was compared with Worthanakul et al. [6], on the study of characterization for post-treatment effect of bagasse ash for silica extraction, reveal almost the same result observed where acid washing method improved the composition of silica in the ash. But, the silica composition obtained by Worthanakul et al. was higher which is achieved at 89% [6]. Silica content of bagasse and its ash vary depending on the type of soil, environment and harvesting period and other process involve in sugarcane plantation.

**Fourier transform infrared spectroscopy analysis**

The functioning group for the commercial sodium silicate and extracted sodium silicate from SCBA was illustrated in Figure 2. The comparison spectrum structure of commercial sodium silicate and extracted sodium silicate was clearly shown. Theoretically, Fourier transform infrared spectroscopy measures the absorption of infrared spectrum radiation by the sample material versus wavenumber. The infrared absorption bands will identify molecular structures and components exist in the sample. When a sample is irradiated with infrared radiation, absorbed IR radiation usually excites molecules into a higher vibration state. The wavelength of light absorbed by a particular molecule is a function of the energy difference between the at-rest and excited vibration states. The wavelengths that are absorbed by the sample are characteristic of its molecular structure. The functioning group of the single molecules was represented according to the result, absorption bands in the range of 400 $cm^{-1}$ to 4400 $cm^{-1}$ wavenumbers are typically due to functional groups Si, O and H. The patterns of the result obtain almost the same, at peak 969 $cm^{-1}$, the wavenumber represent the Si-O-Si stretching. Both spectrums appear at peak 3239 $cm^{-1}$ confirms the presence of hydroxyl group in the sample. Peak observed at 1646 $cm^{-1}$ confirm the presence of H-O-H (water adsorption) and at peak 871 $cm^{-1}$ confirm the presence of $SiO_4$ tetrahedron. Absorption bands in this region are generally due to intramolecular phenomena and are highly specific to each material. Therefore, all peak that present in commercial sodium silicate also present in extracted sodium silicate from sugarcane bagasse ash.

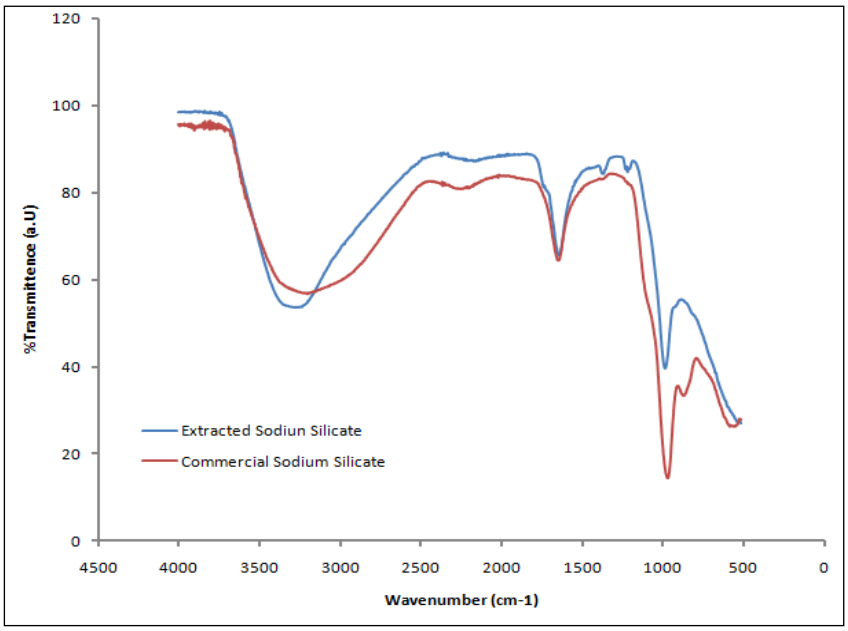



Figure 2. The FTIR spectrums of commercial sodium silicate and extracted sodium silicate from SCBA

**Conclusion**

Four hours burning time for all three different temperatures gave higher silica composition than 2 hours burning time. Amount of silica composition without acid washing method at temperature 600 °C, 800 °C and 1000 °C for 2 hour burning time are 37.76%, 42.47% and 52.38% respectively. While at 4 hours, the amount of silica recorded at 40.25%, 43.62% and 53.05%, respectively. On the other hand, the silica composition for the sugarcane ash that undergoes acid washing method was give the same result, while 4 hours burning time give higher silica amount than 2 hours. An amount of 88.13% is highest composition of silica obtain at temperature 1000 °C for 4 hour with acid washing method. The patterns of the result obtain from Fourier transform-infrared spectroscopy analysis was almost the same, the peak present at 969 $cm^{-1}$, 3239 $cm^{-1}$, 1646 $cm^{-1}$ and 871 $cm^{-1}$ wavenumbers are typically due to present of functional groups Si, O and H, hydroxyl group, Si-O-Si stretching, H-OH (water adsorption) and SiO4

tetrahedron, respectively. Therefore, the property and functional group exist in extracted sodium silicate from sugarcane bagasse ash (SCBA) was same as commercial sodium silicate in the market.

**Acknowledgement**

The present research was made possible through a Research Grant FRGS 5/3 (94/2013) and also facilities and constant encouragement from Faculty of Chemical Engineering, Universiti Teknologi MARA (UiTM) is gratefully acknowledged.

**References**

1. Jorina, F. (2012). What is sugarcane? Access online http://www.ehow.com/about_5426719_sugar-cane.html. Retrieved on 3rd November 2014.
2. Rebitanim, N. Z., Ghani, W. A. W. A. K., Rebitanim, N. A. and Salleh, M. A. M. (2013). Potential applications of wastes from energy generation particularly biochar in Malaysia. Renewable and *Sustainable Energy Reviews*, 21: 694 – 702.
3. Payá, J., Monzó, J., Borrachero, M. V., Díaz-Pinzón, L. and Ordónez, L. M. (2002). Sugar-cane bagasse ash (SCBA): Studies on its properties for reusing in concrete production. *Journal of Chemical Technology and Biotechnology*, 77(3): 321 – 325.
4. Madurwar, M. V, Mandavgane, S. A. and Ralegaonkar, R. V. (2014). Use of sugarcane bagasse ash as brick material. *Current Science*, 107(6): 1044 - 1051.
5. Loh, Y. R., Sujan, D., Rahman, M. E. and Das, C. A. (2013). Sugarcane bagasse-the future composite material: A literature review. *Resources, Conservation and Recycling*, 75: 14 - 22.
6. Worathanakul, P., Payubnop, W. and Muangpet A. (2009). Characterization for post-treatment effect of bagasse ash for silica extraction. *World Academy of Science, Engineering and Technology*, 56: 360 - 362.
7. Sales, A. and Lima, S. A. (2010). Use of Brazilian sugarcane bagasse ash in concrete as sand replacement. *Waste Management,* 30(6): 1114 – 1122.

**Malaysian Journal of Analytical Sciences Vol 21 No 3 2017**

Articles 11-17 are selected papers from the "National Congress on Membrane Technology (NATCOM 2016), 'Membranes Technology for Efficient Separation and Energy Generation', 24 - 25 August 2016, Pulai Spring Resort, Johor Bahru; organised by Advanced Membrane Technology Research Centre, Universiti Teknologi Malaysia, Malaysia."

Guest Editor: Lau Woei Jye

Articles 18-25 are selected papers from the "International Conference on Chemical Engineering and Industrial Biotechnology (ICCEIB 2016), FEW: Emerging for Sustainable Future, 28 - 30 November 2016, Bayou Hotel Malacca; organised by Faculty of Chemical and Natural Resource Engineering, Universiti Malaysia Pahang, Malaysia."

Guest Editor: Siti Kholijah Abdul Mudalip


| | | **Page** |
|---|---|---|
| 1. | ENZYME-LINKED IMMUNOSORBENT ASSAY (ELISA)-BASED-SENSOR FOR DETERMINATION OF BENZO[A]PYRENE IN RIVER WATER USING SCREEN-PRINTED GOLD ELECTRODE<br>(Sensor-berasaskan Ujian Enzim-Pengerap Immuno (ELISA) untuk Pengesanan Benzo[a]pirina dalam Air Sungai Menggunakan Elektrod Emas Skrin Tercetak)<br>*Noor Sheryna Jusoh, Alyza Azzura Abd Rahman Azmi, Azrilawani Ahmad* | 518 |
| 2. | GAMMA RADIATION-INDUCED GRAFTING OF ACETIC ACID ONTO EXPANDED POLY(TETRAFLUOROETHYLENE) MEMBRANES FOR BIOMATERIAL APPLICATIONS<br>(Pencantuman Teraruh Sinaran Gama Asid Asetik ke atas Regangan Membran Poli(tetrafluoraetilena) bagi Aplikasi Biobahan)<br>*Zaitizila Ismail, Norsyahidah Mohd Hidzir, Nur Ain Mohd Radzali, Irman Abdul Rahman* | 527 |
| 3. | BIOACCUMULATION OF SEDIMENTARY ENDOCRINE DISRUPTING CHEMICALS (EDCs) BY THE BENTHIC FISH, *Pleuronectes yokohamae*<br>(Biopenumpukan Bahan Kimia Pengganggu Endokrin (EDCs) oleh Ikan Bentik, *Pleuronectes yokohamae*)<br>*Nurulnadia Mohd Yusoff, Jiro Koyama, Seiichi Uno* | 535 |
| 4. | INTERACTION OF N,N'-BIS[4-[1-(2-HYDROXYETHOXY)] SALICYLIDENE]-PHENYLDIAMINE-NICKEL(II) AND COPPER(II) COMPLEXES WITH G-QUADRUPLEX DNA<br>(Interaksi Antara Kompleks N, N'-Bis [4- [1- (2-Hidroksietoksi)] Saliksalidin] - Fenildiamina-Nikel(II) dan Kuprum(II) Bersama DNA G-Kuadrupleks)<br>*Roshatiara Shamsuddin, Muhammad Ameerullah Sahudin, Nur Hasyareeda Hassan, Nurul Huda Abd Karim* | 544 |
| 5. | MARKOV CHAIN MONTE CARLO METHOD FOR HANDLING MISSING DATA IN AIR QUALITY DATASETS<br>(Kaedah Rantai Markov Monte Carlo Untuk Mengurus Data Hilang Di Dalam Data Kualiti Udara)<br>*Norhazlina Suhaimi, Nurul Adyani Ghazali, Muhammad Yazid Nasir, Muhammad Izwan Zariq Mokhtar, Nor Azam Ramli* | 552 |
| 6. | SYNTHESIS, STRUCTURAL, CHEMICAL PROPERTIES, AND ANTI-BACTERIAL SCREENING | 560 |

OF Sm(III) THIOSEMICARBAZONE COMPLEXES
(Sintesis, Struktur, Sifat-Sifat Kimia, dan Penyaringan Antibakteria bagi Kompleks Sm(III) Tiosemikarbazon)
*Nur Nadia Dzulkifli, Yang Farina, Bohari M.Yamin, Nazlina Ibrahim*

7. SYNTHESIS AND CHARACTERIZATION OF HYDROXYAPATITE FROM BULK SEASHELLS AND ITS POTENTIAL USAGE AS LEAD IONS ADSORBENT 571
(Sintesis dan Pencirian Hidroksiapatit dari Kulit Kerang dan Potensi Sebagai Penjerap Ion Plumbum)
*Marinah Mohd Ariffin, Norhafiza Ilyana Yatim, Sofiah Hamzah*

8. THE ANALYSIS OF THERMAL DECOMPOSITION PRODUCTS GENERATED FROM PORCINE TISSUES EXPOSED TO OUTDOOR BURNING CONDITIONS 585
(Analisis Produk Penguraian Haba Yang Terhasil Daripada Tisu Khinzir Yang Terdedah Kepada Pembakaran Terbuka)
*Gina Francesca Gabriel, Azima Ismail, Atiah Ayuni, Khairul Osman, Noor Hazfalinda Hamzah*

9. METALS CONTAMINATION USING *Polymesoda expansa* (MARSH CLAM) AS BIO-INDICATOR IN KELANTAN RIVER, MALAYSIA 597
(Pencemaran Logam di Sungai Kelantan, Malaysia Menggunakan *Polymesoda expansa* (Lokan) Sebagai Penunjuk Biologi)
*Ong Meng Chuan, Muhammad Izzat Kamaruzaman, Yong Jaw Chuen, Kamaruzzaman Bin Yunus, Joseph Bidai*

10. DEVELOPMENT AND VALIDATION OF A REVERSE PHASE-HIGH PERFORMANCE LIQUID CHROMATOGRAPHY-ULTRAVIOLET METHOD FOR SIMULTANEOUS DETECTION OF CAFFEINE AND PHENOLPHTHALEIN IN WEIGHT REDUCING SUPPLEMENTS 605
(Pembangunan dan Pengesahsahihan Kaedah Fasa Terbalik-Kromatografi Cecair Prestasi Tinggi Ultraungu bagi Pengesanan Kafein dan Fenolftalein Dalam Suplemen Pengurangan Berat Badan)
*Elham Mohammadi Nasr and Lai Chun Wong*

11. REMOVAL OF LEAD(II) FROM AQUEOUS SOLUTION USING POLYACRYLONITRILE/ZINC OXIDE ACTIVATED CARBON NANOFIBERS 619
(Penyingkiran Plumbum(II) daripada Larutan Akues Mengunakan Gentian Nano Karbon Teraktif Poliakrilonitril/Zink Oksida)
*Norfadhilatuladha Abdullah, Muhamad Hanis Tajuddin, Norhaniza Yusof, Juhana Jaafar, Farhana Aziz, Nurasyikin Misdan*

12. COMPARISON ON IN VITRO DEGRADATION OF POLYCAPROLACTONE AND POLYCAPROLACTONE/GELATIN NANOFIBROUS SCAFFOLD 627
(Perbandingan Degradasi In Vitro Bagi Perancah Gentian Nano Polikaprolakton dan Polikaprolakton/Gelatin)
*Lim Mim Mim and Naznin Sultana*

13. EFFECT OF BORE FLUID COMPOSITION ON STRUCTURAL AND PERFORMANCE OF POLYPHENYLSULFONE HOLLOW FIBER MEMBRANE CONTACTOR FOR DEACDIFICATION OF CRUDE PALM OIL 633
(Kesan Komposisi Cecair Lubang pada Struktur dan Prestasi Membran Gentian Geronggang Polifenilsulfona Membran Kontaktor untuk Penyahasidan Minyak Sawit Mentah)
*Noor Hidayu Othman, Ahmadilfitri Md Noor, Mohd Suria Affandi Yusoff, Pei Sean Goh, Ahmad Fauzi Ismail, Woei Jye Lau, Be Cheer Ng, Norafiqah Ismail*

14. A REVIEW OF OILFIELD WASTEWATER TREATMENT USING MEMBRANE FILTRATION OVER CONVENTIONAL TECHNOLOGY 643
(Ulasan Mengenai Rawatan Sisa Medan Minyak Menggunakan Teknologi Membran Penapisan Berbanding Teknologi Konvensional)
*Syarifah Nazirah Wan Ikhsan, Norhaniza Yusof, Farhana Aziz, Nurasyikin Misdan*

15. POLY(EUGENOL SULFONATE) - SULFONATED POLYETHERIMIDE NEW BLENDS MEMBRANE PROMISING FOR DIRECT METHANOL FUEL CELL 659
(Membran Campuran daripada Poli(Eugenol Sulfonat) dan Polieterimida Sulfonat yang Menjanjikan untuk Sel Bahan Api Metanol Langsung)
*Eka Cahya Muliawati, Mardi Santoso, Ahmad Fauzi Ismail, Juhana Jaafar, Mohd. Taufiq Salleh, Silvana Dwi Nurherdiana, Nurul Widiastuti*

16. PRELIMINARY STUDIES ON POWER GENERATION BY *Bacilli E1* USING DUAL CHAMBER MICROBIAL FUEL CELL 669
(Kajian Awal Penghasilan Elektrik oleh *Basilli El* Menggunakan Sel Bahan Api Mikroorganisma Dwi-kebuk)
*Nazlee Faisal Ghazali, Nik Azmi Nik Mahmood, Kamarul Asri Ibrahim, Amir Asyraf Nasaruddin*

17. CORRELATION BETWEEN PROTON CONDUCTIVITY, HYDROPHILICITY, AND THERMAL STABILITY OF CHITOSAN/MONTMORILLONITE COMPOSITE MEMBRANE MODIFIED GPTMS AND THEIR PERFORMANCE IN DIRECT METHANOL FUEL CELL 675
(Hubungan antara Kekonduksian Proton, Sifat Hidrofil dan Kestabilan Termal atas Membran Komposit Kitosan/Montmorillonit dengan Modifikasi GPTMS dan Prestasinya dalam Sel Bahan Api Metanol Langsung)
*Mochammad Purwanto, Lukman Atmaja, M.T. Salleh, Mohamad Azuwa Mohamed, Juhana Jaafar, Ahmad Fauzi Ismail, Mardi Santoso, Nurul Widiastuti*

18. MICROWAVE-ASSISTED EXTRACTION OF PHENOLIC COMPOUND FROM PINEAPPLE SKINS: THE OPTIMUM OPERATING CONDITION AND COMPARISON WITH SOXHLET EXTRACTION 690
(Pengekstrakan Sebatian Fenolik daripada Kulit Nenas dengan Bantuan Gelombang Mikro: Pengoptimuman Keadaan Pengendalian dan Perbandingan dengan Pengekstrakan Soxhlet)
*Nor Halaliza Alias and Zulkifly Abbas*

19. PRELIMINARY STUDY ON Pd-BASED BINARY CATALYSTS SUPPORTED WITH CARBON NANOFIBER FOR THE ELECTROOXIDATION OF GLYCEROL 700
(Kajian Awal ke atas Mangkin Berasaskan Pd Disokong dengan Gentian Nano Karbon untuk Pengoksidaan Elektro Gliserol)
*Norilhamiah Yahya, Siti Kartom Kamaruddin, Nabila Abdul Karim, Mohd Shahbudin Masdar, Kee Shyuan Loh*

20. THE EFFECTS OF DIFFERENT RATIOS OF SONOCHEMICALLY ASSISTED NICKEL OXIDE AND ZIRCONIUM OXIDE CATALYSTS IN SYNGAS PRODUCTION 709
(Kesan-Kesan Pelbagai Nisbah Pemangkin Nikel Oksida dan Zirkonium Oksida dengan Rawatan Sonokimia Terhadap Penghasilan Singas)
*Wan Nurdiyana Wan Amarina, Wong Yee Ching, Taufiq Yap Yun Hin*

21. PRELIMINARY STUDY OF SULFUR DIOXIDE REMOVAL USING CALCINED EGG SHELL 719
(Kajian Awal Penyingkiran Sulfur Dioksida Menggunakan Kulit Telur Yang Di Kalsin)
*Sumathi Sethupathi, Yap Chen Kai, Leong Loong Kong, Yamuna Munusamy, Mohamed Jaber Khalil Bashir, Nurshasabila Iberahim*

22. EXTRACTION OF BIOACTIVE COMPOUNDS (MANGIFERIN) FROM MAHKOTA DEWA (*Phaleria macrocarpa*) FRUITS USING SUBCRITICAL WATER: EFFECT OF PROCESS PARAMETERS ON EXTRACTION YIELD 726
(Pengekstrakan Bahan Bioaktif (Mangiferin) dari Buah Mahkota Dewa (*Phaleria macrocarpa*) Menggunakan Kaedah Air Subgenting: Kesan Parameter Proses Terhadap Hasil Ekstrak)
*Nurmaryam Aini Hashim, Ummi Najihah Md. Hashim, Siti Kholijah Abdul Mudalip, Noorlisa Harun, Fatmawati Adam, Rohaida Che Man, Siti Zubaidah Sulaiman, Zatul Iffah Mohd Arshad, Shalyda Md. Shaarani*

23. ALGAE OIL EXTRACTION FROM FRESHWATER MICROALGAE *Chlorella vulgaris* 735
(Pengekstrakan Minyak Alga Daripada Mikroalga Air Tawar *Chlorella vulgaris*)
*Nurfarahanim Abdullah, Nur Amelia Amran, Nur Hidayah Mat Yasin*

24. $O_3/S_2O_8^{2-}$ OXIDATION OF REACTIVE RED 120: EFFECT OF OPERATIONAL PARAMETERS 745
(Pengoksidaan $O_3/S_2O_8^{2-}$ Terhadap Reactive Red 120: Kesan Parameter Operasi)
*Siti Nasuha Sabri, Che Zulzikrami Azner Abidin, Fahmi Muhammad Ridwan, Ong Soon An, Razi Ahmad, Kow Su Huan*

25. CELLULOSE NANOCRYSTALS WITH ENHANCED THERMAL STABILITY REINFORCED THERMOPLASTIC POLYURETHANE 754
(Nanokristal Selulosa Dengan Ketahanan Haba Yang Tinggi Berasaskan Poliuretina Termoplastik)
*Khairatun Najwa Mohd Amin, Pratheep Kumar Annamalai, Darren Martin*

*Malaysian Journal of Analytical Sciences, Vol 21 No 3 (2017): 518 - 526*
*DOI: https://doi.org/10.17576/mjas-2017-2103-01*

MALAYSIAN JOURNAL OF ANALYTICAL SCIENCES
*Published by The Malaysian Analytical Sciences Society*
ISSN 1394 - 2506

# ENZYME-LINKED IMMUNOSORBENT ASSAY (ELISA)-BASED-SENSOR FOR DETERMINATION OF BENZO[A]PYRENE IN RIVER WATER USING SCREEN-PRINTED GOLD ELECTRODE

## (Sensor-berasaskan Ujian Enzim-Pengerap Immuno (ELISA) untuk Pengesanan Benzo[a]pirina dalam Air Sungai Menggunakan Elektrod Emas Skrin Tercetak)

Noor Sheryna Jusoh, Alyza Azzura Abd Rahman Azmi, Azrilawani Ahmad*

*School of Marine and Environmental Sciences,*
*Universiti Malaysia Terengganu, 21030 Kuala Terengganu, Terengganu, Malaysia*

**Corresponding author: azrilawani.ahmad@umt.edu.my*

Received: 16 August 2016; Accepted: 15 April 2017

**Abstract**

This paper described the surface modification of screen-printed gold electrode using thiol self-assembled monolayer, in combination with enzyme-linked immunosorbent assay (ELISA) format for determination of benzo[a]pyrene (BaP) in water sample. All biomolecules were immobilized on the surface of working electrode to increase the sensitivity of the developed biosensor by applying different types of ELISA. Electrochemical characterizations using cyclic voltammetry (CV) and electrochemical impedance spectroscopy (EIS) were carried out to study the conductivity behavior of the developed biosensor. Based on the results, biomolecules were successfully immobilized and characterized optically and electrochemically. Optical immunoassay with indirect competitive ELISA were developed for the determination of BaP compound which showed the best performance compared to other assay. In optical measurement, normal assay exhibits higher absorbance, implying high bio complex formation. Modification of electrode using 11-MUA was successful due to highest blocking effect for electron transfer process. Determination of BaP in real water samples shows that there no BaP was detected in all samples collected, due to no presence of BaP in all samples.

**Keywords:** surface modification, screen-printed gold electrode, benzo[a]pyrene, water sample

**Abstrak**

Kertas kerja ini menerangkan pengubahsuaian permukaan elektrod emas skrin tercetak menggunakan lapisan mono tepasang menggunakan tiol, dengan kombinasi format ujian enzim-pengerap imuno (ELISA) untuk penentuan benzo[a]pirina (BaP) dalam sampel air. Semua molekul bio telah dipegunkan di atas permukaan elektrod bekerja untuk meningkatkan kepekaan biosensor yang dibangunkan dengan menggunakan pelbagai jenis ELISA. Pencirian elektrokimia menggunakan voltametri kitaran (CV) dan spektroskopi impedans elektrokimia (EIS) telah dilakukan untuk mengkaji tingkah laku kekonduksian biosensor yang dibangunkan. Berdasarkan keputusan yang diperolehi, molekul bio telah berjaya dipegunkan dan dicirikan secara optik dan elektrokimia. Ujian imuno optik dengan ELISA bersaing secara tak langsung telah dibangunkan untuk penentuan sebatian BaP menunjukkan prestasi terbaik berbanding ujian lain. Dalam pengukuran optik, ujian normal mempamerkan keserapan lebih tinggi, menandakan pembentukan kompleks bio yang tinggi. Pengubahsuaian elektrod menggunakan 11-MUA berjaya disebabkan oleh kesan halangan tertinggi bagi proses pemindahan elektron. Penentuan BaP dalam sampel air sebenar menunjukkan tiada BaP dikesan dalam semua sampel yang diambil, kerana ketiadaan BaP dalam semua sampel.

**Kata kunci:** pengubahsuaian permukaan, elektrod emas skrin tercetak, benzo[a]pirina, sampel air

## Introduction

Rapid growing of industries has contributed in the increasing of organic pollutants in the environment. Among the pollutants, polycyclic aromatic hydrocarbons (PAHs) have gained extra attentions in the past years from countless research in various fields. PAHs exist naturally in the environment through a carbonization process or can be man-made by pyrolytic processes [1]. However, most of the PAHs compounds in the environment today are the products from the infinite growing industries and human activities and they enter the environment through the incomplete combustion of fossil fuels such as crude oil or coal. Some compounds of PAHs have been recognized as carcinogenic, mutagenic and teratogenic. The simplest PAHs structure is naphthalene, which is the main ingredient in 'moth ball' or 'naphthalene ball', used to get of insects in closet.

Chromatographic technique such as liquid and gas chromatography were frequently selected to detect PAHs compounds in environment, especially in water samples. The method was certainly convenient for determining many targets analytes at one time, in addition of giving precise and accurate results. However, this method usually required large number of samples and complex sample preparation, which is time consuming. Thus, a lot of studies were conducted to develop simpler methods, yet give good results. The new developed method includes biosensor and immunosensor. Biosensors are analytical devices which are fabricated from the combination of two parts: a biological recognition element such as an antibody, enzyme, receptor, DNA, or cell and transducer that converts the biorecognition process into a measurable physical signal [2]. Immunosensors are one of the biosensors, which are widely investigated and developed over these past years. An immunosensor is an affinity-based biosensor designed to detect the direct binding of an antibody or an antigen [3]. The biological reactions on the surface of electrode will be detected by transducer and then converted into physical signal.

Enzyme-Linked Immunosorbent Assay (ELISA) principle is often used for immobilization of antibodies and antigen in immunoassay for biosensors development. The steps in ELISA involve the attachment of antigens to the surface, the application of antibody to the antigen, the antigen-antibody reactions and finally the addition of substrate. ELISA comes in several types namely indirect, direct, sandwich and competitive ELISA. ELISA is broadly applied in medical [4-6], food industry [7, 8], beverage industry [9] and environmental fields, for example detection of dioxins [10] and PAH compounds [11, 12].

In this study, we focused on the application of ELISA for detecting benzo(a)pyrene (BaP) in river water samples. Biological elements such as coating conjugate and antibodies were immobilized in 96-well plate and on the screen-printed gold electrode (SPGE) using indirect competitive ELISA. This type of assay is commonly applied for determination of 1-hydroxypyrene [13] and phenanthrene [14] because the assay usually gave higher sensitivity results compared to other assays. The performance of the immobilized biomolecules were measured optically and electrochemically. The purpose of this study is to determine the behavior of immobilized biomolecules on the SPGE as well as to test the sensitivity of the competitive assay towards real water samples. Optically, a normal competitive assay would display high selectivity and sensitivity towards BaP due to the interaction of 4D5 monoclonal antibody with BaP molecule. In addition, low current and high resistance were expected for electrochemical measurements due to thick layer embedded on the electrode surface, resulting a slow diffusion of redox probe ions.

## Materials and Methods

### Chemical and materials

Screen-printed gold electrode (SPGE) C220BT were purchased from DropSens, Spain. 11-mercaptoundecanoic acid (11-MUA), ethanol, isopropanol, acetone and isopropanol and acetone were purchased from Merck, Germany. Tris(hydroxymethyl)aminomethane (Tris) and bovine serum albumin (BSA) were purchased from Sigma-Aldrich, USA. Tween 20, diethanolamine, potassium chloride, potassium hexacyanoferrate (III) and potassium hexacyanoferrate (II) trihydrate were purchased from Merck, Germany. *p*-nitrophenyl phosphate was purchased from Sigma, USA. Both goat anti-mouse IgG alkaline phopshatase and 4D5 monoclonal antibody (specific for benzo[a]pyrene) were from Santa Cruz Biotechnology, USA. Adipic acid dihydrazide, N-(3-dimethylaminopropyl)-N'-ethylcarbodiimide hydrochloride (EDC), *N*-hydrosuccinimide (NHS), 9-phenanthrene carboxaldehyde and benzo[a]pyrene were purchased from Sigma-Aldrich, Germany. All reagents are of analytical grade or better.

**Instrumentations**
All experiments involving cyclic voltammetry and electrochemical impedance spectroscopy were conducted at room temperature using AUTOLAB PGSTAT30 (Metrohm, Utrecht, The Netherlands), located at School of Ocean Engineering, UMT. SPGE was connected to the potentiostat by DRP-CAC connector (DropSens, Spain). SPGE was cleaned with Ultrasonic Cleaner JAC Ultrasonic 2010P (Jin Woo Engineering Co. Korea). Mini incubator (VWR, China) was used to incubate samples at 37 °C. Ascent Multiskan ELISA reader (Thermo Scientific, USA), located at Institute of Marine Biotechnology, UMT was used for optical characterization.

**Preparation of gold electrodes**
The C220BT screen printed AuE was ultrasonic cleaned with acetone by isopropanol and lastly ultrasonic cleaned in deionized water for 5 minutes in each solution, respectively [15].

**SAM formation on gold electrodes**
SPGE was immersed in the freshly prepared 5 mM 11-MUA in ethanolic solution for 20 hours. The modified electrode was rinsed with ethanol to remove any unbound molecules. Activation of carboxylic acid terminated-group was done by coupling the modified electrode with 50 mM EDC and 50 mM NHS and this activated-modified SPGE was further used to detect BaP using ELISA principle.

**Preparation of buffer solutions**
Blocking buffer was prepared by dissolving 0.3029 g Tris in deionized water. Then, the prepared solution was used to dissolve 0.5 g BSA. For washing buffer, 0.3029 g Tris was dissolved in deionized water. A total of 50 µL Tris solution was pipetted out and replaced by 50 µL Tween-20. 1 mL *p*-nitrophenyl phosphate (*p*-NPP) substrate was diluted in 9 mL of diethanolamine (DEA).

**Control assays**
BSA-PHEN coating conjugate was synthesized by coupling the adipic acid dihydrazide with BSA, EDC and 9-phenanthrene carboxaldehyde [16]. Control assays were performed to evaluate the performance of optimized biomolecules optically and electrochemically (Table 1). *p*-NPP was only involved in optical measurement.

Table 1. Control assays

| Assay | *p*-NPP Only | Control 1 No Conjugate | Control 2 No Conjugate and 4D5 | Control 3 No 4D5 | Normal Assay |
|---|---|---|---|---|---|
| *p*-NPP (blank) | √ | √ | √ | √ | √ |
| AP Label | X | √ | √ | √ | √ |
| 4D5 | X | √ | X | X | √ |
| Blocking | X | √ | √ | √ | √ |
| BSA-PHEN | X | X | X | √ | √ |

**Indirect competitive assay for benzo(a)pyrene**
For optical characterization, the wells were coated with 50 µL bovine serum albumin-phenanthrene (BSA-PHEN) coating conjugate (n=3) and then incubated for an hour at 37 °C. After incubation, the plate was washed with washing buffer. 50 µL blocking buffer was added into each well and incubated again for one hour at 37 °C. After that, the plate was washed again. Serial dilutions of standard BaP were mixed with 4D5 monoclonal antibody and then were left for 15 minutes to react. The solutions were prepared at concentration two times higher than the desired concentration. Then, 50 µL of each solution was added into the wells and incubated at 37 °C for one hour. After washing, 50 µL of alkaline phosphatase (AP) label antibody was added and allowed to react at 37 °C for an hour. After that, the plate was washed and 200 µL of *p*-NPP substrate was added into each well. The absorbance was read at 405 nm after 60 minutes.

For electrochemical characterization, the working electrodes were coated with 5 µL BSA-PHEN coating conjugate (n=3) and then incubated for an hour at 37 °C. After incubation, the electrodes were washed with washing buffer. 5 µL blocking buffer was added onto each electrode and incubated again for one hour at 37 °C. After that, the electrodes were washed again. Then, 5 µL of serial dilution of standard BaP mixed with 4D5 were added onto the electrodes and incubate at 37 °C for one hour. After washing, 5 µL of AP label antibody was added and allowed to react at 37 °C for an hour. After one hour, the electrodes were washed and measured after 60 minutes.

CV measurements were carried out in 5 mM $[Fe(CN)_6]^{3-/4-}$ in 0.1 M KCl and the applied potential was in the range of -0.2 to 0.6 V versus Ag/AgCl. The scan rate applied was 50 $mVs^{-1}$. For impedance measurements, impedance behavior of the electrode is determined by analyzing the AC voltage and current response at frequencies ranging from 0.1 Hz to 10 kHz. Measurements were carried out in the presence of 5 mM $[Fe(CN)_6]^{3-/4-}$ in 0.1 M KCl at an applied potential of +0.025 V with amplitude of 0.1 V. All measurements were recorded at room temperature.

**Sampling site**

Water sampling was conducted at Semerak River in Tok Bali, Kelantan. The sampling was carried out in January 2016. Five sampling points were selected along the Semerak River (Figure 1). All water samples were collected using grab sampling. Triplicate of water samples were taken at each point. 1 mL of 2 M nitric acid ($HNO_3$) was added into the water samples for preservation. Then the bottles were wrapped with aluminium foil and stored in an ice box. The bottles then were transferred into a 4 °C chiller prior further analysis.

**Measurements on the river water samples**

Indirect competitive assay was applied for optical and electrochemical measurements of blank and spiked (50 and 100 ppm BaP) water samples.

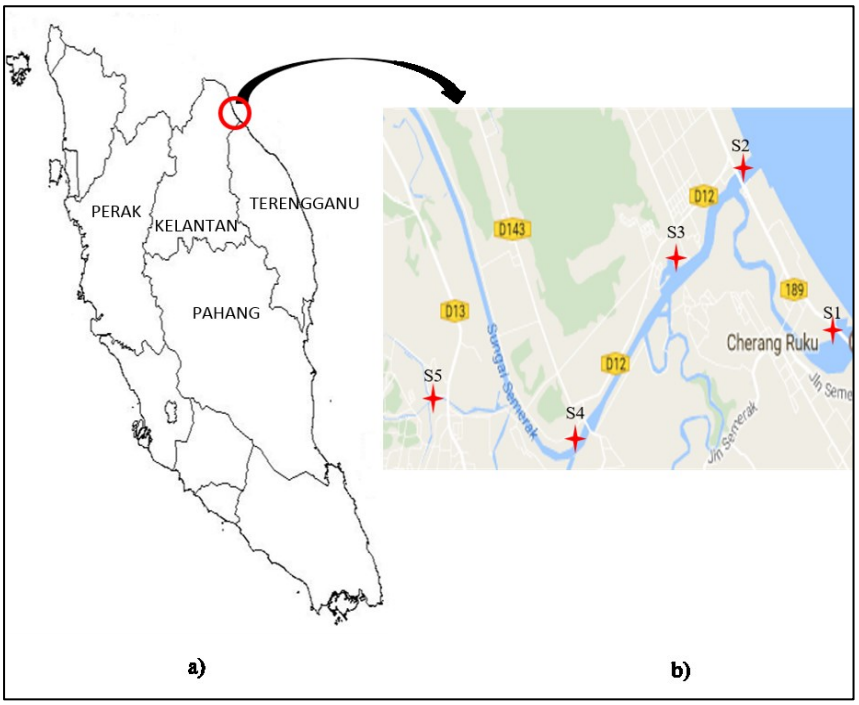



Figure 1. a) Map of Peninsular Malaysia and b) Map of five sampling points along Semerak River. [Scale 1 cm = 2 km]

## Results and Discussion

### Control assays: Optical characterization

Control assays were carried out in order to establish the optimal responses for different substances or antibodies immobilized on the 96 well plates. Figure 2 shows the absorbance for all assays. The effect of BSA-PHEN coating conjugate was studied in Control 1 and it was replaced with coating buffer. Control 2 was performed without BSA-PHEN coating conjugate and 4D5. The effectiveness of optimized AP label antibody was studied in Control 3. There was no specific binding observed for all the controls and it was as expected that the normal assay had the highest absorbance. Thus, it can be concluded that all bio elements must present in order to provide better absorbance reading.

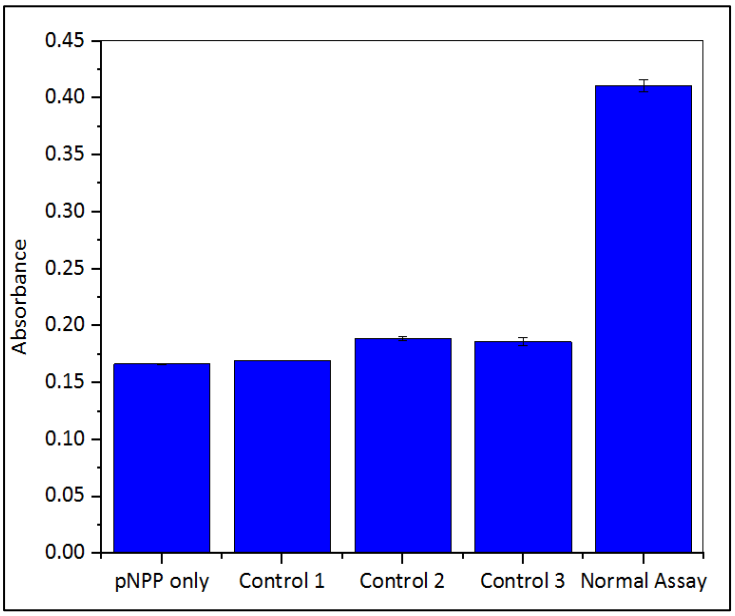



Figure 2. Control assays

### Electrochemical characterization

Electrochemical measurement of the control assay has been conducted without the presence of substrate. Figure 3 and Figure 4 shows the cyclic voltammogram and Nyquist plot of the control assay, respectively. From the voltammogram, low current reading was recorded for all control assays. Redox peaks were appeared in Control 2 and Control 3, which suggested that little redox reaction occurred on the electrode surface, due to formation of thin layers. As expected, normal assay displayed the lowest current reading, which implied high resistance for electron transfer process because of the thick layer appeared due to immobilization of several layers of biomolecules. The CV results were supported by the EIS results. The resistance recorded for normal assay was the highest, due to slow diffusion of the probe ions onto the gold surface [17].

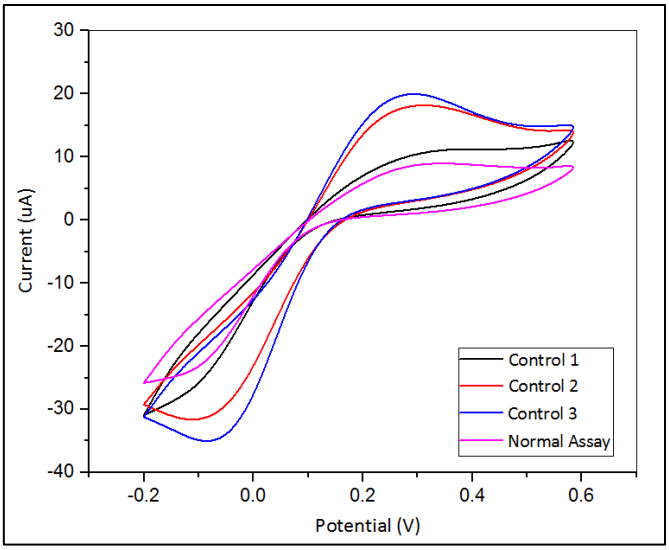



Figure 3. Cyclic voltammograms of control assays on SPGE in 5 mM ferricyanide/ferrocyanide redox probe at scan rate of 50 mV/s

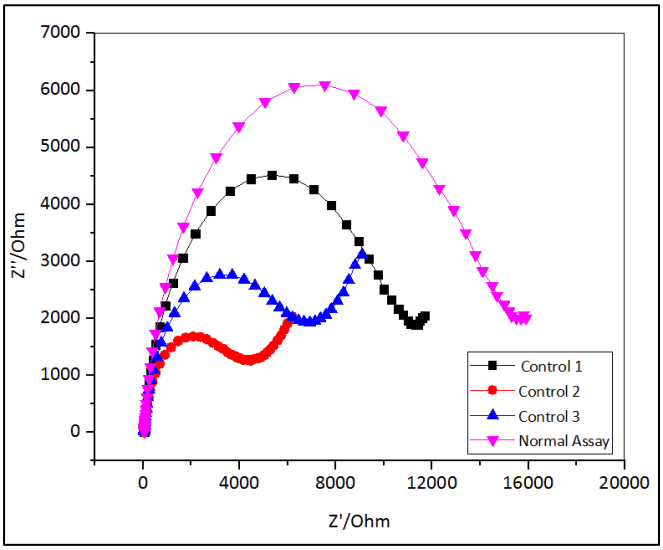



Figure 4. Nyquist plot of control assays on SPGE in 5 mM ferricyanide/ferrocyanide redox probe at 0.025 V and amplitude of 0.1 V

**Indirect competitive assay for benzo(a)pyrene**

The absorbance reading for competitive assay was shown in Figure 5. Different concentrations of BaP were tested to determine the sensitivity of the assay. At 20 ppm of BaP, the absorbance recorded the highest reading, which proved that indirect competitive assay was sensitive at low concentration of BaP. The reading became lower as the concentration of BaP decreased.

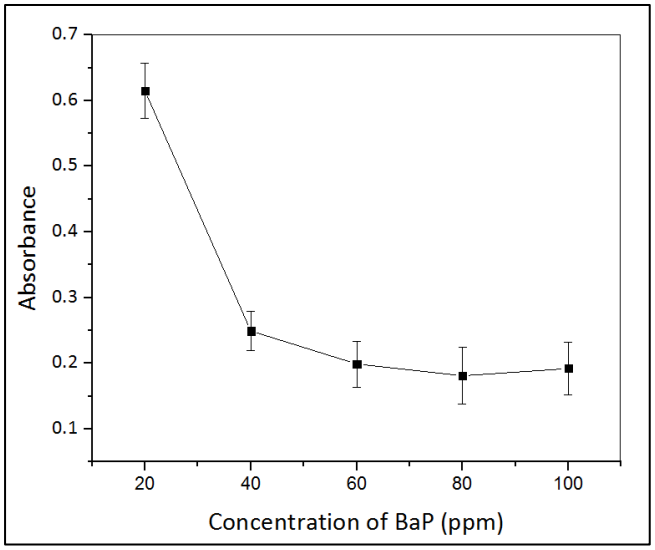



Figure 5. Optical measurement of indirect competitive assay for benzo(a)pyrene

**Measurements on river water samples**

The indirect competitive assay was conducted to study the capability of assay to detect BaP in real water samples. Figure 6 shows the absorbance reading of blank and spiked water samples at five different sampling stations. The lowest absorbance reading was recorded for blank water samples at each station. It is expected because no BaP was presence in the samples. This might be due to the possibility of absence of BaP in the river water during samples collection. However, after the water samples were spiked with 50 ppm and 100 ppm BaP, the absorbance reading significantly increased about two times higher than the blank reading at certain sampling points. In addition, the absorbance for water samples spiked with 50 ppm BaP were much higher than 100 ppm, where the reading was almost the same. The results proved that the assay was sensitive for BaP detection in lower concentration. This is due to less competition of BaP molecules to be attracted by the assay. As the concentration increased, more BaP molecules compete for the binding sites, resulting in low absorbance reading because more binding sites were unoccupied. Compared with lower concentration of BaP, the molecules moved more freely due to many space in the water samples, thus giving enough time for a complete bonding between the assay and the BaP.

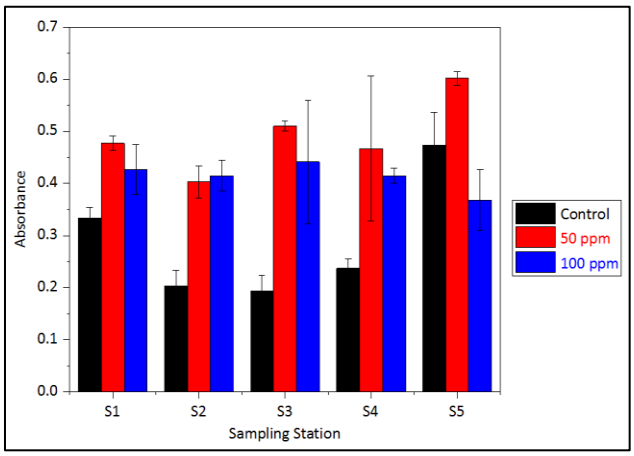



Figure 6. Indirect competitive assay for blank water samples and spiked water samples at five different sampling stations

## Conclusion

Biomolecules were successfully immobilized using indirect competitive ELISA. The optical results displayed active enzymatic reactions occurred with the presence of all biomolecules in the assay. The CV and EIS results verified the immobilization of all elements on SPGE, where high current and low resistance were recorded for normal assay. The immunoassay displayed surprising sensitivity for low concentration of BaP. The optical density recorded for 20 ppm BaP was far higher than other concentrations, which proves the reliability of the immunoassay for detecting the target analytes in lower concentrations of real samples. A test conducted in real water samples verify the sensitivity of the assay, where the optical intensity of lower concentration was higher in most water samples.

## Acknowledgement

The authors would like to extend their gratitude towards the Ministry of Higher Education of Malaysia for financial support through the Research Acculturation Grant Scheme (RAGS) Vote No. 57093 and Universiti Malaysia Terengganu for providing research facilities that were used in this research.

## References

1. World Health Organisation Regional Office for Europe (2000). Polynuclear aromatic hydrocarbons (PAH). Air Quality Guidelines for Europe. Second Edition, Copenhagen: pp. 1 – 24.
2. Van Emon, J. M. (2007). Immunoassay and other bioanalytical techniques. Florida, USA: CRC Press.
3. Moina, C. and Ybarra, G. (2012). Fundamentals and applications of immunosensors. In N. H. L. Chiu (Ed.), Advances in immunoassay technology. Rijeka, Croatia: pp. 65 – 80.
4. Lewis, J. G., Clifford, J. K. and Elder, P. A. (1990). Monoclonal antibodies to pregnanediol-3-glucuronide: Application to a direct enzyme-linked immunosorbent assay of urine. *Steroids*, 55: 314 –318.
5. Chung, M. K., Riby, J., Li, H., Iavarone, A. T., Williams, E. R., Zheng, Y. and Rappaport S. M. (2010). A sandwich enzyme-linked immunosorbent assay for adducts of polycyclic aromatic hydrocarbons with human serum albumin. *Analytical Biochemistry*, 400: 123 – 129.
6. Chung, M. K., Regazzoni, L., McClean, M., Herrick, R. and Rappaport, S. M. (2013). A sandwich ELISA for measuring benzo[a]pyrene-albumin adducts in human plasma. *Analytical Biochemistry*, 435: 140 – 149.
7. Gui, W. J., Liu, Y. H., Wang, C. M., Liang X. and Zhu, G. N. (2009). Development of a direct competitive enzyme-linked immunosorbent assay for parathion residue in food samples. *Analytical Biochemistry*, 393: 88 – 94.
8. Song, J., Yang, H., Wang, Y., Si, W. and Deng, A. (2012). Direct detection of 3-amino-5-methylmorpholino-2-oxazolidinone (AMOZ) in food samples without derivatisation step by a sensitive and specific monoclonal antibody based ELISA. *Food Chemistry*, 135: 1330 – 1336.
9. Perrotta, P. R., Arevalo, F. J., Vettorazzi, N. R. and Zon, M. A. (2012). Development of a very sensitive electrochemical magneto immunosensor for the direct determination of ochratoxin A in red wine. *Sensors and Actuators B: Chemical*, 162: 327 – 333.
10. Van Emon, J. M., Chuang, J. C., Lordo, R. A., Schrock, M. E., Nichkova, M., Gee, S. J. and Hammock, B. D. (2008). An enzyme-linked immunosorbent assay for the determination of dioxins in contaminated sediment and soil samples. *Chemosphere,* 72: 95 – 103.
11. Barcelo, D., Oubina, A., Salau, J. S. and Perez, S. (1998). Determination of PAHs in river water samples by ELISA. *Analytica Chimica Acta*, 376: 49 – 53.
12. Matschulat, D., Deng, A., Niessner, R. and Knopp, D. (2005). Development of a highly sensitive monoclonal antibody based ELISA for detection of benzo[a]pyrene in potable water. *Analyst,* 130: 1078 – 1086.
13. Li, K., Woodward, L. A., Karu, A. E. and Li, Q. X. (2000). Immunochemical detection of polycyclic aromatic hydrocarbons and 1-hydroxypyrene in water and sediment samples. *Analytica Chimica Acta*, 419: 1 – 8.
14. Fahnrich, K. A., Pravda, M. and Guilbault, G. G. (2003). Disposable amperometric immunosensor for the detection of polycyclic aromatic hydrocarbons (PAHs) using screen-printed electrodes. *Biosensors and Bioelectronics*, 18: 73 – 82.
15. Ahmad, A., Lee, P. K. and Jusoh, N. S. (2016). A comparative study of thiols self-assembled monolayers on gold electrode. *Middle-East Journal of Scientific Research.* 24(6):2152 – 2158.

16. Ahmad, A. and Moore. E. (2012). Electrochemical immunosensor modified with self-assembled monolayer of 11-mercaptoundecanoic acid on gold electrodes for detection of benzo[a]pyrene in water. *Analyst*, 137: 5839 – 5844.
17. Mishra, S. K., Kumar, D. and Biradar, A. M. (2012). Electrochemical impedance spectroscopy characterisation of mercaptopropionic acid capped ZnS nanocrystal based bioelectrode for the detection of the cardiac biomarker-myoglobin. *Bioelectrochemistry*, 88: 118 – 126.

*Malaysian Journal of Analytical Sciences, Vol 21 No 3 (2017): 527 - 534*
*DOI: https://doi.org/10.17576/mjas-2017-2103-02*

**MALAYSIAN JOURNAL OF ANALYTICAL SCIENCES**
***Published by The Malaysian Analytical Sciences Society***
**ISSN 1394 - 2506**

# GAMMA RADIATION-INDUCED GRAFTING OF ACETIC ACID ONTO EXPANDED POLY(TETRAFLUOROETHYLENE) MEMBRANES FOR BIOMATERIAL APPLICATIONS

## (Pencantuman Teraruh Sinaran Gama Asid Asetik ke atas Regangan Membran Poli(tetrafluoraetilena) bagi Aplikasi Biobahan)

Zaitizila Ismail, Norsyahidah Mohd Hidzir*, Nur Ain Mohd Radzali, Irman Abdul Rahman

*School of Applied Physics, Faculty of Science and Technology,*
*Universiti Kebangsaan Malaysia, 43600 UKM Bangi, Selangor, Malaysia*

**Corresponding author: syahidah@ukm.edu.my*

Received: 23 November 2016; Accepted: 10 April 2017

**Abstract**

Expanded poly(tetrafluoroethylene) (ePTFE) is used for many applications including in medical applications, such as for facial implants or as artificial vascular valves. However, due to its natural hydrophobic properties, it has limited efficacy in some applications. To be used as a facial implant, ePTFE must be biocompatible to the surrounding living tissues. Therefore, the modification of the ePTFE surface through a radiation-induced grafting technique was introduced in this study. Acetic acid (AA) was used as a monomer grafted onto ePTFE due to its hydrophilic properties. Monomer concentrations and radiation doses were observed to play an important role in the grafting outcomes. A dose of 15 kGy of γ-ray and 20% of AA concentration was observed to be an optimum grafting parameter in this study with the maximum grafting yield of 14 ± 4%. The result also showed a decrease of surface hydrophobicity for grafted ePTFE with the water contact angle decreased 18˚ (from 117˚ to 99˚). No extra band was observed in attenuated total reflectance infrared (ATR-FTIR) spectroscopy for grafted ePTFE, which indicated that grafting might occur only on the very top layer of ePTFE. Analysis from field emission scanning electron microscopy coupled with energy dispersive X-ray (FESEM/EDX) revealed a successful grafting as the oxygen peak can be seen on the treated sample.

**Keywords:** radiation-induced grafting, grafting, expanded poly(tetrafluoroethylene), acetic acid

**Abstrak**

Poli(tetrafluoroetilena) regangan (ePTFE) digunakan dalam pelbagai aplikasi termasuklah dalam aplikasi perubatan, contohnya sebagai implan pada wajah atau sebagai vaskular injap tiruan. Walau bagaimanapun sifat semulajadi ePTFE yang hidrofobik menyebabkan keberkesanannya adalah terhad dalam beberapa aplikasi. ePTFE mestilah mempunyai tahap integrasi biologi yang optimum untuk digunakan sebagai implan wajah. Justeru, pengubahsuaian permukaan ePTFE meggunakan teknik pengkopolimeran menggunakan sinar gama diperkenalkan dalam kajian ini. Asetik asid digunakan sebagai monomer untuk tujuan percantuman dengan ePTFE disebabkan sifatnya yang hidrofilik. Dos sinaran dan kepekatan monomer yang digunakan menunjukkan peranan yang penting dalam peratusan hasil pencantuman. Parameter optimum telah dikenalpasti dalam kajian ini (iaitu dos sinaran 15 kGy dan kepekatan AA sebanyak 20%) dengan menghasilkan nilai cantuman tertinggi sebanyak 14±4%. Hasil juga menunjukkan sifat hidrofobik permukaan ePTFE berkurang sebanyak 18˚ dengan menganalisis sudut permukaan air (iaitu daripada 117˚ menjadi 99˚). Hasil keputusan analisis (ATR-FTIR) tidak menunjukkan sebarang perubahan spektrum berkemungkinan disebabkan pencantuman berlaku pada permukaan ePTFE sahaja. Manakala hasil keputusan daripada analisis (FESEM/EDX) menunjukkan ada pertambahan puncak oksigen di dalam analisis sampel yang telah disinar dan dicantum dengan AA, justeru menunjukkan percantuman berjaya berlaku.

**Kata kunci :** sinaran mengaruh pencantuman, pencantuman, poli(tetrafluoroetilena) rengangan, asetik asid

## Introduction

Poly(tetrafluoroethylene) (PTFE) is widely used in many different industries, such as petrochemical and chemical, electrical, semiconductor, food and beverage, pharmaceutical, and medical industries. The variety of applications of these polymers is possible because PTFE possesses high thermal and chemical stability [1]. This is due to the helical structure of the polymer chain caused by the relatively larger size of fluorine atoms compared to carbon atoms. The PTFE is also naturally hydrophobic, non-reactive, non-polar, and has low surface tension.

Expanded poly(tetrafluoroethylene) (ePTFE) is relatively similar to PTFE, but the difference is in morphology and surface conditions. The ePTFE is proven to be more favourable than the non-expanded version because it has a more porous membrane, excellent dielectric properties, and a drastic reduction in creep, which is a weakness of standard PTFE [2]. In addition, ePTFE is used to make lightweight, waterproof, and breathable fabrics, micro-porous membranes, medical tubes and implants, microwave carriers, industrial sealants, and high-tensile fabrics and cords. Moreover, ePTFE has been reported to perform well as a vascular graft, where its porous property is sufficient to promote endothelial healing with cellular and capillary growth. These properties also make ePTFE one of the best resorbable materials to be used as a tissue implant in the face [3]. However, high hydrophobicity of ePTFE limits the use of this polymer, especially as biomaterial where it is required to make a good integration with the surrounding living tissues. Therefore, its surface properties need to be altered so that it will match the uses of its intended applications [4].

Surface modification of a polymer via grafting techniques can be used to change the properties of any polymer surface so that the desired characteristics can be achieved. Grafting can be described as the covalent attachment process. Currently, there are various grafting techniques available to modify a polymer surface, including chemical treatment [5], photografting [6], radiation [7, 8], and plasma techniques [9]. Radiation-induced graft copolymerisation is one of the grafting techniques that has been well established for almost half a century [10]. These techniques can alter the initial surface of polymeric materials by introducing new functional groups on the backbone of the carbon chain. Many studies have been conducted using the radiation-induced grafting technique in which various monomers have been successfully introduced onto ePTFE, such as acrylic acid [8], itaconic acid [7], and methoxyacrylate phosphate [11]. In the current study, acetic acid (AA) was chosen as the grafting monomer to introduce the carboxylic acid group onto the surface of the ePTFE. The effects of the concentration of the monomer and radiation dose on the grafting outcomes were investigated using various characterisation techniques, including attenuated total reflectance infrared (ATR-FTIR) spectroscopy, field emission scanning electron microscopy (FESEM) coupled with energy dispersive X-ray (EDX) and water contact angle measurements.

## Materials and Methods

### Materials

The ePTFE membranes (0.022 mm thick, dimension of 15 x 10 $mm^2$) were obtained from Pall Corporation under the trade name Zefluor$^{TM}$ (0.5 µm). The membranes were pre-treated with methanol overnight at 40 ˚C to remove contaminants before being dried in the oven to a constant weight. Methanol was obtained from MERCK; AA was purchased from Systerm, and ammonium iron (II) sulphate hexahydrate (Mohr's salt) was obtained from Honeywell Riedel-de Haen.

### Grafting procedure

For the AA grafting experiment, 4 mL of deionised water and 40 mg of Mohr's salt were added to different AA concentrations (2, 10, and 20 w/v %) to form the monomer solution. The ePTFE samples (weight 2 – 3 mg) were placed in the monomer solution. All test tubes were covered using parafilm, and the solution was degassed with nitrogen for 15 minutes to remove the dissolved oxygen from the solution. The test tubes were sealed with caps and parafilm. Samples were then irradiated at ambient temperature using γ-rays (gamma cell 220 excel) with doses of 2 kGy, 5 kGy, 10 kGy, and 15 kGy at a dose rate of 1.8 kGy/h. After the irradiation process, the samples were washed with hot methanol at 40 ˚C for 1 hour to remove any occluded homopolymer or unreacted monomer. Then, the grafted sample was further washed with deionised water three times for 1 hour each and finally left in the water

overnight. The grafted samples i.e., ePTFE-grafted polyacetic acid (ePTFE-g-PAA) were dried in the desiccator jar over 3 days until a constant weight was achieved. The sample grafted with AA was named AA(*m*)*d* where *m* refers to concentration of the monomer and *d* to the dose (e.g., samples grafted in 2% AA at dose of 15 kGy were named AA(2)15).

**Characterisation**

The graft yield was determined from the initial and final weight of samples obtained using the electronic balance (Scaltex SBA31). The graft yield was measured using the formula:

$$\text{Graft yield (\%)} = \left[\frac{(Wf - Wi)}{Wi}\right] \times 100\%, \quad (1)$$

where $W_i$ is the initial weight of the sample and $W_f$ is the weight of grafted sample. The average and standard deviation are reported on triplicate samples.

Water uptake was obtained by immersing the ePTFE and grafted ePTFE in water overnight. The samples were removed from the water, and filter paper was used to remove any surface water before the sample weight was determined. The equilibrium water uptake was calculated using the formula:

$$\text{Water uptake (\%)} = \left[\frac{(Ws - Wd)}{WPAA}\right] \times 100\%, \quad (2)$$

where $W_s$ is the weight of the swollen sample, $W_d$ is the weight of dry sample, and $W_{PAA}$ is the mass of PAA on the grafted membrane. The average and standard deviation are reported on triplicate samples.

The contact angle measurement was performed via a custom-built setup, as previously described [8], using an automated angle goniometer machine (Rama Hart). Samples were placed on a Teflon stage, and 5 µL drops of deionised water were delivered onto the sample surface via a 50 µL glass flat-tip syringe. The measurements were taken at least five times for each sample, and the average measurement was taken.

Attenuated total reflectance infrared (ATR-FTIR) spectroscopy (model Perkin Elmer Spectrum BX) with a resolution of 8 $cm^{-1}$ and wavenumber range 400 $cm^{-1}$ – 4000 $cm^{-1}$ were used in this analysis. A FESEM/EDX analysis (Merlin compact model) was performed on the sample. All samples were coated with platinum for 5 min until a 15 nm thick layer had formed to make the material conductive. The FESEM/EDX analysis was performed under the standard high vacuum mode with the voltage at 3 kV. The morphology of each sample was obtained with various magnifications: 1.00 K x, 3.00 K x, 5.00 K x, and 10.00 K x.

## Results and Discussion

**Effects of grafting parameters on ePTFE and grafted ePTFE**

The increased graft yield after radiation-induced grafting of AA onto ePTFE possibly indicated the success of the grafting process. Table 1 shows the increased graft yield of grafted samples with increased radiation doses and monomer concentrations. At similar concentrations of AA (i.e., 20 w/v %), samples irradiated at higher doses (sample AA(20)15 and AA(20)10) showed higher grafting outcomes at approximately 14% compared to samples that have been irradiated at lower doses (sample AA(20)2) with a graft yield at approximately only 5%. The increased graft yield with higher doses, possibly due to the number of radicals produced at higher doses of radiation, initiated the primary radical of the polymer and monomer unit [12]. Thus, the increased radicals that could take part in the grafting reaction caused the degree of grafting to be increased [13].

In addition, the graft yield was observed to be increased with the increased AA concentrations at 5, 10, and 15 kGy. The percentage of grafting increased approximately 2 – 5% when AA concentrations increased from 2 to 20 w/v% for 5, 10, and 15 kGy. The increased graft yield with monomer concentrations was possibly because the grafting proceeds by a diffusion controlled mechanism, which takes place at the surface of the sample and gradually proceeds further by progressive diffusion of the monomer through the medium of the swollen grafted layer. It is also

assumed that the grafting begins at the polymer surface, then gradually proceeds inward as the grafting zone is swollen by the monomer solution [10, 14].

However, the percentage of grafting in these experiments was lower compared to the study conducted by Hidzir et al. [8], which used acrylic acid as the monomer that showed the highest grafting yield of 36 ± 3% at 20% monomer concentration with a 15 kGy dose. The differences of the percentage of grafting obtained from the previous study compared to the current study were possibly due to the characteristic of the monomer. As AA consists of two carbons that could covalently attach to ePTFE, whereas an acrylic acid has three carbons (Figure 1), only a few carbons of AA can form a bond to the carbon chain of ePTFE, which resulted in lower grafting yield from this monomer. In addition, acrylic acid has an unsaturated bond (i.e., double bond) that could easily break upon irradiation; therefore, more grafting onto ePTFE could easily be obtained with the used of acrylic acid as a monomer.

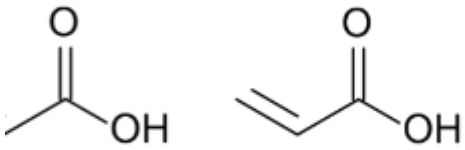



Figure 1. Chemical structure of acetic acid (left) and acrylic acid (right)

Table 1. Characterisation of ePTFE grafted membranes

| Sample | Dose (kGy) | Monomer Concentration (w/v%) | Graft Yield (%) | Water Uptake (%) | Contact Angle $\theta$(°) |
|---|---|---|---|---|---|
| ePTFE | 0 | 0 | 0 | 0 | 117 |
| AA(2)2 | 2 | 2 | 7±4 | 233±58 | na |
| AA(10)2 | 2 | 10 | 7±3 | 250±87 | na |
| AA(20)2 | 2 | 20 | 5±0 | 533±208 | na |
| AA(2)5 | 5 | 2 | 9±3 | 317±161 | na |
| AA(10)5 | 5 | 10 | 7±4 | 600±265 | na |
| AA(20)5 | 5 | 20 | 11±5 | 444±236 | na |
| AA(2)10 | 10 | 2 | 9±4 | 250±132 | 111 |
| AA(10)10 | 10 | 10 | 10±2 | 333±29 | 106 |
| AA(20)10 | 10 | 20 | 14±4 | 372±95 | 104 |
| AA(2)15 | 15 | 2 | 8±5 | 683±126 | na |
| AA(10)15 | 15 | 10 | 10±4 | 733±333 | 103 |
| AA(20)15 | 15 | 20 | 12±2 | 967±76 | 99 |

*na – data not available

**Water uptake and water contact angle analysis of ePTFE and grafted ePTFE**

The percentage of water uptake increased with the increased monomer concentrations and doses. At the highest grafting parameter (i.e., highest dose and monomer concentration used in this study), sample AA(20)15 showed the highest water uptake with 967 ± 76% compared to untreated ePTFE (0% water uptake) and samples that have been grafted at lower doses and monomer concentrations (e.g., sample AA(2)10 with water uptake of 250 ± 132%). This result was in line with the measurement obtained from water contact angle analysis where high hydrophobicity of

ePTFE (117˚) decreased significantly by ~18˚ to became less hydrophobic for grafted samples (sample AA(20)15 with water contact angle of 99˚). The increased water uptake and decreased water contact angle showed that the carboxylic functional group from the AA has successfully grafted onto ePTFE. At higher AA concentrations, more grafting of this carboxylic acid group occurred, thus resulting in a higher percentage of water uptake. The results in this study were similar to the previous studies reported by Wu et al. [4] and Hidzir et al. [8]. According to Wu et al. [4], the ePTFE surface angle can be reduced from 125˚ to 72˚ using the AA plasma deposition procedure. In addition, Hidzir et al. [8] reported that the surface water contact angle obtained is 92˚ for the grafted sample (ePTFE that has been irradiated at a dose of 10 kGy and 40% concentration of acrylic acid).

**Chemical characterisation of ePTFE and grafted ePTFE**

Figure 2(a) shows an FTIR spectra for untreated ePTFE, which displays the σ band at 1208 $cm^{-1}$ and 1154 $cm^{-1}$, which were assigned as the $CF_2$ stretching mode, and the band at 637 $cm^{-1}$ and 555 $cm^{-1}$, which were assigned to the $CF_2$ wagging mode and $CF_2$ deformation mode [8]. No additional band was observed on the sample that has been grafted with AA (e.g., sample AA(20)15) (Figure 2(b)) compared to the untreated sample. In the study by Hidzir et al. [8], the carbonyl band of the carboxylic acid group can be seen at 1716 $cm^{-1}$ , and the hydroxyl groups are present on the band 3000 – 3600 $cm^{-1}$. The undetected presence of the carbonyl group and hydroxyl groups on the spectrum of the current study (sample AA(20)15) is possibly because grafting may only have occurred on the top surface of the ePTFE. The penetration of the FTIR analysis was at the micrometre scale, whereas grafting may have occurred only on the very top surface of the ePTFE. In addition, the grafting obtained in this study was much lower compared to a previous study reported by Hidzir et al. [8].

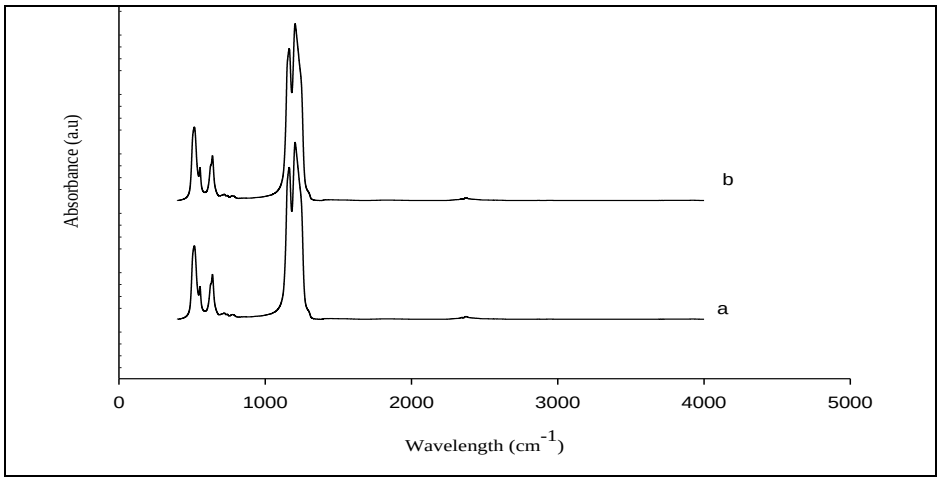



Figure 2. FTIR spectrum sample (a) untreated sample ePTFE and (b) AA(20)15

**Morphology and chemical composition analysis of ePTFE and grafted ePTFE**

Figure 3(a) shows the morphology of the ePTFE, which consists of islands and fibrils. The morphology of the grafted samples was observed to change, with less pores seen after grafting (Figure 3(b-f)). The change of this morphology was because the AA has been covered on the top surface of the ePTFE, resulting in less pores observed.

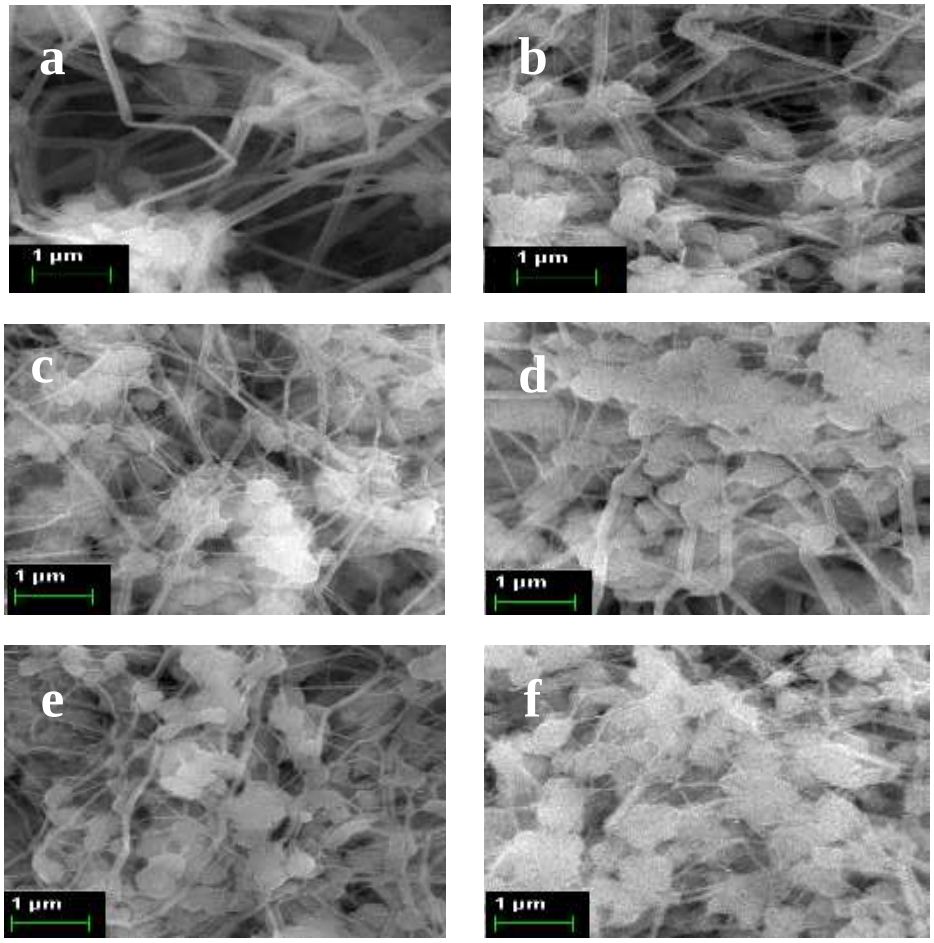



Figure 3. FESEM/EDX analysis of (a) untreated ePTFE, (b) AA(2)10, (c) AA(10)10, (d) AA(20)10, (e) AA(10)15 and (f) AA(20)15. Magnification for all images is 5000x

In addition, more island morphology was observed compared to fibril morphology in samples that have been grafted with higher doses and monomer concentrations (i.e., sample AA(20)15). Morphological changes are possibly due to the increased grafting percentage of AA. High doses and monomer concentrations allows more grafting of the AA onto the ePTFE surface. It was reported that the polymerisation could take place on the membrane surface and inside the pores, particularly when a high grafting degree was obtained [15, 16].

The EDX analysis shows the untreated ePTFE, which only consists of carbon and fluorine (Table 2). Oxygen was observed for the grafted sample (sample (AA(20)15) (Table 2)). In addition, the percentage of carbon weight for the grafted sample was observed to decrease from 22.66% (untreated ePTFE) to 18.92% (Table 2). Similarly, the ratio of carbon to fluorine (C:F) was observed to decrease for the grafted sample (sample AA(20)15) compared to the untreated ePTFE (Table 2). Through previous studies, the ratio of carbon to fluorine (C:F) was reported to decrease, but the ratio of carbon to oxygen (C:O) was increased due to the defluorination and oxidation occurring on the surface and shows the formation of hydrophilic ions on the surface [17].

Table 2. Comparison of elements on untreated ePTFE and sample AA(20)15 from the EDX analysis

| Sample | Element | Weight (%) | Atom (%) |
|---|---|---|---|
| ePTFE | C | 22.66 | 31.67 |
| | F | 77.34 | 68.33 |
| | Total | 100.00 | 100.00 |
| AA(20)15 | C | 18.92 | 26.92 |
| | O | 0.74 | 0.79 |
| | F | 80.34 | 72.29 |
| | Total | 100.00 | 100.00 |

## Conclusion

This study represents the first thorough investigation into gamma irradiation-induced grafting of AA onto ePTFE. It was found that grafting AA increased with higher doses and monomer concentrations. From FESEM/EDX analysis, it was found that grafting was successfully achieved. This grafting has resulted in the change of high hydrophobicity of ePTFE to less hydrophobicity with high water uptake for the grafted sample. This resulted in the desired characteristics of this ePTFE to be used in biomaterial applications, such as for bone tissue, bypass grafts, and artificial valves. However, further analysis, such as *in-vitro* mineralisation and protein adsorption studies, could provide more details on the biocompatibility of this polymer for such applications.

## Acknowledgement

The authors wish to thank School of Applied Physics, UKM especially Nuclear Science Programme, GGPM-2015-038, DLP-2014-011, and FRGS/1/2014/SG06/UKM/02/3 for the funds. The authors acknowledge the facilities and the technical assistance of the Centre of Research and Instrumental, UKM for FESEM/EDX analysis and School of Chemistry and Food Technology, UKM for assistance with FTIR analysis.

## References

1. Cassady, A. I., Hidzir, N. M. and Grøndahl, L. (2014). Enhancing expanded poly(tetrafluoroethylene) (ePTFE) for biomaterials applications. *Journal of Applied Polymer Science*, 131 (15): 40533 - 40547.
2. Kannan, R. Y., Salacinski, H. J., Butler, P. E., Hamilton, G. and Seifalian, A. M. (2005). Current status of prosthetic bypass grafts: A review. *Journal of Biomedical Materials Research Part B. Applied Biomaterials,*74(1): 570 – 581.
3. Wentrup-Byrne, E., Grøndahl, L. and Suzuki, S. (2005). Methacryloxyethyl phosphate-grafted expanded polytetrafluoroethylene membranes for biomedical applications. *Polymer International,* 54 (12): 1581 –1588.
4. Wu, T. H., Chen, K. S., Chen, S. C., Yeh, Y. C. and Shen, L. H. (2008). The Biomedical material of functional ePTFE hydrogels by the cold plasma method and radiation technique. *Advanced Materials Research,* 47–50: 1427 – 1429.
5. Rosli, N. A., Ahmad, I., Abdullah, I. and Anuar, F. H. (2014). Graft copolymerization of methyl methacrylate onto agave cellulose. *Malaysian Journal of Analytical Science,* 18(2): 398 – 404.
6. Naemuddin, N. H., Suradi, S. S., Jamaluddin, J. and Adrus, N. (2015). Photografting of polyacrylamide hydrogel coating onto various polyethylene terephthalate textiles. *Malaysian Journal of Analytical Sciences,* 19(1): 163 – 172.
7. Hidzir, N. M., Lee, Q., Hill, D. J. T., Rasoul, F. and Grondahl, L. (2014). Grafting of acrylic acid-co-itaconic acid onto ePTFE and characterization of water uptake by the graft copolymers. *Journal of Applied Polymer Science*, 132(7):41482 – 41494.
8. Hidzir, N. M., Hill, D. J. T., Martin, D. and Grøndahl, L. (2012). Radiation-induced grafting of acrylic acid onto expanded poly(tetrafluoroethylene) membranes, *Polymer*, 53(26): 6063 – 6071.

9. Hidzir, N. M., Hill, D. J. T., Taran, E., Martin, D. and Grøndahl, L. (2013). Argon plasma treatment-induced grafting of acrylic acid onto expanded poly(tetrafluoroethylene) membranes. *Polymer*, 54(24): 6536 – 6546.
10. Dargaville, T. R., George, G. A., Hill, D. J. T. and Whittaker, A. K. (2003). High energy radiation grafting of fluoropolymers. *Progress in Polymer Science*, 28(9): 1355 – 1376.
11. Chandler-Temple, A., Wentrup-Byrne, E., Whittaker, A. K. and Grøndahl, L. (2010). Graft copolymerization of methoxyacrylethyl phosphate onto expanded poly(tetrafluoroethylene) facial membranes. *Journal of Applied Polymer Science*, 117(6): 3331 – 3339.
12. Yu, L., He, Y., Bin, L. and Yue'e, F. (2003). Study of radiation-induced graft copolymerization of butyl acrylate onto chitosan in acetic acid aqueous solution. *Journal of Applied Polymer Science*, 90(10): 2855 – 2860.
13. Nasef, M. M. (2001). Effect of solvents on radiation-induced grafting of styrene onto fluorinated polymer films. *Polymer International*, 50 (3): 338 – 346.
14. Chandler-Temple, A. F., Wentrup-Byrne, E., Griesser, H. J., Jasieniak, M., Whittaker, A. K. and Grøndahl, L. (2010). Comprehensive characterization of grafted expanded poly(tetrafluoroethylene) for medical applications. *Langmuir*, 26(19): 15409 – 15417.
15. Xu, Z., Wan, L. and Huang, X. (2009). Surface engineering of polymer membranes. Zhejiang University Press, Hangzhou: pp. 82.
16. Freger, V., Gilron, J. and Belfer, S. (2002). TFC polyamide membranes modified by grafting of hydrophilic polymers: An FT-IR/AFM/TEM study. *Journal of Membrane Science*, 209(1): 283 – 292.
17. Pelagade, S. M., Singh, N. L., Rane, R. S., Mukherjee, S., Deshpande, U. P., Ganesan, V. and Shripathi, T. (2012). Investigation of surface free energy for PTFE polymer by bipolar argon plasma treatment. *Journal of Surface Engineered Materials and Advanced Technology*, 2: 132 – 136.

*Malaysian Journal of Analytical Sciences, Vol 21 No 3 (2017): 535 - 543*
*DOI: https://doi.org/10.17576/mjas-2017-2103-03*

MALAYSIAN JOURNAL OF ANALYTICAL SCIENCES
*Published by The Malaysian Analytical Sciences Society*
ISSN 1394 - 2506

# BIOACCUMULATION OF SEDIMENTARY ENDOCRINE DISRUPTING CHEMICALS (EDCs) BY THE BENTHIC FISH, *Pleuronectes yokohamae*

## (Biopenumpukan Bahan Kimia Pengganggu Endokrin (EDCs) oleh Ikan Bentik, *Pleuronectes yokohamae*)

Nurulnadia Mohd Yusoff[1] *, Jiro Koyama[2], Seiichi Uno[2]

[1]*School of Marine and Environmental Sciences,*
*Universiti Malaysia Terengganu, 21030 Kuala Terengganu, Terengganu, Malaysia*
[2]*Faculty of Fisheries,*
*Kagoshima University, Shimoarata 4-50-20, Kagoshima 890-0056, Japan*

**Corresponding author: nurulnadia@umt.edu.my*

Received: 16 August 2016; Accepted: 20 April 2017

**Abstract**

In this study, *Pleuronectes yokohamae (P. yokohamae)* were exposed to the sediment mixed with mixture of nonylphenol (NP), octylphenol (OP), estrone (E1) and 17β-estradiol (E2) which makes up Endocrine Disrupting Chemicals (EDCs). The target compound was detected in water sample, and NP and OP concentrations were found to be the highest, 7.66 µg/L and 0.63 µg/L respectively (E1 and E2 concentrations were below the limit of detection). In pore water on the other hand, NP concentrations recorded the highest with 35.3 µg/L, while concentrations of OP, E1 and E2 were 4.08 µg/L, 0.06 µg/L and 0.18 µg/L respectively. *P. yokohamae* shown rapid and maximum accumulation of NP and OP on day 3, where NP recorded to be 2200 ng/g d.w. and OP 168 ng/g d.w. The recorded BAF values in low and high exposure groups were 0.010 and 0.065 for NP, and 0.065 and 0.084 for OP. The BAF findings recorded, being less than 1 indicated that there were no bioaccumulations in the tested fish of both groups. However, due to their nature of being more predisposed to accumulating EDCs than the water column, the bioaccumulation of contaminant in benthic fish should be continually monitored.

**Keywords**: bioaccumulation, sediment, endocrine disrupting chemical, *Pleuronectes yokohamae*, marbled flounder

**Abstrak**

Dalam kajian ini, campuran bahan kimia pengganggu endokrin (EDC) terdiri daripada nonilfenol (NP), oktilfenol (OP), estron (E1) dan 17β-estradiol (E2) telah dicampur ke dalam sedimen dan didedahkan kepada *Pleuronectes yokohamae (P. yokohamae)*. Sebatian sasaran telah dikesan dalam sampel air dengan kepekatan NP dan OP tertinggi iaitu masing-masing 7.66 µg/L dan 0.63 µg/L (kepekatan E1 dan E2 adalah di bawah had pengesanan), manakala kepekatan tertinggi di dalam air liang ialah 35.3 µg/L untuk NP, 4.08 µg/L untuk OP, 0.06 µg/L untuk E1 dan 0.18 µg/L untuk E2. Kepekatan NP dan OP di dalam *P. yokohamae* meningkat dengan mendadak pada hari 3 dan mencapai kepekatan maksimum 2200 ng/g d.w. dan 168 ng/g d.w. Nilai BAF dalam kumpulan kepekatan rendah dan tinggi ialah 0.010 dan 0.065 untuk NP, dan 0.065 dan 0.084 untuk OP. BAF telah dikira kurang daripada 1 menunjukkan tiada biopenumpukan EDC dalam ikan untuk kedua-dua kumpulan kepekatan. Walaupun begitu, biopenumpukan bahan cemar kepada ikan bentik harus sentiasa dipantau melalui sedimen berikutan kebolehannya menumpuk bahan EDC adalah lebih tinggi berbanding kolum air.

**Kata kunci**: biopenumpukan, sedimen, bahan kimia pengganggu endokrin, *Pleuronectes yokohamae*, marbled flounder

## Introduction

Endocrine Disrupting Chemicals (EDCs) are either estrogenic or natural – the estrogenic chemicals such as nonylphenol (NP), and octylphenol (OP) are mostly industrial byproduct of surfactants in detergents and paints, agricultural dispersing agents, and other industrial applications [1] while natural forms which include 17β-estradiol (E2) and estrone (E1) excreted by humans and livestock, are discharged from sewage treatment works and agricultural run-off into the aquatic ecosystems [2]. As a result, these compounds were frequently reported to disturb the reproductive system in fish such as reduced in testicular growth and formation of eggs in testis [3].

Endocrine disruption in fish occurs as a result of the binding of natural and manmade compounds in the aquatic environment to estrogen receptors, in place of endogenous hormone. The EDCs then alter the enzyme system controlling steroidogenesis, causing mimicking or blocking effects that disrupt normal endocrine pathways [4]. Researchers hypothesised that EDCs could be hydrophobic substances with affinity to bind to particles and accumulate on bottom sediments [5]. EDCs tend to get adsorbed into sediment due to high octanol-water partition coefficient (log Kow), resulting in vulnerability of aquatic organisms to accumulation [6].

*P. yokohamae* resides in sandy-mud bottoms less than 100 m depth [7] and recognised as commercially important species [8]. In Japan, winter is the breeding season of *P. yokohamae*. Both male and female fish reach maturity at the age of 1 year [9]. *P. yokohamae* prey mainly on benthic animals and were reported to accumulate organic compounds such as tributyltin (TBT) [10], 1,1-dichloro-2,2-bis(p-chlorophenyl) ethylene (DDE), hexachlorobenzene (HCB) and polychlorinated biphenyls (PCBs) [11] in the liver. Thus, *P. yokohamae* can serve as a good indicator of EDCs accumulation from sediment.

Bioaccumulation of EDCs has been demonstrated in both field and laboratory-based experiment [12, 13]. To date, nearly all experiments conducted on EDCs apply either the waterborne [14] or intraperitoneal exposure methods [15]. Very few studies adopted dietary and sedimentary exposure. Following this observation, this experiment aims to determine the bioaccumulation factor of EDCs through direct sedimentary uptake. Realising the significance of fisheries as an important commodity and main sources of diet for Japanese people, investigation on potential bioaccumulation of EDCs in fish is undeniably necessary.

## Materials and Methods

### Test organism (*P. yokohamae*)

*P. yokohamae* were purchased from Regional Government Aquaculture Center in Yamaguchi, Japan. They were acclimatized in the laboratory condition for six months to the desired body size and fed with commercial diet. *P. yokohamae* were kept in the water temperature below 25°C as it will die in warm water.

### Sampling of sediment

Approximately ten kilograms of sediment were collected randomly around the Amori River mouth in Kagoshima Bay (Figure 1) on 24 October 2012. Upon arrival at the laboratory, all sediment samples were dried under the sunlight and at room temperature for one week. Prior to spiking with EDCs, the sediment samples were combined and mixed well after sieving using sized 1- mm mesh sieve.

### Preparation of EDCs spiked sediment

Three kilograms of the sieved sediment were transferred into each glass aquarium (60 x 30 x 40 cm) of control, low and high test groups. The mixture of EDCs was then prepared according to Table 1.

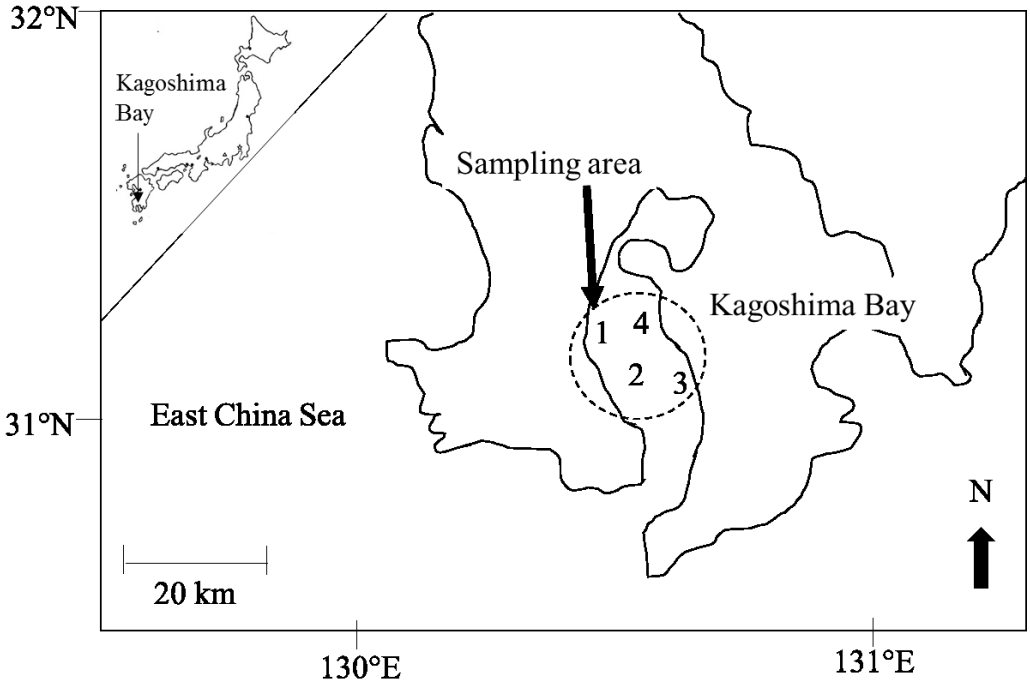



Figure 1. Sediment sampling stations (1, 2, 3 and 4) located in Kagoshima Bay

Table 1. Mean EDCs concentration, ng/g dry weight (d.w.) in control and spiked sediment, n = 2

| EDCs | ng/g dry weight (d.w.) | | |
|---|---|---|---|
| | Control | Low | High |
| NP | 5.09 | 2750 | 30,400 |
| OP | 0.63 | 169 | 1,210 |
| E1 | 2.36 | 1.90 | 10.8 |
| E2 | n.d | 0.83 | 6.70 |

n.d – Not detected

**Exposure scheme**

Before introducing *P. yokohamae*, the sediment in each aquarium (60 x 30 x 40 cm) was flooded and inundated with 60 L of seawater for a week. This condition was maintained in a water-flow-through system. After one week, fifteen of *P. yokohamae* were introduced into each aquarium including the control group. They were fed ad libitum with commercial fish diet twice daily for 14 days of the experimental duration. Sampling of *P. yokohamae* were done on days 0, 3, 7 and 14 while water sampling was done on days 4, 8, 10 and 13. At the end of exposure, sediment and pore-water samples were gathered. The body weight of individual *P. yokohamae* at the initial of exposure ranged from 7.30 g and 8.70 g. During sampling, *P. yokohamae* were anaesthetized using 0.05% 2-phenoxyethanol. The body length and weight were recorded prior to storage of the samples in freezer (-18 °C) until analysis stage. Water parameters such as temperature, dissolved oxygen, pH and salinity were measured periodically using the YSI multiprobe meter.

**Pre-treatment of samples**

After thawing, each benthic fish was weighed into a glass bottle to record the wet weight. The fishes were then freeze dried at -48 °C and 7.8 Pa for 7 days, and immediately after that, the dry weights of fishes were recorded. Sediment samples were treated the same way as benthic fishes. Wet and dry weights of sediments were recorded before and after freeze drying process. Water and pore water samples were analysed on the day of collection.

**EDCs analysis**

EDCs were analysed according to the published procedures in Nurulnadia [16]. After addition of external standard of *p*-n-NP-d4, target chemicals in the freeze-dried benthic fish (weights of homogenate sample ranged from 0.78 to 3.05 g) were ultrasonically extracted twice with 20 mL of methanol for 15 minutes. After centrifugation (4 °C, 760 x g, 10 minutes), the organic layer was collected and transferred into a separating funnel. Later, 3 mL Milli-Q water and 3 mL hexane were added. As lipid interfere with the measurement, they were removed from methanol using 20 mL hexane with 5 minutes shaking. This step was repeated three times. After shaking, hexane layer was discarded, while methanol (denser than hexane) was collected and combined. Methanol was put into the separating funnel again and mixed with 50 mL of 5% sodium chloride (NaCl) and 0.2 mL concentrated hydrochloric acid. The mixture of solvents was extracted twice using 20 mL dichloromethane and 10 min shaking and concentrated to 0.5 mL using a rotary evaporator and gentle stream of nitrogen ($N_2$). The concentrated extract was then replaced with 3 mL hexane and concentrated again to 0.5 mL using $N_2$. This step was repeated three times. Cleaning up process was performed in a 5 mL glass pipette (6 mm i.d. x 17 cm) filled with florisil (containing 3% water) and prewashed with 30 mL hexane. The target chemicals were then eluted with 50 mL hexane-isopropyl alcohol (9:1, v/v). The eluate was later concentrated to dryness using a rotary evaporator and gentle stream of $N_2$. Finally, internal standard (E2-16,16,17- d3) and acetonitrile were added to achieve the final volume of 0.2 mL before liquid chromatography-tandem mass spectrometry (LC-MS/MS) measurement.

Similar procedures were applied for sediment, water and diet samples.

**Measurement using LC-MS/MS-ESI**

LC–MS/MS analysis was carried out using Agilent 1200 LC system (Agilent Technologies, USA) coupled to an API-2000 triple stage quadruple mass spectrometer (Applied Biosystems, USA). The ESI was employed in negative mode. The optimized parameters were set as follows: curtain gas (40 psi), turbo gas (80 psi) and auxiliary gases (80 psi) using nitrogen, CAD gas, 5 psi; ion spray voltage, -4,500 V; and turbo temperature, 400°C. MS/MS measurements were performed in multiple reactions monitoring mode and target chemicals were four EDC compounds as shown in Table 2. The EDCs were analysed by gradient liquid chromatography using a reverse-phase Extend C-18 column (2.1 mm i.d. 9100 mm, 3.5 µm of particle size, Agilent) kept at 40 °C. The mobile phase consisted of solvents A (100% acetonitrile) and B (water containing 0.1% triethylamine, (v/v)).

Quality assurance test was performed using fish diet spiked with 100 ng/g of each EDC standards and internal standard (E2-16,16,17-d3). The EDCs standard extraction and measurement were done as above procedures. Mean percent recovery, as determined from an estimate of the amount of added and recovered, were between 70.0 % and 102.3 %. Analysis were conducted in triplicate (n = 3) with error of all analysis were within ±20 %.

Table 2. Precursor and daughter ions of EDCs and limit of detection by LC-MS/MS-ESI

| EDCs | Precursor Ions, m/z (amu) | Daughter Ions, m/z (amu) | Limit of Detection (ng/g) | |
|---|---|---|---|---|
| | | | Diet (ng/g)[a] | Water (µg/L)[b] |
| NP | 219.0 | 132.9 | 2.67 | 0.54 |
| OP | 205.0 | 132.9 | 0.31 | 0.05 |
| E1 | 269.1 | 145.0 | 1.01 | 0.05 |
| E2 | 271.1 | 144.9 | 1.50 | 0.10 |

[a]Detection limit using 0.3 g diet sample; [b]Detection limit using 0.5 L seawater

**Data analysis**

BAF (bioaccumulation factors) were calculated as the ratio of concentration in biota to sediment [17, 18] using the formula stated below:

$$BAF = \frac{\text{(EDCs concentration at steady state in } \textit{P. yokohamae}\text{)}}{\text{(EDCs concentration in sediment)}} \quad (1)$$

## Results and Discussion

**Water parameters and control sediment**

In the present study, range of water temperature and dissolved oxygen were 12.8 to 14.6 °C and 5.93 to 8.48 mg/L respectively, whereas pH and salinity were 8.01 to 8.08 and 36 to 38 psu respectively. Sediment sample collected from Amori River contains three of the target EDCs as shown in Table 1 (control). Amori River is one of the longest (42.5 km long) river, flowing into Kagoshima Bay, hence it receives large amount of effluent from residential and municipal activities daily. This most likely contributed to some concentrations of NP, OP and E1 in the control sediment. The total organic carbon and total organic nitrogen in sediment were 1.43±0.0.6% and 0.11±0.004% (n=5) respectively.

The concentration of EDCs was measured in the water sample during the exposure test, showing a range of 0.85 and 7.66 µg/L for NP, and 0.49 µg/L and 0.63 µg/L for OP, respectively whereas E1 and E2 concentrations were below the limit of detection. Low concentrations of EDCs were expected to be released into the water as *P. yokohamae* dwell onto the sediment. Low concentrations of EDCs were also recorded in pore water collected right after the exposure period ended (Table 3). In laboratory controlled uptake studies for NP, Bioconcentration factors (BCFs) yielded ranged from 200 to 300 [19, 20] whereas, OP were recorded to be from 250 to 350 [21, 22]. If *P. yokohamae* in this study has bio accumulated the target compound from water, the estimated concentration of NP and OP from maximum value would be approximately 2,300 and 221 ng/g w.w., respectively. However, the maximum wet weight concentrations of NP (532 ng/g w.w.) and OP (45.4 ng/g w.w.) in *P. yokohamae* in this study were recorded much lower than those estimated concentration. Thus, it was assumed that *P. yokohamae* in the present study accumulated EDCs from the spiked sediment.

Table 3. EDCs concentration (µg/L) in pore water, n = 2

| Exposure Group | NP | OP | E1 | E2 |
|---|---|---|---|---|
| Control | 16.9 | n.d | n.d | n.d |
| Low | 11.7 | 0.15 | n.d | n.d |
| High | 35.3 | 4.08 | 0.06 | 0.18 |

n.d – Not detected

**NP and OP concentrations in *P. yokohamae***

As reported in previous study [23], E1 and E2 could not be detected in *P. yokohamae* due to rapid metabolism of the substance in the fish. The accumulation of NP and OP in *P. yokohamae* from the sediment is shown in Figure 2. The concentration is calculated in dry weight (d.w.) basis to ease the determination of bioaccumulation factor (BAF). On day 0, NP and OP were detected in *P. yokohamae* with 114±91 and 34.4±15 ng/g d.w., respectively. Both compounds probably accumulated from commercial diet fed during the acclimatization period [24] as they were measured 27.9±1.77 ng/g d.w of NP and 3.02±0.34 ng/g d.w of OP in the control diet. *P. yokohamae* rapidly accumulated NP and OP on day 3 of exposure period and reached the maximum concentration. The highest concentration of NP in low and high exposure groups were 249 and 2200 ng/g d.w. respectively, whereas the recorded OP concentrations were 56.3 and 168 ng/g d.w. respectively. After day 3, observations shown that the

concentrations declined consistently until the end of experiment. Hence, day 3 was decided as the point at which steady state was reached for both NP and OP and these concentrations were used for the BAF computation.

**Bioaccumulation factors (BAF)**

BAFs were calculated using the concentration of NP and OP at day 3 of each group relative to measured concentration of the respective compound in the spiked sediment (Table 4). BAF values were similar between the low and high exposure groups indicating that the difference in concentration does not affect the bioaccumulation. However, NP and OP were not bio accumulated in *P. yokohamae* as the BAF values less than 1 [23].

Table 4. BAF in low and high exposure groups

| EDCs | Low | High |
|---|---|---|
| NP | 0.010 | 0.065 |
| OP | 0.065 | 0.084 |

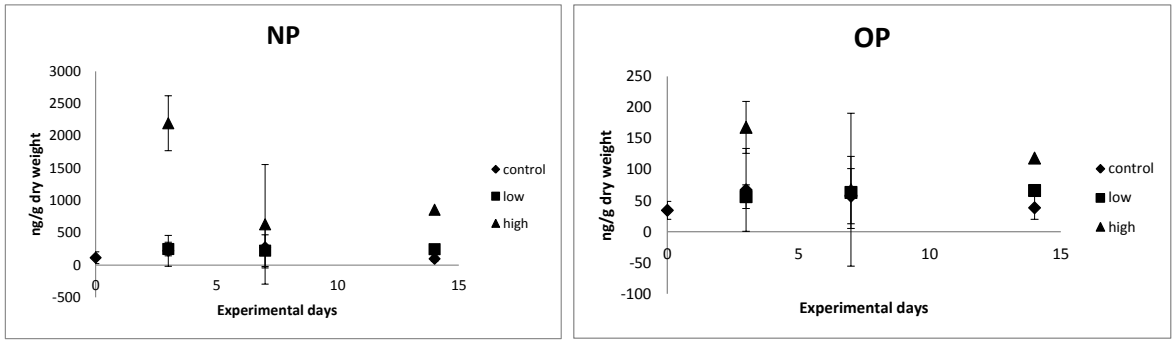



Figure 2. Accumulation of NP and OP (ng/g dry weight) in *P. yokohamae* in control, low and high exposure groups. Error bars indicate the standard deviation (n = 3)

BAF from previous studies are tabulated in Table 5. Based on the values, NP was discovered to be bio accumulated in bluegill, flounder and goby with BAF of 2.33, 6.24 and 27.0, respectively. These fishes were collected near sewage treatment water effluent; thus, it was probable that they may have accumulated NP from the water as well. NP was also found to be bioaccumulated in worm, mussel and bivalve. As sediment-dwelling organism, worms are in direct exposure to the pollutant in sediment – which may cause bioaccumulation [25]; higher concentration of NP in benthic worm compared to sediment was also observed in our previous field study [26]. Meanwhile, mussel and bivalve were sampled in urban and industrial areas [16, 27], hence received NP at frequent term which could lead to bioaccumulation. However, many other studies reported the same results as the present study that NP was not bioaccumulated in fish. In the case of OP on the other hand, no bioaccumulation was observed either in fish or invertebrate.

NP and OP did not bioaccumulate in *P. yokohamae* through the sediment as suggested by BAF values. However, certain aquatic organisms could probably accumulate EDCs (e.g. bluegill, flounder, and goby). This provides an impression that accumulation is probably influenced by species specific. This study was conducted to investigate the extremely high BAF values of EDCs measured in benthic worm compared to sediment samples of Osaka Bay [16]. If the worm accumulated EDCs from the sediment, the fish might accumulate the same compounds. Following this hypothesis, the EDCs have great potentials to be transferred into human as they consume the fish. Therefore, the EDCs measurement in fish from Osaka Bay should be conducted in order to prove the hypothesis.

Table 5. Bioaccumulation factors (BAF) of NP and OP in fishes and invertebrates

| | BAF | | Study Area | Reference |
|---|---|---|---|---|
| | NP | OP | | |
| *Fish* | | | | |
| Bluegill | 2.330 | n.a | Kalamazoo River, US | [28] |
| Flounder | 6.240 | n.a | Tyne Estuary, UK | [29] |
| | 0.042 | 0.960 | Tees Estuary, UK | |
| Various fish | 0.208 | 0.121 | Ebro river basin, Spain | [30] |
| Flatfish | 0.981 | n.a | Southern California Bight | [31] |
| Black seabream | 0.013 | 0.009 | Yundang Lagoon, China | [32] |
| Yellowfin seabream | 0.082 | 0.014 | | |
| Tilapia | 0.303 | 0.073 | | |
| Goby | 27.00 | n.a | North American Pacific Coast estuaries | [12] |
| **Sole (*P. yokohamae*)** | **0.038** | **0.075** | **Lab exposure** | **Present study** |
| *Invertebrate* | | | | |
| Shrimp | 0.002 | n.a | Scheldt estuary, The Netherlands | [33] |
| Bivalve | 6.580 | n.a | Northeast coast of China | [34] |
| Worm | 5.900 | n.a | Lab exposure | [26] |
| Short-necked clam | 0.065 | 0.042 | Yundang Lagoon, China | [32] |
| Mussel | 1.990 | n.a | Venice lagoon, Italy | [27] |

n.a – not available

## Conclusion

*P. yokohamae* in this study rapidly accumulated NP and OP from the sediment until day 3. After that the concentrations of both EDCs decreased to constant level until the end of experiment. E1 and E2 could not be detected in *P. yokohamae* due to rapid metabolism which were proven in our recent study [23]. BAF values for both compounds (NP and OP) indicated bioaccumulation did not occur in *P. yokohamae* after being exposed to EDCs spiked sediment. However, bioaccumulation of EDCs to benthic organism should be continually investigated as sediment can concentrate higher levels of pollutant than the water column.

## Acknowledgement

The present study was partly funded by the EXTEND 2010 Program, Ministry of Environment, Japan.

## References

1. Folmar, L. C., Denslow, N. D., Kroll, K., Orlando, E. F., Enblom, J., Marcino, J., Metcalfe, C. and Guillette Jr., L. J. (2001). Altered serum sex steroids and vitellogenin induction in walleye (*Stizostedion vitreum*) collected near a metropolitan sewage treatment plant. *Archives of Environmental Contamination & Toxicology*, *40*: 392 – 398.
2. Tashiro, Y., Takemura, A., Fujii, H., Takahira, K. and Nakanishi, Y. (2003). Livestock wastes as a source of estrogens and their effects on wildlife of Manko tidal flat, Okinawa. *Marine Pollution Bulletin*, *47*: 143 – 147.
3. Gray, M. A. and Metcalfe, C. D. (1997). Induction of testis-ova in Japanese medaka (*Oryzias latipes*) exposed to p-nonylphenol. *Environmental Toxicology & Chemistry*, 16(5): 1082 – 1086.

4. Tapiero, H., Nguyen, Ba G. and Tew K. D. (2002). Estrogens and environmental estrogens. *Biomedicine & Pharmacotherapy, 56*: 36 – 44.
5. Yu, Z. Q., Xiao, B. H., Huang,W. L. and Peng, P. (2004). Sorption of steroid estrogens to soils and sediments. *Environmental Toxicology and Chemistry,* 23: 531 – 539.
6. David, A., Fenet, H. and Gomez, E. (2009). Alkylphenols in marine environments: distribution monitoring strategies and detection considerations. *Marine Pollution Bulletin,* 58: 953 – 960.
7. Sakamoto, K. (1984). Pleuronectidae righteye flounders. In H. Masuda, K. Amaoka, T. Araga, T. Ueno, & T. Yoshino (Eds.). The Fishes of the Japanese Archipelago Tokyo: Tokai University Press: pp. 336 –340.
8. Park, J. S. (1988). A study on the pleuronectid flounder *Limanda yokohamae* population in Tokyo Bay. PhD Thesis, University of Tokyo, Tokyo (*in Japanese*).
9. Park, J. S. and Simizu, M. (1990). Maturity and spawning season of the *Limanda yokohamae* (Günther) in Tokyo Bay, Japan. *Bulletin of Fisheries Science Institute,* 6, 1 – 6.
10. Takayama, T., Hashimoto, S., Tokai, T. and Otsuki, A. (1995). Measurements of organic tin compounds in fish and crustacean of Tokyo Bay. *Environmental Science*, 8: 1 – 9.
11. Kammann, U., Landgraff, O. and Steinhart, H. (1993). Distribution of aromatic organochlorines in livers and reproductive organs of male and female dabs from the German Bight. *Marine Pollution Bulletin,* 26: 629 – 635.
12. Diehl, J., Johnson, S. E., Xia, K., West, A. and Tomanek, L. (2012). The distribution of 4 nonylphenol in marine organisms of North American Pacific Coast estuaries. *Chemosphere*, 87(5): 490 – 497.
13. Liber, K., Gangl, J. A., Corry, T. D., Heinis, L. J. and Stay, F. S. (1999). Lethality and bioaccumulation of 4-nonylphenol in bluegill sunfish in littoral enclosures. *Environmental Toxicology & Chemistry*, 18: 394 – 400.
14. Thorpe, K. L., Hutchinson, T. H., Hetheridge, M. J., Scholze, M., Sumpter, J. P. and Tyler, C. R. (2001). Assessing the biological potency of binary mixtures of environmental estrogens using vitellogenin induction in juvenile rainbow trout (*Oncorhynchus mykiss*). *Environmental Science & Technology*, 35(12): 2476 – 2481.
15. Arukwe, A., Thibaut, R., Ingebrigsten, K., Celius, T., Goksøyr, A. and Cravedi, J. P. (2000). In vivo and in vitro metabolism and organ distribution of nonylphenol in Atlantic salmon (*Salmo salar*). *Aquatic Toxicology,* 49(4): 289 – 304.
16. Nurulnadia, M. Y., Koyama, J., Uno, S., Kito, A., Kokushi, E., Bacolod, E. T., Ito, K. and Chuman, Y. (2014). Accumulation of endocrine disrupting chemicals (EDCs) in the polychaete *Paraprionospio* sp. from the Yodo River mouth, Osaka Bay, Japan. *Environmental Monitoring & Assessment*, 186(3): 1453 – 1463.
17. Kwok, C. K., Liang, Y., Leung, S. Y., Wang, H., Dong, Y. H., Young, L., Giesy, J. P. and Wong, M. H. (2013). Biota–sediment accumulation factor (BSAF), bioaccumulation factor (BAF), and contaminant levels in prey fish to indicate the extent of PAHs and OCPs contamination in eggs of waterbirds. *Environmental Science & Pollution Research*, 20(12): 8425 – 8434.
18. Melwani, A. R., Greenfield, B. K. and Byron, E. R. (2009). Empirical estimation of biota exposure range for calculation of bioaccumulation parameters. *Integrated Environmental Assessment & Management*, 5(1): 138 – 149.
19. Servos, M. R. (1999). Review of the aquatic toxicity, estrogenic responses and bioaccumulation of alkylphenols and alkylphenol polyethoxylates. *Water Quality Research Journal of Canada,* 34: 123 –177.
20. Staples, C., Mihaich, E., Carbone, J., Woodburn, K. and Klecka, G. (2004). A weight of evidence analysis of the chronic ecotoxicity of nonylpenol ethoxylates, nonylphenol ether carboxylates, and nonylphenol. *Human & Ecological Risk Assessment,* 10: 999 – 1017.
21. Ferreira-Leach, A. M. R. amd Hill, E. M. (2000). Bioconcentration and metabolism of 4-*tert* octylphenol in roach (*Rutilus rutilus*) fry. *Analysis*, 28(9): 789 – 792.
22. Tsuda, T., Takino, A., Muraki, K., Harada, H. and Kojima, M. (2001). Evaluation of 4 nonylphenols and 4-tert-octylphenol contamination of fish in rivers by laboratory accumulation and excretion experiments. *Water Research*, 35(7): 1786 – 1792.
23. Nurulnadia, M. Y., Koyama, J., Uno, S. and Amano, H. (2016). Biomagnification of endocrine disrupting chemicals (EDCs) by *Pleuronectes yokohamae*: Does *P. yokohamae* accumulate dietary EDCs?. *Chemosphere*, 144: 185 – 192.
24. Nurulnadia, M. Y., Koyama, J., Uno, S., Kokushi, E., Bacolod, E. T., Ito, K. and Chuman, Y. (2013). Bioaccumulation of dietary Endocrine Disrupting Chemicals (EDCs) by the Polychaete, *Perinereisnuntia*. *Bulletin of Environmental Contamination & Toxicology*, 91(4): 372 – 376.

25. Mitchelmore, C. L. and Rice, C. P. (2006). Correlations of nonylphenol-ethoxylates and nonylphenol with biomarkers of reproductive function in carp (*Cyprinus carpio*) from the Cuyahoga River. *Science of The Total Environment*, 371(1): 391 – 401.
26. Mäenpää, K. and Kukkonen, J. V. K. (2006). Bioaccumulation and toxicity of 4-nonylphenol (4-NP) and 4-(2-dodecyl)-benzene sulfonate (LAS) in *Lumbriculus variegatus* (Oligochaeta) and *Chironomus riparius* (Insecta). *Aquatic Toxicology*, 77(3): 329 – 338.
27. Pojana, G., Gomiero, A., Jonkers, N. and Marcomini, A. (2007). Natural and synthetic endocrine disrupting compounds (EDCs) in water, sediment and biota of a coastal lagoon. *Environment International*, 33(7): 929 – 936.
28. Kannan, K., Keith, T. L., Naylor, C. G., Staples, C. A., Snyder, S. A. and Giesy, J. P. (2003). Nonylphenol and nonylphenol ethoxylates in fish, sediment, and water from the Kalamazoo River, Michigan. *Archives of Environmental Contamination & Toxicology*, 44(1): 77 – 82.
29. Lye, C. M., Frid, C. L. J., Gill, M. E., Cooper, D. W. and Jones, D. M. (1999). Estrogenic alkylphenols in fish tissues, sediments, and waters from the UK Tyne and Tees estuaries. *Environmental Science & Technology*, 33(7): 1009 – 1014.
30. Lacorte, S., Raldúa, D., Martínez, E., Navarro, A., Diez, S., Bayona, J. M. and Barceló, D. (2006). Pilot survey of a broad range of priority pollutants in sediment and fish from the Ebro river basin (NE Spain). *Environmental Pollution*, 140(3): 471 – 482.
31. Maruya, K. A., Vidal-Dorsch, D. E., Bay, S. M., Kwon, J. W., Xia, K. and Armbrust, K. L. (2012). Organic contaminants of emerging concern in sediments and flatfish collected near outfalls discharging treated wastewater effluent to the Southern California Bight. *Environmental Toxicology & Chemistry*, 31(12): 2683 – 2688.
32. Zhang, X., Gao, Y., Li, Q., Li, G., Guo, Q. and Yan, C. (2011). Estrogenic compounds and estrogenicity in surface water, sediments, and organisms from Yundang Lagoon in Xiamen, China. *Archives of Environmental Contamination & Toxicology*, 61(1): 93 – 100.
33. Verslycke, T. A., Vethaak, A. D., Arijs, K. and Janssen, C. R. (2005). Flame retardants, surfactants and organotins in sediment and mysid shrimp of the Scheldt estuary (The Netherlands). *Environmental Pollution*, 136(1): 19 – 31.
34. Wang, J., Shim, W. J., Yim, U. H., Kannan, N. and Li, D. (2010). Nonylphenol in bivalves and sediments in the northeast coast of China. *Journal of Environmental Sciences*, 22(11): 1735 – 1740.

*Malaysian Journal of Analytical Sciences, Vol 21 No 3 (2017): 544 - 551*
*DOI: https://doi.org/10.17576/mjas-2017-2103-04*

MALAYSIAN JOURNAL OF ANALYTICAL SCIENCES
*Published by The Malaysian Analytical Sciences Society*
ISSN 1394 - 2506

# INTERACTION OF N,N'-BIS[4-[1-(2-HYDROXYETHOXY)] SALICYLIDENE]-PHENYLDIAMINE-NICKEL(II) AND COPPER(II) COMPLEXES WITH G-QUADRUPLEX DNA

## (Interaksi Antara Kompleks N, N'-Bis [4- [1- (2-Hidroksietoksi)] Saliksalidin]-Fenildiamina-Nikel(II) dan Kuprum(II) Bersama DNA G-Kuadrupleks)

Roshatiara Shamsuddin, Muhammad Ameerullah Sahudin, Nur Hasyareeda Hassan, Nurul Huda Abd Karim*

*School of Chemical Sciences and Food Technology, Faculty of Science and Technology, Universiti Kebangsaan Malaysia, 43600 UKM Bangi, Selangor, Malaysia*

**Corresponding author: nurulhuda@ukm.edu.my*

Received: 29 December 2016; Accepted: 28 March 2017

**Abstract**

Binding studies of metal complexes with DNA has attracted many interests due to their importance in cancer therapy and molecular biology. In this study, N,N'-bis[4-[1-(2-hydroxyethoxy)]salicylidene]-phenyldiamine and its metal Ni(II) and Cu(II) complexes have been synthesized and characterized. The complexes were structurally characterized using standard spectroscopic 1D $^{1}$H, 2D COSY, HMQC and $^{13}$C NMR spectroscopy, FTIR spectroscopy and ESI-MS spectrometry. The binding interaction between synthesized metal complexes and G-quadruplex DNA has been investigated using UV/Vis DNA titration study. Ni(II) and Cu(II) complexes bind strongly to G-quadruplex DNA (Kb = (5.42 ± 2.48) x $10^{6}$ $M^{-1}$ and (1.42 ± 2.48) x $10^{6}$ $M^{-1}$ respectively) via end stacking mode. Both complexes show selectivity for G-quadruplex DNA over CT- DNA by 2.15- and 1.82-fold, respectively.

**Keywords**: metal complexes, DNA binding, G-quadruplex DNA

**Abstrak**

Kajian mengenai pengikatan kompleks logam bersama DNA telah menarik perhatian penyelidik disebabkan kepentingannya dalam perubatan terapi kanser dan molekular biologi. Dalam kajian ini, N, N'-bis [4-[1-(2-hidroksietoksi)] saliksalidin]-fenildiamina bersama logam Ni(II) dan Cu(II) kompleks telah berjaya disintesis dan dicirikan. Struktur kompleks telah dicirikan menggunakan spektroskopi piawai 1D $^{1}$H, 2D COSY, HMQC dan spektroskopi $^{13}$C NMR, spektroskopi FTIR dan spektrometri ESI-MS. Pengikatan antara kompleks logam yang disintesis bersama DNA G-kuadruplek telah dikaji dengan menggunakan kajian titratan DNA UV/Vis. Ni(II) dan Cu(II) kompleks memberikatan nilai ikatan yang tinggi kepada DNA G-kuadruplek ((5.42 ± 2.48) x $10^{6}$ $M^{-1}$ dan (1.42 ± 2.48) x $10^{6}$ $M^{-1}$) melalui mod penyusunan akhir. Ni(II) dan Cu(II) kompleks menunjukkan pemilihan pengikatan terhadap G-kuadruplek DNA berbanding CT- DNA dengan 2.15 dan 1.82 kali ganda setiap satu.

**Kata kunci:** kompleks logam, pengikatan DNA, DNA G-kuadruplek

## Introduction

Over this past two decades, DNA have been regarded as primary molecular target for antitumor and antimicrobial drugs [1]. Recently, G-quadruplex DNA have been proposed to be alternative and attractive targets for the development of anticancer drugs. G-quadruplex DNA are found in biologically important regions such as proto-oncogene promoter region, immunoglobulin switch regions and telomeres [2]. Telomere is the end of chromosome

consist of single strand of guanine-rich DNA sequence [3]. The guanine-rich sequences of DNA can fold into quadruply stranded structures known as G-quadruplex DNA [4]. Stabilization of quadruplex DNA by small molecules can inhibit telomerase, an enzyme overexpressed in 85 – 90% of cancerous cell which play important role in cancer cell immortalization [5]. Consequently, there is growing interest in development of G-quadruplex DNA stabilizers. Researchers are focusing on stabilizer that can bind to G-quadruplex DNA with high affinity and selectivity over duplex DNA. Organic compounds have been reported to be a good G-quadruplex DNA stabilizers such as such as anthracene, naphthalene, bipyridine or pyrine [6]. Most of G-quadruplex stabilizers share similar properties such as planar geometry to enable them to π-π stack on the surface of guanine quartet and high solubility in water [7].

Metal complexes have recently emerged to be a new class of G-quadruplex stabilizers. Thus far, metal complexes have included copper, platinum, manganese, nickel, zinc and ruthenium in their design [8-10]. A clear advantage of metal complexes over organic molecules is their varied geometry. The presence of metal ions play a vital role in coordinating ligands into the optimal geometry for G-quadruplex interaction. Metal centre also often possesses a positive charge, which can interact with the electron-rich channel at the centre of the G-quadruplex.

Nickel(II) and copper(II) salphen complexes had been synthesized before and showed ability to selectively stabilize G-quadruplex DNA [4]. Both complexes are reported to have planar geometry with aromatic group that allowed π-π stacking interactions with G-quadruplex DNA [11]. In addition, the presence of substituents such as amines and amino acid group to the metal complexes gave high affinity when interact with G-quadruplex DNA [12]. This is because the substituents played an important role to increase the solubility of the complexes in aqueous media as well as enhancing their ability to bind to G-quadruplex DNA. The attachment of hydroxyl groups to metal complexes have been proposed before by Nurul Huda [13]. The presence of hydrogen bonding can increase the solubility of the complex in buffer and binding energy to G-quadruplex DNA. Thus, a successful strategy to improve the selectivity of complexes have included planar geometry to stack on the surface of guanine quartet and hydroxyl subtituents to improve the solubility of the complexes in water.

Research are still ongoing in finding G-quadruplex DNA with high affinity and selectivity towards G-quadruplex DNA. In this research, we report the synthesis of nickel(II) and copper(II) salphen complex with hydroxyl substituent in order to get good solubility and high binding energy with G-quadruplex DNA. To date, the synthesis and G-quadruplex DNA binding studies of the complexes have not been reported yet. The finding of the research could be useful in designing anticancer drug based on G-quadruplex DNA interaction.

## Materials and Methods

### Chemicals

The chemicals used in this work such as 1,2-phenyldiamine, 2,4-dihydroxybenzaldehyde, nickel(II) acetate tetrahydrate, copper(II) acetate hydrate, 2-chloroethanol and potassium carbonate were purchased from Sigma-Aldrich. Human Telomeric DNA (H-Telo) and Calf thymus DNA (CT-DNA) was purchased from Sigma (USA).

### Physical measurement

The nuclear magnetic resonance (NMR) spectra were recorded in DMSO-d6 by using JEOL JNM-ECP 400 MHz spectrometer. IR spectra were recorded using FTIR Perkin-Elmer GX Model in the spectral range of 4000 – 400 $cm^{-1}$. The mass spectrometry were carried out using Electrospray ionization Mass Spectrometry Bruker Daltonics. DNA binding experiments were carried out in Tris-Potassium chloride (Tris-KCl) buffer at pH 7.4 using PHM 210 measurement, while the UV/Vis absorption spectra were measured on a Shimadzu UV-1650 spectrophotometer using a 1 mL cuvette.

### Synthesis of N,N'-bis-4-(hydroxysalicylidene)-phenylenediamine-nickel(II) complex, [1]

Complex **[1]** was prepared following previous work of the group [4, 14]. All spectroscopic data for the complex are in accordance to literature [14]. 1,2-Phenyldiamine (0.135 g, 1.25 mmol) and 2,4-dihydroxybenzaldehyde (0.345 g, 2.50 mmol) were dissolved in methanol (40 ml) and the reaction mixture was stirred at reflux for 30 min. $Ni(OAc)_2.4H_2O$ (0.622 g, 2.50 mmol) was then added to mixture. A brick-red solid precipitated form immediately.

The reaction was then heated at reflux for a further 4 hour. The solvents was filtered to get brick-red precipitate solid. The solid was washed with ethanol (100 mL), diethyl ether (50 mL) and water (50 mL).

**Synthesis N,N'-bis[4-[1-(2-hydroxyethoxy)]salicylidene]-phenyldiamine-nickel(II) complex, [2]**
Complex **[2]** was prepared following previous work of the group [14]. All spectroscopic data for the complex are in accordance to the literature. A complex nickel(II) salphen (0.251 g, 0.62 mmol), 2-chloroethanol (0.252 g, 3.09 mmol) and $K_2CO_3$ (0.691 g, 4.98 mmol) in DMF solutions (30 mL) was heated at 90 $^oC$ overnight. After that 2-chloroethanol with the same mole was added and the reaction was heated for another 24 hours. After this time the excess salts were removed by filtration and the DMF evaporated under reduced pressure. The resulting dark red solid was recrystallised with DMF: diethylether (1:3) to give as brown red solid.

**Synthesis of N,N'-bis-4-(hydroxysalicylidene)-phenylenediamine-copper(II) complex, [3]**
Synthesis complex copper(II) salphens followed the published method [4]. 1,2-Phenyldiamine (0.135 g, 1.25 mmol) and 2,4-dihydroxybenzaldehyde (0.345 g, 2.50 mmol) were dissolved in methanol (40 mL) and the reaction mixture was stirred at reflux for 30 minutes. $(CH_3COO)_2Cu.H_2O$ (0.499 g, 2.50 mmol) was then added to mixture. A dark green solid precipitated form immediately. The reaction was then heated at reflux for a further 4 hours. The solvents was filtered to get dark green precipitate solid. The solid was washed with ethanol (100 mL), diethyl ether (50 mL) and water (50 mL).

**Synthesis N,N'-bis[4-[1-(2-hydroxyethoxy)]salicylidene]-phenyldiamine-copper(II) complex, [4]**
A complex copper(II) salphen (0.253 g, 0.62 mmol), 2-chloroethanol (0.252 g, 3.09 mmol) and $K_2CO_3$ (0.688 g, 4.98 mmol) in DMF solutions (30 mL) was heated at 90 $^oC$ overnight. After that 2-chloroethanol with the same mole was added and the reaction was heated for another 24 hours. After this time the excess salts were removed by filtration and the DMF evaporated under reduced pressure. The resulting dark green solid was recrystallized with DMF: diethylether (1:3) to give as a dark green solid.

**DNA binding experiments**
The stock solution of DNA was prepared by dissolving DNA in 10 mM of Tris–HCl/ 100 mM KCl buffers at pH 7.4. H-telo DNA was dissolved in 10 mM Tris-HCl/100 mM KCl (pH 7.4) buffer solution. The oligonucleotide were annealed by heating it to 90 ºC for 5 minutes and then cooled to room temperature overnight. CT-DNA dissolved overnight in a 10 mM Tris-HCl /100 mM KCl (pH7.4) buffer solution. Then, the complexes was diluted to 5 mM using DMSO. The absorbtion titration experiments were performed by diluting the complex with buffer to the 30 μM concentrations while increasing DNA concentrations. The intrinsic binding constant (Kb) values were calculated by the following equation 1 [15]:

$$\frac{[DNA]}{(\varepsilon_a-\varepsilon_f)} = \frac{[DNA]}{(\varepsilon_b-\varepsilon_f)} + \frac{1}{Kb(\varepsilon_b-\varepsilon_f)} \quad (1)$$

where [DNA] is the concentration of DNA in base pairs, εa, εf, and εb correspond to the $A_{observed}$/[complex], the extinction coefficient of free complex and the complex in fully bound form, respectively, and Kb is intrinsic binding constant. A plot of [DNA]/ (εa – εf) versus [DNA] will have a slope of 1/(εb – εf) and intercept equal to 1/Kb(εb – εf). Kb is the given ratio of the slope to the intercept.

Percentage hypochromacity was determined using the following equation 2:

$$\text{Hypochromacity (\%)} = \frac{(\varepsilon_b-\varepsilon_f)}{\varepsilon_b} \text{ x } 100 \quad (2)$$

From the equation, Kb of complexes with G-Quadruplex DNA and CT- DNA can be calculated

## Results and Discussion

**Characterization study: N,N'-bis-4-(hydroxysalicylidene)-phenylenediamine-nickel(II) complex**
Yield 0.386 g (77 %). $^1$H NMR (400 MHz, DMSO-$d_6$): δ 6.21 (s, 1H, $H^6$), 6.22 (d, $^3J_{HH}$ = 8.8 Hz , 1H, $H^5$), 7.19 (dd, $^3J_{HH}$ = 6.0 Hz, $^4J_{HH}$ = 3.0 Hz, 1H, $H^1$), 7.41 (d, $^3J_{HH}$ = 8.8 Hz, 1H, $H^4$), 7.99 (dd, $^3J_{HH}$ = 6.0 Hz, $^4J_{HH}$ = 3.0 Hz, 1H,

$H^2$), 8.54 (s, 1H, $H^3$) $^{13}C$ NMR (100 MHz, DMSO-$d_6$) 103.8, 108.4, 114.8, 116.0, 127.1, 136.2, 143.3, 154.9, 165.4, 167.7. IR ($cm^{-1}$): 3527 (OH alcohol/phenol), 3082 (C-H $sp^2$), 1578 (C=N), 1450 (C=C aromatic), 1121 (C-O), 1209 (C-N). ESI(+)-MS m/z calcd for $C_{20}H_{14}N_2NiO_4$ ($M^+$): 404 a.m.u. The a.m.u. Found: $[M+Na]^+$= 427 a.m.u.

**N,N'-bis[4-[1-(2-hydroxyethoxy)]salicylidene]-phenyldiamine-nickel(II) complex, [2]**
Yield: 0.161 g, 64%. $^1H$ NMR (400 MHz, DMSO-d6): δ 3.72 (t, $^3J_{HH}$ = 4.00Hz , 1H, $H^8$), 4.00 (t, $^3J_{HH}$ = 4.00Hz , 1H, $H^7$), 4.96 (s, 1H, $H^9$), 6.32-6.39 (m, 2H, $H^4H^6$), 7.24-7.26 (dd, $^3J_{HH}$ = 8.0 Hz, $^4J_{HH}$ = 4.0 Hz, 1H, $H^1$), 7.46-7.48 (d, $^3J_{HH}$ = 8.6 Hz, 1H, $H^5$), 8.02-8.05 (d, $^3J_{HH}$ = 8.0 Hz, 1H, $H^2$), 8.64 (s, 1H, $H^3$) $^{13}C$ NMR (100 MHz, DMSO-$d_6$) δ 59.79, 70.05, 102.01, 108.02, 115.19, 116.02, 127.23, 135.74, 142.71, 154.86, 165.25, 167. IR ($cm^{-1}$): 3352 (OH alcohol / phenol), 3039 (C-H $sp^2$), 2878 (C-H $sp^3$) 1577 (C=N), 1515 (C=C aromatic), 1127 (C-O), 1196 (C-N). ESI(+)-MS m/z calcd for $C_{24}H_{22}N_2NiO_6$ (M+): 492 a.m.u. The a.m.u. Found: $[M+K]^+$=531, $[M+Na]^+$=515 a.m.u.

**N,N'-bis-4-(hydroxysalicylidene)-phenylenediamine-copper(II) complex, [3]**
Yield 0.386 g (80 %). IR (cm-1): 3350 (OH alcohol / phenol), 3150 (C-H sp2), 1581 (C=N), 1448 (C=C aromatic), 1122 (C-O). ESI(+)-MS m/z calcd for $C_{20}H_{14}CuN_2O_4$ ($M^+$): 409 a.m.u. The a.m.u. Found: $[M+Na]^+$=432 a.m.u.

**N,N'-bis[4-[1-(2-hydroxyethoxy)]salicylidene]-phenyldiamine-copper(II) complex, [4]**
Yield: 0.161 g, 74%. IR (cm-1): 3350 (OH alcohol / phenol), 3100 (C-H $sp^2$), 2929 (C-H $sp^3$) 1575 (C=N), 1482 (C=C aromatic), 1187 (C-O). ESI(+)-MS m/z calcd for $C_{24}H_{22}CuN_2O_6$ ($M^+$): 497 a.m.u. The a.m.u. Found: $[M+K]^+$=536 a.m.u.

The N,N'-bis-4-(hydroxysalicylidene)-phenylenediamine-nickel(II) complex had been successfully synthesized characterized. The attachment of hydroxyl was then carried out by adding 2-chloroethanol in presence of potassium carbonate. The reaction scheme of hydroxyl substituted Nickel(II)- and Copper(II)- salphen complexes **[2]** and **[4]** are illustrated in Figure 1. The synthesis and characterization of complex **[1]**, **[2]** and **[3]** have been reported in our previous work [14]. Synthesis of complex **[4]** yielded 74% product as dark green solid. Complex **[4]** was characterized by means of FTIR and mass spectrometry. Based on IR spectra of the complex **[4]**, absorption bands corresponding to Cu(II) salphen due to stretching vibrations of some functional group such as imine, C-O hydroxyl and C=C for aromatic group are presence. The expected band for imine C=N appears at 1575 $cm^{-1}$ suggested the formation of the salphen complex. The IR spectrum also displayed bands at 3352 $cm^{-1}$, 1482 $cm^{-1}$ and 1187 $cm^{-1}$ for hydroxyl, C=C aromatic and C-O respectively. The attachment of hydroxyl side chain to complex **[2]** to yield complex **[4]** was successful evidence by the presence of absorption band at 2929 $cm^{-1}$ which can be assigned to C-H $sp^3$. The electrospray ionization mass spectrometry (ESI-MS) was carried out to determine the mass-to-charge ratio of complex **[4]**. Spectrum showed that one peak corresponding to complex with adducts ion, which is $[M+K]^+$=536 a.m.u. Since the copper(II) complex is paramagnetic, NMR spectroscopy could not be used to analyze the complex.

**UV-Vis DNA titration**
UV-Vis spectroscopic titration were carried out to gain inside into the binding mode and binding affinity of the complexes with G-Quadruplex and CT- DNA. When a compound exhibit a high binding affinity, it is said to be a powerful binder to DNA and a promising candidate as an anticancer drug. The UV-vis spectra for titration study complex **[2]** with G-Quadruplex DNA is given in Figure 2. As shown, complex **[2**] at 30 μM showed maximum absorption peak at 388 nm. The intensity of complex decreases with addition of G-Quadruplex DNA and red shift can be seen with further addition of DNA. Obviously hypchromicity of 53% was observed along with 10 nm bathochromic shift. The hypochromism effect and bathochromic shifting suggest end stacking for the binding mode of the complex toward G-quadruplex DNA [16].

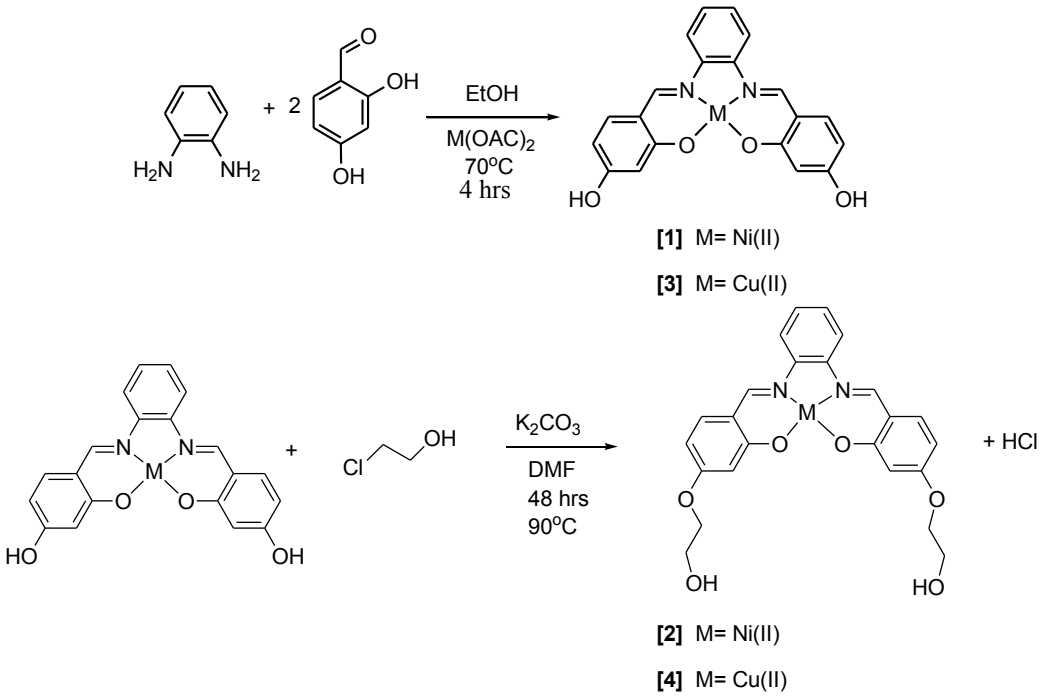



Figure 1. Reaction scheme for N,N'-bis[4-[1-(2-hydroxyethoxy)]salicylidene]-phenyldiamine-nickel(II) and copper(II) complex

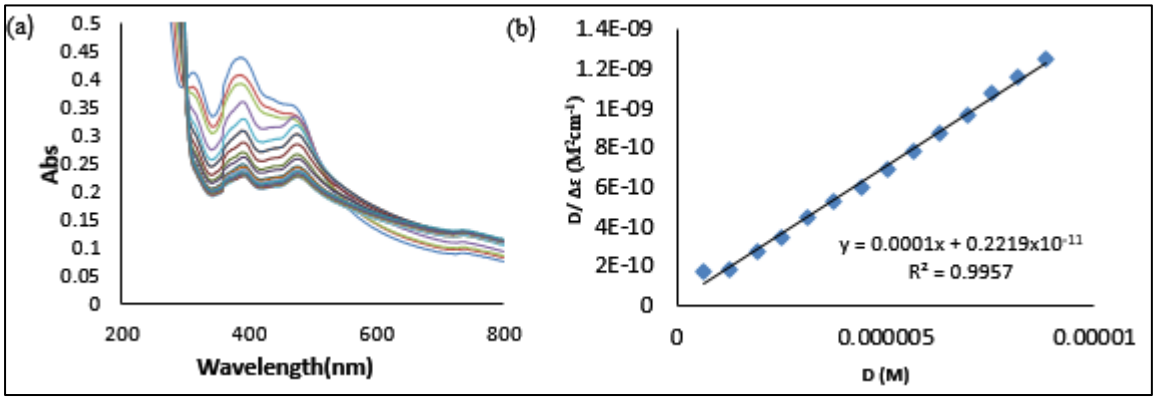



Figure 2. (a) Absorption spectral changes of complex **[2]** (30 μM) in Tris/KCl buffer (pH 7.4) in the absence and presence of increasing concentration of H-Telo (6.30 x $10^{-3}$ mM – 1.3 x $10^{-3}$ mM), (b) The reciprocal plot that fits the absorbance data to obtain the binding constant.

The next binding study is complex **[4]** with G-Quadruplex DNA (Figure 3). Referring to the spectra, complex **[4]** alone at 30 μM showed maximum absorption peak at 385 nm. The intensity of complex decrease with addition of G-Quadruplex DNA and small red shift appeared with further addition of DNA. A hypochromic effect 16% was observed along with 6.5 nm bathochromic shift. The hypochromism effect and bathochromic shifting suggesting the complex possesed end stacking mode binding which is same mode with complex **[2]** when binding to G-quadruplex DNA.

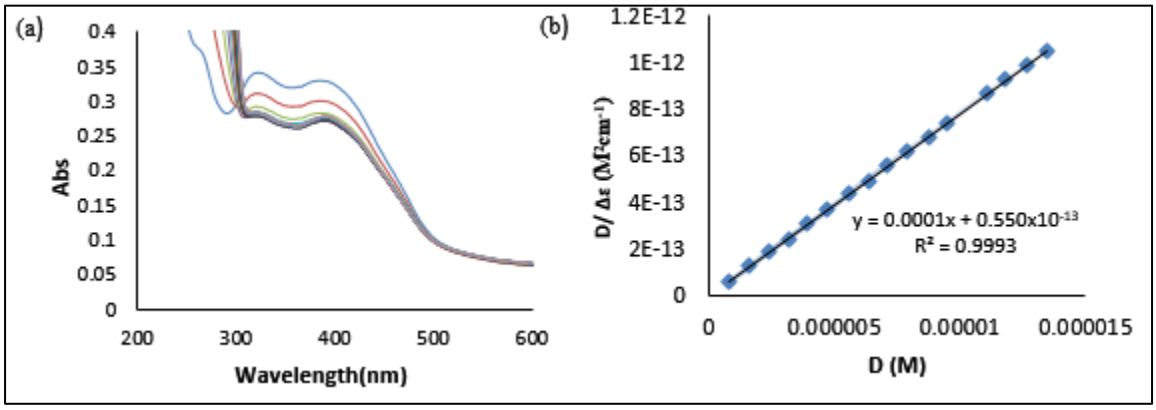



Figure 3. (a) Absorption spectral changes complex **[4]** (30 μM) in Tris/KCl buffer (pH 7.4) in the absence and presence of increasing concentration of H-Telo (7.9 x $10^{-3}$ mM – 13.4 x $10^{-3}$ mM), (b) The reciprocal plot that fits the absorbance data to obtain the binding constant

By using the Scatchard equation (the plot of D/Δεap versus D) the binding constant (Kb) values of the compounds to G-quadruplex DNA were calculated. Complex **[2]** was found to bind to G-quadruplex DNA with higher affinity (Kb= 5.42 ± 2.48 x $10^6$ $M^{-1}$) compared to the complex **[4]** (Kb = 1.42 ± 2.48 x $10^6$ $M^{-1}$). Both new salphen complexes with hydroxyl substituted showed significant improvement on G-quadruplex DNA stabilization ability compared to piperidine substituted metal complexes that have been reported before [5].

For comparison, we also study the binding affinity of both complexes with duplex calf thymus DNA (CT-DNA). The concentration of CT-DNA was determined from UV absorbance at 260 nm (ε = 6600 $cm^{-1}$). The absence of any protein contamination with CT DNA was confirmed from absorption ratio at 260 and 280 nm which was found to be 1.86 [17]. In Figure 4, we can see that upon addition of CT- DNA to complex **[2]**, hypochromicity (29%) of peak absorption can be observed with small red shift (3 nm). From the observations, it is concluded that complex **[2]** have been intercalated to the base pairs of CT-DNA [18].

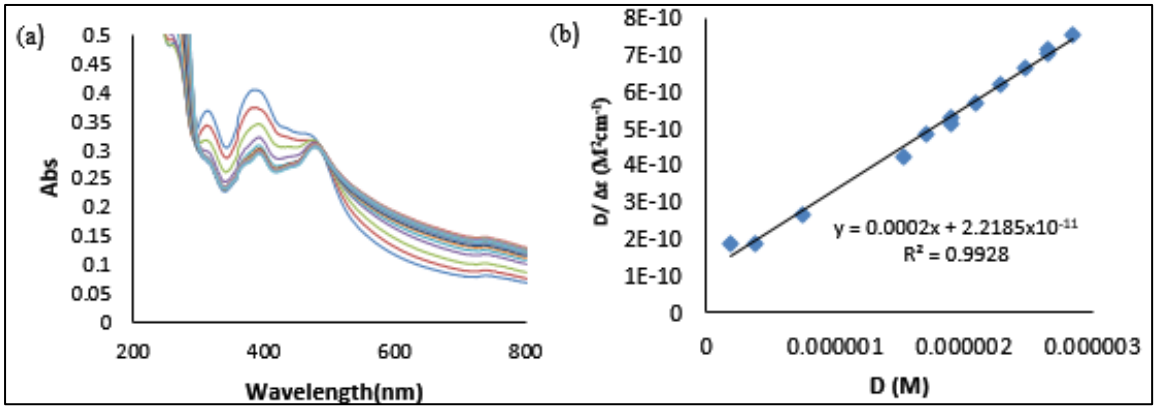



Figure 4. (a) Absorption spectral changes of complex **[2]** (30 μM) in Tris/KCl buffer (pH 7.4) in the absence and presence of increasing concentration of CT-DNA (0.19 x $10^{-3}$ mM – 3.61 x $10^{-3}$ mM), (b) The reciprocal plot that fits the absorbance data to obtain the binding constant

The binding study of complex **[4]** with CT-DNA was shown in Figure 5. Upon addition of CT-DNA to solutions of complex **[4]** the hypochromic (13%) followed by small bathochromic effect (3.5 nm) can be seen. These spectral characteristics suggested moderately intercalative mode binding.

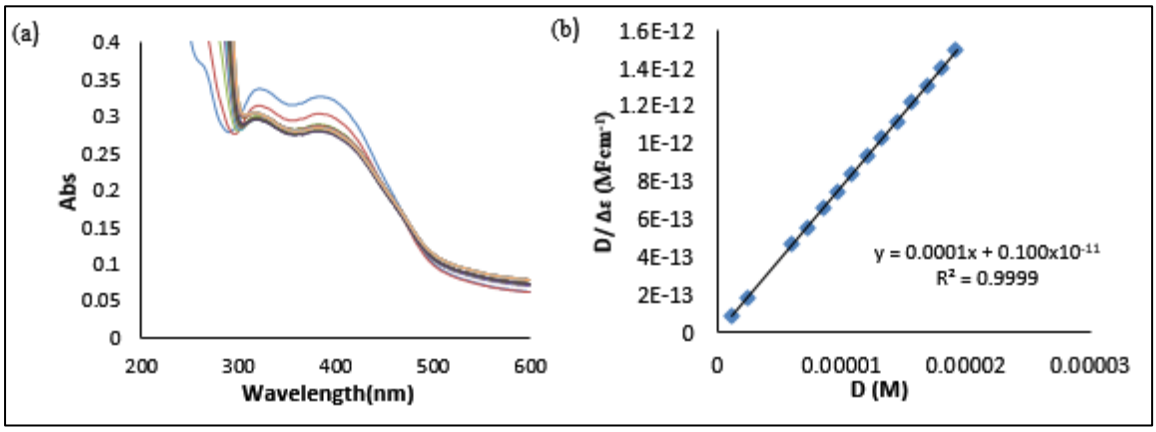



Figure 5. (a) Absorption spectral changes of complex **[4]** (30 µM) in Tris/KCl buffer (pH 7.4) in the absence and presence of increasing concentration of CT-DNA (1.2 x $10^{-3}$ mM – 20.4 x $10^{-3}$ mM), (b) The reciprocal plot that fits the absorbance data to obtain the binding constant.

From the equation, calculated intrinsic binding constant, Kb of complex **[2]** and **[4]** with CT- DNA are 2.51 x $10^6$ ± 0.65 $M^{-1}$ and 7.80 x $10^5$ ± 0.65 $M^{-1}$. Both complexes show selectivity for G-quadruplex DNA over CT- DNA by 2.15- and 1.82-fold, respectively. The presence of hydroxyl substituent on the metal salphen complexes seems to have little effect in the selectivity towards G- quadruplex DNA over CT- DNA.

## Conclusion

N,N'-bis[4-[1-(2-hydroxyethoxy)]salicylidene]-phenyldiamine-nickel(II) complex and N,N'-bis[4-[1-(2-hydroxyethoxy)]salicylidene]-phenyldiamine-copper(II) complex have been successful synthesized and characterized. The DNA binding of complex with G-quadruplex DNA and CT-DNA examine by absorption spectral technique. From the results, the binding constant interaction between complex **[2]** and **[4]** with G quadruplex DNA are (5.42 ± 2.48) x $10^6$ $M^{-1}$ and (1.42 ± 2.48) x $10^6$ $M^{-1}$. Meanwhile, the binding constant of complex **[2]** and **[4]** with CT-DNA are (2.51 ± 0.65) x $10^6$ $M^{-1}$ and (7.80 ± 0.65) x $10^5$ $M^{-1}$ respectively. The UV-Vis titration study suggested that complex **[2]** binds selectively to G-quadruplex DNA over CT-DNA by two folds. Complex **[2]** showed the potential to be a good candidate for anti-cancer drug development via inhibition of telomerase activity.

## Acknowledgement

The authors gratefully acknowledge The National University of Malaysia for providing the research facilities. This work has been carried out with the support of Malaysian Government through Ministry of Higher Education grant GUP-2015-044 and DPP 2014-016.

## References

1. Thomas, P. G., Huw, E. L. W., Katarzyna, I. G., Stephen, R., Neil, J. O., Malcolm, F. G. S., John, E. M. and Mark S. S. (2009). Selectivity of small molecule ligands for parallel and anti-parallel DNA G-quadruplex structures. *Organic and Biomolecular Chemistry*, 7: 4194 – 4200.
2. Xu-Jian, L., Qi-Pin, Q., Yu-Lan, L., Yan-Cheng, L. and Hong L. (2014). Synthesis, antitumor activity and G-Quadruplex DNA/ct-DNA binding property of cationic platinum(II) complex of 2-(4-nitro)-imidazo-[5,6-f][1,10]-phenanthroline. *Indian Journal of Chemistry*, 53: 787 – 792.

3. Hasani, L., Hakimian, F. and Safaei, E. (2014). Spectroscopic investigation on the interaction of copper porphyrazines and phthalocyanine with human telomeric G-Quadruplex DNA. *Biophysical Chemistry*, 187: 7 – 13.
4. Nurul, H. A. K., Oscar, M., Arun, S., Alenxander, J. T., Sushobhan, G., Marina, K. K. and Vilar, R. (2014). Salphen metal complexes as tunable G-quadruplex binders and optical probes. *RSC Advances,* 4: 3355 – 3363.
5. Nancy, H. C., Nurul, H. A. K., Gary, N. P., Mekala, G., Vanessa, P., Alan, K. T., Ramon, V. and Stephen, N. (2012). Molecular basis of structure−activity relationships between salphen metal complexes and human telomeric DNA quadruplexes. *Journal of Medical Chemistry,* 55: 209 − 222.
6. Sofia, G., Inês, R., Filipa, M., Isabel, C. S., Elisabetta, G., Beata, K., Jorge, G-C., Mauro, R., Ramon, V. and António P. (2016). Anthracene-terpyridine metal complexes as new G-quadruplex DNA binders. *Journal of Inorganic Biochemistry*, 160: 275 – 286.
7. Ang, D. L., Harper, B. W., Cubo, L., Mendoza, O., Vilar, R., & Aldrich-Wright, J. (2016). Quadruplex DNA-stabilising dinuclear platinum (ii) terpyridine complexes with flexible linkers. *Chemistry–A European Journal*, 22(7), 2317 – 2325.
8. Taetz, S., Murdter, T. E., Zappc, J., Boettcher, S., Baldes, C., Kleideiter, E., Piotrowska, K., Schaefer, U. F., Klotz, U., Lehr and C.-M. (2008). Decomposition of the telomere-targeting agent BRACO19 in physiological media results in products with decreased inhibitory potential. *International Journal of Pharmaceutics*, 357: 6 – 14.
9. Julie, E. R., Stephen, N. and Ramon, V. (2007). Stabilisation of human telomeric quadruplex DNA and inhibition of telomerase by a platinum phenanthroline complex. *Chemical Communications*, 42: 4366 – 4368.
10. Siti, N. H, Yaakob, R. and Haslina, A. (2016). Synthesis, characterization and DNA binding activity of a potential DNA intercalator. *Malaysian Journal of Analytical Sciences*, 20(4): 760 – 769.
11. Fun, H. K., Kia, R., Mirkhani, V. and Zargoshi, H. (2008). {5, 5-Dihydroxy-2, 2-[o-phenylenebis (nitrilomethylidyne)] diphenolato} nickel (II) dihydrate. *Acta Crystallographica Section E: Structure Reports Online*, 64(9): 1181 – 1182.
12. Verity S. S., Kogularamanan S., Arun S., Andrew J. P. W., David J. M. and Ramon V. (2015). Syntheses of polypyridyl metal complexes and studies of their interaction with quadruplex DNA. *Dalton Transactions (RSC Publishing)*, 44: 3686 – 3700
13. Nurul Huda Abd Karim (2012). Studies towards elucidating the binding modes between metal-salphen complexes and G-quadruplex DNA. Thesis Doctor of Philosophy, Imperial College London.
14. Roshatiara, S. and Nurul Huda, A. K. (2016). Synthesis and characterization of N,N'-bis[4-[1-(2-hydroxyethoxy)]salicylidene]-phenyldiamine-nickel(II)] complex. *AIP Publishing*, 1784: 030007
15. Subbaraj, P., Ramu, A., Raman, N. and Dharmaraja, J. (2015). Synthesis, characterization, DNA interaction and pharmacological studies of substituted benzophenone derived Schiff base metal(II) complexes. *Journal of Saudi Chemical Society*, 19: 207 – 216.
16. Krishnamoorthy, P., Sathyadevi, P., Alan, H. C., Rachel, R. B. and Dharmaraj, N. (2011). Evaluation of DNA binding, DNA cleavage, protein binding and in vitro cytotoxic activities of bivalent transition metal hydrazone complexes. *European Journal of Medicinal Chemistry*, 46: 3376 – 3387.
17. Selamat, N., Heng, L. Y., Hassan, N. I. and Karim, N. H. A. (2016). Synthesis and Characterization of 6, 6'-bis (2-hydroxyphenyl)-2, 2'-bipyridyl ligand and its platinum complex for the interaction with CT-DNA. *Malaysian Journal of Analytical Sciences*, 20(1): 111 – 120.
18. Bordbar, M., Khodaie, F., Tabatabaee, M., Yeganeh-Faal, A., Mehri lighvan, Z. and Mohammad-Ganji, S. (2016). Interaction studies of DNA binding with new Cu(II) complex by spectrophotometric, spectrofluorometric, voltammetric and circular dichroism techniques. *Bulgarian Chemical Communication*, 48(3): 422 – 429.

*Malaysian Journal of Analytical Sciences, Vol 21 No 3 (2017): 552 - 559*
*DOI: https://doi.org/10.17576/mjas-2017-2103-05*

MALAYSIAN JOURNAL OF ANALYTICAL SCIENCES
*Published by The Malaysian Analytical Sciences Society*
ISSN 1394 - 2506

# MARKOV CHAIN MONTE CARLO METHOD FOR HANDLING MISSING DATA IN AIR QUALITY DATASETS

## (Kaedah Rantai Markov Monte Carlo Untuk Mengurus Data Hilang Di Dalam Data Kualiti Udara)

Norhazlina Suhaimi[1], Nurul Adyani Ghazali[1]*, Muhammad Yazid Nasir [1], Muhammad Izwan Zariq Mokhtar [1], Nor Azam Ramli[2]

[1]*School of Ocean Engineering,*
*Universiti Malaysia Terengganu, 21030 Kuala Nerus, Terengganu, Malaysia*
[2]*School of Civil Engineering,*
*Universiti Sains Malaysia, 14300 Nibong Tebal, Pulau Pinang, Malaysia*

**Corresponding author: nurul.adyani@umt.edu.my*

Received: 27 October 2016; Accepted: 18 April 2017

**Abstract**

Missing data are a common problem in raw data especially in air quality datasets. Incomplete data due to machine or instruments failures, changes in the sitting air station monitors, calibration, routine maintenance and human error handling dataset. Multiple imputation of missing value technique was used to deal with selective air quality data by using Markov Chain Monte Carlo (MCMC). Expectation-maximization (EM) algorithm was used to compute the maximum likelihood estimate (MLE), assuming a multivariate normal distribution for the data. In this paper, the air quality monitoring stations selected namely Kemaman, Terengganu and Petaling Jaya, Selangor. The parameters selected were carbon oxide, ground level ozone, sulphur dioxide, nitrogen oxide, nitric oxide and nitrogen dioxide. A total of annual hourly data is 52,704 (8784 x 6 parameters) observations. Result shows that the coefficient of determination for all annual hourly monitoring data is consistently high ($R^2$ = 0.49 – 0.91) and small error (0.0001 – 0.3). Therefore, the multiple imputation technique by using MCMC method provides a good fit imputation and unbiased result of missing value to this data.

**Keywords**: missing data, air quality, multiple imputation, Markov Chain Monte Carlo

**Abstrak**

Data hilang ialah masalah biasa dalam data mentah terutamanya data kualiti udara. Data yang tidak lengkap disebabkan oleh kegagalan alat atau mesin, perubahan tempat stesen udara, kalibrasi, rutin penyelenggaraan dan kesilapan pekerja mengurus data. Teknik pelbagai imputasi digunakan untuk mengisi nilai hilang bagi data kualiti udara yang terpilih dengan menggunakan Markov Chain Monte Carlo. Jangkaan maksimum (EM) algoritma digunakan untuk menjangka kemungkinan maksimum dengan andaian taburan normal dari pelbagai pembolehubah. Dalam kajian ini, stesen kualiti udara yang dipilih ialah Kemaman, Terengganu dan Petaling Jaya, Selangor. Pembolehubah yang dipilih ialah karbon dioksida, ozon paras tanah, sulfur dioksida, nitrogen oksida, nitrik oksida dan nitrogen dioksida. Jumlah data jam tahunan ialah 52,704 (8784 x 6 pembolehubah) pemerhatian. Keputusan menunjukkan penentuan pekali untuk semua data jam tahunan ialah tinggi dan kesilapan kecil. Oleh sebab itu, teknik pelbagai imputasi dengan menggunakan kaedah MCMC menyediakan imputasi yang sangat bagus dan keputusan yang tiada keraguan bagi nilai hilang.

**Kata kunci:** data hilang, kualiti udara, pelbagai imputasi, rantai Markov Monte Carlo

## Introduction

The air pollution in Malaysia has yet reached a critical level at the some areas [1]. However, even outside haze periods, pollution levels occurred despite tight regulations and this is exacerbated by the increase in the number of vehicle, distance travelled and growth in industrial production [1]. The haze phenomenon in Malaysia which contribute to the air pollutant reading including ozone concentration exceeds Malaysian standard [2] have already been observed in some urban [3] and industrial regions of Malaysia [4]. The air quality data was collected from the Air Quality Division of the Department of Environment, Ministry of Natural Resources and Environment of Malaysia. The National Continuous Air Quality Monitoring Network, manual air quality monitoring stations using high volume samplers were also established at the all air monitoring stations [1]. The main pollutants recorded at the Malaysian air quality monitoring stations are ground level ozone ($O_3$), carbon monoxide (CO), nitrogen dioxide ($NO_2$), sulphur dioxide ($SO_2$) and particulate matter of less than 10 microns in size ($PM_{10}$) [1].

Continuously sampling system is necessary to obtain a more reliable and accurate information about the air quality in atmosphere. However, real data are not usually complete that contain missing data. Missing data arise in almost real life datasets especially in air quality dataset. Incomplete data might be because of machine failures or break-down of measurement instruments, changes in the sitting air station monitors, calibration, routine maintenance and reading invalidation or human error handling dataset. Missing data are problematic in statistical analysis; the data will loss of information and efficiency [5], several problems related to data analysis, and bias due to systematic differences between observed and unobserved data [6]. According to Little and Rubin [5], rate of missing data less than 1% are considered trivial, 1 – 5% are manageable, 5 – 15% need powerful method to handle and more than 15% may harm the model's result.

There are various techniques of handling missing data such as interpolation techniques (linear, quadratic, cubic and nearest neighbor interpolation) [7], mean imputation techniques (mean-before after, mean before) [8], hot-deck imputation [9], regression imputation [10], k-nearest neighbor imputation [11]. Multiple Imputation (MI) provides a useful technique for dealing missing value in environmental research [12]. MI technique replaces each missing value with a plausible value that represents the uncertainty the right value to impute [13]. MI gives much better results to handle missing data [14]. The example for multiple imputation is Markov Chain Monte Carlo method [15]. Markov Chain Monte Carlo (MCMC) method was used for the MI procedure because of assuming multivariate normality [16]. Markov chain is a sequence of random variables in the distribution of each variable depends on the value of the previous variable. The expectation-maximization (EM) algorithm is a technique that estimates maximum likelihood for MCMC method [17]. Therefore, the aim of this study focuses on MI technique to replace missing value for air quality data.

## Materials and Methods

This section explains the source of data and process of constructing the multiple imputation technique. We have designed a SAS version 9.0 codes for MI technique.

### Study area

This study involving real secondary data that obtained from the Department of Environmental, Malaysia managed by a private company, Alam Sekitar Malaysia Sdn. Bhd (ASMA). There are two air monitoring stations were studied for this research; Kemaman, Terengganu (S1) and Petaling Jaya, Selangor (S2). Kemaman is developing Malaysian town located at the industrial Kertih Petrochemical Industrial Area in the North and the industrializing and urbanizing Gebeng Industrial Area in the South. The monitoring station was located at Sekolah Rendah Bukit Kuang with coordinate (4°14'21.9"N 103°11'31.8"E). Petaling Jaya, Selangor is located within Klang Valley region and covers an area of 97.2 $km^2$. It's surrounded by residential, commercial and industrial areas leads to a high volume of traffic. The monitoring station was located at Sekolah Rendah Sri Petaling with coordinate (3°08'16.7"N 101°36'29.7"E). Both stations were classified as industrial area although different geographical area. The locations of the continuous air quality monitoring stations for this research are shown in Table 1 and Figure 1.

Table 1. Air quality monitoring stations description

| Air Monitoring Station | Location | Background | Coordinates | |
|---|---|---|---|---|
| | | | Latitude | Longitude |
| S1 | Kemaman, Terengganu | Industrial | $4^0$14'21.9'' N | $103^0$11'31.8''E |
| S2 | Petaling Jaya, Selangor | Industrial | $3^0$08'16.7''N | $101^0$36'29.7''E |

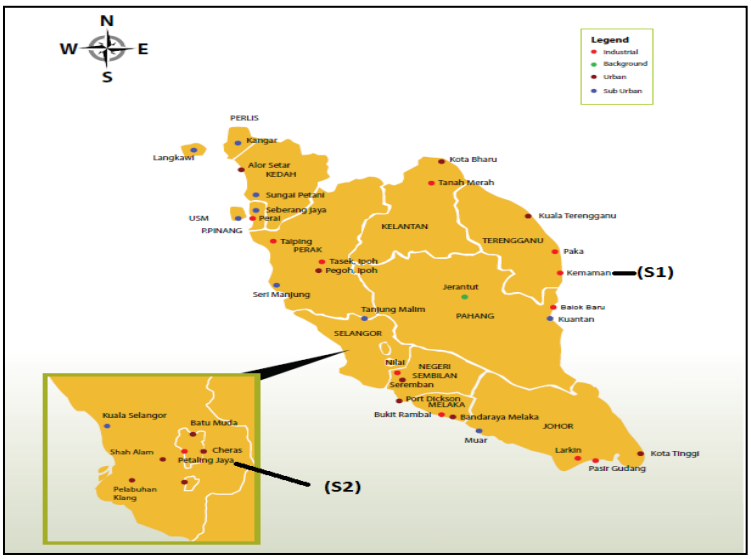



Figure 1. Location of Air Quality Monitoring Stations in Peninsular Malaysia, 2012

**Data acquisition**

Six air pollutants were selected to carry out replacing missing value. The overall air quality data used was collected from January to December for year 2012. The total number of observations is 52,704 records corresponding to the hourly value for each one of the following 6 parameters (8,784 observations x 6 parameters). The highest percentage missing data of parameter for S1 is NO (45.1%) and S2 is $O_3$ (20.4%). Table 2 show the parameters used in this study and percentage of missing data.

Table 2. Parameters used during period of study

| Station | % Missing Data | | | | | |
|---|---|---|---|---|---|---|
| | CO | $O_3$ | $SO_2$ | $NO_X$ | NO | $NO_2$ |
| S1 | 6.9 | 5.3 | 34.4 | 8 | 45.1 | 10.1 |
| S2 | 5.8 | 20.4 | 8.8 | 5.3 | 5.6 | 5.3 |

*CO-Carbon Monoxide, $O_3$-Ozone, $SO_2$-Suphur Dioxide, $NO_x$-Nitrogen oxide, NO-Nitrogen Oxide, $NO_2$-Nitrogen Dioxide*

**Multiple imputation**
The imputation has been performed by Monte Carlo simulation of MCMC method. The expectation-maximization (EM) [17] is a technique that finds maximum likelihood estimates for MCMC method to replace missing data. MCMC method is based on Bayesian inference with missing data by following several steps:

1. Imputation step. Estimate mean and covariance matrix, then simulates the missing values for each observation.
2. Posterior step (P-step). P-step simulates the mean vector and covariance matrix from the imputed step. This is the posterior distribution.

A current parameter estimate $\theta^{(t)}$ at $t^{th}$ iteration, the I-step draws $Y_{mis}^{(t+1)}$ from $p(Y_{mis} \mid Y_{obs}, \theta^{(t)})$ and the P-step draws $\theta^{(t+1)}$ from $p(\theta \mid Y_{obs}, Y_{mis}^{(t+1)})$. Therefore, a Markov chain is created as shown below:

$$(Y_{mis}^{(1)}, \theta^{(1)}), (Y_{mis}^{(2)}, \theta^{(2)}) \tag{1}$$

which converges in distribution to $p(Y_{mis}, \theta \mid Y_{obs})$.

**Performance indicators**
There are four performance indicators were used to explain the efficiency of the imputation method used in this study. The observed data and theoretical data were compared to show the goodness of method for replacing missing values. Four performance indicators were used namely; coefficient of determination ($R^2$), prediction accuracy (PA), mean absolute error (MAE) and root mean squared error (RMSE).

**Coefficient of determination**
The coefficient of determination ($R^2$) explains how much the variability of the imputed data that related with observed data. The value of $R^2$ is between 0 and 1, with value closer to 1 implying a better fit model. The $R^2$ is computed using the following equation 2 [16]:

$$R^2 = \left[ \frac{1}{N} \frac{\sum_{i=1}^{N} \left(P_i - \overline{P}\right)\left(O_i - \overline{O}\right)}{\sigma_p \sigma_o} \right]^2 \tag{2}$$

where N is the number of observations, $O_i$ is observed data, $P_i$ is the imputed data, $\overline{P}$ and $\overline{O}$ are the average of imputed data and observed data, and $\sigma_P$ and $\sigma_O$ are the standard deviation of the imputed data and observed data respectively.

**Prediction accuracy**
The Prediction accuracy (PA) takes on value range from 0 to 1 with closer to 1 describing a better fit model. The equation of PA is given as follows [18]:

$$PA = \sum_{i=1}^{N} \frac{\left[\left(P_i - \overline{P}\right)\left(O_i - \overline{O}\right)\right]}{(N-1)\sigma_P \sigma_O} \tag{3}$$

where N is the number of observations, $O_i$ is observed data, $P_i$ is the imputed data, $\overline{P}$ and $\overline{O}$ are the average of imputed data and observed data, and $\sigma_P$ and $\sigma_O$ are the standard deviation of the imputed data and observed data respectively.

**Mean absolute error**
Mean absolute error (MAE) is the average of the difference between observed data and predicted data. The MAE is computed by Schafer [16]:

$$MAE = \frac{1}{N}\sum_{i=1}^{N}\left|P_i - O_i\right| \tag{4}$$

where N is the number of observations, $O_i$ is observed data, $P_i$ is the imputed data, $\overline{P}$ and $\overline{O}$ are the average of imputed data and observed data, and $\sigma_P$ and $\sigma_O$ are the standard deviation of the imputed data and observed data respectively.

**Root mean squared error**
The root mean squared error (RMSE) is one of the common errors that measure for building of model and testing accuracy of the model. The small value explains the good performance of the model. This error is evaluated by the equation 5 [16]:

$$RMSE = \left(\frac{1}{N}\sum_{i=1}^{N}\left[P_i - O_i\right]^2\right)^{\frac{1}{2}} \tag{5}$$

where N is the number of observations, $O_i$ is observed data, $P_i$ is the imputed data, $\overline{P}$ and $\overline{O}$ are the average of imputed data and observed data, and $\sigma_P$ and $\sigma_O$ are the standard deviation of the imputed data and observed data respectively.

**Multiple imputation efficiency**
The relative efficiency is computed by using $m$ imputation and $\lambda$ as shown in equation 6

$$RE = (1 + \frac{\lambda}{m})^{-1} \tag{6}$$

## Results and Discussion

Table 3 gives the summary of parameters for air quality data. The mean values for both stations and for all parameters are higher than median which indicates that the parameters distributions are skewed to the right. The variance value shows the variability of parameter concentration. The station 1 explained the distribution for CO (sk = 1.36), $SO_2$ (sk = 6.947), $NO_x$ (sk = 2.14), NO (sk = 4.15), and $NO_2$ (sk = 2.08) are highly skewed to the right. Meanwhile, the distribution for $O_3$ (sk = 0.922) is slightly skewed to the right. For the station 2, the distribution for $O_3$ (sk = 1.36), $SO_2$ (sk = 5.23), and NO (sk = 1.55) are highly skewed to the right. Meanwhile, the distribution for CO (sk = 0.93), $NO_x$ (sk = 0.99), and $NO_2$ (sk = 0.94) are slightly skewed to the right. Hence, all parameters are skewed to the right because of nonnegative values. The data was analyzed assuming missing at random because the air quality data was missing being due to the monitoring site down [19].

MI technique was performed by using SAS version 9 with the imputation of m = 5 values for each missing record hence creating five complete datasets. Table 4 shows the relative efficiency of missing data for both stations. The result shows that all parameters are high efficiency very close to 1. This indicates that imputations with five replications are needed for simulation of this data.

Table 5 shows that the parameters give the close fit between the actual data and imputed data because of high value for $R^2$ and PA implying closer to 1. Meanwhile, the errors of the model for both stations are small and closer to 0 for parameters. According to the performance of $R^2$, the highest $R^2$ for both stations is CO parameter in S2 which is 0.906. Meanwhile, the highest performance of PA is NO in S2 which is 0.9513. The smallest RMSE is NO for S1

which is 0.0005 and the smallest MAE is also for NO in S1 which is 0.0002. Although $R^2$ value is quite low for $SO_2$ (0.497) in S1 but the performance of PA is quite high and also given small error. Therefore, this assures us that the MI technique by using MCMC method produced consistent result and suitable for the replace missing value for air quality datasets. It is supported with [20] reported that MI is suitable method to solve the high ratio of missing values for example 43.5% missing data. Another study from [21] shows that MCMC method was more effective than simple mean for the monthly rainfall data in the northern region of Thailand.

Table 3. Details of the two original datasets

| Station | US | CO | $O_3$ | $SO_2$ | $NO_x$ | NO | $NO_2$ |
|---|---|---|---|---|---|---|---|
| S1 | M | 0.35 | 0.021 | 0.0017 | 0.005 | 0.002 | 0.004 |
| | Med | 0.34 | 0.018 | 0.001 | 0.004 | 0.001 | 0.003 |
| | Var | 0.018 | 0.0002 | 0.00001 | 0.00002 | 0.000003 | 0.00001 |
| | Sk | 1.36 | 0.922 | 6.947 | 2.14 | 4.15 | 2.08 |
| S2 | M | 1.17 | 0.015 | 0.0034 | 0.05 | 0.03 | 0.03 |
| | Med | 1.10 | 0.009 | 0.003 | 0.055 | 0.023 | 0.028 |
| | Var | 0.31 | 0.0002 | 0.00001 | 0.001 | 0.001 | 0.0001 |
| | Sk | 0.93 | 1.36 | 5.23 | 0.99 | 1.55 | 0.94 |

**S-Station, US-Univariate Statistic, M-Mean, Med-Median, Var-Variance, Sk-Skewness*

Table 4. Relative efficiency (RE)

| Station | CO | $O_3$ | $SO_2$ | $NO_X$ | NO | $NO_2$ |
|---|---|---|---|---|---|---|
| S1 | 0.99 | 0.99 | 0.95 | 0.97 | 0.97 | 0.98 |
| S2 | 0.99 | 0.98 | 0.99 | 0.99 | 0.99 | 0.99 |

Table 5. The performance indicators for both stations

| Station | Parameter | Performance indicator | | | |
|---|---|---|---|---|---|
| | | $R^2$ | PA | RMSE | MAE |
| S1 | CO | 0.8911 | 0.9439 | 0.0985 | 0.0242 |
| | $O_3$ | 0.8865 | 0.9416 | 0.0061 | 0.0011 |
| | $SO_2$ | 0.4970 | 0.7050 | 0.0016 | 0.0007 |
| | $NO_x$ | 0.8627 | 0.9288 | 0.0017 | 0.0004 |
| | NO | 0.7606 | 0.8721 | 0.0005 | 0.0002 |
| | $NO_2$ | 0.8822 | 0.9392 | 0.0013 | 0.0003 |
| S2 | CO | 0.9060 | 0.9518 | 0.3039 | 0.0652 |
| | $O_3$ | 0.7695 | 0.8771 | 0.0070 | 0.0024 |
| | $SO_2$ | 0.8576 | 0.9260 | 0.0012 | 0.0003 |
| | $NO_x$ | 0.9013 | 0.9494 | 0.0149 | 0.0031 |
| | NO | 0.9050 | 0.9513 | 0.0084 | 0.0015 |
| | $NO_2$ | 0.8859 | 0.9413 | 0.0074 | 0.0016 |

## Conclusion

This paper discussed the use of multiple imputation technique to replace missing values in air quality dataset. The MCMC technique was used. The hourly air quality data was used to test the performance of the imputation technique. The relative efficiency was calculated to examine the accuracy technique for replacing missing values. The result shows that the relative efficiency is high and more than 0.9. Based on the result of performance indicators shows that the MCMC method give the good linear relationship because of $R^2$ and PA are high approaches to 1 for both stations and followed with small errors for RMSE and MAE. Therefore, it can be concluded that MCMC method is suitable method for replacing missing air quality data. MCMC method is also reliable to replace missing value either low or high percentage of missing data. Missing values are always arises, but a proper imputation can help remedy the analysis as much as possible.

## Acknowledgement

This study was funded by Ministry of Higher Education Malaysia under Research Acculturation Collaborative Effort (RACE) Grant Scheme Phase 2/2013. The author would like to thank the Ministry of Education Malaysia for its financial support to carry out this study under the MyBrain15 program. The author also would like to thank the Universiti Malaysia Terengganu for its financial support to carry out this study and Department of Environment (DoE) Malaysia for their permission to utilize air quality data for this study.

## References

1. Department of Environment Malaysia (2012). Malaysia Environmental Quality Report 2012. Kuala Lumpur: Department of Environment, Ministry of Sciences, Technology and the Environment, Malaysia.
2. Awang, M., Jaafar, A. B., Abdullah, A. M., Ismail, M., Hassan, M. N., Abdullah, R., Johan, S. and Noor, H. (2000). Air quality in Malaysia: Impacts, management issues and future challenges. *Respirology,* 5: 183 – 196.
3. Nichol, J. (1998). Smoke haze in South East Asia: A predictable recurrence. *Atmospheric Environment,* 32: 2715 – 2716.
4. Yusoff, N. F. F., Ramli, N. A., Yahaya, A. S., Sansuddin, N., Ghazali, N. A. and AlMadhoun, W. A. (2010). Monsoonal differences and probability distribution of $PM_{10}$ concentration. *Environmental Monitoring and Assessment,* 163: 1 – 4.
5. Little, R. J. and Rubin, D. B. (1987). *Statistical* analysis with missing data*,* New York: John Wiley and Sons.
6. Noor, M. N., Yahaya, A. S., Ramli, N. A. and Mustafa Al Bakri, A. M. (2014). Mean imputation techniques for filling the missing observations in air pollution dataset. *Trans Tech Publications, Switzerland, Key Engineering Materials*: pp. 902 – 908.
7. Batista, G. E. A. P. A. and Monard, M. C. (2003). An analysis of four missing data treatment methods for supervised learning. *Applied Artificial Intelligence,* 17: 519 – 533.
8. Li, D., Deogun, J., Spaulding, W. and Shuart, B. (2004). Towards missing data imputation: A study of fuzzy k-means clustering method. In S Tsumoto, R.Slowinski, J.Komorrowski, & J. W. Grzmala-Busse (Eds), Lecture notes in computer science: Rough sets and current trends in computing. Sweden:Springer-Verlag: pp. 573 – 579.
9. Noor, M. N., Yahaya, A. S, Ramli, N. A. and Abdullah, M. A. A. B. (2008). Estimation of missing values in air pollution data using single imputation techniques. *ScienceAsia,* 34: 341 – 345.
10. Jerez, J. M., Molina, I., GarcÍa-Laencina, P. J., Alba, E., Ribelles, N., Martín, M. and Franco, L. (2010). Missing data imputation using statistical and machine learning methods in real breast cancer problem. *Artificial Intelligence in Medicine,* 50: 105 – 115.
11. Silva-Ramírez E-L., Pino-Mejías R., López-Coello M. and Cubiles-de-la-Vega, M-D. (2011). Missing value imputation on missing completely at random data using multilayer perceptron. *Neural Networks,* 24: 121 – 129.
12. Junninen, H., Niska, H., Tuppurainen, K., Ruuskanen, J. and Kolehmainen, M. (2004). Methods for imputation of missing values in air quality datasets. *Atmospheric Environment,* 38: 2895 – 2907.
13. Rubin, D. B. (1987). Multiple imputation for nonresponse in surveys*,* New York: John Wiley & Sons, Inc.
14. Greenland, S. and Finkle, W. D. (1995). A critical look at methods for handling missing covariates in epidemiologic regression analyses. *American Journal of Epidemiology,* 142: 1255 – 1264.

15. Lu, W-Z. and Wang, D. (2008). Ground-level ozone prediction by support vector machine approach with a cost-sensitive classification scheme. *Science of the Total environment,* 395: 109 – 116.
16. Schafer, J. L. (1997). Analysis of incomplete multivariate data. Chapman and Hall, New York.
17. Little, R. A. and Rubin, B. B. (2002). Statistical analysis with missing data 2nd edition. Wiley, New York: pp. 4 - 22.
18. Chen, J. L., Islam, S. and Biswas, P. (1998). Nonlinear dynamics of hourly ozone concentrations: Nonparametric short term prediction. *Journal of Atmospheric Environment,* 32: 1839 – 1848.
19. Plaia, A. and Bondi, A. L. (2006.) Single imputation method of missing values in environmental pollution data sets. *Atmospheric Environment,* 40: 7316 – 7330.
20. Gómez-Carracedo, M. P., Andrade, J. M., López-Mahlía, P., Muniategui, S. & Prada, D. (2014). A practical comparison of single and multiple imputation methods to handle complex missing data in air quality datasets. *Chemometrics and Intelligent Laboratory Systems,* 134: 23 – 33.
21. Ingsrisawang, L. and Potawee, D. (2012). Multiple imputation for missing data in repeated measurements using MCMC and copulas. *Proceedings of the International Multiconference of Engineers and Computers Scientists*. 14-16 March 2012, Hong Kong.

*Malaysian Journal of Analytical Sciences, Vol 21 No 3 (2017): 560 - 570*
*DOI: https://doi.org/10.17576/mjas-2017-2103-06*

MALAYSIAN JOURNAL OF ANALYTICAL SCIENCES
*Published by The Malaysian Analytical Sciences Society*
ISSN 1394 - 2506

# SYNTHESIS, STRUCTURAL, CHEMICAL PROPERTIES, AND ANTI-BACTERIAL SCREENING OF Sm(III) THIOSEMICARBAZONE COMPLEXES

## (Sintesis, Struktur, Sifat-Sifat Kimia, dan Penyaringan Antibakteria bagi Kompleks Sm(III) Tiosemikarbazon)

Nur Nadia Dzulkifli[1, 2]*, Yang Farina[1], Bohari M.Yamin[1], Nazlina Ibrahim[3]

[1]*School of Chemical Science and Food Technology, Faculty of Science and Technology*
*Universiti Kebangsaan Malaysia, 43600 UKM Bangi, Selangor, Malaysia*
[2]*Department of Chemistry, Faculty of Applied Sciences,*
*Universiti Teknologi MARA, 72000 Kuala Pilah, Negeri Sembilan, Malaysia*
[3]*School of Biosciences and Biotechnology, Faculty of Science and Technology*
*Universiti Kebangsaan Malaysia, 43600 UKM Bangi, Selangor, Malaysia*

**Corresponding author: nurnadia@ns.uitm.edu.my*

Received: 16 August 2016; Accepted: 12 March 2017

**Abstract**

Rare earth complexes can exhibit higher coordination numbers while rare earth metals have the ability to form a multitude of geometries with organic ligands. The ligands, [Sm(III) $(4Acpy4MTSC)_2(4H_2O)Cl]Cl_2$ and [Sm(III) $(4Acpy4ETSC)(5H_2O)Cl_2]Cl$ [4Acpy4MTSC = 4-acetylpyridine 4-methyl-3-thiosemicarbazone; 4Acpy4ETSC = 4-acetylpyridine 4-ethyl-3-thiosemicarbazone] have been synthesised by condensation method. The compounds were structurally characterised by elemental analysis (CHNS), molar conductivity, Fourier Transform Infrared (FT-IR), Nuclear Magnetic Resonance (NMR), Ultraviolet-Visible (UV-Vis), and Thermo-Gravimetric Analysis (TGA). The elemental analysis for the compounds were in a good agreement with the theoretical values. The molar conductivity of the complexes showed electrolyte behaviour and confirmed the presence of counter ions in the structures. The proposed structures of the compounds have been confirmed by NMR, UV-Vis, and TGA. Based on the analysis, the ligands were coordinated to the metal ions through azomethine N and thione S thus, producing bidentate complexes. From the TGA, it is confirmed that a few water molecules have coordinated with metal ions. The X-ray crystallographic structures for the 4Acpy4ETSC, the C=S bond length is shorter than the single bond C-S which is 1.82 Å. It shows that in the solid state, the ligand exists in the thione form. The 4Acpy4ETSC adopted a monoclinic system, $a$ = 10.5922(7), $b$ = 8.9597(6), $c$ = 13.0407, Z = 4. *In vitro* antibacterial tests showed that the complexes have an effective inhibitory effect compared to the ligands because the presence of chloride ions, $Cl^-$ which caused the complexes to be more acidic, can inhibit bacterial growth.

**Keywords**: thiosemicarbazone, samarium(III), antibacterial screening

**Abstrak**

Sebatian kompleks nadir bumi boleh wujud dengan nombor koordinatan yang lebih tinggi dan logam nadir bumi berkeupayaan membentuk pelbagai geometri dengan ligan organik. Sebatian ligan, [Sm(III) $(4Acpy4MTSC)_2(4H_2O)Cl]Cl_2$ dan [Sm(III) $(4Acpy4ETSC)(5H_2O)Cl_2]Cl$ [4Acpy4MTSC = 4-asetilpiridin 4-metil-3-tiosemikarbazon; 4Acpy4ETSC = 4-asetilpiridin 4-etil-3-tiosemikarbazon] telah disintesiskan melalui kaedah kondensasi. Kesemua struktur sebatian telah dicirikan dengan analisis unsur (CHNS), kekonduksian molar, spektoskopi Inframerah Transformasi Fourier (FTIR), Resonans Magnet Nukleus (NMR), Ultralembayung-Sinar Nampak (UV-Vis), dan analisis termogravimetrik (TGA). Data analisis unsur bagi semua sebatian adalah hampir sama dengan nilai-nilai teori. Kekonduksian molar bagi sebatian kompleks menunjukkan sifat elektrolit dan

membuktikan kehadiran ion pembilang dalam struktur sebatian. Struktur jangkaan bagi sebatian telah dibuktikan dengan NMR, UV-Vis, dan TGA. Berdasarkan kepada analisis, ligan berkoordinat dengan ion logam melalui N azometina dan S tion dengan menghasilkan sebatian kompleks bersifat bidentat. Analisis TGA membuktikan kehadiran beberapa molekul air yang berkoordinat dengan ion logam. Struktur kristalografi sinar-X bagi 4Acpy4ETSC, panjang ikatan C=S adalah lebih pendek daripada ikatan tunggal C-S iaitu 1.82 Å. Ini menunjukkan bahawa dalam keadaan pepejal, ligan wujud dalam bentuk tion. 4Acpy4ETSC menghablur dalam sistem monoklinik, $a$ = 10.5922(7), $b$ = 8.9597(6), $c$ = 13.0407, Z = 4. Ujian antibakteria *in-vitro* ke atas sebatian kompleks mempamerkan kesan perencatan yang lebih tinggi berbanding dengan ligan kerana kehadiran ion klorida, Cl- yang menyebabkan kompleks bersifat asid, boleh menghalang pertumbuhan bakteria.

**Kata kunci:** tiosemikarbazon, samarium(III), penyaringan antibakteria

## Introduction

The study of thiosemicarbazone and their complex properties have favoured diverse researches that are related to the biological purposes [1-3]. Previous studies have reported that varied substitutions at the thioamide N atom have a powerful effect on the biological efficiency of the compounds [4]. The restructuring of the thiosemicarbazone framework is intended to get new compounds that will enhance their biological activity and be more reactive as an antibacterial agent [5]. 4-acetylpyridine complexes have the ability to inhibit bacteria cell growth where the activity greatly depends on the nature of the *N*-heterocyclic ring [6]. According to a study conducted by Rosu et al. [7], thiosemicarbazones do not show any bacterial inhibitor properties compared to their complexes against some microorganisms. This is due to chelation between thiosemicarbazones with metal ions that will reduce the metal ion polarity because of the shared positive charge between the donor atoms and metal ions. Moreover, the dispersion of the electrons in the rings may also influence the reactivity of thiosemicarbazones as an antibacterial agent. Thiosemicarbazones consist of C=N and C=S moieties which show favourable coordination towards metal ions [8]. Thiosemicarbazones consist of soft donor atoms; imine N and thiolate S where they act as δ-donor and π-acceptor atoms that can stabilise the oxidation state of metal ions [9]. Thiosemicarbazone commonly reacts with the transition and lanthanide metals to form stable complexes through amine N and thiocarbonyl or thiolate S atoms in which have a few bonding modes such as monodentate, bidentate, and polydentate [10].

In this study, the ligands and Sm(III) complexes were synthesised and characterised by an elemental analysis, molar conductivity, UV-Visible, FT-IR, TGA, NMR and single crystal X-ray diffraction technique. In addition, the antibacterial activity of the compounds were investigated.

## Materials and Methods

All reagents and reactants are of analytical grade and were used as received without further purification. The melting points of the synthesised compound were determined using the Electrothermal IA 9100. The elemental analysis was performed on the CHNS/O Model Fision EA 1180 and Thermo Finnigan Flash EA 1112 Series. 13C and 1H NMR spectra were recorded on a 600 MHz FT-NMR Cryoprobe using DMSO-$d_6$ as solvent and tetramethylsilane as the internal reference. Chemical shifts were recorded in parts per million (δ). Infrared spectra of the ligands were recorded as KBr discs on FTIR Perkin Elmer model GX spectrophotometer in the 4000-400 $cm^{-1}$ range. The thermogravimetric analysis (TGA) of the complexes was recorded on Mettler Toledo model TGA.SDTA 851e. The electronic absorption spectra were recorded on a Shimadzu UV-1650 PC and measured in the range of 200-800 nm in DMF. The molar conductivity was measured with DMF at room temperature using SI Analytic Lab 970 conductivity meter at the concentration of 1 x $10^{-3}$ M.

The determination of the crystal structures of the ligand was carried out on a Bruker Smart APEX CCD area detector diffractometer equipped with graphite mono-chromatised Mo-Kα (λ=0.71073Å) [11]. All data collection was carried out at 296K. Data collection: SMART [12]; cell refinement: SAINT [13]; data reduction: SAINT; program(s) used to solve structure: SHELXTL [14]; program(s) used to refine structure: SHELXTL [14] molecular graphics: SHELXTL [14]; software used to prepare material for publication: SHELXTL and PLATON [15]. Crystallographic data for the compounds Is2MTSC have been deposited with the Cambridge Crystallographic Data Centre, CCDC reference numbers (1007736). This information may be obtained free of charge from The Director, CCDC, 12 Union Road, Cambridge, CB2 1EZ, UK.

**Synthesis of 4Acpy4MTSC and 4Acpy4ETSC**

4Acpy4MTSC: A methanolic solution (10 mL) of 4-acetylpyridine (0.121 g, 10 mmol) was added to a methanolic solution (10 mL) of 4-methyl-3-thiosemicarbazide (0.105 g, 10 mmol) followed by the addition of a few drops of acetic acid. The solution was heated under reflux for 2 hours, filtered and left to dry at room temperature to get the white precipitate which formed after 2 weeks. The 4Acpy4ETSC was synthesised following the same method as 4Acpy4MTSC. Colourless crystals suited for X-ray Crystallography were obtained from methanol by slow evaporation at room temperature after a few weeks. The purity of ligands was checked by TLC and verified by elemental analysis.

**Synthesis of Sm(III) complexes**

$[Sm(III)(4Acpy4MTSC)_2(4H_2O)(Cl)]Cl_2$*:* A methanolic solution (30 mL) of 4-acetylpyridine 4-methyl-3-thiosemicarbazone (0.625 g, 3 mmol) was added dropwise into a methanolic solution (5 mL) of Sm(III) chloride hexahydrate (0.364 g, 1 mmol). The solution was heated under reflux for 3 hours. The yellow precipitate was filtered, rinsed with hot methanol, and dried in the desiccator. The $[Sm(III)(4Acpy4ETSC)_2(5H_2O)(Cl_2)]Cl$ was synthesised following the same method as $[Sm(III)(4Acpy4MTSC)_2(4H_2O)(Cl)]Cl_2$. Their reactions were difficult to be confirmed by the TLC method because of their insolubility in a few organic solvents.

**Antibacterial screening**

Antibacterial activity of the synthesised compounds was tested against Gram-positive bacteria with different species by convenient, low cost, and ease of use method which was disc diffusion. The types of bacteria used for antibacterial screening are as follows: i. *Bacillus subtilis (B. subtilis)*, ii. *Staphylococcus epidermidis (S.epidermidis)*, iii. *Staphylococcus auerus (S. aureus)*, iv. *Bacillus thuringiensis (B. thuringiensis)*, and v. *Methicillin-resistant Staphylococcus aureus (MRSA)*.

## Results and Discussion

**Chemical properties**

The results of the elemental analysis of the compounds are shown in Table 1. The molar conductivity for the complexes was measured in DMF ($10^{-3}$ M) at room temperature. The molar conductance for $[Sm(III)(4Acpy4MTSC)_2(4H_2O)Cl]Cl_2$ showed that the complex was 1:2 electrolyte, while $[Sm(III)(4Acpy4ETSC)(5H_2O)Cl_2]Cl$ was 1:1 electrolyte behaviour. It shows that the complexes have anions, $Cl^-$ outside the metal coordination sphere [16]. The proposed structures for the Sm(III) complexes are shown in Figure 1.

Table 1. Chemical properties of the compounds

| Compounds | Colour | Yield (%) | Composition Percentage, % (Calculated) | | | |
|---|---|---|---|---|---|---|
| | | | C | H | N | S |
| 4Acpy4MTSC | White precipitate | 90 | 51.11 (51.90) | 5.52 (5.81) | 25.48 (26.90) | 14.28 (15.39) |
| 4Acpy4ETSC | Colourless crystal | 92 | 53.64 (54.03) | 5.82 (6.35) | 25.08 (25.20) | 14.08 (14.42) |
| $[Sm(III)(4Acpy4MTSC)_2(4H_2O)(Cl)]Cl_2$ | Yellow precipitate | 83 | 28.89 (29.01) | 4.11 (4.33) | 14.78 (15.03) | 7.69 (8.60) |
| $[Sm(III)(4Acpy4ETSC)_2(5H_2O)(Cl_2)]Cl$ | Yellow precipitate | 89 | 21.82 (22.62) | 4.98 (4.66) | 10.01 (9.59) | 5.27 (5.49) |

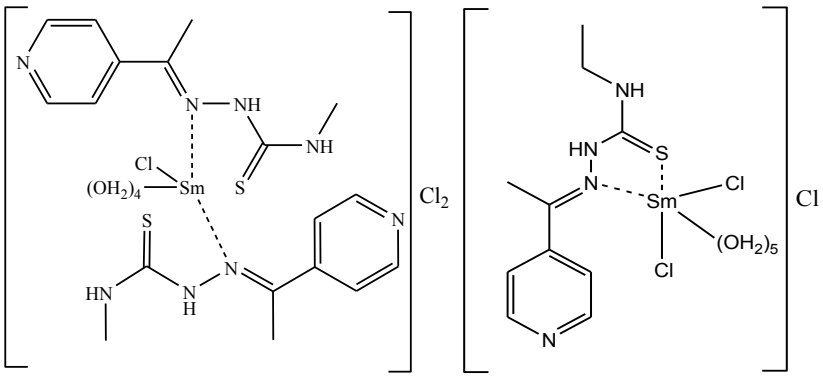


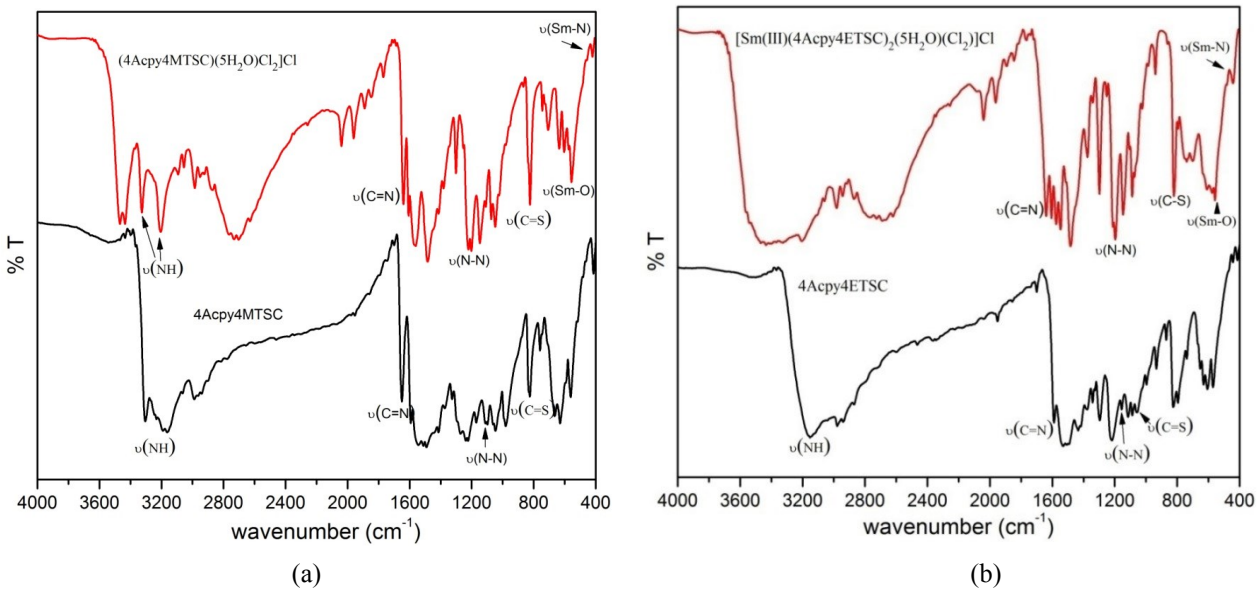

Figure 1. The proposed structures of the Sm(III) complexes

**Infrared spectra**

The infrared spectra of complexes and ligands were reported in the range of 200 – 400 and 400 – 4000 $cm^{-1}$, respectively, as shown in Figure 2. The comparison of stretching bands between the compounds is important to certify the coordination that occurs in the formation of complexes. The stretching band of ν(S-H) in the range of 2600 to 2800 $cm^{-1}$ implies that the ligands exist as tautomeric thione in the solid state [17, 18]. In addition, the presence of an amine group stretching band, ν(NH) in the range of 3150 – 3320 $cm^{-1}$ for the spectra of ligands also proved that ligands remain as thione tautomeric when in the solid state [19]. The absence of thiol stretching band, ν(S-H) in the range 2600 – 2800 $cm^{-1}$ and the existence of thiocarbonyl, ν(C=S) stretching band imply that the ligands will be presented as thione tautomeric in the solid state. Besides that, the existence of an amine, ν(N-H) stretching band at 3193 $cm^{-1}$ (4Acpy4MTSC) and 3151 $cm^{-1}$ (4Acpy4ETSC) also verified that the ligands remain as thione tautomers in the solid state. The stretching band ν(C=N) for the ligands exists at 1589 $cm^{-1}$. While for the complexes, the stretching band of ν(C=N) was shifted to higher wavenumber due to the coordination between the ligands to the metal ion through donor atoms, N-imine [20]. The stretching bands ν(C=S) for the ligand 4Acpy4MTSC and 4Acpy4ETSC showed up at 822 and 826 $cm^{-1}$, respectively. The stretching band was shifted to lower wavenumber, 821 $cm^{-1}$ for [Sm(III) (4Acpy4ETSC)($5H_2O$)$Cl_2$]Cl due to the coordination that occurred between thiocarbonyl sulfur with a metal ion. While the stretching band, ν(C=S) in [Sm(III) (4Acpy4MTSC)($5H_2O$)$Cl_2$]Cl was not shifted as it proved that no coordination occurred through S [21]. The coordination between azomethine, N and thiocarbonyl sulfur to metal ion was verified with the presence of stretching bands, ν(Sm-N) in the range 420 – 442 $cm^{-1}$ [22] and ν(Sm-S) at 353 $cm^{-1}$ [23]. In addition, the existence of two new stretching bands, ν(Sm-Cl) and ν(Sm-O) also showed that chloride ions and water molecules are also coordinated to metal ion to form high stability complexes.

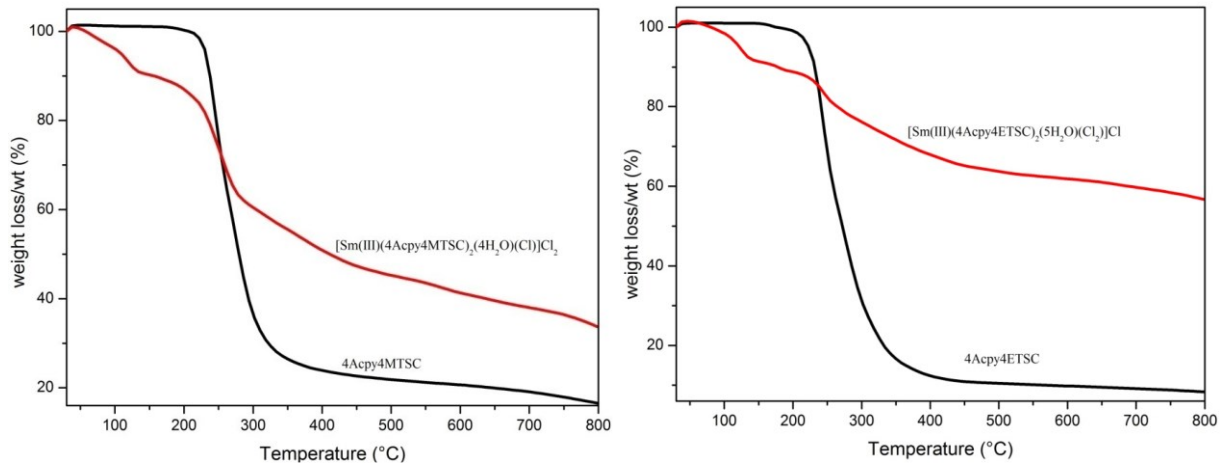
**Thermogravimetric analysis**

The thermogravimetric analysis (TGA) (20 – 800 °C) was recorded for the prepared ligands and complexes to distinguish between the coordinated and hydrate water molecules and study the thermal stability of the compounds. In order to evaluate the thermal stability of the prepared Sm(III) complexes, the TGA plot of the ligands was compared with Sm(III) complexes. The decomposition of the prepared complexes was not fully completed compared to the ligands as the instrument constraints only allow combustion of up to 800 °C. Referring to Figure 3, these complexes will be fully decomposed above 800 °C to produce $MS_2$ or $MO_2$ as a residue. Moreover, water molecules evaporate at less than 100 °C, which is likely that the complexes are not completely dry. Meanwhile, the temperatures between 100 – 300 °C are referred to the loss of water molecules coordinated with Sm(III) ion which can be supported by the proposed structures [24]. The complexes have a higher thermal stability than the ligands because the thermal stability is enhanced when the complexation occurred. Besides that, the decomposition of chloride, $Cl^-$ and nitrate ions, $NO_3^-$ also occurred in this temperature range [25].




(a) (b)

Figure 2. Infrared spectral of (a) 4Acpy4MTSC, (b) 4Acpy4ETSC and Sm(III) complexes




(a) (b)

Figure 3. Thermogram of (a) 4Acpy4MTSC, (b) 4Acpy4ETSC and Sm(III) complexes

**Absorption spectra**

The absorption spectra of the ligands and Sm(III) complexes were determined in DMSO solution ($c$ = 1 x $10^{-5}$ M). The spectra of 4Acpy4MTSC and 4Acpy4ETSC displayed almost similar diagrams in the range of 200 – 400 nm regions. The absorption spectra for 4Acpy4MTSC were composed of three intense absorption peaks at 205.50, 237.50, and 315.50 nm which appointed to n→σ*, π→π*, and n→π*, while 4Acpy4ETSC was composed of four intense bands at 211.00 (n→σ*), 243.50, 253.00 (π→π*), and 320.50 (n→π*). The electronic transitions refer to the presence of azomethine, thioamide, and benzene rings. In addition, according to Tulay et al. [26], electronic

transition, $\pi \rightarrow \pi^*$ refers to the transition of electrons in imine, C = N. The formation of the Sm(III) complexes led to the change in the absorption region (200-400 nm). This is probably because of the conjugation effect caused by the deprotonation of the ligands upon coordination. The spectra of $[Sm(III)(4Acpy4MTSC)_2(4H_2O)(Cl)]Cl_2$ were composed of three intense absorption peaks at 206.00, 233.00, and 315.50 nm which appointed to $n\rightarrow\sigma^*$, $\pi\rightarrow\pi^*$, and $n\rightarrow\pi^*$, while $[Sm(III)(4Acpy4ETSC)_2(5H_2O)(Cl_2)]Cl$ was composed of three intense absorption peaks at 203.50, 235.00, and 315.50 nm which appointed to $n\rightarrow\sigma^*$, $\pi\rightarrow\pi^*$, and $n\rightarrow\pi^*$. The slight shifting of absorption peaks proves that the coordination occurred through azomethine N and thiocarbonyl S [27]. No absorption peak for *f-f* transition appeared in the visible region presumably due to the very weak transition. Besides that, Taha et al. [28] reported that Sm(III) ion is not involved in the absorption of complexes as the *f-f* transition is a Laporte forbidden transition, which is assumed to be too weak to appear in the visible range with low molar absorption coefficient.

**Nuclear Magnetic Resonance analysis**

The results of the Nuclear Magnetic Resonance of the ligands are shown in Table 2.

Table 2. NMR spectra data of the ligands

| Compounds | Type of Protons | Chemical Shift δ (ppm) | Type of Carbons | Chemical Shift δ (ppm) |
|---|---|---|---|---|
| 4Acpy4MTSC | N-$CH_3$ (d) | 3.04-3.05 | -$CH_3$ | 31.65 |
| | N(1)H (s) | 2.49 | C=S | 179.31 |
| | N(2)H (s) | 10.39 | C=N | 150.22 |
| | $CH_3$C=N (s) | 2.28 | $CH_3$C=N | 13.80 |
| | Aromatic (m) | 7.87-8.59 | Aromatic | 121.09, 145.21 |
| 4Acpy4ETSC | -$CH_3$ (t) | 1.13-1.17 | -$CH_3$ | 14.85 |
| | N-$CH_2$ (m) | 3.59-3.66 | -$CH_2$ | 39.05 |
| | N(2)H (s) | 10.30 | C=S | 178.27 |
| | N(1)H (t) | 8.63-8.66 | C=N | 150.23 |
| | $CH_3$C=N (s) | 2.28 | $CH_3$C=N | 13.84 |
| | Aromatic (m) | 7.86-8.59 | Aromatic | 121.09, 145.20, 145.30 |

Based on Table 2, the chemical shift for N(2)H appeared at downfield, 10.39 and 10.30 ppm for 4Acpy4MTSC and 4Acpy4ETSC, respectively, with singlet multiplicity. For 4Acpy4MTSC, the spin multiplicity of N(1)H is a singlet different from the theory, as it should be generating quartet. This is because the presence of $D_2O$ has caused nitrogen protons to exchange with deuterium, then indirectly; the resonance disappears and exists as a singlet. Besides that, from the NMR data, it was revealed that the ligands exist as thione form caused by the absence of S-H protons and existence of C=S and C=N bonds. The protons of the phenyl group also appeared at downfield due to the presence of magnetic anisotropy and resonance effect. The chemical shifts for DMSO deuterated appeared in the range of 2 – 5 ppm. The NMR data proved the proposed structures of ligands as recommended. The complexes have paramagnetic properties and are not suitable for NMR analysis.

**X-ray structure determination**

The molecular structure of the ligand along with the atomic numbering scheme is shown in Figure 4. The crystal data and structure refinement and H-bonding parameters of the ligand are shown in Tables 3 and 4, respectively.

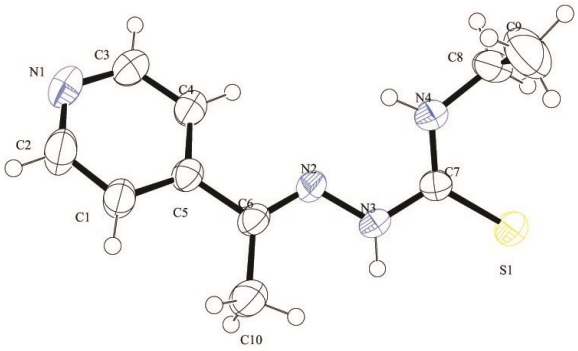



Figure 4. The molecular structure of (4Acpy4ETSC) with the atom labelling scheme. Displacement ellipsoids are drawn at the 50% probability level

Table 3. Crystal data and structure refinement for the ligand, 4Acpy4ETSC

| | **4Acpy4ETSC** |
|---|---|
| Chemical formula | $C_{10}H_{14}N_4S$ |
| Molar mass (g) | 222.31 |
| Crystal system | Monoclinic |
| Space group | $P2_1/c$ |
| *a* (Å) | 10.5922(7) |
| *b* (Å) | 8.9597(6) |
| *c* (Å) | 13.0407 |
| $\alpha$ (°) | 90 |
| $\beta$ (°) | 106.025(2) |
| $\gamma$ (°) | 90 |
| *V* (Å$^3$) | 1189.51(14) |
| Mo K$\alpha$ (Å) | 0.71073 |
| *Z* | 4 |
| D/Mgm$^{-3}$ | 1.241 |
| *F* (000) | 472 |
| Colour | Colourless |
| Shape | Block |
| Crystal size (mm) | 0.35,0.60,0.33 |
| Temperature (*K*) | 302(2) |
| Range $\theta$ (°) | 3.029-28.368 |
| *Goodness of fit on* $F^2$ | 1.048 |
| Indexes R final, $I > 2\sigma(I)$ | 0.0619 |
| Indexes *R* (All data) | 0.1001 |

Table 4. Hydrogen bonding parameters for 4Acpy4ETSC

| | D---H…A | Type | D-H (Å) | H…A (Å) | D…A (Å) | D-H…A(°) |
|---|---|---|---|---|---|---|
| | 4Acpy4ETSC | | | | | |
| i | N(3)---H(3A)…S(1) | Inter | 0.88 | 2.58 | 3.4523 | 173 |
| ii | N(4)---H(4A)…N(2) | Intra | 0.87 | 2.21 | 2.6111 | 108 |
| iii | N(4)---H(4A)…N(1) | Inter | 0.87 | 2.23 | 2.9945 | 146 |
| iv | C(8)---H(8B)…S(1) | Intra | 0.97 | 2.72 | 3.1041 | 104 |
| v | C(10)---H(10C)…N(3) | Intra | 0.96 | 2.45 | 2.8210 | 103 |

Symmetry codes: i. 1-x,-y,-z, and ii. -x,1/2+y,1/2-z

For 4Acpy4ETSC, pyridine ring N1/C1/C2/C3/C4/C5, as shown in Figure 4, is planar with a maximum deviation of 0.014 Å for the C5 atom from the least square plane. Thiourea moiety, S1/N3/N4/C7 is planar with a maximum deviation of atoms at 0.009 Å C7 from the least square plane. 4Acpy4ETSC ligand is connected with hydrogen bonds as listed in Table 2 to form 1D chain along the *b* axis. Referring to Table 5, for azomethine moiety, C(6)-N(2) and S(1)-C(7) is a double bond in which the bond length varies with the theoretical value. This is due to the effect of conjugation and delocalisation of electron density in the molecule [29].

Table 5. Selected bond lengths and angles for 4Acpy4ETSC

| Bond | Bond Length (Å) | Bond | Bond Angles (°) |
|---|---|---|---|
| S(1)-C(7) | 1.6803 | C(2)-N(1)-C(3) | 115.81 |
| N(1)-C(2) | 1.3262 | C(7)-N(4)-C(8) | 124.41 |
| N(1)-C(3) | 1.3281 | N(1)-C(3)-C(4) | 124.34 |
| N(2)-N(3) | 1.3777 | S(1)-C(7)-N(4) | 124.32 |
| N(4)-C(8) | 1.4566 | N(3)-N(2)-C(6) | 119.30 |
| N(4)-C(7) | 1.3229 | N(3)-C(7)-N(4) | 116.39 |
| N(3)-C(7) | 1.3596 | N(2)-N(3)-C(7) | 118.39 |
| N(2)-C(6) | 1.2741 | N(1)-C(2)-C(1) | 124.45 |
| | | N(2)-C(6)-C(5) | 114.83 |
| | | S(1)-C(7)-N(3) | 119.27 |
| | | N(4)-C(8)-C(9) | 112.26 |

**Antibacterial screening**

The synthesised compounds tested for their *in vitro* antibacterial activity against Gram-positive bacteria by disc diffusion method and their diameters of the zones inhibition are listed in Table 6. From the observation, it can be concluded that the complexes are more active as antibacterial agent compared to the ligands. This phenomenon is caused by the presence of chelation between metal ion with the ligands in which will lower the polarity of metal ion caused by the partial sharing between positively charged metal ions with the donor atoms, N and O [30]. This will increase the chelation lipophilic properties of the metal ion which will indirectly increase the penetration abilities of the complexes through the cell walls of microorganisms. Increasing the lipophilic properties of the complexes will inhibit the growth of bacteria [31]. In addition, when the metal ions or complexes were adsorbed onto the bacteria wall, they will indirectly inhibit the respiration cell and protein production process. Hence, this phenomenon will inhibit the growth of the bacteria. Besides that, the complexes showed that the inhibitory activities are more active compared to the ligands due to the presence of chloride ions, $Cl^-$ that are acting as electron withdrawing group

which causes them to be more acidic. In addition, due to the high degree of solubility of these compounds in the solvent DMSO, they are easily absorbed into the cells of bacteria through the membrane [32].

Table 6. Antibacterial activity of ligands and Sm(III) complexes

| **Compounds** | ***B. Subtilis*** | ***S. Epidermidis*** | ***S. Aureus*** | ***B. Thuringiensis*** | ***MRSA*** |
|---|---|---|---|---|---|
| | **Diameter of the Zones of Inhibition (cm)** | | | | |
| 4Acpy4MTSC | 0.65 | 0.70 | 0.65 | 0.65 | 0.65 |
| 4Acpy4ETSC | 0.65 | 0.70 | 0.60 | 0.65 | 0.70 |
| $[Sm(III)(4Acpy4MTSC)_2(4H_2O)(Cl)]Cl_2$ | 1.00 | 0.90 | 1.00 | 1.10 | 0.65 |
| $[Sm(III)(4Acpy4ETSC)_2(5H_2O)(Cl_2)]Cl$ | 0.90 | 0.90 | 0.80 | 0.80 | 0.60 |

## Conclusion

Two ligands and complexes were successfully synthesised and the proposed structures were supported by the elemental analysis, infrared, UV-Vis, molar conductivity, TGA, and X-ray Crystallographic study. The ligands exist as thione form in the solid state, which were proven by the X-ray Crystallographic study. The complexes showed 1:2 and 1:1 electrolytic behaviour for 4Acpy4MTSC and 4Acpy4ETSC, respectively, with molecular formula of $[Sm(III)\ (4Acpy4MTSC)_2(4H_2O)Cl]Cl_2$ and $[Sm(III)\ (4Acpy4ETSC)(5H_2O)Cl_2]Cl$. From the infrared and UV-Vis spectra, it can be seen that the ligands are coordinated with Sm(III) through azomethine N and thiocarbonyl, S as recommended by the proposed structures. The existence of coordinated $H_2O$ molecules with Sm(III) was proven by TGA which supported the proposed structures. An antibacterial screening implies that the Sm(III) complexes exhibit higher antibacterial activity compared to the ligands. These performances are due to the presence of chloride ions, $Cl^-$ which caused the complexes to be more acidic and therefore, inhibit bacterial growth.

## Acknowledgement

The authors would like to thank the Faculty of Science and Technology, Universiti Kebangsaan Malaysia and the Centre for Research and Instrumentation (CRIM) for the research facilities, provision of laboratory facilities, and technical assistance. This study is financially supported by the research grant from GUP-2012-022, FRGS/2/2013/ST01/UKM/01/2, Universiti Teknologi MARA (UiTM) and scholarship from MyBrain15.

## References

1. Demoro, B., De, A. R. F. M., Marques, F., Matos, C. P., Otero, L., Costa, Pes, J., Santos, I., Rodriguez, A., Moreno, V., Lorenzo, J., Gambino, D. and Tomaz, A. I. (2013). Screening organometallic binuclear thiosemicarbazone ruthenium complexes as potential anti-tumour agents: cytotoxic activity and human serum albumin binding mechanism. *Dalton Transactions*, 42(19): 7131 – 7146.
2. Atalay, T. and Akgemci, E. G. (1998). Thermodynamic studies of some complexes of 2-benzoylpyridine 4-phenyl-3-thiosemicarbazone. *Turkish Journal of Chemistry*, 22: 123 – 128.
3. Seda, S., Baybars, K., Fatma, K. and Sevgi, H. B. (2009). Theoretical and spectroscopic studies of 5-fluoro-isatin-3-(*N*-benzylthiosemicarbazone) and its zinc(II) complex. *Journal of Molecular Structure*, 917: 63 – 70.
4. Bernhardt, P. V., Sharpe, P. C., Islam, M., Lovejoy, D. B., Kalinowski, D. S. and Richardson, D. R. (2008). Iron chelators of the dipyridylketone thiosemicarbazone class: precomplexation and transmetalation effects on anticancer activity. *Journal of Medicinal Chemistry*, 52(2): 407 – 415.
5. Nguyen, T. B. Y., Pham, C. T., Trieu, T. N., Abram, U. and Nguyen, H. H. (2015). Syntheses, structures and biological evaluation of some transition metal complexes with a tetradentate benzamidine/thiosemicarbazone ligand. *Polyhedron,* 96: 66 – 70.
6. Matesanz, A. I., Tapia, S. and Souza, P. (2016). First 3,5-diacetyl-1,2,4-triazol derived mono(thiosemicarbazone) and its palladium and platinum complexes: Synthesis, structure and biological properties. *Inorganica Chimica Acta,* 445: 62 – 69.

7. Rosu, T., Pahontu, E., Pasculescu, S., Georgescu, R., Stanica, N., Curaj, A., Popescu, A. and Leabu, M. (2010). Synthesis, characterization antibacterial and antiproliferative activity of novel Cu(II) and Pd(II) complexes with 2-hydroxy-8-R-tricyclo[7.3.1.0.$^{2,7}$] tridecane-13-one thiosemicarbazone. *European Journal of Medicinal Chemistry,* 45: 1627 – 1634.
8. Feng, L., Shi, W., Ma, J., Chen, Y., Kui, F., Hui. Y. and Xie, Z. (2016). A novel thiosemicarbazone Schiff base derivative with aggregation-induced emission enhancement characteristics and its application in $Hg^{2+}$ detection. *Sensors and Actuators B: Chemical,* 237: 563 – 569.
9. Hosseini-Yazdi, S. A., Hosseinpour, S., Khandar, A. A., Kassel, W. S. and Piro, N. A. (2015). Copper(II) and nickel(II) complexes with two new bis(thiosemicarbazone) ligands: Synthesis, characterization, X-ray crystal structures and their electrochemistry behavior. *Inorganica Chimica Acta,* 427: 124 – 130.
10. Shahsavani, E., Khalaji, A. D., Feizi, N., Kucerakova, M. and Dusek, M. (2015). Synthesis, characterization, crystal structure and antibacterial activity of new sulfur-bridged dinuclear silver(I) thiosemicarbazone complex $[Ag_2(PPh_3)_2(\mu\text{-S-Brcatsc})_2(n^1\text{-S-Brcatsc})_2](NO_3)_2$. *Inorganica Chimica Acta,* 429: 61 – 66.
11. Awang, N. W., Hasbullah, S. A., Yusoff, S. F. M. and Yamin, B. M. (2014). *N*-[Ethyl(2-hydroxyeth-yl)carbamothioyl]-3-fluorobenzamide. *Acta Crystallographica Section E: Structure Reports Online*, 70(5): 570.
12. Bruker (2009). SMART, SAINT and SADABS. Bruker AXS Inc., Madison, Wisconsin, USA.
13. Bruker (2008). APEX2, SAINT and SADABS. Bruker AXS Inc., Madison, WI.
14. Sheldrick, G. M. (2008). A short history of SHELX. *Acta Crystallographica Section A: Foundations of Crystallography*, 64(1), 112 – 122.
15. Spek, A. L. (2009). Structure validation in chemical crystallography. *Acta Crystallographica Section D: Biological Crystallography*, 65(2): 148 – 155.
16. Seleem, H. S., Emara, A. A. and Shebl, M. (2005). The relationship between ligand structures and their Co(II) and Ni(II) complexes: Synthesis and characterization of novel dimeric Co(II)/Co(III) complexes of bis(thiosemicarbazone). *Journal of Coordination Chemistry,* 58(12): 1003 – 1019.
17. Rai, D. K. and Singh, A. (2013). Synthesis, characterization and catalytic activity of transition metal complexes with thiosemicarbazone core ligand. *Indian Journal of Science Research,* 4(2): 129 – 133.
18. Liu, Y. Y., Ma, J. F. and Yang, J. (2007). Syntheses and structures of Zn(II) and Ni(II) complexes of 4-N-(acetylacetone amine)acetophenonehiosemicarbazone. *Journal Coordination of Chemistry,* 60(14): 1579 – 1586.
19. Chatterjee, M. and Ghosh, S. (1998). Vanadium(III) complexes of salicylaldehyde thiosemicarbazones. *Transition Metal Chemistry,* 23: 355 – 356.
20. Agata, T. K. (2014). On the verification of binding modes of *p*-dimethylaminobenzaldehyde with mercury(II). The solid state studies. *Journal of Molecular Structure,* 1072: 284 – 290.
21. Bisceglie, F. Pinelli, S., Alinovi, R., Goldoni, M. and Mutti, A. (2014). Cinnamaldehyde and cuminaldehyde thiosemicarbazones and their copper(II) and nickel(II) complexes: A study to understand their biological activity. *Journal of Inorganic Biochemistry,* 140: 111 – 125.
22. Brindha, G. & Vijayanthimala, R. (2015). Synthesis, characterization of novel Copper(II), nickel(II) complexes of *N*-substituted thiosemicarbazides: Evaluation of anti-bacterial, anti-fungal and anti-cancer activities. *Journal of Chemical and Pharmaceutical Research,* 7(3): 225 – 231.
23. Silva, J. G. D., Wardell, S. M. S. V., Wardell, J. L. and Beraldo, H. (2009). Zinc(II) complexes of 2-pyridine-derived *N*(4)-*p*-tolylthiosemicarbazones: Study of in vitro antibacterial activity. *Journal of Coordination Chemistry,* 62(9): 1400 – 1406.
24. Poyraz, M., Sari, M., Ney, A. G., Demirci, F., Demirayak, S. and Sahin, E. 2008. Synthesis, characterization and antimicrobial activity of a Zn(II) complex with 1-(1H-benzoimidazol-2-yl)-ethanone thiosemicarbazone. *Journal of Coordination Chemistry,* 61(20): 3276 – 3283.
25. El-Asmy, A. A., El-Gammal, O. A. and Saleh, H. S. (2008). Spectral, thermal, electrochemical and analytical studies on Cd(II) and Hg(II) thiosemicarbazone complexes. *Spectrochimica Acta Part A,* 71: 39 – 44.
26. Tulay, B-D., Musa, S., Esin, K., Mustafa, O., Bahri, U. and Resat, A. (2015). Synthesis and antioxidant activities of transition metal complexes based 3-hydroxysalicylaldehyde-S-methylthiosemicarbazone. *Spectrochimica Acta Part A: Molecular and Biomolecular Spectroscopy,* 138: 866 – 872.
27. Kenawy, I. M., Hassanien, M. M., Abdel-Rhman, M. H., Zaki, R. R. and Rashed, H. S. (2016). Synthesis and characterization of Hg(II) and Cd(II) complexes derived from the novel acenaphthaquinone-4-phenyl thiosemicarbazone and its CPE application. *Egyptian Journal of Basic and Applied Sciences,* 3(1): 106 – 117.

28. Taha, Z. A., Ajlouni, A. A. M. and Momani, W. A. (2012). Structural, luminescence and biological studies of trivalent lanthanide complexes with *N*,*N*'-Bis(2-Hydroxynaphthylmethylidene)-1,3-propanediamine Schiff base ligand. *Journal of Luminescence,* 132: 2832 – 2841.
29. Stanojkovic, T. P., Kovala-Demertzi, D., Primikyri, A., Garcia-Santos, I., Castineiras, A., Juranic, Z. and Demertzis, M. A. (2010). Zinc(II) complexes of 2-acetyl pyridine 1-(4-fluorophenyl)-piperazinylthiosemicarbazone: Synthesis, spectroscopic study and crystal structures – Potential anticancer drugs. *Journal of Inorganic Biochemistry,* 104: 467 – 476.
30. Waleed, M. A. M. (2013). A study of *in vitro* antibacterial activity of lanthanides complexes with a tetradentate Schiff base ligand. *Asian Pacific Journal of Tropical Biomedicine,* 3(5): 367 – 370.
31. Obaleye, J. A., Adediji, J. F. and Adebayo, M. A. (2011). Synthesis and biological activities on metal complexes of 2,5-diamino-1,3,4-thiadiazolederivedfrom semicarbazide hydrochloride. *Molecules,* 16(7): 5861 – 5874.
32. Sankaraperumal, A., Karthikeyan, J., Shetty, A. N. and Lakshmisundaram, R. (2013). Nickel(II) complex of *p*-[*N*.*N*-bis(2-chloroethyl)amino]benzaldehyde-4-methylthiosemicarbazone: Synthesis, structural characterization and biological application. *Polyhedron*, 50: 264 – 269.

*Malaysian Journal of Analytical Sciences, Vol 21 No 3 (2017): 571 - 584*
*DOI: https://doi.org/10.17576/mjas-2017-2103-07*

MALAYSIAN JOURNAL OF ANALYTICAL SCIENCES
*Published by The Malaysian Analytical Sciences Society*
ISSN 1394 - 2506

# SYNTHESIS AND CHARACTERIZATION OF HYDROXYAPATITE FROM BULK SEASHELLS AND ITS POTENTIAL USAGE AS LEAD IONS ADSORBENT

## (Sintesis dan Pencirian Hidroksiapatit dari Kulit Kerang dan Potensi Sebagai Penjerap Ion Plumbum)

Marinah Mohd Ariffin[1]*, Norhafiza Ilyana Yatim[1], Sofiah Hamzah[2]

[1]*School of Marine and Environmental Sciences*
[2]*School of Ocean Engineering*
*Universiti Malaysia Terengganu, 21300 Kuala Terengganu, Malaysia*

**Corresponding author: erin@umt.edu.my*

Received: 16 August 2016; Accepted: 27 March 2017

**Abstract**

In the present work, hydroxyapatite (HAP) powder was successfully synthesized *via* the thermal decomposition and subsequent wet precipitation (with different experimental reaction times of 3, 5, 24, 48, and 72 hours of bulk seashells. We found that the reaction time during wet precipitation stage affected the physical and chemical properties of HAPs adsorbents. HAP synthesized with a reaction time of 48 hours showed the highest removal of $Pb^{2+}$ ions (99.1%) and is highly potential to be used as bio adsorbent material in heavy metal wastewater treatment.

**Keywords**: hydroxyapatite, seashell, wet precipitation, lead

**Abstrak**

Di dalam kajian ini, serbuk hidroksiapatit (HAP) telah berjaya disintesis dari kulit kerang melalui proses penguraian termal dan diikuti oleh teknik pemendakan basah (dengan masa tindakbalas kajian 3, 5, 24 dan 72 jam). Kajian mendapati masa tindakbalas mempengaruhi ciri-ciri fizikal dan kimia penjerap HAP. HAP yang disintesis dengan masa tindakbalas selama 48 jam menunjukkan peratusan penyingkiran ion $Pb^{2+}$ tertinggi (99.1%) dan berpotensi untuk digunakan sebagai bahan penjerap-bio bagi pemulihan logam berat di dalam air sisa.

**Kata kunci**: hidroksiapatit, kulit kerang, pemendakan basah, plumbum

## Introduction

Water contamination often occurs due to anthropogenic activities such as manufacturing industries and agriculture. The untreated wastes from these activities are discharged directly into the environment, causing adverse impact on both the environment and human. Lead is one of the harmful pollutants which can cause irreversible neurological harms, e.g. kidney diseases, nervous disorders and reproductive toxicity [1]. The main factors contributing to lead contamination are from pipes, batteries, cable sheathing, and lead sheets [2]. The Ministry of Health Malaysia set the benchmark for both raw and drinking water quality index, with a maximum acceptable value of lead at 0.05 mg/L and 0.01 mg/L, respectively [3]. Various conventional methods have been introduced to remove heavy metals from wastewater, including chemical precipitation, membrane filtration, ion exchange, carbon adsorption, and co-precipitation/adsorption [4]. However, due to operational demerits, high cost of the treatment, the generation of

toxic chemical sludge and incomplete removal of the pollutants, the conventional methods are least favourable [5]. Therefore, in search of alternatives, many researchers have applied regenerated natural wastes to produce an efficient and low cost treatment technology for heavy metal treatment.

Nowadays, studies using hydroxyapatite, $Ca_{10}(PO_4)_6(OH)_2$, (HAP) are being rapidly conducted and due to its versatility, it is applied in various fields such as biomedical application [6, 7], bone tissue engineering [8, 9], and wastewater treatment [10 – 12]. In addition, HAP has appealed a great deal of attention as a good adsorbent. It is highly stable under reducing and oxidizing conditions and possesses various favourable surface characteristics, such as surface functional groups, acidity and basicity, surface charge, hydrophilicity and porosity. The heavy metal sorption takes place through ionic exchange reaction, surface complexation with phosphate, calcium and hydroxyl groups and/or co-precipitation of new partially soluble phases [13].

HAP, also commonly known as calcium phosphate ceramic or bioceramic, exhibits similar structure and composition to the mineral phase of bones and teeth. Every year, 63,000 metric ton of shell fish wastes are generated worldwide and about 70% of this total weight is represented by clam shells. Easily available and abundant in nature, a renovation of these clam shell wastes into value-added HAP can be highly profitable [14]. HAP can also be produced from other natural calcium sources, e.g. corals, eggshell [15], cuttlefish shells, natural gypsums, bovine bones and seashells [16]. Various HAP production methods are developed: preparation methods such as hydrothermal method [17], microwave-assisted hydrothermal rapid synthesis [18], combustion method [19], precipitation, sol-gel technique, multiple emulsion, biomimetic deposition technique and electro deposition approach [20]; experimental conditions can also be modified according to the needs of applications prior to use. The type of source, method of preparation and different conditions will create HAP with different chemical and physical properties.

Therefore, in the present work, HAP was produced from marine waste *via* straightforward analysis technique by controlling the reaction time taken to produce high quality of HAP adsorbent in optimum condition. The changes of physical and chemical characteristics of the resulting HAP were discussed. The produced HAP is a potential lead-removal adsorbent, removing lead from contaminated water, thus curbing water pollution due to anthropogenic activities by converting wastes into valuable material.

## Materials and Methods

### Instrument

The purity of HAP adsorbents was examined by X-ray diffraction (XRD) using Cu Kα radiation (λ¼1.5406 Å) on a SmartLab X-ray diffractometer (Rigaku). Fourier Transform infrared (FTIR) spectroscopy technique using potassium bromide (KBr) pellet method was conducted using Perkin Elmer Spectrum 2000 FT-IR Spectrometer to define the information functional groups of HAP present in adsorbents. The adsorbent surface morphologies were studied using scanning electron microscope (SEM) (JEOL model JSM-6360 LA), and analysed using Brunauer, Emmett, and Teller (BET) analysis (Micromeritics, ASAP-2020). An Inductively Couple Plasma-Optical Emission Spectroscopy (ICP-OES) Shimadzu was used for $Pb^{2+}$ analysis.

### Raw material and chemical

Bulk seashells were randomly collected from Teluk Ketapang beach, Terengganu. Standard solution (1000 mg/L of lead) was prepared from lead (II) nitrate, $Pb(NO_3)_2$ (Merck, Germany) and used as stock solution of Pb(II). The working solutions of lower concentrations were prepared by dilutions series. All standard solutions were stored in refrigerator at 4 °C. Ammonium hydrogen dibasic was supplied by Merck, Germany. Deionised water was purified by Purelab Ultra, ELGA with Millipore 18.2 μΩ. All reagents used were of analytical grade.

### Synthesis of hydroxyapatite

Bulk seashells were cleaned and dried in oven at 60 °C overnight. After crushed and pulverized, the seashell powder was calcined at 1000 °C for 1 hour in a furnace. HAP 3 was synthesized by slowly adding 150 mL of dissolved diammonium hydrogen phosphate solution to the 150 mL of calcined seashell powder with a Ca/P ratio of 1.68. The solution was then stirred at room temperature for 3 hours. The resulting precipitate was filtered using nylon cellulose filter paper (pore size = 0.25 μm) and extensively washed with deionized water to neutralize the

precipitate. Subsequently, the HAP 3 was dried in oven at 100 °C overnight. Finally, the HAP 3 was sieved at a size range of less than 38 µm before being stored in tight container for further analyses. This experimental procedure was repeated to produce HAP 5, HAP 24, HAP 48 and HAP 72 by changing the reaction time during stirring from 3 to 5, 24, 48 and 72 hours. The physical and chemical characterizations of the HAPs powders produced were examined. The chemical reaction involved in the experiment is stated as equation 1 and 2 below:

$$CaCO_3 \xrightarrow{1000\ ^\circ C} CaO + CO_2 \quad (1)$$

$$10CaO + 6(NH_4)_2HPO_4 + 4H_2O \longrightarrow \underset{\text{Hydroxyapatite}}{Ca_{10}(PO_4)_6(OH)_2} + 12NH_4OH \quad (2)$$

**Adsorption method**

Batch adsorption experiment was conducted to study the $Pb^{2+}$ ions adsorption performance of different types of HAPs adsorbents. The experiments were conducted by mixing HAP adsorbent (0.4 g) in 200 mL of lead (II) nitrate solution (25 mg/mL) in a 250 mL Schott bottle. The solutions were equilibrated using controlled mechanical shaker at 150 rpm in room temperature. The aliquot supernatant was collected at fix time intervals (0, 15, 30, 60, 120, 150, 180, 210 and 240 minutes). The concentration changes of $Pb^{2+}$ were determined using ICP-OES.

The percentage of lead removal (% R), quantity adsorbed by adsorbent ($q_t$) and adsorption capacity of adsorbent ($q_e$) were calculated using equation 3, 4 and 5, respectively:

$$\% R = [(C_0-C_e)/C_0] \times 100\% \quad (3)$$
$$q_e = (C_0-C_{eq})\ V/\ (M) \quad (4)$$
$$q_t = (C_0-C_t)\ V/\ (M) \quad (5)$$

where, $C_0$, $C_t$ and $C_{eq}$ are the initial, at time t (min) and equilibrium concentration of heavy metal ion in the solution (mg/L), respectively. The $q_e$ is the adsorption capacity in (mg/g), $q_t$ is the amount of lead adsorbed at time (mg/g), V is the total volume of the solution (L) and M is the amount of composite adsorbent (g).

**Kinetic and equilibrium modelling**

The effect of initial concentrations of adsorbate, $Pb^{2+}$ (25, 50, 75, 100, 125, 150, and 200 mg/L) was observed. In each batch experiment, 200 mL of aqueous metal ion solution of desired concentration was prepared and a fix weight of adsorbent, 0.4 g was added. The mixed solution was equilibrated with controlled mechanical shaker at 150 rpm. Supernatants were collected at various time intervals (0, 15, 30, 60, 120, 150, 180, 210 and 240 minutes), and the concentration of lead was determined using ICP-OES analysis. All experiments were carried out in triplicates and the mean values were presented.

Study of kinetic models is important to define the mechanism involved in the adsorption process of adsorbate onto adsorbent in aqueous solution. The kinetic models by Lagergren's pseudo-first order and McKay and Ho's pseudo-second order models were used to the analysis data [5]. The linear equation of pseudo-first and pseudo-second are expressed in equation 6 and 7, correspondingly.

$$\log (q_e - q_t) = \log q_e - (k_1/2.303)t \quad (6)$$
$$t/q_t = 1/k_2 q_e^{\ 2} + t/q_e \quad (7)$$

where $q_e$ is the amount of lead adsorbed by the absorbent at equilibrium at specific time $q_t$ (mg/g). $k_1$ ($min^{-1}$) is the biosorption rate constant of pseudo-first-order sorption. The graph of pseudo-first order was plotted as log ($q_e$-$q_t$) versus t, and the linear graph for pseudo-second-order was plotted as t/qt against t. The pseudo-second order model rate constant, $k_2$ (g/mg min) and $q_e$ was obtained from the intercept and slope of the linear graph plotted. From the equation 8, the initial biosorption rate, h (mg/g min) was calculated from the value obtained using pseudo-second-order as stated below:

$$h\ (mg/g\ min) = k_2 q_e^2 \quad (8)$$

The equilibrium adsorption isotherm is important in designing a biosorption system. The relationship between the adsorbent and adsorbate in equilibrium can be described from the type of adsorption isotherms data plotted. In this study, the lead adsorption of HAP 48 adsorbent was tested using Langmuir and Freundlich isotherm models. The Freundlich and Langmuir isotherm are represented in equation 9 and 10 as below:

$$\log q_e = \log K_F + (1/n) \log C_e \quad (9)$$
$$C_e/q_e = (1/Q_0 b) + (C_e/Q_0) \quad (10)$$

where $q_e$ is the amount of adsorbate adsorbed at equilibrium (mg/g) and $C_e$ is the equilibrium solute concentration (mg/L). Value of $K_F$ and 1/n are Freundlich constants, that related to the adsorption capacity and adsorption intensity of the adsorbent which are can be directly obtained from the intercept and slope of the linear plot of log $q_e$ against log $C_e$. Value of b is the Langmuir constant related to the energy of biosorption (L/mg), $q_m$ is the maximum sorption capacity corresponding to complete monolayer coverage (mg/g). These b and $Q_0$ were obtained from the intercept and slope, respectively from the linear plot of $C_e/q_e$ over $C_e$.

The favourable nature of adsorption can be expressed in terms of dimensionless separation factor of equilibrium parameter, which is shown in equation 10 below [22].

$$R_L = 1/1+bC_0 \quad (11)$$

## Results and Discussion

### Physical characterizations

Figure 1 depicts the diffractograms of different types of HAPs produced at different reaction times. The broad peaks indicate an amorphous structure. This result is consistent with previous study, in which non-calcined HAP produced broad peaks as a result of poor crystallinity structure [23]. The reflection patterns of HAP 3, HAP 24, HAP 48 and HAP 72 matched the XRD pattern of hydroxyapatite [$Ca_{10}(PO_4)_6(OH)_2$] (JCPDS standard No. 74–565). HAP 5 powder showed the presence of calcite peak matching the XRD pattern of carbonate hydroxyapatite, syn [$Ca_{10}(PO_4)_3(CO_3)_3(OH)_2$] (JCPDS standard No. 19–272). The highest peak of HAP was at $31.9^0$ and the adsorbent of HAP 48(315) showed the highest intensity, indicating the high purity of HAP 48 compared to others adsorbents (i.e. HAP 24(313), HAP 72(295), HAP 3(286) and HAP 5(258)). The calcite peak of HAP 5 at 29.42° is considered as an intermediate product in the conversion of seashell (calcium carbonate) to calcium oxide. The production of HAP increased with reaction time and conversion is completed with the disappearance of the diffraction line of calcite [24].

Figure 2 illustrates the FTIR spectra of different types of HAP. A broad peak at 1031 – 1033 $cm^{-1}$ demonstrated the stretching modes of P-O bonds of phosphate group ($PO_4^{3-}$) in the HAP structure. The peak at 602 $cm^{-1}$ and 563 $cm^{-1}$ were due to the bending modes of P–O bonds in phosphate groups [25]. A broad peak at 3421 – 3441 $cm^{-1}$ were assigned to the hydroxyl group (-OH) vibration [26]. A weak band of functional group of carbonate, $CO_3^{2-}$ exhibited in the region 1419 – 1455 and 873 – 875 $cm^{-1}$ corresponded to the B-type carbonate substitution of the $PO_4$ groups in the HAP structure [27]. The lower intensity of the carbonate bands of HAP 72 and HAP 48 showed that they were purer compared to other HAPs.

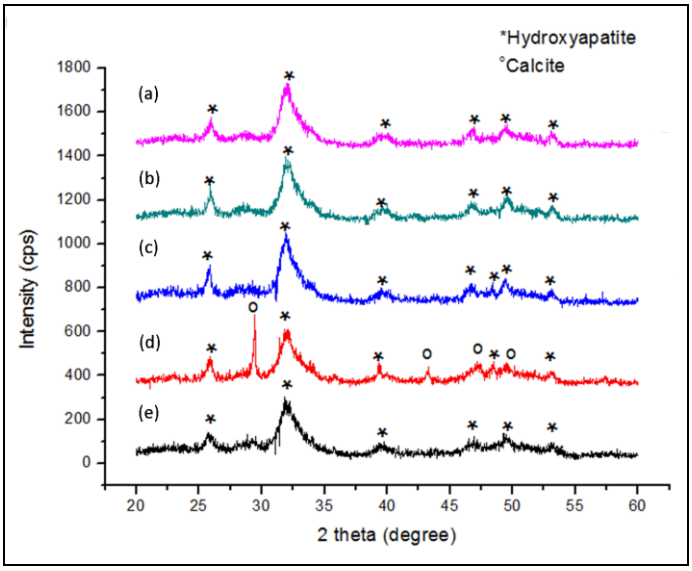



Figure 1. The XRD diffractogram of the HAP adsorbents. (a) HAP 72, (b) HAP 48, (c) HAP 24, (d) HAP 5 and (e) HAP 3

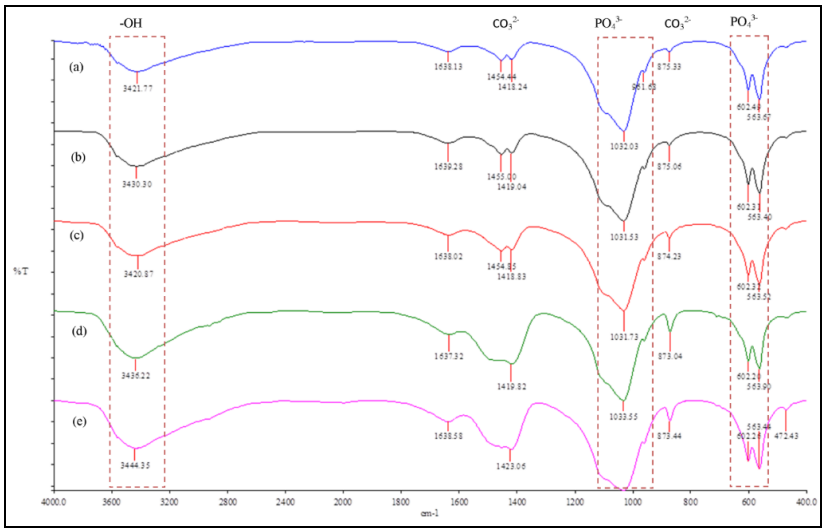



Figure 2. The FTIR spectra of HAP adsorbents. (a) HAP 72, (b) HAP 48, (c) HAP 24, (d) HAP 5 and (e) HAP 3

Based on these observations, the synthesis of HAP was successful based on the existence of the main functional groups of HAP, i.e. the hydroxyl group and phosphate group in each spectrum of HAP adsorbents. The reaction time exerted effects on the composition of the resulting HAP, which was clearly reflected from the band intensity of functional groups that appear in all spectra. A reaction time of 48 hours and 72 hours produced purer HAP structure, indicating that the reaction time is positively correlated with the conversion process of calcium carbonate, $CaCO_3$ to hydroxyapatite, HAP molecule.

The surface and texture porosity of the HAPs were determined by nitrogen adsorption/desorption measurements at 77 K and the results of BET analysis are presented in Table 1. The data have shown that the reaction time was

inversely proportional to the value of BET surface area. The HAP 3 exhibited the highest surface area, 126.51 $m^2/g$ while HAP 72 = gave the lowest value of BET surface area, 66.91 $m^2/g$. A possible explanation for this might be due to the agglomerate process that produced larger cluster of particles [28].

Table 1. The BET surface area, average pore volume and pore diameter of HAPs

| Type of Adsorbent | BET Surface Area ($m^2/g$) | Average Pore Volume ($cm^3/g$) | Average Pore Diameter (nm) |
|---|---|---|---|
| HAP 3 | 126.6 | 0.482 | 13.05 |
| HAP 5 | 87.8 | 0.330 | 12.77 |
| HAP 24 | 76.6 | 0.438 | 20.53 |
| HAP 48 | 74.6 | 0.389 | 17.99 |
| HAP 72 | 66.9 | 0.347 | 17.12 |

Figure 3 presents the isotherm graphs of HAPs produced at different reaction times. As shown in this figure, all the HAPs illustrated the physisorption isotherm type IV, indicating a mesoporous structure (2 – 50 nm in diameter). This type of isotherm was determined based on the shape of hysteresis loop formed during capillary condensation process occurred in the mesoporous structures [29]. Based on Figure 3, the hysteresis loops of HAPs at relative pressure ($P/P_0$) from 0.55 to 1.0 were of Type H4, thus indicating the presence of narrow-slit like pore pattern in the absorbents' structures.

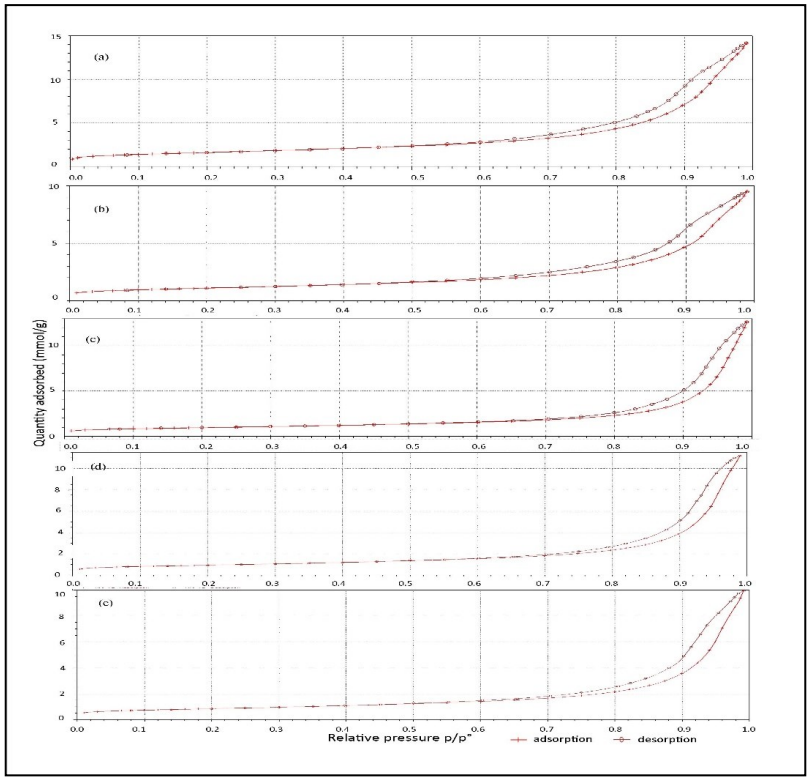



Figure 3. The nitrogen adsorption and desorption isotherm of HAP adsorbents. a) HAP 3, b) HAP 5, c) HAP 24, d) HAP 48 and e) HAP 72

The HAP formation was governed by the nucleation and growth process. By increasing the reaction time, more spaces are available for HAP particles growth, thus producing more surface for the attachment of nucleate particles [30]. Figure 4 showed the typical SEM images of the prepared HAP adsorbents. All the synthesized HAPs showed irregular shapes and were accumulated in bulky sizes due to the uneven surface of HAP and the formation of plat-like shape that overlapped each other. The morphology of HAP varies when using high temperature, carbonate sources, and the solvent extraction [31].

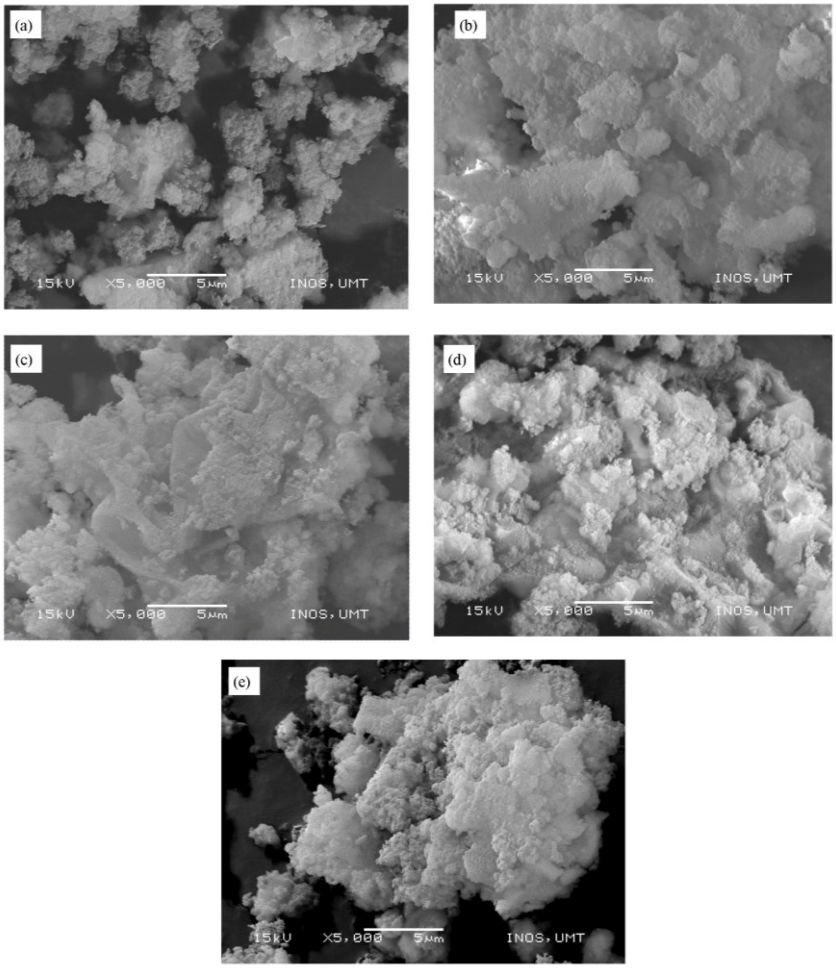



Figure 4. The scanning electron microscope (SEM) micrograph image of HAPs adsorbent at 5,000x magnifications. a) HAP 3,b) HAP 5, c) HAP 24, d) HAP 48 and e) HAP 72

**Selection of optimum HAP adsorbent**

The removal of lead ($Pb^{2+}$) by synthesized HAP adsorbents showed similar trends due to the similarities in their main chemical compositions (Figure 5). The selection of optimum adsorbent was based on the slope of the graph during the first 50 minutes of contact time, with HAP48 showing the steepest of slope followed by HAP72 > HAP3 > HAP24 > HAP5.

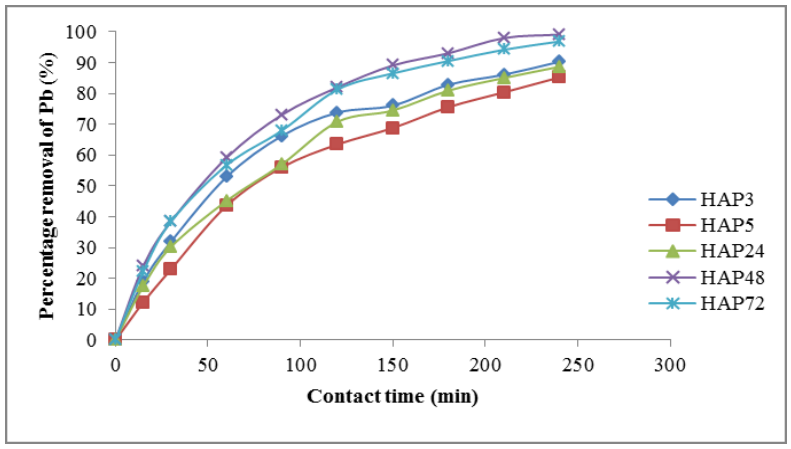



Figure 5. Removal of lead ($Pb^{2+}$) (%) by prepared HAP adsorbents. (adsorbent dose: 0.4 g; initial concentration and volume of $Pb^{2+}$: 25 mg/L, 200 mL)

The capability of HAP48 to absorb metal ($Pb^{2+}$) was the highest (12.28 mg/g), followed by HAP72 (11.62 mg/g), HAP3 (11.6 mg/g), HAP24 (10.28 mg/g) and HAP5 (10.4 mg/g). This result is similar to the XRD diffractogram (Figure 1), demonstrating the purity of HAP48 compared to the other adsorbents. It is clear that the time of reaction affected the chemical properties of HAP adsorbent by influencing the availability of active sites to adsorb the metal ions. Consequently, HAP48 adsorbent was determined as the optimum adsorbent for subsequent studies. HAP derived from seashells are used in wastewater treatment as fluoride removal [32], sulfur removal [33], and dye removal [34]. The HAP produced from similar source is also applied in other fields such as fluorescence-quenching platform for cancer cell detection [35], bone tissue engineering [36], and body implant application [37].

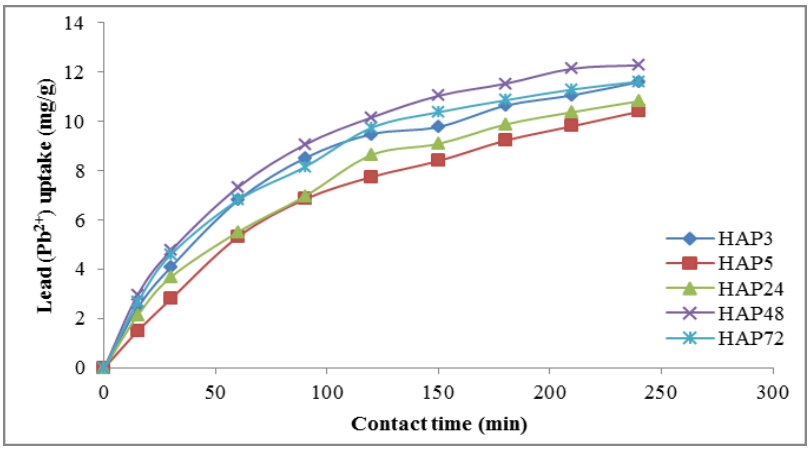



Figure 6. Effect of contact time on metal uptake ($Pb^{2+}$) by HAP adsorbents. (adsorbent dose: 0.4 g; initial concentration and volume of $Pb^{2+}$: 25 mg/L, 200 mL)

**Effect of initial metal ions concentration and contact time**

Metal adsorption by the absorbent is influenced by the initial concentration of $Pb^{2+}$ ion. Form the Figure 7, the adsorption of lead has occurred rapidly in the first 30 min and can be seen from the steep of slope at 0 to 30 minutes of contact time and subsequently, the system achieved equilibrium point after 90 minutes. This situation was due to the reduced availability of binding sites and the external sites were occupied [38].

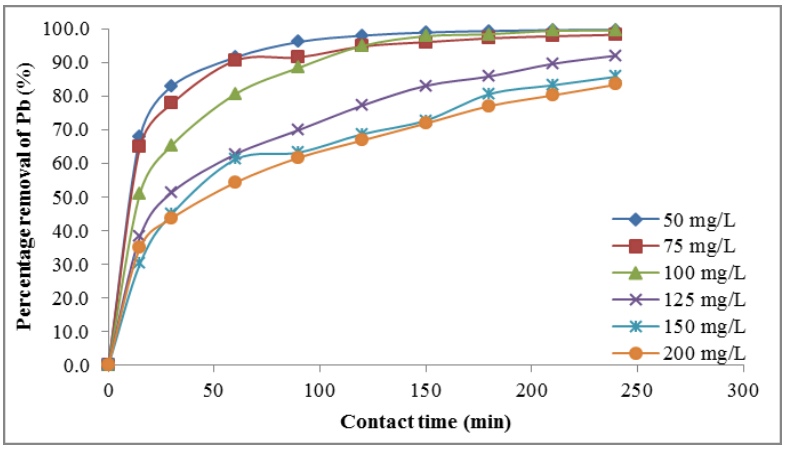



Figure 7. Effect of initial concentration of Pb on the percentage removal of ($Pb^{2+}$) (mg/g) by HAP48 adsorbent. (adsorbent dose: 0.4 g; volume of $Pb^{2+}$: 200 mL)

From Figure 8, the lowest initial concentration of $Pb^{2+}$ (50 mg/mL) achieved equilibrium in the shortest time compared to other higher initial concentrations in terms of the quantity of metal adsorbed ($Pb^{2+}$). During low initial concentration, metal ions are adsorbed by HAP on specific active sites. As the initial concentration of metal increases, so was the adsorption rate. The lowest initial concentration of $Pb^{2+}$ achieved equilibrium fastest is due to the static weight of adsorbent [39].

The maximum uptake of $Pb^{2+}$ by HAP48 achieved equilibrium at 60 minutes of contact time for initial concentration of 50 mg/L (20.87 mg/g) and 75 mg/L (31.18 mg/g). However, higher initial concentration required longer contact time to achieve equilibrium, 120 minutes for concentration 100 mg/L, 150 minutes for 125 mg/L, 180 minutes for 150 and 200 mg/L with the increased of adsorption capacity, 43.94 mg/g, 49.09 mg/g, 58.31 mg/g, and 73.77 mg/g, respectively. This similar pattern was also reported from previous study on methylene blue adsorption using activated carbon discovered from pineapple leaf [22].

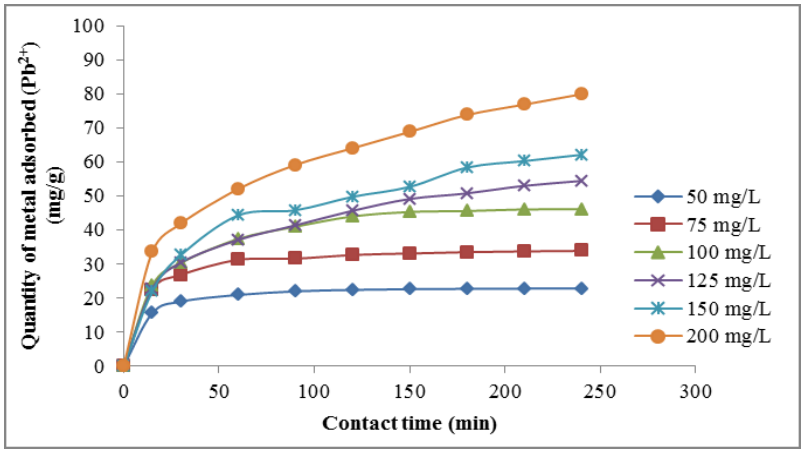



Figure 8. Effect of initial concentration of Pb on the quantity of metal adsorbed ($Pb^{2+}$) (mg/g) by HAP48 adsorbent. (adsorbent dose: 0.4 g; volume of $Pb^{2+}$: 200 mL)

**Kinetic adsorption study**

The adsorption experiment data of lead was fitted to pseudo-first-order and second-order as shown in Figure 9. The value of $R^2$ of linear equation approaches value 1 designates that the respective equation corresponds well to the experimental data [22]. Therefore, the kinetic adsorption was fitted well to the pseudo-second-order model, with $R^2$ value of 0.9994 for the bio adsorption system. This model, based on the chemisorption mechanism for metal ions interaction with adsorbent surface, was suggested as the rate-limiting step in HAP48 adsorbent [40]. This mechanism also described the physicochemical interactions between the two phases [41].

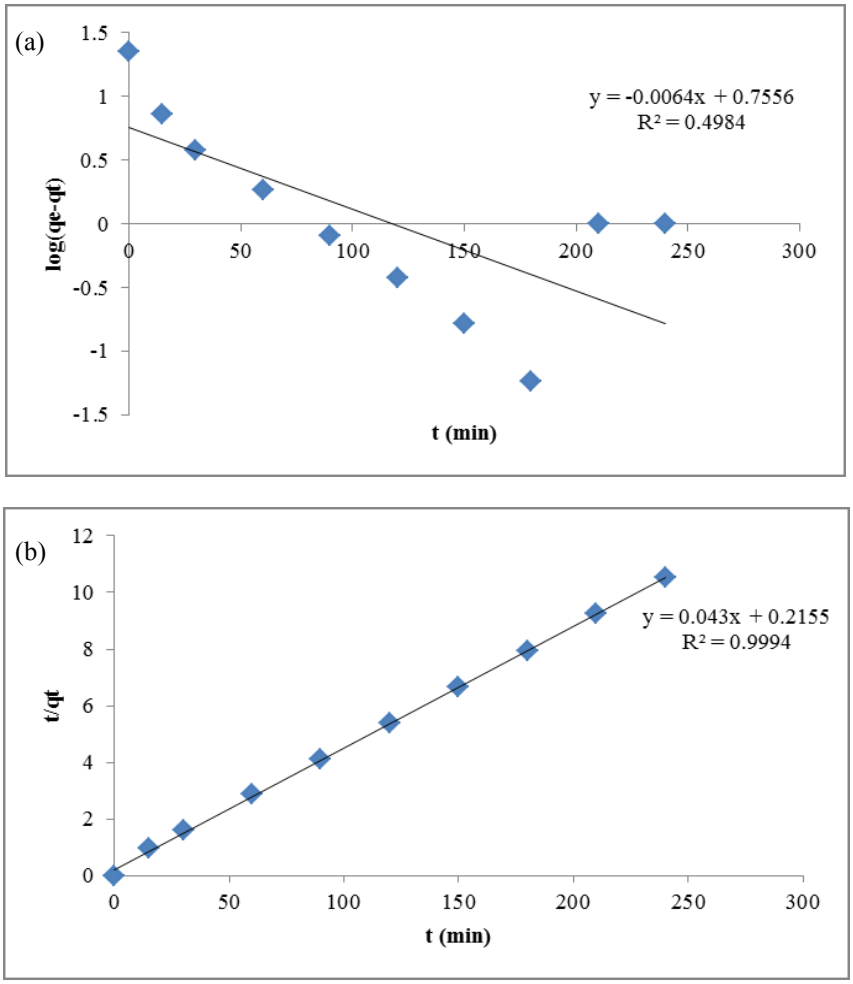



Figure 9. Pseudo-first-order (a) and pseudo-second-order (b) for kinetics model of $^{Pb2+}$ adsorption onto HAP48

Initial concentration was inversely proportional to the adsorption rate, $k_2$ and displayed in Table 2. Even increasing of initial concentration was decreasing the rate constant, $k_2$, the adsorption capacity, $q_e$ was showed increasing trend. Similar pattern to the work on lead removal using modified coconut shells [42].

**Equilibrium adsorption study**

The linear plots for both isotherms are shown in Figure 10. It clearly presented that the adsorption data were well fitted with Langmuir isotherm, with $R^2$= 0.973 compared to Freundlich isotherm ($R^2$ = 0.865). The Langmuir model describes the formation of a monolayer adsorbate on the outer surface of the adsorbent, and no more adsorption

takes place once a saturation value is reached [43]. The $R_L$ value of 0.013 (Table 3) indicates that the adsorption of $Pb^{2+}$ onto HAP48 was favourable ($0 < R_L < 1$) and had strong interaction with each other.

Table 2. The pseudo-second-order kinetic parameters for lead removal by HAP48 adsorbent

| $C_{0\ (mg/L)}$ | $q_{e\ (mg/g)}$ | $k_2$ (g/mg min) | h (mg/ g min) | $R^2$ |
|---|---|---|---|---|
| 50 | 23.26 | 0.0086 | 4.640 | 0.999 |
| 75 | 34.48 | 0.0047 | 5.593 | 0.999 |
| 100 | 48.54 | 0.0016 | 3.837 | 0.996 |
| 125 | 57.47 | 0.0008 | 2.493 | 0.984 |
| 150 | 65.79 | 0.0006 | 2.488 | 0.978 |
| 200 | 84.03 | 0.0005 | 3.285 | 0.978 |

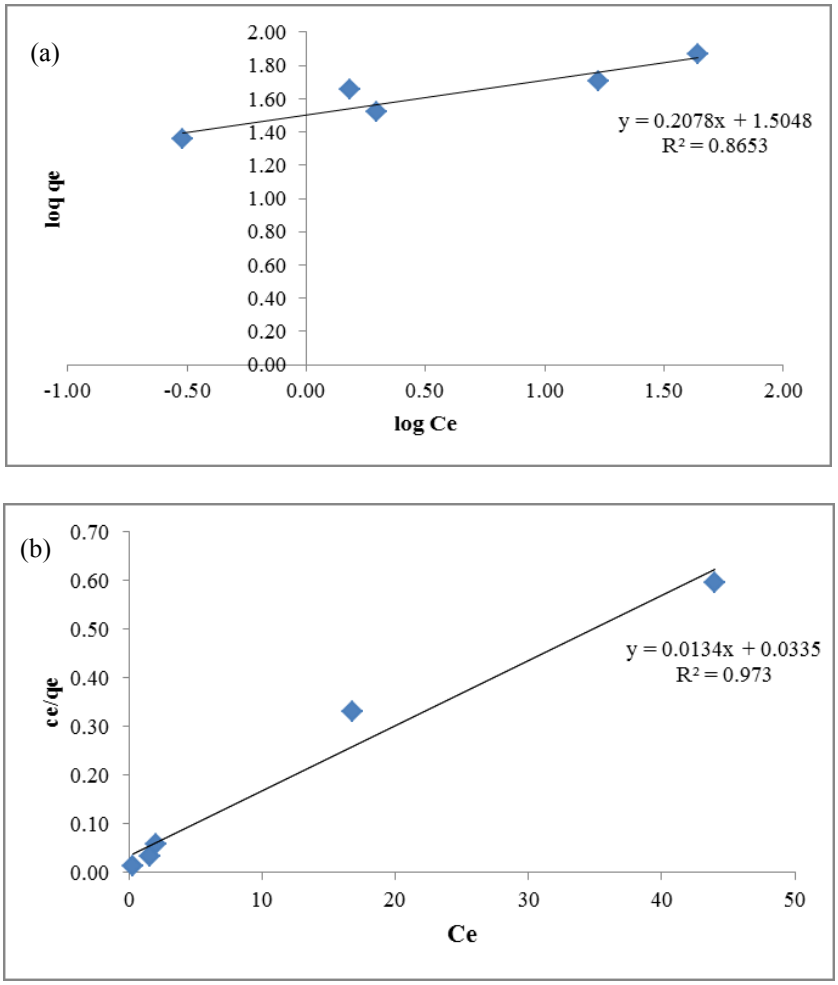



Figure 10. Freundlich (a) and Langmuir (b) adsorption isotherm models of $Pb^{2+}$ adsorption onto HAP 48

Table 3. Freundlich and Langmuir isotherms constants of lead ($Pb^{2+}$) biosorption onto HAP 48 adsorbent

| **Freundlich Constants** | | | **Langmuir Constants** | | | |
|---|---|---|---|---|---|---|
| **$K_F$** | **n** | **$R^2$** | **$q_m$ (mg/g)** | **b (L/mg)** | **$R^2$** | **$R_L$** |
| 31.97 | 4.812 | 0.8653 | 74.63 | 0.4 | 0.973 | 0.013 |

The maximum sorption capacity, $q_m$ of HAP48 was 74.63 mg/g. Using dead calcareous skeletons (CS) as calcium carbonate source, maximum adsorption capacities of 26.5 and 38.5 mg/g for the Cd(II) and Pb(II) column, respectively were achievable [44]. However, *Anadara inaequivalvis* seashells powder had higher biosorption capacity of Cu(II) and Pb(II) (330.2 and 621.1 mg/g, respectively) [38]. The obtained result was postulate to be affected by the orthorhombic crystal structure of aragonite and the condition of the experiment conducted.

The interaction mechanism between $Pb^{2+}$ ions and HAP48 adsorbent was determined via dissolution and precipitation process. The chemisorption interaction had occurred via the formation of new chemical bonding between adsorbate and adsorbent surface and was explained in the chemical reactions below [45]:

$$Ca_{10}(PO_4)_6(OH)_2 + 14H_2^+ \longrightarrow 10Ca^{2+} + 6H_2PO_4^- + 2H_2O \text{ (Dissolution process)} \quad (12)$$

$$10Pb^{2+} + 6H_2PO_4^- + 2H_2O \longrightarrow 14H_2^+ + Pb_{10}(PO_4)_6(OH)_2 \text{ (Precipitation process)} \quad (13)$$

## Conclusion

In this study, a worthwhile bio adsorbent from marine bio-waste, HAP48 bio-adsorbent was successfully synthesized with optimal characteristics for the application of the removal of lead from contaminated water. Though the resulting HAP resembles that found naturally in terms of its composition, this continuous research efforts have produced new economic synthesis approaches and can be applied in future research. For subsequent study, the produced HAP will be combined with other potential adsorbents, as well as its absorbent ability in other multi-metal ions, adsorbent reusability and its production on pilot scale.

## Acknowledgement

The authors would like to Thank and gratitude to Universiti Malaysia Terengganu for providing the facilities to conduct this research.

## References

1. Sutherland, A. M. C. A., Milner, E. F., Kerby, R. C. and Teindl, H. (1990). Lead. Ullmann's Encyclopedia of Industrial Chemistry. VCH Verlagsgesellschaft: pp. 193 – 257.
2. Das, S., Raj, R., Mangwani, N., Dash, H. R. and Chakraborty, J. (2014). Heavy metals and hydrocarbons: Adverse effects and mechanism of toxicity. Microbial Biodegradation and Bioremediation. Elsevier Inc: pp 24 – 54.
3. Engineering Services Division (2017). Drinking water quality standard. Acess online http://kmam.moh.gov.my/public-user/drinking-water-quality-standard.html. Accessed on 12 January 2017.
4. Bailey, S. E., Olin, T. J., Bricka, R. M. and Adrian, D. D. (1999). A review of potentially low-cost sorbents for heavy metals. *Water Research*, 33(11): 2469 – 2479.
5. Mudhoo, A., Garg, V. K. and Wang, S. (2011). Removal of heavy metals by biosorption. *Environmental Chemistry Letters*, 10(2): 109 – 117.
6. Shepherd, J. H., Friederichs, R. J. and Best, S. M. (2015). Synthetic hydroxyapatite for tissue engineering applications. Hydroxyapatite (HAP) for biomedical applications. Elsevier Ltd: pp. 235 – 267.
7. Camaioni, A., Cacciotti, I., Campagnolo, L. and Bianco, A. (2015). Silicon-substituted hydroxyapatite for biomedical applications. Hydroxyapatite (HAP) for biomedical applications. Elsevier Ltd: pp. 343 – 373.

8. Milovac, D., Gallego, G., Ivankovic, M. and Ivankovic, H. (2014). PCL-coated hydroxyapatite scaffold derived from cuttle fish bone: Morphology, mechanical properties and bioactivity. *Materials Science & Engineering C,* 34: 437 – 445.
9. Zhang, X. and Vecchio, K. S. (2006). Creation of dense hydroxyapatite (synthetic bone) by hydrothermal conversion of seashells. *Materials Science & Engineering C,* 26(8): 1445 – 1450.
10. Corami, A., Mignardi, S. and Ferrini, V. (2007). Copper and zinc decontamination from single- and binary-metal solutions using hydroxyapatite. *Journal of Hazourdous Materials,* 146(1–2): 164 – 170.
11. Minh, D. P., Tran, N. D., Nzihou, A. and Sharrock, P. (2013). Hydroxyapatite gel for the improved removal of $Pb^{2+}$ ions from aqueous solution. *Chemical Engineering Journal*, 232: 128 – 138.
12. Prabhu, S. M., and Meenakshi, S. (2014). Synthesis of surface coated hydroxyapatite powders for fluoride removal from aqueous solution. *Powder Technology*, 268: 306 – 315.
13. Mobasherpour, I., Salahi, E. and Pazouki, M. (2012). Comparative of the removal of $Pb^{2+}$, $Cd^{2+}$ and $Ni^{2+}$ by nano crystallite hydroxyapatite from aqueous solutions: Adsorption isotherm study. *Arabian Journal Chemistry*, 5(4): 439 – 446.
14. Bramhe, S., Kim, T. N., Balakrishnan, A. and Chu, M. C. (2014). Conversion from biowaste *Venerupis* clam shells to hydroxyapatite nanowires. *Materials Letters*, 135: 195 – 198.
15. Wu, S.-C., Tsou, H.-K., Hsu, H.-C., Hsu, S.-K., Liou, S.-P. and Ho, W.-F. (2013). A hydrothermal synthesis of eggshell and fruit waste extract to produce nanosized hydroxyapatite. *Ceramics International,* 39(7): 8183 – 8188.
16. Sanosh, K. P., Chu, M.-C., Balakrishnan, A., Kim, T. N. and Cho, S.-J. (2009). Utilization of biowaste eggshells to synthesize nanocrystalline hydroxyapatite powders. *Materials Letters,* 63(24–25): 2100 –2102.
17. Aminian, A., Solati-Hashjin, M., Samadikuchaksaraei, A., Bakhshi, F., Gorjipour, F., Farzadi, A., Moztarzadeh, F. and Schmücker, M. (2011). Synthesis of silicon-substituted hydroxyapatite by a hydrothermal method with two different phosphorous sources. *Ceramics International,* 37(4): 1219 –1229.
18. Zhao, J., Zhu, Y., Cheng, G., Ruan, Y., Sun, T., Chen, F., Wu, J., Zhao, X. –Y., and Ding, G. (2014). Microwave-assisted hydrothermal rapid synthesis of amorphous calcium phosphate nanoparticles and hydroxyapatite microspheres using cytidine 5'-triphosphate disodium salt as a phosphate source. *Materials Letters,* 124: 208 – 211.
19. Zhao, J., Dong, X., Bian, M., Zhao, J., Zhang, Y., Sun, Y., Chen, J. and Wang, X. (2014). Solution combustion method for synthesis of nanostructured hydroxyapatite, fluorapatite and chlorapatite. *Applied Surface Science,* 314: 1026 – 1033.
20. Nayak, A. K. (2010). Hydroxyapatite synthesis methodologies: An overview. *International Journal of ChemTech Research*, 2(2): 903 – 907.
21. Ofomaja, A. E. (2011). Kinetics and pseudo-isotherm studies of 4-nitrophenol adsorption onto mansonia wood sawdust. *Industrial Crops and Products*, 33(2): 418 – 428.
22. Mahamad, M. N., Zaini, M. A. A. and Zakaria, Z. A. (2015). Preparation and characterization of activated carbon from pineapple waste biomass for dye removal. *International Biodeterioration & Biodegradation*, 102: 274 – 280.
23. Rujitanapanich, S., Kumpapan, P. and Wanjanoi, P. (2014). synthesis of hydroxyapatite from oyster shell via precipitation. *Energy Procedia*, 56: 112 – 117.
24. Wu, S.-C., Hsu, H.-C., Wu, Y.-N. and Ho, W.-F. (2011). Hydroxyapatite synthesized from oyster shell powders by ball milling and heat treatment. *Materials Characterization,* 62(12): 1180 – 1187.
25. Singh, A. (2012). Hydroxyapatite, a biomaterial: Its chemical synthesis, characterization and study of biocompatibility prepared from shell of garden snail, *Helix aspersa*. *Bulletin of Materials Science,* 35(6): 1031 – 1038.
26. Ge, H., Zhao, B., Lai, Y., Hu, X., Zhang, D., and Hu, K. (2010). From crabshell to chitosan-hydroxyapatite composite material via a biomorphic mineralization synthesis method. *Journal of Materials Science: Materials in Medicine.* 21(6): 1781 – 1787.
27. Putro, J. N., Handoyo, N., Kristiani, V., Soenjaya, S. A., Ki, O. L., Soetaredjo, F. E., Ju, Y. –H. and Ismadji, S. (2014). *Pomacea sp* shell to hydroxyapatite using the ultrasound–microwave method (U–M). *Ceramics International,* 40(7): 11453 – 11456.
28. Spivak, D. A. (2005). Optimization, evaluation, and characterization of molecularly imprinted polymers. *Advanced Drug Delivery Reviews*, 57(12): 1779 – 1794.

29. Ariffin, M. M., Yatim, N. I. and Tahir, N. M. (2015). Selective surface characteristics and extraction performance of a nitro-group explosive molecularly imprinted polymer. *Malaysian Journal of Analytical Sciences*, 19(3): 574 – 585.
30. Zhang, X. and Vecchio, K. S. (2007). Hydrothermal synthesis of hydroxyapatite rods. *Journal of Crystal Growth,* 308(1): 133 – 140.
31. Sofronia, A. M., Baies, R., Anghel, E. M., Marinescu, C. A. and Tanasescu, S. (2014). Thermal and structural characterization of synthetic and natural nanocrystalline hydroxyapatite. *Materials Science and Engineering C*, 43: 153 – 163.
32. Terasaka, S., Kamitakahara, M., Yokoi, T. and Matsubara, H. (2015). Ability of hydroxyapatite synthesized from waste oyster shells to remove fluoride ions. *Materials Transactions,* 56(9): 1509 – 1512.
33. Mahidin, M., Gani, A., Muslim, A., Husin, H., Hani, M. R., Syukur, M., Hamdan, Khairil, K. and Rizal, S. (2016). Sulfur removal in bio-briquette combustion using seashell waste adsorbent at low temperature. *Journal of Engineering and Technological Sciences,* 48(4): 465 – 481.
34. Suteu, D. and Rusu, L. (2012). Removal of methylene blue dye from aqueous solution using seashell wastes as biosorbent. *Environmental Engineering and Management Journal,* 11(11): 1977 – 1985.
35. Zhang, Y., Liu, W., Banks, C. E., Liu, F., Li, M., Xia, F. and Yang, X. (2014). A fluorescence-quenching platform based on biomineralized hydroxyapatite from natural seashell and applied to cancer cell detection. *Scientific Reports,* 4: 7556.
36. Zhang, X. and Vecchio, K. S. (2013). Conversion of natural marine skeletons as scaffolds for bone tissue engineering. *Frontiers of Materials Science,* 7(2): 103 – 117.
37. Narayanan, R., Dutta, S. and Seshadri, S. K. (2006). Hydroxy apatite coatings on Ti-6Al-4V from seashell. *Surface and Coatings Technology,* 200(16–17): 4720 – 4730.
38. Bozbaş, S. K., and Boz, Y. (2016). Low-cost biosorbent: *Anadara inaequivalvis* shells for removal of Pb(II) and Cu(II) from aqueous solution. *Process Safety and Environmental Protection*, 103: 144 – 152.
39. El-Sayed, G. O., Dessouki, H. A. and Ibrahiem, S. S. (2011). Removal of Zn (II), Cd (II) and Mn (II) from aqueous solutions by adsorption on maize stalks. *Malaysian Journal of Analytical Sciences,* 15(1): 8 – 21.
40. Lee, S. H., and Shrestha, S. (2014). Application of micellar enhanced ultrafiltration (MEUF) process for zinc (II) removal in synthetic wastewater: Kinetics and two-parameter isotherm models. *International Biodeterioration and Biodegradation,* 95: 241 – 250.
41. Robati, D. (2013). Pseudo-second-order kinetic equations for modeling adsorption systems for removal of lead ions using multi-walled carbon nanotube. *Journal of Nanostructure in Chemistry,* 3(1): 55 – 61.
42. Largitte, L. and Lodewyckx, P. (2015). Modeling the influence of the operating conditions upon the sorption rate and the yield in the adsorption of lead (II). *Microporous and Mesoporous Materials*. 202: 147 – 154.
43. Igberase, E., Osifo, P. and Ofomaja, A. (2014). The adsorption of copper (II) ions by polyaniline graft chitosan beads from aqueous solution: Equilibrium, kinetic and desorption studies. *Journal of Environmental Chemical Engineering,* 2(1): 362 – 369.
44. Lim, A. P., and Aris, A. Z. (2014). Continuous fixed-bed column study and adsorption modeling: Removal of cadmium (II) and lead (II) ions in aqueous solution by dead calcareous skeletons. *Biochemical Engineering Journal,* 87: 50 – 61 .
45. Mousa, S. M., Ammar, N. S. and Ibrahim, H. A. (2016). Removal of lead ions using hydroxyapatite nano-material prepared from phosphogypsum waste. *Journal of Saudi Chemical Society*, 20(3): 357 –365.

*Malaysian Journal of Analytical Sciences, Vol 21 No 3 (2017): 585 - 596*
*DOI: https://doi.org/10.17576/mjas-2017-2103-08*

MALAYSIAN JOURNAL OF ANALYTICAL SCIENCES
*Published by The Malaysian Analytical Sciences Society*
ISSN 1394 - 2506

# THE ANALYSIS OF THERMAL DECOMPOSITION PRODUCTS GENERATED FROM PORCINE TISSUES EXPOSED TO OUTDOOR BURNING CONDITIONS

## (Analisis Produk Penguraian Haba Yang Terhasil Daripada Tisu Khinzir Yang Terdedah Kepada Pembakaran Terbuka)

Gina Francesca Gabriel, Azima Ismail, Atiah Ayuni, Khairul Osman, Noor Hazfalinda Hamzah*

*Forensic Science Program, Faculty of Health Sciences,*
*Universiti Kebangsaan Malaysia, 43600 UKM Bangi, Selangor, Malaysia*

**Corresponding author: raviera@yahoo.com*

Received: 28 August 2016; Accepted: 16 March 2017

**Abstract**

Volatile products commonly known as pyrolytic products, are thermal decomposition products generated from the various fuels that are present at a fire scene due to heat exposure. When a fire scene involves human remains, the volatile species generated from the remains can be mistaken with others residues due to the presence of interfering products or ignitable liquid residues from the fire scene. Knowledge of the type of products generated from human remains in real life fire scenarios is crucial under these circumstances. Thus, this study was executed to test the robustness and validity of the pyrolytic data generated from porcine tissue under indoor laboratory burning conditions to those generated under outdoor burning conditions. Porcine bone samples were burnt under outdoor conditions until the ignition of fat occurred (temperatures exceeding 250 °C). The pyrolytic products generated were absorbed onto activated carbon tablets that were incubated in an oven for 16 hours at 80 °C and then desorbed with pentane and injected into the Gas Chromatography-Mass Spectrometry (GC-MS). The 60 pyrolytic profiles obtained were in the range of *n*-alkanes, *n*-alkenes, *n*-aldehydes, aromatics and nitriles, similar to those obtained from the indoor laboratory burning data but with the additional presence of *n*-aldehydes. Results from this study has indicated that the human pyrolytic data model generated indoors is a good representative of outdoor burning conditions and has also successfully clarified the inconsistencies in terms of the presence and absence of *n*-aldehydes from porcine and human pyrolytic data.

**Keywords:** thermal decomposition, porcine bone, pyrolytic products, activated carbon tablet, gas chromatography-mass spectrometry

**Abstrak**

Sebatian meruap mudah kebiasaannya dikenali sebagai produk pirolitik merupakan produk penguraian menggunakan haba yang terhasil daripada pelbagai jenis bahan api yang terdapat di sekitar kawasan kebakaran disebabkan oleh pendedahan kepada haba. Apabila terdapat sisa kebakaran yang melibatkan tulang manusia, spesis sebatian mudah meruap yang dikesan boleh disalah anggap dengan sisa lain disebabkan produk luar atau pun sisa cecair mudah terbakar. Oleh yang demikian, kajian ini bertujuan untuk mengenalpasti ketepatan dan kesahihan data pirolitik yang terhasil daripada tisu khinzir melalui pembakaran secara tertutup di dalam makmal dengan pembakaran secara terbuka. Tulang khinzir dibakar secara terbuka sehingga suhu nyalaan pembakaran lemak tulang berlaku (suhu melebihi 250 °C). Produk pirolisis yang dijana diserap menggunakan penjerapan karbon teraktif dalam bentuk tablet dengan menggunakan inkubator selama 16 jam pada suhu 80 °C dan seterusnya dinyaherap dengan pentana dan dianalisis menggunakan Kromatografi Gas-Spektrometri Jisim (GC-MS). Sejumlah 60 jenis produk pirolitik yang terhasil adalah sebatian kompaun *n*-alkana, *n*-alkena, *n*-aldehid, aromatik dan sebatian nitril. Produk yang terhasil adalah sama dengan data pembakaran di dalam makmal tetapi dengan penambahan kehadiran *n*-aldehid. Keputusan kajian ini menunjukkan bahawa model data pirolitik manusia yang terhasil daripada pembakaran dalam makmal boleh menjadi rujukan yang baik untuk

situasi kebakaran terbuka, dan berjaya menjelaskan percanggahan dari segi kehadiran dan ketiadaan *n*-aldehid daripada data pirolitik khinzir dan manusia.

**Kata kunci:** penguraian menggunakan haba, tulang khinzir, produk pirolitik, penjerapan karbon teraktif, kromatografi gas-spektrometri jisim

## Introduction

Fire is often used as a tool to conceal and destroy evidence of a crime, particularly in terms of obscuring the detection of human remains [1, 2] as it is commonly believed that fire or the effects of fire can completely destroy any forensic evidence present. When a human body is exposed to fire, a variety of physical, chemical and biological changes are exerted to the muscles, tissues and bony structure of the body [3 – 5]. These changes can indefinitely pose difficulty to a fire investigator, in locating and identifying human remains, if any, at a fire scene. Moreover, it is a daunting task to differentiate between small fragments of bone or teeth that are severely burnt and/or dismembered from charred fragments of fire debris [3, 4], even for trained anthropologies [3]. This is due to the similarity in overall appearance for both components, especially when mixed together with various fuel loads at the fire scene. The lack of knowledge and experience in locating these burnt remains, in addition to the limited research data available in identifying the pyrolytic profile of burnt human remains [6] as opposed to the vastly known and readily available pyrolytic database of ignitable liquid residue (ILR) could potentially lead investigators to a false positive or false negative conclusion [7].

Previous work in the field of pyrolytic data from human and porcine tissue were conducted by DeHaan et al. [8], in which they determined the presence of *n*-alkanes, *n*-aldehydes, *n*-alkenes and aromatic compounds from these samples burnt in a contained microfurnace at 300 °C, 500 °C and 700 °C, respectively. In the recent work conducted by Agu [9] and Gabriel [7] on human and porcine tissue exposed to an open flame but under controlled laboratory conditions, identified the consistent presence of volatile compounds in the range of *n*-alkanes, *n*-alkenes, aromatic alkenes, *n*-alkyl-benzenes and nitriles when exposed to temperatures between 500 °C to 800 °C. No *n*-aldehydes were present at these temperature ranges as opposed to DeHaan et al.'s [8] work. However, both Gabriel [7] and Agu [9] identified the presence of *n*-aldehydes at pre-ignition temperatures (below 300 °C). Variations in temperature, methodologies and particularly exposure conditions (indoor and outdoor, contained and open) could certainly cause these documented discrepancies in the pyrolytic profile obtained from human and porcine tissue.

This paper addresses these issues, by testing the robustness of the pyrolytic data and key indicators established from porcine tissue under controlled laboratory conditions to those generated from outdoor conditions. The similarity and differences in terms of the chemical fingerprint of thermal decomposition products from porcine tissue; as a representation of human tissue [7, 8], exposed under both; indoor laboratory and outdoor conditions were analysed, compared and reported.

## Materials and Methods

This study is an extension of the work executed by Gabriel [7], who conducted indoor laboratory burning using porcine bone. This study adapted similar experimental procedures but varied the conditions to outdoor burning.

### Standard test mixture

A 1 mg/mL standard solution (Sigma Aldrich, UK) containing 12 high purity compounds; benzene, toluene, octane, ethyl-benzene, *p*-xylene, propyl-benzene, decane, butyl-benzene, dodecane, tridecane, tetradecane and pentadecane, were prepared and placed into six individual gas chromatography (GC) vials (Agilent, UK). The six vials were then placed into an auto-sampler of a Gas Chromatography-Mass Spectrometry (GC-MS) (Shimadzu, UK) and injected into the instrument. Information from the individual peak area and retention time of each compound provided data that was then used to test the robustness of the instrument and analysis by revealing the relative standard deviation (RSD) values.

### GC-MS condition

The temperature of the injector was maintained at 250 °C, set to splitless mode with a 20:1 split ratio and 32.7 mL/min split flow. A 128-0122 DB-1MS column (22 mm length × 0.2 mm inner diameter × 0.33 $\mu$m film

thickness) (Crawford Scientific, UK) was used in this experiment. Helium was used as a carrier gas, flowing at a constant rate of 1 mL/min. The oven temperature was set at 40 °C and held for five minutes, then ramped at 15 °C/min to reach the final temperature of 280 °C and held for two minutes. The temperature of the detector was maintained at 250 °C. Data collected from the GC-MS analysis were identified based on their *m/z* values that were matched against the standard test mixture and National Institute of Standards and Technology (NIST) (NIST/EPA/NIH Mass Spectral Library).

**Sample preparation**

Porcine femur bones in the range between five to six months of age were utilised in this work, purchased from the Kajang Wet Market, Selangor. The bones were labelled according to the date purchased and stored in a laboratory freezer at -21°C. Before cutting, the bones were defrosted at room temperature for 30 to 40 minutes. The epiphysis of each bone was detached using a bench vice and a hacksaw in order to reduce variations in the composition of the bone samples that could potentially alter the resultant pyrolytic data [7]. Scissors and tweezers were used to remove any residual soft tissues on the bone. The remaining diaphysis was then cut into 25 ± 1.5 g sizes as recommended in the indoor laboratory burning experiment, to be the optimum size for best pyrolytic data. Each 25 ± 1.5 g bone fragment was then placed into individual 125 mL aluminium tin can (WA Products, UK) respectively. The process above was repeated until six 25 ± 1.5 g bone samples were obtained.

**Thermal decomposition process**

The outdoor burning experiment was set up at the Forensic Science Simulation Site, UKM, Bangi, Selangor. A retort stand was placed on a flat ground and the tin can (with the lid removed) containing the bone sample was clamped onto it to hold it in place during the burning process. The sample was heated using a portable gas canister burner (Sigma Aldrich, UK) placed under the tin can at approximately 3 cm from the tip of the canister to the base of the tin. A k-thermocouple connected to a digital thermometer model 6802 II (Signstek Ltd, London) was used to monitor the temperature of the bone sample during pyrolysis. The sample was allowed to burn until the ignition of fat occurred and was allowed to burn for five minutes thereafter. Ten seconds before the five minute mark, the gas canister and k-thermocouple were removed swiftly and an empty lid was placed over the tin can in order to extinguish the flame. The covered tin can containing the burnt sample was then left to cool at room temperature for four minutes as recommended in the indoor laboratory burning experiment.

The empty lid was then replaced with another lid containing an activated carbon tablet, which was hooked onto a paper clip and held on the lid with the use of magnets. The tin was sealed shut and incubated in oven for 16 hours at 80 °C [10]. After the incubation process, the activated carbon tablet was removed and placed into a 1 mL GC vial (Agilent, UK) and desorbed with 1 mL of pentane. The GC vial containing the desorbed activated carbon in pentane was then introduced into the GC-MS. The entire process was repeated until six sets of results were obtained. The similarities and differences in terms of volatile compound detected in outdoor burning conditions were then compared to the results obtained from the indoor laboratory burning conditions.

## Results and Discussion

Porcine tissue was chosen as a representative of human tissue as Gabriel [7], Agu [9] and DeHaan et al. [8] identified clear similarities with minor differences in the pyrolysis products generated across both tissues. Porcine bone, in particular, possesses the closest resemblance to human bone as compared to other animals [11] in terms of its morphology, bone remodelling process and structure [12, 13], diameter and the area of femoral cross-sectional, structure of lamella bones and regeneration rate [11].

Across the six replicates, volatile compounds in the range of $C_7$ to $C_{17}$ *n*-alkanes and $C_4$ to $C_{17}$ *n*-alkenes as well as *n*-cycloalkanes, aromatics, *n*-alkyl-benzenes, $C_5$-$C_6$ *n*-aldehydes, nitriles, furans, disulfide alcohol and dienes were detected, as displayed in Table 1. Table 1 also shows the volatile compounds that are consistently present across all six replicates of burnt porcine bone samples, namely; $C_8$ to $C_{15}$ *n*-alkanes and $C_4$ to $C_{16}$ *n*-alkenes together with *n*-cycloalkanes, aromatics, *n*-alkyl-benzenes, $C_5$ *n*-aldehyde and a nitrile. Six individual Total Ion Chromatograms (TIC) for each set are illustrated in Figure 1 till Figure 6, respectively.

Table 1. Volatile compounds generated from six outdoor burning of porcine bone samples. A tick represents that the compound is present in the sample

| No | Retention Time (min) | Compound | Set | | | | | |
|---|---|---|---|---|---|---|---|---|
| | | | 1 | 2 | 3 | 4 | 5 | 6 |
| 1. | 1.12 | 1-butene | ✔ | ✔ | ✔ | ✔ | ✔ | ✔ |
| 2. | 1.81 | methyl-cyclopentane | ✔ | ✔ | ✔ | ✔ | ✔ | ✔ |
| 3. | 1.88 | butanenitrile | | ✔ | ✔ | ✔ | ✔ | ✔ |
| 4. | 1.99 | benzene | ✔ | ✔ | ✔ | ✔ | ✔ | ✔ |
| 5. | 2.08 | cyclohexane | | ✔ | ✔ | ✔ | | ✔ |
| 6. | 2.23 | pentanal | ✔ | ✔ | ✔ | ✔ | ✔ | ✔ |
| 7. | 2.41 | 1-heptene | ✔ | ✔ | ✔ | ✔ | ✔ | ✔ |
| 8. | 2.49 | 3-methyl-butanitrile | ✔ | ✔ | ✔ | ✔ | ✔ | ✔ |
| 9. | 2.56 | heptane | ✔ | ✔ | ✔ | ✔ | ✔ | ✔ |
| 10. | 2.63 | 2-heptene | ✔ | ✔ | ✔ | ✔ | ✔ | ✔ |
| 11. | 2.70 | 2-ethyl-furan | | ✔ | ✔ | ✔ | | ✔ |
| 12. | 2.75 | 3-heptene | | ✔ | ✔ | ✔ | ✔ | ✔ |
| 13. | 2.85 | methyl-cyclohexane | | ✔ | ✔ | ✔ | | ✔ |
| 14. | 2.93 | dimethyl-disulfide | ✔ | | ✔ | ✔ | ✔ | ✔ |
| 15. | 3.05 | ethyl-cyclopentane | | ✔ | ✔ | ✔ | | ✔ |
| 16. | 3.49 | toluene | ✔ | ✔ | ✔ | ✔ | ✔ | ✔ |
| 17. | 3.75 | cycloheptene | | ✔ | ✔ | ✔ | ✔ | ✔ |
| 18. | 4.13 | hexanal | ✔ | | ✔ | ✔ | | ✔ |
| 19. | 4.47 | 1-octene | ✔ | ✔ | ✔ | ✔ | ✔ | ✔ |
| 20. | 4.78 | 3-methyl-1-heptene | | ✔ | ✔ | ✔ | | ✔ |
| 21. | 4.86 | octane | ✔ | ✔ | ✔ | ✔ | ✔ | ✔ |
| 22. | 5.00 | 2-octene | ✔ | ✔ | ✔ | ✔ | ✔ | ✔ |
| 23. | 5.27 | 4-octene | | ✔ | ✔ | ✔ | ✔ | ✔ |
| 24. | 5.72 | propyl-cyclohexane | | ✔ | ✔ | ✔ | | ✔ |
| 25. | 6.10 | 1,8-nonadiene | | ✔ | ✔ | ✔ | | ✔ |
| 26. | 6.19 | ethyl-benzene | ✔ | ✔ | ✔ | ✔ | ✔ | ✔ |
| 27. | 6.42 | *o*-xylene | | ✔ | ✔ | ✔ | | ✔ |
| 28. | 6.60 | 2-butyl-furan | | ✔ | ✔ | ✔ | | ✔ |
| 29. | 6.82 | benzo-cycobutene | | ✔ | ✔ | ✔ | | ✔ |
| 30. | 6.92 | *p*-xylene | | ✔ | ✔ | ✔ | | ✔ |
| 31. | 7.23 | 1-nonene | ✔ | ✔ | ✔ | ✔ | ✔ | ✔ |
| 32. | 7.47 | nonane | ✔ | ✔ | ✔ | ✔ | ✔ | ✔ |
| 33. | 7.53 | 3-nonene | | ✔ | ✔ | ✔ | ✔ | ✔ |
| 34. | 7.68 | 4-nonene | | ✔ | ✔ | ✔ | | ✔ |
| 35. | 7.92 | 3-cyclohexyl-1-cyclohexene | | ✔ | ✔ | ✔ | ✔ | ✔ |
| 36. | 8.01 | ethyl-cylopentane | | ✔ | ✔ | ✔ | | ✔ |
| 37. | 8.15 | propyl-benzene | ✔ | ✔ | ✔ | ✔ | ✔ | ✔ |
| 38. | 8.23 | 3,4-nonadiene | | ✔ | ✔ | ✔ | ✔ | ✔ |
| 39. | 8.57 | 1-ethyl-4-methyl-benzene | | ✔ | ✔ | ✔ | | ✔ |
| 40. | 8.83 | 2-pentyl-furan | ✔ | | ✔ | ✔ | ✔ | ✔ |
| 41. | 8.98 | 1-decene | ✔ | ✔ | ✔ | ✔ | ✔ | ✔ |
| 42. | 9.03 | nonanol | | | ✔ | ✔ | | ✔ |

Table 1 (cont'd). Volatile compounds generated from six outdoor burning of porcine bone samples. A tick represents that the compound is present in the sample

| No | Retention Time (min) | Compound | Set | | | | | |
|---|---|---|---|---|---|---|---|---|
| | | | 1 | 2 | 3 | 4 | 5 | 6 |
| 43. | 9.16 | decane | ✔ | ✔ | ✔ | ✔ | ✔ | ✔ |
| 44. | 9.72 | butyl-benzene | ✔ | ✔ | ✔ | ✔ | ✔ | ✔ |
| 45. | 10.33 | 1-undecene | ✔ | ✔ | ✔ | ✔ | ✔ | ✔ |
| 46. | 10.47 | undecane | ✔ | ✔ | ✔ | ✔ | ✔ | ✔ |
| 47. | 10.96 | pentyl-benzene | ✔ | ✔ | ✔ | ✔ | ✔ | ✔ |
| 48. | 11.45 | 1-dodecene | ✔ | ✔ | ✔ | ✔ | ✔ | ✔ |
| 49. | 11.58 | dodecane | ✔ | ✔ | ✔ | ✔ | ✔ | ✔ |
| 50. | 12.47 | 1-tridecene | ✔ | ✔ | ✔ | ✔ | ✔ | ✔ |
| 51. | 12.58 | tridecane | ✔ | ✔ | ✔ | ✔ | ✔ | ✔ |
| 52. | 13.39 | 1-tetradecene | ✔ | ✔ | ✔ | ✔ | ✔ | ✔ |
| 53. | 13.49 | tetradecane | ✔ | ✔ | ✔ | ✔ | ✔ | ✔ |
| 54. | 14.26 | 1-pentadecene | ✔ | | ✔ | | | ✔ |
| 55. | 14.35 | pentadecane | ✔ | ✔ | ✔ | ✔ | ✔ | ✔ |
| 56. | 14.78 | 1-hexadecene | ✔ | ✔ | ✔ | ✔ | ✔ | ✔ |
| 57. | 15.15 | hexadecane | ✔ | ✔ | ✔ | ✔ | | ✔ |
| 58. | 15.73 | 1-heptadecene | ✔ | | ✔ | ✔ | | ✔ |
| 59. | 15.92 | heptadecane | ✔ | ✔ | ✔ | ✔ | | ✔ |
| 60. | 17.13 | hexadecanitrile | | ✔ | ✔ | ✔ | | |

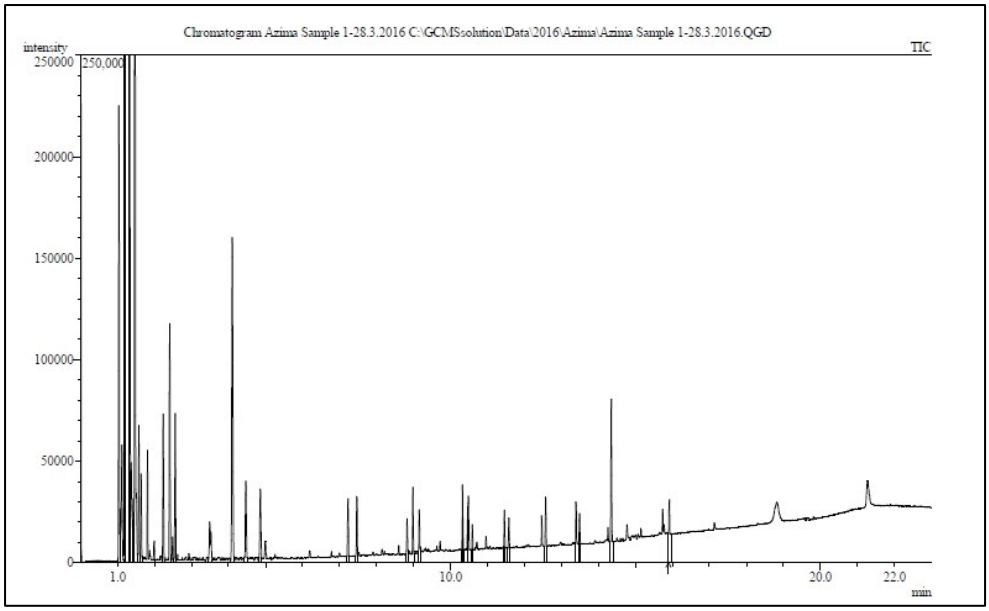



Figure 1. TIC of burned porcine bone (Set 1)

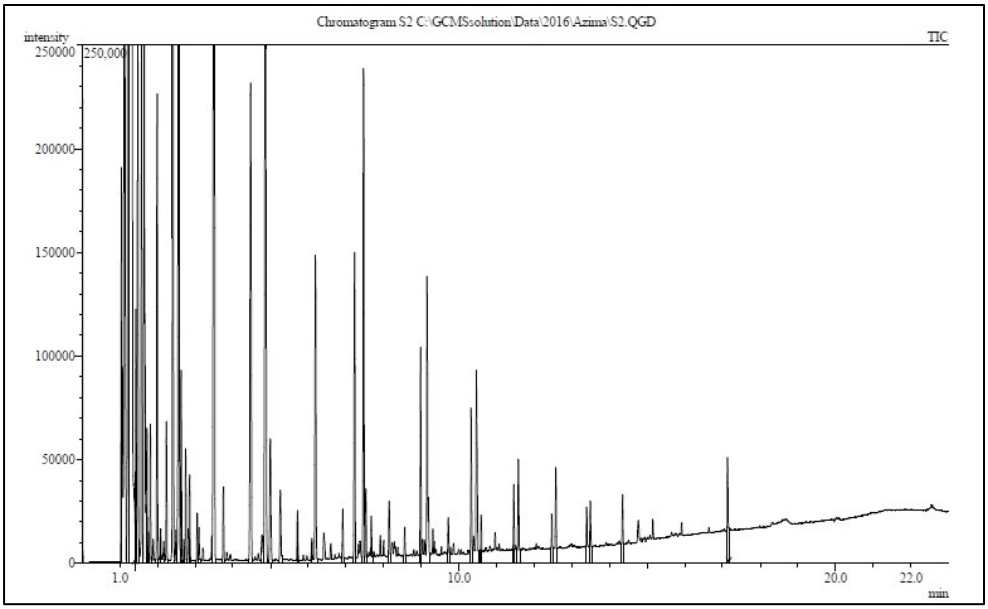



Figure 2. TIC of burned porcine bone (Set 2)

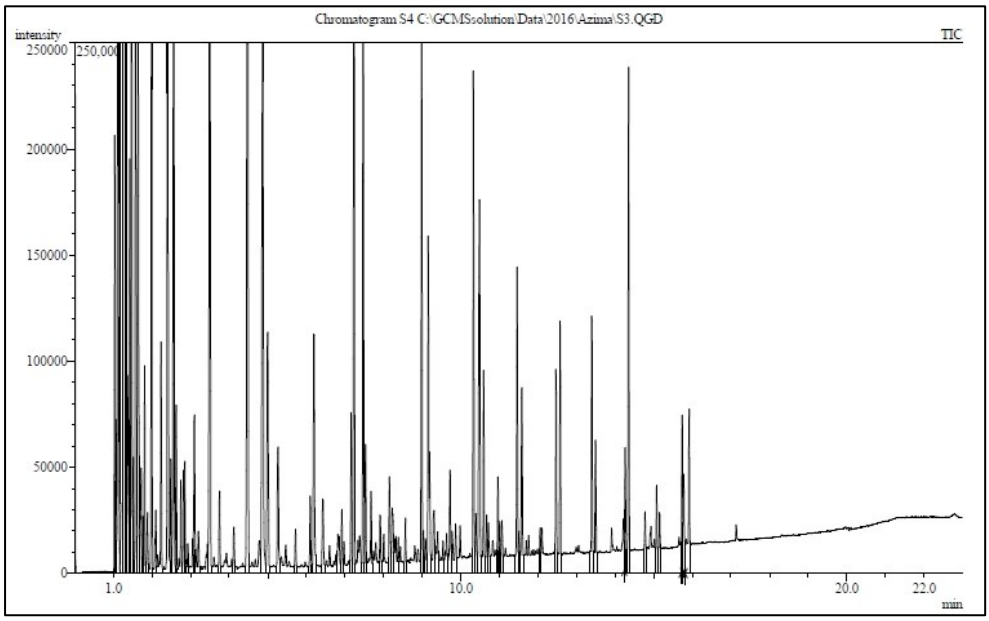



Figure 3. TIC of burned porcine bone (Set 3)

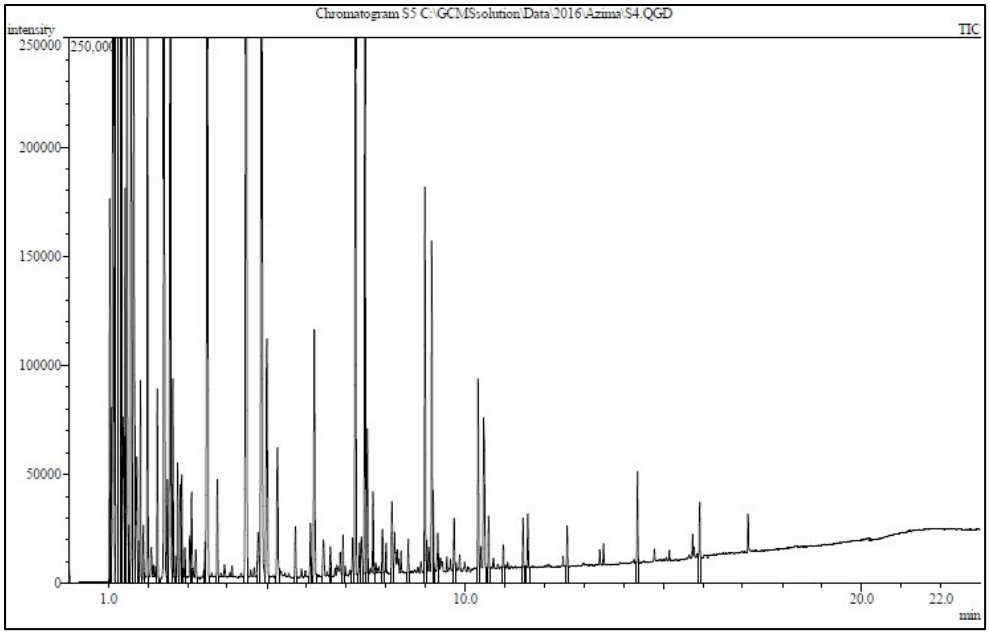



Figure 4. TIC of burned porcine bone (Set 4)

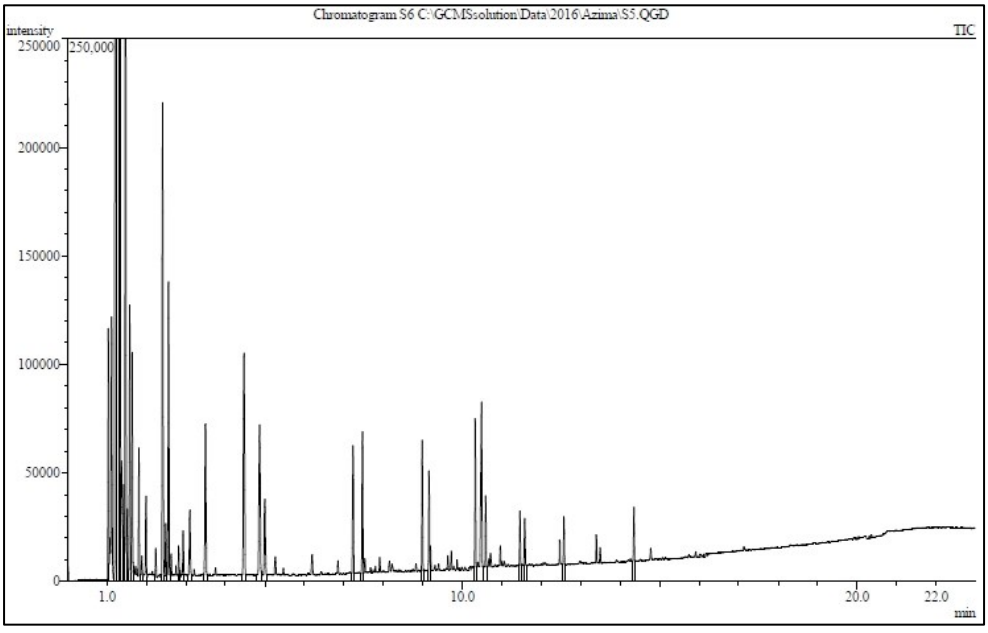



Figure 5. TIC of burned porcine bone (Set 5)

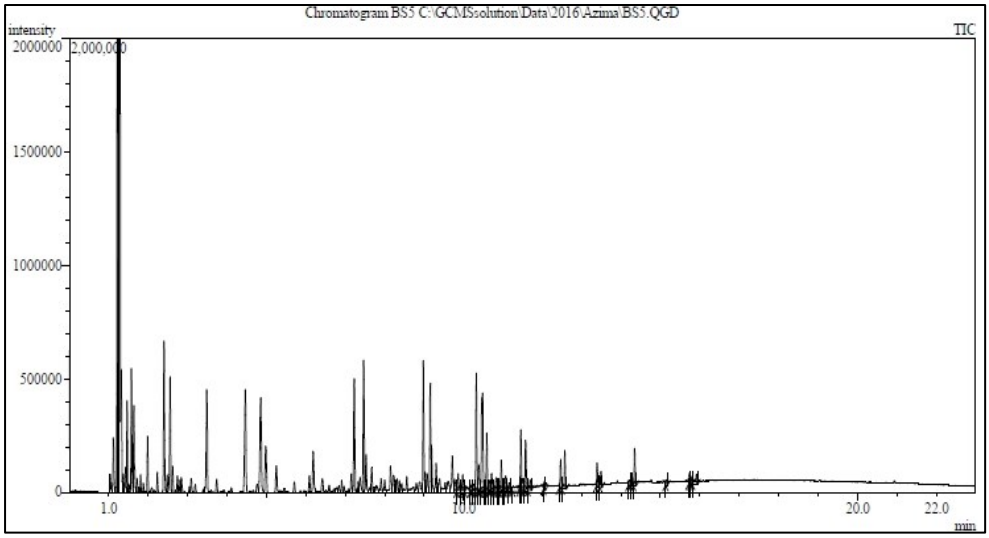



Figure 6. TIC of burned porcine bone (Set 6)

While majority of the compounds appeared in at least four of the total six repetitions, alcohol (nonanol), *n*-alkene (1-pentadecene) and nitrile (hexadecanitrile) only appeared in three or less repetitions. Meanwhile, hexadecanitrile was only present in three out of the six repetitions, although a small peak in every chromatogram with *m/z* values of 38 and 44 were consistently detected across six repetitions. It's absence could potentially be due to the decomposition and fragmentation of hexadecanitrile into smaller daughter fragments that rendered it undetectable in the GC-MS. Similar to the indoor burning data in Gabriel's research [7], this work (Table 1) also documented the presence of dimethyl-disulfide and dienes, although inconsistently across the repetitions. The present of furan in this work could be due to the variation in the environmental conditions exposed particularly the auto-ignition of fat that occurred multiple times in one complete cycle of burning as shown in Figure 7(a).

Higher temperature with broader exposure durations have been documented in the literature to cause the volatilization of low vapour pressure (higher molecular weight) *n*-alkanes and *n*-alkenes [14]. Although this experiment attained sufficient temperatures to volatilise these compounds, the inconsistencies in the presence of high molecular weight *n*-alkanes and *n*-alkenes in this work (Table 1) could be due to the short length of exposure and multiple ignitions experienced, as illustrated in Figure 7(a).

The differences in the time-temperature profiles of six replicates of porcine bone samples across indoor laboratory and outdoor burning conditions are illustrated in Figure 7. The initial temperature of all laboratory samples in Figure 7(b) increased rapidly and attained temperatures above 250 °C after seven minutes. This was not the case for outdoor samples in Figure 7(a) as most samples attained temperatures of 250 °C within one minute. In Figure 7(a), it is clearly seen that the ignition of fat occurred several times for sets 1, 2 and 4, but died down almost instantly before the final ignition that lasted for five minutes. It is noted that the ignition of fat in set 2 occurred once at 300 seconds but instantly died off and ignited again at 500 seconds. This was not the case for laboratory burning as the ignition of fats occurred once and could sustain itself for five minutes as shown in Figure 7(b). This occurrence could be due to the variation in the concentration of oxygen that is largely controlled by wind conditions in outdoor burning [15]. On the contrary, in indoor burning, the supply of oxygen was steady and controlled throughout the entire experiment, facilitating a steady and long-lasting flame [16]. It is also noted in Figure 7(b) that the maximum temperature attained in indoor burning was above 700 °C. As for the outdoor burning, the maximum temperature attained as illustrated in Figure 7(a) was only 580 °C. The differences in temperatures attained could also be due to the variations in oxygen availability that could alter the burning efficiency [15, 16].

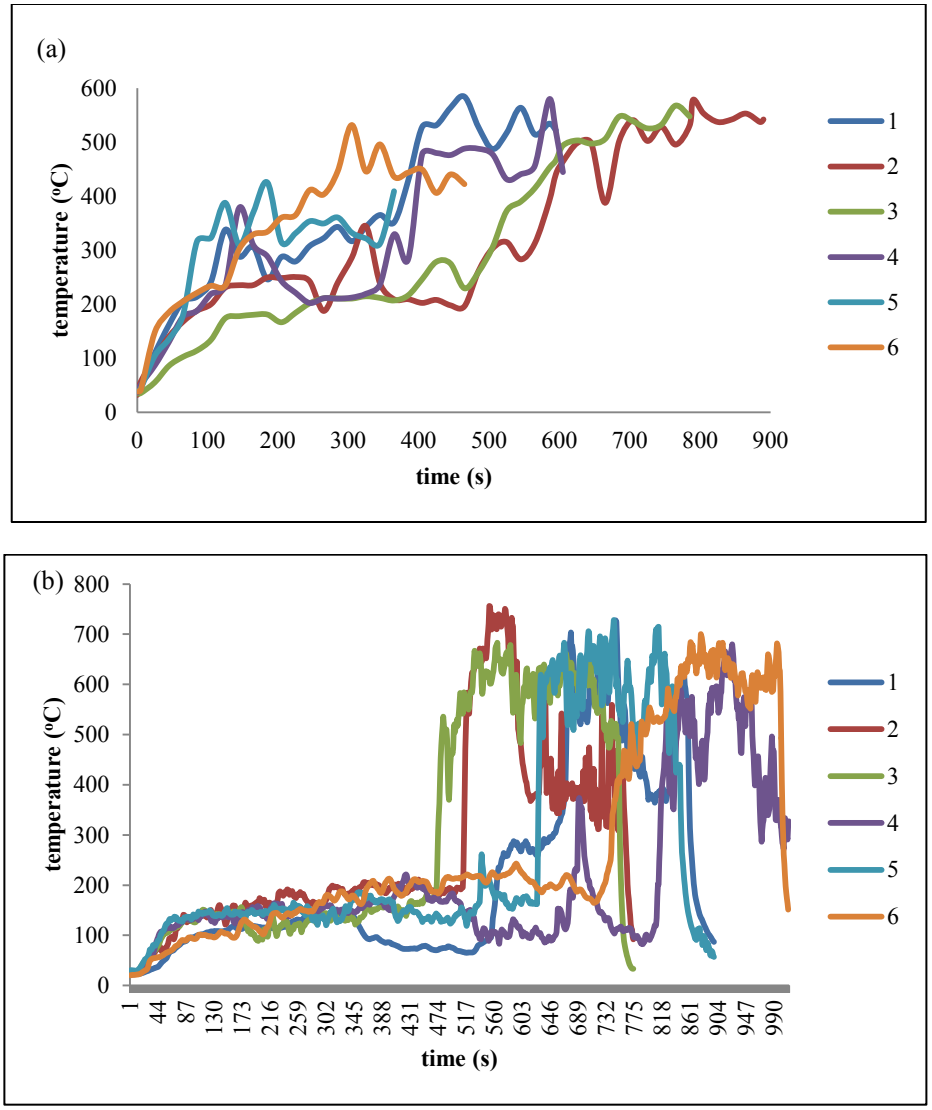



Figure 7. Overlay of six time-temperature profiles of **(a)** outdoor burning condition and (b) indoor laboratory burning condition [7]

Pyrolysis products generated from the outdoor burning of porcine bone samples that consistently appeared across six repeats were found to be similar with those generated from indoor laboratory burning condition as displayed in Table 2. These include $C_8$ to $C_{16}$ *n*-alkanes and *n*-alkenes (1-octene, octane, 1-nonene, nonane, 1-decene, decane, 1-undecene, undecane, 1-dodecene, dodecane, 1-tridecene, tridecane, 1-tetradecene, tetradecane, pentadecane, 1-hexadecene) and aromatic compounds (benzene, toluene, ethyl-benzene, propyl-benzene). Five volatile compounds that were detected consistently in this work but not consistent in indoor laboratory burning are methyl-cyclopentane, 3-methyl-butananitrile, 2-octene, butyl-benzene and pentyl-benzene. The presence of *n*-aldehydes (pentanal and hexanal) in this work was the major differences noted in terms of pyrolytic profiles when compared to indoor laboratory burning condition. No *n*-aldehydes were detected from indoor laboratory burning of porcine bone samples that were exposed to temperatures above auto-ignition (250 °C) [7] under longer burning durations above 900 seconds.

Similar findings were also noted by Purevsuran et al. [17] for their samples that were exposed to temperatures above 500 to 700 °C under extended burning durations of about 4 to 5 hours. However, *n*-aldehydes were detected in the pre-ignition samples (temperatures below 300 °C) in Gabriel's work [7] under indoor laboratory burning conditions. Contrary to Gabriel [7] and Purevsuran et al.'s [17] finding, DeHaan et al. [8] detected the present of straight chain *n*-aldehydes at high temperature (above 700 °C) but with shorter burning durations of ten seconds. The presence or absence of *n*-aldehydes as a by-product of pyrolysis from porcine bone samples is largely related to the temperature in which the samples were exposed; higher temperature induces the decomposition and oxidation of *n*-aldehydes into smaller compounds and renders it undetectable by the instrument [8, 9]. The presence of *n*-aldehyde in this work may be due to the lower temperature profiles experienced by the sample and the multiple ignitions as illustrated in Figure 7(a). Besides temperature, the exposure duration also plays an important role in the detection of *n*-aldehydes [7]. In the indoor laboratory burning conditions [7] and in Purevsuren et al.'s [17] work, burning occurred for extended periods of more than 900 seconds and 4 hours respectively as compared to DeHaan et al.'s work [8] (ten seconds) and the outdoor burning conditions in this work (800 seconds), where burnings were shorter, thus preserving the *n*-aldehydes from being decomposed or totally consumed during the burning process [7].

Table 2. Comparison of pyrolysis products that were detected consistently across six sets of repeats between indoor and outdoor burning conditions [7]

| No. | Compound (Outdoor Burning) | Compound (Indoor Laboratory Burning) |
|---|---|---|
| 1. | 1-butene | **benzene** |
| 2. | methyl-cyclopentane | **toluene** |
| 3. | **benzene** | **1-octene** |
| 4. | pentanal | **octane** |
| 5. | 3-methyl-butanitrile | **ethyl-benzene** |
| 6. | **toluene** | *p*-xylene |
| 7. | **1-octene** | **1-nonene** |
| 8. | **octane** | **nonane** |
| 9. | 2-octene | **propyl-benzene** |
| 10. | **ethyl-benzene** | **1-decene** |
| 11. | **1-nonene** | **decane** |
| 12. | **nonane** | **1-undecene** |
| 13. | **propyl-benzene** | **undecane** |
| 14. | **1-decene** | **1-dodecene** |
| 15. | **decane** | **dodecane** |
| 16. | butyl-benzene | **1-tridecene** |
| 17. | **1-undecene** | **tridecane** |
| 18. | **undecane** | **1-tetradecene** |
| 19. | pentyl-benzene | **tetradecane** |
| 20. | **1-dodecene** | 1-pentadecene |
| 21. | **dodecane** | **pentadecane** |
| 22. | 1-tridecene | **1-hexadecene** |
| 23. | **tridecane** | hexadecane |
| 24. | **1-tetradecene** | 1-heptadecene |
| 25. | **tetradecane** | heptadecane |
| 26. | **pentadecane** | hexadecanitrile |
| 27. | **1-hexadecene** | |

*bold text refer to the compound that appeared for both condition

## Conclusion

Indoor laboratory burning conditions generated consistent results in terms of the pyrolysis products generated and the time-temperature profiles in comparison to outdoor burning conditions. Pyrolytic data generated in this work were determined to be in the range of *n*-alkanes, *n*-alkenes, *n*-aldehydes, aromatics and nitrile compounds, similar to those obtained from indoor laboratory burning but with the additional presence of *n*-aldehydes. Results from this study has indicated the human pyrolytic data model generated indoors to be a good representative of outdoor conditions and has also successfully clarified the inconsistencies in terms of the presence and absence of *n*-aldehydes from porcine and human pyrolytic data. The use of activated carbon tablet as a substitute of activated carbon strip (ACS) for the adsorption of pyrolytic products is also highlighted in this work.

In terms of future prospects, pyrolytic experiments using other parts of the porcine carcass would be an advantage. This will reveal further information about the type and consistency of pyrolysis products generated by different types of tissues in a fire. In addition, it would also be particularly interesting to explore the origin of porcine tissues that have been subjected to burning in the presence of ignitable liquids and clothing material. Data generated from this process would be helpful in identifying the effects of interfering products that can possibly be generated, if any, on the key indicators of human remains in the presence of contaminants.

## Acknowledgement

The authors would like to appreciate Faculty of Health Sciences, Universiti Kebangsaan Malaysia for the facilities and support that are provided for this study. We would also like to extend our gratitude to The Centre for Water Research and Analysis (ALIR), UKM for collaboration in providing the facilities which is a freezer to store the bone samples.

## References

1. Fanton, L., Jdeed, K., Tilhet-Coartet, S. and Malicier, D. (2006). Criminal Burning. *Forensic Science Institute,* 158 (2-3): 87 – 93.
2. Porta, D., Poppa, P., Regazzola, V., Gibelli, D., Schillaci, D. R., Amadasi, A., Magli, F. and Cattaneo, C. (2013). The importance of an anthropological scene of crime investigation in the case of burnt remains in vehicles: 3 case studies. *American Journal of Forensic Medicine and Pathology,* 34(3): 195 – 200.
3. Ubelaker, D. H. (2009). The forensic evaluation of burned skeletal remains: A synthesis. *Forensic Science Institute,* 183 (1-3): 1 – 5.
4. Knight, B. and Saukko, P. J. (2004). Knight's Forensic Pathology. Third ed. Edward Arnold Publisher Ltd, London.
5. Holden, J. L., Phakey, P. P. and Clement, J. G. (1995). Scanning electron microscope observations of heat-treated human bone. *Forensic Science Institute,* 74 (1-2): 29 – 45.
6. National Centre For Forensic Science (NCFS). (2006). Substrate database. University of Central Florida.
7. Gabriel, G. F. (2015). The analysis and discrimination of pyrolysis products from biological and non-biological sources. *Central of Forensic Science, Department of Pure and Applied Chemistry*. University of Strathclyde.
8. DeHaan, J. D., Brien, D. J. and Large, R. (2004). Volatile organic compounds from the combustion of human and animal tissue. *Science and Justice,* 44 (4): 223 – 236.
9. Agu, K. (2011). Investigation of the thermal degradation products of bone. *Centre for Forensic Science, Department of Pure Science and Apllied Chemistry*. University of Strathclyde.
10. American Society for Testing and Materials (ASTM) International E1412-07 (2012). Standard practice for separation of ignitable liquid residues from fire debris samples by passive headspace concentration with activated charcoal. *American Society for Testing and Materials (ASTM) International.* West Conshohocken, PA.
11. Pearce, A. I., Richards, R. G., Milz, S., Schneider, E. and Pearce, S. G. (2007). Animal models for implant biomaterial research in bone: A review. *Europe Cells and Materials Journal,* 13: 1 – 10.
12. Mosekilde, L., Kragstrup, J. and Richards, A. (1987). Compressive strength, ash weight, and volume of vertebral trabecular bone in experimental fluorosis in pigs. *Calcified Tissue International,* 40(6): 318 –322.
13. Thorwarth, M., Schultze-Mosgau, S., Kessler, P., Wiltfang, J. and Schlegel, K. A. (2005). Bone regeneration in osseous defects using a resorbable nanoparticular hydroxyapatite. *Journal of Oral and Maxillofacial Surgery,* 63(11): 1626 – 1633.

14. Stauffer, E. (2003) *C*oncept of pyrolysis for fire debris analysis. *Science and Justice.* 43 (1): 29-40.
15. National Fire Protection Association (NFPA). (1990). Fire Protection Handbook. *National Fire Protection Association (NFPA),* Standard Publishing Company.
16. Welker, J. R. and Sliepcevich, C. (1966). Burning rates and heat transfer from wind-blown flames. *Fire Technology,* 2(3): 211 – 218.
17. Purevsuren, B., Avid, B., Garelmaa, T., Davaajay, Y., Morgan, T., Herod, A. and Kandiyoti, R. (2004). The characterisation of tar from the pyrolysis of animal bones. *Fuel,* 83 (7-8): 799 – 805.

*Malaysian Journal of Analytical Sciences, Vol 21 No 3 (2017): 597 - 604*
*DOI: https://doi.org/10.17576/mjas-2017-2103-09*

MALAYSIAN JOURNAL OF ANALYTICAL SCIENCES
*Published by The Malaysian Analytical Sciences Society*
ISSN 1394 - 2506

# METALS CONTAMINATION USING *Polymesoda expansa* (MARSH CLAM) AS BIO-INDICATOR IN KELANTAN RIVER, MALAYSIA

## (Pencemaran Logam di Sungai Kelantan, Malaysia Menggunakan *Polymesoda expansa* (Lokan) Sebagai Penunjuk Biologi)

Ong Meng Chuan[1]*, Muhammad Izzat Kamaruzaman[1], Yong Jaw Chuen[1], Kamaruzzaman Bin Yunus[2], Joseph Bidai[3]

[1]*School of Marine and Environmental Sciences, Universiti Malaysia Terengganu, 21030 Kuala Terengganu, Malaysia*
[2]*Department of Marine Science, Kulliyyah of Science, International Islamic Universiti Malaysia, Bandar Indera Mahkota, 25200 Kuantan, Pahang, Malaysia*
[3]*Institute of Oceanography and Environment, Universiti Malaysia Terengganu, 21030 Kuala Terengganu, Malaysia*

**Corresponding author: ong@umt.edu.my*

Received: 7 August 2016; Accepted: 13 April 2017

**Abstract**

Bivalve, such as marsh clam (*Polymesoda expansa*) feed by filtering most of the suspended particle in water that surrounding them. Lots of elements being trap into their body via this feeding habit including pollutant such as trace metals. Unfortunately, these marsh clams were taken directly by human as their daily diet. Due to its ability to filter water, marsh clam was used to monitor the level of trace metals in aquatic system in significant place such as industrial area. Therefore, this study was carried out at Kelantan River near to the industrial area in Pengkalan Chepa, Kelantan, Malaysia. A total of 80 marsh clams were collected from 4 different sites to represent a different environmental condition. The in-toto of the marsh clam were dissected and digest with suprapur nitric acid by using Teflon Bomb method. Six metals were determined by using Inductively Coupled Plasma Mass Spectrometry including chromium, iron, copper, cadmium, lead and zinc. The highest mean concentration of all metals studied (Cr 45.03 µg/g dry weight; Fe 1.28 µg/g dry weight; Cu 21.8 µg/g dry weight; Cd 1.15 µg/g dry weight; Pb 2.31 µg/g dry weight; Zn 898 µg/g dry weight) in the marsh clam tissue was recorded at station 4 which is near to the industrial area discharge. Whereas, those concentration were lower at Station 1 and Station 2, which located at the upstream and far from the industrial area discharge. On the other hand, the size of marsh clam does not significantly correlate to the concentration of selected trace metals. Level of selected metals in some the samples were exceeded the permissible limit provide by Malaysia Food Safety and Food Regulation 1985 especially marsh clam collected from station near to industrial area. Therefore, marsh clam collected for consumption near to industrial area need to be continuously monitor to prevent any acute effect on human health risk.

**Keywords:** Kelantan River, marsh clam, metals, permissible limit, human health risk

**Abstrak**

Kerang seperti lokan (*Polymesoda expansa*) memperolehi makanan melalui proses penapisan zarah-zarah terampai di dalam air di sekeliling mereka. Banyak unsur-unsur elemen yang terperangkap di dalam badan mereka melalui tabiat makan ini termasuklah logam surih. Malangnya, lokan ini telah diambil oleh manusia dan dijadikan sebagai diet harian mereka. Disebabkan keupayaan lokan ini untuk menapis air, lokan telah digunakan untuk memantau tahap pencemaran logam berat di dalam persekitaran akuatik terutamanya di kawasan perindustrian. Oleh itu, kajian ini telah dijalankan di Sungai Kelantan berhampiran dengan kawasan perindustrian di Pengkalan Chepa, Kelantan, Malaysia. Sebanyak 80 lokan yang dikutip dari 4 kawasan

penyampelan untuk mewakili keadaan persekitaran yang berbeza. Keseluruhan tisu lembut lokan tersebut telah dikeluarkan dan dicerna dengan menggunakan kaedah Teflon bom dengan bantuan asid nitric suprapur. Kepekatan 6 logam telah ditentukan menggunakan spekrometri jisim gandingan aruhan plasma termasuk logam kromium, ferum, kuprum, cadmium, plumbum dan zink. Purata kepekatan logam yang dikaji (Cr 45.03 µg/g berat kering; Fe 1.28 µg/g berat kering; Cu 21.8 µg/g berat kering; Cd 1.15 µg/g berat kering; Pb 2.31 µg/g berat kering; Zn 898 µg/g berat kering) di dalam tisu lokan tersebut dicatatkan di stesen 4 yang terletak berhampiran dengan pelepasan sisa kawasan perindustrian. Kepekatan logam adalah lebih rendah di dalam lokan yang dikutip dari Stesen 1 dan Stesen 2 yang terletak di hulu sungai dan jauh daripada kawasan pelepasan sisa perindustrian. Selain itu, saiz lokan tidak mempengaruhi kadar kepekatan logam yang dikaji. Tahap kepekatan logam yang dikaji didapati melebihi had yang ditetapkan oleh Peraturan Makanan Malaysia 1985 terutamanya lokan yang dikutip dari stesen berhampiran kawasan perindustrian. Oleh itu, lokan berhampiran kawasan perindustrian perlu dipantau untuk mengelakkan apa-apa kesan akut kepada risiko kesihatan manusia.

**Kata kunci**: Sungai Kelantan, lokan, logam berat, had dibenarkan, risiko kesihatan manusia

## Introduction

Heavy metals are a metallic chemical element that has a high density and are toxic or poisonous at low concentrations [1]. Living organisms need a certain amounts of some metals, including calcium, copper, iron, manganese, molybdenum, vanadium, strontium, and zinc in order to keep the metabolism activities inside the body functioning well [2,3]. However, heavy metals are also dangerous because they tend to bio-accumulate in the body of the organism [4].

Heavy metals have been recognized as a severe pollutant to the environment due to its hazardous effects. Industrial and agricultural activities were reported as the major sources of the accumulation of pollutants in the aquatic environment, including the sea [5, 6]. These lethal wastes in the sea are highly probable to be accumulated in the sediments and marine organisms, including shellfish and consequently transfer to human beings through the food chain [7]. Shellfish are consumed by human beings and if accumulate large quantities of some metals from the water through daily consumption. It is important to determine the concentration of heavy metals in shellfish in order to evaluate the possible risk of the consumption for human health [8]. Shellfish contain quite great concentrations of carotenoids [9], low levels of fat and essential amino acids and also possess a relatively high content of vitamins and minerals [10]. For an example, bivalves have a much higher concentration of vitamins such as folate, cobalamin and minerals [10]. Today, it is generally accepted that fish and shellfish are important in a healthy and balanced human diet [11].

However, the evaluation of the risks and benefits of the consumption of these products has been particularly controversial. Even though, shellfish are very important human foods, but they exposed to chemicals in polluted and contaminated waters [12]. Toxicologists tend to relate shellfish as a major vector for toxic substances of metal trace elements and persistent organic pollutants [13]. The bioaccumulation of heavy metals by fish and shellfish make these food items can be a rich source of metal [14]. The interactions of heavy metals with usual elements form diet have an important role in acute and chronic toxicity [15].

Among the common approaches used to study environmental contamination, the use of bivalve mollusk as bio-indicator species has proved to be a valuable and informative technique [16]. This approach has been particularly developed in temperate areas, whereas in sub-tropical and tropical areas the scarcity of available information makes the identification of species that could be used as suitable bio-indicators is difficult [17]. This study was conducted to evaluate the concentration of selected heavy metals accumulated in the seashell and beside to determine the size of seashells toward the concentration of metals in the seashell.

## Material and methods

### Sample collection

The seashells, ranged from 54 to 80.9 mm were collected in the mangrove area of the Kelantan River, located in Kota Bharu, Kelantan (Figure 1) during June 2013 in four different sampling stations. Sampling station 1 and 2 locate before industrial area, meanwhile station 3 and 4 locate near to industrial area. Various type of industries

including food canning and manufacture of plastics. Sediment attached to the seashell was washed thoroughly by the *in-situ* water. All samples were stored in low temperature before the seashells were dissected in the laboratory.

**Sample analysis**

In the laboratory, the sample was washed with distilled water. Prior to analysis, the samples were classified, weighted, and the length measured using vernier caliper and all of the soft tissue were removed from their shells by using ceramic scalpel blades and then thoroughly rinsed to remove any extraneous impurities. The total weight and wet weight were recorded on the data sheet.

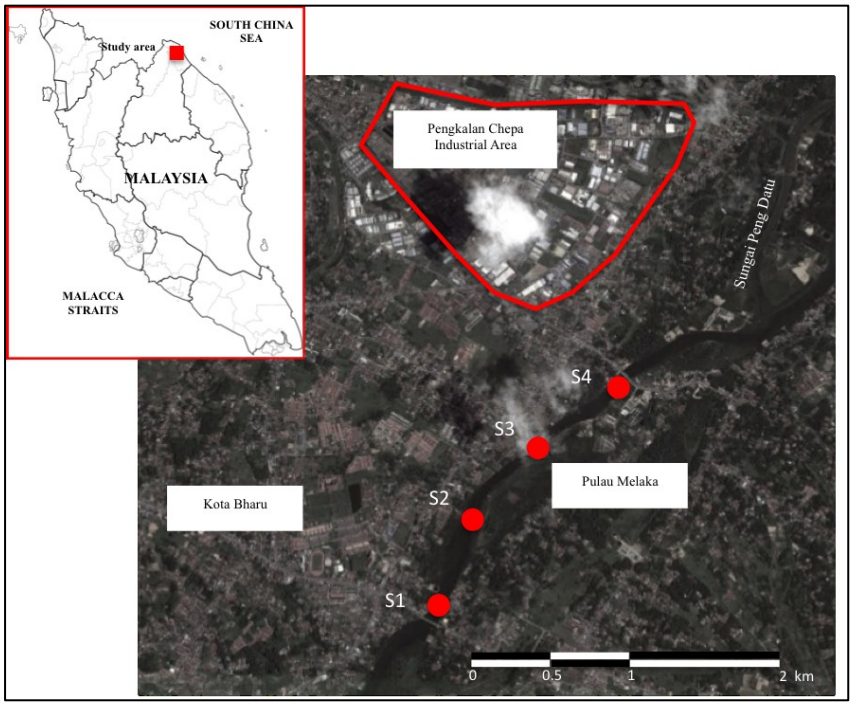



Figure 1. The sampling stations (Sungai Peng Datu, Kelantan) near to Kota Bharu city and Kampung Pulau Melaka

**Analytical method**

The soft tissue is weighted approximately to 0.05 g (dry sample) in Teflon digestion container. Suprapur nitric acid was added into each of the samples and let to predigest. Standard reagent, SRM1566 Oyster Tissue and blank were done simultaneously. After that, the container is covered and place in a stainless steel bomb, which is sealed with screw closure to avoid any acid leakage and store in the oven. The sample was heated in oven temperature for 7 hours at 100 °C in order to digest the sample completely. After cooling, the solution is transferred into a centrifuge tube diluted with deionized water to 10 mL. The metals content, then measured by inductively-coupled plasma mass spectrometry (ICP-MS).

**Statistical analysis**

The statistical analysis, t-test of SPSS software is used to investigate the variation in trace elements concentration in the organisms and the sampling site. The levels of significance of the statistical analyses are set at 0.05.

## Results and Discussion

### Average concentration of heavy metal in marsh clam

Table 1 shows the overall results obtained from this study. Generally, cadmium (Cd), lead (Pb) and zinc (Zn) relatively are higher in station 4. Station 4 is the station that locates near to the end of the river and also near to the industrial area. However, concentration of chromium (Cr) in station 2 is the lowest among all. Approaching to industrial area, the concentrations of metal seem to be increased. This shows the industrial area may affect the selected metal concentration inside the river and uptake by the clam.

Table 1. The average concentration of each metals in each station

| Sample ID | Cr (μg $g^{-1}$) | Fe (μg $g^{-1}$) | Cu (μg $g^{-1}$) | Cd (μg $g^{-1}$) | Pb (μg $g^{-1}$) | Zn (μg $g^{-1}$) |
|---|---|---|---|---|---|---|
| Station 1 (non-industrial area) | | | | | | |
| Average | 44.60 ± 0.05 | 0.50 ± 0.05 | 13.10 ± 0.05 | 0.54 ± 0.05 | 1.17 ± 0.05 | 323.65 ± 0.05 |
| Std. Dev. | 32.06 ± 0.05 | 0.50 ± 0.05 | 9.72 ± 0.05 | 0.45 ± 0.05 | 0.61 ± 0.05 | 296.60 ± 0.05 |
| Station 2 (non-industrial area) | | | | | | |
| Average | 25.05 ± 0.05 | 1.08 ± 0.05 | 17.89 ± 0.05 | 0.88 ± 0.05 | 1.89 ± 0.05 | 510.86 ± 0.05 |
| Std. Dev. | 14.89 ± 0.05 | 0.61 ± 0.05 | 9.19 ± 0.05 | 0.34 ± 0.05 | 0.91 ± 0.05 | 197.50 ± 0.05 |
| Station 3 (industrial area) | | | | | | |
| Average | 45.90 ± 0.05 | 1.04 ± 0.05 | 24.99 ± 0.05 | 0.91 ± 0.05 | 1.84 ± 0.05 | 752.00 ± 0.05 |
| Std. Dev. | 62.24 ± 0.05 | 0.46 ± 0.05 | 7.34 ± 0.05 | 0.44 ± 0.05 | 0.66 ± 0.05 | 293.51 ± 0.05 |
| Station 4 (industrial area) | | | | | | |
| Average | 45.03 ± 0.05 | 1.28 ± 0.05 | 21.81 ± 0.05 | 1.15 ± 0.05 | 2.31 ± 0.05 | 898.40 ± 0.05 |
| Std. Dev. | 29.60 ± 0.05 | 0.46 ± 0.05 | 7.51 ± 0.05 | 0.68 ± 0.05 | 0.83 ± 0.05 | 390.06 ± 0.05 |

Previous study shows the significant value that has been done in certain areas which may be affected by different physical and biological factor. Differences of value between the current study and previous study determined the toxicity of the area and may give harmful to human society and community through ingestion and consumption. Previous report shows there are four metals that have been studied along the Strait of Malacca. Several fishes have been catch and well preserved together with several cockles (*Anadara granosa*) [18]. However, there are only two same metals which previous report and this report have used include cadmium and lead. Previous study shows higher concentration of cadmium rather than in this study range from 25.1 μg $g^{-1}$ to 47.0 μg $g^{-1}$ [18]. This could be due to the fact that the habitat of *Anadara granosa* that are living at the bottom of the sea, nearly in the sediment where various kinds of hazardous and toxic substances are accumulated [19]. Lead in previous study showed much lower than the current study (0.19 μg $g^{-1}$ to 0.28 μg $g^{-1}$). *Anadara granosa* from Malacca's Straits was used as background comparison as there is no study that's been established around the Kelantan River.

A previous study in 1998, the report shows that the heavy metal concentrations of the bivalve *Anadara (Senilia) senilis* show a clearly distinct effect of size, small individuals having greater concentrations than large cockles [19]. Results should therefore be normalized for size before attempting any geographical or temporal comparison. In this study, statistically significant differences in metal concentrations of cockles between localities and years are explained by differences in the size distribution of the samples. Five types of metals studied in previous study show that than this study as the concentration is 309 μg $g^{-1}$. In the previous study conduct during 1980, the concentration in the cockles is much lower than in this research [20].

Generally, the levels in industrial area were higher compared to non-industrial area station. For example, the average concentration of Cu was 18 μg $g^{-1}$ at Station 2 and 25 μg $g^{-1}$ at Station 3, respectively. This clearly indicates the influence of aquatic environments [21] as well as surrounding human activities at a specific point of time may contribute to the accumulation of trace metals in marine organisms. Copper is one of the metals that is introduced

into the aquatic environment through a number of natural methods. Copper is also a very useful substance for man. When these uses occur, some of that Cu is also presented in the aquatic environment [22]. In this study, the concentration of Cu in each sample is still below 30 μg $g^{-1}$ and in safety level. Highest level of Cu was observed at station 4. Thus, the accumulation of heavy metals in the aquatic environments has been associated with urban runoff, sewage treatment plants, industrial effluents and wastes, mining operations, boating activities, domestic garbage dumps and agricultural fungicide runoff [23].

On the other hand, the concentration of Cr is high and almost the same except for Station 2. The decrease of concentration may influence by the degradation of Cr by the biological process of marine organisms [24] or there are less human activity and production that contribute to the increase of Cr concentration. Although the graph shows the high concentration in both non-industrial area, yet it is considered as low. Besides, Cr has low toxicity and no adverse effects were observed at intakes of 1000 to 2000 μg/day by human [25]. Due to the lack of adequate data, the EU Scientific Committee for Food (2003) has not suggested a Tolerable Upper Intake Level (UL) for Cr. The same conclusion was reported by the US Food and Nutrition Board and the UK Expert Group on Vitamins and Minerals [25].

For the iron (Fe) in the clam samples, the highest percentage of concentration can be observed in samples at station 4. Similar with other metals, Fe also was carried through the stream and accumulates at the end of the river bank. Station 2 and 3 shows almost same value, probably due to the station located close to the industrial area. Surface and river runoff from the industrial area may contribute to the amount of the Fe present in the river.

The concentration pattern of cadmium (Cd) is likely same as concentration of Fe and Pb. The highest concentration of Cd exceeding safety level can be found in station 4 and lowest concentration of Cd can be found in station 1. Although Cd is not widely used in human activities, but Cd is the essential component in the manufacture of solder, electrical supplies, batteries, phosphors in the production of televisions, anti-corrosive coatings for metals and bearing alloys [26]. However in this study, the Cd may come from natural resource as there are no specific industries utilized Cd present in the area of sampling located.

For lead metal (Pb), the highest level was observed in an industrial area in station 4 and exceeding safety levels of human consumption while in lowest level can be found at Station 1. Station 4 has the highest concentration of Pb because of the accumulation of the heavy metal at the end of river bank [27]. It is because the industrial area may also contribute to the amount of the Pb concentration at Station 4. Pb is well known metal used in industry as paint, coating agent and storage of batteries. Although Pb is not harmful to human at low level, but if the amount takes more than the body can handle, the body will show some of the known symptoms of Pb poisoning such as headache, irritability, abnormal pain and various symptoms related to the nervous system.

The data about the zinc metal (Zn) show that all sampling stations exceed the safety level of human consumption, 150 μg $g^{-1}$. Station 4 in industrial area shows the highest concentration of Zn in each sample. Excess level Zn has been accumulating at the end of the river and the source may come from the industrial area. The evidence in station 3 shows the concentration of zinc in higher than in non-industrial area (Station 1 and 2). Large doses of consuming zinc taken by mouth even for a short time can cause stomach cramps, nausea, and vomiting. Zinc is well known as metal that easily found dumped by villager in this river such as roof, barrel and component of car.

**Correlation of length and weight and the concentration of heavy metals**

From the tabular data of correlation between length of seashell and concentration of heavy metal, it was concluded that the heavy metal concentrations in the bivalve *Polymesoda expansa* are not related based on sample size (Figure 2 and 3). Small individuals having higher concentrations than large seashells and some small seashells also have lower concentration of metals than a large one or called as a growth dilution effect. The concentration of metals in samples is not directly proportional to the size, but regarding to the geographical or temporal comparison. In this study, statistically significant differences for concentration of metals in seashells between localities and years are clarified by differences in the size distribution of the samples. The areas itself give important in determining the status of metal toxicity in the current study. Moreover, the concentration levels of zinc, lead, cadmium and iron

shows that the highest concentration within the range of 60 mm to 70 mm of seashell's length, meanwhile for chromium and copper, the highest concentration can be found in the seashells with the range of 70 mm to 80 mm.

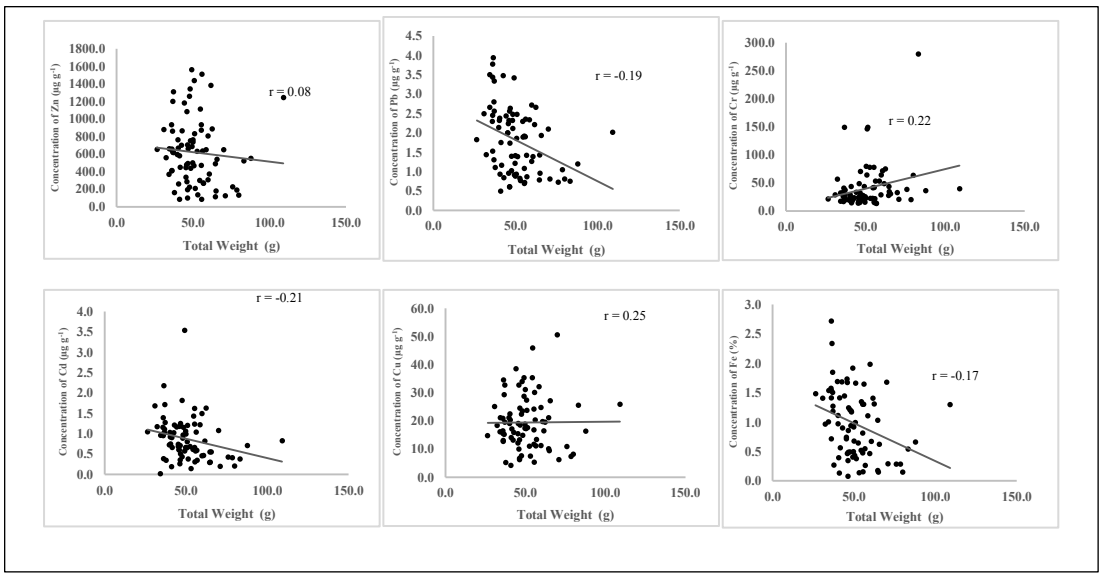



Figure 2. Correlation between weight of clam and the concentration of metals

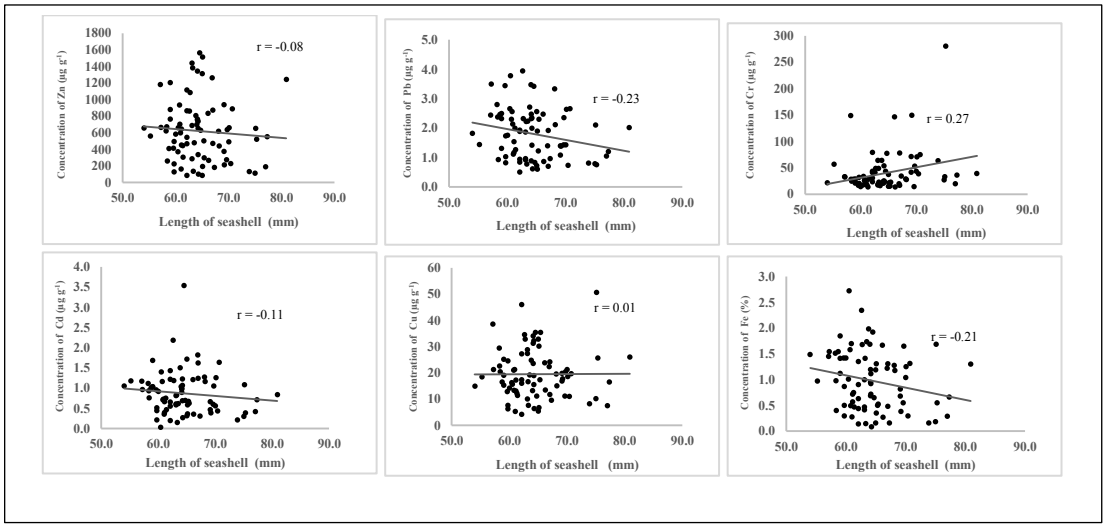



Figure 3. Correlation between length of clam and the concentration of metals

## Conclusion

The concentration of metal in non-industrial and industrial area is most likely same and can determine that the industrial area use safe and work in accordance with the standards set. The metals in the river is not totally come from the industries but may come from rural activities. Vehicle and metal-based barrel dumping are also contribute to the increase of the concentration. The size of clam also play role in determining the concentration of heavy metal

inside their body but limited to certain type of metals. From the correlation graph, some of metals are increase through size or length but some of metals are also decrease directly with size. However, there are some researchers claimed that the behavior of the seashell itself will 'consume' less if the area is really polluted. The gasping rate is decrease and less medium like water pass through the body. From the preliminary data obtained, the marsh clams at Kelantan River are still safe to be consumed. However, continuous consume the organism may lead to Zn poisoning due to the level of Zn is higher compare to standard values. Therefore, an intensive studies include water and sediment quality or other organism should be considered in order to obtain a better conclusion for metal pollution in Kelantan River.

**Acknowledgement**

This research was conducted with funding from the Ministry of Higher Education Malaysia (MOHE), under the Niche Area Research Grant Scheme (NRGS) project number 53131. The authors wish to express their gratitude to Oceanography and Biodiversity Laboratory, School of Marine and Environmental Sciences teams for their invaluable assistance and providing the facilities to carry out the research. We are grateful to our editors and referees for their invaluable comments that helped improve this manuscript.

**References**

1. Cid, B. P., Boia, C., Pombo, L., and Rebelo, E. (2001). Determination of trace metals in fish species of the Ria de Aveiro (Portugal) by electro thermal atomic absorption spectrometry. *Food Chemistry*, 75(1): 93 – 100.
2. Araya M, Pizarro F, Olivares M, Arredondo M, Gonzalez M. and Mendez, M. (2006). Understanding copper homeostasis in humans and copper effects on health. *Biology Research,* (39): 183 – 187.
3. Harris, E. D. (2001). Copper homeostasis: the role of cellular transporters. *Nutrition Revision*, (59): 281 – 285.
4. Ryan, N. H. (2012). What You Should Know About Heavy Metals. Retrieve from: http://www.bewholebewell.com/articles/WhatYouShouldKnowAboutHeavyMetals.pdf. Date access 26 September 2013.
5. Freedman, B. (1989). Environmental Ecology. The impact of pollution and other stresses on ecosystem structure and function. London: Academic Press, (4): pp. 13 – 16.
6. Jordao, C. P., Pereira M.G., Bellato C. R., Pereira, J. L., and Matos, A. T. (2002). Assessment of water systems for contaminants from domestic and industrial sewages. *Environmental Monitoring Assessment*, (8): 33 – 36.
7. Tuzen, M. (2003). Determination of heavy metals in fish samples of the middle Black Sea (Turkey) by graphite furnace atomic absorption spectrometry. *Food Chemistry*, (13): 17 – 21.
8. Castro-González, M. I. and Méndez-Armenta, M. (2008). Heavy metals: implications associated to fish consumption. *Environmental Toxicology and Pharmacology*, (26): 263 – 271.
9. Britton, G., Liaaen-Jensen, S. and Pfander, H. (2009). Carotenoids: Nutrition and Health. Birkhauser Verlag. United States.
10. Holland, B., Brown, J. and Buss, D. H., (1993). Fish and Fish products. Royal Society of Chemistry and Ministry of Agriculture. *Fisheries and Food*, (2): 36 – 37.
11. World Health Organization. (2003). Concise International Chemical Assessment Document 55. Polychlorinated biphrnyls: human health aspect. Retrieve from: http://www.inchem.org/documents/cicads/ cicads/ cicad55.htm#10.0. Date access 26 September 2013.
12. Ikem, A. and Egiebor, N. O. (2005). Assessment of trace elements in canned fishes (Mackerel, Tuna, Salmon, Sardines and Herrings) marketed in Georgia and Alabama (United States of America). *Journal of Food Composition and Analysis*, (3): 34 – 37.
13. Guerin, T., Chekri, R., Vastel, C., Sirot, V., Volatier, J., Leblanc, J. and Noel, L. (2011). Determination of 20 trace elements in fish and other seafood from the French market. *Food Chemistry*, (11): 12 –16.
14. Boscolo, R., Cacciatore, F., Berto, D. and Giani, M. (2007). Polychlorinated biphenyls in clams Tapes philippinarum cultured in the Venice Lagoon (Italy): Contamination levels and dietary exposure assessment. *Food and Chemical Toxicology*, (45): 1065 – 1075.
15. Leblanc J. C., Guerin T., Noel L., Calamassi-Tran G., Volatier J. C. and Verger P. (2005). Dietary exposure estimates of 18 elements from the 1st French total diet study. *Food Additives and Contaminants*, (9): 22 – 25.
16. Goldberg, E. D., Koide, M., Hodge, V., Flegal, A. R. and Martin, J. H. (1983). U. S. Mussel Watch: 1977-1978 results on trace metals and radionuclides. *Estuarine, Coastal and Shelf Science*, (12): 42 –45.

17. Phillips, D. J. (1991). Selected trace elements and the use of biomonitors in subtropical and tropical marine ecosystems. In Reviews of Environmental Contamination and Toxicology. Springer New York: pp. 105 – 129.
18. Alina, M., Azrina, A., Mohd Yunus, A. S., Mohd Zakiuddin, S., Mohd Izuan Effendi, H. and Muhammad Rizal, R. (2012). Heavy metals (mercury, arsenic, cadmium, plumbum) in selected marine fish and shellfish along the straits of Malacca. *International Food Research Journal*, (19): 135 – 140.
19. Joiris, C. R., Azokwu, M. I., Otchere, F. A. and Ali, I. B. (1998). Mercury in the bivalve *Anadara (Senilia) senilis* from Ghana and Nigeria. *Science of the Total Environment*, (224): 181 – 188.
20. Orren, M. J., Eagle, G. A., Hennig, H. F, Green, A. (1980). Variations in trace metal content of the mussel Choromytilus meridionalis (Kr.) with season and sex. *Marine Pollution Bulletin*, (11): 253 – 257.
21. Zhang, I. and Wong, M. H. (2007). Environmental mercury contamination in China: Sources and impacts. *Environmental International*, (33): 108 – 121.
22. Lewis, A. G. (1995). Copper in water and aquatic environments, International Copper Association, LTD. New York, NY: pp. 1 – 2.
23. Agency for Toxic Substance and Disease Register (2003). Toxicological profile for arsenic. US Department of Health and Humans Services, Public Health Human Services, Centres for Diseases Control, Atlanta.
24. Ehrlich H. L. (1996). How microbes influence mineral growth and dissolution: Chemical and biological control on mineral growth and dissolution kinetics, American chemical society meeting. *Chemical Geology*, (132): 5 – 9.
25. Scientific Committee on Food (2003). Tolerable upper intake level of trivalent chromium. SCF/CS/NUT/UPPLEV/67 Final. European Commission. Health & Consumer Protection Directorate-General. Retrieve from http://europa.eu.int/comm/food /fs/sc/scf/out80_en.html, 2003. Date access 3 April 2014.
26. Hardy D. H., Myers J. and Stokes C. (2008) Heavy metals in North Carolina soils: Occurrence and significance. North Carolina Department of Agriculture and Consumer Services. Retrieve from: www.ncagr.gov/agronomi/. Date access on 28 March 2014.
27. Kamaruzzaman, B. Y., Shuhada, N. T., Akbar, B., Shahbudin, S., Jalal, K. C. A., Ong, M. C., Al-Barwani, S. M. and Goddard, J. S. (2011). Spatial concentrations of lead and copper in bottom sediments of Langkawi coastal area, Malaysia. *Research Journal in Environmental Science*, (5): 179 –186.

*Malaysian Journal of Analytical Sciences, Vol 21 No 3 (2017): 605 - 618*
*DOI: https://doi.org/10.17576/mjas-2017-2103-10*

**MALAYSIAN JOURNAL OF ANALYTICAL SCIENCES**
***Published by The Malaysian Analytical Sciences Society***
**ISSN 1394 - 2506**

# DEVELOPMENT AND VALIDATION OF A REVERSE PHASE-HIGH PERFORMANCE LIQUID CHROMATOGRAPHY-ULTRAVIOLET METHOD FOR SIMULTANEOUS DETECTION OF CAFFEINE AND PHENOLPHTHALEIN IN WEIGHT REDUCING SUPPLEMENTS

## (Pembangunan dan Pengesahsahihan Kaedah Fasa Terbalik-Kromatografi Cecair Prestasi Tinggi Ultraungu bagi Pengesanan Kafein dan Fenolftalein Dalam Suplemen Pengurangan Berat Badan)

Elham Mohammadi Nasr and Lai Chun Wong*

*Department of Pharmaceutical Chemistry, School of Pharmacy, International Medical University, 57000 Kuala Lumpur, Malaysia*

**Corresponding author: laichunwong@imu.edu.my*

Received: 13 May 2016; Accepted: 12 April 2017

**Abstract**

A reversed-phase high performance liquid chromatography analytical method with variable wavelength detection was developed for the simultaneous detection of caffeine and phenolphthalein in weight reducing supplements. Chromatographic separation was achieved with a C18 reversed-phase column using a gradient elution of methanol and an ammonium acetate buffer (pH 5; 25 mM), with the detector wavelength set at 254 nm. The method was validated according to The International Conference on Harmonisation of Technical Requirements for Registration of Pharmaceuticals for Human Use guidelines. The method was proven to be linear over a concentration of 10 – 100 µg/mL for both caffeine and phenolphthalein, with mean correlation coefficients of 1.000 and 0.999, respectively. The limit of detection for caffeine and phenolphthalein was 0.77 µg/mL and 0.47 µg/mL respectively, while the limit of quantification for caffeine and phenolphthalein was 2.35 µg/mL and 1.44 µg/mL, resspectively. The percentage relative standard deviation for both intra and inter-day precision was less than 2%. The mean recovery values were calculated as 105.84% and 113.58% for caffeine and phenolphthalein. In addition, the method was proven to be robust when deliberate changes in flow rate, buffer pH and organic mobile phase composition were tested.

**Keywords**: caffeine, phenolphthalein, high performance liquid chromatography, validation, weight reducing supplement

**Abstrak**

Satu kaedah analitikal kromatografi cecair prestasi tinggi (KCPT) fasa terbalik dengan pengesanan pada pelbagai panjang gelombang telah dibangunkan untuk pengesahan kafein dan fenolftalein dalam suplemen pengurangan berat badan. Pemisahan kromatografik dicapai dengan turus fasa terbalik C18 menggunakan kecerunan elusi metanol dan penampan ammonium asetat (pH 5; 25 mM), pada panjang gelombong λ = 254 nm. Kaedah ini telah ditentusahkan mengikut garis panduan harmonisasi persidangan antarabangsa keperluan teknikal untuk pendaftaran famaseutikal bagi pengunaan manusia. Kaedah ini dibuktikan linear dalam julat kepekatan larutan piawai kafein dan fenolftalein di antara 10 – 100 µg/mL dengan nilai pekali korelasi ($R^2$) 1.000 dan 0.999 untuk masing – masing bagi kafein dan fenolftalein. Had pengesanan bagi kafein dan fenolftalein masing-masing ialah 0.77 µg/mL and 0.47 µg/mL. Keputusan had kuantifikasi bagi kafein dan fenolftalein masing-masing ialah 2.35 µg/mL and 1.44 µg/mL. Peratus relatif sisihan piawai bagi ketepatan intra dan antara hari yang diukur ialah kurang dari nilai 2%. Nilai min pemulihan semula yang dikira bagi kafein dan fenolftalein masing-masing ialah 105.84 dan 113.58%. Kaedah ini juga dibuktikan teguh apabila perubahan dalam kadar aliran, pH panampan dan komposisi fasa bergerak diuji.

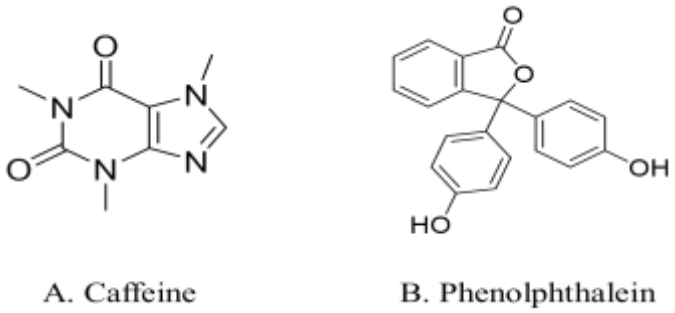
**Kata kunci:** kafein, fenolftalein, kromatografi cecair prestasi tinggi, pengesahsahihan, suplemen pengurangan berat badan

## Introduction

Obesity is a worldwide health epidemic. It is reported that among adults aged 18 and above, 11% of men and 15% of women were obese in 2014 [1]. Because of the health risks associated from being overweight, and also pressure from society to have a slim and attractive body, weight reducing supplements are popular worldwide among both men and women. The majority of these weight reducing supplements are marketed as being derived from phytotherapeutic formulations and are advertised as being natural and safe. Unfortunately this is not the case in reality, as there have been many reports worldwide of weight reducing supplements being adulterated with undeclared prescription pharmaceuticals and banned substances to enhance their efficiency [2–11].

In the US, the Food and Drug Administration (FDA) has detected the presence of adulterants such as sibutramine, fenproporex, fluoxetine, bumetanide, furosemide, phenytoin, rimonabant, cetilistat and phenolphthalein in various weigh reducing products sold over the counter (OTC) and online [12]. We are interested in developing a simple and fast HPLC method to quantify caffeine and phenolphthalein, as these compounds are popular choices as adulterants due to their relatively cheap price and easy accessibility. Phenolphthalein, a synthetic compound, was a stimulant laxative used for the treatment of constipation and for bowel evacuation until 1999, when the FDA reclassified the drug as 'not generally safe and effective' after studies indicated that it presented a potential carcinogenic risk [13]. Since then, the United Kingdom has changed the status of phenolphthalein from OTC to prescription agent, while European countries such as Italy and France have suspended the use of it in prescription and OTC pharmaceutical preparations [14, 15].

Caffeine is a natural product found in the leaves, seeds, and fruits of more than 60 plants [16]. As a stimulant, caffeine was reported to be one of the most used drugs for slimming purposes [3]. Consuming caffeine increases energy expenditure, making the individual more alert and hence more active, leading to weight loss [17]. Caffeine has also been proposed to counteract the decrease in metabolic rates, and may also act as an appetite suppressant. Although complications due to caffeine toxicity are rare, excessive consumption of caffeine can lead to health problems such as sleep disruption, headache, nausea, anxiety, and even caffeine-induced cardiac arrhythmia [18,19]. The chemical structures of caffeine and phenolphthalein are shown in Figure 1 below.




A. Caffeine B. Phenolphthalein

Figure 1. Chemical structures of the adulterants of interest (a) Caffeine (1,3,7-trimethyl-3,7-dihydro-1H-purine-2,6-dione) and (b) Phenolphthalein (3,3-Bis(4-hydroxyphenyl)-2-benzofuran-1(3H)-one)

In this paper, the development and validation of a reversed-phase high performance liquid chromatography-ultra violet (RP-HPLC-UV) analytical method to detect caffeine and phenolphthalein in weight reducing supplements was investigated. The developed method was validated according to The International Conference on Harmonisation of Technical Requirements for Registration of Pharmaceuticals for Human Use (ICH) guidelines [20]. Among the existing analytical methods reported in the literature to detect caffeine and phenolphthalein simultaneously are ultra-high performance liquid chromatography (UHPLC) and liquid chromatography-mass

spectroscopy (LC-MS) [9, 21]. Recently, an article was published reporting a HPLC-UV method for quantitative determination of six adulterant drugs, including caffeine and phenolphthalein, in slimming supplements [22]. However, the published method uses different HPLC parameters from our study. The method which we have developed can be applied to analytical laboratories in developing countries which are only equipped with HPLC-UV instrumentation to screen and quantify for caffeine and phenolphthalein in weight reducing supplements.

## Materials and Methods

### Chemicals and reagents

Caffeine (≥99.0%) and phenolphthalein (ACS reagent), used as standards, were purchased from Sigma Aldrich and Merck, respectively. HPLC-grade methanol and ammonium acetate (>99%) was obtained from Fischer Scientific. The mobile phase was filtered through a 0.45 µm nylon membrane filter and ultrasonically degassed before use. Other reagents, including glacial acetic acid, were of analytical grade. Ultrapure water was prepared using an atrium® 611 Ultrapure Water System (Sartorius, Germany).

### Instrumentation and chromatographic system

Method development and validation was performed on a 1200 series HPLC (Agilent Technologies, US), interfaced with a binary pump (G1312A, Agilent Technologies, US), degasser (G1379B, Agilent Technologies, US), variable wavelength detector (VWD) (Agilent Technologies, US) and manual injector (G1328B, Agilent Technologies, US). The HPLC was interfaced to a Hewlett-Packard L1908 computer equipped with ChemStation System (version 2008) software.

The chromatography method was developed using a C18 Hypersil GOLD column (150 mm x 4.6 mm internal diameter, 5 µm particle size) at room temperature. The mobile phase was composed of (A) an ammonium acetate buffer 25 mM solution adjusted to pH 5 with glacial acetic acid and (B) methanol with a gradient elution programme, as shown in Table 1. The mobile phase was delivered at a flow rate of 1.1 mL/min. The injection loop volume was 20 µl. The detection wavelength was set at 254 nm.

Table 1. Gradient elution profile used in HPLC system

| Time (min) | 0 | 1 | 3 | 5 | 10 |
|---|---|---|---|---|---|
| A (%) | 90 | 90 | 60 | 45 | 45 |
| B (%) | 10 | 10 | 40 | 55 | 55 |

A = ammonium acetate buffer (pH 5; 25 mM); B = methanol

### Preparation of stock standard solution

Stock standard solutions of 1 mg/mL caffeine and phenolphthalein were prepared separately in HPLC grade methanol. The resulting stock solutions were sonicated and filtered using a 0.2 µm nylon syringe filter.

### Preparation of mixed standard and mixed working solution

Mixed standard solution in concentration 100 µg/mL was prepared from the stock standard solutions. Using this tertiary solution, mixed working solutions of 10, 20, 40, 60 and 80 µg/mL were prepared by diluting with the appropriate amount of methanol. All solutions were prepared in HPLC grade methanol, stored in a refrigerator (4 $^{o}$C) and brought to room temperature before use.

### Preparation of blank sample

The blank sample for validation of specificity was prepared according to methods modified from the literature [5, 10]. A herbal weight reducing supplement purchased from a local pharmacy was considered as a blank sample. The capsule was opened, and 0.1 g of powder was weighed. The powder was then extracted with 25 mL of HPLC grade methanol by sonication for 10 minutes. The mixture was then centrifuged at 10 000 rpm for five minutes, and the

supernatant was then collected and filtered through a 0.2 µm nylon syringe filter. The blank sample was stored at 4 ºC in the refrigerator and brought to room temperature before injection into the HPLC.

**System suitability tests**

System suitability tests were carried out before performing validation parameters. The following system suitability tests were performed: peak symmetry, number of theoretical plates, resolution and capacity factor.

**Method validation**

The method validation was performed according to ICH guidelines for the following parameters: specificity, linearity, limit of detection (LOD), limit of quantification (LOQ), accuracy, precision, and robustness. Stability of a mixed working solution at a 50 µg/mL concentration was also investigated.

**Specificity**

Specificity is defined as the ability to assess unequivocally the analytes in the presence of components which may be expected to be present. Specificity was determined by injecting blank samples into the HPLC system to test for interference of a complex matrix of the blank samples with caffeine and phenolphthalein peaks. Blank samples used were OTC weight reducing supplements.

**Linearity of the calibration curve**

The linearity of the calibration curves were constructed by analysing mixed working solutions of caffeine and phenolphthalein. Six concentrations of mixed working solutions containing them ranging from 10 µg/mL to 100 µg/mL were prepared. The linearity was obtained by the injection of the mixed standard working solutions at each concentration in triplicates (n = 3), and the results were expressed as the mean of the triplicates.

**Limit of detection and limit of quantification**

The LOD is defined as the lowest analyte concentration of a sample that can be detected by the analyst, while LOQ is the lowest analyte concentration which can be quantitatively detected with accuracy and acceptable precision. The LOD is expressed as 3.3δ/S, and LOQ is expressed as 10δ/S, where S refers to the slope of the calibration curve and δ refers to the standard deviation of the response. The value of δ was determined from the residual standard deviation of the calibration curve.

**Accuracy**

The accuracy of the method, expressed as percentage recovery (% recovery), was established via spiking studies. The % recovery values were evaluated by spiking blank samples with low, medium and high levels of caffeine and phenolphthalein standards. The concentrations of caffeine standard spiked into the samples were 11, 22 and 33 µg/mL, while the concentrations of phenolphthalein standard spiked were 10.44, 20.88 and 31.32 µg/mL. Each standards of the same concentration was injected into the HPLC in triplicates (n = 3) and the results are expressed as the mean of the triplicates. The % recovery values were established by calculating the ratio of the experimentally determined concentration of each analytes spiked into the blank samples to its theoretical amount (equation 1):

$$\% \text{ Recovery} = \frac{(\text{Recovered concentration of analytes})}{(\text{Theoretical concentration of analytes})} \text{ x } 100\% \quad (1)$$

**Precision**

Precision is the measure for the relative errors of the method and is expressed as the percentage relative standard deviation (% RSD) for intra-day precision (repeatability) and inter-day precision (intermediate precision). To find the intra-day precision, mixed working solutions at low, medium and high concentrations were injected consecutively in the same day. Each sample of a similar concentration was injected in triplicates (n = 3), and the results were expressed as the mean of the triplicates. To find the inter-day precision, the process to do so was repeated where injections of mixed working standard solutions at low, medium and high concentrations were performed over three consecutive days. Each sample of a similar concentration was injected in triplicates (n = 3), and the results were expressed as the mean of the triplicates.

**Stability of mixed standard solution**
A mixed working solution of concentration 50 µg/mL was prepared fresh. The stability of this solution was checked after 24 hours under refrigerated conditions (4 °C).

**Robustness**
The robustness of the method was determined by analysing the mixed standard solution after deliberate changes in flow rate (± 0.2 mL/min), buffer pH (± 0.2 units) and organic content of the mobile phase (± 2.0%). System suitability was applied after each of the above mentioned changes. The method is considered robust for the parameter tested if it conforms to the system suitability tests.

**Preparation of representative samples**
The representative samples were prepared according to similar method employed to prepare the blank sample. Five weight reducing supplements in the form of capsules and powder were purchased from the Kuala Lumpur area (products A, B, C, D and E). The filtered solution of product A was diluted by 10 times with HPLC grade methanol before injection into the HPLC to obtain concentrations within the calibration range. No dilutions were required for the other samples before injection into the HPLC. All solutions were injected in triplicate.

**Liquid-liquid extraction (LLE)**
To clean-up product E, 0.05 g of the product was weighed and dissolved in 20 mL sodium carbonate solution. Solids were removed by filtering, and the filtrate collected into a separating funnel. The filtrate was extracted with dichloromethane (20 mL x 3), the dichloromethane fractions pooled into a round bottom flask and the solvent removed using a rotary evaporator. The residue left in the round bottom flask was reconstituted with 10 mL of HPLC grade methanol and filtered through a 0.2 µm nylon syringe filter prior to injection into the HPLC.

## Results and Discussion

**Selection and optimisation of the method**
The chromatographic method was optimised during the method developing stage by trying different mobile phase compositions and flow rates. The final method was obtained using an ammonium acetate buffer (pH 5; 25 mM) as an aqueous mobile phase and methanol as an organic mobile phase at a flow rate of 1.1 mL/min. The buffer was used as an aqueous mobile phase to obtain good peak shape and a constant retention time, as caffeine and phenolphthalein contains pH sensitive functional groups [23, 24]. Additional peaks were observed when ammonium acetate buffer pH 5 was substituted with ammonium acetate buffer pH 3.8 and pH 5.8 (Figures 2a and 2b). The optimum wavelength allowing for sensitive detection for both caffeine and phenolphthalein was set at 254 nm based on literature [9, 10, 25].

The elution gradient begins with 10% methanol and 90% buffer. After one minute a linear gradient is started where 40% methanol composition is reached after 2 minutes from the time of gradient. A second linear gradient is then applied where methanol composition increases to 55% after 2 minutes and kept constant for 5 minutes until caffeine and phenolphthalein elutes out at 5.61 minutes and 8.78 minutes respectively. The separation achieved using the experimental conditions described are presented in Figure 2c. The following system suitability test parameters were performed: peak symmetry, number of theoretical plates, resolution and capacity factor (Table 2). All system suitability test parameters were found to be within the ICH requirements.

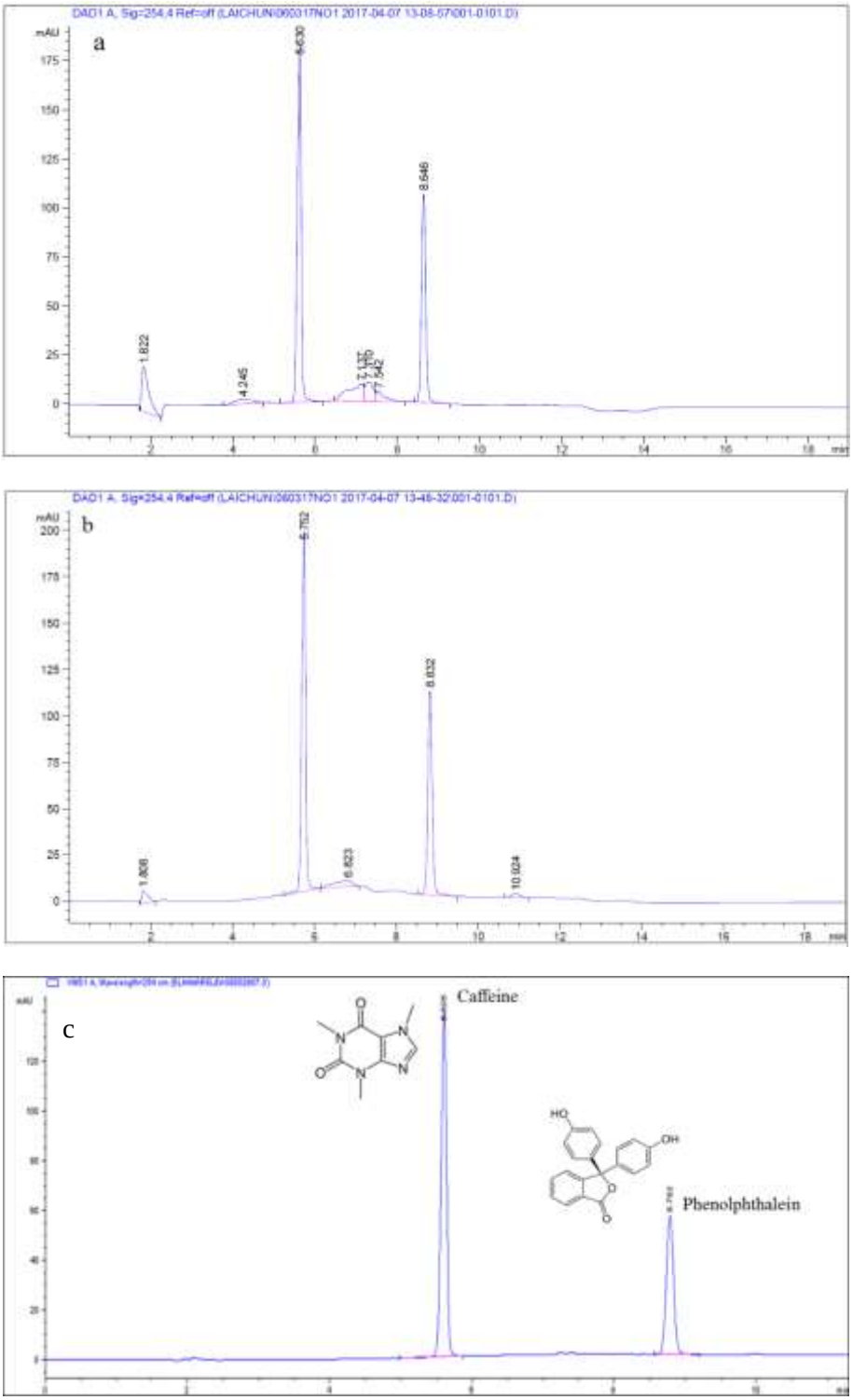



Figure 2. The HPLC chromatogram of mixed working solution (50 µg/mL) under chromatographic conditions of the developed method with ammonium acetate buffer at (a) pH 3.8; (b) pH 5.8 and (c) pH 5

Table 2. System suitability test parameters

| **Parameters** | **Caffeine** | **Phenolphthalein** | **ICH Requirement** |
|---|---|---|---|
| Numbers of theoretical plate | 43 442 | 58 100 | > 10 000 |
| Peak symmetry | 1.5 | 1.3 | < 2 |
| Retention factor (min) | 2.18 | 4.04 | - |
| Precision (%RSD, n = 6) | 1.32 | 1.49 | < 2 % |
| Resolution (R) | 26.125 | 26.125 | > 1.5 |

**Validation criteria of the HPLC method: Specificity**

Specificity was indicated by the absence of any endogenous interference at retention times close to the peaks of interest, as evaluated by chromatograms of blank samples and blank samples spiked with analytes. Retention times for caffeine and phenolphthalein in the spiked sample were 5.652 minutes and 8.987 minutes respectively. In the blank sample, no interfering peaks were found at the retention times of caffeine and phenolphthalein (Figure 3).

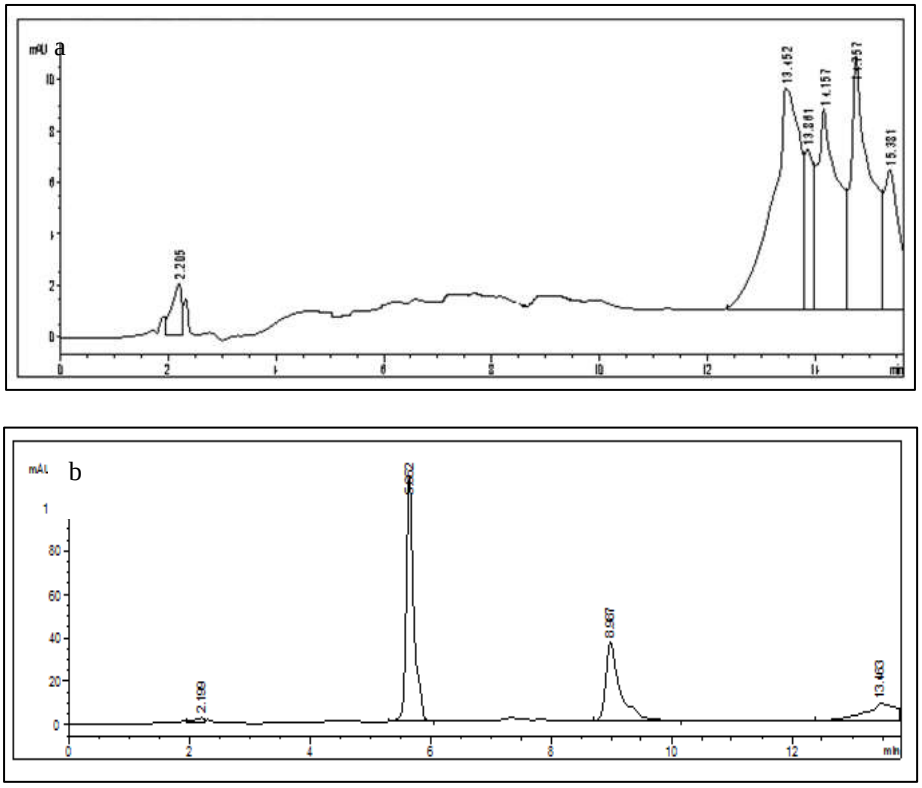



Figure 3. Representative chromatograms for (a) blank sample and (b) blank sample spiked with caffeine (50 µg/mL) and phenolphthalein (50 µg/mL)

**Linearity**

The calibration curves for caffeine and phenolphthalein were plotted using ordinary least-square linear regression over the concentration range 10 µg/mL to 100 µg/mL (Figure 4). A linear relationship was established between the peak area and analyte concentrations over the range tested, and it was confirmed by the correlation coefficient ($R^2$) value where $R^2$ values were higher than 0.990. The slope and intercept of the calibration curve was calculated, and the following linear equation was obtained: y = 22.751x + 66.613 for caffeine and y = 11.352x + 5.716 for phenolphthalein. Therefore, it can be concluded that the calibration curves for caffeine and phenolphthalein is linear within the range 10 µg/mL to 100 µg/mL.

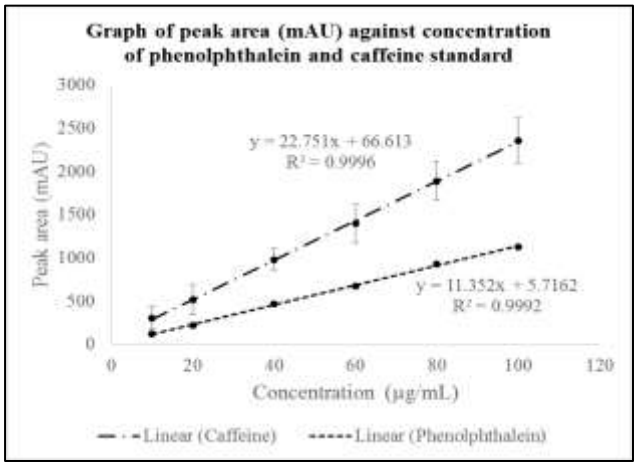



Figure 4. Calibration curve for caffeine and phenolphthalein in concentration range 10 – 100 µg/mL

**Limit of detection and limit of quantification**

The LOD for both caffeine and phenolphthalein determined from the residual standard deviation of the regression line was found to be 0.77 µg/mL and 0.47 µg/mL, respectively. The LOQ for caffeine and phenolphthalein determined from the residual standard deviation of a regression line was found to be 2.35 µg/mL and 1.44 µg/mL, respectively. The LOD and LOQ values for caffeine were found to be comparable with those reported in a previous study using HPLC-UV (0.75 µg/mL and 2.25 µg/mL respectively) [22]. However, the LOD and LOQ values for phenolphthalein obtained in this study were higher than the values reported in the previous study (0.1 µg/mL and 0.3 µg/mL, respectively) [22]. The higher LOD and LOQ values for phenolphthalein could be attributed by the different wavelength used in our study (254 nm) compared to the previous one (220 nm).

**Accuracy**

The percentage recovery values of caffeine and phenolphthalein at low, medium and high concentrations are summarised in Table 3. The mean percentage recovery values for caffeine and phenolphthalein in the range of concentration tested were found to 105.84% and 113.58% respectively. The method was proven to be accurate in measuring caffeine and phenolphthalein in the concentrations tested, where the measured concentration values were close to the true values.

**Precision**

The intra-day precisions for caffeine and phenolphthalein were found to be between 0.67 – 1.99% and 0.80 – 1.55%, respectively, while the inter-day precisions for caffeine and phenolphthalein over three consecutive days were between 0.67 – 1.99% and 0.80 – 1.79%, respectively. In both cases, percentage RSD values were found well within the 2% limit. Therefore, the method is proven to be repeatable and is capable of producing consistent results regardless of whether the analysis is made in the same or on different days. The percentage RSD values for precision are summarised in Table 4.

Table 3. Accuracy of the HPLC method expressed as percentage recovery (% recovery), determined using spiking (three spike levels) experiment

| Spike Levels | Compound | Spiked (Theoretical) µg/mL | Spiked (Found) µg/mL | % Recovery (n = 3) |
|---|---|---|---|---|
| Low | Caffeine | 11.00 | 11.49 | 104.45 ± 3.82 |
| | Phenolphthalein | 10.44 | 12.54 | 120.11 ± 4.50 |
| Medium | Caffeine | 22.00 | 23.78 | 108.07 ± 0.59 |
| | Phenolphthalein | 20.88 | 23.79 | 113.94 ± 0.43 |
| High | Caffeine | 33.00 | 34.65 | 105.00 ± 0.64 |
| | Phenolphthalein | 31.32 | 33.42 | 106.70 ± 0.93 |

Table 4. Intra-day and inter-day precision of the HPLC method to detect and quantify caffeine and phenolphthalein, measured on three consecutive days

| Day | Compound | % RSD |
|---|---|---|
| 1 | Caffeine | 0.68 – 1.14% |
| | Phenolphthalein | 0.84 – 1.55% |
| 2 | Caffeine | 1.22 – 1.48% |
| | Phenolphthalein | 1.00 – 1.52% |
| 3 | Caffeine | 1.41 – 1.85% |
| | Phenolphthalein | 0.93 – 1.79% |

**Stability of mixed working standard solution**

Mixed working standard solution (50 µg/mL) was found to be stable over up to 24 hours under refrigeration conditions (4 °C). Stability values for caffeine and phenolphthalein were 99.0 ± 0.9% and 97.4 ± 2.5%, respectively. The stability values are summarised in Table 5 below.

Table 5. Stability of mixed working standard solution at 4°C after 24 hours

| Solution | Compounds | Stability (%) (n = 3) |
|---|---|---|
| Mixed working solution (50 µg/mL) | Caffeine | 99.0 ± 0.9 |
| | Phenolphthalein | 97.4 ± 2.5 |

**Robustness**

System suitability parameters (precision, peak symmetry, number of theoretical plates, retention factor and resolution) remained within the acceptable limit range [20,26,27] after deliberate changes in the three robustness parameters tested (Table 6). This indicates robustness of method for flow rate ± 0.2 mL/min, buffer pH ± 0.2 units and organic content ± 2.0%.

**Analysis of representative samples**

Five herbal weight reducing supplements (products A, B, C, D and E) were purchased from the Kuala Lumpur area. All the products were advertised by the manufacturers to be derived from natural plant sources. The concentrations of caffeine and phenolphthalein quantified in the products are summarised in Table 7 below. Phenolphthalein was

detected in two of the five products. Product A was found to contain the highest amount of phenolphthalein, about 40 mg per capsule. The chromatogram of product A is shown in Figure 5 below. As the instruction on the product label recommends three capsules daily, a consumer may be ingesting up to 120 mg of phenolphthalein a day. The typical dose for adults before it was withdrawn as a laxative was 30 – 200 mg, and it was not recommended to exceed 270 mg [28]. Phenolphthalein has been detected as an undeclared drug in weight reducing supplements around the world in concentrations ranging from 48.20 – 1167 mg/capsule of mg/pill [2, 29] and 13.8 – 45.4 mg/g [5]. It is expected that adulteration of weight reducing products with phenolphthalein will be identified more frequently in the future, as phenolphthalein is widely available in laboratories and is cheap.

Table 6. System suitability parameters after deliberate changes in flow rate, buffer pH and buffer organic content of the mobile phase

| **Parameter** | | **Compound** | **Precision (% RSD) n = 6** | **Peak Symmetry** | **Number of Theoretical Plates** | **Retention Factor** | **Resolution** |
|---|---|---|---|---|---|---|---|
| Flow rate, mL/min | 0.9 | Caffeine | 1.53 | 1.3 | 48 771 | 2.59 | 25.35 |
| | | Phenolphthalein | 1.39 | 1.2 | 53 313 | 4.66 | |
| | 1.3 | Caffeine | 2.80 | 1.4 | 41 145 | 1.89 | 25.89 |
| | | Phenolphthalein | 2.54 | 1.2 | 57 037 | 3.64 | |
| Buffer pH | 4.8 | Caffeine | 4.10 | 1.3 | 18 719 | 2.19 | 21.08 |
| | | Phenolphthalein | 2.52 | 1.4 | 57 110 | 4.07 | |
| | 5.2 | Caffeine | 3.83 | 1.2 | 22 693 | 2.19 | 22.28 |
| | | Phenolphthalein | 4.08 | 1.2 | 58 254 | 4.07 | |
| Organic Content | +2% | Caffeine | 2.57 | 1.8 | 15 374 | 2.10 | 19.91 |
| | | Phenolphthalein | 3.53 | 1.3 | 76 249 | 4.84 | |
| | -2% | Caffeine | 3.58 | 1.5 | 17 140 | 2.28 | 21.99 |
| | | Phenolphthalein | 0.01 | 1.4 | 49 863 | 4.45 | |

Table 7. Amount of caffeine and phenolphthalein measured in weight reducing supplements purchased from Kuala Lumpur

| **Product** | **Formulation** | **Analysis of Weight Reducing Supplements** | | |
|---|---|---|---|---|
| | | **Analyte** | **Concentration (mg/g)** | **Amount Consumed per Sachet/Capsule (mg)** |
| A | Capsule | Caffeine | 1.51 ± 0.038 | 0.49 ± 0.012 |
| | | Phenolphthalein | 126.82 ± 0.46 | 40.73 ± 0.14 |
| B | Capsule | Caffeine | ND | ND |
| | | Phenolphthalein | 0.76 ± 0.002 | 0.63 ± 0.002 |
| C | Capsule | Caffeine | ND | ND |
| | | Phenolphthalein | ND | ND |
| D | Capsule | Caffeine | ND | ND |
| | | Phenolphthalein | ND | ND |
| E | Powder | Caffeine | 2.16 ± 0.12 | 43.28 ± 2.48 |
| | | Phenolphthalein | ND | ND |

ND: Not detected

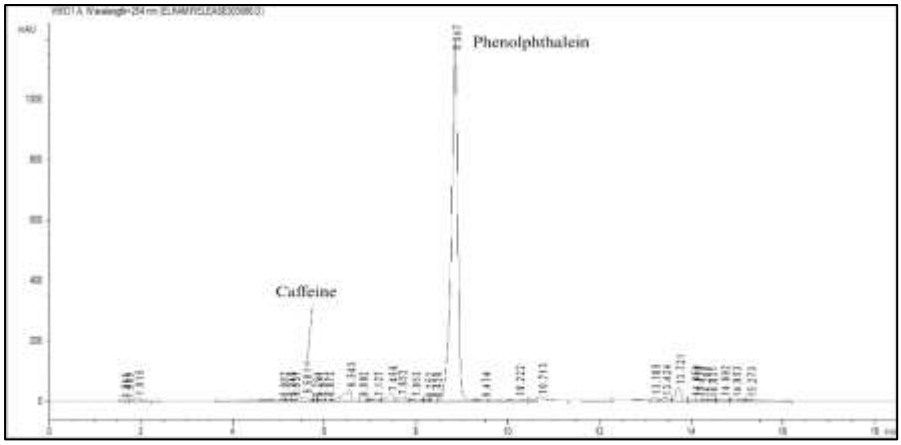



Figure 5. HPLC chromatogram of Product A. Caffeine and phenolphthalein elutes out at 5.581 and 8.847 minutes, respectively

Caffeine is classified by the FDA as generally recognised as safe (GRAS), with a toxic dose being over 10 g for an average adult. Caffeine was detected in two of the products, and the concentration measured to be within the safe limit. Further clean-up of product E was attempted by the LLE method to improve the reliability of caffeine measurement due to the complicated matrix in the product (Figure 6). The extraction method is as described in the materials and methods section. Product E was dissolved in basic solution prior to extraction of caffeine with dichloromethane. Water soluble impurities and tannins (if present) remained in the basic solution. As observed from the chromatogram in Figure 7, LLE may be an effective clean-up method for products with complicated matrices. However, it should be noted that products suspected to be adulterated with phenolphthalein should be dissolved in water instead of basic solution, as phenolphthalein contains acidic phenolic groups.

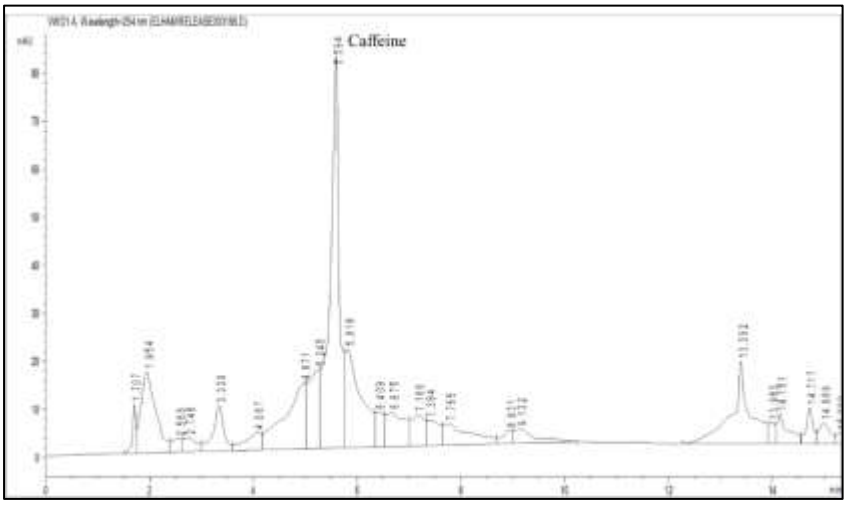



Figure 6. HPLC chromatogram of Product E before LLE. Caffeine elutes out at 5.594 minutes

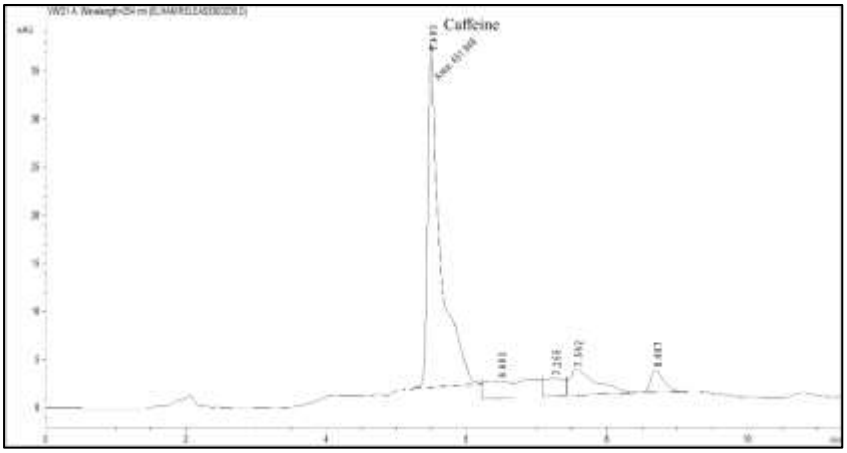



Figure 7. HPLC chromatogram of Product E after LLE. Caffeine elutes out at 5.493 minutes

## Conclusion

A RP-HPLC-UV analytical method with variable wavelength detection was developed and validated for the simultaneous detection of caffeine and phenolphthalein in weight reducing supplements. Out of five supplements screened, two products were found to be adulterated with phenolphthalein. The validation was performed according to ICH guidelines. The HPLC method developed is selective, accurate, precise, robust and relatively fast (10 minutes). Moreover, the use of ammonium acetate buffer combined with methanol allows the transfer to a mass spectrometer, leading to a more thorough investigation in case of any doubt. The method can be easily adapted for rapid detection of caffeine and phenolphthalein in herbal products in quality control laboratories with a HPLC instrument.

## Acknowledgement

This work was supported by the International Medical University (Project ID No.: MAPC I1/2013 (4)). The authors would like to thank Dr. Ng Sook Han for her assistance in supervising Ms Elham Mohammadi Nasr.

## References

1. Arroyo-Johnson, C and Mincey, K. D. (2016). Obesity epidemiology worldwide. *Gastroenterology Clinics*, 45(4): 571 – 579.
2. Ancuceanu, R., Dinu, M. and Arama, C. (2013). Weight loss food supplements: Adulteration and multiple quality issues in two products of chinese origin. *Farmacia*, 61(1): 28 – 44.
3. de Carvalho, L. M., Martini, M., Moreira, A. P., de Lima, A. P., Correia, D., Falcão, T., Garcia, S. C., de Bairros, A. V., do Nascimento, P. C. and Bohrer, D. (2011). Presence of synthetic pharmaceuticals as adulterants in slimming phytotherapeutic formulations and their analytical determination. *Forensic Science International*, 204(1-3): 6 – 12.
4. Ioset, J. R., Raoelison, G. E. and Hostettmann, K. (2003). Detection of aristolochic acid in chinese phytomedicines and dietary supplements used as slimming regimens. *Food and Chemical Toxicology*, 41(1): 29 – 36.
5. Wang, J., Chen, B. and Yao, S. (2008). Analysis of six synthetic adulterants in herbal weight-reducing dietary supplements by LC electrospray ionization-MS. *Food Additives & Contaminants. Part A, Chemistry, Analysis, Control, Exposure & Risk Assessment*, 25(7): 822 – 830.
6. Shi, Y., Sun, C., Gao, B. and Sun, A. (2011). Development of a liquid chromatography tandem mass spectrometry method for simultaneous determination of eight adulterants in slimming functional foods. *Journal of Chromatography A*, 1218(42): 7655 – 7662.
7. Haneef, J., Shaharyar, M., Husain, A., Rashid, M., Mishra, R., Siddique, N. A. and Pal, M. (2013). Analytical methods for the detection of undeclared synthetic drugs in traditional herbal medicines as adulterants. *Drug Testing and Analysis*, 5(8): 607 – 613.

8. Dunn, J. D., Gryniewicz-Ruzicka, C. M., Mans, D. J., Mecker-Pogue, L. C., Kauffman, J. F., Westenberger, B. J. and Buhse, L. F. (2012). Qualitative screening for adulterants in weight-loss supplements by ion mobility spectrometry. *Journal of Pharmaceutical and Biomedical Analysis*, 71: 18 – 26.
9. Rebiere, H., Guinot, P., Civade, C., Bonnet, P. and Nicolas, A. (2012). Detection of hazardous weight-loss substances in adulterated slimming formulations using ultra-high-pressure liquid chromatography with diode-array detection. *Food Additives & Contaminants. Part A, Chemistry, Analysis, Control, Exposure & Risk Assessment*, 29(2): 161 – 171.
10. Deconinck, E., Verlinde, K., Courselle, P. and Beer J. O. (2012). A validated ultra high pressure liquid chromatographic method for the characterisation of confiscated illegal slimming products containing anorexics. *Journal of Pharmaceutical and Biomedical Analysis*, 59: 38 – 43.
11. Phattanawasin, P., Sotanaphun, U., Sukwattanasinit, T., Akkarawaranthorn, J. and Kitchaiya, S. (2012). Quantitative determination of sibutramine in adulterated herbal slimming formulations by TLC-image analysis method. *Forensic Science International*, 219: 96 – 100.
12. Food and Drug Administration. Drugs (2009). Available from: http://www.fda.gov/Drugs/ResourcesForYou/ Consumers/QuestionsAnswers/ucm136187.htm. Date acces on 1 April 2017.
13. Dunnick, J. K. and Hailey, J. R. (1996). Phenolphthalein exposure causes multiple carcinogenic effects in experimental model systems. *Cancer Research*, 56(21): 4922 – 4926.
14. World Health Organization (1998). World drug information. *Essential Medicines and Pharmaceutical Policies*, 12(1): 1 – 21.
15. International Agency on Research for Cancer (2000). Some antiviral and antineoplastic drugs, and other pharmaceutical agents. *IARC Monographs on the Evaluation of Carcinogenic Risks to Humans*, 76: 387 – 415.
16. Barone, J. J. and Roberts, H. (1984). Human consumption of caffeine. *Caffeine*, 59 – 73.
17. Diepvens, K., Westerterp, K. R. and Westerterp-Plantenga, M. S. (2007). Obesity and thermogenesis related to the consumption of caffeine, ephedrine, capsaicin, and green tea. *American Journal of Physiology - Regulatory, Integrative and Comparative Physiology*, 292(1): 77 – 85.
18. Snel, J. and Lorist, M. M. (2011). Effects of caffeine on sleep and cognition. *Progress in Brain Research*, 190: 105 – 117.
19. Cannon, M. E., Cook, C. T. and McCarthy, J. S. (2001). Caffeine-induced cardiac arrhythmia: An unrecognised danger of healthfood products. *Medical Journal of Australia*, 174(10): 520 – 521.
20. International Conference on Harmonisation (1996). Guidance for industry Q2B validation of analytical procedures: Methodology: pp. 1 – 10.
21. Zheng-Fei, P. (2011). Determination of caffeine, phenolphthalein and sibutramine illegally added to weight loss functional food with UPLC/MS/MS. *China Tropical Medicine*, 11(9): 1116 – 1117.
22. Hammadi, R. and Almardini, M. A. (2014). A fully validated HPLC-UV method for quantitative and qualitative determination of six adulterant drugs in natural slimming dietary supplements. *International Journal of Pharmaceutical Sciences Review and Research*, 29(1): 171 – 174.
23. National Center for Biotechnology Information (2004). Caffeine. Available from: http://pubchem.ncbi. nlm.nih.gov/summary/summary.cgi?cid=2519. Acesss online on 1 April 2017.
24. National Center for Biotechnology Information (2005). Phenolphthalein. Available from: http://pubchem.ncbi. nlm.nih.gov/summary/summary.cgi?cid=4764. Access online on 1 April 2017.
25. Rahim, A. A., Nofrizal, S. and Saad, B. (2014). Rapid tea catechins and caffeine determination by HPLC using microwave-assisted extraction and silica monolithic column. *Food Chemistry*, 147: 262 – 288.
26. Shabir, G. (2003). Validation of high-performance liquid chromatography methods for pharmaceutical analysis. understanding the differences and similarities between validation requirements of the US Food and Drug Administration, the US Pharmacopeia and the International Conference on Harmonization. *Journal of Chromatography A*, 987(1-2): 56 – 66.
27. Center for Drug Evaluation and Research CDER (1994). Reviewer guidance-validation of chromatographic methods: pp. 1 – 30.
28. U.S. Department of Health and Human Services. (2016). 14th Report on carcinogens (phenolphthalein). National Toxicology Program.

29. Khazan, M., Hedayati, M., Kobarfard, F., Askari, S. and Azizi, F. (2014). Identification and determination of synthetic pharmaceuticals as adulterants in eight common herbal weight loss supplements. *Iranian Red Crescent Medical Journal*, 16(3): 15344 - 15350.

*Malaysian Journal of Analytical Sciences, Vol 21 No 3 (2017): 619 - 626*
*DOI: https://doi.org/10.17576/mjas-2017-2103-11*

MALAYSIAN JOURNAL OF ANALYTICAL SCIENCES
*Published by The Malaysian Analytical Sciences Society*
ISSN 1394 - 2506

# REMOVAL OF LEAD(II) FROM AQUEOUS SOLUTION USING POLYACRYLONITRILE/ZINC OXIDE ACTIVATED CARBON NANOFIBERS

## (Penyingkiran Plumbum(II) daripada Larutan Akues Mengunakan Gentian Nano Karbon Teraktif Poliakrilonitril/Zink Oksida)

Norfadhilatuladha Abdullah[1,2], Muhamad Hanis Tajuddin[1,2], Norhaniza Yusof[1,2]*,Juhana Jaafar[1,2], Farhana Aziz[1,2], Nurasyikin Misdan[3]

[1]*Advanced Membrane Technology Research Centre (AMTEC)*
[2]*Faculty of Chemical and Energy Engineering (FCEE)*
*Universiti Teknologi Malaysia, 81310 Skudai, Johor Bahru, Malaysia*
[3]*Faculty of Engineering Technology,*
*Universiti Tun Hussein Onn Malaysia, 86400 Parit Raja, Johor, Malaysia*

**Corresponding author: norhaniza@petroleum.utm.my*

Received: 26 August 2016; Accepted: 8 January 2017

**Abstract**

This study aimed to prepare activated carbon nanofibers (ACNFs) from polyacrylonitrile (PAN) and zinc oxide (ZnO) via electrospinning process for removal of lead from aqueous solution. The ACNFs/ZnO were characterized in term of its morphological changes, specific surface area and functional groups analysis using Field Emission Scanning Electron Microscope (FESEM), Brunauer–Emmett–Teller (BET) and Fourier Transform Infrared (FTIR) analysis, respectively. The results showed that the specific surface area (SSA) of the ACNFs/ZnO were higher than the neat ACNFs which were 163.04 $m^2/g$ as compared to 67.6 $m^2/g$, accordingly. FESEM analysis illustrated that composite ACNFs possessed more compact fibers with presence of ZnO beads and smaller fiber diameter whereas neat ACNFs possessed more aligned nanofibers with larger fiber diameter. Adsorption study showed that the composite ACNFs possessed higher capacity which was 120.3 mg/g as compared to 77.6 mg/g of neat ACNFs. This excellent adsorption performance of ACNFs PAN/ZnO exhibits the potential of this composite adsorbent to solve the environmental issue of heavy metal contamination.

**Keywords**: activated carbon, activated carbon nanofiber, adsorption capacity, lead adsorption

**Abstrak**

Kajian ini bertujuan untuk menyediakan gentian-nano karbon teraktif (ACNFs) daripada poliakrilonitril (PAN) and zink oksida melalui proses putaran-elektro untuk menyingkirkan plumbum (II) daripada larutan akues. ACNFs/ZnO dicirikan berdasarkan perubahan morfologi, luas permukaan spesifik, dan analisis kumpulan berfungsi mengunakan Mikroskopi Elektron Pengimbasan Pancaran Medan (FESEM), Brunauer–Emmett–Teller (BET) dan Inframerah Transformasi Fourier (FTIR). Keputusan kajian menunjukkan luas permukaan spesifik (SSA) komposit ACNFs adalah lebih tinggi berbanding ACNFs tanpa logam oksida iaitu 163.04 $m^2/g$ berbanding 67.6 $m^2/g$. Analisis FESEM menunjukkan komposit ACNFs mempunyai gentian lebih padat dengan kehadiran manik zink oksida and mempunyai diameter gentian lebih kecil manakala ACNFs tanpa logam oksida mempunyai gentian lebih tersusun dengan diameter gentian yang lebih besar. Ujian penjerapan menunjukkan bahawa penyingkiran Pb(II) menunjukkan kapasiti penjerapan yang lebih tinggi, iaitu 120.0 mg/g berbanding 77.6 mg/g oleh ACNFs tanpa ZnO. Hasil kajian ini menunjukkan potensi PAN/ZnO ACNFs sebagai penjerap untuk menyelesaikan isu pencemaran logam berat dalam persekitaran.

**Kata kunci:** karbon teraktif; gentian nano karbon teraktif, kapasiti penjerapan, penjerapan plumbum

## Introduction

Recently, contamination of water by heavy metals has becomes a major concern among researchers. Their exposure towards human and enviroment could cause acute effects due to their non-degradable property and their rapid bio-accumulation into body system [1]. In water, some heavy metals that are commonly present are cadmium, arsenic, copper, iron, manganese and lead. Out of these hazardous heavy metals, the removal of lead (Pb) has been extensively studied. In general, the major athrophogenic source of Pb disposal is mainly from industry, such as from leaded gasoline, leaded pipes, building construction, radiation shields, battery industries as well as lead smelting and bearings [2]. The effects of Pb exposure are well documented in which even a very small amount of Pb will results acute effects to nervous system, hematopoeitic system, cardicac and vascular system, metabolism, reproductive system and immune system [3]. To date, the maximum contaminant level (MCL) of Pb in drinking set by World Health Organization (WHO) and US Environmental Protection Agency (USEPA) is 15 µg/L [3]. With the increasing development of industrilization, the amount of Pb being released into water streams will aggravate. Therefore, the elevated amount of Pb in water is an important matter to be concerned.

Due to hazardous exposure of Pb on human and environment, there are various techniques have been implied for its removal from water streams; such as coagulation-flocculation, precipitation, ion exchange, membrane technology and adsorption [4]. Among the mentioned methods, adsorption stands as a promising techniques for removing heavy metals in which the process is relatively simple, effective and economic. In brief, adsorption is a process whereby the adsorbents are attached on the surface of solid or adsorbent [4]. There are wide range of adsorbents have been used for removal of Pb(II) such as natural products, zeolite, aluminosilicate, peat, clay, and activated carbon [5]. Among the wide range adsorbents, carbon-based materials particularly activated carbon (ACs) has become as one of the commonly used adsorbent for Pb(II) adsorption ascribed by their highly porous and high specific surface area [5]. In recent years, studies have been focusing on the development of activated carbon in nanofiber form (ACNFs). The developed ACNFs have been reported to possess smaller pore diameter with more concentrated pore size distribution which this properties are required for adsorption process [5].

There are several methods can be used to fabricate nanofibers such as melt fibrillation, island-in-sea, electro-spinning and gas jet technique [6]. Nevertheless, it seems that electro-spinning process as shown in Figure 1 provides more advantages in term of high production rate and relatively low in cost as compared to the other techniques mentioned previously. To prepare electrospun ACNFs, polymer polyacrylonitrile (PAN) serves as an excellent carbon precursor as it has high carbon yield as compared to other carbon precursors [6]. Recently, many researchers had focused on incorporating various metal oxides such as magnesium oxide, iron oxide, zinc oxide, aluminium oxide and manganese oxide as additive in the dope suspension of ACNFs [7]. Adding metal oxides such as zinc oxide can enhance adsorption capacity as it is reported that these additives can improve the properties of the ACNFs [8,9]. Thus, the aim of this study is to fabricate ACNFs based polyacrylonitrile (PAN) as carbon precursor and zinc oxide as additive by electrospinning process. The prepared ACNFs were evaluated based on its physicochemical properties as well as it adsorptive performance towards Pb(II) from aqueous solution.

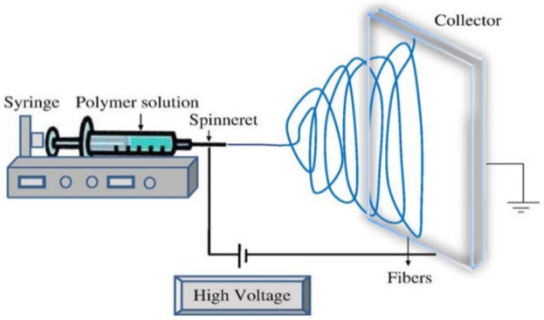



Figure 1. Schematic setup for electrospinning process [7]

## Materials and Methods

### Materials

Polyacrylonitrile (PAN) with molecular weight of 150kDa was purchased from Sigma Aldrich (USA). Similarly, N,N-Dimethylformamide (DMF) and zinc oxide (ZnO) powder with 99% purity were purchased from Alfa Aesar. Stock solution of Pb(II) was prepared using lead nitrate ($Pb^2NO^3$) powder (Sigma Aldrich, USA) while the pH of heavy metal solution was adjusted by using 0.1mol of NaOH and HCl.

### Preparation of PAN-ZnO nanofibers by electrospinning

Initially, dope solution of PAN-ZnO was prepared by stirring 5 wt.% of ZnO powder with N-N dimethylformamide (DMF) for 5 hours followed by addition of 10 wt.% polyacrylonitrile (PAN). The mixture was again continuously stirred for another 24 hours to obtain a homogenous solution. The dope solution was later subjected to electrospinning process under the electric field of 12kV, suspension rate of 1.0mL/hour and distance of 20 cm. The collected nanofibrous mats were allowed to dry for at least a day prior to carbonization and activation process.

### Preparation of PAN-ZnO ACNFs

The PAN-ZnO nanofibrous mats were later subjected to three pyrolysis processes: 1) stabilization; 2) carbonization and 3) activation following procedure [10]. The nanofibers were stabilized in pure air at temperature of 250 $^oC$ for 4 hours with heating rate of 1 $^oC$/min. For the carbonization process, the process was carried out in nitrogen gas at temperature of 325 $^oC$ for 1.5 hours with heating rate of 3 $^oC$ /min. Lastly, the carbonized nanofibers were activated at a heating rate of 3 $^oC$/min with under carbon dioxide until temperature at 425 $^oC$. The physicochemical properties of the end product which is activated carbon nanofibers (ACNFs) was characterized as described in section 2.4. Figure 2 shows the procedures of ACNFs fabrication.

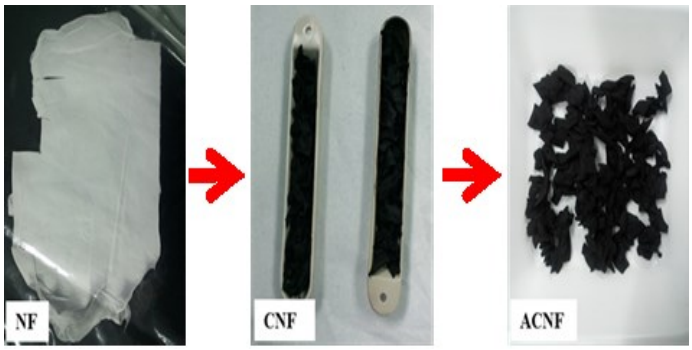



Figure 2. Preparation of nanocomposite ACNFs/ZnO

### Characterization

In this study, characterizations were carried out in term of specific surface area (SSA), morphological structures and functional groups analysis by BET, FESEM-EDX and FTIR, respectively. To analyze the specific surface area of NFs and ACNFs, the specific surface area was determined by using automatic Tristar 3000 volumetric system.The surface morphologies of the ACNFs were examined using Field Emission Scanning Electron Microscopy (FESEM) respectively. The samples were placed on a staph and were sputtered with gold prior of FESEM analysis. The distribution and presence of Zn particles were analyzed by EDX, which was conducted by using the images captured by FESEM analysis. The functional groups present in PAN-ZnO ACNFs were identified using ATR-FTIR spectrometer (Model: IRTRACE100, Shimadzu). The samples were scanned by single-reflectance ATR accessory with IRTRACER100. The sample was prepared by cutting it into a small pieces and scanning at a wavelength 400 $cm^{-1}$ to 4000 $cm^{-1}$.

**Pb(II) adsorption study**

The adsorptive performance of ACNFs on lead removal was conducted by studying the effect of initial pH and initial concentration. In every sample, 0.01 g of neat ACNFs and composite ACNFs was added into 10 mL Pb(II) solution. The solution was agitated for 48 hours in rotary shaker. The pH was adjusted using 0.1 mol of NaOH and HCI. The equilibrium concentrations of each samples was measured by filtering the samples and analyzed using Atomic Absorption Spectrometer (AAS) (model 4100ZL, Perkin Elmers).

The removal efficiency, R(%) and adsorption capacity of prepared PAN-ZnO ACNFs were calculated using equation 1 and 2, respectively [9]:

$$R(\%)= (C_o-C_e)/C_o \times 100 \quad (1)$$

$$q_e\ (mg/g)=(C_o-C_e)V/m \quad (2)$$

where $C_o$ is initial concentration of metal (mg/L); $C_e$ is equilibrium concentration of metal (mg/L); $V$ is volume of solution in (L) and $m$ is mass of adsorbent.

**Adsorption isotherm**

Adsorption isotherm analysis was conducted to analyze the adsorption behavior of ACNFs for the removal of Pb(II) ions from aqueous solution. The linear equations of Langmuir and Freundlich models are described from equation 3 and 4, respectively [9].

$$C_e/q_e = 1/Q_{max}b + C_e/Q_{max} \quad (3)$$

where $q_e$ is amount of Pb (II) adsorbed to adsorbent (mg/g); $C_e$ is equilibrium concentration of metal (mg/L). $Q_{max}$ is maximum adsorption capacity (mg/g) and $b$ is the Langmuir constant.

$$\ln q_e = \ln KF + (1/n) \ln C_e \quad (4)$$

$q_e$ is amount of Pb (II) adsorbed to adsorbent (mg/g); $C_e$ is equilibrium concentration of metal (mg/L); $K_F$ is the Freundlich constant (mg/g) and $1/n$ is parameter related to adsorption intensity.

## Results and Discussion

**Characterizations of PAN-ZnO ACNFs**

***Specific surface area***

Table 1 shows the specific surface area (SSA) of ACNFs and ACNFs/ZnO after activation process. From the table, it can be seen that addition of ZnO in the ACNFs increased the specific surface area from 67.60 $m^2/g$ for neat ACNFS to 163.04 $m^2/g$ for composite ACNFs/ZnO. The larger specific surface area could be resulted from the role of metal oxides (in our study, ZnO) that acts as catalyst that accelerates the process of carbonization and activation. As results, more pores were created which contributes to larger specific surface area [8]. Nevertheless, the SSA obtained by both ACNFs were lower as compared to the studies reported elsewhere [9]. It is believed that the carbonization and activation process of the ACNFs might be incomplete, and thus contributed to low SSA when analyzed by BET analysis. Thus, longer duration of activation and carbonization might be required.

Table 1. Specific surface area of NFs and ACNFs

| Sample | Specific Surface Area (S.S.A) ($m^2/g$) | |
|---|---|---|
| | Before Activation | After Activation |
| Neat ACNFs | 9.13 | 67.60 |
| ACNFs/ZnO | 8.91 | 163.04 |

***SEM/FESEM – EDX analysis***

The structural morphologies of neat ACNFs and composite ACNFs are shown in Figure 3. It can be seen that the neat ACNFs possessed more aligned and straight fibers while the PAN-ZnO ACNFs showed more compact arrangement with bent surfaces. The result obtained is in agreement to study conducted by Imtiaz et al. where the activation process and the presence of ZnO led to cross-sectional shrinkage and causing the surface of fibers became rougher and more compact [11]. It can also be seen that there are white spots present alongside the fibers (as indicated by circle marks) which this could be referred as ZnO which is dispersed as beads alongside the PAN-ZnO nanofibers. Dispersion of ZnO beads further supported with EDX mapping as depicted in Figure 4 confirmed that ZnO exists in the ACNFs.

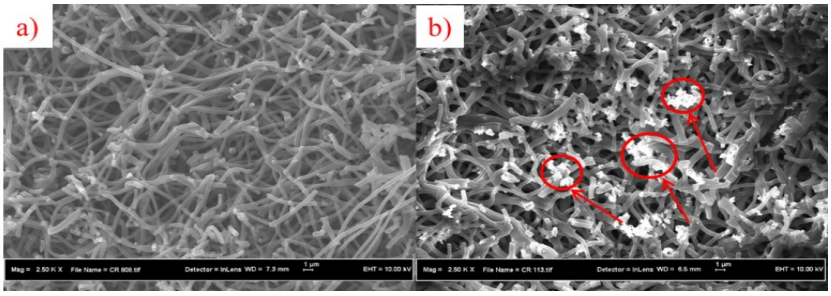



Figure 3. Structural morphologies of a) neat ACNFs and b) PAN-ZnO ACNFs

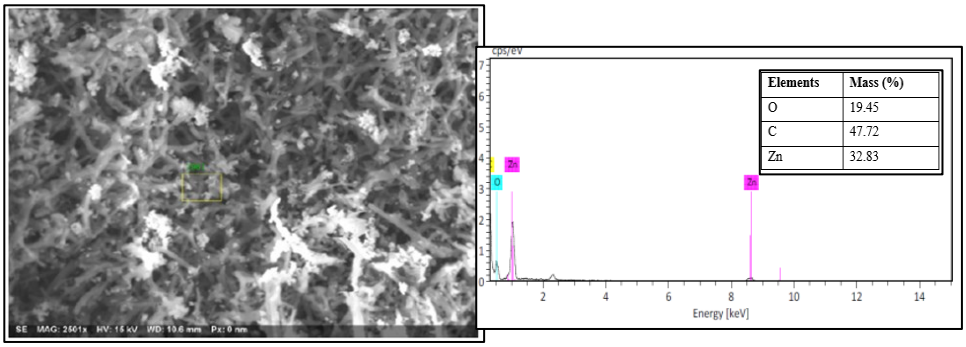



Figure 4. EDX mapping and elemental analysis of PAN-ZnO ACNFs

***FTIR analysis***

Figure 5 displays the FTIR spectrum of neat and PAN/ZnO based ACNFs. It can be seen that the activation process removed nitrile groups (C≡N) and methylene group ($CH_2$), only carbon and hydrogen remain as observed at wavelength peaks of 1573 $cm^{-1}$ and 1250 $cm^{-1}$ indicating aromatic C-C groups and alkyl halides C-H groups [9]. In addition, absorption peak at 436.5$cm^{-1}$ was identified as Zn-O, indicating the presence of ZnO nanoparticles in the composite ACNFs [11]. The result is supported by EDX-mapping as displayed by Figure 4 previously, which showing the presence of elements Zn.

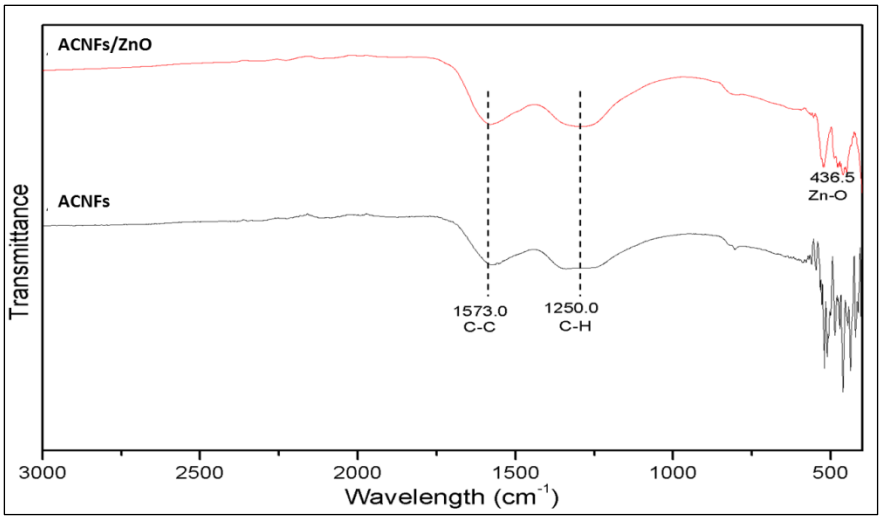



Figure 5. FTIR spectrum of ACNFs and ACNFs/ ZnO

**Adsorptive performance of ACNFs on Pb removal**

***Effect of pH***

The adsorption of Pb(II) on ACNFs/ZnO at different pH (1.0 to 6.0) was conducted and the results are shown in Figure 6. The pH values higher than 6 was not tested in order to avoid precipitation of Pb(II) with $OH^-$ ions which will form lead salts as well as to avoid any inaccuracy [11]. It can be seen from the figure that increasing pH of the Pb solution increased the removal efficiency. For neat ACNFs, the removal efficiency of Pb is 20.1% (pH 1.0) to 99.4% (pH 4.0). After pH 4.0, there is no increment of removal was obtained. Therefore, the optimum pH of Pb(II) removal on ACNFs is from pH 4.0 to pH 6.0. Similarly, for ACNFs/ZnO, increasing the pH caused a gradual increase of Pb(II) removal from 20.0% (pH 1.0) to 99.4% (pH 6.0) in which the optimum pH for removal of Pb on ACNFs/ZnO is at pH 6.0. From the pH study, it can be seen that both ACNFs and ACNFs/ZnO have good removal efficiency which was more than 99.0%. From the trend shown by both ACNFs, it is evident that the removal of Pb(II) is strongly related to pH which is related to the protonation of the functional groups existed in ACNFs. In acidic condition, low adsorption efficiency was achieved due to the competition between H+ and metal ions for active sorption sites while at higher pH value, thus permitting the attraction between the metal ions and the surface of the adsorbent [8, 9].

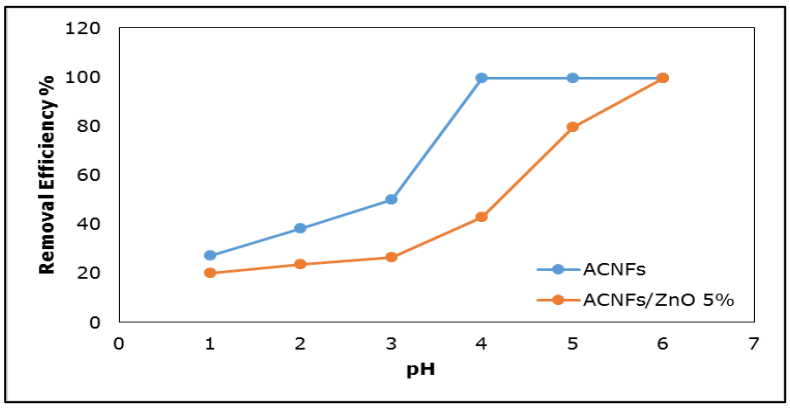



Figure 6. Effects of pH on removal of Pb(II)

***Effect of initial concentration***

Figure 7 depicts the removal of Pb(II) by neat and PAN-ZnO ACNFs with respect to different initial concentration (10 – 121 mg/L) of Pb(II) solution. For both ACNFs, it can be seen that the percentage of adsorption capacity increased with the increase of initial concentration. The highest adsorption capacity achieved for neat ACNFs was 77.60 mg/g. whereas the highest adsorption capacity achieved for ACNFs/ZnO 5% was 120.3 mg/g. For carbon-based adsorbents, the adsorptive capabilities are contributed surface area, pore volume as well as minor role of surface functional groups which adsorb the ions. For the adsorption process, enhancing the former features is necessary as higher SSA and pore volume facilitate the adsorption process due to the availability of more binding sites [11]. As discussed in the previous section, the SSA of ACNFs/ZnO were higher than the neat ACNFS. Thus, the higher adsorption capacity may be attributed to the higher number of active sites provided by ZnO. It is possible that addition of ZnO increased the active adsorption sites that increase the adsorption capacity of composite ACNFs towards Pb(II) [9]. The satisfactory adsorption capacity also contributed due to the fact that ZnO itself is adsorbent and very favorable towards sorption of heavy metals [9].

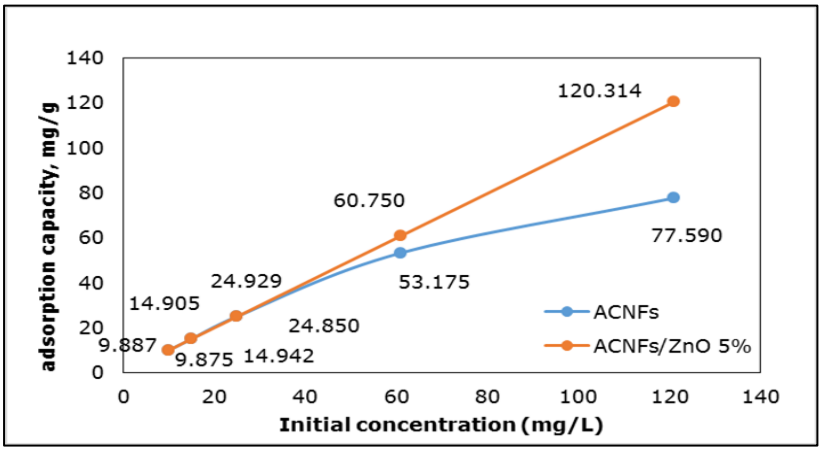



Figure 7. Effect of initial concentration

**Adsorption isotherm study**

In order to evaluate the mechanism of adsorption occurred on the surface of adsorbent, Langmuir and Freundlich isotherm models were applied and the results are presented in Table 2. As refer to Table 2, the $R^2$ values from Freundlich model (0.960) for ACNFs was higher than Langmuir model (0.608). Similar results were obtained for ACNFs/ZnO in which the $R^2$ values from Freundlich model (0.958) was higher than Langmuir model (0.939). Thus, Freundlich isotherm model is best fitted to describe the adsorption behaviour that took place between the ACNFs and ACNFs/ZnO with Pb(II) ions. From that, it is assumed that the attachment of Pb(II) ions occurred at heterogeneous surface of the neat ACNFs and ACNFs/ZnO [11].

Table 2. Langmuir and Freundlich isotherm parameters

| Adsorbent | Langmuir Model | | | Freundlich Model | | |
|---|---|---|---|---|---|---|
| | $Q_{max}$ (mg/g) | b (L/mg) | $R^2$ | K (mg/g) | 1/n | $R^2$ |
| ACNFs | 54.6 | 0.778 | 0.608 | 9.314 | 0.882 | 0.960 |
| ACNFs/ZnO | 169.5 | 1.594 | 0.939 | 2.920 | 0.011 | 0.958 |

## Conclusion

In this study, the feasibility of ACNFs/ ZnO to remove Pb(II) from aqueous solution was demonstrated. The specific surface area was increased by addition of zinc oxide in the ACNFs component. Under SEM analysis the ACNFs/ZnO were found to have compact arrangement with dispersion of Zn beads. The adsorption studies revealed that the removal was dependant on pH and the adsorption mechanism were best fitted to be described by Freundlich model with the highest adsorption capacity in this study was 120.3 mg/g.

## Acknowledgement

The authors would like to acknowledge the financial support from Malaysian Ministry of Education (Higher Institution Centre of Excellence) and Universiti Teknologi Malaysia under Grant No. R.J090301.7846.4J179 and Q.J130000.2546.12H54. The authors would also like to acknowledge the technical and management support from Research Management Centre (RMC), Universiti Teknologi Malaysia.

## References

1. Sheet, I., Kabbani, A. and Holail, H. (2014). Removal of heavy metals using nanostructured graphite oxide, silica nanoparticles and silica/graphite oxide composite. *Energy Procedia,* 50: 130 – 138.
2. Flora, G., Gupta, D. and Tiwari, A. (2012). Toxicity of lead: A review with recent updates. *Interdisciplinary Toxicology*, 5:47 – 58.
3. Ghazy, S. E. and Ragab, A. H. (2007). Removal of lead ions from aqueous solution by sorptive-flotation using limestone and oleic acid. *Iranian Journal of Chemistry and Chemical Engineering*, 26: 83 – 92.
4. Fu, F. and Wang, Q. (2010). Removal of heavy metal ions from wastewaters: A review. *Journal of Environmental Management*, 92: 407 – 418.
5. Wang, G., Pan, C., Wang, L., Dong, Q., Yu, C., Zhao, Z. and Qiu, J. (2012). Activated carbon nanofiber webs made by electrospinning for capacitive deionization. *Electrochimica Acta*, 69: 65 – 70.
6. Nataraj, S. K., Yang, K. S. and Aminabhavi, T. M. (2012). Polyacrylonitrile-based nanofibers – A state-of-the-art review. *Progress Polymer Science*, 37: 487 – 513.
7. Ramakrishna, S., Fujihara, K., Teo, W., Yong, T., Ma, Z. and Ramaseshan, R. (2013). Electrospun nanofiber: Solving global issues. *Materials Today*, 9(3): 40 – 50.
8. Dadvar, S., Tavanai, H. and Morshed, M. (2012). Effect of embedding MgO and $Al_2O_3$ nanoparticles in the precursor on the pore characteristics of PAN based activated carbon nanofibers. *Journal of Analytical and Applied Pyrolysis,* 98: 98 – 105.
9. Faghihian, H., Kooravand, M. and Atarodi, H. (2013). Synthesis of a novel carbon nanofiber structure for removal of lead. *Korean Journal of Chemical Engineering*, 30: 357 – 363.
10. Norhaniza, Y., Dipak, R., Ismail, A. F. and Takeshi, M. (2016). Microstructure of polyacrylonitrile-based activated carbon fibers prepared from solvent-free coagulation process. *Journal of Applied Research and Technology*, 14: 54 – 61.
11. Imtiaz, A. and Rafique, U. (2011). Synthesis of metal oxides and its application as adsorbent for the treatment of wastewater effluents. *International Journal of Chemical and Environmental Engineering*, 2(6): 400 – 405.

*Malaysian Journal of Analytical Sciences, Vol 21 No 3 (2017): 627 - 632*
*DOI: https://doi.org/10.17576/mjas-2017-2103-12*

MALAYSIAN JOURNAL OF ANALYTICAL SCIENCES
*Published by The Malaysian Analytical Sciences Society*
ISSN 1394 - 2506

# COMPARISON ON *IN VITRO* DEGRADATION OF POLYCAPROLACTONE AND POLYCAPROLACTONE/GELATIN NANOFIBROUS SCAFFOLD

## (Perbandingan Degradasi *In Vitro* Bagi Perancah Gentian Nano Polikaprolakton dan Polikaprolakton/Gelatin)

Lim Mim Mim[1] and Naznin Sultana[1,2]*

[1]*Department of Clinical Sciences, Faculty of Biosciences and Medical Engineering*
[2]*Advanced Membrane Technology Research Center*
*Universiti Teknologi Malaysia, 81310 Johor Bahru, Johor, Malaysia*

**Corresponding author: naznin@biomedical.utm.my*

Received: 26 August 2016; Accepted: 8 January 2017

**Abstract**

Tissue engineering has emerged to provide a new medical therapy in helping tissue regrowth and regeneration by employing scaffold as an artificial supporting structure for cellular growth. Many polymers have been utilized in the fabrication of these artificial scaffolds, but there is still a need to fabricate hydrophilic nanofibrous scaffold with appropriate degradation rate. In this study, polycaprolactone (PCL) and polycaprolactone/gelatin (PCL/Ge) 70:30 nanofibrous scaffolds were fabricated using electrospinning technique and compared on *in vitro* degradation rate to determine a more suitable scaffold for skin tissue engineering application. *In vitro* degradation was evaluated by morphological changes, water uptake, and chemical bonding until 12 weeks. Result shows that both PCL and PCL/Ge (70:30) nanofibrous scaffolds were degraded after 8th week. However, the degradation rate of PCL nanofibrous scaffold is slower and does not has obvious morphological changes. PCL/Ge (70:30) nanofibrous scaffold with faster degradation rate have the potential for skin tissue engineering application.

**Keywords**: tissue engineering, nanofibrous scaffold, *in vitro* degradation, polycaprolactone, polycaprolactone/gelatin

**Abstrak**

Kejuruteraan tisu muncul untuk menyediakan terapi perubatan baru dalam membantu pertumbuhan semula tisu dengan menggunakan perancah sebagai struktur sokongan tiruan untuk pertumbuhan selular. Banyak polimer telah digunakan dalam penghasilan perancah ini, namun masih wujud permintaan terhadap penghasilan perancah gentian hidrofilik yang bersaiz nano dengan kadar degradasi yang sesuai. Dalam kajian ini, gentian perancah nano polikaprolakton (PCL) dan polikaprolakton/gelatin (PCL/Ge) 70:30 telah dihasilkan dengan teknik putaran elekron dan kadar degradasi *in vitro* dibandingkan untuk menentukan perancah yang lebih sesuai bagi aplikasi kejuruteraan tisu kulit. Degradasi *in vitro* telah dinilai melalui perubahan morfologi, penyerapan air, dan ikatan kimia kedua-dua gentian perancah nano sehingga 12 minggu. Keputusan menunjukkan kedua-dua PCL dan PCL/Ge (70:30) gentian perancah nano telah degradasi selepas minggu ke-8. Walau bagaimanapun, kadar degradasi gentian perancah nano PCL adalah lebih perlahan dan tiada perubahan morfologi yang jelas. Gentian perancah nano PCL/Ge (70:30) dengan kadar degradasi yang lebih cepat mempunyai potensi dalam bidang kejuruteraan tisu kulit.

**Kata kunci:** kejuruteraan tisu, perancah gentian nano, degradasi *in vitro*, polikaprolakton, polikaprolakton/gelatin

## Introduction

Tissue engineering is an interdisciplinary field that uses life sciences and engineering principles to develop biological substitutes for example fibrous scaffold for improving, maintaining and restoring the function of tissues

or organs. Skin tissue engineering has been developed recently due to the limitations of autografts and allografts such as availability of healthy autologous skin, infections, and scarring. The emergence of skin tissue engineering facilitates the treatment of patients with deep dermal injuries, deep skin burns, and skin related disorders [1]. Skin tissue engineering aims to promote the healing of wounds [2], repair, and promote the regeneration of skin tissue with reduced scarring [1] by applying fibrous scaffold on the wounds.

There are many techniques of scaffold fabrication. One of the techniques which is simple and cost effective for fibrous scaffold fabrication is electrospinning technique [3]. Electrospinning, a technique that utilises electrostatic forces to produce fibers has been emerging from 100 years ago [4]. This technique is versatile to spin a wide range of materials such as polymers, composites, and ceramics into extremely thin fibers ranging from micrometers to a few nanometers [5]. These thin fibers mimic the structural dimension of extracellular matrix (ECM) of tissues and organs [4]. Moreover, small dimension of fibers provides high surface area to volume ratio for cellular growth [4]. The product of electrospinning is called electrospun fiber or electrospun membrane or fibrous scaffold. Electrospinning technique is able to fabricate nano-sized fibrous scaffolds which mimic ECM of skin for skin tissue engineering.

To fabricate scaffold, biomaterials such as biodegradable polymers are widely used as the material of scaffold. Using biodegradable polymer as scaffold, it will provide an adequate support for cells and degrade at a rate coincide with tissue growth. Biodegradable polymers are divided into biodegradable synthetic polymers and natural polymers. In this study, biodegradable synthetic polymer, polycaprolactone (PCL) and natural polymer, gelatin (Ge) were used. Both polymers were Food and Drug Administration (FDA) approved to be safe for human body [6, 7].

Some studies observed that PCL fibrous scaffolds caused a reduction in the ability of cell attachment, migration, proliferation, and differentiation [8]. Cell affinity towards synthetic polymer is usually poorer than natural polymer. PCL has the advantages of biodegradable and biocompatibility, but it has lower hydrophilicity, slower degradation rate, and lack of surface cell-recognition sites [9]. Ge is a natural polymer derived from collagen, the main structural component of ECM of skin. It is hydrophilic and has faster degradation rate. Previous study had investigated Ge and blending of Ge with poly(L-lactic acid)-co-poly(ε-caprolactone) (PLACL) for the application of skin tissue engineering [10, 11]. Ge fibrous scaffold has the potential for dermo-epidermal composite skin substitute [10]. Blending of poly(L-lactic acid)-co-poly(ε-caprolactone) (PLACL)/Ge is favorable for cell infiltration [11]. However, an appropriate degradation rate is also an important characteristic for skin tissue engineering application. In this study, Ge is selected to be blended with PCL to achieve a desired fibrous scaffold for the aim to increase the degradation rate. PCL and PCL/Ge (70:30) nanofibrous scaffolds were compared on *in vitro* degradation to choose a suitable scaffold for skin tissue engineering application.

## Materials and Methods

Polymer Ge Type A in powder form (~300 g Bloom) from porcine skin, PCL with molecular weight 70,000 – 90,000, formic acid (≥ 95%), and phosphate buffered saline (PBS, P-3813, pH 7.4) were obtained from Sigma Aldrich (St. Louis, MO). PCL and PCL/Ge with weight ratio 70:30 were dissolved in formic acid. Both solutions were electrospun to fabricate nanofibrous scaffolds by using electrospinning technique. Degradation of PCL and PCL/Ge (70:30) nanofibrous scaffolds was evaluated by morphological changes and water uptake. Nanofibrous scaffolds were sectioned into 1 x 1cm$^2$, weighted, and incubated at 37 ºC in 10 ml PBS. After 4, 8, and 12 weeks of incubation, nanofibrous scaffolds were washed with distilled water to remove residual buffer salts. Nanofibrous scaffolds were blotted dry with tissue paper to remove excess water and weighted. Water uptake of nanofibrous scaffolds was calculated using the following equation 1 [12].

$$\text{Water Uptake } (\%) = \frac{W_w - W_d}{W_d} \times 100 \quad (1)$$

where $W_w$ is weight of scaffold after incubation, $W_d$ is weight of scaffold before incubation.

This process was repeated for three times for each time point. The average and standard deviation of water uptake was plotted against degradation time. Nanofibrous scaffolds were dried at room temperature until a constant weight

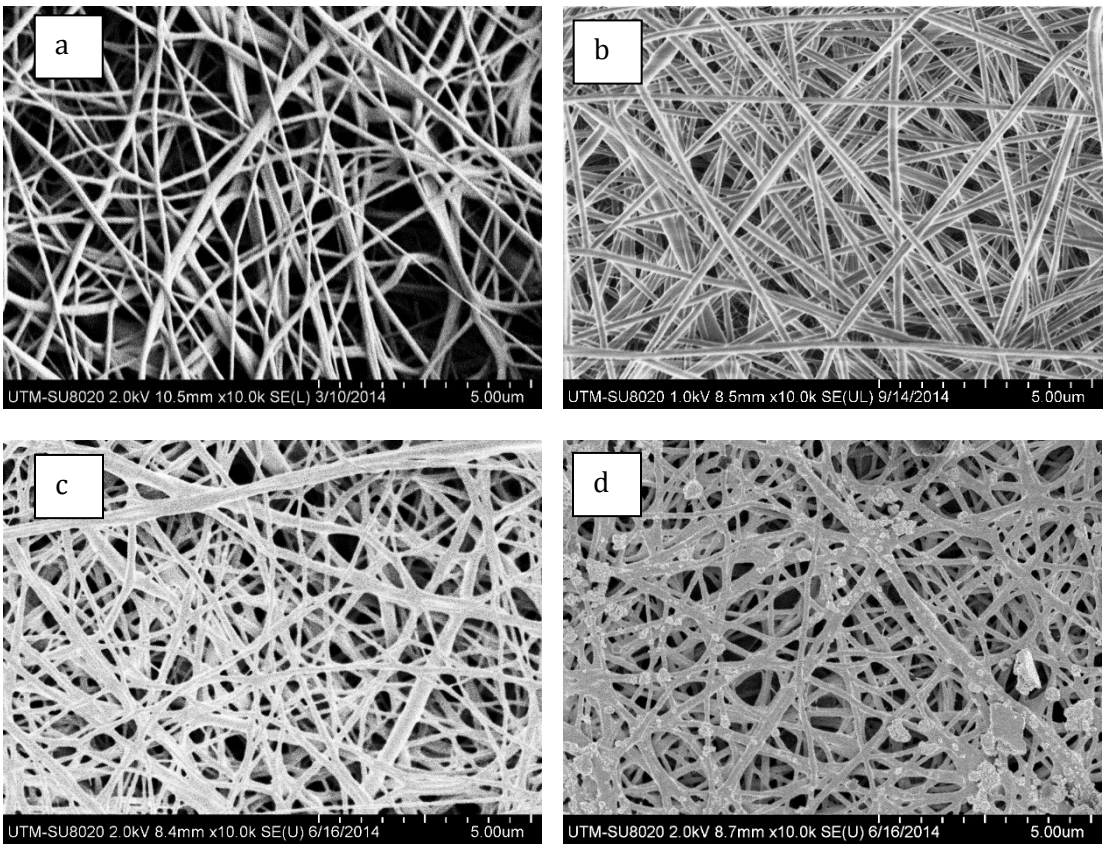
had achieved and coated with gold for the preparation to be viewed under field emission scanning electron microscope (FESEM). Morphological changes of the fibers after degradation for 8 and 12 weeks were determined by FESEM images.

Chemical bonding analysis of both PCL and PCL/Ge nanofibrous scaffolds was performed by using an attenuated total reflectance (ATR) spectroscopy (Perkin-Elmer Series, USA Modal) in the range of 4000 – 400 $cm^{-1}$.

## Results and Discussion

PCL and PCL/Ge (70:30) scaffolds were fabricated using electrospinning technique by using formic acid as solvent. 14% w/v of PCL and PCL/Ge (70:30) in formic acid formed fibrous scaffold with nanosized diameter. Previous study had reported that the average fiber diameter of PCL and PCL/Ge (70:30) fibrous scaffolds were 88.02 ± 27.83 nm and 155.60 ± 41.13 nm [13]. The contact angle of as-fabricated PCL was 112.30 ± 8.14 and 43.83 ± 0.06 for PCL/Ge. Both nanofibrous scaffolds were compared on *in vitro* degradation. Biodegradable scaffolds are usually degraded and replaced by new tissue. Ideally, the rate of degradation should match the rate of tissue regeneration or tissue growth in vitro and in vivo [9, 14, 15]. In this study, PCL and PCL/Ge (70:30) nanofibrous scaffolds were incubated in PBS at 37 ºC for 12 weeks.

Figure 1 illustrates the morphological changes of PCL and PCL/Ge (70:30) nanofibrous scaffolds before incubation and after 8 and 12 weeks of incubation. From the FESEM images, there was no broken fiber was observed. The fiber diameters of PCL and PCL/Ge increased after absorbing water at different degradation period which is referred as "swelling".



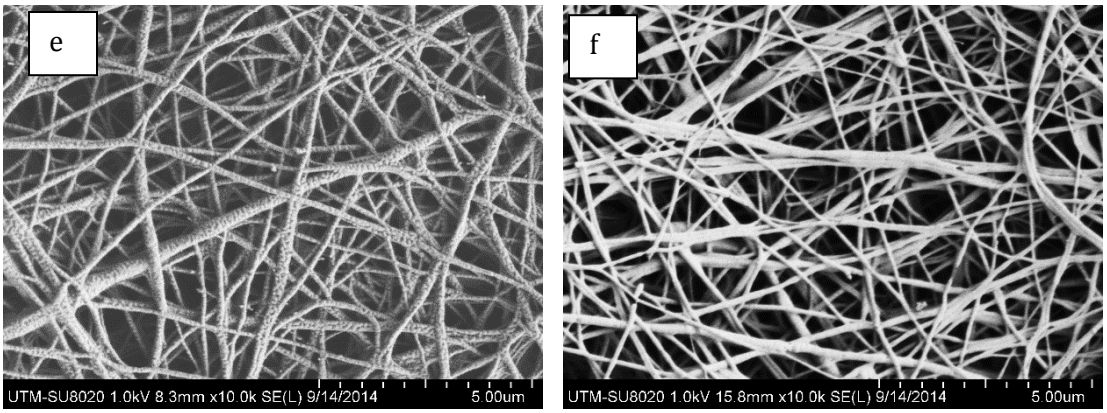



Figure 1. FESEM images of PCL (left) and PCL/Ge (70:30) (right) nanofibrous scaffolds for *in vitro* degradation (a, b) before degradation, (c, d) after 8 weeks, (e, f) after 12 weeks

Water uptake percentage of PCL and PCL/Ge (70:30) nanofibrous scaffold was also studied for 4, 8, and 12 weeks to evaluate the rate of degradation. Figure 2 shows the percentage of water uptake.

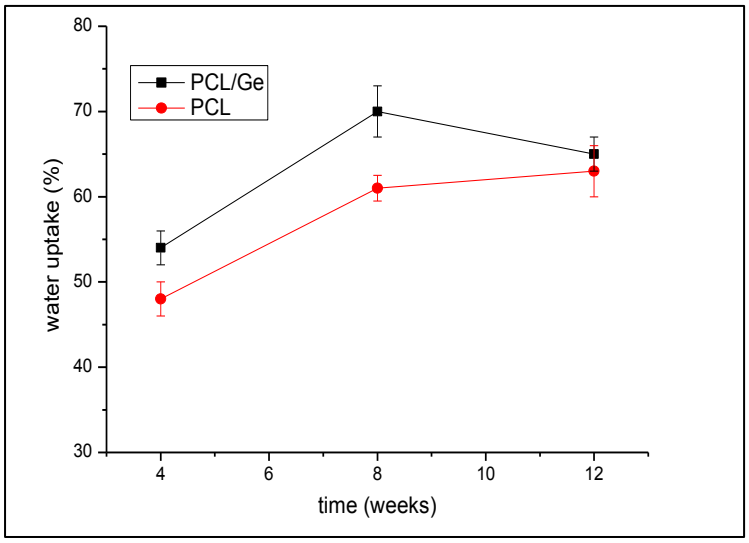



Figure 2. Water uptake percentage of PCL and PCL/Ge (70:30) nanofibrous scaffolds after degradation for 4, 8, and 12 weeks

With increasing time, water uptake percentage of PCL nanofibrous scaffold was increasing, but water uptake percentage of PCL/Ge (70:30) nanofibrous scaffold decreased at week 8. In overall, percentage of water uptake of PCL/Ge nanofibrous scaffold was higher than PCL nanofibrous scaffold due to the presence of an amide bond. Amide bond of Ge presence in PCL/Ge scaffold is able to form hydrogen bonds with water molecules. Hence, PCL/Ge nanofibrous scaffold is hydrophilic and takes up more water. However, from the result, percentage of water uptake decreased at week 8 as nanofibrous scaffolds were started to degrade. Degradation of amide bond decreases its ability to form hydrogen bonds with water molecules. Hence, percentage of water uptake was decreased.

Chemical structure of both PCL and PCL/Ge (70:30) nanofibrous scaffolds are investigated using ATR. Figure 3 shows the ATR spectra of PCL and PCL/Ge nanofibrous scaffolds before and after degradation.

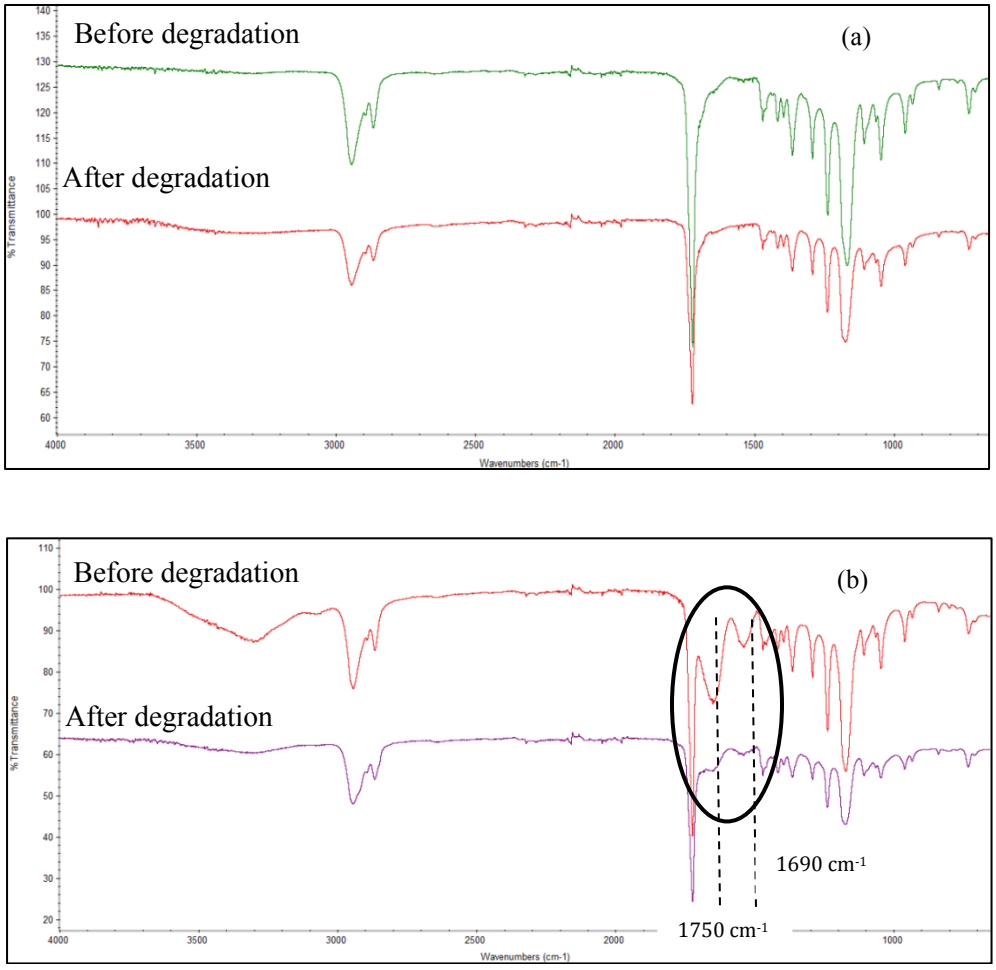



Figure 3. Chemical structure analysis of nanofibrous scaffolds before and after degradation for 8 weeks (a) PCL and (b) PCL/Ge

PCL is a polyester containing ester (C=O-O) groups and cyclic alkyl groups. It can be observed in Figure 3 (a) that there are three prominent absorption peaks displayed in both polycaprolactone (PCL) spectra before and after degradation. Absorption band at around 2900 and 2800 $cm^{-1}$ are attributed to asymmetric and symmetric $sp^3$ C-H stretching, 1730 – 1750 $cm^{-1}$ is assigned to C=O-O, and 1150 $cm^{-1}$ is indicated the presence of C-O group. The difference between these two spectra is that the loss of concentration of PCL proven by decreasing of the PCL intensity in the spectrum after degradation.

In Figure 3 (b), it is clearly seen that the absorption peak of carboxylate group (C=O-O, around 1730 – 1750 $cm^{-1}$), amide group (C=O-N, 1690 $cm^{-1}$) and carbonyl group (1150 $cm^{-1}$) reduced after the 8$^{th}$ week. It is proven that the PCL/Ge degraded in PBS solution. Hence, the water absorption capacity was decreased due to the loss of carboxylate, amide and carbonyl groups which can form hydrogen bonding with water molecules.

Both PCL and PCL/Ge nanofibrous scaffolds were degraded after 8$^{th}$ week. However, the degradation rate of PCL nanofibrous scaffold is slower and does not has obvious morphological changes. PCL has been known for its slow

degradation rate which can degraded up to 3 – 4 years [6]. After adding Ge, degradation rate has increased. Type of the chemical bond and water uptake are the most important factors that will influence the rate of degradation of a scaffold [15, 16].

## Conclusion

In this study, nanofibrous scaffolds of PCL and PCL/Ge with weight ratio 70:30 were produced. The results reported in this study demonstrated that the degradation rate of PCL/Ge (70:30) nanofibrous scaffold was faster than PCL nanofibrous scaffold. PCL nanofibrous scaffold with slow degradation rate is more suitable to be used for long-term implantation and long-term drug delivery carrier while PCL/Ge (70:30) nanofibrous scaffold might have the potential to be used for skin tissue engineering application.

## Acknowledgement

The authors would like to acknowledge MOHE for the GUP Tier 1 grants (Vot: 12H24) and HiCOE grant (Vot: 4J191) as well as lab facilities of Universiti Teknologi Malaysia (UTM).

## References

1. Priya, S. G., Jungvid, H. and Kumar, A. (2008). Skin tissue engineering for tissue repair and regeneration. *Tissue Engineering Part B: Reviews*, 14(1): 105 – 118.
2. Mansbridge, J. (2008). Skin tissue engineering. *Journal of Biomaterial Science, Polymer Edition*, 19(8): 955 – 968.
3. Zhang, Y., Ouyang, H., Lim, C. T., Ramakrishna, S. and Huang, Z. M. (2005). Electrospinning of gelatin fibers and gelatin/PCL composite fibrous scaffolds. *Journal of Biomedical Materials Research Part B*, 72(1): 156 – 165.
4. Sill, T. J. and von Recum, H. A. (2008). Electrospinning: applications in drug delivery and tissue engineering. *Biomaterials*, 29(13), 1989 – 2006.
5. Goh, Y. F., Shakir, I. and Hussain, R. (2013). Electrospun fibers for tissue engineering, drug delivery, and wound dressing. *Journal of Materials Science*, 48(8): 3027 – 3054.
6. Gelatin Manufacturers Institute of America (2012). Gelatin Handbook. Access from Dostupné z: www. gelatin-gmia.com/images/GMIA_Gelatin_Manual_2012.pdf.
7. Woodruff, M. A. and Hutmacher, D. W. (2010). The return of a forgotten polymer – polycaprolactone in the 21st century. *Progress Polymer Science*, 35(10), 1217 – 1256.
8. Kim, C. H., Khil, M. S., Kim, H. Y., Lee, H. U. and Jahng, K. Y. (2006). An improved hydrophobicity via electrospinning for enhanced cell attachment and proliferation. *Journal of Biomedical Materials Research Part B*, 78(2): 283 – 290.
9. Ghasemi-Mobarakeh, L., Prabhakaran, M. P., Morshed, M., Nasr-Esfahani, M.-H. and Ramakrishna, S. (2008). Electrospun poly(ε-caprolactone)/gelatin nanofibrous scaffolds for nerve tissue engineering. *Biomaterials*, 29(34): 4532 – 4539.
10. Powell, H. and Boyce, S. (2008). Fiber density of electrospun gelatin scaffolds regulates morphogenesis of dermal–epidermal skin substitutes. *Journal of Biomedical Materials Research Part A*, 84(4): 1078 – 1086.
11. Chandrasekaran, A. R., Venugopal, J., Sundarrajan, S. and Ramakrishna, S. (2011). Fabrication of a nano-fibrous scaffold with improved bioactivity for culture of human dermal fibroblasts for skin regeneration. *Biomedical Materials,* 6(1): 015001.
12. Sultana, N. and Khan, T. H. (2012). In vitro degradation of PHBV scaffolds and nHA/PHBV composite scaffolds containing hydroxyapatite nanoparticles for bone tissue engineering. *Journal of Nanomaterials*, 2012: 1 – 12.
13. Lim, M. M., Sun, T., and Sultana, N. (2015). In vitro biological evaluation of electrospun polycaprolactone/ gelatine nanofibrous scaffold for tissue engineering. *Journal of Nanomaterials,* 2015: 1 – 11.
14. Chang, H.-I. and Wang, Y. (2011). Cell responses to surface and architecture of tissue engineering scaffolds: In Tech Open Access Publisher: pp. 569 – 588.
15. Cui, W., Li, X., Zhou, S. and Weng, J. (2008). Degradation patterns and surface wettability of electrospun fibrous mats. *Polymer Degradation and Stability*, 93(3): 731 – 738.
16. Sultana, N. and Kadir, M. R. A. (2011). Study of in vitro degradation of biodegradable polymer based thin films and tissue engineering scaffolds. *African Journal of Biotechnology*. 10(81): 18709 – 18715.

*Malaysian Journal of Analytical Sciences, Vol 21 No 3 (2017): 633 - 642*
*DOI: https://doi.org/10.17576/mjas-2017-2103-13*

MALAYSIAN JOURNAL OF ANALYTICAL SCIENCES
*Published by The Malaysian Analytical Sciences Society*
ISSN 1394 - 2506

# EFFECT OF BORE FLUID COMPOSITION ON STRUCTURAL AND PERFORMANCE OF POLYPHENYLSULFONE HOLLOW FIBER MEMBRANE CONTACTOR FOR DEACDIFICATION OF CRUDE PALM OIL

## (Kesan Komposisi Cecair Lubang pada Struktur dan Prestasi Membran Gentian Geronggang Polifenilsulfona Membran Kontaktor untuk Penyahasidan Minyak Sawit Mentah)

Noor Hidayu Othman[1,2]*, Ahmadilfitri Md Noor[1], Mohd Suria Affandi Yusoff[1], Pei Sean Goh[2], Ahmad Fauzi Ismail[2], Woei Jye Lau[2], Be Cheer Ng[2], Norafiqah Ismail[2]

[1]*Sime Darby R&D Centre Downstream,*
*42960 Pulau Carey, Selangor, Malaysia*
[2]*Advanced Membrane Technology Research Centre (AMTEC),*
*Universiti Teknologi Malaysia, 81310 UTM Skudai, Johor Darul Takzim, Malaysia*

**Corresponding author: noor.hidayu.othman@simedarby.com*

Received: 26 August 2016; Accepted: 8 January 2017

**Abstract**

The present work is aimed to study the influence of membrane internal structure on the extracting performance of hollow fiber membrane contactor system in removing free fatty acid (FFA) from crude palm oil (CPO). Polyphenylsulfone (PPSU) hollow fiber membrane were prepared via wet spinning method. Different bore fluid composition were employed mainly consisted of distilled water in combination with 0, 20, 30 and 40 wt.% N-methyl-2pyrrolidone (NMP). The resulting membranes structure were characterized for membrane morphology, membrane wettability and membrane pore size. The used of pure distilled water as membrane BF had created a large macrovoid structure with uniform and tiny finger-liked morphology at the outer membrane layer. Meanwhile, the present of NMP in BF composition had obviously changed the internal layer of 14PPSU membrane to more interconnected double-layers of finger-liked morphology. However, there are not much different in membrane wettability and pore size of 14PPSU membrane were recorded. All PPSU hollow fiber membranes were further evaluated for deacidification performance through membrane contactor with sodium hydroxide (NaOH) as liquid extractant. 14PPSU-100:0 membrane contactor that prepared from100% distilled water as BF composition demonstrated the highest FFA removal of 16.54% without soap formation in oil permeate stream.

**Keywords**: polyphenylsulfone, membrane contactor, sodium hydroxide, free fatty acids, crude palm oil

**Abstrak**

Hasil kerja ini bertujuan untuk mengkaji pengaruh struktur dalaman membran kepada prestasi pengekstrakan gentian geronggang membran kontaktor sistem dalam mengeluarkan asid lemak bebas (FFA) daripada minyak sawit mentah (MSM). Membran polifenilsulfona gentian geronggang telah disediakan melalui teknik fasa balikan basah. Komposisi cecair lubang yang berbeza telah digunakan dimana sebahagian besarnya terdiri daripada air suling dengan kombinasi 0, 20, 30 dan 40 wt.% berat N-metil-2pirolidon (NMP). Struktur membran yang dihasilkan telah diperincikan kepada morfologi membran, kebolehbasahan membran dan saiz liang membran. Penggunaan air suling tulen sebagai cecair lubang telah mewujudkan struktur ruang makro dengan morfologi seperti jejari kecil dan sekata pada lapisan luar membran. Sementara itu, kehadiran NMP dalam komposisi cecair lubang dengan jelas telah mengubah lapisan dalaman membran 14PPSU untuk saling berhubung diantara dua lapisan morfologi jejari. Walau bagaimanapun, tiada perbezaan ketara pada kebasahan dan saiz liang membran 14PPSU telah direkodkan. Semua membran PPSU gentian geronggang telah dinilai pada prestasi penyahasidan melalui membran kontaktor bersama natrium hidroksida (NaOH) sebagai cecair pengekstrak. Membran 14PPSU-100:0 kontaktor yang dihasilkan daripada 100% air suling

sebagai komposisi cecair lubang telah menunjukkan penyingkiran FFA tertinggi sebanyak 16.54% tanpa pembentukan sabun dalam aliran minyak.

**Kata kunci:** polifenilsulfona, kontaktor membran, natrium hidroksida, asid lemak bebas, minyak sawit mentah

## Introduction

In palm oil industry, refining process involves the removal of undesirable constituents such as FFA, phospholipid, colour pigment and trace elements from crude palm oil (CPO) in order to achieve the required quality and stability of refined oil. Chemical and physical refining processes are the most common methods that has been applied in palm oil industry. Deacidification or the removal of free fatty acid (FFA) are conducted at different processing stage between these two refining approached. In chemical refining, the FFA is removed during neutralization stage in the formed of soapstock after reacted with sodium hydroxide (NaOH). In physical refining, the FFA is removed during deodorization stage by steam distillation at high temperature of 260 – 265 °C [1]. However, several drawbacks are identified from conventional refining processes such as high energy usage, losses of neutral oil and large amount of water and chemical usage had heavily produced a contaminated effluents [2].

Membrane technology is one of new deacidification approaches that can be further explore in order to overcome the drawbacks of conventional deacidification practices. It is due to advantages of low energy consumption, mild temperature operation and retention of nutrients and other desirable components [3]. Nevertheless, FFA in principle is almost impossible to be removed by membranes itself due to smaller molecular size of FFA (<300 Da) than the triglycerides (~900 Da). Theoretically, the ideal process would be to use a precise membrane pores size that could effectively separate the FFAs from the triglycerides [4].

In order to overcome the abovementioned limitation, membrane contactor technology is chosen for deacidification of CPO due to the advantages of liquid-liquid mass transfer without dispersion of one phase within another. In membrane contactors system, the membrane separation is fully integrated with another separation technology called extraction process in order to exploit the benefits of both technologies in improving the removal of FFA from CPO. The fluids to be contacted are flowed on the opposite sides of the membrane and the fluid/fluid interface forms at the mouth of each membrane pore. Mass transfer occurs by diffusion across the interface. The driving force for separation is a concentration rather than a pressure gradient; indeed only a very small pressure drop across the membrane is required to ensure that the fluid/fluid interface remains immobilized at the mouth of the pore [5].

Polyphenylsulfone (PPSU) membrane was chosen as a main polymer for membrane contactor system. Although PPSU is relatively new in the polysulfone family, it has a vast potential in various membrane applications, such as fuel cell [6], pervaporation [7], gas separation [8] and water treatment process [9]. PPSU that comprises sulfone moieties, ether linkages and biphenyl group in its repeat group have the highest impact strength compared with the other family members [10]. It presents superior resistant to hydrolysis and plasticization of stress cracking. The robustness of PPSU membrane in terms of physical durability and high tolerance to chemical resistance has standout as a remarkable polymer candidate, which could be potentially developed for further use in CPO deacidification [7].

A dry-jet wet spinning method usually employed a tube-in-orifice spinneret that transfer the nascent fiber through an air gap before it enters the coagulation bath. The shell surface structure can be controlled by the air gap length and the environment of the surrounding including relative humidity, temperature, organic vapor etc. Whereas, the bore fluid (BF) composition controlled the bore side structure [11]. Dong et al. [12] investigated the effect of various membrane fabrication parameters on the structure and separation performance of hollow fiber (HF) membrane for gas separation. They found that increasing NMP to water in BF composition had suppressed the finger-liked macrovoids and the sponge-like structure becomes predominant. Feng et al. [13] investigated on the PVDF-HF membrane fabrication using various N-methyl-2-pyrrolidone (NMP) aqueous solutions as an inner coagulant. They found that the PVDF membrane morphology had gradually shifted from a double-skin to a single-skin structure with the increased in NMP concentration.

The aimed of current research work is to study the influence of membrane internal structure at different BF composition (water/NMP) on the extracting performance of membrane contactor. It is generally known that changing the BF composition will change the membrane internal structure due to low solvent/non solvent exchange rate upon addition of solvent into bore fluid. The addition of NMP into BF composition could delay the demixing process, produce more porous membrane structure and better mass transport of solute (FFA) towards the liquid extractant for effective deacidification of CPO. NaOH is used as liquid extractant in PPSU membrane contactor system due to high affinity towards FFA. The interfacial contact between NaOH and CPO that immobilized in the membrane pores could serve as a good platform in extracting the FFA without contaminating the CPO with soap formation. Hence, it could prevent the oil loss throughout the process as well as an attractive solution towards "solvent-free" technology.

## Materials and Methods

### Materials

PPSU membrane polymer was purchased from Sigma-Aldrich. N-methyl-2pyrrolidone (NMP) was bought from Merck and used as a solvent in membrane dope solution and bore fluid composition. CPO was obtained from Sime Darby Jomalina Sdn. Bhd. (Telok Panglima Garang, Selangor,Malaysia). Sodium Hydroxide (NaOH) was used as liquid extractant for membrane contactor system. All chemicals used in this work were received without further treatment.

### Preparation of dope solution

Three membrane dope solution were prepared from a combination of 14% PPSU membrane and 86% NMP. Both polymer and solvent were mixed thoroughly under constant mechanical stirring at 60 $^{o}$C for 1 day in order to produce a homogenous solution. Then the formulated dope solution was degassed before spinning to remove the micro-bubbles.

### Fabrication of PPSU hollow fiber membrane

The HF membranes were fabricated according to the well-known wet spinning method. The dope was place in a stainless steel dope reservoir (volume: 1 liter) that was subsequently pump to the spinneret by a gear pump. The dope reservoir that contains polymer solution was kept under nitrogen pressure as a precaution against cavitation in the line to the pump. Then a pulse-free BF was fed into the inner tube of the spinneret by a syringe pump. Once the spinning dope and the BF met at the tip of the spinneret, they went into the external coagulation bath after going through zero air gap. The details spinning parameter of HF membrane is shown in Table 1. The nascent fibers were then passed through the washing/treatment bath before collected properly by a wind-up drum.

### Membrane post-treatment

The as-spun fibers were cut in pieces of approximately 40 cm in length and immersed in water bath at room temperature for 1 day to remove residual solvent from the membrane structure. Then the nascent HF membrane were post-treated with water/ ethanol (1:1) solution for 30 minutes, followed by pure ethanol solution for another 30 minutes to prevent fiber shrinkage. Finally, the fibers were hang vertically and air dried at room temperature for about 1 day before membrane characterization and preparation of membrane module.

### Membrane contactor module

A total of 100 pieces of HF membrane were potted inside the PVC pipe for membrane contactor performance testing. An epoxy adhesive resin (Polyurethane E-30CL Loctite) was used as the potting resin. This resin was chosen due to its suitable cure times, low viscosity and proper adhesion with the PVC and steel tubing. Table 2 shows the detail specification of HF membrane contactor module.

### Membrane characterization

PPSU membrane cross-sectional images was observed using table-top scanning electron microscope (SEM, Model: TM 3000, Hitachi). All specimens were freeze-dried and coated with an ultra-thin layer of gold before characterisation. Prior to analysis, a piece of hollow fiber was immersed in a liquid nitrogen and fractured carefully in order to create a perfect cross section.

Table 1. Spinning parameters for fabrication of PPSU-HF membrane

| Spinning Parameter | Composition |
|---|---|
| Spinning solution | 14PPSU/86NMP |
| Bore fluid composition | Distilled water/ NMP |
| (a) 14PPSU-80:20 | 80/20 |
| (b) 14PPSU-70:30 | 70/30 |
| (c) 14PPSU-60:40 | 60/40 |
| Inner diameter of spinneret (mm) | 0.55 |
| Outer diameter of spinneret (mm) | 1.25 |
| Air gap (mm) | 0 |
| Dope extrusion rate ($cm^3$/min) | 7.2 |
| Bore fluid flow rate (ml/min) | 2.2 |
| Take-up rate (rpm/min) | 24 |
| Spinning temperature (°C) | 27 |
| External coagulant | Distilled water |
| Coagulation bath temperature (°C) | 25 |

Table 2. Specification of HF membrane contactor module

| Membrane Specification | Value |
|---|---|
| Module i.d. (mm) | 35 |
| Module length (mm) | 400 |
| Fiber o.d. (mm) | 0.55 |
| Fiber i.d. (mm) | 1.25 |
| Effective fiber lengh (mm) | 330 |
| No. of fibers | 100 |

The membrane wettability property of HF membrane was evaluated by sessile drop method using contact angle goniometer (Model: OCA15Plus, Dataphysics, Germany) equipped with images processing software. A total of 10 contact angle measurement were recorded from each sample to get more accurate and average reading.

The field emission scanning electron microscopy (FESEM) (Hitachi model S-900) was used to capture the membrane images with magnifications ranging from 10,000 to 50,000. The electron beam was accelerated under a 3.0 kV in the vacuum chamber. The images obtained from the FESEM were analyzed by the software 'AnalySIS' provided by Soft Imaging System. The pores area was measured by encircling the membrane pores.

**Lab-scale hollow fiber membrane contactor system**

Figure 1 shows a schematic diagram of membrane contactor system for CPO deacidification. The pressure was set at 0.1 bar for both CPO stream (1) and NaOH stream (2). Initially, CPO was subjected to pre-treatment process to remove gums (phospholipids) before deacidification process. The treated CPO was heated and maintained at 50 to 60°C when passing through membrane contactor module within the membrane housing (shell-side), whereas the NaOH was circulated inside the lumen (tube-side) of PPSU membrane (Figure 2). The interfacial contact between CPO and NaOH occurred at the mouth of membrane pores for FFA extraction towards the liquid extractant. 200 ml permeate oil was collected every 30 min time interval for 3 hours for FFA and soap content analysis.

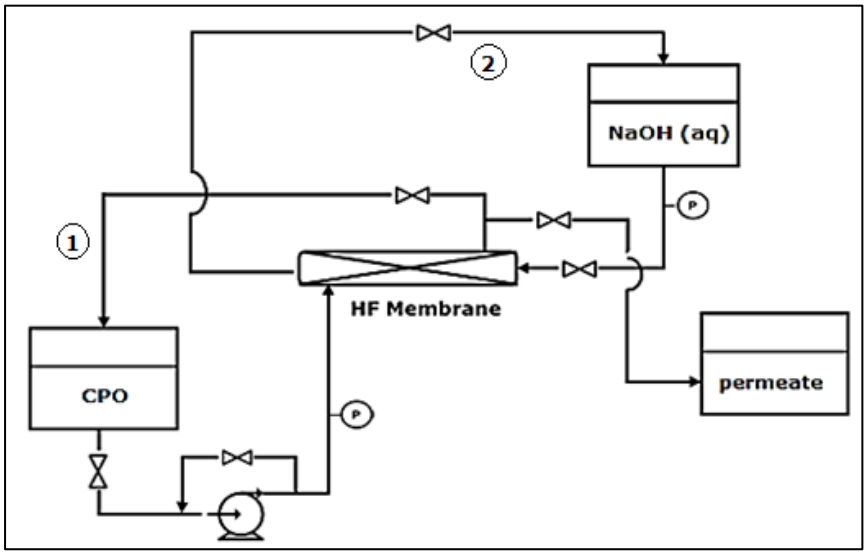



Figure 1. Schematic diagram of HF membrane contactor system

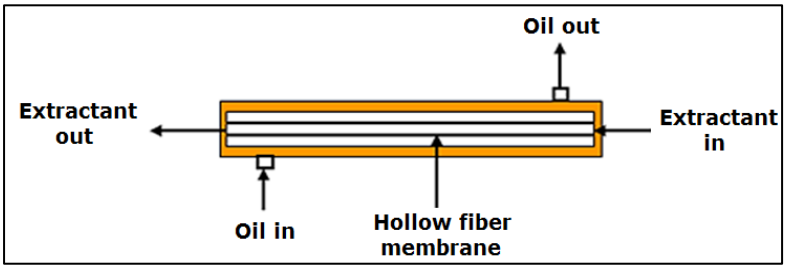



Figure 2. Flow direction of CPO stream and NaOH stream within a membrane housing

**Oil analysis**

Free fatty acid (FFA) and soap content in the oil samples was determined according to the American Oil Chemists' Society (AOCS) Official Method – Ca 5a-40 and Cc 17-95, respectively.

**Statistical analysis**

Statistical analysis software (Minitab 17) was used to perform statistical analysis for R-square and P-value. The analysis of variance (ANOVA) with Tukey pairwise comparison was performed to determine the significant difference at $P < 0.05$. Analysis was conducted in triplicates.

## Results and Discussion

**Membrane morphology**

The influence of internal coagulant on HF membrane properties has been investigated by many researchers. It was found that the addition of solvent into the internal coagulant significantly reduced the precipitation rate. The formation of hollow fiber is based on the solvent/non-solvent exchange mechanism. The used of distilled water as membrane BF due to significant concentration gradient results in a rapid exchanged mechanism. The exchanged mechanism is significantly slower when the BF contains solvent [14, 15].

The most two important parameters that influences the membrane properties are type of solvent and polymer concentration in membrane dope solution. 14PPSU-100 HF membrane that fabricated using 100% distilled water as BF composition had produced a tiny finger-liked morphology near the outer membrane surface with a large macrovoid structure in the central core membrane layer as shown in Figure 3 (a). The present of 20% NMP in combination with 80% distilled water as BF composition had changed the internal structure of 14PPSU-80:20 HF membrane to a prominent double-layer finger-liked morphology with bigger microvoid structure at the inner membrane layer compared to the outer part (Figure 3b). Apparently, the double-layer finger-liked morphology of 14PPSU-70:30 HF membrane became thicker especially at the inner membrane layer with the present of 30% NMP in membrane BF while the bottom structures of skin layer remains unchanged (Figure 3c). Further increased of solvent (40%NMP/ 60% distilled water) in membrane BF composition made 14PPSU-60:40 HF membrane became more porous compared to 14PPSU-70:30 HF membrane with more uniform and interconnected finger-liked morphology between the inner and outer membrane layers.

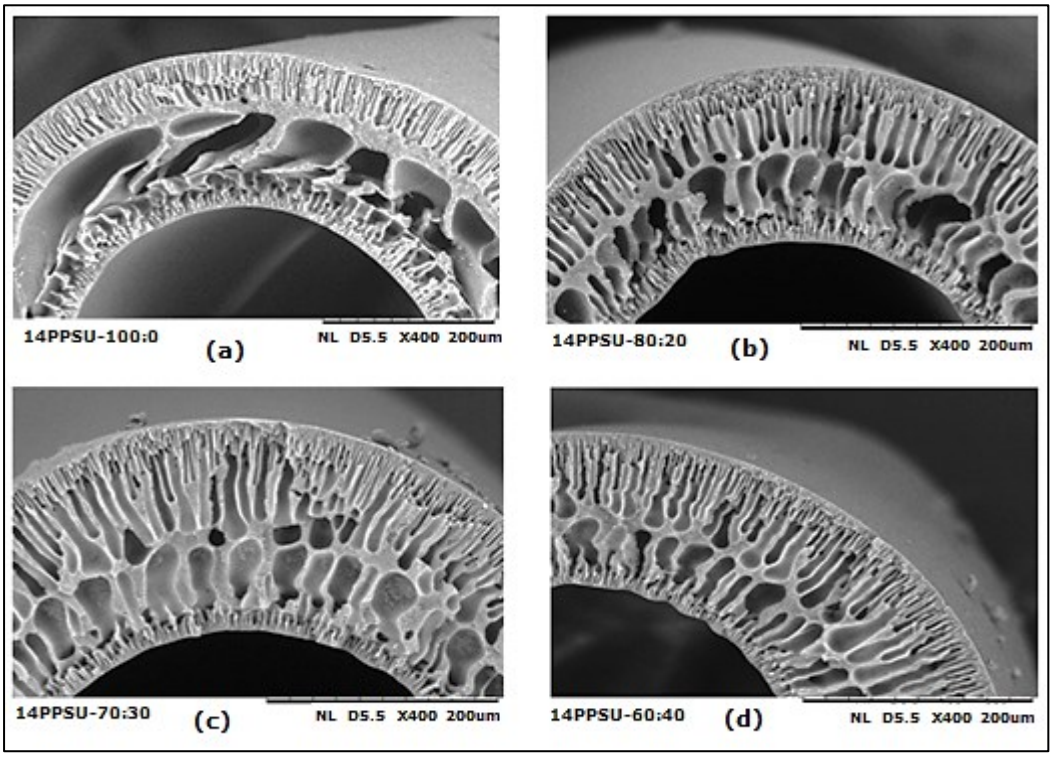



Figure 3. SEM cross-sectional images (400X magnification) of 14PPSU with different bore fluid ratio of water: NMP (a) 100:0 (b) 80:20 (c) 70:30 (d) 60:40

These is an agreement with Rahbari-sisakht et al. [15] which explained that as NMP concentration in the BF increased, the inner surface becomes more porous because the solvent out flux from the polymer solution phase to the coagulant phase is suppressed in the presence of solvent (NMP) in the coagulant. As the consequences, a large amount of NMP remains at the polymer solution/coagulant interface, preventing the formation of dense skin layer. However, the results obtained was contradict with finding from Feng et al. [13].They found that increased in NMP concentration had shifted a double-skin to a single-skin structure of PVDF hollow fiber membrane. It may due to different membrane polymer have different membrane morphology that acted differently although membrane fabrication is subjected to similar BF composition.

**Membrane wettability**

Table 3 shows the membrane contact angle of 14PPSU membrane at different water/NMP as BF composition. It can be observed that more than 20% NMP present in BF composition had significantly ($P<0.05$) reduced the hydrophobicity of 14PPSU membrane from 85.23° (0% NMP) to 81.46°(30% NMP) and 81.11° (40% NMP), respectively.

Table 3. Membrane contact angle of 14PPSU membrane at different bore fluid composition of water: NMP

| Membrane | Contact Angle (0) |
|---|---|
| 14PPSU-100:0 | $85.23 \pm 0.77^{A}$ |
| 14PPSU-80:20 | $83.54 \pm 1.57^{A}$ |
| 14PPSU-70:30 | $81.46 \pm 0.70^{B}$ |
| 14PPSU-60:40 | $81.11 \pm 1.52^{B}$ |

Each value in table represents the mean ± standard deviation of sample analysis from triplicate analysis. Mean within column with different superscripts letter A, B are significantly different ($P < 0.05$).

**Membrane pore size**

Table 4 shows the range and mean pore size of 14PPSU membrane characterized by images analysis from FESEM micrograph. Statistically, the present of 20%NMP in BF composition had significantly ($P<0.05$) increased the mean pore size of 14PPSU membrane from 24.81nm to 30.49nm, respectively. However, further increased in NMP composition resulted in a fluctuation of membrane pore size but it has no significant different ($P<0.05$) from 14PPSU produced from 100% distilled water as BF composition. A poor correlation ($R2=0.2898$) was recorded between the different in BF composition and membrane pore size of 14PPSU membrane.

Table 4. Membrane pore size of 14PPSU membranes at different BF composition (H2O: NMP)

| Membrane | Range Pore Size (nm) | Mean Pore Size (nm) |
|---|---|---|
| 14PPSU-100:0 | 22.3 to 31.3 | $24.81 \pm 3.07^{B}$ |
| 14PPSU-80:20 | 22.3 to 35.7 | $30.49 \pm 6.51^{A}$ |
| 14PPSU-70:30 | 17.8 to 26.8 | $23.59 \pm 2.78^{B}$ |
| 14PPSU-60:40 | 22.3 to 32.97 | $26.01 \pm 3.92^{AB}$ |

Each value in table represents the mean ± standard deviation of sample analysis from triplicate analysis. Mean within column with different superscripts letter A, B are significantly different ($P < 0.05$).

**PPSU membrane contactor performance: FFA removal and soap formation**

The selection of proper BF composition had a big impact on the membrane contactor performance in removing the FFA. As shown by Figure 4, 14PPSU-100 had the most promising results with high initial FFA removal of 12% after 30 min, followed by 12.86% FFA removal after 120 min and up to 16.54% FFA removal after 180 min of permeate collected throughout the process although there are some fluctuation in between the time intervals. Unfortunately, changing the internal membrane structure by adding the NMP into BF composition had tremendously reduced the deacidification performance of membrane contactor system. It can be seen clearly a significant ($P<0.05$) reduction in FFA removal when NMP was added into BF composition. 14PPSU-80:20 did not favour FFA removal at all. Meanwhile both 14PPSU-70:30 and 14PPSU-60:40 had only 2.5% and 2.3% FFA removal, respectively after 3 hours permeate collection. Although the present of NMP in BF composition had

slightly changed the membrane hydrophobicity and membrane pore size, a predominant changed in internal membrane structure from a large macrovoid with tiny finger-like morphology on the upper membrane layer (BF: 100% distilled water) to interconnected double-layers finger-like morphology had reduced the immobilisation of CPO towards NaOH at the mouth of membrane pores. It may due to the reduction in CPO volume localisation inside the internal membrane structure. Besides, the present of central core skin layer that separated double-layer finger-liked morphology had created a barrier and obstructing the mass transfer of FFA towards NaOH.

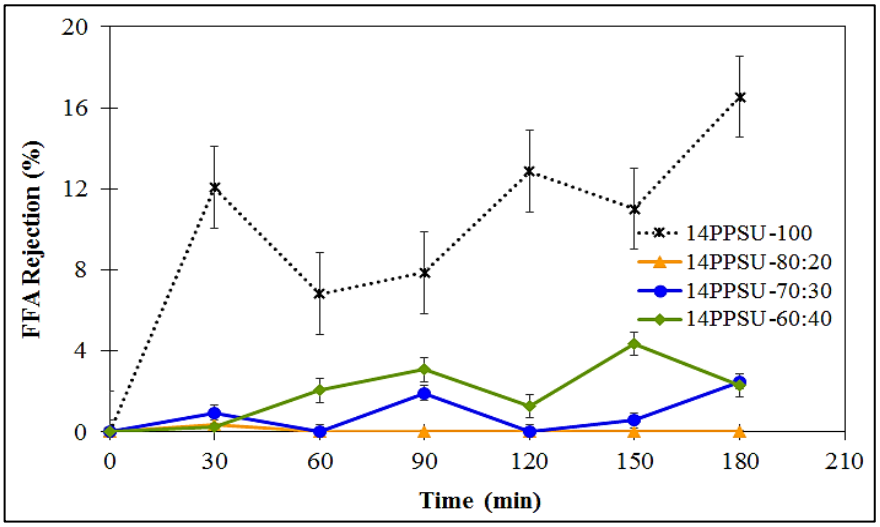



Figure 4. FFA rejection of 14PPSU membranes at different bore fluid composition

For the practical application, it is of great importance to ensure that the membrane contactor system could remove FFA from feed CPO without contaminating the permeate oil with soap formation to avoid neutral oil loss. PPSU is chosen in this study due to its hydrophobicity that allows the oil to wet the membrane layer and prevent the NaOH from penetrating into CPO stream. Besides, the operating pressure for both CPO and NaOH stream was properly established to facilitate FFA extraction and limit the penetration between the two separated streams at the membrane interface only. Although the deacidification performance was not favourable with the present of NMP in BF composition, but the robustness of all PPSU membrane with regards to chemical resistance cannot be denial. Table 5 showed that no soap formation was detected in all permeate samples throughout 3 hours operation.

Table 5. Soap content analysis of permeate oil sample collected from membrane contactor performance

| **Membrane Modules** | **Soap Content (ppm)** | | | |
|---|---|---|---|---|
| | **14PPSU-100 (water)** | **14PPSU-80:20 (water: NMP)** | **14PPSU-70:30 (water: NMP)** | **14PPSU-60:40 (water: NMP)** |
| Feed oil | n/a | n/a | n/a | n/a |
| Permeate: After | | | | |
| 30 min | nil | nil | nil | nil |
| 60 min | nil | nil | nil | nil |
| 90 min | nil | nil | nil | nil |
| 120 min | nil | nil | nil | nil |
| 150 min | nil | nil | nil | nil |
| 180 min | nil | nil | nil | nil |

## Conclusion

It can be concluded that proper selection of BF composition employed during membrane fabrication had provides a big different for the performance of membrane contactor system in removing the FFA in CPO. Different BF composition employed during membrane fabrication had prominently changed the internal membrane structure of 14PPSU membrane with slightly changed in membrane wettability and membrane pore size. The combination of distilled water/NMP in BF composition had changed the internal layer of 14PPSU membrane from tiny finger-liked morphology with larger macrovoid structure to more interconnected double-layers finger-liked morphology. For CPO deacidification process, 100% distilled water was the most suitable BF composition in producing 14PPSU-HF membrane due to its promising results with the highest FFA removal of 16.54% recorded without soap formation. For future work in this research area, it is recommended to investigate on the effect of dope extrusion rate (DER) during spinning process in order to understand the rheological influence of phase inversion in membrane production and separation performance of HF membrane contactor system.

## Acknowledgement

The author (N.H. Othman) is thankful to Sime Darby Research Sdn. Bhd. for supplying crude palm oil and other financial support, and to the members of Advanced Membrane Technology Centre (AMTEC), UTM Skudai, Johor for technical support. P.S. Goh and A.F. Ismail would like to acknowledge HiCOE Grants 4J182 and 4J204 under Ministry of Higher Education for the financial support.

## References

1. Bhosle, B. and Subramanian, R. (2005). New approaches in deacidification of edible oils – A review. *Journal of Food Engineering,* (69): 481 – 494.
2. Gibon, V., Greyt, W. and Kellens, M. (2007). Palm oil refining. *European Journal of Lipid Science and Technology,* (109): 315 – 335.
3. Koseoglu, S. S and Engelgau, D. E. (1990). Membrane application and research in the edible oil industry: An assessment. *Journal of the American Oil Chemists' Society,* (67): 239 – 249.
4. Cheryan, M. (2005). Membrane technology in the vegetable oil industry. *Membrane Technology,* (2): 5 – 7.
5. Hwang, S. and Gabelman, A. (1999). Hollow fiber membrane contactors. *Journal of Membrane Science,* (159): 61 – 106.
6. Decker, B., Hartmann, C.-T., Carver, P. I., Keinath, S. E. and Santurri, P. R. (2010). Multilayer sulfonated polyhedral oligosilsesquioxane (S-POSS) sulfonated polyphenylsulfone (S-PPSU) composite proton exchange membranes. *Chemistry of Materials*, 22(3): 942 – 948.
7. Jullok, N., Darvishmanesh, S., Luis, P. and Van der Bruggen, B. (2011). The potential of pervaporation for separation of acetic acid and water mixtures using polyphenylsulphone Membranes. *Chemical Engineering Journal,* 175: 306 – 315.
8. Weng, T.-H. , Tseng, H.-H. and Wey, M.-Y. (2008). Preparation and characterisation of PPSU/PBNPI blend membrane for hydrogen separation. *International Journal of Hydrogen Energy*, 33(15): 4178 – 4182.
9. Sani, N., Lau, W. and Ismail, A. F. (2015). Morphologies and separation characteristics of polyphenylsulfone-based solvent resistant nanofiltration membranes: Effect of polymer concentration in casting solution and membrane pretreatment condition. *Korean Journal of Chemical Engineering*, 32(4): 743 – 752.
10. Scheirs, J. (2000). Compositional and failure analysis of polymers: A practical approach. John Wiley & Sons. England.
11. Liu, Y., Koops, G. H. and Strathmann, H. (2003). Characterization of morphology controlled polyethersulfone hollow fiber membranes by the addition of polyethylene glycol to the dope and bore liquid solution. *Journal of Membrane Science,* 223: 187 – 199.
12. Dong, G., Li, H. and Chen, V. (2010). Factors affect defect-free matrimid hollow fiber gas separation performance in natural gas purification. *Journal of Membrane Science*, 353: 17 – 27.
13. Feng, R. C., Wang, H. and Zhang, L. S. (2011). Diverse morphologies of PVDF hollow fiber membranes and their performance analysis as gas/liquid contactors. *Journal of Applied Polymer Science*, 119: 1259 – 1267.
14. Rahbari-sisakht, M., Ismail, A. F. and Matsuura, T. (2012). Effect of bore fluid composition on structure and performance of asymmetric polysulfone hollow fiber membrane contactor for $CO_2$ Absorption. *Separation and Purification Technology*, 88: 99 – 106.

15. Yan, J. and Lau, W. (1998). Effect of internal coagulation morphology of polysulfone hollow fiber membranes. *Separation and Science Technology,* 33(1): 33 – 55.

*Malaysian Journal of Analytical Sciences, Vol 21 No 3 (2017): 643 - 658*
*DOI: https://doi.org/10.17576/mjas-2017-2103-14*

**MALAYSIAN JOURNAL OF ANALYTICAL SCIENCES**
***Published by The Malaysian Analytical Sciences Society***
**ISSN 1394 - 2506**

# A REVIEW OF OILFIELD WASTEWATER TREATMENT USING MEMBRANE FILTRATION OVER CONVENTIONAL TECHNOLOGY

## (Ulasan Mengenai Rawatan Sisa Medan Minyak Menggunakan Teknologi Membran Penapisan Berbanding Teknologi Konvensional)

Syarifah Nazirah Wan Ikhsan[1,2], Norhaniza Yusof [1,2]*, Farhana Aziz[1,2], Nurasyikin Misdan[3]

[1]*Advanced Membrane Technology Research Centre (AMTEC)*
[2]*Faculty of Chemical and Energy Engineering (FCEE)*
*Universiti Teknologi Malaysia, 81310 UTM Skudai, Johor, Malaysia*
[3]*Faculty of Engineering Technology,*
*Universiti Tun Hussein Onn Malaysia, 86400 Parit Raja, Johor, Malaysia*

**Corresponding author: norhaniza@petroleum.utm.my*

Received: 26 August 2016; Accepted: 8 January 2017

**Abstract**

The oil and gas industry has been a constant developing industry as it is of importance to the maintenance of industrial civilization in its current configuration and play vital roles in many other industries. Some oil and gas industry operations have been accountable of water contamination through by-results of refining and oil slicks. One of the biggest by-products that have raised a critical environment concern is oilfield produced water. Oilfield produced water (OPW) is coproduced aqua liquid phase which originate from well alongside oil phases in normal production process. The content of OPW consists of different type of organic and inorganic mix. Discarding this kind of wastewater can lead to surface pollution especially on water sources as well as soil. Hence, to meet environmental regulations as well as reuse and recycling of produced water, many researchers have focused on treating oily saline produced water. Conventional technologies used to treat produced water consist of clarifiers, dissolved air flotation, hydro cyclones, and disposable filters/absorbers. Typically, additional chemicals for coagulation or settling are needed which are expensive and are incapable of achieving recently required standards of cleanliness. Therefore, researchers have swung to membrane filtration plans because of their capability to minimize extra expenses and surpass issues connected with current advances. Thus, the purpose of this review is to highlight the current and developed membrane technology used in treating the oilfield produced wastewater and its current progress.

**Keywords**: oilfield produced water, membrane filtration, mixed matrix membrane, oily wastewater

**Abstrak**

Industri minyak dan gas telah menjadi industri membangun berterusan kerana ia adalah penting untuk mengekalkan tamadun perindustrian dalam konfigurasi semasa dan memainkan peranan penting dalam banyak industri lain. Sesetengah operasi industri minyak dan gas telah dipertanggungjawabkan ke atas pencemaran air melalui tindakan penapisan dan minyak tumpahan. Salah satu yang produk sampingan yang terbesar yang telah menimbulkan kebimbangan persekitaran kritikal adalah air yang dihasilkan medan minyak. Air yang dihasilkan dari medan minyak (OPW) adalah dihasilkan bersama fasa cecair dan fasa minyak yang berasal dari telaga minyak dalam proses pengeluaran normal. Kandungan OPW terdiri daripada pelbagai jenis campuran organik dan bukan organik. Pembuangan jenis air sisa ini boleh membawa kepada pencemaran permukaan terutamanya kepada sumber air dan tanah. Oleh itu, untuk memenuhi peraturan-peraturan alam sekitar serta penggunaan semula dan kitar semula air yang dihasilkan, ramai penyelidik telah memberi tumpuan kepada merawat air masin yang dihasilkan dari medan minyak ini. Teknologi konvensional yang digunakan untuk merawat air yang dihasilkan terdiri daripada clarifiers, pengapungan udara terlarut, siklon hidro dan penapis boleh guna/penyerap. Biasanya, bahan kimia tambahan untuk pembekuan

atau pemendakan yang diperlukan yang agak mahal dan tidak mampu mencapai piawaian semasa kebersihan air. Oleh itu, penyelidik telah beralih kepada teknologi membran pemisahan kerana keupayaannya untuk mengurangkan perbelanjaan tambahan dan mengatasi isu-isu yang berkaitan dengan kemajuan semasa. Oleh itu, tujuan ulasan ini adalah untuk mengetengahkan teknologi membran semasa dan maju yang digunakan dalam merawat air sisa medan minyak yang dihasilkan dan kemajuan semasa teknologi ini.

**Kata kunci:** sisa medan minyak, penapisan membran, membran matriks campuran, air sisa berminyak

## Introduction

The fast growth of oil and gas industry is usually closely related to its vital role in the maintenance of industrial civilization in its current configuration. Virtually almost all economic sectors depend intensely on oil and gas. This ever-emerging industry has raised concern for many nations, mainly because its processes generate large volume of liquid waste [1].

Some oil and gas industry operations have overseen water contamination through by-results of refining and oil slicks. The oil and gas industry the biggest industrial source of discharges of volatile organic compounds (VOCs) which is a gathering of chemicals that add to the arrangement of ground-level ozone and this has raised many concern over the century. One of the biggest by-products that have raised a critical environment concern is oilfield produced water. Produced water is the aqueous liquid phase that is co- produced from a producing well along with oil phases during normal production process. Oilfield produced water contains different types of organic and inorganic contents. Discharging produced water can pollute surface and underground water and soil [1].

In recent years, it is found that universally produced water production is evaluated at around 250 million barrels each day. Since universally produced water production is more than production of oil, water cut has risen to 70%. Because of expanding volume of this waste everywhere throughout the world, the destiny and impact of releasing created water on natural has as of late turned into a noteworthy issue of ecological [2]. Figure 1 shows the estimation of onshore and offshore produced water production since 1990 until 2015. Ferro and Smith [3] forecasted that the production of oilfield produced water will be increased ultimately by years and this has been proven as the oil and gas industry has become a major industry since the early 2000s. The increasing demand in oil and gas industry has increased the production of wastewater which has in turned raised concern in terms of environmental safety.

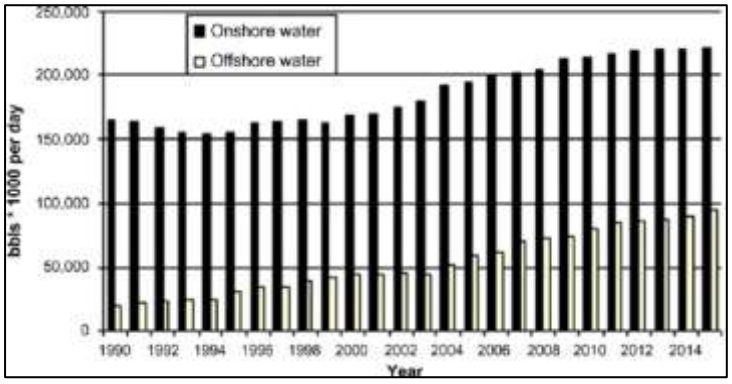



Figure 1. The estimation of produced water since 1990 until 2015 [3]

Historically, produced water was discarded in vast evaporation ponds. In any case, this has turned into an undeniably inadmissible disposal technique from both ecological and social viewpoints. Generally, produced water is often viewed as an industrial waste and coal seam gas (CSG) producers which are currently required to employ

any type of useful re-utilization for it. Currently, more-exacting environmental standards have led to greater efforts being made to treat produced water. Per Malaysia's Environmental Law, Environmental Quality Act, 1974, the Malaysia Environmental Quality (Sewage and Industrial Effluents) Regulations, 1979, 1999, 2000, the limit for oil and grease disposal in the water is 10 mg/L whereby the COD limit is 100 mg/L.

Hence, to meet environmental regulations as well as reuse and recycling of produced water, many researchers have focused on treating oily saline produced water [1]. There are several main contaminants of concern in the produced water which include high level of total dissolved solids (TDS), oil and grease (O&G), suspended solids (SS), dispersed oil, dissolved and volatile organic compounds, heavy metals, radionuclides, dissolved gases, and bacteria.

Generally, treatment of produced water from oilfield involved several stages that include pre-treatment to remove the bulk oil and gas as well as other coarse particle, main treatment that remove small droplets and particles, polishing treatment to remove ultra-small particles and finally optional tertiary treatment to removed dissolved matters and gases. There are different types of treatment that can be employed to achieve those treatments. The treatment of produced water is conventionally expensive and time consuming as capital cost of physical methods and cost of chemicals for chemical treatment of hazardous sludge is high [1]. The main aim in treatment of oilfield produced water is to remove hydrocarbon components. Table 1 shows the summary of type of treatment used in stages involved in treatment of produced water in a simple water treatment plant.

In produced water technologies, there are a few requirements that needed to be addressed to achieve high performance and separation. High recovery is desirable to decrease waste volume and disposal. Besides that, high rejections of contaminants are favored to meeting the stringent discharge requirements. In addition to that, a dynamic treatment should be very robust and comprises of low maintenance to reduce labor and supervision requirement. The treatment should also be flexible whereas it can handle high variation in water quality and quantity. Furthermore, in modular aspect, the technology should have small footprint as well as minimal disturbance.

Table 1. General overview of stages of oily wastewater treatment

| **Stages** | **Treatment** |
|---|---|
| Primary | Physicochemical |
| Secondary | Biological combined with physicochemical |
| Tertiary | Treating the sample for reuse |
| Finishing | Sludge treatment (natural/mechanical) |

Thus, with environmental regulations in concern and in effort to reduce cost, more researchers are focusing in coming up with novel technique in treating the oily wastewater which aims to reduce the cost as much as possible [4]. Domestic and foreign research institutions have tirelessly studied the matter in-depth and discussed on oily wastewater treatment methods, and the goal is both include of removal of a large amount of oil, considering the removal of dissolved organic matter, suspended solids, soaps, pH, sulfide, ammonia, etc. [5]. Customary physical-chemical strategies utilized for the treatment of oilfield produced water are frequently inadmissible since they are centered around the division of the dispersed oil or the expulsion of disintegrated organic pollutants from the aqueous stage with no synthetic change [6]. Although the produced water is a complex mixture of different contaminations, but, by using suitable and effective technologies it can be treated for various reclamation and re-use alternative options [7].

The environmental concerns regarding oilfield produced water usually due to the polluting impact which caused by numerous aliphatic and aromatic hydrocarbons, polycyclic aromatic hydrocarbons, phenols, and other chemical products. Current technologies used to treat produced water consist of clarifiers, dissolved air flotation, hydrocyclones and disposable filters/absorbers. Typically, without using the technologies, additional expensive

chemicals for coagulation or settling, these technologies are not capable of achieving recently required standards of cleanliness. Thus, operating expenses that enhanced and increased volumes of hazardous waste are produced. Even after a primary process of separation from the oil, the water still contains drops of oil in emulsion in concentrations as high as 2000 mg/L, necessitating further treatment before it may be discharge [8].

**Conventional treatment methods of oilfield produced water**

There are several conventional methods used to treat oily produced water that has been employed since decades before. The methods include flotation, coagulation, and biological treatment. Both flotation and coagulation are physicochemical method whereas biological treatments make use of anaerobic and aerobic method to reduced COD and BOD levels in the wastewater. However, the conventional treatment methods mentioned are not efficient enough especially when the sample involved has oil droplets that dispersed finely and low in concentration. The conventional way of produced water purification before was primarily involve the separation of oil and water physically by making use of gravity and the effluent was subsequently dump to the environment [9].

Due to different content in oily wastewater, the traditional methods are often failed in obtaining high separation result [10]. Besides that, most of the conventional techniques are only suitable for pretreatment of wastewater for in-situ reuse. It is not as versatile and dynamic hence there's a need for greater and more reliable treatments methods. The refractory nature of oily wastewater has made it difficult for the traditional technique to fully treat it and high success rate is often impossible.

**Flotation**

Flotation is a process of separating small particles of various materials by treatment with chemicals in water to make some particles adhere to air bubbles and rise to the surface for removal while others remain in water. The conventional dissolved gas flotation system is as depicted in figure 2. Flotation has shorter retention time and higher loading rate. This method has better separation efficiency in removing smaller and lighter particles [11].

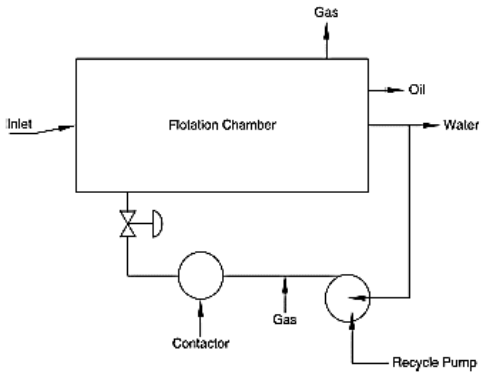



Figure 2. Conventional dissolved gas flotation systems [12]

However, for wastewater containing emulsified oil it is difficult to separate small bubble. There are several factors that is sensitive to the process and can affect the effectiveness of the process which includes pH, pressure, and feed rate. To improve the performance of floatation process, the process parameters and conditions or characteristics of floatable particles need to be determined properly [13]. This made the method more tedious, time consuming and multiple use of instruments and mechanism will increase the cost greatly.

**Coagulation**

Coagulation is a method which makes use of coagulants which destabilized the colloids by neutralizing the forces that keep them apart as depicted in Figure 3. This method usually coupled with flocculation which aims to agglomerate the fine particles and colloids into larger particles to reduce turbidity. The process comprised of two

stages which involve rapid mixing of dispersed coagulant into water and followed by flocculation for agglomeration of small particles into well define flocs via gentle agitation. This method has simple design, low energy consumption, easy operation and quite versatile as it can be used in different stages of wastewater treatment [14]. This method employed the usage of coagulants and the most extensively used coagulants in wastewater treatment include aluminium sulphate and polyaluminium chloride. Table 2 shows the most widely used coagulants in treatment of oily wastewater. Its mechanism is determined greatly on coagulant selection, dosage, wastewater characteristics and treatment technique.

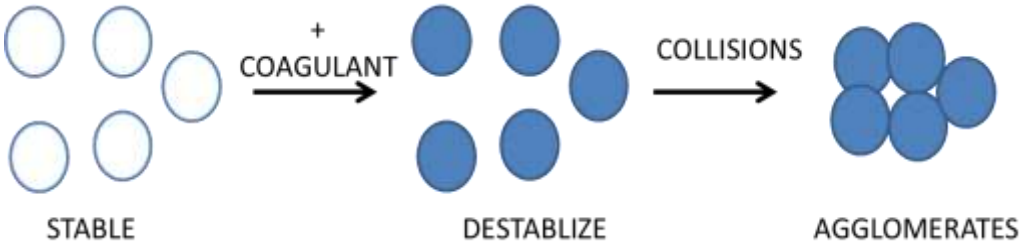



Figure 3. Basic mechanism of coagulation [15]

Table 2. Commonly used coagulant for treatment of oilfield produced water

| **Coagulant** | **Properties** |
|---|---|
| Aluminium sulfate | Inorganic salt, water soluble and act as medium strong acid which reacts with alkalis and attacks many metals in presence of water |
| Ferric chloride | Inorganic salt, water soluble, $FeCl_3$ in slightly basic water reacts with the hydroxide ion to form a floc of iron(III) hydroxide, or more precisely formulated as $FeO(OH)^-$, that can remove suspended materials |
| Polyaluminum chloride | polymeric structure, totally soluble in water, work extremely well at low raw water temperatures |

Dosage plays large roles in effectiveness of this method as overdosing the coagulant can cause the particles to restabilized. The use of chemical coagulant can rise another concern in terms of toxicity of alum and polymeric based coagulant whereby it has posed hazard to health. Overdosing of alum in wastewater treatment may lead to high residual of aluminium concentration [16].

Zhang Jin et al. [17] has employed coagulant utilization in treatment of oily wastewater and found that the coagulant has affected the filtration flux in their combined experimental methods. They found that by using coagulant, the filtration flux improved which mainly due to coalescence between the droplets taken together and the consequent the size of emulsion. However, the excess dosage of coagulant has also found to be the reason behind flux decrement.

**Biological treatment**

Biological treatments make use of microbial metabolism so that the water was dissolved colloidal organic pollutants into harmless substances. The use of anaerobic and facultative digestion has been employed to overcome the oily effluent pollution. Activated sludge process has been the mainstay of wastewater treatment however it is a very energy consuming process. Biological conversion of organic wastes which includes oily wastewater involves four fundamental phenomena which are hydrolysis, fermentation, acefogenesis and methanogenesis [18].

Biological treatments are usually considered as secondary treatment whereby it involves aerobic and anaerobic processes. The employment of mixed bacterial culture has demonstrated to be more advantageous in comparison with pure culture due to synergistic interactions among members of the associations [19]. Due to characteristics of poor nutrients of nitrogen and phosphorus, low BOD/COD ratio, high toxicity, oilfield produced water is difficult to be treated by a simple biological treatment [20].

Lu et al. [21] has developed a field pilot treatment system that employed hydrolysis acidification/bio-contact oxidation system (HA/BCO) as shown in Figure 4 at which air used to produce oxygen-saturated conditions was supplied to the two aerobic tanks through air diffusers, located at the bottom of the tanks, to supply sufficient oxygen to the biomass and to stir the liquid as well as to exfoliate the aged biofilm. The system can achieve the ratio of $BOD_5$ to COD of 0.24 which is around 65% COD removal efficiency and showed an overall hydrocarbon waste removal efficiency of 68%. Their study proved that biological treatment can be a cheap alternative however yet to prove its efficiency in overall treatment of oilfield produced water.

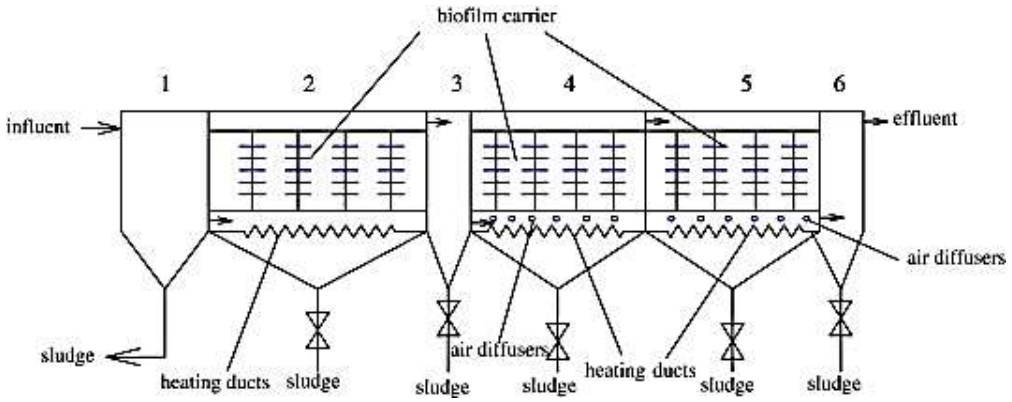



Figure 4. Schematic diagram of the HA/BCO setup. 1. Settling tank a; 2. Anoxic tank; 3. Settling tank b; 4. Aerobic tank a; 5. Aerobic tank b; 6. Settling tank [21]

**Membrane technologies in oilfield produced water treatment**

Precise investigations of membrane marvels can be followed to the eighteenth century rationalist researchers. Through the nineteenth to mid twentieth hundreds of years, membranes had no modern or business utilizes, however were utilized as research center instruments to create physical/synthetic speculations [26].

Preparatory tests utilizing membrane innovation included isolating certain gasses and were at first led in 1950 [22]. The success of these membrane applications prompted the improvement and use of 219 membrane units in refineries around the globe until roughly 1993 [33], after which extra applications have been produced and utilized. Table 3 shows the advancements of membrane technologies utilization in treatment of OPW. For oilfield produced water treatments, there are many studies that have been conducted showing promising results via application of membrane technology which further details and examples are discussed in next sections.

**Type of membrane filtration process**

Researchers have swung to membrane filtration plans because of their capability to minimize extra expenses and transfer issues connected with current advances. Polymeric and ceramic membranes are found to be effective in separating the oils, emulsions, and silts from the produced water [8]. The membrane pressure driven procedure depends on the pore size of the layer to isolate the sample segments as indicated by their pore sizes [24]. membrane based operations tested so far include microfiltration (MF), ultrafiltration (UF), nanofiltration (NF) and reverse osmosis (RO). Also, the coalition of membrane based procedures has been examined as an effective device to treat the produced water to meet the quality benchmarks of environmental standards [25].

Table 3. Advancement in membrane utilizations for OPW purification

| Reference | Study | Inference |
|---|---|---|
| White et al. [27] | Polyimide membrane for separation of solvents from lube oil | Separate small molecules of methyl ethyl ketone solvent from lube oil |
| Buffle et al. [28] | A generalized description of aquatic colloidal interactions: The three-colloidal component approach | Utilization of UF Membrane for the development of filtration process that led to the upgrade visbroken residual products by UF during thermal cracking |
| Yu et al. [29] | Treatment of oily wastewater by organic–inorganic composite tubular ultrafiltration (UF) membranes | After UF treatment, there's significant decrement of oil and suspended solid content |
| Zhang et al. [30] | Development of a sulfated Y-doped nonstoichiometric zirconia/polysulfone composite membrane for treatment of wastewater containing oil | Oil retention is 99.16% and oil concentration in the permeation is 0.67 mg/L |
| Salahi et al. [31] | Nano-porous membrane process for oily wastewater treatment: Optimization using response surface methodology | Nano-porous membrane is efficient for the treatment of petroleum refinery waste water |
| Huang et al. [32] | Treatment of oily waste water by PVP grafted PVDF ultrafiltration membranes | Ultrafiltration performance of oil wastewater was improved greatly and flux recovery of PVDF–PVP membranes cleaned using NaOH solution exceeded 90%. |

**Microfiltration**

Microfiltration (MF) is a kind of physical filtration process where a polluted liquid is gone through an exceptional pore-sized layer to partitioned microorganisms and suspended particles from procedure fluid. It has significant applications in simple dead-end filtration for water, sterile fruit juices and wine, and aseptic pharmaceuticals [33]. However, not all applications that benefit from MF operate successfully in the dead-end mode. Recent innovation in microfiltration has mainly concerned the development of cross-flow filtration technology and membranes [26]. Thus, MF need to be coupled to other methods to achieved successful result.

There are numbers of research done in investigating the effectiveness of MF membrane on treatment of oily wastewater. Studies done by Kiss et al. [34] found that the oil emulsion can be separated with MF PTFE membrane however the retention has been decreased in presence of emulsifier due to arrest of oil coalescence.

A study done by Nandi et al. [60] confirmed that the MF membrane can be used for treatment of oil water emulsion to yield permeate containing oil concentration less than 10 mg/L. Some other research focused on the flux decline of the membrane to evaluate the effectiveness of MF membranes. Modeling of permeation flux decline during MF of oily wastewater in membrane with experimental results is important in evaluating membrane fouling [35].

Besides that, research done by Wang et al. [36] observed that for the treatment of factory emulsified oily wastewater, MF membrane could not be fully regenerated by using conventional cleaning method and combination of filtration with interval aeration would enhance the performance of the membrane. Hence, the use of MF operations would most likely result in better separation performance if coupled with other operations.

**Ultrafiltration**

Ultrafiltration uses a finely porous membrane to separate water and micro solutes from macromolecules and colloids. The average pore diameter of the membrane is in the 10 – 1000 ˚A range. Compared to conventional method, the use of ultrafiltration method is more energy saving and have consistent product quality. Typical filtration processes for emulsified oily wastewater can reach an oil rejection rate of 80 – 99% [37]. The application of ultrafiltration (UF) to the separation of oil emulsions (O/W) from oily wastewater streams has been extensively examined and it is observed that the ability of UF membranes in separating oil in water emulsions with high TOC rejection [39]. There are few researches has recorded successful application of UF membrane in treating wastewater.

Recently Abdullah et al. [40] has successfully synthesized a new type of adsorptive microporous UF membranes that were composed of an organic polysulfone (PSf) and inorganic HFO nanomaterial and has helped in removal of lead in the wastewater. Meanwhile Luo et al. [41] has employed ultrafiltration of oil-water separation using triangle-shape tri-bore hollow fibre membrane from sulfonated PSf and the result has shown that the water permeates after filtration are very clear with low turbidity. These researches show the promising ability of UF in oil-water separation and there are different opportunities in enhancing its ability even further.

**Nanofiltration**

Nanofiltration is a membrane filtration-based strategy that utilizes nanometer estimated barrel shaped through-pores that go through the membrane at 90°. Nanofiltration membrane has pore sizes ranging from 1 – 10 nanometers, smaller than that used in microfiltration and ultrafiltration, but just larger than that in reverse osmosis (RO). NF generally focused to expel just divalent and bigger particles. Monovalent particles, for example, sodium and chloride will go through a nanofiltration film, in this way a considerable lot of its uses include de-salting of the procedure stream.

This promising procedure has pulled in expanding consideration over late years because of the advancement of new applications in the few regions, for example, material industry (expulsion of color from waste wash water), paper, plating industry (constraining of consumption of clean water by reusing waste water similarly as the release waters don't contain too high measures of monovalent particles), drinking water generation and so forth.

**Reverse osmosis**

Reverse Osmosis (RO) utilizes a semipermeable film to evacuate particles, atoms, and bigger particles from drinking water. In reverse osmosis, a connected weight is utilized to overcome osmotic weight, a colligative property, that is driven by substance potential contrasts of the dissolvable, a thermodynamic parameter. The utilization of RO innovation in wastewater treatment has been accounted for since the 1970s. RO is the finest partition membrane process accessible, with pore sizes range from 0.0001 µm to 0.001 µm. RO can hold generally all atoms aside from water and because of the measure of the pores, the required osmotic weight is essentially more prominent than that for MF. Figure 5 depicts the commonly employed RO membrane used for water treatment. Due to both RO and NF small size pores, they are not preferable in treatment of oily wastewater.

Al-Jeshi et al. [42] has conducted an experiment to test the ability of RO membranes to treat water containing up to 50% (by volume) of oil and to evaluate the effect of oil contamination on membrane performance whereby it is found that the RO membrane employed can only treat wastewater with up to 50% oil contamination. Besides having questionable ability in separation of oil in water emulsion, the high-pressure pump supplies the pressure needed to push water through the membrane, even as the membrane rejects the passage of salt through it which makes the process make use of more energy compared to other separation methods.

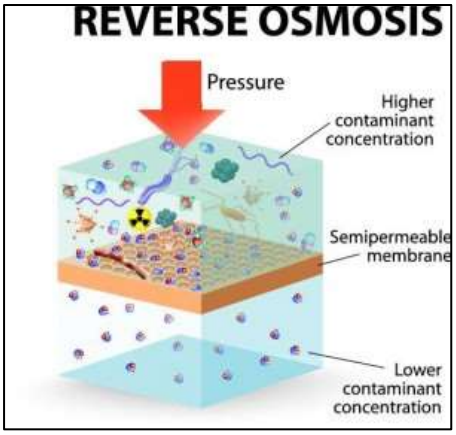



Figure 5. Mechanism of RO [42]

**Type of membrane for oilfield produced water treatment: Polymeric membrane**

Polymeric membrane is usually classified as synthetic membrane and is the most widely used in oil-in-water separation. Polymeric membranes, many organic polymers including crystalline and amorphous, glassy, and rubbery, are suitable membrane fabrication that targets oil-in-water separation. The preparation methods involve phase inversion, interfacial reaction, coating, stretching and etcetera [43]. Synthetic membranes such as polymeric membranes are the most commercially utilized membrane in oily wastewater separation with estimated sales of $2 billion in 2003 worldwide. Utilization of synthetic membranes in purification of oily wastewater such as produced water has better performance compared to the organic membranes. As compared to its biological or organic counterparts, polymeric membrane possesses variety of advantages especially in industrial application such as oil-in-water separation. Due to its wide variability of barrier structures and properties, polymeric membrane has ultimately been the first choice in development of oily wastewater treatment technologies. Its robustness has given the possibility to control the density, size, size distribution, shape and vertical alignment of membrane pores making it easier to be customized to suit the need of any certain application.

The ability of the polymeric membranes to be designed accordingly and with wide rooms for customization has given it upper hand in competing with its organic counterparts. Currently, there are two commercially designs used using polymeric membrane. Membrane filters are usually manufactured as flat sheet stock or as hollow fibers and then formed into one of several different types of membrane modules [44]. Polymeric membranes are generally classified by the nature of the materials, the membrane morphology, geometry, preparation method, separation regime and processes.

The polymeric membrane possessed three significant structural magnitudes namely thermocular, microcrystalline and colloidal. Thermocular level of the membrane is like the chemical nature of the polymer and it is responsible for the membrane's microcrystalline nature. The microcrystalline is the level at which play an important part for both the transport and mechanical properties of the membrane; and finally, the colloidal that involved macromolecules aggregation and affect the pores properties such as pore size, size distribution, density, and void volume [45]. The utilization of polymeric membrane in purification of oilfield produced water is still limited and only few literatures have been done using it as sample feed. There are a few researches that have been done in applying polymeric membranes and integrating it into the treatment technologies of oilfield produced water.

Xu and Drewes [45] in their report has tested thin-film composite polyamide membranes at which was applied in two standard laboratory cross-flow membrane filtration units to purify the water sample collected at a natural gas production facility in Eastern Montana. Their research was focused on salt rejection, iodide recovery and operating performance at which they employed bench-scale filtration tests and in situ characterization techniques to examine the viability of the selected membrane in multi-beneficial use of produced water. The research has concluded that

the studied polymeric membranes having high salt rejection and permeability, provide a viable technique for produced water treatment and beneficial reuse.

Besides that, Mondal et al. [46] have employed three layers' membrane distillation system which consists of polyester, polysulfone and polyamide to purify produced water that was obtained from three different sources. The membranes have different surface roughness and rejection behavior for the oily feeds. In their study, they had determined the variation of permeate flux with time during dead end filtration. Their results conclude that the usage of different polymeric membranes have given positive output at which all three successfully displayed minimum reduction of flux after tested with produced water. They have also concluded that membrane filtration could be a viable process for produced water treatment.

Besides tested on its own, the polymeric membrane has also been integrated to different technologies to further improve the system's performance. Qiao et al. [47] has developed a pilot-scale plant involving aeration tank, air floatation, sand filter and UF has been designed and performance characteristics of the hybrid process have been studied for treatment of oilfield produced water. The UF membrane used was a PVC alloy hollow fiber membrane. Their research resulted in the SS and oil removal in the UF unit of about 70% and 90%, respectively, and their respective contents in the effluent of UF are less than 0.5 mg/L and 1.0 mg/L meet the required standard for discharging or injection water.

A. Fakhru'l-Razi et al. [7] had employed two different polymeric membranes namely polyethersulfone (PES) and polyvinylidene fluoride (PVDF) in their membrane sequencing batch reactor which their coupled with utilization of isolated tropical halophilic microorganisms. It was found that the isolated microorganisms played an important role in the biodegradation of the pollutants and membrane separation was required for ensuring a stable permeate quality. They research has proven that it is possible to employ polymeric membrane in treatment of produced water.

**Ceramic membrane**

Ceramic membrane has reputable ability in treatment oily wastewater especially in oilfield produced water. It has excellent membrane reliability and stability which contribute to its high operation safety. Commonly, ceramic membrane has an asymmetrical structure with a viable top layer framed by coating or casting. Figure 2 shows the theoretical portrayals of ceramic membrane which are usually asymmetrical [48]. Sol-gel process usually produces typical ceramic membranes. In this process, particle dispersions are forced to agglomerate. To produce continuous and porous layers, particles of decreasing size are deposited and the membrane is sintered at extreme temperature. This resulted in asymmetric structure of the membrane. Pore size and characteristics of the selective layers of the membrane may be customized by using grain size and type of particles as basis.

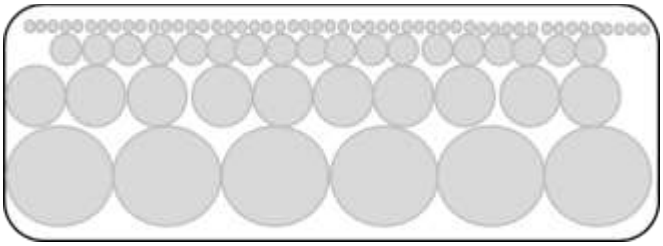


Figure 6. Theoretical portrayals of asymmetrical ceramic membrane

Lately, there is a developing enthusiasm for utilizing ceramic membrane for oily wastewater treatment since organic membranes affected by polar solvents, chlorinated solvents, and high oil fraction. Weschenfelder et al. [49] in their research have evaluated the commercialized Zirconium ($ZiO_2$) performance in treating oilfield wastewater using synthetic oil effluent. The membrane performance was tested in laboratory and results shows that the membrane could generate a permeate stream with an oil and grease content lower than 5 mg/L, which enables the reuse of

water. The research also shows that the cost estimation of using the ceramic membrane and it is found that there's increase of cost in using the membrane.

On the other hand, M. Ebrahimi et al. [8] has done characterization of five different ceramic membranes for oilfield produced water treatment which include MF and UF $Al_2O_3$ and MF and UF $TiO_2$ membranes and concluded that the tested membrane has been proven to be cost efficient for oil removal from oilfield produced water. However, the membranes have failed to reach an acceptable level of removed TOC. Their research has also highlighted the obstacles in treatment of produced water using membrane technologies which include membrane fouling, reduced trans-membrane flux and membrane cleaning.

Abadi et al. [50] have also employed tubular ceramic MF membrane using ($\alpha$-$Al_2O_3$) in treatment of refinery oily wastewater. Their research has resulted in 95% TOC removal efficiency which abides to the National Discharge Standard. They proposed the system to replace the conventional methods as it has higher efficiency rate as well as better separation for oil in water emulsions.

Li and Lee [48] in their research have also utilized ceramic membrane in purification of produced water. Their research investigates the micro- and mesoporous inorganic membranes, specifically clay membranes and zeolite membranes, on desalination of produced water. The study utilizes few ceramic membranes from different materials such as macroporous a-alumina (pore size ¼ 0.2 mm, Pall), disk-shaped stainless steel (0.5 mm, Mott), and Zr-coated stainless steel (pore size ¼ 0.1 mm, Pall), MFI-type zeolite membranes on porous a-alumina supports and laboratory fabricated clay membranes. The research concluded that microporous ceramic membranes are very effective for reducing concentrations of oil and suspended solids from produced water whereby clay and zeolite are microporous materials that show promising application in novel membrane fabrications that have potential for use in produced water deionization. MFI-type zeolite membranes formed on commercial tubular substrates give over 99% ion rejection at a water flux of approximately 10 $kg/m^2h$.

Besides using ceramic membrane on its own, there's also interest in coupling the ceramic membrane with other operation. Rahman et al. [51] has developed cross flow membrane bioreactor which utilizes hollow tubular alumina membranes in refining oily wastewater from refinery. They set up a laboratory-scale bioreactor comprised mainly of tubular ceramic membranes, aeration tank, and circulation pump. Their investigations resulted in COD removal efficiency of more than 93% and performance of the unit when operated with MLSS of 3000 mg/L was impressive with changing the influent mass loading from 30 to 65 g/day.

Different points of interest of ceramic membranes are identified with the capacity to treat slick waters without extra chemicals and its resistance against mechanical, thermal, and chemical stress, permitting a superior recovery of the layer with harsh chemical cleanings [49]. The essential preferred standpoint of utilizing ceramic membrane is the capacity to achieve the current regulatory treatment goals with no chemical pretreatment [8]. Besides that, benefits of ceramic membranes include bigger pore and enhanced hydrophilic surface which leads to higher fluxes, compared to organic membranes. The mechanical, thermal, and chemical resistance of the ceramic membrane has helps in increasing performance membrane and enhances the recovery.

Their ability to stand in harsh environment has open the way for ceramic membranes to be used in produced water purification [37]. For example, the zeolite membranes have high tolerance of organic solutions, excellent corrosion resistance, and very reliable under harsh operating conditions, i.e., high temperatures, high surface shear rates, or the presence of oxidative solvents [48].

However, utilization of ceramic membrane has its own challenges. There's always need to curb the problems regarding sealing which often caused by the thermal expansion of ceramic membrane and module housing. Besides that, its mechanical built which naturally more brittle makes it more sensitive and require a more tedious and careful handling. This diminishes its ability to be fully automated when integrated into other operation.

Notwithstanding that, the significant obstruction including ceramic film is flux misfortunes. Focused polarization frames close to the film surface amid the partition procedure which is administered by liquid science, membrane

properties and hydrodynamics [48]. Furthermore, conventionally the commercialized ceramic membranes (such as $Al_2O_3$, $SiO_2$, $ZrO_2$, and $TiO_2$) are too expensive for oil in water emulsion treatment [52].

**Advantages of membrane technologies and current challenge in treatment of oilfield produced water**

The usage of membrane filtration technologies such as UF, MF and NF has posed several advantages in treatment of oilfield produced water. Firstly, the technology is more widely applicable across a range of industries such as off shore and on shore oil exploration. The operation is practically easy to handle and require minimal supervision. In addition to that it can be fully automated to eliminate labor and human error. Besides that, operators have turned to membrane filtration schemes due to their potential to minimize additional costs and disposal issues [8]. The transport selectivity of the membrane is a unique characteristic that draws attention for its utilization in OPW purification.

Membrane systems can dominate over more complex treatment systems in terms of treating oily wastewater that is high in oil content, small particle size with flow rates more than 150 $m^3$/h. This is much preferable especially for medium and large offshore platforms. Besides that, utilization of membrane technologies has eliminated the usage of chemical additives and coagulant making it more environmental friendly and cost effective [1].

Membranes are favored over other technologies for water treatment, such as disinfection, distillation, or media filtration because, in principle, they require no chemical additives, thermal inputs, or require regeneration of spent media [53]. In addition to that, due to simple operation and mechanism, the utilization of membrane technology has also opened the opportunities to the building of small and compact treatment plant. These possibilities are even more favorable especially in offshore facilities which often have limited space. Membrane equipment has also smaller footprints which contribute to its environmental friendly properties.

Besides having simple operational mechanism, membrane has high reusability properties which allow recycling of selected waste streams. This reduces operational cost as well as increased the sustainability in terms of resources and energy. The use of membrane operation can be independent without pre- or post-treatment which eliminates extra costs and making it more economically feasible.

In addition to that, there's vast opportunity of mixing the membrane with other technologies to further improve its performance. Its robustness allows rooms for further improvement and integration in development of better performing treatment technology. Being a versatile technology, employment of membrane can open more doors towards enhanced and excellent purification of wastewater especially produced water. Their reliability can be exploited to be adopted in the petroleum industry to satisfy the industry requirement for discharge and reuse standards [33]. Table 4 depicted the advantages of membrane technology over conventional method.

Despite its robust and versatile characteristics, membrane technology has stumbled across various challenges that hinder its performance in purification of oilfield produced water. One of the major hindrances of membrane technology is fouling. Fouling is caused by buildup of materials which can take up different form such as adsorption, pore blockage, deposition, and gel formation [55].

Fouling caused severe decline of flux which deter the membrane performance. It also contributes to the difficulties in membrane cleaning which add up extra steps in the treatment operation. Based on the sample to be treated, causes of fouling may vary. For oilfield produced water treatment, contaminants such as alumina, ammonia, organic matter, scale compounds, boron and silica can be the ones that contribute to membrane fouling during the treatment process [23].

These chemicals can lead to scaling at which concentration will increase and change the ph. This will lead precipitation of salt and hydroxide which are the main factors for scaling. Other than that, the accumulation of small molecules might tend to have strong interactions with some polymeric membranes. For instance, anti-foaming agents such as polypropylene glycols have tendency to strongly adhere to certain polymeric membrane and thus promotes pore blocking [56].

Table 4. Comparison between conventional method and membrane technology

| **Conventional Method** | **Membrane Technology** |
|---|---|
| Conventional techniques are only suitable for pre-treatment of wastewater for in-situ reuse [54] | Less complex & preferable for medium and large offshore platforms. [58] |
| Large amount of energy and chemical additives required, economically unfit and lower size molecules difficult to settle down [54] | No chemical additives, thermal inputs, or regeneration of spent media [54] |
| Very slow and complex process and required more place [58] | Simple operational mechanism [59] |
| Often involved spent chemical that in return add on to the chemical pollutants [59] | High reusability properties which allow recycling of selected waste streams [54] |
| Limited room for improvement as most of the technique are rigid and exacting [59] | Robust, allows rooms for further improvement and integration in development of better performing treatment technology [60] |

Besides fouling, another drawback that membrane technology possessed is sludge formation. This challenge often emerges in membrane bioreactor (MBR) which involved activated sludge removal. MBRs can be broadly defined as systems integrating biological degradation of waste products with membrane filtration [58]. This system has been integrated broadly in treatment of refinery wastewater as well as in upstream processing in oil and gas industry. The sludge form will eventually be released to the sea which in turns contribute to the severe sea pollution and pose harm to the surrounding ecosystem.

Drawbacks such as fouling and sludge formation can affect the performance of the membrane operations as it deters the transmembrane pressure as well as membrane flux. Pore blocking will also cause the membrane to function poorly after a few usages. In addition to that, there's need to add in membrane cleaning stage for the membrane to be reused. The cleaning stage might involve chemicals and additives which in turns will add on the pollutants in the final effluent from the technology.

## Conclusion

Oilfield produced water has delicate and complex content and may vary depends on different factors. Each location has their own complex content making it difficult to develop technologies that can suit each one of the produced water. This has made it one of the toughest wastewater to be treated. However, with its extended versatility and vast opportunities its offer has made membrane filtration as one of the most suitable technology to be employed in purification of produced water. The readiness of membrane technology to be customized and integrated into other existing technologies making it possible to treat the complex oilfield produced water. Despite being simple in terms of operation, employment of membrane technology has greatly improved the separation of different components in oilfield produced water. It has been the greatest contender in terms of purification performance compared to other conventional and existing technologies. It has enabled the utilization of single treating unit with little to no need of pre or post treatment stage. Being highly customized, the membrane technologies offer different rooms for the development of better and enhanced purification system for reusing and filtration of oilfield produced water. It is a highly potential technology that should be explored more in future.

## Acknowledgement

The authors gratefully acknowledge financial support from Ministry of Higher Education under Higher Institution Centre of Excellence scheme (Grant Number: R. J090301.7846.4J180 and R. J090301.7846.4J179) and Universiti Teknologi Malaysia under GUP grant (Grant Number: Q. J130000.2546.12H54).

**References**


1. Ahmadun, F., Alireza P., Luqman C. A., Awang Biak, D. R., Madaenic S. S. and Zainal Abidin, Z. (2009). Review of technologies for oil and gas produced water treatment. *Journal of Hazardous Materials*, 170 (1-2): 530 – 551.
2. Tellez, G. T., Nirmalakhandan, N. and Gardea-Torresdey, J. L. (2002).. Performance evaluation of an activated sludge system for emoving petroleum hydrocarbons from oilfield produced water. *Advances in Environmental Research*, 6(4): 455 – 470.
3. Ferro, B. D. and Smith, M. (2016). Global onshore and offshore water production. http://www.touchoilandgas.com/global-onshore-offshore-water-a7137-. Accessed online 20 May 2016.
4. Bjarne, N. (2003). Developments in membrane technology for water treatment. *Desalination*, 153: 355 – 360.
5. Hayat, S., Iqbal A., Azam, Z. M., Ahmad, A., Inam, A. and Samiullah. (2002). Effect of long-term application of oil refinery wastewater on soil health with special reference to microbiological characteristics. *Bioresource Technology*, 84(2): 159 – 163.
6. Jaramillo-Gutiérrez, M. I., Rivero, E. P., Cruz-Díaz, M. R., Nino-Gómez, M. E. and Pedraza-Avellaa, J. A. (2016). Photoelectrocatalytic hydrogen production from oilfield-produced wastewater in a filter-press reactor using $TiO_2$-based photoanodes. *Catalysis Today*, 266: 17 – 26.
7. Fakhru'l-Razi, A., Pendashteh A., Zainal Abidin, Z., Abdullah L. A., Awang Biak, D. R. and Madaeni, S. S. (2010) Application of membrane-coupled sequencing batch reactor for oilfield produced water recycle and beneficial re-use. *Bioresource Technology*, 101(18): 6942 – 6949.
8. Ebrahimi, M., Ashaghi, S., Engel, L., Willershausen, D., Mund, P., Bolduan, P. and Czermak, P. (2009). Characterization and application of different ceramic membranes for the oil-field produced water treatment. *Desalination*, 245(1-3): 533 – 540.
9. Witze, A. (2015)., Race to unravel Oklahoma's artificial quakes. *Nature*, 520(7548): 418 – 419.
10. Gryta, M., Karakulski, K. and Morawski, A.W. (2001). Purification of oily wastewater by hybrid UF/MD. *Water Resources*, 53(15): 3665 – 3669.
11. Saththasivam, J., Loganathan, K. and Sarp, S. (2016). An overview of oil-water separation using gas flotation systems. *Chemosphere*, 144: 671 – 680.
12. Arnold, K. E. and Stewart, M. (2008). Surface production operations-design of oil handling systems and facilities. Gulf Publishing Co, Houston, Texas.
13. Ran, J., Liu, J., Zhang, C., Wang, D. and Li, X. (2013). Experimental investigation and modeling of flotation column for treatment of oily wastewater. *International Journal of Mining Science and Technology*, 23(5): 665 – 668.
14. Teh, C. Y., Yeong W. T. and Ching J. J. (2014). Optimization of agro-industrial wastewater treatment using unmodified rice starch as a natural coagulant. *Industrial Crops and Products*, 56: 17 – 26.
15. Gregory, J., (2006). Particles in water: Properties and processes. London: IWA Pub: Boca Raton, CRC Press Taylor & Francis.
16. Yang, C. L. (2007). Electrochemical coagulation for oily water demulsification. *Separation and Purification Technology*, 54(3): 388 – 395.
17. Zhang, J., Sun, Y. X., Huang, Z. F., Liu, X. Q. and Meng, G. Y. (2006). Treatment of phosphate-containing oily wastewater by coagulation and microfiltration. *Journal of Environmental Science*, 18(4): 629 – 633.
18. Sadhukhan, J., Lloyd, J. R., Scott, K., Premier, G. C., Yu, E. H., Curtis, T. and Head, I. M. (2016). A critical review of integration analysis of microbial electrosynthesis (Mes) systems with waste biorefineries for the production of biofuel and chemical from reuse of $CO_2$. *Renewable and Sustainable Energy Reviews*, 56: 116 – 132.
19. Cerqueira, V. S., Hollenbach, E. B., Maboni, F., Vainstein, M. H., Camargo, F. A., Do Carmo R. P. M. and Bento, F. M. (2011). Biodegradation potential of oily sludge by pure and mixed bacterial cultures. *Bioresource Technology*, 23: 11003 – 11010.
20. Liu, G., Zhengfang, Y., Kun, T., and Zhang, Y. (2013). Biotreatment of heavy oil wastewater by combined upflow anaerobic sludge blanket and immobilized biological aerated filter in a pilot-scale test. *Biochemical Engineering Journal*, 72: 48 – 53.
21. Lu, M., Zhang, Z., Yu, W., and Wei, Z. (2009). Biological treatment of oilfield-produced water: A field pilot study. *International Biodeterioration & Biodegradation*, 63(3): 316 – 321.

22. Weller, S. and Steiner, W. A. (1950). Engineering aspect of separation gases: Fractional permeation. *Chemical Engineering Progression*, 46: 585 – 590.
23. Alzahrani, S. and Mohammad, A. W. (2014). Challenges and trends in membrane technology implementation for produced water treatment : A review. *Journal of Water Process Engineering*, 4: 107 – 133.
24. Sonune, A. and Ghate, R. (2004) Developments in wastewater treatment methods. *Desalination*, 167: 55 – 63.
25. Macedonio, F., Ali, A., Poerio, T., El-Sayed, E., Drioli, E. and Abdel-Jawad, M. (2014). Direct contact membrane distillation for treatment of oilfield produced water. *Separation and Purification Technology*, 126: 69 – 81.
26. Baker, R. W. (2000). Membrane technology and applications. John Wiley & Sons Ltd, California.
27. White, L. S., Wang, I. F. and Minhas, B. S. (1993). Polymide membranes for separation of solvents from lube oil, US Patent 5,364,166.
28. Buffle, J., Wilkinson K. J., Stoll, S., Filella, M. and Zhang, J., (1998). A generalized description of aquatic colloidal interactions: The three colloidal component approach. *Environmental Science Technology*, 32(19): 2887 – 2889.
29. Yu, S. L., Lu, Y., Chai, B. X. and Liu, J. H., (2006). Treatment of oily wastewater by organic-inorganic composite tubular ultrafiltration (UF) membranes. *Desalination*, 196(1-3): 76 – 83.
30. Zhang, Y., Cui, P., Du, T., Shan, L. and Wang, Y. (2009). Development of a sulfated Y-doped nonstoichiometric zirconia/polysulfone composite membrane for treatment of wastewater containing oil. *Separation and Purification Technology*, 70(2): 153 – 159.
31. Salahi, A., Noshadi, I., Badrnezhad, R., Kanjilal, B. and Mohammadi, T. (2013). Nano-porous membrane process for oily wastewater treatment: optimization using response surface methodology. *Journal of Environmental Chemical Engineering*, 1(3): 218 – 225.
32. Huang, X., Wang, W., Liu, Y., Wang, H., Zhang, Z., Fan, W. (2015). Treatment of oily wastewater by PVP grafted PVTF ultrafiltration membranes. *Chemical Engineering Journal*, 273: 421 – 429.
33. Bernardo, P. and Drioli E. (2010). Membrane technology: Latest application in refinery and petrochemical field. *Comprehensive Membrane Science and Engineering*, 1: 211 – 239.
34. Kiss, Z. L, Laszlo, T., Zita, S., Sandor, B., Cecilia, H. and Zsuzsanna, L. (2013). Treatment of model oily waste water by microfiltration. *Periodica Polytechnica Chemical Engineering*, 57(1-2): 21 – 24.
35. Shokrkar, H., Salahi, A., Kasiri, N. and Mohammadi, T. (2012). Prediction of permeation flux decline during MF of oily wastewater using genetic programming. *Chemical Engineering Research and Design*, 90(6): 856 – 853.
36. Wang, Y., Xu, C., Zhang, J., Yin, J. and Wang, H. (2009). Investigation of microfiltration for treatment of emulsified oily wastewater from the processing of petroleum products. *Desalination*, 249(3): 1223 – 1227.
37. Zhang, H., Zhong, Z. and Xing, W. (2013). Application of ceramic membranes in the treatment of oilfield-produced water:effects of polyacrylamide and inorganic salts. *Desalination*, 309: 84 – 90.
38. Juang, R. S. and Jiang, J. D. (1994). Application of batch ultrafiltration to the separation of W/O emulsions in liquid surfactant membrane processes. *Journal of Membrane Science*, 96(3): 193 – 203.
39. Khulbe, K. C, Feng, C. Y. and Matsuura, T., (2008). Synthetic polymeric membrane. Springer-Verlag Berlin Heidelberg, Ottawa.
40. Abdullah, N., Gohari, R. J., Yusof, N., Ismail, A. F., Jaafar, J. and Lau, W. J. (2016). Polysulfone/hydrous ferric oxide ultrafiltration mixed matrix membrane: Preparation, characterization and its adsorptive removal of lead(II) from aqueous solution. *Chemical Engineering Journal*, 289: 28 – 37.
41. Luo, L., Gang H., Chung, T, Weber, M., Staudt, C. and Maletzko, C. (2015). Oil/water separation via ultrafiltration by novel triangle-shape tri-bore hollow fibre membranes from sulfonated polyphenylenesulfone. *Journal of Membrane Science*, 476: 162 – 170.
42. Al-Jeshi, S. and Anne N. (2008). An experimental evaluation of reverse osmosis membrane performance in oily water. *Desalination*, 228(1-3): 287 - 294.
43. Ren, J. and Rong, W. (2011). Preparation of polymeric membranes. Handbook of Environmental Engineering, 13: 47 - 100.
44. Solanki, S. J. and Desai, R. N. (2013) Polymer membrane technology. *International Journal of Engineering Science and Innovative Technology*, 2(2): 400 - 403.
45. Xu, P., and Drewes, J. E. (2006). Viability of nanofiltration and ultra-low pressure reverse osmosis membranes for multi-beneficial use of methane produced water. *Separation and Purification Technology*, 52(1): 67 - 76.

46. Mondal, S. and Wickramasinghe, S. R. (2008). Produced water treatment by nanofiltration and reverse osmosis membranes. *Journal of Membrane Science*, 322(1): 162 - 170.
47. Qiao, X., Zhang, Z., Yu, J. and Ye, X. (2008). Performance characteristics of a hybrid membrane pilot-scale plant for oilfield-produced wastewater. *Desalination*, 225(1-3): 113 – 122.
48. Li, L. and Lee, R. (2009). Purification of produced water by ceramic membranes: material screening, process design and economics. *Separation Science and Technology*, 44(15): 3455 - 3484.
49. Weschenfelder, S. E., Louvisse, A. M. T., Borges, C. P., Meabe, E., Izquierdo, J. and Campos, J. C. (2015). Evaluation of ceramic membranes for oilfield produced water treatment aiming reinjection in offshore units. *Journal of Petroleum Science and Engineering*, 131: 51 - 57.
50. Abadi, H., S. R., Sebzari, M. R., Hemati, M., Rekabdar, F. and Mohammadi, T. (2011). Ceramic membrane performance in microfiltration of oily wastewater. *Desalination*, 265(1): 222 - 228.
51. Rahman, M. M. and Muhammad, H. A. (2006). Performance of a crossflow membrane bioreactor (cf-mbr) when treating refinery wastewater. *International Congress on Membranes and Membranes Processes*, 191(1-3): 16 - 26.
52. DeFriend, K. A. , Wiesner, M. R., and Barron A. R. (2003). Alumina and aluminate ultrafiltration membranes derived from alumina nanoparticles. *Journal of Membrane Science*, 224(1-2): 11 - 28.
53. Pendergast, M. T. M. and Hoek, E. M. V (2011). A review of water treatment membrane technologies. *Energy and Environmental Science*, 4: 1946 - 1971.
54. Munirasu, S., Abu Haija, M. and Banat, F. (2016). Use of membrane technology for oilfield and refinery produced water treatment - A review. *Process Safety and Environmental Protection*, 100: 183 - 2002.
55. Field, R. (2010). Fundamentals of fouling. *Membranes for Water Treatment*, 4: 1 - 23.
56. Scott, K. (1995). Handbook of industrial membranes. Elsevier, New York.
57. Cicek, N., Dionysiou, D., Suidan, M. T., Ginestet, P., and Audic, J. M. (1999). Performance deterioration and structural changes of a ceramic membrane bioreactor due to inorganic abrasion. *Journal of Membrane Science*, 163(1): 19 - 28.
58. Hua, F. L, Tsang, Y. F, Wang, Y. J, Chan, S. Y., Chua, H. and Sin, S. N. (2007). Performance study of ceramic microfiltration membrane for oily wastewater treatment. *Chemical Engineering Journal*, 128(2-3): 169 - 175.
59. Muric, A., Petrinic, I. and Christensen, M. L. (2014). Comparison of ceramic and polymeric ultrafiltration membranes for treating wastewater from metalworking industry. *Chemical Engineering Journal*, 255: 403 - 410.
60. Nandi, B. K, Moparthi, A., Uppaluri, R. and Purkait, M. K. (2010). Treatment of oily wastewater using low cost ceramic membrane: comparative assessment of pore blocking and artificial neural network models. *Chemical Engineering Research and Design*, 88(7): 881 - 892.

*Malaysian Journal of Analytical Sciences, Vol 21 No 3 (2017): 659 - 668*
*DOI: https://doi.org/10.17576/mjas-2017-2103-15*

MALAYSIAN JOURNAL OF ANALYTICAL SCIENCES
*Published by The Malaysian Analytical Sciences Society*
ISSN 1394 - 2506

# POLY(EUGENOL SULFONATE) - SULFONATED POLYETHERIMIDE NEW BLENDS MEMBRANE PROMISING FOR DIRECT METHANOL FUEL CELL

## (Membran Campuran daripada Poli(Eugenol Sulfonat) dan Polieterimida Sulfonat yang Menjanjikan untuk Sel Bahan Api Metanol Langsung)

Eka Cahya Muliawati[1,2], Mardi Santoso[2], Ahmad Fauzi Ismail[1,3], Juhana Jaafar[1,3], Mohd. Taufiq Salleh[1,3], Silvana Dwi Nurherdiana[2], Nurul Widiastuti[2]*

[1]*Advanced Membrane Technology Research Centre (AMTEC), Universiti Teknologi Malaysia, 81310 UTM Skudai, Johor Bahru, Johor, Malaysia*
[2]*Department of Chemistry, Faculty of Mathematics and Natural Sciences, Institut Teknologi Sepuluh Nopember, Surabaya, Indonesia*
[3]*Faculty of Petroleum and Renewable Energy Engineering, Universiti Teknologi Malaysia, 81310 UTM Skudai, Johor Bahru, Johor, Malaysia*

**Corresponding author: nurul_widiastuti@chem.its.ac.id*

Received: 26 August 2016; Accepted: 8 January 2017

**Abstract**

A new polymeric membrane blended from sulfonated polyetherimide (SPEI) and poly(eugenol sulfonate) (PES) was prepared as proton exchange membrane (PEM) for direct methanol fuel cell (DMFC). The membrane was characterized by Fourier Transform Infrared Spectroscopy (FTIR), thermogravimetric analysis (TGA) and Scanning Electronic Microscopy (SEM). Ion exchange capacity (IEC), proton conductivity, methanol barrier, water uptake, water contact angle and mechanical strength of the membrane was also being determined. The new PES/SPEI membrane with 3 wt.% PES and 20 wt.% SPEI show higher IEC, water uptake, proton conductivity and methanol barrier properties as compared to Nafion 117 membrane. As a conclusion, the results indicate that the SPEI/PES membrane has potential to be employed as PEM for DMFC application.

**Keywords**: sulfonated polyetherimide, poly(eugenol sulfonate), blend membrane, direct methanol fuel cell

**Abstrak**

Membran polimer baru diperbuat daripada campuran polieterimida sulfonat (SPEI) dan poli(eugenol sulfonat) (PES) telah disediakan sebagai membran pertukaran proton (PEM) untuk sel bahan api metanol langsung (DMFC). Membran ini telah dianalisis menggunakan Spektroskopi Inframerah Transformasi Fourier (FTIR), analisis termogravimetri (TGA) dan Mikroskop Imbasan Elektron (SEM). Sifat membran seperti kapasiti pertukaran ion (IEC), kekonduksian proton, halangan metanol, penyerapan air, sudut sentuhan air dan kekuatan mekanikal juga telah ditentukan. Membran baru PES/SPEI dengan 3 wt.% PES dan 20 wt.% SPEI telah menunjukkan nilai IEC, pengambilan air, kekonduksian proton dan halangan metanol yang lebih tinggi berbanding membran Nafion 117. Sebagai kesimpulan, hasil kajian menunjukkan bahawa membran SPEI/PES mempunyai potensi untuk digunapakai sebagai PEM untuk aplikasi DMFC.

**Kata kunci:** polieterimida sulfonat, poli(eugenol sulfonat), membran campuran, sel bahan api metanol langsung

## Introduction

The Direct Methanol Fuel Cell (DMFC) is one of the attractive fuel cell type for mobile application which is clean technology to the environment, having high efficiency, portable, and can be operated at relatively low temperatures

[1]. The key component in DMFC is proton exchange membrane, with respect to development of cell performance via an increase conductivity and a reduction of methanol permeability [2 – 5]. Perfluorosulfonic acid (PFSA) membrane, under Nafion commercial brand is a type (Proton Exchange Membrane) PEM that has been used widely with high proton conductivity, low dimensional change in water, and excellent cell performance in various environments [6 – 8]. However, Nafion membranes are expensive and lose their proton conductivity and durable properties at high temperature (>80 $^{o}$C) [5 – 11]. Therefore, many researchers have endeavored to develop inexpensive membranes for higher operation temperature and lower methanol permeability such as a variety of polymer blends.

The use of polymer blends means to combine two different characteristics then improving the comprehensive properties and modification of a matrix [5, 9 – 13]. Among many types of blend membranes, the sulfonated polymer organic blend membranes show many attractive properties. Polymer blend membranes described as organic materials are new class of interesting materials that exhibit improved proton conductivity and reduced methanol permeability when applied in DMFC. Many researchers have investigated the alternative cheap materials with new hydrocarbon polymers synthesized, or blended with a methanol hating material [11, 13, 16]. The improvement progress in the membrane for DMFC has been gradually made by physical and chemical changes of polymer materials, such as rigidity of main chains, length of side chains, equivalent weight of proton donors and concentration of introduced hydrophilic groups like sulfonic and phosphoric acids in the membranes [12]. The increase of concentration of those groups in the membranes produces more water clusters, which would be able to repair the controlled proton transport, water and methanol crossovers.

In previous study [7, 15], the preparation and characterization of a new type of proton exchange membrane based on SPEI, which was obtained by directly synthesis from sulfonated monomer, have been described. The conductivity values for the SPEI copolymers at ion exchange capacity around 0.553 meq/g were 0.0014 S/cm at 25 °C, indicating that they are promising candidates for PEM materials [7].

In this study, we have reported a new blend membranes material from sulfonated polyetherimide and poly(eugenol sulfonate) who has never done. Poly(eugenol sulfonate) have been aromatic phenol units provide high performance properties such as considerable mechanical strength, thermal stability and chemical resistance, while the flexible sulfonate linkages provide good processability [14].

## Materials and Methods

### Materials

All the membranes characterized were prepared in the laboratory with polyetherimide and methyl-2-pyrrolidone (NMP) supplied by Sigma–Aldrich, Eugenol supplied by Merck, and Nafion 117 membrane was purchased from DuPont Co.

### Synthesis of poly(eugenol sulfonate)

Poly(eugenol sulfonate) was synthesized from eugenol according to a previous study. Poly(eugenol sulfonate) (PES) is made from a mixture of concentrated sulphuric acid, eugenol and $PbSO_4$ in a steam bath at a temperature of 90 °C. The results are analysed with an infrared spectrophotometer [14].

### Sulfonation of polyetherimide

The synthesis sulfonated polyetherimide **(**SPEI) was carried out by the previous procedure. First, 10 g of PEI was dissolved in dichloroethane (50 mL) at 60 °C for 5 hours. The solution was kept at room temperature for 1 hour. Chlorosulfonic acid (2.06 mL) in dichloroethane (35 mL) was added drop-wise to the polymer solution under vigorous stirring for 45 minutes. The product was dissolved in DMAc after 2 hours, and the polymer solution was precipitated in isopropanol. The product was filtered and washed with isopropanol three times to remove impurities, and dried in an oven at 50 °C for 48 hours. The results were characterized with an infrared spectrophotometer [7, 15, 17].

**Preparation of membrane**
The polymer blended membranes were prepared with three different mass ratios of SPEI (15%, 20%, 25%) and three different mass ratio of SPEI: PES blend (15: 3, 20: 3, 25: 3)%. PES and SPEI were simultaneously dissolved in NMP to form 15 wt.% solutions with stirring at 60 °C for 12 hours. After cooled to room temperature, the resulting polymer solutions were cast on glass plates and dried in a room temperature for 12 hours. Then immersed to sulfic acid for 12 hours.

**Characterization of blend membranes**
FTIR spectra of the membranes were measured by in the range of 4000 – 400 $cm^{-1}$. The samples were dried at 80 °C for 1 hour before measurement. The surface and cross-section morphology of the blend membranes were examined with a Zeuss field emission scanning electron microscope. All the samples for cross-sectional view were fracture in liquid nitrogen. The mechanical properties of the blend membranes were measured by a tensile machine (Instron 5567, TA Instruments Co.) at room temperature. The samples were tested at elongation with rate of 5.0 mm $min^{-1}$. All membranes were tested five times to obtain an average value.

The contact angle (CA), of the membrane surface was measured using a Optima Surface Analysis System (AST Products Inc., Billerica, MA). Sample coupons with an area of about 5 cm x 1.5 cm were prepared by cutting to pieces at random locations within the membrane sheet. The sample was placed on a glass plate and fixed with a tape. A drop of distilled water was then placed on the sample surface using a microsyringe (Hamilton Company, Reno, NV). The CA was measured within a 30 s period after the water drop was placed. The CA was measured at 10 different spots on each membrane sample coupon and the values averaged.

Thermal stability of the samples was characterized using thermogravimetric analysis (TGA). Dry sample was ground into fine powder and the sample was placed in a platinum pan. The analysis was carried out at a heating rate of 10 °C $min^{-1}$ over 30 – 700 °C temperature range under air atmosphere. The sample powder was prepared in the pin stub holder and coated with gold for analysis.

**Water uptake and swelling ratio**
The membranes were dried at 80 $^{o}$C under vacuum for 24 hours and the dry weights of the samples were weighed. Subsequently, the membranes were immersed in deionized water for 24 hours at room temperature. After quickly wiping off the water adhered to the surface of the membranes, the weight and dimension of wet membranes were measured. The water uptake and swelling ratio could be determined according to the following equation 1 and 2 [18] :

$$\text{Water uptake} = \frac{W_{wet}-W_{dry}}{W_{dry}} \times 100\% \quad (1)$$

where $W_{wet}$ and $W_{dry}$ are the weight of membranes in wet and dry state, respectively.

$$\text{Swelling ratio} = \frac{L_{wet}-L_{dry}}{L_{dry}} \times 100\% \quad (2)$$

where $L_{wet}$ and $L_{dry}$ are the length of membranes in wet and dry condition, respectively [19].

**Ion exchange capacity**
The ion exchange capacity (IEC) of membranes was obtained by titration method. The dry membranes were immersed in the 1 mol $L^{-1}$ NaCl solution for 24 hours. This solution was titrated by 0.01 mol $L^{-1}$ NaOH with phenolphthalein as the indicator. The IEC of the samples was calculated by following equation 3:

$$IEC = \frac{V_{NaOH}-C_{NaOH}}{W_d} \times 100\% \quad (3)$$

where $V_{NaOH}$ is the volume of consumed NaOH solution, $C_{NaOH}$ is the concentration of NaOH solution and $W_d$ is the weight of the dry membrane [17].

**Methanol permeability and proton conductivity**

Methanol permeability was determined using a two-compartment diffusion cell. Compartment A was filled with 1 M methanol solution and compartment B was filled with deionized water. The membrane was placed between compartment A and B. Samples from compartment B were taken out every 30 minutes for 6 hours to determine its methanol concentration using high-performance liquid chromatography (HPLC). The methanol permeability values were determined by using equation 4 [18].

$$P = \left(\frac{\Delta C_B}{\Delta t}\right)\left(\frac{LV_B}{AC_A}\right) \quad (4)$$

P is methanol permeability of the membrane ($cm^2.s^{-1}$), $\Delta C_B/\Delta t$ is the slope variation of methanol concentration in compartment B as a function of time (mol $L^{-1}.s^{-1}$), $L$ is the thickness of the membrane (cm), $V_B$ is the volume of the water at compartment A ($cm^3$), $A$ is the membrane surface area ($cm^2$), and $C_A$ is the concentration of methanol in the cell A (mol $L^{-1}$). The proton conductivity of the membrane was measured using electrochemical impedance spectroscopy (EIS), at a frequency of 1-$10^6$ Hz. The proton conductivity values were calculated using equation 5;

$$\sigma = \frac{L}{R \times A} \quad (5)$$

where $\sigma$ is the proton conductivity of the membrane (S $cm^{-1}$), $L$ is the membrane (cm), $A$ is the membrane surface area ($cm^2$), and $R$ is the membrane resistance (Ω) [18].

## Results and Discussion

**Fourier transform infrared spectroscopy**

Fourier transform infrared spectroscopy (FTIR) spectra of PES+SPEI polymer blend membranes are shown in Figure 1. As for the SPEI, PES, and PES+PEI membranes, the bands at 708 $cm^{-1}$, 1071 $cm^{-1}$, 1279 $cm^{-1}$ are assigned to the stretching vibration of $–SO_3H$ groups [7, 9]. Furthermore, the broad band in the SPEI, PES and SPEI+PES spectra around 3600 $cm^{-1}$ was assigned to O–H vibration associated with the interaction between sulfonic acid groups and water molecules. This is confirmed that the sulfonic acid groups are successfully introduced to the resulting polymer. The hydrophilic clusters formed by the sulfonic acid groups could broaden the proton transfer channels. The bands for the stretching vibration of the C-N groups of SPEI can be observed at 1467 $cm^{-1}$ and the stretching vibration of the C=O groups of SPEI and PES can be seen at 1650 $cm^{-1}$.

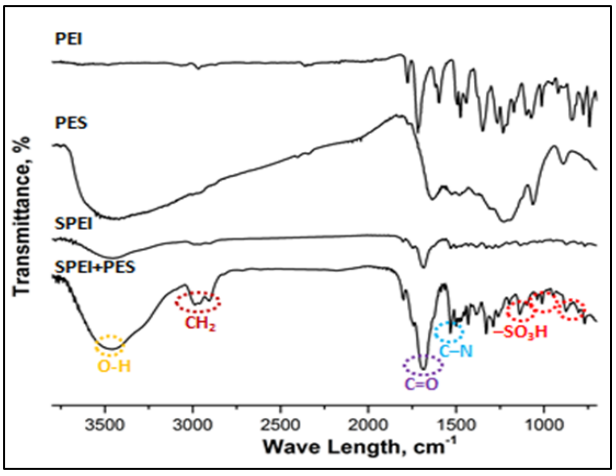



Figure 1. FTIR spectra of membranes

**Mechanical properties**

The mechanical strength of the blend membranes is significant for DMFC application to assure its stability as the electrolyte passes across the membrane. The mechanical strength of SPEI membrane and the blend membranes (SPEI-PES) were measured at room temperature.

As shown in Figure 2, the blend membranes show higher tensile strength along with the decrease of SPEI. The tensile strength rises from 13.9 to 30.7 MPa with the content of SPEI decrease from 25 to 15%. The tensile strength decrease from 31 to 13 MPa with the content of SPEI increase from 15 to 25% with added 3% PES. Such enhancement in tensile strength is due to the ionic crosslinking and close packed molecules in sulfonated blend membranes. However, the ionic crosslinking also reduces molecular flexibility, hence the blend membranes become more fragile and the elongation at break is decreased [9].

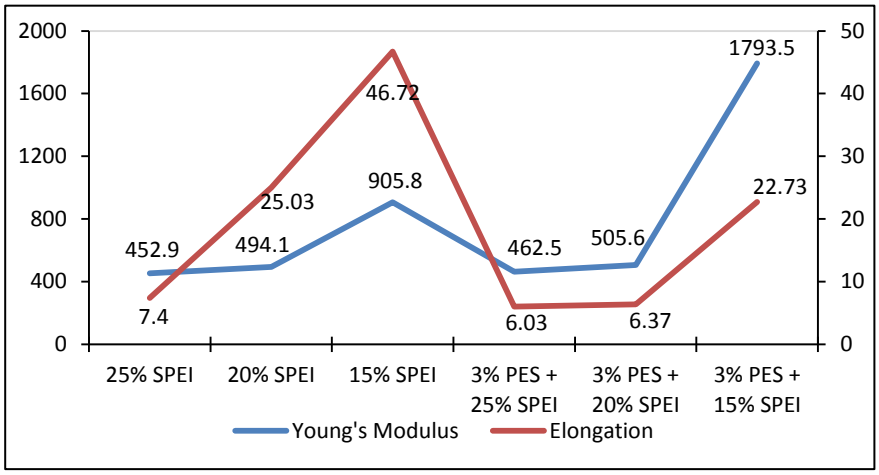



Figure 2. The mechanical properties of membranes

**Physically properties**

The water uptake, methanol uptake, swelling ratio, IEC and contact angle are important parameters for a membrane to be characterized. These properties of polymer blend membranes are presented in Figure 3. Many significant properties of the membrane, such as proton conductivity and water uptake, are related to IEC [9]. Ionic exchange capacity (IEC) is defined as the fixed milli equivalents of exchangeable group per gram of polymer, which is usually considered to correspond to the amount of sites for proton transfer and has great relation to the proton conductivity [5]. IEC depends on the content of free sulfonic acid groups in the membrane [9]. It can be seen that the IEC of the blend membranes increase with increase amount of the SPEI and also addition PES. One reason is due to the content of SPEI increase with the increase of sulfuric acid group of added PES.

Water uptake is another important parameter for ion exchange membrane. It has a great influence on the proton conductivity and dimensional stability of the membrane [9]. High water uptake can improve the proton conductivity [9]. As expected, hydrophilic side groups in SPEI and PES improve the amount of free sulfonic acid groups by polymer blend interactions. High content of SPEI leads water uptake increase, indicating the increase of hydrophilicity within the blend membranes. Moreover, the formation of cross-linked network structure increase free volume in blend membranes for water molecules which leads to water uptake increase. The swelling ratio reflects dimensional stability, and the lower swelling ratio is required for keeping membrane dimensional stable for a long time. Similar to the water uptake, all blend membranes show develop swelling ratio with increase of the SPEI and PES added [5, 9]. Therefore, it needs optimization composition of polymer. 20% (% weight ratio) SPEI/ 3% PES are the best compositions.

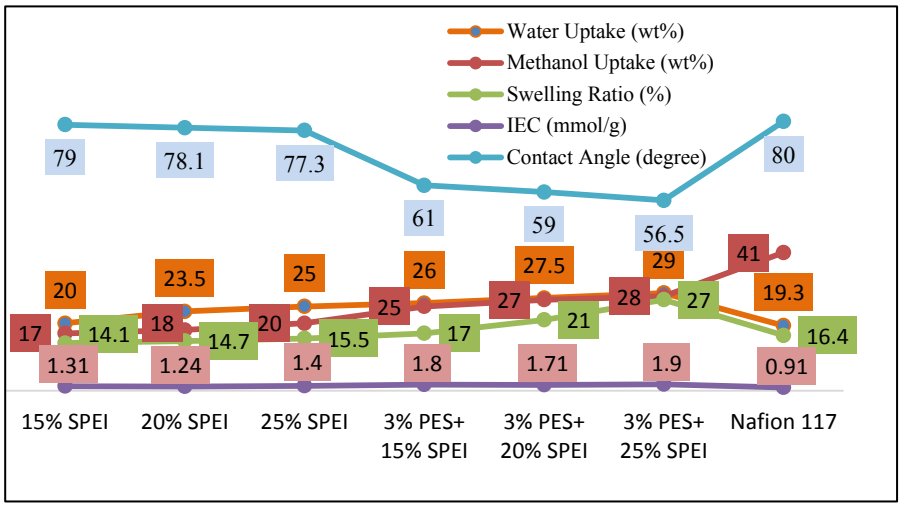



Figure 3. The physical properties of membranes

Permeability of methanol is a crucial parameter for DMFC, which represents the ability to prevent the crossover of positive and negative electrolytes [9]. Since DMFC uses methanol as fuel, low methanol permeability PEM would contribute to high efficiency fuel usage and low fuel loss [18]. Diffusion of methanol across the membrane will lead to self-discharge of the cell [9]. In this study, the methanol permeability of blend membranes and Nafion 117 membrane was measured. The calculated methanol permeability and proton conductivity are illustrated in Table 1.

Table 1. Methanol permeability and proton conductivity of pure PEI and PEI-PES membranes

| **Membranes** | **Proton Conductivity ($S.cm^{-1}$)** | **Methanol Permeability ($\times 10^{-7} cm^2.s^{-1}$)** |
|---|---|---|
| PES 20% | 0.0010 | 5.75 |
| SPEI 15% | 0.0018 | 11 |
| SPEI 20% | 0.0078 | 10 |
| SPEI 25% | 0.0069 | 13 |
| SPEI 20%-PES 3% | 0.0080 | 15 |
| Nafion® 117 | 0.0900 | 25 |

According to Table 1, all the blend membranes have lower methanol permeability than Nafion 117 membrane. However, methanol permeability can be improved by increasing hydrophilic polymer from sulfonic group addition. It caused the free volume of polymers will be bigger, which will result higher in their permeability's [9, 20].

In general, the smaller of contact angle indicates increasing hydrophilicity of the samples. Figure 3 illustrates the contact angles of the SPEI, PES, SPEI+PES significantly decrease because the presence of hydroxyl and sulfonic groups. Moreover, another important reason is the SPEI and PES possesses a high degree of sulfonic and hydrophilicity. This finding confirms the result of the water absorption of the membranes. This following Figure 4, provides information of the interactions between SPEI and PES membrane.

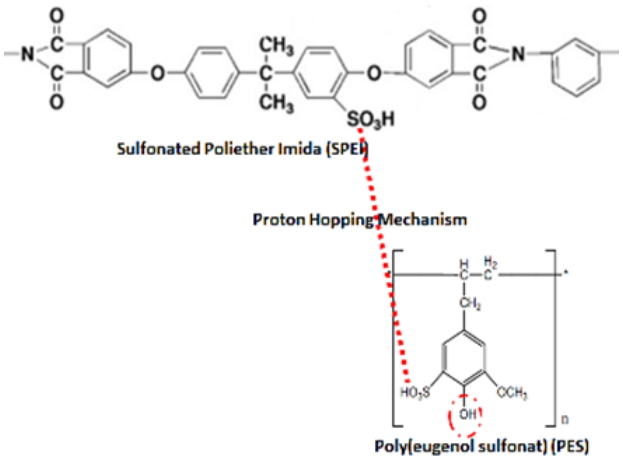



Figure 4. The interactions between SPEI and PES

Protons are largely transferred through the PEMs either as water-solvated species or by passing from one water molecule to another; hence, the ability of PEMs to imbibe large amounts of water molecules enhances the proton conductivity in the most cases. This effect is related to sufficient number of ionic sites and polar functional groups and also better formation and connection of proton-conducting channels in PEMs containing acid-bearing functionalities as well as higher dissociation degree of the ionic groups as the proton-conducting sites [21]. This statement is consistent as the Figure 4 contained polar functional groups such as $–SO_3H$ and –OH. With the sulfonate group will occur stepping proton from the one sulfonate group to another or called as proton hopping mechanism [21].

**Thermo gravimetric analysis**

Figure 5 illustrates the Thermo gravimetric analysis (TGA) curves of the membranes that under went both the dry method (slide casting and then vacuum), and wet method (spin coating and then waterbath), respectively. The changes in the sample weight with different temperatures under nitrogen flow using a standard temperature program with two steps were used for the TGA obtained at 550, 600, and 650 $^oC$ at a heating rate of 1 $^oC$ /min.

In Figure 5, it can be observed that the SPEI begins weight loss at around 200 $^oC$, followed by a final decomposition that began slowly around 450 $^oC$ after heating. The thermal decomposition of organic polymers is characterized by the breaking of the main chains [9] and different thermal degradation routes of SPEI. The decomposition of PES and PES+SPEI membranes weight significantly decreases after the temperature reaches approximately 550 $^oC$.This result may be due to the evaluation of a cleavage of the benzene ring of the SPEI and PES precursor. Consequently, the PEI-PES membrane can be expected to possess higher thermal stability characteristics compared to pure PEI membrane. Therefore, the resultant blend membrane is stable at desired operating temperatures (<100 $^oC$) for DMFC application.

**Morphology of the membranes**

Figure 6 shows the SEM images of SPEI and SPEI-PES particles. It appears that before the blending process, the 20% SPEI particles surfaces were less smooth and corrugated because casting solution is not perfect as shown in Figure 6 (a). After being blended with 3% PES (see Figure 6 (b)), the PES particles were dispersed and smooth its surface. These images prove that the PES has been successfully incorporated and dispersed into the SPEI. Also Figure 6 (c) and (d), with the elemental composition is given in Table 2, show the incorporation and dispersion of $–SO_3H$ groups on SPEI+PES. Oxygen, nitrogen, sulfuric elements present are important for bonding formation with organic polymer, enhancing the mechanical strength of its blending membrane, and developing the pathway for protons, thus consequently increase the membrane proton conductivity [18].

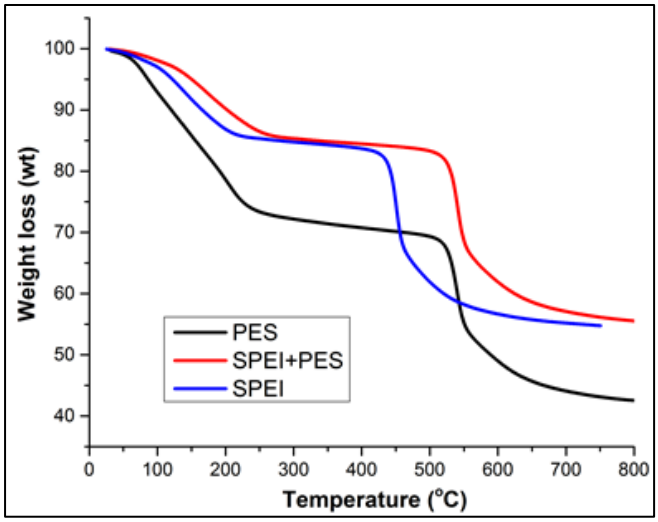



Figure 5. TGA curves SPEI, PES and SPEI+PES

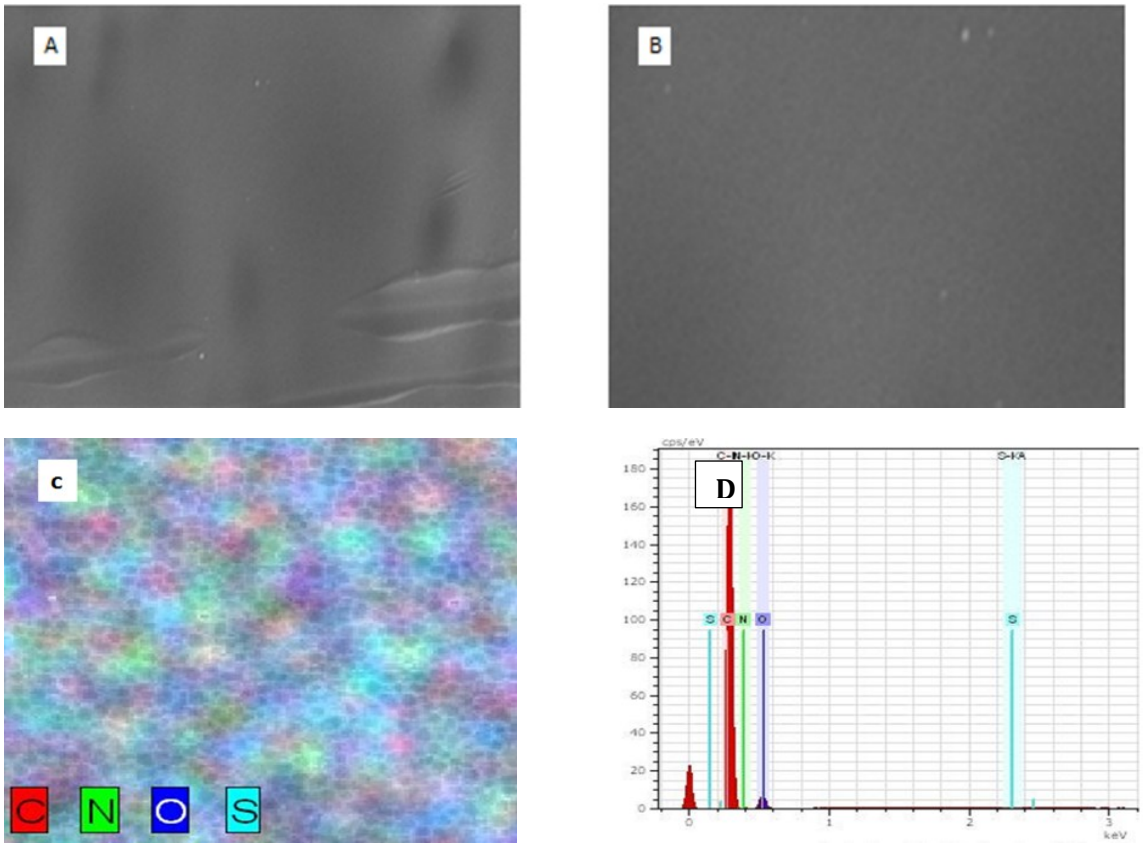



Figure 6. SEM images of (a) 20%SPEI, (b) 20%SPEI+3%PES, (c) Elements map and (d) EDX spectra of 20%SPEI+PES3%

Table 2. Elemental composition of 20%SPEI+PES3%

| E1 | AN | Series | Unn. C (wt.%) | Norm. C (wt.%) | Atom. C (at.%) | Error (%) |
|---|---|---|---|---|---|---|
| C | 6 | K-series | 70.84 | 70.84 | 76.11 | 21.5 |
| N | 7 | K-series | 4.01 | 4.01 | 3.70 | 1.6 |
| O | 8 | K-series | 24.92 | 24.92 | 20.10 | 7.9 |
| S | 16 | K-series | 0.23 | 0.23 | 0.09 | 0.0 |

## Conclusion

The blended membrane of SPEI and PES was successfully prepared using solution casting method. SEM images showed the evidence of PES incorporation and disperse into the PEI polymer matrix. The water uptake for SPEI-PES membranes increase as the increasing of SPEI concentration. The DMFC with blended membranes shows higher proton conductivity 0.008 $S.cm^{-1}$ and low methanol permeability $15 \times 10^{-7}$ $cm^2.s^{-1}$, which is better than the costly Nafion 117 membrane. Based on the obtained results, it can be concluded that PEI membrane blending with PES can be potentially used as promising polymer electrolyte membrane for DMFC applications.

## Acknowledgement

The authors would like to acknowledge the Indonesian Ministry of Research and Higher Education for providing scholarship for pursuing Doctoral Degree for Eka Cahya Mulyawati in the Department of Chemistry, Institut Teknologi Sepuluh Nopember and financial support under research grant "Penelitian Disertasi Doktor" number 1444/E3/LT/2017. The authors also would like to express gratitude to the Ministry of Science, Technology and Innovation (MOSTI) Malaysia and Ministry of Higher Education for the financial support from the grants with the vote number of R.J130000.7942.4S507, R.J130000.7809.4F592 and Q.J130000.2509.05H52, and also to the research management centre (RMC), Universiti Teknologi Malaysia for supporting the research management activities.

## References

1. Ma, C. C. M., Hsiao, Y. H., Lin, Y. F., Yen, C. Y., Liao, S. H., Weng, C. C. and Weng, F. B. (2008). Effects and properties of various molecular weights of poly(propylene oxide) oligomers/Nafion® acid–base blend membranes for direct methanol fuel cells. *Journal of Power Sources*, 185(2): 846 –852.
2. Yang, T. and Liu, C. (2011). SPEEK/sulfonated cyclodextrin blend membranes for direct methanol fuel cell. *International Journal of Hydrogen Energy*, 36(9): 5666 – 5674.
3. Tsai, J. C. and Lin, C. K. (2011). Acid-base blend membranes based on Nafion®/aminated SPEEK for reducing methanol permeability. *Journal of the Taiwan Institute of Chemical Engineers*, 42(2): 281 –285.
4. Muthumeenal, A., Neelakandan, S., Kanagaraj, P. and Nagendran, A. (2016). Synthesis and properties of novel proton exchange membranes based on sulfonated polyethersulfone and N-phthaloyl chitosan blends for DMFC applications. *Renewable Energy*, 86: 922 – 929.
5. Yang, T. (2009). Composite membrane of sulfonated poly(ether ether ketone) and sulfated poly(vinyl alcohol) for use in direct methanol fuel cells. *Journal of Membrane Science*, 342(1): 221 – 226.
6. Lufrano, F., Baglio, V., Staiti, P. and Antonucci, V. (2008). Polymer electrolytes based on sulfonated poly-sulfone for direct methanol fuel cells. *Journal of Power Sources*, 179(1): 34 – 41.
7. Rajagopalan, M., Jeon, J. H. and Oh, I. K. (2010). Electric-stimuli-responsive bending actuator based on sulfonated polyetherimide. *Sensors and Actuators B: Chemical*, 151(1): 198 – 204.
8. Awang, N., Ismail, A. F., Jaafar, J., Matsuura, T., Junoh, H., Othman, M. H. D. and Rahman, M. A. (2015). Functionalization of polymeric materials as a high performance membrane for direct methanol fuel cell: A review. *Reactive and Functional Polymers*, 86: 248 – 258.
9. Liu S., Wanga L., Ding Y., Liu B., Han X., Song Y. (2014). Novel sulfonated poly(ether ether keton)/ poly-etherimide acid-base blend membranes for vanadium redox flow battery applications. *Electrochimica Acta*, 130: 90 – 96.

10. Jung, H. Y., and Park, J. K. (2007). Blend membranes based on sulfonated poly(ether ether ketone) and poly (vinylidene fluoride) for high performance direct methanol fuel cell. *Electrochimica Acta*, 52(26): 7464 – 7468.
11. Kim, D. J., Lee, H. J. and Nam, S. Y. (2014). Sulfonated poly(arylene ether sulfone) membranes blended with hydrophobic polymers for direct methanol fuel cell applications. *International Journal of Hydrogen Energy*, 39(30): 17524 – 17532.
12. Jung, B., Kim, B. and Yang, J. M. (2004). Transport of methanol and protons through partially sulfonated polymer blend membranes for direct methanol fuel cell. *Journal of Membrane Science*, 245(1): 61 – 69.
13. Arnett, N. Y., Harrison, W. L., Badami, A. S., Roy, A., Lane, O., Cromer, F., Dong, L. and McGrath, J. E. (2007). Hydrocarbon and partially fluorinated sulfonated copolymer blends as functional membranes for proton exchange membrane fuel cells. *Journal of Power Sources*, 172(1): 20 – 29.
14. Handayani, D. S. (2002). Sulfonasi dan polimerisasi eugenol. *Alchemy Jurnal Penelitian Kimia*, 1(2): 48 – 54.
15. Guhathakurta, S. and Min, K. (2009). Influence of crystal morphology of 1H-1, 2,4-triazole on anhydrous state proton conductivity of sulfonated bisphenol A polyetherimide based polyelectrolytes. *Polymer*, 50(4): 1034 – 1045.
16. Maier, G. and Meier-Haack, J. (2008). Sulfonated aromatic polymers for fuel cell membranes. In Fuel cells II. Springer Berlin Heidelberg: pp. 1 – 62.
17. Shen, L. Q., Xu, Z. K., Liu, Z. M. and Xu, Y. Y. (2003). Ultrafiltration hollow fiber membranes of sulfonated polyetherimide/polyetherimide blends: Preparation, morphologies and anti-fouling properties. *Journal of Membrane Science*, 218(1): 279 – 293.
18. Purwanto, M., Atmaja, L., Mohamed, M. A., Salleh, M. T., Jaafar, J., Ismail, A. F., Santoso, M. & Widiastuti, N. (2016). Biopolymer-based electrolyte membranes from chitosan incorporated with montmorillonite-cross linked GPTMS for direct methanol fuel cells. *RSC Advances*, 6(3): 2314 – 2322.
19. Liu, S., Wang, L., Ding, Y., Liu, B., Han, X. and Song, Y. (2014). Novel sulfonated poly(ether ether keton)/ polyetherimide acid-base blend membranes for vanadium redox flow battery applications. *Electrochimica Acta*, 130: 90 – 96.
20. Jaafar, J., Ismail, A. F. and Matsuura, T. (2009). Preparation and barrier properties of SPEEK/Cloisite 15A®/ TAP nanocomposite membrane for DMFC application. *Journal of Membrane Science*, 345(1): 119 – 127.
21. Tohidian, M., Ghaffarian, S. R., Shakeri, S. E., Dashtimoghadam, E. and Hasani-Sadrabadi, M. M. (2013). Organically modified montmorillonite and chitosan–phosphotungstic acid complex nanocomposites as high performance membranes for fuel cell applications. *Journal of Solid State Electrochemistry*, 17(8): 2123 – 2137.

*Malaysian Journal of Analytical Sciences, Vol 21 No 3 (2017): 669 - 674*
*DOI: https://doi.org/10.17576/mjas-2017-2103-16*

MALAYSIAN JOURNAL OF ANALYTICAL SCIENCES
*Published by The Malaysian Analytical Sciences Society*
ISSN 1394 - 2506

# PRELIMINARY STUDIES ON POWER GENERATION BY *Bacilli E1* USING DUAL CHAMBER MICROBIAL FUEL CELL

## (Kajian Awal Penghasilan Elektrik oleh *Basilli El* Menggunakan Sel Bahan Api Mikroorganisma Dwi-kebuk)

Nazlee Faisal Ghazali[1]*, Nik Azmi Nik Mahmood[1], Kamarul Asri Ibrahim[2], Amir Asyraf Nasaruddin[1]

[1]*Department of Bioprocess and Polymer Engineering*
[2]*Department of Chemical Engineering*
*Faculty of Chemical and Energy Engineering,*
*Universiti Teknologi Malaysia, 81310 Johor Bahru, Johor, Malaysia*

**Corresponding author: nazlee@utm.my*

Received: 26 August 2016; Accepted: 8 January 2017

**Abstract**

Microbial fuel cell (MFC) is a developed technology to utilize microbial degradation ability and turned the degradation products to electricity. One of the limiting factor that contributes to the performance level of MFC is the microorganism used in the MFC. In the present research, *Bacilli E1* has been tested for its ability to utilize glucose and converted it to electricity in dual chamber MFC. The MFC operated using E1 produced a maximum average of open circuit voltage (OCV) of 0.8 V. Meanwhile, by inserting a 1000 Ω resistance in the MFC circuit, produced a stable voltage of 0.1 V and calculated current and power were 0.2 ± 0.017 mA and 0.1 $Wm^{-2}$ Comparison of glucose based voltage production between individual and mixed culture shows similar pattern of voltage profile and since individual CC did not show any significant increase of OCV, it was concluded that *Bacilli E1* plays major role in the present MFC for power production.

**Keywords**: microbial fuel cell, *bacilli*, glucose

**Abstrak**

Sel bahan api berasaskan mikrob (MFC) adalah satu teknologi terbangun yang menggunakan keupayaan mikroorganisma mendegradasi dan menukarkan produk degradasi kepada elektrik. Antara yang menjadi faktor penghad yang menyumbangkan kepada tingkat prestasi MFC adalah mikroorganisma yang digunakan di dalam MFC. Dalam kajian ini, *Bacilli E1* telah diuji keupayaannya untuk menggunakan glukosa dan menukarkannya kepada elektrik dalam dwikebuk MFC. MFC yang dijalankan dengan menggunakan E1, telah menghasilkan voltan litar terbuka (OCV) sebanyak 0.8 V. Manakala, dengan memasukkan rintangan sebanyak 1000 Ohm dalam litar MFC menghasilkan voltan yang stabil berjumlah 0.1 V serta jumlah arus dan kuasa yang dikira adalah masing-masing 0.2 ± 0.017 mA dan 0.1 $Wm^{-2}$. Perbandingan antara penghasilan voltan daripada glukosa menggunakan individu dan kultur campuran adalah hampir serupa dan memandangkan CC secara individu tidak menunjukkan sebarang kenaikan dalam OCV, maka kesimpulan dibuat bahawa *Bacilli E1* memainkan peranan besar dalam MFC yang dijalankan untuk penghasilan kuasa..

**Kata kunci:** sel bahan api berasaskan mikrob, *bacilli*, glukosa

## Introduction

Microorganism(s) which has the ability to oxidize organic compounds to carbon dioxide, protons and electrons which the electrons are then been transferred to electrodes is called 'electricigens' [1, 2]. Electricigens are known to

convert organic waste into protons and electrons directly from the waste itself or with help of different alternative mechanism(s). However, in the advances in microbiology and biotechnology, some of the microorganisms have been identified as 'super bug' that mainly referred as unique microbes that can perform electron transfer directly with the aid of appendages equipped on the microorganisms or some natural surface proteins on the microbes. For example, *Geobacter* sp. [3] has been reported to possess appendage-like accessory called nanowire that can attach to electrodes and directly transferred electrons without any aid of other chemical substance or physical means. Recently, *Geobacter sulfurreducens* KN400 mutants were discovered to produce high current densities in pure cultures [4]. The addition of *Shewanella* sp. and *Pseudomonas* sp. diversified the types of unique microorganisms that each of one of them possesses different capacity of power generating mechanism(s).

Naturally, microorganism(s) competes to use substrate available in order to survive in their micro-environment and this may be a challenge in bioreactor like an MFC. However, there were reports of more than two microbes present in an MFC and able to produce way better or more or less similar power value to individual microbes [5, 6]. Previously, it was conducted by our research team on immobilized cells which were individual microbes been immobilized separately and then mixed in a single chamber MFC and produced comparable power to other MFC trials to date [7].

In the present research, a bacilli species has been isolated from anaerobic digester of a local waste water treatment plant (designated as E1) and been tested for its ability to initiate electricity production in a MFC. In addition, the *Bacilli E1* was mixed with another microorganisms which is known not able to conduct any voltage production as a control. The data will be presented on its open circuit and closed-circuit condition using a structurally designed MFC which was based on the principle of a dual chamber reactor separated by a proton-exchange membrane.

## Materials and Methods

### Microorganism characterization

*Bacilli E1* was isolated from an anaerobic digester of wastewater treatment system in a local palm oil mill in Pasir Gudang, Johor. Briefly, wastewater samples were diluted several times with sterile distilled water and dilutions were plated onto nutrient agar and incubated in an anaerobic jar (Thermo scientific Oxoid) supplemented with a commercially available Anaerogen sachet (Oxoid) which provides anaerobic conditions. Emerging microbes were then re-isolated in the same conditions and selected for MFC trials. Meanwhile, *Clostridium cellulolyticum* ATCC35319 (designated as CC) a strictly anaerobic microorganism has been purchased from American Type Culture Collection (ATCC).

Both microbes were subjected to standard simple staining and gram staining. Briefly, for simple staining, the microbes were heat-fixed onto a glass slide and one drop of methylene blue stain (Merck) was added to the glass slide for staining. Meanwhile, gram staining was conducted by fixing individual microbes onto a glass side and stained with sequential steps of different solutions (crystal violet, iodine, and safranin) which was purchased as kit from Merck Milipore.

### MFC preparation

Stock *Bacilli E1* and *CC* cell suspensions were maintained in -80 $^{\circ}$C previously and thawed prior to use. An amount 12.5 mL each of the cell suspension were transferred into a freshly prepared MFC containing 10% glucose in 0.1 M Potassium phosphate (Kpi) buffer with a pH of 7. All chemicals were analytical grade and sterilized through autoclaving prior to use.

### MFC operation

An acrylic dual chamber MFC was designed with a total volume of 250 mL for each chamber. In addition, anodic chamber was filled with 0.1 M Kpi, pH 7.0 mixed with cell suspension *Bacilli E1* and glucose as described previously or otherwise mixed of *E1* and *CC* for comparison. As for the cathodic chamber, 0.005 M of potassium permanganate in 0.1 M Kpi, pH 7, was added. Both chamber was equipped with rectangular shaped reticulated carbon cloth with a surface area of 20 $cm^2$. Meanwhile, a Nafion membrane (117) was pre-treated and set in between the chambers to separate them. The MFC was operated for three days to analyze the MFC performance in electrical production or voltage values with no resistant applied in between anode and cathode or indicated as open

circuit voltage (OCV). In addition, after OCV values were stable, different resistant values were applied in between the anode and cathode and voltage values were measured or indicated as closed-circuit voltage (CCV). Both OCV and CCV were monitored and recorded using an auto-logged multimeter.

**Closed-circuit voltage analysis**

CCV obtained was then calculated for power and current using the general equation (1 and 2) by Ohm's Law;

$$V = IR \quad (1)$$

$$P = V^2R \quad (2)$$

where V is the voltage obtained, I is the current calculated from V and resistant applied designated as R. P is the calculated power. All MFC trials were done in duplicates.

## Results and Discussion

**General characterization**

Simple and gram staining reveals that the microbe designated as E1 was bacilli in shape as shown in Figure 1. In addition, the gram staining shows that *Bacilli E1* was gram negative. In the group of 'electricigens' so far, there is no generalization that 'electricigens' are gram negative in nature but it is known from literature that generally in the MFC, these microbes tend to form electroactive biofilms on the anodic electrode [7, 8, 9] and it was also observed that after a period of time, biofilm formed on the anodic surface (data not shown). It was shown in several MFC trials that these electricigens within the attached biofilm on the anodic electrodes, capable of donating electrons or receiving electrons from electrodes, via extracellular electron transfer within the MFC environment [10]. However, it was difficult to explore how the electron transfer occurs in the vicinity of *Bacilli E1* without further dissections of the electron transfer process. In the next section, *Bacilli E1* capability in producing electricity will be discussed.

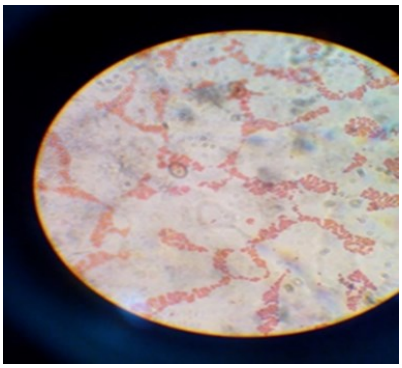


Figure 1. *Bacilli* E1 stained as gram negative

**Open circuit voltage**

Basically, OCV cannot be evaluated as indicator of the MFC performance but merely indicates of potential existence. Figure 2 (a) shows that a maximum average of 0.8 (V) was produced using *Bacilli E1* but *CC* did not show any changes in OCV values and produced less potential difference. Furthermore, similar maximum average of 0.8 (V) was observed for using a mixture of both microbes in the same MFC. This observation proved that the presence of E1 is needed to ensure the possibility of electrical activity initiated in the MFC. However, the OCV start-up seems to shift rapidly for mixed culture which an indication of possible fast degradation though there was no test done in access of the degradation products content. In addition, thermodynamically, the OCV value can be evaluated as the cell electron motive force ($E_{mf}$) which is a maximum achievable voltage without taking account on the losses due internal resistance in the system [11, 12]. From the present results, $E_{mf}$ = 0.8 V was achieved after 5

to 6 hours of operation and stabilized for almost 50 hours as shown Figure 2a. In contrast, as later shown, with current presents, the maximum voltage produced was much less than 0.8 V.

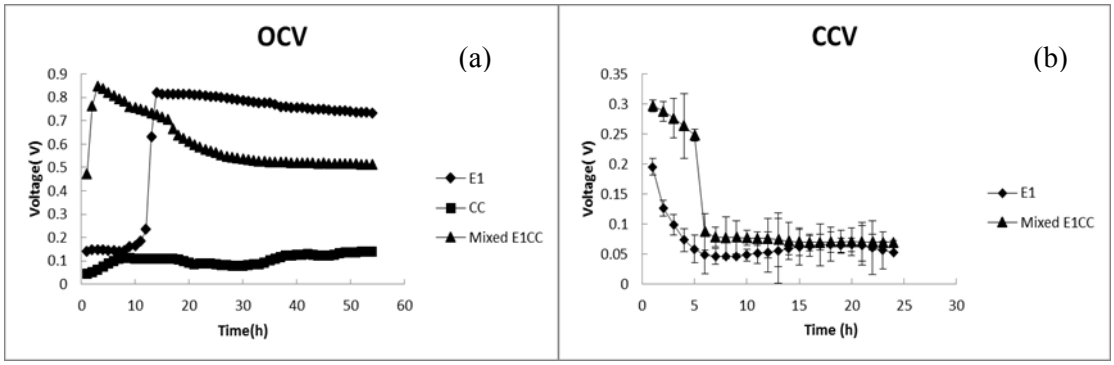



Figure 2. Voltage production in open and close circuit conditions (a) the open circuit voltage (OCV) profile and (b) shows the closed-circuit settings with 1000 Ohm as the resistant applied

**Closed circuit voltage**

The presence of load or resistant, at 1000 Ohm showed a rapid voltage drop (from 0.3 V to approximately 0.1 V) using the mixed culture which an indication of higher current densities produced (based on Ohm's Law) with maximum average calculated value of 0.2 ± 0.017 mA. In contrast, more stable voltage was activated after approximately 5 hours, mainly after large internal resistant and external resistant were equal [13]. It was reported previously more than 50% glucose carbon was discharged as carbon dioxide gas, acetate and various soluble products [14]. Meanwhile, it was also reported that the glucose metabolism within the fuel cell was a combination of both aerobic and anaerobic conditions which also means that the varieties of ionic components produced would probably lead to high internal resistance [12, 13, 14]. However, to synthesize the true source of high internal resistance that occurs in a particular MFC, further comparison in terms of type of membranes, electrolyte used and electrodes type should be conducted [15].

Meanwhile, Table 1 shows comparison of some established lab-scale MFC with the present tested MFC. Based on calculation, the presence dual chambered MFC for mixed culture used produced approximately 0.1 $Wm^{-2}$. The power density obtained was comparable to most sugar-based MFC but the differences in value are due to different materials of electrodes, the microbes used and independent design (anode surface area, volume, etc.) [16] which influence the performance of the MFC.

Table 1. Comparison of different studies of sugar-based MFC

| Type of MFC | Substrate or Fuel | Mode of Operation | Power ($Wm^{-2}$) | References |
|---|---|---|---|---|
| Dual chamber | Date syrup | Batch | 0.065 | [17] |
| Dual chamber | Date syrup | Batch | 0.052 | [18] |
| Dual chamber | Glucose | Fed-batch | 3.6 | [19] |
| Dual chamber | Glucose | Batch | 0.1 | Current work |

## Conclusion

It was revealed that *Bacilli E1* was able to be used for electricity production using microbial fuel cell (MFC). The highest OCV obtained by single microorganism *Bacilli E1* was 0.8 V and the CCV value with 1000 Ohm resistant produced a stable 0.1 V with calculated current of 0.2 ± 0.017 mA.

## Acknowledgement

We wish to acknowledge Universiti Teknologi Malaysia (UTM) for providing the facilities and venue for us to conduct the present research and also platform for students to participate in this study. We also like to acknowledge the technical staff in Department of Bioprocess and Polymer Engineering, UTM for the technical and analysis provision. This work was supported by Ministry of Higher Education (MOHE), grant no. FRGS (PY2014/04052). Also we would like to acknowledge UTM for GUP grant (PY2016/06351).

## References

1. Lovely, D. R. (2006). Microbial energizers: Fuel cells that keep on going. *Microbe,* 1(7): 323 – 329.
2. Logan, B. E. (2009). Exoelectrogenic bacteria that power microbial fuel cells. *Nature Review Microbiology,* 7: 375 – 381.
3. Poddar, S. and Khurana, S. (2011) Geobacter: The electric microbe! efficient microbial fuel cells to generate clean, cheap electricity. *Indian Journal of Microbiology,* 51(2): 240 – 241.
4. Yi, H., Nevin, K. P., Kim, B. C., Franks, A. E., Klimes, A., Tender, L. M. and Lovley, D. R. (2009). Selection of a variant of Geobacter sulfurreducens with enhanced capacity for current production in microbial fuel cells. *Biosensors and Bioelectronics*, 24(12): 3498 – 3503.
5. Zain, S.M., Rosiani, N.S., Hashim, Anuar, N., Suja, F., Daud, W. R. W. and Basri, N. E. A. (2011) Microbial fuel cells using mixed cultures of wastewater for electricity generation. *Sains Malaysiana,* 40(9): 993 – 997.
6. Ren, Z., Ward, T. E., and Regan, J. M. (2007) Electricity production from cellulose in a microbial fuel cell using a defined binary culture. *Environmental Science and Technology*, 41: 4781 – 4786.
7. Mesran, H., Mamat, S., Pang, Y. R., Hong, T. Y., Muneera, Z, Ali, M. A, Ghazali, N. F. M. and Mahmood, N. A. N. (2014). Preliminary studies on immobilized cell-based microbial fuel cell system on its power generation performance. *Journal of Asian Scientific Research,* 4(8): 428 – 435.
8. Mohan, S. V., Raghavulu, S. V. and Sarma, P. N. (2008). Influence of anode biofilm growth on bioelectricity production in a single chambered mediatorless microbial fuel cell using anaerobic consortia. *Biosensor and Bioelectronics*, 24: 41 – 47.
9. Franks, A. E, Malvankar, N. and Nevin, K. P. (2010). Bacterial biofilms: The powerhouse of a microbial fuel cell. *Biofuels,* 1(4): 589 – 604.
10. Kiely, P. D., Call, D. F., Yates, M. D., Regan, J. M. and Logan, B. E. (2010). Anodic biofilms in microbial fuel cells harbor low numbers of higher-power-producing bacteria than abundant genera. *Applied Microbiol and Biotechnology,* 88: 371 – 380.
11. Semenec, L. and Franks, A. E. (2015). Delving through electrogenic biofilms: From anodes to cathodes to microbes. *AIMS Bioengineering,* 2(3): 222 – 248.
12. Logan, B. E., Hmelers, B., Rozendal, R. A., Schroeder, U., Keller, J., Freguia, S., Aelterman, P., Verstratete, W. and Rabaey, K. (2006). Microbial fuel cells: Methodology and technology. *Environmental Science and Technology,* 40 (17): 5181 – 5192.
13. Harnisch, F. and Schrçder, U. (2009). Selectivity versus mobility: Separation of anode and cathode in microbial bioelectrochemical systems. *ChemSusChem,* 2: 921 – 926.
14. Vazquez-Larios, A. L., Solorza-Feria, O., Vazquez-Huerta, G., Rios-Leal, E., Rinderknecht-Seijas, N. and Poggi-Varaldo, H. M. (2011). Internal resistance and performance of microbial fuel cells: influence of cell configuration and temperature. *Journal of New Materials for Electrochemical Systems,* 14(2), 99-105.
15. Thurston, C. F., Bennetto, H. P., Delaney, G. M., Delaney, G., Mason, J. R., Roller, S. D. and Stirling, J. L. (1985). Glucose metabolism in a microbial fuel cell. stoichiometry of product formation in a thionine-mediated proteus vulgaris fuel cell and its relation to coulombic yields. *Journal of General Microbiology,* 131: 1393 – 1401.
16. Zhang, P. Y. and Liu, Z. L. (2010). Experimental study of the microbial fuel cell internal resistance. *Journal of Power Sources*, 195(24): 8013 – 8018.

17. Jafary, T., Ghoreyshi, A. A., Najafpour, G. D., Fatemi, S. and Rahimnejad, M. (2013). Investigation on performance of microbial fuel cells based on carbon sources and kinetic models. *International Journal of Energy Research,* 37: 1539 – 1549.
18. Ghoreyshi, A. A., Jafary, T., Najafpour, G. D. and Haghparast, F. (2011) Effect of type and concentration of substrate on power generation in a dual chambered microbial fuel cell. World Renewable Energy Congress 2011. Lingkoping, Sweden: pp. 1174 – 1181.
19. Rabaey, K., Lissens, G., Siciliano, S. D. and Verstraete, W. (2003). A microbial fuel cell capable of converting glucose to electricity at high rate and efficiency. *Biotechnology Letters*, 25: 1531 – 1535.

*Malaysian Journal of Analytical Sciences, Vol 21 No 3 (2017): 675 - 689*
*DOI: https://doi.org/10.17576/mjas-2017-2103-17*

MALAYSIAN JOURNAL OF ANALYTICAL SCIENCES
*Published by The Malaysian Analytical Sciences Society*
ISSN 1394 - 2506

# CORRELATION BETWEEN PROTON CONDUCTIVITY, HYDROPHILICITY, AND THERMAL STABILITY OF CHITOSAN/MONTMORILLONITE COMPOSITE MEMBRANE MODIFIED GPTMS AND THEIR PERFORMANCE IN DIRECT METHANOL FUEL CELL

## (Hubungan antara Kekonduksian Proton, Sifat Hidrofil dan Kestabilan Termal atas Membran Komposit Kitosan/Montmorillonit dengan Modifikasi GPTMS dan Prestasinya dalam Sel Bahan Api Metanol Langsung)

Mochammad Purwanto[1,2], Lukman Atmaja[3]*, M.T. Salleh[2], Mohamad Azuwa Mohamed[2], Juhana Jaafar[2], Ahmad Fauzi Ismail[2], Mardi Santoso[3], Nurul Widiastuti[3]

[1]*Institut Teknologi Kalimantan, Kampus ITK Karang Joang, Balikpapan 76127, Indonesia*
[2]*Advanced Membrane Technology (AMTEC) Research Centre, Universiti Teknologi Malaysia, 81310 UTM Johor Bahru, Johor, Malaysia*
[3]*Department of Chemistry, Institut Teknologi Sepuluh Nopember, ITS Sukolilo, Surabaya 60111, Indonesia*

**Corresponding author: lukman_at@chem.its.ac.id*

Received: 26 August 2016; Accepted: 8 January 2017

**Abstract**

Chitosan based inorganic hybrid membrane is a promising organic–inorganic hybrids for the development of high performance proton exchange membrane (PEM). The immobilization of modified montmorillonite (MMT) using GPTMS within chitosan matrix would possess superior physicochemical characteristics due to more hydrogen bonding formation introduced by GPTMS. Therefore, higher number hydrogen bond formation can be expected in Ch/MMT-GPTMS membrane rather than in pure Ch membrane. A fully hydrated membrane at elevated temperatures is desirable for efficient proton conduction in the membranes. It remains a critical challenge to maintain proper hydration of the membranes for the operation of the direct methanol fuel cell (DMFC). The microstructure obtained by SEM for composites showed that filler was successfully incorporated and relatively well dispersed in the chitosan polymer matrix. The role of surface modification of MMT filler by GPTMS have increase the functional group that can form hydrogen bonding which suitable for interaction with water. High water uptake is favourable for high performance PEM to facilitate great numbers of protons hopping and diffusion through the membrane. In addition, greater hydrogen bonding formation would lead to the tighter packing of composite membrane, resulting in higher bonding strength and higher thermal resistance. The Ch/MMT-GPTMS composite membrane with 5 wt% filler loading exhibited the best proton conductivity are 4.66 $mScm^{-1}$, with water contact angle value of 64.73°. A maximum power density of 0.24 $mWcm^{-2}$ was obtained with a 2M methanol feed. The relationship of water contact angle, water upake, membrane swelling, thermal stability, and proton conductivity shown suitable trend, it means that all quality of them are related to the hydrophilicity properties.

**Keywords:** chitosan, montmorillonite, (3-glycidoxypropyl) trimethoxysilane, direct methanol fuel cel

**Abstrak**

Kitosan berasaskan membran hibrid tak organik ialah kacukan organik-tak organik yang menjanjikan pembangunan pertukaran proton membran berprestasi tinggi (PEM). Montmorillonit (MMT) pegun diubahsuai menggunakan GPTMS dalam matriks

kitosan akan mempunyai ciri-ciri fiziko-kimia unggul kerana lebih pembentukan ikatan hidrogen yang diperkenalkan oleh GPTMS. Oleh itu, pembentukan jumlah ikatan hidrogen yang lebih tinggi boleh dijangka pada membran Ch/MMT-GPTMS bukannya pada membran Ch tulen. Setiap membran terhidrat sepenuhnya pada suhu tinggi adalah diperlukan untuk pengaliran proton cekap dalam membran. Ia kekal sebagai cabaran kritikal untuk mengekalkan penghidratan membran untuk operasi sel bahan api metanol langsung (DMFC). Mikrostruktur diperolehi melalui SEM untuk komposit menunjukkan bahawa pengisi telah berjaya digabungkan dan tersebar di dalam matriks polimer kitosan. Peranan pengubahsuaian permukaan MMT pengisi oleh GPTMS telah meningkatkan kumpulan berfungsi yang boleh membentuk ikatan hidrogen yang sesuai untuk berinteraksi dengan air. Pengambilan air yang tinggi adalah baik untuk PEM yang berprestasi tinggi bagi membantu proton bergerak dan penyebaran melalui membran. Di samping itu, pembentukan ikatan hidrogen yang lebih besar akan membawa kepada pembungkusan membran komposit yang lebih ketat, menyebabkan kekuatan ikatan dan rintangan haba yang lebih tinggi. Membran komposit Ch/MMT-GPTMS dengan 5% berat pengisi mewujudkan kekonduksian proton terbaik iaitu 4.66 $mScm^{-1}$, dengan nilai sudut sentuhan air ialah 64.73°. Ketumpatan kuasa maksimum ialah 0.24 $mWcm^{-2}$ telah diperolehi dengan suapan 2M metanol. Hubungan sudut sentuhan air, serapan air, pengembangan membran, kestabilan haba, dan kekonduksian proton menunjukkan corak yang sesuai, ia bermaksud semua kualiti yang terhasil adalah berkaitan sifat hidrofilik.

**Kata kunci:** kitosan, montmorillonit, (3-glisidoksipropil) trimetoksisilana, sel bahan api metanol langsung

## Introduction

Fuel cells are considered as green, reliable and highly efficient power generation technology in the current century. Among the different types of fuel cells, direct methanol fuel cell (DMFC) are promising candidates for portable devices or transportation applications in view of their high energy density, simplified system design, low emission, low temperature and pressure operation and high efficiency [1,2]. Polymer electrolyte membranes (PEM), a crucial component in the DMFC separating the cathode and anode, function as proton conductor as well as methanol separator between the cathode and anode [3]. In fact, the performance of DMFC is profoundly connected to PEM, wherein the electrochemically generated protons transport from anode to cathode electrodes. Perfluorosulfonic acid membranes (Nafion©) are widely used as PEM for DMFC applications, owing to good chemical and thermal resistance and high ionic conductivity [4,5]. However, these membranes suffer from drastic high methanol diffusion, high cost and rapid dehydration with decreasing proton conductivity at high temperatures. The high methanol diffusion causes loss of fuel, reduced fuel efficiency, reduced cathode voltage and excess thermal load in the cell [4,6,7].

Chitosan is considered to be the second most abundant polysaccharide in the world after cellulose which can be renewed and produced by utilizing marine waste such as shrimp, crab, lobster, and fish shells [8,9]. Chitosan can also be prepared from fungal cell walls via fermentation technology [10]. Chitosan is a polyaminosaccharide with good mechanical strength, biodegradable, and nontoxic properties [11,12]. Chitosan is not directly available in nature, however, it can be easily generated through the process of deacetylation of chitin by a strong alkali [8]. In the recent years, the comprehensive utilization of chitosan as bio-based polymer has drawn elevated attention for various functional hybrid materials with tremendous properties for various applications such as medicine, pharmaceutical, food industries, waste water treatment and energy [13–17].

It has been reported that the reinforcement of nanomaterial in bio-polymeric matrices has greatly improved the physicochemical, mechanical and thermal stability characteristic of resultants bio-polymer nanocomposites [18–20]. Recently, the incorporation of layered silicates and in particular montmorillonite (MMT) in chitosan has been extensively studied [21–24]. The use of MMT as a filler in bio-polymer is interesting due to its environmental and economic importance. MMT has several advantages including easy to obtain, having a large specific surface area, chemical resist, having strong absorption capability, and having good cation exchange capacity, and having good adhesive capability [25–28].

MMT as an inorganic material cannot collaborate perfectly with organic polymer, because the surface layer of montmorillonite cannot interact maximally with the organic portion of the polymer. Organophilization process is one of the promising methods to improve the interaction of MMT in polymer matrices [29,30]. Huang and co-workers prepared carboxymethyl chitosan/organically MMT with enhanced thermal stability and antimicrobial activity with complexation with copper ion [22]. Wang et al. developed an organic-inorganic composite using chitosan as the polymer matrix and zeolite as inorganic filler [31]. Their study indicated that by using (3-

glycidoxypropyl) trimethoxysilane (GPTMS) to modify the zeolite surface, the new developed composite membrane was able to achieve denser and high thermal stability.

In this study, we prepared chitosan/MMT-GPTMS composite membrane by utilizing dried shrimp shell powder as chitosan source and acetic acid as solvent. The surface modification process of MMT using (3-glycidoxypropyl) trimethoxysilane (GPTMS) would provide excellent compatibility with chitosan membrane.The immobilization of modified MMT using GPTMS within chitosan matrix would possess superior psychochemical characteristics due to more hydrogen bonding formation introduced by GPTMS. Therefore, higher number hydrogen bond formation can be expected in Ch/MMT-GPTMS membrane rather than in pure Ch membrane. A fully hydrated membrane at elevated temperatures is desirable for efficient proton conduction in the membranes. It remains a critical challenge to maintain proper hydration of the membranes for the operation of the DMFC. The aim of this study is to analyse a relationship between proton conductivity, hydrophilicity, and thermal stability of chitosan/montmorillonite composite membrane modified GPTMS as the electrolyte membrane for direct methanol fuel cell. The morphological structure and functional groups was analysed by SEM and FTIR. The thermal stability TGA/DTG and The hydrophilicity properties was investigated by water contact angle, water uptake (WU) and membrane swelling (MS). The proton conductivity, methanol permeability, DMFC single cell are carried out to determine the overall membrane performance for DMFC applications.

## Materials and Methods

### Materials

Shrimp shell waste of *Penaeusmonodon* was used the chitosan source. Montmorillonite (MMT K-10, S.A 220 – 270 $m^2/g$) powder, (3-glycidoxypropyl) trimethoxysilane (GPTMS)and phosphotungstic acid (PTA, $H_3PW_{12}O_{40}$. $xH_2O$, MW: 2880.05) were purchased from Sigma-Aldrich. Sodium hydroxide (NaOH), hydrochloric acid (HCl), methanol (MeOH), acetic acid, in pure analytical grade were purchased from Merck. The distilled water was used throughout the study.

### Extraction of chitosan matrix and MMT modification

Chitosan was extracted according to the approach reported in the literature [32], with four step process includes preparation, deproteination, demineralization and deacetylation. First step, shrimp shell waste was driedat 60 $^oC$ and then it was grinded until it became dried shrimp shell powder. Second step, dried shrimp powder was added into 3.5% NaOH solution with a ratio of 1:10 (w/v) under continuous stirring for 2 hours at 65 $^oC$. Then, the mixture was filtered and the outcome was washed until pH 7 and dried at 105 $^oC$. Third step, the dried powder was then demineralized using 1 M HCl, stirred for 30 minutes at 65 $^oC$ with a ratio of 1 : 15 (w/v), washed, and dried. The results of demineralization process is dry powder form, called chitin. The chitin powder obtained was then run through the deacetylation process in last process, using 50% NaOH solution, stirred for four hours at 120 $^oC$ with a ratio of 1:10 (w/v), washed, and dried until it became dried powder called chitosan.

The modification of MMT sample was performed using the surface hydroxyl groups of MMT by dehydration process and condensation with GPTMS. MMT powder, GPTMS and toluene were mixed in a reactor with weight ratio 1:2:20. The reaction was carried out at refluxing temperature of toluene (110 °C) and stirred for 24 hours. After being washed with ethanol for three times, the sample was soaked in a solution of 0.1 M HCl for 24 hours at room temperature. The precipitate then was filtered and washed with demineralized water until neutral. Finally, the precipitate was dried in the oven at 100 °C for four hours. The surface-modified MMT was designated as MMT-GPTMS.

### Membrane fabrication

Chitosan powder was dissolved in 25 mL of 2% acetic acid, and stirred at 80 °C and 400 rpm. Another 25 mL of 2% acetic acid was used to dilute MMT-GPTMS powder and ultrasonic treatment for 30 minutes. Then, both mixtures were mixed together and stirred for 30 minutes at 80 °C. After that, the mixture was given an ultrasonic treatment for 30 minutes, stopped for 30 minutes, and then, an ultrasonic treatment was carried out again for 30 minutes. After degasification, the mixture was then caston glass panel and dried at room temperature for 48 hours. The detached membrane was then immersed in 1 M NaOH for 15 minutes before being washed with distilled water until neutral pH was achieved.The membrane then immersing in 2% w/v of PTA solution for 24 hours, and then washed

repeatedly with distilled water to remove the remaining PTA acid before being dried at room temperature for 24 hours[33,34]. The pristine chitosan membranes and MMT unmodified was synthesized by the same process.

**Membrane characterization**

Fourier Transform Infrared Spectroscopy (FTIR) was used to analyse the structure and functional group. The disk containing 0.1 – 0.2 g sample and 0.5 – 1.0 g of fine grade KBr was mixed and crushed into powder, and pellets were formed with a hydraulic press. All measurements were scanned within the waverange of 650 – 4000 $cm^{-1}$. The morphological structural of the resultant material was analysed by means of Scanning Electron Microscopy (SEM) Bruker analysis. The sample powder was prepared in a pin stub holder and coated with gold before the analysis. Thermo gravimetric analysis (TGA) was carried out using a Mettler Toledo 851e TGA/DTG thermogravimetric analyser at a heating rate of 10 $^{o}C\ min^{-1}$ under air flow of 30 mL $min^{-1}$ from room temperature to 800 $^{o}C$.

Water uptake (WU) were conducted by measuring the weights of membranes under fully hydrated and completely dried conditions. A detail procedure was reported previously [31]. Water uptake was calculated using equation (1).

$$WU(\%) = \frac{W_{wet} - W_{dry}}{W_{dry}} \times 100 \quad (1)$$

where $W_{dry}$ and $W_{wet}$are the membrane weight before and after immersion in gram, respectively. The membrane swelling (MS) was defined as follows (equation 2):

$$MS(\%) = \frac{L_{wet} - L_{dry}}{L_{dry}} \times 100 \quad (2)$$

where $L_{wet}$ and $L_{dry}$ are the thickness of wet and dry membranes, respectively.

The hydrophilicity property of membrane studied based on water contact angle (WCA) measurement. The water contact angle was determined by using a contact angle goniometer (OCA15Pro, Data Physics), equipped with image-processing software. This instrument was used to evaluate the degree of membrane hydrophilicity via sessile drop technique. The proton conductivity of the membrane was measured using electrochemical impedance spectroscopy (EIS), at a frequency of 1-$10^6$ Hz. The proton conductivity values were calculated by using equation (3)[34].

$$\sigma = \frac{L}{R \times A} \quad (3)$$

where $\sigma$ is proton conductivity of the membrane (S $cm^{-1}$), $L$ is the membrane (cm), $A$ is the membrane surface area ($cm^2$), and $R$ is the membrane resistance (Ω).

Methanol permeability was determined by using a two-compartment diffusion cell. Compartment A was filled with 1 M MeOH solution and compartment B was filled with deionized water. The membrane was placed between compartment A and B. Samples from compartment B were taken out every 30 minutes for 3 hours, to determine its methanol concentration using High Performance Liquid Chromatography (HPLC). The methanol permeability values were determined by using equation (4) [34].

$$P = \left(\frac{\Delta C_B}{\Delta t}\right)\left(\frac{LV_B}{AC_A}\right) \quad (4)$$

$P$ is methanol permeability of the membrane ($cm^2.s^{-1}$), $\Delta C_B/\Delta t$ is the slope variation of methanol concentration in compartment B as a function of time ($mol.L^{-1}.s^{-1}$), $L$is the thickness of the membrane (cm), $V_B$ is the volume of the water at compartmentB ($cm^3$), $A$ is the membrane surface area ($cm^2$), and $C_A$ is the concentration of methanol in the cell A ($mol.L^{-1}$).

To evaluate the cell performance of the DMFC, a membrane electrode assembly (MEA) was made by catalyst-coated membranes were sandwiched within gas diffusion layers, inside the test single cell. The Pt-Ru/C with 40 wt.% Pt + 20 wt% Ru/C and the Pt/C catalyst with 20 wt.% Pt were used as the anodic and cathodic catalyst,

respectively. The active area of the cells was 2.5 cm x 2.5 cm. The MEA was hot-pressed at 105 $^{o}$C and 5 MPa for 1 min. The performance of the single cell was measured at room temperature with a Fuel Cell Test Autolab instrument. 2 M MeOH solution with a flow rate of 20 mLmin$^{-1}$ and oxygen with a flow rate of 0.5 Lmin$^{-1}$ were used [35].

## Results and Discussion

### Biopolymer extraction and modification process

Figure 1 shows the FTIR spectra of chitin and chitosan. The peak at 3514 cm$^{-1}$ described of stretching vibration -OH group and as seen as the characteristic peaks of the chitin which is at 3298, 3155, 1579 cm$^{-1}$ derived from stretching vibration group NH (-NHCOCH$_3$) and at 2970 cm$^{-1}$ for absorption of a methyl group (-CH$_3$), but lost in the spectra of chitosan, however presence overlapping of stretching vibration –OH and –NH group at 3508 cm$^{-1}$. The characteristic of chitosan shown the reduce of the peak at 1670 and 1622 cm$^{-1}$ attributed from stretching vibration of C=O group on the cluster NHCOCH$_3$ chitin, shown that the removal of the acetyl group into the amine group due to the process of deacetylation. This phenomenon was supported by the loss of a methyl group (-CH$_3$) from the amide (-NHCOCH$_3$) which are known from the absorption loss at 2970 cm$^{-1}$. The typical characteristic of chitosan is visible at 1662 cm$^{-1}$ shows the bending vibration of NH amine (-NH$_2$) [36]. The peaks at 2945, 1429 and 929 cm$^{-1}$ in chitosan spectra assigned to stretching vibration of methylene -CH$_2$-, C-N stretching vibration, and buckling vibration –C-O-C- showed glucopyranose ring, respectively, similar peak also presence in chitin spectra.

The functional group analysis of MMT before and after modification using FTIR sre presented in Figure 1. Two peaks at 3440 and 1640 cm$^{-1}$ corresponded to the –OH stretching and bending vibrations of H–O–H on the MMT surface, respectively. The GPTMS modification has reduced the intensity of -OH stretching bond vibration of pure MMT, as a result of the consumption of the MMT hydroxyl groups by condensing with the silanol groups, and meanwhile the surface of the MMT occurred decreasing of the water adsorption [33]. The characteristic peaks at 2940 cm$^{-1}$ is corresponded to C–H valence vibration for epoxy ring from GPTMS structure.

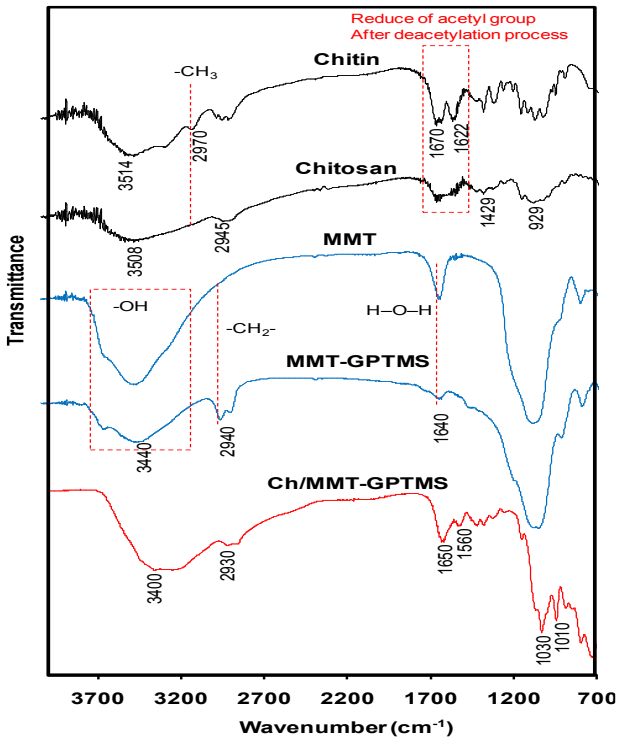



Figure 1. FTIR spectra of MMT, MMT-GPTMS, Chitin, Chitosan and Ch/MMT-GPTMS composite membrane

The filler modification process is illustrated in Figure 2(a). The modification process starts with hydrolysis of the three labile metoxy groups attached to silicon atom. The –OH group for the hydrolysis process was contributed by water present on the MMT surface. Then, a reactive silanol group is formed, which can bind together with other silanol groups to be oligomers at condensation step. The third step is to attach the oligomers via hydrogen bonding with –OH groups on MMT surface. Finally, termination reaction of epoxy groups with HCl acid solution catalytic, resulting in hydroxyl group formation at the end side of GPTMS[37,38].

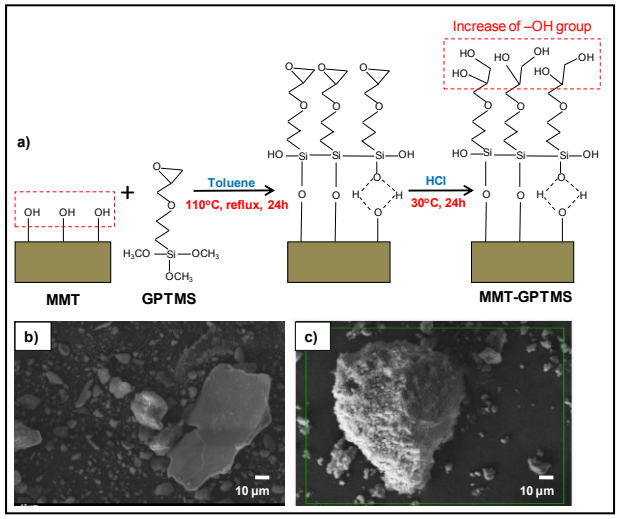



Figure 2. Illustration scheme of MMT modification process by GPTMS (a) and SEM image (b) MMT and (c) MMT-GPTMS

Figure 2 (b, c) shows the SEM images for MMT and MMT-GPTMS surface. The MMT surfaces are smooth and flat, but after the modification process, the MMT-GPTMS surface becomes rough and overgrown soft granules are spread almost evenly on the MMT-GPTMS surface (Figure 2b). This indicates that GPTMS has been successfully incorporated on the surface of MMT, showing good interlocking interaction. SEM and FTIR results confirmed that the MMT particles were successfully modified using GPTMS to form MMT-GPTMS filler.

**Physicochemical and thermal stability of membrane**

The FTIR spectra of Ch/MMT-GPTMS composite membrane presented in Figure 1. Two peaks at 3400 $cm^{-1}$ and 1650 $cm^{-1}$ which are attributed to hydroxyl group and amide groups, indicating that the characteristics of chitosan still exist as a matrix in composite membrane. The peaks at 2930 $cm^{-1}$ were assigned to $–CH_2$ stretching, and the two bands at 1030 $cm^{-1}$ and 1010 $cm^{-1}$ for chitosan matrix were merged and shifted towards 1030 $cm^{-1}$ in MMT-GPTMS filled composite membranes due to the overlapping of Si–O band with the C–O stretching band [16].The SEM images for pure chitosan membrane, Ch/MMT and Ch/MMT-GPTMS composite membrane are presented in Figure 3.

As can be seen in Figure 3(a), the pure chitosan membrane shows a void free dense structure. Meanwhile, Figure 3(b) shows the MMT agglomeration between the chitosan polymer matrix, which is due to the incompatibility between inorganic and organic material. Better interfacial morphology was able to be achieved after the MMT modification using GPTMS, thus improving the compatibility between chitosan organic polymer and MMT-GPTMS inorganic filler, and reducing the MMT-GPTMS agglomeration, as shown in Figure 3(c) [33,38]. The incompatibility between chitosan organic polymer and MMT inorganic filler has caused the phase separation in Ch/MMT 5 membrane, thus the agglomeration of MMT particles are formed (Figure 3(e)). However, the cross-section image of Ch/MMT-GPTMS 5 shows that the MMT-GPTMS filler was well dispersed inside the chitosan

polymer matrices with no visible agglomeration occurred (Figure 3(f)). This proves that the addition of GPTMS on the surface of MMT filler was able to increase the compatibility between the chitosan matrix and MMT-GPTMS filler.

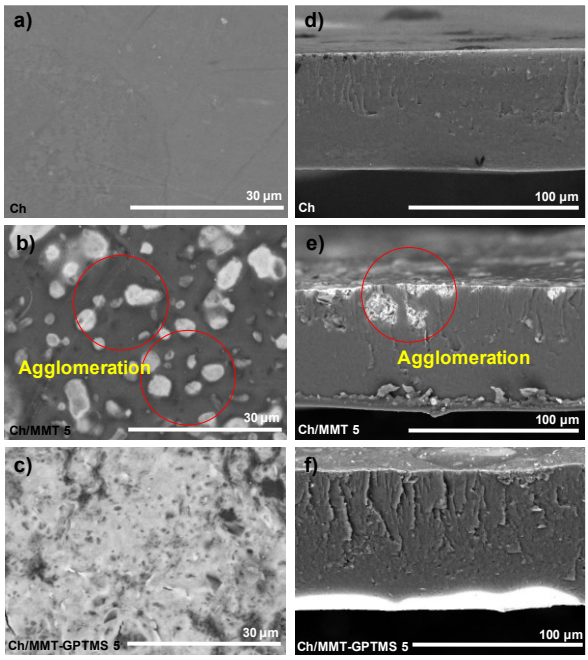



Figure 3. SEM images of (a) pristine Ch, (b) Ch/MMT, and (c) Ch/MMT-GPTMS membrane, (d), (e), and (f) showed the cross section of chitosan, Ch/MMT and Ch/MMT-GPTMS membrane, respectively

The TGA analysis was carried out to evaluate the thermal stability of the pure chitosan, Ch/MMT and Ch/MMT-GPTMS. The TGA and DTG curves in Figure4 show that all membranes followed almost identical degradation mechanism since there were miniscule difference in $T_{10\%}$, $T_{30\%}$, $T_{50\%}$, and $T_{max}$, as shown in Table 1. As shown in the Figure 4 all membranes show three stages of weight loss, the first stage that happens below 175 $^{o}$C which was attributed to the evaporation of absorbed water[14,39]. The second stage happens at 175 – 400 $^{o}$C interval because of the chitosan polymer chain degradation, and the last stage happens after 400 $^{o}$C due to the decomposition of residual organic group [31]. It has been reported that the decomposition of montmorillonite clay is not complete until 800 $^{o}$C [39]. Therefore, it is believed that the incorporation of inorganic filler might fill the gaps between the chitosan polymer matrixes, thus making the chain becomes tighter and increases the strength of the chitosan polymer chain. This occurrence might attribute to the increasing of thermal stability characteristics of Ch/MMT and Ch/MMT-GPTMS membrane compared to its parent chitosan membrane as shown in Figure 4. As can be seen in Table 1, the neat chitosan exhibited the lowest in residual percent, while the Ch/MMT-GPTMS exhibited the higest. The incorporation of GPTMS has improved the interaction of MMT with chitosan by introducing more functional groups, so increasing of thermal stability of Ch/MMT-GPTMS composite membrane. These results are in good agreement with previously reported values for chitosan composites [14].

Furthermore, Figure 4 suggested that the Ch/MMT-GPTMS membrane has lower weight loss percentage compared to the Ch/MMT membrane. The greater hydrogen bond formation was expected in Ch/MMT-GPTMS membrane rather than in Ch/MMT membrane (As can be illustrated in Figure 5(a) and (b)). Thus, the greater hydrogen bonding formation would improve the interaction of MMT filler within chitosan polymer matrices. Consequently, the

Ch/MMT-GPTMS membrane becomes tighter and stronger than Ch/MMT membrane, thus giving the Ch/MMT-GPTMS membrane higher thermal stability characteristics compared to Ch/MMT membrane.

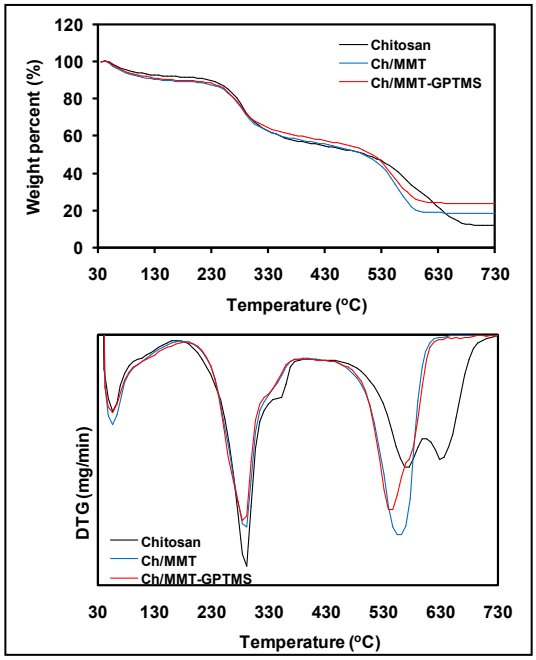



Figure 4. TGA and DTG curves for pristine chitosan, Ch/MMT, and Ch/MMT-GPTMS membrane.

Tabel 1. Thermal Stability Data of Ch, Ch/MMT, and Ch/MMT-GPTMS composite membrane

| Sample | $T_{10}$% (°C) | $T_{30}$% (°C) | $T_{50}$% (°C) | DTG peak, $T_{max}$ (°C) | | | Residu at 730 °C (%) |
|---|---|---|---|---|---|---|---|
| | | | | $T_{max}^{1}$ | $T_{max}^{2}$ | $T_{max}^{3}$ | |
| Chitosan | 220.9 | 298.4 | 500.9 | 56.4 | 290.6 | 575.7 | 12.1 |
| Ch/MMT | 122.2 | 290.3 | 498.5 | 56.3 | 290.3 | 561.7 | 18.9 |
| Ch/MMT-GPTMS | 144.6 | 298.1 | 514.5 | 56.4 | 290.3 | 546.3 | 23.8 |

Similar observations also have been reported by Wang and co-worker with CS/Zeolite and CS/Zeolite-GPTMS composite membrane [31]. In their study, the CS/Beta-GPTMS membrane showed a little higher thermal stability than the CS/Beta membrane. It has been suggested that the organic chains and –OH groups on the surface of the GPTMS-modified zeolite beta particles can enhance the interactions between the zeolite beta and chitosan molecules, which decelerate the decomposition of the chitosan main chain. Wang and co-workers had reported the strong interaction of MMT filler in the CS matrix to form flocculated structure in Ch/MMT composite. Since one chitosan unit possesses one amino and two hydroxyl functional groups, these functional groups can form hydrogen bonds with the silicate hydroxylated edge groups from montmorillonite filler, which lead to the strong interaction between matrix and MMT layers [40]. The same phenomenon of interaction polymer clay composite has been reported [41], the layer of biopolymer is adsorbed by means of a hydrogen bonding mechanism, since the hydroxyl functional groups in surface of the MMT has been already balanced by functional groups of the chitosan layer as a matrix.

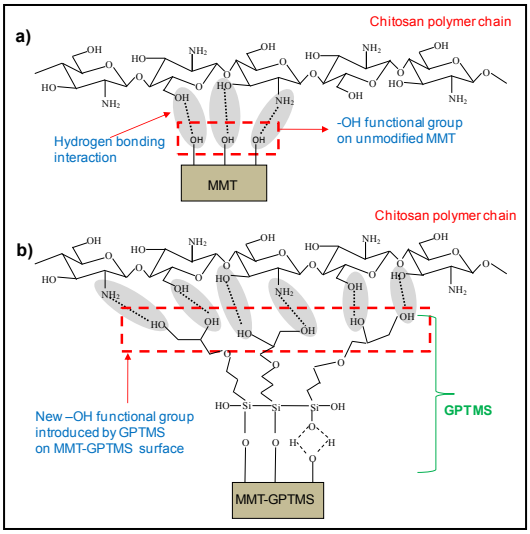



Figure 5. Plausible schematic diagram illustrates the bonding formation between chitosan parent polymer and its filler for (a) Ch/MMT and(b) Ch/MMT-GPTMS composite membranes

**Water uptake, membrane swelling and hydrophilic properties**

The hydrophilic property of membrane was studied based on water contact angle (WCA), water uptake (WU) and membrane swelling (MS). The water uptake has a profound effect on proton transport and dimensional stability of proton conducting membranes. The high water uptake is favorable for high performance PEM to facilitate great numbers of protons hopping and diffusion through the membrane. The water uptake and membrane swelling for chitosan, Ch/MMT and Ch/MMT-GPTMS is shown in Table 2. The water uptake for pure chitosan membrane is 72.9%, after the incorporated of inorganic filler the water uptake decreased at 54.5% and 62.1% for Ch/MMT and Ch/MMT-GPTMS, respectively. The similar trend has been reported in previous study, the water uptake for Ch/Zeolite composite membrane showed a decrease as the zeolite filler load increased [31]. In addition, Madaeni and co-worker reported in previous study where the water uptake for PVA composite membrane decreased by incorporated filler [42].

Table 2. Water uptake and membrane swelling for chitosan, Ch/MMT and Ch/MMT-GPTMS

| Membrane | Water Uptake (%) | Membrane Swelling (%) |
|---|---|---|
| Chitosan | 72.9 | 23.7 |
| Ch/MMT 5 | 54.5 | 18.5 |
| Ch/MMT-GPTMS 5 | 62.1 | 19.7 |
| Ch/MMT-GPTMS 10 | 53.9 | 18.1 |
| Ch/MMT-GPTMS 15 | 49.2 | 17.9 |

The high water uptake of chitosan membrane showing better hydrophilic trend, compared to Ch/MMT composite membrane which presence decreased the water uptake. This phenomenon suggested to the dynamic water contact angle of pristine chitosan and Ch/MMT 5 composite membrane are plotted in Figure 6. It was found that the initial contact angle of pristine chitosan showed a better hydrophilicity than Ch/MMT 5 (35.9$^{o}$ compared to 82.8$^{o}$). This results established that lower contact angle showed a better hydrophilicity, thus notably indicating that hybrid

membrane presented an enhanced hydrophilicity or decrease of hydrophilicity depends to addition inorganic filler [31, 42, 43].

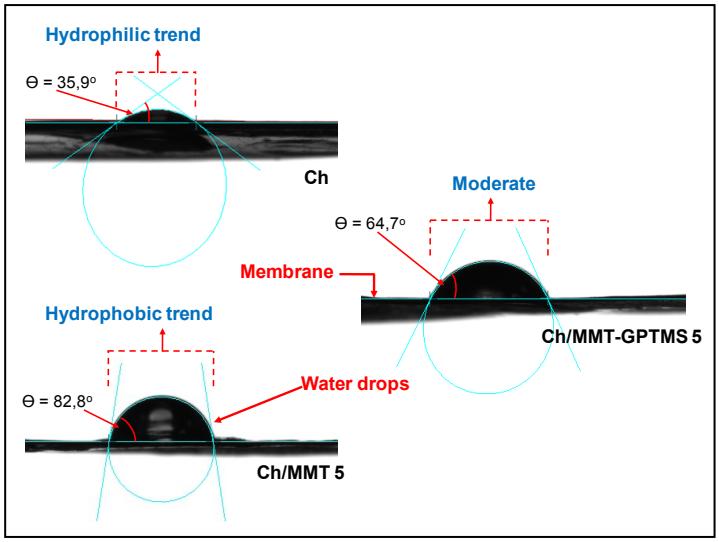



Figure 6. Water contact angle Ch, Ch/MMT and Ch/MMT-GPTMS

In another part, for direct methanol fuel cell application, membrane with high hydrophilic properties are very crucial to be able to hold existence of water because the proton will be transported along the water channel created in the membrane composite, however the hydrophobic properties also crucial to reduce methanol permeation rate which causes decrease of membrane efficiency. Therefore the moderate membrane is very suitable for this application, for get high proton conductivity and low methanol permability as previous study [31, 38]. Thus, in this study, we were able to prepare composite membrane with moderate properties, Ch/MMT-GPTMS 5 with water uptake at 62%, suggested to the equilibrium water contact angle, at 64.7$^{o}$ (Figure 6).

As seen as Table 2, shows the water uptake as a function of the membrane swelling of the chitosan, Ch/MMT and Ch/MMT-GPTMS membranes. As compared to pristine chitosan, high water uptake values were characterized for Ch/MMT and Ch/MMT-GPTMS composite membranes, but all of them showed low membrane swelling. The targeted membranes should be modest water uptake values and low membrane swelling ratios. These results revealed that the role of surface modification by GPTMS in Ch/MMT-GPTMS composite can be expected to possess higher thermal stability characteristics and lower membrane swelling, compared to pure Ch and Ch/MMT membrane. Therefore, the resultant composite membrane is stable at desired operating temperatures (<100 $^{o}$C) for DMFCs application.

**Proton conductivity, methanol permeability and DMFC performance**

Proton conductivity is one of the most essential requirement to enable membranes to be applicable in DMFC. The efficiency of the proton transfer within the PEM is therefore related either as water solvated species or the number of ionic sites, polymer functional groups and microstructure formation in the PEM through the interconnection between proton-conductive channels/species in the membranes [44]. The proton conductivity for chitosan and composite membranes are listed in Table 3. As seen as Table 3, the proton conductivity of hydrated plain chitosan membrane was 2.4 mS cm$^{-1}$ and increase with incorporated of MMT loading 5% in composite membrane, at 2.7 mScm$^{-1}$. The composite membrane Ch/MMT-GPTMS 5 is able to achieve maximum proton conductivity of 4.7 mScm$^{-1}$, an increase from 2.7 mScm$^{-1}$ exhibited by the Ch/MMT 5. The phenomenon can be explained that, the surface modification of MMT using GPTMS make an increase of hydroxy group, thus it can improve interaction

between the –OH group of MMT-GPTMS filler with hydroxy group and amine group of biopolymer chitosan via hydrogen bonding. High interaction in membrane structure provides additional conduction site for proton to be transported, thus increases the proton conductivity of the membrane.

Table 3. Proton conductivity and methanol permeability for chitosan, Ch/MMT and Ch/MMT-GPTMS

| **Membrane** | **Proton Conductivity ($mScm^{-1}$)** | **Methanol Permeability ($x\ 10^{-7}\ cm^2\ s^{-1}$)** |
|---|---|---|
| Chitosan | 2.4 | 4.9 |
| Ch/MMT 5 | 2.7 | 4.7 |
| Ch/MMT-GPTMS 5 | 4.7 | 3.0 |
| Ch/MMT-GPTMS 10 | 4.3 | 3.2 |
| Ch/MMT-GPTMS 15 | 4.1 | 7.6 |

Ch, MMT and GPTMS are able to establish channels of hydrophilic or water bulk phase which allows the protons to be transported via vehicle mechanism in the form of hydronium ions [44–46]. It has been suggested that, electrostatic interaction in the membranes which contain the abbundance hydroxy group and presence of $–NH_3^+$ allows the proton transferred along the ionic bonds and hydrogen bonds by "jumping" from one functional group to another. The incorporation of modified MMT (MMT-GPTMS) within the chitosan matrix has given chance for more protons to transport in Ch/MMT-GPTMS membrane, so that the proton conductivity of the membrane is higher than the Ch/MMT membrane. However, higher filler load had led to agglomerations problem in composite membrane, hence reduce of both water content and effectiveness of filler to provide conduction site for proton at the same time, thus decrease the proton conductivity of the membrane. The proton conductivity decrease after 10% loading filler at 4.3 $mScm^{-1}$ and 4.1 $mScm^{-1}$ for Ch/MMT-GPTMS 10 and Ch/MMT-GPTMS 15, respectively (Table 3). This results established that a better hydrophilicity and high thermal stability are important characteristics to be able to hold water and reduce of hidration phenomenon. The proton will be transported along the water channel created in the membrane composite by hydronium ions. The existence of water has a profound effect on proton transport and dimensional stability of proton conducting membranes.

The methanol permeability of the chitosan and composite membranes at room temperature is shown in Table 3. The role of GPTMS for MMT modification process in composite membranes exhibited low methanol permeability until 3.0 x $10^{-7}cm^2s^{-1}$ for Ch/MMT-GPTMS 5. This results lower than that of pristine chitosan (4.9 x $10^{-7}cm^2s^{-1}$) and Ch/MMT (4.7 x $10^{-7}cm^2s^{-1}$). It is suggested that, existense of GPTMS attributed hydrophobic characterstic in morphology membrane structure, shown incline hydrophobicity with increasing of initial contac angle (Figure 6), and in the other hand the MMT-GPTMS structure that has a quite wide and long ratio which creates longer diffusion path for methanol permeate [47]. The methanol permeability of Ch/MMT-GPTMS is obtained the lowest with the MMT-GPTMS filler loading at 5%, but increased slightly with 10% filler load, then an increase in the permeability of methanol is significant when the filler loading was increased to 15%. This phenomenon can be explained that, the matrix and filler need good collaboration with a specific composition, especially with addition of GPTMS included in the layer structure of the membrane can support the interaction between the inorganic filler and biopolymer matrix. Therefore, the precise composition of composite membrane will have a good structure, more dense and has the ability to reduce of methanol diffusion. The increase of the methanol permeability of Ch/MMT-GPTMS 15 more than a double of Ch/MMT-GPTMS 10 is due to the excess of filler load showing a low interaction distribution in membrane structure, therefore it caused agglomeration. This phenomenon led to the presence of pin hole in the composite membrane, which provide greater opportunities for methanol to diffuse into the membrane structure, thus the methanol permeability is significanly increased. The similar trend also can be found in previous study [31].

The DMFC responses of Ch/MMT-GPTMS composite membrane compared with Ch/MMT at room temperature with 2M methanol consentrations and oxygen flow at the 2 mL/min is represented in Figure 7. The cell performance

based on Ch/MMT composite membrane in terms of power density was 5.01 x $10^{-2}$ mW/cm$^2$, and increase of the cell performance for Ch/MMT-GPTMS until 24.87 x $10^{-2}$ mW/cm$^2$. Clearly, the higher cell performance based on Ch/MMT-GPTMS membrane was attributed to the fact that more hydrogen bonding and water content to achieve proton conductivity comparable to Ch/MMT-GPTMS because the hydrophilic characteristics. In the Ch/MMT-GPTMS composite membrane, the proton transport can occur from $H_3O^+$ as proton donor to $H_2O$ as acceptor on the membrane structure. Uniform distribution and optimum water content within the composite membrane is critical for the continuous proton transfer pathway with minimum resistance.

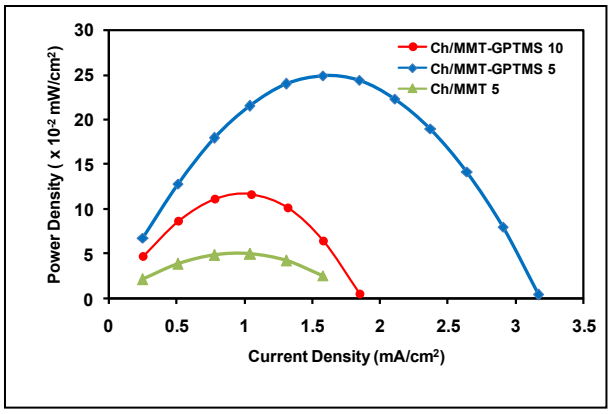



Figure 7. DMFC performance of composite membrane

## Conclusion

A composite membrane was obtained through using solution casting method, and GPTMS was introduced into the system to increase of matrix and filler interaction. The properties of the composite membranes, such as thermal stability, hydrophilicity and proton conductivity were significantly improved. The Ch/MMT-GPTMS showed excellent proton conductivities varying from 4.1 to 4.7 mS cm$^{-1}$ at 25 °C, which are higher compared to pristine chitosan and Ch/MMT. The Ch/MMT-GPTMS composite membrane with 5 wt% filler load exhibited the best proton conductivity are 4.7 mScm$^{-1}$, with water contact angle value of 64.7$^o$ and shown maximum power density of 0.24 mWcm$^{-2}$ was obtained with a 2M methanol feed. In this study it was known that water contact angle, membrane swelling, thermal stability, and proton conductivity show suitable trend, it means that all quality of them are related to the hydrophilicity properties.

## Acknowledgement

The author (Mochammad Purwanto) would like to express gratitude to the Ministry of Science, Technology and Innovation (MOSTI) Malaysia for the grants with vote number of R.J130000.7809.4F592, Q.J130000.2509.05H52 and R.J130000.7942.4S507 for the financial support and to the research management centre (RMC), UTM for supporting related research management activities.

## References

1. Yuan, T., Pu, L., Huang, Q., Zhang, H., Li, X. and Yang H. Yang. (2014). An effective methanol-blocking membrane modified with graphene oxide nanosheets for passive direct methanol fuel cells. *Electrochimica Acta*, 117: 393 – 397.
2. Sadrabadi, M. M. H., Dashtimoghadam, E., Majedi, F. S., Kabiri, K., Solati-Hashjin, M. and Moaddel, H. (2010). Novel nanocomposite proton exchange membranes based on Nafion and AMPS-modified montmorillonite for fuel cell applications. *Journal of Membrane Science,* 365(1–2): 286 –293.
3. Cui, Z., Xing, W., Liu, C., Liao, J. and Zhang, H. (2009). Chitosan/heteropolyacid composite membranes for direct methanol fuel cell. *Journal of Power Sources*, 188(1): 24 – 29.

4. Jung, D. H., Cho, S. Y., Peck, D. H., Shin, D. R. and Kim, J. S. (2003). Preparation and performance of a Nafion/montmorillonite nanocomposite membrane for direct methanol fuel cell. *Journal of Power Sources*. 118(1-2): 205 – 211.
5. Lu, J. L., Fang, Q. H., Li, S. L. and Jiang, S. P. (2013). A novel phosphotungstic acid impregnated meso-Nafion multilayer membrane for proton exchange membrane fuel cells. *Journal of Membrane Science,* 427: 101 – 107.
6. Lufrano, F., Baglio, V., Staiti, P., Antonucci, V., and Arico, A. S. (2013). Performance analysis of polymer electrolyte membranes for direct methanol fuel cells. *Journal of Power Sources*, 243: 519 –534.
7. Wang J. and Wang, L. (2014). Preparation and properties of organic-inorganic alkaline hybrid membranes for direct methanol fuel cell application. *Solid State Ionics*, 255: 96 – 103.
8. Younes, I., Ghorbel-Bellaaj, O., Nasri, R., Chaabouni, M., Rinaudo, M. and Nasri, M. (2012). Chitin and chitosan preparation from shrimp shells using optimized enzymatic deproteinization. *Process Biochemistry,* 47(12): 2032 – 2039.
9. Sagheer, F. A., Al-Sughayer, M. A., Muslim, S. and Elsabee, M. Z. (2009). Extraction and characterization of chitin and chitosan from marine sources in Arabian Gulf. *Carbohydrate Polymer,* 77(2): 410 – 419.
10. Chatterjee, S., Adhya, M., Guha, A. K. and Chatterjee, B. P. (2005). Chitosan from Mucor rouxii: production and physico-chemical characterization. *Process Biochemistry,* 40(1): 395 – 400.
11. Krishna Rao, K. S. V., Ramasubba Reddy, P., Lee, Y.-I, and Kim, C. (2012). Synthesis and characterization of chitosan–PEG–Ag nanocomposites for antimicrobial application. *Carbohydrate Polymer,* 87(1): 920 – 925.
12. Croisier, F. and Jérôme, C. (2013). Chitosan-based biomaterials for tissue engineering. *European Polymer Journal,* 49(4): 780 –792.
13. Bhattacharyya, R. and Ray, S. K. (2014). Micro- and nano-sized bentonite filled composite superabsorbents of chitosan and acrylic copolymer for removal of synthetic dyes from water. *Applied Clay Science,* 101: 510 – 520.
14. Lewandowska, K., Sionkowska, A., Kaczmarek, B. and Furtos, G. (2014). Characterization of chitosan composites with various clays. *International Journal of Biological Macromolecules,* 65: 534 – 541.
15. Liu, Y., Yang, S. and Niu, W. (2013). Simple, rapid and green one-step strategy to synthesis of graphene/carbon nanotubes/chitosan hybrid as solid-phase extraction for square-wave voltammetric detection of methyl parathion. *Colloids Surface B: Biointerfaces*. 108: 266 – 270.
16. Olad, A. and Farshi Azhar, F. (2014). The synergetic effect of bioactive ceramic and nanoclay on the properties of chitosan–gelatin/nanohydroxyapatite–montmorillonite scaffold for bone tissue engineering. *Ceramic International,* 40(7): 10061 – 10072.
17. El Ichi, S., Zebda, A., Alcaraz, J. P., Laaroussi, A., Boucher, F., Boutonnat, J., Reverdy-Bruas, N., Chaussy, D., Belgacem, M. N., Cinquin, P. and Martin, D. K. (2015). Bioelectrodes modified with chitosan for long-term energy supply from the body. *Energy and Environmental Science,* 8(3): 1017 –1026.
18. Sabaa, M. W., Abdallah, H. M., Mohamed, N. A. and Mohamed, R. R. (2015). Synthesis, characterization and application of biodegradable crosslinked carboxymethyl chitosan/poly(vinyl alcohol) clay nanocomposites. *Materials Science and Engineering C,* 56: 363 – 373.
19. Petersson, L., Kvien, I. and Oksman, K. (2007). Structure and thermal properties of poly(lactic acid)/cellulose whiskers nanocomposite materials. *Composite Science Technology,* 67(11–12): 2535 –2544.
20. Mohamed, M. A., Salleh, W. N. W., Jaafar, J., Ismail, A. F., Mutalib, M. A, Sani, N. A. A., Asri, S. E. A. M. and Ong, C. S. (2016). Physicochemical characteristic of regenerated cellulose/N-doped $TiO_2$ nanocomposite membrane fabricated from recycled newspaper with photocatalytic activity under UV and visible light irradiation. *Chemical Engineering Journal,* 284: 202 – 215.
21. Grigoriadi, K., Giannakas, A., Ladavos, A. K. and Barkoula, N. M. (2015). Interplay between processing and performance in chitosan-based clay nanocomposite films. *Polymer Bulletin,* 72(5): 1145 – 1161.
22. Huang, Y., Huang, J., Cai, J., Lin, W., Lin, Q., Wu, F. and Luo, J. (2015). Carboxymethyl chitosan/clay nanocomposites and their copper complexes: Fabrication and property. *Carbohydrate Polymer,* 134: 390 – 397.
23. Hong, S. I., Lee, J. H., Bae, H. J., Koo, S. Y., Lee, H. S., Choi, J. H., Kim, D. H., Park, S.-H. and Park, H. J. (2011). Effect of shear rate on structural, mechanical, and barrier properties of chitosan/montmorillonite nanocomposite film. *Journal of Applied Polymer Science,* 119(5): 2742 –2749.
24. Oguzlu, H. and Tihminlioglu, F. (2010). Preparation and barrier properties of chitosan-layered silicate nanocomposite films. *Macromolecule Symposium*, 298 (1): 91 – 98.

25. Ludueña, L., Morán, J. and Alvarez, V. (2015). Biodegradable polymer/claynanocomposites. in eco-friendly polymer nanocomposites, 75th Edition, V. K. Thakur and M. K. Thakur, Eds. Springer India. pp. 109 –135.
26. Liu, X., Hu, M. and Hu, Y. (2008). Chemical composition and surface charge properties of montmorillonite. *Journal of Central South University Technology,* 15(2): 193 – 197.
27. Zhu, J., Tian, M., Zhang, Y., Zhang, H. and Liu., J. (2015). Fabrication of a novel 'loose' nanofiltration membrane by facile blending with Chitosan–Montmorillonite nanosheets for dyes purification. *Chemical Engineering Journal,* 265: 184 – 193.
28. Liu, B., Wang, X., Yang, B. and Sun, R. (2011). Rapid modification of montmorillonite with novel cationic Gemini surfactants and its adsorption for methyl orange. *Materials Chemistry and Physics,* 130(3): 1220 – 1226.
29. Huskić, M., Brnardić, I., Žigon, M. and Ivanković, M. (2008). Modification of montmorillonite by quaternary polyesters. *Journal of Non Crystalline Solids*, 354(28): 3326 – 3331.
30. Jiratumnukul, N., Manowanna, P. and Premmag, N. (2012). Modified bentonite clay in UV-curable coating applications. *Engineering Journal,* 16(3): 13 – 18.
31. Wang, Y., Jiang, Z., Li, H., and Yang, D. (2010). Chitosan membranes filled by GPTMS-modified zeolite beta particles with low methanol permeability for DMFC. *Chemistry Engineering Process, Process Intensification,* 49(3): 278 – 285.
32. Trisnawati, E., Andesti, D. and Saleh, A. (2013). Pembuatan kitosan dari limbah cangkang kepiting sebagai bahan pengawet buah duku dengan variasi lama pengawetan. *Jurnal Teknologi Kimia,* 19(2): 17 – 26.
33. Wang, Y., Yang, D., Zheng, X., Jiang, Z. and Li, J. (2008). Zeolite beta-filled chitosan membrane with low methanol permeability for direct methanol fuel cell. *Journal Power Sources*, 183(2): 454 – 463.
34. Tohidian, M., Ghaffarian, S. R., Shakeri, S. E., Dashtimoghadam, E. and Hasani-Sadrabadi, M. M. (2013). Organically modified montmorillonite and chitosan-phosphotungstic acid complex nanocomposites as high performance membranes for fuel cell applications.*Journal of Solid State Electrochemistry,* 17(8): 2123 – 2137.
35. Cui, Z., N. Li, X. Zhou, C. Liu, J. Liao, S. Zhang and W. Xing. (2007). Surface-modified Nafion membrane by casting proton-conducting polyelectrolyte complexes for direct methanol fuel cells. *Journal of Power Sources,* 173(1): 162 – 165.
36. Kumari, S. and Rath, P. K. (2014). Extraction and characterization of chitin and chitosan from (Labeo rohit) fish scales. *Procedia Materials Science*, 6: 482 – 489.
37. Duan, J. K., Shao, S. X., Jiang, L., Li, Y., Jing, P. K. and Liu, B. P. (2011). Nano-attapulgite functionalization by silane modification for preparation of covalently-integrated epoxy/TMPTMA Nanocomposites. *Iranian Polymer Journal,* 20(11): 855 – 872.
38. Wu, H., Zheng, B., Zheng, X., Wang, J., Yuan, W. and Jiang, Z. (2007). Surface-modified Y zeolite-filled chitosan membrane for direct methanol fuel cell. *Journal of Power Sources*, 173(2): 842 – 852.
39. Dos Santos, B. R., Bacalhau, F. B., Pereira, T. D. S., Souza, C. F. and Faez, R. (2015). Chitosan-montmorillonite microspheres: A sustainable fertilizer delivery system. *Carbohydrate Polymer,* 127: 340 – 346.
40. Wang, S. F., Shen, L., Tong, Y. J., Chen, L., Phang, I. Y., Lim, P. Q. and Liu, T. X. (2005). Biopolymer chitosan/montmorillonite nanocomposites: Preparation and characterization. *Polymer Degradation and Stability,* 90(1): 123 – 131.
41. Darder, M., Colilla, M. and Ruiz-Hitzky, E. (2005). Chitosan-clay nanocomposites: Application as electrochemical sensors. *Applied Clay Science,* 28(1–4): 199 – 208.
42. Madaeni, S. S., Amirinejad, S. and Amirinejad, M. (2011). Phosphotungstic acid doped poly(vinyl alcohol)/poly(ether sulfone) blend composite membranes for direct methanol fuel cells. *Journal of Membrane Science,* 380(1–2): 132 – 137.
43. Gosalawit, R., Chirachanchai, S., Shishatskiy, S. and Nunes, S. P. (2008). Sulfonated montmorillonite/sulfonated poly(ether ether ketone) (SMMT/SPEEK) nanocomposite membrane for direct methanol fuel cells (DMFCs). *Journal of Membrane Science*, 323(2): 337 – 346.
44. Lee, S. H., Choi, S. H., Gopalan, S. A., Lee, K. P. and Anantha-Iyengar, G. (2014). Preparation of new self-humidifying composite membrane by incorporating graphene and phosphotungstic acid into sulfonated poly(ether ether ketone) film. *International Journal of Hydrogen Energy*, 39(30): 17162 –17177.
45. Xiao, Y., Xiang, Y., Xiu, R. and Lu, S. (2013). Development of cesium phosphotungstate salt and chitosan composite membrane for direct methanol fuel cells. *Carbohydrate Polymer,* 98(1): 233 – 240.

46. Cui, Z., Liu, C., Lu, T. and Xing, W. (2007). Polyelectrolyte complexes of chitosan and phosphotungstic acid as proton-conducting membranes for direct methanol fuel cells. *Journal of Power Sources*, 167(1): 94 – 99.
47. Lin, H., Zhao, C. Ma, W., Shao, K., Li, H., Zhang, Y. and Na, H. (2010). Novel hybrid polymer electrolyte membranes prepared by a silane-cross-linking technique for direct methanol fuel cells. *Journal of Power Sources*, 195(3): 762 – 768.

*Malaysian Journal of Analytical Sciences, Vol 21 No 3 (2017): 690 - 699*
*DOI: https://doi.org/10.17576/mjas-2017-2103-18*

MALAYSIAN JOURNAL OF ANALYTICAL SCIENCES
*Published by The Malaysian Analytical Sciences Society*
ISSN 1394 - 2506

# MICROWAVE-ASSISTED EXTRACTION OF PHENOLIC COMPOUND FROM PINEAPPLE SKINS: THE OPTIMUM OPERATING CONDITION AND COMPARISON WITH SOXHLET EXTRACTION

## (Pengekstrakan Sebatian Fenolik daripada Kulit Nenas dengan Bantuan Gelombang Mikro: Pengoptimuman Keadaan Pengendalian dan Perbandingan dengan Pengekstrakan Soxhlet)

Nor Halaliza Alias[1]* and Zulkifly Abbas[2]

[1]*Faculty of Chemical Engineering,*
*Universiti Teknologi MARA, 40450 Shah Alam, Selangor, Malaysia*
[2]*Department of Physics, Faculty of Science,*
*Universiti Putra Malaysia, 43400 Serdang, Selangor, Malaysia*

**Corresponding author: norhalaliza@salam.uitm.edu.my*

Received: 28 November 2016; Accepted: 5 February 2017

**Abstract**

A new method of extraction by using a microwave has been widely used in the extracting of bioactive compound from plants. In this research**,** the pineapple (*Ananas comosus L., Merr*) wastes (namely skin) has been chosen as it contains a very high phenolic compound and provide a good source of antioxidant to human's health. The three parameters varied were the microwave power, the types of solvent extraction and the extraction temperature. Each of the samples was evaluated for the Total Phenolic Compound (TPC) and Antioxidant Activity (AA). The aims of this study are to obtain the optimum operating condition of Microwave-Assisted Extraction (MAE) in the extraction of phenolic compound from pineapple skins and to compare the extraction yield between MAE and Soxhlet Extraction (SE) method. From the results, it was found that the optimum condition was at 750 W microwave power, 60 °C operating temperature and with the solvent ratio of ethanol: water (50-50) by volume**.** At this optimum condition, the TPC observed was 207.72 mg GAE/g dw, whereas for the $EC_{50}$, DPPH value obtained was the lowest, 13.2 mg/mL. MAE has proven that this method is comparable to SE, with the TPC obtained was 28.78 mg GAE/g dw and $EC_{50}$ of 2.78 mg/L, respectively.

**Keywords**: pineapple skin, microwave-assisted extraction, microwave power, total phenolic compound, antioxidant activity

**Abstrak**

Satu kaedah baru pengekstrakan dengan menggunakan gelombang mikro telah digunakan secara meluas di dalam pengekstrakan sebatian bioaktif daripada tumbuhan. Di dalam kajian ini, sisa (kulit) nenas (*Ananas comosus L., Merr*) telah dipilih kerana ia mengandungi sebatian fenolik yang tinggi dan menyediakan sumber antioksidan yang baik kepada kesihatan manusia. Tiga parameter boleh ubah iaitu kuasa gelombang mikro, jenis pelarut pengekstrakan dan suhu pengekstrakan. Setiap sampel telah dinilai untuk jumlah sebatian fenolik (TPC) dan aktiviti antioksidan (AA). Tujuan kajian ini adalah untuk mendapatkan keadaan pengendalian optimum oleh bantuan gelombang mikro (MAE) di dalam pengekstrakan sebatian fenolik daripada sisa nenas dan membandingkan hasil pengekstrakan di antara MAE dan pengekstrakan Soxhlet (SE). Daripada keputusan, telah didapati bahawa keadaan optimum adalah pada kuasa gelombang mikro 750 W, pengendalian suhu 60 °C dan nisbah pelarut etanol: air (50-50) mengikut isipadu. Pada keadaan optimum ini, TPC yang dicerap adalah 207.72 mg GAE/g dw, manakala untuk $EC_{50}$, DPPH telah didapati pada nilai yang paling rendah, iaitu 13.2 mg/mL. MAE telah membuktikan bahawa kaedah ini setanding dengan SE, dengan TPC diperoleh adalah masing – masing 28.78 mg GAE/g dw dengan $EC_{50}$ 2.78 mg/L.

**Kata kunci:** kulit nenas, gelombang mikro terbantu, kuasa gelombang mikro, jumlah sebatian berfenol, aktiviti antioksidan

## Introduction

Phytochemicals are the major bioactive compounds which usually available in fruits and vegetables. Usually, the plants phenolics are found in both edible and non-edible parts of the plants and was reported to have multiple biological effects, including antioxidant activity [1]. In the recent years, the phenolics compound, or known as polyphenolics have become one of the interest due to their ability to act as a powerful antioxidant [2]. An antioxidant is a group of compounds which are able to delay or inhibit the oxidation lipids or other biomolecules and hence could prevent or repair the damaged body cells that is oxidized by the oxygen [3,4] and it has beneficial effects on metabolism.

The source of antioxidants can be synthetic or natural based. Due to the adverse effect of the synthetic antioxidant, there is an increasing attention to develop a new approach by using natural antioxidant, which is mostly, comes from fruits and vegetables [5,6]. Studies have revealed that daily intake of natural antioxidant will help to reduce the risk of those common diseases such as cancer, cardio and cerebro-vascular diseases [7].

In industry, normally the processing fruits will leave behind a large amount of fruits residue, such as peels, seeds, pulp, bean, rind and skin. The disposal of these fruit wastes can create the pollution problem to the environment [8]. In order to overcome this problem, the recovery of the fruit residues is one of the best alternatives. This is because the output from this recovery could be used in pharmaceutical industry, food and cosmetic [9]. In the past few years, the research on the phenolic compounds and antioxidant activity in fruits residues has been conducted on guava leaves [4], mango seed kernel [10], cantaloupe residue (leaf, stem, skin, seed and flesh) [11], bean [12], peanut skins [13], peels of mangosteen, rambutan and pomegranate [14] and citrus mandarin peels [15] and the residue of Kinnow (seed and peel), Litchi (seed and pericarp), grape seed and banana peel [8].

The pineapple, also known as *Ananas comosus L., Merr*, by-products is not exempted because it consists of peels, stem, pulp and leaves as it's residual. As one of the most important fruits in the world, the pineapple is the leading edible member of the *Bromeliacea*'s family [16]. It contains a good nutrient which gives benefit to human's health. This is because the pineapple contains a very high amount of phenolics compound [6, 16 – 20]. Several studies have been conducted in the extracting of phenolic compound from pineapple with different methods such as by using Soxhlet extraction unit [8, 21], magnetic stirrer [6, 19, 22] and orbital shaker (incubator shaker) [20].

In the recent technology of extraction, the microwave-assisted extraction (MAE) has been introduced. As compared to the conventional method, namely Soxhlet extraction unit, the MAE has a lot of advantages in the extraction process such as higher extraction rate, less extraction time, less solvent needed and can produce better product with lower cost [23]. This extraction method has been done on *Berberis asiatica* leaves [24], chokeberries (*Aronia melanocarpa*) [25], bark extracts [26], asparagus, cauliflower, celery, and chicory wastes [27], longan peel [28], bean [29], citrus mandarin peel [30], peanut skin [31] and many more.

This research is the extension research which has been done before where the pineapple wastes (namely skin) has been extracted for the analysis of phenolic compounds and antioxidant activity [17]. In this preliminary research, the parameters varied were only the temperature of extraction and the type of solvent used in the extraction, whereas the microwave power has been fixed at 250 W. From this research, it was found that the optimum condition at 250 W of microwave power was at 30 °C by using the deionized water as the extraction solvent, with the optimum value of phenolic compound and antioxidant activity ($EC_{50}$) were 206.46 mg GAE/g dw and 13.65 mg/mL, respectively. It indicated that the higher the phenolic value, the lower the $EC_{50}$, the better the antioxidant property. Thus, it was proven that the pineapple could serve as the potential candidate in becoming one of the best natural antioxidant [17]. However, based on the previous study the microwave power was just fixed at one value only, which was at 250 W. Thus, the effect of the variation in the usage microwave power has not been studied. Therefore, in this research, the microwave power will be varied, as well as the extraction temperature and the types of solvent used. The outcome of this result should reveal the optimum condition of MAE in the extracting of pineapple wastes and the results will be compared with the Soxhlet Extraction Method.

## Materials and Methods

### Material

The skin of the pineapple (waste) was peeled for the sample preparation [17].

### Sample preparation

The samples (skin) obtained were washed, frozen, dried and grounded. Each sample was weight at 5 g each before the extraction process [17].

### Microwave-assisted extraction

The extraction process was conducted at three different parameters, namely, the microwave power (500 W, 750 W and 1000 W), temperature (30 °C, 60 °C and 90 °C) and the type of solvent used (100% ethanol, 50% ethanol in deionized water and 100% deionized water). About 1 mL of sample was mixed with 50 mL of solvent. The extraction time was 20 minutes. The extract obtained was then analyzed for total phenolic compound and antioxidant activity [17].

### Total phenolic compound

The total phenolic compound was measured using the Folin-Ciocalteu method [32]. The results were expressed in milligram of Gallic Acid Equivalent (GAE)/gram of dry weight sample of pineapple (mg GAE/g dw). All samples were analyzed in duplicates [17].

### Scavenging activity on DPPH radical

The scavenging activity or antioxidant activity of the extract was analyzed by 2,2'-diphenyl-1-picrylhydrazyl radical (DPPH) [33,34,35]. All tests were performed in duplicates [17].

### Sample statistical analysis

All the experiments were conducted in duplicates and the mean was calculated using MS Excel [17].

### Soxhlet extraction

A total volume of solvent 250 mL (50 mL of ethanol in 200 mL of deionized water) was used in the Soxhlet experiment. The solvent was mixed with 5 g of sample and refluxed for 5 hours at 78 °C. After the extraction process, the supernatant was separated from the solvent by using the rotary evaporator for 15 minutes. The supernatant was then tested for total phenolic content and scavenging activity on DPPH radical analysis.

## Results and Discussion

### Effect of microwave power

The MAE is the process whereby the polar solvent which in contact with the solid samples is heated by using microwave energy [36], thus reducing the extraction time and amount of solvent consumed. The mechanism of MAE in the extracting of phenolic compound can be explained by a phenomenon. In the extraction process, the dried plant used normally will contain small traces of moisture. When the microwave energy is absorbed, this energy will be change to heat and thus the moisture starting to evaporate. This evaporated water will cause the pressure to increase inside the cell wall and lead to the rupture of the cell in the sample. Eventually, the active compound will be released from the rupture cell into the surrounding solvent and increasing the extraction yield [37].

In this research, there were three effects that have been studied. The first effect or parameter was the microwave power used in the extraction. The values were ranged from 250 W to 1000 W. For each of the microwave power value, the total phenolic compound and antioxidant activity of the pineapple waste were evaluated. Based on the previous research, a standard calibration curve was prepared to get the value of phenolic compound. The graph showed a linear relationship, whereby the gallic acid were ranged from 50 – 500 mg/L, with a correlation coefficient ($R^2$) of 0.97 [17].

From the preliminary study, the optimum condition at 250 W microwave power had been obtained at 30 °C operating temperature by using deionized water as solvent. The study has proven that at 120 °C operating

temperature, both phenolic compound and $EC_{50}$ (defined as the concentration of antioxidant required for 50% scavenging of DPPH radicals, is a parameter widely used to measure antioxidant activity value from antioxidant activity) marked a deteriorated value [17]. Therefore, in this study the temperatures were varied from 30 °C to 90 °C only.

Table 1 showed the extraction condition at 500 W microwave power. At 30 °C operating temperature by using ethanol as the solvent, the phenolic compound was 165 mg GAE/g dw, whereas the antioxidant value, which reported as $EC_{50}$, the value was 21.68 mg/mL. Meanwhile, by using the deionized water at 30 °C operating temperature, the phenolic compound increased to 177.24 mg GAE/g dw. The $EC_{50}$ value at this condition was 15.07 mg/mL. As the temperature increased to 60 °C, there was a remarkable increase for the phenolic compound, 200.63 mg GAE/g dw and a sharply decrease for $EC_{50}$ value, 14.59 mg/mL. The solvent used was ethanol in deionized water (50-50). At the highest operating temperature, which was at 90 °C the phenolic compound and $EC_{50}$ recorded were 184.56 mg GAE/g dw and 14.84 mg/mL, respectively. The trends showed that as the temperature increase, the phenolic compound increased until 60 °C but then decrease at 90 °C. This was contradicting with the trends in $EC_{50}$, whereby as the temperature increase, the $EC_{50}$ dropped at 60 °C but then inclined to 90 °C. From 500 W microwave power, the optimum value was obtained at 60 °C by using ethanol in deionized water (50-50). The phenolic compound and $EC_{50}$ value recorded at this condition were 200.63 mg GAE/g dw and 14.59 mg/mL, respectively. $EC_{50}$ value is a parameter to measure the antioxidant activity. It is also known as the concentration of antioxidant required for 50% scavenging of DPPH radicals. The smaller value of $EC_{50}$, the higher antioxidant activity of the plant extracts [38]. Therefore, the higher the phenolic compound, the lower the $EC_{50}$ value, the better the antioxidant property of the pineapple skins.

Table 1. Total phenolic compound and DPPH radical scavenging of the extract at the microwave power of 500 W with different temperatures and solvents

| **Temperature (°C)** | **Types of Solvent** | **Phenolic compound (mg GAE/g dw)** | **$EC_{50}$ (mg/mL)** |
|---|---|---|---|
| 30 | Ethanol | 165.23 | 21.68 |
| 30 | Water | 177.24 | 15.07 |
| 60 | Ethanol-Water (50-50) | 200.63 | 14.59 |
| 90 | Ethanol-Water (50-50) | 184.56 | 14.84 |

The extraction at 750 W microwave power was shown in Table 2. As compared to the operating microwave power at 500 W, generally the readings of phenolic compound at 750 W were much higher. The phenolic compound recorded at 30 °C using ethanol as solvent was 186.25 mg GAE/g dw and the $EC_{50}$ value obtained was 16.51 mg/mL. Similar trends go to the operating temperature of 30 °C using deionized water, the phenolic compound was higher compared to the solvent with pure ethanol. In general, the phenolic compound at 30 °C operating temperature using deionized water was higher both in 250 W and 500 W microwave power. Meanwhile, by using the ethanol in deionized water as a solvent, the phenolic compound at 60 °C and 90 °C were 207.72 mg GAE/g dw and 182.34 mg GAE/g dw, respectively. The value of $EC_{50}$ was recorded at 13.2 mg/mL for 60 °C operating temperature. At 90 °C, the $EC_{50}$ was a slightly higher at 14.38 mg/mL. Thus, the optimum condition at 750 W was at 60 °C by using ethanol in deionized water.

On the other hand, Table 3 showed the total phenolic compound and $EC_{50}$ value at 1000 W microwave power of extraction. Overall, the readings of phenolic compound at 1000 W microwave power were slightly decreased as compared to 750 W. At 30 °C operating temperature, the phenolic compound and $EC_{50}$ value were recorded at 165.54 mg GAE/g dw and 84.03 mg/mL, respectively. Those values were analysed by using ethanol as the solvent. Meanwhile, at 60 °C operating temperature by using deionized water as the solvent, there was a small inclined in the phenolic compound reading, 187.74 mg GAE/g dw. The $EC_{50}$ value for the antioxidant activity was recorded at 16.41 mg/mL. There were a tremendous decreased in the phenolic compound value for both at 60 °C and 90 °C

operating temperature, which recorded at 163.32 mg GAE/g dw and 79.8 mg GAE/g dw, respectively. The same pattern of depreciation could be observed in the $EC_{50}$ value which depicted at 22.15 mg/mL and 65.96 mg/mL for 60 °C and 90 °C operating temperature, respectively. The optimum value at 1000 W microwave power was obtained at 30 °C operating temperature by using deionized water as solvent.

Table 2. Total phenolic compound and DPPH radical scavenging of the extract at the microwave power of 750 W with different temperatures and solvents

| Temperature (°C) | Types of Solvent | Phenolic compound (mg GAE/g dw) | $EC_{50}$ (mg/mL) |
|---|---|---|---|
| 30 | Ethanol | 186.25 | 16.51 |
| 30 | Water | 195.68 | 15.02 |
| 60 | Ethanol-Water (50-50) | 207.72 | 13.20 |
| 90 | Ethanol-Water (50-50) | 182.34 | 14.38 |

Table 3. Total phenolic compound and DPPH radical scavenging of the extract at the microwave power of 1000 W with different temperatures and solvents

| Temperature (°C) | Types of Solvent | Phenolic Compound (mg GAE/g dw) | $EC_{50}$ (mg/mL) |
|---|---|---|---|
| 30 | Ethanol | 165.54 | 84.03 |
| 30 | Water | 187.74 | 16.41 |
| 60 | Ethanol-Water (50-50) | 163.32 | 22.15 |
| 90 | Ethanol-Water (50-50) | 79.80 | 65.96 |

In any plant extraction, the extraction yield might be reduced if the high microwave power is applied. This is due to the degradation or decomposes of thermal sensible compound. Generally, as the microwave power increase, the extraction yield will be increase linearly, up to a certain limit, before it starts to decrease or become insignificant [39 – 42]. Microwave power supplies the heating directly to the sample and will assist the MAE to break down the plant cell so that the active compound (analyte) could diffuse from the plant and dissolve in the solvent [43].

From the four-optimized microwave power that have been discussed above based on the reading of phenolic compound and $EC_{50}$ value, the most optimum microwave power was determined at 750 W. The operating temperature was at 60 °C and ethanol in deionized water was used as the solvent. At this optimum condition, the highest value of phenolic compound was recorded at 207.72 mg GAE/g dw, wheareas the antioxidant activity, $EC_{50}$ value was obtained at the lowest value of 13.20 mg/mL.

**Effect of operating temperature**

The second effect observed in this study was the effect of the extraction temperature. The value of temperature was ranged from 30 °C up to 90 °C for all the samples. The temperature and microwave power are interconnected. This is because as the temperature increases, the solvent power will be increases as well due to the decreasing in viscosity and surface tension [37]. However, there will be always a limit of the operating temperature for all the plants and fruits tested before the phenolic compound starts to degrade. A report has claimed that at a very high microwave power such as 1000 W, the extraction yield of the flavonoids from Radix astragali roots has been decreased if the extraction temperature was higher than 110 °C [40]. Another investigation found that the phenolic compound extracted from Oolong tea has been increased with the increasing extraction temperature and the optimum temperature was obtained at 170 °C [44].

According to our preliminary research, the reading of the phenolic compound was increased with the increasing temperature, but slightly decreased at 90 °C and declined sharply at 120 °C due to the thermal degradation [17, 43]. Since the extraction at 120 °C has proven to be the worst among all the temperatures tested, therefore in this research the focus of temperatures was between 30 °C to 90 °C. In general, the trends in operating temperature were the same for all the microwave power tested. This is proved by the result from Table 1, 2 and 3. Nevertheless, out of all the operating temperature, the value of the antioxidant activity, $EC_{50}$ showed the highest value at 30 °C by using ethanol as the extraction solvent for all microwave power. This showed that the condition was not suitable to extract the phenolic compound from the pineapple skins. Therefore, the most suitable temperature to extract the phenolic compounds from the pineapple wastes was at 60 °C at 750 W microwave power.

**Effect of solvent extraction**

Among the most commonly used solvent for the extraction of phenolics compound from fresh fruits or plants at different concentration in water are such as ethanol, methanol, ethyl acetate, propanol, acetone and dimethylformamide [45,46]. The percentage of polyphenolic yield produced from plant materials is depending on the solubility of the phenolic compounds in the solvent used for the extraction. In other words, the solvent types used in the extraction process is very important as well as its polarity [22]. For example, in the extraction of phenolic compounds from grape skin and seed, methanol has been used as the solvent and it has been proven that the yield of polyphenolic was higher as compared to ethanol, but the latter extract had stronger antioxidant properties [47]. Generally, ethanol is the most common solvent used and acts as a good microwave absorber to extract the bioactive compounds from plants [48]. Based on the result, by referring to the all powers and temperatures shown in Table 1, 2 and 3, the highest yield of phenolic compounds was obtained by using ethanol in deionized water as the solvent, at 750W microwave power and 60 °C of operating temperature. The $EC_{50}$ value recorded was also the lowest at this condition. A study has been reported that by addition of water to the solvent has increased the yield [49]. Several organic solvents should be prepared in the aqueous solution form before it is used as a solvent extraction. This is because with the presence of water in the organic solvent, it can improve the penetration of the solvent into the plant cell and hence, could increase the heating efficiency [50].

**Comparison between microwave-assisted extraction method and the soxhlet extraction method**

From the study of the three effects that have been discussed, the optimum condition for microwave power, operating temperature and solvent extraction were 750 W, 60 °C and ethanol in deionized water, respectively. This condition was then compared with the conventional method, namely Soxhlet extraction, by using the ethanol in deionized water as a solvent. The time taken for the Soxhlet extraction was 2 hours [51], whereas for the MAE needed only 20 minutes of extraction time.

Based on Figure 1, there was a significant different in phenolic compound value by using Soxhlet extraction, which was recorded at 28.78 mg GAE/g dw as compared to the MAE [51]. The results of phenolic compound are comparable since the value obtained by using the MAE was much higher at 207.72 mg GAE/g dw. On the other hand, Figure 2 shows that the value for $EC_{50}$ for Soxhlet extraction was lower, 2.78 mg/mL compared to 13.20 mg/mL by using MAE. As discussed in the previous section, the lower the $EC_{50}$, the greater the antioxidant activity. Even though the $EC_{50}$ value of Soxhlet extraction is lower compared to MAE, but based on the value of phenolic compound obtained, it has proven that MAE is an effective method compared to Soxhlet extraction. This is in line with the advantages of MAE which only consumed less solvent and has shorter extraction time [52]. Higher extraction rate in fruits, vegetables, foods and beans have been reported in several studies by using MAE compared to the Soxhlet extraction [53,54,55]. Lower yield, high amount of solvent used and continuous operation time of 6 or 12 hours make the Soxhlet is not the best extraction method. The long operating hours will lead to the increasing of the operational cost [56].

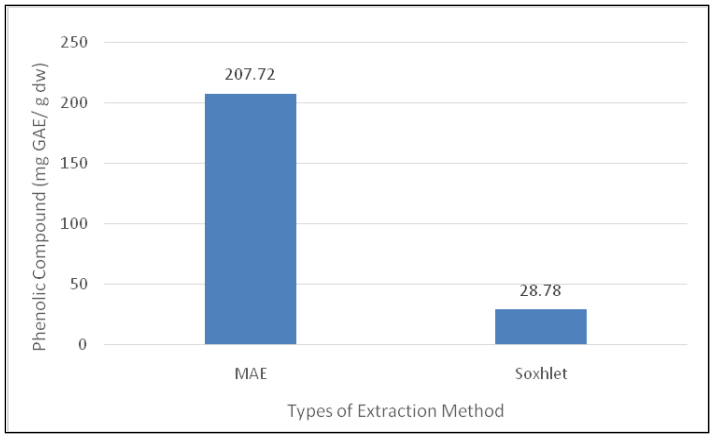



Figure 1. Comparison of total phenolic compound extracted using microwave-assisted extraction and soxhlet method

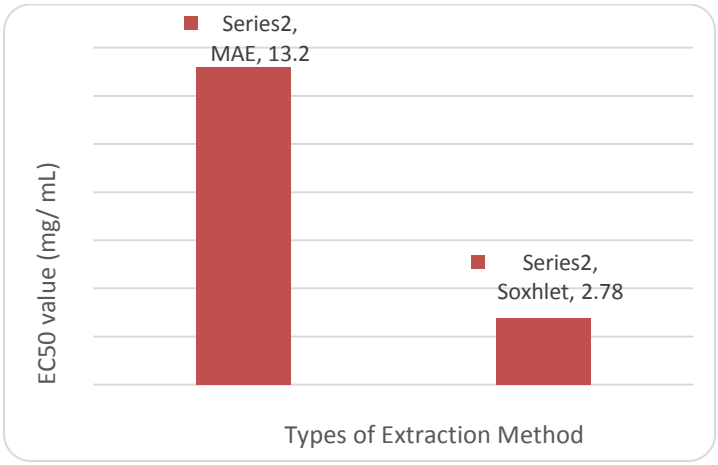



Figure 2. Comparison of DPPH radical scavenging value using microwave-assisted extraction and soxhlet method

## Conclusion

Microwave-assisted extraction (MAE) is an alternative technique of extraction which provides higher yield, shorter time and less solvent used. In this research, three parameters were varied, namely, the microwave power, extraction temperature and solvent type. Based on the results, the optimum condition has been achieved at 750 W of microwave power, 60 °C of operating temperature and ethanol in deionized water was used as the solvent. At this optimum condition, the phenolic compound was obtained at the highest yield, which was 207.72 mg GAE/g dw, whereas the antioxidant activity or $EC_{50}$ value was at the lowest, 13.2 mg/mL. The higher the phenolic compound, the lower the $EC_{50}$ value, the better the antioxidant properties of the fruits or plants. Thus, the pineapple skins could become one of the good sources of antioxidant, which are renewable and environmental friendly compared to the commercial antioxidant. As compared to the Soxhlet extraction method, MAE exhibits more efficient method with a higher extraction of phenolic compound value.

## Acknowledgement

The author would like to acknowledge the financial supports from the Research Management Institute (RMI) Universiti Teknologi MARA, Shah Alam (600-RMI/ST/DANA 5/3/Dst (301/2011) and Faculty of Chemical

Engineering, Universiti Teknologi MARA, Shah Alam. A special thanks to the Faculty of Science, Universiti Putra Malaysia and Faculty of Chemical Engineering, Universiti Teknologi MARA, Shah Alam for the assistance of laboratory staffs in this project.

**References**

1. Cook, N. C. and Sammon S. (1996). Flavanoids chemistry, metabolism, cardioprotective effects and dietary sources. *Nutritional Biochemistry*, 7: 66 – 76.
2. Karakaya, S., El, S. and Ta, A. A. (2001). Antioxidant activity of some foods containing phenolic compounds. *International Journal of Food Sciences and Nutrition*, 52: 501 – 508.
3. Shahidi, F. and Naczk, M. (2004). Phenolics in food and nutraceuticals. CRC Press, Boca Raton, FL.
4. Tachakittirungrod, S., Okonogi, S. and Chowwanapoonpohn, S. (2007). Study on antioxidant activity of certain plants in Thailand: mechanism of antioxidant action of guava leave extract. *Journal of Food Chemistry*, 103(2): 381 – 388.
5. Frankel, E. N. (2007). Antioxidant in food and biology: Facts and fiction. *USA: The Oily*.
6. Amzad Hossain, M. and Mizanur Rahman, S. M. (2011). Total phenolics, flavanoids and antioxidant activity of tropical fruit pineapple. *Journal of Food Research International*, 44: 672 – 676.
7. Renaud, S. C., Gueguen, R., Schenker, J. and d'Houtaud, A. (1998). Alcohol and mortality in middle-aged men from France. *Epidemiology*, 9: 184 – 188.
8. Neha, B., Harinder Singh, O., Dewinder Singh, U. and Ramabhau Patil, P. (2011). Total phenolic compound and antioxidant capacity of extracts obtained from six important fruit residues. *Journal of Food Research International*, 44: 391 – 396.
9. Makris, D. P., Boskou, G. and Androkopoulus, N. K. (2007). Recovery of antioxidant phenolics from white vinification solid by-products employing water/ethanol mixtures. *Bioresource Technology*, 98: 2963 – 2967.
10. Maisuthisakul, P. and Gordon, M. H. (2009). Antioxidant and tyrosinase inhibitory activity of mango seed kernel by-product. *Journal of Food Chemistry*, 117: 332 – 341.
11. Hajar, I. I., Wei Chan, K., Abdalbasit, A. M. and Maznah, I. (2010). Phenolic compound and antioxidant activity of cantaloupe (*Cucumis melo*) methanolic extract. *Journal of Food Chemistry*, 119: 643 – 647.
12. Sutivisedsak, N., Cheng, H. N., Willett, J. L., Lesch, W. C., Tangsrud, R. R. and Atanu, B. (2010). Microwave-assisted extraction of phenolics from bean (*Phaseolus vulgaris, L.*). *Journal of Food Research International*, 43: 516 – 519.
13. Tameshia, S. B., Parameswarakumar, M., Kequan, Z. and Sean, O. (2010). Microwave-assisted extraction of phenolic antioxidant compounds from peanut skin. *Journal of Food Chemistry*, 120: 1185 – 1192.
14. Okonogi, S., Duangrat, C., Anuchpreeda, S., Tachakittirungrod, S. and Chowwanapoonpohn, S. (2007). Comparison of antioxidant capacities and cytotoxicities of certain fruit peels. *Journal of Food Chemistry*, 103: 839 – 846.
15. Khizar, H., Sarfraz, H., Shabbar, A., Umar, F., Baomiao, D., Shuqin, X., Chengsheng, J., Xiaoming, Z. and Wenshui, X. (2009). Optimized microwave-assisted extraction of phenolic acids from citrus mandarin peels and evaluation of antioxidant activity in vitro. *Journal of Separation and Purification Technology*, 70: 63 – 70.
16. Atul, U., Jeewan, P. L. and Shinkichi, T. (2010). Utilization of pineapple waste: A review. *Review in Journal of Food Science,* 6: 10 – 18.
17. Alias, N. H. and Zulkifly, A. (2013). Preliminary investigation on the total phenolic compound and antioxidant activity of pineapple wastes via microwave-assisted extraction at fixed microwave power. *IEEE Symposium on Business, Engineering and Industrial Application*: pp. 423 – 427.
18. Kongsuwan, A., Suthiluk, P., Theppa korn, T., Srilaong, V. and Setha, S. (2009). Bioactive compounds and antioxidant capacities of *Phulae* and *Nanglae* pineapple. *Asian Journal of Food and Agro-Industry, Special Issue*: 44 – 50.
19. Adhikarimayum, H., Kshetrimayum, G. and Maibam, D. (2010). Evaluation of antioxidant properties of phenolics extracted from Ananas comosus l. *notulae scientia niologicae. Academic Press*: pp. 68 –71.
20. Anynda, Y. and Lee-Fong, S. (2014). A comparative study of the antioxidant properties of three pineapples (*Ananas comosus L.*) varieties. *Journal of Food Studies*, 3 (1): 40 – 56.
21. de oliveira, A. C., Valentim, I. B., Silva, C. A., Bechara, E. J. H., de Barros, M. P., Mano, C. M. and Goulart, M. O. F. (2009). Total phenolic compound and free radical scavenging activities of methanolic extract powders of tropical fruit residues. *Journal of Food Chemistry*, 115: 469 – 475.

22. Alothman, M., Bhat, R. and Karim, A. A. (2009). Antioxidant capacity and phenolic compound of selected tropical fruits from malaysia, extracted with different solvent. *Journal of Food Chemistry*, 115: 785 – 788.
23. Glanzer, K., Sanglo, A. and Valko, K. (1986). Microwave extraction – a novel sample preparation method for chromatography. *Journal of Chromatography*, 371: 299 – 306.
24. Belwal, T., Bhatt, I. D., Rawal, R. S. and Pande, V. (2017). Microwave-assisted extraction (MAE) conditions using polynomial design for improving antioxidant phytochemicals in *Berberis asiatica* Roxb. Ex DC leaves. *Journal of Industrial Crops and Products*, 95: 393 – 403.
25. Simic, V. M., Rajkovic, K. M., Stojicevic, S. S., Velickovic, D. T., Nikolic, N. C., Lazic, M. L. and Karabegovic, I. T. (2016). Optimization of microwave-assisted extraction of total polyphenolic compounds from chokeberries by response surface methodology and artificial neural network. *Journal of Separation and Purification Technology*, 160: 89 – 97.
26. Bouras, M., Chadni, M., Barba, F. J., Grimi, N., Bals, O. and Vorobiev, E. (2015). Optimization of microwave-assisted extraction of polyphenols from *Quercus* bark. *Journal of Industrial Crops and Products*, 77: 590 – 601.
27. Baiano, A., Bevilacqua, L., Terracone, C., Conto, F. and Del Nobile, M. A. (2014). Single and interactive effects of process variables on microwave-assisted and conventional extractions of antioxidants from vegetable solid wastes. *Journal of Food Engineering*, 120: 135 – 145.
28. Pan, Y., Wang, K., Huang, S., Wang, H., Mu, X., He, C., Ji, X., Zhang, J. and Huang, F. (2008). Antioxidant activity of microwave-assisted extract of Longan (*Dimocarpus Longan Lour.*). *Journal of Food Chemistry*, 106: 1264 – 1270.
29. Sutivisedsak, N., Cheng, H.N., Willett, J. L., Lesch, W. C., Tangsrud, R. R. and Biswas, A. (2010). Microwave-assisted extraction of phenolics from bean (*Phaseolus vulgaris L.)*. *Journal of Food Research International*, 43: 516 – 519.
30. Hayat, K., Hussain, S., Abbas, S., Farooq, U., Ding, B., Xia, S., Jia, C., Zhang, X. and Xia, W. (2009). Optimized microwave-assisted extraction of phenolic acids from citrus mandarin peels and evaluation of antioxidant activity in vitro. *Journal of Separation and Purification Technology*, 70: 63 – 70.
31. Ballard, T. S., Mallikarjunan, P., Zhou, K. and O'Keefe, S. (2010). Microwave-assisted extraction of phenolic antioxidant compounds from peanut skins. *Journal of Food Chemistry*, 120: 1185 – 1192.
32. Singleton, V. L., Orthofer, R. and Lamuela-Raventos, R. M. (1999). Analysis of total phenols and other oxidation substrates and antioxidants by means of Folin-Ciocalteu reagent. *Methods in Enzymology*, 299: 152 – 178.
33. Brand, W. W., Cuvelier, M. E. and Berset, C. (1995). Use of a free radical method to evaluate antioxidant activity. *Lebensmittel-Wissenschaft und Technologie*, 20: 25 – 30.
34. Sanchez-Moreno, C., Larrauri, J. A. and Saura-Calixto, F. (1998). A procedure to measure the antiradical efficiency of polyphenols. *Journal of Food and Science and Agriculture*, 76: 270 – 276.
35. Blois, M. S. (1958). Antioxidant determinations by the use of a stable free radical. *Nature*, 26: 1199 –1200.
36. Luque de Castro, M. D. and Luque Garcia, J. L. (2002). Acceleration and automation of solid sample treatment. *Amsterdam: Elsevier*: pp. 218.
37. Mandal, V., Mohan, Y. and Hemalatha, S. (2007). Microwave-assisted extraction - an innovative and promising extraction tool for medicinal plant research. *Pharmacognosy Reviews*, 1(1): 7 – 18.
38. Maisuthisakul, P., Suttajit, M. and Pongsawatmanit, R. (2007). Assessment of phenolic compound and free radical-scavenging capacity for some Thai indigeneous plants. *Journal of Food Chemistry*, 72(2): 145 – 171.
39. Mandal, V. and Mandal, S. C. (2010). Design and performance evaluation of a microwave-based low carbon yielding extraction technique for naturally occurring bioactive triterpenoid: Oleanolic acid. *Biochemical Engineering Journal*, 50(1-2): 63 – 70.
40. Xiao, W., Han, L. and Shi, B. (2008). Microwave-assisted extraction of flavanoids from *Radix astragal*. *Separation and Purification Technology*, 62: 614 – 618.
41. Chemat, S., Ait-Amar, H., Lagha, A. and Esveld, D. C. (2005). Microwave-assisted extraction kinetics of terpenes from Caraway seeds. *Chemical Engineering and Processing: Process Intensification*, 44 (12): 1320 – 1326.
42. Kwon, J. H., Belanger, J. M. R., Pare, J. R. J. and Yaylayan, V. A. (2003). Application of the Microwave-Assisted Process (MAP$^{TM}$) to the fast extraction of ginseng *Saponins*. *Food Research Institute*, 36: 491 – 498.

43. Chung-Hung, C., Rozita, Y., Gek-Cheng, N. and Fabian Wai-Lee, K. (2011). Microwave-assisted extractions of active ingredients from plants. *Journal of Chromatography A*, 1218: 6213 – 6225.
44. Tsubaki, S., Sakamoto, M. and Azuma, J. (2010). Microwave-assisted extraction of phenolic compounds from tea residues under autohydrolytic conditions. *Journal of Food Chemistry*, 123(4): 1255 – 1258.
45. Antolovich, M., Prenzler, P., Robards, K. and Ryan, D. (2000). Sample preparation in the determination of phenolic compounds in fruit. *Journal of Analyst*, 125: 989 – 1009.
46. Luthria, D. L. and Mukhopadhyay, S. (2005). Influence of sample preparation on assay of phenolic acids from eggplant. *Journal of Agriculture and Food Chemistry*, 54: 41 – 47.
47. Casazza, A. A., Aliakbarian, B., Mantegna, S., Cravotto, G. and Perego, P. (2010). Extraction of phenolics from *Vitis Vinifera* wastes using non-conventional techniques. *Journal of Food Engineering*, 100: 50 – 55.
48. Zhou, H. Y. and Liu, C. Z. (2006). Microwave-assisted extraction of solanesol from tobacco leaves. *Journal of Chromatography A*, 1129: 135 – 139.
49. Escribano-Bailon, M. T. and Santos-Buelga, C. (2003). Polyphenol extraction from foods. In *C. Santos*-Buelga and G. Williamson (Eds.). Methods in polyphenol analysis, UK. *The Royal Society of Chemistry*: pp. 1 – 16.
50. Alfaro, M. J., Belanger, J. M. R., Padilla, F. C. and Pare, J. R. J. (2004). Influence of solvent, matrix dielectric properties and applied power on the liquid-phase microwave-assisted processes (MAP$^{TM}$) extraction of ginger (*Zingiber officinale*). *Journal of Food Research International*, 36(5): 499 – 504.
51. Hatam, S. F., Suryanto, E. and Abidjulu, J. (2013). Aktivitas antioksidan dari ekstrak kulit nenas (*Ananas comosus (L) Merr*). *Pharmacon, Jurnal Ilmiah Farmasi*, 2(1): 2310 – 2315.
52. Zhou, T., Xiao, X. H., Wang, J. Y., Chen, J. L., Zhu, X. F., He, Z. F. and Li, G. K. (2012). Evaluation of microwave-assisted extraction for aristolochic acid from *aristolochiae fructus* by chromatographic analysis coupled with nephrotoxicity studies. *Journal of Biomedical Chromatography*, 26: 166 – 171.
53. Diange, R. G., Foster, G. D. and Khan, S. U. (2002). Comparison of soxhlet and microwave-assisted extraction for the determination of fenitrothion residues in beans. *Journal of Agriculture and Food Chemistry*, 50: 3204 – 3207.
54. Pan, X., Niu, G. and Liu, H. (2003). Microwave-assisted extraction of tea-polyphenols and tea caffeine from green tea leaves. *Journal of Chemical Engineering Process*, 42: 129 – 133.
55. Singh, S. B., Foster, G. D. and Khan, S. U. (2004). Microwave-assisted extraction for the simultaneous determination of thiamethoxam, imidacloprid and carbendazim residues in fresh and cooked vegetable samples. *Journal of Agriculture and Food Chemistry*, 52: 105 – 109.
56. Setiawan, C., Purnomo, H. and Kusnadi, J. (2013). Application of microwave-assisted extraction on teak (*Tectona grandis*) leaves antioxidant extraction. *Research Journal of Pharmaceutical, Biological and Chemical Sciences*, 4(3): 1012 – 1018.

*Malaysian Journal of Analytical Sciences, Vol 21 No 3 (2017): 700 - 708*
*DOI: https://doi.org/10.17576/mjas-2017-2103-19*

**MALAYSIAN JOURNAL OF ANALYTICAL SCIENCES**
***Published by The Malaysian Analytical Sciences Society***
**ISSN 1394 - 2506**

# PRELIMINARY STUDY ON Pd-BASED BINARY CATALYSTS SUPPORTED WITH CARBON NANOFIBER FOR THE ELECTROOXIDATION OF GLYCEROL

## (Kajian Awal ke atas Mangkin Berasaskan Pd Disokong dengan Gentian Nano Karbon untuk Pengoksidaan Elektro Gliserol)

Norilhamiah Yahya[1]*, Siti Kartom Kamaruddin[2,3], Nabila Abdul Karim[2], Mohd Shahbudin Masdar[3], Kee Shyuan Loh[2]

*[1]Malaysian Institute of Chemical and Bioengineering Technology, Universiti Kuala Lumpur, 78000 Alor Gajah, Melaka, Malaysia*
*[2]Fuel Cell Institute*
*[3]Department of Chemical and Process Engineering Universiti Kebangsaan Malaysia, 43600 UKM Bangi, Selangor, Malaysia*

**Corresponding author: norilhamiah@unikl.edu.my*

Received: 28 November 2016; Accepted: 5 February 2017

**Abstract**

In this study, Aurum (Au) was used as the second metal in palladium catalyst (Pd) and carbon nanofiber (CNF) as catalyst support for glycerol oxidation. Second metal and catalyst support will help to improve catalytic activity and decrease adsorbed oxidation intermediates species. Carbon nanofiber supported PdAu nanoparticles was synthesized by using trisodium citrate as stabilizing agent and sodium borohydride as reducing agent. Physicochemical characterizations of the catalyst were performed by X-ray Diffraction (XRD), Transmission Electron Microscope (TEM), Field Emission Scanning Electron Microscope (FESEM) and Brunauer-Emmett-Teller (BET) to study the nature of the catalysts. The electrochemical activity for oxidation of glycerol on PdAu/CNF was evaluated in half cell under alkaline media by cyclic voltammetry potentiostat. The densities and mass activity obtained from half-cell analysis were 73.81 mA $cm^{-2}$ @ 492.04 mA $mg^{-1}$, 63.82 mA $cm^{-2}$ @ 425.44 mA $mg^{-1}$ and 55.73 mA $cm^{-2}$ @ 371.54 mA $mg^{-1}$ for PdAu/CNF, Pd/CNF and Au/CNF, respectively in 1 M KOH + 0.5 M glycerol electrolyte. The electrochemical study, exhibited the superior performance of bimetallic PdAu/CNF catalyst as compared to monometallic Pd/CNF. This indicate that the electronic coupling between Pd and Au can promote the electrocatalytic activity for glycerol oxidation.

**Keywords:** PdAu, carbon nanofiber, glycerol oxidation, alkaline media

**Abstrak**

Dalam kajian ini, Au telah digunakan sebagai logam kedua dalam pemangkin paladium dan gentian nano karbon sebagai sokongan pemangkin kepada pengoksidaan gliserol. Logam kedua dan sokongan pemangkin akan membantu meningkatkan aktiviti pemangkin dan mengurangkan perjerapan spesis pertengahan pengoksidaan. PdAu dengan disokong oleh gentian nano karbon telah disintesis dengan menggunakan trisodium sitrat sebagai ejen penstabil dan natrium borohidrat sebagai agen penurunan. Pencirian fizikal-kimia pemangkin telah dijalankan oleh pembelauan sinar-X (XRD), Mikroskop Elektron Penghantaran (TEM), Mikroskop Imbasan Elektron (FESEM) dan Brunauer-Emmett-Teller (BET) untuk mengkaji sifat pemangkin. Aktiviti elektrokimia untuk pengoksidaan gliserol pada PdAu/CNF dinilai dalam sel separuh di bawah media beralkali dengan menggunakan kitaran voltammetri potentionstat. Ketumpatan arus dan berat aktiviti yang diperolehi daripada analisis sel separuh adalah 73.81 mA $cm^{-2}$ @ 492.04 mA $mg^{-1}$, 63.82 mA $cm^{-2}$ @ 425.44 mA $mg^{-1}$ dan 55.73 mA $cm^{-2}$ @ 371.54 mA $mg^{-1}$ masing-masing untuk PdAu/CNF, Pd/CNF dan Au/CNF, dalam 1 M KOH + 0.5 m gliserol elektrolit. Kajian elektrokimia, mempamerkan

prestasi unggul pemangkin PdAu/CNF berbanding dengan Pd/CNF and Au/CNF. Ini menunjukkan bahawa gandingan elektronik antara Pd dan Au boleh menggalakkan aktiviti elektrokatalitik untuk pengoksidaan gliserol.

**Kata kunci:** PdAu, gentian nano karbon, oksidasi gliserol, media beralkali

## Introduction

Fuel Cell is one of the alternative energy use to generate electricity without any combustion. Direct Alcohol Fuel Cell in which use methanol and ethanol can be applied in small electronic appliances like hand phone, laptop, camera and lamp. The use of methanol in the fuel cell can be absolutely no doubt, while the use of ethanol has increasing attention among researchers. However, properties of methanol that has high toxicity[1-2] and high volatility of ethanol [3] make both fuels unsuitable as a fuel for the commercialization of fuel cell [4]. One alternative proposed currently is glycerol, to replace methanol in fuel cell application. The growing biodiesel market in Malaysia as Malaysia is the world's largest producer of palm oil will lead to surpass the capacities of glycerol as a by-product. Fuels such as glycerol have drawn an attention because they are renewable from biomass production, less harmful, have high energy density, low vapor pressure, low cost, and easy storage and transportation needs [5-6].

Glycerol is feed at the anode side of fuel cell where the oxidation reaction of glycerol occurs to produce carbon dioxide, electrons and protons. To complete the full reaction in fuel cell, the electrons are pass through the electronic circuit while the proton are permeated through membrane both to cathode side. At the cathode is where the oxygen reduction reaction occurs to complete the cell and produce electricity. However, the oxidation of glycerol quite complicated in which the partial oxidation will produce unwanted products such as glyceraldehyde, 1,3-dihydroxyacetone, glyceric acid, hydroxypyruvic acid, tartronic acid, mesoxalic acid, formic acid, ocilic acid and glycolic acid [7, 9 -11]. All these partial oxidation products are not desirable as these products will reduce the performance single fuel cell. Thus, the catalyst selection for the glycerol oxidation is important to increase overall performance fuel cell. The main problem with glycerol oxidation is the potential of generation intermediates species during anodic oxidation of glycerol which might be poison the catalyst surface [12]. Due to this, selection of catalyst is the critical issue in order to increase the activity of glycerol oxidation in anode side and at the same time minimize the cost of the fuel cell itself. Up until now, there are several catalysts use to study the oxidation of glycerol such as platinum. The use of platinum has brought stability issue as another intermediate product of carbon monoxide poisoning the platinum surface by adsorbing too strong on the platinum surface.

Bimetallic electrocatalysts have been used as catalysts in this study, which the purpose is related to the decreased load of the noble metal and combine with secondary metals (normally transition metal). This combination will enhance the electrocatalytic activity of bimetallic mixtures in terms of electrocatalytic activity of bimetallic mixtures in terms of current density and tolerance to the carbon monoxide poisoning effect [13,14]. Several previous literatures, reported the effectiveness PdAu bimetallic as the electrocatalyst. Bimetallic containing gold show higher activity and selectivity in helping to oxidize CO resulting from the reaction intermediate with more efficient even below room temperature in oxidation of ethanol [15,16,17]. Therefore, bimetallic palladium-Aurum (PdAu) is used to study the activity of oxidation reaction of glycerol. The Pd-Au is supported to the carbon nanofiber (CNF) so that the catalyst can evenly distributed and to reduce the usage of metal for glycerol oxidation reaction but at the same time have higher catalyst activity. This study will focus on PdAu supported with carbon nanofiber, which believed can give high durability and stability to the catalyst as this bimetallic catalyst has high a tendency to agglomerate. This paper reports the synthesis, physicochemical and electrochemical characterization analysis of Pd/CNF, Au/CNF and PdAu/CNF for glycerol oxidation in half cell.

## Materials and Methods

### Materials

To carry out this research all precursor metal salts and chemicals such as tetrachloroauric acid ($HAuCl_4 \cdot 4H_2O$), palladium chloride ($PdCl_2$), trisodium citrate ($Na_3Ct$), sodium borohydride ($NaBH_4$), carbon nanofiber, sodium hydroxide and glycerine has been purchased from Sigma-Aldrich (USA).

**Preparation of catalysts using reduction method**

In brief, the synthesized catalyst was modified from the previous study [17], where 0.05 M $PdCl_2$ (Sigma-Aldrich) (in 0.1 M HCl) was mixed together with 0.05 M of $AuCl_3 \cdot HCl \cdot 4H_2O$ (Sigma- Aldrich) bring a total solution of 15 mL. The mixed solution was added to some amount of trisodium citrate in drop wise manner. Subsequently, the above solution was added drop-wise to a stirred CNF slurry (isopropanol and deionized water) and stirred for 2 hours. Next, the reduction of the metal precursors is carried out using an appropriate amount of freshly prepared ice-cold sodium borohydride ($NaBH_4$) and the solution was stirred overnight at 10 ºC. Longer reaction time is needed to allow the sodium borohydride as it has strong reducing abilities to react with metal precursors to form product. The molar ratio of $NaBH_4$ to metal ions was taken as 5:1. The solid was filtered and washed with deionized water several times and dried at 80 ºC overnight.

**X-ray diffraction analysis**

XRD is a powerful method used to give the crystallinity of the metal synthesis. The samples data were collected at 2θ from 20° to 90°. While FESEM and TEM provide the information about size, size distribution, dispersion and the morphology of various shapes of particles. The morphology of the synthesized catalysts was observed by using FESEM model Zeiss/SUPRA 55VP. The electron microscope specimens have been prepared by dispersing the small amount of catalyst in ethanol and casting it by dropping the solution onto the copper-grids. BET analysis provides on determination the precise specific area evaluation of materials by nitrogen multilayer adsorption measured as a function of relative pressure using a fully automated analyzer. The technique encompasses external area and pore area evaluation to determine the total specific area evaluation to determine the total specific area in $m^2/g$ yielding important information in studying the effects of surface porosity and particle size in many applications.

**Cyclic voltammetry analysis**

Cyclic voltammetry is a type of potential dynamic electrochemical measurement. All apparatus for cyclic voltammetry measurement was performed by using Autolab (PGSTAT101) electrochemical workstation under room temperature. The catalyst ink solution was carefully transferred onto the glassy carbon electrode by using micropipette and then leave dried under room temperature. The electrochemical characterization of three types of catalysts was studied by a cyclic voltammetry (CV) test in the potential range -0.7 to 0.4 V in 50 $mVs^{-1}$ in 1 M KOH and at scan rate 50 $mVs^{-1}$ in 0.5 M glycerol/1 M KOH solution. Both solution was de-oxygenated by bubbling with $N_2$ at 200 mL $min^{-1}$ for 30 minutes before taking any measurement of glycerol oxidation reaction.

## Results and Discussion

Phase analysis by X-ray diffraction (XRD) goes beyond elemental composition to characterize the crystalline forms present and understand the alloy structure of bimetallic nanoparticles. Figure 1 showed the XRD patterns of the catalyst samples. The XRD patterns confirmed the presence of target metal in catalyst samples of Pd/CNF, Au/CNF and PdAu/CNF and fit well their characteristic of face centered cubic (fcc) patterns. The $2\theta$ angle of the diffraction meter was stepped from 20° to 90° [18]. The first strong peak for all catalyst samples with value 25.83° referred to the carbon (002) facet of the carbon nanofiber support. The diffraction peaks in catalyst sample Pd/CNF exhibited the characteristic face-centred cubic crystalline structure of Pd-based material with $2\theta$ values of 39.84°, 46.53°, 67.53°, and 81.61°correspond to the (111), (200), (220) and (311) of the metallic palladium face respectively. The diffraction peaks of Au/CNF are 38.08°, 44.21°, 77.80°, 65.01° correspond to the (111), (200), (220) and (311) facets of Au crystals respectively. Meanwhile, for catalyst sample of PdAu/CNF shows that the both metal has form metal alloyed particles since there is only a single peak. The diffraction peak positions for PdAu/CNF, move which located between two wavelengths at each monometallic nanoparticle for Pd and Au. This indicates that, Au has entered Pd lattice and form a homogeneous substitution alloy [19].

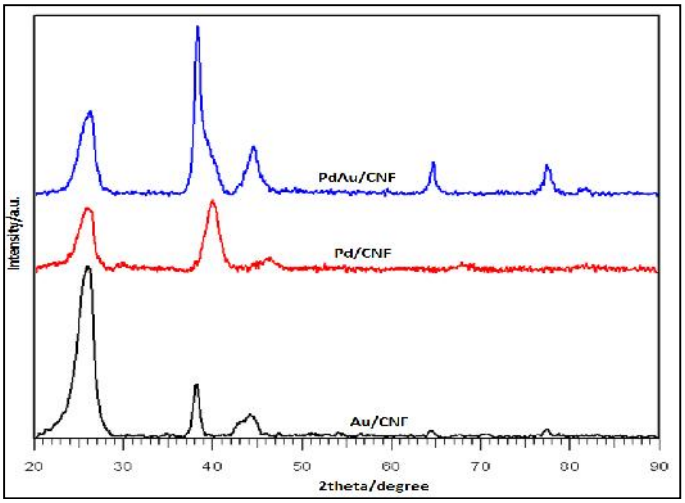



Figure 1. XRD patterns of PdAu/CNF, Au/CNF and Pd/CNF catalysts

BET analysis has been conducted to evaluate the specific area of the catalyst support to ensure the pore of the support has been filled in the catalyst. Specific surface area for CNF before catalyst deposition is 370$m^2$/g. Table 1 shows the BET analysis of surface areas for all catalyst samples. From the Table 1 shown that the value of BET has decrease after deposition of catalysts on CNF surface. The metal catalyst has been successfully deposited onto the surface of CNF support. This is due to metal catalyst reduced onto the support and blocks some microspores which leads to a decreased BET surface area.

Table 1. Crystal size, particles size and surface area of the Pd/C, Au/C and PdAu/CNF based on XRD, TEM and BET analysis

| **Catalyst** | **XRD** | **TEM** | **BET Surface Area ($m^2$/g)** |
|---|---|---|---|
| | **Crystallite Size (nm)** | **Particle Size (nm)** | |
| Pd/CNF | 6.0 | 5.7 | 24 |
| Au/CNF | 8.7 | 7.5 | 20 |
| PdAu/CNF | 4.4 | 4.8 | 26 |

Figure 2a-c shows the FESEM image of porous structure of the prepared Pd, Au and PdAu supported with carbon nanofiber. The images reveal a three-dimensional image of the catalysts surface and shows the equilibrium forms of small metal crystallites on the dispersed on the support. Meanwhile Figure 3d-f shows the TEM images of Pd/CNF, Au/CNF and PdAu/CNF catalyst samples. From TEM images clearly shown that there is no large agglomeration of metal catalysts and supported in CNF. The shape catalysts shown here have ununiformed particle size but still in dimension of nanometre. The determination of activity catalyst not only size dependence as the catalyst size become small so as the surface area for active site become large but the distribution of catalyst on CNF also important. The CNF as catalyst support help increase in catalyst distribution so that the active site for reaction happen also increase.

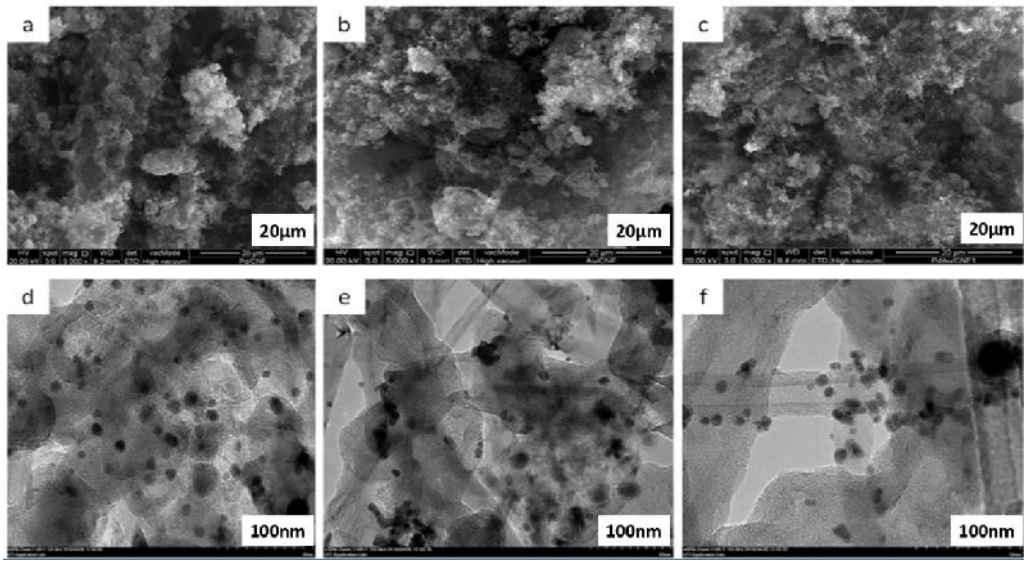



Figure 2. FESEM images of catalysts a) Pd/CNF b) Au/CNF and c) PdAu/CNF. TEM images of d) Pd/CNF, e) Au/CNF and f) PdAu/CNF catalyst

**Electrochemical analysis of cyclic voltammetry**

The performance of catalysts in glycerol oxidation reaction (GOR) was evaluated in terms of two aspects: (1) onset potential ($E_{on}$); indicative of the catalytic activity over glycerol oxidation reactions, (2) forward anodic specific peak current density ($I_f$); showing the catalyst maximum performance. To get acquiring qualitative information for catalysts activity in alkaline media, CV experiment is carried out in 1.0 M NaOH. The CV behaviour of Pd-based catalyst was preliminarily investigated in 1.0 M KOH without the presence of glycerol as shown in Figure 3. As this analysis is conducted under alkaline environment it can be found that the onset of the oxide formation and the peak potential of the oxide reduction for PdAu/CNF shifted to more negative potentials which exhibit the chemisorption of OH on the Pd at a negative potential. Glycerol is a complex molecule, due to this the oxidation of glycerol in alkaline medium can form numbers of possible oxide/hydrous or oxide/hydroxyl surface molecules. This is having been described in reduction wave [20]. Based on the previous study the major electrooxidation of glycerol by using Pd catalyst in alkaline media can be described as equation 1 – 3 follow [3];

$$Pd + OH^- \leftrightarrow Pd - (OH)_{ads} + e^- \quad (1)$$

$$Pd + C_2H_3\ OH\ _2 - CH_2\ OH\ + 3OH^- \leftrightarrow Pd - (C_2H_3(OH)_2 - CO)_{ads} + 3H_2O + 3e^- \quad (2)$$

$$Pd{-}(OH)_{ads} + Pd - (C_2H_3(OH)_2 - CO)_{ads} \rightarrow C_2H_3(OH)_2 - COOH + 2Pd \quad (3)$$

$$C_2H_3(OH)_2 - COOH + OH^- \rightarrow C_2H_3(OH)_2 - COO^- + H_2O \quad (4)$$

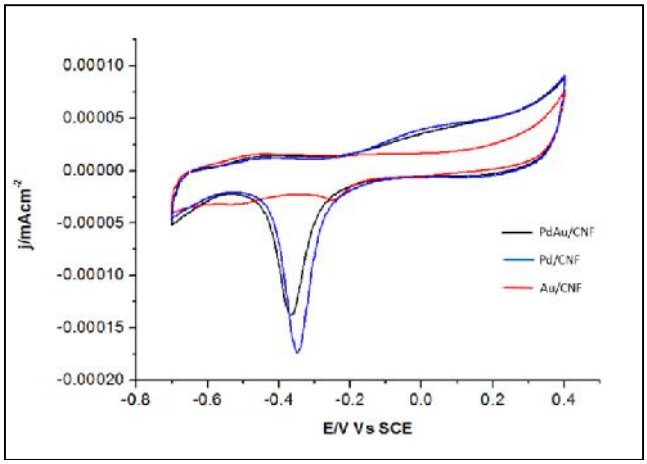



Figure 3. Cyclic voltammogram of PdAu/CNF in 1 M KOH solution at room temperature with the scan rate of 50 mV/s

Figures 4 shows the CV scans for Pd/CNF, Au/CNF and PdAu/CNF catalyst for glycerol oxidation in 1.0 M KOH solution containing 0.5 M glycerol in the potential range -0.7V to 0.4V. In these CV scans, a peak is an indication of surface interaction or reaction between some species and catalyst. In the positive-going (forward scan), is attributed to the electrooxidation of glycerol on the catalysts. Meanwhile, during the reverse scan there is a secondary oxidation peak which associated with incomplete oxidation of carbonaceous residues from the glycerol in forward scan. Between three synthesized catalysts, the bimetallic catalyst which is PdAu/CNF shows the best performance towards glycerol oxidation in alkaline media compare with Pd/CNF and Au/CNF in terms of onset potential and current density. The onset potential ($E_{on}$) is -0.45 for Pd/CNF, -0.46 for Au/CNF and -0.48 for PdAu/CNF, while the peak current density ($I_f$) for PdAu/CNF is 73.81mA $cm^{-2}$ which is highest compare to Pd/CNF and Au/CNF. The results in forward scan shows that the addition of Au in Pd form bimetallic catalyst can significantly improve the catalytic activity of Pd for glycerol oxidation in alkaline media.

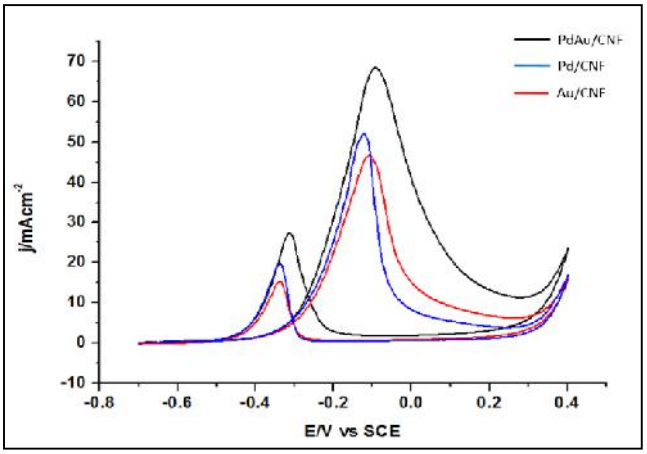



Figure 4. Cyclic voltammograms of Pd/CNF and PdAu/CNF for the electrooxidation of 0.5 M glycerol using 1.0 M KOH as an electrolyte scan rate of 50 mV/s

The actual performance glycerol oxidation in alkaline media has been summarized in Table 2. Based on Table 2, the onset potential ($E_{on}$) of glycerol oxidation with PdAu/CNF catalyst reveal more negative value compared to Pd/CNF and Au/CNF. This indicates, the significant enhancement oxidation kinetic activity for glycerol by addition of Au. With the addition of Au making the adsorption of oxygen species such as OH occurs at much lower potential than on monometallic Pd and Au surface to oxidize CO or adsorbed CO-like carbonaceous species on Pd sites. The addition of Au as second metal in PdAu/CNF also contribute to sufficient oxygen containing species such as OH to remove the adsorbed carbonaceous species and in other way it will beneficial in oxidation of glycerol [19]. Meanwhile the catalyst poisoning against the carbonaceous species can be traced from the forward scan to backward ($I_f/I_r$) scan peak current density ratio as shown in Table 2. The ratio of PdAu/CNF catalyst show higher value compare to Pd/CNF and Au/CNF. Therefore PdAu/CNF show better oxidation of methanol to carbon dioxide during anodic scan and less accumulation of carbonaceous species on the catalyst surface compare to Pd/CNF and Au/CNF [21].

Table 2. Electrocatalytic properties Pd/CNF and PdAu /CNF catalysts for glycerol oxidation

| **Catalyst Types** | **$E_{on}$ V vs SCE** | **$E_p$ V vs SCE** | **Ip (mA cm$^{-2}$)** | **$E_r$ V vs SCE** | **Ir (mA cm$^{-2}$)** | **j (mA mg$^{-1}$)** | **$I_f/I_B$** |
|---|---|---|---|---|---|---|---|
| Au/CNF | -0.46 | -0.071 | 55.73 | -0.29 | 23.14 | 371.54 | 2.40 |
| Pd/CNF | -0.45 | -0.044 | 63.82 | -0.27 | 40.58 | 425.44 | 1.57 |
| PdAu/CNF | -0.48 | -0.091 | 73.81 | -0.32 | 27.94 | 492.04 | 2.64 |

**Chronoamperometric study**

Chronoamperometric study has been employed for 3600s, where the considerable stability and tolerance to poisoning by intermediates species can be tested. Figure 5 shows the chronoamperometry obtained at room temperature in solutions 1.0 M NaOH and 0.5 M glycerol for 3600s. For all three catalysts, we can observe a decay of current value in the time interval measured for the studied electrocatalysts. However, after the initial drops the performance become stable for all the catalyst tested. From Figure 6 shows that the PdAu/CNF demonstrates better stability compared to Pd/CNF and Au/CNF alone, indicating that the present of Au could improve the stability of the catalyst by give a balance adsorption between OH species from Au and species from glycerol adsorption on Pd [22].

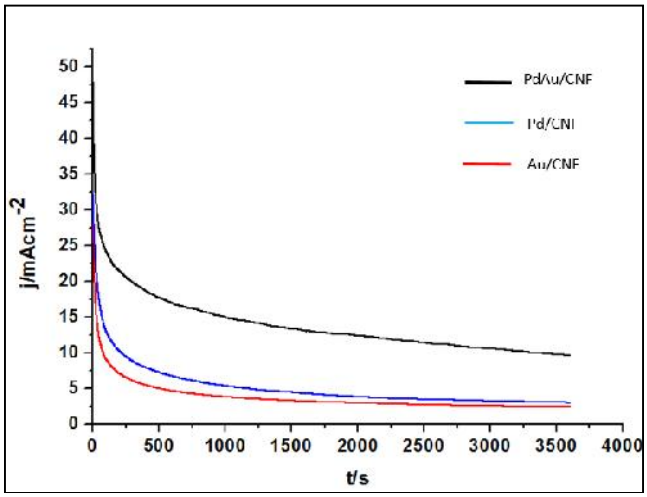



Figure 5. Cyclic voltammograms of Pd/CNF and PdAu/CNF for the electrooxidation of 0.5 M glycerol using 1.0 M KOH as an electrolyte

## Conclusion

In summary, the three types of catalysts namely as Pd/CNF, Au/CNF and PdAu/CNF have successfully synthesize by a facile method. XRD data clearly show the presence of Pd, Au and bimetallic PdAu. The FESEM and TEM image shown that the catalysts distributed on supported catalysts of CNF. The CV results exhibited, PdAu/CNF shows excellent catalytic activities and high stability for glycerol oxidation compared to Pd/CNF and Au/CNF. The onset potential of glycerol oxidation for PdAu/CNF more negative than Pd/CNF and Au/CNF which was attributed to the electronic effect. As well as the current density peak for PdAu/CNF is higher compared to monometallic catalyst. In addition, the $I_f/I_r$ ratio which reflect poisoning species for the oxidation of glycerol shows that bimetallic PdAu/CNF again is higher ratio value which means bimetallic catalyst has higher tolerance to the poisoning species.

## References


1. Li, S. S., Hu, Y. Y., Feng, J. J., Lv, Z. Y., Chen, J. R. and Wang, A. J. (2014). Rapid room-temperature synthesis of Pd nanodendrites on reduced graphene oxide for catalytic oxidation of ethylene glycol and glycerol. *International Journal of Hydrogen Energy*, 39(8): 3730 - 3738.
2. Habibi, E. and Razmi, H. (2012). Glycerol electrooxidation on Pd, Pt and Au nanoparticles supported on carbon ceramic electrode in alkaline media. *International Journal of Hydrogen Energy*, 37(22): 16800 -16809.
3. Su, L., Jia, W., Schempf, A. and Lei, Y. (2009). Palladium/titanium dioxide nanofibers for glycerol electrooxidation in alkaline medium. *Electrochemistry Communications*, 11(11): 2199 - 2202.
4. Kamarudin, M. Z. F., Kamarudin. S. K., Masdar. M. S. and Daud, W. R. W. (2013). Review: Direct ethanol fuel cells. *International Journal of Hydrogen Energy*, 38(22): 9438 - 9453.
5. Bagheri, S., Julkapli, N. M. and Yehye, W. (2015). Catalytic conversion of biodiesel derived raw glycerol to value added products. *Renewable and Sustainable Energy Reviews*, 41: 113 - 127.
6. Dector, A., Cuevas-Muñiz, F. M., Guerra-Balcázar, M., Godínez, L. A., Ledesma-García, J. and Arriaga, L. G. (2013). Glycerol oxidation in a microfluidic fuel cell using Pd/C and Pd/MWCNT anodes electrodes. *International Journal of Hydrogen Energy*, 38(28): 12617 - 12622.
7. Lee, S., Kim, H. J., Choi, S. M., Seo, M. H. and Kim, W. B. (2012). The promotional effect of Ni on bimetallic PtNi/C catalysts for glycerol electrooxidation. *Applied Catalysis A: General*, 429-430: 39 - 47.
8. Fernández, P. S., Martins, M. E., and Camara, G. A. (2012). New insights about the electro-oxidation of glycerol on platinum nanoparticles supported on multi-walled carbon nanotubes. *Electrochimica Acta*, 66: 180 - 187.
9. Geraldes, A. N., Da Silva, D. F., e Silva. L. G. D. A., Spinacé, E.V., Neto, A. O., Dos Santos, M. C. (2015). Binary and ternary palladium based electrocatalysts for alkaline direct glycerol fuel cell. *Journal of Power Sources*, 293: 823 - 830.
10. Rezaei, B., Havakeshian E. and Ensafi A. A. (2014). Fabrication of a porous Pd film on nanoporous stainless steel using galvanic replacement as a novel electrocatalyst/electrode design for glycerol oxidation. *Electrochimica Acta*, 136: 89 - 96.
11. Zhang, M., Nie, R., Wang L, Shi, J., Du, W. and Hou, Z. (2014). Selective oxidation of glycerol over carbon nanofibers supported Pt catalysts in a base-free aqueous solution. *Catalysis Communications*, 55: 5 - 9.
12. Maya-Cornejo, J., Arjona, N., Guerra-Balcázar, M., Álvarez-Contreras, L., Ledesma-García, J. and Arriaga, L. G. (2014). Synthesis of Pd-Cu bimetallic electrocatalyst for ethylene glycol and glycerol oxidations in alkaline media. *Procedia Chemistry*, 12: 19 - 26.
13. Li, S. S., Hu, Y. Y., Feng, J. J., Lv, Z. Y., Chen, J. R. and Wang, A. J. (2014). Rapid room-temperature synthesis of Pd nanodendrites on reduced graphene oxide for catalytic oxidation of ethylene glycol and glycerol. *International Journal of Hydrogen Energy*, 39(8): 3730 - 3738.
14. Mougenot, M., Caillard, A., Simoes, M., Baranton, S., Coutanceau, C., and Brault, P. (2011). PdAu/C catalysts prepared by plasma sputtering for the electro-oxidation of glycerol. *Applied Catalysis B: Environmental*, 107(3-4): 372 - 379.
15. Huang, Z., Zhou, H., Li, C., Zeng, F., Fu, C. and Kuang, Y.(2012). Preparation of well-dispersed PdAu bimetallic nanoparticles on reduced graphene oxide sheets with excellent electrochemical activity for ethanol oxidation in alkaline media. *Journal of Material Chemistry A*, 22(5):1781 - 1785.

16. Thi, B., Lam, X., Chiku, M., Higuchi, E. and Inoue, H. (2015). Preparation of PdAg and PdAu nanoparticle-loaded carbon black catalysts and their electrocatalytic activity for the glycerol oxidation reaction in alkaline medium. *Journal of Power Sources*, 297:149 - 157.
17. Feng, Y., Liu, Z., Xu, Y., Wang, P., Wang, W. and Kong, D. (2013). Highly active PdAu alloy catalysts for ethanol electro-oxidation. *Journal of Power Sources*, 232: 99 - 105.
18. Yang, Z., Liu, L., Wang, A., Yuan, J. and Feng, J. (2016). Simple wet-chemical strategy for large-scaled synthesis of snowflake-like PdAu alloy nanostructures as effective electrocatalysts of ethanol and ethylene glycol oxidation. *Internatinal Journal of Hydrogen Energy*, 42(4): 2034 - 2044. =
19. Yan, W., Tang, Z., Wang, L., Wang, Q., Yang, H., and Chen, S.(2016). PdAu alloyed clusters supported by carbon nanosheets as efficient electrocatalysts for oxygen reduction. *International Journal of Hydrogen Energy*, 42(1): 218 - 227.
20. Qin, Y-H., Jia, Y-B., Jiang, Y., Niu, D. F., Zhang, X. S., Zhou, X. G., Niu, L. and Yuan, W. K. (2012). Controllable synthesis of carbon nanofiber supported Pd catalyst for formic acid electrooxidation. *International Journal of Hydrogen Energy*, 37(9): 7373 - 7377.
21. Simões, M., Baranton, S. and Coutanceau, C. (2010). Electro-oxidation of glycerol at Pd based nano-catalysts for an application in alkaline fuel cells for chemicals and energy cogeneration. *Applied Catalysis B: Environmental*, 93(3-4): 354 - 362.
22. Chen, Z., Wang, S., Lian, C., Liu, Y., Wang, D. and Chen, C. (2016). Nano PdAu bimetallic alloy as an effective catalyst for the Buchwald – Hartwig reaction. *Chemistry of Asian Journal*, 11(3): 351 - 355.

*Malaysian Journal of Analytical Sciences, Vol 21 No 3 (2017): 709 - 718*
*DOI: https://doi.org/10.17576/mjas-2017-2103-20*

MALAYSIAN JOURNAL OF ANALYTICAL SCIENCES
*Published by The Malaysian Analytical Sciences Society*
ISSN 1394 - 2506

# THE EFFECTS OF DIFFERENT RATIOS OF SONOCHEMICALLY ASSISTED NICKEL OXIDE AND ZIRCONIUM OXIDE CATALYSTS IN SYNGAS PRODUCTION

## (Kesan-Kesan Pelbagai Nisbah Pemangkin Nikel Oksida dan Zirkonium Oksida dengan Rawatan Sonokimia Terhadap Penghasilan Singas)

Wan Nurdiyana Wan Amarina[1,2], Wong Yee Ching[1,2]*, Taufiq Yap Yun Hin[3,4]

[1]*Faculty of Agro Based Industry*
[2]*Faculty of Bioengineering and Technology*
*Universiti Malaysia Kelantan, Locked Bag No. 100, 17600 Jeli, Kelantan, Malaysia*
[3]*Centre of Excellence for Catalysis Science and Technology*
[4]*Department of Chemistry, Faculty of Science*
*Universiti Putra Malaysia, 43400 UPM Serdang, Selangor, Malaysia*

**Corresponding author: yeeching@umk.edu.my*

Received: 28 November 2016; Accepted: 5 February 2017

**Abstract**

Heterogeneous catalytic cracking is currently one of the most effective ways for both reducing tar content and enhancing hydrogen ($H_2$) content in syngas at relatively low temperature, besides being environmental friendly. Sonochemical treatment has also been shown to lower reaction times with enhanced reaction rate and enables production of particles with high surface area. Two different types of metal oxides, which are Nickel Oxide (NiO) and Zirconium Oxide ($ZrO_2$) at combinations of 1:1, 1:2 and 2:1 ratios with Zeolite NaY as the supporter were synthesized via sonochemical treatment. The catalysts were then characterized using X-Ray Diffraction (XRD), Temperature Programmed Reduction in $H_2$/Argon (TPR-$H_2$), Brunauer-Emmett-Teller surface measurement (BET), Scanning Electron Microscopy (SEM) and Transmission Electron Microscopy (TEM). From SEM and TEM analysis, nickel tends to agglomerate and form globular shapes, zirconium forms coral-like branching structure and Zeolite NaY forms stacks of cubic clumps. The most promising NiO to $ZrO_2$ ratio for syngas production is 1:1 because it removes the most reactive oxygen during hydrogen reduction at 0.83 $x10^{21}$ atoms/g, has small crystallite size at 56.90 nm and has the highest surface area for maximum contact with the reactants at 506.52 $m^2$/g. Generally, sonochemical treatment also reduces the catalysts crystallite size (54.83 nm) and increases the catalysts surface area (506.52 $m^2$/g) and oxygen removal (0.83 $x10^{21}$ atoms/g) as well as lowers the reduction temperature (637 K) which is favourable in term of production cost.

**Keywords**: heterogeneous catalysts, nickel oxide, zirconium oxide, zeolite, syngas

**Abstrak**

Perekahan pemangkin heterogen adalah salah satu cara terkini yang paling efektif untuk mengurangkan kandungan tar dan juga meningkatkan kandungan hidrogen ($H_2$) di dalam singas pada suhu rendah, di samping mesra alam sekitar. Rawatan sonokimia juga telah dibuktikan dapat mengurangkan masa tindak balas di samping meningkatkan kadar tindak balas dan membolehkan penghasilan partikel dengan luas permukaan yang tinggi. Dua jenis besi oksida berbeza, iaitu Nikel Oksida (NiO) dan Zirkonium Oksida ($ZrO_2$) dalam kombinasi nisbah 1:1, 1:2 dan 2:1 dan Zeolit NaY sebagai penyokong dihasilkan melalui rawatan sonokimia. Katalis – katalis tersebut kemudian dianalis menggunakan pembelauan sinar-X (XRD), Penurunan Suhu Berprogram (TPR-$H_2$), pengukuran permukaan Brunauer-Emmett-Teller (BET), Mikroskop Imbasan Elekron (SEM) dan Mikroskop Elektron Transmisi (TEM). Daripada analisis SEM dan TEM, nikel cenderung untuk bergumpal dan membentuk glob besar, zirkonium membentuk struktur seperti karang bercabang dan Zeolit NaY membentuk lapisan kubik. Nisbah NiO kepada $ZrO_2$ yang paling

berpotensi adalah 1:1 kerana ia menyingkirkan banyak oksigen yang reaktif semasa reduksi hidrogen pada kadar 0.83 $x10^{21}$ atom/g, mempunyai saiz kristal yang kecil iaitu 56.90 nm dan mempunyai luas permukaan yang paling tinggi pada 506.52 $m^2/g$ untuk kontak maksimum dengan bahan tindak balas. Umumnya rawatan sonokimia juga mengurangkan saiz kristal katalis (54.83 nm) dan meningkatkan luas permukaan pemangkin (506.52 $m^2/g$) dan juga penyingkiran oksigen (0.83 $x10^{21}$ atom/g) di samping mengurangkan suhu penurunan (637K) di mana ia adalah baik untuk penjimatan kos pengeluaran.

**Kata kunci:** pemangkin heterogen, nikel oksida, zirkonium oksida, zeolit, singas

## Introduction

The depletion of world petroleum reserves and increased environmental concerns has stimulated the search for the alternative renewable fuels that are capable of fulfilling an increasing energy demand. The biomass fuels represent an abundantly available and renewable energy resource with $CO_2$ neutral impact. It is the only sustainable source of energy and organic carbon for industrial society [1]. Among different processes for their utilization, the biomass gasification is one of the best options in order to optimize the conversion of the chemical energy of the fuel. Instead of using edible biomass (sugars, starches, and vegetable oils) for large scale production of fuels, the development of nonedible biomass (lignocellulosic biomass) permits sustainable and cheaper production of fuels and chemicals without affecting food supplies [1]. Biomass gasification is one of the most promising options for converting lignocellulosic biomass to synthesis gas (syngas), a mixture of CO and $H_2$, which can be used either as a fuel to produce heat and power or as an intermediate in the production of liquid fuels (e.g. diesel fuel, dimethyl ether) and chemicals (e.g. methanol).

Tar is a complex mixture of condensable organic compounds, which includes single ring to 5-ring aromatic compounds along with other oxygen-containing hydrocarbons and complex polycyclic aromatic hydrocarbons (PAHs), which can foul the equipment and cover the surface of catalysts to slow or stop the reaction [2]. Tars present a number of process challenges, including coking of catalysts and condensation on downstream piping, filters, and other equipment. The tar removal cost is as expensive as the overall process to produce syngas [3]. Tars cause severe operational problems associated with their condensation and polymerization. Tar removal is a critical issue in the development of biomass gasification, especially in the Fischer–Tropsch (F–T) synthesis where those impurities can lower the F-T activity in the bio-syngas catalytic conversion [2]. Moreover, a high $H_2$/CO ratio in the gas stream is desirable for F-T synthesis.

Catalytic cracking/reforming is currently one of the most effective ways for both reducing tar content and enhancing $H_2$ content in syngas at relatively low temperature. Recently, conventional homogeneous base catalysts are expected to be replaced in the near future by environmentally friendly heterogeneous base catalysts mainly because of environmental constraints and simplifications in the existing processes. Heterogeneous catalytic is considered as a technology with the highest potential to contribute to the solution of tar decomposition. In addition, the use of a catalyst can enhance the gas yield and promote the reforming reactions of residual hydrocarbons. In heterogeneous reaction, the interaction of methane with metals results in $H_2$ evolution where at temperature above 400K, dehydrogenation of $CH_x$ species becomes fast and the elemental carbon is more stable forming stronger bonds with the metal surface [4].

Several catalytic materials have been studied as additives in fluidized-bed reactor in order to achieve in situ catalytic conditioning of the product gas inside the gasifier reactor. Many works on in-bed catalysts consider dolomite [2,5,6], olivine [3,6], nickel [2,3,5-8] and noble metal (NM) based catalysts [4]. A tar conversion rate of 99% has been achieved by using dolomite and Ni-based catalysts [2]. The catalytic performance of dolomite in tar cracking is directly proportional to the number of surface base sites [3].

Although NMs, such as Ru, Rh, Pd, Pt, and Ir, have been studied extensively for dry reforming reaction, their high cost and limited availability limits their industrial applications [9]. Nickel-based catalyst has been considered as the most suitable due to its fast turnover rates, long-term stability and lower cost [4]. However, the major challenge in many processes involving Ni-based catalyst is deactivation by carbon deposition [2]. Therefore, an effective catalyst that minimizes coke deposition should be developed. Zirconium has been tested as a base catalyst to reform gas containing tarry impurities. Zirconium catalyst works efficiently in decomposing tars, especially heavier

hydrocarbons. In several tests done by Simell and Kurkela [10], zirconium catalysts provided a tar conversion of 60 to 80% at a temperature of about $600^0$C. Zirconium has also been used as support for Ni-based catalyst for syngas production by dry reforming reaction, which enables direct conversion of natural gas into liquid fuels at remote extraction sites [4].

Metal oxides are constituents of the Earth crust and have been catalyzing different important reactions in chemical evolution. They are good adsorbents and efficient catalysts [11]. They consist of dispersed surface metal oxide species and catalytic active sites supported on high surface area oxides [12]. Mixed metal oxide catalysts are used in heterogeneous catalysis for chemical processes and being further developed for their catalytic performance and durability [13]. Supported metal oxide catalysts have been extensively investigated since 1950s. According to Lee and Wachs [14], the surface metal oxide species of supported metal oxide catalysts control the overall catalytic performance such as activity and selectivity. Zirconium oxide ($ZrO_2$) has high thermal stability as a catalyst support. It is proved to be a very good promoter for cobalt catalyst where it enhanced CO conversion rate and C5+ selectivity [2]. A study comparing $Ni/CeO_2$, $Ni/ZrO_2$, and $Ni/CeO_2$-$ZrO_2$ mixed oxide catalysts for methane partial oxidation at 700 °C showed higher activity and coke resistance on the composite supports as compared to the individual metal oxides [6]. Another study using combination of Ni-Ce-$ZrO_2$ catalyst showed high conversions of reactants (97%) and provide high resistance to catalyst deactivation, but still requires a high temperature [4].

Catalytic performances are expected to be improved by the optimization of the catalytic filter system and the use of more active in-bed catalysts. In this study, the catalysts used are two different types of metal oxides, which are Nickel Oxide (NiO) and Zirconium Oxide ($ZrO_2$) with Zeolite supporter. Zeolites have been added to the conventional F-T system in many studies. They have a shape-selective property that restrains the formation of products that are larger than the size of the zeolite channels and result in lighter hydrocarbons. Zeolites acid site can help with cracking, isomerization and aromatization reactions for F-T products [2]. They are also widely used in heterogeneous catalysis because of their well-defined pore structures and capabilities of extremely high surface area and surface acidity [6].

The catalysts used for this study were synthesized via sonochemical treatment. Sonochemically assisted reactions showed lower reaction times with enhanced reaction rate. It enables production of small and high uniform particles sizes with high surface area, metal dispersion and defects that have been shown to play a crucial role in catalysis [15-20]. The utilization of sonochemical treatment in the synthesis of the catalysts was proven to show significant increase in the catalytic activity, stability and selectivity of catalysts [20].

## Materials and Methods

### Preparation of mixed nickel oxide and zirconium oxide catalysts

Mixture of NiO and $ZrO_2$ catalysts was synthesized by conventional impregnation /co-precipitation method by mixing NiO (from Hmbg) and $ZrO_2$ (from Acros Organics) at three different NiO to $ZrO_2$ ratios of 1:1, 1:2 and 2:1 in 100 mL distilled water. The solutions were then sonicated separately for 30 minutes with 2 cm diameter Ti-horn, 20 kHz, 500W probe. The temperature was kept constant at 80 °C. The samples were then cooled to room temperature. The resultant solid (mixture of NiO and $ZrO_2$) was then recovered using centrifuge for 5 minutes at 2000 rpm [21]. It was then subsequently washed with distilled water followed by washing with acetone to remove the by-products [22] before oven dried overnight at 105 °C for 12 hours according to Tao et al. [23].

### Preparation of Zeolite NaY supporter

The supporter used was Zeolite Y sodium (Zeolite NaY), procured from Alfa Aesar. Table 1 showed its mole ratio and surface area.

Zeolite NaY was first treated with sonochemical treatment and the resultant solid was recovered using centrifuge before oven dried overnight at 105 °C. The synthesized mixture of NiO and $ZrO_2$ were then added with Zeolite at a loading of 10g equally, in 100 mL distilled water. The mixture was then stirred on a hot plate with a magnetic stirrer for one hour. The solid was again recovered using centrifuge technique and subsequently washed with distilled water followed with acetone then oven dried overnight at 105 °C for 12 hours [23]. The catalysts mixtures were then calcined in air at 500 °C for 4 hours, yielding a homogeneous catalyst powder, according to Klimova et al. [24]

and Maciel et al. [25]. Calcining the synthesized catalysts powders also removes structure directing agents and other organic substances present in them [26].

Table 1. Mole ratio and surface area of Zeolite NaY

| Zeolite NaY Characterization | $SiO_2$ | $Al_2O_3$ |
|---|---|---|
| Mole ratio | 5.1 | 1 |
| Surface area ($m^2/g$) | 900 | 900 |

**Catalyst characterization**

The catalysts were then characterized through a series of analysis as follows. X-ray diffraction (XRD) analysis was carried out using Shimadzu diffractometer model XRD 6000 at range 2Θ from 5° to 80° in continuous scanning at 2° per minute and sampling pitch of 0.02°. Hydrogen temperature programmed reduction analysis ($H_2$-TPR) was performed using Thermo Fisher Scientific TPDRO 1100 apparatus that was equipped with a thermal conductivity detector (TCD). The total surface areas of the catalysts were then measured using Thermo Electron Sorptomatic 1990 and Quantachrome AS1Win$^{TM}$ Automated Gas Sorption Data Acquisition and Reduction utilizing Brunauer-Emmett-Teller (BET) method. The catalyst samples were degassed at 300 °C for 12 hours. Electron microscopy technique was used to obtain the information on the morphology and size of the catalyst samples by using LEO 1455 Variable Pressure scanning electron microscope (SEM). The particle sizes of the samples were examined using Hitachi H-7100 energy filter transmission electron microscope (TEM).

## Results and Discussion

**X-Ray diffraction analysis**

X'Pert HighScore software from PANalytical B. V. was used to analyze the XRD data. From the XRD data of all samples, the presence of NiO phase appeared consistently at $2\Theta$ = 37.3°, 43.4°, 62.8° and 75.4° (JCPDS File No. 00-022-1189) but the peak intensities are very low. This might be due to high metal dispersion of NiO on the surface of Zeolite NaY due to the effect of sonochemical treatment in improving particles size distribution The presence of $ZrO_2$ phase appeared at multiple degrees = 24°, 24.3°, 28.4°, 31.7°, 34.4°, 35.6°, 40.9°, 49.4°, 50.3°, 50.8°, 54.2°, 55.5°, 58.6° and 62.2° (JCPDS File No. 00-013-0307). While Zeolite NaY showed multiple peaks at 2Θ = 6.4°, 10.5°, 12.2°, 15.9°, 19.0°, 20.6°, 23.0°, 24.0°, 27.3°, 29.9°, 31.1°, 31.7°, 34.4°, 40.9°, 49.4° and 54.2° (JCPDS File No. 00-038-0239). Some of the peaks of $ZrO_2$ and Zeolite NaY seem to overlap with each other and it is quite difficult to distinguish the peaks between the two.

Based from the peak intensities shown in Figure 1, the sonochemically treated catalysts with NiO: $ZrO_2$ ratio of 1:1 shows the lowest peak intensities followed by catalysts ratio 2:1 and 1:2. It seems that equal amount of NiO and $ZrO_2$ contributes to higher dispersion of metal oxides on Zeolite's surface compared to the unequal amounts of NiO and $ZrO_2$. Catalysts ratio 1:2 shows the highest peak intensities where $ZrO_2$ is double the amount of NiO. Since the peaks of $ZrO_2$ are more prominent than NiO, it can be said that $ZrO_2$ is not as well dispersed as NiO on the surface of Zeolite NaY supporter.

Zeolite NaY generally has the highest crystallinity and more defined structures compared to NiO and $ZrO_2$. It is identified to possess cubic crystal system. Its particle size is also the largest compared to NiO and $ZrO_2$ (average of 201 to 493 nm). The size of crystallite can be estimated from the XRD data as shown in Table 2, using Scherrer equation in equation 1 [27],

$$L = K\lambda/\beta.\cos\Theta \quad (1)$$

where L = average crystallite size, K = constant which is normally taken as 0.9, λ = X-ray wavelength, β = peak width of the diffraction profile at half maximum height and Θ can be either in degrees or radians.

Based from Table 2, catalyst ratio 2:1 showed the smallest crystallite size average of 54.83 nm compared to other catalysts with different ratios. This is to be expected since the TEM analysis images also show that Ni has the smallest particle size (average of 6 to 12 nm) and that the high amount of NiO means it is well dispersed on the surface of the catalyst, thus contributing to smaller crystallite size. However, the crystallite size of catalyst 2:1 is not significantly different than catalyst ratio 1:1. While catalyst ratio 1:2 shows the biggest crystallite size due to higher amount of $ZrO_2$.

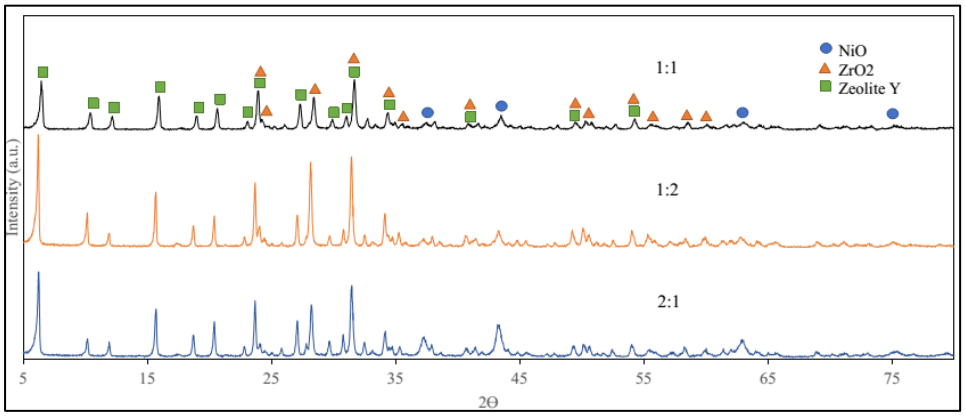



Figure 1. XRD patterns of NiO:$ZrO_2$ catalysts ratio of 1:1, 1:2 and 2:1 treated with sonochemical treatment for 30 minutes

Table 2. Crystallite size average from XRD data (nm)

| **Catalyst** | **Crystallite Size Average (nm)** |
|---|---|
| 1:1 | 56.90 |
| 1:2 | 62.51 |
| 2:1 | 54.83 |

**Temperature programmed reduction (TPR in $H_2$/Ar)**
All catalyst samples produced a single reduction peak at temperature ranging from 637 K to 657 K as shown in Figure 2 and Table 3.

As can be seen in Table 3, catalyst ratio 1:1 removed the highest amount of oxygen at 0.83 $x10^{21}$ atoms/g followed by catalysts ratio 2:1 and 1:2. From the data, it is shown that catalyst ratio 1:1 is the most efficient reactive oxygen removal while catalyst ratio 1:2 is the least efficient with reactive oxygen removal at 0.48 $x10^{21}$ atoms/g. This is also in agreement with the XRD data discussed earlier where catalyst ratio 1:1 with equal distribution of NiO and $ZrO_2$ is well dispersed with small crystallite size. However, catalyst ratio 1:2 and 2:1 have lower $T_{max}$ at 637K and 653K respectively compared to catalyst ratio 1:1 at 657K. Despite the 20K $T_{max}$ difference between catalysts ratio 1:1 and 1:2, catalyst ratio 1:1 has almost double the amount of reactive oxygen removed compared to catalyst ratio 1:2.

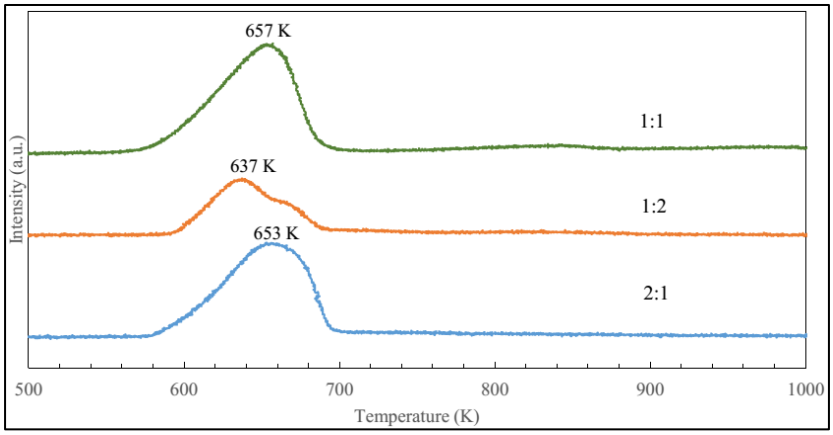


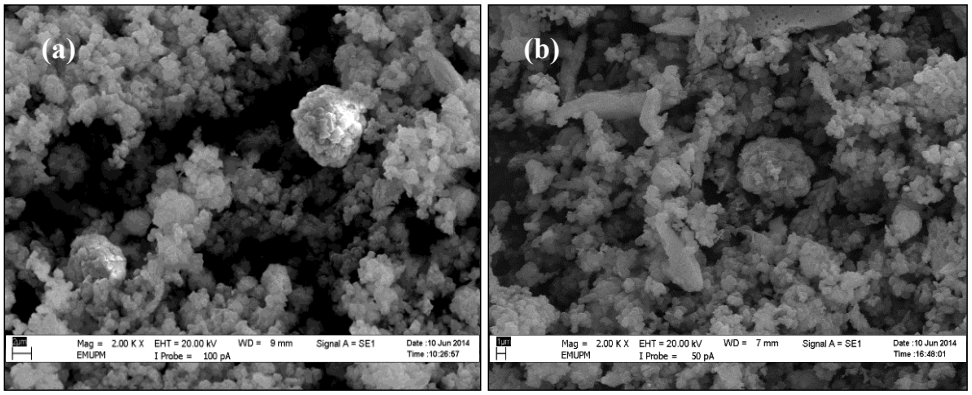

Figure 2. Temperature programmed reduction profiles for NiO: $ZrO_2$ ratio 1:1, 1:2 and 2:1

Table 3. Total amount of oxygen removed from the catalysts by reduction in $H_2$/Ar

| Catalyst | $T_{max}$ (K) | $H_2$ gas adsorbed ($x10^{-3}$ mol/g) | Total $O_2$ removed ($x10^{21}$ atoms/g) |
|---|---|---|---|
| 1:1 | 657 | 1.37 | 0.83 |
| 1:2 | 637 | 0.79 | 0.48 |
| 2:1 | 653 | 1.21 | 0.73 |

**Scanning electron microscope**

In all samples, NiO tends to agglomerate into large globular shape while Zeolite NaY forms stacks of cubic shaped clumps and mostly spread out trough out the entire sample. Generally $ZrO_2$ forms the smallest structures among the other two catalysts. It was seen to be in cylindrical form in coral-like branching structure distributed throughout the sample. Figure 3 shows large globular clumps of NiO surrounded by Zeolite NaY and some smaller coral-like $ZrO_2$ clumps can be seen around it.



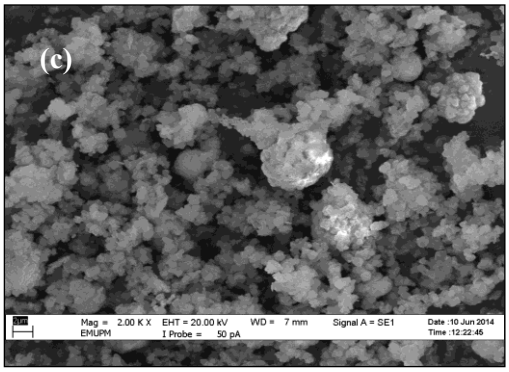
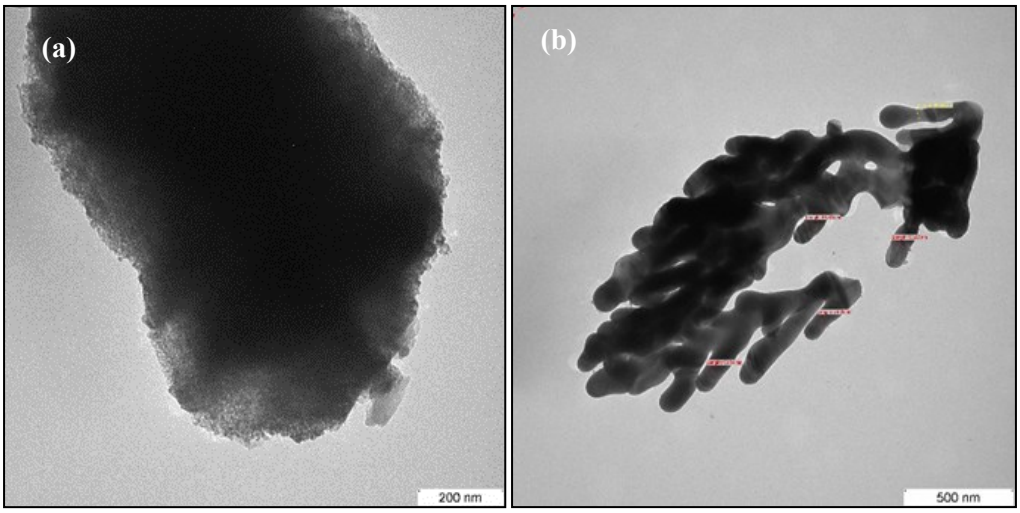



Figure 3. SEM micrograph of sample (a) 1:1, (b) 1:2, and (c) 2:1 at magnification 2000x

Catalyst ratio 1:1 shows NiO agglomerated globular clumps with $ZrO_2$ smaller structures are equally distributed on the surface of Zeolite NaY while catalyst ratio 1:2 shows more and bigger structures of $ZrO_2$ on the surface of the catalyst. Globular clumps of NiO are more apparent in catalyst ratio 2:1, as can be seen in Figure 3.

**Transmission electron microscope**

Figure 4 shows agglomerated NiO particles with sizes ranging from 6 to 12 nm in catalyst ratio 1:1. From the same sample, $ZrO_2$ forms coral-like branching structures with diameters ranging from 74 to 94 nm while crystal-like Zeolite NaY stacks up on each other with diameters ranging from 201 to 493 nm. TEM images shows that $ZrO_2$ average particle size is larger than NiO and this is in agreement with XRD results where catalysts ratio 1:2 also has the highest peak intensities where $ZrO_2$ is double the amount of NiO. Since the peaks of $ZrO_2$ are more prominent than NiO, it can be said that $ZrO_2$ is not as well dispersed as NiO on the surface of Zeolite NaY supporter due to its larger particle size and its branching structures.



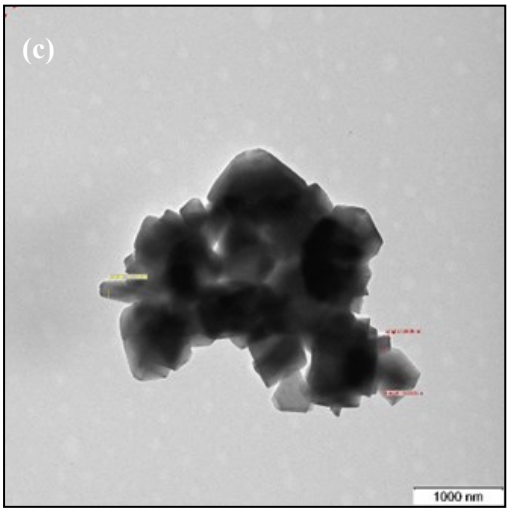



Figure 4. TEM micrograph of catalyst ratio 1:1 of (a) NiO at magnification 100 000x, (b) $ZrO_2$ at magnification 50 000x, and (c) Zeolite at magnification 20 000x

**BET surface area measurement**

Based from Table 4, catalyst with the highest surface area is catalyst ratio 1:1 with surface area of 506.52 $m^2/g$ and the lowest surface area is catalyst ratio 1:2 with surface area of 399.88 $m^2/g$. This is in agreement with the XRD and TPR-$H_2$ data where catalyst ratio 1:1 has well dispersed metal oxides with average crystallite size of 56.90 nm and the highest reactive oxygen removal at 0.83 $x10^{21}$ atoms/g compared to catalysts ratio 1:2 and 2:1.
While catalyst ratio 1:2, with its higher amount of $ZrO_2$ on the surface of Zeolite NaY has reduced the surface area of the catalyst (399.88 $m^2/g$) as well as reduced contact with the active sites thus contributing to low removal of reactive oxygen as presented in previous TPR-$H_2$ section discussion.

The presence of Zeolite NaY supporter and $ZrO_2$ in catalysts was reported by Derekaya and Yasar [28] to give higher surface area compared to the catalysts without their presence. Zeolite NaY also has high surface area (900 $m^2/g$) and well dispersed pore structure. $ZrO_2$ was also implied to act as a surface area agent. However, higher ratio of $ZrO_2$ to NiO is proven to significantly reduce the surface area of the catalysts.

There is also a huge discrepancy between pure Zeolite NaY surface area (900 $m^2/g$) and treated Zeolite NaY surface area. The drying and calcination of catalyst could also possibly affect the total surface area. This also means that both NiO and $ZrO_2$ loading on Zeolite NaY significantly reduced the surface area of Zeolite NaY. This might be due to the effects of sonication treatment which caused the agglomeration of active metal Ni on the surface of Zeolite NaY where it could lead to blockage of pores and reduces the overall surface area of Zeolite NaY [17].

Table 4. Specific BET surface area of NiO: $ZrO_2$ catalysts

| Catalyst | Surface Area ($m^2/g$) |
|---|---|
| 1:1 | 506.52 |
| 1:2 | 399.88 |
| 2:1 | 436.37 |

A summary of comparisons between catalysts ratio 1:1, 1:2 and 2:1 is shown in Table 5.

Table 5. Comparisons of properties between catalysts with different ratio

| Catalyst | Average Crystallite Size (nm) | $T_{max}$ (K) | $H_2$ Gas Adsorbed ($x10^{-3}$ mol/g) | Total $O_2$ Removed ($x10^{21}$ atoms/g) | Surface area ($m^2/g$) |
|---|---|---|---|---|---|
| 1:1 | 56.90 | 657 | 1.37 | 0.83 | 506.52 |
| 1:2 | 62.51 | 637 | 0.79 | 0.48 | 399.88 |
| 2:1 | 54.83 | 653 | 1.21 | 0.73 | 436.37 |

## Conclusion

The catalysts studied, which are NiO and $ZrO_2$ with Zeolite NaY as supporter will help in the study of catalytic cracking/ reforming mechanisms in good quality and cleaner syngas production. However the results are not conclusive yet since syngas evaluation using Temperature Programmed Gasification (TPG) has not been done yet. The results from TPG analysis will determine the performance of the catalysts and will relate with the catalysts characterization data. For now, it can be said that the most promising NiO to $ZrO_2$ catalyst ratio is ratio 1:1 because of the well dispersion of mixed metal oxides on the catalyst surface with small average crystallite size of 56.90 nm, removal of reactive oxygen at the highest rate at 0.83 $x10^{21}$ atoms/g as well as possessing the highest surface area at 506.52 $m^2/g$. Equal distribution of mixed metal oxides on the surface of Zeolite NaY supporter produces favourable characteristics for the production of quality syngas. Higher amount of $ZrO_2$ however causes blockage of the pores, thus reduces the catalyst surface area because of its tendencies to agglomerate and form large branching structures, which produces catalyst of poorer profile compared to catalysts ratio 1:1 and 2:1. From SEM and TEM analysis, NiO tends to agglomerate and form sizable globular shapes, $ZrO_2$ forms coral-like branching structure and Zeolite NaY forms stacks of cubic clumps. From the catalysts characterization data and analysis obtained, catalysts with NiO: $ZrO_2$ ratio of 1:1 seems to be a promising catalyst for producing rich syngas with higher catalytic activity and reaction.

## Acknowledgement

This work was supported by Research Grant R/FRAGS/A07.00/00457A/003/2014/000180 from the Ministry of Higher Education, Malaysia.

## References

1. Serrano-Ruiz, J. C., West, R. M. and Dumesic, J. A. (2010). Catalytic conversion of renewable biomass resources to fuels and chemicals. *Annual Review of Chemical and Biological Engineering*, 1: 79 - 100.
2. Hu, J., Yu, F. and Lu, Y. (2012). Application of Fischer–Tropsch synthesis in biomass to liquid conversion. *Catalysis,* 2(2): 303 – 326.
3. Rownaghi, A. A. and Huhnke, R. L. (2013). Producing hydrogen-rich gases by steam reforming of syngas tar over CaO/MgO/NiO catalysts. *American Chemical Society Sustainable Chemistry & Engineering,* 1: 80 – 86.
4. Havran, V., Dudukovi, M. P. and Lo, C. S. (2011). Conversion of methane and carbon dioxide to higher value products. *Industrial & Engineering Chemistry Research,* 50: 7089 – 7100.
5. Mohammed, M. A. A., Salmiaton, A., Wan Azlina, W. A. K. G., Mohamad Amran, M. S., Omar, R., Taufiq-Yap, Y. H. and Ahmadun, F. R. (2012). Catalytic gasification of empty fruit bunch for enhanced production of hydrogen rich fuel gas. *Pertanika Journal of Science & Technology,* 20(1): 139 – 149.
6. Yung, M. M., Jablonski, W. S. and Magrini-Bair, K. A. (2009). Review of catalytic conditioning of biomass-derived syngas. *Energy & Fuels,* 23: 1874 – 1887.
7. Deghedi, L., Basset, J. -M., Candy, J. -P., Dalmon, J. -A., Dubreuil, A-C. and Fischer, L. (2009). Nanosized bimetallic Ni-Sn and Ni-Zr catalysts prepared by SOMC/M route: Characterization and catalytic properties in styrene selective hydrogenation. *Chemical Engineering Transaction,* 17: 31 – 36.

8. Nakayama, O., Ikenaga, N., Miyake, T., Yagasaki, E. and Suzuki, T. (2010). Production of synthesis gas from methane using lattice oxygen of NiO-$Cr_2O_3$-MgO complex oxide. *Industrial & Engineering Chemistry Research,* 49: 526 – 534.
9. Moon, D. J. (2008). Hydrogen production by catalytic reforming of gaseous hydrocarbons (methane & LPG). *Catalysis Surveys from Asia,* 12(3): 188 – 202.
10. Simell, P. and Kurkela, E. (2007). International Publication No. WO 2007/116121 A1. Helsinki, Finland: World Intellectual Property Organization (WIPO).
11. Kamaluddin. (2013). Role of metal oxides in chemical evolution. In S. K. Chakrabarti, K. Acharyya, & A. Das (Eds.), *AIP Conference Proceedings*, 1543 (1): 90 – 98.
12. Wachs, I. E. and Kim, T. (2009). Oxidation reactions over supported metal oxide catalysts: Molecular/ electronic structure-activity/selectivity relationships. In Jackson, S. D. and Hargreaves, Justin S. J. (Eds). Metal oxide catalysis. WILEY-VCH Verlag GmbH & Co. KGaA. Weinheim, Germany: pp. 487 – 488.
13. Lee, D. W. and Yoo, B. R. (2014). Advance metal oxide (supoorted) catalysts: Synthesis and applications. *Journal of Industrial and Engineering Chemistry,* 20(6): 3947 – 3959.
14. Lee, E. L. and Wachs, I. E. (2009). Use of oxide ligands in designing catalytic active sites. In Ozkan, U. S. (Ed). Design of heterogeneous catalysts: new approaches based on synthesis, characterization and modeling. WILEY-VCH Verlag GmbH & Co. KGaA. Weinheim, Germany.
15. Gole, V. L. and Gogate, P. R. (2012). A review on intensification of synthesis of biodiesel from sustainable feed stock using sonochemical reactors. *Chemical Engineering and Processing,* 53: 1 – 9.
16. Saminda, D., King'ondu, C. K., Pedrick, W., Lakshitha, P. and Suib, S. L. (2012). Direct sonochemical synthesis of manganese octahedral molecular sieve (OMS-2) nanomaterials using cosolvent systems, their characterization, and catalytic applications. *Chemistry of Materials,* 24(4): 705 – 712.
17. Sharifi, M., Haghighi, M. and Abdollahifar, M. (2015). Sono-dispersion of bimetallic Ni-Co over Zeolite Y used in conversion of greenhouse gases $CH_4$/$CO_2$ to high valued syngas. *Journal of Natural Gas Science and Engineering,* 23: 547 – 558.
18. Zhong, Y. L. and Bernasek, S. L. (2011). Mild and efficient functionalization of hydrogen-terminated Si(III) via sonochemical activated hydrosilylation. *Journal of the American Chemical Society,* 133: 8118 – 8121.
19. Chavan, V. P. and Gogate, P. R. (2011). Intensification of synthesis of cumene hydroperoxide using sonochemical reactors. *Industrial & Engineering Chemistry Research.* 50(22): 12433 – 12438.
20. Zhang, X., Jiang, W., Gong, X. and Zhang, Z. (2010). Sonochemical synthesis and characterization of magnetic separable of $Fe_3O_4$/Ag composites and its catalytic properties. *Journal of Alloys and Compounds,* 508(2): 400 – 405.
21. Taufiq-Yap, Y. H., Joshua Hoh, J. R. and Wong, Y. C. (2011). Synthesis of nanostructured vanadium phosphate catalysts using sonochemical route for partial oxidation of n-butane. *Journal of Applied Sciences,* 11(13): 2370 – 2375.
22. Meybodi, S. M., Hosseini, S. A., Rezaee, M., Sadrnezhaad, S. K. and Mohammadyani, D. (2012). Synthesis of wide band gap nanocrystalline NiO powder via a sonochemical method. *Ultrasonics Sonochemistry,* 19: 841 – 845.
23. Tao, J., Zhao, L., Dong, C., Lu, Q., Du, X. and Dahlquist, E. (2013). Catalytic steam reforming of toluene as a model compound of biomass gasification tar using Ni-$CeO_2$/SBA-15 catalysts. *Energies,* 6: 3284 – 3296.
24. Klimova, T., Pena, L., Lizama, L., Salcedo, C. and Gutierrez, Y. (2009). Modification of activity and selectivity of NiMo/SBa-15 HDS catalysts by grafting of different metal oxides on the support surface. *Industrial & Engineering Chemistry Research,* 48: 1126 – 1133.
25. Maciel, C. G., Silva, T. D., Assaf, E. M. and Assaf, J. M. (2013). Hydrogen production and purification from the water-gas shift reaction on CuO/$CeO_2$-$TiO_2$ Catalysts. *Applied Energy,* 112: 52 – 59.
26. Pal, P., Das, J. K., Das, N. and Bandyopadhyay, S. (2013). Synthesis of NaP Zeolite at room temperature and short crystallization time by sonochemical method. *Ultrasonics Sonochemistry,* 20: 314 – 321.
27. Monshi, A., Foroughi, M. R. and Monshi, M. R. (2012). Modified Scherrer equation to estimate more accurately nano-crystallite size using XRD. *World Journal of Nano Science and Engineering,* 2: 154 – 160.
28. Derekaya, F. B. and Yasar, G. (2011). The CO methanation over NaY-Zeolite supported Ni/$Co_3O_4$, Ni/$ZrO_2$, $Co_3O_4$/$ZrO_2$ and Ni/$Co_3O_4$/$ZrO_2$ catalysts. *Catalysis Communications,* 13: 73 – 77.

*Malaysian Journal of Analytical Sciences, Vol 21 No 3 (2017): 719 - 725*
*DOI: https://doi.org/10.17576/mjas-2017-2103-21*

MALAYSIAN JOURNAL OF ANALYTICAL SCIENCES
*Published by The Malaysian Analytical Sciences Society*
ISSN 1394 - 2506

# PRELIMINARY STUDY OF SULFUR DIOXIDE REMOVAL USING CALCINED EGG SHELL

## (Kajian Awal Penyingkiran Sulfur Dioksida Menggunakan Kulit Telur yang Dikalsinkan)

Sumathi Sethupathi[1]*, Yap Chen Kai[1], Leong Loong Kong[2], Yamuna Munusamy[1], Mohamed Jaber Khalil Bashir[1], Nurshasabila Iberahim[1]

*[1]Faculty of Engineering and Green Technology,*
*Universiti Tunku Abdul Rahman, 31900 Kampar, Perak, Malaysia*
*[2]LKC Faculty of Engineering and Science,*
*Universiti Tunku Abdul Rahman, 43000 Kajang, Selangor, Malaysia*

**Corresponding author: sumathi@utar.edu.my*

Received: 28 November 2016; Accepted: 5 February 2017

**Abstract**

The combustion of coal for energy had created severe environmental issues mainly due to the release of particulate matter and flue gases containing sulphur dioxide ($SO_2$) during the processing. At present limestone based adsorbent is used to desulphurize flue gas. Egg shell is a type of food waste and it contains high amount of calcium carbonate which is similar to limestone. In this study, the potential of egg shell as a substitute material to replace commercial limestone based calcium oxide was investigated. Waste egg shell and commercial calcium carbonate (limestone)(CCC) were calcined at various temperatures (750 – 950 ºC) and holding time (2 and 4 hours). The calcined samples were tested for $SO_2$ adsorption using a gas reactor at room temperature with a flow rate of 300 mL/min. The initial concentration of $SO_2$ is 200 ppm. Characterization of the adsorbents will be done using Fourier Transform Infrared (FTIR), Brunauer-Emmett-Teller (BET) and X-ray Diffraction (XRD) to understand the sorption behavior. Calcined egg shell and calcined CCC takes about 110 min and 180 min for saturation. It is noted that calcined egg shell could remove $SO_2$ alike calcined CCC. However, the adsorption capacity of egg shell is lower compared to CCC and this could be due to impurities.

**Keywords**: sulphur dioxide, adsorption, egg shell, calcium carbonate

**Abstrak**

Pembakaran arang batu untuk sumber tenaga telah mewujudkan isu-isu alam sekitar yang teruk disebabkan oleh pembebasan habuk tertentu dan gas serombong yang mengandungi sulfur dioksida ($SO_2$) semasa pemprosesan. Pada masa ini, batu kapur berasaskan serapan digunakan untuk menyingkirkan gas serombong. Kulit telur adalah sejenis sisa makanan dan ia mengandungi jumlah kalsium karbonat yang tinggi dan sama seperti batu kapur. Dalam kajian ini, potensi kulit telur sebagai bahan pengganti untuk menggantikan kalsium oksida daripada batu kapur komersial telah dikaji. Sisa kulit telur dan kalsium karbonat komersial (batu kapur) (CCC) telah dibakar pada pelbagai suhu (750 – 950 ºC) dan masa induk (2 and 4 jam). Sampel yang telah dibakar kemudian diuji untuk penyerapan $SO_2$ menggunakan reaktor gas pada suhu bilik dengan kadar aliran 300 mL/min. Kepekatan awal $SO_2$ adalah 200 ppm. Pencirian serapan dilakukan dengan menggunakan Infra merah Transformasi Fourier (FTIR), Brunauer-Emmett-Teller (BET) dan pembelauan Sinar-X (XRD) untuk memahami keadaan penyerapan itu. Kalsin kulit telur and kalsin CCC masing-masing memerlukan tempoh selama 110 min and 180 min untuk mencapai ketepuan. Ternyata bahawa kalsin kulit telur boleh menyingkirkan $SO_2$ seperti kalsin CCC. Walau bagaimanapun, kapasiti penyerapan kalsin kulit telur lebih rendah berbanding dengan kalsin CCC yang mungkin disebabkan oleh berhadas.

**Kata kunci:** sulfur dioksida, penyerapan, kulit telur, kalsium karbonat

## Introduction

Combustion of the sulphur containing fuel, such as coal and oil, results in the formation of sulphur dioxide ($SO_2$). Flue gas from coal processing is one of the major contributors of $SO_2$ to the environment. It has been reported that a typical coal-fired plant generates about 10,000 tons of $SO_2$ [1]. The releasing of $SO_2$ into the air will bring adverse effects to the human health and environment. Several technologies had been invented to treat $SO_2$ from flue gas before it is being released to the atmosphere. Flue gas desulphurization (FGD) is one of the methods that removes the $SO_2$ content in the flue gas from solid, liquid or gases [2]. Wet desulphurization method using limestone as adsorbent had been used widely due to the high removal efficiency (higher than 90 %) of the $SO_2$ [3]. However, the usage of limestone a depleting natural source for cleaning purpose is not economically viable. Besides using limestone as an adsorbent for FGD, many other types of adsorbents such as activated carbon, activated coke, fly ash have been reported in the literature to remove $SO_2$ [4-6].

Egg shell (ES) is an emerging abundant solid waste from the sources such as poultry, homes, restaurants, and food manufacturing industries [7]. In Malaysia about 642,600 tonnes of egg is produced every year and from this total about 70,686 tons of ES waste is expected to be generated every year [8]. Furthermore, recently in Malaysia egg cracking industries is growing rapidly giving largest chuck of ES. ES usually are disposed to landfills without prior treatment and this indirectly creates negative effect to the environment and human health [9-10]. Many investigations have been conducted to explore usefulness of ES such as ES based fertilizer, cement additive, heavy metal adsorbent, catalyst and collagen [11-13]. However, none have been tested for pollutant gas adsorption.

In present study, waste egg shells were tested as a new material to treat $SO_2$ from flue gases. Egg shells are calcined to calcium oxide (CaO). Calcined ccommercial calcium carbonate ($CaCO_3$) was also used to compare the performance of egg shell waste to commercially available adsorbent.

## Materials and Methods

### Eggshell preparation

ES was collected from the university campus canteen. About 1 kg of waste ES was collected in a day throughout the campus. The collected ES was thoroughly washed to remove any white or yellow egg residue and egg membrane. It is then dried at 105 °C till a constant weight is obtained. Prior to storage, ES powder was sieved to a particle size of 63 µm. This size was chosen to standardize the adsorbent size and preliminary study shows smaller size has better adsorption capacity due large surface area. In order to test the potential ES for $SO_2$ removal, it was further processed to form CaO. The calcination processes were done by varying the calcination temperature (750 – 950 °C) and time (2 and 4 hours). The temperature and time range was chosen based on a preliminary study and literature [8]. Similarly, was done for the commercial calcium carbonate (CCC) (lab grade, 99% purity) purchased from Merck.

### Sulphur dioxide removal

Desulfurization experiments were performed in a laboratory scale of adsorption system with a fixed bed adsorber. Figure 1 shows the illustration of the experimental rig. The height and inner diameter of the reactor are 180 mm and 9 mm. The concentration of $SO_2$ gas was measured using a gas analyzer (Vario Plus Industrial Gas Analyzer, V: 1.78-000). About 0.5 g of adsorbent was placed in the reactor. 200 ppm $SO_2$ and $N_2$ as the balance was passed through the reactor at room temperature. The feed flow through the reactor was controlled at 300 ml/min. The amount of $SO_2$ adsorbed by the prepared adsorbent was expressed in breakthrough curves. Three sets of $SO_2$ adsorption study was done for each sample and the average data was used to plot the breakthrough curves.

The adsorption capacity was calculated based on the breakthrough curve data. The time equivalent to the total or stoichiometric capacity of $SO_2$ was calculated numerically by integrating the following equation 1;

$$t_t = \int_0^{\infty} 1 - \frac{C}{Co}\, dt \qquad (1)$$

Where $t_t$ is the time equivalent to the total or stoichiometric capacity, $t$ is the time, $C$ is the concentration of $SO_2$ at time, $t$ and $Co$ is the feed concentration of $SO_2$. With $t_t$ determined, the amount of adsorbed by adsorbent (the adsorption capacity) was calculated at STP condition from the following equation 2 and 3 [14];

$$q = \frac{Q_f t_t y_f}{m_c} \tag{2}$$

$$q = 1 - \frac{C}{Co} \frac{Q_f t_t y_f}{m_c} \tag{3}$$

where $q$ is the adsorbent sorption capacity, $q_t$ is the breakthrough sorption capacity at 5% from initial concentration, $y_f$ is the mole fraction of $SO_2$ in the feed, $Q_f$ is the volumetric feed flow rate at STP and $m_c$ is the mass of adsorbent used in the bed.

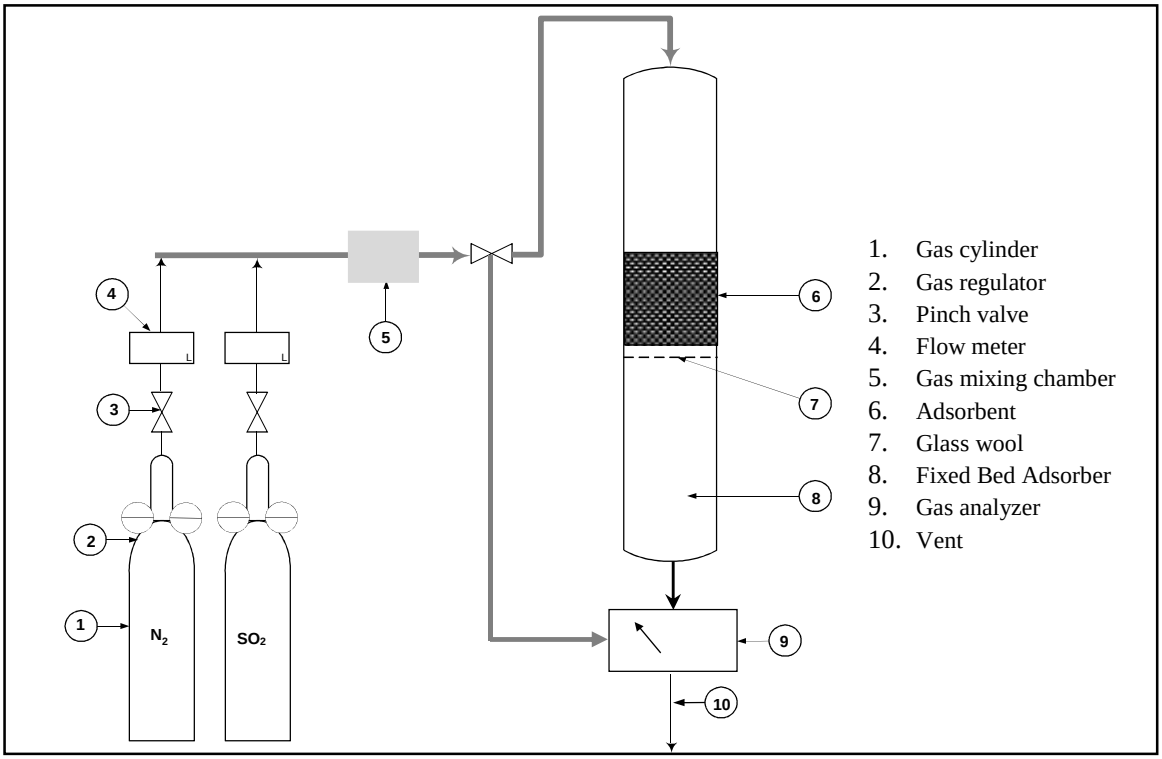



Figure 1. Experimental rig for desulphurization

**Characterization**

In this study, the prepared adsorbent will be characterized to determine their physical and chemical properties. The Fourier Transform Infrared (FTIR) was used to qualitatively identify the functional groups on the surface of ES and CCC using PerkinElmer FT-IR 2000. The spectra were obtained in the range of 400 – 4000 $cm^{-1}$ with a resolution of 4 $cm^{-1}$. The sample preparation consisted of mixing fine powder of each sample with KBr powder. The Brunauer-Emmett-Teller (BET) surface area analysis was done using $N_2$ adsorption and desorption isotherms measured at 77 K using Micromeritics (ASAP 2020 V4.02) volumetric gas adsorption instrument. Prior to measurements, the samples were degassed at 105 °C for 24 hours. The X-ray diffraction patterns of the samples were recorded by XRD-6000, Shimadzu using Cu-Ka radiation. The measurements were made at temperature range of 15 – 70 °C on $2\theta$ with a step size of 0.02°. The diffraction patterns were analyzed using the Joint Committee on Powder Diffraction Standards (JCPDS). CaO crystallite size was calculated using Scherrer equation from the most intense CaO peak at $2\theta$ of 37.6°.

## Results and Discussion

The $SO_2$ adsorption performance by calcined ES and CCC at different temperature and time are shown in Figure 2(a) and 2(b) and Figure 3(a) and 3(b) respectively. The data was plot based on average of three replicates and the difference of each set was less than 4%. The longest time (180 minutes) taken for saturation by CCC was at temperature 900 °C with 2 hours of calcination. The adsorption capacity of this sample was calculated as 3.95 mg/g. It was noticed that as the temperature was increased from 750 to 900 °C the saturation time for CCC increased rapidly. However, at temperature 950 °C the adsorption curve was narrower and almost similar to 900 °C. Further increase in temperature did not show significant changes in the removal efficiency. This is because the maximum conversion of $CaCO_3$ to CaO happens at 900 °C [15]. Thus, any sample prepared at lower temperature is expected to give less adsorption capacity due to incomplete process of $CaCO_3$ calcination.

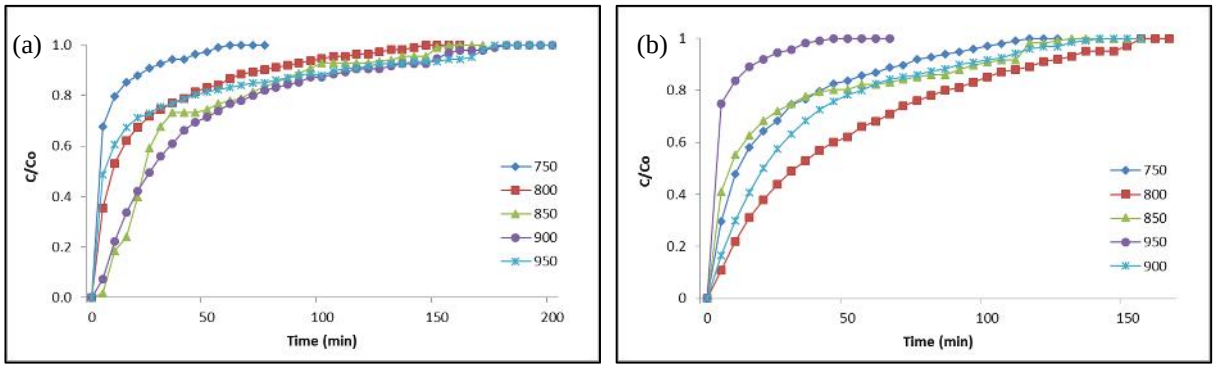



Figure 2. $SO_2$ breakthrough curve at different temperature for CCC at (a) 2 hours and (b) 4 hours of calcination

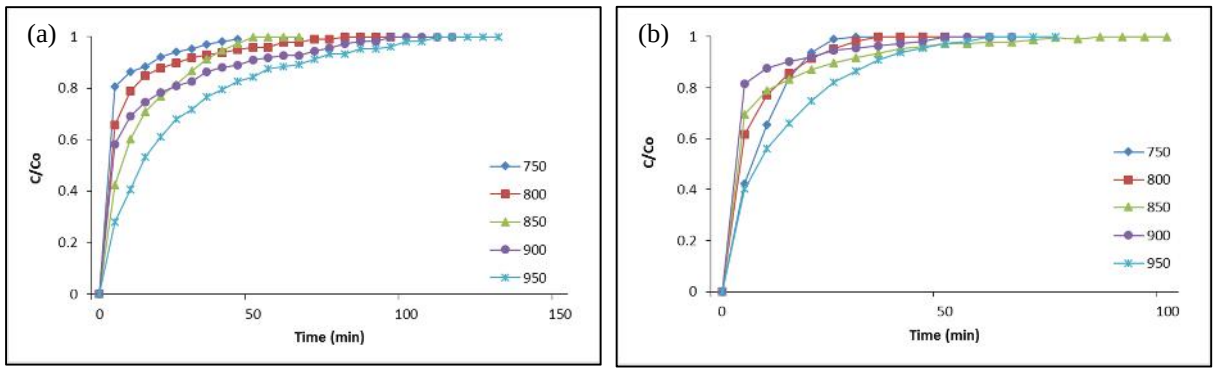



Figure 3. $SO_2$ breakthrough curve at different temperature for egg shell at (a) 2 hours and (b) 4 hours of calcination

Furthermore, it was noticed that further increase in time as shown in Figure 2(b), decreased the removal efficiency and saturation time. This could be due to overheating of the sample. Hu et al. reported that sintering of limestone particle could be the main reason. Limestone particles lost partly their reactivity after a heat treatment at 1123 K. The loss of the reactivity was also dependent on the duration of heat treatment, whereby a longer heat treatment will cause a greater loss of reactivity [16]. Sintering effect can be proven using the surface area data in Table 1. It is clearly seen that the surface area of calcined CCC at higher temperature was lower compared to the best removal sample. The best sample for 4 h of calcination was found to be at 800 °C for CCC. This further proves that increase in time and temperature at certain condition discourages $SO_2$ adsorption by CCC due to the reasons given above.

Table 1. Surface area of CCC, calcined ES and calcined CCC

| Sample | BET Surface Area ($m^2/g$) | CaO Crystallite Size (nm) | Adsorption Capacity (mg/g) |
|---|---|---|---|
| CCC | 1.12 | - | - |
| Eggshell | 0.56 | - | - |
| Calcined CCC – 900-2h | 9.51 | 3.29 | 3.95 |
| Calcined ES – 950-2h | 6.54 | 2.95 | 2.15 |
| Calcined CCC – 900-4h | 7.98 | 3.56 | 3.16 |
| Calcined ES - 950-4h | 4.25 | 3.07 | 1.19 |

A similar trend was observed for calcined ES. It was noticed that the longest saturation time (110 minutes) was achieved at temperature 950 °C and 2 hours of calcination for ES. The adsorption capacity of this sample was calculated as 2.15 mg/g. Overall, it was observed that 4 h of ES calcination, did not improve the saturation time for $SO_2$ removal. Moreover, all adsorbents were not capable of removing 100% $SO_2$, as after a few seconds the $SO_2$ concentration started to increase immediately. The figures did not show any significant breakthrough point. These results most likely reflect the fact that the specific surface area of the adsorbents was low. This can be further proven from the surface area data shown in Table 1. All adsorbents have surface area of less than 10 $m^2/g$. It was reported in the literature that most calcium-based materials have low sorption capacity due to low surface area [17-18].

Figure 4 shows XRD patterns of the best calcined CCC (a) and calcined ES (b). X-ray diffraction pattern of ES and CCC shows 2θ values of CaO at 32.4 and 37.6 when the eggshell was calcined at 950 °C for 2 hours (Figure 4b) and CCC was calcined at 900 °C for 2 hours (Figure 4a) which was indexed to JCPDS 82-1690. Similar peaks were also observed by Piker et al. and Joshi et al. [15,19]. XRD pattern of the calcined CCC (Figure 4a) appeared at almost at the same $2\theta$ angles as that of the calcined ES. However, the peaks intensities of the calcined CCC were higher than those of the ES, suggesting that the CaO crystalline size of CCC was larger than that of the calcined ES. The CaO crystallite size calculated by using Scherrer equation is listed in Table 1. It was denoted that the best sample of calcined CCC generated CaO with a crystalline size of 3.29 nm while ES showed a much lower degree of crystallinity with the size of 2.95 nm for the its best performed sample. This could be also another reason for the poor performance of calcined ES compared to calcined CCC. It had been reported that the commercially available CaO has a larger crystalline size compared to calcined eggshell by other researchers as well [17].

FTIR spectra of the best calcined adsorbent prepared by ES and CCC were analyzed to identify chemical constituents in a compound. Figure 5 shows the functional group peaks of the samples and it was observed that both samples have similar peaks. Two well-defined infrared bands were noticed at about 1424 and 875 $cm^{-1}$. They are characteristics of the C–O stretching and bending modes of calcium carbonate, respectively [17]. Gergely et al. suggested that the OH stretching vibration band at 3639 $cm^{-1}$ is probably related to Ca–O bonds [20]. Furthermore, Joshi et al. suggested that normally stretching vibration associated to water molecule in uncalcined ES is a broad band around 3432 $cm^{-1}$. However, for calcined ES a sharp absorption band appeared at 3640 $cm^{-1}$ suggesting reaction of CaO with OH [15].

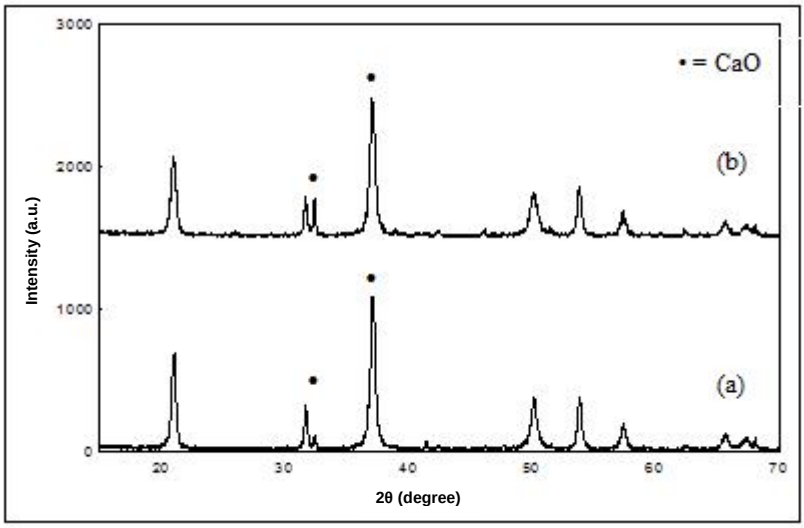



Figure 4. XRD patterns of (a) calcined CCC (900 - 2h) and (b) calcined ES (950 – 2h)

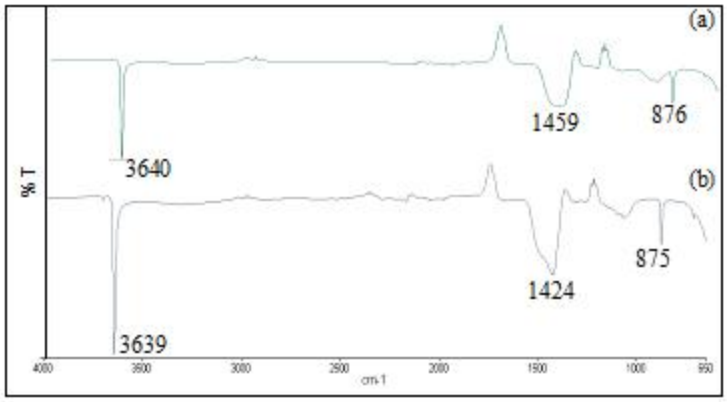



Figure 5. FTIR spectra of (a) calcined CCC (900 - 2h) and (b) calcined ES (950 – 2h)

Joshi et al. reported that peaks at 1424 $cm^{-1}$ and 1459 $cm^{-1}$ were broad and weak identifying reduced mass of the group $CO_3^{2-}$ upon calcination at 900 °C. The trend is identical for this study, suggesting the samples have been transformed to CaO [15]. However, samples were not fully calcined. In order to further understand the main reason for the poorer adsorption capacity by ES comparatively to CCC even though the composition and level of calcination is alike, a detailed study on using XRF and EDX should be done. Impurities may exist in ES which causes a poorer adsorption.

## Conclusion

The purpose of this study is to reutilize waste eggshell into an economic valuable product. The feasibility of ES to substitute limestone a depleting natural resource in flue gas desulphurization was tested. Results proved that ES can be used as a substitute of limestone for $SO_2$ removal. However, the capacity of removal was not as good as CCC. Even though the removal capacity was lower, the potential of ES to remove $SO_2$ was encouraging. The structure, surface area and functional groups of ES were also found to be like CCC. The most efficient calcined ES was found at 950°C for 2h. The adsorption capacity of the best calcined ES was 2.15mg/g. The surface area and crystallinity of the ES plays the major role in the adsorption of $SO_2$. This finding indicates that the CaO derived from the waste ES

is attractive for the use as $SO_2$ sorbent due to its low cost (derived from waste), environmentally friendly and high removal capacity of $SO_2$.

**Acknowledgement**

The authors gratefully acknowledge the financial support from Universiti Tunku Abdul Rahman Research Fund (UTARRF 6200-S57).

**References**

1. Liu, Y., Bisson, T. M., Yang, H. Q. and Xu, Z. H. (2010). Recent developments in novel sorbents for flue gas clean up. *Fuel Processing Technology*, 91: 1175 – 1197.
2. Lawrence, K. W., Norman, C. P. and Hung, Y. T. (2005). Advanced air and noise pollution control. Handbook of Environmental Engineering. Humana Press Inc. New Jersey.
3. Kallinikos, L. E., Farsari, E. I., Spatinos, D. N. and Papayannakos, N. G. (2010). Simulation of the operation of an industrial wet flue gas desulphuriztion system. *Fuel Processing Technology*, 91: 1794 – 1802.
4. Li, J. J., Kobayashi, N. and Hu, Y. Q. (2008). The activated coke preparation for $SO_2$ adsorption by using flue gas from coal power plant. *Chemical Engineering and Processing*, 47: 118 – 127.
5. Rubio, B. and Izquierdo, M. T. (2010) Coal fly ash based carbon for $SO_2$ removal from flue gases. *Waste Management*, 30: 1341 – 1347.
6. Sumathi, S., Bhatia, S., Lee, K. T. and Mohamed, A. R. (2010). Adsorption isotherm models and properties of $SO_2$ and NO removal by palm shell activated carbon supported with cerium (Ce/PSAC). *Chemical Engineering Journal*, 162(1): 194 – 200.
7. Sonenklar, C. (1999). Famous for eggwaste, penn state news. Access online http://news.psu.edu/ story/140891/1999/09/01/research/famous-egg-waste [Date access 21st August 2016].
8. Rohim, R., Ahmad, R., Ibrahim, N., Hamidin, N. and Abidin, C. Z. A. (2014). Characterization of calcium oxide catalyst from eggshell waste. *Advances in Environmental Biology*, 8: 35 – 38.
9. Ho, W. F., Hsu, H. C., Hsu, S. K., Hung, C. W. and Wu, S. C. (2013). Calcium phosphate bioceramics synthesized from eggshell powders through a solid state reaction. *Ceramic International*, 39(6): 6467 –6473.
10. Soares, M. R., Andrade, S. R., Martins, R. C., Quina, M. J. and Quinta-Ferreira, R. M. (2012). Organic biowastes blend selection for composting industrial eggshell by-product: Experimental and statistical mixture design. *Water Science and Technology*, 65(11): 1939 – 1945.
11. Wei, Z., Xu, C. and Li, B. (2009). Application of waste eggshell as low-cost solid catalyst for biodiesel production. *Bioresources Technology*, 100(11): 2883 – 2885.
12. Glatz, P., Miao, Z. and Rodda, B. (2011). Handling and treatment of poultry hatchery waste: Review. *Sustainability*, 3: 216 – 237.
13. Oliveira, D. A., Benelli, P. and Amante, E. R. (2013). A literature review on adding value to solid residue: Eggshell. *Journal of Cleaner Production*, 46: 42 – 47.
14. Cheremisinoff, P. N. (1993). Air pollution control and design for industry. New York.
15. Joshi, G., Devendra, S. R., Bhawna Y. L., Kamal K. B., Pankaj K., Nayan K. and Sanjay K. (2015). Transesterification of jatropha and karanja oils by using waste egg shell derived calcium based mixed metal oxides. *Energy Conversion and Management*, 96: 258 – 267.
16. Hu, G., Dam-Johansen, K., Wedel S. and Hansen, J. P. (2006). Review of the direct sulfation reaction of limestone. *Progress in Energy and Combustion Science*, 32: 386 – 407.
17. Witoon, T. (2011). Characterization of calcium oxide derived from waste eggshell and its application as $CO_2$ sorbent. *Ceramic International*, 37: 3291 – 3298.
18. Lin, R. B., Shih, S. M. (2003). Characterization of $Ca(OH)_2$/fly ash sorbents for flue gas desulphurization. *Powder Technology*, 131: 212 – 222.
19. Piker, A., Tabah, B., Perkas, N. and Gedanken, A. (2016). A green and low-cost room temperature biodiesel production method from waste oil using egg shells as catalyst. *Fuel*, 182: 34 – 41.
20. Gergely, G., Weber, F., Lukacs, I., Toth, A. L., Horvath, Z. E., Mihaly, J. and Balazsi, C. (2010). Preparation and characterization of hydroxyapatite from eggshell, *Ceramic International*, 36: 803 – 806.

*Malaysian Journal of Analytical Sciences, Vol 21 No 3 (2017): 726 - 734*
*DOI: https://doi.org/10.17576/mjas-2017-2103-22*

MALAYSIAN JOURNAL OF ANALYTICAL SCIENCES
*Published by The Malaysian Analytical Sciences Society*
ISSN 1394 - 2506

# EXTRACTION OF BIOACTIVE COMPOUNDS (MANGIFERIN) FROM *MAHKOTA DEWA (Phaleria macrocarpa)* FRUITS USING SUBCRITICAL WATER: EFFECT OF PROCESS PARAMETERS ON EXTRACTION YIELD

## (Pengekstrakan Bahan Bioaktif (Mangiferin) dari Buah *Mahkota Dewa* (*Phaleria macrocarpa*) Menggunakan Kaedah Air Subgenting: Kesan Parameter Proses Terhadap Hasil Ekstrak)

Nurmaryam Aini Hashim, Ummi Najihah Md. Hashim, Siti Kholijah Abdul Mudalip*, Noorlisa Harun, Fatmawati Adam, Rohaida Che Man, Siti Zubaidah Sulaiman, Zatul Iffah Mohd Arshad, Shalyda Md. Shaarani

*Faculty of Chemical Engineering & Natural Resources,*
*Universiti Malaysia Pahang, Lebuh Raya Tun Razak, 26300 Gambang, Pahang, Malaysia*

**Corresponding author: kholijah@ump.edu.my*

Received: 28 November 2016; Accepted: 5 February 2017

**Abstract**

*Mahkota Dewa* (*Phaleria macrocarpa)* is a popular herbal plant that is indigenous to Indonesia and Malaysia. The bioactive ingredients in the plant contain antihistamine, antioxidant, and anti-cancer compound. In this work, experimental study was performed using subcritical water extraction (SWE) method to extract bioactive compound namely mangiferin from *Mahkota Dewa* fruits. A sequential screening strategy using one-factor-at-a-time (OFAT) was carried out at different solid to solvent ratios (30 – 70 g/L), temperatures (50 – 150 °C) and extraction times (3 – 7 hours). The yield of mangiferin extracted was measured using high performance liquid chromatography (HPLC). The results show that the solid to solvent ratio, extraction temperature and time cause significant effect on the mangiferin yield. The best operating conditions for extracting *Mahkota Dewa* fruit with subcritical method is 60 g/L solid to solvent ratio and 100°C extraction temperature for 5 hours with mangiferin yield of 3.202% w/w.

**Keywords**: *Mahkota Dewa*, subcritical water extraction, mangiferin, one factor at a time

**Abstrak**

*Mahkota Dewa* (*Phaleria macrocarpa*) adalah tumbuhan herba yang popular berasal dari Indonesia dan Malaysia. Bahan bioaktif yang boleh didapati dalam ekstrak tumbuhan ini adalah seperti antihistamin, antioksidan, dan juga anti-kanser. Dalam kerja penyelidikan ini, satu eksperimen telah dijalankan dengan menggunakan proses pengekstrakan air subgenting (SWE), untuk mengekstrak bahan bioaktif daripada buah *Mahkota Dewa* iaitu mangiferin. Proses saringan secara berturutan dengan menggunakan kaedah satu-faktor-pada-satu-masa (OFAT) telah dijalankan pada pelbagai nisbah pepejal kepada pelarut (30 – 70 g/L), suhu (50 – 150 °C) dan masa pengekstrakan (3 – 7 jam). Hasil ekstrak mangiferin dianalisis dengan menggunakan kaedah kromatografi cecair berprestasi tinggi (HPLC). Hasil analisa menunjukkan bahawa nisbah pepejal kepada pelarut, suhu pengekstrakan dan masa memberi kesan yang besar ke atas hasil ekstrak mangiferin itu. Parameter eksperimen yang terbaik untuk mengekstrak buah *Mahkota Dewa* dengan menggunakan kaedah subgenting adalah pada nisbah pepejal kepada pelarut 60 g/L dan suhu ekstrak pada 100 °C selama 5 jam dengan hasil ekstrak mangiferin sebanyak 3.202% w/w.

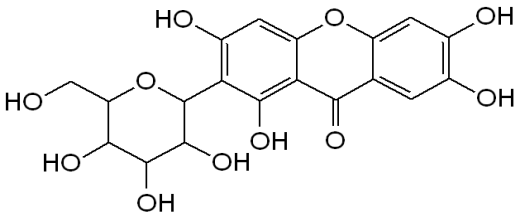
**Kata kunci:** *Mahkota Dewa*, pengekstrakan air subgenting, mangiferin, satu faktor pada satu masa

## Introduction

In Malaysia, more than 2000 plant species exist possess healing properties and extensive potential to be commercialized. *Phaleria macropcarpa* or else known as *Mahkota Dewa* is one of typical herbal plants that are highly in demand nowadays. *Mahkota Dewa* is an Indonesia plant of *Thymelaceae* family that grow in the topical areas of Papua Island [1,2]. Though originated from Indonesia, due to the resemblance of climate, *Mahkota Dewa* can be easily cultivated and discovered in Malaysia. *Mahkota Dewa* as illustrated in Figure 1(a) is a complete tree with stem, leaves, flowers, and also fruits. Normal height for *Mahkota Dewa* tree ranges from 1 to 6 m with productive age ranges from 10 to 20 years [1,3,4]. Its leaves are green and elongated with the length and width ranging from 7 to 10 cm and 3 to 5 cm, respectively. Fruits of *Mahkota Dewa*, as illustrated in Figure 1 (a), are green when unripe and turn to red once ripening. It's brown and anatropous seed exist as 1 to 2 seed per fruit [3]. *Mahkota Dewa* fruits contain ranges of chemical constituents include saponin, flavoid, polyphenol, alkaloid and mangiferin [3,5].



(a)




(b)

Figure 1. (a) *Mahkota Dewa* (*Phaleria macrocarpa*) fruits and (b) molecular structure of Mangiferin

Among the bioactive compounds, mangiferin as illustrated in Figure 1(b), has an extensive range of pharmacological effects including anti-inflammation, antioxidant, anti-diabetic, anti-tumor and also anticancer activity [5–7]. Mangiferin ($C_{19}H_{18}O_{11}$) is reported as a heat stable molecule and it's natural pharmacological active compound has been proven to have various biological benefits [8]. Despite its beneficial bioactive effect, only few researches [5,9] reported the extraction of bioactive compounds from *Mahkota Dewa* using conventional extraction method. Considering the benefits of the plant extraction, it is necessary to explore other alternative method to extract the bioactive compounds.

Extraction method can be further divided into two, which is a conventional and non-conventional method. Conventional techniques is a classical existing techniques based on the extracting power of different solvents in use and also the application of heat and/or mixing towards the target plant [10]. It can be further classified into hydrodistillation, maceration and soxhlet extraction. This technique are still being practiced as a comparison technique to non-conventional methods [10,11]. Non-conventional such as microwave assisted extraction (MAE), ultrasound-assisted extraction (UAE) and subcritical water extraction (SWE) methods are reported to have more advantages compared to the conventional techniques [10,12,13]. These includes environmental friendly and cost efficient due to less usage of synthetic and organic chemical, short operational time, higher yield and good extract quality [10,12–14].

Previous work demonstrates the usage of organic solvent like methanol and ethanol as extraction solvent [15, 16]. Due to long extraction time, low extraction yield, and residual toxic problem, the urge to develop new non-organic solvent-based extraction methods with higher extraction efficiency is needed. Subcritical water extraction (SWE) implements use of green solvent such as water and it is well known as environmental-friendly and non-toxic solvent. Water demonstrates exceptional properties as it has high boiling point for its mass, high polarity and high

dielectric constant [17,18]. SWE promote shorter extraction time, higher quality of extract and lower extraction cost at temperature between 100 °C to 374 °C. By increasing the temperature at moderate pressure, it reduces the surface tension and viscosity, and increasing its diffusion rate causes SWE is comparable to organic solvents [17,19].

Recently, it has been reported that extraction efficiency of triterpenes from dry loquat leaves using SWE method produced yield of 1.7 times higher than those obtained using traditional methods which was soxhlet extraction (SE) [18]. The aim of this research work was to demonstrate the extraction of mangiferin from *Mahkota Dewa* using subcritical water extraction approach. The effect of solid to solvent ratio, temperature, and time on extraction yields of mangiferin was investigated. The results obtained would be useful as alternative experimental design to extract and analysis plant material, for further analysis in form of making the process more efficient and to increase the process economy.

## Materials and Methods

### Materials

Dried *Mahkota Dewa (Phaleria macrocarpa)* fruits were supplied by Ethno Resources Malaysia Sdn. Bhd. (Petaling jaya, Malaysia). *Mahkota Dewa* provided were planted in Selangor, Malaysia. The dried *Mahkota Dewa* was ground with Ultra Centrifugal Mill ZM 200 (Haan, German) to an average size of 500 µm. HPLC grade methanol (99.9% purity) and ortho-phosphoric acid (85% purity) purchased from Permula Chemicals Sdn. Bhd (Kuantan, Malaysia). Mangiferin (1S-1,5-Anhydro-1-(1,3,6,7-tetrahydroxy-9-oxo-9H-xanthen-2-yl)-D-glucitol) standard and 2,2-diphenyl-1-picrylhydrazyl (DPPH) were purchased from Merck (Selangor, Malaysia). All chemicals were used without further purification. Deionized water was prepared using a Milli-Q, Ultrapure Water Purification System (Massachusetts, USA) with a 0.22 mm filter. The 0.2 µm nylon membrane filter and 0.45 µm nylon syringe filter used in sample preparation prior to HPLC analysis were supplied by MHY Energy Resources (Kuantan, Malaysia).

### Subcritical water extraction

A classical approach one-factor-at-a-time (OFAT) was used to determine the optimum range of the selected process parameters during the SWE process. Through this technique, one level of the factor to be investigated was changed over the desired range and at the same time keeping the level of other factors constant [20]. SWE experiments were performed in a 10 cm (W) x 20 cm (H) stainless steel batch Buchiglasuster Kiloclave laboratory pressure vessel reactor system (Uster, Switzerland) as illustrated in Figure 2. The vessel can be operated within temperature range of -20 °C to 250 °C and can hold up sample up to 2 L. This multipurpose pressure reactor is made up from stainless steel and designed for the use of large steel pressure vessel.

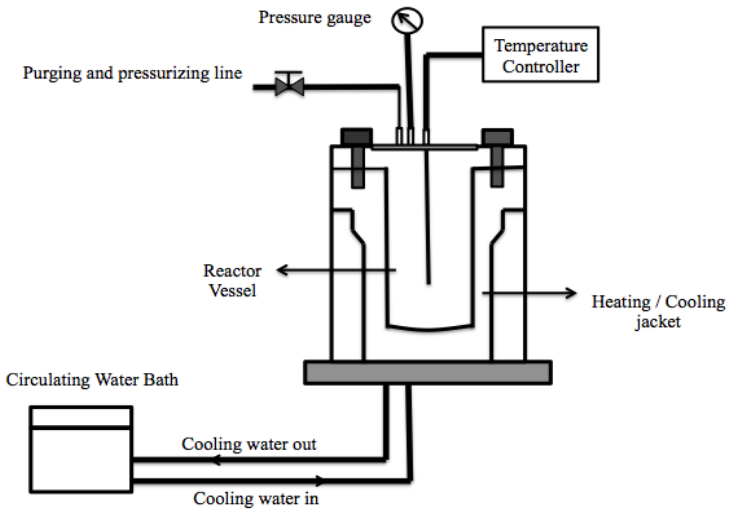



Figure 2. Schematic diagram of Buchiglasuster Kiloclave laboratory reactor system

Process parameters studied were solid to solvent ratio, temperature and extraction time. Summaries of the parameters investigated at different levels are tabulated in Table 1. Dry ground *Mahkota Dewa* fruit sample weighed and placed into the extraction vessel. Exact volume of deionized water (1 L) was added as extraction solvents and mixed thoroughly. Reactor was tightly closed and secured with bolts and nuts. Temperature and time were set at desired value. Once extraction was completed, vessel was allowed to cool to room temperature, 24 °C. Cooling water was supplied using Stuart recirculating cooler RE300RC (Staffordshire, UK). Extract was collected by loosing the nut and bolt of the reactor and then poured into a sample bottle. About 40 mL of the extract was then poured into the centrifuge tube and centrifuged for 30 min at 5000 rpm and the rest of the extract stored in -20 °C refrigerator. Extract supernatant isolated from precipitate and sonicated for 10 minutes to evenly disperse the particle in water. During the sonication, 10 ml of sonicated extract collected then diluted with 20 mL of methanol by using syringes. Mixtures filtered using 0.45 μm nylon syringe filter into Agilent MS analyzed vial kits (California, USA) and analysed using HPLC. All the experiments performed in triplicates.

Table 1. Summary of process parameters for OFAT

| Parameters | Experimental Conditions | Fixed Parameters |
|---|---|---|
| Solid to solvent ratio (g/L) | 30, 40, 50, 60 and 70 | Temperature - 100 °C<br>Time - 5 h |
| Temperature (°C) | 50, 75, 100, 125 and 150 | Solid to solvent ratio - 6:100 g/L<br>Time - 5 h |
| Time (h) | 3, 4, 5, 6 and 7 | Solid to solvent ratio - 6:100 g/L<br>Temperature - 100 °C |

**High performance liquid chromatography analysis**

Chemical compound in *Mahkota Dewa* was determined using HPLC (Agilent Technologies 1100, California, USA). Column used was Zorbax Eclipse Plus C18, Analytical 4.6 X 250 mm, 5 Micron (Agilent Technologies, California, USA). Detection was performed using a diode array detector (DAD). The chromatographic separation was performed at a wavelength of 258 nm. Mobile phase comprises of HPLC grade methanol and 0.1% aqueous phosphoric acid with a ratio of 31:69 and filtered with 0.2 μm nylon membrane filter prior to analysis. Mobile phase flow rate was set at 1.0 mL/min with amount of sample injection of 10 μL. HPLC unit was calibrated with mangiferin standard solution prepared prior to each analysis at different concentrations. Standard solution was prepared by diluting 5.0 mg of mangiferin standard with 10 mL methanol to produced 500 ppm of concentration [5]. This mixture was then diluted into several concentrations (5 to 60 ppm) and was used to construct a calibration curve. HPLC chromatogram of mangiferin standard and *Mahkota Dewa* extract are shown in Figure 3. The relationship between peak area, $x$ and concentration of mangiferin, $y$ can be represented by a linear equation as follows:

$$y = 15.806x \ (R^2 = 0.99482) \quad (1)$$

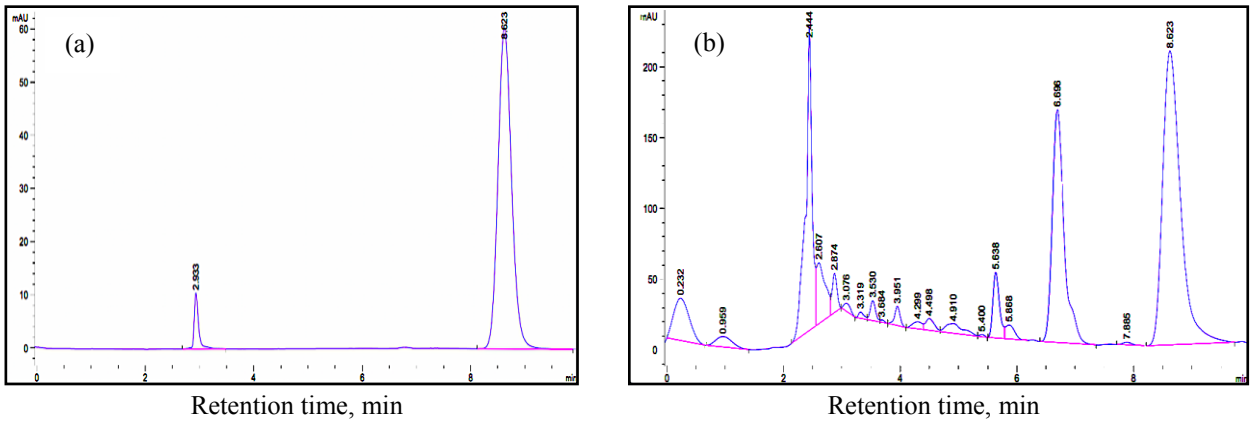



Figure 3. HPLC chromatogram of (a) mangiferin standard and (b) *Mahkota Dewa* extract. The peak at retention time of of 8.623 min was used to estimate the mangiferin yield

## Results and Discussion

### The effect of solid to solvent ratio

The results show that among solid to solvent ratio tested, 60 g/L was most effective. Figure 4 shows the effect of solid to solvent ratio on the mangiferin yield. Mangiferin yield was increased from 0.962% w/w to 1.8718% w/w at solid to solvent ratio of 30 to 60 g/L. However, the mangiferin yield was reduced to 1.524% w/w at the solid to solvent ratio of 70 g/L. The removal of solute require a lot of energy using water as solvent, consequently if more water used in an extraction, it may lead to higher energy consumption [21]. In general, the higher the amount of solid in a solvent would reflect the higher amount extraction yield. This statement is in agreement with the mass transfer principle, where its driving force depends on the concentration gradient between solute and the solvent [22,23]. High solid to solvent ratio produce high concentration gradient, thus cause an increase of diffusion rate, which allows greater extraction of solute by solvent [11,12]. The decrease of mangiferin yield beyond solid to solvent ratio of 60 g/L is probably due to low extraction efficiency, where the solvent was not sufficient enough to dissolve the solute and the equilibrium of solute and solvent was achieved [11]. Equilibrium of solute and solvent defined as a condition where no further changes in either phase will occur for the solid and solvent phases [17,24–26]. Smaller volumes of solvent can lead to incomplete target extraction while larger volumes can make the extraction procedure becomes complex and wasteful. This findings is in agreement with Zhang et al. [27] which stated that the chance of bioactive components come into contact with the extracting solvent is increase with the increase amount of solute and will not continue to increase once equilibrium is reached.

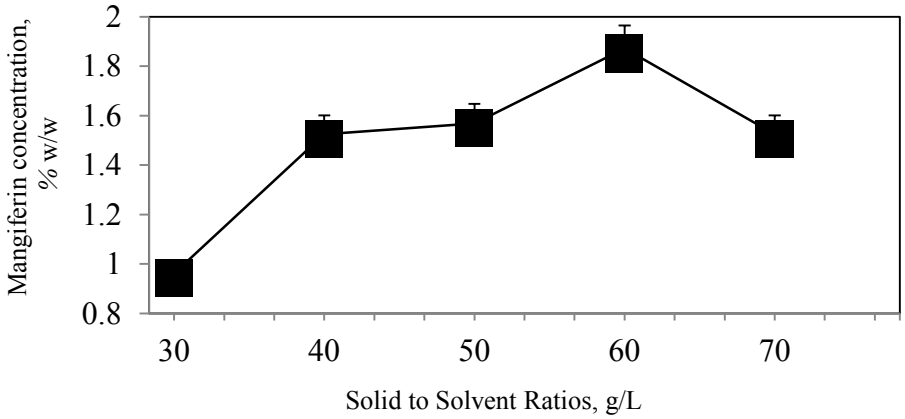



Figure 4. Effects of different solid to solvent ratio on mangiferin yield. The extraction temperature and time were fixed at 100 °C and 5 hours, respectively. Values are mean ± standard deviations

**The effect of temperature**

Figure 5 illustrates the effect of extraction temperatures on the mangiferin yield. It can be seen that the yield of mangiferin increase with the increase of temperature from 50 °C up to 100 °C. The highest mangiferin yield (2.405% w/w) was obtained at extraction temperature of 100 °C. At temperature of 125 °C and 150 °C, a slight decreased of mangiferin yield was observed with the yield of 1.827% w/w and 1.435% w/w, respectively. Both the equilibrium (solubility) and mass transfer rate (diffusion coefficient) can affect the extraction temperature and high temperature is often associated with the increase rate of diffusivity and solubilization of solute but decrease in the viscosity and surface tension of solvent. In theory, the penetrability and solubility of the solvents increased with the increase of the temperature, thus resulting in an increased of extraction efficiency and speed. Increase in yield with respect to increasing temperature is attributed to thermal kinetics of mass transfer and the thermodynamic effect of temperature on solubilization [21]. Therefore, extraction process that performed at high temperature often shows an increment in yield. According to Gbashi et al. [19], it is recommended to extract at the high permitted temperature since low temperature result in low diffusivity and consequently low extraction yield [18–20]. Consistent with previous works yield decreases as operating temperature exceeds 100 °C [21, 30]. The main disadvantage of applying higher temperature is the increase of the solvent boil off and reducing effective contact area between solid and liquid phases. As a result, lower yield of the final extracts [21]. This extraction process aiming to extract mangiferin compound and water temperature does not necessarily have to be high as possible, all of the parameter should be optimized and carefully controlled [31]. It is suggested that the best operational temperature that yield highest amount of mangiferin was at 100 °C with extraction yield of 2.405% w/w.

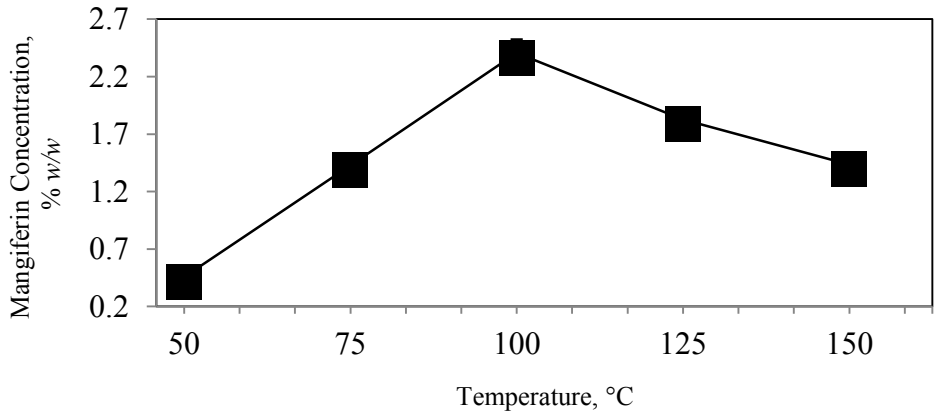



Figure 5. Effects of different temperature on mangiferin yield. The extraction solid to solvent ratio and time were fixed at 60 g/L and 5 h, respectively. Values are mean ± standard deviations

**The effect of time**

The extraction process was carried out at different times with fixed solid to solvent ratio of 60 g/L and temperature of 100 °C. The results illustrated in Figure 6 show a significant increment of extraction yield from extraction time of 3 hours (2.506% w/w) to extraction time of 5 hours (3.202% w/w). Further increase of the extraction time, which is from 6 to 7 hours reduced the mangiferin yield to 2.631% w/w. It is essential to determine the duration of the extraction process required to extract most of the desired bioactive compounds. Under static extraction, equilibrium among the sample components was still bound to the matrix and the water phase, in which the components are already solubilized, might be reached [28,29]. By using this information, suitable duration can be selected and operating cost for the process can be reduced [21]. Based on the result, the efficiency of the extraction time was not increase within 5 hours of extraction and since most bioactive compounds are sensitive to elevated temperature, keeping them for a longer period would lead to the thermal decomposition of the bioactive compounds. For this reason, best extraction time for subcritical water extraction of *Mahkota Dewa* is 5 hours with yield of 3.202% w/w

of mangiferin. This results as further support the finding reported by Tunchaiyaphum et al. [29] and Kim et al. [5] who found that the degradation of extracted compound at prolonged extraction time.

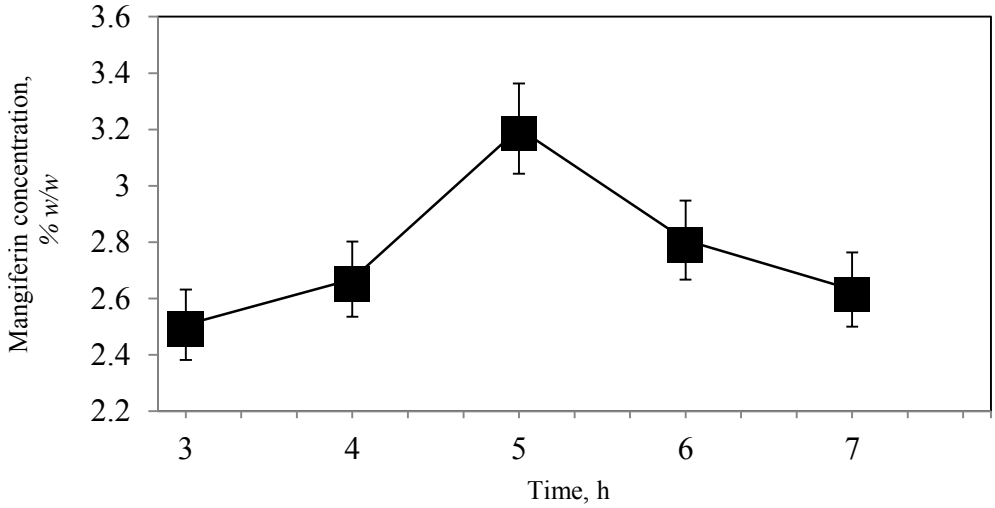



Figure 6. Effects of different time on mangiferin yield. The extraction solid to solvent ratio and temperature were fixed at 60 g/L and 100 °C, respectively. Values are mean ± standard deviations

## Conclusion

The effect of process parameters in extracting mangiferin from *Mahkota Dewa* fruits, i.e., solid to solvent ratio, extraction temperature, and time on a subcritical water extraction (SWE) batch extraction of have been investigated. In general, solid to solvent ratio, extraction temperature, and extraction time was found to show significant effect on the amount of mangiferin extracted from *Mahkota Dewa* fruits. The increased of the solid to solvent ratio, extraction temperature, and extraction time up to certain extent, increased the mangiferin yield. The best operating parameters that produced the highest mangiferin yield of 3.202% w/w) were at 60 g/L of solid to solvent ratios, extraction temperature of 100 °C and extraction time of 5 hours.

## Acknowledgement

The authors are grateful for the financial support from the Ministry of Education Malaysia for Research Acculturation Grant Scheme (Grant No. RDU151402). We also appreciate the Faculty of Chemical and Natural Resources Engineering, Universiti Malaysia Pahang for the research facilities.

## References

1. Anggraini, T. and Lewandowsky, P. (2015). The exotic plants of Indonesia: Mahkota Dewa (*Phaleria macrocarpa*), Sikaduduak (*Melastoma malabathricum* Linn) and Mengkudu (*Morinda citrifolia*) as potent antioxidant sources. *International Journal on Advanced Science Engineering Information Technology,* 5(2): 59 – 62.
2. Tandrasasmita, O. M., Lee, J. S., Baek, S. H. and Tjandrawinata, R. R. (2010). Induction of cellular apoptosis in human breast cancer by DLBS1425, a Phaleria macrocarpa compound extract, via downregulation of PI3-kinase/AKT pathway. *Cancer Biology and Therapy*, 10(8): 814 – 824.
3. Altaf, R., Zaini, M., Asmawi, B., Dewa, A., Sadikun, A. and Umar, M. I. (2013). Phytochemistry and medicinal properties of *Phaleria macrocarpa* (Scheff.) Boerl. extracts. *Pharmacognosy Reviews,* 7(13), 73 – 80.
4. Zhang, Y.-B., Xu, X.-J. and Liu, H.-M. (2006). Chemical constituents from *Mahkota dewa*. *Journal of Asian Natural Products Research*, 8(1–2): 119 – 123.
5. Kim, W., Veriansyah, B., Lee, Y., Kim, J. and Kim, J. (2010). Extraction of mangiferin from Mahkota Dewa (*Phaleria macrocarpa*) using subcritical water. *Journal of Industrial and Engineering Chemistry*, *16*(3), 425 – 430.

6. Dai, J. and Mumper, R. J. (2010). Plant phenolics: Extraction, analysis and their antioxidant and anticancer properties. *Molecules*, 15(10): 7313 – 7352.
7. Mirza, R. H., Chi, N. and Chi, Y. (2013). Therapeutic potential of the natural product mangiferin in metabolic syndrome. *Journal of Nutritional Therapeutics*, 2: 74 – 79.
8. Luo, F., Lv, Q., Zhao, Y., Hu, G., Huang, G. and Zhang, J. (2012). Quantification and purification of mangiferin from Chinese Mango (*Mangifera indica* L.) cultivars and its protective effect on human umbilical vein endothelial cells under $H_2O_2$-induced stress. *International Journal of Molecular Sciences,* 13: 11260 – 11274.
9. Andrean, D., Prasetyo, S., Kristijarti, A. P. and Hudaya, T. (2014). The extraction and activity test of bioactive compounds in *Phaleria macrocarpa* as antioxidants. *Procedia Chemistry*, 9: 94 – 101.
10. Azmir, J., Zaidul, I. S. M., Rahman, M. M., Sharif, K. M., Mohamed, A., Sahena, F., Jahurul, M.H.A., Ghafoor, K., Norulaini, N. A. N. and Omar, A. K. M. (2013). Techniques for extraction of bioactive compounds from plant materials: A review. *Journal of Food Engineering*, *117*(4): 426 – 436.
11. Nayak, B., Dahmoune, F., Moussi, K., Remini, H., Dairi, S., Aoun, O. and Khodir, M. (2015). Comparison of microwave, ultrasound and accelerated-assisted solvent extraction for recovery of polyphenols from Citrus sinensis peels. *Food Chemistry*, 187: 507 – 516.
12. Bimakr, M., Rahman, R. A., Saleena Taip, F., Adzahan, N. M., Islam Sarker, Z. and Ganjloo, A. (2013). Ultrasound-assisted extraction of valuable compounds from winter melon (*Benincasa hispida*) seeds. *International Food Research Journal*, 20(1): 331 – 338.
13. Fazlali, A., Moradi, S. and Hamedi, H. (2015). Studying of optimization condition of rosemary essence extraction with microwave assisted hydro-distillation method. *American Journal of Essential Oils and Natural Products,* 3: 46 – 50.
14. Eikani, M. H., Golmohammad, F. and Rowshanzamir, S. (2007). Subcritical water extraction of essential oils from coriander seeds (*Coriandrum sativum* L.). *Journal of Food Engineering*, 80(2): 735 – 740.
15. Kubátová, A., Miller, D. J. and Hawthorne, S. B. (2001). Comparison of subcritical water and organic solvents for extracting kava lactones from kava root. *Journal of Chromatography A*, 923(1–2): 187 – 194.
16. Lay, M. M., Karsani, S. A., Banisalam, B., Mohajer, S. and Abd Malek, S. N. (2014). Antioxidants, phytochemicals, and cytotoxicity studies on *Phaleria macrocarpa* (Scheff.) Boerl Seeds. *BioMed Research International*, 2014: 1 – 13.
17. Asl, A. H. and Khajenoori, M. (2013). Subcritical water extraction. mass transfer - advances in sustainable energy and environment oriented numerical modeling. InTech Publisher.
18. Erasto, M., Shuang, Z., Zongping, Z. and Jie, C. (2016). Subcritical water extraction of bioactive compounds from dry loquat (*Eriobotrya japonica*) leaves and characterization of triterpenes in the extracts. *African Journal of Biotechnology*, 15(22): 1041 – 1049.
19. Gbashi, S., Adebo, O. A., Piater, L., Madala, N. E. and Njobeh, P. B. (2016). Subcritical water extraction in biological materials. *Separation and Purification Reviews*, 46(1): 21–34.
20. Czitrom, V. (1999). One-factor-at-a-time versus designed experiments. *American Statistical Association*, 53(2): 65 – 74.
21. Mohamad, M., Ali, M. W., Ripin, A. and Ahmad, A. (2013). Effect of extraction process parameters on the yield of bioactive compounds from the roots of *Eurycoma Longifolia*. *Jurnal Teknologi*, 60: 51–57.
22. Saim, N., Osman, R., Azriza, W., Yasin, H. and Hamid, R. D. (2008). Subcritical water extraction of essential oil from coriander (*Coriandrum sativum* L.) seeds. *Malaysian Journal of Analytical Sciences,* 12(1): 22 – 24.
23. Wong, B. Y., Tan, C. P. and Ho, C. W. (2013). Effect of solid-to-solvent ratio on phenolic content and antioxidant capacities of "Dukung Anak" (*Phyllanthus niruri*). *International Food Research Journal*, 20(1): 325 – 330.
24. Toledo, R. (2007). Fundamentals of food process engineering. Springer, Athens, USA.
25. Zhang, S. Q., Bi, H. M. and Liu, C. J. (2007). Extraction of bio-active components from *Rhodiola sachalinensis* under ultrahigh hydrostatic pressure. *Separation and Purification Technology*, 57(2): 277 – 282.
26. Fariza, N., Luqman, C. A., Ky, P., Dayang, R. Ab., Umi, K. and Adawiah, I. (2014). Optimisation of extraction of *Phaleria macrocarpa* leaves. *Medicinal & Aromatic Plants*, *3*(1): 1 – 3.
27. Gong, Y., Zhang, X., He, L., Yan, Q., Yuan, F. and Gao, Y. (2015). Optimization of subcritical water extraction parameters of antioxidant polyphenols from sea buckthorn (*Hippophaë rhamnoides* L.) seed residue. *Journal of Food Science and Technology*, 52(3): 1534 – 1542.

28. Bilek, S. E. (2010). The effect of time, temperature, solvent: solid and solvent composition on extraction of total phenolic compound from dried olive (*Olea europaea* L.) leaves. *The Journal of Food,* 35: 411 –416.
29. Tunchaiyaphum, S., Eshtiaghi, M. N. and Yoswathana, N. (2013). Extraction of bioactive compounds from mango peels using green technology. *International Journal of Chemical Engineering and Applications*, 4(4): 194 – 198.
30. Cacace, J. E. and Mazza, G. (2003). Mass transfer process during extraction of phenolic compounds from milled berries. *Journal of Food Engineering,* 59: 379 – 389.
31. Herrero, M., Mendiola, J. A. and Ib, E. (2003). Subcritical water extraction of bioactive components from algae. *Elsevier*: pp. 534–560.

*Malaysian Journal of Analytical Sciences, Vol 21 No 3 (2017): 735 - 744*
*DOI: https://doi.org/10.17576/mjas-2017-2103-23*

MALAYSIAN JOURNAL OF ANALYTICAL SCIENCES
*Published by The Malaysian Analytical Sciences Society*
ISSN 1394 - 2506

# ALGAE OIL EXTRACTION FROM FRESHWATER MICROALGAE *Chlorella vulgaris*

## (Pengekstrakan Minyak Alga Daripada Mikroalga Air Tawar *Chlorella vulgaris*)

Nurfarahanim Abdullah, Nur Amelia Amran, Nur Hidayah Mat Yasin*

*Faculty of Chemical Engineering & Natural Resources,*
*Universiti Malaysia Pahang, 26300 Gambang, Pahang, Malaysia*

**Corresponding author: hidayahyassin@ump.edu.my*

Received: 28 November 2016; Accepted: 5 February 2017

**Abstract**

This research aims to investigate the optimum condition of oil extraction method to extract maximum oil yield from freshwater microalgae *Chlorella vulgaris*. The modified soxhlet extraction method was used to identify the best solvent systems which are heptane, heptane: methanol (1:1), heptane: methanol (1:2), heptane: ethanol (1:1) and heptane: ethanol (1:2) for extracting the microalgae oil. The effect of different mixing rate (rpm), temperature ($^oC$) and extraction time (hours) were carried out using the optimized solvent system to evaluate the optimum condition of oil extraction. Based on the yield of oil extraction, heptane alone become the best solvent to extract the oil with the yield of 57.5%, followed by heptane: methanol (1:2), heptane: ethanol (1:1), heptane: ethanol (1:2) and heptane: methanol (1:1) with the yield of 47.5%, 44.8%, 43.2% and 41.4%, respectively. Maximum oil quantity of 61.27% was obtained after extracted the *Chlorella vulgaris* biomass using heptane as a solvent at the following optimal conditions: mixing rate of 600 rpm, temperature of 65 °C and extraction time of 5 hours. This study confirmed that an increasing temperature resulted in the increased of oil yield, but at higher temperature (greater than 65 °C), the oil yield was decreasing. Too high of temperature in oil extraction may cause partial decomposition of the microalgae cells and thus lowering the yield of oil extracted.

**Keywords**: soxhlet extraction, oil extraction, freshwater microalgae, *Chlorella vulgaris*, solvent systems

**Abstrak**

Kajian ini bertujuan untuk mengkaji keadaan optimum bagi kaedah pengekstrakan minyak dalam usaha untuk mendapatkan hasil minyak maksimum daripada mikroalga air tawar *Chlorella vulgaris*. Kaedah pengekstrakan soxhlet yang diubah suai digunakan untuk mengenal pasti sistem pelarut yang terbaik iaitu heptana, heptana: metanol (1:1), heptana: metanol (1:2), heptana: etanol (1:1) dan heptana: etanol (1:2) untuk mengekstrak minyak mikroalga. Kesan daripada kadar pencampuran yang berbeza (rpm), suhu ($^oC$) dan masa pengekstrakan (jam) telah dijalankan dengan menggunakan sistem pelarut yang telah dioptimumkan untuk menilai keadaan optimum pengekstrakan minyak. Berdasarkan hasil pengeluaran minyak, heptana bersendirian menjadi pelarut terbaik untuk mengeluarkan minyak dengan hasil sebanyak 57.5%, diikuti oleh heptana: metanol (1:2), heptana: etanol (1:1), heptana: etanol (1:2) dan heptana: metanol (1:1) dengan hasil masing – masing 47.5%, 44.8%, 43.2% dan 41.4%. Kuantiti minyak maksimum 61.27% telah diperolehi selepas biojisim *Chlorella vulgaris* diekstrak menggunakan heptana sebagai pelarut pada keadaan optimum berikut: kadar percampuran 600 rpm, suhu 65 $^oC$ dan 5 jam masa pengekstrakan. Kajian ini mengesahkan bahawa suhu meningkat menyebabkan peningkatan hasil minyak, tetapi pada suhu yang lebih tinggi (lebih daripada 65 $^oC$), hasil minyak telah berkurangan. Suhu yang terlalu tinggi dalam pengekstrakan minyak boleh menyebabkan penguraian sebahagian daripada sel-sel alga dan seterusnya mengurangkan hasil minyak yang dikeluarkan.

**Kata kunci:** pengekstrakan soxhlet, pengekstrakan minyak, mikroalga air tawar, *Chlorella vulgaris*, sistem pelarut

## Introduction

Limitations of fossil fuels have brought the studies of microalgae as the promising raw materials to produce biodiesel. Microalgae appear to be the source of biodiesel production because of the high growth rate without competing for arable land which makes algae an exciting raw material to the sustainable fuel portfolio [1]. Besides, it has the potential to produce more oil as compared to the other raw materials [2] such as rapeseed, soybean, sunflower and palm. Moreover, microalgae biodiesel are non-toxic, highly bio-degradable; contain no sulphur and the left over materials after extracting the oil can be used for ethanol production or as soil fertilizer [3]. In addition, renewable biodiesel produce from microalgae is capable of meeting the global demand for transport fuels and oil productivity of microalgae greatly exceeds the oil productivity of the best producing oil crops such as corns.

Chisti [4] reported that *Chlorella* sp., *Spirulina* sp. and *Nitzschia* sp. are the main microalgae sources that are usually used to produce biodiesel. It is because these three microalgae species produce the highest oil content (% dry weight) among the other species with 28-32% oil content produced by *Chlorella* sp., *Spirulina* sp. produce 50 – 77% oil content and *Nitzschia* sp. produce about 45 – 47% oil content. According to Islam et al. [5], microalgae have received much attention as a new source of renewable energy in the form of biodiesel. However, they are not yet commercially viable because of the high cost of the production process and also limited information available on the parameters affecting extraction of microalgae oil for commercial biodiesel production. For this reason, a vigorous quantification of the extraction parameters is critical to optimize and consequently increase the feasibility of the process.

Oil extraction from algae is a hotly debated topic currently because this process is one of the more costly processes which can determine sustainability of algae-based biodiesel. Various methods to extract the oil from microalgae are available such as expeller/press, solvent extraction and supercritical fluid extraction [2]. Expeller pressing is the method of extracting oil with a mechanical press rather than utilizing a chemical extraction process and this method provides yields of only 65 – 70% of the oil [6] while extraction using supercritical fluid gives very high purity and good product concentration but the operating and investment cost is high [7].

Solvent extraction method is a common and efficient technique for producing oil for biodiesel production since it is recovers almost all the oil and leaves behind only 0.5% to 0.7% residual oil in the raw material [8] and it is also involves the transfer of a soluble fraction from a solid material to a liquid solvent. In addition, this method has a relatively low operating cost compared with supercritical fluid extraction [9]. However, there are certain disadvantages for solvent extraction method such as poor extraction of polar lipids, long time required for extraction and hazards of boiling solvents [10].

In order to obtain maximum amount of oil extraction by using solvent extraction method, the optimum condition of extraction process for all parameters used in this study must be optimized. Therefore, the following objectives should be achieved in this investigation which are i) to investigate the oil extraction of microalgae biomass using five different solvent systems and ii) to assess the efficiency of solvent extraction method with the use of three different parameters such as mixing rate, temperature and extraction time to obtain maximum oil extraction.

## Materials and Methods

### Microalgae

The microalgae *Chlorella vulgaris* was used in this research. A microalgal strain *C. vulgaris* was obtained from Culture Collection of Algae and protozoa (CCAP). *C. vulgaris* appears to be the best choice and the most suitable algae species for producing biodiesel [11]. It is one of the most attractive microalgae species for oil extraction owing to its fast growth and easy cultivation [12]. Besides, the strain became the most favored by researchers [13] since it have a high lipids content and easily growth in the laboratory.

### Media preparation

The unicellular microalgae *C. vulgaris* were actually cultured in Bold's Basal Medium with 3-fold nitrogen and vitamins (BBM) by adding 20 mL of (BBM) (I), 12 mL of BBM (II), and 2 mL each of BBM (III) and BBM (IV) to 2000 mL sterilized distilled water (DW). BBM (I) contain the following compounds per 1 L of DW: 75.0 g of $NaNO_3$, 2.5 g of $CaCl_2.2H_2O$, 7.5 g of $MgSO_4.7H_2O$, 7.5 g of $K_2HPO_4.3H_2O$, 17.5 g of $KH_2PO_4$ and 2.5 g of NaCl,

BBM (II) contained the following compounds per litre of DW: 97.0 mg of $FeCl_3.6H_2O$, 41.0 mg of $MnCl_2.4H_2O$, 5.0 mg of $ZnCl_2$, 2.0 mg of $CoCl_2.6H_2O$ and 4.0 mg of $Na_2MoO_4.2H_2O$, BBM (III) contains 0.12 g of vitamin $B_1$ (Thiaminhydrochloride) per 100 mL DW and BBM (IV) consists of 0.1 g of vitamin $B_{12}$ (Cyanocobalamin) per 100 mL DW.

**Preparation of *Chlorella vulgaris* culture**
The process had been done by using aseptic technique to avoid any contamination towards microalgae and media. The medium and flasks were sterilized in an autoclave, HV-85 (HIRAYAMA, Japan) for 15 minutes at 121$^{o}$C. Approximately, 5 mL of microalgae stock culture was seeded into 2 L Schott bottle filled with 2 L of sterilized DW that contained BBM (I-IV) at 25 $^{0}$C. Two fluorescent lamps were used for continuous lighting and was cultured with continuously aerated for 12 days by bubbling air through it at a constant pressure [13].

**Microalgae harvesting**
The *C. vulgaris* cells were harvested using centrifuge model 5810 R (Eppendorf, Malaysia) at 8000 rpm for 10 minutes. After centrifugation, the clear solution had been discarded and the resulting *C. vulgaris* biomass was rinsed once with de-ionized water to remove residual nutrients [14].

**Microalgae freeze drying**
The extraction was performed on the dry biomass. Therefore, freeze dryer was used to dry the microalgae biomass before the oil extraction was took over. The biomass was dried overnight by using freeze dryer, RP2 V (SGD Serail Argenteuil, France) to measure the cell dry weight [15].

**Destruction of microalgae cells**
Freeze-dried samples of 0.05 g of *C. vulgaris* biomass along with 16.6 mL DW were placed into 250 mL of round bottom flask and then sonicated for 5 minutes to lyse the cells [15].

**Oil extraction**
Solvent extraction method by using modified Soxhlet extraction (SE) was used in the oil extraction process. Modified Soxhlet extraction set up mainly consist of the following apparatus: condenser, retort stand, hot plate stirrer, 1L beaker, tube and 250 mL round bottom flask. Approximately 27.2 mL of solvent systems was used for each 0.05 g of the freeze-dried microalgae biomass in extraction step. Five different solvent systems were used to extract the oil from the *C. vulgaris* biomass which are heptane, heptane: methanol (1:1), heptane: methanol (1:2), heptane: ethanol (1:1) and heptane: ethanol (1:2). The extraction took place about 5 hours to extract oil from microalgae. Magnetic stirrer was used to mix up the biomass with the solvent at mixing rate of 600 rpm and temperature of 65 $^{o}$C. After 5 hours of extraction, the mixture was then centrifuged at 4000 rpm for 2 minutes and resulted in separation into three layers [15]. The upper layer contains only water, while middle layer was biomass and lowest layer was oil-solvent mixture. The lowest layer was collected and evaporated using rotary evaporator model BUCHI Rotavapor R-200 to obtain the microalgae oil. After that, the extraction was executed in different parameters such as mixing rate, temperature and extraction time to enhance the oil yield from *C. vulgaris* biomass using the best solvent from previous result. The details of the experiment are summarized in Table 1.

Table 1. Manipulated and constant variables used in each extraction step

| Experiment | Manipulated Variable | Constant Variables |
|---|---|---|
| 1 | Solvent:<br>Heptane,<br>Heptane: methanol (1:1),<br>Heptane: methanol (1:2),<br>Heptane: ethanol (1:1),<br>Heptane: ethanol (1:2) | Mixing rate: 600 rpm<br>Temperature: 65 $^{o}$C<br>Extraction time: 5 hours |

Table 1 (cont'd). Manipulated and constant variables used in each extraction step

| Experiment | Manipulated Variable | Constant Variables |
|---|---|---|
| 2 | Mixing rate:<br>500, 600, and 700 rpm | Temperature: 65 $^{0}$C<br>Extraction time: 4 hours<br>Solvent[a] |
| 3 | Temperature:<br>55, 65, and 75 $^{0}$C | Solvent[a]<br>Mixing rate[b]<br>Extraction time: 4 hours |
| 4 | Extraction time:<br>4, 6, and 8 hours | Solvent[a]<br>Mixing rate[b]<br>Temperature[c] |

[a] Best solvent from experiment 1
[b] Optimum condition of mixing rate from experiment 2
[c] Optimum condition of temperature from experiment 3

**Determination of oil extraction yield**

After extract the oil, the amount of oil extracted using different solvent systems and parameters was determined by using the following equation 1 [16]:

$$\text{oil extraction yield (\%)} = \frac{\text{weight of oil extraction (g)}}{\text{weight of microalgae biomass (g)}} \text{ x } 100\% \quad (1)$$

## Results and Discussion

**Effect of solvent systems on oil extraction**

The effect of solvent systems on microalgae oil extraction yield is shown in Table 2. The solvents used for the extraction of microalgae biomass showed the different yields. The highest oil extraction yield of 57.5% was achieved from *Chlorella vulgaris* biomass was heptane. Approximately 47.5% of oil extraction yield was achieved using heptane: methanol (1:2). Whereas the yield 44.8% was obtained using heptane: ethanol (1:1). The oil extraction yield for heptane: methanol (1:1) and heptane: ethanol (1:2) was found to be 41.4% and 43.2%, respectively.

Table 2. Effect of various solvent systems on oil extraction yield (%)

| Solvent/Solvent Mixture | Ratio | Oil Extraction (%) |
|---|---|---|
| Heptane | - | 57.5 ± 0.5 |
| Heptane: Methanol | 1 : 1 | 41.4 ± 0.5 |
| Heptane: Methanol | 1 : 2 | 47.5 ± 1.0 |
| Heptane: Ethanol | 1 : 1 | 44.8 ± 0.6 |
| Heptane: Ethanol | 1 : 2 | 43.2 ± 1.0 |

Figure 1 shows the percentage of oil yield obtained for different solvent systems. The extraction yield increase in the following order: H:M (1:1) < H:E (1:2) < H:E (1:1) < H:M (1:2) < H. Oil extraction by heptane alone is found to

be most effective than combination of solvent systems. This observation might be due to the other solvent's physical characteristic distracting the ability of heptane to extract the oil. Therefore, the combination of solvent system between heptane and alcohol are less effective to extract the oil compared to heptane alone.

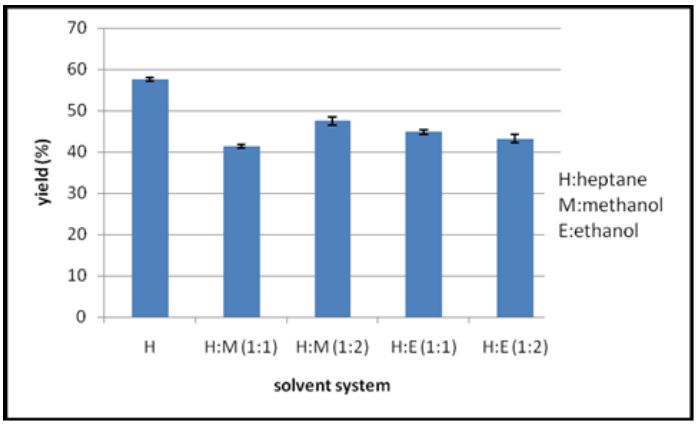



Figure 1. Oil extraction yield with different solvent systems

The selection of the solvent system for oil extraction is an important factor in order to produce the highest yield of oil. Basically, solvent system should have a higher solubility with oil to degrade the cell walls of the microalgae and also to dissolve the oil to enhance the oil yield. However, efficiency of oil extraction yield depends on polarity of the compound and solvent viscosity [17].

The selected solvents were come from two polarity-based classes: polar protic and non-polar. Polar protic solvents usually used to dissolve salt. Generally, these solvents have high dielectric constant and high polarity. The common characteristic of polar protic solvents is hydrogen bond containing hydroxyl group [17] for example water, low molecular weight alcohol such as methanol and ethanol, and the solution that have low molecular-weight carboxylic acid. While, non-polar solvents contain bonds between atoms with similar electronegativities [17] such as carbon and hydrogen. Similar electronegativities mean that small difference between atoms causing less polar bond, thus easier to extract the oil. Alkanes like hexane and heptane are example for this non-polar solvent [18].

Besides, solvent viscosity becomes one of the physical properties that affect the extractability of oil from microalgae. Low-viscosity solvents have a high diffusivity that allows them to easily diffuse into the microalgae biomass to leach out the oil [19].

Based on the research done by Conkerton et al. [20], heptane is the best alternative solvent to replace hexane since the physical properties of heptane is quite similar to hexane which is high stability, low greasy residual and low corrosiveness. Heptane also has a low viscosity and low polarity since it is non-polar group compared to the other solvents. Low viscosity and polarity gave a result of higher yield compare to the other solvent systems.

However, when the heptane is combine with other solvent to extract the oil, the yield of oil extraction become low. This observation is in contrast to the study of Ryckebosch et al. [21] which state that solvent mixture containing a polar and a non-polar solvent could extract a great amount of oil such as a combination of chloroform (non-polar) and methanol (polar). In addition, the result studied by Li et al. [22] also showed a significant difference in extraction efficiency between single and mixture solvent. The oil extraction yield in the mixture was nearly three times higher than when using single solvent.

Despite of these contradict results with Ryckebosch et al. [21] and Li et al. [22], experimental result obtained is similar with Shen et al, [23] where oil recovery was higher in the single solvent. A possible cause for the lower oil

recovery efficiency in mixture solvent may be that small quantities of oils are took over by polar solvent that cannot be extracted by heptane. Besides, the physical properties of solvent systems such as viscosity and polarity might be change due to the mechanism formed by two different solvents with microalgae cells. The combination of solvents may changes the polarity and viscosity of heptane that have an ability to extract the oil, thus may not help to extract the oil as much as heptane alone can extract. However, the combination of solvent systems between heptane and alcohol still can be used as long as it is implied at appropriate proportions of polar and non-polar solvents in order to achieve high oil extraction yields.

**Effect of mixing rate on oil extraction**

The effect of mixing rate on oil extraction is shown in Figure 2. The oil extraction yield in the range of 500 to 700 rpm was evaluated with constant temperature of 4 $^0$C and extraction time of 4 hours. The result obtained shows that the oil yield was increasing with the increase in the mixing rate. The oil extraction yield increased from 54.74% at 500 rpm to 57.86% at 600 rpm. However, at 700 rpm, there was no significant increase in the oil yield where 57.94% of oil can be extracted from *C. vulgaris*.

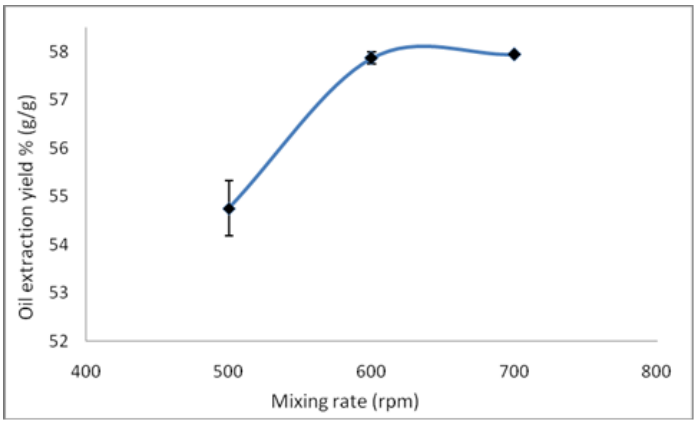



Figure 2. The effect of mixing rate on the oil extraction yield

Mixing rate of the extraction will affects the oil yield of *C. vulgaris*and it is proving by result obtained in Figure 2. Increasing mixing rate will increases the eddy diffusion and the transfer of oil from the slurry form of the microalgae biomass to the solvent mixture [24]. The increasing oil yield shows that the mass transfer plays major role during the extraction process. However, at 700 rpm, the oil yield becomes constant because the extraction has gone completion at 600 rpm and no further increase in oil extraction yield was observed. Thus, it can be concluded that the maximum oil yield was obtained at 600 rpm which is 57.86%.

Similar phenomenon was also found by Suganya and Renganathan [24] that studied the effect of mixing rate on oil extraction from *U. lactuca* using hexane as a solvent and solvent-to-ratio of 5:1. They have extracted oil from 7.81% to 9.36% with the use of mixing rate varying from 200 to 800 rpm. Maximum oil yield was achieved at 500 rpm which is 9.36%. Another research by Kadi and Fellag [25] indicated that the oil extraction from olive foot cake using hexane as a solvent have extracted oil from 6.9% to 7.7% with the use of mixing rate varying from 600 to 1000 rpm and the maximum yield was obtained at 800 rpm which is 7.7%. Even though the optimum mixing rate for both cases were achieved in the range of 500 to 800 rpm, the oil yield obtained from the previous researches is smaller which is between 7.7 to 9.36% compared to the current study (57.86%). The major differences in the oil yield obtained from previous studies and current study is due to the different extraction time used to extract oil from *U. lactuca*, olive foot cake and *C. vulgaris*. Oil yield obtained from *U. lactuca* and olive foot cake were studied for 120 minutes and 10 minutes only, while the extraction time used to obtain the oil yield from *C. vulgaris* is 4 hours which is longer than the extraction time used in previous studies and eventually more oil is extracted in longer extraction time.

**Effect of temperature on oil extraction**

The effect of temperature on the microalgae oil extraction was investigated over the range of 55 to 75 $^0$C from *C. vulgaris* biomass (Figure 3). The increase in temperature from 55 to 65 $^0$C leads to increase in the oil extraction yield from 47.29% to 56.92% while increasing the temperature from 65 $^0$C to 75 $^0$C resulted in decreasing the oil yield from 56.92% to 52.26%.

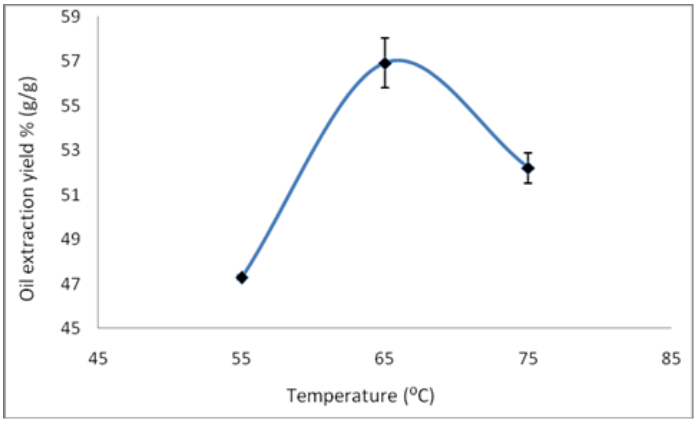



Figure 3. The effect of extraction temperature on the oil extraction yield

At the lower temperature (smaller than 65 $^0$C), the oil extraction yield was found to be increased with an increase in the temperature (Figure 2). This result is due to the enhanced in the dissolution capacity of the solvent system [24]. Moderate increase in temperature can lead to a large decrease in fluid density, with a consequent reduction in solute solubility and volatility which resulted in the increase of oil yield [26]. In addition, the increase in temperature will also accelerate the mass transfer and improve the oil extraction yield [27]. However, the result in Figure 3 shows a decrease in oil yield from temperature of 65 to 75$^0$C. High temperature will affect the solubility of interfering substances in the sample, resulting in lower selectivity of the extracts. Moreover, too high of an extraction temperature may cause partial decomposition of the extracted substances and thus disturb the result of the extracted lipids [28]. From the result obtained in Figure 3, it can be concluded that the maximum oil extraction yield was obtained at temperature of 65 $^0$C which is 56.92%. This result was also found in the study of the effect of temperature on the extraction yield of spearmint (*M. spicata L.*) leaves at 3 different temperature level of 40, 50 and 60 $^0$C [29]. The extraction yield of spearmint leaves increased with temperature and the highest extraction yield (60.57 mg/g) was obtained at 60 $^0$C.

**Effect of extraction time on oil extraction**

In this research, the effect of extraction time on the oil extraction yield of *C. vulgaris* was examined with different time intervals varying from 4 to 8 hours. The result obtained in Figure 4 shows that the oil extraction yield enhanced with the increase of extraction time. The extraction was settled at the optimum mixing rate and temperature from the previous experiment which is 600 rpm and 65 $^o$C, respectively. The oil yield was observed to be increased from 56.09% to 61.27% from 4 hours to 6 hours. However, at 8 hours, the oil yield did not show any significant changes in the extraction where 61.26% of oil can be extracted at that time. Hence, 6 hours was found to be an optimum extraction time for the oil extraction of *C. vulgaris* where the oil obtained is in the maximum yield (61.27%).

It is crucial to determine the optimum extraction time required for the extraction process. As the extraction time increases, the oil yield also increases. The increase in the oil yield is due to the increase of mass transfer of oil [24]. However, at 8 hours, the oil yield becomes constant because the extraction has gone completion at 6hours and no

further increase in oil extraction yield was observed. Thus, it can be concluded that the maximum oil yield was obtained at 6 hours which is 61.27%.

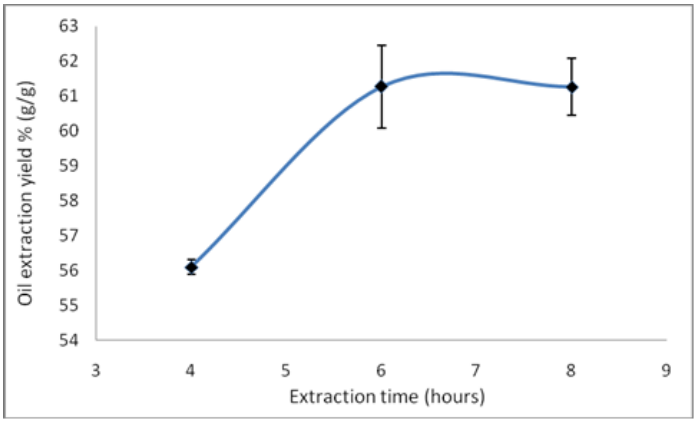



Figure 4. The effect of extraction time on the oil extraction yield

A similar pattern of oil yield produce also was made by McConnel and Farag [30] which studied the extraction of *C. vulgaris* using solvent to dry algae ratio of 30:1 at different time interval varying from 5 to 100 minutes. The optimum time was found to be 60 minutes for maximum production of oil at 2.60 g lipid extracted per 100 g of dry algae. At the extraction longer than 60 minutes, the oil yield obtained is constant. Another research by Suganya and Renganathan [24] was studied the effect of extraction time on the oil yield of *U. lactuca* at different time intervals varying from 20 to 160 min shows that at 140 minutes, the oil was found at the maximum yield which is 10.59% and at extraction time above 140 min did not show any further significant improvement in the extraction.

## Conclusion

The extraction of oil from *Chlorella vulgaris* biomass using heptane showed the highest result compared to the other solvent systems with the yield of 57.5%. By using heptane as solvent system, the maximum oil extraction yield of 61.27% was obtained with optimum conditions of mixing rate of 600 rpm, temperature of 65 $^{0}$C and 5 hours of extraction time from *C. vulgaris*. The result shows that the oil extraction yield increasing with the increase of mixing rate, temperature and extraction time. When the operating condition of the extraction process passes the optimum condition, the oil yield of *C. vulgaris* show no significant increases. The constant oil yield extracted is because the extraction has gone completion at that point. Extraction process should not be done at higher temperature to avoid the decomposition of the microalgae which will affect the result of oil yield obtained.

## Acknowledgement

The authors would like to acknowledge the UMP Research Grant (Grant No. RDU 140390 and RDU 150396) from Universiti Malaysia Pahang, which has fully supported this research.

## References

1. Hannon, M., Gimpel, J., Tran, M., Rasala, B. and Mayfields, S. (2010). Biofuels from alga: Challenges and potential. *Biofuels*, 1(5): 763 – 784.
2. Demirbas, A. (2009). Production of biodiesel from algae oils. *Energy Sources A*, 31: 163 – 168.
3. Demirbas, A. and Demirbas, F. M. (2011). Importance of algae oil as a source of biodiesel. *Energy Conversion and Management*, 52: 163 – 170.
4. Chisti Y. (2007). Biodiesel from microalgae. *Biotechnology Advances*, 25: 294 – 306.
5. Islam, M. A., Brown, R. J., O'Hara, I., Kent, M. and Heimann, K. (2014). Effect of temperature and moisture on high pressure lipid/oil extraction from microalgae. *Energy Conversion and Management*, 88: 307 – 316.

6. Weingarten, H. (2015). What is expeller and why does it matter. Retrieved from http://blog.fooducate.com/2010/12/08/what-is-expeller-pressed-oil-and-why-does-itmatter/http://biofuel. org.uk /second-generation-biofuels.html. Date access 25 November 2015.
7. Mongkholkhajornsilp, D., Donglas, P. L., Elkamel, A., Tepparitoon, W. and Pongamphair, S. (2004). Supercritical $CO_2$ extraction of nimbim from neem seeds-a modeling study. *Journal of Food Engineering*, 71(4): 331 – 340.
8. Niraj, S. T., Sunita, J. R., Renge, V. C., Satish, V. K., Chavan, Y. P. and Bhagat, S. L. (2011). Extraction of oil from algae by solvent extraction and oil expeller method. *International Journal Chemical Science*, 9(4): 1746 – 1750.
9. Ahmad, A. L., Mat Yasin, N. H., Derek, C. J. C and Lim, J. K. (2013). Microfiltration of *Chlorella sp*.: Influence of material and membrane pore size. *Membrane Water Treatment*, 4(2): 143 – 155.
10. Kirolia, A., Bishnoi, N. R. and Singh, R. (2013). Microalgae as a boon for sustainable energy production and its future research and development aspects. *Renewable and Sustainable Energy Review,* 20: 642 – 656.
11. Mata, T. M., Martins, A. A. and Caetano, N. S. (2010). Microalgae for biodiesel production and other applications: A review. *Renewable and Sustainable Energy Review,* 14: 217 – 232.
12. Al-Iwayzy, S. H., Yusaf, T. and Al-Juboori, R. A. (2014). Biofuels from the fresh water microalgae *Chlorella vulgaris* (FWM-CV) for diesel engines. *Energies*, 7: 1829 – 1851.
13. Ahmad, A. L., Mat Yasin, N. H., Derek, C. J. C and Lim, J. K. (2014). Chemical cleaning of a cross-flow microfiltration membrane fouled by microalgal biomass. *Journal of Taiwan Institute of Chemical Engineers*, 45: 233 – 241.
14. Halim, R., Gladman, B., Danquah, M. K. and Webley, P. A. (2011). Oil extraction from microalgae for biodiesel production. *Bioresource Technology*, 102: 178 – 185.
15. Ahmad, A. L., Mat Yasin, N. H., Derek, C. J. C and Lim, J. K. (2014). Comparison of harvesting methods for microalgae *Chlorella vulgaris* sp. and its potential use as a biodiesel feedstock. *Environmental Technology*, 35(17-20): 2244 – 2253.
16. Gutierrez, L. F., Ratti, C. and Belkacemin K. (2008). Effects of drying method on the extraction yields and quality of oils from quebec sea buckhtom (*Hipphophaerhamnoides L.*) seeds and pulp. *Food Chemistry*, 106: 896 – 904.
17. Rezaie, M., Farhoosh, R., Iranshahi, M., Sharif, A. and Golmohamadzadeh, S. (2015). Ultrasonic- assisted extraction of antioxidative compounds from Bene (*Pistacia atlantica subsp. Mutica*) hull using various solvents of different physicochemical properties. *Food Chemistry*, 173: 577 – 583.
18. Reichardt, C. and Welton, T. (2011). Solvents and solvent effects in organic chemistry. John Wiley & Sons.
19. Wijekon, M., Bhat, R. and Karim, A. A. (2011). Effect of extraction solvents on the phenolic compounds and antioxidant activities of bunga kantan (*Etlingera elatior* Jack) inflorescence. *Journal of Food Composition and Analysis*, 24: 615 – 619.
20. Conkerton, E. J., Wan, P. J. and Richard, O. A. (1995). Hexane and heptane as extraction solvents for cottonseed: A laboratory-scale study. *Journal of American Oil Chemical Society*, 72: 963 – 965.
21. Ryckebosch, E., Myuylaert, K. and Foubert, I. (2012). Optimisation of an analytical procedure for extraction of oils from microalgae. *Journal of American Oil Chemical Society*, 89: 189 – 198.
22. Li, Y., Naghdi, F. G., Garg, S., Adarme-Vega, T. C., Thurecht, K. J., Ghafor, W. A., Tannock, S. and Schenk P. M. (2013). A comparative study: the impact of different oil extraction methods on current microalgal oil research. *Microbial Cell Factories*, 13: 1475 – 2859.
23. Shen, Y., Pei, Z. J., Yuan, W. Q. and Mao, E. R. (2009). Effect of nitrogen and extraction method on algae oil yield. *International Journal of Agriculture and Biology Engineering*, 2: 51 – 57.
24. Suganya, T. and Renganathan, S. (2012). Optimization and kinetic studies on algae oil extraction from marine macroalgae *Ulvalactuca*. *Bioresources Technology*, 107: 319 – 326.
25. Kadi, H. and Fellag, H. (2110). Modeling of oil extraction from olive foot cake using hexane. *Grass Aceitas*, 52: 369 – 372.
26. Roop, R. K., Akgerman, A., Dexter, B. J. and Irvin, T. R. (1989). Extraction of phenol from water with supercritical carbon dioxide. *Journal of Supercrital Fluids*, 2: 51 – 56.
27. Wang, L., Yang, B., Du, X. and Yi, C. (2008). Optimization of supercritical extraction of flavonoids from *Puerarialabota*. *Food Chemistry*. 108: 737 – 741.

28. Fang, Z., Smith, R. L. and Qi, X. H. (2015). Production of biofuels and chemicals with ultrasound. *Journal of Food Engineering*, 5: 147 – 148.
29. Bimakr, M., Abdul Rahman, R., Taip, F. S., Ganjiloo, A., MdSalleh, L., Selamat, J., Hamid, A. and Zaidul, A. S. M. (2011). Comparison of different extraction methods for the extraction of major bioactive flavonoid compounds from Spearmint (Menthaspicata L.) leaves. *Food and Bioprocess*, 89: 67 – 72.
30. McConnel, B. and Farag, H. I. (2013). Kinetics study of the solvent extraction of lipids from *Chlorella vulgaris*. *International Journal of Engineering and Technical Research,* 10: 1 – 10.

*Malaysian Journal of Analytical Sciences, Vol 21 No 3 (2017): 745 - 753*
*DOI: https://doi.org/10.17576/mjas-2017-2103-24*

**MALAYSIAN JOURNAL OF ANALYTICAL SCIENCES**
*Published by The Malaysian Analytical Sciences Society*
**ISSN 1394 - 2506**

# $O_3/S_2O_8^{2-}$ OXIDATION OF REACTIVE RED 120: EFFECT OF OPERATIONAL PARAMETERS

## (Pengoksidaan $O_3/S_2O_8^{2-}$ Terhadap Reactive Red 120: Kesan Parameter Operasi)

Siti Nasuha Sabri, Che Zulzikrami Azner Abidin*, Fahmi Muhammad Ridwan, Ong Soon An, Razi Ahmad, Kow Su Huan

*School of Environmental Engineering,*
*Universiti Malaysia Perlis, Kompleks Pusat Pengajian Jejawi 3, 02600 Arau, Perlis, Malaysia*

**Corresponding author: zulzikrami@unimap.edu.my*

Received: 28 November 2016; Accepted: 5 February 2017

**Abstract**

In this research, the decolourisation performance of Reactive Red 120 (RR120) in aqueous solution using $O_3/S_2O_8^{2-}$ was evaluated. RR120 was selected due to high solubility in the aquatic environment. Ozonation ($O_3$) experiments were conducted as a control, to compare the treatment performance after addition of sodium persulphate. The aim of this research is to identify the effect of operational parameters of $O_3/S_2O_8^{2-}$ treatment on colour and COD removal. All experiments were carried out under continuous operation in a bubble column reactor. Operational parameters, namely initial dye concentration, $S_2O_8^{2-}$ dosage, initial pH, and contact time, were manipulated to optimize the performance of $O_3/S_2O_8^{2-}$. The effect of parameters on decolourisation performance was identified based on colour and COD removal. The performance of colour and COD removal in the $O_3$ was also compared with $O_3/S_2O_8^{2-}$ treatment processes. The intermediates were characterized based on its spectra evolution via UV-Vis spectrophotometer. The findings showed on increases in $S_2O_8^{2-}$ dosage that leads to an increase in the decolourisation efficiency. In addition, when the initial concentration increased to 300 mg/L, the decolourisation efficiency decreases as high concentration of azo bond cause the deficiency of the oxidation process. The $O_3/S_2O_8^{2-}$ performance also improved in alkaline pH, in the presence of hydroxyl radical. By comparing these two treatments, $O_3/S_2O_8^{2-}$ obtained better removal efficiency in colour than $O_3$.

**Keywords**: $O_3/S_2O_8^{2-}$, ozonation, decolourisation, Reactive Red 120, persulphate

**Abstrak**

Dalam kajian ini, prestasi penyingkiran warna $O_3/S_2O_8^{2-}$ dinilai terhadap Reactive Red 120 (RR120) dalam larutan akues. RR120 telah dipilih kerana keterlarutan tinggi dalam persekitaran akuatik. Eksperimen pengozonan ($O_3$) telah dijalankan sebagai kawalan, untuk membandingkan prestasi rawatan selepas penambahan natrium persulfat. Tujuan kajian ini adalah untuk mengenal pasti kesan parameter operasi rawatan $O_3/S_2O_8^{2-}$ terhadap penyingkiran warna dan COD. Eksperimen ini telah dijalankan di bawah operasi yang berterusan dalam reaktor turus panjang. Parameter operasi, iaitu kepekatan awal pewarna, dos $S_2O_8^{2-}$, pH awal, dan masa sentuhan, telah dimanipulasikan untuk mengoptimumkan prestasi $O_3/S_2O_8^{2-}$. Kesan parameter terhadap prestasi penyingkiran telah dikenal pasti berdasarkan penyingkiran warna dan COD. Prestasi penyingkiran warna dan COD dalam $O_3$ juga telah dibandingkan dengan proses rawatan $O_3/S_2O_8^{2-}$. Perantaraan daripada RR120 telah dicirikan berdasarkan perubahan spektrum menerusi spektrofotometer UV-Vis. Hasil kajian menunjukkan peningkatan dos $O_3/S_2O_8^{2-}$ membawa kepada peningkatan kecekapan penyingkiran warna. Di samping itu, apabila kepekatan awal RR120 meningkat kepada 300 mg/L, kecekapan peyingkiran warna turut berkurangan, kerana kepekatan ikatan azo meningkat menyebabkan proses pengoksidaan berkurangan. Prestasi $O_3/S_2O_8^{2-}$ juga bertambah baik pada pH alkali, dengan kehadiran radikal hidroksil. Dengan membandingkan kedua-dua perawatan, didapati $O_3/S_2O_8^{2-}$ mempunyai kecekapan penyingkiran warna yang lebih baik daripada $O_3$.

**Kata kunci:** $O_3/S_2O_8^{2-}$, pengozonan, penyingkiran warna, Reactive Red 120, persulfat

## Introduction

Textile industry is one of the largest industries in the world in terms of its production and employment [1]. Dyes are widely used in the textile industries due to favourable characteristics, such as intense colour, water fastness, and uncomplicated application techniques. In the industries, the azo are among the most common synthetic dyes both in terms of the number and amount produced with azo bond groups [2]. Besides, azo dyes account for approximately 60 – 70% of all dyes used in food and textile manufacture [3]. Normally industrial effluent is not treated completely before discharging it into the water bodies such as rivers or lakes. There are many industries come out with their own wastewater treatment plant. But the discharge effluents still do not follow the standard that can discharge to water bodies. Dye wastewater is mainly generated from the wet-processing originates from washing and bleaching in textile industry [4,5]. Dye is a colorant used to dye textile fibres; in other words, it has an affinity to the material to which it is applied to. The colour of dyes is due to the presence of chromophore group, which is also known as auxochoromes and conjugated bond [6]. Azo dye wastewater is comprised of high biological oxygen demand (BOD) and chemical oxygen demand (COD) content, which has the impact on visible colour; obstruct light penetration and oxygen transfer into water bodies. The common methods used in dye wastewater treatment are carbon adsorptions and flocculation processes. Though other parameters can be treated by conventional chemical, physical or biological method, colour remained after treatment. Therefore, the colour problem caused by residual dyes requires more effort and time to study and investigate [2].

Advanced oxidation processes (AOPs) have high efficiency in treating dye wastewater in terms of decolourisation and degradation of refractory pollutants compared to other methods. Over years, ozonation and AOPs involving ozone in combination with hydrogen peroxide ($O_3/H_2O_2$), photolytic $H_2O_2$ oxidation (UV radiation with $H_2O_2$) and advanced fenton became the new technology to treat dyes textile and dyestuff industrial effluent. Now, ozone-based concept treatment has extended to the oxidation processes with sulphate radicals ($SO_4^{\bullet-}$), namely ozone persulphate ($O_3/S_2O_8^{2-}$). This treatment has operational advantages over conventional processes such as suitable for wide pH range, low cost of oxidant precursors, no post treatment steps and complete mineralization of pollutants into harmless products [7]. Lastly, the present research is very significant for the development of the efficient and economical treatment for the mineralization of the industrial dye wastewater. Thus, this current study will investigate the efficiency of $O_3$ and $O_3/S_2O_8^{2-}$ on industrial dye wastewater treatment.

## Materials and Methods

### Materials

The analytical grade diazo RR120 was selected as model due to its common application in industries obtained from Sigma-Aldrich. Its molecular weight and molecular formula is 1,469.98g and $C_{44}H_{24}Cl_2N_{14}O_{20}S_6Na_6$, respectively. The appropriate weight of dye will be dissolve to ultrapure water for the preparation of stock solution. Figure 1 present the chemical structure of the studied dye.

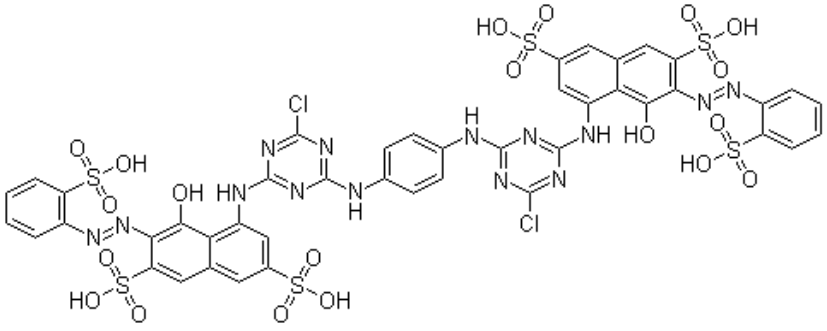


Figure 1. Chemical Structure of RR120 [8]

### Experimental set-up

$O_3$ gas was generated in laboratory and supplied to a 2 L of cylindrical glass reactor connected to 2% of potassium iodide trap which act as $O_3$ destructor. The $O_3$ gas was generated using A2Z (model Z-3G) Ozone Generator which

continuously supplied with purified $O_2$. During experiments, $O_3$ gas constantly flow through a diffuser to produce fine bubbles into 2 L dye sample. For the $O_3/S_2O_8^{2-}$, predetermined $S_2O_8^{2-}$ dosage was added to the dye sample before $O_3$ entered the reactor.

2 L/min $O_2$ flow rate was applied to generate $O_3$ throughout the experiments. Different dosage of 1, 3, and 5 g $S_2O_8^{2-}$ /g dye at pH 7. The $O_3$ and optimum $S_2O_8^{2-}$ dosage were applied to the study of the effects of pH (3, 5, 7, 9, 11), together with the initial concentration of 100 and 300 mg/L. The experiments were conducted at room temperature with different contact time of 0, 1, 2, 3, 4, 5, 10, 15, and 20 minutes. Finally, the samples were withdrawn at definite intervals for analyses.

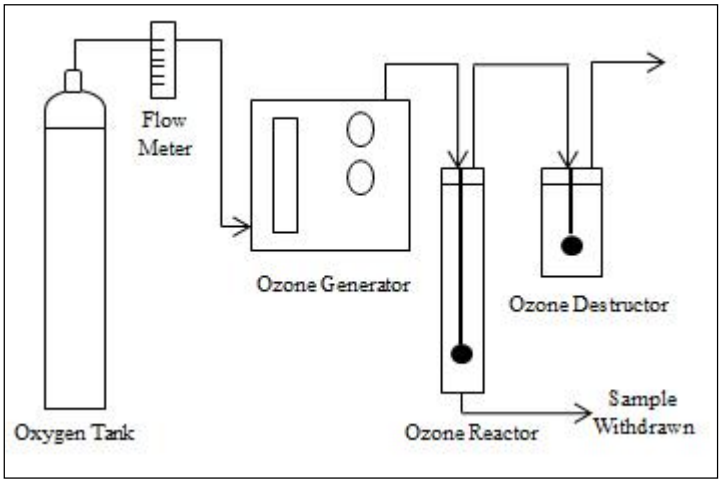



Figure 2. Schematic diagram of experimental set-up for $O_3$ and $O_3/S_2O_8^{2-}$

**Analytical method**

The potassium iodide titration will use to determine the $O_3$ flow rate dye samples. UV-Vis spectrophotometer will be used to analyse the absorbance colour change and dye concentration of the dye samples. The pH value before and after the treatment will be tested by using pH meter (Hannah Instruments H1223). The value of COD will be tested before and after treatment by $O_3/S_2O_8^{2-}$ oxidation with the standard APHA method. HACH DR200 COD reactor and DR2800 spectrophotometer will be used to react and take the COD reading in terms of mg/L, respectively [9]. The COD analysis will repeat for 3 times and the average is calculate. The removal efficiency of COD and colour was determined using Eq. 1.

$$\text{Removal (\%)} = [\ C_i - C_f/C_i\ ] \times\ 100 \quad (1)$$

where $C_i$ and $C_f$ were respectively refer to the initial and final colour and COD concentration.

## Results and Discussion

The comparison of colour and COD removal of RR120 for both treatment methods are based on the optimum operating parameter, where the most favourable condition to achieve highest removal efficiency are at pH 7, 100 mg/L of initial dye concentration and dosage of 5 g $S_2O_8^{2-}$/g dye for $O_3/S_2O_8^{2-}$system. In addition, ozone flow rate was maintained at 2 L/min.

**Effect of initial pH**

The effect of initial pH on the UV-Vis spectra obtained is given in the Figure 3. The visible region reduces rapidly in alkaline condition, might be due to the dissociation of the N=N bonds. The decreasing of the visible region means that there is cleavage of chromophore, which is azo bond that give colour to RR120.

The pH value was known as the important parameters that affect the colour and COD removal. For the initial concentration of 100 mg/L and initial dosage of 5 g $S_2O_8$/g dye, the dye has completely decolourize after 5 minutes of treatments as shown in Figure 4. Various studies showed that solution of pH is directly effect the decomposition of ozone [10]. The ozone molecular remain as the main oxidant at low pH values, while at high pH hydroxyl radicals are formed from ozone decomposition [11]. Since the decolourization of dye can be at different pH in colour effluents, the effects of pH value in the pH range 3 to 11 was studied. The solution of dyes were adjusted by addition of $H_2SO_4$ or NaOH in order to get desired pH. The complete decolourization was observed from pH 3 to 5 and the further to 11. This condition may be explained by the radical way reactions predominated at higher pH values which is efficient in colour removal by equal cleavage of two electron bond [12].

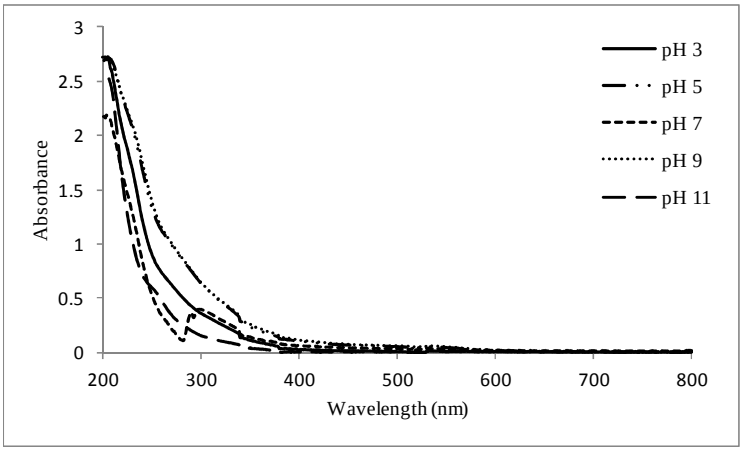



Figure 3. Effect of pH on the UV-Vis spectra

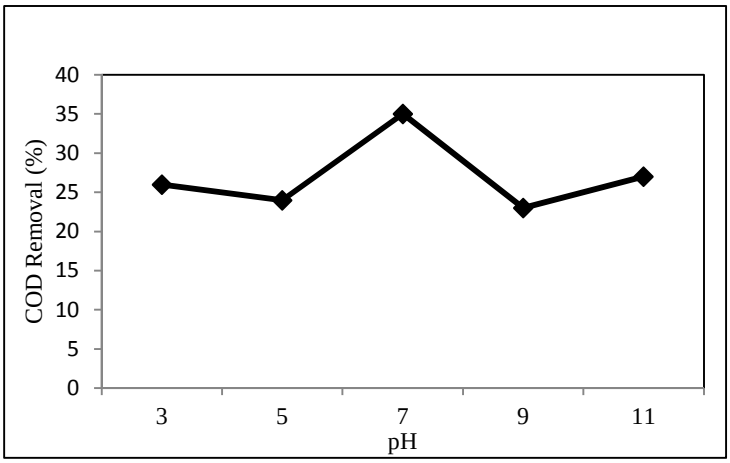



Figure 4. Effect of pH on the COD removal

Figure 4 also presented the COD results obtained for the COD analysis of dye solution after the $O_3/S_2O_8^{2-}$ treatment. COD removal was decreased from pH 3 to 5 and sharply rose to 7. This can explained by reaction between molecular ozone and organic polltant is the predominat mechanism at low pH and took over by hydroxyl radicals at high pH [13]. Therefore, the COD concentration is decreased as pH value increase due to stronger oxidizing power of hydroxyl radicals.

**Effect of initial dosage**

The changes of UV-Vis spectra obtained from the different intial $S_2O_8^{2-}$ dosage are presented in Figure 5. Figure below represented two different trends of wavelength spectrum; the first is before the treatment and the second is after the treatment. After 20 minutes treatment, the peaks of absorbance in the visible region gradually declined resulting the decolourization. Therefore, the decrease of visible region indicate that azo bonds cleavage, while in UV region indicates aromatic such as benzene and naphthalene cleavage.

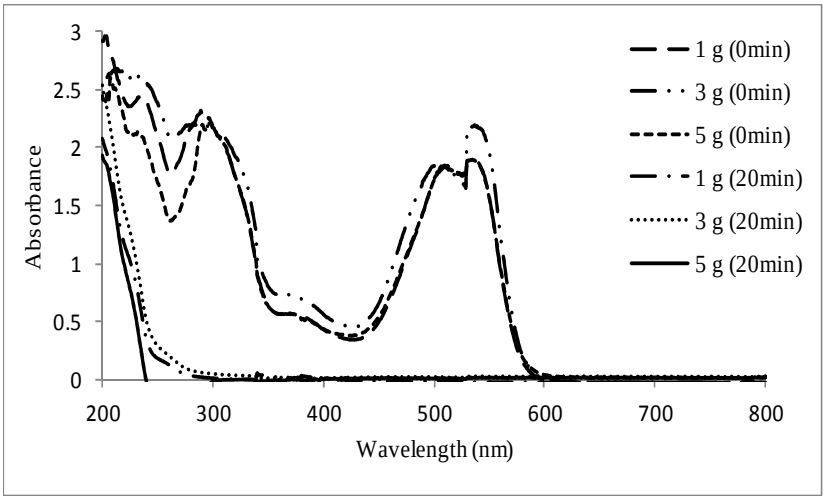



Figure 5. Effect of $S_2O_8^{2-}$ dosage on the UV-Vis spectra

Figure 6 showed that at dosage 5 and 3 g $S_2O_8^{2-}$/g dye, the percentage of colour removal for RR120 almost similar. An amount 5 g $S_2O_8^{2-}$/g dye has 25% COD concentration at 10 min, and 3 g $S_2O_8^{2-}$/g dye achieved after 15 minutes, while dosage 1 g $S_2O_8^{2-}$/g dye only achieved after 20 min of reaction time. Hence, it is necessary to further increase the dosage to various levels in order to investigate the relationship of dosage with colour and COD removal. The initial $S_2O_8^{2-}$ dosage gives a very important effect in the generation of hydroxyl and sulphate radicals for the dye degradation. In general, higher hydroxyl radical concentrations produced from the higher initial dosage which able to decomposes more target compound such as dyes resulting colour and COD removal. In this research, the degradation of dye was evaluate for several initial $S_2O_8^{2-}$ dosage (1, 3, 5 g $S_2O_8^{2-}$/g dye) at constant initial dye concentration and pH. The results indicate that, higher dosage of $S_2O_8^{2-}$ produces higher colour and COD removal. Generally, when $S_2O_8^{2-}$ is added into the ozonation system, the decomposition of $O_3$ into hydroxyl radical accelerated the process and shift the process entirely to an AOPs [14]. Therefore, with the more number of hydroxyl radicals and the presence of sulphate radical, they can attack the azo bond faster than breaking down the sulphonate group and naphthalene ring in dye [15].

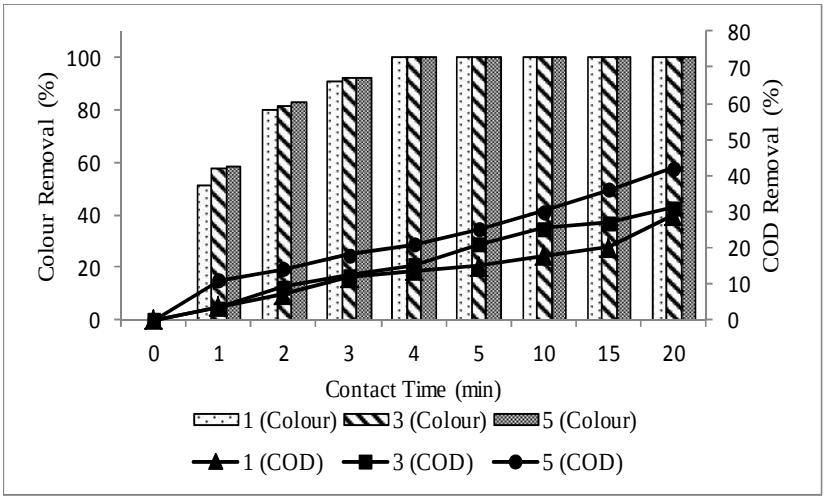



Figure 6. Effect of $S_2O_8^{2-}$ dosage on the colour and COD removal

**Effect of initial dye concentration**

Figure 7 shows the effect of initial dye concentration on the UV-Vis spectra during $O_3/S_2O_8^{2-}$. It can be seen that the intensity of absorbance was reduced sharply after 20 minutes of treatment time for $O_3/S_2O_8^{2-}$, which represents the cleavage of azo bond and resulting in decolourisation. On the other hand, the benzene and naphthalene ring are connected to the azo bond at 212 and 298 nm, respectively in the UV region also showed greatly reduced with $O_3/S_2O_8^{2-}$ treatment. Azo bond will be attacked first before the degradation on the benzene ring or naphthalene. This is because the absorption bands intensities for UV region is degraded more slowly than visible band. Therefore, the colour of RR120 has been disappeared first by breaking azo bond and the followed by oxidation of benzene ring and naphthalene that cannot been see by eyes, but only detected with UV-Vis [16].

In this study, the dye degradation was investigated for several initial concentrations of dye (100 and 300 mg/L) at a constant initial dosage of 5 g $S_2O_8^{2-}$/g dye. Figure 8 illustrated the effect of initial dye concentration on the colour and COD removal during $O_3/S_2O_8^{2-}$ at constant pH which is pH 7. The colour removal efficiency decrease as the concentration of dye increase due to less production of persistent intermediates [12]. The initial dye concentration of 100 mg/L achieved more that 80% of colour removal after 2 minutes, whereas 300 mg/L obtained after 10 minutes. On the other hand, completely decolourisation was presented after 4 and 15 minutes for 100 and 300 mg/L dye concentration, respectively. The initial dye concentration give an important role in the determination of economical use of ozone for decolourisation [10]. Therefore, longer reaction time is needed to completely decolourise higher concentration of dye. Various researches have obtained that the time required for decolourisation of the dye solution is dependent on the initial dye concentration [17]. The COD removal has the same result as colour reduction efficiency. It can be seen that 100 mg/L achieved better COD reduction compared to 300 mg/L dye concentration. The 100 mg/L dye concentration reduced 10% of the COD concentration after 1 min of treatment, whereas 300 mg/L concentration achieved after 3 minutes. In fact, increasing the dye concentration will decreased the pollutant ration of ozone molecules to dye molecules. Therefore, more oxidants needed to be consumed in order to completely degrade the refractory pollutants. The removal rate of COD will increase as the increasing of the treatment contact time. This condition can be explained by the amount of hydroxyl free radicals in dye solutions increase with the reaction time [18].

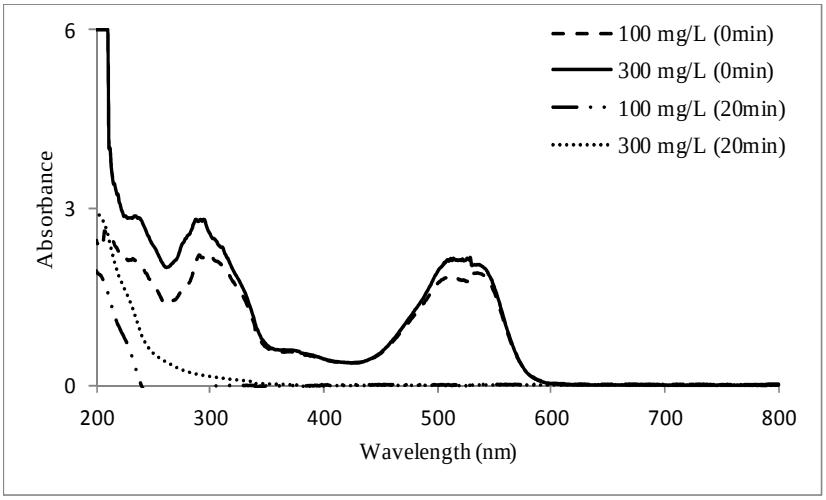



Figure 7. Effect of initial dye concentration on the UV-Vis spectra

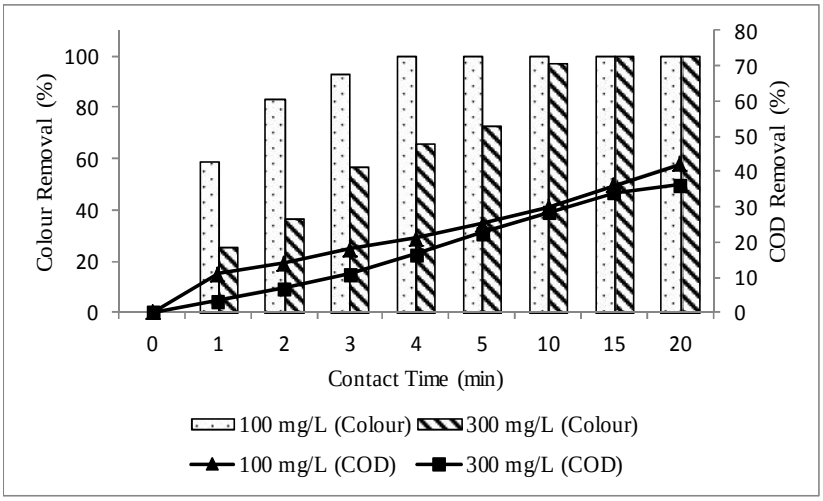



Figure 8. Effect of initial dye concentration on the colour and COD removal

**Comparison of $O_3$ and $O_3/S_2O_8^{2-}$**

Figure 9 showed the colour, and COD removal percentages of RR120 at initial dye concentration 100 mg/L for a different method which are $O_3$ and $O_3/S_2O_8^{2-}$. This graph indicates increasing in reaction time has caused in an increasing in colour and COD removal. The decolourisation of dye occurred faster than the COD removal. This situation may be explained that chromophore may destroyed during treatment and partially mineralized to a smaller fragments [19]. The $O_3/S_2O_8^{2-}$ oxidation achieved completely decolourisation after 4 min, while this condition happened to $O_3$ after 5 min. The results proved that $O_3/S_2O_8^{2-}$ more capability to breakdown the azo bond from the dye structure than the $O_3$ alone. This is because the $O_3/S_2O_8^{2-}$ is involving the generation of two type reactive free radicals, which are hydroxyl radicals and sulphate radical at neutral or basic pH. Both radicals played an important role in this processes in terms of decolourisation. On the other hand, $O_3$ is only able to produce the hydroxyl radicals through the process.

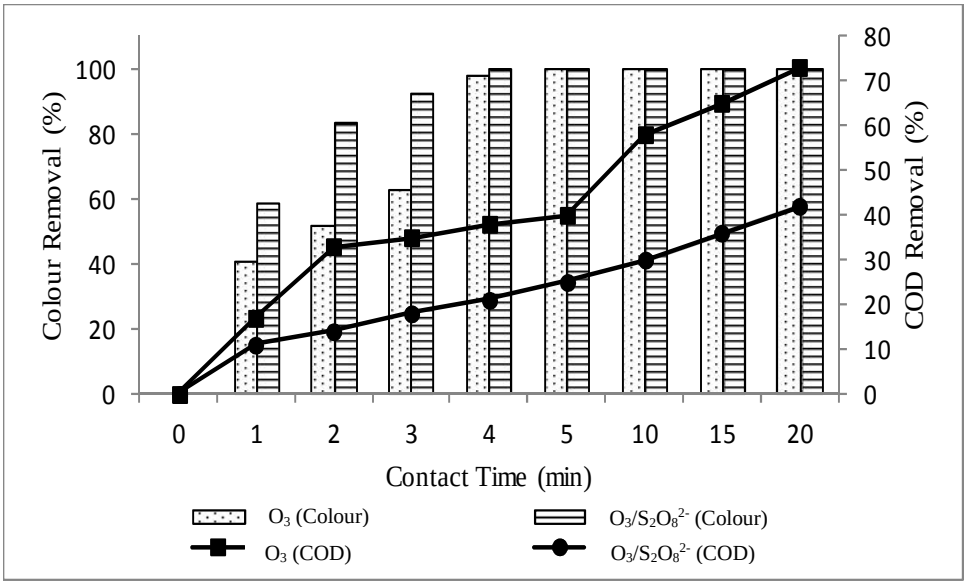



Figure 9. Effect of $O_3$ and $O_3/S_2O_8^{2-}$ on the colour and COD removal

## Conclusion

This study has found that generally, the $O_3/S_2O_8^{2-}$ advanced oxidation treatment provides good performances in the colour removal of the RR120 in water. The initial $S_2O_8^{2-}$ dosage, dye concentration and pH give a very important role in the generation of hydroxyl and sulphate radicals for the dye generations. The results of this investigation show that, the decolourisation was strongly depending on initial $S_2O_8^{2}$ dosage. The decolourisation efficiency increased with increasing $S_2O_8^{2-}$ dosage and reaction time. While, decolourisation efficiency decreased with raising the initial dye concentration.

## Acknowledgement

This work was carried out with the support of Ministry of Higher Education (MOHE), Malaysia for financial support under the grant of FRGS 9003-00513.

## References

1. Wang, Z., Xue, M., Huang, K. and Liu, Z. (2010). Textile dyeing wastewater treatment. Intech Open Acess Publisher: pp. 91 – 116.
2. Muqing, Q., Shou, J., Ren, P. and Jiang, K. (2014). A comparative study of the azo dye reactive Black 5 degradation by UV/$TiO_2$ and photo-fenton processes. *Journal of Chemical and Pharmaceutical Research*, 6(7): 2046 – 2051.
3. Rauf, M. A. and Ashraf, S. S. (2009). Application of advanced oxidation processes (AOP) to dye degradation-an overview. In Dyes and Pigments : New Research. Nova Science Publishers. United Arab Emirates: pp. 260 – 290.
4. Lokesh, K. N. and Kiran, S. R. (2013). Biological methods of dye removal from textile effluents A review. *Journal of Biochemical Technology*, 3(5): 177 – 180
5. Smita, V., Quaff, A. R., Pandey, N. D. and Venkatesh, K. (2014). Decolorization and mineralization of C.I. direct Red 28 Azo dye by ozonation. *Desalination and Water Treatment*, 57(9): 4135 – 4145.
6. Zhang, F., Yediler, A., Liang, X. and Kettrup, A. (2004). Effects of dye additives on the ozonation process and oxidation by-products: A comparative study using hydrolyzed C.I. Reactive Red 120. *Dyes and Pigments*, 60(1): 1–7.

7. Abu Amr, S. S., Aziz, H. A., Adlan, M. N. and Alkasseh, J. M. A. (2014). Effect of ozone and ozone/persulfate processes on biodegradable and soluble characteristics of semiaerobic stabilized leachate. *Environmental Progress & Sustainable Energy*, 33(1): 184 – 191.
8. Sigma Aldrich – Reactive Red 120 (2016). Acess online from http://www.sigmaaldrich.com/catalog/product/sigma/r0378?lang=en&region=MY&gclid=CjwKEAiArfDBRDeyOybg8jd2U4SJAAoE5XqFW4bmf4Mym2M6_ToAcObcO0TA2yKdAJKJkWtwnxoCybrw_wcB
9. American Protect Health Agency (2005). Standard methods for the examination of water and wastewater, 21st edition, Washington DC.
10. Chu, W. and Ma, C. W. (2000). Quantitative prediction of direct and indirect dye ozonation kinetics. *Water Research*, 34(12): 3153 – 3160.
11. Soares, O. S. G. P., Orfao, J. J. M., Portela, D., Vieira, A. and Pereira, M. F. R. (2006). Ozonation of textile effluents and dye solutions under continuous operation: Influence of operating parameters. *Journal of Hazardous Materials*, 137(3): 1664 – 1673.
12. Kazemi, M., Jafar, S. S. M., Ali, B. K. and Mohammad, A. K. (2004). Decolourisation of RR-120 dye using ozone and ozone/UV in a semi-batch reactor. *The Canadian Journal of Chemical Engineering*, 82(6): 1284 – 1288.
13. Poznyak, T., Tapia, R. and Chairez, I. (2006). Effect of pH to the decomposition of aqueous phenols mixture by ozone. *Journal of the Mexican Chemical Society*, 50(1): 28 – 35.
14. Griffini, O. and Iozzelli, P. (1996). The influence of $H_2O_2$ in ozonation treatment: experience of the water supply service of Florence, Italy in Ozone Science Engineering. Taylor and Francis: pp. 117 – 126.
15. Pachhade, K., Sandhaya, S. and Swaminathan, K. (2009). Ozonation of reactive dye, Procion red MX-5B catalyzed by metal ions. *Journal of Hazardous Materials*, 167(1): 313 – 318.
16. Feng, W., Nansheng, D. and Helin, H. (2000). Degradation mechanism of azo dye C. I. RG2 by iron powder reduction and photooxidation in aqueos solutions. *Chemosphere*, 41(8): 1233 – 1238.
17. Sevimli, M. F. and Sarikaya, H. Z. (2002). Ozone treatment of textile effluents and dyes: Effect of applied ozone dose, pH and dye concentration. *Journal of Chemical Technology and Biotechnology*, 77(7): 842 –850.
18. Yang, D. M., Wang, B., Ren, H. Y. and Yuan, J. M. (2012). Effects and mechanism of ozonation for degradation of sodium acetate in aqueous solution. *Water Science and Engineering*, 5(2): 155 – 163.
19. Abidin, C. Z. A., Muhammad Ridwan, F. and Ong, S. A. (2015). Decolourization of an azo dye in aqueous solution by ozonation in a semi-batch bubble column reactor. *ScienceAsia*, 41: 49 – 54.

*Malaysian Journal of Analytical Sciences, Vol 21 No 3 (2017): 754 - 761*
*DOI: https://doi.org/10.17576/mjas-2017-2103-25*

MALAYSIAN JOURNAL OF ANALYTICAL SCIENCES
*Published by The Malaysian Analytical Sciences Society*
ISSN 1394 - 2506

# CELLULOSE NANOCRYSTALS WITH ENHANCED THERMAL STABILITY REINFORCED THERMOPLASTIC POLYURETHANE

## (Nanokristal Selulosa Dengan Ketahanan Haba Yang Tinggi Berasaskan Poliuretina Termoplastik)

Khairatun Najwa Mohd Amin[1]*, Pratheep Kumar Annamalai[2], Darren Martin[2]

[1]*Faculty of Chemical and Natural Resources Engineering,*
*Universiti Malaysia Pahang, Lebuhraya Tun Razak, 26300 Gambang, Kuantan, Pahang, Malaysia*
[2]*Australian Institute for Bioengineering and Nanotechnology (AIBN), Corner College and Cooper Rds (Bldg 75),*
*The University of Queensland, Brisbane QLD 4072 Australia*

**Corresponding author: knajwa@ump.du.my*

Received: 28 November 2016; Accepted: 5 February 2017

**Abstract**

Melt compounding processing approach for incorporating cellulose nanocrystals (CNC) into thermoplastic polyurethane (TPU) has not well been explored. This is primarily due to the poor thermal stability and dispersibility of CNCs. As they are typically obtained from sulphuric acid hydrolysis, they give rise to degradation and discolouration of the extruded nanocomposites. The investigation of this research demonstrates sulphuric acid hydrolysis (CNC-S), phosphoric acid hydrolysis (CNC-P) and a novel non-hydrolytic high energy bead milling method (CNC-MC) into a polyether based thermoplastic polyurethane via melt compounding using twin screw extruder. The TPU film incorporated with CNC-S obviously shows the sign of CNC degradation where TPU film was changed to brown colour. The tensile strength of TPU reinforced with CNC-S, CNC-P and CNC-MC shows 18%, 16% and 14% of improvement at CNC loading of 0 to 1 wt.% upon host polymer. CNCs isolated via mild acid hydrolysis and mechanical milling methods, can be easily processed via large scale melt-processing techniques for reinforcing thermoplastic polyurethane without affecting their physical appearance and elastic properties.

**Keywords**: cellulose nanocrystals, thermoplastic polyurethane, nanocomposites

**Abstrak**

Kajian mengenai penggunaan nanokristal selulosa (CNC) di dalam termoplastik poliuritena (TPU) amat jarang diterokai. Ini adalah kerana CNC mempunyai ketahanan haba yang rendah. CNC yang dihasilkan melalui proses hidrolisis asid sulfurik mudah terdegradasi apabila digabungkan dengan polimer yang melalui proses meramu pencairan umumnya menggunakan suhu pemprosesan yang tinggi. Kajian ini menggunakan CNC yang dihasilkan daripada hidrolisis asid sulfurik (CNC-S), asid fosforik (CNC-P) dan kaedah novel pengisaran manik (CNC-MC) ke dalam poliuretana termoplastik berasaskan berasas polieter melalui proses meramu pencairan. Filem TPU yang digabungkan dengan CNC-S jelas menunjukkan tanda degradasi CNC apabila filem TPU bertukar warna kepada coklat. Kekuatan tegangan TPU diperkukuhkan dengan CNC-S, CNC-P dan CNC-MC menunjukkan 18%, 16% dan 14% peningkatan pada muatan CNC 0-1 wt.% di dalam komposit. CNC yang dihasilkan melalui hidrolisis asid berkekuatan sederhana dan melalui kaedah mekanikal boleh diproses melalui teknik meramu pencairan yang berskala besar dan mampu meningkatkan kekuatan poliuretana termoplastik tanpa menjejaskan penampilan fizikal mereka dan sifat elastiknya.

**Kata kunci:** nanokristal selulosa, poliuritena termoplastik, nanokomposit

## Introduction

Thermoplastic polyurethane (TPU) is a versatile material which has both thermoplastic and elastomeric properties with unique attributes, for instance, melt-process ability, recyclability and easy to mould [1]. One of the methods to improve the properties of TPU is by using reinforcing filler. Recently nanoscale fillers such as clay, carbon nanotubes, metal and metal oxides have been demonstrated to remarkably enhance the thermal, physical and mechanical properties of TPU within very low loading [2-4]. Recently cellulose nanocrystal (CNC) has gained high attention as reinforcing filler due to its key attributes such as very high specific mechanical properties of individual nanocrystals and renewability. Moreover, CNC reinforced polymer nanocomposites can retain the transparency of the polymer matrix [5]. With polyurethanes and different types of nanocellulose particles, remarkable reinforcements have been demonstrated. Specifically at a low volume fraction of CNC, TPU nanocomposites has demonstrated an extraordinary increase in tensile strength without compromising the tensile strain and stiffness of the material [6]. However, their processing involves solvent based methods. Conventional method like solvent casting poses a challenge in terms of production speed and environmental issue due to the high solvent usage [7]. Thus, for TPU industrial scale production, classical melt-processing methods such as compounding, reactive extrusion and moulding are preferred. Melt compounding method which has been explored with other thermoplastics whose fusion temperatures are below 170°C such as poly lactic acid [8] and polyethylene [9], is however limited due to the poor thermal stability, dispersibility of CNCs and degradation in optical transparency of the host for most of the thermoplastics whose processing temperatures are above 170 °C.

Hence, this work focuses on the processing of TPU nanocomposites reinforced with three types of CNCs which were obtained via sulphuric acid hydrolysis (CNC-S), and phosphoric acid hydrolysis (CNC-P) and acid-free high energy bead milling (CNC-MC), via a classical melt compounding method using an intermediate scale twin screw extruder. Their processing and properties enhancement are compared with the nanocomposites processed by solvent casting method.

## Materials and Methods

### Materials

Cellulose source used was Whatman filter paper (Advantec) and commercial microcrystalline cellulose (Avicel PH-101). Sulphuric acid ($H_2SO_4$, 98%) and ortho-phosphoric acid ($H_3PO_4$, 85%) from Merck Australia was used in for acid the hydrolysis process. The TPU grade selected, Texin 990, was purchased from Bayer Materials Science. This grade was specifically selected because it represents one of the highest selling aromatic polyether grades and is employed in a multitude of applications. Dimethylformamide (DMF) was purchased from Merck and used for solvent casting.

### Isolation of cellulose nanocrystals: Acid hydrolysis method

The isolation process using sulphuric acid was adapted from Capadona et al. [10] with some modifications. The solid to liquid ratio for this isolation process was 1:75. Filter paper was blended with deionised water. The sulphuric acid was added slowly under vigorous mechanical stirring to the cooled filter paper until the final solution reached an acid concentration of 32%. Since the acid hydrolysis process is exothermic, while adding acid, ice bath is used to keep the temperature below 20 °C. After the acid addition is complete the reaction is set at 50 °C or higher for a stipulated time. The mixture was then heated to 50 °C for 3.5 hours. The cellulose suspension was cooled to room temperature and was subsequently centrifuged four to five times at 4750 rpm until it became turbid. The cellulose suspension was then dialyses against deionised water until the suspension reached the neutral state. Then the cellulose suspension was ultrasonicated using high intensity ultrasonication (QSonica ultrasonicator) for 30 minutes. Finally, the cellulose suspension was lyophilised using liquid nitrogen and was vacuum freeze dried. The CNC obtained was denoted as CNC-S. Meanwhile, acid hydrolysis of cellulose using $H_3PO_4$ was adapted from Camarero et al. [11], with slight modification, and generally the procedure is very similar to $H_2SO_4$ hydrolysis. This CNC is denoted as CNC-P.

### High energy bead milling method

Isolation of CNC via high energy bead milling (HEBM) was carried out based on the work of Amin et al. [12]. The cellulose source used in this process was microcrystalline cellulose (MCC). Various concentrations of MCC were dispersed in deionised water overnight. Then the dispersion was milled using a laboratory agitator bead mill

(Labstar, Netzsch, Germany). Using various milling times, 0.4 mm of zirconium beads were used to mill the cellulose dispersion at 1000 rpm in a batch process mode. Finally, the resulting suspensions obtained were freeze dried.

**Processing of nanocomposites**

In these nanocomposites, CNC loading levels were 0.5, 1, and 5 wt.% respectively. In melt compounding method, initially CNC and PU resin were mixed physically. TPU nanocomposites reinforced with three types of CNCs were processed by melt-compounding using a ThermoHaake PolyLab twin-screw extruder. The extrudates were pelletised and compression moulded.

In solvent casting process, TPU resin and CNC were individually dissolved in DMF. 0.5 wt.% of CNC in TPU was prepared by mixing the desired amounts of CNC and TPU solution in DMF. The mixture was stirred vigorously for 1 hour at room temperature. The mixture was then sonicated for 2 minutes at 20 kHz. Subsequently, further stirring was undertaken after the sonication process and immediately cast onto a Teflon petri dish. The films were dried under nitrogen purged for 24 hours and subsequently annealed in a vacuum condition at 80 °C for 12 hours. TPU nanocomposites prepared by solvent casting were denoted as SC-TPU/CNC *X* where *X* represents the volume fraction of CNC. TPU nanocomposites processed via the melt compounding process were denoted as MC-TPU/CNC *X*.

**Characterisation and mechanical testing**

The morphology and thermal stability of CNCs were characterised by transmission electron microscopy (TEM) and thermogravimetric analysis (TGA). TGA measurements were carried out on a Mettler Toledo DSC/TGA Star$^e$ system using aluminum crucible standard 40 µL. The samples were heated in a nitrogen atmosphere. The samples were first heated from room temperature to 110 °C, at a heating rate of 10 °C/min, isothermally held for 10 minutes and further heated to 500 °C at a heating rate 5 °C/min.

The mechanical properties of the composites were measured at room temperature on an Instron model 5543 universal testing machine equipped with a 500 N load cell. The tensile and hysteresis tests were cut into dumbbell shapes according to ASTM d-638-M-3. The tests were performed with a gauge length of 14 mm and crosshead speed of 50 mm/min and pneumatic grips were employed to prevent slippage.

## Results and Discussion

**Cellulose Nanocrystals (CNC)**

Figure 1 shows the transmission electron micrographs (a-b) and thermograms (d) of the CNCs obtained via hydrolysis using sulphuric acid (CNC-S), phosphoric acid (CNC-P) and mechanical method (CNC-MC). The dimensions of CNCs were measured from at least 10 particles using ImageJ analytical software. From Figure 1a-c, the 'rod-like' shape CNC can be seen clearly with an average aspect ratio of 13, 10 and 25, for CNC-S, CNC-P and CNC-MC respectively. The HEBM process is more environmentally friendly than the acid hydrolysis methods as it was produced without using any acids, as well as being a more economically viable and scalable approach to produce CNC.

The thermal stability of CNC was determined using TGA and the associated thermograms are shown in Figure 1 (d). It can be clearly seen that CNC-S have the lowest onset degradation temperature ($T_{onset}$) noted at 200 °C as presented in Table 1. In contrast, CNC-P and CNC-MC recorded $T_{onset}$ values of 255 °C and 258 °C, respectively. Despite the well-known advantages of CNC isolated via sulphuric acid hydrolysis in terms of stable aqueous colloidal stability, which is due to the negative sulphate group introduced into the surface of CNC, this method leads to poor thermal stability. The sulphate groups formed are known to promote dehydration reactions and act as flame retardants, but this characteristic also gives rise to a low nanocellulose thermal stability [13,14].

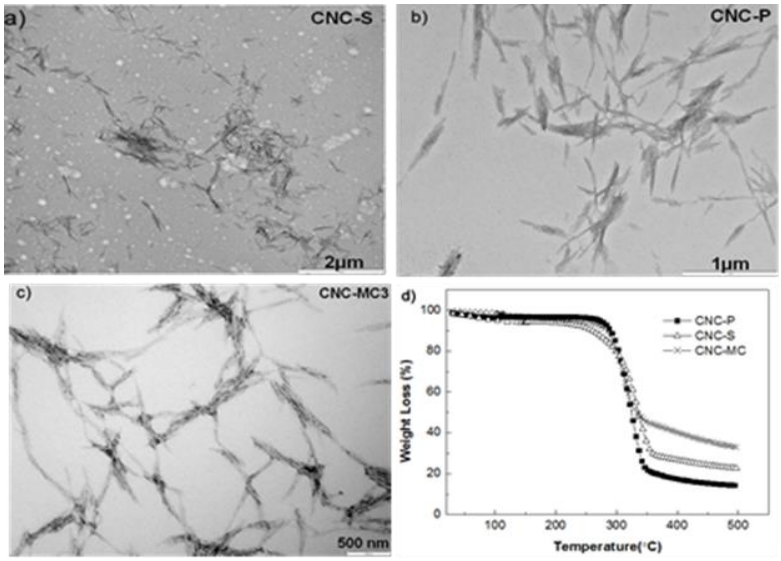



Figure 1. TEM images of CNCs produced from acid hydrolysis; a) CNC-S, b) CNC-P, c) HEBM method (CNC-MC) and d) their corresponding TGA thermograms

On the other hand, CNC-P and CNC-MC isolated from phosphoric acid hydrolysis and HEBM methods both clearly demonstrated a better thermal stability than CNC-S. Possibly phosphate group ($(PO_4)^{3-}$ ) attached on the surface of CNC-P is also able to assist with aqueous colloidal stability, but in this case without affecting the thermal behaviour of CNC [15]. The CNC-MC nanocellulose sample was successfully produced in a green and clean process (without the use of any acids or oxidising agents), and this approach also appears to have contributed to better thermal stability. Importantly, both of these strategies have shifted the onset degradation temperatures well above the typical melt compounding or reactive extrusion temperature window commonly employed for TPU processing with temperature of 180 – 230 °C, depending on the TPU grade and formulation.

Table 1. Dimensions and production yield of CNC isolated from the acid hydrolysis and HEBM methods

| Sample | Length (nm) | Diameter (nm) | Aspect Ratio | Yield (%) | Onset Degradation Temperature ($T_{onset}$)(°C) |
|---|---|---|---|---|---|
| CNC-S | 213 ± 50 | 16 ± 3 | 13 | 81 | 200 |
| CNC-P | 270 ± 135 | 26 ± 13 | 10 | 62 | 255 |
| CNC-MC | 424 ± 90 | 17 ± 4 | 25 | 76 | 258 |

**Physical appearance of TPU nanocomposites**

The influence of different thermal stabilities and surface chemistry of CNC on processing can be clearly observed in Figure 2 from the physical appearance of compression moulded nanocomposite films produced via melt compounding and solvent casting. The TPU/CNC nanocomposite films produced via solvent casting retained the transparency of the host TPU at low 0.5-1 wt.% loading levels for all types of CNCs, and at the higher 5 wt.% loading the nanocomposites with CNC-S and CNC-MC showed just some feint discolouration. The solvent cast nanocomposites with CNC-P were able to retain the transparency of the host TPU even at 5 wt.%. However, very obvious and commercially-unacceptable colour changes to darkening for nanocomposites obtained via melt-compounding can be seen from Figure 2, and the order of extent of discolouration is as follows: TPU control (MC-TPU Control) < Nanocomposites using phosphoric acid hydrolysed CNCs (MC-TPU/CNC-P) << Nanocomposites

using micronised CNCs (TPU/CNC-MC) < Nanocomposites using conventional sulphuric acid hydrolysed CNCs MC-TPU/CNC-S.

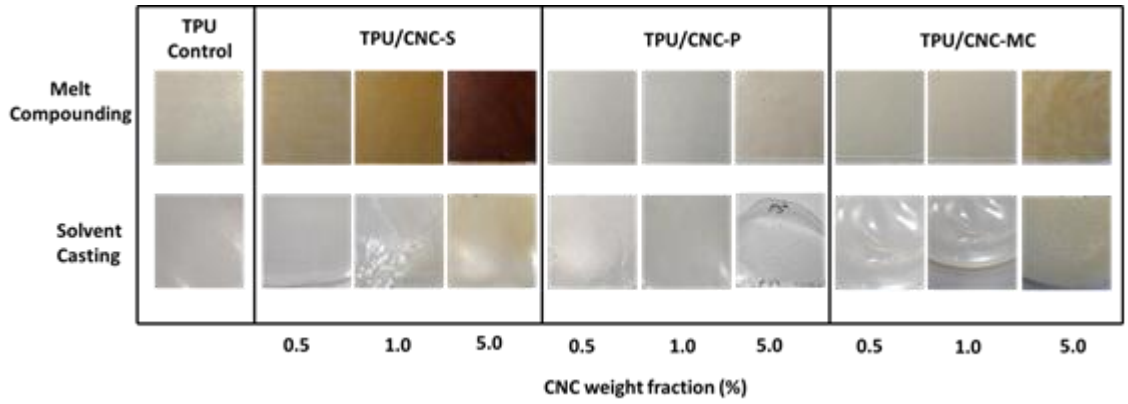



Figure 2. Photographs of TPU control and TPU/CNC nanocomposites processed via solvent casting (bottom) and melt compounding (top)

Even at 0.5 wt.% of CNC-S loading, the light brown colour of nanocomposite films was noticeable. As the processing temperature employed in the extruder was about 225 °C, the CNC isolated from sulphuric acid hydrolysis showed degradation behaviour and darkened. As reported previously, sulphate $(SO_4)^{2-}$ groups, which are present on the surface of CNC might promote the dehydration reactions [14,16,17]. The onset degradation temperature of CNC-P and CNC-MC are 255 and 258 °C, respectively. However, the dispersibility of CNC-P where phosphate groups assist in achieving superior colloidal suspension stability is better than CNC-MC, which also gives rise to the discolouration of nanocomposites incorporating CNC-MC. This strongly suggests that this discolouration in melt compounded TPU nanocomposites is due to relative CNC thermal stability and degradation, which in-turn leads to the aggregation of the less thermally stable nanocellulose.

**Mechanical properties**

The reinforcement effect of the CNCs was investigated by measuring the tensile properties of the TPU control and its nanocomposites, at room temperature. Figure 3 shows the stress-strain curves of TPU control and nanocomposites produced via both processes and the values determined are summarized in Table 2. Obviously, no significant changes in tensile strength upon 0 to 300% of tensile strain were observed for melt compounded material, whereas solvent cast nanocomposites show the increase difference immediately after 50% of strain. The solvent cast TPU control obtained higher tensile strength than melt compounded materials. The reduction mostly contributed by transurethanisation reaction occurred due to the harsh environment in the extrusion process.

The tensile strength of TPU reinforced with CNC-S, CNC-P and CNC-MC shows 18%, 16% and 14% of improvement respectively upon host polymer via melt compounding method. The increase was recorded at CNC loading of 0 to 1 wt.%, as it reached 5 wt.% mechanical properties of the composites was declined. Regarding percolation model related to volume fraction of filler, the percolation threshold for CNC previously has been determined at 1- 2 volume % [18,19] for CNC to form network with polymer matrix which most probably linked by the hydrogen bonding. Thus, in this work, CNC loading at 5 wt. % have been assumed ineffective as reinforcing element to the TPU matrix.

Moreover, elongation and stiffness at the optimum value of tensile strength were also unaffected indicating the soft-segment domain of TPU was not disrupted by the cellulose addition. Furthermore, the reinforcement of CNC was also can be seen from the improvement in toughness and tear strength of TPU nanocomposites. These results indicate that CNCs able to work as an efficient stress transfer medium without disrupting the original function of the TPU microstructure (hard segment and soft segment). Indeed preventing the undesired stiffening with soft domain

was able to maintain the elongation of the TPU composites. The strength of the material fabricated via melt compounding is competent by comparing it with solvent casting process. This also proved that cellulose (CNC-P and CNC-MC) able to be processed with high processing temperature method.

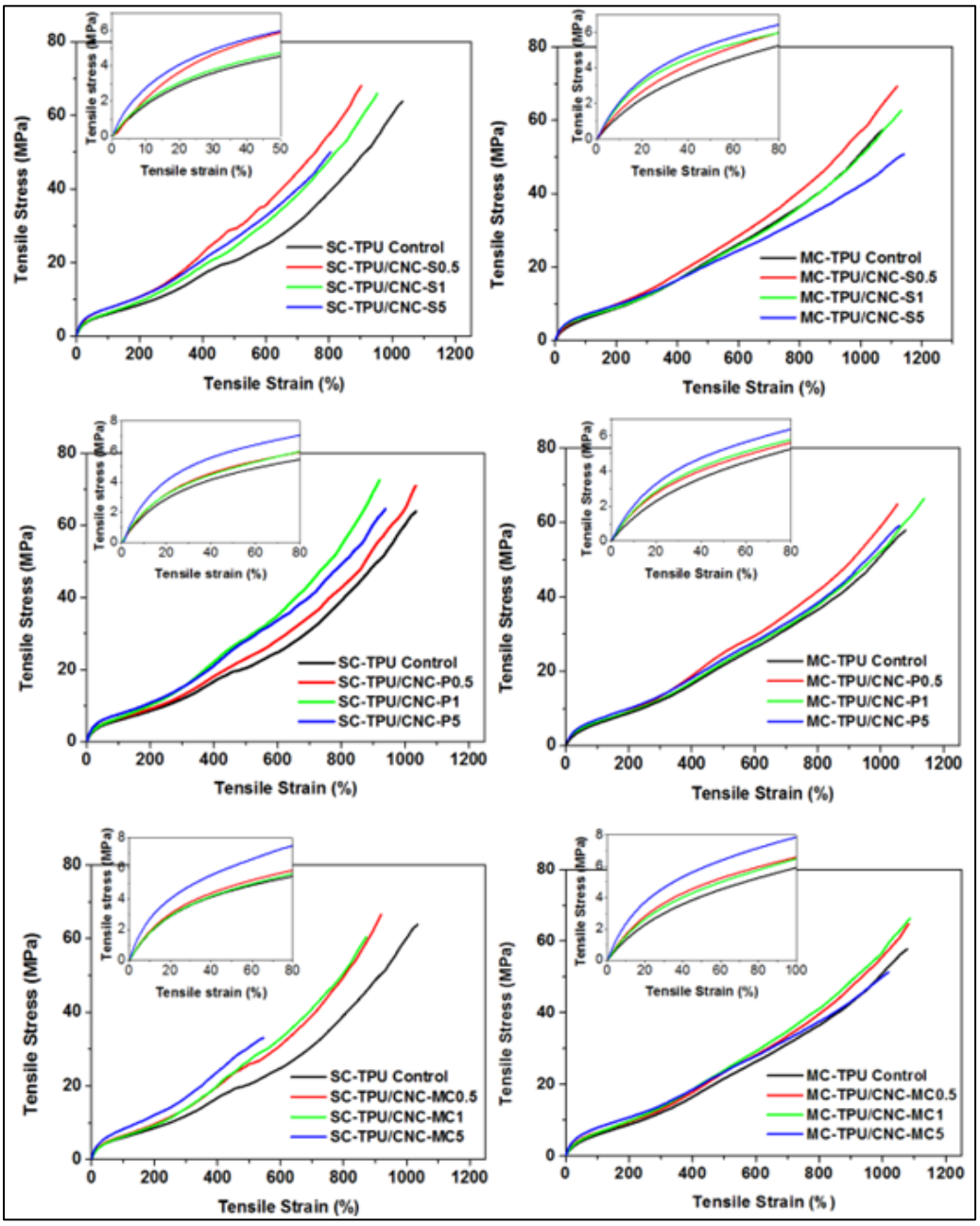



Figure 3. Stress-strain curves TPU nanocomposites fabricated via solvent casting (left column) and melt compounding (right column)

Table 2. Summary of tensile properties of TPU nanocomposites processed via solvent cast (SC) and melt compounding (MC) method.

| Sample | | Tensile Stress (MPa) | Tensile Strain at Break (%) | Modulus (MPa) | Toughness (MPa) | Tear Strength (N/mm) |
|---|---|---|---|---|---|---|
| TPU Control | SC | 64.7 ± 1 | 954.6 ± 33 | 13.6 ± 1 | 258.9 ± 7 | 69.4 ± 15 |
| | MC | 57.7 ± 3 | 1041.3 ± 39 | 11.3± 1 | 261.5 ± 18 | 119.9 ± 4 |
| TPU/CNC-S0.5 | SC | 67.1 ± 8 | 925.7 ± 27 | 17.4 ± 3 | 255.1 ± 35 | 88.6 ± 8 |
| | MC | 67.9 ± 3 | 1115.7 ± 29 | 14.3 ± 1 | 319.3 ± 21 | 118.7± 4 |
| TPU/CNC-S1.0 | SC | 65.8 ± 3 | 964.6 ± 35 | 16.5 ± 3 | 261.9 ± 14 | 96.8 ± 5 |
| | MC | 62.1 ± 2 | 1115.4 ± 26 | 15.0 ± 1 | 295.8 ± 12 | 123.2± 1 |
| TPU/CNC-S5.0 | SC | 49.4 ± 4 | 809.2 ± 49 | 21.6 ± 4 | 183.9 ± 17 | 73.7 ± 11 |
| | MC | 51.3 ± 1 | 1137.5 ± 19 | 17.2 ± 1 | 281.6 ± 9 | 129.1 ± 4 |
| TPU/CNC-P0.5 | SC | 66.0 ± 7 | 994.8 ± 55 | 11.3 ± 4 | 256.2 ± 39 | 70.5 ± 27 |
| | MC | 65.9 ± 2 | 1062.4 ± 24 | 13.5 ± 1 | 296.9 ± 13 | 121.7± 5 |
| TPU/CNC-P1.0 | SC | 66.2 ± 6 | 924.1 ± 21 | 14.0 ± 1 | 243.4 ± 20 | 88.6 ± 3 |
| | MC | 66.8 ± 1 | 1108.8 ± 29 | 14.0 ± 1 | 295.8 ± 12 | 120.9± 2 |
| TPU/CNC-P5.0 | SC | 64.5 ± 7 | 950.8 ± 62 | 20.7 ± 2 | 271.2 ± 40 | 78.9 ± 16 |
| | MC | 59.9 ± 2 | 1063.6 ± 25 | 16.2 ± 1 | 280.8 ± 8 | 123.5 ± 7 |
| TPU/CNC-MC0.5 | SC | 66.9 ± 8 | 956.0 ± 46 | 14.9 ± 2 | 256.3 ± 33 | 85.7 ± 16 |
| | MC | 64.0 ± 2 | 1062.6 ± 30 | 12.6 ± 1 | 290.2 ± 15 | 113.1± 6 |
| TPU/CNC-MC1.0 | SC | 60.4 ± 4 | 822.4 ± 70 | 14.6 ± 2 | 210.3 ± 24 | 81.6 ± 21 |
| | MC | 65.6 ± 2 | 1084.7 ± 5 | 12.4 ± 1 | 305.9 ± 7 | 125.2± 7 |
| TPU/CNC-MC5.0 | SC | 33.2 ± 3 | 583.7 ± 75 | 22.4 ± 4 | 103.3 ± 19 | 83.1 ± 12 |
| | MC | 51.2 ± 1 | 1005.6 ± 20 | 21.1 ± 1 | 247.2 ± 10 | 126.6 ± 4 |

## Conclusion

Three types of CNCs isolated via sulphuric acid hydrolysis (CNC-S), phosphoric acid hydrolysis (CNC-P) and mechanical milling method (CNC-MC) were successfully incorporated into TPU via melt compounding method. These nanocomposites were compared with that processed via conventional solvent casting method. The thermally stable CNCs (CNC-P and CNC-MC) have demonstrated the melt process ability with polyether based thermoplastic polyurethane (TPU) without affecting the optical transparency, whereas, CNC-S has shown the degradation behavior. Remarkable reinforcement effect has been observed for nanocomposites with all the three CNCs, in terms of improvement in tensile strength and toughness without affecting elongation. It can be summarized that CNC isolated via mild acid hydrolysis and an optimized mechanical milling methods, can be easily processed via large scale melt-processing techniques for reinforcing thermoplastic polyurethanes at 0.5-1 wt. % without affecting their physical appearance and elastic properties.

## Acknowledgement

The authors gratefully acknowledge the facilities as well as the scientific and technical assistance of the Centre for Microscopy and Microanalysis, University of Queensland. Khairatun Najwa also thanks to the Ministry of Education Malaysia and Universiti Malaysia Pahang for the financial support.

**References**


1. Barick, A. K., Jung, J. Y., Choi, M. C. and Chang, Y. W. (2013). Thermoplastic vulcanizate nanocomposites based on thermoplastic polyurethane and millable polyurethane blends reinforced with organoclay prepared by melt intercalation technique: Optimization of processing parameters via statistical methods. *Journal of Applied Polymer Science*, 129 (3): 1405 - 1416.
2. Koerner H., Liu, W., Alexander, M., Mirau, P., Dowty, H. and Vaia, R. A. (2005). Deformation–morphology correlations in electrically conductive carbon nanotube - thermoplastic polyurethane nanocomposites. *Polymer*, 46 (12): 4405 - 4420.
3. Kotal, M., Kuila, T., Srivastava, S. and Bhowmick, A. (2009). Synthesis and characterization of polyurethane/Mg-Al layered double hydroxide nanocomposites. *Journal of Applied Polymer Science*, 114 (5): 2691 - 2699.
4. Barick A. and Tripathy D. (2010). Thermal and dynamic mechanical characterization of thermoplastic polyurethane/organoclay nanocomposites prepared by melt compounding. *Materials Science and Engineering: A*, 527(3): 812 - 823.
5. Liu, H., Liu, D., Yao, F. and Wu, Q. (2010). Fabrication and properties of transparent polymethylmethacrylate/cellulose nanocrystals composites. *Bioresource Technology*, 101(14): 5685 -5692.
6. Pei, A., Malho, J. M., Ruokolainen, J., Zhou, Q. and Berglund, L. A. (2011). Strong nanocomposite reinforcement effects in polyurethane elastomer with low volume fraction of cellulose nanocrystals. *Macromolecules*, 44 (11): 4422 - 4427.
7. Jyoti, J., Basu, S., Singh, B. P. and Dhakate, S., (2015). Superior mechanical and electrical properties of multiwall carbon nanotube reinforced acrylonitrile butadiene styrene high performance composites. *Composites Part B: Engineering*, 83: 58 - 65.
8. Oksman, K., Mathew, A., Bondeson, D. and Kvien, I. (2006). Manufacturing process of cellulose whiskers/polylactic acid nanocomposites. *Composites Science and Technology*, 66 (15): 2776 - 2784.
9. Ben Azouz, K., Ramires, E. C., Van den Fonteyne, W., El Kissi, N. and Dufresne, A. (2011). Simple method for the melt extrusion of a cellulose nanocrystal reinforced hydrophobic polymer. *ACS Macro Letters*, 1(1): 236 - 240.
10. Capadona, J. R., Van Den Berg, O., Capadona, L. A., Schroeter, M., Rowan, S. J. and Tyler, D. J. (2007). A versatile approach for the processing of polymer nanocomposites with self-assembled nanofibre templates. *Nature Nanotechnology*, 2(12): 765 - 769.
11. Camarero Espinosa, S., Kuhnt, T., Foster, E. J. and Weder, C. (2013). Isolation of thermally stable cellulose nanocrystals by phosphoric acid hydrolysis. *Biomacromolecules*, 14(4): 1223 - 1230.
12. Amin, K. N. M., Annamalai, P. K., Morrow, I. C. and Martin, D. (2015). Production of cellulose nanocrystals via a scalable mechanical method. *RSC Advances*, 5(70): 57133 - 57140.
13. Wang, N., Ding, E. Y., & Cheng, R. S. (2007). Thermal degradation behaviors of spherical cellulose nanocrystals with sulfate groups. *Polymer*, 48(12): 3486 - 3493.
14. Roman, M. and Winter, W. T. (2004). Effect of sulfate groups from sulfuric acid hydrolysis on the thermal degradation behavior of bacterial cellulose. *Biomacromolecules*, 5(5):1671 - 1677.
15. Salajkova, M. (2013). Wood nanocellulose materials and effects from surface modification of nanoparticles. Thesis Doctor of Philosophy. KTH Royal Institute of Technology.
16. Wang N., Ding, E. and Cheng, R. (2007). Thermal degradation behaviors of spherical cellulose nanocrystals with sulfate groups. *Polymer*, 48(12): 3486 - 3493.
17. Kargarzadeh, H., Ahmad, I., Abdullah, I., Dufresne, A., Zainudin, S. and Sheltami, R. (2012). Effects of hydrolysis conditions on the morphology, crystallinity, and thermal stability of cellulose nanocrystals extracted from kenaf bast fibers. *Cellulose*, 19(3): 855 - 866.
18. Favier, V., Chanzy, H. and Cavaille, J. Y. (1995). Polymer nanocomposites reinforced by cellulose whiskers. *Macromolecules*, 28(18): 6365 - 6367.
19. Dufresne, A., Cavaillé, J. Y. and Helbert, W. (1997). Thermoplastic nanocomposites filled with wheat straw cellulose whiskers. Part II: Effect of processing and modeling. *Polymer Composites*, 18(2): 198 -210.

**Malaysian Journal of Analytical Sciences Vol 21 No 4 2017**

Articles 8 - 15 are selected papers from the "International Conference on Catalysis 2016, 'Frontiers, Challenges and Opportunities in Catalysis', 20 - 21 September 2016, Grand BlueWave Hotel, Johor Bahru, Johor, Malaysia; jointly organised by the Department of Chemistry, Faculty of Science, Universiti Teknologi Malaysia and Academy of Sciences Malaysia."

Guest Editor: Wan Aini Wan Ibrahim

Articles 16 - 20 are selected papers from the "International Workshop on Nanotechnology for Young Scientists 2016, 28 - 30 November 2016, Hotel Bangi Putrajaya, Bandar Baru Bangi, Selangor, Malaysia; organised by Faculty of Science and Technology, Universiti Kebangsaan Malaysia."

Guest Editor: Mohd Amir Radhi Othman

Articles 21 - 26 are selected papers from the "International Conference on Chemical Engineering and Industrial Biotechnology (ICCEIB 2016), 'FEW: Emerging for Sustainable Future', 28 - 30 November 2016, Bayou Hotel Malacca; organised by Faculty of Chemical and Natural Resource." Engineering, Universiti Malaysia Pahang, Malaysia."

Guest Editor: Siti Kholijah Abdul Mudalip


| | | **Page** |
|---|---|---|
| 1. | CHEMICAL SENSOR FOR HYDRAZINE DETECTION USING POLYANILINE THIN FILM<br>(Sensor Kimia Untuk Mengesan Hidrazin Dengan Menggunakan Polyanilina Berbentuk Filem Nipis)<br>*Kavirajaa Pandian Sambasevam, Sharifah Mohamad, Sook-Wai Phang* | 762 |
| 2. | CHITIN AND CHITOSAN EXTRACTION FROM *Portunus pelagicus*<br>(Pengekstrakan Kitin dan Kitosan dari *Portunus pelagicus*)<br>*Norhidayah M. Ahyat, Faridah Mohamad, Azrilawani Ahmad, Alyza A. Azmi* | 770 |
| 3. | NEW COMPOUNDS FROM *Hydnophytum formicarum* YOUNG TUBERS<br>(Sebatian Baru daripada Bonjolan Muda *Hydnophytum formicarum*)<br>*Nur Shafiqa Abdullah, Wan Yaacob Wan Ahmad, Noor Aziiraa Sabri* | 778 |
| 4. | OPTICAL CHEMICAL SENSOR OF Cd(II) IN WATER BASED ON 1-(2-PYRIDYLAZO)-2-NAPHTOL IMMOBILIZED ON POLY(METHYL METHACRYLATE) AND 2-NITROPHENYL OCTYL ETHER MATRIX<br>(Sensor Kimia Optik untuk Penentuan Cd(II) dalam Air Berasaskan 1-(2-Piridilazo)-2-Naftol yang Dipegun dalam Matriks Poli(metil metaakrilat) dan 2-Nitrofenil Oktil Eter)<br>*Moersilah, Dwi Siswanta, Roto Roto, Mudasir Mudasir* | 784 |
| 5. | EFFECT OF NON-IONIC SURFACTANTS TO THE Al(III)-MORIN COMPLEX AND ITS APPLICATION IN DETERMINATION OF Al(III) IONS: A PRELIMINARY STUDY<br>(Kesan Surfaktan Tak-Ionik Kepada Kompleks Al(III)-Morin dan Aplikasinya dalam Penentuan Ion Al(III): Satu Kajian Awal)<br>*Faiz Bukhari Mohd Suah, Musa Ahmad, Faizatul Shimal Mehamod* | 793 |
| 6. | CHARACTERIZATION, CALCULATION OF CALORIFIC VALUES, AND BIO-OIL PRODUCTION VIA THERMOCHEMICAL PROCESSES OF MUNICIPAL SOLID WASTE IN PERLIS, MALAYSIA | 801 |

(Pencirian, Pengiraan Nilai – Nilai Kalorifik dan Pengeluaran Bio-Minyak Melalui Proses Termokimia Sisa Pepejal Perbandaran di Perlis, Malaysia)
*Khairuddin Md Isa, Farizul Hafiz Kasim, Umi Fazara Md Ali, Radzuwan Ab Rashid*

7. ULTRASOUND-ASSISTED SURFACTANT ENHANCED EMULSIFICATION MICROEXTRACTION METHOD COUPLED WITH GAS CHROMATOGRAPHY-MASS SPECTROMETRY FOR THE DETERMINATION OF SELECTED POLYCYCLIC AROMATIC HYDROCARBONS IN AQUEOUS SAMPLES 810
(Kaedah Pengekstrakan Mikro Ultrabunyi dengan Bantuan Surfaktan Meningkatkan Pengemulsian Bergabung dengan Kromatografi Gas-Spektrometri Jisim Bagi Penentuan Polisiklik Aromatik Hidrokarbon Terpilih di dalam Sampel Akueus)
*Siti Farahiyah Ahmad Shater, Noorfatimah Yahaya, Nur Nadhirah Mohamad Zain, Sharlina Mohamad, Farah Wahidah Mohd Hassan, Sazlinda Kamaruzaman, Nor Suhaila Mohamad Hanapi, Mazidatulakmam Miskam*

8. EFFECT OF ONE STEP ACTIVATION KOH MODIFIED CARBON IN DIMETHYL CARBONATE TRANSESTERIFICATION REACTIONS 820
(Kesan Satu Langkah Pengaktifan KOH Terhadap Karbon Terubahsuai dalam Tindak Balas Transesterifikasi dengan Dimetil Karbonat)
*Abdul Rahim Yacob, Nor Wajihan Muda, Muhammad Azam bin Muhammad Zaki*

9. CHARACTERIZATION AND DEACIDIFICATION OF ACIDIC PETROLEUM CRUDE OIL UTILIZING METAL OXIDE CATALYST SUPPORTED ON ALUMINA AND AMMONIATED-POLYETHYLENE GLYCOL SOLUTION 830
(Pencirian dan Penyahasidan Minyak Mentah Petroleum Menggunakan Mangkin Logam Oksida Disokong Dengan Alumina dan Larutan Ammonia-Polietilena Glikol)
*Nurasmat Mohd Shukri, Jafariah Jaafar, Wan Azelee Wan Abu Bakar, Zaiton Abdul Majid*

10. PRODUCTION OF ETHYLENE FROM ETHANOL DEHYDRATION OVER $H_3PO_4$-MODIFIED CERIUM OXIDE CATALYSTS 839
(Penghasilan Etilena Daripada Pendehidratan Etanol Dengan Mangkin Serium Oksida Terubahsuai $H_3PO_4$)
*Soo Ling Chong, Jiah Chee Soh, Chin Kui Cheng*

11. GAS PHASE GLYCEROL DEHYDRATION TO ACROLEIN USING SUPPORTED SILICOTUNGSTIC ACID CATALYST 849
(Penyahhidratan Gliserol Fasa Gas Kepada Akrolein Menggunakan Sokongan Mangkin Asid Silikotungstik)
*Amin Talebian-Kiakalaieh and Nor Aishah Saidina Amin*

12. SYNTHESIS OF MESOPOROUS SODALITE BY MIXED QUATERNARY AMMONIUM CATION TEMPLATES FOR KNOEVENAGEL CONDENSATION REACTION 860
(Sintesis Sodalit Mesoliang dengan Campuran Templat-Templat Kation Amonium Kuaterner untuk Tindak Balas Kondensasi Knoevenagel)
*Mohamad Faiz Othman, Shima Shirani Lapari, Zainab Ramli, Sugeng Triwahyono*

13. PALLADIUM PINCER COMPLEXES AS CATALYSTS FOR SELECTIVE ACTIVATION AND FUNCTIONALIZATION OF 1-PROPANOL 871
(Kompleks Paladium Pincer Sebagai Mangkin untuk Pengaktifan dan Pefungsian Terpilih 1-Propanol)
*Sri Sugiarti and Craig M Jensen*

14. OPTIMIZATION BY BOX-BEHNKEN DESIGN OF *IN-SITU* CARBON DIOXIDE CONVERSION USING LANTHANUM OXIDE 880
(Pengoptimuman Dengan Reka Bentuk Box-Behnken Untuk Penukaran *in-situ* Karbon

Dioksida Menggunakan Lantanum Oksida)
*Salmiah Jamal Mat Rosid, Wan Azelee Wan Abu Bakar, Rusmidah Ali*

15. SYNTHESIS OF ZnO/rGO NANOHYBRID FOR IMPROVED PHOTOCATALYTIC ACTIVITY 889
(Sintesis Nanohibrid ZnO/rGO Untuk Mempertingkatkan Aktiviti Fotopemangkinan)
*Marilyn Yuen Sok Wen, Abdul Halim Abdullah, Lim Hong Ngee*

16. EFFECT OF NICKEL ON BIMETALLIC NANOALLOY CATALYST FOR HYDROGEN GENERATION 901
(Kesan Nikel ke atas Mangkin Nanoaloi Dwilogam bagi Penghasilan Hidrogen)
*Masitah Abdul Halim Azizi, Norliza Dzakaria, Wan Nor Roslam Wan Isahak, Mohd Ambar Yarmo*

17. EFFECT OF RHODIUM ADDITIVE ON THE REDUCTION BEHAVIOUR OF IRON OXIDE IN CARBON MONOXIDE ATMOSPHERE 907
(Kesan Penambahan Rodium Terhadap Tindak Balas Penurunan Ferum Oksida Di Dalam Atmosfera Karbon Monoksida)
*Tengku Shafazila Tengku Saharuddin, Fairous Salleh, Alinda Samsuri, Norliza Dzakaria, Rizafizah Othaman, Mohammad Bin Kassim, Mohammad Wahab Mohammad Hisham, Mohd Ambar Yarmo*

18. EFFECT OF ANNEALING STRATEGY ON IMPROVED PHOTOACTIVITY OF CUPROUS OXIDE NANOWIRE PREPARED USING FACILE FABRICATION STRATEGY FOR SOLAR WATER SPLITTING 914
(Kesan Strategi Pengkalsinan Terhadap Peningkatan Fotoaktiviti Nanowayar Kuprous Oksida Yang Disediakan Menggunakan Cara Mudah Untuk Pembelahan Air Suria)
*Mohd Nur Ikhmal Salehmin, Lorna Jeffery Minggu, Khuzaimah Arifin, Mohammad Bin Kassim*

19. CARBON DIOXIDE SORPTION BY TETRADECYLAMINE SUPPORTED ON SILICA GEL 921
(Serapan Karbon Dioksida Oleh Tetradesilamina Disokong Pada Silika Gel)
*Maratun Najiha Abu Tahari, Azizul Hakim, Tengku Sharifah Marliza, Mohd. Ambar Yarmo*

20. PERFORMANCE ENHANCEMENT OF DYE SENSITIZED SOLAR CELL USING GRAPHENE OXIDE DOPED TITANIUM DIOXIDE PHOTOELECTRODE 928
(Peningkatan Prestasi Bagi Sel Suria Pemeka Warna Menggunakan Grafin Oksida di dalam Titanium Dioksida Sebagai Fotoelektrod)
*Ahmad Muslihin Ramli, Mohd Zikri Razali, Norasikin Ahmad Ludin*

21. EFFECT OF VARIOUS POWER LEVEL AND DIFFERENT RATIO OF FRUIT TO WATER IN OIL PALM FRUITS MICROWAVE STERILIZER 941
(Kesan Pelbagai Tahap Kuasa dan Nisbah Berlainan Buah terhadap Air dalam Pensterilan Gelombang Mikro Buah Kelapa Sawit)
*Norashikin Ahmad Zamanhuri, Norazah Abd Rahman, Noor Fitrah Abu Bakar*

22. DODECYLBENZENE SULFONIC ACID CONCENTRATION EFFECT ON ELECTRICAL AND THERMAL PROPERTIES OF POLYANILINE 950
(Kesan Penumpuan Asid Sulfonik Dodekilbenzena ke atas Sifat Elektrik dan Termal Polianilin)
*Nurul Akmil Mustaffa, Qumrul Ahsan, Mohd Asyadi Azam, Luqman Chuah Abdullah*

23. COMPARISON OF PURIFICATION METHODS TO PURIFY RECOMBINANT BROMELAIN FROM *Escherichia coli* BL21-A1 958
(Perbandingan Kaedah Penulenan Rekombinan Bromelain daripada *Escherichia coli* BL21-A1)

*Zatul Iffah Mohd Arshad, Azura Amid, Faridah Yusof, Siti Zubaidah Sulaiman, Siti Kholijah Abdul Mudalip, Rohaida Che Man, Shalyda Md Shaarani*

24. PERCENTAGE DIFFERENCE OF RESISTIVITY OF NANOPARTICLES IN DETERMINING CRUDE OIL USING SAND-PACK EXPERIMENTAL METHOD 972
(Peratusan Perbezaan Kerintangan Nanopartikel Dalam Penentuan Minyak Mentah Mengunakan Kaedah Ujikaji Pek Pasir)
*Mohd Zulkifli Mohamad Noor, Mariyamni Awang, Sonny Irawan*

25. DETERMINATION OF PHYSICAL CROSSLLINK BETWEEN CARRAGEENAN AND GLYOXYLIC ACID USING DENSITY FUNCTIONAL THEORY CALCULATIONS 979
(Penentuan Ikatan Sambung Silang Fizikal Antara Karagenan dan Asid Glioksilik Menggunakan Pengiraan Teori Fungsi Ketumpatan)
*Siti Hana Abu Bakar and Fatmawati Adam*

26. *Alchemilla vulgaris* AND *Filipendula ulmaria* EXTRACTS AS POTENTIAL NATURAL PRESERVATIVES IN BEEF PATTIES 986
(Ekstrak *Alchemilla vulgaris* dan *Filipendula ulmaria* Sebagai Pengawet Asli dalam Burger Daging)
*Khadijah Husna Abd Hamid, Nurul Aini Mohd Azman, Shalyda Sharaani, Norashikin Zain, Normazlinah Ahmad, Ahmad Ziad Sulaiman, Syed Saufi Tuan Chik, Wan Faizal Wan Ishak, Maria Pillar Almajano Pablos*

*Malaysian Journal of Analytical Sciences, Vol 21 No 4 (2017): 762 - 769*
*DOI: https://doi.org/10.17576/mjas-2017-2104-01*

MALAYSIAN JOURNAL OF ANALYTICAL SCIENCES
*Published by The Malaysian Analytical Sciences Society*
ISSN 1394 - 2506

# CHEMICAL SENSOR FOR HYDRAZINE DETECTION USING POLYANILINE THIN FILM

## (Sensor Kimia Untuk Mengesan Hidrazin Dengan Menggunakan Polyanilina Berbentuk Filem Nipis)

Kavirajaa Pandian Sambasevam[1], Sharifah Mohamad[2], Sook-Wai Phang[3]*

[1]*School of Chemistry and Environment, Faculty of Applied Sciences, Universiti Teknologi MARA, Negeri Sembilan Branch,Kuala Pilah Campus, 72000 Kuala Pilah, Negeri Sembilan, Malaysia*
[2]*Department of Chemistry, Faculty of Science, University of Malaya, 50603 Kuala Lumpur, Malaysia*
[3]*Department of Physical Science, Faculty of Applied Sciences, Tunku Abdul Rahman University College, 53300 Kuala Lumpur, Malaysia*

**Corresponding author: pinkyphang@gmail.com*

Received: 17 August 2016; Accepted: 15 June 2017

**Abstract**

Polyaniline (PANI) doped with dioctyl sodium sulfosuccinate (AOT) was prepared by chemical oxidative polymerization method. This PANI thin film was used as an effective chemical sensor at room temperature for different concentrations of hydrazine (10, 100, 1000 and 10000 ppm) detection. The PANI chemical sensor has shown a good recyclability up to 10 cycles with 2 minutes response time and immediate recovery time. The sensor response was proved by red-shift of the UV-Vis at 780 nm which indicates the transformation of emeraldine salt (ES, conducting state) to leucoemeraldine salt (LES, non-conducting state) of PANI. Besides that, the intensity ratio of $I_{Quinoid}/I_{Benzenoid}$ at FTIR spectroscopy can explicit the predominating benzenoid species that formed as a result of ES interaction with hydrazine. In this study, a very simple and inexpensive sensor setup has been successfully developed for hydrazine detection compare to the complicated traditional chemical sensors.

**Keywords**: polyaniline, hydrazine, dioctyl sodium sulfosuccinate, chemical sensor, conductivity

**Abstrak**

Polianilina (PANI) yang didopkan dengan natrium dioktil sulfosuksinat (AOT) telah disediakan melalui kaedah pempolimeran pengoksidaan kimia. Filem nipis PANI telah digunakan sebagai sensor kimia pada suhu bilik untuk mengesan hidrazin dengan kepekatan yang berbeza (10, 100, 1000 dan 10000 ppm). Sensor kimia PANI telah menunjukkan penggunaan semula sehingga 10 kali dengan masa 2 minit dengan masa pemulihan segera. Keputusan sensor telah dibuktikan dengan peralihan-merah UV-Vis pada 780 nm yang menunjukkan transformasi garam emeraldina (ES, konduktif) kepada garam leukoemeraldina (LES, tidak konduktif). Selain itu, nisbah keamatan $I_{Kuinoid}$ / $I_{Benzenoid}$ di FTIR spektroskopi telah menjelaskan spesies benzenoid lebih banyak sebagai hasil interaksi ES dengan hidrazin. Dalam kajian ini, penyediaan sensor yang sangat mudah dan murah telah berjaya diperkembangkan untuk mengesan hidrazin berbanding dengan sensor kimia tradisional yang rumit.

**Kata kunci:** polianilina, hidrazin, natrium dioktil sulfosuksinat, sensor kimia, konduktiviti

## Introduction

In recent years, there has been growing interest in conducting polymers due to their versatile applications in light emitting diodes, electronic devices, sensors, actuators, catalysis, corrosion protection coatings and microwave

absorption [1-5]. Among the conducting polymers, polyaniline (PANI) is the most promising semiconductor because of its ease of synthesis [6], high conductivity, low cost and good environmental stability [7, 8]. However, the great potential of PANI was masked by few disadvantages such as insolubility, infusibility and hence poor process ability. Attempts have been made to improve its solubility, of which the most widely used strategy is to dope PANI with suitable surfactants such as dodecylbenzene sulphonic acid (DBSA), camphor sulphonic acid (CSA) and etc. [9]. The PANI with improved solubility can be spin coated on an appropriate substrate to be used as a sensing material for toxic compounds such as ammonia, hydrogen peroxide, hydrazine and etc [10].

Hydrazine and its derivatives are commonly known for fuels in explosives, antioxidants, rocket propellants, blowing agents, photographic chemical, corrosion inhibitor, insecticides and plant growth regulators [11]. In spite of this, hydrazines are well known as neurotoxin, carcinogen, mutagen and hepatoxic [12]. Besides that, the exposure of high level of hydrazine can cause irritation to nose, eye, throat, dizziness, nausea, temporary blindness, pulmonary edema and coma, which will eventually endanger the liver, kidneys and central nervous system of humans [13].

Therefore, it has been realized that, effective and sensitive sensing methods need to be explored to detect the hydrazine. Presently, several efforts have been developed towards the rapid, sensitive and selective methods for the detection of hydrazine. The sensing properties of hydrazine have been extensively studied by various methods using different metal oxides, electrodes and semiconductors [14, 15]. Electroanalytical techniques were proven to be relatively direct and effective for the detection of hydrazine [16]. Unfortunately, hydrazine exhibits irreversible oxidation which required large overpotentials at bare carbon electrodes. Recently, various chemically modified electrodes (CMEs) have been prepared and applied in the detection of hydrazine [17-21], which can significantly lower the overpotentials and increase the oxidation current response. However, the tedious preparation method, expensive electrode modification techniques, control on pH of reactants have made these methods cumbersome and thus the door for a fast track, cheap and sensitive methodology is still opened. The preference for a conducting polymer especially PANI over a conventional metal as sensing material stems from several factors such as it can be operated at lower applied voltages and temperatures, unique acid-base chemistry and it interacts more favorably with both organic and inorganic compounds [10].

In this study, PANI was prepared by chemical oxidation method in the presence of dioctyl sodium sulfosuccinate (AOT) as a dopant to improve the solubility and enhance electrical conductivity. A very simple sensor set-up has been utilized and investigated by using UV-Vis, FTIR and conductivity studies to evaluate the response of PANI thin films against different concentrations of hydrazine such as 10, 100, 1000 and 10000 ppm.

## Materials and Methods

### Raw materials

All chemicals such as aniline (Ani) monomer, dioctyl sodium sulfosuccinate (AOT) and ammonium peroxydisulfate (APS) were purchased from Sigma Aldrich. Hydrochloric acid (HCl) 37% was purchased from Lab Scan Sdn. Bhd. Technical grade of toluene was used as a solvent for PANI thin film preparation. Distilled water was used throughout the research. Other reagents were used without purification unless noted.

### Synthesis of PANI

PANI was synthesized by chemical oxidation method at 0 – 5 ˚C. Firstly, 1 mmol of AOT was dissolved in 1 N of HCl followed by the dropwise addition of Ani (1 mmol). Then, 1 mmol of APS solution was added slowly into the solution mixture and the polymerization was preceded for 24 hours. After that, the PANI was washed by distilled water for three times and dispersed in toluene for film preparation by using spin coater.

### Characterizations

The characterizations of PANI films were investigated through ultraviolet-visible (UV-Vis) by using UV-1650 PC spectrometer in the wavelength range of 300 – 900 nm and Fourier transform infrared (FTIR) by using Perkin Elmer RX1 FTIR ATR spectrometer in the range of 4000 – 400 $cm^{-1}$.

**Sensor set-up**

In this study, a simple and cost-effective sensor set-up has been developed by using glass cuvettes. PANI film was immersed into the hydrazine solution in cuvette to determine the response of PANI against hydrazine. Measurements were taken before and after immersion into hydrazine solution using UV-Vis and FTIR spectroscopy and standard four point probe method (model Loresta HP) was used to study the normalized conductivity.

## Results and Discussion

**Characterizations**

UV-Vis spectrum of PANI was shown in Figure 1. The spectrum shows typical characteristic peaks of doped PANI such as π- π* conjugation at 350 nm, shoulder peak at 415 nm which showed enhanced polaronic character and a peak at 779 nm that resembles doped state of quinoid cations [22].

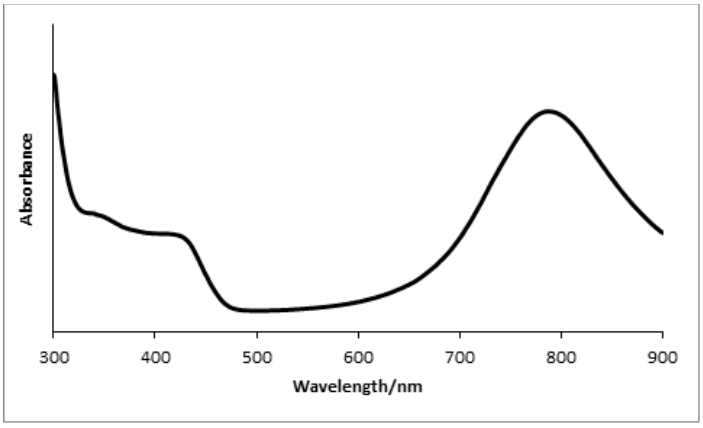



Figure 1. UV-Vis spectrum of doped PANI

The FTIR spectrum of PANI as shown in Figure 2 exhibited few significant peaks at 773 $cm^{-1}$ which corresponds to the C-H bending vibration out of the plane of benzene and 1140 $cm^{-1}$ which attributed to the $NH^{+}$ vibration mode. Meanwhile, 1183 $cm^{-1}$ peak shows the presence of S=O symmetric and 1284 $cm^{-1}$ peak shows asymmetric which arise from AOT dopant and C-N stretching peaks. The structure of PANI was confirmed by the appearance of main characteristic peaks at 1477 $cm^{-1}$ and 1578 $cm^{-1}$. These two peaks contributed to the stretching vibration mode of benzenoid ring and vibration mode of quinoid, respectively [23, 24]. Therefore, UV-Vis and FTIR spectra have confirmed the chemical structure of the resulted PANI.

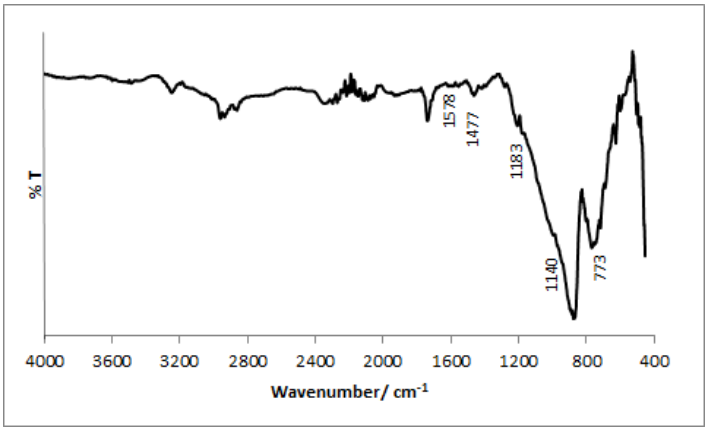



Figure 2. FTIR spectrum of doped PANI

**Sensor measurements**

First of all, the immersion time for PANI into hydrazine was optimized through conductivity study. Figure 3 shows the effect of immersion time for PANI chemical sensor against 100 ppm of hydrazine. The *y*-axis is the normalized conductivity ($\sigma_f/\sigma_i$), where $\sigma_i$ is the initial conductivity of the doped PANI (before immersion) and $\sigma_f$ is the time dependent conductivity of the film after exposed to hydrazine. The PANI thin film has recorded an initial conductivity of $4.883 \times 10^{-2}$ S/cm and it decreased with time after expose to 100 ppm of hydrazine. After 2 minutes of exposure time, the conductivity of PANI film decreased to $2.133 \times 10^{-2}$ S/cm. Besides that, the normalized conductivity decreased insignificantly from the 2nd minute to 5th minute. Therefore, 2 minute was chosen as optimum exposure time of PANI for 100 ppm of hydrazine. PANI exhibits decrease in overall conductivity upon exposure to hydrazine is due to the transformation of conducting state of PANI (emeraldine salt (ES)) to non-conducting state of PANI (leucoemeraldine salt (LES)) [25].

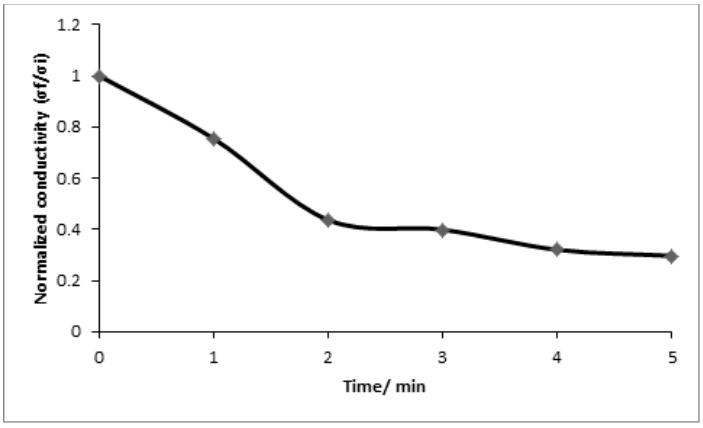



Figure 3. Normalized conductivity of PANI chemical sensor against 100 ppm of hydrazine with respect to time

Figure 4 shows the response of PANI chemical sensor in term of conductivity study against different concentrations of hydrazine such as 10, 100, 1000 and 10000 ppm. The PANI thin films have recorded 2 minutes of response time for 10 - 100 ppm of hydrazine while it showed an immediate response for 1000 - 10000 ppm of hydrazine concentrations. It revealed that the decrease in conductivity for higher concentration of hydrazine is much bigger with shorter response time compare to the lower concentration of hydrazine. It is because of higher concentration of hydrazine will possess higher hydrazinium ions which can dedope the PANI from ES to LES at much faster rate and thus decrease the conductivity of the ES within a shorter response time [18].

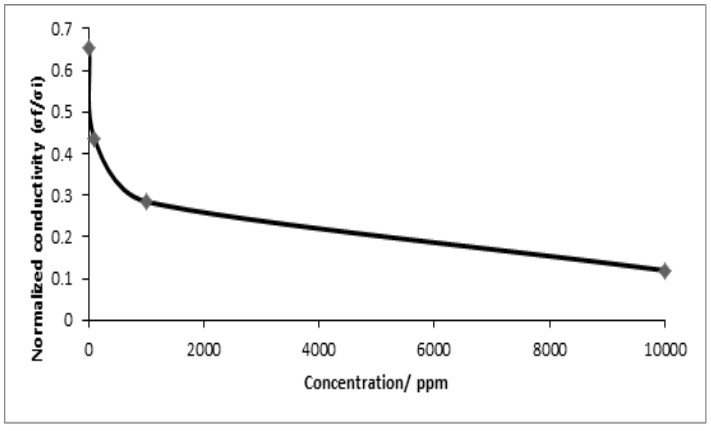



Figure 4. Normalized conductivity of PANI chemical sensor against different concentration of hydrazine

On the other hand, the recyclability of PANI chemical sensor has also been evaluated via conductivity study. According to the theory, conducting state of PANI ES will possess benzenoids and quinoids that can be dedoped by hydrazine to form LES which is an electrical insulator with predominating benzenoid units. Later, LES can be redoped back by an acid to produce ES. Thus, it is known as a reversible interaction between ES and LES with the help of a reducing agent (hydrazine) and acid. Figure 5 shows that the PANI chemical sensor can be recycled up to 10 cycles. The initial conductivity of this film was $3.899 \times 10^{-2}$ S/cm and the conductivity after the $10^{th}$ recycle was $6.167 \times 10^{-1}$ S/cm [26]. It is observed that, the normalized conductivity of PANI chemical sensor is about 15 times higher compare to the initial conductivity. It is due to the role played by the acids that used to redope PANI chemical sensor. Normally, inorganic acids will yield PANI with higher conductivity [26].

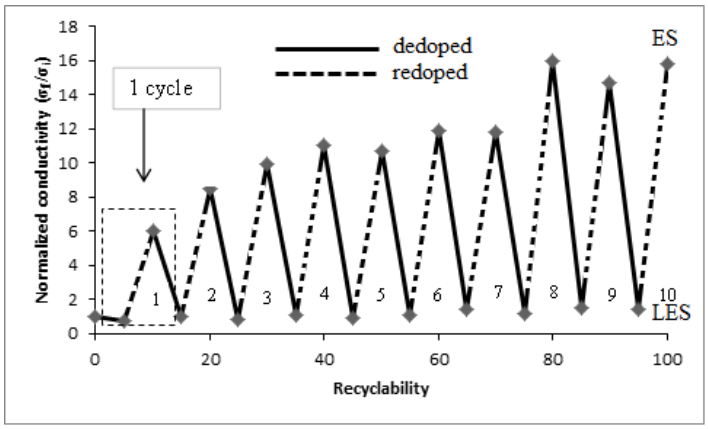



Figure 5. Recyclability of PANI for 100 ppm of hydrazine in terms of conductivity

In this study, for the first time, the UV-Vis and FTIR measurements as the supporting data were used for conductivity study of PANI chemical sensor for hydrazine detection. In the UV-Vis spectra, red-shift can be observed at ~780 nm due to the interaction of ES with hydrazine to form the LES. In general, ES will possess stretched polaron due to the quinoids as shown in the peak at 780 nm. Once the ES dedoped by hydrazine, the stretched polaron will diminish and shows a red shift which indicates the transformation of ES to LES. In Figure 6, low concentration of hydrazine (10 and 100 ppm) exhibited shorter wavelength shift while high concentration of hydrazine (1000 and 10000 ppm) exhibited longer wavelength shift from the initial wavelength of PANI films. This could be explained by the fact that higher concentration of hydrazine will possess higher amount of hydrazinium ions which can readily dedope ES to form the LES compare to the lower concentration of hydrazine which will require more time to interact with ES matrix.

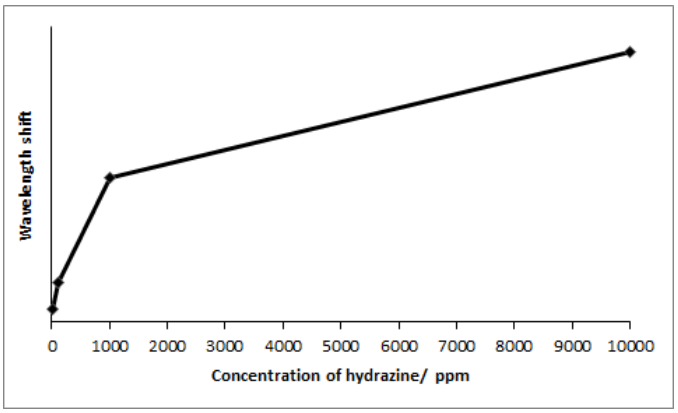



Figure 6. Wavelength shift observed for PANI for different concentration of hydrazine at 780 nm

Figure 7 illustrates the supportive data for recyclability of PANI against 100 ppm of hydrazine as explained by the conductivity data from Figure 3. ES exhibit red shift at polaron stretching around 780 nm upon dedoping by hydrazine which indicates the transformation of ES to LES while blue shift will be observed at polaron stretching when the redoping done by an acid which attributed to the conversion of LES to the conducting state of ES. Thus, Figure 7 clearly confirmed that PANI ES can be recycled up to 10 cycles. This is one of the most important characters of a chemical sensor to be used as a reusable sensor.

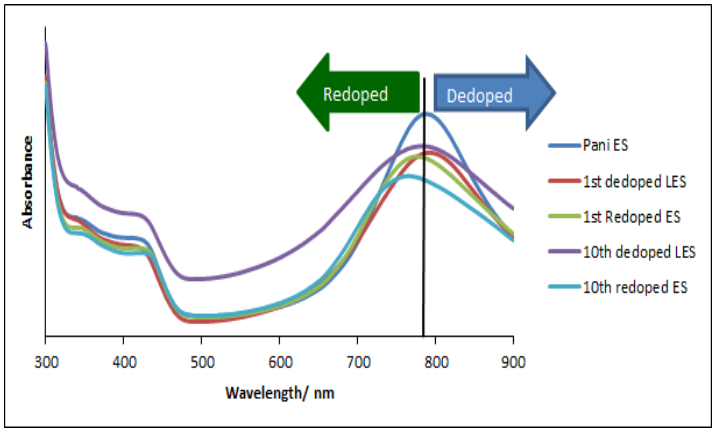



Figure 7. UV-Vis spectra of recyclability of PANI upon dedope by 100 ppm of hydrazine and redope by 1N HCl

Figure 8 shows the PANI sensing response against hydrazine by means of FTIR spectra. In general, PANI shows two significant characteristic peaks at 1477 and 1578 $cm^{-1}$ which corresponds to the benzenoid and quinoid ring stretching, respectively. Thus, the intensity ratio ($I_{1578}/I_{1477}$) of these bands could be used as an indicator for the degree of oxidation of PANI [27]. Table 1 shows the intensity ratio of ES and LES after exposure to different concentrations of hydrazine. It can be observed that, intensity ratio of LES is smaller than of ES for all hydrazine concentration; this shows that, the presence of benzenoid is predominating in the PANI chain which is an important structure of LES. So, these results further prove the changes of ES to LES upon dedope by hydrazine.

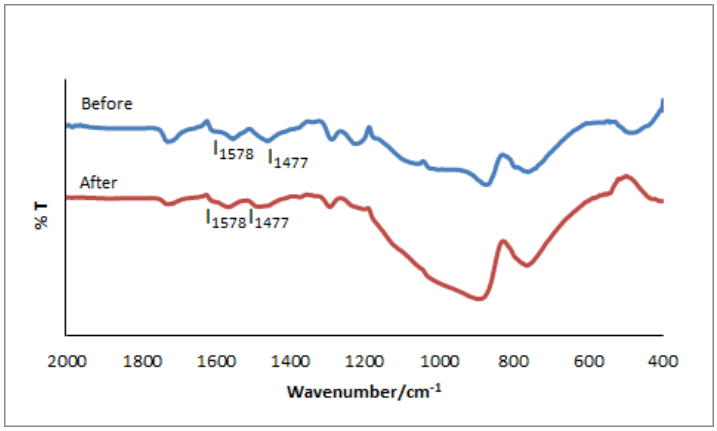



Figure 8. FTIR spectra of PANI before and after exposure with 100 ppm hydrazine

Table 1. FTIR intensity ratio of quinoid/benzenoid for different concentration of hydrazines

| **Concentration of Hydrazine (ppm)** | **ES ($I_{1578}/I_{1477}$)** | **LES ($I_{1578}/I_{1477}$)** |
|---|---|---|
| 10 | 1.00 | 0.99 |
| 100 | 1.00 | 0.99 |
| 1000 | 1.00 | 0.98 |
| 10000 | 1.00 | 0.92 |

## Conclusion

PANI was successfully synthesized and applied as an effective chemical sensor for hydrazine detection. The PANI can detect hydrazine with various concentrations such as 10, 100, 1000 and 10000 ppm with recyclability up to 10 cycles. Besides that, PANI sensor measurements were also shown in terms of UV-Vis wavelength shifts and the PANI ES and LES structural changes via FTIR spectra. In future prospect, the PANI sensor study can be carried out in a dynamic range of hydrazine concentration to determine the limit of detection and limit of quantitation. Besides, that incorporation of metal oxides into the PANI matrix would provide synergetic effects for PANI as a chemical sensor.

## Acknowledgement

The authors would like to show high gratitude for the financial support by UiTM Negeri Sembilan Branch, Kuala Pilah Campus to attend SKAM 29 and University of Malaya (UMRG: RP020A-16SUS) for research purposes.

## References

1. Cui, G., Lee, J. S., Kim, S. J., Nam, H., Cha, G. S. and Kim, H. D. (1998). Potentiometric $pCO_2$ sensor using polyaniline-coated pH- sensitive electrodes. *Analyst*, 123: 1855 – 1859.
2. Karyakn, A. A., Lukachona, L. V., Karyakina, E. E., Orlov, A. V. and Kappachora, G.P. (1999). The improved potentiometric pH response of electrodes modified with processible polyaniline. Application to glucose biosensor. *Analytical Communications*, 36: 153 – 156.
3. Wu, C. G., Bein, T. (1994), Conducting polyaniline filaments in a mesoporous channel host. *Science* 264: 1757-1759.
4. Ahmad, N. and MacDiarmid, A. G. (1996). Inhibition of corrosion of steels with the exploitation of conducting polymers. *Synthetic Metals*, 78: 103 – 110.
5. Rose, T. L., Antonio, S. D., Jilson, M. H., Kron, A.B., Suresh, R. and Wang, F. (1997). A microwave shutter using conductive polymers. *Synthetic Metals*, 85: 1439 – 1440.
6. MacDiarmid, A. G., (1997). Polyaniline and polypyrrole: Where are we headed? *Synthetic Metals*, 84: 27 – 34.
7. MacDiarmid, A. G., Chiang, J. C., Halpern, M., Huang, W. S., Mu, S. L., Somasiri, N. L. D., Wu, W. Q. and Yaniger, S. I. (1985). Polyaniline: Interconversion of metallic and insulating forms. *Molecular Crystals and Liquid Crystals*, 121: 173 – 180.
8. Wang, X., Shao, M., Shao, G., Wu, Z. and Wang, S. (2009). A facile route to ultra-long polyaniline nanowires and the fabrication of photoswitch. *Journal of Colloid Interface and Science*, 332: 74 – 77.
9. Koul, S., Dhawan, S. K., Chandra, S. and Chandra, R. (1997). Conducting polyaniline as a sensor for the detection of HCl vapors. *Indian Journal of Chemistry*, 36A: 901 – 904.
10. Zheng, W., Hu, L., Yoon, L. S. L. and Wong, K.Y. (2016) Copper nanoparticles/polyaniline/graphene composite as highly sensitive electrochemical glucose sensor. *Journal of Electroanalytical Chemistry*, 781: 155 – 160.
11. Umar, A., Rahman M. M., Kim, S. H. and Han, Y. B. (2008). Zinc oxide nanonail based chemical sensor for hydrazine detection. *Chemical Communication*, 2: 166 – 168.
12. Golabi, S. M. and Zare, H. R. (1999). Electrocatalytic oxidation of hydrazine at a chlorogenic acid (CGA) modified glassy carbon electrode. *Journal of Electroanalytical Chemistry*, 465: 168 – 176.
13. Omar, F. S., Numan, A., Duraisamy, N. and Bashir, S. (2017). A promising binary nanocomposite of zinc cobaltite intercalated with polyaniline for supercapacitor and hydrazine sensor. *Journal of Alloys and Compounds*, 716: 96 – 105.

14. Umar, A., Abaker, M., Faisal, M., Hwang, S. W., Baskoutas, S. and Al-Sayari, S. A. (2011). High-yield synthesis of well crystalline α-$Fe_2O_3$ nanoparticles: Structural, optical and photocatalytic properties. *Journal of Nanoscience and Nanotechnology*, 11: 3474 – 3480.
15. Ibrahim, A. A., Dar, G. N., Zaidi, S. A., Umar, A., Abaker, M., Bouzid, H. and Baskouts, S. (2012). Growth and properties of Ag-doped ZnO nanoflowers for highly sensitive phenyl hydrazine chemical sensor application. *Talanta*, 93: 257 – 263.
16. Ravichandran, K. and Baldwin, R. P. (1983), Liquid chromatographic determination of hydrazines with electrochemically pretreated glassy carbon electrodes. *Analytical Chemistry*, 55: 1782 – 1786.
17. Kamyabi, M. A., Shahabi, S., Hosseini, M. H. (2008), Electrocatalytic oxidation of hydrazine at a cobalt (II) Schiff-base-modified carbon paste electrode. *Journal of Electrochemical Society*, 155: 8 – 12.
18. Maleki, N., Safavi, A. and Tajabadi, F. (2008). Palladium nanoparticle decorated carbon ionic liquid electrode for highly efficient electrocatalytic oxidation and determination of hydrazine. *Analytica Chimica Acta*, 611: 151 – 155.
19. Nassef, H. M., Radi, A. E. and O'Sullivan, C. K. (2006). Electrocatalytic oxidation of hydrazine at o-aminophenol grafted modified glassy carbon electrode: Reusable hydrazine amperometric sensor. *Journal of Electroanalytical Chemistry*, 592: 139 – 146.
20. Zare, H. R. and Nasirizadeh, N. (2007), Hematoxylin multi-wall carbon nanotubes modified glassy carbon electrode for electrocatalytic oxidation of hydrazine. *Electrochimica Acta*, 52: 4153 – 4160.
21. Zheng, L. and Song, J. F. (2009). Curcumin multi-walled carbon nantubes modiefied galssy carbon electrode and its electrocatalytic activity towards oxidation of hydrazine. *Sensors and Actuators B-Chemical,* 135: 650 – 655.
22. Koul, S., Chandra, R. and Dhawan, S. K. (2001). Conducting polyaniline composite: a reusable sensor material for aqueous ammonia. *Sensors and Actuators B-Chemical*, 75: 151 – 159.
23. Tai, H., Jiang, Y., Xie, G. and Yu, J. (2010). Preparation, characterization and comparative NH3-sensing characteristic studies of PANI/inorganic oxides nanocomposite thin film. *Journal of Materials Science and Technology*, 26: 605 – 613.
24. Runge, M. B., Dadsetan, M., Baltrusaitis, J., Knight, A. M., Ruesink, T., Lazcano, E. A., Lu, L., Windebank, A. J. and Yaszemski, M. J. (2010). The development of electrically conductive polycaprolactone fumarate-polypyrrole composite materials for nerve regeneration. *Biomaterials*, 31: 5916 – 5926.
25. Virji, S., Kaner, R. B. and Weiller, B. H. (2005). Hydrazine detection by polyaniline using fluorinated alcohol additives. *Chemistry of Materials*, 17: 1256 – 1260.
26. Xing, S., Zhao, C., Jing, S., Wu, Y. and Wang, Z. (2006). Morphology and gas sensing behavior of in situ polymerized nanostructured polyaniline films. *European Polymer Journal*, 42: 2730 – 2735.
27. Choi, B. G., Park, H. S., Im, H. S. and Kim, Y. J. (2008). Influence of oxidation state of polyaniline on physicochemical and transport properties of Nafion/polyaniline composite membrane for DMFC. *Journal of Membrane Science*, 324: 102 – 107.

*Malaysian Journal of Analytical Sciences, Vol 21 No 4 (2017): 770 - 777*
*DOI: https://doi.org/10.17576/mjas-2017-2104-02*

MALAYSIAN JOURNAL OF ANALYTICAL SCIENCES
*Published by The Malaysian Analytical Sciences Society*
ISSN 1394 - 2506

# CHITIN AND CHITOSAN EXTRACTION FROM *Portunus pelagicus*

## (Pengekstrakan Kitin dan Kitosan dari *Portunus pelagicus*)

Norhidayah M. Ahyat, Faridah Mohamad, Azrilawani Ahmad, Alyza A. Azmi*

*School of Marine and Environmental Sciences,*
*Universiti Malaysia Terengganu, 21030 Kuala Nerus, Terengganu, Malaysia*

**Corresponding author: alyza.azzura@umt.edu.my*

Received: 30 March 2017; Accepted: 4 June 2017

**Abstract**

Isolation of chitin and chitosan from natural sources are widely known as they can be used in many applications. Extraction of chitin and chitosan are carried out in exoskeleton of flower crab, *Portunus pelagicus.* Chemical treatments such as demineralization and deproteinzation processes are used for chitin extraction, and followed by deacetylation process of chitin, which is to produce its derivatives that known as chitosan. Characterization of chitin and chitosan has been done using Fourier Transform Infrared (FTIR) Spectroscopy, X-ray diffraction (XRD), CHNS elemental analysis and Thermogravimetric analysis (TGA). Preliminary results of FTIR vibrations patterns showed stretching of hydroxyl (O-H), amine (N-H) and carbonyl (C-O) groups indicated the presence of chitin and chitosan. XRD analysis indicates the crystalline nature of chitin and chitosan. The degree of deacetylation of chitin was characterized using CHNS elemental analyzer. The extracted chitosan will be used as reducing agent for silver nanoparticles synthesis in the future studies.

**Keywords**: crustacean, marine invertebrates, bio-polymers, natural reductant

**Abstrak**

Pengasingan kitin dan kitosan daripada sumber semulajadi telah dikenali secara meluas kerana dapat digunakan dalam banyak aplikasi. Pengekstrakan kitin dan kitosan dari exoskeleton ketam bunga, *Portunus pelagicus* telah dilakukan. Rawatan kimia seperti proses demineralisasi dan proses deprotenisasi telah digunakan untuk pengekstrakan kitin dan diikuti dengan proses deasetilasi daripada ktin untuk penghasilan terbitannya yang dikenali sebagai kitosan. Pencirian kitin dan kitosan telah dilakukan dengan menggunakan Spektoskopi Inframerah Transformasi Fourier (FTIR), pembelauan Sinar X (XRD), analisis unsur CHNS dan analisis termogravimetri (TGA). Dapatan awal getaran FTIR menunjukkan regangan bagi kumpulan hidroksil (O-H), amino (N-H) dan karbonil (C-O) menunjukan kehadiran sebatian kitin dan kitosan. Analisis XRD menunjukkan sifat kristal bagi kitin dan kitosan. Pencirian darjah deasetilasi kitin telah dilakukan menggunakan penganalisis unsur CHNS. Ekstrak kitosan akan digunakan sebagai agen penurun bagi sintesis nanopartikel perak untuk kajian masa hadapan.

**Kata kunci:** krustasea, invertebrata marin, bio-polimer, penurun semulajadi.

## Introduction

Polysaccharides have given many advantages in life science as their unique structure has shown some potential as natural bioactive component. Chitin is the second most abundant of polysaccharides on earth after cellulose that formed a linear chain of acetylglucosamine group. Chitin can be isolated from exoskeleton of crustacean for instance; shrimp shells [1], crab shells [2], fish scales [3], gastropod shell and operculum [4]. Chitin is available in three different forms, which are α, ß and γ forms. In addition, chitin has a compact structure and strong intra and inters molecular hydrogen bonds [5] that may causes the insolubility in most of the organic solvents, thus limit it in many applications, especially in clinical field. Due to this concern, chemical modification on chitin is performed,

which is to increase the solubility. Chitin can be deacetylated or partially deacetylated into chitosan that can be identified by calculating the percentage of degree of deacetylation (DD). Chitin and chitosan represent as white solid, non-toxic, odourless, biodegradable, biocompatible with living tissues and bio-absorbable with antibacterial, free from antigenic effect, polar in nature and can form stable complexes with heavy metals [6,7]. Chitosan has versatile properties that can be used in different fields such as biomedicals [8], tissue engineering [9], textiles [10,11], and food processing industries [12].

In general, three major steps are used in the isolation process. The processes include demineralization, deproteinization and deacetylation. Demineralization is a process of removing inorganic materials from the natural sources (i.e; exoskeleton of invertebrates), using dilute acidic solution. Then, the process is continued with deproteinization process that aided in the protein separation and followed by deacetylation process, which gives the final product of chitosan. Deacetylation process occurred at elevated temperature (in range 105 to 110 $^{o}$C) in concentrated bases solution (40% to 50%) [13 - 15]. Blue swimmer crab, *Portunus pelagicus* (*P. pelagicus*) is a major marine crab that distributed in the coastal water of western South China Sea. In the recent study, extraction of chitin and chitosan from blue swimmer crab, *P. pelagicus* (Figure 1) was conducted using this standard method and the obtained chitosan will be used as reducing agent to chelate metal ion in silver nanoparticles synthesis for upcoming research work.

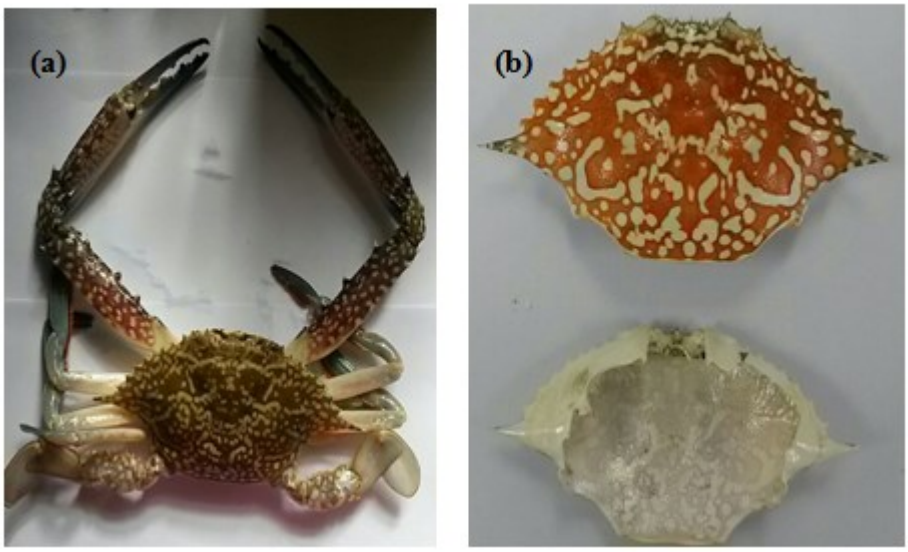



Figure 1. (a) Blue swimmer crab, *P. pelagicus* and (b) its carapace after drying process

## Materials and Methods

### Raw material preparations

Blue swimmer crab, *P. pelagicus* is bought from a local market in Kuala Terengganu, Malaysia. The carapace was scrapped free from any loose tissues, washed, dried and ground (Retsch PM 100) into fine powder with size average of 450 μm.

### Extraction procedures

Chitin was extracted from *P. pelagicus* carapace following method by Sagheer et al. [16] with some modifications. The demineralization process begins by treating the pulverized carapace in 1.0 N hydrochloric acid, HCl solution (1:15 solid-to-solvent ratio, w/v) with constant stirring for 1 hour. No thermal heating used in this process. The deproteinization process was performed by heating the demineralized powder under reflux in 1.0 N sodium hydroxide, NaOH solution (1:15 solid-to-solvent ratio, w/v) at 80 °C for 6 hours. Then, removal colour of the deproteinized powder was conducted in acetone (1:100 solid-to-solvent ratio, w/v) with constant stirring for 24

hours. The purified chitin was filtered, washed to neutrality and dried in oven at 60 °C. White powder of carapace shell was obtained after undergo the demineralization, deproteinization and decolourization processes.

**Chitin deacetylation**
Chitin was deacetylated using traditional thermal heating. The samples was mixed in 50% (w/v) of sodium hydroxide, NaOH at 1:20 solid-to-solvent ratio and stirred for 6 hours at 110 °C. After the deacetylation process, the sodium hydroxide, NaOH was drained off and the pure chitosan was washed with deionized water to neutrality and dried in oven at 60 °C.

**Characterization of chitin and chitosan: Fourier transform infrared spectroscopy**
The vibration of functional groups spectra of chitin and chitosan prepared were analyzed using FTIR spectroscopy. All samples were KBr supported, pressed to result homogenous sample/KBr disc and analyzed over the frequency of 4000 to 400 $cm^{-1}$ at resolution of 4 $cm^{-1}$ using Perkin Elmer Spectrum 100 FT-IR Spectrometer.

**X-ray powder diffractometry**
The XRD measurement of powder samples were carried out using a model of Rigaku MiniFlex II diffractometer equipped with Ni – filtered Cu Kα radiation (λ = 1.5406 Å) as the X-ray source. The diffractometer was set up at 1.25° diverging and receiving slits at 40 kV and 30 mA. Data was collected at a scan rate of 2°/min with the scan angle from 3° to 40°.

**Elemental analysis**
The average degree of deacetylation (DD) of chitosan samples was determined using CH-NS Elemental Analyzer (CHNS Microanalysis / EA1112 CHNS – O Analyzer). The DD% value of chitosan samples were calculated from the following formula:

$$DD\% = [(6.857 - C / N) / 1.7143] \times 100 \quad (1)$$

where C/N is the carbon to nitrogen ratio peak area measured from the elemental composition of the chitosan samples.

**Thermogravimetric analysis**
Thermogravimetric analysis (Perkin Elmer TGA analyzer) were carried out using approximately 20 mg of sample with temperature range of 30 to 600 °C, and with heating rate of 10 °C/min under (30 mL/min) nitrogen atmosphere.

## Results and Discussion

**Extraction of chitin and chitosan**
In this study, extraction of chitin and chitosan from the carapace of crab, *P. pelagicus* was initiated by treatment of crab shells in dilute acidic solution for the removal the inorganic content such as calcium carbonate, $CaCO_3$ from the shells. Bubbles were released after the penetration of the acid on the surface of crab shell indicates the emission of carbon dioxide, $CO_2$ gas. During this treatment, low concentration of acidic solution, which is 15 mL/g of 1.0 N HCl was used to prevent the hydrolysis of chitin structure [17]. Deacetylation process is a conducted, which is to remove the acetyl group in chitin, thus produce chitosan [5]. Bolat et al. [18] reported the chitin and chitosan content for freshwater crab were 6.83% and 4.56%, respectively. In this study, the dry weight of chitin and chitosan contents for the carapace of *P. pelagicus* were 20.24% and 13.56%, respectively and the result is consistent with the result reported by Das et al. [19].

**Characterization of chitin and chitosan: Fourier transform infrared analysis**
Fourier transform infrared (FTIR) spectroscopy is a technique that is used to determine the vibration of functional groups in chitin and chitosan. The FTIR spectra of chitin and chitosan of *P. pelagicus* were examined as shown in Figure 2. Chitin spectrum shows bands at 3447 $cm^{-1}$, 3103 $cm^{-1}$ and 1657 $cm^{-1}$ corresponds to the vibration of hydroxyl, the O–H stretching, aliphatic compound, the $CH_3$ stretching and amide I, the stretching of C=O group, respectively. These peaks are pivotal to observe because they are used to differentiate the formation between chitin and chitosan from the extracted sample. The vibration of Amide III was observed at peak 1314 $cm^{-1}$ due to the

presence of protein content in the chitin complexes. Vibration of N–H stretching that associated with O-H stretching was observed in chitosan FTIR spectrum at band 3447 $cm^{-1}$. The vibration of $-CH_3$ group in chitin spectrum was absence in the FTIR spectrum of chitosan after treating in concentrated NaOH for six hours, thus this finding proved that the acetyl group, $COCH_3$ in chitin backbone was removed during the deacetylation process, thus produced chitosan. Besides, there is no significant between the FTIR spectrum of prepared chitosan and commercial chitosan. Table 1 shows the spectral value of chitin, chitosan and commercial chitosan.

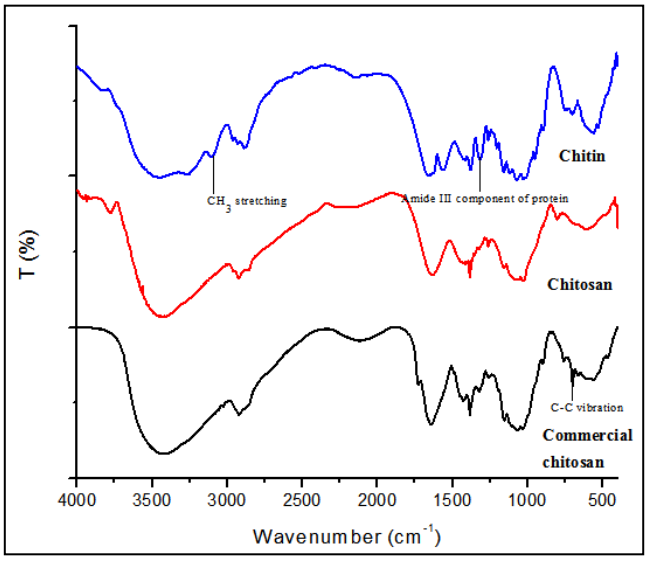



Figure 2. FTIR spectra of chitin, chitosan and commercial chitosan

Table 1. FTIR spectra value of chitin, chitosan and commercial chitosan

| **Assignment** | **Frequency ($cm^{-1}$)** | | |
|---|---|---|---|
| | **Chitin** | **Chitosan** | **Commercial Chitosan** |
| Hydroxyl, O-H stretch (H-bonded) | 3445 | - | - |
| Amine, $NH_2$ stretch and hydroxyl, O-H stretch | - | 3435 | 3429 |
| Amine, N-H stretch | 3264 | - | - |
| Aliphatic compound, $-CH_3$ stretch | 3102 | - | - |
| Aliphatic compound, $-CH_2$ stretch | - | 2924 | 2921 |
| Secondary amide, C=O stretch | 1657 | 1636 | 1643 |
| Amide, N-H bend | 1559 | - | - |
| Aliphatic compound, $-CH_2$ bend | 1417 – 1379 | 1412 - 1384 | 1430 - 1384 |
| Amide III, component of protein | 1314 | - | - |
| Complex vibration of NHCO group | - | 1261 | 1262 |
| C-O-C glycosidic linkage | - | 1160 | 1154 |
| Carbonyl, C-O stretch | - | 1023 | 1070 |
| Ring vibration (C-C) | - | - | 699 |

**X-ray powder diffractometry analysis**

X-ray diffraction analysis is applied to determine the crystallinity structure of extracted chitin and chitosan. In the crystallography study of the prepared samples (Figure 3), the XRD patterns of chitin shows three sharp peaks at 9.3°, 19.4°, 26.0° and a small peak at 13.0°. These peaks often used as reference peaks for α chitin [15, 20 - 21]. In addition, weak reflection of α chitin peak at 26° was observed in the chitosan of *P. pelagicus.* This condition is occurred may due to the partial deacetylation of chitin. Furthermore, strong reflection was observed at 9.3° and 19.2° belongs to chitosan and these peaks were almost similar to the peaks available in the commercial chitosan.

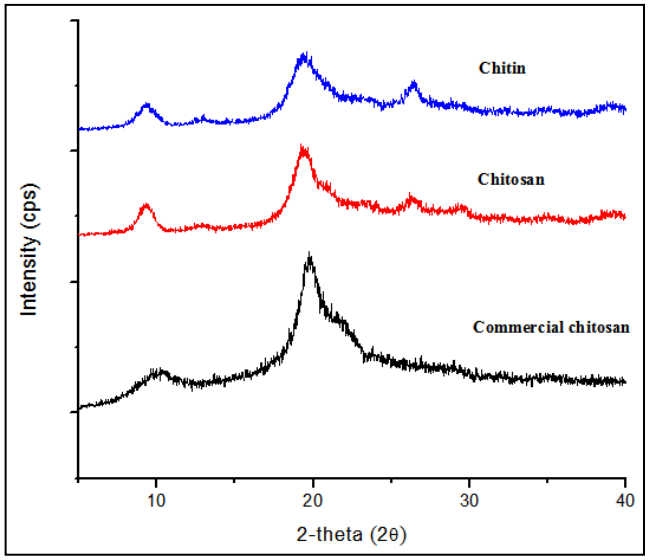



Figure 3. XRD patterns for chitin, chitosan and commercial chitosan

**Elemental analysis**

Table 2 shows the chemical composition of chitin and chitosan. The percentage for carbon, C in chitin and chitosan were 77.67% and 73.93%, respectively. The decreasing value of the C percentage is due to the removal of acetyl groups in the chitin structure. Kaya et al. [22] stated that the theoretical of N percentage for pure chitin is 6.9%. Hence, the N percentage in chitin and chitosan prepared were 9.62% and 12.00%, respectively, which are higher than 6.9% reported in literature. This is due to the present of protein residue in the both samples and supported by the results obtained from FTIR spectra. Furthermore, the two components (C and N) are important to determine the percentage of the DD of the chitosan sample followed by the formula given. The DD of the chitosan of *P. pelagicus* was 40.60% slightly lower than the suggested DD (approximately 50%). However, this might cause by partially deacetylation of chitin and the result is consistent with the crystallinity data obtained.

Table 2. The percentage composition of carbon, nitrogen and hydrogen in chitin and chitosan

| Samples | Carbon (%) | Nitrogen (%) | Hydrogen (%) | C/N |
|---|---|---|---|---|
| Chitin | 77.67 | 9.62 | 12.71 | 8.07 |
| Chitosan | 73.93 | 12.00 | 14.07 | 6.16 |

**Thermogravimetric analysis**

Thermogravimetric analysis (TGA) is conducted, which is to study on thermal degradation of chitin and chitosan. The TGA curves (Figure 4) was observed that chitin and chitosan have two degradation steps. The first stage of degradation chitin and chitosan occurred at temperature range 30 °C to 125 °C and 30 °C to 123 °C with 7% and 12% of weight loss, respectively. This degradation may attribute to the loss of water molecules because the chitin

and chitosan structures have strong affinity towards water and lead dehydration. The second stage of chitin and chitosan degradation begins around 152 °C to 398 °C and 148 °C to 392 °C with 61% and 48% of weight loss, respectively. The second degradation belongs to thermal decomposition of chitin and chitosan. Although the chitin and chitosan prepared shows a similar trend of thermal degradation curves, but chitin has larger decomposition rate as compared to chitosan [15].

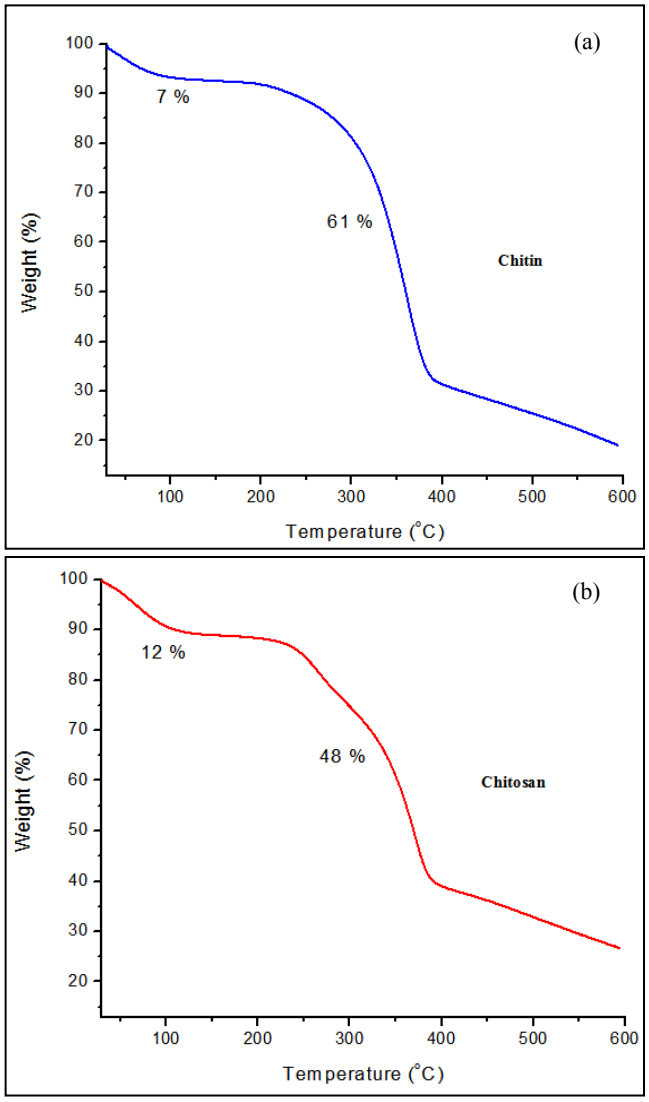



Figure 4. TGA analysis of (a) chitin and (b) chitosan

## Conclusion

Chitin and chitosan were successfully extracted from the carapace of blue swimmer crab, *P. pelagicus* with significant outcomes. Dry weight of chitin and chitosan content were 20.24% and 13.56%, respectively. FTIR analysis confirmed the structural change between chitin and chitosan. Crystallinity analysis revealed the formation of α chitin from the studied species. Partially deacetylation of chitin into chitosan was observed with 40.60% of DD. Additionally, the thermal degradation analysis proved that α chitin exists as a stable structure towards thermal

decomposition than chitosan. It is suggested that chitin and chitosan from the carapace of blue swimmer crab, *P. pelagicus* can be used as potential a reducing agent for synthesizing silver nanoparticles in future studies.

**Acknowledgement**

The authors are thankful to Ministry of Higher Education Malaysia for financial assistant in Research Acculturation Grant Scheme (RAGS) vote no. 57117, Mybrain15 for scholarship sponsor and Universiti Malaysia Terengganu for providing the facilities.

**References**

1. Younes, I., Hajji, S., Frachet, V., Rinaudo, M., Jellouli, K. and Nasri, M. (2014). Chitin extraction from shrimp shell using enzymatic treatment. Antitumor, antioxidant and antimicrobial activities of chitosan. *International Journal of Biological Macromolecules*, 69: 489 – 498.
2. Hajji, S., Ghorbel-bellaaj, O., Younes, I., Jellouli, K. and Nasri, M. (2015). Chitin extraction from crab shells by *Bacillus* bacteria. Biological activities of fermented crab supernatants. *International Journal of Biological Macromolecules*, 79: 167 – 173.
3. Kumari, S. and Kumar, P. (2014). Extraction and characterization of chitin and chitosan from (Labeo rohit) fish scales. *Procedia Materials Science*, 6: 482 – 489.
4. Palpandi, C., Shanmugam, V. and Shanmugam, A. (2009). Extraction of chitin and chitosan from shell and operculum of mangrove gastropod *Nerita (Dostia) crepidularia* Lamarck. *International Journal of Medicine and Medical Sciences*, 1(5): 198 – 205.
5. Abdel-Rahman, R. M., Hrdina, R., Abdel-Mohsen, A. M., Fouda, M. M. G., Soliman, A. Y., Mohamed, F. K., Mohsin, K. and Pinto, T. D. (2015). Chitin and chitosan from Brazilian Atlantic Coast: Isolation, characterization and antibacterial activity. *International Journal of Biological Macromolecules*, 80: 107 –120.
6. Gomes, J. R. B., Jorge, M., and Gomes, P. (2014). Interaction of chitosan and chitin with Ni, Cu and Zn ions : A computational study. *Journal of Chemical Thermodynamics*, 73: 121 – 129.
7. Mohan, C. O., Ravishankar, C. N., Lalitha, K. V. and Gopal, T. K. S. (2012). Effect of chitosan edible coating on the quality of double filleted Indian oil sardine (*Sardinella longiceps*) during chilled storage. *Food Hydrocolloids*, 26: 167 – 174.
8. Jayakumar, R., Prabaharan, M., Nair, S. V. and Tamura, H. (2010). Novel chitin and chitosan nanofibers in biomedical applications. *Biotechnology Advances*, 28 (1): 142 – 150.
9. Shavandi, A., Bekhit, A. E.-D. A., Ali, M. A., Sun, Z. and Gould, M. (2015). Development and characterization of hydroxyapatite/β-TCP/chitosan composites for tissue engineering applications. *Materials Science and Engineering: C*, 56: 481 – 493.
10. Demarchi, C. A., Campos, M. and Rodrigues, C. A. (2013). Adsorption of textile dye Reactive Red 120 by the chitosan–Fe(III)-crosslinked: Batch and fixed-bed studies. *Journal of Environmental Chemical Engineering*, 1(4): 1350 – 1358.
11. Chandrasekar, S., Vijayakumar, S. and Rajendran, R. (2014). Application of chitosan and herbal nanocomposites to develop antibacterial medical textile. *Biomedicine and Aging Pathology*, 4(1): 59 – 64.
12. Bae, M. J., Shin, H. S., Kim, E. K., Kim, J. and Shon, D. H. (2013). Oral administration of chitin and chitosan prevents peanut-induced anaphylaxis in a murine food allergy model. *International Journal of Biological Macromolecules*, 61: 164 – 168.
13. Shanmugam, A., Subhapradha, N., Suman, S., Saravanan, R., Shanmugam, V. and Srinivasan, A. (2012). Characterization of biopolymer "chitosan" from the shell of donacid clam donax scortum (Linnaeus, 1758) and its antioxidant activity. *International Journal of Pharmacy and Pharmaceutical Sciences*, 4 (2): 460 – 465.
14. Puvvada, Y. S., Vankayalapati, S. and Sukhavasi, S. (2012). Extraction of chitin from chitosan from exoskeleton of shrimp for application in the pharmaceutical industry. *International Current Pharmaceutical Journal*, 1(9): 258 – 263.
15. Abdou, E. S., Nagy, K. S. A. and Elsabee, M. Z. (2008). Extraction and characterization of chitin and chitosan from local sources. *Bioresource Technology*, 99: 1359 – 1367.
16. Sagheer, F. A., Al-Sughayer, M. A., Muslim, S. and Elsabee, M. Z. (2009). Extraction and characterization of chitin and chitosan from marine sources in Arabian Gulf. *Carbohydrate Polymers*, 77 (2): 410 – 419.
17. Benhabiles, M. S., Salah, R., Lounici, H., Drouiche, N., Goosen, M. F. A. and Mameri, N. (2012). Antibacterial activity of chitin, chitosan and its oligomers prepared from shrimp shell waste. *Food Hydrocolloids*, 29: 48 –56.

18. Bolat, Y., Bilgin, Ş., Günlü, Izci, L., Koca, D. B., Çetinkaya, S. and Koca, H. U. (2010). Chitin – chitosan yield of freshwater crab (*Potamon potamios,* Olivier 1804) Shell. *Paskitan Veterinanry Journal,* 30 (4): 227 – 231.
19. Das, N. G., Khan, P. A. and Hossain, Z. (1996). Chitin from the shell of two coastal portunid crabs of Bangladesh. *Indian Journal of Fisheries*, 43(4): 413 – 415.
20. Ramasamy, P., Subhapradha, N., Shanmugam, V. and Shanmugam, A. (2014). Extraction, characterization and antioxidant property of chitosan from cuttlebone *Sepia kobiensis* (Hoyle 1885). *International Journal of Biological Macromolecules*, 64: 202 – 212.
21. Kaya, M., Baran, T. and Mentes, A. (2014). Extraction and characterization of α -chitin and chitosan from six different aquatic invertebrates. *Food Biophysics*, 145 – 157.
22. Kaya, M., Baublys, V., Can, E., Šatkauskiene, I., Bitim, B., Tubelyte, V. and Baran, T. (2014). Comparison of physicochemical properties of chitins isolated from an insect (*Melolontha melolontha*) and a crustacean species (*Oniscus asellus*). *Zoomorphology*, 133(3): 285 – 293.

*Malaysian Journal of Analytical Sciences, Vol 21 No 4 (2017): 778 - 783*
*DOI: https://doi.org/10.17576/mjas-2017-2104-03*

MALAYSIAN JOURNAL OF ANALYTICAL SCIENCES
*Published by The Malaysian Analytical Sciences Society*
ISSN 1394 - 2506

# NEW COMPOUNDS FROM *Hydnophytum formicarum* YOUNG TUBERS

## (Sebatian Baru daripada Bonjolan Muda *Hydnophytum formicarum*)

Nur Shafiqa Abdullah, Wan Yaacob Wan Ahmad*, Noor Aziiraa Sabri

*School of Chemical Science and Food Technology, Faculty of Science and Technology*
*Universiti Kebangsaan Malaysia, 43600 UKM Bangi, Selangor, Malaysia*

**Corresponding author: wanyaa@ukm.edu.my*

Received: 16 January 2017; Accepted: 14 June 2017

**Abstract**

The fine powders from young tubers of *Hydnophytum formicarum* were soaked and extracted by Soxhlet in methanol. Both methanol solutions were evaporated with rotary evaporator to yield cold and hot methanol extracts. Chromatographic separation on the extracts by vacuum liquid and radial chromatography gave two new compounds namely hydnophaldehyde [4,4′,10′,13′,14′-pentamethylgona-7′,9′(11′)-dien-17′-yl(6)-2,2-dimethylheptanal] (**1**) and 2-(2′-methoxyphenyl)ethyl palmitate (**2**). The structures of the above compounds were established by interpreting their spectral data of mass, 1-D Nuclear Magnetic Resonance (NMR), 2-D NMR, and Infrared (IR).

**Keywords**: Rubiaceae, *Hydnophytum formicarum*, hydnophaldehyde, 2-(2′-methoxyphenyl)ethyl palmitate

**Abstrak**

Serbuk halus bonjolan muda *Hydnophytum fomicarum* direndam dengan metanol dan diekstrak mengunakan kaedah Soxhlet. Kedua-dua larutan metanol disejat dengan penyejat berputar bagi menghasilkan ekstrak metanol sejuk dan panas. Pemisahan kromatografi terhadap ekstrak tersebut dengan kromatografi cecair vakum dan radial memberikan dua sebatian baru bernama hidnofaldehid [4,4′,10′,13′,14′-pentametilgona-7′,9′(11′)-dien-17′-il(6)-2,2-dimetilheptanal] (**1**) dan 2-(2′-metoksifenil)etil palmitat (**2**). Struktur sebatian di atas disahkan dengan mentafsirkan data spektrum bagi jisimnya, Resonans Magnetik Nuklear (RMN) 1-D, RMN 2-D dan Inframerah (IM).

**Kata kunci:** Rubiaceae, *Hydnophytum formicarum*, hidnofaldehid, 2-(2′-metoksifenil)etil palmitat

## Introduction

Ant-house plants of *Hydnophytum* genus are distributed in Southeast Asia, the Pacific region, and also extending into northern Australia state of Queensland. The plants grow on tree branches and on trunks by their epiphytic attaching tubers that look like the swollen succulent stems are having few woody branches with leaves. The genus comprises 55 species, of which 44 are found in New Guinea [1]. *Hydnophytum formicarum* Jack. (Rubiaceae) forms a symbiotic relationship with ants where its hollow as well as smooth-walled tunnels within the modified stems provide shelter for ant colonies, and in return they provide nutrients to the plants by leaving wastes within the tunnels. In Malaysia, the plant is known as Sarang Semut, Kepala Beruk, and Raja Satong. The tubers of *H. formicarum* have been used in Thai as well as in Malaysian traditional herbal medicine for cancer treatment. To date, only eight known compounds of β-sitosterol, stigmasterol (steroids), protocatechualdehyde, isoliquiritigenin, butein (phenolic compounds), butein [2, 3], sinapinic acid [4] and 7,3',5'-trihydroxyflavanone (flavonoids) [5] were isolated from *H. formicarum* tubers.

Previous study showed that ethanolic and phenolic-rich extracts of *H. formicarum* tubers possessed both antiproliferative activity as well as HDAC inhibitory activity in HeLa cells that are mediated by induction of apoptosis. On the other hand, methanol, methanol-water (1:1), and water extracts of *H. formicarum* showed selective activity against human tumor cell lines, HeLa, and A549. These results support the efficacy of *H. formicarum* tubers for the treatment of cervical cancer, colon cancer, and T-cell leukemia in an alternative medicine. Thanaset et al. stated that sinapinic acid that is isolated from *H. formicarum* tubers, inhibited the growth of HeLa and HT29 cells more effectively than sodium butyrate. However, it inhibited the growth of HCT116 and Jurkat cells less effectively than sodium butyrate. The non-cancer cell line (Vero cells) and breast cancer cell line (MCF-7 cells) appeared to be resistant to both sinapinic acid and sodium butyrate. The growth inhibitory effect of sinapinic acid in HeLa cells was mediated by induction of apoptosis. *Hydnophytum formicarum* tubers-derived 7,3',5'-trihydroxyflavanone could induce the apoptotic cell death of MCF-7 cells by increasing Bax expression level [6]. In view of the above, we embark on the isolation of new compounds from the extracts of *H. formicarum*. In this study, methanol was used for maceration and Soxhlet because more polar compounds can be extracted from the young tubers.

## Materials and Methods

### Instruments

The $^{1}H$ and $^{13}C$-APT NMR spectra were recorded with Avance III 700 MHz Bruker in $CDCl_3$ with the chemical shifts, δ, in ppm and the values of coupling constants, *J*, in Hz. LC-MSToF spectra were taken on the Dionex/Bruker Micro ToFQ and FTIR (ATR) spectra were recorded on the Perkin-Elmer Spectrometer 400 FT-IR/FT-NIR. Column chromatography (Merck 7747; particle size 0.040 – 0.063 mm), vacuum liquid chromatography (Merck 7747; particle size 0.040 – 0.063 mm), radial chromatography (Merck 7749; particle size 0.040 – 0.063 mm), thin layer chromatography (Merck 5554; mesh 230 – 400).

### Plant materials

Young tubers of *Hydnophytum formicarum* were bought in April 2015 from a medicinal plant seller at Kampung Lak Lok, Jertih, Besut, Terengganu. A voucher specimen (UKMB 40312) was deposited at the herbarium of Universiti Kebangsaan Malaysia Bangi (UKMB).

### Extraction and isolation

The air-dried young tubers of *Hydnophytum formicarum* were cut into small pieces and grounded into fine powder by using mechanical grinding machine. The powders (1.04 kg) were then extracted with methanol through two types of extraction: maceration in three days, and Soxhlet for a total of 18 hours. The maceration extraction produced 17.0 g of dark-brown concentrated extract after being evaporated by rotary evaporator. The methanol solution of the extract was extracted by using separatory funnel with *n*-hexane and chloroform to yield extracts of *n*-hexane (9.0 g), chloroform (5.0 g), as well as methanol (3.0 g) [3]. The *n*-hexane extract was subjected to vacuum liquid chromatography (VLC) by using silica gel 7747 (Merck) that eluted with increasing polarity of *n*-hexane and ethyl acetate. The eluents were combined based on their silica gel thin layer chromatography (TLC) 5554 (Merck) profile to give seven fractions (A-G). Fraction B (1.1 g) was further separated by radial chromatography (RC) by using *n*-hexane-ethyl acetate (9:1) to yield nine fractions ($B_1$-$B_9$). The $B_3$ fraction was pure to give 2-(2′-methoxyphenyl) ethyl palmitate (28.0 mg).

Meanwhile, the methanol solution of the Soxhlet extraction was evaporated to give 15.0 g (1.44 %) of a dark-brown extract after solvent removal by a rotary evaporator. The extract was subjected to VLC that eluted with increasing polarity of *n*-hexane and ethyl acetate. The eluents were combined based on their TLC profile to give seven fractions (A-G). Fraction C (1.2 g) was further purified by RC using *n*-hexane-ethyl acetate (7:3) to yield eight fractions ($C_1$-$C_8$). The $C_2$ fraction was pure to give hydnophaldehyde (38.0 mg).

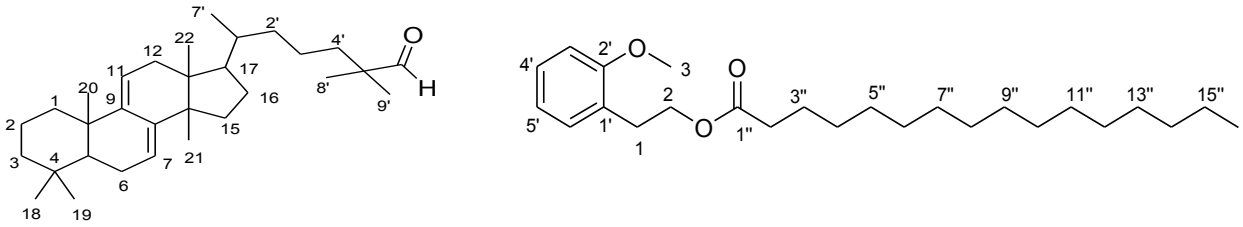
## Results and Discussion

### Characterization Study

Hydnophaldehyde (**1**) (38.0 mg): white needles; $R_f$ = 0.94 (*n*-hexane-ethyl acetate, 7:3); ESI-MS (m/z): 461.3201 $[M+Na]^+$, $C_{31}H_{50}O$; FTIR (ATR) $cm^{-1}$: 2927 and 2870 ($Csp^3$–H), 1698 (C=O aldehyde), 1456 (C=C), 1385 ($Csp^3$-H), 750 ($Csp^2$–H). Data of 1-D and 2-D (HSQC, COSY, HMBC) for $^{1}H$ and $^{13}C$-APT NMR are in Table 1.

2-(2′-Methoxyphenyl)ethyl palmitate (**2**) (28.0 mg): white powders; $R_f$ = 0.69 (*n*-hexane-ethyl acetate, 9:1); ESI-MS (m/z): 413.2417 $[M+Na]^+$, $C_{25}H_{42}O_3$; FTIR (ATR) $cm^{-1}$: 2916 and 2849 (C$sp^3$-H), 1711 (C=O ester), 1458 and 1378 (C$sp^3$-H), 1268 and 1158 (C-O), 1032 (C$sp^2$-H), 1516, 1473 and 1463 (C=C aromatic), 718 (ortho subs. benzene). Data of 1-D and 2-D (HSQC, COSY, HMBC) for $^1$H and $^{13}$C-APT NMR are in Table 2.

Molecular structures of hydnophaldehyde **(1)** and 2-(2′-methoxyphenyl)ethyl palmitate (**2**) as shown in Figure 1.




**1** **2**

Figure 1. Molecular structures of hydnophaldehyde **(1)** and 2-(2′-methoxyphenyl)ethyl palmitate (**2**)

Table 1. Spectral data of 1-D and 2-D NMR (700 MHz, $CDCl_3$) of hydnophaldehyde (1)

| No. | $\delta_C$ | $\delta_H$ (ΣH, *m*, *J* Hz) | COSY | HMBC |
|---|---|---|---|---|
| 1 | 36.9 | - | H-2 | - |
| 2 | 19.8 | - | H-3 | - |
| 3 | 40.7 | - | - | - |
| 4 | 32.8 | - | - | - |
| 5 | 47.0 | - | - | H-7, H-11 |
| 6 | 24.3 | 2.40 (2H, *m*) | H-5 | H-7 |
| 7 | 125.8 | 5.29 (1H, *dd*, *J* = 7.6, 2.4 Hz) | - | - |
| 8 | 141.9 | - | - | - |
| 9 | 138.4 | - | - | - |
| 10 | 39.2 | - | - | H-7, H-11 |
| 11 | 123.3 | 5.35 (1H, *dd*, *J* = 9.0, 2.4 Hz) | H-12 | - |
| 12 | 39.5 | 2.55 (2H, *d*, *J* = 2.4 Hz) | - | - |
| 13 | 47.6 | - | - | - |
| 14 | 50.4 | - | - | - |
| 15 | 34.4 | - | - | - |
| 16 | 39.6 | - | - | - |
| 17 | 52.8 | - | - | H-11 |
| 18 | 26.7 | 0.91 (3H, *s*) | - | - |
| 19 | 26.8 | 0.89 (3H, *s*) | - | - |
| 20 | 21.7 | 1.13 (3H, *s*) | - | - |
| 21 | 23.7 | 1.14 (3H, *s*) | - | - |
| 22 | 17.2 | 1.06 (3H, *s*) | - | - |
| 1′ | 39.0 | - | - | - |

Table 1 (cont'd). Spectral data of 1-D and 2-D NMR (700 MHz, $CDCl_3$) of hydnophaldehyde (1)

| No. | $\delta_C$ | $\delta_H$ (ΣH, *m*, *J* Hz) | COSY | HMBC |
|---|---|---|---|---|
| 2′ | 36.9 | - | - | - |
| 3′ | 23.4 | - | - | - |
| 4′ | 32.7 | - | - | - |
| 5′ | 48.2 | - | - | - |
| 6′ | 207.6 | 9.34 (1H, *s*) | - | - |
| 7′ | 17.5 | 0.98 (3H, *s*) | - | - |
| 8′ | 21.3 | 1.14 (3H, *s*) | - | H-6′ |
| 9′ | 21.7 | 1.17 (3H, *s*) | - | H-6′ |

Table 2. Spectral data of 1-D NMR and 2-D NMR (700 MHz, $CDCl_3$) of 2-(2′-methoxyphenyl) ethyl palmitate (2) and palmitate part of tricosanyl palmitate

| No. | 2-(2′-methoxyphenyl)ethyl palmitate | | | | *Palmitate Part | |
|---|---|---|---|---|---|---|
| | $\delta_C$ | $\delta_H$ (ΣH, *m*, *J* Hz) | COSY | HMBC | $\delta_C$ | $\delta_H$ (ΣH, *m*, *J*) |
| 1′ | 127.0 | - | - | - | - | - |
| 2′ | 157.0 | - | - | - | - | - |
| 3′ | 109.3 | 7.04 (1H, *s*) | H-4′ | H-4′ | - | - |
| 4′ | 144.6 | 7.60 (1H, *d*, *J* = 7.5Hz) | - | H-5′ | - | - |
| 5′ | 123.1 | 7.08 (1H, *d*, *J* = 8.1 Hz) | H-6′ | H-4′ | - | - |
| 6′ | 129.9 | 7.44 (1H, *d*, *J* = 8.3 Hz) | - | H-4′ | - | - |
| 1 | 31.9 | 1.58 (2H, *t*, *J* = 6.8 Hz) | - | - | - | - |
| 2 | 64.6 | 4.19 (2H, *t*, *J* = 6.8 Hz) | H-1 | H-1 | - | - |
| 3 | 56.0 | 3.93 (3H, *s*) | - | - | - | - |
| 1″ | 167.4 | - | - | - | 171.5 | - |
| 2″ | 31.9 | 1.25 (28H, *br*) | - | H-2 | 31.8 | 1.18 (28H, *br*) |
| 3″ | 26.0 | | - | - | 29.6 | |
| 4″ | 29.7 | | - | - | 29.6 | |
| 5″ | 29.6 | | - | - | 29.6 | |
| 6″ | 29.6 | | - | - | 29.6 | |
| 7″ | 29.6 | | - | - | 29.6 | |
| 8″ | 29.4 | | - | - | 29.6 | |
| 9″ | 29.4 | | - | - | 29.6 | |
| 10″ | 29.4 | | - | - | 29.4 | |
| 11″ | 28.8 | | - | - | 29.6 | |
| 12″ | 28.4 | | - | - | 29.6 | |
| 13″ | 29.7 | | - | - | 29.6 | |
| 14″ | 26.0 | | - | - | 29.6 | |
| 15″ | 22.7 | | - | - | 22.6 | |
| 16″ | 14.1 | 0.88 (3H, *t*, *J* = 6.9 Hz) | - | H-14″, H-15″ | 14.3 | 0.81 (3H, *t*, *J* = 6.3 Hz) |

Source: *[7]

Spectral data of $^{1}H$ and $^{13}C$-APT NMR as well as 2-D NMR in Table 1 confirmed that the compound is hydnophaldehyde or 4,4′,10′,13′,14′-pentamethylgona-7′,9′(11′)-diene-17′-yl(6)-2,2-dimethylheptanal. The ESI-MS gave molecular ion at *m/z* 461.3201 $[M+Na]^{+}$, which corresponded to the molecular formula $C_{31}H_{50}O$. To the best of our knowledge, hydnophaldehyde (steroid) that is isolated from *Hydnophytum formicarum* is a new compound. Based on Prachayasittikul et al, protocatechualdehyde (phenolic) has been isolated from *H. formicarum*. The presence of aldehydes among others in the phytochemical screening of *H. formicarum* ethanol extract supports the existence of hydnophaldehyde in the plant [8]. Figure 2 below shows the correlations between carbon and proton as well as proton and proton from the respective HMBC and COSY spectral data of hydnophaldehyde in Table 1.

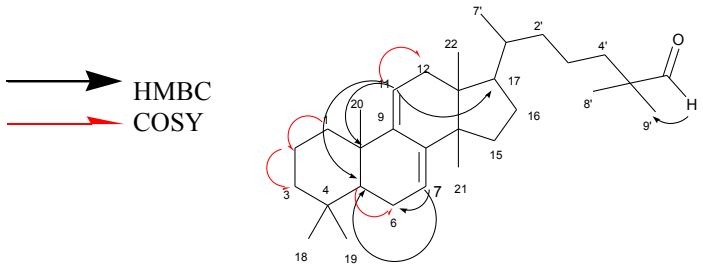



Figure 2. HMBC and COSY correlations of hydnophaldehyde (1)

The NMR spectral data ($^{1}H$ and $^{13}C$-APT) in Table 2 is in agreement that it is compound that is named as 2-(2′-methoxyphenyl) ethyl palmitate. The ESI-MS exhibited molecular ion at *m/z* 413.2417 $[M+Na]^{+}$, which is matched with the molecular formula $C_{25}H_{42}O_3$. A 107 species in Rubiaceae family that composed fatty acids in leaves proved that 2-(2′-methoxyphenyl) ethyl palmitate as an ester of palmitic acid is present in *Hydnophytum formicarum* [9]. Figure 3 shows the HMBC and COSY correlations of 2-(2′-methoxyphenyl) ethyl palmitate.

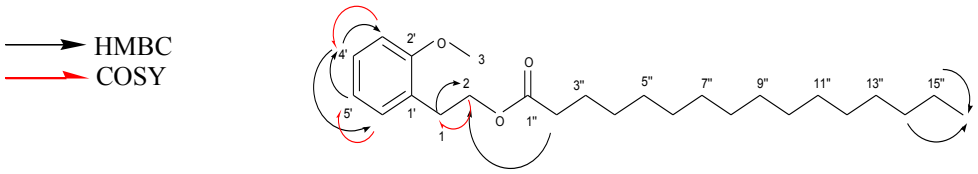



Figure 3. HMBC and COSY correlations of 2-(2′-methoxyphenyl)ethyl palmitate (2)

## Conclusion

Chromatographic separation of two methanol extracts that was derived from maceration and Soxhlet of powder for young tubers of *Hydnophytum formicarum* yielded two new compounds of hydnophaldehyde (4,4′,10′,13′,14′-pentamethylgona-7′,9′(11′)-diene-17′-yl(6)-2,2 dimethylheptanal) and 2-(2′-methoxyphenyl)ethyl palmitate. Hydnophaldehyde and 2-(2′-methoxyphenyl) ethyl palmitate can be used to evaluate their biological activities such as for antimicrobial, antioxidants, anti-cancer, and antitumor properties.

## Acknowledgement

We would like to thank the Ministry of Higher Education Malaysia and Universiti Kebangsaan Malaysia (UKM) for the financial support under DLP-2013-018 and LIV-2015-01 grants. Special thanks to School of Chemical Sciences and Food Technology, Faculty of Science and Technology, UKM and Centre for Research and Innovation Management (CRIM), UKM for the technical support on NMR, LC-MSToF and FTIR (ATR) instrumentation.

## References

1. Huxley, C. R. and Jebb, M. H. P. (1991). The tuberous epiphytes of the Rubiaceae 1: A new subtribe - The Hyd nophytinae. Blumea. National Botanic Gardens Glasnevin. Dublin, Ireland. 36: 1 – 20.

2. Prachayasittikul, S., Buraparuangsang, P., Worachartcheewan, A., Isarankura-Na-Ayudhya, C., Ruchirawat, S. and Prachayasittikul, V. (2008). Antimicrobial and antioxidative activities of bioactive constituents from *Hydno phytum formicarum* Jack. *Molecules (Basel, Switzerland)*, 13(4): 904 – 921.
3. Prachayasittikul, S., Pingaew, R., Yamkamon, V., Worachartcheewan, A., Wanwimolruk, S., Ruchirawat, S. an d Prachayasittikul, V. (2012). Chemical constituents and antioxidant activity of *Hydnophytum formicarum* Jack. *International Journal of Pharmacology,* 8(5): 440 – 444.
4. Thanaset, S., Suwatchai, M., Somprasong, K., Suporn, N., Prasan, S., Chanokbhorn, P., Arpa, S. and Banchob, S. (2013). Histone deacetylase (HDAC) inhibitory and antiproliferative activities of phenolic-rich extracts deriv ed from the rhizome of *Hydnophytum formicarum* Jack: Sinapinic acid acts as HDAC inhibitor. *BMC Complem entary and Alternative Medicine,* 13: 232 – 243.
5. Abdullah, H., Pihie, A. H. L. and Hohmann, J. (2009). Release of cytochrome c in MCF-7 cells treated with 7,3' ,5'-trihydroxyflavanone of *Hydnophytum formicarum*. *Biomedical & Pharmacology Journal,* 2(1): 1 – 6.
6. Abdullah, H., Pihie, A.H.L., Hohmann, J. and Molnar, J. (2010). A natural compound from *Hydnophytum formi carum* induces apoptosis of MCF-7 cells via up-regulation of Bax. *Cancer Cell International,* (10): 14 – 23.
7. Alam, P., Ali, M. and Aeri, V. (2011). Isolation of four new phytoconstituents from the roots of *Albizzia lebbec k* Benth. *Der Pharmacia Lettre,* 3(6): 74 – 81.
8. Darwis, D., Hertini, T. and Samito, E. (2014). The effects of *Hydnophytum formicarum* ethanolic extract towar d lymphocyte, vero and T47d cells proliferation in vitro. *Journal of Applied Pharmaceutical Science,* 4(6): 103- 109.
9. Mongrand, S., Badoc, A., Patouille, B., Lacomblez, C., Chavent, M. and Bessoule, J. J (2005). Chemotaxonom y of the rubiaceae family based on leaf fatty acid composition. *Phytochemistry*, 66(5): 549 – 559.

*Malaysian Journal of Analytical Sciences, Vol 21 No 4 (2017): 784 - 792*
*DOI: https://doi.org/10.17576/mjas-2017-2104-04*

**MALAYSIAN JOURNAL OF ANALYTICAL SCIENCES**
*Published by The Malaysian Analytical Sciences Society*
**ISSN 1394 - 2506**

# OPTICAL CHEMICAL SENSOR OF Cd(II) IN WATER BASED ON 1-(2-PYRIDYLAZO)-2-NAPHTOL IMMOBILIZED ON POLY(METHYL METHACRYLATE) AND 2-NITROPHENYL OCTYL ETHER MATRIX

## (Sensor Kimia Optik untuk Penentuan Cd(II) dalam Air Berasaskan 1-(2-Piridilazo)-2-Naftol yang Dipegun dalam Matriks Poli(metil metaakrilat) dan 2-Nitrofenil Oktil Eter)

Moersilah[1,2], Dwi Siswanta[1], Roto Roto[1], Mudasir Mudasir[1]*

[1]*Department of Chemistry, Faculty of Mathematics and Natural Sciences, Universitas Gadjah Mada, Sekip Utara, Yogyakarta, 55281 Indonesia*
[2]*Department of Chemistry, Faculty of Mathematics and Science, State University of Jakarta, Jl. Pemuda No. 10 Jakarta Timur, Jakarta, Indonesia*

**Corresponding author: mudasir@ugm.ac.id*

Received: 18 January 2017; Accepted: 22 May 2017

**Abstract**

An optical chemical sensor for determination of Cd(II) in aqueous solution has been developed by immobilizing 1-(2-pyridylazo)-2-naphtol (PAN) in poly(methyl methacrylate) (PMMA) as a matrix and 2-nitrophenyl octyl ether (NPOE) as a plasticizer. The adsorption of Cd(II) causes the color of the membrane to change from yellow to red-orange with the maximum absorbance ($\lambda_{max}$) at 556 nm. The sensor membrane gives the best response towards Cd(II) ion at pH 8.5, after 120 minutes of contact time, at 2 ppm Cd(II), and 2 mL solution. A linear Cd(II) calibration curve can be developed in the concentration range of 0.8 - 1.8 ppm with $R^2$ = 0.960. The limit of the detection and limit of quantification are 0.041 ppm and 0.126 ppm, respectively. The molar absorptivity is found to be 2.3 x $10^5$ L $mol^{-1}$ $cm^{-1}$. The proposed sensor membrane has been applied to the determination of Cd(II) in the river water with internal standard addition method. The observed percent recovery is in the range of 100.24 – 107.52%.

**Keywords**: optical chemical sensor, 1-(2-pyridylazo)-2-naphtol, Cd(II) analysis, poly(methyl methacrylate)

**Abstrak**

Reagen 1-(2-piridilazo)2-naftol (PAN) yang dipegun dalam poli(metil metaakrilat) (PMMA) dengan 2-nitrofenil oktil eter (NPOE) sebagai pemplastik untuk sensor kimia optik bagi penentuan ion Cd(II) dalam larutan akues telah dibangunkan. Jerapan ion Cd(II) telah menyebabkan penukaran warna dari kuning menjadi merah-oren dengan serapan maksimum pada ($\lambda_{max}$) iaitu 556 nm. Membran sensor memberikan tindak balas maksimum apabila dicelupkan dalam larutan Cd(II) pada pH 8.5, selepas 120 minit masa sentuhan pada kepekatan 2 ppm Cd(II) dan 2 ml isipadu larutan. Berdasarkan kajian yang dijalankan, julat linear lengkung kalibrasi kepekatan ion Cd(II) ialah 0.8 - 1.8 ppm dan nilai $R^2$ = 0.960. Had pengesanan dan pengkuantitian yang diperolehi masing – masing ialah 0.041 ppm dan 0.126 ppm. Daya penyerapan molar dikira pada 2.3 x $10^5$ L $mol^{-1}$ $cm^{-1}$. Membran sensor ini telah dikaji untuk menentukan kepekatan Cd(II) dalam air sungai yang dipaku kaesah larutan piawai dalam. Ia telah menghasilkan pemulihan semula pada nilai 100.24 – 107.52%.

**Kata kunci**: Sensor kimia optik, 1-(2-piridilazo)2-naftol, analisis Cd(II), poli(metil metaakrilat)

## Introduction

Cadmium (Cd) is one of the heavy metals that can pollute the environment even in a trace amount. Cd(II) ion in water also has a significant influence towards water quality and public health. The maximum permitted contents of Cd in waste and drinking water are 0.1 and 0.05 ppm, respectively [1]. Cd is harmful to health since it is both toxic and carcinogenic [2-4]. Therefore, a simple, rapid, sensitive and low-cost method of analysis is required for monitoring Cd(II) content in the environment.

The conventional standard methods for metal determination are atomic absorption spectrophotometer (AAS) and Flame-AAS [5, 6]. These methods are sensitive and selective. However, it is relatively expensive and requires a skilled person to do the job. The chemo-optic sensor is an alternative method for metal analysis. It is part of the green analytical methods since it can significantly reduce energy consumption, organic solvents, and gas emission. Therefore, it is much more environmentally friendly [7-10].

Several studies on optical chemical sensors have been carried out based on the immobilization of colored complexing reagents in an appropriate polymer membrane. For example, an optical chemical sensor for Cd(II) determination has been developed using various techniques such as in cellulose acetate membrane by immobilization of 1-(2-piridilazo)-2-naftol (PAN) [11], 2-amino-cyclopentene-1-dithiocarboxylic acid (ACDA) [12], and dithizone [13]. Immobilization of PAN in the poly-methyl methacrylate membrane has been applied in the determination of Cd(II), Ni(II), Cu(II), Zn(II), Pb(II), and Co(II) [14, 15]. Also, polyvinyl chloride (PVC) based chemo-optic sensor as a matrix for pyridylazo resorcinol (PAR) using tributhyl phosphate (TBP) as a plasticizer for Th(III) determination has also been described by Ensafi and Fouldagar [16].

1-(2-piridilazo)-2-naftol (PAN) possesses azo-nitrogen and OH groups (Figure 1). It reacts with transition metals to form a colorful complex. PAN is an unselective coloring reagent. However, its selectivity over other metal ions can be enhanced by adjusting the pH of the solution in accordance with the targeted metal ions [17]. Cd(II) in alkaline media forms a stable color complex with PAN, which can be extracted into organic solvents [17, 18].

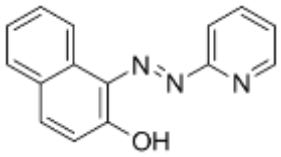



Figure 1. Molecular structure of PAN

In this study, we have developed a chemo-optic Cd(II) sensing method, which is simple, safe, inexpensive, environmentally friendly and oriented to green analytical chemistry. The sensing membrane is developed based on immobilization of PAN in poly-methyl methacrylate (PMMA) membrane using 2-nitrophenyl octyl ether (NPOE) as plasticizer.

## Materials and Methods

### Chemicals and instruments

Cadmium(II) nitrate [$Cd(NO_3)_2$], sodium hydroxide (NaOH), hydrochloric acid (HCl), copper(II) chloride ($CuCl_2$), zinc(II) nitrate [$Zn(NO_3)_2$], nickel(II) nitrate [$Ni(NO_3)_2$], iron(III) chloride ($FeCl_3$) and tetrahydrofuran (THF) were obtained from Merck. 1-(2-pyridylazo)-2-naphtol (PAN) and 2-nitrophenyl octyl ether (NPOE) were analytical grades and purchased from Sigma-Aldrich. Poly-methyl methacrylate (PMMA) was obtained by synthesis with an average molecular weight of about 220,000. The double distilled water was used as a solvent throughout the UV-Visible spectrophotometric measurements. The pH of the solution was adjusted by drop wise addition of either 0.10 M NaOH or 0.10 M HCl and monitored by using Thermo Scientific (ORION 4 STAR, pH-ISE Portable) pH-meter. A Shimadzu UV-Visible spectrophotometer UV-2450 model and A Shimadzu FTIR spectrophotometer, Prestige-21 type model, were used to measure the UV-Visible and FTIR spectra.

**Preparation of sensor membrane**
The sensor membrane was prepared by dissolving 0.4000 g PMMA, 0.0100 g PAN, and 120 µL NPOE in 10 mL THF, and stirring the mixture at a constant speed for 5 hours at room temperature. Subsequently, the reaction mixture was poured into a casting glass (5 cm × 12 cm) and kept at room temperature for 10 – 12 hours, until all the solvent evaporated. The membranes were released from the cast, washed with distilled water, dried at room temperature, and cut into rectangle shape (0.8 cm × 2 cm). The membrane thickness was c.a. 0.05 mm.

**Characterization of sensor membrane**
The FTIR spectra of PAN, NPOE, PMMA and PMMA-PAN membrane were recorded using A Shimadzu FTIR spectrophotometer.

**Determination of optimum pH**
The optimum pH was determined by measuring the absorbance of membranes that were previously soaked in 2 mL solution containing 2 ppm of the Cd(II) ion in the pH range of 7.0 – 9.0 for a defined time. The optimum pH was indicated by maximum absorbance at 556 nm.

**Range of linearity**
The linear range of absorbance of Cd(II)-PAN complex was studied at Cd(II) concentration of 0.2 – 2.0 ppm.

**Interfering ions**
The interfering ions including Cu(II), Zn(II), Ni(II), and Fe(III) were studied by measuring the absorbance of the solution in the presence of the interfering cations and Cd(II) in the concentration ratio of 1:1 at 556 nm and pH 8.5.

**Application in water sample**
The membrane was applied for analysis of Cd(II) in the stream water of "Kali Code" flowing across the City of Yogyakarta, Indonesia. A measured 100 mL of river water sample was acidified using $HNO_3$ 1.0 M until pH about 3, filtered off and stored in a propylene bottle at room temperature. For Cd(II) determination, the pH of the sample solution was adjusted to pH 8.5 by adding NaOH 0.1 M solution. Note: "Kali Code" is the name of the river that flows across City of Yogyakarta, Indonesia, starting from Merapi Mountain in the north to the Indian Ocean in the south.

## Results and Discussion

**Supporting matrix stability and sensor membrane response toward Cd(II)**
PMMA was chosen as a supporting matrix for PAN due to its hydrophobicity, transparency, resistance to acid, base and salt solutions [19], and low absorbance in the UV-Vis range [20]. These will keep the sensor membrane stable during analysis of Cd(II) in water and allow quantitative analysis by UV-Vis spectrophotometry.

As a ligand, PAN can form a colorful complex ion with a number of cations, that are Cd(II) [11, 14], Co(II) [15], Cr(III) [21]. The complex ions of PAN with those cations are formed through the coordination bond between -OH and azo-nitrogen groups of the phenolic ring with the cations. Based on known stoichiometry, the Cd(II)/PAN molar ratio is 1:2 [17, 22]. The reaction of metal complex formation is displayed in Figure 2.

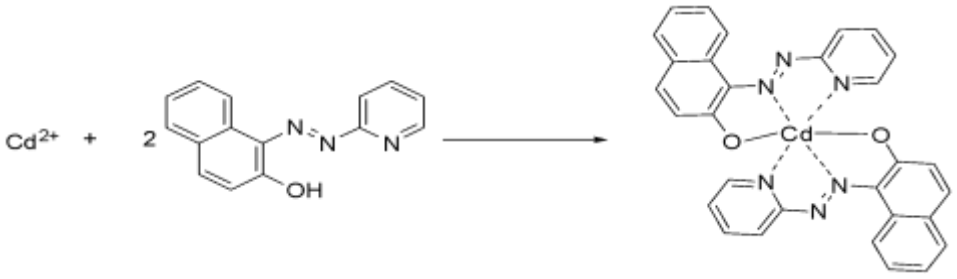



Figure 2. Reaction scheme for the complex formation of Cd(II) – PAN

**Membrane characterization**

The FTIR spectra of PAN immobilized in the membrane matrix are shown in Figure 3. It is clearly shown in the Fig. 3d that PAN has been successfully incorporated into the membrane. The peak at 3441 $cm^{-1}$ indicates a stretching vibration of –OH group of naphtol, whereas the peak at 2338 $cm^{-1}$ is due to the N=N group. The medium peak at 1605 $cm^{-1}$ is attributed to the N=O bond. Further, the peak at 1250 $cm^{-1}$ suggests the presence of $C_{aryl}$-O-$C_{alkyl}$ group. Both peaks reveal the existence of NPOE as a plasticizer in the membrane.

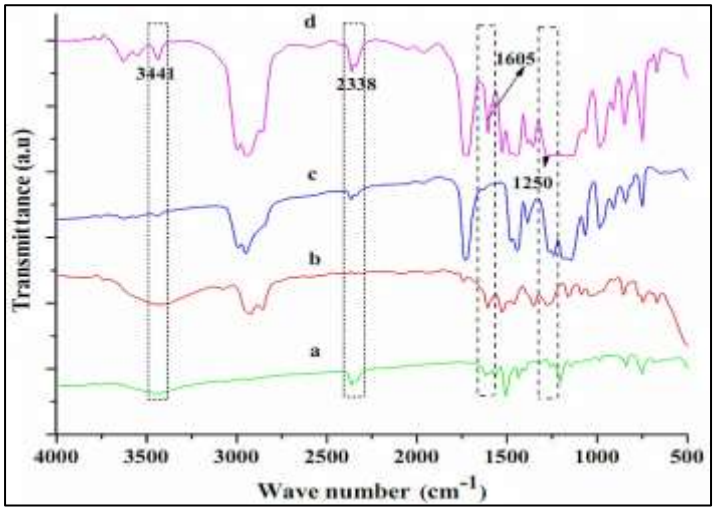



Figure 3. Infrared spectra of the membrane components (a) PAN, (b) NPOE, (c) PMMA and (d) PMMA-PAN membrane

**The effect of pH on sensing performance**

The pH of the test solutions plays an important role in obtaining a better membrane performance. The analyte solution has been subjected to pH variation, from 7.0 to 9.0. Figure 4 suggests that the solution pH of 8.5 gives the best response. It has been previously reported in many works that the best pH for Cd(II)-PAN complex formation is at pH 8.7 – 10 with $\lambda_{max}$ of 540 – 570 nm [17,22] or $\lambda_{max}$ of 550 – 560 nm [18]. In case of optimum pH of Cd(II)-PAN complex formation in the membranes, it has also been reported that the optimum pH in the PVC membrane using NPOE as plasticizer is at pH 8.0 and $\lambda_{max}$ of 558 nm [23]. Similarly, the optimum pH in the cellulose triacetate membrane using TEHP as a plasticizer is at pH 7.5 with $\lambda_{max}$ of 553 nm [11]. Therefore, our result of optimum pH at 8.5, is in good agreement with previously reported works. For this study, the absorbance of the membrane was recorded after 105 – 125 min of reaction.

Furthermore, at optimum pH, the amount of $OH^-$ ion in the solution is larger and the donor atom in the ligand tends to release $H^+$ ion (deprotonated) and thus becomes partially negative-charged species ($L^-$). This condition enhances the reaction between $Cd^{2+}$ or $[Cd(OH)]^+$ in the solution and PAN ligand in the matrix to form $CdL_2$. On the other hand, at lower pH, large amount of $H^+$ in the solution causes the formation of free metal ion ($M^{n+}$) and the hydroxyl group in the ligand remains protonated. This situation causes the interaction between metal ion and ligand much more difficult to occur due to charge repulsion between positive metal ion and positively protonated ligand. At higher pH (> 9.0), the absorbance is getting smaller possibly due to leaching process of PAN ligand from the membrane matrix as indicated by the red-color change of the solution. For all of the tested pH, the absorbance has been observed to reach its maximum value after 180 min of reaction.

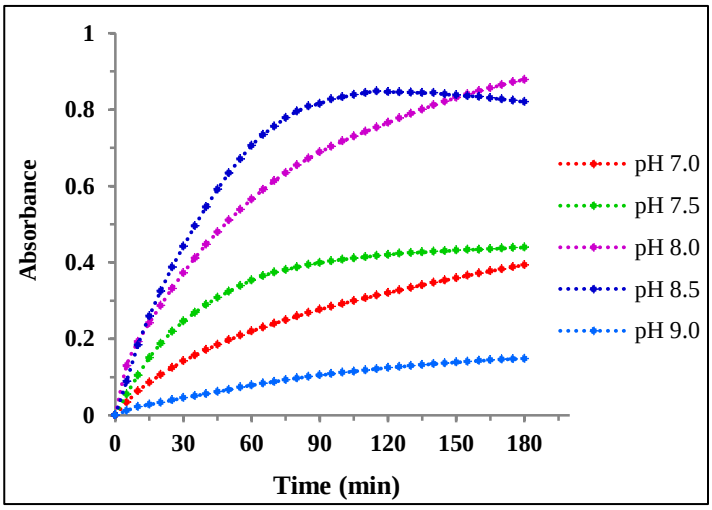



Figure 4. The response of sensor membrane at different pH with cadmium concentration of 2 ppm (n=3)

**Range of linearity**

The linear range of the sensor membrane for Cd(II) analysis was examined. The Cd(II) concentration was set at 0.2 – 2.0 ppm and the obtained data are shown in Figure 5. The absorbance linearly increases along with the increasing in the Cd(II) concentration, from 0.08 – 1.8 ppm. From the curve, it has been obtained that the detection limit of Cd(II) is 0.041 ppm with $R^2 = 0.960$.

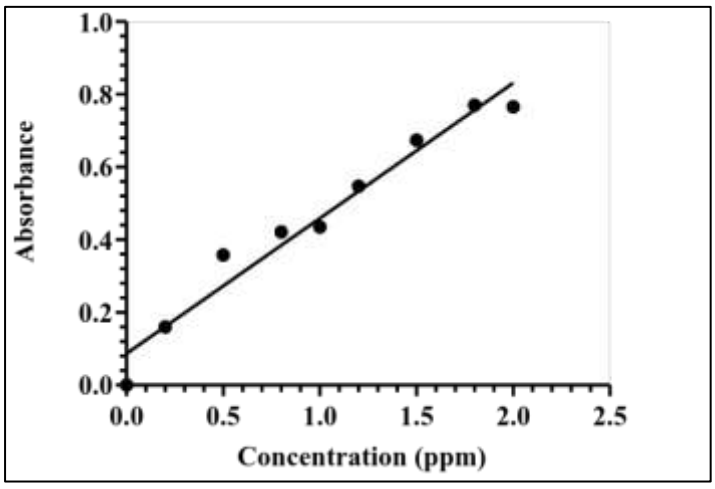



Figure 5. Calibration curve of Cd(II) sensor membrane. The absorbance was recorded at λ 556 nm

**Response of sensor membrane**

The UV-Vis spectra of sensing membrane before and after contact with Cd(II) solution are displayed in Figure 6. Before contact with Cd(II) solution, the sensor membrane has maximum absorbance ($\lambda_{max)}$ at 466 nm, and after contact with Cd(II) solution at pH 8.5, it shifts to 556 nm. The formation of complex Cd(II)-PAN in the sensor membrane exhibits significant bathochromic shift from 466 to 556 nm. It has been reported that the $\lambda_{max}$ of PAN and Cd(II)-PAN complex in chloroform is 470 nm and between 540 – 570 nm, respectively [22]. The slight difference in our results may be due to the sensitivity of PAN in different environments that lead to shift in $\lambda_{max}$

when it packs in the solid membrane matrices [24]. It is noteworthy to note that the cation permeability in the polymer matrix is lower than that in the solution. This may also cause the shift of $\lambda_{max}$.

For comparison, it has been reported that the $\lambda_{max}$ of PAN and Cd(II)-PAN complex in the CTA membrane is observed at 466 and 553 nm, respectively. The membrane was prepared by solvent mixing of 10 mL dichloromethane and 10 mL chloroform, and dried for 48 hours. By using this reported membrane, it has been found that the linear range of Cd(II) calibration curve was in the range of 0.01 – 5.0 ppm and the equilibrium time for complex formation was achieved after 150 minutes of reaction at pH 7.5 [11]. It is, therefore, obvious that our results is superior than those previously reported, especially in term of response time (120 minutes), required sample size (2 mL only), less usage solvent and shorter evaporation time, meaning that the preparation of the sensing membrane in our study produces less waste, reduces gas emission and needs shorter analysis time.

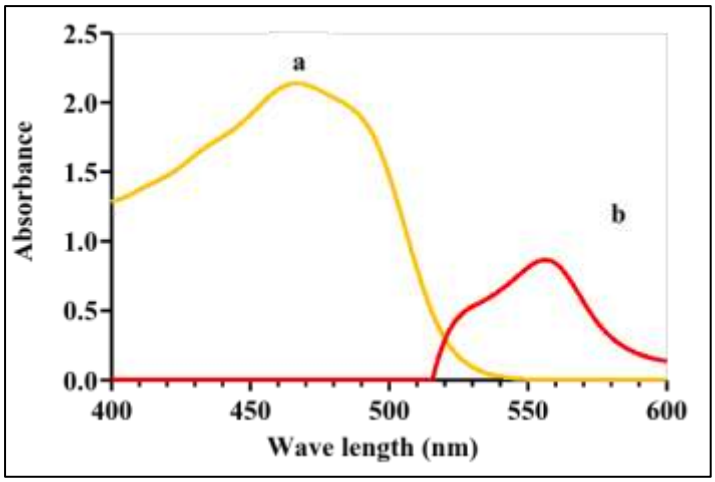



Figure 6. Absorption spectra of sensor membrane before (a) and after (b) contact with 2 ppm Cd(II) solution at pH 8.5

After contact with Cd(II) solution, the membrane color changes from yellow to red-orange as shown in Figure 7. The color intensity of the membrane increases along with the increase of the concentration of Cd(II) in the solution.

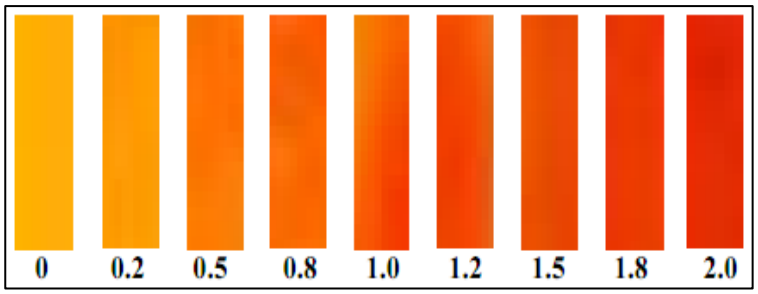



Figure 7. Progress of sensor membrane color change along with increase in Cd(II) concentration

**Effect of the other cations**

The response of the membrane towards Cd(II) ion in the presence of other cations such as Cu(II), Zn(II), Ni(II) and Fe(III) was tested. The experiment was conducted at the optimized conditions of Cd(II) analysis. The membrane was immersed separately in each solution containing both the interfering cation and Cd(II) ion at pH 8.5 for 120

min. The mole ratio of Cd(II)/interfering cation was set at 1:1, and the absorbance was measured at 556 nm. The results of the study are presented in Table 1.

Table 1. Effect of other cations on the sensing response

| No. | Cation | %Error* |
|---|---|---|
| 1. | Cu(II) | -18.92 |
| 2. | Zn(II) | 9.56 |
| 3. | Ni(II) | 2.05 |
| 4. | Fe(III) | 7.06 |
| 5. | Cu, Zn, Ni, Fe(III) | 33.35 |

*% Error was calculated using equation, $\{(A_{Cd(II)\text{-}cation} - A_{Cd(II)})/A_{Cd(II)}\} \times 100$ % [25] $A_{Cd(II)\text{-}cation}$ is the absorbance of sensor membrane in Cd(II) solution containing interference cation, and $A_{Cd(II)}$ is the absorbance of sensor membrane in Cd(II) solution without interference cation.

From Table 1, it is easily understood that the co-existence of Cu(II) in the solution causes the negative error (decrease in absorbance) of about 19% against the absorbance of single solution containing Cd(II)-PAN complex. It has been reported that Cu(II) ion can form stable complex, Cu(II)-PAN with PAN but the optimum condition of the complex formation is at pH 3.2 with $\lambda_{max}$ of 550 nm [17], while the optimum complex formation for Cd(II)-PAN is at pH 8.5. Because of the large difference in the formation pH of Cu(II)-PAN and Cd(II)-PAN complexes, it is expected that the competition between the two cations to interact with PAN not occur in the solution. The 19% decrease in absorbance of Cu(II)-PAN is most likely due to the decrease in the diffusion of the Cd(II) in the membrane sensor caused by the presence of Cu(II) ion.

Unlike Cu(II), the co-presence of Zn(II), Ni(II) and Fe(III) in the solution shows positive errors (increase in absorbance). From the literature, it is known that the best pH for the formation of Zn(II)-PAN and Ni(II)-PAN complexes is at pH 10 [22] and pH 4 – 10 [17], respectively. The Zn(II)-PAN in chloroform have $\lambda_{max}$ at 550 – 570 nm, which is quite close to the $\lambda_{max}$ of Cd(II)-PAN complex. Therefore, it is understandable that the co-existence of Zn(II) in the Cd(II) solution causes the absorbance of Cd(II)-PAN complex to increase.

Similarly, Fe(III)-PAN complex in chloroform can readily form at pH 4 – 8, with $\lambda_{max}$ at 775 nm [18, 22]. The closeness of the pH for the Fe(III) complexation with that of Cd(II) causes the competition between the two cations to form related complex with the ligand, hence the co-existence of Fe(III) in the solution contributes to the increase in the absorbance of the solution containing Cd(II)-PAN.

The co-addition of Cu(II), Zn(II), Ni(II), and Fe(III) altogether in the Cd(II) solution shows a large positive increase in absorbance of about 37%, which is much higher than the sum of individual effect. This may be explained from the point of view that the formation of Zn(II)-PAN, Ni(II)-PAN and Fe(III)-PAN is more dominant/favourable compared to the formation of Cu(II)-PAN when they are present altogether, as a result, the negative effect of Cu(II) vanishes and only positive effect is observed when the four cations exist together in the Cd(II) solutions.

**Analytical application of real samples**

The developed membrane has been applied to the analysis of Cd(II) in the river water of "Kali Code". Since most of the samples do not contain Cd(II) ion, for this purpose we have used internal addition standard method and the results are displayed in Table 2. From the table, it is clearly shown that the membrane produces a good percentage of recovery in the range of 100.25 – 107.52%. It is also observable from the table that Cd(II) content in the sample taken from location 1 and 2 could not be detected and only river water taken from location 3 contains sub-ppm of Cd(II). This result can easily be understood by considering the position of sampling points. Location 3 is located in the point where the river of "Kali Code" starts leaving city of Yogyakarta, meaning that the river water taken from this sampling point has received many waste such as domestic and industrial activities available along the river side

across the city of Yogyakarta. Some of the waste may contain heavy metals including Cd(II), therefore we detected Cd(II) in this sample. On the other hand, sampling points of location 1 and 2 are in the remote area, which is far away from domestic and industrial activities, therefore it is relatively still free from any pollutants, and this is becoming the reason that we could not detect the presence of Cd(II) ion in these two samples.

Table 2. Results of the Cd(II) analysis in the river water samples

| No. | River Water Sample | Cd(II) in Water Sample (ppm) | Added Cd(II) (ppm) | Cd(II) Found (ppm) | Recovery (%) |
|---|---|---|---|---|---|
| 1. | Location 1 | Not detected | 1 | 1.075 ± 0.041 | 107.52 |
| 2. | Location 2 | Not detected | 1 | 1.068 ± 0.008 | 106.78 |
| 3. | Location 3 | 0.046 | 1 | 1.002 ± 0.005 | 100.25 |

Notes: "Kali Code" is the name of river that flows across the City of Yogyakarta, Indonesia, starting from Merapi Mountain in the north to the Indian Ocean in the south. Location 1: 15 km from Merapi Mountain (before entering Yogyakarta City). Location 2: 13.5 km from location 1 (start entering Yogyakarta City). Location 3: 6.7 km from location 2 (before leaving Yogyakarta City).

## Conclusion

A chemo-optical sensing membrane for Cd(II) analysis has been developed by immobilization of PAN in a matrix of PMMA using NPOE as a plasticizer. The obvious change in membrane color after contact with analyte suggests the possible application of the method for qualitative detection and the linear response of absorbance along with the change in the analyte concentration provides its application in quantitative analysis. The membrane has been successfully applied to the analysis of Cd(II) in the natural water with satisfactory results as indicated by good percentage of recovery. The proposed optical chemical sensor membrane can be used as an alternative method for detection and determination of Cd(II) in ground water as well as in waste water, which offers simple, cheap, save and environmentally friendly technique. In the future, the developed sensing membrane can also be applied in periodic monitoring of Cd(II) pollution in water and may be developed for *in-situ* field analysis. Another possible prospective application is to develop membrane as "Cd(II) analytical kit", which can be used for quick and real time assessment of Cd(II) in the polluted area.

## Acknowledgement

The first author, Moersilah, would like to acknowledge the Ministry of Education and Culture, The Republic of Indonesia for providing doctoral scholarships. The authors thank Universitas Gadjah Mada Indonesia for the research support and facilities.

## References

1. Mirzaei, M. and Pili, H. B. (2015). Potentiometric determination of cadmium using coated platinum and PVC membrane sensors based on N, N′-bis (salicylaldehyde) phenylenediamine (salophen). *Journal of Analytical Chemistry*, 70 (6): 731 – 737.
2. Manahan, S. and Manahan, S. E. (2009). Environmental Chemistry, Ninth Edition. CRC Press, London: pp. 200 – 239.
3. van der Perk, M. (2006). Soil and water contamination: from molecular to catchment scale. CRC Press, London: pp. 125 – 137.
4. Urek, Š. K., Frančič, N., Turel, M. and Lobnik, A. (2013). Sensing heavy metals using mesoporous-based optical chemical sensors. *Journal of Nanomaterials*, 8: 1 – 13.
5. da Silva, M. C. H., da Silva, L. H. M. and Paggioli, F. J. (2005). A novel micellar medium using triblock copolymer for cobalt determination. *Analytical Sciences*, 21 (8): 933 – 937.
6. Ensafi, A. A., and Shiraz, A. Z. (2008). The combination of solid phase extraction and flame atomic absorption spectrometry for trace analysis of cadmium. *Brazilian Journal of Analytical Chemistry*, 19 (1): 11–17.

7. Manahan, S. E. (2006). Green chemistry and the ten commandments of sustainability. 2nd edition. ChemChar Research, Inc, Columbia: pp.159 – 176.
8. Koel, M., and Kaljurand, M. (2006). Application of the principles of green chemistry in analytical chemistry. *Pure and Applied Chemistry*, 78(11): 1993 – 2002.
9. Tobiszewski, M., Mechlińska, A. and Namieśnik, J. (2010). Green analytical chemistry – theory and practice. *Chemical Society Reviews*, 39(8): 2869 – 2878.
10. Wardencki, W. and Namiesnik, J. (2002). Some remarks on gas chromatographic challenges in the context of green analytical chemistry. *Polish Journal of Environmental Studies*, 11(2): 185 – 187.
11. Tharakeswar, Y., Kalyan, Y., Gangadhar, B., Kumar, K. S. and Naidu, G. R. (2012). Optical chemical sensor for screening cadmium (II) in natural waters. *Journal of Sensor Technology*, (2): 68 – 74.
12. Ensafi, A. A., and Isfahani, Z. N. (2011). A simple optical sensor for cadmium ions assay in water samples using spectrophotometry. *Journal of Analytical Chemistry*, 66(2): 151 – 157.
13. Tavallali, H. and Kazempourfard, F. (2009). Determination of cadmium ions by designing an optode based on immobilization of dithizone on a triacetylecelluose membrane in polluted soil and water samples. *Journal of the Korean Chemical Society*, 53(2): 144 – 151.
14. Gavrilenko, N. A. and Saranchina, N. V. (2009). Analytical properties of 1-(2-pyridylazo)-2-naphthol immobilized on a polymethacrylate matrix. *Journal of Analytical Chemistry*, 64(3): 226 – 230.
15. Gavrilenko, N A, Saranchina, N. V. and Gavrilenko, M. A. (2015). A colorimetric sensor based on a polymethacrylate matrix with immobilized 1-(2-pyridylazo)-2-naphthol for the determination of cobalt. *Journal of Analytical Chemistry*, 70(12): 1475 – 1479.
16. Ensafi, A. A and Fouladgar, M. (2014). A new sensitive optical bulk test-system for thallium based on pyridylazo resorcinol. *Journal of Analytical Chemistry*, 69(2): 143 – 148.
17. Ueno, K., Imamura, T. and Cheng, K. L. (1992). Handbook of Organic Analytical Reagent. 2nd edition, CRC Press Inc, Tokyo: pp. 209 – 368.
18. De, A. K., Khopkar, A. K. and Chalmers, S. M. (1970). Solvent extraction of metals. Van Nostrand Reinhold Company, London: pp. 117 – 124.
19. Mohr, G. J. (2004). Polymers for optical sensors', in Baldini, F., Chester, A. N., Homola, J. and Martellucci, S. (ed.), Optical chemical sensor, Springer, The Netherland: pp. 297 – 322.
20. Hsu, S. L. (1999). Poly(methyl methacrylate), in Mark, J. E. (ed.), Polymer data handbook. Oxford University Press, Inc., Oxford: pp. 655 – 657.
21. Moghimi, A. (2011). Cr(III) selective PVC membrane electrodes based on schiff base 1-(2-pyridylazo)2-naphtol complex as an ionophore. *Middle-East Journal of Scientific Research*, 7(2): 147 –152.
22. Sandell, H. and Onishi, E. B. (1978). Photometric determination of traces of metals general aspects 4th edition, John Wiley and Sons, Inc., New York: pp. 449 – 487.
23. Moersilah, M., Siswanta, D., Roto, R. and Mudasir, M. (2017). PAN-immobilized PVC-NPOE membrane for environmentally friendly sensing of Cd(II) ions. *Indonesian Journal of Chemistry*, 17(1): 1 – 6.
24. Donagh, C. Mc., Burke, C. S. and MacCraith, B. D. (2008). Optical chemical sensors, *Chemical Reviews*, 108(2): 400 – 422.
25. Sombatsri, S., Wittayakun, J., Sanai, K. and Kajsanthia, K. (2012). An optical sensing film for the determination of Co(II) based on disodium-1-nitroso-2-naphthol-3,6-disulfonate immobilized in chitosan film. *Sensor and Actuator B: Chemical*, 166 – 167: 772 – 776.

*Malaysian Journal of Analytical Sciences, Vol 21 No 4 (2017): 793 - 800*
*DOI: https://doi.org/10.17576/mjas-2017-2104-05*

MALAYSIAN JOURNAL OF ANALYTICAL SCIENCES
*Published by The Malaysian Analytical Sciences Society*
ISSN 1394 - 2506

# EFFECT OF NON-IONIC SURFACTANTS TO THE Al(III)-MORIN COMPLEX AND ITS APPLICATION IN DETERMINATION OF Al(III) IONS: A PRELIMINARY STUDY

## (Kesan Surfaktan Tak-Ionik Kepada Kompleks Al(III)-Morin dan Aplikasinya dalam Penentuan Ion Al(III): Satu Kajian Awal)

Faiz Bukhari Mohd Suah[1]*, Musa Ahmad[2], Faizatul Shimal Mehamod[3]

[1] *School of Chemical Sciences,*
*Universiti Sains Malaysia, 11800 Minden, Pulau Pinang, Malaysia*
[2] *Faculty of Science & Technology,*
*Universiti Sains Islam Malaysia, Bandar Baru Nilai, 71800 Nilai, Negeri Sembilan, Malaysia*
[3] *School of Fundamental Science,*
*Universiti Malaysia Terengganu, 21030 Kuala Terengganu, Terengganu, Malaysia*

**Corresponding author: fsuah@usm.my*

Received: 5 October 2016; Accepted: 11 May 2017

**Abstract**

A simple and sensitive spectrofluorimetric method for the determination of Al(III) based on the formation of Al-Morin-Triton X-100 ternary complex is described. The effect of other non-ionic surfactants, such as Tween 80, Tween 20 and octylglucoside (OG) on fluorescence analysis were also studied. The addition of Triton X-100 makes feasible the fluorimetric determination of submicrogram quantities of Al(III). The complex was excited at 410 nm and the fluorescence signal was measured at 495 nm. Maximum fluorescence signal was produced at pH 4.0 (acetic acid-acetate buffer), with 0.6% Triton X-100 and $1.35 \times 10^{-3}$ mol $L^{-1}$ Morin. The calibration graph is linear up to 7 mg $L^{-1}$ and the detection limit is 0.022 mg $L^{-1}$. The relative standard deviation is 1.81% for Al(III) at 5 mg $L^{-1}$. It was found that Zn(II) and $F^-$ produced highest interference.

**Keywords:** aluminum determination, fluorescence analysis, non-ionic surfactants, Triton X-100, Morin

**Abstrak**

Satu kaedah penentuan Al(III) secara spektrofluorimetri yang mudah dan sensitif berasaskan kepada pembentukan kompleks ternari Al-Morin-Triton X-100 dilaporkan. Kesan beberapa surfaktan tak-ionik yang lain seperti Tween 20, Tween 80 dan ositilglukos (OG) terhadap analisis berpendarflour turut dikaji. Penambahan Triton X-100 telah membolehkan penentuan secara pendarflour Al(III) dijalankan sehingga kepada kuantiti submikrogram. Kompleks teruja pada 410 nm dan isyarat pendarflour diukur pada 495 nm. Isyarat pendarflour maksimum dihasilkan pada pH 4.0 (menggunakan penimbal asetik asid-asetat), dengan 0.6% Triton X-100 dan 1.35 x $10^{-3}$ mol $L^{-1}$ morin. Graf kalibrasi adalah linear sehingga 7 mg $L^{-1}$ dan had pengesanan pula adalah 0.022 mg $L^{-1}$. Sisihan piawai relatif bagi penentuan 5 mg $L^{-1}$ Al(III) ialah 1.81%. Didapati juga ion Zn(II) dan $F^-$ menghasilkan gangguan bacaan yang tertinggi.

**Kata Kunci**: penentuan aluminum, analisis fluorimetrik, surfaktan tak-ionik, Triton X-100, Morin

## Introduction

It is known that Al(III) is a minor component in natural waters, its concentration being largely controlled by its low solubility, with typical levels in the range 0.5 – 5 µg $L^{-1}$ in seawater and 10–140 µg $L^{-1}$ in fresh waters [1]. As for

drinking water, the World Health Organization (WHO) has set the standard permissible level of Al(III) in drinking water at 200 μg $L^{-1}$ [2]. Al(III) ions also present several neurotoxic effects, and it has been suspected that Al(III) may be responsible for the cause of Alzheimer's disease, toxic effects on patients with renal failure and bone softening [3]. Sensitive analytical procedures are therefore required to study and monitor its level in the environment and its toxicology. While several methods have been developed for the determination of Al(III), spectrophotometry [4–6] and spectrofluorimetry [7–10] are the preferred techniques due to their simplicity, high precision and accuracy, high sensitivity, low cost and widespread availability of equipment.

Surfactants have been successfully used to improve current analytical techniques and in developing new ones. In micellar media, the sensitivity, selectivity and stability constants of reactions are greatly enhanced, and metal complex reactions are among them. As for fluorometric analysis, the intensity of molecular fluorescence is greatly influenced by the solvent effect and the presence of quenching impurities in the solvent. In some cases, it is possible to enhance the fluorescence and minimize the interferences by the incorporation of surfactants into the solution to be studied. The reasons for the increased fluorescence intensity in micellar solutions are not fully understood. Several mechanisms have been proposed by various authors. According to Sanz-Medel et al. in 1987, it is most likely due to (i) the effect of solubilization of neutral chelates and ligands within the micellar aggregates and (ii) the interaction of ionic complexes with surfactant molecules and aggregates having opposite charge [11]. Alternatively, Hinze et al. in 1984 proposed that the effect of the micelle appeared to result from the protection of the metal chelate from quenching in the bulk solvent [12]. From the literature, we have found that the use of cationic and anionic surfactants has little impact on enhancing the intensity of the metal–morin complexes; on the contrary, those surfactants decrease the fluorescence intensity and create unstable ternary complexes [13–15]. Therefore, we have decided to focus only on the use of non-ionic surfactants.

This paper investigated the reaction of Al(III) and morin in the presence of polyoxyethylene(9.5)-*t*-octyl-phenol (Triton X-100) and its potential for the determination of aqueous Al(III). The influences of various non-ionic surfactants on the fluorescence intensity of the Al(III)–Morin complex and their characteristics were also studied.

## Materials and Methods

### Instrument

Fluorescence spectra were obtained using Perkin-Elmer LS55 fluorescence spectrometer operated with 5.0 nm for excitation and emission slits.

### Reagents

All chemicals used were analytical grade unless stated otherwise. All solutions were prepared by using MilliQ distilled deionized water. Reagents used in this study were aluminum potassium sulphate dodecahydrate (Merck), morin (Fluka), polyoxyethylene(9.5)-t-octyl-phenol (Triton X-100), (Fluka), polyoxyethylene (20)sorbitol monolaurate (Tween 20), (BDH), polyoxyethylene(20)sorbitol mono-oleate (Tween 80), (BDH), octylglucoside (OG), (BDH) and ethanol 95% (Hmbg. Chemical).

The Al(III) stock solution (10 $mgL^{-1}$) was prepared daily by dissolving 0.1758 g of aluminium potassium sulphate dodecahydrate in water, adding 1% (v/v) sulphuric acid and diluting to 1 L with water. The morin solution ($5.0 \times 10^{-3}$ mol $L^{-1}$) was prepared by dissolving 0.1691 g of morin in 85 mL of 95% ethanol and diluting to 100 mL with water. All surfactants were used without further purification. The surfactants used in this study were prepared by diluting the surfactants to the percent required with water.

All of the buffer solutions (acetic acid-sodium-acetate buffer system), standard solutions for Al(III), ethanolic morin solution and non-ionic surfactants were prepared at room temperature of 25°C. The pH was measured to a pH of ± 0.01 with a Hanna Instrument model HI 2211 pH Meter.

### General procedure

To a solution containing 2 mL of Al(III), add 2 mL of buffer, 1 mL of morin solution ($1.35 \times 10^{-5}$ mol $L^{-1}$) and 3 mL of aqueous 0.6% v/v Triton X-100 solution. The mixture was diluted to volume in 25 mL standard flask with MilliQ water. The sample should be shaken briskly immediately prior to measurement the fluorescence. The fluorescence

intensity was measured at 495 nm, with excitation at 410 nm. All measurements were carried out three times, unless stated otherwise.

## Results and Discussion

An initial study was carried out to identify the level of the fluorescence enhancement obtained from a variety of non-ionic surfactants. It was found that sustained and superior enhancement was observed with the use of Triton X-100 compared with the other non-ionic surfactants (Figure 1). It is obvious that certain operational and preparation difficulties could be encountered with some surfactants, e.g. OG. High-viscosity materials were difficult to dissolve and could lead to phase separation if left overnight. Therefore, vigorous shaking of the samples must be performed immediately after the addition of the surfactant and again before the fluorescence measurements to obtain a homogeneous micelle system. Based on the degree of enhancement and the ease of operation, Triton X-100 was selected for further study.

The significance of the order of reagent addition was also examined. It was found that the fluorescent enhancement and its maximum intensity did not depend on this. The order of addition chosen was as follows: an aliquot of Al(III), the addition of acetic acid–acetate ion buffer solution, followed by morin solution and finally an aqueous Triton X-100 solution.

In common with all fluorescence techniques, the sensitivity is basically determined by the choice of an appropriate tool and working conditions. In this study, the experimental precision and sensitivity were found to be very dependent on reagent mixing. Therefore, the solutions should be briskly mixed immediately prior to measuring the fluorescence intensity.

The emission spectra of the Al(III)–morin complex in the presence of non-ionic surfactants are shown in Figure 1. It was found that the addition of Triton X-100 produced about fivefold enhancement and stabilization of fluorescence. The maximum fluorescence was obtained at 495 nm, corresponding to excitation at 410 nm. The enhancement of the fluorescent emission of Al–morin–Triton X-100 is owing to the surfactant's capabilities to (i) increase the solubility of hydrophobic species; (ii) create the microenvironment capable of producing a favourable polarity and acid–base equilibrium that in turn enhance its fluorescence efficiency and (iii) adopt a structure that protects the fluorescence of the analyte from external quenching. In addition, the unique structure of Triton X-100, which has a much shorter hydrophobic tail than the three other surfactants (Tween 20, Tween 80 and OG), also plays a massive role in enhancing the fluorescent emission of the ternary complex. According to Simoncic and Kert [16], the short hydrophobic tail of Triton X-100 can increase the hydrophobicity of the ternary complex and at the same time increases the attractive force (including van der Waals attraction between hydrocarbon parts) between Al(III) and morin. Therefore, it was found that Triton X-100 is also capable of enhancing the fluorescent emission compared with other non-ionic surfactants due to its distinctive structure, increasing the complex's hydrophobicity and the attractive force between Al(III) and morin.

Red-shifts (of around 20 nm) were observed in the fluorescence spectra of the Al(III) complexes in the presence of Triton X-100 and Tween 20. The red-shifts of $\lambda_{em}$ in the presence of non-ionic surfactants show that the contact between the Al(III) complex and non-ionic surfactants causes the excited state of the complex molecule to transform. According to Carrion Dominguez and Cirugeda [17], the Al(III) complexes may be fixed by the non-ionic surfactant, thus made more rigid and therefore the fluorescence quantum yield is increased.

The effect of the reaction variables on the fluorescence of the Al(III)–morin–Triton X-100 system was also studied. The fluorescence intensity of the Al(III)–morin–Triton X-100 system was measured over a variety of pH conditions in the range 2.0 – 7.0. The optimum pH was 4.0 (Figure 2) and the buffer solutions were prepared from acetic acid and sodium acetate. The result, (optimum pH at 4.0) was almost the same as reported in the literature, which used morin as the indicator but Genapol PF-20 as the surfactant [18]. Intensity measurements were recorded at the excitation and emission wavelengths giving the maximum intensity. In addition, these results were blank-corrected to minimize contributions from the variable composition buffer components.

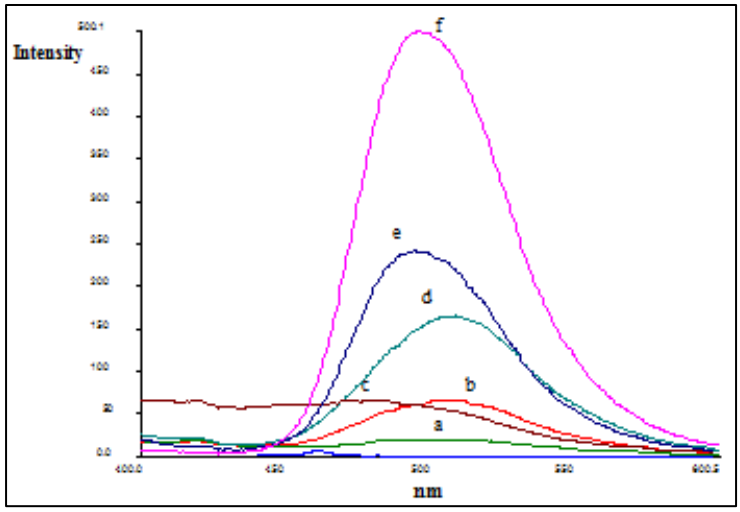



Figure 1. Emission spectra of (a) Al(III), (b) morin, (c) Al-morin-Tween 80, (d) Al-morin, (e) Al-morin-tween 20 and (f) Al-morin-Triton X-100. Conditions: Al(III) 5 mg $L^{-1}$; morin concentration $1.35 \times 10^{-5}$ mol $L^{-1}$; Triton X-100 0.6 % v/v; pH 4.0; $\lambda_{ex}$ 410 nm; $\lambda_{em}$ 495 nm

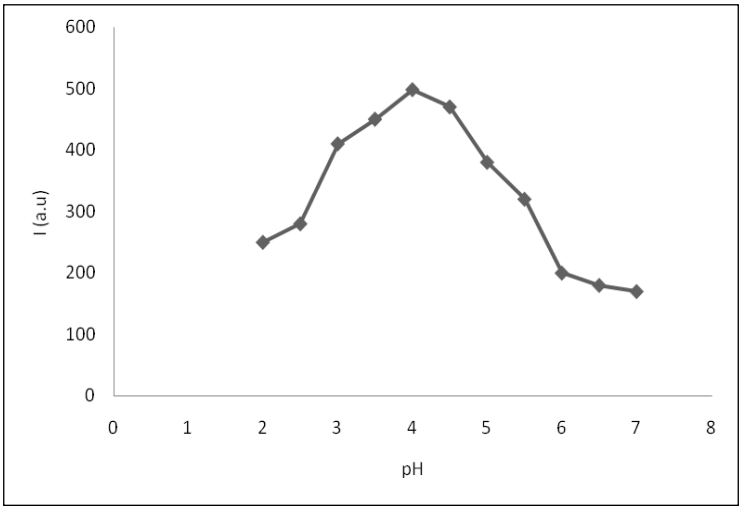



Figure 2. Effect of pH on the fluorescence intensity obtained from a 5 mg $L^{-1}$ Al(III) solution. Conditions: morin concentration $1.35 \times 10^{-5}$ mol $L^{-1}$; Triton X-100; 0.6 % v/v

The influence of the concentration of Triton X-100 on fluorescence intensity was studied with fixed concentration of Al(III) and morin and variable concentrations of Triton X-100 between 0 and 0.8% v/v. It was observed that as the Triton X-100 concentration increased, the fluorescence intensity increased until it reached 0.6% v/v (Figure 3). These gradual increases are attributable to the increased viscosity produced at the higher concentrations.

As mentioned by Hinze et al. in 1984, the metal complex and ligand compete in their interaction with the surfactant [12]. The ligand requires a surfactant concentration only slightly higher than the critical micelle concentration to achieve optimum interaction with the surfactant, whereas the complex requires a significantly higher concentration to yield maximum fluorescence. The viscous effect at high surfactant concentrations is not appreciable for morin alone. In all cases, the increase in fluorescence of the complex is much higher than with morin alone.

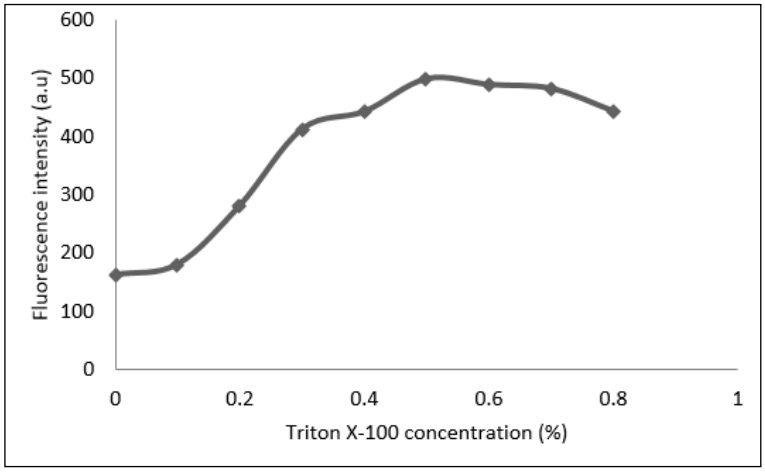



Figure 3. Effect of Triton X-100 concentration on the fluorescence intensity. Conditions: Al(III) 5 mg $L^{-1}$; morin concentration 1.35 $\times 10^{-5}$ mol $L^{-1}$; Triton X-100 0.6 % v/v; pH 4.0; $\lambda_{ex}$ 410 nm; $\lambda_{em}$ 495 nm

Figure 4 shows the effect of morin concentration at a fixed concentration of Al(III) (5 mg $L^{-1}$) and Triton X-100 (0.6% v/v). The fluorescence intensity of the complex is almost constant in the morin concentration range 1.35 $\times$ $10^{-5}$ – 1.70 $\times$ $10^{-5}$ mol $L^{-1}$. This optimum concentration range was achieved because these morin concentrations were sufficient to yield the Al(III)–morin complex in the presence of Triton X-100. This concentration (1.35 $\times$ $10^{-5}$ mol $L^{-1}$) was therefore employed for further studies.

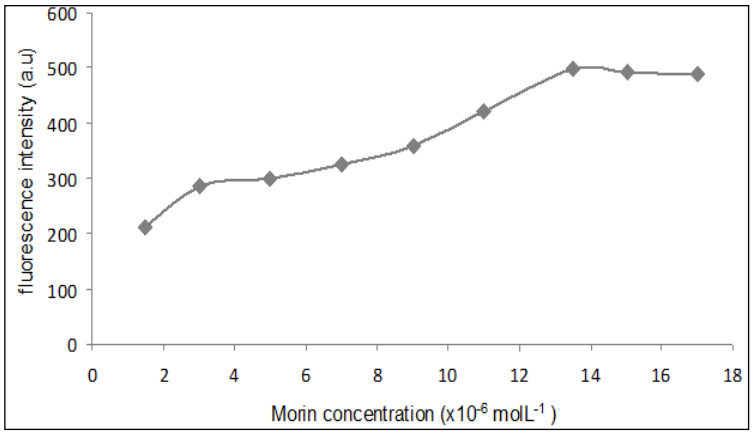



Figure 4. Effect of morin concentration to the formation of Al-morin-Triton X-100 complex. Conditions: Al(III), 5 mg L-1; Triton X-100, 0.6 % v/v

In addition, it is expected that a decrease in fluorescence intensity at higher morin concentrations will occur [19]. This is due to the higher self-quenching effect (the tendency of ions to collide with each other) that occurs between Al(III) and morin at higher concentrations of morin.

The calibration curve of Al(III) concentration versus relative fluorescence intensity ($(I - I_0)/I_0$) is shown in Figure 5, where $I$ was the measured fluorescence intensity at any Al(III) concentration and $I_0$ was the intensity in the absence of Al(III).

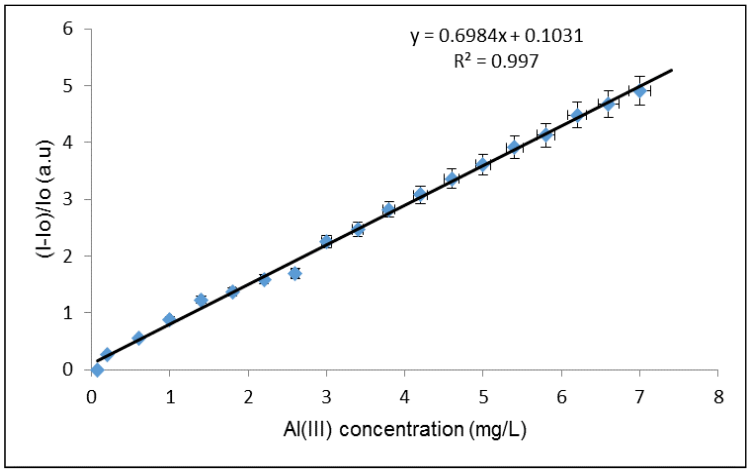



Figure 5. Calibration curve for Al(III)-morin-Triton X-100 complex system. Conditions: Al(III) 5 $mgL^{-1}$; morin concentration $1.35 \times 10^{-5}$ mol $L^{-1}$; Triton X-100 0.6 % v/v; pH 4.0; $\lambda_{ex}$ 410 nm; $\lambda_{em}$ 495 nm

The morin–Triton X-100 complex exhibited a linear emission response to Al(III) in the concentration range of $1.30 \times 10^{-6} - 2.59 \times 10^{-4}$ mol $L^{-1}$ (0.035 – 7.0 mg $L^{-1}$) with a correlation coefficient of $r = 0.997$. The detection limit (the concentration of the metal ion giving a signal equal to the blank signal plus three standard deviations of the blank) was found to be 0.022 mg $L^{-1}$. The calculated relative standard deviation, R.S.D., for eight replicate analyses of a sample containing 5 mg $L^{-1}$ of Al(III) was 1.81%.

The effect of various species present in the samples was studied too. A sample containing 2 $mgL^{-1}$ Al(III) was prepared in the presence of 10 $mgL^{-1}$ of Mg(II), Cu(II), Zn(II), Fe(III), Ca(II), Ba(II), $Cl^-$, $F^-$ and $SO_4^{2-}$. The results shown in Table 1 indicate little or no interference is observed in the presence of Mg(II), Ca(II), Ba(II), $Cl^-$ and $SO_4^{2-}$. However, Cu(II) Zn(II) and Fe(III) gave lower recovery due to slight quenching effect of these species on the fluorescence intensity of the Al(III)–morin–Triton X-100 complex. Interference from Fe(III) is expected since the ionic radius of Fe(III) is similar to the Al(III) ion. As for Cu(II) and Zn(II) ions, the interferences are due to the tendency of morin to form Cu(II)–morin and Zn(II)–morin complexes. However, the recovery could be improved with an introduction of 1,10-phenanthroline for reducing or eliminating the interferences of Fe(III) and hydroxylamine for Cu(II) to the samples as the masking agents [20]. As for the significant interference from $F^-$, it is also predicted since Al(III) forms a stable complex with this anion. Therefore, it is recommended that large amount of Be(II) as berilium chloride should be tried as to improve the recovery of Al(III) [21].

Table 1. Effect of interfering species on the recovery of 2 mg $L^{-1}$ Al(III) ion. Conditions: morin $1.35 \times 10^{-5}$ mol $L^{-1}$; Triton X-100 0.6 % v/v.

| **Species Added (10 $mgL^{-1}$)** | **Recovery ± R.S.D%** |
|---|---|
| $Mg^{2+}$ | 106.5 ± 1.8 |
| $Cu^{2+}$ | 70.2 ± 1.1 |
| $Zn^{2+}$ | 62.8 ± 1.2 |
| $Fe^{3+}$ | 68.8 ± 1.2 |
| $Ca^{2+}$ | 97.9 ± 1.2 |
| $Ba^{2+}$ | 102.8 ± 1.6 |
| $Cl^-$ | 105.2 ± 1.2 |
| $F^-$ | 45.6 ± 1.8 |
| $SO_4^{2-}$ | 104.4 ± 1.1 |

## Conclusion

The procedure described in this research offers a substantial improvement compared to other method, which utilizing an extraction steps in determination of Al(III) by fluorescence method. The use of Triton X-100 has eliminates the need to use an additional extraction steps for the sensitive and selective determination of Al(III). A five-fold sensitivity increased in the fluorimetric determination of Al(III) using morin was obtained by the addition of Triton X-100. The optimum conditions obtained at pH 4.0 in the presence of $1.35 \times 10^{-5}$ mol $L^{-1}$ morin and 0.6% v/v Triton X-100. A wide calibration range of $1.30 \times 10^{-6} – 2.59 \times 10^{-4}$ mol $L^{-1}$ (0.035 – 7.0 mg $L^{-1}$) and the detection limit of 0.022 mg $L^{-1}$ were achieved too by using the proposed method. Further study will be taken to apply this method to determine Al(III) ion in the real samples.

## Acknowledgements

The authors would like to acknowledge financial support from Ministry of Higher Education of Malaysia (Grant FRGS 1/2011/ST/USIM/01/1) and Universiti Sains Islam Malaysia (Grant PPP/FST-05-12711) for this work.

## References

1. Tria, J. C. V. Butler, E. C. V. Haddad, P. R. and Bowie, A. R. (2007). Determination of aluminium in natural water samples. *Analytica Chimica Acta,* 588: 153 – 165.
2. Dilleen, J. W. Birch, B. J. and Hagget, B. G. D. (1999). Electrochemical detection of aluminium using single-use sensors. *Analytical Communications,* 36: 363 – 365.
3. Flaten, T. P. (2001). Aluminium as a risk factor in Alzheimer's disease, with emphasis on drinking water. *Brain Research Bulletin,* 55(2): 187 – 196.
4. Ghavami, R., Najafi, A. and Hemmateenejad, B. (2008). Chemometrics-assisted spectrophotometric methods for simultaneous determination and complexation study of Fe(III), Al(III) and V(V) with morin in micellar media. *Spectrochima Acta Part A*, 70: 824 – 834.
5. Carpani, I. Scavetta, E. and Tonelli, D. (2004). Spectrophotometric determination of aluminium and nickel. *Annali di Chimica,* 94: 365 – 372.
6. Guray, T. Uysal, U. D. Gedikbey, T. and Huseyinli, A. A. (2005). 2, 2', 3,4-tetrahydroxy-3'-sulpho-5'-nitroazobenzene for spectrophotometric determination of aluminium in pharmaceutical suspensions and granite. *Analytical Chimica Acta,* 545: 107 – 112.
7. Hernandez, F. H. and Esriche, J. M. (1984). Fluorimetric determination of aluminium with morin after extraction with isobutyl methyl ketone. Part I. Fluorescence of the aluminium-morin complex in an isobutyl methyl ketone- ethanol- water system. *Analyst,* 109: 1585 – 1588.
8. Brach-Papa, C. Coulomb, B. Théraulaz, F. Van Loot, P. Boudenne, J. L. Branger, C. and Margaillan, C. (2004). Fluorimetric determination of aluminium in water by sequential injection through column extraction. *Analytical and Bioanalytical Chemistry,* 378: 1652 – 1658.
9. Al-Kindy, S. M. Z. Suliman, F. O. and Salama, S. B. (2003). A sequential injection method for the determination of aluminium in drinking water using fluorescence enhancement of the aluminum–morin complex in micellar media. *Microchemical Journal,* 74: 173 – 179.
10. Alonso-Mateos, A. Almendral-Parra, M. J. Curto-Serrano, Y and Rodríguez-Martín, F. J. (2008). Online monitoring of aluminium in drinking water with fluorimetric detection. *Journal of Fluorescence,* 18: 183 – 192.
11. Sanz-Medel, A. De La Campa, R. F. and Garcia Alonso, J. I. (1987). Metal chelate fluorescence enhancement in micellar media: mechanisms of surfactant action. *Analyst,* 112: 493 – 497.
12. Hinze, W. L. Singh, H. N. Baba, Y. and Harvey, N. G. (1984). Micellar enhanced analytical fluorimetry. *Trends in Analytical Chemistry,* 3: 193 – 199.
13. Howard, A. G. Coxhead, A. J. Potter, I. A. and Watt, A. P. (1986). Determination of dissolved aluminium by the micelle-enhanced fluorescence of its lumogallion complex. *Analyst,* 111: 1379 –1382.
14. Diaz Garcia, M. E. and Sanz-Medel, A. (1986). Dye-surfactant interactions: A review. *Talanta,* 33: 255 – 264.
15. Nakahara, Y. Kida, T. Nakatsuji, Y. and Akashi, M. (2004). A novel fluorescent indicator for $Ba^{2+}$ in aqueous micellar solutions. *Chemical Communications,* 2: 224 – 225.
16. Simoncic, B. and Kert, M. (2008). Influence of the chemical structure of dyes and surfactants on their interactions in binary and ternary mixture. *Dyes and Pigments,* 76: 104 – 112.

17. Carrion Dominguez, J. L. and Cirugeda, M. D. L. G. (1987). Spectroscopic study of the aluminium/lumogallion system in the presence of non-ionic surfactants. *Analytical Chimica Acta,* 198: 53 – 61.
18. Escriche, J. M., Cirugeda, M. D. L. G. and Hernandez, F. H. (1983). Increase in the sensitivity of the fluorescent reaction of the complexing of aluminium with morin using surfactant agents. *Analyst,* 108: 1386 – 1391.
19. Hernandez, F. H. Esriche, J. M. and Andreu, M. T. G. (1986). Enhancement of the fluorescence of the zinc-morin complex by non-ionic surfactant. *Talanta*, 33: 537 – 540.
20. Ren, J. L. Zhang, J. Luo, J. Q. Pei, X. K. and Jiang, Z. X. (2001). Improved fluorimetric determination of dissolved aluminium by micelle-enhanced lumogallion complex in natural waters. *Analyst*, 126: 698 – 702.
21. Zhang, J. Xu, H. and Ren, J. L. (2000). Fluorimetric determination of dissolved aluminium in natural waters after liquid–liquid extraction into n-hexanol. *Analytical Chimica Acta*, 405: 31 – 42.

*Malaysian Journal of Analytical Sciences, Vol 21 No 4 (2017): 801 - 809*
*DOI: https://doi.org/10.17576/mjas-2017-2104-06*

MALAYSIAN JOURNAL OF ANALYTICAL SCIENCES
*Published by The Malaysian Analytical Sciences Society*
ISSN 1394 - 2506

# CHARACTERIZATION, CALCULATION OF CALORIFIC VALUES, AND BIO-OIL PRODUCTION VIA THERMOCHEMICAL PROCESSES OF MUNICIPAL SOLID WASTE IN PERLIS, MALAYSIA

## (Pencirian, Pengiraan Nilai – Nilai Kalorifik dan Pengeluaran Bio-Minyak Melalui Proses Termokimia Sisa Pepejal Perbandaran di Perlis, Malaysia)

Khairuddin Md Isa[1,2]*, Farizul Hafiz Kasim[2], Umi Fazara Md Ali[1], Radzuwan Ab Rashid[3]

[1]*School of Environmental Engineering,*
*Universiti Malaysia Perlis, P.O Box 77, d/a Pejabat Pos Besar 01007, Kangar, Perlis, Malaysia*
[2]*Centre of Excellence for Biomass Utilisation,*
*Universiti Malaysia Perlis, Kompleks Pengajian Jejawi 3, 02600 Jejawi, Perlis, Malaysia*
[3]*Faculty of Languages and Communication,*
*Universiti Sultan Zainal Abidin, 21300 Kuala Nerus, Terengganu, Malaysia*

**Corresponding author: khairudin@unimap.edu.my*

Received: 9 January 2017; Accepted: 13 June 2017

**Abstract**

Municipal solid wastes (MSW) collected from Padang Siding Landfill, Perlis were segregated and characterized in the laboratory. The main components of MSW found are paper, plastic, glass and large proportion of organic waste. Moisture content was measured for all the components. Paper and yard wastes recorded the highest percentage of 26.7% and 28.8%, respectively. Thermogravimetric analysis (TGA) shows that the thermal degradation of MSW samples ranged from 200 $^{o}$C to 800 $^{o}$C, indicating fast decomposition occurred at 370 $^{o}$C, 430 $^{o}$C and 700 $^{o}$C. Traditional method shows a lower error compared to the physical method in calculating the calorific values (CV) for MSW. Bio-oil production via fast pyrolysis route gave higher liquid yield of ~35% with high oxygen content of ~49 – 53%. Heavy oil recovered from hydrous pyrolysis experiments gave low yield of ~7 – 13%, however with low oxygen content of ~11 – 18%.

**Keywords**: Municipal solid waste, thermogravimetric analysis, calorific value, pyrolysis, hydrous pyrolysis

**Abstrak**

Sisa pepejal perbandaran (SPP) dikumpulkan dari tapak pelupusan Padang Siding, Perlis. Bahan buangan ini diasingkan dan dikategorikan di dalam makmal. Komponen utama MSW yang ditemui adalah kertas, plastik, kaca dan sebahagian besar sisa organik. Kandungan kelembapan diukur untuk semua komponen di mana kertas dan sisa dari laman telah mencatatkan peratus tertinggi sebanyak 26.7% dan 28.8% masing-masing. Analisis termogravimetrik menunjukkan degradasi terma sampel MSW adalah antara 200 $^{o}$C hingga 800 $^{o}$C, menunjukkan penguraian cepat berlaku pada 370 $^{o}$C, 430 $^{o}$C dan 700 $^{o}$C. Kaedah tradisional menunjukkan ralat yang lebih rendah berbanding dengan kaedah fizikal dalam mengira nilai kalorifik untuk SPP. Pengeluaran bio-minyak melalui laluan pirolisis pantas memberikan hasil cecair yang lebih tinggi ~35% dengan kandungan oksigen yang tinggi ~ 49 – 53%. Minyak berat diperoleh daripada eksperimen pirolisis berair memberikan hasil yang rendah ~ 7 – 13%, walau bagaimanapun dengan kandungan oksigen yang rendah ~ 11 – 18%.

**Kata kunci:** Sisa pepejal perbandaran, analisa termogravimetrik, nilai kalorifik, pirolisis, pirolisis berair

## Introduction

Municipal solid waste (MSW), also known as urban solid waste, is a type of waste that predominantly comes from household waste (domestic waste) with a small portion of commercial waste collected by municipality of a particular area. Generally, the solid waste is defined as the household's refusal and non-hazardous solid waste from industrial, commercial and institutional establishments, such as hospitals, market and yard wastes, and street sweepings [1]. MSW is a heterogeneous material and its physical composition is dependent on socio-economic level and climatic conditions [2].

Perlis Indera Kayangan is the smallest state in Malaysia which is located at the northern part of the Peninsular Malaysia. Its population is 227,025 as of 2010. The increase in population and industrial activities in Perlis has resulted in serious environmental problems including air quality deterioration, water and land pollutions. The amount of solid wastes generated in Perlis is approximately 221 tonnes/day [3]. The most popular disposal practice for MSW is landfilling. Landfilling is a universal solution that provides ultimate waste disposal and can be implemented easily. However, the setback of this approach is that it requires a large piece of land and does not employ the concepts of reduction and conversion of MSW. The MSW disposal in Perlis is located at Padang Siding landfill with an area approximately 50.876 hectare. Landfills face the problems of overfilling, overflowing of leachates leading to pollution of water resources, and uncontrolled dust emissions adversely affecting the human environment [4].

In order to justify the feasibility of energy recovery for the use of renewable energy, it is very important to determine the calorific value (CV) of MSW. Bomb calorimeter can be used for calorimetric measurement in which combustion is conducted under conditions of constant volume. Other important methods are physical composition and traditional methods where the energy content can be calculated using physical and proximate analysis, respectively.

One option of utilizing the MSW is energy recovery through various processes, such as combustion, pyrolysis, liquefaction and refuse-derived fuel [5]. Several researchers have pyrolyzed biomass residue to produce bio-oil under certain conditions [6 – 8]. Bio-oil is dark brown liquid which has a high heating value that can be used as fuels in boiler, diesel engines for power generation, or upgraded to produce fuels and bulk chemicals. However, direct usage of bio-oil as conventional fuels may present some difficulties due to high viscosity, poor heating value, corrosiveness and instability. The comparison of pyrolysis and hydrous pyrolysis of MSW has not been done in earlier studies and this study attempts to fill in the gap. The comparison is beneficial for engineers and policy makers to design an alternative solution for MSW.

A large portion of the waste has significant energy potential which can be utilized. The energy recovered can also reduce emissions that would otherwise be produced by other energy systems, such as fossil fuel thermal power plants [9]. An important criterion for the success of waste management plan is the accurate data on the quality and quantity of the waste generation. With this data, proper management strategies can be planned and put into actions. The data can also be used to predict the future trends of the quantity and quality of the MSW. This allows the authorities to take anticipating measures to manage MSW generated properly [10].

In order to justify the feasibility of energy recovery for the use of renewable energy, it is very important to determine the calorific value (CV) of MSW. Bomb calorimeter can be used for calorimetric measurement in which combustion is conducted under the condition of constant volume. Other important methods are physical composition and traditional methods where the energy content can be calculated using physical and proximate analysis, respectively.

In Perlis, there is less data available on the potential of MSW to be used as energy sources. To fill in the gap, this study was conducted to segregate and characterize the main components of MSW in the state. The energy contents of MSW generated were calculated. The production of bio-oil was performed via thermochemical conversion processes to investigate its potential to be used as a renewable energy.

## Materials and Methods

### Sample preparation

The solid waste samples were collected at Padang Siding landfill in Arau, Perlis. The sampling was carried out randomly at 5 different locations within the 0.12 $km^2$ landfill area of 0.6 m depth. These samples were brought back to the laboratory for analysis. The manual segregation process was conducted to calculate the MSW's components. After the completion of segregation, all the samples were mixed, washed (with water) and oven dried at 105 $^oC$ for 12 hours to eliminate external moisture. The samples (except glass) were shredded and sieved to obtain uniform size less than 1.5 mm for further experimental works. This sample was used for TGA analysis and pyrolysis experiments.

### Moisture-content determination

The collected samples were oven-dried at 105 $^oC$ for 5 hours to measure moisture-content. All the moisture content values used in this research were based on the wet basis, unless otherwise stated. The percentage of moisture content was calculated as follow:

$$Moisture\ (\%) = \left[\frac{Wet\ weight - dry\ weight}{Wet\ weight}\right] \text{ x } 100\% \quad (1)$$

### Thermogravimetric analysis

The thermogravimetric analysis was carried out by using a TGA/DSC 1 Mettler Toledo. The weight loss and the rate of weight loss were recorded continuously under dynamic conditions, as functions of time or temperature, in the range of 25 to 900 $^oC$. Purified nitrogen gas was used for the pyrolysis with a flow rate of 150 ml/min. The heating rate of 20 $^oC$/min was selected for this test. The temperature was increased to the setting value of 900 $^oC$ at the pre-selected heating rate and it was kept constant at this value until steady conditions were obtained.

### Proximate analysis

Proximate analysis was performed according to ASTM D2974 [11] using the thermogravimetric analyzer (TGA/DSC 1, Mettler Toledo) for determination of moisture, volatile matter, fixed carbon and ash in MSW. The experiment was performed under inert nitrogen gas and purified air with a constant flow rate of 150 ml/min and the heating rate of 20 $^oC$. The samples were weighed directly into the alumina crucible and the temperature was kept at isothermal for 0.5 minutes until a steady condition was obtained before ramping to the desired temperature [12]. The experiments were replicated at least twice to obtain reproducibility.

### Calorific value (CV)

The calorific values (CVs) of the samples were determined by using a bomb calorimeter (Model: C2000 basic, IKA co, Germany). The calculation was also made according to the model developed by Khan and Abu Ghrarah [13] as reported by Abu-Qudais and Abu-Qdais [5].

$$E = 23\ [F + 3.6\ (PA)] + 160\ (PL) \quad (2)$$

where E is the energy content of MSW (Btu/lb), PL is the percentage of plastic by weight, F is the percentage of food waste by weight and PA is the percentage of paper waste by weight.

For comparison, a traditional model reported by Abu-Qudais and Abu Qdais [5] had also been employed as follows:

$$E\ (Kcal/kg) = 45B - 6W \quad (3)$$

where B is the combustible volatile matter in MSW (%) and W is the water percentage weight on dry basis (%).

### CHNO analyses

The elemental analyses of the oils were determined using Thermo Electron FlashEA 1112 elemental analyser. Vanadium pentoxide (2-3 mg) was used to determine the Sulphur content and the amount of Sulphur found was too small and negligible for the calculation of this research.

**Pyrolysis experimental procedure**

Fast pyrolysis was conducted in a fixed-bed reactor as in our previous study [7]. The experimental device consisted of a tube reactor with a volume of 250 $cm^3$, equipped with a K-type thermocouple , an electric heater, a nitrogen cylinder, a cold trap, water bath and product effluent. The condensation temperature was set at 0 $^oC$ for all experiments. The amounts of sample used in all experiments were 5 mg per run. The bio-oil yield was collected from oil collector and weighed to calculate the percentage. For all experiments, whenever the pyrolysis temperature was reached, it was immediately cooled down to 100 $^oC$ within 4 minutes. Experiments were repeated 5 times to ensure the reproducibility of the results.

Nitrogen flow rate and condensation temperature were kept constant at 100 $cm^3$/min and 0 $^oC$, respectively. The pyrolysis experiments were conducted using fixed bed pyrolyser at pyrolysis temperature of 470 $^oC$, particle size of 0.60 mm, holding time at 1 minute. Experiments were repeated 5 times to ensure the reproducibility of the results.

**Hydrous experimental procedure**

Hydrous experiments were conducted using a Parr 4740 series stainless steel (75 ml cylindrical) pressure vessel at pre-set temperatures (380, 420 and 480 $^oC$) for 1 hours. After sealing the vessel and attaching the pressure gauge, it was purged 10 times with nitrogen gas to remove the air, and then 2 bar of nitrogen gas was introduced to provide an inert atmosphere. The reactor was heated in a fluidised sand bath. Temperature was monitored by an additional K-type thermocouple which was connected to a computer and recorded every 10 s. The reacted product washing procedure had been reported in the previous study [14]. Hydrous pyrolysis was also conducted at 380, 420 and 480 $^oC$ with sample to water mass ratio of 1:6, using 75 ml reactor for 1 hour. The pressures recorded for these experiments were in the range of 280 – 300 bar.

## Results and Discussion

**Waste segregation and moisture content**

Table 1 shows the average compositions after the segregation process. Plastic and glass were the highest proportion in the samples collected with approximately 46%. Similarly, papers contributed approximately 21%, ranked as the third largest component. The other smallest components were polystyrene, yard wastes and wood with 1.4%, 3.5% and 8.0%, respectively. Food waste consists of approximately 12%, as such, it can be inferred that the management of organic waste has not been properly done.

Table 1. Characterization of MSW from Padang Siding landfill

| Sample | Food Waste (%) | Paper (%) | Plastic (%) | Polystyrene (%) | Rubber (%) | Yard waste (%) | Glass (%) | Wood (%) |
|---|---|---|---|---|---|---|---|---|
| 1 | 37.80 | 1.50 | 13.90 | 1.20 | 24.70 | 6.40 | 0.00 | 14.50 |
| 2 | 2.80 | 4.00 | 15.40 | 2.20 | 11.30 | 7.80 | 46.20 | 10.20 |
| 3 | 12.50 | 16.80 | 14.20 | 0.60 | 6.90 | 0.00 | 43.90 | 5.20 |
| 4 | 5.30 | 24.70 | 48.40 | 2.70 | 0.00 | 0.00 | 11.50 | 7.40 |
| 5 | 0.00 | 56.20 | 12.40 | 0.30 | 0.00 | 3.40 | 24.90 | 2.90 |
| Average | 11.68 | 20.64 | 20.86 | 1.40 | 8.58 | 3.52 | 25.3 | 8.04 |

Note: Mud and gravel had been removed from the samples

Moisture contents of the MSW components are summarized in Table 2. As expected, paper, polystyrene, and yard wastes had the highest proportion with 26.7%, 25.0%, and 28.8%, respectively. Rubber had the lowest percentage of moisture with 10.2%. The high moisture content is normally attributed to the climate of the area. Perlis is a tropical climate state with a large amount of rainfall obtained throughout the year. The annual rainfall is approximately 2,700 mm and may increase up to 6,000 mm in the catchment region. On top of this, the average air humidity in Perlis is above 80% [15].

Table 2. Moisture content of MSW components from Padang Siding, Perlis Landfill

| Waste Components | Wet weight (kg) | Dry weight (kg) | Moisture Content (%) |
|---|---|---|---|
| Food waste | 0.780 | 0.682 | 12.6 |
| Paper | 0.030 | 0.022 | 26.7 |
| Plastic | 0.286 | 0.238 | 16.8 |
| Polystyrene | 0.024 | 0.018 | 25.0 |
| Rubber | 0.510 | 0.458 | 10.2 |
| Yard waste | 0.132 | 0.094 | 28.8 |
| Wood | 0.300 | 0.268 | 10.7 |

**Proximate and TGA analysis**

Proximate analysis was carried out in order to determine the moisture content (dry basis), volatile matter content, fixed carbon content and ash content in the waste samples. The analysis was conducted for the combination of yard wastes, plastic, paper, polystyrene, wood and rubber. Table 3 tabulates the proximate analysis for 5 samples collected from Padang Siding Landfill. Volatile matter had 68% in average and offered high percentage of condensable gas. The thermochemical conversion method is the best option as condensable gas is promising in amount. The proximate analysis conducted in previous studies set in Penang, Malaysia, shows that the investigated MSW comprised of 44.66% of moisture content, 44.55% of volatile matter, 8.56% of ash content and 2.23% of fixed carbon content [16]. Typically, based on the proximate percentages range for moisture content in residential, MSW is about 15% to 40%, volatile matter comprises approximately 40% to 60% and the range for fixed carbon is from 4% to 15% [17].

Table 3. Proximate analysis of MSW from Padang Siding landfill[a]

| Variable (wt. %) | Sample | | | | | Average |
|---|---|---|---|---|---|---|
| | 1 | 2 | 3 | 4 | 5 | |
| Moisture content | 7 | 10 | 5 | 7 | 5 | 7 |
| Volatile matter | 53 | 71 | 68 | 71 | 79 | 68 |
| Fixed carbon | 10 | 7 | 10 | 10 | 2 | 8 |
| Ash content | 30 | 12 | 17 | 12 | 14 | 17 |

Note: [a] dry basis

The TG analysis is usually used for thermal characterization, calculation of the pyrolysis conversion and evaluation of reactivity and kinetic parameters [7]. In this research, the purpose of TG analysis was to look into the degradation profile for MSW. Figure 1 shows the thermal decomposition of MSW. The initial curve indicates that there was moisture loss of up to 105 $^{o}$C. The decomposition was gradually increased starting from 200 $^{o}$C until it had a fast decomposition reaching 350 $^{o}$C. Up to 400 $^{o}$C, the remaining residue was 40% and about 60% was decomposed. The decomposition produced approximately 15 to 17% of ash content. This result is in agreement with the waste compositions described earlier. The carbon residues ranged between 10 to 17% pose significant carbon deposition during refinery upgrading (e.g. catalytic cracking), whereas the values above 20% are considered problematic. The decomposition trend was observed to be influenced by the waste compositions, such as paper, wood and plastic. For each TG experiment, the weight loss of MSW as a function of temperature cannot be simulated by considering a single decomposition reaction [18]. The remaining others slowly degraded over 350 $^{o}$C until 800 $^{o}$C. They are 4 zones indicated as A, B, C and D in thermogravimetric curve and this is presented clearly in the DTG curve.

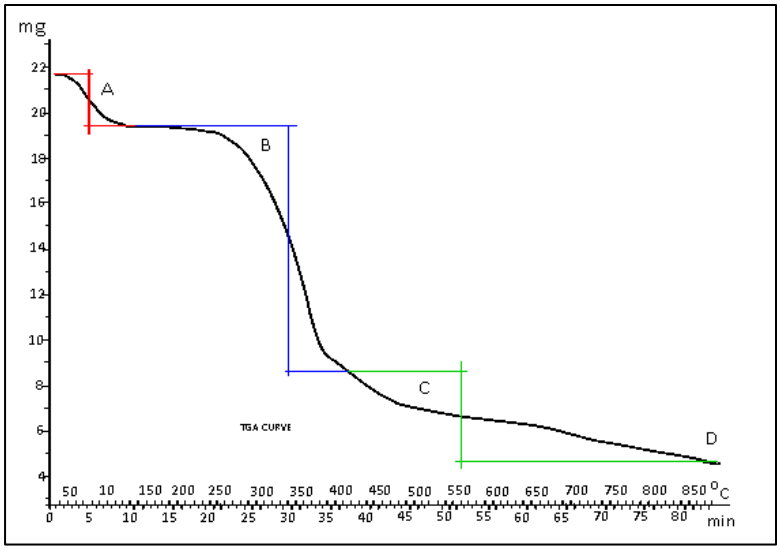



Figure 1. TGA curves for MSW samples

Figure 2 shows the DTG evolution profiles for MSW samples. Zone A indicated moisture loss curve while Zones B, C and D were attributed to the waste compositions. The fast decomposition occurred at three regions which were at 350 °C, 430 °C and 700 °C. The fast decomposition at zone B was caused by the degradation of materials, such as wood and yard wastes. Based on the DTG evolution profiles, material at zone B started to decompose at temperature ranging from 200 °C to about 400 °C, with $T_{max}$ at 350 °C. It was followed by the degradation of plastic and the fast decomposition was shown at C. Zone C recorded the burn-out temperature starting from 400 °C and ended at 480 °C. The more stable materials, such as rubber, gradually degraded and recorded fast decomposition at 700 °C. Small percentage of rubber contributed to the small peak at 700 °C. The burn-out temperature occurred at 600 °C with $T_{max}$ at 750 °C. The differences in the DTG profiles showed the difference in the complexity of MSW components. Shen and Qinlei reveal three steps in their previous study due to the emission and combustion of the volatiles with the char combustion [19].

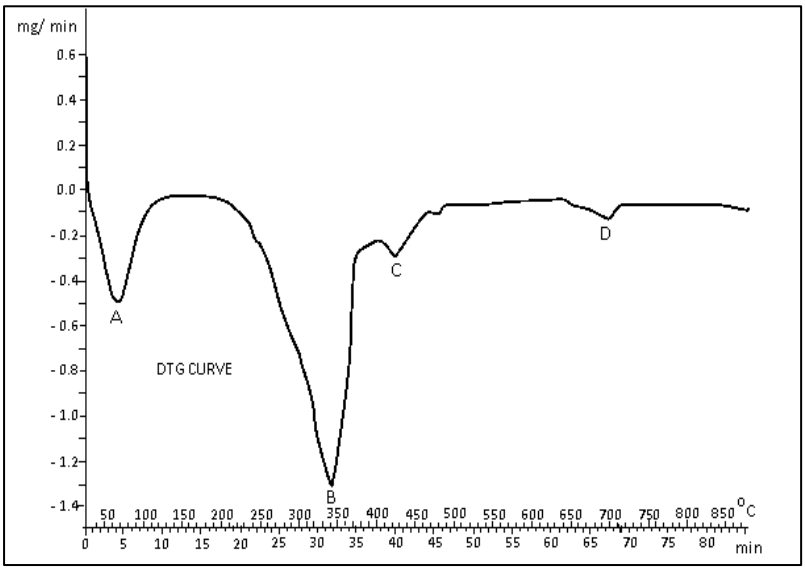



Figure 2. DTG curves for MSW samples

**Calorific values (CVs)**

Table 4 shows the calorific values of MSW by using bomb calorimeter, calculations employing physical composition and proximate analysis techniques. The calorific values ranging from 2200 to 4500 kcal/kg were obtained for all samples by using bomb calorimeter. Sample No. 4 had the highest value while sample No.1 recorded the lowest. Kathirvale et al. reported that the calorific values of the Malaysian MSW ranged between 1500 and 2600 kcal/kg [20]. The CVs calculated employing physical composition gave values ranging from 1601 to 5550 kcal/kg while proximate analysis technique gave values ranging from 2343 to 4000 kcal/kg. In physical composition, sample No. 4 gave the highest value with 5550 kcal/kg. This was attributed to the composition of paper and plastic and it is in agreement with PL/PA ratio as reported by Abu-Qudais and Abu-Qdais [5]. Traditional method shows a lower error compared to the physical method. The result from traditional method analysis is useful in calculating CVs in MSW study compared to the physical method.

Table 4. Comparison of CVs determined by different methods

| Waste Sample | Calorific Value (kcal/kg) | | |
|---|---|---|---|
| | Bomb Calorimeter | Physical Composition | Traditional Method |
| 1 | 2200 | 1802 | 2343 |
| 2 | 2500 | 1601 | 3135 |
| 3 | 3451 | 2212 | 3030 |
| 4 | 4500 | 5550 | 4000 |
| 5 | 3480 | 3717 | 3525 |

**Thermochemical processes**

The pyrolysis experiments were conducted using fixed bed pyrolyser at pyrolysis temperature of 470 $^{o}$C and the bio-oil produced was ~ 35%. The hydrous pyrolysis were conducted at 380, 420 and 480 $^{o}$C to investigate the effect of temperature on product distribution (Figure 3). The high gas yield obtained at 480 $^{o}$C (42%) had resulted in the decrease of liquid products due to the further thermal decomposition [21]. As decomposition to form gas occurred when the temperature had increased to 480 $^{o}$C, the oil plus water yield decreased to 42%. Of this, 6% was recovered as heavy oil while approximately 10 – 12% of heavy oil was recovered at 380 and 420 $^{o}$C.

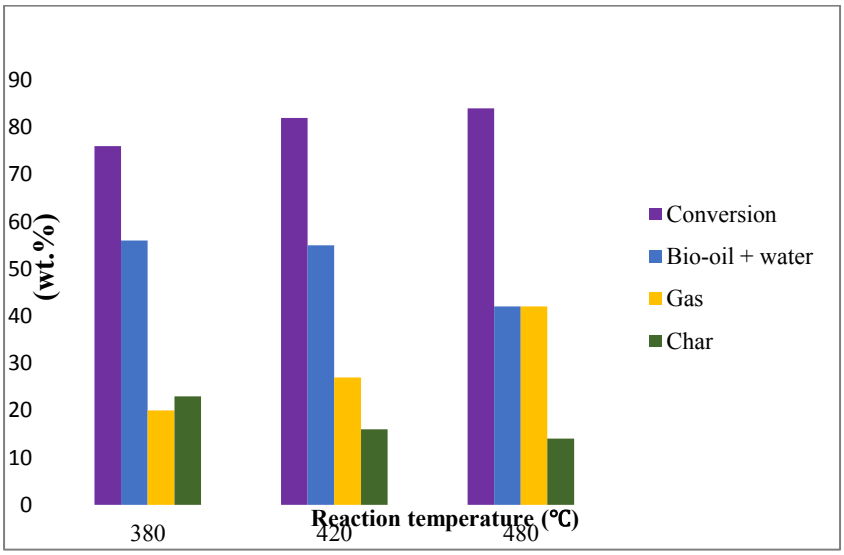



Figure 3. Effect of reaction temperature on product yields using MSW sample to water mass ratio of 1:6 for 1 hour

Table 5 presents the elemental compositions of the bio-oils and heavy oils obtained from pyrolysis and hydrous experiments. An increase in temperature gave low oxygen contents (~11%) for heavy oil from hydrous pyrolysis and bio-oils obtained from direct fast pyrolysis had high oxygen content (~49 – 53%).

Table 5. Elemental analyses of bio-oils and heavy oils from pyrolysis and hydrous pyrolysis experiments

| Runs | Samples | C (%) | H (%) | N (%) | *O (%) |
|---|---|---|---|---|---|
| Pyrolysis | Bio-oil 1 | 42.0 | 7.0 | 0.3 | 50.7 |
| | Bio-oil 2 | 43.0 | 6.9 | 0.4 | 49.7 |
| | Bio-oil 3 | 40.0 | 7.0 | 0.3 | 52.7 |
| Hydrous pyrolysis | Heavy oil (380 $^{o}$C) | 74.0 | 6.8 | 0.6 | 18.6 |
| | Heavy oil (420 $^{o}$C) | 77.0 | 7.1 | 0.6 | 15.3 |
| | Heavy oil (480 $^{o}$C) | 81.0 | 7.3 | 0.5 | 11.2 |

*Oxygen by difference

## Conclusion

The MSW in Perlis mainly consists of plastic and paper followed by food waste, wood, yard waste and polystyrene. Referring to the wide range of wastes, the thermogravimetric analysis displays a broad range of degradation temperature starting from 200 $^{o}$C to 800 $^{o}$C. DTG curves illustrate the fast decompositions that occurred at 350 $^{o}$C, 430 $^{o}$C and 700 $^{o}$C which represent different waste components. For each TG experiment, the weight loss of MSW due to temperature cannot be simulated by considering a single decomposition reaction. CVs calculation employing traditional method gave a lower error compared to the physical method. The physical composition method could be employed for MSW CVs calculation if the MSW compositions are influenced by ratio of plastic to paper. Bio-oil production via fast pyrolysis route gave higher liquid yield of ~35% with high oxygen content of ~49 – 53%. Heavy oil recovered from hydrous pyrolysis experiments gave low yield of ~7 –12%, however with low oxygen content of ~11 – 18%.

## Acknowledgement

The researchers thank Universiti Malaysia Perlis for funding this work.

## References

1. Hannan, M. A., Arebey, M., Basri, H. and Begum, R. A. (2010). Intelligent solid waste bin monitoring and management system. *Australian Journal of Basic and Applied Sciences*, 4(10): 5314 – 5319.
2. Cheng, H. and Hu, Y. (2010). Municipal solid waste (MSW) as a renewable source of energy: Current and future practices in China. *Bioresource Technology*, 101(11): 3816 – 3824.
3. Johari, A., Alkali, H., Hasyim, H., Ahmed, S. and Mat, R. (2014). Municipal solid waste management and potential revenue from recycling in Malaysia. *Modern Applied Science*, 8(4): 37 – 49.
4. Syed, A. K. S. A., Abidin, H. Z., Sulaiman, M. R., Khoo, K. H. and Ali, H. (2008). Combustion characteristics of Malaysian municipal solid waste and predictions of air flow in a rotary kiln incinerator. *Journal of Material Cycles Waste Management,* 10: 116 – 123.
5. Abu-Qudais, M. and Abu-Qdais, H. A. (2000). Energy content of municipal solid waste in Jordan and its potential utilization. *Energy Conversion & Management,* 41(9), 983 – 991.
6. Isa, K. M., Ying, L. J., Saad, S. A., Kasim, F. H. and Rahim, M. A. A. (2016). Pyrolysis of oil palm fronds in a fixed bed reactor and optimisation of bio-oil using Box-Behnken Design. *Journal of Advanced Research in Fluid Mechanics and Thermal Sciences,* 27(1), 12 – 18.
7. Isa, K. M., Daud, S., Hamidin, N., Ismail, K. and Kasim, F. K. (2011). Thermogravimetric analysis and the optimisation of bio-oil yield from fixed-bed pyrolysis of rice husk using response surface methodology (RSM). *Industrial Crops and Products*, 33(2): 481 – 487.

8. Chen, X., Chen, Y., Yang, H., Chen, W., Wang, X. and Chen, H. (2017). Fast pyrolysis of cotton stalk biomass using calcium oxide, *Bioresource Technology*, 233: 15 – 20.
9. Liamsanguan, C. and Gheewala, S. H. (2007). Environmental assessment of energy production from municipal solid waste incineration. The International Journal of Life Cycle Assessment, 12(7): 529 – 536.
10. Kathirvale, S. Yunus, M. N. M., Sopian, K., Samsuddin, A. H. and Rakmi, A.R. (2002). Comprehensive characteristic of the municipal solid waste generated in Kuala Lumpur. *In Proceedings of the Regional Symposium on Environment and Natural Resources*, Kuala Lumpur, Malaysia: pp. 359 – 368.
11. Annual Book of ASTM Standards, D2974 volume 5.05. The American Society for Testing and Material (ASTM), Philadelphia, PA.
12. Ismail, K., Zakaria, Z. and Ishak, M. A. M. (2005). *Proceeding of 22nd, International Pittsburgh Coal Conference*, Pittsburgh, USA.
13. Khan, A. M. Z. and Abu Ghrarah, Z. H. (1991). New approach for estimating energy content of municipal solid waste. *Journal Environmental Engineering*, 117(3), 376 – 380.
14. Isa, Md. K., Snape, C. E., Uguna, C. and Meredith, W. (2015). High conversions of miscanthus using sub- and supercritical water above 400 $^{o}$C. *Journal of Analytical and Applied Pyrolysis*, 113: 646 – 654.
15. Hamatschek, E., Tee, S. S. and Faulstich, M. (2010). Current practice of municipal solid waste management in Malaysia and the potential for waste-to-energy implementation. *ISWA World Congress,* 1 – 13.
16. Chai, S. P. and Zakaria, R. (2006). Investigation of combustion characteristic of municipal solid waste from Penang State Malaysia. 4th *International Conference on Combustion, Incineration/Pyrolysis and Emission Control: Waste to Wealth*, Kyoto, Japan.
17. Tchobanoglous, G., Theisen, H. and Vigil, A. S. (1993). Integrated solid waste management, engineering principles and management issues. Mc Graw-Hill, New York.
18. Garcia, A. N., Marcilla, A. and ont, R. (1995). Thermogravimetric kinetic study of the pyrolysis of municipal solid waste. *Thermochimica Acta*, 254: 277 – 304.
19. Shen, B. and Qinlei. (2006). Study on MSW catalytic combustion by TGA. *Energy Conversion & Management,* 47(11-12): 1429 – 1437.
20. Kathirvale, S., Yunus, M. N. M., Sopian, K. and Samsuddin, A. H. (2003). Energy potential from municipal solid waste in Malaysia. *Renewable Energy*, 29(4): 559 – 567.
21. Onsri, K., Prasassarakich, P. and Ngamprasertsith, S. (2010). Co-liquefaction of coal and used tire in super-critical water. *Energy Power Engineering*, 2: 95 – 102.

*Malaysian Journal of Analytical Sciences, Vol 21 No 4 (2017): 810 - 819*
*DOI: https://doi.org/10.17576/mjas-2017-2104-07*

**MALAYSIAN JOURNAL OF ANALYTICAL SCIENCES**
*Published by The Malaysian Analytical Sciences Society*
**ISSN 1394 - 2506**

# ULTRASOUND-ASSISTED SURFACTANT ENHANCED EMULSIFICATION MICROEXTRACTION METHOD COUPLED WITH GAS CHROMATOGRAPHY-MASS SPECTROMETRY FOR THE DETERMINATION OF SELECTED POLYCYCLIC AROMATIC HYDROCARBONS IN AQUEOUS SAMPLES

## (Kaedah Pengekstrakan Mikro Ultrabunyi dengan Bantuan Surfaktan Meningkatkan Pengemulsian Bergabung dengan Kromatografi Gas-Spektrometri Jisim Bagi Penentuan Polisiklik Aromatik Hidrokarbon Terpilih di dalam Sampel Akueus)

Siti Farahiyah Ahmad Shater [1], Noorfatimah Yahaya[1]*, Nur Nadhirah Mohamad Zain[1], Sharlina Mohamad[1], Farah Wahidah Mohd Hassan[1], Sazlinda Kamaruzaman[2], Nor Suhaila Mohamad Hanapi[3], Mazidatulakmam Miskam[4]

[1]*Integrative Medicine Cluster, Advanced Medical and Dental Institute (AMDI), Universiti Sains Malaysia, Bertam, 13200 Kepala Batas, Penang, Malaysia*
[2]*Department of Chemistry, Faculty of Science, Universiti Putra Malaysia, 43400 UPM Serdang, Selangor, Malaysia*
[3]*Faculty of Applied Sciences, Universiti Teknologi MARA, 40450 Shah Alam, Selangor, Malaysia*
[4]*School of Chemical Sciences, Universiti Sains Malaysia, 11800 Penang, Malaysia*

**Corresponding author: noorfatimah@usm.my*

Received: 29 March 2017; Accepted: 20 June 2017

**Abstract**

A simple and rapid microextraction method termed as ultrasound-assisted surfactant enhanced emulsification microextraction (UASEME) was developed for the determination of fluoranthene (FLU) and phenanthrene (PHE) in aqueous samples followed by gas chromatography-mass spectrometry (GC-MS). Six important parameters, that affect the extraction efficiency of polycyclic aromatic hydrocarbons (PAHs) were evaluated and the results were as follows; extraction solvent (toluene), volume of extraction solvent (30 µL), surfactant (Tween 20), volume of surfactant (15 µL), extraction time (2 minutes) and with no salt addition. Under the optimum conditions, the method showed good linearity over the concentration range from 1 – 1000 µg $L^{-1}$ with correlation coefficients ($R^2 \geq 0.9932$), acceptable limits of detection (0.3 µg $L^{-1}$) and limits of quantification (1.0 µg $L^{-1}$) for both analytes. Good relative recovery values, in the range of 91.75 – 104.1%, were obtained for tap water samples. The relative standard deviations (RSDs) were 1.62 – 10.32% ($n$ = 3). The proposed method was applied for the determination of FLU and PHE in tap water and sugarcane juices.

**Keywords:** ultrasound-assisted, surfactant, emulsification, polycyclic aromatic hydrocarbons, gas chromatography-mass spectrometry

**Abstrak**

Satu kaedah pengekstrakan mikro yang mudah dan cepat disebut kaedah ultrabunyi-dibantu surfaktan diperkuat pengemulsian dibangunkan bagi penentuan fluorantin (FLU) dan fenantrin (PHE) di dalam sampel akueus diikuti oleh kromatografi gas-spektrometri jisim (GC-MS). Enam parameter penting, mempengaruhi kecekapan pengekstrakan hidrokarbon aromatik polisiklik

(PAH) telah dinilai dan keputusan adalah seperti berikut; pengekstrakan pelarut (toluena) jumlah pelarut pengekstrakan (30 µL), surfaktan (Tween 20), jumlah surfaktan (15 µl), masa pengekstrakan (2 minit) dan tanpa tambahan garam. Di bawah keadaan yang optimum, kaedah ini menunjukkan kelinearan baik pada julat kepekatan 1 –1000 µg $L^{-1}$ dengan pekali korelasi ($R^2 \geq$ 0.9932) dan had pengesanan yang diterima (0.3 µg $L^{-1}$) dan had kuantifikasi (1.0 µg $L^{-1}$) untuk kedua-dua analit. Nilai perolehan semula yang baik dalam julat 91.75 – 104.1%, telah diperoleh bagi sampel air paip. Sisihan piawai relatif (RSDs) adalah 1.62 – 10.32% ($n$ = 3). Kaedah yang dicadangkan telah digunakan untuk penentuan FLU dan PHE dalam sampel air paip dan jus tebu.

**Kata kunci:** ultrabunyi-dibantu, surfaktan, pengemulsian, polisiklik aromatik hidrokarbon, kromatografi gas-spektrometri jisim

## Introduction

Polycyclic aromatic hydrocarbons (PAHs) are organic compounds with two or more benzene rings categorized by the European Union (EU) and the US Environmental Protection Agency (US EPA) as priority pollutants due to their mutagenic and carcinogenic properties [1]. PAHs are ubiquitous in the environment and have mainly been found in the process of incomplete combustion of oil spill, fossil fuels, wood and etc [2]. Fluoranthene (FLU) and phenanthrene (PHE) are listed as priority pollutants by the US EPA and the action and risk levels of FLU and PHE are described in the Dutch Government Quality Standards for the assessment soil and water contamination [3]. Since PAH compounds exist at very low concentrations in the environment and the presence of a high level of matrix interferences in samples, the determination of these compounds in environmental samples is complicated. Thus, a fast and effective sample pre-treatment method is critical to eliminate major interferences and enrich the target analytes before instrumental analysis.

Liquid-liquid extraction (LLE) [4] and solid phase extraction (SPE) [4, 5] are conventional sample preparation methods that have been employed for the determination of PAHs. However, these classical pre-concentration methods involve several phase operations with the consumption of large volumes of toxic organic solvent that lead to environment-unfriendly processes [6]. Researchers are devoted to the development of a microextraction method to overcome these problems as it is environmental friendly and consumes a minimum amount of organic solvent. Several microextraction methods have been developed for the determination of PAH compounds including liquid phase microextraction (LPME) [7], static- liquid phase microextraction (S-LPME) [8] and ultrasound assisted emulsification microextraction (UAEME) [9]. Although there are various established analytical methods nowadays, the application of microextraction on sugarcane samples is still unexplored. A micro implementation of liquid-liquid extraction (LLE), namely liquid-phase microextraction (LPME) has become a very popular sample pre-treatment technique because it combines extraction and enrichment of target analytes with a relatively inexpensive cost, is easy to operate and nearly solvent-free [10].

Ultrasonic-assisted emulsification microextraction (UAEME) is developed for the extraction of organic compounds from water samples [11]. This method has proven to be an efficient tool in the formation of the emulsification phase and acceleration of mass transfer between two immiscible phases [12]. A relatively new method is developed using surfactants as the emulsifier in the UAEME method for detection of selected carbamate compounds in water samples [13]. Surfactants are known as surface active agents since they have both hydrophilic and hydrophobic moieties [13]. Due to their amphiphilic structure, they are able to react both in water and immiscible phases and thus can be used as emulsifiers to enhance the dispersion of the water-immiscible phase into the aqueous phase [13]. The newly introduced method incorporated with the surfactant has greatly shortened the time of extraction required due to the effective combination of surfactant and ultrasound radiation [14]. USAEME has been previously employed for the determination of poly-brominated flame retardants in water samples [13] and for determination of PAHs in water samples [15, 16]. In the UASEME method, the extraction procedure is carried out under the simultaneous actions of ultrasound radiation and surfactant, shortening the time for analysis [13]. Ultrasound radiation leads to the fragmentation of one of the phases, resulting in the rapid emulsification of the mixture [9].USAEME provides very high extraction efficiencies in a short time, since the high contact surface between both liquids facilitates the mass transfer from the sample solution to the extraction solvent [9]. This developed method provides many advantages such as excellent enrichment factors, simplicity, stability, easy to operate, low cost and low consumption of organic solvents [15].

In this study, a new microextraction method termed UASEME incorporated with Tween 20 was developed prior to GC-MS determination of FLU and PHE in tap water and sugarcane juice samples. Six parameters were optimized including the type of extraction solvent, type of surfactant, volume of extraction solvent, volume of surfactant, salt addition and extraction time. Based on the results obtained, the proposed method is applicable for the analysis of selected PAHs in aqueous matrices due to its simplicity, efficiency and sensitivity. To the best of our knowledge, there is no paper reported on the determination of FLU and PHE in aqueous matrices using this method.

## Materials and Methods

### Chemicals and reagents

Fluoranthene (FLU) and phenanthrene (PHE) (Figure 1) were obtained from Toronto Research Chemicals INC (Toronto, Canada). HPLC-Grade toluene, n-hexane, iso-octane, and 1-octanol were purchased from QReC Asia Sdn. Bhd. (Selangor, Malaysia). Analytical grade surfactants (Tween 80, Tween 20 and DC193C) were purchased in their chemically pure form from Fisher Scientific (Selangor, Malaysia). Ultrapure water of 18.2 MΩ was purified by a Sartorious system, model Arium 611 D1 (Stedim Biotech, Gottingen, Germany). Stock standard solutions (1000 µg $L^{-1}$) of FLU and PHE were prepared in a solvent mixture of methanol and acetonitrile (1:1) and stored in the dark at 4 °C. The working standard solutions were prepared daily by the dilution of stock solution in ultrapure water prior to extraction and analysis.

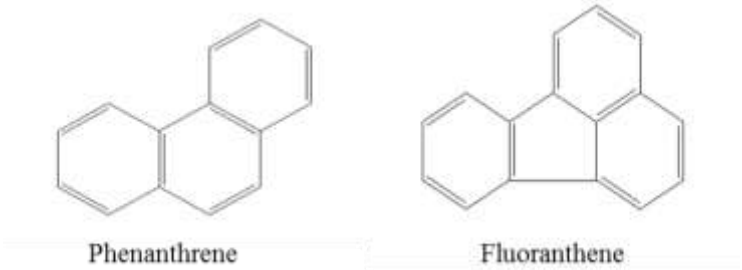



Figure 1. 2D-structures of selected polycyclic aromatic hydrocarbons

### GC-MS operating conditions

All analyses were performed using Agilent GC system Model 7890A with mass spectrometry analyser Model 5975C (Palto Alto, USA). Helium gas was used with a constant flow rate of 1mL $min^{-1}$. Splitless injections were performed at 250 °C and the volume of injection was 1 µL. The chromatographic condition was carried out on an Agilent HP 5-MS column (30 m x 0.25 mm I.D., 0.25 µm film thickness). The oven temperature applied was initially programmed at 150 °C for 3 minutes. After that, the temperature was raised up to 250 °C at 10 °C per minute. The transfer line and ion source temperature were fixed at 280 °C. Data were collected and quantified in the scan of the mass spectrometer analyzer. The retention time of PHE and FLU were recorded under optimized chromatographic conditions at 8.90 and 11.75 minutes, respectively. Electron impact mass spectra were recorded at 70 eV and the detector voltage was set at 1.0 kV. The chromatographic data were processed using MSD Chemstation E.01.01 Agilent Technology software.

### Samples collection

The optimized UASEME method was applied to the analysis of aqueous matrices. Tap water samples were obtained from the laboratory in the Integrative Medicine Cluster, Advanced Medical and Dental Institute, Universiti Sains Malaysia, Penang. Sugarcane juice samples were purchased from street vendors and local stores in Kedah and Penang, Malaysia. The sugarcane juice samples were centrifuged for 15 minutes at 3500 rpm prior to extraction. The pellet layer was discarded before the microextraction procedure. The samples were filtered through a 0.45 µm Whatman nylon membrane filter to remove unwanted particles and stored in refrigerator (4 °C) prior to use.

### Ultrasound-assisted surfactant enhanced emulsification microextraction

The ultrasound-assisted surfactant enhanced emulsification microextraction (UASEME) procedure is illustrated in Figure 2. Firstly, 15 µL of Tween 20 was added into a 10-mL volumetric flask followed by the addition of 30 µL toluene. Then, 10 mL sample solution spiked with PAHs was immediately added into the volumetric flask. Next, the

mixture was sonicated for 2 minutes. After sonication, two immiscible phases were formed and 20 µL of the upper layer was collected using a micro syringe. Finally, the clean extract was diluted with 80 µL of methanol prior to GC-MS analysis. Quantification for all data was calculated based on the peak area of analytes.

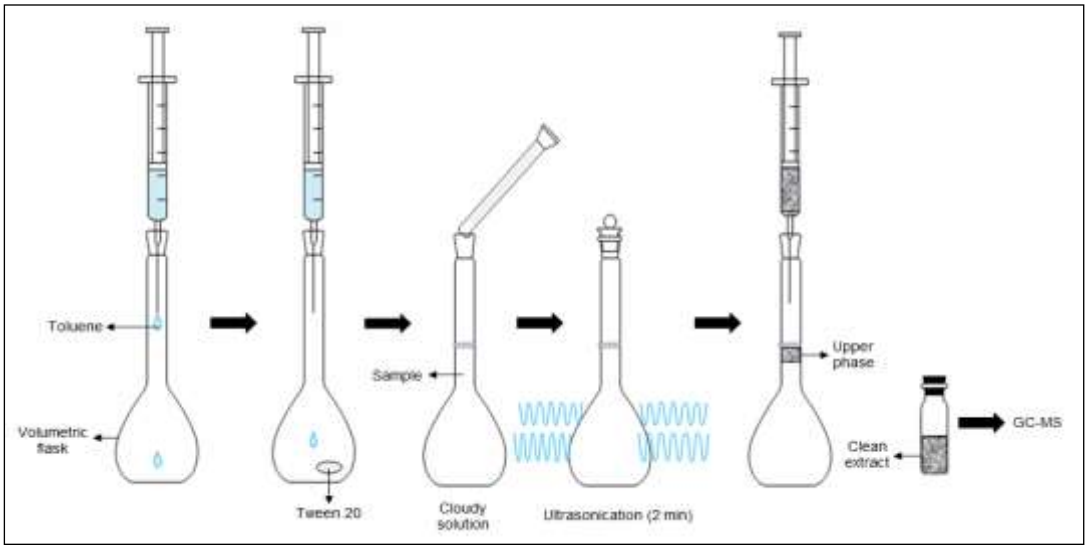



Figure 2. Schematic of UASEME procedure

## Results and Discussion

### Optimization of UASEME procedure

In order to obtain the optimum extraction and detection conditions for FLU and PHE, several parameters that potentially affect the extraction performance of UASEME were thoroughly investigated, namely type and volume of extraction solvent, type and concentration of surfactant, extraction time and salt addition. All optimization parameters were conducted in triplicates using 1000 µg $L^{-1}$ of PHE and FLU spiked in water.

### Effect of type and volume of extraction solvent

A good selection of extraction solvent should meet some important criteria such as (a) less dense than water; (b) low solubility in water; and (c) able to form a stable emulsion system in the presence of an emulsifier after sonication and has the ability to extract the targeted analytes [12, 13]. In this study, four solvents were tested namely toluene, n-hexane, iso-octane and 1-octanol. The result showed that toluene gave the highest extraction efficiency compared to other solvents (Figure 3a). This might probably due to the lower viscosity of toluene, which leads to a rapid and efficient emulsification process [15]. Thus, toluene was selected as the extraction solvent for subsequent experiments.

To optimize the volume of extraction solvent, different volumes of toluene (20, 25, 30, 35, 40, 45, 50, and 55 µL) were evaluated. The results indicated that the peak areas of all analytes reached maximum when using 30 µL of toluene as extraction solvent (Figure 3b). However, the peak areas of all analytes decreased gradually when more volume of toluene was used. This may be due to the dilution effect; as the amount of extraction solvent is increased, the volume of the floating phase (upper phase) will also increase [17]. Therefore, 30 µL of toluene as extraction solvent was used for further analysis.

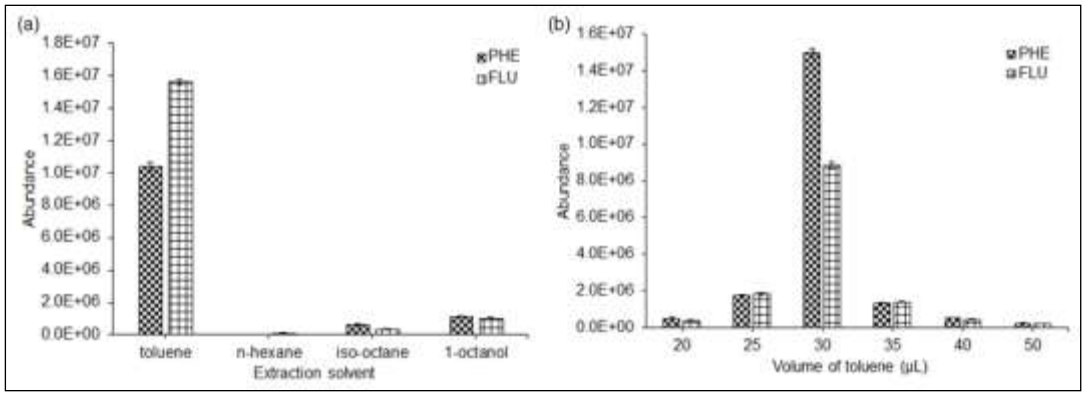



Figure 3. Effect of extraction solvent (a) and volume of toluene (b) on UASEME methods on the extraction of PHE and FLU from spiked water (n = 3 in each case)

**Effect of type and volume of surfactant**

The selection of a suitable surfactant is very crucial in order to obtain higher extraction efficiency for the targeted analytes. Under ultrasound radiation, the surfactant enhances the rate of emulsification process between the water-immiscible extraction solvent and aqueous solution. Upon completion of emulsification process, the extraction solvent is dispersed as fine droplets in the sample solution, which accelerate the mass transfer process of the analytes from the aqueous phase to the organic phases. A suitable hydrophilic-lipophilic balance (HLB) is the primary criterion for the selection of surfactant. The effects of three non-ionic surfactants (Tween 20, Tween 80 and DC193C) on the extraction efficiency of UASEME were investigated. The results showed that Tween 20 gave the highest extraction efficiency for both analytes compared to without the use of surfactant, DC193C and Tween 80 (Figure 4a). The occurrence of this phenomenon may be due to the hydrophobic properties of Tween 20 which interact ideally with the non-polar FLU and PHE compounds. A strong hydrophobic interaction between Tween 80 and PAHs contributed to less extraction efficiency of analytes toward the extraction solvent as indicated by the suppression of GC-MS chromatographic responses.

The volume of surfactant is important in the UASEME method as it will affect the mass transfer rate of the analytes. The effect of Tween 20 amount used was investigated by varying its volume from 0 to 25 µL. Based on the results obtained (Figure 4b), the extraction efficiency began to decrease as the volume of Tween 20 increased. This was probably due to the fractionation of the analytes which was incorporated into the micelle when the surfactant concentration was higher than the CMC, thus increasing the solubility of analytes in the sample solution [18]**.** Therefore, 15 µL of Tween 20 was used in the subsequent extractions.

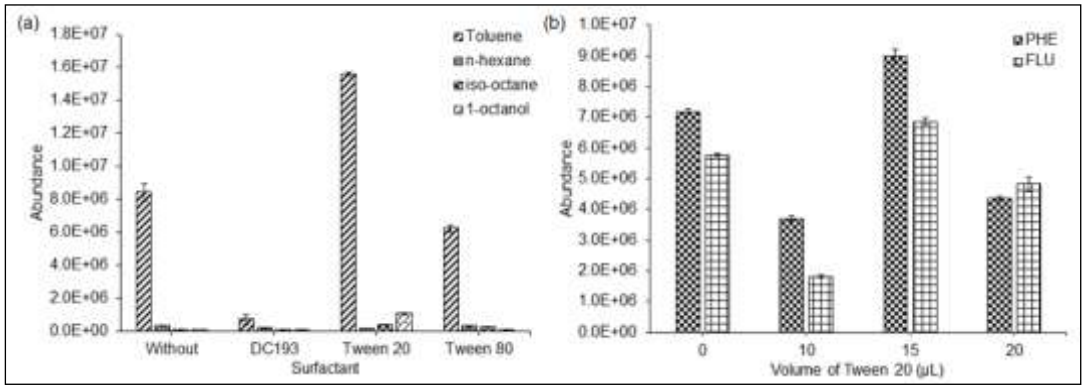



Figure 4. Effect of surfactant (a) and volume of Tween 20 (b) on UASEME methods on the extraction of PHE and FLU from spiked water sample (n = 3 in each case)

**Effect of extraction time and salt addition**

In this study, the interval time from the beginning of the emulsification to the moment before the injection into the vial is known as the ultrasound extraction time. The effect of extraction time in this method was studied over the range from 0 to 5 minutes with other experimental conditions kept constant (Figure 5a). The results showed that the peak area increased continuously from 0 to 2 minutes of extraction time. It revealed that the contact surface between the extraction solvent and aqueous sample was infinitely larger [14]. However, when the extraction time was prolonged to 3 minutes, the extraction efficiency of the analytes decreased. This occurrence was probably due to the longer sonication time which produced heat to the sample vial and caused the analytes' degradation [19]. Hence, 2 minutes was used as the optimum extraction time in the UASEME method.

Generally, the addition of salt into the sample solution may reduce the solubility of polar analytes and enhance their partitioning into the extraction solvent or organic phase. The effect of the NaCl addition on the UASEME method's efficiency was evaluated and studied in the range from 0 to 12% (w/v). The results showed that there was no significant increment with the addition of salt during UASEME (Figure 5b) due to the relatively non-polar characteristics of FLU and PHE. Hence, no salt was added in the subsequent UASEME method analysis.

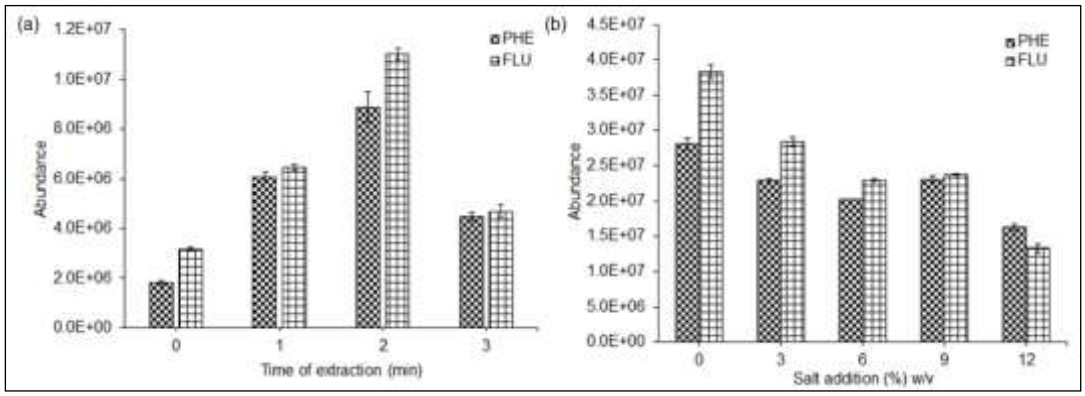



Figure 5. Effect of extraction time (a) and salt addition (b) on UASEME methods on the extraction of PHE and FLU from spiked water sample (n = 3 in each case)

**Method validation**

The analytical performance of the proposed UASEME method was evaluated in terms of its linearity, limits of detection (LODs), limits of quantification (LOQs), precision and recovery under the optimized extraction conditions. Method validation was carried out based on the ICH Harmonised Tripartite Guideline [20]. The calibration curves were plotted in the concentration range between 1 to 1000 µg $L^{-1}$ using at least five spiked concentrations in distilled water. Good linearity was observed for PHE and FLU with the coefficient of determination, $R^2$ of 0.9932 and 0.9968, respectively (Table 1). LODs were calculated as three times the signal-to-noise ratio (S/N = 3) and LOQs were measured as ten times the signal-to-noise ratio (S/N = 10). The LODs and LOQs for PHE and FLU obtained in this study were 0.3 and 1.0 µg $L^{-1}$, respectively. Under the optimized UASEME conditions, the enrichment factors (EFs) of 21.8 and 30.6 were obtained for PHE and FLU, respectively. EF was calculated using the following Equation 1:

$$EF = C_1/C_0 \quad (1)$$

where $C_1$ and $C_0$ are the final concentrations of analytes found in the clean extract and initial concentration in the original sample solution, respectively.

Table 1. Validation data of UASEME method for selected polycyclic aromatic hydrocarbons in spiked water samples

| Analyte | Linear Range (μg $L^{-1}$) | Linear Equation | $R^2$ | LOD (μg $L^{-1}$) | LOQ (μg $L^{-1}$) | EF |
|---|---|---|---|---|---|---|
| PHE | 1 – 1000 | y = 15419 x + 13043 | 0.9932 | 0.3 | 1.0 | 21.8 |
| FLA | 1 – 1000 | y = 5609.9 x - 34604 | 0.9968 | 0.3 | 1.0 | 30.6 |

The analytical characteristics of the proposed UASEME method were compared with other reported methods for the analysis of PAHs in water samples (Table 2). Although the developed method produced a lower sensitivity of analytes compared to most methods used for PAHs determination, the use of 30 μL of toluene and 15 μL of Tween 20 in UASEME is more environmentally friendly and beneficial as an alternative microextraction method for the analysis of PAHs in aqueous samples. In addition, the proposed method is rapid and the extraction process can be accomplished within 5 min, which is useful for routine analyses of PAHs.

Table 2. Comparison of UASEME method with other previously reported methods

| Instrument | Sample Preparation | LOD (μg $L^{-1}$) | Precision (RSD) | Recovery (%) | References |
|---|---|---|---|---|---|
| GC-MS[a] | UASEME[d] | 0.3 | 1.62 – 10.32 | 91.75 – 104.1 | This work |
| GC-MS | SPME[e] | 0.001 – 0.029 | < 20 | - | [21] |
| HPLC-FLD[b] | SBSE[f] | 0.0002 – 0.0015 | 3.2 – 12.8 | 60.1 – 86.8 | [22] |
| GC-MS | USAEME[g] | 0.001 – 0.036 | < 8 | > 92 | [16] |
| GC-MS | AF-LPME[h] | 0.01 – 0.04 | 6.1 – 9.2 | 92.9 – 104.7 | [23] |
| GC-FID[c] | HSME[i] | 4 – 41 | 0.7-19.5 | - | [24] |

[a] Gas chromatography-mass spectrometry,
[b] High performance liquid chromatography-fluorescence detection,
[c] Gas chromatography-flame ionization detection,
[d] Ultrasound-assisted surfactant enhanced emulsification microextraction,
[e] Solid-phase microextraction,
[f] Stir bar sorptive extraction,
[g] Ultrasound-assisted emulsification-microextraction,
[h] Agarose film liquid phase microextraction,
[i] Headspace solvent microextraction

**Real sample analysis**

To evaluate the applicability of the proposed method, the procedure was performed as an analysis of PAHs in one tap water and nine sugarcane juice samples. Analyses of these samples were conducted under the optimum conditions of UASEME. From the blank analyses, no PHE and FLU were detected in all samples. The non-spiked and spiked tap water samples were analysed in triplicate and the typical chromatograms of blank and spiked samples at 100 μg $L^{-1}$ are shown in Figure 6. The accuracy of the developed method was determined by spiking analytes at three different concentration levels (1, 50 and 100 μg $L^{-1}$) into the tap water samples. The relative recovery was calculated as the percentage of mean values of the extracted PAHs peak area (triplicates) against the peak area of PAHs derived from the calibration curve. Table 3 shows a recovery of 91.75 – 104.1% for both analytes with RSDs of 1.62 – 10.32%. The obtained results demonstrated that the proposed UASEME method is applicable for low and high concentrations of PAHs in aqueous matrices.

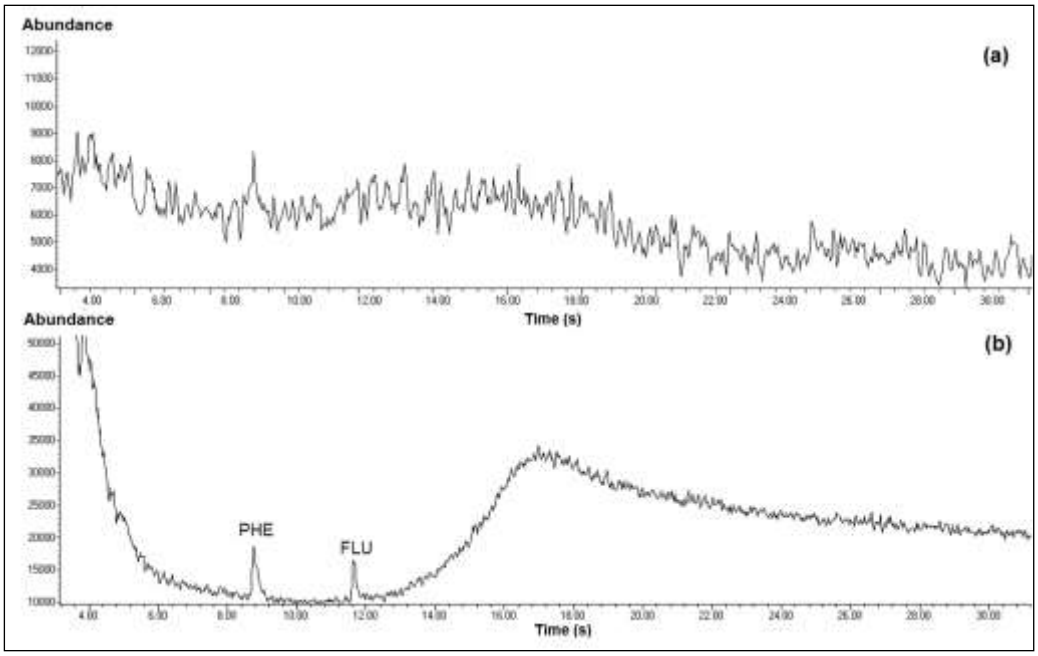



Figure 6. GC-MS chromatograms of PAHs obtained by UASEME under optimized conditions (a) blank tap water (b) spiked tap water at 100 µg $L^{-1}$

Table 3. Recoveries obtained in determination of phenanthrene and fluoranthene in spiked tap water samples by UASEME

| Analyte | Spiked level (µg $L^{-1}$) | Intraday Precision (% RSD), (n = 3) | Concentration Found (µg $L^{-1}$) | Recovery (%) (n = 3) |
|---|---|---|---|---|
| PHE | 0 | - | nd | - |
| | 1 | 6.24 | 0.92 | 91.75 |
| | 50 | 5.71 | 48.84 | 97.67 |
| | 100 | 1.62 | 99.5 | 99.50 |
| FLA | 0 | - | nd | - |
| | 1 | 10.32 | 0.94 | 93.88 |
| | 50 | 9.63 | 49.80 | 99.59 |
| | 100 | 5.08 | 104.1 | 104.1 |

nd: not detected

## Conclusion

In brief, the results indicated that the UASEME method can be used as a simple and efficient sample preparation technique for trace analysis of PAHs in aqueous samples prior to GC-MS analysis. This method also uses a minimum amount of extraction solvent and surfactant for each extraction. Therefore, the new UASEME method can be potentially used as an alternative 'green' microextraction for the detection of PAHs in aqueous matrices. Future investigations can be focused on the combination of the developed method with other microextraction methods such as dispersive micro-solid phase extraction and magnetic solid phase extraction to improve the sensitivity and detection limits of the studied analytes.

**Acknowledgements**

The authors gratefully acknowledge Universiti Sains Malaysia and the Ministry of Education Malaysia for financial support through the Short-Term Grant (304.CIPPT.6313197) and Fundamental Research Grant Scheme (FRGS - 203.CIPPT.6711484).

**References**

1. Rezvani-Eivari, M., Amiri, A., Baghayeri, M. and Ghaemi, F. (2016). Magnetized graphene layers synthesized on the carbon nanofibers as novel adsorbent for the extraction of polycyclic aromatic hydrocarbons from environmental water samples. *Journal of Chromatography A*, 1465: 1 - 8.
2. Wu, Y., Xia, L., Chen, R. and Hu, B. (2008). Headspace single drop microextraction combined with HPLC for the determination of trace polycyclic aromatic hydrocarbons in environmental samples. *Talanta*, 74 (4): 470 - 477.
3. Hossain, M. A., Yeasmin, F., Mizanur Rahman, S. M. and Rana, M. S. (2016). Gas chromatograph-mass spectrometry determination of carcinogenic naphthalene, anthracene, phenanthrene and fluorene in the Bangsai river water of Bangladesh. *Arabian Journal of Chemistry*, 9: 109 - 113.
4. Caruso, M. and Alaburda, J. (2009). Optimization of the benzo (A) pyrene determination procedure in cachaça. *Journal of the Brazilian Chemical Society*, 20(3): 502 - 508.
5. Da Porto, C. and Moret, S. (2007). Comparison of polycyclic aromatic hydrocarbons (PAHs) between smoked marc spirits and whiskies. *Food and Chemical Toxicology*, 45(10): 2069 - 2071.
6. Hosseini, M. H., Rezaee, M., Mashayekhi, H. A., Akbarian, S., Mizani, F. and Pourjavid, M. R. (2012). Determination of polycyclic aromatic hydrocarbons in soil samples using flotation-assisted homogeneous liquid-liquid microextraction. *Journal of Chromatography A*, 1265: 52 - 56.
7. Reza, M., Zanjani, K., Yamini, Y., Shariati, S. and Ake, J. (2007). A new liquid-phase microextraction method based on solidification of floating organic drop. *Analytica Chimica Acta*, 585(2): 286 - 293.
8. Hou, L. and Lee, H. K. (2002). Application of static and dynamic liquid-phase microextraction in the determination of polycyclic aromatic hydrocarbons. *Journal of Chatomatography* A, 976(1-2): 377 - 385.
9. Cacho, J. I, Campillo, N., Viñas, P. and Hernández-córdoba, M. (2016). Evaluation of the contamination of spirits by polycyclic aromatic hydrocarbons using ultrasound-assisted emulsification microextraction coupled to gas chromatography – mass spectrometry. *Food Chemistry*, 190: 324 - 330.
10. Wang, Y., Kwok, Y. C., He, Y. and Lee, H. K. (1998). Application of dynamic liquid-phase microextraction to the analysis of chlorobenzenes in water by using a conventional microsyringe. *Analytical Chemistry*, 70 (21): 4610 - 4614.
11. Regueiro, J., Llompart, M., Garcia-Jares, C., Garcia-Monteagudo, J. C. and Cela, R. (2008). Ultrasound-assisted emulsification-microextraction of emergent contaminants and pesticides in environmental waters. *Journal of Chromatography A*, 1190 (1-2): 27 - 38.
12. Fontana, A. R., Wuilloud, R. G., Martínez, L. D. and Altamirano, J. C. (2009). Simple approach based on ultrasound-assisted emulsification-microextraction for determination of polibrominated flame retardants in water samples by gas chromatography-mass spectrometry. *Journal of Chromatography A*, 1216 (1): 147 - 153.
13. Wu, Q., Chang, Q. and Wu, C. (2010). Ultrasound-assisted surfactant-enhanced emulsification microextraction for the determination of carbamate pesticides in water samples by high performance liquid chromatography. *Journal of Chromatography A*, 1217(11): 1773 - 1778.
14. Veyrand, B., Brosseaud, A. and Sarcher, L. (2013). Development of a novel ultrasound-assisted surfactant-enhanced emulsification microextraction method and its application to the analysis of eleven polycyclic aromatic hydrocarbons at trace levels in water. *Journal of Chromatography A*, 391(2): 363 - 393.
15. Saleh, A., Yamini, Y., Faraji, M., Rezaee, M. and Ghambarian, M. (2009). Ultrasound-assisted emulsification microextraction method based on applying low density organic solvents followed by gas chromatography analysis for the determination of polycyclic aromatic hydrocarbons in water samples. *Journal of Chromatography A*, 1216(39): 6673 - 6679.
16. Ozcan, S., Tor, A. and Aydin, M. E. (2010). Determination of polycyclic aromatic hydrocarbons in waters by ultrasound-assisted emulsification-microextraction and gas chromatography-mass spectrometry. *Analytica Chimica Acta*, 665(2): 193 - 199.

17. Sanagi, M. M., Abbas, H. H., Ibrahim, W. A. W. and Aboul-Enien, H. Y. (2012). Dispersive liquid-liquid microextraction method based on solidification of floating organic droplet for the determination of triazine herbicides in water and sugarcane samples. *Food Chemistry*, 133(2): 557 - 562.
18. Tseng, W., Chen, P. and Huang, S. (2014). Optimization of two different dispersive liquid – liquid microextraction methods followed by gas chromatography – mass spectrometry determination for polycyclic aromatic hydrocarbons (PAHs) analysis in water. *Talanta*, 120: 425 - 432.
19. Mukdasai, S., Thomas, C. and Srijaranai, S. (2014). Two-step microextraction combined with high performance liquid chromatographic analysis of pyrethroids in water and vegetable samples. *Talanta*, 120: 289 - 296.
20. ICH Harmonised Tripartite Guideline Validation of Analytical Procedures. (1994). Text and Methodology. https://www.ich.org/fileadmin/Public_Web_Site/ICH_Products/Guidelines/Quality/Q2_R1/Step4/Q2_R1__Guideline.pdf [Access online 20 January 2015].
21. King, A. J., Readman, J. W. and Zhou, J. L. (2004). Determination of polycyclic aromatic hydrocarbons in water by solid-phase microextraction-gas chromatography-mass spectrometry. *Analytica Chimica Acta*, 523(2): 259 - 267.
22. Bourdat-Deschamps, M., Daudin, J. J. and Barriuso, E. (2007). An experimental design approach to optimise the determination of polycyclic aromatic hydrocarbons from rainfall water using stir bar sorptive extraction and high performance liquid chromatography-fluorescence detection. *Journal of Chromatography A*, 1167(2): 143 - 153.
23. Sanagi, M. M., Loh, S. H., Wan Ibrahim, W. A., Hasan, M. N. (2012). Agarose film liquid phasemicroextraction combined with gas chromatography-mass spectrometry for the determination of polycyclic aromatic hydrocarbons in water. *Journal of Chromatography A*, 1262: 43 - 48.
24. Shariati-Feizabadi, S., Yamini, Y. and Bahramifar, N. (2003). Headspace solvent microextraction and gas chromatographic determination of some polycyclic aromatic hydrocarbons in water samples. *Analytica Chimica Acta*, 489(1): 21 - 31.

*Malaysian Journal of Analytical Sciences, Vol 21 No 4 (2017): 820 - 829*
*DOI: https://doi.org/10.17576/mjas-2017-2104-08*

MALAYSIAN JOURNAL OF ANALYTICAL SCIENCES
*Published by The Malaysian Analytical Sciences Society*
ISSN 1394 - 2506

# EFFECT OF ONE STEP ACTIVATION KOH MODIFIED CARBON IN DIMETHYL CARBONATE TRANSESTERIFICATION REACTIONS

## (Kesan Satu Langkah Pengaktifan KOH Terhadap Karbon Terubahsuai dalam Tindak Balas Transesterifikasi dengan Dimetil Karbonat)

Abdul Rahim Yacob*, Nor Wajihan Muda, Muhammad Azam bin Muhammad Zaki

*Department of Chemistry, Faculty of Science*
*Universiti Teknologi Malaysia, 81310 Skudai, Johor, Malaysia*

**Corresponding author: manrahim@kimia.fs.utm.my*

Received: 20 September 2016; Accepted: 16 May 2017

**Abstract**

In this work one step activation was introduced to potassium hydroxide (KOH) modified palm kernel shells. Various concentration of potassium hydroxide was used to activate and impregnate palm kernel shell before calcined at 600 $^{o}$C for 2 hours. All the prepared samples were characterized using Fourier Transform Infrared spectroscopy (FTIR), Nitrogen Adsorption Analysis and Field Emission Scanning Electron Microscope (FESEM), respectively. The basicity and basic strength of the prepared samples were determined using back titration methods. Following the preparation, the samples were used as base heterogeneous catalyst in palm oil transesterification reaction using dimethyl carbonate (DMC). Analysis of the products were performed using Gas Chromatography-Flame Ionization Detector (GC-FID) while to check the possibility of leaching, that is the presence of potassium in the biodiesel X-ray Fluorescence (XRF) spectroscopy was used. FTIR analysis of the raw palm kernel shell showed the presence of various functional groups. However, after the activation most of the functional groups were eliminated. A high BET surface area of 1054 $m^2$/g was obtained from 10% AC/K, while the BET surface area for 15%, 20% and 25% AC/K decreases. This study shows, as the percentage of one step activation potassium doped carbon increases, the basic strength increases and followed by the increase in biodiesel production with leaching free reaction. The percentage conversion of biodiesel for 10% AC/KOH, 15% AC/KOH, 20% AC/KOH and 25% AC/KOH calculated were 35%, 45%, 63% and 67%, respectively.

**Keywords**: one step activation, dimethyl carbonate, biodiesel, leaching free

**Abstrak**

Dalam kajian ini pengaktifan satu langkah diperkenalkan dengan menggunakan kalium hidroksida (KOH) terubahsuai tempurung kelapa sawit. Pelbagai kepekatan kalium hidroksida digunakan bagi mengaktifkan dan menepukan tempurung kelapa sawit sebelum dikalsin pada 600 $^{o}$C selama 2 jam. Kesemua sampel yang telah disediakan dianalisis mengunakan teknik spektroskopi Inframerah Transformasi Fourier (FTIR), Analisis Penjerapan Nitrogen dan Mikroskopi Medan Pancaran Imbasan Elektron (FESEM). Kebesan dan kekuatan bes sampel yang disediakan ditentukan melalui pentitratan kembali. Sampel yang telah disediakan digunakan sebagai pemangkin bes heterogen untuk transesterifikasi minyak kelapa sawit dengan dimetil karbonat (DMC). Hasil yang didapati dianalisis dengan menggunakan Gas Kromatografi – Pengesan Pengionan Nyala (GC-FID) manakala untuk mengkaji kemungkinan larut resap iaitu kehadiran kalium dalam biodiesel, spektroskopi sinar-X pendarflour (XRF) digunakan. Analisis FTIR tempurung kelapa sawit mentah menunjukkan kehadiran pelbagai kumpulan berfungsi. Walaubagaimanapun, selepas pengaktifan dan karbonisasi, kebanyakan kumpulan berfungsi ini telah disingkirkan. Luas permukaan BET yang tinggi iaitu 1054 $m^2$/g telah diperolehi daripada 10% AC/KOH, manakala luas permukaan BET untuk 15%, 20% dan 25% AC/KOH menurun. Hasil kajian menunjukkan apabila peratus penepuan karbon dalam pengaktifan satu langkah oleh kalium meningkat, kekuatan bes turut meningkat diikuti oleh peningkatan hasil biodiesel dalam tindak balas bebas

larut resap. Peratus penukaran biodiesel untuk 10% AC/K, 15% AC/K, 20% AC/K dan 25% AC/K adalah masing-masing 35%, 45%, 63% dan 67%.

**Kata kunci:** pengaktifan satu langkah, dimetil karbonat, biodiesel, bebas larut resap

## Introduction

Activated carbons (AC) are important material, which have been widely used in various industrial applications, which include separation/purification of liquid or gas and removal of heavy metal [1]. In the preparation of heterogeneous catalyst, activated carbon has proved to be highly effective as catalyst support. Activated carbon can be produced from a variety of raw material mostly coal and agricultural by products or lignocellulosic materials. Production of activated carbon from agricultural by products is preferable since it is more cost effective. There are numerous study regarding the production of activated carbon from agricultural by products such as coconut shell [2, 3], pistachio nut shell [4], sugar cane Bagasse [5], olive stones [6] and macadamia nut-shell [7]. Palm kernel shell (PKS) is one of the most abundant agricultural waste produce since palm oil industry is one of the major industries in Malaysia. Hence, palm kernel shell would be a better choice to be utilized for the raw material in the production of activated carbons.

Due environmental concerns, biodiesel has received many attentions to be used as an alternative diesel fuel since it has a unique advantage such as being biodegradable, non-toxic and suitable for domestic production. Biodiesel is a mono alkyl ester of long chain fatty acids obtain from transesterification reaction of triglyceride such as vegetable oil or animal fat with simple alcohol as shown in Figure 1.

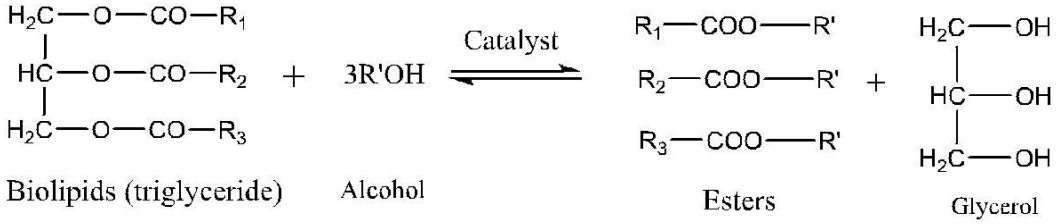



Figure 1. Transesterification of triglyceride with alcohol

Glycerol is produce as the undesired by product in this reaction. The separation process of glycerol could be costly and technically difficult. In this study dimethyl carbonate (DMC) will be introduced as a reagent to replace alcohol in the transesterification reaction. Free glycerol biodiesel can be obtained because fatty acid glycerol carbonates (FAGCs) is form and can be easily remove from the biodiesel as shown in Figure 2.

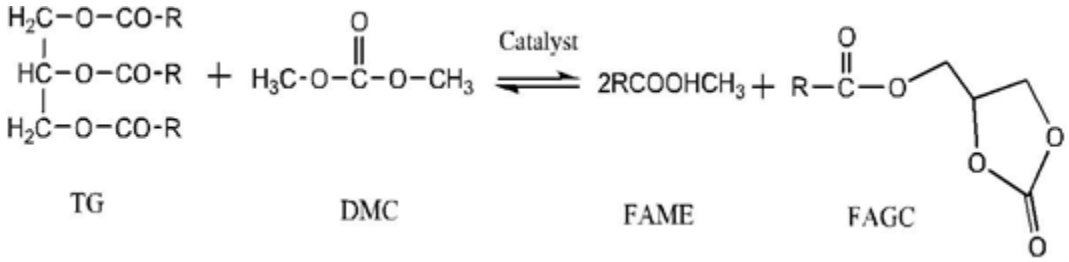



Figure 2. Transesterification of triglyceride with DMC

Another problem normally occur in the production of biodiesel is leaching [8]. In conventional method, normally part of the alkali metal catalyst would leach into the biodiesel, thus reducing the biodiesel quality. The removal of

the catalyst would require a series of repeated washing and this will contribute to environmental problem. By immobilizing the catalyst in a suitable support can prevent the leaching problem and therefore separation can be easily done through centrifugation or filtration.

In this study, activated carbon from palm kernel shell was produced through one-step activation using potassium hydroxide (KOH) as activating agent Potassium doped activated carbon (AC/K) were then tested as a potential heterogeneous base catalyst in production of biodiesel from palm oil. In addition, by considering the advantages offered by DMC, it was chosen as a reagent and reactant in this reaction replacing alcohol.

## Materials and Methods

This locally available palm kernel shell (PKS) were collected from the Kulai palm oil mill. Refined oil was purchased from local markets. Potassium hydroxide (KOH), n-hexane, n-heptane were purchased from QREC while dimethyl carbonate and 37% HCL were purchased from MERCK.

### Preparation of AC/K catalyst

The base activation was carried out by using a liquid state KOH impregnation at different concentration. KOH solution at 10%, 15%, 20%, and 25% concentration were prepared by dissolving KOH pallets in deionized water in a 100-mL volumetric flask. About 10g of dried PKS were impregnated with different percentage concentration of KOH in a hot plate and stirred for 5 hours and dried in an oven overnight at 100 $^{o}$C. The impregnated carbon was further calcined in a furnace at 600 $^{o}$C for 2 hours and finally dried in an oven for 24 hours. All the samples were labeled as 10% AC/K, 15% AC/K, 20% AC/K and 25% AC/K according to the respective KOH percentage concentration.

### Transesterification reaction with DMC

The reaction was conducted by mixing the palm oil and DMC with a 1:9 ratio in a two-necked 250-mL round bottom flask immersed in paraffin oil to control the temperature. The flask is equipped with a reflux and a magnetic stirrer. Firstly, the catalyst was added to the DMC and vigorously stirred with slight heating for 30 minutes until completely dissolved. About 10 g of palm oil were added into the mixture of catalyst and DMC then the mixture was refluxed at temperature close to the boiling point of DMC (80 – 90$^{o}$C). The reaction condition for are based on methodology reported by previous study [9,10]. After reflux, the mixture allowed to cool at room temperature and transferred into 15ml centrifuge tube. The mixture was centrifuged at 3000rpm for 30 minutes to separate the excess DMC and catalyst from the solution. The biodiesel was then collected for characterization by filtering out the catalyst.

All materials were characterized using Thermogravimetric Analyzer (TGA), Fourier Transform Infrared (FTIR), Nitrogen Adsorption Analysis-(BET) surface area, Field Emission Scanning Electron Microscope (FESEM) and Energy Dispersive X-ray fluorescence (XRF). While the transesterification reaction of palm oil with DMC to produce biodiesel was performed using gas chromatography – flame ionization (GC – FID) and Gas Chromatography – mass spectrometry (GC-MS).

## Results and Discussion

### Thermogravimetry analysis of raw palm kernel shell

Thermogravimetry analysis (TGA) is commonly used to study the thermal decomposition of agricultural by product. Raw palm kernel shell was first analyzed using diamond TG/DTA Perkin Elmer to estimate the optimum carbonization temperature for the activation process. Figure 3 shows the TGA thermogram of raw-PKS subjected in a temperature range 50 – 800 $^{o}$C at a heating rate of 10 $^{o}$C/min under air flow and nitrogen gas flow.

From the thermogram shown in Figure 3, there are various weight losses which can be separated into four different stages from stage I to IV. During stage I, 11.5% of weight loss occurred at the temperature of 50 – 130 $^{o}$C. This is due to the elimination of moisture in the raw material. Major weight loss of 47.4% occurs at temperature range from 240 – 360 $^{o}$C which is at stage II. It is assumed that the decomposition of the major components of lignocellulose biomass including hemicellulose, cellulose and lignin occur at this stage [11]. In stage III, at temperature of 360 °C to 450 °C, it shows the final decomposition or weight loss which corresponding to lignin decomposition and

charcoal oxidation. The percentage weight lost recorded at this region were 16% and it is believed that most of these lignocellulosic materials in raw-PKS were decomposed. As reported by some researchers, lignin was gradually lost at temperature from 200 °C to 720 °C [12].

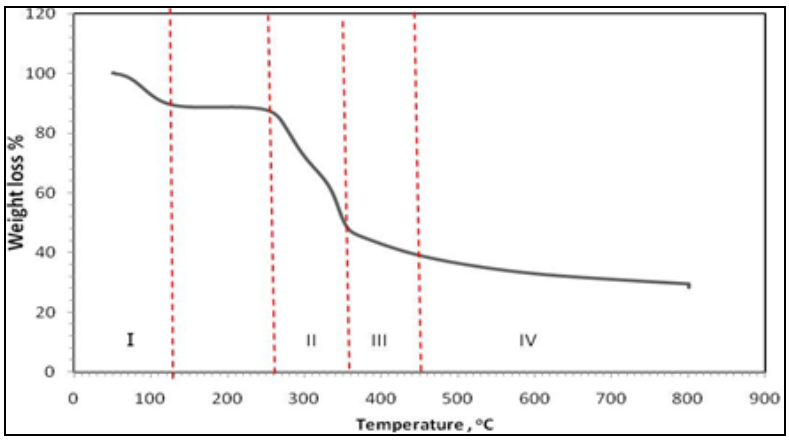



Figure 3. TGA curve of raw PKS

No significant change in weight loss on the stage IV for at which the temperature is around 450 °C. Total weight loss occurs at 800 °C. This is probably caused by the formation of volatile tar as the predominant product during the volatilization [13]. It is also believed that the organic compound in raw samples was completely carbonized at 500 °C. To ensure complete decomposition of organic compounds and liberation of volatile temperature for activation of activated carbon was set at 600 °C.

**Fourier transfer infrared spectroscopy analysis**

Fourier transfer infrared spectroscopy (FTIR) was employed to identify the variety of functional group presence in the raw-PKS and activated carbon. It also provides information on the effect of the activation process that has been carried out as an evidence of the phase transformation which occurred in both raw-PKS and AC/K catalyst. Figure 4 shows the spectra of raw-PKS and the prepared 10%, 15%, 20% and 25% AC/K catalyst.

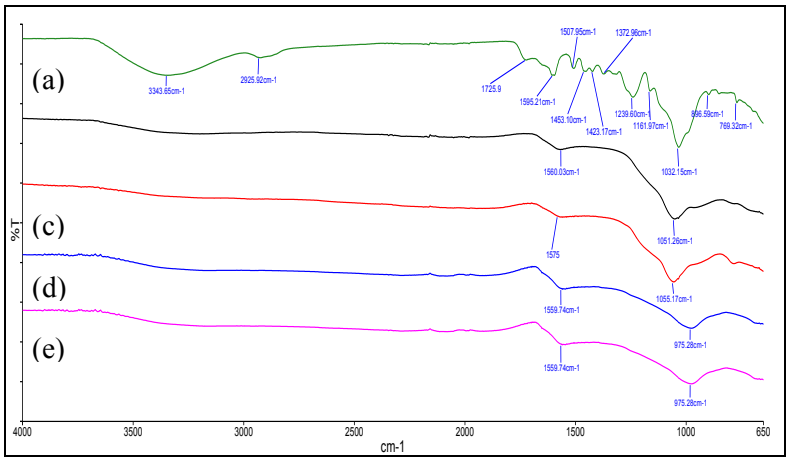



Figure 4. FTIR spectrum of (a) raw-PKS (b) 10%AC/K (c) 15%AC/K (d) 20%AC/K (e) 25%AC/K

Raw-PKS shows additional extra bond compares to AC/K. These extra bands are at 3343 $cm^{-1}$ which is usually assign to hydrogen bond OH group [6]. The absorption band at 2025.92 $cm^{-1}$ which was due to the C-H stretching in

methyl and methylene groups. This band is different to the C-H vibrations band for $–CH_3$-and $CH_2=$, which are located around 1372.96 $cm^{-1}$ and 1453.10 $cm^{-1}$, and is very useful for identifying the methylene and methyl groups in each compound [14]. Moreover, peak at 1735 $cm^{-1}$ which represents the stretching of (C=O) carbonyl groups. The bands at 1595.21 $cm^{-1}$, 1507.95 $cm^{-1}$ and 1423 $cm^{-1}$ indicated the presence of C=C stretching of aromatic compounds. Another peak at 1239.90 $cm^{-1}$ and a subsequent small rise in 1161.97 $cm^{-1}$ could be assigned to the stretching of C-O in ester, ethers or phenol groups. The strong band at 1032.15 $cm^{-1}$ could be attributed to the (C-OH) alcohols group. From the analysis of the FTIR spectrum, carbonyl group, ether, esters, alcohols and the phenol groups can be suggested as the main oxygen group present in the raw PKS. This result supported by the thermogram of TGA analysis. The spectrum of raw PKS is quite similar to the study reported by previous study [15].

However, for the prepared AC/K at 10%, 15%, 20% and 25% concentration spectra illustrated less absorption peak compared with raw-PKS. From the spectra, it can be observed that most of the absorption peaks of functional groups were disappeared. This phenomenon might be explained as the process of carbonization in which most of the functional group presented in the raw-PKS were evaporated as volatile materials upon heating which indicated the activation process have taken place [16]. The spectra of prepared 10%, 15%, 20% and 25% AC/K showed a decreasing trend in the broad peak of C-O around 900-1300 $cm^{-1}$ and the C=C absorption band around 1500 –1650 $cm^{-1}$. This result in agreement by the previous studies [11, 17] indicating that by increasing the amount of activating agent, the activation reaction would increase and more weak bonds disappeared by thermal degradation.

**Nitrogen adsorption analysis**

The single point nitrogen gas adsorption characterization was performed to study the surface area of the prepared AC/K catalyst. The specific BET surface area, SBET of 10% AC/K, 15% AC/K, 20% AC/K and 25% AC/K samples are shown in Figure 5.

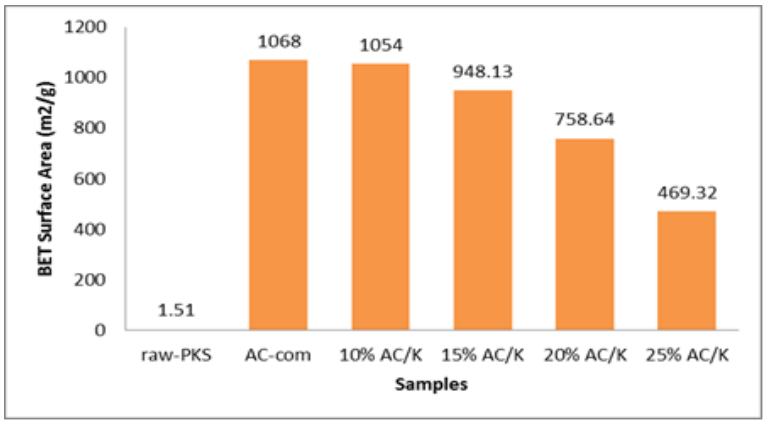



Figure 5. Single point BET surface area of raw PKS, AC-Com and prepared AC/K

Lowest surface area is shown in the raw-PKS which is 1.51 $m^2/g$. This is because of the dense structure of raw-PKS with lack of pores. After activation, there is an increase in the surface area of the activated carbon. This shows that potassium hydroxide, KOH successfully act as an activating agent. However, there is a significant reduction in the specific BET surface area as the percentage concentration of KOH loading increases from 10% to 25%. Further increased in percentage of KOH loading caused the surface area of other activated carbons to decrease. The reduction of BET surface area may be caused by the filling of potassium hydroxide molecules into the pores of the activated carbon. The excessive amounts of KOH would promote a vigorous gasification reaction and diminished the carbon framework leading to a dramatic decrease of accessible area. Besides, an excessive KOH molecule might decompose following the reactions in equation 1 and 2 [18,19].

$$2KOH \rightarrow K_2O + H_2O \quad (1)$$

$$H_2O + C \rightarrow CO + H_2 \quad (2)$$

**Field emission electron microscope**

The morphological structure of raw-PKS and AC/K was characterized by field emission electron microscope (FESEM). Information on the structural change in the raw-PKS before and after activation we thoroughly studied. Figure 6 shows the FESEM micrographs of raw-PKS with 2.50KX magnifications. A dense and planar image with some occasional cracks can be seen. This mainly due to high percentage composition of lignin, a phenolic polymer that provides structural strength to the plant and give its hard and rough wood like structure.

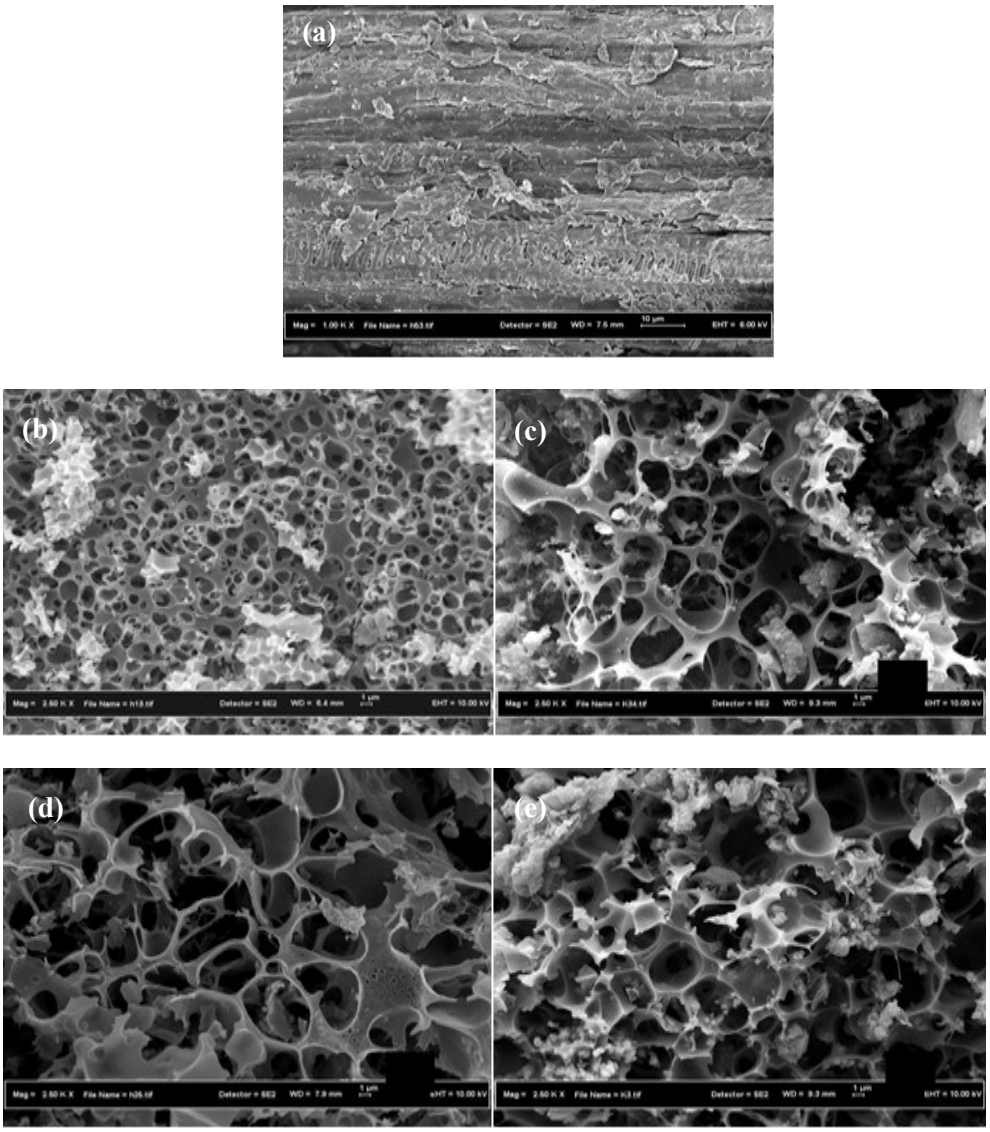



Figure 6. FESEM image of (a) raw PKS (b) 10%, (c) 15%, (d) 20% and (e) 25% AC/K with magnification of 2.50KX

Figure 6 (a – d) shows the FESEM micrograph at 2.50KX magnification of prepared AC/K at 10%, 15%, 20% and 25% concentration respectively. The FESEM micrographs reveal the presence of cavities and pores with different size and shapes. The development of pore and cavities in the AC/K is the result of the release of volatile

components and the evaporation of KOH from the spaces, which were previously occupied by the reagent. Pore structure is one of the important characteristic in the heterogeneous catalysis process as the pore structure helps in the dispersion of the catalytic species throughout the carbon and thus increasing the catalytic performance [20]. The development of porosity by KOH activation is associated with the gasification reaction and formation of potassium species such as potassium dioxide, potassium carbonate and hydrogen [21]. However, as the percentage concentration of potassium hydroxide increase, a larger and wider pore can be seen. Beyond the optimum value, the excessive KOH would promote vigorous gasification reaction and may cause the excessive carbon burn-off, which can destroy the carbon framework, which collapse of some pore walls leading to a dramatic decrease of accessible area [22].

**Back titration analysis**

Determination of the amount of the basic site of the prepared AC/KOH catalyst was performed by the back titration method. This method was suggested in determining the amount of basic site of the bulk catalyst [23]. This analysis is important to identify the best prepared AC/KOH. Their basicity should be known first before applying as a catalyst for transesterification reaction. Figure 7 shows the amount of basic sites recorded in millimole per gram for the prepared 10% AC/K, 15% AC/K, 20% AC/K and 25% AC/K, respectively.

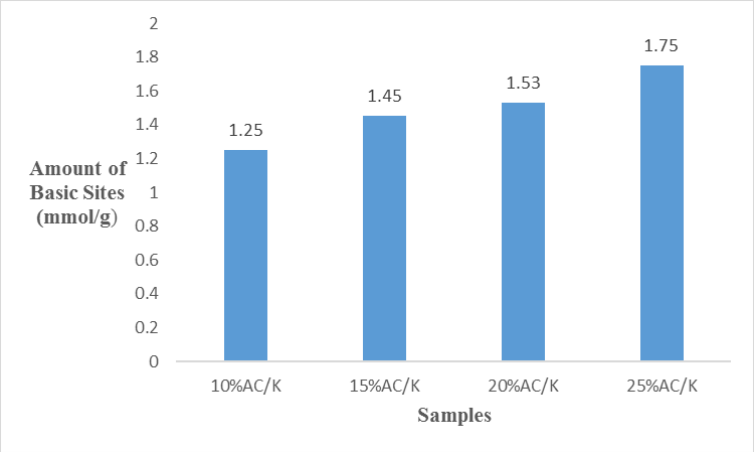



Figure 7. Amount of basic site of prepared AC/K catalyst

From the Figure 7, 25% AC/K shows highest amount of basic site of 1.75 mmol/g, follow by 20% AC/K and 15% AC/K, which have a basic site of 1.53 and 1.45 mmol/g respectively. While for 10% AC/K it shows a lower basic site of 1.25 mmol/g. It was found that the basic site increase with increase of percentage of KOH concentration. In addition, KOH can decompose into potassium species such as potassium oxide that acts as active site, which probably contribute to the basicity of the catalyst. Thus, increase the amount of KOH loading will probably increases the production of active site. This result in agreement with studies reported by Intarapong et al. [24], which found that the basicity and the activity of the catalyst increased with increased of the potassium loading to the $ZrO_2$.

**Analysis and determination of transesterification product**

The biodiesel obtained from the reaction process was analyzed to investigate the effectiveness of 10%, 15%, 20% and 25% AC/K as catalyst to catalyze the transesterification reaction of palm oil with DMC. Gas chromatography method was used for analysis and for the confirmation of the components in biodiesel produced. The biodiesel, which is fatty acid methyl esters (FAMEs), was firstly analyzed by GC-FID to determine the percentage conversion.

Figure 8 shows typical example of the GC chromatogram of the FAMEs. The elution order for the FAMEs obtain in the transesterification reaction with different percentage concentration catalyst is similar. The composition of FAME obtained including Methyl myristate (C14:0), Methyl palmitate (C16:0), Mehyl stearate (C18:0), Methyl

oleate (C18:1) and Methyl linoleate (C18:2). Methyl palmitate and Methyl oleate are the main methyl esters for palm oil biodiesel. While Methyl myristate, Methyl stearate and Methyl limoleate exist in small percentage of the biodiesel. This data agrees with data reported in previous works [25,26].

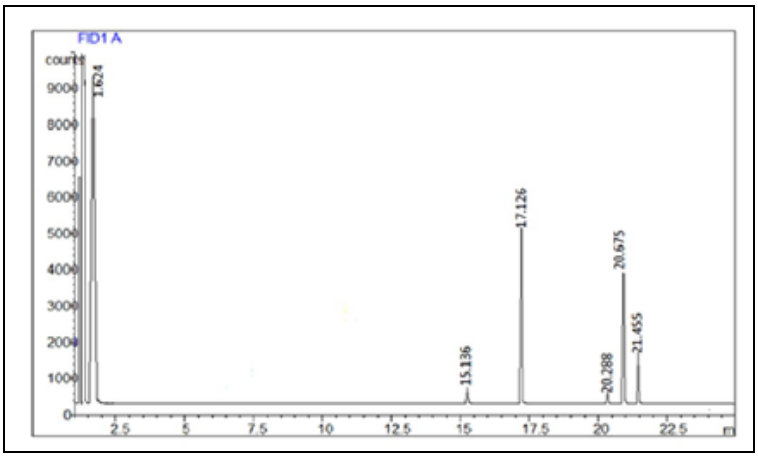



Figure 8. GC chromatograms of biodiesel using 25% AC/K catalyst

From the chromatogram obtained, percentage conversion of the biodiesel was calculated. Besides that, X-ray Fluorescence (XRF) analysis were done to determine the possibility of potassium leaching into the biodiesel after the reaction. Table 3.1 shows percentage conversion and the potassium content in the biodiesel produced from prepared 0% AC/K, 10% AC/K, 15% AC/K, 20% AC/K and 25% AC/K.

Table 1. Percentage conversion and potassium content of the biodiesel

| Samples | Percentage Conversion (%) | Potassium (wt.%) |
|---|---|---|
| AC-Com | 0 | ND |
| 10%AC/K | 35 | ND |
| 15%AC/K | 45 | ND |
| 20%AC/K | 63 | ND |
| 25%AC/K | 67 | ND |

ND: not detected

An increasing trend can be seen in the percentage conversion of biodiesel. For 10% AC/K, 15% AC/K, 20% AC/K and 25% AC/K the percentage conversion of biodiesel were 35%, 45%, 63% and 67% respectively. As the basicity of the catalyst used increase, the percentage conversion also increases. In addition, this proved that the production of biodiesel does not always depend on the surface area of the catalyst as reported in previous studies [26, 27]. As for the XRF analysis, it shows that there is no potassium content detected in the biodiesel after the reaction. This showed that by using DMC, the alkali catalyst in the one step activated KOH modified carbon do not dissolve or leach out into the reaction medium.

## Conclusion

The prepared AC/K KOH was identified and could be an effective and potential heterogeneous base catalyst in transesterification of palm oil and DMC. The used of DMC in this reaction can prevent the leaching of KOH into the biodiesel and the transesterification produced glycerol free-FAME. The percentage conversion of biodiesel for

10% AC/K, 15% AC/K, 20% AC/K and 25% AC/K were 35%, 45%, 63% and 67%, respectively. Highest percentage conversion was obtained from 25% AC/K, although it has the lowest surface area compared with others. This showed that, the production of methyl ester in biodiesel not always depend on the large surface area. In addition, from the study, it shown that the basicity and the basic strength of the prepared AC/K play an important role in the catalytic performance of the catalyst. Increase in the basicity and basic strength of the catalyst. Higher percentage loading of potassium increased the basicity of the catalyst, which gives a significant impact to the percentage conversion of biodiesel.

**Acknowledgement**

The authors gratefully acknowledge the Chemistry Department, University Teknologi Malaysia and the International Conference on Catalyst (iCAT 2016) in helping for publication of this work.

**References**

1. Largitte, L., Brudey, T., Tant, T., Dumesnil, P. C. and Lodewyckx, P. (2015). Comparison of the adsorption of lead by activated carbons from three lignocellulosic precursors. *Microporous and Mesoporous Materials*, 219: 265 – 275.
2. Mohd Iqbaldin, M. N., Khudzir, I., Mohd Azlan, M. I., Zaidi, A. G., Surani, B. and Zubri, Z. (2013). Properties of coconut shell activated carbon. *Journal of Tropical Forest Science*, 25(4): 497 – 503.
3. Govind Raj, K. and Alias Joy, P. (2015). Coconut shell based activated carbon–iron oxide magnetic nanocomposite for fast and efficient removal of oil spills. *Journal of Environmental Chemical Engineering*, 3(3): 2068 – 2075.
4. Xu, J., Gao, Q., Zhang, Y., Tan, Y., Tian, W., Zhu, L. and Jiang, L. (2014). Preparing two-dimensional microporous carbon from pistachio nutshell with high areal capacitance as supercapacitor materials. *Scientific Reports*, 4: 5545 – 5551.
5. Foo, K. Y., Lee, L. K. and Hameed, B. H. (2013). Preparation of activated carbon from sugarcane bagasse by microwave assisted activation for the remediation of semi-aerobic landfill leachate. *Bioresource Technology*, 134: 166 – 172.
6. Bohli, T., Ouederni, A., Fiol, N. and Villaescusa, I. (2015). Evaluation of an activated carbon from olive stones used as an adsorbent for heavy metal removal from aqueous phases. *Comptes Rendus Chimie*, 18(1): 88 – 99.
7. Rodrigues, L. A., De Sousa Ribeiro, L. A., Thim, G. P., Ferreira, R. R., Alvarez-Mendez, M. O. and Coutinho, A. D. R. (2013). Activated carbon derived from macadamia nut shells: an effective adsorbent for phenol removal. *Journal of Porous Materials*, 20 (4): 619 – 627.
8. Di Serio, M., Tesser, R., Casale, L., D'apos;Angelo, A., Trifuoggi, M. and Santacesaria, E. (2010). Heterogeneous catalysis in biodiesel production: the influence of leaching. *Topics in Catalysis*, 53(11-12): 811 – 819.
9. Fabbri, D., Bevoni, V., Notari, M. and Rivetti, F. (2007). Properties of a potential biofuel obtained from soybean oil by transmethylation with dimethyl carbonate. *Fuel*, 86 (5-6): 690 – 697.
10. Zhang, L., Sheng, B., Xin, Z., Liu, Q. and Sun, S. (2010). Kinetics of transesterification of palm oil and dimethyl carbonate for biodiesel production at the catalysis of heterogeneous base catalyst. *Bioresource Technology*, 101(21): 8144 – 8150.
11. Buasri, A., Chaiyut, N., Loryuenyong, V., Phakdeepataraphan, E., Watpathomsub, S. and Kunakemakorn, V. (2013). Utilization of biodiesel wastes as a bioresource for the preparation of activated carbon. *International Journal of Applied Physics and Mathematics*, 3(3): 173 – 177.
12. Hayashi, J., Horikawa, T., Takeda, I., Muroyama, K. and Nasir Ani, F. (2002). Preparing activated carbon from various nutshells by chemical activation with $K_2CO_3$. *Carbon*, 40(13): 2381 – 2386.
13. Hanapi, S. Z., Masrom, N. I. and Yacob, A. R. (2010). Tungsten carbide synthesis by microwave-induced alloying using phosphoric acid activated palm kernel shell carbon. *Journal of Materials Science and Engineering,* 4(4): 68 – 73.
14. Shoaib, M. and Al-Swaidan, H.M. (2015). Optimization and characterization of sliced activated carbon prepared from date palm tree fronds by physical activation. *Biomass and Bioenergy*, 73: 124 – 134.
15. Misnon, I. I., Zain, N. K. M., Aziz, R. A., Vidyadharan, B. and Jose, R. (2015). Electrochemical properties of carbon from oil palm kernel shell for high performance supercapacitors. *Electrochimica Acta*, 174: 78 – 86.

16. Yacob, A. R., Majid, Z. A., Sari, R. and Dasril, D. (2008). Comparison of various sources of high surface area carbon prepared by different types of activation. *Malaysian Journal of Analytical Sciences*, 12(1): 264 – 271.
17. Mopoung, S., Moonsri, P., Palas, W. and Khumpai, S. (2015). Characterization and properties of activated carbon prepared from tamarind seeds by KOH activation for Fe(III) adsorption from aqueous solution. *The Scientific World Journal*, 2015: 1 – 9.
18. Ahmadpour, A. and Do, D. D. (1997). The preparation of activated carbon from macadamia nutshell by chemical activation. *Carbon*, 35(12): 1723 – 1732.
19. Cao, Q., Xie, K. C., Lv, Y. K. and Bao, W. R. (2006). Process effects on activated carbon with large specific surface area from corn cob. *Bioresource Technology*, 97(1): 110 – 115.
20. Konwar, L. J., Boro, J. and Deka, D. (2014). Review on latest developments in biodiesel production using carbon-based catalysts. *Renewable and Sustainable Energy Reviews*, 29: 546 – 564.
21. Gu, Z. and Wang, X. (2013). Carbon materials from high ash biochar: A nanostructure similar to activated graphene. *American transactions on Engineering & Applied sciences*, 2(1): 15 – 34.
22. Jin, H., Lee, Y. S., and Hong, I. (2007). Hydrogen adsorption characteristics of activated carbon. *Catalysis Today*, 120(3-4): 399 – 406.
23. Intarapong, P., Iangthanarat, S., Phanthong, P., Luengnaruemitchai, A. and Jai-In, S. (2013). Activity and basic properties of KOH/mordenite for transesterification of palm oil. *Journal of Energy Chemistry*, 22 (5): 690 – 700.
24. Intarapong, P., Iangthanarat, S., and Luengnaruemitchai, A. (2014). Biodiesel production from palm oil using potassium hydroxide loaded on $ZrO_2$ catalyst in a batch reactor. *Chiang Mai Journal of Science*, 41(1): 128 – 137.
25. Ivanoiu, A., Schmidt, A., Peter, F., Rusnac, L. M., and Ungurean, M. (2011). Comparative study on biodiesel synthesis from different vegetables oils. *Chemical Bulletin of "POLITEHNICA" University (Timisoara).*, 56 (70): 94 – 98.
26. Irmawati, R., Shafizah, I., Sharina, A.N., and Ahangar, H. A. (2014). Transesterification of palm oil by using silica loaded potassium carbonate ($K_2CO_3/SiO_2$) catalysts to produce fatty acid methyl esters (FAME). *Energy and Power*, 4(1): 7 – 15.
27. Singh, A. K. and Fernando, S. D. (2008). Transesterification of soybean oil using heterogeneous catalysts, *Energy & Fuels*, 9(5): 2067 – 2069.

*Malaysian Journal of Analytical Sciences, Vol 21 No 4 (2017): 830 - 838*
*DOI: https://doi.org/10.17576/mjas-2017-2104-09*

MALAYSIAN JOURNAL OF ANALYTICAL SCIENCES
*Published by The Malaysian Analytical Sciences Society*
ISSN 1394 - 2506

# CHARACTERIZATION AND DEACIDIFICATION OF ACIDIC PETROLEUM CRUDE OIL UTILIZING METAL OXIDE CATALYST SUPPORTED ON ALUMINA AND AMMONIATED POLYETHYLENE GLYCOL SOLUTION

## (Pencirian dan Penyahasidan Minyak Mentah Petroleum Menggunakan Mangkin Logam Oksida Disokong Alumina dan Larutan Ammonia Polietilena Glikol)

Nurasmat Mohd Shukri, Jafariah Jaafar*, Wan Azelee Wan Abu Bakar, Zaiton Abdul Majid

*Department of Chemistry, Faculty of Science,*
*Universiti Teknologi Malaysia, 81310 UTM Johor Bahru, Johor, Malaysia*

**Corresponding author: jafariah@kimia.fs.utm.my*

Received: 20 September 2016; Accepted: 16 May 2017

**Abstract**

The presence of naphthenic acid (NA) in petroleum crude oil may cause serious corrosion problem for refinery processing equipment. In this work, an alternative method to remove NA is investigated based on the catalytic deacidification reaction to achieve the target of lowering the total acid number (TAN) as required by PETRONAS to be less than 1. Ammoniated polyethylene glycol ($NH_3$-PEG) was formulated as a deacidifying agent with various concentrations ranging from 100 – 1000 mg/L for crude oil. Cerium oxide based catalyst supported on alumina was synthesized via wet impregnation method and characterized using X-ray diffraction spectroscopy (XRD), Brunauer–Emmett–Teller (BET) and thermogravimetry analysis-differential thermal analysis (TGA-DTA). Parameters such as amount of basic chemical dosing, type of metal oxides, catalyst calcination temperature and reusability of catalyst on the removal of NA was studied. The results showed the TAN value for crude oil was reduced by 70.6% to a TAN of 0.74 mg KOH/g by using 1000 mg/L of $NH_3$-PEG dosing aids by $Ce/Al_2O_3$ catalyst calcined at 1000 $^oC$.

**Keywords**: total acid number, naphthenic acid, metal oxide catalyst, ammoniated polyethylene glycol, alumina

**Abstrak**

Kehadiran asid naftenik (NA) dalam minyak mentah boleh menyebabkan masalah hakisan yang serius kepada peralatan pemprosesan penapisan. Di dalam kajian ini, satu kaedah alternatif untuk menyingkir NA telah disiasat berdasarkan tindak balas penyahasidan pemangkin untuk mencapai sasaran jumlah nombor asid (TAN) kurang daripada 1 seperti yang dikehendaki PETRONAS. Larutan ammonia polietilena glikol ($NH_3$-PEG) telah diformulakan sebagai ejen penyahasidan dengan pelbagai kepekatan antara 100 – 1000 mg/L. Mangkin serium oksida disokong dengan alumina telah disintesis menggunakan kaedah pengisi tepuan basah dan dicirikan menggunakan spektroskopi pembelauan sinar-X (XRD), Brunauer–Emmett–Teller (BET) dan analisis termogravimetri – analisis pengkamiran terma (TGA-DTA). Parameter seperti jumlah dos kimia bes, jenis logam oksida, suhu pengkalsinan mangkin dan kebolehgunaan mangkin terhadap penyingkiran NA telah dikaji. Hasil kajian menunjukkan nilai TAN bagi minyak mentah telah dikurangkan sebanyak 70.6% kepada TAN 0.74 mg KOH/g dengan menggunakan 1000 mg/L dos $NH_3$-PEG dibantu oleh mangkin $Ce/Al_2O_3$ dikalsinkan pada 1000 $^oC$.

**Kata kunci:** nombor jumlah asid, asid naftenik, mangkin, ammonia polietilena glikol, alumina

## Introduction

The initial concern about naphthenic acid corrosion dates back to the previous century, and it keeps drawing the attention of refineries until today [1]. Naphthenic acid (NA) is a complex mixture of cyclic or acyclic aliphatic organic compounds characterized by a carboxyl reactive group [2] and constitutes about 50 wt.% of the total acidic compounds in crude oil [3].Total acid number (TAN) refers to the amount of NA found in the crude oil and was measured using ASTM D664 method. TAN represents milligram of KOH per gram liquid needed to neutralize 1 g of acid present in the sample. If the acidic species in the petroleum cannot be removed during the refinement, it will influence the quality of the final product, causing problems, equipment failures, and environmental pollution. Several efforts are focused on the development of the current approaches to refine acidic crudes by blending with non-acidic crudes so that the TAN of the blend is no higher than about 0.5 mg KOH/g [4]. The drawback of this approach is that it limits the amount of acidic crude that can be processed. The acidic crudes can be treated with inorganic bases such as potassium and sodium hydroxide to neutralize the acids [5]. This approach, however, forms an emulsion which is very difficult to break and undesirably leaves potassium or sodium in the treated crude. Catalytic removal of NA has been studied for many years. It has been reported that transition metal catalyst could reduce the acidity of crude oil under hydrogen atmosphere but, this process consumes large amounts of hydrogen [6] and it has not been commercialized yet. In order to solve this problem, the catalytic deacidification process was investigated in this work by using different metal oxides as catalyst supported on alumina to assist in the deacidification process together with the $NH_3$-PEG as basic chemical agent.

## Materials and Methods

### Materials

All the materials were purchased from QRëC™ and used without further treatment. 2-propanol and toluene were used as extraction solvents. Ammonia solution 28% mixed with polyethylene glycol (MW 300, 400 and 600) were used as deacidifying agents. Phenolphthalein indicator solution, 1% in ethanol was used as an indicator in the deacidification process. Potassium hydroxide pellets and barium hydroxide were used as titrants. The feedstock used in this study was crude oil obtained from Petronas Penapisan Melaka, Malaysia labelled as crude B with a TAN of 2.52 mg KOH/g.

### Preparation of 0.4 % $NH_3$-PEG

Ammonia solution (40 mL) was added dropwise into a sample bottle containing 9.96 mL polyethylene glycol. The mixture of $NH_3$-PEG was vigorously stirred using a magnetic bar for an hour. The reaction of $NH_3$ with PEG to form $NH_3$-PEG was hastened by soaking the bottle in an ice bath. The solution, which was then ready for blending with the crude oil, was set aside in a dark bottle to avoid sunlight penetration.

### Catalyst preparation

The catalyst was synthesized by wet impregnation method according to the report by Toemen et al. [7].The required amount of cerium nitrate in a beaker was dissolved with a small amount of distilled water. The solution was then mixed via continuous stirring using a magnetic bar for 30 minutes at ambient temperature to homogenize the mixture. Alumina beads with diameters of between 4 to 5 mm were used as support material. The support was dipped into the catalyst solutions for 24 hours and then transferred onto an evaporating dish lined with glass wool. Subsequently, it was aged in an oven at 80 – 90 $^oC$ for 24 hours to eliminate moisture and allow coating of the metal on the surface of the supported catalysts.

This was followed by calcination in the furnace at 400, 700, 900 and 1000 $^oC$ for 5 hours using a ramp rate of 10 $^oC$/min to eliminate all metal precursors, excess water and impurities. The developed catalysts were analyzed by BET, FESEM-EDX and XRD to characterize the physicochemical properties of the catalyst.

### Catalysts characterization

Potential catalyst was characterized by several techniques to study its physicochemical properties. The information obtained is highly useful in order to understand the relationship between the properties and its catalytic performance towards the deacidification activity. In this research, the characterization techniques used were X-ray diffraction spectroscopy (XRD), Brunauer–Emmett–Teller (BET) and thermogravimetry analysis-differential thermal analysis (TGA-DTA).

**Total acid number (TAN) determination**

An amount 0.2 g crude B was measured and placed in a titration beaker. As much as 40 mL of the titration solvent, which is a mixture of toluene: 2-propanol: distilled water (50:49.5:0.5) was poured into the crude oil sample in the titration beaker. After that, 100 ppm of 4% $NH_3$–PEG solution together with the prepared catalyst was added into 0.1 – 0.15 g crude oil sample. The solution was heated to 35 – 40 $^{o}$C to stimulate the catalyst in the mixture. The petroleum crude oil sample was then titrated with potassium hydroxide solution (0.01 mol/L). Total acid number value for crude B (TAN = 2.52 mg KOH/g) was determined by semi-micro color indicator titration method. The indicator used was phenolphthalein solution (0.1 mL), the end-point for the titration method was indicated when the stable red color was observed. The titration method was performed on crude B before and after the catalytic deacidification technology. In order to express the results, TAN value of the sample was calculated in milligrams of potassium hydroxide per gram of sample (mg KOH/g) by using the equation below (Equation 1):

$$\text{TAN} = \frac{56.1 \times c \times (V_{KOH} - V_B)}{m} \quad (1)$$

where c is the concentration of the standard volumetric potassium hydroxide solution (in mol/L), $V_{KOH}$ is the volume of titrant required for the determination (in mL), $V_B$ is the volume of titrant required for the blank test, (in mL), and m is the mass of the test portion (in gram).

## Results and Discussion

**Catalytic deacidification of Crude B: Effect of different molecular weight of PEGs**

The deacidification activities for crude B increased significantly when using PEG with molecular weights of 300, 400, 600 and 1500 as shown in Figure 1. This observation is proven by the decrease in TAN values of crude B along these PEGs. Lower TAN values of 1.68mg KOH/g were obtained for crude B by using both MW PEG of 600 and 1500. These results showed that the deacidification activities for crude B were decreased by using these PEGs. However, in this work, PEG with MW 600 was chosen as the solvent for deacidification agent due to higher percentage of NA removal for crude B and its cheaper cost compared to other PEGs.

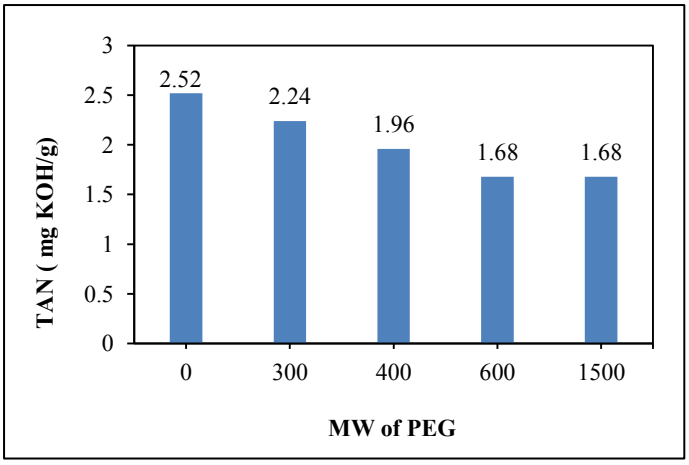



Figure 1. Effect of the different molecular weights of PEG on TAN values of crude B. [Initial TAN value for crude B (2.52 mg KOH/g)]

**Effect of different basic chemical dosing**

The deacidification performances of different dosing amount of $NH_3$-PEG in the range of 100-2500 mg/L were compared in order to select a suitable dosing amount for removal of naphthenic acid in the crude oil sample and the result is presented in the Figure 2.

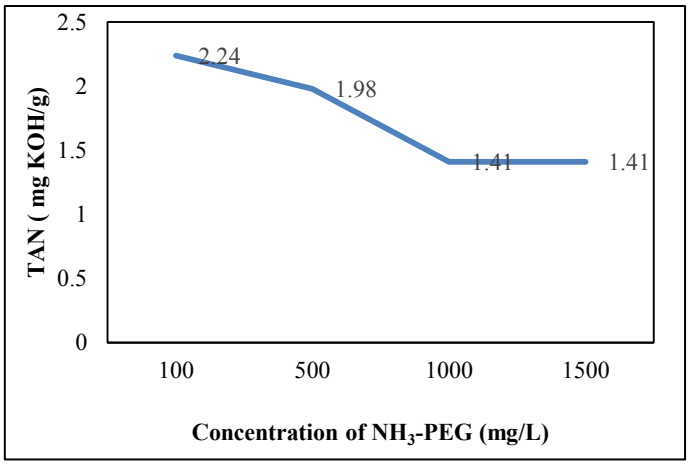



Figure 2. Effect of different dosing amount of $NH_3$-PEG on the TAN value.

It could be seen from Figure 2, the TAN number of crude B decreased with increasing dosing amounts of $NH_3$-PEG. When the dosing rose to 1000 mg/L the TAN number was decreased to 1.41 mg KOH/g and after that the curve become flat. The amount of dosing employed in the study should be appropriate enough to react with the NA in the crude oil B, because huge amounts of $NH_3$-PEG may form a stable emulsion, which would probably stabilize the NA in crude B and reduce the deacidification reaction. Even though high concentration of $NH_3$-PEG was added, there is no change of the TAN value. This explained that using 1000 mg/L is sufficient to deacidify the acid in crude B because if the concentration was increased more than 1000 mg/L it will cause operational difficulties and waste.

**Effect of different metal oxides and calcination temperatures of catalyst**

In the preparation of the catalyst, the types of metal oxide catalyst and calcination temperatures are determinant of catalyst activity. The catalytic deacidification was carried out under reaction temperature ranging between 35 to 40$^{o}$C with addition of 100-1000 mg/L of $NH_3$-PEG dosing in the presence of $Ce/Al_2O_3$, $Zn/Al_2O_3$ and $Sn/Al_2O_3$ catalysts calcined at different temperatures of 400, 700 and 1000$^{o}$C for 5 h. Figure 3 portrays the effect of different metal oxide catalysts prepared at different calcination temperatures towards the catalytic deacidification process.

A noticeable difference was recorded for the catalytic deacidification process fulfilling the expected target of TAN to be less than one. An increase in the calcination temperature for all catalysts from 400 to 1000 $^{o}$C caused a decrease of the TAN value for crude B. For these studies, the $Ce/Al_2O_3$ catalyst calcined at 1000 °C gave the lowest value of TAN of 0.74 mg KOH/g followed by $Sn/Al_2O_3$ catalyst calcined at 1000 $^{o}$C (TAN = 1.68 mg KOH/g) and $Zn/Al_2O_3$ catalyst calcined at 1000 $^{o}$C with a TAN of 1.41 mg KOH/g. As for the $Ce/Al_2O_3$ catalyst, the calcination temperature below than 1000 $^{o}$C cannot reduce the TAN value below than one due to incomplete metal oxide formation and the amorphous properties of this catalyst which produced less amount of basic surface active sites available for the catalytic deacidification reaction. However, an increase in the calcination temperature up to 1000 $^{o}$C for this catalyst managed to reduce the TAN below than one due to its polycrystallinity properties as shown in XRD data which generated a larger amount of total basic surface active sites led to a successful catalytic deacidification reaction. Furthermore, excellent redox properties of CeO due to the very fast reduction of $Ce^{4+}/Ce^{3+}$ as reported by Ayastuy et al. [8] results in the formation of oxygen vacancies at the surface, making the NA removal more efficient. Thus, Ce calcined at 1000 $^{o}$C was chosen as the catalyst to be further optimized in this study.

**Reusability testing over $Ce/Al_2O_3$ catalyst**

The potential $Ce/Al_2O_3$ catalyst calcined at 1000 $^{o}$C was tested several times under optimum reaction conditions in order to study the reusability of this catalyst. It was tested by using the same catalyst until the catalyst was deactivated. After one catalytic reaction was completed, the catalyst was rinsed with 2-propanol to remove any adsorbed naphthenic acid compounds. The catalyst was then dried in an oven at 80 $^{o}$C and re-used for the second reaction. The process was repeated for the next consecutive run. Figure 4 shows the plot of reusability testing over

$Ce/Al_2O_3$ catalyst. It can be seen that the TAN value was maintained (0.74 mg KOH/g) until the fifth cycle. However, the catalyst started to deactivate (spent catalyst) at the sixth testing as a slight decrease in the activity is seen as indicated by the increasing TAN value to 0.84 mg KOH/g.

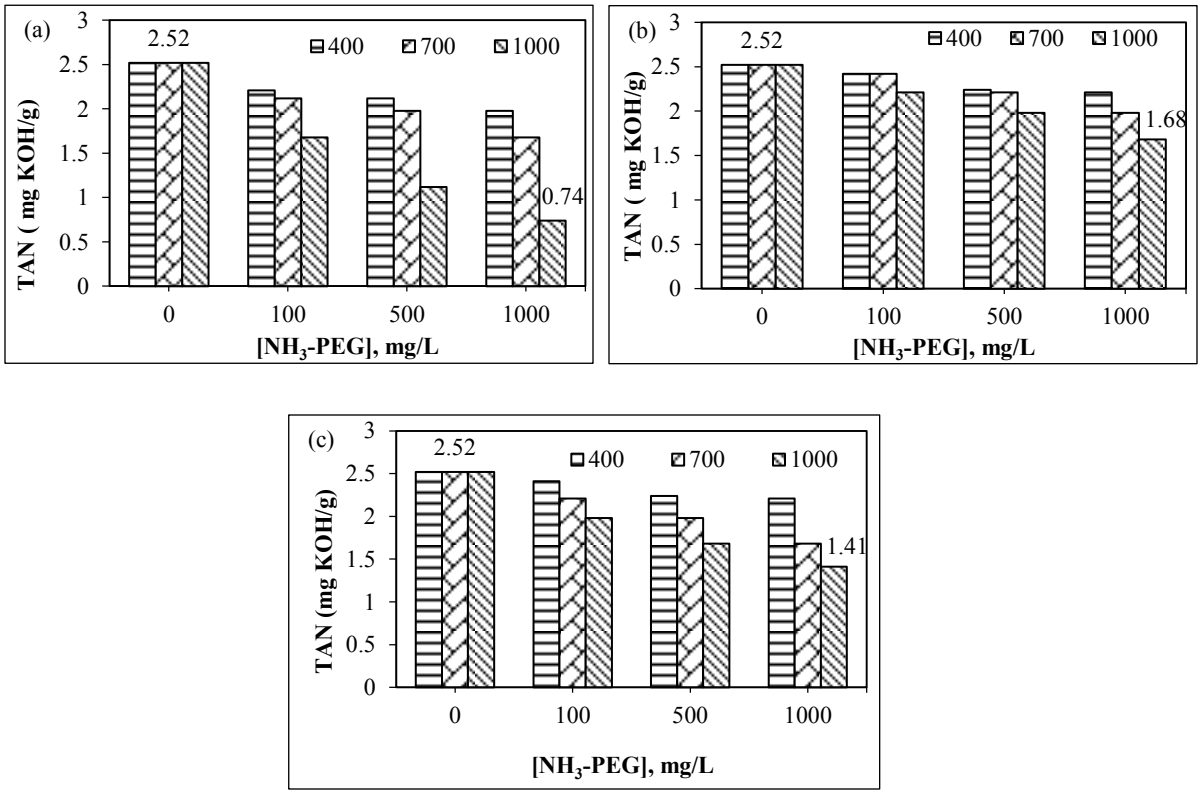



Figure 3. Effect of a) Ce, ) Zn and c) Sn catalysts supported on alumina calcined at 400, 700 and 1000 $^oC$ on the reduction of TAN value

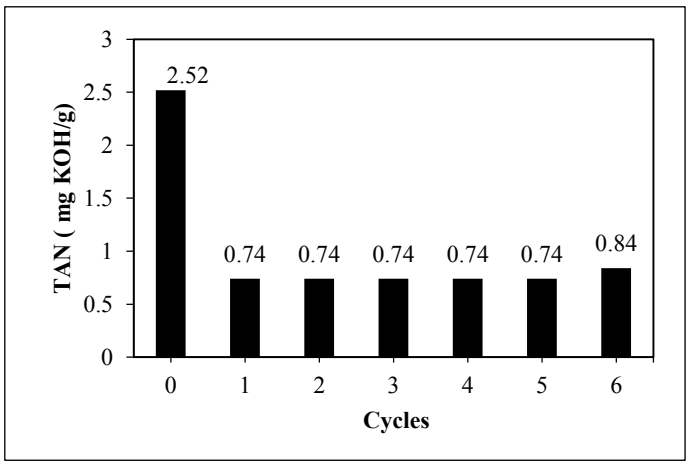



Figure 4. TAN value for six cycles of catalytic deacidification. Reaction conditions: Catalyst = $Ce/Al_2O_3$, calcination temperature of catalyst: 1000 $^oC$.

**Characterization of the potential catalyst: TGA-DTA**

After aging the catalysts which had been prepared by wetness impregnation method in an oven for 24 hours at 80 – 90 ◦C, the catalyst was analyzed by using TGA-DTA. Figure 5 shows the TGA thermogram of $Ce/Al_2O_3$ catalyst which illustrate four significant weight lost curves which occurred at 80, 130, 250 and 480 ◦C.

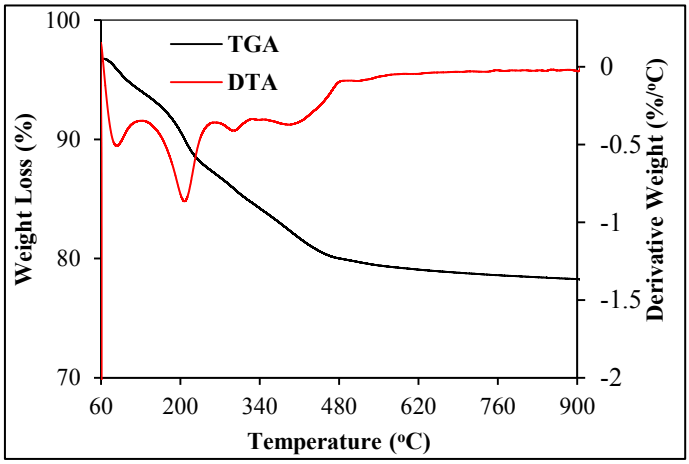



Figure 5. TGA-DTA thermogram of $Ce/Al_2O_3$ catalyst after aging in an oven for 24 hours at 80 – 90 °C.

The total weight loss for this sample is 16.69%. Freewater molecule and nitrate compound was removed from the supported catalyst starting from a temperature of 80 °C until 340 °C. Meanwhile at 480 °C onward; nitrate compounds and surface hydroxyl molecule were decomposed from the samples [9]. From this investigation, the calcination temperature of 400 °C is insufficient to remove all the nitrate compounds that originate from the metal precursor. This observation is in agreement with the results shown in "effect of different metal oxides and calcination temperatures of catalyst" in which using $Ce/Al_2O_3$ catalyst calcined at 400 °C, the TAN value of crude B cannot be reduced to lower than one as the catalyst calcined at this temperature resulted in incomplete formation of metal oxide.

**BET analysis**

One of the most characteristic properties of the surface of a solid is its ability to adsorb gases and vapors. The potential catalyst of fresh and spent $Ce/Al_2O_3$ were characterized by nitrogen adsorption analysis. Table 1 summarizes their BET surface area and BJH desorption average pore diameter.

Table 1. BET surface area and BJH desorption average pore diameter of the fresh and spent forms of $Ce/Al_2O_3$ catalyst

| Condition | SBET ($m^2g^{-1}$) | Pore Diameter (A) |
|---|---|---|
| Fresh | 70 | 19 |
| Used | 62 | 25 |

Isotherm shape depends on the solid porous texture. Figure 6 shows the NA isotherm of fresh and used $Ce/Al_2O_3$ catalyst. NA/desorption isotherm of $Ce/Al_2O_3$ catalyst prepared exhibit the characteristic of mesoporous structure with Type IV with incorporation of some mesopores with the presence of hysteresis loop type H3. Results showed that the surface area of used catalyst (70 $m^2/g$) was slightly decreased than fresh $Ce/Al_2O_3$ catalyst (62 $m^2/g$) probably due to some surface areas which were covered with contamination from crude oil during catalytic

deacidification reaction. However, this occurrence does not affect the catalytic activity after using for one time as proved by catalytic deacidification in reusability testing.

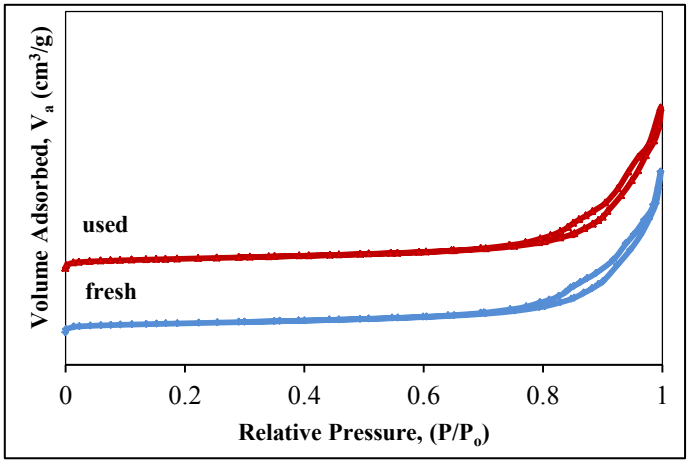



Figure 6. Nitrogen adsorption-desorption isotherms for fresh and used $Ce/Al_2O_3$ catalyst

Figure 7 shows the pore size distribution curves of the fresh and used $Ce/Al_2O_3$ catalyst calcined at temperature of 1000°C. The pore size distributions calculated from the desorption branch by the Barret–Joyner–Halenda (BJH) method were very similar for both samples, presenting a very wide pore distribution covering the range of 19–40 nm.

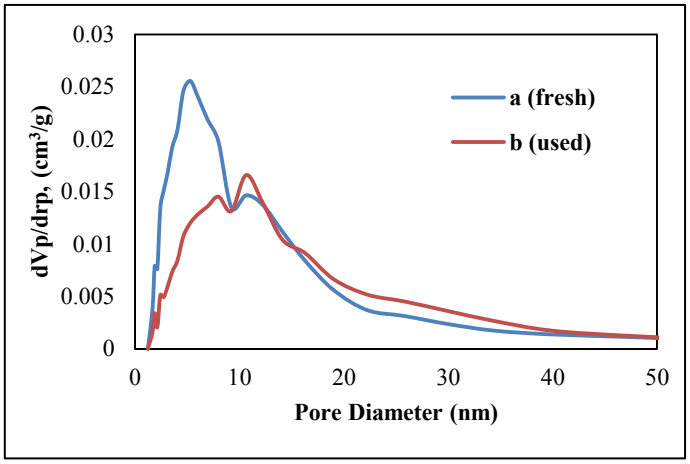



Figure 7. Pore size distribution of a) fresh and b) used $Ce/Al_2O_3$ catalyst calcined at 1000 °C for 5 hours

**XRD analysis**

In order to confirm the reusability of the $Ce/Al_2O_3$ catalyst, the diffractograms of fresh and used $Ce/Al_2O_3$ catalysts, both calcined at 1000 °C for 5 hours are compared in Figure 8 to investigate any transformation that occurred on the surface of this catalyst before and after being used (after 1st catalytic testing) in the catalytic deacidification process of crude B. Both diffractograms displayed the polycrystallinity phase dominated by the $CeO_2$ (fcc) species and some of the alumina orthorhombic (o) phase. The $CeO_2$ species for both fresh and used catalysts showed 2θ valuesat 28.6, 47.5, 56.5, 32.9, 76.6 and 78.9°. Meanwhile the alumina orthorhombic phase occurred at 2θ of 67.3 and 36.5°. This data shows that no change in the diffractograms of both fresh and used catalysts occurs which indirectly prove that

the $Ce/Al_2O_3$ catalyst possesses a higher thermal stability, smaller rate of deactivation and higher reusability.This is shown via the reusability testing, whereby the catalyst can be used up to the fifth cycle with an excellent catalytic deacidification activity.

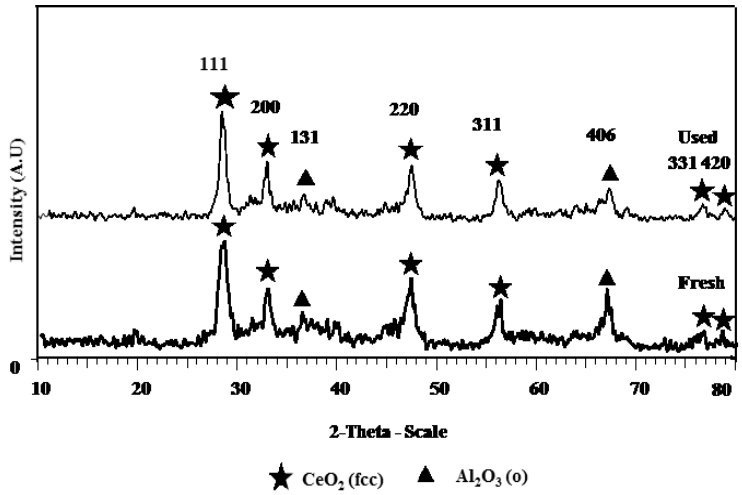



Figure 8. XRD diffractograms of fresh and used $Ce/Al_2O_3$ catalysts calcined at 1000 $^oC$ for 5 hours

## Conclusion

The technology applied was successful in meeting the PETRONAS benchmark of a TAN less than 1 mg KOH/g for crude oil B. The result from the catalytic deacidification process revealed that $Ce/Al_2O_3$ catalyst prepared at a calcination temperature of 1000 $^oC$ has the potential to enhance the reduction of TAN in crude oil. Physical characterization by BET analysis showed that this catalyst has the largest surface area. This revelation is significant as a greater surface area offers more surface-active sites for catalytic deacidification to take place. Furthermore, XRD diffractograms portrayed unchanged composition after this catalyst is used in the catalytic deacidification reaction which indirectly proved that this catalyst possesses a higher thermal stability, smaller rate of deactivation and higher reusability.

## Acknowledgement

The authors gratefully acknowledge Universiti Teknologi Malaysia (UTM), Ministry of Education (MOE), for the financial support given under Fundamental Research Grant Scheme (FRGS, Vote no.: 4F225) and Ministry of Science, Technology and Innovation (MOSTI) for MyBrain 15 scholarship to Nurasmat Mohd Shukri.

## References

1. Slavcheva, E., Shone, B. and Turnbull, A. (1999). Review of naphthenic acid corrosion in oil refining. *British Corrosion Journal* 34(2): 125 – 131.
2. Brient, J. A., Wessner, P. J. and Doyle, M. N. (2000). Naphthenic Acids. In: Kirk-Othmer Encyclopedia of Chemical Technology. John Wiley and Sons, Inc.
3. Saad,O. M., Gasmelseed, G. A. and Hamid, A. H. M. (2014). Separation of naphthenic acid from Sudanese crude oil using local activated clays. *Journal of Applied and Industrial Sciences*, 2(1): 14 –18.
4. Halbert, T. R., Riley, K. L., Trachte, K. L. and Vannauker, D. L. (1999). Process for reduction of total acid number in crude oil. US Patent 5,910,242. pp. 1 – 6.
5. Braccknell, S. N. D. and Osborne, C. G. (2002). Process for deacidifying a crude oil system.US Patent 6,464,859. pp. 1 – 6.
6. Shi, L. J., Shen, B. X. and Wang, G.Q. (2008). Removal of naphthenic acids from Beijing crude oil by forming ionic liquids. *Energy Fuels*, 22: 4177 – 4181.

7. Toemen, S. Bakar, W. A. W. A. and Ali, R. (2014). Investigation of $Ru/Mn/Ce/Al_2O_3$ catalyst for carbon dioxide methanation: Catalytic optimization, physicochemical studies and RSM. *Journal of the Taiwan Institute of Chemical Engineers,* 45 (5): 2370 – 2378.
8. Ayastuy, J. L., Fernandez-Puertas, E., Gonzalez-Marcos, M. P. and Gutierrez-Ortiz, M. A. (2012). Transition metal promoters in $CuO/CeO_2$ catalysts for CO removal from hydrogen streams. *International Journal of Hydrogen Energy*, 37: 7385 –7397.
9. Alouche, A. (2008). Preparation and characterization of copper and/or cerium catalysts supported on alumina or ceria. *Jordan Journal of Mechanical and Industrial Engineering,* 2: 111 – 116.

*Malaysian Journal of Analytical Sciences, Vol 21 No 4 (2017): 839 - 848*
*DOI: https://doi.org/10.17576/mjas-2017-2104-10*

MALAYSIAN JOURNAL OF ANALYTICAL SCIENCES
*Published by The Malaysian Analytical Sciences Society*
ISSN 1394 - 2506

# PRODUCTION OF ETHYLENE FROM ETHANOL DEHYDRATION OVER $H_3PO_4$-MODIFIED CERIUM OXIDE CATALYSTS

## (Penghasilan Etilena Daripada Pendehidratan Etanol Dengan Mangkin Serium Oksida Terubahsuai $H_3PO_4$)

Soo Ling Chong[1], Jiah Chee Soh[1], Chin Kui Cheng[1,2]*

[1]*Faculty of Chemical & Natural Resources Engineering*
[2]*Centre of Excellence for Advanced Research in Fluid Flow*
*Universiti Malaysia Pahang, 26300 Kuantan, Pahang, Malaysia*

**Corresponding author: chinkui@ump.edu.my*

Received: 20 September 2016; Accepted: 16 May 2017

**Abstract**

Production of ethylene from ethanol dehydration was investigated over $H_3PO_4$ (10 wt.% to 30wt.%)-modified cerium oxide catalysts synthesized by wet impregnation technique. The prepared catalysts were characterized using scanning electron microscope (SEM), $N_2$ adsorption-desorption method, X-ray diffraction (XRD), Fourier transform infrared spectroscopy (FTIR) and thermogravimetric analysis (TGA) for the physicochemical properties. The ethanol catalytic dehydration was carried out in a fixed-bed reactor at 673-773 K and at ethanol partial pressure of 33 kPa. The effects of phosphorus loading on catalyst and reaction temperatures were investigated in terms of catalytic activity towards product selectivity and yield. Overall, the selectivity and yield of ethylene increased with the temperature and phosphorus loading. The highest ethylene selectivity and yield were 99% and 65%, respectively, at 773 K and 33 kPa over the 30 wt.% $H_3PO_4$-modified cerium oxide.

**Keywords**: ethylene production, ethanol dehydration, $H_3PO_4$ modification, cerium oxide

**Abstrak**

Penghasilan etilena daripada pendehidratan etanol telah dikaji dengan mangkin serium oksida terubahsuai $H_3PO_4$ (10 wt.% hingga 30 wt.%) yang dihasilkan melalui kaedah pengisitepuan. Mangkin disediakan telah dicirikan menggunakan mikroskop elektron imbasan (SEM), kaedah penjerapan-nyahjerapan $N_2$, pembelauan sinar-X (XRD), spektroskopi inframerah transformasi Fourier (FTIR) dan analisis termogravimetri (TGA) untuk mengetahui sifat fizikokimia mangkin. Tindak balas pendehidratan etanol dengan mangkin dilakukan di dalam reaktor turus terpadat pada julat suhu 673 – 773 K dan tekanan separa etanol 33 kPa. Pengaruh muatan $H_3PO_4$ dan suhu tindak balas kimia dalam pendehidratan etanol telah dikaji. Secara keseluruhan, kepilihan dan hasil etena meningkat dengan muatan $H_3PO_4$ dan suhu tindak balas kimia. Kepilihan dan hasil etena tertinggi masing-masing ialah 99% dan 65% pada 773 K dan 33kPa untuk mangkin serium oksida terubahsuai $H_3PO_4$ 30 wt.%.

**Kata kunci:** penghasilan etilena, pendehidratan etanol, pengubahsuaian $H_3PO_4$, serium oksida

## Introduction

The increasing demand of ethylene is due to its uses in producing polyethylene, one of the primary components in the most of the plastic and in petrochemical industry [1]. Besides that, ethylene acts as precursors for surfactant chemicals such as ethylene oxide or ethylene glycol. With increased demand, global ethylene production has grown at an average rate of almost 4.5% per year from 2009 – 2014. Currently steam cracking of hydrocarbon from fossil fuel is still dominating the production market because of the high production cost and energy consumption

associated with catalytic dehydration pathway. Due to the increasing demands for energy, stricter environmental regulations, and continued depletion of fossil feedstock, alternative and renewable energy resources have attracted increased interest in recent research. In the view of potential limitations of ethylene availability from the current sources, catalytic dehydration of ethanol (especially bioethanol) to ethylene has become a completely renewable process for producing ethylene [2].

Ethanol dehydration is a process in which water molecules are removed, or the equivalent of water molecules removed from ethanol to produce ethylene when heated together with catalyst. There are two reactions that occur in parallel during catalytic dehydration of ethanol as in Equation (1) to (2):

$$C_2H_5OH \leftrightarrow C_2H_4 + H_2O \qquad +44.9 \text{ kJ/mol} \qquad (1)$$

$$2C_2H_5OH \leftrightarrow C_2H_5OC_2H_5 + H_2O \qquad -25.1 \text{ kJ/mol} \qquad (2)$$

The low temperature favors the side reaction to produce diethyl ether; in contrast, higher reaction temperature is theoretically favoring the main reaction (ethanol dehydration). The dehydration reaction is endothermic and need 390 calories per gram of ethylene produced. The temperature of diethyl ether formation is mainly between 423 K and 573 K, while ethylene formation is favoured between 593 K and 773 K.

Acidic catalysts are often used in ethylene production from ethanol dehydration. The traditional homogeneous catalysts used are sulfuric acid or phosphoric acid in almost all industrial scale processes [1]. The former usually requires higher reaction temperatures and yields lower ethylene selectivity [3]. Due to the low yield and byproducts formation, sulfuric acid and phosphoric acid have been replaced by heterogeneous catalysts such as alumina.

Many studies have been carried out with different technologies and using various acidic heterogeneous catalysts such as alumina, silica, zeolites, metal oxides and heteropolyacids [4 - 7]. Among those studied catalysts, gamma alumina ($\gamma$-$Al_2O_3$) and HZSM-5 zeolite have drawn the most attention for their high activity and selectivity. HZSM-5 has been widely used in alcohol dehydration reactions due to its uniform pore structure, high surface area, and adjustable acidity. Low reaction temperature (>473 K) favors the reaction towards ethylene production from ethanol dehydration over HZSM-5. HZSM-5 can achieve 60 – 80% ethylene yield at relatively low reaction temperature (473 – 573 K) [8]. Besides of the reaction temperature, the catalyst surface acidity is a significant catalytic performance factor. HZSM-5 has high concentration of strong acidic sites, which exist at low Si/Al ratios helps in ethylene production. However, the high acidity also leads to render HZSM-5 zeolite unstable and low anti-coking property [9]. On the contrary, $\gamma$-$Al_2O_3$ has high surface area (50 –300 $m^2 g^{-1}$) and thermal stability up to 873 K that make it widely used in industrial. The ethanol dehydrate over $\gamma$-$Al_2O_3$ can achieve greater than 90% to form ethylene. The disadvantage of $\gamma$-$Al_2O_3$ is high reaction temperature needed for ethanol catalytic dehydration. Another problem is that water can deactivate active sites on $\gamma$-$Al_2O_3$ and inhibit the formation rate of ethylene and diethyl ether [10].

The weak acid centers and relatively strong acid centers of the catalyst are the active sites of ethanol intramolecular dehydration to ethylene [6]. However, the strong acid centers can easily lead to ethylene polymerization. Hence, surface acidity of catalyst need to adjust using additives to improve catalyst stability and high ethylene selectivity. In continuation of discovering new catalyst for ethanol catalytic dehydration, we report the use of ceria-based catalysts for the aforementioned reaction. The use of cerium oxide as the support bring advantages such as its high oxygen mobility associated with oxygen vacancies and oxygen storage capacity. Due to the high effectiveness of cerium oxide used as a support and the (phosphostic acid ad), many studies have been carried out by employing cerium oxide as catalyst for ethanol conversion reactions especially steam reforming reactions [11 - 15]. As mentioned earlier , the surface acidity of catalyst is improtant in this reaction. Thus, pure $CeO_2$ catalysts as well as phosphoric acid ($H_3PO_4$) doped $CeO_2$ catalysts were prepared to study the behavior of $CeO_2$ towards kinetics of ethanol dehydration.

Therefore, the aim of this study is to investigate the feasibility of ethanol dehydration over $H_3PO_4$-modified cerium oxide catalysts on new catalyst application for this reaction. The synthesized catalysts were characterized using

scanning electron microscope (SEM), energy dispersion X-ray spectroscopy (EDX), $N_2$ adsorption-desorption method, X-ray diffraction (XRD), Fourier transform infrared spectroscopy (FTIR) and thermogravimetric analysis (TGA) for the physicochemical properties.

## Materials and Methods

### Catalysts preparation

Cerium nitrate salt $Ce(NO_3)_2$ was procured from Sigma-Aldrich, USA. The ceria support was prepared by thermal decomposition of $Ce(NO_3)_2.6H_2O$ at 873 K for 2 hours and then crushed to powder. The modified cerium oxide phosphate catalyst (10PA-$CeO_2$) was prepared by impregnating the 10 wt.% aqueous solution of $H_3PO_4$ into 90 wt.% of the ceria support followed immediately by magnetic stirring for 3 hours. The solution was then magnetic-stirred for 3 hours under ambient condition. Thereafter, the impregnated catalyst was oven-dried for 12 hours at 373 K. During the first 6 hours of the drying process, the catalyst was manually stirred using a glass rod for each hour to maintain relative homogeneity of the slurry. Post 12 hours, the calcination of the dried catalyst was carried out in a muffled furnace model Carbolite RHF1400 for 5 hours at 773 K with heating rate of 5 K $min^{-1}$. The catalyst was then cooled to room temperature and ground for physicochemical characterization and reaction studies. The resulting 20PA-$CeO_2$ and 30PA-$CeO_2$ were prepared by the similar procedure with 20 wt.% and 30 wt.% of phosphoric acid, respectively.

### Catalyst characterization

The fresh modified cerium oxide phosphate catalysts were characterized using several methods. The phase structure of the catalysts was characterized by X-ray diffraction (Rigaku Miniflex Instrument) using X-ray source from CuKα (λ=1.542 Å) at 30 kV and 15 mA. $N_2$ physisorption was conducted to determine the textural property of the synthesized catalysts. The information about the surface morphology of the catalyst and the elemental chemical compositions were determined using SEM analysis employing Hitachi TM3030Plus with a magnification of 5kx which was also equipped with energy-dispersive X-ray spectroscopy (EDX). Thermogravimetric-difference thermal analysis (TG) technique of samples before and after reaction was carried out to monitor the thermal profile of fresh and spent catalysts. Fourier Transform Infrared Spectroscopy (FTIR) (Perkin Elmer Spectrum 100) was also employed to determine the nature of chemical bonding of the catalysts.$NH_3$-TPD was carried out in a ThermoFinnigan TPDRO 1100. The catalyst was pre-treated with $N_2$ at 423 K for 15 minutes. $NH_3$-TPD is used to determine the amount of acidic sites and their distribution in strength. The adsorption of $NH_3$ was carried out at room temperature for 45 min and after saturation was achieved, $N_2$ was purged in to eliminate the $NH_3$ that remained in the gas phase. Analysis of desorption of $NH_3$ was done under the flow of helium at temperature of 323 to 1273 K, at the rate of 20 K $min^{-1}$.

### Catalytic activity

The reaction was conducted in a fixed-bed reactor at ethanol partial pressure of 33 kPa with WHSV of 240 $h^{-1}$, in the temperature range of 673 – 773K. The reactor was loaded with 0.3 g of catalyst and introduced with pure ethanol (≥99.9%) with a HPLC pump. The gaseous products were collected and identified using GC to identify the quantity of targeted product. The GC instrument used was Shimadzu GC-2014 with two packed column, column temperature and flame ionizer detector temperature at 333 K and 473 K, respectively. Ethanol conversion and products selectivity were calculated by Equation (3) and (4), respectively [16, 17]:

$$X_{Ethanol} = \frac{\sum \text{Total gas products},F_i}{2 \text{ x molar flow rate of ethanol in the feed}} \text{ x } 100 \quad (3)$$

$$S_i = \frac{F_{C_2H_4}}{\Sigma \text{ Total gas products},F_i} \times 100 \quad (4)$$

where F is define as molar flow rate and *i* is refer to $C_1$, $C_2$, $C_3$, $C_4$ and $C_5$ species.

## Results and Discussion

### Catalyst characterization

Figure 1 illustrates XRD diffractogram of $CeO_2$ and 10, 20, 30PA-$CeO_2$. Based on Figure 1, the high intensity peaks recorded at 2θ readings of 28.6°, 33.1°, 47.48° and 56.36° which corresponding to (111), (200), (220) and

(311) crystal planes respectively.The XRD patterns obtained of the synthesized catalysts were compared with the standard data for $CeO_2$ (JCPDS card No. 34-0394).This also indicated that the $CeO_2$'s structure maintained well for all modified catalysts [18]. The structure of catalysts became less crystalline as affected by $H_3PO_4$ loading. There are additional small peaks found for 20PA-$CeO_2$ and 30PA-$CeO_2$ at 2θ readings of 21°, 27° and 43° which can be ascribed to $CeP_2O_7$ species (JCPDS card No. 30-0164). $CeP_2O_7$ is a crystalline product in which every Ce atom is joined to six oxygen and every P to four oxygen, with a connectivity of four and six. The P atoms are joined in pairs through shared O atom to form $P_2O_7^{4-}$ units, each of it shared its six remaining oxygen with the $CeO_6$ octahedral. The appearance of $CeP_2O_7$ is normally occurred when cerium oxide reacted with phosphoric acid at temperature around 623 K to 1073 K. In this case, the modified cerium oxide phosphate catalysts were prepared at 773 K in a furnace which causes the formation of $CeP_2O_7$ species [19].

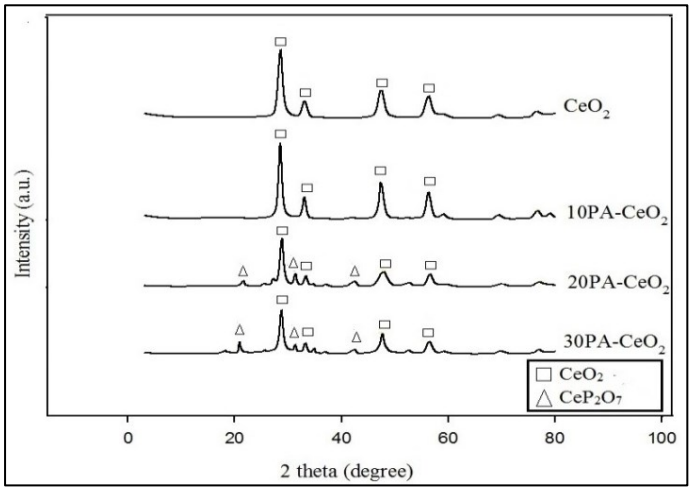



Figure 1. X-ray diffraction profiles of $CeO_2$ and $H_3PO_4$-modified $CeO_2$ catalysts

SEM micrographs of modified cerium oxide phosphate catalysts at 20 µm resolution are shown in Figure 2. Based on the Figure 2, most of the samples were agglomerated together. The SEM images shown in Figure 2 reveal the morphology of all samples is similar with formation of irregular and bulky surface which is typical of thermally-synthesized wet impregnated catalyst. Meanwhile, it is clearly proved that the addition of $H_3PO_4$ did not alter the surface morphology of the catalysts, and that the $H_3PO_4$ has blended intimately with the $CeO_2$ support to form a single phase.

The fresh catalysts were also subjected to the FTIR scanning and the spectra collected are shown in Figure 3. The spectra were recorded in the wave number that ranged 4000 – 400 $cm^{-1}$. Significantly, transmission band representing N-O stretch which normally can be found at wavenumber 3000 $cm^{-1}$ is absent in Figure 3. This indicates that the entire nitrate group was successfully removed during the thermal decomposition of nitrate-salt to yield pure $CeO_2$. The transmission band at wave number 550.73 $cm^{-1}$ represents the Ce-O stretch. In addition, the bands at wavenumber around 900 – 1000 $cm^{-1}$ represent the O=P=O asymmetric stretching modes of phosphate or polyphosphate species[20]. As shown in Figure 3, the intense band found around 1000 – 1600 $cm^{-1}$ increase as the loading of phosphorus increase. This is due to the introduction of phosphorus onto the $CeO_2$ catalyst whereby the O=P=O asymmetric increases. The same results observed in previous study [21]. This proves that introduction of $H_3PO_4$ has been successfully carried out.

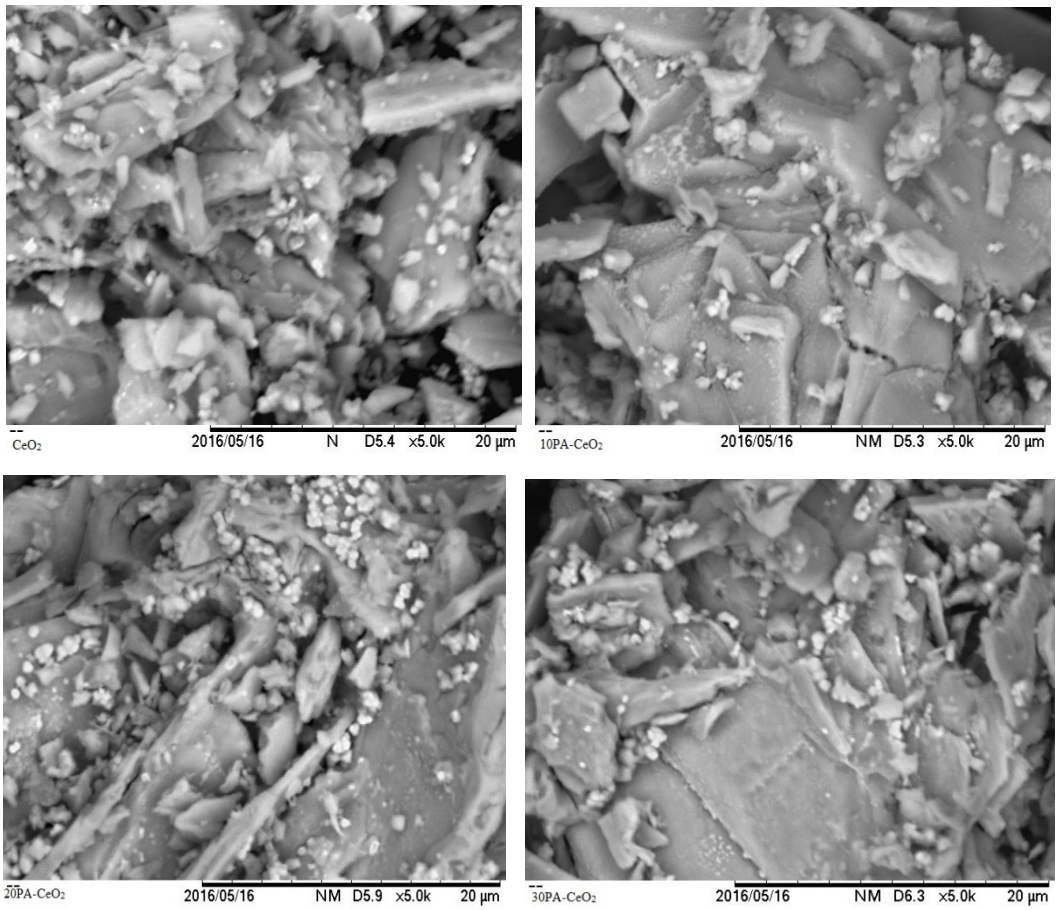



Figure 2. SEM images of $CeO_2$ and $H_3PO_4$-modified $CeO_2$ catalysts

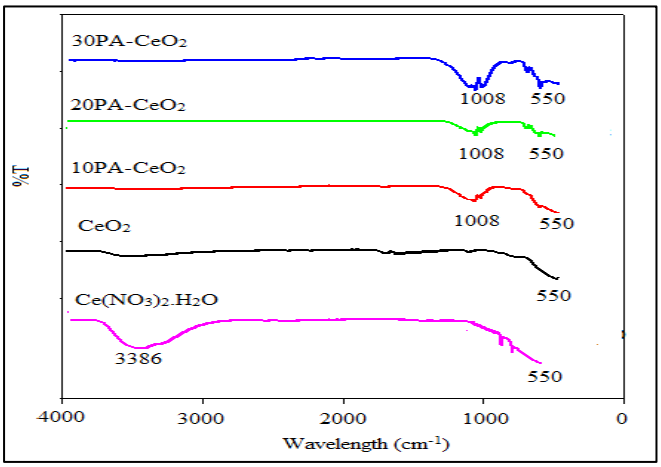



Figure 3. FTIR results of $CeO_2$ and $H_3PO_4$-modified $CeO_2$ catalysts

Table 1 provides the BET specific surface area, mesopore volume and pore diameter of pure $CeO_2$ and $H_3PO_4$-modified $CeO_2$ catalysts that were obtained from $N_2$ physisorption. Both the BET specific surface area and

mesopore volume decreased with $H_3PO_4$ loading, to the tune of nearly 90% reduction for the 30 wt.% $H_3PO_4$ loading. The reduction of pore dimension or pore blockage of the $CeO_2$ by the introducing of phosphoric acid in the treatment [22]. In contrast, the pore diameter recorded an increment, from 14.0 nm improved to 18.8 nm when the $H_3PO_4$ weight was increased. This could be due to the creation of wider pore mouth on the surface of $CeO_2$ resulting from the acid attack that occurred at the employed calcination temperature.

Table 1. Textural properties of the $CeO_2$ and $H_3PO_4$-modified $CeO_2$ catalysts

| Fresh Catalyst | BET Specific Surface Area ($m^2\ g^{-1}$) | Pore Volume ($cm^3\ g^{-1}$) | Pore Diameter (nm) |
|---|---|---|---|
| $CeO_2$ | 71.6 | 0.2545 | 14.0 |
| 10PA-$CeO_2$ | 35.5 | 0.1461 | 16.3 |
| 20PA-$CeO_2$ | 20.2 | 0.0833 | 16.3 |
| 30PA-$CeO_2$ | 9.9 | 0.0461 | 18.8 |

Thermo-desorption profiles of $NH_3$ were carried out to determine the acid-base properties of the as-synthesized catalysts. The acid strength can be categorized into weak acidic site (373-523 K), moderate acidic site (523-673 K) and strong acidic site (673- 823 K), respectively, based on the desorption temperature. Table 2 shows the resulting acid amount of $CeO_2$ and $H_3PO_4$-modified $CeO_2$ catalysts. From Table 2, it can be observed that there are three types of acid sites with variable amounts, at 819 μmol $g^{-1}$, 188 μmol $g^{-1}$ and 548 μmol $g^{-1}$, respectively, for weak, moderate and strong acids found in $CeO_2$ catalyst. The introduction of $H_3PO_4$ generates moderate acid sites by suppressing the strong acid sites of $CeO_2$. The amount of moderately-strong acid site has increased substantially, increasing incrementally to 837 μmol $g^{-1}$ for 10PA- $CeO_2$, 1238 μmol $g^{-1}$ for 20PA- $CeO_2$ and 1532 μmol $g^{-1}$ for 30PA- $CeO_2$, respectively. This may be due to the nature of $H_3PO_4$, which is a moderately-strong acid with pKa value of 6.9 x $10^{-3}$. Moreover, the strong acid site which was inititally present on the surface of pure $CeO_2$ was dimishing with the $H_3PO_4$ loading, decreased from 548 μmol $g^{-1}$ for pure $CeO_2$ to just 284 μmol $g^{-1}$ for 30PA-$CeO_2$ catalyst. As the loading of phosphoric acid on $CeO_2$ increases, the total acid amount increases.

Table 2. The total surface acidity and acid strength distribution of $CeO_2$ and $H_3PO_4$-modified $CeO_2$ catalysts

| Catalysts | Acid Amount (μmol $g^{-1}$) | | | Total Acid Amount (μmol $g^{-1}$) |
|---|---|---|---|---|
| | Weak Acid Site (373-523 K) | Moderate Acid Site (523-673 K) | Strong Acid Site (673-823 K) | |
| $CeO_2$ | 819 | 188 | 548 | 1555 |
| 10PA-$CeO_2$ | 850 | 837 | 413 | 2100 |
| 20PA-$CeO_2$ | 838 | 1238 | 385 | 2461 |
| 30PA-$CeO_2$ | 823 | 1532 | 284 | 2639 |

**Catalytic performances of modified cerium oxide phosphate catalysts**

Table 3 shows the product distribution over $CeO_2$ and 10, 20, 30PA- $CeO_2$ catalyst at different reaction temperature and ethanol partial pressure 33 kPa. Cerium oxide catalyst presented lowest catalytic performance among all synthesized catalysts. The pure $CeO_2$ catalyst, under the same reaction condition as aforementioned, the conversions recorded were 1.25%, 2.45% and 6.89%, respectively. This reveals that the acidity amount found in $CeO_2$cannot protonate the hydroxyl group of $C_2H_5OH$ which explains its low activity. The selectivity decreases with the increasing reaction temperature. This is due to higher hydrocarbons formation with almost 35% at 773 K. $CeO_2$ presents highest number of strong acidic sites which lead to the higher hydrocarbons formation [16], [22]. Hence, there were over 45% of hydrocarbons formed over $CeO_2$ catalyst at high temperature.

Table 3. Product distributions of ethanol dehydration over $CeO_2$ and $H_3PO_4$-modified $CeO_2$ catalysts at 33 kPa and 673 – 773 K

| Variable | $CeO_2$ | | | 10PA-$CeO_2$ | | | 20PA-$CeO_2$ | | | 30PA-$CeO_2$ | | |
|---|---|---|---|---|---|---|---|---|---|---|---|---|
| | Temperature (K) | | | Temperature (K) | | | Temperature (K) | | | Temperature (K) | | |
| | 673 | 723 | 773 | 673 | 723 | 773 | 673 | 723 | 773 | 673 | 723 | 773 |
| Ethanol conversion (%) | 1.23 | 2.45 | 6.89 | 4.79 | 8.96 | 29.90 | 9.39 | 35.73 | 41.31 | 15.97 | 38.02 | 59.74 |
| Selectivity (%) | | | | | | | | | | | | |
| Ethylene | 68.71 | 53.76 | 47.20 | 47.2 | 54.60 | 70.39 | 94.11 | 95.35 | 98.33 | 96.14 | 98.55 | 99.21 |
| Higher hydrocarbons | | | | | | | | | | | | |
| $C_3$ | 0.28 | 0.81 | 3.25 | 0.01 | 1.18 | 0.28 | 0 | 0.01 | 0.01 | 0 | 0.01 | 0.01 |
| $C_4$ | 7.73 | 21.13 | 22.93 | 0.14 | 6.32 | 2.17 | 0.2 | 0.14 | 0.11 | 0.2 | 0.11 | 0.14 |
| $C_5$ | 19.78 | 0 | 8.01 | 0.44 | 4.01 | 3.78 | 3.30 | 0.44 | 1.12 | 3.30 | 1.12 | 0.44 |
| $C_6$ | 0 | 14.90 | 0.10 | 0 | 0 | 0.14 | 0 | 0 | 0 | 0 | 0 | 0 |

The ethanol conversion, ethylene selectivity and total acid amountwere correlated for the synthesized catalysts in Figure 4. Upon doing with $H_3PO_4$, the ethylene selectivity and ethanol conversion increase as the loading of $H_3PO_4$ increase. The addition of $H_3PO_4$ into $CeO_2$ catalyst causes the amount of strong acidic sites decrease. This change suppresses the formation of higher hydrocarbons and improves the ethylene production. Although 10PA-$CeO_2$ did not present a high catalytic performance with low ethanol conversion 4.79%, 8.96% and 29.90% for 673 K, 723 K and 773 K, respectively, but it showed increasing trend in terms of catalytic performance as compared to pure $CeO_2$. This indicates that the surface acidity of 10PA-$CeO_2$ was unable to catalyze the formation of products. Among all $CeO_2$ and $H_3PO_4$-modified $CeO_2$ catalysts, the 30PA-$CeO_2$ catalyst showed the best catalytic performance. On this catalyst, the products are dominated by ethylene under all reaction condition with over 95% of ethylene selectivity.

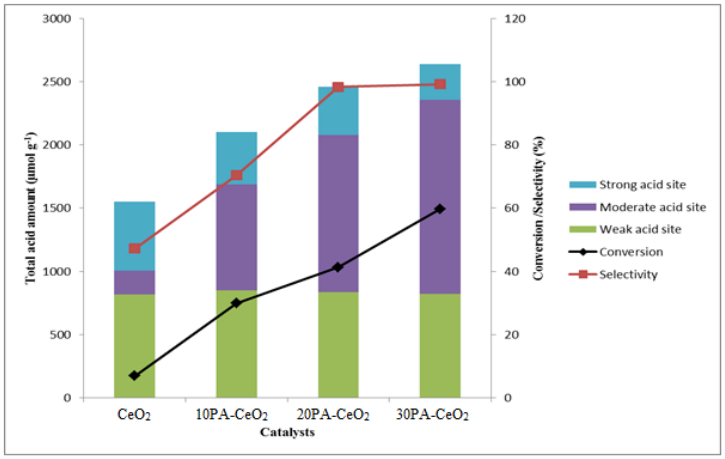



Figure 4. Relationship between catalytic performances and acid amounts

The presence of moderate weak acidic sites in this catalyst helps to suppress the formation of higher hydrocarbons meanwhile improved the ethylene production and selectivity. Besides that, based on the $N_2$ physisorption results $CeO_2$ has a large BET surface area and high porosity which lead to the $C_2H_5OH$ molecules would have voyage

profound into the arrangement of passage systems that exists in the pristine $CeO_2$. The blockage of pore volume after the addition of $H_3PO_4$ helps in reducing the multiple adsorptions of ethanol whereby results in the improvement in ethylene selectivity [22].

In addition, 10, 20 and 30PA-$CeO_2$ present an increasing trend in both ethanol conversion and ethylene selectivity as the temperature increases. Among all the $CeO_2$ and $H_3PO_4$-modified $CeO_2$ catalysts, 30PA-$CeO_2$ catalyst showed the best catalytic performance. With increasing reaction temperature, both ethanol conversion and ethylene selectivity increased, *viz*. conversion of ethanol increased from 15.97% at 673 K to 59.74% at 773 K, whilst the ethylene selectivity improved from a low of 96.14% at 673 K to 99% at 773 K. This showed that the dehydration activity of 30PA-$CeO_2$ catalyst improved with reaction temperature. This indicates that $H_3PO_4$ functioned more effectively with reaction temperature, *i.e*. its acidity property can be tailored to the reaction temperature and thus, able to protonate the hydroxyl group of $C_2H_5OH$ molecule.

**Post reaction study**

Among all $CeO_2$ and $H_3PO_4$-modified $CeO_2$ catalysts, 30PA-$CeO_2$ catalysts showed the best catalytic performance. The 30PA-$CeO_2$ catalyst was collected for post reaction characterization. The used 30PA-$CeO_2$catalysts at different reaction temperatures (673 K, 723 K and 773 K) were collected and were subjected to further examinations. Figure 5 shows the SEM image of the post-reaction 30PA-$CeO_2$ catalysts. It can be visualized that there are not much changes to the catalysts' morphology. In addition, no visible carbon formation was found after the reaction. This result suggests that the addition of 30wt% phosphoric acid enhance the stability of catalysis by weakening the strong acidic sites into moderate weak acidic sites. This prevent the double bond which is π bond found in $C_2H_4$ is electron rich from being attracted toward the acidic catalyst surface and form single C-C bond which lead to coke formation [23].

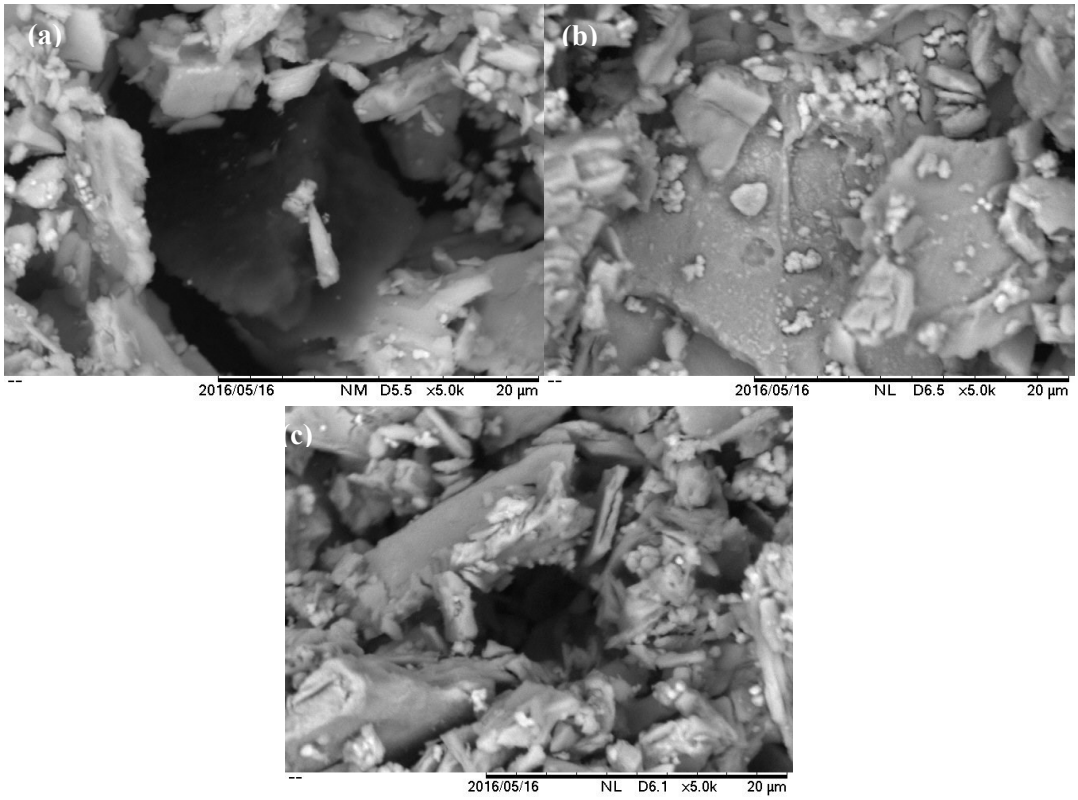



Figure 5. SEM images of 30PA-$CeO_2$ catalysts at ethanol partial pressure 33 kPa and (a) 673 K (b) 723 K and (c) 773 K.

TG analysis was performed to study the thermal profile of the spent 30PA-$CeO_2$ catalysts. The TG analysis was performed from 298 K to 1173 K, each time. As shown in Figure 6, weight loss in the used catalyst at all reaction temperatures are small. Indeed, the total weight loss of used 30PA-$CeO_2$ at reaction temperature 673 K was about 0.84 wt.%. For the used 30PA-$CeO_2$ catalyst at reaction temperatures of 723 K and 773 K, the weight losses at 873 K and 1073 K were 0.86 wt.% and 0.915 wt.%, respectively. This weight loss can be ascribed to the loss of water in catalyst and was consistent with the SEM results where no visible carbon formation was found. The results obtained also indicate that 30PA-$CeO_2$ catalyst was thermally stable.

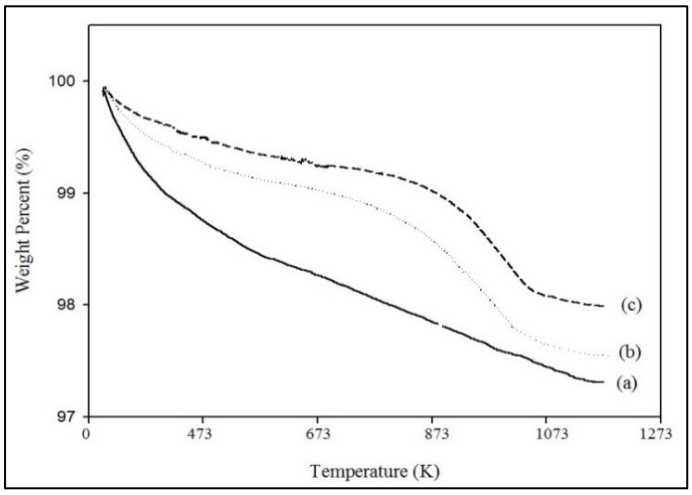



Figure 6. TGA profiles of used 30PA- $CeO_2$ catalysts at (a) 673 K, (b) 723 K and (c) 773 K

## Conclusion

This project focuses on the catalytic performance of ethanol to ethylene on $H_3PO_4$-modified $CeO_2$ (various loadings of $H_3PO_4$) catalysts and the influences of $H_3PO_4$ on ethanol conversion over the synthesized catalysts. The addition of phosphorus acid to the $CeO_2$ catalyst improved the catalytic performance and catalyst stability for ethanol dehydration to ethylene. These improvements are due to the tuned acid sites and reduction of BET specific surface areaby preventing coke formation and blocking the accessibility of reactants to the acid sites.The $H_3PO_4$-modified $CeO_2$ catalysts showed increasing trend in ethanol conversion and ethylene selectivity with the loading of phosphorus. The post reaction analyses on the 30PA-$CeO_2$ catalyst (the best performing catalyst) also showed that the introduction of $H_3PO_4$ acid has helped in maintaining coke-free surface that would have otherwise caused catalyst deactivation. This can be attributed to the mild acidity sites available on the 30PA-$CeO_2$ catalyst.

## Acknowledgement

We thank Universiti Malaysia Pahang for providing UMP Short Term Grant RDU160335 to support this work.

## References

1. Morschbacker, A. (2009). Bio-ethanol based ethylene.*Polymer Review*, 49 :79 – 84.
2. Takahara, I., Saito, M., Inaba, M. and Murata, K. (2005). Dehydration of ethanol into ethylene over solid acid catalysts.*Catalysis Letters*, 10(3–4): 249 – 252.
3. Fan, D., Dai, D.-J., and Wu, H.-S. (2012). Ethylene formation by catalytic dehydration of ethanol with industrial considerations. *Materials (Basel)*, 6(1): 101 – 115.
4. Aguayo, A. T., Gayubo, A. G., Atutxa, A., Valle, B. and Bilbao, J. (2015). Regeneration of a HZSM-5 zeolite catalyst deactivated in the transformation of aqueous ethanol into hydrocarbons. *Catalysis Today*, 107 – 108: 410 – 416.

5. Phung, T. K., Radikapratama, R., Garbarino, G., Lagazzo, A., Riani, P. and Busca, G. (2015). Tuning of product selectivity in the conversion of ethanol to hydrocarbons over H-ZSM-5 based zeolite catalysts. *Fuel Processing Technology*, 137: 290 – 297.
6. Phung,T. K., Proietti Hernández, L.,Lagazzo, A. and Busca, G. (2015). Dehydration of ethanol over zeolites, silica alumina and alumina: Lewis acidity, Brønsted acidity and confinement effects. *Applied Catalysis A General*, 493: 77 – 89.
7. Varisli, D., Dogu, T. and Dogu, G. (2007). Ethylene and diethyl-ether production by dehydration reaction of ethanol over different heteropolyacid catalysts. *Chemical Engineering Science*, 62: 5349 – 5352.
8. Madeira, F. F., Gnep, N. S., Magnoux, P., Maury, S. and Cadran, N. (2009). Ethanol transformation over HFAU, HBEA and HMFI zeolites presenting similar Brønsted acidity. *Applied Catalysis A General*, 367(1–2): 39 – 46.
9. Zhan, N., Hu, Y., Li, H., Yu, D., Han, Y. and Huang, H. (2010). Lanthanum-phosphorous modified HZSM-5 catalysts in dehydration of ethanol to ethylene: A comparative analysis. *Catalysis Communications*, 11(7): 633 – 637.
10. DeWilde, J. F., Chiang, H., Hickman, D., Ho, C. R., and Bhan, A. (2013). Kinetics and mechanism of ethanol dehydration on $\gamma$-$Al_2O_3$: Tthe critical role of dimer inibition. *ACS Catalysis*, 3(4): 798 – 807.
11. Cai, W., Wang, F.,Zhan, E.,Van Veen, A. C., Mirodatos, C. and Shen,W. (2008). Hydrogen production from ethanol over Ir/$CeO_2$ catalysts: A comparative study of steam reforming, partial oxidation and oxidative steam reforming. *Journal of Catalysis*, 257(1): 96 – 107.
12. Diagne, C., Idriss, H. and Kiennemann, A. (2002). Hydrogen production by ethanol reforming over Rh/$CeO_2$–$ZrO_2$ catalysts. *Catalysis Communications*, 3(12): 565 – 571.
13. Mudiyanselage, K., Al-Shankiti, I., Foulis, A., Llorca, J. and Idriss, H. (2016). Reactions of ethanol over $CeO_2$ and Ru/$CeO_2$ catalysts. *Applied Catalysis B Environmental*, 197: 198 - 205.
14. Wang, H., Ye, J., Liu, Y., Li, Y. and Qin, Y. (2007). Steam reforming of ethanol over $Co_3O_4$/$CeO_2$ catalysts prepared by different methods. *Catalysis Today*, 129(3–4): 305 – 312.
15. Zhang, B., Tang, X., Li, Y., Cai, W., Xu, Y. and Shen, W. (2006). Steam reforming of bio-ethanol for the production of hydrogen over ceria-supported Co, Ir and Ni catalysts. *Catalysis Communications*, 7(6): 367–372.
16. Ramesh, K., Jie, C., Han, Y. F. and Borgna, A. (2010). Synthesis, characterization, and catalytic activity of phosphorus modified H-ZSM-5 catalysts in selective ethanol dehydration. *Industrial Engineering Chemistry Research*, 49(9): 4080 – 4090.
17. Zhang, X., Wang, R., Yang, X. and Zhang, F. (2008). Comparison of four catalysts in the catalytic dehydration of ethanol to ethylene. *Microporous Mesoporous Materials*, 116(1–3): 210 – 215.
18. Yacob, A. R., Bello, A. M. and Kabo, K. S. (2016). The effect of polyoxyethylene (40) stearate surfactant on novel synthesis of mesoporous $\gamma$-alumina from Kano kaolin. *Arabian Jounal of Chemistry*, 9(2): 297 –3 04.
19. White, K. M., Lee, P. L., Chupas, P. J., Chapman, K. W., Payzant, E. A., Jupe, A. C., Bassett, W. A., Zha, C. S. and Wilkinson, A. P. (2008). Synthesis, symmetry, and physical properties of cerium pyrophosphate. *Chemistry of Materials*, 20(11): 3728 – 3734.
20. Armaroli, T., Busca, G., Carlini, C., Giuttari, M., Raspolli Galletti, A. M. and Sbrana, G. (2000). Acid sites characterization of niobium phosphate catalysts and their activity in fructose dehydration to 5-hydroxymethyl-2-furaldehyde. *Journal of Molecular Catalysis A Chemical*, 151(1): 233 – 243.
21. Brandão, R. F., Quirino, R. L., Mello,V. M., Tavares, A. P., Peres, A. C.,Guinhos, F., Rubim, J. C. and Suarez, P. A. Z. (2009). Synthesis, characterization and use of $Nb_2O_5$ based catalysts in producing biofuels by transesterification, esterification and pyrolysis. *Journal of the Brazilian Chemical Society*, 20(5): 954 – 966.
22. Ramesh,K., Hui, L. M., Han,Y. F., and Borgna, A. (2009). Structure and reactivity of phosphorous modified H-ZSM-5 catalysts for ethanol dehydration. *Catalysis Communications*, 10(5): 567 – 571.
23. Zaera, F. (2001). Probing catalytic reactions at surfaces. *Progress Surface Science*, 69(1):1 – 98.

*Malaysian Journal of Analytical Sciences, Vol 21 No 4 (2017): 849 - 859*
*DOI: https://doi.org/10.17576/mjas-2017-2104-11*

MALAYSIAN JOURNAL OF ANALYTICAL SCIENCES
*Published by The Malaysian Analytical Sciences Society*
ISSN 1394 - 2506

# GAS PHASE GLYCEROL DEHYDRATION TO ACROLEIN USING SUPPORTED SILICOTUNGSTIC ACID CATALYST

## (Penyahhidratan Gliserol Fasa Gas Kepada Akrolein Menggunakan Sokongan Mangkin Asid Silikotungstik)

Amin Talebian-Kiakalaieh and Nor Aishah Saidina Amin*

*Chemical Reaction Engineering Group (CREG), Faculty of Chemical and Energy Engineering, Universiti Teknologi Malaysia, 81310 Johor Bahru, Johor, Malaysia*

**Corresponding author: noraishah@cheme.utm.my*

Received: 20 September 2016; Accepted: 16 May 2017

**Abstract**

The gas phase dehydration of glycerol to acrolein over a series of supported silicotungstic acid (HSiW) on γ-$Al_2O_3$ nanoparticle ($W_{10}$-Al, $W_{20}$-Al, $W_{30}$-Al and $W_{40}$-Al) has been investigated. The catalysts were characterized by temperature programmed desorption, nitrogen adsorption–desorption, thermogravimetric analysis, X-ray diffraction, field-emission scanning electron microscopy and energy dispersive X-ray techniques. The large pore diameters (>21 nm) of the prepared catalysts alleviated the coke deposition effect. The acidity of the samples increased from 2 to 2.6 mmol/g.cat by varying HSiW loadings from 10 to 40 wt.% on γ-$Al_2O_3$ nanoparticle. The highest acrolein yield achieved was 74.1% at 94% glycerol conversion over $W_{20}$-Al catalyst for 10 wt% glycerol feed concentration and 300 ˚C reaction temperature in 3 hours. The combined physicochemical characteristics of $W_{20}$-Al made it more superior compared with other samples in the current study.

**Keywords**: acrolein, dehydration, glycerol, supported silicotungstic acid

**Abstrak**

Penyahhidratan gliserol fasa gas kepada akrolein dengan menggunakan satu siri asid silikotungstik disokong (HSiW) terhadapnanopartikel γ-$Al_2O_3$ ($W_{10}$-Al, $W_{20}$-Al, $W_{30}$-Al, dan $W_{40}$-Al) telah dikaji. Mangkin-mangkin tersebut dicirikan oleh penyahjerapan suhu terprogram, penjerapan-penyahjerapan nitrogen, analisis termogravimetrik, pembelauan sinar X, mikroskop pengimbasan elektron pancaran medan, dan teknik penyerakan tenaga sinar X. Diameter liang besar (>21 nm) bagi mangkin yang disediakan dapat mengurangkan kesan pemendapan kok. Keasidan sampel meningkat daripada 2 hingga 2.6 mmol/g.cat dengan mengubah beban HSiW daripada 10 hingga 40 wt.% pada nanopartikel γ-$Al_2O_3$. Hasil akrolein tertinggi yang dicapai adalah 74.1% pada 94% penukaran gliserol terhadap mangkin $W_{20}$-Al bagi 10 wt.% kepekatan suapan gliserol dan 300 °C suhu tindak balas dalam masa 3 jam. Ciri-ciri gabungan fizikokimia $W_{20}$-Al menjadikannya lebih unggul berbanding sampel lain dalam kajian semasa.

**Kata kunci: a**krolein, penyahhidratan, gliserol, asid silikotungstik disokong

## Introduction

Production of value added chemicals from renewable sources as substitute for conventional petroleum-based processes is a hot issue recently. The huge glycerol availability due to large scale production of biodiesel worldwide provides spectacular opportunities for researchers to evaluate its application as a bio-renewable feedstock in future refineries [1, 2]. In addition, glycerol characteristics such as bio-degradability, non-toxicity, and its multi functional structure made it as one of the top 12 most important bio-based chemicals in the world [3]. Glycerol can be used in

production of more than 2000 value-added chemicals [4, 5]. One of the most important products which can be produce from glycerol during a bio-based process is acrolein which is a substitute for petroleum based propylene oxidation process [6]. Acrolein is one of the versatile intermediates in chemical industry due to its wide utilization for acrylic acid, superabsorbent polymer, 1,3-propanediol, and many more polymers or polyesters production.

Wide ranges of studies have been reported for application of solid acid catalysts such as heteropoly acids [7 – 9], zeolites [10, 11], and metal oxides [12 – 14] in gas or liquid phases of glycerol dehydration to acrolein during the last decade, but still there is no catalyst which exhibit long-term stability without severs deactivation with prospect for industrialization. Among various reported catalysts, supported heteropoly acid (HPA) is attracted much attention due to its stronger acidity (Bronsted acidic sites) and higher activity compared to other catalysts. It is reported that the Bronsted acidic site is more effective than Lewis acidic site for acrolein production [15]. The low specific surface area (1 – 10 $m^2/g$) and thermal stability are the main limitations of HPAs. Therefore, to overcome these drawbacks HPAs are often support on a carrier such as alumina, zirconia, and silica. Alumina showed better results due to strong electrical interaction with HPAs and also enhancement of their thermal stability [16]. However, application of $Al_2O_3$ nanoparticles as a support for HPAs is never reported before. Suitable pore structure and high surface acidity are the key components for higher activity of catalyst for acrolein production [17, 18].

One of the main obstacles for industrialization of bio-based glycerol dehydration to acrolein is fast deactivation of catalyst by coke deposition. For example, the Cs-HPW catalyst is reported as the highest active catalyst in gas phase dehydration of glycerol to acrolein with 98% acrolein selectivity at 100% glycerol conversion, but this catalyst only could last for a few hours and its activity dropped dramatically beyond this time [19]. Some catalyst characteristics such as small pore diameter, very strong acidic sites, and high reaction temperature promote coke deposition [16]. Various researchers proposed different methods for slowing down or eliminating the coke deposition on the catalyst surface such as co-feeding of oxygen or hydrogen. However, this process may increase the probability of explosive conditions or oxidation of products which finally decrease the acrolein selectivity. Besides, some other researchers studied the catalyst structure by addition of noble metals to improve catalyst activity and stability [20, 21]. The main objective of this study is to synthesize a supported HSiW catalyst with $\gamma$-$Al_2O_3$ nanoparticles for the first time to obtain a catalyst with high surface acidity, large specific surface area, large pore diameter and high thermal stability for increasing glycerol conversion and its selectivity to acrolein.

## Materials and Methods

### Catalyst preparation

A series of catalysts with various HSiW loadings (10, 20, 30, and 40 wt.%) on $\gamma$-$Al_2O_3$ were prepared by the incipient-wetness impregnation method. In this method, aqueous HSiW solutions were added drop-wise to the $\gamma$-$Al_2O_3$ nanoparticles support. The slurries were rigorously stirred for 12 h followed by drying at 110 ˚C for 18 hours. The HSiW-$Al_2O_3$ supported catalysts were denoted as $W_{10}$-Al, $W_{20}$-Al, $W_{30}$-Al, and $W_{40}$-Al for 10, 20, 30 and 40 wt.% of HSiW loading, respectively.

### Characterization

Nitrogen adsorption/desorption at -196 ˚C was employed to determine the BET specific surface area, pore volume, and average pore diameter (Thermo Scientific, SURFAR). Prior to analysis, the sample was degassed under vacuum at 200 ˚C for 4 hours for purification and complete removal of adsorbed moisture. The BJH method was used for average pore diameter calculation. Thermogravimetric analysis (TG-DTA) of prepared catalyst was performed using a THERMO TGA instrument in a temperature range of 30 to 800 ˚C with a ramp rate of 10 K/min under nitrogen flow. The morphology of the samples was observed by Field Emission Scanning Electron Microscopy (FESEM, HITACHI, SU-8000) with the STEM detector. The total acidity of the prepared catalysts was determined by temperature programmed desorption of ammonia ($NH_3$-TPD) using the Micrometrics Auto Chem II instrument. A specific amount of catalyst was dried at 200 ˚C for 1 hour by saturation of $NH_3$ at 60 ˚C for 0.5 hour before the physically adsorbed $NH_3$ was removed by helium purging at 60 ˚C for 0.5 hour. X-ray diffraction (XRD) was used to determine the structure of the prepared catalysts and to evaluate the degree of crystallinity. The XRD patterns were obtained by D5000 Siemens instrument using Cuk$\alpha$ radiation (40 kev, 40 mA). The patterns were scanned in the 2$\theta$ range of 10 – 80˚ (step width 0.05˚, 1s per step).

**Catalytic reaction**

The gas phase dehydration of glycerol was conducted under atmospheric pressure in a vertical fixed bed quartz reactor (30 cm length, 11 mm i.d.) using 0.5 – 1 g catalyst sandwich between plugs of glass wool. Prior to reaction, the catalyst was pretreated at 300 ˚C under nitrogen ($N_2$) flow (1200 ml/h) for 1 hour. Liquid aqueous solution of glycerol (10 wt.%) introduced to the pre-heater (300 ˚C) by a syringe pump for complete vaporization and then swept into the reactor with 2 ml/h flow rate. Gas hourly speed velocity (GHSV) of the inert carrier gas was 1200 $h^{-1}$. The products and unconverted glycerol were condensed in a water-ice–salt bath (-5 ˚C) and collected each hour for analysis. n-Butanol was added to the condensed products as internal standard. The final solution was analyzed by a gas chromatograph (GC), which equipped with capillary column (DB Wax; 30 m × 0.53 mm × 0.25 μm) and FID detector. To achieve effective product separation, the column was held at 40 ˚C for 4 minutes before the temperature was ramped up to 200 ˚C with a rate of 12 K/min. The glycerol conversion, product selectivities and yields are defined by equations (1) to (3):

$$Con_{Gl}(\%) = \frac{M_{Gl,\ in\ \ feed} - M_{Gl,\ in\ \ outlet}}{M_{Gl,\ in\ \ feed}} \times 100\% \quad (1)$$

$$Sel_N(\%) = \frac{M_{C\ \ in\ \ product}}{M_{C\ \ in\ \ Gl,\ \ feed} - M_{C\ \ in\ \ Gl,\ \ outlet}} \times 100\% \quad (2)$$

$$Yield_N(\%) = Con_{Gl}(\%) \times Sel_N(\%) \quad (3)$$

where, $M_{Gl}$, $M_C$, $Con_{Gl}$, $Sel_N$, and $Yield_N$ are moles of glycerol, moles of carbon for each product, glycerol conversion, selectivity and yield of each product (N), respectively.

## Results and Discussion

**Surface area and pore structure analysis**

The textural characteristics, specific surface area ($S_{BET}$), pore volume ($V_P$), average pore diameter ($D_P$) of supported HSiW catalysts derived from nitrogen physisorption isotherms are presented in Table 1. The specific surface areas of bulk γ-$Al_2O_3$ and HSiW are 143.2 and 8.2 $m^2/g$, respectively. By increasing the HSiW loading from 10 to 40 wt.% on the γ-$Al_2O_3$, the surface areas of the prepared catalysts decreased from 140.5 to 76.6 $m^2/g$. The reduction of surface area during the catalyst preparation steps was due to the plugging of pores by agglomeration [22], crystallization of active compounds (HSiW), and formation of monolayer HSiW surface with less surface area [23]. Impregnation of HSiW on γ-$Al_2O_3$ also led to reduction of pore volume from 0.5 to 0.2 $cm^3/g$ for pure γ-$Al_2O_3$ to $W_{40}$-Al. In fact, the highest amount of HSiW loading on alumina diminished approximately 50% of the pore volume. The average pore diameter seems to be not effected and it remained stable with about 21 nm.

Table 1. Bulk and supported samples surface area ($S_{BET}$), pore volume (Pv), and pore diameter (Pd)

| Catalyst | $S_{BET}$ ($m^2/g$) | $V_p$ ($cm^3/g$) | $D_p$ (nm) |
|---|---|---|---|
| HSiW | 8.2 | 0.02 | 10.3 |
| $Al_2O_3$ | 143.2 | 0.5 | 22.5 |
| $W_{10}$-Al | 140.5 | 0.4 | 21.0 |
| $W_{20}$-Al | 125.7 | 0.4 | 21.5 |
| $W_{30}$-Al | 115.7 | 0.4 | 21.1 |
| $W_{40}$-Al | 76.6 | 0.2 | 21.6 |

**Acidity ($NH_3$-TPD)**

The prepared catalysts were analyzed by temperature programmed desorption of ammonia ($NH_3$-TPD) to determine the amount and strength of acidity (Table 2 and Figure 1). The strength of acid sites was divided into three categories of weak (150 – ≤300 ˚C), medium (300 – ≤450 ˚C), and strong (>450 ˚C). The position and area of the TPD peaks are closely related to the acid amount and strength [24]. The total acidity of bulk HSiW and γ-$Al_2O_3$

were 1.62 and 1.2 mmol/g.cat, respectively. The HSiW possessed the highest acid strength due to its weak and strong acidic sites compared to the $\gamma$-$Al_2O_3$ with only weak acidity.

Table 2. $NH_3$-TPD acidity of bulk and supported silicotungstic acid catalysts

| Cat | Weak (100 – 300 ˚C) | | Medium (300 – 450 ˚C) | | Strong (>450 ˚C) | | Total[c] |
|---|---|---|---|---|---|---|---|
| | Peak (˚C)[a] | Acidity[b] | Peak (˚C) | Acidity | Peak (˚C) | Acidity | |
| HSiW | 131 & 250 | 0.02 | - | - | 530 | 1.6 | 1.62 |
| $Al_2O_3$ | 127 & 287 | 1.2 | - | - | - | - | 1.2 |
| $W_{10}$-Al | 132 | 1 | 300 | 1 | - | - | 2 |
| $W_{20}$-Al | 137 | 0.5 | 301 | 1.8 | - | - | 2.3 |
| $W_{30}$-Al | 135 | 0.5 | 311 | 2 | - | - | 2.5 |
| $W_{40}$-Al | 136 | 0.6 | 317 | 2 | - | - | 2.6 |

[a] Peak position, [b]Acid amount ($NH_3$/Cat, mmol/g), [c] Total acidity (mmol/g.cat)

The acidity increased significantly from 2 to 2.6 mmol/g.cat by increasing the HSiW loading from 10 to 40 wt.% on $\gamma$-$Al_2O_3$. All the samples displayed two peaks at 135 and 300 ˚C which related to the weak and medium acidic sites. Also, the strength of the medium acid sites was higher than the weak ones. For instance, the $W_{30}$-Al and $W_{40}$-Al approximately have 4 times (2 mmol/g.cat) stronger medium acidic sites than their weak acidic sites (0.5-0.6 mmol/ g cat). Also, $NH_3$ peak positions of weak and medium acidity showed small shifts from 132 – 136 ˚C and 300 – 317 ˚C which confirmed increasing the acidic cites strength (Figure 1). The main reason is the electric interaction between HSiW and support ($\gamma$-$Al_2O_3$). In fact, during the impregnation process the hydroxyl groups on the surface of $\gamma$-$Al_2O_3$ were protonated with water which caused a positive charged surface. Finally, the HSiW addition leads an electric interaction. The strength of this interaction depends on the type of support which is stronger for alumina [7, 16].

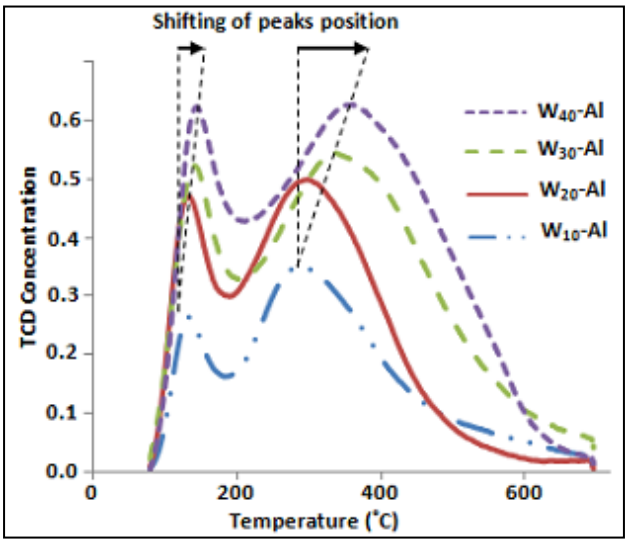



Figure 1. $NH_3$-TPD profiles of supported ($W_{10\text{-}40}$-Al) samples

**X-ray diffraction**

The X-ray diffraction (XRD) patterns of the supported HSiW (10 – 40 wt.%) on $\gamma$-$Al_2O_3$ nanoparticles are shown in Figure 2. The pure HSiW illustrates three main peaks (2$\theta$ = 10.9˚, 25.5˚, and 34.7˚) which attributed to its Keggin

anions. Besides, the diffraction peaks related to the pure γ-$Al_2O_3$ appeared at $2\theta$ = 18.75˚, 36.9˚, 44.2˚ and 67.3˚. However, increasing the HSiW loading from 10 to 40 wt.% on the support caused a reduction in diffraction peaks of γ-$Al_2O_3$ and also the reduction magnitude surged. It is noted that none of the supported catalysts illustrates peaks attributed to the HSiW Keggin structure, which demonstrated high dispersion of HSiW on the support. Similar results reported previously [25 – 27]. The main reason for highly uniform dispersion of HSiW on the γ-$Al_2O_3$ surface is the size of the Keggin anions (D = 1.2 nm) and the large specific surface area of γ-$Al_2O_3$ nanoparticles ($S_{BET}$ = 143.2 $m^2$/g). Atia et al. [16] mentioned that only >80 wt.% HSiW loading can saturate the support surface. In fact, XRD can detect HSiW crystals whenever high concentration of HSiW saturate the γ-$Al_2O_3$ surface and then some HSiW molecules cannot reach the support meso-pores and crystallise as separate phase.

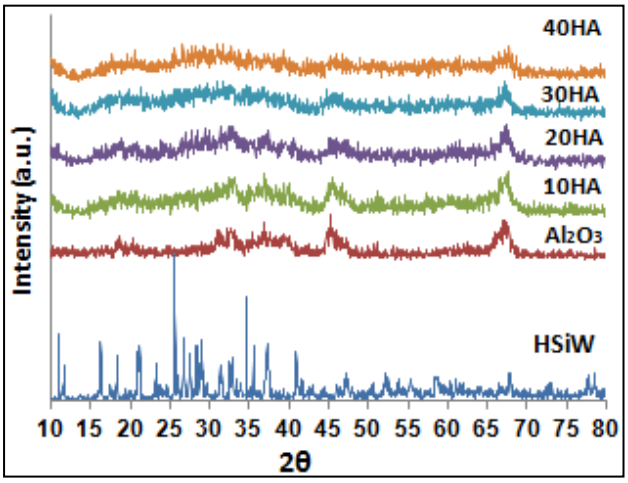



Figure 2. XRD patterns of the pure and supported prepared catalysts

**Thermal stability**

Figure 3 displays the TG-DTA curves of pure γ-$Al_2O_3$, HSiW, and supported $W_{20}$-Al samples. It can clearly be seen that pure γ-$Al_2O_3$ lost weight with heating from 30 to 800 ˚C. The alumina DTA curves exhibits a broad band peak at 70 ˚C which related to the loss of physically adsorbed water. Afterwards, only a little weight loss observed at 250 ˚C which attributed to the dehydroxylation of hydroxyl groups. Both TG and DTA curves of the bulk HSiW registered three steps of weight losses. The first two weigh losses of 8% and 3% at 85 and 200 ˚C, respectively are referred to the loss of physically absorbed water and removal of water from HSiW hydrated heteropoly acid [28, 29]. However, the third weight loss (1%) at 500 ˚C related to decomposition of the HSiW Keggin anions [16]. Further loading of $WO_3$ led to new broad band at 3500 $cm^{-1}$ crystallite planes, respectively.

Finally the prepared $W_20$-Al catalyst shows one broad peak at 80 ˚C corresponds to the loss of physically adsorbed water (DTA curve). The second weight loss observed at 350 ˚C which attributed to the removal of structural water molecules. However, no important structural changes were observed in the rest of analysis which confirmed high thermal stability of the $W_{20}$-Al sample. In fact, this high stability of $W_{20}$-Al catalyst was referred to the electronic interaction between HSiW and γ-$Al_2O_3$ [7, 24]. Scheme 1 depicts different decomposition steps of HSiW and it clearly confirmed that full decomposition happened in >500 ˚C and the second weight loss of $W_{20}$-Alat 350 ˚C was not the decomposition peak. Remarkably, the prepared catalyst showed high stability even in high temperatures compared to some similar catalysts in previous studies such as HSiW/SBA-15, 30%HSiW-Al, 20%HSiW/A5, 20%HSiW/AS4 which were unstable at temperatures above 480 ˚C [16, 20, 24].

$$H_4SiW_{12}O_{40}nH_2O \xleftrightarrow[<200\ \ ^\circ C]{-nH_2O} H_4SiW_{12}O_{40} \xleftrightarrow[>500\ \ ^\circ C]{-2H_2O} SiW_{12}O_{38} \rightarrow 12WO_3 + SiO_2$$

Scheme 1. Different steps of silicotungstic acid thermal decomposition

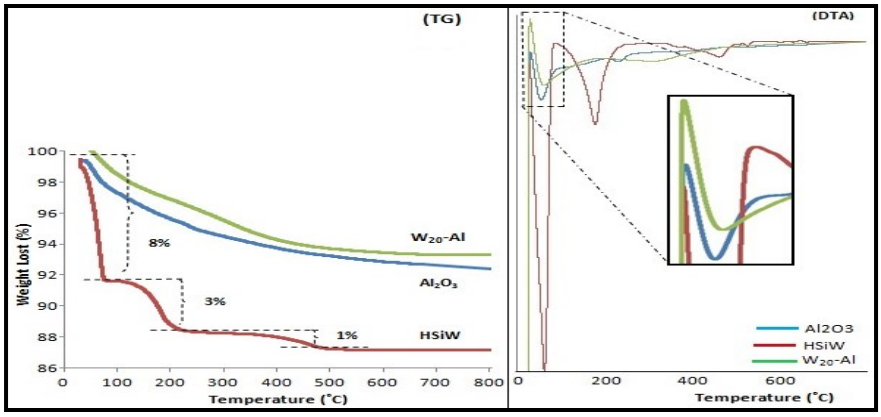



Figure 3. TG-DTA plots for non-supported and supported silicotungstic acid catalysts

**Morphological analysis**

The surface morphology of the fresh and used $W_{20}$-Al samples was examined by FESEM (Figure 4). HSiW seems to be dispersed on the external surface of the alumina and filling the voids between the particles with in a gain (Figure 4a-b). As results the specific surface area decreased from 143.2 to 125.7 $m^2/g$ for pure γ-$Al_2O_3$ and $W_{20}$-Al catalyst respectively according to the BET results.Fortunately, no dramatic change in catalyst surface morphology was observed after dehydration reaction (Figure 4c-d). Indeed, FESEM study demonstrated that the catalyst morphological characteristics remain unaffected during the reaction due to high hydrothermal stability of catalyst (confirmed by TGA results), similar results reported elsewhere [30 – 32].The EDX analysis results related to the fresh $W_{20}$-Al sample are exhibited in Figure 4e. The EDX mapping confirms an extremely uniform distribution of alumina (Figure 4f) and tungsten (Figure 4g) elements throughout the $W_{20}$-Al catalyst. In addition, the EDX analysis reveals 71.83% and 17.34% weight percentages of Al and HSiW in this catalyst which found to be very close to the theoretical values of 80 and 20 wt% of γ-$Al_2O_3$ and HSiW, respectively (Figure 4h).

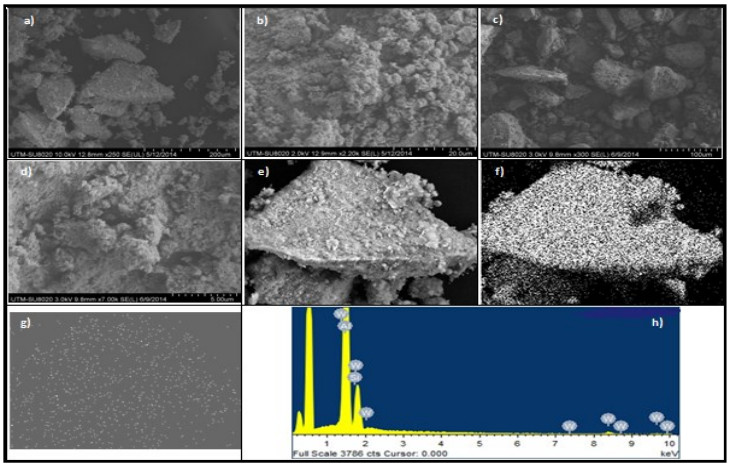



Figure 4. Field emission scanning electron microscopy of fresh and used supported *$W_{20}$-Al* catalyst (a-b), used *$W_{20}$-Al*catalyst (c-d), and EDX mapping analysis of the fresh catalyst: (e) EDX mapping, (f) alumina, (g) tungsten, and (h) EDX mapping result

**Catalytic performance**

Application of bulk samples (HSiW and γ-$Al_2O_3$) in gas phase dehydration of glycerol could not obtain more than 38.1% selectivity of acrolein. These results demonstrate that the strong Lewis acid sites samples (γ-$Al_2O_3$) and even

the strong Bronsted acid site catalyst (HSiW) were not suitable for high acrolein selectivity. Indeed, the strong Lewis acid sites increase the byproducts production and the strong Bronsted acids enhanced coke formation on catalyst surface. Therefore, impregnation of HSiW on support ($\gamma$-$Al_2O_3$) is required to increase the glycerol conversion and acrolein selectivity.

The gas phase dehydration of glycerol to acrolein was investigated by the $\gamma$-$Al_2O_3$ supported HSiW (10 to 40 wt.%) catalyst at different temperatures (280, 300, and 320 ˚C) in 3 hours reaction time (Table 3). The results indicated that increasing the HSiW loading from 10 to 20 wt.% led to higher acrolein selectivity but HSiW loading above 20% slightly reduce the selectivity of acrolein or remained constant. Indeed, impregnation of HSiW on $\gamma$-$Al_2O_3$ caused a significant increase in catalyst activity compared to the pure HSiW due to increase in the total amount of catalytically active protons in the supported catalyst. On the other hand, well dispersed catalyst provides higher accessibility of glycerol molecules to the active compounds of supported catalyst. However, the main reason for reduction of acrolein selectivity or catalyst activity for HSiW loading above 20 wt.% is deposition of a huge amount of active compounds (HSiW) over $\gamma$-$Al_2O_3$ which cause second surge in the acid strength. Consequently, the coke deposition process on the surface of catalyst increase which has negative effect on acrolein selectivity [33].

The highest acrolein selectivity of 74.1% obtained over the $W_{20}$-Al supported catalyst with 94% glycerol conversion at 300 ˚C. Also, increasing the temperature from 280 to 320 ˚C has significant impact on glycerol conversion. The reaction conversion increased from 90% to 97% for 280 to 320 ˚C, respectively. All the reaction products such as ethanal, propanol, acetic acid, and hydroxyacetone selectivities are summarized in Table 3.

Table 3. Catalytic performance of the bulk and supported (10 to 40 wt.%) silicotungstic acid on nano sized alumina for glycerol dehydration to acrolein[a]

| Catalyst | T (˚C) | X (%) | Y (%)[b] | Selectivity (%) | | | | | | | |
|---|---|---|---|---|---|---|---|---|---|---|---|
| | | | | AC[c] | Eth[d] | Pr[e] | Ace[f] | Hyd[g] | Ala[h] | Aca[i] | Total |
| Blank | 300 | 56 | 11.6 | 20.7 | - | - | 3.8 | 22.9 | - | 18.3 | 65.7 |
| $Al_2O_3$ | 300 | 80 | 30.2 | 37.7 | 0.2 | 0.2 | 3.8 | 7.6 | 2.7 | 1.2 | 53.5 |
| HSiW | 300 | 85 | 32.4 | 38.1 | 4.2 | 5.9 | 4.5 | 16.6 | 5.1 | 11.2 | 85.6 |
| $W_{10}$-Al | 280 | 89 | 50.6 | 56.8 | 6.9 | 5.5 | 4.5 | 12.5 | 1.5 | 3.8 | 91.5 |
| | 300 | 92 | 55.4 | 60.2 | 4.5 | 4.2 | 3.4 | 10.7 | 1.3 | 6.1 | 90.6 |
| | 320 | 93 | 50.8 | 54.6 | 8.7 | 3.3 | 3.9 | 14.1 | 1.9 | 6.3 | 92.7 |
| $W_{20}$-Al | 280 | 90 | 64.2 | 71.3 | 2.2 | 2.1 | 3.1 | 3.6 | 4.1 | 8.3 | 94.7 |
| | 300 | 94 | 69.7 | 74.1 | 1.1 | 1.1 | 2.4 | 3.3 | 5.8 | 5.3 | 93.2 |
| | 320 | 97 | 60.7 | 62.6 | 3.9 | 4.9 | 5.6 | 5.6 | 5.5 | 6.7 | 94.7 |
| $W_{30}$-Al | 280 | 87 | 53.2 | 61.1 | 4.9 | 3.6 | 5.3 | 7.9 | 4.1 | 5.8 | 92.8 |
| | 300 | 91 | 60.9 | 66.9 | 4.1 | 4.9 | 5.4 | 6.1 | 1.3 | 6.1 | 94.8 |
| | 320 | 93 | 55.6 | 59.7 | 5.2 | 5.9 | 4.8 | 6.2 | 8.5 | 4.8 | 95.2 |
| $W_{40}$-Al | 280 | 86 | 55.8 | 64.8 | 5.4 | 4.3 | 5.9 | 5.9 | 1.5 | 6.5 | 94.4 |
| | 300 | 88 | 56.3 | 64.0 | 5.2 | 5.2 | 4.4 | 7.9 | 1.8 | 6.4 | 94.8 |
| | 320 | 95 | 58.8 | 61.9 | 4.6 | 4.1 | 3.6 | 9.5 | 1.2 | 7.2 | 92.1 |

[a] Reaction condition: Feed: 2 ml/h, 10 wt% aqueous glycerol solution, Carrier gas: 20 ml/min, Reaction temperature: 300˚C, Time on Stream (TOS = 3 h), 0.5 g catalyst weight. [b] Acrolein yield, [c] Acrolein, [d] Ethanal, [e] Propanal, [f] Hydroxyacetone, [g] Allyl alcohol, [h] Acetic acid.

The strong interaction between HSiW and $\gamma$-$Al_2O_3$ is required for long-life stability of catalyst [34]. The TG-DTA results demonstrated the strong binding between HSiW and $\gamma$-$Al_2O_3$ with high catalyst stability. In addition, the

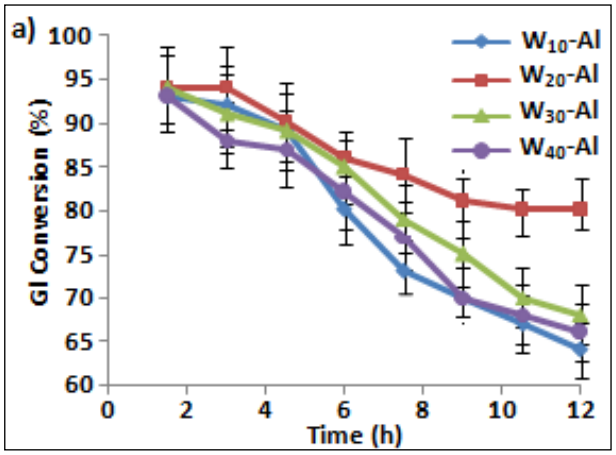
BET results also indicated that supported $W_{20}$-Al catalysts have large pore diameter (> 21nm) which is one of the main reason for high stability of this catalyst. In fact, pore size >4 nm providing a required space for Keggin anions (D = 1.2 nm) and also increase the interaction between adsorbed glycerol molecules and Keggin units [16]. Furthermore, large pore diameter significantly reduces the effect of internal mass transfer limitations [35].

The glycerol conversion related to all the prepared catalysts decreased steadily during 12 hours reaction time. However, $W_{20}$-Al recorded the least conversion reduction among all the tested samples (Figure 5a). The acrolein selectivities for all four samples are exhibited in Figure 5b. All samples exhibit dramatic reduction in acrolein selectivity except for the most active and stable catalyst, $W_{20}$-Al, which displayed a difference of only 11.6% from 74.1 to 62.5%. The $W_{20}$-Al sample was more active than $W_{10}$-Al due to the approximately 2 times stronger medium acidic sites (1.8 mmol/g.cat) of $W_{20}$-Al compared to the $W_{10}$-Al (1 mmol/g.cat). However, $W_{20}$-Al only showed 0.2 mmol/g.cat less medium acidity compared to the $W_{30}$-Al and $W_{40}$-Al samples. In fact, the $W_{20}$-Al, $W_{30}$-Al and $W_{40}$-Al samples showed similar nature of acidity (high medium acid strength). The differences in the total acidity of these samples were only 0.2 – 0.3 mmol/g.cat.

$$\text{The number of acid sites} = \left(\frac{Total\ \ acidity\ \ (NH_3 - TPD)}{Surface\ \ area\ \ (BET)}\right)\left(\frac{mmol}{m^2}\right) \quad (4)$$

for $W_{20}$-Al was lower than the $W_{30}$-Al and $W_{40}$-Al samples. The number of acid sites increased from 0.018 to 0.034 mmol/$m^2$ by surging the HSiW loading from 20 to 40 wt.%. In fact, the $W_{40}$-Al sample registered double acid sites amount (0.034 mmol/$m^2$) compared to the$W_{20}$-Al. Therefore, the main reason for significant reduction of catalyst activity for $W_{30}$-Al and $W_{40}$-Al samples was higher number of active sites which enhance the coke deposition process on the catalyst surface and deactivate the catalyst faster.

As stated in Table 3 and Figure 5b the acrolein selectivity for $W_{30}$-Al and $W_{40}$-Al samples were initially high; however, as more coke was deposited on the catalyst surface, the selectivity dwindled during 12 hours of reaction time. Consequently, the optimum amount of HSiW loading was found to be 20 wt.%. For above 20 wt.% HSiW loading, the catalyst activity remained stable in the first hour of reaction, but then its activity and acrolein selectivity declined dramatically (Figure 5a-b). Figure 5c exhibits long-term stability of $W_{20}$-Al catalyst during 30 hours reaction time. The stability of $W_{20}$-Al sample with 61.8% acrolein selectivity at 78% glycerol conversion prevailed up to 30 hours.



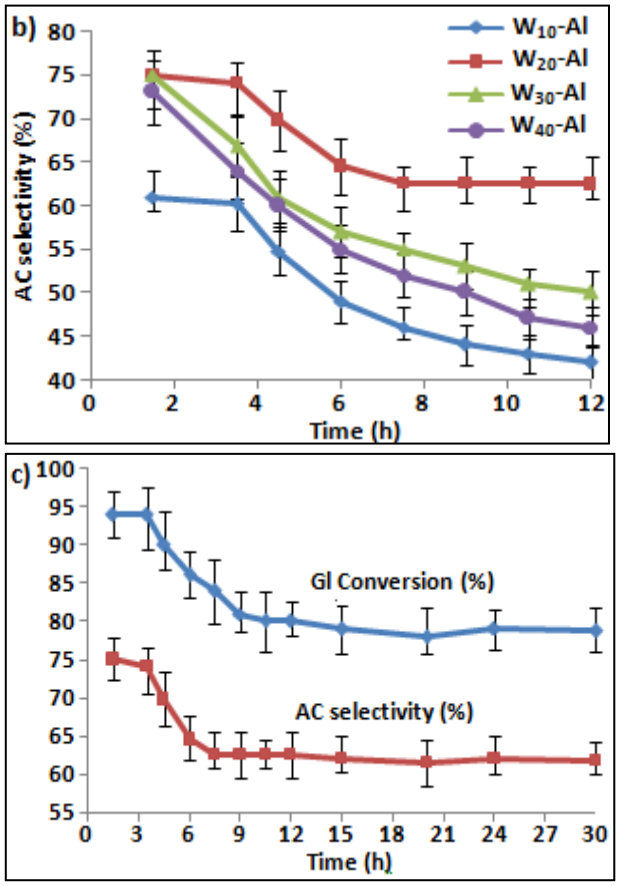



Figure 5. (a) Glycerol conversion versus time and (b) Acrolein selectivity versus time for W10-Al, W20-Al, W30-Al, and W40-Al samples at 300 ˚C, 12 hours reaction time, 2 ml/h glycerol feed, and 20 ml/min carrier gas flow (c) Long-term stability investigation of W20-Al sample in 30 hours

## Conclusion

A series of supported silicotungstic acid on aluminum oxide nanoparticle catalysts were prepared and examined in gas phase dehydration of glycerol to acrolein at different temperatures (280, 300, and 320 ˚C). The $W_{20}$-Al catalyst could achieved 74.1% acrolein selectivity with 94% glycerol conversion at optimum reaction condition of 300 ˚C temperature, 10 wt.% glycerol feed concentration and 0.5 wt.% catalyst amount. The characterization results prove that the $W_{20}$-Al large pore diameter (21.5 nm) was the key component for long-life stability of catalyst. In addition, high surface acidity, medium acid cite strength and availability of acid sites on the surface of $W_{20}$-Al catalysts led to the highest acrolein selectivity and glycerol conversion among all the synthesized samples.

## Acknowledgement

The authors would like to express their since gratitude to the Ministry of Science Malaysia for funding the project 03-01-06-SF0963 under Ministry of Science Malaysia (MOSTI). The first author (A. Talebian-Kiakalaieh) is thankful to Universiti Teknologi Malaysia for the postdoctoral fellowship under Vot 02E80.

## References

1. Liu, L., Ye, X. P. and Bozell, J. J. (2012). A comparative review of petroleum-based and bio-based acrolein production. *ChemSusChem*, 5(7): 1162 – 1180.

2. Talebian-Kiakalaieh, A., Amin, N. A. S. and Hezaveh, H. (2014). Glycerol for renewable acrolein production by catalytic dehydration. *Renewable and Sustainable Energy Reviews*, 40: 28 – 59.
3. Tan, H.W., Aziz, A. R. A. and Aroua, M. K. (2013). Glycerol production and its applications as a raw material: A review. *Renewable and Sustainable Energy Reviews*. 27: 118 – 127.
4. Yadav, G. D., Chandan, P. A. and Gopalaswami, N. (2012). Green etherification of bioglycerol with 1-phenyl ethanol over supported heteropolyacid. *Clean Technologies and Environmental Policy,* 14(1): 85 – 95.
5. Garcia, J. I., Garcia-Marin, H. and Pires, E. (2014). Glycerol based solvents: synthesis, properties and applications. *Green Chemistry*, 16: 1007 – 1033.
6. Thomas, J. M. (2014). Heterogeneous catalysis and the challenges of powering the planet, securing chemicals for civilised life, and clean efficient utilization of renewable feedstocks. *ChemSusChem*, 7(7): 1801 – 1832.
7. Katryniok, B., Paul, S., Capron, M., Belliere-Baca, V., Rey, P. and Dumeignil, F. (2012). Regeneration of silica -supported silicotungstic acid as a catalyst for the dehydration of glycerol. *ChemSusChem*, 5 (5): 1298 – 1306.
8. Kang, T. H., Choi, J. H., Bang, Y., Yoo, J., Song, J. H., Joe, W., Choi, J. S. and Song. I. K. (2015). Dehydration of glycerin to acrolein over $H_3PW_{12}O_{40}$ heteropolyacid catalyst supported on silica-alumina. *Journal of Molecular Catalysis A: Chemistry*, 396: 282 – 289.
9. Ma, T., Yun, Z., Xu, W., Chen, L., Li, L., Ding, J. and Shao. R. (2016). Pd-$H_3PW_{12}O_{40}$/Zr-MCM-41: An efficient catalyst for the sustainable dehydration of glycerol to acrolein. *Chemical Engineering Journal*, 294: 343 – 352.
10. Costa, B. O. D., Peralta, M. A. and Querini, C. A. (2014). Gas phase dehydration of glycerol over, lanthanum-modified beta-zeolite. *Applied Catalysis A: General*, 472: 53 – 63.
11. Park, H., Yun, Y. S., Kim, T. Y., Lee, K. R., Baek, J. and Yi. J. (2015). Kinetics of the dehydration of glycerol over acid catalysts with an investigation of deactivation mechanism by coke. *Applied Catalysis B: Environment*, 176: 1 – 10.
12. Estevez, R., Lopez-Pedrajas, S., Blanco-Bonilla, F., Luna, D. and Bautista, F. M. (2015). Production of acrolein from glycerol in liquid phase on heterogeneous catalysts. *Chemical Engineering Journal*, 282: 179 – 186.
13. Garcia-Sancho, J. A. C. C., Merida-Robles, J. M. M., Gonzalez, J. S., Moreno-Tost, R. and Maireles-Torres, P. (2016). $WO_3$ supported on Zr doped mesoporous SBA-15 silica for glycerol dehydration to acrolein. *Applied Catalysis A: General*, 516: 30 – 40.
14. Feng, X., Yao, Y., Su, Q., Zhao, L., Jiang, W., Ji, W. and Au. C. (2015). Vanadium pyrophosphate oxides: The role of preparation chemistry in determining renewable acrolein production from glycerol dehydration. *Applied Catalysis B: Environment*, 164: 31 – 39.
15. Tao, L. Z., Chai, L. H., Zuo, Y., Zheng, W. T., Liang, Y. and Xu, B. Q. (2010). Sustainable production of acrolein: Acidic binary metal oxide catalysts for gas-phase dehydration of glycerol. *Catalysis Today*, 158: 310 – 316.
16. Atia, H., Armbruster, H. and Martin, A. (2008). Dehydration of glycerol in gas phase using heteropolyacid catalysts as active compounds. *Journal of Catalysis*, 258: 71 – 82.
17. Stosic, D, Bennici, S., Sirotin, S., Calais, C., Couturier, J. L., Dubois, J. L., Travert, A., Auroux, A. (2012). Glycerol dehydration over calcium phosphate catalysts: Effect of acidic–basic features on catalytic performance. *Applied Catalysis A: General*, 447: 124 – 134.
18. Gu, Y., Cui, N., Yu, Q., Li, C. and Cui, Q. (2012). Study on the influence of channel structure properties in the dehydration of glycerol to acrolein over H-zeolite catalysts. *Applied Catalysis A: General*, 429: 9 – 16.
19. Alhanash, A., Kozhevnikova, E. F. and Kozhevnikov, I. V. (2010). Gas-phase dehydration of glycerol to acrolein catalysed by caesiumheteropoly salt. *Applied Catalysis A: General*, 378: 11 – 18.
20. Haider, M. H., Dummer, N. F., Zhang, D., Miedziak, P., Davies, T. E., Taylor, S. H., Willock, D. J., Knight, D. W., Chadwick, D. and Hutchings, G. H. (2012). Rubidium- and caesium-doped silicotungstic acid catalysts supported on alumina for the catalytic dehydration of glycerol to acrolein. *Journal of Catalysis*, 286: 206 – 213.
21. Yun, D., Kim, T. Y., Park, D. S., Yun, Y. S., Han, J. W. and Yi, J. (2014). A tailored catalyst for the sustainable conversion of glycerol to acrolein: Mechanistic aspect of sequential dehydration. *ChemSusChem*, 7(8): 2193 – 2 201.
22. Atia, H., Armbruster, U. and Martin, A. (2011). Influence of alkaline metal on performance of supported silicotungstic acid catalysts in glycerol dehydration towards acrolein. *Applied Catalysis A. General*, 393: 331 – 339.

23. Said, A. E. A., El-Wahab, M. M. M. A. and Alian. A. M. (2007). Catalytic performance of Brønsted acid sites during esterification of acetic acid with ethyl alcohol over phosphotungestic acid supported on silica. *Journal of Chemical Technology and Biotechnology,* 82: 513 – 523.
24. Katryniok, B., Paul, S., Capron, M., Lancelot, C., Bellere-Beca, V., Rey, P. and Dumeignil, F. A. (2010). A long-life catalyst for glycerol dehydration to acrolein. *Green Chemistry*, 12: 1922 – 1925.
25. Badday, A. S., Abdullah, A. Z. and Lee, K. (2013). Ultrasound-assisted transesterification of crude Jatropha oil using alumina-supported heteropolyacid catalyst. *Applied Energy*, 105: 380 – 388.
26. Hernández-Cortez, J. G., Martinez, L., Soto, L., López, A., Navarrete, J. and Manríquez, M. (2010). Liquid phase alkylation of benzene with dec-1-ene catalyzed on supported 12-tungstophosphoric acid. *Catalysis Today*, 150: 346 – 352.
27. Shringarpure, P. A. and Patel, A. (2011). Supported undecatungstophosphate: An efficient recyclable bi-functional catalyst for esterification of alcohols as well as selective oxidation of styrene. *Chemical Engineering Journal*, 173: 612 – 619.
28. Hondnett, B. H. and Moffat, J. B. (1984). Application of temperature-programmed desorption to the study of heteropoly compounds: Desorption of water and pyridine. *Journal of Catalysis*, 88: 253 – 263.
29. Pizzio, L. R. and Blanco, M. N. (2007). A contribution to the physicochemical characterization of nonstoi-chiometric salts of tungstosilicic acid. *Microporous Mesoporous Materials*, 103: 40 – 47.
30. Zhu, S., Gao, X., Zhu, Y., Zhu, Y., Xiang, X., Hu, C. and Li, Y. (2013). Alkaline metals modified Pt–$H_4SiW_{12}O_{40}/ZrO_2$ catalysts for the selective hydrogenolysis of glycerol to 1,3-propanediol. *Applied Catalysis B: Environment*, 140: 60 – 67.
31. Zhu, S., Zhu, Y., Hao, S., Zheng, H., Mo, T. and Li, Y. (2012). One-step hydrogenolysis of glycerol to bio-propanols over Pt–$H_4SiW_{12}O_{40}/ZrO_2$ catalysts. *Green Chemistry*, 14: 2607 – 2616.
32. Yadav, G. D. and Tekale, D. P. (2014). Selective mono-isopropylation of ,3-propanediol with isopropyl alcohol using heteropoly acid supported on K-10 clay catalyst. *Catalysis Today*, 237: 54 – 61.
33. Talebian-Kiakalaieh, A., Amin, N. A. S. and Zaki, Y. Z. (2016). Gas phase selective conversion of glycerol to acrolein over supported silicotungstic acid catalyst. *Journal of Industrial Chemical Engineering*, 34: 300 – 312.
34. Kozhevnikov, I. V. (1998). Catalysis by heteropoly acids and multicomponent polyoxometalates in liquid-phase reactions. *Chemical Reviews*, 98: 171 – 198.
35. Tsukuda, E., Sato, S., Takahashi, R. and Sodesawa, T. (2007). Production of acrolein from glycerol over silica-supported heteropoly acids. *Catalysis Communication*, 8(9): 1349 – 1353.

*Malaysian Journal of Analytical Sciences, Vol 21 No 4 (2017): 860 - 870*
*DOI: https://doi.org/10.17576/mjas-2017-2104-12*

MALAYSIAN JOURNAL OF ANALYTICAL SCIENCES
*Published by The Malaysian Analytical Sciences Society*
ISSN 1394 - 2506

# SYNTHESIS OF MESOPOROUS SODALITE BY MIXED QUATERNARY AMMONIUM CATION TEMPLATES FOR KNOEVENAGEL CONDENSATION REACTION

## (Sintesis Sodalit Mesoliang dengan Campuran Templat-Templat Kation Amonium Kuaterner untuk Tindak Balas Kondensasi Knoevenagel)

Mohamad Faiz Othman, Shima Shirani Lapari, Zainab Ramli*, Sugeng Triwahyono

*Department of Chemistry, Faculty of Science,*
*Universiti Teknologi Malaysia, 81310 UTM Johor Bahru, Johor, Malaysia*

**Corresponding author: zainabr@utm.my*

Received: 20 September 2016; Accepted: 16 May 2017

**Abstract**

Sodalite (SOD) is a microporous zeolite with pore size about 2.8 Å which limits its role as catalyst for the reaction involving bulky molecules. To overcome this disadvantage, mesotemplate can be added to create mesoporosity in the synthesis of SOD. A series of SOD samples was synthesized using dual templates approach by mixing tetrapropylammonium hydroxide (TPAOH) with different quaternary ammonium cations. The samples were characterized using X-ray Diffraction (XRD), Fourier Transformation Infrared (FTIR) and $N_2$ adsorption analysis. From $N_2$ adsorption analysis, only SOD sample prepared by mixing TPAOH with organosilane (SOD-TO) showed the characteristic of mesoporosity with a narrow pore size distribution peak centered at *ca.* 66 Å. The basicity properties of all SOD samples were evaluated by Hammett indicators test and back titration method. While, the basicity property of SOD-TO was compared with the microporous SOD (Na-SOD) using TPD-$CO_2$ analysis. All SOD samples were tested in the Knoevenagel condensation reaction of benzaldehyde and diethyl malonate, giving diethyl-2-benzylidenemalonate as the main product. The results showed that SOD-TO catalyst which possessing the highest amount of basicity and the highest surface area with mesoporosity character gave the highest percentages of conversion and yield of Knoevenagel reaction.

**Keywords:** sodalite, basic catalyst, dual templates approach, mesoporous sodalite, Knoevenagel condensation reaction

**Abstrak**

Sodalit (SOD) ialah zeolit mikroliang dengan liang bersaiz sekitar 2.8 Å yang menghadkan peranannya sebagai mangkin untuk tindak balas yang melibatkan molekul – molekul yang besar. Untuk mengatasi kekangan ini, mesotemplat boleh ditambahkan dalam sintesis SOD bagi mengwujudkan mesoliang dalam SOD. Satu siri SOD telah disintesis menggunakan pendekatan dwi templat dengan campuran tetrapropilamonium hidroksida (TPA) dengan pelbagai kation amonium kuaterner. Semua sampel telah dicirikan menggunakan pembelauan sinar-X (XRD), Inframerah Tranformasi Fourier (FTIR) dan analisis penjerapan $N_2$. Daripada analisis penjerapan $N_2$, sampel SOD yang disintesis hasil campuran TPA dengan organosilana (SOD-TO) sahaja yang menunjukkan ciri-ciri mesoliang dengan puncak penyebaran sempit saiz liang berpusat di *ca.* 66 Å. Ciri-ciri kebesan untuk semua sampel SOD telah dinilai menggunakan ujian petunjuk Hammett dan kaedah titratan berbalik. Manakala, ciri-ciri kebesan SOD-TO telah dibandingkan dengan SOD mikroliang (Na-SOD) menggunakan analisis TPD-$CO_2$. Semua sampel SOD telah diuji dalam tindak balas kondensasi Knoevenagel antara benzaldehid dan dietil malonat yang menghasilkan dietil-2-benzilidenemalonat sebagai hasil utama. Keputusan menunjukkan mangkin SOD-TO yang mempunyai jumlah kebesan dan luas permukaan yang paling tinggi dengan kehadiran ciri mesoliang dalam strukturnya memberikan peratusan penukaran dan hasil yang paling tinggi bagi tindak balas Knoevenagel.

**Kata kunci:** sodalit, mangkin bes, pendekatan dwi templat, sodalit mesoliang dan tindak balas kondensasi Knoevenagel

## Introduction

Zeolites are microporous crystalline aluminosilicate solids made up from corner-sharing of $SiO_4^-$ and $AlO_4^-$ tetrahedra. These tetrahedra are linked together by sharing all the oxygen atoms, forming a uniformly pores or channels of molecular dimensions [1]. Microporous zeolites are widely used as catalysts in organic catalytic reactions due to their excellent catalytic performance such as large surface area, environment friendly, easy work-up and shape-selectivity [2]. However, in reactions involving large molecules, the sole presence of micropores in zeolites limit the diffusion of large molecules and lead to poor catalytic performance [3]. Therefore, many studies have been focusing on synthesizing zeolites with proper pore size in order to accelerate the conversion of large molecules. One of the best strategies is by synthesizing a new zeolite that consists of micropores and mesopores (2 – 50 nm) in one material. This strategy leads to the formation of hierarchical porous zeolites or also known as mesoporous zeolites [4]. Mesoporous zeolites offer some advantages such as fast diffusion and accessible for large molecules [5].

There are many methods to introduce mesopores in the zeolite structure. The most common methods used are post-synthetic method and templating method [6]. Desilication and dealumination are examples of post-synthetic method. This method has some drawbacks such as reducing the number of active sites and non-uniform nature of the mesopore formation [7]. Recently, the synthesis of mesoporous zeolites has been done by templating methods. This can be achieved by introducing various templates such as “hard” or “soft” templates into the zeolites during the synthesis process. This low cost method allowed reducing in the number of synthetic steps during the preparation [8]. Among these two templates, soft templating approach has been widely used for synthesizing mesoporous zeolites. Some examples of soft templates are surfactants and polymers [9]. The major advantage by using soft templates is the easily removed of the templates by a calcination process [10]. Instead of using single soft template, the mesopore zeolites can also be synthesized by mixing two soft templates. This strategy is known as dual templates method by which the small molecular template is used as structure directing agent whereas the large molecular template is used to create mesopores [11].

The formation of mesoporous zeolites gives lots of advantages in many applications especially in various catalytic reactions. They are primarily useful in improving the catalytic performances of conventional zeolites that having only micropores [12]. Some examples of catalytic reactions that used mesoporous zeolites are cracking, alkylation, isomerization and hydrogenation [13]. Knoevenagel condensation reaction is another example of catalytic reactions being catalyzed by mesoporous zeolites (alkaline X and Y zeolites) [14]. This reaction involved the condensation of carbonyl compounds with active methylene and catalyzed by a base catalyst. Some important intermediates produced from Knoevenagel condensation reactions have significant applications in industries such as therapeutic drugs, perfumes and cosmetics [15].

In this work, we focused on the synthesis of mesoporous sodalite (SOD). SOD is an example of zeolite, consisting of a four membered ring with the smallest pore openings size of about 2.8 Å in the zeolite family. In addition, SOD is an example of basic zeolite with high aluminium content (Si/Al = 1) and high stability in basic solution [16]. However, the presence of ultrafine micropores in its structure limit only to the reaction involving small reactants. Therefore, this work is expected to solve the problem by synthesizing mesoporous SOD in order to catalyze Knoevenagel condensation reaction involving large reactants. This mesoporous SOD was synthesized by dual templates approach using different quaternary ammonium cation templates and mixed with tetrapropylammonium hydroxide (TPAOH). The catalyst activity was tested in the Knoevenagel condensation reaction of benzaldehyde with diethyl malonate.

## Materials and Methods

### Catalyst preparation

A series of SOD samples were prepared by following the molar ratio of the previous study; $1.7SiO_2$: 15NaOH: $Al_2O$: $80H_2O$: 0.3templates [17]. First, sodium hydroxide solution was prepared by dissolving NaOH pellets (NaOH; Merck; 15 g) in distilled water (18 mL). The NaOH solution was then divided into two portions equally.

One portion of the NaOH solution was mixed with fume silica ($SiO_2$; Fluka; 1.28 g) to form silicate solution. The other portion was mixed with sodium aluminate ($NaAlO_2$; Riedel-de Haë; 1.28 g) to form aluminate solution. Next, tetrapropylammonium hydroxide (TPAOH; Merck; 0.85 mL) was added into the silicate solution followed by dimethyloctadecyl[3-(trimethoxysilyl)propyl] ammonium chloride (Organosilane; Sigma-Aldrich; 2.09 mL). The mixture was stirred until clear solution was formed. The resulting solution was then added dropwise into the aluminate solution and stirred of about 1 hour. The resulting solution formed was transferred into stainless steel autoclave and heated at 150 °C for 24 hours for the precipitation of SOD. The SOD product was collected by filtration and washed using distilled water until the filtrate solution reached to pH 7. The product was then dried at 60 °C overnight and calcined at 550 °C for 6 hours.

The procedures were repeated for different mixture of templates: the mixture of TPAOH with cetyltrimethylammonium bromide (CTAB; Fisher Scientific), dodecyltrimethylammonium bromide (DTAB; Sigma-Aldrich) and dimethyldioctadecylammonium bromide (DDAB; Sigma-Aldrich). As comparison, microporous SOD (Na-SOD) was synthesized using the same method without the presence of templates.

**Characterizations**
X-ray diffraction (XRD) patterns were recorded on powder diffractometer (Bruker Advance D8, 40 kV, 10 mA) using a Cu-Kα radiation source in the range of 5 – 50°. The FTIR analysis was recorded in the range of 400 to 4000 $cm^{-1}$ using Perkin Elmer 1600 series spectrometer. The BET analysis of the samples was determined by $N_2$ adsorption-desorption isotherms using a Micromeritics ASAP 2010 instrument. The samples were outgassed at 90 °C for 1 hour and heated up again at 350 °C for 4 hours before being subjected to $N_2$ adsorption. The surface area measurement was derived from the Brunauer – Emmett - Teller (BET) theory and the pore size distributions based on Barrett, Joyner and Halenda (BJH) theory.

**Basicity measurements**
Basicity of all SOD samples was determined using Hammett indicators and back titration method. In the case of the former, the procedure was followed from previous study with some modifications [18]. An activated solid SOD sample was shaken with 2 mL solution of Hammett indicators in ethanol and left to equilibrate. The color changed was noted. The following Hammett indicators were used; bromothymol blue ($pK_a$ = 7.2), phenolphthalein ($pK_a$ = 8.2) and 4-nitroaniline ($pK_a$ = 18.4).

In the back titration method, an amount of activated solid SOD sample was suspended in 10 mL of distilled water. It was shaken and left for 1 day. After one day, the solution was filtered. Then, the filtrate was mixed with 5 mL of 0.05 M HCl (Qrëc). The resulting solution was next titrated against 0.02 M of KOH (Qrëc) using phenolphthalein as the indicator. End point was noted when the colorless color of the phenolphthalein changed to pink.

Basicity comparison between Na-SOD sample and mesoporous SOD with highest BET surface area was done by Temperature Program Desorption of $CO_2$ (TPD-$CO_2$) using AutoChem II 2920 Micromeritics Chemisorption analyzer. Sample was heated in a stream of He gas at the flow rate of 20 mL/min to 500 $^oC$ at the heating rate of 10 $^oC$/min for 2 hours and then cooled to 50 $^oC$. After cooling, the $CO_2$ gas was introduced at the rate of 20 mL/min for 30 minutes. After that the gas flow was changed to He as carrier gas. The TPD-$CO_2$ was carried out in the temperature range of 50 to 1000 $^oC$ at heating rate of 10 $^oC$/mL and He rate of 20 mL/min.

**Catalytic testing**
Knoevenagel condensation reaction of benzaldehyde and diethyl malonate was carried out in this study. The catalyst samples were first activated at 500 °C for 2 hours. Equimolar solutions of benzaldehyde (0.02 mol) and diethyl malonate (0.02 mol) were added into a 50 mL round bottom glass reactor. The 0.05 g catalyst powder was then added to the solution. $N_2$ gas was then bubbled through the solution to remove dissolved oxygen to avoid formation of benzoic acid. Lastly, the solution was connected to the condenser and refluxed in an oil bath at 150 °C for 24 hours with stirring. Products of reaction were separated and analyzed using Gas Chromatography model Agilent 6890N Series equipped with flame ion detector (FID) using Ultra-1 column. Meanwhile, the components of the product produced in the reaction were identified by using Gas Chromatography-Mass Spectroscopy (GC-MS) model Perkin Elmer Clarus 680.

## Results and Discussion

### Catalyst characterizations

Figure 1 shows the XRD patterns of the as-synthesized SOD samples. The patterns exhibited six diffraction peaks at 2θ = 14.10°, 24.40°, 31.60°, 34.70°, 37.60° and 48.80° correspond to $d_{[110]}$, $d_{[211]}$, $d_{[310]}$, $d_{[222]}$, $d_{[321]}$ and $d_{[330]}$ planes respectively. These patterns are assigned to SOD crystal phase pattern after comparing with the previous study [19]. Among the SOD samples, SOD-TO showed broader XRD peaks which indicated a smallest crystallite size in its structure. In some cases, mixture of phases could be seen for SOD. It can be observed that the XRD pattern for SOD-TDDAB sample produced two peaks at certain 2θ. However, the extra peaks could not be identified and not matched with other type of zeolites. As for other SOD samples, peaks with high intensity were observed. The diffraction peak at (211) corresponding to the most intense peak was selected to calculate the crystallite size using Debye-Scherrer equation. The results correspond to the crystallite size of all SOD samples are shown in Table 1. The values suggested that all SOD samples were composed of nano-sized crystals. In addition, the values also suggested that the crystallite size increases as the wideness of the diffraction peak decreases. The SOD-TO sample has the smallest crystallite size as compared with other SOD samples which indicated that this sample consists of a highly nanocrystalline nature of the framework due to the presence of small crystallite size.

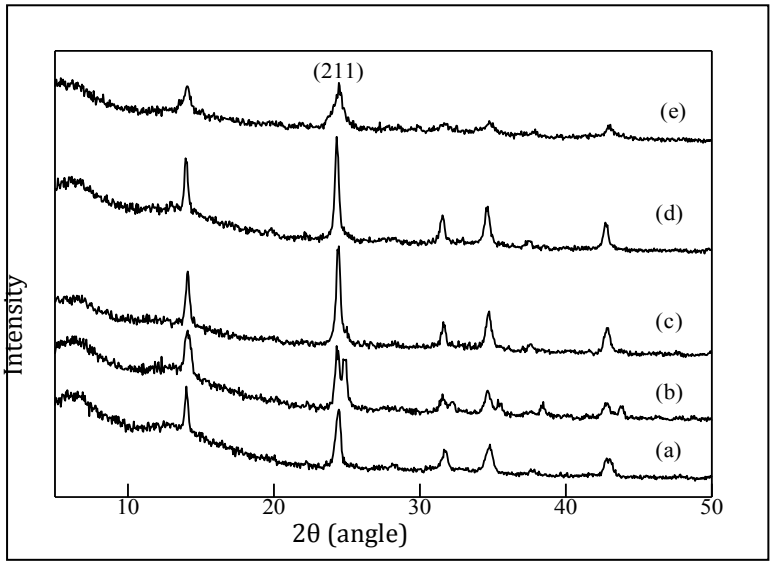



Figure 1. XRD diffractograms of (a) Na-SOD, (b) SOD-TDDAB, (c) SOD-TCTAB, (d) SOD-TDTAB and (e) SOD-TO

Table 1. Crystallite size of all SOD samples

| Samples | Crystallite size (nm) |
|---|---|
| Na-SOD | 18 |
| SOD-TDDAB | 23 |
| SOD-TCTAB | 25 |
| SOD-TDTAB | 26 |
| SOD-TO | 17 |

Figure 2 shows the IR spectra of as-synthesized SOD samples. Each SOD sample showed a broad absorption band at around 980 $cm^{-1}$. This band can be assigned to the internal vibration of T-O-T (T = Si or Al) asymmetric stretch.

However, except SOD-TO sample, all other SOD samples showed additional absorption band at around 920 $cm^{-1}$. This band could be assigned to the Si-O stretching mode of surficial silanol group (Si-OH). This band might be produced due to the hydroxylation of silica upon exposure to water. In addition, each of SOD samples showed absorption bands in the region of 650 – 740 $cm^{-1}$ that can be due to the symmetric stretch of T-O-T (T = Si or Al). While, the absorption band around 450 – 465 $cm^{-1}$ represents the internal vibration of T-O-T bending (T = Si or Al). The characteristic absorption band at 428 – 436 $cm^{-1}$ also represent the vibrations of T-O-T (T = Si or Al) bending that related to the pore opening of the SOD unit. The absorption bands discussed are related to the characteristic of SOD framework as found by previous study [20].

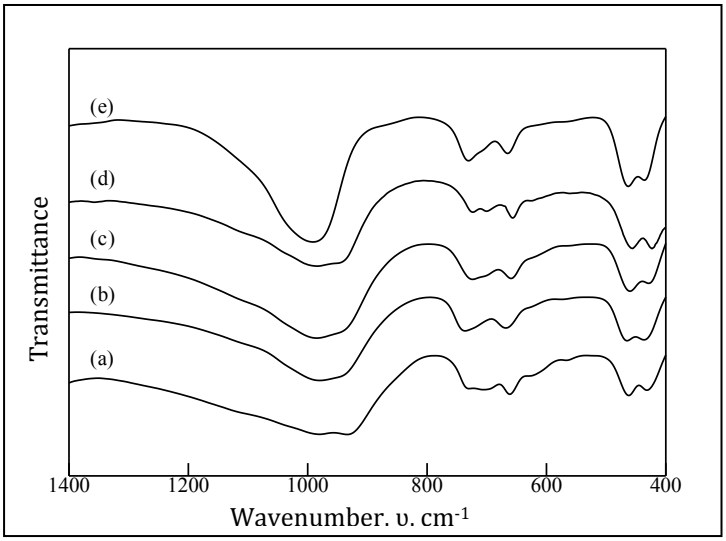



Figure 2. IR spectra of (a) Na-SOD, (b) SOD-TDDAB, (c) SOD-TCTAB, (d) SOD-TDTAB and (e) SOD-TO

Figure 3 shows the BET adsorption-desorption isotherm of all SOD samples while Figure 3B shows the BJH pore size distributions of all SOD samples. Based on Figure 3A, the BET adsorption-desorption isotherm of the SOD-TO sample (see Figure 3 (e)) exhibited type IV isotherm with a H1 type hysteresis loop which was typical of mesoporous solids. This hysteresis loop produced was due to the capillary condensation in mesopore channels. As for other SOD samples, the isotherms can be classified as type II isotherm with a non-uniform type H3 hysteresis loop. While, the Na-SOD sample produced type II isotherm with type H2 hysteresis loop. Thus, only SOD-TO sample showed the successfully formation of mesoporosity in its structure based on the obtained isotherm. The presence of mesoporous structure in the SOD-TO sample was confirmed with a narrow pore size distribution peak centered at *ca.* 66 Å as shown in Figure 4 (e). In addition, the higher specific surface area and larger pore volume were attributed to the presence of mesoporous structure in the SOD-TO as shown in Table 2. As for other SOD samples, they exhibited broader pore size distributions ranging from 30 Å to 475 Å and some even extended to the macropore range. This suggested that those samples inhibited the characteristic of an ordered mesoporous solid with very low BET surface area as shown in Table 2.

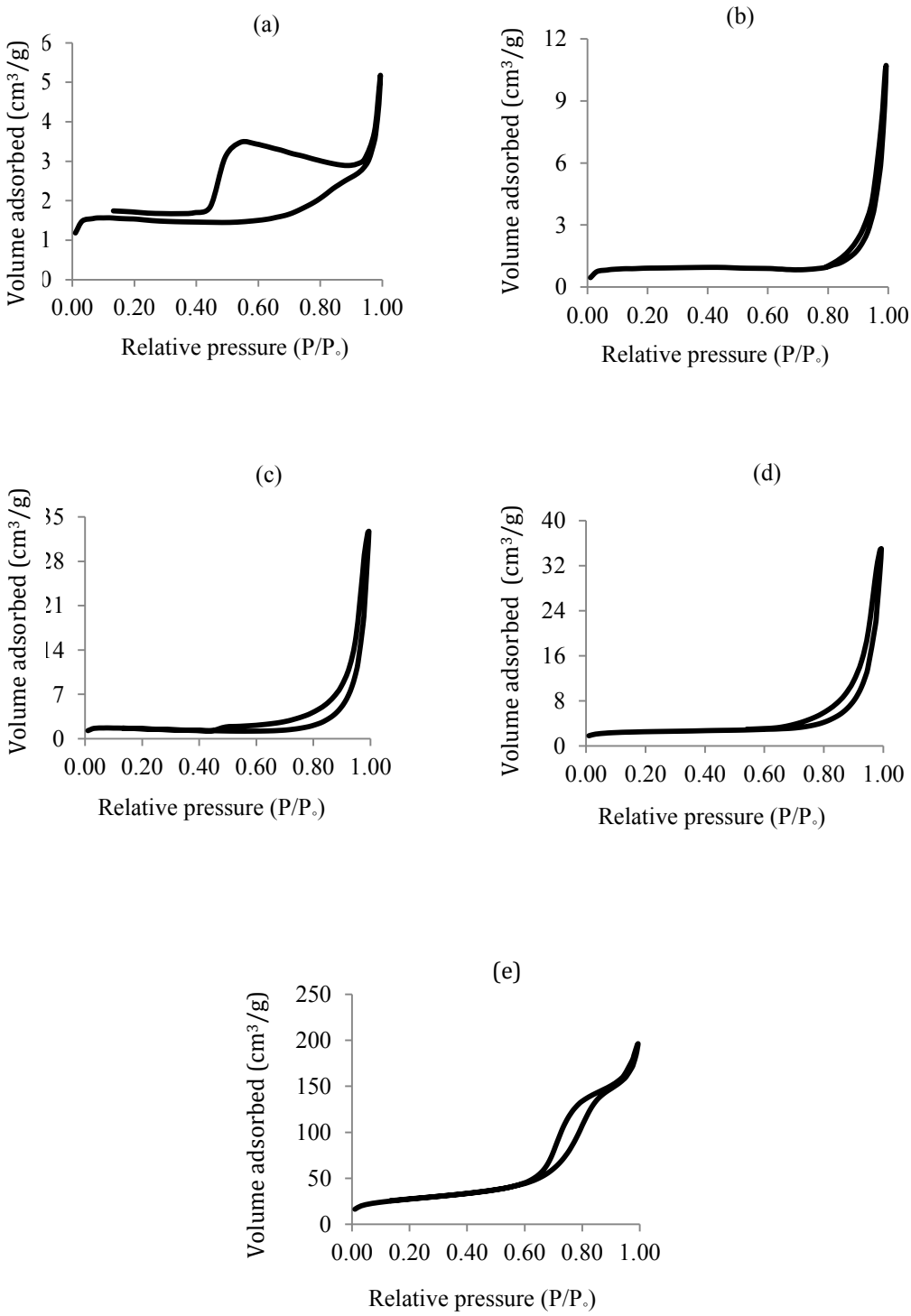
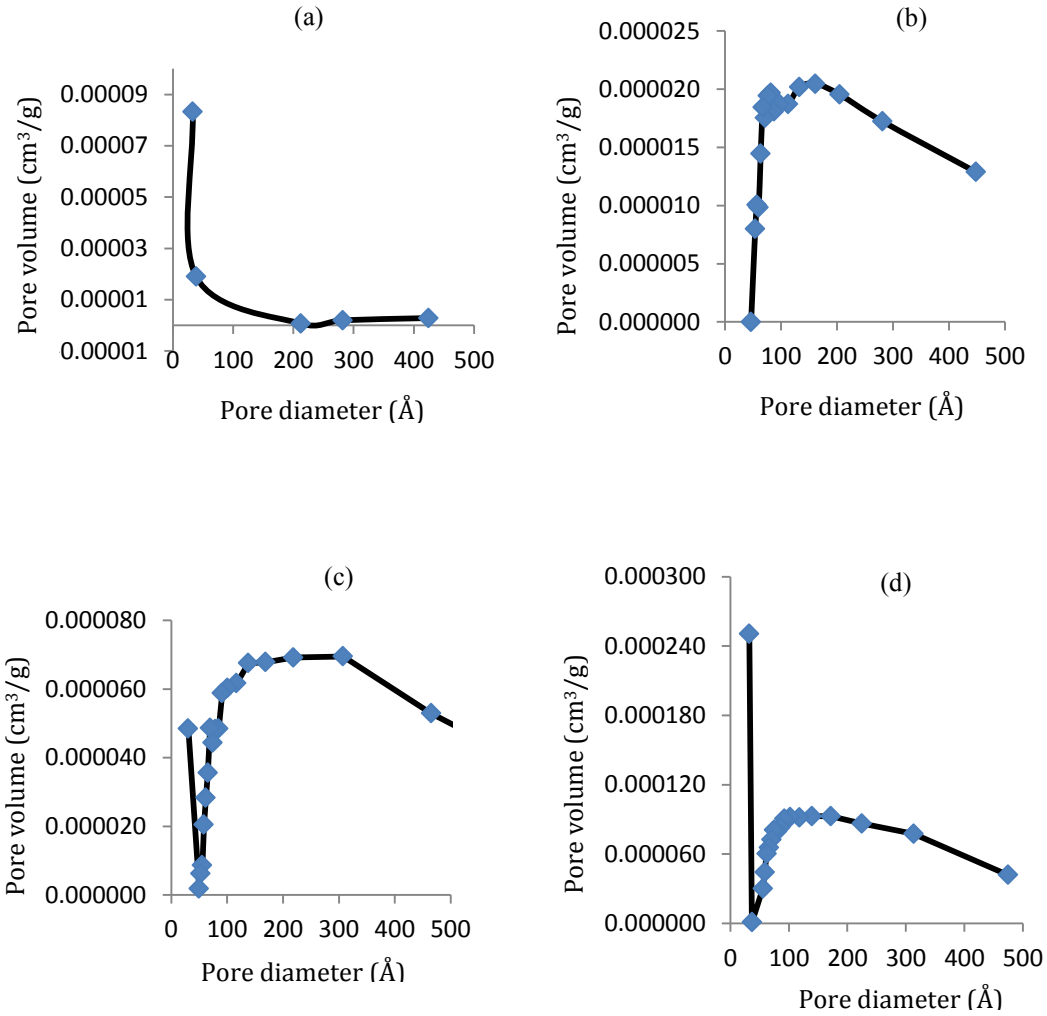



Figure 3. BET adsorption-desorption isotherm of (a) Na-SOD, (b) SOD-TDDAB, (c) SOD-TCTAB, (d) SOD-TDTAB and (e) SOD-TO

Table 2. $N_2$ adsorption-desorption data of all SOD samples

| Samples | BET Surface Area, $S_{BET}$ ($m^2/g$) | t-plot Micropore Area ($m^2/g$) | External Surface Area, $S_{Ext}$ ($m^2/g$) | BJH Desorption Cumulative Volume of Pores ($cm^3/g$) |
|---|---|---|---|---|
| Na-SOD | 6.8 | 6.0 | 0.8 | 0.007 |
| SOD-TDDAB | 3.3 | 2.4 | 0.9 | 0.012 |
| SOD-TCTAB | 6.8 | 5.8 | 0.9 | 0.051 |
| SOD-TDTAB | 9.1 | 6.6 | 2.5 | 0.049 |
| SOD-TO | 94.2 | 19.2 | 75.0 | 0.285 |



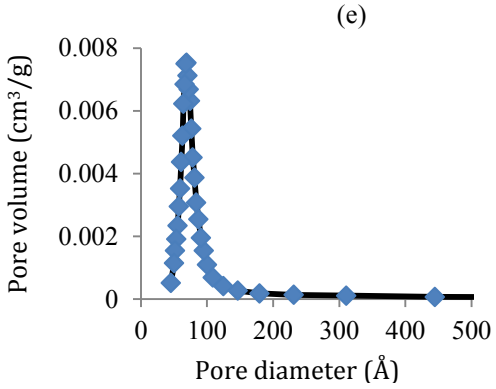



Figure 4. BJH pore size distributions of (a) Na-SOD, (b) SOD-TDDAB, (c) SOD-TCTAB, (d) SOD-TDTAB and (e) SOD-TO

**Basicity measurements**

The basic strength of the SOD samples was estimated by using Hammett indicators. A change in color was observed for bromothymol blue from orange to dark blue and colorless to pink for phenolphthalein indicators. None of the samples were able to change the color of 4-nitroaniline. Hence, the strength of the basicity of all SOD samples prepared in this study was estimated in the range: $8.2 \leq pKa \leq 18.4$ as shown in Table 3.

Table 3. Basic strength of all SOD samples

| Samples | Hammett Indicators | | | Basic Strength |
|---|---|---|---|---|
| | Bromothymol Blue | Phenolphthalein | 4-nitroaniline | |
| Na-SOD | +* | + | -* | $8.2 \leq pKa \leq 18.4$ |
| SOD-TDDAB | + | + | - | $8.2 \leq pKa \leq 18.4$ |
| SOD-TCTAB | + | + | - | $8.2 \leq pKa \leq 18.4$ |
| SOD-TDTAB | + | + | - | $8.2 \leq pKa \leq 18.4$ |
| SOD-TO | + | + | - | $8.2 \leq pKa \leq 18.4$ |

*(+) = color changed, (-) = color unchanged

The similar strength of all the samples suggested that the basicity strength is contributed by the type of counter cation used and not the porosity. In this study, similar alkali cation which was $Na^+$ was used as the counter cation during the synthesis of all sodalite samples.

The amount of basicity of the SOD samples was evaluated by back titration method. Results found that the average amount of basicity of all SOD samples synthesized with the presence of templates is more than two fold higher than the SOD synthesized without the presence of templates, Na-SOD as shown in Table 4. Among the SOD samples synthesized with the presence of templates, it was found that the SOD-TO sample possess the highest average amount of basicity as compared with other SOD samples. This result indicated that the highest basic sites were present in the SOD-TO sample and lead to the highest amount of basicity. This could be due to the mesopore structure present in the sample, which more accessible of the reactant for the basic sites.

Table 4. Average amount of basicity of all SOD samples

| Sample | Amount of Basicity (mmol/g) | | | Average Amount of Basicity (mmol/g) |
|---|---|---|---|---|
| | (i) | (ii) | (iii) | |
| Na-SOD | 0.60 | 0.80 | 0.80 | 0.73 |
| SOD-TDDAB | 1.72 | 1.76 | 1.76 | 1.75 |
| SOD-TCTAB | 1.64 | 1.68 | 1.68 | 1.67 |
| SOD-TDTAB | 1.68 | 1.72 | 1.72 | 1.71 |
| SOD-TO | 1.80 | 1.80 | 1.84 | 1.81 |

Comparison of the strength and the amount of basicity for mesoporous SOD-TO and microporous Na-SOD samples were measured using TPD-$CO_2$ analysis. The basicity profiles of SOD-TO and Na-SOD samples are presented in Figure 5. Four peaks were found for the SOD-TO sample which centred at 131.7, 210.4, 688.8 and 895.4 °C with the amount of $CO_2$ desorbed of 0.1098, 1.0632, 0.2789 and 0.4242 mmol/g, respectively. Meanwhile, three peaks were observed for the Na-SOD sample which centred at 142.0, 723.5 and 875.5 $^oC$ with the amount of $CO_2$ desorbed of 0.0867, 0.4278 and 0.2946 mmol/g, respectively.

Since the activation temperature of the catalyst for the catalytic study was carried out at 500 °C, thus the amount of $CO_2$ desorbed was compared in the range of temperature below 500 °C. It was observed that at temperature below 500 °C, the amount of $CO_2$ desorbed for the SOD-TO sample was higher than that of the Na-SOD sample. In this study, the peaks with broader width and high peak area for the SOD-TO sample was found at around 300 °C. This suggested that within this range of temperature, more $CO_2$ was desorbed from SOD-TO sample. From the results, at temperature below 500 °C, the amount of basic site for the SOD-TO sample is higher than the Na-SOD sample. This phenomenon should be due to the presence of mesoporosity in the SOD-TO sample that leads to the increase in the basic sites available for $CO_2$ to react. Thus, more $CO_2$ is physically attached within the mesopores channels of the SOD-TO sample. It is also suggested that the interaction of $CO_2$ with the basic site in the mesopore channels is not very strong and can be easily detached at lower temperature

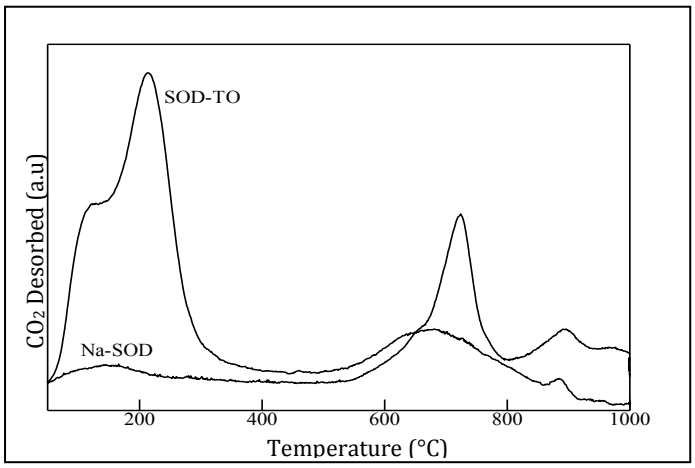
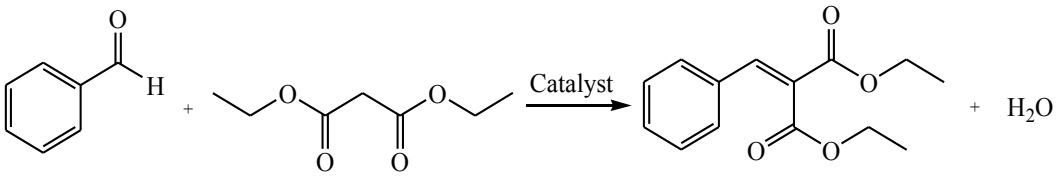



Figure 5. TPD-$CO_2$ analysis for the SOD-TO and Na-SOD samples

**Catalytic activity study**

The catalytic activity of all SOD samples was tested as base catalysts in the reaction Knoevenagel condensation reaction between benzaldehyde and diethyl malonate. The reaction was expected to give an enone which was diethyl-2-benzylidenemalonate as the major product as shown in Scheme 1.




Benzaldehyde Diethyl-malonate Diethyl-2-benzylidenemalonate

Scheme 1. Equation of Knoevenagel condensation reaction between benzaldehyde and diethyl malonate

Since the results of the reaction showed that the reactants were converted into products, it was suggested that all SOD catalysts synthesized in this study were active for the Knoevenagel condensation reaction. As shown in Scheme 1, it was deduced that only one product produced from the reaction. However, two side products were obtained from this reaction. The most probable compounds produced as side products belong to ethyl cinnamate as a major side product and diethyl 2, 2- bis(hydroxy(phenyl)methyl) malonate as a minor side product. The reactivity of the SOD catalysts was studied in term of percentages of conversion and selectivity. Besides, the percentage of yield for all SOD catalysts was calculated based on the major product. The percentages of yield, conversion and selectivity of the SOD catalysts are listed in Table 5. SOD-TO produce the highest percentage of conversion (96.29%) followed by SOD-TDDAB (95.84%), Na-SOD (95.63%), SOD-TDTAB (42.02%) and SOD-TCTAB (13.25%) after 24 hours reaction. The higher percentage conversation of SOD-TO could be due to the higher possibility of reactants to access to the active basic sites present in their mesopores. In addition, the SOD-TO catalyst possessed the higher amount of basicity indicated the higher amount of the active basic sites is available. From Table 5, the SOD-TO catalyst showed the highest percentage of yield for the major product as compared with other SOD catalysts which was 34.80%.

Table 5. Percentages of conversion, selectivity and yield of all SOD catalysts

| Sample | Conversion (%) | Selectivity (%) | | | Yield (%) |
|---|---|---|---|---|---|
| | | Major Product | Major Side Product | Minor Side Product | |
| Na-SOD | 95.63 | 18.66 | 61.05 | 20.29 | 17.84 |
| SOD-TDDAB | 95.84 | 22.88 | 68.11 | 9.01 | 21.93 |
| SOD-TCTAB | 13.25 | 72.30 | 0.91 | 26.79 | 9.58 |
| SOD-TDTAB | 42.02 | 59.83 | 3.15 | 37.02 | 25.14 |
| SOD-TO | 96.29 | 36.14 | 45.66 | 18.20 | 34.80 |

## Conclusion

Mesoporous sodalite (SOD-TO) was successfully synthesized in the presence of tetrapropylammonium hydroxide (TPAOH) and organosilane templates using molar oxide ratio of $1.7SiO_2$: $15NaOH$: $Al_2O_3$: $80H_2O$: 0.3 templates. On the other hand, the rest of sodalite samples synthesized using TPAOH mixed with quaternary ammoniums other than organosilane, only produced microporous sodalite. All the as-synthesized samples showed the XRD patterns of sodalite phase indicating the successful formation of sodalite phase crystal. While, FTIR results revealed that all absorption patterns shown by all the as-synthesized samples are related to the characteristic of sodalite framework. From $N_2$ adsorption analysis, SOD-TO showed the successful formation of mesoporosity contains mesoporous-microporous hierarchical structure with the highest BET surface area. All the as-synthesized sodalite samples

showed the basicity strength in the range: $8.2 \leq pKa \leq 18.4$ with mesoporous SOD-TO sample showed the highest amount of basicity. TPD-$CO_2$ analysis found that the mesoporous SOD-TO sample gave higher strength and amount of basic sites than the Na-SOD sample at temperature below 500°C. The SOD-TO catalyst with the highest amount of basicity and the highest surface area is most active, giving the highest percentages of conversion and yield in the Knoevenagel condensation reaction of benzaldehyde and diethyl malonate.

**Acknowledgements**

Authors would like to thank Universiti Teknologi Malaysia (UTM) and Ministry of Higher Education (MOHE) for financial assistant under GUP Vot No QJ13000.2526.06H70.

**References**

1. Weckhuysen, B. M. and Yu, J. (2015). Recent advances in zeolite chemistry and catalysis. *Chemical Society Reviews,* 44 (20): 7022 – 7024.
2. Arya, K. and Tomar, R. (2015). Microporous zeolite catalyst system: An eco-approach for regioselective synthesis of pyrimidobenzimidazoles. *Research on Chemical Intermediates,* 41(6): 3389 – 3400.
3. Zhao, J., Wang, G., Qin, L., Li, H., Chen, Y. and Liu, B. (2016). Synthesis and catalytic cracking performance of mesoporous zeolite Y. *Catalysis Communications,* 73: 98 – 102.
4. Mukti, R. R., Kamimura, Y. and Chaikittisilp, W. (2011). Hierarchically porous ZSM-5 synthesized by nonionic- and cationic-templating routes and their catalytic activity in liquid-phase esterification. *ITB Journal of Science,* 43 (1): 59 – 72.
5. Zhu, J., Meng, X. and Xiao, F. (2013). Mesoporous zeolites as efficient catalysts for oil refining and natural gas conversion. *Frontiers of Chemical Science and Engineering,* 7(2): 233 – 248
6. Wei, Y., Parmentier, T. E., de Jong, K. P. and Zecevic, J. (2015). Tailoring and visualizing the pore architecture of hierarchical zeolites. *Chemical Society Reviews,* 44(20): 7234 – 7261.
7. Vernimmen, J., Meynen, V. and Cool, P. (2011). Synthesis and catalytic applications of combined zeolitic/mesoporous materials. *Beilstein Journal of Nanotechnology,* 2: 785 – 801.
8. Moliner, M. (2012). Direct synthesis of functional zeolitic materials. *ISRN Materials Science,* 2012: 1 –24.
9. Chen, Z., Zhang, J. and Yu, B. (2015). Amino acid mediated mesopore formation in LTA zeolites. *Journal of Materials Chemistry A,* 4(6): 2305 – 2313.
10. Jiao, W. Q., Fu, W. H. and Liang, X. M. (2014). Preparation of hierarchically structured Y zeolite with low Si/Al ratio and Its applications in acetalization reactions. *RSC Advances,* 4(102): 58596 – 58607.
11. Emdadi, L., Wu, Y., Zhu, G., Chang, C. C., Fan, W., Pham, T. and Liu, D. (2014). Dual template synthesis of meso- and microporous MFI zeolite nanosheet assemblies with tailored activity in catalytic reactions. *Chemistry of Materials,* 26(3): 1345 – 1355.
12. Na, K. and Somorjai, G. A. (2014). Hierarchically nanoporous zeolites and their heterogeneous catalysis: Current status and future perspectives. *Catalysis Letters,* 145(1): 193 – 213.
13. Jie, Z., X. M. and Fengshou, X. (2013). Mesoporous zeolites as efficient catalysts for oil refining and natural gas conversion. *Frontiers of Chemical Science and Engineering,* 7(2): 233 – 248.
14. Corma, A., Fornés, V. and Martín-Aranda, R. M. (1990). Zeolites as base catalysts: Condensation of aldehydes with derivatives of malonic esters. *Applied Catalysis,* 59(1): 237 – 248.
15. Muralidhar, L. and Girija, C. R. (2014). Simple and practical procedure for knoevenagel condensation under solvent-free conditions. *Journal of Saudi Chemical Society,* 18(5): 541 – 544.
16. Yao, J., Zhang, L., and Wang, H. (2008). Synthesis of nanocrystalline sodalite with organic additives. *Materials Letters,* 62(24), 4028 – 4030.
17. Shanbhag, G. V., Choi, M., Kim, J. and Ryoo, R. (2009). Mesoporous sodalite: A novel, stable solid catalyst for base-catalyzed organic transformations. *Journal of Catalysis,* 264(1): 88 – 92.
18. Rahul, R., Satyarthi, J. K. and Srinivas, D. (2011). Lanthanum and zinc incorporated hydrotalcites as solid base catalysts for biodiesel and biolubricants production. *Indian Journal of Chemistry-Section A,* 50: 1017 – 1025.
19. Treacy, M. M. J. and Higgins J. B. (2001). Collection of simulated XRD powder patterns for zeolites. Elsevier, Amsterdam.
20. Yao, J., Wang, H., Ratinac, K. R., and Ringer, S. P. (2006). Formation of colloidal hydroxy-sodalite nanocrystals by the direct transformation of silicalite nanocrystals. *Chemistry of Materials,* 18(6): 1394 – 1396.

*Malaysian Journal of Analytical Sciences, Vol 21 No 4 (2017): 871 - 879*
*DOI: https://doi.org/10.17576/mjas-2017-2104-13*

MALAYSIAN JOURNAL OF ANALYTICAL SCIENCES
*Published by The Malaysian Analytical Sciences Society*
ISSN 1394 - 2506

# PALLADIUM PINCER COMPLEXES AS CATALYSTS FOR SELECTIVE ACTIVATION AND FUNCTIONALIZATION OF 1-PROPANOL

## (Kompleks Paladium Pincer Sebagai Mangkin untuk Pengaktifan dan Pefungsian Terpilih 1-Propanol)

Sri Sugiarti[1]* and Craig M Jensen[2]

[1]*Department of Chemistry, Faculty of Mathematics and Natural Sciences, Bogor Agricultural University, 16680 Bogor, Indonesia*
[2]*Department of Chemistry, University of Hawaii at Manoa, Honolulu, 96822 Hawaii, United States*

**Corresponding author: sri.sw07@gmail.com*

Received: 20 September 2016; Accepted: 16 May 2017

**Abstract**

Selective activation and functionalization of saturated C-H bonds in the original Shilov system used a combination of $PtCl_4^{2-}$ and $PtCl_6^{2-}$ in aqueous solution to transform methane into methanol and/or methyl chloride. On the other hand, palladium phosphinito PCP pincer halides ($PdX\{C_6H_3\text{-}2,6\text{-}(OPr^i_2)_2\}$, X=Cl, Br, I) have been developed for the Heck reactions of aryl halide, and they are believed to operate by an alternative Pd(II)/Pd(IV) mechanism, made this catalyst potentially used for the Shilov type reaction. Palladium pincer complexes showed selectivity for terminal functionalization of 1-propanol at lower temperature. Successful substitution of $PtCl_4$ by the less expensive oxidation system, $CuCl_2$ and air was achieved. In the presence of $CuCl_2$, the Wacker-like oxidation is apparently involved in the reaction. The phosphorous donor palladium pincer complexes showed better activity and selectivity than other types of palladium pincer complexes such as NCN-Pd-Br and SCS-Pd-Cl.

**Keywords**: C-H bonds activation, palladium pincer complexes, 1-propanol, selective functionalization, Shilov system

**Abstrak**

Pengaktifan dan pefungsian terpilih ikatan C-H tepu pada sistem asal Shilov menggunakan kombinasi larutan akueus daripada $PtCl_4^{2-}$ dan $PtCl_6^{2-}$ untuk mengubah metana menjadi metanol dan/atau metil klorida. Selain itu, paladium fosfinito PCP pincer halida ($PdX\{C_6H_3\text{-}2,6\text{-}(OPr^i_2)_2\}$, X=Cl, Br, I) telah digunakan untuk tindak balas Heck daripada aril klorida, dan dipercayai beroperasi melalui mekanisme alternatif Pd(II)/Pd(IV), menjadikan mangkin ini berpotensi untuk digunakan pada tindak balas jenis Shilov. Kompleks – kompleks paladium pincer menunjukkan kepilihan terhadap pefungsian terminal 1-propanol pada suhu rendah. Kejayaan penggantian $PtCl_4$ oleh sistem pengoksidaan yang lebih murah iaitu $CuCl_2$ dan udara telah dicapai. Dengan kehadiran $CuCl_2$, tindak balas pengoksidaan Wacker terlibat secara tidak langsung. Kompleks pincer paladium dengan penderma fosforus menunjukkan aktiviti dan kepilihan yang lebih baik dibandingkan dengan jenis lain dari kompleks paladium pincer, seperti NCN-Pd-Br dan SCS-Pd-Cl.

**Kata kunci**: pengaktifan ikatan C-H, kompleks paladium pincer, 1-propanol, pefungsian terpilih, sistem Shilov

## Introduction

Selective activation and functionalization of C-H bonds in alkanes is one of the biggest challenging problems in chemistry. The abundant saturated hydrocarbons are underutilized and require an efficient method to transform

them into more valuable products [1, 2]. Alkanes are not readily able to participate in chemical reactions because they have no empty orbital of low energy or filled orbital of high energy [3]. Several practical processes can be used to convert alkanes directly into more valuable products. However, they usually require harsh conditions that are difficult to control to prevent conversion of the alkanes into the thermodynamically stable and unattractive products carbon dioxide and water.

It was reported that low valent precious metal complexes will oxidatively add to alkane C-H bonds to give an alkyl hydride. The attempt to activate and functionalize C-H bond of alkanes was first reported by Shilov in 1970 [4]. The reaction has been found to be selective for the least substituted carbon of the alkane. The system which is now known as the "Shilov-system" is platinum catalyzed C-H bond activation and functionalization in aqueous media. In Shilov chemistry, the C-H bond is activated and functionalized by metal complexes with unique selectivity. Activation and functionalization at the terminal position is preferred. The use of 1-propanol as a substrate gives several advantages, it is possible to distinguish whether the pincer complexes catalyze a Shilov-type reaction or if only a Fenton-type reaction occurs. In the Shilov system, the main product would be 1,3-propanediol, while the formation of 1,2-propanediol would indicate that a radical reaction had taken place. Another advantage is that it is miscible in aqueous media. Thus the reactions can be carried out in simple glassware and at atmospheric pressure [5]. The general equation and the proposed mechanism of the reaction are as follow (equation 1 and Figure 1):

$$R\text{-}H + H_2O + PtCl_6^{2-} \xrightarrow[120\ ^oC]{\text{catalyst } PtCl_4^{2-}} R\text{-}OH\ (+\ R\text{-}Cl) + PtCl_4^{2-} + 2HCl \qquad (1)$$

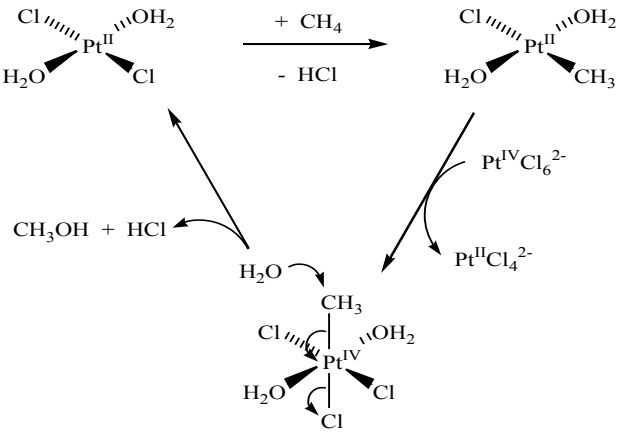



Figure 1. Proposed catalytic cycle for the platinum-catalyzed oxidation of alkanes in aqueous solution

As seen in Figure 1, the C-H activation is catalytic in Pt(II). It is also shown that the Shilov system requires a stoichiometric amount of Pt(IV) as oxidant which is one of the drawbacks of this system. Also, the presence of metallic platinum promotes the over-oxidation of the Shilov reaction's product. Pt(IV) plays dual roles in the reaction, as stoichiometric oxidant and also to prevent the formation of metallic platinum by suppressing the disproportionation of Pt(II), another drawback of the Shilov system [5]. Introducing a strong chelating ligand such as a pincer ligand into the platinum complex would be expected to stabilize Pt(II) from undergoing disproportionation. The use of pincer platinum complexes in the Shilov-type reaction has been reported [6, 7]. The most interesting result is that Pt(IV) can be replaced by the cheaper, $CuCl_2$ oxidant. However, the activity of pincer complexes to catalyze Shilov-type chemistry is reduced upon this substitution [8]. This leads to the exploration of the use of different metal pincer complexes as catalysts.

Previously, in Heck reaction, palladium pincer complexes were proposed to proceeds through Pd(II)/Pd(IV) chemistry rather than the typical Pd(0)/Pd(II) cycles [9]. It is arguable that palladium pincer complexes might proceed through Pd(II)/Pd(IV) cycles when applied in the Shilov-type system in the analogy to the platinum analogs. Here we report the development of palladium pincer complexes as catalysts for alkane hydroxylation. Four types of pincer complexes seen in Figure 2 were tested in the Shilov reaction to see if minor changes in the ligand would have any effect on the catalytic activity. Furthermore, the possibility of using $CuCl_2$ as primary oxidant was also investigated.

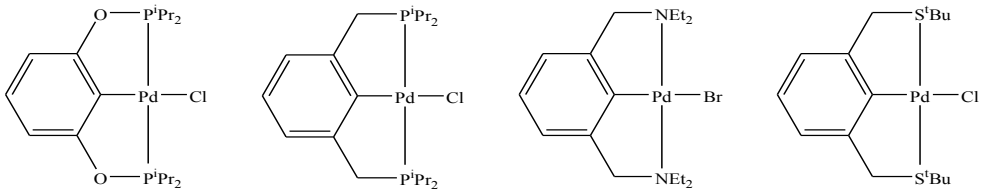



Figure 2. Pincer palladium complexes tested as hydroxylation catalysts

## Materials and Methods

### Materials

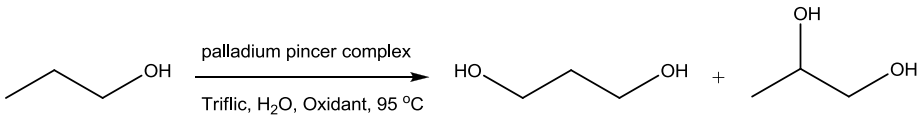
$PtCl_4$ (Pressure Chemicals), $K_2PtBr_6$ (Pressure Chemicals), trifluoromethanesulfonic acid (Aldrich), trifluoroacetic acid (Aldrich), acetic acid (Aldrich), 1-propanol (Fisher Scientific), $CuCl_2{\cdot}2H_2O$ (Fisher Scientific), $Cu(OAc)_2.H_2O$ (Fischer Scientific), hydrochloric acid (Aldrich) and hydrogen peroxide (30%, Fisher Scientific) were used as purchased. Complexes **1** [9], **2** [10], **3** [11] and **4** [12] were prepared according to the published procedures.

### Hydroxylation of 1-propanol catalysed by palladium pincer complexes

Water (3 ml), trifluoromethanesulfonic acid or trifluoroacetic acidoracetic acidorhydrochloric acid (3.33 mmol), the complex **1** or other type of palladium pincer complexes (0.18 mmol), and oxidant ($PtCl_4$, $K_2PtBr_6$, $CuCl_2{\cdot}2H_2O$, $Cu(OAc)_2.H_2O$) were added to a round bottom flask equipped with a condenser. 1-propanol was added portion wise over a 4 hours period (4 x 1 ml, total 56 mmol). The flask was heated in the range from 65 to 95 $^oC$ and the mixture was treated dropwise with 30% hydrogen peroxide at the rate of 1.0 to 2.0 ml/hour from a syringe pump. After eight hours, the resulting mixture was analyzed by gas chromatography – mass spectrometry (GC-MS).

## Results and Discussion

In order to test the reactivity of palladium pincer complexes in Shilov type chemistry, the original oxidant, $PtCl_4$, was used coupled with $H_2O_2$ as co-oxidant, as seen on equation 2. De Vries et al. used $H_2O_2$ to oxidized Pt(II) to Pt(IV) in the presence of the strong acid trifluoromethanesulfonic acid [5]. The result is shown on Table 1.




(2)

Table 1. Hydroxylation of 1-propanol with palladium pincer complexes[a]

| Entry | Catalyst | Rate of $H_2O_2$ (ml/h) | Time (hour) | TON[b] | | $^{31}$P NMR[c] (ppm) |
|---|---|---|---|---|---|---|
| | | | | 1,3-diol | 1,2-diol | |
| 1 | 1 | 1.0 | 1 | - | - | 188 |
| 2 | 1 | 2.0 | 2 | Trace | No | 65 |
| 3 | 1 | 1.9 | 3.5 | 5 | 2 | 65 |
| 4 | 2 | 1.9 | 3.5 | 4 | 1.8 | 65 |
| 5 | 3 | 1.9 | 0.5 | 1 | 0.4 | - |
| 6 | 4 | 1.9 | 1 | 2 | 1 | - |
| 7 | - | 1.0 | 4 | - | - | - |
| 8 | - | - | 5 | - | - | - |

[a]All reactions were carried out in the presence of $PtCl_4$ and $H_2O_2$ unless otherwise noted. The resulting mixtures were analyzed by GC. Nevertheless, the formation of 1,3-diol and 1,2-diol conformed by $^1$H and $^{13}$C NMR [b]TON is the average of three runs. TON=mol of product/(mol of palladium complex + mol of $PtCl_4$) [c] $^{31}$P NMR at 65 ppm corresponds to phosphorous oxide and at 188 ppm corresponds to complex **1**.

The rates of the addition of $H_2O_2$ must be controlled as such to prevent the formation of Pt(0), a black precipitate resulting from the disproportionation of Pt(II), once Pt(IV) is reduced to Pt(II) in the cycle. Apparently, at lower rates of $H_2O_2$, complex **1** quickly underwent redox reaction with $PtCl_4$ but not following the Shilov reaction's pathway as no 1,3-propanediol was formed. Result on 1$^{st}$ entry showed that the rate of $H_2O_2$ at 1 ml/h was not fast enough to oxidize Pt(II) to Pt(IV). The rate of $H_2O_2$ addition to 2 ml/h resulted in the decomposition of complex **1** as shown by $^{31}$P NMR. Slightly reduced rate of $H_2O_2$ addition at 1.9 ml/h resulted in similar yield to that observed previously using the analogous platinum complex as catalyst.

Unlike the platinum analog, the Shilov reaction with the palladium pincer complexes showed ligand dependency. Changing the atom donor from phosphorous to nitrogen or sulphur resulted in poor turnover numbers. Unfortunately, the reaction only lasted 3.5 hours before the PCP pincer complex decomposed into a detectable black precipitate. Blank tests in the presence of $PtCl_4$, entry 7 and 8, confirmed that the product only formed in the presence of the catalyst. Even though the Shilov reaction is dominant, the formation of radical products was also significant as shown by the presence of 1,2-propanediol. The ratio between 1,3-propanediol and 1,2-propanediol is 3:1. It was considered that the higher reaction temperature of 95 $^oC$ might promote the formation of radical products. Experiments carried out at the lower temperature of 65 $^oC$ are presented in Table 2.

Table 2. Hydroxilation of 1-propanol in the presence of complex 1 at 65 $^oC$ [a]

| Entry | Oxidant | Acid | TON | |
|---|---|---|---|---|
| | | | 1,3-diol | 1,2-diol |
| 1 | $PtCl_4$ | Triflic | 3 | 0.8 |
| 2 | $PtCl_4$ | Trifluoroacetic | 3 | 0.8 |
| 3 | $PtCl_4$ | Acetic | 1 | 4 |
| 4 | $PtCl_4$ | Triflic[b] | 2 | 0 |

[a] Reactions were carried out in the presence of $H_2O_2$ as secondary oxidant. TON is the average of three runs. Catalysis with complex **2** showed very similar results with complex **1**. Complex **3** and **4** always decomposed prematurely. [b] In the presence of 1 ml THF

Reducing the temperature resulted in reduced solubility of $PtCl_4$ compounds and in turn gave less turnover number. Introducing different acids was done to solve this problem with no success. However, a new conclusion was made that in the presence of acetic acid more radical product was formed.

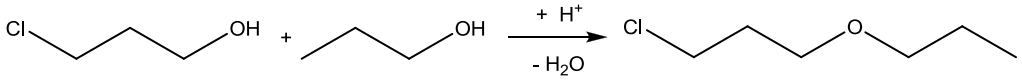
A critical drawback with the Shilov reaction is the use of expensive Pt metal as oxidant. Substituting Pt with another cheaper redox metal is desirable. The best candidate was $CuCl_2$. In the catalytic reaction of the Wacker process, $CuCl_2$ is widely known to do redox reactions with Pd [13, 14]. Introducing $CuCl_2$ to the reaction almost did not result in any type of products as shown in Table 3. Apparently $H_2O_2$ oxidized the catalyst at a higher rate than the redox reaction between $CuCl_2$ and palladium pincer complexes. Introducing another source of copper, $Cu(OAc)_2$, resulted in a very significant turnover number of products. However, as mention earlier, acetic ion promotes the formation of radical reaction as more than twice as much 1,2-propanediol was formed.

Table 3. Impact of copper salt in the presence of complex 1[a]

| Entry | Oxidant | Additive | TON[b] | |
|---|---|---|---|---|
| | | | 1,3-diol | 1,2-diol |
| 1 | $CuCl_2$ | Triflic | Trace | - |
| 2 | $Cu(OAc)_2$ | Triflic | 15 | 45 |
| 3 | $Cu(OAc)_2$ | Trifluoroacetic | 17 | 41 |
| 4 | $Cu(OAc)_2$ | Acetic | Trace | Trace |
| 5 | $Cu(OAc)_2$ | - | Trace | Trace |

[a] Reactions were carried out in the presence of $H_2O_2$ at 0.5 ml/h. The temperature of the reactions was 65 $^oC$. [b] TON is the average of three runs. TON = mol of diol/mol of palladium complex. Similar results were showed by complex **2.** Complex **3** and **4** produced only trace amount of product

Information from the Wacker system led to a better understanding of the Shilov reaction in the presence of palladium pincer complexes and $CuCl_2$ [13, 14]. The reaction was then carried out in the presence of $CuCl_2$, water, HCl and at temperature of 65$^oC$ to give two kinds of products 1,3-propanediol and 3-chloro-1-propanol. However, the GC spectrum showed neither one of those expected products. Instead, one very dominant peak appeared at a higher retention time as shown in Figure 3. Mass spectrum fragmentation study showed that the compound at 10.46 minutes is a chloro compound. The compound at 10.46 minutes has m-1 at 135. Apparently 3-chloro-1-propanol compound was formed but in the acidic solution it quickly reacts with the starting material to form an ether compound, as seen on equation 3.




(3)

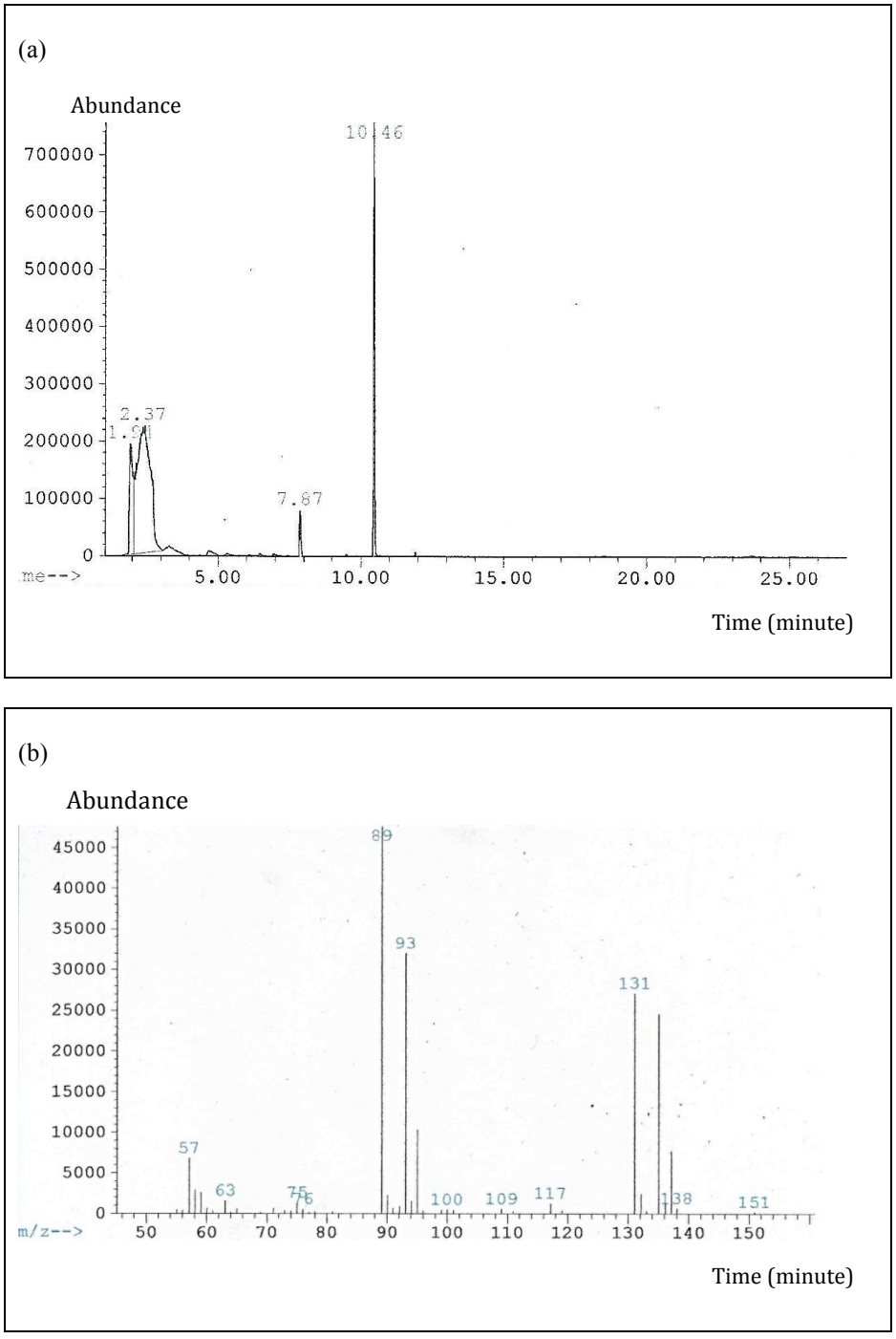



Figure 3. GC spectrum of (a) the Wacker-type reaction of hydroxylation of 1-propanol and (b) the mass spectrum of ether complex at retention time of 10.46 minutes

The appearance of ether in the products led to a conclusion that there is a Lewis acid present in the solution, as alcohol would be converted to ether in the presence of a strong acid or Lewis acid [15]. Figure 3(b) features a peak

at 93 that belongs to the 3-chloro-1-propanol which also results from loss of 43 molecular mass or a fragment of $CH_3CH_2CH_2$-. Detailed on mass fragmentation of ether compound can be seen Figure 4 below.

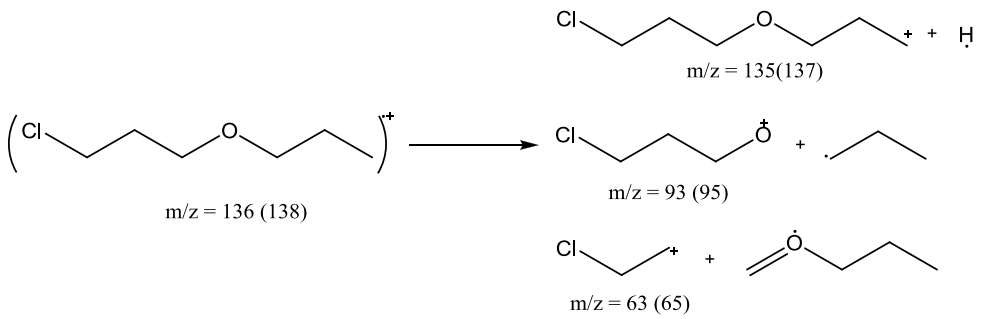



Figure 4. Detailed on mass fragmentation of ether compound

Experiments showed that the ether compound can be obtained in the presence of HCl and $CuCl_2$ or complex **1**, suggesting that complex **1** acts as a catalyst in Shilov type chemistry as well acting as a Lewis acid [16]. Therefore, reducing the catalyst loading, consequently reducing the amount of Lewis acid, was expected to reduce the rate of formation of ether. Figure 5 shows the result from reaction with lower catalyst loading of complex 1.

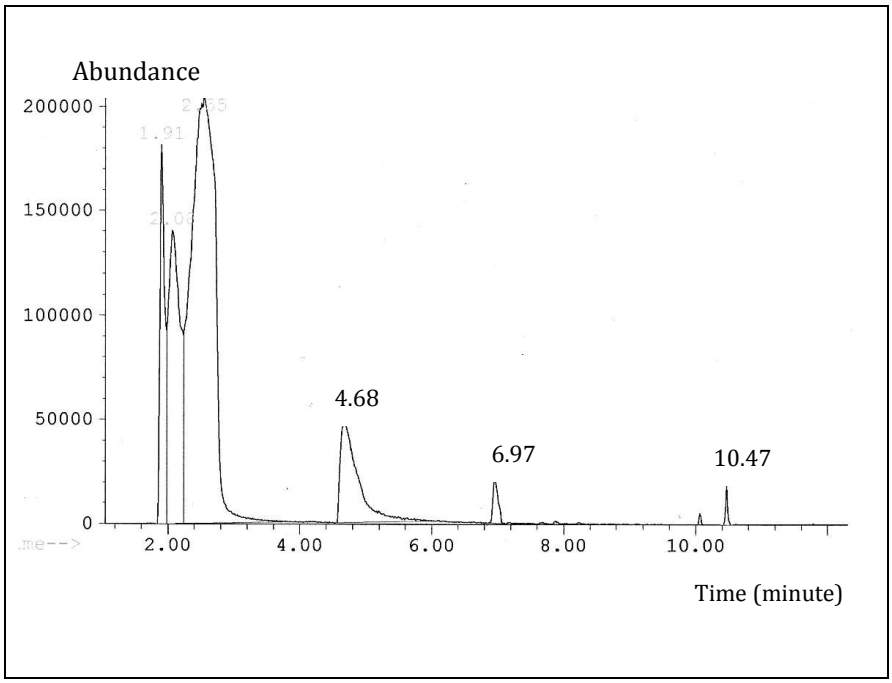



Figure 5. Hydroxylation of 1-propanol at lower catalyst loading

The peak at 4.68 minutes is 3-chloro-1-propanol complex with turnover number of 23. This is the highest turnover number that was attained in all of the Shilov-type experiments with palladium pincercomplexes. Furthermore, this condition was the best in terms of not producing radical reactions. The dominance of 3-chloro 1-propanol in the products suggests that in the presence of $CuCl_2$, the nucleophilic attack by $OH^-$ is less effective. This phenomenon is also known in the Wacker process where use of $CuCl_2$ as oxidant instead of CuCl results in product dominated by

chloro compound [17]. One concern with using $CuCl_2$ and HCl system in our reaction is that since the dominant product is the chloro compound and the source of chloride in the system is either $CuCl_2$ or HCl or both, then as the reaction progresses, the concentration of $CuCl_2$ or HCl will decrease. Less $Cl^-$ might reduce the re-oxidation of Cu(I) complex into Cu(II) complex, and eventually slow down the reaction.

## Conclusion

Palladium pincer complexes are catalysts for Shilov-type chemistry by showing selectivity for terminal functionalization of 1-propanol at lower temperature. A cheaper alternative oxidant $CuCl_2$ and air was successfully applied, adapted from the Wacker process. The phosphorous palladium pincer complexes showed better activity and selectivity than other types of palladium pincer complexes such as NCN-Pd-Br and SCS-Pd-Cl.

## References


1. Konnick, M. M., Hashiguchi, B. G., Devarajan, D., Boaz, N. C., Gunnoe, T. B., Groves, J. T., Gunsalus, N., Ess, D. H., Periana, R. A. (2014). Selective CH functionalization of methane, ethane, and propane by perfluoroarene iodine(III) complex. *Angewandte Chemie,* 126(39): 10658 – 10662.
2. Labinger, J. A. and Bercaw, J. E. (2002). Understanding and exploiting C-H bond activation. *Nature*, 417: 507 – 514.
3. Crabtree, R. H. (2004). Organometallic alkane CH activation. *Journal of Organometallic Chemistry*, 689 (24): 4083 – 4091.
4. Shilov, A. E. and Shul'pin G. B. (1997). Activation of C-H bonds by metal complexes. *Chemical Reviews*, 97(8): 2879 – 2932.
5. DeVries, N., Roe, D. C., Thorn, D. L. (2002). Catalytic hydroxylation using chloroplatinum compounds. *Journal of Molecular Catalysis A: Chemical*, 189 (1): 17 – 22.
6. Jensen, C. M. (1999). Irridium PCP complexes: Highly active and robust catalysts for novel homogenous aliphatic dehydrogenation. *Chemical Communications*, 24: 2443 – 2449.
7. Morales-Morales, D., Redon, R., Yung, C. and Jensen, C. M. (2004). Dehydrogenation of alkanes catalyzed by an irridium phosphinito PCP pincer complex. *Inorganica Chimica Acta*, 357(10): 2953 – 2956.
8. Wang, Z., Sugiarti, S., Morales, C. M., Jensen, C. A. and Morales-Morales, D. (2006). Catalytic hydroxylation of 1-propanol by platinum NCN and PCP pincer complexes using $CuCl_2$ as oxidant. *Inorganica Chimica Acta*, 359(6): 1923 – 1928.
9. Morales-Morales, D., Grause, C., Kasaoka, K., Redon, R., Cramer, R. E. and Jensen, C. M. (2000). Highly efficient and regioselective production of trisubstituted alkenes through Heck couplings catalyzed by a palladium phosphinito PCP pincer complex.*Inorganica Chimica Acta*, 300: 958 – 963.
10. Ohff, M., Ohff, A., van der Boom, M. E. and Milstein, D. (1997). Highly active Pd(II) PCP-type catalysts for the Heck reaction. *Journal of the American Chemical Society*, 119: 11687 – 11688.
11. Van Beek, J. A. M., Van Koten, G., Dekker, G., Wissing, E., Zoutberg, M. C., Stam, C. H. (1990). Synthesis and reactivity towards diiodine of palladium(II) and platinum(II) complexes with non-cyclic and cyclic ligands $(C_6H_3\{CH_2NR^1R^2\}_2$-2,6)- End-on diiodine platinum(II) bonding in macrocyclic $[PtI(C_6H_3\{CH_2NMe(CH_2)_7MeNCH_2\}$-2,6)$(\eta^1$-$I_2)]$. *Journal of Organometallic Chemistry*, 394: 659 – 678.
12. Errington, J., McDonald, W. S. and Shaw, B. L. (1980). Cyclopalladation of $C_6H_4(CH_2SBu^t)_2$-1,3 and the crystal structure of $[PdCl\{C_6H_3(CH_2SBu^t)_2$-2,6]. *Journal of the Chemical Society-Dalton Transactions*: 2312 – 2314.
13. Smidt, J., Hafner, W., Jira, R., Sedlmeier, J., Sieber, R., Ruttinger, R. and Kojer, H. (1959). Katalytische umsetzungen von olefinen an platinmetall-verbindungen das consortium verfahren zur herstellung von acetaldehyd. *Angewandte Chemie*, 71(5): 176 – 182.
14. Keith, J. A., Nielsen, R. J., Oxgaard, J. and Goddard, W. A. (2007). Unraveling the Wacker oxidation mechanisms. *Journal of the American Chemical Society*, 129(41): 12342 – 12343.
15. Jaworski, M. A., Vega, S. R., Siri, G. J., Casella, M. L., Salvador, A. R. and Lopez, A. S. (2015). Glycerol etherification with benzyl alcohol over zirconia catalysts. *Applied Catalysys A: General*, 505: 36 – 43.
16. Dijkstra, H. P., Meijer, M. D., Patel, J., Kreiter, R., van Klink, G. P. M., Lutz, M., Spek, A. L., Canty, A. J. and van Koten, G. (2001). Design and performance of rigid nanosize multimetallic cartwheel pincer compounds as Lewis acid catalysts. *Organometallics*, 20(14): 3159 – 3168.

17. Tsuji, J. (1984). Synthetic applications of palladium catalyzed oxidation of olefins to ketones. *Synthesis,* 1984(05): 369 – 384.

*Malaysian Journal of Analytical Sciences, Vol 21 No 4 (2017): 880 - 888*
*DOI: https://doi.org/10.17576/mjas-2017-2104-14*

MALAYSIAN JOURNAL OF ANALYTICAL SCIENCES
*Published by The Malaysian Analytical Sciences Society*
ISSN 1394 - 2506

# OPTIMIZATION BY BOX-BEHNKEN DESIGN OF IN-SITU CARBON DIOXIDE CONVERSION USING LANTHANUM OXIDE

## (Pengoptimuman Dengan Reka Bentuk Box-Behnken Untuk Penukaran In-Situ Karbon Dioksida Menggunakan Lantanum Oksida)

Salmiah Jamal Mat Rosid, Wan Azelee Wan Abu Bakar*, Rusmidah Ali

*Department of Chemistry, Faculty of Science,*
*Universiti Teknologi Malaysia, 81310 Skudai, Johor Bahru, Johor, Malaysia*

**Corresponding author: wazelee@kimia.fs.utm.my*

Received: 20 September 2016; Accepted: 16 May 2017

Lanthanum oxide based catalyst was revealed as one of potential catalyst to convert carbon dioxide to wealth product methane in simulated natural gas. To produce higher conversion of carbon dioxide, the Response Surface Methodology utilizing Box-Behnken design (BBD) was used to optimize the lanthanum oxide based catalysts by three critical parameters which were calcination temperature, based ratio and catalyst dosage. The maximum $CO_2$ conversion was achieved at 1000 $^oC$ calcination temperature using 7 g of catalyst for 60% based loading. The optimization result from BBD is in good agreement with experimental data. The optimize parameters gave 99% of $CO_2$ conversion determined using Fourier Transformation Infrared (FTIR) and yielded about 50% of $CH_4$ at reaction temperature of 400 °C. X-ray Diffraction (XRD) analysis showed an amorphous structure with $RuO_2$ as active species and Field Emission Scanning Electron Microscope (FESEM) illustrated the catalyst surface was covered with small and dispersed particles with undefined shape. EDX analysis revealed that when the calcination temperature was increased, the mass ratio of Ru increased.

**Keywords**: Box-Behnken design, optimization, response surface methodology, lanthanum oxide

**Abstrak**

Mangkin asas lanthanum oksida adalah salah satu mangkin berpotensi menukarkan karbon dioksida kepada produk metana yang banyak dalam simulasi gas asli. Untuk menghasilkan penukaran karbon dioksida yang tinggi, kaedah gerak balas permukaan menggunakan reka bentuk Box-Behnken (BBD) untuk mengoptimumkan mangkin asas lantanum oksida oleh tiga parameter kritikal yang mana suhu kalsin, nisbah asas, dan dos mangkin. Maksimum penukaran $CO_2$ dicapai pada suhu kalsin 1000 $^oC$ menggunakan 7 g mangkin untuk 60% nisbah asas. Keputusan pengoptimuman dari BBD adalah selari dengan data eksperimen. Parameter yang optimum memberikan 99% penukaran $CO_2$ apabila ditentukan menggunakan Inframerah transformasi Fourier (FTIR) dan menghasilkan 50% metana pada suhu tindak balas 400 $^oC$. Analisis pembelauan sinar-X (XRD) menunjukkan struktur amorfus dengan $RuO_2$ sebagai aktif spesis dan Mikroskop Imbasan Elektron Pancaran Medan ( FESEM ) menunjukkan permukaan mangkin diselaputi dengan partikel yang bersaiz kecik dan terserak sekata tanpa bentuk. Analisis EDX menunjukkan apabila suhu kalsin meningkat, nisbah jisim Ru meningkat.

**Kata kunci:** reka bentuk Box-Behnken, pengoptimuman, kaedah gerak balas permukaan, lantanum oksida

## Introduction

Nowadays, industrial pollution control has facing challenges when industrial demands have been increased which would affect the environment and social sustainability. Therefore, new technologies are needed to reduce $CO_2$ emission at high efficiency to meet the requirement of Kyoto Protocol which has limited the greenhouse gas

emission to the environment. Natural gas is one of demanding industrial request for the fuel transportation. However, the higher percentage of $CO_2$ content in natural gas has been decreased the quality and price of natural gas.

Recently, the removal of these sour gases via chemical conversion techniques becomes the most promising technique. Catalysts for the $CO_2$ methanation have been extensively studied because of their application in the conversion of $CO_2$ gas to produce methane, which is the major component in natural gas [1]. Methanation of carbon dioxide is the reaction for chemical fixation of carbon dioxide that is considerably faster than the reactions to form other hydrocarbons or alcohols. Thus, the methanation reaction is suited for treating a huge amount of carbon dioxide [2]. Besides, methanation has received attention from a viewpoint of environmental protection because the emission of $CO_2$ in the atmosphere brings about global warming by the greenhouse effect and these harmful gases can simultaneously be converted to useful methane gas [3]. This process can increase the purity and quality of the natural gas without wasting the undesired components but fully used them to produce high concentration of methane.

From the previous study, trimetallic Ru/Co/La (5:35:60)/$Al_2O_3$ calcined at 1000 $^oC$ showed a promising performance with 99% of $CO_2$ conversion and 50% $CH_4$ formation [4]. This observation showed that $La_2O_3$ is able to increase adsorption of $CO_2$ to the surface of catalyst. Other than that, Wan Abu Bakar et al. also reported that when cobalt oxide doped with noble metal (platinum), it gives higher $CO_2$ conversion with 70% and yielded 47% methane [5]. This can be concluded that noble metal would increase the cobalt reducibility in catalyst supported on alumina [6]. Therefore, in this paper, the potential catalyst was optimized to determine the optimum parameters for Ru/Co/La (5:35:60)/$Al_2O_3$ to obtain higher $CO_2$ conversion and $CH_4$ formation by using Box-Behnken design.

## Materials and Methods

### Catalyst preparation

Wet impregnation method was used to prepare $Al_2O_3$ supported catalyst by impregnating the catalyst solution on $Al_2O_3$ beads support. Then, alumina beads with diameter of 3 mm was immersed into the catalysts solution for 20 minutes and it was then dried at 80 $^oC$ for 24 hours and calcined at 400 $^oC$, 700 $^oC$, 900 $^oC$, 1000 $^oC$, and 1100 $^oC$ for 5 hours. For catalytic activity measurements, reactions of methanation were performed from ambient temperature up to 400 $^oC$ with temperature rate of 5 $^oC$/ min. $CO_2$ and $H_2$ gases were introduced into the reactor system in a stoichiometric ratio of 1:4. Screening on the product gas stream was done by using FTIR analysis.

### Characterization

The surface morphology and physical properties of the catalysts were characterized by Field Emission Scanning Electron Microscope (FESEM) – Energy Dispersion X-ray (EDX), and X-ray Diffraction (XRD). The surface morphology of the samples was analyzed using Zeiss Supra 35VP FESEM with the energy of 2.0 kV and 50 000 x magnification couple with EDX analyzer and 1500x magnification. Prior to the analysis, the sprinkled sample was coated with gold as conducting material by gold sputter at $10^{-1}$ Mbar using Bio Rad Polaron Division SEM coating system machine. The XRD patterns of the powder samples were recorded at 2θ between $10^o$ to $80^o$ using a Bruker Advance D8 with Siemens 5000 diffractometer. The Cu $K_\alpha$ radiation operates at 40 kV and 40 mA with $\lambda = 1.5418$ Å.

### Design of experiment

A three variables Box-Behnken design for response surface methodology were used to study the effect of calcination temperature ($^oC$), Based loadings (%), and catalyst dosage (g) on catalytic activity of methanation reaction using Design Expert Software, version 7.1 (Stat-Ease Inc., USA). Analysis of variance, ANOVA, is a statistical decision-making tool used for detecting any differences in average performances of tested parameters [7]. Analysis of variance (ANOVA) was used to check the adequacy of the model for the responses in the experimentation.

## Results and Discussion

### Characterization: X-ray diffractogram analysis for lanthanum oxide based catalyst

Figure 1 shows the diffractogram of Ru/Co/La (5:35:60)/$Al_2O_3$ calcined at 400 °C, 700 °C, 900 °C, 1000 °C and 1100 °C. XRD diffractogram for calcination temperature of 400 ºC showed very low degree of crystallinity and an amorphous phase. This could be attributed to the alumina support which can be assigned at $2\theta$ of 66.47 ° ($I_{100}$) as $Al_2O_3$ with cubic phase. Tang et al. claimed that the support only exhibits broad diffraction peaks when calcined at below 500 ºC [8].

For Ru/Co/La (5:35:60)/$Al_2O_3$ calcined at 700 °C, the diffractogram also showed an amorphous peak indicating the atom are arranged almost in a regular pattern. At calcination temperature of 700 °C, three peaks of $Al_2O_3$ with cubic phase were appeared at $2\theta$ = 45.83 ° ($I_{100}$), 66.97 ° ($I_{100}$), and 60.45 ° ($I_{75}$). Furthermore, at 900 °C calcination temperature exhibited of $Al_2O_3$ cubic phase which could be observed at $2\theta$ values of 67.034º ($I_{100}$), 45.863º ($I_{100}$), and 37.604º ($I_{80}$). The shifting peaks occurred due to decrease lattice spacing parameter which can be supported by decreasing lattice value from 0.991 Á (110) to 0.246 Á (440) [9]. The peaks for cobalt oxide were only observed at 32.173º ($I_{662}$). Formation of new peak which belong to $RuO_2$ with tetragonal phase were revealed at the $2\theta$ values of 28.135º ($I_{999}$), and 35.793º ($I_{751}$).The diffractograms of catalyst calcined at 1000 °C and 1100 °C exhibited similar peaks with the catalyst calcined at 900 °C. Nevertheless, the diffractogram of catalyst calcined at 1100 °C showed few new peaks. Three of them were at $2\theta$ values of 33.958º, 36.146º, and 42.741º which were assigned to the lanthanum aluminium oxide with hexagonal phase. Other peaks corresponding to the alumina corundum with rhombohedral phase could be observed at $2\theta$ values 43.347º and 57.492º. From the overall diffractograms, it could be suggested that the calcination temperature affects the performance of catalytic activity by increasing of crystal lattice in order to produce narrower peaks [10].

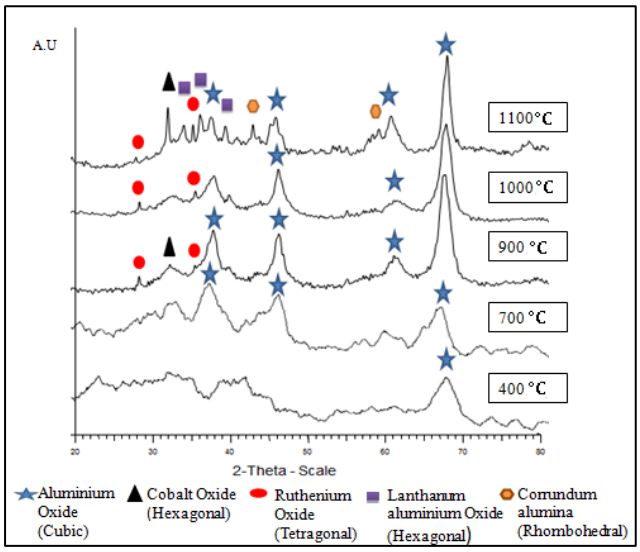



Figure 1. Diffractogram of various calcination temperatures of Ru/Co/La (5:35:60)/$Al_2O_3$ catalysts

### Field emission scanning electron microscope analysis for lanthanum oxide based catalyst

The micrographs of the supported catalysts showed a rough surface morphology. In general, there was no significant change in morphologies for the entire sample after calcination. A typical FESEM micrograph for Ru/Co/La (5:35:60)/$Al_2O_3$ sample is illustrated in Figure 2. From the micrograph in Figure 2, the surface particles of the fresh catalyst agglomerated, possibly due to the calcination process. The particles were in spherical shape. It was also noted that the pore of the catalyst is slightly visible. When it is small particle, the surface area is higher thus, adsorption process easy to occur. This is in a good agreement with the XRD analysis which exhibited very broad peaks denoting an amorphous character for the Ru/Co/La (5:35:60)/$Al_2O_3$ catalyst. Nevertheless, the catalyst Ru/Co/La (5:35:60) /$Al_2O_3$ calcined at 1100 °C showed many square shaped particles were formed on

the catalyst surface. This square shaped was belong to $Al_2O_3$ rhombohedral phase as shown in the XRD diffractogram in Figure 1 as similarly discussed by Mat Rosid et al. [4].

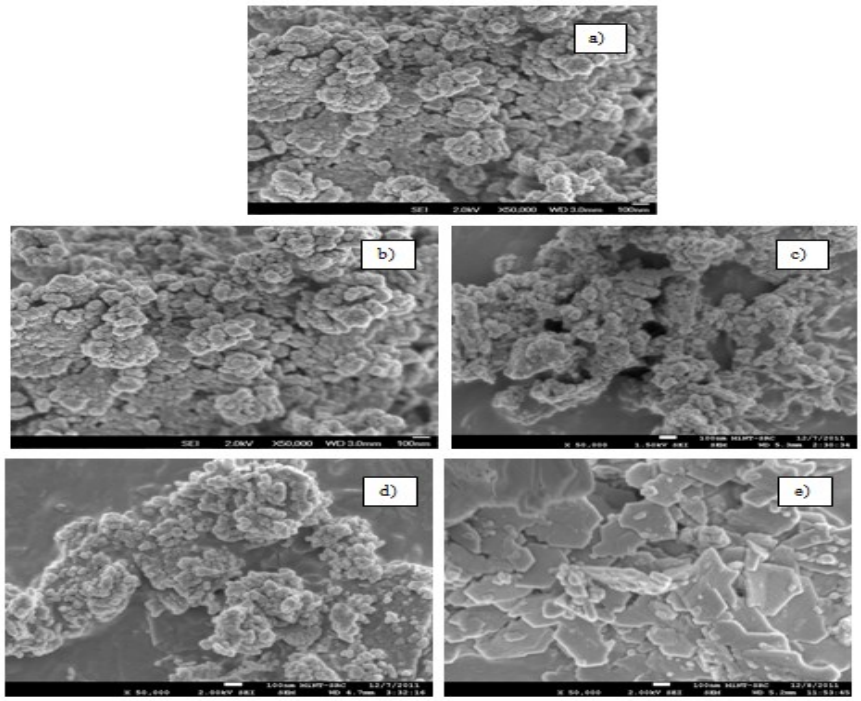



Figure 2. FESEM micrographs of Ru/Co/La (5:35:60)/$Al_2O_3$ catalyst calcined at a) 400 $^oC$, b) 700 $^oC$, c) 900 $^oC$, d) 1000 $^oC$ and e) 1100$^oC$ for 5 hour in 50000x magnification

**Energy dispersive X-ray analysis for lanthanum oxide based catalyst**

Table 1 shows the elemental composition of the EDX analysis for Ru/Co/La (5:35:60)/$Al_2O_3$ catalyst calcined at 400 $^oC$, 700 $^oC$, 900 $^oC$, 1000 $^oC$ and 1100 $^oC$. From the table, it was observed that atomic ratio of Al is quite high which suggested that the catalyst surface is dominated by the Al from the support. The entire elements were detected on the catalyst surface. At 1000 $^oC$ calcination temperature, the La and Co revealed the higher atomic ratio compared to Ru. It might due to Ru have been incorporated into the pore of alumina. Although the tiny amount of atomic mass of Ru on the catalyst surface, it still enhances the high catalytic activity towards methanation reaction [11].

Table 1. Elemental composition from EDX analysis at various calcination temperatures for 5 hours

| **Calcination Temperature ($^oC$)** | **Atomic Ratio (%)** | | | | |
|---|---|---|---|---|---|
| | **Al** | **O** | **La** | **Co** | **Ru** |
| 400 | 35.72 | 44.14 | 4.58 | 1.69 | 0.13 |
| 700 | 36.48 | 42.68 | 3.16 | 1.81 | 0.35 |
| 900 | 36.89 | 52.47 | 5.94 | 1.89 | 0.40 |
| 1000 | 32.83 | 20.73 | 11.45 | 7.38 | 0.42 |
| 1100 | 43.96 | 40.28 | 8.57 | 5.56 | 0.47 |

**Catalytic activity measurement: Effect of calcination temperature**

From the catalytic screening of $CO_2$ conversion, the potential catalysts which was Ru/Co/La/$Al_2O_3$ catalyst was proceed with different calcination temperatures to elucidate the optimum calcination temperature on the potential catalyst. The catalytic activity is summarized in Table 2. The Ru/Co/La/$Al_2O_3$ catalyst showed an increasing catalytic activity with Co as a dopant with increasing calcination temperature. It was possibly due to the Ru enhance the dispersion of Co on the catalyst surface. It also has been reported by Kok et al. that $La^{3+}$ promotes for the formation of new active sites while Ru could increase the degree of Co reduction and this improve the catalytic activity [12]. According to Perego and Villa, calcination process would give some effects towards the catalyst such as loss of chemically bonded water or CO, modified the texture and structure through sintering, generate active phase and stabilize the mechanical properties [13].

Table 2. Percentage conversion of $CO_2$ in $CO_2/H_2$ methanation reaction catalyzed by lanthanum oxide based catalysts with dopant (Co) and co-dopant (Ru) after calcined at different temperatures for 5 hours

| **Catalyst** | **Calcination Temperature (°C)** | **Reaction Temperature (°C)** | | | | | |
|---|---|---|---|---|---|---|---|
| | | **100** | **200** | **250** | **300** | **350** | **400** |
| | | **% Conversion of $CO_2$** | | | | | |
| Ru/Co/La (5:35:60)/$Al_2O_3$ | 400 | 2.18 | 14.69 | 25.62 | 29.45 | 30.79 | 32.89 |
| | 700 | 4.30 | 33.04 | 66.93 | 70.09 | 74.83 | 89.09 |
| | 900 | 3.93 | 18.73 | 59.34 | 73.21 | 82.11 | 91.03 |
| | 1000 | 9.98 | 35.23 | 54.76 | 68.41 | 78.67 | 98.87 |
| | 1100 | 10.36 | 38.04 | 60.74 | 73.98 | 87.41 | 94.22 |

**Effect of based loadings**

The plot effect of based loadings is shown in Figure 3. The results obtained showed that when the based loading of La was increased, the $CO_2$ conversion was decreased. This might due to excessive amount of La has been blocking the active surface on catalyst. This re supported with He et al. 2011 [14] and Mat Rosid et al. 2015 [15] which have stated that excessive amount of based loading will enhance the particle to nucleate which will inhibit the growth of crystal on active site. Therefore, the optimum based loading was obtained at 60%.

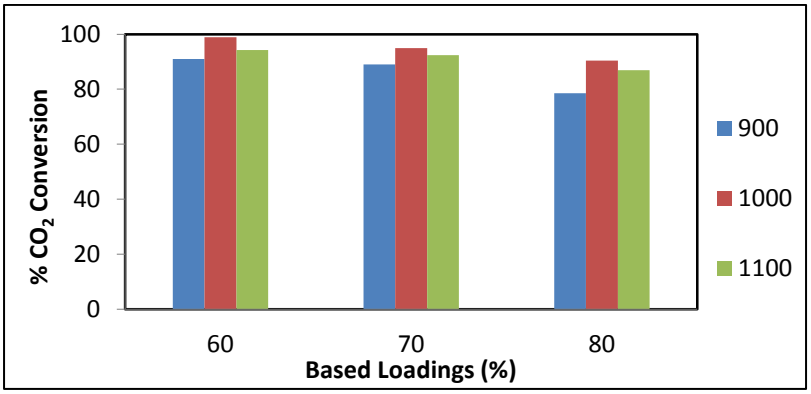



Figure 3. Catalytic performance of $CO_2$ conversion from methanation reaction over Ru/Co/La/$Al_2O_3$ catalyst calcined at 900 °C, 1000 °C and 1100 °C for 5 hours with various based loadings

**Effect of catalyst dosage**

Catalyst dosage is one of the parameter that affects the catalytic activity. Figure 4 shows that when the catalyst dosage is increase, the $CO_2$ conversion is increased. This is in agreement with Londhe and Gupta study which stated that when the catalyst dosage is increased, the fraction of the gases adsorbed over catalyst surface and the reaction products formed is increased [16].

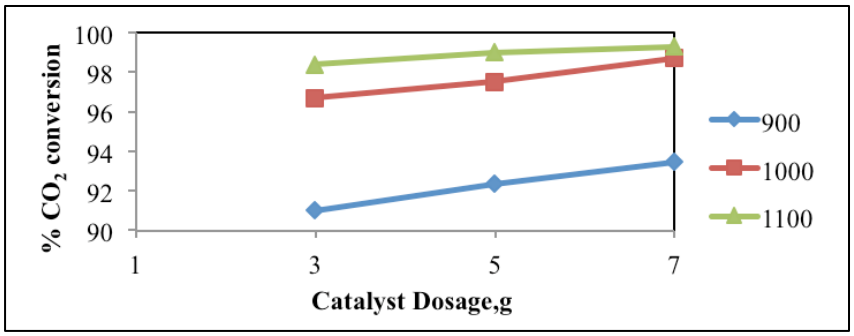



Figure 4. Catalytic performance of $CO_2$ conversion from methanation reaction over $Ru/Co/La/Al_2O_3$ catalyst calcined at 900 $^oC$ , 1000 $^oC$ and 1100 $^oC$ for 5 hours with various catalyst dosages

**Methane gas formation**

The formation of methane over the potential catalyst showed low percentage of methane at lower temperature which yielded 2.74% and 8.51% at 200 $^oC$ and 250 $^oC$, respectively. However, when the reaction temperature reached 300 $^oC$, the percentage formation of methane yielded 43.40% of $CH_4$. The increased of methane formation was 50% at 400 $^oC$ reaction temperature as discussed by Mat Rosid et al. [4].

**Statistical analysis: Box-Behnken design**

The selection of levels was carried out based on the results obtained in the preliminary study. Table 3 shows the experiment design for $CO_2$ conversion with 17 runs of experiment. The predicted values are accordance with actual value from the experimental data. Results obtained after carrying out ANOVA is presented in Table 4. The Model F-value of 122.87 implies the model was significant. Values of "Prob > F" less than 0.0500 indicate model terms are significant. In this case A, B, $A^2$, $B^2$ are significant model terms. Values greater than 0.1000 indicate the model terms are not significant. From the ANOVA, it can be observed that catalyst dosage (c) is not a significant model terms. This can be supported from the experimental data which showed that the $CO_2$ conversion (Figure 4) does not highly differ for each catalyst dosage. The "Lack of Fit F-value" of 0.28 implies the Lack of Fit is not significant relative to the pure error. Non-significant lack of fit is good.

Table 3. Experiment design for $CO_2$ conversion and results response

| Run | Calcination Temperature A ($^oC$) | Based Loadings B (%) | Catalyst Dosage C (g) | $CO_2$ Conversion (%) | |
|---|---|---|---|---|---|
| | | | | Actual | Predicted |
| 1 | 900 | 70 | 3 | 90.80 | 90.85 |
| 2 | 1000 | 60 | 7 | 98.87 | 98.79 |
| 3 | 1000 | 70 | 5 | 93.45 | 93.46 |
| 4 | 900 | 70 | 7 | 93.30 | 93.42 |
| 5 | 1100 | 80 | 5 | 90.30 | 90.38 |
| 6 | 1000 | 70 | 5 | 93.84 | 93.46 |
| 7 | 1000 | 80 | 7 | 93.00 | 92.97 |

Table 3 (cont'd). Experiment design for $CO_2$ conversion and results response

| Run | Calcination Temperature A ($^oC$) | Based Loadings B (%) | Catalyst Dosage C (g) | $CO_2$ Conversion (%) | |
|---|---|---|---|---|---|
| | | | | Actual | Predicted |
| 8 | 1000 | 80 | 3 | 94.56 | 94.64 |
| 9 | 900 | 60 | 5 | 92.00 | 91.92 |
| 10 | 1000 | 70 | 5 | 93.00 | 93.46 |
| 11 | 1100 | 70 | 7 | 93.50 | 93.45 |
| 12 | 1000 | 70 | 5 | 93.80 | 93.46 |
| 13 | 1000 | 60 | 3 | 97.80 | 97.83 |
| 14 | 1000 | 70 | 5 | 93.80 | 93.46 |
| 15 | 1100 | 70 | 3 | 94.40 | 94.24 |
| 16 | 900 | 80 | 5 | 90.50 | 90.37 |
| 17 | 1100 | 60 | 5 | 97.70 | 97.83 |

Table 4. ANOVA table (partial sum of squares) for response surface model (response: $CO_2$ conversion)

| Source | Sum of Squares | df | Mean Square | F Value | p-Value (Prob>F) |
|---|---|---|---|---|---|
| Model | 102.99 | 9 | 11.44 | 122.87 | <0.00001 Significant |
| A-Calcination Temp | 17.46 | 1 | 17.46 | 187.51 | <0.00001 |
| B-Ratio | 40.55 | 1 | 40.55 | 435.33 | <0.00001 |
| C-Catalyst Dosage | 0.25 | 1 | 0.25 | 2.67 | 0.1464 |
| AB | 8.70 | 1 | 8.70 | 93.44 | <0.0001 |
| AC | 0.19 | 1 | 0.19 | 2.08 | 0.1926 |
| BC | 1.73 | 1 | 1.73 | 18.57 | 0.0035 |
| $A^2$ | 21.51 | 1 | 21.51 | 230.96 | <0.0001 |
| $B^2$ | 8.58 | 1 | 8.58 | 92.09 | <0.0001 |
| $C^2$ | 5.79 | 1 | 5.79 | 62.12 | 0.0001 |
| Residual | 0.65 | 7 | 0.093 | | |
| Lack of Fit | 0.11 | 3 | 0.038 | 0.28 | 0.8390 not significant |
| Pure Error | 0.54 | 5 | 0.13 | | |
| Cor Total | 103.64 | 16 | | | |
| Std. Dev | 0.31 | | $R^2$ | 0.9937 | |
| Mean | 93.62 | | Adj $R^2$ | 0.9856 | |
| CV | 0.33 | | Pred $R^2$ | 0.9745 | |
| PRESS | 2.65 | | Adeq Precision | 35.968 | |

To modify regression model accuracy, the ultimate model equation in terms of coded factors after excluding the insignificant items was obtained as follows:

$$CO_2 \text{ conversion} = 93.46 + 1.48A - 2.25B - 0.18C - 1.47AB - 0.22AC - 0.66BC - 2.26A^2 + 1.43B^2 + 1.17C^2$$

**Optimization of parameters by Box-Behnken design**

The optimization of critical parameters was run to obtain highest $CO_2$ conversion by using numerical hill-climbing algorithms. The $CO_2$ conversion was set to 99% and all parameters was kept in range. The optimum parameters were verified experimentally and it give almost exact value of $CO_2$ conversion as suggested by Box-Behnken design.

## Conclusion

The Box-Behnken design was successfully applied for the optimization of catalytic methanation reaction to give the optimum parameters to obtain highest $CO_2$ conversion. The maximum $CO_2$ conversion was achieved at 1000 $^oC$ calcination temperature using 7 g of catalyst for 60% based loading. The optimize parameters gave 99% of $CO_2$ conversion determined using FTIR and yielded about 50% of $CH_4$ at reaction temperature of 400 °C. The active species in this methanation reaction was $RuO_2$ as observed in X-ray Diffraction (XRD) analysis and Field Emission Scanning Electron Microscope (FESEM) illustrated the catalyst surface was covered with small and dispersed particles with undefined shape. EDX analysis revealed that when calcination temperature increased, the mass ratio of Ru increased.

## Acknowledgement

We are grateful to the Universiti Teknologi Malaysia, Ministry of Higher Education (MOHE), Malaysia for the financial support given under the GUP, Vot 04H97 and Ministry of Science, Technology and Innovation (MOSTI) for human capital assistance.

## References

1. Wan Abu Bakar, W. A., Othman, M. Y., Ali, R. and Yong, C. K. (2008). Nickel oxide based supported catalysts for the in-situ reactions of methanation and desulfurization in the removal of sour gases from simulated natural gas. *Catalysis Letters,* 128: 127 – 136.
2. Inui, T. (1996). Highly effective conversion of carbon dioxide to valuable compounds on composite catalysts. *Catalysis Today*, 29: 329 – 337.
3. Hayakawa, T., Suzuki, S., Nakamura, J., Uchijima, T., Hamakawa, S., Suzuki, K., Shishido, T. and Takehira, K. (1999). $CO_2$ reforming of $CH_4$ over Ni/perovskite catalysts prepared by solid phase crystallization method. *Applied Catalysis A,* 18: 271 – 285.
4. Mat Rosid, S. J., Wan Abu Bakar, W. A. and Ali, R. (2015). Physicochemical study of supported cobalt-lanthanum oxide based catalysts for $CO_2/H_2$ methanation reaction. *Clean Technology Environmental Policy*, 17 : 257 – 264.
5. Wan Azelee, W. A. B, Rusmidah, A., Abdul Aziz, A. K., Salmiah Jamal, M. R and Nurul Shefeeqa M. (2012). Catalytic methanation reaction over alumina supported cobalt oxide doped noble metal oxides for the purificati on of simulated natural gas. *Journal of Fuel Chemistry and Technology,* 40(7): 822 – 830.
6. Bianchi (2001). TPR and XPS investigations of $Co/Al_2O_3$ catalysts promoted with Ru, Ir and Pt. *Catalysis Letters.* 76(3): 155 – 159.
7. Montgomery D. C. (1999). Experimental design for product and process design and development. *The Statistician*, 48(2): 159 – 177.
8. Tang, Q., Huang, X., Wu, C., Zhao, P., Chen, Y. and Yang, Y. (2009). Structure and catalytic properties of K-doped manganese oxide supported on alumina. *Journal of Molecular Catalysis A: Chemical*, 306: 48 – 53.
9. Makinson, J. D, Lee, J. S, Magner, S. H, De Angelis, R. J, Weins, W. N. and Hieronymus, A. S. (2000). X-ray diffraction signatures of defects in nanocrystalline materials. *Advances in X-ray Analysis*, 42: 407 – 411.
10. Mat Rosid, S. J, Abu Bakar, W.A.W. and Ali, R. (2013). Methanation reaction over samarium oxide based catalysts. *Malaysian Journal of Fundamental and Applied Sciences*, 9(1): 28 – 34.
11. Panagiotopoulou, P., Kondarides, D. I. and Verykios, X. E. (2009). Selective methanation of CO over supported Ru catalysts. *Applied Catalysis B: Environmental,* 88(3-4): 470 – 478.

12. Kok, E., Scott, J., Cant, N. and Trimm D. (2011). The impact of ruthenium, lanthanum and activation conditions in the methanation activity of alumina-supported cobalt catalysts. *Catalysis Today*, 164: 297 – 301.
13. Perego, C. and Villa, P. (1997). Catalyst preparation methods. *Catalysis Today*, 34 (3-4): 281 – 305.
14. He, Z. Huang, C. Wang, Q. Jiang, Z. Chen, S. and Song S. (2011). Preparation of a praseodymium modified Ti/ $SnO_2$- Sb/$PbO_2$ electrode and its application in the anodic degradation of the azo dye acid black 94. *Internation al Journal of Electrochemical Science,* 6: 4341 – 4354.
15. Salmiah, J. M. R., Wan Azelee, W. A. B. and Rusmidah, A. (2015). Optimization of preseodymium oxide based catalysts for methanation reaction of simulated natural gas using box-behnken design. *Jurnal Teknologi (Science & Engineering),* 75:1: 55 – 65.
16. Londhe, V. P. and Guota, N. M. (1998). Recent advances I n basic and applied aspects of industrial catalysis. *Studies in Surface Science and Catalysis,* 113: 375 – 381.

*Malaysian Journal of Analytical Sciences, Vol 21 No 4 (2017): 889 - 900*
*DOI: https://doi.org/10.17576/mjas-2017-2104-15*

MALAYSIAN JOURNAL OF ANALYTICAL SCIENCES
*Published by The Malaysian Analytical Sciences Society*
ISSN 1394 - 2506

# SYNTHESIS OF ZnO/rGO NANOHYBRID FOR IMPROVED PHOTOCATALYTIC ACTIVITY

## (Sintesis Nanohibrid ZnO/rGO Untuk Mempertingkatkan Aktiviti Fotopemangkinan)

Marilyn Yuen Sok Wen[1], Abdul Halim Abdullah[1,2]*, Lim Hong Ngee[1]

[1]*Department of Chemistry, Faculty of Science*
[2]*Materials Science and Characterization Lab., Institute of Advanced Technology*
*Universiti Putra Malaysia, 43400 UPM Serdang, Selangor, Malaysia*

**Corresponding author: halim@upm.edu.my*

Received: 20 September 2016; Accepted: 16 May 2017

**Abstract**

Nanohybrids of zinc oxide/reduced graphene oxide (ZnO/rGO) with varying graphene oxide content were prepared via precipitation and were subsequently utilised in the photodegradation of methyl orange (MO) under UV light irradiation. The prepared photocatalysts were characterized by X-ray Diffraction (XRD), Field Emission Scanning Electron Microscopy (FESEM), Transmission Electron Microscopy (TEM) and Raman spectroscopy. The surface area and the band gap energy of the photocatalysts were determined by the Brunauer-Emmett-Teller method and UV-visible spectroscopic analysis. The ZnO/rGO nanohybrids produced had smaller particle sizes and lower band gap energy than that of ZnO. All the ZnO/rGO nanohybrids demonstrated better photocatalytic efficiency in the photodegradation of MO compared to ZnO. ZnO/rGO10 exhibited the highest photocatalytic activity with a rate constant that was four times higher than pure ZnO and about 40% enhancement in the photocatalytic activity for the removal of methyl orange within 3 hours. The enhanced photocatalytic performance of the ZnO/rGO photocatalysts was due to the efficient transfer of photogenerated electrons to the graphene sheet that inhibited the recombination of electron-hole pairs.

**Keywords**: zinc oxide, reduced graphene oxide, nanohybrid, precipitation method, photocatalysis

**Abstrak**

Nanohibrid zink oksida/grafin oksida terturun (ZnO/rGO) dengan kandungan grafin oksida yang berbeza telah disediakan melalui kaedah pemendakan dan seterusnya digunakan dalam fotodegradasi metil jingga (MO) di bawah sinaran cahaya UV. Fotopemangkin yang disediakan telah dicirikan dengan menggunakan pembelauan sinar-X (XRD), mikroskopi pengimbasan elektron (FESEM), mikroskopi transmisi elekron (TEM) dan spektroskopi Raman. Luas permukaan dan tenaga jurang jalur fotomangkin telah ditentukan menggunakan kaedah Brunauer-Emmett-Teller dan analisis spektroskopi UV-sinar nampak. Nanohibrid ZnO/rGO yang terhasil mempunyai saiz zarah yang lebih kecil dan tenaga jurang jalur yang lebih rendah berbanding dengan ZnO. Nanohibrid ZnO/rGO mempamerkan kecekapan fotopemangkinan yang lebih tinggi dalam fotodegradasi MO berbanding dengan ZnO. ZnO/rGO10 mencatatkan aktiviti fotopemangkinan yang tertinggi dengan pemalar kadar empat kali ganda lebih tinggi daripada ZnO dan peningkatan 40% dalam aktiviti fotopemangkinan degradasi metil jingga dalam masa 3 jam. Peningkatan prestasi fotopemangkinan pemangkin ZnO/rGO adalah disebabkan oleh kecekapan pemindahan fotojanaan elektron ke lembaran grafin yang seterusnya menghalang penggabungan semula pasangan elektron-lubang.

**Kata kunci:** zink oksida, grafin oksida terturun, nanohibrid, kaedah pemendakan, fotopemangkinan

## Introduction

Water pollution due to effluents from textile industries, especially dyes is a cause of serious concern. It is estimated that 1% to 15% of the dye is lost during the dyeing processes which is subsequently released into natural water resources and the wastewater system [1]. When released into the water, dyes may change the colour of the water, impact light penetration and reduce the solubility of gases [2].This in turn, has a serious impact on the aquatic ecosystem. Dyes are also stable and difficult to be biodegraded due to their synthetic origins and complex aromatic structures [3]. Hence, it is important to treat water resources and wastewaters containing such organic pollutants. Photocatalysis has long been introduced as a means of water decontamination [4]. Photocatalysis involves utilizing electron- hole pairs generated upon the irradiation of light to degrade organic molecules adsorbed on the surface of the photocatalyst [5]. This green technique can be performed in an ambient environment and may also oxidize organic carbon into carbon dioxide [6].

The use of zinc oxide (ZnO) as a photocatalyst has several advantages including a low production cost, wide band gap (~3.37 eV), high stability and catalytic activity, better sensitivity in UV light and the presence of its many active sites with high surface reactivity [7-9]. However, the fast recombination of the electron-hole pairs of ZnO has limited its catalytic efficiency [10]. Recently, many attempts have been carried out to enhance the performance of ZnO photocatalysts by modifications with noble metal loading, ion doping or the incorporation of electron-accepting materials to extend the light absorption range to the visible light region or to suppress the electron–hole recombination process [11].

Graphene, a two-dimensional (2D) single-layered carbon sheet with an $sp^2$ network of carbon atoms has excellent conductivity, good chemical stability, mechanical flexibility, a high mobility of charge carriers and a large specific surface area [12].These properties enable graphene to be an ideal support in combination with semiconductor photocatalysts. Graphene can be prepared by reducing graphene oxide (GO) [13]. The presence of oxygen-containing functional groups on the surface of the reduced graphene oxide (rGO) also makes graphene an excellent supporting material by anchoring strongly to the metal oxide nanostructure [14, 15].

Many methods have been used to fabricate ZnO photocatalysts hybridised with rGO, including solvothermal [16], chemical deposition [11], hydrothermal [15, 17, 18] and sol- gel [19] methods. Herein, we report a simple precipitation method to prepare ZnO/rGO nanohybrids with zinc acetate dihydrate and graphene oxide (GO) as the starting materials, and ammonia as both the precipitator and reductant. This study is focused on determining the effect of rGO on the structure and photocatalytic activity of ZnO.

## Materials and Methods

### Materials

Zinc acetate dihydrate ($(CH_3COO)_2Zn.2H_2O$) and 25% ammonia solution ($NH_3$) were purchased from Merck. Methyl orange (MO) ($C_{14}H_{14}O_3N_3SNa$), a model pollutant, was obtained from Bendosen. All chemicals were used without further purification.

### Synthesis of graphene oxide

GO was synthesized using a modified Hummers method [20]. In a typical experiment, graphite flakes, $H_2SO_4$:$H_3PO_4$ (320:80 ml) and $KMnO_4$ (18g) were mixed together under magnetic stirring. The mixture was stirred for 3 days to allow the oxidation of graphite, where the colour of the mixture changed from dark purplish green to dark brown. The colour of the mixture changed to bright yellow after the addition of $H_2O_2$ solution. The graphite oxide formed was washed three times with 1M HCl aqueous solution and repeatedly with deionized water using a centrifugation force of 10,000 g until wash-water with a pH of 4 – 5 was obtained.

### Preparation of ZnO/rGO nanohybrid photocatalyst

The ZnO/rGO nanohybrid was synthesized by mixing 10 ml of 1mg/ml GO with 100 ml 0.3M zinc acetate dihydrate solution followed by the addition of ammonia solution until a pH 10 of was achieved. The precipitate was later filtered and washed several times with deionised water and dried overnight in an oven at 100 °C. The dried powder was then calcined at 400 °C for 2 hours and labelled as ZnO/rGO10. In order to study the effect of GO content on the physicochemical properties and photocatalytic activity, three different nanohybrids were prepared by

changing the initial volume of the GO solution. ZnO/rGO nanohybrids with a volume ratio of 5:100, 10:100 and 20:100 of GO and Zinc acetate dihydrate solution were denominated as ZnO/rGO5, ZnO/rGO10 and ZnO/rGO20. For comparison, pure zinc oxide (ZnO) was also obtained using the same method without adding any GO.

**Characterization**

The phase and crystallinity of the samples were analysed using Philips PW 3040/60 MPD X-ray diffractometer with Ni-filtered $CuK_{\alpha}$ radiation. The X-ray diffraction (XRD) pattern were recorded in the 2θ range of 20° - 80° at a scanning rate of 2°/min. The surface morphology of the samples was studied using Field Emission Electron Microscopy (FESEM) (FEI Nova Nanosem 230 combined with EDX) and Transmission Electron Microscopy (TEM) (Hitachi H-7100). The surface area of the samples was determined using a BET surface area analyzer (BELSorp Mini II). Raman spectroscopy (WITec Alpha 300R) was used to study the disordered crystal structure of the carbon based material and to confirm the presence of rGO. Diffuse reflectance spectra were recorded using a Shimadzu UV-3600 spectrophotometer in order to determine the band gap energy of the prepared samples.

**Photocatalytic activity experiment**

The photocatalytic performance of the prepared photocatalysts was evaluated in the photodegradation of methyl orange (MO) under the illumination of a 6W UVA lamp for 3 hours. In a typical experiment, 0.5g of photocatalyst was suspended in a photoreactor containing 500 ml of MO solution (10 ppm). The resultant solution was magnetically stirred in the dark for 30 minutes to reach an adsorption-desorption equilibrium prior to UV irradiation. An amount 5 ml of test samples were taken at predetermined time intervals and were immediately filtered with a 0.45 µm cellulose nitrate filter. The concentration of MO in the test samples was determined (Perkin Elmer Lambda 35 UV-Vis Spectrometer) at a wavelength of 464.3 nm.

## Results and Discussion

**X-ray diffraction**

Figure 1 displays the XRD patterns of pure ZnO and ZnO/rGO nanohybrid photocatalysts. The diffraction peaks observed in the XRD pattern of the prepared photocatalysts were consistent with the hexagonal wurtzite phase of ZnO (JCPDS No. 36-1451). The peaks at 2θ=31.8°, 34.4°, 36.2°, 47.5°, 56.6°, 62.8°, 66.4°, 68.0°, 69.1°, 72.5° and 77.0° are associated with the 100, 002, 101, 102, 110, 103, 200, 112 and 203 crystalline planes of ZnO, respectively. However, no characteristic peak for rGO was observed in the XRD patterns due to its low content and its relatively low diffraction intensity compared to ZnO [21-23]. The average crystallite size of ZnO and the ZnO/rGO nanohybrid photocatalysts was calculated using Scherrer's equation and the data is shown in Table 1. It was also observed that the intensity of the diffraction peaks of the ZnO/rGO nanohybrids decreased as the rGO content increased. This indicated that the crystallinity of ZnO deteriorated as the concentration of ZnO in the ZnO/rGO nanohybrids decreased when compared to pure ZnO [24]. Kuo and co-workers [25] reported that an increase in the concentration of the dopant led to the formation of stresses because of the difference in ionic size of zinc and the dopant. ZnO/rGO nanohybrids were observed to have smaller crystallite sizes when compared to pure ZnO. This was due to the presence of the dopant, (rGO) which hindered the growth of crystal grains[26].

Table 1. Physical characteristics of ZnO and ZnO/rGO nanohybrids.

| Photocatalyst | Crystallite Size (nm) | Surface Area ($m^2g^{-1}$) | Band Gap Energy (eV) |
|---|---|---|---|
| ZnO | 43 | 5.15 | 3.16 |
| ZnO/rGO5 | 32 | 7.78 | 3.05 |
| ZnO/rGO10 | 36 | 9.70 | 3.08 |
| ZnO/rGO20 | 32 | 7.48 | 3.05 |

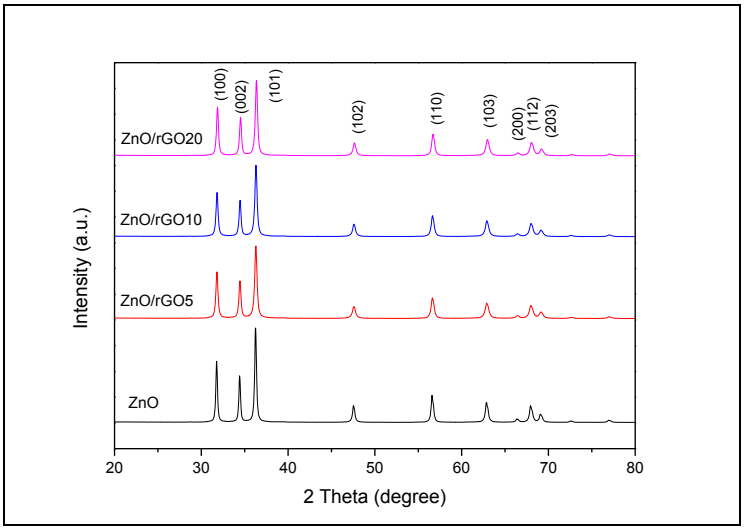



Figure 1. XRD patterns of ZnO and ZnO/rGO nanohybrid photocatalysts

**Morphology**

The surface morphology of the ZnO and ZnO/rGO nanohybrid photocatalysts, determined using TEM and FESEM, is shown in Figures 2 and 3, respectively. TEM images revealed the presence of ZnO on the surface of the graphene sheet. The ZnO nanoparticles were nearly spherical in shape, self-assembled and were randomly distributed on the graphene sheets. The formation of spherical ZnO nanoparticles could have been due to the addition of $OH^-$ that increased the reaction rate, thus forming more nuclei in a short time [5]. The two- dimensional graphene sheets were not perfectly flat but rough with wrinkles. EDX were used to distinguish the components present in the samples. As shown in Figure 4, carbon (C), zinc (Zn) and oxygen (O) were the main elements present in the ZnO/rGO nanohybrid photocatalysts with no unexpected elements being detected. This confirmed the purity of the samples.

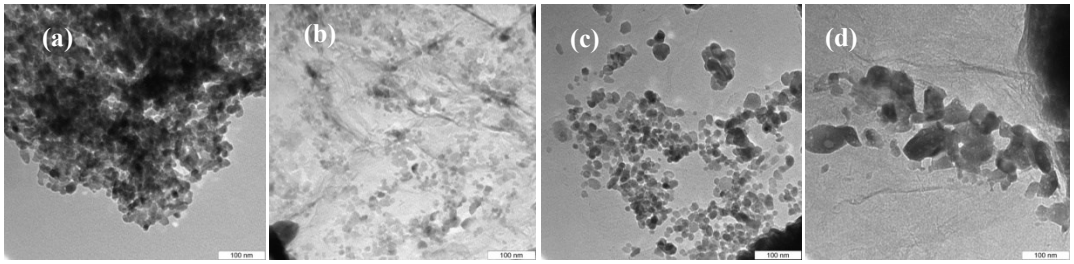



Figure 2. TEM images of (a) ZnO, (b) ZnO/rGO5, (c) ZnO/rGO10 and (d) ZnO/rGO20

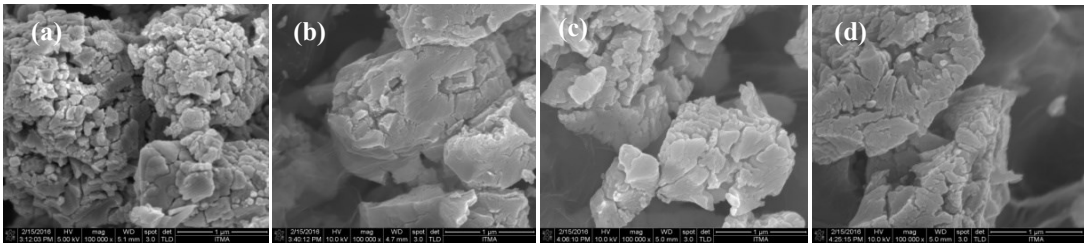



Figure 3. FESEM images of (a) ZnO, (b) ZnO/rGO5, (c) ZnO/rGO10 and (d) ZnO/rGO20

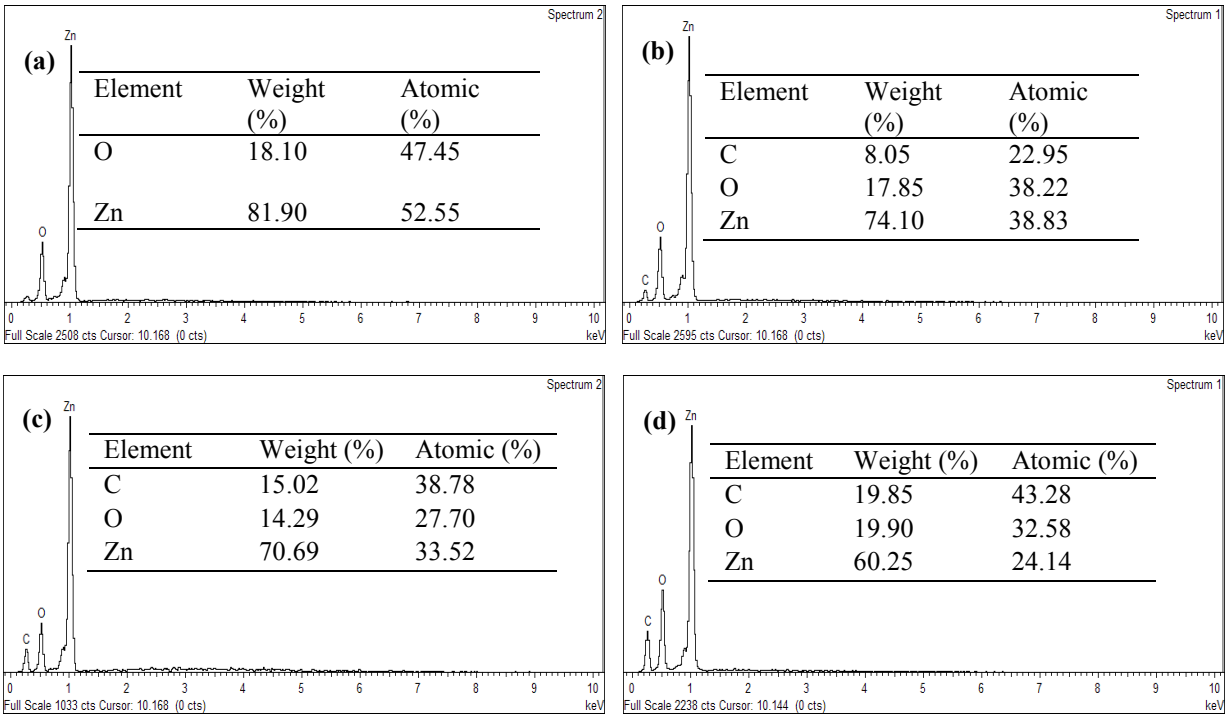
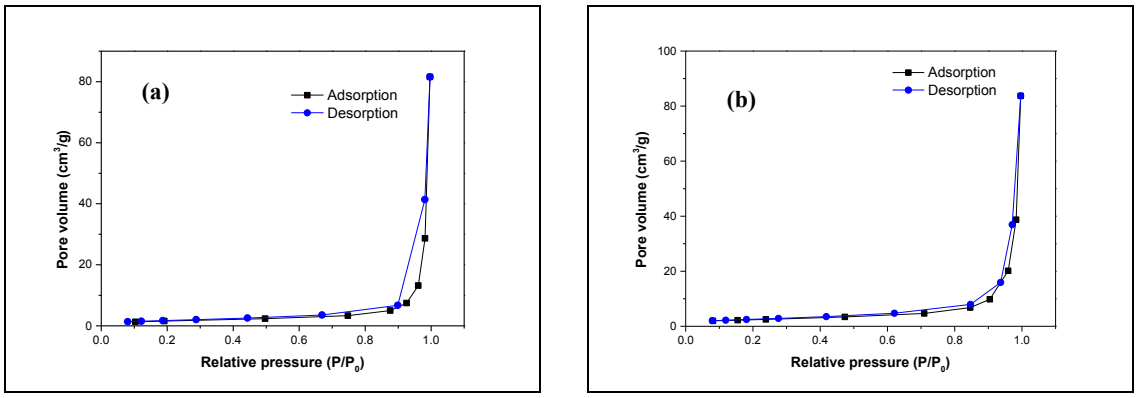



Figure 4. EDX spectra of (a) ZnO, (b) ZnO/rGO5, (c) ZnO/rGO10 and (d) ZnO/rGO20

**Surface area and porosity**

The BET surface areas of the ZnO and ZnO/rGO nanohybrid photocatalysts were obtained from the nitrogen adsorption- desorption isotherm and the results are represented in Table 1. Both the ZnO and ZnO/rGO nanohybrid photocatalysts met the type V $N_2$ adsorption- desorption isotherms with H3 hysteresis loop where there was a weak adsorbent- adsorbate interaction. The high adsorption at a relative pressure $P/P_0$ close to 1.0 also suggested the formation of large mesopores and macropores. Meanwhile, the presence of type H3 loop suggested the occurrence of macropores which are not completely filled with pore condensate [27]. It was observed that there was an improvement in the surface area of the ZnO/rGO nanohybrids compared to ZnO where graphene was incorporated. The nanohybrids were expected to have better photocatalytic performance than ZnO as the high surface area enhanced the efficient adsorption and transfer of organic molecules in a photochemical reaction via π-π conjugation between the organic molecules and graphene sheet [28].



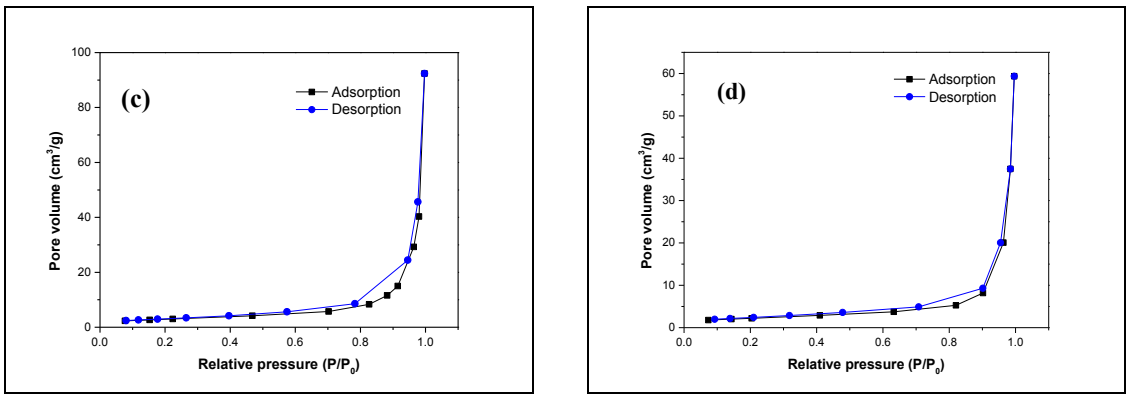



Figure 5. Nitrogen adsorption-desorption isotherm of (a) ZnO (b) ZnO/rGO5 (c) ZnO/rGO10 and (d) ZnO/rGO20

**Raman spectroscopy**

Figure 6 shows the Raman spectra of GO, rGO and ZnO/rGO10. The characteristic Raman peaks of all three samples showed similar D and G band structures of carbon, which was 1362 $cm^{-1}$ and 1605 $cm^{-1}$; 1352 $cm^{-1}$ and 1605 $cm^{-1}$; 1355 $cm^{-1}$ and 1605 $cm^{-1}$ for GO, rGO and ZnO/rGO10, respectively. The D band refers to the presence of disorder in the graphene structure while the G band refers to the presence of an $sp^2$ carbon type structure [29]. The D band in ZnO/rGO10 was slightly blue shifted by 7 $cm^{-1}$ compared to GO. This was due to the interaction between ZnO and rGO [28]. Similar D and G bands for rGO and ZnO/rGO10 also suggested that the structure of rGO was maintained in the nanohybrid. However, there was a change in the electronic conjugation state of the GO as indicated by the change in the G and D band intensities after being incorporated into ZnO [12, 30]. The intensity ratios ($I_D/I_G$) increased from 0.87 in GO to 0.98 in ZnO/rGO10 implying that the GO was successfully reduced and more $sp^2$ domains (graphene sheets) had formed [31]. This also indicated that the introduction of ZnO increased the defects or disorders in the GO sheet [32], hence confirming the formation of the ZnO/rGO nanohybrid.

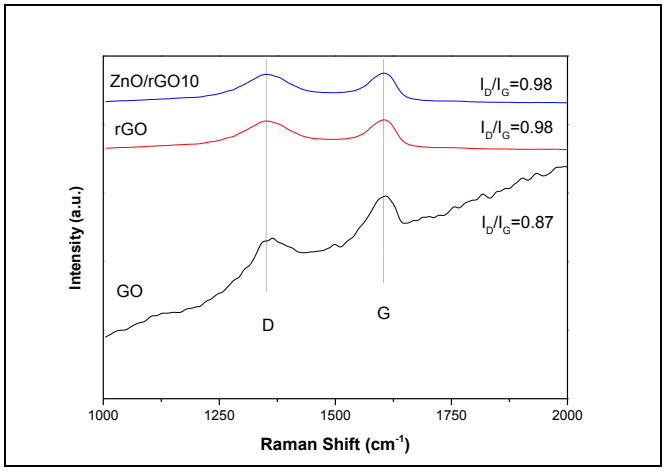



Figure 6. Raman spectra of GO, rGO and ZnO/rGO10

**UV- visible diffuse reflectance spectroscopy**

Figure 7 shows that both ZnO and ZnO/rGO nanohybrids had similar maximum absorptions at 360 nm. There was an enhancement in the absorption intensity of the ZnO/rGO nanohybrids corresponding to the increase in GO

content in both the UV and visible regions as a result of the increase in the surface electric charge of the oxides and the modification of the fundamental process of electron- hole pair formation during irradiation [33, 34]. The band gap energy of both ZnO and ZnO/rGO nanohybrids were determined by the extrapolation of the linear relationship between $(\alpha hv)^2$ and hv [35]:

$$(\alpha hv)^2 = K\ (hv\ -\ E_g) \tag{1}$$

where $\alpha$ is the absorption coefficient, $K$ is the proportionality constant and $v$ is the frequency of photons.

A plot of $(\alpha hv)^2$ as a function of photon energy, $hv$ for all samples is illustrated in Figure 7 with the band gap values listed in Table 1. The band gap energy of pure ZnO was slightly higher than that of the ZnO/rGO nanohybrids. The reduction in band gap energy could be attributed to the formation of Zn-O-C chemical bonds in the nanohybrid [17, 36, 37]. This also indicated that the presence of graphene influenced the electronic energy level of the ZnO nano-particles. As the band gap energy reduced, more photons were prone to be absorbed by the nanohybrid which in turn would enhance the photocatalytic efficiency.

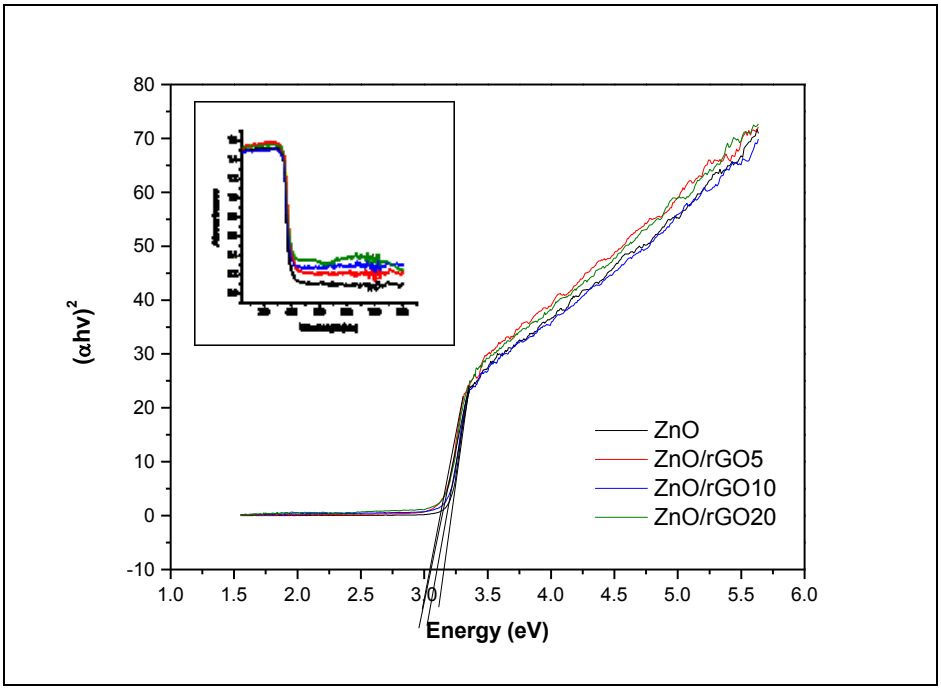



Figure 7. The plots of $(\alpha hv)^2$ versus $hv$ and UV spectrum (inset) for ZnO, ZnO/rGO5, ZnO/rGO10 and ZnO/rGO20

**Photocatalytic activities**

The photocatalytic performance of both the ZnO and ZnO/rGO nanohybrid photocatalysts were evaluated by degrading methyl orange under the irradiation of UV light and the results are depicted in Figure 8. By comparison, only 53% of MO was degraded using pure ZnO after 180 minutes of irradiation. However, the ZnO/rGO nanohybrids were found to show more prominent photocatalytic efficiency, with 80%, 97% and 77% of MO photodegraded for ZnO/rGO5, ZnO/rGO10, and ZnO/rGO20, respectively.

In principle, the photocatalytic degradation of MO by ZnO and ZnO/rGO nanohybrids is an interface process and follows the Langmuir-Hinshelwood model where it obeys the following assumptions: (i) limited adsorption sites on the catalyst's surface, (ii) monolayer coverage of the catalyst surface with single adsorptions on each site, (iii) reversible adsorption reactions, (iv) homogeneous catalyst surface and (v) zero interactions between the molecules

adsorbed[38]. In this study, $H_2O$, $O_2$ and dye (MO) were adsorbed on the surface of the catalyst in adjacent sites. The reaction then occurred between the adsorbed molecules and the radicals generated before the products ($CO_2$ and $H_2O$) were desorbed from the catalyst's surface.

$$ZnO + h\nu \rightarrow e_{CB^-} + h^+_{VB} \quad (2)$$

$$H_2O + h^+_{VB} \rightarrow OH\bullet + H^+ \quad (3)$$

$$O_{2(ads)} + eCB^- \rightarrow O_2^{\bullet -} \quad (4)$$

$$OH^-_{(ads)} + h^+_{VB} \rightarrow OH_{(ads)}\bullet \quad (5)$$

$$OH_{(ads)}\bullet + OH\bullet \rightarrow H_2O_2 \quad (6)$$

$$H_2O_2 + O_2^{\bullet -} \rightarrow OH\bullet + OH^- + O_2 \quad (7)$$

$$Dye_{(ads)} + OH\bullet \rightarrow CO_2 + H_2O \quad (8)$$

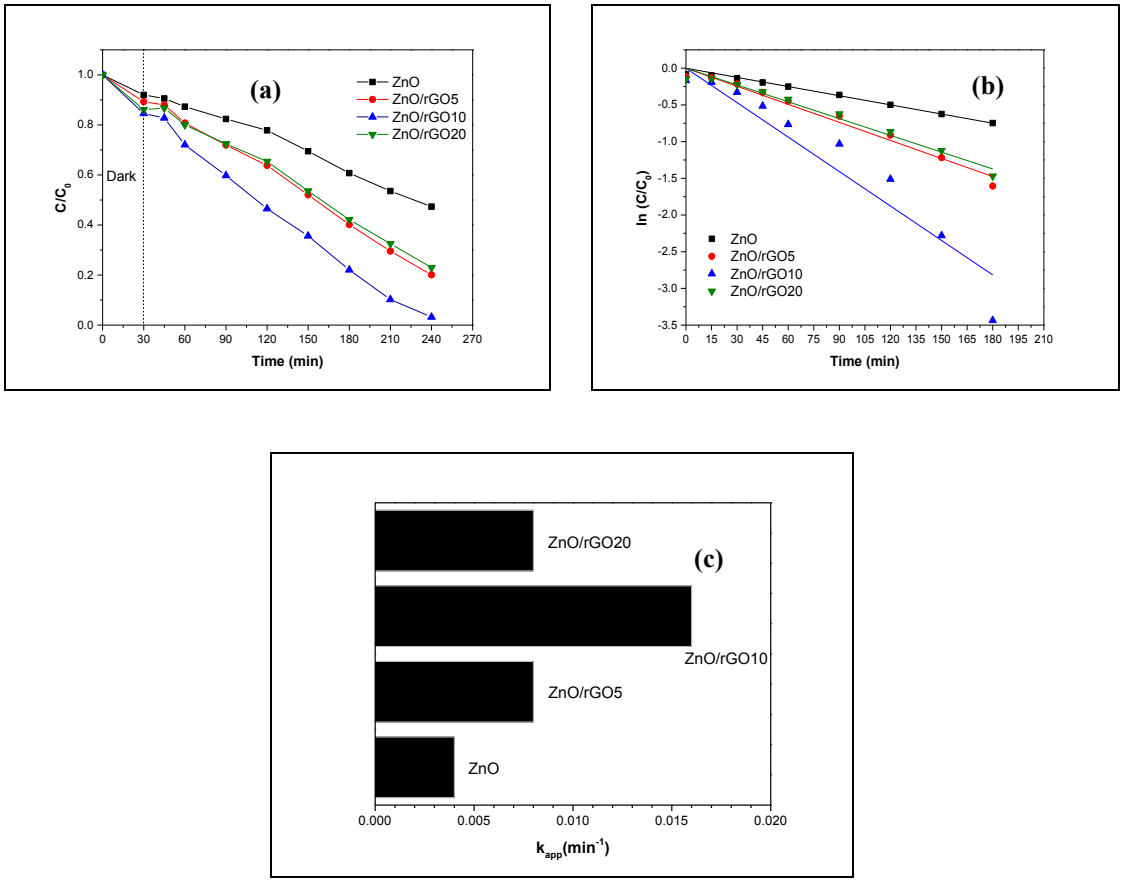



Figure 8. Photodegradation of MO by pure ZnO and ZnO/rGO nanohybrid photocatalysts: (a) reaction profile (b) kinetics and (c) apparent rate constant [condition: 0.5 g of photocatalyst, 10 ppm MO, pH = 6.6]

The data for the photocatalytic degradation of MO was fitted to the Langmuir-Hinshelwood kinetics model and the plot of $\ln(C/C_0)$ vs time (Figure 8b) showed that the photodegradation of MO followed a pseudo first order reaction. The pseudo first order kinetics for MO degradation was calculated as follows:

$$\ln(C/C_0) = \_kt \quad (9)$$

where C (mg/L) is the initial concentration of MO, $C_0$ (mg/L) is the concentration of MO at time t (min) and *k* ($min^{-1}$) is the pseudo first order rate constant. The apparent rate constants, $k_{app}$, were determined from the slope of the plot and is illustrated in Figure 8c. It was clear that the ZnO/rGO nanohybrid photocatalysts exhibited higher photocatalytic activities than pure ZnO. The photocatalytic activity increased as the GO content increased until it reaches the optimum, in the order of ZnO/rGO10 > ZnO/rGO5 > ZnO/rGO20 > ZnO. ZnO/rGO10 had the best photocatalytic activity with a kinetic rate constant 0.016 $min^{-1}$, which was four times higher than pure ZnO. The results were comparable with that reported in literature [21, 28].

The enhancement in the photocatalytic performance of the ZnO/rGO nanohybrids could be attributed to the strong interactions between ZnO and rGO and the defect sites of graphene. Graphene, with a two- dimensional conjugation structure [39], acted as an excellent electron acceptor. When ZnO was irradiated with UV light, the electrons were excited from the valence band to the conduction band, leaving behind holes in the valence band. These excited electrons could also be transferred from the conduction band of ZnO to the graphene sheet. The effective transfer of photoelectrons from the conduction band of ZnO to graphene prolonged the electron-hole pairs recombination hence promoting the separation of electron- hole pairs of ZnO [40, 41]. More charge carriers were produced from the reactive species which eventually helped in the degradation of MO [42]. The schemetic mechanism of the photocatalysis is shown in Figure 9. Moreover, the ZnO/rGO nanohybrid had a smaller particle size, larger surface area and lower band gap energy compared to ZnO. Such structural changes in ZnO increased the light absorption and the adsorption of MO on the surface of the catalyst; hence increasing the photocatalytic activity of the photocatalysts. However, a high content of GO (ZnO/rGO20) led to a decrement in the photocatalytic activity. Gayathri and co-workers [43] have reported that, at a higher graphene content, the graphene sheets tended to clasp together and appeared like multi-layer graphene after heat treatment. Excess GO also caused a shielding of the active sites on the catalyst surface, and led to the scattering of photons [31, 44, 45]. Since the light absorption of the photocatalyst was reduced, the excitation efficiency of ZnO was also lowered, consequently reducing the photocatalytic activity of the photocatalysts.

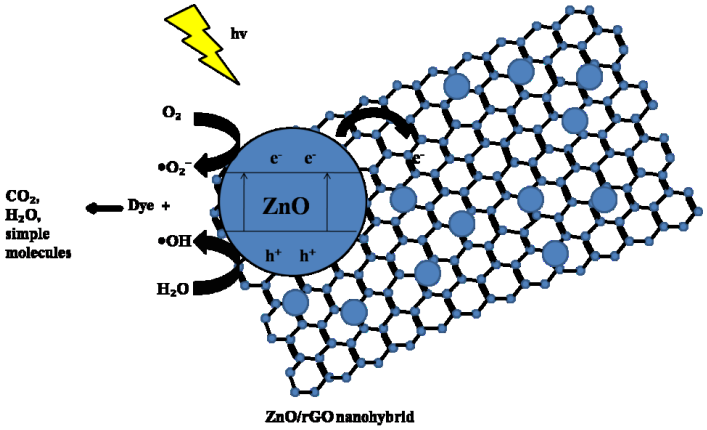



Figure 9. Mechanism of photodegradation

## Conclusion

A series of ZnO/rGO nanohybrids with different GO content was successfully synthesized via a simple and inexpensive precipitation method. The ZnO particles were formed on the surface of the graphene sheet. The presence of GO during the synthesis inhibited the crystal growth of ZnO that led to the formation of smaller-sized ZnO particles. ZnO/rGO nanohybrids showed better photodegradation activity compared to ZnO in degrading methyl orange due to their smaller particle sizes and lower band gap energy. ZnO/rGO10 exhibited the highest photocatalytic activity with a kinetic rate constant that was four times higher than pure ZnO. The enhanced photocatalytic activity of the nanohybrids could be attributed to the presence of rGO, an excellent electron acceptor

which enhanced the active transfer of photogenerated electrons of ZnO to the rGO sheet, thereby retarding the charge carrier recombination, thus enhancing the charge separation.

**Acknowledgements**

The authors would like to thank Universiti Putra Malaysia (UPM) and the Malaysian Government under the Malaysian Exploratory Research Grant Scheme (ERGS-5527187) and UPM-Graduate Research Fellowship award for the financial support for this work.

**References**

1. Zainal, Z., Hui, L. K., Hussein, M. Z., Taufiq-Yap, Y. H., Abdullah, A. H. and Ramli, I. (2005). Removal of dyes using immobilized titanium dioxide illuminated by fluorescent lamps. *Journal of Hazardous Materials,* 125(1): 113 - 120.
2. Lin, W.-C., Yang, W.-D. and Jheng, S.-Y. (2012). Photocatalytic degradation of dyes in water using porous nanocrystalline titanium dioxide. *Journal of the Taiwan Institute of Chemical Engineers,* 43(2): 269 - 274.
3. Chowdhury, S. and Balasubramanian, R. (2014). Graphene/semiconductor nanocomposites (GSNs) for heterogeneous photocatalytic decolorization of wastewaters contaminated with synthetic dyes: A review. *Applied Catalysis B: Environmental,* 160: 307 - 324.
4. Palanisamy, B., Babu, C., Sundaravel, B., Anandan, S. and Murugesan, V. (2013). Sol–gel synthesis of mesoporous mixed $Fe_2O_3$/$TiO_2$ photocatalyst: Application for degradation of 4-chlorophenol. *Journal of Hazardous Materials,* 252: 233 - 242.
5. Ahmad, M., Ahmed, E., Hong, Z., Xu, J., Khalid, N., Elhissi, A. and Ahmed, W. (2013). A facile one-step approach to synthesizing ZnO/graphene composites for enhanced degradation of methylene blue under visible light. *Applied Surface Science,* 274: 273 - 281.
6. Shaari, N., Tan, S. and Mohamed, A. (2012). Synthesis and characterization of CNT/Ce-$TiO_2$ nanocomposite for phenol degradation. *Journal of Rare Earths,* 30(7): 651 - 658.
7. Zhu, L.-P., Liao, G.-H., Huang, W.-Y., Ma, L.-L., Yang, Y., Yu, Y. and Fu, S.-Y. (2009). Preparation, characterization and photocatalytic properties of ZnO-coated multi-walled carbon nanotubes. *Materials Science and Engineering: B,* 163(3): 194 - 198.
8. Klanwan, J., Akrapattangkul, N., Pavarajarn, V., Seto, T., Otani, Y. and Charinpanitkul, T. (2010). Single-step synthesis of MWCNT/ZnO nanocomposite using co-chemical vapor deposition method. *Materials Letters,* 64(1): 80 - 82.
9. Saleh, T. A., Gondal, M., Drmosh, Q., Yamani, Z. and Al-Yamani, A. (2011). Enhancement in photocatalytic activity for acetaldehyde removal by embedding ZnO nano particles on multiwall carbon nanotubes. *Chemical Engineering Journal,* 166(1): 407 - 412.
10. Sakthivel, S., Geissen, S.-U., Bahnemann, D., Murugesan, V. and Vogelpohl, A. (2002). Enhancement of photocatalytic activity by semiconductor heterojunctions: α-$Fe_2O_3$, $WO_3$ and CdS deposited on ZnO. *Journal of Photochemistry and Photobiology A: Chemistry,* 148(1): 283 - 293.
11. Li, B., Liu, T., Wang, Y. and Wang, Z. (2012). ZnO/graphene-oxide nanocomposite with remarkably enhanced visible-light-driven photocatalytic performance. *Journal of Colloid and Interface Science,* 377(1): 114 - 121.
12. Wang, Z.-I., Xu, D., Huang, Y., Wu, Z., Wang, L.-M. and Zhang, X.-B. (2012). Facile, mild and fast thermal-decomposition reduction of graphene oxide in air and its application in high-performance lithium batteries. *Chemical Communications,* 48(7): 976 - 978.
13. Liu, Y., Han, G., Li, Y. and Jin, M. (2011). Flower-like zinc oxide deposited on the film of graphene oxide and its photoluminescence. *Materials Letters,* 65(12): 1885 - 1888.
14. Ameen, S., Akhtar, M. S., Seo, H.-K. and Shin, H. S. (2013). Advanced ZnO–graphene oxide nanohybrid and its photocatalytic applications. *Materials Letters,* 100: 261 - 265.
15. Zhou, X., Shi, T. and Zhou, H. (2012). Hydrothermal preparation of ZnO-reduced graphene oxide hybrid with high performance in photocatalytic degradation. *Applied Surface Science,* 258(17): 6204 -6211.
16. Leng, Y., Wang, W., Zhang, L., Zabihi, F. and Zhao, Y. (2014). Fabrication and photocatalytical enhancement of ZnO-graphene hybrid using a continuous solvothermal technique. *The Journal of Supercritical Fluids,* 91: 61 - 67.

17. Xu, S., Fu, L., Pham, T. S. H., Yu, A., Han, F. and Chen, L. (2015). Preparation of ZnO flower/reduced graphene oxide composite with enhanced photocatalytic performance under sunlight. *Ceramics International,* 41(3): 4007 - 4013.
18. Marlinda, A., Huang, N. M., Muhamad, M. R., An'amt, M., Chang, B. Y. S., Yusoff, N., Harrison, I., Lim, H. N., Chia, C. and Kumar, S.V. (2012). Highly efficient preparation of ZnO nanorods decorated reduced graphene oxide nanocomposites. *Materials Letters,* 80: 9 - 12.
19. Fu, D., Han, G., Chang, Y. and Dong, J. (2012). The synthesis and properties of ZnO–graphene nano hybrid for photodegradation of organic pollutant in water. *Materials Chemistry and Physics,* 132(2): 673 - 681.
20. Ming, H. N. (2010). Simple room-temperature preparation of high-yield large-area graphene oxide. *International Journal of Nanomedicine,* 6: 3443 - 3448.
21. Zhang, Y., Chen, Z., Liu, S. and Xu, Y.-J. (2013). Size effect induced activity enhancement and anti-photocorrosion of reduced graphene oxide/ZnO composites for degradation of organic dyes and reduction of Cr(VI) in water. *Applied Catalysis B: Environmental,* 140: 598 - 607.
22. Chen, Y.-L., Hu, Z.-A., Chang, Y.-Q., Wang, H.-W., Zhang, Z.-Y., Yang, Y.-Y. and Wu, H.-Y. (2011). Zinc oxide/reduced graphene oxide composites and electrochemical capacitance enhanced by homogeneous incorporation of reduced graphene oxide sheets in zinc oxide matrix. *The Journal of Physical Chemistry C,* 115(5): 2563 - 2571.
23. Moussa, H., Girot, E., Mozet, K., Alem, H., Medjahdi, G. and Schneider, R. (2016). ZnO rods/reduced graphene oxide composites prepared via a solvothermal reaction for efficient sunlight-driven photocatalysis. *Applied Catalysis B: Environmental,* 185: 11 - 21.
24. Samadi, M., Shivaee, H. A., Zanetti, M., Pourjavadi, A. and Moshfegh, A. (2012). Visible light photocatalytic activity of novel MWCNT-doped ZnO electrospun nanofibers. *Journal of Molecular Catalysis A: Chemical,* 359: 42 - 48.
25. Kuo, S.-Y., Chen, W.-C., Lai, F.-I., Cheng, C.-P., Kuo, H.-C., Wang, S.-C. and Hsieh, W.-F. (2006). Effects of doping concentration and annealing temperature on properties of highly-oriented Al-doped ZnO films. *Journal of Crystal Growth,* 287(1): 78 - 84.
26. Selvam, N. C. S., Narayanan, S., Kennedy, L. J. and Vijaya, J. J. (2013). Pure and Mg-doped self-assembled ZnO nano-particles for the enhanced photocatalytic degradation of 4-chlorophenol. *Journal of Environmental Sciences,* 25(10): 2157 - 2167.
27. Thommes, M., Kaneko, K., Neimark, A. V., Olivier, J. P., Rodriguez-Reinoso, F., Rouquerol, J. and Sing, K. S. (2015). Physisorption of gases, with special reference to the evaluation of surface area and pore size distribution (IUPAC Technical Report). *Pure and Applied Chemistry,* 87 (9-10): 1051 - 1069.
28. Kavitha, M., Pillai, S. C., Gopinath, P. and John, H. (2015). Hydrothermal synthesis of ZnO decorated reduced graphene oxide: Understanding the mechanism of photocatalysis. *Journal of Environmental Chemical Engineering*, 3:1194 - 1199.
29. Omar, F. S., Nay Ming, H., Hafiz, S. M. and Ngee, L. H. (2014). Microwave synthesis of zinc oxide/reduced graphene oxide hybrid for adsorption-photocatalysis application. *International Journal of Photoenergy,* 2014: 1 - 8.
30. Huang, K., Li, Y., Lin, S., Liang, C., Wang, H., Ye, C., Wang, Y., Zhang, R., Fan, D. and Yang, H. (2014). A facile route to reduced graphene oxide–zinc oxide nanorod composites with enhanced photocatalytic activity. *Powder Technology,* 257: 113 - 119.
31. Peng, Y., Ji, J. and Chen, D. (2015). Ultrasound assisted synthesis of ZnO/reduced graphene oxide composites with enhanced photocatalytic activity and anti-photocorrosion. *Applied Surface Science,* 356: 762 - 768.
32. Song, Y., Shao, P., Tian, J., Shi, W., Gao, S., Qi, J., Yan, X. and Cui, F. (2016). One-step hydrothermal synthesis of ZnO hollow nanospheres uniformly grown on graphene for enhanced photocatalytic performance. *Ceramics International,* 42(1): 2074 - 2078.
33. Lv, T., Pan, L., Liu, X., Lu, T., Zhu, G. and Sun, Z. (2011). Enhanced photocatalytic degradation of methylene blue by ZnO-reduced graphene oxide composite synthesized via microwave-assisted reaction. *Journal of Alloys and Compounds,* 509(41): 10086 - 10091.
34. Nipane, S., Korake, P. and Gokavi, G. (2015). Graphene-zinc oxide nanorod nanocomposite as photocatalyst for enhanced degradation of dyes under UV light irradiation. *Ceramics International,* 41 (3): 4549 - 4557.
35. Yakuphanoglu, F. (2010). Electrical characterization and device characterization of ZnO microring shaped films by sol–gel method. *Journal of Alloys and Compounds,* 507(1): 184 - 189.

36. Tien, H. N., Khoa, N. T., Hahn, S. H., Chung, J. S., Shin, E. W. and Hur, S. H. (2013). One-pot synthesis of a reduced graphene oxide–zinc oxide sphere composite and its use as a visible light photocatalyst. *Chemical Engineering Journal,* 229: 126 - 133.
37. Morales-Torres, S., Pastrana-Martínez, L. M., Figueiredo, J. L., Faria, J. L. and Silva, A. M. (2013). Graphene oxide-P25 photocatalysts for degradation of diphenhydramine pharmaceutical and methyl orange dye. *Applied Surface Science,* 275: 361 - 368.
38. Khezrianjoo, S. and Revanasiddappa, H. (2012). Langmuir-Hinshelwood kinetic expression for the photocatalytic degradation of Metanil Yellow aqueous solutions by ZnO catalyst. *Chemical Sciences Journal,* 3: 1 - 7.
39. Liu, Q., Liu, Z., Zhang, X., Yang, L., Zhang, N., Pan, G., Yin, S., Chen, Y. and Wei, J. (2009). Polymer photovoltaic cells based on solution-processable graphene and P3HT. *Advanced Functional Materials,* 19(6): 894 - 904.
40. Yang, Y. and Liu, T. (2011). Fabrication and characterization of graphene oxide/zinc oxide nanorods hybrid. *Applied Surface Science,* 257(21): 8950 - 8954.
41. Herring, N. P., Almahoudi, S. H., Olson, C. R. and El-Shall, M. S. (2012). Enhanced photocatalytic activity of ZnO–graphene nanocomposites prepared by microwave synthesis. *Journal of Nanoparticle Research,* 14(12): 1 - 13.
42. Wang, X., Zhi, L. and Müllen, K. (2008). Transparent, conductive graphene electrodes for dye-sensitized solar cells. *Nano Letters,* 8(1): 323 - 327.
43. Gayathri, S., Jayabal, P., Kottaisamy, M. and Ramakrishnan, V. (2014). Synthesis of ZnO decorated graphene nanocomposite for enhanced photocatalytic properties. *Journal of Applied Physics,* 115(17): 173504.
44. Chen, Z., Zhang, N., and Xu, Y.-J. (2013). Synthesis of graphene–ZnO nanorod nanocomposites with improved photoactivity and anti-photocorrosion. *CrystEngComm,* 15(15): 3022 - 3030.
45. Sarkar, S. and Basak, D. (2013). The reduction of graphene oxide by zinc powder to produce a zinc oxide-reduced graphene oxide hybrid and its superior photocatalytic activity. *Chemical Physics Letters,* 561: 125 - 130.

*Malaysian Journal of Analytical Sciences, Vol 21 No 4 (2017): 901 - 906*
*DOI: https://doi.org/10.17576/mjas-2017-2104-16*

MALAYSIAN JOURNAL OF ANALYTICAL SCIENCES
*Published by The Malaysian Analytical Sciences Society*
ISSN 1394 - 2506

# EFFECT OF NICKEL ON BIMETALLIC NANOALLOY CATALYST FOR HYDROGEN GENERATION

## (Kesan Nikel ke atas Mangkin Nanoaloi Dwilogam bagi Penghasilan Hidrogen)

Masitah Abdul Halim Azizi[1], Norliza Dzakaria[2], Wan Nor Roslam Wan Isahak[1]*, Mohd Ambar Yarmo[2]

[1]*Department of Chemical and Process Engineering, Faculty of Engineering and Built Environment*
[2]*School of Chemical Science and Food Technology, Faculty of Science and Technology*
*Universiti Kebangsaan Malaysia, 43600 UKM Bangi, Selangor, Malaysia*

**Corresponding author: wannorroslam@ukm.edu.my*

Received: 28 November 2016; Accepted: 27 April 2017

**Abstract**

A mesoporous Fe-Ni catalyst was prepared by microwave combustion method by using glycine as a fuel to help the combustion occur in the microwave. The bimetallic catalyst synthesized was intend to accelerate the production of hydrogen via decomposition of formic acid. The hydrogen produced supposedly can substitute the energy source used now especially from fossil fuels to contribute to the reduction of greenhouse effect. The catalyst sample was characterized by powder X-ray diffraction (XRD), scanning electron microscopy (SEM) and $N_2$ adsorption-desorption isotherm (BET). From the BET isotherms, a type IV isotherm was observed, indicate the presence of mesoporous solid. XRD diffractograms of Fe-Ni have well-defined diffraction patterns with strong and sharp diffraction peaks, indicating that they are crystalline. The SEM images show the presence of voids and pores in the sample and spongy structure which also consisted of very fine crystalline. The selectivity for $H_2$ formation using the prepared bimetallic catalyst was achieved ranging of 94 to 99% for 120 minutes at optimum conversion of formic acid and merely at room temperature.

**Keywords**: iron nickel catalyst, hydrogen energy, microwave combustion method, $H_2$ selectivity

**Abstrak**

Mangkin Fe-Ni yang bersifat mesoporos telah disediakan dengan menggunakan kaedah pembakaran oleh gelombang mikro dengan bantuan glisin sebagai bahan bakar. Mangkin dwilogam yang disintesis bertujuan untuk mempercepatkan penghasilan hidrogen melalui penguraian asid formik. Hidrogen yang dihasilkan diharapkan dapat menggantikan sumber tenaga yang digunakan dewasa ini terutama daripada bahan api fosil supaya dapat mengurangkan kesan rumah hijau. Sampel mangkin dicirikan dengan pembelauan sinar-X (XRD), mikroskopi pengimbasan elektron (SEM), dan isoterma penyerapan-penyahjerapan $N_2$ (BET). Daripada isoterma BET, isoterma jenis IV telah dikenalpasti, menandakan kehadiran pepejal mesoporos. Difraktogram XRD bagi Fe-Ni menunjukkan corak yang terbentuk dengan puncak yang baik dan tajam, menunjukkan mangkin tersebut merupakan hablur. Imej SEM menunjukkan kehadian ruang dan pori di dalam sampel dan berstruktur span dimana ia juga terdapat hablur yang sangat halus. Keterpilihan terhadap penghasilan gas $H_2$ menggunakan mangkin dwilogam FeNi adalah 94 – 99% pada masa tindak balas 120 minit pada peratus penukaran asid fomik yang optimum pada suhu bilik.

**Kata kunci:** mangkin ferum nikel, tenaga hidrogen, kaedah pembakaran gelombang mikro, kepilihan $H_2$

## Introduction

Global warming has been continuously increases the attention among scientists and the earth community. This popular problem was resulted from both human activity and natural variability [1]. The emission of greenhouse and

toxic gases such as NOx and $SO_2$ to the atmosphere is the main reason of global warming other than environmental pollution due to the combustion of fossil fuel [2]. This all things happened because the source of energy nowadays is mainly from fossil fuels and scientist has found a way to change from petroleum to hydrogen as a new technology of energy source.

Hydrogen as a future energy carrier is very dependable due to its clean combustion pathways and high gravimetric energy density [3]. However, hydrogen has a very low volumetric energy density at atmospheric conditions [4]. To obtain a balanced gravimetric and volumetric hydrogen storage density, pure hydrogen can be stored in compressed gases or liquid form. Formic acid has been recognized as a potential hydrogen storage material due to its high gravimetric energy density, nontoxicity, and can be safely handled in aqueous solution [4]. This organic compound which is in liquid form at room temperature has limited uses including as a preservative and antifungal agent and it's also contribute in the production of leather and could act as a lime scale remover [5]. Levulinic acid production from cellulosic biomass [6, 7] and glucose [8, 9] will produce formic acid as a side product and due to the redundancy of formic acid, it makes sense that we utilize the acid to make something useful for the earth and mankind.
To produce hydrogen, formic acid needs to react in the present of catalyst. Formic acid can undergo two path of reaction that is dehydration (1) and dehydrogenation (2).

$$HCOOH \longrightarrow H_2O + CO \quad \Delta G_{298K} = -14.9 \text{ kJ mol}^{-1} \tag{1}$$
$$HCOOH \longrightarrow H_2 + CO_2 \quad \Delta G_{298K} = -35.0 \text{ kJ mol}^{-1} \tag{2}$$

Carbon monoxide that liberated from reaction (1) is toxic to fuel cell catalysts which will reduce the catalytic performance [4, 10]. In order to avoid formic acid undergoing dehydration, the type of active catalyst used in the reaction at low temperature must be taken into account. Flaherty et al. [11] in their studies on decomposition of formic acid on the molybdenum (Mo) and molybdenum carbide (C-Mo) surfaces show that at 350 – 450 K, dehydration is the dominant pathway on clean Mo (110) with ~5% or less formic acid undergoing dehydrogenation, while C-Mo (110) selectively promotes 70 – 75% of hydrogen. Hence, the type of catalyst use is very important and here, we report the characteristic of nanoalloy catalyst at different ratio of Fe and Ni composition.

## Materials and Methods

### Synthesis of bimetallic nanoalloy catalysts

All chemicals were of analytical grades and were used without further purification. Fe-Ni bimetallic catalysts were prepared by microwave combustion method with the weight percentage (wt%) of Fe to Ni as 99:1, 97:3 and 95:5. In order to prepare $NiFe_2O_4$, $Fe(NO_3)_2.9H_2O$ and $Ni(NO_3)_2.6H_2O$ with ratio stated before were mixed in a crucible porcelain in the presence of glycine as fuel. The mixture was then put into a microwave with a power of 240 W for 3 minutes. The voluminous sponge-like product was produced and washed with distilled water and ethanol. The washed product was dried at 115 ºC in an oven for 24 hours. The product was then reduced in hydrogen gas at 500 ºC for 1 hour to get Fe-Ni bimetallic. The compositions of final obtained catalysts are (100-x)Fe:xNi (x = 0, 1, 3 and 5) in weight percentage ratio, which labelled as F100, FN991, FN973 and FN955, respectively.

### Characterization of catalyst

Brunauer-Emmett-Teller (BET) surface area of every catalyst were analysed by $N_2$ adsorption and desorption isotherms. In this research, the BET instrument used was Micromeritics ASAP 2020. Samples were degassed at 350 ºC for 4 hours prior to the analysis and $N_2$ adsorption was carried out at -196 ºC. X-ray diffraction (XRD) diffractogram of the produced catalysts were recorded on a Bruker AXS D8 Advance using a Cu Kα radiation source (40 kV, 40 mA). Scans were taken over the 2θ range from 10º to 80º and wavelength, λ = 0.154 nm. 1 gram of sample was put on sample holder. The data obtain from the analysis was compared with standard peak data reported by Joint Committee on Powder Diffraction Standard (JCPDS) to get the structure and identity of the sample. The surface morphology of the catalyst was observed by variable pressure scanning electron microscopy (VPSEM).

**Decomposition of formic acid and product analysis**

Catalytic decomposition of formic acid by the produced catalyst was performed at room temperature (25 ºC) in a closed reactor containing formic acid with 50% concentration. The produced gases were analyzed using gas chromatography equipped with thermal conductivity detector (GC-TCD). The gases were collected from a gas bag connected to the reactor every 30 minutes and the volume released were recorded until 120 minutes.

## Results and Discussion

Table 1 shows the BET surface area of the synthesized catalyst. The BET surface area of the catalysts ranging from 5.64 to 9.02 $m^2/g$. The low surface area is due to the high temperature of the reaction in the microwave [12]. The surface area of the catalysts are gradually decreases as the percentage of Ni in the catalyst increase. The $N_2$ adsorption-desorption isotherms of the catalysts are shown in Figure 1. For all of them, a type IV isotherm is observed, indicate the presence of mesoporous solids [13]. A similar result has also been reported by Feyzi et al. (2010) [14] in the study of iron nickel oxide Fischer-Tropsch synthesis (FTS) catalyst. This result may be due to the electronic structure of the catalyst. Having greater surface area does not guarantee the excellency of catalytic activity as reported by Mandal et al. [15]. As in our work, F100 has larger BET surface area than FN991 but in term of $H_2$ selectivity, FN991 was more efficient than F100 as stated in Figure 4.

Table 1. Surface properties of catalyst

| Catalyst | $S_{BET}$ ($m^2/g$) | $V_{pore}$ ($cm^3/g$) | $d_{pore}$ (Å) |
|---|---|---|---|
| F100 | 9.02±0.09 | 0.048±0.010 | 235.30±2.0 |
| FN991 | 7.69±0.04 | 0.034±0.009 | 171.80±2.0 |
| FN973 | 7.30±0.05 | 0.028±0.007 | 182.81±2.0 |
| FN955 | 5.64±0.08 | 0.026±0.007 | 257.65±2.0 |

$S_{BET}$: BET surface area; $V_{pore}$: total pore volume;
$d_{pore}$: average pore diameter

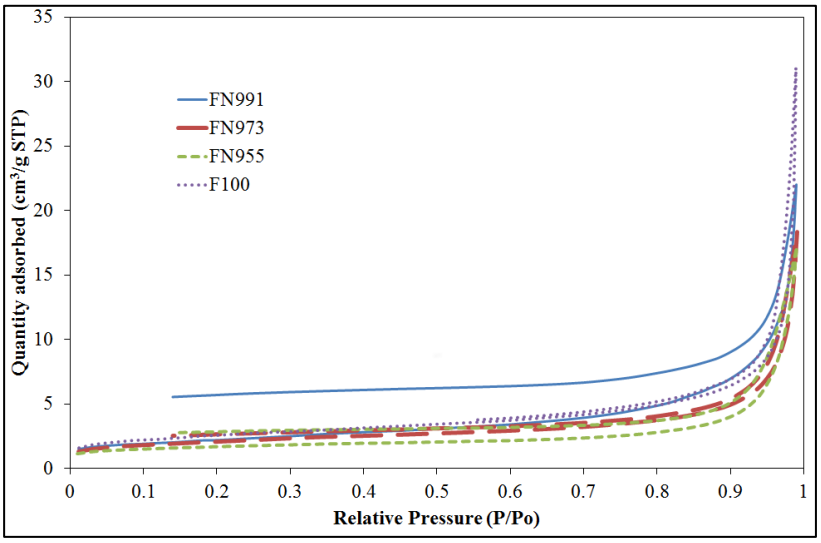



Figure 1. BET analysis of $N_2$ adsorption-desorption isotherms

XRD diffractograms for fresh Fe and FeNi bimetallic catalysts are shown in Figure 2. The XRD pattern of all the samples have well-defined diffraction patterns with strong and sharp diffraction peaks, indicating that they are crystalline. For F100 catalyst, two phases were detected; Fe (JCPDS file: 03-065-4899) and $Fe_3O_4$ (JCPDS file:

01-080-6402). For the Fe-Ni catalysts, besides the diffraction peaks of FeNi (JCPDS file: 01-080-7663), the diffraction peak of $Fe_3O_4$ also detected. A comparatively low intensity of $Fe_3O_4$ phase was detected on FN991 catalyst than other percentage ration. This indicate that low nickel composition is easy to reduce to form pure metallic.

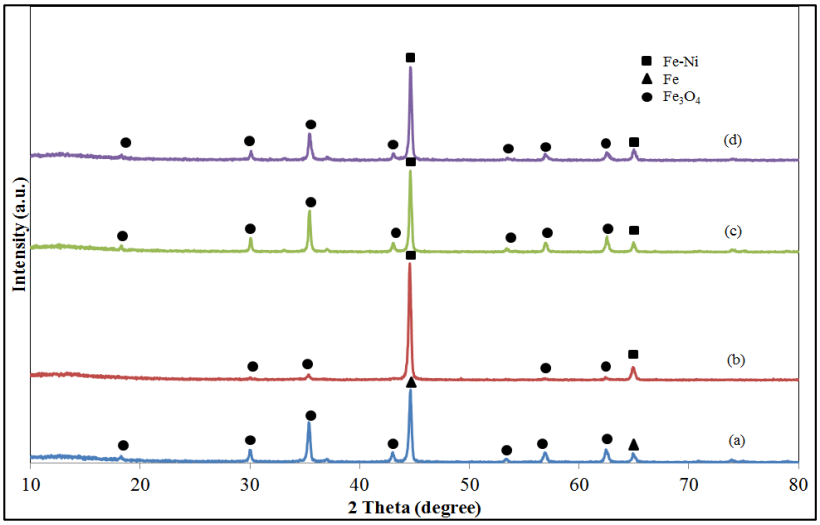
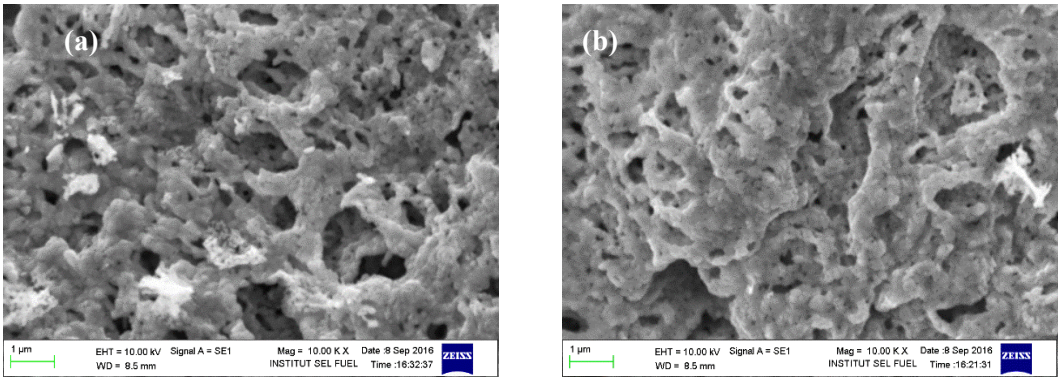



Figure 2. XRD diffractograms of prepared (a) F100, (b) FN991, (c) FN973 and (d) FN955

The SEM images in Figure 3 (a-d) show the porous structures of the prepared Fe and FeNi catalysts by microwave combustion method. Their morphological characteristics were investigated by variable pressure scanning electron microscope (VPSEM). As can be seen in Figure 3, the SEM images show the presence of voids and pores in the samples, which can be attributed to the release of large amount of gas during the combustion process. The sample has a spongy structure and one can see that the formation of multigrain agglomeration consisted of very fine crystallite.



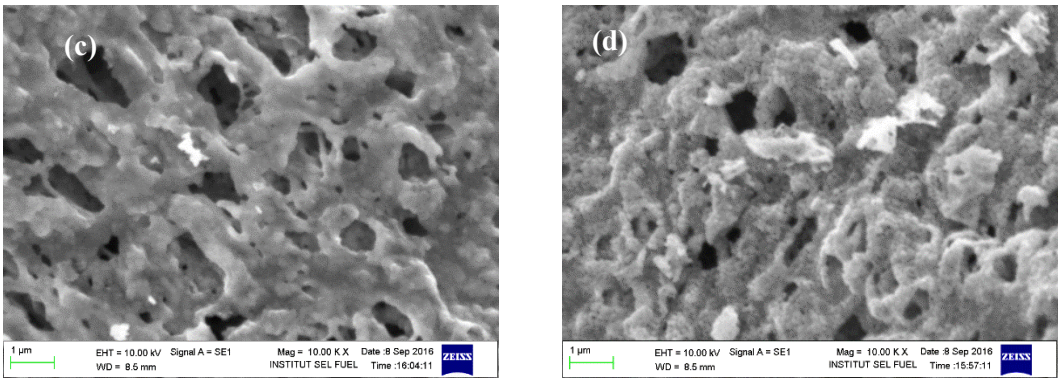



Figure 3. SEM images of prepared (a) F100, (b) FN991, (c) FN973 and (d) FN955

Figure 4 shows the graph of $H_2$ production against time. As the time increases, the activity of catalyst decreases. The FN973 catalyst was showed a significant decrement in activity compared to other catalysts. This degradation of the catalysts activity is due to the decreases of formic acid concentration during the reaction process which some of them consumed and decompose into hydrogen and carbon dioxide [4]. It was found that the FN991 catalyst showed the most excellent $H_2$ selectivity. The selectivity for $H_2$ formation was 94-99% even at maximum conversion of formic acid.

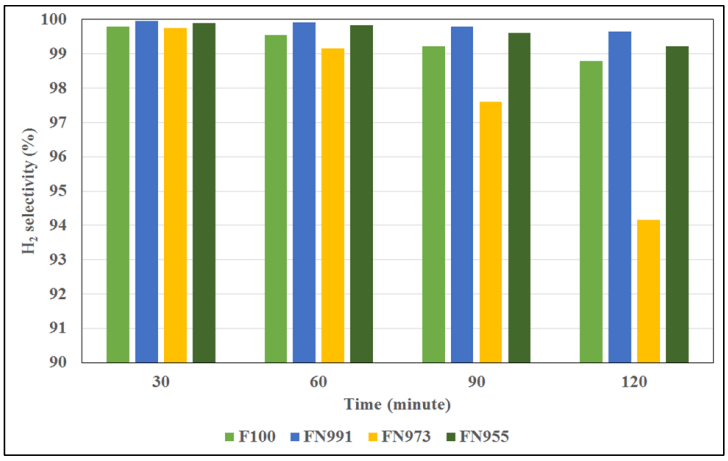



Figure 4. Production of $H_2$ for 120 minutes

## Conclusion

In this study three bimetallic alloy have been successfully prepared by microwave combustion method using glycine as a fuel. The doping of Ni in the catalyst increase the activity of the produced catalyst. FeNi bimetallic were found to be an active catalyst for the formic acid decomposition at room temperature to produce hydrogen with selectivity ranging of 94 – 99% for 120 minutes at room condition. The lower Ni content at 1 wt.% showed a relatively higher selective to hydrogen rather than produce $CO_2$ gas. The utilization of low cost transition metal such as Fe and Ni to produce catalyst for dehydrogenation of formic acid may represent a new approach to develop an efficient catalyst.

## Acknowledgement

Authors would like to thanks Ministry of Higher Education and Universiti Kebangsaan Malaysia (UKM) for funding this project under research grant number FRGS/1/2015/SG01/UKM/02/2 and DIP-2016-010 respectively,

Centre of Research and Innovation Management (CRIM), UKM and Fuel Cell Institute, UKM for instruments facilities.

**References**

1. Jian-bin, H., Shao-wu, W., Yong, L. U. O., Zong-ci, Z. and Xin-yu, W. E. N. (2012). Debates on the causes of global warming. *Advances in Climate Change Research*, 3(1): 38 – 44.
2. El Naggar, A. M. A., Awadallah, A. E. and Aboul-Enein, A. A. (2016). Novel intensified nano-structured zero-valente nickel alloy based catalyst for hydrogen production via methane catalytic decomposition. *Renewable and Sustainable Energy Reviews*, 53: 754 – 765.
3. Montandon-Clerc, M., Dalebrook, A. F. and Laurenczy, G. (2015). Quantitative aqueous phase formic acid dehydrogenation using iron(II) based catalysts. *Journal of Catalysis,* 343: 62 – 67.
4. Wang, Z. L., Ping, Y., Yan, J. M., Wang, H. L. and Jiang, Q. (2014). Hydrogen generation from formic acid decomposition at room temperature using a NiAuPd alloy nanocatalyst. *International Journal of Hydrogen Energy*, 39(10): 4850 – 4856.
5. Jia, L., Bulushev, D. A. and Ross, J. R. H. (2014). Formic acid decomposition over palladium based catalysts doped by potassium carbonate. *Catalysis Today*, 259: 453 – 459.
6. Morone, A., Apte, M. and Pandey, R. A. (2015). Levulinic acid production from renewable waste resources: bottlenecks, potential remedies, advancements and applications. *Renewable and Sustainable Energy Reviews*, 51: 548 – 565.
7. Yan, K., Jarvis, C., Gu, J. and Yan, Y. (2015). Production and catalytic transformation of levulinic acid: A platform for speciality chemicals and fuels. *Renewable and Sustainable Energy Reviews*, 51: 986 – 997.
8. Ramli, N. A. S. and Amin, N. A. S. (2015). Fe/HY zeolite as an effective catalyst for levulinic acid production from glucose: characterization and catalytic performance. *Applied Catalysis B: Environmental*, 163: 487 – 498.
9. Zhi, Z., Li, N., Qiao, Y., Zheng, X., Wang, H. and Lu, X. (2015). Kinetic study of levulinic acid production from corn stalk at relatively high temperature using $FeCl_3$ as catalyst : A simplified model evaluated. *Industrial Crops & Products*, 76: 672 – 680.
10. Tedsree, K., Li, T., Jones, S., Chan, C. W. A., Yu, K. M. K., Bagot, P. A. J., Marquis, E. A., Smith, G. D. W. and Tsang, S. C. E. (2011). Hydrogen production from formic acid decomposition at room temperature using a Ag-Pd core-shell nanocatalyst. *Nature Nanotechnology*, 6(5): 302 – 307.
11. Flaherty, D. W., Berglund, S. P. and Mullins, C. B. (2010). Selective decomposition of formic acid on molybdenum carbide: a new reaction pathway. *Journal of Catalysis*, 269(1): 33 – 43.
12. Kooti, M. and Sedeh, A. N. (2012). Glycine-assisted fabrication of zinc and manganese ferrite nanoparticles. *Scientia Iranica*, 19(3): 930 – 933.
13. Gregg, S. J. and Sing, K. S. W. (1982). Adsorption, surface area and porosity. Academic Press, New York.
14. Feyzi, M., Mirzaei, A. A. and Bozorgzadeh, H. R. (2010). Effects of preparation and operation conditions on precipitated iron nickel catalysts for Fischer-Tropsch synthesis. *Journal of Natural Gas Chemistry*, 19(3): 341 – 353.
15. Mandal, K., Bhattacharjee, D. and Dasgupta, S. (2015). Synthesis of nanoporous PdAg nanoalloy for hydrogen generation from formic acid at room temperature. *International Journal of Hydrogen Energy*, 40(14): 4786 – 4793.

*Malaysian Journal of Analytical Sciences, Vol 21 No 4 (2017): 907 - 913*
*DOI: https://doi.org/10.17576/mjas-2017-2104-17*

MALAYSIAN JOURNAL OF ANALYTICAL SCIENCES
*Published by The Malaysian Analytical Sciences Society*
ISSN 1394 - 2506

# EFFECT OF RHODIUM ADDITIVE ON THE REDUCTION BEHAVIOUR OF IRON OXIDE IN CARBON MONOXIDE ATMOSPHERE

## (Kesan Penambahan Rodium Terhadap Tindak Balas Penurunan Ferum Oksida Di Dalam Atmosfera Karbon Monoksida)

Tengku Shafazila Tengku Saharuddin[1], Fairous Salleh[2], Alinda Samsuri[3], Norliza Dzakaria[2], Rizafizah Othaman[2], Mohammad Bin Kassim[2], Mohammad Wahab Mohammad Hisham[2], Mohd Ambar Yarmo[2]*

[1]*Faculty of Science and Technology,*
*Universiti Sains Islam Malaysia, 71800 Nilai, Negeri Sembilan, Malaysia*
[2]*School of Chemical Sciences and Food Technology, Faculty of Science and Technology,*
*Universiti Kebangsaan Malaysia, 43600 UKM Bangi, Selangor, Malaysia*
[3]*Centre for Defense Foundation Studies,*
*Universiti Pertahanan Nasional Malaysia, Kem Sungai Besi, 57000 Kuala Lumpur, Malaysia*

**Corresponding author: ambar@ukm.edu.my*

Received: 28 November 2016; Accepted: 27 April 2017

**Abstract**

This study was carry out to investigate the effect of 3% rhodium on the reduction behaviour of iron oxide by (10%, v/v) carbon monoxide in nitrogen as a reductant. The Rh/$Fe_2O_3$ samples were prepared by impregnation method and the reduction behavior of Rh/$Fe_2O_3$ and pure $Fe_2O_3$ were investigated by using temperature programmed reduction (TPR). The prepared samples and the reduced phases were characterized by X-ray diffraction spectroscopy (XRD). The results indicate that Rh/$Fe_2O_3$ give a better reducibility compared to $Fe_2O_3$ with a complete reduction at 650 °C, which is 250 °C lower than $Fe_2O_3$. The TPR results indicate that the reduction of $Fe_2O_3$ proceed in three steps reduction ($Fe_2O_3$ → $Fe_3O_4$ → FeO → Fe) with $Fe_3O_4$ and FeO as intermediate states while for Rh/$Fe_2O_3$ as the TPR result showed the overlapping of second and third peak ($Fe_3O_4$ → FeO and FeO → Fe) at higher temperature. Addition of Rh may possibly reduce the formation of stable FeO that stable at higher temperature by accelerates the direct reduction of $Fe_3O_4$→ Fe so the reduction process of $Fe_2O_3$ become faster. The XRD pattern shows the diffraction peaks of Rh/$Fe_2O_3$ is more intense with improved crystallinity for the characteristic peaks of $Fe_2O_3$ compared to pure $Fe_2O_3$. No visible sign of rhodium particles peaks in the XRD spectrum that indicates the Rh particles loaded onto the iron oxide are well dispersed. The well dispersed Rh onto the iron oxide and the ability to reduce the sintering effect to the iron oxide also has been confirmed by FESEM. The study shows that addition of Rh gives a better reducibility of iron oxide is also due to the ability of Rh to interact with CO as confirmed by the thermodynamic data with higher surface area compared to $Fe_2O_3$.

**Keywords**: temperature programmed reduction, rhodium, ferum oxide, carbon monoxide

**Abstrak**

Kajian ini dijalankan untuk melihat pengaruh 3% rodium kepada kelakuan penurunan ferum oksida di mana karbon monoksida (10%, v/v) di dalam nitrogen digunakan sebagai agen penurunan. Sampel Rh/$Fe_2O_3$ disintesis menggunakan kaedah impregnasi dan kelakuan penurunan dikaji menggunakan teknik suhu penurunan berprogram (TPR). Fasa - fasa yang terbentuk dicirikan menggunakan teknik pembelauan sinar X (XRD). Keputusan menunjukkan Rh/$Fe_2O_3$ memberikan kelakuan penurunan yang lebih baik berbanding $Fe_2O_3$ sahaja dengan penurunan lengkap berlaku pada suhu 650 °C dimana suhu penurunan berkurangan sebanyak 250 °C berbanding suhu penurunan lengkap $Fe_2O_3$. Profil TPR menunjukkan bahawa penurunan ferum oksida melalui tiga langkah tindak balas penurunan ($Fe_2O_3$ → $Fe_3O_4$ → FeO → Fe) dengan $Fe_3O_4$ dan FeO merupakan fasa perantara, sementara, Rh/$Fe_2O_3$ pada suhu penurunan tinggi menunjukkan pertindihan diantara puncak kedua dan puncak ketiga ($Fe_3O_4$ → FeO and FeO → Fe). Penambahan Rh didapati mengurangkan penghasilan FeO yang stabil pada suhu tinggi dengan

menggalakkan penurunan terus $Fe_3O_4$→ Fe menjadikan tindak balas penurunan lebih cepat. Difraktogram XRD bagi Rh/$Fe_2O_3$ menunjukkan peningkatan pada kehabluran puncak $Fe_2O_3$ berbanding ferum oksida tulen. Tiada puncak tambahan diperhatikan dimana ia menjelaskan bahawa zarah Rh yang dimuatkan pada ferum oksida telah tersebar dengan baik. Penyerakan yang baik oleh Rh di atas ferum oksida telah menunjukkan pengurangan kesan pensinteran terhadap ferum oksida yang telah dibuktikan melalui FESEM. Kajian menunjukkan penambahan Rh memberikan kesan yang baik kepada proses penurunan ferum oksida berdasarkan kebolehan Rh untuk berinteraksi dengan gas CO yang telah disahkan oleh pengiraan termodinamik dan peningkatan kepada luas permukaan berbanding $Fe_2O_3$ tulen.

**Kata kunci:** suhu penurunan berprogram, rodium, ferum oksida, karbon monoksida

## Introduction

The reduction behaviour of the iron species were highly important in such application in industry and some chemical processes [1, 2]. The reduction process of $Fe_2O_3$ is not a simple process which may include several steps relies on factors such as temperature, concentration reduction gas used, particle size, crystallinity and additives [3]. This reduction process of iron oxide involves several possible structural changes and complex compositions in the intermediate oxides such as hematite ($Fe_2O_3$) → magnetite ($Fe_3O_4$) → wüstite (FeO) → iron (Fe) and in most cases the reactions were usually simultaneous [2]. Pineau et al. investigate the effect of temperature on the reduction behaviour of iron oxide and proposed several reduction routes depending on the formation of metastable wüstite [4]. The reduction of $Fe_2O_3$ to metallic Fe can be a two-step ($Fe_2O_3$→ FeO → Fe) or three-step mechanisms ($Fe_2O_3$→ FeO → Fe) depending on temperature and affected the formation of metastable wüstite [5]. When the reduction temperature reached 570 °C and above, magnetite can be reduced to wüstite so higher temperature is needed to its reduction to metal iron [6].

In this study, we will focus on the addition of other element which is rhodium for the purpose of improving the reduction behaviour of $Fe_2O_3$. Good performance of Rh on the reduction behaviour of iron oxide has also been studied by Seak et. al. [7] using $H_2$ as a reductant. Their study revealed that Rh additive can promote the reduction corresponding to the reduction of $Fe_2O_3$→$Fe_3O_4$ as the reduction temperature at this transition was obviously decreased. Thus, we will report the results of an attempt to understand the influence of Rh species on the reduction behavior of the iron oxide with CO as a reductant.

## Materials and Methods

### Materials

Iron(III) oxide (99%) and Rhodium(III) nitrate (99%) were obtained from Sigma Aldrich Chemical Company and the gas mixture of 10% CO in nitrogen was obtained from MOX.

### Catalyst preparation

The addition of 3% Rh (w/w, %) on $Fe_2O_3$ was prepared by impregnating $Fe_2O_3$ powder with aqueous solution containing rhodium cation additives. The $Fe_2O_3$ powder was directly impregnated into 50 ml distilled water corresponding metal cation additives in the above proportion and stirred vigorously for 4 hours at room temperature. The impregnated sample was dried at 110 °C overnight and subsequently calcined at 600 °C for 3 hours.

### Characterization

Temperature programmed reduction (TPR) measurements using a Micromeritic Autochem 2920 Chemisorption Analyzer apparatus; a feed of 10% CO in $N_2$ at a flow rate of 20 mL $min^{-1}$ (STP) was used as reducing gas. The 50 mg of samples were heated up to 900 °C, at a rate of 10 °C $min^{-1}$ were applied to the samples. The carbon monoxide consumption was monitored using a thermal conductivity detector (TCD). Phase characterization was carried out by X-ray diffraction (XRD) Bruker AXS D8 Advance type with X-ray radiation source of Cu Kα (40 kV, 40 mA) to record the 2θ diffraction angle from 10 – 80 degree at wavelength (λ = 0.154 nm) to observe the lattice of the structures and were matched with standard diffraction (JCPDS) files. Physical surface analysis (Brunauer–Emmett–Teller, BET) of nitrogen adsorption at 77 K (liquid nitrogen) was conducted using a Micromeritics ASAP 2010 instrument to obtain the adsorption isotherm of each sample. The calcined sample of Rh/$Fe_2O_3$ and $Fe_2O_3$ were degassed at 350 °C for 6 hours before the BET surface area analyses were done. The Brunauer–Emmett–Teller

(BET) surface areas were calculated from the isotherms. FESEM images were obtained using Merlin Ultra High Resolution FESEM operating with 3.0 kV.

## Results and Discussion

### Thermodynamic consideration data

Table 1 shows the thermodynamic data of iron oxide and rhodium oxide reduction process in CO atmosphere. Sequenced of three steps iron oxide reduction by using carbon monoxide are listed in the table as Eq. 1 to 3 together with the reduction process of rhodium oxide to rhodium metal as Eq. 4. The thermodynamic calculations based on the Gibbs free energy change due to the reactions below and the equilibrium composition of the oxides indicates all equations as written are favourable within the range that also has been mentioned by Svoboda and Bexter [8].

Table 1. Thermodynamics data of iron oxide reduction process in CO atmosphere

| Reactions | | ΔH ($kJmol^{-1}$) | ΔS ($Jmol^{-1}K^{-1}$) | ΔG ($kJmol^{-1}$) | T (°C) | Reaction Possibility |
|---|---|---|---|---|---|---|
| $3Fe_2O_3 + CO \rightarrow 2Fe_3O_4 + CO_2$ | (1) | -47 | +47 | -88 | 600 | Favourable |
| $Fe_3O_4 + CO \rightarrow 3FeO + CO_2$ | (2) | +19 | +53 | -26 | 600 | Favourable |
| $FeO + CO \rightarrow Fe + CO_2$ | (3) | -12 | -18 | +4 | 600 | Favourable |
| $Rh_2O_3 + 3CO \rightarrow 2Rh + 3CO_2$ | (4) | -564.5 | -9 | -556 | 600 | Favourable |

### Isotherm adsorption of $N_2$

The result indicates that the impregnation of $Fe_2O_3$ with rhodium nitrate (5.26 $m^2/g$) shows the BET surface area was larger than pure $Fe_2O_3$ (4.67 $m^2/g$). The higher BET surface area of $Rh/Fe_2O_3$ may contribute to the higher rate of reduction as mentioned by Hu et al. [9] as they mentioned that higher specific surface area was also an important factor which provide more unsaturated surface coordination sites exposed to the gas which may result in the increasing of the activity.

### Crystallinity studies

Figure 1 shows the X-ray diffraction patterns of prepared samples $Rh/Fe_2O_3$ and pure $Fe_2O_3$ before reduction with CO in nitrogen (10%, v/v). The characteristic peaks are consistent with the standard data of rhombohedral ($\alpha$-$Fe_2O_3$, JCPDS 33-0664) with the 2θ $Fe_2O_3$ main peaks revealed the presence of contribution at about 24.2, 33.2, 35.7, 40.9, 49.5, 53.5, 57.2, 62.4, 64.2, 72.4 and 75.7 with crystallite phases of (0,1,2), (1,0,4), (1,1,0), (1,1,3), (0,2,4), (1,1,6), (0,1,8), (2,1,4), (3,3,0), (10,1,0), (2,2,0), respectively. The diffraction peaks show improvement in the crystallinity when loading with Rh with no additional peak that can be explained by a high dispersion of the Rh particles, formation of non-crystalline compounds, compounds giving the same diffraction peaks as those of $Fe_2O_3$ or the amount of the Rh dopant may be too small to be detected significantly as suggested by Lorente et al. [10].

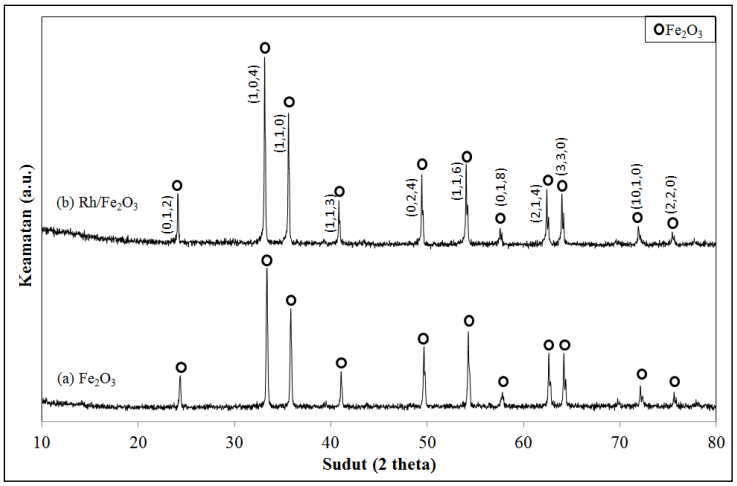



Figure 1. XRD diffractograms of (a) $Fe_2O_3$ and $Rh/Fe_2O_3$ after calcined at 600 °C

To investigate the role of Rh in the reduction behavior of $Fe_2O_3$ in CO atmosphere, all samples were collected according to the TPR pattern when the reduction of $Rh/Fe_2O_3$ in CO is assumed to be finished at 650 °C and also at 900 °C for comparison purposes. From the results display in Figure 2, $Rh/Fe_2O_3$ exhibit a complete reduction at temperature 650 °C with only metallic Fe diffraction peak observed (iron, JCPDS 65-4899). Meanwhile, for $Fe_2O_3$ the reduction accomplished only when the temperature reached 900 °C as it still exhibited a remaining unreduced $Fe_3O_4$ (magnetite, JCPDS 71-6336) and FeO (wustite, JCPDS 80-0686) at reduction temperature of 650 °C.

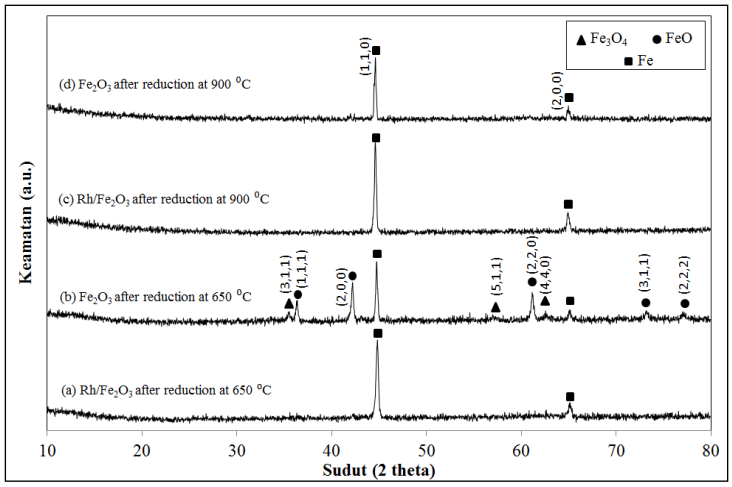



Figure 2. XRD diffractograms of $Rh/Fe_2O_3$ after reduction at (a) 650 °C and (c) 900 °C and $Fe_2O_3$ at (c) 650 °C and (d) 900 °C by CO

**Catalyst characterization by TPR**

The TPR pattern of non-isothermal CO reduction for $Rh/Fe_2O_3$ and $Fe_2O_3$ were shown in Figure 3. For $Fe_2O_3$, 3 reduction peaks were observed at temperature 361 °C, 509 °C and 807 °C which known to reflect the reduction reaction of iron oxides and proceeds the 3 steps reduction of $Fe_2O_3 \rightarrow Fe_3O_4 \rightarrow FeO \rightarrow Fe$. The results are in agreement with the XRD diffractogram as shown before. Meanwhile, $Rh/Fe_2O_3$ also showed one sharp peak at early reduction temperature represents the first stage reduction of $Fe_2O_3 \rightarrow Fe_3O_4$. Nevertheless, as the temperature increased, a broad reduction peak was observed at 565 °C which may represents the overlapping of several reduction steps

before completed to form metallic Fe. Based on the TPR profile together with the XRD diffractogram, $Rh/Fe_2O_3$ exhibited better reducibility compared to $Fe_2O_3$ as the reduction of $Rh/Fe_2O_3$ to metallic Fe completed at 650 °C compared to a much higher temperature (900 °C) of completion for $Fe_2O_3$ without Rh additive. According to Datta et al. [11], addition of other element as a dopant may activates the dissociation of CO and promotes the breaking of Fe-O and contribute to the enhancement of the reducibility process. Thus, the involvement of rhodium element in the structure of iron oxide inhibit the formation of FeO which is stable at higher temperature, thus promotes the direct reduction of $Fe_3O_4 \rightarrow$ Fe and accelerates the reduction process of $Fe_2O_3$. Moreover, Rh itself is favourable to react with CO as in agreement with the thermodynamic data of Eq. 4 as mentioned in Table 1 if compared to $Fe_2O_3$ alone.

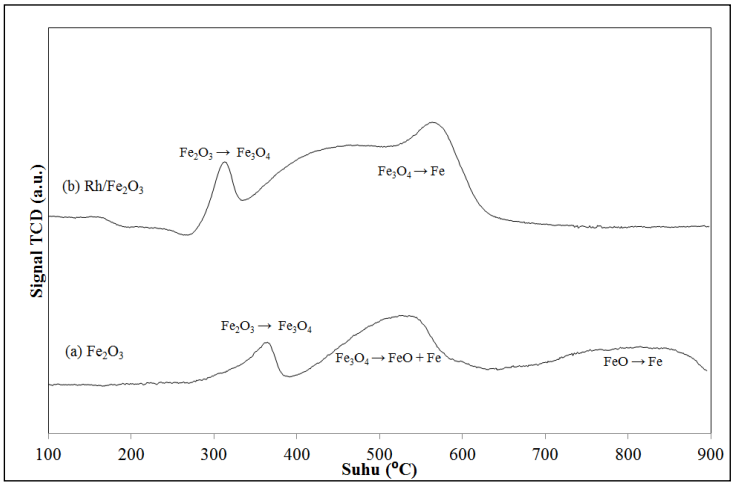



Figure 3. TPR profile of (a) $Fe_2O_3$ and (b) $Rh/Fe_2O_3$ in CO atmosphere

**Catalyst characterization by FESEM**

Figure 4 and Figure 5 show the FESEM images of $Fe_2O_3$ and $Rh/Fe_2O_3$ samples before and after the reduction process in 10% CO atmosphere as seen in magnification (20000x). It is clearly observed from the FESEM image that at reduction temperature of 650 °C, the particle size of $Fe_2O_3$ are slightly bigger that caused by sintering of iron oxide, while $Rh\text{-}Fe_2O_3$ sample showed no big changes in particles size compare with before and after the reduction process. Smaller in particles observed after reduction at 650 °C for $Rh/Fe_2O_3$ may contribute to better reducibility of $Fe_2O_3$.

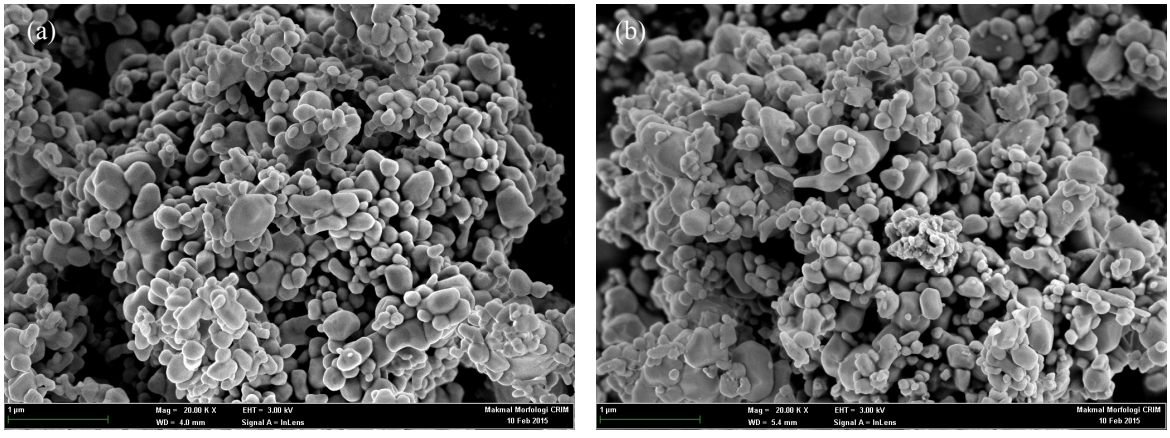



Figure 4. FESEM image of (a) prepared $Fe_2O_3$ and (b) prepared $Rh/Fe_2O_3$ calcined at 600 °C

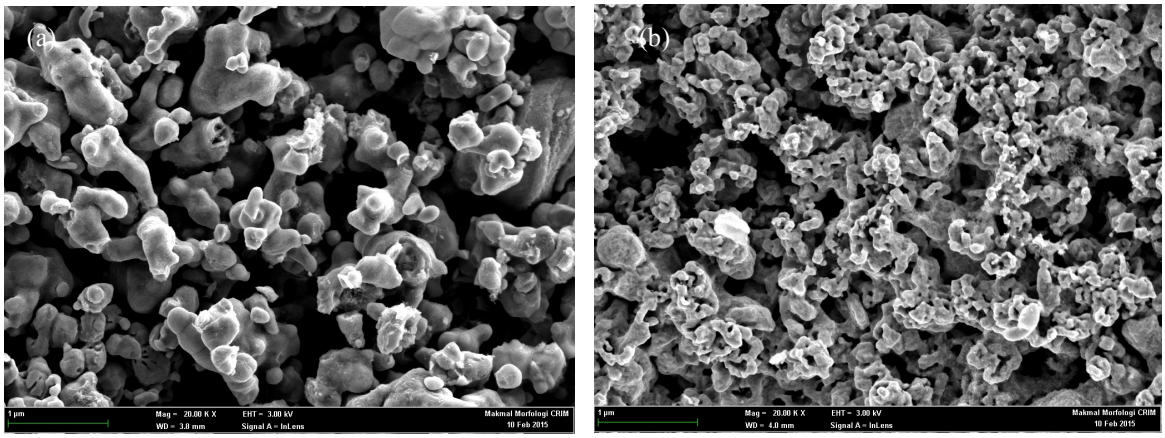



Figure 5. FESEM image of the surface of particle of (a) $Fe_2O_3$ and (b) Rh-$Fe_2O_3$ reduction at 650 °C in 10% CO atmosphere

## Conclusion

The reduction behaviour of Rh added to the $Fe_2O_3$ in CO as a reductant was investigated and compared using TPR and XRD. Addition of Rh to the iron oxide showed the effect on enhancing the reduction process in CO atmosphere. The reduction process completed 250 °C lower compared to $Fe_2O_3$ with XRD patterns showed only metallic Fe peak at 650 °C. Rhodium species played important role on lowering the reduction temperature due to well dispersed of the Rh particle, good interaction with CO as prove by the thermodynamic data and higher of surface area.

## Acknowledgement

The author wish to thank Ministry of Higher Education (MOHE) for funding this project under research grant number BKBP-FST-K003323-2014, FRGS/2/2013/TK06/UKM/02/3, ETP-2013-066, TD-2014-024 & Centre of Research and Innovation Management CRIM-UKM for instruments facilities.

## References

1. Jozwiak, W. K., Kaczmarek, E., Maniecki, T. P., Ignaczak, T. P. and Maniukiewicz, W. (2007). Reduction behavior of iron oxides in hydrogen and carbon monoxide atmospheres. *Applied Catalysis A: General,* 326(1): 17 – 27.
2. Lorente, E., Herguido, J. and Peña, J. A. (2011). Steam-iron process: Influence of steam on the kinetics of iron oxide reduction. *International Journal of Hydrogen Energy,* 36(21): 13425 – 13434.
3. Jian-Ming, P., Pei-Min, G., Pei Z., Chao-Zhen, C. and Dian-Wei, Z. (2009). Influence of size of hematite powder on its reduction kinetics by $H_2$ at low temperature. *Journal of Iron and Steel Research, International,* 6(5): 7 – 11.
4. Pineau, Kanari N. and Gaballah, I., (2007). Kinetics of reduction of iron oxides by $H_2$. *Thermochimica Acta,* 456(2): 75 – 88.
5. Kuo, Y., Hsu, W., Chiu, P., Tseng, Y. and Ku, Y. (2013). Assessment of redox behavior of nickel ferrite as oxygen carriers for chemical looping process. *Ceramics International,* 39: 5459 – 5465.
6. Ramadan, W., Zaki, M. I., Fouad, N. E. and Mekhemer, G. H. (2014). Particle characteristics and reduction behavior of synthetic magnetite. *Journal of Magnetism and Magnetic Materials*, 355: 246 –253.
7. Seak, Y., Chun, J., Hee, D. and Ho, Y. (2006). Hydrogen storage characteristics using redox of M/$Fe_2$ $O_3$ (M = Rh , Ce and Zr) mixed oxides. *World Hydrogen Energy Conference Proceeding*, 3: 2 – 8.
8. Svoboda, K. and Baxter, D. (2007). Thermodynamic possibilities and constraints for pure hydrogen production by iron based chemical looping process at lower temperatures. *Energy Conversion and Management,* 48: 3063 – 3073.

9. Hu, C., Gao, Z. and Yang, X. (2007). Facile synthesis of single crystalline α-$Fe_2O_3$ ellipsoidal nanoparticles and its catalytic performance for removal of carbon monoxide. *Materials Chemistry and Physics,*104: 429 – 433.
10. Lorente, E., Peña, J. A. and Herguido, J. (2009). Separation and storage of hydrogen by steam-iron process: Effect of added metals upon hydrogen release and solid stability. *Journal of Power Sources*, 192(1): 224 – 229.
11. Datta, P., Rihko-Struckmann, L., K. and Sundmacher, K. (2014). Quantification of produced hydrogen in a cyclic water gas shift process with mo stabilized iron oxide. *Fuel Processing Technology,* 128: 36 –42.

*Malaysian Journal of Analytical Sciences, Vol 21 No 4 (2017): 914 - 920*
*DOI: https://doi.org/10.17576/mjas-2017-2104-18*

MALAYSIAN JOURNAL OF ANALYTICAL SCIENCES
*Published by The Malaysian Analytical Sciences Society*
ISSN 1394 - 2506

# EFFECT OF ANNEALING STRATEGY ON IMPROVED PHOTOACTIVITY OF CUPROUS OXIDE NANOWIRE PREPARED USING FACILE FABRICATION STRATEGY FOR SOLAR WATER SPLITTING

## (Kesan Strategi Pengkalsinan Terhadap Peningkatan Fotoaktiviti Nanowayar Kuprous Oksida Yang Disediakan Menggunakan Cara Mudah Untuk Pembelahan Air Suria)

Mohd Nur Ikhmal Salehmin[1], Lorna Jeffery Minggu[1]*, Khuzaimah Arifin[1], Mohammad Bin Kassim[1,2]

[1]*Fuel Cell Institute*
[2]*School of Chemical Sciences and Food Technology, Faculty of Science and Technology*
*Universiti Kebangsaan Malaysia, 43600 UKM Bangi, Selangor, Malaysia*

**Corresponding author: lorna_jm@ukm.edu.my*

Received: 28 November 2016; Accepted: 27 April 2017

**Abstract**

$Cu_2O$ photocathode such as nanowire (NW) have shown to improve photoactivity than that nanoparticle thin film counterpart. This enhancement is attributed to enhanced photocatalytic reaction due to increase in surface active area and effective radial charge diffusion. However, the photoelectrochemical performance of reported work were rather low which need an improvement prior protection. In this study, $Cu_2O$ nanowire photocathode was fabricated using sequential wet chemical oxidation method and annealing under inert condition. Focusing on annealing step, the transformation of precursor $Cu(OH)_2$ nanowire to $Cu_2O$ nanowire undergone multistep annealing with a different ramping rate under inert condition. The highest photocurrent was then compared with photocurrent generated from $Cu_2O$ NW prepared with direct annealing strategy. With multistep annealing, the best photoelectrochemical performance was obtained from $Cu_2O$ NW prepared at the highest ramping rate which is 1.2 folds better than that obtained with single step annealing. The photocurrent enhancement obtained in this study was attributed to favourable morphology improving light trapping. Overall, the ampleness of material source, non-toxic, simple fabrication and excellent photocatalytic performance are the pre-requisite to realize solar hydrogen production.

**Keywords**: cuprous oxide nanowire, photocurrent, water-splitting, hydrogen production

**Abstrak**

Fotokatod $Cu_2O$ yang berstrukturkan nano wayar (NW) telah menunjukkan aktiviti foto yang lebih baik berbanding filem nipis. Prestasi fotomangkin yang baik ini disumbang oleh peningkatan luas permukaan yang aktif dan keberkesanan pengaliran cas. Walaubagaimanapun, prestasi fotoelektrokimia yang telah dilaporkan masih lagi rendah dan memerlukan penambahbaikan sebelum penyalutan sebagai perlindungan untuk kestabilan fotokatod. Dalam kajian ini, $Cu_2O$ NW fotokatod telah disintesis menggunakan oksidasi kimia dan pengkalsinan dalam keadaan lengai. Pada peringkat pengkalsinan, transformasi pemula $Cu(OH)_2$ nanowayar kepada $Cu_2O$ nanowayar telah melalui beberapa langkah pengkalsinan dengan kadar pengkalsinan yang berbeza. Fotoarus yang tertinggi akan dibandingkan dengan fotoarus yang terhasil daripada $Cu_2O$ nanowayar yang disediakan menggunakan pengkalsinan terus. Pada pengkalsinan berperingkat, prestasi fotoelektrokimia yang terbaik didapati daripada $Cu_2O$ NW yang disediakan pada kadar pengkalsinan yang paling tinggi iaitu 1.2 kali ganda lebih baik berbanding yang didapati daripada pengkalsinan terus. Peningkatan fotoarus yang terhasil daripada kajian ini telah disumbangkan oleh kesan morfologi bahan yang berkeupayaan menyerap cahaya secara efektif. Keseluruhannya, keberadaan sumber bahan yang mencukupi, tidak toksik, cara penyediaan yang mudah, serta prestasi fotomangkin yang bagus adalah keperluan untuk merealisasikan penghasilan hidrogen dari tenaga suria.

**Kata kunci**: nanowayar kuprous oksida, fotoarus, pembelahan air, penghasilan hidrogen

## Introduction

The photocatalytic performance of $Cu_2O$ photocathode for photoelectrochemical application can be enhanced by nanostructuring owing to its high surface area for photocatalytic reaction and alleviated issue of mismatch between the intrinsic carrier diffusion length [1, 2] and the light absorption depth near the band gap [3]. This single metal oxide was theoretically estimated to produce approximately -15 mA/cm$^2$ and photoconversion efficiency of 18% based on the AM 1.5 spectrum [4]. As photocathode, recent research trend has been attempts to fabricate the photocathode with nanowire (NW) arrays film [5-8] and stabilize it using facile technique and inexpensive protective material, respectively [4, 9-12]. Prior to stabilization, priority should be given to improve the photocurrent generation that can be tapped from the photoharvester of $Cu_2O$ film. This step is crucial to compensate photocurrent reduction which might be due to poor charge transportation between overlayers or any deleterious effect of the film after the coating treatment [9, 13-15]. $Cu_2O$ NW can be fabricated using sequential wet chemical oxidation method (WCOM) [1, 6, 11, 16] followed by annealing under inert condition as one of the method which promotes facility and high quality. This method is initiated with the fabrication of $Cu(OH)_2$ NW as precursor using WCOM [17] before transforming to $Cu_2O$ NW through annealing under inert condition. Focusing on the annealing process, the transformation of the precursor to $Cu_2O$ NW involved dehydration and deoxidization step [17, 18]. Therefore it needs a multistep of annealing to provide each step with a complete transformation from $Cu(OH)_2$ to CuO through dehydration and ultimately CuO to $Cu_2O$ through deoxidization.

Through literature survey on PEC application, there was only one single study which we know of following similar annealing strategy for $Cu_2O$ NW fabrication from $Cu(OH)_2$ NW precursor [19]. However, this study only managed to achieve photocurrent of -2.05 mA/cm$^2$ at 0.265 V vs. RHE which was produced from the sample annealed at 700 $^oC$ for 2 hours. The low photocurrent could be due to diminishing NW structure at high annealing temperature, thus decreased surface active area for photocatalytic reaction. Other reported studies with similar material and strategy deemed to practise a direct annealing since no details were mentioned on annealing step [5, 6, 8, 12, 16]. As far as photocurrent generation is concerned, the highest photocurrent ever reported for bare $Cu_2O$ from WCOM was -4.07 mA/cm$^2$ at 0V vs. RHE. This PEC performance was achieved using WCOM and direct annealing at 500 $^oC$ for 2 hours under Argon flow [10]. Based on the maximum theoretical measurement of photocurrent for $Cu_2O$ photocathode mentioned above, there is indeed more room for improvement.

Therefore, in this study, an annealing with multistep strategy was used to affect an improved $Cu_2O$ NW photocathode with excellent PEC performance. Since the effect of annealing temperature [5, 10], and holding time [8] were well studied, hence we investigated the effect of multistep ramping rate at 500 $^oC$ for 2 hours. For comparison, a direct annealing was conducted under similar annealing parameter that affect the highest photocurrent.

## Materials and Methods

### The fabrication of $Cu(OH)_2$ NW

In most recent studies, $Cu(OH)_2$ NW was prepared using an established method proposed by Zhang et. al. [17]. However, in this study, the growth solution was modified by the addition of $NH_3$. Briefly, a sheet of copper foil as substrate of 1 cm$^2$ was cleaned in acetone, ethanol, and double distilled water ($ddH_2O$) for 5 minutes each, consecutively. The wet Cu foils were then dried with nitrogen flow prior to immersion in growth solution. The growth solution composed of 2.67 M NaOH (Amreck), 0.133 M $(NH_4)_2S_2O_8$ (Sigma), and 4.26% $NH_3$ (Merck), were dissolved in $ddH_2O$ as reaction media. After 25 minutes of reaction, blue film appeared covering the substrate indicating the growth of $Cu(OH)_2$ NW. Then, the grown film was rinsed with $ddH_2O$ and dried in air.

### The conversion of $Cu(OH)_2$ NW to $Cu_2O$ NW

The as-prepared $Cu(OH)_2$ NW film was then subjected for annealing to be converted to $Cu_2O$ NW under $N_2$ flow. Three levels of ramping rate at 1, 3, and 5 $^oC$/min were carried out to reach final temperature of 500 $^oC$ for 2 hours. Routinely, the furnace was first evacuated with vacuum and followed by nitrogen sparging alternately for 3 cycles. Then, from room temperature, the furnace was first raised to 120 $^oC$ with 5 $^oC$/min ramping rate and held at 120 $^oC$

for 60 minutes before ramped up to 180 $^{o}$C for 1 hour and held for another 1 hour. With different ramping rate as mentioned, the temperature was finally raised to 500 $^{o}$C and held for another 2 hours before cooling down. For comparison on PEC performance, a direct annealing (without multistep) was conducted at the pre-determined ramping rate under similar annealing condition. For simplicity, hereafter, the $Cu_2O$ NW sample prepared with multistep annealing at 1, 3, and 5 $^{o}$C/min ramping rate were denoted as $Cu_2O$-(1 $^{o}$C/min), $Cu_2O$-(3$^{o}$C/min), and $Cu_2O$-(5$^{o}$C/min), respectively. Whereas sample labelled with $Cu_2O$-(5 $^{o}$C/min)(D.A) stands for $Cu_2O$ NW which prepared with direct annealing strategy at 5 $^{o}$C/min.

**Structural characterization**

The morphology of the samples was characterized using a Variable Pressure Scanning Electron Microscope (VPSEM). The crystallinity of the samples were determined by X-ray diffractometer (XRD) (Bruker D8 Advance), using Cu Kα radiation. Whereas, the UV-vis diffuse reflectance spectra were determined with a spectrophotometer (Perkin Elmer, Lambda 950).

**Photoelectrochemical measurement**

The photoresponse of the samples were measured using three electrodes configuration contained in a photocell with expose area of 0.196 cm$^2$. The fabricated photoelectrode was assigned as working electrode, Ag/AgCl as reference electrode, and platinum as counter electrode. Cu tape was connected to photoelectrode sample and clamped before it is filled with electrolyte. Those electrodes were immersed in 0.5 M $Na_2SO_4$ solution which was purged with Argon for 10 minutes prior to measurement. The photocurrent measurement was acquired under AM 1.5 Xenon light irradiation at 100 mW/cm$^2$. The photocurrent density was then determined as a result of subtraction between light and dark current and divided by the sample's exposed area.

## Results and Discussion

**Characterization of $Cu_2O$ NW film**

The transformation of $Cu(OH)_2$ NW to $Cu_2O$ NW depicts a morphology changes from a straight-standing $Cu(OH)_2$ NW to bendy and segmented $Cu_2O$ NW (Figure 1). The changes can be seen started at 180 $^{o}$C (Figure 1b) where a straight NW of $Cu(OH)_2$ NW was appeared bendy and the films turned black (insert (1b). As temperature increased to 500 $^{o}$C at different ramping rate and held for 2 hours, a dramatic change on the NW strand was noticed (Figure 1c, 1d, and 1e) indicating $Cu_2O$ NW was produced as evidenced from XRD analysis Figure 2. It was reported that the curly and bendy NW after annealing was due to the stress of phase changes resulted from oxygen separation from the lattice of CuO [8].

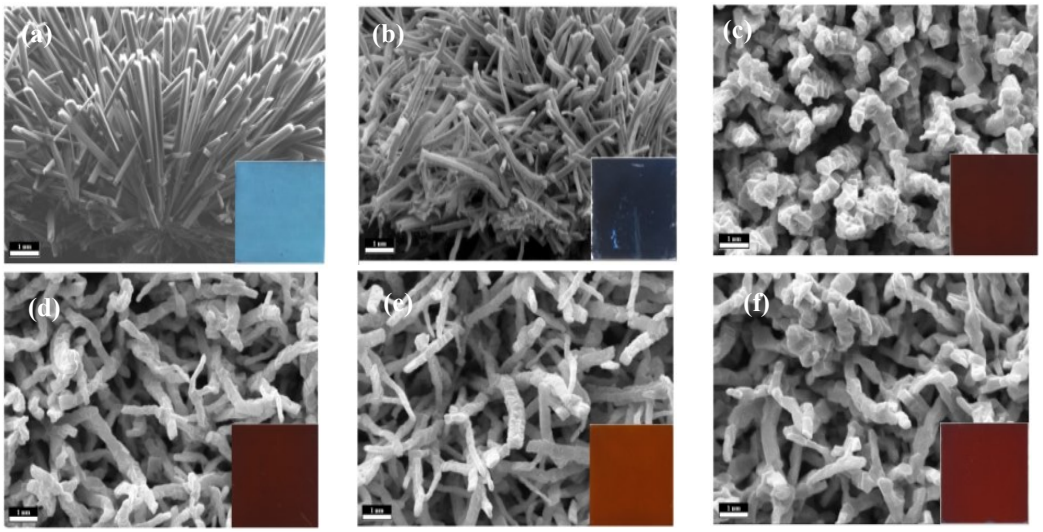



Figure 1. SEM images of a) $Cu(OH)_2$ NW, b) CuO NW, $Cu_2O$ NW prepared at multistep annealing with different ramping rate at c) 1 $^{o}$C/min, d) 3 $^{o}$C/min, e) 5 $^{o}$C/min, and f) without multistep $Cu_2O$ NW-(5 $^{o}$C/min) (D.A)

The phase transformation from CuO to $Cu_2O$ is explainable with deoxidization reaction where oxygen molecules was removed from the CuO lattice and reducing the ionic state from 2 to 1 becoming $Cu_2O$ [17]. Along with morphology changes, the NW dimension also changed accordingly as tabulated in Table 1.

Table 1. The dimension of nanowire before and after annealing measured using ImageJ software

| Samples | Length (µm) | Width (µm) |
|---|---|---|
| $Cu(OH)_2$ NW | 5.60 ± 0.20 | 0.40 ± 0.02 |
| $Cu_2O$-(1 $^oC$/min) | 2.72 ± 0.14 | 0.82 ± 0.14 |
| $Cu_2O$-(3 $^oC$/min) | 3.12 ± 0.09 | 0.45 ± 0.01 |
| $Cu_2O$-(5 $^oC$/min) | 4.07 ± 0.08 | 0.39 ± 0.08 |
| $Cu_2O$-(5 $^oC$/min)(D.A) | 3.33 ± 0.07 | 0.56 ± 0.04 |

The results obtained here can be concluded that, the length and width of NW arrays were shortened and widen as the ramping rate decreased. This observation is attributed to agglomeration of NW structure affected by long annealing time imposed by the lowest ramping rate. A long annealing time induced the increase in crystal size which is in agreement with reported study [8]. On the other hand, samples annealed at higher ramping rate has shorter annealing time and were not severely impacted by agglomeration, hence appeared to be the longest NW. Although $Cu_2O$-(5 $^oC$/min)(D.A) sample was prepared with the shortest annealing time, its NW length is shorter than that measured for $Cu_2O$-(5 $^oC$/min). This shows that during the multisteps annealing the different holding time at different temperatures affected the agglomeration rate differently than during direct annealing. Furthermore, it is reported that the curly and bendy NW after annealing was due to the stress of phase changes resulted from oxygen separation from the lattice of CuO [8].

In Figure 2, an overlayer of XRD pattern of the samples pre and post annealing are displayed. A distinct XRD pattern of each sample reflecting a complete transformation from Cu to $Cu(OH)_2$, CuO and subsequently to $Cu_2O$ after annealing. $Cu_2O$ is known with dominant peak of 111 phase which claimed to be responsible for good PEC performance [5, 20]. This particular peak has increased in intensity as the ramping rate decreased which remarked an improved crystallinity with longer annealing time (Figure 2). Contrastingly, the $Cu_2O$-(5 $^oC$/min)(D.A) has shown a higher peak intensity than that obtained by $Cu_2O$-(5 $^oC$/min). The peculiar results on NW dimension and crystallinity demonstrated by $Cu_2O$-(5 $^oC$/min)(D.A) sample might be clarified through the study of effect of annealing temperature on dominant peak intensity through direct annealing strategy.

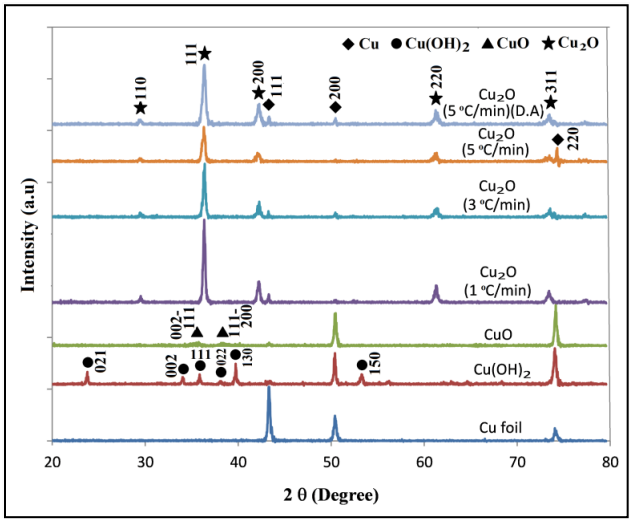



Figure 2. The overlayer of XRD pattern of samples pre and post annealing

The photoabsorption of the annealed samples were measured using diffuse reflectance spectrophotometry (Figure 3a). The higher reflectance indicates lower light absorption. Therefore, in this study, $Cu_2O$-(5 $^oC$/min) has the higher capacity in absorbing light than $Cu_2O$-(1 $^oC$/min) specifically within 300 – 500 nm light spectrum frame. This observation has the correlation with the morphology which structured at different ramping rate. As mentioned earlier, short and bulky NW arrays were made of large crystal which featured with low surface area to volume ratio. Dimensionally, it did not encourage high light absorption capacity. Long and slim NW arrays, on the other hand, were made of small crystal which structured at relatively shorter annealing time, thus enhancing light trapping efficiency. These observations are in line with the previous reported study with similar research material and strategy [8]. In order to determine the band gap of each $Cu_2O$ NW sample, Kubelka Munk-plotting function was used against band gap energy [21]. From the K-M plotting (Figure 3b), a very close band gap for all samples were extrapolated to be 2.05 ± 0.01 eV. The obtained band gap values are consistent with reported value and within the favourable band gap frame (1.8-2.1 eV) for PEC application as suggested by Murphy et al. [22].

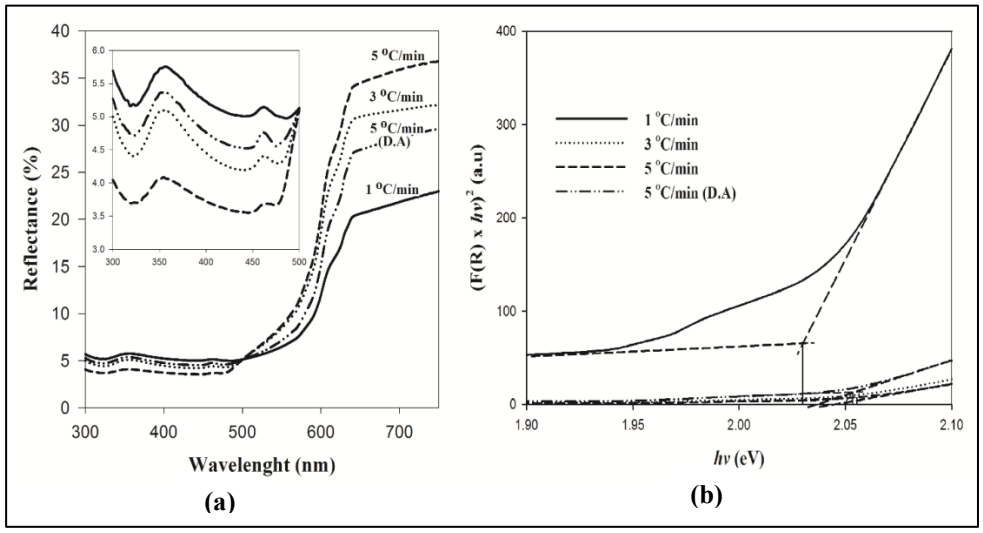



Figure 3. Diffuse reflectance spectra of a) $Cu_2O$ NW prepared at different ramping rate and annealing step; the insert shows the light reflectance value within a light spectrum frame, b) the corresponding Kubelka-Munk plot for the $Cu_2O$ NW-(1$^oC$/min), $Cu_2O$ NW-(3$^oC$/min), and $Cu_2O$ NW-(5$^oC$/min), and $Cu_2O$ NW-(5 $^oC$/min)(D.A)

**Photocurrent measurement**

The photocurrent appears to be influenced by the morphology of the NW which was affected by the ramping rate (Figure 2). A longer and thinner NW produced by a higher ramping rate (shorter time) enhanced photocurrent. Although the XRD peak intensity reduced with the higher ramping rate (shorter annealing time), this does not seem to reduce the photocurrent. Therefore, the NW morphology appears to have more effect on the photocurrent than the XRD peak intensity. This is shown by $Cu_2O$-(5 $^oC$/min) produced the highest photocurrent which benefitted from the long and slimmer NW which concomitantly provides high surface active area [23, 24], and improved radial charge diffusion for a better photocatalytic reaction [23, 25]. As the band gaps are very similar (Figure 3b), the photocurrent appears to be influenced solely by the morphology of the NW. Whereas, a lower ramping rate (longer annealing time) produced shorter and wider NW resulting in lower photocurrent. Even though the direct annealing strategy ($Cu_2O$-(5 $^oC$/min)(D.A)) has the shortest annealing time, but the photocurrent produced was significantly lower than that obtained by the sample $Cu_2O$-(5 $^oC$/min). This can also be observed from the NW morphology as well, where $Cu_2O$-(5 $^oC$/min)(D.A) has shorter and wider NW compared to$Cu_2O$-(5 $^oC$/min). Furthermore, $Cu_2O$-(5 $^oC$/min)(D.A) reflects light higher than $Cu_2O$-(5 $^oC$/min)(D.A) which explained the photocurrent reduction as shown in Figure 4. Eventhough $Cu_2O$-(5 $^oC$/min)(DA) was prepared at the shortest annealing time, however the multistep annealing used in the $Cu_2O$-(5 $^oC$/min) preparation improved the NW morphology which resulted in enhanced

photocurrent. This result suggested that multistep annealing is critical to affect complete phase transformation during the course of annealing.

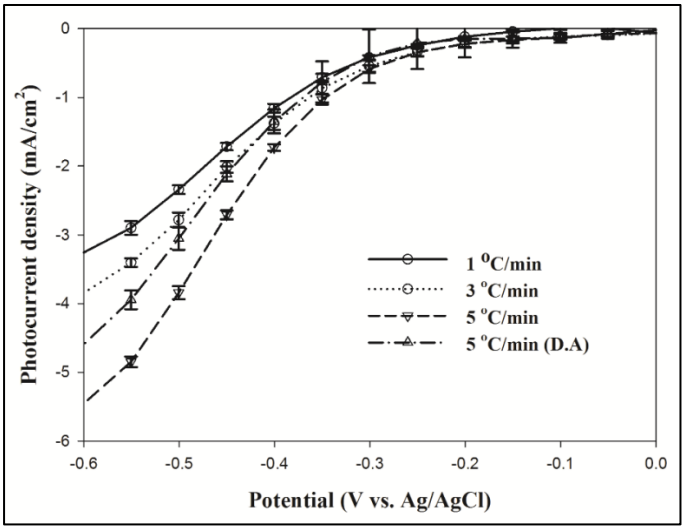



Figure 4. Photocurrent measurement generated from $Cu_2O$ annealed at different ramping rate and annealing step

## Conclusion

In this study, the photoactivity of $Cu_2O$ NW was markedly influenced by the effect of ramping rate which found to be analogous with the effect of annealing time. With longer and slimmer NW, $Cu_2O$-(5 $^o$C/min) sample exhibited the highest photoabsorption and photocatalytic activity, thus resulted with the highest photocurrent generation relative to the other $Cu_2O$ sample. This study also suggesting that a multistep annealing is necessary to prepare a good quality of $Cu_2O$ NW photocathode. Technically, this low cost and simple fabrication technique for $Cu_2O$ NW photocathode was adequate to produce a highly efficient photoelectrode for PEC system. The next step is to stabilize the $Cu_2O$ NW from photocorrosion problem which remain the biggest challenge.

## Acknowledgement

This work was financially supported by DLP-2014 008 & FRGS/1/2014/SG01/UKM/02/1.

## References

1. Hacialioglu, S., Meng, F. and Jin, S. (2012). Facile and mild solution synthesis of $Cu_2O$ nanowires and nanotubes driven by screw dislocations. *Chemical Communications,* 48(8): 1174 – 1176.
2. De Jongh, P., Vanmaekelbergh, D. and Kelly, J. (1999). $Cu_2O$: Electrodeposition and characterization. *Chemistry of Materials,* 11(12): 3512 – 3517.
3. Engel, C. J., Polson, T. A., Spado, J. R., Bell, J. M. and Fillinger, A. (2008). Photoelectrochemistry of Porous P-$Cu_2$o Films. *Journal of the Electrochemical Society,* 155(3): 37 – 42.
4. Paracchino, A., Laporte, V., Sivula, K., Grätzel, M. and Thimsen, E. (2011). Highly active oxide photocathode for photoelectrochemical water reduction. *Nature materials,* 10(6): 456 – 461.
5. Hsu, Y.-K., Yu, C.-H., Chen, Y.-C. and Lin, Y.-G. (2013). Fabrication of coral-like $Cu_2O$ nanoelectrode for solar hydrogen generation. *Journal of Power Sources,* 242: 541 – 547.
6. Hsu, Y.-K., Yu, C.-H., Chen, Y.-C. and Lin, Y.-G. (2013). Synthesis of novel $Cu_2O$ micro/nanostructural photocathode for solar water splitting. *Electrochimica Acta,* 105: 62 – 68.
7. Luo, J., Steier, L., Son, M.-K., Schreier, M., Mayer, M. T. and Grätzel, M. (2016). $Cu_2O$ nanowire photocathodes for efficient and durable solar water splitting. *Nano Letters,* 16(3): 1848 – 1857.

8. Li, C., Li, Y. and Delaunay, J.-J. (2013). A novel method to synthesize highly photoactive $Cu_2O$ microcrystalline films for use in photoelectrochemical cells. *ACS Applied Materials & Interfaces,* 6(1): 480 – 486.
9. Zhang, Z., Dua, R., Zhang, L., Zhu, H., Zhang, H. and Wang, P. (2013). Carbon-layer-protected cuprous oxide nanowire arrays for efficient water reduction. *ACS Nano,* 7(2): 1709 – 1717.
10. Li, Y., Zhang, X., Chen, H. and Li, Y. (2015). Thermal conversion synthesis of $Cu_2O$ photocathode and the promoting effects of carbon coating. *Catalysis Communications,* 66: 1 – 5.
11. Dubale, A. A., Su, W.-N., Tamirat, A. G., Pan, C.-J., Aragaw, B. A., Chen, H.-M., Chen, C.-H. and Hwang, B.-J. (2014). The synergetic effect of graphene on $Cu_2O$ nanowire arrays as a highly efficient hydrogen evolution photocathode in water splitting. *Journal of Materials Chemistry A,* 2(43): 18383 –18397.
12. Tilley, S. D., Schreier, M., Azevedo, J., Stefik, M. and Graetzel, M. (2014). Ruthenium oxide hydrogen evolution catalysis on composite cuprous oxide water-splitting photocathodes. *Advanced Functional Materials,* 24(3): 303 – 311.
13. Paracchino, A., Mathews, N., Hisatomi, T., Stefik, M., Tilley, S. D. and Grätzel, M. (2012). Ultrathin films on copper(I) oxide water splitting photocathodes: A study on performance and stability. *Energy & Environmental Science,* 5(9): 8673 – 8681.
14. Morales-Guio, C. G., Tilley, S. D., Vrubel, H., Grätzel, M. and Hu, X. (2014). Hydrogen evolution from a copper (i) oxide photocathode coated with an amorphous molybdenum sulphide catalyst. *Nature Communications,* 5: 1 – 7.
15. Li, C., Hisatomi, T., Watanabe, O., Nakabayashi, M., Shibata, N., Domen, K. and Delaunay, J.-J. (2015). Positive onset potential and stability of $Cu_2O$-based photocathodes in water splitting by atomic layer deposition of a $Ga_2O_3$ buffer layer. *Energy & Environmental Science,* 8(5): 1493 – 1500.
16. Lin, C.-Y., Lai, Y.-H., Mersch, D. and Reisner, E. (2012). $Cu_2O|NiO_X$ nanocomposite as an inexpensive photocathode in photoelectrochemical water splitting. *Chemical Science,* 3(12): 3482 –3487.
17. Zhang, W., Wen, X., Yang, S., Berta, Y. and Wang, Z. L. (2003). Single-crystalline scroll-type nanotube arrays of copper hydroxide synthesized at room temperature. *Advanced Materials,* 15(10): 822 – 825.
18. Lu, C., Qi, L., Yang, J., Zhang, D., Wu, N. and Ma, J. (2004). Simple template-free solution route for the controlled synthesis of $Cu(OH)_2$ and CuO nanostructures. *The Journal of Physical Chemistry B,* 108(46): 17825 – 17831.
19. Kargar, A., Partokia, S. S., Niu, M. T., Allameh, P., Yang, M., May, S., Cheung, J. S., Sun, K., Xu, K. and Wang, D. (2014). Solution-grown 3D $Cu_2O$ networks for efficient solar water splitting. *Nanotechnology,* 25(20): 1 – 9.
20. Kim, T. G., Oh, H.-B., Ryu, H. and Lee, W.-J., (2014). The study of post annealing effect on $Cu_2O$ thin-films by electrochemical deposition for photoelectrochemical applications. *Journal of Alloys and Compounds,* 612: 74 – 79.
21. Wilkinson, F. (1986). Diffuse reflectance flash photolysis. *Journal of the Chemical Society, Faraday Transactions 2: Molecular and Chemical Physics,* 82(12): 2073 – 2081.
22. Murphy, A., Barnes, P., Randeniya, L., Plumb, I., Grey, I., Horne, M. and Glasscock, J. (2006). Efficiency of solar water splitting using semiconductor electrodes. *International Journal of Hydrogen Energy,* 31(14): 1999 – 2017.
23. Dai, P., Xie, J., Mayer, M. T., Yang, X., Zhan, J. and Wang, D. (2013). Solar hydrogen generation by silicon nanowires modified with platinum nanoparticle catalysts by atomic layer deposition. *Angewandte Chemie International Edition,* 52(42): 11119 – 11123.
24. Walter, M. G., Warren, E. L., McKone, J. R., Boettcher, S. W., Mi, Q., Santori, E. A. and Lewis, N. S. (2010). Solar water splitting cells. *Chemical Reviews,* 110(11): 6446 – 6473.
25. Dai, P., Li, W., Xie, J., He, Y., Thorne, J., McMahon, G., Zhan, J. and Wang, D. (2014). Forming buried junctions to enhance the photovoltage generated by cuprous oxide in aqueous solutions. *Angewandte Chemie International Edition,* 53(49): 13493 – 13497.

*Malaysian Journal of Analytical Sciences, Vol 21 No 4 (2017): 921 - 927*
*DOI: https://doi.org/10.17576/mjas-2017-2104-19*

MALAYSIAN JOURNAL OF ANALYTICAL SCIENCES
*Published by The Malaysian Analytical Sciences Society*
ISSN 1394 - 2506

# CARBON DIOXIDE SORPTION BY TETRADECYLAMINE SUPPORTED ON SILICA GEL

## (Serapan Karbon Dioksida Oleh Tetradesilamina Disokong Pada Silika Gel)

Maratun Najiha Abu Tahari[1]*, Azizul Hakim[1], Tengku Sharifah Marliza[2], Mohd. Ambar Yarmo[1]

[1]*School of Chemical Science and Food Technology, Faculty of Science and Technology, Universiti Kebangsaan Malaysia, 43600 UKM Bangi, Selangor, Malaysia*
[2]*Catalysis Science and Technology Research Centre, Faculty of Science, Universiti Putra Malaysia, 43400 UPM Serdang, Selangor, Malaysia*

**Corresponding author: maratunnajiha@gmail.com*

Received: 28 November 2016; Accepted: 27 April 2017

**Abstract**

Carbon dioxide emissions generated from fossil fuel-based power plants and other industries has reached 400 ppm in atmosphere. This negatively impact the environment, infrastructures and wildlife in particular. A lot of efforts are needed to produce $CO_2$ gas sorbent in order to reduce high $CO_2$ concentration. Therefore, porous silica gel (SG) is modified with amine compound for carbon dioxide capture. Calcinated silica gel functionalized with tetradecylamine (TDA) using wet impregnation has been developed as a porous media. The prepared sorbents is characterized by $N_2$ physisorption technique Brunauer-Emmet-Teller analysis (BET). Significant changes in physical properties of the sorbents further ascertained the dispersion of TDA on the internal channels and external surface of the SG. Reactivity of porous sorbent towards $CO_2$ was evaluated using isothermal $CO_2$ adsorption desorption technique. This study shows 65TDA/SG enable to adsorb $CO_2$ in the highest capacity which is 23.22 $cm^3$ $CO_2$ per gram sorbent. Moreover, $CO_2$ capture consists of two type sorption which are physisorption and chemisorption. 55TDA/SG is the best sorbent in capturing $CO_2$ by chemisorption (19.62 $cm^3$ $CO_2$ per gram adsorbent).

**Keywords:** **t**etradecylamine, modified silica gel, carbon dioxide, chemisorption, physisorption

**Abstrak**

Pembebasan karbon dioksida terhasil daripada plan penghasilan tenaga berasaskan bahan api fosil dan pelbagai industri telah mencecah kepekatan 400 ppm di atmosfera. Perkara ini memberi kesan negatif kepada alam sekitar, infrastruktur dan kehidupan liar khasnya. Pelbagai usaha diperlukan untuk menghasilkan penjerap gas $CO_2$ dalam usaha untuk merendahkan kepekatan $CO_2$ yang semakin meningkat ini. Oleh itu, silika gel berliang (SG) telah di ubahsuai dengan sebatian amina untuk pemerangkapan karbon dioksida. Silika gel yang telah dikalsin akan difungsikan dengan teteradesilamina (TDA) menggunakan kaedah impregnasi basah telah dibangunkan sebagai media berliang. Penjerap yang dihasilkan akan dicirikan dengan teknik jerapan fizikal $N_2$ iaitu analisis Brunauer-Emmet-Teller (BET). Perubahan ciri fizikal yang ketara pada penjerap mengukuhkan lagi sebaran TDA pada permukaan dalam liang dan juga permukaan luaran SG. Kereaktifan penjerap berliang terhadap $CO_2$ telah dinilai menggunakan teknik penjerapan dan penyahjerapan isoterma $CO_2$. Hasil kajian ini menunjukkan bahawa 65TDA/SG mampu menjerap $CO_2$ dalam kapasiti yang tertinggi sebanyak 23.22 $cm^3$ $CO_2$ per gram penjerap. Tambahan, pemerangkapan $CO_2$ terdiri daripada dua jenis serapan iaitu serapan fizikal dan jerapan kimia. Penjerap 55TDA/SG adalah penjerap terbaik dalam pemerangkapan $CO_2$ secara jerapan kimia (19.62 $cm^3$ $CO_2$ per gram penjerap).

**Kata kunci:** tetradesilamina, SG di ubahsuai, karbon dioksida, jerapan kimia, serapan fizikal

## Introduction

In the era of globalization, carbon dioxide ($CO_2$) is well known as a main greenhouse gas. This gas is released into the atmosphere from human activities, industrial development including fossil fuel burning, chemical and petrochemical manufacturing [1]. Indoor air pollutants (IAPs) included that $CO_2$ is the representative pollutant of indoor air quality and its concentration is associated with the human activities while the outdoor concentrations of $CO_2$ range from 350 – 450 ppm. Therefore, studies have been done to collect $CO_2$ gas to be used as fuel feedstock and other chemicals. The great effort in reducing concentration of $CO_2$ in atmosphere is more important rather than lowering concentration of $CO_2$ gas emission [2]. The accumulated $CO_2$ traps the earth's heat, thus creating global warming which has already altered weather patterns and further increasing sea levels due to the melting of the polar iceberg. There were several works reported in reducing $CO_2$ concentration by capture and separate the $CO_2$ gas. There are different unit operations such as liquid absorption phenomena [3], solid adsorption [4-6], cryogenic techniques and selective diffusion through polymer, metallic or ceramic membranes [7].

Therefore, research in developing $CO_2$ sorbents must be taken in order to reduce the concentration of $CO_2$ in the atmosphere. Amines are the most widely used organic chemicals for $CO_2$ capture due to their basicity. This allows them to react with acidic $CO_2$ to form a carbamate compounds. This reaction known as chemisorption. Previous study, straight chain alkylamine with C18 known as octadecylamine was developed as $CO_2$ sorbent. Octadecylammonium octadecylcarbamate ion pairs (alkylammonium alkylcarbamate) was formed on contact with dry $CO_2$ [8]. Belmabkhout et al. [9] reported, under dry conditions, carbamate with $CO_2$/N stoichiometry ratio of 0.5 is formed. This means two amine groups are needed in interact with one $CO_2$ molecule on the adsorbent surfaces as reported by Gray et al. [10] (refer Equation 1).

$$\underset{\text{alkylamine}}{2\,RNH_2} + \underset{\text{carbon dioxide}}{CO_2} \longrightarrow \underset{\text{alkylacarbamate}}{RNHCO_2^-} + \underset{\text{alkylammonium}}{RNH_3^+} \quad (1)$$

Nowadays, porous materials are widely used as supporter such as silica dioxide, silica gel, activated carbon and many more [1, 2, 4, 6]. Supporter is important to improve stability of the amine compound. Besides, porous materials have an ability to interact with $CO_2$ gas through physical interaction (physisorption). In this study, physical and chemical modifications at the external surface or internal channels of the supporter (silica gel, SG) using organic functional groups (tetradecylamine, TDA, $C_{14}H_{31}N$) have drawn much attention. The synthesized sorbents were characterized by Brunauer-Emmet-Teller analysis (BET).

## Materials and Methods

Modification of silica gel (SG) by tetradecylamine (TDA) represented as TDA/SG was done through wet impregnation method with few modifications [11]. Silica gel powder (Fluka) was calcined at 600 °C for 3 hours before impregnation process with various percentage of TDA (ALDRICH®, 97%) and chloroform, $CHCl_3$ (SYSTERM®, 99 – 99.4%) as a solvent. After stirring for 4 hours in a closed system, the mixture was rested for 1 hour before sonication (S 4000-010 Sonicator 4000) and afterward evaporated in air for one night. The process followed by drying at 45 °C for 4 hours in a vacuum oven. Lastly, the adsorbents were physically characterized by $N_2$ adsorption desorption isothermal and reactivity towards $CO_2$ measured by $CO_2$ adsorption desorption isothermal at 30 °C using BET technique (Micrometiric ASAP 2020).

## Results and Discussion

The sorption capacity of $CO_2$ on prepared sorbents were measured by $CO_2$ isothermal adsorption desorption using BET technique at 30 °C. Referring to Figure 1 and 2, unmodified SG was able to captured 9.39 $cm^3$ $CO_2$ / g sorbent. This capacity is higher than another two modified SG, 5 and 15TDA/SG. Addition of 5-15 % TDA will prevent direct interaction of $CO_2$ towards SG due to formation of mono or multilayers TDA on SG surfaces. This happened during wet impregnation process in which mixture of TDA and chloroform were able to wet entire surface of SG including external and internal surfaces (small pores of SG). After drying process, chloroform was evaporated and TDA layers formed on the SG surfaces. It was clearly shown that pure SG is enable to adsorb $CO_2$. According to addition of 15 to 65 % TDA, the amount of $CO_2$ uptake increased proportional to the TDA percent loaded. The capacity of $CO_2$ gradually increased from 13.21 up to 23.22 $cm^3$ $CO_2$ / g sorbent. However, $CO_2$ uptake by the SG modified with 75 % TDA was reduced drastically and lower than 45TDA/SG sorbent.

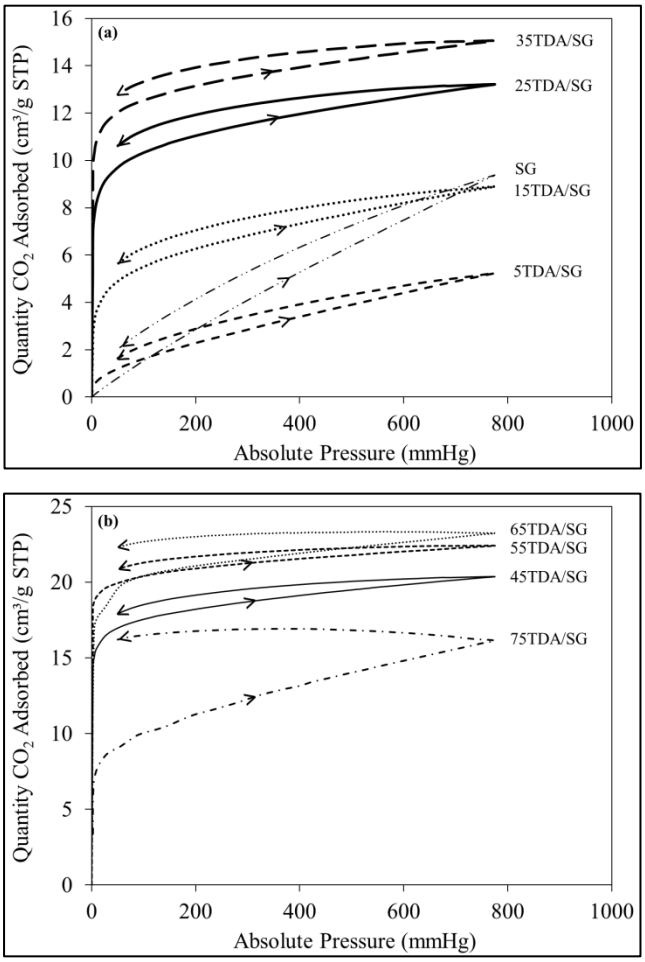



Figure 1. $CO_2$ adsorption-desorption isotherms of SG and modified SG with (a) SG, 5TDA/SG, 15TDA/SG, 25TDA/SG and 35TDA/SG and (b) 45TDA/SG, 55TDA/SG, 65TDA/SG and 75TDA/SG

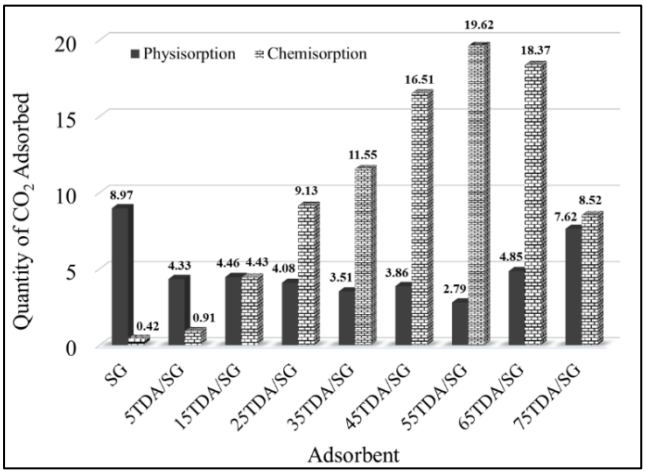



Figure 2. Quantity of $CO_2$ adsorbed physically and chemically measured by $CO_2$ adsorption desorption isothermal using BET technique

At a very low pressure, $CO_2$ sorption curve is very sharp and increased drastically around 0 – 20 mmHg. Formation of linear curve can be seen at higher pressure (more than 20 mmHg). This pattern is just applicable for modified SG whereas $CO_2$ sorption curve for unmodified SG sorbent was increased gradually without linear curve at the higher pressure. Shaw et al. [12] reported a very sharp sorption curve at the initial pressure showed that sorption of $N_2$ gas occurred in the small pores which known as micropores. Referring to Table 1, measured surface value t-$plot_{mic}$ for SG is 12.89 $m^2/g$ and this proved SG contained small pores in micro size known as micropores. In this research which involved $CO_2$ gas, the very sharp curve proved that the $CO_2$ gas were able to enter the micropores of SG. It happened due to strong interaction between internal SG channels (micropores surfaces) towards $CO_2$ gas. This interaction known as physical interaction or so called physisorption. However, drastically increased $CO_2$ uptake at the initial sorption also clarified chemical reaction that formed between $CO_2$ and TDA molecules. This chemical reaction also known as chemisorption and can produce another compounds such as alkylcarbamate and alkylammonium. Bacsik et al. [13] suggested highest amount of $CO_2$ uptake happened at highest pressure and lower temperature by modified silica with (3-aminopropyl) methyldiethoxysilane (APMDES) was referred to chemical adsorption of $CO_2$.

There are two lines on the sorption curve which refers to adsorption (->-) and desorption (-<-) line. Adsorption line starts from 0-760 mmHg whereas desorption line is vice versa (760 – 0 mmHg). Referring to the curve, we found desorption line is not converge with the adsorption line at lower pressure. This explained by changing pressure of the system was unable to fully desorp the captured $CO_2$ gas. Usually, this refers to $CO_2$ gas that entered micropores and chemically bonded with the TDA molecules. Energy (usually heat energy) is needed to break these chemical bonds. Therefore, captured $CO_2$ gas can be desorbed and sorbent can be used again in capturing $CO_2$.

Table 1. Effect of percent TDA loading towards SG surface properties

| **Adsorbent** | **$S_{BET}$ ($m^2/g$)** | **t-$plot_{mic}$ ($m^2/g$)** | **$V_t$ ($cm^3/g$)** | **$W_D$ (Å)** |
|---|---|---|---|---|
| SG | 246.17 | 12.89 | 1.2 | 174.9 |
| 5 TDA/SG | 194.7 | n.d | 0.9 | 121.8 |
| 15TDA/SG | 159.6 | n.d | 0.7 | 111.2 |
| 25TDA/SG | 128.8 | n.d | 0.5 | 91.5 |
| 35TDA/SG | 113.2 | n.d | 0.4 | 87.9 |
| 45TDA/SG | 81.4 | n.d | 0.2 | 81.0 |
| 55TDA/SG | 61.3 | n.d | 0.2 | 73.0 |
| 65TDA/SG | 48.8 | n.d | 0.1 | 71.0 |
| 75TDA/SG | 29.2 | n.d | 0.1 | 67.5 |

n.d = note detected

Figure 2 shows quantity of $CO_2$ adsorbed that measured by adsorption desorption of $CO_2$ using BET technique. As discussed earlier, $CO_2$ sorption at initial pressure (0 – 20 mmHg) was corresponded to chemisorption and physisorption in the micropores. Therefore, by subtracting capacity of $CO_2$ at the highest pressure (760 mmHg) to the value at lower pressure, the amount of $CO_2$ captured by physical interaction can be measured. $CO_2$ uptake by physisorption on SG was the highest compared to other sorbents with value 8.97 $cm^3$ $CO_2$/g sorbent. This value explained that SG is a porous material which able to attract and capture $CO_2$ gas in the SG pores through physical interaction. The absence of sharp sorption curve at the initial pressure proven physisorption was primarily occurred compared to chemisorption (0.42 $cm^3$ $CO_2$/g sorbent).

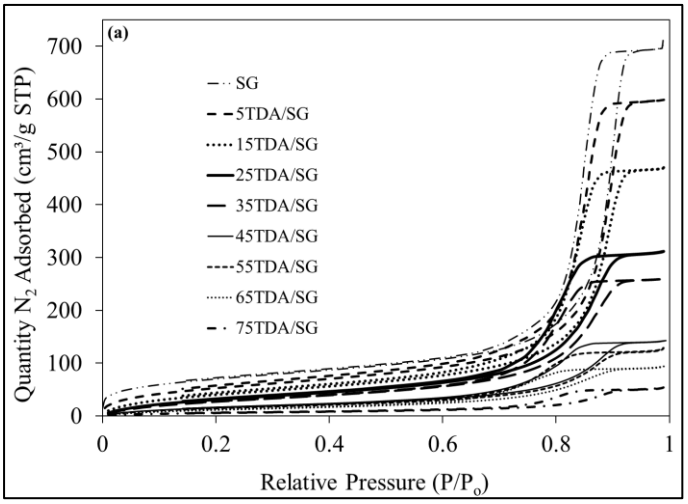
Addition of TDA from 5 to 55 % exhibited an increasing capacity of chemisorption from 0.91 to 19.62 $cm^3$ $CO_2$/g sorbent. Meanwhile, capacity of physisorption was reduced gradually with increasing percent of TDA. This clarified as amine was loaded onto SG, the pores of SG are filled with amine layers hence increasing the steric hindrance for

physisorption of $CO_2$ to occur and more $CO_2$ affinity sites were exposed for chemisorption to take place [14]. Thus, it is suggested that the higher sorption of $CO_2$ on modified SG also due to more chemisorption process occurred in the internal channels and external surfaces ($CO_2$–TDA chemical interaction/reaction).

However, capacity of $CO_2$ sorption by SG loaded with 5 and 15% TDA are not improve significantly compared to ability of pure SG since the presence of TDA layers on the internal SG pores have reduced the $CO_2$–SG physisorption and yet improved chemisorption. Conversely, $CO_2$ uptake by chemisorption on higher percent TDA loading (65 and 75TDA/SG) was declined to 8.52 $cm^3$ $CO_2$/g sorbent whereas capacity of physisorption was take place by increased up to 7.62 $cm^3$ $CO_2$/g sorbent. Hence, addition of high amount of amine (more than 55% TDA) is not require due to formation of amine double or multilayer on the SG surfaces which reducing amount of active sites and further dropping the ability of formation alkylammonium alkylcarbamate compounds [15].

Amine modified SG was further examined using physisorption analysis (Micrometiric ASAP 2020). BET surface area, micropore surface area (t-$plot_{mic}$), pore volume and pore width values was summarized in Table 1. Figure 3(a) shows $N_2$ adsorption and desorption isotherms of all adsorbents. According to IUPAC (1972), the hysteresis curve of all adsorbents is type A where the mesopores are cylindrical in shape [16]. At the earlier stage of the sorption, which is involving low pressure, the adsorption of a single/mono layer of $N_2$ happened inside pores and followed by adsorption of multiple layers at higher relative pressures. Based on the isotherms, as the TDA loading percentage increases, the quantity of $N_2$ sorbed will decreases. This is due to physical changes that occurred on the SG surface after the impregnation of TDA. According to rapid pore filling theory, the long chain molecules (TDA) can rapidly fill into the mesopores. Consequently, it creates pore blockage and resulted in the lowering of the quantity of $N_2$ adsorbed which is directly refers to the decreasing in BET surface area.

Referring to Figure 3(b), average pore diameter appeared as a peak for each sorbent. The highest peak was the SG without any loading while the lowest peak was the 75TDA/SG. The average pore width of SG is 174.9 Å, which refers to the aperture or diameter of the mesopores. When the SG was modified with 35% TDA, the average pore width shifted to a lower value (100.42 Å) since the formation of TDA layer on the inner wall of the mesopores. This result suggests that more molecules are able to get into the pores during modification even though TDA is a straight and long chain molecules. Moreover, the addition of 75% TDA shows drastically decreased in pore volume which is from 1.2 to 0.1 $cm^3$/g (Figure 3(c)). This explains the rapid entrance of amine molecules into the pores making the empty spaces to be filled with that amine molecules [17, 18]. Therefore, the decreasing values of average pore width are proportional with the total volume of the pores.



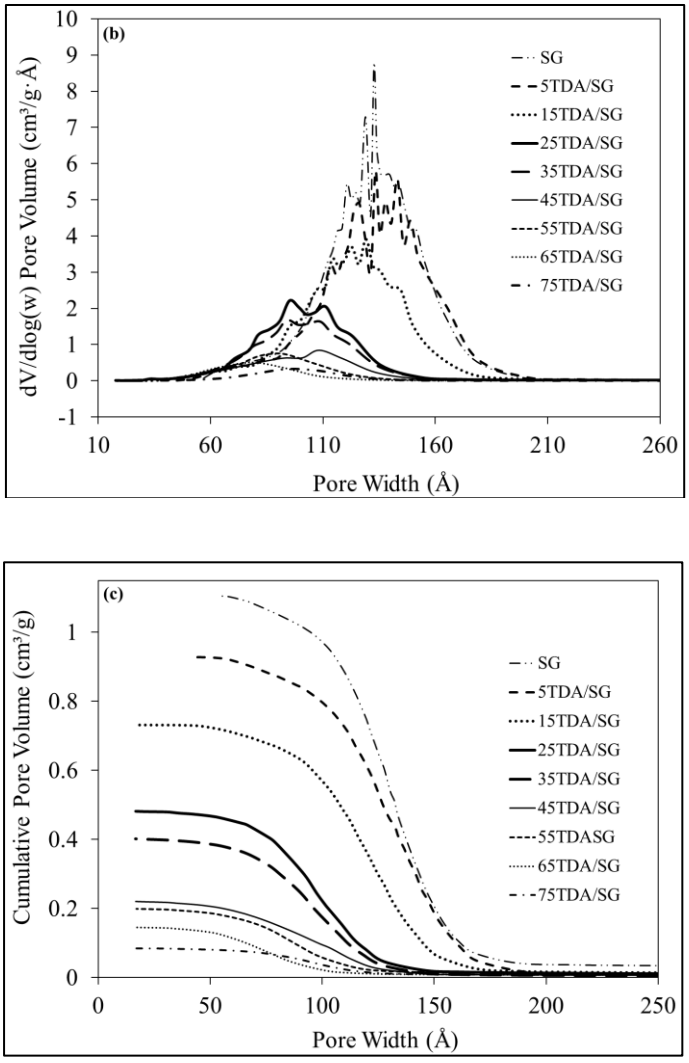



Figure 3. Surface properties of SG and modified SG (5TDA/SG, 15TDA/SG, 25TDA/SG, 35TDA/SG, 45TDA/SG, 55TDA/SG, 65TDA/SG and 75TDA/SG by BET technique with (a) $N_2$ adsorption desorption isotherms, (b) Pore size distributions and (c) Cumulative pore volume of sorbents.

## Conclusion

$CO_2$ gas can be captured by prepared sorbent which is SG modified with different percentage of TDA. $CO_2$ isothermal adsorption desorption analysis shows that capturing $CO_2$ gas involved two types of sorption (physisorption and chemisorption). SG is a porous material acts as supporter and able to physically capture $CO_2$ gas whereas modified SG are mainly undergo chemically capture $CO_2$ gas. Moreover, 55TDA/SG was the optimum sorbent due to its ability in capturing highest amount of $CO_2$ through chemisorption. It is very important in order to increase retention time of $CO_2$ on the sorbent before it finally being desorb at different time and place (good for transport purposes). Various amount of TDA loading resulted in great changes in physical properties of the adsorbents in term of BET surface area, average pore diameter and total pore volume of adsorbents. Therefore, all significant changes happened actually ascertained the existence of TDA on the SG surfaces by wet impregnation method.

**Acknowledgment**

Authors would like to thanks Ministry of Higher Education and Universiti Kebangsaan Malaysia for funding this project under research grant number BKBP-FST-K003323-2014, STGL-008-2012, ETP-2013-066, TD-2014-024 and Centre of Research and Innovation Management (CRIM) for the instruments facilities.

**References**

1. Pevida, C., Plaza, M. G., Arias, B., Fermoso, J., Rubiera, F. and Pis, J. J. (2007). $CO_2$ capture by adsorption with nitrogen enriched carbons. *Fuel*, 86: 2204 – 2212.
2. Lee, S. C., Hsieh, C. C., Chen, C. H. and Chen, Y. S. (2013). $CO_2$ adsorption by y-type zeolite impregnated with amines in indoor air. *Aerosol Air Quality Research,* 13: 360 – 366.
3. Samanta, A. and Bandyopadhyay, S. S. (2009). Absorption of carbon dioxide into aqueous solution of piperazine activated 2-amino-2-methyl-1-propanol. *Chemical Engineering Science,* 64: 1185 – 1194.
4. Anson, A., Lina, C. C. H., Kuznickia, S. M. and Sawadab, J. A. (2009). Adsorption of carbon dioxide, ethane and methane on titanosilicate type molecular sieves. *Chemical Engineering Sc*ience, 64: 3683 –3687.
5. An, H., Feng, B. and Su, S. (2011). $CO_2$ capturer by electrothermal swing adsorption with activated carbon fibre materials. *International Journal of Greenhouse Gas Control,* 5: 16 – 25.
6. Zhao, G. Y., Aziz, B. and Hedin, N. (2010). Carbon dioxide adsorption on mesoporous silica surfaces containing amine-like motifs. *Applied Energy,* 87: 2907 – 2913.
7. Brunetti, A., Scura, F., Barbier, G. and Drioli, E. (2010). Membrane technology for $CO_2$ separation. *Journal of Membrane Scienc*e, 359: 115 – 125.
8. Tahari, M. N. A. and Yarmo, M. A. (2014). Adsorption of $CO_2$ on silica dioxide catalyst imoregnated with various alkylamine. *AIP Conference Proceeding*, 1614: 334 – 341.
9. Belmabkhout, Y., Serna-Guerrero, R. and Sayari, A. (2010). Amine-bearing mesoporous silica for $CO_2$ removal from dry and humid air. *Chemical Engineering Science*, 65: 3695 – 3698.
10. Gray, M., Soong, Y., Champagne, K. J., Pennline, H., Baltrus, J. P., Stevens Jr., R. W., Khatri, R., Chuang, S. S. C. and Fiburn, T. (2005). Improved immobilized carbon dioxide capture sorbents. *Fuel Processing Technology*, 36: 1449 – 1455.
11. Knowles, G. P., Graham, J. V., Delaney S. W. and Chaffe, A. L. (2005). Aminopropyl-functionalized mesoporous silica as $CO_2$ adsorbents. *Fuel Processing Technology*, 86: 1435 – 1448.
12. Shaw, D. J. (1980). Introductio to Colloid and Surface Chemistry. 3rd Edition. Liverpool: Butterworth & Co Ltd.
13. Bacsik, Z., Ahlsten, N., Ziadi, A., Zhao, G., Garcia-Bennett, A. E., Martin-Matute, B. and Hedin, N. (2001). Mechanisme and kinetics for sorption of $CO_2$ on bicontinuous mesoporous silica modified with n-Propylamine. *Langmuir* 27: 11118 - 11128.
14. Tahari, M. N. A., Hakim, A., Wahab, M. and Yarmo, M. A. (2016). Modification of porous materials by saturated fattry amine as $CO_2$ capturer. *International Journal of Chemical Engineering and Applications,* 6: 2 – 7.
15. Chernyshova, I. V. (2011). Near infrared spectroscopic characterization of surface hydroxyl groups on hydrothermally treated silica gel. *International Journal of Chemical and Environment Engineering*, 2 (1): 27 – 32.
16. Belman, N., Israelachvili, J. N., Li, Y., Safinya, C. R., Bernstein, J. and Golan, Y. (2009). The temperature-dependent structure of alkylamines and their corresponding alkylammonium-alkylcarbamates. *Journal of the American Chemical Society*, 131(25): 9107 – 9113.
17. International Union of Pure and Applied Chemistry (1972). Manual of symbols and terminology, colloid and surface chemistry. *Pure Applied Chemistry*, 31: 578.
18. Kamarudin, K. S. N. and Alias, N. (2013). Adsorption performance of MCM-41 impregnated with amine for $CO_2$ removal. *Fuel Processing Technology*, 106(41): 332 – 337.

*Malaysian Journal of Analytical Sciences, Vol 21 No 4 (2017): 928 - 940*
*DOI: https://doi.org/10.17576/mjas-2017-2104-20*

MALAYSIAN JOURNAL OF ANALYTICAL SCIENCES
*Published by The Malaysian Analytical Sciences Society*
ISSN 1394 - 2506

# PERFORMANCE ENHANCEMENT OF DYE SENSITIZED SOLAR CELL USING GRAPHENE OXIDE DOPED TITANIUM DIOXIDE PHOTOELECTRODE

## (Peningkatan Prestasi Bagi Sel Suria Pemeka Warna Menggunakan Grafin Oksida di dalam Titanium Dioksida Sebagai Fotoelektrod)

Ahmad Muslihin Ramli, Mohd Zikri Razali, Norasikin Ahmad Ludin*

*Solar Energy Research Institute,*
*Universiti Kebangsaan Malaysia, 43600 UKM Bangi, Selangor, Malaysia*

**Corresponding author: sheekeen@ukm.edu.my*

Received: 28 November 2016; Accepted: 27 April 2017

**Abstract**

Dye-sensitized solar cell (DSSCs) is one of the photovoltaic cells that have attracted extensive research over decade. In this study, different weight percentage (wt.%) of graphene oxide (GO) was used with titanium dioxide ($TiO_2$) as photoelectrode in DSSCs. GO was synthesized by simplified Hummer's method at ambient temperature. The amount of GO in composite film are designed from 0.0 wt.%, 0.4 wt.%, 0.6 wt. % and 0.8 wt.%. The prepared samples were characterized by Field Emission Scanning Electron Microscopy (FESEM), X-ray Diffraction (XRD), Atomic Force Microscopy (AFM) and Incident Photon to Current Efficiency (IPCE). The photocurrent-voltage characteristics of the fabricated dye sensitized solar cells were examined using a solar simulator under 100 mW/cm$^2$ AM 1.5 xenon illumination. The results indicated that optimum the power conversion efficiency (PCE) was obtained for the device doped with 0.6 wt.% GO with the short circuit current density ($J_{sc}$), open circuit voltage ($V_{oc}$) and PCE of 9.8 mA/cm$^2$, 0.7 V and 3.7 %, respectively. It was observed that the introduction of 0.6 wt.% GO into $TiO_2$ photoelectrode has successfully increased the performance of DSSCs as much as 28% compared to the sample without GO. This is due to the increment in dye absorption and enhanced electron transportation as proven by IPCE analysis.

**Keywords**: dye sensitized solar cells, graphene oxide, photoelectrode, power conversion efficiency, titanium dioxide

**Abstrak**

Sel suria pemeka warna (DSSCs) adalah salah satu sel fotovolta yang telah menarik minat penyelidik sejak kebelakangan ini. Dalam kajian ini, peratusan berat grafin oksida (GO) yang berbeza telah digunakan bersama titanium dioksida ($TiO_2$) sebagai fotoelektrod di dalam DSSCs. GO telah disintesis dengan kaedah Hummer dipermudah pada suhu persekitaran. Jumlah GO dalam filem komposit telah ditetapkan dari 0.0 wt.%, 0.4 wt.%. 0.6 wt.% dan 0.8 wt.%. Sampel-sampel yang disediakan telah dicirikan dengan menggunakan analilsis Mikroskopi Imbasan Pancaran Medan Elektron (FESEM), Analisis Pembelauan sinar-X (XRD), Analisis Mikroskopi Daya Atom (AFM) dan analisis kejadian foton kepada keberkesanan pembawa arus (IPCE). Ciri – ciri fotoarus-voltan bagi sel suria pemeka warna telah diperiksa menggunakan simulator suria dengan intensiti dikawal pada 100 mW/cm$^2$ AM 1.5 pengcahayaan. Keputusan menunjukkan bahawa kecekapan penukaran kuasa (PCE) yang optimum telah dicatatkan oleh peranti DSSC yang ditambah 0.6 wt.% GO, dengan ketumpatan arus litar-pintas ($J_{sc}$), voltan litar-terbuka ($V_{oc}$) dan PCE masing-masing adalah 9.8 mA/cm$^2$, 0.7 V dan 3.7 %. Ini jelas menunjukkan bahawa penambahan 0.6 wt.% GO ke dalam $TiO_2$ fotoelektrod telah meningkatkan kecekapan prestasi bagi DSSCs sebanyak 28% berbanding dengan sampel tanpa GO. Peningkatan ini disebabkan oleh peningkatan penyerapan pewarna dan pengangkutan elektron seperti yang dibuktikan dalam analisis IPCE.

**Kata kunci**: sel suria pemeka warna, grafin oksida, fotoelektrod, kecekapan penukaran kuasa, titanium dioxide

## Introduction

Dye sensitized solar cells (DSSCs), the third generation of photovoltaic are currently proposed as the alternative to the conventional silicon solar cells. This is due to its low production cost, simple manufacturing procedures and practically under ambient condition with acceptable power conversion efficiency [1-3]. Generally, a monolayer of organic dye is attached to mesoporous metal oxide semiconductor with wide band-gap. The incident light is absorbed by the dyes and electrons are excited, and then injected into the conduction band of the metal oxide semiconductor. The electrons are then transported across the $TiO_2$ nanoparticles layer to the anode (current collector) and later, pass through the external circuit. The sensitizer is regenerated by the organic hole conductor which transport the positive charges to the counter electrode [4]. As a wide band gap semiconductor material, $TiO_2$ is commonly used as photoelectrode in DSSCs due to its abundances, low cost, good chemical stability, non-toxicity, and etc. [5]. It functions as a dye loader, electron acceptor and electron transporter in DSSCs. However, the particles sizes of $TiO_2$ in photoelectrode films are too small to support any space charge and form inner electric field, causing transportation of electrons in the $TiO_2$ porous film is a random process of electron diffusion and hopping [6]. These electron transportations modes encourage to electron recombination with oxidized states of dye or oxidized particles in electrolyte. The transportation of electrons was disturbed and thus decreased the photoelectric conversion efficiency (PCE) of DSSCs [7]. Currently, numerous ways are being explored by researchers to enhance the electron transportation in photoelectrodes and reduce the charge recombination in order to increase the performances of DSSCs. According to Yen et al. [8], both of the $V_{oc}$ and $J_{sc}$ can be enhanced by incorporating carbon nanotubes (CNTs) into $TiO_2$ to form compound photoelectrode. However, this enhancement is limited by poor contact between $TiO_2$ with CNT. In order to optimize the structure of photoelectrode in DSSCs, three different layers of TiO2 were designed by Hu et al. [9]. These layers including small pore size films, larger pore size films, and light-scattering particles. Their results show that DSSCs with optimized microstructures had better lightscattering effects and gaining a higher PCE compared to conventional DSSCs. Recently, a study was reported by Bai et al. [10] to enhance the electron transfer by introducing a new type of photoelectrode architecture. The photoelectrode was prepared by in situ direct growth of ZnO nanowires within a $TiO_2$ nanoparticle film through a hydrothermal process. The results show that by embedding an optimal amount of ZnO in $TiO_2$, it can enhance the PCE remarkably from 6.65% to 8.44%. Mane et al. [11] was reported the recombination between electron and oxidized dye as well as $I^{3-}$ in the electrolyte was reduced by introducing a core−shell structure by using the layer-by layer deposition to coat a 30 nm ZnO layer on $TiO_2$ film. The ZnO layer acts as an energy barrier to block electron transportation out of $TiO_2$, then reducing the recombination and increased the PCE from 3.31% to 4.51%.

Recently, the extensive investigation has been carried out on the graphene-based composite nanomaterials because of the synergistic effects of the different functional components in the composites. With excellent electron mobility and large specific area, graphene can be incorporated into $TiO_2$- based DSSCs photoelectrode as electron transport enhancer and support material for PCE improvement [12-14]. Numerous synthetic methods to produce graphene/$TiO_2$ composites as photoelectrode materials have been developed [15], and the positive effects of the incorporated graphene have been revealed and summarized in the following two main aspects: (1) increased dye adsorption and (2) significant longer exciton lifetime. The incorporation of graphene gives rise to the porosity of the anode films, which increases the surface area for more dye adsorption sites, therefore enhancing the dye loading and the light harvesting efficiency. Furthermore, graphene dispersed in $TiO_2$ matrix forms a continuous 2D conduction network. The photogenerated electrons in the network can be effectively transported across the $TiO_2$ matrix, which reduce the charge recombination, and extending the electron lifetime [13]. In this study, different amount of graphene oxide (GO) was doped with $TiO_2$ as the photoelectrode in DSSCs. The influences of different wt.% of GO on the photovoltaic parameters were studied. It exhibited that GO improved the $J_{sc}$, $V_{oc}$ and PCE of DSSCs in comparison to control device. The device with optimum doping concentration of 0.6 wt.% GO exhibited $J_{sc}$ = 9.80 mA/cm$^2$, $V_{oc}$ = 0.72 V and FF = 53.2 %, resulting in a PCE of 3.7 %.

## Materials and Methods

### Materials

Graphite nanopowder (400nm – 1.2µm, 99.9%) and titanium dioxide nanopowder ($TiO_2$, anatase, 99.5%, 15 nm) were purchased from US Research Nanomaterials. Potassium permanganate ($KMnO_4$, 99.9%), sulfuric acid ($H_2SO_4$, 98%), phosphoric acid ($H_3PO_4$, 85%), hydrogen peroxide ($H_2O_2$, 30 %), hydrogen chloride (HCl, 37%),

polyethylene glycol ($M_w$ =10,000) from Sigma Life Science, nitric acid ~70.0%, triton X-100 purchased from Sigma-Aldrich, iodolyte AN-50 from Solaronix and platinum paste PT-1 from Dyesol company.

**Synthesis of graphene oxide**

GO was synthesized using simplified Hummer's method at ambient temperature [16] as illustrated in Figure 1. Oxidation of graphite was carried out by mixing $H_2SO_4$:$H_3PO_4$ (72:8 mL), graphite nanopowder: $KMnO_4$ (0.72 g), and $KMnO_4$ (3 g) using a magnetic stirrer. After adding all the materials slowly, the one-pot mixture was left for stirring for 3 days at ambient temperature to allow the oxidation of graphite. The colour of the mixture changed from dark purplish green to dark brown. Several drop of $H_2O_2$ solution was added to stop the oxidation process, and the colour of the mixture changed to bright yellow, indicating a high oxidation level of graphite. The graphite oxide formed was washed three times with 1 M of HCl aqueous solution and repeated with deionized water until a pH 4 – 5 was achieved. The washing process was carried out using simple decantation of supernatant via a centrifugation technique with a centrifugation speed 10,000 rpm and 10 minutes. During the washing process with deionized water, the graphite oxide experienced exfoliation, which resulted in the thickening of the graphene solution, forming a GO paste.

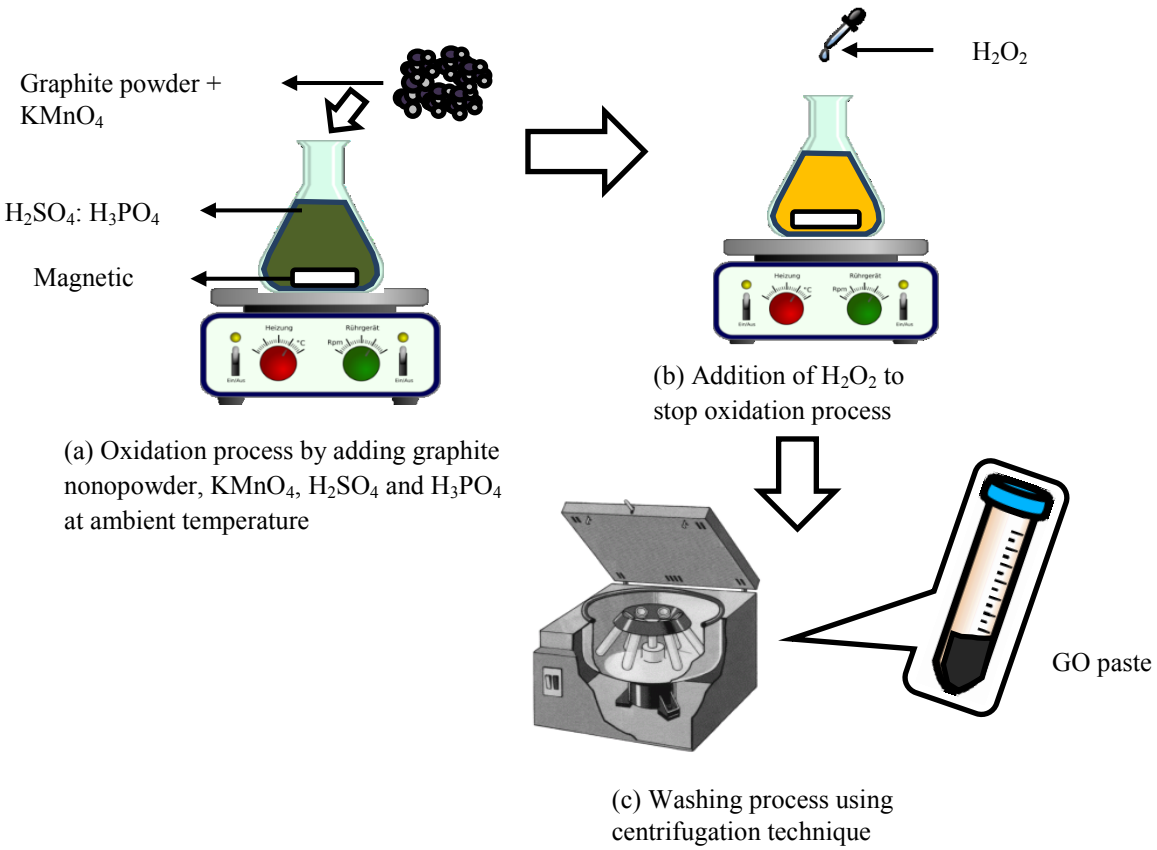



Figure 1. Synthesis of graphene oxide at ambient temperature

**Graphene oxide/$TiO_2$ preparation**

Graphene oxide paste was heated on hot plate at 70 °C for 15 minutes to remove the water. An amount 3 g of $TiO_2$ nanopowder, polyethylene glycol (PEG, $M_w$ =10,000), 0.13 ml nitric acid and 4ml distilled water were stirred well in the mortar for half an hour until a uniform paste formed. After that, several drops of Triton X-100 were added to

the paste and stirred another 30 minutes to get shiny and uniform paste. 0.4 wt.% of GO was put into the paste and the procedures were repeated by using 0.6 wt.% and 0.8 wt.% of GO. $TiO_2$ paste without GO also prepared as the control sample.

**Fabrication of DSSCs**

A complete DSSC device requires working electrode (photoelectrode) and the counter electrode (Figure 2). In the preparation of working electrode for DSSC, conductive substrate (FTO) (8 ohm/cm$^2$) was used. FTO substrate was cleaned by ultrasonic bath in acetone, ethanol and distilled water for 15 minutes each and was dried using nitrogen gas. GO/$TiO_2$ paste was deposited on FTO and form into a thin film using doctor blade technique. Single layer of magic tape was used to control the thickness and active area of GO/$TiO_2$. The active area of photoelectrode is 1.0 cm$^2$. The photoelectrode was annealed at 450 °C for 30 minutes, then was cooled down to 100 °C and followed by immersion in 0.03 mM N719 dye solution. After 24 hours immersion, photoelectrode was cleaned using ethanol to remove the excess dye in the GO/$TiO_2$ nanoparticle. In the preparation of counter electrode, platinum paste was deposited on the FTO substrates by doctor blade technique, and annealed at 450 °C for 30 minutes. The DSSC sample was assembled by sandwiching electrolyte layer between the GO/$TiO_2$ photoelectrode and Pt-coated conductive glass counter electrode. The electrodes were separated using U-shape Surlyn film and were pressed heated.

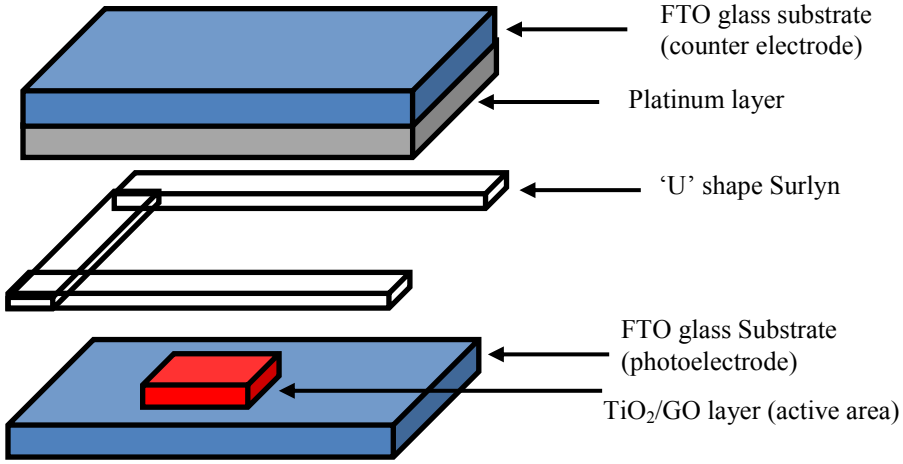



Figure 2. Fabrication of DSSC

**Characterization**

The micro-morphologies and energy-dispersive X-ray (EDX) of the GO and GO/$TiO_2$ was observed with field emission scanning electron microscope (FESEM) instrument (Zeisz Supra: 15 kV). The X-ray diffraction patterns of the samples were obtained by using X-ray diffractometer (Bruker D8 Advance). The average surface roughness of the thin film was determined by atomic force microscopy (AFM). Incident photon to current efficiency was analyzed using G300 instrument with simulated AM 1.5 xenon illumination. The current-voltage curves and power conversion efficiency of the cell was measured by light-current-voltage (LIV) Tester model Keithley 2400 with 100mW/cm$^2$ light output.

## Results and Discussion

**Morphology and structure analysis**

Figure 3 (a) and (b) show the field emission scanning electron microscopy (FESEM) images of synthesized GO at different magnification. Common process in chemical oxidation of graphite used ice bath during the initial addition of $KMnO_4$ and heating during the oxidation stage. But, the high temperature during the oxidation process reduces the size of GO produced [17]. In this study, the average lateral dimension of GO is obtained between about 600 –

900 nm, as shown in Figure 3 (b). According to Zhao et al. the electrical resistivity of GO sheets with large area is much lower compared to small GO sheets [18]. Figure 4 (a), (b) and (c) show the FESEM images of GO/$TiO_2$ thin films with different concentration of GO. As shown in Figure 4 (a), (b) and (c), GO/$TiO_2$, the porosity and specific surface area increased by increasing the concentration of GO in $TiO_2$. Several reports have shown that incorporation of GO into $TiO_2$ photoelectrode resulted in a coarse and porous surface, as a result of unique 2D structure of GO [19-21]. The evaporation of $H_2O$ in GO during the annealing process at 450 °C resulted in an increase of GO/$TiO_2$ thin film porosity from volume shrinkage [6]. The porous structure of thin film increase light scattering, dye absorptions and enhance the photovoltaic properties [6, 22]. However, previous study reported the optimal porosity for the photoelectrode was considered to be between 50% and 60% [23]. The compact structure will destruct the produced film that has many porous and crack at the surface of the film. The EDX analysis used to study the appearance elements of GO at 0.4 wt.%, 0.6 wt.% and 0.8 wt.% mixed with $TiO_2$. Based on the GO nanosheet film, the appearance peaks of C and O are 78.8% and 21.2% respectively, as shown in Figure 5(a) After annealed at 450 °C , the C element in 0.4%, 0.6% and 0.8% GO/$TiO_2$ samples were 2.7%, 4.0% and 4.3% respectively. The percentage of C element slightly increased due to the increment of GO percentage in $TiO_2$.

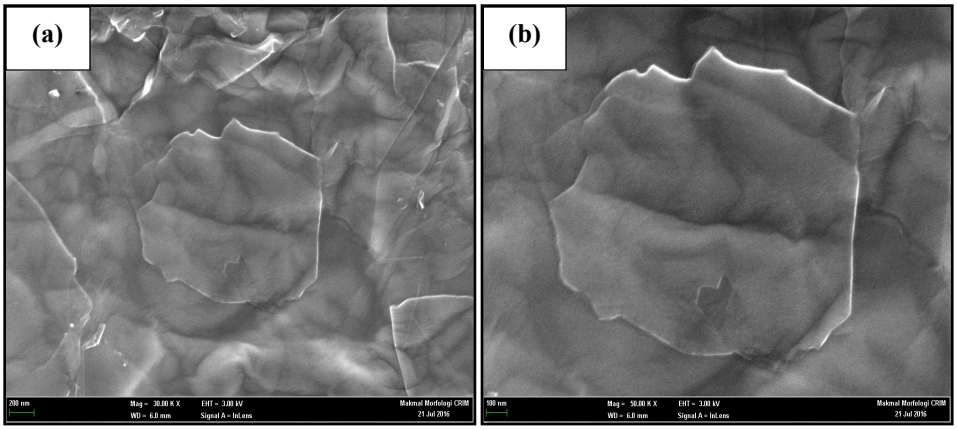
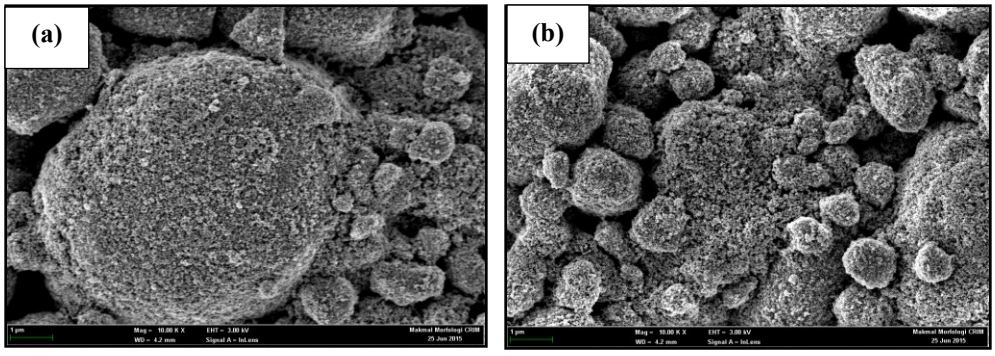



Figure 3. The FESEM images of synthesized (a) GO at low magnification and (b) GO at high magnification



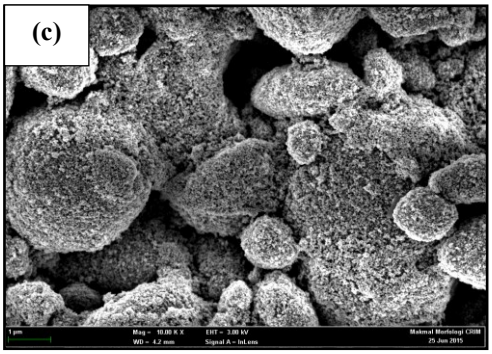



Figure 4. The FESEM images of GO/$TiO_2$ thin film with (a) 0.4, (b) 0.6 and (c) 0.8 wt.% of GO

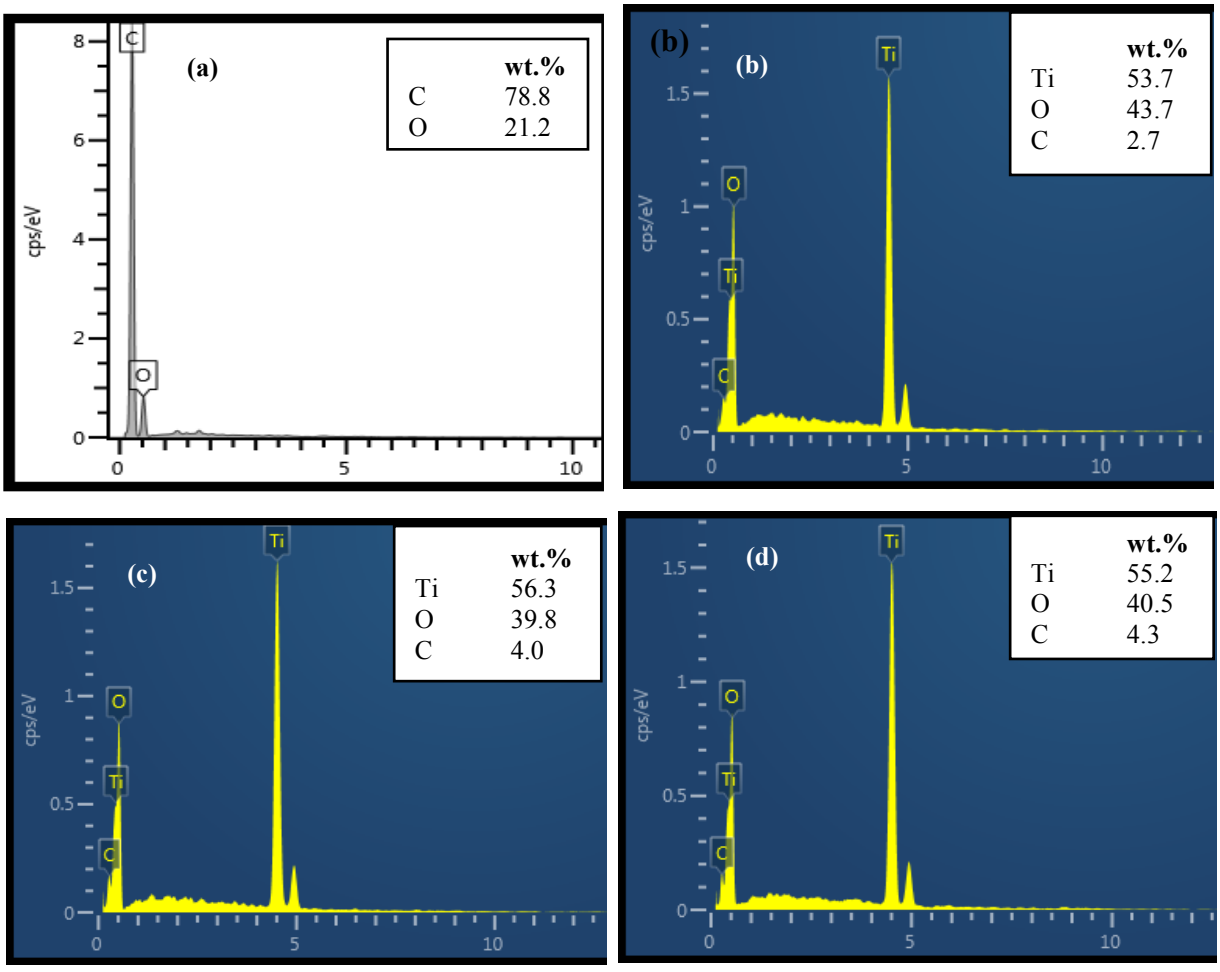



Figure 5. EDX analysis for (a) GO, GO/$TiO_2$ thin film with (b) 0.4 wt.%, (c) 0.6 wt.%, and (d) 0. 8 wt.% of GO

The morphology characterizations from AFM analysis are used to examine the surface roughness of the different percentage of GO doped in $TiO_2$ thin film. Figure 6(a), 6(b), and 6(c) and 6(d) show the three-dimensional surface morphology of the GO/$TiO_2$ thin films with 0.0 wt.%, 0.4 wt.%, 0.6 wt.% and 0.8 wt.% of GO, respectively. Based on the Table 1, the surface roughness values of 0.0 wt.%, 0.4 wt.%, 0.6 wt.% and 0.8 wt.% working electrode are 20.1 nm, 25.2 nm, 35.1 nm and 39.3 nm respectively. The high surface roughness indicates that GO/$TiO_2$ thin film exhibited high surface area, which in turn will give a greater absorption of the dye.

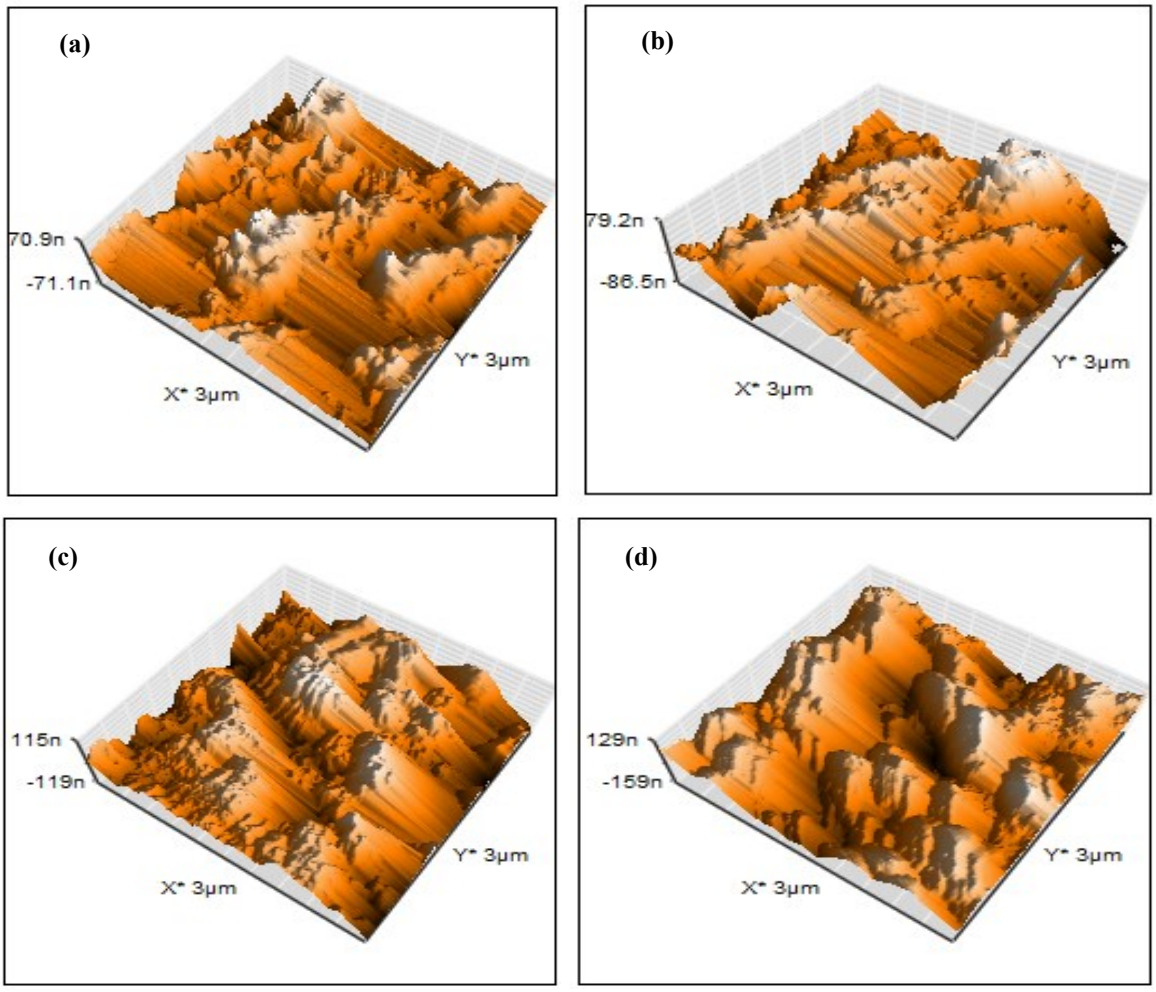



Figure 6. Topography AFM images of GO/$TiO_2$ film containing (a) 0.0 wt.%, (b) 0.4 wt.%, (c) 0.6 wt.% and 0.8 wt. % graphene oxide

Table 1. Roughness average parameter of thin films.

| Sample | Doping concentration of GO (wt.%) | Average Surface Roughness (nm) |
|---|---|---|
| (a) | 0.0 | 20.1 |
| (b) | 0.4 | 25.2 |
| (c) | 0.6 | 35.1 |
| (d) | 0.8 | 39.3 |

**X-ray diffraction analysis**

The results from XRD measurement are shown in Figure 7. The XRD pattern for $TiO_2$ shows obvious anatase phase with a characteristic peak of (1 0 1), (1 1 2), (2 0 0), (1 0 5), and (2 1 1). A small amount of rutile phase also are found in this pattern which assigned to (1 0 1) and (1 1 1) plane. The increasing of GO concentration in $TiO_2$ resulted in slight decrement of reflection peak intensity. However, due to its small content, the presence of GO in GO/$TiO_2$ sample were not detected. [24]**.** The Debye-Scherer formula was used to estimate the particle size as shown in formula equation 1.

$$D = \frac{k\,\lambda}{B\cos\theta} \tag{1}$$

where $\lambda$ is the wavelength of 1.492 nm, $B$ is the full width at half-maximum of the main peak and $\theta$ is the main peak position divided by 2 [6]. The results of crystallite size were shown in Table 2.

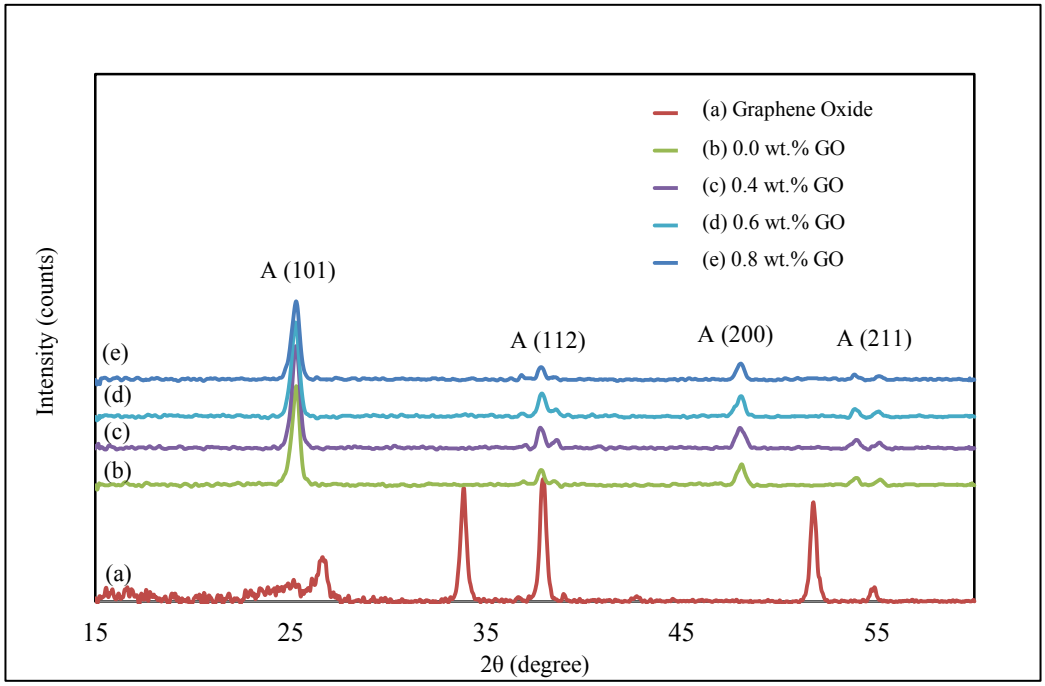



Figure 7. XRD pattern of GO and different concentration of GO/$TiO_2$ films

Table 2. The crystallite size for $TiO_2$ and GO/$TiO_2$ samples

| Samples | Doping Concentration of GO (wt.%) | Crystallite Size (nm) |
|---|---|---|
| (b) | 0.0 | 29.36 |
| (c) | 0.4 | 29.29 |
| (d) | 0.6 | 29.27 |
| (e) | 0.8 | 27.08 |

**DSSCs performance studies**

IPCE is the ratio of the number of electrons in the external circuit produced by an incident photon at a given wavelength [25]. The generation of IPCE is explained by three main factors: (1) the light-harvesting efficiency of dyes, (2) the efficiency of electron injection and (3) the efficiency of collecting photo injected electrons at the FTO substrate. In DSSC, it primarily responds to the wavelength of visible light in the 300 – 800 nm regions. Figure 8 shows the IPCE spectra of DSSC different concentration of GO doped $TiO_2$ photoelectrode. The dye that reacted at a wavelength of 500 – 600 nm had the highest quantum number, which is corresponding to the absorption peak of N719 dye [26]. The fabricated DSSCs exhibited a maximum absorption peak at ~515 nm, which mainly originated from the light-harvesting of the N719 dyes adsorbed by the photoelectrode films upon light illumination. The highest IPCE value of fabricated DSSCs was recorded by GO/$TiO_2$ 0.6 wt.%, with 51.49%, while the GO/$TiO_2$ 0.0 wt.%, 0.4 wt.%, and 0.8 wt.% showed low IPCE values of 42.89 %, 47.14 % and 48.89 %, respectively. The IPCE percentage increased by adding GO with concentration 0.4 wt.% and 0.6 wt.%, but slightly decreased by further adding GO with 0.8 wt.% concentration. The enhancement of IPCE value is caused by the increasing in specific surface areas of the GO/$TiO_2$ materials, which results in a considerably higher dye molecules loading and the ability to convert more photons to electrons. On the other hand, the lower IPCE value in GO/$TiO_2$ 0.8 wt.% indicates the electron-collection efficiency at the $TiO_2$/FTO substrate is poor due to too porous structure of photoelectrode. [27].

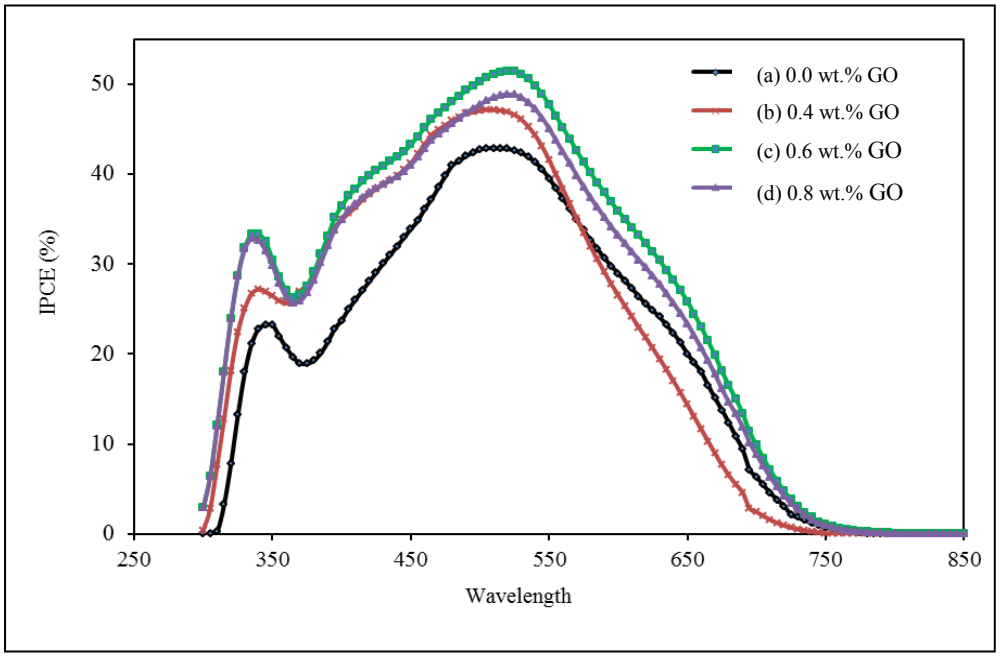



Figure 8. IPCE spectra of DSSC using different concentration of GO in $TiO_2$ photoelectrode

Table 3. IPCE parameter of DSSC

| Sample | Doping Concentration of GO (wt.%) | IPCE (%) |
|---|---|---|
| (a) | 0.0 | 42.89 |
| (b) | 0.4 | 47.14 |
| (c) | 0.6 | 51.49 |
| (d) | 0.8 | 48.89 |

Figure 9 shows the *J–V* curve of the DSSCs under varying illumination intensity of 100 mW $cm^{-1}$ (AM1.5G). The photovoltaic parameters of $TiO_2$ and GO/$TiO_2$ were summarized in Table 4. Based on the photovoltaic parameters in Table 4, the $J_{sc}$ and PCE of GO/$TiO_2$ DSSCs increased compared to the standard DSSC (without GO). This increment is similar to that reported in previous studies [28]. The highest $J_{sc}$ and PCE were obtained at 0.6 wt.% of GO in $TiO_2$ DSSC, with the value of 9.8 mA/$cm^2$ and 3.7%, respectively. $J_{sc}$ are mostly established by good charge injection from the excited state of dye into the GO/$TiO_2$ photoanode and great charge transport [29]. The $J_{sc}$ of GO/$TiO_2$ from 0.0 wt.% to 0.8 wt.% was recorded as 8.1, 8.6, 9.1 and 8.7mA/$cm^2$, respectively. The increasing of $J_{sc}$ and efficiency is due to following reasons: (a) improve the electron transfer efficiency from $TiO_2$ film to FTO substrate [30-32] and (b) reduce the charge recombination rate and resistance [33 – 37]. However, the value of $J_{sc}$ and PCE decrease with a further increase the percentage of GO up to 0.8 wt.%. This may be due to the porosity became too large to act as a kind of recombination center instead of providing an electron pathway that resulted in longer charge migration routes or electron contacting directly with FTO to form a dark current due to more graphene oxide surrounding $TiO_2$ nanoparticles [25].

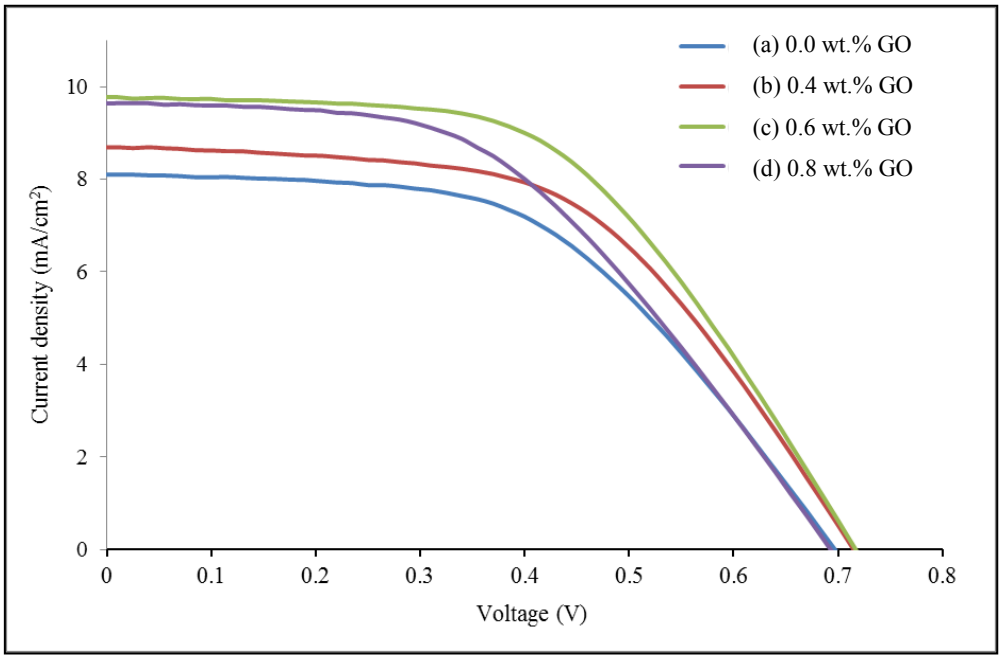



Figure 9. *J-V* curves of the DSSC with various wt.% of GO under illumination of simulated AM 1.5G sunlight at 100 mW/$cm^2$

Table 4. The photovoltaic parameter of DSSC for $TiO_2$ and GO/$TiO_2$

| **Doping Concentration of GO (wt.%)** | $V_{oc}$ **(V)** | $J_{sc}$ **(mA/cm²)** | **Fill Factor (%)** | **Efficiency, IPCE (%)** |
|---|---|---|---|---|
| 0.0 | 0.68 | 8.1 | 51.8 | 2.9 |
| 0.4 | 0.69 | 9.6 | 48.0 | 3.2 |
| 0.6 | 0.72 | 9.8 | 53.2 | 3.7 |
| 0.8 | 0.72 | 8.7 | 53.8 | 3.3 |

## Conclusion

Graphene oxide (GO) was successfully synthesized at ambient temperature and GO was doped with $TiO_2$ as photoelectrode. The results of DSSC showed that the doping of 0.6 wt.% graphene oxide into $TiO_2$ paste enhanced the photoelectric conversion efficiency (PCE) by 28% compared to standard DSSC. The increment is due to increase in dye absorption and enhanced electron transportation. However, further increase in GO concentration in $TiO_2$ can cause the decrease the efficiency of DSSC due to too porous structure of photoelectrode and lead to charge recombination.

## Acknowledgements

This research was supported by the Ministry of Higher Education Malaysia and Universiti Kebangsaan Malaysia under the Look East Policy (LEP) Grant (LEP 2.0/14/UKM/NT/03/1 and Arus Perdana (AP-2015-014). This research also was presented at UKM-ISESCO-COMSAT International Workshop on Nanotechnology for Young Scientists (IWYS2016) on Monday, 28 November 2016.

## References

1. O'Regan, B. and Grätzel, M. (1991). A low-cost, high-efficiency solar-cell based on dye-sensitized colloidal $TiO_2$ films. *Nature*, 353: 737 – 740.
2. Gong, J., Liang, J. and Sumathy, K. (2012). Review on dye-sensitized solar cells (DSSCs): fundamental concepts and novel material. *Renewable Sustainable Energy Reviews*, 16: 5848 – 5860.
3. Zhang, S., Yang, X., Numata, Y. and Han, L. (2013). Highly efficient dye-sensitized solar cells: Progress and future challenges. *Energy Environment Science,* 6: 1443 – 1464.
4. Smestad, G.P. and Grätzel, M. (1998). Demonstrating electron transfer and nanotechnology: A natural dye-sensitized nanocrystalline energy converter. *Journal of Chemical Education*, 75: 752 – 756.
5. Grätzel, M. (2004). Conversion of sunlight to electric power by nanocrystalline dye-sensitized solar cells. *Journal of Photochemistry and Photobiology*, 164: 3 − 14.
6. Fang, X., Li, M., Guo, K., Hu, Y. Z., Liu, X., Chen, B. and Zhao, X. (2012). Improved properties of dye-sensitized solar cells by incorporation of graphene into the photoelectrodes. *Electrochimica Acta*, 65: 174 – 178.
7. Tang, B., Hu, G., Gao, H. and Shi, Z. (2013). Three-dimensional graphene network assisted high performance dye sensitized solar cells. *Journal of Power Sources,* 234: 60 – 68.
8. Yen, C. Y., Lin, Y. F., Liao, S. H., Weng, C. C., Huang, C. C., Hsiao, Y. H., Ma, C. C. M., Chang, M. C., Shao, H., Tsai, M. C., Hsieh, C. K., Tsai, C.H. and Weng, F. B. (2008). Preparation and properties of a carbon nanotube-based nanocomposite photoanode for dye-sensitized solar cells. *Nanotechnology,* 19(37): 375305.
9. Hu, L. H., Dai, S. Y., Weng, J., Xiao, S. F., Sui, Y. F., Huang, Y., Chen, S., Kong, F., Pan, X. and Liang, L. (2007). Microstructure design of nanoporous $TiO_2$ photoelectrodes for dye sensitized solar cell modules. *Journal of Physical Chemistry B,* 111: 358 − 362.
10. Bai, Y., Yu, H., Li, Z., Amal, R., Lu, G. Q. M. and Wang, L. (2012). In-situ growth of a ZnO nanowire network within a $TiO_2$ nanoparticle film for enhanced dye-sensitized solar cell performance. *Advance Material*, 24: 5850 − 5856.
11. Mane, R. S., Lee, W. J., Pathan, H. M. and Han, S. H. (2005). Nanocrystalline $TiO_2$/ZnO thin films: fabrication and application to dye sensitized solar cells. *Journal of Physical Chemistry B*, 109: 24254 − 24259.
12. Sun, S., Gao, L. and Liu, Y. (2010). Enhanced dye-sensitized solar cell using graphene-$TiO_2$ photoanode prepared by heterogeneous coagulation. *Applied Physics Letters,* 96: 083113.
13. Yang, N. L., Zhai, J. Wang, D., Chen, Y. S. and Jiang, L. (2010). Two-dimensional graphene bridges enhanced photoinduced charge transport in dye-sensitized solar cells. *ACS Nano*, 4(2): 887 – 894.
14. Zhu, C. Z., Wang, S. J. P., Xing, L. Y., Fang, X., Zhai, Y. M. and Dong, S. J. (2010). One-pot, water-phase approach to high-quality graphene/$TiO_2$ composite nanosheets. *Chemical Communications*, 46(38): 7148 – 7150.
15. Tang, Y. B., Lee, C. S., Xu, J., Liu, Z. T., Chen, Z. H., He, Z. B., Cao, Y. L., Yuan, G.D., Song, H. S., Chen, L. M. Luo, L. B., Cheng, H. M. Zhang, W.J., Bello, I. and Lee, S. T. (2010). Incorporation of graphenes in nanostructured $TiO_2$ films via molecular grafting for dye-sensitized solar cell application. *ACS Nano*, 4(6): 3482 – 3488.

16. Huang, N. M., Lim, H. N., Chia, C. H., Yarmo, M. A. and Muhamad, M. R. (2011). Simple room-temperature preparation of high-yield large-area graphene oxide. *International Journal of Nanomedicine*, 6: 3443 – 3448.
17. Su, C. Y., Xu, Y. and Zhang, W. (2009). Electrical and spectroscopic characterizations of ultra-large reduced graphene oxide monolayers. *Chemistry of Materials*, 21: 5674 – 5680.
18. Zhao, J., Pei, S., Ren, W., Gao, L. and Cheng, H. M. (2010). Efficient preparation of large-area graphene oxide sheets for transparent conductive films. *ACS Nano*, 4: 5245 – 5252.
19. Yen, M., Hsiao, M., Liao, S., Liu, P., Tsai, H., Ma, C., Pu, N. and Ger, M. (2011). Preparation of graphene/multi-walled carbon nanotube hybrid and its use as photoanodes of dye-sensitized solar cells. *Carbon*, 49: 3597 – 3606.
20. He, Z., Guai, G., Liu, J., Guo, C., Loo, J., Li, C. and Tan, T. (2011). Nanostructure control of graphene composited $TiO_2$ by a one-step solvothermal approach for high performance dye-sensitized solar cells. *Nanoscale*, 3: 4613 – 4616.
21. Yen, C., Lin, Y., Hung, C., Tseng, Y., Ma, C., Chang, M. and Shao, H. (2008). The effects of synthesis procedures on the morphology and photocatalytic activity of multiwalled carbon nanotubes/$TiO_2$ nanocomposites. *Nanotechnology*, 19: 045604.
22. Wang, H., Leonard, S. L. and Hu, Y. H. (2012). Promoting effect of graphene on dye-sensitized solar cells. *American Chemical Society, Industrial and Engineering Chemistry Research*, 51: 10613 – 10620.
23. Kopidakis, N., Benkstein, K. D., Van de Lagemaat J. and Frank, A. J. (2003). Transport-limited recombination of photocarriers in dye-sensitized nanocrystalline $TiO_2$ solar cells. *Journal of Physical Chemistry B*, 107: 11307 – 11315.
24. Kim, D. Y., Joshi, B. N., Park, J. J., Lee, J. G., Cha, Y. H., Seong, T. Y., Noh, S. I., Ahn, H. J., Al-Deyabe, S. S. and Yoon, S. S. (2014). Graphene-titania films by supersonic kinetic spraying for enhanced performance of dye sensitized solar cells. *Ceramics International,* 40: 11089 – 11097.
25. Salam, Z., Vijayakumar, E., Subramania, A., Sivasankar, N. and Mallick, S. (2015). Graphene quantum dots decorated electrospun $TiO_2$ nanofibers as an effective photoanode for dye sensitized solar cells. *Solar Energy Materials and Solar Cells*, 143: 250 – 259.
26. Chang, J., Yang, J., Ma, P., Wu, D., Tian, L., Gao, Z., Jiang, K. and Yang L. (2012). Hierarchical titania mesoporous sphere/graphene composite, synthesis and application as photoanode in dye sensitized solar cells. *Journal of Colloid and Interface Science,* 394: 231 – 236.
27. Liu, R., Yang, W. D. and Qiang, L. S. (2012). Enhanced efficiency for dye-sensitized solar cells using a surface-treated photo-anode. *Journal of Power Sources*, 199: 418 – 425.
28. Tang, Y. B., Lee, C. S., Xu, J., Liu, Z. T., Chen, Z. H., He, Z., Cao, Y. L., Yuan, G., Song, H. Chen, L., Luo, L., Chen, H. M., Cheng, W., Zhang, J., Bello, I. and Lee, S. T. (2010). Incorporation of graphenes in nanostructured $TiO_2$ films via molecular grafting for dye-sensitized solar cell application. *ACS Nano*, 4: 3482 – 3488.
29. Wang, P., Wang, J., Wang, X., Yu, H., Yu, J., Lei, M. and Wang, Y. (2013). One-step synthesis of easy-recycling $TiO_2$–rGO nanocomposite photocatalysts with enhanced photocatalytic activity. *Applied Catalysis B: Environmental,* 132: 452 – 459.
30. Zhang, H., Lv, X., Li, Y., Wang, Y. and Li, J. (2010). P25-graphene composite as a high performance photocatalyst. *American Chemical Society Nano*, 4: 380 – 386.
31. Luan, X., Chen, L., Zhang, J., Qu, G., Flake, J. C. and Wang, Y. (2013). Electrophoretic deposition of reduced graphene oxide nanosheets on $TiO_2$ nanotube arrays for dye-sensitized solar cells. *Electrochimica Acta*, 111: 216 – 222.
32. Tsai, T. H., Chiou, S. C. and Chen, S. M. (2011). Enhancement of dye-sensitized solar cells by using graphene-$TiO_2$ composites as photoelectrochemical working electrode. *International Journal of Electrochemical Science,* 6: 3333 – 3343.
33. Andrade, L., Sousa, J., Ribeiro, H. A. and Mendes, A. (2011). Phenomenological modeling of dye-sensitized solar cells under transient conditions. *Solar Energy*, 85: 781 – 793.
34. Shu, W., Liu, Y., Peng, Z., Chen, K., Zhang, C. and Chen, W. (2013). Synthesis and photovoltaic performance of reduced graphene oxide-$TiO_2$ nanoparticles composites by solvothermal method. *Journal of Alloys and Compounds*, 563: 229 – 233.
35. Yang, N., Zhai, J., Wang, D., Chen, Y. S. and Jiang, L. (2010). Two-dimensional graphene bridges enhanced photoinduced charge transport in dye sensitized solar cells. *ACS Nano*, 4: 887 – 894.

36. Zhao, J., Wu, J., Yu, F., Zhang, X., Lan, Z. and Lin, J. (2013). Improving the photovoltaic performance of cadmium sulfide quantum dots-sensitized solar cell by graphene/titania photoanode. *Electrochimica Acta,* 96: 110 – 116.
37. Koide, N., Islam, A., Chiba, Y. and Han, L. (2006). Improvement of efficiency of dye-sensitized solar cells based on analysis of equivalent circuit. *Journal of Photochemistry and Photobiology A. Chemistry*, 182: 296 – 305.

*Malaysian Journal of Analytical Sciences, Vol 21 No 4 (2017): 941 - 949*
*DOI: https://doi.org/10.17576/mjas-2017-2104-21*

MALAYSIAN JOURNAL OF ANALYTICAL SCIENCES
*Published by The Malaysian Analytical Sciences Society*
ISSN 1394 - 2506

# EFFECT OF VARIOUS POWER LEVEL AND DIFFERENT RATIO OF FRUIT TO WATER IN OIL PALM FRUITS MICROWAVE STERILIZER

## (Kesan Pelbagai Tahap Kuasa dan Nisbah Berlainan Buah terhadap Air dalam Pensterilan Gelombang Mikro Buah Kelapa Sawit)

Norashikin Ahmad Zamanhuri*, Norazah Abd Rahman, Noor Fitrah Abu Bakar

*Faculty of Chemical Engineering,*
*Universiti Teknologi MARA, 40450 Shah Alam, Selangor, Malaysia*

**Corresponding author: shikin282103@gmail.com*

Received: 28 November 2016; Accepted: 5 February 2017

**Abstract**

The aim of this paper is to investigate the effect of using various power level and different ratio of fruit to water in microwave sterilizer in order to acquire the shortest time of the fruit to be completely detached from the spikelet. Normally, the palm oil fruits processing uses steam heating for sterilization of oil palm fruit brunches. The conventional steam treatment of sterilization produces large amount of waste water from the palm oil mill process. Also, this process is classifying as crucial process with the intention of inactivate the lipolytic enzyme as prevention to the increase of free fatty acids (FFA) in oil. Therefore, microwave irradiation is used in this research for solving this problem and improving of palm oil fruit quality prior to extraction of crude palm oil (CPO). The optimal condition was 800W for 6 minutes of 100% strip of fruit from the spikelet with 1:0.5 ratio by means of 4.08% of FFA. It can be concluded that microwave radiation is suitable for quick detachment of the fruitlet from the spikelet and fruit loosening performed without kernels started to turn brown and appeared dehydrated. Throughout the trial, the quality of the oil extracted from the microwave sterilized spikelets in terms of the FFA percentage was acceptable. The quality of the oil is excellent, with free fatty acids of the crude oil generally below 5%.

**Keywords**: oil palm fruits, sterilisation, microwave, stripping, free fatty acids

**Abstrak**

Tujuan kertas ini adalah untuk mengkaji kesan menggunakan pelbagai tahap kuasa dan nisbah yang berbeza buah-buahan terhadap air dalam pensterilan gelombang mikro untuk memperoleh masa yang singkat buah-buahan terpisah lengkap daripada spikelet itu. Biasanya, pemprosesan buah kelapa sawit menggunakan pemanasan stim untuk tujuan pensterilan. Rawatan wap konvensional pensterilan menghasilkan sejumlah besar air sisa daripada proses kilang minyak sawit. Juga, proses ini diklasifikasikan proses sebagai penting dengan niat untuk menyahaktifkan enzim lipolitik sebagai pencegahan kepada peningkatan asid lemak bebas (FFA) dalam minyak. Oleh itu, penyinaran gelombang mikro digunakan dalam kajian ini untuk menyelesaikan masalah dan meningkatkan kualiti buah kelapa sawit sebelum pengekstrakan minyak sawit mentah (MSM). Keadaan optimum adalah 800W untuk 6 minit daripada 100% lerai buah dari spikelet dengan nisbah 1: 0.5 bagi 4.08% FFA. Dapat disimpulkan bahawa radiasi gelombang mikro adalah sesuai untuk peleraian cepat buah dari spikelet dan ia dapat dilakukan tanpa biji mula bertukar coklat dan kelihatan kering. Sepanjang ujikaji, kualiti minyak yang diekstrak daripada gelombang mikro disterilkan dari segi peratusan FFA boleh diterima. Kualiti minyak adalah yang baik, dengan asid lemak bebas minyak mentah biasanya di bawah 5%.

**Kata kunci:** buah kelapa sawit, pensterilan, gelombang mikro, pelucutan, asid lemak bebas

## Introduction

Malaysia is one of the countries that successfully beneficiaries of the oil palm industry and being responsible for uprising this industry globally through significant contributions and continuous commitment. In summary, oil palm processing in mill involves the receiving of fresh fruit bunches from the plantations, sterilizing and separating of the bunches to free the palm fruits, digesting and mashing of the fruits and pressing out the crude palm oil, clarification, purification, drying and storage[1, 2]. Pre-treatments are occasionally crucial with the purpose of overcome difficulties in material handling throughout subsequent processing steps. Sterilization process of oil palm fruits is categorize as the –first step in palm oil milling process prior to extract crude palm oil as well as identified steam treatment. At this moment, the conditions to apply sterilization is within range of 15 -45 psi of pressure, 70 – 90 min of cooking time and at temperature more than 100 °C [3, 4].

Crude palm oil (CPO) generated from this current process has good quality. Nonetheless, palm oil mill effluent (POME) known as hazardous to the surroundings has produced abundant waste water [5]. POME will be generated from three main sources for each tonne, sterilizer condensate, sludge separator and hydrocyclone waste with 27%, 44% and 29%, respectively [6, 7]. Even though POME is a non-toxic liquid waste with horrible smell and its chemical oxygen demand (COD) and biochemical oxygen demand (BOD) value are relatively high, thus the great cost of treatment was required to meet environmental standard [8]. To solve the problem of the generated POME, alternative methods may also be encountered throughout microwave oven to apply as a treatment to the oil palm fruits with the minimal water usage.

In the conventional milling process, fresh fruit bunches are loaded in cages and pushed into sterilizers where they are cooked. The process seizures oil quality deterioration due to enzymatic activity. Enzymatic lipolysis of the oil, which may result in a rise of free fatty acids (FFA) in the fruits, is halted immediately upon sterilization of the bunches. High amount of free fatty acids that the oil might become unfit for human consumption without appropriate refining. Sterilisation also facilitates the stripping of fruits from the bunch and the extraction of oil and kernel. At present, screw press and hydraulic presser technology has been carried out in palm oil mill processing [7, 9] that is completed after the fresh fruit bunches run through steam treatment. However, current method carried out in mill for oil extraction, generates residual oil or leftover oil about 3-7%, which is eventually gathered as POME and proven to be dangerous to the environment [10, 11]. Therefore, an effort is thus made in this study to look into the prospect of utilization of microwave heating for the first stage of the process.

Numerous experiments have established that the solventised fibres from soxhlet extraction were discovered to be very dry, brittle and completely decolourised, indicating complete exhaustion of oil [3, 12-15] . The clarification step in the conventional palm oil milling process which uses large amount of water, was fully omitted, bringing to cleaner and higher quality crude palm oil. Oil with higher content of vitamin E and carotenes produce from this solvent extraction method, will be more stable and having longer shelf life. The current pretreatment using microwave could also offer as an alternative route for phytonutrients recovery. It is also a clean technology due to minimal water effluent discharge. They also wrap up that milling would then be a process not only for the recovery of trapped crude palm oil in fibres after digesting process, but also for the recovery of high value added nutraceuticals too. This would enhance the economics of palm oil production.

To the best of our comprehension, the influence of microwave extraction *cum* sterilisation for the crude palm oil from oil palm fruits has not been reported yet. And also, less emphasis on stripping irradiation time of the sterilised oil palm bunch at various power levels, ratio and quality of the fruits after microwave sterilization is reported in published literature. Thus, the aims of the present research are: (1) to study the effect of using various power level to improve the stripping efficiency with shorter irradiating time or comparable to conventional method, (2) to discover effect of different ratio of fruit to water in microwave sterilizer in order to get the the shortest time of the fruit to be completely detached from the spikelet as well as good mesocarp and kernel condition. For this purpose, all parameters were individually investigated and then combined and optimized, finally (3) to analyse the quality of the oil extracted from the microwave sterilized oil palm spikelets in terms of the FFA percentage whether acceptable, below 5% [14, 15].

## Materials And Methods

### Materials

Fresh palm fruit was obtained from local oil palm plantation from open areas in Selangor, Malaysia. Fresh fruit bunch was chopped into fruit spikelets and 200g of each was weighed [12]. The sample was kept in a dry place ready for sterilization [16]. It is of utmost importance that the chopped fruits to be subjected to immediate sterilization in order to deactivate the lipase activity [17]. The FFA content from the fruit spikelets with major damage can reach above 5% if there was no pre- treatment process done immediately [13].

### Microwave sterilisation experiments

Only several spikelet of bunch were selected and weighed before undergoing microwave heating (microwave oven Panasonic Commercial, model: NN-ST651M, 1000 Watt frequency of 2450 MHz) for 2 minutes intervals time until 100% stripping reach. The trials were repeated 3 times for 100, 300, 400, 600 and 800W of microwave power level. The condition and appearance of the center of the kernel was noted. The fruits at the spikelets were detached with a slight push of a finger [12, 16] until the fruits were completely detached from the spikelet. The stripping efficiency was then determined according to Equation 1.

$$\%\ \text{Stripping Efficiency}, S_{\text{eff}} = \frac{F_l}{F_l + F_r} \text{x} 100\% \quad (1)$$

where $S_{eff}$, the percentage of stripping efficiency, $F_l$, the number of fruits loosened from the spikelet after stripping, and $F_r$, the number of fruits remained at the spikelet after stripping.

In addition, study is necessary on a combined system by using combination of moisture and heat in a microwave so that sterilisation can be conducted at shorter time with 100% fruits stripping efficiency. Effect of water ratio (m:v) at 1:0.5, 1:1 and 1:2 was also investigated for each batch of microwave revealing duration, where the ratio is fruits mass (gram) to water volume (ml). As the exposure duration of dry microwave was extended, there was significant increase in drying, cracking and browning effect on the mesocarp and kernel. This step on combination of moisture and heat in a microwave is essential to give them the initial moisture throughout sterilization process with very minimal water added [19 – 21]. The important benefit of a microwave is the 'time efficiency'. So, the energy and time are saved.

The percentage of free fatty acids was measured by means of Soxhlet extraction, where 20 g of mesocarp oil palm was weighed into a cellulose thimble(30mm x 77 mm, Whatman, Maidstone, UK) and placed in a Soxhlet device. Most mesocarp samples should be predried at 102 ± 2 °C for 1–2 hours to optimize the oil extraction. Water in the sample can decrease the efficiency of the solvent extraction, resulting in low fat recoveries. Two hundred milliliters of hexane (at 63 – 65 °C) were used as the solvent and the extraction was performed for 4 - 6 hours until the yellow color has disappeared [13, 18].

### Determination of free fatty acid content

The free fatty acid content was measured using the titration method as written in the MPOB Test Method [23] with some modification [13]. An amount 2 g of preheated oil (about 50 °C) was weighed in a clean beaker and mixed with 50 ml Isopropyl alcohol. The solution was neutralized by titration of 0.100 N sodium hydroxide (NaOH). The percentage of FFA content was calculated using this Eq. (2):

$$\%\text{FFA} = \frac{25.6 \text{x} V \text{x} N}{w} \quad (2)$$

where: $V$ = volume of sodium hydroxide used, $N$ = 0.1005 N Normality (concentration) of sodium hydroxide used, $w$ =Weight of oil used

## Results and Discussion

### Preliminary study: Optimization of microwave power level

Figures 1 shows effect on stripping efficiency of oil palm spikelet in relation various microwave power level of 100 to 800 Watt with fruit spikelets mass of 200 g. It can be observed that, the shortest time to reach completely fruits

detachment is at 800 Watt for only 4 minutes and the lengthiest irradiating time to reach 100% stripping is at 100 Watt. Immediate microwave sterilization is the ultimate importance in order to deactivate the lipase activity that later will increase the FFA percentage. In most of the microwave study, power and material always represent by power density which expressed number of power applies to the oil palm fruits sample per gram. High power density expressed effectiveness of moist microwave sterilization process due to maximum microwave energy being absorbed by small sample [24]. Overheating of the bunch portions will further deteriorate the stripping efficiency [18] as indicated by declining stripping trend as the heating time was prolonged after achieving highest stripping efficiency after 12 minutes for 2 kW, after 14 minutes for 1.5 kW and after 16 minutes for 1 kW. For microwave sterilization studied by [24], the stripping efficiency at elevated power level are 27%, 58.5% and 61%, after 16 minutes of exposure time.

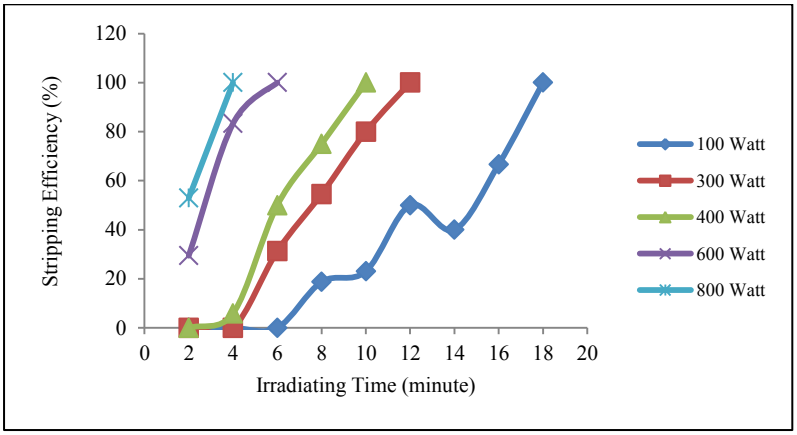



Figure 1. Effects on stripping efficiency of oil palm spikelet in relation various microwave power level of 100 to 800 Watt

Determination of microwave power level was decided after conducting several preliminary works, where researcher discovered that, the highest power level (1000 Watt) will contribute to low fruits quality, on the other hand at low power level (300 and 100 Watt) will be responsible for lengthy of time required for fruit detachments. As can be seen, power level workedin this study is medium level, within the range of 400, 600 and 800 Watt at irradiating time less than 10 minutes with oil palm fruits completely detached from the bunches.This results are similarly with previous work conducted by other researchers from[12, 21, 22]. These results also proved that microwave radiation is suitable to be used for fruit detachment from the bunch since the abscission region has higher dielectric properties [18] due to high moisture content as compared to other parts of the fruitlet. The high moisture content and conduction loss from ionic constituents were the two main contributing factors. Their results indicated that the ultimate of the moisture content is exactly positioned at the abscission region. Undeniably, the moisture content under a microwave treatment is important, since water is an excellent absorber of microwave energy [26]. This strong absorption provides the increase of the temperature inside the sample and then the break of the mesocarp positioned at pedicel by the *in-situ* water known as abscission zone [27], followed by the evaporation of water vapour. For that reason, the proposed microwave power level that will applicable in this research is medium range 400, 600 and 800 Watt.

**Effect of water ratio on stripping efficiency**

The purpose of addition of waterto fruits spikelet is to implement a combined system that using combinations moisture heat with microwave with the intention of sterilisation can be carried at shorter time with 100% fruits stripping efficiency and give good quality of CPO. Figure 2 exhibits effect on irradiating time in relation to fruit mass to water volume at with 1:0 , 1:1 and 1:2 (m:v). As can be observed, power level worked in this study is medium level, within the range of 400, 600 and 800 Watt. Obviously, at microwave power 400 Watt, it takes lengthy time to reach completely fruits detached with ratio of fruit mass to water volume at 1:2. Waves are absorbed

by the oil palm spikelets, some are reflected and the remaining unabsorbed power is dissipated into the water vessel, which is placed in a container in the microwave cavity. The microwave powers lower than 450 W were in favour of the best water retention capacities [28].

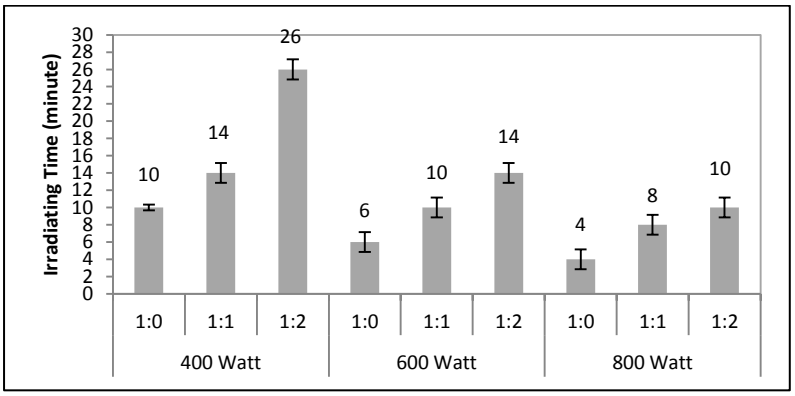



Figure 2. The irradiating time from medium power levels of microwave sterilization. Ratio fruit mass to water volume at with 1:0 , 1:1 and 1:2 (m:v)

Definitely, the moisture content under a microwave treatment is critical, since water is an outstanding absorber of microwave energy [26 - 29]. This strong absorption delivers the increase of the temperature inside the sample and then the rupture of the mesocarp and kernel cells by the *in situ* water, followed by the evaporation of water vapour. However, huge water adding in the vessel will interfere the stripping process time the oil palm fruits. To the best of our knowledge, implementation a combined system that using combinations moisture heat with microwave technique has never been applied for the oil palm fruits sterilisation. For that reason, through adding water will improve the kernel condition and mesocarp as well.

**Effect of microwave exposure on quality of palm oil**

The quality of crude palm oil (CPO) can be indicated from chemical properties such as free fatty acids content. Figure 3 presented FFA percentage with medium range power level microwave and ratio. CPO normally contains free fatty acids which need to be eliminated as part of the refining process. Obviously, Figure 3 summarizes at power 600 W and 800 W the maximum free fatty acids percentage are 4.04 and 4.08, respectively with ratio 1:0. As can be seen also in the Figure 3, the trend of FFA percentage increased at 400 Watt. However, after increasing microwave power the FFA trend percentage was decreased. Throughout the trial, the quality of the oil extracted from the oil palm fruit spikelets in terms of the free fatty acid percentage was acceptable i.e below 5%, varying from 1.02 to 4.08%. However it should be kept as low as possible for nicer oil quality of palm oil and lower refining cost [28 – 30]. It is also important in oil extraction to have an suitable microwave irradiation power setting as high power can degrade volatile compounds and the plant material itself [30, 31]. The fruits consequently need to be heated immediately after harvest to inactivate the lipase and to prevent an unacceptable level of free fatty acids in the oil. The enzyme is activated upon abscission of the fruit and also when the fruit is bruised.

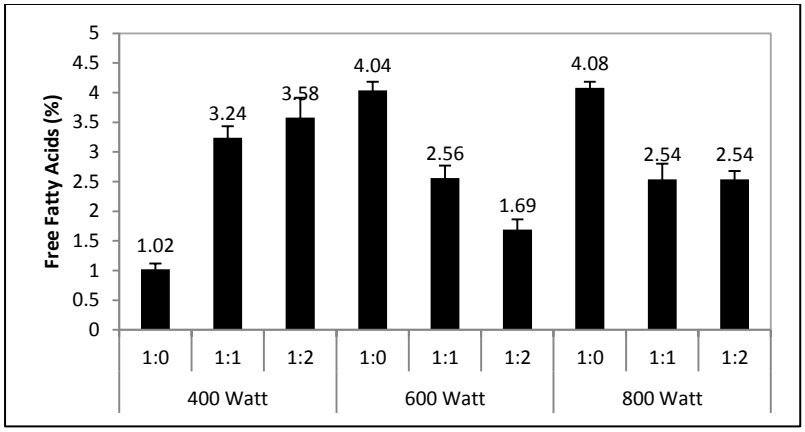



Figure 3. Effects of different fruit mass to water volume ratio on free fatty acids percentage. Microwave sterilised process was performed at different: irradiation power in medium range 400, 600 and 800 Watt

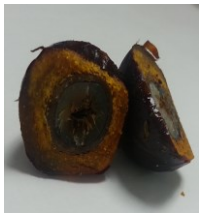
**Physical appearance of microwave treated palm fruits**

Table 1 indicates the physical appearance of oil palm spikelet in relation to microwave heating period at water ratio 1:0 and 1:0.5. The extension of microwave exposure with fruit to water ratio (m:v) of 1:0.5 was not discovered to burn kernel and mesocarp as observed in Table 1 even though at 800 Watt. The purpose of studying minimal water to the oil palm fruit spikelets is to distinguish the kernel condition once microwave irradiation. Production of water vapour and caramel-like aroma was also recognised for all microwavable exposure conditions. The removal of water was part of the heating process [32, 21]. Indeed, the moisture content under a microwave treatment is critical, since water is an excellent absorber of microwave energy [36]. This mechanism is led to the drying effect and justifiable for the cracked, hardened and desiccated mesocarp [3].

Table 1. Physical appearance of oil palm fruits after microwave sterilisation by: (a) 1:0, (b) 1:0.5 ratio

| **Power (W)** | **Ratio (m:v) (g:ml) (fruit mass: water volume)** | | | |
|---|---|---|---|---|
| | **(a) 1:0** | | **(b) 1:0.5** | |
| | **Empty Spikelet and Mesocarp** | **Kernel** | **Empty Spikelet and Mesocarp** | **Kernel** |
| 400 |  |  |  |  |
| 600 |  |  |  |  |

Table 1 (cont'd). Physical appearance of oil palm fruits after microwave sterilisation by: (a) 1:0, (b) 1:0.5 ratio

| Power (W) | Ratio (m:v) (g:ml) (fruit mass: water volume) | | | |
|---|---|---|---|---|
| | (a) 1:0 | | (b) 1:0.5 | |
| | Empty Spikelet and Mesocarp | Kernel | Empty Spikelet and Mesocarp | Kernel |
| 800 |  |  |  |  |

The mesocarp of fresh palm fruits has a fibrous-like texture which is yellowish- orange, hard and possesses a sweet fragrant. The seed or kernel is a single, hard and white in colour. As the exposure duration was extended with water ratio 1:0, there was significant increase in drying, cracking and browning effect on the mesocarp and kernel especially. It was observed that microwave exposure has greater effect on the kernel than mesocarp [25, 37]. There was almost slight drying and browning effect upon 2 min exposure with various power level and fruit mass to water ratio (m:v). Although kernels started to turn brown and appeared drier after several minute of exposure with fruit to water ratio of 1:0.5, 1:1 and 1:2, the mesocarp undergoes negligible browning. Therefore, thecondition and appearance of microwave exposed oil palm fruits after reaching 100% strip from the spikelets at 800 Watt and ratio 1:0.5 were denoted in Table 1(b). It shows good quality of white in colour kernel as compared to kernel in Table 1(a) at same power level.

## Conclusion

In this research paper, the effect of using various power leveland ratio of fruit to water as well as analyze the quality of extracted oil have been presented and discussed. It has been shown that, medium power range of 400, 600 and 800 Watt enhance the stripping efficiency with shorter irradiating time. The optimum condition of this research was 6 min of irradiating time at 800 Watt and 1:0.5 ratio to reach completely fruit loosening and exhibits good quality of white in colour kernel with 4.08% of FFA. It was found that the microwave sterilisation can be completed at shorter time with 100% fruits stripping efficiency supplementary with minimum water ratio and this suggests further works especially on the understanding of the microwave interaction with the spikelet during irradiation with the intention ofextraction the oil. During the experimental, the quality of the oil extracted in terms of the free fatty acid percentage was acceptable, varying from 1.02 to 4.08%. With the help of microwave mechanism, in future clean crude palm oil extraction can be done completed without toxic organic solvents in minutes instead of hours with various advantages.

## Acknowledgement

The authors gratefully acknowledge the financial support received from Ministry Higher Education of Malaysia through Research Acculturation Grant Scheme (RAGS) (600-RMI/RAGS 5/3 (77/2013)), Lestari (600-IRMI/DANA 5/3/LESTARI (0033/2016)), Research Management Institute (RMI) and Faculty of Chemical Engineering, Universiti Teknologi MARA, Shah Alam, Selangor, Malaysia.

## References

1. Osei-Amponsah, C., Visser, L., Adjei-Nsiah, S., Struik, P. C., Sakyi-Dawson, O. and Stomph, T. J. (2012). Processing practices of small-scale palm oil producers in the Kwaebibirem District, Ghana: A diagnostic study. *NJAS-Wageningen Journal of Life Sciences*, 60: 49 – 56.

2. Awalludin, M. F., Sulaiman, O., Hashim, R. and Nadhari, W. N. A. W. (2015). An overview of the oil palm industry in Malaysia and its waste utilization through thermochemical conversion, specifically via liquefaction. *Renewable and Sustainable Energy Reviews*, 50: 1469 – 1484.
3. Vincent, C. J., Shamsudin, R. and Baharuddin, A. S. (2014). Pre-treatment of oil palm fruits: A review. *Journal of Food Engineering*, 143: 123 – 131.
4. Hansen, S. B., Padfield, R., Syayuti, K., Evers, S., Zakariah, Z. and Mastura, S. (2015). Trends in global palm oil sustainability research. *Journal of Cleaner Production*, 100, 140 – 149.
5. Basiron, Y. and Weng, C. K. (2004). The oil palm and its sustainability. *Journal of Oil Palm Research*, 16(1): 1 – 10.
6. Lam, M. K. and Lee, K. T. (2011). Renewable and sustainable bioenergies production from palm oil mill effluent (POME): win–win strategies toward better environmental protection. *Biotechnology Advances*, 29(1): 124 – 141.
7. Owolarafe, O. K. and Oni, O. A. (2011). Modern mill technology and centralised processing system, an alternative for improving performance of palm oil mills in Abia State, Nigeria. *Technology in Society*, 33(1): 12 – 22.
8. Ahmad, A. L., Ismail, S. and Bhatia, S. (2003). Water recycling from palm oil mill effluent (POME) using membrane technology. *Desalination*, 157(1-3): 87 – 95.
9. Sanagi, M. M., See, H. H., Ibrahim, W. A. W. and Naim, A. A. (2005). Determination of carotene, tocopherols and tocotrienols in residue oil from palm pressed fiber using pressurized liquid extraction-normal phase liquid chromatography. *Analytica Chimica Acta*, 538(1): 71 – 76.
10. Sivasothy, K., Hwa, R. M. T. T. Y. and Basiron, Y. (2006). Continuous sterilization: The new paradigm for modernizing palm oil milling. *Journal of Oil Palm Research*, 2006: 144 – 152.
11. Norulaini, N. N., Ahmad, A., Omar, F. M., Banana, A. A. S., Zaidul, I. M. and Kadir, M. O. A. (2008). Sterilization and extraction of palm oil from screw pressed palm fruit fiber using supercritical carbon dioxide. *Separation and Purification Technology*, 60(3): 272 – 277.
12. Chow, M. C. and Ma, A. N. (2007). Processing of fresh palm fruits using microwaves. *Journal of Microwave Power and Electromagnetic Energy*, 40(3), 165 – 173.
13. Fatin, S. A., Rosnah, S. and Yunus, R. (2014). Effect of chopping oil palm fruit spikelets on the free fatty acid content release rate and its mechanical properties. *International Journal of Research in Engineering and Technology*, 3(1): 511 – 516.
14. Tan, C. H., Ghazali, H. M., Kuntom, A., Tan, C. P. and Ariffin, A. A. (2009). Extraction and physicochemical properties of low free fatty acid crude palm oil. *Food Chemistry*, 113(2), 645 – 650.
15. Cheng, S. F. and Chuah, C. H. (2011). Microwave pretreatment: A clean and dry method for palm oil production. *Industrial Crops and Products*, 34(1): 967 – 971.
16. Sarah, M. and Taib, M. R. (2013). Microwave sterilization of oil palm fruits: Effect of power, temperature and d-value on oil quality. *Journal of Medical and Bioengineering*, 2(3): 129 – 133.
17. Ali, F. S., Shamsudin, R. and Yunus, R. (2014). The effect of storage time of chopped oil palm fruit bunches on the palm oil quality. *Agriculture and Agricultural Science Procedia*, 2: 165 – 172.
18. Sukaribin, N. and Khalid, K. (2009). Effectiveness of sterilisation of oil palm bunch using microwave technology. *Industrial Crops and Products*, 30(2): 179 – 183.
19. Arimi, J. M., Duggan, E., O'Sullivan, M., Lyng, J. G. and O'Riordan, E. D. (2010). Effect of moisture content and water mobility on microwave expansion of imitation cheese. *Food Chemistry*, 121(2), 509 – 516.
20. McLoughlin, C. M., McMinn, W. A. M., & Magee, T. R. A. (2000). Microwave drying of pharmaceutical powders. *Food and Bioproducts Processing*, 78(2): 90 – 96.
21. Bayramoglu, B., Sahin, S. and Sumnu, G. (2008). Solvent-free microwave extraction of essential oil from oregano. *Journal of Food Engineering*, 88(4): 535 – 540.
22. Zhao, S. and Zhang, D. (2014). Supercritical $CO_2$ extraction of Eucalyptus leaves oil and comparison with Soxhlet extraction and hydro-distillation methods. *Separation and Purification Technology*, 133: 443 – 451.
23. Siew, W. L., Tan, Y. A. and Tang, T. S. (1995). Methods of test for palm oil and palm oil products: Compiled by Siew Wai Lin, Tang Thin Sue, Tan Yew Ai. Palm Oil Research Institute of Malaysia.
24. Sarah, M., Taib, M. R. and Adamu, A. (2014). Enzymatic inactivation of oil palm fruits: Comparison of microwave irradiation and steam bath process. *Jurnal Teknologi*, 65: 55 – 60.

25. Nokkaew, R. and Punsuvon, V. (2014). Sterilization of oil palm fruits by microwave heating for replacing steam treatment in palm oil mill process. *Advanced Materials Research*, 1025: 470 – 475.
26. Lucchesi, M. E., Chemat, F. and Smadja, J. (2004). Solvent-free microwave extraction of essential oil from aromatic herbs: comparison with conventional hydro-distillation. *Journal of Chromatography A*, 1043(2): 323 – 327.
27. Li, Y., Fabiano-Tixier, A. S., Vian, M. A. and Chemat, F. (2013). Solvent-free microwave extraction of bioactive compounds provides a tool for green analytical chemistry. *TrAC Trends in Analytical Chemistry*, 47: 1 – 11.
28. Ghanem, N., Mihoubi, D., Kechaou, N. and Mihoubi, N. B. (2012). Microwave dehydration of three citrus peel cultivars: Effect on water and oil retention capacities, color, shrinkage and total phenols content. *Industrial Crops and Products*, 40: 167 – 177.
29. Virot, M., Tomao, V., Ginies, C., Visinoni, F. and Chemat, F. (2008). Microwave-integrated extraction of total fats and oils. *Journal of Chromatography A*, 1196: 57 – 64.
30. Benmoussa, H., Farhat, A., Romdhane, M. and Bouajila, J. (2016). Enhanced solvent-free microwave extraction of Foeniculum vulgare Mill. essential oil seeds using double walled reactor. *Arabian Journal of Chemistry,* Article in Press.
31. Chong, C. L. and Sambanthamurthi, R. (1993). Effects of mesocarp bruising on the rate of free fatty acid release in oil palm fruits. *International Biodeterioration & Biodegradation*, 31(1): 65 – 70.
32. Mba, O. I., Dumont, M. J. and Ngadi, M. (2015). Palm oil: Processing, characterization and utilization in the food industry–A review. *Food bioscience*, 10: 26 – 41.
33. Takagi, S. and Yoshida, H. (1999). Microwave heating influences on fatty acid distributions of triacylglycerols and phospholipids in hypocotyl of soybeans (glycine max L.). *Food Chemistry*, 66(3), 345 – 351.
34. Filly, A., Fernandez, X., Minuti, M., Visinoni, F., Cravotto, G. and Chemat, F. (2014). Solvent-free microwave extraction of essential oil from aromatic herbs: from laboratory to pilot and industrial scale. *Food Chemistry*, 150: 193 – 198.
35. Chandrasekaran, S., Ramanathan, S. and Basak, T. (2013). Microwave food processing—A review. *Food Research International*, 52(1): 243 – 261.
36. Lucchesi, M. E., Smadja, J., Bradshaw, S., Louw, W. and Chemat, F. (2007). Solvent free microwave extraction of *Elletaria cardamomum* L.: A multivariate study of a new technique for the extraction of essential oil. *Journal of Food Engineering*, 79(3): 1079 – 1086.
37. Umudee, I., Chongcheawchamnan, M., Kiatweerasakul, M. and Tongurai, C. (2013). Sterilization of oil palm fresh fruit using microwave technique. *International Journal of Chemical Engineering and Applications*, 4(3), 111 – 113.

*Malaysian Journal of Analytical Sciences, Vol 21 No 4 (2017): 950 - 957*
*DOI: https://doi.org/10.17576/mjas-2017-2104-22*

MALAYSIAN JOURNAL OF ANALYTICAL SCIENCES
*Published by The Malaysian Analytical Sciences Society*
ISSN 1394 - 2506

# DODECYLBENZENE SULFONIC ACID CONCENTRATION EFFECT ON ELECTRICAL AND THERMAL PROPERTIES OF POLYANILINE

## (Kesan Penumpuan Asid Sulfonik Dodekilbenzena ke atas Sifat Elektrik dan Termal Polianilin)

Nurul Akmil Mustaffa[1]*, Qumrul Ahsan[1], Mohd Asyadi Azam[1], Luqman Chuah Abdullah[2]

[1]*Faculty of Manufacturing Engineering,*
*Universiti Teknikal Malaysia Melaka, Hang Tuah Jaya, 76100 Durian Tunggal, Melaka, Malaysia*
[2]*Material Processing and Technology Laboratory, Institute of Advance Technology,*
*Universiti Putra Malaysia, 42400 UPM Serdang, Selangor, Malaysia*

**Corresponding author: akmil.mustaffa@gmail.com*

Received: 28 November 2016; Accepted: 5 February 2017

**Abstract**

Polyaniline (PANI) doped with various concentration of dedocylbenzene sulfonate acid (DBSA) were prepared by oxidative polymerization with presence of ammonium persulfate. Emerald green PANI powder obtained were characterized by Fourier transform infrared spectroscopy (FTIR), differential scanning calorimetry (DSC), and carried out electrical conductivity test. In this research, the conductivity and thermal properties of PANI has been changed with the effect of doping. With increasing concentration of DBSA, the conductivity raises up to certain concentration (1.65 mmol of DBSA), afterwards with further increase of DBSA concentration, conductivity value declines and reaches to a value lower than that of pristine PANI. The similar trend is also observed for enthalpy values (ΔH) determined by DSC of pristine PANI and DBSA doped PANIs' which may attribute the effect of concentration of DBSA on molecular arrangement in PANI. Results from polymeric structure obtained from FTIR clearly indicate the disruption in bond when PANI doped with DBSA and it may indicate that the DBSA changes molecule structure of PANI in term of segmented local structure of polymer.

**Keywords**: polyaniline, advanced material, dodecylbenzene sulfonate acid, conductivity, differential scanning calorimetry

**Abstrak**

Polianilin (PANI) didopkan dengan pelbagai kepekatan asid sulfonat dodekilbenzena (DBSA) telah disediakan dengan kaedah pempolimeran oksidatif dengan kehadiran ammonium persulfat. Serbuk hijau zamrud PANI yang diperolehi dicirikan oleh spektroskopi inframerah Fourier (FTIR), kalorimeter imbasan pembeza (DSC), dan ukuran kekonduksian. Dalam kajian ini, didapati bahawa kekonduksian haba dan sifat – sifat PANI telah ditukar sebagai kesan daripada pendopan. Dengan peningkatan kepekatan DBSA, kekonduksian juga meningkat sehingga kepekatan tertentu (1.65 mmol daripada DBSA). Kemudian, kekonduksian berkurangan dengan peningkatan kepekatan DBSA selanjutnya. Keputusan PANI daripada DSC, yang mengandungi nilai entalpi yang berbeza (ΔH) menunjukkan bahawa DBSA tidak mengubah struktur molekul PANI dari segi segmen struktur tempatan polimer dan ΔH juga menunjukkan ke arah kesan kepekatan DBSA pada susunan molekul dalam PANI.

**Kata kunci:** polianilin, bahan termaju, asid sulfonat dodekilbenzena, konduktiviti, kalorimeter imbasan pembeza

## Introduction

Now days, conductive polymers are widely used in electric and electronic devices. Among the conductive polymers, polyaniline (PANI) conquers a place of special interest in alternative to metal and semiconducting material [1].

Through the past 20 years, a variety of different conducting polymers have been found and studied [2]. From the commercial viewpoint, these polymers show promise for the invention of materials for numerous applications; they be able to replace metals and semiconductors, because their feature in conductivity, low density, and easy processability. Polyaniline (PANI) a representatives from the family of conducting polymers is well-known by easy synthesis and high environmental stability. Interest about PANI (Figure 1) is evidenced by the fact that the field of conducting polymers has concerned scientists from such varied areas of interest as electrochemistry, materials science, synthetic chemistry, polymer science, solid state physics, electrical and electronics engineering.

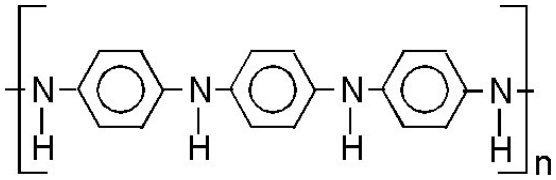


Figure 1. Polyaniline molecule structure

The attention has been paid in studying conducting polymers because these polymers have aromatic rings - and nitrogen-substituted derivatives which can be readily synthesized. Rings and derivatives can exist in several different oxidation states these in principle can be doped by various dopants through non-redox processes or by partial chemical or electrochemical oxidation. DBSA has been widely used as dopant which also acts as a surfactant and a protonating agent [3], especially in emulsion polymerizations [4] where the PANI performs as a semiconductor. Preparation of PANI–DBSA colloids [5] to polymerize PANI is a doping process for adding impurities to intrinsic semiconductors (PANI) to change their electrical properties. However, the doping process sometime will affect directly or indirectly to the conductivity of PANI. Hence, the concentration of dopant also have maximum limit that will contribute to lower in conductivity because of the restricted electron delocalization. The study of polymeric materials by thermal analysis has become increasingly popular in today's analytical laboratory because it will give more information about molecule arrangement and defect in crystal structure.

Therefore, in this research focusing more on the DBSA effect without using strong acid to alter the acidic condition of PANI during polymerization. DBSA doped PANI were characterized using four point probe method for conductivity, differential scanning calorimeter (DSC) for thermal analysis and Fourier Transforms Infrared spectrometer (FTIR).

## Materials and Methods

### Materials

Aniline chloride and hydrochloric acid (HCl) (37%) were collected from Merck, Ammonium peroxydisulfate and dodecylbenzene sulfonic acid ($C_{18}H_{30}NaO_3S$) were collected from Sigma-Aldrich.

### Synthesis of PANI

The pristine PANI was synthesized (direct oxidation) by the polymerization of aniline hydrochloride and ammonium peroxydisulfate without addition of dodecylbenzene sulfonic acid (DBSA). The aniline hydrochloride and ammonium peroxydisulphate ($(NH_4)_2S_2O_8$) was dissolved in 100 mL of distilled water separately. Both solutions were precooled at 9 °C for 12 hours and were mixed in a beaker, briefly stirred and left at rest to polymerize in a refrigerator at 9 °C for 24 hours. While for DBSA doped PANI was synthesized by the polymerization of aniline hydrochloride in different concentrations of aqueous DBS acid solutions. Aniline hydrochloride (purum; 5.18 g, 40 mmol) was added in aqueous DBS acids (0.8, 1.65, 2.0, and 2.5 mmol) of 100 mL solution. The reaction conditions for synthesis of PANI-DBSA are given in Table 1. Ammonium peroxydisulphate (purum; 11.42 g, 50 mmol) was dissolved in distilled water to prepare another 100 mL of solution. Both solutions were precooled (9 °C, 12 hours) and were mixed in a beaker, briefly stirred, and left at rest to polymerize in refrigerator at 9 °C for 24 hours. Afterwards the PANI precipitate (emeraldine salt) was collected on a filter, washed three times with 100 ml of 0.2 M HCl acid followed by 100 mL of acetone. Later salt was dried in vacuum at 60 °C for 24 hours.

Table 1. Reaction conditions for synthesis of PANI-DBSA

| Code | Monomer | Oxidant | Dopant | Volume of Dopant (mmol) | Temperature |
|---|---|---|---|---|---|
| $DBSA_1$ | | | | 0.8 | |
| $DBSA_2$ | | | | 1.2 | |
| $DBSA_3$ | Aniline | $(NH_4)_2S_2O_8$ | $C_{18}H_{30}NaO_3S$ | 1.6 | 9 °C |
| $DBSA_4$ | | | | 2.0 | |
| $DBSA_5$ | | | | 2.5 | |

**Characterization: Fourier Transformation Infrared analysis**
FTIR (FT/IR-6100; JASCO) analysis was conducted to confirm the presence of functional group in pristine PANI and PANI-DBSA. PANI granules powder was grounded to obtain fine particles. All spectra were recorded at ambient temperature and the analysis was performed at wavelength range from 400 $cm^{-1}$ to 4000 $cm^{-1}$ at scanning speed of 2 mm $s^{-1}$ with aperture size of 7.1 mm.

**Conductivity**
For conductivity measurement, PANI powders are firstly press into a pellet form by using hydraulic presser to make less than 1mm samples. Then, conductivity measurements, using the four-point probe technique (ASTM D-991-89) were performed upon pressed pellets of the starting material. The measurements were made using a Jandel four-point probe.

**Thermal scanning**
Differential Scanning Calorimetry (Perkin Elmer model DSC 7) were conducted in nitrogen atmosphere at a temperature range of 30-300 $^{\circ}C$ with a heating rate of 20 $^{\circ}C$/min

## Results and Discussion

**Fourier transforms infrared spectroscopy**
FTIR is used to observe the changes in PANI bonding structure. From Figure 2, the strong peak observed at ~1600 $cm^{-1}$ is related to C=C conjugate. This peaks are shown in pristine PANI, PANI-$DBSA_3$ and PANI-$DBSA_5$ at 1608, 1617 and 1612 $cm^{-1}$, respectively. The adsorption band at around 1380 $cm^{-1}$ (blue circle) corresponds to group of sulphoamide formed after doping with DBSA, for that reason only PANI-$DBSA_3$ AND PANI-$DBSA_5$ spectra shows slightly broad peaks base on sulphoamide structure present in their molecule. The major peaks at 1360 –1250 $cm^{-1}$ correspond to quinone and benzene ring stretching deformations as correspond to aromatic amide in PANI structure. The adsorption band at 1306 $cm^{-1}$ corresponds to $\pi$-electron delocalization induced in polymer via protonation. The PANI-$DBSA_3$ and PANI-$DBSA_5$ spectra also show the adsorption band correspond to covalent sulphonates at 1095 and 1084 $cm^{-1}$ as shown in the red circle. The main functional group of PANI is 1,4-disubstituded benzene which found at 820,814, and 810 $cm^{-1}$ for pristine PANI, PANI-$DBSA_3$ and PANI-$DBSA_5$, respectively. The various peaks in the range of 700 to 500 $cm^{-1}$ are correspond to main aromatic component of PANI's. Table 2, shows the absorption FTIR peaks collected from pristine PANI, PANI-$DBSA_3$ and PANI-$DBSA_5$ as compare to reference values [6].

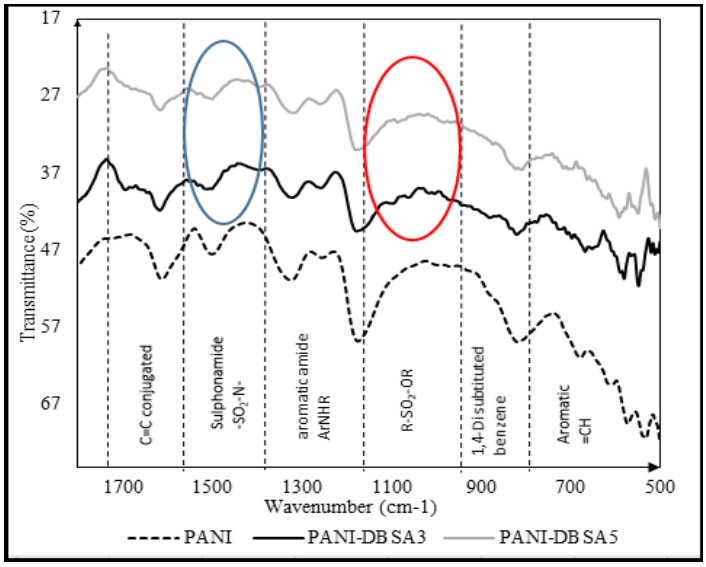



Figure 2. FTIR specra of Pristine PANI, PANI-DBSA$_3$, and PANI-DBSA$_5$.

Table 2. Comparision of absorption peaks in the synthesis pristine PANI, PANI-DBSA$_3$ and PANI-DBSA$_5$.

| **Functional Group** | **Peaks (cm$^{-1}$)** | | | |
|---|---|---|---|---|
| | **Reference [6]** | **Pristine PANI** | **PANI-DBSA$_3$** | **PANI DBSA$_5$** |
| C=C conjugated | ~1600 | 1608 | 1617 | 1612 |
| Sulphonamide $SO_2$-N < | 1380 | - | 1387 | 1389 |
| Primary or secondary aromatic amide ArNHR | 1360-1250 | 1252 | 1254 | 1257 |
| Covalent sulphonates, R-SO2-OR | 1020-850 | - | 1095 and 1059 | 1084 and 969 |
| 1,4-Disubstituded benzene | 860-780 | 814 | 820 | 810 |

**Conductivity**

Electrical conductivity of PANI doped with various concentration of DBSA were determined by using four point probe analysis and their values are shown in Figure 3. The highest conductivity after doping with DBSA is 13. 37S/cm. The graph shows conductivity of pristine PANI decrease when DBSA$_1$ is introduce to the polymerization system. It is may be due to the polymerization of PANI are disturbed and segmental molecule structure not properly arranged. Furthermore, after addition of 1.2 and 1.65 mmol of DBSA, the trend shows by increasing of amount of DBSA, the conductivity is increased. Moreover, PANI-DBSA$_3$ AND PANI-DBSA$_4$ shows almost similar value of conductivity before the conductivity decreases at PANI-DBSA$_5$. PANI itself is consisting of benzoid and oxidized quinoid units [7]. The conduction of electricity in PANI is due to conjugation in the backbone of the polymer in the benzoid and quinoid units. Due to overlapping of conjugated π-electrons, there develops valance and conduction bands throughout the backbone of the PANI.

This can be explained as the presence of DBSA in polymerization, as "holder" to hold the aniline micelles monomer in aqueous medium as schematic representation shown in Figure 4. Aniline ion (phenyl-$NH_3^+$) resides between the individual sodium dodecyl sulphate (SDS) near the shell of micelle complexes with sulfate ion. The aniline molecule are oriented with phenyl substitution (hydrophobic nature of DBSA) to be the core of micelle and the $NH_3^+$ to the outer side of micelle. During the polymerization process, the aniline ion is polymerized into the micelle

together with DBSA after being oxidized by APS. Therefore, the increasing of amount of DBSA will increase the aniline ion attached together to formed a large size of micelle, hence enlargement of polymer chain. The longer chains of PANI formed, the higher conductivity of PANI as the present of large amount of the conjugated ion in the polymer chains. The formed chains also arranged in a segment, and the segmental local structure of polymer are shorten.

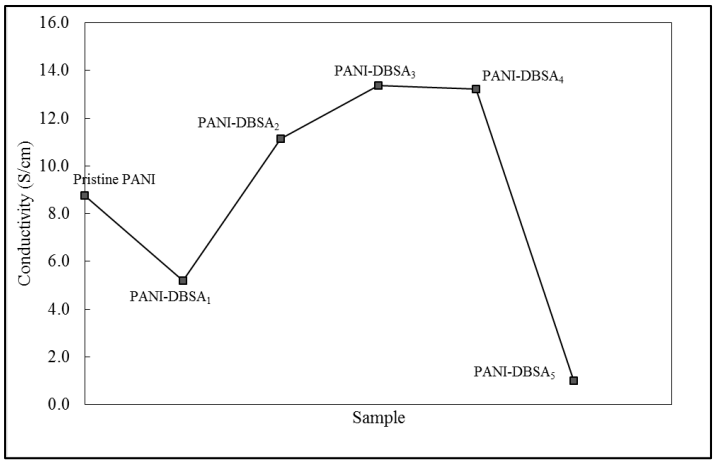



Figure 3. Conductivity of PANI-DBSA

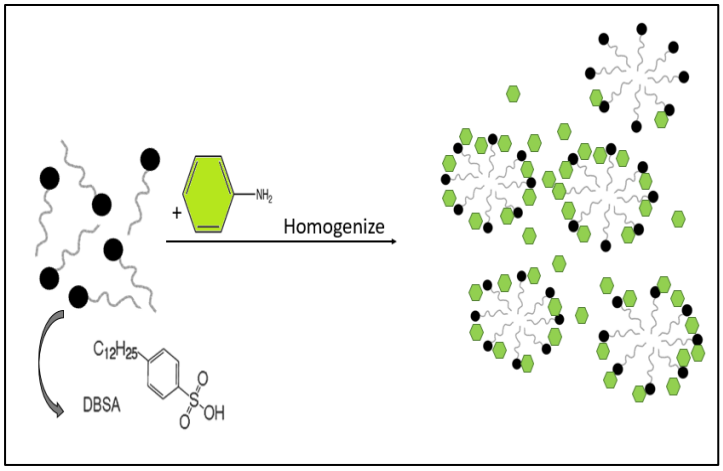



Figure 4. Probable reaction mechanism of micelles SDS and aniline during polymerization

On the other hand, the excessive amount of DBSA (as increased to 2.0 and 2.5 mmol of DBSA) shows the decreasing in conductivity. It can be inferred that the DBSA also act as surfactant in the system. The excessive amount of sodium dodecyl sulphate (SDS) ion, will capture more aniline ion to be in one large micelle before oxidation occurs.

After addition of APS, the longer chains formed during oxidative polymerization process. However, as stated by Khohklov in 1981, the longer chains formed during polymerization, the higher possibility the polymer chains will collapse [8]. The collapse polymer chains or a Gaussian coil starts to aggregate, resulting in a homogeneously dense sausage-like shape. After several times, the minimization of interfacial area drives this sausage-like shape to

condense and shorten until, at the final stage, a globule is formed [9]. The collapse phenomena creates chains disordered (globule) and resulting in dislocated of conjugated π-electrons hence lower the conductivity. The decrease in conductivity also could be assigned to the dominating role of ion association over free ion formation which decreases the number of charge carriers for conduction [10].

**Differential scanning calorimetry**

From DSC thermogram in Figure 5, we can determined the onset temperature of melting point, peak temperature that represent the melting point of the polymer, and the enthalpy of fusion, ΔH by calculating area under the graph. Table 3 shows the DSC thermogram data for Pristine PANI and PANI-DBSA.

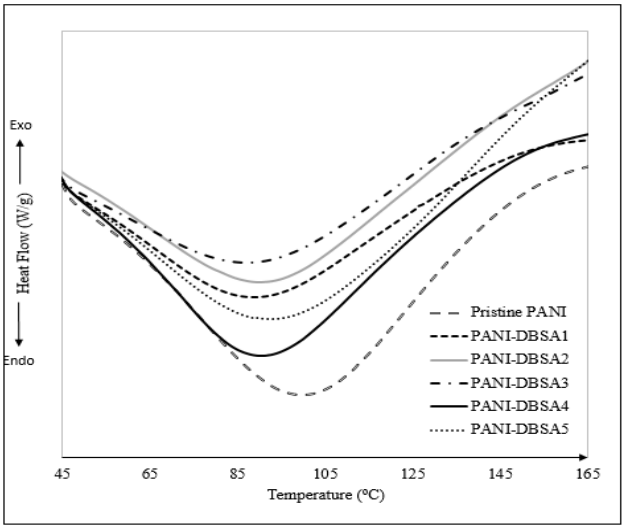



Figure 5. DSC thermogram of Pristine PANI and PANI-DBSAs

Table 3. DSC thermogram data for Pristine PANI and PANI-DBSA

| Sample | Onset Temperature ($T_o$), $^oC$ | Melting temperature ($T_m$), $^oC$ | Enthalpy of Fusion (ΔH), J/g |
|---|---|---|---|
| Pristine PANI | 50.31 | 97.77 | 210.2908 |
| PANI-$DBSA_1$ | 42.31 | 87.22 | 219.7509 |
| PANI-$DBSA_2$ | 41.60 | 86.85 | 158.4879 |
| PANI-$DBSA_3$ | 41.56 | 84.16 | 136.6957 |
| PANI-$DBSA_4$ | 40.34 | 88.27 | 157.8515 |
| PANI-$DBSA_5$ | 40.73 | 89.15 | 187.4384 |

In semi-crystalline polymer like PANI, a broad melting curve is the normal DSC thermogram, thus make separating melting from simultaneous crystallization or crystalline reorganization can be difficult [10]. The onset temperature usually indicates the starting point PANI's molecules start to change their state from solid to rubbery state. The PANI's molecules become soften and crystalline portions start to move transitionally [11]. As increasing in amount of DBSA during polymerization of PANI, the onset temperature is decreasing shows the presence of DBSA has altered the chains length make it easily to adsorbed heat to disturb ordered molecule regions. Though, sample PANI-$DBSA_5$, shows the onset temperature increase slightly compare to PANI-$DBSA_4$, it shows insignificant value because the differences is too small. The melting point of the pristine PANI and PANI-DBSAs shows the same trend as onset temperature. In addition of DBSA, the melting point slightly decreased compare to pristine PANI.

In Figure 6, the enthalpy of fusion shows indirectly proportional to the value of conductivity. It can be enlightened that the amount of DBSA doped PANI affect the conductivity and thermal properties of PANI. The value enthalpy of fusion (ΔH) corresponds to the normalized peak area in joules per gram (J/g) and a result of crystal imperfection [12]. The increase in conductivity with ΔH is interpreted in terms of hopping mechanism between co-ordination sites, local structural relaxation and segmental motion of polymer [13]. Thus the segmental local structures of polymer are shorten with increasing in amount of DBSA in polymerization of PANI. This can be assure as the ΔH are decreasing as increasing in amount of DBSA. However, as concentration of DBSA is increase up to 2.0 mmol, the ΔH shows slightly increased. This is may be due to the PANI local structure has been increased and the segmental motion are stiffer thus increase heat required to vibrate the PANI structure.

Moreover, increasing amount of DBSA shows no independent influence to melting point of PANI. This may be due to the amount of DBSA are very small to influence the melting point even though the ΔH shows a great significant value.

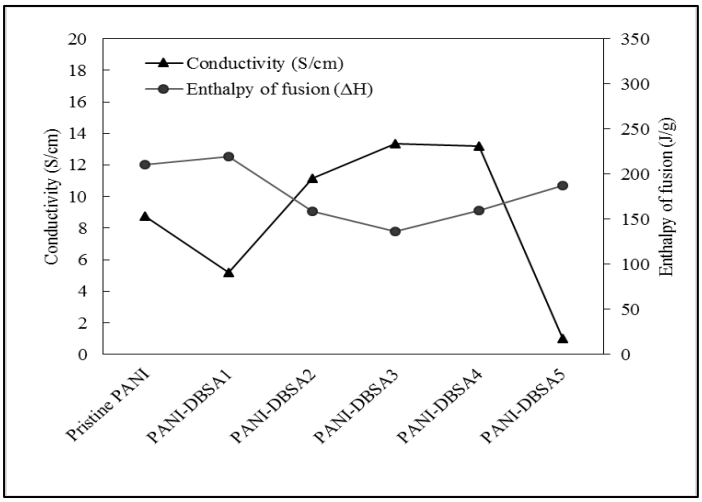



Figure 6. Graph of enthalpy and conductivity versus amount of DBSA in PANI

## Conclusion

Polyaniline was prepared by chemical synthesis using DBSA as the surfactant. The spectra of PANI-DBSA has the important significant peaks of DBSA after doping procedure. For synthesized PANI-DBSA, FTIR spectra shows the dopant peaks as the interaction with PANI structure. The electrical conductivity measurement has shown that electrical conductivity of pristine PANI is 8.77 S/cm and addition of DBSA as dopant in PANI polymerization has increased the conductivity up to 13.37 S/m. Based on DSC results, DBSA has a strong effect as it can lowered the ΔH values of PANI-DBSA$_1$ to PANI-DBSA$_3$ but increases at PANI-DBSA$_4$ and PANI-DBSA$_5$ as the doping give an effect on PANI molecular arrangement.

## Acknowledgement

The support of the Ministry of Higher Education (Malaysia) for Mybrain15 scholarship is kindly acknowledged.

## References

1. Basavaraja, C., Pierson, R., Kim, J. H. and Huh, D. S. (2008). Microscopic studies of polyaniline-poly-n-isopropylacrylamide/alumina composites containing dodecylbenzene sulfonic acid. *Bulletin of the Korean Chemical Society*, 29(9): 1699 – 1704.
2. Skotheim, T. A. (1986). Handbook of Conducting Polymer, Marcel Dekker, New York.

3. Saini, P. and Choudhary, V. (2015). Structural, spectral and thermal properties of bulky organic sulfonic acids doped polyanilines and antistatic performance of its melt blend. *Indian Journal of Pure & Applied Physics*, 53(5): 320 – 327.
4. Wang, Y., Ji, H., Shi, H., Zhang, T. and Xia, T. (2015). Fabrication and characterization of stearic acid/polyaniline composite with electrical conductivity as phase change materials for thermal energy storage. *Energy Conversion and Management*, 98: 322 – 330.
5. Wallace, G. G., Spinks, G. M. and Teasdale, P. R. (1997). Conductive electroactive polymers; intelligent materials systems. Lancaster: Technomic.
6. Socrates, G. (2004). Infrared and Raman characteristic group frequencies: tables and charts. John Wiley & Sons.
7. Molapo, K. M., Ndangili, P. M., Ajayi, R. F., Mbambisa, G., Mailu, S. M., Njomo, N., Masikini, M., Baker, P. and Iwuoha, E. I. (2012). Electronics of conjugated polymers (I): polyaniline. *International Journal of Electrochemical Science*, 7(12): 11859 – 11875.
8. Khokhlov, A. R. (1981). Theory of the polymer chain collapse for the d-dimensional case. *Physica A: Statistical Mechanics and its Applications*, 105(1-2): 357 – 362.
9. Abrams, C. F., Lee, N. K. and Obukhov, S. P. (2002). Collapse dynamics of a polymer chain: Theory and simulation. *EPL (Europhysics Letters)*, 59(3): 391.
10. Hatakeyama, T. and Quinn, F. X. (1999). Thermal analysis: fundamentals and applications to polymer science. , 2nd Edition, John Wiley & Sons.
11. Menczel, J. D. and Prime, R. B. (2014). Thermal analysis of polymers: fundamentals and applications. John Wiley & Sons.
12. Pitchimani, R., Zheng, W., Simon, S. L., Hope-Weeks, L. J., Burnham, A. K. and Weeks, B. L. (2007). Thermodynamic analysis of pure and impurity doped pentaerythritol tetranitrate crystals grown at room temperature. *Journal of Thermal Analysis and Calorimetry*, 89(2): 475 – 478.
13. Imre, Á. W., Schönhoff, M. and Cramer, C. (2008). A conductivity study and calorimetric analysis of dried poly (sodium 4-styrene sulfonate)/poly (diallyldimethylammonium chloride) polyelectrolyte complexes. *The Journal of Chemical Physics*, 128(13): 134905.
14. Wang, Y., Ji, H., Shi, H., Zhang, T. and Xia, T. (2015). Fabrication and characterization of stearic acid/polyaniline composite with electrical conductivity as phase change materials for thermal energy storage. *Energy Conversion and Management*, 98: 322 – 330.
15. Mustaffa, N. A., Ahsan, Q., Azam, M. A. and Abdullah, L. C. (2016). Effect of dodecylbenzene sulfonic acid dopant concentration on the synthesis of polyaniline. *Jurnal Teknologi.*

*Malaysian Journal of Analytical Sciences, Vol 21 No 4 (2017): 958 - 971*
*DOI: https://doi.org/10.17576/mjas-2017-2104-23*

MALAYSIAN JOURNAL OF ANALYTICAL SCIENCES
*Published by The Malaysian Analytical Sciences Society*
ISSN 1394 - 2506

# COMPARISON OF PURIFICATION METHODS TO PURIFY RECOMBINANT BROMELAIN FROM *Escherichia coli* BL21-A1

## (Perbandingan Kaedah Penulenan Rekombinan Bromelain daripada *Escherichia coli* BL21-A1)

Zatul Iffah Mohd Arshad[1,2*], Azura Amid[2], Faridah Yusof[2], Siti Zubaidah Sulaiman[1], Siti Kholijah Abdul Mudalip[1], Rohaida Che Man[1], Shalyda Md Shaarani[1]

[1]*Faculty of Chemical Engineering & Natural Resources, Universiti Malaysia Pahang, 26300 Gambang, Pahang, Malaysia*
[2]*Bioprocess and Molecular Engineering Research Unit, Department of Biotechnology Engineering, Faculty of Engineering, International Islamic University Malaysia, P.O. Box 10, 50728 Kuala Lumpur, Malaysia*

**Corresponding author: zatul@ump.edu.my*

Received: 28 November 2016; Accepted: 5 February 2017

**Abstract**

Recombinant bromelain is a cysteine protease that can be exploited for its protease activity in food and pharmaceutical applications. The aim of this study was to compare different purification methods aqueous two-phase system (ATPS), ammonium sulphate precipitation, ion exchange, affinity, and gel filtration chromatography) for the recombinant bromelain purification from *Escherichia coli* BL21-A1. From the SDS-PAGE analysis, all methods produced band with molecular weight between 50 to 55 kDa. Among the methods used, the ATPS purification consisting of 13% (w/w) of PEG6000 and 11% (w/w) potassium phosphate at pH 7.0 was chosen as the best purification method. The method produced 16.39 ± 0.03 % of yield, purification fold of 5.35 ± 0.11, and specific activity of 3.47 ± 0.11 unit/mg of recombinant bromelain. This proposed study can be used as a platform for large-scale downstream processing of recombinant bromelain in industry.

**Keywords**: recombinant bromelain, purification, chromatography, aqueous two-phase system

**Abstrak**

Rekombinan bromelain adalah sisteina protease yang boleh dieksploitasi dalam aplikasi makanan dan farmaseutikal. Tujuan kajian ini adalah untuk membandingkan kaedah penulenan yang berbeza dengan menggunakan sistem akueus dua fasa (ATPS), pemendakan amonium sulfat, pertukaran ion, afiniti dan gel penapisan kromatografi untuk penulenan rekombinan bromelain daripada *Escherichia coli* BL21-A1. Daripada analisis SDS-PAGE, semua kaedah menghasilkan jalur dengan berat molekul antara 50 hingga 55 kDa. Antara kaedah yang digunakan, sistem akueus dua fasa (ATPS) yang terdiri daripada 13% (w/w) PEG6000 dan 11% (w/w) kalium fosfat pada pH 7.0 telah dipilih sebagai kaedah penulenan yang terbaik. Kaedah ini mendapat 16.39 ± 0.03% hasil, kadar penulenan 5.35 ± 0.11, dan aktiviti rekombinan bromelain sebanyak 3.47 ± 0.11 unit/mg. Kajian ini dicadangkan boleh digunakan sebagai platform untuk pemprosesan hiliran rekombinan bromelain secara besar-besaran dalam industri.

**Kata kunci:** rekombinan bromelain, penulenan, kromatografi, sistem akueus dua fasa

## Introduction

Bromelain is a plant protease that is commercially obtained from stem, fruit, and waste of pineapple plant [1]. Bromelain is notable for being used in multitude industrial applications such as meat tenderization, food, beverages, and pharmaceuticals, hence increases its market demand [2]. However, there is a rising argument whether pineapple

crop should be selected for food or bromelain extraction. Besides, the processing of pineapple crop to produce bromelain generates bulk waste that eventually leads to environmental issues. Considering the significance of economic, efficient production and downstream processing of bromelain, recombinant bromelain was successfully expressed in various hosts, including *Escherichia coli* BL21-A1 [3], *E.coli* BL21 DE3pLysS [4] and *Brassica rapa* [5]. Our research group has successfully cloned the stem bromelain from *Ananas comosus* into the pENTR/TEV/D-TOPO vector and subcloned it into the pDEST17 expression vector. Later, *E. coli* BL21-A1 was transformed with the expression vector [3] and was cultivated in a batch process using auto-induction media [6]. The recombinant bromelain is an intracellular enzyme and remains abundantly in the cytoplasm of the *E. coli* cells. Therefore it is vital to develop a reliable, efficient, and cost-effective purification process to purify the recombinant bromelain after cell disruption process using ultrasonication method [7].

Commonly, recombinant bromelain was purified using affinity chromatography under native condition [3, 8]. An instrument such as AKTA prime plus® (GE Healthcare, USA) provides a quick design to facilitate affinity chromatography purification as the plasmid vector of recombinant bromelain has a unique polyhistidine (His6) tag [3]. It was reported that, the recombinant bromelain purified from *E. coli* BL21-A1 has a molecular weight of 50 – 55 kDa and exhibited optimum proteolytic activity at pH 4.6 [3]. In the majority of food industry, the enzyme is added in bulk quantity. The enzyme purified by Amid et al. [3] was only produced in a small amount (~200 µl) and could not be used for large scale food-related processes. Therefore, there is a need to develop a purification protocol that accompanies higher recovery, lower cost, and shorter processing time. Aqueous two-phase system (ATPS) is one of the alternative purification methods which involves a mixing of two polymers or one polymer and one salt under specific condition to form a phase separation. Due to its low cost and high recovery, ATPS purification method has been addressed previously by other researchers for the purification of recombinant protein [9, 10] and bromelain from pineapple plant [1].

To date, recombinant bromelain has not been extracted by aqueous two-phase technique, which could be promising in the bromelain research. In this paper, we compare the purification efficiency of ammonium sulfate precipitation, aqueous two-phase system, ion exchange chromatography, affinity chromatography, and gel filtration chromatography. Purified recombinant bromelain was further evaluated using SDS-PAGE analysis and enzyme assay with Nα-CBZ-L-lysine *ρ*-nitrophenyl ester (LNPE) as substrate.

## Materials and Methods

### Media and culture condition

The cultivation of *E. coli* BL21-A1 [3] was conducted in a batch fermentation using auto-induction method [6]. Approximately 10 ml of starter medium supplemented with 100 µg/ml ampicillin was inoculated with single colony of *E. coli* BL21-A1 harbouring the bromelain gene and incubated for 16 hours at 37 °C with shaking at 300 rpm in an incubator shaker (CERTOMAT® IS, Sartorius, Germany). 1 L of ZYM medium [11], supplemented with 100 µg/ml ampicillin, was inoculated with 10 ml of starter culture and incubated in an incubator shaker (CERTOMAT® IS, Sartorius, Germany) for 12 hours at 37 °C with shaking at 250 rpm until the $OD_{600nm}$ reached 0.6-1.0. After 12 hours, the cells were harvested by centrifugation (4 °C, 16000 x g, and 15 min) (Heraeus Multifuge X1R, Thermo Scientific, USA), and the cell pellet was stored at -20 °C until further used. The cell pellet was suspended in lysis buffer at a ratio of 1 g to 5 ml of lysis buffer before cell disruption by sonication technique (20% amplitude and first cycle for 130 ml/min) [7]. The lysate was then centrifuged at 16000 x g for 45 min (Heraeus Multifuge X1R, Thermo Scientific, USA) to obtain a clear supernatant for further analysis.

### Enzyme activity assay

The enzymatic assay was based on continuous spectrophotometric rate determination method. The proteolytic activity of recombinant bromelain was measured using Nα-CBZ-L-lysine *ρ*-nitrophenyl ester (LNPE) as a substrate at 44 °C and pH 4.6. Initially, 2.60 ml of LNPE buffer was mixed and incubated with 100 µl of enzyme solution for approximately 3 min. Then, 100 µl of 50 mM LNPE substrate was added and mixed by inversion. The absorbance measurement of enzymatic reaction was measured spectrophotometrically for 5 min at 340 nm using a microplate reader (Thermo Scientific, USA). One unit of enzyme activity corresponds to the release of 1.0 µmole of ρ-nitrophenyl ester from the LNPE substrate per min after reaction with bromelain [12]. The hydrolysis of substrate was monitored at the selected wavelength starting 50 sec after the addition of enzyme in order to allow enough time

for the assay medium to reach 44 °C. Initial velocity measurements were obtained from the data recorded over the next 300 sec (5 min), where linearity was maintained. The results were plotted as ΔAbs per min versus amount of enzyme. The slope of this line, together with the molar absorption coefficient obtained as described in equation 1, allowed us to calculate enzyme activity in terms of units/mg protein as below:

$$\frac{\left(\frac{\Delta A_{340nm}}{\text{min Test}} - \frac{\Delta A_{340nm}}{\text{min Blank}}\right) \times 2.8 \times DF}{6.32 \times 0.1} \quad (1)$$

where the values of 2.8, 6.32, 0.1 and DF denote the assay volume in milliliters, the millimolar extinction coefficient of ρ-nitrophenol at 340 nm, the volume of enzyme used in milliliters, and the dilution factor, respectively. Assays were carried out in triplicate.

**Protein assay**
Protein content was measured based on the Bradford method using Bio-Rad Protein Assay (Bio Rad, Germany). Absorbance was measured at a wavelength of 595 nm using a microplate reader. (Thermo Scientific, USA). Bovine serum albumin was used as a standard for the protein assay [13]. Assays were carried out in triplicate.

**Sodium dodecyl sulfate-polyacrylamide gel electrophoresis**
Purified samples from ATPS were analyzed by using sodium dodecyl sulfate-polyacrylamide gel electrophoresis (SDS-PAGE) [14]. The ATPS samples were diluted two times before applying to 12% resolving gel and 4% stacking gel. After electrophoresis was performed at 200 V, 700 mA for 37 min, the gels were stained using silver stain or Coomassie blue.

**Ammonium sulfate precipitation**
Protocol for ammonium sulfate precipitation was adopted from Grodzki et al. [15]. The precipitation of the recombinant bromelain was performed by slow addition of ammonium sulfate to the crude cell lysate at 4 °C. Initially, solid ammonium sulfate was slowly added to achieve a final concentration of 30% (w/v). The mixture was incubated for 30 minutes with continuous stirring. After the ammonium sulfate was completely dissolved, the mixture was centrifuged at 4 °C and 16000 x g for 15 minutes (Heraeus Multifuge X1R, Thermo Scientific, USA). Precipitate was discarded, and the recombinant bromelain in supernatant was collected. The supernatant was subjected to further precipitation by slowly adding ammonium sulfate to achieve a final concentration of 60% (w/v). The solution was stirred and incubated overnight at 4 °C to reach equilibrium. The precipitated protein was collected for chromatography analysis after centrifugation at 16000 x g for 15 minutes. The weight of saturated ammonium sulfate in gram that was required for salting out the protein is given in Equation 2.0 [15] as follows:

$$g = Volume\ of\ sample\ (ml) \times 0.515 \frac{g}{ml} \times \frac{(S_2 - S_1)}{1 - S_2} \quad (2)$$

where $S_2$ and $S_1$ are final saturation (%) and initial saturation (%), respectively. The value of 0.515 g/ml denotes the solubility of ammonium at 4 °C. The ammonium sulfate has a molecular weight of 131.14 g/mol, and 100% saturation of ammonium salt at 4 °C corresponds to 3.93 M, therefore the solubility of ammonium sulfate at 4 °C is 0.515 g/ml.

**Ion-exchange chromatography**
Ion exchange chromatography using AKTA Prime Plus® (GE Healthcare, UK) was performed to purify recombinant bromelain. A glass column connected to AKTA Prime Plus® (GE Healthcare, UK) with an inner diameter of 1 cm and the length of 10 cm was packed with DEAE-Sepharose FF® with 5.5 $cm^3$ column volume and equilibrated with 100 mM of Tris at pH 9.0 followed by 5 ml sample loading from 0.16 g recombinant bromelain produced from 60% ammonium sulfate precipitation process at a flow rate of 1 ml/min. After that, the column was washed with the same buffer. A stepwise elution experiment was performed with elution buffer of 100 mM of Tris and 700 mM NaCl at pH 9.0. Finally, the eluates were analyzed for their enzyme activity, specific activity, total protein content and purification fold.

**Affinity chromatography**

Affinity purification was conducted using AKTA Prime Plus® (GE Healthcare, UK). A glass column connected to AKTA Prime Plus® (GE Healthcare, UK) with an inner diameter of 1 cm and 10 cm length was packed with 5.5 $cm^3$ column volume of Ni-NTA agarose and equilibrated with equilibration buffer (50 mM of $NaH_2PO_4$, 300 mM NaCl and 10 mM of imidazole) at pH 8.0. The protein precipitate (0.16 g) from 60% of ammonium sulfate precipitation process was suspended in 5 ml equilibration buffer and was loaded into the packed column at a flow rate of 1 ml/min. After the unbound protein was washed with washing buffer (50 mM of $NaH_2PO_4$, 300 mM NaCl and 20 mM of imidazole, pH 8.0), the desired protein was eluted with a stepwise elution using elution buffer (50 mM of $NaH_2PO_4$, 300 mM NaCI and 250 mM of imidazole, pH 8.0). Collected fractions were analyzed by enzyme activity, specific activity, total protein content, and purification fold.

**Gel filtration chromatography**

A glass column connected to AKTA Prime Plus® (GE Healthcare, UK) with an inner diameter of 2.5 cm and 100 cm length was packed with 375.57 $cm^3$ column volume of Sephacryl S-200® and equilibrated with two column volumes of 100 mM Tris buffer, pH 7.0. Recombinant bromelain sample (0.16 g) from 60% of ammonium sulfate precipitation was applied to the packed column at a flow rate of 1 ml/min and washed with two column volumes of the same buffer until no other proteins were eluted. Purified proteins were analyzed for enzyme activity, specific activity, total protein, and purification fold.

**Aqueous two-phase system**

Stock solution of PEG 1500, 2000, 4000, 6000, 8000 and potassium phosphate was prepared with 50% (w/w) concentration. Potassium phosphate solution was prepared using specified ratios of $K_2HPO_4$ and $KH_2PO_4$ to achieve pH 7.0. ATPS was prepared in a graduated tube by adding 20% (w/w) of recombinant bromelain lysate, known weight of the PEG stock solution, potassium phosphate stock solution at definite pH, and deionized water to reach a total of 50% (w/w) concentration of ATPS. The mixture was mixed thoroughly for 3 minutes using a Vortex mixer. Phase separation was achieved by centrifugation at 1000 × g for 10 minutes at 25 ºC. Then, the top and bottom phases were collected for assay analysis. In order to evaluate the purification process, a purification factor (PF) and partition coefficient ($K_E$) recovered in the bottom and top phases were calculated according to the equation below:

$$PF = \frac{SA_e}{SA_i} \tag{3}$$

where $SA_e$ is a specific activity of each phase and $SA_i$ is an initial specific activity of crude lysate. The partition coefficient ($K_E$), was defined as follows:

$$K_E = \frac{A_T}{A_B} \tag{4}$$

where $A_T$ and $A_B$ are the enzyme activity in the top and the bottom phase, respectively.

## Results and Discussion

**Ammonium sulfate precipitation**

In many cases, ammonium sulfate precipitation is often used as a preliminary purification of crude cell lysates to remove unwanted proteins prior to use of expensive columns in chromatography technique for its easy operation and economic practicality. Crude lysate of recombinant bromelain obtained after cell lysis was subjected to ammonium sulfate precipitation. It was hypothesized that most of the recombinant bromelain would be susceptible to precipitate from crude cell lysate in the presence of between 30% to 60% ammonium sulfate. The percentages were relative to a saturated solution (100%), which was equal to 3.93 M at 4 °C. Hence, the concentration was between 1.179 M and 2.358 M. The recombinant bromelain was found to precipitate at 60% of saturation with specific activity and purification fold of 0.03 ± 0.03 unit/mg and 0.05-fold, respectively. SDS-PAGE analysis shown in Figure 1 indicates the size of precipitated recombinant bromelain is approximately 50 – 55 kDa [3]. From Figure 1, we could see that most of the unwanted proteins have been removed after ammonium sulfate precipitation process.

This finding was in conformity with the previous works by Devakate et al. [16], stating that the bromelain from the pineapple fruit plant was precipitated at a saturation level of 40 – 60% with 2.81-fold purity. Soares et al. [17] also recovered bromelain at saturation range of 20 to 40% with purification fold of 4.4 using ammonium sulfate and ethanol precipitation. However, the purification fold of precipitated recombinant bromelain in the current work was lower than those of the native precipitated bromelains obtained by Devakate et al. [16] and Soares et al. [17]. The presence of more than one contaminant proteins precipitated with recombinant bromelain at saturation level of 40 – 60% (Figure 1) decrease the purification fold. Therefore, further purification steps such as chromatography purification were needed to obtain a pure protein sample with high purification fold. Besides, there was an absence of carbohydrate moiety in recombinant proteins produced in *E. coli* and folding anomalies might occur due to the inability of *E. coli* to perform post-translational modifications, therefore potentially resulted in modification of enzyme activity [18].

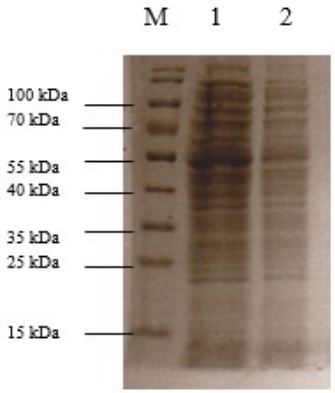
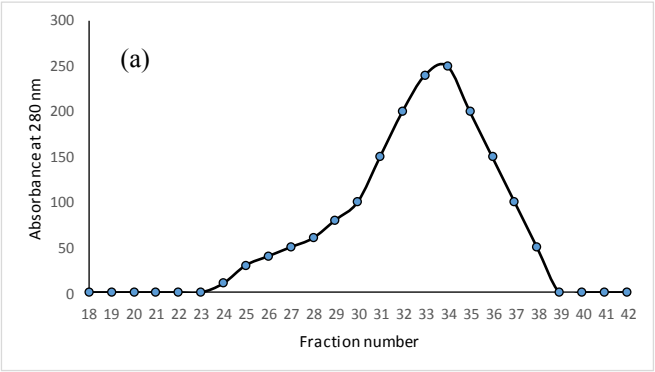



Figure 1. SDS-PAGE of purified recombinant bromelain using ammonium sulfate precipitation. Lane M: the standard molecular weight. Lane 1: crude cell lysate containing recombinant bromelain. Lane 2: 60 % ammonium sulfate precipitation. The position of recombinant bromelain is at estimated size of 50-55 kDa [3].

**Ion-exchange chromatography**

Ion-exchange chromatography was employed to purify the recombinant bromelain. A stepwise elution experiment was performed using binding buffer containing 100 mM of Tris at pH 9.0 and elution buffer containing 100 mM of Tris with 700 mM NaCl at pH 9.0. A chromatogram of recombinant bromelain purified using DEAE Sepharose is shown in Figure 2. From the elution profile shown in Figure 2, a prominent peak appears at fraction 33. All fractions under the peak were pooled and assayed for protein content and enzyme activity. The pooled fractions exhibited specific activity and purification fold of 0.094 unit/mg and 0.14, respectively. The fractions were analyzed by SDS-PAGE (Figure 2).



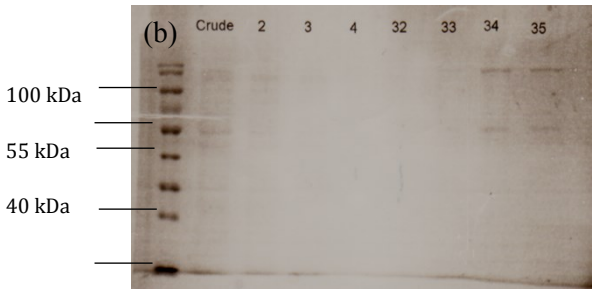
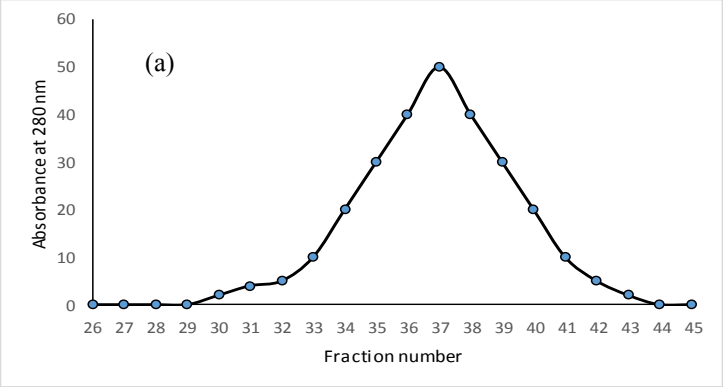



Figure 2. Chromatogram of the purified bromelain from ion exchange chromatography using DEAE Sepharose resin (a). The SDS-PAGE analysis of recombinant bromelain from ion exchange chromatography (b). 1 ml fraction was collected at a flow rate of 1 ml/min. The position of recombinant bromelain is at estimated size of 50-55 kDa [3]

**Affinity chromatography**

Affinity chromatography was conducted for purification of recombinant bromelain using AKTA prime plus® system. Equilibrium buffer used contained 50 mM of $NaH_2PO_4$, 300 mM NaCl, and 10 mM imidazole at pH 8.0. Washing buffer contained 50 mM of $NaH_2PO_4$, 300 mM NaCl, and 20 mM of imidazole buffer, pH 8.0. Elution buffer contained 50 mM of $NaH_2PO_4$, 300 mM NaCl, and 250 mM imidazole at pH 8.0. A chromatogram of recombinant bromelain purified using Ni-NTA agarose resin is shown in Figure 3. The recombinant bromelain pooled from fractions 33 to 37 exhibited specific activity and purification fold of 1.77 ± 0.02 unit/mg and 2.72-fold, respectively and appeared on the SDS-PAGE at the expected size of 50 – 55 kDa (Figure 3). The purification conditions are in accordance with the research presented by Amid et al. [3] and Bala et al. [8].



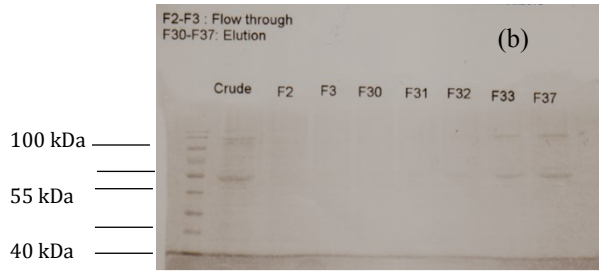
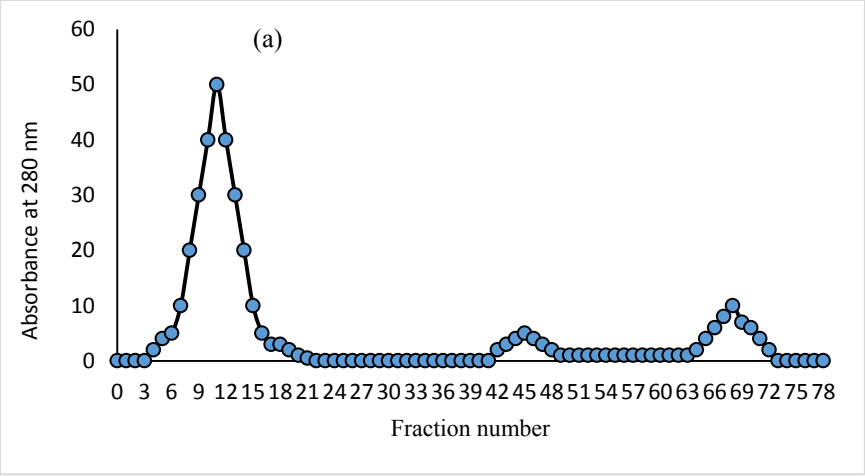



Figure 3. Chromatogram (a) and SDS-PAGE analysis (b) of the purified samples from affinity chromatography using Ni-NTA agarose resin. Equilibrium buffer contained 50 mM of $NaH_2PO_4$, 300 mM NaCl, and 10 mM imidazole at pH 8.0. Washing buffer contained 50 mM of $NaH_2PO_4$, 300 mM NaCl, and 20 mM of imidazole buffer, pH 8.0. Elution buffer contained 50 mM of $NaH_2PO_4$, 300 mM NaCl, and 250 mM imidazole at pH 8.0. 1 ml fraction was collected at a flow rate of 1 ml/min. The position of recombinant bromelain is at estimated size of 50 – 55 kDa [3].

**Gel filtration chromatography**

Gel filtration chromatography is a separation technique based on the size of the protein. The protein precipitated from the 60% of ammonium sulfate precipitation process was subjected to gel filtration chromatography using Sephacryl S-200® resin and a total of 78 fractions were collected (Figure 4). From the chromatogram, it can be seen that there was a high peak after washing step from fractions 9 to 20, followed by a broad absorbance peak from fractions 42 to 72 (Figure 4). The ammonium sulfate precipitation step removed the majority of protein contaminants and the remaining unwanted proteins were separated based on size by gel filtration beads. Thus, recombinant bromelain with 55 kDa was eluted first. The specific activity and purification fold obtained after gel filtration purification were 2.00 ± 0.51 unit/mg and 3.08 ± 0.79-fold, respectively. The SDS-PAGE analysis from Figure 4 shows that the recombinant bromelain pooled from fractions of 11 to 14 has an apparent molecular weight of 50 – 55 kDa.



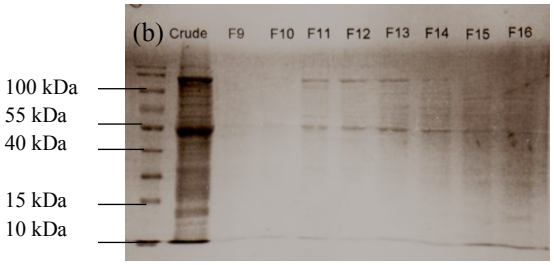



Figure 4. Chromatogram (a) and SDS-PAGE (b) analysis of the purified samples from gel filtration chromatography using Sephacryl S-200® resin. Equilibrium, washing and elution buffers contained 100 mM Tris buffer, pH 7.0. 5 ml fractions were collected at a flow rate of 1 ml/min. The position of recombinant bromelain is at estimated size of 50-55 kDa [3]

The SDS-PAGE analysis was also performed for the remaining peak from fractions 27 to 78, however, no protein band was visible, indicating that no impurities present in the sample. Costa et al. [19] performed ion exchange chromatography prior to gel filtration chromatography to purify bromelain with a molecular weight of 30 kDa from pineapple stem residue. The gel-filtration resin used was Sephadex®G-50. Suh et al. [20] employed gel filtration chromatography to estimate the molecular weight of bromelain as 32.5 and 37 kDa from pineapple fruit and stem, respectively using Sephadex G-200 resin. Hence, it can be concluded that the combination of low-resolution (ammonium sulfate precipitation) and high-resolution (chromatography) methods are most likely provide a higher purity of desired protein.

**Aqueous two-phase system**

In order to determine the best ATPS extraction conditions for the recovery and purification of recombinant bromelain, different molecular weight of PEG was used. The influence of PEG with different molecular weights (1500, 2000, 4000, 6000, and 8000) at constant volume ratio of 1.0 was investigated for the purification of recombinant bromelain. Most recombinant bromelain partitioned in all two phase systems to PEG-rich top phase and salt rich bottom phase. It is because, in a PEG-salt system, phase separation is caused by the volume exclusion effect of the polymer and salting-out effect of salt [21].

Table 1 shows the partition coefficient ($K_E$), purification fold (PF), and enzyme activity recovery of recombinant bromelain in the PEG-rich top phase. The PEG1500/phosphate and PEG2000/phosphate systems exhibited relatively small partition coefficient, purification fold and enzyme activity recovery of recombinant bromelain compared to other three systems investigated (PEG4000, PEG6000 and PEG8000). One explanation for this observation is that high molecular weight of PEG has high hydrophobicity and thus increases the salting-out characters that drive the partition of recombinant bromelain to the upper phase [22]. Conversely, low molecular weight of polymer attracts the migration of contaminant proteins to the top phase and causes a decrease in remaining free volume available for the recombinant bromelain to occupy [23]. Thus, the $K_E$, PF, and enzyme activity recovery values at the top phase were significantly reduced. Bekale et al. [24] had proved by using molecular modelling technique that PEG6000 was strongly adsorbed on bovine serum albumin (BSA) and human serum albumin (HSA) through hydrophobic binding compared with PEG3000. The interaction of polymer-enzyme in ATPS has led to the equilibration between polymer hydrophobicity and salting-out force that explains the preference of recombinant bromelain to migrate to the upper segment [25].

The highest $K_E$ (1.63), PF (5.35), and enzyme activity recovery (53.25%) were obtained in a system consisting of 11% (w/w) of potassium phosphate and 13% (w/w) of PEG6000. Even though the system with the composition of 11% (w/w) PEG8000 and 12% (w/w) potassium phosphate has a high partition coefficient, its purification fold and enzyme activity recovery were found to be low. The purification fold represents the specific activity of purified protein over the specific activity of crude lysate. Thus, high purification fold for the ATPS of 11% (w/w) of potassium phosphate and 13% (w/w) of PEG6000 indicated high specific activity and purity. The molecular weight of partitioned protein may influence the composition of polymer and salt. Ketnawa et al. [1] had successfully

partitioned bromelain from pineapple peels using the system containing 18% (w/w) PEG6000 and 17% (w/w) $MgSO_4$. Ramakrishnan et al. [26] observed that the enzyme recovery of lipase from *Enterococcus faecium* MTCC5695 was increased with the increase of PEG molecular weight from 1000 to 8000. The purified sample from the top phase (PEG-rich) was subjected to SDS-PAGE analysis. All of the purified samples were run on SDS-PAGE under reducing conditions (Figure 5). The protein bands observed at 50-55 kDa represent the molecular weight of recombinant bromelain.

Table 1. The effect of molecular weight to the partition coefficient ($K_E$) and purification fold (PF). (Note: PP: potassium phosphate, PEG: polyethylene glycol)

| **MW of PEG** | **Composition (PP/PEG) % (w/w) at $V_R = 1$** | **$K_E$** | **PF** | **Enzyme Activity Recovery (%)** |
|---|---|---|---|---|
| 1500 | 11/13 | 0.61 ± 0.12 | 0.72 ± 0.61 | 28.31 ± 1.84 |
| | 12/15 | 0.31 ± 0.00 | 0.12 ± 0.32 | 16.40 ± 0.45 |
| | 13/16 | 0.04 ± 0.01 | 0.05 ± 0.05 | 2.58 ± 0.64 |
| | 14/17.5 | 0.14 ± 0.03 | 0.14 ± 0.14 | 7.44 ± 1.05 |
| 2000 | 11/12 | 1.89 ± 0.09 | 0.95 ± 0.00 | 35.36 ± 0.43 |
| | 12/14 | 0.55 ± 0.03 | 1.00 ± 0.02 | 38.29 ± 1.02 |
| | 14/16 | 0.35 ± 0.06 | 0.28 ± 0.01 | 12.67 ± 0.69 |
| | 15/17 | 0.16 ± 0.02 | 0.30 ± 0.01 | 13.36 ± 0.69 |
| 4000 | 10/10 | 2.15 ± 0.16 | 1.24 ± 0.03 | 32.41 ± 1.23 |
| | 11/10 | 0.51 ± 0.03 | 1.49 ± 0.02 | 32.96 ± 0.79 |
| | 12/12 | 1.21 ± 0.18 | 1.31 ± 0.03 | 28.47 ± 1.10 |
| | 13/13 | 2.42 ± 0.42 | 3.23 ± 0.02 | 71.46 ± 0.68 |
| 6000 | 11/13 | 1.63 ± 0.05 | 5.35 ± 0.11 | 53.25 ± 0.91 |
| | 12/14 | 0.64 ± 0.02 | 3.12 ± 0.06 | 45.38 ± 0.58 |
| | 13/15 | 0.72 ± 0.02 | 2.59 ± 0.00 | 46.95 ± 0.22 |
| | 14/16 | 1.80 ± 0.07 | 2.01 ± 0.03 | 48.26 ± 0.94 |
| 8000 | 10/11 | 22.99 ± 0.14 | 0.73 ± 0.08 | 11.56 ± 2.06 |
| | 11/12 | 26.73 ± 0.35 | 3.00 ± 0.11 | 34.77 ± 1.89 |
| | 12/13 | 0.70 ± 0.03 | 2.24 ± 0.05 | 26.37 ± 0.88 |
| | 14/15 | 1.24 ± 0.09 | 3.12 ± 0.02 | 58.72 ± 0.51 |

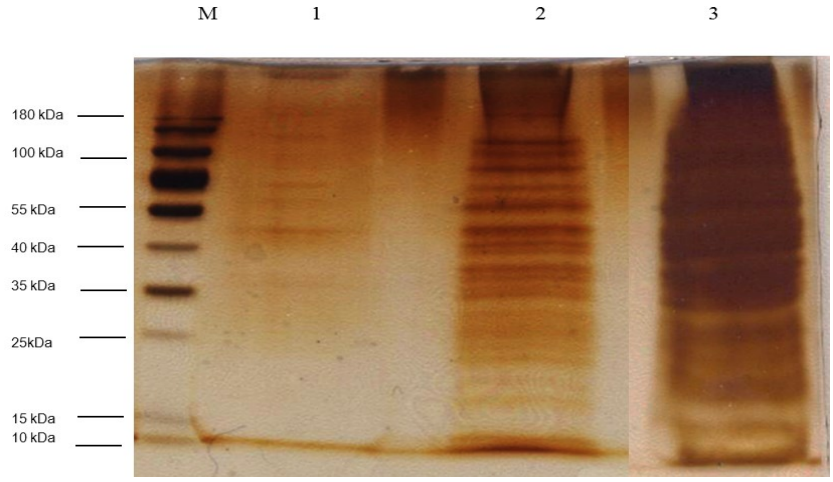



Figure 5. SDS-PAGE analysis for purified recombinant bromelain by ATPS purification techniques. Lane M corresponds to protein marker, lane 1 is the top phase (PEG-rich), lane 2 is the bottom phase (salt-rich), and lane 3 is the crude cell lysate containing recombinant bromelain. The position of recombinant bromelain is at estimated size of 50 – 55 kDa [3].

**Comparison of purification by ATPS and chromatographic techniques**

The purification efficiency of the recombinant bromelain from various purification methods is summarized in Table 2. The chromatography process for the purification of recombinant bromelain has been well explained by Amid et al. [3]. In chromatography purification, the crude extract from cell lysis process was subjected to ammonium sulfate precipitation to concentrate and precipitate the recombinant bromelain. Later, the precipitated protein was dissolved in equilibrium buffer, depending on the type of chromatography (affinity, ion exchange, and gel filtration) used. In contrast, ATPS purification was performed directly after centrifugation in which the crude extract from cell lysis was applied to the PEG6000-potassium phosphate extraction stage.

Table 2. Purification efficiency of recombinant bromelain by different purification methods.

| Purification Methods | Volume (ml) | Total Protein (mg) | Total Activity (units) | Specific Activity (units/mg) | Purification Folds | Yield (%) |
|---|---|---|---|---|---|---|
| Crude | 200 | 304.96 ± 0.00 | 197.49 ± 0.00 | 0.65 ± 0.00 | 1.00 ± 0.00 | 100 ± 0.00 |
| Ammonium sulphate precipitation | 50 | 36.05 ± 0.00 | 1.16 ± 0.00 | 0.03 ± 0.03 | 0.05 ± 0.00 | 0.59 ± 0.02 |
| Affinity (Ni-NTA agarose) chromatography | 3 | 0.13 ± 0.00 | 0.23 ± 0.00 | 1.77 ± 0.02 | 2.72 ± 0.00 | 0.12 ± 0.00 |
| Ion-exchange (DEAE Sepharose) chromatography | 11 | 5.29 ± 0.01 | 0.49 ± 0.01 | 0.09 ± 0.00 | 0.14 ± 0.00 | 0.25 ± 0.00 |

Table 2 (cont'd). Purification efficiency of recombinant bromelain by different purification methods.

| Purification Methods | Volume (ml) | Total Protein (mg) | Total Activity (units) | Specific Activity (units/mg) | Purification Folds | Yield (%) |
|---|---|---|---|---|---|---|
| Gel filtration (Sephacryl S-200®) chromatography | 20 | 0.05 ± 0.00 | 0.10 ± 0.00 | 2.00 ± 0.51 | 3.08 ± 0.79 | 0.05 ± 0.01 |
| Aqueous two-phase system | 20 | 3.02 ± 0.00 | 10.50 ± 0.00 | 3.47 ± 0.11 | 5.35 ± 0.11 | 16.39 ± 0.03 |

In this study, Ni-NTA agarose chromatography (affinity) resulted in purity and specific activity of 2.72-fold and 1.77 ± 0.02 unit/mg, respectively. Meanwhile, DEAE Sepharose chromatography (ion exchange) achieved 0.09 unit/mg and 0.14-fold, respectively. The Sephacryl S-200® chromatography produced specific activity of 2.00 ± 0.51 unit/mg with 3.08 ± 0.79-fold. However, the ATPS purification (13% (w/w) of PEG6000 and 11% (w/w) potassium phosphate, pH 7.0) produced favourable value of purification fold (5.35±0.11-fold) compared with that produced after Ni-NTA agarose chromatography (2.72-fold) and Sephacryl S-200® chromatography (3.08 ± 0.79 fold). With respect to yield percentage, ATPS process exhibited higher yield (16.39 ± 0.03%) compared to ammonium sulphate precipitation (0.59 ± 0.02%), DEAE Sepharose chromatography (0.25%), Ni-NTA agarose chromatography (0.12%), and Sephacryl S-200® chromatography (0.05 ± 0.01%). The yield is defined as the amount of purified protein (total units) divided by the initial amount of protein (defined as 100%).

From economic analysis point of view as stated in Table 3, it can be summarized that ATPS method exhibited the second lowest operating cost with shorter operating time (30 minutes) over chromatographic methods. Among the chromatography methods used, gel filtration chromatography appeared to exhibit higher operating cost due to long separation time (72 hours), causing an increment of buffer usage. Affinity chromatography was positioned as the second most costly method owing to the expensive resin and chemicals used within 1 hour operation time. In terms of reusability, the resin can be re-used up to 100 times only, with an additional cost of using sodium hydroxide, sodium chloride, nickel sulphate, and EDTA for stripping and regenerating the resin after each run. In the case of ATPS, the polymer and salt cannot be recycled as they were part of the final purified enzyme [23]. Such economic and operation analysis provides understanding for further research, and the ATPS process is proven to be a cost-effective, time-saving, and a higher recovery method that may be scaled up for industrial purpose. The purification method should be selected based on the complexity and the application of the recombinant bromelain. In many cases, it is not necessary to have the protease preparation in high purity form, especially for the commercial use such as in food, cosmetics, and textile industries [2]. Therefore, the purification method is aimed to obtain an active protease preparation in high recovery and high yield for industrial purpose. However, for some pharmaceutical uses, the protease must be highly purified. High purity protease is almost invariably expensive due to the purification intricacy to get rid of undesirable contaminating substances. For that reason, this study enables producers and researchers to choose the desired level of protease purity, thereby further reducing the cost of the production process.

Table 3. Direct comparison between chromatography and ATPS methods for the downstream processing of recombinant bromelain

| **Parameter** | **Ammonium Sulfate** | **Ion Exchange** | **Affinity** | **Gel Filtration** | **ATPS** |
|---|---|---|---|---|---|
| Operation | Batch | Batch and semi-batch | Batch and semi-batch | Batch and semi-batch | batch |
| Processing time | 24 hours | 1 hour | 1 hour | 72 hours | 30 minutes |
| Cost of the resin | - | DEAE Sepharose: USD 7.84/7ml | Ni-NTA: USD 121.03/7 ml | Sephacryl S-200®: USD 184/200 ml | - |
| Cost of the column | | Flow Adaptor (1.0 cm): USD 191.99 Econo Column (1 cm x 10 cm): USD 69.82 | Flow Adaptor (1.0 cm): USD 191.99 Econo Column (1 cm x 10 cm): USD 69.82 | Flow Adaptor (1.5cm): USD 191.99 Econo Column (2.5 x 100 cm): USD 71.26 | - |
| Cost of the chemicals (per kg) | Ammonium sulfate: USD 151.24 | Tris: USD 197.85 NaCl: USD 118.15 | Imidazole: USD 614.55 NaCl: USD 118.15 $NaH_2PO4$: USD 280.98 | Tris: USD 197.85 | $K_2HPO_4$: USD 173.45 $KH_2PO_4$: USD 210.21 PEG6000: USD 42.42 |
| Cost of the operation per system | USD 151.24 | USD 585.65 | USD 1396.52 | USD 645.10 | USD 426.08 |

## Conclusion

The ATPS, ammonium sulfate precipitation, and chromatographic procedures for downstream processing of recombinant bromelain were investigated. Our study clearly demonstrated that ATPS process was proven to be a cost-effective (USD 426.08), time-saving (30 min), and high-recovery method (16.39 ± 0.03%) that may be scaled up for industrial purpose. The optimum conditions of ATPS system comprised of 13% (w/w) of PEG6000 and 11% (w/w) potassium phosphate at pH 7.0 which resulted 3.47 ± 0.11 unit/mg, and 5.35 ± 0.11-fold for the specific activity, and purification fold, respectively. Herein, ATPS can be a potential technique for the purification of single step separation and avoid multistep purification like ammonium sulfate precipitation and chromatography process.

## Acknowledgement

This study was supported by the Techno Fund grant (TF1001 F046) by Ministry of Agriculture Malaysia. We are grateful to the International Islamic University of Malaysia (IIUM) for providing the laboratories facilities.

## References

1. Ketnawa, S., Chaiwut, P. and Rawdkuen, S. (2011). Extraction of bromelain from pineapple peels. *Food Science and Technology International*, 17(4): 395 – 402.
2. Arshad, Z. I. M., Amid, A., Yusof, F., Jaswir, I., Ahmad, K. and Loke, S.P. (2014). Bromelain: An overview of industrial application and purification strategies. *Applied Microbiology and Biotechnology*, 7283 – 7297.

3. Amid, A., Ismail, N. A., Yusof, F., Salleh, H. M. (2011). Expression, purification, and characterization of a recombinant stem bromelain from *Ananas comosus*. *Process Biochemistry*, 46(12): 2232 – 2239.
4. George, S., Bhasker, S., Madhav, H., Nair, A. and Chinnamma, M. (2014). Functional characterization of recombinant bromelain of *Ananas comosus* expressed in a prokaryotic system. *Molecular Biotechnology,* 56(2): 166 – 174.
5. Jung, Y-J., Choi, C-S., Park, J-H., Kang, H-W., Choi, J-E., Nou, I-S., Lee, S-Y. and Kang, K. K. (2008). Overexpression of the pineapple fruit bromelain gene (BAA) in transgenic Chinese cabbage (Brassica rapa) results in enhanced resistance to bacterial soft rot. *Electronic Journal of Biotechnology*, 11(1): 1 –8.
6. Jamaluddin, M. J. A., Amid, A., Azmi, A. S. and Othman, M. E. F. (2014). Screening of important autoinduction medium composition for high biaomass production of E. coli expressing recombinant bromelain. *Journal of Pure and Applied Microbiology,* 8(1): 741 – 750.
7. Arshad, Z. I. M, Amid, A., Othman, M. E. F. (2015). Comparison of different cell disruption methods and cell extractant buffers for recombinant bromelain expressed in *E.Coli* Bl21-A1. *Jurnal Teknologi,* 77(24): 83 – 87.
8. Bala, M. (2011). Recovery of recombinant bromelain from *Escherichia coli* BL21-AI. *African Journal of Biotechnology,* 10(81):18829 – 18832.
9. Mohammadi, H. S., Mostafavi, S. S., Soleimanib, S., Bozorgian, S., Pooraskari, M. and Kianmehr, A. (2015). Response surface methodology to optimize partition and purification of two recombinant oxidoreductase enzymes, glucose dehydrogenase and D-galactose dehydrogenase in aqueous two-phase systems. *Protein Expression and Purification*, 108: 41 – 47.
10. Jacinto, M. J., Soares, R. R. G., Azevedo, A. M., Chu, V., Tover, A., Conde, J. P. and Aires-Barros, M. R (2015). Optimization and miniaturization of aqueous two phase systems for the purification of recombinant human immunodeficiency virus-like particles from a CHO cell supernatant. *Separation and Purification Technology*, 154: 27 – 35.
11. Studier, F. W. (2005). Protein production by auto-induction in high-density shaking cultures. *Protein Expression and Purification*, 41(1): 207 – 234.
12. Heinrickson, R. L. and Kézdy, F. J. (1976). Acidic cysteine protease inhibitors from pineapple stem. In: Laszlo L, editor. *Methods in Enzymology,* 740 – 751.
13. Bradford, M. M. (1976). A rapid and sensitive method for the quantitation of microgram quantities of protein utilizing the principle of protein-dye binding. *Analytical Biochemistry,* 72(1–2): 248 – 254.
14. Laemmli, U. K. (1970). Cleavage of structural proteins during the assembly of the head of bacteriophage T4. *Nature*, 227(5259): 680 – 685.
15. Grodzki, A. C. and Berenstein, E. (2010). Antibody purification: Ammonium sulfate fractionation or gel filtration. *Immunocytochemical Methods and Protocols* Totowa, NJ: Humana Press. pp. 15 – 26.
16. Devakate, R. V., Patil, V. V., Waje, S. S. and Thorat, B. N. (2009). Purification and drying of bromelain. *Separation and Purification Technology*, 64(3): 259 – 264.
17. Soares, P. A. G., Vaz, A. F. M., Correia, M. T. S., Pessoa, A. and Carneiro-Da-Cunha, M. G. (2012). Purification of bromelain from pineapple wastes by ethanol precipitation. *Separation and Purification Technology*, 98: 389 – 395.
18. Walsh, G. (2002). Proteins biochemistry and biotechnology. John Wiley & Sons Ltd.
19. Costa, H. B., Fernandes, P. M. B., Romão, W. and Ventura, J. A. (2014). A new procedure based on column chromatography to purify bromelain by ion exchange plus gel filtration chromatographies. *Industrial Crops and Products*, 59: 163 – 168.
20. Suh, H. J, Lee, H., Cho, H.Y. and Yang, H. B. (1992). Purification and characterization of bromelain isolated from pineapple. *Hanguk Nonghwa Hakhoe,* 35: 300 – 307.
21. Nam, S. H., Walsh, M. K. and Yang, K.Y. (2016). Comparison of four purification methods to purify cysteine protease from Asian pear fruit (*Pyrus pyrifolia*). *Biocatalysis and Agricultural Biotechnology*, 5: 86 – 93.
22. Raja, S. and Murty, V. R. (2013). Liquid-liquid equilibria of aqueous two-phase systems containing PEG + sodium citrate+ water at various pH. *Journal of Chemical Science and Technology,* 2(4):169 – 174.
23. Aguilar, O., Albiter, V., Serrano-Carreón, L. and Rito-Palomares, M. (2006). Direct comparison between ion-exchange chromatography and aqueous two-phase processes for the partial purification of penicillin acylase produced by *E. coli*. *Journal of Chromatography B,* 835(1–2): 77 – 83.
24. Bekale, L., Agudelo, D. and Tajmir-Riahi, H. A. (2015). The role of polymer size and hydrophobic end-group in PEG–protein interaction. *Colloids and Surfaces B Biointerfaces,* 130:141 – 148.

25. Ng, H. S, Tan, C. P, Chen, S. K., Mokhtar, M. N., Ariff, A. and Ling, T. C. (2011). Primary capture of cyclodextrin glycosyltransferase derived from *Bacillus cereus* by aqueous two phase system. *Separation and Purification Technology*, 81(3): 318 – 324.
26. Ramakrishnan, V., Goveas, L. C., Suralikerimath, N., Jampani, C., Halami, P. M. and Narayan, B. (2016). Extraction and purification of lipase from Enterococcus faecium MTCC5695 by PEG/phosphate aqueous-two phase system (ATPS) and its biochemical characterization. *Biocatalysis and Agricultural Biotechnology*, 6: 19 – 27.

*Malaysian Journal of Analytical Sciences, Vol 21 No 4 (2017): 972 - 978*
*DOI: https://doi.org/10.17576/mjas-2017-2104-24*

MALAYSIAN JOURNAL OF ANALYTICAL SCIENCES
*Published by The Malaysian Analytical Sciences Society*
ISSN 1394 - 2506

# PERCENTAGE DIFFERENCE OF RESISTIVITY OF NANOPARTICLES IN DETERMINING CRUDE OIL USING SAND-PACK EXPERIMENTAL METHOD

## (Peratusan Perbezaan Kerintangan Nanopartikel Dalam Penentuan Minyak Mentah Mengunakan Kaedah Ujikaji Pek Pasir)

Mohd Zulkifli Mohamad Noor[1]*, Mariyamni Awang[2], Sonny Irawan[2]

[1]*Faculty of Chemical Engineering & Natural Resources,*
*Universiti Malaysia Pahang, 26300 Gambang, Pahang, Malaysia*
[2]*Department of Petroleum Engineering,*
*Universiti Teknologi PETRONAS, 32610 Bandar Seri Iskandar, Perak, Malaysia*

**Corresponding author: mzulkifli@ump.edu.my*

Received: 28 November 2016; Accepted: 5 February 2017

**Abstract**

Nanoparticle with its nanoscale can be used as a data collector in every part of the development of the petroleum field. By having a hydrophilic condition for the nanoparticles, it can move to the targeted area in the water zone. The hydrophilic condition will differentiate between oil zone and water zone. The objective of the study is to use the hydrophilic nanoparticles to detect the oil and water zones using sand-pack displacement test. An experiment using the sand-pack method was done to show that the hydrophilic nanoparticles can be used to collect data. The nanoparticles used were aluminum oxide ($Al_2O_3$) and nickel zinc ferrite oxide (NiZnFeO). The results showed that for NiZnFeO, at 3-inch distance from the injection point, the percentage difference increased from 15% to 25%, while for $Al_2O_3$, the nanoparticles also showed the same increment but different in values, which were from 6% to 15%. This is shown by the significant change of resistivity percentage at the 3-inch distance. To conclude, the use of both types of nanoparticles that have hydrophilic nanoparticles can show the significant changes for resistivity at internal short front face of well reservoir with oil zone only.

**Keywords**: nanoparticles, formation characterization, sand-pack displacement, resistivity

**Abstrak**

Nanopartikel dengan skala nano boleh digunakan sebagai pengumpul data di setiap bahagian pembangunan bidang petroleum. Dengan adanya keadaan hidrofilik untuk nanopartikel, ia boleh bergerak ke kawasan yang disasarkan di zon air. Keadaan hidrofilik akan membezakan antara zon minyak dan zon air. Objektif kajian ini adalah untuk menggunakan nanopartikel hidrofilik untuk mengesan zon minyak dan air menggunakan ujian pek pasir. Satu eksperimen menggunakan kaedah pek pasir dilakukan untuk menunjukkan bahawa nanopartikel hidrofilik boleh digunakan dalam mengumpul data. Nanopartikel yang digunakan adalah aluminium oksida ($Al_2O_3$) dan nikel zink ferit oksida (NiZnFeO). Hasil kajian menunjukkan bahawa untuk NiZnFeO, pada jarak 3 inci dari sudut suntikan, perbezaan peratusan meningkat daripada 15% kepada 25%, manakala bagi $Al_2O_3$, nanopartikel juga menunjukkan kenaikan yang sama tetapi berbeza dalam nilai iaitu dari 6% kepada 15%. Ini ditunjukkan oleh perubahan yang ketara peratusan kerintangan pada jarak 3 inci. Kesimpulannya, penggunaan kedua-dua jenis nanopartikel yang mempunyai nanopartikel hidrofilik boleh menunjukkan perubahan signifikan bagi kerintangan muka depan pendek dalaman takungan baik dengan zon minyak sahaja.

**Kata kunci:** nanopartikel, penentuan formasi, pengaliran pek pasir, kerintangan

## Introduction

In the oil and gas industry, nanotechnology has been applied for approximately more than 50 years in many branches like exploration, drilling, production, Enhanced Oil Recovery (EOR), as well as refining and processing [1]. There are many tools used in well logging and one of the most important logging tools is resistivity logging. Resistivity logging has been widely used in well logging. It is one of the useful induction logging combination tools that have been enhanced by replacing the short normal quantitative interpretation [2]. It is also known as electric logging tool. The resistivity logging consists of two types of logging systems, which are dual lateral log and induction log. At present, resistivity logging uses both types of logs but the most commonly used logging is the induction logging. Besides that, the dual lateral log is used as a combination with the induction log for resistivity logging. Therefore, the quality of resistivity measurements is increased for the logging [3].

Research that focuses on nanoparticles used in well logging has not been attempted so far. Nevertheless, excellent works have been carried out on the Enhanced Oil Recovery (EOR). The nano particles are used to increase oil recovery via the EOR method [4]. Injected nanoparticles in the formation will somehow push the leftover oil in the formation to the wellbore for recovery and it has been proven in some recent studies. The idea is by mixing the nanoparticles with water and they will increase the electrical properties of the water. Furthermore, it is known that metal oxide nanoparticles do have good electrical properties that can change the electrical properties of the water. Therefore, the resistivity of water is altered by adding nanoparticles into it. Hence, the motivation for the use of nanoparticles in well logging becomes a more interesting study to be conducted. The low resistivity condition for oil and brine water can be solved by conducting the current research.

The conditions of low resistivity and low contrast pay on the resistivity are also termed as wet condition [5, 6] and it is considered as a limitation in logging tool resolution that has to be looked into. Although low resistivity and low contrast pay can be grouped together, they are actually different. Low resistivity pay is a deep resistivity log curves of approximately 1 to 10 ohm. They are also known as the mixing combination of shale content, mineralogy, macro and micro-porosity, and bed thickness. On the other hand, low contrast pay lacks resistivity contrast between pay zones or good area or best formation with oil zones and flanking shale or wet zones. It is a problem when a logging tool passes through a zone that contains fresh water or water in an area of low salinity. As salinity decreases, the conductivity becomes lower and the path for movement of electrical properties becomes weaker and it will attribute to more resistance. Therefore, the resistivity of the water leg should be high enough to record the data for resistivity between pay zone and wet zone, which is difficult to differentiate [5, 7, 8].

Furthermore, there are also some other factors, for example, the geological aspect factor. They are laminated clean sand with shales, silts or shale sands, clay-couted sand, gloucanite sand, sands with interstitial disperse clay, sand with disseminated pyrite, or other conductive minerals [8]. The geological factor has become a big factor with a combination of bed thickness, grain size, mineralogy, structure of formation, clay distribution, and water salinity. Thus, the conventional logging tool shows poor resolution [8, 9] as the formation or the sand is shown as shale due to the lower value of its cut-off zones. With that, the formation is grouped as low contrast and low resistivity reservoir [7].

On finding the resistivity of formation in the reservoir, a resistivity tool is used. There are two types of resistivity package tools, which are Dual Lateral log (DLL) and Induction log. They respond to real rock and all petro-physical analysis to find water saturation, hence, they follow the Archie's Law [12-16]. In fresh water, there is no conductive medium due to the non-ionic solution of the fresh water. So, when resistivity logging is done in fresh water, very high resistivity data are recorded. Therefore, it can be said that the fresh water is poor in conducting electrical current flow. On the other hand, water with saline and rich in mineral is more conductive due to the ionic materials contained in the water and the salinity of the water itself contributes to the conductive liquid. With this principle, the resistivity is conducted to measure the conductive formation in finding the best reservoir with high pay. Basically, most of the sedimentary rocks are very poor in conductive flow [14]. So, most of the conductivity fluid is brine water with ionic salt minerals.

Hence, the condition of low resistivity with low contrast pay needs to be altered, and one of the ways is by introducing nanoparticles. This is because nanoparticles are materials that are nano in size and the use of nanoparticles has become an interesting method to be incorporated within the research. Besides that, the size of pore and grain in nanoparticles makes it a good injector for formation. The size of pore and grain in a formation is minute, thus, only small particles with good permeability can penetrate the formation [17]. A study conducted by Yu et al. [17] showed that the size of pore and grain is a vital factor and it depends on the coating material for the nanoparticles. In selecting the nanoparticles, it needs to be based on polar and non-polar conditions of the nanoparticles because the nanoparticles need to be hydrophilic so that they can be immiscible into the brine, while oleophilic to be immiscible into the hydrocarbon oil. The main reason for the increasing interest within the industry is due to the numerous advantages that the nanotechnology brings. Known success of implementation of nanoparticles has been documented since its inception. Matteo et al. [18] reported that nanoparticles, when combined with smart fluids, can be deployed as very sensitive downhole sensors for extreme pressure, stress, and temperature. Innovative corrosion-resistant material solution can also be processed with the help of nanotechnology. It extends the lifespan and efficiency of drilling systems and when applied as a corrosion inhibitor for pipelines, nano-layer can act through the creation of permanent molecular layer, thus, can help to reduce HCl or $H_2S$ corrosion.

## Materials and Methods

### Materials

The nanoparticles used were metal oxide nanoparticles with the purity of 99% and purchased from the US Research Nanomaterials, Inc. USA. The nanoparticles are nickel zinc ferrite oxide (NiZnFeO) and aluminum oxide ($Al_2O_3$). Meanwhile, the crude oil sample for the crude oil injection was taken from the Malacca Petronas Refinery plant and the crude oil sample was collected upon receiving it from shipment. The properties of the crude oil are shown in Table 1 below. The sand-pack was fabricated with a cylindrical column prospexglass with 3 points interval distance to measure the resistivity as shown in Table 2 below. The sand-pack fabrication model is also shown in Table 2 below. The resistivity measurements were made using the Keithley Multimeter from the Keithley Instrument, Inc. Cleveland, Ohio USA and recorded using ExceLINX software by the Keithley Instrument. The unit for resistivity will be in ohm.

Table 1. Crude oil Properties

| Crude Oil type | Properties | Value | Unit |
|---|---|---|---|
| Tapis | Density | 0.7665 (T = 90 °C) | g/cm$^3$ |
| | Viscosity | 1.11 (T = 90 °C) | cP |
| | Flash point | 5 | °C |
| | Boiling point | 84 - 398 | °C |
| | Chemical composition | Crude oil – 99%<br>Benzene – 1% | Percentage |

Table 2. Sand-pack model dimension and experimental condition

| Material and Equipment | Descriptions | | |
|---|---|---|---|
| Horizontal Sand-pack | Length | 12 inch | Channel Resistance distance taken<br>- Interval Distance 1: 3 inch<br>- Interval Distance 2: 6 inch<br>- Interval Distance 3: 9 inch<br>All Interval distance from inlet. |
| | Diameter | 2.5 inch | |
| | Type of sand | Batik Beach Manjung sand (40 micrometer in size) | |

**Preparation of nanoparticles**

Preparation of nanoparticles with concentration of 1000ppm. The nanoparticles, NiZnFeO and $Al_2O_3$, were prepared using a 100 mL beaker. The nanoparticles were weighted before being mixed with 100 mL of distilled water to produce nano-fluid. In order to make the nanoparticles suspended in the distilled water, the nano-fluid produced needs to control its pH value of 8.

Before the nanoparticles were injected into the sand-pack, the sand-pack needs to be pre-prepared first. The cylindrical column that is being fabricated need to be packed with sand. The collected sand needs to be washed with distilled water and dried a few times to make sure that there are no salt contaminations present in the sand. The sand-pack needs to be packed uniformly. After packing, the sand-pack experimental setup was prepared. The setup is shown in Figure 1.

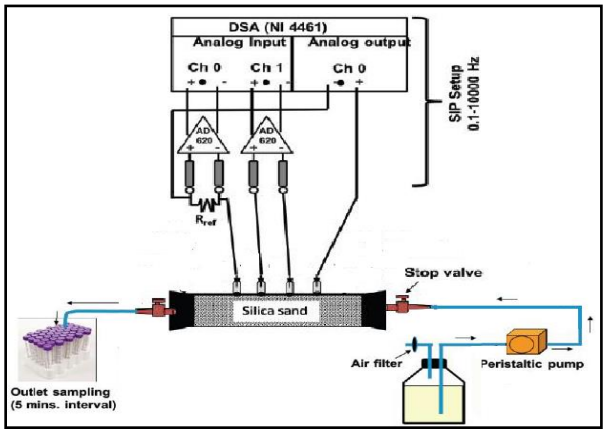



Figure 1. Experimental setup for the sand-pack

Once the process complete, the sand-pack was saturated with 7000 ppm of brine. A fully saturated sand-pack with brine is achieved when there are no more bubbles present in the outlet. After that, the first measurement of resistivity was taken in order to record the resistivity measurement before the injection of nanoparticles.

The injections of nanoparticles were done for 0.25, 0.50, 0.75, and 1.00 pore volume of injection. Each injection's volume was 60 mL and the resistivity measurement was taken after 5 minutes of each injection to make sure that the fluid movement inside the sand-pack was in a static condition without any outlet at the outlet stream.

## Results and Discussion

The 7000 ppm brine is a typical low salinity water in the Malay Basin [7]. The concentration of nanoparticles is 1000 ppm. Properties of the sand-pack are shown in Table 1 and results of the effects of NiZnFeO and $Al_2O_3$ nanoparticles are given in Table 3 and 4, respectively. As proposed, the resistivity of the brine/water phase showed a reduction from the initial values for NiZnFeO nanoparticles injection by 14.59, 3.94, and 1.82% at 3, 6, and 9-inch range, respectively, at the 0.25 pore volume injection of the sand-pack in Table 3 and Figure 2(A). When the experiments were conducted with different pore volumes, the resistivity readings agreed with our expected results. The nanoparticles moved along the interval distance causing a reduction in resistivity and at the pore volume of 1, the changes increased because the nanoparticles were suspended between the 3 to 9-inch ranges. It was proven from the measurement of outlet from the test that the amount got it only 0.01 ppm in the outlet collected.

Table 3. Resistivity change in sand pack after injection of 1000 ppm NiZnFeO nanoparticles (measurement taken every 5 minutes of injection finish)

| **Pore Volumes Injected** | **0.25** | | | **0.50** | | | **0.75** | | | **1.00** | | |
|---|---|---|---|---|---|---|---|---|---|---|---|---|
| Interval distance from inlet (inch) | 3 | 6 | 9 | 3 | 6 | 9 | 3 | 6 | 9 | 3 | 6 | 9 |
| % Change in resistivity of water zone | 14.59 | 3.94 | 1.82 | 12.72 | 3.93 | 3.96 | 12.47 | 3.98 | 1.98 | 2.43 | 10.93 | 14.04 |

On the other hand, for the $Al_2O_3$ nanoparticles, as shown in Table 4 and Figure 2(b), the initial values of the injected nanoparticles were 5.7, 1.94, and 1.62 % at 3, 6, and 9-inch range, respectively, at the 0.25 pore volume injection of the sand-pack. When it went to all of the interval distances, it showed the same patent of decreasing value in terms of percentage difference. It proved that the $Al_2O_3$ had good hydrophilic nanoparticles for the movement of nanoparticles in the brine/water. The difference can be used to differentiate the oil and water zones for log measurements. Within the water zone, the reduction in resistivity indicated that the nanoparticles and traveled along the core, but the heterogeneity in the sand-pack had resulted in uneven resistivity drops.

Table 4. Resistivity change in sand pack after injection of 1000 ppm $Al_2O_3$ nanoparticles (measurement taken every 5 minutes of injection finish)

| **Pore Volumes Injected** | **0.25** | | | **0.50** | | | **0.75** | | | **1.00** | | |
|---|---|---|---|---|---|---|---|---|---|---|---|---|
| Interval distance from inlet (inch) | 3 | 6 | 9 | 3 | 6 | 9 | 3 | 6 | 9 | 3 | 6 | 9 |
| % Change in resistivity of water zone | 5.7 | 1.94 | 1.62 | 9.53 | 2.24 | 1.58 | 11.20 | 4.83 | 1.35 | 15.26 | 5.26 | 2.88 |

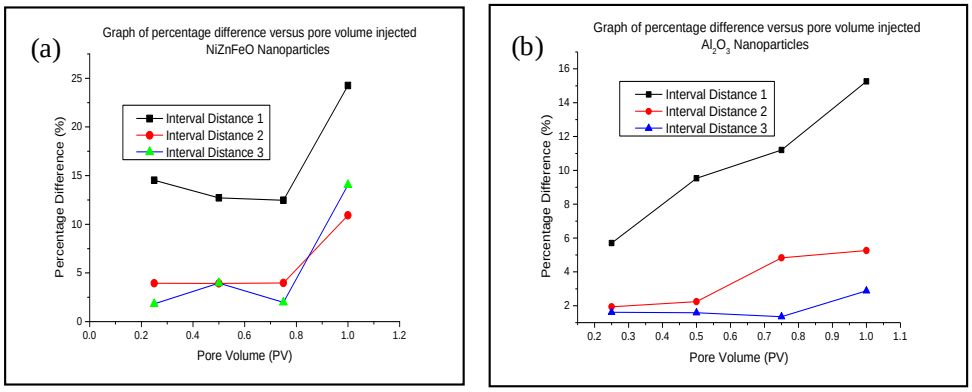



Figure 2. Percentage difference of resistivity value with difference pore volume for a) NiZnFeO and b) $Al_2O_3$ nanoparticles injection

Both nanoparticles in the experiments showed interests in the water zone. Therefore, the use of both nanoparticles has made it possible to differentiate between the oil and water zones. The results also showed that only a small pore volume was needed to determine the changes. For example, the NiZnFeO nanoparticles with only 0.5 pore volume of injected nanoparticles can detect the difference in the targeted zone. The same goes for the $Al_2O_3$ nanoparticles. Other than that, a 6-inch traveling distance for the nanoparticles was good enough to show the changes that happened. This condition is suitable for both NiZnFeO and $Al_2O_3$ nanoparticles.

## Conclusion

It can be concluded that oil zone can be determined using nanoparticles. It is proven by looking at the penetrations done by the NiZnFeO and $Al_2O_3$ nanoparticles in the sand-pack at 0.25 and 0.50 pore volume. The NiZnFeO and $Al_2O_3$ nanoparticles were injected and resistivity changes were recorded at the interval distance stated. NiZnFeO and $Al_2O_3$ nanoparticles showed the same patent for the percentage difference of resistivity at 3 and 6-inch injections. It can be seen from the percentage difference at 0.25 and 0.50 pore volume of injection. Both nanoparticles favored hydrophilic nanoparticles that went to water zone. Therefore, by having a system with oil water system that is low in contrast during log determination, the nanoparticles will choose the water zone and expose the oil zone. In this case, the oil zone can be determined while making changes for the water zone only. The targeted production zone for oil zone can be clearly stated and determined.

## Acknowledgement

The research was funded by the E-science programme of the Malaysian Ministry of Science, Technology, and Innovation. M. Zulkifli M. Noor's study is made possible by Universiti Malaysia Pahang. We would like to thank Universiti Teknologi PETRONAS for the full access to the excellent laboratory facilities and the staff of the Centre of Research in Enhanced Oil Recovery (COREOR) for providing other support services.

## References

1. Kong, X. and Ohadi, M. (2010). Applications of micro and nano technologies in the oil and gas industry - overview of the recent progress. *Abu Dhabi International Petroleum Exhibition and Conference, Society of Petroleum Engineers*, 1-4 November, Abu Dhabi, UAE, SPE-138241.
2. Riboud, J. and Schuster, N. A. (1971). Well logging techniques, 13-18 June, *8th World Petroleum Congress*, WPC-14237.
3. Ellis, D.V. (2007). Well logging for earth scientists. 2nd edition, Dordrecht, *The Netherlands: Springer*. 17: 692.
4. Fletcher, A. and Davis, J. (2010). How EOR can be transformed by nanotechnology, in *SPE Improved Oil Recovery Symposium 2010, Society of Petroleum Engineers.* Tulsa, Oklahoma, USA, 1:152 – 167
5. Sneider, R. M. B. and Kulha, J. T. (1993). Low-resistivity, low-contrast productive sands. *AAPG Database*, 33: 1 – 4.
6. Kulha, J. T. (2004). Low Resistivity, Low-Contrast Pays. *Houston Geological Society Bulletin*, 41(9): 11.

7. Hamada, G. M., Al-Blehed, M. S., and Al-Awad, M. N. J. (1999). Determining petrophysical properties of low resistivity reservoirs using nuclear magnetic resonance logs. *SPE Annual Technical Conference and Exhibition*, 3-6 October, Houston, Texas, SPE 56789.
8. Stolper, K. (1994). Identify potential low-resistivity pay using visual rock analysis, *Houston Geological Society Bulletin*, 37(4): 32.
9. Heavysege, R. G. (2002). Formation evaluation of fresh water shaly sands of the Malay basin, offshore Malaysia. *SPWLA 43rd Annual Logging Symposium*, Oiso, Japan, 1–14.
10. Amin, N. C. A. R. (2012). Evaluation of low resistivity low contrast reservoir. Dissertation Universiti Teknologi PETRONAS.
11. Boyd, A., Darling, H. and Tabanou, J. (1995). The lowdown on low-resistivity pay. *Oilfield Review*, 7(3): 4 – 18.
12. Asquith, G. B. and Gibson, C. R. (1982). Basic well log analysis for geologists. Methods in exploration series. Tulsa, Okla., USA: *American Association of Petroleum Geologists*. 7: 216.
13. Darling, T. (2005). Well logging and formation evaluation. Gulf drilling guides. Amsterdam; Boston Burlington, MA: Elsevier. Gulf Professional Publication, 9: 326.
14. Crain, E. R. R. (2001). Crain's petrophysical handbook - 3rd Millennium Edition. Online Shareware Petrophysics Training and Reference Manual.
15. Worthington, P. F. (2011). The petrophysics of problematic reservoirs. *Journal of Petroleum Technology*. 63(12): 88 – 97.
16. Archie, G. E. (1942). The electrical resistivity log as an aid in determining some reservoir characteristics. *Society of Petroleum Engineers: Transactions of the AIME*, 143(1): 54 – 62.
17. Yu, H., Kotsmar, C., Yoon, K. Y., Ingram, D. R., Johnston, K. P., Bryant, S. L. and Huh, C. (2010). Transport and retention of aqueous dispersions of paramagnetic nanoparticles in reservoir rocks. In *SPE Improved Oil Recovery Symposium. Society of Petroleum Engineers*, Tulsa, Oklahoma, USA, 2: 1027-1047.
18. Matteo, C., Candido, P., Vera, R. and Francesca, V. (2012). Current and future nanotech applications in the oil industry. *American Journal of Applied Sciences*, 9(6): 784 – 793.

*Malaysian Journal of Analytical Sciences, Vol 21 No 4 (2017): 979 - 985*
*DOI: https://doi.org/10.17576/mjas-2017-2104-25*

MALAYSIAN JOURNAL OF ANALYTICAL SCIENCES
*Published by The Malaysian Analytical Sciences Society*
ISSN 1394 - 2506

# DETERMINATION OF PHYSICAL CROSSLLINK BETWEEN CARRAGEENAN AND GLYOXYLIC ACID USING DENSITY FUNCTIONAL THEORY CALCULATIONS

## (Penentuan Ikatan Sambung Silang Fizikal Antara Karagenan dan Asid Glioksilik Menggunakan Pengiraan Teori Fungsi Ketumpatan)

Siti Hana Abu Bakar and Fatmawati Adam*

*Faculty of Chemical Engineering & Natural Resources,*
*Universiti Malaysia Pahang, 26300 Gambang, Pahang, Malaysia*

**Corresponding author: fatmawati@ump.edu.my*

Received: 28 November 2016; Accepted: 5 February 2017

**Abstract**

Film of carrageenan and glyoxylic acid has been produced with an aim for hard capsule application through manipulation of physical crosslink. In this paper, the computational calculation has been used through utilization of density functional theory to predict the possible location of the physical crosslink in the conjugate complex between carrageenan and glyoxylic acid (film of carrageenan and glyoxylic acid). The calculations for pure kappa carrageenan (k-carrageenan), glyoxylic acid and conjugate complex were carried out using Gaussian 09W; and analysis of molecular electrostatic potential (MESP) was carried out using Gaussview 5. The molecular electrostatic surface potential (MESP) for optimized structure for k-carrageenan and glyoxylic acid have been generated with the red region represents the most negative electrostatic potential which can be found around oxygen and sulphur atoms for the carrageenan molecule. While the blue region that represents the most positive electrostatic potential which can be found around the hydrogen atom far from the double bond oxygen atoms in glyoxylic acid. Therefore, both of this regions may interact and form physical crosslink via hydrogen bond interaction.

**Keywords**: computational analysis, hard capsule, Gaussian 09W, molecular electrostatic potential, hydrogen bond

**Abstrak**

Filem karagenan dan asid glioksilik telah dihasilkan untuk aplikasi kapsul keras melalui manipulasi kaedah ikatan sambung silang fizikal. Di dalam kertas penyelidikan ini, pengiraan komputer menggunakan teori fungsi ketumpatan telah digunakan untuk mengenalpasti lokasi ikatan sambung silang fizikal yang terbentuk di dalam kompleks kappa-karagenan dan asid glioksilik. Penggiraan teori telah dilakukan untuk struktur kappa-karagenan, asid glioksilik dan kompleks kappa-karagenan-asid glioksilik menggunakan perisian Gassian 09W; dan analisis keupayaan elektrostatik molekul (MESP) dilakukan menggunakan perisian Gaussview 5. Ikatan sambung silang dapat ditentukan berdasarkan gambar-gambar MESP yang dihasilkan. Ikatan sambung silang tersebut dapat dilihat melalui interaksi antara keupayaan elektrostatik negatif (atom oksigen, dan sulfur di dalam karagenan) dan keupayaan elektrostatik positif (atom hydrogen di dalam asid glioksilik). Maka, kedua – dua bahagian ini mempunyai interaksi dan membentuk sambung silang fizikal melalui interaksi ikatan hidrogen

**Kata kunci:** analisis pengiraan, kapsul keras, Gaussian 09W, keupayaan elektrostatik molekul, ikatan hidrogen

## Introduction

Kappa carrageenan (k-carrageenan) is an anionic sulphate polysaccharide with interesting pharmacology properties such as ability to inhibit hepatitis A viruses [1]. It has been used by in various studies to produce drug delivery carrier such as hydrogel [2, 3, 4], shell of microcapsules [5], and beads [6] which normally has prolonged drug release properties. This prolonged drug release properties is due to the swelling capability of k-carrageenan film such as been reported by Hezaveh and Muhammad [2] that non-crosslink k-carrageenan hydrogel can swelled up to 16% after soaked for 35 hours in pH 7 solution. While, this study aims to produce the hard capsule using k-carrageenan which require to disintegrate in less than 15 minutes. Therefore to achieve this aim, the crosslink method has been used with physical crosslink establishment as a main target. This physical crosslink can promote rapid swelling of k-carrageenan hard capsule and ensure its ability to disintegrate as required by US pharmacopeia [7]. According to Hiemstra et al. [8], physical crosslink is a mild crosslink or interaction such as hydrogen bond interaction in which its network can be easily disrupted due to changes in the external environment. At present, the interaction studies Adam et al. [9] and Karavas et al. [10] used the computational chemistry to simulate and calculate the establishment of the interaction through calculation of radial diffusion function (RDF) and interaction energy for hydrogen bond established in the system.

In this paper, the computational study using quantum mechanics concept will be presented. The quantum mechanics calculation was carried out to determine the particular atoms involved in the physical crosslink establishment between k-carrageenan and glyoxylic acid. The electron and proton donor site can be determine and conjugate complex k-carrageenan – glyoxylic acid was set at the selected site. This then may indicate the suitability of physical cross-linked carrageen to be developed as hard capsule application. In addition the effect of physical crosslink to the k-carrageenan molecule may further investigate.

## Materials and Methods

### Quantum Mechanics Calculation

The density functional theory (DFT) calculations have been carried out using Gaussian 09W software at B3LYP (Becke's three-parameter functional [11] and nonlocal correlation of LYP expression [12]) level of theory; with basis set of 6-31G. The geometry optimization and frequency calculations for pure k-carrageenan, glyoxylic acid and physical crosslink conjugate complex of k-carrageenan-glyoxylic acid (GaSc) were executed with the selected functional and correlation function. The molecule electronic surface potential (MESP) of k-carrageenan and glyoxylic acid has been generated from the geometry optimization calculation. Through this MESP, determination of the physical crosslink conjugate complex has been drawn and calculated for it optimum geometry. The crosslink point between k-carrageenan and glyoxylic acid was measured to ensure its can be categorized as hydrogen bond through calculation of interaction energy produced using Equation 1 below. While the absolute difference in muliken charges of optimized conjugate complex k-carrageenan-glyoxylic acid and k-carrageenan may indicate the probability of scission of chains. This scission effect may promote mechanical fracture (crack) of film. Figure 1 illustrates the quantum mechanics calculations steps that were carried out in this study.

$$\text{Interaction energy} = \text{ESCF complex} - \{\text{ESCF polysaccharide} + \text{ESCF crosslinker agent}\} \quad (1)$$

-

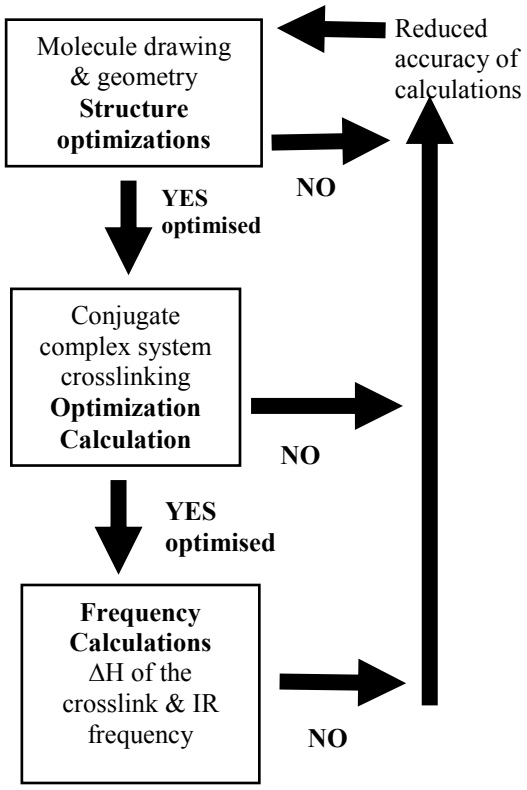
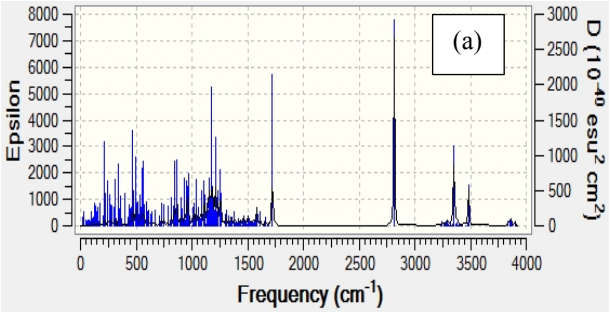



Figure 1. Summary of calculations steps using Gaussian 09W in this study

## Results and Discussion

The IR spectrum (Figure 2) for optimized k-carrageenan and glyoxylic acid molecules were generated from the frequency calculation. The frequency calculation was carried out after the molecules has been optimized. The positive value of vibration produced and for k-carrageenan and glyoxylic acid may indicate that the molecules geometry optimize calculation has managed to found the stationary point of the local minima on the potential energy surface. This validation technique has been suggested by Kumar et al. [13] in their quantum study of azelaic acid.



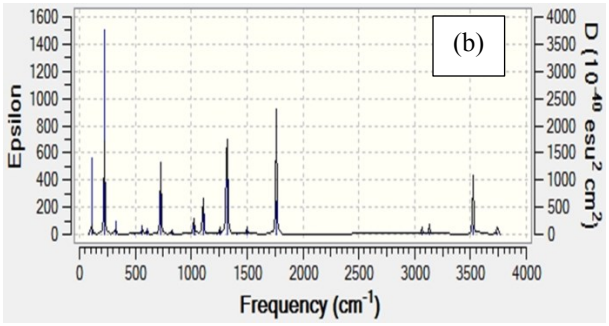



Figure 2. IR spectrum generated for optimized (a) kappa carrageenan molecule, and (b) glyoxylic acid molecule

In Figure 3 (a) and (b), the molecule electronic surface potential (MESP) for optimized k-carrageenan and glyoxylic acid illustrate the charge distributions of molecule with different values of the electrostatic surface potential at the surface. The potential increases (electron rich) in the order blue<green<yellow<orange<red. Knowledge of the charge distribution of the molecule which illustrated by electrostatic surface potential of molecule can be used to predict how molecule react to the other molecule such as suggested by Rawat and Singh [14]. Figure 4(a) shows that the negative regions in k-carrageenan are mainly localized on the oxygen and sulphur atoms which agreed with suggestion by Kumar et al. [13]. They suggested that the shapes of the electrostatic potential surface is influenced by the structure and charge density distributions in the molecule with sites close to the oxygen atom, showing region of most negative electrostatic potential. While in the glyoxylic acid, the positive regions are localized at the hydrogen atoms from hydroxyl functional group. Therefore, the physical crosslink may establish between the red region of k-carrageenan and blue region of glyoxylic acid or vice versa. The k-carrageenan will serve as an electron donor with glyoxylic acid will serve as a proton donor to establish the hydrogen bond. Tanak [15] also found negative potential site generated around Sulphur molecule using the BL3YP calculation for 4,5-bis(tert-butylsulfanyl)phthalonitrile and may serve as electron donor.

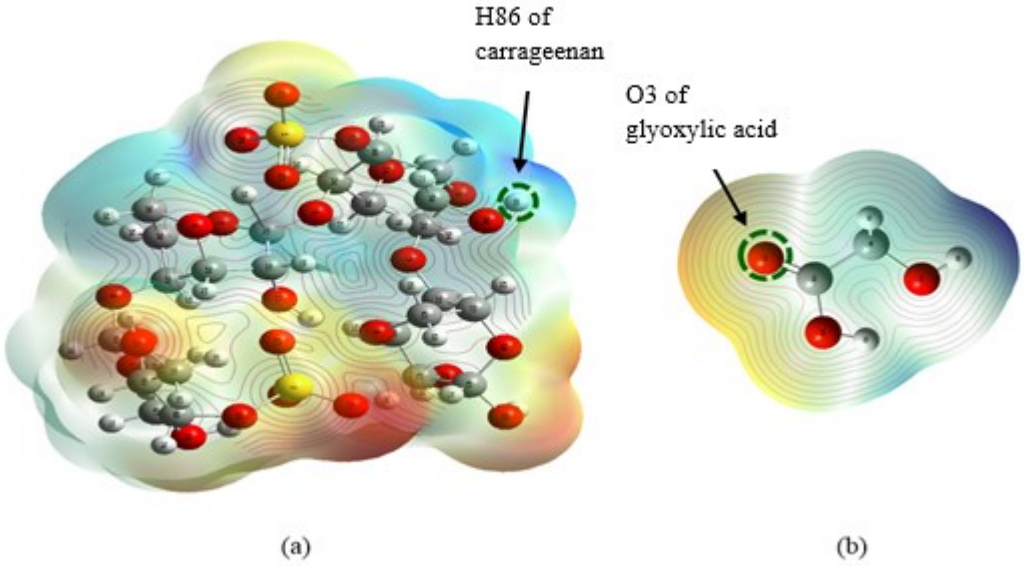



Figure 3. The molecular electrostatic potential (MESP) analysis for optimized molecule structure of (a) k-carrageenan and (b) glyoxylic acid

In this calculation the interaction between H86 of k-carrageenan and O3 of glyoxylic acid has been set up at the length of 2.2 Å at the beginning of calculation. The hydrogen bond has been established between H86 --- O3 with bond length of 1.90 Å (Figure 4) after optimization step completed for conjugate complex k-carrageenan-glyoxylic acid. According to Karavas et al. [10] the hydrogen bond length established in their Gaussian calculation for k-carrageenan and fluvastatin is around 1.897 Å. While Adam et al. [9] calculated hydrogen bond length of 1.75 Å for interaction between ethanol and patchouli in their molecular dynamic simulation. Therefore, the hydrogen bond established in this calculation is around the acceptable ranged. The hydrogen bond is the strongest intermolecular interaction [16, 17], which as physical crosslink, it may produce stable hard capsule shell that may promote disintegration.

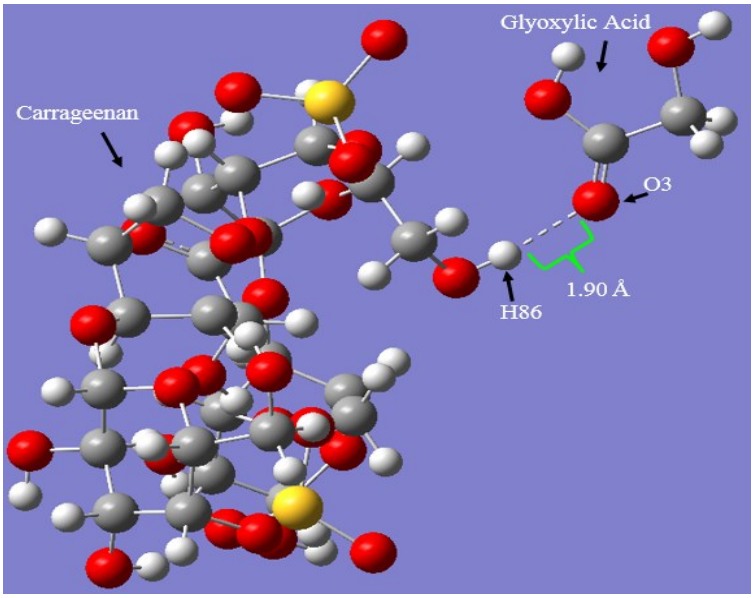



Figure 4. Hydrogen bond point between H86 --- O3 generated from the optimization calculation

The self-consistent field (SCF) energy values for optimized k-carrageenan, glyoxylic acid and conjugate complex k-carrageenan-glyoxylic acid were tabulated in Table 1. This study calculated -75.735 kJ $mol^{-1}$ for interaction energy of hydrogen bond between k-carrageenan and glyoxylic acid using 6-31G basis set. While Karavas et al. [10] calculated -318 kJ $mol^{-1}$ for the interaction energy of hydrogen bonding between iota carrageenan and (API) fluvastatin using basis set of 6-31G **(d.p) with ** as diffusion function and (d,p) as polarization function. This additional functionals may produce better result however due to computer constraint, this study only use basis set of 6-31G without additional functions. Meanwhile Reichardt and Welton [18] reported that a strong hydrogen bond interaction energy for hydrofluoric acid (HF---HF) is -155 kJ $mol^{-1}$. Thus the interaction energy calculated in this study may indicate that hydrogen bond established in the conjugate complex of k-carrageenan-glyoxylic acid weaker and can promote disintegration as well.

Table 1. SCF energy value for optimized k-carrageenan, glyoxylic acid and conjugate complex k-carrageenan-glyoxylic acid

| **Component** | **SCF energy for optimized molecule (kJ $mol^{-1}$)** |
|---|---|
| k-Carrageenan | -938 9839.095 |
| Glyoxylic acid | -798 961.796 |
| k-Carrageenan – glyoxylic acid | -1 018 876.626 |
| Interaction energy (ΔSCF energy) | -75.735 |

Another parameter that generated from this DFT calculations is the muliken charges of the molecule (Table 2). Sakaguchi et al. [19] reported that absolute ΔMulliken atomic charge can be used to predict the ionic degree of the covalent bond comprising polymer main chain. They concluded that the higher absolute ΔMulliken atomic charge, the higher ionic degree or ionic yield. While Gao et al. [20] suggest that the ionic degree indicates the hardness of covalent bond. Lower ionic degree may induce the scission of polymer chains. Therefore the absolute ΔMulliken atomic charge of 0.492 may induce the scission that promote further disintegration of hard capsule at C32 – O5 (Figure 5).

Table 2. Mulliken atomic charges, and absolute Mulliken atomic charges (ΔMC) obtained for optimized k-carrageenan and conjugate complex of k-carrageenan-glyoxylic acid.

| Component | C32 | O5 | C34 | ΔMC C32 – O5 | ΔMC O5 – C34 |
|---|---|---|---|---|---|
| k-Carrageenan | -1.850 | 0.180 | 0.617 | 2.030 | 0.437 |
| k-Carrageenan - glyoxylic acid | 0.054 | -0.442 | 0.691 | 0.492 | 1.133 |

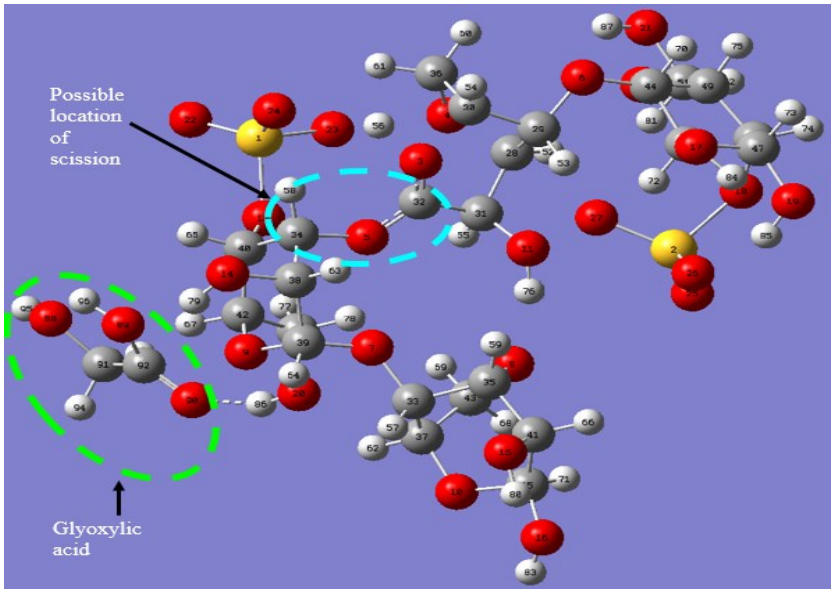



Figure 5. Probability of scission effect in conjugate complex k-carrageenan-glyoxylic chains

## Conclusion

The DFT calculations to determine the physical crosslink establishment has been successfully carried out and generated positive value of vibrations indicate calculations are at the global minima. The calculated interaction energy for established hydrogen bond is -75.735 kJ $mol^{-1}$. While generated MESP for k-carrageenan and glyoxylic acid indicate that both molecules have the electron and proton donor site which can establish the hydrogen bond as physical crosslink. Furthermore the absolute ΔMulliken atomic charge of may suggest scission effect toward main covalent bond in k-carrageenan and thus further promote disintegration of hard capsule. It is recommended that a higher accuracy calculations should be carried out through addition of diffusion and polarization functions to the basis set used in this work.

**Acknowledgements**

The authors would like to acknowledge support from the Ministry of Science Technology and Innovation via EScience Grant Scheme: UMPRDU 140504 and Universiti Malaysia Pahang (FKKSA & FIST) for the computer lab facilities. Special thanks to Assoc. Prof. Dr. Ku Halim Ku Bulat (Univerisiti Malaysia Terengganu) and Dr. Saifful Kamaluddin Muzakir (FIST, UMP) for all the quantum mechanics guidance.

**References**

1. Girond, S., Crance, J. M., Van Cuyck-Gandre, H., Renaudet, J. and Deloince, R. (1991). Antiviral activity of carrageenan on hepatitis A virus replication in cell culture. *Research in Virology*, 142: 261 – 270.
2. Hezaveh, H. and Muhamad, I. I. (2013). Modification and swelling kinetic study of kappa-carrageenan-based hydrogel for controlled release study. *Journal of the Taiwan Institute of Chemical Engineers*, 44(2): 182 – 191.
3. Hezaveh, H. and Muhamad, I. I. (2013b). Controlled drug release via minimization of burst release in pH-response kappa-carrageenan/polyvinyl alcohol hydrogels. *Chemical Engineering Research and Design*, 91(3): 508 – 519.
4. Meena, R., Prasad, K. and Siddhanta, K. (2009). Development of a stable hydrogel network based on agar-kappa-carrageenan blend cross-linked with genipin. *Food Hydrocolloids*, 23: 497 – 509.
5. Briones, A. V. and Sato, T. (2010). Encapsulation of glucose oxidase (GOD) in polyelec-trolyte complexes of chitosan–carrageenan. *Reactive and Functional Polymer,* 70: 19 – 27.
6. Ozsoy, Y. and Bergisadi, N. (2000). Preparation of mefenamic acid sustained release beads based on kappa-carrageenan. *Bollettino Chimico Farmaceutico*, 139: 120 – 123.
7. USP 30 (2007). United States Pharmacopeia, chapter 701: 276 – 277.
8. Hiemstra, C., Zhong, Z., Dijikstra, P. and Feijen, J. (2009). Stereocomplexed PEG-PLA hydrogels in hydrogels: Biological properties and applications. Roland Barbucci (Editor). Springer-Verlag Italia, Milan, Italy.
9. Adam, F., A. Bakar, S. H., M. Yusoff, M. and Tajuddin, S. N. (2013). Molecular dynamic simulation of the patchouli oil extraction process. *Journal of Chemical and Engineering Data*, 59: 183 – 188.
10. Karavas, E., Koutris, E., Papadopoulos, A. G., Sigalas, M. P., Nanaki, S., Papageorgiou, G. Z., Achillas, D. Z. and Bikiatris, D. N. (2014). Application of density functional theory in combination with FTIR and DSC to characterise polymer drug interactions for the preparation of sustained release formulations between fluvastatin and carrageenans. *International Journal of Pharmaceutics*, 466: 211 – 222.
11. Becke, A. D. (1993). Density-functional thermochemistry. III. The role of exact exchange. *Journal of Chemical Physics,* 98: 5648 – 5652.
12. Lee, C., Yang, W. and Parr, R.G. (1988). Development of the Colle–Salvetti correlation-energy formula into a functional of the electron density. *Physical Review B*, 37: 785 – 789.
13. Kumar, A., Narayan, V., Prasad, O. and Sinha, L. (2012). Monomeric and dimeric structures, electronic properties and vibrational spectra of azelaic acid by HF and B3LYP methods. *Journal of Molecular Structure,* 1022: 81 – 88.
14. Rawat, P. and Singh, R. N. (2015). Synthesis, conformational, spectroscopic and chemical reactivity analysis of 2-cyano-3-(1H-pyrrol-2-yl)acrylohydrazide using experimental and quantum chemical approaches. *Journal of Molecular Structure*, 1082: 118 – 130.
15. Tanak, H. (2015). Molecular structure, spectroscopic and DFT computational studies on 4,5-bis(tert-butylsulfanyl)phthalonitrile. *Journal of Molecular Structure*, 1090: 86 – 92.
16. Suchocki, J. (2000). Conceptual chemistry: Understanding our world of atoms & molecules. 3rd edition. Pearson Benjamin, USA.
17. Reger, D. L, Goode, S. R. and Ball, D. W. (2010) Chemistry: principles and practice. Brooks/Cole: Cengage Learning, Canada.
18. Reichardt, C. and Welton, T. (2011). Solvents and solvents effects in organic chemistry. John Wiley & Sons Publication, USA.
19. Sakaguchi, M., Makino, M., Ohura, T. and Iwata, T. (2014). The correlation between the ionic degree of covalent bond comprising polymer main chain and the ionic yield due to mechanical fracture. *Polymer,* 55(8), 1917 – 1919.
20. Gao, F., He, J., Wu, E., Liu, S., Yu, D., Li, D., Zhang, S. and Tian, Y. (2003). Hardness of covalent crystals. *Physical Review Letters,* 91: 015502.

*Malaysian Journal of Analytical Sciences, Vol 21 No 4 (2017): 986 - 995*
*DOI: https://doi.org/10.17576/mjas-2017-2104-26*

MALAYSIAN JOURNAL OF ANALYTICAL SCIENCES
*Published by The Malaysian Analytical Sciences Society*
ISSN 1394 - 2506

# *Alchemilla vulgaris* AND *Filipendula ulmaria* EXTRACTS AS POTENTIAL NATURAL PRESERVATIVES IN BEEF PATTIES

## (Ekstrak *Alchemilla vulgaris* dan *Filipendula ulmaria* Sebagai Pengawet Asli dalam Burger Daging)

Khadijah Husna Abd Hamid[1], Nurul Aini Mohd Azman[1]*, Shalyda Sharaani[1], Norashikin Zain[1], Normazlinah Ahmad[1], Ahmad Ziad Sulaiman[1], Syed Saufi Tuan Chik[1], Wan Faizal Wan Ishak[1], Maria Pillar Almajano Pablos[2]

[1]*Chemical and Natural Resources Engineering Faculty, University Malaysia Pahang, Lebuhraya Tun Razak, 26000 Gambang, Pahang, Malaysia*
[2]*Department of Chemical Engineering, Technical University of Catalonia, Avigunda Diagonal 647, Barcelona 08028, Spain*

**Corresponding author: ainiazman@ump.edu.my*

Received: 28 November 2016; Accepted: 5 February 2017

**Abstract**

*Alchemilla vulgaris* (AV) and *Filipendula ulmaria* (FU) are European medicinal plants possess bioactive compounds that exhibit many pharmacological benefits in human. The present work aims to assess two plants ethanolic extract; AV and FU of their antioxidant activities as natural preservative in beef patties. All plant samples were analysed using total polyphenol content (TPC), their antioxidant activities using Trolox Equivalent Antioxidant Capacity (TEAC), Ferric Reducing Antioxidant Power (FRAP), color and TBARS (Thiobarbituric acid reactive substances) analysis to measure their potential as synthetic preservative in muscle food. The antioxidant activity of FU and AV extracts measured with TEAC were 88.46 and 68.21 mmol of Trolox (TE)/g Dry Weight (DW) respectively. Whereas, FRAP assay were 44.6 and 40.12 mmol of TE/g DW for FU and AV extracts. The effect of lipid oxidation of beef patties were measured with adding 0.1% (w/w) of lyophilise FU and AV and Butylated hydroxytoluene (BHT) packed in modified atmosphere (MAP) (80% v/v $O_2$ and 20% v/v $CO_2$) for 14 days storages. FU and AV treated samples showed no significant different compared with BHT ($p>0.05$). Beef patties treated with 0.1% (w/w) FU showed minimum changes in red color and formation of metmyoglobin throughout storages ($p<0.05$). These results indicate that these edible plants extract are promising sources of natural antioxidants and can potentially be used as functional preservatives in meat products.

**Keyword**: *Alchemilla vulgaris*, *Filipendula ulmaria*, antioxidant, free radicals, polyphenol

**Abstrak**

*Alchemilla vulgaris* (AV) dan *Filipendula ulmaria* (FU) merupakan tumbuhan perubatan Eropah mempunyai sebatian bioaktif yang boleh memberi kesan positif farmakologi terhadap manusia. Kajian ini bertujuan menganalisa kedua-dua tumbuhan; AV dan FU terhadap aktiviti antioksidan dan sebagai pengawet semula jadi dalam model makanan. Aktiviti antioksidan di dalam FU dan AV ekstrak menggunakan analisis keupayaan antioksidan setara Trolox (TEAC) masing-masing adalah 88.46 dan 68.21 mmol Trolox/g bahan kering. Sebaliknya, aktiviti antioksidan oleh ujian kuasa antioksidan penurunan ferik (FRAP) adalah 44.6 dan 40.12 mmol Trolox/g bahan kering bagi ekstrak FU dan AV. Kesan aktiviti antioksidan disukat dalam burger daging yang mempunyai 0.1% (w/w) lyophilise FU dan AV tidak menunjukkan perbezaan yang ketara berbanding dengan 0.1% BHT apabila disimpan dalam pembungkusan MAP (80% $O_2$ dan 20% $CO_2$ v/v) selama 14 hari ($p> 0.05$). Burger daging yang dirawat dengan 0.1% (w/w) FU menunjukkan perubahan minimum pada warna merah dan pembentukan metmyoglobin sepanjang penyimpanannya ($p <0.05$). Keputusan ini menunjukkan bahawa ekstrak tumbuhan yang boleh dimakan ini menjanjikan satu sumber antioksidan semulajadi yang berpotensi untuk digunakan sebagai bahan pengawet di dalam produk daging.

**Kata kunci:** *Alchemilla vulgaris*, *Filipendula ulmaria*, antioksidan, radikal bebas, polifenol

## Introduction

Over the last decades, the development of ready-to-serve foods products posed new challenges from modern consumer to satisfy and optimized the food cost, appearance and most importantly about the food safety and nutritional values. Moreover, customers recently have been gaining interest in formulation of foodstuff that are healthy and functional, least chemical additives and preferably with natural ingredient [1].Therefore, the food manufacturing industries nowadays are very keen to venture in the variety of healthy food products innovation as new market demand and stimulate purchasing. The use of synthetic antioxidant such as butylated hydroxyanisole (BHA), butylated hydroxytoluene (BHT) and tert-butylhydroquinone (TBHQ) in food formulation developed health concern by public due their possible toxicological effects that may contribute too many diseases [2].

Lipid oxidation occurs in meat product affects the sensory characteristics such as colour, flavour, odour and texture, also causes the loss of nutritional value and the generation of toxic reaction products such as malonaldehyde (MDA) [3]. Alternatively, partial substitution of meat preservatives using natural preservatives had been studied in past years [4 – 8]. Soltanizadeh et al. [9] demonstrated the use of 3% (w/w) of Aloe Vera improved most quality characteristic that satisfy consumer acceptability. Soya, rosemary, thyme, oregano, broccoli and *Gentiana lutea* are among healthy substitute in the meat patties role as natural preservatives [10 –14]. Hence, it conclude that the natural edible plants responsible to many antioxidant actions may linked to the various type of actives ingredients including polyphenol.

*Alchemilla vulgaris* (AV) and *Filipendula ulmaria* (FU) are perennial herbs in the family Rosaceae, widely spread around Europe and Western Asia. They displayed excellent antioxidant activity and many pharmacological benefits in human [15]. AV is well known for their antioxidant activities probably due to the high phenolic contents (rutin, tannins, antocianidins, flavonoids, flavonol, phenolic acid and kempherol) [15 –18]. The plant extract exhibited different pharmacological roles, such as astringent, antidiarrheal, diuretic, depurative, intestinal antiseptic, bacteriostatic and bactericidal, tonic, anti-arthritic and cancer deterrent [19]. Moreover, FU showed relevant biological activity as astringent, antacid, anti-ulcer, anti-rheumatic, immunomodulatory and cytotoxic properties with various polyphenol compositions [15, 20, 21]. Many authors demonstrated the present of numbers of phenolic constituent including derivatives salicylates, flavonols and ellagitannins that contributed to the biological activities in the plant extract [22, 23]. Moreover, both these plants could act as antioxidants and antimicrobials in food, acting as natural additives that increased food shelf life as well as adding health benefits to potential consumers.

However, the antioxidant activity of AV and FU leaves extract towards lipid oxidation has not been fully determined. Thus, our goals were (1) to quantify the phenolic compounds in AV and FU leaves extract (2) to evaluate the antioxidant activity of AV and FU leaves extract using in Trolox equivalent antioxidant capacity (TEAC) assays and Ferric Reducing Antioxidant Power (FRAP) (3) to demonstrate the ability of AV and FU leaves extract to inhibit lipid deterioration and their effect toward red color changes in meat patties.

## Materials and Methods

### Materials

Commercial dried AV and FU was kindly supplied by Pàmies Hortícoles (Balaguer, Spain), a registered herbal company. All reagents and solvents used were of analytical grade and obtained from Panreac (Barcelona, Spain) and Sigma Aldrich (Gillingham, England).

### Extraction of plants extract

Dried roots of AV and FU were finely ground using a standard kitchen food processor. Ground plants were extracted with 50:50 (v/v) ethanol: water in the ratio 1:10 (w/v). The extractions were performed at 60 ± 1°C for 24 hours, in the dark with constant stirring. The plants extract solutions were recovered by filtration using Whatman Filter paper, 0.45 µm. Part of the supernatant were taken for subsequent use to determine the antioxidant activities. The volume of the remaining supernatant was measured and the excess of ethanol was removed under vacuum using

a rotary evaporator (Buchi Re111, Switzerland) and kept frozen at -80°C for 24 hours. All extracts were dried in a freeze dryer (Unicryo MC2L -60 b°C, Germany) under vacuum at -60 °C for 3 days to remove moisture.

**Determination of the total phenolic content**

The Folin-Ciocalteu method was used to determine the total phenolic content (TPC) as reported by Santas et al. [23]. Mixtures of 7.7% sample, 4% Folin reagent and 30.8% of saturated sodium carbonate solution final concentrations were diluted with the sample with 1:25 (v/v). Finally, final mixture was diluted with Milli-Q water, shaken and incubated in the dark for 1 hour. Absorbance at 765 nm was measured using a microplate reader (Fluostar Omega, BMG Labtech, Ortenberg, Germany) against water as a blank. Gallic acid was used to prepare a standard calibration, and the results were expressed as mg of Gallic acid equivalents/g dry weight (mg GAE/g DW).

**Determination of the Trolox equivalent antioxidant capacity assay**

The antioxidant activities against $ABTS^{\bullet+}$ radical of plants extract were measured by using a modified TEAC assay, as described by Azman et al. [14]. $ABTS^{\bullet+}$ radical cation (7 mM, final concentration) was dissolved before adding potassium sulphate (2.45 mM, final concentration) and allowing the mixture to stand in the dark up to 16 hours. Phosphate Buffer Solution (PBS, 10 mM) with the $ABTS^{\bullet+}$ radical cation were incubated at room temperature for 30 minutes before used. Then, the mixture of the $ABTS^{\bullet+}$ radical cation was adjusted to an absorbance of 0.73 ± 0.2 nm, using a microplate reader (Fluostar Omega, BMG Labtech, Ortenberg, Germany). The TEAC values for the different concentrations of each compound were interpolated from the Trolox calibration curve and expressed as milligrams of Trolox equivalent per gram of dry weight sample (mg TE/g DW sample).

**Determination of the ferric reducing antioxidant power**

The FRAP method was introduced by Benzie et al. [24] and implemented with some modifications. The FRAP solution was prepared in proportions of 10:1:1 of 300 mmol/L acetate buffer (pH 3.6), 10 mmol/L, 2,4,6-tripyridyl-s-triazine (TPTZ) in 40 mmol/L hydrochloric acid (HCl) and 20 mmol/L iron(III) chloride ($FeCl_3$), respectively. FRAP solution was incubated at 37 °C for 20 minutes before it was mixed with the adequate dilution of the extract. The absorbance was measured at 593 nm using a microplate reader. Results were compared with the Trolox calibration curve, and concentrations were expressed as micromoles of Trolox equivalents per gram dried weight of sample (mmol of TE/g DW).

**Determination of antioxidant activity in food model: Preparation of beef patties**

The lean meat of male cows slaughtered in accordance with approved guidelines of the Animal Ethics Committee was supplied by local market. The meat was collected 7 days after slaughter to allow it to mature and was kept at approximately -20 °C for further treatment. Fat and joint tissues from lean meat were trimmed off lean meat (2000 g) and the meat was minced through 8 mm industrial plates. Then, the minced meat was divided into 4 batches (w/w) and were mixed with 1.5% of sodium chloride (NaCl) and either i) control (no addition), ii) 0.1% butylated hydroxytoluene (BHT), iii) 0.1% FU lyophilise, iv) 0.1% AV lyophilise. All batches were mixed vigorously for 2 minutes to attain an even distribution of additives throughout the meat. Each sample was moulded into smaller portions (about 20 g each), stuffed and packed with polystyrene B5-37 (Aerpack) trays and placed in BB4L bags (Cryovac) of low gas permeability (8–12 $cm^3$ $m^{-2}$ over 24 hours). The air in the trays was flushed with 80:20 (v/v) oxygen: carbon dioxide ($O_2$:$CO_2$) by EAP20 mixture (Carburos Metalicos, Barcelona) using packaging. Samples were stored in the dark at 4 ± 2 $^oC$ for 2 weeks to analyse the oxidation for thiobarbituric acid reactive substances (TBARS) method. Every measurement was carried out in triplicate each day.

**TBARS assay**

TBARS measurement was used to measure the extent of lipid oxidation over the storage period as described by Grau et al. [25]. The samples (1 g) were weighed in a tube and mixed with 3 g/L aqueous ethylenediamine-tetraacetic acid (EDTA) in ratio 1:1 (w/v). Then, the sample was immediately mixed with 5 mL of thiobarbituric acid reagent using an Ultra-Turrax (IKA, Germany); 32000 rpm speed, for 2 min. All procedures were carried out in the dark and all samples were kept in ice. The mixture was incubated at 97 ± 1 $^oC$ in hot water for 10 minutes and shaken for 1 minute during the process to form a homogeneous mixture. The liquid sample was recovered by filtration (Whatman Filter paper, 0.45 μm) after the sample was cooled for 10 minutes. The absorbance value for each sample was measured at 531 nm using a spectrophotometer. The TBARS value was calculated from a

malonaldehyde (MDA) standard curve prepared with 1,1,3,3 tetraethoxypropane and analysed by linear regression. All results were reported in mg malonaldehyde per kg of sample (mg MDA /kg sample).

**Percentage of metmyoglobin**

The metmyoglobin method was based on the method developed by Xu et al. [26]. An amount 5 g beef patties were homogenized with 25mL of ice-cold 0.04 M phosphate buffer (pH 6.8) for 15 second using homogenizer (Ultra-Turrax, IKA, Germany), which was set at speed setting 2 (18000 rpm). The homogenate was allowed to stand in 4 $^{o}$C for 1 hourr and centrifuged at 4500 g for 20 minutes at 4 $^{o}$C using a high-speed freezing centrifuge (GI-20G, Anke, Shanghai, China). The absorbance of the filtered supernatant was read at 572, 565, 545, and 525 nm with a spectrometer (Fluostar Omega, BMG Labtech, Germany). The percentage of metmyoglobin was determined using the formula; MetMb (%) = [-2.514(A572/A525) + 0.777(A565/A525) + 0.8(A545/A525) + 1.098] x 100

**Statistical analysis**

A one-way analysis of variance (ANOVA) was performed using Minitab 16 software program ($\alpha$=0.05). The results were presented as mean values (n $\geq$3).

## Results and Discussion

**Extraction yield, total polyphenols and antioxidant activity assays**

The European herbs were tested for their polyphenol content and antioxidant ability. Ethanol is used as extraction solvent because is recognized as a GRAS (Generally Recognized as Safe) component that safely used in the food industry application [27]. Rababah et al. [28] reported temperature of 60 $^{o}$C found to be the best for extracting phenolic compounds in most common herbs including oregano, thyme and terebinth. In addition, 70% (w/w) ethanol extract is used to extract the bioactive compound of AV and FU for acetylcholinesterase and tyrosinase inhibitory assay for treatment of neurodegenerative disorder in human [15].

Table 1 illustrated the extraction yield, phenolic compound and antioxidant activity of AV and FU in 50% (w/w) aqueous solvent extract. Generally, AV showed higher yield, phenol content and antioxidant activity than FU extract. The phenolic content value of the AV and FU extracts showed positive correlation to the antioxidant activity value in TEAC and FRAP assays. The total phenolic content of AV and FU extracts allowed the estimation of all phenolic acids, flavonoids, anthocyanin, non-flavonoids and many classes of polyphenol compounds present in the samples. The obtained results are in agreement with Neagu et al. [15] which found phenolic content of AV and FU are 112.33 µg/mL and 103.00 µg/mL using 70% ethanol solvent. The authors also identified amount of proanotcyanidins and flavonoes in the plants extract. Previous research finding correlates the total phenolic content with antioxidant activity which may contributes many pharmacological actions in plants extract [23].

Table 1. Extraction yield, TPC and antioxidant activity of AV and FU extracts in ethanol aqueous

| **Activities Plant extract** | **Extraction solvent 50:50 (v/v) EtOH:$H_2O$** | |
|---|---|---|
| | **FU** | **AV** |
| Extraction yield (%) | 32.1 ± 0.03 | 30.4 ± 0.01 |
| Total phenolic content (mg GAE/g DW) | 122.11 ± 0.12 | 96.43 ± 0.2 |
| TEAC (mmol of TE /g DW) | 88.46 ± 0.83 | 68.21 ± 0.33 |
| FRAP (mmol of TE/g DW) | 44.6 ± 0.19 | 40.12 ± 0.11 |

*Mean value n = 3 and the standard deviation for each assay is less than 5%. Gallic Acid Equivalent (GAE), Trolox Equivalent (TE), Dry Weight (DW)

Nevertheless the *in-vitro* antioxidant activity of TEAC assay gave higher antioxidant activity values of compared to the FRAP assay in both plant extracts. The assay value indicated the extracts potency to scavenge the long-life radical cation ABTS•+ generated in the assay [29]. Research finding from Kiselova et al. [17] showed the antioxidant activity of AV extract in TEAC assay that has strong correlation with the polyphenol content ($r^2$ = 0.92). Moreover, Barros et al. [20] observed FU extract using acetone showed highest value in TEAC assay compare with

methanol and water. Meanwhile, FRAP assay showed the antioxidant ability of polysaccharides in the plant extracts react with a colorless Fe(III) to generate a colored Fe(II)–tripyridyltriazine form which can measured at 593 nm absorbance. A number of *in-vitro* antioxidant studies has been carried out including TEAC, Oxygen Radical Absorbance Capacity (ORAC) and 2,2-diphenyl-1-picrylhydrazyl (DPPH) radical scavenging shown antioxidant activity potential in the AV and FU extracts [15, 30, 31]. However, to the best of our knowledge this is the first report of antioxidant activity extract from AV and FU assessed using FRAP method. Sufficient amount of studies have reported the antioxidant activities of AV and FU due to the various polyphenol compositions such as rutin quercetin, synaptic acid and chlorogenic acid. These compounds exert radical scavenging behavior towards free radical mainly reactive radical species (ROS) that could be explain in the FRAP and TEAC value during this study.

**Antioxidant activity in food model**

Many strategies on laboratory scale have been developed to improve the stability of shelf life in food models including adding amount of natural extracts that have similar effect as synthetic preservative. The effect of AV and FU on inhibiting lipid oxidation in muscle food has not been described. The oxidation in meat patties was measured in second stage of oxidation, secondary oxidation products (TBARS). In addition the change in color and % metmyoglobin were measured as physically resemble the freshness of the meat.

**TBARS analysis in beef patties**

The study carried out using modified atmosphere packaging for beef patties that was similar to the real packaging in the market. Hence, higher oxygen concentrations in MAP mixtures of 60 – 80% $O_2$ and 20 – 40% $CO_2$ are commonly used in beef product packaging for retail display in the market. Figure 1 shows lipid oxidation in different burger samples during the 2 weeks of storage. Thiobarbituric acid reactive substances (TBARS) as an indicator of secondary phase of lipid oxidation occurs in the sample are measured based on mg of malondialdehyde per kg of the sample. The secondary lipid oxidation is responsible for the alteration of flavor, rancid odor and the undesirable taste in foods [42]. The initial amount of malonaldehyde on day 0 to day 3 varied in the range of 0.1 – 0.2 mg/kg of the sample and no significant differences were observed among the burger samples. Starting day 3 onwards control sample showed the highest TBARS value among samples treated antioxidant ($p > 0.05$). During the 14 days of storage, lipid oxidation proceeded in the control sample and reached 3.90 mg malonaldehyde/kg sample.

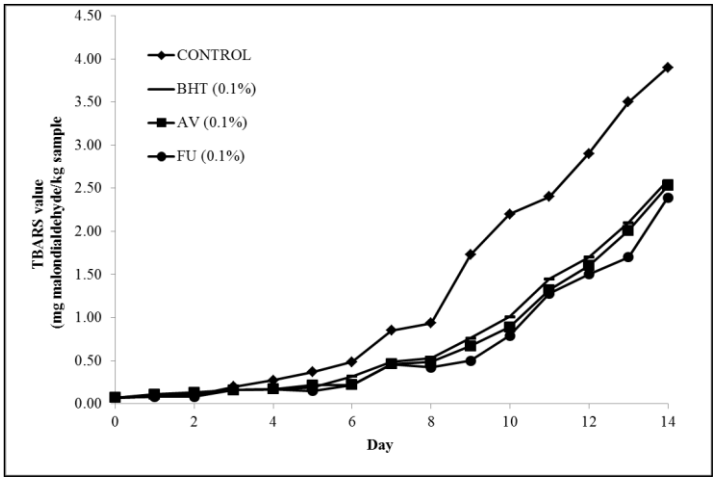



Figure 1. Changes in TBARS values (mg malodialdehyde/kg sample) of control and sample containing different concentrations (0.1% w/w) of AV and FU extract and BHT extract in MAP atmosphere during 14 days storages at 4 ± 1 °C without light. Each sample was measured in triplicate and the average standard deviation for each sample was less than 5%.

In general, the levels of lipid oxidation in beef patties increased over time and followed the order: 0.5% FU < 0.5% AV < 0.5% BHT < Control. The presence of control atmosphere with high oxygen packaging (MAP) resulted in higher TBARS and increased the oxidation rate in muscle food [29, 32, 33]. No statistical difference was observed between sample treated with antioxidant throughout the 14 days storages, however the TBARS value of both samples showed significant difference compared to control samples($p<0.05$). From Figure 1, the antioxidant potential of AV and FU extract at different storages days showed that the plants have activity equivalent to synthetic antioxidant, BHT ($p>0.05$). 0.1% BHT was added as comparison with natural antioxidant beside the FDA guidelines for using BHT is ≥ 200 ppm in meat product [29].

The effect of AV and FU extract on the lipid oxidation in meat has never been reported before. The active properties of AV and FU attributed to various phenolic acid including flavonols, flavonoids-glucosides, isoflavones, ellagitannins and sinapic acid which prevent propagation of lipid oxidation [15]. The antioxidant activity of phenolic compound is closely related to the hydroxyl group linked to the aromatic ring which is capable donating hydrogen atoms with electrons and neutralizing free radicals. This mechanism blocks further degradation of active oxidizing from such as MDA, which can be measured by TBARS method [34]. The study confirmed the potential of AV and FU extract to inhibit the lipid degradation in beef patties.

**Colour and % Metmyoglobin**

Figure 2 illustrated the color changes in meat patties were significantly affected by two plant extracts and BHT. The change of meat color is an important factor that impacts visual attraction in consumers. Normally, the colour analysis parameters collected using Minolta Chroma Meter CR-400 represent the lightness (L*), redness (a*), yellowness (b*) of the meat surface. However, only a* value are shown in this study due to red color is important color parameter in evaluating meat oxidation. The decrease in redness color makes meat product unacceptable to consumer [35]. In all samples, the a*value decreased as storage time progressed and the red color of control faded very rapidly. The natural color of the plant extract influenced the a*value of the meat at the first 3 days showed significant different from BHT and control ($p <0.05$). At the end of storages, the redness value of control sample was significantly lower than the antioxidant treated sample. 0.1% BHT displayed highest value of a* until 5 days storages and declined gradually onwards ($p <0.05$). This finding was expected as BHT role as synthetic antioxidant which used to retain colour and delaying lipid oxidation in the meat. Sample treated with 0.1% AV exhibited the redness color at the highest value after 14 days storages ($p <0.05$), whereas FU sample showed no significant different of a* value with BHT sample. Therefore, the AV and FU at 0.1% (w/w) extracts as natural preservatives potentially preserved the redness color of the meat and displayed the potentially useful in prolonging the shelf life of the meat product.

Meanwhile Figure 3 presents the effect of natural plants extract and BHT on relative metmyoglobin percentage in beef patties. A significant correlation between metmyoglobin (MetMb) percentage and the redness color features were analysed previously [29, 36]. The MetMb percentage increased as the storage time increased throughout the 14 days refrigeration, whereas the control showed the highest MetMb value compared to all samples. Initial mean MetMb percentage was 23.9 ± 0.17 on 0 day and gradually increase until 7 days with no significant different for all samples ($p >0.05$). After 7 days onwards MetMb percentage increased progressively and sample treated with AV exhibited the lowest value significantly at 14 days storages ($p <0.05$). FU and BHT samples showed no significant different throughout the storage period, whereas the AV sample showed even superior to such synthetic antioxidant as BHT. According to Kim et al. [33], the MetMb percentage should not exceed 40%, especially when considering consumer acceptance and AV meat sample was satisfied this limit until day 7.

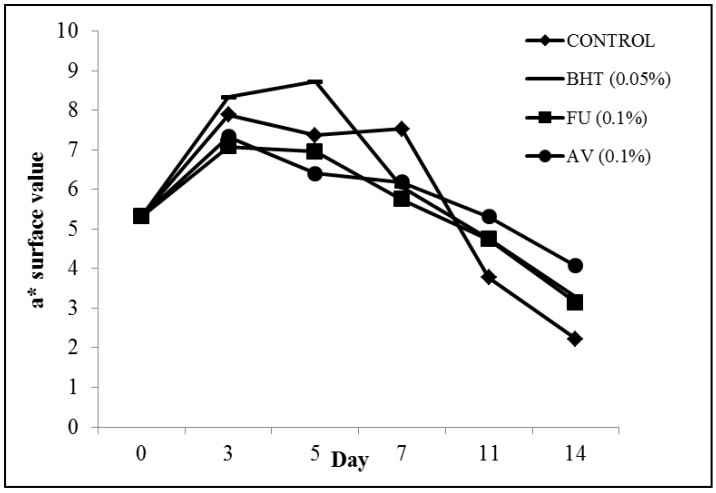



Figure 2. Changes in a* values of control and sample containing different concentrations (0.1% w/w) of AV and FU extract and BHT extract in MAP atmosphere during 14 days storages at 4 ± 1 °C without light. Each sample was measured in triplicate and the average standard deviation for each sample was less than 5%

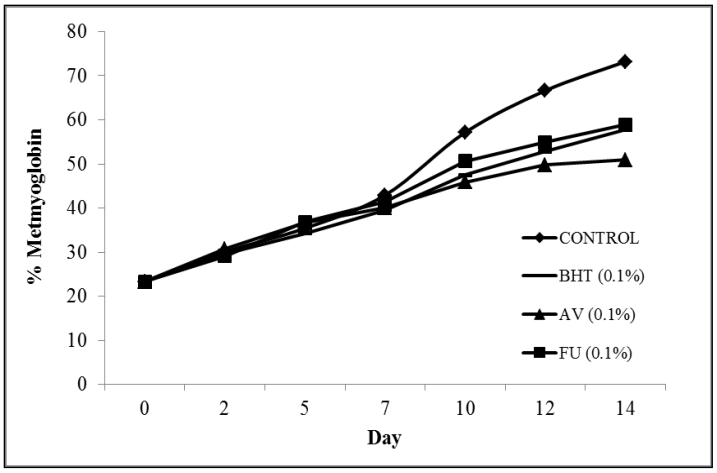



Figure 3. Changes in metmyoglobin percentage of control and sample containing different concentrations (0.1% w/w) of AV and FU extract and BHT extract in MAP atmosphere during 14 days storages at 4 ± 1°C without light. Each sample was measured in triplicate and the average standard deviation for each sample was less than 5%

A number of studies examined the effect of different antioxidant on the meat color and demonstrated the lipid oxidation decrease the redness color of the meat [8, 14, 37]. Xu et al. [26] have proposed that the chemical reaction influences discoloration act as a catalyst of lipid oxidation. Free radicals produced by lipid oxidation in meat are susceptible to initiating the reaction of oxidizing oxymyoglobin (red colour, measured by a*value in Figure 2) to metmyoglobin (brown colour, analysed by relatively formation of metmyoglobin in Figure 3) which results in the discolouration of meat. Hence, the overall changes of % metmyoglobin were inversely proportional to the value of redness (a*). The scavenging ability of samples treated with antioxidant can reduce the oxidation of metmyoglobin acting as scavengers of hydroxyl radicals produced from oxidation of oxymyoglobin. The 0.1% of FU extract displayed the lowest metmyoglobin percentage and capable to preserve redness color specifically compared to

synthetic antioxidant, BHT. However, color deterioration and lipid oxidation very dependent on the test system, including the influenced of salt, sample preparation, temperature, oxygen composition, storage time and packaging condition. Thus, modified atmosphere (MAP) at control gas composition of the meat packaging is important to reduce the variable that affect the meat shelf life.

The present study investigates the antioxidant activity potential of two medicinal plants –AV and FU – as inhibitor of lipid oxidation in muscle foods, which there is no data in the literature with this regard. The most bio active composition of the plants are the same may due to the same family of Rosaceae, however, the activity values tested are different. Numerous researches founds high content of polyphenol compounds in both FU and AV ethanolic extract, could be explained as antioxidant activity role in preventing lipid deterioration similar as BHT [15,38,39]. The plants contain polyphenol compounds that showed close behavior of antioxidant activity relevant in the study, which are rutin, quercetin, chlorogenic acid and synaptic acid. Rutin and quercetin are responsible exhibit significant pharmacological actives including anti-oxidation, whereas quercetin exert radical scavenging behavior that benefits in many neurodegenerative diseases by mitigating cellular damage induces by radical oxygen species (ROS)[40]. While, Chlorogenic acid (CGA) is a polyphenolic components associate to free radical scavenging and antioxidant activities towards hydrogen peroxide and amyloid beta [41]. The present of synapic acid present has also radical scavenging properties beside the behavior or anti-apotopic and anti-inflammatory [42].

## Conclusion

The aqueous extract of FU and AV plants exhibited different levels of phenolic content and antioxidant activity measured by TEAC and FRAP assays. Therefore, the antioxidant activity of FU and AV extract in the Trolox Equivalent Antioxidant Capacity (TEAC) were 88.46 and 68.21 mmol of TE/g DW respectively while the ferric reducing antioxidant power (FRAP) antioxidant activity for FU and AV extracts were 44.6 and 40.12 mmol of TE/g DW respectively. This study revealed the first time of radical scavenging activity has been evaluated in FU and AV extract using FRAP method. Addition of 0.1% (w/w) lyophilise FU and AV as an antioxidant in beef patties inhibited lipid oxidation during 14 days of storage in MAP atmosphere at 4 ± 1 °C without light. 0.1% (w/w) FU and AV decreased the discoloration of meat after 14 days of storage ($p < 0.05$) while FU showed no significant different of color changes in beef patties with BHT (synthetic antioxidant) sample. Thus, this study showed that the AV and FU as a potential antioxidant sources for natural preservatives in prolonging the shelf life of the food products.

## References

1. Carocho, M. and Isabel, C. F. R. F. (2013). A review on antioxidants, prooxidants and related controversy: natural and synthetic compounds, screening and analysis methodologies and future perspectives. *Food and Chemical Toxicology,* 51: 15 – 25.
2. Jayathilakan, K., Sharma, G. K., Radhakrishna, K. and Bawa, A. S. (2007). antioxidant potential of synthetic and natural antioxidants and its effect on warmed-over-flavour in different species of meat. *Food Chemistry,* 105: 908 – 916.
3. Tan, W. and Shelef, L. A. (2002). Effects of sodium chloride and lactates on chemical and microbiological changes in refrigerated and frozen fresh ground pork. *Meat Science,* 62(1): 27 – 32.
4. Triki, M., Herrero, A. M., Jiménez-Colmenero, F. and Ruiz-Capillas, C. (2013). Effect of preformed konjac gels, with and without olive oil, on the technological attributes and storage stability of merguez sausage. *Meat Science,* 93(3), 351 – 360.
5. Salminen, H., Kurt, H. and Jochen, W. (2013). Oil-in-water emulsions as a delivery system for n-3 fatty acids in meat products. *Meat Science,* 93(3): 659 – 667.\
6. Qi, S. and Delong, Z. (2013). Lotus seed epicarp extract as potential antioxidant and anti-obesity additive in chinese cantonese sausage. *Meat Science,* 93(2): 257 – 262.
7. Moarefian, M., Barzegar, M. and Sattari, M. (2013). Cinnamomum zeylanicum essential oil as a natural antioxidant and antibactrial in cooked sausage. *Journal of Food Biochemistry,* 37(1): 62 – 69.
8. Martín-Sánchez, A. M., Gelmy, C., Estrella, S., José, V., Jamel, B. and José, Á. P. (2013). Date palm by-products as a new ingredient for the meat industry: Application to pork liver pâté. *Meat Science,* 93 (4): 880 – 887.

9. Soltanizadeh, N. and Hossein, G. (2014). Qualitative improvement of low meat beef burger using aloe vera. *Meat Science,* 99: 75 – 80.
10. Iturriaga, L., Olabarrieta, I. and Martínez, D. M. I. (2012). Antimicrobial assays of natural extracts and their inhibitory effect against listeria innocua and fish spoilage bacteria, after incorporation into biopolymer edible films. *International Journal of Food Microbiology,* 158 (1): 58 – 64.
11. McBride, N. T. M., Sean, A. H. and Joe, P. K. (2007). Comparative addition of rosemary extract and additives on sensory and antioxidant properties of retail packaged beef. *International Journal of Food Science & Technology,* 42 (10): 1201 – 1207.
12. Campagnol, P. C. B., Dos Santos, B. A., Wagner, R., Terra, N. N. and Pollonio, M. A. R. (2013). The effect of soy fiber addition on the quality of fermented sausages at low – fat content. *Journal of Food Quality*, 36(1): 41 – 50.
13. Banerjee, R., Verma, A. K., Das, A. K., Rajkumar, V., Shewalkar, A. A. and Narkhede, H. P. (2012). Antioxidant effects of broccoli powder extract in goat meat nuggets. *Meat Science*, 91(2): 179 – 184.
14. Azman, N. A. M., Michael, H. G., Monika, S., Francisco, S. and María, P. A. (2014). Use of lyophilised and powdered *Gentiana lutea* root in fresh beef patties stored under different atmospheres. *Journal of the Science of Food and Agriculture*, 95(9): 1804 – 1811.
15. Neagu, E., Paun, G., Albu, C. and Radu, G. L. (2015). Assessment of acetylcholinesterase and tyrosinase inhibitory and antioxidant activity of *Alchemilla vulgaris* and *Filipendula ulmaria* extracts. *Journal of the Taiwan Institute of Chemical Engineers*, 52: 1 – 6.
16. Condrat, D., Mosoarca, C., Zamfir, A., Crişan, F., Szabo, M. and Lupea, A. (2010). Qualitative and quantitative analysis of gallic acid in *Alchemilla vulgaris, Allium ursinum, Acorus calamus* and *Solidago virga-aurea* by chip-electrospray ionization mass spectrometry and high performance liquid chromatography. *Open Chemistry*, 8(3): 530 – 535.
17. Kiselova, Y., Ivanova, D., Chervenkov, T., Gerova, D., Galunska, B. and Yankova, T. (2006). Correlation between the in vitro antioxidant activity and polyphenol content of aqueous extracts from Bulgarian herbs. *Phytotherapy Research*, 20(11): 961 – 965.
18. Plotnikov, M. B., Aliev, O. I., Andreeva, V. Y., Vasil'ev, A. S. and Kalinkina, G. I. (2006). Effect of *Alchemilla vulgaris* extract on the structure and function of erythrocyte membranes during experimental arterial hypertension. *Bulletin of Experimental Biology and Medicine*, 141(6): 708 – 711.
19. Spiridonov, N. A., Konovalov, D. A. and Arkhipov, V. V. (2005). Cytotoxicity of some Russian ethnomedicinal plants and plant compounds. *Phytotherapy Research*, 19(5): 428 – 432.
20. Barros, L., Alves, C. T., Dueñas, M., Silva, S., Oliveira, R., Carvalho, A. M., Henriques, M., Santos-Buelga, C. and Ferreira, I. C. (2013). Characterization of phenolic compounds in wild medicinal flowers from Portugal by HPLC–DAD–ESI/MS and evaluation of antifungal properties. *Industrial Crops and Products,* 44: 104 – 110.
21. Blazics, B., Papp, I. and Kéry, Á. (2010). LC–MS qualitative analysis and simultaneous determination of six Filipendula salicylates with two standards. *Chromatographia*, 71(1): 61 – 67.
22. Azman, N. A. M., Sara, P., Lluís, F., Luis, J. and Maria, P. A. (2014). Radical scavenging of white tea and its flavonoid constituents by electron paramagnetic resonance (EPR) spectroscopy. *Journal of Agricultural and Food Chemistry,* 62(25): 5743 – 5748.
23. Santas, J., Carbo, R., Gordon, M. and Almajano, M. (2008). Comparison of the antioxidant activity of two spanish onion varieties. *Food Chemistry,* 107(3): 1210 – 1216.
24. Benzie, I. F. and Strain, J. J. (1996). The ferric reducing ability of plasma (FRAP) as a measure of 'antioxidant power': The FRAP assay. *Analytical Biochemistry,* 239(1): 70 – 76.
25. Grau, A., Guardiola, F., Boatella, J., Barroeta, A. and Codony, R. (2000). Measurement of 2-thiobarbituric acid values in dark chicken meat through derivative spectrophotometry: Influence of various parameters. *Journal of Agricultural and Food Chemistry,* 48(4): 1155 – 1159.
26. Xu, Z., Tang, M., Li, Y., Liu, F., Li, X. and Dai, R. (2010). Antioxidant properties of Du-zhong (*Eucommia ulmoides Oliv.*) extracts and their effects on color stability and lipid oxidation of raw pork patties. *Journal of Agricultural and Food Chemistry*, 58(12): 7289 – 7296.
27. Fernández-Agullóa, A., Pereira, E., Freire, M. S., Valentão, P., Andrade, P. B., González-Álvarez, J. and Pereira, J. A. (2013). Influence of solvent on the antioxidant and antimicrobial properties of walnut (*Juglans regia* l.) green husk extracts. *Industrial Crops and Products,* 42: 126 – 132.

28. Rababah, T. M., Banat, F., Rababah, A., Ereifej, K. and Yang, W. (2010). Optimization of extraction conditions of total phenolics, antioxidant activities, and anthocyanin of oregano, thyme, terebinth, and pomegranate. *Journal of Food Science*, 75(7): 626 – 632.
29. Azman, N., Maria, G., Luis, J., Lluis, F. and María, P. A. (2015). The effect of convolvulus arvensis dried extract as a potential antioxidant in food models. *Antioxidants,* 4: 170 – 184.
30. Oktyabrsky, O., Vysochina, G., Muzyka, N., Samoilova, Z., Kukushkina, T. and Smirnova, G. (2009). Assessment of anti-oxidant activity of plant extracts using microbial test systems. *Journal of Applied Microbiology,* 106(4): 1175 – 1183.
31. Shilova, I. V., Semenov, A. A., Suslov, N. I., Korotkova, E. I., Vtorushina, A. N. and Belyakova, V. V. (2009). Medicinal plants chemical composition and biological activity of a fraction of meadowsweet extract. *Pharmaceutical Chemistry Journal,* 43(4): 4 – 9.
32. Martínez, L., Djenane, D., Cilla, I., Beltrán, J. A. and Roncalés, P. (2006). Effect of varying oxygen concentrations on the shelf-life of fresh pork sausages packaged in modified atmosphere. *Food Chemistry*, 94(2): 219 – 225.
33. Kim, S. J., Min, S. C., Shin, H. J., Lee, Y. J., Cho, A. R., Kim, S. Y. and Han, J. (2013). Evaluation of the antioxidant activities and nutritional properties of ten edible plant extracts and their application to fresh ground beef. *Meat Science,* 93(3): 715 – 722.
34. Lin, Y., Huang, M., Zhou, G., Zou, Y. and Xu, X. (2011). Prooxidant effects of the combination of green tea extract and sodium nitrite for accelerating lipolysis and lipid oxidation in pepperoni during storage. *Journal of Food Science*, 76(5): 694 – 700.
35. Renerre, M. (2000). Review: biochemical basis of freshmeat color. *Proceedings of the 45th International Congress of Meat Science and Technology*: pp. 344 – 352.
36. Dai, Y., Miao, J., Yuan, S. Z., Liu, Y., Li, X. M. and Dai, R. T. (2013). Colour and sarcoplasmic protein evaluation of pork following water bath and ohmic cooking. *Meat Science*, 93(4): 898 – 905.
37. Skowyra, M., Falguera, V., Gallego, G., Peiró, S. and Almajano, M. P. (2014). Antioxidant properties of aqueous and ethanolic extracts of tara (*Caesalpinia spinosa*) pods in vitro and in model food emulsions. *Journal of the Science of Food and Agriculture*, 94(5): 911 – 918.
38. Rompel, A., Fischer, H., Meiwes, D., Büldt-Karentzopoulos, K., Magrini, A. and Eicken, C. (1999). Substrate specificity of catechol oxidase from lycopus europaeus and characterization of the bioproducts of enzymic caffeic acid oxidation. *FEBS Letters,* 445: 103 – 110.
39. Momtaz, S., Mapunya, B. M., Houghton, P. J., Edgerly, C., Hussein, A., Naidoo, S. and Lall, N. (2008). Tyrosinase inhibition by extracts and constituents of Sideroxylon inerme L. stem bark, used in South Africa for skin lightening. *Journal of Ethnopharmacology*, 119(3): 507 – 512.
40. Jiménez-Aliaga, K., Bermejo-Bescós, P., Benedí, J. and Martín-Aragón, S. (2011). Quercetin and rutin exhibit antiamyloidogenic and fibril-disaggregating effects in vitro and potent antioxidant activity in APPswe Cells. *Life Science,* 89: 939 – 945.
41. Almeida, I. F., Fernandes, E., Lima, J. L., Valentao, P., Andrade, P. B. and Seabra, R. M. (2009). Oxygen and nitrogen reactive species are effectively scavenged by *Eucalyptus globulus* leaf water extract. *Journal of Medicinal Food,* 12: 175 – 183.
42. Lee, H. E., Kim, D. H., Park, S. J., Kim, J. M., Lee, Y. W., Jung, J. M., Lee, C. H., Hong, J. G.., Liu, X., Cai, M. and Park, K. J. (2012). Neuroprotective effect of sinapic acid in a mouse model of amyloid β1-42 protein-induced alzheimer's disease. *Pharmacology Biochemistry and Behaviour,* 103: 260 – 266.

**Malaysian Journal of Analytical Sciences Vol 21 No 5 2017**

Articles 17 - 25 are selected papers from the "International Conference in Organic Synthesis 2016 (ICOS2016), 'From Fundamental Research to Industrial Applications', 21 - 24 August 2016, Riverside Majestic Hotel, Kuching, Sarawak, Malaysia; organised by Institute of Science, Universiti Teknologi MARA (UiTM)."

Guest Editor: Mohd Fazli Mohammat


| | | Page |
|---|---|---|
| 1. | PERFORMANCE OF SOLAR PHOTOCATALYSIS AND PHOTO-FENTON DEGRADATION OF PALM OIL MILL EFFLUENT<br>(Prestasi Fotopemangkinan dan Degradasi Foto-Fenton Menggunakan Sinar Suria ke atas Efluen Kilang Minyak Kelapa Sawit)<br>*Devagi Kanakaraju, Nurul Liyana Binti Ahmad, Noorfaezah Binti Mohd Sedik, Sylvester Gan Hsien Long, Tay Meng Guan, Lim Ying Chin* | 996 |
| 2. | SYNTHESIS AND X-RAY SINGLE CRYSTAL STUDY OF 3-DIBUTYNYL AND 4-DIPENTYNYL PYRIDINE-2,6-DICARBOXYLATE<br>(Sintesis dan Kajian Sinar-X Hablur Tunggal 3-dibutinil dan 4-dipentinil piridina-2,6-dikarboksilat)<br>*Nawwar Hanun Abdul Malek, Mohammad Fadzlee Ngatiman, Bohari M. Yamin, Nurul Izzaty Hassan* | 1008 |
| 3. | BREAKDOWN OF HYDROGEN SULFIDE IN SEAWATER UNDER DIFFERENT RATIO OF DISSOLVED OXYGEN / HYDROGEN SULFIDE<br>(Penguraian Hidrogen Sulfida dalam Air Laut dengan Nisbah Oksigen Terlarut / Hidrogen Sulfida yang Berbeza)<br>*Hii Yii Siang, Norhayati Mohd Tahir2, Abdul Malek, Mohd Azlan Md Isa* | 1016 |
| 4. | ANTI-PROLIFERATIVE EFFECT OF *Aerva javanica* EXTRACTS ON MCF7 AND MDA-MB-231 BREAST CANCER CELL LINES<br>(Kesan Anti-proliferatif Ekstrak *Aerva javanica* Ke Atas Titisan Sel Kanser Payudara MCF7 dan MDA-MB-231)<br>*Nagla Mustafa Eltayeb, Ghada Mustafa Eltayeb, Salizawati Muhamad Salhimi* | 1028 |
| 5. | SYNTHESIS, CRYSTAL STRUCTURE AND COORDINATION CHEMISTRY OF DI-2-PYRIDYLMETHANEAMMINE-BASED CHELATING LIGANDS WITH CADMIUM SALTS<br>(Sintesis, Struktur Hablur dan Kimia Koordinatan Ligan Pengkelat Berasaskan Di-2-Piridilmetanaamina dengan Garam Kadmium)<br>*Maisara Abdul Kadir and Christopher James Sumby* | 1036 |
| 6. | PREPARATION OF DATE SEED ACTIVATION FOR SURFACTANT RECOVERY<br>(Penyediaan Biji Kurma Teraktif Untuk Pemulihan Surfaktan)<br>*Nurul' Ain Binti Jamion, Nor Haziqah Binti Abd Hafiff, Nurul Huda Abd Halim, Sheikh Ahmad Izzaddin Sheikh Mohd Ghazali, Jamil Mohamed Sapari* | 1045 |
| 7. | ISOLATION AND CHARACTERISATION OF MICROPLASTIC ABUNDANCE IN *Lates calcarifer* FROM SETIU WETLANDS, MALAYSIA<br>(Pemisahan dan Pencirian Plastik-Mikro di dalam *Lates calcarifer* dari Tanah Bencah Setiu, Malaysia) | 1054 |

*Yusof Shuaib Ibrahim, Ruthra Rathnam, Sabiqah Tuan Anuar, Wan Mohd Afiq Wan Mohd Khalik*

8. EXTRACTION AND CHARACTERIZATION OF CELLULOSE FROM AGRICULTURAL RESIDUE - OIL PALM FRONDS 1065
(Pengekstrakan dan Pencirian Selulosa daripada Bahan Buangan Pertanian - Pelepah Kelapa Sawit)
*Siti Rasila Ainaa Mohd Rasli, Ishak Ahmad, Azwan Mat Lazim, Ainon Hamzah*

9. DEGRADATION OF IMAZAPYR AND IMAZAPIC IN AQUEOUS SOLUTIONS AND SOIL UNDER DIRECT SUNLIGHT 1074
(Degradasi Imazapyr dan Imazapic dalam Larutan Akueus dan Tanah di bawah Cahaya Matahari)
*Siti Norashikin Mohamad Shaifuddin, Hazilia Hussain, Hamzah Fansuri Hassan, Nazri Che Dom, Razi Ikhwan Md Rashid*

10. CALCIUM CONTENT OF LIME MORTARS FROM 19th CENTURY CHURCH RUINS IN THE PHILIPPINES USING VOLUMETRIC ANALYSIS 1080
(Kandungan Kalsium Mortar Batu Kapur dari Runtuhan Gereja Abad Ke 19 di Filipina Menggunakan Analisis Volumetrik)
*Jan-Michael C. Cayme and Aniano N. Asor, Jr*

11. A NEW AUTOMATED GAS CHROMATOGRAPHY/SOLID PHASE MICROEXTRACTION PROCEDURE FOR DETERMINING α-FLUORO-β-ALANINE IN URINE 1091
(Kaedah Baru Pengekstrakan Mikro Fasa Pepejal/Kromatografi Gas Berautomatik untuk Penentuan α-Fluoro-β-Alanina di dalam Urin)
*Stefano Dugheri, Alessandro Bonari, Ilenia Pompilio, Matteo Gentili, Manfredi Montalti, Nicola Mucci, Giulio Arcangeli*

12. RESPONSE SURFACE METHODOLOGY OPTIMIZATION OF OIL REMOVAL USING BANANA PEEL AS BIOSORBENT 1101
(Pengoptimuman Kaedah Gerak Balas Permukaan Untuk Penyingkiran Minyak Menggunakan Kulit Pisang sebagai Penjerap-Bio)
*Najaa Syuhada Mohamad Thani, Rozidaini Mohd Ghazi, Norhisyam Ismail*

13. SINTESIS DAN PENCIRIAN HIDROGEL TERBIODEGRADASI BERASASKAN BAKTERIA SELULOSA MENGGUNAKAN TEKNIK RADIASI ULTRA LEMBAYUNG 1111
(Synthesis and Characterization of Biodegradable Bacterial Cellulose Based Hydrogels Using Ultra Violet Curable Radiation)
*Norhanisah Jamaludin dan Azwan Mat Lazim*

14. INCORPORATION OF GRAPHENE INTO COUNTER ELECTRODE TO ENHANCE THE PERFORMANCE OF DYE-SENSITIZED SOLAR CELLS 1120
(Pengabungan Grafin dalam Elektrod Lawan untuk Meningkatkan Prestasi Sel Suria Terpeka Pewarna)
*Aisyah Bolhan and Norasikin Ahmad Ludin*

15. PERFORMANCE ANALYSIS OF SIMPLIFIED SILICON SOLAR CELL ON *P*-TYPE CRYSTALLINE SILICON WAFER 1127
(Analisis Prestasi Bagi Sel Suria Silikon Teringkas Ke Atas Silikon Wafer Kristal Jenis-*P*)
*Wan Zulhafizhazuan, Suhaila Sepeai, Cheow Siu Leong, Kamaruzzaman Sopian , Saleem H. Zaidi*

16. INFRA-RED INVESTIGATION ON SILICON SOLAR CELLS 1134

(Kajian Inframerah ke atas Sel-sel Suria Silikon)
*Nurfarizza Surhada Mohd Nasir, Suhaila Sepeai, Cheow Siu Leong, Kamaruzzaman Sopian, Saleem H.Zaidi*

17. SYNTHESIS AND ANTIBACTERIAL STUDY OF ORGANOTIN(IV) COMPLEXES CONTAINING HYDRAZINOPYRIDINE LIGAND 1143
(Sintesis dan Kajian Antibakteria Kompleks Organostanum(IV) yang Mengandungi Ligan Hidrazinopiridin)
*Dayang Norafizan A. Chee, Monica Lulo Rodis, Norziah Saat, Zainab Ngaini, Ainaa Nadiah Abdul Halim*

18. SYNTHESIS, CHARACTERIZATION AND ANTIMICROBIAL PROPERTIES OF COPPER(II) COMPLEX OF HETEROCYCLIC LIGANDS 1151
(Sintesis, Pencirian dan Ciri Antimikrob Kuprum(II) Kompleks dengan Ligan Heterosiklik)
*Rabuyah Ni, Mohammad Isa Mohamadin, Vivien Jong Yi Mian*

19. ISOLATION AND SYNTHESIS OF PINOCEMBRIN AND PINOSTROBIN FROM *Artocarpus odoratissimus* 1156
(Pemencilan dan Sintesis Pinocembrin dan Pinostrobin dari *Artocarpus odoratissimus*)
*Nyotia Nyokat, Khong Heng Yen, Ahmad Sazali Hamzah, Isabel Fong Lim, Aimi Suhaili Saaidin*

20. IRON(II) COMPLEX OF ANTHRAQUINONE: SYNTHESIS, STRUCTURAL ELUCIDATION AND ANTIMICROBIAL ACTIVITY 1162
(Komplek Ferum(II) Antrakuinon: Sintesis, Penentuan Struktur Organik dan Aktiviti Antimikrob)
*Nur Dzaina Zaidel, Vivien Jong Yi Mian, Mohammad Isa Mohamadin*

21. SYNTHESIS, CHARACTERIZATION AND ANTIBACTERIAL ACTIVITIES OF HYDRAZONE SCHIFF BASE COMPOUNDS AND ITS DERIVATIVES 1168
(Sintesis, Pencirian dan Aktiviti Antibakteria Sebatian Bes Schiff Hidrazon dan Terbitannya)
*Ruwaida Asyikin Abu Talip, Meng Guan Tay, Hashimatul Fatma Hashim*

22. STEREOSELECTIVE REDUCTION OF 1-BENZYL-3,3-DIMETHYL-5-METHYLENEPYRROLIDINE-2,4-DIONE USING SODIUM BOROHYDRIDE WITH SELECTED METAL CHLORIDES 1176
(Tindak Balas Penurunan Stereoselektif 1-Benzil-3,3-Dimetil-5-Metilenapirolidina-2,4-Dion Menggunakan Natrium Borohidrat Dengan Logam Klorida Terpilih)
*Nor Saliyana Jumali, Zurina Shaameri, Habsah Mohamad, Ahmad Sazali Hamzah*

23. SYNTHESIS AND ANTIBACTERIAL ACTIVITY OF AZO AND ASPIRIN-AZO DERIVATIVES 1183
(Sintesis dan Aktiviti Antibakteria Terhadap Azo dan Terbitan Azo-Aspirin)
*Zainab Ngaini and Ho Boon Kui*

24. SYNTHESIS, MODIFICATION, CHARACTERIZATION AND BIOLOGICAL ACTIVITY OF 3-HYDROXYBENZALDEHYDESALICYLHYDRAZIDE 1195
(Sintesis, Modifikasi, Pencirian dan Aktiviti Biologi 3-Hidroksibenzaldehidesalisilhidrazida)
*Nornadia Jasin, Meng Guan Tay, Hashimatul Fatma Hashim*

25. ONE-POT MANNICH BASE SYNTHESIS USING TASK SPECIFIC PROTIC IONIC LIQUIDS 1203
(Sintesis Bes Mannich Tunggal Menggunakan Cecair Ionik Terkhusus)
*Sabahat Sardar, Cecilia Devi Wilfred, Jean Marc Leveque*

*Malaysian Journal of Analytical Sciences, Vol 21 No 5 (2017): 996 - 1007*
*DOI: https://doi.org/10.17576/mjas-2017-2105-01*

MALAYSIAN JOURNAL OF ANALYTICAL SCIENCES
*Published by The Malaysian Analytical Sciences Society*
ISSN 1394 - 2506

# PERFORMANCE OF SOLAR PHOTOCATALYSIS AND PHOTO-FENTON DEGRADATION OF PALM OIL MILL EFFLUENT

## (Prestasi Fotopemangkinan dan Degradasi Foto-Fenton Menggunakan Sinar Suria ke atas Efluen Kilang Minyak Kelapa Sawit)

Devagi Kanakaraju[1]*, Nurul Liyana Binti Ahmad[1], Noorfaezah Binti Mohd Sedik[1], Sylvester Gan Hsien Long[1], Tay Meng Guan[1], Lim Ying Chin[2]

[1]*Department of Chemistry, Faculty of Resource Science and Technology, Universiti Malaysia Sarawak, 94300 Kota Samarahan, Sarawak, Malaysia*
[2]*School of Chemistry and Environment, Faculty of Applied Sciences, Universiti Teknologi MARA, 40450 Shah Alam, Selangor, Malaysia*

**Corresponding author: kdevagi@unimas.my*

Received: 16 August 2016; Accepted: 5 April 2017

**Abstract**

Palm oil mill effluent (POME) contains significant amounts of organic matter, solids, and grease or oil, which requires appropriate treatment prior to being discharged into the environment. In this study, solar radiation was investigated as a possible source of photon in the solar $TiO_2$ and ZnO photocatalysis, and solar photo-Fenton treatments to reduce the chemical oxygen demand (COD) in POME. The results indicated that solar photo-Fenton was more efficient in reducing COD levels compared to dark Fenton and indoor photo-Fenton. The highest removal was recorded at 89% in the presence of 1:30 ratio of $Fe^{2+}$:$H_2O_2$ under acidic pH (~2.8) after 3 hours of solar exposure. Increased concentrations of $H_2O_2$ have greatly influenced the COD removal. Additionally, solar $TiO_2$ photocatalysis (pH~3.7; $TiO_2$ = 0.1 g/L) has outperformed solar photolysis and solar ZnO photocatalysis in reducing COD levels in POME. With successive increase of $TiO_2$ from 0.02 to 0.1 g/L, the removal of COD had linearly increased from 54.3% to 88.5% after 5 hours of solar exposure. Based on the investigated conditions, the optimum $TiO_2$ concentration of 0.1 g/L was concluded. In conclusion, solar $TiO_2$ photocatalysis and solar photo-Fenton can be applied as possible means to reduce the organic loads in POME.

**Keywords:** advanced oxidation process, organic matter, reduction, solar, titanium dioxide

**Abstrak**

Efluen kilang minyak kelapa sawit (POME) mengandungi jumlah bahan organik, pepejal dan gris atau minyak yang ketara yang memerlukan rawatan sesuai sebelum ia boleh disalurkan ke persekitaran. Dalam kajian ini, sinar suria dikaji sebagai salah satu sumber foton dalam fotopemangkinan $TiO_2$ dan ZnO sinar suria dan rawatan foto-Fenton menggunakan sinar suria untuk mengurangkan keperluan oksigen kimia (COD) dalam POME. Keputusan kajian menunjukkan foto-Fenton menggunakan sinar suria adalah lebih berkesan dalam menurunkan COD berbanding dengan Fenton bercahaya dalam dan Fenton tanpa cahaya. Penyingkiran tertinggi yang dicatatkan ialah 89% menggunakan nisbah $Fe^{2+}$:$H_2O_2$ sebanyak 1:30 dalam pH berasid (~2.8) selepas pendedahan kepada sinar suria selama 3 jam. Peningkatan kepekatan $H_2O_2$ sangat mempengaruhi penyingkiran COD. Tambahan pula, fotopemangkinan $TiO_2$ menggunakan sinar suria (pH~3.7; $TiO_2$ = 0.1 g/L) menunjukkan prestasi yang lebih baik berbanding dengan fotolisis dan fotopemangkinan ZnO menggunakan sinar suria dalam mengurangkan kandungan COD dalam POME. Peningkatan $TiO_2$ secara berturutan dari 0.02 ke 0.1 g/L meningkatkan penyingkiran COD secara linear daripada 54.3% ke 88.5% selepas pendedahan kepada sinar suria selama 5 jam. Berdasarkan keadaan eksperimen yang dikaji dapat dirumuskan bahawa kepekatan optimum $TiO_2$ ialah sebanyak 0.1 g/L. Kesimpulannya, teknik fotopemangkinan $TiO_2$ sinar suria dan Fenton sinar suria boleh digunakan untuk mengurangkan kandungan organik dalam POME.

**Kata kunci**: proses pengoksidaan termaju, bahan organik, penurunan, sinar suria, titanium dioksida

## Introduction

Malaysia is known as the world's largest palm oil exporter. The palm oil industry has made significant contribution to the country's economic revenue. The global demand for palm oil, particularly for crude palm oil and its related products, such as palm oil and palm kernel oil, is rapidly growing. Consequently, the palm oil industry is generating a significant amount of waste, namely palm oil mill effluents (POME). Approximately 44 million tons of POME was generated in 2008 in Malaysia [1]. Typically, raw POME is brownish in colour and contains elevated levels of organic matter, such as total solids (405,000 mg/L) and grease/oil (6000 mg/L), as well as high biochemical oxygen demand (BOD) (25,000 mg/L) and chemical oxygen demand (COD) (50,000 mg/L) [2, 3]. POME is also known to be highly acidic (pH 3.8 – 4.5) and biodegradable in nature. The open ponding system is currently used by 85% of palm oil mill operators, as the potential method to treat POME [1], due to its biodegradable nature. A ponding system comprises of a series of anaerobic, facultative and aerobic treatments. This type of system demands vast area of lands, requires lengthy treatment periods (up to 40 – 60 days) for effective treatments to be achieved, and it releases bad odour, despite its ease of operation [4, 5]. A previous study has reported that this biological treatment process is rather inefficient in treating POME [2]. It contributes to various environmental issues due to the high loadings of BOD and COD, while a low pH of POME renders the conventional treatment technique inefficient.

In recent times, advanced oxidation processes (AOPs) have been considered as suitable methods to treat effluents in various wastewaters. AOPs are based on short-lived hydroxyl radicals (HO•), which are powerful oxidizing agents that can decompose organic compounds in water [6]. AOPs, such as photocatalysis, ozonation, wet oxidation, and photo-Fenton have been documented to efficiently eliminate or mineralize organic pollutants in different types of wastewaters such as textile wastewater [7], pharmaceutical wastewater [8, 9], and pulp mill wastewater [10]. In this study, titanium dioxide ($TiO_2$) and zinc oxide (ZnO) photocatalysis, and photo-Fenton oxidation have been narrowed down as suitable methods to reduce the organic loads in POME. The photo-Fenton process uses Fenton reagents ($H_2O_2$ and $Fe^{2+}$) in the presence of light to produce HO• radicals. This process involves the oxidation of ferrous ions ($Fe^{2+}$) to ferric ions ($Fe^{3+}$) in an acidic aqueous solution to produce HO• radicals, which will trigger the oxidation of organic compounds. It is important to keep the solution at pH 3 because the Fenton reaction works best in an acidic condition [11].

In the case of $TiO_2$ and ZnO photocatalysis, photon illumination ($\lambda$<400 nm) onto the $TiO_2$ and ZnO surfaces, of greater than or equal to the band gap energy, will result in the formation of electron-hole pairs. These pairs will be involved in the oxidative and reductive reactions with molecules present at/or near the surface of the semiconductor [12]. Both $TiO_2$ and ZnO have similar band gap energy of 3.2 eV [13]. Nonetheless, $TiO_2$ is the most applied photocatalyst in various environmental applications, primarily due to its non-toxicity, low cost, and photostability. ZnO, despite being highly photosensitive and absorbs a larger portion of the solar spectrum compared to $TiO_2$, suffers from photocorrosion in acidic aqueous solution and the formation of $Zn(OH)_2$ on its surface due to dissolution [13]. Thus, photocatalysis is of special interest since sunlight can be used as a photon source. Solar ZnO and $TiO_2$ photocatalysis can be activated by sunlight of lower than 390 nm, while photo-Fenton oxidation requires sunlight of up to 500 nm. The degradation of organic pollutants using AOPs with sunlight as the energy source is advantageous in lowering costs. Previous studies on solar photo-Fenton [14], and solar ZnO and $TiO_2$ photocatalysis [15,16] have recognized the roles of these mechanisms in reducing or degrading organic compounds in wastewater effluents. Nonetheless, there remains a paucity of knowledge regarding the feasibility of these treatments on POME. Aris et al. [17] reported that solar photo-Fenton has resulted in a better COD and colour from biologically treated POME compared to ambient photo-Fenton. On the other hand, $TiO_2$ photocatalysis was able to reduce the COD level of POME to 78% within 20 hours of irradiation [18].

This study aims to assess the efficiency of solar ZnO photocatalysis, solar $TiO_2$ photocatalysis, and solar photo-Fenton in reducing the COD level of POME. The dependence of solar photodegradation rate on intrinsic parameters, such as ZnO and $TiO_2$ concentrations, and the ratio of $Fe^{2+}$:$H_2O_2$ was investigated.

## Materials and Methods

### Sample collection

The POME samples used in this study were collected during the month of November 2014, from SALCRA Palm Oil Mill Plant located in Bau, Sarawak, Malaysia. The POME samples were collected from the cooling ponds of the palm oil mill, and stored in polyethylene bottles. The air-tight bottles were transported to the laboratory and kept refrigerated at 4 °C until further analysis. Characterization and solar photocatalytic oxidation treatments were performed using diluted POME.

### Characterization of palm oil mill effluents

Diluted POME was used for water quality analysis. Distilled water was used to dilute 1 mL of POME effluent to 1000 mL. The levels of biological oxygen demand ($BOD_5$), chemical oxygen demand (COD), total suspended solids (TSS), and dissolve oxygen (DO) were determined. All analyses were performed according to the Standard Methods of Water and Wastewater Treatment [19].

### Solar photodegradation of palm oil mill effluents

POME solar photodegradation study was conducted on the ground floor of the Faculty of Resource Science and Technology, Universiti Malaysia Sarawak, Malaysia. All solar treatments were performed for 2 – 5 hours on sunny days. Beakers filled with diluted POME and the required quantities of reagents were exposed to sunlight under continuous magnetic stirring. The beaker used for solar study was covered with a polyethylene wrap to avoid evaporation. A portable digital Lux meter (TEX 1335) was used to measure the intensity of sunlight. Temperature, pH, and solar intensity were periodically measured during periods of solar exposure. The recorded sunlight intensity and temperature during all solar experiments had ranged from 30 to 180 Klux and 30 to 38 °C, respectively. The temperatures recorded during the solar photo-Fenton and solar ZnO and $TiO_2$ photocatalysis had varied from 28 to 38 °C. In the case of indoor photo-Fenton experiments, the recorded temperatures had varied from 23 to 24.5 °C. All experiments were performed in duplicate. COD reduction was calculated using Equation 1:

$$\text{COD reduction } (\%) = \frac{\text{COD}_{\text{initial}} - \text{COD}_{\text{final}}}{\text{COD}_{\text{initial}}} \text{x } 100 \quad (1)$$

### Palm oil mill effluent concentration for treatment

As the concentration of POME in the photocatalytic treatments would affect the overall COD removal efficiency, three dilution ratios (POME: water) were considered: 1:10, 1:100 and 1:1000. Diluted POME sample of 1:10 ratio (Figure 1a) appeared to be more brownish, thicker, and murkier compared to the other diluted samples (Figure 1b and 1c). To ensure the maximum performance of the photocatalysts or reagents in these treatments, and to ensure adequate light penetration, the dilution ratio of 1:1000 was used. At high pollutant initial concentrations, all catalytic sites are occupied [20].

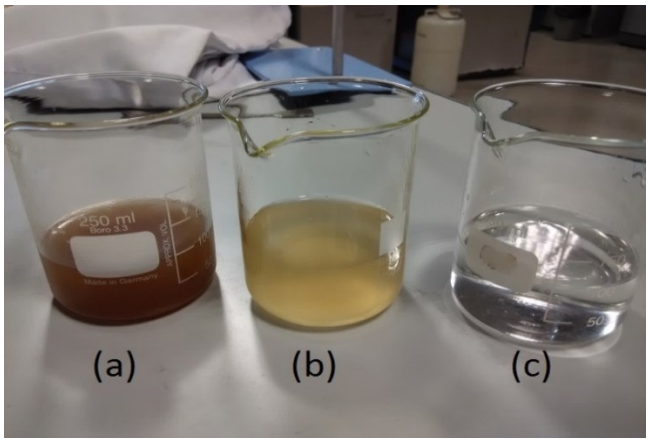



Figure 1. Photograph of diluted POME solutions (POME: water) (a) 1:10, (b) 1:100, and (c) 1:1000

**Treatment of palm oil mill effluent using solar photocatalysis**

Solar ZnO and $TiO_2$ photocatalysis were conducted by varying the concentrations of $TiO_2$ and ZnO from 0.02 to 0.2 g/L and 0.5 to 4 g/L, respectively in 150 mL of diluted POME (1:1000). The mixture of POME and photocatalyst (either ZnO or $TiO_2$) was magnetically stirred for 30 minutes in a dark environment (covered with polyethylene wrap) to establish equilibrium between the two substances. Then, the reaction slurry in the beaker was uncovered before being exposed to direct sunlight. The beaker was magnetically stirred during solar exposure and sample collection was done at pre-determined intervals using a syringe. A parallel control experiment (without photocatalyst) was also conducted. Supernatant obtained *via* filtration was used for COD analysis.

**Treatment of palm oil mill effluent using solar photo-Fenton**

Indoor photo-Fenton (laboratory) treatments with ambient light and solar photo-Fenton treatments were performed to compare their efficiency in reducing COD levels in POME. The concentration of $Fe^{2+}$ was kept constant, while the concentration of $H_2O_2$ was varied in the photo-Fenton experiments. Similar ratios of Fenton reagents, $Fe^{2+}$:$H_2O_2$, which include 1:10, 1:20, 1:30, and 1:40, were investigated for both treatments. The pH of the solution mixture was kept in the range of pH 2 to 3 by adding $H_2SO_4$ accordingly. Then, the mixture was continuous stirred in the laboratory to ensure homogeneity. It was subsequently exposed to sunlight. Samples were collected at fixed intervals. At the end of the solar exposure period, the pH of the sample was adjusted to range between pH 11 and 12 by adding NaOH pellets. The sample was stirred again for 15 minutes before being left overnight to ensure the decomposition of $H_2O_2$. After the sample has stood overnight, filtration was performed, which was followed by COD analysis. A blank sample (POME only) was also exposed to sunlight alongside the photo-Fenton treatment. Similar procedures were applied for photo-Fenton treatments in the laboratory. In this case, the source of photon was from the visible light in the laboratory. The beaker used for dark Fenton treatment was wrapped with aluminium foil to prevent any form of light from penetrating the reaction mixture.

**Characterization**

Analytical grade $TiO_2$ photocatalysts (99.8% trace metals basis, anatase) and ZnO were supplied by Sigma-Aldrich and Bendosen, respectively. The crystal phase of the $TiO_2$ and ZnO samples were determined using the X-ray Diffraction (XRD, PaNalytical X'pert Pro) method with Cu Kα radiation ($\lambda = 0.154$ nm) in the scanning range of $2\theta$ between 10° and 80°, at a rate of 0.04° per second. The accelerating voltage and applied current were 45 kV and 40 mA, respectively. Field emission scanning electron microscopy (FESEM) was performed using the Carl Zeiss, SUPRA 40VP Scanning Microscope to analyse the surface morphology of the samples. A low electron beam voltage of 5 kV was used. Therefore, no coating was required prior to imaging.

## Results and Discussion

**Characteristics of palm oil mill effluent**

Table 1 lists the results of pH, $BOD_5$, COD, and TSS. POME is a thick brownish colloidal mixture of water, oil, and fine suspended solids. The pH of POME was found to be acidic, resulting from the organic acids produced during the fermentation process [5]. This indicates that raw POME is unsuitable to be directly discharged into water bodies as the permissible level set by DOE falls between 5 and 9 (Table 1). The BOD and COD values obtained in this study implied the elevated levels of organic matters in POME. A comparison between the obtained values and those outlined by the effluent discharge standard of the Environmental Quality Act 1974 [5], showed that these values had exceeded the permissible levels. The ratio of $BOD_5$/COD, which is normally used to express the biodegradability of wastewater, was calculated to determine whether POME could be biodegraded using biological treatments [21]. Clearly, the obtained $BOD_5$/COD ratio of 0.10 (Table 1) implied that POME was not suitable to be biodegraded using biological treatments. The characterization of POME suggested that the open ponding system, as practiced by palm oil mill operators, has failed to reduce these parameters to comply with the discharge limits set by the Environmental Quality Act 1974. Based on the obtained $BOD_5$/COD ratio, this method is inefficient to improve the water qualities of POME to an acceptable level. Therefore, other treatments must be sought.

Table 1. Characteristics of POME

| Parameter | Mean ± SD | Effluent discharged standard for crude palm oil (Environmental Quality Act 1974)* |
|---|---|---|
| pH | 4.85 ± 0.05 | 5-9 |
| $BOD_3$, 30°C (mg/L) | 7600 ± 15.2 | 100 |
| COD (mg/L) | 73 150 ± 124.5 | 1000 |
| $BOD_5$/COD | 0.10 | NA |
| TSS (mg/L) | 18 000 ± 5000 | 400 |

*Parameters Limit of Environmental Quality (Prescribed Premises) (Crude Palm Oil) (Amendment) Regulation 1997, and NA: Not applicable

**Reducing chemical oxygen demand using solar heterogeneous photocatalysis**

Two types of photocatalyst, $TiO_2$ and ZnO were applied during the solar heterogeneous photocatalytic treatment of POME. The effect of photolysis (without photocatalyst) was studied for two reasons: (i) to act as a control, and (ii) to confirm the contribution of solar heterogeneous photocatalysis towards reducing COD level. COD reduction, by means of photolysis, has ranged between 7 to 29%, thus indicating that the presence of $TiO_2$ or ZnO is crucial to reduce the COD level in POME.

An optimum concentration of photocatalyst under studied experimental conditions is an important factor towards achieving efficient removal of COD. Thus, the effect of $TiO_2$ (0.02 to 0.2 g/L) and ZnO (0.5 to 2.0 g/L) concentrations on the reduction of COD was studied. The same experimental conditions were applied for both photocatalytic treatments, where 150 mL of diluted 1:1000 POME was exposed under sunlight for 5 hours. The optimum concentration of photocatalyst was then fixed for other parameters studied. Figure 2 shows the percentage of COD reduction after 5 hours of solar $TiO_2$ photocatalysis. As expected, the percentage of COD reduction was increased from 54.3 to 88.5% concomitantly with the increased amount of $TiO_2$ from 0.02 to 0.1 g/L. However, further increase of $TiO_2$ to 0.2 g/L has yielded only 40% of COD reduction. Under the studied experimental conditions, 0.1 g/L of $TiO_2$ has led to a maximum reduction of 88.5% of COD (Figure 2). $TiO_2$ concentrations of higher than the optimum value (0.1 g/L) could increase the opacity of the suspension due to the excess amount of photocatalyst. Furthermore, penetration of solar radiation could have been impeded by the excess catalysts [22], contributing to the retardation of COD reduction. With 0.1 g/L of $TiO_2$, COD was reduced from 73,150 mg/L to 8,000 mg/L after 5 hours of solar exposure (Figure 3).

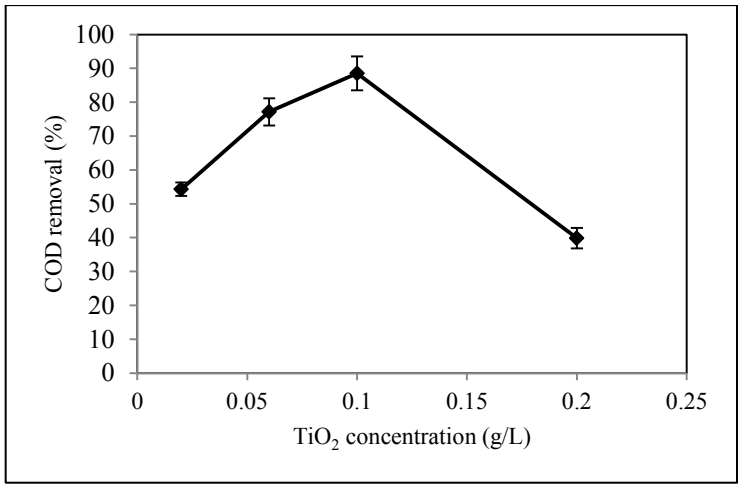



Figure 2. Effect of $TiO_2$ concentration on COD reduction efficiency using solar $TiO_2$ photocatalysis (error bars indicate standard deviation)

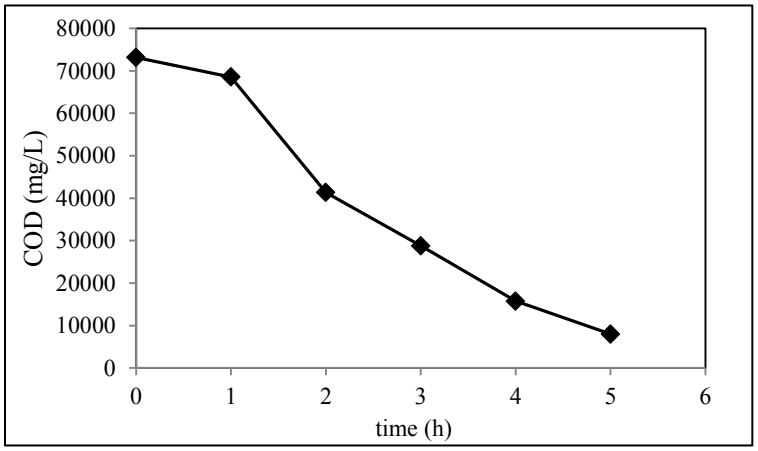



Figure 3. Reduction of COD with the optimum concentration of $TiO_2$ (0.1 g/L) using solar $TiO_2$ photocatalysis

In the case of ZnO, the percentage of COD reduction has increased from 26.3 to 60.5% with increased ZnO concentration, from 0.5 to 2 g/L (Figure 4). Further increase of ZnO concentration to 4 g/L has resulted in the declining percentage of COD reduction to 36.6%. The reasons elucidated for $TiO_2$ photocatalysis could also be applied to the phenomenon observed during the ZnO photocatalysis. When the performances of ZnO and $TiO_2$ photocatalysis were compared based on the effect of photocatalyst concentration on COD reduction, the latter has demonstrated better reduction efficiency under the investigated experimental conditions. The higher percentage of COD reduction of 88.5% was achieved with a low $TiO_2$ concentration (0.1 g/L). In contrast, 2 g/L of ZnO was required to obtain the maximum percentage of COD reduction of 60.5%. Several studies have reported that ZnO photocatalysis had performed better than $TiO_2$ photocatalysis for pollutant degradation [16, 23] because ZnO can absorb a larger fraction of the solar spectrum compared to $TiO_2$. However, in this study, the performance of $TiO_2$ was superior to ZnO.

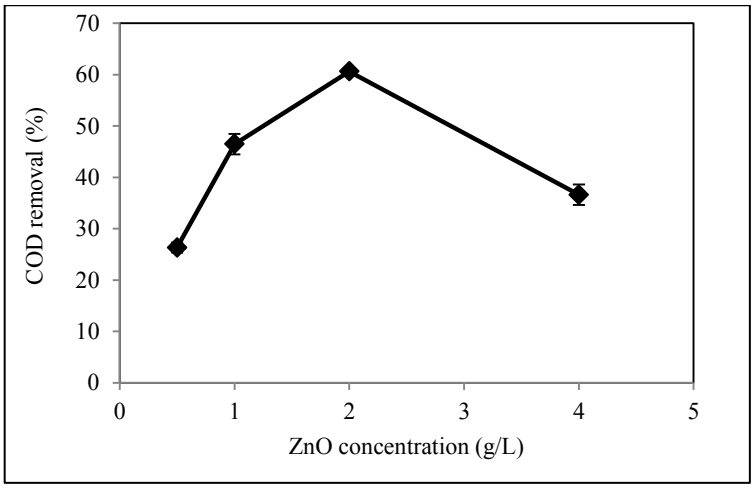



Figure 4. Effect of ZnO concentration on COD reduction efficiency using solar ZnO photocatalysis (error bars indicate standard deviation)

The performance of photocatalysts in degrading organic matter is known to be closely linked to their synthetic nature. The XRD patterns in Figure 5 clearly corresponded to the typical pure anatase $TiO_2$. The existence of strong crystalline peaks at $2\theta$ values of 25.3°, 37.6°, 48.0°, 53.9°, and 54.9°, which corresponded to the crystal planes of

(101), (004), (200), (105), and (211), respectively, were indicative of pure anatase $TiO_2$ (Figure 5a). As for ZnO, the crystalline peaks at $2\theta$ values of 31.8°, 34.4°, 36.2°, and 47.5° corresponded to the crystal planes of (100), (002), (101), and (102), respectively. These peaks were indicative of the predominant crystalline phase of ZnO (Figure 5b). FESEM images were also acquired for the commercial $TiO_2$ and ZnO, as shown in Figure 6. Figure 6a shows the surface of $TiO_2$ to be smooth and spherical in shape, with slightly varied particle sizes. Meanwhile, ZnO particles were predominantly rod-shaped (Figure 6b). Irregular sizes of ZnO particles in spherical and rectangular shapes can also be observed.

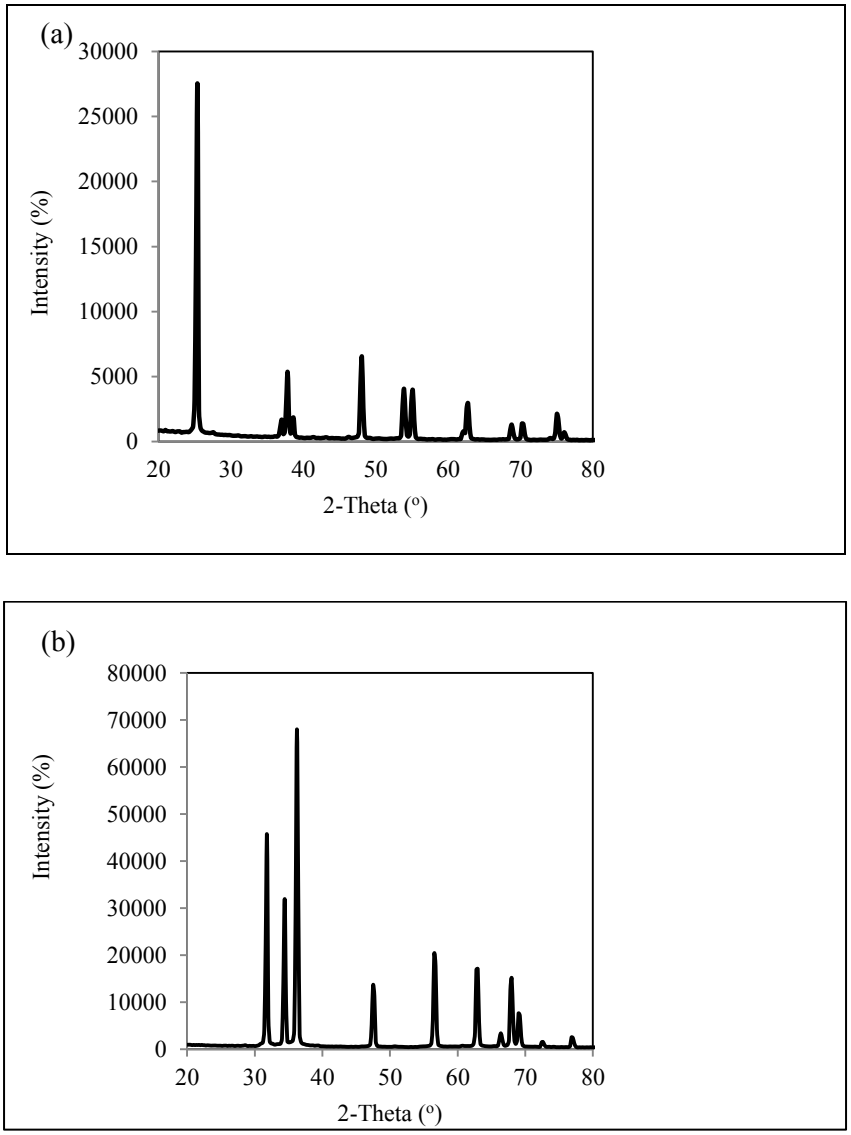



Figure 5. Comparison of XRD patterns between commercial: (a) $TiO_2$, and (b) ZnO

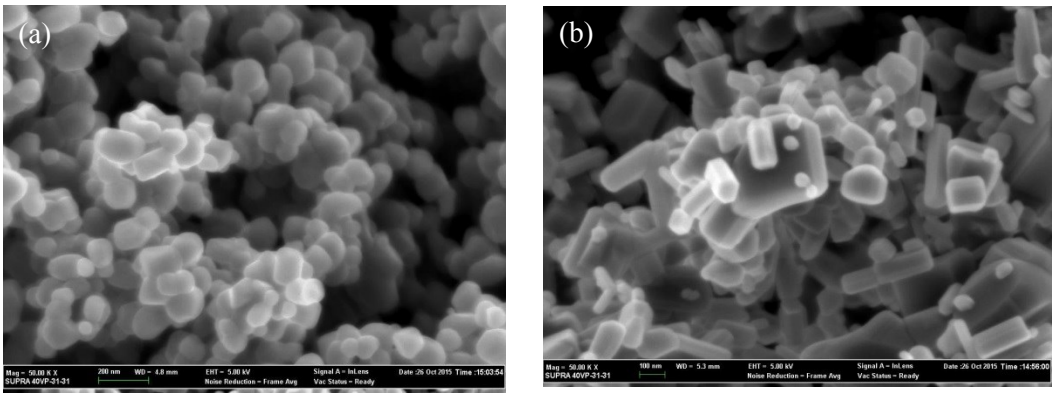



Figure 6. FESEM images of commercial: (a) $TiO_2$, and (b) ZnO

High crystallinity and non-porosity of both ZnO and $TiO_2$ could have contributed to the oxidation or mineralization of the organic matter in POME. The Brunauer-Emmett-Teller specific surface areas ($S_{BET}$) for $TiO_2$ and ZnO were 55 $m^2/g$ and 25 $m^2/g$, respectively. The average particle size of $TiO_2$ could also be estimated from the $S_{BET}$ by assuming that all particles have the same spherical size and shape. The particle size, $D$ is given by Equation 2 [24]:

$$D = \frac{6000}{S_{BET} \times \rho} \quad (2)$$

where $\rho$ is the true density for $TiO_2$, which in this study, was 4.2 g/mL and the estimated particle size was 26 nm. However, estimating the particle size of ZnO from Equation 2 would be inaccurate as ZnO has distinct irregular shapes, ranging from rod to rectangular. By using the Image J software, the particle size of ZnO was estimated to be 300 – 400 nm, with some 46 – 50 nm spherical particles. In this study, COD removal efficiencies could largely be attributed to fine spherical nanoparticles that have higher surface areas compared to the larger particles. With its smaller particle size, $TiO_2$ could absorb more photon and subsequently, more active sites were created, where more hydroxyl radicals were induced to enhance COD removal. In contrast, ZnO has lower absorption potential due to its relatively larger particle size. A similar observation was also made by Rojviroon et al. [25] and Vineetha et al. [26].

The performance of solar photocatalytic reaction is greatly influenced by pH and the concentration of catalyst [27]. In this study, solar ZnO and $TiO_2$ photocatalysis were performed without any pH adjustment. POME is known to be very acidic in nature. In this study, pH adjustment was not considered as it will increase the cost of treatment. Nonetheless, pH readings were recorded during sample collection to investigate whether there was any direct relationship between the pH of the suspension and COD reduction. The pH values of the collected samples during this treatment ranged between 1.2 and 4.9. The recorded mean pH for the highest percentage of COD reduction, which was attained using 0.1 g/L $TiO_2$, was at 3.68. Higher $TiO_2$ loading of 0.2 g/L had not only resulted in a very acidic pH (~1.2), it had also produced the lowest percentage of COD reduction. The aggregation of $TiO_2$ particles at 0.2 g/L could have reduced the ability of the suspension to absorb light [24], thus affecting the percentage reduction of COD. In addition, $TiO_2$ photocatalytic oxidation of POME may also produce other intermediary or degradation products, which could also have been acidic in nature, and directly affected COD reduction. Hence, this study has shown that COD reduction in POME is possible by means of solar $TiO_2$ photocatalysis without any prior pH adjustments and a small amount of $TiO_2$.

**Reduction of chemical oxygen demand by solar photo-Fenton**

Solar photo-Fenton treatment was conducted by varying the $Fe^{2+}$: $H_2O_2$ ratio to investigate its effect on COD reduction efficiency. Experiments were conducted by varying the concentrations of $H_2O_2$ in difference ratios of $Fe^{2+}$:$H_2O_2$ (1:10, 1:20, 1:30, and 1:40). A predetermined volume of NaOH was added to the samples at the end of the photo-Fenton treatments. The NaOH will lead to the formation of iron precipitate, $(Fe(OH)_3)$, which could accelerate the decomposition of $H_2O_2$. The precipitation of $Fe(OH)_3$ was observed to be slightly reduced in samples treated *via* photo-Fenton. To avoid the interference of excess $H_2O_2$ in the COD analysis, titration with potassium

permanganate was conducted to ensure the complete decomposition of excess $H_2O_2$. In the presence of $H_2O_2$, manganese(VII) was reduced to colourless manganese(II), as shown in Equation 3.

$$2KMnO_4 + 5H_2O + 3H_2SO_4 \leftrightarrow K_2SO_4 + 2MnSO_4 + 8H_2O + 5O_2 \quad (3)$$

Blank diluted POME (1:1000) was added with $FeSO_4 \bullet 7H_2O$ and $H_2O_2$ separately (without both reacting simultaneously) to determine the effect of the addition of these reagents on COD reduction. POME samples that contained $H_2O_2$ had turned bright red immediately after the addition of Ferroin indicator, thus no titration was performed on these samples. POME samples with $FeSO_4 \bullet 7H_2O$ had required similar amount of ferrous ammonium sulphate as the blank sample during titration. This observation implies that the addition of these reagents did not affect the experimental results of COD reduction in the photo-Fenton treatment.

The amount of Fe(II) catalyst was fixed, while the amount of $H_2O_2$ was varied to determine its optimum ratio. Ferrous ions react rapidly with $H_2O_2$ to produce a large amount of HO• radicals (Equation 4). Based on the properties of this catalyst, only a small amount was required to speed up the reaction. Higher loadings of ferrous ions may only contribute to the waste of chemical.

$$H_2O + Fe^{3+} + h\nu \rightarrow HO\bullet + H^+ + Fe^{2+} \quad (4)$$

Figure 7 shows the reduction of COD using dark Fenton, indoor photo-Fenton and solar photo-Fenton after 3 h of reaction time. Dark Fenton oxidation has contributed to COD reduction percentage that ranged between 20 to 45%. The COD reduction efficiency was increased when the ratio of $H_2O_2$ concentration was increased from 1:10 to 1:30 for both indoor (50 – 78%) and solar photo-Fenton (62 – 89%) treatments. When the ratio was increased to 1:40, COD reduction efficiency had declined to 40% for indoor photo-Fenton and 56% for solar photo-Fenton. The excessive $H_2O_2$ loading could have resulted in the production of $HO_2\bullet$ radicals, which are less productive, compared to HO• radicals (Equation 5). $HO_2\bullet$ radicals could also have formed with the incorporation of HO• radicals in $H_2O_2$ (Equation 6). In addition, the HO• radicals could have recombined to form $H_2O_2$, without favouring any reactions (Equation 7). Based on Figure 7, the reaction was concluded to be optimized when the $Fe^{2+}$:$H_2O_2$ ratio was 1:30. With this ratio, the maximum percentages of COD reduction of 78% (from 73,000 to 16,000 mg/L) and 89% (from 73,400 to 7,855 mg/L) were obtained with indoor photo-Fenton and solar photo-Fenton treatments, respectively after 3 h of reaction time (Figure 8). A comparison of COD reductions between dark Fenton oxidation, solar photo-Fenton, and indoor photo-Fenton has shown that photon is necessary to activate the Fenton reagents. COD reduction using dark Fenton oxidation was rather low, although the trend was similar to those observed in the photo-Fenton treatments (indoor and solar).

$$H_2O_2 + HO\bullet \rightarrow HO_2\bullet + H_2O \quad (5)$$

$$HO\bullet + H_2O_2 \rightarrow HO_2\bullet + H_2O \quad (6)$$

$$HO\bullet + HO\bullet \rightarrow H_2O_2 \quad (7)$$

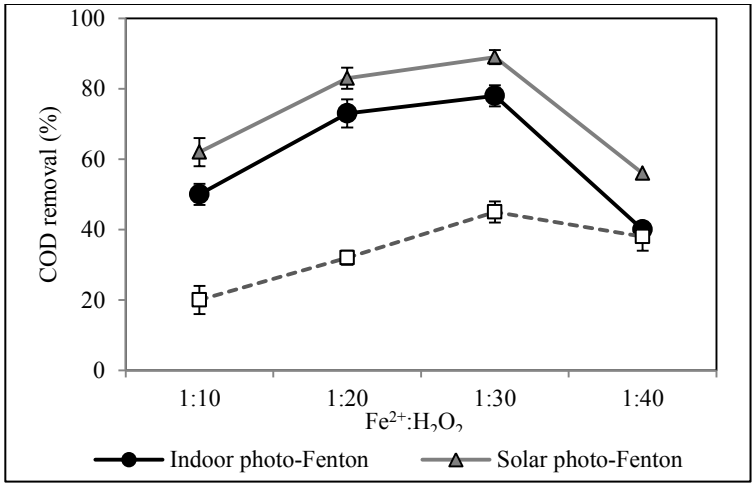



Figure 7. Reduction of COD by dark Fenton, solar photo-Fenton, and indoor photo-Fenton processes

In a Fenton treatment, pH plays an important role. The optimal pH condition in a Fenton reaction system is between 2.8 and 3.0 [28]. Therefore, the pH of POME solutions during each treatment was kept between 2.8 and 2.9. The purpose of the acidic pH is to avoid the precipitation of iron, which might interfere with the absorption of solar irradiation by the exposed medium. Prevention of iron precipitation will lead to the continuous photoreduction of ferric iron complexes at a longer wavelength.

In this study, solar photo-Fenton was found to be more efficient than indoor photo-Fenton. This result was in agreement with the findings reported by Aris et al. [17]. Several other studies have also concluded that solar photo-Fenton had performed better than other AOPs in various conditions, such as for textile effluent [29] and pharmaceutical wastewater [30]. The findings from the present study suggested that solar photo-Fenton should be considered as a valuable option for the reduction of COD in POME.

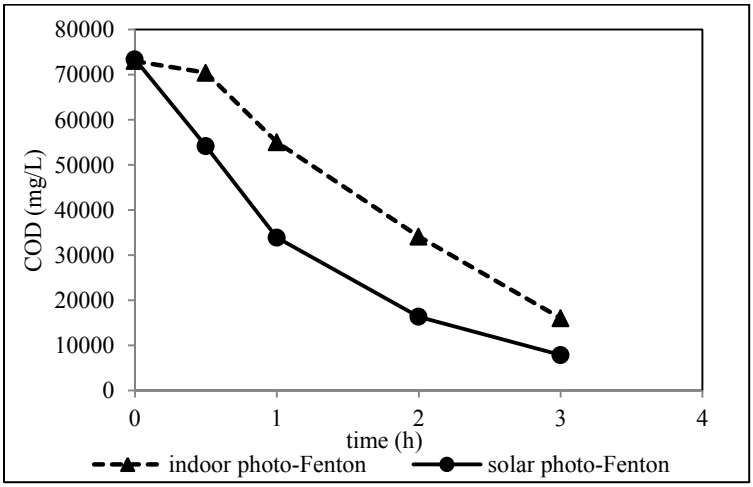



Figure 8. Reduction of COD by solar photo-Fenton and indoor photo-Fenton using the optimum $Fe^{2+}$:$H_2O_2$ ratio (1:30)

## Conclusion

A higher percentage of COD reduction was accomplished with solar photo-Fenton compared to indoor photo-Fenton and dark Fenton under similar solar exposure time. The reduction of COD in POME was found to be governed by the concentration of the photocatalyst in solar ZnO and $TiO_2$ photocatalysis. On the other hand, $H_2O_2$ concentration was the determinant for better solar photo-Fenton and indoor photo-Fenton treatments. In addition, the pH value in photo-Fenton systems has also played an important role, where the optimum pH value was found to be between 2.8 and 2.9. Decreasing the pH to 1.2 or increasing the pH to an alkaline level may result in poor COD reduction. Both solar photo-Fenton and solar $TiO_2$ photocatalysis were able to produce up to 89% of COD reduction. Nevertheless, solar photo-Fenton took only 3h of exposure time to achieve the highest reduction compared to solar $TiO_2$ photocatalysis that took up to 5h to achieve a similar level. This study has shown that the reduction of COD in POME generated from palm oil milling activities can be performed using solar photo-Fenton and $TiO_2$ photocatalysis. Thus, solar photo-Fenton and $TiO_2$ photocatalysis can be considered as pre-treatment steps prior to the biological treatment.

## Acknowledgement

The authors would like to thank Mr. Krishan Singh, Mill Manager of Bau Palm Oil Mill Sdn Bhd, Sarawak, Malaysia for providing the samples. The authors would also like to acknowledge the financial support by the Ministry of Education Malaysia under the Research Acculturation Collaborative Effort programme [RACE/b(1)/1245/2015(01)] and the Fundamental Research Grant Scheme [FRGS/SG01 (01)/1204/2014(05)].

.

## References

1. Wu, T. Y., Mohammad, A. W., Jahim, J. M. and Anuar, N. (2010). Pollution control technologies for the treatment of palm oil mill effluent (POME) through end-of-pipe processes. *Journal of Environmental Management*, 91(7): 1467 – 1490.
2. Ahmad, A. L., Ismail, S. and Bhatia, S. (2005). Optimization of coagulation-flocculation process for palm oil mill effluent using response surface methodology. *Environmental Science & Technology*, 39(8): 2828 – 2834.
3. Ujang, Z., Salmiati, S. and Salim, M. R. (2010). Microbial biopolimerization production from palm oil mill effluent (POME). Institute of Environmental and Water Resource Management (IPASA), Universiti Teknologi Malaysia.
4. Setiadi, T. and Djajadiningrat, A. (1996). Palm oil mill effluent treatment by anaerobic baffled reactors: recycle effects and biokinetic parameters. *Water Science and Technology*, 34 (11): 59 – 66.
5. Rupani, P. F., Singh, R. P., Ibrahim, M. H. and Esa, N. (2010). Review of current palm oil mill effluent (POME) treatment methods: vermicomposting as a sustainable practice. *World Applied Sciences Journal*, 11(1): 70 – 81.
6. Legrini, O., Oliveros, E. and Braun, A. M. (1993). Photochemical processes for water treatment. *Chemical Reviews*, 93(2): 671 – 698.
7. Soares, P. A., Silva, T. F., Manenti, D. R., Souza, S. M., Boaventura, R. A. and Vilar, V. J. (2014). Insights into real cotton-textile dyeing wastewater treatment using solar advanced oxidation processes. *Environmental Science and Pollution Research*, 21(2): 932 – 945.
8. Klavarioti, M., Mantzavinos, D. and Kassinos, D. (2009). Removal of residual pharmaceuticals from aqueous systems by advanced oxidation processes. *Environment International*, 35(2): 402 – 417.
9. Kanakaraju, D., Motti, C. A., Glass, B. D. and Oelgemöller, M. (2014). Photolysis and $TiO_2$-catalysed degradation of diclofenac in surface and drinking water using circulating batch photoreactors. *Environmental Chemistry*, 11(1): 51 – 62.
10. Lucas, M. S., Peres, J. A., Amor, C., Prieto-Rodríguez, L., Maldonado, M. I. and Malato, S. (2012). Tertiary treatment of pulp mill wastewater by solar photo-Fenton. *Journal of Hazardous Materials*, 225: 173 – 181.
11. Babuponnusami, A. and Muthukumar, K. (2014). A review on Fenton and improvements to the Fenton process for wastewater treatment. *Journal of Environmental Chemical Engineering*, 2(1): 557 – 572.
12. Chong, M. N., Jin, B., Chow, C. W. and Saint, C. (2010). Recent developments in photocatalytic water treatment technology: A review. *Water Research*, 44(10): 2997 – 3027.
13. Lam, S. M., Sin, J. C., Abdullah, A. Z. and Mohamed, A. R. (2012). Degradation of wastewaters containing organic dyes photocatalysed by zinc oxide: A review. *Desalination and Water Treatment*, 41(1-3): 131 – 169.

14. Vilar, V. J., Pinho, L. X., Pintor, A. M. and Boaventura, R. A. (2011). Treatment of textile wastewaters by solar-driven advanced oxidation processes. *Solar Energy*, 85 (9): 1927 – 1934.
15. Pereira, J. H., Reis, A. C., Queirós, D., Nunes, O. C., Borges, M. T., Vilar, V. J. and Boaventura, R. A. (2013). Insights into solar $TiO_2$-assisted photocatalytic oxidation of two antibiotics employed in aquatic animal production, oxolinic acid and oxytetracycline. *Science of the Total Environment*, 463: 274 – 283.
16. Chekir, N., Benhabiles, O., Tassalit, D., Laoufi, N. A. and Bentahar, F. (2015). Photocatalytic degradation of methylene blue in aqueous suspensions using $TiO_2$ and ZnO. *Desalination and Water Treatment*, 57(13): 1 – 7.
17. Aris, A., Siew, O. B., Kee, K. S. and Ujang, Z. (2008). Tertiary treatment of palm oil mill effluent using fenton oxidation. *Malaysian Journal of Civil Engineering*, 20(1): 12 – 25.
18. Ng, K. H. and Cheng, C. K. (2015). A novel photomineralization of POME over UV-responsive $TiO_2$ photocatalyst: Kinetics of POME degradation and gaseous product formations. *RSC Advances*, 5(65): 53100 – 53110.
19. American Public Health Association (1999), American Water Works Association, Water Pollution Control Federation, & Water Environment Federation. *Standard Methods for the Examination of Water and Wastewater* (Vol. 2). 18th Ed. American Public Health Association.
20. Carp, O., Huisman, C. L. and Reller, A. (2004). Photoinduced reactivity of titanium dioxide. *Progress in Solid State Chemistry*, 32(1): 33 – 177.
21. Badawy, M. I., Gohary, F. E., Ghaly, M. Y. and Ali, M. E. M. (2009). Enhancement of olive mill wastewater biodegradation by homogeneous and heterogeneous photocatalytic oxidation. *Journal of Hazardous Materials*, 169(1): 673 – 679.
22. Gaya, U. I. and Abdullah, A. H. (2008). Heterogeneous photocatalytic degradation of organic contaminants over titanium dioxide: a review of fundamentals, progress and problems. *Journal of Photochemistry and Photobiology C: Photochemistry Reviews*, 9(1): 1 – 12.
23. Sakthivel, S., Neppolian, B., Shankar, M. V., Arabindoo, B., Palanichamy, M. and Murugesan, V. (2003). Solar photocatalytic degradation of azo dye: Comparison of photocatalytic efficiency of ZnO and $TiO_2$. *Solar Energy Materials and Solar Cells*, 77(1): 65 – 82.
24. Raj, K. and Viswanathan, B. (2009). Effect of surface area, pore volume and particle size of p25 titania on the phase transformation of anatase to rutile. *Indian Journal of Chemistry,* 48: 1378 – 1382.
25. Rojviroon, O., Rojviroon, T. and Sirivithayapakorn, S. (2014). Study of COD removal efficiency from synthetic wastewater by photocatalytic process. *Environmental Engineering Research,* 19(3): 255 – 259.
26. Vineetha, M. N., Matheswaran, M. and Sheeba, K. N. (2013). Photocatalytic colour and COD removal in the distillery effluent by solar radiation. *Solar Energy,* 91: 368 – 373.
27. Malato, S., Fernández-Ibáñez, P., Maldonado, M. I., Blanco, J. and Gernjak, W. (2009). Decontamination and disinfection of water by solar photocatalysis: recent overview and trends. *Catalysis Today*, 147(1): 1 – 59.
28. Oturan, M. A. and Aaron, J. J. (2014). Advanced oxidation processes in water/wastewater treatment: principles and applications. A review. *Critical Reviews in Environmental Science and Technology*, 44 (23): 2577 – 2641.
29. Manenti, D. R., Soares, P. A., Silva, T. F., Módenes, A. N., Espinoza-Quiñones, F. R., Bergamasco, R., Boaventura, R.A. and Vilar, V. J. (2015). Performance evaluation of different solar advanced oxidation processes applied to the treatment of a real textile dyeing wastewater. *Environmental Science and Pollution Research*, 22(2): 833 – 845.
30. Klamerth, N., Rizzo, L., Malato, S., Maldonado, M. I., Agüera, A. and Fernández-Alba, A. R. (2010). Degradation of fifteen emerging contaminants at $\mu gL^{-1}$ initial concentrations by mild solar photo-Fenton in MWTP effluents. *Water Research*, 44(2): 545 – 554.

*Malaysian Journal of Analytical Sciences, Vol 21 No 5 (2017): 1008 - 1015*
*DOI: https://doi.org/10.17576/mjas-2017-2105-02*

MALAYSIAN JOURNAL OF ANALYTICAL SCIENCES
*Published by The Malaysian Analytical Sciences Society*
ISSN 1394 - 2506

# SYNTHESIS AND X-RAY SINGLE CRYSTAL STUDY OF 3-DIBUTYNYL AND 4-DIPENTYNYL PYRIDINE-2,6-DICARBOXYLATE

## (Sintesis dan Kajian Sinar-X Hablur Tunggal 3-dibutinil dan 4-dipentinil piridina-2,6-dikarboksilat)

Nawwar Hanun Abdul Malek [1], Mohammad Fadzlee Ngatiman[2], Bohari M. Yamin[1], Nurul Izzaty Hassan[1]*

[1]*School of Chemical Sciences and Food Technology, Faculty of Science and Technology*
[2]*Centre for Research and Instrumentation Management,*
*Universiti Kebangsaan Malaysia, 43600 UKM Bangi, Selangor, Malaysia*

**Corresponding author: drizz@ukm.edu.my*

Received: 7 March 2017; Accepted: 19 July 2017

**Abstract**

Two pyridine-2,6-dicarboxylates each containing butynyl and pentynyl at position 2 and 6 were synthesized by esterification of 2,6-pyridinedicarbonyl dichloride with *N*-alkyne alcohol. All compounds were characterized by using nuclear magnetic resonance spectroscopy (NMR), infrared spectroscopy (IR) and mass spectrometry (MS) techniques. Crystallographic studies showed that both compounds, 3-dibutynyl pyridine-2,6-dicarboxylate **(3a)** and 4-dipentynyl pyridine-2,6-dicarboxylate **(3b)** crystallized in monoclinic system with same space group of C 2/c.

**Keywords**: diester macrocyclic, esterification, X-Ray structural study

**Abstrak**

Dua sebatian piridina dikarboksilat, 3-dibutinil dan 4-dipentinil pada kedudukan 2 dan 6 telah berjaya disintesiskan dengan tindak balas pengesteran di antara 2,6-piridinadikarbonil diklorida dengan *N*-alkuna alkohol. Setiap sebatian berjaya dicirikan dengan teknik spektroskopi resonans magnetik nuklear (RMN), infra merah (IR) dan spektrometri jisim (MS). Kajian kristalografi menunjukkan sebatian 3-dibutinil piridina-2,6-dikarboksilat **(3a)** dan 4-dipentinil piridina-2,6-dikarboksilat **(3b)** terhablur dalam sistem monoklinik dengan kumpulan ruang C 2/c.

**Kata kunci:** makrosiklik diester, tindak balas pengesteran, kajian struktur sinar-X

## Introduction

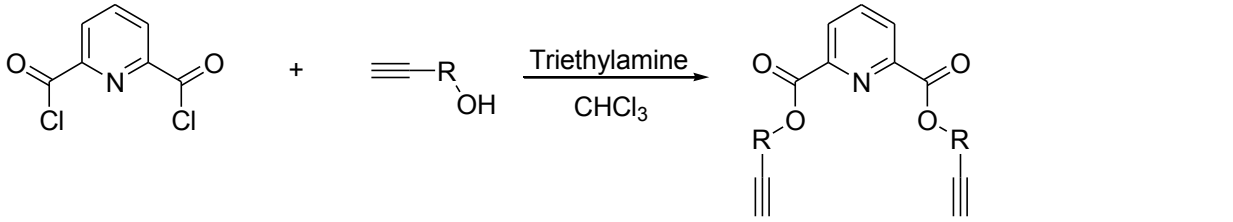
The synthesis study of macrocyclic has been rapidly developed for almost 40 years [1]. The design of this compound can be varies depending on the linker being used such as pyridine, benzene or aliphatic chain. The side chain can be functional group of ester, ether, thiourea, alkyne and alkene [2-7]. Various derivatives have been reported due to straightforward preparation and potential in biological activities and medicine.

Macrocyclic compound is an important reference compound in chemistry studies such as complexation to metal due to existence electron donating atom in the ligand [8-9]. Some of macrocyclic derivatives have been reported showing great capability in antibacterial, anticancer and HIV treatment [10-14]. Besides that, macrocyclic compounds contained alkene or alkyne ligands have been studied in recent trend of metathesis reaction. This

reaction has been shown to facilitate several complicated reaction steps especially in natural product synthesis such as lactones and marine alkaloid nakadomarin A [15].

Esters are commonly synthesized from the condensation reaction between carboxylic acid and alcohol with the loss of water. The esters can also be prepared by other reactions using acid anhydrides, acid chloride, unsaturated hydrocarbon, amides, nitriles, ethers, aldehydes, ketones, alcohols, and ester itself. The synthesis of these macrocyclic were carried out by esterification reaction with acyl chloride and alkyne alcohol in the presence of triethylamine as a base. The nitrogen's lone pair of triethylamine assisted the deprotonation of hydrogen at hydroxyl to initiate the esterification reaction.

This is demonstrated in the present work where pyridine acyl chloride was reacted with alkyne alcohol to form pyridine bridged diester macrocyclic followed by 3- and 4-dialkyne to form 3-dibutynyl pyridine-2,6-dicarboxylate **3a** and 4-dipentynyl pyridine-2,6-dicarboxylate **3b**, respectively (Scheme 1). With the help of X-ray structure, we could see either the presence of lone pair of nitrogen pyridine, position of the ester on ring or the *sp* hybridization of alkyne would give effect on geometry of the isomers. Following this, the designing of next product for future study, especially in complexation or metathesis reaction become facile. Thus, the synthesis, characterization and X-ray structures of the isomers are presented.




**1** **2** **3a/3b**

**3a** R= $CH_2CH_2$

**3b** R= $CH_2CH_2CH_2$

Scheme 1. Synthesis of N-dialkyne pyridine-2,6-dicarboxylate, 3a and 3b at ambient temperature with percentage yield of 76% and 63%

## Materials and Methods

### Materials

2,6-pyridinedicarbonyl dichloride, 3-butyn-1-ol, 4-pentyn-1-ol, triethylamine, chloroform, cyclohexane and ethyl acetate were purchased from Sigma Aldrich. Other chemicals were analytical grades and used as received.

### Instruments

The reactions were monitored by thin-layer chromatography (TLC) using 0.25 mm silica gel plates (Merck Kieselgel $60F_{254}$ UV indicator). Column chromatography was performed using silica gel Merck Kieselgel (230-400 mesh). The NMR spectra were recorded by Bruker spectrometer at 400 MHz for $^1$H NMR using tetramethylsilane (TMS) as internal standard and 100 MHz for $^{13}$C NMR. The coupling constant (*J*) are given in Hz. IR spectra were recorded in the range of 4000-370 $cm^{-1}$ using a Perkin Elmer Spectrum GX with samples prepared as KBr pellets. The melting point was determined by using Barnstead Electrothermal IA9000 Series Melting Point Apparatus with oven temperature range ambient to 400 °C. The Mass spectrometry was recorded by Bruker MicroToF Q with method of direct infuse and source type electro-spray ionization (ESI).

### Synthesis of *N*-dialkyne pyridine-2,6-dicarboxylate

2,6-pyridinedicarbonyl dichloride (4.9 mmol, 1g) was dissolved in 25 mL chloroform inside the one-neck round bottom flask. Alkyne alcohol solution (9.8 mmol) is added into the mixture followed with 2.1 mL of triethylamine. The mixture was stirred at 0 °C for 10 minutes and continued stir at room temperature for 18 hours. The mixture

then dried under vacuum and the residue purified by flash chromatography (cyclohexane/ethyl acetate) to give colorless crystal upon evaporation. The crystals are suitable for X-ray study.

## Results and Discussion

**Representative data for synthesis 3-dibutynyl pyridine-2,6-dicarboxylate, 3a**

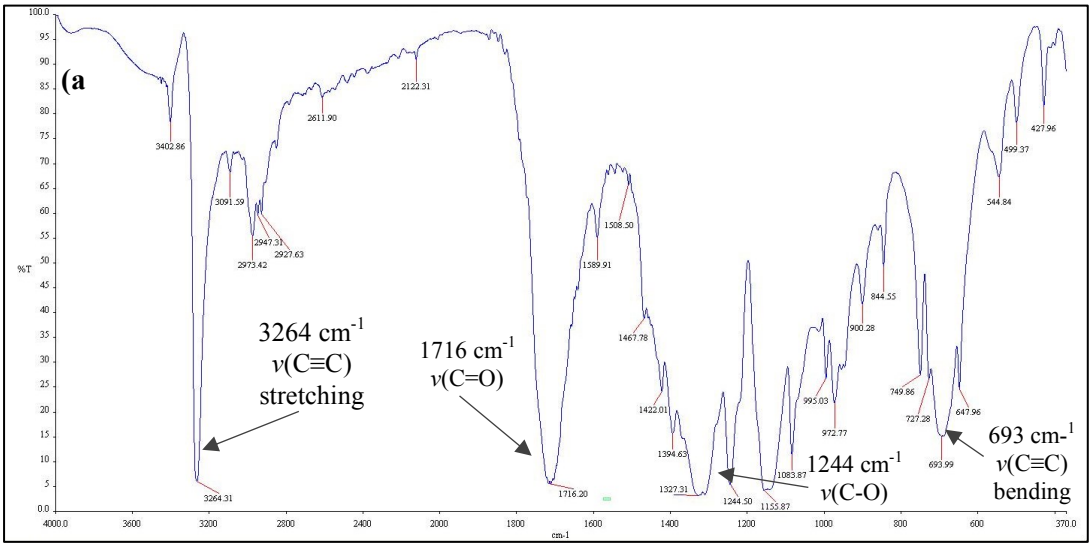
The compound was obtained as colorless crystal in 76% yield after recrystallization. Mp 86 - 87 °C. IR (KBr pellets) υ/cm$^{-1}$: 3264 (stretching C≡C), 1716 (C=O), 1327 (Ar-N), 1244 (C-O), 693 (bending C≡C).; $^{1}$H NMR (400 MHz; $CDCl_3$) $\delta_{H\ 2.06}$ (2H, s, C≡CH), 2.73 (4H, t, J= 6.8, 2xC$H_2$C≡C*H*), 4.52 (4H, t, J= 7.2, 2xO$CH_2CH_2$C≡CH), 8.02 (1H, t, J=7.6, ArH), 8.30 (2H, d, J=7.6, 2xArH). $^{13}$C NMR (100 MHz; $CDCl_3$) $\delta_C$ 18.9 ($CH_2$C≡CH), 63.6 (O-*C*$H_2$), 70.3 (*C*≡CH), 79.5 (*C*≡CH), 128.2 (Ar*C*H), 138.4 (Ar*C*H), 148.1 (Ar*C*), 164.1 (*C*=O). HRMS (ES$^+$) m/z calculated for $C_{15}H_{13}NO_4Na$ $[M+Na]^+$ 294.2578, found 294.0740.

**Representative data for synthesis 4-dipentynyl pyridine-2,6-dicarboxylate, 3b**

The compound was obtained as colorless crystalline in 63% yield after recrystallization. Mp 80 - 82 °C. IR (KBr pellets) υ/cm$^{-1}$: 3278 (stretching C≡C), 1736 (C=O), 1288 (Ar-N), 1237 (C-O), 693 (bending C≡C). $^{1}$H NMR (400 MHz; $CDCl_3$) $\delta_{H\ 2.01}$ (2H, s, C≡CH), 2.09 (4H, **t**, J= 8, 2xC$H_2$C≡C*H*), 2.41 (4H, q, J= 4, 2x$CH_2CH_2$C≡CH), 4.54 (4H, t, J=8, 2xO-$CH_2CH_2CH_2$C≡CH), 8.02 (1H, t, J=8, ArH), 8.27 (2H, d, J=8, 2xArH). $^{13}$C NMR (100 MHz; $CDCl_3$) $\delta_C$ 15.27 ($CH_2$C≡CH), 27.45 (O-$CH_2$-$CH_2$)64.70 (O-$CH_2$), 69.26 (C≡CH), 82.87 (C≡CH), 127.90 (ArCH), 138.25 (ArCH), 148.44 (ArC), 164.51 (C=O). HRMS (ES+) m/z calculated for $C_{17}H_{17}NO_4Na$ $[M+Na]^+$ 322.3109, found 322.1158.

**Characterization**

The infrared spectra for both ester macrocyclic isomers, **3a** and **3b** showed the presence of the stretching frequency at 3264 and 3278 cm$^{-1}$ due to the existence of terminal alkyne. The peak at 1716 and 1740 cm$^{-1}$ are the stretching frequencies for the *v* (C=O). For the peak at 1327 and 1288 cm$^{-1}$ are referred to aromatic amine of the pyridine and peak at 1244 and 1237 cm$^{-1}$ are for the ether group. Sharp peak at 693 and 654 cm$^{-1}$ are referring to bending mode of the terminal alkyne. Figure 1(a) display the IR spectrum of **3a** and (b) for compound **3b**.



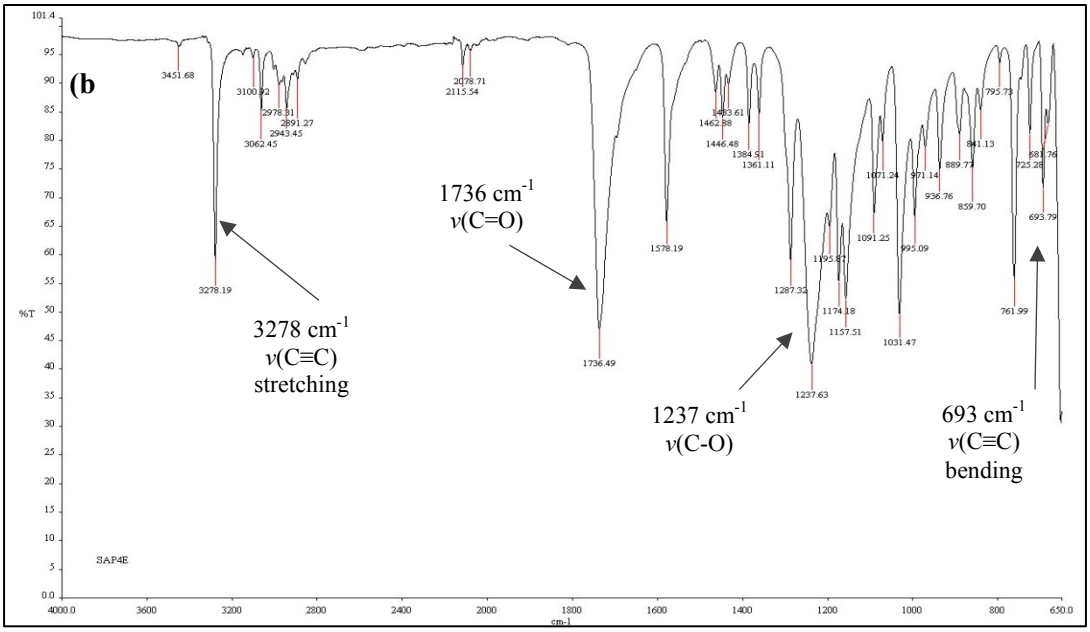



Figure 1. The IR spectrum of (a) **3a** and (b) **3b**

The chemical shifts of the pyridine rings protons for the both isomers are similar and appeared as a dublet at 12.0 and a triplet at 11.0 ppm, respectively. The terminal alkynes protons for the compounds **3a** and **3b** were found in the range of 1.0-2.0 ppm. The chemical shifts of the methylene protons near the alkyne ($-CH_2C\equiv CH$) appeared at the range of 2.07-5.02 ppm while the methylene protons's chemical shifts are found at 4.50 ppm. In the $^{13}C$ NMR spectra, the carbon chemical shifts of C=O is found at 174.0 ppm, respectively for the both isomers. The aromatic pyridine carbon chemical shifts of the isomers appeared in the range of 124.5-136.0 ppm. The chemical shift for the terminal alkyne observed at the range of 21.1-43.8 ppm. The value of molecular ion peak found in mass spectrometry for **3a** and **3b** are agreed with the expected molecular weight, respectively.

**X-ray crystallographic study**

The colorless crystals of **3a** and **3b** are crystallized in monoclinic system with same space group of C 2/c. The crystallographic data are summarized in Table 1.

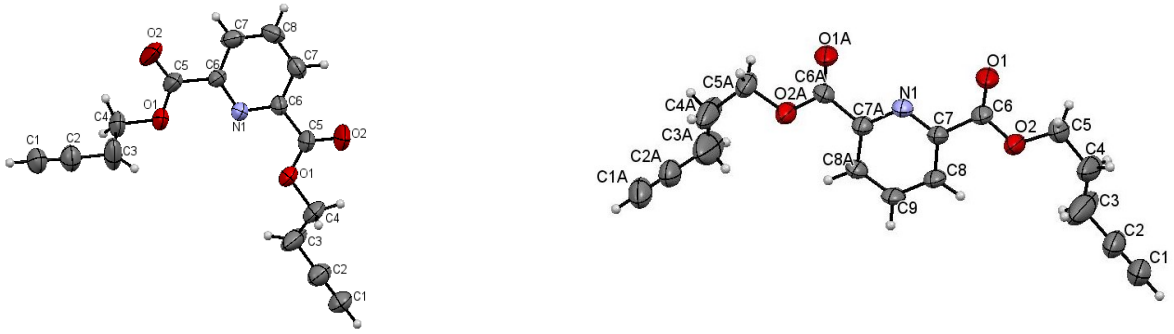
Table 1. Crystal data and structure refinement for the compounds **3a** and **3b**.

| **Crystal Parameters** | **3a** | **3b** |
|---|---|---|
| CCDC deposition number | 1535752 | 1536022 |
| Empirical formula | $C_{15}H_{11}NO_4$ | $C_{17}H_{17}NO_4$ |
| Formula weight | 269.25 | 299.31 |
| Temperature | 303(2) K | 303(2) K |
| Wavelength | 0.71073 Å | 0.71073 Å |
| Crystal system | Monoclinic | Monoclinic |
| Space group | C 2/c | C 2/c |
| Unit cell dimensions | a = 13.2710(16) Å | a = 24.577(4) Å |
| | b = 11.7023(14) Å | b = 6.3136(9) Å |
| | c = 8.9657(10) Å | c = 10.5608(14) Å |
| | α = 90° | α = 90° |
| | β = 102.672(4)° | β = 99.562(5)° |
| | γ = 90° | γ = 90° |

Table 1 (cont'd). Crystal data and structure refinement for the compounds **3a** and **3b**.

| **Crystal Parameters** | **3a** | **3b** |
|---|---|---|
| Volume | 1358.5(3) $Å^3$ | 1616.0(4) $Å^3$ |
| Z | 4 | 4 |
| Density (calculated) | 1.316 $Mg/m^3$ | 1.230 $Mg/m^3$ |
| Absorption coefficient | 0.097 $mm^{-1}$ | 0.088 $mm^{-1}$ |
| F(000) | 560 | 632 |
| Crystal size | 0.480 x 0.300 x 0.130 $mm^3$ | 0.480 x 0.160 x 0.080 $mm^3$ |
| Theta range for data collection | 3.053 to 24.972° | 3.334 to 24.966° |
| Index ranges | -15<=h<=15,<br>-13<=k<=13,<br>-9<=l<=10 | -28<=h<=28,<br>-7<=k<=7,<br>-12<=l<=12 |
| Reflections collected | 18132 | 16291 |
| Independent reflections | 1197 [R(int) = 0.0714] | 1420 [R(int) = 0.0988] |
| Completeness to theta | 99.9 % | 99.9 % |
| Max. and min. transmission | 0.988 and 0.955 | 0.993 and 0.959 |
| Refinement method | Full-matrix least-squares on $F^2$ | Full-matrix least squares on $F^2$ |
| Data / restraints / parameters | 1197 / 0 / 92 | 1420 / 1 / 101 |
| Goodness-of-fit on $F^2$ | 1.071 | 1.372 |
| Final R indices [I>2sigma(I)] | R1 = 0.0734,<br>wR2 = 0.1969 | R1 = 0.1094,<br>wR2 = 0.2461 |
| R indices (all data) | R1 = 0.1031,<br>wR2 = 0.2305 | R1 = 0.1695,<br>wR2 = 0.2763 |
| Largest diff. peak and hole | 0.391 and -0.322 e.$Å^{-3}$ | 0.735 and -0.587 e.$Å^3$ |

Figure 2 shows the structure molecular with labels of the molecules **3a** and **3b**. Both molecules with the pyridine linker and both side chains groups, respectively adopt a cis-cis against the C=O bond. The two molecules have asymmetric unit of ½ independence molecule generated since they are centrosymmetric across the N1/C8 and N1/C9 atoms.




**3a** **3b**

Figure 2. ORTEP diagrams of compund 3a and 3b drawn at 50% probability displacement ellipsoids

Compound **3a** possess a planar geometry by its pyridine ring N1/(C6-C8)/C6a-C7a) with the ester C4-C5/O1-O2 and C4a-C5a/O1a-O2a with maximum deviation of 0.016 Å for atom C4. The pyridine and ester groups are

perpendicular with the alkyne side chain with dihedral angle to the ester at C5/O1/C4/C3 with -139.8(4)°. As for compound **3b**, all atoms are in planar with maximum deviation at C8 with 0.052(4) Å. The bond lengths and angles are in normal ranges for both compounds (Table 2).

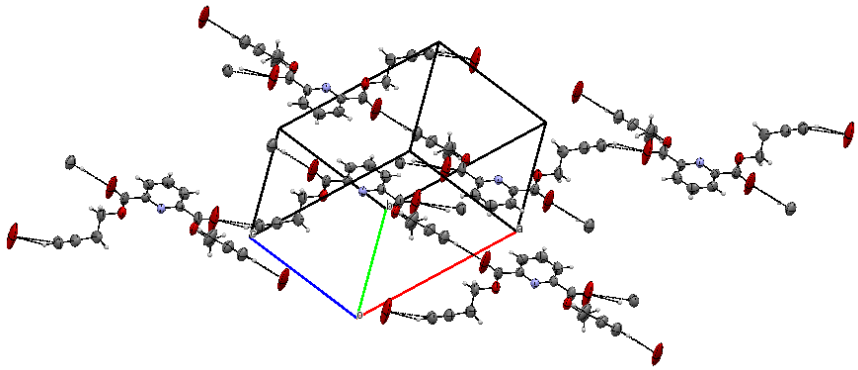
Table 2. Selected Bond Lengths (Å) and Bond Angles (°) for Compounds **3a** and **3b**

| **Compound 3a** | | **Compound 3b** | |
|---|---|---|---|
| **Bond** | **Dist.** | **Bond** | **Dist.** |
| O1—C5 | 1.300 (4) | O1—C6 | 1.193(5) |
| O1—C4 | 1.456 (4) | O2—C6 | 1.327(5) |
| O2—C5 | 1.177 (4) | O2—C5 | 1.458(6) |
| N1—C6#1 | 1.332(3) | N1—C7 | 1.337(5) |
| N1—C6 | 1.333 (3) | N1—C7#1 | 1.337(5) |
| C1—C2 | 1.166 (5) | C1—C2 | 1.127(8) |
| C2—C3 | 1.463 (5) | C2—C3 | 1.405(10) |
| C3—C4 | 1.455 (6) | C3—C4 | 1.504(8) |
| C5—C6 | 1.492 (4) | C4—C5 | 1.449(9) |
| C6—C7 | 1.386 (5) | C6—C7 | 1.493(6) |
| C7—C8 | 1.360 (4) | C7—C8 | 1.391(6) |
| C8—C7#1 | 1.360 (4) | C8—C9 | 1.369(6) |
| | | C9—C8#1 | 1.369(6) |
| **Angle** | **(°)** | **Angle** | **(°)** |
| C5—O1—C4 | 116.5 (3) | C6—O2—C5 | 117.1(4) |
| C6#1—N1—C6 | 115.8 (4) | C7—N1—C7#1 | 117.1(5) |
| C1—C2—C3 | 178.1 (4) | C1—C2—C3 | 169.7(10) |
| C4—C3—C2 | 112.2 (3) | C2—C3—C4 | 115.9(8) |
| C3—C4—O1 | 108.2 (3) | C5—C4—C3 | 123.2(7) |
| O2—C5—O1 | 123.4(3) | C4—C5—O2 | 109.7(5) |
| O2—C5—C6 | 121.5(3) | O1—C6—O2 | 122.6(5) |
| O1 —C5 —C6 | 115.2(3) | O1—C6—C7 | 126.1(4) |
| N1 —C6 —C7 | 123.8(3) | O2—C6—C7 | 111.3(4) |
| N1 —C6 —C5 | 119.0(3) | N1—C7—C8 | 123.0(5) |
| C7 —C6 —C5 | 117.2(3) | N1—C7—C6 | 115.3(4) |
| C8 —C7 —C6 | 118.9(3) | C8—C7—C6 | 121.6(4) |
| C7#1—C8 —C7 | 118.7(4) | C9—C8—C7 | 119.0(5) |
| | | C8#1—C9—C8 | 118.9(6) |

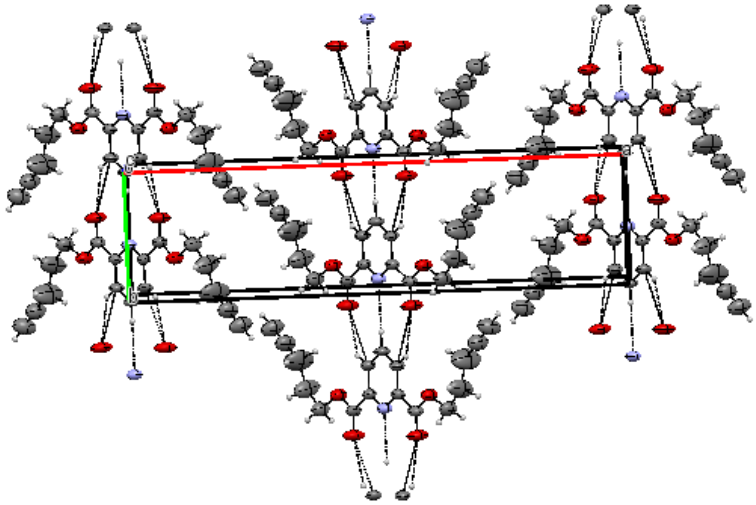
In the crystal structure, the **3a** molecule is linked by C1—H1···O2 intermolecular hydrogen bond. In contrast with molecule **3b**, linked by nitrogen of pyridine with the hydrogen methine of C9 pyridine, N1···H9—C9 and oxygen carbonyl and hydrogen methine of C8 pyridine, C8—H8···O1 (Table 3). The intermolecular hydrogen bond for molecule **3a** and **3b** formed a network of polymorph at b-axis and c-axis (Figure 3).

Table 3. Hydrogen Bond Lengths (Å) and Bond Angles for Compounds **3a** and **3b**

| **Compound** | **D—H·····A** | **D—H** | **H·····A** | **D·····A** | **D—H·····A** | **Symmetry code** |
|---|---|---|---|---|---|---|
| **3a** | C1—H1·····O2#2 | 0.93 | 2.25 | 3.131(6) | 159 | ½-x, ½+y, -1/2-z |
| **3b** | C8—H8·····O1$1#2 | 0.93 | 2.51 | 3.182(6) | 129.3 | -x+2, y, -z+1/2 |
| | C9—H9·····N1#2 | 0.93 | 2.60 | 3.531(8) | 180 | 2x, y-1, z |



**3a**



**3b**

Figure 3. Polymorph network of molecule at b-axis (**3a**) and c-axis (**3b**). The dash line indicates the intermolecular hydrogen bond

## Conclusion

The ester macrocyclic 3-dibutynyl-2,6-pyridine dicarboxylate and 4-dipentynyl-2,6-dicarboxylate were successfully synthesized by condensation reaction and fully characterized using spectroscopic techniques. Both compounds were crystallized in the solvent system of cyclohexane and ethyl acetate for purification and afforded colorless and needle-liked crystals. The observation on CCDC data has no record on these compounds. Both compounds have monoclinic system with space group of C 2/c but different geometry as **3b** showed fully geometry planar. The intermolecular hydrogen bond gave the compounds a polymorph network in the crystal structure. The terminal alkynes on both compounds are suitable metathesis reaction. Thus, further study on the metathesis reaction and optimization to obtain cyclic compounds are in progress.

## Acknowledgement

The authors thank the Ministry of Higher Education of Malaysia and Universiti Kebangsaan Malaysia for the research grant GUP-2016-059. The assistance of Mr Mohammad Fadzlee bin Ngatiman at Centre of Research and

Instrumentation Management. One of the authors, Nawwar Hanun would like to thank the Ministry of Higher Education of Malaysia for the Mybrain15 scholarship.

**References**

1. Newkome, G. R., Sauer, J. S., Roper, J. M. and Hager, D. C. (1976). Construction of synthetic macrocyclic compounds possesing subheterocyclic rings, specifically pyridine, furan and thiophene. *Chemical Review,* 77: 513 – 597.
2. Garren E. Maas, G. E., Bradshaw, J. S., Izatt, R. M. and Christensen, J. J. (1977). Synthesis of a new series of macrocyclic polyether-diester ligands. *Journal of Organic Chemistry,* 42: 3937 – 3941.
3. Bradshaw, J. S. and Thompson, M. D. (1978). Synthesis of macrocyclic polyether-diester compounds with an aromatic subcyclic unit. *Journal of Organic Chemistry,* 43: 2456 – 2460.
4. Potts, K. T., Cipullo, M. J., Ralli, P. and Theodoridis, G. (1982). Synthesis of 2,6-disubstituted pyridines, polypyridinyls and annulated pyridines. *Journal of Organic Chemistry,* 47: 3027 – 3038.
5. Zhao, H. and Hua, W. (2000). Synthesis and characterization of pyridine-based polyamido-polyester optically active macrocycles and enantiomeric recognition for d- and l- amico acid methyl ester hydrochloride. *Journal of Organic Chemistry,* 65: 2933 – 2938.
6. Vedernikov, A. N., Pink, M. and Caulton, K. G. (2003). Design and synthesis of tridentate facially chelating ligands of the [2.n.1]-(2,6)-pyridinophane family. *Journal of Organic Chemistry,* 68: 4806 –4814.
7. Newkome, G. R., Patri, A. K., Holder, E. and Schubert, U. S. (2004). Synthesis of 2,2'-bipyridines: versatile building blocks for sexy architectures and functional nanomaterials. *European Journal of Organic Chemistry,* 2004(2): 235 – 254.
8. Kolthoff, I. M. (1979). Application of macrocyclic compounds in chemical analysis. *Analytical Chemistry,* 51: 1 – 22.
9. Bradshaw, J. S., Maas, G. E., Lamb, J. D., Izatt, R. M. and Christensen, J. J. (1980). Cation complexing properties of synthetic macrocyclic polyether-diester ligands containing the pyrdine subcyclic unit. *Journal of the American Chemical Society,* 2: 467 – 474.
10. Al-Salahi, R. A., Al-Omar, M. A. and Amr, A. E. E. (2010). Synthesis of new macrocyclic polyamides as antimicrobial agent candidates. *Molecules,* 15: 6588 – 6597.
11. El-Salam, O. I. A., Al-Omar, M. A., Fayed, A. A., Flefel, E. M. and Amr, A. E. E. (2012). Synthesis of new macrocyclic polyamides as antimicrobial agent candidates. *Molecules,* 17: 14510 – 14521.
12. Kuz'min, V. E., Lozitsky, V. P., Kamalov, G. L., Lozitskaya, R. N., Zheltvay, A. I., Fedtchouk, A. S. and Kryzhanovsky, D. N. (2000). Analysis of the structure – anticancer activity relationship in a set of Schiff bases of macrocyclic 2,6-bis(2- and 4-formylaryloxymethyl)pyridines. *Acta Biochimica Polonica*, 47: 867 – 875.
13. Santini, C., Pellei, M., Gandin, V., Porchia, M., Tisato, F. and Marzano, C. (2003). Advances in copper complexes as anticancer agents. *Chemical Review*, 114(1): 815 – 862.
14. Rusconi, S., Cicero, M. L., Viganò, O., Sirianni, F., Bulgheroni, El., Ferramosca, S., Bencini, A., Bianchi, A., Ruiz, L., Cabrera, C., Martinez-Picado, J., Supuran, C. T. and Galli, M. (2009). New macrocyclic amines showing activity as HIV entry inhibitors against wild type and multi-drug resistant viruses. *Molecules*, 14: 1927 – 1937.
15. Fürstner,A., Guth, O., Rumbo, A. and Seidel, G. (1999). Ring closing alkyne metathesis. Comparative investigation of two different catalyst systems and application to the stereoselective synthesis of olfactory lactones, azamacrolides, and the macrocyclic perimeter of the marine alkaloid nakadomarin A. *Journal of American Chemical Society*, 121: 11108 – 11113.

*Malaysian Journal of Analytical Sciences, Vol 21 No 5 (2017): 1016 - 1027*
*DOI: https://doi.org/10.17576/mjas-2017-2105-03*

**MALAYSIAN JOURNAL OF ANALYTICAL SCIENCES**
*Published by The Malaysian Analytical Sciences Society*
**ISSN 1394 - 2506**

# BREAKDOWN OF HYDROGEN SULFIDE IN SEAWATER UNDER DIFFERENT RATIO OF DISSOLVED OXYGEN / HYDROGEN SULFIDE

## (Penguraian Hidrogen Sulfida dalam Air Laut dengan Nisbah Oksigen Terlarut / Hidrogen Sulfida yang Berbeza)

Hii Yii Siang[1]*, Norhayati Mohd Tahir[2], Abdul Malek[3], Mohd Azlan Md Isa[3]

[1]*School of Fisheries and Aquaculture Science*
[2]*School of Marine and Environmental Sciences*
*University Malaysia Terengganu, 21030 Kuala Nerus, Terengganu, Malaysia*
[3]*Sapura Kencana Energy Inc., Level 6, Menara Sapura Kencana Petroleum, Solaris Dutamas, Jalan Dutamas 1, 50480 Kuala Lumpur, Malaysia*

**Corresponding author: hii@umt.edu.my*

Received: 29 November 2016; Accepted: 8 August 2017

**Abstract**

Breakdown of hydrogen sulfide ($H_2S$) in seawater is highly dependent on both the concentration of dissolved $H_2S$ and dissolved oxygen (DO). A simple correlation was found in the $H_2S$ dissociation and ratio of [DO/$H_2S$]. When the [DO/$H_2S$] ratio is more than one, $H_2S$ breakdown rapidly, resulting in a short half-life of $H_2S$ in the seawater (in a time scale of minute). When the dissolved oxygen is not a limiting factor, $H_2S$ breakdown in a first order reaction. Nevertheless, when [DO/$H_2S$] ratio is less than 1, $H_2S$ breakdown in the seawater becomes slower, resulting in a longer $H_2S$ half-life (in a time scale up to hours). In this case, the $H_2S$ breakdown in a pseudo-second order reaction. This pseudo-second order reaction is commonly reported by other investigators. This study also investigated the relation between the concentration of dissolved $H_2S$ and pH changes during $H_2S$ dissociation in the seawater. The pH is lowered with increasing concentration of initial $H_2S$ in the seawater but appears to reach an asymptotic low value of about 4 as the dissolved $H_2S$ approaches its saturation limit in the seawater at about 2,500 mg $L^{-1}$.

**Keywords:** hydrogen sulfide, dissolved oxygen, oxidation, seawater, $H_2S$ dissociation

**Abstrak**

Penguraian hidrogen sulfida ($H_2S$) dalam air laut sangat bergantung kepada kepekatan kedua-dua $H_2S$ terlarut dan oksigen terlarut (DO). Satu kolerasi mudah telah ditemui antara penguraian $H_2S$ dan nisbah [DO/$H_2S$]. Apabila nisbah [DO/$H_2S$] melebihi satu, penguraian $H_2S$ adalah cepat, menyebabkan separuh hayat $H_2S$ yang pendek dalam air laut (dalam skala masa minit). Dalam keadaan yang mana oksigen terlarut bukan faktor penghad, penguraian $H_2S$ merupakan tindak balas tertib pertama. Namun, apabila nisbah [DO/$H_2S$] kurang daripada satu, penguraian $H_2S$ dalam air laut menjadi lambat, menyebabkan separuh hayat $H_2S$ yang lebih lama (dalam skala masa jam). Dalam kes ini, penguraian $H_2S$ adalah tindak balas pseudo tertib kedua. Tindak balas pseudo tertib kedua ini biasa dilaporkan oleh ramai penyelidik. Kajian ini turut menyiasat hubung kait antara kepekatan $H_2S$ terlarut dan perubahan pH semasa penguraian $H_2S$ dalam air laut. Nilai pH jadi rendah dengan peningkatan kepekatan awal $H_2S$ dalam air laut tapi ia mencapai nilai asimptot yang rendah dalam lingkungan 4 apabila kepekatan $H_2S$ terlarut menghampiri had ketepuannya dalam air laut pada kepekatan 2,500 mg $L^{-1}$.

**Kata kunci:** hidrogen sulfida, oksigen terlarut, pengoksidaan, air laut, penguraian $H_2S$

## Introduction

Hydrogen Sulfide ($H_2S$) gas is one of the potential contaminant found in oil and gas production. $H_2S$ is normally formed in oil and/or gas reservoirs through the decomposition of organic matter under anaerobic condition by microbes. Typically, such $H_2S$ will be removed from the main hydrocarbon stream and disposed off to increase the sales value of the sweetened hydrocarbon. In the ocean, $H_2S$ is mainly formed through geochemical processes during deep sea volcanic activities including hydrothermal vents [1]. When $H_2S$ is present in the seawater in dissolved form, it dissociates into hydrosulfide ($HS^-$), which is the product of the first dissociation equilibrium ($K_{a1}$). The second dissociation equilibrium ($K_{a2}$) produces the sulfide ion ($S^{2-}$). $H_2S$ is a weak acid, with $pK_{a1}$ being reported by various investigators in the order of 7.0 [2-5] and $pK_{a2}$ in the order of 12.5 [6]. Due to the first dissociation of $H_2S$ to $HS^-$, the concentration of aqueous $H_2S$ will decrease with increasing pH in water. At pH 7.0, the concentration ratio of the aqueous $H_2S$ to $HS^-$ is approximately 1:1. As the pH increases beyond 7.0, the ratio of the concentration of $HS^-$ to aqueous $H_2S$ increases. Sulfide ion ($S^{2-}$), which is the product of the second dissociation becomes significant, only when pH is above 12.

The hydrosulfide ion is susceptible to oxygenation reactions under aerobic condition in seawater. The oxygenation of $HS^-$ is rather complex, involving a multitude of chemical reactions, producing various intermediate and final products, amongst others, the following possible reactions 1 – 3 [7, 8]:

$$2HS^- + 3O_2 \rightarrow 2SO_3^{2-} + 2H^+ \quad (1)$$

$$HS^- + 2O_2 \rightarrow SO_4^{2-} + H^+ \quad (2)$$

$$2HS^- + 2O_2 \rightarrow S_2O_3^{2-} + H_2O \quad (3)$$

In the presence of relatively high concentration of dissolved oxygen (DO), the ion species of sulfite ($SO_3^{2-}$) is stable. Even so, some of the $SO_3^{2-}$ species would also be oxidized to sulfates ($SO_4^{2-}$) [7, 9]. Hence, it is apparent that the actual overall oxidation rate of $H_2S$ in seawater varies depending on the conditions studied. A simplified gross measure of the overall breakdown of $H_2S$ in seawater due to various reactions shown above can be depicted by the $H_2S$ half-life; which is a measure of the time taken to lower the $H_2S$ concentration from its initial value to half the initial value. Various publications have provided different $H_2S$ half-life values, depending on the reaction conditions investigated. Göte and Alexander [10] reported that the $H_2S$ half-life of about 17 minutes at constant dissolved oxygen concentration of 5.4 mg $L^{-1}$ and 25 °C in seawater. Sharma and Yuan [11] reported $H_2S$ half-life of 25 minutes for treated domestic wastewater initially containing about 6 mg $L^{-1}$ of $H_2S$ and 8 mg $L^{-1}$ DO, while Asaoka et al. [12] reported an *in-situ* half-life of approximately 50 minutes in the Etajima Bay, which contains about 28 mg $L^{-1}$ of sulfide.

Decomposition of the $H_2S$ becomes more complicated when microbial degradation is also taking place [13] or when catalytic metals are present [14]. Oxidized metals such as Fe(III), Mn(III) and Mn(IV), for example, are efficient catalysts to overcome the kinetic barrier for the chemical oxidation of sulfides [15]. The interaction of all these factors in the seawater leads to unpredictable outputs in the tropical marine environment. It is apparent that the half-life of $H_2S$ dissociation in such waters is quite complex and dependent on the physical chemical properties as well as biological assemblage of the seawater. Thus, whenever the rate of $H_2S$ decomposition is the intended subject, invariably there is a need to conduct *in-situ* verification using the actual seawater source. Understanding the rate of $H_2S$ breakdown in seawater is important in environmental management as it plays an important role in toxicity and ecological footprint of the toxic gas in the marine environment. Hence, this paper describes the experiments undertaken to determine the rate of $H_2S$ breakdown in seawater obtained from the Terengganu offshore, as representative of the offshore water of Peninsular Malaysia. The study includes analysis to derive appropriate rate equations and rate constant(s) for the $H_2S$ breakdown in seawater as well as estimations of the dissociation half-life. In addition, the effect of $H_2S$ dissociation on the pH of the resultant solution is of particular interest. In freshwater, the dissolution of $H_2S$ into $HS^-$ ions generate protons, which effectively lowers the pH of the solution. However, in seawater, the natural alkalinity of the seawater tends to counteract the lowering of the pH through various carbonaceous compounds in the seawater carbonate equilibrium. This can result in a complex, non-linear pH correlation with concentration of $H_2S$ dissolution. In this study, it is desired to establish an empirical relationship between the effect of $H_2S$ dissolution and resultant pH of the seawater solution.

## Materials and Methods

### Materials

Seawater used in this experiment was collected from the South China Sea off Terengganu. The seawater was then filtered and acclimatized for one week before use. 1 L Kipps apparatus was used to produce the hydrogen sulfide ($H_2S$) gas used in this study. In the Kipps apparatus, excess pyrite ($Fe_2S$) was allowed to react with hydrochloric acid (20%) to generate $H_2S$ gas. The gas was bubbled into 1 L oxygen-free deionized water for 24 hours to produce an approximately 2000 mg $L^{-1}$ $H_2S$ aliquot for the subsequent experiments. Oxygen free water was prepared by purging deionized water with pure nitrogen at 30 mL $s^{-1}$ for 40 minutes. High Purity oxygen and nitrogen (> 99 %) gases were used in this study. All the chemicals used in the study were of analytical grade and supplied by Merck Co.

### Determination of hydrogen sulfide in seawater

Hydrogen sulfide ($H_2S$) probe (MS-AQUA) was used to monitor $H_2S$ concentration in the experiments. Analysentechnik GmbH develops the amperometric MS-AQUA $H_2S$ micro sensor for *in-situ* determination of dissolved $H_2S$ or Total sulfide in aqueous solution within a pH range of 0 to 8. Other than the ion sensitive electrode (ISE), the MS-AQUA is the only method for *in-situ* [$H_2S$/ Total Sulfide] measurement. MS-AQUA is more relevant as compared to the other ISEs because the workable pH range of MS-AQUA is more relevant to the study undertaken. The accuracy and the concentration of the MS-AQUA below 3 mg $L^{-1}$ is essentially better than the other ISEs. Table 1 shows the technical data extracted from the technical manual of the sensor. The $H_2S$ probe was pre-calibrated by the manufacturer and was validated with standard solutions by comparing the concentration obtained from the probe and the standard methods (APHA 4500-$S^{2-}$F., Iodometric method and APHA 4500-$S^{2-}$H, calculation of unionized $H_2S$) [16]. Dissolved oxygen and pH were determined by using YSI 550a and the pH probe of the MS-AQUA respectively.

Table 1. Technical specification of MS-AQUA $H_2S$ probes used in the study

| Technical Specification | Range |
|---|---|
| Measurement range | |
| • Type I* | • 10 µg $L^{-1}$ – 3 mg $L^{-1}$ $H_2S$ |
| • Type II | • 50 µg $L^{-1}$ – 10 mg $L^{-1}$ $H_2S$ |
| • Type III* | • 500 µg $L^{-1}$ – 50 mg $L^{-1}$ $H_2S$ |
| Accuracy of the sensor | 2 % |
| Temperature range | 0°C – 30°C |
| pH range | 0 – 8 |
| Salinity range | < 40 ppt (g $L^{-1}$) |
| Signal Interference | |
| • Carbon dioxide | Up to 25.38% |
| • Methane | Up to 5.78% |
| • Hydrogen | Up to 0.544% |
| • Ammonia | Up to 1000 ppm |
| • Carbon monoxide | Up to 92 ppm |
| • Carbon disulfide | Up to 5% |
| • Acetic acid | Up to 1 mol $L^{-1}$ |
| • Dimethyl sulfide | Up to 10% |
| • Ethanol | Up to 10% |

* Sensors used in this study

APHA Method 4500–$S^2$-F [16] was also used to validate the reading from the probe as well as to determine those concentration that fell beyond the measurement range of the MS-AQUA. In the case where the $H_2S$ level exceeded the measurement range, water sample was collected from the experimental chamber by using syringe acted as a

piston to drive water sample out of the vessel. Samples drawn out from the experiment was analyzed for its pH and $H_2S$ level right after sampling. Briefly, 20 mL of iodine solution (0.025 N) followed by 2 mL 6N HCl was poured into a 500 mL flask. An amount 200 mL sample was discharged under the solution surface into the flask. More iodine solution was added if the color of the iodine disappeared. The sample was then back-titrated with standard sodium thiosulfate solution (0.025 N). A few drops of starch solution were added as indicator for the end point (disappearance of blue color). The concentration of total sulfide was then calculated, taking into account the dilution factor during titration. The concentration of unionized $H_2S$ is then calculated by multiplying the dissociation factor at the measured pH with the total sulfides as stipulated in APHA Method 4500–$S^2$-H [16].

**Breakdown of hydrogen sulfide in seawater**

Experimental chamber as shown in Figure 1 was used in this study. The chamber consists four major components; 1. $H_2S$, temperature and pH probes, 2. Aliquot injection port, 3. Dissolved oxygen probes, and 4. Magnetic bar and stirrer. The experimental chamber was incubated in a 20 L water bath. The reactor vessel was first filled with 2 L of seawater. Pure oxygen and nitrogen from gas cylinders were used to adjust the level of dissolved oxygen in the seawater. 50 mL syringe was used to inject concentrated $H_2S$ aliquot through the injection port into the reactor. The volume of concentrated $H_2S$ solution injected into the reactor was obtained based on dilution equation ($M_1V_1 = M_2V_2$) to make up the desired $H_2S$ concentration. The volume of injection was limited to less than 2% of the total reactor volume. No head space was permitted in the chamber throughout the experiment. In order to avoid leakages, all ports were sealed with silicon glue. Magnetic bar and stirrer (300 rpm) were used to homogenize the aliquot and seawater in the experimental vessel. The experiments were conducted in the laboratory at 28°C, pH 8.0 and 30 ppt. Experiment started one minute after injection of the $H_2S$ aliquot. This is to ensure sample homogeneity in the vessel. Readings were recorded continuously by using a camcorder and then manually transferred into excel spreadsheet. The data were then used to determine the reaction order, rate and constant. All the experiments were conducted in triplicate.

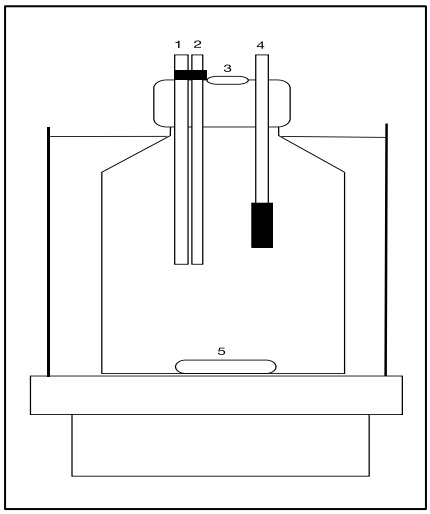



Figure 1. Experimental setup for investigation of $H_2S$ removal in seawater. 1. $H_2S$, temperature and pH probes, 2. Aliquot injection port, 3. Dissolved oxygen probe, 4. Magnetic bar and stirrer

**$H_2S$ solubility and pH changes in seawater**

Prior to the main $H_2S$ breakdown rate experiments, solubility of the $H_2S$ in seawater was tested using the experimental setup as shown in Figure 2. In the experiment, $H_2S$ gas generated from Kipps apparatus was bubbled through the seawater at 28°C, 30 ppt and pH 8.0 in a 2 L vessel through port 2. Port 4 is the vent for excess gas. During sample withdrawal, port 4 was clipped and the syringe (5) was used as a piston to drive water sample out of the vessel through port 3. The concentration of the $H_2S$, temperature, pH and dissolved oxygen were determined

immediately. The experiments were conducted in a 20 L water bath for consistent temperature at 28 °C (±0.5 °C). All the experiments were conducted in three replicates.

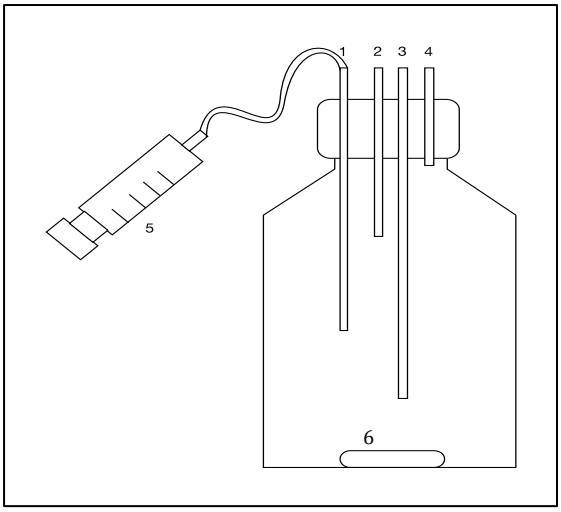



Figure 2. Experimental setup for investigating hydrogen sulfide solubility. 1. Piston inlet for sampling, 2. Gas inlet from Kipps apparatus, 3. Sample outlet, 4. Excess gas exhaust, 5. Syringe, 6. Magnetic bar

**Determination of reaction order, rate constant and half-life**

Data obtained from $H_2S$ breakdown experiments were used to determine the reaction order, rate constant and half-life of the $H_2S$ removal. Reaction kinetics were studied based on computation procedure of Han et al. [17]. The reaction orders, rate constants and half-life were obtained by using graphical method. In the case where the dissolved oxygen is in excess, the reaction constant and the breakdown rate of the $H_2S$ would resemble the pseudo-first order ($K_1$) reaction as (4):

$$\frac{d[H_2S]}{dt} = -K_1[H_2S]_t \quad (4)$$

Where, $[H_2S]_t$ is define as concentration of hydrogen sulfide at time t and $K_1$ is define as rate constant.

While, the reaction constant and the breakdown rate of the $H_2S$ resemble a second order reaction, it represented as (5):

$$\frac{d[H_2S]}{dt} = -K_2[H_2S]_t[O_2]_t \quad (5)$$

where, $[H_2S]_t$ is define as concentration of hydrogen sulfide at time t, $[O_2]_t$ is define as concentration of dissolved oxygen at time t and $K_2$ is rate constant.

The reaction constant for second order reaction, $K_2$, can be assessed by dividing $K_1$ with $[O_2]_t$. $K_1$ can also be derived from the concentration graphs by computing the gradient of the $H_2S$ concentration over the linear portion of the decline and dividing by the average concentration of $H_2S$ over the considered range. Comparing equations (4) and (5), $K_2$ can be estimated from $K_1/[O_2]$. Since the DO concentration in the seawater for the case of lower DO/ $H_2S$ concentration ratio is expected to decline in tandem with the breakdown of $H_2S$, estimation of $K_2$ in this case, is applicable only over a narrow time range where the DO concentration within that time range does not resulted in a significant differences in $K_2$ and $K_1$. In this study, such approximations are restricted to the first few minutes of the experiments, where the $H_2S$ concentration decline is still linear and the DO has not declined more than 50% of its

initial concentration. Integrating equation (5) provides a mathematical estimate of the $H_2S$ dissociation half-life for the experiments (equation 6 - 8):

$$\int \frac{\mathrm{d[H2S]}}{\mathrm{[H2S]}}\mathrm{dt} = -1 \int K_2 [O_2]$$
$$\frac{1}{[O_2]_o - [H_2S]_o} \ln \frac{[O_2]_t [H_2S]_o}{[O_2]_o [H_2S]_t} = K_2 t \quad (6)$$

When $[O_2]_o$ is much higher than $[H_2S]_o$, $[O_2]_o \sim [O_2]_t$, equation (6) become (7)

$$\frac{1}{[O_2]_t} \ln \frac{[H_2S]_o}{[H_2S]_t} = K_2 t$$

$$[H_2S]_t = [H_2S]_o e^{-[O_2]_t K_2 t} \quad (7)$$

Half-life can be determined based on equation (7), as $[H_2S]_t = 0.5[H_2S]_o$, thus

$$t_{1/2} = \frac{ln0.5}{-K_2[O_2]_o} \quad (8)$$

**Statistical analysis**

Paired t-test was performed to compare if there is significant different in the reading obtained from $H_2S$ probe (MS-AQUA) and the standard methods [16]. The statistical analysis was performed by using open source software, R statistics version 3.3.2.

## Results and Discussion

**Validation of $H_2S$ probe**

Data obtained by using the $H_2S$ probe (MS-AQUA) was cross checked with APHA 4500-$S^{2-}$F standard method. Experiments and analysis on different concentration of $H_2S$ standard solution was conducted to validate the corresponding measurement on the sensor. Results obtained from the probe were not significantly different (paired t-test, $p>0.05$) from those obtained by using APHA standard method and there is a correlation between the data values. (Pearson, $P < 0.05$, $R^2 = 0.9974$). Figure 3 shows the correlation of $H_2S$ concentration obtained by using probe and the standard method. Validation of the $H_2S$ probe is important because the probe is considered new in the market and there are only few reports on its efficiency in measurement. The probe is responsive towards $H_2S$ even it exceeded the measurement range recommended by the manufacturer although the last two points in the validation curve (Figure 3) starts showing deviation from the proportionality.

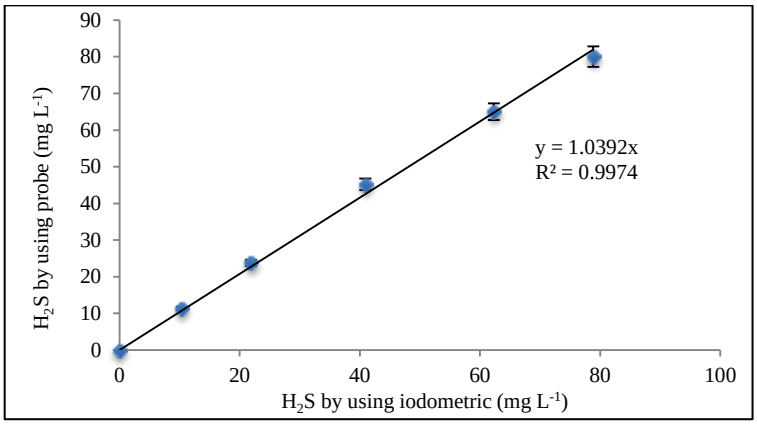



Figure 3. $H_2S$ Probe (MS-AQUA) measurement correlated with concentration determined by using APHA standard methods (4500-$S^{2-}$F and APHA 4500-$S^{2-}$H)

**$H_2S$ solubility and pH changes in seawater**

When $H_2S$ was continuously bubbled into the seawater, the seawater pH dropped from an initial value of pH 8.01 down to pH 4.27 as the $H_2S$ concentration was approaching 2312 mg $L^{-1}$ (Figure 4). At 28 °C, the concentration of $H_2S$ was saturated at about 2500 mg $L^{-1}$ in 30 ppt seawater in the experiments. It is anticipated that $H_2S$ would equilibrate and evolve into the vapor space at the saturation state. Hence, the $H_2S$ concentration used in this study was limited to 1500 mg $L^{-1}$ to reduce experimental errors and in terms of safety consideration.

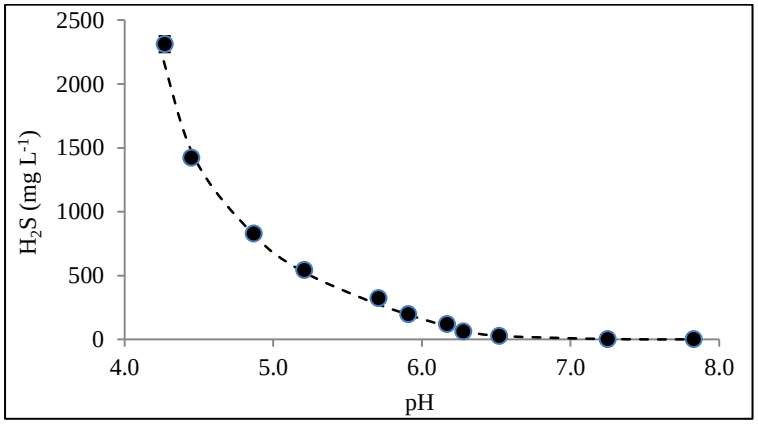
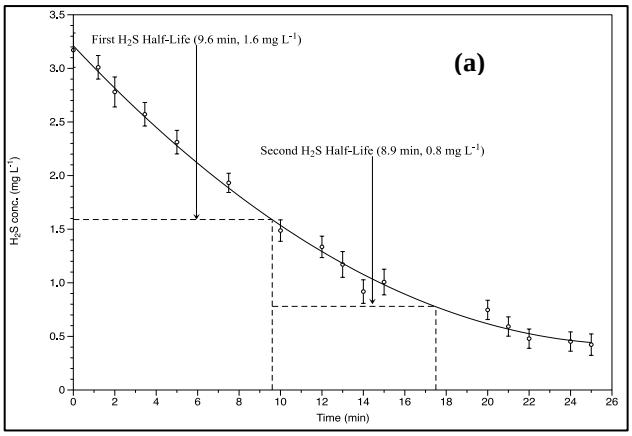



Figure 4. Effect of hydrogen sulfide concentration on seawater pH

**Hydrogen sulfide breakdown in seawater at different [DO]/[$H_2S$] ratio**

In the presence of excess dissolved oxygen in seawater, dissolved hydrogen sulfide ($H_2S$) is oxidized rapidly in the seawater. Figure 5 shows the $H_2S$ breakdown against time in seawater under aerobic condition. At an initial dissolved oxygen of 10.2 mg $O_2$ $L^{-1}$ (Figure 5a), the $H_2S$ decomposed from initial 3.2 mg $L^{-1}$ into half of its initial concentration at 1.6 mg $L^{-1}$ in about 10 minutes when the ratio of [DO/$H_2S$] is 3.4 (Figure 5a). The $H_2S$ concentration was further decomposed in the seawater. The subsequent half-life of the $H_2S$ concentration 1.6 to 0.79 mg $L^{-1}$ was about 9 minute. We repeated the experiment by introduced an initial concentration of 5.2 mg$L^{-1}$ $H_2S$ under a [DO/$H_2S$] ratio of 3.2 (Figure 5b) at an initial dissolved oxygen of 17.4 mg $O_2$ $L^{-1}$, after 10.6 minutes, the $H_2S$ concentration dropped to half of its initial concentration. The $H_2S$ concentration in this experiment further decomposed to 1.3 mg$L^{-1}$ after 10.4 minutes. In both experiments, the dissolved oxygen remained above 4 mg$L^{-1}$ at the end of the experiments. On average, $H_2S$ breakdown at 9.9 ± 0.8 minute in the seawater when dissolved oxygen is in excess. The $H_2S$ breakdown reaction appears to be a first order reaction, when the dissolved oxygen is not a limiting factor.



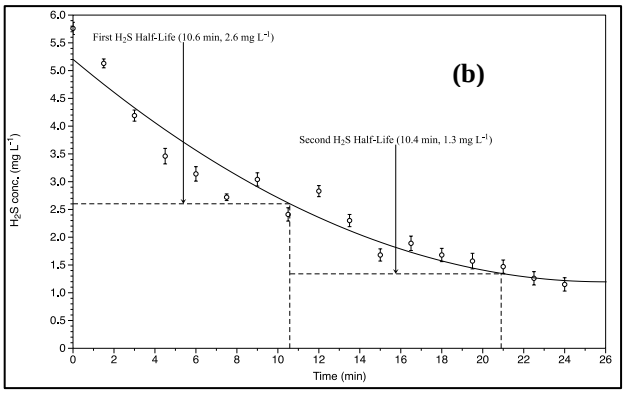



Figure 5. Hydrogen sulfide breakdown in the seawater at (a) initial dissolved oxygen of 10.2 mg $L^{-1}$, [$DO/H_2S$] ratio 3.4 (b) initial dissolved oxygen of 17.4 mg $L^{-1}$, [$DO/H_2S$] ratio 3.2

**Hydrogen sulfide breakdown in seawater at low [$DO/H_2S$] molarity ratio**

Under low [$DO/H_2S$] molarity ratio, as the hydrogen sulfide ($H_2S$) is oxidized, the concentration of DO in the seawater decreased in tandem with the decrease in $H_2S$ concentration. In this case, $H_2S$ breakdown no longer resemble a first order reaction due to the dissolved oxygen depletion in the seawater. The $H_2S$ breakdown is rather regulated by the availability of the dissolved oxygen. Figure 6 shows a typical $H_2S$ concentration decline as it is reacted with DO under a low [$DO/H_2S$] concentration ratio. The $H_2S$ half-life at initial conditions of the experiment was estimated based on equation (4) provided earlier. Further experiments were conducted at low [$DO/H_2S$] ratios to derive the correlations of $H_2S$ breakdown in seawater and determine the approximate $H_2S$ half-life under those conditions. The experiments were conducted such that the [$DO/H_2S$] molarity ratio range spanned from less than 0.1 to above 10. This would provide adequate evidence of any correlation between the concentration ratio and the dissociation half-life. Table 3 below provides the measured $H_2S$ half-life for various [$DO/H_2S$] ratio.

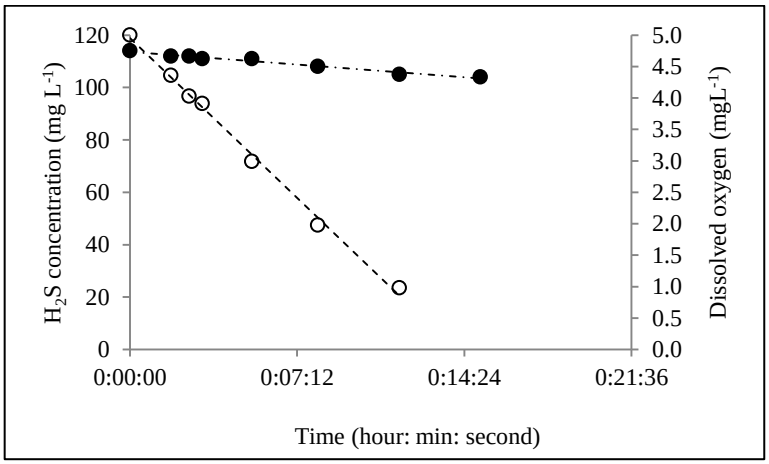



Figure 6. Typical hydrogen sulfide breakdown in seawater at low [$DO/H_2S$] concentration ratio [$H_2S$ initial concentration = 114 mg $L^{-1}$; DO initial concentration = 5 mg $L^{-1}$]. Open blank circle indicates dissolved oxygen while filled circle indicates concentration of hydrogen sulfide in seawater

Table 3. $H_2S$ Half-life at various [DO/$H_2S$] ratio

| [DO/$H_2S$] Ratio | $H_2S$ Initial Conc. (mg $L^{-1}$) | DO Initial Conc. (mg $L^{-1}$) | $H_2S$ Half-life (min) |
|---|---|---|---|
| 0.05 | 114.0 | 5.0 | 82.1 |
| 0.16 | 92.7 | 14.0 | 35.7 |
| 0.49 | 43.2 | 20.0 | 17.3 |
| 3.41 | 3.2 | 10.2 | 10.3 |
| 12.02 | 1.5 | 16.4 | 3.3 |

As can be seen from Table 3 and Figure 7, the $H_2S$ half-life versus [DO/$H_2S$] concentration ratio reveal a non-linear regression. The log transformed half-life and [DO/$H_2S$] ratio showed a significant regression ($P < 0.05$, $y = -0.54x + 1.16$, $R^2 = 0.9687$). Figure 7 shows the $H_2S$ half-life plotted against the molarity ratio of [DO/$H_2S$] in a log-log plot. The relationship between the [DO/$H_2S$] versus $H_2S$ half-life resembles an inverse relationship, where decomposition of $H_2S$ is very much dependent on the presence of dissolved oxygen in the seawater. Based on Figure 7, when [DO/$H_2S$] concentration ratio is lower than 0.07, the $H_2S$ half-life will extend beyond hour. When the [DO/$H_2S$] ratio is higher than 1.1, the $H_2S$ half-life will fall within 10 minutes.

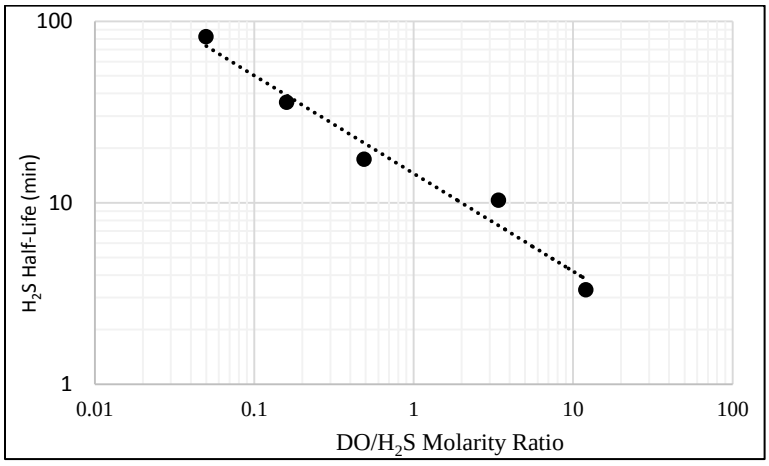



Figure 7. Hydrogen sulfide half-life versus the molarity ratio of [DO/$H_2S$] in a log-log plot

Table 4 shows a compilation of $H_2S$ half-life reported in various reports. The $H_2S$ half-life reported ranged from 17 minutes up to 55 days. Our current finding is consistent with the previous reports which reported that oxidation of $H_2S$ resembles a first order reaction in seawater when the dissolved oxygen is high and unlimited and becomes a second order reaction when dissolved oxygen is depleting [7, 8]. Nevertheless, both group of researchers reported that oxidation of $H_2S$ in seawater involved a series of complicated processes that are dependent on the composition and conditions of seawater. Different seawater conditions; which include physical, chemical and biological parameters is interacting and will influent $H_2S$ breakdown in the seawater.

Pos et al. [18] reported $H_2S$ in seawater subjects to photo-oxidation that had a half-life of 45 ± 15 minutes in Biscayne Bay water and 147 ± 15 minutes in the Gulf stream while Heitmann and Blodau [19] reported oxidation and incorporation of $H_2S$ by dissolved organic matter in seawater. Luther et al. [20] reported a complicated inorganic and biological mediated processes in the fate of $H_2S$ in the seawater environment. To the best of our survey, we have not encounter any comprehensive report that reveals the total interaction of physical, chemical and

biological factors into the $H_2S$ breakdown in seawater and the complicated interaction is probably the reasons that lead to various $H_2S$ half-life reported in the seawater.

Table 4. $H_2S$ breakdown half-life reported in seawater

| **Medium** | **Experimental Conditions** | **Half-Life** | **References** |
|---|---|---|---|
| Seawater | Temperature = 28 °C<br>Salinity = 30 ppt<br>Hydrogen sulfide = 1.5 – 114 mg $L^{-1}$<br>DO = 5 – 16.4 mg $L^{-1}$ | 3.3 – 82.1 min | Present study |
| Seawater | Temperature = 9.8 °C<br>Salinity = 30.27 ppt<br>Total sulfide = 2.0 mg $L^{-1}$<br>DO = DO: Total sulfide ratio from 8 - 2<br>pH = 9.6 | 6-28 h | [7] |
| Seawater | Temperature = 25 °C<br>Salinity = 35 ppt<br>$H_2S$ = 0.85 mg $L^{-1}$<br>pH = 8.0 | 26 h | [8] |
| Seawater | Temperature = 25 °C<br>Salinity = Not reported<br>$H_2S$ = Not reported<br>DO = 3.8 ml/l<br>pH = Not reported | 17 min | [10] |
| Seawater | Temperature = Not reported<br>Salinity = 30 ppt<br>$H_2S$ = 20 mg $L^{-1}$<br>DO = Not reported<br>pH = Not reported | 45 min | [11] |
| NaCl solution | Temperature = 25 °C<br>Salinity = Not reported<br>$H_2S$ = Not specified<br>DO = Saturation<br>pH = 12 | 55 day | [20] |
| Artificial seawater | Temperature = Not reported<br>Salinity = 16.5 ppt<br>$H_2S$ = 25 mg $L^{-1}$<br>DO = Not reported<br>pH = Not reported | 57 min | [21] |
| Seawater | Not reported | 2 – 5 h | [22] |
| Seawater | Temperature = Not reported<br>Salinity = Not reported<br>$H_2S$ = 513 µg $L^{-1}$<br>DO = Not reported<br>pH = 9.6 | 30 min | [23] |

## Conclusion

Hydrogen sulfide ($H_2S$) breakdown in seawater is highly dependent on the concentration of dissolved $H_2S$ and the concentration of dissolved oxygen (DO). The rate of $H_2S$ breakdown can be generally estimated based on the molarity ratio of [DO/$H_2S$]. At high [DO/$H_2S$] ratio (> 1), the $H_2S$ breakdown rate can be rapid, resulting in short half-life of $H_2S$ dissociation (within 10 minutes). Under this circumstance where the dissolved oxygen is not a limiting factor in the $H_2S$ oxidation, the breakdown rate appears as a first order reaction. However, when the ratio of [DO/$H_2S$] ratio is lower than 0.07, the breakdown rate became slower, resulting in longer half-life of $H_2S$ breakdown (more than an hour's). In this case, the breakdown rate displays a second order reaction form, which concurred with reports from other investigators. This study also investigated relation between the dissolved $H_2S$ content and pH changes in the seawater. The pH of seawater became lowered with increasing initial $H_2S$ concentration in the seawater. It reached an asymptotic low value of about 4 as the dissolved $H_2S$ content approaches its saturation limit in the seawater at about 2,500 mg $L^{-1}$.

## Acknowledgement

The authors would like to thank Sapura Kencana Energy Inc. for supporting the study.

## References

1. Karl, D. M. (1995). The microbiology of deep sea thermal vents. CRC Press, New York, pp. 299.
2. Ellis, A. J. and Golding, R. M. (1959). Spectrophotometric determination of the acid dissociation constants of hydrogen sulphide. *Journal of the Chemical Society*, 1959: 127 – 130.
3. Savenko, V. S. (1977). The dissociation of hydrogen sulfide in seawater. *Oceanology*, 16: 347 – 350.
4. Barbero, J. A., McCurdy, K. G. and Tremaine, P. R. (1982). Apparent molal heat capacities and volumes of aqueous hydrogen sulfide and sodium hydrogen sulfide near 25°C: The temperature dependence of $H_2S$ ionization. *Canadian Journal of Chemistry*, 60(14): 1872 – 1880.
5. Millero, F. J., Plese, T. and Fernandez, M. (1988). The dissociation of hydrogen sulfide in seawater. *Limnology and Oceanography*, 33(2): 269 – 274.
6. Zavodnov, S. S., and Kryukov, P. A. (1960). The value of the second dissociation constant of hydrogen sulfide. *Bulletin of the Academy of Sciences of the USSR, Division of Chemical Science*, 9(9): 1583 –1585.
7. Cline, I. D. and Richards, F. A. (1969). Oxygenation of hydrogen sulfide in seawater at constant salinity, temperature and pH. *Environmental Science and Technology*, 3(9): 838 – 843.
8. Millero, F. J., Hubinger, S., Fernandez, M. and Garnett, S. (1987). Oxidation of $H_2S$ in seawater as a function of temperature, pH, and ionic strength. *Environmental Science and Technology*, 21(5): 439 –443.
9. Chen, K. Y. and J. C. Morris. (1972). Kinetics of oxidation of aqueous sulphide by $O_2$. *Environmental Science and Technology*, 6(6): 529 – 537.
10. Göte, H. Ö. and Alexander, J. (1963). Oxidation rate of sulfide in seawater, a preliminary study. *Journal of Geophysical Research*, 68(13): 3995 – 3997.
11. Sharma, K. R. and Yuan, Z. (2010). Kinetics of chemical sulfide oxidation under high dissolved oxygen levels. *Proceedings of 6th International Conference of Sewer Processes and Networks*: 1 – 3.
12. Asaoka S., Yamamoto, T., Takahashi, Y., Yamamoto, H., Kim, K. H. and Orimoto, K. (2012). Development of an on-site simplified determination method for hydrogen sulfide in marine sediment pore water using a shipboard ion electrode with consideration of hydrogen sulfide oxidation rate. *Interdisciplinary Studies on Environmental Chemistry - Environmental Pollution and Ecotoxicology*, 6: 345 – 352.
13. Baumgartner, L. K., Reid, R. P., Dupraz, C., Decho, A. W., Buckley, D. H., Spear, J. R., Przekop, K. M. and Visscher, P. T. (2006). Sulfate reducing bacteria in microbial mats: changing paradigms, new discoveries. *Sedimentary Geology*, 185: 131 – 145.
14. Poulton, S. W., Krom, M. D., Raiswell, R. and Raiswell, R. (2004). A revised scheme for the reactivity of iron (oxyhydr)oxide minerals towards dissolved sulfide. *Geochimica et Cosmochimica Acta*, 68: 3703 – 3715.
15. Yao, W., and Millero, F. J. (1996). Oxidation of hydrogen sulfide by hydrous Fe(III) oxides in seawater. *Marine Chemistry*, 52: 1 – 16.
16. American Public Health Association (2005). Standard methods for examination of water and wastewater, American Public Health Association, W.W.A, Washington, D.C.

17. Han, K., Chu, T., Hirst, J., Smith, I. W. M., Canneaux, S., Kim, Y., Calvo, F., de la Lande, A. Skodje, R. T., Kawai, S., Petters, B., Kapral, R., Kim, H. J., Zhao, Y., Yan, Y., Zhang J., Swiatla-Wojcik, D., Bertrand, P., Varandas, A. J. S., Borgis, D., Senthilkumar, K., Hase, W. L. and Gao, J. (2013). Reaction rate constant computations: Theories and applications. *Royal Society of Chemistry*, London pp. 572.
18. Pos, W. H., Milne, P. J., Riemer, D. D. and Zika, R. G. (1997), Photoinduced oxidation of $H_2S$ species: A sink for sulfide in seawater, *Journal of Geophysical Research*, 102(11): 12831 – 12837.
19. Heitmann, T., and Blodau, C. (2006). Oxidation and incorporation of hydrogen sulfide by dissolved organic matter. *Chemical Geology*, 235(1): 12 – 20.
20. Luther, G. W., Findlay, A. J., MacDonald, D. J., Owings, S. M., Hanson, T. E., Beinart, R. A., and Girguis, P. R. (2011). Thermodynamics and kinetics of sulfide oxidation by oxygen: A look at inorganically controlled reactions and biologically mediated processes in the environment. *Frontiers in Microbiology*, 2(62): 1 – 9.
21. Dermendzhieva N., Razkazova-Velkova E., Martinov M., Ljutzkanov L. and Beschkov V. (2013). Oxidation of sulfide ions in model solutions of seawater using of metal catalysts built in carbon matrix. *Journal of Chemical Technology and Metallurgy*, 48(5): 465 – 468.
22. Almgren T., Dyrssen D., Elgquist B. and Johansson H. (1976). Dissociation of hydrogen sulfide in seawater and comparison of pH scale. *Marine chemistry*, 4: 289 – 297.
23. Aumond V., Waeles M., Salaün P., Gibbon-Walsh K., van den Berg C. M. G., Sarradin P. and Riso R. D. (2012). Sulfide determination in hydrothermal seawater samples using a vibrating gold micro-wire electrode in conjunction with stripping chronopotentiometry. *Analytica Chimica Acta*, 753: 42 – 47.

*Malaysian Journal of Analytical Sciences, Vol 21 No 5 (2017): 1028 - 1035*
*DOI: https://doi.org/10.17576/mjas-2017-2105-04*

MALAYSIAN JOURNAL OF ANALYTICAL SCIENCES
*Published by The Malaysian Analytical Sciences Society*
ISSN 1394 - 2506

# ANTI-PROLIFERATIVE EFFECT OF *Aerva javanica* EXTRACTS ON MCF7 AND MDA-MB-231 BREAST CANCER CELL LINES

## (Kesan Anti-proliferatif Ekstrak *Aerva Javanica* Ke Atas Titisan Sel Kanser Payudara MCF7 dan MDA-MB-231)

Nagla Mustafa Eltayeb[1, 2], Ghada Mustafa Eltayeb[3], Salizawati Muhamad Salhimi[1]*

[1]*School of Pharmaceutical Sciences,*
*Universiti Sains Malaysia, 11800 USM, Penang, Malaysia*
[2]*Tropical Medicine Research Institute (TMRI),*
*National Centre for Research (NCR), Khartoum, Sudan*
[3]*Faculty of Clinical and Industrial Pharmacy,*
*National University-Sudan, Khartoum 11111, Sudan*

**Corresponding author: saliza@usm.my*

Received: 16 August 2016; Accepted: 25 July 2017

**Abstract**

In this study, the medicinal plant *Aerva javanica* was sequentially extracted with n-hexane, chloroform and 80% methanol using maceration technique. The anti-proliferative effect of the three extracts was assessed on two different breast cancer cell lines, MDA-MB-231 and MCF7, using MTT assay. 1, 1-diphenyl-2-picryl-hydrazyl (DPPH) scavenging activity assay was used to assess the antioxidant activity of the three extracts. The result showed that the chloroform extract exerted an inhibitory effect in a concentration dependent manner on both cancer cell lines with $IC_{50}$ values of 32.7 ± 0.7 µg/ml and 40.9 ± 2 µg/ml on MDA-MD-321 and MCF7 respectively. 80% methanol extract exhibited cytotoxic effect on MCF7 with $IC_{50}$ value of 96.6 ± 2.9 µg/ml, whereas had no cytotoxic effect on MDA-MB-231 cell line ($IC_{50}$ > 200 µg/ml). n-hexane extract found to be less cytotoxic against both cancer cell lines with $IC_{50}$ values of 178.3 ± 3.7 and 196.9 ± 2.8 µg/ml on MDA-MB-231 and MCF7, respectively. The highest $IC_{50}$ value for scavenging activity was shown by 80% methanol extract (46.5 ± 2.2 µg/ml) followed by chloroform extract (78.3 ± 3.6 µg/ml). On the other hand, the extract prepared in n-hexane showed no scavenging activity effect ($IC_{50}$ > 1000 µg/ml). *Aerva javanica* possesses moderate anti-proliferative activity against human breast cancer cell lines with some cytoselectivity towards MDA-MB-231 compare to MCF7 cells. Further studies are needed to identify the potential anticancer component (s) from *Aerva javanica*.

**Keywords**: MTT assay, *Aerva javanica*, MCF7, MDA-MB-231

**Abstrak**

Dalam kajian ini, tumbuhan ubatan *Aerva javanica* telah diekstrak secara berturutan dengan n-heksana, kloroform dan 80% metanol menggunakan teknik pemaseratan. Kesan anti-proliferatif daripada tiga ekstrak dinilai pada dua titisan sel kanser payudara yang berbeza iaitu MDA-MB-231 dan MCF7, menggunakan ujian MTT. Ujian aktiviti hapus sisa DPPH telah digunakan untuk menilai aktiviti antioksidan daripada tiga ekstrak. Keputusan menunjukkan bahawa ekstrak kloroform memberikan kesan perencatan bergantung kepekatan ke atas kedua-dua jenis sel kanser dengan nilai-nilai $IC_{50}$ 32.7 ± 0.7 µg/ml dan 40.9 ± 2 µg/ml pada MDA-MD-321 dan MCF7 masing-masing. Ekstrak 80% metanol menunjukkan kesan sitotoksik ke atas MCF7 dengan nilai $IC_{50}$ 96.6 ± 2.9 µg/ml, tetapi tidak memberikan kesan sitotoksik ke atas MDA-MB-231 ($IC_{50}$ > 200 µg/ml). Ekstrak n-heksana didapati kurang sitotoksik terhadap kedua-dua titisan sel kanser dengan nilai-nilai $IC_{50}$ 178.3 ± 3.7 dan 196.9 ± 2.8 µg/ml masing-masing ke atas MDA-MB-231 dan MCF7. Aktiviti hapus sisa yang tertinggi ditunjukkan oleh ekstrak 80% metanol ($IC_{50}$ 46.5 ± 2.2 µg/ml ) diikuti dengan ekstrak kloroform ($IC_{50}$ 78.3 ± 3.6 µg/ml). Berbeza dengan ekstrak n-heksana yang tidak menunjukkan kesan aktiviti hapus sisa ($IC_{50}$ > 1000 µg/ml). *Aerva javanica* mempunyai aktiviti anti-proliferatif

sederhana terhadap titisan sel kanser payudara manusia dan lebih selektif terhadap sel-sel MDA-MB-231 berbanding MCF7. Kajian lanjut diperlukan untuk nengenalpasti komponen yang berpotensi sebagai anti-kanser daripada *Aerva javanica*.

**Kata kunci**: Ujian MTT, *Aerva javanica*, MCF7, MDA-MB-23

## Introduction

Breast cancer is the most common type of cancer and the main cause of cancer death among women in both developed and developing countries. It accounts for 25% of all cancer diagnosed cases and 15% of all cancer female deaths [1]. New advances in research have produced medications for treating different stages of breast cancer. These chemically synthesized agents while being effective, often have some major side effects such as loss of appetite, muscle and joint pain, weakness, dizziness, vaginal bleeding, hair thinning and weight loss. The huge demand for herbal medicines is due to their wide biological activities, higher safety and lower costs [2]. Plants have shown an important role in the development of cancer therapy. Vincristine and vinblastine from *Catharanthus roseus* and paclitaxel from the bark of the Pacific yew tree, *Taxus brevifolia* are well known examples of plant-based anti-cancer drugs [3]. Investigating medicinal plants to explore traditional medicines could lead to the development of novel drugs.

*Aerva javanica* is a medicinal plant belongs to Amaranthaceae family [4]. It is a perennial herb extensively found in various regions of the tropical world. It is native to Africa, but can also be found in some Asian countries [5]. In Sudan, *A. javanica* plant or *Ras Elshaieb* as locally known has been used in traditional medicine in different parts of the country. In North Kordofan Province the plant is used for treating ulcers, wounds, abdominal pain and as anti-plasmodial. In the White Nile province, the plant is used against snake bites, breast cancer and rheumatism [6].

Phytochemical analysis studies of *A. javanica* revealed the presence of different important phytochemical constituents which include flavonoids, alkaloids, triterpenes anthraquinones, coumarins, diterpenes, triterpenes, sterol, saponins, carbohydrates, tannins and polyphenols [7, 8, 9].

In Sudan, *A. javanica,* is considered as an important traditional medicinal plant and has been used for treating various diseases, including cancer; however, its anti-cancer properties have not been investigated yet. The main objective of this study was to screen three *A. javanica* extracts for their cytotoxic effects on MCF7 (estrogen-receptor positive) and MDA-MB-231 (estrogen- receptor negative) breast cancer cell lines and to assess the antioxidant activities of the different extracts.

## Materials and Methods

### Reagents and chemicals

Dulbecco's modified eagle medium (DMEM), fetal bovine serum (FBS), penicillin/streptomycin and trypsin-EDTA were purchased from Gibco, USA. 3-(4,5-Dimethylthiazol-2-yl)- 2,5diphenyl tetrazolium bromide (MTT) reagent, phosphate buffered saline tablets, dimethyl sulfoxide (DMSO) and 1,1-diphenyl-2-picryl-hydrazyl (DPPH) were obtained from Sigma-Aldrich, Germany.

### Plant sample collection and identification

The whole plant of *Aerva javanica* was collected from Nile river banks, state of Khartoum, Sudan, in November 2015. The plant was authenticated by the plant taxonomist Yahya Suliman Mohamed and voucher specimen was deposited in the herbarium of Medicinal and Aromatic Plants Research Institute (MAPRI) – National Center for Research, Khartoum, Sudan.

### Plant extraction

The whole plant was dried under shade for two weeks and then was grounded to make a fine powder. Powdered whole plant (500 g) was macerated sequentially with n-hexane, chloroform and 80% methanol for 3 days at 50 °C. The ratio of raw material to solvent was 1:10. The extracts were filtered through Whatmann No. 1 filter paper and concentrated using rotary evaporator at 50 °C, and then all the extracts were put in oven at 50 °C until complete dryness. The stock solutions of the extract were prepared at 10 mg/ml and kept at 4 °C until use.

**Cell culture**
Human breast adenocarcinoma cell lines MCF7 and MDA-MB-231 were originally obtained from American Type Culture Collection (ATCC, Rockville, MD, USA). MCF7 and MDA-MB-231 cells were grown in DMEM supplemented with 10% fetal bovine serum and 1% penicillin/streptomycin. All cell lines were incubated in a humidified incubator at 37 °C under an atmosphere containing 5% $CO_2$. The cells were sub cultured when nearly confluent using 0.25% trypsin-EDTA.

**Cell viability assay**
Cell viability and proliferation were assessed by MTT (3-[4,5-dimethylthiazol-2-yl]-2,5 diphenyltetrazolium bromide) dye reduction assay. In brief, the cells were seeded in a 96-well plate ($3 \times 10^3$ cell/well for MCF7 and $5 \times 10^3$ cell/well for MDA-MB-231) and treated with different concentrations of the extracts (6.25 – 200 µg/ml) for 48 hours. MTT solution (5 mg/ml in PBS) was added (20 µl/well) and incubated for 3 hours. The formazan crystals formed by the viable cells were dissolved by adding 200 µl/well DMSO. Optical density was measured at 570 nm wavelength (reference filter 630 nm) using an ELISA plate reader (TECAN, sunrise). Cell survival rates were expressed as the percentage of untreated controls, and the 50% inhibitory concentrations ($IC_{50}$) of the extracts were calculated.

**1, 1-diphenyl-2-picryl-hydrazyl (DPPH) free radical analysis**
1,1-diphenyl-2-picrylhydrazyl (DPPH) assay was carried out to evaluate the scavenging activity of the extracts. The stock solution of DPPH was prepared at a concentration of 200 µM in absolute methanol while stock solutions of the extracts were prepared at a concentration of 10 mg/ml. 100 µl of DPPH was dispensed in 96-well plate and immediately, 100 µl of samples were added at final concentrations of 12.5, 25, 50, 100, 200 and 400 µg/ml. Ascorbic acid was used as positive control. Methanol alone and methanol with DPPH were used as blank and negative control, respectively. The mixtures were incubated for 30 minutes in the dark and then the absorbance was measured at 517 nm using TECAN microplate reader (Tecan sunrise). The dose response curves were obtained and then used to calculate the median inhibitory concentration ($IC_{50}$). The results were expressed as mean ± SEM (n = 6).

**Statistical analysis**
All of the cytotoxic and antioxidant experiments in the study were carried out for at least three times in triplicate and results were expressed as mean ± standard deviation (SD). One-way analysis of variance (ANOVA) and Dunnet's Multiple Comparison Test were used to assess $IC_{50}$ values and cytotoxicity data. $P < 0.05$ was considered as statistically significant.

## Results and Discussion

**Extraction**
Extraction efficiencies (% yield) of the three solvents, n-hexane, chloroform and 80% methanol showed significant differences ($P < 0.05$). The maximum extraction yield was shown by 80% methanol (2.8 %) followed by n-hexane (1.1 %) and chloroform (0.6%). Figure 1 shows the extraction yields of the different solvents.

**(4,5-dimethylthiazole-2-yl)-2,5-diphenyl tetrazolium bromide (MTT) assay**
The three extracts exhibited variations in their cytotoxic effect on the two examined breast cancer cell lines with different $IC_{50}$ values. The chloroform extract showed the lowest $IC_{50}$ values of 32.7 ± 0.7 and 40.9 ± 2 µg/ml on MDA-MB-231 and MCF7, respectively. 80% methanol extract exhibited cytotoxic effect on MCF7 with $IC_{50}$ value of 96.6 ± 2.9 µg/ml, while had no cytotoxic effect on MDA-MB-231 cell line ($IC_{50}$ > 200 µg/ml). The n-hexane extract showed high $IC_{50}$ concentrations for both cancer cell lines (Table 1).

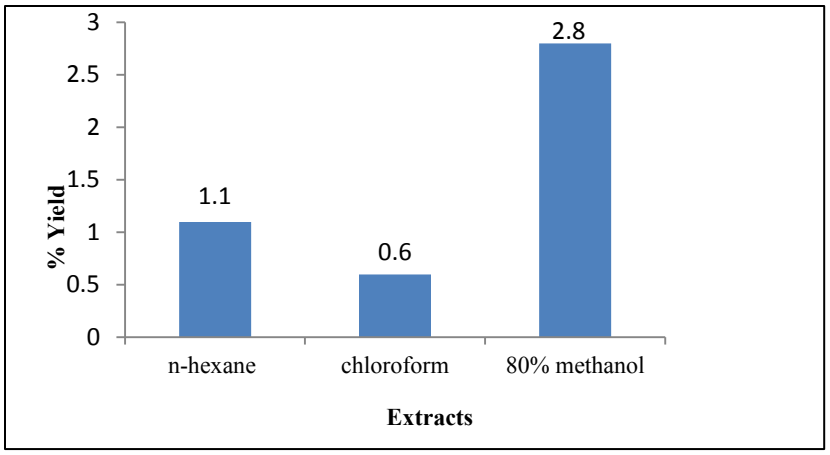



Figure 1. Extraction yields of *Aerva javanica* using the three different solvents

Table 1. $IC_{50}$ (µg/ml) values of the three extracts against the two cancer cell lines

| Extracts | IC $_{50}$ value (µg/ml) | |
|---|---|---|
| | MCF7 | MDA-MB-231 |
| n-Hexane | 196.9 ± 2.8 | 178.3 ± 3.7 |
| Chloroform | 40.9 ± 2.3 | 32.7 ± 0.7 |
| 80% Methanol | 96.6 ± 2.9 | > 200 |

The results are presented as mean ± SEM. Each experiment was repeated three times; (n =3)

The chloroform extract exerted moderate cytotoxic activity in a concentration dependent manner on both cancer cell lines MDA-MB-231 and MCF7 cell line (Figure 2). Unexpectedly, the cytotoxic effect of the extract was more potent in the highly invasive breast cancer cell line; MDA-MB-231.

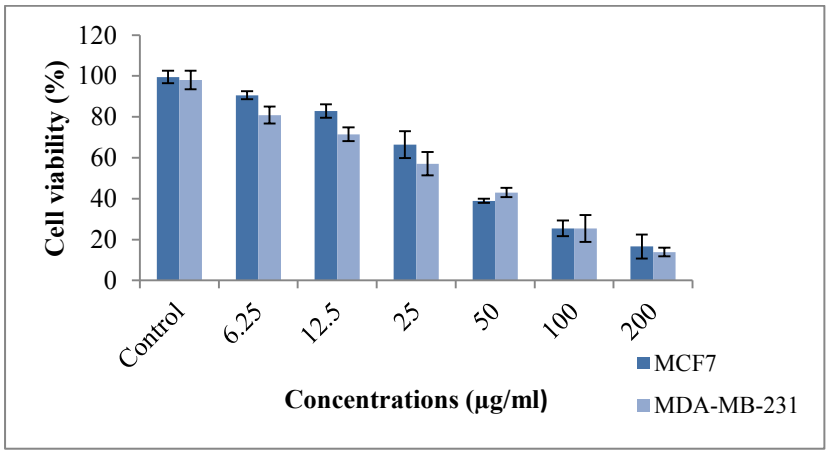
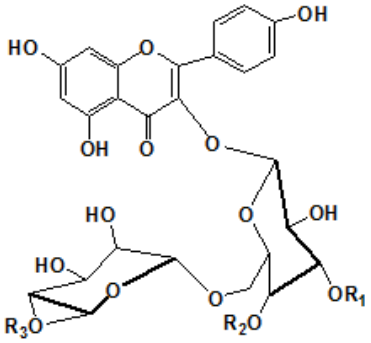



Figure 2. Effect of *A. javanica* chloroform extract on MDA-MB-231 and MCF7 cell viability. The cells were treated with different concentrations and DMSO as a control for 48 h and the cell viability was tested using MTT assay

The pharmacological effects of medicinal plants can be attributed to their main constituents such as alkaloids, flavonoids, coumarins, lignans, saponins and saccharides. Flavonoids are considered as an important phytochemical, with various anti-cancer activities. It has been reported that many flavonoids significantly decrease cancer cell viability via the upregulation of caspase activity [10]. The flavonols, kaempferols and kaempferol glycosides are found in a variety of plants and plant-derived foods [11, 12, 13]. Several reports have shown that kaempferol and/or some kaempferol glycosides induce cell death in a variety of cancer cells from different tissues, including human leukemia cell lines [14] and breast cancer cell lines [15 – 18]. Many flavonol glycosides have been isolated from *A. javanica* as major phytoconstituents [9].

Recently, three kaempferol glycosides have been isolated from *A. javanica* flowers, namely, kaempferol-3-O-b-D-[4000-E-p-coumaroyl-a-L-rhamnosyl(1→6)]-galactoside (1), kaempferol-3-O-b-D-[4000-E-p-coumaroyl-a-L-rhamnosyl(1→6)]-(300-E-p-coumaroyl)-galactoside (2), and kaempferol-3-O-b-D-[4000-E-p-coumaroyl-a-L-rhamnosyl(1→6)]-(400-E-p-coumaroyl)- galactoside (3) [19]. Figure 3 shows the structure of the three acylated flavonoid glycoside compounds isolated from *A. javanica*.




1: R1 = R2 = H, R3 = *E*-*p*-coumaroyl
2: R1 = *E*-*p*-coumaroyl, R2 = H, R3 = *E*-*p*-coumaroyl
3: R1 = H, R2 = R3 = *E*-*p*-coumaroyl

Figure 3. Structure of the three acylated flavonoid glycoside compounds isolated from *A. javanica*

Coumarins are an important medicinal phytochemicals present in different medicinal plants. Coumarins have a wide range of biological activities including anticancer properties [20]. Both natural and synthetic coumarins exhibited potent anticancer activity against various types of cancer, including breast cancer with low toxicity and good selectivity [20]. Figure 4 shows the coumarin structure. Previous study revealed the presence of coumarins in *A. javanica* chloroform fraction; however, no coumarin compounds have been isolated from the plant yet [8].

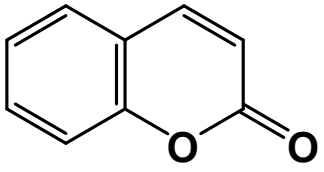



Figure 4. The structure of coumarin

The anti-proliferative effect exhibited by the chloroform extract in this study could be due to the presence of one or both of these important phytochemicals. Further studies are needed to identify the bioactive compounds that present in *A. javanica* chloroform extract and to elucidate the mechanism of action for these compounds. Our results showed that *A. javanica* chloroform extract was more cytotoxic to MDA-MB-231 than MCF7 cell line. The

differences in susceptibility of different tumor cell lines have been shown by several research groups [21, 22, 23]. The differential response of these two cancer cell lines could be due to the differences in their signaling pathway responsible for the cytotoxic effect [23]. It should be noted that the MDA-MB-231 cell line does not express the estrogen receptor [24] and the fact that the extract showed cytotoxic effect on this cell line indicates that estrogen-receptor signaling pathway is not required in its mode of action. This is very interesting since many conventional drugs that are used in the treatment of breast cancer, such as tamoxifen, raloxifene and toremifene require estrogen-receptor to exert their cytotoxic effect [25]. Furthermore, the response of estrogen-receptor negative subtype of breast cancer to conventional drugs is very poor [24, 26]. The possible molecular mechanisms underlying the differential responses of MCF-7 and MDA-MB-231 cells to the cytotoxic effects of *A. javanica* need to be further investigated.

**Antioxidant activity**

The results obtained from DPPH free radical scavenging activity assay in this study showed that the 80% methanol extract demonstrated the most potent antioxidant activity (46.5 ± 3 µg/ml) followed by chloroform extract (78.3 ± 4 µg/ml), whereas the extract prepared from n-hexane showed poor DPPH scavenging activity as the $IC_{50}$ value estimated to be more than 1000 µg/ml (Table 2).

Table 2. $IC_{50}$ values of the three extracts of *Aerva javanica* evaluated for DPPH scavenging activity

| Extract | DPPH ($IC_{50}$ µg/ml) |
|---|---|
| n-Hexane | > 1000 |
| Chloroform | 78.3 ± 3.6 |
| 80% Methanol | 46.5 ± 2.2 |
| Ascorbic acid | 3.3 ± 3.9 |

The 80% methanol extract contains significantly high free radical scavenging activity. Thus, it was found that free radical scavenging activity increased with the increase of the solvent polarity. This observation strongly supports previous results [27] as the methanol extract contains the highest amount of phenolic compounds. Phenolic compounds are known to be powerful antioxidants; they possess scavenging ability due to their hydroxyl groups [28]. So, in the present study, the antioxidant activity of the hydroalchoholic extract was possibly due to its high phenolic content.

## Conclusion

The result of the present study concludes that *Aerva javanica* shows moderate cytotoxic effect on two different breast cancer cell lines with some cytoselectivity towards MDA-MB-231 compare to MCF7 breast cancer cell line. The plant also exerts moderate free radical scavenging activity. Further studies are needed to identify the potential anticancer component(s) from this medicinal plant and to determine the mechanism(s) of action underlying its cytotoxicity.

## Acknowledgement

We wish to acknowledge Universiti Sains Malaysia (USM) and The World Academy of Sciences (TWAS) for TWAS-USM Postgraduate Fellowship (FR number 3240275091) and financial support to Nagla. Authors also wish to acknowledge Universiti Sains Malaysia for the financial support for this project through RUI grant (1001/PFARMASI/8011003).

## References

1. Torre, L. A., Bray, F., Siegel, R. L., Ferlay, J., Lortet-Tieulent, J. and Jemal, A. (2015). Global cancer statistics, 2012. CA: *A cancer journal for clinicians*, 65(2): 87 – 108.
2. Khan, M. K., Ansari, I. A. and Khan, M. S. (2013). Dietary phytochemicals as potent chemotherapeutic agents against breast cancer: Inhibition of NF-κB pathway via molecular interactions in rel homology domain of its precursor protein p105. *Pharmacognosy Magazine*, 9 (33): 51 – 57.

3. Cragg, G. M. and Newman, D. J. (2005). Plants as a source of anti-cancer agents. *Journal of Ethnopharmacology*, 100(1): 72 – 79.
4. Khan, M. A., Khan, M. A., Hussain, M. and Mujtaba, G. (2012). Medicinal plants used in folk recipes by the inhabitants of Himalayan region Poonch Valley Azad Kashmir (Pakistan). *Journal of Basic and Applied Sciences*, 8: 35 – 45.
5. Judd, W. S., Campbell, C. S., Kellogg, E. A., Stevens, P. F. and Donoghue, M. J. (1999). Plant systematics: A phylogenetic approach. *Ecologia Mediterranea*, 25(2): 215.
6. Elsaeed, A., Mohamed, O. S. A. and Ahmed, R., H. (2015). Anti-Inflammatory effects of *Aerva Javanica* (Burm.f.) Schult. against carrageenan induced paw oedema in albino rats. *Journal of forest products & Industries*, 4(1): 17 – 20.
7. Radwan, H. M, Nazif, N. M. and Hamdy, A. A. (1999). The lipid and flavonoidal constituents of *Aerva javanica* (var.bovi) Webb in Hook. F and their antimicrobial activity. *Egyptian Journal of Pharmaceutical Sciences*, 40: 167 – 178.
8. Abbas, N. O., Ahmed El Imam, Y. M. and Abdelmageed, M. A. M. (2014). The Phytochemical analysis of the ethanolic extract of Sudanese *Aerva javanica* (Burm.f.) juss. *World Journal of Pharmaceutical Research*, 4 (6): 2253 – 2263.
9. Chawla, P., Chawla, A. M. I. T., Vasudeva, N. E. E. R. U. and Sharma, S. K. (2012). A review of chemistry and biological activities of the genus Aerva–a desert plant. *Acta Poloniae Pharmaceutica*, 69: 171 – 177.
10. Sepehr, M. F., Jameie, S. B. and Hajijafari, B. (2011). The *Cuscuta kotschyana* effects on breast cancer cells line MCF7. *Journal of Medicinal Plants Researc*h, 5 (27): 6344 – 6351.
11. Chen, A. Y. and Chen, Y. C. (2013). A review of the dietary flavonoid, kaempferol on human health and cancer chemoprevention. *Food Chemistry*, 138(4): 2099 – 2107.
12. Liu, R. H. (2013). Health-promoting components of fruits and vegetables in the diet. *Advances in Nutrition: An International Review Journal*, 4(3): 384 – 392.
13. Kim, S. H. and Choi, K. C. (2013). Anti-cancer effect and underlying mechanism(s) of kaempferol, a phytoestrogen, on the regulation of apoptosis in diverse cancer cell models. *Toxicological Research*, 29(4): 229 – 234.
14. Dimas, K., Demetzos, C., Mitaku, S., Marselos, M., Tzavaras, T. and Kokkinopoulos, D. (2000). Cytotoxic activity of kaempferol glycosides against human leukaemic cell lines in vitro. *Pharmacological Research*, 41(1): 83 – 86.
15. Kang, G. Y., Lee, E. R., Kim, J. H., Jung, J. W., Lim, J., Kim, S. K. and Kim, K. P. (2009). Downregulation of PLK-1 expression in kaempferol-induced apoptosis of MCF-7 cells. *European Journal of Pharmacology*, 611(1): 17 – 21.
16. Kim, B. W., Lee, E. R., Min, H. M., Jeong, H. S., Ahn, J. Y., Kim, J. H. and Cho, S. G. (2008). Sustained ERK activation is involved in the kaempferol-induced apoptosis of breast cancer cells and is more evident under 3-D culture condition. *Cancer Biology and Therapy*, 7(7): 1080 – 1089.
17. Oh, S. M., Kim, Y. P. and Chung, K. H. (2006). Biphasic effects of kaempferol on the estrogenicity in human breast cancer cells. *Archives of Pharmacal Research*, 29(5): 354 – 362.
18. Tomczyk, M., Drozdowska, D., Bielawska, A., Bielawski, K. and Gudej, J. (2008). Human DNA topoisomerase inhibitors from *Potentilla argentea* and their cytotoxic effect against MCF-7. *Die Pharmazie-An International Journal of Pharmaceutical Sciences*, 63(5): 389 – 393.
19. Mussadiq, S., Riaz, N., Saleem, M., Ashraf, M., Ismail, T. and Jabbar, A. (2013). New acylated flavonoid glycosides from flowers of *Aerva javanica*. *Journal of Asian Natural Products Research*, 15 (7): 708 – 716.
20. Klenkar, J. and Molnar, M. (2015). Natural and synthetic coumarins as potential anticancer agents. *Journal of Chemical and Pharmaceutical Research*, 7(7): 1223 – 1238.
21. Jafarian-Dehkordi, A., Emami, S. A., Saeidi, M. and Sadeghi, H. (2004). Cytotoxicologic studies of the extracts of Iranian *Juniperus sabina* and *Platycladus orientalis* on Cancer Cells. Journal of Research in Medicinal Sciences, 5: 205 – 209.
22. Monajemi, R., Oryan, S., Haeri-Roohani, A., Ghannadi, A. and Jafarian, A. (2005). Cytotoxic effects of essential oils of some Iranian Citrus peels. Iran Journal of Pharmaceutical Research, 3:183 – 187.
23. Jia, T., Zhang, L., Duan, Y., Zhang, M., Wang, G., Zhang, J. and Zhao, Z. (2014). The differential susceptibilities of MCF-7 and MDA-MB-231 cells to the cytotoxic effects of curcumin are associated with the PI3K/Akt-SKP2-Cip/Kips pathway. *Cancer cell international*, 14 (1): 126 – 140.

24. Brenton, J. D., Carey, L. A., Ahmed, A. A. and Caldas, C. (2005). Molecular classification and molecular forecasting of breast cancer: ready for clinical application? *Journal of Clinical Oncology*, 23 (29): 7350 – 7360.
25. Department of Health and Human Services. National Institutes of Health, National Cancer Institute, USA. (2012). Hormone therapy for breast cancer. https://cancer.gov/types/breast/breast-hormone-therapy-fact-sheet. [Access online on 20 January 2017].
26. Klinakis, A., Szabolcs, M., Chen, G., Xuan, S., Hibshoosh, H. and Efstratiadis, A. (2009). Igf1r as a therapeutic target in a mouse model of basal-like breast cancer. *Proceedings of the National Academy of Sciences*, 106(7): 2359 – 2364.
27. Munir, H. and Sarfraz, R. A. (2014). Medicinal attributes of *Aerva javanica* native to pothohar plateau. *Pakistan journal of life and social sciences*, 12(2): 80 – 86.
28. Kähkönen, M. P., Hopia, A. I., Vuorela, H. J., Rauha, J. P., Pihlaja, K., Kujala, T. S. and Heinonen, M. (1999). Antioxidant activity of plant extracts containing phenolic compounds. *Journal of Agricultural and Food Chemistry*, 47(10): 3954 – 3962.

*Malaysian Journal of Analytical Sciences, Vol 21 No 5 (2017): 1036 - 1044*
*DOI: https://doi.org/10.17576/mjas-2017-2105-05*

MALAYSIAN JOURNAL OF ANALYTICAL SCIENCES
*Published by The Malaysian Analytical Sciences Society*
ISSN 1394 - 2506

# SYNTHESIS, CRYSTAL STRUCTURE AND COORDINATION CHEMISTRY OF DI-2-PYRIDYLMETHANEAMINE-BASED CHELATING LIGANDS WITH CADMIUM SALTS

## (Sintesis, Struktur Hablur dan Kimia Koordinatan Ligan Pengkelat Berasaskan Di-2-Piridilmetanaamina dengan Garam Kadmium)

Maisara Abdul Kadir[1]* and Christopher James Sumby[2]

[1]*School of Fundamental Science,*
*Universiti Malaysia Terengganu, 21030 Kuala Nerus, Terengganu, Malaysia*
[2]*School of Physical Sciences, Centre for Advanced Nanomaterials,*
*The University of Adelaide, Adelaide, South Australia 5005, Australia*

**Corresponding author: maisara@umt.edu.my*

Received: 16 August 2016; Accepted: 17 July 2017

**Abstract**

Chelating ligands play a prominent role as organic linker in the construction of multinuclear complexes due to their strong binding to metal ions. Thus, in this study, two new bridging ligands with chelating arms, namely 1,3-*N,N'*-[bis(di(pyridin-2-yl)methyl)]isophthalamide (L1) and 1,4-*N,N'*-bis[(di(pyridin-2-yl)methyl)]terephthalamide (L2) were successfully synthesized and characterized using Fourier Transform Infrared (FTIR), $^{1}$H and $^{13}$C Nuclear Magnetic Resonances ($^{1}$H and $^{13}$C NMR) and X-ray crystallography. Reaction of L1 and L2 with metal salts gave two multinuclear cadmium complexes, with formula molecules $[\{CdCl_2(CH_3OH)(L1)CdCl_2\}_2]$ and $[(CdBr_2)_2(L_2)(CH_3OH)_2]$, respectively. X-ray crystallography reveals that ligands L1 and L2 used all four nitrogen donors from di-2-pyridylmethaneamine units to chelate with cadmium ions in forming stable multinuclear complexes. The complexes are also stabilized by supramolecular interactions such as hydrogen bonding and pi-pi stacking, as observed in the crystal packing.

**Keywords**: crystal, chelating ligands, synthesis, pi stacking, supramolecular

**Abstrak**

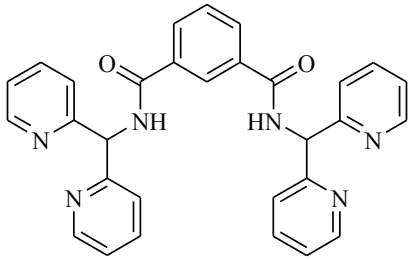
Ligan pengkelat memainkan peranan penting sebagai penghubung organik dalam pembentukan kompleks multinuklear kerana ikatan yang kuat terhadap ion logam. Oleh itu, dalam kajian ini, dua ligan penghubung baharu yang mempunyai kumpulan pengkelat, iaitu 1,3-*N,N'*-[bis(di(piyridin-2-il)metil)]isoptalamida (L1) dan 1,4-*N,N'*-bis[(di(piridin-2-il)metil)]tereptalamida (L2) telah berjaya disintesis dan dicirikan menggunakan analisis Inframerah Transformasi Fourier (FTIR), $^{1}$H dan $^{13}$C Resonan Magnetik Nuklear ($^{1}$H dan $^{13}$C RMN) dan kristalografi sinar-X. Kajian kimia koordinatan ligan L1 dan L2 dengan garam logam menghasilkan dua kompleks multinuklear kadmium dengan formula molekul masing-masing adalah $[\{CdCl_2(CH_3OH)(L1)CdCl_2\}_2]$ dan $[(CdBr_2)_2(L_2)(CH_3OH)_2]$. Kajian hablur kristalografi sinar-X menunjukkan bahawa ligan L1 dan L2 menggunakan empat atom penderma nitrogen dari di-2-piridilmetanaamina unit untuk berikatan pada ion kadmium dalam menghasilkan kompleks multinuklear yang lebih stabil. Kompleks ini turut distabilkan oleh interaksi supramolekul seperti ikatan hidrogen dan interaksi pertindihan pi-pi sebagaimana yang dilihat dalam padatan hablur.

**Kata kunci:** hablur, ligan pengkelat, sintesis, pertindihan pi, supramolekular

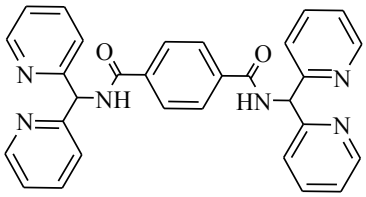
## Introduction

The use of bridging ligands that have the capacity to chelate each metal centre bridged by the ligand is important to improve the stability of multinuclear complexes or enhance metal–metal interactions [1-4]. Steel and co-workers for instance, have reported many complexes derived from the bridging ligands containing di-2-pyridyl chelating motifs such as di-2-pyridylamine (dpa) based bridging heterocyclic ligands with silver(I), copper(II) and palladium(II) [2-5]. On reaction with silver salts, the ligands act as divergent bridging unit, with only two of the four pyridine rings involved in the coordination to form 1-D coordination polymers. Conversely, on reaction with copper(II) and palladium(II), the ligand uses all four nitrogen donors to coordinate with the metal centres and form stable discrete dinuclear complexes [5]. Along with this interest, significant efforts have been paid to generate bridging ligands with flexible di-2-pyridyl chelating moieties [6-9]. The additional spacer at di-2-pyridyl chelating moieties is important not only to confer flexibility but also to minimise the potential for hydrolysis that plagues other related compounds described in the literature [2,4,5]. Also, by using flexible bridging ligands, a diverse range of complexes and crystal packing can be obtained.

Di-2-pyridylmethaneamine (dpma), is the example of flexible chelating ligand that consists of methylene spacer between di-2-pyridyl rings and amine. (Figure 1). Dpma compound has been studied by Trilla and co-workers in 2006 and has shown potential as recyclable catalyst in Suzuki cross coupling reactions [10]. Before that, it was synthesized and the coordination chemistry with ruthenium salts was investigated by Chang et al. [11]. However, it was a little surprise to discover that this chelating compound is less explored particularly as bridging ligands unit, and the reason behind this little attention was not mentioned in any reports. Therefore, in line with our interest to expand the repertoire of bridging ligands containing flexible pyridyl moieties available for studies [12-13] and to explore their coordination chemistry of the type of ligands, we have produced another two new doubly bidentate bridging ligands with dpma units appended to isophthalamide (L1) and terephthalamide (L2) core, as shown in Figure 1.




L1




L2

Figure 1. The structure of two new doubly bidentate bridging ligands L1 and L2 described in this study

Basically, di-2-pyridylmethane chelating unit can coordinate to metal centres through three coordination modes, which are chelating, monodentate or bridging. Between the three modes, predominant coordination mode of the di-2-pyridyl motif is to chelate to particular metal centre through the two nitrogen donor atoms (Figure 2). Therefore, this study is carried out to further investigate the chelating potential of the bridging ligands and identify the chelating modes preferred by compounds L1 and L2, respectively.

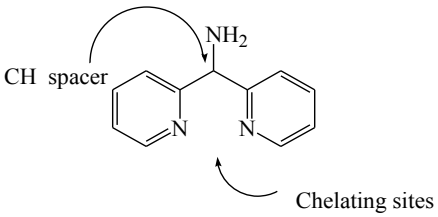



Figure 2. Molecular structure of di-2-pyridylmethaneamine (dpma) with CH spacer and metal ion chelating sites

## Materials and Methods

### Instrumentations

Elemental analyses were performed by the Campbell Microanalytical Laboratory at the University of Otago, Dunedin, New Zealand. Infrared spectra were collected on a Perkin Elmer Spectrum BX Infrared spectrometer as KBr disks. Nuclear Magnetic Resonances (NMR) spectra were recorded on Varian Gemini 300MHz NMR spectrometer at 23 ºC using a 5 mm probe. $^{1}$H NMR spectra recorded in deuterated chloroform ($CDCl_3$-$d_6$); $^{1}$H NMR spectra recorded in $CDCl_3$-$d_6$ which was referenced to the solvent peak: 7.24 ppm. $^{13}$C NMR spectra were all referenced to their solvent peaks: $CDCl_3$, 77.23 ppm. Electrospray (ES) mass spectra were recorded using a Finnigan LCQ mass spectrometer by preparing serial dilutions of a 1 mg/mL solution of the compound. Crystals were analyzed by single crystal X-ray crystallography using Oxford Diffraction X-calibur at 150(2) K.

### Syntheses of the ligands: 1,3-*N,N'*-[bis(di-(pyridin-2-yl)methyl)]isophthalamide (L1)

Isophthaloyl chloride (0.55 g, 2.8 mmol) was dissolved in dichloromethane (40 mL). Then, di-(2-pyridyl)methylamine (1.01 g, 5.5 mmol) and triethylamine (0.76 mL, 5.5 mmol) were added to the solution and heated at reflux for 72 hours. The solvent was removed in vacuo to give a brown solid which was collected, washed with diethyl ether, dried and recrystallized from ethanol to give **L1** as a light brown solid (0.90 g, 63%).

### 1,4-*N,N'*-bis[(di(pyridin-2-yl)methyl)]terephthalamide(L2)

Terephthaloyl chloride (0.30 g, 1.5 mmol) was dissolved in dichloromethane (40 mL). Then, di-(2-pyridyl)methylamine (0.55 g, 3.0 mmol) and triethylamine (0.41 mL, 3.0 mmol) were added to the solution and heated at reflux for 72 hours. The solvent was removed in vacuo to give a brown solid of **L2**. The solid was washed with diethyl ether, dried and recrystallized from ethanol to give **L2** as a fine brown solid (0.43 g, 57%).

### Syntheses of the cadmium complexes: [{$CdCl_2(CH_3OH)(L1)CdCl_2$}$_2$]

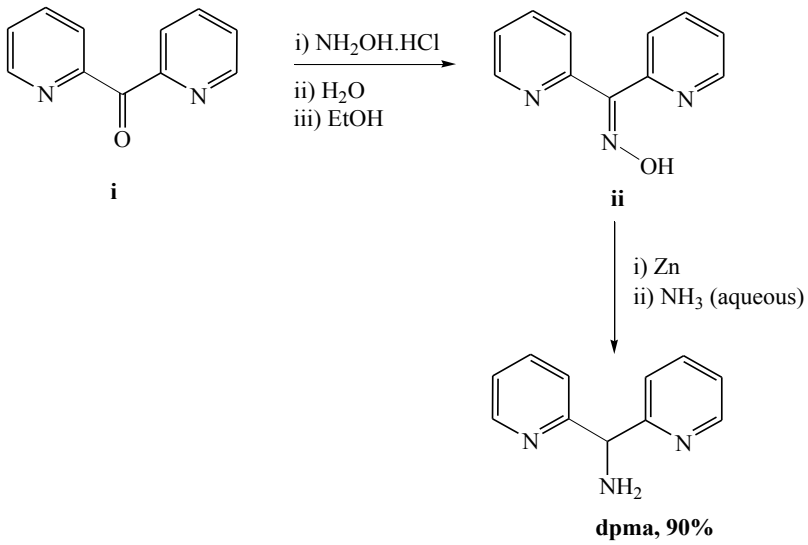
A solution of $CdCl_2$ (0.037 g, 0.20 mmol) was dissolved in methanol (5 mL), heated for 20 minutes, before being added dropwise to a solution of L1 (0.051 g, 0.10 mmol) which was dissolved in methanol (10 mL). The colourless solution was further heated for 45 minutes before being left to evaporate at room temperature. After three weeks, the solution afforded [{$CdCl_2(CH_3OH)(L1)CdCl_2$}$_2$] as colourless crystals in low yield (0.015 g, 16%).

### [$(CdBr_2)_2(L_2)(CH_3OH)_2$]

A solution of $CdBr_2$ (0.0195 g, 0.072 mmol) was dissolved in water (5 mL), heated for 20 minutes, before being added dropwise to a solution of L2 (0.0180 g, 0.036 mmol) in methanol-acetonitrile (15 mL). The colourless solution was heated for 45 minutes and left to evaporate at room temperature. After a week, the solution afforded [$(CdBr_2)_2(L2)(CH_3OH)_2$] as colourless crystals in good yield (0.012 g, 75%).

## Results and Discussion

Di-2-pyridylmethaneamine (dpma) was synthesized by using reductive amination methods which requires two steps of reactions as described in the literature procedures [14]. In the first step of the method, di-2-pyridyl ketone (i) was treated with hydroxylamine to produce di-2-pyridyl ketone oxime (ii) and reduced by zinc powder in aqueous ammonia to give di-2-pyridylmethaneamine (dpma) in 90% yield (Scheme 1).




Scheme 1. Synthesis of dpma from di-2-pyridyl ketone

After the dpma compound was obtained, it was further reacted with isopthalolyl chloride and terephthaloyl chloride in dry dichloromethane to give two new doubly bidentate bridging ligands, namely 1,3-*N,N'*-[bis(di(pyridin-2-yl)methyl)]isophthalamide (L1) and 1,4-*N,N'*-bis[(di(pyridin-2-yl)methyl)]terephthalamide (L2), respectively. The products were subjected for elemental analysis and the results obtained (Table 1) show good agreement between theoretical and experimental data of L1 and L2, as proposed earlier in Figure 1.

Table 1. Elemental analysis data for compounds L1 and L2

| Compounds | C(%) | | H(%) | | N(%) | |
|---|---|---|---|---|---|---|
| | Calcd. | Found | Calcd. | Found | Calcd. | Found |
| L1 | 71.98 | 70.13 | 4.83 | 4.98 | 16.79 | 15.63 |
| L2 | 71.98 | 71.83 | 4.83 | 4.08 | 16.79 | 16.05 |

In the IR spectra of the ligands, strong absorbance bands which were indicated at 1650 – 1652 $cm^{-1}$ were assigned to C=O stretching of the amide moieties. Strong bands of NH stretches which were observed at range 3211 – 3217 $cm^{-1}$ confirmed the formation of amide coupling that generate the respective bridging ligands. In similar to the IR spectra, the $^{1}H$ NMR of compound L1 and L2 also showed all resonances that were consistent with the expected 2-fold symmetric disubstituted compound. The NH peaks were observed at range 8.87 – 8.96 ppm, respectively. The difference in chemical shift in either IR and NMR spectra of L1 and L2 was due to the different conformations of the amides about the 1,3 and 1,4-phenyl cores. This different was also reported in our previous study using terephathaloyl and isophthaloyl based moieties [13]. The electrospray mass spectrum showed peaks at m/z 501.1 and 522.4, which corresponded to $[L1+H]^+$ and $[L1+Na]^+$. Meanwhile, a peak at m/z 501.2 which corresponding to $[L2+H]^+$ and $[L2+Na]^+$ was observed at m/z 523.2 in a low relative abundance.

In order to determine the molecular structure of the ligands, compounds L1 and L2 were dissolved in hot ethanol and left to evaporate at room temperature. Crystals of L2 were obtained in two weeks and subjected for X-ray crystallography while L1 remain as brown powder. Compound L2 crystallizes in the triclinic space group *P*-1, with one molecule of ligand L2 in the asymmetric unit. The phenyl core is planar, although the amide groups are twisted

slightly out of the plane of the ring (torsion angles 119.60 and 117.05°). The two di-2-pyridyl units are further twisted relative to the phenyl, as shown in Figure 3.

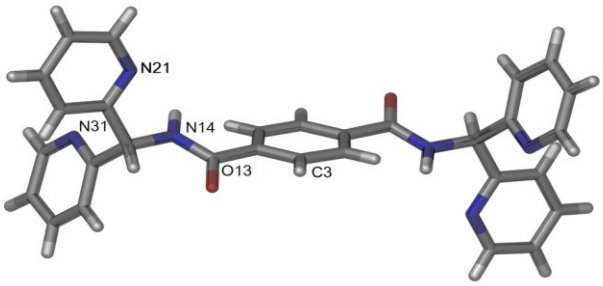



Figure 3. The perspective view of the asymmetric unit of L2

As observed in the crystal structure, the two pyridyl rings are not co-planar. The rings are arranged in *trans* conformations which brought the nitrogen atoms from the two pyridyl rings closer. This conformation has been observed in a crystal structure of a related chelating ligand, namely 1,2-bis(di-pyridylaminomethyl)benzene [2]. The packing of L2 is stabilized by supramolecular interaction (C-H···π) between the hydrogen atom from the phenyl ring and the pendant pyridine with H-centroid distance of 2.788 Å (Figure 4). This distance is closed to other edge-on C-H···π interaction distances reported for other compounds [15].

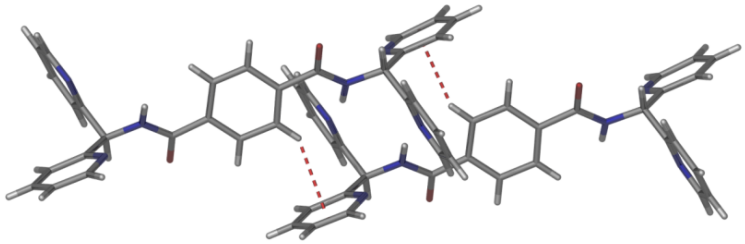


Figure 4. The extended view of compound L2 with a C-H···π interaction showing by dashed line

To further understand the types of structures and coordination chemistry of L1 and L2, these ligands were reacted with a range of metal salts to provide variety geometries and coordination numbers for the metal component. Reaction with selected metal salts such as copper, cobalt, palladium and zinc chloride produced only oils or oily solids that were not further characterized or could not be crystallized. Further attempts at these reactions using different ratios (1:1 and 1:2 metal-to-ligand ratios) and different solvent mixtures generally failed to give cleanly isolatable products. Fortunately, reaction of L1 and L2 with cadmium chloride and cadmium bromide gave products in crystals form, highly suitable for X-ray crystallography.

**X-ray crystallography of cadmium complexes**

Complex of L1, with formula molecule $[\{CdCl_2(CH_3OH)(L1)CdCl_2\}_2]$ crystallizes in the triclinic space group *P*-1, with one molecule of L1, two cadmium atoms, four coordinated chloride anions and one coordinated methanol molecule in the asymmetric unit (Figure 5). The Cd-N bond lengths are in the range 2.318(5) - 2.371(5)Å which are similar to many previous literature studies [15-20]. This complex has two cadmium atoms with trigonal bipyramidal geometries, although the cadmium atoms have quite different donor sets. Cd(1) is coordinated by two nitrogen atoms from the pendant pyridyl rings of L1, two chloride atoms (one bridging and one monodentate), while the second cadmium atom Cd(2) is coordinated by two nitrogen atoms from the pyridyl rings of L1, two chloride atoms and one methanol molecule. In similar manner to related ligands, [17] ligand L1 uses all four nitrogen donors to

coordinate with the cadmium atoms. The distance between Cd1-Cd2 is 6.40 Å, while the distance between the two cadmium atoms bridged by the chloride anions is much shorter at 3.68 Å. The coordination mode of L1 in this complex has quite a different motif compared with complexes incorporating other ligands based on a 1,3-phenyl core, such as 1,3-bis(di-2-pyridylaminomethyl)benzene [2]. In previous work, reaction of this ligand with silver nitrate gave discrete [1+1] metallo-macrocycle complex, while reaction with silver perchlorate and silver hexafluorophosphate gave 1-D coordination polymers [17]. The previous study revealed that ligand 1,3-bis(di-2-pyridylaminomethyl)benzene acted as a divergent bridging unit, with only two of the four pyridine rings involved in the coordination to form the complexes.

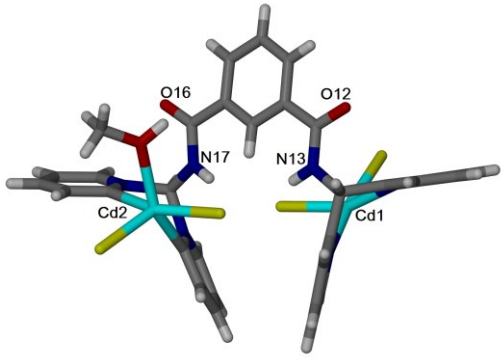



Figure 5. A perspective view of the asymmetric unit of complex [{$CdCl_2(CH_3OH)(L1)CdCl_2$}$_2$]

The extended view of complex L1 shows that the bridging chloride atoms connect the two dinuclear units to form a dimer as shown in Figure 6.

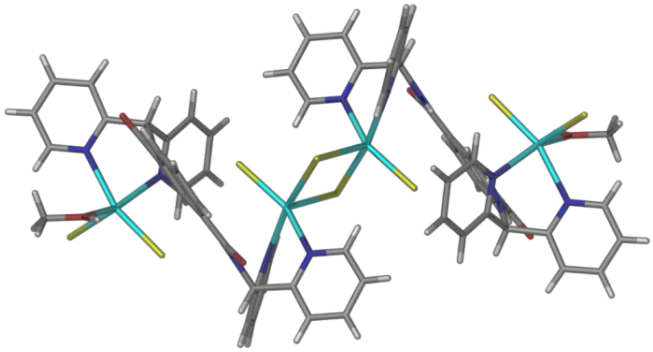


Figure 6. An exended view of complex [{$CdCl_2(CH_3OH)(L1)CdCl_2$}$_2$]

Complex with L2 was obtained in 75% yield by slow evaporation of a methanol-acetonitrile solution containing L2 and cadmium bromide. Single, rectangular, block-shaped crystals of complex L2 were separated from the clump and subjected to single crystal X-ray crystallography. The structure obtained by X-ray crystallography reveals the formation of a dinuclear complex, [$(CdBr_2)_2(L2)(CH_3OH)_2$]. In contrasts to the complex above, this complex crystallizes in the monoclinic space group, $P2_1/c$ with half a molecule of L2, one cadmium atom, two coordinated bromide anions and one coordinated methanol in the asymmetric unit (Figure 7). In this structure, the ligand acts as a tetradentate bridge to link two cadmium atoms and form a discrete dinuclear complex with a 2:1 metal to ligand ratio. The cadmium atom has distorted trigonal bipyramid geometry with one of the chelating pyridyl and one coordinated methanol donor occupying the axial positions. The monodentate pyridine donors twist back towards the core of the ligands in the similar manner to that observed in the dinuclear complexes described earlier. The Cd-N

distances are between 2.3119(19) – 2.365(9)Å, typical for such entities. By contrast to complexes of L1, the chelating rings in this complex is twisted by ca. 63.3° from the plane of the central phenyl core, which is approximately three times greater than the torsion angles observed in previous complexes reported by us [17]. Due to the para substitution of the central arene core, complex of L2 have a considerably longer Cd-Cd distance (12.261 Å) than those observed in complex of L1. In the crystal structure, it was seen that the discrete complexes were connected to each other by intermolecular hydrogen bonding interactions between the oxygen of the carbonyl group and the coordinated methanol solvent ($d$ = 1.903Å) to form 1-dimensional hydrogen bond chains (Figure 8). The crystallographic data for the three crystals compounds described in this study is listed in Table 2 for reference.

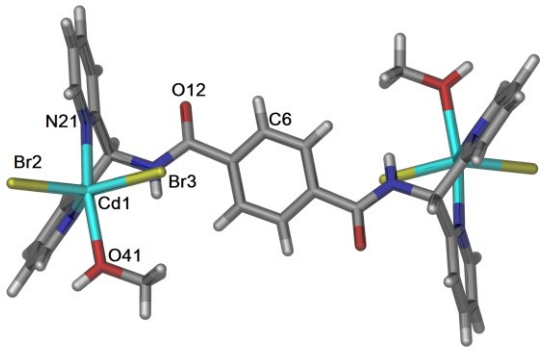



Figure 7. A perspective view of complex $[(CdBr_2)_2(L2)(CH_3OH)_2]$

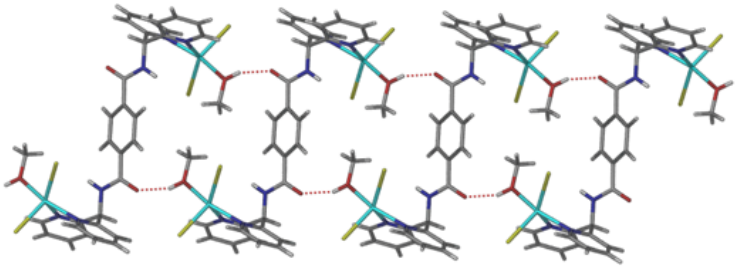


Figure 8. A perspective view of the 1-dimensional hydrogen bonded chains in complex $[(CdBr_2)_2(L2)(CH_3OH)_2]$

The crystal structure of compounds L2, and two new complexes have been deposited to Cambridge Crystallograpic Data Centre (CCDC) with reference number 1042070, 1042068 and 1042069, respectively.

Table 2. Crystal data for ligand L2 and complexes of L1 and L2, respectively

| **Compounds** | **L2** | **$[\{CdCl_2(CH_3OH)(L1)CdCl_2\}_2]$** | **$[(CdBr_2)_2(L2)(CH_3OH)_2]$** |
|---|---|---|---|
| Empirical Formula | $C_{30}H_{24}N_6O_2$ | $C_{31}H_{28}Cd_2Cl_4N_6O_3$ | $C_{32}H_{32}Br_4Cd_2N_6O_4$ |
| Formula weight | 500.55 | 899.19 | 1109.08 |
| Crystal system | Triclinic | Triclinic | Monoclinic |
| Space group | *P*-1 | *P*-1 | $P2_1/c$ |
| *a* (Å) | 8.4621(4) | 10.0062(6) | 9.4783(2) |
| *b* (Å) | 8.8809(5) | 13.7799(9) | 13.8293(3) |

Table 2 (cont'd). Crystal data for ligand L2 and complexes of L1 and L2, respectively

| **Compounds** | **L2** | **[{$CdCl_2(CH_3OH)(L1)CdCl_2\}_2$]** | **[$(CdBr_2)_2(L2)(CH_3OH)_2$]** |
|---|---|---|---|
| *c* (Å) | 9.7782(5) | 13.9357(8) | 14.3145(3) |
| α (º) | 68.479(5) | 64.558(6) | 90 |
| β (º) | 72.112(5) | 81.854(5) | 107.028(3) |
| γ (º) | 69.326(5) | 82.060(5) | 90 |
| Volume ($^3$) | 626.13(6) | 1711.23(18) | 1794.06(7) |
| *Z* | 1 | 2 | 2 |
| Density calculated ($Mg/m^3$) | 1.328 | 1.745 | 2.053 |
| Absorption coeficient ($mm^{-1}$) | 0.087 | 1.597 | 1.685 |
| F(000) | 262 | 888 | 1068 |
| Crystal size ($mm^3$) | 0.41x0.26x0.09 | 0.12x0.14x0.06 | 0.43x0.04x0.03 |
| Theta range for data (º) | 2.29 – 29.63 | 2.48 – 29.81 | 2.69– 29.92 |
| Reflections collected | 12303 | 8293 | 4736 |
| Observed reflections [I>2s(I)] | 6245 | 5989 | 3676 |
| Data/restraints/ parameters | 6245/3/343 | 8293/0/416 | 4736/0/218 |
| Goodness-of-fit on $F^2$ | 0.902 | 1.074 | 0.932 |
| $R_1$ [I>2s(I) | 0.0341 | 0.0630 | 0.0226 |
| $wR_2$ (all data) | 0.0780 | 0.1851 | 0.0479 |
| Largest diff. peak and hole ($e.Å^{-3}$) | 0.233 and -0.198 | 3.664 and -2.101 | 0.569 and -0.594 |

## Conclusion

The synthesis and coordination chemistry of doubly bidentate bridging ligands with dpma units have been successfully explored. It was confirmed from this study that ligands L1 and L2 used all four nitrogen donor atoms from dpma chelating units to bind with the cadmium ions, and forming stable multinuclear complexes. Like other ligands incorporating two di-2-pyridylmethyl chelating motifs, ligands L1 and L2 readily bridge two metals with bidentate chelation at each metal centre. The work described in this paper could be further expanded by finding conditions to limit hydrolysis of the ligands upon reaction with other metal salts, as from this study, only cadmium complexes can be isolated.

## Acknowledgments

The authors greatly acknowledge scientific and financial supports from Universiti Malaysia Terengganu, Ministry of Higher Education Malaysia and the University of Adelaide.

## References

1. Sumby C. J. (2011). Bridging ligands comprising two or more di-2-pyridylmethyl or amine arms: alternatives to 2,2'- bipyridyl-containing bridging ligands. *Coordination Chemistry Review,* 255: 1937 – 1967.

2. Antonioli B., Clegg J. K., Bray D. J., Gloe K., Gloe K., Kataeva O. N., Lindoy L. F., McMurtrie J. C., Steel P. J., Sumby C. J. and Wenzela M. (2006). Silver(I) complexation of linked 2,2'-dipyridylamine derivatives. Synthetic, solvent extraction, membrane transport and X-ray structural studies. *Dalton Transaction*, 40: 4783 – 4794.
3. Sumby C. J. and Steel P. J. (2007). Steel Mono- and dinuclear ruthenium complexes of bridging ligands incorporating two di-2-pyridylamine motifs: Synthesis, spectroscopy and electrochemistry. *Polyhedron,* 26: 5370 – 5381.
4. Antonioli B., Bray D. J., Clegg J. K., Gloe K., Gloe K., Jager A., Jolliffe K. A., Kataeva O. N, Lindoy L. F., Steel P. J., Sumby C. J. and Wenzel M. (2008). Interaction of copper(II) and palladium(II) with linked 2,2-dipyridylamine derivatives: Synthetic and structural studies. *Polyhedron,* 27: 2889 – 2898.
5. Sumby C. J. and Steel P. J. (2007). Coordination chemistry of di-2-pyridylamine-based bridging heterocyclic ligands: A structural study of coordination polymers and discrete dinuclear complexes. *Inorganic Chimica Acta,* 360: 2100 – 2114.
6. Philip, V., Suni, V., Kurup., P. R. M. and Nethai, M. (2005). Novel binuclear copper(II) complexes of di-2-pyridine ketone *N*(4)-methyl, *N*(4)-phenylthiosemicarbazone: Structural and spectral investigation, *Polyhedron*, 24: 1133 – 1142.
7. Suni, V., Kurup, P. R. M. and Nethaji, M. (2007). Structural and spectral investigation on some new Ni(II) complexes of-di-2-pyridyl ketone *N*(4)-phenylthiosemicarbazone. *Polyhedron,* 26: 3097 – 3102
8. Wu, S. H., Zhong, Y. W. and Yao J. (2013). 2,3-di(2-pyridyl)-5-phenylpyrazine: ANN-CNN-type bridging ligand for dinuclear transition-metal complexes. *Chemistry Asian Journal,* 8: 1504 – 1513
9. Zhong, Y. W, Wu, S. H., Burkhardt, S. E. and Abruna H. D. (2011). Mononuclear and dinuclear ruthenium complexes of 2,3-di-2-pyridyl-5,6-diphenylpyrazine: Synthesis and spectroscopic and electrochemical studies. *Inorganic Chemistry,* 50: 517 – 524.
10. Trilla, M., Pleixats, R., Man, M. W. C., Bied, C. and Moreau, J. J. E. (2006). Hybrid organic–inorganic silica materials containing di(2-pyridyl)methylamine–palladium dichloride complex as recyclable catalysts for Suzuki cross-coupling reactions. *Tetrahedron*, 47: 2399 – 2403.
11. Chang, J., Plummer, S., Berman, E. S. F., Striplin, D. and Blauch, D. (2004). Synthesis and characterization of bis(di-2-pyridylmethanamine)ruthenium(II). *Inorganic Chemistry,* 43: 1735 – 1742.
12. Kadir, M. A, Ramli, R., Kassim, N., Mansor, N., Sumby, C. J. (2015). Synthesis, structural and spectroscopic studies of palladium(II) metallo-macrocyles containing ancillary blocking ligands and *N,N'*-2,6-bis(3-pyridylmethyl)pyridine dicarboxamide. *Malaysian Journal of Analytical Sciences*, 19(3): 520 – 530.
13. Idris, N. S. B., Kadir, M. A. and Khandaker, M. M. (2017), Synthesis, characterization and coordination chemistry of *N,N'*-bis(3-pyridylmethyl)benzene-1,4-dicarboxamide with palladium and ruthenium salts. *Asian Journal of Chemistry*, 29(7): 1459 – 1462.
14. Renz, M., Hemmert, C. and Meunier, B. (1998). Synthesis of bis(di-2-pyridylmethyl)amine (BDPMA) by a novel one-pot multi-step reductive amination with molecular sieves and Zn/i-PrOH. *European Journal of Inorganic Chemistry*, 30: 1271 – 1273.
15. Kitagawa, S., Kitaura, R. and Noro, S. I. (2004). Functional porous coordination polymers. *Angewante Chemistry International Edition*, 43: 2334 – 2375.
16. Liu, T. F., Lu, J. and Cao R. (2010). Coordination polymers based on flexible ditopic carboxylate or nitrogen-donor ligands. *Crystal Engineering Communication,* 12: 660 – 670.
17. Abdul-Kadir, M., Clements, P. R., Hanton, L. R., Hollis, C. A. and Sumby C. J. (2012). Pre-organisation or a hydrogen bonding mismatch: Silver(I) diamide ligand coordination polymers versus discrete metallo-macrocyclic assemblies. *Supramolecular Chemistry,* 24: 627 – 640.
18. Abdul-Kadir, M., Hanton, L. R. and Sumby, C. J. (2011). Self-assembled metallo-macrocycle based coordination polymers with unsymmetrical amide ligands. *Dalton Transaction,* 40: 12374 – 12380.
19. Abdul-Kadir, M., Hanton, L. R. and Sumby, C. J. (2012). Building blocks for coordination polymers: self-assembled cleft like and planar discrete metallo macrocyclic complexes. *Dalton Transaction*, 41: 4497 – 4505.
20. Kadir, M. A., Mansor, N., Yusof, M. S. M. and Sumby, C. J. (2014). Synthesis and crystal structure of *N*-6-[(4-pyridylamino) carbonyl]-pyridine-2-carboxylic acid methyl ester zinc complex. *Complex Metals*, 1: 32 – 37.

*Malaysian Journal of Analytical Sciences, Vol 21 No 5 (2017): 1045 - 1053*
*DOI: https://doi.org/10.17576/mjas-2017-2105-06*

MALAYSIAN JOURNAL OF ANALYTICAL SCIENCES
*Published by The Malaysian Analytical Sciences Society*
ISSN 1394 - 2506

# PREPARATION OF DATE SEED ACTIVATION FOR SURFACTANT RECOVERY

## (Penyediaan Biji Kurma Teraktif Untuk Pemulihan Surfaktan)

Nurul' Ain Binti Jamion*, Nor Haziqah Binti Abd Hafiff, Nurul Huda Abd Halim, Sheikh Ahmad Izzaddin Sheikh Mohd Ghazali, Jamil Mohamed Sapari

*Department of Chemistry, Faculty of Applied Sciences,*
*Universiti Teknologi MARA, 72000 Kuala Pilah, Negeri Sembilan, Malaysia*

**Corresponding author: ain7059@ns.uitm.edu.my*

Received: 16 August 2016; Accepted: 5 September 2017

**Abstract**

Surfactants also known as surface-active agents are one of the water pollutants that can lead to the deterioration of the environment. In this study, activated carbon was prepared from date seeds (DAC) by using phosphoric acid as an activating agent. The activation process was carried out at 500 °C for two hours. DAC was characterized by Fourier-Transformed Infrared Spectrometer (FTIR), Field Emission Scanning Electron Microscopy (FESEM), Energy-Dispersive X-Ray Spectroscopy (EDX) and Nitrogen Adsorption at 77 K. The BET surface area of DAC was 1187 $m^2/g$. The adsorption capacities of surfactants (CTAB and TX-100) were determined. This study showed that the adsorption capacity of CTAB (23.0724 mg/g) onto DAC was greater than TX-100 (11.3868 mg/g). The adsorption process between both surfactants onto DAC was done by physisorption through electrostatic forces. Thus, this study showed that the date seeds have a greater tendency to be microporous activated carbon and an adsorbent for surfactants recovery.

**Keywords**: activated carbon, phosphoric acid, date seed

**Abstrak**

Bahan aktif permukaan juga dikenali sebagai surfaktan adalah salah satu bahan pencemar air yang boleh membawa kepada kemerosotan alam sekitar. Dalam kajian ini, karbon teraktif telah disediakan daripada biji kurma (DAC) dengan menggunakan asid fosforik sebagai ejen pengaktifan. Proses pengaktifan telah dilakukan pada suhu 500 °C selama dua jam. Karbon teraktif (DAC) telah dicirikan oleh Spektroskopi Inframerah Transformasi Fourier (FTIR), Mikroskopi Medan Pancaran Imbasan Elektron (FESEM), Sebaran Tenaga Sinar-X (EDX) dan penjerapan gas nitrogen pada suhu 77 K. Luas permukaan BET kawasan DAC adalah 1187 $m^2/g$. Kapasiti penjerapan surfaktan (CTAB dan TX-100) telah dikaji. Kajian ini menunjukkan bahawa kapasiti penjerapan CTAB (23.0724 mg/g) pada DAC adalah lebih tinggi daripada TX-100 (11.3868 mg/g). Proses penjerapan antara bagi kedua-dua surfaktan DAC adalah secara penjerapan fizikal melalui daya elektrostatik. Oleh itu, kajian ini menunjukkan bahawa biji kurma mempunyai kecenderungan yang lebih besar sebagai karbon teraktif berliang mikro dan bahan penjerap yang baik untuk pemulihan surfaktan.

**Kata kunci:** karbon teraktif, asid fosforik, biji kurma

## Introduction

The deterioration of environment in the process of economic growth has started to give impact on mankind. Lack of knowledge to deal with pollution and incapability of the natural environment to decompose unnatural generated element have made the occurrence of pollution inevitable. One of the environmental pollutions that needs to be

made aware of is water pollution which happens because of human activities such as raw sewage discharge [1]. Raw sewage is wastewater that comes from residential areas, industries, and agricultural processes. It contains a wide variety of contaminants and can be hazardous to human and animal if untreated.

Surface-active agent or also known as surfactant is one of the common water pollutants that comes from the production of detergents, fabric softeners, emulsifiers, paints, and adhesive. It is discharged to the sewer system upon application [2]. About 50 % of surfactants consumption comes from detergents and cleaners. Another source of surfactants contamination comes from surfactants dispersants for fuel oil spillages. These surfactants are resistant to bio-degradation by bacteria and have a toxic effect upon breakdown [3]. Synthetic surfactants also do not biodegrade sufficiently in the treatment plant, even when they are left for a long time [4]. Hence, the amount of surfactants must be reduced to an acceptable level before being discharged into the body of water.

Currently, there are a few techniques to remove surfactant from wastewater, which include biosorption [5], biodegradation [3], oxidation [6], adsorption [7], ultra-filtration, and ion-exchange [8]. Among these techniques, the adsorption method is easy to implement and low in cost while some of the adsorbents can be reused. Activated carbon is one of the efficient adsorbents that can be used in the adsorption method because it has a large specific surface area and pH-independent capacity with strong carbon–surfactant interaction. The combination of a large specific surface area and pH-independent means that activated carbon has a large adsorption capacity in order to remove the surfactants, which make it as effective adsorbents in removing surfactants from wastewater [9].

Activated carbons are carbonaceous materials characterized by their extraordinary large specific surface areas and well-developed porosity [10]. However, the commercial activated carbons are quite costly to purchase as they use high cost precursors such as petroleum residue, wood, coal, peat, and lignite that are non-renewable [11]. Hence, other sources of activated carbon such as from agricultural by-product were studied. By using agricultural by-product, the reliance on raw materials and cost can be reduced [12]. In recent years, there is a growing research interest in the agriculture by-product that is chosen based on price, purity, potential extent of its activation and also stability of its supply such as corncob [13], rice husk [14], olive seed [15], sugarcane bagasse [16] and date seeds [17].

Date seeds are one of the lignocellulosic materials from agriculture by-products that come from the date fruit which is mostly grown in the Middle East Asia, North African, and North American desert regions [18]. Dates are composed of fleshy pericarp and seed are mostly used in the food industries to manufacture various products such as date powders, syrup, and juice, chocolate coated dates and date confectionery [19]. Upon consumption or usage for the manufacturing process, the seeds are removed from the date fruit. Hence, there is an availability to use the date stones as raw materials to produce activated carbon [20] as Malaysia has increased the number of imported dates from 7.339 to 17.756 metric tonnes from 2005 to 2015 [21].

Thus, in this study, date seeds were choose as the raw material to prepare activated carbon based on the stated criteria for surfactants recovery.

## Materials and Methods

### Materials

Date seeds were used as the raw material. The chemicals used in this study are 85% ortho-phosphoric acid ($H_3PO_4$), cetyltrimethylammonium bromide (CTAB), TritonX-100 (TX100), deionised water, sodium hydroxide (NaOH) and distilled water.

### Preparation of activated carbon

The date seeds were collected by purchasing one box of dates from the market. The date pericarps were removed to obtain the seeds used as the raw material. An amount of about 100.00 g of date seeds were then washed thoroughly with tap water and dried under the sunlight. Next, the date seeds were soaked with 250 mL of 30% aqueous solution phosphoric acid for 24 hours to give acidic conditions to the seeds (pre-treated process). Then, the date seeds were washed with distilled water and dried under room temperature [22].

After that, the pre-treated date seeds were impregnated with 85% of concentrated phosphoric acid with the ratio of 2:1 (200 mL of phosphoric acid : 100 g of date seed). Next, the mixtures were heated by using a hot plate in a temperature range between 70 °C to 90 °C for 4 hours or until they appeared to be apparently semi-dried in the fume cupboard. The drying procedure was continued in the oven for 24 hours with the temperature at 110 °C [22].

Then, the activation process was modified based on a previous study where the samples were carried out in the muffle furnace at 500 °C for two hours [17]. Lastly, the activated carbon samples were washed with distilled water and tested with the pH meter until it was neutral. Finally, the prepared activated carbon were kept in the desiccator and used for characterization and adsorption studies [22]. The prepared activated carbons were named as date activated carbon (DAC).

**Characterization of activated carbon**

DAC was characterized by FTIR (Perkin Elmer model FTIR spectrum 100) to determine the fundamental vibrations bands at mid infrared region (4000 – 400 $cm^{-1}$). The Field Emission Scanning Electron Microscope with Energy Dispersive X-ray (FESEM-EDX) Spectroscopy (Hitachi SU8020) was used to examine the surface morphology and confirm the elements present in DAC. Meanwhile, multiple point nitrogen adsorptions analysis (BET) was used to determine the surface area of DAC.

**Adsorption capacity of activated carbon**

Cationic and non-ionic surfactants which are cetyltrimethylammonium bromide (CTAB) and TritonX-100 (TX100) were used to study the adsorption capacity onto DAC. Deionized water was used for making up the solution. About 0.5 g of DAC was weighed in 50 mL conical flasks, and then each surfactants solution was pipetted into the conical flasks, which were wrapped with parafilm and placed into an electronic bath shaker. The shaker was set at a constant speed of 100 rpm for 2 hours. After that, the mixture was filtered and 10 mL of the filtrates were diluted into a 50 mL volumetric flask and filled up with deionized water [22]. The solutions were analysed with T80+ UV/Visible Spectrometer instrument. The concentration of CTAB was determined by measuring the UV absorbance at $\lambda_{max}$ 193 nm while the concentration of TX100 at $\lambda_{max}$ 223 nm.

## Results and Discussion

**Percent yield of DAC**

The product yield of the DAC from 100 g of raw date seeds were calculated using Equation 1 as follows:

$$Yield\ \% = \frac{W_2}{W_1} \times 100 \quad (1)$$

where $W_1$ is the initial weight of date seeds (100 g) and $W_2$ is the final weight of date seeds after activation and carbonization. The percent yield of the DAC in this study was 47.12%. The result of percentage yield may be affected by the impregnation ratio and activation temperature used in the preparation steps [23]. In keeping with Prahas et al., the impregnation ratio is a crucial parameter that affects the quality of the carbon. The presence of excess phosphoric acid in the impregnation process promoted gasification of char and increased the total weight loss of carbon [24]. The presence of phosphoric acid was supported by the FTIR and EDX analyses.

**Characterization of DAC: Fourier transfrom infrared spectroscopy**

The adsorption frequency of the raw date seeds and DAC was studied using FTIR spectrometer instrument. The spectra obtained in this study are shown in Figure 1. The functional groups present in the raw date seeds and DAC spectrum listed in Table 1.

From the raw date seed spectrum, it shows that there was a broad hydroxyl group (O-H) peak at 3375.25 $cm^{-1}$ which may result from the water molecules, because date seeds contains hemicellulose and cellulose in their fiber. However, the hydroxyl peak disappeared at DAC spectrum due to loss of water moisture when the date seeds were carbonised. There was also the presence of alkanes group (C-H) peak stretch at 2924.91 $cm^{-1}$ and 2851.92 $cm^{-1}$. This indicated the presence of carbon and hydrogen in the date seeds. The adsorption band present at 1746.77 $cm^{-1}$ was the carbonyl group (C=O), which stretch showed the presence of oxygen. Lastly, the presence of adsoption present

peak at 1647.97 $cm^{-1}$ corresponded to the C=C double bond stretching that showed alkenes or aromatic group compound also present in the date seeds.

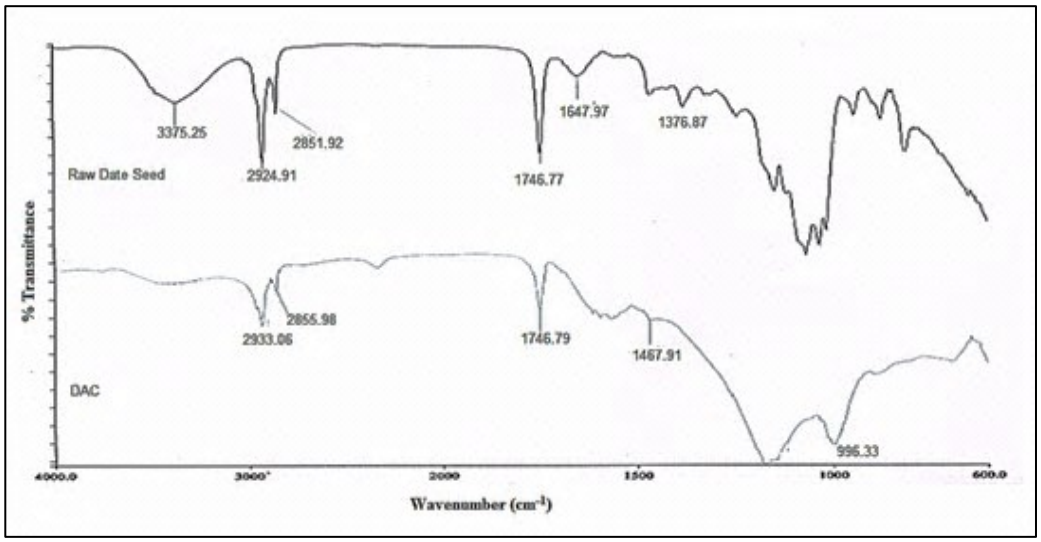



Figure 1. FTIR spectrum of raw date seed and DAC

Table 1. Functional group present in raw date seeds and DAC spectrum

| Sample | Functional Group | Wavenumber ($cm^{-1}$) |
|---|---|---|
| Raw Date Seed | O-H streching | 3375.25 |
| | C-H streching | 2924.91, 2851.92 |
| | C=O streching | 1746.77 |
| | C=C streching | 1647.97 |
| DAC | C-H streching | 2933.06, 2855.98 |
| | C=O streching | 1746.79 |
| | P-O-C streching | 1467.91, 996.33 |

The functional group of DAC showed the presence of alkanes group (C-H) stretching absorption bands at 2933.06 $cm^{-1}$ and 2855.98 $cm^{-1}$, respectively. The presence of carbonyl group (C=O) peak can be also seen in DAC at absorption band 1749.13 $cm^{-1}$. Besides, bands at 1467.91 $cm^{-1}$ and 996.33 $cm^{-1}$ indicated the stretching of carbon bonded to P-O groups of phosphates [24]. The P-O functional group was present due to the use of phosphoric acid in the preparation process of activated carbon.

From the FTIR results, it is shown that the appearance and disappearance of functional groups in the raw date seeds and DAC happened due to the carbonization and impregnation process that took place at the high temperature of 500 °C [24].

**Field emission scanning electron microscope**

In this study, the surface morphology of the DAC was obtained from Field emission scanning electron microscope (FESEM). The micrographs of DAC sample with magnifications 1.00Kx and 1.50Kx are shown in Figures 2(a) and 2(b), respectively. From both micrographs, the pores of DAC were shown homogenously distributed and well

developed on the external surface. The pores are seen to be uniformly developed in the mixture of oval and circle patterns. This was due to the activation process which involved the used of phosphoric acid as an activating agent, which helped to create more pores in the activated carbon and thus increased the surface area and pores volume. These were proven by the nitrogen gas adsorption results where the surface area of DAC was 1187 $m^2/g$, which was higher compared to 682 $m^2/g$ activated carbon from date stem activated with pure steam at 450 °C [17]. Other than that, the micrographs also observe the presence of white particles inside some of the pores and scattered over the surface which are the ash [22].

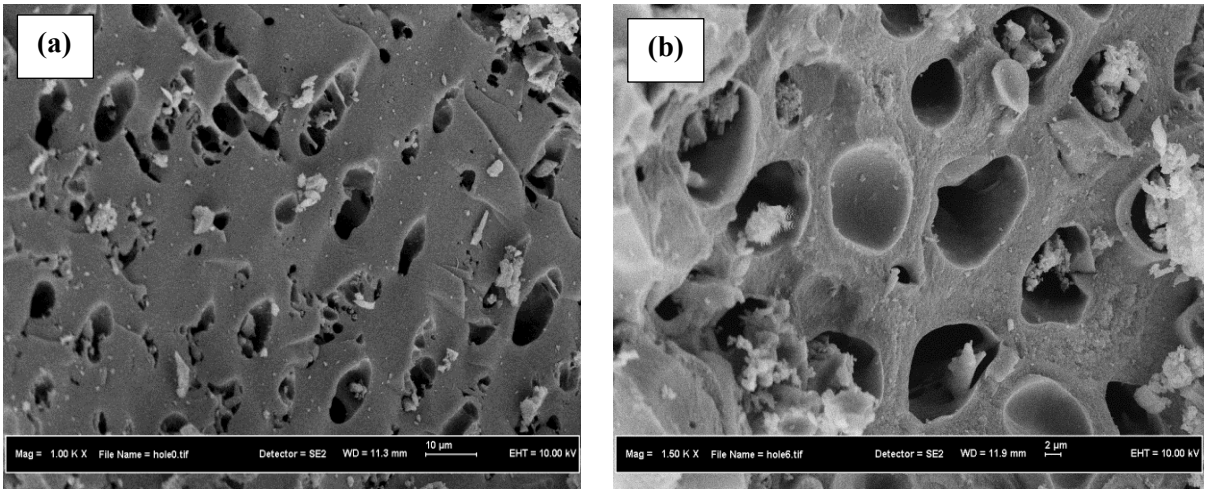



Figure 2. (a) DAC with magnification 1.00Kx and (b) DAC with magnification 1.50Kx

**Energy dispersive X-ray spectroscopy**

In this study, Energy dispersive X-ray (EDX) was used to determine the surface composition of the DAC. The spectrum obtained from EDX is shown in Figure 3 and element percentage is summarised in Table 2. From Table 2, the presence of 79.78% carbon (C), 13.10% oxygen (O), and 7.12% phosphorus (P) on the surface of the DAC can be seen. The high percentage of carbon indicated that the volatile organic compounds in the date seeds were reduced and resulted in char containing a higher content of fixed carbon [11]. Phosphorus element was present on the DAC due to the activating agent used in this study which was phosphoric acid. This indicated that phosphorus compounds were strongly bound to the oxygen and carbon and therefore not easily removed by washing, either with the cold or hot distilled water [17].

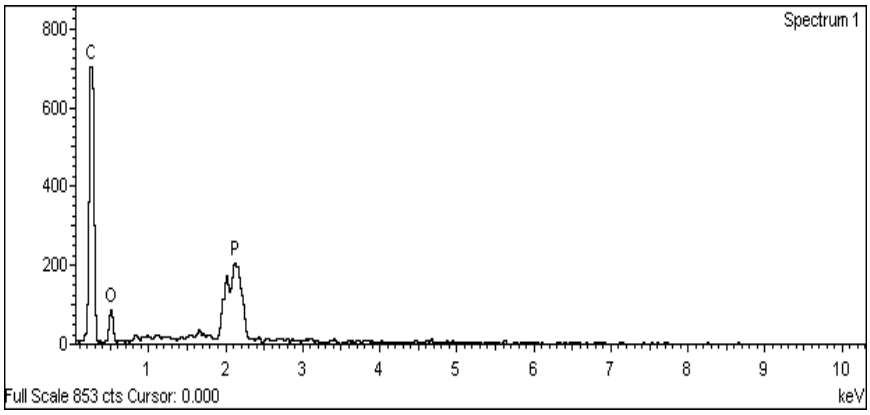



Figure 3. EDX spectrum for DAC

Table 2. Composition of elements presence on the DAC surface

| Element | Weight Percentage (%) | |
|---|---|---|
| | Weight | Atomic |
| Carbon | 79.78 | 86.37 |
| Oxygen | 13.10 | 10.64 |
| Phosphorus | 7.12 | 2.99 |

**Nitrogen gas adsorption analysis**

The solid-gas adsorption study was determined using BET surface area model and adsorption isotherm. The BET surface area ($S_{BET}$) was carried out by using nitgogen gas analysis at 77 K. The results are shown in Table 3.

Table 3. The specific surface area, average pores diameter and total pores volume of DAC

| Sample | Specific surface area, $S_{BET}$ ($m^2/g$) | Total pores volume, $V$ ($cm^3/g$) | Average pores diameter, $d$ (Å) |
|---|---|---|---|
| DAC | 1187 | 0.482 | 16.21 |

From the results, the $S_{BET}$ of the DAC activated by $H_3PO_4$ was high which was 1187.6844 $m^2/g$ compared to the date seeds that used other activation agents such as ferric chloride (780 $m^2/g$) [25] and calcium acetate (702 $m^2/g$) [26]. This indicated that $H_3PO_4$ was a good activating and dehydrating agent as the process of dehydrating the raw material helped in the development of the higher surface area by penetrating deep into the raw material. The total pores volume of the DAC was 0.482 $cm^3/g$ with the average pores diameter of 16.21 Å, indicating that micropores were present ($d$ < 20 Å) [27].

The adsorption isotherm result for DAC is shown in Figure 4. From the results, it is shown that the physisorption isotherm was Type I isotherm, also known as Langmuir isotherm according to IUPAC classification [27]. The isotherm showed that the adsorption was reversible and the amount of gas adsorbed was approaching the limiting value as $P/P_o \rightarrow 1$. This indicated that the DAC consisted of micropores with a micropores filling mechanism.

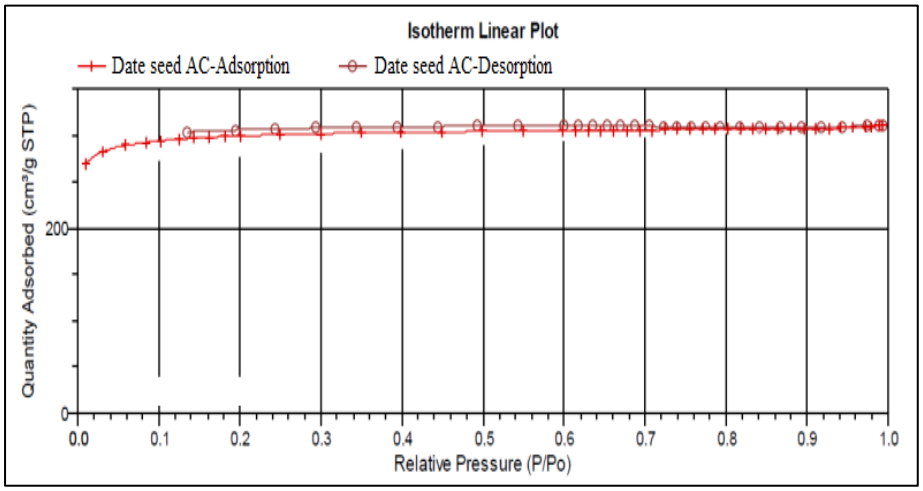



Figure 4. Adsorption isotherm of DAC

Based on the pores size distribution graph (Figure 5), DAC sample also had macropores represented by a small shoulder peak in between pore width of 50 Å to 60 Å [27]. This result can be explained by the activation process where the phosphoric acid used can enhance and produce relatively large pores [28]. It was revealed that DAC exhibited a well-developed porous network structure which contained macropores. This porosity is an advantage for DAC where large sized pores will act as feeder during the adsorption process [17].

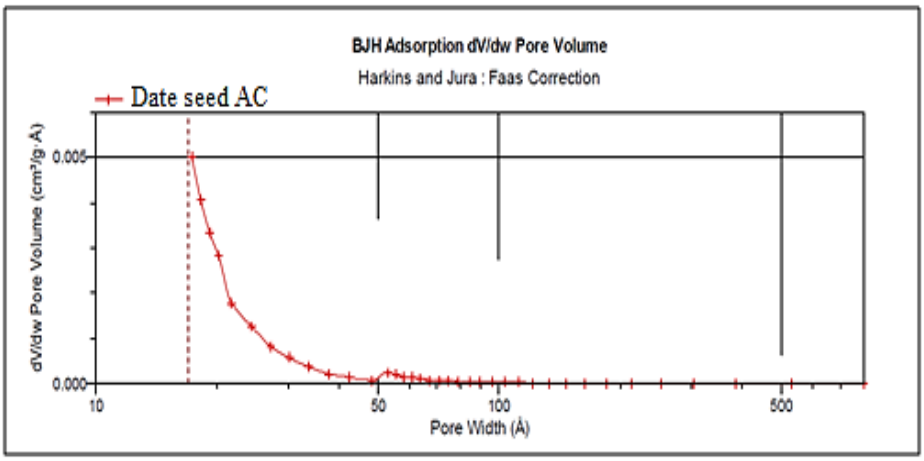



Figure 5. Pores size distribution plot of DAC

**Adsorption capacity of activated carbon**

In this adsorption study, two types of surfactants were used, namely CTAB and TX-100. Both adsorptions were performed at room temperature (28°C). The adsorption capacities of DAC for both surfactants are shown in Table 4.

Table 4. Adsorption capacity of CTAB and TX-100 onto DAC

| Type of surfactants | Adsorption capacity, $q_e$ (*x/m*) | Adsorption's percentage (%) |
|---|---|---|
| CTAB | 23.0724 mg $g^{-1}$ | 92.33 |
| TX-100 | 11.3868 mg $g^{-1}$ | 95.63 |

From the results, it is shown that CTAB adsorption capacity was higher (23.0724 mg $g^{-1}$) compared to TX-100 (11.3868 mg $g^{-1}$). The difference in the adsorption capacity could be due to the charge of the surfactants. CTAB carried positively charged hydrophilic part which could be easily attracted and adsorbed to the surface of negatively DAC. The DAC was supported by the EDX result which consisted of phosphorus element that carried the $P^{3-}$ charge from phosphoric acid, $H_3PO_4$. This phenomenon explained that CTAB molecules formed a monolayer coverage on DAC surface at equilibrium through the van der Waal's forces (electrostatic forces) [29]. Nevertheless, the low adsorption capacity of TX-100 was because it is a non-ionic surfactant that not carry any charged on the hydrophilic part. Thus, TX-100 is difficult to adsorb on a charged surface. However, in order to increase the adsorption of TX-100 onto the surface, it needs enough energy adsorption force such as increasing the temperature to overcome the strong interaction of water molecules with DAC surface [30].

## Conclusion

According to all the data obtained, date seeds could be a good precursor in order to prepare an activated carbon. The preparation of DAC by using the high concentration of phosphoric acid (85%) with the ratio 2:1 as the chemical activating agent at low activation and carbonization temperature (500 °C) contributed a well-developed porosity.

Apart from that, DAC showed a high surface area from this method of preparation. Thus, these characteristics directly enhanced the adsorption process of surfactants onto DAC, especially for CTAB due to the electrostatic force. Therefore, activated carbon prepared from date seeds (DAC) has shown its availability to be a good adsorbent in surfactant recovery.

**Acknowledgements**

The authors would like to acknowledge the Department of Chemistry at the Faculty of Applied Sciences, Universiti Teknologi MARA Kuala Pilah Campus, Negeri Sembilan for the facilities provided, as well as all the students and laboratory staff for their continuous help.

**References**

1. Hitam, M. B. and Borhan, H. B. (2012). FDI, growth and the environment: Impact on quality of life in Malaysia. *Procedia - Social and Behavioral Sciences*, 50: 333 – 342.
2. Clara, M., Scharf, S., Scheffknecht, C. and Gans, O. (2007). Occurrence of selected surfactants in untreated and treated sewage. *Water Research*, 41(19): 4339 – 4348.
3. Scott, M. J. and Jones, M. N. (2000). The biodegradation of surfactants in the environment. *Biochimica et Biophysica Acta (BBA) – Biomembranes,* 1508 (1–2): 235 – 251.
4. Harwell, J. H., Sabatini, D. A. and Knox, R. C. (1999). Surfactants for ground water remediation. *Colloids and Surfaces A: Physicochemical and Engineering Aspects,* 151: 255 – 268.
5. Aksu, Z. (2005). Application of biosorption for the removal of organic pollutants: A review. *Process Biochemistry,* 40 (3–4): 997 – 1026.
6. Zsilák, Z., Fónagy, O., Szabó-Bárdos, E., Horváth, O., Horváth, K., and Hajós, P. (2014). Degradation of industrial surfactants by photocatalysis combined with ozonation. *Environmental Science and Pollution Research,* 21(19): 11126 – 11134.
7. Schouten, N., Van Der Ham, L. G. J., Euverink, G-J. and Haan, A. B. (2007). Selection and evaluation of adsorbents for the removal of anionic surfactants from laundry rinsing water. *Water Research,* 41: 4233 – 4241.
8. Kowalska, I. (2008). Surfactant removal from water solutions by means of ultrafiltration and ion-exchange. *Desalination,* 221: 351 – 357.
9. Krivova, M. G., Grinshpan, D. D. and Hedin, N. (2013). Adsorption of CnTABr surfactants on activated carbons. *Colloids and Surfaces A: Physicochemical and Engineering Aspects,* 436: 62 – 70.
10. Al-Qodah, Z. and Shawabkah, R. (2009). Production and characterization of granular activated carbon from activated sludge. *Brazilian Journal of Chemical Engineering*, 26: 127 – 136.
11. Yahya, M. A., Al-Qodah, Z. and Ngah, C. W. Z. (2015). Agricultural bio-waste materials as potential sustainable precursors used for activated carbon production: A review. *Renewable and Sustainable Energy Reviews,* 46: 218 – 235.
12. Qin, C., Chen, Y. and Gao, J. M. (2014). Manufacture and characterization of activated carbon from marigold straw (*Tagetes erecta L*) by $H_3PO_4$ chemical activation. *Materials Letters,* 135: 123 – 126.
13. Song, M., Jin, B., Xiao, R., Yang, L., Wu, Y., Zhong, Z. and Huang, Y. (2013). The comparison of two activation techniques to prepare activated carbon from corn cob. *Biomass and Bioenergy,* 48: 250 – 256.
14. Cheenmatchaya, A. and Kungwankunakorn, S. (2014). Preparation of activated carbon derived from rice husk by simple carbonization and chemical activation for using as gasoline adsorbent. *International Journal of Environmental Science and Development*: 171 – 175.
15. Nouri, H. and Ouederni, A. (2013). Modeling of the dynamics adsorption of phenol from an aqueous solution on activated carbon produced from olive stones. *International Journal of Chemical Engineering and Applications*, 4(4): 254 – 261.
16. Amin, N. K. (2008). Removal of Reactive Dye from Aqueous Solutions by Adsorption onto Activated Carbons Prepared from Sugarcane Bagasse Pith. *Desalination,* 223(1–3): 152 – 161.
17. Hadoun, H., Sadaoui, Z., Souami, N., Sahel, D. and Toumert, I. (2013). Characterization of mesoporous carbon prepared from date stems by $H_3PO_4$ chemical activation. *Applied Surface Science,* 280: 1 – 7.
18. Danish, M., Hashim, R., Ibrahim, M. N. M. and Sulaiman, O. (2014). Optimized preparation for large surface area activated carbon from date (*Phoenix dactylifera L.*) stone biomass. *Biomass and Bioenergy,* 61: 167 – 178.
19. Rahman, M. S., Kasapis, S., Al-Kharusi, N. S. Z., Al-Marhubi, I. M. and Khan, A. J. (2007). Composition characterisation and thermal transition of date pits powders. *Journal of Food Engineering,* 80: 1 – 10.

20. Haimour, N. M. and Emeish, S. (2006). Utilization of date stones for production of activated carbon using phosphoric acid. *Waste Management,* 26: 651 – 660.
21. The International Nut and Dried Fruit Council Foundation (INC). (2017). Nuts & Dried Fruits Statistical Yearbook 2016/2017. pp 56.
22. Jamion, N. A and Mohamed, S. M. (2014). Characterization of activated carbon from sugar cane husk. *Applied Mechanics and Materials,* (699): 1006 – 1011.
23. Demiral, I. and Aydin Ş. C. (2016). Preparation and characterisation of activated carbon from pumpkin seed shell using $H_3PO_4$. *Anadolu University Journal of Science and Technology-A Applied Sciences and Engineering*, 17(1): 125 – 138.
24. Prahas, D., Kartika, Y., Indraswati, N. and Ismadji, S. (2008). Activated carbon from jackfruit peel waste by $H_3PO_4$ chemical activation: Pore structure and surface chemistry characterization. *Chemical Engineering Journal*, 140(1–3): 32 – 42.
25. Theydan, S. K. and Ahmed, M. J. (2012). Adsorption of methylene blue onto biomass-based activated carbon by $FeCl_3$ activation: Equilibrium, kinetics, and thermodynamic studies. *Journal of Analytical and Applied Pyrolysis,* 97: 116 – 122.
26. Awwad, N. S., El-Zahhar, A. A., Fouda, A. M. and Ibrahium, H. A. (2013). Removal of heavy metal ions from ground and surface water samples using carbons derived from date pits. *Journal of Environment Chemical Engineering*, 1: 416 – 423.
27. International Union of Pure and Applied Chemistry (1994). Recommendations for the characterization of porous solids. *Pure and Applied Chemistry,* 66(8): 1739 – 1758.
28. Puziy, A. M., Poddubnaya, O. I., Martinez-Alonso, A., Suarez-Garcia, F. and Tascon, J. M. D. (2002). Synthetic carbons activated with phosphoric acid, porous structure. *Carbon,* 40: 1507 – 1519.
29. Martinez-Costa, J. I. and Leyva-Ramos, R. (2017). Effect of surfactant loading and type upon the sorption capacity of organobentonite towards pyrogallol. *Colloids and Surfaces A: Physicochemical Engineering Aspects,* 520: 676 – 685.
30. Huang, L., Maltesh, C. and Somasundaran, P. (1996). Adsorption behavior of cationic and nonionic surfactant mixtures at the alumina–water interface. *Journal of Colloid and Interface Science,* 177: 222 – 228.

*Malaysian Journal of Analytical Sciences, Vol 21 No 5 (2017): 1054 - 1064*
*DOI: https://doi.org/10.17576/mjas-2017-2105-07*

MALAYSIAN JOURNAL OF ANALYTICAL SCIENCES
*Published by The Malaysian Analytical Sciences Society*
ISSN 1394 - 2506

# ISOLATION AND CHARACTERISATION OF MICROPLASTIC ABUNDANCE IN *Lates calcarifer* FROM SETIU WETLANDS, MALAYSIA

## (Pemisahan dan Pencirian Plastik-Mikro di dalam *Lates calcarifer* dari Tanah Bencah Setiu, Malaysia)

Yusof Shuaib Ibrahim*, Ruthra Rathnam, Sabiqah Tuan Anuar, Wan Mohd Afiq Wan Mohd Khalik

*School of Marine and Environmental Sciences,*
*Universiti Malaysia Terengganu, 21030 Kuala Nerus, Terengganu, Malaysia*

**Corresponding author: yusofshuaib@umt.edu.my*

Received: 20 July 2017; Accepted: 14 September 2017

**Abstract**

The presence of microplastics (<1 mm) in wild and cage-cultured Asian sea bass (*Lates calcarifer*) was successfully studied. Fish samples were collected from Setiu Wetlands in October 2016. Microplastics were isolated from fish samples using the alkaline solution method (10 M of NaOH solution). Microplastics were sorted visually according to their shapes and colours after being observed under dissecting microscope. A total of 4,498 pieces of microplastics were identified and threadlike shape was the most abundant microplastic particles found during this study. The identification of functional groups in the composition of microplastics was achieved using Fourier transform infrared (FTIR) spectroscopy. Microplastics, with the presence of strong peaks at $\upsilon$=3342 $cm^{-1}$ (N-H str), 1510 $cm^{-1}$ (N-H bend) and $\upsilon$=1706 $cm^{-1}$ (C=O str) are associated with the materials consist of polyamide. Additionally, peaks related to the polyvinyl alcohol groups are recorded at $\upsilon$= 3321 – 4323 $cm^{-1}$ (O-H str), 1706 $cm^{-1}$ (C=O str), 1219 $cm^{-1}$ (O-H wag) and $\upsilon$=1028 – 1128 $cm^{-1}$ (C-O str). The abundance levels of microplastics ingested by wild and cage-cultured fishes are statistically significantly different, $p < 0.05$.

**Keywords:** Asian sea bass, fish ingestion, microplastics, polymer, wetland environment

**Abstrak**

Kemunculan plastik-mikro (<1 mm) di dalam ikan siakap liar dan sangkar ternakan (*Lates calcarifer*) telah berjaya dikaji. Sampel ikan diambil dari tanah bencah Setiu semasa bulan Oktober 2016. Plastik-mikro telah diasingkan daripada sampel ikan mengunakan kaedah larutan beralkali (10 M larutan NaOH). Plastik-mikro telah diasingkan secara visual dibawah mikroskop mengikut perbezaan warna dan bentuk. Sejumlah 4,498 pecahan plastik-mikro telah dikenalpasti dan bentuk benang merupakan partikel yang paling kerap dijumpai semasa kajian ini dijalankan. Pengenalpastian kumpulan berfungsi bagi komposisi plastik-mikro telah dicapai menggunakan spektroskopi FTIR. Analisis plastik-mikro menunjukkan kehadiran puncak yang jelas pada $\upsilon$=3342 $cm^{-1}$ (N-H str), 1510 $cm^{-1}$ (N-H bend) dan $\upsilon$=1706 $cm^{-1}$ (C=O str) bagi komposisi polimer kumpulan poliamida. Tambahan, puncak yang menunjukan kehadiran kumpulan polivinil alkohol dicatatkan pada $\upsilon$= 3321 – 4323 $cm^{-1}$ (O-H str), 1706 $cm^{-1}$ (C=O str), 1219 $cm^{-1}$ (O-H wag) dan $\upsilon$=1028 – 1128 $cm^{-1}$ (C-O str). Aras kehadiran plastik-mikro yang dihadam oleh ikan liar dan sangkar ternakan adalah berbeza secara signifikan, $p < 0.05$.

**Kata kunci:** ikan siakap, penghadaman oleh ikan, plastik-mikro, polimer, persekitaran tanah bencah

## Introduction

Microplastics are generally defined as plastics with size less than 1 mm in diameter [1], which makes much easier for them to be displaced into biota. Despite no possibility of danger regarding microplastics and marine organisms recorded at this stage, there is a great concern about the potential risks that microplastics may pose to organisms via

ingestion, which is then transferred to food chain and ultimately poses risks to human health. Studies over the past decades have shown that microplastics are widespread in the marine environment including sea surface, shoreline or sea bed, and their abundance has increased annually.

Microplastics could have both physical and chemical effects on the organisms that ingest the pollutant. If ingested, microplastics may pass through the gut or retained in the digestive tract [2]. Fibres may knot or clump and it could be hazardous if the passage of food is blocked. The accumulation of debris in the digestive tract leads to the difficulty in breathing as some plastic particles could choke the organism. According to Ivar do Sul et al. [3], microplastics accumulation occurred through the food web, from the smallest organisms like plankton to the largest fish.

In fact, small-sized microplastics have a great potential to be ingested by a wide range of marine organisms including fish. A great variety of fish species across the world have been proven to ingest synthetic polymers. For instance, a total of 35% of five mesopelagic and one epipelagic fish species from the North Pacific were found to have ingested plastics with an average of 2.1 pieces of plastic per fish [4]. Meanwhile, three different species of bottom-feeding catfish were investigated in a Brazilian estuary and as a result, 17 – 33% of the sampled fishes had ingested plastics [5]. Lusher et al. [6] in their work found that ten fish species from the English Channel had ingested microplastics (both pelagic and demersal species), with a total of 37% of the sample studied was affected.

Foekema et al. [7] found that only 2.6% of the fish from the North Sea contained microplastics, but this was after excluding textile fibres from their data analysis. Of the seven-species investigated, five of the subjects studied contained plastics. Atlantic cod (*Gadus morhua*) was one of the species studied and the abundance levels varied depending on the location, in which 0 – 15% of the individuals contained microplastics. A recent study carried out by Rummel et al. [8] also found relatively low plastic content in fish (both pelagic and demersal species) from the North Sea and the Baltic Sea, where 5.5% of all fishes were affected by this pollutant. To date, no study has cited the comparison of microplastic particles between two fishes derived from different habitat locations.

In Malaysia, the research exploration related to the issue of microplastics is still limited. To the best of our knowledge, there are several studies documenting the occurrence of microplastic in mangrove sediment [9], sandy beaches [10], and bivalves [11]. Indeed, there have been no studies documenting the ingestion of microplastics among estuarine fishes of Malaysia.

*Lates calcarifer* or commonly known as the Asian sea bass in Malaysia is a commercial fish found in great abundance along the estuary of Setiu Wetlands, Terengganu. They are found in both open environment and cage-cultured by the local fishermen. This area has nine distinctive ecosystems namely beach, sea, mudflat, river, lagoon, estuary, island, coastal forest, and mangroves. Thus, Setiu Wetlands is the only wetland in Malaysia that can be found with a great diversity of ecosystems [12]. The presence of microplastic particles in the lower trophic level organisms such as bivalves has been proven in our previous work [11] and the abundance levels are remarkably high in this area. Thusly, this extended work conveys the ubiquity of microplastics in the upper trophic level in order to understand the translocation, which could further be found in human body.

Therefore, the main goal of this study is to evaluate the abundance levels of microplastics ingested by estuarine fish with different life habits (wild and cage-cultured). Physical and chemical characterisations were carried out to identify the main shape and colour of microplastics, polymer composition, and their relationship towards spatial variation.

## Materials and Methods

### Sample collection

Cage-cultured and wild *L. calcarifer* (n = 4) were caught from Setiu Wetlands in October 2016. Each location was coordinated and illustrated as shown in Table 1 and Figure 1, respectively. Wild *L. calcarifer* was collected using a drift net (100 m length × 2 m width) located at Stations 3 and 4, where the net was left overnight. Meanwhile, cage-cultured *L. calcarifer* was purchased from a local fisherman at the aquaculture site. The weight of each sample was

set in the range of 300 – 400 g regardless of their habitual area. The samples were kept in a cool box filled with ice cubes before the samples were transferred to the laboratory for further analysis.

Table 1. The coordinate of sampling location in Setiu Wetlands

| Station | Latitude (N) | Longitude (E) |
|---|---|---|
| 1 (Cage Cultured) | 05° 37'10.34 | 102° 47'31.51 |
| 2 (Cage Cultured) | 05° 39'03.80 | 102° 44'55.32 |
| 3 (Wild) | 05° 41'30.77 | 102° 41'54.98 |
| 4 (Wild) | 05° 43'21.08 | 102° 47'31.51 |

**Sample preparation**

In the laboratory, the fish samples were thawed at room temperature and general biological parameters such as length (cm) and weight (g) were measured. The gastrointestinal tract for each sample was removed by dissection as described in previous works reported by Lusher et al. [6] and Rocha-Santos and Duarte [13]. In general, each sample was cut from the top of the oesophagus through the end of the gastrointestinal tract, which was then digested and stored individually in a 250-mL glass jar containing 80% ethanol solution until further identification. Plastic materials were not used throughout this study as it would cause cross contamination and generate bias in the final result.

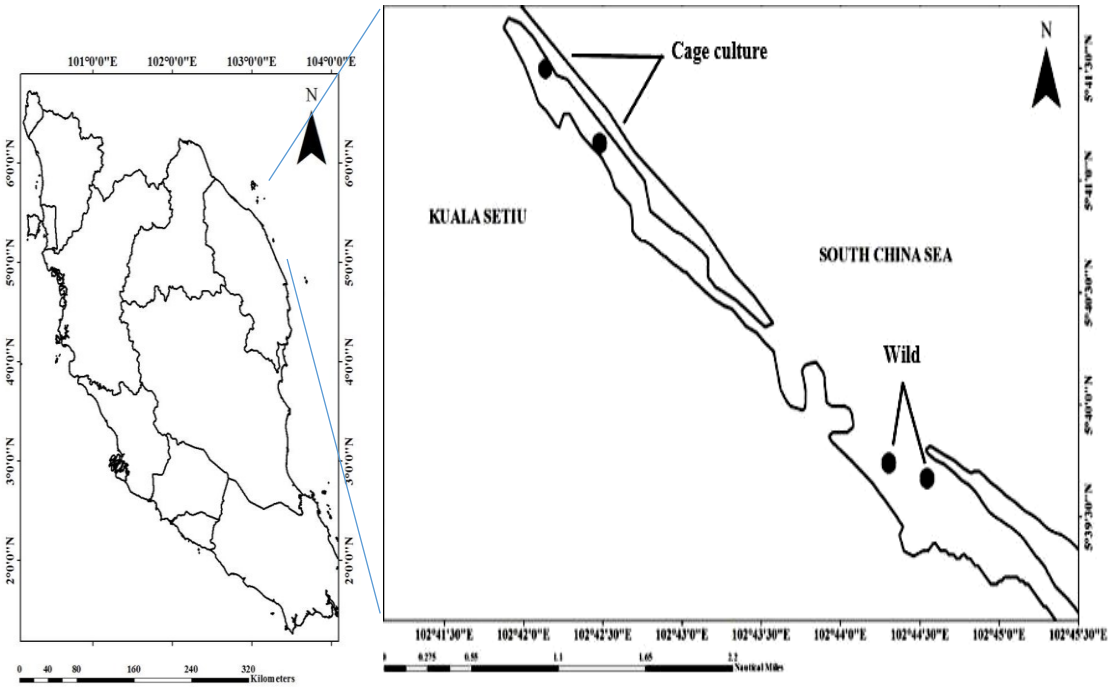



Figure 1. Location of sampling activity in Setiu Wetlands (on left side is map of Peninsular Malaysia)

**Digestion procedure**

The samples were digested using the alkaline method as described by Cole et al. [14] in their work. An amount of 10 M of sodium hydroxide (NaOH) was chosen as the digestion solution and introduced into the beaker containing the gastrointestinal tract. Later, the 50 – 60 g digested samples were placed in a water bath with the temperature set at 60 °C and shaken constantly (130 rpm) during the incubation period in order to speed up the digestion process. The digestion steps were carried out in triplicate. After 21 days, the digestion solution was filtered and analysed using a stereoscopic microscope (Leica ZOOM 2000, Cole-Palmer, IL, USA) to observe the presence of microplastic materials.

**Microplastic sorting and identification**

The sorted microplastics were photographed and the maximum length, colour, and shape (threadlike, fragment or spherical) were noted using a dissecting microscope (Olympus SZX7, Olympus Corp. Tokyo, Japan). Particles which presented the characteristic features of synthetic polymers were identified as microplastics (mouldable items with consistent thickness and colour which do not break when pressed with stainless forceps). In case of doubt, a hot metal tip was applied on the object. The collected microplastics were kept in individual glass urine bottles pertaining to its original shape. Centrifugation process was carried out to enhance the separation of the microplastic particles from the supernatant before further analysis.

Fourier transform infrared spectroscopy (FTIR) (IR Tracer-100, Perkin Elmer, MA, USA) was used to identify the functional groups associated with polymer chemical properties. Microplastic particles were analysed using attenuated total reflection (ATR) in the mid-IR range of 4000 – 650 $cm^{-1}$ and 18 scans per analysis. One-way ANOVA was performed to evaluate the significant level of microplastic abundance among location and shape types. Differences at $p < 0.05$ were considered statistically significant. Statistical analyses (one-way ANOVA) and Pearson correlation were conducted using SPSS statistical package Version 23.0.

## Results and Discussion

**Microplastic abundance**

The microplastic size collected in this study was recorded between 4.3 and 15.7 µm with an average length of 50.1 µm. The total number of microplastics found in all samples was 4,498. The highest abundance of microplastics was found in the gastrointestinal tract of wild *L. calcarifer* containing 1,260 and 1,277 of digested and microplastic particles, respectively. Meanwhile, the lowest level of ingestion was recorded in cage-cultured fish samples, with a total of 1,961 microplastic fragments in both samples. The microplastic abundance observed between wild and cage-cultured *L. calcarifer* was statistically significant at $p < 0.05$. Most of the microplastics found had threadlike shape with distinctive colours (i.e. black, blue, red, green, purple, orange or colourless).

Figure 2 and Figure 3 show the shape and colour distribution of the microplastic particles isolated from the gastrointestinal tracts of *L. calcarifer* during this study, respectively. Black threadlike shape was the most abundant microplastic particle found in both cage-cultured and wild *L. calcarifer* at different sampling locations, followed by transparent and blue threadlike shapes. The image of microplastic captured under dissecting microscope is presented in Figure 4. Statistical analysis also elucidated that the microplastic abundance based on the colour observed was significantly different between sample type and station at $p < 0.05$.

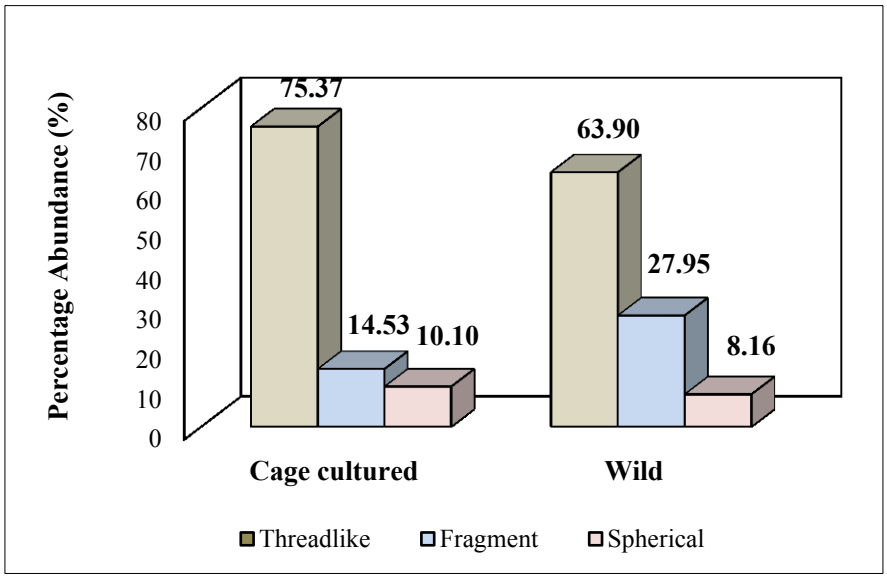



Figure 2. Percentage abundance (%) of microplastic based on shapes between cage cultured and wild *L. calcarifer* from Setiu Wetlands

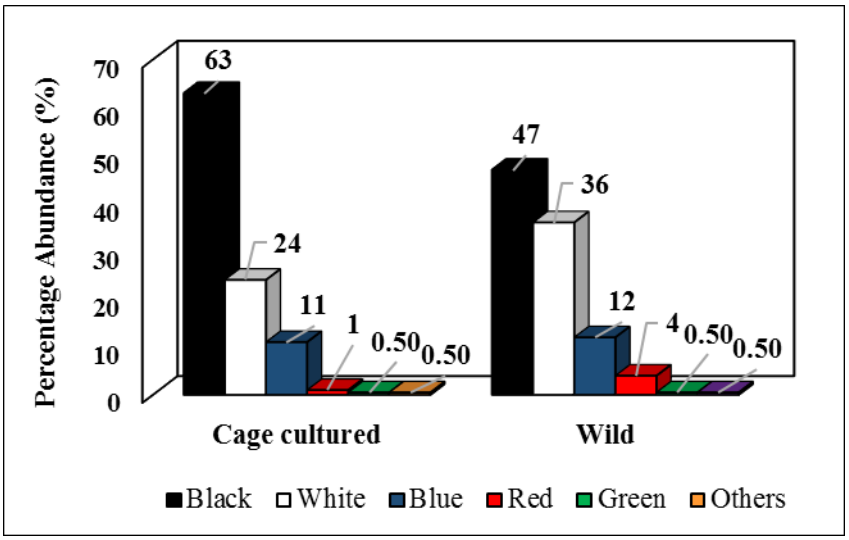



Figure 3. Percentage abundance (%) of microplastic based on colours between cage cultured and wild *L. calcarifer* from Setiu Wetlands

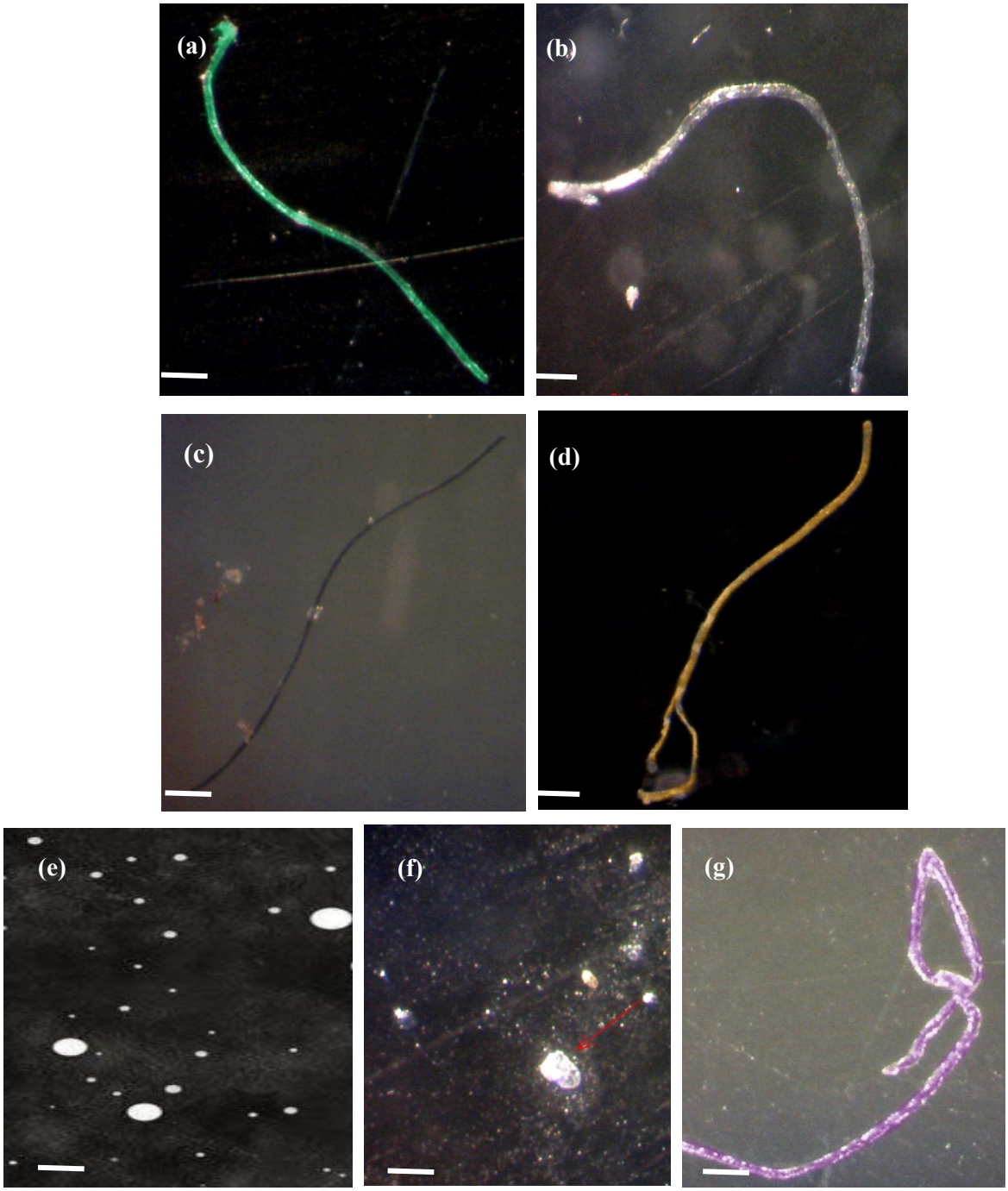



Figure 4. The shapes and colours of microplastic found in cage cultured and wild *L. calcarifer* a) green threadlike b) transparent threadlike, c) black threadlike, d) orange threadlike, e) white spherical, f) white fragment, and g) purple threadlike. Scale bars: 0.1 mm

**Characterisation of microplastics**

The FTIR spectra associated to microplastics are shown in Figure 5 and Figure 6. The collected microplastic particles identified by FTIR spectroscopy analysis proposed that the microplastics found in both wild and cage-cultured *L. calcarifer* were mostly polyamide (PA) (Figure 5) and polyvinyl alcohol (PVA) (Figure 6). In Figure 5, the functional group associated towards microplastic composition shows a strong peak at 3342 $cm^{-1}$ for N-H stretching vibrations from the terminal amine group. Additionally, the N-H bending shows the vibration at ν=1510 $cm^{-1}$. The absorption band at ν=2852 $cm^{-1}$ may be attributed to C-H aliphatic stretching modes, with the band at ν=1428 $cm^{-1}$ matches with the bending of C-$H_2$ vibrations, showing the existence of alkyl chains in the collected microplastics. These findings are in agreement with the previous works reported by Charles et al. [15] and Pavia et al. [16] to elucidate the composition of nylon (polyamide). The band at ν=1706 $cm^{-1}$ corresponds to the C=O carbonyl stretching group vibration, which implies a small part of swaying vibration in the microplastic sample obtained.

The FTIR spectra of PVA carrying all major peaks related to hydroxyl and acetate groups were observed during this study (Figure 6), and similar to the pure PVA spectra recorded by Mansur et al. [17] and Nicodom [18] in their research. The bands observed at ν=3321 – 3423 $cm^{-1}$ are linked to the stretching of O–H from the intermolecular and intramolecular hydrogen bonds, which is suggested due to the high hydrophilic forces among PVA polymeric chains [19]. The vibrational band observed at ν=2840 – 3000 $cm^{-1}$ refers to the stretching of C–H from alkyl groups. Moreover, the arrangement of carbonyl, C=O, which can be distributed randomly along the alkyl chain demonstrated by the bands showed around ν=1706 $cm^{-1}$, is due to the stretching of C=O from the acetate group remaining from PVA [20]. This overlaps with the O-H bending peak [17]. The peaks between ν=1174 and 1219 $cm^{-1}$ show the C-$H_2$ wagging and C-O carboxyl stretching at ν=1028–1128 $cm^{-1}$ vibration absorptions. Thus, it indicates the amorphous and crystalline nature of PVA [17, 20]. PVA is usually amorphous, albeit can be found as a semicrystalline structure for some products. Therefore, this band has been used previously as an indicator for PVA structure as semicrystalline synthetic polymer [17, 21].

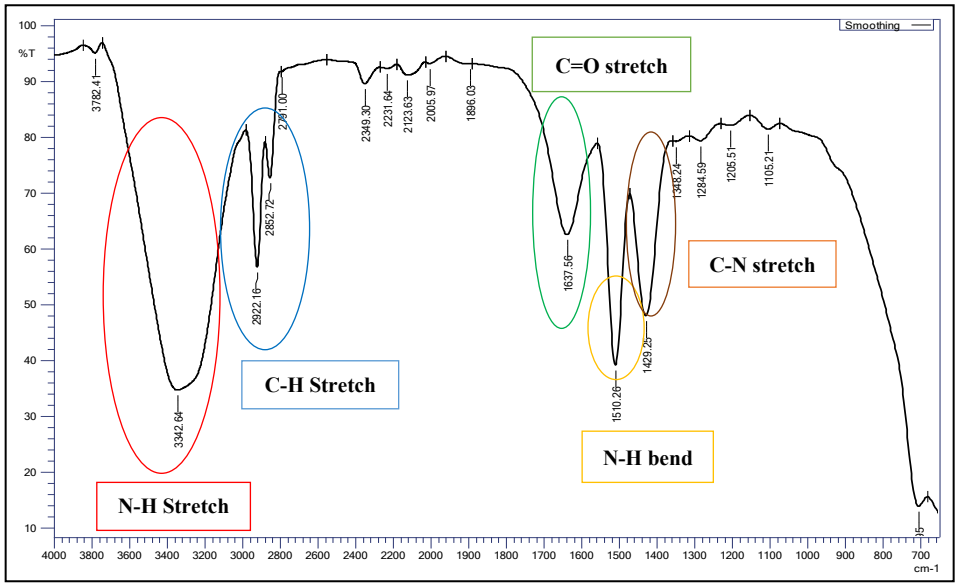



Figure 5. FT-IR spectrum showing the functional group associated to polyamide composition

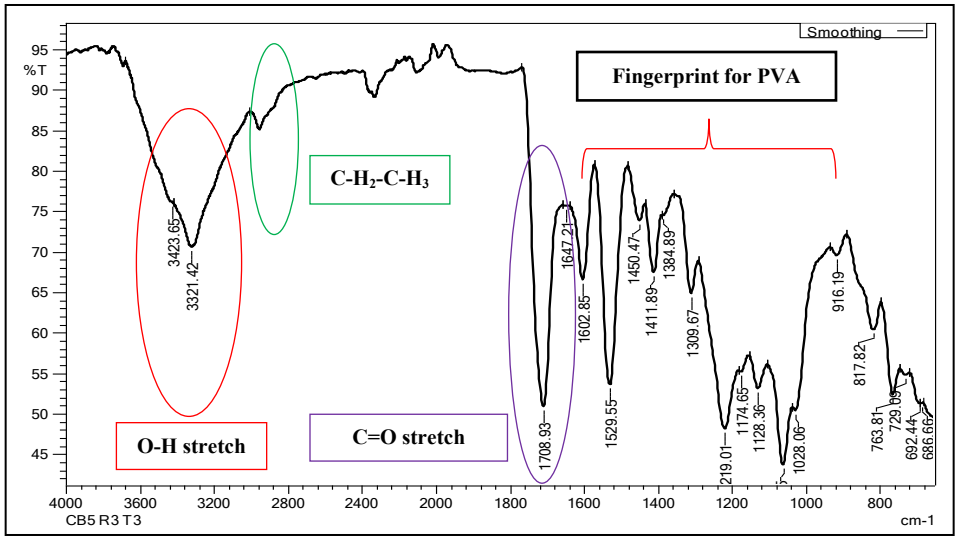



Figure 6. FT-IR spectrum showing the functional group associated to polyvinyl alcohol composition

**Spatial variation**

In this study, wild fish showed significantly higher abundance of microplastics than cage-cultured fish ($p < 0.05$). Microplastic ingestion is closely related to different feeding strategies [22, 23, 24]. Brandao et al. [25] suggested that fouling and high density plastics are examples of items that can be ingested by fish through feeding habitat. In this case, this ingestion is probably linked to the normal feeding activity of the fish. Wild fishes of *L. calcarifer* are known to feed on various preys emerging from different locations and environment as they drift all over the estuary. In contrast, cultured fishes are known to have feeding activities limited to their aquaculture area.

Feeding habitat also plays an important role in the ingestion of debris and lead to the increase of the abundance or bioavailability of microplastics. Higher abundance may be related to different habitats of fishes, and the presence of plastic debris near the seabed is normally high [26]. Referring to Figure 1, the sampling locations of wild and cage-cultured *L. calcarifer* are far from each other. Cage-cultured fishes were collected northwards from Setiu Wetlands, adjacent to the settlement area. Meanwhile, wild fishes were caught nearer to the passage of South China Sea, where several fishermen boats and ships commute in and out of the wetland. The area sampled for wild species has a possibility of higher microplastic particle content in water column as it could be transported from the sea via ocean current and wind. Distinctive habitat also contributes to the difference in microplastic ingestion of the fishes.

The highest microplastic recorded in the gastrointestinal tract of both wild and cage-cultured species is threadlike form; however, the colour coated or additives do not really determine the types of microplastics [27]. Besides the likely contribution from fisheries to the billions of synthetic fibres in the water column, fibres are common in the aquatic environments to which they are delivered in large concentration via wastewater outflow. Browne et al. [28] suggested that the possible sources of fibres in the marine environment are related to the discharge from the sewage sludge or fishing industry, which makes it as the main factor contributing to the emerging microplastics. In fact, cage-cultured fishes ingested more threadlike particles compared to wild species of *L. calcarifer*, probably resulting from the disintegration of nets used in the aquaculture ponds. In contrast, the fragment type was reported remarkably higher in quantity for wild fishes, as it could be denser than water, expected to sink and therefore being accidentally ingested by wild *L. calcarifer*. Pearson correlation also exhibits strong relationship between threadlike and fragment ($r = 0.90$) but weak towards spherical shape ($r = 0.18$).

The main polymers found are PA and PVA, where both polymers are slightly denser than water. The standard type of cage used for fish aquaculture, which is made up of synthetic materials, explains the higher number of PA existed in the gastrointestinal tract of cage-cultured species. PA is one of the major materials used to manufacture the nets. In addition, the chances of natural food supply in cages are much less; hence a regular stock of food is necessary.

The foods are usually composed of raw materials of animals such as small fish heads and inner organs. Thus, there is a higher possibility for the presence of microplastics in cage-cultured species, which is caused by the foods fed. Higher PVA inhabits wild species due to its property that is denser than water and disintegrated fragments from the settlement of abandoned fishing gears and nets on the bottom floor. Furthermore, the existence of human settlements is believed to have contributed to the large volume of microplastic waste, particularly from domestic activities.

**Comparison with literature studies**

Since this study is considered as the first report for estuary fishes, the occurrence of polymer type was compared with previously documented literature. A study carried out in the Norwegian coast explicates that the polyester materials become the major fraction of microplastics observed in fish gut samples [29]. Microplastic abundance high in this area is closely linked to high density of population and anthropogenic activities (Bergen City Harbour). Polyester materials were believed to be derived from polypropylene rope, synthetic clothing, and other polyester products. Moreover, it accounted for 88% of the microplastics found in full stomach samples, which leads to the understanding that the materials are retained longer in the fish body similar to their foods. The comparison of the main polymers found in fish samples is tabulated in Table 2.

In Durban Harbour, 72.8% of the microplastics were observed in mullet samples. Polystyrene is one of the polymer subjects found in this study, but it only contributed 7.3% of the total plastics [30]. The most abundant is in fibre form with white colour. It is worth to note that the correlation between plastic ingestion and fish length or size is not significantly different. The source of pollution especially the emergence of fibres is believed to have originated from domestic or industrial discharge nearby. Meanwhile, recent studies reported by Pazos et al. [31] and Güven et al. [32] indicated that the emergence of a new contaminant affects the multispecies of fishes collected in estuary and coastal areas, respectively. Fibres become the prevalent type of microplastics found in both areas.

Table 2. Comparison of polymer type found in microplastics debris in this study and literature

| Species | Study area | Polymer Identifed | Reference |
|---|---|---|---|
| *Gadus morhua* | Norwegian coast, Norway | Polyester | [29] |
| *Mugil cephalus* | Durban Harbour, South Africa | Polystyrene | [30] |
| Multi species[a] | Rio de la Plata estuary, Brazil | - | [31] |
| Multi species[b] | Mediterranean coast, Turkey | Polypropylene, Polyethylene, Polyester | [32] |
| *Lates calcarifer* | Setiu Wetland, Malaysia | Polyamide and Polyvinyl alcohol | This study |

[a] 11 species fish, [b] 28 species fish

## Conclusion

In this present study, microplastic ingestion has been reported to be pervasive in the gastrointestinal tract of both wild and cage-cultured species of *L. calcarifer* from Setiu Wetlands, Terengganu. The abundance of microplastics is higher in wild species compared to cage-cultured species, which is linked to the dynamics of habitat and feeding activity. PA and PVA are the main polymer compositions found in the gastrointestinal tract of the fishes examined. To the best of our knowledge, the result reported in this study is the first evidence of estuarine fish contaminated by microplastics. Therefore, we highly recommend that in future work, the whole gastrointestinal tract and digestion process should be used in the investigation of microplastic pollution in fish and also not limited to Asian sea bass species only.

## Acknowledgement

The authors are thankful to the Ministry of Higher Education (MOHE) and Universiti Malaysia Terengganu for the financial research grant FRGS 59457. The authors would also like to extend the gratitude to Prof. Dr. Norhayati Mohd. Tahir, Assoc. Prof. Dr. Siti Aishah Abdullah (School of Marine and Environmental Sciences) and Dr.

Shumpei Iehata (School of Fisheries and Aquaculture Sciences) for their valuable assistance and guideline while conducting this research.

**References**

1. Browne, M. A., Underwood, A. J., Chapman, M. G., Williams, R., Thompson, R. C. and van Franeker, J. A. (2015). Linking effect of anthropogenic debris to ecological impacts. *Proceedings of the Royal Society B: Biological Sciences*, 28: 2014 – 2929.
2. Browne, M. A., Dissanayake, A., Galloway, T. S., Lowe, D. M. and Thompson, R. C. (2008). Ingested microscopic plastic translocates to the circulatory system of the mussel, *Mytilus edulis* (L.). *Environmental Science & Technology*, 42: 5026 – 5031.
3. Ivor Do Sul, J. A., Costa, M. F., Barletta, M. and Cysneiros, F.J. (2013). Pelagic microplastics around an archipelago of the Equatorial Atlantic. *Marine Pollution Bulletin*, 75: 305 – 307.
4. Boerger, C. M., Lattin, G. L., Moore, S. L. and Moore, C. J. (2010). Plastic ingestion by planktivorous fishes in the North Pacific Central Gyre. *Marine Pollution Bulletin*, 60(12): 2275 – 2278.
5. Possatto, F. E., Barletta, M., Costa, M. F., do Sul, J. A. I. and Dantas, D. V. (2011). Plastic debris ingestion by marine catfish: An unexpected fisheries impact. *Marine Pollution Bulletin*, 62(5): 1098 –1102.
6. Lusher, A. L., McHugh, M. and Thompson, R. C. (2013). Occurrence of microplastics in gastrointestinal tract of pelagic and demersal fish from the English Channel. *Marine Pollution Bulletin*, 67: 94 – 99.
7. Foekema, E. M., De Gruijter, C., Mergia, M. T., van Franeker, J. A., Murk, A. J. and Koelmans, A. A. (2013). Plastic in north sea fish. *Environmental Science & Technology*, 47(15): 8818 – 8824.
8. Rummel, C. D., Löder, M. G., Fricke, N. F., Lang, T., Griebeler, E. M., Janke, M. and Gerdts, G. (2016). Plastic ingestion by pelagic and demersal fish from the North Sea and Baltic Sea. *Marine Pollution Bulletin*, 102(1): 134 – 141.
9. Barasarathi, J., Agamuthu, P., Emenike, C. U. and Fauziah, S. H. (2014). Microplastic abundance in selected mangrove forest in Malaysia. *In Proceeding of the ASEAN Conference on Science and Technology*, pp. 1 – 5.
10. Noik, V. J. and Tuah, P. M. (2015). A first survey on the abundance of plastics fragments and particles on two sandy beaches in Kuching, Sarawak, Malaysia. *In IOP Conference Series: Materials Science and Engineering,* 78(1): 012035.
11. Ibrahim, Y. S. (2016). Microplastics ingestion by *Scapharca cornea* at Setiu Wetland, Terengganu, Malaysia. *Middle-East Journal of Scientific Research*, 24: 2129 – 2136.
12. Amin, N. M. and Hasan, F. A. (Eds.). (2003). Setiu Wetlands: Tranquility amidst plenty, 1st Ed. Kolej Universiti Sains dan Teknologi Malaysia: Kuala Terengganu, Malaysia.
13. Rocha-Santos, T. and Duarte, A. C. (2015). A critical overview of the analytical approaches to the occurrence, the fate and the behavior of microplastics in the environment. *TrAC Trends in Analytical Chemistry*, 65: 47 – 53.
14. Cole, M., Webb, H., Lindeque, P. K., Fileman, E. S., Halsband, C. and Galloway, T. S. (2014). Isolation of microplastics in biota-rich seawater samples and marine organisms. *Scientific Reports*, 4: 4528.
15. Charles, J., Ramkumaar, G. R., Azhagiri, S. and Gunasekaran, S. (2009). FTIR and thermal studies on nylon-66 and 30% glass fibre reinforced nylon-66. *Journal of Chemistry*, 6: 23 – 33.
16. Pavia D. L., Lampman G. M., Kriz G. S. and Vyvyan J. R. (2008). Infrared Spectroscopy, In: Introduction to Spectroscopy. Brooks/Cole: CA, USA.
17. Mansur, H. S., Sadahira, C. M., Souza, A. N. and Mansur, A. A. (2008). FTIR spectroscopy characterization of poly(vinyl alcohol) hydrogel with different hydrolysis degree and chemically crosslinked with glutaraldehyde. *Materials Science and Engineering: C,* 28: 539 – 548.
18. Nicodom Ltd (2007). Nicodom libraries: poly vinyl alcohol. Retrieved from http://www.ftir-polymers.com. [Access date: 21st March 2017].
19. Hassan, C. M. and Peppas N. A. (2000). Structure and applications of poly (vinyl alcohol) hydrogels produced by conventional crosslinking or by freezing/thawing methods. *Advance Polymer Science*, 153: 37 – 65.
20. Mansur H. S. Orélice R. L. and Mansur A. A. P (2004). Characterization of poly (vinyl alcohol)/poly(ethylene glycol) hydrogels and PVA-derived hybrids by small-angle X-ray scattering and FTIR spectroscopy. *Polymers*, 45: 7193 – 7202.
21. Hennink W. E. and Nostrum C. F. (2002) Novel crosslinking methods to design hydrogels. *Advance Drug Delivery Reviews*, 17: 13 – 36.

22. Anastasopoulou, A., Mytilineou, C., Smith, C. J. and Papadopoulou, K. N. (2013). Plastic debris ingested by deep-water fish of the Ionian Sea (Eastern Mediterranean). *Deep Sea Research Part I: Oceanographic Research Papers,* 74: 11 – 13.
23. Battaglia, P., Pedà, C., Musolino, S., Esposito, V., Andaloro, F. and Romeo, T. (2016). Diet and first documented data on plastic ingestion of *Trachinotus ovatus* L. 1758 (Pisces: Carangidae) from the Strait of Messina (central Mediterranean Sea). *Italian Journal of Zoology*, 83: 121 – 129.
24. Romeo, T., Pietro, B., Pedà, C., Consoli, P., Andaloro, F. and Fossi, M. C. (2015). First evidence of presence of plastic debris in stomach of large pelagic fish in the Mediterranean Sea. *Marine Pollution Bulletin*, 95: 358 – 361.
25. Brandão, M. L., Braga, K. M. and Luque, J. L. (2011). Marine debris ingestion by Magellanic penguins, *Spheniscus magellanicus* (Aves: Sphenisciformes), from the Brazilian coastal zone. *Marine Pollution Bulletin*, 62: 2246 – 2249.
26. Woodall, L. C., Sanchez-Vidal, A., Canals, M., Paterson, G. L., Coppock, R., Sleight, V. and Thompson, R. C. (2014). The deep sea is a major sink for microplastic debris. *Royal Society Open Science*, 1: 140 – 317.
27. Andrady, A. L. (2011). Microplastic in the marine environment. *Marine Pollution Bulletin*, 62: 1596 – 1605.
28. Browne, M. A., Crump, P., Niven, S. J., Teuten, E., Tonkin, A., Galloway, T. and Thompson, R. (2011). Accumulation of microplastic on shorelines worldwide: sources and sinks. *Environmental Science & Technology*, 45(21): 9175 – 9179.
29. Bråte, I. L. N., Eidsvoll, D. P., Steindal, C. C. and Thomas, K. V. (2016). Plastic ingestion by Atlantic cod (*Gadus morhua*) from the Norwegian coast. *Marine Pollution Bulletin*, 112(1): 105 – 110.
30. Naidoo, T., Smit, A. J. and Glassom, D. (2016). Plastic ingestion by estuarine mullet Mugil cephalus (Mugilidae) in an urban harbour, KwaZulu-Natal, South Africa. *African Journal of Marine Science*, 38(1): 145 – 149.
31. Pazos, R. S., Maiztegui, T., Colautti, D. C., Paracampo, A. H. and Gómez, N. (2017). Microplastics in gut contents of coastal freshwater fish from Río de la Plata estuary. *Marine Pollution Bulletin*, 122 (1–2): 85 – 90.
32. Güven, O., Gökdağ, K., Jovanović, B. and Kıdeyş, A. E. (2017). Microplastic litter composition of the Turkish territorial waters of the Mediterranean Sea, and its occurrence in the gastrointestinal tract of fish. *Environmental Pollution*, 223: 286 – 294.

*Malaysian Journal of Analytical Sciences, Vol 21 No 5 (2017): 1065 - 1073*
*DOI: https://doi.org/10.17576/mjas-2017-2105-08*

MALAYSIAN JOURNAL OF ANALYTICAL SCIENCES
*Published by The Malaysian Analytical Sciences Society*
ISSN 1394 - 2506

# EXTRACTION AND CHARACTERIZATION OF CELLULOSE FROM AGRICULTURAL RESIDUE - OIL PALM FRONDS

## (Pengekstrakan dan Pencirian Selulosa daripada Bahan Buangan Pertanian - Pelepah Kelapa Sawit)

Siti Rasila Ainaa Mohd Rasli[1], Ishak Ahmad[2], Azwan Mat Lazim[2], Ainon Hamzah[1]*

[1]*School of Biosciences and Biotechnology, Faculty of Science and Technology*
[2]*School of Chemical Sciences and Food Technology, Faculty of Science and Technology*
*Universiti Kebangsaan Malaysia, 43600 UKM Bangi, Selangor, Malaysia*

**Corresponding author: ainonh@gmail.com*

Received: 4 March 2017; Accepted: 22 August 2017

**Abstract**

Cellulose from oil palm fronds (OPF) was extracted using a cost-effective method combining physical treatment (high pressure steaming) and repeated chemical treatments (alkali and bleaching). Alkali and bleaching treatments were performed using low concentrations of sodium hydroxide and sodium chlorite, respectively. High levels of cellulose were successfully extracted, with 4 grams of cellulose for every 10 grams of raw oil palm fronds. The morphology of the cellulose was investigated using variable pressure scanning electron microscope (VPSEM). Fourier transform infrared spectroscopy (FTIR), X-ray diffraction (XRD) and thermogravimetric analyser (TGA) were used for structural analysis. The extracted cellulose was found to have smaller diameter (8 – 10 µm) and smoother surface compared to the untreated fibres. The results from FTIR, XRD and TGA indicate that the hemicelluloses and lignin were extensively removed from the isolated cellulose. Alkali treatment helped in removal of hemicelluloses, while bleaching assisted in delignification. The extracted cellulose showed high crystalline index of 68.75% and degradation temperature of 350 $^{o}$C resulted from removal of lignin and hemicelluloses via alkali and bleaching treatments.

**Keywords:** *Elaeis guineensis*, high pressure steaming, alkali treatment, bleaching treatment, cellulose

**Abstrak**

Selulosa telah diekstrak daripada pelepah kelapa sawit dengan menggunakan kaedah yang menjimatkan kos iaitu gabungan kaedah fizikal (pemanasan pada tekanan tinggi) dan rawatan kimia (alkali dan pelunturan). Rawatan alkali dilakukan dengan menggunakan sodium hidroksida manakala rawatan pelunturan pula dilakukan dengan menggunakan sodium klorit. Kedua-dua bahan kimia tersebut digunakan pada kepekatan yang rendah. Sebanyak 4 gram selulosa berjaya diekstrak daripada setiap 10 gram pelepah kelapa sawit. Morfologi selulosa yang diekstrak telah dikaji dengan menggunakan mikroskopi elektron pengimbas tekanan berubah-ubah (VPSEM). Manakala spektroskopi inframerah transformasi Fourier (FTIR), analisis belauan sinar-X (XRD) dan analisis termogravimetri (TGA) telah digunakan bagi tujuan menganalisis struktur selulosa. Selulosa yang diekstrak mempunyai diameter yang lebih kecil (8 – 10 µm) dan permukaan yang lebih licin berbanding gentian yang tidak dirawat. Hasil daripada FTIR, XRD dan TGA menunjukkan bahawa hemiselulosa dan lignin telah dibuang dalam jumlah yang tinggi selepas rawatan-rawatan tersebut dijalankan. Rawatan alkali membantu membuang hemiselulosa manakala rawatan pelunturan pula membantu membuang lignin daripada sampel. Selulosa yang diekstrak mempunyai tahap kristal yang tinggi iaitu 68.75% dan suhu degradasi yang tinggi iaitu 350 $^{o}$C berikutan daripada pembuangan hemiselulosa dan lignin selepas rawatan alkali dan pelunturan dilakukan.

**Kata kunci:** *Elaeis guineensis*, pemanasan pada tekanan tinggi, rawatan alkali, rawatan pelunturan, selulosa

## Introduction

*Elaeis guineensis*, commonly known as oil palm, is one of the main crops in Malaysia and is widely planted all over the country, especially in Sabah, Sarawak and Johor. With oil palm covering about 4.49 million hectares. Malaysia is the world's second largest palm oil exporter, accounting for 39% of the world palm oil production [1]. The oil palm plantation industry contributes to huge amount of agricultural wastes (lignocellulosic biomass) every year such as the OPFs from thinning, replanting and pruning processes. The huge amounts of waste generated from the oil palm industry have led to concerns over the managements of the wastes. The most common disposal methods for such agricultural waste include use in mulching or leaving it to decompose naturally in the plantation area. These practices are harmful to the environment. The decomposing OPFs interfere with plantation processes and serve as pest breeding sites [2], especially for insects like rhinoceros beetles.

Natural plant fibres are made up of cellulose, amorphous polymers (hemicelluloses and lignin) and small number of extractives. Cellulose is a naturally occurring hydrophilic polymer and is the main substance that makes up plant cell walls and contributes to the physical stability of the cells [3]. Thus, cellulose is probably the most abundantly available organic compound on Earth. Cellulose does not dissolve in water, and has high crystallinity and high molecular weight [4].

The OPFs are composed of 58% cellulose, 24% hemicelluloses, 5% lignin, 8% extractives and 5% ashes [5]. The amount of cellulose in the OPF is higher than other waste parts (leaves and empty fruit bunches) of oil palm trees [6].

The accumulating amount of the agricultural waste or OPFs could serve as an inexpensive cellulose source compared to wood, that could be exploited for many uses and purposes. The common uses of cellulose are in paper, film, textiles, building material and food additives production. Recent studies have shown strong interest in this organic polymer due to its superior characteristics, such as high water absorption capacity [7] and large surface areas, compared to other biomaterials. Besides the traditional uses of cellulose, some of the latest cellulose-based innovations are focusing on solving environmental problems, such as cellulose-based absorbents for oil spills and heavy metal pollution on water or land [8]. Additionally, there have been studies on the uses of cellulose in bio-based filters for industrial [9] and municipal wastewater treatment [10].

The extraction of cellulose from oil palm fronds using an inexpensive method could serve as an alternative environmental friendly way of managing the largely produced agricultural wastes. The purpose of this study was to extract the cellulose from oil palm fronds using a cost-effective method, namely a combination of physical and chemical methods. The physical method used was the high pressure steaming, while the chemical methods were alkali and bleaching treatments. Then, the extracted cellulose was characterized using a variable pressure scanning electron microscope (VPSEM), Fourier transmission infrared (FTIR), thermogravimetric analyser (TGA), and X-ray diffraction (XRD).

## Materials and Methods

### Materials

Fresh Oil Palm Fronds (OPFs) were collected from the MPOB (Malaysian Palm Oil Board), Bangi, Selangor. The chemical reagents used were sodium hydroxide (NaOH) and sodium chlorite ($NaClO_2$). To assist in physical treatment, an autoclave (Hirayama, HVE50) was used.

### Pre-treatment

The collected OPF were cut into smaller pieces (15 – 20 cm) before dried at room temperature for 3 days. The dried OPFs were then ground into smaller size of 5 – 6 cm and soaked in water for 3 days. The water was changed daily. The samples were then rinsed with distilled water several times to remove dirt and sand particles. Then, the samples were autoclaved at 121$^{o}$C, 21 psi for 15 minutes. The dark brown supernatant was removed and the samples were washed with distilled water a few times until clear water was observed. The OPFs were dried at room temperature and ground into 1 – 2 cm pieces.

**Extraction of OPF-cellulose**
Cellulose extraction from OPF was done using the method from Chan et al. [11] with some modifications. The autoclaved and dried samples were treated with 4% sodium hydroxide (NaOH) at 80 $^{o}$C for 2 hours with continuous stirring. Then, a bleaching treatment was applied using 1.7% sodium chlorite ($NaClO_2$) at pH 4.5 and 80 $^{o}$C for 4 hours with continuous stirring. The alkali and bleaching treatments were repeated three and four times, respectively. The ratio of sample to solvent was 5:100 (g/mL). After each treatment, the samples were rinsed few times using distilled water. The extracted cellulose was dried in an oven at 60 $^{o}$C and the dried weight of the cellulose was determined.

**Characterization: Variable pressure scanning electron microscope**
The morphological studies of extracted cellulose from OPF were carried out with a variable pressure scanning electron microscope (Leo 1450VP/ Zeiss)

**Fourier transmission infrared spectroscopy**
The chemical investigation of functional groups in extracted cellulose from OPF was done using Fourier Transmission Infra-Red Spectroscopy (Perkin Elmer Spectrum 400 FT-IR/FT-NIR and Spotlight 400 Imaging System).

**X-ray diffraction**
The crystallinity of the extracted cellulose was studied using an X-ray diffractometer (Bruker/D8 Advance). The crystalline index was determined based on the method by Segal [12] using the following equation:

$$X_c = \frac{I_{002} - I_{am}}{I_{002}} \text{ x } 100 \quad (1)$$

where $X_c$ is the crystalline index, $I_{002}$ is the peak intensity of crystalline materials and $I_{am}$ is the peak intensity of amorphous materials.

**Thermogravimetric analysis**
Thermogravimetric analysis was carried out using Mettler Toledo thermogravimetric analyser (TGA/SDTA 85-F) to measure the thermal stability of all samples. Measurements were made with a nitrogen gas flow of 10 mL min$^{-1}$ and heated from room temperature to 600 $^{o}$C with heating rate of 10 $^{o}$C min$^{-1}$.

## Results and Discussion

**Extraction of OPF-cellulose**
The combination of physical and chemical methods succeeded in extracting high total cellulose yield, 40% (w/w) on a dry weight basis. The pre-treatment of samples by high pressure steaming played a role in removing loose substances from the surface of the fibres and assisted in penetration of the alkali and bleaching reagents by reducing the polymerization degree of the fibres.

**Morphological analysis**
The colour of the raw oil palm frond fibres changed from brown to white after treatment (Figure 1). The extracted cellulose fibres had smaller diameters (8 – 10 µm) and smoother surfaces compared to the untreated fibres, which had diameters ranging from 150 to 300 µm and rough surfaces (Figure 2).

Both colour and morphological changes were due to removal of lignin and other extractives during high pressure steaming and bleaching treatments, resulting in lighter colour and smoother surface of the fibres, respectively. The colour of wood is determined by the phenolic substances (lignin and extractives). The removal of extractives caused a slight colour change, while removal of lignin caused a more significant colour change [13]. The removal of the binding substance also induced the dispersal of the fibre bundles into individual fibres by cleavage of the bonds between the hemicelluloses and lignin, producing fibres with smaller diameters. A smoother surface of the extracted cellulose resulted from all the treatments (high pressure steaming, alkali and bleaching treatments) which removed impurities from the surface of the fibres.

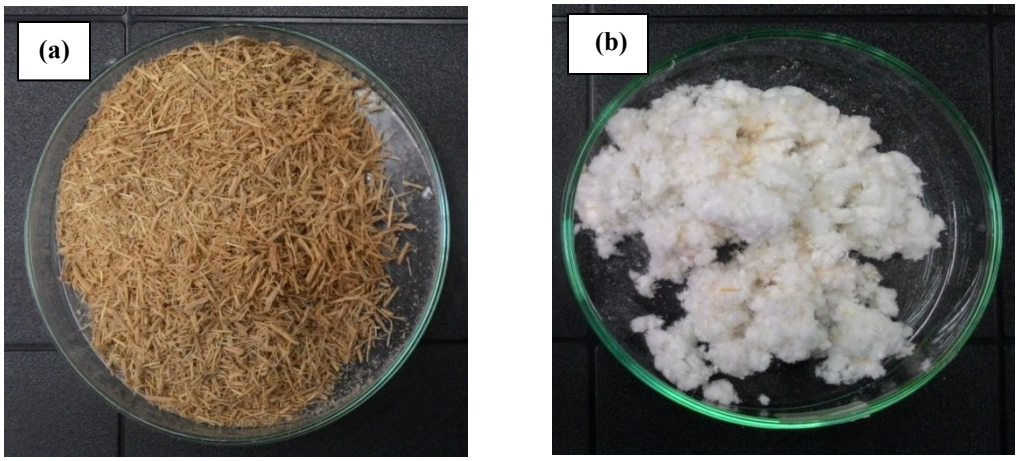



Figure 1. Ground oil palm fronds. (a) Before treatments and (b) after treatments

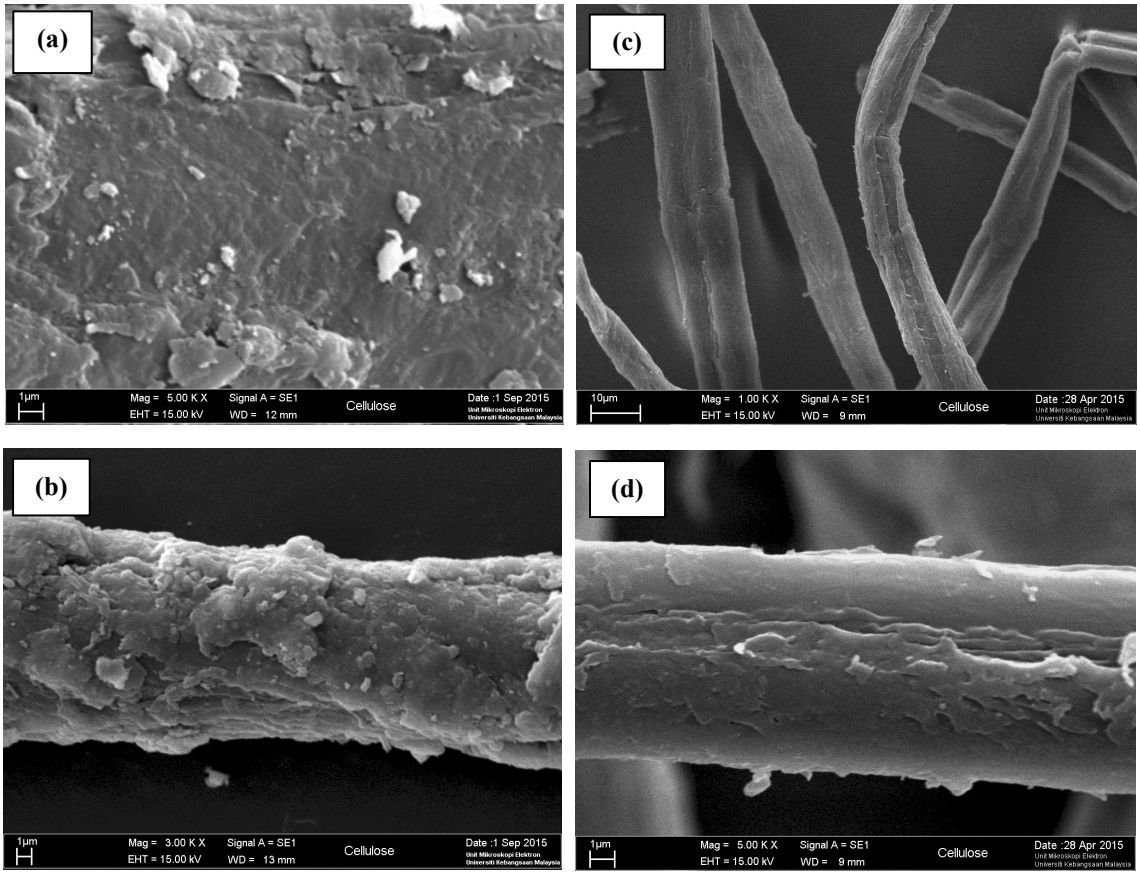



Figure 2. Variable pressure scanning electron microscope micrographs of oil palm frond samples. (a) and (b) before treatments, while (c) and (d) after treatments

**FTIR spectroscopy analysis**

The FTIR results (Figure 3) suggest the complete removal of the functional groups of both lignin and hemicelluloses from the extracted cellulose. The peak 1246.70 $cm^{-1}$ (C-O-C, aryl-alkyl-ether) which is the ether bond between the hydroxyl groups of lignin and the carbohydrates in the raw OPF was completely removed after alkali treatment. This indicates the complete removal of the hemicelluloses. Meanwhile, the intensity of the peak 1594.81 $cm^{-1}$ (C=C of lignin aromatic ring) was reduced after alkali treatment and completely removed after bleaching. As reported by Johar et al. [14], the alkali treatment removed hemicelluloses and other impurities from the raw samples, while partially removed the cementing material of lignin.

The peaks at 897.86 $cm^{-1}$ and 3318.87 $cm^{-1}$ were attributed to the ß-glycosidic linkage of cellulose and adsorbed water in the samples, respectively. The peaks at 2922.03 $cm^{-1}$ and 1031.86 $cm^{-1}$ indicate the C-H and C-O groups of the cellulose. The high pressure steaming treatment softened the lignin and released it from the cell wall to the fibre surface. This physical treatment played a role in increasing the accessible surface area and size of cell wall pores for penetration of the alkali and bleaching reagents.

The alkali treatment removed hemicelluloses from the sample through hydrolysis of glycosidic bonds in hemicelluloses and led to the cleavage of the ester bonds between the hydroxyl groups of lignin and the carboxyl groups of the hemicelluloses. Hemicelluloses are susceptible to the two degradation reactions by alkali reactions due to the high number of end-groups resulted from low polymerization level. The hemicelluloses were released from the fibres and complete removal was achieved by the repeated washing of the samples with distilled water.

Delignification of the fibres was achieved by complete removal of the lignin on the fibre surface. The lignin was degraded by the bleaching treatments using an oxidising agent, sodium chlorite which oxidized the ether bonds between the hydroxyl groups of lignin and the carbohydrates. The most common chemicals used in bleaching process are hydrogen peroxide, oxygen, and sodium chlorite. Sodium chlorite is the most effective for bleaching without reducing total carbohydrate [15]. Acidified sodium chlorite has been reported to cleave the phenolic ether bonds in plant cell walls at high temperatures [16]. The bleaching treatment also removed remaining hemicelluloses by oxidation reactions that cleaved the glycosidic linkages of the residues [15].

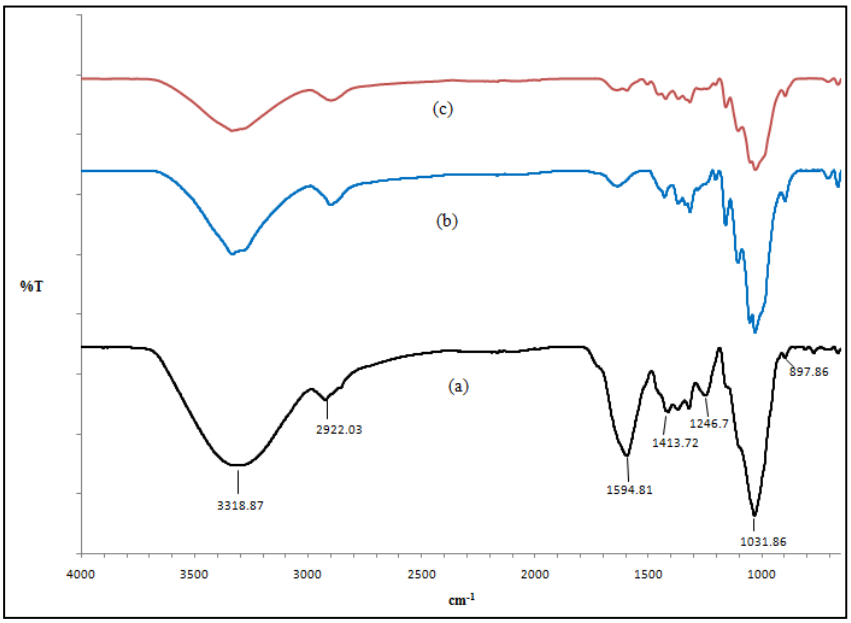



Figure 3. Fourier transmission infrared spectroscopy spectra of the extracted cellulose from oil palm fronds: (a) raw oil palm frond, (b) after alkali treatment and (c) after bleaching treatment

**X-ray diffraction measurements**

Cellulose is made of diverse crystalline arrangements which result from the hydrogen bonding of the hydroxyl groups. The major peaks (22.6º) in the X-ray diffractogram are attributed to the crystalline structure of the cellulose, while the low intensity at 18º reflects the amorphous background of the samples.

X-ray diffraction results (Figure 4) show a crystalline index of 24.31% for the raw oil palm fronds, which progressively increased after alkali treatment (52.46%) and bleaching treatment (68.75%). The crystalline index values of all samples are listed in Table 1. The increasing crystalline index of the samples after alkali and bleaching treatments were due to progressive removal of the hemicelluloses and lignin. According to Sheltami et al. [17], the crystallinity level of cellulose is influenced by removal of amorphous polymers.

The crystalline index of the extracted cellulose is higher compared to the 57.19% reported by Syamani et al. [18] for the extracted cellulose from oil palm fronds by pulping and bleaching using hydrogen peroxide. The amount of cellulose is higher due to higher removal of the amorphous polymers via alkali and sodium chlorite bleaching treatments. In addition, the major peaks progressively became sharper after each treatment, reflecting the greater distinguished crystalline structure of the samples.

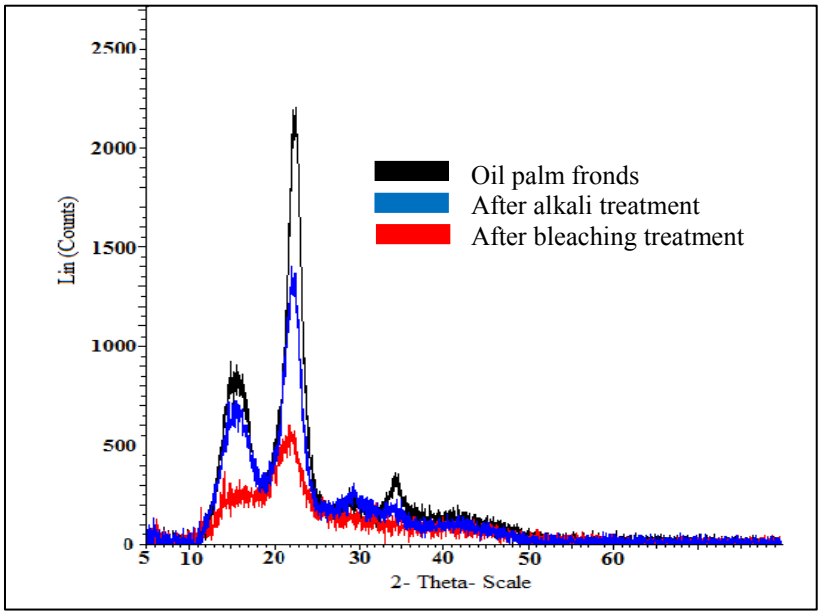



Figure 4. X-ray diffraction patterns for raw oil palm frond, after alkali treatment and after bleaching treatment

Table 1. Crystalline index of the oil palm fronds at different stages of treatment

| **Samples** | ***2θ*(am)(º)** | ***2θ*(002)(º)** | **Xc(%)** |
|---|---|---|---|
| Oil palm fronds | 18.5 | 22 | 24.31 |
| After alkali treatment | 18.8 | 22.5 | 52.46 |
| After bleaching treatment | 18.5 | 22.2 | 68.75 |

**Thermogravimetric analysis**

Both TG (Figure 5) and DTG curves (Figure 6) showed the thermal stability of the raw, alkali-treated and bleached samples. All three samples showed initial weight loss at temperature lower than 100 $^{o}$C which attributed to the water evaporation from the samples which was the moisture adsorbed to the fibre. After bleaching, weight reduction increased due to the hydrophilic nature of the cellulose, which had a higher level of moisture compared to the raw and alkali-treated samples.

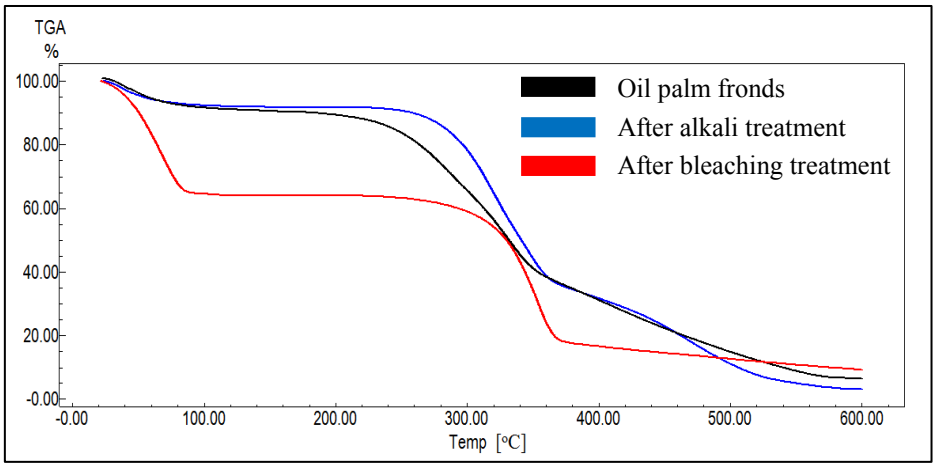



Figure 5. Residual mass (TG) curves of raw oil palm frond, after alkali treatment and after bleaching treatment

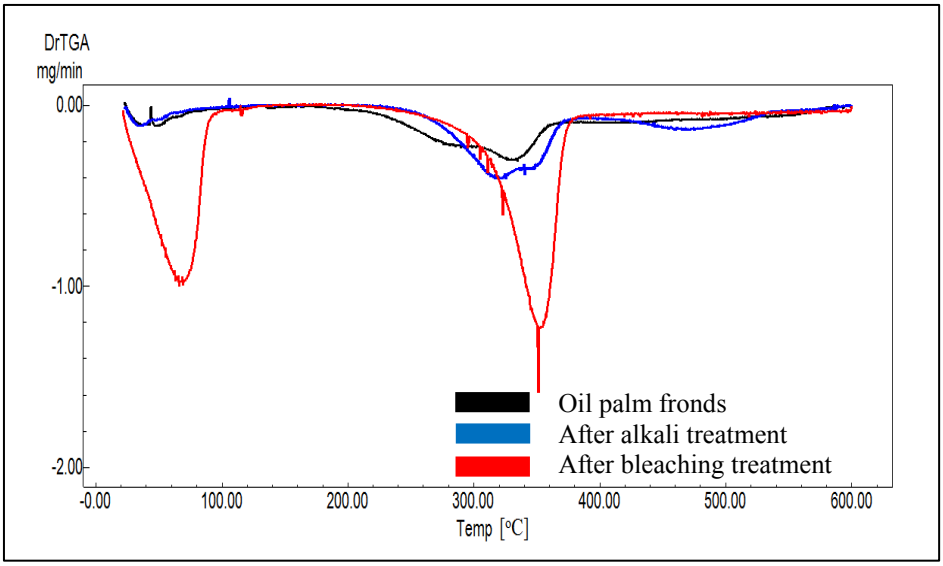



Figure 6. Differential residual mass (DTG) curves of raw oil palm frond, after alkali treatment and after bleaching treatment

For the raw and alkali-treated samples, there were small broad peaks at 280 $^{o}$C and 320 $^{o}$C before the major peak, reflecting the low molecular weight compounds, hemicelluloses and lignin [19]. These peaks were completely removed after bleaching treatment.

The major peaks of the DTG curves demonstrate the degradation temperatures of the samples. The bleached sample showed highest degradation temperature at 350 $^{o}$C compared to the raw and alkali-treated samples, which degraded at 330 $^{o}$C and 345 $^{o}$C respectively. The progressively increased degradation temperature of the samples after each treatment was due to the progressive removal of lignin and hemicelluloses. Hemicelluloses and lignin had lower decomposition temperatures compared to cellulose [20]. This was due to the higher crystallinity of the cellulose, which increased the thermal stability of the sample [21].

However, the bleached sample showed highest weight loss at the decomposition temperature. Meanwhile, the raw and alkali-treated samples retained higher residual mass. This was due to the presence of the lignin and ashes within the raw and alkali-treated samples [22]. Ashes were regenerated after the samples were burnt, causing only slight weight reduction of the samples [14]. These thermal analysis results are quite consistent with the results obtained from the FTIR and crystallinity measurements.

## Conclusion

Cellulose was successfully extracted from oil palm fronds using a cost-effective method, with a combination of physical treatment and low concentration chemical methods. High amounts of cellulose (40% w/w) were successfully extracted with a high crystalline index (68.75%) and thermal stability (350 $^{o}$C), demonstrating extensive removal of amorphous polymers from the samples. The extraction of cellulose from the oil palm fronds could be exploited on a larger scale and serve as a proper practice for agricultural waste management. Further research should be carried out to study the mechanical properties of cellulose, including tensile strength and moisture regain, for better understanding on the potential uses of the OPFs cellulose.

## Acknowledgement

The authors would like to express their gratitude to Universiti Kebangsaan Malaysia (GUP-2014-081) for their financial support.

## References

1. Malaysian Palm Oil Council (2015). Malaysia palm oil industry. http://www.mpoc.org.my/Malaysia_Palm_Oil_Industry.aspx. [Access online 13 April 2015].
2. Altieri, M. A., Nicholls, C. I. and Fritz, M. A. (2014). Manage insects on your farm. Sustainable Agriculture Research and Education (SARE), Maryland: pp. 15 – 17.
3. Duchemin, B., Thuault, A., Vicente, A., Rigaud, B., Fernandez, C. and Eve, S. (2012). Ultrastructure of cellulose crystallites in flax titles fibres. *Cellulose*, 19(6): 1837 – 1854.
4. Kuutti, L. (2013). Cellulose, starch and their derivatives for industrial applications. VTT Technical Research Centre of Finland, Finland: pp. 35 – 37.
5. Sabrina, S. M. S., Roshanida, A. R. and Norzita, N. (2013). Pretreatment of oil palm fronds for improving hemicelluloses content for higher recovery of xylose. *Jurnal Teknologi (Sciences & Engineering)*, 62(2): 39 – 42.
6. Sulaiman, O., Salim, N., Nordin, N. A., Hashim, R., Ibrahim, M. and Sato, M. (2012). The potential of oil palm trunk biomass as an alternative source for compressed wood. *Bioresources*, 7(2): 2688 – 2706.
7. Kala, D. R., Rosenani, A. B., Fauziah, C. I., and Thorirah, L. A. (2009). Composting oil palm wastes and sewage sludge for use in potting media of ornamental plants. *Malaysian Journal of Science*, 13: 77 – 91.
8. Nguyen, S. T., Feng, J., Le, N. T., Le, A. T. T., Hoang, N., Tan, V. B. C. and Duong, H. M. (2013). Cellulose aerogel from paper waste for crude oil spill cleaning. *Industrial and Engineering Research*, 52: 18386 – 13891.
9. He, Z., Meng, M., Yan, L., Zhu, W., Sun, F., Yan, Y., Liu, Y. and Liu, S. (2015). Fabrication of new cellulose acetate blend imprinted membrane assisted with ionic liquid ((BMIM)Cl) for selective adsorption of salicylic acid from industrial wastewater. *Separation and Purification Technology*, 145: 63 – 74.

10. Nataraj, S. K., Roy, S., Patil, M. B., Nadagouda, M. N., Rudzinski, W. E. and Aminabhavi, T. M. (2011). Cellulose-acetate-coated α-alumina ceramic composite tubular membranes, for wastewater treatment. *Desalination*, 281: 348 – 353.
11. Chan, C. H., Chia, C. H., Zakaria, S., Ahmad, I. and Dufresne, A. (2013). Production and characterization of cellulose and nano-crystalline cellulose from Kenaf Core Wood. *Bioresources*, 8(1): 785 – 794.
12. Segal, L., Creely, J. J., Martin, A. E. and Conrad, C. M. (1959). An empirical method for estimating the degree of crystallinity of native cellulose using the X-ray diffractometer. *Textile Research Journal*, 29(10): 786 – 794.
13. Chen, Y., Tshabalala, M., A., Gao, J., Stark, N. M. and Fan, Y. (2014). Colour and surface chemistry changes of pine wood flour after extraction and delignification. *Bioresources*, 9(2): 2937 – 2948.
14. Johar, N., Ahmad, I. and Dufresne, A. (2012). Extraction, preparation and characterization of cellulose fibres and nanocrystals from rice husk. *Industrial Crops and Products*, 37: 93 – 99.
15. Park, J., Shin, H., Yoo, S., Zoppe, J. O. and Park, S. (2015). Delignification of lignocellulosic biomass and its effect on subsequent enzymatic hydrolysis. *Bioresources*, 10(2): 2732 – 2743.
16. Wells, B., Mccann, M., C., Shedletzky, E., Delmer, D. and Roberts, K. (1994). Structural features of cell walls from tomato cells adapted to grow o the herbicide 2,6-dichlorobenzonitrile. *Journal of Microscopy*, 173: 155 – 164.
17. Sheltami, R. M., Abdullah, I., Ahmad, I., Dufresne, A. and Kargarzadeh, H. (2012). Extraction of cellulose nanocrystals from mengkuang leaves (*Pandanus tectorius*). *Carbohydrate Polymers*, 88: 772 – 779.
18. Syamani, F. A., Subyakto, S. and Suryani, A. (2015). Changes in oil palm frond fibre morphology, cellulose crystallinity and chemical functional groups during cellulose extraction phases. *Chemistry and Materials Research*, 7: 105 – 114.
19. Neto, W. P. F., Silverio, H. A., Dantas, N. O. and Pasquini, D. (2013). Extraction and characterization of cellulose nanocrystals from agro-industrial residue – Soy hulls. *Industrial Crops and Products*, 42: 480 – 488.
20. Morán, J. I., Alvarez, V. A., Cyras, V. P. and Vázquez, A. (2008). Extraction of cellulose and preparation of nanocellulose from sisal fibers. *Cellulose,* 15: 149 – 159.
21. Abe, K., Iwamoto, S. and Yano, H. S. (2009). Obtaining cellulose nanofibers with a uniform width of 15 nm from wood. *Biomacromolecules*, 8(10): 3276 – 3278.
22. Fahma, F., Iwamoto, S., Hori, N., Iwata, T. and Takemura, A., (2011). Effect of pre-acid- hydrolysis treatment on morphology and properties of cellulose nanowhiskers from coconut husk. *Cellulose*, 18: 443 – 450.

*Malaysian Journal of Analytical Sciences, Vol 21 No 5 (2017): 1074 - 1079*
*DOI: https://doi.org/10.17576/mjas-2017-2105-09*

MALAYSIAN JOURNAL OF ANALYTICAL SCIENCES
*Published by The Malaysian Analytical Sciences Society*
ISSN 1394 - 2506

# DEGRADATION OF IMAZAPYR AND IMAZAPIC IN AQUEOUS SOLUTIONS AND SOIL UNDER DIRECT SUNLIGHT

## (Degradasi Imazapyr dan Imazapic dalam Larutan Akueus dan Tanah di bawah Cahaya Matahari)

Siti Norashikin Mohamad Shaifuddin[1], Hazilia Hussain[1]*, Hamzah Fansuri Hassan[2], Nazri Che Dom[1], Razi Ikhwan Md Rashid[1]

[1]*Department of Environmental Health and Safety*
[2]*Department of Basic Sciences, Faculty of Health Sciences*
*Universiti Teknologi MARA, 42300 UiTM Puncak Alam, Selangor, Malaysia*

**Corresponding author: hazilia@puncakalam.uitm.edu.my*

Received: 25 January 2017; Accepted: 3 July 2017

**Abstract**

Photolytic degradation of imazapyr and imazapic in aqueous solutions (pH 3, 7 and 9) and soil under direct sunlight were studied. A total of 0.1 mL of aqueous solutions containing herbicides were collected at 0, 1, 2 and 3 days and were directly analyzed using high performance liquid chromatography equipped with ultraviolet detector (HPLC-UV) without further clean-up process. Soils that were treated with herbicides were sampled at seven different days (0, 1, 5, 10, 16, 23 and 30). The photolytic results showed that imazapyr and imazapic degraded faster in solutions compared to soils (> 90%). Photolysis of imidazolinone herbicides became more effective as the pH value increased. The half-lives for imazapyr and imazapic degradation on soil surface under sunlight were calculated at 126 days and 85.56 days, respectively. Low degradation of imazapyr and imazapic in soil becomes a concern since it may contribute to the persistency of imidazolinone herbicides in this media. The use of these herbicides should be planned well to reduce the risk of herbicides leaching into groundwater and posing risk to non-target crops and organism.

**Keywords**: photolysis, imazapyr, imazapic, aqueous solutions, soil

**Abstrak**

Kajian degradasi fotolitik bagi imazapyr dan imazapic dalam larutan akueus (pH 3, 7 dan 9) dan tanah di bawah cahaya matahari telah dijalankan. Sebanyak 0.1 mL cecair larutan yang mengandungi racun rumpai telah diambil pada hari 0, 1, 2 dan 3 dan terus dianalisis menggunakan kromatografi cecair berprestasi tinggi dengan pengesan ultra-ungu (HPLC-UV) tanpa melalui sebarang proses pembersihan. Tanah yang telah dicampurkan dengan racun rumpai telah disampelkan pada tujuh hari yang berbeza (0, 1, 5, 10, 16, 23 dan 30). Keputusan fotolitik menunjukkan imazapyr dan imazapic lebih cepat terurai di dalam cecair berbanding dengan tanah (>90%). Fotolisis racun rumpai imidazolinon adalah lebih berkesan apabila pH meningkat. Jangka masa separuh hayat untuk imazapyr dan imazapic terurai di permukaan tanah di bawah cahaya matahari masing-masing adalah 126 dan 85.56 hari. Degradasi rendah bagi imazapyr dan imazapic dalam tanah telah menjadi suatu kebimbangan kerana ia boleh menyumbang kepada pengekalan racun rumpai imidazolinon di dalam media ini. Penggunaan racun rumpai ini perlu dirancang dengan sebaiknya bagi mengurangkan risiko untuk racun larut terlesap ke dalam air bawah tanah dan menimbulkan risiko kepada tanaman dan organisma yang bukan sasarannya.

**Kata kunci:** fotolisis, imazapyr, imazapic, larutan akueus, tanah

## Introduction

As one of the main contributors to Malaysian economy, the agriculture sector takes up a major part of the land used in this country [1]. Additionally, Malaysian government has invested millions of ringgit to ensure this sector is well developed and this includes introducing modern agricultural input such as herbicides [2]. This contributes to the increase of herbicide application in Malaysian agricultural areas [1]. Herbicide is the most common method used to prevent or control the unwanted weeds in agricultural areas. Not only that, it is also used to maintain the quality of crops and reduce the percentage of yield losses [2]. Some common examples of herbicides are 2,4-D dimethylamine, paraquat, glyphosate and propanil [1]. However, the use of herbicide is harmful in certain quantities as some herbicides may leach into the root zone once they are introduced into the environment. Consequently, this can either result in better weed control or cause damage to surrounding environment as not all of the applied chemicals are able to reach the target site [3]. Therefore, it is very important to understand the fate of the chemicals in the environment.

Currently, commercial herbicides containing two active ingredients (imazapyr and imazapic) are widely used in rice field area to control the growth of weedy rice [4, 5]. The growth of weedy rice in rice field affects the annual rice yield in Malaysia [2, 6] and this contributes to economic loss among farmers [3]. Thus, the combination of imidazolinone-tolerant rice (IMI-TR) seeds developed by MARDI and BASF (Malaysia) with a single application of imazapyr/ imazapic in rice field area [4, 5] are found to be able to reduce weed management cost and yield higher quality of rice [6]. Imazapyr and imazapic belong to imidazolinone group that can eliminate subjected weeds by inhibiting the action of plant enzyme acetohydroxyacid synthase (AHAS) and interfering with their growth [7, 8].

The applications of imidazolinone herbicides are assumed to be environmentally safe because of their low toxicity effects on mammals as well as being highly effective with a very low application rate [4, 9, 10]. This in turn reduces the amount of herbicides released into the environment and ecosystem [6]. However, the application of herbicides in rice field for a long period of time may give rise to several environmental issues. One of the environmental concerns is the persistency of imidazolinone herbicide in soil [11 – 14] and groundwater [15]. Since these herbicides are able to remain for a long period of time in the environment, it may pose risks to non-target organisms such as fish [16, 17].

There are many factors affecting the persistency of herbicides molecule in the environment and these may include sorption, volatilisation, leaching and degradation (abiotic and biotic) [3, 14]. Photodegradation may play an important role for the breakdown of herbicides in environment because all pesticides are susceptible to this process to a certain degree [3]. Since imazapyr and imazapic are applied to foliage or soil surface, they are more prone to break down by sunlight [3]. Therefore, the aims of this study were to determine the capability of imazapyr and imazapic herbicides to break down under direct sunlight as well as to calculate their half-life in aqueous solutions and soil surface.

## Materials and Methods

### Chemicals

Imazapyr and imazapic with 99.5% and 99.9% purity respectively were purchased from Active Advance Technology Company. Acetonitrile (ACN) grade for liquid chromatography (LC), acetic acid, monopotassium phosphate and sodium hydroxide (NaOH) were obtained from Merck (Malaysia). Potassium biphthalate, borax and hydrochloric acid (HCl) were purchased from Juara Saintifik (Malaysia). Imazapyr and imazapic solutions were prepared by dissolving the weighed herbicide in ACN.

### Preparation of buffer solutions

Three different buffer solutions (pH 3, 7 and 9) were prepared based on United States Environmental Protection Agency's (USEPA) Fate, Transport and Transformation Test Guidelines [18]. The buffer solutions were prepared by mixing 0.1N HCl with 0.1M potassium biphthalate (pH 3); 0.1N NaOH with monopotassium phosphate (pH 7); and 0.025 M borax with 0.1N HCl for pH 9. All buffers solutions and glassware used in this experiment were sterilised by using autoclave [9].

**Photolysis of imazapyr and imazapic in aqueous solutions**

Outdoor photodegradation experiments for imazapyr and imazapic in aqueous solutions and soil were conducted in greenhouse at Universiti Teknologi MARA Puncak Alam Campus. The photolysis activity was tested for individual and mixture of the herbicides using USEPA protocol [19]. All three prepared buffer solutions were then treated with herbicide solution in order to obtain 10 µg $mL^{-1}$ of imazapyr and imazapic concentration respectively as well as a mixture of imazapyr and imazapic in the ratio of 1:3. 10 mL buffered solutions of herbicide (pH 3, 7 and 9) were placed in three different sterilized glass test tubes before being exposed under sunlight. All these solutions were prepared in triplicate along with two control samples. The average temperatures during experimental days were varied between 26 ºC to 36 ºC. The sunlight intensity was also measured during the exposure. An amount of 0.1 mL of aliquots was pipetted aseptically from each test tube on day 0, 1, 2 and 3 into 2 mL amber vials for further analysis with High Performance Liquid Chromatography (HPLC) [20].

**Photodegradation of imazapyr and imazapic on soil**

For this research, the study of photodegradation on soil surface was carried out in reference to USEPA Guideline [21]. A soil sample was collected from the surface layer (0 to 10 cm) from the field. The sample was air-dried at room temperature, passed through 2 mm sieve and was later autoclaved at 121ºC twice [9]. An amount 5 grams of sterilized soil was weighed into sterile petri dish and herbicide solution was applied on the top of spread soil to obtain the initial concentration of 5 µg $g^{-1}$. For control samples, the petri dishes containing soil-herbicide were wrapped with aluminum foil to keep out light and maintain darkness. The samples were exposed to the sunlight and then were collected at 0, 1, 5, 10, 16, 23 and 30 days. Three exposed and control samples were sampled for each sampling day and transferred into sterile centrifuge tube for herbicides extraction. Herbicides were extracted from the soil samples by shaking 20 mL of 0.5 M NaOH and centrifuging at 2000 rpm for 10 minutes. These steps were repeated twice. The decanted supernatants were filtered through 0.45 µm filter and were analyzed directly using HPLC [20].

**HPLC analysis**

An Agilent 1200 High Performance Liquid Chromatography equipped with UV detector was used for quantification of imazapyr and imazapic residues [20]. The wavelength for the detector was set up at 251 nm. ACN: acidified water (pH 2.88) (35:65, v/v) was used as mobile phase with flow rate of 1.0 mL $min^{-1}$ while for chromatography, An Agilent Zorbax SB-C18 column (4.6 mm i.d. x 250 mm, 5 µm) was used.

**Data analysis**

The percentages of imazapyr and imazapic degradation were calculated using equation 1 [22]:

$$\text{Photodegradation (\%)} = (C_0 - C_t)/C_0 \times 100\% \quad (1)$$

Calculations for imidazolinone herbicides half-life were performed using kinetic equation 2 and 3, respectively [9, 19, 23]:

$$\ln (C_0/C_t) = kt \quad (2)$$

$$t_{1/2} = 0.693/k \quad (3)$$

where, $C_0$ refers to the initial concentration of herbicide, $C_t$ represents the herbicide concentration at time *t*, k is photolytic rate constant, and $t_{1/2}$ exemplifies the half-life.

## Results and Discussion

**Photolysis of imidazolinone herbicides in aqueous solutions**

The results for degradation of imidazolinone herbicides in aqueous solutions were shown in Table 1. These findings suggested that both imazapyr and imazapic herbicides were able to completely degrade (> 90%) within 72 hours under direct sunlight (light intensity ranged 162 to 1059 watt/$m^2$). The half-life values of imazapyr under direct sunlight were 16.54 hours (pH 3), 12.42 hours (pH 7) and 12.18 hours (pH 9). Imazapic was found to have half-lives of 32.35 hours, 10.06 hours and 10.76 hours in pH 3, 7 and 9, respectively. Trials on combination of both

herbicides under acidic pH level showed that imazapyr was completely degraded within 24 hours while imazapic residue was calculated at 20.94 percent within 72 hours.

Table 1. Photolysis of imidazolinone herbicides under direct sunlight in buffer solutions

| **Sampling Days** | **Percentage of Residues (%)** | | | | | | | | |
|---|---|---|---|---|---|---|---|---|---|
| **Herbicide** | **Imazapyr** | | | **Imazapic** | | | **Imazapyr: Imazapic (1:3)** | | |
| **pH solution** | **3** | **7** | **9** | **3** | **7** | **9** | **3** | **7** | **9** |
| 0 | 100 | 100 | 100 | 100 | 100 | 100 | 100:100 | 100:100 | 100:100 |
| 1 | 65.87 | 23.73 | 23.69 | 55.89 | 17.42 | 17.09 | 0:51.76 | 25.29:16.80 | 26.03:17.39 |
| 2 | 15.98 | 5.01 | 4.09 | 28.83 | 5.91 | 2.10 | 0:30.29 | 4.04:2.16 | 4.74:2.74 |
| 3 | 4.89 | 1.80 | 1.67 | 21.38 | 0.72 | 0.97 | 0:20.94 | 1.39:0.88 | 1.68:1.08 |

Results presented in Table 1 suggested that pH values of buffer solutions affected the photolysis rate for imazapyr and imazapic. Degradation rate of imidazolinone herbicides tested increased as pH increased, which was in agreement with previous studies [23, 24, 25]. This might be due to the effect of higher molar absorption coefficients at higher pH value [24]. Imazapyr and imazapic herbicides were more rapidly degraded in solution compared to on soil surface (Table 1 and Table 2). However, the photolysis rate of imidazolinone herbicides in actual water samples might be slower due to the presence of light screening compounds such as humic acid and natural organic matter (NOM) [3, 26].

**Photodegradation of imidazolinone herbicides on soil**

The percentages of photodegradation of two imidazolinone herbicides were tabulated in Table 2. Imazapic had a higher degradation rate ($t_{1/2}$= 85.56 days) compared to imazapyr ($t_{1/2}$= 126 days). The ability of these herbicides to remain longer might be due to the properties of the soil itself which absorbed the photons, therefore reducing the availability of photons to degrade the herbicides compounds [9, 27]. Previous study showed that imazapyr and imazapic had an enhanced adsorption and a lower desorption in rice field soil due to the presence of high clay content and organic matter [28], especially at low pH value. The soil sample used consisted of 57.50% clay, 37.50% silt, 0.90% sand, 4.26% total organic carbon and a pH of 5.29. Since the soil sample used in this study had the properties of high clay content and organic matter which were similar to a previous study [28], it suggested that these two imidazolinone herbicides were tightly bound to soil particles. This indicated that very little of these compounds were available for degradation via photolytic activity. Moreover, air-drying step of soil sample preparation in this study might cause an increase in soil-herbicide binding as the soil water content decreased [27]. Once the herbicides penetrated underneath the soil surface, the photodegradation activity became low [27] and this might contribute to their persistency in the environment. Since imazapyr and imazapic were able to remain longer in the soil, these herbicides also had a higher probability to leach into groundwater as reported previously [14, 29].

Table 2. Photodegradation of imidazolinone herbicides on soil exposed with direct sunlight

| **Sampling Days** | **Percentage of Residues (%)** | | |
|---|---|---|---|
| **Herbicide** | **Imazapyr** | **Imazapic** | **Imazapyr: Imazapic (1:3)** |
| 0 | 100 | 100 | 100: 100 |
| 1 | 98.24 | 92.77 | 98.69: 97.07 |
| 5 | 96.99 | 90.88 | 95.25: 94.20 |
| 10 | 94.52 | 87.66 | 93.58: 93.25 |
| 16 | 93.18 | 83.03 | 91.30: 92.01 |
| 23 | 92.04 | 81.03 | 87.73: 83.53 |
| 30 | 84.75 | 78.40 | 78.12: 81.16 |

## Conclusion

Photodegradation of imidazolinone herbicides could be an important factor for their breakdown in the environment as demonstrated in the tabulated results. Degradation of imazapyr and imazapic in aqueous solutions were faster compared to on soil surface under direct sunlight. Low photolytic degradation in soil became a concern since it might pose risk to non-target crops and organisms. Further study on biotic degradation might expand new angle in this field since microbe could be used as a degrading organism to break down imidazolinone herbicides, especially under anaerobic condition. The approach in this paper could be taken as a general applied method to analyses other degraded pollutants, especially those that had similar functional group.

## Acknowledgement

The authors would like to acknowledge the research grant from Universiti Teknologi MARA (LESTARI 21/2016) for supporting this research.

## References

1. Ismail, B. S., Sameni, M. and Halimah, M. (2011). Evaluation of herbicide pollution in the Kerian ricefields of Perak. Malaysia. *World Applied Sciences Journal*, 15(1): 5 – 13.
2. Fuad, M. J., Junaidi, A. B., Habibah, A., Hamzah, J., Toriman, M. E., Lyndon, N., Er, A. C., Selvadurai, S. and Azima, A. M. (2012). The impact of pesticides on paddy farmers and ecosystem. *Advances in Natural and Applied Sciences*, 6(1): 65 – 70.
3. Tiryaki, O. and Temur, C. (2010). The fate of pesticide in the environment. *Journal of Biological & Environmental Sciences*, 4(10): 29 – 38.
4. Azmi, M., Azlan, S., Yim, K. M., George, T. V. and Chew, S. E. (2012). Control of weedy paddy in direct-seeded paddy using the clearfield production system in Malaysia. *Pakistan Journal of Weed Sciences Research,* 18: 49 – 53.
5. Idris, R. (2012). Dua gen baru dihasilkan MARDI akhiri belenggu padi angin. http://www.bharian.com.my/articles/DuagenbarudihasilkanMARDIakhiribelenggupadiangin/Article/print_html. [Access online 19 December 2012].
6. Hidayatul, N., Anusar, S., Mazlan, N., Ahmad, E., Engku, K., Juraimi, A. S. and Yusop, M. R. (2014). Comparative study of vegetation and reproductive growth. *Journal of International Society for Southeast Asian Agricultural Sciences*, 20(1): 41 – 51.
7. Hess, F. G., Harris, J. E., Pendino, K. and Ponnock, K. (2001). Imidazolinone. In: handbook of pesticide toxicology. Academic Press, San Diego: pp. 1641 – 1651.
8. Colquhoun, J. (2001). How herbicides work: Uptake, translocation, and mode of action. http://osuext.intermountaintech.org/download/how herbicides work.pdf. [Access online 18 December 2012].
9. Ramezani, M., Oliver, D. P., Kookana, R. S., Gill, G. and Preston, C. (2008). Abiotic degradation (photodegradation and hydrolysis) of imidazolinone herbicides. *Journal of Environmental Science and Health, Part B: Pesticides, Food Contaminants, and Agricultural Wastes*, 43(2): 105 – 112.
10. Tan, S., Evans, R. R., Dahmer, M. L., Singh, B. K. and Shaner, D. L. (2005). Imidazolinone-tolerant crops: History, current status and future. *Pest Management Science*, 61: 246 – 257.
11. Rotterdam Convention (2001). Interim secretariat for rotterdam convention on the prior informed consent procedure for certain hazardous chemicals and pesticides in international trade - PIC CIRCULAR XIV. http://www.pic.int/Portals/5/en/Circular/CIRC14EN.pdf. [Access online 13 February 2013].
12. Carrier, M., Perol, N., Herrmann, J.-M., Bordes, C., Horikoshi, S., Paisse, J. O., Baudot, R. and Guillard, C. (2006). Kinetics and reactional pathway of imazapyr photocatalytic degradation influence of ph and metallic ions. *Applied Catalysis B: Environmental,* 65: 11 – 20.
13. Bundt, A. C., Avila, L. A., Pivetta, A., Agostinetto, D., Dick, D. P. and Burauel, P. (2015). Imidazolinone degradation in soil in response to application history. *Planta Daninha,* 33(2): 341 – 349.
14. Souza, M. F., Neto, M. D. C., Marinho, M. I., Saraiva, D. T., Faria, A. T., Silva, A. A. and Silva, D. V. (2016). Persistence of imidazolinones in soils under a clearfield system of rice cultivation. *Planta Daninha,* 34(3): 589 – 596.
15. Börjesson, E., Torstensson, L. and Stenström, J. (2004). The fate of imazapyr in a Swedish railway embankment. *Pest Management Science,* 60 (6): 544 – 549.

16. Moraes, B. S., Clasen, B., Loro, V. L., Pretto, A., Toni, C., Antonio de Avila, L., Marchesan, E., Luiz de Oliveira Machado, S., Zanella, R. and Reimche, G. B. (2011). Toxicological response of *Cyprinus Carpio* after exposure to a commercial herbicide containing imazethapyr and imazapic. *Ecotoxicology and Environmental Safety,* 74: 328 – 335.
17. Golombieski, J. I., Sutili, F. J., Salbego, J., Seben, D., Gressler, L. T., da Cunha, J. A., Gressler, L. T., Zanella, R., Vaucher, R. A., Marchesan, E. and Baldisserotto, B. (2016). Imazapyr+imazapic herbicide determines acute toxicity in silver catfish *Rhamdia quelen*. *Ecotoxicology and Environmental Safety*, 128 (2016): 91 – 99.
18. United States Environmental Protection Agency (2008). Fate, transport and transformation test guidelines. EPA 712-C-08-012; Prevention, pesticides and toxic substances (7101). OPPTS 835.2120 hydrolysis. https://www.regulations.gov/document?D=EPA-HQ-OPPT-2009-0152-0009. [Access online 1 January 2014].
19. United States Environmental Protection Agency (1998). Fate, transport and transformation test guidelines. EPA 712-C-98-060; Prevention, pesticides and toxic substances (7101). OPPTS 835.2210 Direct photolysis rate in water by sunlight. https://www.regulations.gov/document?D=EPA-HQ-OPPT-2009-0152-0011. [Access online 1 January 2014].
20. Shaifuddin, S. N. M., Hussain, H. and Hassan, H. F. (2016). Optimization of extraction and detection method for imazapyr and imazapic residues in water, soil and fish tissue samples using high performance liquid chromatography. *Jurnal Teknologi,* 78(6-7): 43 – 48.
21. United States Environmental Protection Agency (USEPA). (2008). Fate, transport and transformation test guidelines. EPA 712-C-08-015; Prevention, pesticides and toxic substances (7101). OPPTS 835.2410 photodegradation on soil. https://www.regulations.gov/document?D=EPA-HQ-OPPT-2009-0152-0015. [Access online 1 January 2014].
22. Abdullah, A. H., Peng, W. T. and Hussein, M. Z. (2016). Degradation of methylene blue dye by CuO-$BiVO_4$ photocatalysts under visible light irradation. *Malaysian Journal of Analytical Sciences*, 20(6): 1338 – 1345.
23. Harir, M., Gaspar, A., Frommberger, M., Lucio, M., El Azzouzi, M., Martens, D., Kettrup, A. and Schmitt-Kopplin, P. (2007). Photolysis pathway of imazapic in aqueous solution: Ultrahigh resolution mass spectrometry analysis on intermediates. *Journal of Agricultural and Food Chemistry,* 55(24): 9936 – 9943.
24. Pandiselvi, V., Sathiyanarayanan, S., Ayyappan, S. and Ramesh, A. (2012). Investigations on the photolysis of imazethapyr in aqueous solutions under direct sunlight by HPLC UV and LC-MS/MS-ESI – application of green alga as a potential biomarker. *International Journal of Chemistry Research*, 3(1): 45 – 51.
25. Mallipudi, N. M., Stout, S. J., da Cunha, A. R. and Lee, A. (1991). Photolysis of imazapyr (AC 243997) herbicide in aqueous media. *Journal of Agricultural and Food Chemistry*, 39(2): 412 – 417.
26. Espy, R., Pelton, E., Opseth, A., Kasprisin, J. and Nienow, A. M. (2011). Photodegradation of the herbicide imazethapyr in aqueous solution: Effects of wavelength, pH, and natural organic matter (NOM) and analysis of photoproducts. *Journal of Agricultural and Food Chemistry*, 59: 7277 – 7285.
27. Curran, W. S., Loux, M. M., Liebl, R. A. and Simmons, F. W. (1992). Photolysis of imidazolinone herbicides in aqueous solution and on soil. *Weed Science,* 40: 143 – 148.
28. Shaifuddin, S. N. M., Hussain, H., Hassan, H. F., Dom, N. C. and Rashid, R. I. M. (2016). Adsorption and desorption of imazapyr and imazapic in soils. http://learningdistance.org/rcstss2016/public/site/rcstss2016_abstracts_ST_final_secured.pdf. [Access online 2 January 2017].
29. Mazlan, A. Z., Hussain, H. and Zawawi, M. A. M. (2016). Assessment of imazapic presence in surface water and groundwater in paddy field area. *Jurnal Teknologi,* 78(5-5): 33 – 37.

*Malaysian Journal of Analytical Sciences, Vol 21 No 5 (2017): 1080 - 1090*
*DOI: https://doi.org/10.17576/mjas-2017-2105-10*

MALAYSIAN JOURNAL OF ANALYTICAL SCIENCES
*Published by The Malaysian Analytical Sciences Society*
ISSN 1394 - 2506

# CALCIUM CONTENT OF LIME MORTARS FROM 19th CENTURY CHURCH RUINS IN THE PHILIPPINES USING VOLUMETRIC ANALYSIS

## (Kandungan Kalsium Mortar Batu Kapur dari Runtuhan Gereja Abad Ke 19 di Filipina Menggunakan Analisis Volumetrik)

Jan-Michael C. Cayme* and Aniano N. Asor, Jr

*Chemistry Department, College of Science,*
*De La Salle University, 2401 Taft Avenue, Malate, Metro Manila, Philippines*

**Corresponding author: jm_cayme@yahoo.com*

Received: 12 April 2017; Accepted: 25 July 2017

**Abstract**

A calcium determination method for lime mortars in old church ruins is described. Two volumetric analysis methods were employed: titration using EDTA solution, and with $KMnO_4$ solution. The binder fraction with sieve size (<0.075mm) was used for titration which is abundant in $CaCO_3$ as established by Fourier-Transform Infrared Spectroscopy (FTIR) technique. The mortar sample from Misamis Oriental yields a mean calcium concentration of 59.60% ± 4.64 and 60.48% ± 6.68 for EDTA and $KMnO_4$, respectively, while the Metro Manila mortar sample is 73.54% ± 2.68 for EDTA and 73.33% ± 6.88 for $KMnO_4$. Two tailed *t*-test and *F*-test analysis confirm that there is no statistical difference between EDTA and $KMnO_4$ methods in determining the calcium content. Atomic Absorption Spectroscopy (AAS) technique validated the mean concentration values obtained from each method with less than 6.4% difference. The proposed titration methods are simple, rapid and sufficiently precise, without the use of expensive analytical instruments. This study is a good alternative method to easily determine the amount of calcium in historic lime mortars which is valuable in heritage conservation work and restoration of old structures in the Philippines.

**Keywords:** lime mortar, titration, Fourier transform infrared spectroscopy, atomic absorption spectroscopy, cultural heritage conservation

**Abstrak**

Satu kaedah penentuan kalsium untuk mortar batu kapur dalam runtuhan gereja lama telah dibincangkan. Dua kaedah analisis volumetrik telah dibangunkan; pentitratan menggunakan larutan EDTA dan $KMnO_4$. Pecahan mengikut saiz ayak (<0.075mm) telah digunakan untuk pentitratan yang kaya dengan $CaCO_3$ yang telah ditentukan oleh teknik inframerah transformasi Fourier (FTIR). Sampel mortar batu kapur dari Misamis Oriental menghasilkan purata kepekatan kalsium 59.60% ± 4.64 dan 60.48% ± 6.68 untuk masing-masing EDTA dan $KMnO_4$, manakala sampel mortar batu kapur Metro Manila adalah 73.54% ± 2.68 untuk EDTA dan 73.33% ± 6.88 untuk $KMnO_4$. Analisis ujian-t dan ujian-F mengesahkan bahawa tidak ada perbezaan signifikan antara kaedah EDTA dan $KMnO_4$ dalam penentuan kandungan kalsium. Teknik spektroskopi serapan atom (AAS) telah menentusahkan nilai kepekatan yang diambil dari setiap kaedah memberikan perbezaan kurang daripada 6.4%. Kaedah pentitratan yang dicadangkan adalah mudah, cepat dan cukup tepat, tanpa menggunakan instrumen analisis mahal. Kajian ini merupakan alternatif yang baik dengan mudah menentukan kandungan kalsium dalam mortar batu kapur bersejarah yang berharga dalam kerja-kerja pemuliharaan warisan dan pemulihan struktur lama di Filipina.

**Kata kunci:** mortar kapur, pentitratan, spektroskopi inframerah transformasi Fourier, spektroskopi serapan atom, pemuliharaan warisan budaya

## Introduction

The overall amount of calcium is an important parameter for replicating historic lime-based mortars for restoration work. Calcium is the principal chemical element found in binders which is the component of mortars responsible for holding together the different stone and sand aggregates. Binders are essentially composed of lime or $CaCO_3$ produced by burning limestone. In the Philippines, lime can also be obtained from crushed seashells and corals [1]. The temperature and manufacturing process of lime is crucial in determining the mortar's physical properties and mechanical behaviour. Specifically, the crystal arrangement, porosity and the lime's reactivity when water is added (slaking) will be affected [2, 3]. The absence of standard methodologies in lime preparation in the past, as well as the lack of detailed documentation on its manufacture in the Philippines, have produced old lime-based mortars which are non-uniform and varied in chemical compositions relative to its location. Hence, proper scientific investigation to understand conventional lime-making techniques in the past based on calcium content is crucial for proper conservation work of historic structures in the Philippines.

This study describes the amount of calcium in a lime-based historic mortar from church ruins built during the Spanish Colonial Period in the Philippines. The country was under Spanish rule for almost 400 years from 1521 to 1898 and was heavily influenced by Roman Catholic traditions. The church ruin in Misamis Oriental in the southern island of Mindanao was built during the mid-1800's [4] while the one collected from Metro Manila, which is the capital city of the Philippines, was constructed in the early 1800's [5]. These sites were chosen for this study because of their different geographical locations, hence, different raw materials used in its construction. It also represents the unique building-making methods characteristic of the Jesuits (Misamis Oriental) and the Franciscans (Metro Manila) which are major Catholic religious orders during the Spanish Era in the Philippines.

Complexometric titration using ethylenediaminetetraacetic acid (EDTA) and oxidation-reduction (redox) titration with potassium permanganate ($KMnO_4$) were the techniques utilized to quantify the amount of calcium in the historic mortar samples from Misamis Oriental and Metro Manila. The accuracy of these methods was confirmed using atomic absorption spectroscopy (AAS). Statistical analysis (*t*-test and *F*-test) was also employed to determine if both titration methods yield comparable results. EDTA can be completely deprotonated to the anion, $EDTA^{4-}$ in basic solution, to form a 1:1 complex with the calcium ions present in the lime mortar sample as shown in equation (1). Since EDTA is a stronger complexing agent than the indicator, Eriochrome black T (EBT), it will displace the calcium-EBT complex forcing the indicator to return to its original form (blue color) marking the endpoint of the titration.

$$CaCO_3 + EDTA^{4-}_{(aq)} \rightarrow Ca(EDTA)^{2-}_{(aq)} + CO_3^{2-}_{(aq)} \quad (1)$$

The redox reaction between oxalic acid and $KMnO_4$ is another method to detect the amount of calcium in old mortar samples. Calcium was precipitated with oxalate ion and dissolved in dilute acid as represented by equation (2). The liberated oxalic acid was titrated with $KMnO_4$ as shown in equation (3), which is a strong oxidizing agent. Due to the intense color of the permanganate ion, it is already sufficient in detecting the endpoint of the titration. The permanganate ion which forms a $Mn^{+7}$ oxidation state was reduced to manganese ion with an oxidation state of $Mn^{+2}$ while carbon was oxidized from $C^{+3}$ to a $C^{+4}$ oxidation states.

$$CaC_2O_{4(aq)} + 2H^+_{(aq)} \rightarrow Ca^{2+}_{(aq)} + H_2C_2O_{4(aq)} \quad (2)$$

$$5H_2C_2O_{4(aq)} + 2MnO_4^-{}_{(aq)} + 6H^+_{(aq)} \rightarrow 10CO_{2(g)} + 8H_2O_{(l)} + 2Mn^{2+}_{(aq)} \quad (3)$$

Different complexometric and redox titration methods were applied for limestone [6, 7] using a variety of titrants and colored indicators, such as disodium EGTA, calcon and EBT indicators [8, 9], and azochromotropic acid derivative indicators [10]. Potentiometric titration using calcium sensitive electrodes [11] was also reported in literature, as well as flow-injection analysis [12] and atomic absorption spectroscopy methods [13]. Calcium oxide was determined in lime mortars by titrating with EDTA and methylene blue indicator [14]; however, the sample preparation and analysis are different from this study. In general, none of these reported methods were applied directly on historic lime-based mortars whose chemical properties were influenced by the local manufacturing process.

## Materials and Methods

### Mortar samples

The lime-based mortar samples were collected from two different sites in the Philippines. One sample was acquired from the southern Mindanao Island at Misamis Oriental in April 2015 and the other was obtained from the northern Luzon Island at Metro Manila, where the capital city of the Philippines is located (Figure 1), in April 2014. Each respective sample was found within the ruins of old Catholic churches built in the 19$^{th}$ century. The sample from Misamis Oriental (8.2g) was gently scraped-off from a coral-stone wall ruin, which is believed to be part of the church's window arch, while the Metro Manila sample (14.7g) was taken from a loose brick fragment wall believed to be a segment of the old church foundation. The mortars used in the analysis were removed from its surrounding materials at an approximate depth of about 0.5 to 1.5 cm from its surface to prevent contamination. Both mortars are made entirely of lime binder which was evident from its powdery texture.

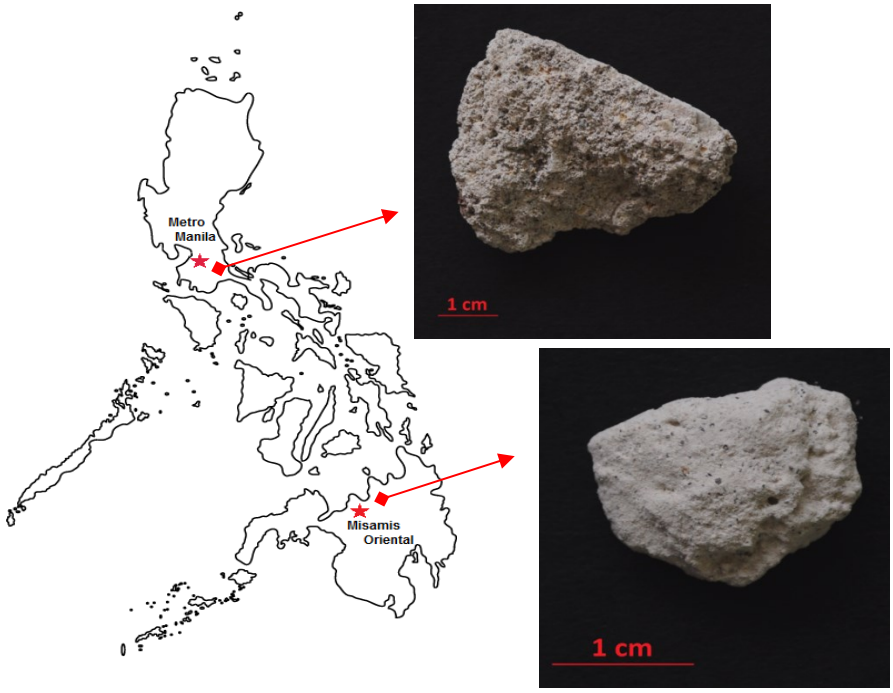



Figure 1. Location map showing the collection site at Misamis Oriental and Metro Manila. Inset photos show the historical lime mortars used for this study

Each mortar samples (between 4.0 to 8.0g) were gently pulverized into small pieces and disaggregated, ensuring that the original texture of the aggregate is not lost in this process. The crushed materials were sieved through sizes of 4.750, 2.360, 1.180, 0.600, 0.425, 0.250, 0.150 and 0.075 mm using a USA Standard Testing Sieve ASTME11 Specification. Fractions smaller than 0.075 mm and retained in the "pan" were also included. Efficient separation of the different fractions was achieved by having the sieves shaken in a mechanical shaker (US Tyler brand) for 5 minutes. The resulting fractions were individually weighed and labelled according to their respective retained sieve size.

### Analysis by Fourier transform infrared spectroscopy

For both mortar samples, a small portion of sieved fraction retained in the "pan" (<0.075mm) was mixed, grounded, and pressed together with KBr powder to form a thin and transparent pellet. The ratio of sample relative to the amount of KBr is about 1 to 2%. Pure analytical grade $SiO_2$ (Sigma-Aldrich) and $CaCO_3$ (Unichem, 98%) were also pelletized with KBr. The IR spectrum was recorded using a Thermo Scientific Nicolet 6700 FT-IR

Spectrophotometer in the finger print region 2400 – 400$cm^{-1}$ with a resolution of 4 $cm^{-1}$ and 32 scans per spectrum [15]. The spectrum was reported as absorbance relative to the wave number.

**Titration with EDTA solution: Standardization of EDTA**
The EDTA solution was prepared by mixing 2.0g EDTA powder (Himedia, 99.5%), 1.0g of NaOH (Unichem, 96%) and 0.15g of $MgCl_2 \cdot 2H_2O$ (Qualikems, 99%). It was diluted with distilled water in a 1L volumetric flask. All chemical reagents are analytical grade.

**Preparation of standard analyte**
The analyte was prepared by measuring 0.20g of oven dried (110$^0$C for 24 hours.) analytical grade $CaCO_3$ (Unichem, 98%) in three separate 100 mL beakers. Concentrated analytical grade HCl (Macron) was added drop wise until 6.0 mL. This was followed by the addition of 50.0mL distilled water and boiled in water bath for 5 minutes. The solution was transferred into a 250 mL volumetric flask after cooling and diluted with distilled water.

A 25.0 mL aliquot was pipetted in three individual 250 mL Erlenmeyer flasks and combined with 10.0 mL of ammonium buffer and 5 drops of EBT indicator (Merck). A titration set-up was assembled and the $CaCO_3$ solution in the flask was titrated with EDTA solution in the burette until the first appearance of a persistent clear blue color, marking the endpoint of the titration. The concentration of EDTA was calculated in molarity.

**Preparation of unknown analyte**
About 0.10 to 0.15g of mortar samples from the sieve size left in the pan (<0.075mm) were dried in an oven for 24 hours at 110 $^0$C. Drop-wise addition of concentrated HCl was done directly on the sample until dissolution was complete. It was then boiled in 50 mL distilled water, cooled and diluted to the mark with distilled water in a 250 mL volumetric flask. A 25.0 mL aliquot portion was titrated with the standardized EDTA solution until the appearance of a persistent clear blue color with EBT indicator. Three replicate trials were done. The concentration of calcium in the unknown sample was reported in terms of its percentage composition.

**Titration with $KMnO_4$ solution: Standardization of $KMnO_4$**
The $KMnO_4$ solution was prepared by dissolving 1.58g analytical grade $KMnO_4$ powder (Univar, 99%) in 50.0 mL distilled water and diluted in a 1L volumetric flask.

**Preparation of standard analyte**
A dried (110 $^0$C for 2 hours) $Na_2C_2O_4$ (Unichem, 99.8%) measuring about 0.22g was placed in a 500.0 mL beaker and dissolved in 250.0 mL 0.75M $H_2SO_4$ (Macron). It was heated and maintained at a temperature between 80 – 90 $^0$C, while being titrated with the prepared $KMnO_4$ solution. The appearance of a persistent pink color marks the end point of the titration. Three trials were done. A blank sample was also prepared by using 0.75M $H_2SO_4$ and titrated directly with $KMnO_4$. The volume obtained (0.2 mL) was subtracted from the volume of titrant acquired with the sample. The concentration of $KMnO_4$ was calculated and expressed in molarity.

**Preparation of unknown analyte**
The sieved fractions retained in the "pan" were dried for 3 hours at 120 $^0$C in an oven and cooled. About 0.25 – 0.30g were obtained for each dried mortar sample and placed in separate 250 mL beakers. To dissolve the solid samples, 20.0 mL drop-wise addition of concentrated analytical grade HCl (Macron) was carefully done. This was followed by mixing 40.0 mL distilled water and stirred for 10 minutes at room temperature (30 $^0$C) until all carbon dioxide was removed from the solution.

A 20.0 mL aliquot of the digested mortar samples was added with 3 drops of saturated bromine water and gently boiled for 3 minutes. Each sample portion was diluted with 20.0 mL distilled water, boiled and added with 15.0 mL of hot 6% (w/v) $(NH_4)_2C_2O_4$ (Mallinckrodt, 99%) solution. To precipitate the $CaC_2O_4$, 6M $NH_3$ (Merck, 25%) solution was added slowly until color changes from an intermediate yellow-orange or pH range from 4.5 – 5.5. The solution was allowed to stand for 20 minutes and filtered. The precipitate was washed several times with 5.0 mL of cold water to induce the formation of more precipitates.

The $CaC_2O_4$ precipitate from each trial was dissolved in 15.0 mL distilled water and 7.0 mL 3M $H_2SO_4$ in a beaker. It was heated and maintained at a temperature between 80 – 90 $^0$C while being titrated with the standardized $KMnO_4$. A blank volume was titrated (0.20 mL) and subtracted from the volume of $KMnO_4$ consumed. The percentage of calcium in the mortar samples was computed.

**Calcium determination by atomic absorption spectroscopy**

Calibration curves were prepared by diluting a commercially available 1000 ppm analytical standard grade calcium solution (Fluka) to concentrations of 0.10, 0.30, 0.50, 0.80 and 1.0 ppm, respectively, in separate 50 mL volumetric flasks. The concentration range assures that the calibration curve is linear as required by Beer's Law. A chemical suppressant (2.5 mL, 5.0% w/v strontium nitrate, $Sr(NO_3)_2$) were also added to each standard solution before diluting to the mark with distilled water. Absorbance readings were recorded in a Shimadzu AA-6300 Atomic Absorption Spectrophotometer in an air-acetylene gas mixture at a detection wavelength of 423 nm. Three replicate measurements were performed. Distilled water was used as solvent blank during the experiment [16].

For the mortar samples, 0.20 mL aliquot portion from the original 250 mL EDTA digested binder fraction (< 0.075 mm) was added with 0.50 mL of 5.0% $Sr(NO_3)_2$ in separate 100 mL volumetric flasks. The same AAS parameters mentioned in the preparation of the calcium standard curve were followed afterwards.

## Results and Discussion

**Particle size distribution in mortars**

The mechanical separation of different grain sizes in the mortar samples was achieved through sieve analysis. The relative sizes of the particles and their distribution in the mortar are related to their engineering behaviour [17]. Figure 2 shows the relationship between the mesh size and the percentage of particles retained in a specific sieve for both lime mortar samples. Based on the American Society for Testing and Materials (ASTM, 1980) classification system, the sample from Misamis Oriental is generally composed of fine sand aggregates since most of its weight retained in the 0.250 mm and 0.150 mm sieve sizes, respectively. The Metro Manila sample, however, is mainly made up of medium to fine sand aggregates due to more particles distributed within the sieve size range of 0.600 mm to 0.250 mm, respectively. The absence of particles retained in the 4.750 mm sieve size for the Misamis Oriental sample was compensated by a higher percentage amount of binder fraction from the "pan" (<0.075 mm) [18] which is comparable in weight with the 0.150 mm sieve size. This is in contrast with the Metro Manila sample which has a well-represented particle size distribution, hence, a relatively lower percentage of the binder fraction was observed. There was no evidence which may suggest that the aggregates in both mortar samples are calcitic ($CaCO_3$) in nature.

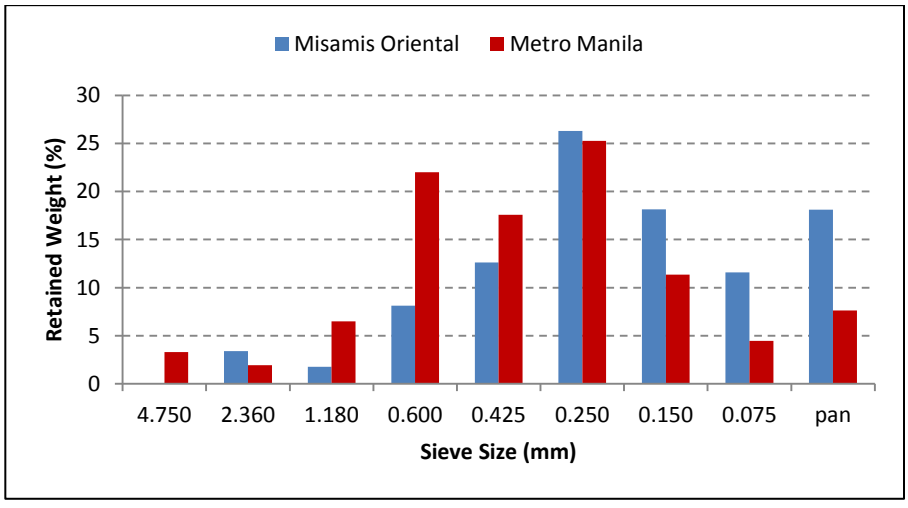



Figure 2. Grain size weight distributions of the mortar samples

To know if the old mortar samples were manufactured with good representations of each particle sizes, a gradation curve was plotted as shown in Figure 3. From this logarithmic plot, the important basic parameters of effective size ($D_{10}$), uniformity coefficient ($C_u$) and coefficient of curvature ($C_c$) were computed. $D_{10}$ is defined as the value for the grain size diameter (D) that passed through the sieve at 10% and was extrapolated on the graph. To compute for $C_c$ and $C_u$, the values for $D_{30}$ and $D_{60}$, or 30% and 60% of particles that passed through the sieve, respectively, were also obtained. The results were tabulated in Table 1 for each mortar samples. Since the values for $C_c$ are within the ranges of 1 to 3 and have $C_u$ values that are greater than 4, both Misamis Oriental and Metro Manila samples are considered as well-graded [19].

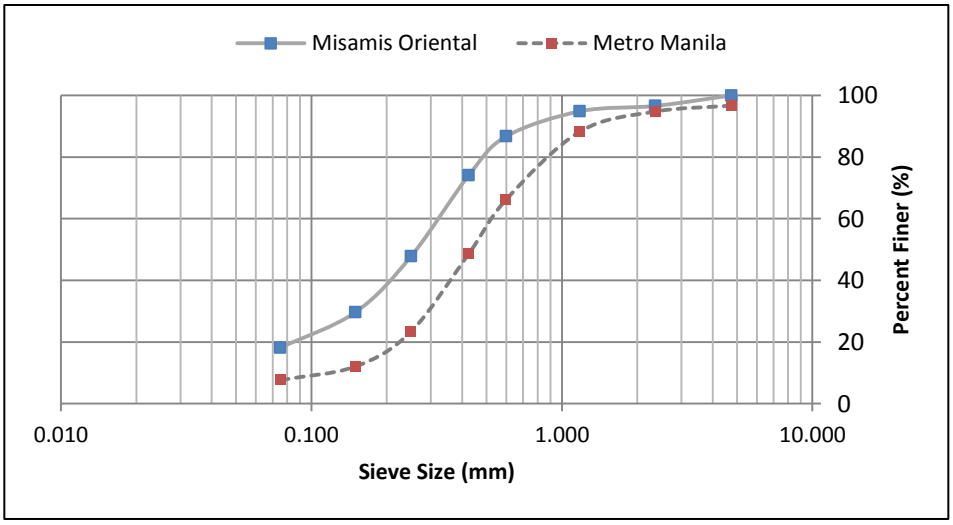



Figure 3. Particle size gradation curve of the mortar samples

Table 1. Soil parameters used for classification of mortar samples

| Parameters | Mortar Samples | |
|---|---|---|
| | Misamis Oriental | Metro Manila |
| $D_{10}$ | [a]0.040 | 0.125 |
| $D_{30}$ | 0.150 | 0.300 |
| $D_{60}$ | 0.325 | 0.525 |
| [b]$C_u$ | 8.13 | 4.20 |
| [c]$C_c$ | 1.73 | 1.37 |

[a]determined by extrapolation, [b]greater than 4, [c]between 1-3

**Binder characterization by Fourier transformation infrared spectroscopy**

There are evidences from X-ray diffraction (XRD) studies that peak intensities corresponding to calcite increases relative to the other minerals present in lime mortars as the sieve size decreases [18]. Hence, the finest fraction which was retained in the "pan" (<0.075 mm) is considered to be the binder fraction and concentrated with $CaCO_3$. Figure 4 shows the infrared spectrum of the mortar sample's binder fractions (<0.075) compared with pure calcium carbonate and pure silicon dioxide. These will serve as IR absorption standards for comparing the old lime mortar sample with sand (composed of $SiO_2$) and lime (mainly contains $CaCO_3$), respectively, which are raw materials in its manufacture. For calcium carbonate, the characteristic IR absorption peaks are the C-O in-plane bending ($\upsilon 4$) at 712 $cm^{-1}$ and C-O out-of-plane bending ($\upsilon 2$) at 876 $cm^{-1}$. These sharp peaks are suitable in determining the presence of $CaCO_3$ because few compounds absorb strongly at this wavenumber. Furthermore, the broad peak at 1419 $cm^{-1}$ is

attributed to the C-O asymmetric stretching (υ3) of $CaCO_3$. The most intense absorption bands of silicon dioxide are centered at 1082 $cm^{-1}$ assigned to the asymmetric stretching mode of Si-O-Si, 795 $cm^{-1}$ which is the symmetric stretching mode of Si-O-Si and the bending vibrations of Si-O-Si centered at 463 $cm^{-1}$, respectively [20,21]. Based on the IR spectrum in Figure 4, the binder fractions from both mortar samples have absorption peaks that are very similar with the bands of calcium carbonate. The absence of peaks attributed to silicon dioxide confirms that the binder fraction in the mortar sample is purely $CaCO_3$. Hence, this fraction was targeted for digestion with acid and titrated with EDTA and $KMnO_4$ to determine the calcium content.

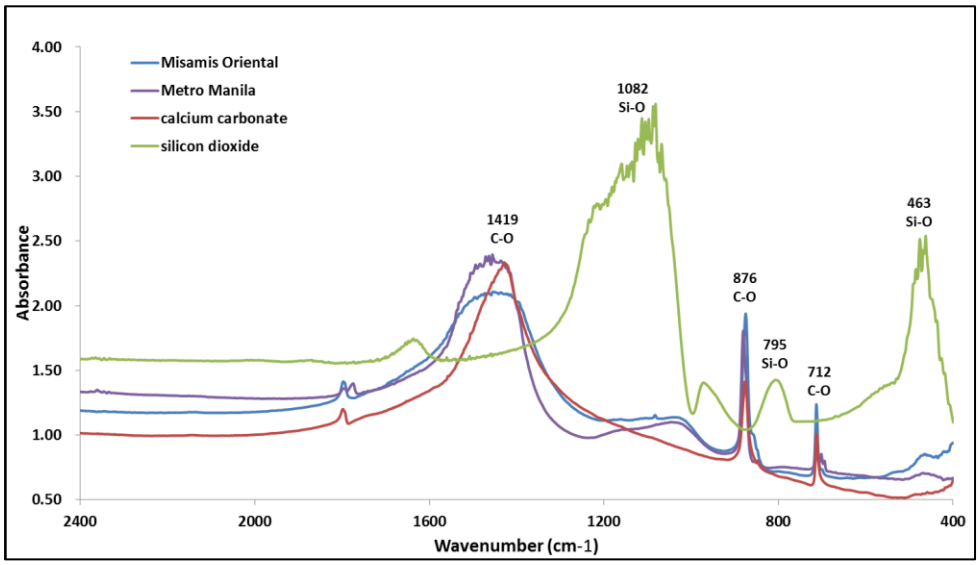



Figure 4. Spectrum of mortar fractions retained in pan (<0.075 mm) taken at finger print region (2400 – 400 $cm^{-1}$)

**Analysis of EDTA titration**

The mean value obtained from the standardization of EDTA solution using pure analytical grade $CaCO_3$ was 4743 ± 132.9 µM at 95% confidence level. The standard deviation of 1.49 x $10^{-5}$ indicates that the concentration of each trial run is precise. From this standardized EDTA concentration, mortar samples from Misamis Oriental and Metro Manila were titrated. Results show that calcium content of the binder fraction for Metro Manila sample (73.54%) is higher compared to the Misamis Oriental sample (59.60%), representing a difference of 13.94%. This implies that the lime material used for making mortars were sourced from different locations which is highly possible because the church ruins are geographically apart. Absence of direct trade of raw materials between Metro Manila and Misamis Oriental was also inferred. Moreover, difference in mortar preparation techniques may contribute to this variation. Since the Misamis Oriental church ruin is located on a promontory, probably sea shells or corals may have been used as sources of lime which accounts to the observed difference.

Table 2 shows the important parameters used to determine the percentage of calcium in the Misamis Oriental sample. Binder fractions in mortars are expected to be homogenously mixed [1, 5]. Therefore, a 95% confidence level for the mean calcium content of 59.60% ± 4.64 gives a range of 54.96% to 64.24%. This percentage represents the true amount of calcium in the entire mortar sample obtained from the site. The percentage calcium from each trial is also within the 95% confidence limits. Since the coefficient of variation is 3.14%, which is less than the acceptable percentage of 5%, the values from this titration are considered precise [22].

Table 2. Calcium content of Misamis Oriental sample using EDTA

| Mass of Mortar Sample (g) | Trial | Volume of EDTA Consumed (mL) | Concentration of Ca (ppm) | Mass of Ca (g) | % Ca (w/w) in Sample | Mean (w/w) and Standard Deviation |
|---|---|---|---|---|---|---|
| 0.1079 | 1 | 32.70 | 248.62 | 0.06216 | 57.60 | 59.60% ± 4.64* |
| | 2 | 34.80 | 264.59 | 0.06615 | 61.30 | (1.87) |
| | 3 | 34.00 | 258.50 | 0.06463 | 59.89 | |

* at 95% confidence level

Results from Table 3 shows that the Metro Manila sample has a 95% confidence level for the mean calcium content of 73.54% ± 2.68 or a calcium percentage range of 70.86% to 76.22%. Hence, the actual calcium content for the entire Metro Manila mortar sample obtained from the site should be within this interval range. The individually measured calcium concentration per trial also falls in these confidence limits. The titration of the Metro Manila sample was considered to be more precise than the Misamis Oriental sample based on the smaller confidence interval value which is attributed to random errors brought about by the visual determination of the end point color. The computed coefficient of variation (1.47%) supports this higher precision compared to the Misamis Oriental titration. Samples from both sites yielded mean calcium contents that are statistically consistent with each other suggesting that EDTA titration can be used for old lime mortar samples.

Table 3. Calcium content of Metro Manila sample using EDTA

| Mass of Mortar Sample (g) | Trial | Volume of EDTA Consumed (mL) | Concentration of Ca (ppm) | Mass of Ca (g) | % Ca (w/w) in Sample | Mean (w/w) and Standard Deviation |
|---|---|---|---|---|---|---|
| 0.1027 | 1 | 39.30 | 298.80 | 0.07470 | 72.74 | 73.54% ± 2.68* |
| | 2 | 39.50 | 300.32 | 0.07508 | 73.11 | (1.08) |
| | 3 | 40.40 | 307.16 | 0.07679 | 74.77 | |

* at 95% confidence level

**Analysis of $KMnO_4$ titration**

The $KMnO_4$ solution was first standardized using sodium oxalate and the mean concentration is 10660 ± 640.5 μM at a 95% confidence level. Precision for the standardization method was considered high due to the small value ($2.58 \times 10^{-4}$) of the standard deviation. The results of $KMnO_4$ titration on the Misamis Oriental sample shown in Table 4 is consistent with the mean calcium concentration values obtained from EDTA titration and differs only by 1.47 units. However, the confidence limits (± 6.68) and standard deviation equal to 2.69 is higher compared to that of the EDTA titration. This is due to the tedious process of crystallization and in maintaining the temperature during the titration which may introduce random errors in the system. Nevertheless, the measured calcium concentration values per replicate are within the allowable confidence limits and the coefficient of variation (4.45%) is still less than 5%, making the titration process precise.

Table 4. Calcium content of Misamis Oriental sample using $KMnO_4$

| Mass of Mortar Sample (g) | Trial | Volume of $KMnO_4$ Consumed (mL) | Mass of Ca (g) | % Ca (w/w) in Sample | Mean (w/w) and Standard Deviation |
|---|---|---|---|---|---|
| 0.03597 | 1 | 20.50 | 0.02190 | 60.87 | 60.48% ± 6.68* |
| | 2 | 21.20 | 0.02264 | 62.95 | (2.69) |
| | 3 | 19.40 | 0.02072 | 57.61 | |

* at 95% confidence level

The same pattern of consistency was also observed for $KMnO_4$ titration of Metro Manila sample shown in Table 5 compared to the results of EDTA titration and differs by 0.286 units. A high confidence limit value (± 6.88) and standard deviation (2.77) were also obtained from the Metro Manila sample supporting the idea that $KMnO_4$ titration method is more prone to random errors. A coefficient of variation of 3.78% and calcium concentration values per replicate, which are within the given confidence limits, make the data obtained precise and reliable.

Table 5. Calcium content of Metro Manila sample using $KMnO_4$

| Mass of Mortar Sample (g) | Trial | Volume of $KMnO_4$ Consumed (mL) | Mass of Ca (g) | % Ca (w/w) in Sample | Mean (w/w) and Standard Deviation |
|---|---|---|---|---|---|
| 0.03423 | 1 | 23.80 | 0.02542 | 74.26 | 73.33% ± 6.88* |
| | 2 | 24.20 | 0.02585 | 75.51 | (2.77) |
| | 3 | 22.50 | 0.02403 | 70.21 | |

* at 95% confidence level

**Comparison of EDTA and $KMnO_4$ titration methods**

Results of the two tailed *t*-test for two independent means performed on the Misamis Oriental mortar samples indicate that at 95% confidence level, the calculated *t* ($t_{calc}$) is 0.4653 which is less than the critical *t* ($t_{table}$) value of 2.776 for 4 degrees of freedom. Hence, the null hypothesis ($H_0$) is accepted and the two titration methods, EDTA and $KMnO_4$, are not significantly different at $p < 0.05$. For the Metro Manila mortar samples, the same *t*-test yielded a $t_{calc}$ value of 0.1242 which is also less than the $t_{table}$ (2.776) for a 95% confidence and 4 degrees of freedom. The null hypothesis is therefore accepted and there is no significant difference between the calcium concentrations resulting from the EDTA and $KMnO_4$ titration [23, 24].

The precision of the two different titration methods was evaluated using the *F*-test. For the Misamis Oriental mortar samples, the computed *F*-value ($F_{calc}$) is 2.07 and for the Metro Manila sample $F_{calc}$ is equal to 6.58. Since both $F_{calc}$ values did not exceed the tabulated critical value of *F* for a 95% confidence level at two degrees of freedom (19.0), there is statistically no significant difference between the standard deviations of the EDTA and $KMnO_4$ titration methods for both mortar samples [23].

The *t*-test and *F*-test analysis proves that the EDTA and $KMnO_4$ titration methods done in this study will provide the same analytical results and the observed difference are attributed entirely to random errors and not to systematic errors. This shows that both methods are comparable and either method is effective in determining the concentration of calcium on old lime mortar samples.

**Atomic absorption spectroscopy analysis of calcium**

AAS was used to further validate the results of the titration methods in determining the amount of calcium on the old mortar sample's binder fraction. Table 6 shows that the calcium concentration obtained in the AAS of the Misamis Oriental sample differs by about 1.2 to 2.3 units from the titration methods or a percentage difference of

about less than 3.9%. The Metro Manila sample however differs from the titration method by about 4.3 to 4.8 units which translates to a percentage difference of roughly less than 6.4% from the titration methods. These percentage differences are statistically acceptable considering the comparison is between a classical method and an instrumental method [25].

Table 6. Summary of AAS data for calcium content

| Sample Site | Trial | Mass of Sample (g) | Absorbance | % Ca | Mean and Standard Deviation |
|---|---|---|---|---|---|
| Misamis Oriental | 1 | 0.1079 | 0.0538 | 61.09 | 58.21% ± 6.31* (2.54) |
| | 2 | 0.1079 | 0.0506 | 57.19 | |
| | 3 | 0.1079 | 0.0499 | 56.34 | |
| Metro Manila | 1 | 0.1027 | 0.0640 | 77.26 | 78.11% ± 4.82* (1.94) |
| | 2 | 0.1027 | 0.0664 | 80.33 | |
| | 3 | 0.1027 | 0.0636 | 76.74 | |

* at 95% confidence level

## Conclusion

The calcium content of the binder fractions in the historic lime mortar samples were determined quantitatively using EDTA and $KMnO_4$ titration. This serves as a very useful baseline information for future renovation work of historic structures in the Philippines. Lime mortars are not manufactured the same since the two church ruins in this study have no direct relation with each other and are geographically apart. Both EDTA and $KMnO_4$ titration methods yielded comparable results and have high precision based on the statistical tests performed and supported by AAS data in this study. Hence, both titration techniques can be applied for calcium analysis of historic mortars. Furthermore, the approach of analyzing the sieved fractions separately is not common in literature, especially since the analysis of calcium content in this study was focused on the finest fraction (<0.075mm) which makes it unique. This study could be utilized readily for routine analysis of calcium in lime mortars that is simple, reproducible and cost-effective.

## Acknowledgement

The authors would like to convey their sincere gratitude to the Chemistry Department of the De La Salle University, Manila for the generous support in equipment use and for subsidizing the chemical reagents in this study. The helpful insights and assistance of the following persons are highly appreciated: Dr. Glenn Alea, Mr. Michael Ajero and Dr. Maria Carmen Tan. The authors would also like to acknowledge Ms. Mutya N. Reynancia, English Program Coordinator and Advanced English Proficiency Training Coordinator of the General Education Department of the Far Eastern University Diliman, Quezon City for her expertise in editing this article.

## References

1. Jose, Jr., R. T. (2003). *Palitada*: Skin of the church. In: Zero In: Skin surface essence. Ateneo Art Gallery, Ayala Foundation, Inc., Eugenio Lopez Foundation, Inc., and Museum Pambata Foundation, Inc.: pp. 27 –28.
2. Elert, K., Rodriguez-Navarro, C., Sebastian Pardo, E., Hansen, E. and Cazallo, O. (2002). Lime mortars for the conservation of historic buildings. *Studies in Conservation*, 47: 62 – 75.
3. Moropoulou, A., Bakolas, A. and Aggelakopoulou, E. (2000). The effects of limestone characteristics and calcinations temperature to the reactivity of the quicklime. *Cement and Concrete Research,* 31: 633 – 639.
4. Neri, L. M. (2011). A report on the archaeological survey along the coastal area of Misamis Oriental, Philippines. *Hukay (Journal for Archaeological Research in Asia and the Pacific),* 16: 1 – 27.
5. Javellana, S. J. R. B. (2010). La Casa de Dios, The legacy of Filipino-Hispanic churches in the Philippines. Pasig: Ortigas Foundation, Inc.: pp. 184 – 187.

6. Cheng, K. L., Kurtz, T. and Bray, R. H. (1952). Determination of calcium, magnesium, and iron in limestone. *Analytical Chemistry*, 24(10):1640 – 1641.
7. Skoog, D. A., West, D. M., Holler, F. J. and Crouch, S. R. (2013). Fundamentals of analytical chemistry, 9th Ed. Brooks/Cole, Cengage Learning: pp. 991 – 994.
8. Page, J. O. (1968). Compleximetric determination of calcium in impure calcium carbonate and limestone. *Analytica Chimica Acta,* 42: 233 – 238.
9. Malmstadt, H. V. and Hadjiioannou, T. P. (1958). Rapid and accurate automatic titration of calcium and magnesium in dolomites and limestones use of EDTA titran and automatic derivative spectrophotometric end-point termination. *Analytica Chimica Acta*, 19: 563 – 569.
10. Rathore, D. P. S., Kumar, M. and Bhargava, P. K. (1997). Complexometric determination of calcium and magnesium in dolomite, limestone, magnesite, phosphatic and silicate matrices using azochromotropic acid derivative as an indicator. *Chemia Analityczna (Warsaw)*, 42: 725 – 728.
11. Hadjiioannou, T. P. and Papastathopoulous, D. S. (1970). EDTA titration of calcium and magnesium with calcium-selective electrode. *Talanta*, 17(5): 399 – 406.
12. De Oliveira, W. and Mendes, A. (1987). Determination of calcium and magnesium in limestone and dolomite by enthalpimetric flow-injection analysis. *Talanta*, 34(6): 543 – 546.
13. Robinson, P. (1980). Determination of calcium, magnesium, manganese, strontium, sodium and iron in the carbonate fraction of limestones and dolomites. *Chemical Geology*, 28: 135 – 146.
14. Middendorf, B., Hughes, J. J., Callebaut, K., Baronio, G. and Papayianni, I. (2005). Investigative methods for the characterisation of historic mortars. Part 2: Chemical characterization. *Materials and Structures,* 38: 771 – 780.
15. Pires, J. (2015). Simple analysis of historical lime mortars. *Journal of Chemical Education*, 92: 521 –523.
16. Cayme, J. M. and Asor, Jr, A. N. (2015). Extraction methods for quantifying iron, calcium and magnesium in a historic brickwork produced during the Spanish Colonial Period in the Philippines. *KIMIKA*, 26(1): 28 – 38.
17. Reddy, B.V.V. and Gupta, A. (2008). Influence of sand gradation on the characteristics of mortars and soil cement block masonry. *Construction and Building Materials*, 22: 1614 – 1623.
18. Miranda, J., Carvalho, A. P. and Pires, J. (2012). Assessment of the binder in historical mortars by various techniques. *Archaeometry*, 54(2): 267 – 277.
19. Holtz, R. and Kovacs, W. (1981). An introduction to geotechnical engineering. Prentice-Hall, Inc, New Jersey.
20. Cayme, J. M., Asor, Jr, A. N., Alano, M. K. A. T. and Miranda, E.T. (2016). Chemical characterization of historical brickwork of the church convento in Pagsanjan, Laguna. *KIMIKA*, 27(1): 30 – 41.
21. Music, S., Filipovic-Vincekovic, N. and Sekovanic, L. (2011). Precipitation of amorphous $SiO_2$ particles and their properties. *Brazilian Journal of Chemical Engineering*, 28(1): 89 – 94.
22. Couto, M. F., Peternelli, L. A. and Barbosa, M. H. P. (2013). Classification of the coefficients of variation for sugarcane crops. *Ciencia Rural, Santa Maria*, 43(6): 975 – 961.
23. Limentani, G. B., Ringo, M. C., Ye, F., Bergquist, M. L. and McSorley, E. O. (2005). Beyond the t-test: Statistical equivalence testing. *Analytical Chemistry*, 77(11): 221 – 226.
24. Lung, K. R., Gorko, M. A, Llewelyn, J. and Wiggins, N. (2003). Statistical method for the determination of equivalence of automated test procedures. *Journal of Automated Methods and management in Chemistry*, 25(6): 123 – 127.
25. Miller, J. C. and Miller, J. N. (1993). Statistics for analytical chemistry, 3rd Ed. Ellis Horwood PTR Prentice Hall, New York: pp. 5 – 10.

*Malaysian Journal of Analytical Sciences, Vol 21 No 5 (2017): 1091 - 1100*
*DOI: https://doi.org/10.17576/mjas-2017-2105-11*

MALAYSIAN JOURNAL OF ANALYTICAL SCIENCES
*Published by The Malaysian Analytical Sciences Society*
ISSN 1394 - 2506

# A NEW AUTOMATED GAS CHROMATOGRAPHY/SOLID PHASE MICROEXTRACTION PROCEDURE FOR DETERMINING α-FLUORO-β-ALANINE IN URINE

## (Kaedah Baru Pengekstrakan Mikro Fasa Pepejal/Kromatografi Gas Berautomatik untuk Penentuan α-Fluoro-β-Alanina di dalam Urin)

Stefano Dugheri[1]*, Alessandro Bonari[2], Ilenia Pompilio[2], Matteo Gentili[3], Manfredi Montalti[2], Nicola Mucci[2], Giulio Arcangeli[2]

*[1]Laboratorio di Igiene e Tossicologia Industriale,*
*Azienda Ospedaliero-Universitaria Careggi, Firenze, Italy*
*[2]Dipartimento di Medicina Sperimentale e Clinica,*
*Università degli Studi di Firenze, Firenze, Italy*
*[3]Giotto Biotech Srl, Sesto Fiorentino, Italy*

**Corresponding author: stefano.dugheri@unifi.it*

Received: 15 February 2017; Accepted: 16 June 2017

**Abstract**

In industrial hygiene, biomarkers maintain their promise to reveal the true extent of occupational exposure. The environmental limit values proposed by industrial hygienist associations are more than biological, health-based values indicating professional hazards to humans. High-throughput screening of samples is therefore the strategy of choice to detect occupational exposure biomarkers, yet it requires user-friendly apparatus that give relatively prompt results while ensuring high degrees of selectivity, precision, accuracy and automation, particularly in preparation processes. In light of the above, this contribution describes a novel gas chromatography/triple quadrupole mass spectrometry/positive chemical ionisation approach for determining urinary α-fluoro-β-alanine, a metabolite of 5-fluorouracil, the most widely employed antineoplastic drug. In this new procedure chromatography's sensitivity is combined with the user-friendliness of alkyl chloroformate/trialkyloxonium on-sample derivatizations followed by solid-phase microextraction sampling, to which is added the quantitative accuracy afforded using a specific isotope-labelled internal standard. The quantification limit for α-fluoro-β-alanine was 25.4 µg/L. Intra- (3.8%) and inter-session (4.5%) repeatability was also evaluated. This method serves to identify suitable risk-control strategies for occupational hygiene conservation programs.

**Keywords:** α-fluoro-β-alanine, solid phase microextraction, gas chromatography, occupational medicine

**Abstrak**

Dalam industri kesihatan, penanda biologi mengekalkan peranannya untuk mendedahkan sejauh mana keselamatan pekerjaan. Nilai had persekitaran yang dicadangkan oleh persatuan industri kesihatan melebihi daripada aspek biologi, iaitu tahap berasaskan kesihatan yang menunjukkan bahaya kepada manusia. Melalui saringan sampel, pemilihan strategi penting untuk mengesan pekerjaan yang terdedah kepada penanda biologi, maka alatan mesra pengguna yang memberikan keputusan segera disamping memastikan nilai kepilihan, kejituan, ketepatan dan bersifat automatik perlulah menjadi sebahagian proses tersebut. Sehubungan itu, sumbangan kajian ini adalah membincangkan kaedah novel kromatografi gas/spektrometri jisim caturkutub ganda tiga/pengionan kimia positif digunakan untuk penentuan α-fluoro-β-alanina di dalam urin, iaitu metabolit 5-fluorourasil yang digunakan secara meluas sebagai dadah antineoplastik. Melalui prosedur baru ini, sensitiviti kromatografi digabungkan bersama menggunakan kloroformat/trialkiloksonium di ikuti oleh pensampelan pengekstrakan mikro fasa pepejal, di mana ketepatan kuantitatif analisis didorong oleh penggunaan larutan piawai internal berlabel isotop. Had kuantifikasi α-fluoro-β-

alanina ialah 25.4 µg/L. Kebolehulangan intra- (3.8%) dan inter- (4.5%) juga telah di uji. Kaedah ini menyediakan strategi kawalan penilaian risiko yang sesuai untuk program pemuliharaan kesihatan pekerjaan.

**Kata kunci:** α-fluoro-β-alanina, pengekstrakan mikro fasa pepejal, kromatografi gas, pekerjaan perubatan

## Introduction

5-fluorouracil has been one of the most frequently used antineoplastic drugs in the world for more than 20 years, and it is still considered to be among the most active cytostatic agents in advanced colorectal cancer as well as for malignancies of the head and neck [1]. In Italy, more than 400 kg are being administered each year [2]. In addition to the therapeutic effects, however, many side effects are known, such as leukopenia, stomatitis, diarrhea, nausea, thrombocytopenia and a decrease in erythrocyte precursors in the marrow [3, 4]. Several groups of workers, such as oncology nurses involved in the preparation and administration of this antineoplastic drug, as well as personnel employed in pharmaceutical plants, are occupationally exposed to this substance. In the processes of health risk-assessment at work, biological monitoring of occupational exposure often plays a central role in identifying the suitable risk-control strategies and hygiene conservation programs. The availability of a highly-sensitive, compound-selective and validated analytical method for measuring a suitable marker of occupational exposure would allow personnel to know the true extent of exposure.

Although the bio-transformation of 5-fluorouracil in humans was described 30 years ago, when a patient study found that 80% of the dose is quickly excreted in urine as α-fluoro-β-alanine (FBAL), no governmental industrial hygienist association has ever mentioned FBAL health-based values as indicators of human professional exposure to this anti-cancer drug. In the field of occupational medicine, few analytical methods have been published to measure urinary FBAL, and their very low number of positive biological samples demonstrates the need to adopt more sensitive analytical methods. The existing assays have limitations, namely: their complexity, their use of solvents, and/or the need for clean-up steps to extract and eliminate interfering compounds from the urine, all of which involved lengthy manual operations, bigger costs, uncertainty in the determination analysis, and the possible loss of analyte. For these reasons, simultaneous and more sensitive assay methods than those available were needed; furthermore, many researchers have called for standardization of analytical factors affecting FBAL determination [2, 5 – 12].

Sample preparation remains one of the more time-consuming and error-prone aspects of analytical chemistry. Over the last 10 years, miniaturization has attracted much attention and has driven solvent and sample savings, sample enrichment, rapid sample preparation, and easier automation. Solid-phase microextraction (SPME) analysis is considered one of the major advances that shaped 20$^{th}$ century analytical chemistry [13]. It integrates sampling, extraction, concentration and sample introduction into a single step, without any polluting, organic solvent for extraction [14-17].

Accordingly, we sought to simplify sample treatment by using the SPME technique. The efficiency of alkyl chloroformate/trialkyloxonium on-sample derivatizations has been demonstrated, as has the success of quantitative determination by gas chromatography (GC) coupled with triple quadrupole-mass spectrometry (QpQ-MS)/positive chemical ionisation (PCI). By combining these procedures, we propose a new user-friendly apparatus which provides relatively prompt results with high degrees of selectivity, precision and accuracy.

## Materials and Methods

### On-sample propyl chloroformate-trimethyloxonium tetrafluoroborate (TMO) derivatizations

To convert the FBAL (CAS n. 867-84-5, Cat. n. F0185, TCI Europe) into related N-propyl carbamate, 100 µL of propyl chloroformate (CAS n. 109-61-5, Cat. n. 249467, Aldrich) derivatizating agent was added to a 20.0 mL vial containing 0.5 mL of urine and 10 µL of 2,3,3-D3 (R, S)-3-amino-2-fluoropropanoic acid (FBAL-D3) internal standard (IS) water solution (5 µg/mL) and continuously agitated for 30 minutes with a magnetic stirring bar. To convert the FBAL carboxyl group, derivatization with TMO (CAS n. 420-37-1, Cat. n. 281077, Aldrich) was performed in two steps at room temperature with agitation, after previous dilution with 1.5 mL of water. About 20 mg of sodium carbonate ($Na_2CO_3$) were added and within 4 minutes approximately 30 mg of solid TMO were added in two aliquots. After 1 minute, the solution was neutralized with about 15 mg of sodium bicarbonate ($NaHCO_3$).

This procedure was repeated. Finally, sodium chloride (0.5 g) was added for salting out and the vials were processed for on-line or off-line extraction.

**On-line headspace (HS-SPME) and xyz robotic apparatus**
Automation of the GC procedure was achieved using a new Flex autosampler (EST Analytical, Fairfield, USA). For HS-SPME absorption, samples were incubated at 60 °C with a pulsed agitation (on for 2 s at 500 rpm and off for 4 s), before the polyacrylate (PA) 85 μm SPME fiber (Cat. n. 57305, Supelco) was inserted into the vial, under the same temperature/agitation conditions. After absorption, the SPME fiber was introduced into the GC injector port by *xyz* autosampler.

**Off-line HS-SPME sampling and *xyz* robotic apparatus**
The SPME Multi Off-Line Sampler (Chromline, Prato, Italy) is a holder designed to be used with FFA SPME fibers; in our case PA 85 μm SPME FFA (Cat. n. FFA 57294-U, Supelco) were used. The holder acts as a support when exposing the SPME fiber in the vial, after which it is placed on the plate of the 15-position magnetic stirrer (Chromline) at 60 °C. After exposure, the FFA is removed from the Multi Off-Line Sampler and placed into the 45-position Multi Fiber eXchange (MFX, Chromline, Prato, Italy), which performs automated exchanges of the fibers. For desorption the fiber is put into a Flex *xyz* autosampler (EST Analytical) with GC instrumentation equipped with Merlin Microseals (Cat. n. 24817-U, Sigma-Aldrich). A connection with the Laboratory Information Management System (Bika Lab System) provides a user-programmable suite of options.

**GC/QpQ-MS**
Analyses were performed with a Varian 3900 GC equipped with electronic flow control and a Varian 320-QpQ-MS (Varian Inc.) detector. A MEGA-5-MS fused silica capillary column (internal diameter 0.25 mm, length 30 m and film thickness 0.25 μm, Cat. No. MS-5-025-025-30, MEGA, Legnano, Italy) was used. For desorbing the analytes, the SPME fiber was introduced into the 1177 Varian GC injector port.

**Synthesis of FBAL-D3**
FBAL-D3 was synthesized following the protocol reported by Gani et al. [18] with slight modifications. First, DL-Serine D3 (850 mg, 8 mmol) was suspended in dry methanol (16 mL) in a nitrogen ($N_2$) atmosphere. After cooling down the suspension with an ice bath, thionyl chloride (1.635 mL, 12.5 mmol) was added slowly. The mixture was stirred for 10 minutes then warmed to room temperature (r.t.) and stirred for 1 hour. Evaporation of the solvent afforded an oily residue. Secondly, DL-Serine D3 methyl ester (980 mg, 8 mmol), benzyl bromide (2 mL, 16.8 mmol), $NaHCO_3$ (3.336 g, 40 mmol), dry tetrahydrofuran (THF) (10 mL) and dry dimethyl sulfoxide (3.2 mL) were placed in a flask in an $N_2$ atmosphere and heated to 80 °C. After 5 hours, the reaction was completed. The mixture was diluted with ethyl acetate (EtOAc) and washed with water three times, dried over sodium sulfate and concentrated. The residue was purified by flash column chromatography on silica gel (hexane/EtOAc 5:1, then 4:1), resulting in 1.44 g of pure product. Third, a solution of DL-serine D3 *N,N*-dibenzylamino methyl ester (1.20 g, 4.0 mmol) in dry THF (20 mL) was added slowly to a solution of diethylaminosulfur trifluoride (0.6 mL, 4.8 mmol) in dry THF (20 mL) at r.t in an $N_2$ atmosphere and stirred for 30 minutes.

Ice and EtOAc were added to the solution followed by solid $NaHCO_3$ until effervescence ceased. The aqueous phase was extracted with EtOAc. The organic phases were combined, washed with water three times and dried on $Na_2SO_4$. The solvent was removed under reduced pressure (r.p.). Fourth, DL-α-Fluoro-β-*N,N*-dibenzyl alanine D3 methyl ester (970 mg, 3.2 mmol) was dissolved in absolute ethanol (50 mL) and 1M HCl (1 eq); to this solution 10% Pd/C (100 mg) was added. The mixture was stirred in a hydrogen atmosphere for two days, then filtered on Celite and washed with ethanol. The alcohols were concentrated under r.p. and treated with 6M HCl for 90 min. The solvent was removed under r.p. and the residue dissolved in water and applied to a column of Amberlite IR45 (OH) using water as eluent. After 100 mL of eluent, the solution was concentrated under r.p. and precipitated from water/acetone, obtaining pure FBAL-D3 as a white solid (236 mg, 50% yield).

**Method validation**
Calibration samples were prepared and analyzed to obtain a calibration curve. Six calibration samples were obtained (30, 60, 120, 240, 480, 960 μg/L) and six analyses for each of the calibration samples were performed. Least-square

linear regression (LSLR) analysis was used to estimate slopes (m) and intercepts (b) of calibration lines y = mx + b, where y is the ratio between the chromatographic area of the analyte and the relative IS, and x the concentration of FBAL (μg/L of urine). The limit of detection (LOD) of the assay was calculated according to the following equation 1:

$$LOD = (3SE_b + b)/m \quad (1)$$

where $SE_b$ is the internal standard error of the intercept [19]. The precision of the assay (as a coefficient of variation, CV%) was based on both within-session and inter-session repeatability. Accuracy was evaluated by the recoveries (calculated from the percentage ratio between the measured and the nominal concentration solutions) at all concentrations used for the calibration plot. Values of accuracy were then compared with the requirements of the US Food and Drug Administration for analytical method validation.

## Results and Discussion

In previous studies, the oft-reported use of solvents and/or clean-up steps were necessary to extract and eliminate most of the interfering compounds from the urine. These procedures resulted in many manual operations, uncertainty of the determination, higher overall costs of the method, and possible analyte loss. Accordingly, we developed a method where the HS-SPME technique was applied after on-sample derivatization, and then coupled with quantitative determination via GC/QpQ-MS. Four fundamental aspects motivated this choice.

### HS-SPME

The first objective was to develop derivatization conditions on HS-SPME technologies to obtain compounds which are not only stable under a variety of conditions, but also easily amenable to sampling, to GC separation, and to MS identification. Since FBAL determination in urine by this technique for previous alkylchloroformate/ trialkyloxonium derivatizations had not been previously reported, the equilibrium and kinetics of the reaction product, with regards to SPME, had to be both theoretically explored and experimentally proven. In a previous work [20], the HS-SPME technique had been used in a three-phase process in which a liquid polymeric coating, a headspace and an aqueous solution were involved. The mass (n) of analytes absorbed by the coating after the equilibrium has been reached is related to the overall equilibrium of analytes in the three-phase system as follows in equation 2:

$$N = (C_0V_1V_2K_1K_2)/(K_1K_2V_1 + K_2V_3 + V_2) \quad (2)$$

where $K_1$ is the SPME coating/HS partition coefficient, $K_2$ is the HS/aqueous matrix partition coefficient, $C_0$ is the initial concentration of the analyte in the aqueous solution, and $V_1$, $V_2$ and $V_3$ are the volumes of the coating, the aqueous solution, and the HS, respectively. Since the K values of the analytes (where $K = K_1 \times K_2$) are often very close to the octanol–water partition coefficient ($K_{ow}$), and $K_2 = K_H/RT$, where $K_H$ is Henry's constant ($C_0$, concentration gas phase/$C_0$, concentration liquid phase). It follows that the equilibrium is controlled by $K_{ow}$ and $K_H$ values. The values $K_{ow}$ and $K_H$ can be found in the literature or calculated, and in this way, it is possible to know in advance whether the HS-SPME method offers some advantages or vice versa. Moreover, the constant of distribution estimated from physicochemical tables or by using the structural unit contribution method can anticipate trends in SPME analysis.

For example, Performs Automated Reasoning in Chemistry (ARChem, Danielsville, Georgia, USA) is a physicochemical calculator that uses computational algorithms based on the fundamental chemical structures to foresee a wide variety of reactivity parameters strictly based on molecular structure. The $K_H$ of the N-propyl carbamate/methyl ester FBAL-derivate was 0.13 atm $cm^3$/mol (Table 1), which agreed with that reported by Pacenti et al. [21]; this confirmed that HS-SPME is efficient under such conditions.

Table 1. Physical properties and partition coefficients of N-propyl carbamate/methyl ester FBAL-derivates evaluated using SPARC software

| SMILES strings | $T_{eb}$ (°C) | $D_{water}$ ($cm^2/s$) | $D_{air}$ ($cm^2/s$) | $K_H$ (atm $m^3$/mol) | $K_{ow}$ (Log) | $P_{vap}$ (log(atm)) |
|---|---|---|---|---|---|---|
| O=C(NCC(F)C(=O)OC)OCCC | 271.8 | $6.52*10^{-6}$ | 0.0483 | $1.25*10^{-7}$ | 1.31 | -5.3 |

**Alkyl chloroformate derivatization conditions**

Chloroformates have been widely used to convert amines into carbamates in aqueous media. One-step treatment of amino acids with chloroformates and alcohols of the same alkyl with catalysis by pyridine met the basic criteria required for an ideal procedure: very simple sample handling in aqueous solutions and derivatization completed within a few seconds with microliter amounts of reagent of negligible cost [22 – 25]. Modification in the reaction conditions towards using reagents with different alkyls appeared to be useful [26, 27] in enabling researchers to prepare a wide variety of esters tailored to the analytical needs of specific tasks. In our method, we decided to carry out such derivatization in water, without using any alcoholic solvent, in order to avoid the formation of undesired side products as those described by Wang et al. [28].

A novel approach to the derivatization of carboxylic groups by the use of TMO, a methyl group of oxonium ions reacts with the anion of the carboxylic group to form methyl ester. This method employs a sample derivatization technique to convert polar substances into hydrophobic compounds, whose volatility is sufficiently high for HS-SPME/GC determination. Trialkyloxonium ions (Meerwein salts), $R_3O^+$, with various counterions such as $SbF_6^-$, $BF_4^-$, $SbCl_6^-$ and $PF_6^-$, are excellent alkylating agents for nucleophiles containing such heteroatoms as N, O, or S [17, 21, 29 – 31]. The application of TMO as a methylating agent together with propyl chloroformates as agent without catalysis by pyridine was implemented in this work. The reaction, occurring under mild conditions at room temperature, is completed in a few minutes (Figure 1).

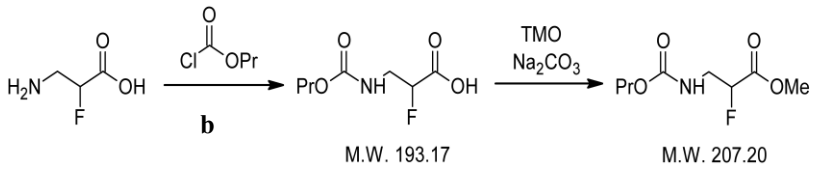



Figure 1. (a) FBAL and (b) propyl chloroformate reaction to related (c) alkyl chloroformate and subsequent trialkyloxonium derivatization which forms (d) FBAL-N-propyl carbamate-methylester

**$^1$H-NMR analysis of propyl chloroformate/TMO derivatization**

The reaction of FBAL and propyl chloroformate was investigated by NMR spectroscopy in D2O, in order to ensure the conversion of the amino group into the corresponding propyl carbamate. The sample was placed in a clear tube and analyzed by a Varian Gemini NMR instrument at 200 MHz. Following the addition of sub stoichiometric quantities of propyl chloroformate, a new set of signals appeared immediately, as the intensity of the reagent's signals decreased, until completely disappearing when a stoichiometric amount of the chloroformate was added. This confirms that FBAL spontaneously reacts with propyl chloroformate in aqueous phase in a quantitative yield. After alkalization of the same solution with $Na_2CO_3$, TMO was added stepwise till a stoichiometric amount was reached. NMR spectra showed an increasing signal of methyl ester until the reagent was completely converted.

**Choice of GC/QpQ-MS/Positive Chemical Ionization (PCI)**

In this work, PCI was used for the analysis of FBAL-derivates to increase the signal intensity of the molecular ions, and then coupled with QpQ-MS during Selected Reaction Monitoring (SRM) to increase their selectivity compared to the background matrix. For PCI we selected methane as the reactive gas, which produced a few fragments of FBAL, as the parent ion was m/z 208 $(M+H)^+$ as peak to be used as precursor ion in QpQ-MS (Figure 2).

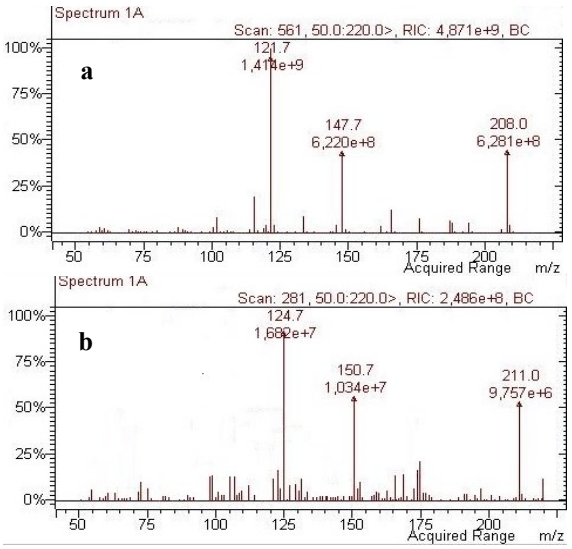



Figure 2. GC/SCAN-MS/PCI spectrum of FBAL (a) and FBAL-D3 (b)

The GC and QpQ-MS/PCI parameters are displayed in Table 2. As indicated in Table 3, the resulting calibration curves for FBAL were linear in the investigated range, showing a correlation coefficient >0.99.

Table 2. GC and QpQ-MS/PCI parameters

| **GC conditions** | |
|---|---|
| Injection | 300°C, 2:1 split mode. Liner 0.75 mm i.d. |
| Oven | 50°C (1 min) increased at 10 °C/min to 180 °C and 30 °C/min to 300°C (2 min). (Run time 20.00 min) |
| Column flow | Helium (99.999%) at a flow rate of 1.2 mL/min |
| Retention times | FBAL (12.141 min) FBAL-D3 (12.131 min) |
| GC interface | 280 °C |
| **MS parameters** | |
| Mode | Positive CI |
| Filament | Electron energy, 70 eV. Filament current, 50 µA |
| Source | Temperature, 200 °C. Pressure, 8 Torr |
| CI reagent | Methane |
| Collision gas | CID gas, Argon. CID gas pressure, 2.00 mTorr |
| Collision energy | FBAL, 5 eV. FBAL-D3, 10 eV |
| **SRM transition** | |
| FBAL-derivate | Fragments Q1>Q3 (208>148, quantification) |
| | Fragments 208>122 (unspecific response was obtained in urine samples) |
| FBAL-D3-derivate | Fragments Q1>Q3 (211>125, quantification) |

Table 3. Calibration curve, accuracy and precision (coefficient of variation) of the FBAL analytical method

| **FBAL (Nominal Concentration, µg/L)** | **FBAL (Measured Concentration, µg/L)** |
|---|---|
| 30 | 21.0 |
| 60 | 46.6 |
| 120 | 109.8 |
| 240 | 230.4 |
| 480 | 463.1 |
| 960 | 937.4 |
| LSLR parameters | m = 0.0287, b = 0.2403 |
| Coefficient of Correlation | 0.992 |
| Standard Error | 0.054 |
| LOD (µg/L) | 7.7 |
| LOQ (µg/L) | 25.4 |
| Within-session accuracy (%) | 4.3 |
| Within-session repeatability (%) | 3.8 |
| Inter-session repeatability (%) | 4.5 |

Accuracy was within 15% of the theoretical concentration, in line with the requirement of the US Food and Drug Administration. The new SPME Multi Off-Line Sampler proposed in this study integrates the MFX (Figure 3).



Figure 3. SPME Multi Off-Line Sampler holder

Several preparation steps immediately before sample injection have been automated, allowing just-in-time sample preparation. Below is an example of the advantages of using an SPME FFA Multi Off-Line Sampler: calculate an extraction time of 40 minutes for FBAL-derivate equilibrium in a three-phase SPME system plus an analysis time of 20 minutes (Figure 4).

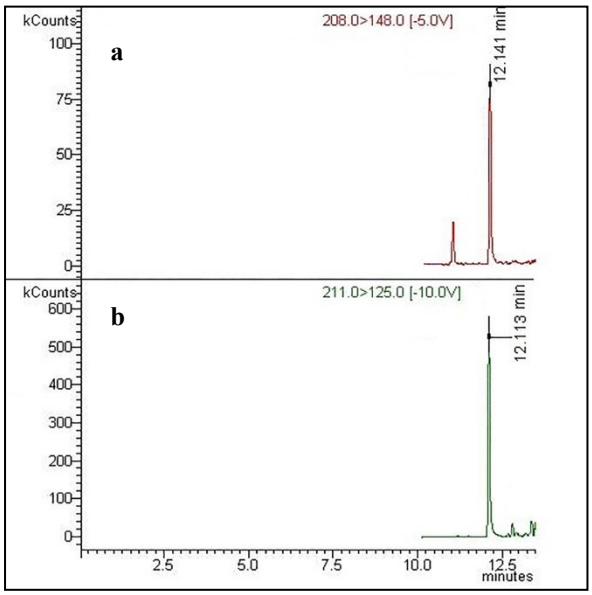



Figure 4. GC chromatograms of FBAL- (a) and FBAL-D3- (b) derivate

The results are excellent, with a reduction in total analysis time of 725 minutes (30 samples processed), compared to conventional SPME on-line analysis (Figure 5).

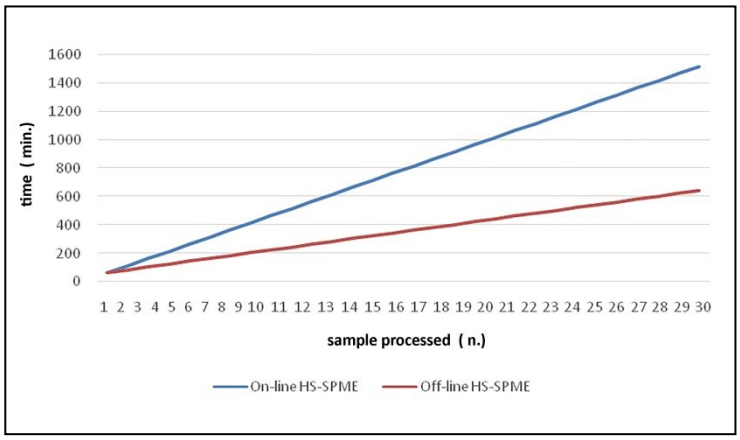



Figure 5. Off-Line vs. On-Line SPME extraction

## Conclusion

Our data suggests that automated SPME extraction coupled with GC/QpQ-MS/PCI is a viable alternative for FBAL analyses. Customized, automatized MS apparatus for high-throughput screening are not only user-friendly, but they reduce the costs of monitoring occupational health hazards. New sample preparation techniques are currently being increasingly explored because of the considerable need for information management, the automation of sample preparation, and the integration of data management into the analytical process. Lastly, we expanded the application of this methodology by carrying out analyses of other amino acids.

**Acknowledgements**

We thank the Azienda Ospedaliero-Universitaria Careggi (Florence, Italy), one of the largest polyclinics in Italy, for allowing us access to the wards and their employees, and particularly Fabrizio Niccolini, Daniela Tognoni and Anna Maria Tognoni, for enduring our presence and participating in the study. Furthermore, the authors gratefully acknowledge Marco Colpo for statistical analysis support.

**References**

1. Breda, M. and Barattè, S. (2010). A review of analytical methods for the determination of 5-fluorouracil in biological matrices. *Analytical Bioanalytical Chemistry*, 397(3): 1191 – 1201.
2. Rubino, F. M., Verduci, C., Buratti, M., Fustinoni, S., Campo, L., Omodeo-Salè, E., Giglio, M., Iavicoli, S., Brambilla, G. and Colombi, A. (2006). Assay of urinary alpha-fluoro-beta-alanine by gas chromatography-mass spectrometry for the biological monitoring of occupational exposure to 5-fluorouracil in oncology nurses and pharmacy technicians. *Biomedical Chromatography*, 20(3): 257 –266.
3. Nair, K. L., Jagadeeshan, S., Nair, S. A. and Kumar, G. S. (2011). Biological evaluation of 5-fluorouracil nanoparticles for cancer chemotherapy and its dependence on the carrier, PLGA. *International Journal of Nanomedicine*, 6:1685 – 1697.
4. Jaferian, S., Negahdari, B. and Eatemadi, A. (2016). Colon cancer targeting using conjugates biomaterial 5-flurouracil. *Biomedicine & Pharmacotherapy*, 84: 780 – 788.
5. Sessink, P. J., Timmersmans, J. L., Anzion, R. B. and Bos, R. P. (1994). Assessment of occupational exposure of pharmaceutical plant workers to 5-fluorouracil. *Journal Occupational Medicine,* 36(1):79-83.
6. Anderson, D., Kerr, D. J., Blesing, C., and Seymour, L. W. (1997). Simultaneous gas chromatographic-mass spectrophotometric determination of alpha-fluoro-beta-alanine and 5-fluorouracil in plasma. *Journal of Chromatography B: Biomedical Sciences and Applications*, 688(1): 87 – 93.
7. Licea-Perez, H., Wang, S. and Bowen, C. (2009). Development of a sensitive and selective LC-MS/MS method for the determination of alpha-fluoro-beta-alanine, 5-fluorouracil and capecitabine in human plasma. *Journal of Chromatography. B, Analytical Technologies in the Biomedical and Life Sciences*, 877(11-12): 1040 – 1046.
8. Ndaw, S., Denis, F., Marsan, P., d'Almeida, A. and Robert, A. (2010). Biological monitoring of occupational exposure to 5-fluorouracil: urinary α-fluoro-β-alanine assay by high performance liquid chromatography tandem mass spectrometry in health care personnel. *Journal of Chromatography. B, Analytical Technologies in the Biomedical and Life Sciences*, 878(27): 2630 – 2634.
9. Bos, R. P., Weissenberger, B. F. J. and Anzion, R. B. M. (1998). α-Fluoro-β-alanine in urine of workers occupationally exposed to 5-fluorouracil in a 5-fluorouracil producing factory. *Biomarkers*, 3(1): 81 – 87.
10. Furuhata, T., Kawakami, M., Okita, K., Kimura, Y., Kihara, C., Tsuruma, T., Ohmura, T., Yamaguchi, K., Hata, F., Katsuramaki, T., Sasaki, K. and Hirata, K. (2006). Plasma level of a 5-fluorouracil metabolite, α-fluoro-β-alanine correlates with dihydropyrimidine dehydrogenase activity of peripheral blood mononuclear cells in 5-fluorouracil treated patients. *Journal of Experimental and Clinical Cancer Research*, 25(1): 79 – 82.
11. Yoshida, J., Koda, S., Nishida, S., Nakano, H., Tei, G. and Kumagai, S. (2013). Association between occupational exposure and control measures for antineoplastic drugs in a pharmacy of a hospital. *Annals of Occupational Hygiene*, 57(2): 251 – 260.
12. Poupeau, C., Tanguay, C., Plante, C., Gagné, S., Caron, N. and Bussières, J. F. (2016). Pilot study of biological monitoring of four antineoplastic drugs among Canadian healthcare workers. *Journal of Oncology Pharmacy Practice*, April:1-10.
13. Handley, J. and Harris, C. M. (2001). Great ideas of a decade. *Analytical Chemistry*, 73(23): 660 – 666.
14. Bianchi, F., Bisceglie, F., Dugheri, S., Arcangeli, G., Cupelli, V., Del Borrello, E., Sidisky, L. and Careri, M. (2014). Ionic liquid-based solid phase microextraction necklaces for the environmental monitoring of ketamine. *Journal of Chromatography A*, 1331: 1 – 9.
15. Sassolini, A., Dominici, C., Saurini, M. T., Guidotti, M., Cenciarelli, O., Malizia, A., Ludovici, G. M., Gabbarini, V., Gabriele, J., Bellecci, C., Palombi, L. and Gaudio, P. (2015). Development of a SPME-GC-MS based methods for analysis of organochlorinated smoke agents in soil and its applications in a former military site samples. *Malaysian Journal of Analytical Sciences*, 19(6): 1179 – 1186.
16. Kremser A., Jochmann, M. A., and Schmidt, T. C. (2016). SPME Arrow-evaluation of a novel solid-phase microextraction device for freely dissolved PAHs in water. *Analytical and Bioanalytical Chemistry*, 408(3): 943 – 952.

17. Dugheri, S., Bonari, A., Pompilio, I., Mucci, N., Montalti, M. and Arcangeli, G. (2016). Development of new gas chromatography/mass spectrometry procedure for the determination of hexahydrophthalic anhydride in unsaturated polyester resins. *RASĀYAN Journal of Chemistry*, 9(4): 657 – 666.
18. Gani, D., Hitchcock, P. B. and Young, D. W. (1985). Stereochemistry of catabolism of the DNA base thymine and of the anti-cancer drug 5-fluorouracil. *Journal of the Chemical Society, Perkin Transactions*, 1: 1363 – 1372.
19. Miller, J. C. and Miller, J. N. (1984). Statistics for analytical chemistry, Ellis Horwood: Chinchester, 4: pp. 96.
20. Zhang, Z. and Pawliszyn, J. (1993). Headspace solid-phase microextraction. *Analytical Chemistry*, 65(14): 1843 – 1852.
21. Pacenti, M., Dugheri, S., Villanelli, F., Bartolucci, G., Calamai, L., Boccalon, P., Arcangeli, G., Vecchione, F., Alessi, P., Kikic, I. and Cupelli V. (2008). Determination of organic acids in urine by solid-phase microextraction and gas chromatography-ion trap tandem mass spectrometry previous 'in sample' derivatization with trimethyloxonium tetrafluoroborate. *Biomedical Chromatography*, 22(10): 1155 – 1163.
22. Hušek, P. (1998). Chloroformates in gas chromatography as general purpose derivatizing agents. *Journal of Chromatography B: Biomedical Sciences and Applications*, 717(1-2): 57 – 91.
23. Hušek, P., Švagera, Z., Hanzlíková, D., Řimnáčová, L., Zahradníčková, H., Opekarová, I. and Šimek, P. (2016). Profiling of urinary amino-carboxylic metabolites by in-situ heptafluorobutyl chloroformate mediated sample preparation and gas chromatography-mass spectrometry. *Journal of Chromatography A*, 1443: 211 – 232.
24. Bianchi, F., Dugheri, S., Musci, M., Bonacchi, A., Salvatori, E., Arcangeli, G., Cupelli,V., Lanciotti, M., Masieri, L., Serni, S., Carini, M., Careri, M. and Mangia, A. (2011). Fully automated solid-phase microextraction-fast gas chromatography-mass spectrometry method using a new ionic liquid column for high-throughput analysis of sarcosine and N-ethylglycine in human urine and urinary sediments. *Analytica Chimica Acta*, 707(1-2): 197 – 203.
25. Naccarato, A., Gionfriddo, E., Sindona, G. and Tagarelli, A. (2014). Development of a simple and rapid solid phase microextraction-gas chromatography-triple quadrupole mass spectrometry method for the analysis of dopamine, serotonin and norepinephrine in human urine. *Analytica Chimica Acta*, 810: 17 –24.
26. Makita, M., Yamamoto, S. and Kõno, M. (1976). Gas-liquid chromatographic analysis of protein amino acids as N-isobutyloxycarbonylamino acid methyl esters. *Journal of Chromatography*, 120(1): 129 –140.
27. Makita, M., Yamamoto, S., Sakai, K. and Shiraishi, M. (1976). Gas-liquid chromatography of the N-isobutyloxycarbonyl methyl esters of non-protein amino acids. *Journal of Chromatography*, 124: 92 –96.
28. Wang, J., Huang, Z. H., Gage, D. A. and Watson, J. T. (1994). Analysis of amino acids by gas chromatography-flame ionization detection and gas chromatography-mass spectrometry: simultaneous derivatization of functional groups by an aqueous-phase chloroformate-mediated reaction. *Journal of Chromatography A*, 663(1): 71 – 78.
29. Meerwein, H., Hinz, G., Hofmann, P., Kroning, E. and Pfeil, E. (1937). Über Tertiäre Oxoniumsalze, I. *Journal für praktische Chemie*, 147(10-12): 257 – 285.
30. Liebich, H. M. and Gesele, E. (1999). Profiling of organic acids by capillary gas chromatography-mass spectrometry after direct methylation in urine using trimethyloxonium tetrafluoroborate. *Journal of Chromatography A*, 843(1-2): 237 – 245.
31. Amazzini, S., Onor, M., Pagliano, E., Mester, Z., Campanella, B., Pitzalis, E., Bramanti, E. and D'Ulivo, A. (2015). Determination of thiocyanate in saliva by headspace gas chromatography-mass spectrometry, following a single-step aqueous derivatization with triethyloxonium tetrafluoroborate. *Journal of Chromatography A*, 1400: 124 – 130.

*Malaysian Journal of Analytical Sciences, Vol 21 No 5 (2017): 1101 - 1110*
*DOI: https://doi.org/10.17576/mjas-2017-2105-12*

MALAYSIAN JOURNAL OF ANALYTICAL SCIENCES
*Published by The Malaysian Analytical Sciences Society*
ISSN 1394 - 2506

# RESPONSE SURFACE METHODOLOGY OPTIMIZATION OF OIL REMOVAL USING BANANA PEEL AS BIOSORBENT

## (Pengoptimuman Kaedah Gerak Balas Permukaan Untuk Penyingkiran Minyak Menggunakan Kulit Pisang sebagai Penjerap-Bio)

Najaa Syuhada Mohamad Thani[1], Rozidaini Mohd Ghazi[1]*, Norhisyam Ismail[2]

[1]*Faculty of Earth Science,*
*Universiti Malaysia Kelantan Jeli Campus, 17600 Jeli, Kelantan, Malaysia*
[2]*Department of Chemistry, Faculty of Science,*
*Uni versiti Teknologi Malaysia, 81310, Skudai Johor Bharu, Johor, Malaysia*

**Corresponding author: rozidaini@umk.edu.my*

Received: 21 February 2017; Accepted: 24 August 2017

**Abstract**

Improper waste management of oil causes environmental pollution particularly water pollution. Conventional method in treating oil contaminants are expensive and have low removal efficiency, hence the use of natural adsorbent is suggested because of its reliability and affordability. This study aimed to use banana peel as a biosorbent for oil removal and the application of response surface methodology to identify the optimum conditions of oil removal. The adsorptive capacity of household wastes derived from banana peel towards oil were studied by using different parameters such as oil concentration, adsorbent dosage and contact time. Maximum oil adsorption of 98.86% was achieved using banana peel. The optimum conditions for oil removal were found at a dosage of 4.94 g, for 10.29 hours contact time and the initial oil concentration as high as 8.74%. The rate of oil adsorption was mathematically described as a function of experimental parameters and was modelled through response surface methodology via Box-Behnken design. The results showed that the responses of oil adsorption were significantly affected by the quadratic term of oil concentration, adsorbent dosage and contact time. The statistical analysis was performed by ANOVA which indicated good correlation of experimental parameters.

**Keywords**: banana peel, oil removal, response surface methodology

**Abstrak**

Pengurusan sisa minyak yang tidak teratur menyebabkan pencemaran alam sekitar terutamanya pencemaran air. Kaedah konvensional untuk merawat pencemaran minyak adalah mahal dan tahap penyingkiran minyaknya adalah rendah, maka penggunaan penjerap semulajadi adalah dicadangkan kerana kebolehannya menyerap minyak dan lebih menjimatkan. Matlamat kajian ini adalah untuk menggunakan kulit pisang sebagai biopenjerap untuk penyingkiran minyak dan aplikasi kaedah gerak balas permukaan untuk mengenal pasti keadaan optimum kapasiti penyingkiran minyak. Kapasiti penjerapan daripada sisa rumah yang diambil daripada kulit pisang terhadap minyak telah dikaji dengan menggunakan parameter yang berbeza seperti kepekatan minyak, kuantiti penjerap dan tempoh masa. Penjerapan minyak secara maksimum, pada kadar 98.86% telah dicapai oleh kulit pisang. Keadaan optimum untuk menyingkirkan minyak adalah pada kadar 4.94 g, 10.29 jam dan kepekatan minyak sebanyak 8.74%. Kadar penjerapan minyak telah diterangkan secara matematik dalam fungsi parameter eksperimen dan telah dimodelkan melalui reka bentuk Box-Behnken (kaedah gerak balas permukaan). Hasil kajian menunjukkan bahawa tindak balas penjerapan minyak sangat dipengaruhi oleh kepekatan minyak, kuantiti penjerap dan tempoh masa. Analisis statistik ANOVA menunjukkan korelasi yang baik bagi setiap parameter eksperimen.

**Kata kunci:** kulit pisang, penyingkiran minyak, kaedah gerak balas permukaan

## Introduction

Water pollution affects not only individual living species, but also populations and entire functioning ecosystems that exist in the water. Oil and grease is toxic to some aquatic organisms. The oil film also prevents oxygen transfer from the atmosphere and causes low dissolved oxygen levels in the water [1]. Cities spend billions of dollars every year unplugging or replacing grease-blocked pipes, repairing pump stations, and cleaning up costly and illegal wastewater spills [2].

Conventional methods to remove oil and grease are the use of skimming tanks, oil and grease traps and interceptors in treatment plants. The main disadvantage of these methods is low efficiency of removal [1]. Biosorption process involves a solid phase (sorbent) and a liquid phase (solvent, normally water) containing a dissolved species to be sorbed (sorbate, e.g. oil). Due to the higher 'affinity' of the sorbent for the sorbate species the latter is attracted into the solid and bound there by different mechanisms [3]. The production of biosorbent will save cost, be environmentally friendly, effective in treating oil pollution, minimization of sludge upon usage and ability of regeneration of biosorbent [4]. Other study for oil removal has been conducted by Vlaev et al. [5], using rice husk ash, where at a given temperature, black rice husk ash sorbed more crude oil than diesel fuel. Hussein et al. [6], studied about carbonized peat bagasse where the result showed that the fibres extracted from bagasse and carbonized at 300 °C for 2 hours were found to have a high performance for sorption, recovery and recycling of heavy oils, even the viscous ones. Peat-based sorbents has been tested by Cojocaru et al. [7], where the removal efficiency of 99.21% was achieved. Sawdust has also been tested, where oleic acid grafted sawdust (OGSD) had the best sorption capacity for crude oil as well as weathered oil [8]. In addition, a study on sugarcane bagasse conducted by Brandao et al. [9] showed great potential when it was able to adsorb up to 99% of oil. Said et al. [10] tested grafted raw bagasse in pure oil, and sorption capacity of 3g/g was achieved after about 15 minutes. A study on vegetable fibres also showed a very high degree of hydrophobicity and oil sorption capacity of approximately 85 g oil/g sorbent in 24 hours [11].

Response surface methodology (RSM) is an effective statistical technique for optimizing complex processes. It can reduce the number of experimental trials needed to evaluate multiple parameters and their interactions. Moreover, Box-Behnken design (BBD), as a type of response surface design, is also widely used in many research work [12]. RSM is a very effective technique for this study because it presents statistical models which can be used to know the relationship between the parameters that have been optimized [13].

Hence, the goal of this study is to utilize banana peel as a biosorbent for oil removal and the application of RSM to identify the optimum conditions of oil removal. By considering the initial concentration of oil, biosorbent dosage and contact time, a regression model for surface area (response) was developed.

## Materials and Methods

### Materials

Cooking oil was used as a synthetic oil wastewater. The solvent used was n-Hexane (95% pure, Bendosen). The water used was distilled water that was produced in the Environmental Science Laboratory, Universiti Malaysia Kelantan. Banana peels were collected from a local store in Jeli, Kelantan.

### Untreated banana peel (UBP)

Banana peels were separated from the fruit gently, washed thoroughly with distilled water to remove other inorganic impurities. Then, it was dried under sun light for 5 days and heated using an oven (Model FD115, Binder, Korea) at 70 °C for 1 hour. The dried banana peels were then cut into small pieces, ground using a blender and sieved with 200 – 400 μm.

### Treated banana peel (TBP)

The method was the same with untreated banana peel but the dried banana peel was then treated with 0.5M hydrochloric acid for 24 hours at speed rate of 4 rpm. The modified banana peel was washed several times with deionized water to remove any excess acid. It was dried for 24 hours at 60 °C in an oven before starting the experiments.

**Biosorption studies**
Different biosorption studies were carried out for contact time, biosorbent dosage and oil concentration, and how the parameters influenced the biosorption process, all of this was performed at room temperature.

The experiments were conducted in a 250-ml conical flask containing 100 ml of synthetic oil wastewater (oil-in-water mixture). The sample was prepared by mixing cooking oil and distilled water using a blender following the desired concentrations. The synthetic oil wastewater with different percentages was treated differently with various quantities of biosorbent for a desired time, in an incubated shaker at a speed of 150 rpm.

At the end of the treatment, the biosorbent was removed from the oil and water mixture by passing it through cloth coffee filters. The concentration of oil before and after treatment was calculated using gravimetric method. The control experiment was the flask without biosorbent.

**Gravimetric-based methods**
100 ml of synthetic oil wastewater was added in a clean separatory funnel. The acidity of the sample was adjusted at pH 2 or less by adding 4 ml hydrochloric acid solution, 6.0 N (1:1). It was then serially extracted three times with n-hexane in a separatory funnel.

After separating the solvent (now containing oil) from the water sample, it was placed into a round bottom flask, which has been weighed beforehand. It then underwent a distillation process to remove n-hexane. After that, the flask was placed in an oven for 12 hours at 106 °C to evaporate excess water. After the solvent was evaporated, the flask now containing the residual oil is dried and weighed. Knowing the weight of the empty flask, the amount of residual oil can be calculated [14].

**Screening of biosorbent**
The experiments were conducted in a 250-ml conical flask containing 100 ml of 1:1 ratio oil and water mixture, prepared by mixing cooking oil with distilled water using a blender and its pH was measured.

The synthetic oil wastewater with 50% w/v concentration was treated with 0.5g of UBP and TBP for 3 hours, in an orbital shaker (Model SI-300/300R/600/600R, JEIO TECH, Korea) at a speed of 150 rpm. At the end of the treatment, biosorbents were filtered by passing them through cloth coffee filters. The concentration of oil before and after treatment was calculated using the gravimetric method.

The percentage of oil removal and the uptake capacity of the biosorbent for each different oil concentration were calculated. The results were then used to decide which high and low concentration of oil will be used in RSM for optimization.

The percentage (%) removal oil and amount of oil adsorbed by banana peel (qe) was calculated by equation (1) and (2), respectively:

$$\text{Oil removal concentration (\%)} = \frac{100\,(C_0 - C_e)}{C_0} \quad (1)$$

$$q_e = \frac{(C_0 - C_e)}{m}\,V \quad (2)$$

where $C_0$ is the initial oil concentration (mg/L) and $C_e$ is the concentration of oil left (mg/L), $V$ the solution volume (L) and $m$ is the mass of biosorbent (g). All adsorption experiments were duplicated and the mean values were used in data analysis.

**Experimental design and optimization using response surface methodology**
Three different parameters namely oil concentration (0.5 – 10 %), biosorbent dosage (0.5 – 5g) and contact time (1 – 24 hours) were selected as the critical variables. The experiments were randomly conducted and the measurements of percentage of oil removal for each experiment were calculated. A software package by Design Expert Version 6.0.8 was used to fit the second-order model.

The effects of oil concentration, biosorbent dosage and contact time at three variable levels (-1, 0, 1) in the reaction were evaluated in Table 1:

Table 1. Ranges of the factors investigated using Box–Behnken Design

| Variables | Symbols | Levels | | |
|---|---|---|---|---|
| | | -1 | 0 | 1 |
| Oil Concentration (%) | A | 0.5 | 5.25 | 10 |
| Biosorbent dosage (g) | B | 0.5 | 2.75 | 5 |
| Contact time (h) | C | 1 | 12.5 | 24 |

To determine the relationship between the preparation variables and the responses under consideration, the data collected must be analysed by a statistical approach of using regression equations. For regression equation, the preparation variables were coded according to equation (3):

$$y = \beta_0 + \sum_n^k \beta_i \, x_i + \sum_n^k \beta_{ii} \, x_i^2 + \sum_n^k \beta_{ij} x_i \, x_j + \varepsilon \quad (3)$$

where $y$ is the response (dependent variables), $\beta_0$ is constant coefficient, $\beta_1$, $\beta_{ii}$ and $\beta_{ij}$ are the regression coefficients for linear, quadratic and interaction terms, respectively, whereas $x_i$ and $x_j$ are the independent variables, while $\varepsilon$ is the error [15].

## Results and Discussion

### Screening of biosorbent for oil removal

From the bar chart (Figure 1), UBP adsorbed oil more efficiently with the higher percentage oil removal of 31.63%, whereas TBP with 5.675% of oil concentration. The surface activity of banana peels is mainly due to the presence of carboxyl, hydroxyl and amide groups on its surface and the high surface area of banana peels adds to the property and makes it an excellent and economic adsorbent, for water purification processes [16]. As shown by the result, UBP adsorbed better than TBP, so UBP was then used in RSM for the optimization process.

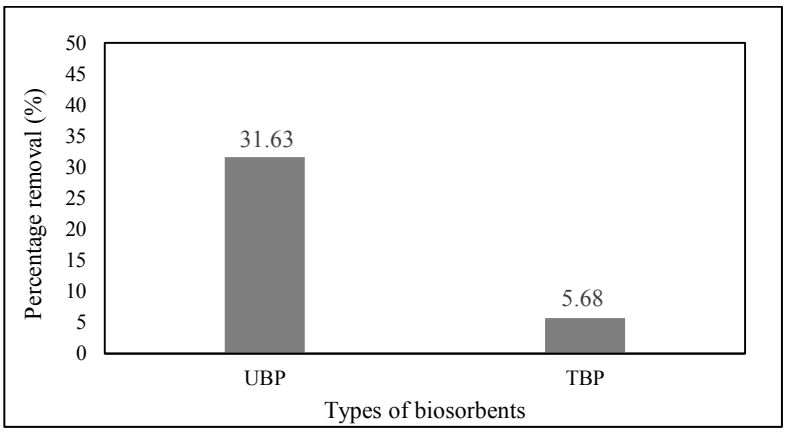



Figure 1. Percentage oil removal and uptake capacity of biosorbents

### RSM experiments and model fitting

The results for the actual values acquired from the response from the experimental runs and the predicted values obtained from the generated quadratic model that corresponded to the percentage removal of oil are tabulated in Table 2.

Table 2. Design of RSM and its actual and predicted values

| Std | Factor 1 A: Oil Concentration (%) | Factor 2 B: Dosage (g) | Factor 3 C: Time (hour) | Percentage Oil Removal (%) | |
|---|---|---|---|---|---|
| | | | | Actual Value | Predicted Value |
| 1 | 0.5 | 0.5 | 12.5 | 65.72 | 66.91 |
| 2 | 10 | 0.5 | 12.5 | 67.72 | 69.54 |
| 3 | 0.5 | 5 | 12.5 | 63.72 | 61.89 |
| 4 | 10 | 5 | 12.5 | 92.91 | 91.72 |
| 5 | 0.5 | 2.75 | 1 | 19.57 | 23.59 |
| 6 | 10 | 2.75 | 1 | 83.10 | 86.49 |
| 7 | 0.5 | 2.75 | 24 | 94.29 | 90.89 |
| 8 | 10 | 2.75 | 24 | 64.48 | 60.46 |
| 9 | 5.25 | 0.5 | 1 | 79.47 | 74.25 |
| 10 | 5.25 | 5 | 1 | 89.44 | 87.24 |
| 11 | 5.25 | 0.5 | 24 | 97.10 | 99.29 |
| 12 | 5.25 | 5 | 24 | 98.26 | 103.47 |
| 13 | 5.25 | 2.75 | 12.5 | 88.91 | 91.48 |
| 14 | 5.25 | 2.75 | 12.5 | 88.55 | 91.48 |
| 15 | 5.25 | 2.75 | 12.5 | 92.58 | 91.48 |
| 16 | 5.25 | 2.75 | 12.5 | 91.97 | 91.48 |
| 17 | 5.25 | 2.75 | 12.5 | 95.38 | 91.48 |

The maximum removal efficiency of oil was found to be 98.25%. The best fitting model was established by a regression analysis. The following equation is a regression model with the experimental results in terms of coded factors:

$$Y = 91.4756 + 8.1154A + 4.2906B + 10.3175C - 22.324A^2 + 3.3721B^2 - 3.7837C^2 + 6.7993AB - 23.333AC - 2.201BC \quad (4)$$

where $Y$ is the percentage oil removal (%), A is oil concentration (%), B is the biosorbent dosage (g) and C is the contact time of biosorbent to oil (hour).

**Regression model and Analysis of Variance (ANOVA)**
Statistical testing of the model was performed with the Fisher's statistical test for analysis of variance (ANOVA), as shown in Table 3.

The significance of each model is assessed from the coefficient ($R^2$) which is found to be 0.97. The high coefficient of determination between the predicted and experimental adsorption activities confirmed that the quadratic polynomial model was adequate to explain the actual relationship between the response and the significant variables.

The F statistic value of 29.63 implies that the model is significant and there is only a 0.01% chance that the model could occur due to noise. The significance of each term in this model is also evaluated by P value (Prob > F) that was less than 0.05. This was supported by a P-value which confirmed that the quadratic model was statistically significant and sufficient to explain the actual relationship between the response and the significant variables.

Table 3. Analysis of variance for the response of the uptake capacity for cooking oil

| Source | Sum Squares | Degrees Freedom | Mean Square | F Value | Prob > F (P-value) |
|---|---|---|---|---|---|
| Model | 6127.18 | 9 | 680.80 | 29.63 | < 0.0001 |
| A | 526.87 | 1 | 526.87 | 22.93 | 0.0020 |
| B | 147.28 | 1 | 147.28 | 6.41 | 0.04 |
| C | 851.61 | 1 | 851.61 | 37.06 | 0.0005 |
| $A^2$ | 2099.95 | 1 | 2099.95 | 91.39 | < 0.0001 |
| $B^2$ | 47.88 | 1 | 47.88 | 2.08 | 0.20 |
| $C^2$ | 60.28 | 1 | 60.28 | 2.62 | 0.15 |
| AB | 184.92 | 1 | 184.92 | 8.05 | 0.03 |
| AC | 2177.72 | 1 | 2177.72 | 94.78 | < 0.0001 |
| BC | 19.38 | 1 | 19.38 | 0.84 | 0.39 |
| Residual | 160.84 | 7 | 22.98 | | |
| Lack of Fit | 128.91 | 3 | 42.97 | 5.38 | 0.07 |
| Pure Error | 31.93 | 4 | 7.98 | | |
| Corrected Total | 6288.02 | 16 | | | |

$R^2$ = 0.98, Coefficient of variation = 5.94, Adj $R^2$= 0.94, Pred $R^2$= 0.66, Adeq precision = 21.73

The ANOVA test indicates that the F-value for the lack of fit (5.38) was lower than the tabulated value, suggesting that the lack of fit was insignificant relative to the pure error, thereby indicating the data in the experimental domain was well represented by the model. There is a 6.68% chance that a "Lack of Fit F-value" this large could occur due to noise.

**Effect of process variables on the percentage removal of cooking oil**

Figure 2 below illustrates the effect of the process variables, namely oil concentration, biosorbent dosage and contact time on the percentage removal of cooking oil.

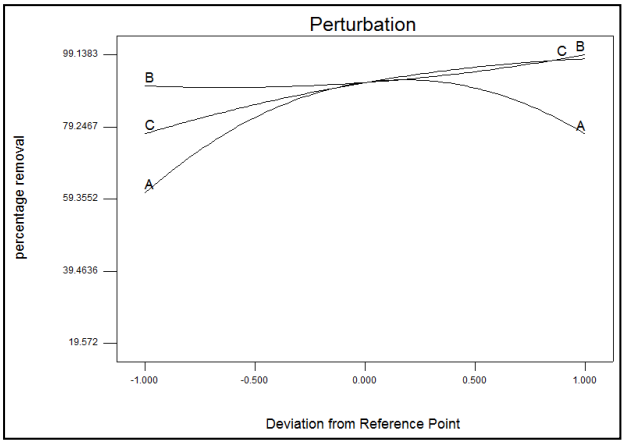



Figure 2. Deviation of reference point for the oil concentration, biosorbent dosage and contact time on the percentage removal of cooking oil

The percentage removal of cooking oil increased at first but then decreased with the increase of (A) oil concentration, whereas the percentage removal of cooking oil showed an upward trend with the increase of (B) biosorbent dosage into the oil. From the figure, it can also be seen that the increase in (C) contact time of biosorbent with oil also increased the percentage removal of oil.

**Effect of oil concentration and biosorbent dosage**

Figure 3 illustrates the response surface curve and contour plot for the oil concentration (A) and biosorbent dosage (B), and their mutual interaction on the percentage removal of cooking oil by UBP.

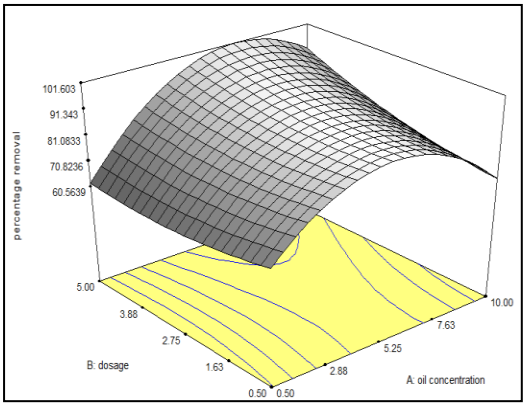



Figure 3. Effect of oil concentration (A) and biosorbent dosage (B) response surface plot on percentage removal of oil

It has been found that the efficiency of biosorbents to adsorb oil initially increases with increasing oil concentration. At lower oil concentrations in the solution, the oils would interact with the sorbent and thus facilitated adsorption whereas at higher concentrations, more oils are left un-absorbed in the solution due to the saturation of the binding sites [17].

The increasing initial oil concentration would decrease oil removal efficiency. This must be caused by the decrease in surface area of the biosorbent due to the increasing of the amount of oil adsorbed per unit weight of biosorbent [18].

At high initial concentration, the gradient between the solution sample and the center of particle enhances oil diffusion through the film surrounding the particle and in the porous network of the biosorbent. Eventually, as time goes by, the adsorbed oil will start to clog the pores near the outer surface so oil residue can no longer diffuse to the active sites deep within the interior surface [19].

**Effect of oil concentration and time**

Figure 4 illustrates the response surface curve and contour plot for the oil concentration (A) and time (C), and their mutual interaction on the percentage removal of cooking oil by UBP.

It was observed that the interactions of the two reaction parameters, oil concentration (A) and time (C) were significant because of the small p-value (< 0.0001) that is less than 0.05. Increasing the contact time between the biosorbent and oil significantly elevated the percentage removal of oil. It can be concluded that the reaction time had a positive effect on percentage removal of oil. Hence, the prolonged contact time increased the probability of effective collisions between oil and biosorbent. In addition, at longer mixing time, breakage of the oil droplets are enhanced, thus reducing the diameter of the oil droplets (emulsification) which leads to more interfacial area for the adsorption to occur and encourages the adsorption of residue oil by biosorbent [19]. Therefore, interaction time between the oil molecule and biosorbent particles is very important in oil removal.

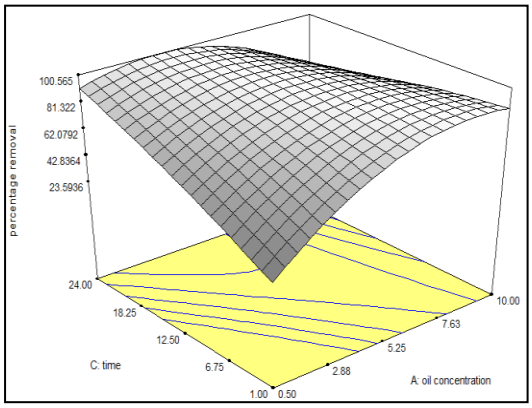



Figure 4. Effect of oil concentration (A) and time (C) response surface plot on percentage removal of oil

The increased rate of percentage removal of oil is due to the larger surface area of the biosorbents being available at the beginning of adsorption of oil. The increasing contact time increased the oil adsorption and it remains constant after equilibrium is reached [20]. However, contact time plays an important role only at the beginning of oil adsorption, and is less important near equilibrium. At near equilibrium, only a small increase in oil removal is observed due to limited availability of biosorbent surfaces for oil entrapment [13].

**Effect of biosorbent dosage and time**

Figure 5 illustrates the response surface curve and contour plot for the biosorbent dosage (B) and time (C), and their mutual interaction on the percentage removal of oil by UBP.

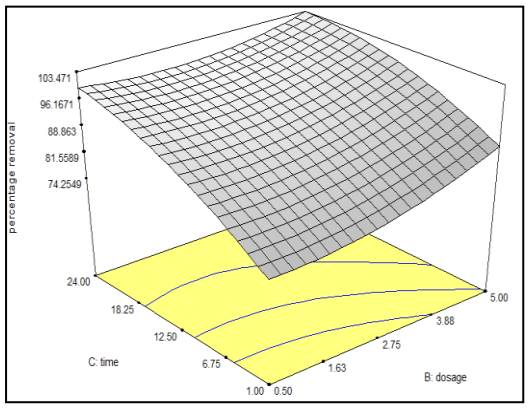



Figure 5. Effect of dosage (B) and time (C) response surface plot on percentage removal of oil

It could be noted that for both an increase in contact time and the biosorbent dosage, the percentage removal increases. An increase in biosorbent dosage results in more binding sites available for the oil molecules to be adsorbed, whereas, an increased contact time provides enough time for the molecules to bind on the adsorbent sites. Adsorption is a surface related phenomenon, at equilibrium most of the oil molecules were adsorbed on the surface and in the intermolecular pores of the adsorbent [21]. Hence, at higher dosage, the oil adsorbed are higher due to the availability of more empty binding sites as compared to lower dosages which has less binding sites to adsorb the same amount of oil in the adsorbate solution [17].

The increase in active sites will lead to a higher percentage removal but with lowered oil uptake per unit of adsorbent. This is due to the abundancy of active sites available on biosorbent for oil to be adsorbed at a higher dosage, thus leading to a higher interaction between oil particles and adsorbent [22]. However, saturated oil binding sites occurred with the increasing biosorbent dosage. In addition, saturation effect also reduces the efficiency of oil removal when maximum sorption capacity is reached [23].

**Optimum conditions and model verification**

The optimum condition for percentage of oil removal is shown in Table 4. The model capable of predicting the maximum adsorption capacity showed that the optimum condition for the oil removal were concentration of oil at 8.74%, with a dosage of 4.94 g and a duration of 10.29 hours. Under these conditions, the predicted adsorption capacity was 99.18% which was in good agreement with the experimental value of 98.86%.

The obtained results were found to be relatively close to the predicted percentage removal and this confirmed the eligibility of the quadratic model suggested by the software. Thus, RSM with appropriate experimental design could be effectively applied to optimize the process parameters in this investigation.

Table 4. Optimum conditions for percentage of oil removal

| Number | Oil Concentration (%) | Dosage (g) | Time (h) | Actual Percentage Removal (%) | Predicted Percentage Removal (%) |
|---|---|---|---|---|---|
| 1 | 8.74 | 4.94 | 10.29 | 98.86 | 99.18 |

## Conclusion

The optimum conditions of UBP as oil adsorbent were obtained as follows; oil concentration 8.74%, dosage 4.94 g, time 10.29 hours. Under these optimum conditions, the predicted value from the model is 99.18% and the obtained result was 98.86% and this indicates the successful development model because of a small deviation error. Statistical optimization on UBP production was successfully performed using RSM via DOE software by conducting a BBD by varying the activation temperature and contact time.

UBP can benefit the oil pollution issue with a more affordable solution and this can also reduce the abundance of household waste problems. The use of UBP in oil removal needs to be further investigated to promote large-scale use of non-conventional adsorbents. The uses of UBP for wastewater treatment applications today are strongly recommended due to their local availability, technical feasibility, engineering applicability, and cost effectiveness. Undoubtedly, UBP can benefit commercial purposes in the future.

## Acknowledgement

The authors acknowledge the Ministry of Higher Education (MOHE) and Universiti Malaysia Kelantan (UMK) for funding the project through NRGS Grant (R/NRGS/A0700/00413A/006/2014/000150).

## References

1. Hebbar, A. H. and Jayantha, K. S. (2013). Oil and grease removal from wastewater using laterite as an adsorbent material. *International Journal of Emerging Technology and Advanced Engineering*, 3(5): 654 – 657.
2. Pawlak, Z., Rauckyte, T. and Oloyede, A. (2008). Oil, grease and used petroleum oil management and environmental economic issues. *Journal of Achievements in Materials and Manufacturing Engineering*, 26(1): 11 – 17.
3. El-Nafaty, U. A., Muhammad, I. M. and Abdulsalam, S. (2013). Biosorption and kinetic studies on oil removal from produced water using banana peel. *Civil and Environmental Research*, 3(7): 125 – 136.
4. Volesky, B. and Holan, Z. R. (1994) Biosorption of lead and nickel by biomass of marine algae. *Biotechnology and Bioengineering*, 43 (11): 1001 – 1009.
5. Vlaev, L., Petkov, P., Dimitrov, A. and Genieva, S. (2011). Cleanup of water polluted with crude oil or diesel fuel using rice husks ash. *Journal of the Taiwan Institute of Chemical Engineers*, 42(6): 957 – 964.

6. Hussein, M., Amer, A. and Sawsan, I. I. (2009). Oil spill sorption using carbonized pith bagasse. application of carbonized pith bagasse as loose fiber. *Global NEST Journal*, 11(4): 440 – 448.
7. Cojocaru, C., Macoveanu, M. and Cretescu, I. (2011). Peat-based sorbents for the removal of oil spills from water surface: Application of artificial neural network modelling. *Colloids and Surfaces A: Physicochemical and Engineering Aspects*, 384 (1-3): 675 – 684.
8. Banerjee, S. S., Joshi, M. V. and Jayaram, R. V. (2006). Treatment of oil spill by sorption technique using fatty acid grafted sawdust. *Chemosphere*, 64(6): 1026 – 1031.
9. Brandao, P. C., Souza, T. C., Ferreira, C. A., Hori, C. E. and Romanielo, L. L. (2010). Removal of petroleum hydrocarbons from aqueous solution using sugarcane bagasse as adsorbent. *Journal of Hazardous Materials*, 175(1-3): 1106 – 1112.
10. Said, A., Ludwick, A. G. and Aglan, H. A. (2009). Usefulness of raw bagasse for oil absorption: A comparison of raw and acylated bagasse and their components. *Bioresource Technology*, 100(7): 2219 – 2222.
11. Annunciado, T. R., Sydenstricker, T. H. D. and Amico, S. C. (2005). Experimental investigation of various vegetable fibers as sorbent materials for oil spills sorbent materials for oil spills. *Marine Pollution Bulletin*, 50(11): 1340 – 1346.
12. Yi, J., Wang, Z., Bai, H., Yu, X., Jing, J. and Zuo. L. (2015). Optimization of purification, identification and evaluation of the in vitro antitumor activity of polyphenols from Pinus *koraiensis pinecones*. *Molecules*, 20 (6): 10450 – 10467.
13. Kadir, S., Matali, S., Mohamad, N. F. and Rani, N. H. A. (2014). Preparation of activated carbon from oil palm empty fruit bunch (EFB) by steam activation using response surface methodology. *International Journal of Materials Science and Applications*, 3(5): 159 – 163.
14. Yang, M. (2011). Produced water. Springer, Glasgow: pp. 57 – 88.
15. Salamatinia, B., Zinatizadeh, A., Kamaruddin, A. and Abdullah, A. Z. (2006). Application of response surface methodology for the optimization of Cu and Zn removals by sorption on pre-treated oil palm frond (OPF). *Iranian Journal of Chemical Engineering*, 3(2): 73 – 84.
16. Singhal, S., Agarwal, S., Bahukhandi, K., Sharma, R. and Singhal, N. (2014). Bio-adsorbent: A cost-effective method for effluent treatment. *International Journal of Environmental Sciences and Research,* 3(1): 151 – 156
17. Abdel-Ghani, N. and El-Chaghaby, G. (2014). Biosorption for metal ions removal from aqueous solutions: A review of recent studies. *International Journal of Latest Research in Science and Technology*, 3(1): 24 – 42.
18. Alkhalssi, R. M., Saeed, E. A. and Khalid, M. G. (2014). Treatment of emulsified oil in produced water from oil wells by adsorption on to corn-cob as sorbent. *Nahrain University, College of Engineering Journal*, 17(1): 83 – 90.
19. Ahmad, A. L., Sumathi, S. and Hameed, B. H. (2005). Adsorption of residue oil from palm oil mill effluent using powder and flake chitosan: Equilibrium and kinetic studies. *Water Research*, 39(12): 2483 – 2494.
20. Kumar, P. S. and Kirthika, K. (2009). Equilibrium and kinetic study of adsorption of nickel from aqueous solution onto bael tree leaf powder. *Journal of Engineering Science and Technology*, 4(4): 351 – 363.
21. Mohammed, S. A., Faisal, I. and Alwan, M. M. (2011). Oily wastewater treatment using expanded beds of activated carbon and zeolite. *Journal of Chemical and Petroleum Engineering*, 12(1): 13.
22. Sidik, S. M., Jalil, A. A., Triwahyono, S., Adam, S. H., Satar, M. A. H. and Hameed, B. H. (2012). Modified oil palm leaves adsorbent with enhanced hydrophobicity for crude oil removal. *Chemical Engineering Journal*, 203: 9 – 18.
23. Rajakovic V., Aleksic, G. and Rajakovic, L. (2008). Governing factors for motor oil removal from water with different sorption materials. *Journal of Hazardous Materials*, 154(1-3): 558 – 563.

*Malaysian Journal of Analytical Sciences, Vol 21 No 5 (2017): 1111 - 1119*
*DOI: https://doi.org/10.17576/mjas-2017-2105-13*

MALAYSIAN JOURNAL OF ANALYTICAL SCIENCES
*Published by The Malaysian Analytical Sciences Society*
ISSN 1394 - 2506

# SINTESIS DAN PENCIRIAN HIDROGEL TERBIODEGRADASI BERASASKAN BAKTERIA SELULOSA MENGGUNAKAN TEKNIK RADIASI ULTRA LEMBAYUNG

## (Synthesis and Characterization of Biodegradable Bacterial Cellulose Based Hydrogels Using Ultra Violet Curable Radiation)

Norhanisah Jamaludin dan Azwan Mat Lazim*

*Pusat Pengajian Sains Kimia dan Teknolohi Makanan,*
*Fakulti Sains dan Teknologi,*
*Universiti Kebangsaan Malaysia, 43600 UKM Bangi, Selangor, Malaysia*

**Corresponding author: azwanlazim@ukm.edu.my*

Received: 16 January 2017; Accepted: 16 July 2017

**Abstrak**

Hidrogel terbiodegradasi berasaskan selulosa bakteria (BC) daripada *nata de coco* dihasilkan melalui proses radiasi ultra lembayung terawat. Selulosa bakteria (BC) telah digabungkan bersama akrilamida (AM) pada nisbah yang berbeza. N,N-metilena bisakrilamida (BIS) dan kalium persulfat (KPS) kemudiannya ditambah untuk mensintesis hidrogel dengan nisbah 5% w/v (hidrogel A) dan 10% w/v (hidrogel B). Hidrogel berasaskan AM juga turut disintesis dengan label hidrogel pemalar. Dalam kajian ini, akrilamida (AM) bertindak sebagai monomer dan terikat pada struktur tulang belakang selulosa. Kalium persulfat (KPS) bertindak sebagai bahan pemula cahaya di mana ianya membantu dalam menghasilkan radikal bebas dan N,N-metilena bisakrilamida (BIS) pula berfungsi sebagai agen pentaut silang. Berdasarkan penggunaan teknik radiasi dan bahan pemula cahaya, tindak balas yang terlibat adalah pempolimeran radikal bebas. Lima analisis telah dilakukan bagi mencirikan hidrogel A dan B iaitu ujian pengembangan menggunakan lima larutan penimbal pH, analisis struktur kimia, analisis gravimetri termal (TGA), analisis kalorimetri pengimbasan pembezaan (DSC) dan analisis pembelauan sinar-X. Morfologi permukaan bagi kedua – dua hidrogel A dan B juga telah ditentukan menggunakan analisis mikroskopi pengimbasan elektron (SEM). Hasil analisis telah menunjukkan kewujudan liang – liang terbuka dalam hidrogel A adalah lebih banyak berbanding dengan hidrogel B.

**Kata kunci:** hidrogel, selulosa bakteria, ultra lembayung terawat

**Abstract**

A rapid biodegradable hydrogel made up of bacterial cellulose (BC) from *nata de coco* was prepared by curing it under the ultra violet (UV) radiation. Bacterial cellulose (BC) is grafted with acrylamide (AM) at different proportions. Potassium persulphate (KPS) and N,N-methylene bisacrylamide (BIS) are added to synthesize hydrogels at the ratio of 5% w/v (hydrogel A) and 10% w/v (hydrogel B). Acrylamide hydrogel is also synthesized as a control hydrogel. In this research, acrylamide acts as a monomer that binds itself to the cellulose backbone while potassium persulfate (KPS) as an intiator where it produces free radicals. The N,N-methylene bisacrylamide (BIS) is used as a cross linker. Here, free radical polymerization is involved. Several analyses have been done to characterise hydrogel A and B which are swelling test in five different buffer solutions, chemical structure analysis, thermal gravimetry analysis (TGA), diffrential scanning calorimetry (DSC) and X-ray diffraction (XRD). The surface morphology for both hydrogel A and B are also determined by using scanning electron microscopy (SEM) analysis. The images found that the pores in hydrogel A were more than in hydrogel B.

**Keywords:** hydrogel, bacterial cellulose, curable ultra violet

## Pengenalan

Hidrogel merupakan bahan polimer yang boleh menyerap sejumlah besar air tanpa ia melarut dalamnya [1]. Hidrogel merupakan gel kimia yang distabilkan oleh jaringan paut silang secara kovalen [2]. Polimer hidrogel boleh dikategorikan kepada dua kelas iaitu sintetik dan berasaskan bahan semulajadi [3]. Sejak bermulanya kajian berkaitan hidrogel, ia telah menjadi salah satu bahan polimer yang paling banyak dikaji terutamanya dalam bidang biologi. Malah, disebabkan oleh kesedaran terhadap teknologi hijau dan bio-serasi pada masa kini, kebanyakan hidrogel diperbuat daripada sumber semulajadi dan salah satunya adalah selulosa. Penggunaan selulosa sedikit sebanyak dapat mendorong penghasilan hidrogel yang mempunyai sifat ketulenan, keseragaman dan juga kekuatan mekanikal yang tinggi [4].

Selulosa merupakan salah satu sumber semulajadi yang banyak dan mudah untuk didapati di muka bumi. Selulosa terbahagi kepada dua jenis iaitu daripada sumber bakteria dan tumbuhan [5]. Secara kimianya, selulosa bakteria (BC) adalah sama seperti selulosa tumbuhan (PC) walaupun mempunyai struktur makromolekular dan sifat fizikal yang berbeza. Selulosa dari kedua-dua sumber ini terikat pada ikatan 1,4-β-glukosidik yang menjadikan kadar penghabluran selulosa adalah tinggi dan tidak mudah larut dalam air. Walau bagaimanapun, biosintesis BC menghasilkan fiber bersaiz nano dengan magnitud dua kali ganda lebih kecil berbanding dengan fiber PC. Oleh itu, selulosa bakteria menunjukkan jaringan fiber ultra halus yang berkebolehan untuk menyerap air dengan banyak dan mempunyai daya ketegangan yang lebih tinggi daripada PC [6]. Salah satu selulosa yang biasa digunakan dalam industri makanan adalah selulosa bakteria (BC). Selulosa bakteria boleh dihasilkan daripada pelbagai sumber dan salah satu contoh BC adalah *nata de coco*. *Nata de coco* merupakan sejenis pencuci mulut berbentuk kiub gelatin dan berwarna putih. Secara asasnya, kiub gelatin tersebut diperbuat daripada air kelapa melalui proses fermentasi oleh organisma *Acetobacter xylinium* [6].

Oleh kerana hidrogel menawarkan pelbagai aplikasi [7], maka kajian ke atas hidrogel telah mendapat perhatian umum dan dijalankan secara meluas. Sebagi contoh, hidrogel telah digunakan sebagai medium penghantaran ubat dalam sistem tubuh manusia [8], bahan penjerap, salutan [7] dan nanoreaktor. Bagi menghasilkan suatu hidrogel yang terbaik, kaedah yang dipilih mestilah efektif bagi mengurangkan kos serta menjimatkan masa. Antara kaedah yang pernah digunakan untuk mensintesis hidrogel adalah kaedah sinaran gamma, sinaran alur elektron, gelombang mikro dan kaedah kimia [9].

Seperti yang telah diketahui, kebanyakan hidrogel yang telah dihasilkan adalah berasaskan polimer sintetik. Walaupun ia telah digunakan secara meluas, namun, polimer sintetik merupakan bahan yang tidak boleh diperbaharui dan proses penghasilannya yang rumit turut menyebabkan kos untuk menghasilkannya adalah tinggi. Malah, polimer sintetik juga merupakan bahan yang tidak mesra alam dan tidak boleh terbiodegradasi [9]. Sesetengah daripada bahan kimia yang digunakan dalam penghasilan hidrogel adalah toksik, dan jika tidak dirawat dengan sempurna ia akan menyumbang kepada pencemaran alam sekitar. Oleh yang demikian, kini kajian yang dijalankan adalah lebih bertumpu kepada penghasilan produk mudah terbiodegradasi dan mesra alam.

Memandangkan tiada kajian berkaitan penghasilan hidrogel terbiodegradasi berasaskan nata de coco dengan menggunakan teknik radiasi ultra lembayung terawat pernah dilakukan, ini merupakan satu peluang yang baik untuk meneroka dan mengkaji teknik tersebut. Ini kerana kaedah ini menawarkan satu teknik yang mudah, boleh alih dan kos efektif berbanding kaedah radiasi gamma, alur elektron serta gelombang mikro yang memerlukan tempat khas dan mahal. Oleh itu, kajian ini dilakukan bertujuan untuk mensintesis hidrogel berasaskan selulosa bakteria dengan menggunakan teknik radiasi ultra lembayung terawat. Hidrogel yang dibangunkan menggunakan teknik ini kemudiannya akan dianalisa serta dicirikan terhadap hidrogel dengan menggunakan ujian pengembangan, analisis spektroskopi inframerah transformasi Fourier (ATR-FTIR), kalorimetri pengimbasan pembezaan (DSC), analisis gravimetri termal (TGA), pembelauan sinar-X (XRD) dan mikroskopi pengimbasan elektron (SEM). Hasil kajian diharapkan akan menjadi kaedah alternatif bagi membangunkan hidrogel dan digunakan dengan lebih meluas.

## Bahan dan Kaedah

### Bahan

Selulosa bakteria yang disediakan daripada *nata de coco* (diperoleh dari industri makanan Kuala Selangor, Malaysia) yang telah ditulenkan dan dikisar. Bahan kimia seperti akrilamida (AM), kalium persulfat (KPS), penaut

silang N,N-metilena bisakrilamida 99% (BIS), natrium hidroksida (NaOH) dan urea diperoleh daripada pembekal Sigma-Aldrich, larutan penimbal dan air suling.

**Penyediaan serbuk selulosa bakteria daripada *nata de coco***
Penyediaan serbuk selulosa bakteria telah dilakukan mengikut kaedah yang dilaporkan oleh Halib et al. [6]. *Nata de coco* terlebih dahulu dibasuh dengan menggunakan air suling sebelum direndam dalam air suling yang telah dididihkan. Kemudian, natrium hidroksida akan dimasukkan dan dibiarkan semalaman dengan tujuan membolehkan sisa protein dalam *nata de coco* akan terlarut dalam air suling. Seterusnya, ianya dibasuh dengan menggunakan air untuk membuang sisa protein yang terlarut dalam air rendaman *nata de coco*. Proses diteruskan dengan merendamnya dalam air suling didih selama 2 jam sebelum dibasuh. Langkah ini diulangi sehingga nilai pH yang diperoleh adalah neutral. *Nata de coco* yang telah ditulenkan akan dikisar dengan menggunakan pengisar bahan basah sebelum dikeringkan dalam oven. Kepingan *nata de coco* yang telah kering dikisar dengan menggunakan pengisar kering untuk mendapatkan serbuk selulosa yang halus.

**Penyediaan hidrogel selulosa bakteria**
Penghasilan hidrogel terbiodegradasi di mana selulosa bakteria (BC) bertindak sebagai ko-monomer telah dilakukan dengan menggunakan kaedah yang digunakan oleh Pandey dan Amin [10]. Larutan selulosa bakteria (BC) disediakan dengan menyerakkan serbuk BC ke dalam 8% larutan NaOH dan 4% larutan urea. Sampel kemudiannya disimpan di dalam peti sejuk beku pada suhu 4 °C selama 24 jam. Larutan beku ini kemudiannya dikacau untuk menghasilkan larutan BC yang homogany.

Sebanyak 10 mL larutan selulosa bakteria dimasukkan ke dalam bikar bersama dengan pengacau bermagnet untuk proses pengacauan. Proses pengacauan ini dibiarkan selama 3 minit tanpa adanya proses pemanasan untuk memastikan larutan selulosa bakteria adalah homogen. Akrilamida (AM) kemudiannya ditimbang sebelum dicampurkan ke dalam larutan selulosa bakteria (BC). Berdasarkan kajian penyelidikan terdahulu [6,10] nisbah akrilamida yang dipilih dan digunakan dalam kajian ini adalah sebanyak 5% (w/v) (hidrogel A) dan 10% (w/v) (hidrogel B). Proses pengacauan diteruskan lagi setelah akrilamida dimasukkan. Setelah akrilamida larut sepenuhnya, kalium persulfat (KPS) dimasukkan ke dalam larutan BC di mana KPS bertindak sebagai bahan pemula cahaya. Nisbah berat KPS yang dimasukkan telah ditetapkan kepada 5% daripada nisbah berat akrilamida yang digunakan. N,N-metilena bisakrilamida (BIS) kemudiannya dicampurkan setelah kalium persulfat telah larut sepenuhnya. Dalam kajian ini, BIS berfungsi sebagai agen pentaut silang. Nisbah berat BIS yang dicampurkan ke dalam larutan pula telah ditetapkan kepada 10% daripada nisbah berat akrilamida yang digunakan.

Apabila kesemua bahan telah larut sepenuhnya, proses pengacauan dihentikan. Campuran tadi kemudiannya dimasukkan ke dalam piring petri kaca dan diradiasikan dengan menggunakan teknik radiasi ultra lembayung (instrumen UV kristal terawat model MKD-UV-800 Photo, USA) selama 360 saat. Hidrogel yang telah diradiasi kemudiannya dimasukkan ke dalam ketuhar pada suhu 40 – 45 °C selama semalaman untuk proses pengeringan.

**Ujian pengembangan**
Ujian pengembangan hidrogel dilakukan dengan menggunakan larutan penimbal pada pH yang berbeza bertujuan untuk mengetahui kesan pH yang berlainan terhadap hidrogel. Oleh itu, lima larutan penimbal dengan nilai pH 3, 5, 7, 9 dan 12 telah disediakan. Hidrogel kemudiannya direndam di dalam larutan penimbal ini dan beratnya akan ditimbang pada setiap selang lima minit selama 1 jam. Ujian ini dijalankan pada suhu bilik dan sebarang perubahan diperhatikan. Nisbah pengembangan hidrogel dikira dengan menggunakan persamaan seperti berikut:

$$\% S = Mt - MoMo\ x\ 100\% \quad (6)$$

di mana $Mo$ (g) adalah jisim asal hidrogel dan $Mt$ (g) adalah jisim hidrogel yang telah mengembang pada masa t (minit).

**Spektroskopi inframerah transformasi fourier**
Kajian ini telah menggunakan Jumlah Pantulan Teratenuat-Spektroskopi Inframerah Transformasi Fourier (Perkin Elmer, USA) sebagai salah satu analisis yang dijalankan terhadap hidrogel bakteria selulosa. Instrumen ini

digunakan untuk mengenal pasti kumpulan berfungsi dalam hidrogel bakteria selulosa.

**Analisis gravimetri termal-kalorimetri pengimbasan pembezaan**
Analisis gravimetri termal adalah berdasarkan kepada ukuran perubahan jisim dalam keadaan sampel dipanaskan, disejukkan ataupun pada suhu malar. Selain daripada jisim sampel, TGA-DSC (Mettler Toledo, USA) juga boleh digunakan untuk mengukur aliran haba sampel. Hal ini membolehkan instrumen ini mengesan perubahan termal yang tidak melibatkan perubahan jisim seperti peleburan, peralihan kaca dan peralihan pepejal-pepejal. Malah, isyarat DSC juga boleh dinilai secara kuantitatif sekaligus membolehkan peralihan dan entalpi tindak balas ditentukan.

**Pembelauan sinar-X**
Analisis pembelauan sinar-X (D8 Advance, Bruker, USA), secara teorinya elektron dalam medan elektromagnet ulang-alik akan berayun pada frekuensi yang sama. Apabila alur sinar-X mengenai atom, elektron di sekitar atom akan mula berayun pada frekuensi yang sama dengan alur yang masuk.

**Mikroskopi pengimbasan elektron**
Mikroskopi pengimbasan elektron (JSM 5610, JEOL, USA) merupakan instrumen saintifik yang menggunakan alur elektron bertenaga tinggi untuk menentukan morfologi objek pada skala yang sangat kecil terutamanya dalam bidang biologi, perubatan dan sains bahan [11].

## Keputusan dan Perbincangan

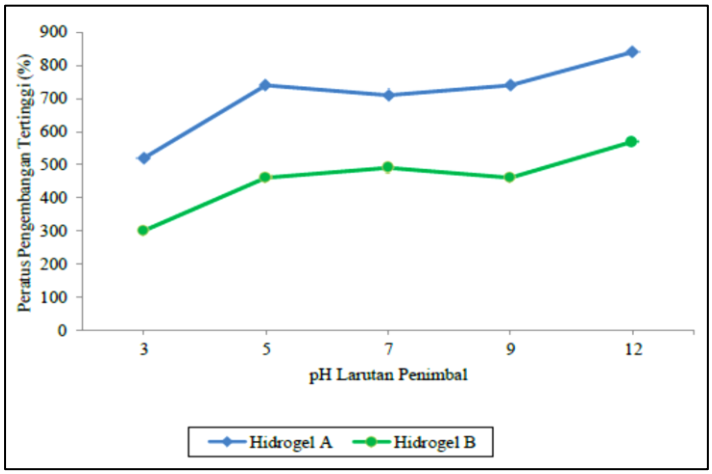
**Kesan pH ke atas peratus pengembangan hidrogel**
Peratus pengembangan tertinggi bagi kedua-dua hidrogel A dan hidrogel B pada setiap pH telah dicatatkan seperti dalam Jadual 1 di atas. Berdasarkan peratus pengembangan ini, graf perbandingan bagi kedua – dua hidrogel A dan B kemudiannya telah diplot seperti dalam Rajah 1.

Jadual 1. Perbandingan peratus pengembangan tertinggi bagi kedua-dua hidrogel untuk setiap nilai pH

| pH | Peratus Pengembangan Tertinggi Hidrogel (%) | | |
|---|---|---|---|
| | Hidrogel A | Hidrogel B | Perbezaan |
| 3 | 520 | 300 | 220 |
| 5 | 740 | 460 | 280 |
| 7 | 710 | 490 | 220 |
| 9 | 740 | 460 | 280 |
| 12 | 840 | 570 | 270 |

Merujuk kepada graf dalam Rajah 1, dapat dilihat berlakunya penurunan peratus pengembangan bagi kedua –dua hidrogel pada pH yang berbeza. Bagi hidrogel A, peratus pengembangan hidrogel pada pH 3 adalah 520% dan meningkat sehingga 740% pada pH 5. Namun, peratus pengembangan hidrogel ini telah menurun kepada 710% dalam larutan penimbal pH 7. Kemudian, peratus pengembangan hidrogel A kembali meningkat sehingga 740% pada pH 9 dan seterusnya 840% pada pH 12. Keputusan yang diperoleh adalah signifikan dengan keputusan yang pernah dilaporkan sebelum ini [12].

Bagi hidrogel B pula, peratus pengembangan tertinggi hidrogel pada pH 3 adalah 300%. Peratus pengembangan ini semakin meningkat pada pH 5 dengan nilai peratus sebanyak 460% dan seterusnya 490% pada pH 9. Walau bagaimanapun, peratus pengembangan hidrogel ini telah menurun sehingga 460% pada pH 9 sebelum kembali meningkat pada pH 12 dengan 570%. Menerusi Jadual 1 dan Rajah 1, dapat dilihat hidrogel A iaitu hidrogel dengan nisbah AM kepada selulosa bakteria 5% w/v mempunyai daya serapan yang lebih tinggi daripada hidrogel B dalam semua nilai pH. Hal ini menunjukkan kadar pengembangan hidrogel A adalah lebih cepat berbanding dengan hidrogel B.




Rajah 1. Graf peratus pengembangan tertinggi (%) terhadap pH bagi hidrogel A dan hidrogel B

Peratus pengembangan kedua-dua hidrogel A dan B yang tertinggi adalah pada larutan penimbal pH 12. Hal ini kerana, larutan dengan nilai pH yang tinggi akan menyebabkan kumpulan $-CONH_2$ dihidrolisiskan. Apabila kumpulan $-CONH_2$ dihidrolisis, penolakan antara kumpulan karboksilat yang bercas akan berlaku sekaligus memanjangkan ikatan polimer. Hal ini akan mewujudkan ruang yang besar dalam hidrogel untuk menyerap air dan meningkatkan pengembangan hidrogel. Walau bagaimanapun, apabila hidrogel telah mencapai tahap serapan air yang maksima, ianya akan menyebabkan hidrogel tersebut menjadi rapuh dan mudah pecah.

Secara keseluruhannya, kedua-dua hidrogel menunjukkan kebolehan menyerap air yang baik. Nilai peratus pengembangan hidrogel yang paling minimum adalah 520% bagi hidrogel A manakala sebanyak 300% bagi hidrogel B. Berdasarkan Rajah 1, nilai peratus pengembangan paling minimum bagi kedua-dua hidrogel ini adalah pada pH 3.

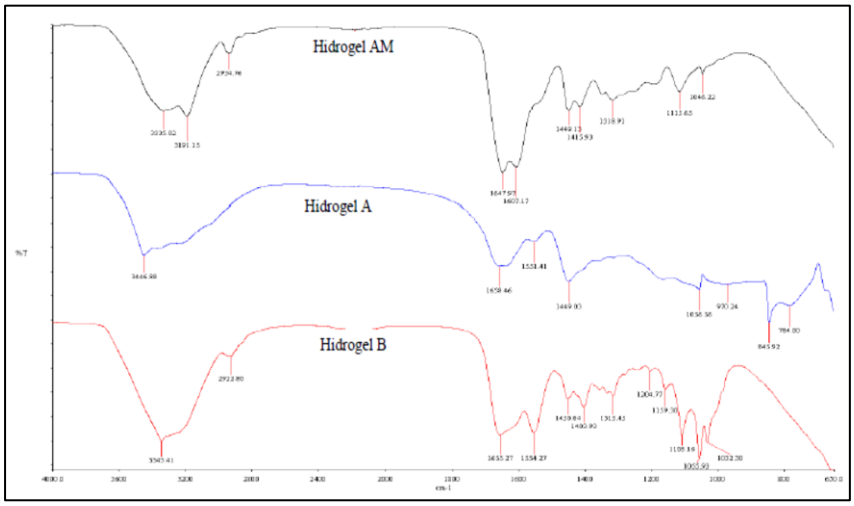
**Spektroskopi inframerah transformasi fourier**

Kajian berdasarkan Rajah 2 di atas, spektrum menunjukkan ketiga – tiga hidrogel mempunyai puncak utama yang hampir sama tetapi ketara berbeza dari segi keamatannya. Hal ini kerana interaksi yang berlaku antara jaringan selulosa bakteria dan akrilamida sewaktu pembentukan hidrogel bagi ketiga-tiga jenis hidrogel adalah sama.

Spektrum inframerah untuk kedua-dua hidrogel A dan B menunjukkan puncak keamatan masing-masing pada sekitar 3362 $cm^{-1}$ dan 3343 $cm^{-1}$ yang mewakili kumpulan –OH bagi selulosa yang mempunyai ikatan hidrogen. Selain itu, spektrum hidrogel B mempunyai puncak pada 2922 $cm^{-1}$ yang menunjukkan kesan regangan $-CH_2$ dari kumpulan $-CH_2OH$ yang terdapat dalam selulosa bakteria [6]. Manakala, puncak 1658 $cm^{-1}$ bagi hidrogel A dan 1655 $cm^{-1}$ bagi hidrogel B terhasil daripada getaran C=O kumpulan $–CONH_2$ yang terdapat dalam akrilamida.

Malah, pembentukan puncak 1658 $cm^{-1}$ bagi hidrogel A dan 1655 $cm^{-1}$ bagi hidrogel B telah menunjukkan bahawa berlakunya hidrolisis poliakrilamida yang membawa kepada penukaran kumpulan $-CONH_2$ kepada $–COO^-$ [8]. Kedua-dua spektrum bagi hidrogel A dan B juga telah menunjukkan puncak keamatan pada julat 3500 – 3100 $cm^{-1}$ yang mewakili kumpulan N-H dalam akrilamida. Getaran regangan C-O-C dalam ikatan eter selulosa bakteria pula ditunjukkan pada puncak 1165 $cm^{-1}$ bagi hidrogel A dan 1159 $cm^{-1}$ bagi hidrogel B.

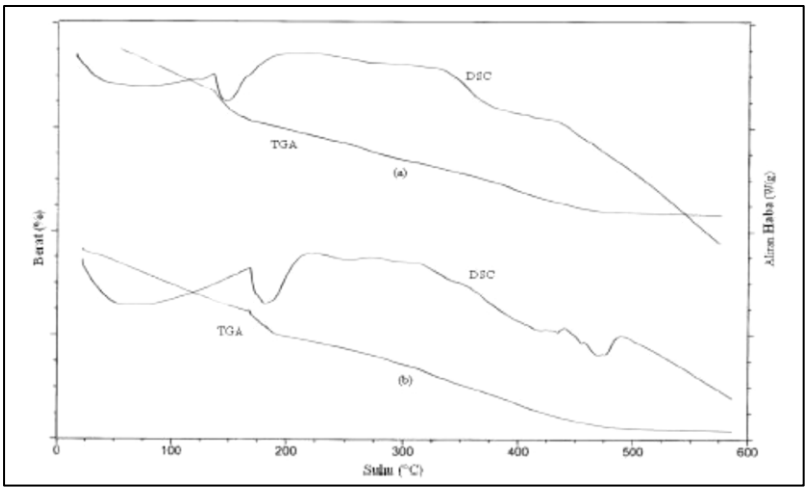
Jika dibandingkan dengan hidrogel A dan B, spektrum bagi hidrogel akrilamida mempunyai puncak yang lebih tajam pada 1647 $cm^{-1}$. Puncak yang terhasil ini adalah disebabkan oleh kehadiran kumpulan C=O dalam ikatan bersama amida. Selain itu, puncak 2934 $cm^{-1}$ pula menunjukkan kesan regangan $-CH_2$ daripada kumpulan $-CH_2OH$. Malah turut dapat diperhatikan juga kehadiran kumpulan N-H dalam spektrum hidrogel akrilamida pada julat 3500 – 3100 $cm^{-1}$ [13].




Rajah 2. Perbandingan spektrum inframerah bagi ketiga-tiga hidrogel di mana a) hidrogel AM b) hidrogel A dan c) hidrogel B

**Analisis gravimetri termal-kalorimetri pengimbasan pembezaan**

Analisis perbandingan keluk kalorimetri pengimbasan pembezaan dan analisis gravimetri termal (DSC/TGA) bagi hidrogel A dan B dapat dilihat seperti yang ditunjukkan dalam Rajah 3 di bawah. Berdasarkan keluk TGA, dapat dilihat bahawa kadar kehilangan berat maksimum bagi hidrogel A berlaku dalam julat suhu 150 – 200 °C manakala bagi hidrogel B pula berlaku dalam julat suhu 175 – 200 °C. Pada julat suhu 475 – 600 °C pula, keluk kedua-dua hidrogel A dan B menunjukkan tiada kehilangan berat berlaku seiring dengan penurunan nilai peralihan menghampiri peleburan.




Rajah 3. Perbandingan keluk TGA-DSC bagi a) hidrogel B dan b) hidrogel A

Manakala, puncak yang terhasil pada keluk DSC bagi kedua-dua hidrogel berkemungkinan disebabkan oleh peralihan fasa yang berkaitan dengan pembentukan dan pemutusan jaringan selulosa bakteria [14]. Menurut Halib et al. [6], selulosa bakteria mempunyai banyak kumpulan hidroksil di mana kumpulan ini akan bertindak balas dengan air untuk membentuk ikatan hidrogen sekaligus membolehkan hidrogel selulosa bakteria mengembang. Berdasarkan

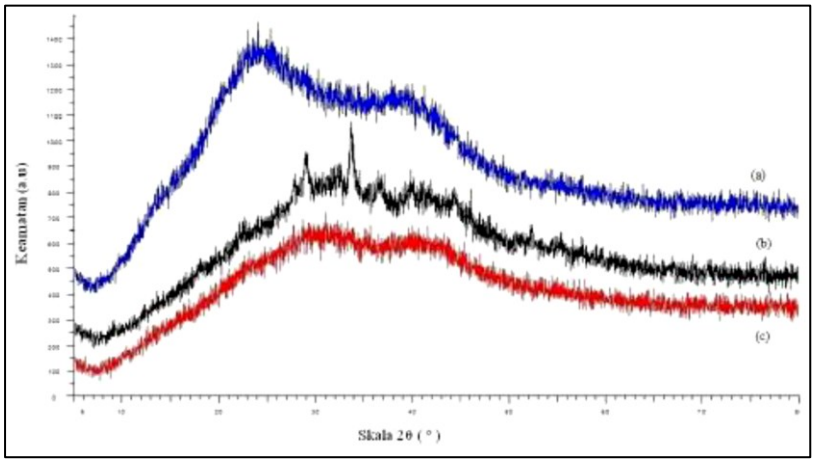
keluk DSC, nilai peralihan kaca bagi hidrogel A berlaku dalam julat suhu 175 – 225 °C manakala nilai peralihan kaca bagi hidrogel B berlaku dalam julat suhu 150 – 200 °C. Hal ini menunjukkan bahawa hidrogel A mempunyai kestabilan terma yang lebih tinggi berbanding hidrogel B kerana peningkatan jumlah molekul air yang terikat pada selulosa bakteria akan meningkatkan nilai peralihan kaca. Perbandingan nilai peralihan kaca dan pengurangan berat maksimum bagi kedua-dua hidrogel dapat dilihat dengan lebih jelas seperti dalam Jadual 2 di bawah.

Jadual 2. Perbandingan termogram bagi kedua-dua hidrogel A dan B

| **Nisbah hydrogel** | **Nilai pengurangan berat maksimum/ Nilai peralihan kaca ($^{o}$C)** | |
|---|---|---|
| | **TGA** | **DSC** |
| Hidrogel A | 150 – 200 | 175 – 225 |
| Hidrogel B | 175 – 200 | 150 – 200 |

**Pembelauan sinar-X**

Dalam kajian ini, analisis pembelauan sinar-X telah digunakan untuk mencirikan peratusan penghabluran hidrogel berasaskan selulosa bakteria [15]. Rajah 4 telah menunjukkan perbandingan peratus penghabluran antara hidrogel akrilamida, hidrogel A dan juga hidrogel B.




Rajah 4. Perbandingan peratus penghabluran di antara hidrogel a) hidrogel akrilamida, b) hidrogel A dan c) hidrogel B

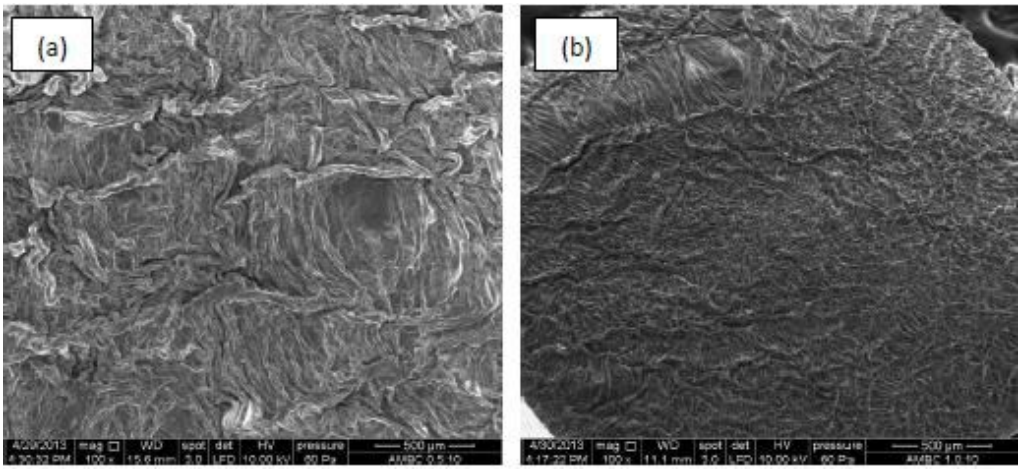
Berdasarkan Rajah 4 di atas, spektrum menunjukkan puncak keamatan bagi hidrogel A adalah hampir sama seperti hidrogel B. Tetapi, hidrogel A mempunyai beberapa puncak puncak yang lebih tinggi dan tajam jika dibandingkan dengan puncak bagi hidrogel B yang kelihatan lebih luas. Puncak keamatan hidrogel B yang lebar dan luas menunjukkan bahawa hidrogel ini mengandungi lebih banyak komponen amorfus. Manakala, puncak keamatan hidrogel A yang lebih tajam pula menunjukkan peratus penghabluran bagi hidrogel A adalah lebih tinggi berbanding dengan hidrogel B.

Rajah 4 juga menunjukkan hidrogel akrilamida mempunyai puncak yang lebih tinggi dan kurang lebar berbanding dengan hidrogel A dan juga hidrogel B. Hal ini menunjukkan peratus penghabluran bagi hidrogel akrilamida adalah lebih tinggi. Walau bagaimanapun, peratus penghabluran yang terlalu tinggi boleh mendorong kepada peningkatan kadar kerapuhan hidrogel [16].

**Mikroskopi pengimbasan elektron**

Dalam kajian ini, analisis mikroskopi pengimbasan elektron (SEM) telah digunakan untuk membandingkan

morfologi permukaan antara hidrogel A dan juga hidrogel B. Berdasarkan Rajah 5, morfologi permukaan kedua – dua hidrogel menunjukkan wujudnya liang – liang terbuka dalam hidrogel. Kewujudan liang – liang ini membolehkan proses penyerapan air berlaku dari semua arah sekaligus dapat menentukan tahap keporosan hidrogel [12].




Rajah 5. Mikrograf SEM bagi hidrogel berasaskan selulosa di mana a) hidrogel A dan b) hidrogel B

Berdasarkan ujian pengembangan, didapati hidrogel A mempunyai nilai peratus pengembangan yang lebih tinggi berbanding hidrogel B. Hal ini kerana hidrogel A mempunyai tahap keporosan yang lebih tinggi memandangkan liang – liang yang terdapat dalam hidrogel A adalah lebih banyak dan besar daripada hidrogel B.

## Kesimpulan

Hidrogel berasaskan selulosa boleh diketengahkan sebagai bahan bio untuk diaplikasikan dalam pelbagai bidang seperti kejuruteraan tisu, penghantaran ubat dan komponen elektronik. Berdasarkan kajian yang telah dan sedang dijalankan, hidrogel berasaskan selulosa bakteria telah berjaya dihasilkan dengan menggunakan teknik ultra lembayung terawat. Teknik telah menghasilkan sampel hidrogel berasaskan selulosa bakteria bagi dengan ciri-ciri yang setara dengan sampel yang dihasilkan menggunakan sinar gamma dan sinar alur elektron (EB). Malah teknik ini menawarkan satu kaedah yang murah dan mudah sebagai alternatif kaedah konvensional dan teknik radiasi yang lain.

## Rujukan

1. Schacht, E. H. (2004). Polymer chemistry and hydrogel systems. *Journal of Physics: Conference Series,* 3: 22 – 28.
2. Hoffman A. S. (2002). Hydrogels for biomedical applications. *Advanced Drug Delivery Reviews,* 43: 3 – 12.
3. Langer, R. and Peppas, N. A. (2003). Advances in biomaterials, drug delivery, and bionanotechnology. *Bioengineering, Food, And Natural Products,* 49(2003): 2990 – 3006.
4. Brown, R. M., Jr. (2004). Cellulose structure and biosynthesis: What is on the store for the 21st Century? *Journal of Polymer Science: Part A: Polymer Chemistry,* 42(3): 487 – 495
5. Sannino, A., Demitri, C. and Madaghiele, M. (2009). A review on biodegradable cellulose-based hydrogels: Design and applications. *Materials,* 2(2009): 353 – 373.
6. Halib, N., Amin, M. C. I. M. and Ahmad, I. (2012). Physicochemical properties and characterization of nata de coco from local food industries as a source of cellulose. *Sains Malaysiana,* 41(2): 205 – 211.
7. Azman, I., Mutalib, S. A., Yusoff, S. F. M., Fazry, S., Noordin, A., Kumaran, M. and Lazim, A. M. (2016). Novel dioscorea hispida starch-based hydrogels and their beneficial use as disinfectants. *Journal of Bioactive and Compatible Polymers,* 31(1): 42 – 59.

8. Amin, M. C. I. M., Abadi, A. G., Ahmad, N., Katas, H. and Jamal, J. A. (2012). Bacterial cellulose film coating as drug delivery system: Physicochemical, thermal and drug release properties. *Sains Malaysiana,* 41(5): 561 – 568.
9. Amin, M. C. I. M., Ahmad, N., Halib, N. and Ahmad, I. (2012). Synthesis and characterization of thermo- and pH-responsive bacterial cellulose/acrylic acid hydrogels for drug delivery. *Carbohydrate Polymers,* 88(2): 465 – 473.
10. Pandey, M. and Amin, M. C. I. M. (2012). Accelerated preparation of novel bacteria cellulose/acrylamide-based hydrogel by microwave irradiation. *International Journal of Polymeric Materials,* 62: 402 – 405.
11. Voutou, B. and Stefanaki, E. C. (2008). Electron microscopy: The basics. *Physics of Advanced Materials Winter School, 2008:* pp. 1 – 11.
12. Halib, N., Amin, M. C. I. M. and Ahmad, I. (2010). Unique stimuli responsive characteristics of electron beam synthesized bacterial cellulose/acrylic acid composite. *Journal of Applied Polymer Science,* 116: 2920 – 2929.
13. Lampman, G. M., Pavia, D. L., Kriz, G. S. and Vyvyan, J. R. (2010). *Introduction to Spectroscopy*. United States of America: Brooks/Cole Cengage Learning.
14. Jager, H. J. and Prinsloo, L. C. (2001). The dehydration of phosphates monitored by DSC/TGA and in situ Raman spectroscopy. *Thermochimica Acta,* 376: 187 – 196.
15. Prevey, P. S. (2009). X-ray diffraction characterization of crystallinity and phase composition in plasma-sprayed hydroxylapatite coatings. *Journal of Thermal Spray Technology,* 9(3): 369 – 376.
16. Scintag Inc. (1999). Chapter 7: Basic of X-ray diffraction. www.scintag.com [Access online 10 Mei 2013].

*Malaysian Journal of Analytical Sciences, Vol 21 No 5 (2017): 1120 - 1126*
*DOI: https://doi.org/10.17576/mjas-2017-2105-14*

MALAYSIAN JOURNAL OF ANALYTICAL SCIENCES
*Published by The Malaysian Analytical Sciences Society*
ISSN 1394 - 2506

# INCORPORATION OF GRAPHENE INTO COUNTER ELECTRODE TO ENHANCE THE PERFORMANCE OF DYE-SENSITIZED SOLAR CELLS

## (Pengabungan Grafin dalam Elektrod Lawan untuk Meningkatkan Prestasi Sel Suria Terpeka Pewarna)

Aisyah Bolhan and Norasikin Ahmad Ludin*

*Solar Energy Research Institute (SERI)*
*Universiti Kebangsaan Malaysia, 43600 UKM Bangi, Selangor, Malaysia*

**Corresponding author: sheekeen@ukm.edu.my*

Received: 12 April 2017; Accepted: 1 September 2017

**Abstract**

Platinum (Pt) is a conventional material for counter electrodes of dye-sensitized solar cells (DSSCs) due to its excellent electrocatalytic activity in the redox process. However, the high cost of Pt motivates researchers to search for composite materials of Pt to reduce its consumption. This study is aimed to reduce Pt usage by incorporating reduced graphene oxide (rGO) with Pt of different ratios in counter electrode thin films and to determine the optimum ratio with the highest efficiency. A DSSC-based platinum/rGO (Pt/rGO) counter electrode composite was fabricated using doctor-blade method. X-ray diffraction analysis was performed to examine the crystallite structure of the Pt/rGO thin film. The optimum ratio was found to be 70:30 of Pt:rGO, with current–voltage characterization showing an efficiency of 5.5%, open-circuit voltage of 0.739 V, current density of 12.5 mA/cm$^2$, and fill factor of 59.24%.

**Keywords**: counter electrode, dye-sensitized solar cell, graphene, platinum, thin film

**Abstrak**

Platinum (Pt) adalah bahan konvensional untuk elektrod lawan sel suria terpeka pewarna (DSSC) memandangkan ia mempunyai aktiviti pemangkinan-elektro dalam proses redoks yang sangat baik. Namun begitu, harga Pt sangat mahal mendorong para pengkaji untuk mencari bahan komposit Pt yang boleh mengurangkan penggunaannya. Kajian ini menumpukan pengurangan penggunaan Pt dengan menggabungkannya dengan grafin oksida terturun (rGO) dengan Pt dalam filem nipis elektrod lawan pada nisbah berbeza dan untuk menentukan nisbah paling optimum yang meningkatkan kecekapan. DSSC berasaskan komposit elektrod lawan platinum/grafin oksida (Pt/rGO) telah difabrikasikan menggunakan kaedah *doctor blade*. Analisis Pembelauan sinar-X (XRD) telah dijalankan untuk memeriksa struktur kristal pada filem nipis Pt/rGO. Nisbah optimum yang dicapai adalah 70:30 kepada Pt:rGO dimana pencirian arus-voltan (*I-V*) menunjukkan nilai kecekapan ialah 5.5%, dengan nilai litar voltan terbuka $V_{oc}$, ketumpatan arus $J_{sc,}$ dan faktor mengisi *FF*, masing-masing dengan nilai 0.739 V, 12.5 mA/cm$^2$ dan 59.24 %.

**Kata kunci:** elektrod lawan, sel suria terpeka pewarna, grafin, platinum, filem nipis

## Introduction

Over the past decade, green and renewable energy sources have been explored and used [1] to reduce $CO_2$ emissions [1-3]. Several types of renewable energy include hydro, wind, and solar or photovoltaic (PV). Among these sources, PV is the third most valued energy source that leads to the intense development of PV cell technology in recent years [1]. The sun is the best source of energy among the renewable or non-renewable energy because it provides 174,000 TW per year to the earth [4]. In other words, the energy from the sun should be utilized optimally. Ongoing

intense research is currently still being conducted for PV energy sources. Currently, PV energy sources have three generations of solar cell. The first generation is the silicon solar cell, in which the power conversion efficiency achieved 25% [5]. Presently, the silicon solar cell has dominated the market, but the high production cost has limited the spread of cell application. The second generation is the compound solar cell, in which gallium arsenide reached 28% [6] efficiency and cadmium telluride attained 20% [6, 7]. However, similarly the second generation also bears a high cost of production, which leads to the third generation. The third generation consists of dye-sensitized solar cells (DSSCs), organic solar cell, and quantum dots solar cells [8]. Third generation cells have lower cost production than conventional solar cell and have green technology that minimizes the environmental effect.

DSSC is one of the third generations of PV devices that gained the attention from most researchers. DSSC has several important parts that make up the cells; these parts include the titanium dioxide ($TiO_2$) photoanode, which helps excite the electron to the covalent bond; platinum (Pt) counter electrode, which acts as a catalyst in redox process; ruthenium dye (N719), which acts as a sensitizer that absorbs photon from light; and iodide electrolyte, which helps transfer the electron between two electrodes and also works in the redox process [9, 10]. Pt is a catalyst material that helps in reducing the triiodide ions into an iodide ion at counter electrode and electrolyte interface [11]. A faster rate of reducing the triiodide ions results in fast electron charge transfer. However, Pt is corrosive toward iodide electrolyte and is commercially expensive [12]. Therefore, replacing Pt with other materials or reducing Pt consumption using Pt composite materials is crucial. In addition, it is necessary to find the material that has a high electrocatalytic activity compared with Pt.

Recently, graphene has attracted much attention as a counter electrode material because of its electrical properties, corrosive resistance, low cost, and abundance [13]. The rGO structure is a three-dimensional network and has an oxygen-containing functional group that contributes to the electrocatalytic activity of rGO counter electrode [14]. Graphene is considered as a promising composite material with Pt. Hence, several ratios of composite Pt/rGO thin films were prepared in the starting ratio of the weight of the Pt to rGO 99:1 as the first ratio. The ratio of the rGO and the Pt will continuously increase and decrease, respectively. This paper focuses on determining the optimum ratio of rGO that can be incorporated into the Pt-based DSSC while reducing the use of Pt to achieve higher efficiency than Pt-based DSSC.

## Materials and Methods

### Materials

$TiO_2$ (WER2-0, Solaronix) was used as photoanode thin film, platinum paste PT-1 was purchased from Dyesol-Australia, and rGO-B026 purchased from graphenea were used as the counter electrode thin films. The N719 ruthenium dye sensitizer purchased from Dyesol were diluted with ethanol to form 0.3 mM solution mixture. Iodide electrolyte (Iodolyte, AN-50) performed as an electrolyte. An 8 $\Omega$ $cm^{-2}$ FTO glass substrate (FTO Tec 8, Dyesol) and 15 $\Omega$ $cm^{-2}$ FTO thin film (FTO Tec 15, Dyesol) will function as a counter electrode and photoanode glass substrate, respectively. Surlyn (Meltonix) is an adhesive material that helps photoanode and counter electrode glass substrate to attach together.

### Preparation of the counter electrode thin films

Pt/rGO CE thin films were prepared with commercially available Pt paste and rGO powder. The Pt/rGO thin films were prepared as the ratio of the weight of Pt to rGO are 99:1, 95:5, 90:10, 85:15, 80:20, 75:25, 70:30, and 65:35. The Pt paste and rGO powder were ultrasonicated by the ultrasonic bath for approximately 15 minutes to create homogeneous composite mixture. Then, the mixture was stirred for another 15 minutes using the magnetic stirring bar and pasted onto the glass substrate of the 1.5 cm × 2 cm, 8 $\Omega$ $cm^{-2}$ fluorine-doped tin oxide (FTO) using doctor-blade method. Pt/rGO CE thin films were annealed for 30 minutes at 450 °C.

### Fabrication of the DSSC

$TiO_2$ photoanode thin films were also prepared using the doctor-blade method, and the thin films were then immersed in the N719 ruthenium dye for 16 h with an active area of 0.25 $cm^2$. The photoanode and counter electrode were attached together by using a warm press machine to melt the Surlyn placed between the two electrodes. The active area part was injected with iodide electrolyte through the aperture between the electrodes. Then, the aperture was sealed to complete the fabrication of DSSC.

## Results and Discussion

### X-ray diffraction analysis

The X-ray diffraction (XRD) pattern of Pt, composite Pt/rGO of different ratio, and rGO are illustrated in Figure 1. Pt has been observed to have a prominent peak at (111) plane attributed to 39.8° with JCPDS of 03-065-2868. The Pt peak decrease until ratio 90:10 and rise slightly at ratio 85:15 before decreasing again at ratio 80:20 as the weight ratio of rGO increases. rGO has a weak intensity, shown in J of Figure 1, where the *hkl* plane of (006) attribute to 26.6° with JCPDS of 00-026-1076. $SnO_2$ diffraction angle is 26.5°, which is close to the rGO at (110) plane. The presence of Pt has concealed the rGO peak when Pt is mixed with the rGO. This process resulted in no visible rGO peak for the XRD pattern of Pt/rGO CE thin film. Thus, Pt is more crystallized than rGO. The crystallite size for each CE thin film can be calculated using Debye–Scherrer equation as in (1) [15],

$$D = \frac{0.9\lambda}{\beta \cos\theta} \tag{1}$$

where $D$ is the crystallite size, $\lambda$ is the wavelength, $\beta$ is the full width at the half maximum in radians, and $\theta$ is the diffraction angle. The crystallite sizes of the CE have been calculated, and the plotted graph is depicted in Figure 2. From the graph, the crystallite size increase until ratio of Pt:rGO is 95:5 and the crystallite size began to fluctuate at the range 29 – 36 nm approximately until ratio of Pt:rGO is 75:25. The crystallite size continues to decrease again at the ratio of Pt:rGO 70:30 although the amount of rGO keeps increasing. The larger the size of crystallite leads to high surface roughness of the thin films. The higher surface roughness of the thin film contributes to large surface area that instigates the high conductivity of the counter electrode thin film. Thus, from Figure 2 we can determine that counter thin film of Pt/rGO with ratio 80:20 has better conductivity among other due to large size of crystallite.

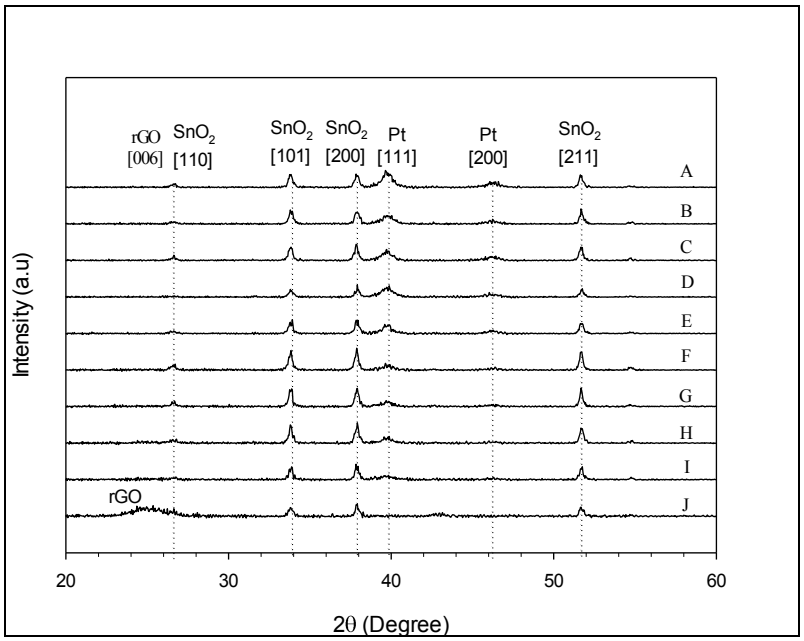



Figure 1. XRD of CE thin film. A is Pt. B–I is Pt:rGO with ratio 99:1, 95:5, 90:10, 85:15, 80:20, 75:25, 70:30, and 65:35. J is rGO

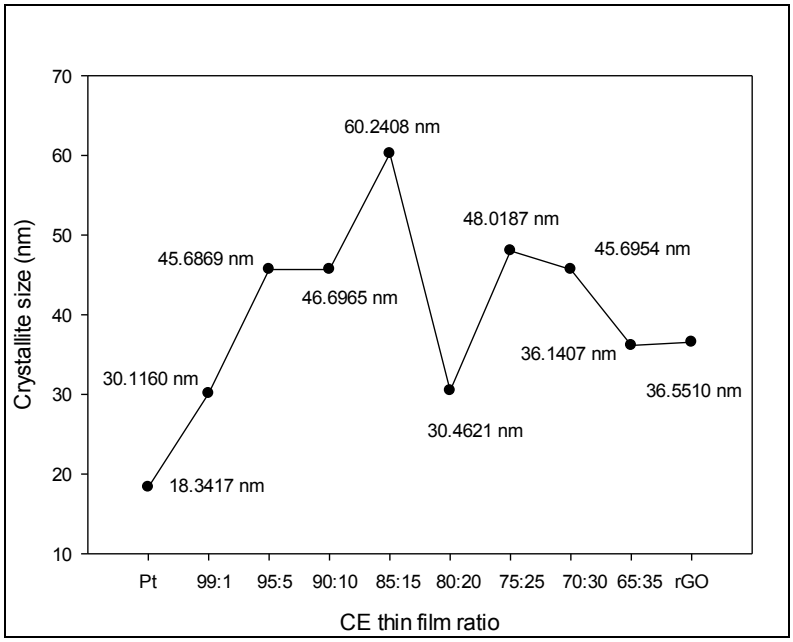
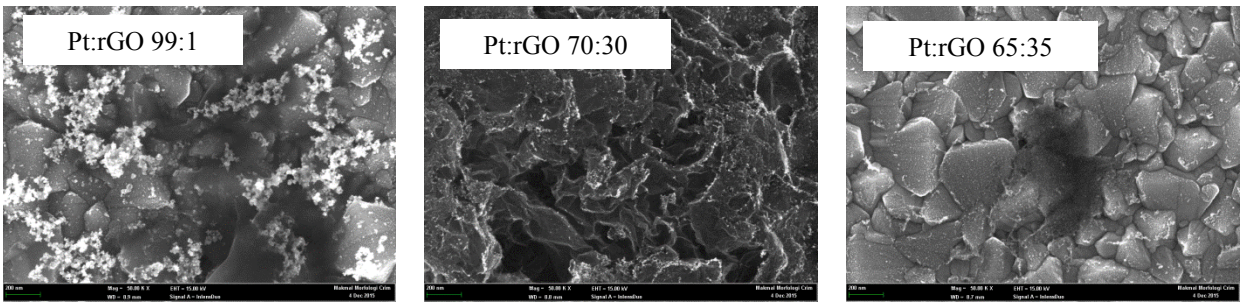



Figure 2. Crystallite size for Pt, rGO, and Pt:rGO at various ratios CE thin film

**Field emission scanning electron microscopy analysis**

The field emission scanning electron microscopy (FESEM) images of the thin films are used to study the morphology of the composite Pt:rGO counter electrode thin films (Figure 3). Pt is observed to have nano-like particle that spread homogeneously on the FTO glass substrate, and rGO is a nanosheet that has randomly aggregated. The three ratios of composite Pt/rGO thin films of the counter electrode are displayed in Figure 3. The Pt:rGO of ratio 99:1 is the first ratio, where we can observe that Pt nanoparticles are more than the rGO nanosheets. The Pt nanoparticles decrease with the increase of the rGO, and the Pt:rGO of ratio 70:30 is the optimum ratio with higher efficiency. In ratio 70:30, the Pt nanoparticles were well blended in the rGO nanosheets. When the rGO increases, the Pt nanoparticle can no longer blend with the rGO nanosheets as presented in Figure 3. In ratio 65:35, we hardly observe the Pt nanoparticle and a small amount of rGO nanosheets attached to FTO glass substrate.



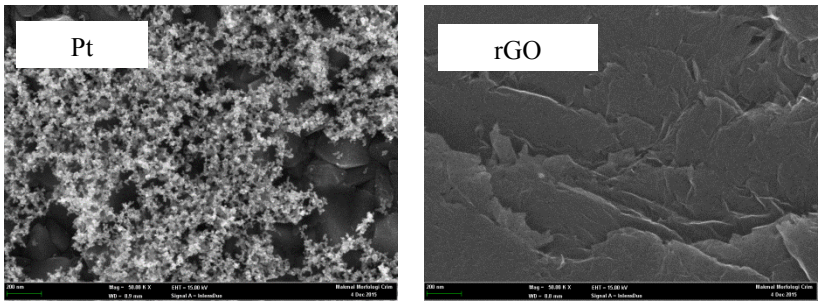



Figure 3. FESEM image of Pt, rGO, Pt:rGO of 99:1, 70:30, and 65:35

**Current-voltage analysis**

Figure 4 shows the current–voltage characterization for the DSSC with a different type of CE. The efficiency of the DSSC can be calculated by Martinson et al. [16] using equation 2:

$$\eta = \frac{VocJscFF}{Pin} \tag{2}$$

where $\eta$ is the efficiency of the device equals to the product of $V_{oc}$, $J_{sc}$, and FF divided by an $V_{oc}$ of 100 mW/cm$^2$ under AM 1.5 ($P_{in}$). The *I–V* curve for rGO is the lowest with $J_{sc}$ of 8.40 mA/cm$^2$ and an $V_{oc}$ of 0.62 V, resulting in poor efficiency of 1.97% as presented in Table 1. It can be seen that the conductivity of the thin film increase as the value of $J_{sc}$ increase following the increase of the amount of rGO. This is due to the rGO is more conductivity than Pt, the adding of the rGO improves the conductivity of the thin films. The *I–V* curve of Pt/rGO-based DSSC of ratio 70:30 shows high $J_{sc}$ (12.50 mA/cm$^2$) with $V_{oc}$ of 0.74 V, resulting in high efficiency of 5.5 %, which is better than Pt-based DSSC. Table 1 summarizes all the *I–V* curve parameter of DSSC. Therefore, the addition of the rGO in CE thin film increases the efficiency of the DSSC until the ratio of Pt:rGO of 70:30. The efficiency decreases when more rGO is added. Thus, 70:30 is the optimum ratio of rGO that can be incorporated with Pt as a CE material.

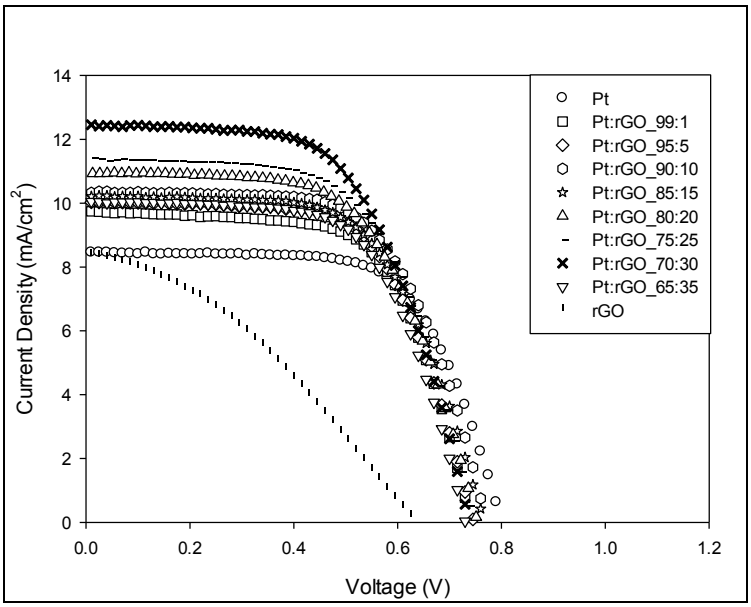



Figure 4. *I–V* Characterization of DSSC

Table 1. *I–V* characterization parameter of DSSC with Pt CE, various ratio of Pt:rGO, and rGO

| Counter electrode | $V_{oc}$ (V) | $J_{sc}$ (mA/cm$^2$) | *FF* (%) | $\eta$ (%) |
|---|---|---|---|---|
| rGO | 0.62 | 8.40 | 37.30 | 1.97 |
| Pt | 0.80 | 8.43 | 66.23 | 4.46 |
| Pt:rGO 99:1 | 0.74 | 9.73 | 64.59 | 4.67 |
| Pt:rGO 95:5 | 0.75 | 10.00 | 64.07 | 4.8 |
| Pt:rGO 90:10 | 0.77 | 10.30 | 63.55 | 5.10 |
| Pt:rGO 85:15 | 0.77 | 10.20 | 61.59 | 4.80 |
| Pt:rGO 80:20 | 0.75 | 10.90 | 60.66 | 5.00 |
| Pt:rGO 75:25 | 0.74 | 11.40 | 61.80 | 5.20 |
| Pt:rGO 70:30 | 0.74 | 12.50 | 59.24 | 5.50 |
| Pt:rGO 65:35 | 0.73 | 10.10 | 63.18 | 4.70 |

## Conclusion

The composite of Pt/rGO counter electrode thin films with different ratios were successfully prepared using doctor-blade method annealed at 450 °C for 30 min. The ratio of Pt/rGO that has been prepared were 99:1, 95:5, 90:10, 85:15, 80:20, 75:25, 70:30, and 65:35. The pattern of the increase and decrease of the efficiency of the DSSCs is observable after reaching the optimum ratio. Pt and rGO CE thin film are also prepared using the same technique as references. The Pt/rGO of ratio 70:30 shows the highest efficiency of 5.5% with the $J_{sc}$ value of 12.50 mA/cm$^2$, $V_{oc}$ value of 0.74 V, and FF is 59.24. The Pt counter electrode-based DSSC incorporated with rGO has higher efficiency at an optimum ratio of 70:30 in comparison with the Pt efficiency, which is 4.46%. The objective to reduce the use of Pt in the counter electrode of DSSC is achieved.

## Acknowledgment

This study is supported by the Centre for Research and Instrumentation (CRIM), Universiti Kebangsaan Malaysia and the Ministry of Higher Education Malaysia under Look East Policy (LEP) Grant (LEP 2.0/14/UKM/NT/03/1). We would like to thank the Solar Energy Research Institute (SERI) Colloquium 2015 for providing the platform to the discussion session and disseminating the findings.

## References

1. Karimi, M., Mokhlis, H., Naidu, K., Uddin, S., Bakar, A. H. A. (2016). Photovoltaic penetration issues and impacts in distribution network – a review. *Renewable and Sustainable Energy Review*, 53: 594 – 605.
2. Hua, Y., Oliphant, M. and Hu, E. J. (2016). Development of renewable energy in Australia and China: A comparison of policies and status. *Renewable Energy*, 85: 1044 – 1051.
3. Kardooni, R., Yusoff, S. and Kari, F. (2016). Renewable energy technology acceptance in Peninsular Malaysia. *Energy Policy*, 88: 1 – 10.
4. Smil, V. (1991). General energetics: Energy in the biosphere and civilization. John Wiley: New York, pp. 240.
5. Green, M., Emery, K., Hishikawa, Y., Warta, W. and Dunlop, E. (2015) Solar cell efficiency tables (Version 45). *Progress in Photovoltaics Research and Application*, 23: 1 – 9
6. Yella, A., Lee, H., Tsao, H., Yi, C., Chandiran, A., Nazeeruddin, M., Diau, E., Yeh, C., Zakeeruddin, S. and Gratzel, M. (2011). Porphyrin-sensitized solar cells with cobalt (II/III)–based redox electrolyte exceed 12 percent efficiency. *Science*, 334: 629 – 634.
7. Mathew, S., Yella, A., Gao, P., Humphry-Baker, R., Curchod, B., Ashari-Astani, N., Tavernelli, I., Rothlisberger, U., Nazeeruddin, M. and Gratzel, M. (2014). Dye-sensitized solar cells with 13% efficiency achieved through the molecular engineering of porphyrin sensitizers. *Nature Chemistry*, 6: 242 – 247.

8. Sugaya, T., Numakami, O., Oshima, R., Furue, S., Komaki, H., Amano, T., Matsubara, K., Okano, Y. and Niki, S. (2012). Ultra-high stacks of InGaAs/GaAs quantum dots for high efficiency solar cells. *Energy and Environmental Science*, 5 (3): 6233 – 6237
9. Yue, G., Lin, J-Y., Tai, S-Y., Xiao, Y. and Wu, J. (2012). A catalytic composite film of $Mos_2$/graphene flake as a counter electrode for Pt-free dye-sensitized solar cells. *Electrochimica Acta*, 85: 162 – 168.
10. Wu, J., Lan, Z., Lin, J., Huang, M., Huang, Y., Fan, L. and Luo, G. (2015). Electrolytes in dye-sensitized solar cells. *Chemical Reviews*, 115(5): 2136 – 2173.
11. Guai, G. H., Song, Q. L., Guo, C. X., Lu, Z. S., Chen, T., Ng, C. M. and Li, C. M. (2012). Graphene-Pt/ITO counter electrode to significantly reduce Pt loading and enhance charge transfer for high performance dye-sensitized solar cell. *Solar Energy*, 86: 2041 – 2048.
12. Yun, S., Liu, Y., Zhang, T. and Ahmad, S. (2015). Recent advances in alternative counter electrode materials for Co-mediated dye-sensitized solar cells. *Nanoscale*, 7: 11877 – 11893.
13. Duan, X., Gao, Z., Chang, J., Wu, D., Ma, P., He, J., Xu, F., Gao, S. and Jiang, K. (2013). $CoS_2$-graphene composite as efficient catalytic counter electrode for dye-sensitized solar cell. *Electrochimica Acta*, 114: 173 – 179.
14. Hoshi, H., Tanaka, S. and Miyoshi, T. (2014). Pt-graphene electrodes for dye-sensitized solar cells. *Materials Science and Engineering B*, 190: 47 – 51.
15. Lipson, H. and Steeple, H. (1970). Interpretation of X-ray powder diffraction pattern. Macmillan, London.
16. Martinson, A. B. F., Goes, M. S., Santiago, F. F., Bisquert, J., Pellin, M. J. and Hupp, J. T. (2009). Electron transport in dye-sensitized solar cells based on ZnO nanotubes: Evidence for highly efficient charge collection and exceptionally rapid dynamics. *Journal of Physical Chemistry A*, 113: 4015 – 4021.

*Malaysian Journal of Analytical Sciences, Vol 21 No 5 (2017): 1127 - 1133*
*DOI: https://doi.org/10.17576/mjas-2017-2105-15*

MALAYSIAN JOURNAL OF ANALYTICAL SCIENCES
*Published by The Malaysian Analytical Sciences Society*
ISSN 1394 - 2506

# PERFORMANCE ANALYSIS OF SIMPLIFIED SILICON SOLAR CELL ON *P*-TYPE CRYSTALLINE SILICON WAFER

## (Analisis Prestasi Bagi Sel Suria Silikon Teringkas Ke Atas Silikon Wafer Kristal Jenis-*P*)

Wan Zulhafizhazuan*, Suhaila Sepeai, Cheow Siu Leong, Kamaruzzaman Sopian , Saleem H. Zaidi

*Solar Energy Research Institute (SERI),*
*Universiti Kebangsaan Malaysia, 43600 UKM Bangi, Selangor, Malaysia*

**Corresponding author: wanzulhafizhazuan@gmail.com*

Received: 12 April 2017; Accepted: 1 September 2017

**Abstract**

Crystalline silicon (c-Si) wafers are the dominating substrate materials for solar cells in current photovoltaic (PV) industry. Silicon (Si) wafer with positive-type (*p*-type) based solar cells dominates almost 95% of the global PV market. Recent goal in Si solar cell industry is focusing on cost reduction through inexpensive manufacturing processes. Standard manufacturing process of Si solar cell fabrication consist of damage removal, cleaning, texturing, phosphorus oxytrichloride ($POCl_3$) diffusion, anti-reflective coating (ARC) deposition, metallization by screen printing technique, firing and light current-voltage (LIV) testing. These fabrications line are time–consuming and high temperature process which lead to high manufacturing cost. This study presents the simplification of Si solar cell fabrication on *p*-type Si wafer. Simplified fabrication process eliminates the ARC deposition by plasma enhanced chemical vapour deposition (PECVD). Simplified Si solar cell was fabricated without silicon nitride (SiN) as ARC layer. In commercial solar cell, both pyramid texture on Si wafer and SiN have been used to reduce reflectance and enhanced the light absorption. From the reflectance measurement, it can be seen that SiN and pyramid texture shows an average reflectance curve. The efficiency obtained by commercial, fabricated and simulated solar cells were 17.09%, 9.44% and 9.67%, respectively. From the simulation study, it is proven that the low efficiency of simplified solar cell was attributed by low minority carrier lifetime of *p*-type Si wafer.

**Keywords**: crystalline silicon solar cell, *p*-type Si wafer, anti-reflective coating, minority carrier life time, PC1D simulation

**Abstrak**

Kepingan silikon kristal (c-Si) adalah bahan substrat yang mendominasi sel suria untuk industri fotovolta (PV) masa kini. Sel suria berasaskan kepingan silikon (Si) berjenis-*p* menguasai hampir 95% daripada pasaran PV global. Matlamat terkini dalam industri sel suria Si memfokuskan kepada pengurangan kos melalui proses pembuatan yang murah. Piawai pembuatan fabrikasi sel suria Si terdiri daripada penyingkiran kotoran, pembersihan, pentekstur an, penyerapan fosforus oksitriklorida ($POCl_3$), pemendapan lapisan anti-pantulan (ARC), penyaduran dengan teknik percetakan skrin, pembakaran dan ujian cahaya arus-voltan (LIV). Proses fabrikasi piawai ini memakan masa dan menggunakan suhu tinggi yang menyebabkan kos pengeluaran yang tinggi. Kajian ini membentangkan peringkasan proses fabrikasi sel suria Si di atas Si wafer jenis-*p*. Proses fabrikasi teringkas ini membuang proses pemendapan ARC oleh pengendapan kimia dipertingkat plasma (PECVD). Sel suria Si teringkas telah difabrikasi tanpa lapisan silikon nitrida (SiN) sebagai ARC. Dalam sel suria komersial, tekstur piramid pada Si wafer dan SiN telah digunakan untuk mengurangkan pantulan dan meningkatkan penyerapan cahaya. Dari pengukuran pantulan, SiN dan tekstur piramid menunjukkan pantulan yang agak sama. Kecekapan yang diperolehi oleh sel suria komersial, diringkas dan simulasi adalah masing-masing pada 17.09%, 9.44% dan 9.67%. Daripada kajian simulasi, ia membuktikan bahawa kecekapan yang rendah bagi sel suria teringkas adalah disebabkan oleh jangka hayat pembawa minoriti yang rendah pada Si wafer jenis-*p*.

**Kata kunci:** kristal silikon sel suria, kepingan silikon jenis-*p*, lapisan anti-pantulan, jangka hayat pembawa minoriti, simulasi PCID

## Introduction

Solar cell is a semiconductor device which converts sunlight into electricity. Silicon (Si) is the most developed and widely used element in manufacturing solar cells. It is an indirect bandgap semiconductor and can be doped by impurities such as boron or phosphorus to form highly conductive positive or negative regions. It also absorbs light over a broad spectral range from ultra-violet (UV) to near infra-red (NIR) range. Si is a non-toxic material and the second most abundant element (after oxygen) on earth with a concentration of 28% [1]. The Si solar cell essentially has three functional elements: (a) absorption of sunlight to form electron-hole ($\bar{e}$-*h*) generation pairs, (b) an internal electric field (*p*-*n* junction) to separate $\bar{e}$-*h* pairs, and (c) external electrical contacts to extract current [2]. The Si wafer itself acts as the light absorber to generate $\bar{e}$-*h* pairs. The junction inside the semiconductor prevents $\bar{e}$-*h* pairs from recombination and guides oppositely charged carriers to respective electrical contacts. Finally, the contacts act as wires to carry photo-generated current into a load. Market review reveals that *p*-type wafer based solar cell dominates almost 95 % of the worldwide PV market [3].

Figure 1(a) shows the standard manufacturing process in solar cell fabrication that consist of damage removal, texturing, junction formation by phosphorus oxytrichloride ($POCl_3$) diffusion, Silicon nitride (SiN) deposition as ARC, metallization by screen printing technique, firing and IV testing. SiN is widely used as ARC layer in commercial c-Si solar cell deposited by PECVD. ARC deposition and diffusion processes consumed 50% to 70% energy from total energy consumption in solar cells fabrication process [4]. In addition, SiN uses silane toxic gas while $POCl_3$ diffusion requires temperature of 1000 °C for junction formation. High temperature process leads to high fabrication cost, meanwhile SiN deposition is a toxic-based process. Therefore, this study presents simplified fabrication process for c-Si solar cell on *p*-type wafers. This process eliminates the use of SiN as ARC layer (Figure 1(b)). Previous study has presented the *in-situ* oxidation process of silicon dioxide ($SiO_2$) as ARC layer [5]. However, in this paper, we presented performance evaluation of Si solar cell without ARC layer by experiment and PC1D simulation. Solar cell simulation model PC1D is used to understand dependence of solar cell performance on wafer and process parameters.

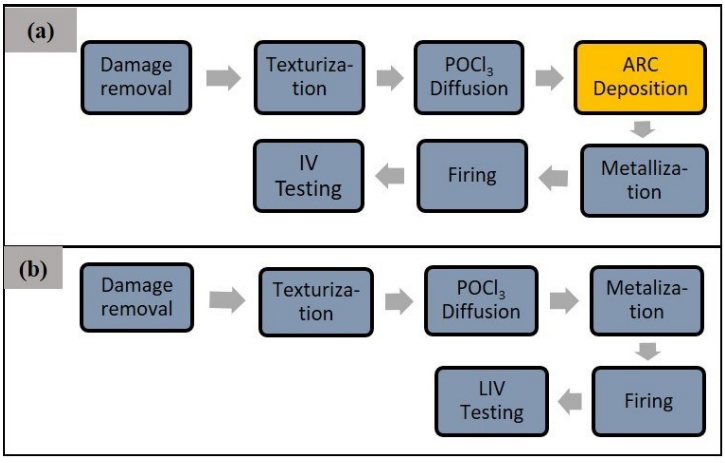



Figure 1. Comparison of (a) standard manufacturing process for Si solar cell fabrication, and (b) fabrication process for simplified Si solar cell on *p*-type Si wafer. There is an elimination of ARC deposition process in simplified Si solar cell

## Materials and Methods

### Fabrication of simplified *p*-type Si solar cell

Figure 2(a) schematically describes the commercial solar cell configuration, meanwhile Figure 2(b) describes simplified solar cell configuration without ARC layer. The saw damage in as-cut boron wafers was removed by etching in 10% sodium hydroxide (NaOH) solution. A mixture of 6000 ml deionized (DI) water and 600 g of NaOH

was prepared in Pyrex beaker and the solution was heated to 70 $^{o}$C. Si wafers were fully immersed into heated solution for 10 minutes. This process removes surface saw damage and other contaminants from the wafering process. The etched wafers are rinsed in DI water and immersed in dilute hydrofluoric (HF) solution to remove native oxide. Appropriately processed wafers will exhibit shiny surface and are completely hydrophobic. An alkaline solution is highly effective in creating a uniform texture for the texturing process on <100> crystalline orientation. A mixture of isopropyl alcohol:potassium hydroxide:deionized water (IPA:KOH:$H_2O$) was prepared based on volume ratio 5:1:123. The solution was heated up at 70 $^{o}$C. The saw-damage removed wafers are immersed in this solution for 30 minutes. Finally, the wafer is rinsed in DI water and immersion in 10% HF solution. With appropriate texture process, surface appearance is grey and shiny at large oblique angles due to high reflection of <111> crystalline facets. Such rough surfaces enhance light trapping and reduce reflection.

A *p-n* junction is formed based phosphorous diffusion with liquid source $POCl_3$ solution. A vapour solution containing $POCl_3$ is transported to a high temperature quartz furnace to form Phosphorous Oxide film on the Si wafer surface. Next, the metallic pastes were screen printed on both the front and rear surfaces of the Si wafer. At the front, Ag paste is screen printed and dried in low temperature oven at 200 ºC for 10 minutes. Following front surface screen printing, rear surface is screen printed by with an Al paste and dried in low temperature oven at 200 ºC for 10 minutes. The drying process removes excess organic solvent from the pastes and provides stable adhesion between paste and wafer surfaces. The aim of this process is to form low resistance ohmic contacts between metallic films and Si. In this process, wafers were placed on the top of the conveyer belt and passes through six temperature zones. Each of temperature zones is heated up by infrared quartz lamps. The finished solar cells were characterized by light current-voltage (LIV) measurement system and quantum efficiency (QE) measurement systems using Keithley 237.

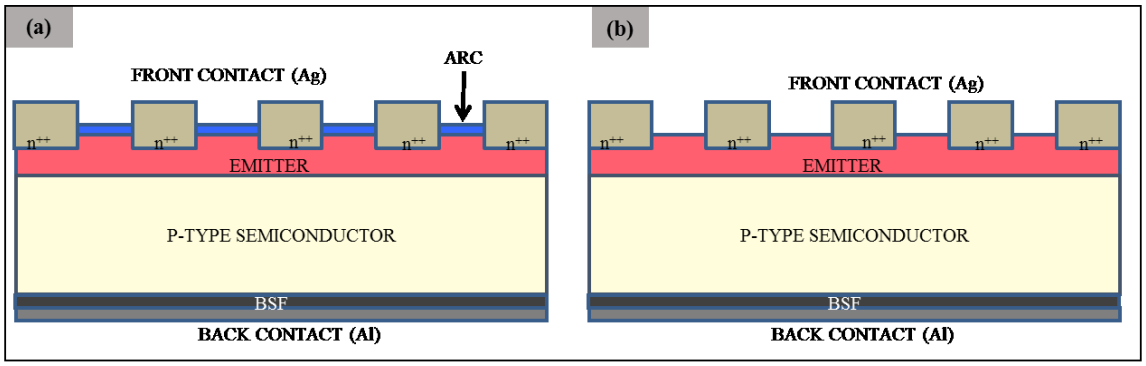



Figure 2. Schematic diagram for device configuration of (a) commercial p-type Si solar cell; and (b) simplified *p*-type Si solar cell

**PC1D simulations of simplified *p*-type Si solar cell**

PC1D simulation software was used to simulate performance of *p*-doped wafer solar cell in terms of critical solar cell parameters such as bulk conductivity, front surface field and minority carrier lifetime [6]. Figure 2 described the differences schematic configuration between (a) ARC and (b) non-ARC solar cell configuration. Non-ARC simulation was carried out for 100 $cm^2$ area p type silicon solar cell with fixed series resistance, shunt conductance, and 200-$\mu$m wafer thickness. Pyramidal texture was assumed with fixed 10 % front surface reflectance. Base contact and internal conductor were respectively set at 0.0015 Ω and 0.3 S [7]. Bulk conductivity concentrations were varied in $1.513\times10^{11}/cm^3$ to $1.513\times10^{16}/cm^3$ range. The front surface emitter doping concentration was varied from $1.27\times10^{17}/cm^3$ to $1.27\times10^{22}/cm^3$. The minority carrier lifetime was varied from 0.001 $\mu$s to 1000 $\mu$s. Finally, the front surface recombination velocity was varied in $1\times10^{6}$ cm/s to 100 cm/s. Table 1 shows the details of simulation parameters.

Table 1. Simplied Si solar cell parameters in PC1D simulation

| **Parameters** | **Value and Unit** |
|---|---|
| Device area | 100 $cm^2$ |
| Front surface texture depth | 3 $\mu$m/ 54.74° |
| Rear surface texture depth | 3 $\mu$m/ 54.74° |
| Front / Rear surface coating enabled | Yes |
| Internal / external optical reflectance | 10% |
| Base contact | 0.015 Ω |
| Internal conductor | 0.3 S |
| Thickness | 200 $\mu$m |
| Material | Silicon (Si) |
| Carrier mobilities for electron and holes ($\mu_e$ /$\mu_h$) | 1450 $cm^2$/Vs 413 $cm^2$/Vs |
| Dielectric constant | 11.9 |
| Band gap | 1.124 eV |
| Intrinsic conc. At 300K | $1\times10^{10}$ $cm^{-3}$ |
| Absorption coefficient | Silicon |
| Free carrier absorption enabled | Yes |
| P-type background doping | $1.513\times10^{16}$ $cm^{-3}$ |
| 1st front diffusion: *n*-type | $1\times10^{17}$ $cm^{-3}$ |
| 2nd front diffusion | - |
| 1st rear diffusion: *p*-type | $1\times10^{19}$ $cm^{-3}$ |
| Bulk recombination | 0.1 $\mu$s |
| Front surface recombination | 10 cm/s |
| Rear surface recombination | 10 cm/s |
| Temperature | 25°C |
| Base circuit | -0.8 to 0.8 V |
| Collector circuit | Zero |

## Results and Discussion

The investigation on reflectance measurement has been performed to investigate the photon reflection of pyramid texture Si wafer and SiN as ARC layer. Scanning electron microscopy (SEM) images of pyramid textured and ~70 nm thin SiN layer on Si wafer shown in Figure 3(a) and Figure 3(b). In commercial solar cell, both pyramid texture and SiN layer have been used to reduce light reflectance and enhanced photon absorption. Figure 4 shows the reflectance measurement of planar (un-textured) wafer, textured wafer and SiN layer on Si wafer. The high reflectance shown by planar wafer indicates that the light is highly reflected on un-textured and non-ARC wafer. Therefore, the planar wafer is not appropriate in Si solar cell fabrication as it has high photon and reflection losses. Meanwhile, textured wafer and SiN layer shows an average performance on reflectance measurement. This average performance of the reflectance measurement proves that non-ARC Si solar cell can potentially produce a good performance output of solar cell compared to commercial solar cell.

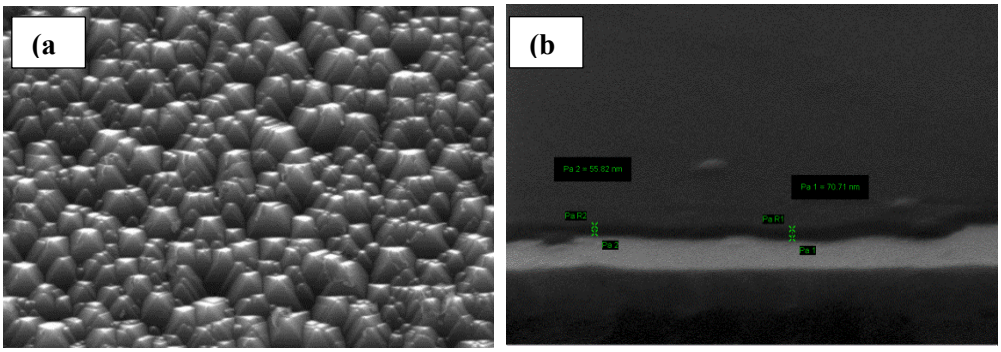



Figure 3. SEM images of (a) pyramid texture on Si wafer, and (b) SiN layer as ARC on commercial Si solar cell

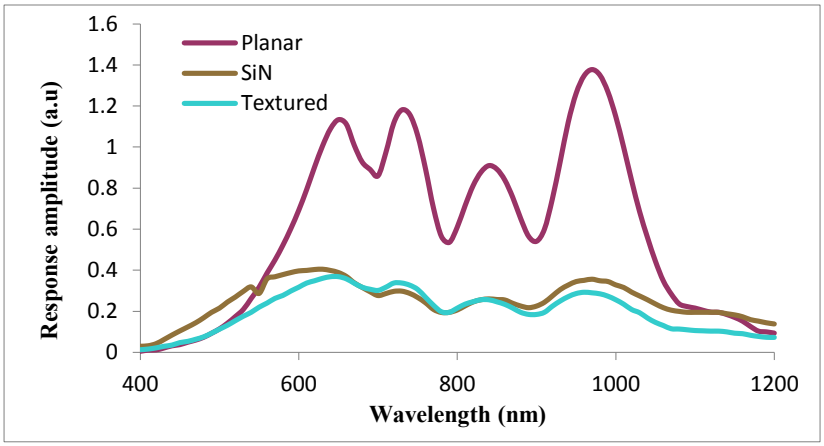



Figure 4. Reflectance measurement on planar wafer, textured wafer and SiN layer on Si wafer

Figure 5 plots current-voltage (I-V) measurements at air mass (AM) 1.5 illumination for commercial solar cell, fabricated and simulated simplified Si solar cell on *p*-type Si wafer. Table 2 summarizes the solar cells performances. In Figure 5, the commercial solar cell as reference cell exhibits significantly superior performance in comparison with simplified solar cell. The efficiency obtained by commercial, fabricated and simulated solar cells were 17.09%, 9.44% and 9.67%, respectively. The commercial solar cell has textured Si wafer and SiN layer as ARC, while fabricated simplified solar cell is non-ARC solar cell and textured. It can be seen that there is a sub-standard performance between commercial and non-ARC solar cell with ~8% of difference in solar cell efficiency. This proves that non-ARC solar cell can still produce a function solar cell without SiN layer. These findings raise up an approach to have the non-toxic solar cell at low fabrication cost.

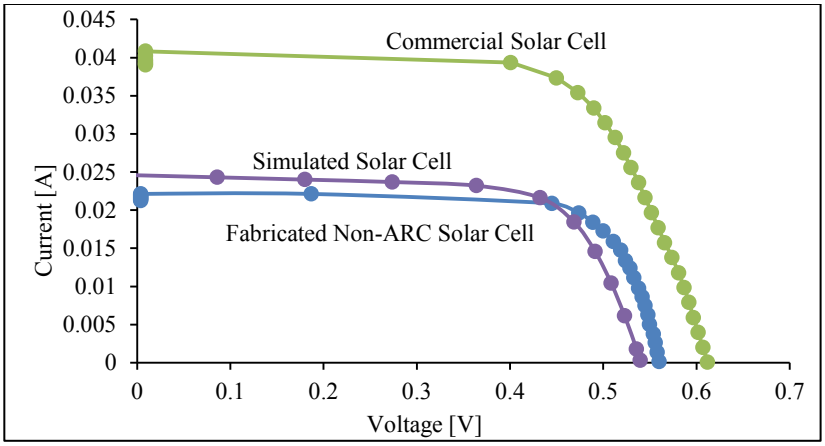



Figure 5. I-V curve of commercial, simulated and fabricated solar cell under AM 1.5 illumination

Table 2. Solar cell performances of commercial, fabricated and simulation solar cell

| **Device Performances** | **Commercial Solar Cell** | **Fabricated Solar Cells** | **Simulated Solar Cell** |
|---|---|---|---|
| Voc (V) | 0.612 | 0.56 | 0.50 |
| Isc [A] | 0.041 | 0.02 | 0.025 |
| FF | 0.671 | 0.7467 | 0.724 |
| Efficiency (%) | 17.09 | 9.44 | 9.67 |

The minority carrier lifetime of *p*-type Si wafer has been varied in PC1D simulation at 0.15 $\mu$s, 0.6 $\mu$s and 1.1 $\mu$s to investigate the significance of the lifetime to the simplified solar cells performance. The lack performance of fabricated simplified solar cell can be attributed to the relatively poor minority carrier lifetimes of *p*-type Si wafers. Figure 6 shows minority carrier lifetime at 0.15 $\mu$s, 0.6µs and 1.1 $\mu$s resulting solar cell efficiency of 10.34%, 12.30% and 13.03% respectively. This result indicated that the front surface emitter field is able to collect large majority light-generated $\bar{e}$-*h* pairs prior to recombination. However, poor lifetime means that a majority of $\bar{e}$-*h* pairs are lost to recombination prior to collection by the junction. *I-V* curve in Figure 5 and 6 shows a good agreement.

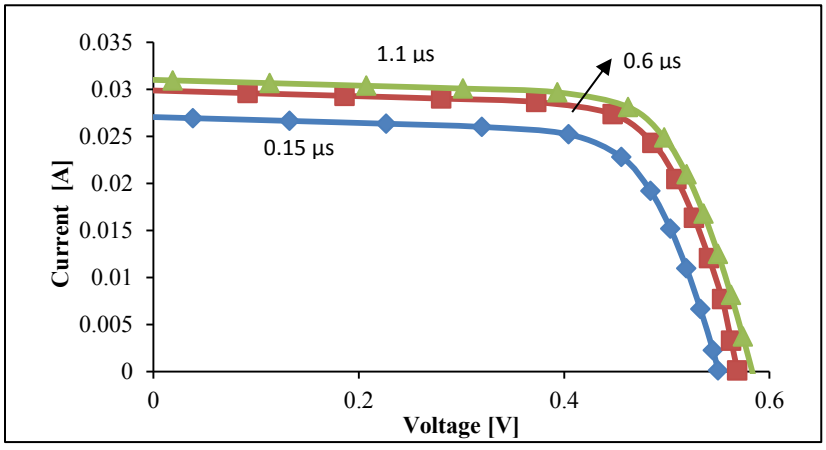



Figure 6. *I-V* response of simulated simplified solar cell with a variation of minority carrier lifetime at 0.15 $\mu$s, 0.6 $\mu$s and 1.1 $\mu$s by PC1D simulation

In addition, this behaviour can be explained in terms of electron-hole pair diffusion across the 200 $\mu$m thickness of the solar cell. Diffusion length is related to lifetime by the equation (1).

$$L_{DIFF} = (\tau * D)^{1/2} \quad (1)$$

where $\tau$ is minority carrier lifetime in second and $D$ is Si diffusivity in $m^2$/sec; for Si, $D=8.8\times10^{-5}$ $m^2$/sec. Therefore, for $\tau$=0.001 $\mu$s, $L_{DIFF}$=0.3 $\mu$m which is 667 times smaller than wafer thickness; therefore, almost all $\bar{e}$-$h$ pairs are likely to be lost to recombination. In contrast, for $\tau$=500 $\mu$s, $L_{DIFF}$=210 $\mu$m, which is larger than wafer thickness; therefore, almost all $\bar{e}$-$h$ pairs will likely reach junction prior to recombination [7]. Ergo, higher efficiency of simplified solar cell can be achieved by using higher minority carrier lifetime of Si wafer. Higher lifetime wafers can produce an average performance of simplified solar cell similar as commercial solar cell that has SiN layer.

## Conclusion

Simplified Si solar cells or non-ARC solar cell have been fabricated and modelled in PC1D. The efficiency obtained by fabricated and simulated solar cells were 9.44% and 9.67%, respectively. The commercial solar cell with ARC layer shows an efficiency of 17.09%. Good agreement is observed between the experimental and simulation results. The low efficiency of the fabricated solar cell has been attributed to the no ARC layer and poor minority carrier lifetime of Si wafer. However, the efficiency of simplified solar cell and the reflectance measurements shows that non-ARC Si solar cell potentially produce an average performance output of solar cell compared to commercial solar cell. Therefore, high minority carrier lifetime is required in order to produce high efficiency of simplified solar cell. This work also contributes to the simple approach of solar cell fabrication at low cost.

## Acknowledgement

The author would like to acknowledge various financial supports from PRGS/1/13/TK07/UKM/01/1, and GGPM-2014-048.

## References

1. Asim, N., Sopian, K., Ahmadi, S., Saeedfar, K., Alghoul, M. A., Saadatian, O. and Zaidi, S. H. (2012). A review on the role of materials science in solar cells. *Renewable and Sustainable Energy Reviews*, 16(8): 5834 – 5847.
2. Hahn, G. and Joos, S (2014). In chapter one: State-of-the-art industrial crystalline silicon solar cells. Advances in photovoltaics: Part 3. Willeke, G. and Weber, E. (Editors), 90: pp 1 – 72.
2. Burgers, A R. Naber, R. C. G., Carr, J. J., Barton, P. C. C., Geerligs, L. J. J., Jinfeng, X., Li, G., Weiping, S., An, H., Hu, Z., Venema, P. R. and Vlooswijk, H. G. (2010). 19% efficiency n-type Si solar cells made in pilot production. *25th European Photovoltaic Solar Energy Conference and Exhibition*: 1106 – 1109.
3. Poliskie, M. (2013). Solar manufacturing environmental design concepts for modules. McGraw-Hill.
4. Leong, C. S., Sopian, K. and Zaidi, S. H. (2013). Oxide passivated low reflection nano-structured solar cell. *In Photovoltaic Specialists Conference (PVSC), 2013 IEEE 39th*: pp. 1260 – 1264.
5. Information from Faculty of Engineering, UNSW Sydney (2015). Access from https://www.engineering.unsw.edu.au. [Date access January 2016].
6. Sepeai, S., Zaidi, S. H., Desa, M. K. M., Sulaiman, M. Y., Ludin, N. A., Ibrahim, M. A. and Sopian, K. (2013). Design optimization of bifacial solar cell by PC1D simulation. *Journal of Energy Technologies and Policy*, 3(5): 1 – 11.

*Malaysian Journal of Analytical Sciences, Vol 21 No 5 (2017): 1134 - 1142*
*DOI: https://doi.org/10.17576/mjas-2017-2105-16*

MALAYSIAN JOURNAL OF ANALYTICAL SCIENCES
*Published by The Malaysian Analytical Sciences Society*
ISSN 1394 - 2506

# INFRA-RED INVESTIGATION ON SILICON SOLAR CELLS

## (Kajian Inframerah ke atas Sel-sel Suria Silikon)

Nurfarizza Surhada Mohd Nasir, Suhaila Sepeai*, Cheow Siu Leong, Kamaruzzaman Sopian, Saleem H.Zaidi

*Solar Energy Research Institute (SERI)*
*Universiti Kebangsaan Malaysia, 43600 UKM Bangi, Selangor, Malaysia*

**Corresponding author: suhailas@ukm.edu.my*

Received: 12 April 2017; Accepted: 1 September 2017

**Abstract**

Increasing reliance on carbon-based fossil fuel is likely to cause irreversible damage to global environment. Crystalline silicon (Si) based on pollution free photovoltaic (PV) electricity generation technology is expected to play a dominant role in this electricity generation transition from carbon to silicon. Since Si wafer represents almost 50% of the PV conversion cost, thinner wafers are highly effective at reducing the production cost. Therefore, there is an urgent need to develop alternative device configurations and processing methods for thinner Si wafer. Si wafer has to go through cleaning process, thinning process, textured process and partially transparent technique. In this work optical transmission through Si is investigated as a function of wafer thickness. For this improved performance, surface morphology, optical properties and the optical transmission near band gap is measured with custom-designed rear infra-red (IR) transmission measurement system. Si wafer with the textured surface have more light absorption than the as-cut and planar Si wafer.

**Keywords**: optical transmission, thin silicon wafers, infrared light, light absorption

**Abstrak**

Peningkatan kebergantungan terhadap penggunaan bahan bakar berasaskan sumber karbon mengakibatkan pencemaran alam sekitar. Fotovolta (PV) sifar pencemaran berasaskan silikon kristal merupakan teknologi tenaga elektrik generasi terkini dijangkakan menjadi sumber yang mendominasi perubahan sumber bahan api berasaskan karbon kepada silikon. Tambahan pula, kepingan silikon meliputi 50% kos keseluruhan pembuatan PV, pengurangan kos yang efektif didapati melalui penipisan kepingan.. Oleh itu, kaedah alternatif kepada pembaharuan bagi konfigurasi sistem penipisan silikon harus di cadangan. Kepingan silikon harus melalui proses pembersihan, proses penipisan, proses tekstur dan teknik separa telus. Dalam kajian hubungan di antara ketebalan kepingan silicon dan maklumat optik diteliti. Bagi meningkatkan prestasi, morfologi permukaan, sifat optik, dan penghantaran optik menghampiri jurang jalur diukur dengan menggunakan sistem pengukuran penghantaran gelombang IR.

**Kata kunci**: penghantaran optik, kepingan silikon nipis, cahaya inframerah, penyerapan cahaya

## Introduction

Silicon wafer-based photovoltaic module production has been growing over 30% since the last decade [1]. Generally, the cost of Si accounts for almost 50% of a photovoltaic panel [2]. Historically, a pathway to reduce cost has been realized by economic use of Si in the form of thinner substrates; current Si wafer is in 150 – 200 $\mu$m thickness [3]. Si PV technology is almost exclusive based on mono-facial solar cells in which light is incident from the front surface with the back surface completely metallized. The bifacial solar cell is an emerging solar cell configuration in which electrical grid patterns are identical on both front and back surfaces. This device

configuration has the potential to generate more power by capturing scattered light from the rear surface than the mono-facial solae cell. The challenging problems in bifacial solar cell is to ensure that the photo-generated electron-hole ($\bar{e}$-$h$) pairs absorbed near the back surface are collected by the front surface emitter prior to recombination. This experiment can be done by using appropriate surface texturing methods, light trapping can be enhanced and absorption in the rear-infrared (NIR) [4-6]. The optical properties of a broad range of different bifacial configurations with varying surface morphologies and rear side reflectors have been extensively investigated in the literature. Although wafer thickness reduction translates into smaller recombination losses and large open circuit voltages; absorption is reduced as well [7].

These considerations have led to extensive research on performance limiting factors in amorphous [8], multi-crystalline [9], and single crystalline solar cells [10, 11]. Due to its indirect band gap, crystalline silicon has weak optical absorption particularly in the range (~900 – 1100) nm. Therefore, in solar cell studies aimed at increasing the efficiency, the primary goal is to enhance light absorption while minimizing recombination losses. Surface texturing aimed at enhanced absorption in silicon has been extensively investigated by geometrical optic [12]. Geometrical textures reduce reflection light into the semiconductor. Despite their effectiveness and industrial applications, geometrical texturing schemes suffer from several disadvantages that limits their effectiveness. Some of those are listed below [13]:

i) Wet-chemical alkaline anisotropic etching used to form random pyramids in (100) oriented crystal is not effective in texturing of flow cost multi-crystalline (mc-Si) wafers, ii) Anti-reflection films have a resonant structure which limits their effectiveness to a narrow range of angles and wavelength, iii) Sufficient IR absorption in thin film ( < 10 $\mu$m) silicon solar cells is not possible with geometrical optics based texturing.

Light trapping schemes based on geometrical optics considerations have been developed for enhancing oblique coupling beyond narrow angle range of (~16°) defined as $sin^{-1}(1/n)$, where $n$ is the refractive index of silicon [14]. In general, the required feature dimensions for geometrical optical path length enhancement are optical wavelength, therefore their applicability to thinner wafers is impractical. Periodically textured surfaces based on diffractive [15] and waveguide optics [16] have been shown to significantly enhance optical absorption. For a weakly absorptive medium, statistical analysis by Yablonovitch [17] and optical analysis of scattering from a lambertian surface predicted absorption enhancement in textured surfaces by (~$4n^2$) over a planar surface, where $n$ is the refractive index of the material. Absorption in such structure is opposed to conventional horizontal, thin-film waveguide structures as proposed by Sheng [18].

In literature application of diffractive and physical optics structures aimed enhancement of optical absorption in thin Si films and solar cells have been reported with good results [19 – 28]. Lambertian schemes and related geometrical optics-based ray tracing approached were applied to both amorphous silicon [29] and crystalline silicon solar cells [30] with successfully results. A lambertian surface capable of filling all the available $k$-space with light beams of equal intensity is difficult to achieve in practice. A close approximation is a randomly textured surface supporting sub-wavelength features. Therefore, the random surface can be described by Fourier summation-over a large number of periods. Although the resulting diffractive scattering ensures almost complete filling of the $k$-space. Light incident on such surfaces normally is diffractively scattered over a broad angular range determined by using equation 1 below

$$\theta_{\mathrm{m,i}}=\sin^{-1}(m_{\mathrm{i}}\lambda/nd_{\mathrm{i}}) \tag{1}$$

where $n$, $d_{\mathrm{i}}$ represents the $m^{\mathrm{th}}$ diffraction order corresponding to the spatial period $d_{\mathrm{i}}$ and $n$ is Si refractive index. Optical path length in geometrical optics is simply the sum of number of passes through a thin film of thickness, $t$. For a single grating the total optical path length enhancement is given by summing over the lengths of all transmitted diffraction order (equation 2):

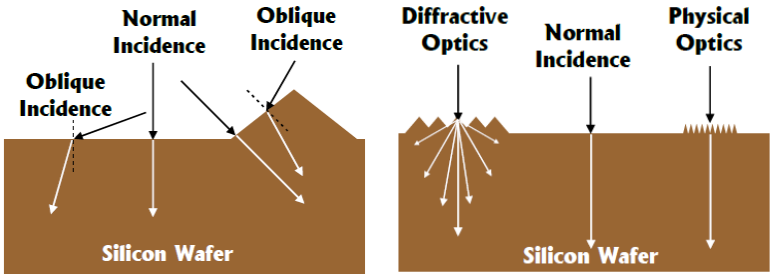
$$d_{\mathrm{opt}}^{\mathrm{grating}} = \sum i\ \gamma_{\mathrm{i}} d_{\mathrm{i}} \tag{2}$$

where $\gamma_i$ is fraction of incident energy coupled into diffractive, $d_i$. For a normally propagating zero order, $d_0$ is identical to *t*; for the diffraction orders the optical path is *t*/cos $\theta_{ij}$ where $\theta_i$ the angle of propagation of the $i^{th}$ diffraction order. For a random sub-wavelength diffractive surface the total optical path length is summed over all grating (*i*); each of which generates diffraction orders (*j*) as defined as (equation 3):

$$d_{opt}^{random} = \sum_{i,j} \gamma_{i,j} d_{i,j} \quad (3)$$

Comparison of the three cases (planar, single period and random surface) illustrate that an appropriately designed random surface is highly effective in filling the *k*-space and therefore in reaching the $4n^2$ enhancement limit.

For a good solar cell it is crically important that all of the incident energy to be scattered into obliquely propagating transmitted orders in order to enhance optical path length hence increase absorption rate. This can be achieved for feature dimensions either substaintially larger (Figure. 1(a)) or comparable or substaintially smaller than optical wavelength (Figure. 1 (b)). The first configuration refers to geometrical optics, the second to diffractive optics, and the third to physical optics. In the physical optics approach deeply etched subwavelength structures are created in three dimensions, on the surface and through the substrate. Rigorous coupled wave analysis [14] has been used to calculate optical absorption in these 3D grating structures. Physical optics also described in terms of subwavelength surfaces (sws) essentially acting as multi-layer anti-reflection films [31]. Structures play no role in optical path length enhancement. In this paper, near IR transmission in (~800 – 1700) nm spectral range for planar and randomly textured Si wafers have been investigated for Si wafers with thickness of (~200 $\mu$m).




(a) (b)

Figure 1. Schematic description of light, interaction with surface features (a) optical wavelength and (b) either or optical wavelength for convenience reflected (diffracted beams are not shown).

## Materials and Methods

Single crystalline silicon (c-Si) wafer with thickness about (~200 $\mu$m) is used. *P*-type Si wafers with resistivity ranging between (0.5-3.0) Ω.cm with doping density between $10^{10}$ to $10^{16}$ were used. The silicon (Si) wafer was initially cleaned by dipping into solution of hydrofluoric acid (HF) and nitric acid ($HNO_3$) in a ratio of 1:100 for 10 minutes. After rinsing with deionized water, it was then dipped into HF and water in a ratio of 1:50 for 1 minute. The wafer was immersed in 10% potassium hydroxide (KOH) at a temperature of 70 – 80 ℃ for 5 minutes. Subsequently, the wafer was repeatedly cleaned in HF:$H_2O$ for 1 minute. Then the wafers were rinsed with deionized water for about 2 minutes and dried with nitrogen gas. Etching process led to the decrease in thickness of Si wafers. Figure 2(a) shows an etching process by using KOH solution. Si wafer with damage removal needs to go through the texturing process with ratio of 1:5:125. The texturing process is a combination of 4 g of KOH pallets, 20 ml of isopropanol and 90 ml of deionized ( DI ) water. The Si wafer will be laminated by using the laminator. Then, the laminated wafer will be transferred into a beaker which contained 10% KOH solution.

The estimated time would be 1 hour and 45 minutes at the temperature of 70 – 80 ℃. Next, the IR transmission data will be measured. Figure 2(b) shows the etching process by using HF:$HNO_3$ with a ratio of 1:10. Then, Si wafer-textured were dipped in a solution of HF:$HNO_3$ with ratio of 1:10 for 1 hour and 45 minutes. Then, the wafers were

rinsed and dried with nitrogen gas. The IR transmission data is recorded from (600 – 1200) nm wavelength with sub-wavelength 25 nm. Figure 2(c) shows a process flow for paste Black Etching Surface (BES) paste process on silicon wafer with 200 $\mu$m thickness. Next, the oxidation process was applied to the Si wafers. The time estimated to produce the oxide layer approach 350 Å is 1 hour and 30 minutes at the temperature 1100 ℃. The Si wafers size were then cut into 4 cm x 4 cm.The BES paste contains level of carbon black and *n*-methyl-2-pyrrolidone by EMD Chemicals Company is placed onto the mask and at the same time the Si wafer is placed under the mask. After that, the etched Si wafer is heated in the furnace at the temperature of 350 ℃ for 90 seconds. Next, Si wafer is soaked in 1% KOH for 1 minute at 40 ℃. After the BES paste is peeled out from the Si wafer, the Si wafer is placed into 10% KOH solution for 1 hour and 15 minutes at 70 ℃. Then, the Si wafer is rinsed using deionized (DI) water and dried with nitrogen gas.

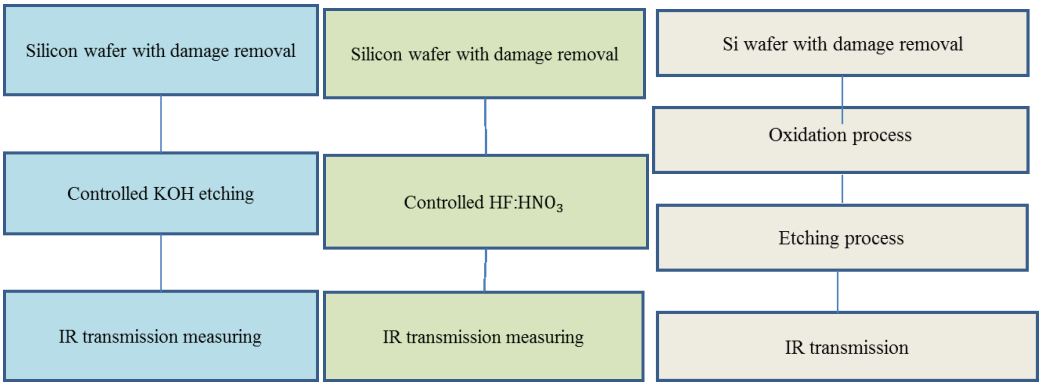



Figure 2. (a) Process flow for KOH etching process on silicon wafer with 200−µm thickness (b) Process flow for HF:$HNO_3$ etching process on silicon wafer with 200−$\mu$m thickness (c) Process flow for BES paste process on silicon wafer with 200−$\mu$m thickness.

A simple experimental setup based on optical configuration described in Figure 3 has been developed for characterization of near IR transmission as a function of wavelength. This system is designed to measure optical transmission system in near and far infrared (IR) range specifically for the wavelength. A computer controlled IR monochromator is used to vary wavelength in the desired range. Spectrally variable light from te monochromator is incident normally on the sample under measurement (SUM). The transmitted light from the sum is collected focusing lens onto an InGaAs photodetector. The output from photodetector is connected to a lock-in amplifier, which is connected to a computer. Intensity variation as a function of wavelength is measured with a LABVIEW based computer programme.

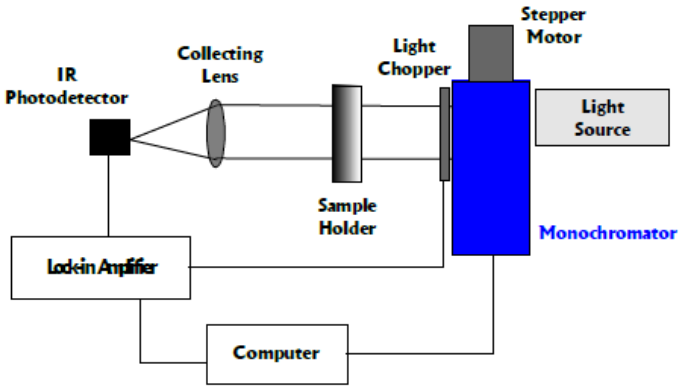



Figure 3. Schematic diagram for IR transmission measurement system

**Results and Discussion**

In order to reduce the reflectivity of the surface and to trap the light in solar cell, texturing process by using KOH solution have developed good achievement in capturing the light.In this work, thining process include KOH etching pocess whereas the Si wafers were immersed in 10 % KOH solution with different time eching such as 30, 60, 90 and 180 minutes. In figure. 4 shows the surface morphology from scanning electron microscope (SEM) analysis for KOH-etched surface. Table 1 conclude that the SEM data at 30 minutes the Si wafer reduced to 58. 4 $\mu$m and the etching rate is 1.94 $\mu$m/ min. Table 2 summarize from surface profiler at 30 minutes the Si wafer reduced to 31.24 $\mu$m and the etching rate is 1.04 $\mu$m/min. These etch results show that etch rate is significantly slowed as etch time increase, this may be attributted to loss of water in the solution to the evaporation resulting in a higher KOH concentration which in turn, slow the etch rate.

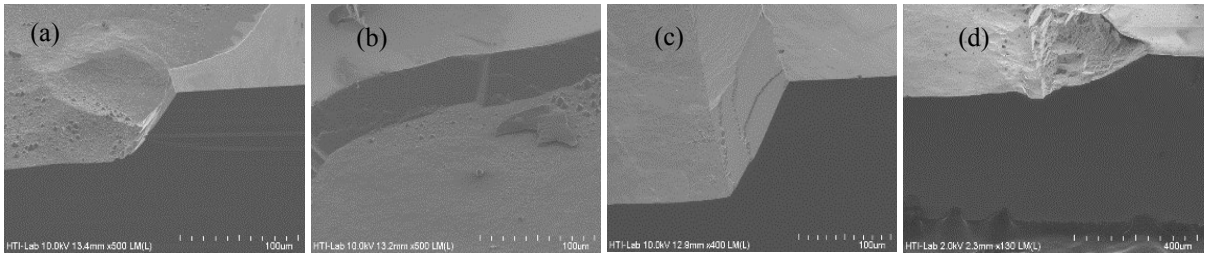



Figure 4. Topographical images for KOH-etched Si surfaces for etching times of 30 minutes (a), 60 minutes (b), 90 minutes (c) and 180 minutes (d)

Table 1. Result of the thickness for KOH etching vs time from SEM data

| Samples (minutes) | Thickness ($\mu$m) | Etching Rate ($\mu$m/min) |
|---|---|---|
| 30 | 58.4 | 1.94 |
| 60 | 41.3 | 0.63 |
| 90 | 97.3 | 1.08 |
| 180 | 135.2 | 0.75 |

Table 2. Result of the thickness for KOH etching vs time from surface profiler

| Samples (minutes) | Thickness ($\mu$m) | Etching Rate ($\mu$m/min) |
|---|---|---|
| 30 | 31.238 | 1.04 |
| 60 | 58.056 | 0.96 |
| 90 | 91.862 | 1.02 |
| 180 | 213.18 | 1.18 |

Figure 5 shows Si wafer surface after through the KOH etching process. Etching of Si in orientation-dependent alkaline solutions is very well characterized. The etch anisotropy of the alkaline solutions basically results from the fewer surface Si-OH bonds per unit cell on <111> compared to <100> and <110> surfaces. Due to this, it leads to higher energy to break bonds of the <111> surface Si atoms. This anisotropy effect is employed to generate V-grooves in <100> Si wafers using openings in an appropriate mask such as an oxide layer. The wafer release two

configurations: a) through holes and b) no holes. According to these results, it show that an oxide layer on Si wafer is not uniformly grown. Figure 5(a) shows the morphology of Si wafer at area with holes by using AMSCOPE 3.0 MD400E digital microscope and Figure 5(b) shows the morphology of Si wafer with partially holes.

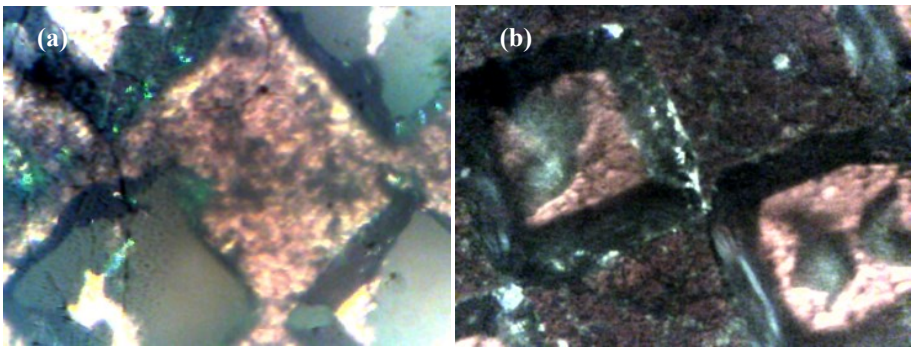
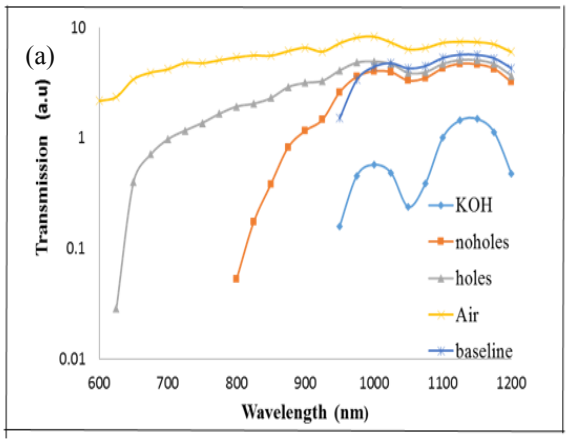



Figure 5. MD400E digital microscope pictures after through KOH etching process (a) the morphology of Si wafer at area with through holes and (b) morphology of Si wafer with partially holes.

Figure 6 shows plots as recorded transmission data as a function of wavelength: comparison transmission response in air and the Si wafer with damage removal known as a baseline have also been plotted. The transmission responses have been plotted on a log scale due to several orders of magnitude variation in transmitted signal. Transmission through air in (yellow line) is has the highest value. The transmission through Si wafer with holes (gray line) is second highest due to lack of absorption of wafer. However, light can be transmitted through Si wafer without reflections. Therefore, the transmission of the Si wafer is highest than planar wafers. Transmission through Si wafer with partially holes (orange line) can trap light and transmit less. Moreover, the Si wafer surface becomes more textured compared with holes. This is due to the increase of light absorption in a textured surface. Transmission through relatively planar polished sample (dark blue line) is lower absorption in a planar and non-textured surface. The sample thickness reaches approximately at (~180 $\mu$m) after going through the damage removal process. Therefore, more light will be reflected. The transmission through Si wafer with KOH-textured etching process is the lowest in 1000 – 1200 nm range (bright blue). The wafer with KOH etching is completely textured with estimated thickness of (~ 80 $\mu$m). The absorption of incident light is enhanced due to texture-based trapping. The Si wafer with 10% KOH have high quality of absorption light in IR wavelength. The surface texture also significantly enhances the light trapping in the long wavelength region, 800 – 1000 nm.



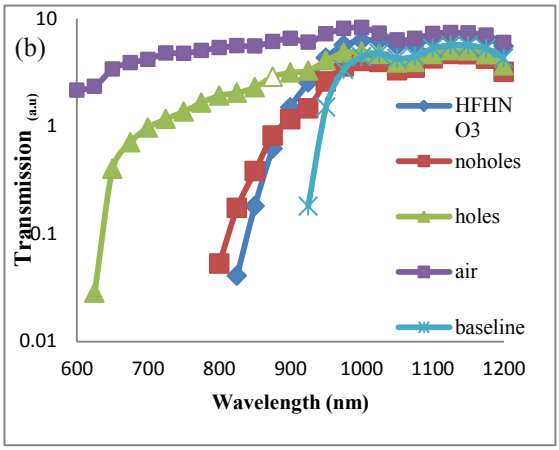



Figure 6. Comparison of optical transmission measurements a) with KOH and BES paste etching method and b) with HF:$HNO_3$ and BES paste etching method.

Figure 6(b) plots as recorded transmission data as a function of wavelength; comparison transmission response in air without Si wafer and the Si wafer with damage removal known as a baseline have also been plotted. The transmission responses have been plotted on a log scale orders of magnitude variation in transmitted signal. Transmission through air (yellow line) is highest. Transmission through Si wafer with holes (grey line) is lower than through air due to lack of absorption in wafer. However, light can transmit through wafer directly without reflection. Therefore, the transmission of the Si wafer is higher than planar wafers. Transmission through Si wafer with no holes (orange line) is reduced due to Si wafer surfaces. Moreover, the Si wafer surfaces had become more textured as the absorption of light increases. Transmission through Si wafer with HF:$HNO_3$ solution at 1:10 ratio (bright blue line) is lower due to its surface. As etching time increase, the Si wafer thickness is reduced to make it thinner. However, as etching time increased wafer starts to develop substantial texture and no longer planar. Therefore, the absorption of light is higher due to surface texturing.

## Conclusion

A simple IR spectral transmission system based on InGaAs photodetector and monochromator was successfully developed for spectral optical measurement. Based on feature dimensions, incident light interaction can be described in terms of geometrical, diffractive and physical optics. The thinner, textured-Si wafer gives the lowest transmission due to a combination of low reflection and diffractive scattering. A more detailed analysis in terms of measured thickness and surface textured will be reported elsewhere.

## Acknowledgement

This work was supported by the Malaysia Ministry of Science Technology and Innovation (MOSTI) and Universiti Kebangsaan Malaysia under the grant UKM-SPKP-CRIM-PK01-B001.

## References

1. Maycock, P., (2003). PV market update. *Renewable Energy World,* 6(4): 84.
2. Munzer, K. A., Holdermann, K. T., Schlosser, R. E. and Sterk, S. (1999). Thin monocrystalline silicon solar cells. *IEEE Transactions on Electron Devices*, 46(10): 2055 – 2061.
3. Tiedje, T., Yablonovitch, E., Cody, G. D. and Brooks, B. G. (1984). Limiting efficiency of silicon solar cells. *IEEE Transactions on electron devices*, 31(5): 711 – 716.
4. Cuevas, A. (1999). The effect of emitter recombination on the effective lifetime of silicon wafers. *Solar Energy Materials and Solar Cells*, 57(3): 277 – 290.
5. Pan, A. C., Del Cañizo, C. and Luque, A. (2009). Characterization of up-converter layers on bifacial silicon solar cells. *Materials Science and Engineering: B*, 159: 212 – 215.

6. Frank, J., Rüdiger, M., Fischer, S., Goldschmidt, J. C. and Hermle, M. (2012). Optical simulation of bifacial solar cells. *Energy Procedia,* 27: 300 – 305.
7. Yamamoto, K., Yoshimi, M., Suzuki, T., Nakata, T., Sawada, T., Nakajima, A. and Hayashi, K. (2000). Large-area and high efficiency a-Si/poly-Si stacked solar cell submodule. *In Photovoltaic Specialists Conference, 200 0. Conference Record of the Twenty-Eighth IEEE*: pp. 1428 – 1432.
8. Hebling, C., Glunz, S. W., Schumacher, J. O. and Knobloch, J. (1997). High efficiency (19.2%) silicon thin-film solar cells with interdigitated emitter and base front-contacts. *In 14th European Photovoltaic Solar Energy Conference*, 2318.
9. Yamamoto, K. (1999). Very thin film crystalline silicon solar cells on glass substrate fabricated at low temperature. *IEEE Transactions on Electron Devices*, 46(10): 2041 – 2047.
10. Miles, R. W., Zoppi, G. and Forbes, I. (2007). Inorganic photovoltaic cells. *Materials Today*, 10(11): 20 – 27.
11. Green, M. A. (1995). Silicon Solar Cells: Advanced Principles and Practice. Bridge Printery, Sydney.
12. Green, M. A. and Keevers, M. J. (1995). Optical properties of intrinsic silicon at 300 K. *Progress in Photo-voltaics: Research and Applications,* 3(3): 189 – 192.
13. Craighead, H. G., Howard, R. E. and Tennant, D. M. (1980). Textured thin-film Si solar selective absorbers using reactive ion etching. *Applied Physics Letters*, 37(7): 653 – 655.
14. Southwell, W. H. (1983). Gradient-index antireflection coatings. *Optics Letters*, 8(11): 584 – 586.
15. Heine, C. and Morf, R. H. (1995). Submicrometer gratings for solar energy applications. *Applied Optics*, 34 (14): 2476 – 2482.
16. Azhari, A. W., Goh, B. T., Sepeai, S., Khairunaz, M., Sopian, K. and Zaidi, S. H. (2013). Synthesis and characterization of self-assembled, high aspect ratio nm-scale columnar silicon structures. *In Photovoltaic Specialists Conference (PVSC), 2013 IEEE 39th*: pp. 0530 – 0534.
17. Yablonovitch, E. (1982). Statistical ray optics. *Journal of the Optical Society of America*, 72(7): 899 –907.
18. Sheng, P. (1984). Optical absorption of thin film on a Lambertian reflector substrate. *IEEE Transactions on Electron Devices*, 31(5): 634 – 636.
19. Zaidi, S. H., Ruby, D. S., DeZetter, K. and Gee, J. M. (2002). Enhanced near IR absorption in random, RIE-textured silicon solar cells: The role of surface profiles. *In Photovoltaic Specialists Conference, 2002. Conference Record of the Twenty-Ninth IEEE*: pp. 142 – 145.
20. Zaidi, S. H. and Brueck, S. R. (1997). Si texturing with sub-wavelength structures. *In Proceedings of the 1997 IEEE 26th Photovoltaic Specialists Conference. IEEE*: pp. 171 – 174.
21. Zaidi, S. H., Gee, J. M. and Ruby, D. S. Ruby (2000). Plama texturing for multicystalline Si solar cells. *In Proceedings of the 2000. Conference Record of the Twenty-Eighth IEEE Photovoltaic Specialists*: pp. 75 – 78.
22. Zaidi, S. H., Matzke, C., Koltunski, L. and DeZetter, K. (2005). Absorption in thin Si films with randomly formed subwavelength structures. *In Photovoltaic Specialists Conference, 2005. Conference Record of the Thirty-first IEEE*: pp. 1145 – 1148.
23. Jahanshah, F., Prinja, R., Anderson, J., Manginell, R., Amin, N., Sopian, K. and Zaidi, S. H. (2008). An investigation of three-dimensional texturing in silicon solar cells for enhanced optical absorption. *In Photo-voltaic Specialists Conference, 2008. 33rd IEEE*: pp. 1 – 5.
24. Zaidi, S. H., Marquadt, R., Minhas, B. and Tringe, J. W. (2002). Deeply etched grating structures for enhanced absorption in thin c-Si solar cells. *In Photovoltaic Specialists Conference, 2002. Conference Record of the Twenty-Ninth IEEE:* pp. 1290 – 1293.
25. Zaidi, S. H., Ruby, D. S. and Gee, J. M. (2001). Characterization of random reactive ion etched-textured silicon solar cells. *IEEE Transactions on Electron Devices*, 48(6): 1200 – 1206.
26. Sandoval, S. G., Khizar, M., Modisette, D., Anderson, J., Manginell, R., Amin, N., Sopian, K. and Zaidi, S. H. (2010). Optical absorption in microstructured crystalline silicon thin films. *In Photovoltaic Specialists Conference (PVSC), 2010 35th IEEE:* pp. 001597 – 001600.
27. Azhari, A. W., Goh, B. T., Sepeai, S., Khairunaz, M., Sopian, K. and Zaidi, S. H. (2013). Synthesis and characterization of self-assembled, high aspect ratio nm-scale columnar silicon structures. *In Photovoltaic Specialists Conference, 2013 IEEE 39th*: pp. 0530 – 0534.
28. Deckman, H. W., Wronski, C. R., Witzke, H. and Yablonovitch, E. (1983). Optically enhanced amorphous silicon solar cells. *Applied Physics Letters*, 42(11): 968 – 970.
29. Campbell, P. and Green, M. A. (1987). Light trapping properties of pyramidally textured surfaces. *Journal of Applied Physics*, 62(1): 243 – 249.

30. Goetzbeger, A. (1981): Optical confinement in thin Si solar celss by diffuse back reflectors. *Proceeding of the 15th IEEE Photovoltaic Specialist Conference*: pp. 867 – 870.
31. Zubel, I. and Kramkowska, M. (2001). The effect of isopropyl alcohol on etching rate and roughness of (1 0 0) Si surface etched in KOH and TMAH solutions. *Sensors and Actuators A: Physical*, 93(2): 138 – 147.

*Malaysian Journal of Analytical Sciences, Vol 21 No 5 (2017): 1143 - 1150*
*DOI: https://doi.org/10.17576/mjas-2017-2105-17*

MALAYSIAN JOURNAL OF ANALYTICAL SCIENCES
*Published by The Malaysian Analytical Sciences Society*
ISSN 1394 - 2506

# SYNTHESIS AND ANTIBACTERIAL STUDY OF ORGANOTIN(IV) COMPLEXES CONTAINING HYDRAZINOPYRIDINE LIGAND

## (Sintesis dan Kajian Antibakteria Kompleks Organostanum(IV) yang Mengandungi Ligan Hidrazinopiridin)

Dayang Norafizan A. Chee*, Monica Lulo Rodis, Norziah Saat, Zainab Ngaini, Ainaa Nadiah Abdul Halim

*Department of Chemistry, Faculty of Resource Science and Technology,*
*Universiti Malaysia Sarawak, 94300 Kota Samarahan, Sarawak, Malaysia*

**Corresponding author: dnorafizan@unimas.my*

Received: 21 August 2016; Accepted: 27 July 2017

**Abstract**

Nowadays, the studies on organotin(IV) complexes with hydrazone ligand become more interesting due to their potential in various applications including medicinal area. In our recent studies, four new organotin(IV) complexes $MeSnCl_2(C_{12}H_{12}N_4)$ (**2**), $BuSnCl_2(C_{12}H_{12}N_4)$ (**3**), $PhSnCl_2(C_{12}H_{12}N_4)$ (**4**) and $Ph_2SnCl(C_{12}H_{12}N_4)$ (**5**) were synthesized by the direct reaction of methyl-2-pyridylketone-2-hydrazinopyridine ligand (**1**) and organotin(IV) chloride(s) in absolute methanol. These complexes have been characterized by UV-Visible, FT-IR, $^1H$ and $^{13}C$ NMR spectroscopies. All of the synthesized compounds were screened for antibacterial activity against *Escherichia coli* and *Staphylococcus aureus*. However, the complexes showed weak activity against the bacteria compared to the free ligand.

**Keywords**: hydrazone ligand, spectral studies, coordination, biological potential

**Abstrak**

Pada masa ini, kajian tentang kompleks organostanum(IV) dengan ligan hidrazon semakin menarik kerana sangat potensinya dalam banyak aplikasi termasuk bidang perubatan. Dalam kajian ini, empat organostanum(IV) kompleks iaitu $MeSnCl_2(C_{12}H_{12}N_4)$ (**2**), $BuSnCl_2(C_{12}H_{12}N_4)$ (**3**), $PhSnCl_2(C_{12}H_{12}N_4)$ (**4**) dan $Ph_2SnCl(C_{12}H_{12}N_4)$ (**5**) telah disintesis melalui tindak balas terus metil-2-piridilketon-2-hidrazinopiridin ligan dan organostanum(IV) klorida di dalam metanol. Kesemua kompleks telah dicirikan oleh kajian spektrum UV-nampak, FTIR, $^1H$ dan $^{13}C$ RMN. Semua sebatian yang disintesis telah diuji untuk aktiviti antibakteria terhadap *Escherichia coli* dan *Staphylococcus aureus*. Walaubagaimanapun, kompleks menunjukkan aktiviti yang agak lemah menentang bakteria berbanding ligan bebas.

**Kata kunci**: ligan hidrazon, kajian spektra, koordinasi, potensi biologi

## Introduction

Schiff base metal complexes containing hydrazone group have been studied extensively due to the interesting ligand systems containing different donor sites in heterocyclic rings. Hydrazones are the organic molecule that usually bonded to the metal atom through nitrogen and oxygen but also there was through sulphur atom. These hydrazone chelate derivatives also act as good potential oral drugs to cure the genetic disorders for example thalassemia [1]. Besides, hydrazones have many pharmacological properties including anti-tubercular activities and iron scavenging [2, 3]. The biochemical activity of organotin compounds commonly depend on the structure of the molecule and the coordination number of the tin atoms [4]. Organotin(IV) complexes are known to stimulate therapeutic effects on

various tumor cells [5]. Besides, Sharma and Kaushik [6] found that they are suitable as wood preservatives and active either towards Gram-positive or Gram-negative bacteria.

Thus, there are many of previous researchers reported on the potential of hydrazone metal complexes in biological activities. Bendre et al. [7] have been produced copper(II) complexes of 1,3-bis(2'-pyridyl)-1,2-diaza-2-butene and all of the synthesized compounds showed inhibition activities against mushroom tyrosinase. A few years later, organotin(IV) complexes with vitamin-$K_3$-2-hydrazinopyridine have been successfully synthesized and evaluated for toxicity and anti-termitic potential by Affan et al. [8]. The result indicated that ligand and organotin(IV) moderately active against *Artenia salina* and *Coptotermes* sp. Again, organotin(IV) complexes with *ortho*-vanillin-2-hydrazinopyridine exhibited better toxicity against *A. salina* and moderate to high activity against four types of bacteria which were *Bacillus cereus, Staphylococcus aureus, Escherichia coli* and *Enterobacter aerogenes* [9]. Evidently, the transition metal and organotin(IV) complexes with 2-hydrazinopyridine derivatives showed many potentials especially in biological activities studies.

Therefore, it is our interest to synthesize, characterize and evaluate the antibacterial activities of organotin(IV) complexes with methyl-2-pyridylketone-2-hydrazinopyridine. This is because this ligand contains N,N-donor atoms which are also still limited, plus the Sn-N coordination bond formed with complexes was believed to contribute to the antibacterial activities of the complexes.

## Materials and Methods

### Preparation of methyl-2-pyridylketone-2-hydrazinopyridine ligand (1)

A solution of methyl-2-pyridylketone (0.242 g, 0.002 mol) in ethanol (10 mL) was added dropwise to a refluxing ethanolic solution of 2-hydrazinopyridine (0.218 g, 0.002 mol). Three drops of concentrated sulphuric acid were added to the reaction mixture, which was later refluxed for 3 hours. Next, the reaction mixture was allowed to cool to room temperature for one hour. The pink precipitate formed were filtered off and the filtrate was evaporated until milky yellow colour precipitate form. The milky yellow precipitate obtained was recrystallized by slow evaporation of hot absolute ethanol solution at room temperature.

### Synthesis of [$MeSnCl_2(C_{12}H_{12}N_4)$] (2)

The ligand ($C_{12}H_{12}N_4$) (**1**) (0.212 g, 0.001 mol) was dissolved in hot absolute methanol (10 mL) in a Schlenk round bottom flask. A methanolic solution of methyltin(IV) chloride (0.240 g, 0.001 mol) was added dropwise into the resulting mixture causing the solution to change from orange to red in colour. The solution was refluxed further for another 5 hours and allowed to cool to room temperature. The precipitate formed was filtered and finally dried in vacuum over silica gel overnight. The methyltin(IV) complex was obtained as shiny red precipitate by recrystallization from methanol.

### Synthesis of [$BuSnCl_2(C_{12}H_{12}N_4)$] (3)

Complex **3** was synthesized using the same procedure as **2** with organotin(IV) chloride (0.282 g, 0.001 mol).

### Synthesis of [$PhSnCl_2(C_{12}H_{12}N_4)$] (4)

Complex **4** was synthesized using the same procedure as **2** with organotin(IV) chloride (0.302 g, 0.001 mol).

### Synthesis of [$Ph_2SnCl(C_{12}H_{12}N_4)$] (5)

Complex **5** was synthesized using the same procedure as **2** with organotin(IV) chloride (0.343 g, 0.001 mol).

### Antibacterial activity

The antibacterial activity of ligand (**1**) and its complexes (**2-5**) were studied against *Escherichia coli* O157:H7 and *Staphylococcus aureus* using turbidimetric kinetic method [10]. The inoculums could grow on media containing nutrient broth at 37 °C with permanent shaking at 250 rpm for 18 hours. 7 mL of culture medium with increasing concentration of the compounds dissolved in DMSO were inoculated with 0.14 mL of inoculums and the mixture was shaken again at 250 rpm at 37 °C. The solvent was used as negative control and the clinical antibiotic, amoxicillin was used as positive control. Aliquots of each replicate were taken at every 1 hour interval for 6 hours and the transmittance (T) was registered in a Metertech Plus SP-830 UV-Visible spectrophotometer. The

antibacterial activity was determined by graph as ln Nt which related to the number cfu/mL (colony forming units/mL) for the bacteria versus time.

## Results and Discussion

**Characterization study: Methyl-2-pyridylketone-2-hydrazinopyridine ligand (1)**

Yield: 0.321g, 70%. M.p: 82-83 °C. UV-Visible (DMSO) $\lambda_{max}$(nm): 331. IR ($\nu_{max}$ $cm^{-1}$) (KBr): 3343 (NH), 1605 (C=N), 994 (N-N), 776 (pyridine in plane). $^1$H NMR (DMSO-$d_6$, 500 MHz) δ: 9.98 (s, 1H, NH), 8.55 (d, 1H, py-$H_6$), 7.68-8.16 (m, 3H, py-$H_3$-$H_5$), 6.84-7.32 (m, 3H, pyridine ring), 2.39 (s, 3H, $CH_3$) ppm. $^{13}$C NMR (DMSO-$d_6$, 500 MHz) δ: 157.21 (1C, ***C***=N), 107.34-155.80 (10C, pyridine ring), 11.33 (1C, $H_3$***C***–C=N) ppm.

**[$MeSnCl_2(C_{12}H_{12}N_4)$] (2)**

Yield: 0.391 g, 87%. M.p: 285-287°C. UV-Visible (DMSO) $\lambda_{max}$(nm): 331, 499. IR ($\nu_{max}$ $cm^{-1}$) (KBr): 3069 (NH), 1599 (C=N–N=C), 1001 (N-N), 781 (pyridine in plane), 566 (Sn–C), 414 (Sn–N). $^1$H NMR (DMSO-$d_6$, 500 MHz) δ: 10.18 (s, 1H, NH), 8.55 (d, 1H, py-$H_6$), 8.06-8.36 (m, 3H, py-$H_3$-$H_5$), 2.58 (s, 3H, $CH_3$), 1.57 (s, 3H, Sn-$CH_3$) ppm. $^{13}$C NMR (DMSO-$d_6$, 500 MHz) δ: 157.11 (1C, ***C***=N), 113.58-144.59 (10C, pyridine ring), 12.14 (1C, $H_3$***C***–C=N) 12.70 (1C, Sn-***C***$H_3$) ppm.

**[$BuSnCl_2(C_{12}H_{12}N_4)$] (3)**

Yield: 0.320 g, 65%. M.p: 253-254°C. UV-Visible (DMSO) $\lambda_{max}$(nm): 331, 500. IR ($\nu_{max}$ $cm^{-1}$) (KBr): 3049 (NH), 1597 (C=N–N=C), 997 (N-N), 771 (pyridine in plane), 565 (Sn–C), 417 (Sn–N). $^1$H NMR (DMSO-$d_6$, 500 MHz) δ: 9.96 (s, 1H, NH), 8.77 (d, 1H, py-$H_6$), 7.96-8.33 (m, 3H, py-$H_3$-$H_5$), 6.74-7.75 (m, 4H, pyridine ring) 2.58 (s, 3H, $CH_3$), 0.95-2.25 (m, 9H, Sn-$CH_2CH_2CH_2CH_3$) ppm. $^{13}$C NMR (DMSO-$d_6$, 500 MHz) δ: 157.24 (1C, ***C***=N), 113.51-144.82 (10C, pyridine ring), 12.17 (1C, $H_3$***C***–C=N) ppm 30.09, 28.56, 25.20, 13.74 (4C, Sn-***C***$H_2$***C***$H_2$***C***$H_2$***C***$H_3$).

**[$PhSnCl_2(C_{12}H_{12}N_4)$] (4)**

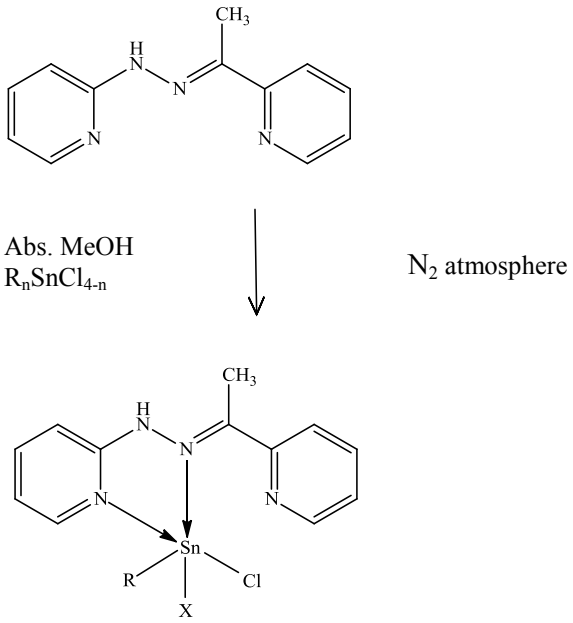
Yield: 0.352 g, 85%. M.p: 268-269°C. UV-Visible (DMSO) $\lambda_{max}$(nm): 332, 406. IR ($\nu_{max}$ $cm^{-1}$) (KBr): 3070 (NH), 1598 (C=N–N=C), 1000 (N-N), 778 (pyridine in plane), 566 (Sn–C), 445 (Sn–N). $^1$H NMR (DMSO-$d_6$, 500 MHz) δ: 9.96 (s, 1H, NH), 8.55 (d, 1H, py-$H_6$), 7.65-7.69 (m, 5H, Sn-$C_6H_5$), 6.66-8.35 (m, overlapping of pyridine-H and phenyl ring protons of phenyl ring attached to the center tin(IV) atom), 2.65 (s, 3H, $CH_3$) ppm. $^{13}$C NMR (DMSO-$d_6$, 500 MHz) δ: 157.08 (1C, ***C***=N), 113.74-144.37 (pyridine ring/Sn-***C***$_6H_5$, 15C), 12.12 (1C, $H_3$***C***–C=N) ppm.

**[$Ph_2SnCl(C_{12}H_{12}N_4)$] (5)**

Yield: 0.256 g, 46%. M.p: 269-270 °C. UV-Visible (DMSO) $\lambda_{max}$(nm): 331, 496. IR ($\nu_{max}$ $cm^{-1}$) (KBr): 3068 (NH), 1598 (C=N–N=C), 999 (N-N), 778 (pyridine in plane), 566 (Sn–C), 446 (Sn–N). $^1$H NMR (DMSO-$d_6$, 500 MHz) δ: 9.95 (s, 1H, NH), 8.55 (d, 1H, py-$H_6$), 7.28-7.93 (m, 10H, Sn-$(C_6H_5)_2$), 6.66-8.35 (m, overlapping of pyridine-H and phenyl ring protons of phenyl ring attached to the center tin(IV) atom), 2.65 (s, 3H, $CH_3$) ppm. $^{13}$C NMR (DMSO-$d_6$, 500 MHz) δ: 157.33 (1C, ***C***=N), 113.76-148.40 (22C, pyridine ring/Sn-$(***C***_6H_5)_2$, 12.13 (1C, $H_3$***C***–C=N) ppm.

**Synthesis**

The methyl-2-pyridylketone-2-hydrazinopyridine (**1**) was initially synthesized by the acid-catalyzed condensation reaction of methyl-2-pyridylketone with 2-hydrazinopyridine in ethanolic solution in 1:1 mole ratio. Afterwards, four new organotin(IV) complexes (**2-5**) were synthesized by direct reaction of organotin(IV) chloride(s) with ligand (**1**) under nitrogen atmosphere. The organotin(IV) complexes were prepared as shown in Scheme 1. All the newly synthesized organotin(IV) complexes were coloured solids and soluble in DMSO, pyridine and DMF.




R=Me X=Cl (**2**)
R=Bu X=Cl (**3**)
R=Ph X=Cl (**4**)
R=Ph X=Ph (**5**)

Scheme 1. Synthesis route of organotin(IV) complexes (**2-5**)

**UV-visible spectra**

The absorption spectrum of ligand (**1**) was recorded in methanol with concentration of $1x10^{-4}$ M at room temperature. There is only one absorption band appeared at $\lambda_{max}$ of 331 which are suggested to be causes by n-$\pi$* transition of imine group. The electronic absorption spectra of complex (**2-5**) were also recorded in DMSO at room temperature. The first peak at 331-332 nm region is attributed to n-$\pi$* transition which has bathochromic shift suggested the free imine (>C=N) group of ligand (**1**) is coordinated to the tin(IV) atoms. Another new peak in the range 496-502 nm indicated the complexation occurred via ligand-to-metal transfer (LMCT) transition [11].

**Infrared spectra**

To clarify the mode of the ligand coordination to the tin centre, IR spectra in the range of 4000 – 400 $cm^{-1}$ were recorded. The IR spectrum of ligand (**1**) in showed the peak appeared at 3343 $cm^{-1}$ was assigned to NH strectching bond. Another important stretching bands are at 1605 and 994 $cm^{-1}$ which are assigned to υ(C=N), υ(N–N) and υ(pyridine in plane), respectively.

Upon complexation, the stretching vibration azomethine (C=N) is shifted to the lower frequency in all complexes (**2-5**) indicating that azomethine nitrogen is involved in coordination with tin(IV) ion [1]. The υ(N–N) stretching vibration value also shifted to the higher frequency which is 997-1001 $cm^{-1}$ compared to the free ligand further supporting that the coordination of azomethine nitrogen to the Sn(IV) atom. A very strong band of υ(pyridine in plane) also showed increases in its value after complexation compared to the free ligand which is 776 $cm^{-1}$. The band of υ(pyridine in plane) went to the higher frequencies at 778 – 781 $cm^{-1}$ in all complexes (**2-5**), indicating that the pyridyl ring nitrogen involved in coordination to the Sn(IV) atom. This is probably because of the occurrence of electron reduction upon complexation [8].

Besides, a new band has been identified at 414 – 446 $cm^{-1}$ in all the organotin complexes (**2-5**) confirming that there were Sn–N bond have been formed and showed that the coordination occurred at azomethine nitrogen and pyridine-N atom. Furthermore, the new band of υ(Sn–C) also indicating that alkyl or aryl group coordinated to the Sn(IV) atom [8].

**$^{1}$H NMR spectra**

The ligand (**1**) showed resonance signals at 9.98, 8.55, 7.68 – 8.16, 6.84 – 7.32 and 2.39 ppm due to the NH, py-$H_6$, py-$H_3$-$H_5$, pyridine ring and $H_3C$–C=N respectively. The $^{1}$H NMR spectra of complexes (**2-5**) were also successfully obtained. Upon complexation, the NH resonance signals for the complex (**2**) shifted to the downfield region (10.18 ppm) while complexes (**3-5**) shifted to the upfield region (9.95 – 9.96 ppm). This showed the occurrence of complexation NH–C=N nitrogen atom to the tin(IV) atom. The py-$H_6$ signal shifted to downfield region at 8.55 – 8.87 ppm compared to the free ligand (**1**) in all complexes (**3-5**), suggesting the involvement of pyridyl ring nitrogen atom in the coordination to tin(IV). Other signals for pyridine ring protons were also shifted to the downfield region but the signals could not be identified properly because of the overlapping of pyridyl ring protons. The $H_3C$–C=N resonance signal for complexes (**3-5**) shifted to the downfield region (2.58 – 2.65 ppm) compared to the free ligand (**1**) also supported the complexation of $H_3C$–C=N nitrogen atom to the tin(IV) atom. In complex (**2**), a sharp resonance signal appeared as singlet at 1.57 ppm attributed to methyl group attached to tin(IV) atom. The resonance signals were appeared at 0.95 – 2.25 ppm in spectra of complex (**3**) assigned to the butyl group attached to tin(IV) atom. Complexes (**4**) and (**5**) exhibited multiplet signals in the region of 7.28 – 7.93 ppm due to the Sn-Ph protons.

**$^{13}$C NMR Spectra**

The $^{13}$C NMR spectrum of free ligand (**1**) showed the resonance signals at 157.21, 107.34 – 155.80 and 11.33 are due to the $\delta$(***C***=N), $\delta$(pyridine ring) and ($H_3$***C***−C=N), respectively. After complexation, the carbon signals of the ***C***=N group shifted to the 157.08 – 157.33 ppm in the complexes (**2-5**) when comparing to the ligand (**1**), indicating participation of the ***C***=N group in coordination to the tin(IV) atom. Besides, the coordination of ligand (**1**) to the tin(IV) atom can be observed through the chemical shifts shown by $H_3$***C***−C=N in the free ligand (**1**) was observed at 11.33 ppm which were shifted to down field region at 12.12 – 12.17 ppm. These observations indicated that the azomethine-N is coordinated to the tin(IV) moiety [12]. The $\delta$ value of carbon atoms in pyridine ring slightly shifted to upfield in the complexes (**2-5**) as compared to the free ligand showed that the pyridine ring nitrogen coordinated to the Sn(IV) atom.

The methyl group attached to the tin(IV) core appeared at 12.70 ppm in complex (**2**). The butyl group attached to the organotin(IV) moiety in complex (**3**) gave four resonance signals at 30.09, 28.56, 25.20 and 13.74 ppm. Apart from that, the phenyl group in complexes (**4**) and (**5**) probably overlapped with pyridine ring from ligand (**1**) and result to the appearance of the resonance signals at 113.74 – 148.40 ppm.

**Antibacterial activity**

The antibacterial activities of ligand (**1**) and its complexes (**2-5**) were assayed at the concentration 50, 80, 100 ppm against bacteria *E. coli* O157:H7 and *S. aureus* at 37 °C. The antibacterial activities of ligand (**1**) and complexes (**2-5**) were compared with DMSO and amoxicillin as a control. All the synthesized compounds demonstrated a quite similar of bacteriostatic activities upon introduction at different concentrations. The equation of $\ln N_t = 27.1 - 8.56T$ was used to indicate the condition of the microbial specific growth and the amount of drug concentration used. The graph of control showed inactive for antibacterial activity, when tested against *E. coli*. The effect of ligand (**1**) and complexes (**2-5**) was also further shown by their minimum inhibitory concentrations (MIC). The MIC of these compounds were determined by extrapolating the concentration at the zero growth rate of *E. coli* (μ=0). Compound with the MIC value >200 ppm is not suitable to be used as antibacterial agent for clinical purpose [13]. The MIC of these compounds were determined by extrapolating the concentration at the zero-growth rate of bacteria (μ=0).

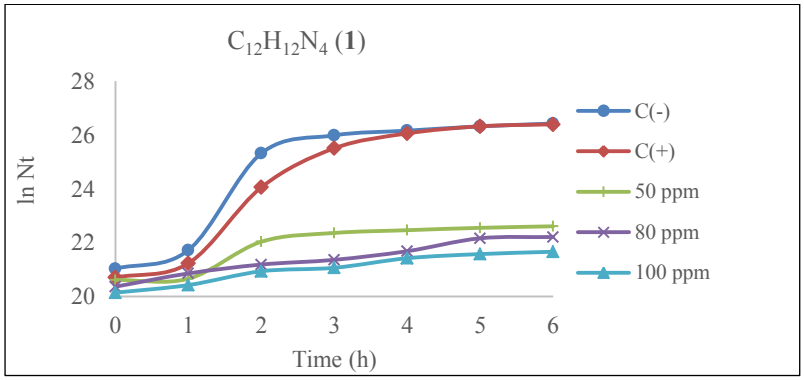
Table 1 shows the MIC values for all synthesized compounds. According to the table, MIC value for ligand (**1**) was lower than 200 ppm, while all complexes (**2-5**) were greater 200 ppm. Based on the results, almost all organotin complexes (**2-5**) showed weak activities against *E. coli* and *S. aureus*. Meanwhile, the antibacterial activity of the

ligand (**1**) showed relatively better antibacterial activity than all of the complexes. Among all of the complexes, complex (**5**) showed the moderate activity against the bacteria strain. Hence, the coordination of tin(IV) atom to the ligand did not raise much of the antibacterial activities. The presence of phenyl group in the complexes (**4**) and (**5**) bonded with the tin atom can improve the antibacterial activity, however in this scenario it is turned out into moderate activity. This is due to the presence of steric hindrance which is preventing the active sites to contact receptor site of the bacteria [9].

Table 1. MIC of ligand (**1**) and complexes (**2-5**)

| **Compound** | **MIC (ppm)** | |
|---|---|---|
| | ***E. coli*** | ***S. aureus*** |
| $C_{12}H_{12}N_4$ (**1**) | 128 | 160 |
| $[MeSnCl_2(C_{12}H_{12}N_4)]$ (**2**) | >200 | 339 |
| $[BuSnCl_2(C_{12}H_{12}N_4)]$ (**3**) | >200 | 372 |
| $[PhSnCl_2(C_{12}H_{12}N_4)]$ (**4**) | >200 | >200 |
| $[Ph_2SnCl(C_{12}H_{12}N_4)]$ (**5**) | 463 | 204 |
| Amoxicillin | >200 | 85 |

In addition, the chloride ion(s) in the structure of the complexes (**2-5**) should be improved the antibacterial activity due to the ability of chloride(s) ion to kill the microbes by inhibiting the multiplication of the bacteria through blockage of the bacteria active sites [9]. However, the presence of the chloride(s) ion in this complexes series did not contribute much to the activity of the complexes. Generally, all the synthesized compounds also more effective against Gram positive bacteria. When comparing the MIC values of the compounds with the clinical antibiotic, amoxicillin, all of the compounds have better activities against *E. coli* but weak activities against *S. aureus*. Figure 1 and 2 shows the inhibition activities of compounds (**1-2**) towards *E. coli* shown as ln $N_t$ for *E. coli* growth *vs.* time and inhibition activities of compounds (**1-2**) towards *S. aureus* shown as ln $N_t$ for *S. aureus* growth *vs.* time, respectively.



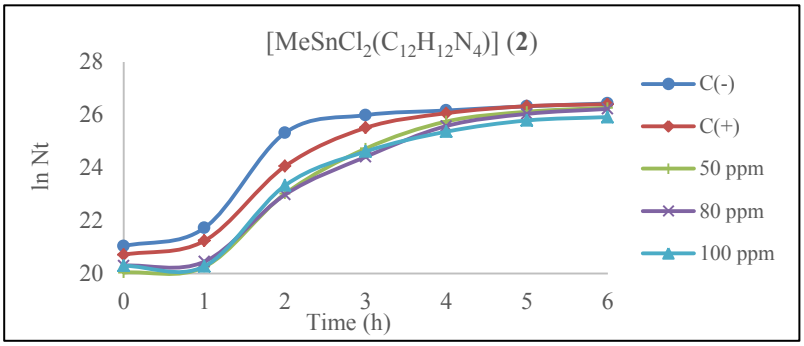



Figure 1. Inhibition activities of compounds (**1**-**2**) towards *E. coli* shown as ln $N_t$ for *E. coli* growth *vs.* time

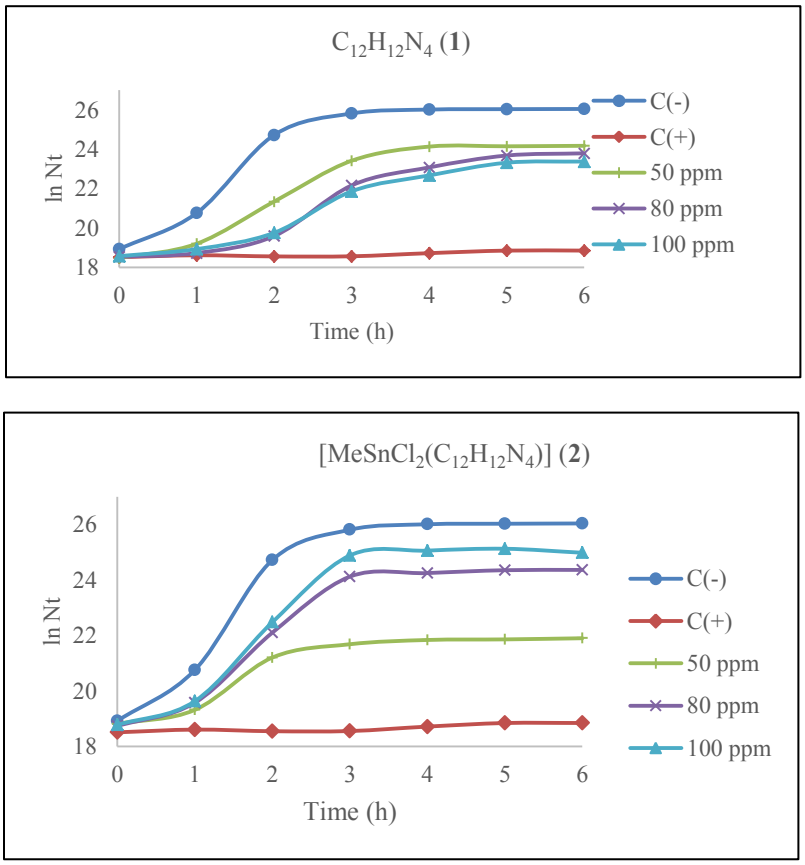



Figure 2. Inhibition activities of compounds (**1**-**2**) towards *S. aureus* shown as ln $N_t$ for *S. aureus* growth *vs.* time

## Conclusion

From the spectral analysis, it is suggested the bonding of ligand to the Sn(IV) atom was at the azomethine nitrogen (C=N) and pyridyl nitrogen atoms. The antibacterial activity evaluation showed that the complexation does not raise the antibacterial activities of the complexes in this study since ligand showed better activity than all of the

complexes. Therefore, it is recommended to investigate more on structure-activity relationship in order to improve the activity of the complexes and screened the antibacterial activities against more than one species of bacteria.

**Acknowledgment**

The authors would like to thank for the financial support provided from research grant of Universiti Malaysia Sarawak (UNIMAS) (RAGS/ST01(1)/1040/2013(07)) and all the person involved in this study.

**References**

1. Datta, A., Huang, J. and Machura, B. (2012). Octahedral complexes of cobalt(III) and nickel(II) incorporating with unsymmetrical NNO-donor hydrazone ligand: Synthesis and structural aspects. *Journal of Chemical Crystallography,* 42(7): 691 – 696.
2. Suvapura, L. N, Young, K. S., Sung, O. B and Ammireddy. (2012). Review on analytical and biological applications of hydrazones and their metal complexes. *E-Journal of Chemistry,* 9(3): 1288 – 1304.
3. Seleem, H. S. and Mousa, M. A. (2011). Ligand substitution reactions of a phenolic quinolyl hydrazone; oxidovanadium (IV) complexes. *Chemistry Central Journal,* 5(47): 1 – 7.
4. Graisa, A., Farina, F Y., Yousif, E. and Kassem, M. (2008). Synthesis and characterization of some diorganotin(IV) complexes of N-toyl-m-nitrobenzohydroxamic acid. *Journal of Engineering and Applied Sciences,* 3(6): 47 – 50.
5. Szorcsik, A., Nagy, L., Gajda-Schrantz, K., Pellerito, L., Nagy, E. Nagy and Edelmann, F. T. E. (2002). Structural studies on organotin(IV) complexes formed with ligands containing {S, N, O,} donor atoms. *Journal of Radioanalytical and Nuclear Chemistry,* 252(3): 523 – 530.
6. Sharma, R. and Kaushik, N. K. (2004). Thermal studies on some organotin(IV) complexes with piperidine and 2-aminopyrdithiocarbamates. *Journal of Thermal Analysis and Colorimetry,* 78(2004): 953 – 964.
7. Bendre, R. Murugkar, A., Padhye, S., Kulkami, P and Karve, M. (1998). Synthesis and characterization of coordinatively unsaturated copper(II) complexes of 1,3-bis(2'-pyridyl)-1,2-diaza-2-butene and their antityrosinase activity. *Metal Based Drugs* 5(2): 59 – 66.
8. Affan, M. A., Chee, D. N. A, Ahmad, F. B., J. I., Yamin, M. Y and Hitam, R. B. (2010). Synthesis, characterization and biological activities of organotin(IV) complexes with vitamin $K_3$-2-hydrazinopyridine: X-ray crystal structure of vitamin $K_3$-2-hydrazinopyridine [VHzP]. *Research Journal of Pharmaceutical, Biological and Chemical Sciences* 1(4): 158 – 172.
9. Sam, N., Affan. M. A., Salam, M. A., Ahmad, F. B. and Asaruddin, M. R. (2012). Synthesis, spectral characterization and biological activities of organotin(IV) complexes with *ortho*-vanillin-2-hydrazinopyridine (VHP). *Open Journal of Inorganic Chemistry,* 2: 22 – 27.
10. Li, R. C., Nix, D. E. and Schentag, J. J. (1993). New turbidimetric assay for quantitation of visible bacterial densities. *Antimicrobial Agents Chemotherapy,* 37(2): 371 – 374.
11. Affan, M. A., Foo, I. P. P., Ahmad, F. B., Sim, E. U. H. and Hapipah, M. A. (2009). Synthesis, structural characterization and toxicity studies of novel organotin(IV) complexes derived from benzoylacetone isonicotinylhydrazone ($H_2$BAS): X-ray crystal structure of [$Me_2$Sn(BAS)]. *Malaysian Journal of Analytical Sciences,* 13(1): 73 – 85.
12. Salam, M. A., Affan, M. A., Arafat, M. A., Saha, R. and Nasrin, R. (2013). Synthesis, characterization and antibacterial activities of organotin(IV) complexes with 2-acetylpyridine-*N*(4)-cyclohexylthiosemicarbazone (HAPCT). *Heteroatom Chemistry,* 24(1): 43 – 52.
13. Pappano, N. B., Centorbi, O. P. and Ferretti, F. H. (1994). Determination of the responsible molecular zone for the chalcones bacteriostatic activity. *Revista de Microbiologia,* 24: 168 – 174.
14. Arslan, H., Duran, N., Borekci, G., Ozer, C. K. and Akbay, C. (2009). Antimicrobial activity of some thiourea derivatives and their nickel & copper complexes. *Molecules,* 10(14): 519 – 527.

*Malaysian Journal of Analytical Sciences, Vol 21 No 5 (2017): 1151 - 1155*
*DOI: https://doi.org/10.17576/mjas-2017-2105-18*

MALAYSIAN JOURNAL OF ANALYTICAL SCIENCES
*Published by The Malaysian Analytical Sciences Society*
ISSN 1394 - 2506

# SYNTHESIS, CHARACTERIZATION AND ANTIMICROBIAL PROPERTIES OF COPPER(II) COMPLEX OF HETEROCYCLIC LIGANDS

## (Sintesis, Pencirian dan Ciri Antimikrob Kuprum(II) Kompleks dengan Ligan Heterosiklik)

Rabuyah Ni*, Mohammad Isa Mohamadin, Vivien Jong Yi Mian

*Faculty of Applied Sciences,*
*Universiti Teknologi MARA, Kampus Samarahan 2, 94300 Kota Samarahan, Sarawak, Malaysia*

**Corresponding author: abuyani2201@gmail.com*

Received: 21 August 2016; Accepted: 27 July 2017

**Abstract**

Copper(II)-*β*-mangostin complex was prepared by 2:1 molar reaction of ligand, *β*-mangostin and copper(II) acetate in one-pot reaction. The resulting complex, $[CuL_2(H_2O)_2]$ has been characterized by using spectroscopic techniques. Ligand and its metal complex were tested against *Escherichia coli*, *Pseudomonas aeruginosa*, *Proteus vulgaris*, *Klebsiella pneumonia* and *Salmonella pneumoniae* bacteria to assess on their antibacterial properties using Minimum Inhibitory Concentrations (MICs) and Minimum Bactericidal Concentrations (MBCs) method. The UV-Vis result showed that the complex has an octahedral geometry. The general formula $[ML_2(H_2O)_2]$, in which L = *β*-mangostin, is determined from UV-Vis, FTIR and CHNS data. Ligands were completely inactive against bacteria whereas the copper(II) *β*-mangostin complex has significant action on bacteria, indicating that it has a good potential as bactericide.

**Keywords**: *β*-mangostin, copper(II) complex, antimicrobial, xanthones

**Abstrak**

Kompleks kuprum(II)-*β*-mangostin disediakan dengan nisbah 2:1 mol antara ligand, *β*-mangostin dan kuprum asetat dalam tindak balas satu-bekas. Kompleks yang dihasilkan, $[CuL_2(H_2O)_2]$ dicirikan dengan menggunakan teknik spektroskopik. Ligan dan logam kompleks diuji ke atas bakteria *Escherichia coli*, *Pseudomonas aeruginosa*, *Proteus vulgaris*, *Klebsiella pneumonia* and *Salmonella pneumoniae* untuk menilai tindak balas bakteria menggunakan kaedah Kepekatan Perencatan Minimum (KPM) dan kaedah Kepekatan Bakteria Minimum (KBM). Keputusan UV-Vis menunjukkan kompleks mempunyai geometri oktahedron. Formula umum $[ML_2(H_2O)_2]$, yang mana L = *β*-mangostin ditentukan dari data UV-Vis, FTIR dan CHNS. Ligand sepenuhnya tidak aktif ke atas bakteria, manakala komplex kuprum(II) *β*-mangostin memberikan tindak balas yang signifikan ke atas bakteria, menunjukkan ia mempunyai potensi yang baik sebagai bactericide.

**Kata kunci**: *β*-mangostin, kuprum(II) kompleks, antimikrob, xanthones

## Introduction

Transition metal ions such as copper(II), iron(II), iron(III) and zinc(II) have been known for many years to exert wide biological activity, for example against tumor cells [1]. Also chromones, flavonoid and coumarins have been known for similar properties. These two facts have attracted the attention of researchers to check whether metal complexes are more effective against anticancer and antibacterial than free ligands.

Copper is an essential trace mineral present in all body tissues. Copper works with iron to help the body to form red blood cells and increase the iron absorption. It also helps to keep the blood vessels, nerves, immune system and bones healthy. Copper has a major role in the production of the very reactive hydroxyl radical through the Fenton and Haber-Weiss reaction. Copper(II) can binds and manifests large hyperchromic and bathochromic shifts in the molecular absorption spectra [2].

Another class of less explored naturally occurring ligands are xanthones. These bioactive compounds are hetero-tricyclic compounds originally isolated as secondary metabolites from plants and microorganisms. Previous phytochemical studies on *Garcinia mangostana* have resulted in isolation of more than 50 xanthones. The major components in *Garcinia mangostana* are xanthones, such as $\alpha$-mangostin, $\beta$-mangostin, and $\gamma$-mangostin [3]. The xanthone derivatives has a remarkable effect on antiulcerogenic, antifungal activity, antibacterial activity, inhibitors of proteinkinase, anticancer activity, antioxidant and anti-inflammatory [4], which depend on their wide range of structures modified by substituents on the ring [5].

Simultaneously, synthetic and medicinal chemistry studies of xanthones derivative have been performed [6]. In contrast, there are only a few reports that deal with complexation of metal ions with xanthones derivatives. So far, complexation having xanthones as a ligand only involve synthetic xanthones. The synthetic xanthone was prepared via reaction dihydroxyxanthone with crown ether [7] or piperidinyl [8], respectively. The macrostructure of crown ether helps to stabilize the Cu(II) complexes formed whereas piperidinyl structure contributed basicity properties to encourage formation of Cu(II) and Zn(II) complexes with simple oxygenated xanthones.

In this work, the isolated $\beta$-mangostin from *Garcinia mangostana* will be used as a ligand to synthesize a new metal complex having copper(II) as the central metal. The newly synthesized compound will be tested for antimicrobial properties. Isolated $\beta$-mangostin was inactive against antimicrobial [9] and anticancer [10]. The inclusion of copper(II) could alter the overall structure of newly formed synthesized compound and thus can increase the biological properties of the compound.

## Materials and Methods

### Materials

All the chemicals used were Analar grade. Copper(II) acetate and ethanol were used as received.

### Extraction, Isolation and Purification of β-mangostin

Around 5-6 kg barks samples of *Garcinia mangostana* were obtained from Sarawak. 2.3 kg of powdered air-dried stem barks samples from *Garcinia mangostana* was macerated with chloroform for 48 hours at room temperature. The solvent was removed under reduced pressure using a rotavapor. The crude chloroform extract was isolated using Liquid Vacuum Chromatography and afforded 27 fractions. Same $R_f$ values on the TLC plates of $\beta$-mangostin were combined. The purity of $\beta$-mangostin was determined using Agilent HPLC Series 1260 Infinity.

### Synthesis of Cu(II) complexes

The procedure to obtain metal complex was adopted from established method by Bukhari et al. [11]. 0.589 mmol of copper(II) acetate was dissolved in ethanol. Then, 0.1178 mmol of $\beta$-mangostin was added and the colour of the solution was olive green. The mixture was refluxed for 3 hours. After refluxed, the mixture solution was filtered and washed with ethanol for few times. The filtrate was evaporated at room temperature. The resulting complex has been characterized using UV-VIS, Fourier Transformation Infrared (FTIR) and CHNS.

### Instrumentations

Ligand, $\beta$-mangostin and its metal complex were determined using Gas Chromatography – Mass Spectrometry (GCMS), Nuclear Magnetic Resonance (NMR), UV-Visible, Fourier Transformation Infrared (FTIR), High Performance Liquid Chromatography (HPLC) and CHNS analyser.

Elemental analyses (C, H and N) was performed on elemental analyser Model vario MICRO cube. Infrared spectra of $\beta$-mangostin and its metal complex were recorded on a Perkin-Elmer Frontier FTIR using KBr pellet in the

spectral range of 4000-400 $cm^{-1}$. Electronic spectra of the ligands and its metal complexes will be carried out by using Perkin-Elmer Model Lambda 25.

$^{1}H$ and $^{13}C$ NMR measurements were obtained on Bruker at 400 MHz, a 5 mm probe head in acetone-$d_6$ at room temperature. HPLC analysis for *β*-mangostin was carried out on Agilent G1316A (150 mm x 4.6 mm, 5 μm) column, the mobile phase was (80:20, v/v) acetonitrile/water mixture at room temperature with 1 mL $min^{-1}$ flow rate and a 5 *μl* injection loop. Detection was performed with a UV detector in HPLC at 320 nm. The xanthone scaffold having good absorption at this wavelength and only a few number of other compounds absorb making 320 nm wavelength for xanthone detection [12].

**Antimicrobial activities**

Antibacterial test for ligand and synthesized compound were carried out using Minimum Inhibitory Concentrations (MICs) and Minimum Bactericidal Concentrations (MBCs) method. The following bacteria were used as test organisms: *Escherichia coli*, *Pseudomonas aeruginosa*, *Proteus vulgaris*, *Klebsiella pneumonia* and *Salmonella pneumoniae*.

## Results and Discussion

**Structural elucidation of β-mangostin**

Fraction 11 until 13 from previous vacuum column chromatography were fractionated using gravity column chromatography yielded *β*-mangostin. Recrystallization from chloroform yielded yellow needle crystals with melting point of 174 – 175 °C (Lit. 175 – 176 °C [13]). The $R_f$ value was 0.575 using a solvent system of chloroform. The molecular ion peak was found at m/z 424 indicating a molecular formula of $C_{25}H_{28}O_6$. Figure 1 showed the structure of *β*-mangostin. The UV-Visible spectrum exhibited characteristic absorption bands of xanthone at $\lambda_{max}$ (ethanol) 244, 259, 315 and 355 nm. The IR spectrum showed the presence of hydroxyl group at 3399 $cm^{-1}$ and a chelated carbonyl group at 1648 $cm^{-1}$. The absorption band situated at 1600, 1571, 1458 and 1278 $cm^{-1}$ are related to carbon vibration in benzene rings. The purity of isolated *β*-mangostin was 98% determined from HPLC analysis.

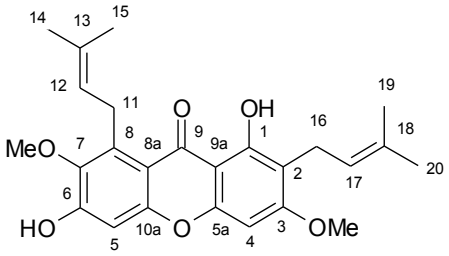



Figure 1. *β*-mangostin

$^{1}H$-NMR and $^{13}C$-NMR data were compared with reported data by Shen et al. [15]; Al-Massarani et al. [16] and Syam et al. [17]. The $^{1}H$ NMR spectrum showed the presence of one chelated hydroxyl group at δ 13.66. In addition, typical signals of four allylic methyl groups at $\delta_H$ 1.67 (3H, s, H-14), 1.84 (3H, s, H-15), 1.65 (3H, s, H-19) and 1.79 (3H, s, H-20); two pairs of methylene proton at $\delta_H$ 4.15 (2H, d, $J$ = 6.6 Hz, H-11) and 3.34(2H, d, $J$ = 7.2 Hz, H-16); and two olefinic protons at 5.22 (2H, t, $J$ = 7.3 Hz, H-12) and 5.29 (2H, t, $J$ = 6.7 Hz, H-17) were observed in the $^{1}H$ NMR spectrum.

The $^{13}C$ NMR spectrum gave a total of twenty five carbons which was validated for the molecular formula, $C_{25}H_{28}O_6$. A signal at $\delta_C$182.0 indicated a carbonyl group in the middle ring. Meanwhile, the methoxyl carbons signals were observed at $\delta_C$ 55.7 and $\delta_C$ 60.5. The locations of the two prenyl moieties were located at the C-2 ($\delta_C$110.9) and C-8 ($\delta_C$137.3). In the COSY spectrum the nature of the allylic and homoallylic coupling systems within the isoprene unit was clearly demonstrated. It showed correlation between the olefinic proton of C-12 and benzylic proton of C-11, and the germinal dimethyl group of C-14 and C-15. The same correlations above were also

observed for the other prenyl moiety.

**Physical properties of Cu(II) complexes**

Metal complexes involving *β*-mangostin and copper metal produced green complex which was stable at room temperature. The ligand, *β*-mangostin (L) on interaction with copper(II) acetate yields complex corresponding to the general formula $[ML_2(H_2O)_2]$. The analytical data showed that the metal to ligand ratio is 1:2. (Yield 72%) Analytical calculation for $CuL_2(H_2O)_2$ (MW = 946 $gmol^{-1}$): C=62.6%, H=5.4%. Found: C=63.4%, H=6.1%.

**Spectroscopic study of Cu(II) complexes**

IR spectra of *β*-mangostin has shifted in υ(C=O) peak from 1648 $cm^{-1}$ to 1615 $cm^{-1}$ and the Δυ(ligand – complex) is 33 [7, 8]. These absorption frequencies demonstrated that the group has lost its original characteristics and formed a coordinative bond with Cu(II) ion. Thus, this shows that the electron density in the carbonyl is slightly decreased probably due to back bonding process. Free OH stretching at 3399 $cm^{-1}$ was absent and replaced with a broad υ(OH) which was observed at 3438 $cm^{-1}$ indicating coordination of water with *β*-mangostin. These data suggested that the oxygen of the carbonyl and hydroxyl have formed a coordination bond with the $Cu^{2+}$ cation.

Another significant difference between the ligand and its metal complex was observed from UV spectrum. The UV spectrum of copper(II) complex shows a broad band at 22 000 $cm^{-1}$ ($\lambda_{max}$, 450 nm) which presumably corresponded to *d-d* transition with octahedral arrangement [18]. The chelation of Cu(II)-*β*-mangostin complex with bidentate ligand occurred with hydroxyl and carbonyl group at $C_9$ and $C_1$ respectively. The proposed structure of the complex was shown in Figure 2. The chelation formation in this study was similar to Farhan [19] and Wang et al. [7].

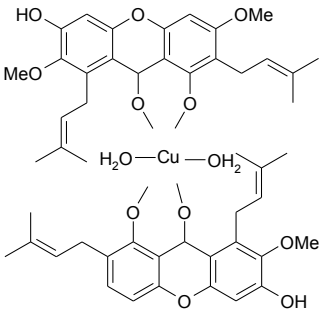



Figure 2. The proposed structure of Cu(II)-*β*-mangostin

**Antimicrobial properties**

*β*-mangostin was classify as inactive against the five bacteria tested. This antimicrobial result of *β*-mangostin was similar to Angia et al. [9]. Whereas the copper(II) complex showed weak inhibition with MIC value of 900 μg/ml to *Pseudomonas aeruginosa*, *Proteus vulgaris*, *Klebsiella pneumonia* and *Salmonella pneumoniae* but moderate inhibition with MIC value of 450 μg/ml towards *Escherichia coli*. The MIC value for positive control, streptomycin sulphate is 7.03 μg/ml for all bacteria used.

## Conclusion

Copper(II)-*β*-mangostin complex, $[CuL_2(H_2O)_2]$ was successfully synthesized with an octahedral geometry. The copper(II) complex showed more potent antimicrobial activity compared to ligand itself. This finding could lead to the development of new metal based bioactive compounds with enhanced antimicrobial properties, suitable for medical application and cosmetic products.

## Acknowledgment

Authors are highly thankful to the Faculty of Applied Sciences, Universiti Teknologi MARA, Campus Samarahan 2, Sarawak and Ministry of Higher Education for given Fundamental Research Grant Scheme (FRGS) grant (FRGS/1/2014/ST01/UiTM/02/3) to support this study.

**References**

1. Grazul, M., and Budzisc, E. (2009). Biological activity of metal ions complexes of chromones, coumarines and flavones. *Coordination Chemistry Review*, 253: 2588 – 2598.
2. Panhwar, Q.K., Memon S. and Bhanger, M.I. (2010). Synthesis, characterisation, spectroscopic and antioxidant studies of Cu(II)-morin Complex. *Journal of Molecular Structure,* 967: 47 – 53.
3. Aisha, A. F. A., Abu-Salah, K. M., Ismail, Z. and Abdul Majid, A. M. S. (2013). Determination of total xanthones in *Garcinia mangostana* fruit rind extracts by ultraviolet (UV) spectrophotometry. *Journal of Medicinal Plant Research,* 7(1): 29 – 35.
4. Yoshwathana, N. and Estiaghi, M. N. (2015). Optimization of subcritical ethanol extraction for xanthone from mangosteen pericarp. *International Journal of Chemical Engineering and Application,* 6(2): 115 – 119.
5. Sylvain V. T. Sob, H. K., Wabo, A. T., Tchinda, P., Tane, B. T. and Ngadjui, Y. Y. (2010). Anthraquinones, sterols, triterpenoids and xanthones from Cassia obtusifolia. *Biochemical Systematics and Ecology*, 38: 342 – 345.
6. Shagutfa, and Ahmad, I. (2016). Recent insight into the biological activities of synthetic xanthone derivatives, *European Journal of Medicinal Chemistry*, 116: 267 – 280.
7. Shen, R., Wang, P. and Tang, N. (2009). Synthesis, crystal structure, DNA-binding properties and cytotoxic activity of the copper(II) complex involving xanthone. *Journal of Fluorescence*, 19: 1073 –1082.
8. Wang, H.F., Shen, R. and Tang, N. (2009). Synthesis and characterization of the Zn(II) and Cu(II) piperidinyl isoeuxanthone complexes: DNA-binding and cytotoxic activity. *European Journal of Medicinal Chemistry*, 44: 4509 – 4515.
9. Angia, V., Bakhtiar, A. and Arbain, D. (2015). The isolation of xanthones from trunk latex *of Garcinia mangostana* Linn. and their antimicrobial activities. *Indonesian Journal Chemistry*, 15(2): 187 – 193.
10. Fei, X., Jo, M, Lee, B., Han, S.B., Lee, K., Jung, J.K., Seo, S.Y. and Kwak, Y.S. (2014). Synthesis of xanthone derivatives based on $\alpha$-mangostin and their biological evaluation for anticancer agents. *Bioorganic & Medicinal Chemistry Letters*, 21: 2062 – 2065.
11. Bukhari, S. B., Memon, S., Tahir, M. M. and Bhanger M. I. (2009). Synthesis, charaterisation and antioxidant activity copper-quercetin complex. *Spectrochimica Acta*, 71: 1901 – 1906.
12. Destandau, E., Toribio, A., Lafosse, M., Pecher, V., Lamy, C. and Andre, P. (2009). Centrifugal partition chromatography directly interfaced with mass spectrometry for the fast screening and fractionation of major xanthones in *Garcinia mangostana*. *Journal of Chromatography A*, 1216: 1390 – 1394.
13. Ee, G. C. L., Daud, S., Taufiq Yap, Y. H., Ismail, N. H. and Rahmani, M. (2006). Xanthones from *Garcinia mangostana* (Guttiferae). *Natural Product Research*, 20: 1067 – 1073.
14. Gopalakrishnan, G., Banumathi, B. and Suresh, G. (1997). Evaluation of the antifungal activity of natural xantones from *Garcinia mangostana* and their synthetic derivatives. *Journal Natural Product,* 60: 519 – 524.
15. Sen, A. K. Sarkar, K. K., Mazumder, P. C., Banerji, N., Uusvuori, R. and Hase, T. A. (1982). The structure of garcinones A, B and C: Three new xanthones from *Garcinia mangostana*. *Phytochemistry,* 21:1747 – 1750.
16. Al-Massarani, S. M., El Gamal, A. A., Al-Musayeib, N. M., Mothana, R. A., Basudan, O. A., Al-Rehaily, A. J., Farag, M., Assaf, M. H., El Tahir, K. and Maes, L. (2013). Phytochemical, antimicrobial and antiprotozoal evaluation of Garcinia mangostana pericarp and $\alpha$-mangostin, Its major xanthone derivative. *Molecules,* 18: 10599 – 10608.
17. Syam, S., Bustaman, A. Abdullah, R., Sukari, M. A, Hashim, N. M., Yahayu, M., Hassandarvish, P. and Abselwaheb, S. I. (2014). Cytotoxic and oral acute toxicity studies of $\beta$-mangostin isolated from Cratoxylum arborescens. *Phcog Journal*, 6: 47 – 56.
18. Yousef, T. A., Abu El-Raesh, G. M, Al-jahdali, M. and El-Rakhawy, E. R. (2014). Synthesis, spectral characterization and biological evaluation of Mn(II), Co(II), Ni(II), Cu(II), Zn(II) and Cd(II) complexes with thiosemicarbazone ending by pyrazole and pyridyl rings. *Spectrochimica Acta Part A: Molecular and Biomolecular Spectroscopy*, 129: 163 – 172.
19. Farhan, S. A. (2013). Study on the interaction of copper(II) complex of morin and its antimicrobial effect. *International Journal Chemistry of Sciences*, 11(3): 1248 – 1255.

*Malaysian Journal of Analytical Sciences, Vol 21 No 5 (2017): 1156 - 1161*
*DOI: https://doi.org/10.17576/mjas-2017-2105-19*

MALAYSIAN JOURNAL OF ANALYTICAL SCIENCES
*Published by The Malaysian Analytical Sciences Society*
ISSN 1394 - 2506

# ISOLATION AND SYNTHESIS OF PINOCEMBRIN AND PINOSTROBIN FROM *Artocarpus odoratissimus*

## (Pemencilan dan Sintesis Pinocembrin dan Pinostrobin dari *Artocarpus odoratissimus*)

Nyotia Nyokat[1], Khong Heng Yen[1]*, Ahmad Sazali Hamzah[2], Isabel Fong Lim[3], Aimi Suhaili Saaidin[2]

[1]*School of Chemistry and Environmental Studies, Faculty of Applied Sciences, Universiti Teknologi MARA, 94300 Kota Samarahan, Sarawak, Malaysia*
[2]*Institute of Science, Universiti Teknologi MARA, 40450 Shah Alam, Selangor, Malaysia*
[3]*Department of Paraclinical Sciences, Faculty of Medicine and Health Sciences, Universiti Malaysia Sarawak, 94300 Kota Samarahan, Sarawak, Malaysia*

**Corresponding author: khonghy@sarawak.uitm.edu.my*

Received: 21 August 2016; Accepted: 27 July 2017

**Abstract**

*Artocarpus odoratissimus* is native to Borneo and Mindanao Island. In Sarawak, it is locally known as Terap. Previous studies showed *Artocarpus* species are rich in phenolic compounds, including flavonoids, stilbenoids and arylbenzofurons. The chemical profile of the indigenous plants from Sarawak, such as *A. odoratissimus* has not been studied intensively and the analyses of medicinal properties have not been explored. Thus, a phytochemical study is carried out on the root extracts of *A. odoratissimus* using various chromatographic methods and it has led to the isolation of two known flavonoids, namely pinocembrin (**1**) and pinostrobin (**2**). The structures are identified by comparison of their $^{1}$H and $^{13}$C NMR data with those reported in the literature. Flavonoid molecule incorporated as multifunctional in the pharmaceutical industry. It has a vast range of pharmacological activities, such as antimicrobial, anti-inflammatory, antioxidant, and anticancer activities. Pinocembrin and pinostrobin which are successfully synthesized with 2-hydroxy,4,6-methoxyacetphenone and benzaldehyde as starting materials were discussed.

**Keywords**: *Artocarpus odoratissimus*, terap, pinocembrin, pinostrobin

**Abstrak**

*Artocarpus odoratissimus* berasal dari Borneo dan Pulau Mindanao. Di Sarawak ia dikenali sebagai Terap. Kajian terdahulu menunjukkan yang spesis *Artocarpus* kaya dengan sebatian fenolik, termasuk flavonoid, stilbenoid dan arilbenzofuron. Profil kimia tentang tumbuhan yang berasal dari Sarawak, seperti *A. odoratissimus* masih belum dikaji secara intensif dan analisis tentang khasiat perubatan masih belum lagi diterokai. Oleh itu, kajian fitokimia yang telah dilakukan ke atas krud ekstrak akar *A. odoratissimus* dengan menggunakan pelbagai kaedah kromatografi telah berjaya memencilkan dua sebatian flavonoid, iaitu pinosembrin (**1**) dan pinostrobin (**2**). Bentuk struktur telah dikenal pasti melalui perbandingan data $^{1}$H dan $^{13}$C NMR dengan kajian literatur. Molekul flavonoid mempunyai pelbagai fungsi di dalam industri farmaseutikal. Ia mempunyai aktiviti farmakologi yang sangat meluas seperti antimikrob, anti-radang, antioksidan, dan antikanser. Pinosembrin dan pinostrobin yang telah berjaya disintesis dengan menggunakan 2-hidroksi,4,6-metoksiasetofenon dan benzaldehid sebagai bahan pemula telah dibincangkan.

**Kata kunci**: *Artocarpus odoratissimus*, terap, pinosembrin, pinostrobin

## Introduction

*Artocarpus odoratissimus* is native to Borneo. It is cultivated in the Philippines and is also found in the wild abundantly in Brunei Darussalam, Sabah and Sarawak [1]. *Artocarpus* species are used as traditional medicines such as treatment against inflammation, malarial fever, diarrhea, diabetes and tapeworm infection. According to Jagtap and Bapat [2] compounds from *Artocarpus* species exhibited diverse biological activities including antibacterial, antitubercular, antiviral, antifungal, antiplatelet, antiarthritic, tyrosinase inhibitory and cytotoxicity. Some *Artocarpus* species are used as traditional medicines. For example *Artocarpus odoratissimus* (terap) is used by local communities in Sarawak as an antidote against centipede and scorpion stings by applying the ash from the leaves on the wounds, while for treatment of scabies the ash is added with a little amount of coconut oil [3]. Ee et al. [4] reported that the isolation of a new prenylated pyranoflavone derivatives, artosimmin and traxateryl acetate. Artosimmin exhibited significant cytotoxicity against cancer cell lines (HL-60 and MCF-7) and showed antioxidant properties.

*Artocarpus* species also rich in phenolic compounds, including flavonoids, stilbenoids and arylbenzofurons. Most of the pharmacological effects can be explained by the presence of phenolic compounds [5]. However, there are very few studies on the *Artocarpus* species from Sarawak, therefore it would be interesting to develop a chemical profile of such Sarawakian species. Thus, a phytochemical study is carried out on the root extracts of *Artocarpus odoratissimus* using various chromatographic methods and it has led to the isolation of two known flavonoids, namely pinocembrin and pinostrobin.

Pinocembrin is a flavanone, a type of flavonoid. It is an antioxidant found in damiana, honey, and propolis. Pinocembrin is a major flavonoid molecule incorporated as multifunctional in the pharmaceutical industry. Its vast range of pharmacological activities has been well studied including antimicrobial, anti-inflammatory, antioxidant, and anticancer activities. Pinocembrin has potential as a drug to treat cerebral ischemia, neurodegenerative diseases, cardiovascular diseases and atherosclerosis as well as other clinical conditions [6]. Pinocembrin also exhibits various interesting biological activities such as antibacterial [7], antifungal [8] and anti-inflammatory [9], [10]. Furthermore, pinocembrin plays a pivotal role in prevention and cure of various neurodegenerative diseases, such as Alzheimer's disease (AD), Parkinson's disease and other neuronal dysfunctions [11].

Pinostrobin is a potent flavonoid inducer of mammalian phase 2 chemoprotective and antioxidant enzymes [12]. Pinostrobin isolated from *Polygonum lapathifolium* nodosum could quickly penetrate through cytoplasm to the cellular nucleus of the cultured cells and gives intensive apoptotic response in stimulating leukemic cells *in vitro*. As such, it may be considered as a good candidate for a leukemia chemopreventic agent [13]. Pinostrobin from Temu Kunci (*Kaempferia pandurata* Roxb) has anticancer activity againts benzo(a)pyrene-induced fibrosarcoma cancer on mice *in vivo* [14]. With increasing concentration, pinostrobin caused a gradual leakage, also contributing to breakage of the envelope and virus inactivation. Treatment effect of oral pinostrobin *in vivo* showed that pinostrobin possesses definite therapeutically effect in the development of lesion score [15].

The interest in the biological properties of pinocembrin and pinostrobin attracted the intense synthetic efforts towards the synthesis of various derivatives compounds. By synthesis we can also save the usage of natural resources of raw material.

## Materials and Methods

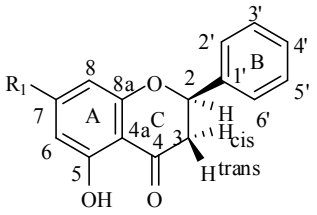
### Plant materials

The root of *Artocarpus oddoratissimus* was collected from Kampung Krokong Pisa, Bau Sarawak. Voucher specimen of the plant is kept in the School of Chemistry and Environmental Studies, Faculty of Applied Sciences at the Universiti Teknologi MARA (UiTM) Kota Samarahan 2 Campus, Sarawak, Malaysia.

### Extraction and isolation

The air-dried root (722.14 g) of *Artocarpus odoratissimus* was extracted by a cold extraction method for 24 hours and repeated thrice using n-hexane, ethyl acetate and methanol as solvents. The removal of solvents under reduced pressure gave hexane (AORH), ethyl acetate (AOREA), and methanol (AORM) crude extracts respectively. The crude extracts were fractionated using silica gel vacuum liquid chromatography (VLC) with a stepwise gradient

solvents system such as hexane, hexane-ethyl acetate, ethyl acetate-methanol and methanol, followed by column chromatography to give major fractions. Fractions with spots of the same $R_f$ values were combined and rechromatographed in appropriate solvent systems until pure isolates were obtained. The crude ethyl acetate root afforded two known flavonoids namely pinocembrin **(1)** and pinostrobin **(2)** (Figure 1)




| R1 | |
|---|---|
| **1** | OH |
| **2** | $CH_3$ |

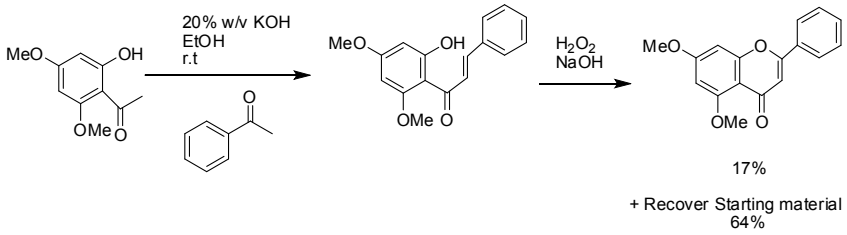
Figure 1. Structure of compounds (**1-2**) isolated from *A. odoratissimus*

**Synthesis of pinocembrin and pinstrobin: Synthesis of 2-hydroxy-4,6-dimethoxychalcone via Claisen-Schmidt condensation**

20% of aqueous KOH (2 mmol) was added to a solution of benzaldehyde (4 mmol) and 2-hydroxy-4,6-dimethoxyacetophenone (4 mmol) in $C_2H_5OH$ (25 mL). The reaction mixture was stirred at room temperature untill completion of reaction (monitored by TLC). The reaction mass was then poured into ice water and neutralized with aqueous 10% HCl solution. The precipitate was filtered, washed with excess of water, dried and recrystallized from methanol to obtain pure 2-hydroxy-4,6-dimethoxy chalcones.

**Synthesis of flavonol**

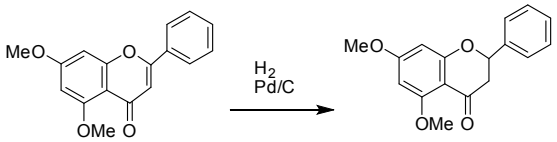
A suspension of a mixture of powdered 2-hydroxy-4,6-dimethoxychalcone (0.10 g, 0.45 mmol) in EtOH, an aq. NaOH solution (8 M, 1.0 ml) and a 30% hydrogen peroxide solution (0.25 g) was stirred at room temperature for 2 hours. The crude product was filtered off, washed with water to give flavonol (Scheme 1). Recrystallization of the crude product from MeOH gave pure compound.




Scheme 1. Formation of flavonol

**Formation of flavanone via hydrogenation reaction**

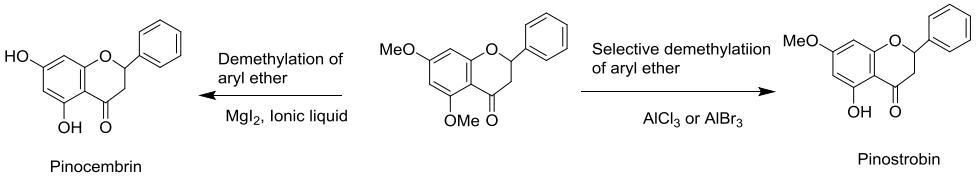
The reaction involves hydrogenation of flavonol to form flavanone (Scheme 2).




Scheme 2. Formation of flavanone

**Demethylation of aryl methyl ethers**

To a solution of aryl methyl ether (1.0 mmol) in [BMIM]$BF_4$ (2 mL) was added magnesium iodide (0.42 g, 1.5 mmol). The reaction mixture was stirred at 50 $^oC$ for 4 – 7 hours. After addition of 5% aqueous sodium thiosulfate (10 mL), the product was extracted with ether (2 × 10 mL), washed with brine (5 mL), and extracted with ether (2 × 10 mL), washed with brine (5 mL), and dried over $MgSO_4$. The solvent was removed in vacuo and the crude mixture was purified by silica gel chromatography using ethyl ether: hexane (1:3) as eluent to give the desired phenolic product (Scheme 3).




Scheme 3. Formation of phenolic product

## Results and Discussion

The extraction and separation from the root extract of *Artocarpus odoratissimus*, afforded two flavonoids, which were identified and characterized as pinocembrin **(1)** and pinostrobin **(2)** based on data comparison literature.

**Characterization study: Pinocembrin (1)**

White yellowish crystalline; mp 201-202 °C; IR (KBr) $\nu_{max}$ $cm^{-1}$: 3435 (Ar-H stretching), 1744 (C=O ester), 1497, 1578 (C=C Aromatic), 1248 (C-O) and 976 (=C-H) $cm^{-1}$; EI-MS m/z (% rel. int.); 256 (100) [$M^+$ $C_{15}H_{12}O_4$], 238 (14), 179 (70), 152 (80), 124 (45), 104 (18), 77 (20), 69 (20) and 51(9); $^1$H NMR (400 MHz; $CDCl_3$): δ 2.86 (3-cis), 3.10 (3-trans), 5.43 (2H, t, J=6.7), 6.03 (H-6), 6.03 (H-8), 7.41-7.49 (H-2'-H6'), 12.07 (C-5-OH). $^{13}$C NMR (100 MHz; $CDCl_3$): δ 43.37 (C-3), 79.18 (C-2), 95.56 (C-8), 96.81 (C-6), 102.97 (C-4a), 126.16 (C-2', C-6'), 128.87 (C-3', C-4', C-5'), 138.42 (C-1'), 163.11 (C-8a), 164.34 (C-5), 195.65 (C-4).

**Pinostrobin (2)**

Colorless crystal; mp 100-102 °C; IR (KBr) $\nu_{max}$ $cm^{-1}$: 3467 (Ar-H stretching), 1741 (C=O ester), 1497, 1578 (C=C Aromatic), 1538, 1360 (C-O) and 968 (=C-H) $cm^{-1}$; EI-MS m/z (% rel. int.); 270 (90) [$M^+$ $C_{16}H_{14}O_4$], 269 (50), 252 (8), 193 (100), 166 (80), 138 (50), 110 (18), 95 (35), 78 (15) and 51 (20);. $^1$H NMR (400 MHz; $CDCl_3$): δ 2.81 (3-cis), 3.86 (C-7-OMe), 3.10 (3-trans), 5.43 (2H, t, J=6.7), 6.03 (H-8), 6.04 (H-6), 7.28-7.49 (H-2'-H6'), 12.07 (C-5-OH). $^{13}$C NMR (100 MHz; $CDCl_3$): δ 43.36 (C-3), 55.60 (C-7-OMe), 79.25 (C-2), 95.49 (C-6, C-8), 103.20 (C-4a), 126.17 (C-2', C-6'), 128.92 (C-3', C-4', C-5'), 138.30 (C-1'), 163.16 (C-5), 164.36 (C-7), 164.63 (C-8a), 195.79 (C-4).

Compound (**1**) was obtained as white yellowish crystalline with melting point 201 – 202 °C. The mass spectrum showed the molecular ion peak at m/z 256, indicated the formal formula $C_{15}H_{12}O_4$. In the $^1$H NMR, one proton singlet at δ 12.07 sited the free hydroxyl at position 5 with H-bridge to O at the carbonyl at position 4. Two doublets at δ 6.03 attributed to meta H-6 and H-8. A five-proton multiplet at δ 7.41 – 7.49 confirmed the non-substitution of the B-ring. Two doublet-doublet of one proton each at δ 2.86 and δ 3.10 attributable to H-3 (*cis*) and H-3(*trans*), respectively. The $^{13}$C NMR spectrum showed 15 carbons signals including one methylene, eight methine and six quaternary carbon atoms.

Compound (**2**) was obtained as colorless crystal with melting point 100 – 102 °C. The mass spectrum showed the molecular ion peak at m/z 270 indicating that the compound had the formula $C_{16}H_{14}O_4$. The IR spectrum showed the presence of aromatic stretch at 3467 $cm^{-1}$, carbonyl group, ester (C=O) at 1741 $cm^{-1}$ as well as an olefin functional group (C-O) at 1538 $cm^{-1}$ . In the $^1$H NMR, a methoxy group was seen as a singlet at δ 3.86. A one-proton singlet at δ 12.07 sited the free hydroxyl at position 5 with H-bridge to O at the carbonyl at position 4. The $^{13}$C NMR

spectrum showed 16 carbons signals including one methyl, one methylene, 8 methine and 6 quaternary carbon atoms. Among these signals the carbon signal of methoxy group is clearly assigned due to the presence of chemical shift 55.60.

The Claisen-Schmidt condensation of 2-hydroxy-4,6-dimethoxyacetophenone with benzaldehyde under basic condition (KOH 50%) in ethanol proceeded smoothly to furnish 2-hydroxy-4,6-dimethoxychalcone in excellent yield, (97.1%). The cyclisation of 2-hydroxy-4,6-dimethoxychalcone in ethanol and aqueous sodium hydroxide solution and a 30% hydrogen peroxide solution gave flavonol and the hydrogenation of flavonol produced flavanone. The reaction of aryl methyl ether and magnesium iodide gave pinocembrin and with aluminum trichloride gave pinostrobin as product.

## Conclusion

The isolation of *Artocarpus odoratissimus* root extract had successfully led to two known flavonoids, namely pinocembrin and pinostrobin. These compounds were then successfully synthesized with 2-hydroxy-4,6-dimethoxyacetphenone and benzaldehyde as starting materials. The identification of compounds was carried out using spectroscopic methods: Infrared (IR) spectroscopy, Nuclear Magnetic Resonance (NMR) spectroscopy and Gas Chromatography Mass Spectroscopy (GC-MS) and a comparison with the literature data of compound.

## Acknowledgment

The authors would like to acknowledge the financial assistance provided by the Ministry of Higher Education, under Research Grant of (600-RMI/TRGS 5/3/(1/2014)-2) and (600-RMI/RAGS 5/3 (95/2013). The authors also extended their thanks to Research Management Institute, Universiti Teknologi MARA (UiTM), Malaysia for their excellent support and assistance.

## References

1. Subhadrabandhu, S. (2001). Under-utilized tropical fruits of Thailand (English): Thailand. Regional Office for Asia and the Pacific.
2. Jagtap, U. B. and Bapat, V. A. (2010). *Artocarpus*: a review of its traditional uses, phytochemistry and pharmacology. *Journal of Ethnopharmacology,* 129(2): 142 – 166.
3. Chai, P. K. (2006). Medicinal plants of Sarawak. Lee Ming Press, Kuching: pp. 212.
4. Ee, C. L. G., Teo, S. H., Rahmani, M., Lim, K. C., Lim, M. Y. and Bong, F. J. C. (2010). Artosimmin-a potential anti-cancer lead compound from *Artocarpus odoratissimus*. *Letters in Organic Chemistry* 7(3): 240 – 244.
5. Hakim, E. H., Achmad, S. A., Juliawaty, L. D., Makmur, L., Syah, Y. M., Aimi, N., Kitajima, M. and Ghisalberti, E. L. (2006). Prenylated flavonoids and related compounds of the Indonesian *Artocarpus* (Moraceae). *Journal of Natural Medicine,* 60: 161 – 184.
6. Liu, R., Li, J. Z., Song, J. K., Zhou, D., Huang, C., Bai, X. Y., Xie, T., Zhang, X., Li, Y. J., Wu, C. X. and Zhang, L. (2014). Pinocembrin improves cognition and protects the neurovascular unit in Alzheimer related deficits. *Neurobiology of Aging* 35(6): 1275 – 1285.
7. Drewes, S. E. and van Vuuren, S. F. (2008). Antimicrobial acylphloroglucinols and dibenzyloxy flavonoids from flowers of *Helichrysum gymnocomum*. *Phytochemistry,* 69(8): 1745 – 1749.
8. López, A., Ming, D. S. and Towers, G. N. (2002). Antifungal activity of benzoic acid derivatives from *Piper lanceaefolium*. *Journal of Natural Products*, 65(1): 62 – 64.
9. Sala, A., Recio, M. C., Schinella, G. R., Máñez, S., Giner, R. M., Cerdá-Nicolás, M. and Ríos, J. L. (2003). Assessment of the anti-inflammatory activity and free radical scavenger activity of tiliroside. *European Journal of Pharmacology*, 461(1): 53 – 61.
10. Arslan, S., Ozbilge, H., Kaya, E. G. and Er, O. (2011). *In vitro* antimicrobial activity of propolis, BioPure MTAD, sodium hypochlorite, and chlorhexidine on *Enterococcus faecalis* and *Candida albicans*. *Saudi Medical Journal,* 32(5): 479 – 483.
11. Essa, M. M., Vijayan, R. K., Castellano-Gonzalez, G., Memon, M. A., Braidy, N. and Guillemin, G. J. (2012). Neuroprotective effect of natural products against Alzheimer's disease. *Neurochemical Research* 37(9): 1829 – 1842.

12. Fahey, J. W. and Stephenson, K. K. (2002). Pinostrobin from honey and Thai ginger (*Boesenbergia pandurata*): A potent flavonoid inducer of mammalian phase 2 chemoprotective and antioxidant enzymes. *Journal of Agricultural and Food Chemistry*, 50(25): 7472 – 7476.
13. Smolarz, H. D., Mendyk, E., Bogucka-Kocka, A. and Kockic, J. (2006). Pinostrobin–an anti-leukemic flavonoid from *Polygonum lapathifolium* L. ssp. nodosum (Pers.) *Dans. Zeitschrift für Naturforschung C* 61(1-2): 64 – 68.
14. Adi Parwata, O., Sukardiman, S. and Widhiartini, A. (2014). Isolasi dan aktivitas antikanker pinostrobin dari Temu Kunci (*Kaempferia pandurata* Roxb) terhadap fibrosarkoma mencit hasil induksi benzopiren. *Journal of Chemistry* 8(2): 243 – 250.
15. Wu, N., Kong, Y., Zu, Y., Fu, Y., Liu, Z., Meng, R. and Efferth, T. (2011). Activity investigation of pinostrobin towards herpes simplex virus-1 as determined by atomic force microscopy. *Phytomedicine,* 18(2): 110 – 118.

*Malaysian Journal of Analytical Sciences, Vol 21 No 5 (2017): 1162 - 1167*
*DOI: https://doi.org/10.17576/mjas-2017-2105-20*

**MALAYSIAN JOURNAL OF ANALYTICAL SCIENCES**
***Published by The Malaysian Analytical Sciences Society***
**ISSN 1394 - 2506**

# IRON(II) COMPLEX OF ANTHRAQUINONE: SYNTHESIS, STRUCTURAL ELUCIDATION AND ANTIMICROBIAL ACTIVITY

## (Komplek Ferum(II) Antrakuinon: Sintesis, Penentuan Struktur Organik dan Aktiviti Antimikrob)

Nur Dzaina Zaidel, Vivien Jong Yi Mian*, Mohammad Isa Mohamadin

*Faculty of Applied Sciences*
*Universiti Teknologi MARA, 94300 Kota Samarahan, Sarawak, Malaysia*

**Corresponding author: vivien@sarawak.uitm.edu.my*

Received: 21 August 2016; Accepted: 27 July 2017

**Abstract**

Our continuing interest in anthraquinone had led the researchers to look at the synthesis of metal complex by reacting our major compound, nordamnacanthal with transition metal, Fe(II). Fe(II)-nordamnacanthal complex had been synthesized successfully via telescoping synthesis/ one-pot reaction. The ligand and its metal complex were established by 1D and 2D nuclear magnetic resonance spectroscopy, UV-Visible, CHNS analyzer, gas chromatography mass spectrometry and infrared analysis. They were evaluated for their antimicrobial activity using minimum inhibitory concentration (MIC) and minimum bactericidal concentration (MBC). Fe(II)-nordamnacanthal complex showed stronger inhibition against *Pseudomonas aeruginosa* at the concentration of 450 μg/mL while *Proteus vulgaris*, *Klebsiella pneumoniae* and *Salmonella pneumoniae* at the concentration of 225 μg/mL compare to nordamnacanthal. In this work, the synthesized compound, Fe(II)-nordamnacanthal showed better antimicrobial activity compared to the ligand itself.

**Keywords**: nordamnacanthal, transition metal Fe(II), Fe(II)-nordamnacanthal complex, antimicrobial activity

**Abstrak**

Kesinambungan perhatian kami terhadap antrakuinon telah membawa kami untuk melihat kepada sintesis kompleks logam dengan menghasilkan tindak balas sebatian utama kami, nordamnacanthal dengan logam peralihan, Fe(II). Kompleks Fe(II)-nordamnacanthal telah berjaya disintesiskan melalui teleskop sintesis/tindak balas satu-periuk. Sebatian dan kompleks logam dikenalpasti melalui 1D dan 2D spektroskopi resonan magnetik nukleus, UV-Vis, CHNS, kromatografi gas spektometri jisim dan analisis inframerah. Sebatian dan kompleks logam tersebut telah dinilai untuk aktiviti antimikrob dengan menggunakan kepekatan perencatan minimum (MIC) dan minimum kepekatan bakteria (MBC). Kompleks Fe(II)-nordamnacanthal menunjukkan perencatan yang kuat terhadap *Pseudomonas aeruginosa* pada kepekatan 450 μg/mL manakala *Proteus vulgaris*, *Klebsiella pneumoniae* dan *Salmonella pneumoniae* pada kepekatan 225 μg/mL berbanding dengan nordamnacanthal. Dalam kajian ini, sebatian yang disintesis, kompleks Fe(II)-nordamnacanthal menunjukkan aktiviti antimikrob lebih baik berbanding dengan sebatian itu sendiri.

**Kata kunci**: nordamnacanthal, logam peralihan Fe(II), kompleks Fe(II)-nordamnacanthal, aktiviti antimikrob

## Introduction

Anthraquinones are biocompounds that are widely obtained from fungi and higher plant families [1, 2]. Anthraquinones have nearly one thousand known compounds, which contain different types of substituents at different positions, leading to a large variety of pharmacological activities [3, 4]. The bioactivities of these

compounds can be attributed to their structure. Presence of substituents namely OH group and carbonyl group on the ring structure of anthraquinones opens up a possibility of forming a coordinated bond with metal ions. The inclusion of transition metal ion is expected to increase the planarity of the compound thus will enhanced the bioactive properties of the new prepared complexes. Anthraquinones structures also plays an important role in the cancer activity as it allows for many sites for the phenolic group substituents on the bridged benzene rings on either side of the carbonyl bridge, while still maintaining its aromaticity. This allows for intercalation of the anthraquinones to DNA in cells, as well as hydrogen bonding between the carbonyl and ether bridges with amino acid residues in enzymes [5].

Similarly, the anthraquinones' structure also plays an important role in the cancer activity of *Morinda citrifolia* as it allows for many sites for the phenolic group substituents on the bridged benzene rings on either side of the carbonyl bridge, while still maintaining its aromaticity. This allows for intercalation of the anthraquinones to DNA in cells, as well as hydrogen bonding between the carbonyl and ether bridges with amino acid residues in enzymes [2].

The underlying bioactive role of such compounds relates to the intracellular interaction of the compounds with DNA molecule with one of the effects is leading to the damaged of the cell. Such disruptive consequence is an inhibitor to the continuous growth of cell and thus resulting in cell death [6]. The inclusion of transition metal complexes namely copper, zinc and iron could enhance such bioactive role of the compounds. This is particular as the presence of such metals could alter the overall structure of the newly formed complex and thus can increase the affinity of the compound to DNA [7, 8].

This could result in the improvement of biological activities of the compounds. This research was carried out on *Morinda citrifolia* and focused on isolation of anthraquinones from the *Morinda citrifolia* stem bark extract and synthesize of Fe(II) complex which is having anthraquinones as ligands.

## Materials and Methods

### Plant material

An amount 5 – 6 kg of stem barks sample of *Morinda citrifolia* were collected from Sarawak. Herbarium voucher specimens were prepared.

### Extraction, isolation and purification

The plant was allowed to air-dry in the laboratory and then the dried sample was grinded. Powdered air-dried samples (2 – 3 kg) were extracted by soaking the sample with organic solvents in sequential polarity which started with hexane and followed by ethyl acetate, chloroform and methanol. The samples were allowed to stand for 48 hours and the process was repeated twice at 48 hours-interval.

The extract from each solvent extraction was filtered and concentrated using a rotavapor under vacuum pressure. The extracts were purified using liquid vacuum column (KCV) chromatography, gravity column chromatography and chromatoron. Fractions which were obtained from the isolation were purified using the gravity column chromatography and chromatotron using hexane and chloroform with ratio (6:4) as a solvent system to obtain the major compound, nordamnacanthal.

### Preparation of the metal complex

Fe(II)-nordamnacanthal complex was synthesized by reacting the major compound, nordamnacanthal, 0.0500 g, 0.1864 mmol with an ethanolic solution 30 mL of 0.0186 g, 0.0932 mmol iron(II) acetate. The mixture was stirred and refluxed for 3 hours. Brown precipitate was yielded during the reflux. It was allowed to cool at the room temperature and was filtered. The solid was washed with ethanol and then air-dried.

### Instrumentation

The ligand, nordamnacanthal and its metal complex were established by gas chromatography mass spectrometry (GCMS), nuclear magnetic resonance (NMR), UV-Visible spectra, Fourier transformation infrared spectrophotometer and CHNS elemental analyzer.

**Bioassay (antimicrobial)**

Antimicrobial nordamnacanthal and Fe(II)-nordamnacanthal were evaluated using minimum inhibitory concentration (MIC) determines by broth micro dilution method using 96-well microplates against the 5 bacteria, *Escherichia coli, Salmonella pneumoniae, Pseudomonas aeruginosa, Proteus vulgaris and Klebsiella pneumonia*. The MIC will be tested according to Güllüce et al. [9]. Nutrient broth was prepared and autoclaved. 3.6 mg of ligand and its metal complex were weighed and dissolved in 2 mL DMSO (Stock solution, 1800 µg/mL).

The inoculated of the microbial strains were prepared from 24 hours broth cultures and suspensions were adjusted to 0.5 McFarland standard turbidity. The sterile nutrient broth was added (100 µg/mL) to wells in row B to H. The stock solution was added (100 µg/mL) to row A and B. The well mixture of nutrient broth and sample at row B were transferred to each well in order to obtain a twofold serial dilution of stock samples (1800, 900, 450, 225, 112.5, 56.25, 28.13 and 14.07 µg/mL). 100 µg/mL of the last row of the well need was removed out. The prepared bacteria were added (100 µg/mL) to all wells (A to H). T96-wells plate were covered with lid, sealed and incubated at 37 ˚C for 24 hours. The microbial growth was observed by turbidity and present of pallet at the bottom.

Minimum bactericidal concentration (MBC) method was used to extend evaluating the results of MIC by determine the number of surviving organism by observing the growth of bacteria. MBC is defining as the number concentration at which 99% of the bacteria were killed. The solution at the clearest stage/concentration in the 96-wells plate (during MIC analysis) were taken out and spread on the plate containing agar using sterilized metal loop. The plates were sealed and incubated at 37 ˚C for 24 hours. The plates were observed. The plate was clear during observation, means the bacteria are not growth and the MBC result is the same as MIC. Meanwhile, if the agar turns cloudy or not clear, MBC result showed concentration one step lower than MIC.

## Results and Discussion

**Structural elucidation of nordamnacanthal**

Nordamnacanthal was isolated via column chromatography (CC) and recrystallised from chloroform as an orange-yellow solid and with the melting point of 217 – 218 °C Temperature of this compound ranging 218 –220 °C was reported by Prista et al. [10]. The phenolic nature of this compound was indicated by the positive $FeCl_3$ test. The difference can be noticed from the molecular ion peak at m/z 268, which corresponds to the molecular formula $C_{15}H_8O_5$. Strong peak at m/z 240 was due to the α-cleavage of the bond to the carbonyl group also occurred in nordamancanthal. The difference of the two compounds can also be observed from the UV spectrum where the absorption wavelength of nordamnacanthal was centered at 246 nm while another was shifted longer wavelength at 290 nm. This is due to the pi-pi* transition in the aromatic rings. There was also an additional weak absorption at 420 nm that indicating the hydroxyl group. The IR spectrum showed strong absorption bands at $\nu$= 3071, 1667, 1573, 1456, 1309 and 1262 $cm^{-1}$ were due to the presence of the hydroxyl group, chelated carbonyl group and the C-O stretch, respectively.

The $^1H$ NMR spectrum showed a singlet signal of aromatic proton ($\delta_H$ 7.34, H-4) and two doublet of doublets protons ($\delta_H$ 8.32, H-5 and H-8) and two multiplets at $\delta_H$ 7.84 (H-6 and H-7). The five signals at aromatic range displayed signals for a 1,2,3-trisubstituted aromatic ring. The assignments were made according to the equivalent protons values of the two protons and their coupling constant values which were 7.3 and 1.8 Hz. These values also confirmed the occurrence of the orto coupling and meta coupling among these protons. The characteristic $^{13}C$ NMR spectra revealed a normal skeleton of anthraquinone attached by two hydroxyl, and a formyl group.

Additional information from the HMBC proved the assignment of the formyl group in the structure, the $^3J$ coupling between the aldehyde proton at $\delta_H$ 10.50 and C-3 ($\delta_C$ 169.2), and $\delta_C$ 168.1 (C-1) with the one proton singlet at $\delta_H$ 7.34 was assigned as H-4. Besides, the substituents in the ring A were identified to have the two hydroxyl groups at position 1 and 3, and the formyl group at position 2. The positions of these substituents were confirmed by the two one-proton singlets at $\delta_H$ 14.06 and 12.68, that represented the chelated hydroxyl protons.

**Characterization of Metal Complex**

The structure of Fe(II)-nordamnacanthal complex was established through the elemental analysis CHNS, IR and UV-Visible spectral data. The synthesis of metal complex was carried out by reacting our major compound,

nordamnacanthal with transition metal, Fe(II). Fe(II)-nordamnacanthal complex had been synthesized successfully via telescoping synthesis/ one-pot reaction. The ligand, nordamnacanthal (L) on interaction with iron(II) acetate. The analytical data show that the metal to ligand ratio is 1:2. (yield 42%). Elemental analysis was found to be C (39.97%); H (3.514%); N (0.2777%) and S (0.06%). Calculated for Fe(II)-nordamnacanthal complex: C (40.00%); H (3.111%); N (0.0%) and S (0.0%). The Fe(II)-nordamnacanthal complex showed molecular ion peak at m/z 450, supported the formation of the complex.

IR spectra of the free ligand, nordamnacanthal (Figure 1) was compared with the IR spectra of the metal complex. IR spectra of ligand showed a strong band at 3071 $cm^{-1}$ that is assigned to the OH group while the band is gone in the spectra of Fe(II) complex indicating the coordination of the hydroxyl group through the deprotonation. Broad absorption band at 3429 $cm^{-1}$ in the spectra of Fe (II) complex may show the presence of $H_2O$ stretching vibration. The band position of ν (C=O) group appeared at 1658 – 1667 $cm^{-1}$ range in the spectra of the free ligand was shifted by in the spectra of the complex, indicating the coordination of C=O of the ring to the Fe ion. While the additional peaks a very low frequency in IR spectra of Fe(II)-nordamnacanthal complex at 463.05 $cm^{-1}$ was attributed to *ν*(M-O), which was supported the formation of the complex [11].

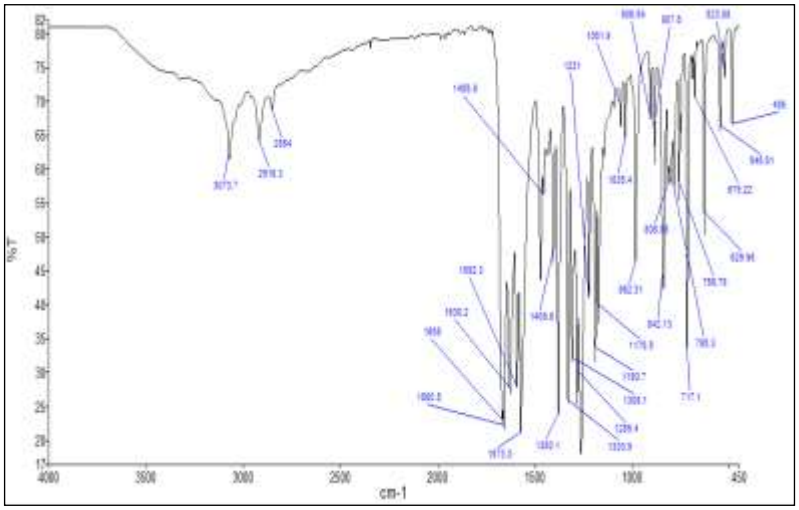



Figure 1. FTIR spectrum of nordamnacanthal

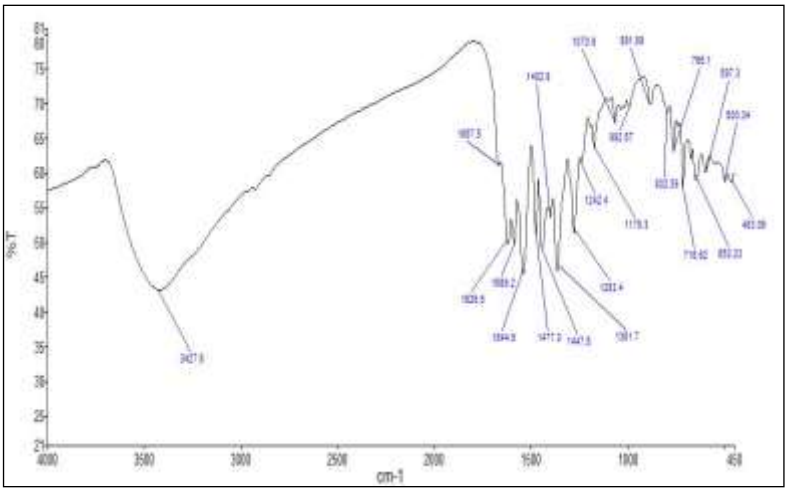



Figure 2. FTIR spectrum of Fe(II)-nordamnacanthal complex

The UV-Vis absorption spectra of nordamnacanthal (Figure 3) showed bands at 258.21 and 268.71 nm, which are due to $\pi \rightarrow \pi^*$ intra ligand transitions. The absorption band were shifted from 258.21 to 274.70 and 268.13 to 309.89 respectively in UV-vis spectra of Fe (II)-nordamnacanthal complex (Figure 4) and additional absorption at 421.78 was shifted to 548.05 nm in Fe (II)-nordamnacanthal complex may be due to a metal-to-ligand charge transfer [12]. Based on these results, ligand nordamnacanthal was confirmed coordinate with Fe(II) metal.

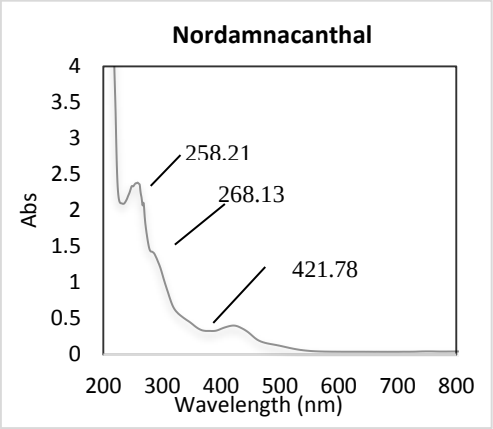



Figure 3. UV VIS spectra of nordamnacanthal

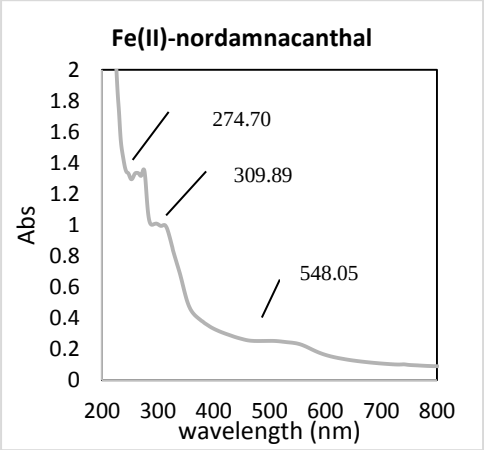



Figure 4. UV VIS Spectra of Fe(II)-nordamnacanthal complex

**Antimicrobial activity**

Antimicrobial activity of the ligand, nordamnacanthal and synthesized compound, Fe(II)-nordamnacanthal complex were compared. They were evaluated for the antimicrobial activity using minimum inhibitory concentration (MIC) and minimum bactericidal concentration (MBC). Fe(II)-nordamnacanthal complex showed stronger inhibition against *Pseudomonas aeruginosa* at the concentration of 450 μg/mL whereas *Proteus vulgaris, Klebsiella pneumoniae* and *Salmonella pneumoniae* at the concentration of 225 μg/mL compared to nordamnacanthal. In this work, the synthesized compound, Fe(II)-nordamnacanthal complex showed better antimicrobial activity compared to the ligand itself.

## Conclusion

Fe(II)-nordamnacanthal complex had been synthesized successfully based on the telescoping synthesis/ one-pot reaction. The synthesized compound, Fe (II)-nordamnacanthal complex showed better antimicrobial activity compared to the ligand itself.

## Acknowledgment

The study was financially supported by FRGS grant (FRGS/1/2014/ST01/UiTM/02/3). The authors would like to extend our sincere appreciation to Faculty Applied Science, UiTM Kampus 2 Samarahan, Sarawak for providing materials and chemicals needed to conduct this study successfully.

## References

1. Jing J. W., Barbara J. S. and Wei Z. (2011). Cytotoxic effect of xanthones from pericarp of the tropical fruit mangosteen (*Garcinia mangostana* Linn.) on human melanoma cells. *Food and Chemical Toxicology*, 49: 2385 – 2391.
2. Jittra K., Siriporn S., Pattiyaa L., Pranee R. and Chawanee T. (2013). Xanthone and anthraquinone-type mycotoxins from the scale insect fungus *Aschersonia marginata* BCC 28721. *Tetrahedron Letters*, 54: 3813 – 3815.
3. Arno R. N. D., Michel F. T., Hippolyte K. W., Gerold J., Guang-Zhi Z., Peter W.r, Ning-Hua T. and Pierre T. (2014). Two new anthraquinone dimers from the stem bark of *Pentas schimperi* (Rubiaceae) *Phytochemistry Letters*, 8: 55 – 58.
4. West, B. J., Palmer, S. K., Deng, S. and Palu, A. K. (2012). Antimicrobial activity of an iridoid rich extract from" morinda citrifolia" fruit. *Current Research Journal of Biological Sciences*, 4(1): 52 – 54.
5. Kamiya, K., Hamabe, W., Tokuyama, S. and Satake, T. (2009). New anthraquinone glycosides from the roots of Morinda citrifolia. *Fitoterapia*, 80(3): 196 – 199.
6. Mani G., Rangasamy L., Sethu R., Anvarbatcha R., Mohamad A. A. and Mallayan P. (2012) Interaction of mixed ligand copper(II) complexes with CT-DNA and BSA: Effect of primary ligand hydrophobicity on DNA and protein binding and cleavage and anticancer activities. *Polyhedron*, 52: 924 – 938.
7. Li, V.S., Choi, D., Wang, Z., Jimenez, L.S., Tang, M.S., Kohn, H. (1996) Role of the C-10 Substituent in Mitomycin C-1−DNA Bonding. *Journal of American Chemical Society 118*: 2326-2331.
8. Zin, Z. M., Abdul-Hamid, A. and Osman, A. (2002). Antioxidative activity of extracts from Mengkudu (*Morinda citrifolia* L.) root, fruit and leaf. *Food Chemistry*, 78(2): 227 – 231.
9. Güllüce, M., Sökmen, M., Şahin, F., Sökmen, A., Adigüzel, A. and Özer, H. (2004). Biological activities of the essential oil and methanolic extract of *Micromeria fruticosa* (L) Druce ssp serpyllifolia (Bieb) PH Davis plants from the eastern Anatolia region of Turkey. *Journal of the Science of Food and Agriculture*, 84(7): 735 – 741.
10. Prista, L. N., Roque, A. S., Ferreira, M. A. and Alves, A. C. (1965). Chemical study of *Morinda geminate*. I. isolation of morindone, damnacanthal, nor-damnacanthal and rubiadin-1-methyl ether. *Garcia de Orta*, 13: 19 – 38.
11. Panhwar, Q. K. and Memon, S. (2014). Synthesis of Cr(III)-morin complex: characterization and antioxidant study. *The Scientific World Journal*, 2014: 1 – 8.
12. Ran, X. G., Wang, L. Y., Cao, D. R., Lin, Y. C. and Hao, J. (2011). Synthesis, characterization and *in vitro* biological activity of cobalt(II), copper(II) and zinc(II). Schiff base complexes derived from salicylaldehyde and D, Lselenomethionine. *Applied Organometallic Chemistry*, 25: 9 – 15.

*Malaysian Journal of Analytical Sciences, Vol 21 No 5 (2017): 1168 - 1175*
*DOI: https://doi.org/10.17576/mjas-2017-2105-21*

MALAYSIAN JOURNAL OF ANALYTICAL SCIENCES
*Published by The Malaysian Analytical Sciences Society*
ISSN 1394 - 2506

# SYNTHESIS, CHARACTERIZATION AND ANTIBACTERIAL ACTIVITIES OF HYDRAZONE SCHIFF BASE COMPOUNDS AND ITS DERIVATIVES

## (Sintesis, Pencirian dan Aktiviti Antibakteria Sebatian Bes Schiff Hidrazon dan Terbitannya)

Ruwaida Asyikin Abu Talip[1]*, Meng Guan Tay[1], Hashimatul Fatma Hashim[2]

[1]*Department of Chemistry, Faculty of Resource Science and Technology*
[2]*Department of Molecular Biology, Faculty of Resource Science and Technology*
*Universiti Malaysia Sarawak, 94300 Kota Samarahan, Sarawak, Malaysia*

**Corresponding author: ruwaidaasyikinabutalip@gmail.com*

Received: 21 August 2016; Accepted: 27 July 2017

**Abstract**

Biological activities (e.g. antibacterial) of hydrazone compound have received much attention from the synthetic chemists since last two decades. Herein, we would like to report the synthesis pathways as well as the spectroscopic characterization of three etherified hydrazone Schiff base compound, which were initiated from 2-hydroxyacetophenone. Hydrazone Schiff base compound was obtained through condensation reaction between 2-hydroxyacetophenone with benzhydrazide. Meanwhile the etherified derivatives of hydrazone Schiff base were prepared *via* Williamson ether synthesis under reflux condition. All the synthesized compounds were characterized using Fourier transformation infrared, UV-Vis and $^1$H nuclear magnetic resonance spectroscopy. In addition, the antibacterial activities of these compounds were also conducted using disc diffusion method against *Bacillus cereus* and *Escherichia coli*. The results are discussed in this present paper.

**Keywords:** hydrazone Schiff base, etherified derivatives, antibacterial

**Abstrak**

Aktiviti biologi (contoh: antibakteria) sebatian hidrazon telah menerima banyak perhatian daripada ahli kimia sintetik sejak dua dekad yang lalu. Di sini, kami ingin melaporkan kaedah sintesis serta pencirian spektroskopi tiga hidrazon yang telah di eterifasi, dimulakan dari 2-hidroksiasetofenon. Bes-Schiff hidrazon telah diperolehi melalui tindak balas pemeluwapan antara 2-hidroksiasetofenon dengan benzihidrazida. Sementara itu, terbitan yang telah di eterifasi daripada bes Schiff hidrazon telah disediakan melalui kaedah sintesis eter Williamson di bawah keadaan refluks. Semua sebatian yang disintesis dicirikan menggunakan inframerah transformasi Fourier, spektroskopi UV-Vis dan $^1$H magnetik nukleus resonan. Di samping itu, aktiviti antibakteria sebatian ini juga dijalankan dengan menggunakan kaedah cakera penyebaran terhadap *Bacillus cereus* dan *Escherichia coli*. Keputusan dibincangkan dalam kajian ini.

**Kata kunci**: bes Schiff hidrazon, terbitan yang telah dieterifasi, antibakteria

## Introduction

Hydrazones generally are prepared by reacting a stoichiometric amount of hydrazide (R-NH-$NH_2$) and a carbonyl (C=O) compound in suitable solvent under reflux condition [1]. Hydrazone Schiff base compounds and complexes have attracted considerable amount of attention since last two decades due to their pharmaceutical activities such as antiproliferative effect, antimicrobial, antibacterial, antifungal, anti-inflammatory [2], anticonvulsant, antitubercular, antiviral, antioxidative effects and inhibition of tumor growth [3]. These biological activities enable the hydrazone

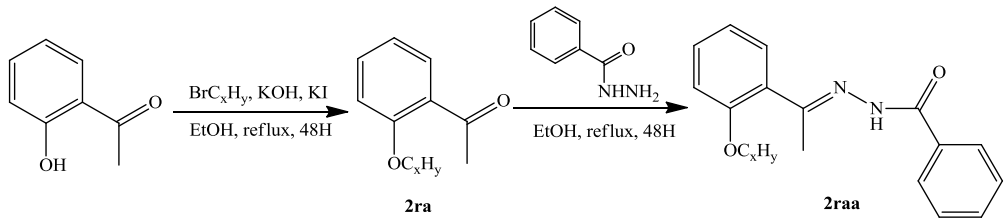
compounds and their complexes are suitable to be used as herbicides, insecticides, nematicides, rodenticides and plant growth regulators [4].

On the other hand, compounds with long carbon chain i.e. $C_8$ and above, received much interest from the researchers as they were reported to bear the potential as organogels in nanostructure formation [5], surfactant and in antibacterial [6]. In addition, the existence of the long carbon chain in the structure was reported to support the ability of the molecule to self-assemble into various architectures, enhance lipophilicity and antibacterial properties of the compound [6].

In this project, we report the synthesis of three hydrazone Schiff base compounds bearing carbon chains of $C_8H_{17}$, $C_{10}H_{21}$ and $C_{12}H_{25}$. The compounds were prepared by reacting etherified ketones with benzhydrazide *via* condensation reaction as shown in Scheme 1. Antibacterial study using disc diffusion method was conducted to find the correlation between the presences of long carbon chain with the antibacterial properties of the compound.

## Materials and Methods

All $^1$H Nuclear Magnetic Resonance (NMR) spectra were recorded by 500 MHz of JEOL ECA-500 using $CDCl_3$ and DMSO-$d_6$ as solvent and TMS as internal standard for $^1$H NMR. UV-Vis spectra were recorded using Jasco V-630 spectrophotometer. The Fourier Transformation Infrared (FTIR) were recorded using Thermo Scientific Nicolet iS10.




| Compound | x | y |
|---|---|---|
| **2ra8** | 8 | 17 |
| **2ra10** | 10 | 21 |
| **2ra12** | 12 | 23 |
| **2raa8** | 8 | 17 |
| **2raa10** | 10 | 21 |
| **2raa12** | 12 | 23 |
| **2raa** | 0 | 1 |

Scheme 1. Synthesis of hydrazone Schiff base compound and its derivatives

**Synthesis of etherified ketone: Synthesis of 2ra8**

1-Bromooctane (0.01mol) was added dropwise to the yellow ethanolic solution of 2-hydroxyacetophenone (0.01mol). Pellet of potassium hydroxide (0.01 mol) and powder of potassium iodide (1 g) were added into the mixture prior before mixture was heated under reflux for 48 hours. The resulting solution which appeared in red liquid was cooled, filtered and extracted using water and diethyl ether obtaining a thick yellow liquid. Yield: 60%.

**Synthesis of 2ra10**

The experimental procedure is similar to that in synthesis of **2ra8** except 1-bromooctane was replaced with 1-bromodecane. Compound **2ra10** was obtained as thick yellow liquid. Yield: 52%.

**Synthesis of 2ra12**

The experimental procedure is similar to that in synthesis of **2ra8** except 1-bromooctane was replaced with 1-bromododecane. Compound **2ra12** was obtained as thick yellow liquid. Yield: 75%.

**Synthesis of derivatives of hydrazone Schiff base: Synthesis of 2raa8**
Benzhydrazide (0.001 mol) was dissolved in 20 ml hot ethanol in a round bottom flask. To the ethanolic solution of benzhydrazide, yellow liquid of **2ra8** (0.001 mol) was added dropwise with constant stirring and heating. The mixture was heated under reflux for 48 hours in ethanol. Resulting yellow liquid was cooled and after 3 days slow evaporation, white solid obtained. Yield: 56%, white solid.

**Synthesis of 2raa10**
The experimental procedure is similar to that in synthesis of **2raa8** except **2ra8** was replaced with **2ra10** (0.001 mol). Yield: 60%, pale yellow solid.

**Synthesis of 2raa12**
The experimental procedure is similar to that in synthesis of **2raa8** except **2ra8** was replaced with **2ra12** (0.001 mol). Yield: 45%, yellow solid.

**Synthesis of parent compound, 2-hydroxyacetophenonebenzhydrazone, 2raa**
The experimental procedure is similar to that in synthesis of **2raa8** except **2ra8** was replaced with 2-hydoxyacetophenone. Yield: 89%, white powder.

**Antibacterial evaluation of the compounds**
The assay was carried out on the parent compound (**2raa**) and the derivatives (**2raa8 – 2raa10**) using disc diffusion method [7]. One colony of *Bacillus cereus* ATCC 33019 from a streak plate was inoculated in 20 ml of Luria-Bertani broth. After 16 hours of incubation, the optical density of the inoculums was measured and further diluted to achieve McFarland standard of 0.5. Using sterile cotton swab, agar plate was uniformly swabbed with diluted inoculums of the bacteria before sterile filter paper (6 mm) which were impregnated with different concentrations of **2raa** and the derivatives **2raa8-2raa10** (0.16%-0.2%) using DMSO as solvent were placed on the agar. The measurements of the inhibitory zones (mm) were taken after 24 hours of incubation. The procedures were conducted in another set for *Escherichia coli* ATCC 35150 and were performed in triplicate.

## Results and Discussion

**FTIR spectroscopy**
The parent compound namely, 2-hydroxyacetophenonebenzhydrazone (**2raa**) was prepared by reacting 2-hydroxyacetophenone with benzhydrazide under reflux using ethanol as solvent, whereas for the preparation of derivatives of hydrazone Schiff base compound, the starting material, 2-hydroxyacetophenone, was reacted with bromoalkane of C8, C10 and C12 carbons chain in the presence KOH and KI to obtain etherified ketones **2ra8 – 2ra12** (Scheme 1). The presence of long carbon chain in the compounds were indicated by the presence of C-H alkane stretching band in range of 2925.26 and 2852.54 $cm^{-1}$ in IR spectrum [8]. The OH stretch that presence in the starting material ketone is no longer detected in the etherified ketone, **2ra8 – 2ra12** (Figure 1).

The etherified ketones, **2ra8 – 2ra12** were then reacted with benzhydrazide under reflux using ethanol as the solvent to obtain the derivatives of hydrazone Schiff base compounds, **2raa8 – 2raa12**. The formation of the hydrazone Schiff base compounds were supported by the presence of stretching band at 3204 $cm^{-1}$attributed to the presence of N-H moiety in the hydrazone Schiff base [3]. On top of N-H band, the appearance of C=N stretching at 1600 $cm^{-1}$ also supported the formation of hydrazone Schiff base [3]. The major difference between parent ligand and the derivatives is the presence of alkane stretch at 2922.23 to 2825.42 $cm^{-1}$[8].

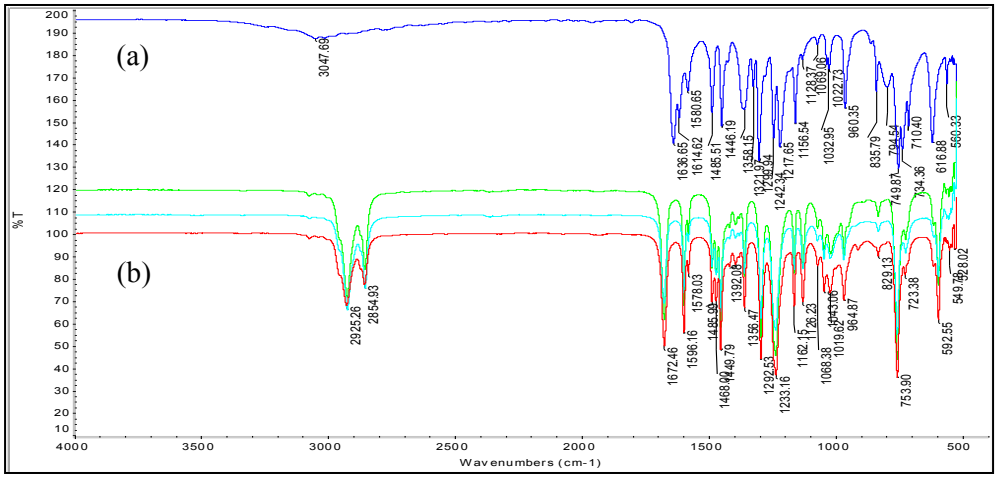



Figure 1. Infrared spectra of (a)starting material, 2-hydroxyacetophenone, (b)etherified 2-hydroxyacetophenone, **2ra8 – 2ra12**

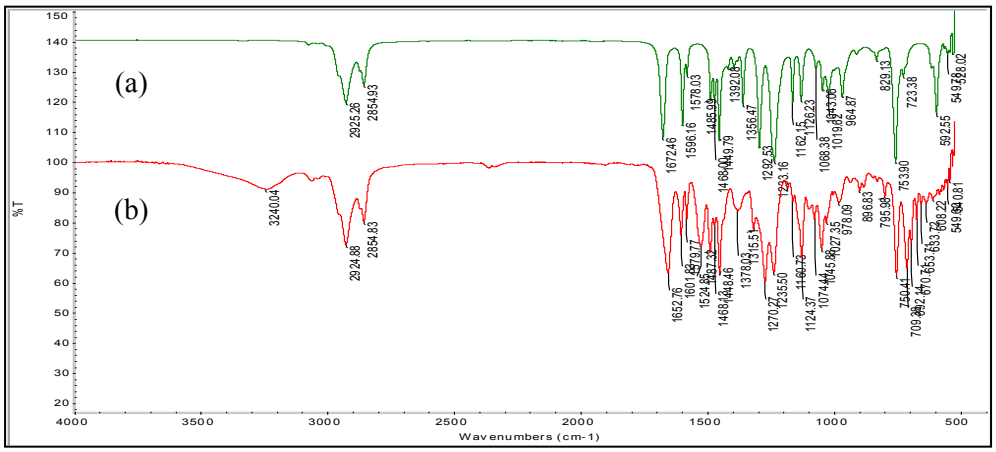



Figure 2. Infrared spectra of (a) etherified ketone, **2ra8** and (b) derivatives of Schiff base, **2raa8**

Table1. Summary of IR spectra stretches of the compounds

| | ***v*(NH) cm$^{-1}$** | ***v*(alkane) cm$^{-1}$** | ***v*(C=O) cm$^{-1}$** | ***v*(C=N) cm$^{-1}$** | ***v*(N-N) cm$^{-1}$** |
|---|---|---|---|---|---|
| 2-octyloxyacetophenone (**2ra8**) | - | 2925.26, 2854.93 | 1672.46 | - | - |
| 2-decyloxyacetophenone (**2ra10**) | - | 2923.25, 2853.57 | 1673.00 | - | - |
| 2-dodecyloxyacetophenone (**2ra12**) | - | 2922.31, 2852.54 | 1673.50 | - | - |
| 2-octyloxyacetophenone benzhydrazone (**2raa8**) | 3240.04 | 2925.88, 2854.83 | 1652.76 | 1601.80 | 896.00 |
| 2-decyloxyacetophenone benzhydrazone (**2raa10**) | 3239.09 | 2923.60, 2853.69 | 1654.94 | 1602.20 | 897.00 |
| 2-dodecyloxyacetophenone benzhydrazone (**2raa12**) | 3248.21 | 2922.23, 2825.42 | 1655.74 | 1600.40 | 881.00 |
| 2-hydroxyacetophenone benzhydrazone (**2raa**) | 3205.95 | - | 1647.71 | 1604.13 | 894.00 |

**UV-Vis**

The UV-Visible electronic spectra of parent compound, **2raa** and derivatives **2raa8 – 2raa12** were measured at room temperature in ethanol solution within range 200 to 800 nm. The data is summarized in Table 2. UV-Vis spectrum for **2raa** showed 2 peaks (Figure 3) at 283 and 328 nm which attributed toπ to π* and n to π* transitions indicating the presence of benzene ring and amino C=N respectively [7].

Table 2. Electronic absorption spectra data of the hydrazone Schiff base 2raa and derivatives

| Compound | $\lambda_m$(nm) |
|---|---|
| **2raa** | 283, 328 |
| **2raa8** | 273, 375 |
| **2raa10** | 274, 375 |
| **2raa12** | 275, 375 |

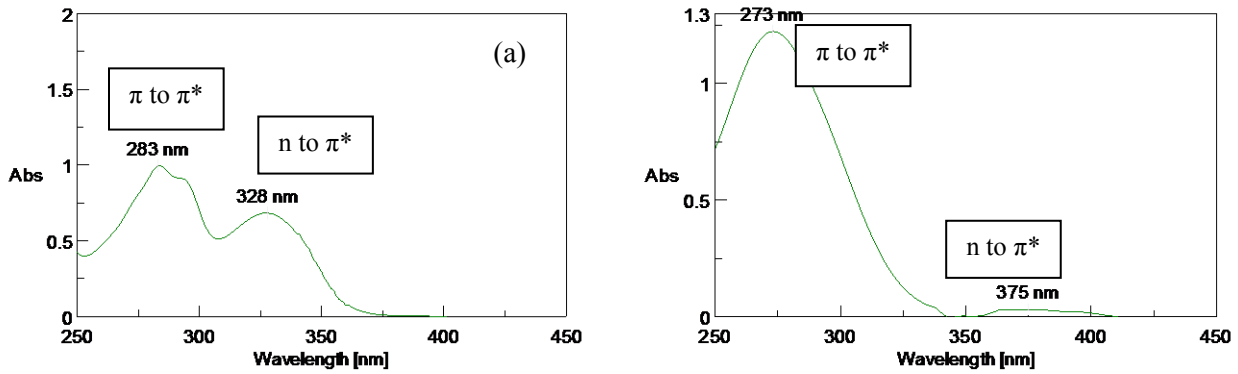



Figure 3. Electronic spectra of (a) parent compound (**2raa**), (b) derivative of Schiff base compound (**2raa8**)

Comparing the spectra of parent ligand and the derivatives, the peak of the derivatives shifted to a higher wavelength which is from 283 to 375 nm indicating the presence of long carbon chain in the moiety. It is known that the presence of electron donating group as substituent in aromatic molecule has significant effect on the absorption band in electronic spectra [8]. Long carbon chain is a donating group in which it decreased the energy gap between LUMO and HOMO in molecular orbital of azomethine C=N hence resulting in lower energy, increasing the wavelength as shown in the electronic spectra of the derivatives.

**Nuclear magnetic resonance spectroscopy**

Comparing the NMR spectra of starting material, 2-hydroxyacetophenone and etherified ketone, **2ra8 – 2ra12**, the presence long carbon chains in the **2ra8 – 2ra12** moiety were indicated by the presence of signals in range of 4.04 – 0.82 ppm [6] and disappearance of OH signal of hydroxyl group at meta position of starting material. Etherified ketones, **2ra8 – 2ra12** were reacted with benzhydrazide to form the derivatives of hydrazone Schiff base, **2raa8 – 2raa12** which were indicated by the presence of aromatic proton in the range of 7.56 – 6.97 ppm with the total number of nine protons [6] representing two benzene rings in the structure of the derivatives and also the presence of NH signal at 8.90 ppm [9]. The summary was tabulated in Table 3.

Table 3. Summary of significant $^{1}$H NMR spectral data for compounds

| Compounds | Chemical Shifts, $\delta$(ppm) | | | | |
|---|---|---|---|---|---|
| | OH | NH | CH aromatic | $CH_3$ | Alkane |
| **2ra8** | - | - | 7.71 – 6.91 (d, t) | 2.61 (s) | 4.01 (t) 1.82 – 0.85 (d, t) |
| **2ra10** | - | - | 7.73 – 6.93 (d, t) | 2.61 (s) | 4.02 (t),1.83 – 0.87 (d, t) |
| **2ra12** | - | - | 7.22 – 6.88 (d, t) | 2.60 (s) | 4.0 (t), 1.84 – 0.84 (d, t) |
| **2raa8** | - | 8.9 (s) | 7.56 – 7.01 (d, t) | 2.39 (s) | 3.99 (t), 1.72 – 0.84 (d, t) |
| **2raa10** | - | 8.93 (s) | 7.56 – 6.97 (d, t) | 2.39 (s) | 3.98 (t), 1.71 – 0.74 (d, t) |
| **2raa12** | - | 8.93 (s) | 7.56 – 7.01 (d, t) | 2.38 (s) | 3.97 (t), 1.78 – 0.84 (d, t) |
| **2raa** | 13.37 (s) | 11.34 (s) | 7.96 – 6.91 (d, t) | 3.35 (s) | 13.37 (s) |

*s: singlet, d: duplet, t: triplet*

**Antibacterial activities**

Disc diffusion method was used to evaluate the antibacterial properties of the hydrazone Schiff base compound, **2raa** and its long carbon chain derivatives, **2raa8 – 2raa12**. Gram positive bacteria, *Bacillus cereus* ATCC 33019 and gram-negative bacteria, *Escherichia coli* ATCC 35150 were used in this study. Compounds **2raa** and **2raa8 – 2raa12** were dissolved into the concentration of 0.16 to 0.020% using DMSO and the diameters of inhibition of the compounds were measured in mm unit. Inhibitions less than 10 mm is considered weak and insignificant, whereas more than 10mm is considered moderate and more than 16 mm is considered significant [10]. For *Bacillus cereus*, the derivatives of Schiff base, **2raa8 – 2raa12** showed better antibacterial properties than the parent compound (**2raa**) at all concentrations (Table 4).

Table 4. Results of antibacterial properties of compounds against *Bacillus cereus* ATCC 33019

| Compound | Diameter of Inhibition Zone (mm) | | | | |
|---|---|---|---|---|---|
| | Concentrations of Compounds in DMSO | | | | |
| | DMSO only | 0.16% | 0.08% | 0.04% | 0.02% |
| **2raa** | - | 10 | - | - | - |
| **2raa8** | | 15 | 12 | 11 | 10 |
| **2raa10** | | 15 | 10 | 10 | 10 |
| **2raa12** | | 11 | - | - | - |

The azomethine group of Schiff base compound is known to possess antibacterial properties as the group have the ability to form H bond with the intracellular components of the bacteria and interfere with the normal cell activity thus lead to the cell death [11]. The presence of long chain in moiety of the compound has increased the lipophilicity of the compound thus assist in the penetration through the peptidoglycan of the bacteria [6]. Synergistically, the effect of these two factors has enhanced the antibacterial properties of the compound. At the concentration of 0.16%, **2raa8** and **2raa10** showed better inhibition than **2raa12**. The antibacterial activity was found to increase with longer chain carbon until certain length where it reached cutoff effect where long chain no longer serves it purpose (as antibacterial agent) [6]. Hence, we can see that at 12 carbon compound namely **2raa12** has weaker inhibition compared to **2raa8** and **2raa10** at 0.16%. **2raa12** also showed insignificant inhibition at 0.02 – 0.08% concentration of compound. Meanwhile antibacterial screening against *Escherichia coli* showed that at all concentrations the incorporation of long chains into the compound (Table 5) has increased the antibacterial activities compared to the parent compound (**2raa**).

Table 5. Results of antibacterial properties of compounds against *Escherichia coli* ATCC 35150

| Compound | Diameter of Inhibition Zone (mm) | | | | |
|---|---|---|---|---|---|
| | Concentrations of Compounds in DMSO | | | | |
| | DMSO only | 0.16% | 0.08% | 0.04% | 0.02% |
| **2raa** | - | - | - | - | - |
| **2raa8** | | 11 | 10 | 10 | - |
| **2raa10** | | 16 | - | - | - |
| **2raa12** | | 16 | 14 | 12 | 11 |

## Conclusion

Hydrazone Schiff base compound and its long derivatives were successfully synthesized and characterized using $^{1}$H NMR, UV-Vis and FTIR. Antibacterial activities of the compounds were evaluated against *Bacillus cereus* and *Escherichia coli* using disc diffusion method where long carbon chain derivatives of hydrazone Schiff base (**2raa8 – 2raa12**) showed considerable antibacterial properties compared to the parent compound (**2raa**). The cooperative effect in between the ability of azomethine group of Schiff base compound to disrupt the normal processes of the bacterial cell by forming H bond with the intracellular components of the bacterial cell and the enhancement in the lipophilicity of the compound by the incorporation of long carbon chain into the moiety of the Schiff base compound that allow easy penetration through the peptidoglycan of the bacterial cell has increased the antibacterial properties of derivatives of the hydrazone Schiff base compound. This can be observed through the antibacterial activities result where the zone inhibition of Schiff base compound was increase upon incorporation of long carbon chain into the moiety of the compound.

## References

1. Solomon, T. W. G. and Fryhle, C. B. (2011). Organic chemistry asia: John Wiley & Sons (Asia) Private Limited.
2. Charles, D., Turner, J. H. and Redmond, C. (2005). Karyotypic profiles of women after clomiphenecitrate therapy. *International Journal of Obstetrics and Gynecology*, 80: 264 – 270.
3. Alhadi, A. A., Shaker, S. A., Yehye, W. A., Mohd Ali, H. and Abdullah, M. A. (2011). Synthesis, magnetic and spectroscopic studies of Ni(II), Cu(II), Zn(II) and Cd(II) complexes of a newly Schiff base derived from 5-bromo-2-hydroxybezylidene)-3,4,5 trihydroxybenzohydrazide. *Bulletin Chemical Society Ethiopia,* 26(1): 95 – 101.
4. Shelke, V. A., Jadhav, S. M., Shankarwar, S. G., Munde, A. S. and Chondhekar, T. K. (2011). Synthesis, characterization, antibacterial and antifungal studies of some transition and rare earth metal complexes of n-benzylidene-2-hydroxybenzohydrazide. *Bulletin Chemical Society Ethiopia,* 25(3), 381 – 391.
5. Tan, C., Su, L., Lu, R., Xue, P., Bao, C., Liu, X. and Zhao, Y. (2006). A family of low molecular weight organogelators based on long chain substituted benzoic acid hydrazides. *Journal of Molecular Liquids,* 124: 32 – 36.
6. Birnie, C. R., Malamud, D. and Schaare, R. L. (2000). Antimicrobial evaluation of *n*-alkyl betaines and *n* alkyl-*n*,*n*-dimethylamine oxides with variations in chain length. *American Society for Microbiology,* 44(9): 2514 – 2517.
7. Osowole, A. A. (2012). Synthesis, spectroscopic characterization, in-vitro antibacterial and anti proliferative activities of some metal(ii) complexes of 3,4-dihydronaphthalen-1(2h) one schiff base. *Experimental Clinical Sciences International Online Journal*, 11: 338 – 345.
8. Meng Guan, T., Zainab, N., Norazilawati, M. S., Siong Wan, F. and Mee Hing, T. (2011). A convenient way for the etherification of p-hydroxyacetophenone. *Research Bulletin, Faculty of Resource Science and Technology*, 2: 8 – 9.

9. Prasanna, M. K. and Kumar, K. P. (2013). Synthesis, characterisation and evaluation of antitumour and antifungal activities of transition metal complexes of 4-pyridinecarboxylic acid [(2-hydroxyphenyl) methylene] hydrazide and its 5-methoxy derivative. *International Journal Pharmceutical Biomedicine Science*, 4(1): 24 – 29.
10. Nam, S., Kang, S. and Chang, J. (2007). Synthesis and photopolymerization of photoreactive mesogens based on chalcone. *Macromolecular Research*, 15(1): 74 – 81.
11. Joseyphus, S. and Nair, M. (2008). Antibacterial and antifungal studies on some Schiff base complexes of zinc(II). *The Korean Society of Mycology*, 36(2): 93 – 98.

*Malaysian Journal of Analytical Sciences, Vol 21 No 5 (2017): 1176 - 1182*
*DOI: https://doi.org/10.17576/mjas-2017-2105-22*

MALAYSIAN JOURNAL OF ANALYTICAL SCIENCES
*Published by The Malaysian Analytical Sciences Society*
ISSN 1394 - 2506

# STEREOSELECTIVE REDUCTION OF 1-BENZYL-3,3-DIMETHYL-5-METHYLENEPYRROLIDINE-2,4-DIONE USING SODIUM BOROHYDRIDE WITH SELECTED METAL CHLORIDES

## (Tindak Balas Penurunan Stereoselektif 1-Benzil-3,3-Dimetil-5-Metilenapirolidina-2,4-Dion Menggunakan Natrium Borohidrat Dengan Logam Klorida Terpilih)

Nor Saliyana Jumali[1]*, Zurina Shaameri[2], Habsah Mohamad[3], Ahmad Sazali Hamzah[2]

[1]*Department of Chemistry, Kulliyyah of Science*
*International Islamic Universiti Malaysia, 25200 Indera Mahkota, Kuantan, Malaysia*
[2]*Institute of Science*
*Universiti Teknologi Mara, 40450 Shah Alam, Selangor, Malaysia*
[3]*Institute of Marine Biotechnology*
*Universiti Malaysia Terengganu, 21030 Kuala Nerus, Terengganu, Malaysia*

**Corresponding author: norsaliyana@iium.edu.my*

Received: 21 August 2016; Accepted: 27 July 2017

**Abstract**

1-benzyl-3,3-dimethyl-5-methylenepyrrolidine-2,4-dione is an intermediate product produced in the synthesis towards the natural bioactive compound, zopfiellamide A. This compound was synthesized via four main steps including dimethylations, addition with $CuBr_2$, cyclization with benzylamine and reaction with formaldehyde. The corresponding intermediate was an α,ß-unsaturated ketone having *exo*-alkene group, and it was subjected to reduction using sodium borohydride and selected metal chlorides. In this study, the effect and the hydride transfer mechanism of sodium borohydride-metal chlorides system in the reduction of 1-benzyl-3,3-dimethyl-5-methylenepyrrolidine-2,4-dione was investigated based on the stereochemical outcome of the product.

**Keywords**: stereoselective, reduction, metal borohydride, exo-alkene

**Abstrak**

1-benzil-3,3-dimetil-5-metilenapirolidina-2,4-dion ialah produk perantara yang terhasil di dalam sintesis terhadap sebatian aktif semulajadi, zopfiellamide A. Sebatian ini telah disintesis melalui empat langkah utama termasuklah metilasi berganda, penambahan kepada kuprum bromida, pengkitaran dengan benzilamina dan tindak balas dengan formaldehid. Sebatian perantara ini merupakan keton α,ß-tidaktepu yang mempunyai kumpulan ekso-alkena, dan ia telah didedahkan kepada penurunan menggunakan natrium borohidrida dan logam klorida terpilih. Di dalam kajian ini, kesan dan mekanisma perpindahan hidrida oleh sistem natrium borohidrida-logam klorida di dalam menurunkan 1-benzil-3,3-dimetil-5-metilenapirolidina-2,4-dion telah dikaji berdasarkan stereokimia produk yang terhasil.

**Kata kunci:** stereoselektif, penurunan, logam borohidrida, ekso-alkena

## Introduction

Reduction is one of the important reaction in chemistry. Several functional groups such as aldehydes, ketones, carboxylic acids, esters, lactones, amides, lactams, imines and ammonium salts can be reduced by using an

appropriate reducing agent. Sodium borohydride ($NaBH_4$) is one of the reducing agent which offers good selectivity and have better solubility in most common organic solvents [2]. Its non-hazardous property allow its application in the efficient synthesis of (*R*)-salmeterol, which used to prevent bronchospasm in asthma patient [1]. It also have been used in industry to synthesized *d*-Biotin, also known as vitamin H, which is important additional nutrient for humans and animals [2].

Besides, $NaBH_4$ is also very versatile reducing agent. Its strength and selectivity can be altered by changing its countercation with other metal [3, 4]. For example, zinc-borohydride ($Zn(BH_4)_2$) can be prepared *in-situ* by adding $ZnCl_2$ into a THF slurry of $NaBH_4$ or to a glyme solution [5]. $Zn(BH_4)_2$ was known as a chemoselective reducing agent which capable of reducing ketones in the presences of enone [4, 5]. Its stereoselectivity was due to better coordinating ability of $Zn^{2+}$ lewis acid [4] via chelation-controlled [1, 5]. Meanwhile, similar reduction systems such as the $NaBH_4/CaCl_2$ reduction system, had been utilized in the reduction of phenacyl phenylglycinol derivatives, in which this reaction gave predominantly one diastereomers [1]. Another reducing reagent which offers excellent chemoselectivity is $Ce.Cl_3.7H_2O/NaBH_4$ which also known as Luche reagent. Davis et al. had used this reagent and was successfully reduced pyrrolidine enone to allylic alcohol in 83% yield [6].

In this study, 1-benzyl-3,3-dimethyl-5-methylenepyrrolidine-2,4-dione (**1**) was subjected to reduction using $NaBH_4$, with and without the presence of metal salts. The metal salts used in this study were $CaCl_2$, $ZnCl_2$, $MgCl_2$ and $MnCl_2$ respectively. $NaBH_4$/metal chloride reduction systems were produced by adding $NaBH_4$ to the reaction mixture containing these metal salts. The effectiveness and the stereochemical control of these reduction systems was mainly depends on the metals used. The stereochemical outcome of the product will reveal the influence and the effect of these metals in the reduction mechanism.

## Materials and Methods

### General

$^1H$ and $^{13}C$ Nuclear Magnetic Resonane (NMR) spectra were measured at 300 and 75 MHz, respectively. The NMR spectra were recorded in deuterated solvents on Bruker NMR 300 MHz, and the assignments were made on the basis of chemical shifts expressed in δ (ppm) units. Infrared spectra were recorded at Perkin Elmer instruments, Spectrum 2000 or Spectrum One, both in the spectral range of 4000 to 400 $cm^{-1}$. All samples were prepared using the KBr sampling method. Melting points were determined by either an Electrothermal melting point apparatus and were uncorrected. Polarimetry was performed using a Bellingham + Stanley Ltd ADP 410 Polarimeter with a cell of 10 cm in length and 4 mm internal diameter and the observed rotation was measured at 589 nm.

### General procedure for reduction using $NaBH_4$.

$NaBH_4$ (0.05 g, 1.57 mmol) was added in one portion into a cooled solution of 1-benzyl-3,3-dimethyl-5-methylenepyrrolidin-2,4-dione (**1**) (0.30 g, 1.31 mmol) in anhydrous methanol (30 ml), at 0 °C under nitrogen atmosphere. The mixture was stirred at 0 °C for four hours. The solvent was evaporated, and the residue was dissolved with DCM and partitioned against $NH_4Cl$ solution. The organic fraction was collected, washed with water, dried over anhydrous $MgSO_4$, filtered and concentrated in vacuum.

### General procedure for reduction using $NaBH_4$/metal chloride system.

Metal chloride (2.0 eq) was added into a stirred solution of 1-benzyl-3,3-dimethyl-5-methylenepyrrolidin-2,4-dione (**1**) (1.0 eq) in anhydrous methanol (20 ml). The mixture was stirred at room temperature under nitrogen atmosphere for 30 minutes. The mixture was then cooled to 0 °C and $NaBH_4$ (1.0 eq) was slowly added and stirred for another 30 minutes (except for $ZnCl_2$, the reaction was stirred for overnight). The solvent was evaporated and the doughy residue was extracted with DCM and partitioned against $NH_4Cl$ solution. The organic fraction was collected, washed with water, dried over anhydrous $MgSO_4$, filtered and concentrated in vacuum.

### (*R*)-(-)-1-Benzyl-3,3,5-trimethylpyrrolidine-2,4-dione (2 and its C5 epimer, 2a)

These products were obtained from the reduction using $NaBH_4$, $NaBH_4/CaCl_2$ and $NaBH_4/MnCl_2$ systems. The product was purified through column chromatography with hexane and ethyl acetate in 1:1 ratio.

**(*R*)-(+)-1-Benzyl-3,3,5-trimethylpyrrolidine-2,4-dione (2)**
This product was obtained from the reduction using $NaBH_4/MgCl_2$ and $NaBH_4/ZnCl_2$ systems. The product was purified through column chromatography with hexane and ethyl acetate in 1:1 ratio.

## Results and Discussion

**Characterization study: (*R*)-(-)-1-Benzyl-3,3,5-trimethylpyrrolidine-2,4-dione**
The mixture was obtained as a white powder, m.p: 102.5 °C. IR v $cm^{-1}$: 3246 (OH stretch), 2927 (C-H stretch), 1658 (C=O), 1417 (C-C Ar stretch), 1101 (C-O stretch). Compound **2**; δH ($CDCl_3$, 300 MHz): 1.19 (3H, s, $CH_3$), 1.22 (3H, s, $CH_3$), 1.34 (3H, s, $CH_3$), 3.68 (1H, s, $CHCH_3$), 4.25 - 4.30 (1H, d, J = 15.9 Hz, CHHPh), 4.59 (1H, br s, OH enol), 4.74 – 4.79 (1H, d, J = 18.0 Hz, CHHPh), 7.23-7.32 (5H, m, Ar H). $^{13}C$ ($CDCl_3$, 75 MHz): 18.74 ($CH_3$), 23.39 ($CH_3$), 24.32 ($CH_3$), 42.00 ($CH_2Ph$), 42.89 (quat. C), 79.16 ($CHCH_3$), 87.56 (quat. C-alkene), 126.64, 126.86, 128.07 (Ar CH), 138.43 (quat. Ar C), 180.42 (C=O). C5 epimer, **2a**; δH ($CDCl_3$, 300 MHz): 1.13 (3H, s, $CH_3$), 1.24 (3H, s, $CH_3$), 1.26 (3H, s, $CH_3$), 3.85 (1H, s, $CHCH_3$), 4.26 – 4.31 (1H, d, J = 15.0 Hz, CHHPh), 4.59 (1H, br s, OH enol), 4.67 – 4.72 (1H, d, J = 15.0 Hz, CHHPh), 7.23-7.32 (5H, m, Ar H). $^{13}C$ ($CDCl_3$, 75 MHz): 18.35 ($CH_3$), 21.00 ($CH_3$), 23.82 ($CH_3$), 41.51 ($CH_2Ph$), 43.69 (quat. C), 82.44 ($CHCH_3$), 90.85 (quat. C-alkene), 126.63, 127.11, 128.01 (Ar CH), 138.65 (quat. Ar C), 178.90 (C=O). M/S: Requires $M^+$ 231.13; Found (1) $M^+$ 231.1, $C_{14}H_{17}NO_2$, m/z: 91.1, 134.1, 70.1, 99.1; Found (2) $M^+$ 231.2, $C_{14}H_{17}NO_2$, m/z: 91.1, 131.1, 65.1, 174.1.

**(*R*)-(+)-1-Benzyl-3,3,5-trimethylpyrrolidine-2,4-dione (2)**
The product obtained as a white precipitate m.p: 106.2 °C. IR v $cm^{-1}$: 3246 (OH stretch), 2927 (C-H stretch), 1658 (C=O), 1417 (C-C Ar stretch), 1101 (C-O stretch). Compound **2** and its enol tautomer; δH ($CDCl_3$, 300 MHz): 1.19 (3H, s, $CH_3$), 1.22 (3H, s, $CH_3$), 1.34 (3H, s, $CH_3$), 3.68 (1H, s, $CHCH_3$), 4.25 – 4.30 (1H, d, J = 15.9 Hz, CHHPh), 4.60 (1H, br s, OH enol), 4.74 – 4.79 (1H, d, J = 15.0 Hz, CHHPh), 7.23-7.33 (5H, m, Ar H). $^{13}C$ ($CDCl_3$, 75 MHz): 18.74 ($CH_3$), 23.38 ($CH_3$), 24.32 ($CH_3$), 42.00 ($CH_2Ph$), 42.90 (quat. C), 79.18 ($CHCH_3$), 87.57 (quat. C-alkene), 126.64, 126.87, 128.07 (Ar CH), 138.44 (quat. Ar C), 180.42 (C=O). M/S: Requires $M^+$ 231.13; Found (1) $M^+$ 231.2, $C_{14}H_{17}NO_2$,; m/z: 91.1, 134.1, 70.1, 175.1. Found (2) $M^+$ 231.1, m/z: 91.1, 131.1, 65.1, 96.8.

In this study, the reduction of 1-benzyl-3,3-dimethyl-5-methylenepyrrolidine-2,4-dione (**1**) was performed according to Fraga and Barreiro's method [3]. A reduction of (**1**), with $NaBH_4$ without metal chloride was served as a control reaction. The result obtained was used to evaluate the effect of metal chloride in the reduction mechanism. In this reduction, compound (**2**) was furnished as a white powder in 34% yield.

In the reduction using $NaBH_4$/metal chloride system, one portion of $NaBH_4$ was added to a solution containing (**1)** and one equivalent of anhydrous metal chloride, in anhydrous methanol. The mixture was stirred at 0 ºC for 30 minutes except for $ZnCl_2$, whereby the reaction was stirred for overnight. The products were purified through column chromatography and the results were presented in Table 1.

Table 1. Reduction of 1-Benzyl-3,3-dimethyl-5-methylenepyrrolidine-2,4-dione (**1**) using $NaBH_4$/metal chloride systems

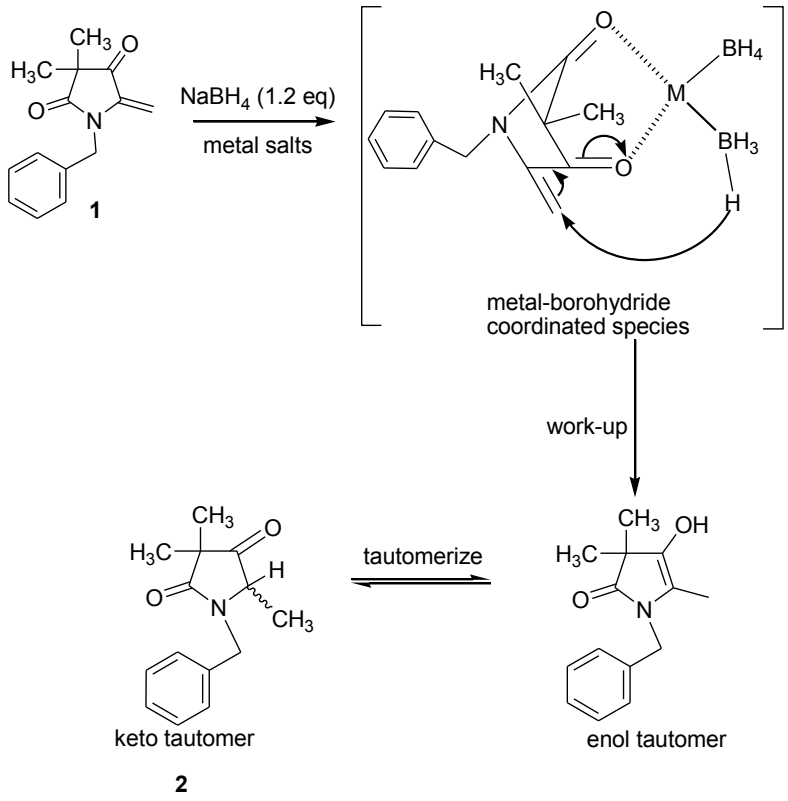
| Condition | Yield (%) |
|---|---|
| $NaBH_4$, anh. $CaCl_2$, anh. MeOH (0 ºC, 30 minutes) | 62 |
| $NaBH_4$, anh. $MnCl_2$, anh. MeOH (0 ºC, 30 minutes) | 73 |
| $NaBH_4$, anh. $MgCl_2$, anh. MeOH (0 ºC, 30 minutes) | 45* |
| $NaBH_4$, anh. $ZnCl_2$, anh. MeOH (0 ºC, overnight) | 40* |

*Notes: *no repeating signals were observed in the NMR spectrum*

The results showed that the presence of these metal chloride did not affect the product outcome, instead had increased the yields of compound (**2**). In all cases, 1,4-addition product was predominate over 1,2-reduction product. The reduction systems employed had given a chemoselective product. The reduction occurred

chemoselectively at ß–carbon at C5 (*exo*-alkene) rather than at the carbonyl carbon at C3 position. Normally, isolated alkene did not undergo reduction with $NaBH_4$ due to lack of polarity, however, in this case, this enone group was activated by an electron withdrawing group present in this compound (carbonyl group). The delocalization of electrons through resonance increases the electrophilicity of this ß-carbon, enable the hydride (nucleophile) to mainly transfer to this position.

In terms of the reaction mechanism, the expected metal-borohydride coordinated species was involved during the hydride transfer, which led to the formation of product [3]. In this proposed reaction mechanism, $NaBH_4$ was reacted with metal chloride (as chelating agent) to form metal-borohydride coordinated complex. This complex had formed a chelation between both oxygen of the carbonyl at C4 and the oxygen of carbonyl amide at C2. Since the electrophilicity of the ß-carbon was increased, the hydride was transferred to this carbon. The usual work-up procedure was led to the formation of enol tautomer of compound (**2)**, which then tautomerized to its keto tautomer, (**2)** (refer to Scheme 1).




Scheme 1. Proposed reduction mechanism for $NaBH_4$/ metal chloride systems

Based on $^1H$ and $^{13}C$ NMR spectra, the reduction of prochiral compound (**1**) using $NaBH_4$, $NaBH_4/CaCl_2$ and $NaBH_4/MnCl_2$ systems showed poor stereochemical control compared to $NaBH_4/MgCl_2$ and $NaBH_4/ZnCl_2$ reduction systems. The spectrum for reduction using $NaBH_4$, $NaBH_4/CaCl_2$ and $NaBH_4/MnCl_2$ systems, showed repeated signals, which indicates the presence of a mixture of compound **2** and its C5 epimer (**2a**). In Figure 1, two sets of signals (doublets of doublets) attributed to benzylic protons were observed; one set resonated at $\delta_H$ 4.25 – 4.30 and $\delta_H$ 4.74 – 4.78; and a second set resonated at $\delta_H$ 4.26 – 4.31 and $\delta_H$ 4.67 – 4.72 respectively. Two singlets which correspond to methine protons at C5 and C5'were resonated at $\delta_H$ 3.68 and 3.85. Repeating signals for methyl protons at C13, C14, C15, C13', C14' and C15'also appeared between $\delta_H$ 1.13 to 1.34. All 10 H's of aromatic protons for the mixture were observed between $\delta_H$ 7.22 – 7.30. The appearance of a broad signal at $\delta_H$ 4.59 was

indicated the presence of enol tautomer, in which the signal was corresponds to the hydroxyl proton at C4 (see Figure 1).

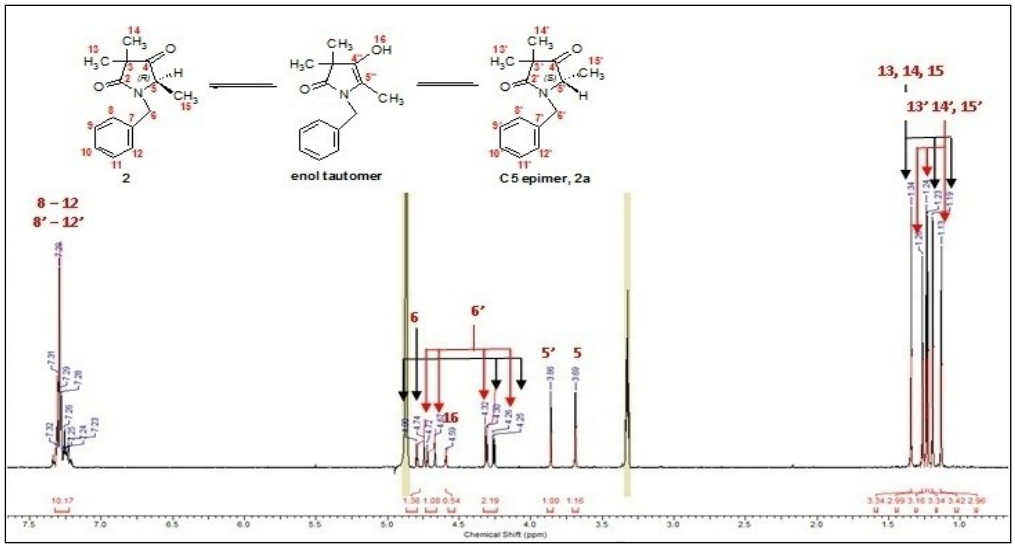



Figure 1. $^{1}$H NMR spectra for reduction using $NaBH_4$, $NaBH_4/CaCl_2$ and $NaBH_4/MnCl_2$ systems

The $^{13}$C NMR spectrum for reduction using $NaBH_4$, $NaBH_4/CaCl_2$ and $NaBH_4/MnCl_2$ systems in Figure 2 also show similar repeating pattern. The signals for methyl (at C13, C14, C15, C13',C14'and C15'), benzylic (C6 and C6') and methine (C5 and C5') carbons were observed between δ 18.35 to 24.32; δ 41.51 and 42.00; and δ 79.16 and 82.44 respectively. The enol's quatenary carbon (C5") was resonated at δ 87.56. Signals for aromatic protons also repeated around δ 126.63–138.65. In this spectrum, only two carbonyl carbon signals at C2 and C2', were observed. Two signals for carbonyl carbon at C4 and C4', does not appear in this spectrum. This might be due to rapid tautomerization process between keto and enol form of compound (**2**), which causes the signals hard to be detected. The enol's quaternary carbon (at C-5'") can be observed at δ 87.57.

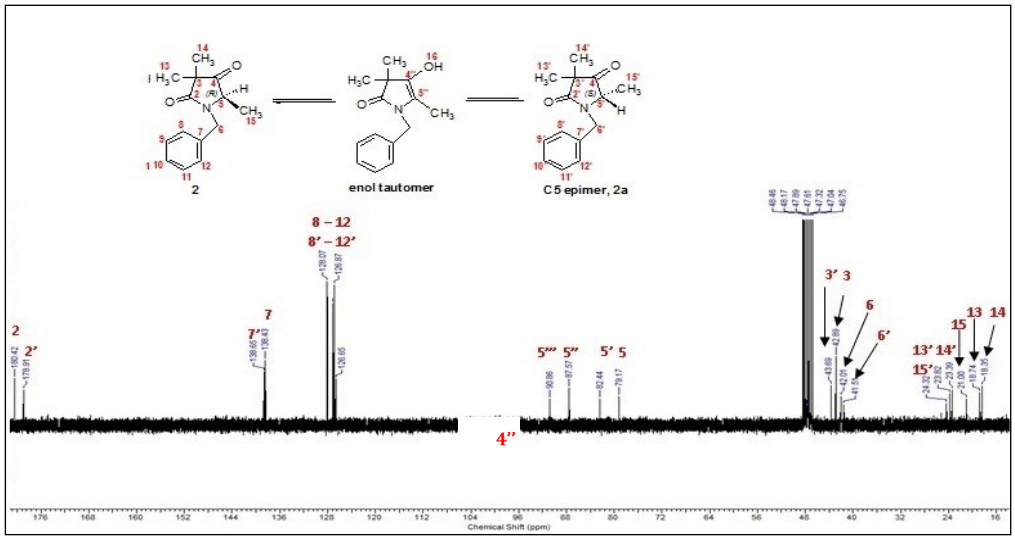



Figure 2. $^{13}$C NMR spectra for reduction using $NaBH_4$, $NaBH_4/CaCl_2$ and $NaBH_4/MnCl_2$ systems

Meanwhile, the reduction of prochiral compound (**1**), with $NaBH_4/MgCl_2$ and $NaBH_4/ZnCl_2$ reduction systems, was resulted in a single compound (**2**) (stereoselective reaction). Both $^1H$ and $^{13}C$ NMR spectra in Figure 3 and 4, showed no repeated signals. This result concludes that, the presences of respective metal chloride in the reducing systems impart better stereochemical control in the reduction mechanism.

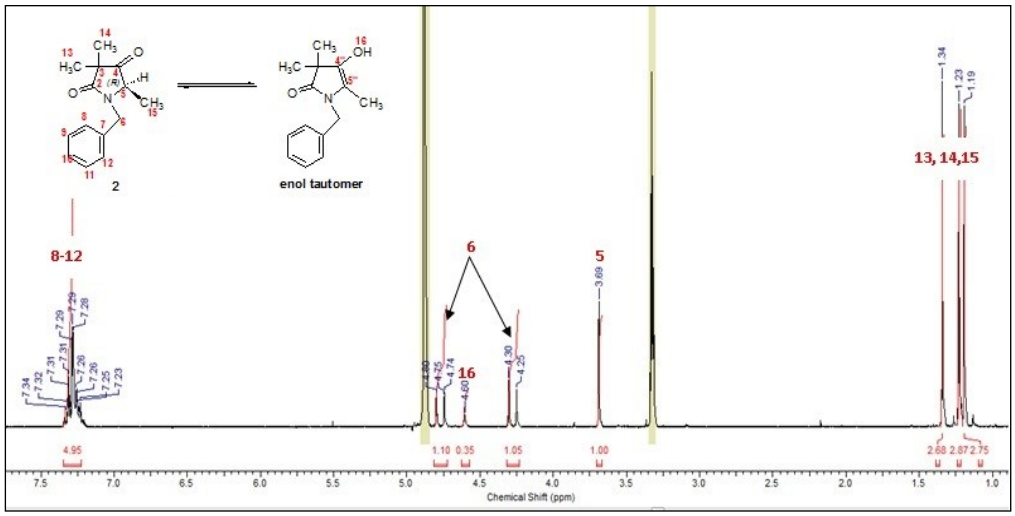



Figure 3. $^1H$ NMR spectra for reduction using $NaBH_4$, $NaBH_4/MgCl_2$ and $NaBH_4/ZnCl_2$ systems

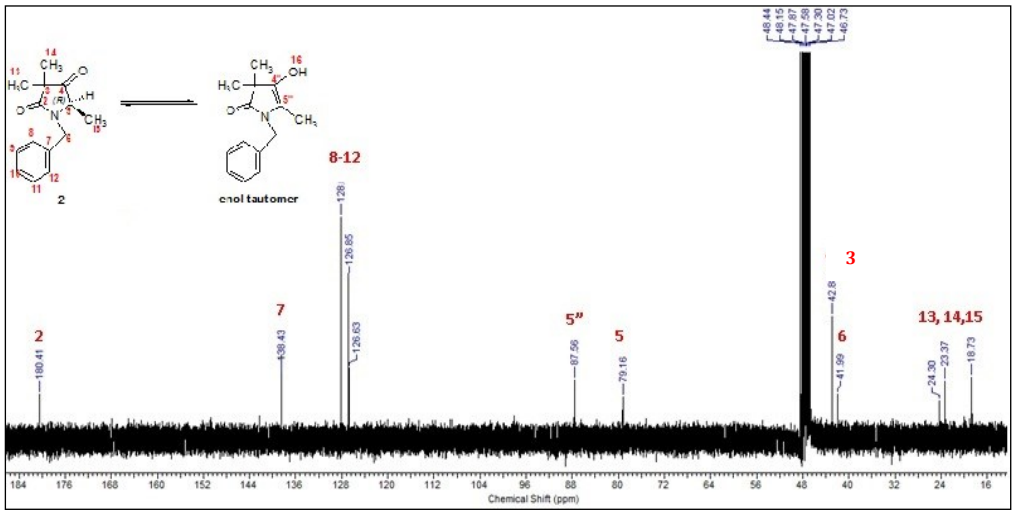



Figure 4. $^{13}C$ NMR spectra for reduction using $NaBH_4/MgCl_2$ and $NaBH_4/ZnCl_2$ reduction system

The stereoselectivity of these reduction systems also can be explained in terms of the size and the chelation effect of the metal countercation used. In this study, bigger countercation ($Ca^{2+}$ and $Mn^{2+}$ is bigger than $Mg^{2+}$ and $Zn^{2+}$ respectively) resulted in a mixture as compared to smaller countercation. This might be due to the small size of countercations ($Mg^{2+}$ and $Zn^{2+}$) have better coordinating ability which imparts selectivity control during the hydride transfer mechanism [4]. This allows the hydride to transfer mainly on one side only (*si*-face) and produce compound (**2**). Meanwhile, big size of countercations cannot perfectly occupy (poor coordinating ability) certain position at a

certain time, and thus caused the hydride to transfer equally from both sides (*re*- or *si*-face). This led in a racemic mixture of compound (**2**) and its C5 epimer, (**2a**) (50:50 ratio based on $^1$H NMR spectra).

## Conclusion

The reduction of prochiral compound (**1**) using $NaBH_4$, $NaBH_4/CaCl_2$, $NaBH_4/MnCl_2$, $NaBH_4/MgCl_2$ and $NaBH_4/ZnCl_2$ reduction systems, had resulted in a chemoselective reduction. However, only reduction using $NaBH_4/MgCl_2$ and $NaBH_4/ZnCl_2$ systems showed high stereoselectivity as the systems produced only a single compound. In the evaluation on the effect of metal chloride in the reduction mechanism, it can be deduced that big countercation has low stereochemical control and resulted in a mixture due to poor coordinating ability in comparison with small countercations.

## Acknowledgement

We would like to thank the Universiti Teknologi MARA (UiTM) for providing the facilities to conduct this research, and also International Islamic University Malaysia (IIUM) and Kementerian Pengajian Tinggi Malaysia for the fellowship.

## References

1. Bream, R. N., Ley, S. V., McDermott, B. and Procopiou, P. A. (2002). A mild enantioselective synthesis of (*R*)-salmeterol via sodium borohydride-calcium chloride asymmetric reduction of a phenacyl phenylglycinol derivative. *Journal of Chemical Society, Perkin Transaction. I*, 20: 2237 –2242.
2. Windey, G., Seper, K. and Yamamoto, J. H. (2003), Chemoselective and stereoselective reductions with modified borohydride reagents. *ChemInform*, 34(1): 15 – 18.
3. Fraga, C. A. and Barreiro, E. J. (1995). Studies toward the diastereoselective reduction of 2-alkoxycarbonyl-2-allyl-cyclopentanone derivatives with boron hydrides. *Synthetic Communications*, 25(8): 1133 – 1144.
4. Narasimhan, S. and Balakumar, R. (1998). Synthetic applications of zinc borohydride. *Aldrichimica Acta*, 31(1): 19 – 26.
5. Oishi, T. and Nakata, T. (1984). An introduction of chiral centers into acyclic systems based on stereoselective ketone reduction. *Accounts of Chemical Research*, 17(9): 338 – 344.
6. Davis, F. A., Zhang, J., Qiu, H. and Wu, Y. (2008). asymmetric synthesis of cis- and trans-2,5-disubstituted pyrrolidines from 3-oxo pyrrolidine 2-phosphonates: synthesis of (+)-preussin and analogs. *Organic Letters*, 10(7): 1433 – 1436.

*Malaysian Journal of Analytical Sciences, Vol 21 No 5 (2017): 1183 - 1194*
*DOI: https://doi.org/10.17576/mjas-2017-2105-23*

MALAYSIAN JOURNAL OF ANALYTICAL SCIENCES
*Published by The Malaysian Analytical Sciences Society*
ISSN 1394 - 2506

# SYNTHESIS AND ANTIBACTERIAL ACTIVITY OF AZO AND ASPIRIN-AZO DERIVATIVES

## (Sintesis dan Aktiviti Antibakteria Terhadap Azo dan Terbitan Azo-Aspirin)

Zainab Ngaini and Ho Boon Kui*

*Department of Chemistry,*
*Faculty of Resource Science and Technology,*
*Universiti Malaysia Sarawak, 94300 Kota Samarahan, Sarawak, Malaysia*

**Corresponding author: boonkui98@hotmail.com*

Received: 21 August 2016; Accepted: 27 July 2017

**Abstract**

A series of azo derivatives (**1a-e**) were synthesized *via* coupling reaction with of overall yield 58 – 72% while aspirin-azo derivatives (**2a-e**) were prepared by esterification reaction of aspirin and azo derivatives (**1a-e**) with overall yield 38 – 75%. In this study, the structures of synthesized compounds were characterized using elemental analysis (CHN), nuclear magnetic resonance ($^{1}$H NMR and $^{13}$C NMR) and Fourier Transform Infrared (FTIR) spectroscopy. The synthesized compounds were tested on antibacterial activity against *Escherichia coli* ATCC 25922 and *Staphylococcus aureus* S48/81 *via* turbidimetric kinetic method. The azo derivative–substituted fluorine, **1d** showed the highest antibacterial activities against *Escherichia coli* ATCC 25922 and *Staphylococcus aureus* S48/81 compared with other synthesized compounds. However, synthesized aspirin–azo derivatives (**2a-e**) showed weak antibacterial activity against tested bacteria due to bulky molecular structure thus hindered the penetration into bacterial cell wall.

**Keywords**: aspirin, azo derivatives, turbidimetric kinetic, *Escherichia coli* ATCC 25922, *Staphylococcus aureus* S48/81

**Abstrak**

Satu siri terbitan azo **(1a-e)** telah dihasilkan melalui tindak balas gandingan dengan hasil keseluruhan 58 – 72% dan terbitan azo-aspirin **(2a-e)** telah disediakan melalui tindak balas esterifikasi aspirin dan terbitan azo **(1a-e)** dengan hasil keseluruhan 38 – 75%. Dalam kajian ini, struktur sebatian yang dihasilkan dicirikan menggunakan analisis unsur (CHN), resonans magnetik nukleus ($^{1}$H NMR dan $^{13}$C NMR) dan spektroskopi inframerah transformasi Fourier . Kesemua sebatian yang dihasilkan telah diuji pada aktiviti anti-bakteria terhadap *Escherichia coli* ATCC 25922 dan *Staphylococcus aureus* S48 / 81 melalui kaedah kinetik turbidimetrik. Terbitan azo tertukarganti fluorin **1d** menunjukkan aktiviti antibakteria tertinggi terhadap *Escherichia coli* ATCC 25922 dan *Staphylococcus aureus* S48/81 berbanding dengan sebatian lain. Walau bagaimanapun, terbitan azo aspirin **(2a-e)** menunjukkan aktiviti anti-bakteria yang lemah terhadap bakteria diuji disebabkan oleh struktur molekul yang besar itu telah menghalang penembusan ke dalam dinding sel bakteria.

**Kata kunci**: aspirin, terbitan azo, kinetik turbidimetrik, *Escherichia coli* ATCC 25922, *Staphylococcus aureus* S48/81

## Introduction

Aspirin is a white crystalline weak acidic product that has analgesic and anti-inflammatory properties [1, 2]. It is also used to prevent cardiovascular disease and cancer. The compound has an antiplatelet effect by inhibiting the production of thromboxane, which under normal circumstances binds platelet molecules together to create a patch over damaged walls of blood vessels [3]. However, aspirin may cause some side effects such as vomiting and

stomach bleeding after prolonged usage [4]. Research on aspirin has been studied extensively. Chemical modification of aspirin and its derivatives have improved its pharmacological properties with less gastrointestinal toxicity [5]. Aspirin derivatives were also reported to apply many biological activities such as antibacterial [6], antithrombic [7], antiplatelet and anticancer properties [8].

Azo is a compound which consist of either an aryl or alkyl group functional group (R-N=N-R'). The most stable azo drivatives contain two aryl groups. The presence of N=N functional group is claimed to contribute to various applications in food [9], paints [10] and cosmetics [11]. In addition, azo derivatives have been reported to play important roles in many biological processes such as antibacterial [12], antifungal [13], antiviral [14] and anticancer activities [15], which stimulate the interest in the synthesis of a series compound containing aspirin with azo moiety.

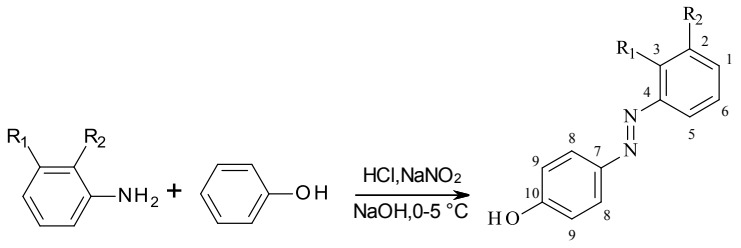
In this paper, we report the synthesis of aspirin-azo derivatives **2a-e** by reaction of aspirin with azo derivatives **1a-e** *via* esterification. The preparation of halogenated azo derivatives **1a-e** was carried out *via* diazotiation followed by coupling reaction. The antibacterial activity of the synthesized azo derivatives **1a-e** and aspirin-azo derivatives **2a-e** against *Escherichia coli* ATCC 25922 and *Staphylococcus aureus* S48/81 have also been characterized.

**Materials and Methods**

Melting point was measured by Stuart SMP3 melting point apparatus and the elemental analysis was determined by flash EA1112 analyzer. IR spectra ($\nu$/cm$^{-1}$) were recorded on a Perkin Elmer GX spectrometer with potassium bromide pellet (KBr). $^{1}$H and $^{13}$C NMR spectra were recorded at 500 MHz on a JEOL.ECA NMR spectrometer.

**General method to synthesis of azo derivatives 1a-e**

The general method for synthesizing azo derivatives **1a-e** was shown in (Scheme 1). A mixture of HCl (2 M, 6 mL) and aniline derivatives (0.46 g, 5 mmol) was added with sodium nitrite solution (1 M, 2 mL) in water at 0 –5 °C slowly. Sodium hydroxide (0.4 g, 10 mmol) and phenol (0.47 g, 5 mmol) dissolved in water (10 mL) stirred and cooled to 0 – 5 °C. The diazo salt compound was added slowly into phenol solution at 0 – 5 °C and stirred for 40 minutes. The mixture was acidified by adding 2 M HCl. The precipitate formed was filtered and washed with cold water. The crude product was purified by crystallization from hot ethanol to give **1a-e**.




**1a-e**

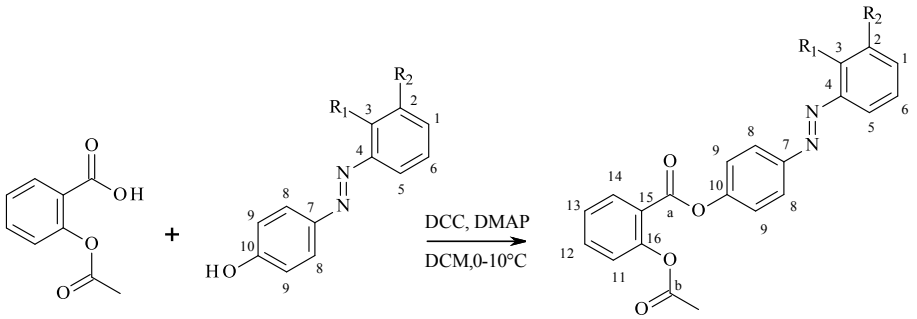
**1a**, $R_1$=H, $R_2$=H
**1b**, $R_1$=H, $R_2$=F
**1c**, $R_1$=H, $R_2$=Cl
**1d**, $R_1$=F, $R_2$=H
**1e**, $R_1$=Cl, $R_2$=H

Scheme 1. Synthesis of azo derivatives **1a-e**

**General method to synthesis of aspirin-azo derivatives 2a-e**

The aspirin-azo derivatives **2a-e** can be synthesized from the reaction of aspirin and azo derivatives **1a-e** *via* esterification reaction (Scheme 2). Azo derivatives **1a-e**, (3 mmol) was dissolved in dichloromethane (20 mL) and added into the flask a solution containing acetylsalicylic acid (0.54 g, 3 mmol) in dichloromethane (20 mL) under ice batch. The mixture was added with dicyclohexylcarbodiimide (DCC) (0.62, 3 mmol) followed by N,N-

dimethyl-4-aminopyridine (DMAP) (0.37 g, 3 mmol). The reaction mixture was stirred for 4 hours at 0 – 10 ˚C and product formation was accompanied by thin layer chromatography (TLC) analysis using ethyl acetate/hexane (1:4). The white precipitate of by-product (dicyclohexylurea) was filtered off under suction. The filtrate was allowed to be evaporated under vacuum to form precipitate. The precipitate was purified by flash column chromatography on silica gel, using hexane as eluent. The product formed was recrystallized from hot ethanol to give **2a-e**.




**1a-e**

**1a**, $R_1$=H, $R_2$=H
**1b**, $R_1$=H, $R_2$=F
**1c**, $R_1$=H, $R_2$=Cl
**1d**, $R_1$=F, $R_2$=H
**1e**, $R_1$=Cl, $R_2$=H

**2a-e**

**2a**, $R_1$=H, $R_2$=H
**2b**, $R_1$=H, $R_2$=F
**2c**, $R_1$=H, $R_2$=Cl
**2d**, $R_1$=F, $R_2$=H
**2e**, $R_1$=Cl, $R_2$=H

Scheme 2. Synthesis of aspirin-azo derivatives **2a-e**

**Antibacterial screening**

The antibacterial activities of the synthesized compounds were studied against *E. coli* and *S. aureus*. *Escherichia coli* was cultured on Luria–Bertani (LB) broth and incubated at 37 $^{o}$C for 24 hours with shaking at 250 rpm in order to be used as inoculums. Transmittances (T) were recorded in UV-Visible spectrophotometer. Erlenmeyer flasks containing 100 ml of culture medium added with 50 ppm, 80 ppm and 100 ppm concentrations of compounds and inoculated with 0.99 ml of inoculums and stirred in a culture chamber at 37 ºC with 180 rpm. Aliquots were extracted at 1 hour intervals for 6 hours and transmittances (T) were recorded in a UV-Visible spectrophotometer at 560 nm wavelength. T values were extrapolated to the number of cfu/ml (colony forming units/ml) for *E. coli* expressed in ln $N_t$. The antibacterial screening was repeated by replaced with *S. aureus* [16].

## Results and Discussion

**Characterization study**

The structures of **1a-e** and **2a-e** were confirmed by CHN elemental analysis, FTIR, $^{1}$H and $^{13}$C NMR spectroscopy. The FTIR spectra of **1a-e** and **2a-e** showed that the peak observed at 1491 – 1450 cm$^{-1}$ was associated to *v*(N=N). The peak observed at 1605 – 1583 cm$^{-1}$ was attributed to aromatic (C=C), while the peak at 764 – 749 cm$^{-1}$ and 918 – 752 cm$^{-1}$ were corresponded to *ortho*-substituted of halogen atom and *meta*-substituted of halogen atom, respectively [17]. In addition, **2a-e** showed that disappearance of *v*(O-H) peak at 3300 – 3000 cm$^{-1}$ and two new strong absorption peaks found at 1772 – 1732 cm$^{-1}$ indicated the presence of *v*(C=O) stretching of ester bond proved that the reaction was completed.

The $^{1}$H and $^{13}$C NMR spectroscopy were further confirmed the targeted structures of **1a-e** and **2a-e**. In the $^{1}$H NMR spectra of **1a-e** and **2a-e**, the aromatic protons were observed at δ 8.2 – 6.9 ppm. The $^{1}$H NMR spectra of **1a-e** showed the presence of OH group was resonated as singlet at δ 10.4 – 10.3 ppm (DMSO-$d_6$) and δ 5.8 – 5.6 ppm ($CDCl_3$), while $^{1}$H NMR spectra of **2a-e** showed the presence of -$CH_3$ appeared as singlet was observed at δ 2.28 –

2.26 ppm. The $^{13}C$ NMR spectra of **2a-e** revealed the -$CH_3$ at δ 20.8 – 20.7 ppm. Whereas, the C=O was observed at δ 169.5 – 162.0 ppm. Other the resonance of aromatic carbon **1a-e** and **2a-e** were observed at δ 163.5 – 95.6 ppm.

**[(phenyl)diazenyl]phenol (1a)**
(0.67 g, 68%) yellow solid m.p. 169-171℃. (Found: C, 72.59; H, 5.02; N, 14.02 % $C_{12}H_{10}N_2O$ Requires C, 72.73; H, 5.05; N, 14.14 %); $R_f$ 0.55 (1:4 EA/ hexane) IR: $\nu_{max}$ (thin film/$cm^{-1}$) 3068 (OH), 1583 (C=C aromatic), 1454 (N=N), 1218 (C-N), 1137 (C-O), 678, 763, 835 (C-H), $^1H$ NMR (500 MHz, DMSO-$d_6$) $^{\delta}H$ (ppm): 10.31 (s, 1H, OH) 7.82-7.80 (m, 4H, Ar-$H_{3,7}$) 7.57-7.48 (m, 3H, Ar-$H_{1, 2, 5}$) 6.94 (d, J = 8.6 Hz, 2H, Ar-$H_8$), $^{13}C$ NMR (125 MHz, DMSO-$d_6$) $^{\delta}C$ (ppm): 160.9 (Ar-$C_9$), 152.1 (Ar-$C_4$), 145.2 (Ar-$C_6$), 130.5 (Ar-$C_1$), 129.3 (Ar-$C_2$), 124.9 (Ar-$C_7$), 122.1 (Ar-$C_3$), 115.9 (Ar-$C_8$).

**3-[(E)-(Florophenyl)diazenyl]phenol (1b)**
(0.70 g, 65%) yellow solid m.p. 128 – 129℃. (Found: C, 66.53; H, 4.30; N, 12.87% $C_{12}H_9N_2OF$ requires C, 66.67; H, 4.17; N, 12.96%); $R_f$ 0.58 (1:4 EA/ hexane) IR: $\nu_{max}$ (thin film/$cm^{-1}$) 3157 (OH), 1588 (C=C aromatic), 1450 (N=N), 1239 (C-N), 1145 (C-O), 840, 785, 673 (C-F), $^1H$ NMR (500 MHz, DMSO-$d_6$) $^{\delta}H$ (ppm): 10.42 (s, 1H, OH) 7.81 (d, J = 8.6 Hz, 2H, Ar-$H_8$) 7.61 – 7.54 (m, 3H, Ar-$H_{1, 3, 5}$) 7.33 (t, J = 7.2 Hz, 1H, Ar-$H_6$) 6.95 (d, J = 8.6 Hz, 2H, Ar-$H_9$), $^{13}C$ NMR (125 MHz, DMSO-$d_6$) $^{\delta}C$ (ppm): 163.5 (Ar-$C_2$), 161.6 (Ar-$C_{10}$), 153.5 (Ar-$C_4$), 144.8 (Ar-$C_7$), 130.9 (Ar-$C_6$), 125.0 (Ar-$C_8$), 119.6 (Ar-$C_5$), 116.8 (Ar-$C_1$), 115.9 (Ar-$C_9$), 106.9 (Ar-$C_3$).

**3-[(E)-(Chlorophenyl)diazenyl]phenol (1c)**
(0.79 g, 68%) red solid m.p. 140 – 141℃. (Found: C, 61.51 ; H, 3.86; N, 12.01% $C_{12}H_9N_2OCl$ requires C, 61.94; H, 3.87; N, 12.04%); $R_f$ 0.54 (1:4 EA/ hexane) IR: $\nu_{max}$ (thin film/$cm^{-1}$) 3253 (OH), 1596 (C=C aromatic), 1476 (N=N), 1253 (C-N), 1151 (C-O), 833, 788, 675 (C-Cl), $^1H$ NMR (500 MHz, DMSO-$d_6$) $^{\delta}H$ (ppm): 10.44 (s, 1H, OH) 8.08 (s, 1H, Ar-$H_3$) 7.86 – 7.81 (m, 4H, Ar-$H_{1, 5, 8}$) 7.36 (t, J =7.7 Hz, 1H, Ar-$H_6$) 6.94 (d, J = 9.2 Hz, 2H, Ar-$H_9$), $^{13}C$ NMR (125 MHz, DMSO-$d_6$) $^{\delta}C$ (ppm): 161.8 (Ar-$C_{10}$), 153.4 (Ar-$C_4$), 145.3 (Ar-$C_7$), 134.3 (Ar-$C_2$), 131.4 (Ar-$C_1$), 130.2 (Ar-$C_6$), 125.5 (Ar-$C_8$), 122.3 (Ar-$C_3$), 120.7 (Ar-$C_5$), 116.3 (Ar-$C_9$).

**2-[(E)-(Florophenyl)diazenyl]phenol (1d)**
(0.67g, 62%) orange solid m.p. 104 – 105℃. (Found: C, 65.99; H, 4.10; N, 12.88% $C_{12}H_9N_2OF$ requires C, 66.67; H, 4.17; N, 12.96%); $R_f$ 0.56 (1:4 EA/ hexane) IR: $\nu_{max}$ (thin film/$cm^{-1}$) 3303 (OH), 1585 (C=C aromatic), 1480 (N=N), 1212 (C-N), 1142 (C-O), 753 (C-F), $^1H$ NMR (500 MHz, DMSO-$d_6$) $^{\delta}H$ (ppm): 10.43 (s, 1H, OH), 7.81 (d, J = 8.6 Hz, 2H, Ar-$H_5$), 7.66 (t, J= 7.7 Hz, 1H, Ar-$H_1$), 7.53 (d, J = 8.2 Hz, 1H, Ar-$H_8$), 7.45 (d, J = 8 Hz, 1H, Ar-$H_2$), 7.31 (t, J = 7.2 Hz, 1H, Ar-$H_6$), 6.95 (d, J = 8.6 Hz, 2H, Ar-$H_9$), $^{13}C$ NMR (125 MHz, DMSO-$d_6$) $^{\delta}C$ (ppm): 115.9 (Ar-$C_9$), 117.0 (Ar-$C_2$), 117.1(Ar-$C_8$), 117.9 (Ar-$C_5$), 124.1 (Ar-$C_6$), 125.5 (Ar-$C_1$), 131.8 (Ar-$C_4$), 140.9 (Ar-$C_7$), 147.6 (Ar-$C_3$), 159.1 (Ar-$C_{10}$).

**2-[(E)-(Chlorophenyl)diazenyl]phenol (1e)**
(0.67g, 58%) orange solid m.p. 112 – 113℃. (Found: C, 61.32; H, 3.76; N, 11.95% $C_{12}H_9N_2OCl$ requires C, 61.94; H, 3.87; N, 12.04%); $R_f$ 0.53 (1:4 EA/ hexane) IR: $\nu_{max}$ (thin film/$cm^{-1}$) 3301 (OH), 1588 (C=C aromatic), 1483 (N=N), 1238 (C-N), 1139 (C-O), 754 (C-Cl), $^1H$ NMR (500 MHz, $CDCl_3$) $^{\delta}H$ (ppm): 7.92 (d, J = 8.6 Hz, 2H, Ar-$H_8$), 7.66 (d, J = 7.4 Hz, 1H, Ar-$H_5$), 7.53 (d, J = 7.4 Hz, 1H, Ar-$H_2$), 7.34 (m, 2H, Ar-$H_{1,6}$), 6.95 (d, J = 8.6 Hz, 2H, Ar-$H_9$), 5.72 (s, 1H, OH), $^{13}C$ NMR (125 MHz, DMSO-$d_6$) $^{\delta}C$ (ppm): 161.6 (Ar-$C_{10}$), 148.1 (Ar-$C_4$), 145.5 (Ar-$C_7$), 133.1 (Ar-$C_1$), 131.6 (Ar-$C_2$), 130.6 (Ar-$C_6$), 127.9 (Ar-$C_3$), 125.4 (Ar-$C_5$), 117.5 (Ar-$C_8$), 116.1 (Ar-$C_9$).

**[(phenyl)diazenyl]phenylaspirinate (2a)**
(0.81 g, 75%) pale yellow solid m.p. 168 – 170℃. (Found: C, 69.97; H, 4.46; N, 7.67% $C_{12}H_9N_2OI$ requires C, 70.0; H, 4.17; N, 7.78%); $R_f$ 0.64 (1:4 EA/ hexane) IR: $\nu_{max}$ (thin film/$cm^{-1}$) 1736, 1763 (C=O), 1604 (C=C aromatic), 1481 (N=N), 1249 (C-N), 1183 (C-O), 762, 686 (C-H) $^1H$ NMR (500 MHz, DMSO-$d_6$) $^{\delta}H$ (ppm): 8.20 (d, J = 9.2 Hz, 1H, Ar-$H_{14}$), 8.01 (d, J = 9.2 Hz, 2H, Ar-$H_7$), 7.91 (d, J = 8.6 Hz, 2H, Ar-$H_3$), 7.79 (t, J= 7.7 Hz, 1H, Ar-$H_{13}$), 7.64 – 7.58 (m, 3H, Ar-$H_{1, 2, 5}$), 7.51 (t, J = 7.8Hz, 1H, Ar-$H_{13}$), 7.48 (d, J= 8.6 Hz, 2H, Ar-$H_8$), 7.35 (d, J = 8 Hz, 1H, Ar-$H_{11}$), 2.27 (s, 3H, -$CH_3$), $^{13}C$ NMR (125 MHz, DMSO-$d_6$) $^{\delta}C$ (ppm): 169.3 ($C_b$=O), 162.4 ($C_a$=O), 152.4

(Ar-$C_4$), 151.9 (Ar-$C_9$), 149.8 (Ar-$C_6$), 150.5 (Ar-$C_{10}$), 135.3 (Ar-$C_{12}$), 131.9 (Ar-$C_1$), 131.7 (Ar-$C_{14}$), 129.5 (Ar-$C_2$), 126.6 (Ar-$C_{13}$), 124.2 (Ar-$C_{11}$), 124.0 (Ar-$C_7$), 122.9 (Ar-$C_3$), 122.6 (Ar-$C_8$), 121.9 (Ar-$C_{15}$), 20.8 (-$CH_3$).

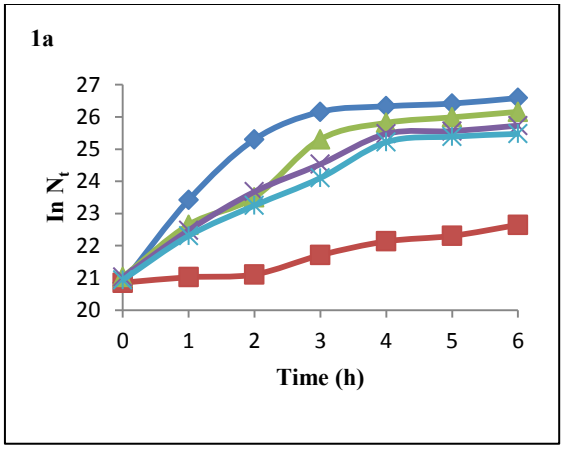
**3-[(E)-(Florophenyl)diazenyl]phenylaspirinate (2b)**
(0.62 g, 55%) pale yellow solid. m.p. 150 – 151℃. (Found: C, 66.61; H, 4.04; N, 7.33% $C_{21}H_{15}N_2O_4F$ requires C, 66.67; H, 3.97; N, 7.41%); $R_f$ 0.65 (1:4 EA/ hexane) IR: $\nu_{max}$ (thin film/$cm^{-1}$) 1768, 1742 (C=O), 1592 (C=C aromatic), 1453 (N=N), 1244 (C-N), 1186 (C-O), 914, 884, 785 (C-F), $^1$H NMR (500 MHz, DMSO-$d_6$) $^\delta$H (ppm): 8.20 (d, J = 7.5 Hz, 1H, Ar-$H_{15}$), 8.03 (d, J = 8.6 Hz, 2H, Ar-$H_8$), 7.83 – 7.79 (m, 2H, Ar-$H_{6, 14}$), 7.71-7.66 (m, 2H, Ar-$H_{3, 5}$), 7.54 – 7.45 (m, 4H, Ar-$H_{1, 9, 13}$) 7.35 (d, J = 8.0 Hz, 1H, Ar-$H_{12}$), 2.27 (s, 3H, -$CH_3$), $^{13}$C NMR (125 MHz, DMSO-$d_6$) $^\delta$C (ppm): 169.3 ($C_b$=O), 163.7 ($C_a$=O), 162.4 (Ar-$C_2$), 161.6 (Ar-$C_4$), 153.4 (Ar-$C_{10}$), 152.8 (Ar-$C_{11}$), 150.5 (Ar-$C_7$), 149.9 (Ar-$C_{13}$), 135.4 (Ar-$C_{15}$), 131.9 (Ar-$C_6$), 131.4 (Ar-$C_{14}$), 126.6 (Ar-$C_{12}$), 124.3 (Ar-$C_8$), 123.1 (Ar-$C_9$), 121.9 (Ar-$C_{16}$), 120.51 (Ar-$C_5$), 117.9 (Ar-$C_1$), 107.6 (Ar-$C_3$), 20.8 (-$CH_3$).

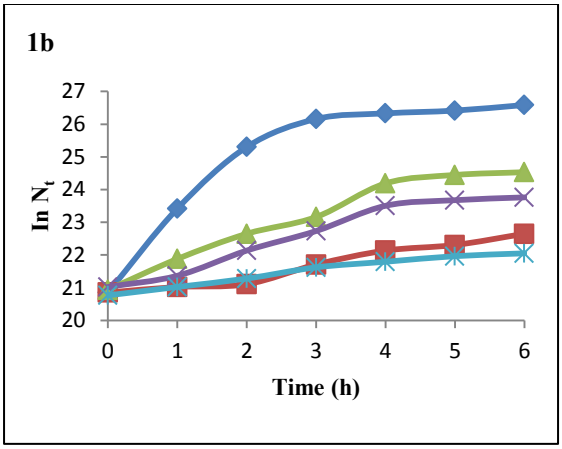
**3-[(E)-(Chlorophenyl)diazenyl]phenylaspirinate (2c)**
(0.57 g, 48%) pale yellow solid m.p. 153 – 154℃. (Found: C, 63.39; H, 3.78; N, 7.04% $C_{21}H_{15}N_2O_4Cl$ requires C, 63.88; H, 3.80; N, 7.10%); $R_f$ 0.62 (1:4 EA/ hexane) IR: $\nu_{max}$ (thin film/$cm^{-1}$) 1760, 1733 (C=O), 1605 (C=C aromatic), 1484 (N=N), 1248 (C-N), 1184 (C-O), 785, 885, 918 (C-Cl), $^1$H NMR (500 MHz, DMSO-$d_6$) $^\delta$H (ppm): 8.20 (d, J = 7.6 Hz, 1H, Ar-$H_{15}$), 8.03 (d, J = 8.60 Hz, 2H, Ar-$H_8$), 7.92 – 7.90 (m, 2H, Ar-$H_{3, 14}$), 7.79 (t, J = 7.7 Hz, 1H, Ar-$H_6$), 7.68 – 7.66 (m, 2H, Ar-$H_{1, 5}$), 7.55 – 7.50 (m, 3H, Ar-$H_{9, 13}$), 7.35 (d, J = 8.0 Hz, 1H, Ar-$H_{12}$), 2.27 (s, 3H, -$CH_3$), $^{13}$C NMR (125 MHz, DMSO-$d_6$) $^\delta$C (ppm): 169.2 ($C_b$=O), 162.4 ($C_a$=O), 152.8 (Ar-$C_4$), 150.5 (Ar-$C_{10}$), 149.7(Ar-$C_{11}$), 135.4 (Ar-$C_7$), 134.2 (Ar-$C_{13}$), 131.9 (Ar-$C_2$), 131.3 (Ar-$C_1$), 131.2 (Ar-$C_{15}$), 126.6 (Ar-$C_6$), 124.3 (Ar-$C_{14}$), 124.1 (Ar-$C_{12}$), 123.1 (Ar-$C_8$), 122.6 (Ar-$C_3$), 121.9 (Ar-$C_9$), 121.6 (Ar-$C_5$), 121.0 (Ar-$C_{16}$), 20.7 (-$CH_3$).

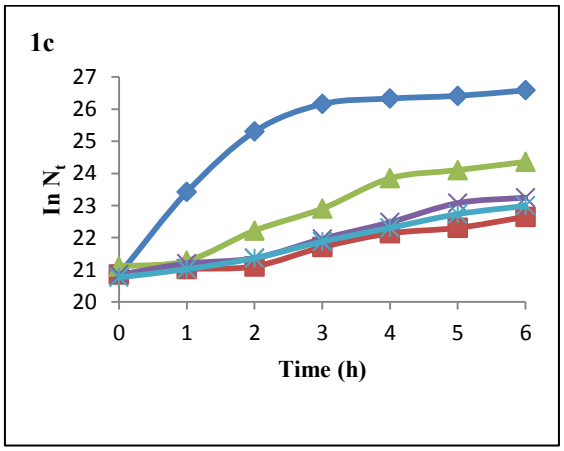
**2-[(E)-(Florophenyl)diazenyl]phenylaspirinate (2d)**
(0.45 g, 40%) pale yellow 123 – 124℃. (Found: C, 66.52; H, 3.91; N, 7.22% $C_{21}H_{15}N_2O_4F$ requires C, 66.67; H, 3.97; N, 7.41%); $R_f$ 0.62 (1:4 EA/ hexane) IR: $\nu_{max}$ (thin film/$cm^{-1}$) 1755, 1732 (C=O), 1588 (C=C aromatic), 1481(N=N), 1250 (C-N), 1181 (C-O), 762 (C-F), $^1$H NMR (500 MHz, DMSO-$d_6$) $^\delta$H (ppm): 8.20 (d, J = 8.6 Hz, 1H, Ar-$H_{15}$), 8.02 (d, J = 6.9 Hz, 2H, Ar-$H_8$), 7.79 (1H, t, J= 8.6 Hz, Ar-$H_1$), 7.74 (t, J= 8.6 Hz, 1H, Ar-$H_{14}$), 7.62 (t, J = 6.9 Hz, 1H, Ar-$H_{13}$), 7.54 – 7.49 (m, 4H, Ar-$H_{5, 6, 9}$), 7.39 – 7.35 (m, 2H, Ar-$H_{2, 12}$), 2.27 (s, 3H, -$CH_3$), $^{13}$C NMR (125 MHz, DMSO-$d_6$) $^\delta$C (ppm): 169.3 ($C_b$=O), 162.4 ($C_a$=O), 160.4 (Ar-$C_3$), 158.4 (Ar-$C_{10}$), 152.8 (Ar-$C_{11}$), 150.6 (Ar-$C_7$), 150.0 (Ar-$C_4$), 139.7 (Ar-$C_{13}$), 135.4 (Ar-$C_1$), 133.8 (Ar-$C_{15}$), 131.9 (Ar-$C_{14}$), 126.6 (Ar-$C_6$), 125.1 (Ar-$C_5$), 124.3 (Ar-$C_{12}$), 123.1 (Ar-$C_8$), 121.9 (Ar-$C_9$), 117.5 (Ar-$C_{16}$), 117.3 (Ar-$C_2$), 20.8 (-$CH_3$).

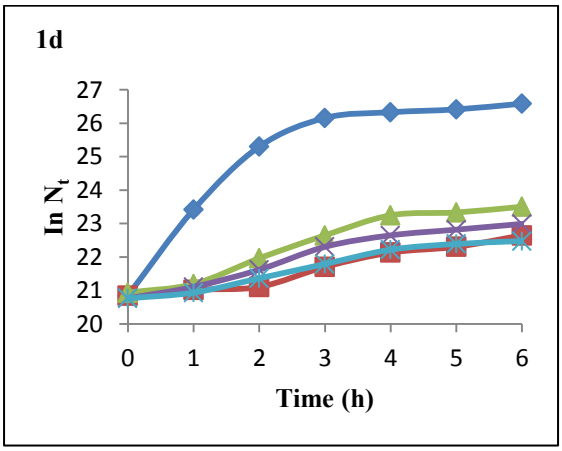
**2-[(E)-(Chlorophenyl)diazenyl]phenylaspirinate (2e)**
(0.54 g, 46%) orange solid m.p. 119 – 120℃. (Found: C, 63.66; H, 3.76; N, 6.98% $C_{21}H_{15}N_2O_4Cl$ requires C, 63.88; H, 3.80; N, 7.10%); $R_f$ 0.62 (1:4 EA/ hexane) IR: $\nu_{max}$ (thin film/$cm^{-1}$) 1770, 1742 (C=O), 1591 (C=C aromatic), 1482(N=N), 1244 (C-N), 1184 (C-O), 753 (C-Cl), $^1$H NMR (500 MHz, DMSO-$d_6$) $^\delta$H (ppm): 8.21 (d, J = 8.0 Hz, 1H, Ar-$H_{15}$), 8.04 (d, J = 8.6 Hz, 2H, Ar-$H_8$) 7.80 (t, J = 7.8 Hz, 1H, Ar-$H_{14}$), 7.74 (d, J = 8.0 Hz, 1H, Ar-$H_5$), 7.70 (1H, d, J = 8.0 Hz, Ar-$H_2$), 7.58 (t, J = 7.8 Hz, 1H, Ar-$H_{13}$), 7.55 – 7.48 (m, 4H, Ar-$H_{1, 6, 9}$), 7.36 (d, J = 7.5 Hz, 1H, Ar-$H_{12}$), 2.28 (s, 3H, -$CH_3$), $^{13}$C NMR (125 MHz, DMSO-$d_6$) $^\delta$C (ppm): 169.4 ($C_b$=O), 162.1 ($C_a$=O), 152.6 (Ar-$C_4$), 150.2 (Ar-$C_{10}$), 149.5 (Ar-$C_{11}$), ), 147.4 (Ar-$C_7$), 135.4 (Ar-$C_{13}$), 133.9 (Ar-$C_1$), 132.8 (Ar-$C_{15}$), 131.9 (Ar-$C_2$), 130.9 (Ar-$C_3$), 128.2 (Ar-$C_6$), 126.6 (Ar-$C_{14}$), 124.5 (Ar-$C_{12}$), 124.3 (Ar-$C_5$), 123.2 (Ar-$C_8$), 121.5 (Ar-$C_9$), 117.6 (Ar-$C_{16}$), 20.8 (-$CH_3$).

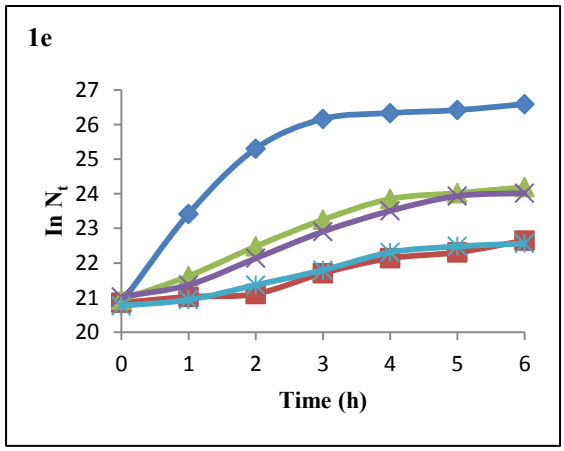
**Antibacterial screening**
The inhibition activity of **1a-e** and **2a-e** against *E. coli* and *S. aureus* are shown in Figure 1 and Figure 2, respectively. Most halogenated azo derivatives **1b-e** showed good antibacterial activities against *E. coli* and *S. aureus* at all concentration (50, 80 and 100 ppm). However, **2a-e** only showed good inhibition activity against bacteria at high concentrations (100 ppm). The effects of synthesized compounds tested at three different concentrations (50, 80 and 100 ppm) are further revealed by minimum inhibitory concentration (MIC) values. The MIC value of **1a-e** and **2a-e** were determined by extrapolating the concentration to zero growth rates of *E. coli* and *S. aureus* [16].

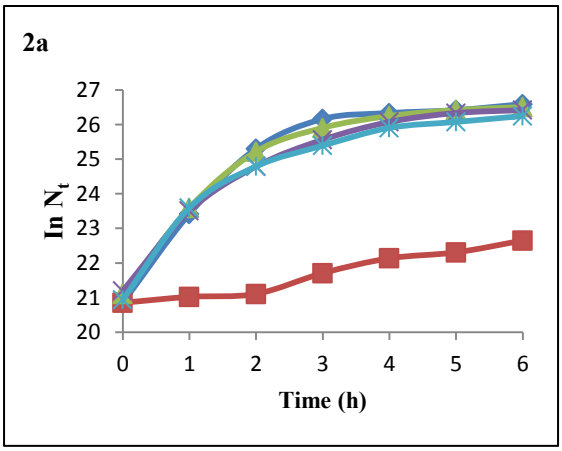

1a
ln $N_t$
Time (h)


1b
ln $N_t$
Time (h)


1c
ln $N_t$
Time (h)


1d
ln $N_t$
Time (h)


1e
ln $N_t$
Time (h)


2a
ln $N_t$
Time (h)

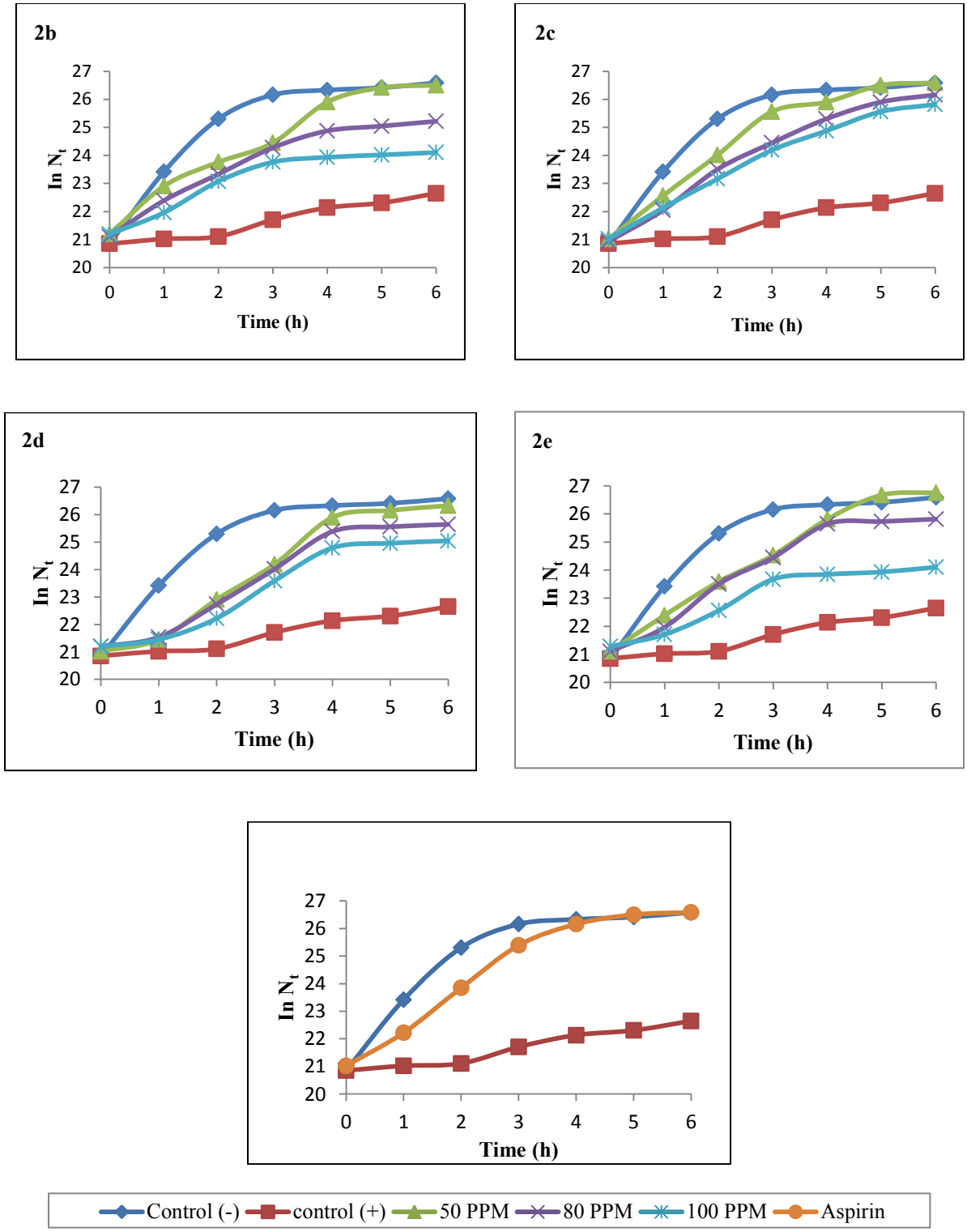
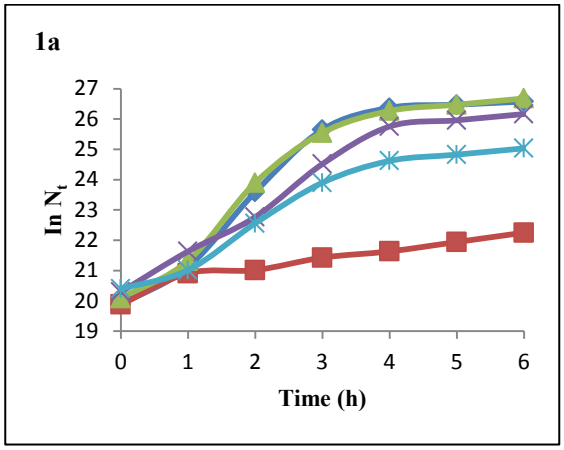
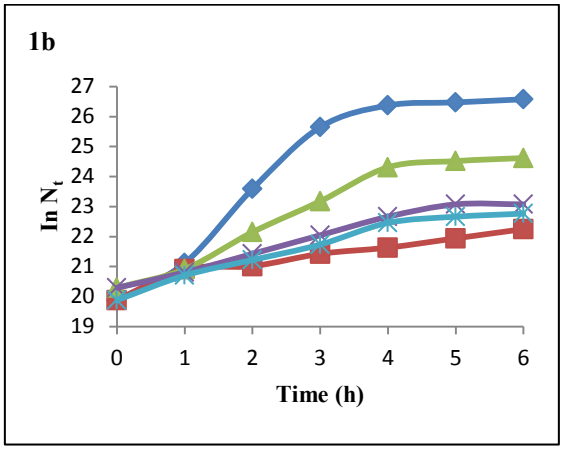
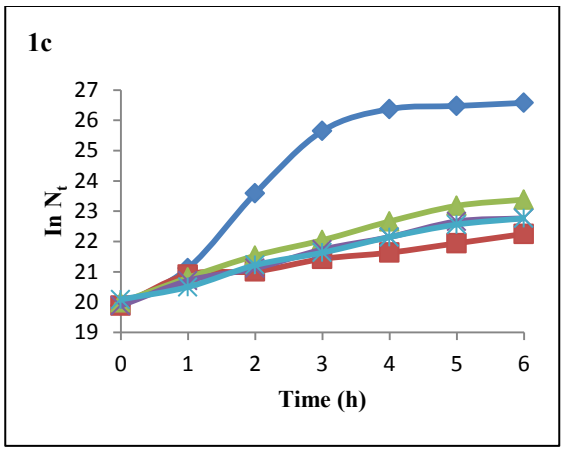
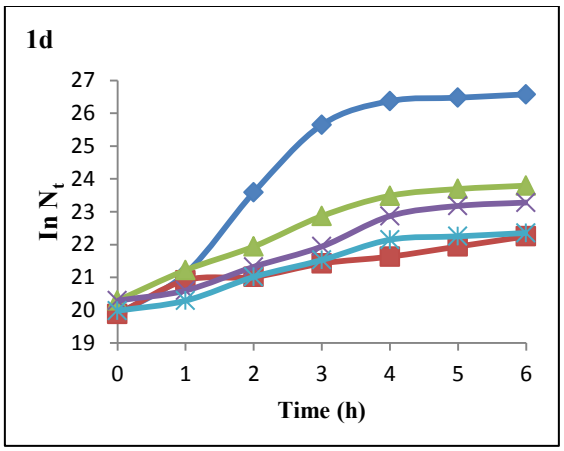


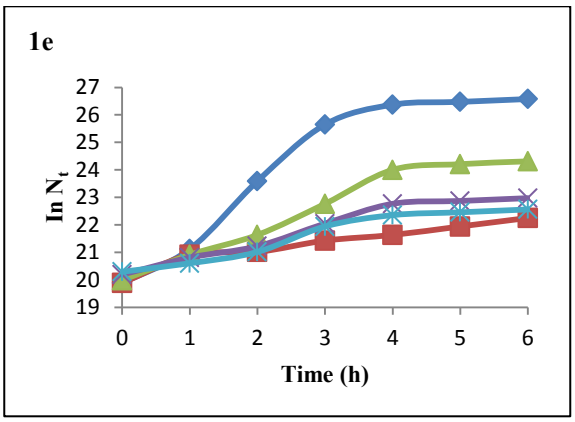

Figure 1. Inhibition activity of **1a-e** and **2a-e** against *E. coli* shown as In $N_t$ for *E. coli* growth versus time.

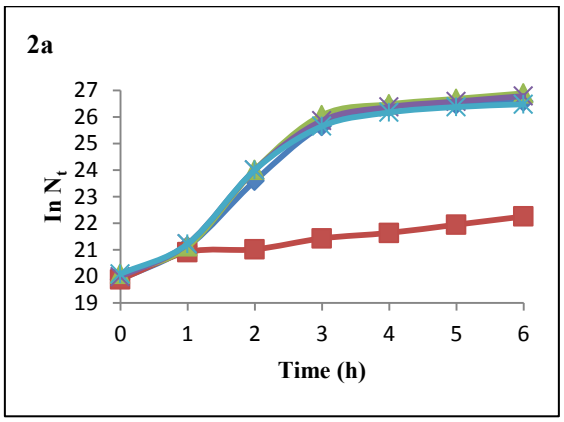

1a
ln N$_t$
Time (h)


1b
ln N$_t$
Time (h)


1c
ln N$_t$
Time (h)


1d
ln N$_t$
Time (h)


1e
ln N$_t$
Time (h)


2a
ln N$_t$
Time (h)

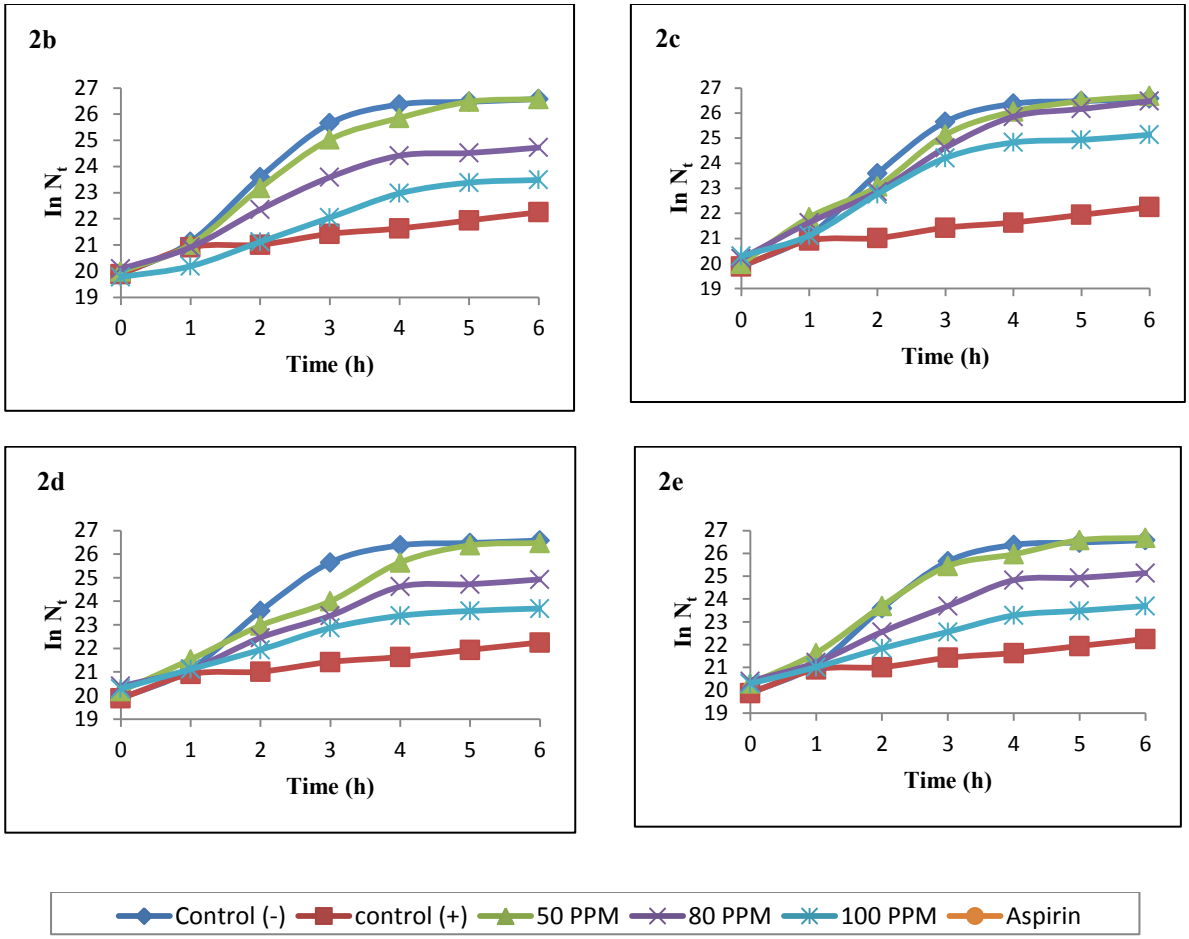



Figure 2. Inhibition activity of aspirin, **1a-e** and **2a-e** against *S. aureus* shown as In $N_t$ for *S. aureus* growth versus time

Based on the MIC values shown in Table 1, the MIC values showed that all halogenated azo derivatives **1b-e** exhibited very good bacteriostatic activities against *E. coli* and *S. aureus* compared to **1a** (without halogen substituent). All the synthesized halogenated azo derivatives **1b-e** demonstrated good inhibition against *E. coli* (MIC < 220 ppm) and *S. aureus* (MIC < 220 ppm), which indicated that these compounds are a potential antibacterial agent [18]. Among these compounds, **1d** (*ortho* fluorine atom substituent) gave the best inhibition with MIC values of 108 ppm and 132 ppm against *E. coli* and *S. aureus*, respectively. These results in agreement with Saeed et al. and Yarovenko et al. which reported that the halogen group and N=N played important roles in antibacterial activities [19, 20]. Furthermore, compounds consist of phenyl groups and halogen atoms have also revealed that those with more lipophilic character could easily penetrates the cell wall of microorganism [21, 22]. The azo derivatives **1b-e** consists of -N=N- group can be protonated under acidic condition to react with the phosphate group on the polysaccharide peptidoglycan layer of bacteria, which hinder the formation of cell wall [23, 24]. Patrick also reported that the halogenated compound was involved in inhibition of bacteria *via* interaction of halogen with receptor of enzyme [25]. In addition, The -N=N- and OH group in the synthesized halogenated azo derivatives **1b-e** interacts with active site on the enzyme of *E. coli* and *S. aureus* through hydrogen bond formation, thus inhibit the growth of bacteria [26].

For compound **2a-e**, only **2b** and **2d-e** exhibited good antibacterial activity against *E. coli* and *S. aureus* compared to **2a** (without halogen substituent) and aspirin. It is because the presence of halogen substituent and N=N in

molecular structure has contributed to antibacterial activities. The **2d** and **2e** substituted with fluorine and chlorine atoms, respectively at *ortho* position are more active to inhibit towards *E. coli* and *S. aureus* compared to compounds substituted with halogen atom at *meta* position. These results also revealed the same finding in which the halogen substituted at different position may have effect on the antibacterial activity as reported Lee et al. [27]. Furthermore, presence of more phenyl ring in molecular structure might also result in bulkiness. Therefore, it is more difficult to penetrate into bilayer of phospholipid *E. coli* and *S. aureus* [28].

Table 1. Minimum inhibitory concentration (MIC ppm) for compound **1a-e** and **2a-e**

| Compounds | MIC (ppm) | |
|---|---|---|
| | ***E. coli*** | ***S. aureus*** |
| Aspirin | >220 | >220 |
| **1a** | >220 | >220 |
| **1b** | 113.4 | 150.2 |
| **1c** | 111.3 | 139.0 |
| **1d** | 108.5 | 132.3 |
| **1e** | 117.3 | 138.3 |
| **2a** | >220 | >220 |
| **2b** | 180.9 | 194.1 |
| **2c** | > 220 | > 220 |
| **2d** | 156.3 | 199.5 |
| **2e** | 167.0 | 198.9 |
| Ampicillin (+) | 92.9 | 124.2 |

## Conclusion

In conclusion, there are two series of azo derivatives **1b-e** and aspirin-azo derivatives **2b-e** were synthesized and screened for their antibacterial activities. The results showed that all halogenated azo derivatives **1b-e** exhibited better antibacterial activities against both gram-negative bacteria and gram-positive bacteria when compared to all aspirin- azo derivatives **2b-e**. The esterification of aspirin with azo derivatives **1b-e** had increased the bulkiness of the molecular structure causing the steric hindrance, thus avoid the molecular structure from binding to the active site of bacteria. In addition, the bulky structure has caused difficulty to penetrate into the cell wall of bacteria. Azo derivatives **1d** bearing fluorine atom gave excellent antibacterial properties and gave the lowest MIC value due to the smaller size of fluorine.

## Acknowledgements

The authors would like to thank university Malaysia Sarawak and Ministry of Higher Education for financial support of this project through grant FRGS/(ST01(02)/968/2013(09).

## References

1. Richard, C. B. (2012). Aspirin and the prevention of venous thromboembolism. *New England Journal of Medicine*, 366: 2028 – 2030.
2. Cemel, A. and Ahmet, S. (2008). Rapid and simultaneous determination of acetylsalicylic acid, paracetamol and their degradation and toxic impurity product by HPLC in pharmaceutical dosage forms. *Journals Medical Science*, 38: 167 – 173.
3. Warner, T. D., Nylander, S. and Whatling, C. (2011). Anti-platelet therapy: cyclo-oxygenase inhibition and the use of aspirin with particular regard to dual anti-platelet therapy. *British Journal of Clinical Pharmacology*, 1365 – 2125.
4. Vane, J. R. and Botting, R. M. (2003). The mechanism of action of aspirin. *Thrombosis Research*, 110: 255 – 258.

5. Cicala, C., Ianaro, A., Fiorucci, S., Calignano, A., Bucci, M. and Gerli, R. (2000). NO-naproxen modulates inflammation, nociception and downregulates T cell response in rat Freund's adjuvant arthritis. *British Journal of Pharmacology*, 130: 1399 – 1405.
6. Al-Bakri, A. G., Othman, G. and Bustanji, Y. J. (2009). The assessment of the antibacterial and antifungal activities of aspirin, EDTA and aspirin-EDTA combination and their effectiveness as antibioflim agents. *Applied Microbiology*, 107(1): 280 – 296.
7. Huang, L., MacKenzie, G. G., Ouyang, N., Sun, Y., Xie, G., Johnson, F., Komninou, D. and Rigas, B. (2011). The novel phospho-non-steroidal anti-inflammatory drugs, OXT-328, MDC-22 and MDC-917, inhibit adjuvant-induced arthritis in rats. *British Journal of Pharmacology*, 162(7): 1521 – 1533.
8. Joseph, S., Nie, T., Huang, L., Zhou, H., Atmakur, K., Gupta, R. C., Johson, F. and Rigas, B. (2011). Structure-activity relationship study of novel anticancer aspirin-based compounds. *Molecular Medicine Reports*, 4(5): 891 – 899.
9. Hinks, D., Freeman, H. S., Nakpathom, M. and Sokolowska, J. (2000). Synthesis and evaluation of organic pigments and intermediates. 1. Nonmutagenic benzidine analogs. *Dyes and Pigments*, 44: 199 –207.
10. Simu, G. M. and Kurunczi, L. (2008). Influence of temperature and of the electrolyte concentration in the dyeing process of a cellulosic fibre with a disazo direct dye. *Chemical Bulletin*, 53(67): 153 – 155.
11. Ahmed, A. E. I., Hay, J. N., Bushell, M. E., Wardell, J. N. and Cavalli, G. (2008). Biocidal polymer (I): Preparation and biological activity of some novel biocidal polymers based on uramil and its azo-dyes. *Reactive and Functional Polymers*, 68(1): 248 – 266.
12. Khalid, A, Arshad. M. and Crowley, D. E. (2008). Accelerated decolorization of structurally different azo dyes by newly isolated bacterial strains. *Applied Microbiology*, 78: 361 – 369.
13. Raghavendra, K. R. and Kumar, K. A. (2013). Synthesis of some novel azo dyes and their dyeing, redox and antifungal properties. *International Journal of ChemTech Research*, 5(2): 1756 – 1760.
14. Tonelli, I. M., Vazzana, B., Jasso, V., Boida, F., Sparatore, P., Lacolla, G., Sanna, G., Giliberti, B., Busonera, P., Farci, C. I. and Loddo, R. (2009). Antiviral and cytotoxic activities of aminoarylazo compounds and aryltriazene derivatives. *Bioorganic and Medicinal Chemistry*, 17: 4425 – 4440.
15. Ho, B. K., Ngaini, Z. Neilsen, P. M., Hwang, S. S., Linton, R. E., Kong, E. L., and Lee, B. K. (2017). Synthesis and Anticancer Activities of 4-[(Halophenyl)diazenyl]phenol and 4-[(Halophenyl)diazenyl]phenyl Aspirinate Derivatives against Nasopharyngeal Cancer Cell Lines. *Journal of Chemistry*, 2017: 1-7.
16. Pappano, N. B., Puig de Centorbi, O., Debattista, N. B., Calleri de Milan, C., Borkowski, E. J. and Ferretti, F. H. (1985). Kinetic of the bacteriostatic activity of natural and synthetic chalcones on a strain *Staplylococcus aureus*. *Revista Argentina De Microbiologia*, 17: 27 – 32.
17. Solomons. T. W. G. and Fryhle, C. B. (2003). Organic Chemistry (8th edition). *John Wiley & Sons*: USA.
18. Arslan, H., Duran, N., Borekei, G., Oxer, C. K. and Akbay, C. (2009). Antimicrobial activity of some thiourea derivatives and their nickel & copper complexes. *Molecules*, 10(14): 519 – 527.
19. Saeed, A., Abbas, N., Rafique, H., Rashid, S. and Hammed, A. (2009). Synthesis characterization and antibacterial activity of some 1-aroyl-3-aryl thiourea. *Chemistry*, 18(5): 152 – 158.
20. Yarovenko, V. N., Lysenko, O. V. and Krayushkin, M. M. (1993). Synthesis of derivatives 2-amino-1,3,4-oxadiazole-5- hydroxamic acid. *Chemistry of Heterocyclic Compounds*, 29(4), 452 – 454.
21. Ansari, M. M., Deshmukh, S.P., Khan, R. and Musaddiq, M. (2014). Synthesis antimicrobial and anticancer evaluation of 1-aryl-5-(o-methoxyphenyl)-2-S-benzyl isothiobiurets. *International Journal of Medicinal Chemistry*, 2014: 1 – 5.
22. Hoey, A. J., Jackson, C. M., Pegg, G. G. and Sillence, M. N. (1996). Characteristics of cyanopindolol analogues active at the beta (3)-adrenoceptor in rat ileum. *British Journal of Pharmacology*, 119: 564 – 568.
23. Brown, S., Santa, M. J. P. and Walker, S. (2013). Wall teichoic acids of gram-positive bacteria. *Annual Review of Microbiology*, 67(1): 313 – 336.
24. Zhong, Z., Xing, R., Liu, S., Wang, L., Cai, S. B. and Li, P. C. (2008). Synthesis of acyl thiourea derivatives of chitosan and their antimicrobial activities in vitro. *Carbohydrate research*, 334(3): 566 –570.
25. Patrick, G. L. (2009) Medicinal chemistry (4th edition). Oxford University Press Inc: Asia.
26. Khalaf, Y. H. (2008). Synthesis a number of azo compounds derived from guanine and studying their biological activity on pathogenic bacteria. *Journal of Al-Anbar University for Pure Science*, 2(3): 38 – 45.
27. Li, J., Rao, X. P., Shang, S. B., Gao, Y. Q. and Song, J. (2012). Synthesis and antibacterial activity of amide derivatives from acrylopimaric acid. *Bioresources*, 7(2): 1961 – 1971.

28. Fernandez, E. R., Manzano, J. L., Benito, J. J., Hermosa, R., Monte, E. and Criado, J. J. (2005). Thiourea, triazole and thiadiazine compounds and their metal complexes as antifungal agents. *Journal of Inorganic Biochemistry*, 99: 1559 – 1572.

*Malaysian Journal of Analytical Sciences, Vol 21 No 5 (2017): 1195 - 1202*
*DOI: https://doi.org/10.17576/mjas-2017-2105-24*

MALAYSIAN JOURNAL OF ANALYTICAL SCIENCES
*Published by The Malaysian Analytical Sciences Society*
ISSN 1394 - 2506

# SYNTHESIS, MODIFICATION, CHARACTERIZATION AND BIOLOGICAL ACTIVITY OF 3-HYDROXYBENZALDEHYDESALICYLHYDRAZIDE

## (Sintesis, Modifikasi, Pencirian dan Aktiviti Biologi 3-Hidroksibenzaldehidesalisilhidrazida)

Nornadia Jasin[1]*, Meng Guan Tay[1], Hashimatul Fatma Hashim[2]

[1]*Department of Chemistry, Faculty of Resource Science and Technology*
[2]*Department of Molecular Biology, Faculty of Resource Science and Technology*
*Universiti Malaysia Sarawak, 94300 Kota Samarahan, Sarawak, Malaysia*

**Corresponding author: nornadiajasin@gmail.com*

Received: 21 August 2016; Accepted: 27 July 2017

**Abstract**

A series of hydrazone Schiff base (compounds **S**, **S8**, **S10** and **S12**) were synthesized by condensation reaction of salicylhydrazide with 3-hydroxybenzaldehyde, 3-(octyloxy)benzaldehyde, 3-(decyloxy)benzaldehyde and 3-(dodecyloxy) benzaldehyde, respectively. Herein, the addition of alkane numbers are reported using successful Williamson etherification method by reacting 3-hydroxybenzaldehyde with bromooctane, bromodecane and bromododecane, respectively. All compounds were characterised using Fourier Transform Infrared and $^1$H Nuclear Mangnetic Resonance spectroscopic. The compounds were assayed to antibacterial activity against Gram-positive and Gram-negative bacteria using *Bacillus cereus* and *Escherichia coli* by disc diffusion method. Interestingly, among the compounds tested **S8** showed a strong inhibition against *Escherichia coli* and none of the compounds tested show significant result against *Bacillus cereus*.

**Keywords**: 3-hydroxybenzaldehyde, Williamson etherification, hydrazone Schiff base, antibacterial activity

**Abstrak**

Satu siri bes Schiff hidrazon (sebatian **S**, **S8**, **S10** dan **S12**) telah disintesis mengunakan tindakbalas pemeluwapan oleh salisilhidrazida dengan 3-hidroksibenzaldehid, 3-(oktiloksi)benzaldehid, 3-(deciloksi)benzaldehid dan 3-(dodeciloksi) benzaldehid. Di sini, penambahan nombor alkana juga telah dilaporkan menggunakan kaedah pengeteran Williamson yang berjaya daripada tindak balas 3-hidroksibenzaldehid dengan bromooktana, bromodekana dan bromododekana. Semua sebatian telah dicirikan menggunakan spektroskopi inframerah transformasi Fourier dan $^1$H nukleus magnetik resonan. Sebatian yang terhasil telah diuji dengan aktiviti antibakteria terhadap bakteria Gram-positif dan Gram- negatif menggunakan *Bacillus cereus* dan *Escherichia coli* dengan kaedah cakera resapan. Menariknya, diantara sebatian yang telah diuji, **S8** menunjukkan perencatan yang kuat terhadap *Escherichia coli* dan tiada sebatian menunjukkan hasil yang ketara terhadap *Bacillus cereus*.

**Kata kunci**: 3- hidroksibenzaldehid, pengeteran Williamson, bes Schiff hidrazon, aktiviti antibakteria

## Introduction

Hydrazone Schiff base compounds have been widely reported regarding its effectiveness in biological activities including antibacterial [1], antifungal, antituberculosis [2], anticancer and antimalarial activities [3]. This is due to the presence of azomethine C=N group. The nitrogen atom of the schiff base contains a lone pair electron with $sp^2$ hybridised orbital that contributes to various biological and chemical properties [4]. In most cases, the structure of hydrazone Schiff base is the main factor in controlling the biological activites. As some reports demostrated that the antibacterial activity of some compounds enhanced by controlling the lipophilicity [5, 6], stereochemistry and the

nucleophilicity of the compounds [5]. Due to this reason, in order to increase the lipophilic ability of the compound which increasing the antibacterial property, Williamson etherification method was introduced to prolong the side chains of parent ligands by addition of C8, C10 and C12 alkyl chains in the compounds.

In this study, we herein report the synthesis, modification, characterization and antibacterial studies of hydrazone shiff base namely 3-hydroxybenzaldehyde salicylhydrazide, 3-(octyloxy)benzaldehyde salicylhydrazide, 3-(decyloxy)benzaldehyde salicylhydrazide and 3-(dodecyloxy)benzaldehyde salicylhydrazide.

## Materials and Methods

### Materials and characterizations

3-hydroxybenzaldehyde, salicylhydrazide, 1-bromooctane, 1-bromodecane and 1-bromododecane were obtained from Sigma Aldrich and Fluka. All chemicals and solvent were used as received without further purification. The infrared spectra were recorded using Thermo Scientific/Nicolet iS10 Fourier Transform Infrared spectrophotometer. The $^{1}H$ and $^{13}C$ NMR spectrum were recorded on a JEOL ECA-500 MHz NMR spectrometer and the chemical shift were reported relative to TMS and were referenced *via* residual proton NMR resonances of the appropriate diturated solvent (DMSO-$d_6$: 2.50 ppm).

### Etherification of 3-hydroxybenzaldehyde (T) to 3-alkoxybenzaldehyde (T8 – T12)

3-alkoxybenzaldehydes were prepared by a reported method with slightly alteration using 1-bromooctane, 1-bromodecane and 1-bromododecane [7]. The reaction was prepared by addition of ethanolic 3-hydroxybenzaldehyde (0.488g, 4 mmol) solution, anhydrous $K_2CO_3$ (1.035g, 7.5 mmol) and corresponding n-alkyl bromide (6 mmol) into the round bottom flask with present of KI and 20 ml of absolute ethanol as a solvent. The reaction mixture was heated under reflux for 20 hours and allowed to cool at room temperature. Then, the solution was transferred into separatory funnel and distilled water was added into the mixture and oily layer of 3-alkoxybenzaldehyde was formed. The mixture was extracted twice with diethyl ether (2 x 15 ml). Lastly, 5% NaOH solution (10 ml) was added into the mixture and distilled water was used to alter the mixture into pH 7. The oily ether extract was collected and dried under room temperature.

### Synthesis of 3-hydroxybenzaldehydesalicylhydrazide (S) and 3-alkoxybenzaldehydesalicylhydrazide (S8 – S12)

Salicylhydrazide (0.304g, 2 mmol) was dissolved in 20 ml of absolute ethanol in a round bottom flask with constant stirring. Ethanolic solution of 3-hydroxybenzaldehyde (**T**) or 3-alkoxybenzaldehydes (**T8 – T12**) (3 mmol) was then added dropwise into the mixture. The reaction mixture was refluxed with constant stirring for 20 hours and allowed to cool at room temperature. The precipitate formed was filtered and washed several times with ethanol and dried *in vacuo*.

### Antibacterial screening

Compounds **S**, **S8**, **S10** and **S12** were screened for their antibacterial property using disc diffusion method against *Bacillus cereus* and *Escherichia coli*. These bacteria were inoculated and incubated into Luria Bertani (LB) broth for 16 hours in an incubator at 37 °C. The culture was then diluted with a fresh LB broth and adjusted to 0.168 at wavelength of 550 nm in a UV-Vis spectrophotometer which represent 2.0 x $10^6$ (CFU/ml). A sterile cotton swab was lightly dipped into the culture and evenly inoculated into LB agar. After that, sterile 6mm paper disc was placed on agar in equal distance. Subsequently, 20 µl of compounds at 250 ppm in EtOH were dispensed individually to each of the disc and EtOH itself was tested to act as control. The agar plate was incubated at 37 °C for 24 hours. The presence of inhibition zone was recorded and measured in diameter (mm).

## Results and Discussion

### Characterization study: 3-octyloxybenzaldehyde (T8)

Colour: Oily yellowish brown. Yield: 57%. Main IR peaks ($cm^{-1}$): ν(C-H) aliphatic ($CH_2$) 2924, ν(C-H) alkanes ($CH_3$) 2854, ν(C=O) 1697, ν(C-O) 1260. $^{1}H$ NMR (DMSO-$d_6$, ppm): 9.96 (s, 1H, HC=O); 7.49 – 7.21 (m, 4H, $H_{aromatic}$); 4.02 – 3.99 (t, 2H, HC-O); 1.42 – 1.23 (m, 15H, $H_{alkanes}$): $^{13}C$ NMR (DMSO-$d_6$, ppm): 192.97 (HC=O); 159.20 (C-O); 137.65 – 113.59 (aromatic); 67.75 – 13.98 (aliphatic).

**3-decyloxybenzaldehyde (T10)**
Colour: Oily yellowish brown. Yield: 59%. Main IR peaks ($cm^{-1}$): ν(C-H) aliphatic ($CH_2$) 2922, ν(C-H) alkanes ($CH_3$) 2853, ν(C=O) 1697, ν(C-O) 1260. $^1$H NMR (DMSO-$d_6$, ppm): 9.95 (s, 1H, HC=O); 7.50 – 7.22 (m, 4H, $H_{aromatic}$); 4.01 – 3.98 (t, 2H, HC-O); 1.38 – 1.23 (m, 17H, $H_{alkanes}$): $^{13}$C NMR (DMSO-$d_6$, ppm): 192.93 (HC=O); 159.20 (C-O); 137.64 – 113.53 (aromatic); 67.73-13.96 (aliphatic).

**3-dodecyloxybenzaldehyde (T12)**
Colour: Oily yellowish brown. Yield: 60%. Main IR peaks ($cm^{-1}$): ν(C-H) aliphatic ($CH_2$) 2921, ν(C-H) alkanes ($CH_3$) 2852, ν(C=O) 1699, ν(C-O) 1260. $^1$H NMR (DMSO-$d_6$, ppm): 9.96 (s, 1H, HC=O); 7.49 – 7.24 (m, 4H, $H_{aromatic}$); 4.02 – 3.99 (t, 2H, HC-O); 1.39 – 1.21 (m, 19H, $H_{alkanes}$): $^{13}$C NMR (DMSO-$d_6$, ppm): 192.95 (HC=O); 159.20 (C-O); 137.64 – 113.54 (aromatic); 67.74 – 13.98 (aliphatic).

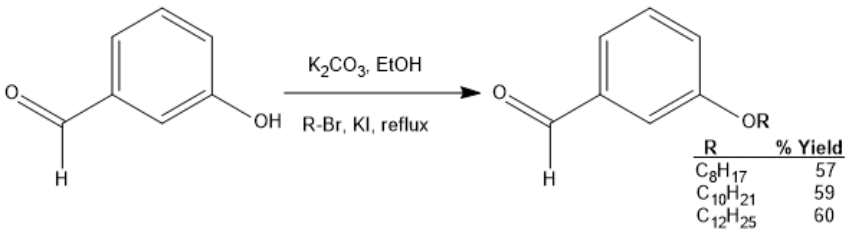
**3-hydroxybenzaldehydesallycylhydrazide (S)**
Colour: White fluffy paper-like structure. Yield: 98%. Main IR peaks ($cm^{-1}$): ν(NH) 3255, ν(O-H) 3059, ν(C=O) 1643, ν(C=N) 1611, ν(N-N) 1147. $^1$H NMR (DMSO-$d_6$, ppm): 8.36 (s, 1H, HC=N); 9.69 (s, 1H, NH); 11.84 (s, 2H, OH); 7.89 – 6.83 (m, 8H, $H_{aromatic}$): $^{13}$C NMR (DMSO-$d_6$, ppm): 148.77 (C=N); 157.74 (C-O); 135.43 –116.01 (aromatic).

**3-octyloxybenzaldehydesallycylhydrazide (S8)**
Colour: White needle shape crystal. Yield: 89%. Main IR peaks ($cm^{-1}$): ν(NH) 3246, ν(O-H) 3045, ν(C-H) aliphatic ($CH_2$) 2916, ν(C-H) alkanes ($CH_3$) 2846, ν(C=O) 1658, ν(C=N) 1627, ν(C-O) 1278, ν(N-N) 1145. $^1$H NMR (DMSO-$d_6$, ppm): 8.42 (s, 1H, HC=N); 10.28 (s, 1H, NH); 11.89 (s, 1H, OH); 7.92 – 6.98 (m, 8H, $H_{aromatic}$); 4.01 – 3.98 (t, 2H, HC-O); 1.41 – 1.25 (m, 15H, $H_{alkanes}$): $^{13}$C NMR (DMSO-$d_6$, ppm): 148.50 (C=N); 159.02 (C-O); 135.56 – 116.06 (aromatic); 67.54 – 14.00 (aliphatic).

**3-octyloxybenzaldehydesallycylhydrazide (S10)**
Colour: White granules. Yield: 92%. Main IR peaks ($cm^{-1}$): ν(NH) 3246, ν(O-H) 3049, ν(C-H) aliphatic ($CH_2$) 2918, ν(C-H) alkanes ($CH_3$) 2849, ν(C=O) 1658, ν(C=N) 1626, ν(C-O) 1278, ν(N-N) 1147. $^1$H NMR (DMSO- $d_6$, ppm): 8.41 (s, 1H, HC=N); 10.27 (s, 1H, NH); 11.88 (s, 1H, OH); 7.90 – 6.94 (m, 8H, $H_{aromatic}$); 4.01 – 3.98 (t, 2H, HC-O); 1.41 – 1.24 (m, 17H, $H_{alkanes}$): $^{13}$C NMR (DMSO- $d_6$, ppm): 148.53 (C=N); 159.03 (C-O); 135.56 – 116.01 (aromatic); 67.53 – 14.03 (aliphatic).

**3-octyloxybenzaldehydesallycylhydrazide (S12)**
Colour: White granules. Yield: 93%. Main IR peaks ($cm^{-1}$): ν(NH) 3246, ν(O-H) 3043, ν(C-H) aliphatic ($CH_2$) 2918, ν(C-H) alkanes ($CH_3$) 2847, ν(C=O) 1655, ν(C=N) 1625, ν(C-O) 1277, ν(N-N) 1148. $^1$H NMR (DMSO- $d_6$, ppm): 8.41 (s, 1H, HC=N); 10.27 (s, 1H, NH); 11.89 (s, 1H, OH); 7.92 – 6.93 (m, 8H, $H_{aromatic}$); 4.00 – 3.98 (t, 2H, HC-O); 1.41 – 1.22 (m, 19H, $H_{alkanes}$): $^{13}$C NMR (DMSO- $d_6$, ppm): 148.51 (C=N); 159.02 (C-O); 135.55 – 115.99 (aromatic); 67.52 – 14.01 (aliphatic).

**Spectroscopic studies: Etherification of 3-hydroxybenzaldehyde**
The yield of 3-(alkoxy)benzaldehyde from the reaction of 3-hydroxybenzaldehyde with 1-bromooctane, 1-bromodecane and 1-bromododecane, respectively were shown in Scheme 1. All figures shown were corresponding to T8 and S8, while the rest of the data were tabulated in Table 1 till Table 3.




Scheme 1. Etherification of 3-hydroxybenzaldehyde

Table 1. Data of infrared spectroscopy ($cm^{-1}$)

| Compound | ν(NH) | ν(O-H) | ν(C-H) aliphatic ($CH_2$) | ν(C-H) alkanes ($CH_3$) | ν(C=O) | ν(C=N) | ν(C-O) | ν(N-N) |
|---|---|---|---|---|---|---|---|---|
| T8 | - | - | 2924 | 2854 | 1697 | - | 1260 | - |
| T10 | - | - | 2922 | 2853 | 1697 | - | 1260 | - |
| T12 | - | - | 2921 | 2852 | 1699 | - | 1260 | - |
| S | 3255 | 3059 | - | - | 1643* | 1611 | - | 1147 |
| S8 | 3246 | 3045 | 2916 | 2846 | 1658* | 1627 | 1278 | 1145 |
| S10 | 3246 | 3049 | 2918 | 2849 | 1658* | 1626 | 1278 | 1147 |
| S12 | 3246 | 3043 | 2918 | 2847 | 1655* | 1625 | 1277 | 1148 |

*Due to present of another C=O at salicylhydrazide side

Table 2. Data of $^{1}H$ NMR spectroscopy (ppm)

| Compound | HC=O | HC=N | NH | OH | $H_{aromatic}$ | $H_{alkanes}$ |
|---|---|---|---|---|---|---|
| T8 | 9.96 s | - | - | - | 7.49 – 7.21m | 1.42 – 1.23 m |
| T10 | 9.95 s | - | - | - | 7.50 – 7.22 m | 1.38 – 1.22 m |
| T12 | 9.96 s | - | - | - | 7.49 – 7.24 m | 1.39 – 1.21 m |
| S | - | 8.36 s | 9.69 s | 11.84 s | 7.89 – 6.83 m | - |
| S8 | - | 8.42 s | 10.28 s | 11.89 s | 7.92 – 6.98 m | 1.41 – 1.25 m |
| S10 | - | 8.41 s | 10.27 s | 11.88 s | 7.90 – 6.94 m | 1.41 – 1.24 m |
| S12 | - | 8.41 s | 10.27 s | 11.89 s | 7.90 – 6.93 m | 1.41 – 1.22 m |

Table 3. Data of $^{13}C$ NMR spectroscopy (ppm)

| Compound | HC=O | HC=N | C-O | $C_{aromatic}$ | $C_{aliphatic}$ |
|---|---|---|---|---|---|
| T8 | 192.97 | - | 159.20 | 137.65-113.59 | 67.75-13.98 |
| T10 | 192.93 | - | 159.20 | 137.64-113.53 | 67.73-13.96 |
| T12 | 192.95 | - | 159.20 | 137.64-113.54 | 67.74-13.98 |
| S | - | 148.77 | 157.74 | 135.43-116.01 | - |
| S8 | - | 148.50 | 159.02 | 135.56-116.06 | 67.54-14.00 |
| S10 | - | 148.53 | 159.03 | 135.56-116.01 | 67.53-14.03 |
| S12 | - | 148.51 | 159.02 | 135.55-115.99 | 67.52-14.01 |

The IR spectrum of **T8** in Figure 1 shows the disappearance of ν(-OH) peak compared to the IR spectrum of 3-hydroxybenzaldehyde at 3194 $cm^{-1}$ and the appearance of new peaks attributed to ν(-$CH_3$) alkyl chain in range of 2854 and 2924 $cm^{-1}$. The intensity of the peaks is depended on the length of an alkyl chain presence in the compounds; the longer alkyl chains the stronger intensity of the peak and *vice versa*.

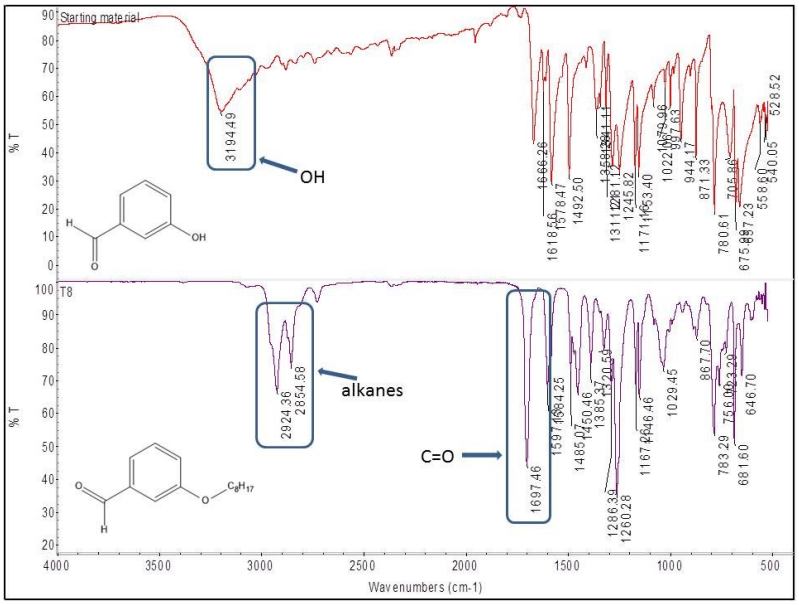



Figure 1. IR spectra of 3-hydroxybenzaldehyde (top) and T8 (bottom)

Similarly, the $^{1}$H NMR spectra of the three etherified products (i.e. $^{1}$H NMR spectrum of **T8** in Figure 2) showed the disappearance of $OH^{-}$ signal at 10.10 ppm and the existence of new proton signals for the alkoxy group at the high field region (δ: 1.00 – 4.00 ppm) has indicated the success of the etherification of 3-hydroxybenzaldehyde.

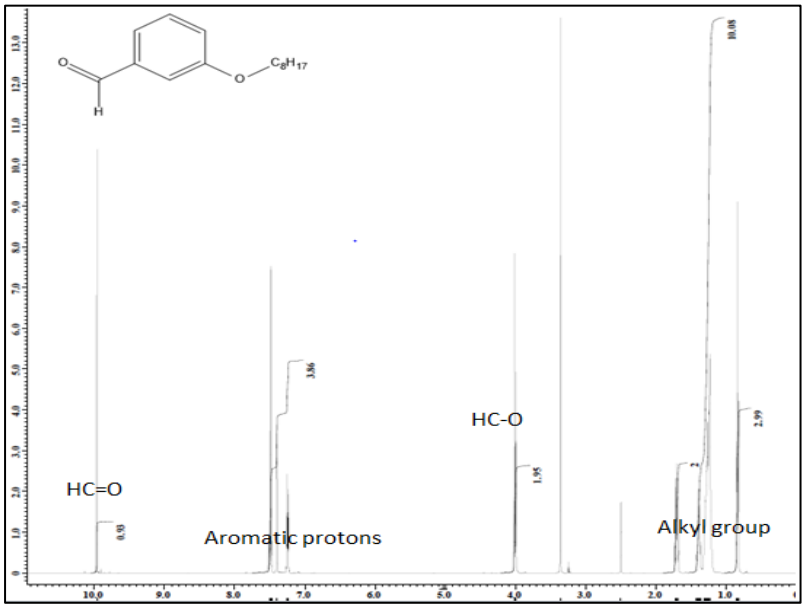
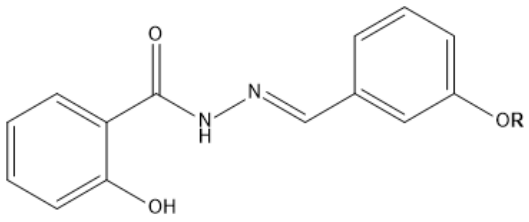



Figure 2. $^{1}$H NMR spectrum of T8

**Characterization of hydrazone Schiff base**
The yield of 3-(alkoxy)benzaldehydesalicylhydrazide were shown in Scheme 2.




| R | % Yield |
|---|---|
| H | 98 |
| $C_8H_{17}$ | 89 |
| $C_{10}H_{21}$ | 92 |
| $C_{12}H_{25}$ | 93 |

Scheme 2. Percentage yield of 3-(alkoxy)benzaldehydesalicylhydrazide

The IR spectrum of **S8** is shown in Figure 3. The disappearance of ν(C=O) peak in 3-(octyloxy)benzaldehyde at 1697 $cm^{-1}$ and appearance of new peaks at 1627, 3045 and 3246 $cm^{-1}$ was attributed to ν(C=N) stretching, ν(-OH) and ν(-NH) of **S8**, respectively.

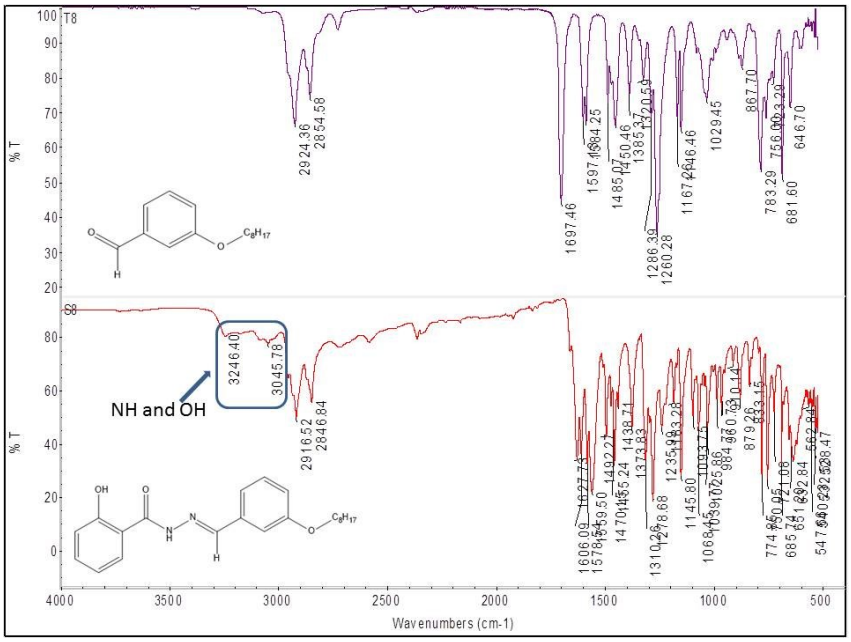



Figure 3. IR spectra of T8 (top) and S8 (bottom)

The $^1$H NMR spectrum of **S8** is shown in Figure 4. Similarly, the formation of **S8** can be represented by the deshielded of HC=N resonance at 8.42 ppm. This is due to the formation of C=N from C=O. In addition, the appearance of new peaks at 10.28 and 11.89 ppm confirmed the presence of NH and OH supporting the formation of **S8**.

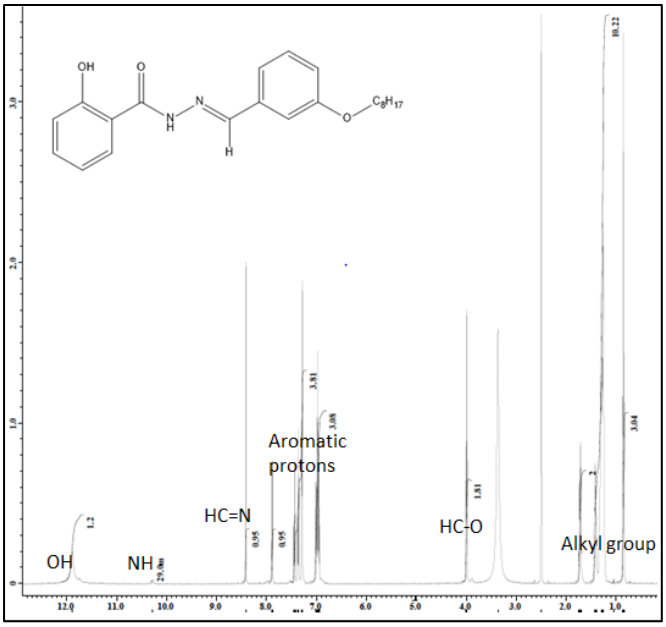



Figure 4. $^{1}$H NMR spectrum of **S8**

**Antibacterial screening**

The antibacterial activity of hydrazine Schiff base compounds **S**, **S8**, **S10** and **S12** were examined using disc diffusion method and the result were illustrated in Figure 5. The results show that, there is no significant inhibition of all the tested compounds to the activity of gram-positive bacteria represented by *Bacillus cereus*. On the other hand, there were strong inhibitions shown for the gram-negative bacteria, *Escherichia coli*. The increase of carbon chains in the structure has enhanced the inhibitory of bacteria activity. However, the activity showed slightly decrease as the length of carbon chain extended to C12. By these results, it is suggested that the moderate carbon chain size of lipophilic substituents might be vital for the optimal antimicrobial activity.

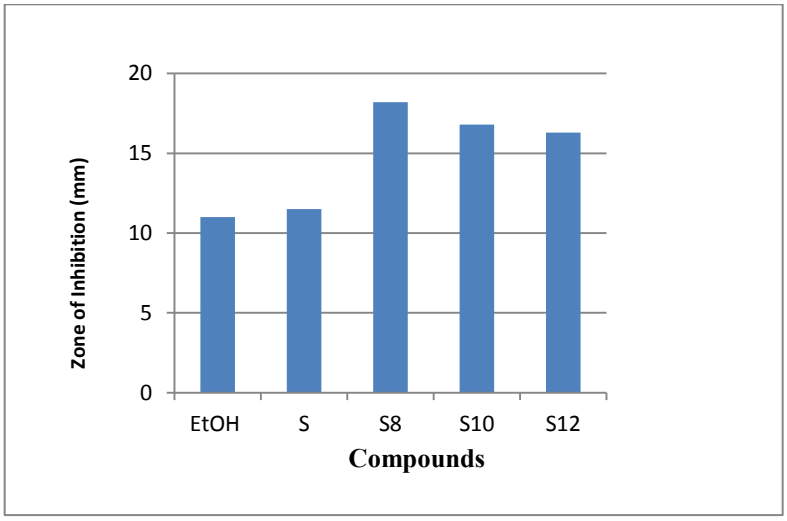



Figure 5. Antibacterial activity against *Escherichia coli*

## Conclusion

Hydrazone shiff base 3-hydroxybenzaldehyde salicylhydrazide (**S**), 3-(octyloxy)benzaldehyde salicylhydrazide (S8), 3-(decyloxy)benzaldehyde salicylhydrazide (**S10**) and 3-(dodecyloxy)benzaldehyde salicylhydrazide (**S12**) were successfully synthesised and characterized using FTIR, $^{1}$H NMR and $^{13}$C NMR. The presence of long carbon chain in the structure has enhanced the antibacterial activity which in good agreement with lipophilic effect. However, the result suggested that there is an optimum carbon chain number that give the highest inhibitory effect in antibacterial grow for gram-negative bacteria while non affect can be observed in gram-positive tested bacteria.

## Acknowledgement

The authors would like to express their sincere appreciation to Malaysian Ministry of Higher Education for financial support under the research grant number of RAGS/ST01/(1)/1038/2013/(05).

## References

1. Khanmohammadi, H., Abnosi, M. H., Hosseinzadeh, A. And Erfantalab, M. (2008). Synthesis, biological and computational study of new Schiff base hydrazones bearing 3-(4-pyridine)-5-mercapto-1,2,4-triazole moiety. *Spectrochimica Acta Part A*, 71: 1474 – 1480.
2. Hearn, M. J., Cynamon, M. H., Chen, M. F., Coppins, R., Davis, J., Kang, H. J. O., Noble, A., Sekine, B. T., Terrot, M. S., Trombino, D., Thai, M., Webster, E. R. and Wilson, R. (2009). Preparation and antitubercular activities in vitro and in vivo of novel Schiff base of isoniazid. *European Journal of Medicinal Chemistry*, 44: 4169 – 4178.
3. Walcourt, A., Loyevsky, M., Lovejoy, D. B., Gordeuk, V. R. and Richardson, D. R. (2004). Novel aroylhydrazone and thiosemicarbazone iron chelators with anti-malarial activity against chloroquine-resistant and –sensitive parasites. *The International Journal of Biochemistry & Cell Biology*, 36: 401 –407.
4. Mishra, N., Poonia, K. and Kumar, D. (2013). An overview of biological aspects of Schiff base metal complexes. *International Journal of Advancements in Research & Technology*, 2(8): 52 – 66.
5. Devinsky, F. and Gorrod, J. W. (1987). Microsomal N-oxidation of long chain N,N-dimethylalkylamines: Quantitative structure-activity relationships. *European Journal of Drug Metabolism and Pharmacokinetics*, 12: 267 – 273.
6. Park, K. D., Park, Y. S., Cho, S. J., Sun, W. S., Kim, S. H., Jung, D. H. and Kim, J. H. (2004). Antimicrobial activity of 3-O-acyl-(-)-epicatechin and 3-O-acyl-(+)-catechin derivatives. *Planta Medica*, 70: 272 – 276.
7. Tay, M. G., Ngaini, Z., Sarih, N. M., Foo, S.W. and Tiong, M. H. (2011). A convenient way for the etherification of *p*-hydroxyacetophenone. *Research Bulletin, Faculty of Resource Science and Technology*, *Universiti Malaysia Sarawak*: pp. 1 – 3.

*Malaysian Journal of Analytical Sciences, Vol 21 No 5 (2017): 1203 - 1209*
*DOI: https://doi.org/10.17576/mjas-2017-2105-25*

MALAYSIAN JOURNAL OF ANALYTICAL SCIENCES
*Published by The Malaysian Analytical Sciences Society*
ISSN 1394 - 2506

# ONE-POT MANNICH BASE SYNTHESIS USING TASK SPECIFIC PROTIC IONIC LIQUIDS

## (Sintesis Bes Mannich Tunggal Menggunakan Cecair Ionik Terkhusus)

Sabahat Sardar*, Cecilia Devi Wilfred, Jean Marc Leveque

*Fundamental and Applied Sciences*
*Universiti Teknologi PETRONAS, Teronoh, Perak, Malaysia*

**Corresponding author: sba.qau@gmail.com*

Received: 21 August 2016; Accepted: 27 July 2017

**Abstract**

Three-component Mannich reaction of ketones, aromatic aldehydes and aromatic amines was catalyzed by four Bronsted acidic ionic liquids comprising of iodide and borate at room temperature. Ionic liquid have been used as catalyst and solvent to produce some Mannich bases in high yield (75%) and shorter reaction time (20 minutes). Work up has been facilitated by simple extraction with water to recover ionic liquid for recycling up to four times without any significant loss in activity.

**Keywords**: Mannich bases, Bronsted acidic ionic liquids, 1-methylimidazole, 1,3-propane sultone, 1,4-butane sultone

**Abstrak**

Tindak balas tiga komponen Mannich iaitu keton, aldehid aromatik dan amina aromatik telah dimangkinkan oleh empat cecair ionik Bronsted berasid yang terdiri daripada iodida dan borat pada suhu bilik. Cecair ionik telah digunakan sebagai pemangkin dan pelarut untuk menghasilkan beberapa bes Mannich dengan hasil yang tinggi (75%) dan masa tindak balas yang lebih pendek (20 minit). Kerja pengekstrakan telah dipermudah dengan menggunakan air dan boleh dikitar semula sehingga empat kali tanpa sebarang kehilangan aktiviti yang penting.

**Kata kunci**: bes Mannich, asid Bronsted cecair ionik, 1-metilimidazol, 1,3-propana sulton, 1,4-butana sulton

## Introduction

Multicomponent reactions have been proven to be an economic and facile approach for building of complex molecules in one synthetic step. A remarkable diversity can be achieved by varying the starting materials. Such appealing reactions offer an elegant course for synthesis of carbon-carbon and carbon-hetero atom linkages with high atom economy, simple methodology and high selectivity in one-pot procedure [1]. Mannich reaction is a fundamental method for a formation of β-amino carbonyl compounds of synthetic intermediates for natural product synthesis (alkaloids and polyketides) and in pharmaceutical industry [2]. The conventional catalysts for the synthesis of classical Mannich bases are mainly organic and mineral acids such as acetic acid [3], proline [4], p-dodecylbenzenesulfonic acid [5] and lewis acids [6]. These reactions conditions often lead to problems like difficulty in product separation, harsh reaction conditions, long reaction durations, toxicity and pollution [7]. Further development lead to the usage of other catalysts such as pTSA, BDMS, $HClO_4$-$SiO_2$, TMSCl, Amberlyst-15, carbon based solid acid, $AuCl_3$-$PPh_3$, $InCl_3$, silica supported sulphuric acid, $NbCl_5$, bismuth (III) chloride, sulfamic acid, boric acid, sucrose charsulfunic acid, $Zn(OTf)_2$, etc. [8]. The drawbacks include: large amount of

catalyst, expensive catalyst, high waste production, long reaction duration and ultimately low yield. [9]. Lanthanide triflate in acetonitrile or dichloromethane has also been reported for Mannich reaction catalysis [10].

In contribution to green chemistry, many studies reported on employing traditional volatile and flammable solvents to benign alternatives such as non-volatile solvent, supercritical system, aqueous media or solventless conditions. In this context, Mannich type reactions have also been reported in water [10]. In current years, ionic liquids (ILs) have been used as an environmentally benign solvents, efficient catalysts and a promising substitutes for volatile organic solvents and traditionally used acid/ base catalysts in construction of organic moieties [11, 12]. Use of organic solvents in reaction mixture usually leads to serious safety issues such as volatility, flammability and toxicity [12, 13]. The use of ionic liquids as reaction media offers a convenient solution to both solvent emission and catalytic recycling problems [10]. Beside high activity and selectivity, these versatile liquids are center of interest as they possess unique properties such as flexibility, high stability in air and water, easy separation and purification processes, reusability, non-volatility, non-flammability, noncorrosive nature, controlled immiscibility, low toxicity, low vapour pressure, low viscosities, high thermal and chemical stabilities [14-16]. Recently work on Mannich reaction is being carried out using ionic liquids [17, 18].

The present study emphasizes on employing ionic liquids as catalyst and solvents to overcome issues associated with traditional catalysts and organic solvents. In this approach, a green procedure has been proposed for synthesis of Mannich bases using acetophenone, aromatic aldehydes and anilines as starting materials. To the best of our knowledge, Mannich reaction catalyzed by ILs bearing imidazolium sultone as cation; and iodide and borate as anions are unprecedented. The reaction proceeded at faster rate with higher yield of desired Mannich bases using the synthesized ionic liquids. The effect of cations and anions in addition to the influence of additional carbon atom on sultone moiety was also been investigated.

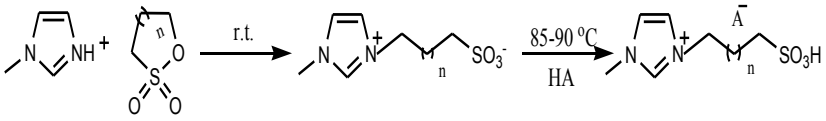
## Materials and Methods

### Chemicals

All the reacting molecules used such as 1,3-propane sultone, 1,4-butane sultone, *N*-methylimidazole, hydriodic acid, boric acid, acetonitrile, aromatic amines, aromatic aldehydes, acetophenone and cyclohexanone were purchased from Sigma Aldrich and used without any purification procedure. Melting points of the Mannich bases were determined in open capillaries and are uncorrected. NMR spectra were recorded on 400 MHz NMR Joel spectrometer using $D_2O$ and $CDCl_3$ as solvents. IR spectra were recorded in Nicolet FTIR spectrometer (400 – 4000 $cm^{-1}$).

### Synthesis of ionic liquids

The task specific ionic liquids have been synthesized by using an analogous method as reported in literature [19-21] with slight modifications. 1,3-propane sultone and 1,4-butane sultone were reacted with *N*-methylimidazole in equimolar ratio affording the respective zwitter ions that were then converted to ILs by acidification with two protic acids (Scheme 1). The corresponding ILs were used further without any purification.



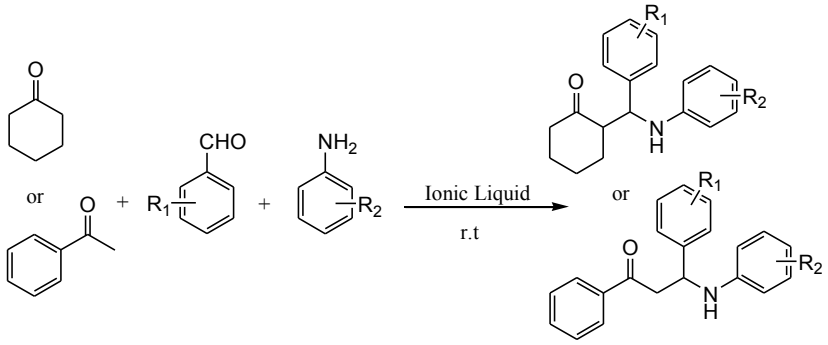

where $A^- = I^-, B(OH)_4^-$, n= 1 and 2

Scheme 1. Reaction scheme for IL synthesis

### Mannich reaction: A typical procedure

Cyclohexanone (10 mmol), benzaldehyde (10 mmol), aniline (10 mmol) and 5 mmol of catalyst were taken in round bottom flask at 25 $^oC$ (Scheme 2) [22]. The completion of reaction was determined using TLC. For work up, some amount of water was added and extraction with ethyl acetate was done. The excess solvent was evaporated via rotary evaporator to afford solid product which was recrystallized from acetonitrile and dried under vacuum until

constant weight was obtained. At the end, the aqueous layer containing IL was vacuum dried at 70 °C to reuse ionic liquid for future use. The synthesized compounds were then characterized using IR and NMR. The spectral analysis along with physical data (melting points) was consistent with those reported in literature.




Scheme 2. Mannich reaction catalyzed by imidazolium based ionic liquids ($R_1$ and $R_2$ are mentioned in Table 4)

## Results and Discussion

The ionic liquids were synthesized by the reaction of methyl imidazole with 1,3-propane sultone and 1,4-butane sultone for preparation of Mannich bases. Spectral analysis confirmed the structure of synthesized ILs. these synthesized ILs were used to catalyze Mannich reaction using acetophenone/ cyclohexanone (10 mmol), benzaldehyde (10 mmol) and aniline (10 mmol) as model substrates at room temperature (Scheme 2).

The reaction mixture gradually turned to highly viscous material within 30 minutes. The reaction work up was done by addition of a small amount of water followed by extraction with ethyl acetate and finally evaporation of organic solvent. For purification, the synthesized Mannich bases were recrystallized from acetonitrile and the aqueous layer was further dried for recycling ionic liquid. Among the four protic ILs 75% of Mannich base was obtained as highest yield by 1-methyl-3-(3-sulfopropyl)-imidazolium borate ([mimps]HBO) in 20 minutes (Table 1).

Table 1. Effect of ionic liquid on yield of Mannich base[a]

| Entry | Catalyst | Solvent Used | Reaction Time (min) | Isolated Yield (%) |
|---|---|---|---|---|
| 01 | - | -, EtOH[b, c, d] | 120 | NR[a,b, c, d] |
| 02 | [mimps]I | -, EtOH[b, c, d] | 120 | NR[a,b, c, d] |
| 03 | [mimbs]I | -, EtOH[b, c, d] | 120 | NR[a,b, c, d] |
| 04 | [mimps]HBO | - | 20 | 75 |
| 05 | [mimbs]HBO | - | 30 | 69 |

[a] Reaction conditions: cyclohexanone (10 mmol), benzaldehyde (10 mmol), aniline (10 mmol), catalyst (5 mmol) r.t.
[b] yield in presence of solvent
[c] yield obtained at 60 °C
[d] yield obtained at 80 °C

The reaction with $I^-$ as anion, was also carried out with ethanol using same IL as catalyst using different temperatures but the results obtained were insignificant (Table 1). It was observed that IL based on propane sultone gave better yield than butane sultone based IL (entries 4 and 5 in Table 1). Furthermore it was also found that the IL formed from weak acid ($H_3BO_3$) gave better yield as compared to the IL which was formed from strong acid (HI).

This observation might be rationalized on basis of pKa, which depicts that the reaction is catalyzed by conjugate bases ($I^-$ and $B(OH)_4^-$) of the protic acids (HI and $H_3BO_3$).

For determining the amount of IL used, the reaction of cyclohexanone (10 mmol), benzaldehyde (10 mmol), aniline (10 mmol) was catalyzed under variable amounts of [mimps]HBO at room temperature. It was found that the yields of the Mannich base was increased with the increase in the amount of [mimps]HBO (Table 2), where 5 mmol was found as an optimal amount.

Table 2. Effect of amount of ionic liquid on Mannich reaction

| Entry | Ionic Liquid (mmol) | Reaction Time (min) | Isolated Yield (%) |
|---|---|---|---|
| 01 | 0 | 24 h | 0 |
| 02 | 1 | 30 | 66 |
| 03 | 3 | 30 | 71 |
| 04 | 5 | 30 | 75 |
| 05 | 7 | 30 | 74 |
| 06 | 9 | 30 | 75 |

Mannich reaction was also conducted in polar and non-polar organic solvents to check the effect of solvent on the yield of product formed for estimation of the best reaction conditions. Herein the reaction of cyclohexanone, benzaldehyde and aniline was selected as standard reaction. It was found that the reaction in which no solvent was used gave the highest yield of 75% among the solvents selected showing that the ionic liquid may act as dual-reagent without need of any external solvent (Table 3).

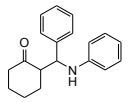
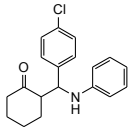
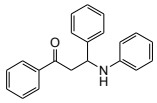
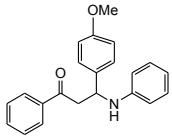
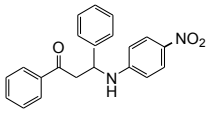
Table 3. Effect of ionic liquid/solvent on Mannich reaction[a]

| Entry | Ionic Liquid/Solvent | Isolated Yield |
|---|---|---|
| 01 | [mimps]HBO | 75 |
| 02 | [mimps]HBO/$H_2O$ | 70 |
| 03 | [mimps]HBO/$C_2H_5OH$ | 69 |
| 04 | [mimps]HBO/$CH_2Cl_2$ | 61 |
| 05 | [mimps]HBO/$C_6H_6$ | 39 |

[a] Reaction conditions: cyclohexanone (10 mmol), benzaldehyde (10 mmol), aniline (10 mmol), [mimps]HBO (5 mmol) r.t.

The Mannich reaction was further investigated with different aromatic aldehydes and anilines using [mimps]HBO. It was observed that aromatic aldehyde with electron-donating group produced higher yield of Mannich base as compared to that of electron withdrawing group (Table 4). In case of aromatic anilines, both electron withdrawing and electron-donating groups have been reported to be equally valuable for Mannich reaction [7]. The synthesis of Mannich bases was confirmed by physical and spectroscopic data and was found in good agreement with the previous reports.

Table 4. Preparation of –amino ketones using [mimps]HBO as catalyst

| Entry | $R_1$ | $R_2$ | H-Active Molecule | Product | Yield (%) | mp ($^oC$) (lit. mp) [ref] |
|---|---|---|---|---|---|---|
| 01 | H | H | $(CH_2)_5CO$ |  | 75 | 114 – 115 (115 – 116) [24] |
| 02 | 4-chloro | H | $(CH_2)_5CO$ |  | 73 | 133 – 134 (134 – 135) [25] |
| 03 | H | H | $C_6H_5CO$ |  | 75 | 168 – 169 (169 – 171) [26] |
| 04 | 4-methoxy | H | $C_6H_5CO$ |  | 74 | 150 – 151 151 – 152 [27] |
| 05 | H | 4-$NO_2$ | $C_6H_5CO$ |  | 72 | 184 – 186 183 – 185 [27] |

Regarding the reusability of ionic liquid, it was found that the IL could be successfully reused up to four cycles without considerable loss of activity (Table 5).

Table 5. Reusability of [mimps]$CH_3COO$ for Mannich reaction

| Entry | Cycle | % Yield |
|---|---|---|
| 1 | I | 75 |
| 2 | II | 75 |
| 3 | III | 74 |
| 4 | IV | 74 |

**Spectral analyses of Zwitter ions and ionic liquids: 1-methylimidazolium-3-(3-propylsulfonate)**
$^1$H NMR (400 MHz, $D_2O$): $\delta$ (ppm) 2.24 (2H, m), 2.73 (2H, t *J*=7.32 Hz), 3.92 (3H, s), 4.24 (2H, t *J*=7.24 Hz), 7.37 (1H, s), 7.45 (1H, s), 8.87 (1H, s); $^{13}$C NMR (400 MHz, $D_2O$): $\delta$ (ppm) 25.5 ($CH_3$), 38.7 ($CH_2$), 48.2 ($CH_2$), 49.5 ($CH_2$), 124.1 (C=C), 126.3 (C=C), 139.1 (C=N); IR ($cm^{-1}$): 3093 C-H stretching (alkene), 1654 C=N stretching (imine), 1456 $CH_2$ bending, 1178 and 1158 S=O stretching (sulfonate), 1034 S=O stretching (sulfoxide).

**1-methyl-3-(3-sulfopropyl)-imidazolium iodide**
([mimps]I, Table 2, entry 2): $^1$H NMR (400 MHz, $D_2O$): $\delta$ (ppm) 2.18 (2H, m), 2.78 (2H, t *J*=7.23 Hz), 3.75 (3H, s), 4.22 (2H, t), 6.37 (1H, s), 6.45 (1H, s), 7.67 (1H, s); $^{13}$C NMR (400 MHz, $D_2O$): $\delta$ (ppm) 22.9 ($CH_3$), 37.9 ($CH_2$), 50.4 ($CH_2$), 56.8 ($CH_2$), 122.9 (C=C), 123.1 (C=C), 137.2 (C=N); IR ($cm^{-1}$): 3090 C-H stretching (alkene), 1685 C=N stretching (imine), 1560 C=C stretching (cyclic alkene), 1453 $CH_2$ bending, 1160 S=O stretching (sulfonate), 1020 S=O stretching (sulfoxide).

**1-methyl-3-(4-sulfobutyl)-imidazolium iodide**
([mimbs]I, entry 3): $^{1}$H NMR (400 MHz, $D_2O$): $\delta$ (ppm) 1.61 (2H, m), 1.88 (2H, m), 2.81 (2H, t *J*=6.98 Hz), 3.73 (3H, s), 4.12 (2H, t *J*=6.86 Hz), 7.32 (1H, s), 7.38 (1H, s), 8.61 (1H, s); $^{13}$C NMR (400 MHz, $D_2O$): $\delta$ (ppm) 21.3 ($CH_3$), 28.2 ($CH_2$), 37.7 ($CH_2$), 52.1 ($CH_2$), 57.6 ($CH_2$), 122.6 (C=C), 122.8 (C=C), 137.4 (C=N); IR ($cm^{-1}$): 3090 C-H stretching (alkene), 1685 C=N stretching (imine), 1560 C=C stretching (cyclic alkene), 1453 $CH_2$ bending, 1161 S=O stretching (sulfonate), 1020 S=O stretching (sulfoxide).

**1-methyl-3-(3-sulfopropyl)-imidazolium borate**
([mimps]HBO, entry 4): $^{1}$H NMR (400 MHz, $D_2O$): $\delta$ (ppm) 2.19 (2H, m), 2.78 (3H, s), 3.75 (2H, t *J*=7.24 Hz), 4.23 (2H, t *J*=7.16 Hz), 7.32(1H, s), 7.38 (1H, s), 8.61 (1H, s); $^{13}$C NMR (400 MHz, $D_2O$): $\delta$ (ppm) 23.6 ($CH_3$), 36.3 ($CH_2$), 50.3 ($CH_2$), 56.5 ($CH_2$), 121.2 (C=C), 121.5 (C=C), 137.5 (C=N); IR ($cm^{-1}$): 3159 C-H stretching (alkene), 1640 C=N stretching (imine), 1574 C=C stretching (cyclic alkene), 1392, 1163 S=O stretching (sulfonate), 1035 S=O stretching (sulfoxide).

**1-methyl-3-(4-sulfobutyl)-imidazolium borate**
([mimbs]HBO, entry 5): $^{1}$H NMR (400 MHz, $D_2O$): $\delta$ (ppm) 1.61 (2H, m), 1.91 (2H, m), 2.82 (2H, t *J*=7.24 Hz), 3.78 (3H, s), 4.14 (2H, t *J*=7.31 Hz), 7.35 (1H, s), 7.41 (1H, s), 8.61 (1H, s); $^{13}$C NMR (400 MHz, $D_2O$): $\delta$ (ppm) 20.03 ($CH_3$), 27.2 ($CH_2$), 36.9 ($CH_2$), 47.9 ($CH_2$), 49.2 ($CH_2$), 121.8 (C=C), 122.6 (C=C), 136.3 (C=N); IR ($cm^{-1}$): 3157 C-H stretching (alkene), 1641 C=N stretching (imine), 1575 C=C stretching (cyclic alkene), 1165 S=O stretching (sulfonate), 1038 S=O stretching (sulfoxide).

## Conclusion

Present methodology deals with a useful and effective way for synthesis of Mannich bases at room temperature in short reaction duration (20 minutes) and good yield (75%) using ILs as dual reagents. The reported synthetic method can be expected as an environmentally green procedure that might give valuable organic transformations by substituting conventional volatile, toxic and flammable organic solvents with ILs. Simple experimental and work up conditions along with reusability of IL can contribute a new method of green chemistry concept.

## References


1. Mukhopadhyay, C., Rana, S. and Butcherb, R. J. (2010). An ionic liquid {[secbmim]$^{+}$Br$^{-}$} as a "dual reagent catalyst" for the multicomponent synthesis of (quinilinyl- and isoquinolinyl- amino) alkylnaphthols, their bis-analogs and a facile route to naphthoxazines. *ARKIVOC*, 10: 291 – 304.
2. Balasubramaniam, S. and Aidhen, I. S. (2008). The growing synthetic utility of the weinreb amide, *Synthesis,* 2008(23): 3707 – 3738.
3. Mogilaiah, K. and Kanksiah, G. (2002). Synthesis and antibacterial activity of novel Mannich bases containing 1,8-naphthyridine moiety. *Indian Journal Heterocyclic Chemistry,* 11: 282 – 286.
4. List, B. (2000). The direct catalytic asymmetric three-component Mannich reaction. *Journal of American Chemical Society*, 122: 9336 – 9338.
5. Manabe, K., Mori, Y and Kobayashi, S. (2001). Three-component carbon-carbon bond-forming reactions catalyzed by a Bronsted acid-surfactant-combined catalyst in water. *Tetrahedron,* 57: 2537 – 2544.
6. Kobayashi, S., Hamada, T. and Manabe, K. (2002). The catalytic asymmetric Mannich type reactions in aqueous media. *Journal of American Chemical Society,* 124: 5640 – 5641.
7. Zhao, G. and Lu, M. (2012). One-pot green procedure for Mannich reaction catalyzed by task specific ionic liquid. *Chiang Mai Journal of Sci*ence, 39: 49 – 58.
8. Vadivel, P., Maheswari, C. S. and Lalitha, A. (2013). Synthesis of β-amino carbonyl compounds via Mannich reaction using sulfated MCM-41. *International Journal of Innovative Technology and Exploring Engineering,* 2: 2278 – 3075.
9. Hajipoura, A. R. and Rafieeb, F. (2009) Basic ionic liquids. A short review. *Journal of the Iranian Chemical Society,* 6: 647 – 678.
10. Sahoo, S. Joseph, T. and Halligudi, S. B. (2006). Mannich reaction in Bronsted acidic ionic liquids: A facile synthesis of β-amino carbonyl compounds. *Journal of Molecular Catalysis A: Chemical,* 244: 179 – 182.

11. Cole, A. C. Jensen, J. L. Ntai, L. Loan, K. and Forbes, D. C. (2002). Novel Bronsted acidic ionic liquids and their use as dual solvent-catalyst. *Journal of American Chemical Society,* 124: 5962 – 5963.
12. Sapkal, S. B. Shelke, K. F. Madje, B. R. Shingate, B. B. and Shingare, M. S. (2009). 1-butyl-3methyl imidazolium hydrogen sulphate promoted one-pot three-component synthesis of amidoalskyl naphthols. *Bulletin Korean Chemical Society,* 30: 2887 – 2889.
13. Rajendran, A. and Priyadarshini, M. (2010). Synthesis and characterization of a novel ionic liquid (TBA-AMPS) and its applications in Mannich condensation reactions under solvent free conditions. *African Journal of Pure and Applied Chem*istry, 4: 183 – 187.
14. Dyson, P. J. and Geldbach, T. J. (2007). Applications of ionic liquids in synthesis and catalysis. *The Electrochemical Society Interface*, 16(1): 50 – 53.
15. Cserjesi, P., Bako K. B. and Gubicza, N. (2008). Recent trends on application of ionic liquids in organic synthesis. *Hungarian Journal of Industrial Chem*istry, 36: 27 – 34.
16. Rajendran, A., Ramu, S. and Karthikeyan, C. (2011). Green synthesis of some novel N-Mannich bases using environmentally benign catalyst under solvent free conditions. *International Journal of Current Research,* 33: 161 – 167.
17. Qain, H., Kai, W. and Zhen, J. (2016). Ultrasound-promoted synthesis of β-amino carbonyl coumpounds via a Mannich reaction catalyzed by ionic liquids. *Letters in Organic Chemistry,* 13: 143 – 147.
18. Senepak, W., Saeeng, R., Jaratiaroonphong, J., Kasemul, T. and Sirion, U. (2015). Green synthesis of dipyyromethanes in aqueous media catalyzed by $SO_3H$-funtionalized ionic liquids. *Organic & Biomolecular Chemistry*, 14: 1302 – 1310.
19. Kundamudi, K. Elavarasan, P. and Dyson, P. J (2010). Alkylation of p-cresol with tert-butyl alcohol using benign Bronsted acidic ionic liquid catalyst. *Journal of Molecular Catalysis,* 321: 34 – 41.
20. Han, X. and Zhou, L. (2011). Optimization of process variables in the synthesis of butyl butyrate using acid ionic liquid as catalyst. *Journal of Chemical Engineering,* 172: 459 – 466.
21. Dubreuil, J. Bourahla, K. and Rahmouni, M. (2002). Catalyzed esterifications in room temperature ionic liquids with acidic counteranion as recyclable reaction media. *Catalysis Communications,* 3: 185 – 190.
22. Zahao, G., Jiang, T., Gao, H., Han, B., Haung, J. and Sun, D. (2004). Mannich reaction using acidic ionic liquids as catalysts and solvents. *Green Chemistry*, 6(2): 75 – 77.
23. Suryawanshi, N. S., Jain, P., Singhal M. and Khan, I. (2012). Mannich synthesis under ionic liquid [Et3NH][HSO4] catalysis. *IOSR Journal of Applied Chemistry* 1: 18 – 23.
24. Yang, Y. Y., Shou, W. G. and Wang, Y. G. (2006). Synthesis of β–amino carbonyl compounds via a $Zn(OTf)_2$-catalyzed cascade reaction of anilines with aromatic aldehydes and carbonyl compounds. *Tetrahedron,* 62: 10079 – 10086.
25. Fang, D., Fei, Z. and Liu, Z. L. (2009). Functionalized ionic liquids as the recyclable catalyst for Mannich-type reaction in aqueous media. *Catalysis Communications,* 10: 1267 – 1270.
26. Yi, L., Zou, J. H., Lei, H. S. and He, Q. L. (1991). The Mannich reaction of butanone, aromatic aldehydes and aromatic amines. *Synthetic Communications,* 21: 2109 – 2117.
27. Yi, W. B. and Cai, C. (2006). Mannich-type reactions of aromatic aldehydes, anilines and methyl ketones in fluorous biphase systems created by rare earth (III) perfluorooctane sulfonates catalysts in fluorous media. *Journal of Fluorine Chemistry,* 127: 1515 – 1521.

# Malaysian Journal of Analytical Sciences Vol 21 No 6 2017

Articles 11 - 19 are selected papers from the "The 16th Asia-Pacific International Symposium on Microscale Separations and Analysis (APCE 2016), 7-10 November 2016, KSL Hotel & Resort, Johor Bahru, Johor; organised by Universiti Teknologi Malaysia and Malaysian Institute of Chemistry."

Guest Editor: Wan Aini Wan Ibrahim

Articles 20 - 26 are selected papers from the "Malaysia-Thailand-Japan International Conference on Science and Technology (MTJICST), 28 & 29 September 2016, UKM Graduate Centre; organised by Polymer Research Center (PORCE), School of Chemical Sciences and Food Technology, School of Applied Physics, Graduate Centre, Universiti Kebangsaan Malaysia."

Guest Editor: Chia Chin Hua


**Page**

1. FLUORESCENCE AND EVAPORATIVE LIGHT SCATTERING HPLC PROFILING OF INTRACELLULAR ASPARAGINE (N)-LINKED OLIGOSACCHARIDES FROM *Saccharomyces cerevisiae* USING THE *alg8* MUTANT 1210
(Pemprofilan KCPT Pendarfluor dan Penyerakan Cahaya Sejatan Oligosakarida Terpaut-(N) Asparagina Intrasel daripada *Saccharomyces cerevisiae* Menggunakan Mutan *alg8*)
*Iqbal Jalaludin, Amirul Husna Sudin, Ikram Mohd Said, Kamalrul Azlan Azizan, Syarul Nataqain Baharum, Abdul Munir Abdul Murad, Farah Diba Abu Bakar, Nor Muhammad Mahadi, Mark R. Wormald, Dominic S. Alonzi, Mukram Mohamed Mackeen*

2. SYNTHESIS OF BENZOTHIAZOLE DERIVATIVES USING ULTRASONIC PROBE IRRADIATION 1219
(Sintesis Terbitan Benzothiazola Dengan Menggunakan Prob Penyinaran Ultrasonik)
*Su-Yin Kan, Wei Sern Yiong, Fu Siong Julius Yong, Poh Wai Chia*

3. SYNTHESIS OF THIOUREA DERIVATIVES AND BINDING BEHAVIOR TOWARDS THE MERCURY ION 1226
(Sintesis Sebatian Terbitan Tiourea dan Sifat Pengikatan Terhadap Ion Merkuri)
*Fatimatul Akma Awang Ngah, Emma Izzati Zakariah, Nurul Izzaty Hassan, Bohari Yamin, Suhaila Sapari, Siti Aishah Hasbullah*

4. ENCAPSULATION OF GADOLINIUM NANOPARTICLES IN AMINO ACID BASED VESICLES 1235
(Pengkapsulan Nanozarah Gadolinium ke dalam Vesikel Berasaskan Asid Amino)
*Muhammad Zul Azri Muhammad Jamil, Faizal Mohamed, Nur Ratasha Alia Md. Rosli, Irman Abdul Rahman*

5. DIKETOPIPERAZINE PRODUCED BY PSYCHROPHILIC YEAST *Glaciozyma antarctica* PI12 1243
(Diketopiperazin Dihasilkan oleh Yis Psikropilik *Glaciozyma antarctica* PI12)
*Andi Rifki Rosandy, Muntaz Abu Bakar, Nurul Nadiah Abdul Rahman, Abdul Munir Abdul Murad, Azira Muhamad, Rozida Mohd. Khalid*

6. SOLVENT EXTRACTION OF THORIUM FROM RARE EARTH ELEMENTS IN MONAZITE THORIUM CONCENTRATE 1250
(Pengekstrakan Pelarut Torium daripada Unsur Nadir Bumi dalam Pekatan Torium Monazit)
*Wadeeah M. Al-Areqi, Che Nor Aniza Che Zainul Bahri, Amran Ab. Majid, Sukiman Sarmani*

7. PHOTOSTABILITY OF PLASTICIZED POLYVINYL CHLORIDE MEMBRANES: A THEORETICAL 1257

STUDY
(Kestabilan Foto bagi Membran Plastik Polivinil Klorida: Satu Kajian Teori)
*Oksana Fizer, Maksym Fizer, Yaroslav Studenyak*

8. POTENTIOMETRIC STUDY OF RHENIUM(V) COMPLEX FORMATION WITH AZATHIOPRINE AND CEFTRIAXONE 1266
(Kajian Potentiometri Penghasilan Kompleks Rhenium(V) dengan Azatioprina dan Ceftriaxon)
*Gamal Abdelaziz Hussein Gouda, Gomaa Abdelgawad Mohammed Ali*

9. SINTESIS $MnO_2$ NANOBUNGA POROS MENGGUNAKAN TEMPLAT SILIKA-APTES 1276
(Synthesis of Porous $MnO_2$ Nanoflower using Silica-APTES Template)
*Siti Zubaidah Hasan, Mohamed Rozali Othman, Muhammad Rahimi Yusop*

10. EXTRACTION OF METHYLPARABEN IN COSMETICS USING DISPERSIVE LIQUID-LIQUID MICROEXTRACTION BASED ON SOLIDIFICATION OF FLOATING ORGANIC DROP COUPLED WITH GAS CHROMATOGRAPHY FLAME IONIZATION DETECTOR 1289
(Pengekstrakan Metilparaben dalam Kosmetik Menggunakan Pengekstrakan Mikro Cecair-Cecair Serakan Berdasarkan Pemejalan Organik Terampai Berganding dengan Kromatografi Gas Pengesan Nyala Pengionan)
*Dyia Syaleyana Md Shukri, Nurul Asma Hamedan, Nur Shakirah Hussin, Wan Izhan Nawawi*

11. SENSORY EVALUATION AND QUANTITATIVE ANALYSIS OF MINERAL AND HEAVY METAL CONTENT OF PROTEIN SUPPLEMENT INCORPORATED WITH HERBAL EXTRACT 1299
(Penilaian Rasa dan Analisa Kuantitatif Kandungan Mineral dan Logam Berat bagi Makanan Tambahan Protin Digabungkan dengan Ekstrak Herba)
*Noor Azwani Zainol, Nor Farahiyah Aman Nor, HarisunYa'akob, Siti Nor Azlina Abd Rashid, Siti Hajar Mat Sarip, Ramlan Aziz*

12. MOLECULARLY IMPRINTED $TiO_2$ INORGANIC FILM AND PVDF/$TiO_2$ COMPOSITE FILM AS SENSORS FOR THE DETECTION OF CHEMICAL THREAT AGENTS USING QUARTZ CRYSTAL MICROBALANCE 1307
($TiO_2$ Filem Tak Organik dan Filem Komposit PVDF/$TiO_2$ Molekul Tercetak sebagai Sensor untuk Mengesan Agen Kimia Berbahaya Menggunakan Penimbang Mikro Kristal Kuarza)
*Xuan Hao Lin, Kah Sing Chooi, Sam Fong Yau Li*

13. COPPER MODIFIED CARBON NITRIDE AS FLUORESCENCE SENSOR FOR NITRATE IONS 1316
(Karbon Nitrida Terubah Suai Kuprum Sebagai Sensor Pendafluor Ion Nitrat)
*Siti Maryam Jasman, Hendrik O. Lintang, Siew Ling Lee, Leny Yuliati*

14. MOLECULARLY IMPRINTED POLYMER-COATED QUARTZ CRYSTAL MICROBALANCE FOR DETECTION OF PARATHION 1327
(Polimer Molekul Tercetak Saduran Kristal Kuarza Penimbang Mikro bagi Penentuan Parathion)
*Xiamin Cheng, Qihui Zhang, Sam Fong Yau Li, Bin Liu*

15. DETECTION OF BIOMOLECULES BY A NOVEL FLUORESCENCE APTASENSOR BASED ON POLYDOPAMINE SPHERES 1335
(Pengesanan Biomolekul oleh Aptasensor Pendarfluor Novel Berasaskan Sfera Polidopamina)
*Haiyan Li and Sam Fong Yau Li*

16. FLUORESCENCE QUENCHING ON MESOPOROUS CARBON NITRIDE BY PHENOL AND ANILINE 1342

(Pelindapan Pendarfluor pada Karbon Nitrida Mesoliang oleh Fenol dan Anilina)
*Leny Yuliati, Ahmad Hanami Abd Kadir, Siew Ling Lee, Hendrik O. Lintang*

17. EFFECT OF BUFFER COMPOSITION ON THE ANALYSIS OF LIPOPOLYSACCHARIDES FROM *Escherichia coli* 055:B5 AND UT189 BY CAPILLARY ELECTROPHORESIS WITH DIRECT UV DETECTION 1352
(Kesan Komposisi Penimbal ke atas Analisis Lipopolisakarida dari *Escherichia coli* 055:B5 dan UT189 oleh Elektroforesis Kapilari dengan Pengesan UV)
*Fun Man Fung, Min Su, Sam Fong Yau Li*

18. SPECIES AND SEROTYPE-SPECIFIC DETERMINATION OF ENDOTOXINS USING LC-MS 1366
(Penentuan Spesies dan Serotip-Khusus Endotoksin Menggunakan LC-MS)
*Anna Karen Carrasco Laserna, Huatao Feng, Sam Fong Yau Li*

19. SURFACE PLASMON RESONANCE SENSOR FOR DETECTION OF PARATHION METHYL IN WATER 1373
(Sensor Permukaan Plasmon Resonan bagi Pengesanan Parathion Metil di dalam Air)
*Baisheng Chen, Douglas Chiang Yon Chong, Xiamin Cheng, Bin Liu, Sam Fong Yau Li*

20. *IN SITU* HYDROGENATION OF LIQUID EPOXIDIZED NATURAL RUBBER USING DIIMIDE 1380
(Penghidrogenan *In Situ* Getah Asli Cecair Terepoksida Menggunakan Diimida)
*Nur Hanis Adila Azhar, Hamizah Md Rasid, Nur Aidasyakirah Mohd Tahir, Siti Fairus M. Yusoff*

21. ISOLATION OF TWO BOTRYANES FROM *Hypoxylon rickii* AND IDENTIFICATION OF THE ENCODING GENES 1389
(Pemencilan Sebatian Botrien dari *Hypoxylon rickii* dan Pengenalpastian Pengekodan Gen)
*Afnani Alwi, Andi Rifki Rosandy, Farah Diba Abu Bakar, Rozida Mohd Khalid*

22. NANOEMULSION BASED PALM OLEIN AS VITAMIN E CARRIER 1399
(Nanoemulsi Berasaskan Olein Sawit Sebagai Pembawa Vitamin E)
*Suria Ramli, Norhakimah Norhman, Norhidayu Zainuddin, Safiah Mohamad Ja'afar, Irman Abdul Rahman*

23. STUDY ON THE EFFECT OF OIL PHASE AND CO-SURFACTANT ON MICROEMULSION SYSTEMS 1409
(Kajian Kesan Fasa Minyak dan Ko-Surfaktan Terhadap Sistem Mikroemulsi)
*Muhammad Asri Abd Sisak, Rusli Daik, Suria Ramli*

24. TENSILE AND THERMAL BEHAVIOURS OF POLY(LACTIC ACID)/LIQUID NATURAL RUBBER BLEND MATRIX INCORPORATED NICKEL ZINC FERRITE NANOPARTICLES 1417
(Sifat Regangan dan Terma Matriks Adunan Asid Polilaktik/Cecair Getah Asli Diperkuat Nanozarah Nikel Zink Ferit)
*Ruey Shan Chen, Dalila Shahdan, Sahrim Ahmad*

25. CHEMICAL MODIFICATION OF EPOXIDIZED PALM OIL FOR BIOLUBRICANT APPLICATION 1423
(Pengubahsuaian Kimia Minyak Sawit Terepoksida Untuk Aplikasi Biopelincir)
*Nurazira Mohd Nor, Darfizzi Derawi, Jumat Salimon*

26. CHARCOAL BASE METALLIC COMPOSITE ELECTRODE FOR WASTEWATER TREATMENT 1432
(Elektrod Komposit Logam Berasaskan Arang Bagi Rawatan Air Buangan)
*Majd Ahmed Jumaah, Mohamed Rozali Othman, Muhammad Rahimi Yusop, Jumat Salimon, Baydaa Khalaf, Wan Mohd Afiq Wan Mohd Khalik*

*Malaysian Journal of Analytical Sciences, Vol 21 No 6 (2017): 1210 - 1218*
*DOI: https://doi.org/10.17576/mjas-2017-2106-01*

MALAYSIAN JOURNAL OF ANALYTICAL SCIENCES
*Published by The Malaysian Analytical Sciences Society*
ISSN 1394 - 2506

# FLUORESCENCE AND EVAPORATIVE LIGHT SCATTERING HPLC PROFILING OF INTRACELLULAR ASPARAGINE (*N*)-LINKED OLIGOSACCHARIDES FROM *Saccharomyces cerevisiae* USING THE *alg8* MUTANT

## (Pemprofilan KCPT Pendarfluor dan Penyerakan Cahaya Sejatan Oligosakarida Terpaut-(*N*) Asparagina Intrasel daripada *Saccharomyces cerevisiae* Menggunakan Mutan *alg8*)

Iqbal Jalaludin[1], Amirul Husna Sudin[1], Ikram Mohd Said[1,2], Kamalrul Azlan Azizan[2], Syarul Nataqain Baharum[2], Abdul Munir Abdul Murad[3], Farah Diba Abu Bakar[3], Nor Muhammad Mahadi[4], Mark R. Wormald[5], Dominic S. Alonzi[5], Mukram Mohamed Mackeen[1,2]*

[1]*School of Chemical Sciences and Food Technology*
[2]*Institute of Systems Biology (INBIOSIS)*
[3]*School of Biosciences and Biotechnology, Faculty of Science and Technology*
*Universiti Kebangsaan Malaysia, 43600 UKM Bangi, Selangor, Malaysia*
[4]*Malaysia Genome Institute,*
*Jalan Bangi, 43000 Kajang, Selangor, Malaysia*
[5]*Oxford Glycobiology Institute,*
*University of Oxford, South Parks Road, Oxford OX1 3QU, United Kingdom*

**Corresponding author: mukram.mackeen@ukm.edu.my*

Received: 21 June 2017; Accepted: 30 September 2017

**Abstract**

*N*-glycans are biologically important oligosaccharides associated with the asparagine residue that may exist in protein-bound or unbound forms in all eukaryotes (including yeasts) and some bacteria. The- core structure of these oligosaccharides is based on the trimannosyl chitobiose structure resulting from cellular *N*-glycosylation. Preparative-scale amounts of these oligosaccharides are important for chemical, structural and functional studies due to their biological significance. Therefore, we explored a biochemical approach of oligosaccharide preparation using mutant-derived monoglucosylated lipid-linked oligosaccharides (LLOs) required for the assembly of *N*-linked glycoproteins and non-monoglucosylated free-oligosaccharides (fOSs) from misfolded *N*-linked glycoproteins using an *N*-glycosylation (*alg*) mutant of *Saccharomyces cerevisiae*. Oligosaccharide extracts of fOSs and LLOs from the *alg8 S. cerevisiae* mutant lacking the *ALG8* gene were profiled using fluorescence- and evaporative light scattering-based HPLC. LLOs did not produce accumulated levels of the target mutant- related monoglucosylated ($Glc_1Man_9GlcNAc_2$) at 100 ml scale. However, it was possible to detect truncated oligomannose (paucimannose) structures in the fOSs of the *alg8* mutant.

**Keywords**: *N*-linked glycosylation, *N*-glycans, Free oligosaccharides, Lipid-linked oligosaccharides, *Saccharomyces cerevisiae*

**Abstrak**

*N*-glikan merupakan oligosakarida yang penting dalam biologi yang bersekutu dengan residu asparagina yang hadir dalam keadaan terikat atau tidak terikat kepada protein dalam semua eukariot (termasuk yis) dan sesetengah bakteria. Struktur asas oligosakarida ini adalah berdasarkan struktur kitobiose trimanosa yang terhasil melalui pengglikosilan-*N*. Oligosakarida ini penting untuk kajian kimia, struktur dan fungsi disebabkan kepentingan biologinya. Oleh itu, kami telah mengkaji kaedah penyediaan oligosakarida dengan pendekatan biokimia menggunakan yis mutan (*alg*) *Saccharomyces cerevisiae* yang

menghasilkan monoglukosa oligosakarida terpaut-lipid (LLO) yang diperlukan dalam pengumpulan glikoprotein terpaut-*N* dan bukan-monoglukosa oligosakarida bebas (fOS) daripada glikoprotein terpaut-*N* silap lipatan. Ekstrak oligosakarida fOS dan LLO daripada mutan *alg8 S. cerevisiae* tanpa gen *ALG8* telah diprofil menggunakan KCPT-pendarfluor dan pengesan penyerakan cahaya sejatan. LLO didapati tidak menghasilkan sebatian sasaran monoglukosa ($Glc_1Man_9GlcNAc_2$) berkaitan-mutan pada skala 100 ml. Walau bagaimanapun, struktur fOS oligomanosa terpangkas (pausimanosa) boleh dikesan daripada mutan *alg8*.

**Kata kunci:** pengglikosilan terpaut-*N*, *N*-glikan, Oligosakarida bebas, Oligosakarida terpaut-lipid, *Saccharomyces cerevisiae*

## Introduction

Asparagine (*N*)-linked glycosylation is the most widespread form of modification found in secreted glycoproteins of all eukaryotes and some prokaryotes as part of the endoplasmic reticulum-associated degradation (ERAD) pathway [1]. These oligosaccharides are significant in various biological processes such as pathogenesis, development, fertility, protein biosynthesis and folding [2, 3]. The biosynthesis of these naturally occurring oligosaccharides begins in the endoplasmic reticulum (ER) with the assistance of the lipid carrier dolichol-pyrophosphate (Dol-PP) to form a lipid-linked triglucosylated high-mannose type oligomannose *N*-glycan. Subsequently, the Dol-PP lipid-linked oligosaccharide (LLO) is transferred co-translationally by oligosaccharyltransferase (OST) to an asparagine residue of a nascent polypeptide within N-X-S/T sequence (N = asparagine, X = any amino acid except proline, S = serine, T = threonine) to produce $Glc_3Man_9GlcNAc_2$ *N*-linked glycoproteins in the ER. Triglucosylated *N*-glycoproteins are further processed by ER glucosidases I and II to generate monoglucosylated $Glc_1Man_9GlcNAc_2$ and non-glucosylated $Man_9GlcNAc_2$ on partially folded proteins. Both these high-mannose type *N*-glycan structures play a critical role in ERAD-controlled protein folding via interaction with the molecular chaperones calreticulin and calnexin [4]. After the initial phase of biosynthesis and protein folding quality control in the ER, these oligomannoses will be trimmed for either further (1) expansion in the Golgi with other mannose or non-mannose units such as galactose, galactosamine, glucosamine, xylose and sialic acid for secretion as glycoproteins or (2) truncation as protein unbound oligosaccharides in the cytosol and lysosome. Therefore, the lipid-linked and protein-unbound *N*-glycans may represent a naturally occurring source for the scalable production of these oligosaccharides using a biochemical (mutant) approach as opposed to using chemical synthesis. In the ER, units of monosaccharides are linked to each other by the asparagine-linked glycosylation (*ALG) 1* to *14* genes encoding *N*-glycosylation enzymes. Mutations involving *ALG* genes will produce accumulation of the biosynthetically relevant *N*-glycan isomers. For example, absence of the *ALG8* gene that is responsible for the formation of $Glc_2Man_9GlcNAc_2$ will result in the accumulation of the $Glc_1Man_9GlcNAc_2$ *N*-glycan LLO [5]. Therefore, this study explored the production of high-mannose type *N*-glycans using the *alg8* mutant to obtain monoglucosylated and non-glucosylated *N*-glycans.

Among the many uses of obtaining sufficient quantity of *N*-glycans would be for structural/conformational studies such as to probe the critical role N-glycans play in the ERAD pathway [6]. Conformational studies of *N*-glycans is mainly based on NMR and molecular dynamics. The structural determination of glycans is beset by the limited spectral dispersion of 1D NMR ($^1H$ and $^{13}C$ nuclei). Although, using 2D NMR spectroscopy facilitates the process of resonance and linkage assignments, it is still tedious and time-consuming [7]. Isotope labelling especially $^{13}C$ and preparative-scale analysis of *N*-glycans can significantly reduce analytical time and allow higher dimensional 3D and 4D NMR experiments to be carried out as routinely done in protein NMR. Additionally, *N*-glycans can be used as valuable analytical standards or as natural substrates for enzyme assays. The preparative-scale production of glycans is also beneficial for the synthesis of glycoconjugates. For example, glycans can be employed in bioorthogonal click chemistry to tag relevant protein substrates for proteomics analysis combining metabolic engineering and mass spectrometry. These tags facilitate the discovery of biomarkers involved in disease development through the screening of disease-related glycans and glycoproteins [8].

Preparative amounts of *N*-glycans have been produced through total chemical synthesis, chemoenzymatic synthesis and isolation from natural sources [9, 10]. Total chemical synthesis is by far the most challenging especially for larger and/or conjugated glycans such as glycoproteins and glycolipids. *N*-glycans obtained from *N*-linked glycoproteins and LLOs as well as fOS have been analysed in cells. However, the preparative scale production of *N*-glycans in previous reports have been complicated by the enzymatic (PNGase/Endo-H-treatment) or chemical (hydrazinolysis-based) release of *N*-glycans from glycoproteins and tedious solvent-partitioning extractions steps

for LLOs [11]. Commercially obtained PNGase F is expensive, and hydrazine is an explosive hazard for sugar-release at the preparative-scale. Therefore, we investigated the use of LLOs and fOSs from a mutant *Saccharomyces cerevisiae* strain (*alg8*) as source of *N*-glycans to: (1) obviate the need for sugar release and tedious solvent extraction and (2) obtain target *N*-glycans i.e the use of the *alg8* mutant to obtain monoglucosylated structure(s) from LLOs and non-target *N*-glycans from fOSs.

## Materials and Methods

### Reagents

Yeast Nitrogen Base (YNB), selected amino acids, acid-washed glass beads, AG50W-X12 ($H^+$ form), AG2-X8 ($Cl^-$ form) and DEAE-cellulose were kindly gifted by the Oxford Glycobiology Institute, University of Oxford. Water was obtained from The Pacific UP6 TKA system was used to obtain pure water. Other materials were purchased from major vendors such as Sigma and Merck unless stated otherwise.

### Yeast strains and culture conditions

The *Saccharomyces cerevisiae* strains used in this study were BY4743 (MATa/α his3Δ1/his3Δ1 leu2Δ0/leu2Δ0 met15Δ0/MET15 lys2Δ0/LYS2 ura3Δ0/ura3Δ0) and YOR067C BY4743 (MATa/α his3Δ1/his3Δ1 leu2Δ0/leu2Δ0 met15Δ0/MET15 lys2Δ0/LYS2 ura3Δ0/ura3Δ0 Δ*alg8*::kanMX4) from Dharmacon, GE Healthcare. Both yeast strains were grown aerobically in Yeast Nitrogen Base (YNB) medium (100 ml) containing 2% (w/v) glucose and 2% (w/v) selected-amino acids (4 mg/ml histidine, 4 mg/ml uracil, 4 mg/ml methionine and 12 mg/ml leucine) in a rotary shaker (180 rpm) at 30 $^oC$.

### Extraction of LLOs

The LLOs were extracted using a previously described method [12]. The cell pellets were harvested by centrifugation (2500 rpm/ 1200 × *g*, 8 min; same parameters used for the rest of this protocol) and washed using phosphate-buffered saline (PBS) three times. Methanol (10 ml) was added and the cells were transferred into glass tubes (10 ml). Sonication was performed for 10 minutes using a water bath-type sonicator and dried under $N_2$ gas. A chloroform-methanol (2:1; 10 ml) solution was added into the tubes, sonicated, vortexed, centrifuged and the supernatant discarded. The cells were resuspended in methanol again, sonicated for 10 minutes and dried under $N_2$ gas. The chloroform-methanol extraction procedure was repeated, but this time using 10 ml water and subsequently chloroform-methanol-water (CMW) (10:10:3; 10 ml). The supernatants from the final centrifugation were collected for further LLO extraction. For LLO partial purification, each CMW extract was run through a DEAE-cellulose column pre-equilibrated with CMW. After sample loading, the column was washed using 10 bed volumes of CMW followed by 10 bed volumes of 3 mM acetic acid in CMW. Elution was carried out using 10 bed volumes of 300 mM $NH_4OAc$ in CMW. Chloroform (4.3 bed volumes) and water (1.2 bed volumes) were added into the collection tubes, vortexed and centrifuged which resulted in three phases. The upper layer was removed and the remaining layers (middle and lower) were dried using $N_2$ gas. For oligosaccharides released from LLOs, 2 ml of 0.1 N HCl in 50% isopropanol was added into the dried samples, vortexed, incubated for 1 hour at 50 $^oC$ and dried under $N_2$ gas. Butanol-saturated water (1 ml) was added, vortexed. After that, 1 ml of water-saturated butanol was added before centrifugation, and the lower phase was recovered after centrifugation and freeze-dried. The dried residues were resuspended in 1 ml water to which 200 µl of AG50W-X12 ($H^+$ form) was added, vortexed, and centrifuged. The supernatant was collected and added to 200 µl of AG2-X8 ($Cl^-$ form) that was vortexed and then centrifuged. The oligosaccharides released from LLOs were obtained from the recovered supernatant.

### Extraction of fOSs

fOSs were extracted by a previously described method [13]. Briefly, the harvest step was the same as LLO extraction, i.e. cells were recovered by centrifugation and the medium discarded. PBS buffer was added into the tube containing the cells and washed three times. Then, the cells were snap-frozen using liquid nitrogen for 10 seconds and thawed three times. One volume of lysis buffer (100 mM Tris-HCl, pH 7.4 containing 4 mM $MgCl_2$) and acid-washed glass beads were added into the tube, vortexed for 30 seconds (six times) and the cell debris removed by centrifugation. The supernatants were desalted by mixed-bed ion exchange column (0.1 ml of AG50W-X12 [$H^+$ form] over 0.2 ml AG8-X2 [$Cl^-$ form]), pre-equilibrated with 5 × 1 ml water, followed by loading and washing with 4 × 1 ml. The eluate was collected for further analysis.

**Phenol-sulfuric acid assay**

The concentration of oligosaccharides in the extracted fOS samples were determined using the microtiter phenol-sulfuric acid assay (PSA) instead of the conventional tube-based assay [14]. Three types of samples were prepared; blank, standard and samples. The blank was the solvent used for dissolving the standards and samples. A series of known glucose standard concentrations ranging from 0.05 to 1.0 mg/ml was prepared. For each 50 µl sample, 150 µl of concentrated sulfuric acid was added rapidly into a well of a 96-well microplate for maximum mixing. Immediately after acid-mixing, 30 µl of 5% phenol was added followed by incubation at 90 $^{o}$C for 5 minutes using a water bath. The plate was floated carefully to avoid any sample leakage. The plate was cooled for a few minutes and wiped dry to measure the absorbance at 490 nm ($A_{490nm}$) using a microplate reader.

**Carbohydrate fluorescence labelling**

The carbohydrates were labelled with 2-anthranilic acid (2-AA) as previously described [15]. For the labelling reaction, 30 mg of 2-AA was dissolved in 1 ml methanol containing 4% (w/v) sodium acetate trihydrate and 2% (w/v) boric acid, followed by the addition of 45 mg sodium cyanoborohydride addition. Labelling reagent (80 µl) was added to each sample (30 µl) and mixed well before incubation in a heating block for 80 $^{o}$C for 45-60 minutes. The reaction was cooled at room temperature and 1 ml of acetonitrile/water (97:3, v/v) was added. The labelled samples were then further purified using Discovery DPA-6S column pre-equilibrated with 1 column volume of acetonitrile water. The column was washed with 95% acetonitrile after sample loading and eluted with 2 × 0.75 ml of water which was collected.

**Carbohydrate analysis by HPLC-ELSD**

The unlabelled samples were analysed by HPLC (Dionex UltiMate 3000 LC System) using an XBridge™ amide column, 3.5 µm; 4.6 x 250 mm (Waters) coupled to an evaporative light scattering detector (ELSD) PS-ELS 2100 Ice (Polymer Laboratories) connected to nitrogen generator. The detector was set as follows: vaporisation temperature = 55 $^{o}$C; gas flow = 1.6 slm (standard litre per minute); light intensity = 100%; gain = 1.0; nebulisation = 30 $^{o}$C. Solvent A contained 20% 100 mM ammonium acetate, pH 3.85, in Milli-Q water and 80% acetonitrile. Solvent B contained 20% 100 mM ammonium acetate, pH 3.85, in Milli-Q water, 60% Milli-Q water, and 20% acetonitrile. Gradient conditions for carbohydrate analysis were as follows: time = 0 min (t = 0), 86% solvent A (0.8 ml/min); t = 6, 86% solvent A (0.8 ml/min); t = 35, 54.7% solvent A (0.8 ml/min); t = 37, 5% solvent A (0.8 ml/min); t = 39, 5% solvent A (0.8 ml/min); t = 41, 86% solvent A (0.8 ml/min); t = 60, 86% solvent A (0.8 ml/min) [15]. Samples were dissolved in Milli-Q water/acetonitrile (2:8, v/v) and injected using an autosampler (50 µl per injection).

**Carbohydrate analysis by HPLC-FD**

The 2-AA labelled samples were kindly analysed by the Oxford Glycobiology Institute, University of Oxford, United Kingdom using normal phase-HPLC with a 4.6 mm × 250 mm TSK gel-Amide 80 column (5 µm) (Anachem, Luton, Beds, U.K) as described previously [15]. The chromatography system consisted of Waters Alliance 2695 separations module and an in-line Waters 474 fluorescence detector (FD) set at Exλ 360 nm and Emλ 425 nm. Solvent A and B were prepared as described above for the HPLC-ELSD analysis. Gradient conditions for carbohydrate analysis were as follows: time = 0 min (t = 0), 86% solvent A (0.8 ml/min); t = 6, 86% solvent A (0.8 ml/min); t = 35, 54.7% solvent A (0.8 ml/min); t = 37, 5% solvent A (1 ml/min); t = 39, 5% solvent A (1 ml/min); t = 41, 86% solvent A (1 ml/min). Samples were injected in Milli-Q water/acetonitrile (2:8, v/v).

## Results and Discussion

**Yeasts growth**

Monoglucosylated structures of LLOs were expected to be accumulated with the deletion of the *ALG8* gene in the LLO biosynthesis pathway. However, fOS was produced through deglycosylation of misfolded glycoprotein by the enzyme PNGase F. This enzyme is known to be regulated in a growth-dependent manner [13]. Under standard culture and laboratory conditions, wild type *S. cerevisiae* reaches the stationary phase, approximately, after 6 days [16]. Based on this, larger fOSs ($Man_{7-9}GlcNAc_2$) were usually observed at the exponential phase and the presence of these glycans were much reduced after six days of culture [13]. Thus, we generated a growth curve for the parental and mutant yeast strains to harvest cells in the appropriate growth phase. Figure 1 shows the growth pattern of the parental and mutant strains of the yeasts for 4 days. The growth curve intercepted each other after 3 days of

culture the parental strain almost reached the stationary phase by day 3. However, mutant strain still increased after the third day and was expected to reach the stationary phase after 6 days as described previously. Hence, we decided to harvest the cells after 2 days because both yeasts showed a steady increase in growth and the larger glycans are accumulated in this phase.

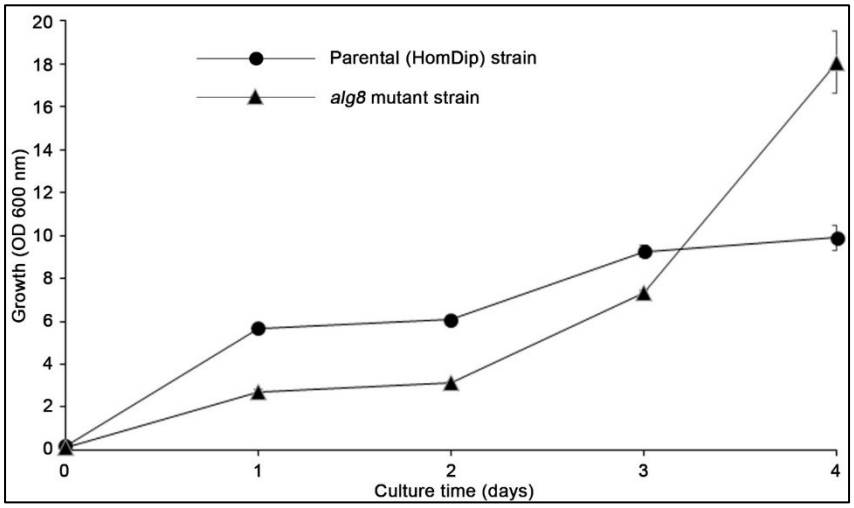



Figure 1. The growth curve of parental (HomDip) and *alg8* mutant strains

**Total concentration of carbohydrates in fOS extracts**

The total concentration of carbohydrates was determined using the PSA assay. A standard curve for quantification was generated using glucose. The linear equation generated from the standard curve shown to calculate sample concentrations was y = 1.115x - 0.008 ($R^2$ = 0.995) (Figure 2). The total oligosaccharide content of only the fOS samples were determined due to the negligible amounts of LLO extracted that were too little to be weighed (< 1 mg) and detection of very weak peaks by fluorescence-based HPLC. Comparison of between the fOS crude extracts of the parent and mutant strains showed that the concentration of carbohydrates was higher in the parent strain than the mutant strain. The values were also comparable to levels to the difference in OD readings measuring growth.

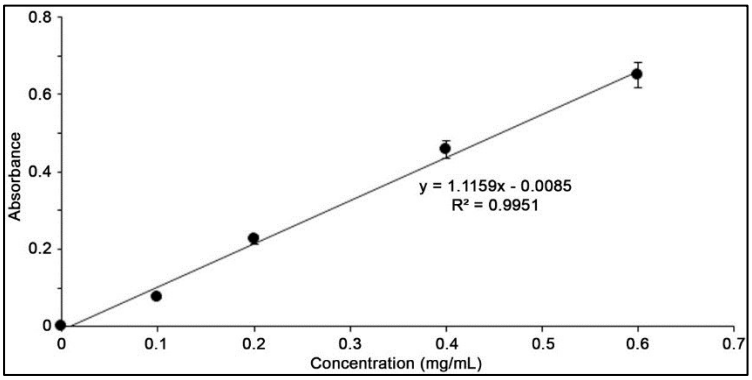



Figure 2. Standard curve of glucose for total carbohydrate content determination (PSA method)

Table 1. Crude samples total carbohydrate concentration of parental and mutant strains

| Samples | Concentration (mg/ml of cell lysate) |
|---|---|
| Parent strain (crude sample) | 2.83 |
| *alg8* mutant strain (crude sample) | 2.06 |

**Analysis of LLOs and fOSs with HPLC-ELSD and HPLC-FD**

HPLC analysis on the samples was carried out using ELSD and FD. The former mode of detection was universal and less sensitive whereas the latter was selective and highly sensitive. The dextran molecular weight ladder standard (0.1 mg/ml), LLOs and fOS extracted from parental and *alg8* mutant strains were analysed and shown in Figures 3 – 6. The HPLC-ELSD and FD chromatograms of the dextran ladder demonstrated good separation of peaks representing carbohydrates (glucose unit: GU) of difference sizes (ELSD: GU1 to GU12; and FD: GU1-GU13). Some of the HPLC-ELSD peaks were broad and slightly spilt. This is most probably a result of different configurations (α/β isomers) of the unlabeled sugar unit at the reducing end [17]. The 2AA-labelled fOS FD chromatogram showed a more complex profile of peaks than the unlabeled fOS ELSD chromatogram (Figures 3 and 5). fOS extract peaks appearing at lower retention times corresponding to ≤ GU3 were abundant in both the ELSD and FD chromatograms. In the FD chromatogram, these peaks were present at extremely high intensities exceeding the detection threshold of fluorescent detection (≥10 000 mV) (data not shown). The profiles suggested that ELS detection was not suitable (insensitive) for carbohydrate profiling on this scale of culture compared to fluorescence detection.

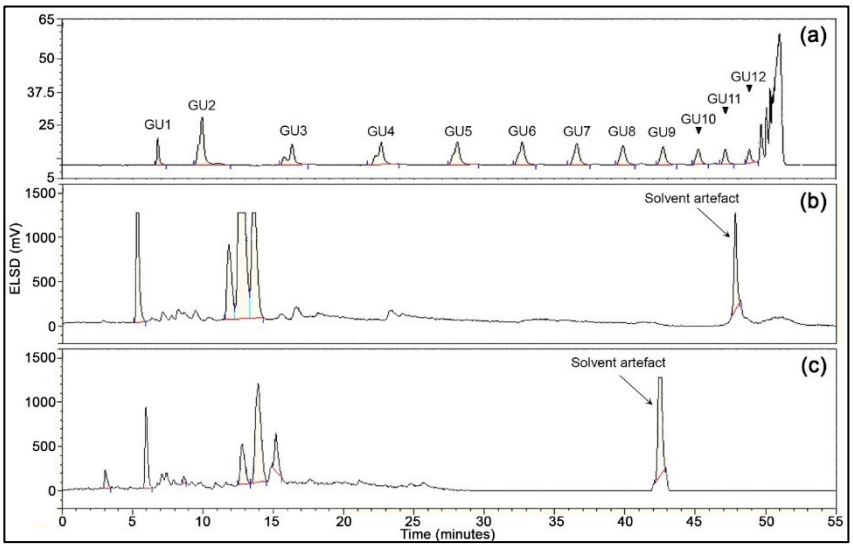



Figure 3. HPLC-ELSD analysis of (a) standard dextran and unlabeled fOS from (b) parental and (c) mutant strains

The major peaks in the HPLC profiles were more abundant in the parental strain. The common present in parent and mutant) abundant peaks present in both the parent and mutant may correspond to β-glucans associated with the cell wall of yeast have been extracted in fOS samples [18]. HPLC peaks were assigned using the glucose unit analysis method via the calculation of GU values calibrated to the dextran mixture standard for comparison to the values of known structures (Figure 6 and 7) [19, 20]. Based on this approach, two additional and abundant peaks with lower GU values were present in the *alg8* mutant. The additional peaks in the mutant had low GU values at 5.30 ($R_t$ = 23.0) and 6.47 ($R_t$ = 27.7) corresponding to the paucimannose *N*-glycans $Man_5GlcNAc_2$ and $Man_6GlcNAc_2$, respectively (Figure 5) [19, 20]. This is due to the truncation of free monoglucosylated $Man_9GlcNAc_2$ from

misfolded *N*-linked glycoproteins by glucosidse II and mannosidases in the ERAD pathway. For the two reported peaks, $Man_6GlcNAc_2$ was trimmed by α-1,2-mannosidase in ER to produce $Man_5GlcNAc_2$. In addition, the known absence of Endoglycosidase-H (Endo-H) in *S. cerevisiae* suggested that the glycan structures should be present with two GlcNAc units instead of one because, under normal circumstances, the presence of Endo-H will cleave chitobiose [21]. Our results show that the accumulation of fOSs from the lysate of *alg8 S. cerevisiae* mutant was more abundant than LLOs at the same scale of culture. Although LLOs did not show accumulation of the target *N*-glycan $Glc_1Man_9GlcNAc_2$, elevated levels of truncated oligomannose (paucimannose) *N*-glycans $Man_5GlcNAc_2$ and $Man_6GlcNAc_2$ were detected in fOSs using the *alg8* mutant.

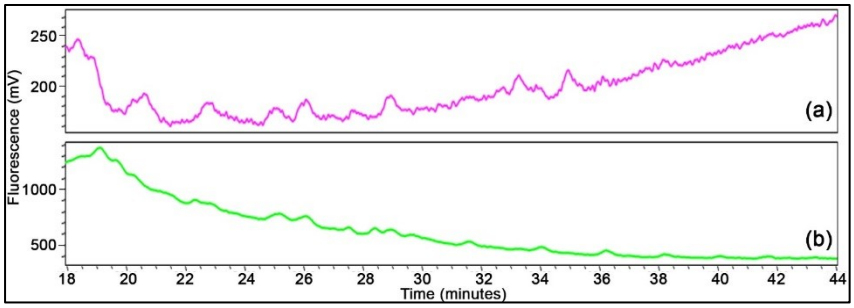



Figure 4. HPLC-FD analysis of 2-AA labelled LLOs from (a) parental and (b) mutant strains

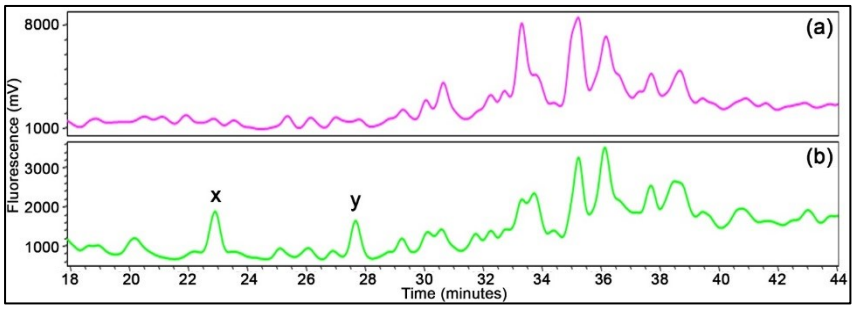



Figure 5. HPLC-FD analysis of 2-AA labelled fOS from (a) parental and (b) *alg8* mutant strains; x = $Man_5GlcNAc_2$ and y = $Man_6GlcNAc_2$

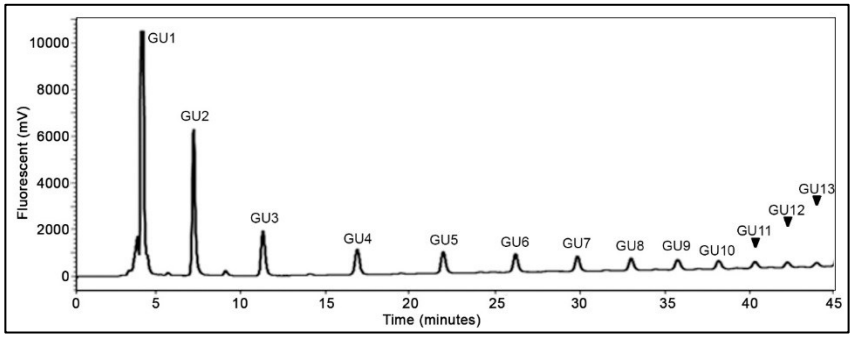



Figure 6. Normal phase-HPLC separation of 2-AA-Dextran with detection by fluorescence

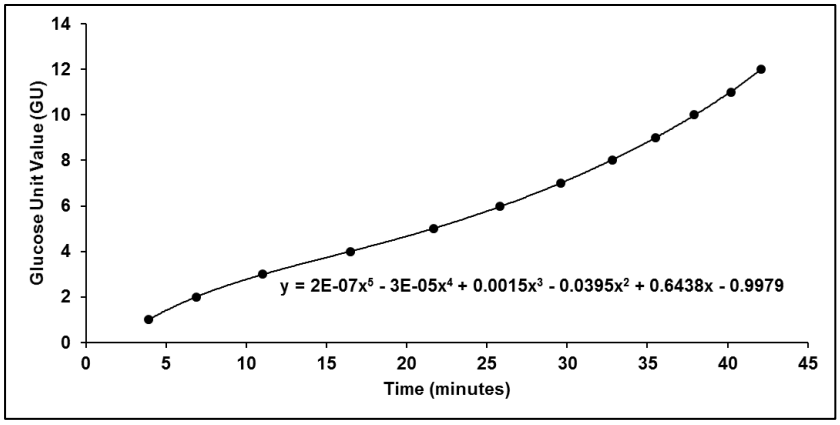



Figure 7. 5th order calibration curve generated from 2-AA-dextran profile for glucose unit (GU) value determination based on HPLC retention times

## Conclusions

fOSs from *S. cerevisiae* afforded higher amounts of oligosaccharides than LLO at the same scale of culture (100 ml). Accumulation of the monoglucosylated $Glc_1Man_9GlcNAc_1$ and/or its mannose-truncated forms was not observed in the LLOs of the *alg8 S. cerevisiae* mutant. However, accumulation of truncated oligomannoses (paucimannoses) $Man_5GlcNAc_2$ and $Man_6GlcNAc_2$ was only observed in the fOS extract of the same mutant.

## Acknowledgements

This work was supported by the Ministry of Higher Education under Grant ERGS/1/2013/STG01/UKM/01/1 and the Malaysia Genome Institute, Ministry of Science, Technology and Innovation Malaysia (MOSTI) under grant 02-05-20- SF0007. The authors also wish to thank the School of Chemical Sciences and Food Technology, School of Bioscience and Biotechnology, Institute of Systems Biology, Universiti Kebangsaan Malaysia and the Oxford Glycobiology Institute, University of Oxford for access to their facilities and technical support.

## References

1. Aebi, M. (2013). *N*-linked protein glycosylation in the ER. *Biochimica et Biophysica Acta - Molecular Cell Research*, 1833: 2430 – 2437.
2. Cheon, Y. and Kim, C. (2015). Impact of glycosylation on the unimpaired functions of the sperm. *Clinical and Experimental Reproductive Medicine*, 42: 77 – 85.
3. Ferris, S. P., Kodali, V. K. and Kaufman, R. J. (2014). Glycoprotein folding and quality-control mechanisms in protein-folding diseases. *Disease Models & Mechanisms*, 7: 331 – 341.
4. Xu, C. and Ng D. T. W. (2015). Glycosylation-directed quality control of protein folding. *Nature Reviews Molecular Cell Biology,* 16: 742 – 752.
5. Runge, K. W. and Robbins, P. W. (1986). A new yeast mutation in the glucosylation steps of the asparagine-linked glycosylation pathway. Formation of a novel asparagine-linked oligosaccharide containing two glucose residues. *Journal of Biological Chemistry,* 261: 15582 – 15590.
6. Mackeen, M. M., Almond, A., Deschamps, M., Cumpstey, I., Fairbanks, A. J., Tsang, C., Rudd, P. M., Butters, T. D., Dwek, R. A. and Wormald, M. R. (2009). The conformational properties of the $Glc_3Man$ unit suggest conformational biasing within the chaperone-assisted glycoprotein folding pathway. *Journal of Molecular Biology*, 387: 335 – 347.
7. Lundborg, M. and Widmalm, G. (2011). Structural analysis of glycans by NMR chemical shift prediction. *Analytical Chemistry,* 83: 1514 – 1517.
8. Zhang, X. and Zhang, Y. (2013). Applications of azide-based bioorthogonal click chemistry in glycobiology. *Molecules*, 18: 7145 – 7159.

9. Kelleher, D. J., Karaoglu, D. and Gilmore, R. (2001). Large-scale isolation of dolichol-linked oligosaccharides with homogeneous oligosaccharide structures: Determination of steady-state dolichol-linked oligosaccharide compositions. *Glycobiology*, 11: 321 – 333.
10. Verostek, M. F., Lubowski, C. and Trimble, R. B. (2000). Selective organic precipitation/extraction of released *N*-glycans following large-scale enzymatic deglycosylation of glycoproteins. *Analytical Biochemistry,* 278: 111 – 122.
11. Roth, Z., Yehezkel, G. and Khalaila, I. (2012). Identification and quantification of protein glycosylation. *International Journal of Carbohydrate Chemistry,* 2012: 1 – 10.
12. Gao, N. (2005). Fluorophore-assisted carbohydrate electrophoresis: a sensitive and accurate method for the direct analysis of dolichol pyrophosphate-linked oligosaccharides in cell cultures and tissues. *Methods*, 35: 323 – 327.
13. Chantret, I., Kodali, V. P., Lahmouich, C., Harvey, D. J. and Moore, S. E. H. (2011). Endoplasmic reticulum-associated degradation (ERAD) and free oligosaccharide generation in *Saccharomyces cerevisiae*. *Journal of Biological Chemistry,* 286: 41786 – 41800.
14. Masuko, T., Minami, A., Iwasaki, N., Majima, T., Nishimura, S. I. and Lee, Y. C. (2005). Carbohydrate analysis by a phenol-sulfuric acid method in microplate format. *Analytical Biochemistry,* 339: 69 – 72.
15. Neville, D. C. A., Coquard, V., Priestman, D. A., te Vruchte, D. J. M., Sillence, D. J., Dwek, R. A., Platt, F. M. and Butters, T. D. (2004). Analysis of fluorescently labeled glycosphingolipid-derived oligosaccharides following ceramide glycanase digestion and anthranilic acid labeling. *Analytical Biochemistry,* 331: 275 – 282.
16. Gray, J. V., Petsko, G. A., Johnston, G. C., Ringe, D., Singer, R. A. and Werner-Washburne, M. (2004). Sleeping beauty: quiescence in *Saccharomyces cerevisiae*. *Microbiology and Molecular Biology Reviews*, 68: 187 – 206.
17. Hossain, T. J., Harada, Y., Hirayama, H., Tomotake, H., Seko, A. and Suzuki, T. (2016). Structural analysis of free *N*-glycans in α-glucosidase mutants of *Saccharomyces cerevisiae*: Lack of the evidence for the occurrence of catabolic α-glucosidase acting on the *N*-glycans. *PLoS One*, 11: e0151891.
18. Hirayama, H., Seino, J., Kitajima, T., Jigami, Y. and Suzuki, T. (2010). Free oligosaccharides to monitor glycoprotein endoplasmic reticulum-associated degradation in *Saccharomyces cerevisiae*. *Journal of Biological Chemistry,* 285: 12390 – 12404.
19. Alonzi, D. S., Neville, D. C. A., Lachmann, R. H., Dwek, R. A. and Butters, T. D. (2008). Glucosylated free oligosaccharides are biomarkers of endoplasmic-reticulum alpha-glucosidase inhibition. *Biochemical Journal,* 409: 571 – 580.
20. Guile, G. R., Rudd, P. M., Wing, D. R., Prime, S. B. and Dwek, R. A (1996). A rapid high-resolution high-performance liquid chromatographic method for separating glycan mixtures and analyzing oligosaccharide profiles. *Analytical Biochemistry,* 240: 210 – 226.
21. Murakami, S., Takaoka, Y., Ashida, H., Yamamoto, K., Narimatsu, H. and Chiba, Y. (2013). Identification and characterization of endo-β-*N*-acetylglucosaminidase from methylotrophic yeast *Ogataea minuta*. *Glycobiology,* 23: 736 – 744.

*Malaysian Journal of Analytical Sciences, Vol 21 No 6 (2017): 1219 - 1225*
*DOI: https://doi.org/10.17576/mjas-2017-2106-02*

MALAYSIAN JOURNAL OF ANALYTICAL SCIENCES
*Published by The Malaysian Analytical Sciences Society*
ISSN 1394 - 2506

# SYNTHESIS OF BENZOTHIAZOLE DERIVATIVES USING ULTRASONIC PROBE IRRADIATION

## (Sintesis Terbitan Benzothiazola Dengan Menggunakan Prob Penyinaran Ultrasonik)

Su-Yin Kan[1], Wei Sern Yiong[2], Fu Siong Julius Yong[3], Poh Wai Chia[2, 3]*

[1]*Faculty of Health Sciences,*
*Universiti Sultan Zainal Abidin, 21030 Kuala Nerus, Malaysia*
[2]*School of Marine and Environmental Science*
[3]*Institute Marine Biotechnology*
*Universiti Malaysia Terengganu, 21030 Kuala Nerus, Malaysia*

**Corresponding author: pohwai@umt.edu.my*

Received: 14 June 2017; Accepted: 17 September 2017

**Abstract**

Benzothiazoles are an important class of pharmaceutical drug with various therapeutic activities. In this work, an efficient and eco-friendly method of synthesizing of benzothiazole derivatives via ultrasonic probe irradiation was described here. Through the improved protocol, the benzothiazole derivatives were prepared with various benzaldehyde and 2-aminothiophenol. The yields were found to be in moderate to good yields, ranging from 65 – 83%. Among the advantages of this procedure as compared to the conventional methods of synthesizing benzothiazoles include simplicity in the procedure, solvent-, catalyst- free reaction and the improved protocol afforded compounds (**4a-4i**) within 20 minutes at room temperature. The current improved protocol could be extended for the synthesis of other bioactive heterocyclic compounds in future work.

**Keywords**: benzothiazole, ultrasound, solvent-free, catalyst-free.

**Abstrak**

Benzotiazola adalah kelas ubat farmaseutikal yang penting dengan pelbagai aktiviti terapeutik. Dalam kajian ini, satu kaedah yang efisien dan mesra alam bagi sintesis terbitan benzotiazola dengan menggunakan prob penyinaran ultrasonik dibincangkan. Melalui kaedah yang ditambahbaik, terbitan benzotiazola dapat disediakan melalui pelbagai benzaldehid dan 2-aminatiofenol. Peratusan hasil produk didapati dari sederhana hingga baik, iaitu antara julat 65 – 83%. Kelebihan protokol ini berbanding dengan kaedah – kaedah konvensional bagi sintesis terbitan benzatiazola, termasuk prosedur yang mudah, tanpa penggunaan pelarut, tanpa pemangkin dan protokol yang ditambahbaik menghasilkan sebatian (4a-4i) dalam masa 20 minit pada suhu bilik. Kaedah yang ditambahbaik kini boleh diperluaskan untuk sintesis sebatian heterosiklik bioaktif lain dalam kajian masa hadapan.

**Kata kunci:** benzotiazola, prob penyinaran ultrasonik, tanpa pengunaan pelarut, tanpa penggunaan pemangkin

## Introduction

Benzothiazoles belong to an important class of pharmaceutical drug that possesses many desirable biological activities, such as antibacterial [1], anticonvulsant [2], anticancer [3], antifungal [4], antimitotic [5], and antitumor [6] properties. Examples of pharmaceutical drugs that contain the benzothiazole moiety include frentizole **1** (an immunosuppressive agent) [7]; ethoxyzolamide **2** (a carbonic anhydrase inhibitor) [8] and riluzole **3** (a registered drug used to treat patients with amyotrophic lateral sclerosis) [9] (Figure 1). In the past, various synthetic pathways for the synthesis of benzothiazole and its derivatives have been reported, including the utilization of microwave

irradiation [10], reusable metal-based catalysis [11], utilization of rare earth based nanocatalyst coupled with ultrasound irradiation [12] and utilization of water in combination with ionic liquid system [13]. Although there is an effort to improve on the efficiency of benzothiazole synthesis, most of these reactions suffer from drawbacks such as less eco-friendly, long reaction time and use of additives in synthesizing benzothiazole derivatives [14]. To that end, method development in the search for a simple and efficient synthetic route for synthesizing bioactive compounds has always been one of the major challenges in organic synthesis research works.

Over the years, the application of ultrasound in chemical synthesis has been an attractive and efficient method, especially to overcome the low reaction rate in chemical synthesis [15]. For instance, a solventless ultrasound-mediated reaction for the synthesis of thiazolo[3,2-a]pyrimidine derivatives have been successfully carried out with good yields [16]. Besides, a shorter reaction time was reported on the production of 2,4,5-trisubstituted imidazoles using Selectfluor™ as catalyst with the employment of ultrasound technique [17]. A green synthesis of sulfonamides with the aid of a natural, efficient and reusable Natrolite nanozeolite catalyst under ultrasound irradiation was also disclosed recently [18]. The utilization of ultrasound in organic reactions can overcome poor mass transfer and interaction between reactants. Through this technique, tremendous amount of energies for chemical activation was supplied by the means of cavitation through bubbles formation, expansion and rupture, which led to a better interaction between reactants [19]. To date, a vast number of useful organic compounds have been generated by using the ultrasound method [20].

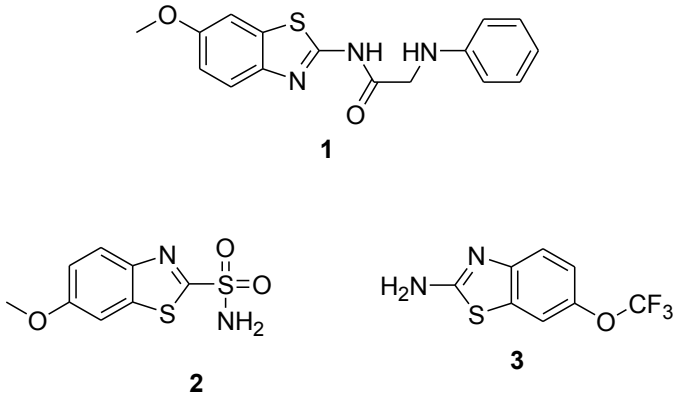
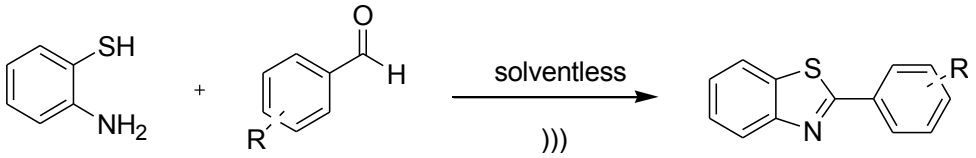



Figure 1. The benzothiazole drugs used for the treatment of various diseases. 1= frentizole. 2 = ethoxyzolamide and 3 = riluzole

In our continuous efforts to search for an efficient method for synthesizing bioactive heterocyclic compounds, herein, we reported on the synthesis of benzothiazole and their derivatives under ultrasound probe irradiation by using 2-aminothiophenol and benzaldehydes as starting materials (Scheme 1).




Scheme 1. Synthetic pathway towards the formation of benzothiazoles

## Materials and Methods

### Materials and instrumentation

All the chemicals and solvents used in this study were of technical grade and were supplied by Merck, Acros Organics and HmbG® chemicals and were used without further purification. These chemicals include

benzaldehyde, 2-chlorobenzaldehyde, 3-chlorobenzldehyde, 4-chlorobenzaldehyde, 2-fluorobenzaldehyde, 4-fluorobenzldehyde, 4-bromobenzaldehyde, 4-isoporpylbenzaldehyde, 4-methoxybenzaldehyde, ethyl acetate, n-hexane and silica gel 60 (0.063-0.200 mm). The FT-IR spectra were recorded using Perkin Elmer 100 FT-IR spectrometer, in spectral range of 4000-400 cm-1. $^{1}$H and $^{13}$C-NMR spectra were recorded on Bruker Avance III 400 spectrometer, with deuterated chloroform as solvent at room temperature at 400 MHz. GC-MS analyses were carried out using Shimadzu QP2010SE. Normal phase GC-MS analysis used a Supelco fused silica capillary column (30 m × 0.25 mm i.d., 0.25 mm film thickness). The aliquot samples were injected directly onto GCMS with methanol as solvent. The oven was held at 50 °C for 5 min, subsequently heated at a gradient of 20 °C/min to 150 °C, 280 °C injector temperature; 100:1 split ratio and 1.0 mL/min flow.

**Synthesis procedure for benzothiazole derivatives 4a-4h.**
2-aminothiophenol (3.00 mmol) was added into benzaldehyde derivatives (3.00 mmol) and the mixture was irradiated under ultrasonic probe for 20 min. The crude product was then purified over silica gel column chromatography (Hexane: Ethyl acetate = 9.5:0.5, v/v) to afford the title compounds **4a-4h** except for compound **4i** which was purified with a different solvent system (Hexane: Ethyl acetate = 8.5:1.5, v/v) over silica gel column chromatography.

## Results and Discussion

**Physical and spectral data**
The spectroscopic data of the synthesized compounds **4a-4i** is as follows:

**(4a)** 2-phenylbenzothiazole
M.p: 112.0 $^{o}$C; IR (cm$^{-1}$): 3064.99, 1589.52-1433.53; $^{1}$H- NMR (ppm): 7.42 (t, 1H), 7.51-7.53 (m, 4H), 7.91-7.93 (d, *J*= 8.0 Hz, 1H), 8.14 (m, 3H); $^{13}$C- NMR (ppm): 122.09, 124.35, 125.48, 126.66, 127.60, 128.07, 130.19, 133.75, 136.06, 152.54, 167.30. GC-MS: m/z 211 [M]$^{+}$.

**(4b)** 2-(2-chlorophenyl) benzothiazole
M.p: 84.0 $^{o}$C; IR (cm$^{-1}$): 3067.21, 1586.06-1441.40, 750.09; $^{1}$H- NMR (ppm): 7.43-7.36 (m, 3H), 7.53-7.51 (m, 2H), 8.12 (d, *J*= 8.1 Hz, 1H), 8.21-8.23 (m, 1H) ; $^{13}$C- NMR (ppm): 121.3, 123.3, 125.4, 126,3, 127.2, 130.6, 131.5, 132.4, 132.5, 136.3, 152.4.4, 164.2 GC-MS: m/z 245 [M]$^{+}$.

**(4c)** 2-(3-chlorophenyl) benzothiazole
M.p: 97.0 $^{o}$C; IR (cm$^{-1}$): 3075.40, 1580.54-1430.01, 751.87; $^{1}$H- NMR (ppm): 7.51-7.34 (d, *J*= 8.0 Hz, 2H), 8.00 (d, *J*= 8.5 Hz, 2H) 8.05 (d, *J*= 8.1 Hz, 1H); $^{13}$C- NMR (ppm): 121.4, 123.4, 125.3, 126,4, 128.6, 129.0, 132.0, 135.1, 137.1, 154.3, 166.4. GC-MS: m/z 245 [M]$^{+}$.

**(4d)** 2-(4-chlorophenyl) benzothiazole
M.p: 117.0 $^{o}$C; IR (cm$^{-1}$): 3065.40, 1543.21-1421.34, 752.34; $^{1}$H- NMR (ppm): 7.21-7.15 (m, 2H), 7.39 (t, *J*= 7.5 Hz, 1H), 7.51 (t, *J*= 7.9 Hz, 1H), 7.86 (d, *J*= 7.9 Hz, 1H), 8.04-8.06 (m, 3H); $^{13}$C- NMR (ppm): 16.3, 121.4, 123.3, 125.4, 126.5, 129.2, 130.2, 135.2, 135.4, 154.3, 163.5, 166.0. GC-MS: m/z 245 [M]$^{+}$.

**(4e)** 2-(2-fluorophenyl) benzothiazole
M.p:67.0 $^{o}$C; IR (cm$^{-1}$): 3055.60, 1590.54-1434.68, 756.79; $^{1}$H- NMR (ppm): 7.21 (d, *J*= 7.5 Hz, 1H), 7.31 (d, *J*= 7.5 Hz, 1H), 7.31 (t, *J*= 7.8 Hz, 2H), 7.45 (m, 3H), 7.93 (d, *J*= 8.1 Hz, 1H), 8.11 (d, *J*= 8.1 Hz, 1H), 8.40, (t, *J*= 7.5 Hz, 1H) ; $^{13}$C- NMR (ppm): 116.3, 121.5, 123.4, 124.5, 124.6, 125.2, 126.2, 129.4, 132.0, 135.6, 152.4, 160.0, 162.1. GC-MS: m/z 229 [M]$^{+}$.

**(4f)** 2-(4-fluorophenyl) benzothiazole
M.p:100.0 $^{o}$C; IR (cm$^{-1}$): 3049.20, 1591.54-1484.22, 829.28; $^{1}$H- NMR (ppm): 7.21 (d, *J*= 7.5 Hz, 1H), 7.31 (d, *J*= 7.5 Hz, 1H), 7.31 (t, *J*= 7.8 Hz, 2H), 7.45 (m, 3H), 7.93 (d, *J*= 8.1 Hz, 1H), 8.11 (d, *J*= 8.1 Hz, 1H), 8.40, (t, *J*= 7.5 Hz, 1H) ; $^{13}$C- NMR (ppm): 116.3, 121.5, 123.4, 124.5, 124.6, 125.2, 126.2, 129.4, 132.0, 135.6, 152.4, 160.0, 162.1. GC-MS: m/z 229 [M]$^{+}$.

**(4g)** 2-(4-bromophenyl) benzothiazole
M.p:131.0 $^{o}$C; IR (cm$^{-1}$): 3005.60, 1604-1408.68, 689.79; $^{1}$H- NMR (ppm): 7.38 (t, *J*= 7.6 Hz, 1H), 7.51 (t, *J*= 7.5 Hz, 1H), 7.66-7.61, (m, 2H), 7.87 (d, *J*= 7.7 Hz, 1H), 7.94 (d, *J*= 8.7 Hz, 2H), 8.05 (d, *J*= 8.1 Hz, 1H) ; $^{13}$C- NMR (ppm): 121.4, 123.3, 125.2, 125,3, 126.4, 128.8, 132.1, 132.4, 135.1, 154.2, 166.5. GC-MS: m/z 288 $[M]^{+}$.

**(4h)** 2-(4-isopropylphenyl) benzothiazole
M.p: 119.0 $^{o}$C; IR (cm-$^{1}$): 2956, 2981, 1602.01-1484.00, 967.89; $^{1}$H- NMR (ppm): 1.25 (d, *J*= 7.3 Hz, 6H), 2.86 (m, 1H), 7.42-7.51, (m, 2H), 7.60-7.63 (m, 2H), 7.74-7.83 (m, 2H), 8.04-8.12 (m, 2H); $^{13}$C- NMR (ppm): 23.5, 34.1, 122.2, 122.5, 125.2, 125.4, 127.3, 128.2, 140.1, 149.0, 149.2, 153.1, 169.4. GC-MS: m/z 253 $[M]^{+}$.

**(4i)** 2-(4-methoxyphenyl) benzothiazole
M.p: 289.0 $^{o}$C; IR (cm$^{-1}$): 3382.00, 1613-1431.00, 811.00; $^{1}$H- NMR (ppm): 7.87-8.06 (m, 4H), 7.51 (t, *J*= 7.3 Hz, 1H), 7.38, (t, *J* = 7.4 Hz, 1H), 7.07 (d, *J*= 8.2 Hz, 2H), 3.8 (s, 3H); $^{13}$C- NMR (ppm): 55.3, 114.6, 122.2, 122.3, 125.1, 125.4, 126.3, 128.7, 134.1, 153.5, 161.6, 167.0. GC-MS: m/z 124.0 $[M]^{+}$.

For the preliminary reaction, the optimized condition was determined by using a model reaction where 2-aminothiophenol and benzaldehyde were reacted in the presence of ultrasound probe irradiation to yield the corresponding product **4a**. Based on the preliminary study, the yield of **4a** has reached a plateau at 51 W power and the reaction yield was recorded at 83 % after 20 min of sonication (Table 1). The synthesis of other benzothiazole derivatives was repeated by using this optimized condition and the improved protocol was also employed for other comparative study.

The effectiveness of the improved protocol was also evaluated by comparing it with ultrasonic bath method and conventional heating method, using the synthesis of **4a** as the model reaction (Table 2). Under the ultrasonic bath method, there was no reaction occurred for the first 20 min at constant room temperature. While, after the reaction proceeded for 30 min, only less than 10 % yield of **4a** was recorded. The main reason for the low yield may due to inadequate heat energy produced in the reaction to agitate the reaction medium and thus required longer reaction time to produce compound **4a**. In contrast, the synthesis of **4a** under conventional heating method has recorded a 60 % yield when the reaction was heated under reflux with methanol as solvent for 6 h. Hence, it is evident that the ultrasound probe irradiation method under solvent- and catalyst-free condition gave the best yield as compared to the ultrasonic bath and conventional heating methods.

Table 1. The ultrasound yields of **4a** under solvent- and catalyst-free conditions

| Entry | Power (W) | Time (min) | Isolated Yield (%) |
|---|---|---|---|
| 1 | 46 | 5 | 60 |
| 2 | 48 | 10 | 70 |
| 3 | 50 | 15 | 73 |
| 4 | 51 | 20 | 83 |
| 5 | 51 | 25 | 83 |
| 6 | 51 | 30 | 83 |
| 7 | 53 | 25 | 83 |

Table 2. The yield of **4a** under ultrasonic bath irradiation and silent condition

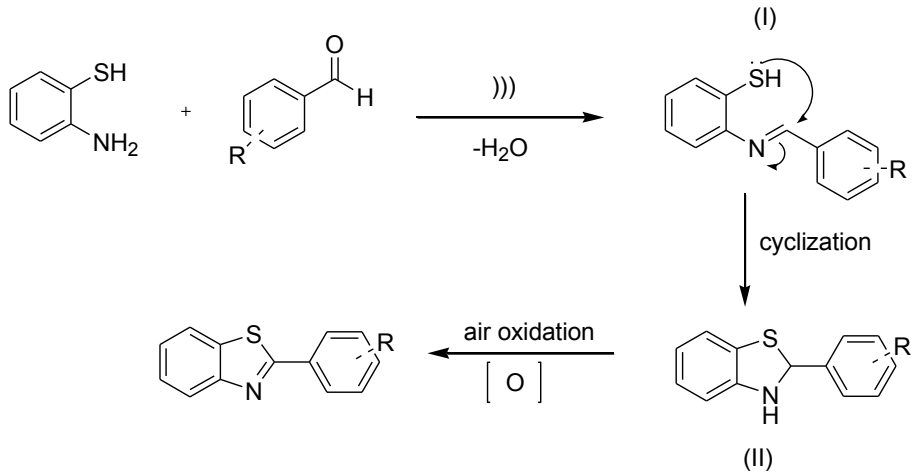
| Time (min) | Isolated Yield (%) | |
|---|---|---|
| | Sonication | Conventional |
| 10 | 0 | - |
| 20 | 0 | - |
| 30 | 7 | - |
| 120 | - | 20 |
| 360 | - | 60 |

Next, we attempt to widen the scope of our study by synthesizing different substituted benzothiazole derivatives by using several electron-donating and electron-withdrawing benzaldehydes under solvent- and catalysts-free ultrasound probe irradiation. As indicated in Table 3, the condensation of different benzaldehydes and 2-aminothiophenol proceeded smoothly under the improved protocol and afforded the title compounds (**4a**-**4i**) in moderate to good yields (65 – 83%) within 20 minutes at room temperature. The electronic effect and the position of the substitution on the benzaldehydes were found to have negligible effect in the reactivity of the synthesis of benzothiazole derivatives (Table 3, **4b** -**4g** vs. **4h**-**4i**). The result of this study was congruent with a previous study on the synthesis of the benzothiazole derivatives using ammonium nickel sulfate in the presence of water assisted by ultrasound irradiation method [21]. The major advantages of this technique include short reaction time, solvent- and catalyst-free reaction condition and the final products were obtained in moderate to good yields in comparison to previous method [11, 12, 13].

Table 3. Isolated yields obtained for compounds **4a-4i**

| Entry | Product No. | R | Isolated Yield (%) | M. P ($^{o}$C) Observed | M. P ($^{o}$C) Reported |
|---|---|---|---|---|---|
| 1 | 4a | H | 83 | 112 | 112-114 [22] |
| 2 | 4b | 2-Cl | 70 | 84 | 84-85 [22] |
| 3 | 4c | 3-Cl | 65 | 97 | 97-98 [22] |
| 4 | 4d | 4-Cl | 65 | 117 | 115-117 [22] |
| 5 | 4e | 2-F | 69 | 67 | 67-68 [22] |
| 6 | 4f | 4-F | 66 | 100 | 98-100 [22] |
| 7 | 4g | 4-Br | 65 | 131 | 129-131 [22] |
| 8 | 4h | 4-$CH(CH_3)_2$ | 65 | 119 | 119 -120 [23] |
| 9 | 4i | 4-$OCH_3$ | 65 | 124 | 123-125 [22] |

A plausible mechanism for the formation of benzothiazole under the ultrasound probe irradiation is depicted in Scheme 2. Under the ultrasound probe irradiation, the nucleophilic attack of 2-aminothiophenol on the carbonyl of benzaldehydes led to the formation of intermediate (I). Subsequently, cyclization reaction occurred to yield the intermediate (II). The air oxidation of intermediate (II) furnish the end-products, which were the benzothiazole derivatives.




Scheme 2. A plausible mechanism for the synthesis of benzothiazole derivatives under ultrasound probe irradiation

## Conclusion

In conclusion, we have demonstrated a simple and efficient protocol for the synthesis of benzothiazole derivatives under ultrasound probe irradiation. The major advantages of this technique include short reaction time, solvent- and catalyst-free reaction condition and the final products were obtained in moderate to good yields. These traits have rendered this method as an alternative way for synthesizing benzothiazole derivatives. In the future, the use of ultrasound probe irradiation under solvent- and catalyst-free condition to synthesize useful bioactive heterocyclic compounds will be further explored in our laboratory.

## Acknowledgement

The author would like to acknowledge the financial support from Ministry of Higher Education Malaysia (RAGS Vot No. 57081) and Universiti Malaysia Terengganu.

## References

1. Rezki, N. (2016). A green ultrasound synthesis, characterization and antibacterial evaluation of 1,4-disubstituted 1,2,3-triazoles tethering bioactive benzothiazole nucleus. *Molecules*, 21: 1 – 13.
2. Gagoria, J., Verma, P. K. and Khatkar, A. (2015). Anticonvulsant and neurological profile of benzothiazoles: a mini-review. *Central Nervous System Agents in Medicinal Chemistry*, 15(1): 11 – 16.
3. Mohamed, L. W., Taher, A. T., Rady, G. S., Ali, M. M. and Mahmoud, A. E. (2017). Synthesis and cytotoxic activity of certain benzothiazole derivatives against human MCF-7 cancer cell line. *Chemical Biology & Drug Design*, 89(4): 566 – 576.
4. Herrera Cano, N., Ballari, M. S., Lopez, A. G. and Santiago, A. N. (2015). New synthesis and biological evaluation of benzothiazole derivates as antifungal agents. *Journal of Agriculture Food Chemistry*, 63(14): 3681 – 3686.
5. Shaik, T. B., Hussaini, S. M., Nayak, V. L., Sucharitha, M. L., Malik, M. S. and Kamal, A. (2017). Rational design and synthesis of 2-anilinopyridinyl-benzothiazole Schiff bases as antimitotic agents. *Bioorganic & Medicinal Chemistry Letters*, 27(11): 2549 – 2558.
6. Gabr, M. T., Ei-Gohary, N. S, Ei-Bendar, E. R. and El-Kerdawy M. M. (2015). New series of benzotiazole and pyrimido[2,1-b]benzothiazole derivatives: Synthesis, antitumor activity, EGFR cyrosine kinase inhibitory activity and molecular modeling studies. *Medicinal Chemistry Research*, 24(2): 860 – 878.
7. Hatfield, S. M., Hartley, L. W. and Schmidtke, J. R. (1982). The immunomodulatory action of frentizole, a novel immunosuppressive agent. *Immunopharmacology*, 5(2): 169 – 179.
8. Drance, S. M. (1960). Ethoxzolamide (cardrase) in the management of chronic simple glaucoma. *Archives Ophthalmology*, 64: 433 – 437.
9. Doble, A. (1996). The pharmacology and mechanism of action of riluzole. *Neurology*, 47: 233 – 241.

10. Chhabra, M., Sinha, S., Barnerjee, S. and Paira, P. (2016). An efficient green synthesis of 2-arylbenzothaizole analogues as potent antibacterial and anticancer agents. *Bioorganic & Medicinal Chemistry Letters*, 26(1): 213 – 217.
11. Chun, S., Yang, S. and Chung, Y. K. (2017). Synthesis of benzothiazoles from 2-aminobenzenethiols in the presence of a reusable polythiazolium precatalyst under atmospheric pressure of carbon dioxide. *Tetrahedron*, 73(25): 3438 – 3442.
12. Ziarati, A., Sobhani-Nasab, A., Rahimi-Nasrabadi, M., Ganjali, M. R. and Badiei, A. (2017). Sonication method synergism with rare earth based nanocatalyst: preparation of NiFe2–xEuxO4 nanostructures and its catalytic applications for the synthesis of benzimidazoles, benzoxazoles, and benzothiazoles under ultrasonic irradiation. *Journal of Rare Earths*, 35(4): 374 – 381.
13. Waseem, M. A., Shireen, Srivastava, A., Srivastava, A., Rahila, and Siddiqui, I. R. (2015). Water and ionic liquid synergy: A novel approach for the synthesis of benzothiazole-2(3H)-one. *Journal of Saudi Chemical Society*, 19(3): 334 – 339.
14. Chen, G.-F., Jia, H.-M., Zhang, L.-Y., Chen, B.-H. and Li, J.-T. (2013). An efficient synthesis of 2-substituted benzothiazoles in the presence of FeCl3/Montmorillonitrile K-10 under ultrasound irradiation. *Ultrasonics Sonochemistry*, 20(2): 627 – 632.
15. Li, J. T., Yin, Y., Li, L. and Sun, M. X. (2010). A convenient and efficient protocol for the synthesis of 5-aryl-1,3-diphenylpyrazole catalyzed by hydrochloric acid under ultrasound irradiation. *Ultrasonics Sonochemistry*, 17(1): 11 – 30.
16. Tan, S. H., Chuah, T. S. and Chia, P. W. (2016). An improved protocol on the synthesis of Thiazolo[3,2-a] pyrimidine using ultrasound probe irradiation . *Journal of Korean Chemical Society*, 60(4): 245 – 250.
17. Heravi, M. R. P., Vessally, E. and Behbehani, G. R. R. (2014). An efficient green MCR protocol for the synthesis of 2,4,5-trisubstituted imidazoles by Selectfluor™ under ultrasound irradiation. *Comptes Rendus Chimie*, 17(2): 146 – 150.
18. Nasrollahzadeh, M., Ehsani, A. and Rostami-Vartouni, A. (2014). Ultrasound-promoted green approach for the synthesis of sulfonamides using natural, stable and reusable Natrolite nanozeolite catalyst at room temperature. *Ultrasonics Sonochemistry*, 21(1): 275 – 282.
19. Li, J.-T., Wang, S.-X., Chen, G.-F. and Li, T.-S. (2005). Some applications of ultrasound irradiation in organic synthesis. *Current Organic Synthesis*, 2(3): 415 – 436.
20. Frizzo, C.P., Scapin, E., Marzari, M.R., München, T.S., Zanatta, N., Bonacorso, H.G., Buriol, L. and Martins, M.A. (2014). Ultrasound irradiation promotes the synthesis of new 1,2,4-triazolo [1,5-a]pyrimidine. *Ultrasonics Sonochemistry*, 21(3): 958 – 962.
21. Pardeshi, S. D., Sonar, J. P., Pawar, S. S., Dekhane, D., Gupta, S., Zine, A. M. and Thore, S. N. (2014). Sonicated assisted synthesis of benaimidazoles, benzoazoles and benzothiazoles in aqueous media. *Journal of Chilean Chemical Society*, 59(1): 2235 – 2340.
22. Gao, Y., Song, Q., Cheng, G. and Cui, X. (2014). KI-catalyzed arylation of benzothiazoles from the coupling of aryl aldehydes with benzothiazoles in neat water. *Organic & Biomolecular Chemistry,* 12(7), 1044 – 1047.
23. Banyopadhyay, P., Sathe, M., Prasad, G. K., Sharma, P. and Kaushik, M. P. (2011). Mesoporous mixed oxide nanocrystal: Efficient and recyclable heterogeneous catalyst for the synthesis of 1, 2-disubstituted benzimidazoles and 2-substituted benzothiazoles. *Journal of Molecular Catalysis A: Chemical*, 341(1): 77 – 82.

*Malaysian Journal of Analytical Sciences, Vol 21 No 6 (2017): 1226 - 1234*
*DOI: https://doi.org/10.17576/mjas-2017-2106-03*

**MALAYSIAN JOURNAL OF ANALYTICAL SCIENCES**
*Published by The Malaysian Analytical Sciences Society*
**ISSN 1394 - 2506**

# SYNTHESIS OF THIOUREA DERIVATIVES AND BINDING BEHAVIOR TOWARDS THE MERCURY ION

## (Sintesis Sebatian Terbitan Tiourea dan Sifat Pengikatan Terhadap Ion Merkuri)

Fatimatul Akma Awang Ngah, Emma Izzati Zakariah, Nurul Izzaty Hassan, Bohari Yamin, Suhaila Sapari, Siti Aishah Hasbullah*

*School of Chemical Sciences and Food Technology,*
*Faculty of Science and Technology,*
*Universiti Kebangsaan Malaysia, 43600 UKM Bangi, Selangor, Malaysia*

**Corresponding author: aishah80@ukm.edu.my*

Received: 19 July 2017 Accepted: 30 September 2017

**Abstract**

Four new thiourea derivatives namely 1-(2-aminophenyl)-3-(naphthlene-1-yl)thiourea, **3a**, *N*-(2-aminophenyl)-*N*-(1-naphthalenyl)thiourea, **3a'**, 1-(3-aminophenyl)-3-(naphthalene-1-yl)thiourea, **3b**, and 1,4-phenylene-bis[3-(*α*-naphthyl)thiourea], **3c** have been synthesized by the reaction of 1-naphthyl isothiocyanate, **1a** with 1,2-phenylenediamine, **2a**, 1,3-phenylenediamine, **2b,** 1,4-phenylenediamine, **2c**. The binding behavior of **3b** for mercury ion was evaluated by 'naked- eye', $^{1}$H Nucleus Magnetic Resonance, Fourier Transformation Infrared, and UV-Vis titration methods. Stoichiometry of the host-guest complexation of **3b** and mercury ion was found to be 1:1 by plotting molar-ratio curves.

**Keywords***:* synthesis, thiourea, sensing, mercury

**Abstrak**

Empat sebatian baru terbitan tiourea iaitu 1-(2-aminofenil)-3-(naftil-1-il)tiourea, **3a**, *N*-(2- aminofenil)-*N*-(1-naftilin-il)tiourea, **3a'**, 1-(3- aminofenil)-3-(naftilin-1-il)tiourea, **3b**, and 1,4-fenilin-bis[3-(*α*-naftil)tiourea], **3c** telah berjaya disintesis melalui tindak balas di antara 1-naftil isotiosianat, **1a** dengan 1,2-fenilenadiamina, **2a**, dan 1,3-fenilenadiamina, **2b** dan 1,4-fenilenadiamina, **2c**. Sifat kelakuan pengikatan sebatian **3b** terhadap ion merkuri dikaji dengan menggunakan kaedah mata kasar, $^{1}$H Resonan Magnetik Nukleus, Infra Merah Transformasi Fourier, dan juga pengtitratan Ultralembayung-Cahaya Nampak (UV-Vis). Stoikiometri kompleks 3b dan ion merkri ditemui pada nisbah 1:1 melalui lengkung nisbah molar yang telah diplot.

**Kata kunci**: sintesis, tiourea, penderia, merkuri

## Introduction

Thiourea, $SC(NH_2)_2$ is a compound that is analogous to urea ($CO(NH_2)_2$), where by the oxygen atom has been replaced with a sulfur atom. It has different properties compared to urea due to the difference in electronegativity between sulfur and oxygen [1]. Thiourea is one of the most important compounds used in relation to metallic electrodes [2]. It can absorb to a metal surface and in so doing block active sites [2]. It is also one of the most important industrial chemical products [3]. The presence of heavy metal ions in the environment is a large problem due to their acute toxicity. They are not biodegradable and harmful to human organs [4]. Among the variety of metal ions, mercury is hugely harmful because its compounds are widely spread in air, soil, and water also can subsequently bio-accumulate through the food chain [5].

Thioureas are also selective analytical reagents, especially for the determination of metals in the presence of other metal ions [6]. Thiourea derivatives with conjugated oxygen or nitrogen donor sites represent some of the most important chelating ligands in coordination chemistry and their metal complexes are useful for homogenous catalysis, chemical vapor deposition, supramolecular chemistry, redox sensing, magnetic materials and so on [7]. Copper is one of the important trace metals and has been used in complexes to disinfect human solids, liquids and also human tissues. The high concentrations of the metals in the environment are harmful and toxic to living organisms [8]. Mercury is very hazardous to the environment and living organisms. It can exist as either an inorganic or organic species in the environment. It can pass through biological membranes and can cause many dangerous conditions like cancer, brain damage and also motion disorder [9]. The thiourea compound can bind with metal ions to make a stable complex due to the sulfur atom's excellent donor properties [10]. Moreover, it is also extremely flexible as a ligand, either neutral, mono-anion or dianions that able to bind to metal center [11]. Metal complexes of thiourea are commonly semi organic materials, in which the organic and inorganic parts of complex confer the advantageous properties of both elements [12].

Thioureas show high biological activity where they act as corrosion inhibitors and antioxidants and are also the component of polymers. In 2006, researchers reported acyl thiourea derivatives are for a wide range of biological activities like bactericidal, fungicidal, herbicidal and insecticidal also possess regulating activity for plant growth [13]. In continuation of our research theme, herein we wish to report the synthesis and characterization of four thioureas based 1,2-, 1,3- and 1,4-phenylenediamine. The binding behavior of **3b** toward mercury ion was investigated by 'naked eyes', $^{1}$H NMR, FTIR and UV–vis titration method.

## Materials and Methods

### Chemicals

This research was using some chemicals such as 1,2-phenylenediamine (Sigma Aldrich), 1,3-phenylenediamine (Sigma Aldrich), 1,4-phenylenediamine (Merck), 1-naphthyl isothiocyanate (Sigma Aldrich), and solvent such as dimethyl sulfoxide (DMSO) and dichloromethane (DCM) from Fisher company. All the chemicals and solvents were used directly without any purification.

### Physical measurement

All reactions were performed under reflux condition. Chemicals and solvents were purchased from Sigma Aldrich and Acros and were used directly without further purification. The compound was analyzed using FTIR Perkin Elmer Model Spectrum GX in the range 400-4000cm$^{-1}$ using KBr method, $^{1}$H and $^{1}$C NMR spectrometer model Bruker Advance 400 MHz, Liquid Chromatography Mass Spectroscopy model Dionex/Bruker MicroToF Q and Ultraviolet visible (UV-vis) CARY Agilent 100.

### Synthesis of 1-(2-aminophenyl)-3-(naphthlene-1-yl)thiourea, 3a

A solution of 1-naphthyl isothiocyanate (0.185 g, 1.00 mmol) and 1, 2-phenylenediamine (0.054 g, 0.50 mmol) in 10 mL dichloromethane (DCM) was refluxed for 23 hours. The white precipitate was filtered out and the pure product was isolated (63 %, 0.092 g).

### Synthesis of N-(2-aminophenyl)-N-(1-naphthalenyl)thiourea, 3a'

A solution of 1-naphthyl isothiocyanate (0.093 g, 0.025 mmol) and 1-(2-aminophenyl)-3-(naphthlene-1-yl)thiourea (**3a**) (0.073 g, 0.025 mmol) in 20 mL DCM was refluxed for 24 hours. The white precipitate was filtered, and the pure product was isolated (85 %, 0.010 g).

### Synthesis of 1-(3-aminophenyl)-3-(naphthalene-1-yl)thiourea, 3b

A solution of 1-naphthyl isothiocyanate (0.705 g, 2.00 mmol) and 1, 3-phenylenediamine (0.109 g, 1.00 mmol) in 20 mL dichloromethane (DCM) was refluxed for 24 hours. The white precipitate was filtered out and the pure product was isolated (82 %, 0.241 g).

**Synthesis of 1,4-phenylene-bis[3-(α-naphthyl)thiourea], 3c**

A solution of 1-naphthyl isothiocyanate (0.927 g, 5.00 mmol) and 1, 4-phenylenediamine (0.270 g, 2.50 mmol) in 20 mL dichloromethane (DCM) was refluxed for 28 hours. The white precipitate was filtered out and the pure product was isolated (95 %, 1.136 g).

**Binding behaviors for compound 3b towards selected metal salts**

The binding experiments were carried out using naked-eye method, FTIR, UV-Vis titration and $^1$H NMR titration. For naked-eye detection, stock solutions (1 x $10^{-3}$ M) of $Fe^{2+}$, $Pb^{2+}$, $Hg^{2+}$, $Ni^{2+}$, $Zn^{2+}$, $Ag^{+}$, $Cu^{2+}$, $Sn^{2+}$ ions and compound **3b** in dimethyl sulfoxide (DMSO) were prepared. 1.0 ml vial containing $Fe^{2+}$ and 1.0 ml of **3b** was mixed together in vials and shaken to ensure homogeneity. The color changes were observed and the data were collected. The experiment was repeated using $Pb^{2+}$, $Hg^{2+}$, $Ni^{2+}$, $Zn^{2+}$, $Ag^{+}$, $Cu^{2+}$, $Sn^{2+}$ ions.

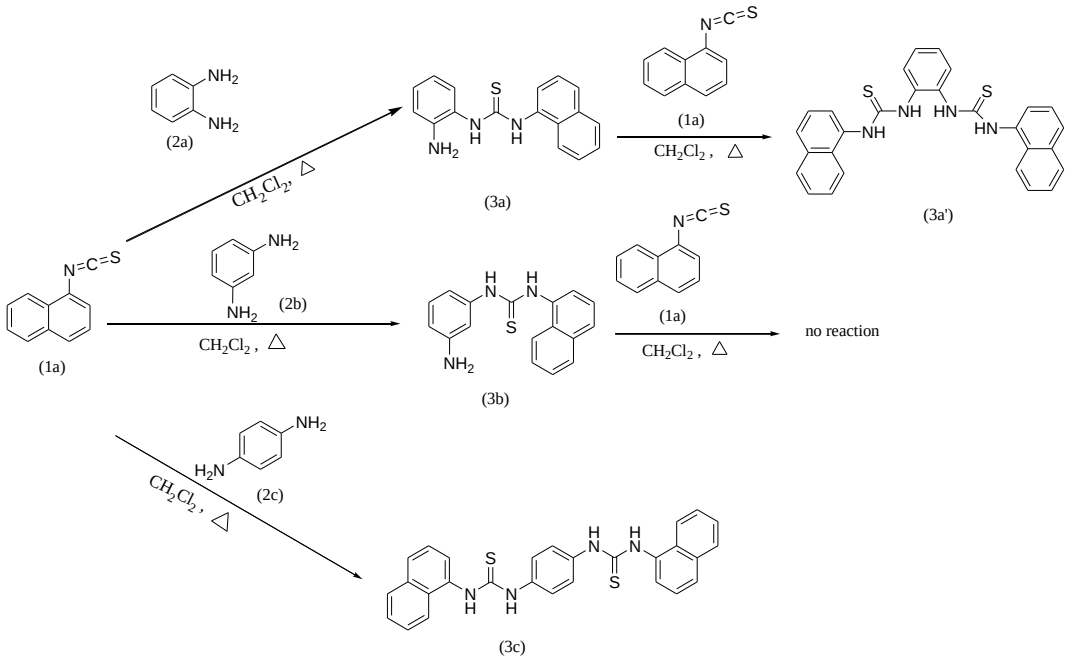
For UV-Vis titrations, 10 ml stock solutions (1 x $10^{-3}$ M) of **3b** and selected metal ions (1 x $10^{-3}$ M) were prepared in DMSO as solvent. The screening of these solutions was conducted on a UV-Vis spectrophotometer. 200 µL of **3b** and 0-600 µL of the mercury ion solution were titrated and directly analyzed using UV-Vis spectrophotometer [5].

For the $^1$H NMR titrations, 300 µL of a stock solution of $Hg^{2+}$ (0 – 0.06 M) was added into 560 µL of stock solution of **3b** (0.03 M) and then was placed in an NMR tube. Both of solutions were in DMSO-$d_6$. The titration solutions were analyzed using $^1$H NMR spectroscopy [14].

For analysis using FTIR spectroscopy, the sample was prepared by using 0.03 M of compound **3b** and 0.03 M of $Hg(OAc)_2$, both in DMSO as solvent.

## Results and Discussion

Compound **3a, 3a', 3b** and **3c** were synthesized by the reaction of ethyl isothiocyanate **1a** with diamines **2a, 2b** and **2c** (Scheme 1).




Scheme 1. Reaction schemes for synthesis of compounds **3a**, **3a'**, **3b** and **3c**

**1-(2-aminophenyl)-3-(naphthlene-1-yl)thiourea, 3a**
Mp: 164.0 – 168.1 ºC. IR (KBr pellet) $\upsilon$($cm^{-1}$): 3467, 3358, 3313, 3145, 3135, 2970, 1595, 1508, 1284, 747. $^{1}$H RMN (DMSO-$d_6$, 400 MHz) δ (ppm): 9.62 (s, 1H, N*H*), 7.21 (s, 1H, N*H*), 8.01 (dd, 2H, J= 7.6 Hz and 7.2 Hz, Ar-*H*), 7.84 (d, 1H, J=8.0 Hz, Ar-*H*), 7.53 (m, 4H, Ar-*H*), 7.11 (d, 1H, J= 7.2 Hz, Ar-*H*), 6.99 (t, 1H, J= 8.0 Hz, Ar-*H*), 6.77 (d, 1H, J= 7.6 Hz, Ar-*H*), 6.60 (t, 1H, J= 7.2 Hz, Ar-*H*), 4.93 (s, 2H, N$H_2$). $^{13}$C RMN (DMSO-$d_6$, 100 MHz) δ (ppm): 182.1 (*C*=S), 144.6 (Ar-*C*), 135.6 (Ar-*C*), 134.3 (Ar-*C*), 127.9 (Ar-*C*), 124.6 (Ar-*C*), 130.5 (Ar-*C*H), 128.9 (Ar-*C*H), 128.5 (Ar-*C*H), 127.2 (Ar-*C*H), 126.6 (Ar-*C*H), 126.5 (Ar-*C*H), 126.1 (2 × Ar-*C*H), 123.5 (Ar-*C*H), 117.0 (Ar-*C*H), 116.4 (Ar-*C*H). LC-MS (ESI) m/z: calculated for $C_{17}H_{15}N_3S$ (293.39), found (M-$H^+$) (292.08) [15].

**N-(2-aminophenyl)-N-(1-naphthalenyl)thiourea, 3a'**
Mp: 165.0 – 169.8 ºC. IR (KBr pellet) $\upsilon$($cm^{-1}$): 3457, 3307, 3129, 2958, 1525, 1500, 1251, 752. $^{1}$H NMR (DMSO-$d_6$, 400MHz) δ (ppm): 10.14 (s, 1H, N*H*), 9.27 (s, 1H, N*H*), 8.01 (m, 3H, Ar-*H*), 7.88 (d, 1H, J=8.0 Hz, Ar-*H*), 7.56 (t, 3H, J= 4.0 Hz, Ar-*H*), 7.48 (d, 2H, J= 3.6 Hz, Ar-*H*). $^{13}$C NMR (DMSO-$d_6$, 100MHz) δ (ppm): 182.1 (*C*=S), 144.6, 134.3, 130.5, 123.5 (4 Ar-*C*), 128.9, 128.5, 127.9, 127.2, 126.6, 126.5, 126.1, 117.0, 116.4 (9 Ar-*C*H). LC-MS (ESI) m/z: calculated for $C_{28}H_{22}N_4S_2$ (478.63), found (477.10).

**1-(3-aminophenyl)-3-(naphthalene-1-yl)thiourea, 3b**
Mp: 117.4 – 121.8 ºC. IR (KBr pellet) υ($cm^{-1}$): 3433, 3345, 3322, 3207, 3043, 1595, 1519, 1225, and 775. $^{1}$H RMN (DMSO-$d_6$, 400 MHz) δ (ppm): 9.62 (d, 2H, J= 5.2 Hz, N*H*), 7.94 (s, 1H, Ar-*H*), 7.84 (d, 1H, J= 8 Hz, Ar-*H*), 7.52 (m, 4H, J= 8, 4 Hz, Ar-*H*), 6.99 (t, 1H, J= 8 Hz, Ar-*H*), 6.65 (d, 1H, J= 8 Hz, Ar-*H*), 6.78 (s, 1H, Ar-*H*), 6.39 (d, 1H, J= 8 Hz, Ar-*H*), 5.12 (s, 2H, N$H_2$). $^{13}$C RMN (DMSO-$d_6$, 100 MHz) δ (ppm): 181.3 (*C*=S), 149.4 (Ar-*C*), 140.2 (Ar-*C*), 135.7 (Ar-*C*), 123.5 (Ar-*C*), 111.4 (Ar-*C*), 134.3 (Ar-*C*H), 130.5 (Ar-*C*H), 129.4 (Ar-*C*H), 128.5 (Ar-*C*H), 127.1 (Ar-*C*H), 126.6 (Ar-*C*H), 126.5 (Ar-*C*H), 126.0 (Ar-*C*H), 126.0 (Ar-*C*H), 112.3 (Ar-*C*H), 110.1 (Ar-*C*H). LC-MS (ESI) m/z: calculated for $C_{17}H_{15}N_3S$ (M+$H^+$) (293.39), found (294.10) [16].

**1,4-phenylene-bis[3-(α-naphthyl)thiourea], 3c**
Mp: 214.3 – 219.1 ºC. IR (KBr pellet) $\nu$($cm^{-1}$): 3325, 3186, 3000, 1542, 1499, 1221, 767. $^{1}$H RMN (DMSO-$d_6$, 400 MHz) δ (ppm): 9.87 (s, 1H, N*H*), 9.77 (s, 1H, N*H*), 7.98 (t, 2H, J= 8.0 Hz, Ar-*H*), 7.86 (d, 1H, J= 6.8 Hz, Ar-*H*), 7.55 (m, 6H, Ar-*H*). $^{13}$C RMN (DMSO-$d_6$, 100 MHz) δ (ppm): 181.6 (*C*=S), 136.5 (Ar-*C*), 135.5 (Ar-*C*), 134.3 (Ar-*C*), 124.7 (Ar-*C*), 130.4 (Ar-*C*H), 128.6 (Ar-*C*H), 127.2 (Ar-*C*H), 126.6 (Ar-*C*H), 126.5 (Ar-*C*H), 126.1 (Ar-*C*H), 125.8 (Ar-*C*H), 124.6 (Ar-*C*H), 123.5 (Ar-*C*H). LC-MS (ESI) m/z: calculate for $C_{28}H_{22}N_4S_2$ (M+$H^+$) (478.63), found (479.1) [17].

**Binding behaviors for 3b towards some selected metal ions**
For the visible observations, the most remarkable color change was observed in the presence of $Hg^{2+}$, $Cu^{2+}$, $Fe^{2+}$, and $Ag^+$ ions. The color changes before and after adding the metal salts into a solution of **3b** are seen in Figure 1 and Table 1. Based on the observation, the colorless solution became dark brown upon the addition of $Hg^{2+}$ (with acetate as counter ion). Next, the screening of **3b** with some selected metals in 2.0 ml solvent was carried out using UV-Vis spectroscopy (Figure 2). Based on the screening, $Hg^{2+}$ was found to show the highest absorption at 260 nm, together with new bands appearing at 305 nm and 370 nm which indicated strong binding behavior of **3b** towards the $Hg^{2+}$ ion. Due to this high affinity, the $Hg^{2+}$ ion was chosen for further titration studies using UV-vis and $^{1}$H NMR titrations.

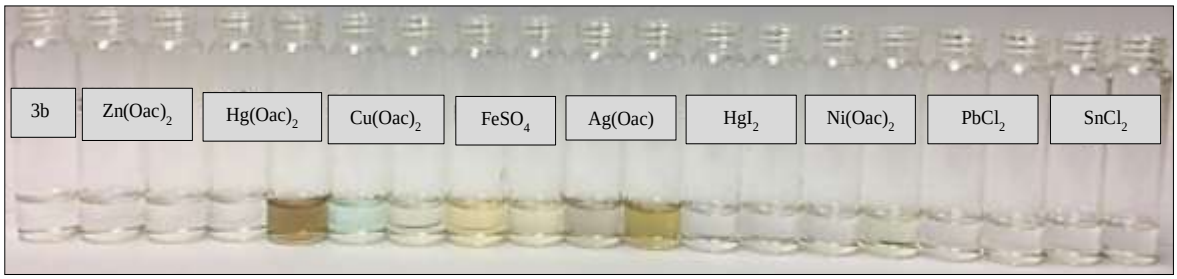



Figure 1. Color changes for naked-eyes sensor of 1-(3-aminophenyl)-3-(naphthalene-1-yl)thiourea, **3b** (1 x $10^{-3}$ M) towards selected metals (1 x $10^{-3}$ M)

Table 1. Color changes before and after adding the metal salts solution into the 1-(3-aminophenyl)-3-(naphthalene-1-yl)thiourea, **3b** solution

| **Metal salts** | **1-(3-aminophenyl)-3-(naphthalene-1-yl)thiourea, 3b (colorless)** |
|---|---|
| $Zn(OAc)_2$ (colorless) | Unchanged |
| $Hg(OAc)_2$ (colorless) | Dark brown |
| $Cu(OAc)_2$ (blue) | Light yellow |
| $FeSO_4$ (yellowish) | Light yellow |
| Ag(OAc) (light grey) | Brown |
| $HgI_2$ (colorless) | Unchanged |
| $Ni(OAc)_2$ (colorless) | Very light yellow |
| $PbCl_2$ (colorless) | Unchanged |
| $SnCl_2$ (colorless) | Unchanged |

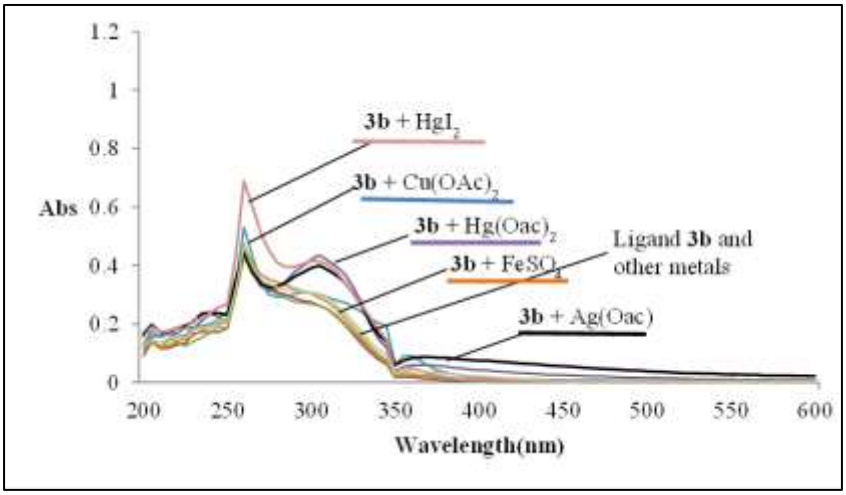



Figure 2. UV-Vis spectra of **3b** (1 x $10^{-3}$ M) with all metal ions (1 x $10^{-3}$ M) in DMSO as solvent

The titration studies of **3b** toward $Hg^{2+}$ ions were performed in DMSO. Figure 3 shows that upon the gradual addition of 25 µL equivalent of $Hg^{2+}$ ($1x10^{-3}$ M) to the 200 µL ligand solution ($1x10^{-3}$ M), new absorption bands at 305 nm and 370 nm appeared with increasing intensity. The absorbance maxima increased linearly with the concentration of $Hg^{2+}$ in a range of 0 – 1.0 M with a correlation coefficient of 0.99306 (Figure 4) after 10 readings. There was an isosbestic point at 280 nm which indicated that there were only two species present at equilibrium [18]. In addition, a new shoulder band appeared at 345 nm, something which relates to the intramolecular charge transfer (ICT) on the thiourea moiety of compound **3b**. The band at 370 nm shows a hyperchromic effect with an increasing amount of $Hg^{2+}$. Based on the UV-Vis titration, we were able to calculate the stoichiometry of the binding interaction between ligand **3b** and $Hg^{2+}$ through the molar-ratio curve method (Figure 4) [19]. The binding ratio of **3b**- $Hg^{2+}$ was 1:1 and the binding constant ($K_d$) was calculated using the nonlinear regression equation using Sigma Plot 12.0 software. The $K_d$ value of **3b**-$Hg^{2+}$ was 1.659 M.

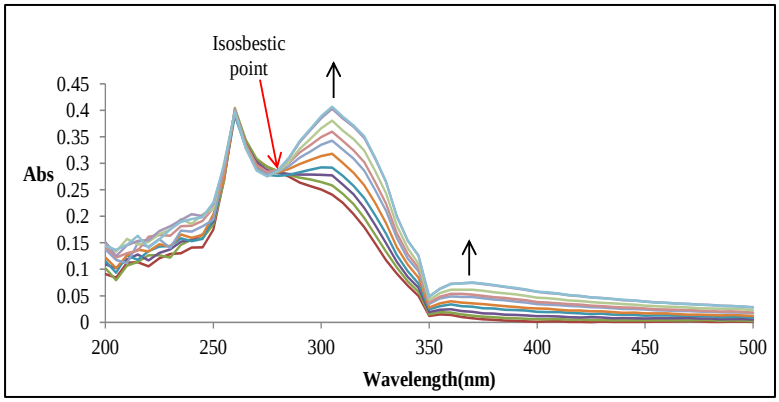



Figure 3. Changes in absorption spectra of **3b** (1 x $10^{-3}$ M) with increasing amount of $Hg^{2+}$ ions ($Hg(OAc)_2$) (1 x $10^{-3}$ M)

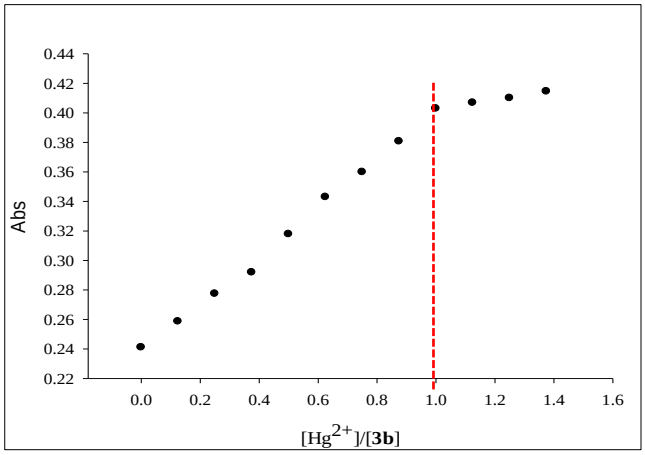



Figure 4. Variation of absorbance at 305 nm versus $[Hg^{2+}]/[\mathbf{3b}]$

To further study the binding behavior, $^1$H NMR titrations were performed in DMSO-$d_6$ (Figure 5). Protons for the two NH of compound **3b** were observed at 9.61 ppm and 9.59 ppm respectively. The integral of the peaks were both 2.00. After gradually adding the $Hg^{2+}$ solution (0 – 0.06 M), the size of the signals decreased and their integration value became less than 1. This was due to the strong interaction between **3b** and $Hg^{2+}$. In addition, the protons for

the $NH_2$ groups in the original spectra for compound **3b** were singlet, but in combination with $Hg^{2+}$ solution, the signal became broader and less intense (integration less than 1.00).

Next, the FTIR spectrum showed that the complex of **3b** and $Hg^{2+}$ showed a decreased intensity for both the CN and C=S groups, whilst a new peak appeared at 998 $cm^{-1}$ (Figure 6) [20]. This peak was due to the complexation of the $Hg^{2+}$ ion and the thiourea moiety. The peaks responsible for the $NH_2$ region disappeared due to the intramolecular charge transfer formed with the thiourea moiety. The proposed reaction mechanism of the **3b**-Hg interaction is shown in Figure 7.

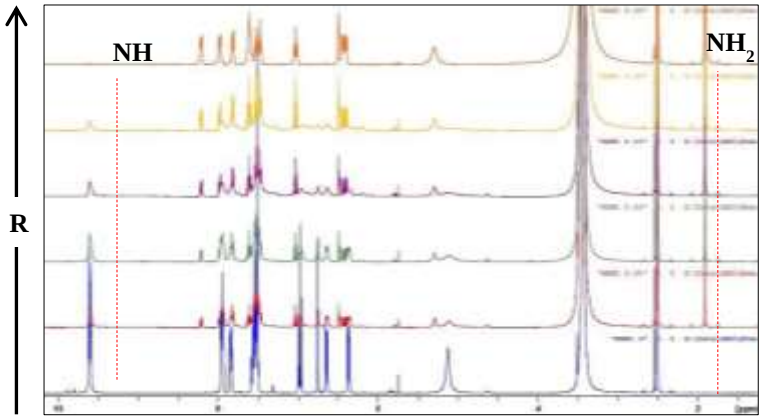



Figure 5. $^1H$ NMR titration of **3b** showing changes in the NH and $NH_2$ chemical shifts of the receptor **3b** (0.03M) with increasing amount of $Hg^{2+}$ (**R**) (0 - 0.06 M) in DMSO-$d_6$

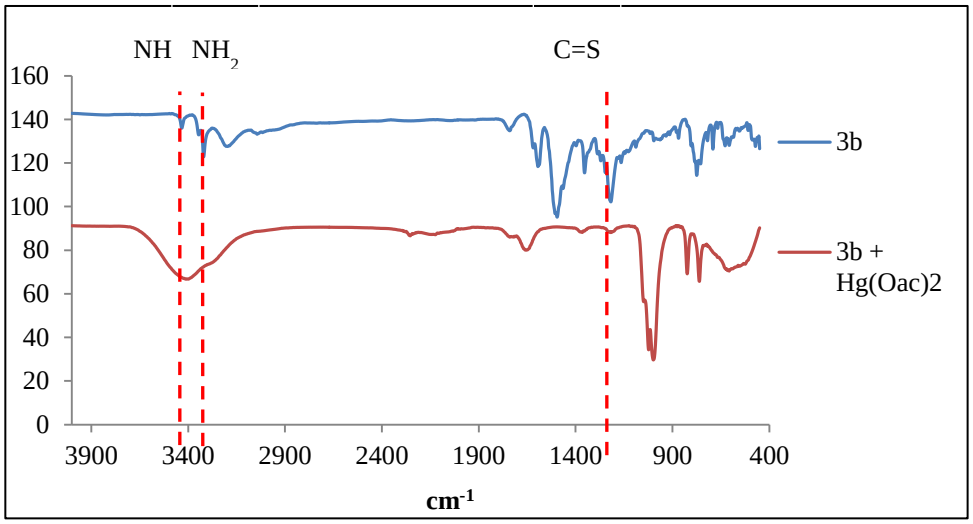



Figure 6. FTIR spectrum of compound **3b** with $Hg(OAc)_2$ solution.

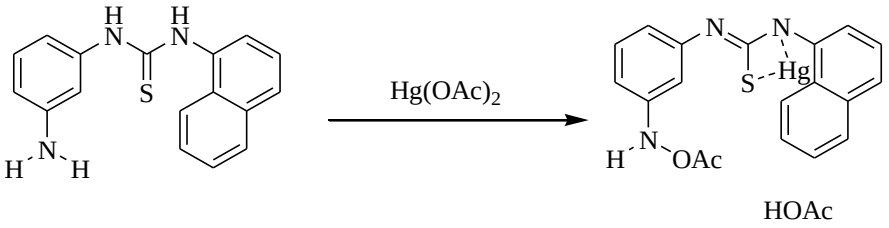



Figure 7. The proposed reaction mechanism of the **3b**-Hg interactions

## Conclusion

In conclusion, we have reported the synthesis of thiourea derivatives, 1-(2-aminophenyl)-3-(naphthlene-1-yl) thiourea (**3a**), N-(2-aminophenyl)-N-(1-naphthalenyl)thiourea (**3a'**), 1-(3-aminophenyl)-3-(naphthalene-1-yl) thiourea (**3b**), and 1,4-phenylene-bis[3-(α-naphthyl)thiourea] (**3c**). Using observation by naked eye, UV-vis titration, FTIR, and $^{1}$H NMR titration methods showed that the binding behavior of compound **3b** towards $Hg^{2+}$ afforded a complex with a 1:1 binding ratio. Future work will be aimed at using compound **3b** for sensor based applications whereby the fate of $Hg^{2+}$ can be tracked in the environment.

## Acknowledgement

The authors thank the Ministry of Higher Education Malaysia for My Master Scholarship, School of Chemical Sciences and Food Technology, National University of Malaysia, Center for Research and Instrumentation (CRIM), Research Grant GUP-2017-086 and everyone that involved in this research.

## References

1. Alkherraz, A. M., Lusta, I. Z. and Zubi, E. A. (2014). Synthesis and use of thiourea derivative (1-phenyl-3-benzoyl-2-thiourea) for extraction of cadmium ion. *International Scholarly and Scientific Research & Innovation,* 8(2): 116 – 118.
2. Zhao, J. and Cui, G. (2011). Study on adsorption and complexation behavior of thiourea on copper surface. *International Journal of Electrochemical Science,* 6: 4048 – 4058.
3. Yahyazahed, A. and Ghasemi, Z. (2013). Synthesis of unsymmetrical thiourea derivatives. *European Chemical Bulletin*, 2(8): 573 – 575.
4. Zhang, Z., Lu, S., Sha, C. and Xu, D. (2015). A single thiourea-appended 1,8-naphthalimide chemosensor for three heavy metal ions: $Fe^{3+}$, $Pb^{2+}$, and $Hg^{2+}$. *Sensors and Actuators*, 208: 258 – 266.
5. Khansari, M. E., Wallace, K. D. and Hossain, M. A. (2013). Synthesis and anion recognition studies of dipodal thiourea-based sensor for anions. *Tetrahedron Letters*, 55: 438 – 440.
6. Singh, A., Bharty, M. K., Bharati, P., Bharti, A., Singh, S. and Singh, N. K. (2015). Synthesis, spectral, thermal and structural characterization of a hexanuclear copper(I) cluster and a cobalt(III) complex of 1-ethyl-3-phenyl-thiourea. *Polyhedron,* 85: 918 – 925.
7. Saad, F. A. (2014). Coordination chemistry of some first row transition metal complexes with multi-dentate ligand (1- benzoyl - 3-(4-methylpyridin -2-yl) thiourea), spectral, electrochemical and x – ray single crystal studies. *International Journal of Electrochemical Science*, 9: 4761 – 4775.
8. Rauf, M. K., Imtiaz-ud-Din, Badshah, A., Gielen, M., Ebihara, M., de Vos, D. and Ahmed, S. (2009). Synthesis, structural characterization and in vitro cytotoxicity and anti-bacterial activity of some copper(I) complexes with N,N'-disubstituted thioureas. *Journal of Inorganic Biochemistry,* 103: 1135 – 1144.
9. Lee, J. Y., Rao, B. A., Hwang, J. Y. and Son, Y. (2015). A novel sensing capabilities and structural modification from thiourea to urea derivative by $Hg(ClO_4)_2$: Selective dual chemodosimeter for $Hg^{2+}$ and $F^-$ ions. *Sensors and Actuators B,* 220: 1070 – 1085.
10. Arslan, H., Duran, N., Borekci, G., Koray, O. and Akbay, C. (2009). Antimicrobial activity of some thiourea derivatives and their nickel and copper complexes. *Molecules,* 14: 519 – 522.

11. Saeed, A., Abbas, N., Ashraf, Z. and Bolte, M. (2013). Synthesis, characterization and antibacterial activity of new 1,2- and 1,4-bis(n'-substituted thioureido)benzene derivatives. *South African Journal of Chemistry*, 66: 273 – 278.
12. Kumari, R. G., Ramakrishnan, V., Carolin, M. L., Kumar, J., Sarua, A. and Kuball, M. (2009). Raman spectral investigation of thiourea complexes. *Spectrochimica Acta Part A*, 73: 263 – 267.
13. Ke, S. Y. and Xue, S. J. (2006). Synthesis and herbicidal activity of n-(o-fluorophenoxyacetyl)thioureas derivatives and related fused heterocyclic compounds. *Arkivoc*, 10: 63 – 68.
14. Odago, M. O., Colabello, D. M. and Lees, A. J. (2010). A simple thiourea based colorimetric sensor for cyanide anion. *Tetrahedron Letters*, 66: 7465 – 7471.
15. Perry, C. J., Holding, K. and Tyrrell, E.. (2008). Simple, novel synthesis for 1-carbamoyl-1*H*-benzotriazole and some of its analogs. *Synthetic Communications*, 38: 3354 – 3365.
16. Awang Ngah, F. A., Lee, Y. H., Hasbullah, S. A. and Hassan, N. I. (2016). Synthesis and characterization of 1-(3-aminophenyl)-3-(naphthalen-1-yl)thiourea and preliminary study towards binding with metal ions. *AIP Conference Proceedings*, 1784 (1): 1 – 8.
17. Zhang, L. P., Shang, X. B., Wu, Q. F., Zhang, Y. and Li, J. P. (2012). Highly efficient method for the synthesis of 1,4-phenylenedithioureas under solvent- and catalyst- free condition promoted by microwave irradiation. *International Journal of Rapid Communication of Synthetic Organic Chemistry*, 42 (7): 1045 – 1052.
18. Kang, J., Lee, J. H., Kim, Y. H., Lee, S. K., Kim, E. Y., Lee, H. G. and Kim, C. (2011). Simple urea/thiourea sensors for the biologically important ions. *Journal of Inclusion Phenomena and Macrocyclic Chemistry*, 70: 29 – 35.
19. Fakhar, I., Yamin, B. and Hasbullah, S.A. (2017). A comparative study of the metal binding behavior of alanine based bis-thiourea isomers. *Chemistry Central Journal*, 11:76. 1 – 16.
20. Wiles, D. M., Gingras, B. A. and Suprunchuk, T. (1966). The C=S stretching vibration in the infrared spectra of some thiosemicarbazones. *Canadian Journal of Chemistry*, 45: 469 – 473.

*Malaysian Journal of Analytical Sciences, Vol 21 No 6 (2017): 1235 - 1242*
*DOI: https://doi.org/10.17576/mjas-2017-2106-04*

MALAYSIAN JOURNAL OF ANALYTICAL SCIENCES
*Published by The Malaysian Analytical Sciences Society*
ISSN 1394 - 2506

# ENCAPSULATION OF GADOLINIUM NANOPARTICLES IN AMINO ACID BASED VESICLES

## (Pengkapsulan Nanozarah Gadolinium ke dalam Vesikel Berasaskan Asid Amino)

Muhammad Zul Azri Muhammad Jamil, Faizal Mohamed*, Nur Ratasha Alia Md. Rosli, Irman Abdul Rahman

*Nuclear Science Programme, School of Applied Physics,*
*Faculty of Science and Technology,*
*Universiti Kebangsaan Malaysia, 43600 UKM Bangi, Selangor, Malaysia*

**Corresponding author: faizalm@ukm.edu.my*

Received: 18 April 2017; Accepted: 12 September 2017

**Abstract**

Production of amino acid based vesicles using sonication method was employed to determine its encapsulation efficacy towards gadolinium(III) nanoparticles as potential drug carrier. The sonication process involved precursor namely sodium N-lauroylsarcosinate hydrate with 1-decanol to produce vesicle in 92 wt.% of water. Gadolinium(III) nanoparticle was then encapsulated into the vesicle system. The structure of $Gd_2O_2CO_3$ nanoparticles was confirmed by X-ray Diffraction technique (XRD). Attenuated Total Reflectance Fourier Transform Infrared (ATR-FTIR) spectroscopy indicates the presence of bonding that formed the vesicles. The size distribution of the obtained gadolinium encapsulated vesicle was examined using Transmission Electron Microscopy (TEM). It has been proven to be a potential nano-sized drug carrier.

**Keywords:** vesicles, encapsulation, gadolinium, sonication, drug carrier

**Abstrak**

Penghasilan vesikel berasaskan asid amino menggunakan kaedah sonikasi telah digunakan dalam menentukan pengkapsulan nanozarah gadolinium(III) yang berpotensi sebagai pembawa dadah. Proses sonikasi melibatkan prekursor natrium N-lauroylsarkosinat hidrat dengan 1-dekanol untuk menghasilkan vesikel dalam 92 wt.% air. Nanozarah gadolinium(III) kemudiannya dikapsulkan ke dalam sistem vesikel. Struktur nanozarah $Gd_2O_2CO_3$ telah disahkan menggunakan teknik pembelauan sinar-X (XRD). Spektroskopi transformasi infra merah Fourier (ATR-FTIR) menunjukkan kehadiran ikatan yang terbentuk ke atas vesikel. Taburan saiz yang nanozarah gadolinium terkapsul ke dalam vesikel dilihat menggunakan mikroskop elektron trasmisi (TEM). Ia telah terbukti berpotensi sebagai pembawa dadah bersaiz nano.

**Kata kunci:** vesikel, pengkapsulan, gadolinium, sonikasi, pembawa dadah

## Introduction

Nanomedicine is defined as a material used for specific diagnostic or therapeutic purposes in the scale range of 1-100 nanometers [1]. These therapeutic carriers have been increasingly used as drug delivery vehicles for the vast advantages that they offer due to their small size and versatility [2]. Gadolinium nanoparticles are very important as nuclear, phosphor, optical and electronic material [3-5]. Gadolinium is another new class of radiation sensitizers [6] because they could be easily viewed *in vivo* through the use of magnetic resonance imaging (MRI). MRI is a popular technique because it has a good soft tissue contrast [7] and high spatial resolution with non-invasive *in vivo* visualization [8]. In clinical use, the size of the nanoparticles has to be small to limit the toxicity due to poor renal clearance which is 6 nm, in order to allow complete and exclusive renal elimination after intravenous injection [9].

Vesicle has already been proven to be important as carrier system and for studying basic biology and medicine related to cell membranes [10]. Vesicle is a bilayer membrane structure consisting of a closed fluid chamber encapsulating aqueous solution [11, 12]. The vesicles were proven to have a good characteristic and potential as a drug delivery vehicles or carrier [13, 14]. In the present investigation, our goal is to encapsulate the gadolinium nanoparticles with amino acid based vesicle. The samples were characterized with various instruments such as transmission electron microscopy (TEM), Fourier transform infrared spectroscopy (FTIR) and X-ray diffraction (XRD).

## Materials and Methods

### Materials

Sodium N-lauroylsarconate with 95% purity was purchased from Across Organics (New Jersey, United States of America), 1-Decanol with 99% purity was purchased from Sigma-Aldrich and Nitric acid with 69.0 – 70.0% purity was purchased from J.T.Baker (Thailand). Gadolinium(III) oxide carbonate was purchased from Sigma-Aldrich with 99.8% trace metals basis. Deionized water was used to prepare all samples.

### Synthesis gadolinium(III) nitrate solutions

In order to obtain mixed assemblies, the required amount of $Gd_2O_2CO_3$ was dissolved in $HNO_3$ to form 5 mol/L concentration of nitrate solution. 0.1 ml nitrate solution was diluted with 500 ml deionized water. The pH of mixture was monitored and adjusted to pH 5 using deionized water. From this stock solution, only 0.08% of nitrate solution was used to synthesize amino acid based vesicles.

### Synthesis of control amino acid based vesicle

Amino acid based vesicles were prepared according to the sonication method as reported previously by Akter et al. [15] and Rosli et al. [13] with several modification. Sodium N-lauroylsarcosinate hydrate was mixed with 1-decanol in a test tube at a molar ratio of 1:2 in 92 wt.% of deionized water. The solution was sonicated for 15 minutes at room temperature using a bath sonicator. To obtain micro emulsion, the solution was vortexed for 5 minutes at 1400 rpm. The solution was then centrifuged for 15 minutes at the speed of 4200 rpm to obtain phase separation. The samples were left undisturbed for a few hours to achieve equilibrium.

### Synthesis of vesicle encapsulating gadolinium(III) nitrate nanoparticles

Vesicle encapsulating gadolinium (III) nitrate nanoparticles was synthesized using the same method used to synthesize control amino acid based vesicle with minor modification, in which the encapsulated gadolinium(III) nitrate nanoparticles was added to the deionised water prior to its addition with surfactant (SNLS and 1-decanol).

### Characterization study

To identify crystalline products, X-ray diffraction (XRD) pattern were collected on a Bruker D8 Advance, using Cu $K\alpha 1$ radiation (40 kV, 40 mA) with a wavelength 1.54060 in 2θ. Attenuated total reflectance infrared (ATR-FTIR) spectra in transmission mode were measured on a Perkin Elmer FTIR Spectrum 400 spectrometer in determining molecular confirmation using pressed KBr tablets in a mortar. The formations of vesicles were characterized using a transmission electron microscope (TEM, Bruker HT7700 electron microscope, operated at 120 kV).

## Results and Discussion

### X-ray diffraction

Based on the x ray diffraction patterns of powdered nanoparticle $Gd_2O_2CO_3$ in Figure 1, three dominant peaks of hexagonal $Gd_2O_2CO_3$ are observed. These peaks consist of peak 250 (at $2\theta \approx 31.8^o$), peak 175 (at $2\theta \approx 27.0^o$) and peak 115 (at $2\theta \approx 46.4^o$). These findings indicated that the nanocrystals consist of crystalline $Gd_2O_2CO_3$ with an excellent peak fitting (JCPDS no. 00-038-0680).

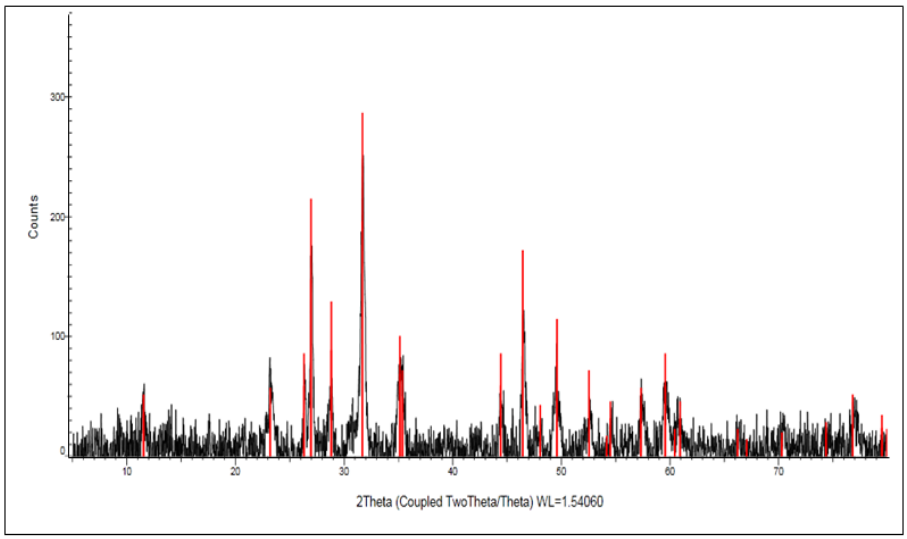



Figure 1. X-ray diffractograms of powdered $Gd_2O_2CO_3$ nanoparticles

**Fourier transform infrared spectroscopy**

The characterization of nanoparticles was performed using FTIR at a wavelength between 500 $cm^{-1}$ to 4000 $cm^{-1}$. The IR spectrum of $Gd_2O_2CO_3$ and $Gd(NO_3)_3$ nanoparticles are shown in Figure 2. The chemical bonds and functional group present in the characterized sample are as listed in Table 1. The peaks at 1100 and 860 $cm^{-1}$ represent carboxylic acids functional group (O-C) and (C-O-H) of $Gd_2O_2CO_3$, respectively. The alkene functional group of the $Gd_2O_2CO_3$ nanoparticles are also present at peak 1400 $cm^{-1}$ (=C-H & $=CH_2$ stretch). Furthermore, a (C-C) stretch (in-ring) of $Gd_2O_2CO_3$ appears as a very strong and sharp peak at 1490 $cm^{-1}$.

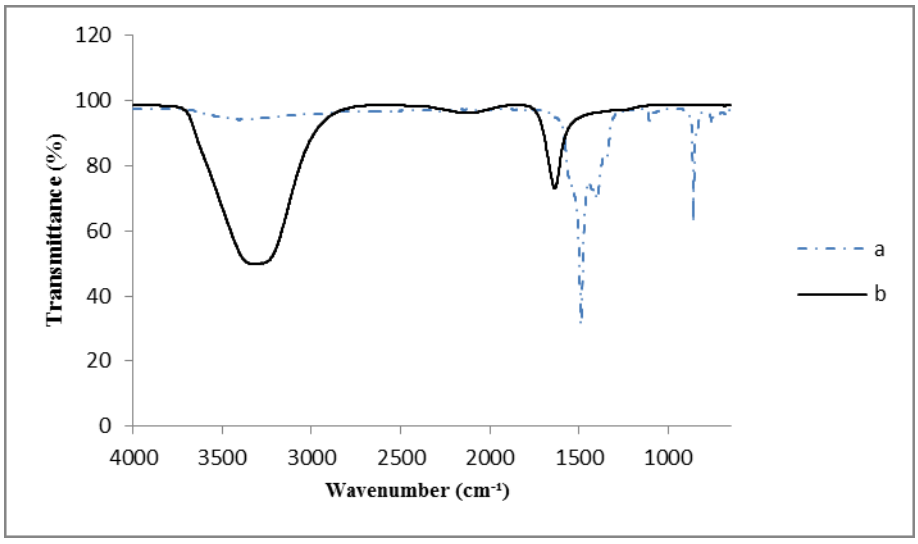



Figure 2. FTIR spectrum of (a) $Gd_2O_2CO_3$ powder and (b) $Gd(NO_3)_3$ solution.

Table 1. Vibrational mode assignment of $Gd_2O_2CO_3$ particles and $Gd(NO_3)_3$ solution

| Modes of vibration | Functional group | Wavenumber ($cm^{-1}$) | |
|---|---|---|---|
| | | $Gd_2O_2CO_3$ | $Gd(NO_3)_3$ |
| O-H stretch (wide,strong) | Hydroxyl | 3406.09 | 3330.65 |
| C≡N stretch | Nitriles | n.d | 2123.61 |
| C=O strecth (strong) | Amides | n.d | 1636.80 |
| H-C-H bend | Alkane | 1488.26 | n.d |
| C-O strecth | Ether | 1395.45 | n.d |
| C-N strecth | Aliphatic amines | 1104.94 | n.d |

n.d Not detected

Besides that, based on the spectrum obtained, C≡N stretch and C=O stretch of $Gd(NO_3)_3$ are also confirmed through the nitrile functional group (at wavelength 2123.61 $cm^{-1}$) and amide functional group (at wavelength 6136.80 $cm^{-1}$). However, these nitrile and amide functional group were not present in $Gd_2O_2CO_3$ compound as there is no use of nitrogen in the preparation of these compounds. The reaction of $Gd_2O_2CO_3$ and $HNO_3$ is shown in equation (1).

$$Gd_2O_2CO_3 + 6HNO_3 \rightarrow 2Gd(NO_3)_3 + 3H_2O + CO_2 \quad (1)$$

Before the synthesis and encapsulation of gadolinium(III) in the vesicle, 1-decanol and sodium N-lauroylsarcosinate hydrate were also characterized using FTIR. The spectrum of 1-decanol and sodium N-lauroylsarcosinate hydrate (SNLS) is shown in Figure 3. The chemical bonds and functional group present in the compound are listed as in Table 2.

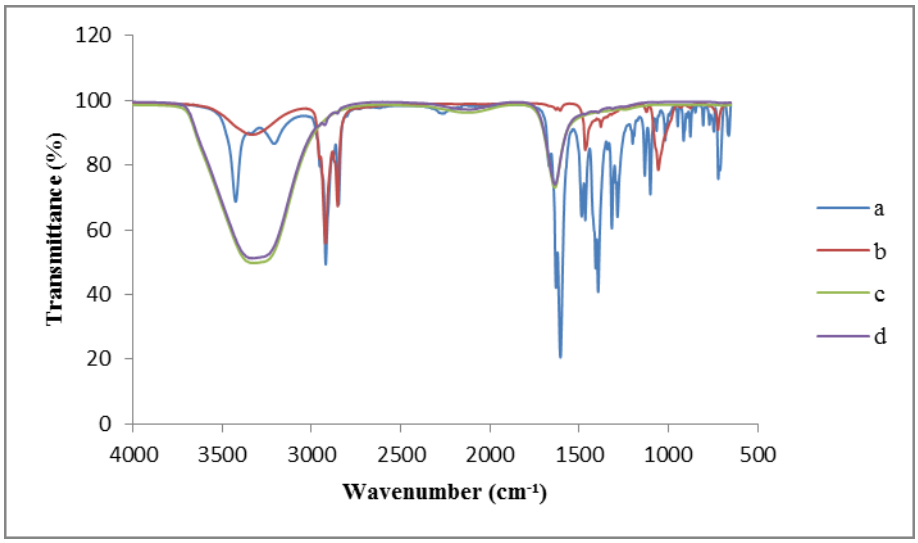



Figure 3. FTIR spectrum of (a) sodium N-lauroylsarcosinate hydrate, (b) 1-decanol, (c) gadolinium (III) nitrate solution and (d) vesicle solution.

Table 2. Vibrational mode assignment of sodium N-lauroylsarcosinate hydrate, 1-decanol, gadolinium (III) nitrate solution and vesicle solution

| Modes of vibration | Functional Group | Wavenumber ($cm^{-1}$) | | | |
|---|---|---|---|---|---|
| | | SNLS | 1-Decanol | $Gd(NO_3)_3$ | Vesicle |
| O-H stretch (wide, strong) | Hydroxyl | 3425.37 | 3341.79 | 3330.65 | 3340.40 |
| C=C-H asymmetric stretch | Alkenes | 3210.79 | n.d | n.d | n.d |
| H-C-H symmetric and asymmetric stretch | Alkanes | 2920.67 | 2922.26 | n.d | n.d |
| C-H bend | Alkanes | 1465.36 | 1465.79 | n.d | n.d |
| C-N stretch | Aliphatic amines | n.d | 1056.42 | n.d | n.d |

n.d Not detected

The strong and wide peak at 3500 – 3200 $cm^{-1}$ represent the O-H stretch from the alcohol group of decanol. Based on the modes of vibration in Table 2, the wavenumber of hydroxyl group for sodium N-lauroylsarcosinate hydrate (SNLS) is 3425.37 $cm^{-1}$ and 3341.79 $cm^{-1}$ for 1-decanol. The formation of vesicle from mixing of SNLS and 1-decanol at molar ratio of 1: 2 is confirmed through the present of strong and wide hydrogen bonding at the wavenumber 3340.40 $cm^{-1}$. Besides that, it is observed that there is a weak mode of asymmetric and symmetric stretch on the methyl group of SNLS and 1-decanol at peak of 2920.67 $cm^{-1}$ and 2922.26 $cm^{-1}$.

In the vesicle formation, strong hydrogen bond occurs between SNLS and 1-decanol. The schematic diagram for interaction between SNLS and 1-decanol is as shown in Figure 4 [15]. The amphiphilic molecules consist of a hydrophilic polar head and hydrophobic non-polar tail [16], which tend to form different structures when environmental changes occur. The nitrogen group also contributes to the formation of vesicles. Since the molecular geometry for nitrogen group is trigonal pyramidal is an evidence for the interaction of strong hydrogen bond which occurs between one SNLS molecule and two decanol molecules. The arrangement of surfactants in the vesicle formed between the interaction of SNLS and decanol in aqueous medium can be seen in Figure 5, in which the hydrophobic tail of surfactants is shielded from aqueous medium whereas the hydrophilic head is in full contact with the medium. Thus, a bilayer structure of vesicle is formed.

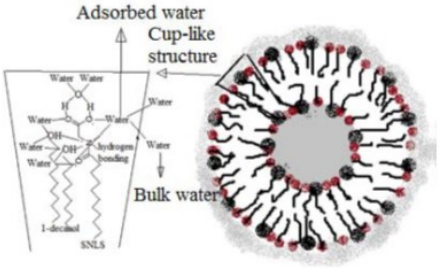



Figure 4. Schematic diagram of hydrogen bonding formation between sodium N-lauroylsarcosinate hydrate (SNLS) and 1-decanol [15] to form a vesicle

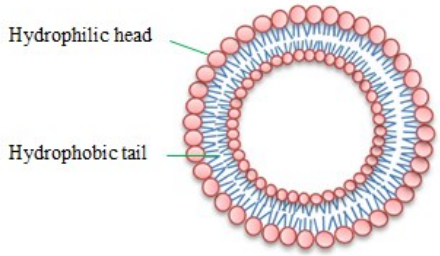



Figure 5. Bilayer structure of vesicle formed through the arrangement of amphiphile surfactants (SNLS and 1-decanol) in aqueous medium

The FTIR spectrum of encapsulated gadolinium(III) nitrate in the vesicle is shown in Figure 6. From the FTIR spectrum, the wavenumber 3500 – 3200 $cm^{-1}$ represent the strong stretch of O-H bond in all samples. In the vesicle encapsulating gadolinium(III) nitrate nanoparticle spectrum, it is observed that there is a slight shift in the O-H bond peak in comparison to the control vesicle and gadolinium(III) nitrate FTIR spectrum. The shift of O-H bond is possibly attributed by the attachment of gadolinium(III) nitrate on the OH group [17]. Besides that, the shift in the peak of gadolinium(III) nitrate nanoparticle was suspected to be encapsulated in the amino acid based vesicles. Further analysis on the morphology of both control vesicle and vesicle encapsulating gadolinium(III) nitrate nanoparticle could be obtained from the transmission electron microscopy (TEM) characterization.

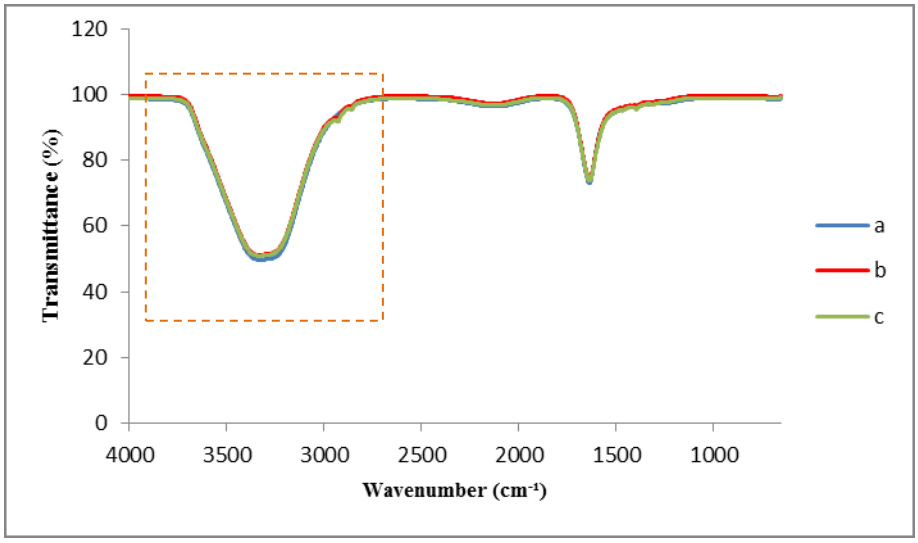



Figure 6. The FTIR spectrum (a) gadolinium(III) nitrate, (b) control vesicle and (c) vesicle encapsulating gadolinium (III) nitrate nanoparticle

**Transmission electron microscopy**

The morphology of synthesized vesicle and its size can be seen in Figure 7. From the TEM images, it is clearly shown that the control vesicle and vesicle encapsulating gadolinium(III) nitrate nanoparticle were formed through the spherical images of vesicle. The size of control vesicle ranged between 70 nm to 200 nm. Whereas, the size of vesicle encapsulating gadolinium nanoparticles ranged between 150 nm to 250 nm in diameter.

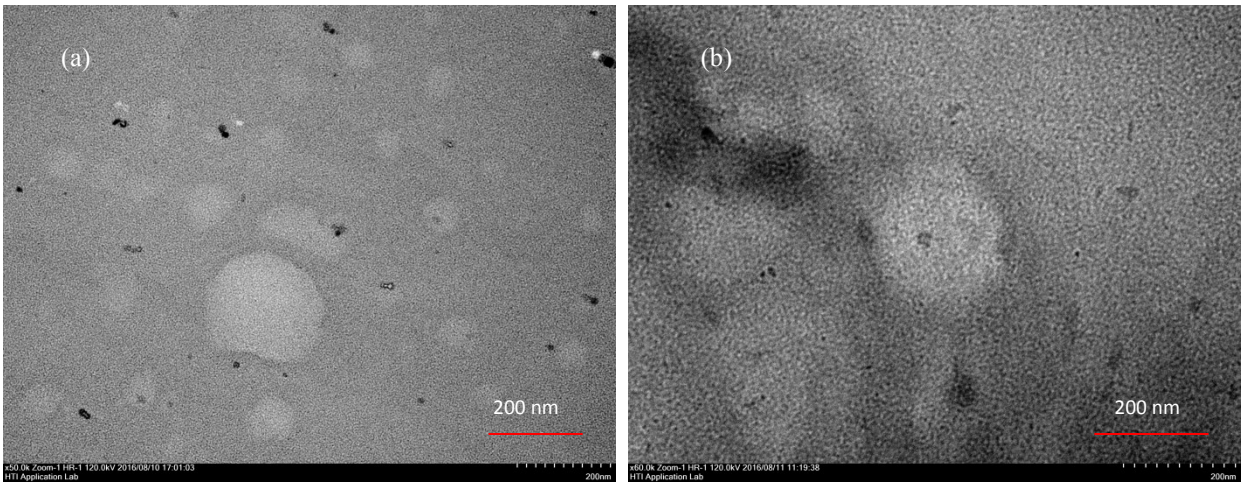



Figure 7. TEM micrograph shows the formation of (a) control vesicle and (b) vesicle encapsulating gadolinium(III) nitrate nanoparticle

Figure 8 shows the morphology of vesicle encapsulating gadolinium(III) nitrate nanoparticles which were stored for two weeks. A globular shape with a size of approximately 3 μm was observed. This shows that probably the synthesized vesicle is not suitable for storage and must be utilized directly after synthesized. This can only be further confirmed through stability test based on zeta potential using dynamic light scattering, which is currently on going.

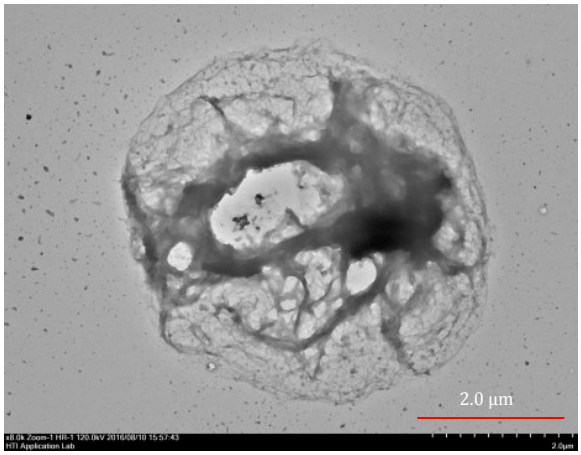



Figure 8. The globular shape was formed after vesicle encapsulating of gadolinium(III) nitrate nanoparticles was stored for two weeks

## Conclusion

Through this study, vesicle encapsulating gadolinium(III) nitrate nanoparticles was synthesized using sonication method. Through chemical molecular conformation and morphological characterization, it is proven that gadolinium(III) nitrate nanoparticles is encapsulated in vesicle. Therefore, this shows that the surfactant used in forming vesicle can be utilized in drug delivery, specifically in carrying encapsulated gadolinium(III) nanoparticle for medical purposes.

**Acknowledgement**

The work was financially supported by the Fundamental Research Grant Scheme (FRGS/2/2014/SG02/UKM/02/1) and University Research Grant (GUP-2016-015). The author thanks the staffs of the Microscope unit and CRIM of National University of Malaysia (UKM) for their assistance in obtaining the TEM, FTIR and XRD images.

**References**

1. Hall, J. B., Dobrovolskaia, M. A., Patri, A. K. and McNeil, S. E. (2007). Characterization of nanoparticles for therapeutics. *Future Medicine*, 2(6): 789 - 803.
2. Cheow, W. S. and Hadinoto, K. (2011). Factors affecting drug encapsulation and stability of lipid–polymer hybrid nanoparticles. *Colloids and Surfaces B: Biointerfaces,* 85(2): 214 - 220.
3. Lussier, J. N., Klemer, D. R., Hawthorn, P. S. and Sobottke, M. D. (1995). Gadolinium vanadate laser. U.S. Patent No. 5,420,876.
4. Kleinlogel, C. and Gauckler, L. (2000). Mixed electronic-ionic conductivity of cobalt doped cerium gadolinium oxide. *Journal of Electroceramics,* 5(3): 231 - 243.
5. Sondermann, T. (1981). Method for manufacturing gadolinium-containing nuclear fuels. U.S. Patent No. 4,278,560.
6. Bernhard, E. J., Mitchell, J. B., Deen, D., Cardell, M., Rosenthal, D. I. and Brown, J. M. (2000). Re-evaluating gadolinium(III) texaphyrin as a radiosensitizing agent. *Cancer Research,* 60(1): 86 - 91.
7. Aisen, A. M., Martel, W., Braunstein, E. M., McMillin, K. I., Phillips, W. A. and Kling, T. (1986). MRI and CT evaluation of primary bone and soft-tissue tumors. *American Journal of Roentgenology,* 146(4): 749 - 756.
8. Park, J.-A., Kim, H.-K., Kim, J.-H., Jeong, S.-W., Jung, J.-C., Lee, G.-H. and Kim, T.-J. (2010). Gold nanoparticles functionalized by gadolinium–DTPA conjugate of cysteine as a multimodal bioimaging agent. *Bioorganic & Medicinal Chemistry Letters,* 20(7): 2287 - 2291.
9. Lux, F., Sancey, L., Bianchi, A., Crémillieux, Y., Roux, S. and Tillement, O. (2015). Gadolinium-based nanoparticles for theranostic MRI-radiosensitization. *Nanomedicine,* 10(11): 1801 - 1815.
10. Szoka Jr, F. and Papahadjopoulos, D. (1980). Comparative properties and methods of preparation of lipid vesicles (liposomes). *Annual Review of Biophysics and Bioengineering,* 9(1): 467 - 508.
11. Zhu, T. F. and Szostak, J. W. (2011). Exploding vesicles. *Journal of Systems Chemistry,* 2(1): 4 - 10.
12. Sankar, V., Ruckmani, K., Jailani, S., Ganesan, K. S. and Sharavanan, S. (2009). Niosome drug delivery system: Advances and medical applications an overview. *Pharmacol Online,* 2: 926 - 932.
13. Rosli, M., Alia, N. R., Mohamed, F. K. K., Sah, M., Syafiq, M. A. and Rahman, I. A. (2014). Effect of gamma radiation on amino acid based vesicle carrying radiosensitizer. *Malaysian Journal of Analytical Sciences,* 18(3): 555 - 561.
14. Cevc, G. (2004). Lipid vesicles and other colloids as drug carriers on the skin. *Advanced Drug Delivery Reviews,* 56(5): 675 - 711.
15. Akter, N., Mohamed, F., Radiman, S. and Reza, M. I. (2012). Vesicles and lamella: Outcome of the changing formation path of a sodium N-lauroylsarcosinate hydrate/1-decanol/water system. *Nature Precedings*, 2012: 1 - 18.
16. Yamamoto, S., Maruyama, Y. and Hyodo, S. A. (2002). Dissipative particle dynamics study of spontaneous vesicle formation of amphiphilic molecules. *The Journal of Chemical Physics,* 116(13): 5842 - 5849.
17. Lim, S.-F., Zheng, Y.-M., Zou, S.-W. and Chen, J. P. (2008). Characterization of copper adsorption onto an alginate encapsulated magnetic sorbent by a combined FT-IR, XPS, and mathematical modeling study. *Environmental Science & Technology,* 42(7): 2551 - 2556.

*Malaysian Journal of Analytical Sciences, Vol 21 No 6 (2017): 1243 - 1249*
*DOI: https://doi.org/10.17576/mjas-2017-2106-05*

MALAYSIAN JOURNAL OF ANALYTICAL SCIENCES
*Published by The Malaysian Analytical Sciences Society*
ISSN 1394 - 2506

# DIKETOPIPERAZINE PRODUCED BY PSYCHROPHILIC YEAST *Glaciozyma antarctica* PI12

## (Diketopiperazin Dihasilkan oleh Yis Psikropilik *Glaciozyma antarctica* PI12)

Andi Rifki Rosandy[1], Muntaz Abu Bakar[1], Nurul Nadiah Abdul Rahman[1], Abdul Munir Abdul Murad[2], Azira Muhamad[3], Rozida Mohd. Khalid[1]*

[1]*School of Chemical Science and Food Technology, Faculty of Science and Technology*
[2]*School of Biosciences and Biotechnology, Faculty of Science and Technology*
*Universiti Kebangsaan Malaysia, 43600 UKM Bangi, Selangor, Malaysia*
[3]*Malaysia Genome Institute (MGI),*
*National Institute of Biotechnology Malaysia, Jalan Bangi, 43000 Kajang, Selangor, Malaysia*

**Corresponding author: rozidakhalid@ukm.edu.my*

Received: 7 June 2017; Accepted: 1 November 2017

**Abstract**

Four diketopiperazine derivatives; cyclo(-Pro-Val) (**1**), (-)-cyclo(-Pro-Tyr) (**2**), (-)-cyclo(-Pro-Phe) (**3**) and (+)-cyclo(-Pro-Leu) (**4**) were isolated from the ethyl acetate extract of *Glaciozyma antarctica* PI12, a cold-adapted yeast that belongs to family Kriegeriales. The compounds were isolated by radial chromatography and thin layer chromatography techniques and the chemical structures were elucidated by infrared (IR), ultraviolet (UV), nuclear magnetic resonance (NMR) spectroscopy and mass spectrometry.

**Keywords:** *Glaciozyma antarctica* PI12, diketopiperazine, Kriegeriales

**Abstrak**

Empat terbitan diketopiperazin; siklo(-Pro-Val) (**1**), (-)-siklo(-Pro-Tir) (**2**), (-)-siklo(-Pro-Phe) (**3**) and (+)-siklo(-Pro-Leu) (**4**) yang dipencilkan daripada ektrak etil asetat *Glaciozyma antarctica* PI12, merupakan yis adaptasi sejuk yang terdiri dari famili Kriegeriales. Sebatian – sebatian terpencil telah diasingkan menggunakan teknik kromatografi pepejal dan kromatografi lapisan nipis dan struktur kimia dijelaskan oleh spektroskopi infra merah (IM), ultra lembayung (UL), resonans magnetik nuklear (RMN) dan spektrometri jisim.

**Kata kunci:** *Glaciozyma antarctica* PI12, diketopiperazin, Kriegeriales

## Introduction

Antarctica is a continent with extreme low temperature and nutrients, with high UV radiation, low water availabilities and frequent freeze-thaw cycle [1]. Therefore, the biology of Antarctica more than other continents, is dominated by microorganisms [2], with a high level of adaptation and able to withstand extreme condition [3]. However, temperature is one of major factors affecting the survival of microorganisms in Antarctica [4]. Cold adapted fungi that grow optimally at temperatures less than 15 °C and cannot grow above 20 °C are called "psychrophilic fungi or cold-adapted fungi" [5]. Since the 1960s, bioactive secondary metabolites have been isolated and structurally characterised from psychrophiles [6] such as bioactive non-ribosomal peptides (NRPs),

compounds derived from the NRP-synthetase that were developed into antibiotics i.e. bacitracin, polymyxin B and E [7].

*Glaciozyma antarctica* PI12 belongs to the family Kriegeriales [8] and was isolated from a marine environment in Antarctica [9]. Recently, this psychrophilic yeast was reclassified from *Leucosporidium antarcticum* to *Glaciozyma antarctica* PI12 [10] and has also been isolated from various locations in Antarctica [11, 12]. *Glaciozyma antarctica* PI12 was widely investigated in recent yearsin most antifreeze protein production and cold-active enzyme, including an extracellular serine proteinase [13]. The main objective of this paper is to describe the isolation and structure characterisation from psychrophilic yeast *G. antarctica* PI12.

## Materials and Methods

### Biological materials

The *G. antarctica* PI12 sample used was a gift from Prof. Dr. Nazalan Najimudin from Universiti Sains Malaysia in Penang, Malaysia. It was identified based on the biochemical characteristics and the sequence of the internal transcribed spacer (ITS) as well as the LSU rRNA (Accession numbers JX89896955 and JX896956) by the National Collection of Yeast Cultures, Norwich, UK. The strain was cultured on Tryptic Soy Agar for 10 days at 4 °C until a single colony was obtained [14]. The culturing of *G. antarctica* PI12 was conducted in collaboration with the Malaysia Genome Institute.

### Cultivation of yeast

10 µL of the *G. antarctica* PI12's glycerol stock was sub-cultured on the Yeast Extract-Peptone-Dextrose (YPD) agar with 50 µg/mL of ampicillin and 50 µg/mL of kanamycin at 12 °C until a single colony was obtained. Next, a starter culture of *G. antarctica* PI12 was prepared by inoculating a single colony of *G. antarctica* PI12 from the agar plate into 10 mL of YPD medium (50 mL falcon tube) with 50 µg/mL of ampicillin and 50 µg/mL of kanamycin. It was then cultured at 12 °C at 180 rpm until mid-log phase (OD600: 1.0 to 1.8) (5 days). Thirdly, a fixed amount ($10^6$ yeast cells/mL) of starter culture was inoculated into 50 mL of YPD medium (three 250 mL of conical flask were used) with two antibiotics, and then cultured at 12 °C at 180 rpm until stationary phase at day 14 [15].

### Extraction and isolation

The production culture was centrifuged (10,000 rpm, 4 °C, 5 min). The supernatant was filtered under vacuum to remove any cells that were not pelleted out and its pH was adjusted to 4.0. The supernatant was extracted thrice with ethyl acetate, and concentrated using a rotary evaporator. The ethyl acetate (EtOAc) extract (200.7 mg) of *G. antarctica* PI12 was subjected to radial chromatography (RC) with 1 mm thickness silica gel on a round glass plate and eluted with the mixtures of dichloromethane (DCM) and methanol (MeOH) with increasing polarity (started with DCM/MeOH, 9.6: 0.4). The eluates showing the same profile on thin layer chromatography (TLC) were combined to give three fractions (I-III). Purification of Fraction I (1-4) (29.7 mg) was carried out using RC with a silica gel plate of 0.5 mm thickness eluted with DCM and MeOH (9.2: 0.8) in 5% polarity increment to yield Compound **1** (1 mg). Purification of Fraction III (5-7) (48.8 mg) was conducted by utilising another RC with silica gel plate of 0.5 mm thickness. Elution with DCM and MeOH (8.4: 1.6) produced Compound **2** (1 mg), Compound **3** (1.5 mg), and Compound **4** (2 mg).

## Results and Discussion

### Characterization study

Cyclo(-Pro-Val) (**1**) is a white amorphous solid. ESI-MS $[M + H]^+$ at *m/z*: 197. IR $\bar{\upsilon}_{max}$ (ATR) $cm^{-1}$: 3191, 2956, 1640, 1453, 1110, 922. $^1H$ NMR (MeOD, 700 MHz) $\delta_H$ (ppm) and $^{13}C$ NMR (MeOD, 175 MHz) $\delta_C$ (ppm) data are tabulated in Table 1.

(-)-Cyclo(-Pro-Tyr) (**2**) is a white amorphous solid. $[\alpha]_D^{20}$ -43.1 (c 0.14, ethanol). ESI-MS $[M + H]^+$ ion at *m/z*: 261. IR $\bar{\upsilon}_{max}$ (ATR) $cm^{-1}$: 3248, 2927, 2853, 1747, 1658, 1449, 1252, 1174, 1114, 1017, 858. $^1H$ NMR (MeOD, 700 MHz) $\delta_H$ (ppm) and $^{13}C$ NMR (MeOD, 175 MHz) $\delta_C$ (ppm) data are tabulated in Table 1.

(-)-Cyclo(-Pro-Phe) (**3**) is a white amorphous solid. $[\alpha]_D^{20}$ -72 (c 0.7, methanol). ESI-MS $[M + H]^+$ ion at *m/z*: 169. IR $\bar{\upsilon}_{max}$ (ATR) $cm^{-1}$: 3357, 2956, 2108, 1647, 1449, 1318 and 1087. $^1H$ NMR (MeOD, 700 MHz) $\delta_H$ (ppm) and $^{13}C$ NMR (MeOD, 175 MHz) $\delta_C$ (ppm) data are tabulated in Table 1.

(+)-Cyclo(-Pro-Leu) (**4**) is a white powder. $[\alpha]_D^{20}$ +28.1 (*c* 0.032, ethanol). ESI-MS $[M + H]^+$ ion at *m/z*: 211. IR $\bar{\upsilon}_{max}$ (ATR) $cm^{-1}$: 3222, 2958, 2930, 2872, 1686, 1676, 1426, 1302, 1275, 1235, 1157, 1102, 1032, 996-919. $^1H$ NMR (MeOD, 700 MHz) $\delta_H$ (ppm) and $^{13}C$ NMR (MeOD, 175 MHz) $\delta_C$ (ppm) data are tabulated in Table 1.

Table 1. $^1H$ and $^{13}C$ NMR data (700 and 175 MHz, MeOD) for compounds **1**-**4**

| Position | APT (ppm) | | | | $^1H$ (*mult*., ΣH)) | | | |
|---|---|---|---|---|---|---|---|---|
| | **1** | **2** | **3** | **4** | **1** | **2** | **3** | **4** |
| 1-N | - | - | - | - | - | - | | - |
| 2 | 165.8 | 165.7 | 165.5 | 167.1 | - | - | - | - |
| 3 | 59.9 | 56.6 | | 53.1 | 3.92 (*d*, 1H) | 4.37 (*m*, 1H) | 4.25 (*t*, 1H) | 4.00 (*t*, 1H) |
| 4-NH | - | - | - | - | 7.93 (*br-s*, 1H) | 7.65 (*s*, 1H) | 7.62 (*s*, 1H) | 7.99 (*br-s*, 1H) |
| 5 | 170.9 | 169.6 | 169.3 | 171.1 | - | - | - | - |
| 6 | 58.7 | 58.7 | 58.6 | 58.9 | 4.11 (*t*, 1H) | 4.05 (*m*, 1H) | 4.14 (*t*, 1H) | 4.18 (*t*, 1H) |
| 7 | 28.3 | 28.0 | 28.0 | 27.9 | 1.82 (*m*, 1H) | 2.33 (*q*, 1H) | 2.29 (*m*, 1H) | 2.12 (*q*, 1H) |
| | | | | | 2.14 (*m*, 1H) | 1.99 (*q*, 1H) | 1.92 (*q*, 1H) | 1.89 (*q*, 1H) |
| 8 | 22.4 | 21.4 | 21.3 | 22.9 | 1.80 (*m*, 1H) | 2.01 (*m* ,1H) | 2.01 (*m* ,1H) | 1.91 (*m*, 1H) |
| | | | | | 1.86 (*m*, 1H) | 1.93 (*m*, 1H) | 1.93 (*m*, 1H) | 1.80 (*m*, 1H) |
| 9 | 45.1 | 44.6 | 44.5 | 45.3 | 3.33 (*t*, 1H) | 3.63 (*m*, 1H) | 3.68 (m, 1H) | 3.36 (*t*, 1H) |
| | | | | | 3.38 (*t*, 1H) | 3.57 (*m*, 1H) | 3.58 (m, 1H) | 3.37 (*t*, 1H) |
| 10 | 28.2 | 36.3 | 36.3 | 38.1 | 2.32 (*m*, 1H) | 3.46 (*dd*, 1H) | 3.47 (dd, 1H) | 1.75 (*t*, 1H) |
| | | | | | | 2.79 (*dd*, 1H) | 2.79 (dd, 1H) | 1.36 (*t*, 1H) |
| 11 | 18.7 | - | - | 24.5 | 0.99 (*d*, 3H) | - | - | 1.85 (*m*, 1H) |
| 12 | 16.7 | - | - | 23.2 | 0.83 (*d*, 3H) | - | - | 0.86 (*d*, 3H) |
| 13 | - | - | - | 22.3 | - | - | - | 0.85 (*d*, 3H) |
| 1` | - | 126.3 | 126.2 | - | - | - | - | - |
| 2`/6` | - | 130.7 | 130.7 | - | - | 7.05 (*dd*, 2H) | 7.02 (dd, 2H) | - |
| 3`/5` | - | 115.0 | 130.3 | - | - | 6.79 (*dd*, 2H) | 6.73 (dd, 2H) | - |
| 4` | - | 156.1 | 128.2 | - | - | 5.35 (*br-s*,1H), -OH | 7.24 (d, 1H) | - |

Compound **1** was isolated as white amorphous solid. Its molecular formula was determined as $C_{10}H_{16}N_2O_2$, obtained by ESI–MS $[M + H]^+$ *m/z* 197. The IR spectrum showed the presence of carbonyl groups from amide (1640 $cm^{-1}$), and also saturated methylene groups at the range of 2956-2889 $cm^{-1}$. The $^{13}C$-APT NMR spectrum showed the location of ten signals representing two quaternary, three methines, three methylenes and two methyls carbons. The double bond equivalent (DBE) value of four indicated that this compound contained two double bonds and two cyclic aliphatic. The most deshielded carbons at $\delta_C$ 170.9 and 165.8 ppm were indicated as an asymmetrical carbonyl group. Three saturated non-equivalent methylenes signals at $\delta_C$ 28.3 (C-7), 22.4 (C-8) and 45.1 (C-9) were attributed to a pyrrolidine ring. A methine carbon at $\delta_C$ 58.7 ppm (C-6) was the specific of methine signal of diketopiperazine alkaloid and another one methine at $\delta_C$ 59.9 ppm (C-3) indicated the presence of a methine existed

between carbonyl and secondary amide while the two non-equivalent gem-dimethyls at $\delta_C$ 18.7 ppm (C-11) and $\delta_C$ 18.7 ppm (C-12) bound a saturated methine at $\delta_C$ 28.2 ppm (C-10).

Meanwhile, 12 proton signals representing 16 protons appeared in the $^1$H-NMR spectrum as shown in Table 1. Six of the signals came from the three non-equivalent methylenes proton at H-7, H-8 and H-9, forming a basic pyrrolidine ring. An aminated methine proton, H-6 ($\delta_H$ 4.11 ppm) resonated as a triplet, indicating that C-6 was adjacent to a methylene group (C-7). Another methine proton at H-10 ($\delta_H$ 2.32 ppm) was resonated as a multiplet, because it was bound to two non-equivalent gem-dimethyls at C-11 and C-12. Comparison of the $^1$H and $^{13}$C-APT NMR spectra of the compound suggested that it was Cyclo(-Pro-Val) (Fig. 1) [16]. Thus, the structure of Cyclo(-Pro-Val) (**1**) was previously isolated from *Aspergillus fumigatus* [17], *Pseudomonas aeruginosa* [18], and *Stenotrophomonas* sp. [19].

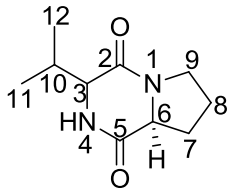



Figure 1. Chemical structure of compound **1**

Compounds **2** and **3** (Figure 2) were found in Fraction III as a UV absorbing spot, which stained to violet with anisaldehyde/sulphuric acid. The $^1$H NMR spectrum of Compound **2** showed two *ortho*-coupled signals at $\delta_H$ 7.05 (H-2', 6') and 6.79 (H-3', 5'), which pointed to an AA'-BB' system of a 1,4-disubstituted aromatic ring, as well as two signals at δ 4.37 and 4.05 for two methines attached to electron withdrawing substituents. The spectrum proton of Compound **2** showed also two doublet of doublets for an ABX system of a methylene group at $\delta_H$ 3.46 and 2.79 ($CH_2$-10), as well as three methylene multiplets ($CH_2$-7) ($\delta_H$ 2.33, 1.99) attached to a heteroatom and $CH_2$-8, 9 ($\delta_H$ 2.01, 1.93, 3.63, 3.57). The ESI mass spectra determined the molecular weight of Compound **2** as 261 Dalton by (+)-ESI mode. The structure was further confirmed as (-)-cyclo(-Pro-Tyr) (**2**) by comparison with an authentic sample and spectra from our collection [20]. (-)-cyclo(-Pro-Tyr) (**2**) was previously isolated from *Pseudomonas fluorescens* GcM5-1A [21], *Streptomyces* sp. H7372 and ML 1532 [22, 23], *Pseudomonas aeruginosa* [18] and *Lysobacter capsici* AZ78 [24]. The difference between Compound **2** and Compound **3** lay on C-4`, where Compound **2** had a hydroxy at C-4` (Figure 2).

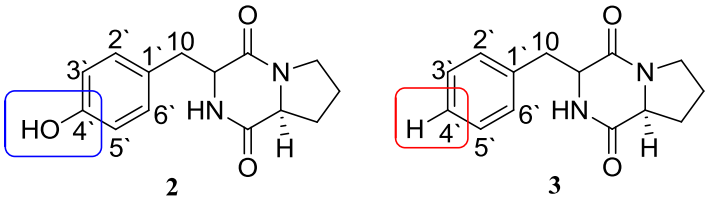



Figure 2. Structure of compounds **2** and **3**

From the spectroscopy data and comparison with the literature, compound **3** was confirmed as (-)-cyclo(-Pro-Phe) (**3**) [17] previously isolated from microbial sources, including *Streptomyces rochei* 87051-3 [16], *Streptomyces sudanensis*. A4.4 [25], *Tyridiomyces formicarum* [26], and *Alternaria alternata* [27].

(+)-Cyclo(-Pro-Leu) (**4**), $[\alpha]_D^{20}$ +28.1 (*c* 0.032, ethanol), was isolated as a white amorphous material with molecular formula $C_{11}H_{18}N_2O_2$, obtained by ESI–MS $[M + H]^+$ *m/z* 211. The IR spectrum showed bands attributed to the aliphatic carbons (2958, 2930, 2872 $cm^{-1}$) and amide (1686, 1676 $cm^{-1}$) functional groups. The $^1$H NMR spectrum

of compound **4** indicated the presence of three methines at H-3, H-6 and H-11; four methylenes at H-7, H-8, H-9 and H-10; and two non-equivalent dimethyls at H-12 and H-13 (Table 1). $^{13}$C NMR spectrum exhibited the presence of 11 carbon signals corresponding to two methyls, four methylenes, three methines and two quaternary carbons. The observation of the quaternary carbons at $\delta_C$ 167.1 (C-2) and 171.1 (C-5) suggested that these carbon signals were due to the carbonyl carbon of the amide groups. The DBE value of four indicated that this compound was containing two double bonds and two cyclic aliphatic. (+)-cyclo(Pro-Leu) (**4**) previously isolated from the Gram-negative Proteobacteria of *Burkholderia cenocepacia* and *Serratia marcescens* [28], *Alternaria alternata* [29], the bacteria *Pseudoalteromonas* sp. [30] and *Vibrio alginolyticus* [31].

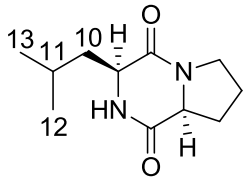



Figure 3. Structure of compounds **4**

## Conclusion

Four diketopiperazine derivatives, i.e. cyclo(-Pro-Val) (Compound**1**), (-)-cyclo(-Pro-Tyr) (Compound **2**), (-)-cyclo(-Pro-Phe) (Compound**3**) and (+)-cyclo(-Pro-Leu) (Compound**4**) were isolated and reported for the first time from psychrophilic yeast *G. antarctica* PI12. All the compounds reported in the present study were not subjected to further bioactivity studies due to insufficient amounts.

## Acknowledgement

We would like to thank the School of Chemical Sciences and Food Technology, Faculty of Science and Technology, Universiti Kebangsaan Malaysia (UKM); Malaysia Genome Institute (MGI) for providing research facilities. We would like also to express our gratitude to the Indonesia Endowment Fund for Education (LPDP) and the Malaysian Ministry of Science and Technology and Universiti Kebangsaan Malaysia for financial support through the following research grants: 02-05-20-SF0007/4 and FRGS-1-2014-SG01-UKM-02-6.

## References

1. Ruisi, S., Barreca, D., Selbmann, L., Zucconi, L. and Onofri, S. (2007). Fungi in Antarctica. *Reviews in Environmental Science and Biotechnology*, 6: 127 – 141.
2. Nienow, J. A. and Friedmann, E. I. (1993). Terrestrial litophytic (rock) communities. In: Friedmann, E. I. (ed). Antarctica microbiology. Wiley-Liss, New York, pp. 343 – 412.
3. Friedmann, E. I. (1993). Antarctic microbiology. Wiley-Liss, New York, pp. 634.
4. Morgan-Kiss, R. M., Priscu, J. C., Pocock, T., Gudynaite-Savitch, L. and Humer, N. P. (2006). Adaptation and acclimation of photosynthetic microorganisms to permanently cold environments. *Microbiology and Molecular Biology Reviews*, 70: 222 – 252.
5. Morgan, R. Y. (1975). Psychrophilic bacteria. *Bacteriological Reviews*, 39: 144 – 167.
6. Giddings, L. A. and Newman, D. J. (2015). Bioactive compounds from terrestrial extremophiles. Springer, New York, pp. 1.
7. Sewald, N. and Jakubke, H. D. (2002). Peptides: Chemistry and biology. NJ: Wiley, Berlin, pp. 119 –124.
8. Di Menna, M. E. (1960). Yeast from Antarctica. *Journal of General Microbiology*, 7: 295 – 300.
9. Fell, J. W., Statzell, A., Hunter, I. L. and Phaff, H. J. (1969). *Leucosporidium* gen. n., the heterobasidiomycetous stage of several yeasts of the genus *Candida. Antonie van Leeuwenhoek*, 35: 433 – 462.
10. Turchetti, B., Thomas-Hall, S. R., Connell, L. B., Branda. E., Buzzini, P., Theelen, B., Müller, W. H. and Boekhout, T. (2011). Psychrophilic yeasts from Antarctica and European glaciers: description of *Glaciozyma* gen. nov., *Glaciozyma martinii* sp. nov. and *Glaciozyma watsonii* sp. nov. *Extremophiles*, 15: 573 – 586.

11. Donachie, S. P. (1995). Ecophysiological description of marine bacteria from Admiralty Bay (Antarctica), and the digestive tracts of selected *Euphausiidae*. Ph.D. Thesis, Department of Antarctic Biology, Polish Academy of Sciences, Warsaw.
12. Connell, L. B., Redman, R., Craig, S., Scorzetti, G., Iszard, M. and Rodriguez, R. (2008). Diversity of soil yeasts isolated from South Victoria Land, Antarctica. *Microbial Ecology*, 56: 448 – 459.
13. Pazgier, M., Turkiewicz, M., Kalinowska, H. and Bielecki, S. 2003. The unique cold-adapted extracellular subtilase from psychrophilic yeast *Leucosporidium antarcticum*. *Journal of Molecular Catalysis B: Enzymatic*, 21: 39 – 42.
14. Hashim, N. H. F., Sulaiman, S., Bakar, F. D. A., Illias, R. M., Kawahara, H., Najimudin, N., Mahadi, N. M. and Murad, A. M. A. (2014). Molecular cloning, expression and characterisation of Afp4, an antifreeze protein from *Glaciozyma antarctica*. *Polar Biology*, 37: 1495 – 1505.
15. Hashim, N. H. F., Bharudin, I., Nguong, D. L. S., Higa, S., Bakar, F. D. A., Nathan, S., Rabu, A., Kawahara, H., Illias. R. M., Najimudin, N., Mahadi, N. M. and Murad, A. M. A. (2013). Characterization of Afp1, an antifreeze protein from the psychrophilic yeast *Glaciozyma antarctica* PI12. *Extremophiles*, 17: 63 – 73.
16. Lee, H. B., Choi, Y. C. and Kim, S. U. (1994). Isolation and identification of Maculosins from *Streptomyces rochei* 87051-3. *Agricultural Chemistry and Biotechnology*, 37(5): 339 – 342.
17. Furtado, N. A. J. C., Pupo, M. T., Carvalho, I., Campo, V. L., Duarte, M. C. T., and Bastos, J. K. (2005). Diketopiperazines produced by an *Aspergillus fumigatus* Brazilian strain. *Journal of the Brazilian Chemical Society*, 16(6B): 1448 – 1453.
18. Vasquez-Rivera, D., González, O., Guzmán-Rodríguez, J., Diaz-Pérez, A. L., Ochoa-Zarzosa, A., Lopez-Bucio, J., Meza-Carmen, V. and Campos-García, G. (2015). Cytotoxicity of cyclodipeptides from *Pseudomonas aeruginosa* PAO1 leads to apoptosis in human cancer cell lines. *BioMed Research International*, 2015: 1 – 9.
19. Jermnak, U., Chinaphuti, A., Poapolathep, A., Kawai, R., Nagasawa, H. and Sakuda, S. (2013). Prevention of aflatoxin contamination by a soil bacterium of *Stenotrophomonas* sp. that produces aflatoxin production inhibitors. *Microbiology*, 159: 902 – 912.
20. Laatsch, H. (2010). AntiBase a data base for rapid dereplication and structure determination of microbial natural products. Wiley-VCH. Germany, Wein-heim.
21. Guo, Q., Guo, D., Zhao, B., Xu, J. and Li, R. (2007). Two cyclic dipeptides from *Pseudomonas fluorescens* GcM5-1A carried by the pine wood nematode and their toxicities to Japanese black pine suspension cells and seedlings in vitro. *Journal of Nematology*, 39(3): 243 – 247.
22. Cheenpracha, S., Borris, R. P., Tran, T. T., Jee, J. M., Seow, H. F., Cheah, H. Y., Ho, C. C. and Chang, L. C. (2011). Three new amides from *Streptomyces* sp. H7372. *Journal of the Brazilian Chemical Society*, 22(2): 223 – 229.
23. Munekata, M. and Tamura, G. (1981). Selective inhibition of SV40-transformed cell growth by diketopiperazines. *Agricultural and Biological Chemistry*, 45(11): 2613 – 2618.
24. Puopolo, G., Cimmino, A., Palmieri, M. C., Giovannini, O., Evidente, A. and I. Pertot, I. (2014). *Lysobacter capsici* AZ78 produces cyclo(L-Pro-L-Tyr), a 2,5-diketopiperazine with toxic activity against sporangia of *Phytophthora infestans* and *Plasmopara viticola*. *Journal of Applied Microbiology*, 117: 1168-1180.
25. Hamza, A. A., Ali, H. A., Clark, B. R., Murphy, C. D. and Elobied, E. A. (2013). Cyclo (L-phenyl, L-prolyl). Diketopiperazines from a newly isolated *Streptomyces sudanensis*. A4.4. *Journal of Biotechnology and Pharmaceutical Research*, 4(1): 1 – 7.
26. Wang, Y., Mueller, U. G. and Clardy, J. (1999). Antifungal diketopiperazines from symbiotic fungus of fungus-growing ant *Cyphomyrmex minitus*. *Journal of Chemical Ecology*, 25(4): 935 – 941.
27. Stierle, A. C., Cardellina, J. H. and Strobelt, G. A. (1988). Maculosin, a host-specific phytotoxin for spotted knapweed from *Alternaria Alternata*. *Proceedings of the National Academy of Sciences of the United States of America*, 85: 8008 – 8011.
28. Yap, A. C., Kok-Gan Chan, K. G. and Choo, Y. M. (2016). Isolation and identification of metabolites from the Gram-negative proteobacteria of *Burkholderia cenocepacia* and *Serratia marcescens*. *Sains Malaysiana*, 45(7): 1073 – 1077.
29. Musetti, R., Polizzotto, R., Vecchione, A., Borselli, S., Zulini, L., D'Ambrosio , M., di Toppi, L. S. and Pertot, I. (2007). Antifungal activity of diketopiperazines extracted from *Alternaria alternata* against *Plasmopara viticola*: An ultrastructural study. *Micron*, 38: 643 – 650.

30. Luis, S. M., Ballesteros, J. and Gutiérrez, M. (2011). Antibacterial constituents from the octocoral associated bacterium *Pseudoalteromonas* sp. *Revista Latinoamericana de Química*, 39: 1 – 2.
31. Wang, X., Huang, Y., Sheng, Y., Su, P., Qiu, Y., Ke, C. and Feng, D. (2017). Antifouling activity towards mussel by small-molecule compounds from a strain of *Vibrio alginolyticus* bacterium associated with Sea Anemone *Haliplanella* sp. *Journal of Microbiology and Biotechnology*, 27(3): 460–470.

*Malaysian Journal of Analytical Sciences, Vol 21 No 6 (2017): 1250 - 1256*
*DOI: https://doi.org/10.17576/mjas-2017-2106-06*

MALAYSIAN JOURNAL OF ANALYTICAL SCIENCES
*Published by The Malaysian Analytical Sciences Society*
ISSN 1394 - 2506

# SOLVENT EXTRACTION OF THORIUM FROM RARE EARTH ELEMENTS IN MONAZITE THORIUM CONCENTRATE

## (Pengekstrakan Pelarut Torium daripada Unsur Nadir Bumi dalam Pekatan Torium Monazit)

Wadeeah M. Al-Areqi*, Che Nor Aniza Che Zainul Bahri, Amran Ab. Majid, Sukiman Sarmani

*Nuclear Science Programme, School of Applied Physics,*
*Faculty of Science and Technology,*
*Universiti Kebangsaan Malaysia, 43600 UKM Bangi, Selangor, Malaysia*

**Corresponding author: walareqi@yahoo.com*

Received: 6 April 2017; Accepted: 20 August 2017

**Abstract**

Solvent extraction is a powerful separation technique in the preparation of nuclear grade thorium. In this study, monazite thorium concentrates produced from Malaysian monazite were used. Thorium was extracted from an aqueous nitric acid medium with TBP (30%) in kerosene and Aliquat-336 (10%) in kerosene, respectively. Constant experimental conditions were used for the extraction in terms of the molarity of nitric acid, concentration of extractants in kerosene, organic/aqueous volumetric ratio, mixing time, and contact time between phases. The stripping process was carried out with distilled water. The determination of thorium and rare earth elements (REEs) in the monazite thorium concentrates and aqueous solutions were performed by using inductively coupled plasma mass spectrometry (ICP-MS). The concentrations of thorium in the thorium concentrate samples were in the range of 11.58 – 83.56%. Three stages of extraction and three stages of stripping were carried out for the extraction of thorium from the REEs in the nitrate solution. The results of the study showed that the thorium extraction efficiency was in the range of 60.96 – 99.75% using TBP (30%) in kerosene and Aliquat-336 (10%) in kerosene. Thorium was stripped from the loaded TBP (30%) in kerosene and Aliquat-336 (10%) in kerosene at an average stripping percentage of 89.04% and 75.75%, respectively. The stripped aqueous solutions were analysed, and it was shown that the thorium content was in the range of 29.49 – 91.28%. This study indicated that both extractants can be successfully used to recover thorium from REEs, but in order to increase the purification of thorium, the extraction and stripping process cycle should be increased.

**Keywords:** thorium, rare earth elements, solvent extraction, monazite thorium concentrate

**Abstrak**

Pengekstrakan pelarut adalah teknik pengasingan yang kuat digunakan untuk mengasingkan torium bergred nuklear. Dalam kajian ini, pekatan torium monazit yang dihasilkan daripada monazit Malaysia telah digunakan. Torium diekstrak daripada medium akues asid nitrik dengan TBP (30%) dalam kerosin dan Aliquat-336 (10%) dalam kerosin. Kondisi eksperimen digunakan iaitu molariti asid nitrik, kepekatan pengekstrak dalam kerosin, nisbah isipadu organik/akues, masa percampuran dan masa sentuhan antara fasa dikekalkan. Proses pelucutan dilakukan menggunakan air suling. Torium dan unsur nadir bumi (REEs) dalam pekatan torium monazit dan larutan akues ditentukan menggunakan spektrometri jisim plasma gandingan teraruh (ICP-MS). Kepekatan torium dalam sampel pekatan torium ditentukan adalah dalam julat 11.58 – 83.56%. Tiga peringkat pengekstrakan dan pelucutan dilakukan untuk mendapatkan torium dari REEs dalam larutan nitrat. Hasil kajian menunjukkan kecekapan pengekstrakan torium adalah dalam julat 60.96 – 99.75% menggunakan TBP (30%) dalam kerosin dan Aliquat-336 (10%) dalam kerosin. Torium telah dilucutkan daripada muatan TBP (30%) dalam kerosin dan Aliquat-336 (10%) dalam kerosin dengan purata peratus pelucutan masing – masing adalah 89.04% dan 75.75%. Larutan akues yang dilucutkan telah dianalisis dan menunjukkan bahawa kandungan torium adalah dalam julat 29.49 – 91.28%. Kajian ini menunjukkan bahawa kedua – dua pengekstrak boleh digunakan dengan berkesan untuk mendapatkan torium daripada REEs tetapi untuk meningkatkan kemurnian torium, pengekstrakan dan kitaran proses pelucutan harus dipertingkatkan.

**Kata kunci**: torium, unsur nadir bumi, pengekstrakan pelarut, pekatan torium monazit

## Introduction

High-purity thorium is required in nuclear technology applications. Nuclear grade thorium is obtained by several industrial processes such as solvent extraction, ion exchange and direct precipitation. Solvent extraction is a powerful separation technique compared to ion exchange and precipitation due to its speed, ease of operation and large throughput [1, 2]. The basis of thorium purification by solvent extraction depends on the solubility of thorium in water and organic solvents by forming complex ions, chalets and solvated species. The sequential transfer between the aqueous and organic phases leads to the purification of thorium.

The most common thorium extraction process is the extraction of thorium nitrate from a solution of nitric acid with TBP (tributyl phosphate) diluted with an aliphatic hydrocarbon such as kerosene or xylene/toluene to reduce the viscosity of the mixture [3]. The purified thorium nitrate, which can be used as a feed material to produce thorium compounds, is converted to thorium oxide or thorium tetrafluoride. Nuclear grade thorium nitrate is obtained with 99% thorium recovery by the solvent extraction process [4].

The extraction of thorium from monazite by solvent extraction was carried out with various organic solvents, e.g. the secondary amine, Adogen 283 [5], Aliquat-336 [6], TBP [7] and primene JM-T [8]. Sato studied the partition of thorium (IV) between aqueous sulphuric acid and solutions of di-(2-ethylhexyl)-phosphoric acid (DEHPA) in kerosene, and also between aqueous sulphuric acid and solutions of long-chain aliphatic amines [9, 10]. Several methods of stripping thorium and rare earths from solvents have been frequently performed. Furthermore, the optimum experimental conditions for the extraction of thorium from a number of elements have been determined in some studies, while the effects of the types and concentrations of the extractants, the settling time between phases, the types and concentrations of the stripping solutions, and the aqueous/organic volumetric ratio have been studied in detail [7, 8].

In this study, thorium concentrates were obtained from Malaysian monazite, which, according to a previous study, contains approximately 2% of thorium [11, 12], where a range of between 6.5 – 7.5% for thorium concentrations and 53.6 – 57.8% for rare earth oxides have also been documented in Malaysian monazite [13]. The objectives of this study were to extract thorium from REEs by TBP (30%) in kerosene and Aliquat-336 (10%) in kerosene, and to determine the thorium purification percentage.

## Materials and Methods

### Materials

All the reagents and chemicals used in this work were of analytical grade, and the extractants used were TBP (tributyl phosphate), which was from Merck Schuchardt OHG, and Aliquat-336 (tricaprylmethylammonium chloride) from Alorich Chemistry. Both extractants were used without further purification. Kerosene, which was used as a diluent, was supplied by R&M Chemicals. Thorium nitrate was obtained from the nuclear science stockpile of Universiti Kebangsaan Malaysia (UKM), and distilled water was used in all the experiments for aqueous solutions**.**

### Solvent extraction procedure

The extraction and stripping experiments were performed using glass bakers and the magnetic stirrer, and then the separation of the organic/aqueous phases was done using a separatory funnel. The sample of Malaysian monazite used in this study was originally from *'amang'* factory in Perak, while the thorium concentrate was obtained from the selective precipitation of a sulphate leach solution of Malaysian monazite using ammonia at a pH of 1.8. Prior to that, the Malaysian monazite was initially processed using hot concentrated sulphuric acid (98%). The concentrations of thorium, uranium and REEs in the aqueous solutions were determined using ICP-MS (ELAN 9000 – Perkin Elmer SCIEX), and the concentration percentages of the elements were calculated from the total concentrations of the elements, which were in μg/g.

An aqueous solution of thorium was prepared by weighing about 0.10 g of thorium concentrate and dissolving it in 4 M of $HNO_3$ in a 100-ml volumetric flask at room temperature. A solution of thorium nitrate was prepared by dissolving 0.10 g of thorium nitrate in 4 M nitric acid in a 100-ml volumetric flask at a molarity of 1.85 x $10^{-3}$. TBP and Aliquat-336 were prepared by diluting 30% of TBP (v/v) in kerosene and 10% Aliquat-336 (v/v) in kerosene, respectively. The extraction experiments were carried out at room temperature.

Constant experimental conditions were maintained for each extractant, whereby the aqueous/organic volumetric ratio was 1:1, and the shaking and settling time was 10 minutes. About 5 ml. of the aqueous solution was mixed with 5 ml. of the organic solvents, and shaken for 10 minutes in bakers. The phases were allowed to settle, and were separated after 10 minutes in a separatory funnel. Three stages of extraction and three stages of stripping were carried out for the extraction of thorium from REEs in a nitrate solution. Each extraction experiment was triplicated.

The concentrations of thorium in the aqueous phase before and after the extraction were determined by ICP-MS, and the extraction percentage, E, was calculated from the distribution ratio, D, using equations 1 and 2, respectively as follows:

$$D = \frac{Co-C}{C}, \quad (1)$$

$$E\% = \frac{DVo}{DVo+Vaq}.100. \quad (2)$$

where $C_o$ and C are the thorium concentrations in the aqueous phase before and after the extraction, respectively, and $V_{aq}$ and $V_o$ are the volumes of the aqueous and organic phases, respectively [6, 7, 14].

The experimental conditions used for the stripping were similar to the conditions for extraction. Distilled water was used as the stripping solution to strip the thorium from the organic phase to the aqueous phase. The stripping percentage was calculated using the concentration of thorium in the aqueous phase after stripping and the concentration of thorium in the organic phase. The flowchart for the solvent extraction of thorium by TBP (30%) in kerosene and by Aliquate-336 (10%) in kerosene is illustrated in Figure 1.

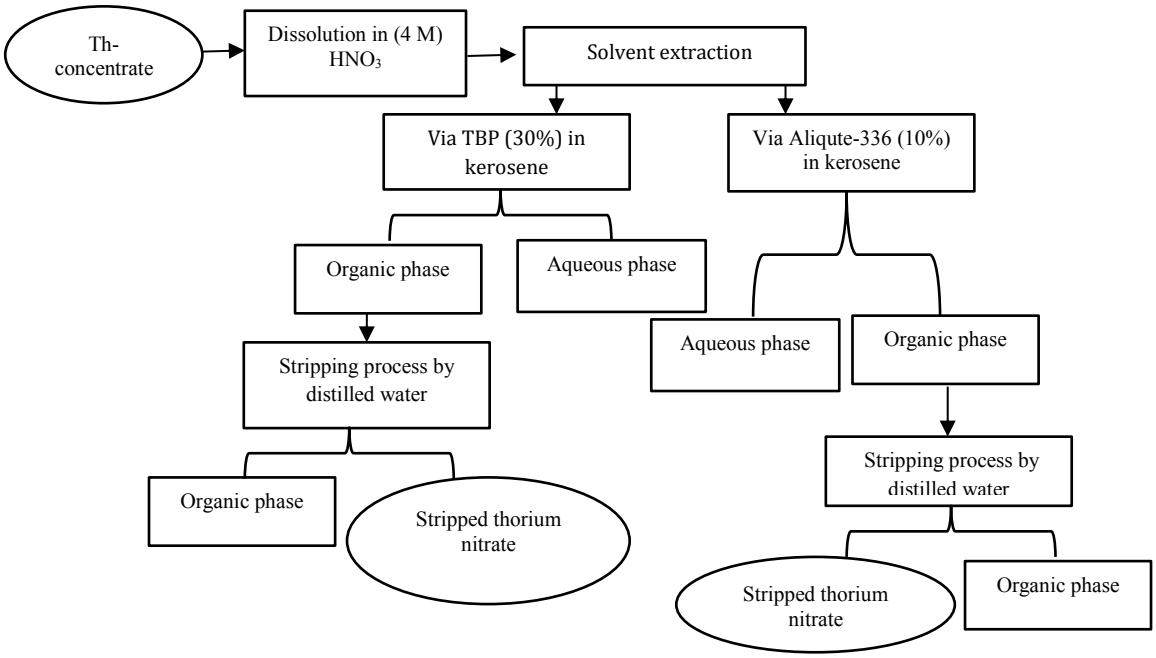



Figure1. Solvent extraction of thorium via TBP (30%) in kerosene and via Aliquate-336 (10%) in kerosene

## Results and Discussion

Monazite, which is a rare-earth and thorium phosphate mineral ((Ce, La, Nd, Th) $PO_4$), are the best primary sources of thorium. Monazite contains 2.5% of thorium and the concentrations of light rare earth elements (LREEs) are more than the concentrations of heavy rare earth elements (HREEs) [15, 16]. Furthermore, monazite concentrates usually contain 5.0 – 10.0% of thorium oxide ($ThO_2$), 0.2 – 0.4% of uranium oxide ($U_3O_8$), 55.0 – 60.0% of rare earth metal oxides, and 24.0 – 29.0% of phosphate ($P_2O_5$) [17].

The results of the analysis of eight monazite thorium concentrate samples are shown in Table 1. It was noticed that the thorium concentration was in the range of 11.58 – 83.56% in the monazite thorium concentrates and the uranium concentration was in the range of 0.04 – 0.63%, which was much lower than the concentrations of thorium and REEs. Meanwhile, the light rare earth elements (LREEs) were in high concentrations compared to the heavy rare earth elements (HREEs) because monazite is originally rich with LREEs and thorium. The Ce content was the highest among the LREEs, and its range was between 4.62 – 41.68%. The La, Nd and Pr contents were lower at 17.86%, 17.54% and 4.83%, respectively. In addition, the rest of the REE concentrations were less than 3.50%.

Table 1. Th, U and REEs concentrations (%) in monazite thorium concentrates samples

| **Analyte/ Sample ID** | **Thc1** | **Thc2** | **Thc3** | **Thc4** | **Thc5** | **Thc6** | **Thc7** | **Thc8** | **Pure Th Nitrate** |
|---|---|---|---|---|---|---|---|---|---|
| Th | 17.05 | 18.38 | 11.58 | 16.09 | 21.89 | 9.81 | 83.56 | 73.02 | 99.86 |
| U | 0.09 | 0.18 | 0.30 | 0.12 | 0.07 | 0.04 | 0.63 | 0.23 | 0.00 |
| **LREEs** | | | | | | | | | |
| La | 13.11 | 12.28 | 14.19 | 15.73 | 14.31 | 17.86 | 2.65 | 4.07 | 0.03 |
| Ce | 38.09 | 37.88 | 36.50 | 36.44 | 36.11 | 41.68 | 4.62 | 10.53 | 0.05 |
| Pr | 4.62 | 4.50 | 4.12 | 4.26 | 4.29 | 4.83 | 0.65 | 1.33 | 0.01 |
| Nd | 17.38 | 15.51 | 13.92 | 16.65 | 15.89 | 17.54 | 3.16 | 4.91 | 0.03 |
| Sm | 3.67 | 2.66 | 2.99 | 3.02 | 2.74 | 3.05 | 0.48 | 1.24 | 0.00 |
| **HREEs** | | | | | | | | | |
| Eu | 0.02 | 0.02 | 0.02 | 0.02 | 0.02 | 0.02 | 0.00 | 0.01 | 0.00 |
| Gd | 2.55 | 2.09 | 2.72 | 0.45 | 0.24 | 0.23 | 0.48 | 1.09 | 0.00 |
| Tb | 0.23 | 0.24 | 0.36 | 2.38 | 1.96 | 2.38 | 0.07 | 0.15 | 0.00 |
| Dy | 0.85 | 1.18 | 2.08 | 0.26 | 0.18 | 0.21 | 0.39 | 0.87 | 0.00 |
| Ho | 0.11 | 0.20 | 0.40 | 1.09 | 0.64 | 0.70 | 0.09 | 0.16 | 0.00 |
| Er | 0.33 | 0.57 | 1.27 | 0.16 | 0.08 | 0.08 | 0.33 | 0.49 | 0.00 |
| Tm | 0.03 | 0.08 | 0.20 | 0.05 | 0.02 | 0.02 | 0.06 | 0.08 | 0.00 |
| Yb | 0.22 | 0.54 | 1.38 | 0.32 | 0.14 | 0.12 | 0.40 | 0.54 | 0.00 |
| Lu | 0.03 | 0.07 | 0.19 | 0.04 | 0.02 | 0.02 | 0.06 | 0.08 | 0.00 |
| Y | 1.60 | 3.61 | 7.78 | 2.92 | 1.41 | 1.41 | 2.37 | 1.21 | 0.01 |

First, thorium was extracted from thorium nitrate solution dissolved in nitric acid by two extractants. The efficiency of the extraction of thorium by the two extractants is displayed in Table 2. The results indicated that under constant experimental conditions, both the TBP (30%) in kerosene and Aliquat-336 (10%) in kerosene were able to successfully extract thorium from pure thorium nitrate solution with an extraction efficiency of 96.92 and 99.84%, respectively, and the extraction efficiency from the thorium concentrates was in the range of 60.96 – 99.75%. From the comparison between the two extractants, Aliquat-336 (10%) in kerosene was more efficient than TBP for the extraction of thorium, and achieved an average extraction efficiency of 95.47% from the thorium concentrates,

while the average extraction efficiency of TBP (30%) was 89.02%. Basically, the extraction of thorium depends on the stability of the thorium-ligand complex in the aqueous phase, and the solubility of the extracted thorium in the organic phase. The extractant type and concentration, mixing time, settling time and organic/aqueous volumetric ratio have an effect on the extraction of thorium.

Table 2. Extraction efficiency % of thorium using TBP (30%) in kerosene and Aliquat-336 (10%) in kerosene

| **Sample ID** | **TBP (30%)** | **Aliquat-336 (10%)** |
|---|---|---|
| | **E%** | **E%** |
| Pure thorium nitrate | 96.92 | 99.84 |
| Thc1 | 94.95 | 99.75 |
| Thc2 | 90.59 | 94.22 |
| Thc3 | 89.44 | 97.72 |
| Thc4 | 88.97 | 97.43 |
| Thc5 | 96.12 | 95.05 |
| Thc6 | 95.13 | 98.48 |
| Thc7 | 96.02 | 99.70 |
| Thc8 | 60.96 | 81.38 |

Furthermore, the stripping results showed that distilled water was a good stripper with TBP (30%) in kerosene and with Aliquat-336 (10%) in kerosene, and it was more successful in stripping thorium from loaded TBP than from loaded Aliquat-336 with an average stripping percentage of 89.04% and 75.75%, respectively (see Figure 2). However, the use of different strippers will increase the efficiency of the stripping, especially when the process involves Aliquat-336. The stripping process depends on the type of stripping agent, the concentration, mixing time, settling time and the organic/aqueous volumetric ratio.

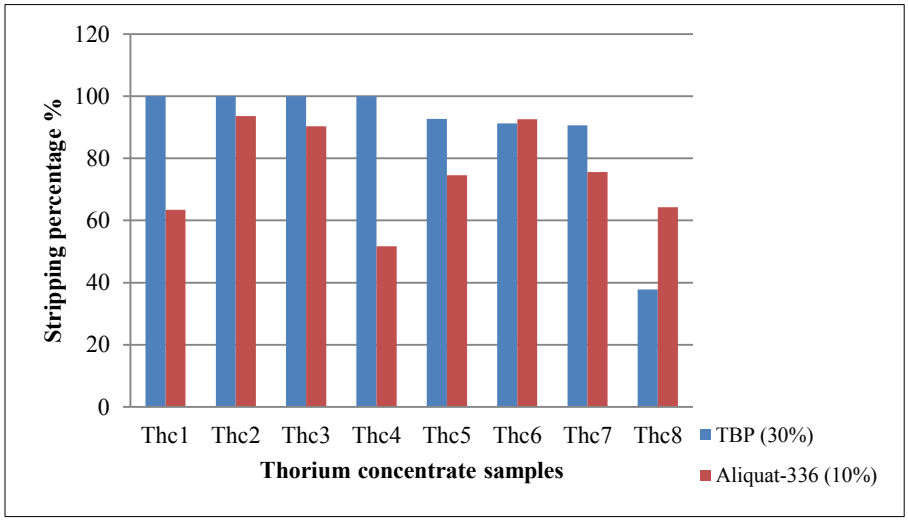



Figure 2. Stripping percentage of thorium by distilled water from loaded TBP (30%) in kerosene and Aliquate-336 (10%) in kerosene

The results of the analysis of the stripped aqueous solutions from loaded TBP and loaded Aliquat-336 for eight thorium concentrate samples are shown in Table 3. It can be seen the thorium purification range using TBP was good at approximately 30.65 – 91.28% compared to 29.49 – 86.90% for Aliquat-336. For uranium, slightly similar concentrations were shown using two extractants, while the REEs were high in the stripped solutions from Aliquat-336 compared to TBP. The study indicated that TBP was more efficient in the purification of thorium from REEs, and three stages of extraction and three stages of stripping were insufficient to obtain high-purity thorium. Therefore, the higher the number of cycles, the higher will be the level of purification.

Table 3. Th, U and REEs ranges content (%) in stripped thorium nitrates from TBP (30%) in kerosene and Aliquat-336 (10%) in kerosene

| **Analyte** | **Aqueous Stripped from TBP (30%)** | **Aqueous Stripped from Aliquat-336 (10%)** |
|---|---|---|
| Th | 30.65 - 91.28 | 29.49 - 86.90 |
| U | 0.20 - 1.97 | 0.21 - 1.18 |
| **LREEs** | | |
| La | 1.01 - 12.73 | 2.68 - 18.27 |
| Ce | 2.37 - 26.26 | 5.24 - 33.73 |
| Pr | 0.29 - 4.15 | 0.51 - 3.52 |
| Nd | 1.15 - 18.16 | 1.72 - 14.51 |
| Sm | 0.28 - 3.76 | 0.30 - 2.52 |
| **HREEs** | | |
| Eu | 0.01 - 1.77 | 0.01 - 0.31 |
| Gd | 0.02 - 2.21 | 0.16 - 1.50 |
| Tb | 0.05 - 2.37 | 0.04 - 1.84 |
| Dy | 0.15 - 1.52 | 0.08 - 0.98 |
| Ho | 0.06 - 0.95 | 0.04 - 0.58 |
| Er | 0.06 - 0.73 | 0.05 - 0.65 |
| Tm | 0.01 - 0.47 | 0.02 - 0.27 |
| Yb | 0.08 - 0.58 | 0.13 - 0.66 |
| Lu | 0.03 - 0.11 | 0.02 - 0.26 |
| Y | 0.07 - 4.76 | 0.09 - 3.39 |

## Conclusion

This study proved that pure thorium can be produced from monazite thorium concentrates by solvent extraction using TBP (30%) and Aliquat-336 (10%) in a nitric acid solution. Thorium was extracted successfully with an extraction efficiency in the range of 60.96 – 99.75% under constant experimental conditions. Aliquat-336 (10%) in kerosene was more efficient than TBP (30%) for thorium extraction, and achieved an average extraction efficiency of 95.47% compared to 89.02% with TBP (30%). Distilled water was able to strip thorium from TBP (30%) and Aliquat-336 (10%), and it was successful in the recovery of thorium, especially from TBP. Thorium purification of up to 91.28% was obtained in the stripped aqueous solutions. The results of this study indicate that both extractants can be used successfully to recover thorium from REEs, but to increase the purification of thorium, the number of extraction and stripping process stages should be increased.

**Acknowledgement**

The authors would like to thank the grant project with reference number FRGS/2013/ST01/UKM/01/2, UKM-GUP-2012-083 and FP0214D052-01 for sponsorship and Nuclear Science Program, Universiti Kebangsaan Malaysia (UKM).

**References**

1. Navratil, J. D. (1986). Solvent extraction in nuclear technology. *Pure & Applied Chemistry*, 58(6): 885 – 888.
2. Patil, C. B., Mohapatra, P. K. and Manchanda, V. K. (2008). Transport of thorium from nitric acid solution by non-dispersive solvent extraction using a hollow fibre contactor. *Desalination*, 232: 272 –280.
3. Abrao, A., Alves de Freitas, A. and Sequeira de Carvalho, F. M. (2001). Preparation of highly pure thorium nitrate via thorium sulfate and thorium Peroxide. *Journal of Alloys and Compounds*, 323: 53 – 56.
4. EUR 17771en. (1997). A present review of the thorium nuclear fuel. Final report, European commission.
5. Hughes, K. C. and Singh, R. (1980). The isolation of thorium from monazite by solvent extraction. *Hydrometallurgy*, 6: 25 – 33.
6. Ali, A. M. I. El-Nadi, Y. A. Daoud, J. A. and Aly, H.F. (2007). Recovery of thorium (IV) from leached monazite solutions using counter-current extraction. *International Journal of Mineral Processing,* 81: 217 – 223.
7. Nasab, M. E., Sam, A. and Milani, S. A. (2011). Determination of optimum process conditions for the separation of thorium and rare earth elements by solvent extraction. *Hydrometallurgy*, 106: 141 – 147.
8. Amaral, J. C. B. S. and Morais, C. A. (2010). Thorium and uranium extraction from rare earth elements in monazite sulphuric acid liquor through solvent extraction. *Minerals Engineering,* 23: 498 – 503.
9. Sato, T. (1965). The extraction of thorium from sulphuric acid solutions by di-(2-ethylhexyl)-phosphoric acid. *Inorganic Nuclear Chemistry*, 27: 1395 – 1403.
10. Sato, T. (1970). The extraction of thorium(IV) from sulphuric acid solutions by long-chain aliphatic amines. *Inorganic Nuclear Chemistry,* 32: 1341 – 1349.
11. AL-Areqi, W. M., Majid, A. A. and Sarmani, S. (2016). Separation and radiological impact assessment of thorium in Malaysian monazite processing. *Malaysian Journal of Analytical Sciences*, 20(4): 770 – 776.
12. Bahri, C. N.A. C. Z., AL-Areqi, W. M., Majid, A. A. and Ruf, M. I. F. M. (2016). Production of rare earth elements from Malaysian monazite by selective precipitation. *Malaysian Journal of Analytical Sciences*, 20(1): 44 – 50.
13. Academy of Sciences Malaysia (2013). Revitalising of rare earth mineral programme in Peninsula Malaysia as a strategic industry. The Academy of Sciences Malaysia (ASM) study report 1/2013.
14. Ayranov, M., Cobos, J., Popa, K. and Rondinella, V. V. (2009). Determination of REE, U, Th, Ba, and Zr in simulated hydrogeological leachates by ICP-AES after matrix solvent extraction. *Journal of Rare Earths,* 27(1): 123 – 127.
15. Cordier, D. J. (2012). Mineral commodity summaries. *U.S. Geological Survey*, 703: 648 – 772.
16. Kabata-Pendias, A. and Mukherjee, A. B. (2007). Trace elements of group 15 (Previously Group Va). *Trace Elements from Soil to Human*, 15: 381 – 399.
17. Gupta, C. K. and Krishnamurthy, N. (1992). Extractive metallurgy of rare earths. *International Materials Reviews*, 37(5): 197 – 248.

*Malaysian Journal of Analytical Sciences, Vol 21 No 6 (2017): 1257 - 1265*
*DOI: https://doi.org/10.17576/mjas-2017-2106-07*

MALAYSIAN JOURNAL OF ANALYTICAL SCIENCES
*Published by The Malaysian Analytical Sciences Society*
ISSN 1394 - 2506

# PHOTOSTABILITY OF PLASTICIZED POLYVINYL CHLORIDE MEMBRANES: A THEORETICAL STUDY

## (Kestabilan Foto bagi Membran Plastik Polivinil Klorida: Satu Kajian Teori)

Oksana Fizer[1], Maksym Fizer[2]*, Yaroslav Studenyak[1]

[1]*Department of Analytical Chemistry*
[2]*Department of Organic Chemistry*
*Faculty of Chemistry,*
*Uzhhorod National University, 88000 Uzhhorod, Ukraine*

**Corresponding author: max.fizer@uzhnu.edu.ua*

Received: 7 March 2017; Accepted: 26 September 2017

**Abstract**

The calculation of spectral shifts in the UV-visible region, and the photostability of polyvinyl chloride membranes plasticized with 1-bromonaphthalene, dibutyl phthalate, dioctyl phthalate, *o*-nitrophenyl octyl ether and tricresyl phosphate, have been systematically investigated using the ZINDO/S method combined with stochastic molecular dynamics with the MMFF94 force field. A Langevin temperature bath was used for the thermostat and the simulation temperature was 298 K during the entire time of the simulation, which was set to 0.6 ns. These methods were employed to predict the molecular structure of the membranes. The absorption wavelengths and the HOMO and LUMO energies of membrane components are reported. In addition, the photostability of the membranes is discussed in the light of the absorption wavelength. Membranes plasticized with tricresyl phosphate and *o*-nitrophenyl octyl ether show less stability under the action of UV irradiation, as they absorb light with higher energy. Membranes plasticized with butyl and octyl esters of phthalic acid are more stable and show very similar behaviour. A membrane plasticized with 1-bromonaphthalene is likely to be the least sensitive to UV irradiation.

**Keywords**: polyvinyl chloride, membrane, molecular dynamics, excited state, photostability

**Abstrak**

Pengiraan anjakan spektra di dalam kawasan ultralembayung-cahaya nampak dan kestabilan foto bagi membran plastik polivinil klorida bersama 1-bromonaftalena, dibutil ftalat, dioktil ftalat, *o*-nitrofenil oktil eter dan tricresil fosfat telah secara sistematik telah dikaji mengunakan kaedah ZINDO/S gabungan molekul dinamik stokastik bersama medan daya MMFF94. Suhu rendaman Langevin telah diguna untuk termostat dan suhu simulasi ialah 298 K bagi keseluruhan masa simulasi, iaitu di tetapkan pada 0.6 ns. Kaedah ini dibangunkan untuk meramal struktur molekul membran berkenaan. Panjang gelombang serapan dan tenaga HOMO dan LUMO membran dilapor. Tambahan lagi, kestabilan foto bagi membran di bincang dari aspek panjang gelombang serapan. Membran plastik bersama tricresil fosfat dan *o*-nitrofenil oktil eter menunjukkan kestabilan yang rendah terhadap penyinaran UV sebagaimana ia menyerap cahaya pada tenaga yang tinggi. Membran plastik bersama butil dan oktil ester asid ftalik adalah lebih stabil dan menunjukkan sifat yang sama. Membran plastik bersama 1-bromonaftalena merupakan membran paling kurang sensitif terhadap penyinaran UV.

**Kata kunci:** polivinil klorida, membran, molekul dinamik, keadaan teruja, kestabilan foto

## Introduction

Ion-selective electrodes (ISEs) with plasticized membranes are widely used in analytical chemistry [1, 2]. ISEs can also be used in environmental analysis [3] and in clinical studies [4, 5]. The main advantages of using ISEs are:

short analysis time, high selectivity, sensitivity, reliability and reproducibility. Moreover, the electrodes in a potentiometer are relatively cheap and not cumbersome, which makes them suitable for use in the field.

Despite all these advantages, some disadvantages are also known, such as the drift in potential and the influence of interference ions [1]. Usually, errors are caused by changes in the membrane's characteristics during the operation of ISEs. The composition, homogeneity and lifetime of a membrane can change due to the leaching of the membrane's components, such as plasticizers or ionophores. Furthermore, degradation of polymeric compounds can be caused by ultraviolet irradiation. Near-UV radiation may be harmful to the plastics and plasticized plastic films [6-8]. The high-energy photons may cause a gradual degradation of the polymer or the plasticizer. Therefore, it is critical to identify the potential resistance properties of a membrane's materials, and to search for molecules that can withstand longer UV exposure. Even a small UV fraction may create major damage in the membrane via radical formation triggering photodegradation of the polymeric materials. This degradation causes a deviation in the conductivity of the ion-selective membrane and a deterioration in the membrane's physical and chemical properties. Therefore, from an application point of view, UV spectra and absorption energies must be considered as design parameters for the selection of materials in the construction of ISEs.

Quantum chemical calculation is a widely used method for the investigation of matter, especially in cases when direct physical measurements are not possible or too time-consuming. Computation and prediction of structure [9, 10], properties [11] and reactivity [12, 13] can readily be performed using various methods. The configuration interaction (CI) method is widely employed for the calculation of electronic spectra and photostability [14, 15].

In this work, we attempt to obtain a new insight into the photostability of five plasticized polymeric membranes. As model objects, we use polyvinyl chloride membranes plasticized with 1-bromonaphthalene (aBN), dibutyl phthalate (DBP), bis(2-ethylhexyl) phthalate also known as dioctyl phthalate (DOP), *o*-nitrophenyl octyl ether (NPOE) and tricresyl phosphate (TCP) [16, 17]. The absorption spectra obtained in this work will provide a valuable data set for other computational studies, and we will also use the data set as a basis for future experimental investigations.

## Materials and Methods

### Computational details

The simulations of the five systems were performed using stochastic molecular dynamics (MD) [18] with the MMFF94 force field [19]. The stochastic integrator uses a type of Langevin temperature bath for the thermostat, and the simulation temperature was 298 K. The total simulation time for each system was 600 ps, with 100 ps for equilibration and 500 ps as the sampling time. Snapshots were generated for each 10 ps period. The relaxation trajectory was obtained, with 50 snapshots for each system.

Using the snapshot geometries as input, the UV-Vis spectra of the five systems were calculated using the ZINDO/S method with the inclusion of all valence electrons [20]. The CI method in combination with the semi-empirical Hamiltonian enables the calculation of the absorption spectra of large organic systems. In the case of each membrane, we calculated a different number of first excited states, in such a way as to accurately describe the wavelength region above 200 nm. The average UV-Vis spectrum was obtained by overlapping all the spectra computed separately for each snapshot.

MD simulations were performed with the TINKER 7.1 package [21]. ZINDO/S calculations were performed with the program ORCA 3.0.3 [22]. The automatic computations for a group of snapshots were realized through the batch script. The Gabedit 2.4.9 program [23] was used to perform overlapping and visualization of the specified range of UV-Vis spectra. A VMD package [24] was used for calculation of the radial distribution function (RDF). Visualization of molecules and molecular orbitals was performed using the Jmol program [25].

## Results and Discussion

### Molecular dynamics simulation of modelled systems

Computations of PVC membrane parameters were performed on small systems that in our opinion can describe membranes in general reasonably well. Each simulated system (Table 1) was a small cluster of two molecules of plasticizer and one molecule of PVC polymer. This composition allows consideration of not only the polymer-

plasticizer interaction but also the interaction between plasticizer molecules. The PVC polymer was modelled as a linear molecule consisting of PVC monomers, $–CH_2$-CHCl-, and terminal H atoms. The size of the PVC molecule was different in each system to maintain the membranes' composition ratios of PVC to plasticizer at approximately 1:1.

Table 1. Simulated systems and their fundamental properties

| # | Number of $-CH_2$-CHCl- | Plasticizer:PVC Ratio (%) | Composition | Atoms | Formula | Weight (g/mol) |
|---|---|---|---|---|---|---|
| 1 | 6 | 52.35 : 47.65 | 2aBN+$PVC_6$ | 74 | $C_{32}H_{34}Br_2Cl_6$ | 791.138 |
| 2 | 8 | 49.93 : 50.07 | 2DBP+$PVC_8$ | 134 | $C_{48}H_{70}Cl_8O_8$ | 1058.689 |
| 3 | 12 | 50.95 : 49.05 | 2DOP+$PVC_{12}$ | 206 | $C_{72}H_{114}Cl_{12}O_8$ | 1533.107 |
| 4 | 8 | 49.34 : 50.66 | 2NPOE+$PVC_8$ | 131 | $C_{45}H_{70}Cl_8N_2O_6$ | 1018.671 |
| 5 | 12 | 49.49 : 50.51 | 2TCP+$PVC_{12}$ | 168 | $C_{66}H_{80}Cl_{12}O_8P_2$ | 1488.720 |

Figure 1 shows the change in total energy at a time during the MD simulation. The chosen integrator provides a reasonable numerical stability. Despite rounding errors and other numerical inaccuracies, the total energies of the systems are relatively well conserved. This shows relative stability and characterizes the chosen method as good enough to obtain reliable geometries. In addition, the thermostat is highly stable, with fluctuations mostly in ±5 K range, and only in a few steps was the deviation in temperature higher than 20 K. Intermolecular interaction energies, on the other hand, fluctuate considerably for each system during the simulation time. This behaviour can be explained in terms of the size of the system components. There is a huge number of possible conformers for these components, and this can cause huge deviations in intermolecular distances and large fluctuations in this type of interaction. Despite rounding errors and other numerical inaccuracies, the total energy of the system is very well conserved (Figure 1).

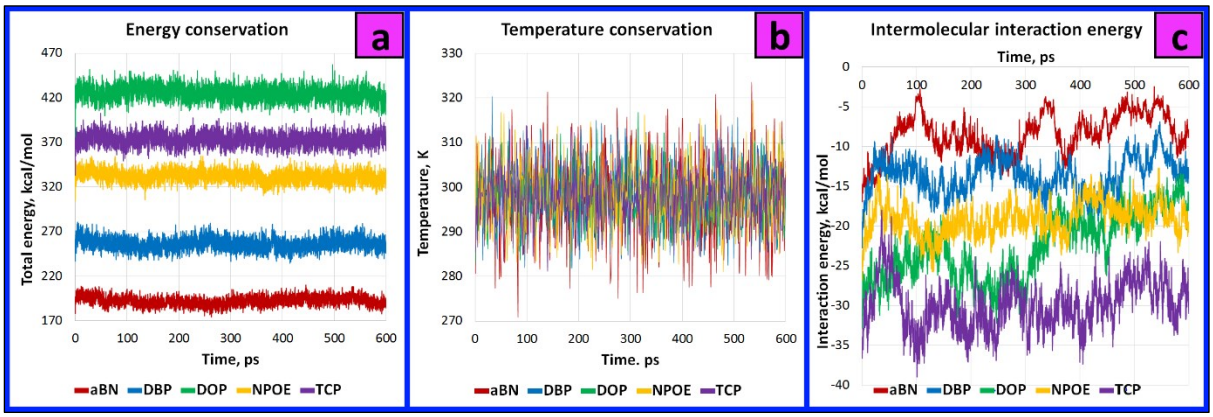



Figure 1. Characteristics of MD simulation (a) conservation of energy, (b) conservation of temperature and (c) intermolecular interaction energy

**1-bromonaphthalene-polyvinyl chloride system**

One of the snapshots of the HOMO and LUMO orbitals is shown in Figure 2. The HOMO of the aBN-PVC complex is located along the naphthalene ring and its energy is –8.00 eV. The LUMO of –0.81 eV is also located in the naphthalene ring. The HOMO–2 and HOMO–1, as well as the LUMO+1 and LUMO+2 of this system are focused on aromatic naphthalene moieties and, among others, also lie in the same energy regions of –9.24 eV, –8.28 eV, –0.71 eV and –0.39 eV respectively. This orbital distributions and energies are not unique to this specific

snapshot but are in general the same for all the generated structures. The RDF is also presented, showing that the average distance between plasticizer molecules and polymer molecules is about 3-15 Å, and the maximal value of the RDF distance during the simulation is 5-7 Å. The distance between 1-bromonaphthalene molecules during the simulation is generally in the range 4-7 Å.

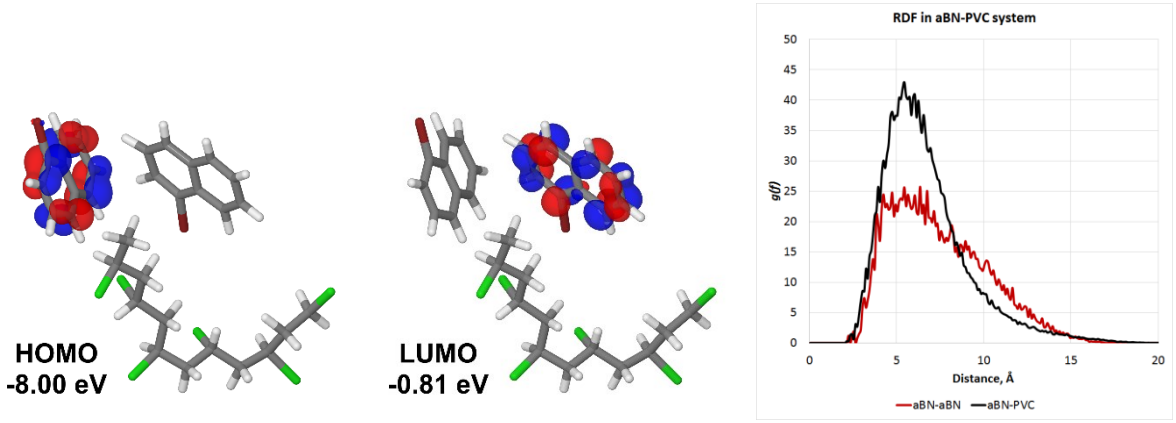



Figure 2. Snapshot geometry with HOMO, LUMO orbitals and RDF for average simulation trajectory of aBN-PVC system

**Dibutyl phthalate-polyvinyl chloride system**

The HOMO and LUMO orbitals of the DBP-PVC system are shown in Figure 3. The HOMO is located along the benzene ring of the phthalic acid fragment and its energy is –9.55 eV. The LUMO, with energy –1.15 eV, is also located on the benzene ring. The HOMO–2, HOMO–1, LUMO+1 and LUMO+2 energies of this system are –9.84 eV, –9.56 eV, –0.96 eV and –0.25 eV respectively. These are also focused on the aromatic phthalic acid moieties of different molecules of DBP. The distribution of orbitals and energies is characteristic for all generated snapshots of the DBP-PVC system. The RDF shows that the average distance between dibutyl phthalate molecules and polyvinyl chloride is in the range 3-17 Å, with the maximum RDF distance in the region of 5-7 Å.

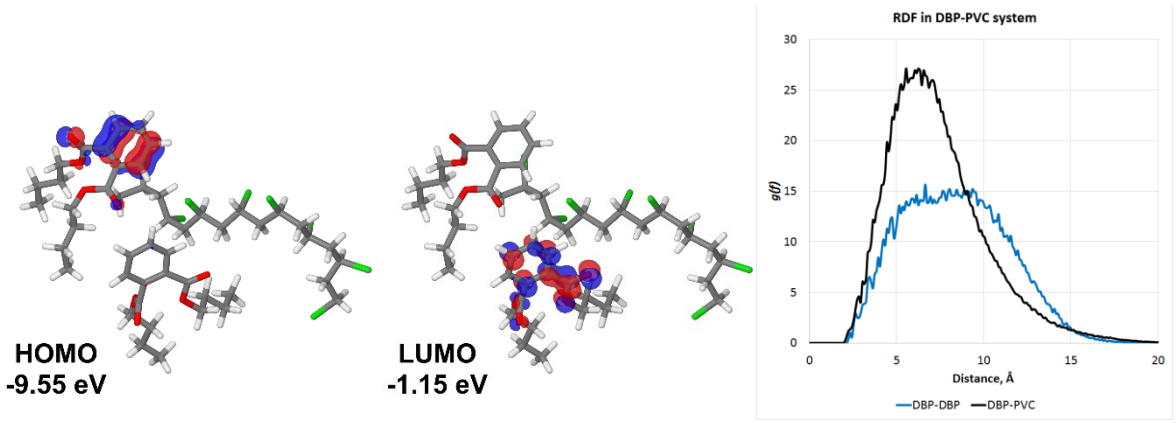



Figure 3. Snapshot geometry with HOMO, LUMO orbitals and RDF for average simulation trajectory of DBP-PVC system

**Dioctyl phthalate-polyvinyl chloride system**

Figure 4 represents the geometry of the DOP-PVC system. The RDF shows that average distance between dioctyl phthalate molecules and polyvinyl chloride is in the range 3-15 Å, with the maximum RDF distance in the region of

6-7 Å. The RDF for the distance between molecules of dioctyl phthalate has a maximum in the region of 5-10 Å. The frontal molecular orbitals can be characterized with the following values of energy: HOMO–2: –9.73 eV, HOMO–1: –9.59 eV, HOMO: –9.29 eV, LUMO: –1.04 eV, LUMO+1: –0.76 eV, LUMO+2: –0.32 eV. All frontier orbitals of the agglomerate are located along the benzene ring of the phthalic acid fragment, similarly to the DBP-PVC system. This can be explained by the similarity in structure and properties of DBP and DOP plasticizers.

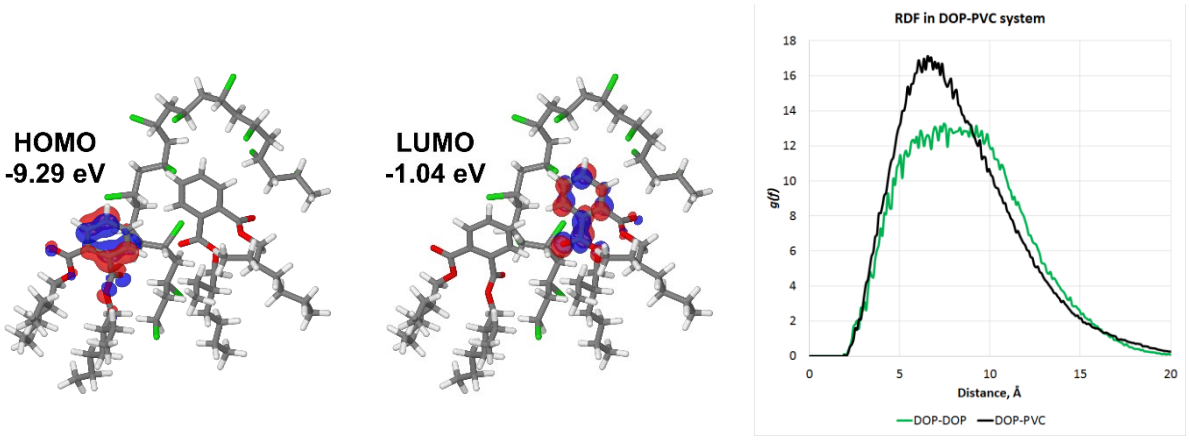



Figure 4. Snapshot geometry with HOMO, LUMO orbitals and RDF for average simulation trajectory of DOP-PVC system

**Nitrophenyl octyl ether-polyvinyl chloride system**

The geometry of the NPOE-PVC system, with HOMO and LUMO orbitals and RDF distances, is represented in Figure 5. During the MD simulation, the maximum distance distribution between NPOE molecules and PVC was about 5-8 Å with a total range of RDF distances of 3-15 Å and a distance between NPOE molecules of around 5-7 Å. The frontal molecular orbitals HOMO–2, HOMO–1, HOMO, LUMO, LUMO+1 and LUMO+2 were characterized by the following values of energy: –9.89 eV, –9.55 eV, –9.42 eV, –3.10 eV, –2.71 eV and –0.34 eV respectively. The HOMO is mostly localized on the phenyl ether moiety, whereas the LUMO is in the region of the nitro group. This is in good agreement with general knowledge about the reactivity of organic molecules.

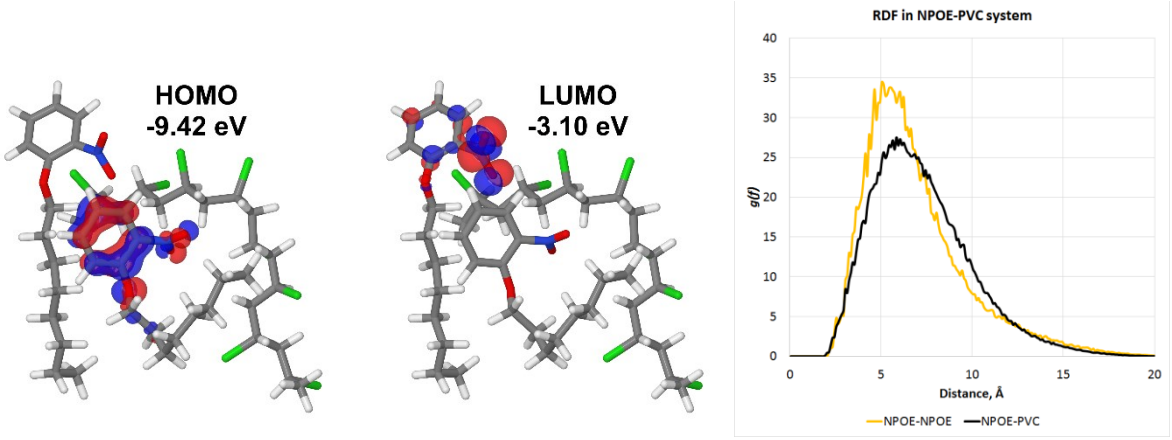



Figure 5. Snapshot geometry with HOMO, LUMO orbitals and RDF for average simulation trajectory of NPOE-PVC system

**Tricresyl phosphate-polyvinyl chloride system**

One of the snapshots of the HOMO and LUMO orbitals is shown in Figure 6. The HOMO of the TCP-PVC complex is located along the methyl phenyl rings of the TCP molecule and its energy is –8.59 eV. The LUMO of 0.07 eV is in the region of the CH-Cl bond of polyvinyl chloride. The HOMO–2 and HOMO–1 are focused on the aromatic moieties of the plasticizer molecules and lie in the same energy regions of –8.65 eV and –8.68 eV, whereas the LUMO+1 and LUMO+2 have energy values of 0.156 eV and 0.163 eV respectively and are located on the PVC molecule. This contrasts with all the other systems described here. To understand this behaviour, we analysed the partial atomic charges for each snapshot, and this showed the transport of a small amount of negative charge from TCP to the PVC chain. The average charge of TCP during the simulation is only –0.01, but this small difference explains the location of unoccupied orbitals and predicts that in the TCP-PVC system the polyvinyl chloride molecule will show more pronounced electrophilic properties. The RDF shows that the average distance between the phosphoric acid ester and the chlorinated polymer is about 3-15 Å, and the maximal value of the RDF distance during the simulation is 4-6 Å.

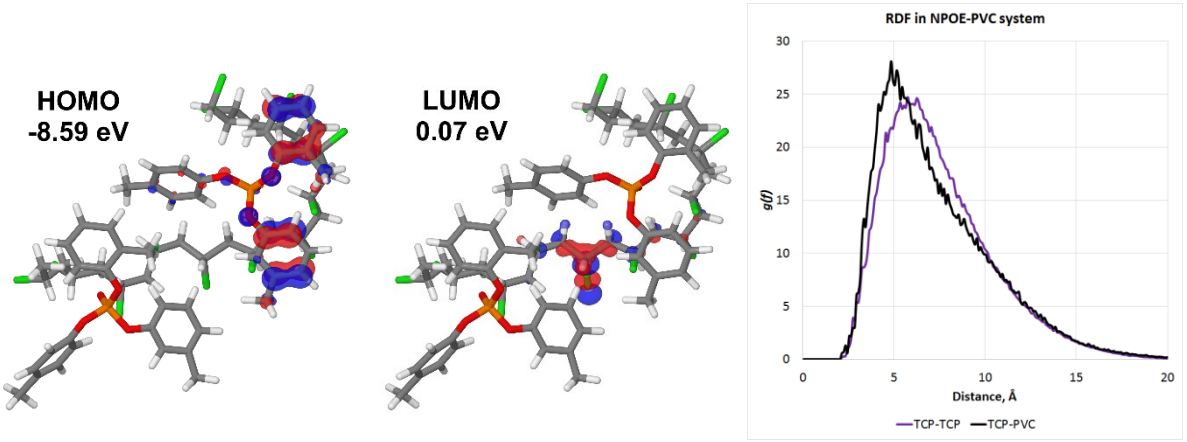



Figure 6. **Snapshot geometry with HOMO, LUMO orbitals and RDF for average simulation trajectory of TCP-PVC system**

**Photochemical stability**

In general, the absorption spectrum of a complex of polyvinyl chloride with a plasticizer molecule containing a phenyl ring is expected to show similarities to a non-substituted benzene molecule. The principal absorption bands in the plasticizer molecules are due to the $\pi \rightarrow \pi^*$ transitions in the benzene moieties. However, these benzene-like transitions are not the same in the modelled systems. This difference can be explained by the influence of another condensed phenyl ring in the 1-bromonaphthalene molecule or by the presence of different substituents and conjugation in the other plasticizers considered.

The detailed graph of the comparisons of the UV-Vis spectra computed using the ZINDO/S method is shown in Figure 7. Variations in the absorption spectra were observed for different plasticizer-polyvinyl chloride systems.

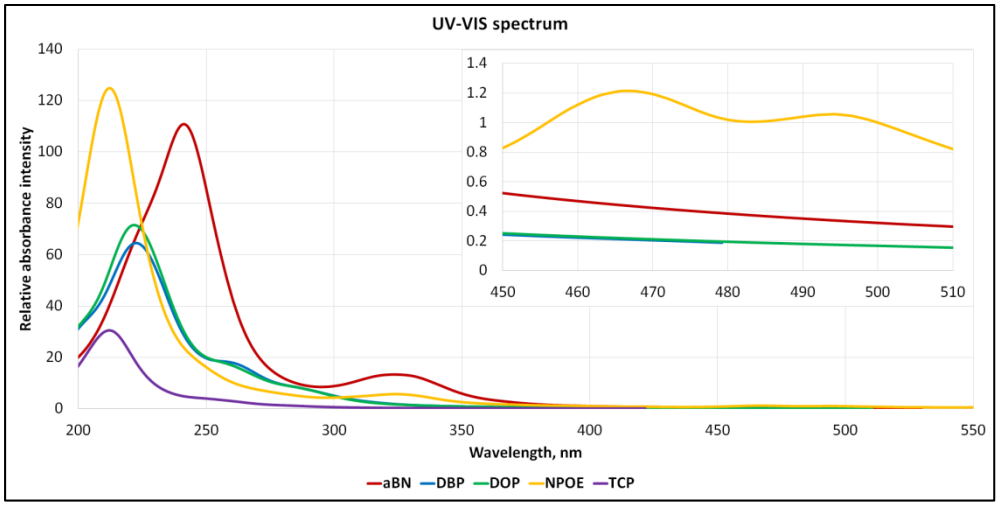



Figure 7. Average UV-Vis spectrum for five systems

**1-bromonaphthalene-polyvinyl chloride system**
In the UV region, three strong absorptions at 221.42 nm (λ1), 241.44 nm (λ2) and 323.45 nm (λ3) were observed. However, no absorption was observed in the visible region. The strongest band appears in the region of 200 nm to 296.05 nm, with an absorption maximum ($\lambda_{max}$) at 241.44 nm (λ2). The absorption band at 323.45 nm (λ3) is in general agreement with UV-Vis spectra of aBN from the NIST database [26]. Experimental data show that the multiple bands in the region of 256 – 320 nm, and the shift of about 30 – 50 nm could be explained by the influence of PVC and by computational error.

**Dibutyl phthalate-polyvinyl chloride system**
Figure 7 shows three prominent bands in the UV region with absorption maxima at 222.66 nm (λ1), 260.57 nm (λ2) and 284.78 nm (λ3) for DBP. The strongest band was observed from 200 nm to 244.44 nm with an absorption maximum at 222.66 nm (λ1). The absorption band at 284.78 nm (λ3) is in very good agreement with experimental UV-Vis spectra of DBP from the NIST database [27], which show bands at 277 nm and 286 nm.

**Dioctyl phthalate-polyvinyl chloride system**
Three strong absorption bands were observed for DOP in the UV region, with absorption maxima at 226.59 nm (λ1), 266.59 nm (λ2) and 284.94 nm (λ3) (Figure 7). The strongest band was observed in the region from 200 nm to 241.88 nm, with an absorption maximum at 226.59 nm (λ1).

**Nitrophenyl octyl ether-polyvinyl chloride system**
The absorption spectrum of the NPOE-PVC system (Figure 7) exhibits one strong and one weak absorption band in the UV region, with absorption maxima at 212.11 nm (λ1) and 324.16 nm (λ2) respectively. In addition, there are two very weak absorption bands in the visible region, with absorption maxima at 466.15 nm (λ1) and 493.88 nm (λ2). This is in a very good agreement with the fact that NPOE is itself yellow, and absorption in the visible region is very close to the predicted absorption.

**Tricresyl phosphate-polyvinyl chloride system**
Two strong absorption bands were observed for the TCP-PVC system in the UV region, with absorption maxima at 212.33 nm (λ1) and 249.16 nm (λ2) (Figure 7). One very weak absorption band at 279.08 nm (λ3) is also present. The strongest band was observed in the region from 200 nm to 240.08 nm with an absorption maximum at 212.33 nm (λ1).

## Conclusion

Calculations have been carried out on five plasticizer-polyvinyl chloride systems, to study their ultraviolet stability in the light of the shift of absorption wavelength with respect to the nature of the plasticizer. The electronic absorption spectra of plasticized membranes, except in the tricresyl phosphate-polyvinyl chloride system, show the strongest absorption band due to the transitions between the energy states HOMO–1→LUMO and HOMO→LUMO+1, which can be assigned as $\pi \rightarrow \pi^*$ transitions. This is due to the presence of two molecules of plasticizer in the systems described, and whereas the HOMO–1 and LUMO correspond to one phenyl/naphthyl ring, the HOMO and LUMO+1 correspond to a transition in another phenyl/naphthyl ring. In the case of the TCP-PVC system, the absorption bands mainly induce transitions of electrons from plasticizer molecules to the polymeric chain.

The principal absorption bands of membranes with TCP and especially with NPOE (considering the much higher relative absorption intensity) show that these membranes are less stable under the action of UV irradiation, as they absorb light with higher energy, causing the bonds to be more easily destroyed. DBP- and DOP-containing systems show very similar behaviour, and they are more stable than the two previously mentioned membranes. A membrane containing 1-bromonaphthalene as a plasticizer is likely to be the least sensitive to UV irradiation.

The methods described show good performance in the study of photostability, and this provides a basis for the future development of computer investigations and quantum chemical simulations in very complex and important objects such as synthetic membrane materials. Furthermore, the presented findings demonstrate that not all placticizers in membranes have the same stability, and therefore testing is needed in each case.

## Acknowledgement

One of the authors (OF) acknowledges the International Visegrad Fund (ID 51700627).

## References

1. Mikhelson, K. N. (2013). Ion-selective electrodes. Springer, Berlin: pp. 1 – 7.
2. Dimeski, G., Badrick T. and St John, A. (2010). Ion selective electrodes (ISEs) and interferences – A review. *Clinica Chimica Acta*, 411 (5 – 6): 309 – 317.
3. Radu, A., Radu, T., McGraw, C., Dillingham, P., Anastasova-Ivanova, S. and Diamond, D. (2013). Ion selective electrodes in environmental analysis. *Journal of Serbian Chemical Society*, 78(11): 1729 – 1761.
4. Yan, R., Qiu, Sh., Tong, L. and Qian, Y. (2016). Review of progresses on clinical applications of ion selective electrodes for electrolytic ion tests: from conventional ISEs to graphene-based ISEs. *Chemical Speciation & Bioavailability*, 28(1 – 4): 72 – 77.
5. Thakur, V. K. and Thakur, M. K. (2015). Handbook of polymers for pharmaceutical technologies, processing and applications (Vol. 2). Scrivener Publishing LLC, USA: p. 211.
6. Wypych, G. (2015). PVC degradation and stabilization. 3rd Edition. ChemTec Publishing, Toronto: pp. 167 – 203.
7. Al Ani K. E. and Ramadhan, A. E. (2010). Plasticization effect on the photodegradation of poly (4-chlorostyrene) and poly(4-bromostyrene) films. *Materials Sciences and Applications*, 1 (6): 358 – 368.
8. Ramadhan, A. E. (2015). Effects of added phthalate plasticizers on photodegradation of irradiated poly(α-methylstyrene) films. *Journal of Polymer Engineering*, 35(2): 159 – 167.
9. Hassan, M. A., Kamarudin, S. K. and Loh, K. S. (2016). Structural study of reduced graphene oxide/polypyrrole composite as methanol sensor in direct methanol fuel cell. *Malaysian Journal of Analytical Sciences*, 20(4): 965 – 970.
10. Bevziuk, K., Chebotarev, A., Snigur, D., Bazel, Ya., Fizer, M. and Sidey, V. (2017). Spectrophotometric and theoretical studies of the protonation of Allura Red AC and Ponceau 4R. *Journal of Molecular Structure*, 1144: 216 – 224.
11. Arifin, K., Daud, W. R. W. and Kassim, M. B. (2016). Molecular and electronic structures of a new ruthenium-tungsten bimetallic complex using density functional theory calculations. *Malaysian Journal of Analytical Sciences*, 20(4): 946 – 954.

12. Fizer, M., Sukharev, S., Slivka, M., Mariychuk, R. and Lendel, V. (2016). Preparation of bisthiourea and 5-Amino-4-benzoyl-1,2,4-triazol-3-thione complexes of copper(II), nickel and zinc and their biological evolution. *Journal of Organometallic Chemistry*, 804: 6 – 12.
13. Fizer, M., Sidey, V., Tupys, A., Ostapiuk, Y., Tymoshuk, O. and Bazel, Y. (2017). On the structure of transition metals complexes with the new tridentate dye of thiazole series: Theoretical and experimental studies. *Journal of Molecular Structure*, 1149: 669 – 682.
14. Praveen, P. L. and Ojha, D. P. (2012). Effect of substituents on electronic spectral shifts and phase stability of liquid crystalline biphenylcyclohexane molecules – A theoretical approach. *Molecular Crystals and Liquid Crystals*, 557(1): 206 – 216.
15. Praveen, P. L. and Ojha, D. P. (2014). Effect of molecular interactions and end chain length on ultraviolet absorption behavior and photo stability of alkoxycinnamic acids: Theoretical models of liquid crystal. *Journal of Molecular Liquids,* 197: 106 – 113.
16. Fizer, O. I. and Studenyak, Y. I. (2014). The behavior of PVC-modified membrane sensors in surfactants solutions. *Scientific Bulletin of the Uzhgorod University. Series Chemistry*, 31(1): 43 – 48.
17. Fizer, O. I. and Studenyak, Y. I. (2015). Potentiometric titration of anionic surfactants in household object. *Naukovij vìsnik Užgorods'kogo unìversitetu. Serìâ Hìmìâ*, 34(2): 55 – 58.
18. Attard, P. (2002). Stochastic molecular dynamics: A combined Monte Carlo and molecular dynamics technique for isothermal simulations. *Journal of Chemical Physics*, 116(22): 9616 – 9619.
19. Halgren, T. A. (1996). Merck molecular force field. I. Basis, form, scope, parameterization, and performance of MMFF94. *Journal of Computational Chemistry*, 17 (5 – 6): 490 – 519.
20. Kotzian, M., Rösch, N. and Zerner, M. C. (1992). Intermediate neglect of differential overlap spectroscopic studies on lanthanide complexes. *Theoretica Chimica Acta*, 81(4): 201 – 222.
21. Ren, P. and Ponder, J. W. (2003). Polarizable atomic multipole water model for molecular mechanics simulation. *The Journal of Physical Chemistry B*, 107(24): 5933 – 5947.
22. Neese, F. (2012). The ORCA program system. *Wiley Interdisciplinary Reviews: Computational Molecular Science*, 2(1): 73 – 78.
23. Allouche, A. R. (2011). Gabedit – A graphical user interface for computational chemistry softwares. *Journal of Computational Chemistry,* 32(1): 174 – 182.
24. Humphrey, W., Dalke, A. and Schulten, K. (1996). VMD – visual molecular dynamics. *Journal of Molecular Graphics*, 14(1): 33 – 38.
25. Jmol 14.4.3. (2016). Jmol: An open-source Java viewer for chemical structures in 3D. http://www.jmol.org/.
26. National Institute of Standards and Technology (2017). NIST Chemistry WebBook, SRD 69. http://webbook.nist.gov/cgi/cbook.cgi?ID=C90119&Units=SI&Mask=400#UV-Vis-Spec. [Access online 28 January 2017].
27. National Institute of Standards and Technology (2017). NIST Chemistry WebBook, SRD 69. http://webbook.nist.gov/cgi/cbook.cgi?ID=C84742&Mask=400#UV-Vis-Spec. [Access online 28 January 2017].

*Malaysian Journal of Analytical Sciences, Vol 21 No 6 (2017): 1266 - 1275*
*DOI: https://doi.org/10.17576/mjas-2017-2106-08*

MALAYSIAN JOURNAL OF ANALYTICAL SCIENCES
*Published by The Malaysian Analytical Sciences Society*
ISSN 1394 - 2506

# POTENTIOMETRIC STUDY OF RHENIUM(V) COMPLEX FORMATION WITH AZATHIOPRINE AND CEFTRIAXONE

## (Kajian Potentiometri Penghasilan Kompleks Rhenium(V) dengan Azatioprina dan Ceftriaxon)

Gamal Abdelaziz Hussein Gouda [1]*, Gomaa Abdelgawad Mohammed Ali [1, 2]

[1]*Chemistry Department, Faculty of Science,*
*Al-Azhar University, 71524 Assiut, Egypt*
[2]*Faculty of Industrial Sciences & Technology,*
*Universiti Malaysia Pahang, Gambang, 26300 Kuantan, Malaysia*

**Corresponding author: ggouda73@mail.ru*

Received: 3 March 2017; Accepted: 17 September 2017

**Abstract**

The behavior of complex formation of Re(V) metal ion with azathioprine (AZ) and ceftriaxone (CE) as medicinal drugs has been investigated potentiometrically in 0.3 M hydrochloric acid. The stability constant of the prepared complexes has been determined and calculated at various temperatures. The obtained results showed that Re(V)-AZ system showed the formation 1:2, 1:3 and 1:4 complexes, while Re(V)-CE showed only 1:1 and 1:2 complexes. The complex formation suggests a successive displacement of the chloride molecules from the coordination sphere of the central ion by the AZ ligand. In addition, the effect of temperature on the complexes formation of Re(V) with AZ and CE was investigated. The entropy and enthalpy changes showed a favorable and exothermic process, respectively. The kinetic parameters of the formation complex process were calculated and discussed.

**Keywords:** rhenium(V), drugs, potentiometry, complex formation, stability constant

**Abstrak**

Tingkah laku penghasilan kompleks ion logam Re(V) dengan azatioprina (AZ) dan ceftriaxon (CE) sebagai ubat – ubatan telah dikaji secara potentiometri dalam 0.3 M asid hidroklorik. Pemalar kestabilan terhadap kompleks yang dihasilkan telah ditentukan dan dikira pada pelbagai tahap suhu. Hasil yang diperoleh menunjukkan bahawa sistem Re(V)-AZ mempamerkan penghasilan kompleks 1:2, 1:3 dan 1:4, sementara Re(V)-CE mempamerkan hanya kompleks 1:1 dan 1:2. Penghasilan kompleks mencadangkan satu anjakan molekul klorida berturut-turut dari lingkungan koordinasi ion tengah oleh ligan AZ. Di samping itu, kesan suhu pada pembentukan kompleks Re(V) dengan AZ dan CE telah dikaji. Perubahan entropi dan entalpi menunjukkan proses yang baik dan eksotermik. Parameter kinetik proses penghasilan kompleks turut dikira dan dibincangkan.

**Kata kunci:** rhenium(V), ubat, potentiometri, penghasilan kompleks, pemalar kestabilan

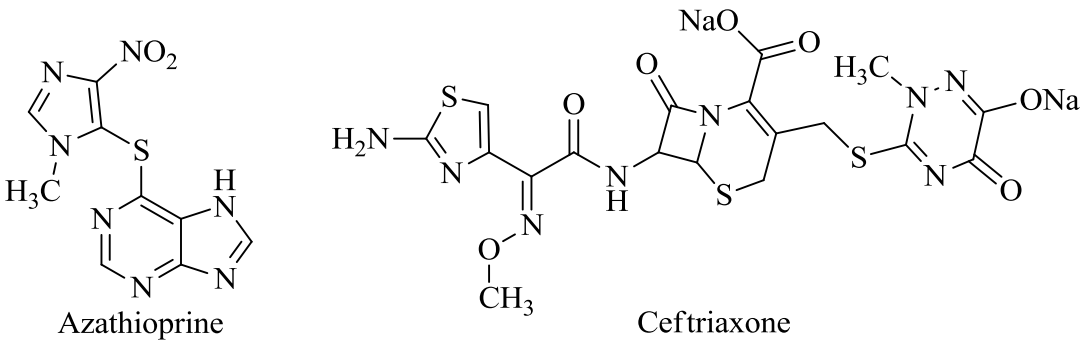
## Introduction

The stability of complexes with medicinal drugs plays a major role in their biological and chemical activities. This is due to that, the medicinal drugs have various functional groups, which can bind to metal ions present in the human body [1, 2]. The azathioprine (AZ) is an immunosuppressive drug used in organ transplantation and autoimmune diseases [3 – 5] while the ceftriaxone (CE) is effective against a wide variety of Gram-positive and Gram-negative bacteria [6 – 9]. Very few works investigated the stability constant and thermodynamic parameters (ΔG, ΔH and ΔS) of Re-Az and Re-CE complexes at different temperatures. The complex formation behavior of AZ with various metal ions has been studied by the potentiometric titration method [10]. AZ is found to form 2:1

complexes with Co(II), Cu(II) and Ni(II), in the stability order of Cu(II) > Ni(II) > Co(II). The effect of various divalent cations on the encapsulation efficiency of gellan gum and to probe the underlying mechanisms responsible for drug loading efficiency. Spherical beads containing AZ were prepared from deacetylated gellan gum by ionotropic gelation method [11]. The anti-rheumatic studies on AZ have also involved its Cu(II) complexes as the possible active form and the stoichiometry and the stability constants of AZ metal complexes, even with that of Cu(II), have been determined [12].

CE is evaluated as a corrosion inhibitor for carbon steel alloys in the presence of 0.5 M hydrochloric acid (HCl) at different concentrations, i.e., 10-50 ppm and different temperatures [13]. Studies of the mechanism, kinetics and thermodynamic constants of VO(II) and Cu(II) complexes with CE in the pH range of 2 – 5 at temperatures of 303, 313, 323 and 333 K, using reversed phase HPLC and ion exchange HPLC were reported [14]. CE degradation in aqueous solution was studied at 310 and 353 K in acidic, basic and neutral conditions. Stability constants of Re(V) metal complexes with selected medicinal drugs adenosine, isoniazid and metformin hydrochloride have been determined using a pH metric titration technique in aqueous HCl at different temperatures and an ionic strength of 0.2 M [15]. The process of complex formation of Re(V) ion with 2-mercapto-pyridine was investigated potentiometrically by evaluating formation the equilibrium and stability constants of the metal complex at the temperature range of 273-338 K [16].

In the present study, the formation equilibrium investigations were extended to the stoichiometry and stability constants of complex formation of AZ and CE (Scheme 1) with Re(V) metal ion in aqueous HCl at different temperatures. Moreover, the kinetic parameters of the complex formation were determined and discussed.




Scheme 1. The chemical structures of the studied drugs

## Materials and Methods

### Materials

Potassium perrhenate ($KReO_4$) and iodine were purchased from Aldrich and Fluka, respectively. $KReO_4$ was converted to $K_2ReOCl_5$ precursor according to the method reported elsewhere [17]. The concentration of metal ion solution was determined spectrophotometrically at wavelength (λ) of 480 nm. A pure AZ and CE drugs were purchased from the local market (El-Nasr Pharm. Chem. Co., Egypt), potassium iodide and HCl (36.4%) was purchased from BDH.

### Titration method

Potentiometric titrations were performed using a R3003 voltage comparator. A platinum plate was used as an indicator electrode. The redox system consisting of AZ and CE was created by oxidizing a small portion of the initial drugs in 0.3 M HCl with 0.1 N iodine solution (0.5 mL). The stepwise complexes of Re(V) with AZ and CE were studied using the Bjerrum method [18, 19]. For this purpose, the redox system consisting of the drugs (0.04192 mol/L) and its oxidized form titrated with a $K_2ReOCl_5$ solution (0.0799 mol/L) in 0.3 M HCl. The

equilibrium ligand concentration ([L]) and the formation function ($\bar{n}$) at each titration point was calculated using the equations (1) and (2) [20, 21], respectively:

$$\log [L] = \frac{E_I - E_i}{1.9837x10^{-4}\,T} + logC_L^l + \frac{1}{2}\, log\frac{V_I}{V_T} \quad (1)$$

$$\bar{n} = \frac{C_L^l - [L]}{C_M} \quad (2)$$

where, $E_I$ and $E_i$ are the initial equilibrium potentials of the system in the absence of metal ion and at the current titration point, $C_L^1$ is the drug initial concentration of, $V_I$ and $V_T$ are the initial and total volumes, respectively, T is the temperature in K and $C_M$ is the concentration of metal ion at each titration point.

The stepwise stability constants (log $K_i$) of the complexes were calculated at half-integer values of the degree of formation. Thus, a large equilibrium constant indicates a highly stable complex. The overall stability constant (βi) defined as the following equation 3 [22]:

$$\log \beta_i = \log K_1 + \log K_2 + \log K_3 \ldots\ldots + \log K_i \quad (3)$$

The log $K_i$ of the complexes was calculated at 288, 298, 308 and 318 K.

The complex formation thermodynamic characteristics such as: enthalpy (ΔH), Gibb's free energy (ΔG) and entropy (ΔS) are a fundamental important properties of understanding of the various factors such as electronic and steric effects, solute-solvent interactions that may influence on the complexes [23]. The thermodynamic parameters of the metal ion complexes at 288, 298, 308, and 318 K were studied. The complex degree of formation was obtained according to the equations (4) and (5) [24, 25]:

$$\boldsymbol{\Delta G = \Delta H - T\Delta S} \quad (4)$$

$$\boldsymbol{\log\, K_i = \frac{-\Delta H}{2.303\,R} + \frac{1}{T} \times \frac{\Delta S}{2.303\,R}} \quad (5)$$

where, R is the ideal gas constant (8.314 J/K mol). ΔH and ΔS were obtained from the intercept and slope of the plot of log $K_i$ against 1/T.

## Results and Discussion

### Potentiometric titration

The metal ion in solution excites as combined with ligands or chelating groups instead of isolated form, giving rise to complexions or coordination compounds. The obtained titration data were analyzed and then stability constant values were calculated [26]. The experimental data show that the equilibrium potential of the redox system increases in the process of potentiometric titration as the metal ion volume increases. During the titration, no precipitates were formed indicating that there is no tendency to form hydroxide complexes [27]. Intense coloration was observed, which indicated the complexes formation. The formation curves were plotted between $\bar{n}$ and -log [L]. The coordination process in the systems Re(V)-AZ and Re(V)-CE in 0.3 M HCl at various temperatures were characterized by the formation curves as displayed in Figure 1.

Re(V) exists in solutions and solids as octahedral species [28, 29]. In this study, the obtained complexes of Re(V) with AZ and CE have a coordination number of six [30, 31]. AZ is considered as neutral and monodentate ligand and the coordination bonds occur between the lone pair of sulfur atom and Re(V) [32]. The Re(V)-AZ system has a maximum value of $\bar{n}$ = 4, this indicates the formation 1:2, 1:3 and 1:4 complexes. While about 1:1 complex has not formed. The complex formation suggests a successive displacement of the chloride molecules from the coordination sphere of the central ion by the AZ and CE ligands [33]. The maximum value of $\bar{n}$ in the Re(V)-CE system was 2, this shows the formation of 1:1 and 1:2 complexes. On the other hand, CE loses one sodium atom and becomes anionic. In case of 1:1 complex, Re(V) unit is coordinated by a mono anionic O,O-bidentate unit of CE ligand, one

CE and three halogens, with Re(V) center in a distorted octahedral environment. The halide ligands are in *cis* positions to each other [34, 35]. The proposed mechanism of the Re(V)-CE complex formation process 1:1 and 1:2 ratios according to the following reaction (Scheme 2). The estimated log $K_i$ values of Re(V) complexes with AZ and CE at different temperatures are listed in Table 1.

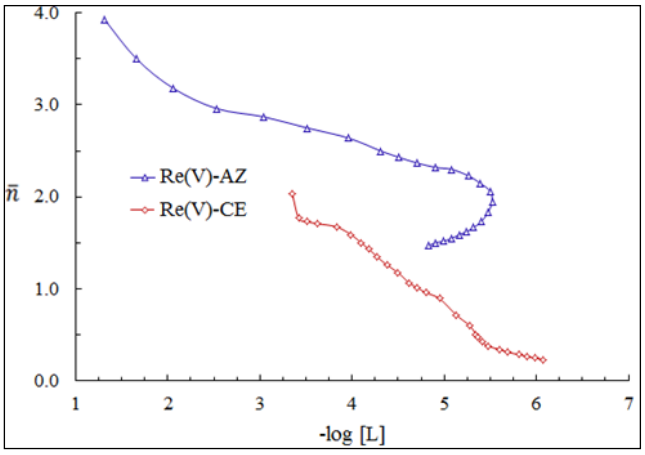
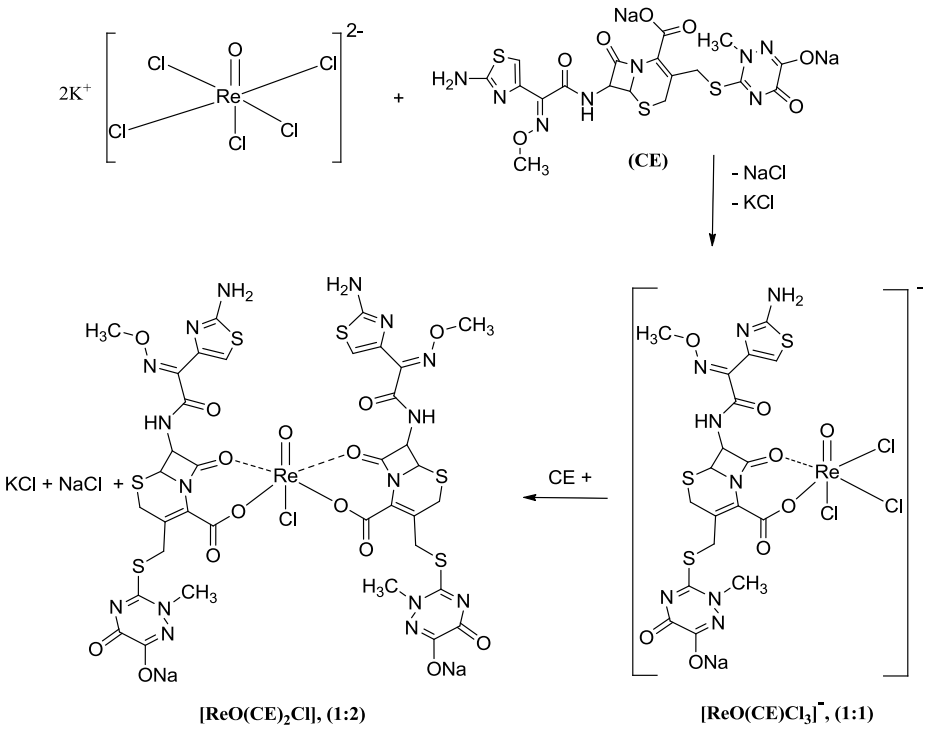



Figure 1. Formation curves of Re(V) complexes with AZ and CE in 0.3 M HCl at 318 K




Scheme 2. The chelation between the $[ReOCl_5]^{2-}$ and CE

Table 1. Stepwise stability constants of Re(V) complexes in 0.3 M HCl

| T (K) | Re(V)-AZ | | | | Re(V)-CE | | |
|---|---|---|---|---|---|---|---|
| | log $K_{2AZ}$ | log $K_{3AZ}$ | log $K_{4AZ}$ | log $\beta_{iAZ}$ | log $K_{1CE}$ | log $K_{2CE}$ | log $\beta_{iCE}$ |
| 288 | 5.93 | 5.30 | 1.82 | 13.05 | 6.66 | 4.95 | 11.61 |
| 298 | 5.84 | 5.13 | 1.77 | 12.72 | 6.34 | 4.67 | 11.01 |
| 308 | 5.32 | 4.66 | 1.72 | 11.63 | 6.11 | 4.33 | 10.44 |
| 318 | 4.91 | 4.31 | 1.66 | 10.84 | 5.35 | 4.10 | 9.45 |

It is observed from Table 1 that, the temperature increase leads to decreasing in log $\beta_i$ values for both AZ and CE. It could be seen from data in all the cases that the differences between $K_1$, $K_2$, $K_3$ and $K_4$ values are found to be high which indicate the formation of the stepwise complex. The value of the ratio of log $K_1$/log $K_2$ or log $K_2$/log $K_3$ is positive in all the cases. This implies that there is no steric hindrance to the addition of a secondary ligand molecule [36]. This is due to the statistically effective and statistically coordination of a second molecule is difficult when compared to the first due to the availability of less number of coordinating sites on the metal ion for the second ligand [37].

**Complexes thermodynamic**

The chemical species in the reaction undergo a change in their concentrations, at the same time. The Gibb's free energy is a function of the concentrations of reactants and products. Entropy is a measure of energy that is unavailable for useful, chemical work. The entropy of an individual species is always positive and tends to be larger for gases than for solids, and for more complex molecules than for simple molecules. The thermodynamic parameters values of Re(V)-AZ and Re(V)-CE complexes have been calculated from the temperature dependent data given in Table 1.

The thermodynamic data were plotted as the values of equilibrium constants (log $K_i$) versus the reciprocal of temperature (1/T) as shown in Figures 2 and 3 for AZ and CE complexes, respectively. All the thermodynamic parameters of the stepwise stability constants of the complexes are given in Table 2.

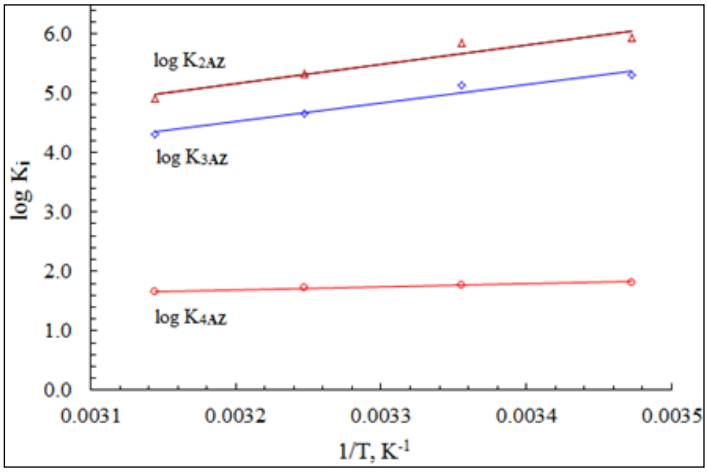



Figure 2. The relations between the values of equilibrium constants (log $K_i$) versus the reciprocal of temperature (1/T) of Re(V)-AZ complexes: log $K_2$ corresponds to $[ReO(AZ)_2Cl_3]$; log $K_3$ corresponds to $[ReO(AZ)_3Cl_2]^+$ and log $K_4$ corresponds to $[ReO(AZ)_4Cl]^{2+}$ species

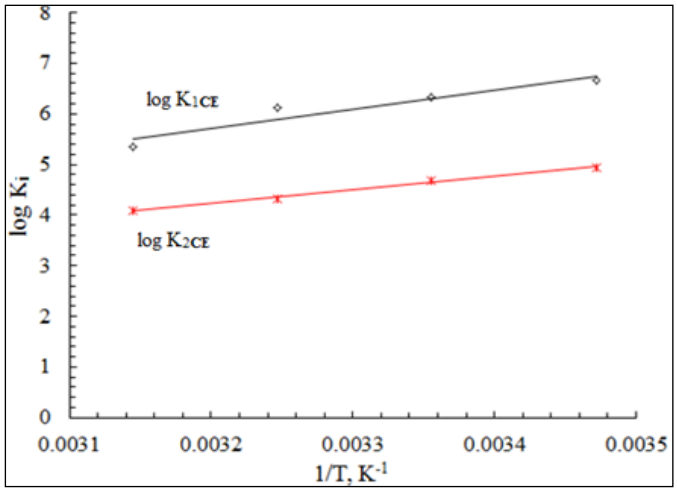



Figure 3. The relations between the values of equilibrium constants (log $K_i$) versus the reciprocal of temperature (1/T) of Re(V)-CE complexes: log $K_1$ corresponds to $[ReO(CE)Cl_3]^-$ and log $K_2$ corresponds to $[ReO(CE)_2Cl]$ species

Table 2. Thermodynamic parameters of Re(V) complexes with AZ and CE in 0.3 M HCl

| **Species** | **– ΔG (kJ/mol)** | **– ΔH (kJ/mol)** | **ΔS (J/K mol)** |
|---|---|---|---|
| $[ReO(AZ)_2Cl_3]$ | 32.32 | 62.36 | –100.78 |
| $[ReO(AZ)_3Cl_2]^+$ | 28.58 | 60.07 | –105.66 |
| $[ReO(AZ)_4Cl]^{2+}$ | 10.08 | 92.76 | 2.71 |
| $[ReO(CE)Cl_3]^-$ | 35.99 | 72.40 | –12.18 |
| $[ReO(CE)_2Cl]$ | 26.51 | 50.70 | –81.60 |

The stepwise formation constants of complexes of the type $ML_n$ (where $M$ is the metal, $L$ is the ligand and $n$ is the number of ligands) decrease in magnitude as $n$ increases. This may be partly explained in terms of the entropy factor. In the case of the formation of octahedral complexes of Re(V)-AZ, the reaction between $K_2[ReOCl_5]$ and AZ involves three successive reactions as the following equations (6-8).

$$K_2[ReOCl_5] + 2AZ \leftrightharpoons [ReO(AZ)_2Cl_3] + 2KCl \quad (6)$$

$$[ReO(AZ)_2Cl_3] + AZ \leftrightharpoons [ReO(AZ)_3Cl_2]Cl \quad (7)$$

$$[ReO(AZ)_3Cl_2]Cl + AZ \leftrightharpoons [ReO(AZ)_4Cl]Cl_2 \quad (8)$$

In equation (6), the two ligands ($n$ = 2) can go into two cites out of five of $K_2[ReOCl_5]$. For equation (8), $n$ = 4 and the fourth ligand can go into one of two sites of $K_2[ReOCl_5]$. This means that there is more randomness in the first step than the fourth one, so ΔS is more positive (2.71), ΔH is more negative (-92.76) and log $K_2$ > log $K_4$ [38]. In addition, there is a dramatic increase in ΔS for adding two compared to adding four monodentate AZ ligands (-100.78 to 2.71 J/K mol) which changed from negative (unfavorable) to positive (favorable). Using the equilibrium constant for the complex formation of Re(V)-CE where the one and two bidentates ligand replace the monodentates chloride ions, it has been found the ΔS decrease (-12.18 to -81.60). The negative change in ΔS indicates a highly solvated metal complex and indicated that the formation of these complexes was entropy favored [39, 40]. ΔH

change for the complexes suggests that all the complexation reactions releasing heat have a negative value (exothermic), favorable at a lower temperature. The metal-ligand binding process is enthalpy driven and metal-ligand bonds are strong [41]. The sign of ΔG indicates the direction in which a reaction moves to reach its equilibrium position. The complexation reactions are thermodynamically favorable when its enthalpy decreases and its entropy increase. Substituting the inequalities $\Delta H < 0$ and $\Delta S > 0$ into the previous equation (4) shows that complexation reactions are thermodynamically favorable and spontaneous when ΔG is negative [42]. Similar trend was obtained for Re(V) with another ligand [38].

**Distribution diagrams**

Mole fractions are commonly used to calculate the concentrations of the individual complexes based on the formation constants. Mole fractions of a form of the complex compressed as the ratio of the concentration of the complex to the total concentration of the metal ion. The distribution diagrams were drawn in the titration where the Re(V) to ligands, mole ratio was 1:1, 1:2, 1:3 and 1:4 at 318 K (Figure 4). It was obtained using Microsoft Excel calculations [43] and the concentration of total metal ions (0.0799 mol/L) was set as 100%.

In Figure 4, the species $[ReO(AZ)_2Cl_3]$ for the system Re(V)-AZ reached a maximum of 2.9%. The second species $[ReO(AZ)_3Cl_2]^+$ and $[ReO(AZ)_4Cl]^{2+}$ reached a maximum of 85.3% and 96.6%, respectively. For Re(V)-CE system, it reached a maximum of 67.5% and 99.89% for $[ReO(CE)Cl_3]^-$ and $[ReO(CE)_2Cl]$ species, respectively. The analysis of the temperature-dependent distribution function shows that the yield of the complexes decreases with increasing the temperature. The analysis of the distribution curves provides the possibility to elucidate the predominance region for some complex depending on temperature and concentration. These results were used to develop optimal methods for the preparation of Re(V) metal ion complexes with AZ and CE in 0.3 M HCl.

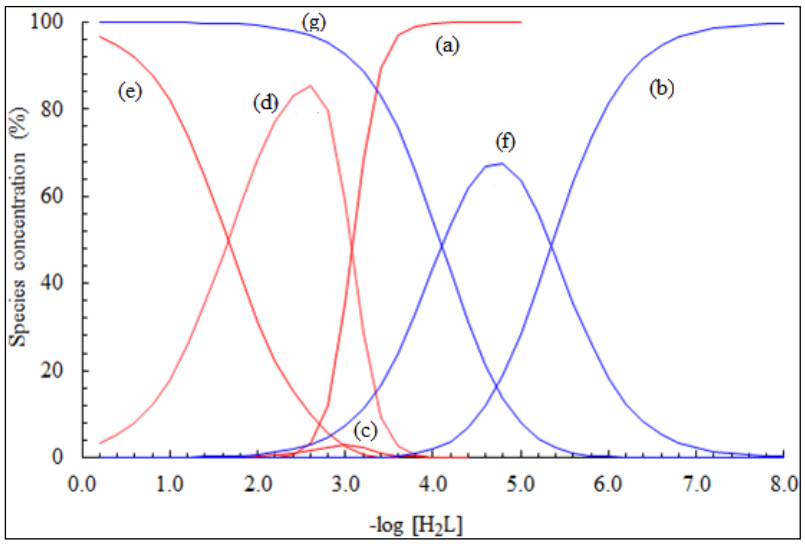



Figure 4. Distribution curves of Re(V) complexes with AZ and CE at 318 K for $[ReOCl_5]^{2-}$ (a) and (b), $[ReO(AZ)_2Cl_3]$ (c), $[ReO(AZ)_3Cl_2]^+$ (d), $[ReO(AZ)_4Cl]^{2+}$ (e), $[ReO(CE)Cl_3]^-$ (f) and $[ReO(CE)_2Cl]$ (g)

## Conclusion

The potentiometric study investigated the behavior of complex formation of Re(V) metal ion with azathioprine (AZ) and ceftriaxone (CE). AZ is a neutral and monodentate ligand and the coordination bonds occur between the lone pair of sulfur atom with Re(V). Re(V)-AZ system has a maximum value of $\bar{n}$ of 4, this showed the formation 1:2, 1:3 and 1:4 complexes. The complex formation suggests a successive displacement of the chloride molecules from the coordination sphere of the central ion by the AZ ligand. The maximum value of $\bar{n}$ in the system of Re(V)-CE was 2, this showed the formation 1:1 and 1:2 complexes. The CE is losing one sodium atom and becomes anionic

ligand. The increasing amount coordinated molecules AZ and CE and the temperature the values log $K_i$ decreases. There is a dramatic increase ΔS for adding two compared to adding four monodentate AZ ligands (-100.78 to 2.71 J/K mol) which change from negative (unfavorable) to positive (favorable). The enthalpy change (ΔH) for the complexes suggests that all the complexation reactions releasing heat have a negative ΔH (exothermic), favorable at low temperatures. ΔG indicates the direction in which a reaction moves to reach its equilibrium position. The above mentioned parameters and results will be useful in understanding the biological behavior of these complexes in the biological applications.

**Acknowledgement**

The authors would like to thank Chemistry department, Faculty of Science, Al-Azhar University, Assiut, Egypt for providing the facilities of this work.

**References**

1. Thomas, G. (2003). Fundamentals of medicinal chemistry. John Wiley & Son Ltd. London, UK.
2. Mendham, J. (2006). Vogels textbook of quantitative chemical analysis. Pearson Education India.
3. Kinlen, L. J. (1985). Incidence of cancer in rheumatoid arthritis and other disorders after immunosuppressive treatment. *American Journal of Medicine,* 78(1): 44 – 49.
4. Fries, J. F., Bloch, D., Spitz, P. and Mitchell, D. M. (1985). Cancer in rheumatoid arthritis: A prospective long-term study of mortality. *American Journal of Medicine,* 78(1): 56 – 59.
5. Kotton, C. N. and Hibberd, P. L. (2009). Travel medicine and the solid organ transplant recipient. *American Journal of Transplantation,* 9(4): 273 – 281.
6. Rind, F. M. A., Laghari, M. G. H., Memon, A. H., Mughal, U. R., Almani, F. N., Memon, K. M. Y. and Maheshwari, M. L. (2008). Spectrophotometric determination of ceftriaxone using 4-dimethylaminobenzaldehyde. *Pakistan Journal of Analytical & Environmental Chemistry,* 9(1): 43 – 48.
7. Al-Momani, I. F. (2001). Spectrophotometric determination of selected cephalosporins in drug formulations using flow injection analysis. *Journal of Pharmaceutical and Biomedical Analysis,* 25(5-6): 751 – 757.
8. Lampros, R., Georgios, P. and Nikolaos, A. (2006). Use of ceftriaxone in patients with severe leptospirosis. *International Journal of Antimicrobial Agents,* 28(3): 259 – 261.
9. Hirn, M., Laitinen, M., Pirkkalainen, S. and Vuento, R. (2004). Cefuroxime, rifampicin and pulse lavage in decontamination of allograft bone. *Journal of Hospital Infection*, 56(3): 198 – 202.
10. Saranjit, S., Monica, G. and Gupta, R. L. (1991). Complexation behaviour of azathioprine with metal ions. *International Journal of Pharmaceutics*, 68(1-3): 105 – 110.
11. Singh, B. N. and Kim, K. H. (2005). Effects of divalent cations on drug encapsulation efficiency of deacylated gellan gum. *Journal of Microencapsulation*, 22(7): 761 – 771.
12. Okoronkwo, A. E. and Aminjanov, A. A. (2005). Study of the step wise complexation processes of rhenium(V) and 2-mercapto pyridine in 6 moles/L HBr. *Oriental Journal of Chemistry*, 21(1): 49 – 57.
13. Al-Sawaad, H. Z. (2013). Evaluation of the ceftriaxone as corrosion inhibitor for carbon steel alloy in 0.5M of hydrochloric acid. *International Journal of Electrochemical Science,* 8(3): 3105 – 3120.
14. Doadrio, A. L., Antonio, M. and Regina, O. (2002). $VO^{2+}$ and $Cu^{2+}$ interactions with ceftriaxone and ceftizoxime: HPLC kinetic studies. *Journal of the Brazilian Chemical Society,* 13(1): 95 – 100.
15. Gouda, G. A. H. (2014). Stability constants of rhenium (V) metal complexes with selected medicinal drugs. *Pyrex Journal of Research in Environmental Studies,* 1(2): 6 – 14.
16. Roberts, N. A. and Robinson, P. A. (1985). Copper chelates of antirheumatic and anti-inflammatory agents: their superoxide dismutase-like activity and stability. *British Journal of Rheumatology,* 24(2): 128 – 136.
17. Jezowska-Trzebiatowska, B., Wajda, S. and Baluka, M. (1968). Structure and properties of technetium and rhenium compounds of the type $[MeVOX_5]^{2-}$ I. Preparation and magnetic and spectrophotometric study. *Journal of Structural Chemistry,* 8(3): 456 – 459.
18. Bjerrum, J. (1941). Metal amine formation in aqueous solution; Hasse P. Son. Copenhagen, Denmark.
19. Irving, H. M. and Rossotti, H. S. (1954). The calculation of formation curves of metal complexes from pH titration curves in mixed solvents. *Journal of the Chemical Society,* 1954: 2904 – 2910.
20. Feiner, A. S. and McEvoy, A. J. (1994). The Nernst equation. *Journal of Chemical Education,* 71(6): 493 – 494.

21. Thompson, M. L. and Kateley, L. J. (1999). The Nernst equation: Determination of equilibrium constants for complex ions of silver. *Journal of Chemical Education,* 76(1): 95 – 96.
22. Heuron, J. Z. and Gilbert, J. B. (1955). New methods for the calculation of association constants of complex ion systems. *Journal of the American Chemical Society,* 77(9): 2594 – 2596.
23. Nair, V. S. K. and Parthasarathy, S. (1971). Studies on metal complexes in aqueous solution-VII: 4-nitro and 4-methyl phthalates of some transition metals. *Journal of Inorganic and Nuclear Chemistry,* 33(9): 3019 – 3020.
24. Ives, D. J. G. (1971). Chemical thermodynamics. Macdonald and Co. Ltd., London, UK.
25. Seaf Elnasr, T. A., Soliman, M. H. and Ayash, M. A. A. (2017). Modified hydroxyapatite adsorbent for removal of iron dissolved in water wells in Sohag, Egypt. *Chemistry of Advanced Materials*, 2(1): 1 – 13.
26. Omar, A. A. and Ali, E. A. (2014). Titanium carboxylate complexes stability constants estimated by four graphical methods. *International Journal of Basic and Applied Sciences,* 3(4): 497 – 503.
27. Golcu, A., Tumer, M., Demirelli H. and Wheatley, R. A. (2005). Cd(II) and Cu(II) complexes of polydentate Schiff base ligands: synthesis, characterization, properties and biological activity. *Inorganica Chimica Acta,* 358(6): 1785 – 1797.
28. Santos, I. G. and Abram, U. (2004). Oxorhenium(V) complexes with thiosemicarbazones. *Zeitschrift für Anorganische und Allgemeine Chemie,* 630(5): 697 – 700.
29. David, J. H., Jonathan, M. W., Catriona, A. M., Victor, L. V., Kevin, J. B. and Paul, S. D. (2016). Synthesis of oxorhenium(V) and oxotechnetium(V) complexes that bind to amyloid-β plaques. *Inorganic Chemistry,* 55(16): 7944 – 7953.
30. Smith, K. J., Ondracek, A. L., Gruhn, N. E., Lichtenberger, D. L., Fanwick, P. E. and Walton, R. A. (2000). A comparative study of the isomers of $ReOCl_3(PMe_3)_2$ and $ReOCl_3(PEt_3)_2$. The isolation and characterization of $ReH_7(PR_3)_2$ and $ReO(OEt)Cl_2$ $(PR_3)_2$ (R= Me or Et) and the photoelectron spectrum of $ReH_7$ $(PMe_3)_2$. *Inorganica Chimica Acta*, 300: 23 – 31.
31. Xiaoyuan, C., Frank, J. F., John, B. W. and Babich, J. Z. (2000). Exploring oxorhenium '3+1' mixed-ligand complexes carrying the S-benzyl-3-[(2-hydroxyphenyl)methylene]dithiocarbazate [ONS]/monothiol [S] donor set: Synthesis and characterization. *Inorganica Chimica Acta,* 307(1-2): 154 – 159.
32. Berthold, N., Hans, P., Francesco, T., Theodosia, M., Peter, L., Hartmut, S. and Chiotellis, E. (2000). Oxorhenium mixed-ligand complexes with the 2,6-dimercaptomethylpyridine ligand. Crystal structure of [2,6-dimercaptomethylpyridinato][p-methoxybenzenethiolato]oxorhenium(V). *Inorganica Chimica Acta,* 304(1): 26 – 32.
33. Conner, K. A., Walton, R. A., Wilkinson, G., Gillard, R. D. and McCleverty, J. A. (1987). Comprehensive coordination chemistry. Pergamon, Oxford, UK.
34. André, G. A., Fernandes, Pedro, M. I. S., Elizeu, S. J., Sebastião, L. S., Alzir, B. A. Abram, U., Ellena, J., Eduardo, C. E. and Victor, D. M. (2008). Rhenium chelate complexes with maltolate or kojate. *Polyhedron*, 27(13): 2983 – 2989.
35. Ondracek, A. L., Fanwick, P. E. and Walton, R. A. (1998). The synthesis, characterization and X-ray crystal structures of the fac-cis and mer-trans isomers of $ReOCl_3(PMe_3)_2$. *Inorganica Chimica Acta,* 267(1): 123 – 126.
36. Mowafak, M. M., Abeer, A. T., Ahmed, E. A. and Mohamed, S. M. (2015). Potentiometric and thermodynamic studies for binary and mixed ligand complexes of some transition metal ions with hydrazone and phenylalanine. *International Journal of Electrochemical Science,* 10(1): 456 – 471.
37. Jamode, V. S. and Kale, A. S. (2007). Stability constant of transition metal ions complex with1-carboxamido-3,5-diaryl-4-aroylpyrazoles. *Asian Journal of Chemistry,* 19(1): 787 – 789.
38. Gouda, G. A. H., Ali, G. A. M. and Seaf-Elnasr, T. A. (2015). Stability studies of selected metal ions chelates with 2-(4-amino-1,5-dimethyl-2-phenyl-1,2-dihydro-pyrazol-3-ylideneamino) phenol. *International Journal of Nanomaterials and Chemistry,* 1(2): 39 – 44.
39. Gouda, G. A. H. and Mahross, M. H. (2016). Potentiometric and quantum chemical studies of some metal complexes with 2-(4-amino-1,5-dimethyl-2-phenyl-1,2-dihydro-pyrazol-3-ylideneamino) phenol. *Global Journal of Multidisciplinary Studies,* 5: 164 – 180.
40. Park, H., Choi, W., Cotton, F. A., Wilkinson, G. and Gaus, P. L. (1995). Basic inorganic chemistry. John Wiley & Sons Inc.
41. Sharmeli, Y. and Lonibala, R. (2009). Thermodynamics of the complexation of n-(pyridin-2-ylmethylene) isonicotinohydrazide with lighter lanthanides. *Journal of Chemical & Engineering Data,* 54(1): 28 – 34.

42. Al-Sarawy, A. A., El-Bindary, A. A., El-Sonbati, A. Z. and Mokpel, M. M. (2006). Potentiometric and thermodynamic studies of azosulfonamide drugs. *Polish Journal of Chemistry,* 80(2): 289 – 295.
43. Martell, A. E. and Motekaitis, R. J. (1989). Determination and use of stability constants. Wiley-VCH, New York, USA.

*Malaysian Journal of Analytical Sciences, Vol 21 No 6 (2017): 1276 - 1288*
*DOI: https://doi.org/10.17576/mjas-2017-2106-09*

MALAYSIAN JOURNAL OF ANALYTICAL SCIENCES
*Published by The Malaysian Analytical Sciences Society*
ISSN 1394 - 2506

# SINTESIS $MnO_2$ NANOBUNGA POROS MENGGUNAKAN TEMPLAT SILIKA-APTES

## (Synthesis of Porous $MnO_2$ Nanoflower using Silica-APTES Template)

Siti Zubaidah Hasan[1], Mohamed Rozali Othman[1,2]*, Muhammad Rahimi Yusop[1]

[1]*Pusat Pengajian Sains Kimia dan Teknologi Makanan*
[2]*Pusat Penyelidikan Air dan Analisis*
*Fakulti Sains dan Teknologi,*
*Universiti Kebangsaan Malaysia, 43600 UKM Bangi, Selangor, Malaysia*

**Pengarang utama: rozali@ukm.edu.my*

Received: 19 May 2017; Accepted: 20 September 2017

**Abstrak**

Tujuan kajian ini dilakukan adalah untuk menyediakan $MnO_2$ poros nano yang mempunyai bentuk nanobunga untuk digunakan sebagai penjerap pewarna sintetik komersial (remazol merah, eriokrom hitam dan metilena biru). Permukaan bahan silika yang telah diubahsuai dengan 3-aminopropil trietoksisilana (APTES) digunakan dalam proses sonokimia pada suhu bilik dengan kehadiran 0.1M $KMnO_4$ untuk menghasilkan komposit silika-$MnO_2$ dan seterusnya $MnO_2$ bersaiz nano selepas proses penyingkiran templat dilakukan. Spektrum FTIR menunjukkan kehadiran getaran $MnO_2$ dalam julat 400 – 600 $cm^{-1}$. Analisis jerap-nyahjerap $N_2$ menunjukkan $MnO_2$ tulen memiliki liang yang bersifat mesoporos 51.9 Å (± 1.4), manakala luas permukaan $MnO_2$ ialah 123.6 $m^2/g$. Penjerap $MnO_2$ nanobunga yang diperolehi menunjukkan kebolehan menjerap pewarna eriokrom hitam dan metilena biru sahaja. Kedua-dua isoterma penjerapan eriokrom hitam dan metilena biru oleh $MnO_2$ menepati ciri-ciri model Langmuir.

**Kata kunci**: sonokimia, logam oksida, jerapan

**Abstract**

The aim of this study is to prepare porous $MnO_2$ nanoflower to be used as an adsorbent for commercial synthetic dyes (remazol red, eriochrome black and methylene blue). The modified surface of the silica with 3-aminopropyl triethoxysilane (APTES) was used in sonochemical process at room temperature in the presence of 0.1M $KMnO_4$ to produce composite silica-$MnO_2$ and later nano-$MnO_2$ after removal of the template. FTIR spectra indicate the presence of $MnO_2$ vibration in the range of 400 – 600 $cm^{-1}$. $N_2$ sorption-desorption analysis showed pure $MnO_2$ is mesopores with the value of 51.9 Å (± 1.4), while the $MnO_2$ surface area is 123.6 $m^2/g$. $MnO_2$ nanoflower adsorbent obtained demonstrate the ability to adsorb dye eriochrome black and methylene blue only. Both adsorption isotherms of eriochrome black and methylene blue by $MnO_2$ meet the characteristics of Langmuir model.

**Keywords**: sonochemical, metal oxides, adsorption

## Pengenalan

Semenjak beberapa tahun kebelakangan ini, sintesis pelbagai logam oksida bersaiz nano menarik perhatian para saintis kerana partikel bersaiz nano mempunyai sifat – sifat yang unik seperti pemangkinan, mekanik, elektronik, magnet, aktif kimia dan sifat optik disebabkan oleh kesan saiznya yang kecil dan luas permukaan yang besar [1-3]. Sintesis logam oksida boleh dilakukan dengan pelbagai kaedah seperti elektrokimia, hidroterma, tindak balas keadaan pepejal, gelombang mikro dan banyak lagi [2, 4 - 9]. Mangan dioksida merupakan salah satu logam oksida

yang digunakan secara meluas sebagai bahan asas dalam pembuatan elektrod dan diaplikasikan dalam pengoksidaan mangkin terpilih. Mangan dioksida banyak digunakan dalam degradasi azo, aplikasi kapasitor elektrokimia dan pemangkinan [10 - 13].

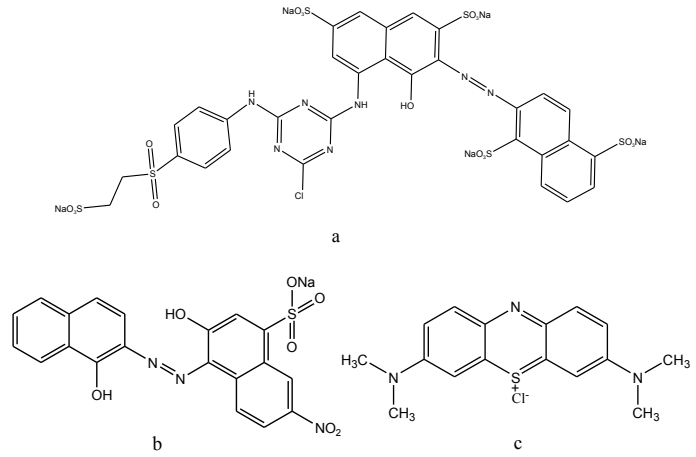
Pewarna organik mempunyai banyak kegunaan dan diaplikasikan dalam bidang pengeluaran dan pemprosesan. Namun, kewujudan sebatian pewarna organik dalam efluen memberikan kesan buruk terhadap alam sekitar. Terdapat 100 000 pewarna komersial yang dihasilkan dan pengeluarannya adalah lebih daripada 700 000 tan setahun [14]. Di Malaysia, menurut sumber industri berjadual (sisa pepejal), industri tekstil hanya menyumbang kira-kira 0.1%. Walau bagaimanapun, jumlah sisa berjadual oleh industri tekstil meningkat sebanyak satu kali ganda iaitu daripada 744 tan (2007) kepada 1559 tan pada tahun 2009 [15]. Pewarna organik sintetik yang dihasilkan biasanya menggunakan bahan kimia yang toksik dan bersifat karsinogenik terhadap ekosistem akuatik dan kehidupan manusia amnya [16, 17]. Kewujudan pewarna organik sintetik di dalam efluen merupakan satu perkara yang tidak diingini. Terdapat beberapa kaedah yang telah dikaji iaitu rawatan secara kimia, biologi dan fizikal. Rawatan secara fizikal iaitu penjerapan dikatakan sebagai satu teknik yang sangat baik dalam rawatan air buangan daripada industri tekstil. Teknik fizikal menarik perhatian saintis kerana kebolehannya menyingkirkan bahan pencemar yang terlalu stabil bagi kaedah biologi. Teknik fizikal seperti penjerapan pewarna dengan menggunakan penjerap logam oksida telah banyak dilakukan [11, 18 - 23].

Objektif kajian ini dilakukan adalah untuk mensintesis $MnO_2$ bersaiz nano menggunakan kaedah sonokimia dengan cara yang mudah dimana templat silika-APTES dicampurkan dengan $KMnO_4$ dan tindak balas dilakukan dalam bekas rendaman ultrasonik pada suhu bilik. Produk yang diperolehi digunakan sebagai penjerap dalam ujian penjerapan pewarna remazol merah, eriokrom hitam dan metilena biru.

## Bahan dan Kaedah Kajian

### Bahan kimia

Bahan jerap yang digunakan ialah pewarna reaktif remazol merah (C.I. 239, tulen 99%), pewarna berasid eriokrom hitam (C.I. 14645, tulen 99%) dan pewarna bes metilena biru (C.I. 52015, tulen 99%) yang diperolehi daripada R & M Chemicals (Rajah 1). Semua bahan kimia lain yang digunakan dalam kajian ini seperti APTES (tulen 98%), silika (tulen 99%), toluena (tulen 99.5%), $KMnO_4$ (tulen 99%) dan NaOH (tulen 98%) diperolehi daripada Sigma Aldrich tanpa dilakukan penulenan terlebih dahulu.




Rajah 1. Struktur molekul sebatian pewarna (a) remazol merah, (b) eriokrom hitam dan (c) metilena biru

### Sintesis bahan poros nano-$MnO_2$

Sintesis $MnO_2$ dilakukan seperti yang telah dilaporkan oleh Hasan et al. [24]. $MnO_2$ yang diperolehi mempunyai morfologi seperti bentuk nanobunga. Refluks dilakukan terlebih dahulu dengan mencampurkan 5 mL APTES ke dalam kelalang bulat (250 mL) yang mengandungi 0.5 g silika dengan kehadiran 50 mL pelarut toluena. Refluks

dilakukan bertujuan mengubahsuai permukaan silika yang hidrofobik kepada hidrofilik dengan memasukkan kumpulan $NH_2$. $MnO_2$ diperolehi dengan melakukan proses sonokimia terhadap templat silika-APTES (12j) dengan kehadiran 5 mL larutan $KMnO_4$ (0.1M). Tindak balas sonokimia dilakukan selama 6 jam pada suhu bilik untuk menghasilkan komposit silika-$MnO_2$. Hasil tindak balas yang diperolehi dituras menggunakan penapis vakum yang menggunakan kertas turas bersaiz 0.45 µm dan dibilas sebannyak tiga kali dengan air nyahion (50 mL setiap kali) sebelum dikeringkan pada suhu 105 ºC selama 9 jam. Setelah kering, proses penyingkiran templat silika keatas mendakan yang diperolehi seterusnya dilakukan dengan merendam hasil yang diperolehi ke dalam 20 mL larutan NaOH (2.0 M) selama 24 jam. Hasil yang diperolehi, iaitu $MnO_2$ tulen dibilas dengan kaedah yang sama seperti sebelum proses penyingkiran templat dilakukan dan dikeringkan pada suhu yang sama.

**Penyediaan larutan pewarna**
Setiap larutan stok pewarna yang berkepekatan 1000 ppm disediakan dengan mencampurkan 1000 mg serbuk pewarna ke dalam 1000 mL air nyahion. Bekas yang berisi larutan pewarna dibalut dengan pembalut aluminium dan disimpan di tempat yang gelap untuk mengelakkan penguraian foto.

**Pencirian penjerap**
Ciri permukaan sampel yang telah dikeringkan terlebih dahulu dianalisis menggunakan mikroskop imbasan elektron (FESEM) daripada jenama Merlin Compact. Ciri-ciri keporosan dan luas permukaan penjerap $MnO_2$ nanobunga ditentukan melalui ujian jerap-nyahjerap $N_2$ menggunakan Micromeritic ASAP 2020 pada -196 ºC. Analisis FTIR dilakukan untuk mengenalpasti getaran kumpulan MnO yang hadir pada nisbah sampel: serbuk KBr (0.5:1) menggunakan alat FTIR berjenama Perkin Elmer model Spectrum BX. Imbasan dilakukan dalam julat 4000 – 400 $cm^{-1}$.

**Ujian penjerapan**
Ujian penjerapan pewarna remazol merah (anionik), eriokrom hitam (anionik) dan metilena biru (kationik) oleh penjerap yang telah disediakan dilakukan menggunakan kaedah kelompok. Sebanyak 0.2 g penjerap seperti bahan pemula (templat silika, silika-APTES dan komposit silika-$MnO_2$) dan $MnO_2$ digunakan dalam ujian penjerapan pewarna dalam tempoh masa sehingga selama 120 minit pada suhu bilik dan pH asal larutan. Perbezaan keamatan serapan setiap pewarna sebelum dan selepas ujian penjerapan diukur menggunakan UV-Vis. Peratus penyahwarnaan dikira menggunakan persamaan di bawah:

$$\% \text{ Penyahwarnaan} = \frac{A_o - A_t}{A_o} \times 100 \quad (1)$$

dimana $A_o$ dan $A_t$ masing-masingnya adalah nilai serapan yang diukur pada panjang gelombang maksimum ($\lambda_{mak}$) kepekatan awal larutan pewarna dan nilai serapan pada waktu *t*. Jumlah bahan jerap yang terjerap pada keadaan keseimbangan, $q_e$ (mg/g) dikira menggunakan persamaan seperti berikut:

$$Q_e = \frac{(C_o - C_e)}{W} \times V \quad (2)$$

dimana $C_o$ adalah kepekatan awal dan $C_e$ adalah kepekatan keseimbangan (mg/L). V adalah isipadu pelarut (L) dan W adalah berat penjerap yang digunakan (g).

**Isoterma penjerapan**
Isoterma penjerapan dilakukan bagi mengkaji potensi penjerapan diantara penjerap dan bahan jerap. Mod isoterma penjerapan yang perlu dikenalpasti ialah Langmuir, Freundlich dan Temkin. Mod Langmuir menentukan hanya satu tapak aktif yang boleh memegang satu molekul bahan jerap, penjerapan berlaku pada tapak homogen penjerap dan interaksi di antara spesis terjerap tidak berlaku. Persamaan linear Langmuir adalah seperti berikut :

$$\frac{C_e}{} = \frac{1}{} + \frac{C_e}{}$$

$$Q_e = Q_{max}b \quad Q_{max} \tag{3}$$

dimana $Q_e$ (mg/g) dan $C_e$ (mg/L) masing-masingnya adalah kapasiti pewarna yang terjerap pada penjerap dan kepekatan pewarna pada keadaan keseimbangan. Manakala mod Freundlich pula menjangkakan penjerapan berlaku pada permukaan yang mempunyai tenaga penjerapan yang berbeza. Persamaan Freundlich adalah seperti berikut:

$$Q_e = K_F C_e^{1/n} \tag{4}$$

dimana $K_F$ ialah pemalar yang terlibat dengan kapasiti penjerapan dan $1/n$ ialah parameter empirik yang menerangkan keheterogenan permukaan atau intensiti penjerapan. Persamaan linear Freundlich adalah seperti berikut:

$$\ln Q_e = \ln K_F + 1/n \, (\ln C_e) \tag{5}$$

Mod Temkin pula menjangkakan haba penjerapan semua molekul berkurang secara linear dengan liputan yang terhasil disebabkan oleh interaksi bahan jerap. Persamaan linear Temkin adalah seperti berikut:

$$Q_e = B \ln A + B \ln C_e, \qquad B = RT/b_T \tag{6}$$

dimana $B$ (J/mol) ialah pemalar yang berkait dengan haba penjerapan dan $A$ (L/g) ialah pemalar pengikat keseimbangan yang merujuk kepada tenaga pengikatan maksimum. $R$ dan $T$ masing-masingnya ialah pemalar gas universal (8.314 J/mol/K) dan suhu pada 298K, manakala $b_T$ ialah pemalar isoterma Temkin.

Sebanyak 50 mL pewarna eriokrom hitam dan metilena biru yang berkepekatan 10 mg/L dicampurkan dengan 0.2 g penjerap $MnO_2$ nanobunga dan eksperimen dilakukan pada suhu bilik pada pH asal larutan pewarna. Selepas tempoh masa tertentu (15, 30, 60, 90 dan 120 minit). 5 mL larutan dikeluarkan dengan menggunakan picagari yang hujungnya disambung dengan penapis membran nilon (0.45 µm). Larutan yang dikeluarkan diukur nilai serapannya pada $\lambda_{max}$ setiap pewarna menggunakan spektrofotometer UV-Vis pada panjang gelombang ($\lambda_{max}$ eriokrom hitam dan metilena biru masing-masingnya ialah 540 dan 664 nm).

**Kinetik penjerapan**

Terdapat dua model kinetik penjerapan yang biasa diaplikasi dalam ujian penjerapan pewarna iaitu model tertib pertama *pseudo* dan tertib kedua *pseudo*. Model tertib pertama *pseudo* diaplikasikan pada peringkat awal proses penjerapan. Persamaan model tertib pertama *pseudo* ialah:

$$\ln (Q_e - Q_t) = \ln Q_e - K_1 t \tag{7}$$

dimana $Q_e$ dan $Q_t$ masing-masingnya ialah kuantiti pewarna yang terjerap (mg/g) pada keseimbangan dan masa tertentu, $t$ (min), $K_1$ ialah pemalar kadar keseimbangan penjerapan tertib pertama *pseudo* ($min^{-1}$). Persamaan model tertib kedua *pseudo* ialah:

$$\frac{t}{Q_t} = \frac{1}{K_2 Q_e^2} + \frac{t}{Q_e} \tag{8}$$

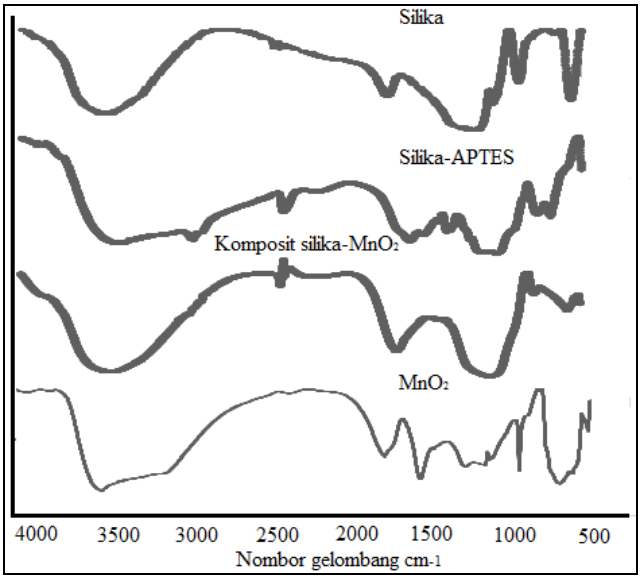
dimana $K_2$ (g/mg/min) ialah pemalar kadar keseimbangan tertib kedua *pseudo*, $Q_e$ (mg/g) ialah kapasiti penjerapan maksimum, dan $Q_t$ (mg/g) ialah kapasiti penjerapan pada masa tertentu, $t$ (min).

Ujian kinetik penjerapan dilakukan dengan menggunakan 50 mL pewarna eriokrom hitam dan metilena biru yang berkepekatan 10 mg/L yang dicampurkan dengan 0.2 g penjerap $MnO_2$ nanobunga dan eksperimen dilakukan pada suhu bilik dan pH asal larutan pewarna. Selepas tempoh masa tertentu (15, 30, 60, 90 dan 120 minit), 5 mL larutan dikeluarkan dengan menggunakan picagari yang hujungnya disambung dengan penapis membran nilon (0.45 µm). Larutan yang dikeluarkan diukur nilai serapannya menggunakan spektrofotometer UV-Vis pada $\lambda_{max}$ setiap pewarna.

**Keputusan dan Perbincangan**

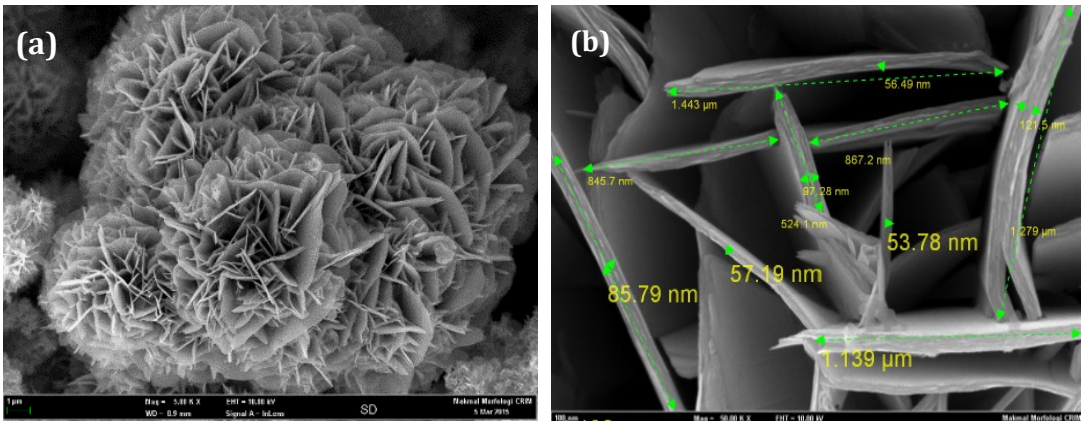
Keberhasilan pengubahsuaian permukaan templat silika dengan APTES dapat diperhatikan dalam spektrum FTIR seperti yang ditunjukkan dalam Rajah 2. Spektrum FTIR silika menunjukkan kehadiran jalur pada 3467 $cm^{-1}$, dimana ini merupakan getaran regangan kumpulan OH yang terikat kepada kumpulan silikon [25]. Manakala jalur pada 1650 $cm^{-1}$ menunjukkan bengkokan kumpulan silanol [25]. Pada jalur 1079 $cm^{-1}$, menunjukkan wujudnya getaran regangan tidak simetri bagi Si-O-Si dalam $SiO_2$, getaran regangan Si-O-Si wujud pada jalur 975 dan 800 $cm^{-1}$, dan getaran bengkokan wujud pada jalur 471 $cm^{-1}$ [25, 26]. Selepas refluks dilakukan, spektrum silika-APTES menunjukkan kehadiran jalur baru di dalam kawasan 3290-3000 $cm^{-1}$ dimana ini merujuk kepada kehadiran getaran regangan kumpulan $NH_2$. Ini membuktikan berlakunya pengikatan antara kumpulan aminopropil dengan silika. Selain itu juga, mod getaran regangan dan bengkokan kumpulan alifatik $CH_2$ masing-masingnya wujud pada jalur 2936 dan 2832 $cm^{-1}$ manakala getaran bengkokan $NH_2$ bagi $SiO_2$-$NH_2$ wujud pada jalur 1574 $cm^{-1}$ [25]. Selepas tindak balas sonokimia, terdapat beberapa jalur baru yang wujud dalam spektrum FTIR komposit silika-$MnO_2$. Jalur 463 $cm^{-1}$ menunjukkan kehadiran getaran Mn-O dan Mn-O-Mn bagi unit $MnO_6$ oktahedron dan jalur pada 3445 dan 1653 $cm^{-1}$ masing-masingnya menunjukkan getaran regangan dan bengkokan kumpulan OH daripada molekul air [27]. Jalur 1067 $cm^{-1}$ menunjukkan kehadiran getaran bengkokan kumpulan OH pada permukaan logam [28].

Selain itu juga, terdapat perbezaan antara spektrum FTIR dimana jalur getaran regangan dan bengkokan kumpulan alifatik $CH_2$ yang wujud pada jalur 2936 dan 2832 $cm^{-1}$ serta getaran bengkokan $NH_2$ bagi $SiO_2$-$NH_2$ yang wujud pada jalur 1574 $cm^{-1}$ sebelum tindak balas sonokimia tidak lagi kelihatan dalam spektrum selepas tindak balas. Ini membuktikan berlakunya pengikatan diantara mangan oksida dan atom nitrogen. Selepas penyingkiran templat dilakukan, spektrum FTIR $MnO_2$ menunjukkan kehadiran getaran Mn-O dan Mn-O-Mn bagi mangan oksida pada nombor gelombang 500 – 800 $cm^{-1}$ [29], dimana getaran Mn-O dan Mn-O-Mn bagi $MnO_2$ ialah 602 $cm^{-1}$. Jalur pada 1468 dan 1405 $cm^{-1}$ wujud selepas proses penyingkiran templat dilakukan kerana spektrum FTIR komposit silika-$MnO_2$ tidak menunjukkan kehadiran jalur ini. Kehadiran jalur ini mungkin disebabkan oleh kumpulan getaran bengkokan OH daripada NaOH yang terikat pada permukaan mangan oksida selepas proses penyingkiran templat dilakukan. Selain itu juga, jalur pada 3467 – 3445 $cm^{-1}$ menunjukkan regangan OH bagi molekul air, jalur pada 1645 – 1695 dan 850 $cm^{-1}$ masing-masingnya menunjukkan getaran bengkokan OH dan getaran bengkokan luar satah OH daripada molekul air, manakala jalur pada 1021, 1186 dan 1068 $cm^{-1}$ merupakan getaran bengkokan OH yang terikat kepada atom Mn [28].

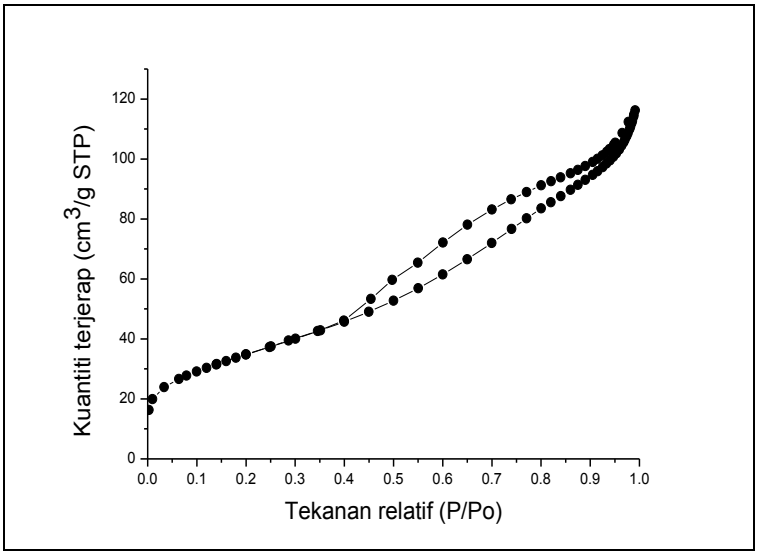



Rajah 2. Spektrum FTIR silika, silika-APTES, komposit silika-$MnO_2$ dan $MnO_2$ nanobunga

Imej SEM bagi penjerap $MnO_2$ adalah seperti yang ditunjukkan dalam Rajah 3 dimana ia menunjukkan morfologi nanobunga yang mempunyai panjang yang tidak sekata iaitu lebih daripada 100 nm dan mencapai 1.5 µm, manakala ketebalannya dalam julat 53 – 122 nm. Rajah 4 menunjukkan graf isoterma jerap-nyahjerap $N_2$ bagi $MnO_2$ yang menunjukkan ia memiliki isoterma jenis II dan IV. Menurut Asouhidou [30], isoterma jenis II merujuk kepada penjerap bukan poros atau makroporos, dimana penjerapan lapisan mono dan lapisan berganda berlaku tanpa had. Isoterma jenis IV pula merujuk kepada bahan mesoporos [31, 32]. Penjerap $MnO_2$ memiliki gelung histeresis jenis $H_3$ dimana pada tekanan relatif (P/Po) yang tinggi, ia tidak mempunyai had penjerapan dan mempunyai liang berbentuk celah. Penjerap ini menunjukkan sifat liang mesoporos dengan saiz liang ialah 51.9 Å (± 1.4). Tambahan lagi penjerap ini menunjukkan luas permukaan yang agak tinggi 123.6 $m^2/g$.




Rajah 3. Mikrograf FESEM $MnO_2$ nanobunga

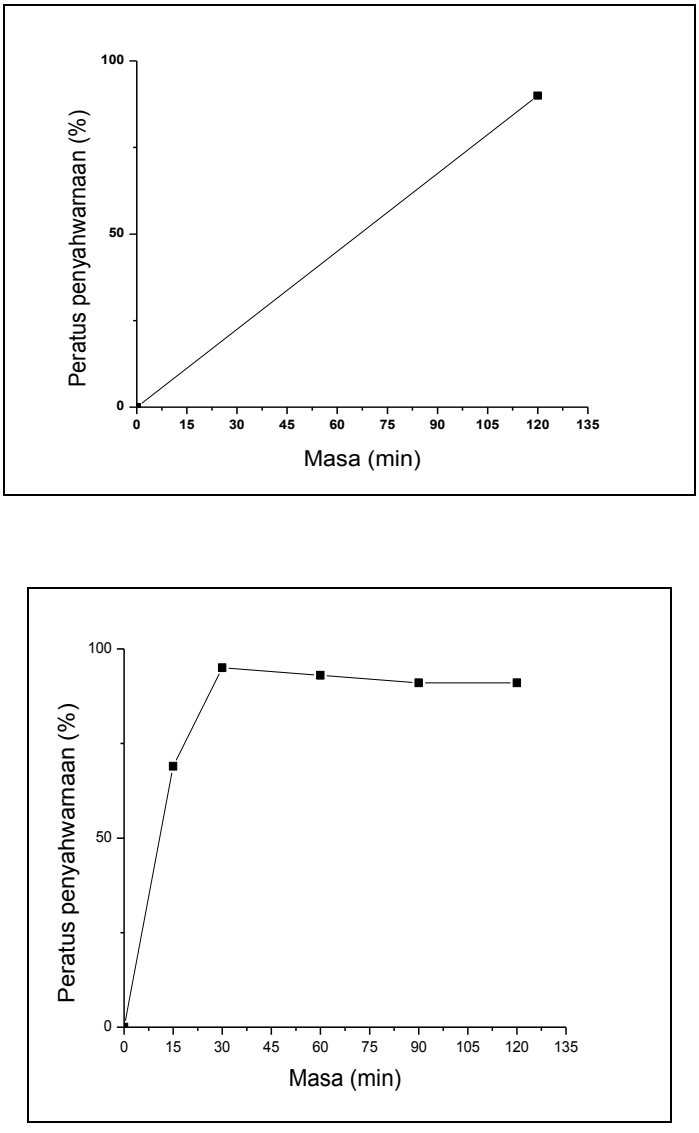



Rajah 4. Graf isoterma jerap-nyahjerap $N_2$ $MnO_2$

Rajah 5 menunjukkan peratus penyahwarnaan pewarna remazol merah oleh penjerap silika-APTES dan komposit silika-$MnO_2$. Tiada penjerapan yang berlaku pada penjerap silika dan $MnO_2$. Perkara ini berlaku kerana silika adalah bersifat hidrofobik dan kumpulan OH yang terikat pada atom logam Mn bagi $MnO_2$ adalah sangat banyak menyebabkan berlakunya peningkatan persaingan antara kumpulan OH dan spesis sulfonat ($SO_3^-$). Ciri – ciri

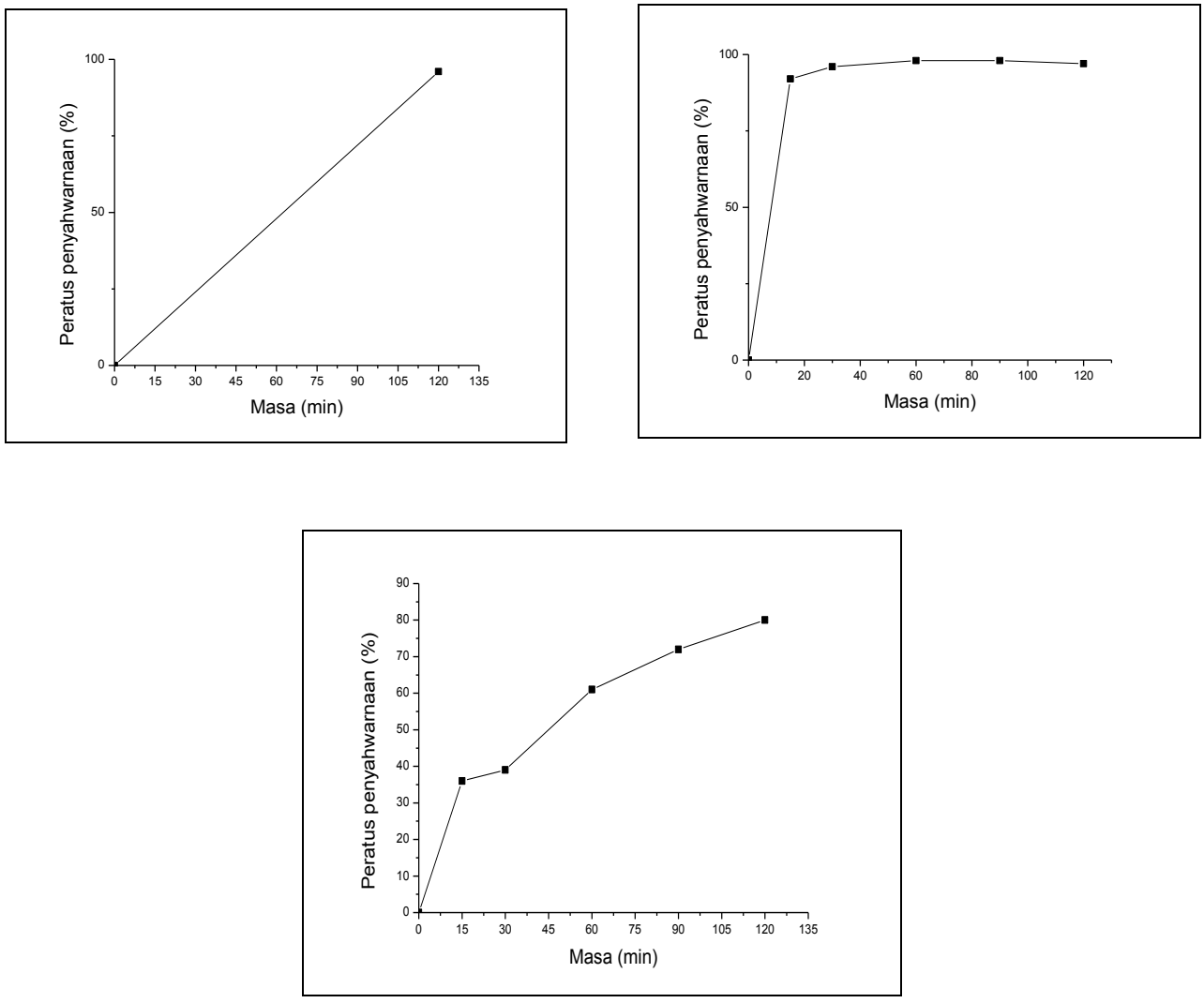
hidrofobik silika menunjukkan ia kalis air kerana struktur dan sifat kimia yang dimilikinya. Apabila air dicampurkan dengan silika, partikel ini menghalang air daripada meresap masuk ke dalam teksturnya. Air hanya bersentuhan dengan hujung partikel lapisan luar bahan. Disebabkan kekurangan daya tarikan, silika menolak molekul air [27].

Peratus penyahwarnaan pewarna reaktif remazol merah adalah sangat tinggi apabila penjerap silika-APTES (90%) dan komposit silika-$MnO_2$ (95%) digunakan. Di sini dapat diperhatikan penjerapan pewarna reaktif remazol merah oleh penjerap komposit silika-$MnO_2$ adalah lebih cepat berlaku berbanding dengan silika-APTES. Penjerap silika-APTES mengambil masa selama 120 minit untuk penyahwarnaan sebanyak 90% tetapi komposit silika-$MnO_2$ mengambil masa 30-40 minit sahaja. Perkara ini berlaku disebabkan oleh perbezaan mekanisme penjerapan yang berlaku pada permukaan penjerap. Mekanisme penjerapan pewarna oleh silika-APTES adalah disebabkan oleh pembentukan ikatan hidrogen manakala penjerapan yang berlaku pada komposit silika-$MnO_2$ adalah disebabkan daya tarikan elektrostatik.



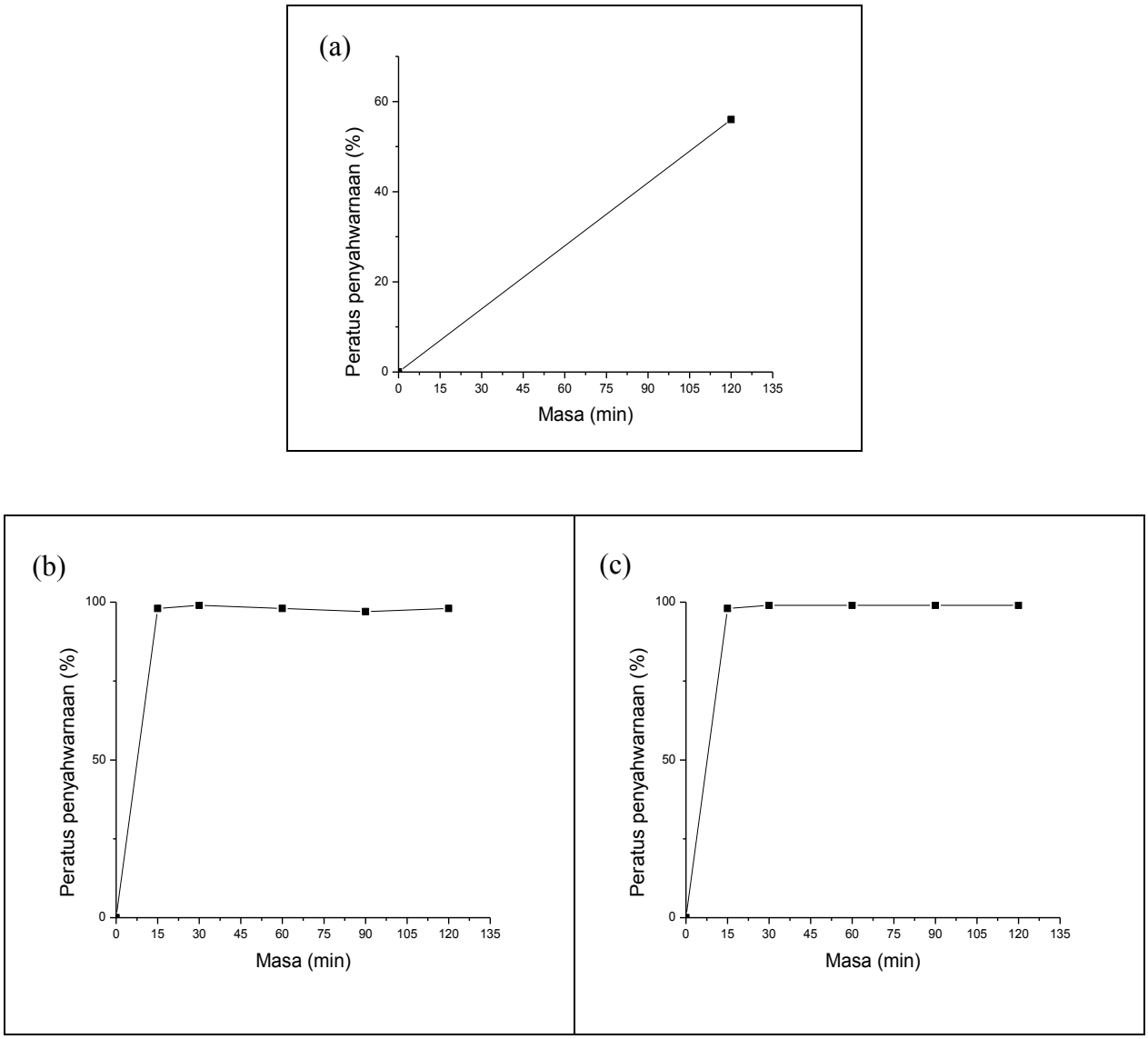

Rajah 5. Penjerapan pewarna reaktif remazol merah oleh (a) silika-APTES dan (b) komposit silika-$MnO_2$

Rajah 6 menunjukkan peratus penyahwarnaan pewarna eriokrom hitam oleh penjerap silika-APTES, komposit silika-$MnO_2$ dan $MnO_2$. Peratus penyahwarnaan pewarna eriokrom hitam oleh silika-APTES, komposit silika-$MnO_2$ dan $MnO_2$ pada minit ke 120 masing-masingnya ialah 96, 97 dan 80%. Perbezaan peratus penjerapan disebabkan oleh mekanisme penjerapan yang berlaku. Mekanisme penjerapan yang berlaku antara eriokrom hitam dengan penjerap silika-APTES ialah ikatan hidrogen manakala penjerapan antara eriokrom hitam dengan penjerap komposit silika-$MnO_2$ adalah disebabkan luas permukaan mangan dioksida yang menyediakan tapak penjerapan dan daya tarikan elektrostatik yang terbentuk antara permukaan penjerap yang bercas negatif dan molekul pewarna yang bercas positif. Penjerapan semakin berkurang apabila penjerap $MnO_2$ digunakan. Hal ini sedemikian kerana permukaan penjerap $MnO_2$ dipenuhi oleh kumpulan OH yang hadir semasa proses penyingkiran templat silika, oleh itu berlaku persaingan antara kumpulan sulfonat daripada eriokrom hitam dan kumpulan OH pada permukaan penjerap $MnO_2$ yang menghadkan bilangan molekul bahan jerap terjerap.




Rajah 6. Penjerapan pewarna anionik eriokrom hitam oleh (a) silika-APTES, (b) komposit silika-$MnO_2$ serta (c) $MnO_2$

Rajah 7 menunjukkan peratus penyahwarnaan pewarna metilena biru oleh penjerap silika-APTES, komposit silika-$MnO_2$ dan $MnO_2$. Peratus penyahwarnaan bagi silika-APTES, komposit silika-$MnO_2$ dan $MnO_2$ pada minit ke 120 masing-masingnya ialah 56, 98 dan 99%. Perbezaan peratus penyahwarnaan adalah disebabkan oleh mekanisme penjerapan yang berbeza. Mekanisme penjerapan pewarna metilena biru oleh penjerap silika-APTES adalah ikatan hidrogen, manakala mekanisme penjerapan metilena biru oleh penjerap komposit silika-$MnO_2$ dan $MnO_2$ adalah disebabkan oleh daya tarikan elektrostatik yang terbentuk antara permukaan penjerap yang bercas negatif dan sebatian pewarna yang bercas positif [33].




Rajah 7. Penjerapan pewarna kationik metilena biru oleh (a) silika-APTES, (b) komposit silika-$MnO_2$ dan (c) $MnO_2$

Secara kesimpulannya, penjerapan oleh penjerap $MnO_2$ hanya berlaku terhadap pewarna eriokrom hitam (anionik) dan metilena biru (kationik) sahaja. Tiada penjerapan berlaku terhadap remazol merah (anionik). Perkara ini berlaku disebabkan kehadiran banyak kumpulan OH pada permukaan penjerap $MnO_2$ yang menghalang penjerapan kumpulan $SO_3^-$ sebatian pewarna pada permukaan penjerap. Sebaliknya pula berlaku terhadap pewarna eriokrom hitam. Walaupun eriokrom hitam terdiri daripada pewarna anionik, namun penjerapan pada permukaan penjerap boleh berlaku. Hal ini sedemikian kerana penjerapan eriokrom hitam pada permukaan penjerap $MnO_2$ disebabkan oleh daya tarikan elektrostatik antara kumpulan $^-OH$ dan $^+NO_2$ sebatian pewarna. Perkara yang sama juga berlaku terhadap pewarna metilena biru. Penjerapan yang berlaku pada permukaan penjerap $MnO_2$ disebabkan oleh daya tarikan elektrostatik antara kumpulan $^-OH$ dan $S^+$ sebatian pewarna.

**Mod isoterma penjerapan**

Mod isoterma penjerapan dipilih berdasarkan nilai pekali korelasi, $R^2$. Nilai $R^2$ merupakan kuantiti yang memberikan kualiti bagi kuasa dua terkecil kepada data asal dimana nilai $R^2$ adalah 1 atau menghampiri 1. Penjerapan eriokrom hitam dan metilena biru oleh $MnO_2$ menepati mod Langmuir dimana masing-masingnya mempunyai nilai $R^2 = 0.9788$ dan 0.9147. Parameter setiap model penjerapan isoterma ditunjukkan dalan Jadual 1.

**Model kinetik penjerapan**

Model kinetik yang dikaji ialah tertib pertama *pseudo*, tertib kedua *pseudo*, tertib kedua dan resapan intrazarah model Weber-Morris. Model kinetik penjerapan dipilih berdasarkan nilai pekali korelasi, $R^2$. Penjerapan eriokrom hitam dan metilena biru oleh penjerap $MnO_2$ masing-masingnya menepati model tertib pertama *pseudo* dan Weber-Morris dengan $R^2 = 0.7482$ dan 0.9902. Parameter model kinetik penjerapan ditunjukkan seperti yang diringkaskan dalam Jadual 2.

Jadual 1. Parameter mod isoterma penjerapan eriokrom hitam dan metilena biru oleh penjerap $MnO_2$

| Model Isoterma | Pembolehubah | Bahan Jerap | |
|---|---|---|---|
| | | Eriokrom Hitam | Metilena Biru |
| Langmuir | $Q_{max}$ ($mgg^{-1}$) | 0.7564 | 3.5804 |
| | $Q_{max}$ b ($Lg^{-1}$) | -0.7268 | 54.3478 |
| | $R^2$ | 0.9788 | 0.9147 |
| Freundlich | $K_F$ ($mgg^{-1}$) | 0.4862 | 1.7462 |
| | 1/n | -0.3045 | 0.4299 |
| | $R^2$ | 0.7365 | 0.7761 |
| Temkin | B ($Jmol^{-1}$) | -0.3187 | 0.8646 |
| | $b_T$ | -7773.9943 | 2865.5702 |
| | $R^2$ | 0.7303 | 0.8350 |

Jadual 2. Parameter model kinetik penjerapan pewarna eriokrom hitam dan metilena biru oleh penjerap $MnO_2$

| **Model Kinetik** | **Eriokrom Hitam** | **Metilena Biru** |
|---|---|---|
| Eksperimen | | |
| $R^2$ | 0.6892 | 0.9902 |
| *Pseudo* tertib pertama | | Tiada data |
| K ($min^{-1}$) | 0.0129 | |
| $R^2$ | **0.7482** | |
| *Pseudo* tertib kedua | | |
| K (L/mg.min) | -0.0762 | -0.0011 |
| $R^2$ | 0.0207 | 0.0010 |
| Tertib kedua | | |
| K (L/mg.min) | -0.0762 | -0.0011 |
| $R^2$ | 0.0207 | 0.0010 |
| Model Weber-Morris | | |
| $K_{int}$ | -0.0072 | 0.0178 |
| $R^2$ | 0.6892 | 0.9902 |

## Kesimpulan

Dalam kajian ini, $MnO_2$ nanobunga berjaya disintesis menggunakan kaedah mudah sonokimia dengan mencampurkan templat silika-APTES dan larutan $KMnO_4$. Produk yang diperolehi mempunyai luas permukaan yang agak tinggi iaitu 123.4 $m^2/g$ dan memiliki sifat liang mesoporos dimana saiz liangnya ialah 51.9 (±1.4) Å. Ujian penjerapan pewarna sintetik organik oleh penjerap $MnO_2$ menunjukkan penjerapan hanya berlaku terhadap eriokrom hitam dan metilena biru sahaja. Penjerapan pewarna oleh $MnO_2$ disebabkan oleh daya tarikan elektrostatik. Isoterma penjerapan menunjukkan penjerapan eriokrom hitam dan metilena biru oleh $MnO_2$ menepati mod Langmuir. Kinetik penjerapan menunjukkan penjerapan eriokrom hitam oleh $MnO_2$ menepati model tertib pertama *pseudo* manakala penjerapan metilena biru oleh $MnO_2$ menepati resapan intrazarah model Weber-Morris.

## Penghargaan

Pengarang menghargai sumbangan yang diberikan oleh geran FRGS/2/2013/SG01/UKM/01/1 dalam menjalankan penyelidikan ini. Selain itu juga, ribuan terima kasih diucapkan kepada Universiti Kebangsaan Malaysia terhadap ruang dan instrumen yang disediakan.

## Rujukan

1. Henglein, A. (1989). Small-particle research: physicochemical properties of extremely small colloidal metal and semiconductor particles. *Chemical Reviews*, 89(8): 1861 – 1873.
2. Suslick, K. S., Choe, S. B., Cichowlas, A. A. and Grinstaff, M. W. 1991. Sonochemical synthesis of amorphous iron. *Nature*, 353(6343): 414 – 416.
3. Emsley, J. (2014). In your element: manganese the protector. *Nature Chemistry*, 6(11): 1026 – 1026.
4. Therese, G. H. A. and Kamath, P. V. (2000). Electrochemical synthesis of metal oxides and hydroxides. *Chemistry of Materials*, 12(5): 1195 – 1204.
5. Titirici, M. M., Antonietti, M. and Thomas, A. (2006). A generalized synthesis of metal oxide hollow spheres using a hydrothermal approach. *Chemistry of Materials*, 18(16): 3808 – 3812.
6. Patil, S. A., Shinde, D. V., Ahn, D. Y., Patil, D. V., Tehare, K. K., Jadhav, V. V., Lee, J. K., Mane, R. S., Shrestha, N. K. and Han, S. H. (2014). A simple, room temperature, solid-state synthesis route for metal oxide nanostructures. *Journal of Materials Chemistry A*, 2(33): 13519 – 13526.

7. Lagashetty, A., Havanoor, V., Basavaraja, S., Balaji, S. D and Venkataraman, A. (2007). Microwave-assisted route for synthesis of nanosized metal oxides. *Science and Technology of Advanced Materials,* 8(6): 484 – 493.
8. Kumar, R. V., Diamant, Y. and Gedanken, A. (2000). Sonochemical synthesis and characterization of nanometer-size transition metal oxides from metal acetates. *Chemistry of Materials*, 12(8): 2301 – 2305.
9. Suslick, K. S., Hyeon, T., Fang, M. and Cichowlas, A. A. (1995). Sonochemical synthesis of nanostructured catalysts. *Materials Science and Engineering A*, 204(1): 186 – 192.
10. Dupont, M., Hollenkamp, A. F. and Donne S. W. (2013). Electrochemically active surface area effects on the performance of manganese dioxide for electrochemical capacitor applications. *Electrochimica Acta*, 104: 140 – 147.
11. Ge, J. and Qu, J. (2003). Degradation of azo dye acid red b on manganese dioxide in the absence and presence of ultrasonic irradiation. *Journal of Hazardous Materials*, 100(1–3): 197 – 207.
12. Ilyas, M. and Saeed, M. (2011). Synthesis and characterization of manganese oxide and investigation of its catalytic activities for oxidation of benzyl alcohol in liquid phase. *International Journal of Chemical Reactor Engineering*, 9(1): A75.
13. Ren, Y., Chen, Z., Cai, Y. and Lin, J. (2011). Electrosynthesis of glyceraldehyde by cyclic nano-$MnO_2$/$Mn^{2+}$ in bipolar membrane-equipped electrolytic cell. *Electrochemistry Communications*, 13(12): 1317 – 1319.
14. Kyzas, G. Z., Fu, J. and Matis, K. A. (2013). The change from past to future for adsorbent materials in treatment of dyeing wastewaters. *Materials*, 6(11): 5131 – 5158.
15. Pang, Y. L. and Abdullah, A. Z. (2013). Current status of textile industry wastewater management and research progress in Malaysia: A review. *CLEAN–Soil, Air, Water*, 41(8): 751 – 764.
16. Manning, B. W., Cerniglia, C. E. and Federle, T. W. (1985). Metabolism of the benzidine-based azo dye direct black 38 by human intestinal microbiota. *Applied and Environmental Microbiol*ogy, 50(1): 10 –15.
17. Nony, C. R. and Bowman, M. C. (1980). Trace analysis of potentially carcinogenic metabolites of an azo dye and pigment in hamster and human urine as determined by two chromatographic procedures. *Journal of Chromatographic Science,* 18(2): 64 – 74.
18. Abdullah, A. H. and Wong, W. Y. (2010). Decolorization of reactive orange 16 dye by copper oxide system. *Sains Malaysiana*, 39(4): 587 – 591.
19. Cui, H. J., Huang, H. Z., Yuan, B. and Fu, M. L. (2015). Decolorization of RhB dye by manganese oxides: effect of crystal type and solution pH. *Geochemical Transactions*, 16(1): 10.
20. Chen, R., Yu, J. and Xiao, W. (2013). Hierarchically porous $MnO_2$ microspheres with enhanced adsorption performance. *Journal of Materials Chemistry A*, 1(38): 11682 – 11690.
21. Cao, J., Mao, Q., Shi, L. and Qian, Y. (2011). Fabrication of γ-$MnO_2$/α-$MnO_2$ hollow core/shell structures and their application to water treatment. *Journal of Materials Chemistry*, 21(40): 16210 –16215.
22. Fei, J., Cui, Y., Yan, X. H., Qi, W., Yang, Y., Wang, K. W., He, Q. and Li, J. B. (2008). Controlled preparation of $MnO_2$ hierarchical hollow nanostructures and their application in water treatment. *Advanced Materials*, 20(3): 452 – 456.
23. Chen, H. and He, J. (2008). Facile synthesis of monodisperse manganese oxide nanostructures and their application in water treatment. *Journal of Physical Chemistry C*, 112(45): 17540 – 17545.
24. Hasan, S. Z., Yusop, M. R. and Othman, M. R. (2015). Sintesis amorfus mangan dioksida ($MnO_2$) nano-poros menggunakan proses sonokimia dan bukan sonokimia. *Malaysian Journal of Analytical Sciences*, 19(2): 388 – 396.
25. Antony, R., David Manickam, S. T., Kollu, P., Chandrasekar, P. V., Karuppasamy, K. and Balakumar, S. (2014). Highly dispersed Cu(II), Co(II) and Ni(II) catalysts covalently immobilized on imine-modified silica for cyclohexane oxidation with hydrogen peroxide. *RSC Advances*, 4(47): 24820 – 24830.
26. Ryu, S. H., Hwang, S. G., Yun, S. R., Cho, K. K., Kim, K. W. and Ryu, K. S. (2011). Synthesis and electrochemical characterization of silica-manganese oxide with a core-shell structure and various oxidation states. *Bulletin of the Korean Chemical Society*, 32(8): 2683 – 2688.
27. Zhao, Y., Li, J., Hu, J., Shu, L. and Shi, X. (2011). Fabrication of super-hydrophobic surfaces with long-term stability. *Journal of Dispersion Science Technology*, 32(7): 969 – 974.
28. Huang, M., Zhang, Y., Li, F. Zhang, L., Ruoff, R. S., Wen, Z. and Liu, Q. (2014). Self-assembly of mesoporous nanotubes assembled from interwoven ultrathin birnessite-type $MnO_2$ nanosheets for asymmetric supercapacitors. *Scientific Reports*, 4: 3878.

29. Ding, K. Q. (2010). Cyclic voltammetrically prepared copper-decorated $MnO_2$ and its electrocatalysis for oxygen reduction reaction *(ORR). International Journal of Electrochemical Science*, 5: 72 – 87.
30. Asouhidou, D. D., Triantafyllidis, K. S., Lazaridis, N. K. and Matis, K. A. (2012). Adsorption of reactive dyes from aqueous solutions by layered double hydroxides. *Journal of Chemical Technology and Biotechnology*, 87(4): 575 – 582.
31. Asouhidou, D. D., Triantafyllidis, K. S., Lazaridis, N. K. and Matis, K. A. (2009). Adsorption of remazol merah from aqueous solutions using APTES and cyclodextrin-modified HMS-type mesoporous silicas. *Colloids and Surfaces A: Physicochemical Engineering Aspects*, 346(1–3): 83 – 90.
32. Santos, D., de Lourdes N. S. M., Costa, J., de Jesus, R., Navickiene, S., Sussuchi, E. and de Mesquita, M. (2013). Investigating the potential of functionalized MCM-41 on adsorption of remazol red dye. *Environmental Science and Pollution Research*, 20(7): 5028 – 5035.
33. Nassar, N. N. and Ringsred, A. (2012). Rapid adsorption of metilena biru from aqueous solutions by goethite nanoadsorbents. *Environmental Engineering Science*, 29(8): 790 – 797.

*Malaysian Journal of Analytical Sciences, Vol 21 No 6 (2017): 1289 - 1298*
*DOI: https://doi.org/10.17576/mjas-2017-2106-10*

MALAYSIAN JOURNAL OF ANALYTICAL SCIENCES
*Published by The Malaysian Analytical Sciences Society*
ISSN 1394 - 2506

# EXTRACTION OF METHYLPARABEN IN COSMETICS USING DISPERSIVE LIQUID-LIQUID MICROEXTRACTION BASED ON SOLIDIFICATION OF FLOATING ORGANIC DROP COUPLED WITH GAS CHROMATOGRAPHY FLAME IONIZATION DETECTOR

## (Pengekstrakan Metilparaben dalam Kosmetik Menggunakan Pengekstrakan Mikro Cecair-Cecair Serakan Berdasarkan Pemejalan Organik Terampai Berganding dengan Kromatografi Gas Pengesan Nyala Pengionan)

Dyia Syaleyana Md Shukri*, Nurul Asma Hamedan, Nur Shakirah Hussin, Wan Izhan Nawawi

*Faculty of Applied Sciences,*
*Universiti Teknologi MARA, 02600 Arau, Perlis, Malaysia*

**Corresponding author: dyia839@perlis.uitm.edu.my*

Received: 16 August 2016; Accepted: 4 November 2017

**Abstract**

A simple and efficient method called dispersive liquid–liquid microextraction based on solidification of floating organic droplets (DLLME-SFO) method coupled with gas chromatography flame ionization detector (GC-FID) was developed for the extraction of methylparaben (MP) in cosmetics. In the optimized DLLME-SFO method, a mixture of n-hexadecane (70 µL) as an extraction solvent and methanol (0.25 mL) as a disperser solvent was rapidly injected into a 5 mL sample solution (pH 6) containing 4 % (w/v) NaCl. After 4 minutes of centrifugation at 4000 rpm, the mixture was separated into two phases with the fine droplets of n-hexadecane floating at the top of the sample solution. Then, the test tube was placed in an ice bath for cooling and solidification purposes. The solidified extract was transferred into a small vial where it melted and injected into GC-FID system. The DLLME-SFO method gave a good linearity over the concentration range from 0.1 – 8 µg/mL with coefficient of estimation ($r^2$) from 0.9996. The method also provides a low limit of detections (LODs) which is 0.0048 µg/mL. Methylparaben was detected in both samples at the concentration level of 0.06 µg/mL for sample 1 and 0.42 µg/mL for sample 2 respectively.

**Keywords:** dispersive liquid–liquid microextraction, solidification of floating organic droplets, gas chromatography flame ionization detector, methylparaben, cosmetic

**Abstrak**

Kaedah yang senang dan berkesan iaitu pengekstrakan mikro cecair-cecair serakan berdasarkan pemejalan organik terampai (DLLME-SFO) berganding dengan kromatografi gas dengan dengan pengesan nyala pengionan (GC-FID) telah dihasilkan bagi penentuan metilparaben dalam alatan kosmetik. Dalam kaedah DLLME-SFO yang telah dioptimumkan, campuran n-heksadekana (70 µL) sebagai pelarut pengekstrak dan metanol (0.25 mL) sebagai pelarut penyebar disuntik segera ke dalam 5 mL larutan sampel (pH 6) yang mengandungi 4% (w/v) NaCl. Selepas pengemparan selama 4 min pada 4000 rpm, campuran terpisah kepada dua fasa di mana titisan halus n-heksadekana terapung di atas larutan sampel. Kemudiannya, tabung uji diletakkan di dalam rendaman ais untuk penyejukan dan pemejalan. Ekstrak yang beku dimasukkan ke dalam vial di mana ia mencair dan disuntik ke dalam sistem GC-FID. Kaedah DLLME-SFO memberikan kelinearan yang baik untuk kepekatan diantara, 0.1 – 8 µg/mL dengan pekali penentuan ($r^2$) 0.9996. Kaedah ini juga menunjukkan had pengesanan (LODs) rendah iaitu 0.0048 µg/mL. Metilparaben telah dikesan dalam kedua-dua sampel pada tahap kepekatan 0.06 µg/mL untuk sampel 1 dan 0.42 µg/mL untuk sampel 2.

**Katakunci:** pengekstrakan mikro cecair-cecair serakan, pemejalan organik terampai, gas kromatografi pengesan pengionan nyala, metilparaben, kosmetik

## Introduction

A preservative is a natural or man-made chemical that is added to several types of products, for example foods, pharmaceuticals, paints, biological samples, wood, beverages and others. It is used to prevent decomposition or any undesirable chemical changes due to microbial activities; hence, products last longer and are safe for use [1, 2]. Hirose and coworkers [3] stated that these preservatives act as either antimicrobials or antioxidants which they will either inhibit the activity of or kill the bacteria, molds, insects and other microorganisms. Antimicrobials are to prevent the growth of molds, yeasts and bacteria while antioxidants keep the products from becoming rancid or developing black spots [4]. They suppress the reaction when the products come in contact with oxygen, heat, and some metals.

Parabens or ester of p-hydroxybenzoic acid are extensively used in formulations of personal care products due to having neutral pH, no perceptible odor or taste, and no discoloration or hardening effect [5]. Generally, parabens are stable in the air, and are resistant to hydrolysis in hot and cold water as well as in acidic solutions ($1 \leq pH < 7$). Despite their benefits, a controversy surrounds the discussion the effect of commonly used parabens, methylparabens (MP), which can cause side effects on consumers and organoleptic alterations in the cosmetics. The studies revealed that the use of parabens may cause cancer, genotoxicity and breast cancer [6, 7, 8]. Parabens are also reported to have side effects on males as it may decrease the reproduction potential, cause infertility and cause skin cancer diseases such as malignant, melanoma and contact eczema. Recently, the use of preservatives in consumer products has been the subject of criticism because of their possible side-effects on human health. According to European Union (EU) and USA legislation, 0.4% (w/w) of single paraben concentration and a maximum of 0.8% (w/w) for the mixture of parabens is allowed in a cosmetic product [9, 10].

There is no doubt that legislation lags behind the market. Numerous amounts of paraben-free cosmetic products have been marketed in recent years. Labels on these products usually claim 0% parabens or paraben-free cosmetics. However, the lack of specific regulation facilitates labeling fraud. Their widespread use makes parabens a group of chemicals to be controlled from an analytical point of view. Information about some analytical methods published for paraben determination can be found in the book edited by Salvador and Chisvert [11] and a review paper by Wang and Liu [12]. Liquid-liquid extraction (LLE), solid phase extraction (SPE), solid-phase microextraction (SPME), and matrix-solid phase dispersion (MSPD) coupled with either gas chromatography (GC) or high performance liquid chromatography (HPLC) have been critically examined for the identification of MP in cosmetics [13-15]. In a conventional LLE there are many well-known drawbacks and limitations, the most important of which are the large volumes of samples and extraction solvents required, and consequently the large amount of wastes generated, as well as the low preconcentration on samples.

Dispersive liquid-liquid microextraction (DLLME) has been introduced for the analysis of organic compounds, inorganic analytes and various types of analytes from different matrices such as water, tissue, biological fluids, and food matrices. DLLME is a miniaturized LLE using microliter volumes of extraction solvent, which is based on the equilibrium distribution process of the target analytes between sample solution and extraction solvent. This method offers simplicity of operation, rapidity, low cost, high recovery, high enrichment factor, and environmental benignity with wide application prospects in trace analysis [16, 17]. In conventional DLLME, the density of extraction solvent should be higher than water. The high density extraction solvents, being mostly halogenated, are generally hazardous to laboratory personnel and are not often compatible with reversed phase high performance liquid chromatography (HPLC).

Recently, a new microextraction method was developed, which is DLLME integrated with the solidification of a floating drop (DLLME-SFO) [18]. In DLLME-SFO, the extraction solvent was collected on the top of the test tube and was then cooled by inserting it into an ice bath for 5 minutes. The solidified extraction solvent was transferred into a suitable vial and immediately melted at room temperature; then it was finally injected into a suitable instrument.

In this work, we present a new application of DLLME-SFO in the extraction of MP in cosmetic creams and separation using GC-FID. In addition, the sample treatment step was employed for the extraction of target analyte in cosmetic creams before DLLME-SFO and thus reducing the matrix effect.

## Materials and Methods

### Chemicals and reagents

Methylparaben standard, 1-undecanol, 1-dodecanol, and *n*-hexadecane were supplied by Sigma-Aldrich (Buchs, Switzerland). HPLC grade of methanol, acetonitrile, and acetone were obtained from Fisher Scientific (UK). Sample pH was adjusted by the addition of diluted sodium chloride from Merck (Darmstadt, Germany). 100 mg $mL^{-1}$ solution was prepared by dissolving analyte in methanol and stored in the refrigerator at 4 ºC before use. This stock solution was diluted with methanol to prepare a series of working solutions. Deionized water was prepared by the use of a Millipore Milli-Q (Milford, MA, USA) reagent water system. pH value was measured using a Cyberscan 510 pH meter; a Hettich (Oxford, UK) model EBA 20 centrifuge was used for phase separation. Two different local cosmetic sunblock's were used as real samples.

### GC conditions

Gas chromatographic (GC-15A, Shimadzu, Japan) analysis was performed with a split or splitless injector system, and a flame ionization detector was used to determine methylparaben. A SPB-50 capillary column (30 m x 0.22 mm i.d., 0.25µm film thickness) was used for chromatographic separation and ultra-pure helium (99.99%, Air products, UK) was used as the carrier gas. The injection port was held at 270 $^{o}$C in the splitless mode with a purge time of 45s. The oven temperature was programmed as follows: initial temperature 130 $^{o}$C (held for 1 min), from 130 $^{o}$C to 230 $^{o}$C at the rate of 10 $^{o}$C/min, and finally held at 230 $^{o}$C for 2 minutes. The FID temperature was maintained at 270 $^{o}$C. Hydrogen gas for FID was generated by a hydrogen generator (OPGU-1500S, Shimadzu, Japan) at a flow rate of 40 mL/min. The flow rate of air for FID was 300 mL/min.

### Sample preparation

Sunblock cream samples (5g) were dissolved into 2:8 mL methanol and deionized water before 1 mL of concentrated HCl was added into the solution and exposed to sonication for 10 minutes. Then, the solution was diluted to 150 mL with deionized water, adjusted to pH 6.0, and then subjected to DLLME-SFO extraction.

### DLLME-SFO procedure

Aqueous solution (5 mL) containing methylparaben (3.0 µg/mL) was placed in a 10-mL test tube. A mixture of *n*-hexadecane (70µL) and methanol (0.25 mL) was rapidly injected into the sample solution using a syringe. A cloudy suspension resulted from dispersion of fine droplets of *n*-hexadecane in the sample solution was then separated by centrifugation for 4 minutes at 4000 rpm. After centrifugation, the test tube was directly put into an ice bath for 5 minutes to solidify the floated *n*-hexadecane. After 5 minutes, the solidified solvent was collected using a small spatula and transferred into a conical vial, where it melted rapidly at room temperature. The floating extraction phase was collected using a microsyringe and 1µL was injected for GC-FID analysis.

## Results and Discussion

### Peak identification

In the GC-FID analysis, methylparaben was detected and eluted at 10.9 minutes (Figure 1). Generally, the area under the peak is directly proportional to its concentration.

### Optimization of DLLME-SFO method

To determine the optimized extraction conditions, the peak area of MP was used to evaluate the extraction efficiency under different conditions. Six parameters were critically examined; types of extraction solvent and disperser solvent, volumes of extraction solvent and disperser solvent, effect of salt concentration and sample pH.

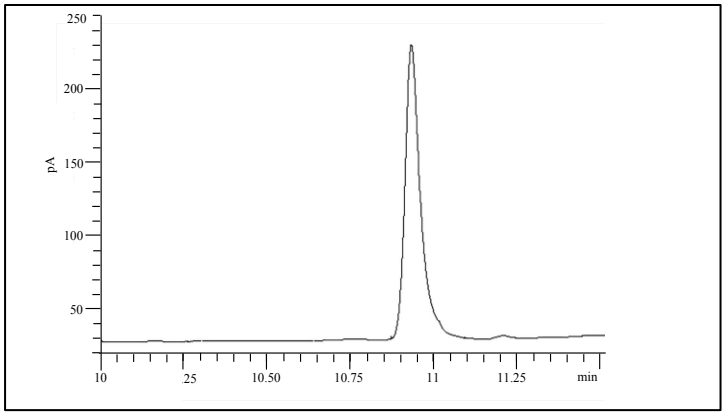



Figure 1. GC-FID chromatogram of MP at concentration 0.5 µg/mL

**Selection of extraction solvents**

An extraction solvent is crucial in the optimization of DLLME-SFO conditions. To achieve the optimum results, the extraction solvent must meet several criteria: high affinity for analytes, lower density than water, low solubility in aqueous solution, low melting point and volatility (Table 1), and perform a good chromatographic behavior [19]. In this study, 1-undecanol, 1-dodecanol, and *n*-hexadecane were tested in DLLME-SFO extraction (Figure 2). The results revealed that *n*-hexadecane showed better extraction efficiency compared to 1-undecanol and 1-dodecanol. Thus, it was selected as an extraction solvent and used in further experiments.

Table 1. Boiling point, melting point and density of extraction solvents [20]

| Extraction Solvent | Boiling Point ($^oC$) | Melting Point ($^oC$) | Density ($g/cm^3$) |
|---|---|---|---|
| 1-Undecanol | 243 | 13-15 | 0.8298 |
| 1-Dodecanol | 98 | 22-24 | 0.8309 |
| *n*-hexadecane | 287 | 18 | 0.7700 |

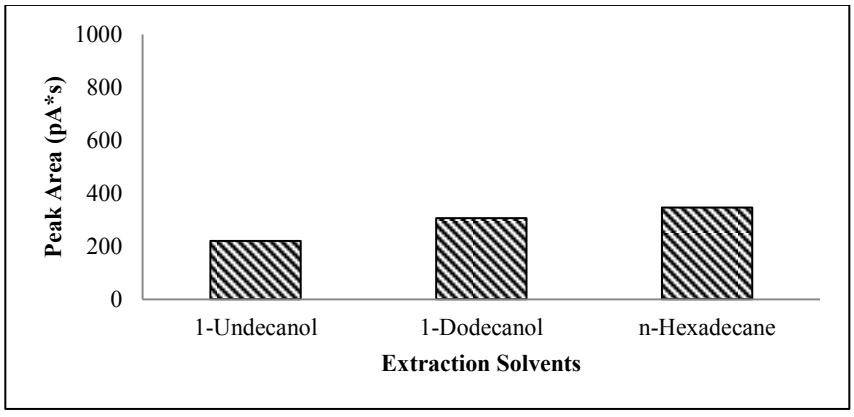



Figure 2. Effect of extraction solvent on extraction efficiency for DLLME-SFO of MP. Concentration of MP 3.00 µg/mL; volume of sample 5 mL (pH 6); volume extractant 70 µL; volume disperser solvent (methanol) 0.25 mL; extraction time 1 min; centrifugation 4000 rpm × 4 min; no salt added

**Selection of disperser solvents**

The miscibility of disperser solvent in diluted cosmetic solution and extraction solvent is one of the criteria that should be considered in order to enable the *n*-hexadecane to be dispersed as a fine particle in aqueous phase to form a cloudy solution (water/disperser solvent/extraction solvent). In such a case, the surface area between extraction solvent and aqueous phase can be definitely large, thus increasing the extraction efficiency [21]. Thereby, acetone, methanol, and acetonitrile were selected for this purpose of study. A series of experiments were conducted by using a mixture of 70 *n*-hexadecane and 0.25 mL of each disperser solvent (Figure 3). According to the obtained results, methanol was selected as the most suitable disperser because of the formation of a cloudy state with very fine droplets and high recovery of analyte.

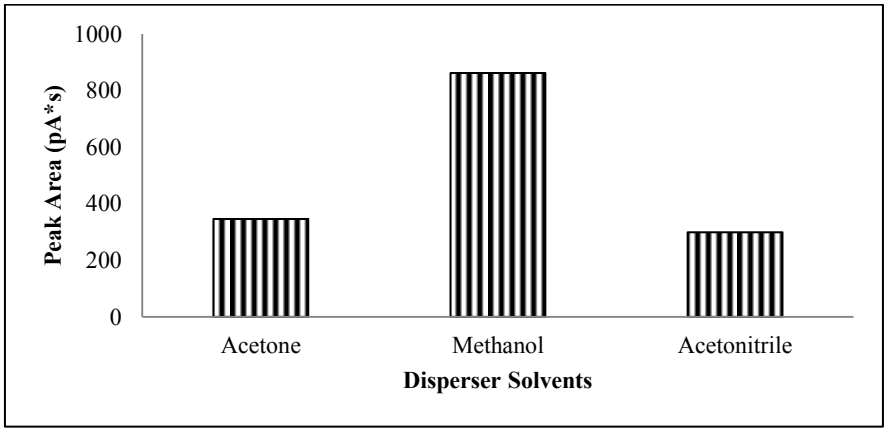



Figure 3. Effect of disperser solvent on extraction efficiency for DLLME-SFO of MP. Concentration of MP 3.00 µg/mL; volume of sample 5 mL (pH 6); volume extractant (*n*-hexadecane) 70 µL; volume disperser solvent 0.25 mL; extraction time 1 min; centrifugation 4000 rpm × 4 min; no salt added

**Effect of volume of extraction solvent**

To study the effect of extraction volume on extraction efficiency in DLLME-SFO method, different volumes of *n*-hexadecane (60, 70, and 80 µL) containing 0.25 mL method were tested. Based on the results in Figure 4, the extraction recoveries decreased when the volume of *n*-hexadecane increased to 80 µL. This is due to the increasing volume of floating phase, and hence lessen the concentration of MP in *n*-hexadecane (dilution factor occurred). Therefore, 70 µL of *n*-hexadecane was chosen as the optimum volume for extraction solvent.

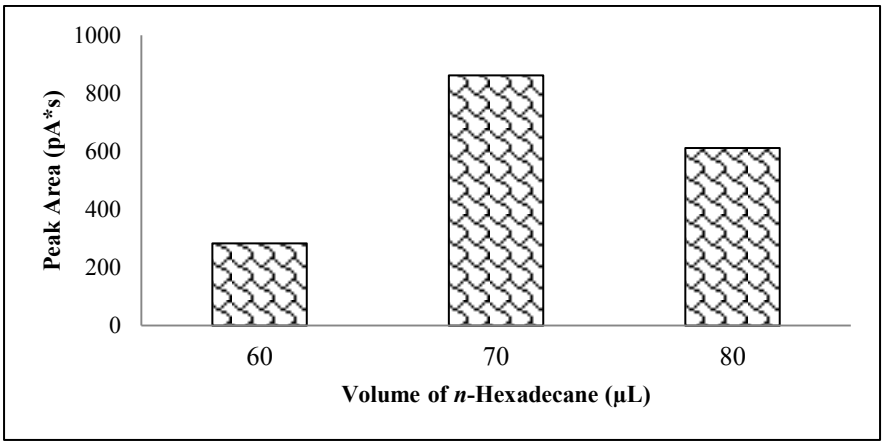



Figure 4. Effect of extraction solvent (*n*-hexadecane) volume for DLLME-SFO of MP. Concentration of MP 3.00 µg/mL; volume of sample 5 mL (pH 6); volume extractant (*n*-hexadecane) 60 - 80 µL; volume disperser solvent (methanol) 0.25 mL; extraction time 1 min; centrifugation 4000 rpm × 4 min; no salt added

**Effect of disperser solvent volume**

The volume of disperser solvent directly affects the formation of cloudy solution (sample solution/disperser solvent/extraction solvent), volume of floated phase, and the degree of dispersion of extraction in aqueous phase and subsequently the overall extraction efficiency. To study the effect of disperser solvent volume on the extraction efficiency in DLLME-SFO method, different volumes of methanol (0.15, 0.25 and 0.50 mL) containing 70 µL of *n*-hexadecane were tested. According to the results in Figure 5, recovery of the analyte increased with the increasing volume of methanol up to 0.25 mL. This may be due to the increasing interaction of MP in water with the increasing volume of methanol. On the other hand, with a large volume of methanol, the solubility of analytes in aqueous phase increased; thus decreased the extraction efficiency. Finally, 0.25 mL of methanol was selected as the volume of disperser solvent in subsequent experiments.

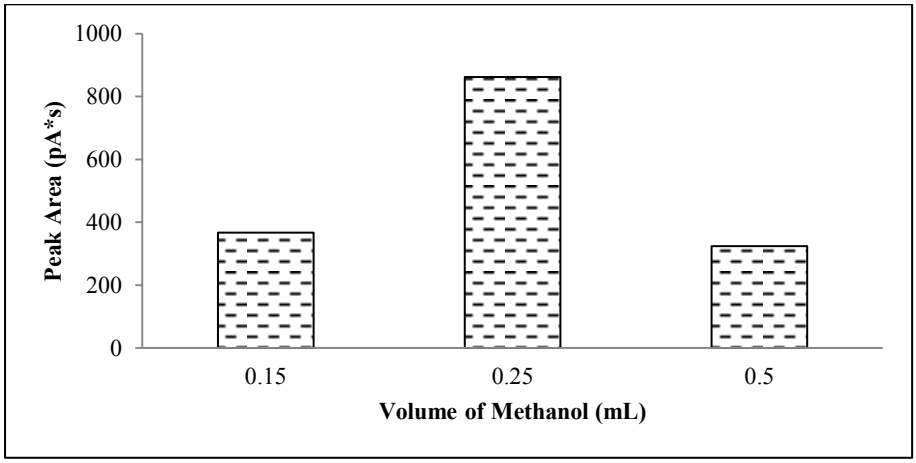



Figure 5. Effect of disperser solvent (methanol) volume for DLLME-SFO of MP. Concentration of MP 3.00 µg/mL; volume of sample 5 mL (pH 6); volume extractant (*n*-hexadecane) 70 µL; volume disperser solvent (methanol) 0.15 - 0.25 mL; extraction time 1 min; centrifugation 4000 rpm × 4 min; no salt added

**Effect of salt concentration**

The function of adding a salt (NaCl) into the sample solution is to increase its ionic strength, decrease the solubility of the analytes in the sample solution and enhance the extraction efficiency [22, 23]. The concentration of salt used in this study was varied between 0 and 8% (w/v) and the effect on the extraction efficiency was investigated. According to the results in Figure 6, the peak areas of MP started to increase with the increasing amount of the NaCl concentration from 0 to 4%. However, with the addition of NaCl to 6%, it shows a dramatic decrease in extraction efficiency and a slight decrease when 8% NaCl was added. This phenomenon can be described regarding the salting-out effect happened in DLLME-SFO. Upon the addition of more than 6% of NaCl, the transportation of the analyte to the extraction solvent is dropped due to the increase of sample viscosity. By increasing the salt concentration, the diffusion of analyte towards organic solvent becomes more difficult; thus, 4% of NaCl was used in next experiments.

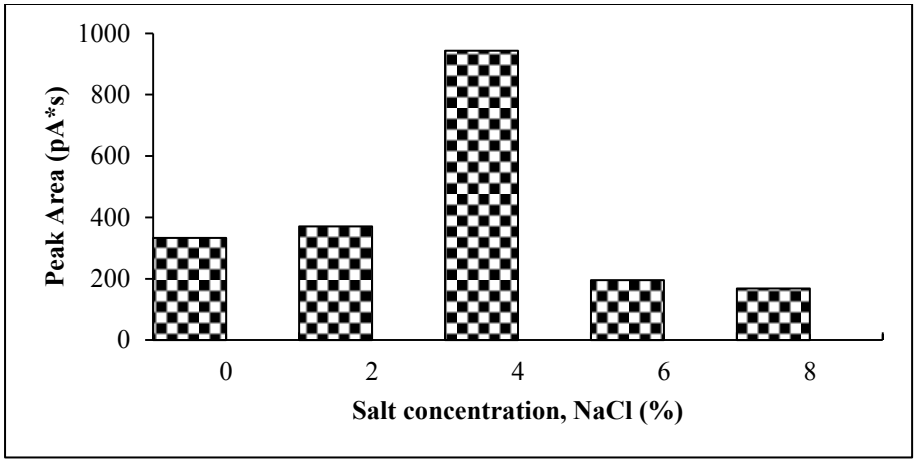



Figure 6. Effect of NaCl for DLLME-SFO of MP. Concentration of MP 3.00 µg/mL; volume of sample 5 mL (pH 6); volume extractant (*n*-hexadecane) 70 µL; volume disperser solvent (methanol) 0.15 - 0.25 mL; extraction time 1 min; centrifugation 4000 rpm × 4 min

**Effect of sample pH**

The pH values of samples can affect the ratio of ionic form to molecular form of the analytes, especially for the analytes which are weak acid or weak alkali. According to Soni et. al. [4], at higher pH values (≥ pH 8), methylparaben is in ionic form and the hydrolysis will occur and make it less to be extracted into organic solvent. Therefore, methylparaben should be extracted at pH values lower than its pKa value (methylparaben, pKa = 8.2) which is less than pH 8. Hence, the pH that was investigated in this study is in the range of 3–7 by adding appropriate sodium hydroxide or hydrochloric acid to the samples. The results illustrated in Figure 8 demonstrate that the optimum extraction efficiency of MP in DLLME-SFO was obtained at pH 6.0.

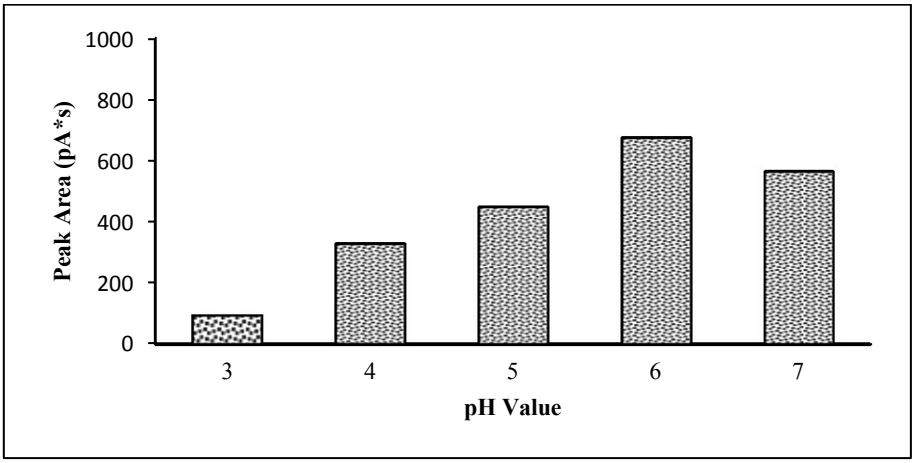



Figure 7. Effect of sample pH for DLLME-SFO of MP. Concentration of MP 3.00 µg/mL; volume of sample 5 mL (pH 6); volume extractant (*n*-hexadecane) 70 µL; volume disperser solvent (methanol) 0.25 mL; NaCl (w/v) 4%; extraction time 1 min; centrifugation 4000 rpm × 4 min

**Method validation and real sample analysis**

The optimized DLLME-SFO conditions which is 70 µL of *n*-hexadecane as extraction solvent, 0.25 mL of methanol as disperser solvent, 4% of NaCl, and pH 6 of sample solution was carried out for the extraction validation in the range of 0.1 – 8 µg/mL. The results showed good linearity and acceptable LODs as summarized in Table 2.

Table 2. Correlation coefficients, LOD and LOQ of samples using GC-FID for DLLME-SFO

| Paraben | Linear Range (µg/mL) | Correlation coefficients, $R^2$ | LOD (µg/mL) | LOQ (µg/mL) |
|---|---|---|---|---|
| Methylparaben | 0.1 – 8 | 0.9996 | 0.082 | 0.272 |

To investigate matrix effects and applicability of the technique on cosmetic samples, the final experiments were carried out on two different brands of sunblock labeled as Sample 1 and Sample 2. These samples were handled exactly according to the steps described in the sample preparation procedure and each sample was carried out with triplicate extraction. According to the chromatograms in Figure 8, MP was detected in both samples at the concentration of 0.06 µg/mL (Sample 1) and 0.42 µg/mL (Sample 2), respectively.

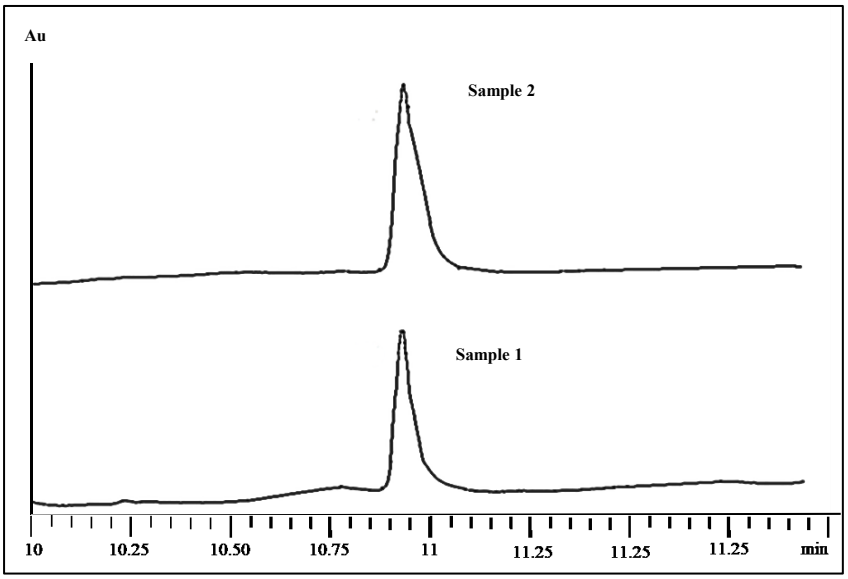



Figure 8. GC-FID chromatograms of DLLME-SFO extracts of Sample 1 and Sample 2

## Conclusion

This study has demonstrated the successful application of DLLME-SFO technique coupled with GC-FID for the determination of methylparaben in cosmetic samples. This method proved to have a high precision and requires a shorter extraction time with a low volume of the lower toxicity of extraction solvent. It is convinced that DLLME-SFO possesses a great potential in the rapid preconcentration of analyte and provides good linearity over the investigated concentration range. Since this is the first time we reported the application of DLLME-SFO in an analysis of methylparaben, with satisfactory results, the system could readily be applied to determine other parabens from different and complex sample matrices, using different analytical instruments. Combination with other microextraction techniques is suggested to enhance the extraction efficiency and sample preconcentration. In addition, simplicity, ease of operation and less consumption of organic solvents are the additional advantages of the method.

## Acknowledgement

The authors acknowledge the research grant IRAGS, provided by the MOHE (600-RMI/DANA 5/3/IRAGS(53/2015) and also Universiti Teknologi MARA for providing the facility.

**References**

1. Kang, S. H. and Kim, H. (1997). Simultaneous determination of methylparaben, propylparaben and thimerosal by high-performance liquid chromatography and electrochemical detection. *Journal of Pharmaceutical and Biomedical Analysis*, 15: 1359 – 1364.
2. Reisch, M. S. (2005). Keeping well-preserved: Cosmetic preservatives makers offer alternatives as widely used parabens come under scrutiny. *Chemical Engineering News*, 25 – 26.
3. Hirose, M., Tanaka, Y., Tamano, H., Tamano, S., Kato, T. and Shirai, T. (1998). Carcinogenicity of antioxidants BHA, caffeic acid, sesamol, 4-methoxyphenol and catechol at low doses, either alone or in combination, and modulation of their effects in a rat medium-term multi-organ carcinogenesis model. *Carcinogenesis*, 19: 207 – 212.
4. Soni, M. G., Burdock, G. A., Taylor, S. L. and Greenberg, N. A. (2002). Evaluation of the health aspects of methylparaben: A review of the published literature. *Food Chemical Toxicology*. 40: 1335 – 1373.
5. Alshana, U., Ertas, N. and Goger, N. G. (2015). Determination of parabens in human milk and other food samples by capillary electrophoresis after dispersive liquid-liquid microextraction with back-extraction. *Food Chemistry*, 181: 1 – 8.
6. Darbre, P. D., Aljarrah, A., Miller, W. R., Coldham, N. G., Sauer, M. J. and Pope, G. S. (2004). Concentrations of parabens in human breast tumours. *Journal of Applied Toxicology,* 24 (1): 5 – 13.
7. Canosa, P., Rodriguez, I., Rubi, E., Bollain, M. H. and Cela, R. (2006). Optimization of a solid-phase microextraction method for the determination of parabens in water samples at low ng per litre level. *Journal of Chromatography A*, 1124 (1-2): 3 – 10.
8. Darbre, P. D. and Harvey, P. W. (2008). Paraben esters: review of recent studies of endocrine toxicity, absorption, esterase and human exposure, and discussion of potential human health risks. *Journal of Applied Toxicology,* 28: 561 – 78.
9. Routledge, E. J., Parker, J., Odum, J., Ashby, J. and Sumpter, J. P. (1998). Some alkyl hydroxy benzoate preservatives (parabens) are estrogenic. *Toxicology and Applied Pharmacology*, 153: 12 – 19.
10. Cabaleiro, N., Calle, I., Bendicho, C. and Lavilla, I. (2014). An overview of sample preparation for the determination of parabens in cosmetics. *Trends in Analytical Chemistry*, 57: 34 – 46.
11. Salvador, A. and Chisvert, A. (2007). Analysis of cosmetic products, Elsevier, Netherlands.
12. Wang, P. and Liu, Y. (2007). Cosmetic preservatives and analysis methods used in China. *Journal of Environmental Health*, 24: 557 – 559.
13. Cabaleiro, N., Calle, I., Bendicho, C. and Lavilla, I. (2013). Current trends in liquid-liquid and solid-liquid extraction for cosmetic analysis: A review. *Analytical Methods*, 5: 323 – 340.
14. Cabaleiro, N., Calle, I., Bendicho, C. and Lavilla, I. (2013). Solid phase extraction and solid-phase microextraction in cosmetic analysis: A review. *Science Letter Journal*, 2: 1 – 21.
15. Malika, J. N. N., Thiruveengadarajan, V. S. and Gopinath, C. (2013). A review on various analytical method developments for the identification of methyl paraben present in cosmetics. *International Journal of Review in Life Sciences*, 3: 5 – 19.
16. Rezaee, M., Assadi, Y., Milani M. R., Hosseini, E., Aghaee, F., Ahmadi, S. and Berijani, S. (2006). Determination of organic compounds in water using dispersive liquid-liquid microextraction. *Journal of Chromatography A*, 1116: 1 – 9.
17. Berijani, S., Assaddi, Y., Anbia. M., Milani, M. R., Hosseini, E. and Aghaee, F. (2006). Dispersive liquid-liquid microextraction combines with gas chromatography-flame photometric detection. very simple, rapid, and sensitive method for the determination of organophosphorus pesticides in water. *Journal of Chromatography A*, 1123: 1 – 9.
18. Leong, M. I. and Huang, S. D. (2008). Dispersive liquid-liquid microextraction method based on solidification of floating organic drop combined with gas chromatography with electron capture or mass spectrometry detection. *Journal of Chromatography A*, 1211: 8 – 12.
19. Juybari, M. B., Mehdinia, A., Jabbari, A. and Yamini, Y. (2011). Dispersive liquid-liquid microextraction based on solidification of floating organic drop followed by gas chromatography-electron capture detector for determination of some pesticides in water samples. *Chromatography Research International*, 2011: 1 – 8.
20. Jamali, M. R., Rahimpour, S. and Rahnama, R. (2012). Determination of cobalt in natural water samples after separation and preconcentration by dispersive liquid-liquid microextraction based on the solidification of floating organic drop. *Applied Chemistry*, 23: 21 – 27.

21. Toraj, A-J., Nazir, F. and Mojtaba, S. (2014). Rapid extraction and determination of amphetamines in human urine samples using dispersive liquid-liquid microextraction and solidification of floating organic drop followed by high performance liquid chromatography. *Journal of Pharmaceutical and Biomedical Analysis*, 94: 145 – 151.
22. Vinas, P., Campillo, N. and Andruch, V. (2015). Recent achievements in solidified organic drop extraction. *Trends in Analytical Chemistry*, 68: 48 – 77.
23. Sanagi, M. M., Abbas, H. H., Ibrahim, W. A. W. and Aboul-Enien, H. Y. (2012). Dispersive liquid-liquid microextraction method based on solidification of floating organic droplet for the determination of triazine herbicides in water and sugarcane samples. *Food Chemistry*, 133: 557 – 562.

*Malaysian Journal of Analytical Sciences, Vol 21 No 6 (2017): 1299 - 1306*
*DOI: https://doi.org/10.17576/mjas-2017-2106-11*

MALAYSIAN JOURNAL OF ANALYTICAL SCIENCES
*Published by The Malaysian Analytical Sciences Society*
ISSN 1394 - 2506

# SENSORY EVALUATION AND QUANTITATIVE ANALYSIS OF MINERAL AND HEAVY METAL CONTENT OF PROTEIN SUPPLEMENT INCORPORATED WITH HERBAL EXTRACT

## (Penilaian Rasa dan Analisa Kuantitatif Kandungan Mineral dan Logam Berat bagi Makanan Tambahan Protin Digabungkan dengan Ekstrak Herba)

Noor Azwani Zainol[1]*, Nor Farahiyah Aman Nor[1], HarisunYa'akob[1,2], Siti Nor Azlina Abd Rashid[1], Siti Hajar Mat Sarip[1], Ramlan Aziz[1,2]

[1]*Institute of Bioproduct Development*
[2]*Faculty of Chemical Engineering*
*Universiti Teknologi Malaysia 81310 UTM Johor Bahru, Johor, Malaysia*

**Corresponding author: azwani@ibd.utm.my*

Received: 7 November 2016; Accepted: 18 September 2017

**Abstract**

Calories-dense products promote weight gain through its healthy ingredients. The incorporation of herbs increased the product's benefit with antioxidant, anti-cancer and anti-aging properties. In this study, the comparison between herbal and non-herbal (commercial products) protein supplements were determined. The sensory evaluation of the protein supplements were done via 9-point hedonic scale. The mineral contents and undesirable toxic metals in the the product were also analysed using Inductively Coupled Plasma-Mass Spectrometry (ICP-MS). The score of hedonic scale indicated that the sweetness and bitterness of the herbal protein supplement were significantly different compared to the commercial products. All samples showed differences in the mineral contents where the herbal protein supplement contributed the highest content of magnesium (Mg) 3643.7 µg/kg, sodium (Na) 8192.3µg/kg and ferum (Fe) 180.7 µg/kg. The ICP-MS analysis result showed traces of heavy metals (cadmium, arsenic, plumbum, mercury) were 1.10 µg/kg, 0.03 µg/kg, 3.00 µg/kg and 5.07 µg/kg, respectively. These results confirmed that the concentrations of heavy metals in the product has not exceeded the maximum standard limit of regulation in Malaysia for Cd (0.3 mg/kg), As (5 mg/kg), Pb (10 mg/kg), and Hg (0.5 mg/kg). Hence, the results might be useful to define the new formulations of these highly consumed protein supplement with health benefits for atheletes.

**Keywords**: protein supplement, mineral content, heavy metal content, hedonic scale

**Abstrak**

Produk-produk padat kalori menggalakkan penambahan berat melalui ramuan-ramuan sihatnya. Penambahan herba meningkatkan kebaikan produk seperti ciri-ciri antioksida, anti-kanser dan anti-penuaan. Di dalam kajian ini, perbandingan di antara makanan tambahan protein berherba dan tidak berherba (produk komersil) telah diperolehi. Ujian rasa terhadap makan tambahan protin ini telah dilakukan melalui 9-titik skala hedonik. Kandungan mineral dan logam toksik yang tidak dikehendaki di dalam produk turut dianalisa menggunakan Spektrometri Jisim-Plasma Ganding Secara Aruhan (ICP-MS). Skor skala hedonik menujukkan kemanisan dan kepahitan makanan tambahan berprotin berbeza secara ketara berbanding produk-produk komersil. Semua sampel menunjukkan perbezaan di dalam kandungan mineral, di mana makanan tambahan protin berherba menyumbang kandungan tertinggi untuk magnesium (Mg) 3643.7 µg/kg, sodium (Na) 8192.3 µg/kg dan ferum (Fe) 180.7 µg/kg. Analisa keputusan ICP-MS menunjukkan kandungan logam berat (kadmium, arsenik, plumbum, merkuri) adalah 1.10 µg/kg, 0.03 µg/kg, 3.00 µg/kg dan 5.07 µg/kg setiap satunya. Hasil ini mengesahkan kepekatan logam berat tidak melebihi piawaian kadar maksimum peraturan Malaysia untuk Cd(0.3 mg/kg), As (5 mg/kg), Pb(10 mg/kg), and Hg (0.5 mg/kg). Oleh itu, keputusan yang

diperolehi mungkin berguna untuk menterjemah formulasi-formulasi baru yang banyak digunakan bagi makanan tambahan protin yang bermanfaat kepada kesihatan untuk atlet.

**Kata kunci:** makanan tambahan protin, kandungan mineral, kandungan logam berat, skala hedonik

## Introduction

The Malaysian sports nutrition industry benefited a 2% value of compound annual growth rate (CAGR) in 2014. Sports nutrition products in Malaysia will continue to have a strong sales demand specifically for men [1]. The increasing number of sports nutrition outlets in major shopping malls will also facilitate sales growth of wide ranges of sports nutritions. Protein supplement, specifically protein shakes is one of the examples of a sport nutrition drink. The protein supplement is added to the diet, mainly as is it contain vitamins, minerals, amino acids, herbs or botanicals, metabolites/constituents/extracts or a combination of any of these ingredients [2]. Sportperson prefers protein supplement as it easy to be prepared as a drink. The protein supplement is also able to speed up the recovery of strained muscles. These features are particularly important for athletes, bodybuilders, or people who need to gain muscle mass and strength while losing fat [3, 4].

The main ingredients used in protein supplement are whey protein, branch chain amino acid (BCAA), sweeteners, creatine, and glutamine. Consuming whey protein is a healthy way to add more protein in the daily diet. The whey protein is a quality protein source; that is absorbed and utilized efficiently by the human body [5]. The whey protein can be digested quickly and performs rapid delivery of amino acid to muscle cell which serves as a building block to increased muscle growth [6]. Meanwhile, the use of beta-alanine is to promote delay in muscle fatigue after workout with regard to the increasing levels of carnosine in intra-muscular. For synergistic effect, creatine is added in order to increase muscle volume and promoting lean body mass as well as increased in post-workout recovery [7]. Apart from that, glutamine promotes durability when connected to high muscle usage [8]. The intake of glutamine allows a person to be actively involved in exercises in longer period and with less fatigue [9].

Currently, there are a lot of protein supplements available in the market which can be used as directed. However, a lot of protein supplements which are commercially available may contain andro-steroids and most of the products are high level in sugar content. Andro-supplements acts like a steroid once it is metabolized by the body and therefore can pose similar kinds of health risks as steroids. The andro-supplements claim to be converted into testosterone in the body to help improve muscle mass. However, in 2004, the U.S. Food and Drug Administration (FDA) declared the andro- supplements are illegal, citing safety concerns [10].

The incorporation of herbs in the formulation of protein supplement is targeted to support a healthy lifestyle while contributing to the growth and maintenance of lean muscle mass. By adding the herbs in the ingredient such as *Eurycoma longifolia* (TA*)* may give a significant effect to sportperson for a long-lasting endurance during performing activities. The *Tongkat Ali* itself can act naturally as andro-supplement, which helps to boost the energy and increases stamina during the workout and/or activity. In parallel, it also promotes wellness with reference to its chemical components which are rich in phytonutrients [11]. Simultaneously, *Tribulus terristeris* has been used to enhance overall health, support healthy libido function and amplify muscle tone [12]. The *Safed muesli (Chlorophytum borivilianum)* is used as an energy booster and generally strengthens body immune system. The addition of herbal extract is also ideal for those who is lacking in consuming vegetables due to rich in vitamins and mineral [13].

Minerals plays an important role to support the metabolism of all living creatures [14]. Mineral contents such as selenium, zinc and copper are essential to maintain the metabolism of the human body; the optimal function for cell growth, healing and the activity of many metabolic processes [15]. Meanwhile, heavy metals such as cadmium, arsenic, lead and mercury can lead to adverse effects, although they are only present in small quantity [16]. Regular consumption of protein supplement may contribute to an increase intake of both mineral and heavy metal contents by the human body [17]. Therefore, it is necessary to give a guideline of the average amount to be consumed safely by the consumers. Contamination of heavy metals in the supplements during preparation and/or the use of heavy metal in the supplements itself is increasing especially when dealing with plants [18, 19]. This contamination might

result in serious health hazards such as dysfunction of kidney and symptoms of chronic toxicity [20, 21] when over consumed.

The innovation of products with healthy ingredients of *Eurycoma longifolia*, *Tribulus terristris* and *Chlorophytum borivilianum* with less sugar content is highly favourable to the sports industry. With balanced combination of fats, proteins, carbohydrates and minerals content, it will help sport persons such as athletes, body builders, and gym-goers to increase muscle size in a healthier way. Since the incorporation of the herbs are relatively new in the market, this study would provides information on the safety guideline of protein supplements with focus on essential mineral content and evaluate the level of heavy metal in the protein supplement. Commercial products of protein supplements were also analysed for its mineral and heavy metal content for comparison. The sensory attributes such as bitterness, sweetness, aftertaste, appearance and overall acceptability were also identified for use in future product formulation.

## Materials and Methods

### Ingredients formulation

The guidelines for the ingredients for the initial product formulation as well as the method of preparation were obtained from a commercial protein supplement. The ingredients chosen for this research were focused on developing the best formulation, with less sugar content and high in essential mineral including protein content. The ingredients of the formulations were obtained from health store at Taman Universiti, Skudai, Johor. Three commercial products categorized as food supplement were purchased for comparison purposes and labeled as sample CML 1, CML 2 and CML 3.

### Preparation of formulated protein supplement

The main herbs used in this product were prepared as follows; *Tongkat Ali* powder were prepared from extracted root part using water with the ratio (1:8 w/v) and then spray dried using spray dryer (Gea Niro, Italy). The spray dried parameter used were as follows : air inlet temperature at 160 °C, feed temperature at 25 °C, air pressure at 17.91 psi and feed flow rate at 4.86 mL/min. The parameter used was at the optimum condition. All other ingredients which formulated were then mixed together using fine grinder until homogenized. The prepared sample were sealed, packed and stored at room temperature for further required test.

### Mineral content and heavy metal analysis: Digestion procedures

For the digestion of the samples, a representative of 0.5 – 1 gram of dry weight sample is digested with 1 mL of 60% analytical grade Nitric acid (Sigma Aldrich, Germany) and ultrapure water (Hitachi, Japan). The digestate was heated using a hot plate under boiling temperature until white vapour appeared. The sample was then diluted with ultrapure water until it reaches a 100-mL final volume. The sample is filtered using 0.25 nylon syringe filter and ready for Inductively Coupled Plasma-Mass Spectrometry (ICP-MS) injection.

For the precise quantification of heavy metal and mineral contents, calibration against synthetic standards was used before running the sample. 1000 µg/kg multi-element standard was used from Perkin Elmer standard solution and diluted to 10, 20, 30, 50 µg/kg and 25 µg/kg as Quality Control (dissolved with 1% nitric acid (Sigma Aldrich, Germany)) for mercury determination Gold (Au) standard solution was used with same concentrations. The data acquisition was done by ICP-MS Software (ELAN 6100, Perkin Elmer).

### ICP-MS instrumentation

The ICP-MS (ELAN 6100, Perkin Elmer) was used for heavy metal and mineral content analysis in the samples. The instrument was setup via an integrated all lines system including; 1000 Watts Inductively Couple plasma radio-frequency (ICP RF) Power. Other conditions were set as follows; plasma flow, auxiliary flow and nebulizer flow, at 15 L $min^{-1}$, 1.5 L $min^{-1}$ and 0.47 L $min^{-1}$, respectively. The samples were introduced after an initial delay of 25 seconds. Afterward, the samples were pumped at the rate of 10 rpm and 25 seconds rinse time. The concentrations were read within 5 seconds for each replicates and an instrument stabilization time of 15 seconds was allowed between the samples.

**Sensory analysis: Subjects**

Fifty subjects consisting of volunteers (comprising of 26 men and 24 women) from University Teknologi Malaysia (UTM) have taken part in the sensory evaluation session. They were led by an experienced facilitator and lasted for 10 minutes. They were given instructions and the objective of the sensory evaluation. The explanation included descriptions of the attributes and their implied acceptability in the two samples; commercial product (CML 1) and formulated protein supplement product (FMD 1). These protein supplements were purposely developed as to compare with the commercial samples.

The attributes generated from the participants included sweetness, bitterness, aftertaste, appearance and overall preference. All five sensory attributes were measured using the 9-point hedonic scale. The scale values ranged from 'Like extremely' to 'dislike extremely', corresponding to the highest and lowest scores of '9' to '1', respectively.

**Sample preparation for sensory evaluation**

Only one of the commercial products was chosen as a comparison with the formulated protein supplement product. The samples were labeled with 3-digit random number and samples were presented simultaneously. Purified water was used to clean the palate. The order of the presentation was balanced and randomised to eliminate contrasting effect and positional bias.

**Statistical analysis**

The sensory scores for the protein supplement were subjected to the analysis of variance (ANOVA) to determine if there were statistically significant ($P \leq 0.05$) preferences in sensory attributes [22]. Tukey's test was used to determine which of the formulation was higly preferred [23, 24].

## Results and Discussion

**Mineral and heavy metal content**

The results of mineral content and heavy metal analysis are presented in Table 1 and Table 2, respectively. Table 1 shows the mineral analysis of CML 1, CML 2, CML 3 and FMD 1. In general (Table 1) sodium and magnesium were the two major components presenet in all of the samples, and followed by ferum. The results obtained for sodium (8192.3 µg/kg), magnesium (3643.7 µg/kg) and ferum (180.7 µg/kg) for formulated protein supplement (FMD 1) were higher compared to the commercial products. Magnesium significantly contributed to the digestive and kidney health level while sodium is important as it isrelated to cardio activities [25]. Ferum is important for its protein transport activities specifically related to the circulatory of blood to the cells [26]. The results obtained from the formulated protein supplement showed a presence of 42.6 µg/kg of zinc, 23.6 µg/kg of manganese, 18.3 µg/kg of chromium, 16.9 µg/kg of copper and 2 µg/kg of selenium. These result was also comparable to the commercial products. Based on the ASEAN Guideline for herbal supplement, the daily dietary intake for adults are as follow; 350 mg of magnesium, 20 mg of ferum, 15 mg of zinc, 3.5 mg of manganese and selenium at 0.2 mg. All of these minerals play an important role in our body as it is related to bioavailability and physiological action where they act as a co-factor in metabolic processes [27].

Table 1. Mineral components of commercial and formulated protein supplement in µg/kg

| Minerals Contents | Protein Supplements | | | |
|---|---|---|---|---|
| | CML 1 | CML 2 | CML 3 | FMD 1 |
| Sodium | 953.3 | 1116.7 | 2645.9 | 8192.3 |
| Ferum | 74.4 | 134.6 | 106.7 | 180.7 |
| Magnesium | 1342.6 | 1378.2 | 2309.8 | 3643.7 |
| Selenium | 0.4 | 0.3 | 0.6 | 2.0 |
| Zinc | 52.6 | 36.0 | 63.8 | 42.6 |
| Manganese | 13.3 | 22.8 | 30.4 | 23.6 |

Table 2. Heavy metals of commercial products and herbal protein supplements in μg/kg

| Heavy Metal contents | Protein Supplements | | | |
|---|---|---|---|---|
| | CML 1 | CML 2 | CML 3 | FMD 1 |
| Plumbum | 2.42[a] | 1.49[a] | 5.87[ab] | 3.00[a] |
| Arsenic | 0.03[a] | 0.05[a] | 0.02[a] | 0.03[a] |
| Mercury | 5.12[a] | 4.80[a] | 5.01[a] | 5.07[a] |
| Cadmium | 0.56[a] | 1.00[ab] | 0.61[a] | 1.10[ab] |
| Chromium | 10.6[a] | 10.0[a] | 7.0[a] | 18.3[ab] |
| Cuprum | 11.2[a] | 15.2[a] | 20.4[ab] | 16.9[a] |

*Means in rows and columns with different superscripts differ ($p \leq 0.05$).

The results obtained in Table 2 refer to the presence of heavy metal content of all protein supplements. In general, mercury, plumbum, cadmium, and arsenic were detected in all samples; however, at a lower detection limit. Based on the National Pharmaceutical Control Bureau (Ministry of Health, Malaysia), the guideline for maximum level permitted for metal contaminant in food product, are as follow; mercury (≤ 0.5 ppm), cadmium (≤ 0.3 ppm), plumbum (≤ 10 ppm), arsenic (≤ 5.0 ppm), chromium (0.5 mg) and copper (2 mg). Plumbum (Pb), cadmium (Cd), arsenic (As) and mercury (Hg) are considered as toxic to human body, therefore, their daily intake via supplements has been restricted. Limitation of intakes of As, Cd, Hg, and Pb were assessed with respect to the safety levels described by various national and public health organizations [28].

**Acceptance of the formulation**

A sensory analysis was carried out at a lab-scale test to verify whether the addition of *Tongkat Ali* herbs would affect the acceptance of the product. In general protein supplement added with herbs was accepted as there is no significant difference compared to the commercial protein supplement where the score were 3.43 and 3.46, respectively as in Table 3. The sensory scores of sweetness, bitterness, aftertaste, appearance and overall acceptability assigned by the panellists were presented in Figure 1. It was observed that the sweetness, bitterness and appearance score were significantly different at ($p \leq 0.05$) as in Table 3. Meanwhile, it was observed that the aftertaste score was not significantly different at ($p \leq 0.05$). The sweetness of the protein supplement needs to be addressed since consumers tend to reduce food intake when they consumed high glucose products. Glucose in solution would be expected to pass rapidly to the small intestine and stimulate the satiety hormones including CCK [29] and polypeptide YY [30]. As a result, this may increase the possibilities of lacking other important nutrients which in turn might increase the risk to health problem. The aftertaste attributes is one of the important attributes as this will affect consumers to like or dislike the products. The component which could also contribute to bitter aftertaste are low-calorie products such as saccharin and acesulfame-K [31]. The low sensory score for the bitterness of the formulated protein supplement was probably because of *Tongkat Ali* powder extract added in the formulation. This bitter tastes in the protein supplement is probably mainly due to the eurycomanone compound in *Tongkat Ali*. Eurycomanone is one of the phytochemical compounds which can be found in *Tongkat Ali* extract and was identified as one type of quassiniods which responsible for the bitter taste [32].

Table 3. Mean sensory scores for protein supplements

| Sensory Attributes | Formulation | |
|---|---|---|
| | Commercial (CML 1) | Formulated (FMD 1) |
| Sweetness | 3.62[a] | 3.07[ab] |
| Bitterness | 3.00[a] | 3.43[ab] |
| Aftertaste | 3.87[a] | 3.67[a] |
| Appearance | 3.83[ab] | 4.03[ab] |
| Overall | 3.43[a] | 3.46[a] |

[ab] There are statistically significant preferences (P ≤0.05) of one sample over the other(s) with respect to the particular sensory attributes if values in the same row carry different superscripts; that is if calculated t-value > tabulated t-value.

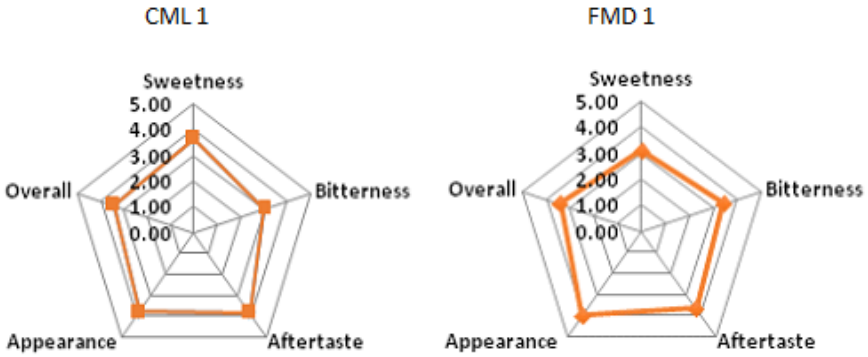



Figure 1. Comparison of sensory attributes for commercial (CML 1) and formulated (FMD 1) product of protein supplements

## Conclusion

Based on the overall results, incorporation of herbal powder significantly affected the bitterness and sweetness of protein supplement products. The addition of herbs in the protein supplement is also important as it increased the mineral intake which is good to promote a healthy diet. Based on the result obtained, protein supplement added with *Tongkat Ali* satisfactorily contribute to nutritional values if compared to other products available in the market. Since there is no significant difference between commercial and formulated product in overall acceptability of the products, it may be concluded that this formulated product may have the potential to be commercial.

## Acknowledgement

The authors sincerely acknowledge the support provided by Platinum Company Sdn. Bhd. and Institute Bioproduct Development, (IBD), UTM, Malaysia for the technical assistance.

## References

1. Euromonitor. (2006). Sports nutrition in Malaysia. Retrieved from www.utm.my/psz\ on 14 January 2017.
2. Barnes, J. (2003). Efficacy and safety of complementary medicines: Fashions, facts and the future. Part 1. Regulation and quality*, British Journal of Clinical Pharmacology, 55*: 226 – 233.
3. Ohtani, M., Sugita, M. and Maruyama, K. (2006). Amino acid mixture improves training efficiency in athletes. *Journal of Nutrition*, 136: 538 – 543S.

4. Sugita, M., Ohtani, M., Ishii, N., Maruyama, K. and Kobayashi K. (2003). Effect of a selected amino acid mixture on the recovery from muscle fatigue during and after eccentric contraction exercise training. *Bioscience, Biotechnology and Biochemistry*, 67: 372 – 375
5. World Health Organization (2004). *WHO traditional medicine strategy 2002–2005*; WHO: Geneva, Switzerland.
6. Carol B. (2010). Whey protein: A functional food. *The Nutrition Practitioner,* 1-8.
7. Haussinger, D., Lang, F. and Gerok, W. (1994). Regulation of cell function by the cellular hydration state. *American Journal of Physiology*, 267: 343 – 355.
8. Newsholme, E. A. (2001). Why is L-glutamine metabolism important to cells of the immune 55 system in health, post-injury, surgery, or infection. *Journal of Nutrition*, 131: 2515 – 2522.
9. Antonio, J. and Street, C. (1999). Glutamine: A potentially useful supplement for athletes. *Canadian Journal of Applied Physiology*, 24(1): 1 – 14.
10. Food and Drug Administration (2009). Public health advisory: the FDA recommends that consumers should not use body building products marketed as containing steroids or steroid-like substances. Retrieved from http://www.fda.gov/Drugs/DrugSafety on 17 January 2017.
11. Marshall, K. (2004). Therapeutic applications of whey protein. *Alternative Medicine Review,* 9(2): 136 – 156.
12. Islam, M. S., Ali, S., Rahman, M., Islam, R., Ali, A., Azad, A. K. and Islam, M. R. (2011). Antidiabetic, cytotoxic activities and phytochemical screening of *Peltophorum pterocarpum* (DC) K. Heyne root. *Journal of Medicinal Plants Research*, 5(16): 3745 – 3750.
13. Pokrywka, A., Obminski, Z., Fijalek, Z., Turek-Lepa, E., Grucza, R. and Malczewska L. (2014). Insights into supplements with *Tribulus terrestris* used by Athletes.
14. Vibhute, B. P., Bhide, D. R., Karadbhajne, V. Y., Kulkarni, A. S. and Khotpal, R. R. (2013). Fatty acid profile of pumpkin and bael seed lipids of Central India Region. *Research and Reviews Journal of Botanical Sciences*, 2(2): 1 – 3.
15. Stitch, S. R. (1957). Trace elements in human tissue. 1. A semi-quantitative spectrographic survey. *Biochemical Journal,* 67: 97 – 103.
16. Ajasa, M. A., Bello, O. M., Ibrahim, O. M., Ogunwande, A. I. and Olawore, O. N. (2004). Heavy metals and macronutrients status in herbal plants of Nigeria. *Food Chemistry.,* 85: 67 – 71.
17. Gosslim, R. E., Smith, R. P., Hodge, H. C. and Braddock, J. E. (1984). *Clinical Toxicology of Commercial Products*, 5th edition; Willians & Wilkins: Baltimore, MD, USA, pp. 437.
18. Schilcher, H. (1987). Possibilities and limitations of phytotherapy. *Pharmaceutish Weekblad – Scientific Edition,* 9(4): 215.
19. Andrew, A. S., Warren, A. J., Barchowsky, A., Temple, K. A., Klei, L., Soucy, N. V., O'Hara, K. A. and Hamilton, J. W. (2003). Genomic and proteomic profiling of responses to toxic metals in human lung cells. *Environmental Health Perspective*, 111: 825 – 835.
20. Shaw, D. Leon, C. Kolev, S. and Murray, V. (1997). Traditional remedies and food supplements. A 5-year toxicological study (1991–1995). *Drug Safety,* 17: 342 – 356.
21. Kreider R. (1999). Dietary supplements and the promotion of muscle growth with resistance exercise. *Sports Medicine*, 27: 97 – 110.
22. Macfie, H. J., Bratchell, N., Grenhoff, K. and Valis, L.V. (1989). Designs to balance the effect of order of presentation and first-order carry-over in hall tests. *Journal of Sensory Studies*, 4: 129 – 132.
23. Kramer, A. and Twigg, B. A. (1970). Quality control for the food industry (3rd Edition). Westport: AVI Publishing Company Incorporation.
24. Larmond, E. (1977). Laboratory methods for sensory evaluation of food. Canadian Government Publishing Centre.
25. Soetan, O. K, Olaiya, C. O and Oyewole O. E. (2010). The importance of mineral elements for humans, domestic animals and plant: A review. *African Journal of Food Science*, 4(5): 200 – 222.
26. National Academy Press. (2001). Institute of Medicine. iron. In: dietary reference intakes for vitamin a, vitamin k, arsenic, boron, chromium, copper, iodine, iron, manganese, molybdenum, nickel, silicon, vanadium, and zinc; pp. 290 – 393.
27. Hathcock, J. N. (2004). Vitamin and mineral safety, 2nd (Edition). Council for responsible nutrition. Washington. pp 169.

28. Bharathi, A., Yan-Hong, W., Duzgoren-Aydin, N. S. and Khan, I. A. (2011). Inorganic elemental compositions of commercial multivitamin/mineral dietary supplements: Application of collision/reaction cell inductively coupled-mass spectroscopy. *Food Chemistry*, 127: 54 – 62.
29. Hall, W. L., Millward, D. J., Long, S. J. and Morgan, L. M. (2003). Casein and whey exert different effects on plasma amino acid profiles, gastrointestinal hormone secretion and appetite. *British Journal of Nutrition*, 89: 239 – 248.
30. Batterham, R. L., Heffron, H., Kapoor, S., Chivers J. E., Chandarana, K. and Herzog, H. (2006). Critical role for peptide YY in protein-mediated satiation and body-weight regulation. *Cell Metabolism*, 4: 223 – 233
31. Kuhn, C., Bufe, B., Winnig, M., Hofmann, T., Frank, O., Behrens, M., Lewtschenko, T., Slack, J. P., Ward, C. D. and Meyerhof, W. (2004). Bitter taste receptors for saccharin and acesulfame-K. *Journal of Neuroscience,* 24(45): 10260 – 10265.
32. Low, B. S., Choi, S. B., Abdul Wahab, H., Das, P. K. and Chan, K. L (2013). Eurycomanone, the major quassinoid in *Eurycoma longifolia* root extract increases spermatogenesis by inhibiting the activity of phosphodiesterase and aromatase in steroidogenesis. *Journal of Ethnopharmacology,* 149(1): 201 – 207.

*Malaysian Journal of Analytical Sciences, Vol 21 No 6 (2017): 1307 - 1315*
*DOI: https://doi.org/10.17576/mjas-2017-2106-12*

MALAYSIAN JOURNAL OF ANALYTICAL SCIENCES
*Published by The Malaysian Analytical Sciences Society*
ISSN 1394 - 2506

# MOLECULARLY IMPRINTED $TIO_2$ INORGANIC FILM AND PVDF/$TIO_2$ COMPOSITE FILM AS SENSORS FOR THE DETECTION OF CHEMICAL THREAT AGENTS USING QUARTZ CRYSTAL MICROBALANCE

## ($TiO_2$ Filem Tak Organik dan Filem Komposit PVDF/$TiO_2$ Molekul Tercetak sebagai Sensor untuk Mengesan Agen Kimia Berbahaya Menggunakan Penimbang Mikro Kristal Kuarza)

Xuan Hao Lin[1], Kah Sing Chooi[1], Sam Fong Yau Li[1, 2]*

[1]*Department of Chemistry,*
*National University of Singapore, 3 Science Drive 3, Singapore 117543, Singapore*
[2]*NUS Environmental Research Institute (NERI),*
*#02-01, T-Lab Building (TL), 5A Engineering Drive 1, Singapore 117411, Singapore*

**Corresponding author: chmlifys@nus.edu.sg*

Received: 7 November 2016; Accepted: 18 September 2017

**Abstract**

In this paper, we report molecularly imprinted $TiO_2$ inorganic film ($MITiO_2$) and PVDF/$TiO_2$ composite film ($MIPTiO_2$) as sensors for the detection of parathion methyl (PTM), a simulant of chemical threat agent (CTA) using quartz crystal microbalance (QCM). PTM was used as a molecular template for the imprinting of the sensor film. The $MITiO_2$ showed a greater response ($\Delta f$ 19 Hz) to 9.88 μM of PTM than that ($\Delta f$ 2 Hz) of the $MIPTiO_2$. The ratios of $TiO_2$/template and PVDF/$TiO_2$/template were optimized. Time for the UV degradation of the template was also optimized. $MITiO_2$ sensor shows good potential for the detection of CTA, other chemical and biochemical pollutants.

**Keywords**: molecularly imprinted polymer, quartz crystal microbalance, sensor, $TiO_2$, parathion methyl

**Abstrak**

Dalam kajian ini, kami melaporkan $TiO_2$ filem tak organik ($MITiO_2$) dan filem komposit PVDF/$TiO_2$ ($MIPTiO_2$) molekul tercetak sebagai sensor untuk mengesan paration metil (PTM), yang merupakan ejen bahan kimia berbahaya (CTA) menggunakan penimbang mikro kristal kuarza (QCM). PTM telah digunakan sebagai templat molekul untuk peneraan filem sensor. $MITiO_2$ menunjukkan tindak balas yang lebih besar ($\Delta f$ = 19 Hz) pada kepekatan 9.88 μM daripada PTM berbanding $MIPTiO_2$ ($\Delta f$ = 2 Hz). Nisbah $TiO_2$/templat dan PVDF/$TiO_2$/templat telah dioptimumkan. Masa untuk degradasi UV bagi templat juga telah dioptimumkan. Sensor $MITiO_2$ menunjukkan potensi yang baik untuk mengesan CTA, serta bahan kimia yang lain dan bahan pencemar biokimia.

**Kata kunci**: polimer molekul tercetak, penimbang mikro kristal kuarza, sensor, $TiO_2$, paration metil

## Introduction

Chemical threat agents (CTA) are toxic synthetic chemicals that can be dispersed in various forms like gas, liquid, aerosol or adsorbed to solid particles [1]. CTA were deployed in war to kill or incapacitate the enemy. Nerve agents are among the most potent of all reported CTA. Nerve agents like Sarin, Tabun and Soman act as inhibitor irreversibly binding to the enzyme acetylcholinestearase, an enzyme that normally destroys and stops acetylcholine, a neurotransmitter. Inhibition of the enzyme would lead to an accumulation of acetylcholine, producing a perpetual

excited state in the nerve (e.g. constant muscle contraction) [2]. The critical effects of this would be the paralysis of the respiratory muscles and inhibition of the respiratory centre in the central nervous system, leading to death of the victim by asphyxiation within minutes [3]. Due to their high toxicity, imperceptibility to senses and rapid action, administration of antidote to victims exposed to such chemicals were often carried out too late. In addition, these CTAs are potential weapons of choice for terrorist organizations that could threaten national security [4]. Thus, there is a need for a highly sensitive and selective sensor to be developed for the detection of such CTAs as a preventive measure.

Various analytical methods had been used in the military and civil agencies for the detection of CTA such as liquid chromatography and gas chromatography [5, 6]. Although these methods are advantageous in terms of having a low limit of detection, they are usually not selective. One selective new method is based on molecular imprinting polymers (MIPs). MIP polymers are synthesized when monomers are polymerized in the presence of template molecules (Figure 1). The functional groups in the monomers would orient toward their counteracting functional groups in the template via forces of interactions like hydrogen bonding, van der Waals interaction and dipole-dipole interactions etc. [7]. Subsequent cross-linking of the polymer would hold the template molecule in place. Upon removal of the template molecules, the remaining cavities that retained the molecular configuration of the template would act as highly specific molecular recognition sites [8].

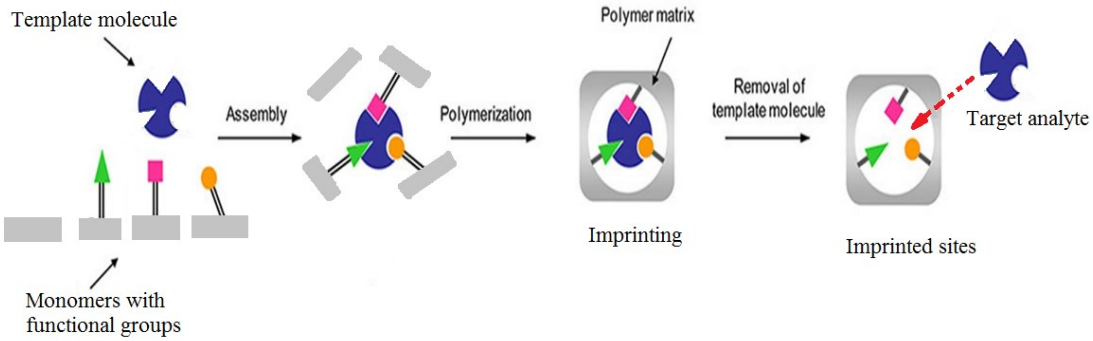



Figure 1. Illustrative formation of molecularly imprinted polymer sensor

A MIP sensor on gold coated AT cut quartz could be coupled with mass sensitive devices such as QCM for the detection of target analyte molecules. A QCM flow cell consists of two electrodes where the MIP sensor sits in between. Resonance frequency of the quartz based sensor with applied voltage is sensitive to mass change. Binding of target analyte molecules onto the molecular cavities on the MIP would lead to an increase in mass which is reflected by a proportional drop in its resonance frequency [9,10,11]. The relationship between change of resonance frequency and change of mass for a QCM sensor could be described by the Sauerbrey equation (eq. 1):

$$\Delta f = -\frac{2f_0^2}{A\sqrt{\rho_q \mu_q}}\Delta m \quad (1)$$

where $\Delta f$ is the frequency change (Hz), $f_0$ is the resonant frequency (Hz), $\Delta m$ is the mass change (g), A is the coated area ($cm^2$), $\rho_q$ is the density of quartz ($g/cm^3$), $\mu_q$ is the shear modulus of quartz ($g/cm\ s^2$).

Hydrophobic PVDF (-($CH_2CF_2$)-) has high affinity to hydrophobic analyte molecules. The polarity of PVDF enables dipole-dipole interaction in addition of Van der Waals interaction with the template molecule. These characteristics, in addition to its chemical and thermal stability, enable PVDF a suitable candidate as the polymer of MIP. PVDF has high affinity to hydrophobic molecules but low affinity to hydrophilic molecules. Therefore, it will be good to include some hydrophilic materials into PVDF so that the final composite sensor could be optimized to bind to both hydrophobic and hydrophilic molecules. $TiO_2$ particles with enriched surface hydroxyl groups could

bind to hydrophilic molecules. In addition, with UV irradiation it could photocatalytically degrade template and analyte molecules which facilitate the template removal and cleaning after analysis. $TiO_2$ particles could be prepared from titanium butoxide ($Ti(OBu)_4$). Upon exposure to moisture, $Ti(OBu)_4$ rapidly undergoes hydrolysis to form $TiO_2$ nano crystals. When $Ti(OBu)_4$ was used alone the rapid formation of the $TiO_2$ particles neighboured the template molecules enabled specific recognition sites to be formed on the MIP [12]. PTM, commonly found in pesticides, was chosen as the template due to its lower toxicity than real CTAs and structure similarity to organophosphorous CTAs like sarin (Figure 2).

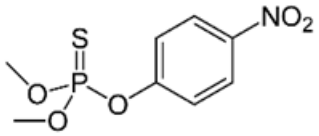



Figure 2. Molecular structure of parathion methyl

Template removal to form MIP is one of the critical and difficult steps. Extra chemicals introduced for template removal may destroy the newly formed molecular cavities. Without extra chemicals introduced, photodegradation have advantages in keeping the molecular cavities not touched with other chemicals during template removal. PTM has been reported to undergo photolysis in the presence of sunlight or more specifically, ultraviolet (UV) light [13]. In addition, metal oxides like titanium dioxide ($TiO_2$) that exhibits high photocatalytic activity have been shown to be able to decompose CTA simulants completely into inorganic products under UV light [14]. Upon absorption of UV light, positively charged holes and negatively charged electrons are generated and these two species can then initiate redox reactions via the generation of reactive species like hydroxyl radicals and superoxides [15]. Therefore, either alone or together with PVDF, photocatalytically active $TiO_2$ could assist the template removal during MIP preparation and sensor post-cleaning after analysis. Here we report molecularly imprinted $TiO_2$ inorganic film and PVDF/$TiO_2$ composite film as sensors for the detection of PTM using QCM. Removal of template molecules was completed through their photocatalytic degradation by the surrounding $TiO_2$ particles under UV irradiation.

## Materials and Methods

### Materials

Polyvinylidene difluoride powder (M.P. 155 – 160 °C) was from Alfa Aesar (Ward Hill, MA). Titanium(IV) butoxide ($Ti(OBu)_4$, reagent grade 97%) was from Sigma Aldrich (St. Louis, MO, USA). Parathion-methyl ($C_{10}H_{14}NO_5PS$, 99.5%) was from Chem Service Inc. (West Chester, PA, USA). N,N-dimethylformamide ($C_3H_7NO$, reagent grade 99.5%) was from Merck (Darmstadt, FR, Germany). Tetrahydrofuran ($C_4H_8O$, reagent grade 99.7%) was from VWR International (Singapore). $TiO_2$ nanoparticles (12 nm) were synthesized according our previously reported sol-gel method from the hydrolysis of $TiOSO_4$ in an alcohol and water mixture [16].

### Preparation of molecularly imprinted PVDF/$TiO_2$ composite sensor (MIP$TiO_2$)

A certain quantity of PVDF powder and PTM were dissolved in DMF. And then $TiO_2$ particles were dispersed into the transparent PVDF/PTM/DMF solution with 10 minutes of sonication. Mass ratios of PVDF, $TiO_2$ nanoparticles and PTM in the ad-mixture were 5:5:1, 2:2:1 and 1:1:1 respectively for different sensors. 20 µL of the ad-mixture was applied onto the gold coated surface of the AT cut quartz crystal chip. After dry at room temperature, the chip was wetted by 700 ppm of potassium bromate aqueous solution and irradiated with monochromatic 365 nm UV light (100 W, mercury lamp, 18 mW/cm$^2$) for a certain period of time for the template degradation. The photocatalytic degradation of parathion methyl was reported before [17, 18]. After template removal the sensor was rinsed with DI water for several times before use.

### Preparation of molecularly imprinted $TiO_2$ film sensor (MI$TiO_2$)

$Ti(OBu)_4$ was used for the preparation of MI$TiO_2$. Due to $Ti(OBu)_4$ sensitive to moisture in air, it was necessary to avoid prolonged exposure of $Ti(OBu)_4$ to the air during the preparation procedures. The reaction vials to be used were first blown with nitrogen gas for 3 minutes to dispel adsorbed moisture on the wall. Then a certain quantity of

$Ti(OBu)_4$ was added into one of the vials and rapidly capped to avoid substantial entry of moisture. THF was then added to the $Ti(OBu)_4$ and the vial was sonicated for 5 minutes to obtain a homogenous solution. Similar procedure was applied when preparing a PTM/THF solution. Then PTM/THF solution was added into $Ti(OBu)_4$/THF solution and mixed well. Subsequently, the mixture was topped up with THF such that the ratio of the total mass (g) of $TiO_2$ and PTM to volume (mL) of THF was 3/1000. Different molar ratios of $TiO_2$/PTM 10:1, 5:1, 2:1 and 1:1 were used to prepare different sensors. The final solution mixture was further sonicated for 5 minutes. 20 μL of the ad-mixture was placed onto the gold surface of quartz chip. When exposure to air, $Ti(OBu)_4$ hydrolyzed to form $TiO_2$ nanocrystallines wrapping PTM template molecules. $Ti(OBu)_4$ hydrolysis process was completed at room temperature after overnight. After complete hydrolysis, the chip was wetted by DI water and irradiated with monochromatic 365 nm UV light (100 W, mercury lamp, 18 $mW/cm^2$) for a certain period of time for the template degradation. Once template molecules were removed, the sensor was rinsed with DI water for a few times and then was ready for use.

**Preparation of non-imprinted polymers (NIP)**

NIPs of PVDF/$TiO_2$ composite and pure $TiO_2$ were prepared using similar procedures but without including template PTM molecules. They were named as PVDF/$TiO_2$ NIP and $TiO_2$ NIP, respectively.

**Evaluation of sensors**

Evaluation of the sensors were conducted using a Q-Sense E4 QCM Analyzer (Biolin Scientific) consisting of a QE 401 Electronics Unit, a QCP 401 Chamber Platform and 4 QFM 401 Flow Modules. The MIP$TiO_2$ and MI$TiO_2$ sensor chips were mounted onto the flow modules and fitted onto the platform in the temperature-controlled chamber with the liquid inlet and outlet tubes connected. The resonance frequencies of the sensor chips were first measured to ensure that with the thickness of the MIP films their resonance frequencies were still within the detection range of QCM. With the chamber's temperature maintained at room temperature (25°C), the liquid flow was started. Deionized water was first introduced into the flow module at 50 μL/min for 5 minutes before increasing to 100 μL/min. Measurement of the frequency change was then started. DI water flow was continued until the frequency has stabilized before PTM analyte solution was introduced. The flow of analyte solution was continued from for about 1.5 hours until the resonance frequency has stabilized before switching to DI water rinsing for 30 minutes. The frequency change was taken at the $70^{th}$ minute after analyte introduction.

## Results and Discussion

**Template removal**

When $TiO_2$ is activated by UV light, holes ($h^+$) are formed in the valence band and electrons ($e^-$) in the conduction band of $TiO_2$. Photogenerated holes and electrons further react with water and oxygen to produce hydroxyl and superoxide radicals. The photocatalytic degradation of PTM was reported before [17, 18]. PTM reacted with hydroxyl radicals to produce paraoxon methyl, which further reacted with hydroxyl radicals to generate p-nitrophenol, hydroquinone, carboxylic acids and other intermediates to final $CO_2$ gas and phosphate ions. To enhance photocatalytic degradation of PTM, electron acceptor bromate was added as an additive. Electron acceptors like $BrO_3^-$ ions removed photogenerated electrons from the conduction band resulting in better electron-hole separation and so photocatalytic efficiency (equation 2) [15]:

$$BrO_3^- + 2H^+ + 2e^- \rightarrow BrO_2\cdot + H_2O \quad (2)$$

Based on previous reports, $TiO_2$ UV photocatalytic degradation of organophosphorous compounds like PTM and diethylphosphoramidate was carried out in the presence of suspended $TiO_2$ particles in an aqueous solution and the time taken for complete photodegradation of these molecules required at least a few hours [14, 18].

**Non-imprinted polymers (NIP)**

PVDF/$TiO_2$ NIP and $TiO_2$ NIP showed some baseline response to 9.88 μM of PTM solution. Mass ratio 1/1 of PVDF/$TiO_2$ was used for the PVDF/$TiO_2$ NIP. Their resonance frequency changes are listed in Table 1. $TiO_2$ NIP had a frequency change of 4.0 Hz, which was lower than that (8.0 Hz) of PVDF/$TiO_2$ NIP although both were low enough as background baseline. Lower NIP response was preferred because lower baseline could enhance detection sensitivity.

Table 1. Response of PVDF/$TiO_2$ NIP and $TiO_2$ NIP to 9.88 μM of PTM solution

| Name of NIPs | Frequency Changes Δf (Hz) |
|---|---|
| PVDF/$TiO_2$* | 8.0 |
| $TiO_2$ | 4.0 |

* Mass ratio of PVDF to $TiO_2$ was 1/1

**MIP$TiO_2$ sensor**

Figure 3 shows the changes of resonance frequency (Δf) of MIP$TiO_2$ sensors with different ratios of PVDF/$TiO_2$/PTM responding to 9.88 μM of PTM aqueous solution before and after template removal. Before template removal MIP$TiO_2$ sensor with 1/1/1 ratio of PVDF/$TiO_2$/PTM in the preparation as-mixture had higher response to PTM than the other two sensors with lower PTM percentage, which could be due to the interactions between template PTM molecules and analyte PTM molecules. However, after template removal by UV irradiation, responses of all the three sensors greatly decreased which could be attributed to two reasons. The first reason was that after UV irradiation, $TiO_2$ may exhibit both natural and permanent superhydrophilicity [19 – 21]. Natural superhydrophilicity was reversible and mainly induced by heating effect of UV light, which dispelled some moisture molecules from $TiO_2$ surface and then the leftover hydrogen bonded moisture molecules spread out thermodynamically to compensate the decrease of surface tension due to the partial loss of water molecules. Permanent superhydrophilicity based on natural superhydrophilicity was mainly attributed to the stabilization layer such as outer $SiO_2$ layer [21] or the PVDF layer in our case to stabilize surface hydroxyl groups. The second reason could be attributed to the appearance of some hydrophilic functional groups on the surface of PVDF after UV irradiation with the existence of $TiO_2$ [22, 23]. Therefore, after template removal by UV irradiation, the sensor surface was highly likely very hydrophilic and so have very weak interaction with hydrophobic PTM molecules, resulting in low response to PTM.

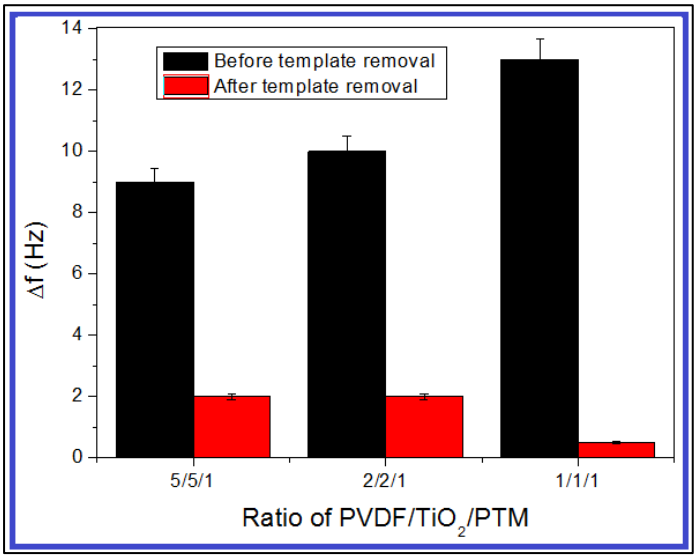



Figure 3. Changes of resonance frequency (Δf) of MIP$TiO_2$ sensors with different ratios of PVDF/$TiO_2$/PTM responding to 9.88 μM of PTM aqueous solution before and after template removal

**$MITiO_2$ sensors**

Figure 4 shows that $MITiO_2$ sensor with $TiO_2$/PTM ratio of 10/1 after template removal had an Δf value of 11.0 Hz responding to 9.88 μM of PTM solution, which was higher than the 4.0 Hz of $TiO_2$ NIP. This demonstrated that PTM molecular cavities were likely imprinted in the $MITiO_2$ sensor. Figure 5 shows the changes of resonance frequency (Δf) of $MITiO_2$ sensors with different ratios of $TiO_2$/PTM responding to 9.88 μM of PTM solution before and after template removal. After template removal, $MiTiO_2$ sensors had higher response to PTM than those before template removal. When ratio of $TiO_2$/PTM was 5/1, the $MITiO_2$ sensor reached the highest response to PTM. When the percentage of template molecules in the preparation ad-mixture was too high, the formed $TiO_2$ film after template removal could easily collapse due to insufficient $TiO_2$ quantity in the film.

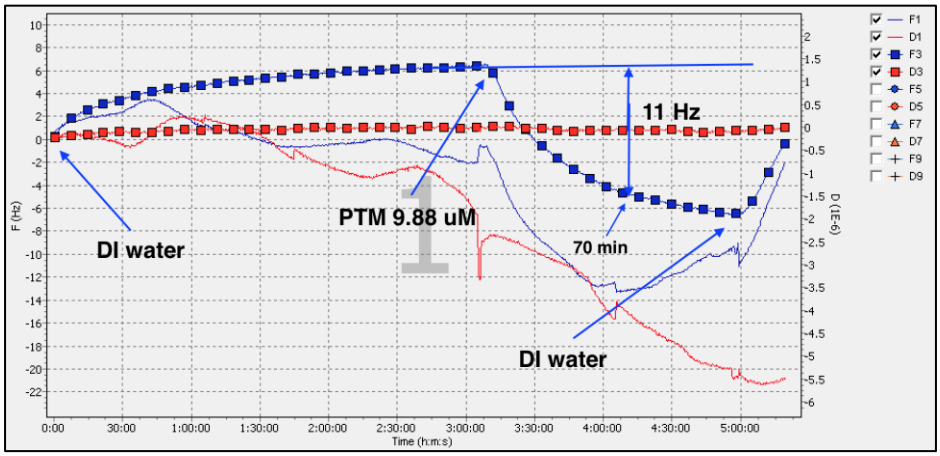



Figure 4. Change of resonance frequency (3rd overtone, i.e. the blue line with squares) of a $MITiO_2$ sensor after template removal; $TiO_2$: PTM = 10:1. The 1st fundamental frequency (the blue line without squares) was not stable and so could be ignored. Red lines were changes of resonance dissipation that were not discussed here.

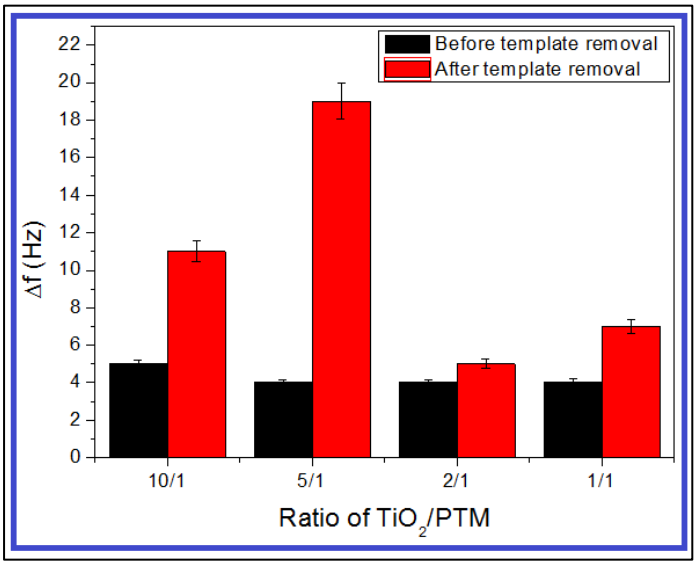



Figure 5. Changes of resonance frequency (Δf) of $MITiO_2$ sensors with different ratios of $TiO_2$/PTM responding to 9.88 μM of PTM solution before and after template removal by UV irradiation for 18 h

Figure 6 shows the changes of resonance frequency (Δf) of $MITiO_2$ sensor with 5/1 ratio of $TiO_2$/PTM with different UV irradiation time during template removal corresponding to 9.88 μM of PTM solution. With longer UV irradiation up to 36 hours, the sensor' response to PTM became weaker than that with only 18 hours of UV exposure. Superhydrophilicity of $TiO_2$ after UV exposure may explain this phenomenon. With 18 hours of UV irradiation, the superhydrophilicity of $TiO_2$ surface may reach a certain level but still could interact with hydrophobic PTM analyte molecules [19 – 21]. With further UV irradiation to 36 hours, the superhydrophilicity of $TiO_2$ surface continuously enhanced to a high level so that hydrophobic PTM analyte molecules had very weak interactions with $TiO_2$, resulting in poor response. Figure 7 further shows that $MITiO_2$ sensor had much higher response to PTM than non-imprinted $TiO_2$ (NIP).

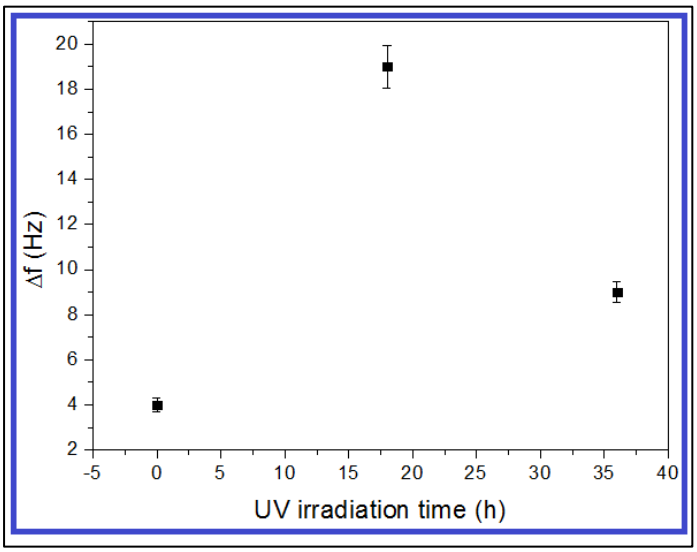



Figure 6. Changes of resonance frequency (Δf) of $MITiO_2$ sensor with 5/1 ratio of $TiO_2$/PTM with different UV irradiation time during template removal responding to 9.88 μM of PTM solution

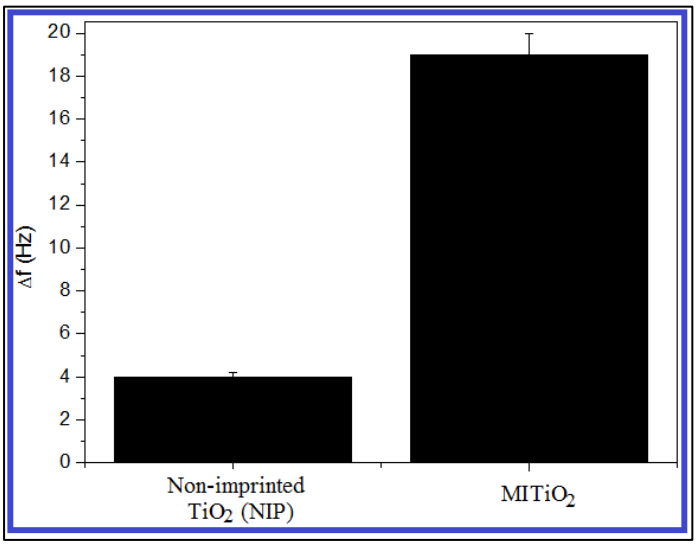



Figure 7. Changes of resonance frequency (Δf) of Non-imprinted $TiO_2$ (NIP) and $MITiO_2$ sensor with 5/1 ratio of $TiO_2$/PTM in the ad-mixture responding to 9.88 μM of PTM solution

## Conclusion

Molecularly imprinted PVDF/$TiO_2$/PTM ($MIPTiO_2$) and $TiO_2$/PTM ($MITiO_2$) sensors were prepared and evaluated for the detection of parathion methyl, a simulant of chemical threat agents. Template PTM molecules were removed via photocatalytic degradation under UV irradiation with the existence of photocatalytically active $TiO_2$ nano crystals. Here we demonstrated that molecular cavities of PTM were formed inside the $MITiO_2$ sensor after PTM template molecules were removed. $MITiO_2$ with a 5/1 mass ratio of $TiO_2$/PTM in the ad-mixture showed promising sensing ability towards PTM analyte molecules after template removal. 18 h of UV irradiation time for template removal was sufficient while 36h was too long that superhydrophilicity of $TiO_2$ dominated and repelled the hydrophobic PTM analyte molecules resulting in lower response to PTM. Molecularly imprinted $MITiO_2$ sensors were suitable for the detection of CTAs and their simulants, such as PTM, with a good sensitivity. However, molecularly imprinted polymers $MIPTiO_2$ were not sensitive enough to be as sensors for CTAs and their simulants, possibly due to the incompatibility between hydrophobic PVDF and hydrophilic $TiO_2$.

## Acknowledgement

The research grant is supported by the Singapore National Research Foundation under its Environmental & Water Technologies Strategic Research Programme and administered by the Environment & Water Industry Programme Office (EWI) of the PUB.

## References

1. Aas, P. (2003). The threat of mid-spectrum chemical warfare agents. *Prehospital and Disaster Medicine,* 18(4): 306 – 312.
2. Stebbins, M. (2016). Type of chemical weapons. Federation of American scientists. Access online http://fas.org/cw/cwagents.htm.
3. Bajgar, J. (2005). Complex view on poisoning with nerve agents and organophosphates. *Acta Medica*, 48(1): 3 – 21.
4. Samuels, R. J. (2006). Encyclopedia of Unites States National Security. Sage Publications, United Kingdom. pp. 117 – 118.
5. Creaser, C. S., Griffiths, J. R., Bramwell, C. J., Noreen, S., Hill, C. A. and Thomas, C. L. P. (2004). Ion mobility spectrometry: A review Part 1 – Structural analysis by mobility measurement. *The Analyst*, 129: 984 – 994.
6. Frishman, G. and Amiray, A. (2000). Fast GC-PFPD system for field analysis of chemical warfare agents. *Field Analytical Chemistry and Technology*, 4(4): 170 – 194.
7. Singh, K., Pasha, A. and Amitha, B. E. (2013). Preparation of molecularly imprinted polymers for heptachlor: An organochloride pesticide. *Chronical Young Scientist*, 4: 46 – 50.
8. Vergara, A. V., Pernites, R. B., Pascua, S., Binag, C. A. and Advincula, P. C., (2012). QCM sensing of a chemical nerve agent analog via electropolymerized molecularly imprinted polythiophene film. *Journal of Polymer Science Part A: Polymer Chemistry*, 50: 675 – 685.
9. Schirhagl, R. (2014). Bioapplications for molecularly imprinted polymers. *Analytical Chemistry,* 86: 250 – 261.
10. Salomaki, M. and Kankare, J. (2007). Modelling the growth processes of polyelectrolyte multilayers using a quartz crystal resonator. *Journal of Physical Chemistry B,* 111(29): 8509 – 8519.
11. Scorrano, S., Mergola, L., Bello, M. P. D., Lazzoi, M. R., Vasapollo, G. and Sole, R. D. (2015). Molecularly imprinted composite membranes for selective detection of 2-deoxyadenosine in urine samples. *International Journal of Molecular Science,* 16: 13746 – 13759.
12. Yang, Z., Yan, J. and Zhang, C. (2012). Piezoelectric detection of bilirubin based on bilirubin-imprinted titania film electrode. *Analytical Biochemistry*, 421: 37 – 42.
13. Wu, C. and Linden, K. G., (2008). Degradation and byproduct formation of parathion in aqueous solutions by UV and UV/$H_2O_2$ treatment. *Water Research,* 42(19): 4780 – 4790.
14. Sun, B., Vorontsov, A. V. and Smirniotis, P. G. (2011). Parametric studies of diethyl phosphoramidate photocatalytic decomposition over $TiO_2$. *Journal of Hazardous Materials,* 186: 1147 – 1153.
15. Armakovid, S. J., Finc-ur, N. L., Sibul, F., Vione, D., Setrajc, J. P. and Abramovic, B. F. (2015). Influence of electron acceptors on the kinetics of metoprolol photocatalytic degradation in $TiO_2$ suspension. a combined experimental and theoretical study. *RSC Advances*, 5: 54589 – 54604.

16. Lin, X. H. and Li, S. F. Y. (2015). Impact of the spatial distribution of sulfate species on the activities of $SO_4^{2-}$/$TiO_2$ photocatalysts for the degradation of organic pollutants in reverse osmosis concentrate. *Applied Catalysis B-Environment,* 170: 263 – 272.
17. Zoh, K. D., Kim, T. S., Kim, J. G., Choi, K. and Yi, S. M. (2006). Parathion degradation and toxicity reduction in solar photocatalysis and photolysis. *Water Science and Technology*, 53(3): 1 – 8.
18. Moctezuma, E., Leyva, E., Palestine, G. and Lasa, H. D., (2007). Photocatalytic degradation of methyl parathion: Reaction pathways and intermediate reaction products. *Journal of Photochemistry and Photobiology A: Chemistry*, 186: 71 – 84.
19. Takeuchi, M., Sakamoto, K., Martra, G., Coluccia, S. and Anpo, M. (2005). Mechanism of photoinduced superhydrophilicity on the $TiO_2$ photocatalyst surface. *Journal of Physical Chemistry B,* 109 (32): 15422 – 15428.
20. Gao, Y. F., Masuda, Y. and Koumoto, K., (2004). Light-excited superhydrophilicity of amorphous $TiO_2$ thin films deposited in an aqueous peroxotitanate solution. *Langmuir,* 20(8): 3188 – 3194.
21. Permpoon, S., Houmard, M., Riassetto, D., Rapenne, L., Berthome, G., Baroux, B., Joud, J. C. and Langlet, M. (2008). Natural and persistent superhydrophilicity of $SiO_2$/$TiO_2$ and $TiO_2$/$SiO_2$ bi-layer films. *Thin Solid Films,* 516(6): 957 – 966.
22. Ye, L. Q., Yang, C. J., Tian, L. H., Zan, L. and Peng, T. Y. (2011). Tunable photocatalytic selectivity of fluoropolymer PVDF modified $TiO_2$. *Applied Surface Science,* 257 (18): 8072 – 8077.
23. Lee, M. J., Ong, C. S., Lau, W. J., Ng, B. C., Ismail, A. F. and Lai, S. O. (2016). Degradation of PVDF-based composite membrane and its impacts on membrane intrinsic and separation properties. *Journal of Polymer Engineering* 36(3): 261 – 268.

*Malaysian Journal of Analytical Sciences, Vol 21 No 6 (2017): 1316 - 1326*
*DOI: https://doi.org/10.17576/mjas-2017-2106-13*

MALAYSIAN JOURNAL OF ANALYTICAL SCIENCES
*Published by The Malaysian Analytical Sciences Society*
ISSN 1394 - 2506

# COPPER MODIFIED CARBON NITRIDE AS FLUORESCENCE SENSOR FOR NITRATE IONS

## (Karbon Nitrida Terubah Suai Kuprum Sebagai Sensor Pendafluor Ion Nitrat)

Siti Maryam Jasman[1], Hendrik O. Lintang[2,3,4], Siew Ling Lee[1, 2], Leny Yuliati[2,3,4]*

[1]*Department of Chemistry, Faculty of Science*
[2]*Centre for Sustainable Nanomaterials, Ibnu Sina Institute for Scientific and Industrial Research*
*Universiti Teknologi Malaysia, 81310 UTM Johor Bahru, Johor, Malaysia*
[3]*Ma Chung Research Center for Photosynthetic Pigments*
[4]*Department of Chemistry, Faculty of Science and Technology*
*Universitas Ma Chung, Malang 65151, East Java, Indonesia*

**Corresponding author: leny.yuliati@machung.ac.id*

Received: 7 November 2016; Accepted: 18 September 2017

**Abstract**

In this study, newly developed copper modified CN composites were prepared and tested as a fluorescence sensor for detection of nitrate ions ($NO_3^-$). The structure and chemical properties of CN and copper modified CN composites were investigated via X-ray diffraction (XRD), Fourier transform infra-red (FTIR), diffuse reflectance ultraviolet-visible (DR UV-Vis) and fluorescence spectroscopies. Three emission sites represented as C=N, C=O and C-N moieties were suggested to contribute as sensing sites in CN and copper modified CN composites. The sensing capabilities of CN and copper modified CN composites toward $NO_3^-$ in the range of 300 to 1800 µM were determined via a quenching technique. The quenching efficiencies ($K_{SV}$) of CN and copper modified CN composites were obtained from the Stern-Volmer plot. Among three emission peaks of CN, C=N sites were found to be the most sensitive site having the strongest interaction with $NO_3^-$. By addition of Cu(0.5 mol%), the $K_{SV}$ of CN was improved from 2.11 x $10^{-4}$ to 5.27 x $10^{-4}$ $\mu M^{-1}$. This study showed that with the addition of copper as modifier, the performance of CN can be improved and the composite can be used as potential fluorescence sensor for the detection of $NO_3^-$.

**Keywords:** copper modified carbon nitride, fluorescence sensor, nitrate ion

**Abstrak**

Dalam kajian ini, karbon nitrida terubah suai kuprum yang baru telah disediakan dan diuji sebagai sensor pendafluor untuk mengesan ion nitrat ($NO_3^-$). Struktur dan sifat kimia bagi CN telah disiasat melalui pembelauan sinar-X (XRD), transformasian infra-merah Fourier (FTIR), spektroskopi pantulan serakan ultralembayung-cahaya nampak (DR UV-Vis) dan spektroskopi pendafluor. Tiga tapak pelepasan diwakili sebagai moiti C=N, C=O dan C-N telah dicadangkan untuk menyumbang sebagai tapak penderiaan CN dan komposit CN terubah suai kuprum. Keupayaan penderiaan CN dan komposit CN terubah suai kuprum terhadap $NO_3^-$ dalam lingkungan 300 hingga 1800 µM telah ditentukan melalui teknik pelindapan. Kecekapan pelindapan ($K_{SV}$) bagi CN dan komposit CN terubah suai kuprum telah diperoleh daripada plot Stern-Volmer. Di antara tiga tapak pelepasan CN, tapak C=N telah ditemui menjadi tapak yang paling sensitif dan mempunyai interaksi paling kuat dengan $NO_3^-$. Dengan penambahan Cu(0.5 mol%), nilai $K_{SV}$ bagi CN telah bertambah baik daripada 2.11 x $10^{-4}$ kepada 5.27 ×$10^{-4}$ $\mu M^{-1}$. Kajian ini menunjukkan bahawa dengan penambahan kuprum sebagai pengubahsuai, prestasi CN boleh ditingkatkan dan komposit tersebut boleh digunakan sebagai potensi sensor pendafluor untuk mengesan $NO_3^-$.

**Kata kunci:** karbon nitrida terubah suai kuprum, sensor pendafluor, ion nitrat

## Introduction

Nitrate ($NO_3^-$) is a widespread contaminant of groundwater which can be easily detected in the environment and cause hazard to human health. The $NO_3^-$ is largely used for food preservative, drinking water and fertilizing agents [1, 2]. Excessive consuming of food and drinking water containing high level of $NO_3^-$ can cause severe risk to human health especially infants. Human may metabolize $NO_3^-$ in blood and finally transform it into carcinogenic nitrosamine causing the condition known as methemoglobinemia or also called as baby blue syndrome [3, 4]. In addition, it has been reported that the healthy human urine range of $NO_3^-$ is in the range of 300 to 1800 μM [5]. Therefore, determination of $NO_3^-$ is an important aspect to human health and environment. Griess reagent has been used widely for detection of $NO_3^-$ ion. Basically, Griess reaction involved several steps starting from reduction of $NO_3^-$ to $NO_2^-$ ion by using vanadium (III) chloride [6]. The mixture was subsequently reacted with sulfanilamide and *N*-(1-naphtyl) ethylenediamine to produce pink coloured azo dye product which strongly absorbed light at 540 nm [5, 7-9]. However, it presents several disadvantages such as using high concentration of hazardous reagent in the reaction, complicated detection procedure and cannot be reused [10]. Thus, development of reusable and sensitive sensor for detection of $NO_3^-$ ion is highly required.

Recently, carbon nitride (CN) has become a current interest because of its unique properties such as non-toxicity, low cost, high photoluminescence intensity [11] and good photostability [12]. CN is a graphite like layered material where *s*-triazine ($C_3N_3$) or tri-*s*-triazine ($C_6N_7$) units connected with amino groups (-NH/$NH_2$) are held together through hydrogen bonds between the amino groups [13, 14]. The principal application of the CN in the environment is mainly in photocatalysis for photodegradation of environmental pollutants [15, 16], while only few studies have been reported on its application in optical detection of environmental pollutant [17-22]. For instances, the CN has been reported to act as fluorescence sensor for detection of $Cu^{2+}$ and $Fe^{3+}$ ions [16-18] and *N*-Nitrosopyrrolidine [19]. Recently, metal-free CN was used as a fluorescence chemical sensor for detection of $NO_3^-$ [23]. Unfortunately, CN alone still has low sensitivity towards the detection of the $NO_3^-$. Therefore, further investigation is still required to improve the performance of the CN.

The objective of this study is to design a sensitive sensing material based CN by improving the sensing sites of the CN for detection of the $NO_3^-$. In order to improve the sensing sites of the CN, copper species was used as the modifier. Copper based material has attracted a great interest due to its low cost as compared to noble metals such as Au, Pt, or Pd. It has been reported that the amino groups from the CN can interact with copper ion to form a stable complex due to the strong coordination force between the amino group and copper ion [24]. Herein, this study reported the modification of the CN by using copper species prepared by impregnation followed by a reduction method. The synthesized composites were demonstrated to show better sensing performances towards the $NO_3^-$.

## Materials and Methods

### Material preparation

CN was prepared by using urea ($CON_2H_4$, Sigma-Aldrich, 98%) as precursor via thermal polymerization technique at 823 k for 4 hours [21, 25]. As for the preparation of composites, certain amount of $Cu(acac)_2$ ($Cu(C_5H_7O_2)_2$, Merck, 99.99%) was dissolved in ethanol and mixed with CN via an impregnation process. The mixture was heated up to 363 K until all the ethanol was evaporated. The obtained solid was underwent thermal hydrogenation process at 473 K for 2 hours under hydrogen flow of 5 ml/min to produce copper species modified CN composites. Composites were denoted as Cu(*x*)/CN composites where *x* showed the mol ratio of Cu to CN, which were fixed at 0.1 and 0.5 mol%. As a reference, the $Cu(acac)_2$ was heated under thermal hydrogenation process at 473 K or 2 hours to obtain Cu metal.

### Characterizations

Properties of CN and Cu(*x*)/CN composites were investigated by several instruments. The structure of the CN and its composite was identified by using powder X-ray difractometer recorded with a Bruker D8 Advanced using Cu Kα irradiation (λ = 1.5406 Å). The surface area of CN and its composites was confirmed by using Brunauer-Emmett-Teller (BET) equation obtained from a Quantachrome NOVA TOUCH $LX^4$. The functional groups present in the CN and its composites were recorded by using a Nicolet iS50 spectroscopy by mixing the samples with potassium bromide as a pellet. The diffuse reflectance UV-Visible (DR UV-Vis) spectra were recorded by using

Shimadzu UV-Vis spectrophotometry (UV-2600) in the range of 250 – 800 nm. The emission spectra were determined via JASCO FP-8500 fluorescence spectrophotometer at room temperature.

**Quenching test**

The interactions between the CN and its composites with $NO_3^-$ were studied via fluorescence spectroscopy at room temperature. The quenching tests were carried out by exposing various concentrations of $NO_3^-$ in the range of 300 to 1800 μM onto the CN and its composites. The various concentrations of $NO_3^-$ (10 μL) were introduced into the sample (0.05 g) and the emission spectra were measured at excitation wavelengths of 277, 320 and 370 nm. The interaction between the samples and the $NO_3^-$ can be observed from the changes in the emission intensity measured at each excitation wavelength and evaluated from the Stern-Volmer plot.

## Results and Discussion

**Characterization of CN and Cu(x)/CN composites**

To investigate the chemical structure and optical properties of CN and its composites, XRD, FTIR, DR UV-Vis and fluorescence spectroscopies measurements were performed. The XRD patterns of CN and its composites are given in Figure 1. The XRD pattern of the prepared Cu metal is also shown as a reference. Cu metal gave three obvious peaks at $2\theta$ of 44.3, 50.4 and 74.1° as the characteristics of copper (0) species (JCPDS no. 00-004-0836), which pattern was virtually the same as the reported one [26]. On the other hand, the CN exhibited two diffraction peaks at $2\theta$ of 13.10 and 27.30°, corresponding to in-planar repeating units and the distance between the nitride pores, respectively [20, 23, 27-30]. The Cu(*x*)/CN composites showed similar diffraction patterns to those of the CN, suggesting that the added Cu might be too low to be detected by XRD or the Cu was highly dispersed on the CN.

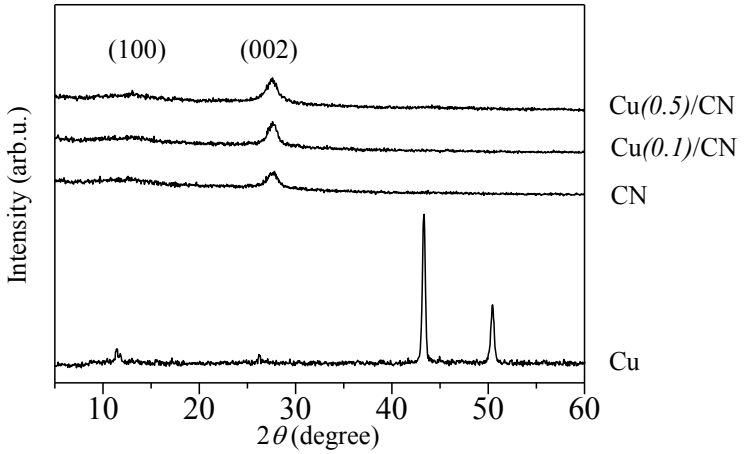



Figure 1. XRD patterns of Cu, CN and Cu*(x)*/CN composites

The FTIR spectra of CN and the Cu*(x)*/CN composites are shown in Figure 2. The CN showed vibration bands at around 3300 – 3400 $cm^{-1}$ that can be attributed to the overlapping bands of primary and secondary amine, *v*(N-H) and *v*(O-H) groups [21-24, 31-35]. The stretching modes of *v*(C-N) heterocycles were observed at 1200 –1700 $cm^{-1}$, while the heterocyclic tri-*s*-triazine ($C_6N_7$) was found at around 809 $cm^{-1}$. Even though the presence of amino groups in the synthesized CN is difficult to be analysed by FTIR spectroscopy, it has been reported by XPS analysis [31]. It was obvious that the Cu(*x*)/CN composite exhibited almost similar peaks to those of the CN, which indicated that the structure of CN was kept to be almost the same even after addition of copper species on the samples, similar to other reported literatures [24, 32].

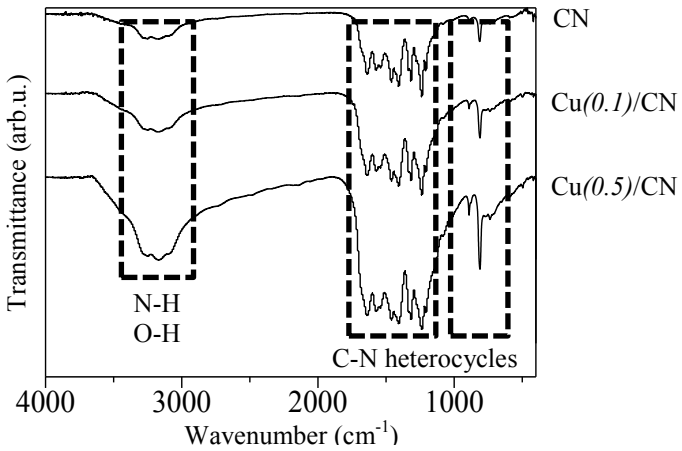



Figure 2. FTIR spectra of CN and Cu*(x)*/CN composites

Figure 3 shows $N_2$ adsorption-desorption isotherms of CN and its composites. It was obvious that they exhibited type III isotherm, which referred to nonporous solids. There were no change occurred on the isotherm when the Cu species were added onto the samples, suggesting that the added copper species did not affect the physical properties of the CN. The BET specific surface areas of CN, Cu *(0.1)*/CN, and Cu *(0.5)*/CN were measured to be 91, 93 and 56 $m^2g^{-1}$, respectively. Addition of 0.1 mol% of Cu did not affect much the specific surface area, but the addition of 0.5 mol% of Cu significantly decreased the specific surface area. The decrease in the surface area has been also reported when $Cu(acac)_2$ was dispersed on the CN [32].

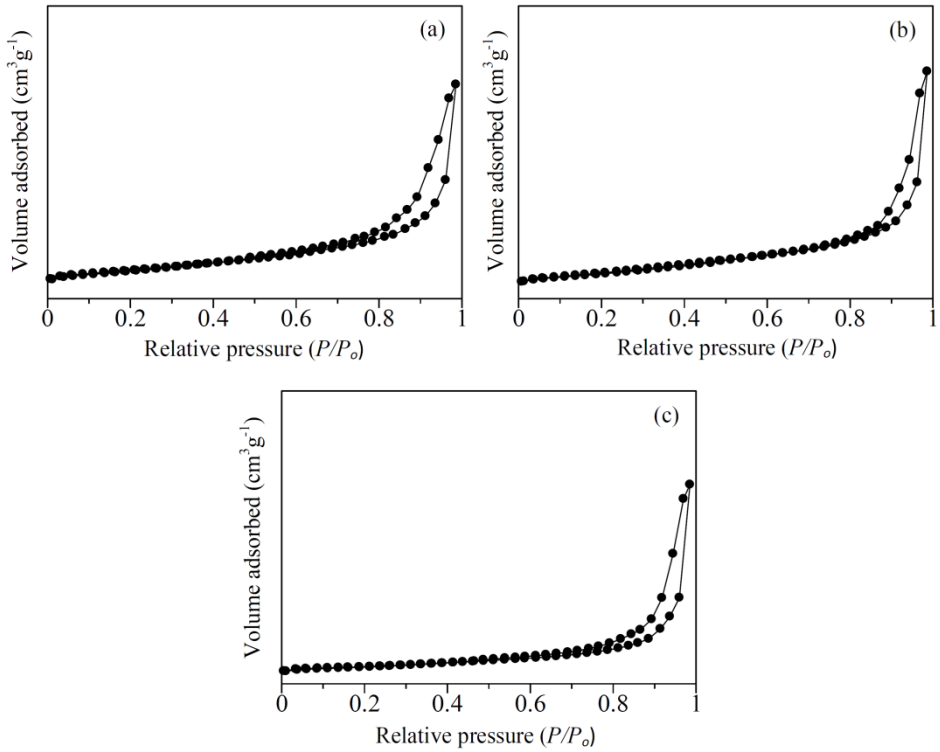



Figure 3. $N_2$ adsorption-desorption of (a) CN, (b) Cu*(0.1)*/CN and (c) Cu*(0.5)*/CN composites

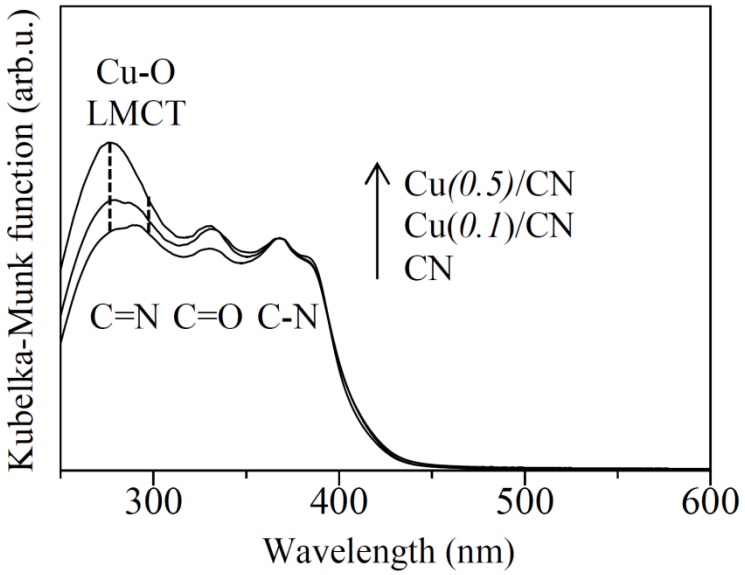



Figure 4. DR UV-Vis spectra of CN and Cu*(x)*/CN composites

The optical properties of CN and its composites were investigated by DR UV-Vis spectroscopy. As shown in Figure 4, CN and its composites exhibited three strong absorption bands at 277, 320 and 370 nm. The peak at 277 nm was corresponded to C=N groups ($\pi$-$\pi$*) in the conjugated aromatic triazine ring [20, 23, 31, 32], while the peak at 320 nm would be related to the presence of C=O moiety ($\pi$-$\pi$* and $n$-$\pi$*) due to the low condensation during the polymerization process of urea [30, 32, 36]. The peak at 370 nm was originated from the C-N terminal moiety ($n$-$\pi$*) [20, 23, 31, 32]. The Cu($x$)/CN composites also gave similar absorption peaks to the CN, but with increased absorption peak intensities below 350 nm. The increase was more prominent for Cu*(x)*/CN composite with higher Cu loading amount. This would be the evidence of the presence of Cu on the samples since the peaks were contributed from the ligand to metal charge transfer (LMCT) transition between Cu and oxygen species in the composites [37].

The fluorescence properties of CN and Cu*(x)*/CN composites were studied by using fluorescence spectroscopy. Similar to the DR UV-Vis spectra, CN and its composites also shows three excitation peaks at 277, 320 and 370 nm, which referred to C=N, C=O and C-N terminal groups, respectively. On the other hand, only one emission peak was observed when CN and its composites were excited at 277, 320 or 370 nm [23]. As can be seen in Figure 5 (a), the intensity of the excitation spectra of the composites decreased with the increase in the loading amount of Cu species. This is believed due to certain interactions occurred between Cu species and CN. The same phenomenon also can be monitored from the emission spectra of CN and its composites at 455 nm for all excitation wavelengths, as can be seen in Figure 5 (b), (c) and (d), which illustrates the emission spectra of CN and its composites when excited at 277, 320 and 370 nm, respectively.

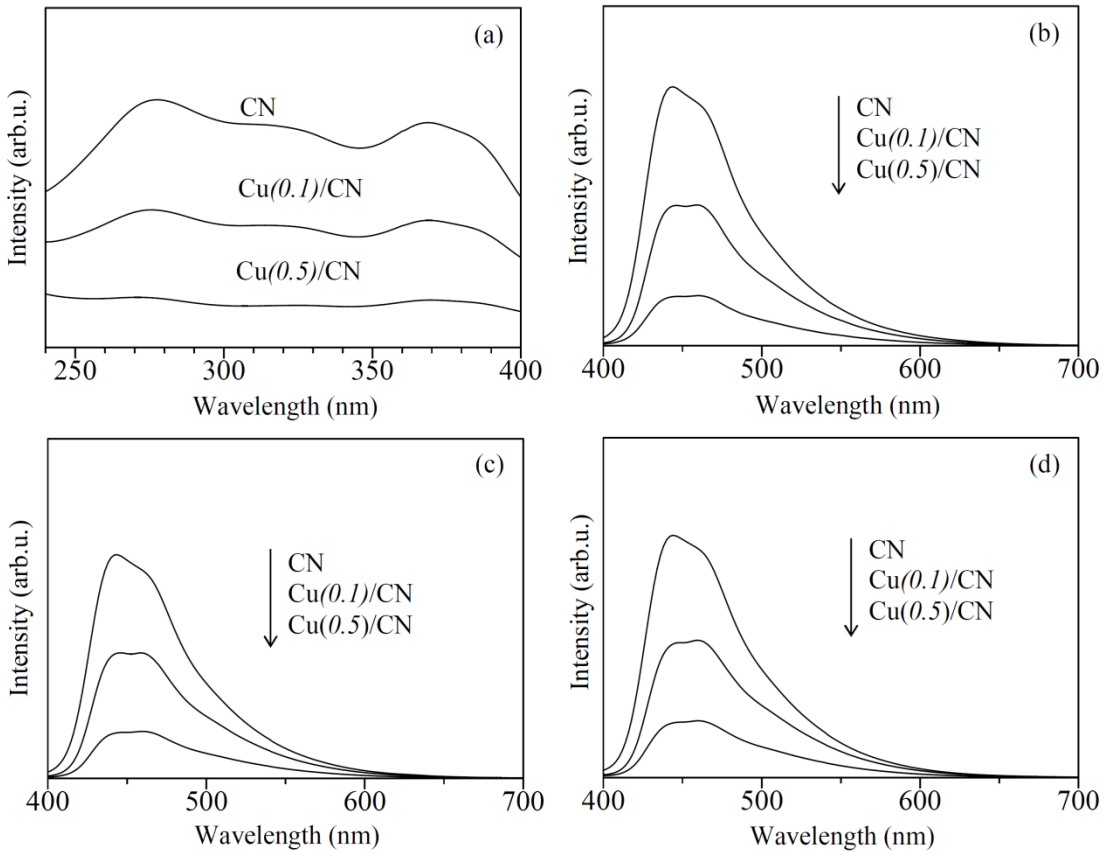



Figure 5. (a) Excitation spectra of CN and Cu*(x)*/CN composites monitored at emission wavelength of 455 nm, and emission spectra of CN and Cu*(x)*/CN composites monitored at excitation wavelengths of (b) 277, (c) 320 and (e) 370 nm

**Sensing performance of CN and Cu(*x*)/CN composites toward $NO_3^-$ ion**

The fluorescence responses of CN and its composites to various concentrations of $NO_3^-$ (300-1800 µM) were studied by using a quenching technique. Since the CN and its composites have three emission sites, which are C=N, C=O and C-N terminal groups, it is important to determine which emission site has the strongest interaction to $NO_3^-$. Figure 6 shows the emission spectra of CN at 277, 320 and 370 nm before and after addition of various concentrations of $NO_3$. Based on the spectra, it is clearly seen that the intensity of CN decreased with the increase of the $NO_3^-$ concentration at all sensing sites, suggesting that the $NO_3^-$ ion interacted with C=N, C=O and C-N terminal sites and acted as a quenching agent to deactivate the emission sites of the CN. It is believed that there is an electrostatic interaction between the CN and its composites with $NO_3^-$ due to different charge between the sensing sites of the sensor samples and the $NO_3^-$ [38]. The same phenomena also can be observed for Cu*(0.1)*/CN and Cu*(0.5)*/CN samples, which spectra are shown in Figures 7 and 8, respectively.

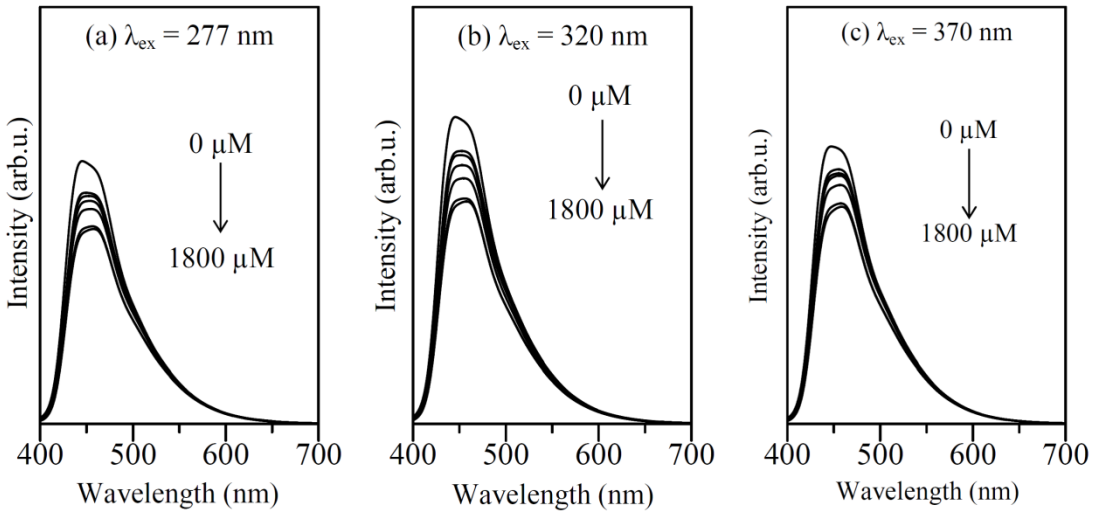



Figure 6. Emission spectra of CN in the absence and presence of $NO_3^-$ with various concentrations, monitored at excitation wavelength of (a) 277, (b) 320 and (c) 370 nm

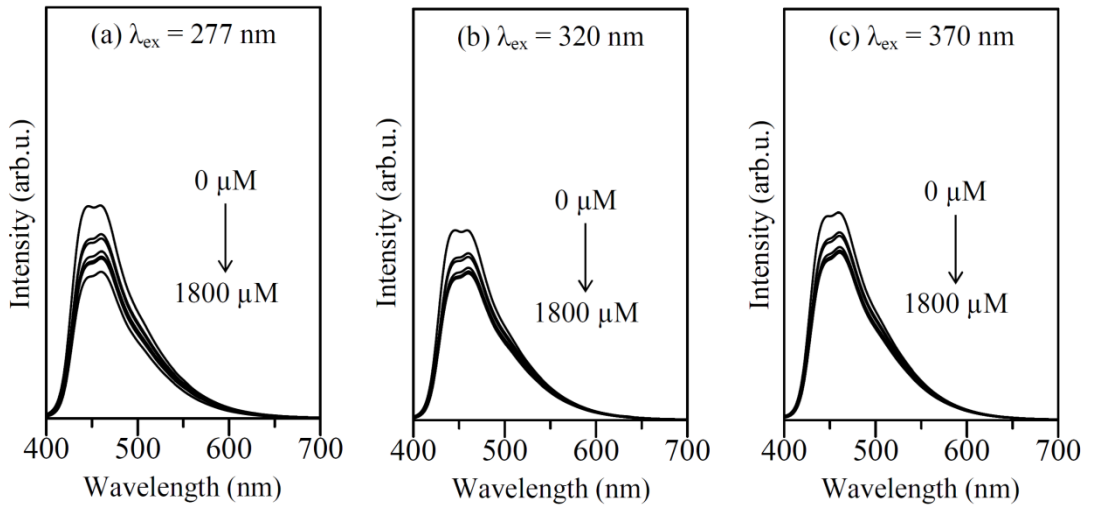



Figure 7. Emission spectra of Cu *(0.1)*/CN in the absence and presence of $NO_3^-$ with various concentrations, monitored at excitation wavelength of (a) 277, (b) 320 and (c) 370 nm

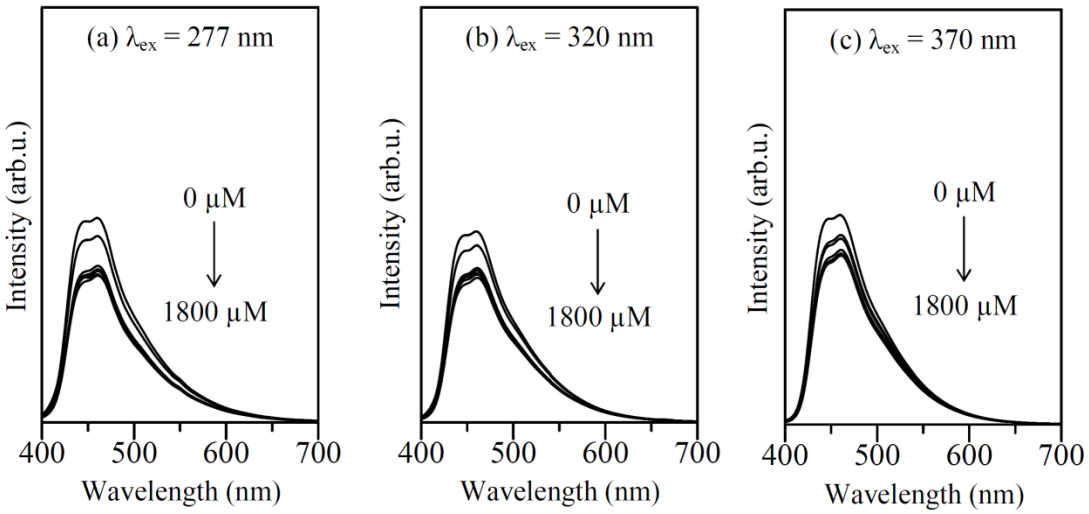



Figure 8. Emission spectra of Cu *(0.5)*/CN in the absence and presence of $NO_3^-$ with various concentrations, monitored at excitation wavelength of (a) 277, (b) 320 and (c) 370 nm

In order to determine the most sensitive sensing sites on the CN and its composites, quenching efficiencies at each sensing sites of the samples need to be calculated. The quenching efficiencies of the sensor can be determined by the relationship between the reduced intensity and the added concentration of $NO_3^-$, which is reflected by the Stern-Volmer equation:

$$I_0/I = K_{SV}[Q] + 1 \quad (1)$$

where $I_0$ is the fluorescence intensity of sensor in the absence of quencher ($NO_3^-$) and $I$ is the fluorescence intensity of sensor in the presence of quencher ($NO_3^-$), $K_{SV}$ is the Stern-Volmer constant which measures the efficiency of quenching and [$Q$] is the concentration of $NO_3^-$.

Among the three sensing sites of the CN and its composites, which are C=N, C=O and C-N terminal groups, the C=N showed the strongest interaction between the samples and the $NO_3^-$ ion. The Stern-Volmer plots of the CN and Cu*(x)*/CN composites for the C=N sites monitored at excitation wavelength of 277 nm are shown in Figure 9. The CN gave almost linear plot to sense $NO_3^-$ ion up to 1800 μM. On the other hand, the Cu *(0.1)*/CN composite and the Cu(*0.5*)/CN composites gave a linear plot up to 1500 and 900 μM, respectively. When the added concentration was higher than these concentration levels, saturation was observed and this was more prominently observed on the Cu(*0.5*)/CN. The addition of Cu was found to give lower concentration range detection, which may be caused by the blocking of the sensing sites by the added Cu species. However, it is clear that the addition of Cu improved the quenching efficiency of the CN. The calculated $K_{SV}$ values of CN, Cu(*0.1*)/CN and Cu(*0.5*)/CN composites at excitation wavelength of 277 nm were $2.11 \times 10^{-4}$, $2.50 \times 10^{-4}$ and $5.27 \times 10^{-4}$ $\mu M^{-1}$, respectively, as summarized in Figure 10. Although detection range on the Cu(*0.5*)/CN composite was lower, obviously the Cu(*0.5*)/CN composite showed almost twofold higher $K_{SV}$ value as compared to the unmodified CN. It is revealed that the presence of copper species improved the performance of CN for the detection of $NO_3^-$ ion. Therefore, it can be concluded that Cu(*x*)/CN composites were potential to be used as a fluorescence sensor for detection of $NO_3^-$ ion.

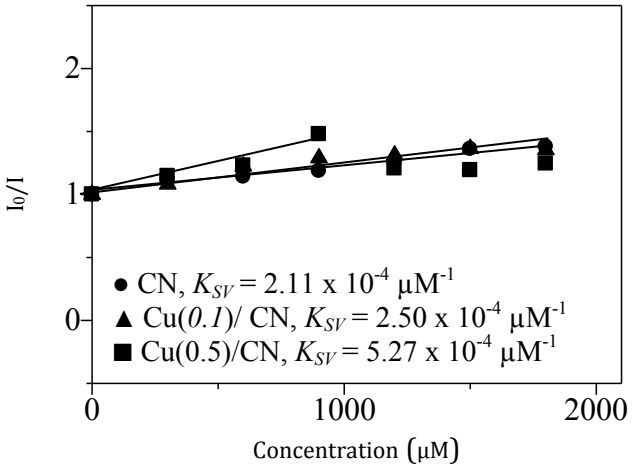



Figure 9. Stern-Volmer plots between the relative emission intensity of CN and Cu(*x*)/CN and the concentration of $NO_3^-$, monitored at excitation wavelength of C=N sites (277 nm)

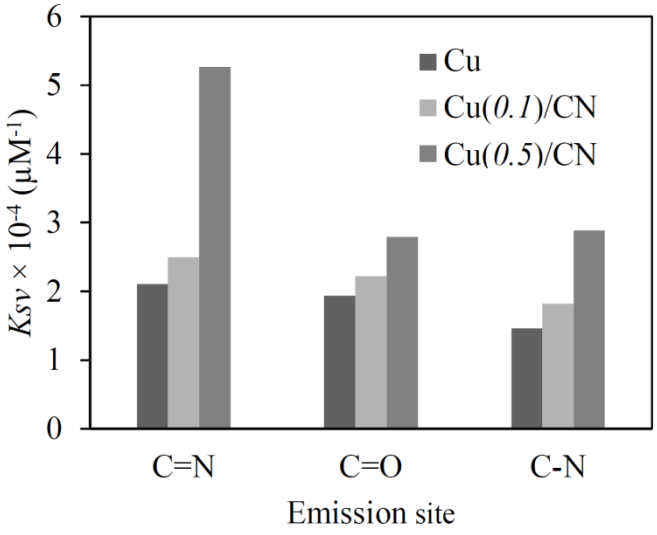



Figure 10. The $K_{SV}$ values for CN and Cu(*x*)/ CN for all the emission sites

## Conclusion

The CN was successfully synthesized via a thermal polymerization technique, while the Cu*(x)*/CN composites were prepared by impregnation of copper species, followed by thermal reduction process. XRD patterns and FTIR spectra did not show any changes, suggesting that the structural properties of CN were not influenced by the addition of copper species onto CN. On the other hand, the DR UV-Vis spectra showed the presence of copper species in the composites in the area below 350 nm, which was due to the LMCT between the copper species and CN. The CN and Cu*(x)*/CN composites exhibited three emission sites, which are C=N, C=O and C-N sites. Among all these emission sites, the C=N site showed the most favorable sensing site for detection of $NO_3^-$ ion. The quenching efficiencies were represented by the $K_{SV}$ values, which values for CN, Cu*(0.1)*/CN and Cu*(0.5)*/CN composites were 2.11 ×$10^{-4}$, 2.50 ×$10^{-4}$ and 5.27 ×$10^{-4}$ µ$M^{-1}$, respectively. Modification with copper species (0.5 mol%) onto the CN improved the quenching efficiency up to two times higher than the unmodified CN. This work clearly demonstrated that the Cu*(x)*/CN composites can be used as a potential fluorescence sensor for detection of $NO_3^-$ ion.

**Acknowledgements**

This work was financially supported by the Ministry of Higher Education (MOHE, Malaysia) and the Universiti Teknologi Malaysia (UTM, Malaysia) through the Research University Grant (Tier-1, cost center code: Q.J130000.2526.10H74). S.M.J also acknowledges financial support from MyBrain15 Scholarship.

**References**

1. Aravamudhan, S. and Bhansali, S. (2008). Development of micro-fluidic nitrate-selective sensor based on doped-polypyrrole nanowires. *Sensors and Actuators B*, 132: 623 – 630.
2. Guadagnini, L. and Tonelli, D. (2008). Carbon electrodes unmodified and decorated with silver nanoparticles for the determination of nitrite, nitrate and iodate. *Sensors and Actuators B,* 188: 806 –814.
3. Ogata, F., Imai, D. and Kawasaki, N. (2015). Adsorption of nitrate and nitrite ions onto carbonaceous material produced from soybean in binary solution system. *Journal of Environmental Chemical Engineering*, 3: 155 – 161.
4. Kim, D., Goldberg, I. B. and Judy, J. W. (2009). Microfabricated electrochemical nitrate sensor using double-potential-step chronocoulometry. *Sensor and Actuators B*, 135: 618 – 624.
5. Trikas, D. (2007). Analysis of nitrite and nitrate in biological fluids by assays based on the Griess Reaction: Appraisal of the Griess Reaction in the L-arginine/nitric oxide area of research. *Journal of Chromatography B*, 851: 51 – 70.
6. Wang, S., Lin, K., Chen, N., Yuan, D. and Ma, J. (2016). Automated determination of nitrate plus nitrite in aqueous samples with flow injection analysis using vanadium (III) chloride as reductant. *Talanta,* 146: 744 – 748.
7. Lee, M., Lee, Y., Soltermann, F. and Gunten, U. V. (2013). Analysis of *N*-nitrosamines and other nitro(so) compounds in water by high-performance liquid chromatography with post-column UV photolysis/Griess reaction. *Water Research,* 47: 4893 – 4903.
8. Ridnour, L. A., Sim, J. E., Hayward, M. A., Wink, D. A., Martin, S. M., Buettner, G. R. and Spitz. D. R. (2000). A spectrophotometric method for the direct detection and quantification of nitric oxide, nitrite and nitrate in cell culture media. *Analytical Biochemistry,* 281: 223 – 229.
9. Bryan, N. S. and Grisham. M. B. (2007). Methods to detect nitric oxide and its metabolites in biological samples. *Free Radical Biology and Medicine*, 43(5): 645 – 657.
10. Kumar, V. V. and Anthony, S. P. (2014). Highly selective silver nanoparticles based label free colorimetric sensor for nitrite anions. *Analytica Chimica Acta,* 842: 57 – 62.
11. Hernandez-Torres, J., Gutierrez-Franco, A., Gonzalez, P. G., Garcia-Gonzalez, L., Hernandez-Quiroz, T., Zamora-Peredo, L., Mendez-Garcia, V. H. and Cisneros-de la Rosa. A. (2016). Photoluminescence and raman spectroscopy studies of carbon nitride films. *Journal of Spectroscopy*, 2016: 1 – 8 .
12. Chai, B., Peng, T., Mao, J., Li, K. and Zan, L. (2012). Graphitic carbon nitride (g-$C_3N_4$)-Pt-$TiO_2$ nanocomposite as an efficient photocatalyst for hydrogen production under visible light irradiation. *Physical Chemistry Chemical Physics,* 14: 16745 – 16752.
13. Yang, S., Gong, Y., Zhang, J., Zhan, L., Ma, L., Fang, Z., Vajtai, R., Wang, X. and Ajayan, P. M. (2013). Exfoliated graphitic carbon nitride nanosheets as efficient catalyst for hydrogen evolution under visible light. *Advanced Material*, 25: 2452 – 2456.
14. Thomas, A. Fischer, A. Goettmann, F. Antonietti, M. Muler, J-O. Schlogl, R. and Carlsson, J. M. (2008). Graphitic carbon nitride materials: Variation of structure and morphology and their use as metal-free catalysts. *Journal of Material Chemistry*, 18: 4893 – 4908.
15. Xia, B., Chu, M., Wang, S, Wang, W., Yang, S., Liu, C. and Luo, S. (2015). Graphene oxide amplified electrochemiluminescence of graphitic carbon nitride and its application in ultrasensitive sensing for $Cu^{2+}$. *Analytical Chemica Acta*, 9: 891:113 - 119.
16. Zhao, Z., Sun, Y. and Dong, F. (2015). Graphitic carbon nitride based nanocomposites: A review. *Nanoscale*, 7: 15 – 37.
17. Lee, E. Z., Jun, Y-S., Hong, W. H., Thomas, A. and Jin, M. M. (2010). Cubic mesoporous graphitic carbon(iv) nitride: an all-in-one chemosensor for selective optical sensing of metal ions. *Angewandte Chemie International Edition,* 49: 9706 – 9710.

18. Tian, J., Liu, Q., Asiri, A. M., Al-Youbi, A. O. and Sun, X. (2013). Ultrathin graphitic carbon nitride nanosheet: A highly efficient fluorosensor for rapid, ultrasensitive detection of $Cu^{2+}$. *Analytical Chemistry,* 85: 5595 – 5599.
19. Zhang, S., Li, J., Zeng, M., Xu, J., Wang, X. and Hu, W. (2014). Polymer nanodots of graphitic carbon nitride as effective fluorescent probes for the detection of $Fe^{3+}$ and $Cu^{2+}$ Ions. *Nanoscale*, 6: 4157 – 4162.
20. Sam, M. S., Lintang, H. O., Sanagi, M. M., Lee, S. L. and Yuliati, L. (2014). Mesoporous carbon nitride for adsorption and fluorescence sensor of *n*-nitrosopyrrolidine. *Spectrochimica Acta Part A: Molecular and Biomolecular Spectroscopy*, 124: 357 – 364.
21. Mane, G. P. Dhawale, D. S. Anand, C. Ariga, K. Ji, Q. Wahab, M. A. Mori, T. and Vinu, A. (2013). Selective sensing performance of mesoporous carbon nitride with a highly ordered porous structure prepared from 3-amino-1,2,4-triazine. *Journal of Materials Chemistry A*, 1: 2913 – 2920.
22. Wang, Q., Wang, W., Lei, J., Xu, N., Gaul, F. and Ju, H. (2013). Fluorescence quenching of carbon nitride nanosheet through its interaction with DNA for versatile fluorescence sensing. *Analytical Chemistry*. 85: 12182 – 12188.
23. Alim, N. S. Lintang, H. O. and Yuliati, L. (2015). Fabricated metal-free carbon nitride characterizations for fluorescence chemical sensor of nitrate ions. *Journal Teknologi*, 76(13): 1 – 6.
24. Wang, N., Han, Z., Fan, H. and Ai, S. (2015). Copper nanoparticles modified graphitic carbon nitride nanosheets as a peroxidase mimetic for glucose detection. *RSC Advances*, 5: 91302 – 91307.
25. Lee, S. C., Lintang, H. O. and Yuliati, L. (2012). A urea precursor to synthesize carbon nitride with mesoporosity for enhanced activity in the photocatalytic removal of phenol. *Chemistry-An Asian Journal*, 7: 2139 – 2144.
26. Cheng, S-L. and Chen, M-F. (2012). Fabrication, characterization, and kinetic study of vertical single-crystalline CuO nanowires on Si substrates. *Nanoscale Research Letters*, 7:119 – 126.
27. Zhu, J., Xiao, P., Li, H. and Carabineiro, S. A. C. (2014). Graphitic carbon nitride: synthesis, properties and application in catalysis. *Applied Materials & Interfaces*, 6: 16449 – 16465.
28. Dong, G., Zhang, Y., Pan, Q. and Qiu, J. (2014). A fantastic graphitic carbon nitride (g-$C_3N_4$) material: Electronic structure, photocatalytic and photoelectronic properties. *Journal of Photochemistry and Photobiology C: Photochemistry Reviews*, 20: 33 – 50.
29. Cui, Y., Tang, Y. and Wang, X. (2015). Template-free synthesis of graphitic carbon nitride hollow spheres for photocatalytic degradation of organic pollutant. *Materials Letters*, 161: 197 – 200.
30. Dai, H., Gao, X., Liu, E., Yang, Y., Hou, W., Kang, L. and Fan, J. (2013). Synthesis and characterization of graphitic carbon nitride submicrospheres using microwave method under mild condition. *Diamond and Related Materials*, 38: 109 – 117.
31. Tiong, P., Lintang, H. O., Endud, S. and Yuliati, L. (2015). Improved interfacial charge transfer and visible light activity of reduced graphene oxide-graphitic carbon nitride photocatalysts. *RSC Advances*, 5: 94029 – 94039.
32. Jasman, S. M., Lintang, H. O. and Yuliati, L. (2017). Enhanced detection of nitrite ions over copper acetylacetonate/polymeric carbon nitride composites. *Macromolecular Symposia*, 371: 84 – 93.
33. Ding, Z., Chen, X., Antonietti, M. and Wang, X. (2011). Synthesis of transition metal-modified carbon nitride polymers for selective hydrocarbon oxidation. *ChemSusChem,* 4: 274 – 281.
34. Luo, J., Cui, Z-C. and Zang, G-K. (2013). Mesoporous metal-containing carbon nitrides for improved photocatalytic activities. *Journal of Chemistry*, 2013: 1 – 6.
35. Mu, T., Huang, J., Liu, Z., Han, B., Li, Z., Wang, Y., Jiang, T. and Gao, H. (2004). Synthesis and characterization of polyester structure carbon nitride. *Journal of Material Research*, 19(6): 1736 – 1741.
36. Liu, J., Zhang, T., Wang, Z. Dawson, G. Chen, W. (2011). Simple Pyrolysis of Urea into Graphitic Carbon Nitride with Recyclable Adsorption and Photocatalytic Activity. *Journal of Materials Chemistry*, 21: 14398 – 14401.
37. Derrien, G., Charnay, C., Zajac, J., Jones, D. J. and Roziere, J. (2008). Copper-containing monodisperse mesoporous silica nanospheres by a smart one-step approach. *Chemistry Communication*, 27: 3118 – 3120.
38. Tang, I. H., Sundari, R., Lintang, H. O. and Yuliati, L. (2016). Polyvinylpyrolidone as a new fluorescent sensor for nitrate ion. *Malaysia Journal of Analytical Sciences*, 20(2): 288 – 295.

*Malaysian Journal of Analytical Sciences, Vol 21 No 6 (2017): 1327 - 1334*
*DOI: https://doi.org/10.17576/mjas-2017-2106-14*

MALAYSIAN JOURNAL OF ANALYTICAL SCIENCES
*Published by The Malaysian Analytical Sciences Society*
ISSN 1394 - 2506

# MOLECULARLY IMPRINTED POLYMER-COATED QUARTZ CRYSTAL MICROBALANCE FOR DETECTION OF PARATHION

## (Polimer Molekul Tercetak Saduran Kristal Kuarza Penimbang Mikro bagi Penentuan Parathion)

Xiamin Cheng[1, 3], Qihui Zhang[2], Sam Fong Yau Li[1, 2]*, Bin Liu[3]

[1]*NUS Environmental Research Institute,*
*5A Engineering Drive 1, T-Lab Building, 117411, Singapore*
[2]*Department of Chemistry,*
*National University of Singapore, 3 Science Drive 3, 117543, Singapore*
[3]*Department of Chemical & Biomolecular Engineering,*
*National University of Singapore, Engineering Drive 4, Blk E5 #02-17, 117585, Singapore*

**Corresponding author: chmlifys@nus.edu.sg*

Received: 7 November 2016; Accepted: 18 September 2017

**Abstract**

Organophosphorus compounds (OPs) as important components of insecticides, pesticides, and chemical threat agents (CTA), have become more and more serious threats to the environment. Real-time monitoring of the threats is an urgent demand for environmental safety. The molecular imprinting polymer (MIP) technique is an attractive method for the generation of polymer-based molecular "memory" for a present target or group of target molecules. In this work, we integrate a novel MIP with quartz crystal microbalance (QCM) to build a simple sensor to selectively monitor OP in water samples in real-time. The MIP system was built up by polymerization of methacryalic acid (MAA) with divinylbenzene (DVB), initiated with 2,2'-azobis(2-methylpropionitrile) (AIBN) in presence of target. The polymer was characterized with FT-IR. Using parathion as a representative template, the MIP was coated on QCM by casting a semi-polymerized solution. The sensor could detect parathion in wide range from 290 ppb to 29 ppm. This sensor is stable, easy to prepare which can be reused and has the potential to be applied other analytes, which are threats to the environment.

**Keywords:** organophosphorus compounds, molecular imprinting polymer, quartz crystal microbalance, parathion

**Abstrak**

Sebatian organofosforus (OPs) adalah kompenen penting bagi racun serangga, racun mahkluk perosak dan agen kimia berbahaya yang telah menjadi ancaman kepada alam sekitar. Pemantauan terhadap ancaman ini telah meningkat berdasarkan kepada keselamatan alam sekitar. Teknik polimer molekul tercetak (MIP) adalah kaedah yang menarik molekul berasaskan polimer yang mempunyai sasaran terhadap molekul tertentu. Dalam kajian ini, MIP tulen bersama penimbang mikro kristal kuarza (QCM) telah disepadu untuk menghasilkan sensor mudah bagi pemantauan terpilih kehadiran OP di dalam sampel air bagi siutuasi sebenar. Sistem MIP telah dibangunkan berdasarkan pempolimeran asid metakrialik (MAA) dan divinilbenzena (DVD), dimulakan dengan kehadiran 2,2'-azobis(2-metilpropionitril)(AIBN) sebagai sasaran. Polimer telah dicirikan menggunakan FT-IR. Menggunakan parathion sebagai templat, MIP disadur ke atas QCM melalui teknik saduran larutan separa polimer. Sensor berupaya mengesan parathio pada julat yang besar dari 290 ppb hingga 29 ppm. Sensor ini adalah stabil, mudah disediakan, dimana boleh diguna semula dan berpotensi untuk diaplikasi terhadap analit lain yang mengancam alam sekitar.

**Kata kunci:** sebatian organofosforus, polimer molekul tercetak, penimbang mikro kristal kuarza, parathion

## Introduction

Pesticides including insecticides are widely used in agriculture activities to provide more food productivity. As important components of pesticide and chemical threat agent (CTA), many organophosphorus compounds (OPs) are generally neurotoxic to all animal and human as cholinesterase inhibitors.[1-3] As shown in Figure 1, a typical organophosporus compound has a phosphorus atom with P=S or P=O bond and phosphate groups. Over-use of OPs has become more and more serious threats to the environment and human health. For example, natural water can be easily contaminated by OPs because it is widely spread and highly fluid, which would result in severe environmental and human health concerns. The residual OPs in food are another traditional problem, which is highly related to human health. To evaluate and control the contamination of OPs in environment, food or other places, many efforts were made on the development of different analytic methods in the last decades, which include chemosensor [4], capillary electrophoresis [5], immunoassay[6] and chromatography-mass spectrometry. Among these methods, the most popular methods are GC and HPLC or in tandem with mass spectrometer [7]. These methods normally are expensive, complex and require skilled personnel to operate. In addition, for trace analysis of complex samples, pre-treatments including separation and enrichment steps are generally required [8].Therefore, sensitive, fast, reliable and easy-handling methods are of great demand.

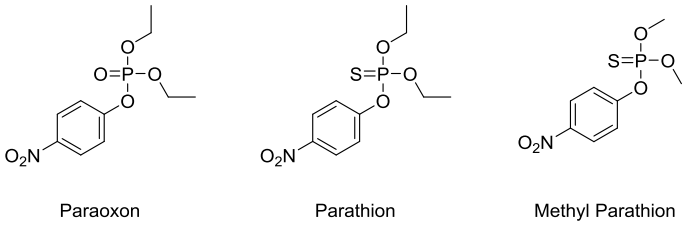



Figure 1. Structures of paraoxon, parathion and methyl parathion

Molecularly imprinted polymer (MIP) has grown fast in the last decades. MIP technique becomes an attractive method to construct of polymer-based molecular recognition elements for a preset target or a group of target molecules. The so-called artificial "enzyme" or "antibody", MIP has many applications, such as separation,[9] sensor [10] and immunoassay [11]. For example, MIPs have been used in selectively separation and enrichment of OPs from complex samples [12, 13]. MIPs have also been reported to make a sensor for Ops detection using electrochemical method by coating the MIPs on electrode [14]. This technique has many advantages including easy preparation, cost-effect, high stability, high affinity and high selectivity [15, 16].

Based on the piezoelectric properties of quartz crystals, the quartz crystal microbalance (QCM) is suitable for trace analysis, as a very sensitive pressure- and mass-sensing device. However, QCM itself has no selectivity. Therefore, different functional materials or chemicals were immobilized on the crystal surface to offer the desired selectivity. According to the well-known Sauerbrey equation, the frequency change of QCM, $\Delta f$, is proportional to the mass of the absorbed target of interest. Therefore, QCM-based sensor has been applied to many research fields, such as vapour analysis and biological analysis [17-19]. For example, an antibody against *A. hydrophila*, which is a bacteria of pathogen, was immobilized on QCM and the mass of target bacteria attached was monitored [20].

Parathion, also known as Folidol, is an organothiophosphate pesticide, which is widely used in agriculture and has high toxicity [21]. In this study, by combination of the sensitivity of QCM and the selectivity of MIP, we have developed a novel on-line biosensor for detection of parathion in water sample.

## Materials and Methods

### Instrument and device

QCM-D experiments were performed on a Q-Sense E4 QCM-D instrument (Q-Sense AB, Västra Frölunda, Sweden) with an AT-cut gold-coated quartz crystal (Model: AC5AP14, Diameter:14.0 mm, Jiaxing JingKong Electonic Co. Ltd, China), which has a response frequency of 5 MHz. All data were recorded at room temperature (25 $^{o}$C). Sauerbrey's equation has been established for the AT-cut gold-coated quartz crystal:

$$\Delta f = -2 f_0^2 . (\rho_q \mu_q)^{-1/2} \Delta m / A \quad (1)$$

$\Delta f$ is frequency shift (Hz) due to the mass change on the crystal, $f_0$ is the resonant frequency (Hz) of the original crystal, $\rho_q$ is the density of quartz crystal (2.648 g. $cm^{-3}$), $\mu_q$ is the shear modulus ($2.947 \times 10^{11}$ $g \cdot cm^{-1} \cdot s^{-2}$) and A is the active electrode area ($cm^2$).

**Chemicals**
Parathion, methacryalic acid (MAA), divinylbenzene (DVB), 2,2'-azobis(2-methylpropionitrile) (AIBN), sulphuric acid (98%), Hydrogen peroxide (30%, w/w) and ethanol (AR grade) are purchased from commercial vendors. Ultra-pure water was processed by Q-POD® ultrapure water dispenser (Merck Millipore) to reach a resistivity of 18.2 MΩ.cm.

**Sample preparation**
The stock solution of parathion was prepared in ethanol. Then the aqueous solution of samples (100 µM, 50 µM, 10 µM, 1 µM, 100 nM and 0 nM) was diluted with ultra-pure water in gradient.

**Sensor fabrication**
Firstly, QCM was soaked in piranha solution (9 mL of conc. sulphuric acid (98%) and 3 mL of hydroperoxide (30%)) for 5 minutes. Then, the crystal was washed thoroughly with ultra-pure water until the water was neutral (pH = 7). It was subsequently flushed with nitrogen flow followed by air-drying for few hours. After cleaning, the crystal is ready for coating without any other treatment.

In a 1.5 mL Eppendorf tube, to a solution of ethanol (178.2 µL), parathion (11.8 µL, 0.34 M), MAA (10.0 µL) and DVB (50.0 µL) was added 1.0 mg of AIBN. The mixture was mixed by vortex for few minutes and bubbled with nitrogen for 5 minutes. Then the sealed tube was incubated at 60 $^oC$ in water-bath for 10 minute until the mixture turned to be slightly muddy. 10.0 µL of the semi-polymerized solution was casted on the gold surface of QCM. The QCM was incubated in oven at 60 $^oC$ overnight to make sure the polymerization was complete. Non-imprinted polymer coated-QCM (NIP@QCM) was prepared in the same way without the template molecule. The sensor was soaked in 30 mL of ethanol with gentle shaking. The solvent was renewed every 6 hours for 4 times. Then the sensor was stored in ultra-pure water with gentle shaking for 1 day.

**Characterization of MIP and NIP**
The polymer (MIP or NIP) in the tube was soaked in ethanol under the same conditions to remove unreacted reagents and target and then dried in vacuum oven. The dried polymer (1 part) was mixed with dried KBr (100 parts). The mixture was ground and the resulted powder was pressed to a transparent pellet. FT-IR spectroscopy was obtained with an ALPHA FTIR Spectrometer (Bruker). The characteristic peaks for the MIP ($cm^{-1}$) included: 3018 (alkene), 2960 (alkane), 2925 (carboxylic acid), 1700 (C=O); NIP ($cm^{-1}$): 3019 (alkene), 2960 (alkane), 2926 (carboxylic acid), 1699 (C=O).

**Analytical procedure**
The detection procedure was monitored on-line with flow rate of 50 µL after the sensor was prepared and installed properly, followed by few pulses of maximum flow rate to remove air bubbles. After each analysis, desorption step was performed in ethanol (30 mL) with gentle shaking. The solvent was renewed every 6 hours for 4 times. Then the sensor was stored in ultra-pure water with gentle shaking for 1 day.

## Results and Discussion

**Design strategy and sensor fabrication**
The design of the sensor is shown in Figure 2a. In the first step, after necessary processes of QCM, the MIP was coated onto the gold electrode surface of the quartz crystal by free radical polymerization. The polymer system includes 4 parts: 1) MAA as functional monomer is used to build the framework of MIP and the carboxylic acid is served as the recognition element via hydrogen-bonding donor; 2) DVB as a cross-linking reagent is used to reinforce the stability of the rigid framework which contributes to the solid "memory" of MIP. DVB also

contributes to recognition by spatial hindrance and hydrophobic interaction to those hydrophobic domains of target including π-π interaction; 3) AIBN is used as initiator; 4) Parathion as the template molecules were mixed in the reaction solution and imbedded in the polymer to create many close-fit cavities with the same size and shape as themselves. By this design, the three-dimensional "memory" of the template was established. Then, in the second step, the template and unreacted reagents were removed by proper repeated washing to generate the cavity specifically for the template. Finally, the sensor was prepared and ready for detection after equilibrium process. The NIP was prepared as a negative control under the same conditions without template. MIP and NIP were characterized with FT-IR spectroscopy.

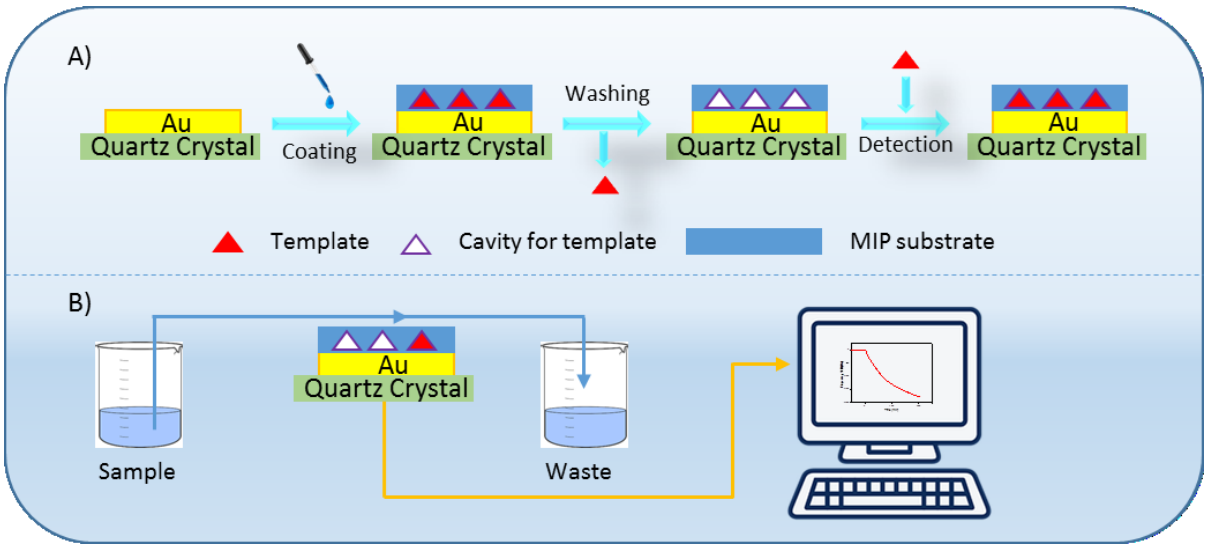



Figure 2. Schematic illustrations of fabrication of the MIP@QCM sensor and detection flow chart

**Fast evaluation of the sensor**

The QCM sensor is based on the piezoelectric properties of quartz crystals which could reflect mass and viscosity changes on the crystal surface. By the aid of the specific nature of MIP, the sensor of MIP@QCM could detect mass of the target captured in samples by reading the corresponding frequency changes according to Sauerbrey's equation in Equation 1. As shown in Figure 2b, in the detection step, the sensor was subjected to the detection of preseted target of MIP. The sample solution was pumped to pass through the surface of MIP@QCM sensor and the frequency shift was monitored in real-time. To rapidly evaluate the response to the target, we performed the detection of water samples in sequence in the interval of 30 minutes, including various concentrations of target from (0.1 to 100 μM or 0.029 to 29 ppm, b to e) as shown in Figure 3a. After 50 minutes of water-rinsing (a), the sensor was brought to resonant frequency ($f_0$). Then frequency of sensor decreased once it was treated with aqueous parathion solution. The frequency remained steady until 10 μM (2.9 ppm) of parathion. By increasing the concentration of parathion, the frequency shifts dramatically enhanced as shown in Table 1. Compared to MIP@QCM sensor, NIP@QCM sensor showed much smaller frequency shifts to the samples. MIP has larger capacity for target as it contained many cavities for binding target molecules, while NIP hold much less target molecules by the nonspecific bonding on the surface. The binding experiment illustrates that the MIP@QCM shows superior specific and sensitive response to the target compared with NIP@QCM.

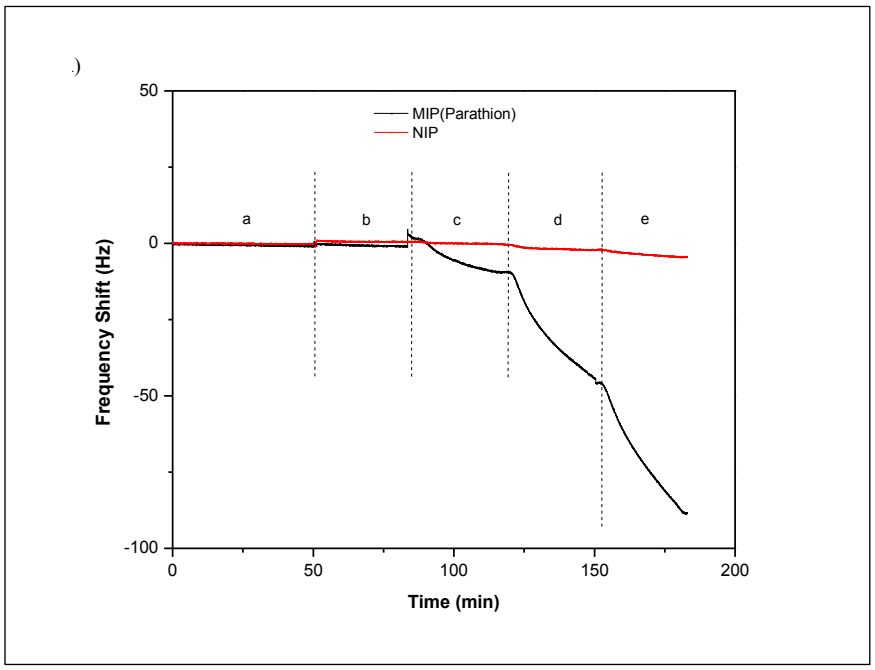



Figure 3. Evaluation of detection of MIP@QCM sensor for parathion against NIP@QCM. A) On-line frequency shift ($\Delta f$, Hz) responses of the sensor for water (a, 50 minutes) and parathion (0.1, 10, 100 µM, b-e) in the interval of 30 minutes. Flow rate: 50 µL/min.

Table 1. The frequency shifts for the corresponding samples.

| **Sample** | **a** | **b** | **c** | **d** | **e** |
|---|---|---|---|---|---|
| Concentration of parathion (µM) | 0 | 0.1 | 10 | 50 | 100 |
| Concentration of parathion (ppm) | 0 | 0.029 | 2.9 | 14.5 | 29 |
| $\Delta f$ of MIP(Hz) | -0.94 | -0.97 | -9.97 | -37.95 | -41.19 |
| $\Delta f$ of NIP(Hz) | -0.14 | 0.36 | -0.36 | -1.78 | -2.6 |

**Performance of the sensor**

After the sensor was evaluated by using aqueous parathion solution, the sensor was further studied to establish the correlation between the frequency shift and sample concentrations. As shown in Figure 4, after 20 min of water flow, the sensor was treated with various concentrations of parathion for 60 min. Compared to the blank sample (0 µM of parathion in water), aqueous parathion solution showed obvious frequency shifts. The calibration curve of frequency shift *vs* concentration of parathion is shown as insert in Figure 4. The limit of detection (LOD) was calculated as 0.83 µM. Table 2 shows the frequency shifts for the corresponding samples.

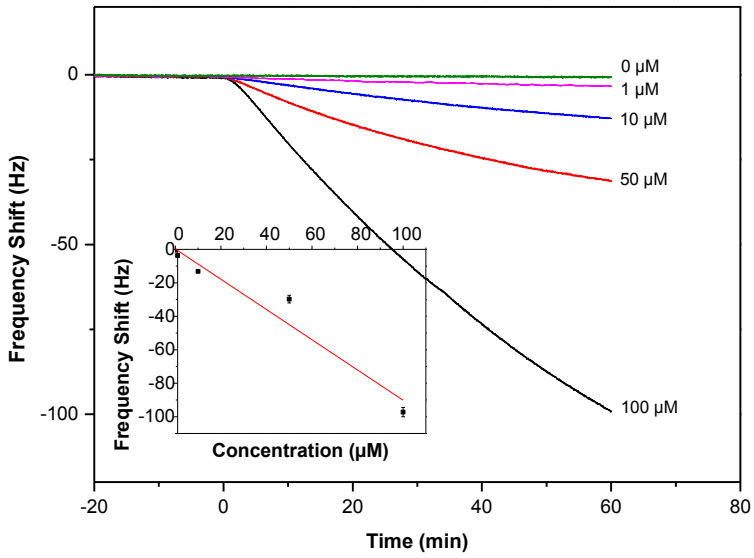



Figure 4. On-line detection of MIP@QCM sensor for parathion. A) On-line frequency ($\Delta f$, Hz) responses of the sensor for parathion (0, 1, 10, 50, 100 μM). 60 minutes of incubation time for each sample. Flow rate: 50 μL/min. Insert: the linear relationship between the frequency shifts against parathion concentration.

Table 2. The frequency shifts for the corresponding samples

| **Concentration of Parathion (μM)** | **0** | **1** | **10** | **50** | **100** |
|---|---|---|---|---|---|
| Concentration of parathion (ppm) | 0 | 0.29 | 2.9 | 14.5 | 29 |
| $\Delta f$ of MIP(Hz) | -0.50 | -3.34 | -12.85 | -31.35 | -99.22 |

**Selectivity of the sensor**

Subsequently the selectivity of MIP (parathion) was evaluated against two analogues – paraoxon and methyl parathion. As shown in Figure 5, the frequency shift of parathion (-30.28 Hz) is much larger than that of methyl parathion (-16.29 Hz) and paraoxon (-11.02 Hz), which indicated MIP (parathion) has higher selectivity to the template (parathion) than to the two analogues. Comparing parathion with paraoxon, MIP (parathion) shows distinct affinities. Although the hydrogen-bonding to the sulphur atom of parathion should be weaker than to the oxygen atom of paraoxon, the dominant interaction is the three-dimensional matching between MIP (parathion) and parathion which is much better for parathion than for paraoxon because of the differences in lone-pair repulsions of sulphur and oxygen atom. Comparing parathion with methyl parathion, the dominant interaction is the differences in three-dimensional matching because of the sizes of ethyl and methyl group. The results indicated that the designed sensor had good selectivity to parathion. Table 3 shows the frequency shifts for the corresponding samples.

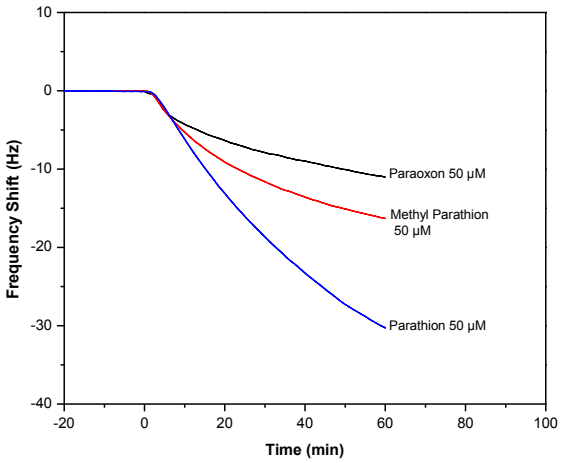



Figure 5. On-line detection of MIP@QCM sensor for parathion against paraoxon and methyl parathion. On-line frequency ($\Delta f$, Hz) responses of the senor parathion (50 µM) against paraoxon (50 µM) and methyl parathion (50 µM). 60 minutes of incubation time for each sample. Flow rate: 50 µL/min. The insets: structures of paraoxon, parathion and methyl parathion.

Table 3. The frequency shifts for the corresponding samples.

| Targets | Paraoxon | Methyl Parathion | Parathion |
|---|---|---|---|
| $\Delta f$ of MIP(Hz) | -11.02 | -16.29 | -30.28 |

## Conclusion

We have developed a novel sensor based on QCM coated with MIPs. The MIP system used methyl methacrylic acid (MAA) as monomer, divinylbenzene (DVB) as cross-linking reagent and azobisisobutyronitrile (AIBN) as initiator. With parathion as the pre-set template, the selectivity experiment showed that the MIP-based QCM sensor could selectively detect parathion in water samples as the MIP offered specific cavity for the template molecule. The sensor has wide detection range (290 ppb ~ 29 ppm) and fast response (60 minutes) to parathion. The sensor is easy to prepare and can be potentially applied to other templates including organophosphorus compounds. The biosensor could potentially be useful for monitoring CTA targets in real water samples.

## Acknowledgement

This research grant (1301-IRIS-021) is supported by the Singapore National Research Foundation under its Environment & Water Research Programme and administered by PUB, Singapore's National Water Agency.

## References

1. Colovic, M. B., Krstic, D. Z., Lazarevic-Pasti, T. D., Bondzic, A. M. and Vasic, V. M. (2013). Acetylcholinesterase inhibitors: Pharmacology and toxicology. *Current Neuropharmacology*, 11(3): 315 – 335.
2. Namba, T. (1971). Cholinesterase inhibition by organophosphorus compounds and its clinical effects. *Bulletin World Health Organization,* 44(1-3): 289 – 307.
3. Delfino, R. T., Ribeiro, T. S. and Figueroa-Villar, J. D. (2009). Organophosphorus compounds as chemical warfare agents: A review. *Journal of the Brazilian Chemical Society*, 20(3): 407 – 428.
4. Obare, S. O., De, C., Guo, W., Haywood, T. L., Samuels, T. A., Adams, C. P., Masika, N. O., Murray, D. H., Anderson, G. A., Campbell, K. and Fletcher, K. (2010). Fluorescent chemosensors for toxic organophosphorus pesticides: A review. *Sensors*, 10(7): 7018 – 7043.

5. Chang, P. L., Hsieh, M. M. and Chiu, T. C. (2016). Recent advances in the determination of pesticides in environmental samples by capillary electrophoresis. *International Journal of Environmental Research and Public Health*, 13(4), 409.
6. Hiramatsu, K., Miura, H., Kamei, S., Iwasaki, K. and Kawakita, M. (1998). Development of a sensitive and accurate enzyme-linked immunosorbent assay (ELISA) system that can replace HPLC analysis for the determination of N 1, N 12-diacetylspermine in human urine. *Journal of Biochemistry*, 124(1): 231 – 236.
7. Wang, X., Qiao, X., Ma, Y., Zhao, T. and Xu, Z. (2013). Simultaneous determination of nine trace organophosphorous pesticide residues in fruit samples using molecularly imprinted matrix solid-phase dispersion followed by gas chromatography. *Journal of Agricultural and Food Chemistry*, 61(16): 3821 – 3827.
8. Pico, Y., Louter, A. J., Vreuls, J. J. and Udo, A. T. (1994). On-line trace-level enrichment gas chromatography of triazine herbicides, organophosphorus pesticides, and organosulfur compounds from drinking and surface waters. *Analyst*, 119(9): 2025 – 2031.
9. Cheong, W. J., Yang, S. H. and Ali, F. (2013). Molecular imprinted polymers for separation science: A review of reviews. *Journal of Separation Science*, 36(3): 609 – 628.
10. Algieri, C., Drioli, E., Guzzo, L. and Donato, L. (2014). Bio-mimetic sensors based on molecularly imprinted membranes. *Sensors*, 14(8): 13863 – 13912.
11. Baggiani, C., Anfossi, L. and Giovannoli, C. (2013). MIP-based immunoassays: State of the art, limitations and perspectives. *Molecular Imprinting*, 1: 41 – 54.
12. Haginaka, J., Tabo, H. and Matsunaga, H. (2012). Preparation of molecularly imprinted polymers for organophosphates and their application to the recognition of organophosphorus compounds and phosphopeptides. *Analytica Chimica Acta*, 748: 1 – 8.
13. Xin, J., Qiao, X., Ma, Y. and Xu, Z. (2012). Simultaneous separation and determination of eight organophosphorous pesticide residues in vegetables through molecularly imprinted solid-phase extraction coupled to gas chromatography. *Journal 0f Separation Science*, 35(24), 3501 – 3508.
14. Zhang, D., Yu, D., Zhao, W., Yang, Q., Kajiura, H., Li, Y., Zhou, T. and Shi, G. (2012). A molecularly imprinted polymer based on functionalized multiwalled carbon nanotubes for the electrochemical detection of parathion-methyl. *Analyst*, 137(11): 2629 – 2636.
15. Yan, M. (2004). Molecularly imprinted materials: Science and technology. CRC press.
16. Ye, L. (2013). Molecular imprinting: Principles and applications of micro-and nanostructure polymers. CRC press.
17. Ward, M. D. and Buttry, D. A. (1990). In situ interfacial mass detection wi piezoelectric transducers. *Science*, 249(4972): 1000 – 1007.
18. Cooper, M. A. and Singleton, V. T. (2007). A survey of the 2001 to 2005 quartz crystal microbalance biosensor literature: Applications of acoustic physics to the analysis of biomolecular interactions. *Journal of Molecular Recognition*, 20(3): 154 – 184.
19. Vashist, S. K. and Vashist, P. (2011). Recent advances in quartz crystal microbalance-based sensors. *Journal of Sensors*, 2011: 1 – 13.
20. Hong, S. R., Kim, M. S., Jeong, H. D. and Hong, S. (2017). Development of real - time and quantitative QCM immunosensor for the rapid diagnosis of Aeromonas hydrophila infection. *Aquaculture Research*, 48(5): 2055 – 2063.
21. Vethanayagam, A. V. A. (1962). Folidol (parathion) poisoning. *British Medical Journal*, 1962): 986 – 987.

*Malaysian Journal of Analytical Sciences, Vol 21 No 6 (2017): 1335 - 1341*
*DOI: https://doi.org/10.17576/mjas-2017-2106-14*

MALAYSIAN JOURNAL OF ANALYTICAL SCIENCES
*Published by The Malaysian Analytical Sciences Society*
ISSN 1394 - 2506

# DETECTION OF BIOMOLECULES BY A NOVEL FLUORESCENCE APTASENSOR BASED ON POLYDOPAMINE SPHERES

## (Pengesanan Biomolekul oleh Aptasensor Pendarfluor Novel Berasaskan Sfera Polidopamina)

Haiyan Li[1] and Sam Fong Yau Li[1, 2]*

[1]*Department of Chemistry,*
*National University of Singapore, 3 Science Drive 3, Singapore 117543, Singapore*
[2]*NUS Environmental Research Institute,*
*5A Engineering Drive 1, T-Lab Building, Singapore 117411, Singapore*

**Corresponding author: chmlifys@nus.edu.sg*

Received: 7 November 2016; Accepted: 18 September 2017

**Abstract**

Aptamers are alternative bio-recognition elements to antibodies, with great advantages, such as high binding affinity and specificity, controllable structures. In this study, a novel fluorescent aptasensor for biomolecules detection has been designed by using aptamer as bio-recognition element and polydopamines as nanoquencher. Bovine catalase protein (BCP) was used as target for assay validation. BCP aptamer was selected based on previous work in our group. Polydopamine spheres (250 – 300 nm) were synthesized by addition of dopamine hydrochloride into a mixture of tris-buffer and isopropyl alcohol with stirring for more than 2 days and size/morphology of spheres has been characterized. The quenching efficiency and sensing performance were examined. It was found that the quenching efficiency was good (> 90%) owing to the interaction between aptamer and polydopamines since FAM labeled ssDNA aptamer could be adsorbed onto polydopamines surface to form a complex, resulting in the quenching of fluorescence. Upon the introduction of BCP, the fluorescence could be retained. The fluorescence intensity increased with the increasing concentration of BCP with the detection limit of 10 nM. Polydopamines could be used as sensing platform in fast and simple way for biomolecules detection and have potential to be extended to other targets.

**Keywords**: biosensors, aptamer, polydopamine, nanoquencher, protein

**Abstrak**

Aptamer adalah elemen alternatif pengecaman-bio terhadap antibodi, dengan kelebihan seperti ikatan keafinan yang kuat dan khusus, kebolehkawalan struktur. Dalam kajian ini, aptasensor pendarflour novel untuk pengesanan biomolekul telah di reka bentuk dengan mengunakan aptameter sebagai elemen pengecaman-bio dan polidopamina sebagai nanoquencher. Protein katalase Bovin (BCP) telah digunakan sebagai sasaran bagi ujian validasi. Aptameter BCP telah dipilih berdasarkan kerja terdahulu. Sfera polidopamina (250 – 300 nm) telah di sistesis melalui penambahan dopamina hidroklorik ke dalam campuran penimbal-tris dan alkohol isopropil dengan pengacauan melebihi 2 hari dan saiz/morfologi juga telah dicirikan. Keberkesanan pemelindapan dan prestasi sensor telah dikaji. Ia di dapati bahawa keberkesanan pemelindapan adalah baik (> 90%) terhadap interaksi antara aptameter dan polidopamina di ketahui bahawa aptamer ssDNA berlabel FAM berupaya menyerap ke dalam permukaan polidopamina untuk membentuk kompleks, menghasilkan pemelindapan pendarfluor. Apabila BCP didedahkan, sifat pendafluor dapat dikekalkan. Keamatan pendafluor meningkat seiring dengan peningkatan kepekatan BCP pada had pengesan ialah 10 nM. Polidopamina boleh digunakan sebagai platfom sensor yang pantas dan mudah bagi pegesanan biomolekul dan berpotensi untuk dikembangkan bagi sasaran lain.

**Kata kunci**: sensor-bio, aptamer, polidopamina, nanoquencher, protein

## Introduction

Detection of biomolecules (biotoxins, proteins) with simple, fast, cost-effective and sensitive assay is crucial to the identification of disease-causing pathogens and water or food contamination, as well as other activities. Challenges remain in accurate and comprehensive detection and quantification of these compounds in short time at low concentrations in complex samples. Catalase is a common acidic protein that can be found in various species and is responsible for the conversion of hydrogen peroxide into water and carbon dioxide [1]. Catalase is identified as a possible bio-indicator of mastitis disease in cattle and could be used to monitor the quality of the milk.

A sensor is a device that transforms chemical or biological information, ranging from the concentration of a specific sample component to total composition analysis, into an analytically useful signal [2]. Bio-recognition elements are the important part for application of biosensors. Aptamers are special nucleic acid sequences that can bind to a wide range of targets, such as proteins, organic molecules, various cell surface receptors, and whole cells. They can be used as alternative bio-recognition elements to antibodies, with great advantages, such as high binding affinity and specificity, controllable structures and stability. Hence aptamers can be an ideal bioreceptor for the detection of biomolecules in environment, food or clinical samples. Biosensor with aptamers as ligands could be called as aptasensor. Conventional methods, such as chromatography-based and MS-based assays, are time consuming, labour intensive and not able to support on site detection. Compared to conventional methods, aptamer based biosensor can offer a sensing platform for fast disease screening and biotoxin monitoring for food and water safety.

Among different transducing systems, fluorescence is a highly sensitive platform for biomolecular detection. Nanomaterials could be used as novel biosensing platforms because of their unique optical, electronic, and catalytic properties [3]. It has been reported that some kind of nanostructures like gold nanoparticles (AuNPs), single-walled carbon nanotubes (SWCNTs), graphene oxide (GO), carbon nanoparticles and polydopamines (PDAs) can quench fluorescent dyes at different emission frequencies, which could eliminate the selection issue of fluorophore-quencher pair in such assay [4-10]. It is demonstrated that PDAs would quench the fluorescence of those fluorophores due to fluorescence resonance energy transfer (FRET) [8, 9]. Furthermore, the monomer dopamine and its oxide quinone, have shown quenching ability towards fluorophores via photoinduced electron transfer (PET) [11]. Polydopamine is a biopolymer which presents excellent biocompatibility and low cytotoxicity since it could be biodegraded in the organism through metabolism [12], which facility its application on biomolecules detection.

In the present work, a fluorescence aptasensor has been developed by taking advantage of specific aptamer and polydopamine sensing platform which is based on the fluorescence recovery due to target recognition. Bovine catalase protein (BCP) was used as target since some biotoxins are under higher biosafety control and BCP can be used as simulant of protein toxins for assay development. BCP aptamer was selected based on previous work in our group [13]. The quenching efficiency of polydopamine was studied and employed for the development of quenching based aptasensing platform.

## Materials and Methods

### Reagents and materials

Dopamine hydrochloride and bovine catalase protein were purchased from Sigma Aldrich (Singapore). FAM dye-labelled ssDNA aptamer (FAM-Aptamer, listed below) ligand of sequence was purchased from Integrated DNA Technologies Pte Ltd (IDT, Singapore) and reconstituted in 10 mM PBS buffer (pH 7.4). Aptamers were renatured using a Bio-Rad DNA engine thermocycler (Bio-Rad, Singapore) by heating to 94 ℃ for 10 minutes and then cooling down to room temperature at rate of 0.5 ℃/s. 10 mM Tris–HCl buffer (pH 7.2) was used and all other reagents were of analytical reagent grade. The water used was purified through a Millipore system.

FAM-Aptamer: 5’-CTT CTG CCC GCC TCC TTC CGA CCT AGC AGT GGA CAT GTG GCA GGG TGA AGT GGC ATC GTC GGA GAC GAG ATA GGC GGA CAC T-3’

### Synthesis of polydopamine

PDAs were synthesized according to previous reported method [14] with some modification. 100 mL of Tris-buffer solution was mixed with 40 mL of isopropyl alcohol (IPA). Then, 120 mg of dopamine hydrochloride was added to the mixed solution. Finally, PDA spheres (PDAs) can be obtained after polymerization under stirring for about 60

hours. The suspension was centrifuged, washed and re-suspended with water for several times. The precipitate was dried in vacuum for sensing experiments. Characterization of PDAs was performed by SHIMADZU IR Prestige21 spectrophotometry for the Fourier transform infrared (FTIR, Japan) and JEOL JSM-6701F Field Emission Scanning Electron Microscope (FESEM, Japan), respectively.

**Quenching and detection process**

The fluorescence emission spectrum was recorded for quenching and detection process with a Gilden Photonics FluoroSENS Fluorometer (United Kingdom). The emission spectra were recorded from 500 to 650 nm at an excitation wavelength of 470 nm, and the fluorescence intensity at 517 nm was used for quantitative analysis. For the quenching process, FAM-aptamer (40 nM) was incubated with PDAs at different concentration for 10 min at room temperature before the fluorescent detection. Then different amount of concentrated catalase solution (2 μM) was added to make BCP at 10, 20, 50, 100, 200, 500 and 1000 nM in the mixtures for detection process respectively. After a gentle mixing, the mixtures were allowed to incubate for 1 hour at 37 ℃ before the fluorescence measurement.

## Results and Discussion

**The sensing scheme of the platform**

The principle of nanomaterial quenching and sensing is shown in Figure 1. 6-carboxyfluorescein (FAM), labelled the aptamer at the 5' end, has strong fluorescence emission. Free fluorophore labelled ssDNA aptamer possess a strong fluorescence emission in the presence of the fluorescein-based dye. PDAs include dihydroxyindole, indoledione, and dopamine units. The interaction between PDAs and ssDNA might be non-covalent binding due to hydrogen bonding, π–π stacking, or charge-transfer complexes between the units of PDA and nucleobases [8, 15, 16]. Thus the introduction of PDAs would result in binding with probe ssDNA to form a complex, resulting in quenching process of the fluorescence due to FRET between PDAs and the fluorescent dye FAM. However, the complementary interaction between protein and aptamer will induce the conformation of aptamer upon the introduction of targets. In consequence, fluorophore labelled aptamer would release from surface of PDAs due to the weakened interaction between them, leading to the recovery of the fluorescence. Hence, the restoration of fluorescence can be applied to the quantitative analysis of target DNA or toxin protein.

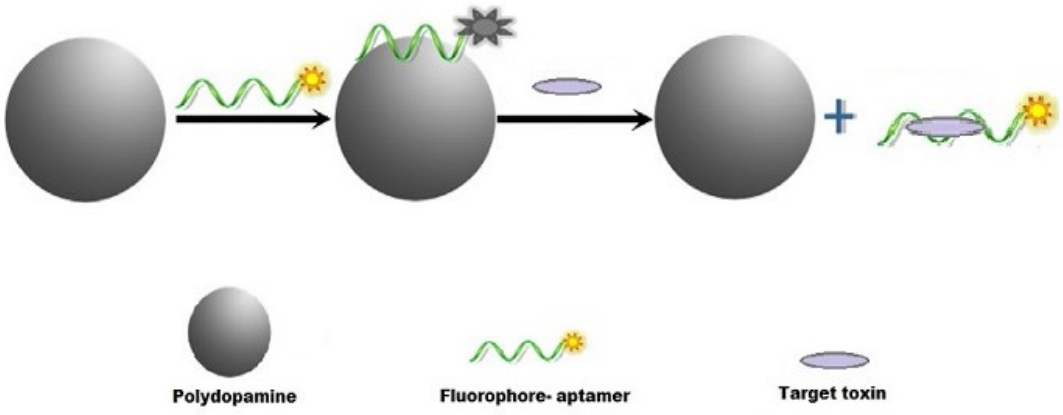



Figure 1. The principle of the sensing of protein

**Characterization of PDAs**

PDA spheres were synthesized in presence of IPA. The morphology and particle size of PDA spheres were characterized by FESEM, shown in Figure 2a. It could be found the size of the obtained PDA spheres is in the 250 – 300 nm range. The FTIR spectrum of PDAs, shown in Figure 2b, gives the characteristic peaks of several functional groups, such as C=O (~1625 $cm^{-1}$), C=C (~1521 $cm^{-1}$) and C–O (~1280 $cm^{-1}$), which also indicate that PDA is a π-

rich polymer. The absorption band at ~3400 $cm^{-1}$ corresponds to the stretching vibrations of –OH and N–H groups in the PDAs.

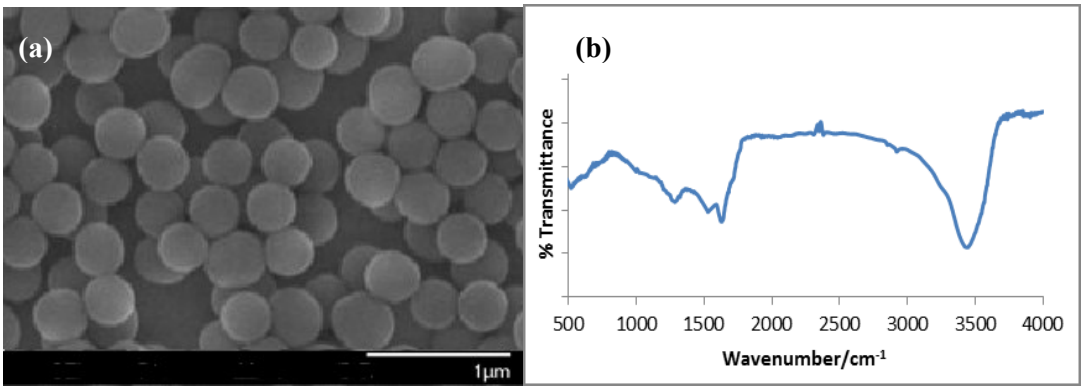


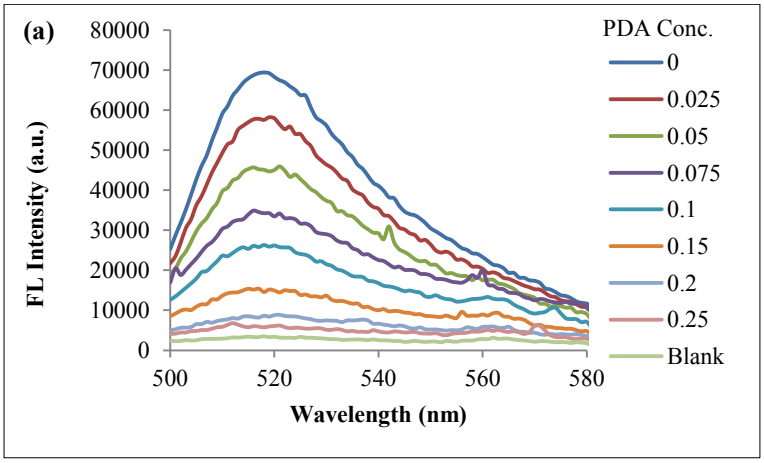

Figure 2. Characterization of PDAs. (a) SEM image and (b) FTIR spectra

**Quenching efficiency**

The feasibility of using PDA as nanoquencher for protein detection was explored. The fluorescence quenching abilities of the PDAs to the FAM-labelled aptamer were evaluated by measurements mixture of aptamer with the PDAs after incubation for 10 min. As shown in the Figure 3a, the emission fluorescence of FAM-aptamer was partly quenched as the introduction of the PDAs. Quenching efficiency (QE) could be calculated as shown in equation 1:

$$\frac{(FLo-FLr)}{FLo} \times 100\% \quad (1)$$

where $FL_o$ and $FL_r$ are fluorescence intensities without and with PDAs, respectively. Quenching efficiency increased with the increasing concentration of PDAs due to complex formation of FAM-Aptamer-PDAs. After PDAs was more than 0.2 mg/mL, the quenching efficiency was more than 90% (Figure 3b) and almost consistent with more PDAs. Thus, 0.2 mg/mL was used for further sensing tests.



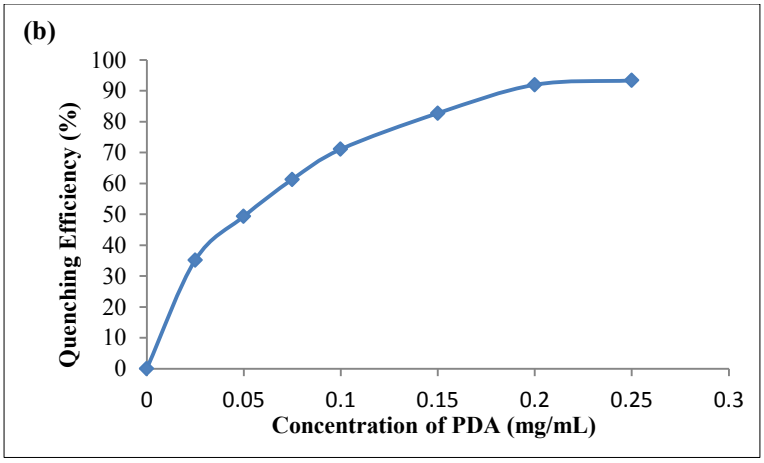
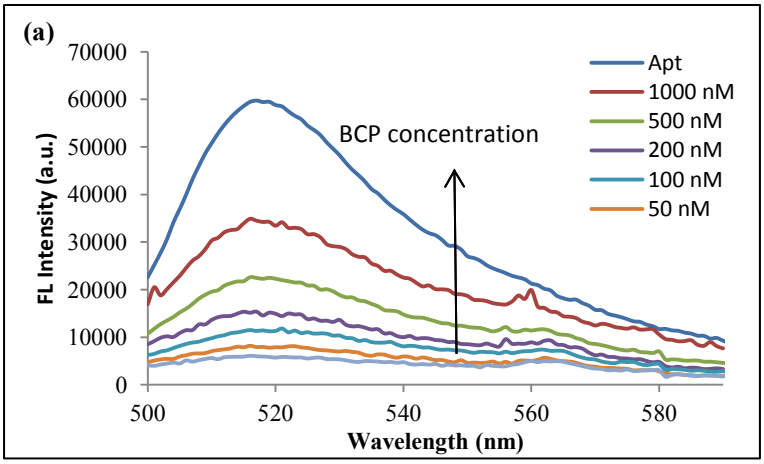



Figure 3. (a) Fluorescence spectra and (b) Quenching efficiency of FAM-aptamer with different concentrations of PDAs

**Detection process**

Fluorescence recovery was observed after the introduction of BCP with incubation time for 1 hour. Figure 4a shows the fluorescence emission spectra of FAM-Aptamer-PDAs in the presence of different concentrations of target. It could be found that more FAM-Aptamer was released which resulting in retained fluorescence with increasing concentration of BCP. By calculating difference of fluorescence intensity in presence and absence of BCP, the calibration curve can be given as shown in Figure 4b. A dynamic range of 10 – 1000 nM was established based on the fluorescence intensity. The limit of BCP detection was estimated to be 10 nM. The relative standard deviation is less than 10%, which exhibits the reproducible results for this detection system. However, the recovery of fluorescence was not high though high concentration of BCP was added which may be caused by affinity problems of aptamer to target or short incubation time for releasing. The further optimization for the detection process would facility the improvement on sensitivity and accuracy.



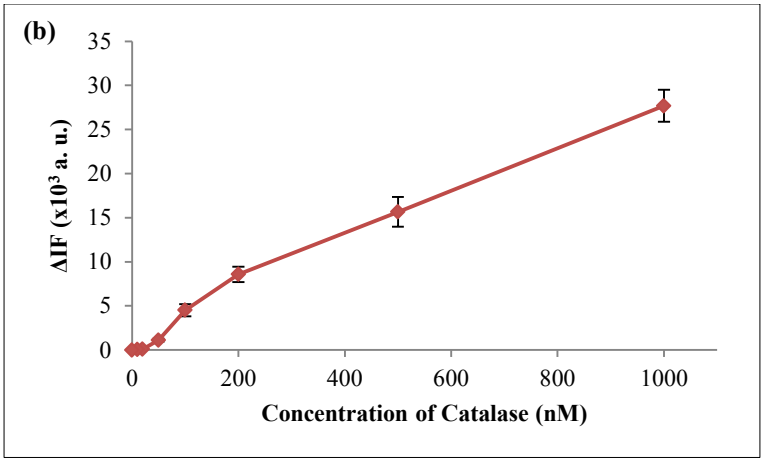



Figure 4. Fluorescence spectra (a) and calibration curve (b) for the FAM-Aptamer-PDAs in the presence of different concentrations of target BCP. Error bars are standard deviation from triplicates trial

## Conclusion

In summary, a fluorescence aptasensor has been developed by taking advantage of specific aptamer and polydopamine sensing platform. It was found that the quenching efficiency was good (> 90%) owing to the interaction between FAM-aptamer and PDAs. The retained fluorescence intensity increased with the increasing concentration of target BCP. The detection limit was confirmed at 10 nM. Further optimization of detection conditions may help to improve sensitivity. Some characterization of the developed sensor, such as interference effect by other compounds, would be performed in further study. PDAs could be used as sensing platform in fast and simple way for proteins detection and have potential to be extended to other targets.

## References

1. Chelikani, P., Fita, I. and Loewen, P. C. (2004). Diversity of structures and properties among catalases. *Cellular and Molecular Life Sciences*, 61(2): 192 – 208.
2. Hulanicki, A., Glab, S. and Ingman, F. (1991). Chemical sensors: Definitions and classification. *Pure and Applied Chemistry*, 63(9): 1247 – 1250.
3. Aragay, G., Pino, F. and Merkoçi, A. (2012). Nanomaterials for sensing and destroying pesticides. *Chemical Reviews*, 112(10): 5317 – 5338.
4. Dubertret, B., Calame, M. and Libchaber, A. J. (2001). Single-mismatch detection using gold-quenched fluorescent oligonucleotides. *Nature Biotechnology*, 19(4): 365 – 370.
5. Yang, R., Jin, J., Chen, Y., Shao, N., Kang, H., Xiao, Z., Tang, Z. W., Wu, Y. R., Zhu, Z. and Tan, W. H. (2008). Carbon nanotube-quenched fluorescent oligonucleotides: Probes that fluoresce upon hybridization. *Journal of the American Chemical Society*, 130(26): 8351 – 8358.
6. Lu, C. H., Yang, H. H., Zhu, C. L., Chen, X. and Chen, G. N. (2009). A graphene platform for sensing biomolecules. *Angewandte Chemie*, 121(26): 4879 – 4881.
7. Duan, Y. F., Ning, Y., Song, Y. and Deng, L. (2014). Fluorescent aptasensor for the determination of Salmonella typhimurium based on a graphene oxide platform. *Microchimica Acta*, 181(5-6): 647 – 653.
8. Qiang, W., Li, W., Li, X., Chen, X. and Xu, D. (2014). Bioinspired polydopamine nanospheres: A superquencher for fluorescence sensing of biomolecules. *Chemical Science*, 5(8): 3018 – 3024.
9. Liu, Q., Pu, Z., Asiri, A. M., Al-Youbi, A. O. and Sun, X. (2014). Polydopamine nanospheres: A biopolymer-based fluorescent sensing platform for DNA detection. *Sensors and Actuators B: Chemical,* 191: 567 – 571.
10. Li, H., Zhang, Y., Wang, L., Tian, J. and Sun, X. (2011). Nucleic acid detection using carbon nanoparticles as a fluorescent sensing platform. *Chemical Communications*, 47(3): 961 – 963.
11. Ji, X., Palui, G., Avellini, T., Na, H. B., Yi, C., Knappenberger Jr, K. L. and Mattoussi, H. (2012). On the pH-dependent quenching of quantum dot photoluminescence by redox active dopamine. *Journal of the American Chemical Society*, 134(13): 6006 – 6017.

12. Liu, Y., Ai, K. and Lu, L. (2014). Polydopamine and its derivative materials: Synthesis and promising applications in energy, environmental, and biomedical fields. *Chemical Reviews*, 114(9): 5057 – 5115.
13. Ashley, J., Ji, K. and Li, S. F. (2012). Selection of bovine catalase aptamers using non – SELEX. *Electrophoresis*, 33(17): 2783 – 2789.
14. Yan, J., Yang, L., Lin, M. F., Ma, J., Lu, X. and Lee, P. S. (2013). Polydopamine spheres as active templates for convenient synthesis of various nanostructures. *Small*, 9(4): 596 – 603.
15. d'Ischia, M., Napolitano, A., Pezzella, A., Meredith, P. and Sarna, T. (2009). Chemical and Structural Diversity in Eumelanins: Unexplored Bio-Optoelectronic Materials. *Angewandte Chemie International Edition*, 48(22): 3914 – 3921.
16. Varghese, N., Mogera, U., Govindaraj, A., Das, A., Maiti, P. K., Sood, A. K. and Rao, C. N. R. (2009). Binding of DNA nucleobases and nucleosides with graphene. *ChemPhysChem*, 10(1): 206 – 210.

*Malaysian Journal of Analytical Sciences, Vol 21 No 6 (2017): 1342 - 1351*
*DOI: https://doi.org/10.17576/mjas-2017-2106-16*

MALAYSIAN JOURNAL OF ANALYTICAL SCIENCES
*Published by The Malaysian Analytical Sciences Society*
ISSN 1394 - 2506

# FLUORESCENCE QUENCHING ON MESOPOROUS CARBON NITRIDE BY PHENOL AND ANILINE

## (Pelindapan Pendarfluor pada Karbon Nitrida Mesoliang oleh Fenol dan Anilina)

Leny Yuliati[1,2,3]*, Ahmad Hanami Abd Kadir[4], Siew Ling Lee[3,4], Hendrik O. Lintang[1,2,3]

[1]*Ma Chung Research Center for Photosynthetic Pigments*
[2]*Department of Chemistry, Faculty of Science and Technology*
*Universitas Ma Chung, Villa Puncak Tidar N-01, Malang 65151, East Java, Indonesia*
[3]*Centre for Sustainable Nanomaterials, Ibnu Sina Institute for Scientific and Industrial Research*
[4]*Department of Chemistry, Faculty of Science*
*Universiti Teknologi Malaysia, 81310 UTM Johor Bahru, Johor, Malaysia*

**Corresponding author: leny.yuliati@machung.ac.id*

Received: 7 November 2016; Accepted: 18 September 2017

**Abstract**

In this study, fluorescence quenching on mesoporous carbon nitride (MCN) was examined in the presence of phenol and aniline. The MCN was synthesized by thermal polymerization of cyanamide using nanocolloidal silica (7 nm) as a hard template and characterized by X-ray diffractometer (XRD), Fourier transform infrared (FTIR), transmission electron microscope (TEM), specific surface area, pore size distribution, and fluorescence spectrophotometer. The MCN showed two excitation wavelengths at 275 and 370 nm, owing to the presence of N=C and N-C terminal groups, respectively. These two excitation wavelengths gave only one emission peak at around 460 nm. Either in the presence of phenol or aniline, the emission intensity of the MCN was confirmed to be quenched in a linear function towards the concentration of phenol or aniline as the quencher molecule. N-C terminal groups were found to have slightly better interactions to phenol and aniline as compared to the N=C groups. Since the emission intensity of MCN was more quenched by phenol molecules than the aniline, it was proposed that the MCN would have stronger interaction to phenol than aniline. This result was also supported by the adsorption data, in which the MCN gave higher adsorption towards phenol than the aniline.

**Keywords**: mesoporous carbon nitride, phenol, aniline, fluorescence quenching, adsorption

**Abstrak**

Dalam kajian ini, pelindapan pendarfluor pada karbon nitrida mesoliang (MCN) telah diperiksa dengan kehadiran fenol dan anilina. MCN telah disintesis secara pempolimeran haba sianamida menggunakan silika nanokoloid (7 nm) sebagai templat keras dan telah dicirikan dengan pembelauan sinar-X (XRD), inframerah transformasi Fourier (FTIR), mikroskop elektron transmisi (TEM), luas permukaan, taburan saiz liang, dan spektroskopi pendafluor. MCN menunjukkan dua panjang gelombang pengujaan pada 275 dan 370 nm oleh kerana kehadiran masing – masing N=C dan N-C sebagai kumpulan terminal. Kedua-dua panjang gelombang pengujaan memberikan hanya satu puncak pelepasan pada kira-kira 460 nm.Sama ada dengan kehadiran fenol atau anilina, keamatan pemancaran daripada MCN disahkan mengalami pelindapan dalam fungsi linear terhadap kepekatan fenol atau anilina sebagai molekul pelindap. Kumpulan terminal N-C didapati mempunyai interaksi lebih baik sedikit untuk fenol dan anilina berbanding dengan kumpulan N=C. Oleh kerana keamatan pemancaran MCN didapati lebih terlindap oleh molekul fenol berbanding dengan anilina, adalah dicadangkan bahawa MCN berinteraksi lebih kuat dengan fenol dibandingkan dengan anilina. Keputusan ini juga disokong oleh data penjerapan, dengan MCN memberikan penjerapan yang lebih tinggi terhadap fenol dibandingkan dengan anilina.

**Kata kunci:** karbon nitrida mesoliang, fenol, anilina, pelindapan pendarfluor, penjerapan

## Introduction

Carbon nitrides (CN) are carbon materials in which some carbon atoms in the graphite-like structure are replaced by some nitrogen atoms in a regular manner. Generally, CN stands for a large family of related compounds ($C_xN_y$) [1 – 3]. Even though the CN has been reported since the 1990s, this material still receives considerable attention because of its versatility until nowadays. The CN is used in various applications while the material is just composed of C, N and H atoms [4]. Other factors that make CN being well explored is because of the abundance of these atoms on earth, non-toxic and easy to be synthesized into a desired shape where the pore of carbon nitride is tunable to form mesoporous carbon nitride (MCN) [1, 5, 6]. MCN has a larger specific surface area than the CN and it facilitated better performance for various applications [7 – 12]. Moreover, CN has many advantageous properties that make it an interesting material, such as high thermal and chemical stability, and great optical properties [13 – 15].

Recently, application of CN and MCN as fluorescence sensor has been a significant interest. Owing to the presence of fluorescent active sites (tri-*s*-triazine units), CN and MCN are potential materials to be used as an optical sensor. Despite of the fact that these materials have a strong fluorescence property, less attention was paid on its sensing ability until there was a report showing the utilities of cubic MCN as all-in-one chemosensor for sensing of trace amount of metal ions in aqueous solution [16]. Since the cubic MCN has the highest sensitivity and selectivity towards copper ions, further modification was also carried out by the research group on the cubic MCN incorporating copper ions for sensing of cyanide ions, which are very poisonous and used abundantly in metal plating industry [17]. CN has been also reported as an efficient fluorosensor for detection of copper ions. It was suggested that the fluorescence quenching was due to strong coordination of the Lewis basic sites on the CN with the Cu ions [18]. Besides metal and cyanide ions, recent studies showed that nitrogen-containing compounds can be also detected by fluorescence quenching. It was reported that MCN was able to be used as a fluorescence sensor for *N*-nitrosopyrrolidone (NPYR) [7]. The surface interaction was proposed to involve electrostatic interactions between the electropositive N and electropositive N at the NPYR molecules and terminal N-C groups of the MCN, respectively. CN was also reported as a fluorescence chemical sensor for nitrate ions [19].

In this study, fluorescence quenching on MCN was investigated in the presence of aromatic compounds, which are phenol and aniline. Phenol is considered as one of the organic pollutants that can be easily found in industrial wastewater [20 – 22]. The wastewater containing phenol may cause the contamination of groundwater and it will give bad effects for ecosystems and also for human. Meanwhile, aniline is also recognized as one of the high priority pollutants that are released from several industries, such as various manufacturers of dyes, and rubber, which caused wide distribution of aniline in the environment [23 – 25]. As an adsorbent, MCN possesses well-ordered porosity, high surface area, and basic groups (NH and $NH_2$) in the structures, which are the important criteria for the removal of organic pollutants. Due to the nitrogen rich structure of MCN with basicity property, it showed remarkable adsorptions towards one of the acidic persistent organic pollutants, *i.e*. phenol [26]. On the other hand, the MCN was also reported showing superior capability to adsorb aniline than the CN and MCM-41 [8, 9]. Therefore, based on these reported studies, the fluorescence quenching on MCN by phenol and aniline is feasible. This study demonstrated that MCN can be also used as a fluorescence sensor for the aromatic compounds.

## Materials and Methods

### Preparation of MCN

The MCN was prepared by a thermal polymerization of cyanamide as the precursor, in the similar way to the method reported in other literatures [7 – 9]. The cyanamide was mixed with the colloidal silica as a hard template 7 nm (mass ratio was 1:1), followed by stirring and heating at 363 K until a white powder was formed. The obtained white powder was ground and then heated at a temperature of 823 K for 4 hours. In order to obtain the MCN, the silica template was removed by treating the MCN powder with the $NH_4HF_2$ solution (4 M, 400 mL) under vigorous stirring and also with ethanol and distilled water. This washing step was repeated for three times. After washing and filtration, the powder was dried at 343 K overnight in an oven.

### Characterizations

The structure of the MCN was determined by an X-ray diffractometer (XRD) on a Bruker D8 Advance Diffractometer at ambient temperature, with a scan rate of 0.05 $s^{-1}$ using Cu-Kα radiation where $\lambda$ equals to

1.5406 Å at 40 kV and 40 mA. To determine the structural information and functional groups of the MCN, a Fourier transform infrared spectroscopy (FTIR) was employed using a FTIR Nicolet iS50 Thermo Scientific. For pellet preparation, a small amount of the MCN was mixed with potassium bromide (KBr) and put under a pellet press. To obtain a better background correction, nitrogen gas was purged into the system before the analysis to remove all humidity. Morphology of the MCN was measured using a transmission electron microscope (TEM) on a JEOL JEM-2100. The MCN powder was first dispersed well in acetone, and then put onto the copper grid to be observed with the TEM. The surface area of the MCN was determined by using the Brunauer-Emmet-Teller (BET) equation, while the pore size of the MCN was determined using the Barret-Joyner-Halenda (BJH) from adsorption-desorption isotherm at 77 K obtained on a Quanta chrome Autosorb-1 instrument. The fluorescence properties were measured using a JASCO Spectrofluorometer FP-8500 to obtain the excitation and emission spectra. The excitation wavelengths used to monitor the emission spectra were 275 and 370 nm, while the emission wavelength used to monitor the excitation spectra was 460 nm. The analysis was carried out at room temperature.

**Fluorescence quenching**

The quenching tests were carried out with various concentrations of phenol and aniline on the MCN (50 mg) at room temperature. The excitation wavelengths at 275 and 370 nm of the MCN were determined by observing the emission spectrum at 460 nm. Meanwhile, the emission wavelength was determined by observing excitation spectra at both excitation wavelengths. From various amounts of phenol solutions (300 – 600 ppm), 20 µL of the solution was taken and then introduced onto the MCN for the quenching test for phenol. The changes in the emission spectra of the MCN were then measured at excitation wavelengths of 275 and 370 nm. As for the quenching test for aniline, the same steps were followed using various concentrations of aniline solution (200 –700 ppm).

**Adsorption tests**

The adsorption process of phenol or aniline onto the MCN was conducted under dark condition using various concentrations of phenol (60 – 400 ppm) and aniline (100 – 500 ppm) at room temperature. Different series of concentrations were selected due to the different behaviors of the observable adsorption. A magnetic bar was put in a 30 mL beaker and 10 mL of phenol or aniline solution was poured into the beaker together with the MCN (50 mg). Inside a closed box, the beaker containing the mixture was placed on the stirring plate and stirred for 6 hours. After filtration and separation from the MCN, the solution was analysed using gas chromatography with a flame ionization detector (GC-FID) on an Agilent 7820AGC-FID. The adsorbed amount was determined by subtracting the initial phenol or aniline with the amounts of remaining phenol or aniline after the adsorption test.

## Results and Discussion

**Properties of MCN**

Shown in Figure 1(a) is the XRD pattern of the prepared MCN, which gave two diffraction peaks at $2\theta$ of 13.1 and 27.4°. The peak at $2\theta$ of 13.1° was corresponding to the distance of 0.66 nm, which indicated the in-planar repeating units and structural packing motif, such as hole-to-hole distance of the nitride pores, while the intense diffraction peak at the $2\theta$ of 27.4° could be indexed as (002) for graphitic materials, giving an interlayer distance of 0.325 nm for the graphite-like stacking of the conjugated aromatic CN layers. This result is in good agreement with values reported elsewhere [4, 7 – 11, 13, 14]. Therefore, it can be concluded that the MCN sample was successfully synthesized.

The functional groups present on the MCN were investigated by FTIR spectroscopy. As shown in Figure 1(b), the absorption peaks of the MCN were observable at the region of 809, 1200 – 1700 and 3000 – 3700 $cm^{-1}$. The bands at 809, 1252, 1319, 1428 and 1646 $cm^{-1}$ could be attributed to the vibration modes of heterocyclic tri-*s*-triazine ring ($C_6N_7$) units, while the broad peak at 3163 $cm^{-1}$ could be assigned to two overlapping bands of stretching modes of N-H and O-H groups [9, 11, 27]. The peak at 2177 $cm^{-1}$ could be attributed to the presence of C≡N or N=C=N group, which was reported in MCN prepared via thermal polymerization reaction [27]. These FTIR spectra supported that the MCN sample was successfully prepared.

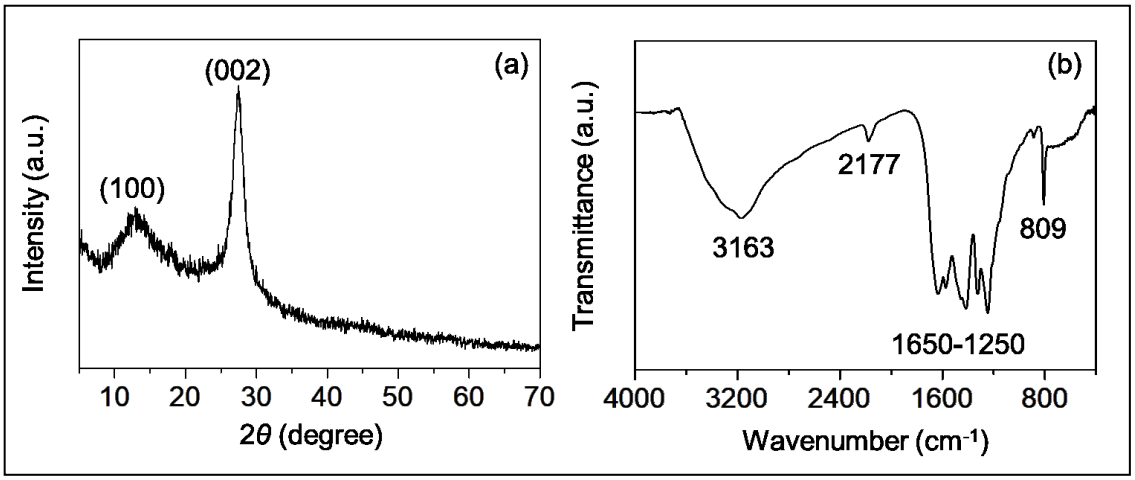



Figure 1. (a) XRD pattern and (b) FTIR spectrum of MCN

The morphology of the prepared MCN was observed by TEM as shown in Figure 2. It can be seen that the MCN has uneven layers due to the graphitic structures of the MCN. Figure 3(a) shows the nitrogen adsorption-desorption isotherms and Figure 3(b) shows the Barrett-Joyner-Halenda (BJH) pore size distribution of the MCN. The results suggested that the MCN has type IV isotherm for mesoporous material with hysteresis loop at relative pressure of 0.5 – 1 due to the capillary condensation in pores. The BET specific surface area of the MCN was determined to be 287 $m^2$ $g^{-1}$. Meanwhile, for BJH pore size distribution, the MCN showed a narrow and sharp pore size of 7 nm. This pore size reflected the size of the silica template that was used for the preparation of the MCN.

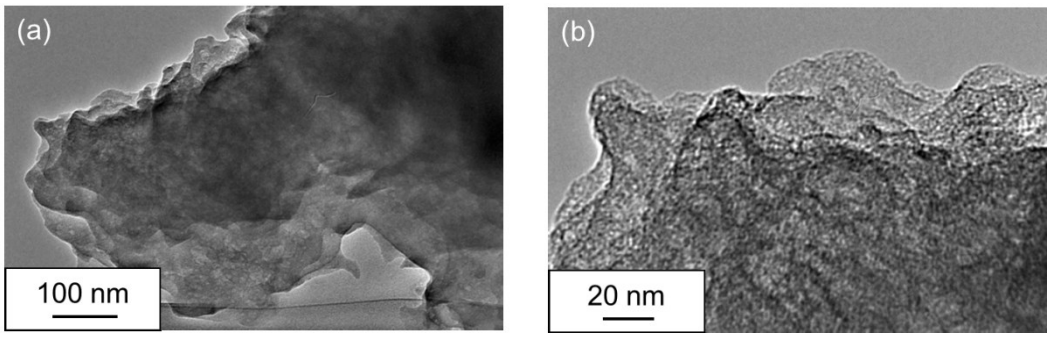



Figure 2. TEM images of MCN shown in different magnification scale bars, (a) 100 nm and (b) 20 nm

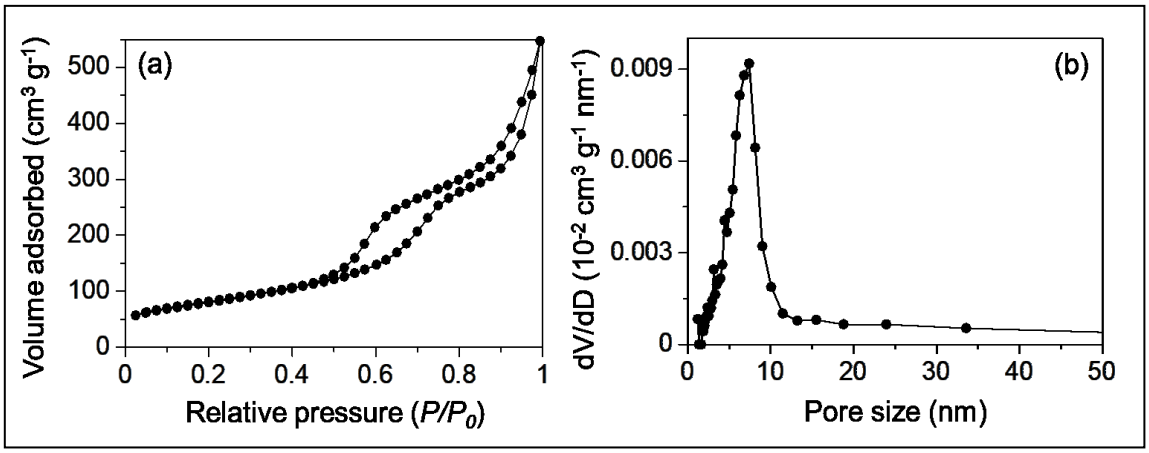



Figure 3. (a) Nitrogen adsorption-desorption isotherm and (b) BJH pore size distribution of MCN

Figure 4(a) displays the excitation spectrum of the MCN. It was clear that the MCN exhibited two excitation peaks at 275 and 370 nm. The excitation peak at 275 nm can be attributed to the $\pi$ to $\pi^*$ electronic transition of the N=C groups in the aromatic 1,3,5-triazine ring of MCN. Meanwhile, the other excitation peak at 370 nm can be attributed to $n$ to $\pi^*$ electronic transition of a terminal N-C group involving lone pairs of nitrogen atoms. As can be seen from Figure 4(b), the MCN gave one emission peak at a wavelength of 460 nm when the MCN was excited either at 275 or 370 nm. These results agree well with previous reports [7, 9, 19].

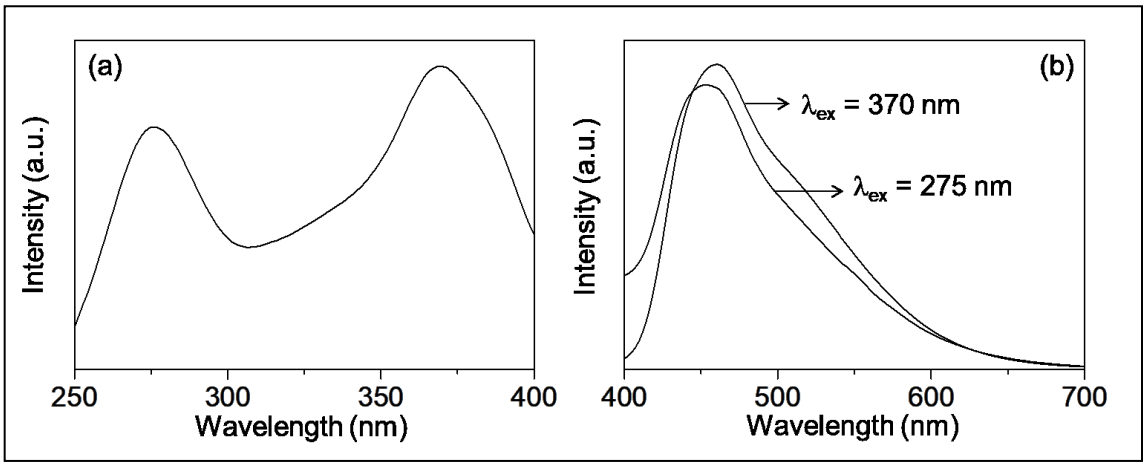



Figure 4. (a) Excitation and (b) emission spectra of MCN that were monitored at emission wavelength of 460 nm and excitation wavelengths of 275 and 370 nm

**Fluorescence quenching**

Quenching tests were conducted on the MCN by the addition of various concentrations of phenol or aniline in order to investigate the sites where the interactions occurred either at N=C groups or terminal N-C groups. The quenching tests were determined by observing the changes in the emission intensity of the MCN sample before and after the addition of phenol or aniline. Since one emission spectrum at around 460 nm was observed for both excitations at 275 and 370 nm, the quenching tests were carried out by monitoring the intensity of the emission peak at 460 nm excited at both excitation wavelengths. As illustrated in Figure 5(a) and (b), the emission intensities of the MCN

excited at both excitation wavelengths of 275 and 370 nm (N=C and terminal N-C emission sites), respectively decreased with the addition of the phenol. This result showed that phenol acted as a quenching agent to deactivate the emission sites. When the added phenol concentration increased, the emission intensity was further decreased. The decrease in the emission intensity would be due to the interactions between the emission sites of MCN at an emission wavelength of 460 nm and the added phenol.

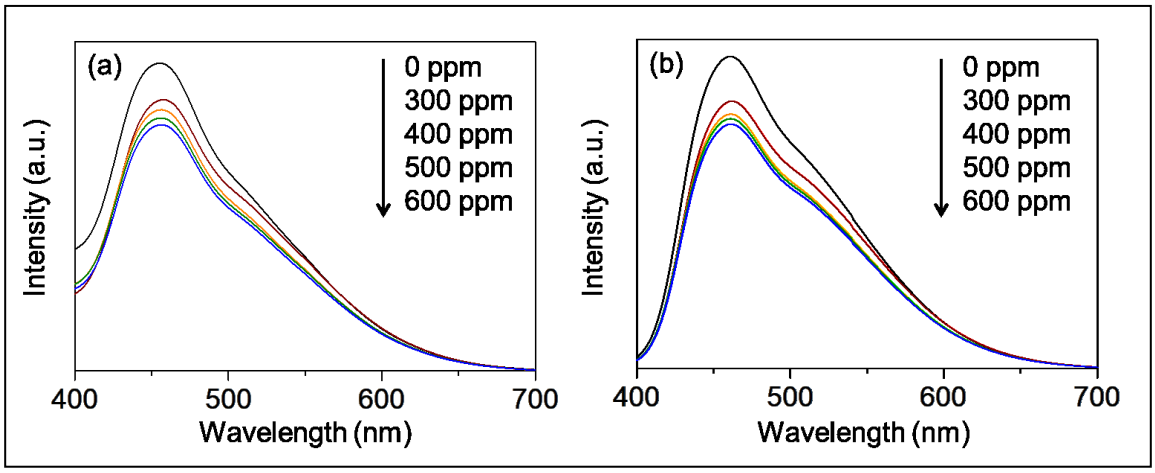



Figure 5. Fluorescence quenching on MCN in the absence and presence of phenol (0–600 ppm) when excited at (a) N=C and (b) terminal N-C groups

In order to have a better understanding about the interaction of MCN with phenol, the quenching results were plotted according to the Stern-Volmer plot following the equation 1:

$$Io/I = K_{SV}[Q] + 1 \quad (1)$$

where $Io$ and $I$ are fluorescence intensities observed in the absence and presence of phenol, $Q$ is the concentration of phenol, and $K_{SV}$ is the Stern-Volmer quenching constant.

Based on the Stern-Volmer equation, the relative emission intensity would be expressed as the function of phenol concentration when the same amount of MCN and the constant illumination intensity were taken in account. Figure 6 shows the Stern-Volmer plots of the relative emission intensity of MCN with various concentrations of phenol. In the range of 300 – 600 ppm, the relative emission intensity excited at both emission sites gave a linear Stern-Volmer plot with the concentrations of phenol. The linear Stern-Volmer plot indicated that the MCN could detect phenol using the fluorescence spectroscopy. Meanwhile, the quenching efficiency of phenol on the emission site of MCN could be obtained from the slope of the linear plot, which was matched to the quenching rate constant ($K_{SV}$ value). It was shown that the $K_{SV}$ values for the emission sites monitored at excitation wavelengths of 275 and 370 nm were $4 \times 10^{-4}$ and $5 \times 10^{-4}$ $ppm^{-1}$, respectively. These results suggested that the emission sites of MCN excited at 275 and 370 nm have almost equal interactions with phenol, which the terminal N-C groups gave slightly better interaction than the N=C groups.

Figure 7(a) and (b) show the changes on the emission intensities excited at 275 and 375 nm, respectively in the presence of aniline. Similar to the phenol addition, the addition of aniline quenched the intensity of the MCN. Aniline also acted as a quenching agent that deactivated the emission sites of MCN. When the concentration of aniline increased, the emission intensity was also further reduced. The decrease in the emission intensity of the MCN suggested that there were interactions between the N=C and terminal N-C emission sites and the aniline. As previously mentioned, the MCN has two excitation sites at 275 and 370 nm, which belong to the N=C groups

($\pi$–$\pi$*) in the aromatic 1,3,5-triazine and the terminal N-C groups ($n$–$\pi$*), respectively. In order to investigate which sites were favoured to the aniline, the Stern-Volmer plot was performed.

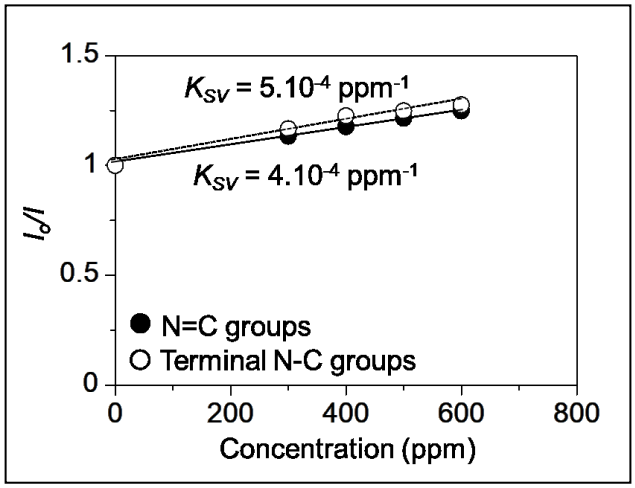



Figure 6. Stern Volmer plots of phenol quenching on MCN at N=C and terminal N-C groups

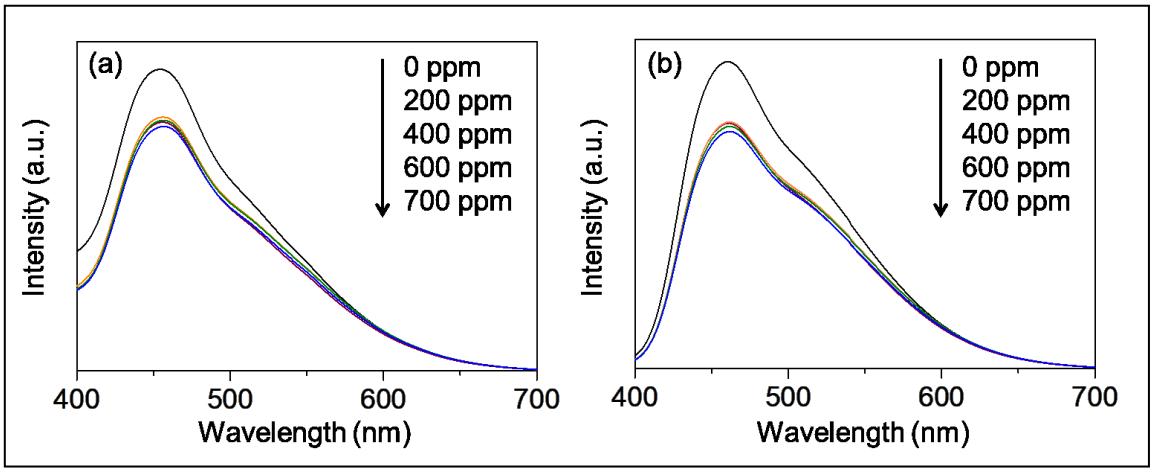



Figure 7. Fluorescence quenching on MCN in the absence and presence of aniline (0 – 700 ppm) when excited at (a) N=C and (b) terminal N-C groups

Shown in Figure 8 is the linear Stern-Volmer plots between the relative emission intensity of MCN with various concentrations of aniline in the range of 200 –700 ppm. Both emission sites, the N=C and terminal N-C groups showed the linear Stern-Volmer plots with the addition of aniline. $K_{SV}$ values obtained were $3 \times 10^{-4}$ and $4 \times 10^{-4}$ ppm$^{-1}$ for the N=C and terminal N-C groups, respectively. The slightly higher $K_{SV}$ value of the terminal N-C group suggested that similar to the results when using phenol as the quencher agent, aniline also favored the terminal N-C groups. Based on the fluorescence quenching tests, it was demonstrated that the MCN showed good interactions with phenol and aniline.

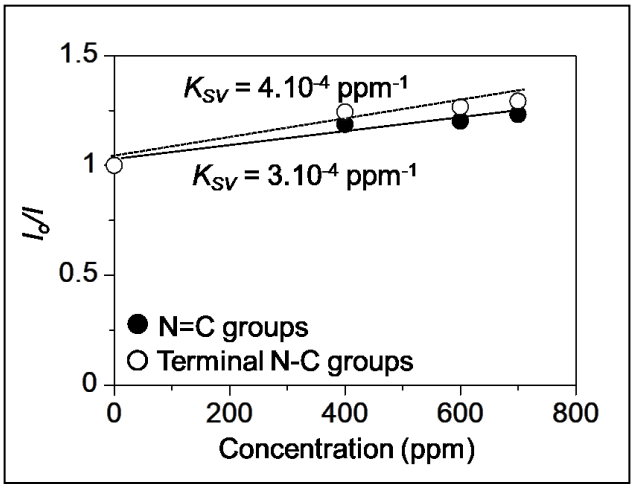



Figure 8. Stern Volmer plots of aniline quenching on MCN at N=C and terminal N-C groups

**Adsorption tests**

Adsorption capability of the MCN towards phenol or aniline was examined by using different concentrations. The adsorption test for phenol was carried out at room temperature with the concentration of phenol was varied from 60 to 400 ppm. Figure 9 presents the results of the adsorption test of phenol on the MCN. The amount of adsorbed phenol increased with the increase of the phenol concentration when it was below 100 ppm. Further increase of the phenol concentration at more than 100 ppm did not affect much the amount of adsorbed phenol. Figure 9 also shows the results of aniline adsorption on the MCN with various concentrations from 100 to 500 ppm. Separated experiments confirmed that no aniline adsorption occurred when the aniline concentration was lower than 100 ppm. At concentration of 100 ppm and above, the MCN showed an increased amount of adsorption with the increase of aniline concentration up to 500 ppm. Compared to the adsorption of phenol, higher amount of aniline was required for MCN to act as an adsorbent.

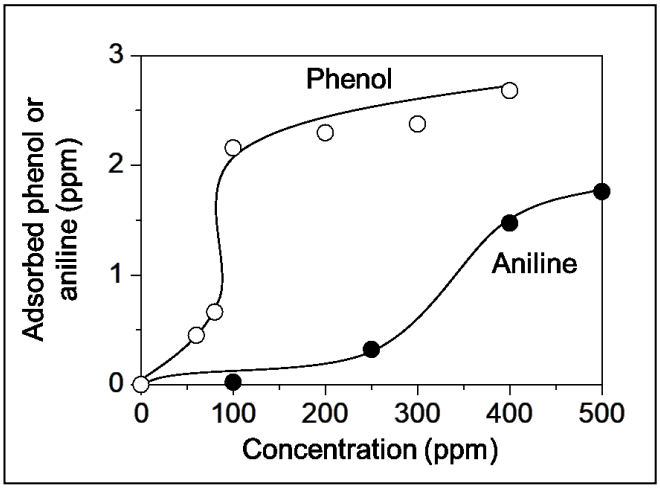



Figure 9. Adsorption of phenol and aniline with various concentrations on MCN at room temperature

From the adsorption test analyses, it can be proposed that phenol and aniline were successfully adsorbed on the MCN. However, under the same concentration for instance at 100 ppm, the MCN gave better adsorption towards phenol than the aniline, which gave adsorbed amounts of 2.16 and 0.02 ppm, respectively. The higher adsorbed

amount of phenol than aniline might be due to the fact that phenol is a weak acid, while aniline is a weak base. Therefore, basicity of the MCN would favor phenol rather than aniline. It can be proposed that phenol would give stronger interaction to the MCN, which in turn gave higher $K_{SV}$ value than the aniline. As has been reported elsewhere [7], the presence of electronegative N at the terminal N-C groups of the MCN provided the possibility for the formation of electrostatic interactions towards the analyte molecules. As phenol is a weak acid, the acid-base electrostatic interactions would occur between the electronegative N at the terminal N-C groups of the MCN and the electropositive phenolic proton. As for aniline, the electrostatic interactions would occur between the electronegative N at the terminal N-C groups of the MCN and the electropositive H at the $NH_2$ group of the aniline, which was less electropositive than the phenolic proton.

## Conclusion

Characterizations by XRD, FTIR, TEM, surface area and pore size analyzer, and fluorescence spectroscopy confirmed that the MCN was prepared successfully by thermal polymerization of cyanamide using nanocolloidal silica as the hard template. The MCN was shown to have good interactions with phenol and aniline, where its emission intensity was quenched almost linearly with the addition of these aromatic compounds. It was obtained that the terminal N-C groups gave slightly higher quenching efficiency than the N=C groups for both phenol and aniline. Phenol gave better interactions towards the emission sites of the MCN, owing to the stronger adsorption of phenol on to the MCN than the aniline caused by the acid-base electrostatic attractive force.

## Acknowledgement

This work was financially supported by the Ministry of Higher Education (MOHE, Malaysia) and the Universiti Teknologi Malaysia (UTM, Malaysia) through Flagship Research University Grant (cost center code: Q.J130000.2426.00G07).

## References

1. Vinu, A. (2008). Two-dimensional hexagonally-ordered mesoporous carbon nitrides with tunable pore diameter , surface area and nitrogen content. *Advanced Functional Materials*, 18(5): 816 – 827.
2. Teter, D. M. and Hemley R. J. (1996). Low-compressibility carbon nitride. *Science*, 271(5245): 53 – 55.
3. Corkill, J. L. and Cohen, M. L. (1993). Calculated quasiparticle band gap of β-$C_3N_4$. *Physical Review B*, 48(23): 17622 – 17624.
4. Goettmann, F., Fischer, A., Antonietti, M. and Thomas, A. (2006). Chemical synthesis of mesoporous carbon nitrides using hard templates and their use as a metal-free catalyst for Friedel-Craft reaction of benzene. *Angewandte Chemie International Edition*, 45(27): 4467 – 4471.
5. Gillan, E. G. (2000). Synthesis of nitrogen-rich carbon nitride networks from an energetic molecular azide precursor. *Chemistry of Materials*, 12(12): 3906 – 3912.
6. Komatsu, T. (2001). Attempted chemical synthesis of graphite-like carbon nitride. *Journal of Materials Chemistry*, 11: 799 – 801.
7. Sam, M. S., Lintang, H. O., Sanagi, M. M., Lee, S. L. and Yuliati, L. (2014). Mesoporous carbon nitride for adsorption and fluorescence sensor of N-nitrosopyrrolidine. *Spectrochimica Acta Part A: Molecular and Bio-molecular Spectroscopy*, 124: 357 – 364.
8. Sam, M. S., Lintang, H. O., Sanagi, M. M., Lee, S. L. and Yuliati, L. (2014). Adsorption of aniline using novel mesoporous carbon nitride. *Advanced Materials Research*, 95: 135–139.
9. Sam, M. S., Tiong, P., Lintang, H. O., Sanagi, M. M., Lee, S. L. and Yuliati, L. (2015). Mesoporous carbon nitride as a metal-free catalyst for the removal of aniline. *RSC Advances*, 5: 44578 – 44586.
10. Lee, S.C., Lintang, H.O. and Yuliati, L. (2012). A urea precursor to synthesize carbon nitride with meso porosity for enhanced activity in the photocatalytic removal of phenol. *Chemistry An Asian Journal*, 7(9): 2139 – 2144.
11. Cui, Y., Zhang, J., Zhang, G., Huang, J., Liu, P., Antonietti, M. and Wang X. (2011). Synthesis of bulk and nanoporous carbon nitride polymers from ammonium thiocyanate for photocatalytic hydrogen evolution. *Journal of Materials Chemistry*, 21: 13032 – 13039.
12. Wang, X., Maeda, K., Chen, X., Takanabe, K., Domen, K., Hou, Y., Fu, X. and Antonietti, M. (2009). Polymer semiconductors for artificial photosynthesis: hydrogen evolution by mesoporous graphitic carbon nitride with visible light. *Journal of the American Chemical Society*, 131(5): 1680 – 1681.

13. Wang, Y., Wang, X. and Antonietti, M. (2012*)*. Polymeric graphitic carbon nitrides as a heterogeneous organo-catalyst: from photochemistry to multipurpose catalysis to sustainable chemistry. *Angewandte Chemie International Edition*, 51(1): 68 – 89.
14. Thomas, A., Fischer, A., Goettmann, F., Antonietti, M., Müller, J.-O., Schlögl, R. and Carlsson, J. M. (2008). Graphitic carbon nitride materials: Variation of structure and morphology and their use as metal-free catalyst. *Journal of Materials Chemistry*, 18(41): 4893 – 4908.
15. Zhang, Y., Mori, T. and Ye, J. (2012). Polymeric carbon nitrides: Semiconducting properties and emerging applications in photocatalysis and photoelectrochemical energy conversion. *Science of Advanced Materials*, 4(2): 282 – 291.
16. Lee, E. Z., Jun, Y. S., Hong, W. H., Thomas, A. and Jin, M. M. (2010). Cubic mesoporous graphitic carbon(IV) nitride: an all-in-one chemosensor for selective optical sensing of metal ions. *Angewandte Chemie International Edition*, 49 (50): 9706 – 9710.
17. Lee, E. Z., Lee, S. U., Heo, N. S., Stucky, G. D., Jun, Y. S. and Hong, W. H. (2012). A fluorescent sensor for selective detection of cyanide using mesoporous graphitic carbon(IV) nitride. *Chemical Communications*, 48(33): 3942 – 3944.
18. Tian, J., Liu, Q., Asiri, A. M., Al Youbi, A. O. and Sun, X. (2013). Ultrathin graphitic carbon nitride nanosheet: a highly efficient fluorosensor for rapid, ultrasensitive detection of $Cu^{2+}$. *Analytical Chemistry*, 85(11): 5595 – 5599.
19. Alim, N. S., Lintang, H. O. and Yuliati, L. (2015). Fabricated metal-free carbon nitride characterizations for fluorescence chemical sensor of nitrate ions. *Jurnal Teknologi*, 76(13): 1 – 6.
20. Dąbrowski, A., Podkościelny, P., Hubicki, Z. and Barczak, M. (2005). Adsorption of phenolic compounds by activated carbon - A critical review. *Chemosphere*, 58(8): 1049 – 1070.
21. Busca, G., Berardinelli, S., Resini, C. and Arrighi, L. (2008). Technologies for the removal of phenol from fluid streams: A short review of recent developments. *Journal of Hazardous Materials*, 160(2-3): 265 – 288.
22. Ahmed, S., Rasul, M. G., Martens, W. N., Brown, R. and Hashib, M.A. (2010). Heterogeneous photocatalytic degradation of phenols in wastewater: a review on current status and developments. *Desalination*, 261(1–2): 3 – 18.
23. Soares, B. G., Amorim, G. S., Souza Jr, F. G., Oliveira M. G. and da Silva, J. E. P. (2006). The *in situ* polymerization of aniline in nitrile rubber. *Synthetic Metals*, 156 (2–4): 91 – 98.
24. Zhao, R., Tan, C., Xie, Y., Gao, C., Liu, H. and Jiang, Y. (2011). One step synthesis of azo compounds from nitroaromatics and anilines, *Tetrahedron Letter*, 52(29): 3805 – 3809.
25. Puig, A., Ormad, P., Roche, P., Sarasa, J., Gimeno, E. and Ovelleiro, J. L. (1996). Wastewater from the manufacture of rubber vulcanization accelerators: Characterization, downstream monitoring and chemical treatment. *Journal of Chromatography A*, 733 (1–2): 511 – 522.
26. Haque, E., Jun, J. W., Talapaneni, S. N., Vinu, A. and Jhung, S. H. (2010). Superior adsorption capacity of mesoporous carbon nitride with basic CN framework for phenol. *Journal of Materials Chemistry*, 20(48): 10801 – 10803.
27. Miller, D. R., Wang, J. and Gillan, E. G. (2002). Rapid, facile synthesis of nitrogen-rich carbon nitride powders. *Journals of Materials Chemistry*, 12(8): 2463 – 2469.

*Malaysian Journal of Analytical Sciences, Vol 21 No 6 (2017): 1352 - 1365*
*DOI: https://doi.org/10.17576/mjas-2017-2106-17*

MALAYSIAN JOURNAL OF ANALYTICAL SCIENCES
*Published by The Malaysian Analytical Sciences Society*
ISSN 1394 - 2506

# EFFECT OF BUFFER COMPOSITION ON THE ANALYSIS OF LIPOPOLYSACCHARIDES FROM *Escherichia coli* 055:B5 AND UT189 BY CAPILLARY ELECTROPHORESIS WITH DIRECT UV DETECTION

## (Kesan Komposisi Penimbal ke atas Analisis Lipopolisakarida dari *Escherichia coli* 055:B5 dan UT189 oleh Elektroforesis Kapilari dengan Pengesan UV)

Fun Man Fung[1], Min Su[1], Sam Fong Yau Li[1,2]*

[1]*Department of Chemistry,*
*National University of Singapore, 3 Science Drive 3, Singapore 117543, Singapore*
[2]*Singapore-Peking-Oxford Research Enterprise (SPORE) Programme,*
*NUS Environmental Research Institute (NERI) #02-01, T-Lab Building (TL), 5a Engineering Drive1 1, Singapore 117411, Singapore*

**Corresponding author: chmlifys@nus.edu.sg*

Received: 7 November 2016; Accepted: 18 September 2017

**Abstract**

Endotoxins are known to many as bacterial toxins. Conventional analysis of endotoxins by capillary electrophoresis-mass spectrometry is laborious and time consuming. A faster capillary electrophoresis method using direct ultraviolet (UV) detection was performed to analyze endotoxins isolated from *Escherichia coli* (*E. coli*) 055:B5 and UT189. In this study, we compared different running buffers and buffer additives to examine the effects of each on the electropherograms obtained. The optimum buffer system was then used to analyze of lipopolysaccharides (LPS) signals from the bacteria *E. coli* 055:B5 (source strain CDC 1644-70), *E. coli* K-235 (source strain ATCC 13027) and *Klebsiella pneumoniae* (source strain ATCC 15380). The data generated for each variant peak showed very good precision and high reproducibility for migration time with percentage RSD values of ≤1.2% (n = 3). Similarly, the percentage RSD for peak areas were ≤5.3% (n = 3) across the three LPS.

**Keywords**: capillary electrophoresis, direct UV, endotoxin, lipopolysaccharides, buffer

**Abstrak**

Endotoksin diketahui sebagai bakteria yang berbahaya. Kaedah konvensional bagi endotoksin oleh elektroforesis kapilari-jisim spektrometri adalah bersifat rumit dan memerlukan tempoh masa yang panjang. Kaedah elektroforesis kapilari yang pantas menggunakan pengesan ultralembayung telah dijalankan untuk menganalisa endotoksin yang dipisahkan dari *Escherichia coli* (E. coli) 055:B5 and UT189. Dalam kajian ini, larutan penimbal yang berbeza telah diuji dan penambahan penimbal dilakukan untuk mengkaji kesan bagi setiap elektropherogram yang terhasil. Sistem penimbal yang optimum kemudian digunakan untuk menganalisa respon lipopolisakarida (LPS) dari bakteria *E. coli* 055:B5 (sumber strain CDC 1644-70), *E. coli* K-235 (sumber strain ATCC 13027) and *Klebsiella pneumoniae* (sumber strain ATCC 15380). Data yang terhasil bagi puncak setiap varian menunjukkan ia adalah jitu dan kebolehulangan yang tinggi bagi masa pemindahan dengan nilai peratus RSD ialah ≤1.2% (n = 3). Begitu juga, peratus RSD bagi luas – luas puncak ketiga – tiga LPS ialah ≤5.3% (n = 3).

**Kata kunci**: elektroforesis kapilari, UV langsung, endotoksin, lipopolisakarida, penimbal

## Introduction

Endotoxins are of great relevance in today's research because most layman would believe that killing bacteria by boiling water alone would ensure toxin-free water. However, endotoxins are released by bacteria after lysis by cell death at high temperature. Endotoxins causes inflammatory reactions and sepsis which can be fatal [1]. Since they are found in high concentrations in wastewater from industries coupled with less than optimal waste treatment [2, 3], the efficiency for the secondary treatment of industry effluents must be addressed.

Endotoxins are found in the cell wall of Gram-negative bacteria. Essentially, endotoxins are major components of the exterior of the outer membrane of the Gram-negative cell wall. Endotoxins are lipopolysaccharides (LPS) and are known to many as bacterial toxins. They are hydrophilic and face outward from the cell membrane and into the medium in which the bacteria is growing [4]. LPS contains major antigens of the bacteria and is the most important target of Gram-negative bacteria for the immune response [5]. Each LPS molecule is unique to a particular Gram-negative bacteria and exhibits much variation in its structure [6] an example shown in Figure 1.

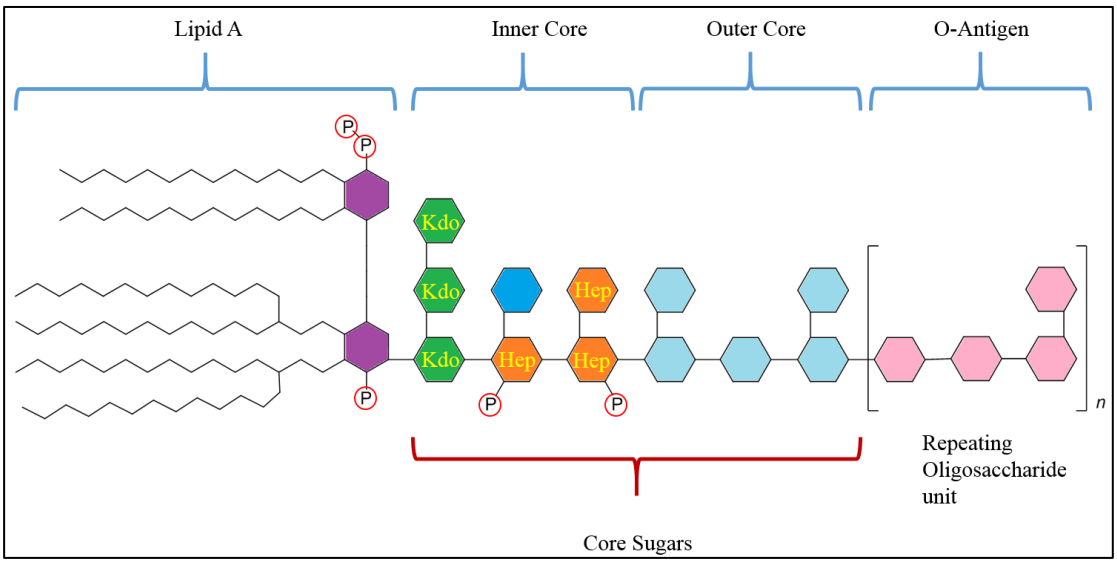



Figure 1. The general structure of lipopolysaccharide molecule, segmented primarily into lipid A, inner core, outer core, and *O*-antigen

Previous research has shown that the heterogeneity of different LPS mixtures enable scientists to distinguish them via mass spectrometric detection [7]. Their differences in molecular weight, size, and connectivity of the branched chains allow the combined use of both online and offline separation techniques [8]. Such distinct structural differences also allow the LPS to be separated via high-performance capillary electrophoresis (CE) for further analysis, as performed by Restaino et al. [9] on the *E. coli* K4 cell surface polysaccharides. LPS from *E. coli* 055:B5 has also been analyzed by CE-UV. However, in the study, only one surfactant, sodium dodecyl sulfate (SDS) was experimented in the running buffer [10]. LPS, being amphiphilic molecules, are prone to aggregation of the repeating oligosaccharide units in the *O*-antigen segment [11, 12]. Without the presence of surfactants, it is perceivable that the LPS form micelles and acquire lower solubility, giving rise to precipitates and lower reproducibility of electropherograms. Thus, it is believed that the migration behavior of LPS will alter when different surfactants are used, depending on the main buffering system. Although work has been performed on the investigation of various concentration of SDS in selected LPS electropherogram [13 – 16], no study has reported the effect of surfactants and buffering system on the LPS extracted from *E. coli* K-235, *E. Coli* UT189 and *Klebsiella pneumoniae*. In this paper, the study of different surfactants and buffering system for the optimization of LPS separation by CE is reported.

## Materials and Methods

### Chemicals

Sodium dodecyl sulfate (SDS), sodium borate, sodium hydroxide were obtained from Merck (Darmstadt, Germany). Buffers were prepared with ultrapure water obtained from Millipore equipment (Millipore, Bedford, MA, USA). Commercially prepared tris(hydroxymethyl)aminomethane (Tris), boric acid, disodium ethylenediaminetetraacetic acid (EDTA) buffer was purchased from Bio-Rad laboratories (Singapore). Poly(ethylene)oxide (PEO, Mr 600 000) was purchased from Sigma-Aldrich (Singapore). 1,4-diaminobutane (DAB) was purchased from Fluka (Münster, Germany).

### Bacteria strains and endotoxins preparation

Lyophilized lipopolysaccharides powders from *E. coli* 055:B5 (Lot #025M4040V) purified by gel-filtration chromatography, E-Toxate™ Endotoxin standard, *E. coli* K-235 purified by gel-filtration chromatography, *Klebsiella pneumoniae* purified by phenol extraction were purchased from Sigma Aldrich. *E. Coli* UT189 was donated by Bau Yi Woo of Department of Chemistry, National University of Singapore.

LPS from *E. Coli* UT189 was prepared by the following procedure: To obtain pure and lyophilized LPS we used the hot phenol–water procedure according to Westphal et al. [17]. Crude LPS was recovered from the combined aqueous phase and subjected to further purification as reported in the conventional method. Purified LPS samples were lyophilized for ~18 h to yield a white-fluffy powder that was used for analysis.

### Instrumentation

All electrophoretic separations were performed on a Beckman Coulter PA 800 plus system (AB Sciex, USA), using photodiode array (PDA) absorbance detection set at 195 nm. Uncoated fused silica capillaries (50 m ID × 360 m OD) were purchased from Polymicro Technologies Inc. (Phoenix, AZ, USA). New capillaries were flushed with 1M NaOH, ultrapure water and background electrolyte (BGE) for 10 minutes each. Preconditioning was performed by flushing with BGE for 3 minutes. The Beckman Coulter's 32 Karat™ version 9.1 software was used for data analysis, data acquisition and peak integration.

### CE–UV experiments

For CE–UV experiments the capillaries were cut to a length of 39 cm. For each capillary, a 0.30 cm transparent window was created by burning the capillary 10 cm from one of the ends. The capillary was burnt with a general butane lighter and the size of the window was consistently maintained by wrapping the capillary with an Aluminum foil with at 0.30 cm aperture. Detection was done using a CE photodiode array detectors (PDA) equipped with a deuterium lamp. The length of this irradiation window was 1 cm and the distance between lamp and capillary about 2 cm. All the measurements were carried out at 16 °C with the applied voltage set at 30 kV. All measurements were carried out at least three times. The LPS was dissolved in the BGE to make up a concentration of 5.0 mg/mL. The various buffering systems applied in this report are summarized in Table 1.

Table 1. Different running buffers used in CE-UV analysis of intact LPSs.

| Number | Buffer System/ BGE | Concentration | pH | Reference |
|---|---|---|---|---|
| 1 | SDS/$Na_2B_4O_7$/$Na_2HPO_4$ | 40 mM/10 mM/40 mM | 9.00 | [9] |
| 2 | SDS/$Na_2B_4O_7$ | 40 mM/10 mM | 9.22 | This study |
| 3 | Tris/Borate/EDTA/PEO | 3.94 mM/0.56 mM/0.013 mM/0.02% | 9.14 | [18] |
| 4 | Tris/Borate/EDTA | 445 mM/445 mM/10 mM | 8.45 | This study |
| 5 | Tris/Borate/EDTA/PEO | 445 mM/445 mM/10 mM/0.02% | 7.77 | This study |
| 6 | $Na_2B_4O_7$ | 50 mM | 9.40 | [19] |
| 7 | $Na_2B_4O_7$/DAB | 50 mM/10 mM | 9.11 | [20] |
| 8 | Tricine | 50 mM | 5.21 | This study |

## Results and Discussion

The LPS isolated from *E. coli* 055:B5 and UT189 were analyzed with the buffering systems consisting of SDS/ $Na_2B_4O_7/Na_2HPO_4$ (40 mM/10 mM/40 mM, pH 9.0) as reported by Restaino et al., although the electropherograms obtained with this buffering system could not ascertain the location of a definitive set of LPS signals, unlike the success reported for *E. coli* K4 [9]. In the electropherograms shown in Figure 2, only that of *E. coli* 055:B5 marginally provides the signature twin signals at migration times of around 6.83 minutes.

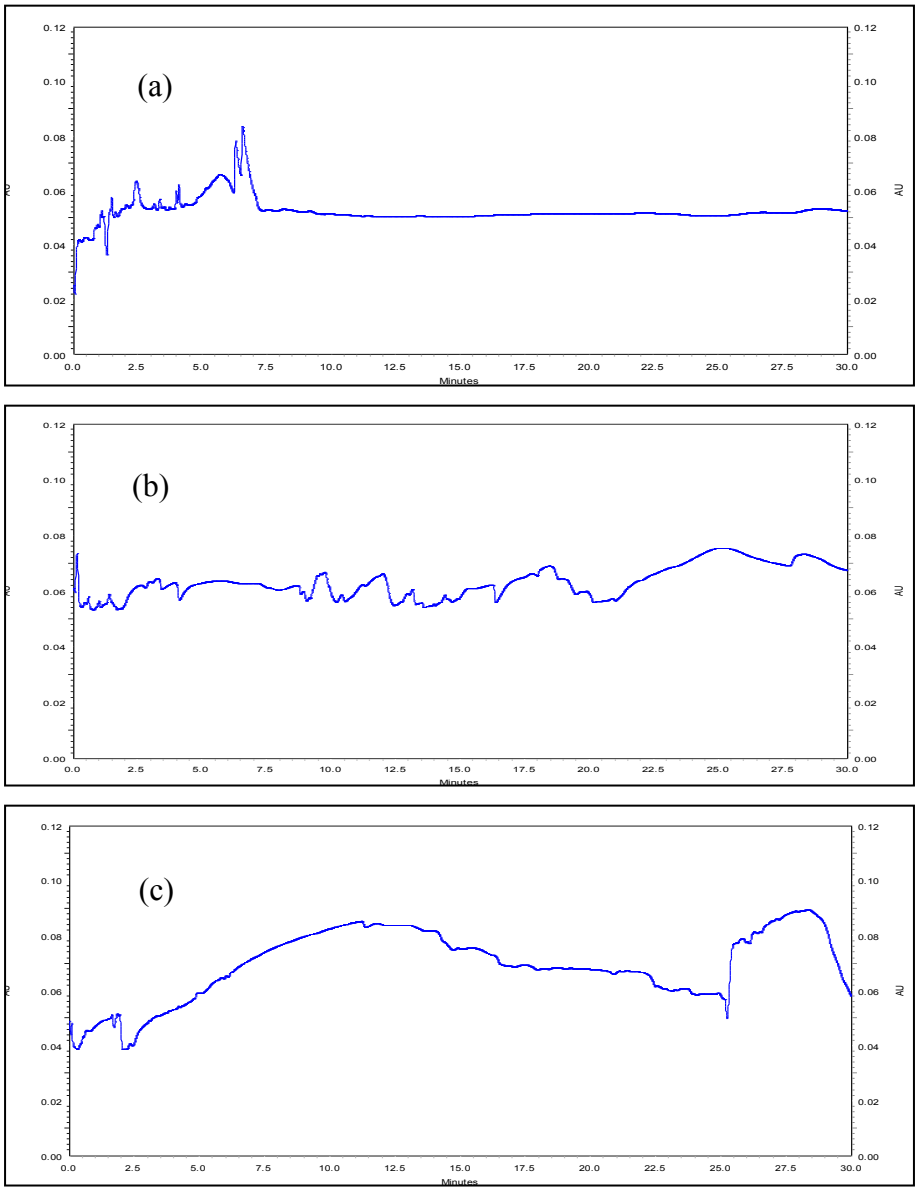



Figure 2. CE-UV electropherograms of lipopolysaccharides from Gram-negative bacteria (A) 055:B5; (B) E-Toxate™; (C) UT189. Running buffer: $SDS/Na_2B_4O_7/Na_2HPO_4$ (40 mM/10 mM/40 mM, pH 9.0). Applied voltage = 30 kV; injection time = 5 s. Capillary dimensions are indicated in experimental section

One of the reasons why the previous buffer system could not give a distinct signal in the electropherograms of LPS E-Toxate™ and UT189 is the solubility of the LPS in the buffer. As mentioned in the introduction, different strains

of bacteria vary in molecular size, and the number of repeat oligosaccharide units (*n* value) in the *O*-antigen segment of the structure. The higher the *n* value, the more likely it is for the oligosaccharide chain to form multiple intramolecular hydrogen bonds (H-bonds) within the *O*-antigen chain, creating an aggregate which may decrease its solubility in selected buffers. The surfactant used according to Restaino et al. was SDS [9], which is an anionic surfactant that increases the overall ionic strength of the buffer. A non-ionic neutral surfactant, polyethylene oxide (PEO), was used as a replacement instead on LPS E-Toxate™ and UT189, by Yu et al. using Tris/$Na_2B_4O_7$/EDTA/PEO (3.94 mM/0.56 mM/0.013 mM/0.02%, pH 9.14) as the buffer system [18]. At this pH, all the ionizable functional groups in the LPS would have been deprotonated, and they carry uniformly negatively charges, giving rise to an increase in charge density, and a more consistent electrophoretic mobility of the LPS. In Figure 3, both electropherograms exhibit the detected LPS signals: at 1.52 minutes for E-Toxate™ and 2.31 minutes for UT189.

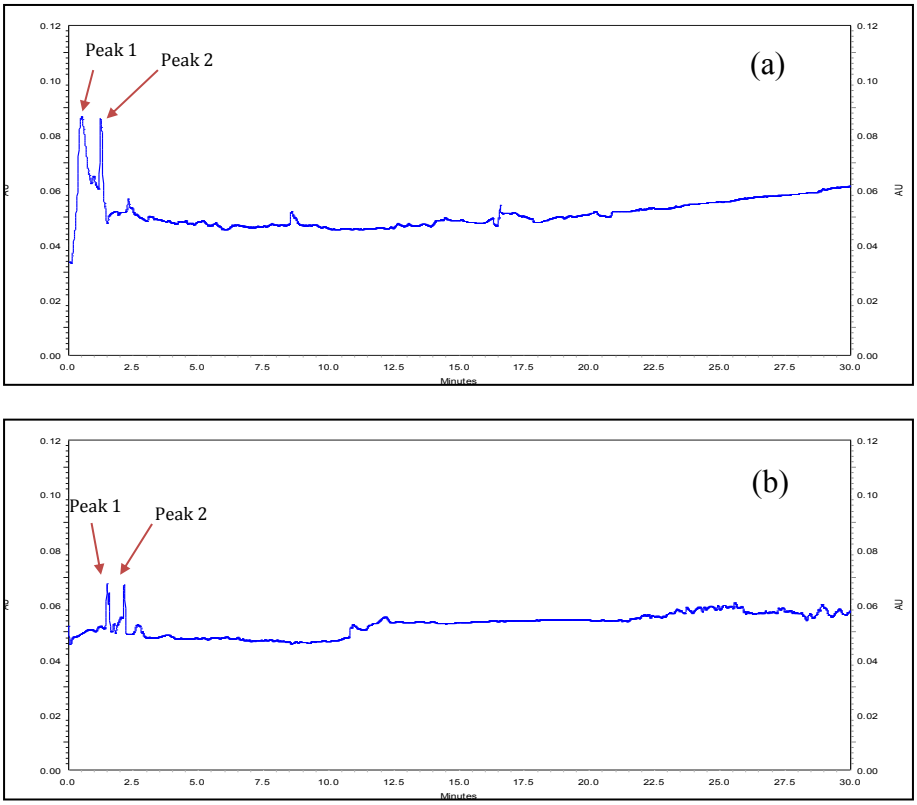



Figure 3. CE-UV electropherograms of lipopolysaccharides from Gram-negative bacteria (A) E-Toxate™; (B) UT189. Running buffer: Tris/$Na_2B_4O_7$/EDTA/PEO (3.94 mM/0.56 mM/0.013 mM/0.02%, pH 9.14). Applied voltage = 30 kV; injection time = 5 s. All other conditions are the same as stated in the experimental section.

The use of PEO in place of SDS has allowed the detection of LPS signals which were previously not seen. However, these LPS signals have relatively short migration times, which means that the use of an electroosmotic flow (EOF) marker will not be accurate. The EOF should preferably produce a signal that has a lower migration time than that of the analytes. This EOF marker signal will have the same relative differences in migration time to the respective analyte signals. Having low migration times for the analytes in this case would mean lower accuracy when comparing the mobilities of the various LPS. The three LPS were then analyzed using a modified buffering system by the use of a commercially purchased Tris/Borate/EDTA (445 mM/445 mM/10 mM, pH 7.77) buffer and the addition of PEO (0.02%). This change in the concentration of the ions and the pH provided the desired effect of delaying the migration time of the LPS signals, as seen in Figure 4. Comparing the electropherograms of the E-

Toxate™, the new buffering system with almost 900 times increase in sodium borate concentration increases the migration time from 1.52 minutes to 2.41 minutes. Likewise for UT189, the migration time increases from 2.31 minutes to 2.92 minutes.

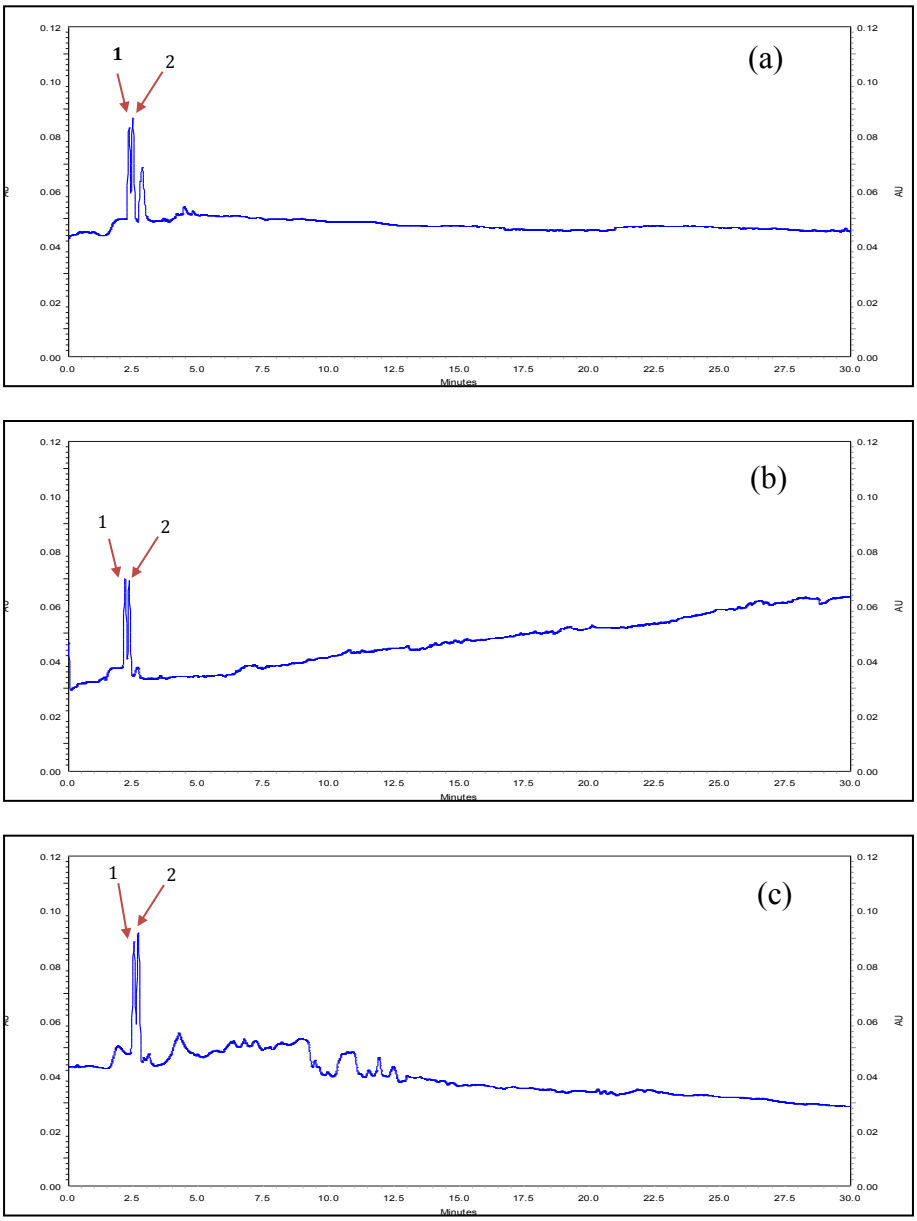



Figure 4. CE-UV electropherograms of lipopolysaccharides from Gram-negative bacteria (A) 055:B5; (B) E-Toxate™; (C) UT189. Running buffer: Tris/$Na_2B_4O_7$/EDTA/PEO (445 mM/445 mM/10 mM/0.02%, pH 7.77). Applied voltage = 30 kV; injection time = 5 s. Capillary dimensions are indicated in experimental section

Although the migration times were prolonged slightly after increasing the Tris/$Na_2B_4O_7$/EDTA concentration, we believed that this can be increased further. The same LPS were subsequently analyzed with the buffer system consisting of Tris/Borate/EDTA (445 mM/445 mM/10 mM, pH 8.45). Without the addition of PEO into this buffer

system, the migration times for all three LPS electropherograms showed marked increment. As shown in Figure 5, the migration times for 055:B5, E-Toxate™ and UT189 increased to 7.10 minute, 6.48 minute and 11.22 minute respectively. The pair of distinctive peaks at migration times of 6.07 (± 0.10) and 6.48 (± 0.10) minutes could be used to identify the presence of E-Toxate™ LPS. These twin peaks showed maximum absorbance at 195 nm in the 3D CE-UV plot (Figure 6).

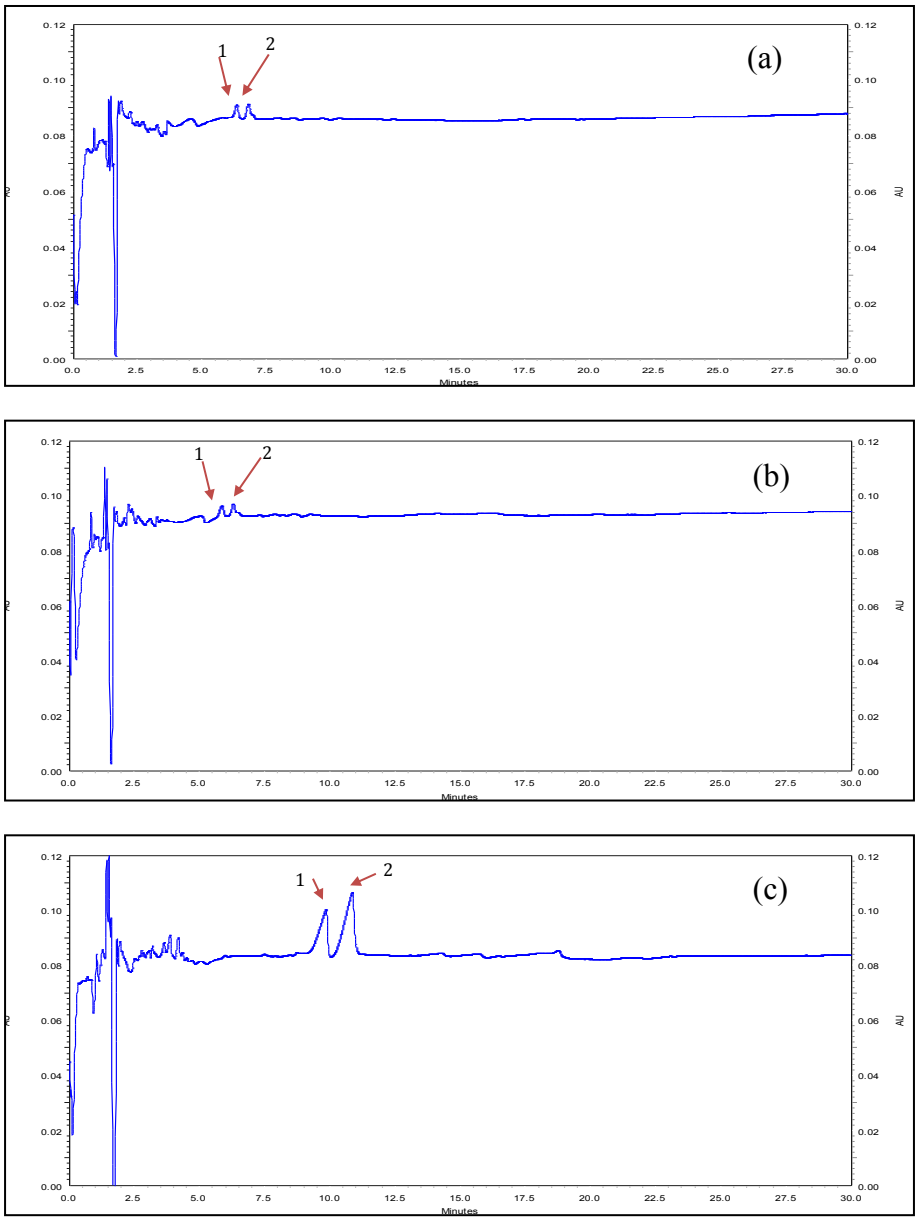



Figure 5. CE-UV electropherograms of lipopolysaccharides from Gram-negative bacteria (A) 055:B5; (B) E-Toxate™; (C) UT189. Running buffer: Tris/$Na_2B_4O_7$/EDTA (445 mM/445 mM/10 mM, pH 8.45). Applied voltage = 30 kV; injection time = 5 s. Capillary dimensions are indicated in experimental section

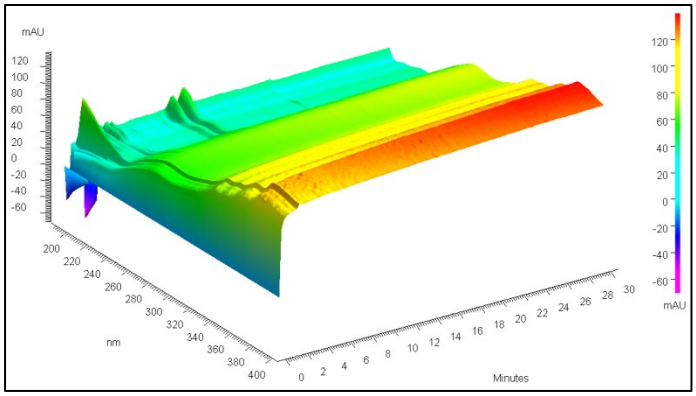
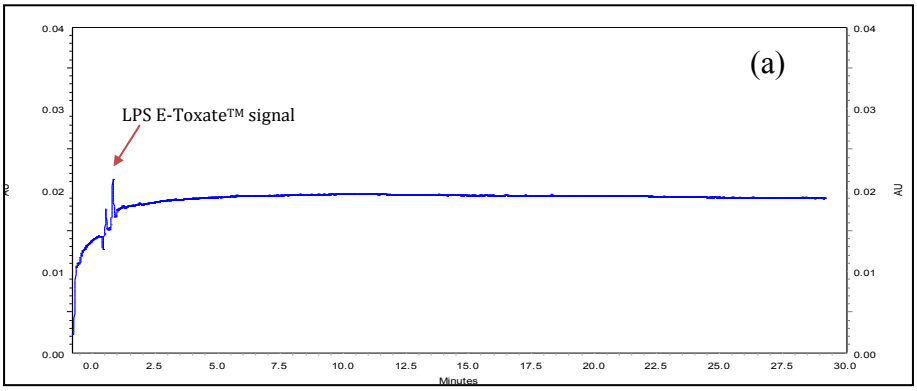



Figure 6. 3-D plot of electropherograms of E-Toxate™ LPS showing the maximum absorbance at 195 nm. Separation condition: buffer - Tris/ $Na_2B_4O_7$/EDTA 445 mM/445 mM/10 mM; pH 8.3. Applied voltage = 30 kV; injection time = 5 s. All other conditions are the same as stated in the experimental section

Venter et al. optimized the running buffer for LPS extracted from *E. coli* (source strain ATCC 25922) using 50 mM borate [19]. In our study, LPS E-Toxate™ was analyzed to check the effect of another surfactant, 1,4-diaminobutane (DAB), on the migration profile of the LPS. In Figure 7, results showed that after the addition of DAB the LPS signals are better resolved. The migration time increased from 1.52 minute to 8.53 minutes after the addition of DAB. This enhancement of resolution can be attributed to the shorter hydrophilic chain of DAB which allows greater interaction and promotes dispersion effect in the oligosaccharides chain of the LPS. Unlike PEO, DAB does not polymerize and form a macromolecule that can interfere with the dispersion of the repeating polysaccharide unit. With the increased London dispersion forces derived from a non-polar macromolecule, PEO exerts less interaction with the oligosaccharides, whose main intermolecular forces of attraction is H-bond. This undesired incompatible effect contrasts with that of DAB which interacts non-covalently primarily by H-bond, and as such it will minimize the aggregation of the sugar units at the *O*-polysaccharide segment. Unfortunately, the addition of DAB causes a significant impedance to the EOF, which results in longer analysis time.



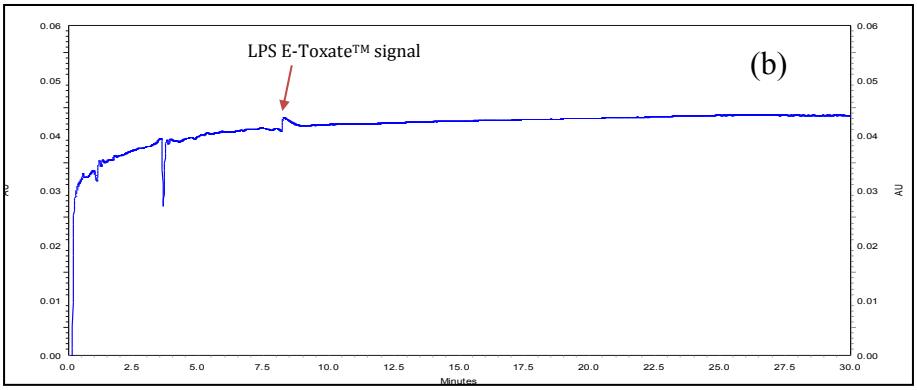
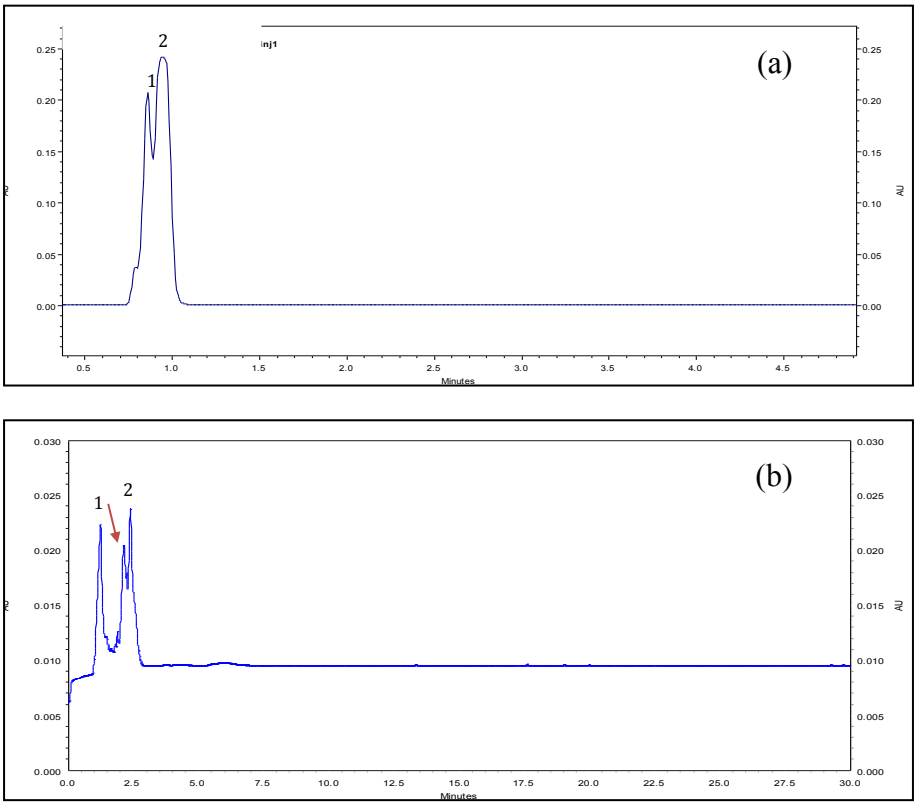



Figure 7. CE-UV electropherograms of lipopolysaccharides from E-Toxate™ (A) Running buffer: $Na_2B_4O_7$ (50 mM, pH 9.40); (B) Running buffer: $Na_2B_4O_7$/DAB (50 mM/10 mM, pH 9.11). Applied voltage = 30 kV; injection time = 5 s. All other conditions are the same as stated in the experimental section

In order to ascertain if SDS works better than DAB in borate buffer system, LPS extracted from *E. coli* 055:B5, E-Toxate™ and *Klebsiella pneumoniae* were analyzed by using SDS/$Na_2B_4O_7$ (40 mM/10 mM, pH 9.22). Figure 8 shows that the baselines for both electropherograms are more stable and exhibit a higher signal-to-noise ratio than that using DAB as the surfactant.



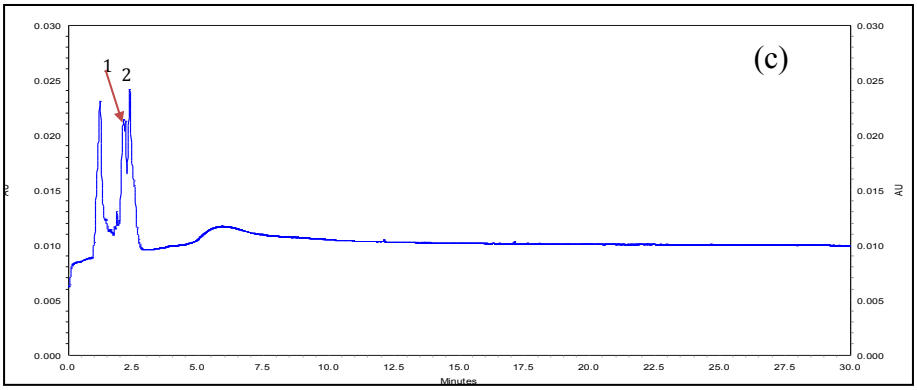



Figure 8. CE-UV electropherograms of lipopolysaccharides from Gram-negative bacteria (A) 055:B5; (B) E-Toxate™; (C) *Klebsiella pneumoniae*. Running buffer: SDS/$Na_2B_4O_7$ (40 mM/10 mM, pH 9.22). Applied voltage = 30 kV; injection time = 5 s. Capillary dimensions are indicated in experimental section

With the buffering system optimized using SDS/$Na_2B_4O_7$ (40 mM/10 mM, pH 9.22), LPS from *E. coli* 055:B5, *E. coli* K-235 and *Klebsiella pneumonia* were analyzed using the same conditions as in the experimental section, and their migration times, peak heights, and peak areas were determined. Each LPS analysis was conducted in triplicates and the results are summarized in Table 2 and Figure 9. The representative electropherograms from these three LPS also indicate the distinct similarity using CE-UV profiling, as shown in Figure 10. Each showing three prominent signals, with the first peak appearing at 1.30 minute, and an overlapping twin peaks at around 2.08 (±0.28) minutes, as shown in an enlarged scale in Figure 11.

The apparent data generated for each variant peak showed very good precision for migration time with percentage RSD values of ≤1.2% (n=3). Similarly, the percentage RSD for peak area values are ≤5.3% (n=3) across different LPS.

Table 2. Summary of data from electropherograms across three LPS types (concentration = 5.0 mg/mL in BGE)

| | | Peak 1 | | | Peak 2 | | |
|---|---|---|---|---|---|---|---|
| | **Sample** | **Migration Time (minutes)** | **Peak Height (mAU)** | **Peak Area** | **Migration Time (minutes)** | **Peak Height (mAU)** | **Average Peak Area** |
| *E. coli* 055:B5 | 1 | 2.12 | 14.1 | 48854 | 2.40 | 17.7 | 90417 |
| | 2 | 2.13 | 14.1 | 45717 | 2.39 | 17.8 | |
| | 3 | 2.12 | 14.1 | 48221 | 2.38 | 17.4 | |
| | Average | 2.12 | 14.1 | 47597 | 2.39 | 17.6 | |
| | RSD (%) | 0.2 | 0.2 | 3.5 | 0.2 | 1.1 | 2.9 |
| *Klebsiella pneumoniae* | 1 | 2.11 | 19.1 | 67284 | 2.36 | 17.8 | 75161 |
| | 2 | 2.14 | 19.2 | 73162 | 2.33 | 18.1 | |
| | 3 | 2.10 | 21.8 | 68765 | 2.30 | 18.1 | |
| | Average | 2.12 | 20.0 | 69737 | 2.33 | 18.0 | |
| | RSD (%) | 1.0 | 7.7 | 4.4 | 1.2 | 1.1 | 5.3 |
| *E. coli* K-235 | 1 | 1.87 | 17.6 | 87752 | 2.37 | 10.0 | 60915 |
| | 2 | 1.85 | 18.1 | 87455 | 2.34 | 10.1 | |
| | 3 | 1.83 | 18.5 | 84463 | 2.32 | 10.1 | |
| | Average | 1.85 | 18.1 | 86556 | 2.34 | 10.0 | |
| | RSD (%) | 0.9 | 2.5 | 2.1 | 1.1 | 0.5 | 2.6 |

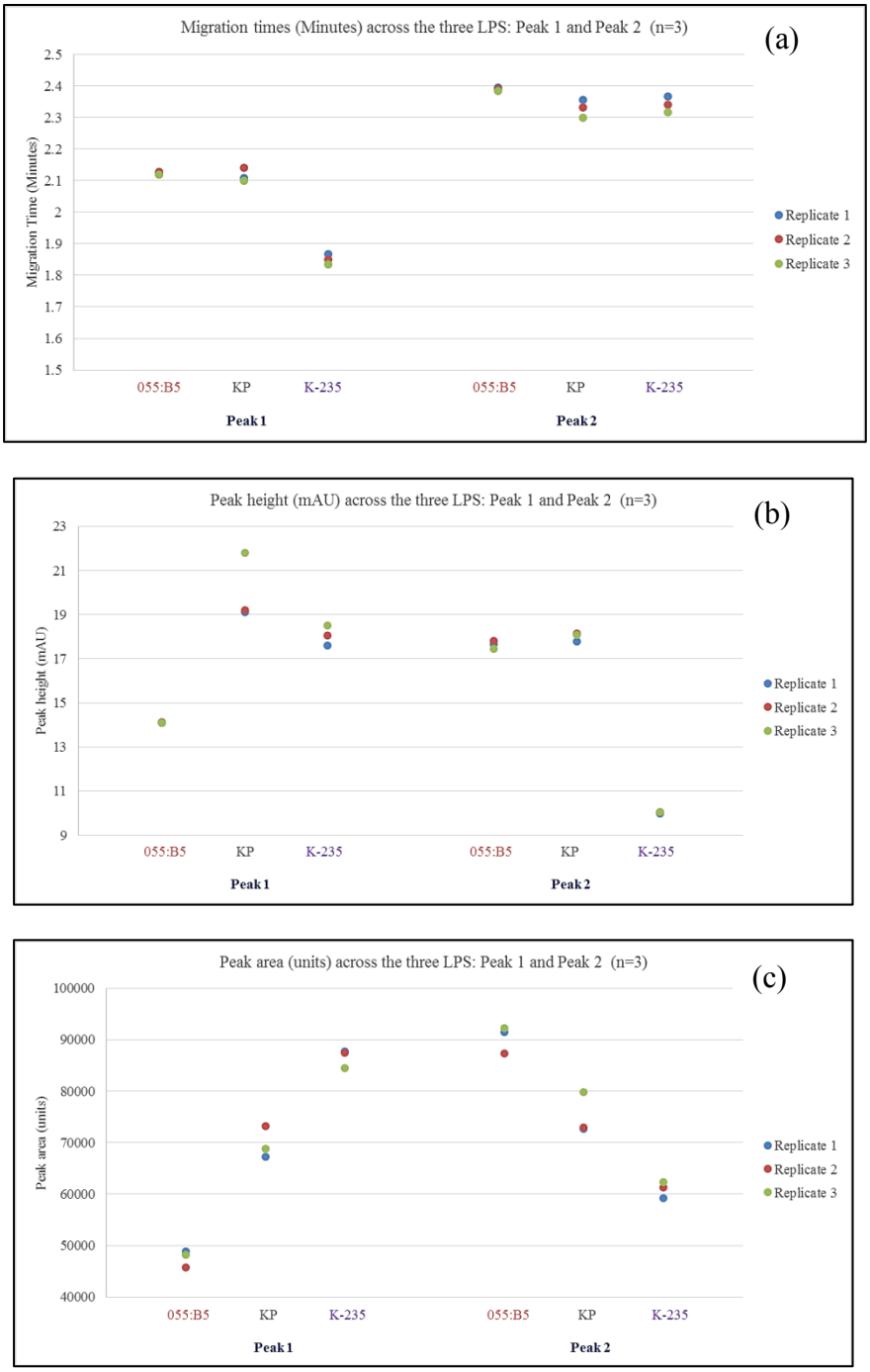



Figure 9. Graphical representation of the reproducibility of the electropherogram peaks of the three LPS analyzed by direct CE-UV detection (A) migration time; (B) peak height; (C) peak area. Running buffer: SDS/$Na_2B_4O_7$ (40 mM/10 mM, pH 9.22). Applied voltage = 30 kV; injection time = 5 s. Capillary dimensions are indicated in experimental section. Legend: 055:B5 (*E. coli* 055:B5); KP (*Klebsiella pneumoniae*); K-235 (*E. coli* K-235)

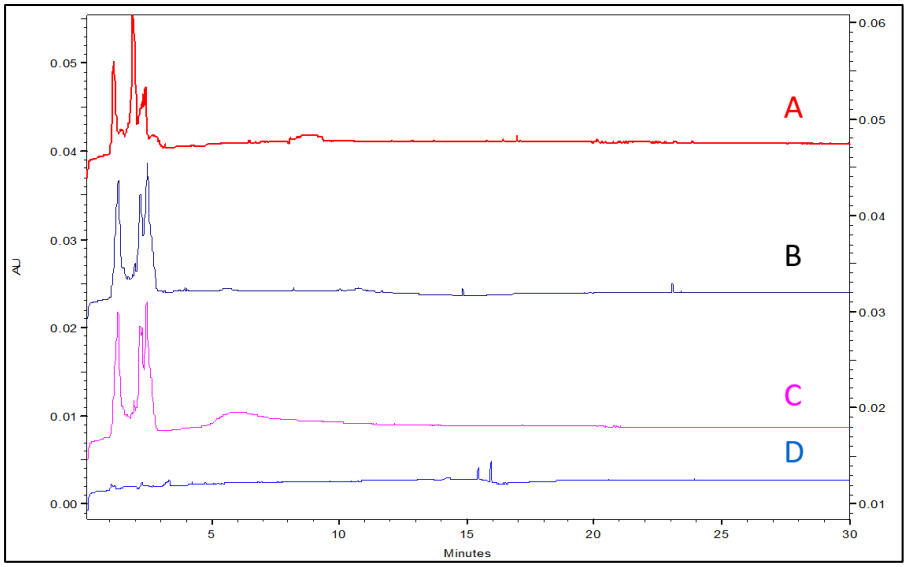



Figure 10. CE-UV electropherograms of lipopolysaccharides from Gram-negative bacteria (A) K-235; (B) 055:B5; (C) *Klebsiella pneumoniae*; (D) Blank buffer. Running buffer: SDS/$Na_2B_4O_7$ (40 mM/10 mM, pH 9.22). Applied voltage = 30 kV; injection time = 5 s. Capillary dimensions are indicated in experimental section

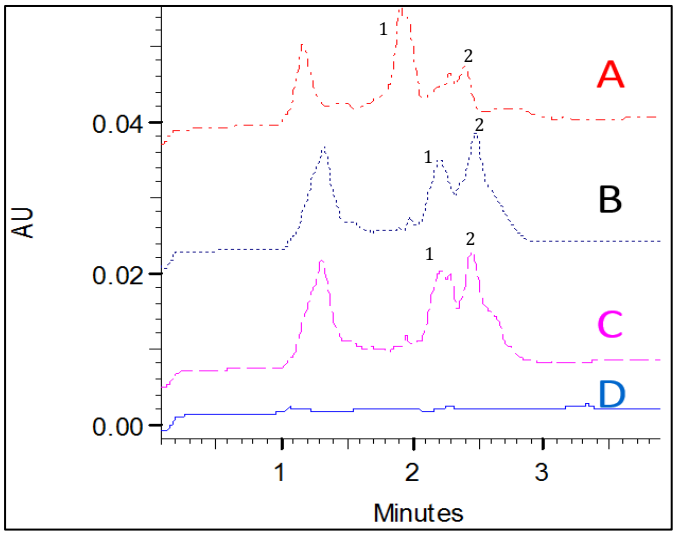



Figure 11. Enlarged electropherograms in the region from 0 to 4 minutes of Figure 10, CE-UV electropherograms of lipopolysaccharides from Gram-negative bacteria (A) K-235; (B) 055:B5; (C) *Klebsiella pneumoniae*; (D) Blank buffer. Running buffer: SDS/$Na_2B_4O_7$ (40 mM/10 mM, pH 9.22). Applied voltage = 30 kV; injection time = 5 s. Capillary dimensions are indicated in experimental section

## Conclusion

Optimization of the electrophoresis buffer was carried out for capillary electrophoresis-direct UV analysis of LPS from *E. coli* 055:B5, K-235, UT189, E-Toxate™, and Gram-negative bacteria *Klebsiella pneumonia*e. We have demonstrated three buffer systems that could provide consistent detectable signals for the separation of LPS. They are (i) Tris/Borate/EDTA (445 mM/445 mM/10 mM); (ii) SDS/$Na_2B_4O_7$ (40 mM/10 mM); (iii) $Na_2B_4O_7$/DAB (50 mM/10 mM). Reproducible electropherograms using the buffering system consisting of SDS/$Na_2B_4O_7$ (40 mM/10

mM, pH 9.22) were obtained for LPS from *E. coli* 055:B5, K-235 and Gram-negative bacteria Klebsiella pneumonia, with percentage RSD values of migration time ≤1.2% (n = 3). The percentage RSD values for peak area are ≤5.3% (n = 3) across different LPS. The optimized buffer system could provide potentially quantitative and qualitative analyzes of these LPS using capillary electrophoresis with direct UV detection.

**Acknowledgement**

This research grant (Grant number 1301-IRIS-026) is supported by the Singapore National Research Foundation under its Environment & Water Research Programme and administered by PUB, Singapore's National Water Agency.

**References**

1. Ramachandran, G. (2014). Gram-positive and gram-negative bacterial toxins in sepsis: A brief review. *Virulence*, 5(1): 213 – 218.
2. Laitinen, S., Kangas, J., Kotimaa, M., Liesivuori, J., Martikainen, P. J., Nevalainen, A., Sarantila, R. and Husman, K. (1994). Workers' exposure to airborne bacteria and endotoxins at industrial wastewater treatment plants. *American Industrial Hygiene Association*, 55(11): 1055 – 1060.
3. Jorgensen, J. H., Lee, J. C. and Pahren, H. R. (1976). Rapid detection of bacterial endotoxins in drinking water and renovated wastewater. *Applied and Environmental Microbiology*, 32(3): 347 – 351.
4. Kastowsky, M., Gutberlet, T. and Bradaczek, H. (1992). Molecular modelling of the three-dimensional structure and conformational flexibility of bacterial lipopolysaccharide. *Journal of Bacteriology*, 174(14): 4798 – 4806.
5. Silhavy, T. J., Kahne, D. and Walker, S. (2010). The bacterial cell envelope. *Cold Spring Harbor Perspectives in Biology*, 2(5): 1 – 16.
6. Kilár, A., Dörnyei, Á. and Kocsis, B. (2013). Structural characterization of bacterial lipopolysaccharides with mass spectrometry and on-and off-line separation techniques. *Mass Spectrometry Reviews*, 32(2): 90 – 117.
7. Lamari, F. N., Gioldassi, X. M., Mitropoulou, T. N. and Karamanos, N. K. (2002). Structure analysis of lipoglycans and lipoglycan-derived carbohydrates by capillary electrophoresis and mass spectrometry. *Biomedical Chromatography*, 16(2): 116 – 126.
8. Volpi, N., Maccari, F. and Linhardt, R. J. (2008). Capillary electrophoresis of complex natural polysaccharides. *Electrophoresis*, 29(15): 3095 – 3106.
9. Restaino, O. F., Cimini, D., De Rosa, M., De Castro, C., Parrilli, M. and Schiraldi, C. (2009). High-performance CE of *Escherichia coli* K4 cell surface polysaccharides. *Electrophoresis*, 30(22): 3877 – 3883.
10. Volpi, N. (2003). Separation of *Escherichia coli* 055: B5 lipopolysaccharide and detoxified lipopolysaccharide by high-performance capillary electrophoresis. *Electrophoresis*, 24(17): 3097 – 3103.
11. Eugene, C. Y. and Hackett, M. (2000). Rapid isolation method for lipopolysaccharide and lipid A from gram-negative bacteria. *Analyst*, 125(4): 651 – 656.
12. Lan, M., Wu, J., Liu, W., Zhang, W., Ge, J., Zhang, H., Sun, J., Zhao, W. and Wang, P. (2012). Copolythiophene-derived colorimetric and fluorometric sensor for visually supersensitive determination of lipopolysaccharide. *Journal of the American Chemical Society*, 134(15): 6685 – 6694.
13. Wu, S. F., Chiu, T. C., Ho, W. L. and Chang, H. T. (2009). Combining capillary electrophoresis with laser-induced fluorescence detection for the analysis of Escherichia coli lysates. *Electrophoresis*, 30(13): 2397 – 2402.
14. Wenz, C., Marchetti-Deschmann, M., Herwig, E., Schröttner, E., Allmaier, G., Trojer, L., Vollmer, M. and Rüfer, A. (2010). A fluorescent derivatization method of proteins for the detection of low-level impurities by microchip capillary gel electrophoresis. *Electrophoresis*, 31(4): 611 – 617.
15. Volpi, N. (2004). Separation of capsular polysaccharide K4 and defructosylated K4 by high-performance capillary electrophoresis. *Electrophoresis*, 25(4-5): 692 – 696.
16. Knudsen, C. B. and Beattie, J. H. (1997). On-line solid-phase extraction–capillary electrophoresis for enhanced detection sensitivity and selectivity: application to the analysis of metallothionein isoforms in sheep fetal liver. *Journal of Chromatography A*, 792(1): 463 – 473.
17. Westphal, O. and Lüderitz, O. (1954). Chemische erforschung von lipopolysacchariden gramnegativer bakterien. *Angewandte Chemie*, 66(13-14): 407 – 417.

18. Yu, L., Yuan, L., Feng, H. and Li, S. F. Y. (2004). Determination of the bacterial pathogen *Edwardsiella tarda* in fish species by capillary electrophoresis with blue light-emitting diode-induced fluorescence. *Electrophoresis*, 25(18-19): 3139 – 3144.
19. Venter, P. and Lues, J. F. R. (2003). Extraction methods for lipopolysaccharides from *Escherichia coli* ATCC 25922 for quantitative analysis by capillary electrophoresis. *International Journal of Food Microbiology*, 84(2): 245 – 250.
20. Giordano, B. C., Muza, M., Trout, A. and Landers, J. P. (2000). Dynamically-coated capillaries allow for capillary electrophoretic resolution of transferrin sialoforms via direct analysis of human serum. *Journal of Chromatography B: Biomedical Sciences and Applications*, 742(1): 79 – 89.

*Malaysian Journal of Analytical Sciences, Vol 21 No 6 (2017): 1366 - 1372*
*DOI: https://doi.org/10.17576/mjas-2017-2106-18*

MALAYSIAN JOURNAL OF ANALYTICAL SCIENCES
*Published by The Malaysian Analytical Sciences Society*
ISSN 1394 - 2506

# SPECIES AND SEROTYPE-SPECIFIC DETERMINATION OF ENDOTOXINS USING LC-MS

## (Penentuan Spesies dan Serotip-Khusus Endotoksin Menggunakan LC-MS)

Anna Karen Carrasco Laserna[1], Huatao Feng[1], Sam Fong Yau Li[1,2]*

[1]*Department of Chemistry, Faculty of Science,*
*National University of Singapore, 3 Science Drive 3, Singapore 11754, Singapore*
[2]*NUS Environmental Research Institute,*
*#02-01 T-Lab Building, 5A Engineering Drive 1, Singapore 117411, Singapore*

**Corresponding author: chmlifys@nus.edu.sg*

Received: 7 November 2016; Accepted: 18 September 2017

**Abstract**

Endotoxins or lipopolysaccharides (LPS) are characteristic components of the outer cellular membrane of Gram negative bacteria, which are recognition targets of immune receptors and are responsible for inciting the bacteria's toxic effects. The toxicity and physiological effects of LPS varies diversely within and across different bacterial species. However, the current standard test for endotoxin analysis, the Limulus Amoebocyte Lysate (LAL) test, can only provide information on the presence of LPS, regardless of which bacteria the LPS is coming from. As implied from the name "lipopolysaccharide", LPS has a lipid and a carbohydrate portion. The carbohydrate component is further subdivided to the core oligosaccharide and the O-antigen polysaccharide chains, which are conserved within species and unique for each serotype, respectively. In this pilot study, we fingerprinted the oligosaccharide units generated from mild acid hydrolysis of the LPS from some serotypes of *Escherichia coli* and *Salmonella*, as well as from *Serratia marcesens* using liquid chromatography coupled to a high resolution mass spectrometer (LC-MS) after labelling them to improve MS ionization. Multivariate analysis showed distinct clustering of samples belonging to each bacterial species and revealed certain features that can be potential species and serotype-specific markers of LPS from the different bacteria under study.

**Keywords:** endotoxins, lipopolysaccharide, oligosaccharide fingerprinting, liquid chromatography – mass spectrometry

**Abstrak**

Endotoksin atau lipopolisakarida (LPS) adalah komponen teras membran selular luaran bakteria Gram negatif yang bertindak untuk mengenalpasti sasaran reseptor imun dan bertanggungjawab menguatkan kesan toksik bakteria tersebut. Terdapat perbezaan dalam ketoksikan dan kesan fisiologi LPS di dalam dan antara spesies bakteria yang berbeza. Walau bagaimanapun, ujian piawai semasa bagi analisis endotoksin, ujian Limulus Amebosit Lisat (LAL), hanya boleh memberikan maklumat mengenai kehadiran LPS tanpa mengira bakteria sumber asal LPS tersebut. Nama lipopolisakarida juga menunjukkan bahawa LPS mempunyai lipid dan sebahagian unsur karbohidrat. Komponen karbohidrat juga terbahagi kepada oligosakarida teras dan rantai polisakarida O-antigen, yang terpelihara di dalam spesies dan unik untuk setiap serotip yang hadir. Dalam kajian rintis ini, kami mengenalpasti unit oligosakarida yang dihasilkan daripada hidrolisis asid lemah LPS dari beberapa serotip dari *Escherichia coli*, *Salmonella* dan juga *Serratia marcescens* menggunakan kromatografi cecair digunakan bersama spektrometri jisim resolusi tinggi (LC-MS) selepas proses pelabelan untuk meningkatkan pengionan MS. Analisis multivariat menunjukkan kelompok tertentu sampel yang datang dari setiap spesies bakteria dan mendedahkan ciri – ciri tertentu yang boleh menjadi spesies yang berpotensi dan penanda serotip spesifik LPS dari bakteria yang berbeza di bawah kajian.

**Kata kunci**: endotoksin, lipopolisakarida, oligosakarida cap jari, kromatografi cecair – spektrometri jisim

## Introduction

Endotoxins or lipopolysaccharides (LPS) are characteristic components of the outer cellular membrane of Gram negative bacteria. In the event of a bacterial infection, they are the recognition targets of the innate immune system and they are responsible for the toxicological effect of the bacteria [1]. When immune cells recognize their presence upon binding, the inflammatory response of the body will be triggered to resolve the infection. However, if the infection is overwhelming, complications may arise such as the development of endotoxic shock [2]. This can lead to multiple organ failure and can be fatal.

LPS is mainly composed of a lipid and a carbohydrate part, thus the name "lipopolysaccharide". Generally, its structure is divided into three main parts: the lipid A, the core oligosaccharide, and the O-polysaccharide or O-antigen chain. The lipid A is made up of ester or amide-linked fatty acid chains of varying lengths that is conserved for each bacterial species and is known to be the active part responsible for the bacteria's toxicity. Changes in its structure can affect the activity of the endotoxin. The core oligosaccharide is further subdivided into an inner and outer core. The inner core mainly consists of unusual sugars such as 3-deoxy-D-manno-octulosonic acid (Kdo) and L-glycero-D-manno-heptose. The outer core consists of more common sugars such as hexoses and hexosamines. The core oligosaccharide is mostly conserved within bacterial species. Lastly, there is the O-polysaccharide or O-antigen chain. It consists of repeating subunits of carbohydrate chains with varying lengths having high specificity for each serotype of the same species. It is the part that binds with immune receptors and induces the antigenic effect, thus the name O-antigen [1, 3]. It can be seen that there is great diversity in the structure of the LPS among different bacterial species and even within the same species. This diversity also results in different innate immune response, different degrees of toxicity, and trigger of different physiological responses to individuals [4].

The current gold standard for LPS analysis is the *Limulus* amoebocyte lysate (LAL) test. The test is based on the agglutination of the amoebocyte lysate obtained from horseshoe crab in the presence of endotoxins. Other methods of endotoxin analysis include rabbit pyrogenic testing, cell and antibody binding assays, molecular binding biosensors, and recombinant bacteriophage binding [5]. For tests like LAL and rabbit pyrogenic testing, there is a concern on sustainability due to their use of animals. Most of these tests are highly sensitive and quantitative. However, they are also mostly non-specific methods of endotoxin detection. They only determine and measure the amount of endotoxin present but do not provide information as to what bacterial species or serotype the endotoxin comes from. On the other hand, there are also assays and biosensors that are highly specific to certain serotypes, thus requiring multiple assays in order to detect the presence of different species and serotypes. Given that different LPS can induce different antigenic and toxicological effects, there is a need for species and serotype-specific determination of LPS.

Chemical fingerprinting has been used in different fields of application for purposes of quality control, authentication, and origin identification [6]. It is based on the understanding that different organisms, species, and even those of the same species raised in different conditions will have their own unique molecular profiles. It can be done using different compounds ranging from DNA to small molecule metabolites and using different analytical platforms. Mass spectrometry (MS)-based analysis are commonly used in fingerprinting as they provide high sensitivity and compound identity information based on mass and fragmentation data. MS analysis is usually coupled with separation techniques such as gas chromatography (GC), liquid chromatography (LC) or capillary electrophoresis (CE) in order to further improve specificity by resolving isomers and increase sensitivity by reducing the number of analytes detected at any given time that may otherwise suppress or interfere with each other. Given that the carbohydrate component of bacterial LPS provides both species and serotype information, we explore the feasibility of fingerprinting different LPS based on their oligosaccharide features.

## Materials and Methods

### Chemicals

The LPS standards of *Salmonella enterica* serotype abortus equi, *Salmonella enterica* serotype minnesota, *Salmonella typhosa*, *Serratia marcesens*, *Escherichia coli* O55:B5, and *Escherichia coli* K-235 were all purchased from Sigma-Aldrich (St. Louis, MO, USA). The reagents 7-(diethylamino) coumarin-3-carbohydrazide (CHH), as well as LC-MS grade formic acid, acetic acid, ammonium formate, and acetonitrile (ACN), were also purchased

from Sigma-Aldrich. Ultrapure water (18.2Ω) was obtained from an UltraClear TWF water purification system by EvoQua (Fahrenberg, Germany).

**Sample preparation**

Each sample of LPS standard was weighed (0.20 ± 0.05 mg) into a centrifuge vial and subjected to mild acid hydrolysis in order to remove the lipid A component. Mild acid hydrolysis was performed by adding 100 µl of 1% acetic acid to the sample followed by heating for 1 hour at 90 ˚C. The samples were then centrifuged, the supernatant was taken and freeze dried. The samples were kept in -80 ˚C until labelling and analysis. The samples were then labelled based on a modification of the method reported by Milic et al. for CHH labelling [7]. Briefly, a volume of 100 µl of 2 mg/ml CHH in 50% ACN was added to the dried LPS hydrolysate. The samples were then incubated in the dark for 3 hours in a temperature controlled shaker at 37 ˚C. All LPS standards were prepared and analyzed in triplicates.

**LC-MS analysis**

The LC-MS analysis was performed using a Dionex Ultimate 3000 RSLC system (Thermo Fisher Scientific, USA) coupled to an AB Sciex Triple TOF 5600 MS (Sciex, USA). Chromatographic separation was done using a Glycan BEH Amide column (Waters, USA) with dimensions of 2.1 x 100 mm and particle size of 1.8 micron. The mobile phase solvents used were 50 mM ammonium formate (pH 4.5) in water (A) and acetonitrile (B), with an initial flow rate of 0.4 ml/min. The gradient program employed for the separation was as follows: 85% B to 50% B for the first 25 minutes, 50 to 30% B from 25 to 27 minutes with a reduction in flow rate to 0.2 ml/min, 0% B at 28 minutes to 30 minutes with flow rate increased to 0.4 ml/min at the end of this step, 0 to 85% B from 30 to 31.5 minutes, and lastly, equilibration for 6.6 minutes. Data acquisition was done in positive electrospray ionization mode. The mass range scanned was from 100 to 2500 Dalton (Da) with an accumulation time of 0.2 second. The nebulizer and heater gases were set at 45 and 50 psi, respectively, the curtain gas was at 30 psi, heater temperature at 450 ˚C, and the ion spray voltage was set to 5,000 volts (V). The declustering potential (DP) was set at 80 V and collision energy (CE) was at 10 V. MS/MS data was obtained using information dependent acquisition (IDA) wherein the 10 highest intensity ions per cycle were subjected to product ion scan at collision energy (CE) of 35 V with CE spread of 15 V. Automated mass calibration was done every three hours using the AB Sciex APCI positive calibration solution (Sciex, USA).

**Data processing and analysis**

The MS data acquisition files were converted to mzXML format using MSConvert (Proteowizard). The files were then uploaded to XCMS online for retention time alignment, peak picking and annotation. The resulting data matrix was exported to Excel for further processing. Peaks common with the reagent blank were removed from the dataset as well as identified isotopic signals. Median normalization was performed to ensure comparability of all samples by reducing the effects of variations from sample weighing and changes in the sensitivity of the instrument through time. All values were log 2 transformed to reduce the effects of variations in high intensity variables and prevent them from masking the contributions of lower intensity variables. Multivariate analysis was performed using SIMCA P+ 12 (MKS Umetrics, Sweden). Principal Components Analysis (PCA) was performed to identify inherent clustering of samples or presence of trends and identify possible outliers. Supervised analysis was also performed using Orthogonal Projection to Latent Structures- Discriminant Analysis (OPLS-DA). Features that are either species or serotype-specific were identified by looking at the contributions plot of the OPLS-DA model.

## Results and Discussion

In this pilot study, we looked at the oligosaccharide fingerprints of two serotypes of *Escherichia coli* (EC O55:B5 and EC K-235), two serotypes of *Salmonella enterica* (minnesota and abortus equi, SEM and SEA), *Salmonella typhosa* (ST), and *Serratia marcesens* (SM). Most carbohydrates do not have functional groups that can be easily used for their detection and they are also not easily ionisable for MS detection. They can be analyzed in negative ionization mode under highly basic conditions but with lower sensitivity. Thus, they are usually derivatized or labelled with moieties that will aid in their detection [8]. Fluorescent reagents like 8-aminopyrene-1,3,6-trisulfonic acid (APTS) and MS ionisable reagents like 2-aminobenzoic acid (2-AB), 2-anthranilic acid (2-AA), and more recently, RapiFluor MS [9], are used to label sugars for detection. However, such reagents require reductive amination in order to react the reducing sugar moiety with the label. It requires the use of a highly toxic reagent,

sodium cyanoborohydride, and an SPE clean-up step. There are also labelling reagents that can react directly with the reducing sugar moiety via hydrazone formation, such as 2-(4-phenethylphenyl)acetohydrazide [10], which allows simpler sample preparation for MS analysis. For this project, we tried the use of a common fluorescent reagent, 7-(diethylamino)coumarin-3-carbohydrazide (CHH) for the labelling of the oligosaccharides via hydrazone formation and subsequent MS detection. It has been previously reported for use in MS analysis of carbonylated lipids [7] given that it can react readily with aldehydes and ketones via the hydrazide moiety and have good ionization in MS with the tertiary amine moiety. We hypothesize that we can also use it to easily tag the reducing sugar moiety of the oligosaccharides and be used for MS analysis of the oligosaccharides. Furthermore, it can also be used for fluorescence detection.

Figure 1 shows the total ion chromatogram (TIC) of the different LPS samples analyzed. It can be seen that each LPS has its own distinct profile. In the chromatographic dimension, there are peaks that appear at the same retention time across different species and serotypes. The use of MS adds another dimension of resolution by differentiating the components eluting at the same retention time based on mass. While this offers better specificity, it also produces a complex data matrix with high dimensionality. Multivariate statistical analysis, commonly used to analyze such data matrices and reveal useful information [11], was used in this study to analyze the complex data matrix.

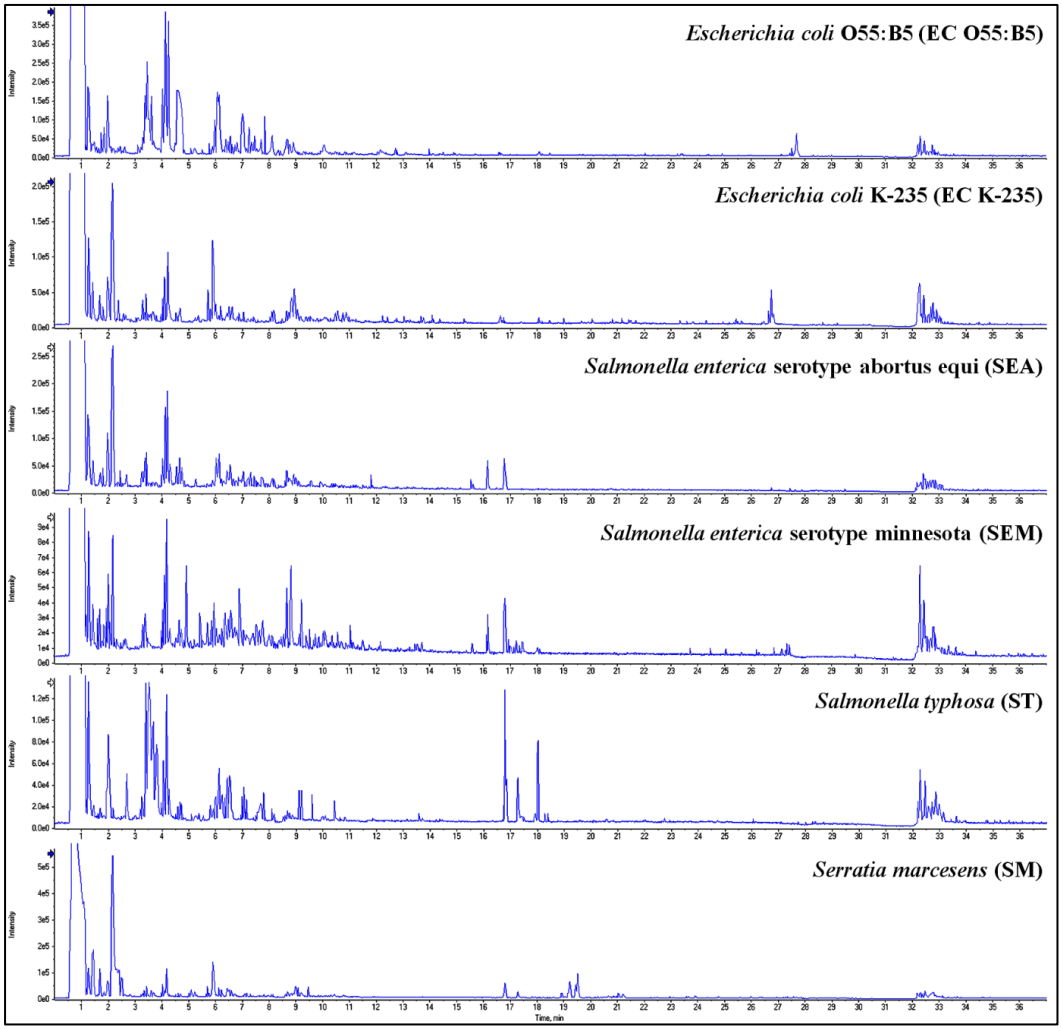



Figure 1. TIC of the different LPS samples labelled with CHH

PCA was used to reduce the high dimensionality of the data to a few components that can account for the variance across the samples. This allows for visualization of inherent groupings and trends in the data. The PCA model generated has a cumulative $R^2X$ value of 0.833 and cumulative $Q^2$ of 0.499. The cumulative $R^2X$ represents the fraction of variation from all the variables (X) that can be explained by the components of the model. The cumulative $Q^2$ is the fraction of the variation that can be predicted by the model through cross-validation using a "leave-one-out" approach [12]. Both serve as measures of the quality of the model. A good model should have $R^2X$ close to 1 with the $Q^2$ approaching or close to the $R^2X$ value. The model has a good cumulative $R^2X$ but low $Q^2$. This can be an indication of the presence of unwanted variance from the variables affecting the model. OPLS-DA, a supervised multivariate analysis technique, can be used to take out the variance that is not related to the class information by putting them into orthogonal component/s and maximize the separation between sample groups (classes). The OPLS-DA model of the dataset has a cumulative $R^2X$ of 0.838, $R^2Y$ of 0.99 and a $Q^2$ of 0.928. $R^2Y$ represents the fraction of variation related to the class information (Y) that can be explained by the components of the model. $Q^2$ in this case, represents variation of Y that can be predicted by the components of the model and it should be as close as possible to the $R^2Y$ [12]. High values of $R^2X$, $R^2Y$, and $Q^2$ show that a good model has been obtained. Cross validation was also done using CV-ANOVA resulting in a p value of $2.35x10^{-12}$ (p value <<< 0.05) showing the high reliability and significance of the model.

Figure 2 shows the score plots of the samples using PCA and OPLS-DA. There is good clustering of the samples for each LPS standard in both plots, indicating good reproducibility of the fingerprints. It can also be observed that the *E. coli* serotypes, EC O55:B5 and EC K-235 are mainly in the lower quadrant, whereas the *Salmonella* species and serotypes, ST, SEA, and SEM, are in the upper quadrant. *Serratia marcescens* (SM) samples are in the middle, between the upper and lower quadrants. It can also be seen that SEM and SEA cluster closer together away from ST, confirming the ability to distinguish species within the same genera using the oligosaccharide features.

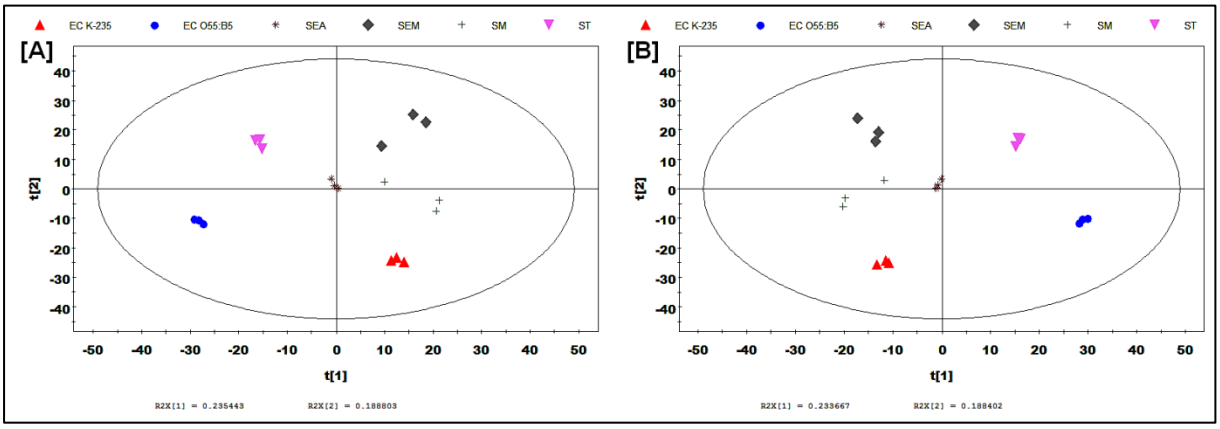



Figure 2. (a) PCA score plot showing the distinct clustering of the LPS samples from different bacterial species and serotypes, and (b) OPLS-DA score plot of the samples

Identification of variables distinct to each serotype and species were identified by looking at contribution plots of the OPLS-DA model. Contribution plots are used to visualize how an observation or group is different from others in model. It displays the differences in scaled units of the observation or group compared to the average of the rest for all variables of the model. Variables with score contribution greater than two were identified as potential species or serotype-specific oligosaccharide feature. This is confirmed by looking at the variable plot for the identified variables. Represented in Figure 3 is an example of a contribution plot showing the variables differentiating SM from the other LPS. The differentiating features are those variables whose scores are above the contribution score cut-off (orange line). The MS and MS/MS information obtained from these species and serotype- differentiating features can be used to develop targeted multiple reaction monitoring (MRM) analysis that will allow the simultaneous determination of LPS coming from different bacterial species and serotypes.

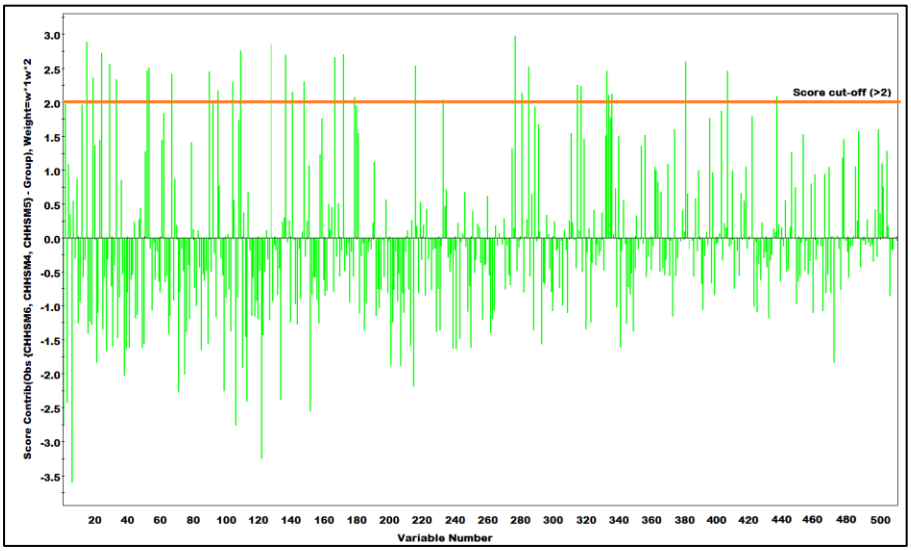



Figure 3. Contribution plot for *Serratia marcesens* (SM)

During the identification of species and serotype-specific features, it was noted that the MS/MS spectra of some of these oligosaccharide features do not have the reporter ions of CHH-labelled compounds (m/z 276 and 244, Figure 4a) [7]. Instead, their MS/MS spectra showed the presence of characteristic HexNAc ions (m/z 204 and 168, Figure 4b) [13], indicating that these oligosaccharide features are unlabelled oliogosaccharides having N-acetylamine moieties. While it is good that such distinct oligosaccharide features can be identified and differentiated based on their characteristic fragmentation pattern, this still highlights the need for further investigation and optimization of the labelling conditions.

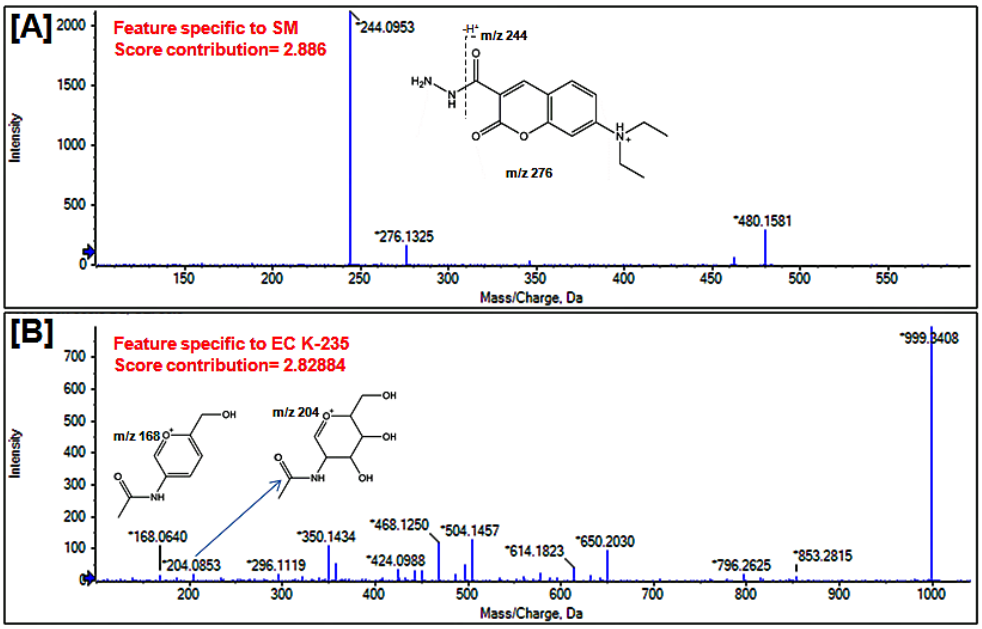



Figure 4. Sample MS/MS spectra of identified distinct oligosaccharide features

## Conclusion

The results of the study demonstrated the feasibility of using oligosaccharide fingerprinting for the species and serotype-specific determination of LPS. Good reproducibility of fingerprints has been obtained across the different bacterial species and serotypes, as shown by the good clustering of samples in the multivariate analysis models. Presence of unlabelled oligosaccharides was found from MS/MS data warranting further improvements in the labelling method. Identified species and serotype-specific oligosaccharide features from the fingerprinting can be used for the development of a targeted method for the simultaneous determination of LPS from different bacteria. It is hoped that this can eventually be used for different applications such as in environmental water and air monitoring, as well as in clinical settings.

## Acknowledgement

The research grant for this study (1301-IRIS-026) is supported by the Singapore National Research Foundation under its Environment & Water Research Programme and administered by PUB, Singapore's National Water Agency. We also acknowledge funding support from NUS and Thermo Fisher through the NUS-Thermo Fisher Strategic Alliance. The authors would also like to thank Ms. Nur Wahdiah Binte Mohamed Safit for the help with the Malay translations.

## References

1. Erridge C., Bennett-Guerrero E. and Poxton I. R. (2002). Structure and function of lipopolysaccharides. *Microbes and Infection,* 4 (8): 837 – 851.
2. Abbott, J. D., Ball, G., Boumpas, D., Bridges, S. L., Chatham, W. and Curtis, J. (2004). Endotoxic shock in rheumatology and immunology therapy. Springer Berlin Heidelberg. pp. 302 – 303.
3. Holst O. (2011). Structure of the lipopolysaccharide core region, in bacterial lipopolysaccharides: structure, chemical synthesis, biogenesis and interaction with host cells, Y.A. Knirel, M.A. Valvano, Editors. Springer Vienna. pp. 21 – 39.
4. Miller S. I., Ernst R. K. and Bader M. W. (2005). LPS, TLR4 and infectious disease diversity. *Nature Review Microbiology,* 3(1): 36 – 46.
5. Das A. P., Kumar P. S. and Swain S. (2014). Recent advances in biosensor based endotoxin detection. *Biosensors Bioelectron,* 51: 62 – 75.
6. Ellis D. I., Brewster V. L., Dunn W. B., Allwood J. W., Golovanov A. P. and Goodacre R. (2012). Fingerprinting food: Current technologies for the detection of food adulteration and contamination. *Chemical Society Reviews,* 41(17): 5706 – 5727.
7. Milic I., Hoffmann R. and Fedorova M. (2013). Simultaneous detection of low and high molecular weight carbonylated compounds derived from lipid peroxidation by electrospray ionization-tandem mass spectrometry. *Analitical Chemistry,* 85 (1): 156 – 162.
8. Ruhaak L.R., Zauner G., Huhn C., Bruggink C., Deelder A. M. and Wuhrer M. (2010). Glycan labeling strategies and their use in identification and quantification. *Analytical and Bioanalytical Chemistry,* 397(8): 3457 – 3481.
9. Lauber M. A., Yu Y-Q., Brousmiche D. W., Hua Z., Koza S. M., Magnelli P., Guthrie, E., Taron, C. H. and Fountain, K. J. (2015). Rapid preparation of released N-glycans for HILIC analysis using a labeling reagent that facilitates sensitive fluorescence and ESI-MS detection. *Analytical Chemistry,* 87(10): 5401 – 5409.
10. Walker S. H., Lilley L. M., Enamorado M. F., Comins D. L. and Muddiman D.C. (2011). Hydrophobic derivatization of N-linked glycans for increased ion abundance in electrospray ionization mass spectrometry. *Journal of American Society Mass Spectrometry,* 22(8): 1309 – 1317.
11. Eriksson L., Antti H., Gottfries J., Holmes E., Johansson E., Lindgren F., Long, I., Lundstedt, T., Trygg, J. and Wold, S. (2004). Using chemometrics for navigating in the large data sets of genomics, proteomics, and metabonomics (gpm). *Analytical and Bioanalytical Chemistry,* 380(3): 419 – 429.
12. Umetrics (2008). User guide to SIMCA-P+ Version 12. M.K.S. Umetrics, Malmo, Sweden.
13. Zhao P., Viner R., Teo C. F., Boons G-J., Horn D. and Wells L. (2011). Combining high-energy C-trap dissociation and electron transfer dissociation for protein O-GlcNAc modification site assignment. *Journal of Proteome Research,* 10(9): 4088 – 4104.

*Malaysian Journal of Analytical Sciences, Vol 21 No 6 (2017): 1373 - 1379*
*DOI: https://doi.org/10.17576/mjas-2017-2106-19*

MALAYSIAN JOURNAL OF ANALYTICAL SCIENCES
*Published by The Malaysian Analytical Sciences Society*
ISSN 1394 - 2506

# SURFACE PLASMON RESONANCE SENSOR FOR DETECTION OF PARATHION METHYL IN WATER

## (Sensor Permukaan Plasmon Resonan bagi Pengesanan Parathion Metil di dalam Air)

Baisheng Chen[1], Douglas Chiang Yon Chong[1], Xiamin Cheng[2, 3], Bin Liu[3], Sam Fong Yau Li[1, 2]*

[1]*Department of Chemistry,*
*National University of Singapore, 3 Science Drive 3, Singapore 117543, Singapore*
[2]*NUS Environmental Research Institute (NERI),*
*#02-01, T-Lab Building (TL), 5A Engineering Drive 1, Singapore 117411, Singapore*
[3]*Department of Chemical & Biomolecular Engineering,*
*National University of Singapore, 4 Engineering Drive 4, Block E5 #02-17, 117585, Singapore*

**Corresponding author: chmlifys@nus.edu.sg*

Received: 7 November 2016; Accepted: 18 September 2017

**Abstract**

A surface plasmon resonance (SPR) sensor based on molecularly imprinted polymer (MIP) was developed for fast detection of chemical threat agents (CTAs) in water. A portable SPR platform provided a very compact-size (L*W*H of 8.5*4.5*4.5 inch) system and the SPR sensor chip was fabricated by a facile process with an inexpensive coating of silver as the SPR material, making possible the sensor chip as a disposal sensor. Using methyl parathion as the simulant of CTA, the developed SPR sensor with the recognition site showed apparent SPR signal than Non-imprinted polymer (NIP) counterpart, suggesting the excellent recognition of the targeted molecules. It also provided a fast responding within 5 minutes with the limit of detection of sub-ppm level.

**Keywords**: molecularly imprinted polymer, surface plasmon resonance, organophosphorus pesticide, chemical threat agents

**Abstrak**

Sensor permukaan plasmon resonans (SPR) berdasarkan polimer molekul tercetak (MIP) telah dibangunkan bagi pengesanan pantas ejen ancaman kimia (CTAs) di dalam air. Sistem platform SPR mudah alih bersaiz padat disediakan (L*W*H 8.5*4.5*4.5 inci) dan cip sensor SPR telah diubahsuai melalui proses mudah dengan salutan murah perak sebagai bahan SPR, menjadikan cip sensor sebagai sensor mudah dilupuskan. Menggunakan parathion metil sebagai sasaran CTA, sensor SPR yang telah dibangunkan dengan bahagian yang dikenalpasti itu menunjukkan isyarat jelas daripada SPR berbanding polimer tak tercetak (NIP), menunjukkan pengenalpastian baik bagi molekul yang disasarkan. Ia juga memberi respons yang cepat dalam masa 5 minit dengan had pengesanan pada aras sub-ppm.

**Kata kunci**: polimer molekul tercetak, permukaan plasmon resonans, racun perosak organofosforus, agen kimia berbahaya

## Introduction

The emerging concerns of terrorists using Chemical Threat Agents (CTAs) has been on the rise which has urged the governments to ensure the water safety before consumption [1, 2]. Organophosphorus compounds (OPs) is used as the simulant of a type of chemical threat agents- nerve agents. The current monitoring method includes gas chromatography-mass spectrometry [3], liquid chromatography-mass spectrometry [4] and micellar electro-kinetic capillary electrophoresis coupled with laser-induced fluorescence (MEKC-LIF) detector [5]. However, these

instruments involved in the monitoring are usually bulky in size, and highly expensive and require highly trained technicians to run the samples, which hinders the application of on-line or on-site monitoring [6]. An alternative monitoring technique is surface plasmon resonance (SPR), which is a phenomenon that occurs when the incident light on a metal film induces the propagation of electron density waves parallel to the metal-dielectric medium interface [7, 8]. SPR system is relatively low-cost and only requires a simple optical setup, rendering a high potential to be suited for on-line/on-site monitoring [9-11].

The recognition of specific CTA molecules requires a highly selective material to provide such capability. Due to their easy synthesis procedures, low cost, and chemical and physical stability in harsh environments, MIPs provide a simple and cost-effective way to fabricate selective recognition elements suitable for chemo-sensors and biosensors [12]. Preparation of MIPs usually involves copolymerizing the template molecule and functional monomers (serving as ligands) with a cross-linker under suitable conditions. The type of cross-linker used influences the morphology of the polymer matrix, and stabilizes the recognition sites. During polymerization, the template and functional monomers will interact and self-assemble to form a polymer network. The MIP will be coated on the silver film of the glass sensor chip with silver film and the template molecule is then removed from the polymer matrix to create complementary three-dimensional cavities for the template. SPR sensors coupled with MIP has been successfully applied in analysing endotoxins [13], waterborne virus [14] and dyeing agents [15] in water.

In this study, an SPR sensor is presented using MIP as the recognition sites for the detection of CTA simulant parathion-methyl. Silver is selected as the SPR coating material since it is known to be more sensitive to changes in refractive indices [16] and reflects more distinctive plasmon resonance bands than gold [17]. The potential of on-line/on-site application of the developed SPR sensor is further discussed.

## Materials and Methods

### Reagents and materials

Analytical grade Parathion-methyl and functional monomer methacrylic acid (MAA) (99%) were purchased from Sigma-Aldrich (Singapore). Absolute ethanol solvent was obtained from VWR Singapore Pte Ltd. and of analytical grade. Initiator 2, 2-azobis (2-methylpropionitrile) (AIBN) (99%) was purchased from Sinopharm Chemical Reagent Co. Ltd. (China) while cross-linker divinylbenzene (>50%) was purchased from Tokyo Chemical Industry Co. Ltd. (Japan). Deionised water (18.2 MΩ, ultrapure) was purified using Milli-Q Integral Water Purification System from Merck Millipore while the index matching oil ($\eta$=1.65) used was provided by PhotonicSys Ltd. (Israel).

### Apparatus and instruments

The SPR system and SPR analysis software (Version: Feb 2016) were from PhotonicSys Ltd. (Israel) and the 40-nm silver film sensor chips were sputter-coated and prepared by the company. The SPR system, as shown in Figure 1, is compact in size with L*W*H of 8.5*4.5*4.5 inch. It uses a diverging laser beam as the light source to illuminate the entire sensor surface in Kretschmann-Raether configuration [18, 19]. A CCD detector is employed to monitor the pattern of dark intensity line on bright background which is corresponding to the SPR dip at an angular range depending on the refractive index of the adjacent analyte [20]. A high precision of SPR signal is subsequently achieved by a forward-projection algorithm based on Radon transform for two-dimensional surface plasmon imaging [21].

For ultra-sonication, the Elmasonic S30H sonicator used was obtained from Elma Schmidbauer GmbH (Germany). The LM530R orbital shaking incubator utilized was purchased from Yihder Technology Co. Ltd. (Taiwan) while the FINEVORTEX vortex mixer was obtained from FINEPCR (South Korea).

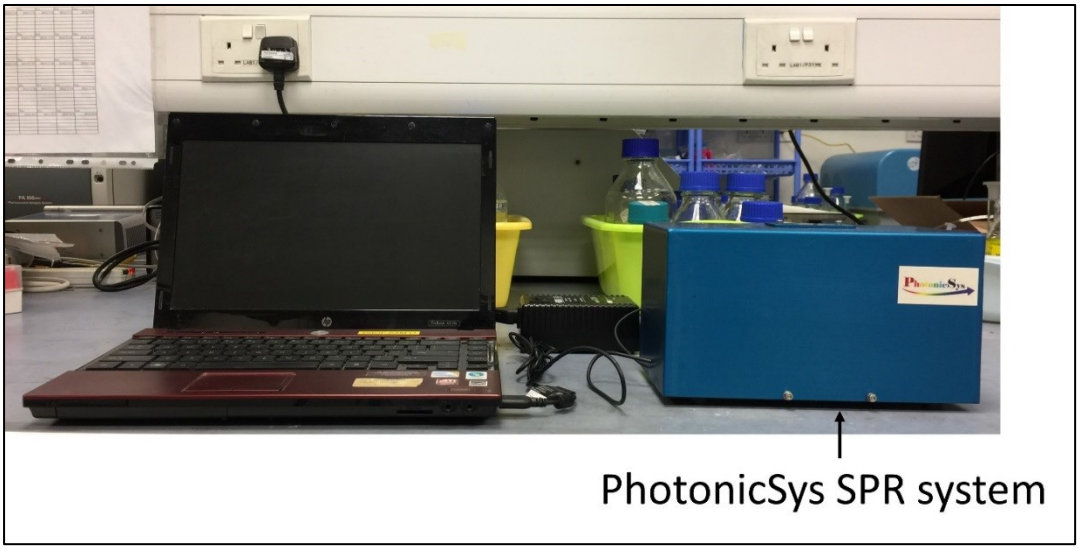



Figure 1. Photo of SPR instrument from PhotonicSys Ltd. connected to a notebook computer via USB

**Preparation of MIP sensor chips**

The MIP polymer comprises four components: MAA as functional monomer, DVB as cross-linker, AIBN as radical initiator and parathion methyl as template molecules. The mechanism behind MIP recognition is based on a combination of bonding. The carboxylic acid in MAA provides hydrogen-bonding donor, while DVB offers better stability of polymer rigidity and hydrophobic interaction with the template molecules.

Molecularly imprinted polymer was prepared by mixing 40 µL of 0.1 M parathion-methyl, 5 µL of MAA, 25 µL of DVB and 0.5 mg of AIBN in 1.5 mL centrifuge tube with 100 µL absolute ethanol. The mixture was ultra-sonicated for 10 minutes to allow thorough mixing. Subsequently, 10 $\mu$L of the MIP solution was drop-coated on a silver sensor chip, which was placed in the oven at 60 ˚C for 6 hours to allow polymerization.

The MIP chip was then soaked in absolute ethanol and left in the orbital shaker for overnight (8-10 hours) to remove the template parathion-methyl molecule from its binding sites in the polymer matrix, shown in Figure 2. The MIP chip was stored in absolute ethanol before measurement to prevent degradation and oxidation of the silver layer. Non-imprinted polymer (NIP) sensor chips were prepared using the same preparation method but without template parathion-methyl.

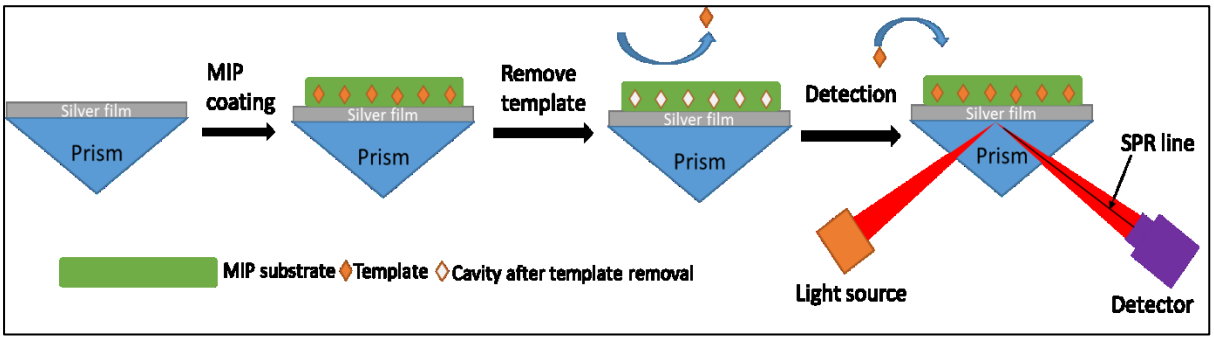



Figure 2. Schematic representation of MIP sensor design

**Preparation of sample solutions**

A 100-ppm parathion methyl solution was prepared by diluting stock solution into a 100-mL volumetric flask with ultrapure water made up to the 100-mL mark. All sample solutions (10 mL each) were prepared accordingly by diluting appropriate volumes of the stock solution in centrifuge sample tubes.

**SPR sensing procedure**

The SPR sensing procedure included the following steps, as illustrated in Figure 3. Firstly, SPR prism was wiped and cleaned with ethanol to remove any dirt or oil residuals. A small amount (approx. 50 µL) of RI matching oil was then applied on the prism. The MIP sensor chip was rinsed with ethanol and followed by deionised water before drying with nitrogen gas.

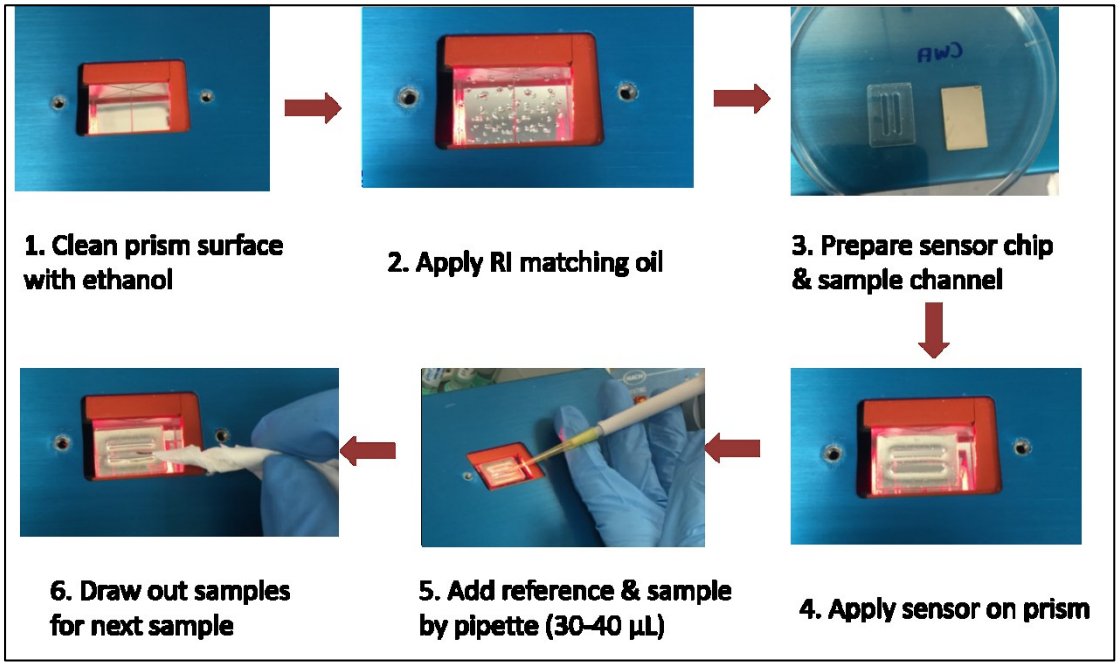



Figure 3. Experimental operation of SPR sensing

The MIP chip was mounted onto the prism by firstly placing the chip on its edge over the prism then carefully lowering it in place using a pair of forceps. It was important to ensure that no dark regions or lines were observed from the camera image. A polydimethylsiloxane (PDMS) sample holder with two identical channels was subentry applied onto the MIP sensor chip and gently pressed to form a sensing substrate.

A reference solution (deionised water) and a sample solution with 30 – 40 µL were added into left and right channels. The channels were rinsed thrice with the respective solution before measurement. The regions of interest (ROIs) were defined by choosing the rectangle cursor and draw the ROI rectangle around the dark line. After each measurement, the solutions were drawn out by a tissue paper on the edge of the channels before adding a new solution.

The software interface allowed the user to view real-time images of the plasmon resonance bands and perform runs based on the difference in RI between the analyte and reference against time [22]. The sensing performance was highly dependent on the image sensor and thus it required optimisation before measurements. The optimised values for image sensor of SPR system was shown in Table 1.

Table 1. Attributes and their respective values of image sensor

| Attributes | Value |
|---|---|
| Brightness | 67 |
| Contrast | 1.28 |
| Exposure | 0.0625 |
| Focus | 50 |
| Gain and saturation | 0 |
| Sharpness | 39 |
| White Balance | 3000 |
| Zoom | 100 |

**Characterization of MIP and NIP**

Both MIP and NIP were soaked in ethanol under same conditions to remove unreacted reagents and dried in a vacuum oven. The respective polymer was then mixed and ground with KBr in 0.99% w/w before being pressed into a transparent pellet. FT-IR spectra were collected using ALPHA FTIR Spectrometer (Bruker). The key infrared peaks for MIP included 3018 $cm^{-1}$ (alkene), 2960 $cm^{-1}$ (alkane), 2925 $cm^{-1}$ (carboxylic acid), and 1700 $cm^{-1}$(carbonyl), while key peaks for NIP included 3019 $cm^{-1}$ (alkene), 2960 $cm^{-1}$ (alkane), 2926 $cm^{-1}$ (carboxylic acid), and 1699 $cm^{-1}$ (carbonyl).

## Results and Discussion

**Detection time**

The SPR sensor in this study was a static-mode sensor which depended on the diffusion of targeted molecules into the cavity of MIP through either binding or space or both interactions. Figure 4a illustrates a real-time image of the SPR sensor of two channel signals. On the left was SPR image of deionised water as the reference, while on the right was SPR image of parathion-methyl as the analyte. Figure 4b is an example of equivalent time of RI signal of the detection of 8 ppm parathion methyl. RI signal increased until it reached a plateau at 300 seconds, i.e. 5 minutes. Similar RI response patterns were observed; therefore 5 minutes was chosen for each test.

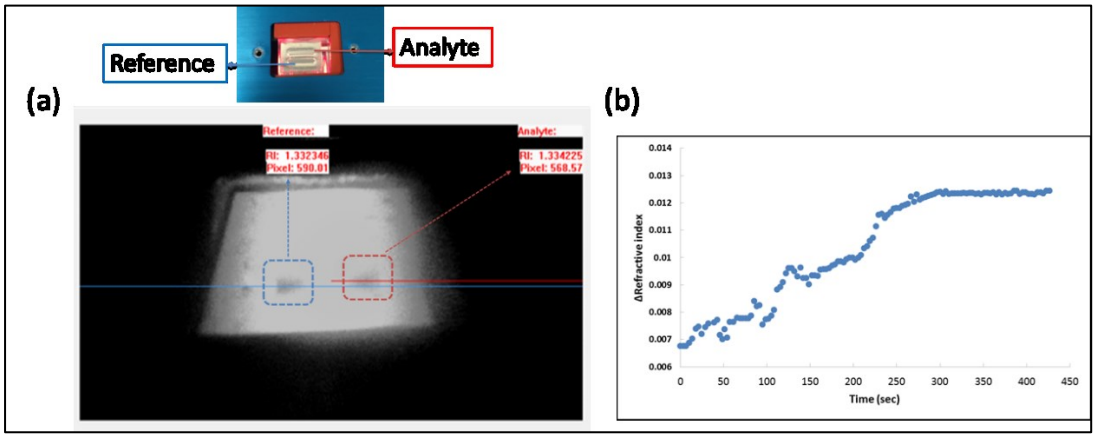



Figure 4. (a) Real-time image of SPR sensing of parathion-methyl and (b) refractive index response relative to time with 8 ppm parathion methyl

**Detection of parathion methyl**

The wavelength of light or the incidence angle at which the SPR is excited, are strong functions of the refractive index of the dielectric medium adjacent to the metal surface, i.e. silver film. The dielectric medium can be a fluid such as water or any other fluids with varying refractive index (RI) due to variations in the concentration in water [22]. The current version of the PhotonicSys SPR system can detect down to $10^{-6}$ refractive index units (RIU).

Different concentration of parathion-methyl was prepared and spiked into water samples before measurements. The RI of molecularly imprinted polymers sensing and non-imprinted polymers sensing were compared. As can be seen from Figure 5, non-imprinted polymer (NIP) showed no apparent signal changes from low concentration to high concentration, whereas MIP showed increased SPR signals (ΔRI) from 2 ppm to 30 ppm and a plateau was observed above 30 ppm. As such, the linear range for the developed SPR sensor was determined to be 2 – 30 ppm with a good correlation ($R^2$ = 0.8783). The limit of detection (LOD), based on the standard deviation of the response and the slope, was calculated to be 13.8 ppm from the calibration curve.

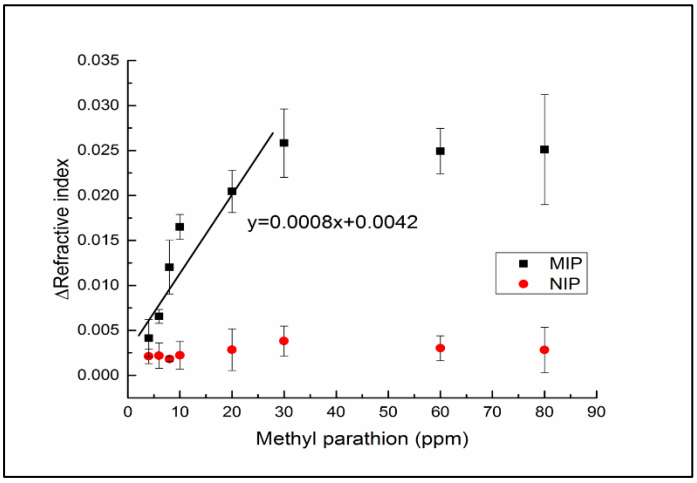



Figure 5. SPR refractive index responses on both imprinted molecular polymer (MIP) and non-imprinted polymer (NIP) toward the injection of different concentrations of methyl parathion in water

## Conclusion

A fast responding (~5 min) SPR sensor based on MIP recognition for the detection of CTA simulant methyl parathion in water has been developed successfully. Due to the portability and fast responding capability, the MIP sensor can be easily deployed for on-site/on-line detection of toxic compounds in water. This method can be easily transferred to measure other organophosphorus compounds in water by adding the organophosphorus compounds as MIP templates. Improvement of sensitivity of SPR sensor can be improved by a flow SPR system. In contrast to the static system, where the interaction is only dependent on the diffusion, a flow SPR system will provide an ever-refreshing interaction of targeted molecules with the developed MIP system. Therefore, the sensitivity can be significantly enhanced. Such flow SPR system will be developed and further tested in our future studies.

## Acknowledgement

This research grant (1301-IRIS-021) is supported by the Singapore National Research Foundation under its Environment & Water Research Programme and administered by PUB, Singapore's National Water Agency.

## References

1. Chenau, J., Fenaille, F., Simon, S., Filali, S., Volland, H., Junot, C., Carniel, E. and Becher, F. (2014). Detection of *Yersinia pestis* in environmental and food samples by intact cell immunocapture and liquid chromatography–tandem mass spectrometry. *Analytical Chemistry*, 86(12): 6144 – 6152.

2. Green, U., Kremer, J. H., Zillmer, M. and Moldaenke, C. (2003). Detection of chemical threat agents in drinking water by an early warning real- time biomonitor. *Environmental Toxicology*, 18(6): 368 – 374.
3. Zhang, J. and Lee, H. K. (2006). Application of liquid-phase microextraction and on-column derivatization combined with gas chromatography–mass spectrometry to the determination of carbamate pesticides. *Journal of Chromatography A*, 1117(1): 31 – 37.
4. Sanagi, M. M., Mokhtar, S. U., Wan Ibrahim, W. A. and Miskam, M. (2011). Determination of organophosphorus pesticides by dispersive liquid-liquid microextraction coupled with gas chromatography-electron capture detection. *Malaysian Journal of Analytical Sciences*, 15(2): 232 – 239.
5. Chang, S. Y., Tseng, W. L., Mallipattu, S. and Chang, H. T. (2005). Determination of small phosphorus-containing compounds by capillary electrophoresis. *Talanta*, 66(2): 411 – 421.
6. Tankiewicz, M., Fenik, J. and Biziuk, M. (2011). Solventless and solvent-minimized sample preparation techniques for determining currently used pesticides in water samples: A review. *Talanta*, 86: 8 – 22.
7. Homola J. and Piliarik M. (2006) Surface plasmon resonance (SPR) sensors. In: Homola J. (eds) Surface plasmon resonance based sensors. Springer Series on Chemical Sensors and Biosensors. Springer, Berlin, Heidelberg.
8. Abdulhalim, I., Zourob, M. and Lakhtakia, A. (2008). Surface plasmon resonance for biosensing: A mini-review. *Electromagnetics*, 28(3): 214 – 242.
9. Yao, G. H., Liang, R. P., Huang, C. F., Wang, Y. and Qiu, J. D. (2013). Surface plasmon resonance sensor based on magnetic molecularly imprinted polymers amplification for pesticide recognition. *Analytical Chemistry*, 85(24): 11944 – 11951.
10. Zhang, P., Chen, Y. P., Wang, W., Shen, Y. and Guo, J. S. (2016). Surface plasmon resonance for water pollutant detection and water process analysis. *TrAC Trends in Analytical Chemistry*, 85: 153 – 165.
11. Olaru, A., Bala, C., Jaffrezic-Renault, N. and Aboul-Enein, H. Y. (2015). Surface plasmon resonance (SPR) biosensors in pharmaceutical analysis. *Critical Reviews in Analytical Chemistry*, 45(2): 97 – 105.
12. Shrivastav, A. M., Usha, S. P. and Gupta, B. D. (2016). Fiber optic profenofos sensor based on surface plasmon resonance technique and molecular imprinting. *Biosensors and Bioelectronics*, 79: 150 – 157.
13. Altintas, Z., Abdin, M. J., Tothill, A. M., Karim, K. and Tothill, I. E. (2016). Ultrasensitive detection of endotoxins using computationally designed nanoMIPs. *Analytica Chimica Acta*, 935: 239 – 248.
14. Altintas, Z., Gittens, M., Guerreiro, A., Thompson, K. A., Walker, J., Piletsky, S. and Tothill, I. E. (2015). Detection of waterborne viruses using high affinity molecularly imprinted polymers. *Analytical Chemistry*, 87(13): 6801 – 6807.
15. Dong, J., Peng, Y., Gao, N., Bai, J., Ning, B., Liu, M. and Gao, Z. (2012). A novel polymerization of ultrathin sensitive imprinted film on surface plasmon resonance sensor. *Analyst*, 137(19): 4571 – 4576.
16. Becker, J. (2012). Plasmons as sensors. Springer Science & Business Media.
17. Lee, K. S. and El-Sayed, M. A. (2006). Gold and silver nanoparticles in sensing and imaging: sensitivity of plasmon response to size, shape, and metal composition. *The Journal of Physical Chemistry B*, 110(39): 19220 – 19225.
18. Isaacs, S. and Abdulhalim, I. (2015). Long range surface plasmon resonance with ultra-high penetration depth for self-referenced sensing and ultra-low detection limit using diverging beam approach. *Applied Physics Letters*, 106(19): 193701.
19. Karabchevsky, A., Tsapovsky, L., Marks, R. S. and Abdulhalim, I. (2013). Study of immobilization procedure on silver nanolayers and detection of estrone with diverged beam surface plasmon resonance (SPR) imaging. *Biosensors*, 3(1): 157 – 170.
20. Karabchevsky, A., Karabchevsky, S. and Abdulhalim, I. (2011). Fast surface plasmon resonance imaging sensor using Radon transform. *Sensors and Actuators B: Chemical*, 155(1): 361 – 365.
21. Karabchevsky, A., Karabchevsky, S. and Abdulhalim, I. (2011). Nanoprecision algorithm for surface plasmon resonance determination from images with low contrast for improved sensor resolution. *Journal of Nanophotonics*, 5(1): 051813 – 051813.
22. PhotoicSys (2015). SPR system user manual (Version 1.0).

*Malaysian Journal of Analytical Sciences, Vol 21 No 6 (2017): 1380 - 1388*
*DOI: https://doi.org/10.17576/mjas-2017-2106-20*

MALAYSIAN JOURNAL OF ANALYTICAL SCIENCES
*Published by The Malaysian Analytical Sciences Society*
ISSN 1394 - 2506

# *IN SITU* HYDROGENATION OF LIQUID EPOXIDIZED NATURAL RUBBER USING DIIMIDE

## (Penghidrogenan *In Situ* Getah Asli Cecair Terepoksida Menggunakan Diimida)

Nur Hanis Adila Azhar[1], Hamizah Md Rasid[1], Nur Aidasyakirah Mohd Tahir[1], Siti Fairus M. Yusoff[1, 2]*

[1]*School of Chemical Science and Food Technology, Faculty of Science and Technology*
[2]*Polymer Research Center (PORCE), Faculty of Science and Technology*
*Universiti Kebangsaan Malaysia, 43600 UKM Bangi, Selangor, Malaysia*

**Corresponding author: sitifairus@ukm.edu.my*

Received: 28 September 2016; Accepted: 6 March 2017

**Abstract**

A low-molecular-weight liquid epoxidized natural rubber (LENR) was prepared through photosensitized degradation of epoxidized natural rubber with 50 mol percent of epoxy content (ENR-50). LENR was modified into hydrogenated liquid epoxidized natural rubber (HLENR) via *in situ* thermal degradation of arylsulfonyl hydrazide as a hydrogenating agent. The chemical structures of LENR and HLENR were characterized using Fourier transform infrared (FTIR) and $^{1}$H nuclear magnetic resonance (NMR) spectroscopies. The thermal behaviour of LENR and HLENR were analysed using thermogravimetric analysis (TGA). The molecular weight and polydispersity index (PDI) of LENR and HLENR were determined using gel permeation chromatography (GPC). The parameter studies on the hydrogenation of LENR were investigated based on the source of diimide, weight ratios of LENR: *p*-toluenesulfonyl hydrazide (TSH), temperature, reaction time and solvent of the reaction. The highest conversion of hydrogenation was achieved at 130 °C for 4 hours reaction time, with 1:1 weight ratio of LENR: TSH using *o*-xylene as a solvent.

**Keywords**: hydrogenation, liquid natural rubber, epoxidized, hydroxylated

**Abstrak**

Getah asli cecair terepoksida (LENR) dihasilkan melalui penguraian fotopemeka yang dijalankan ke atas getah asli terepoksida yang mempunyai 50 mol% kandungan epoksi (ENR-50). LENR dihidrogenkan kepada LENR terhidrogen (HLENR) melalui penguraian terma *in situ* dengan menggunakan agen penghidrogenan iaitu arilsulfonil hidrazida. Struktur kimia LENR dan HLENR dicirikan menggunakan spektroskopi inframerah transformasi Fourier (FTIR) dan resonans magnet nukleus $^{1}$H. Sifat terma LENR dan HLENR dikaji menggunakan analisis termogravimetri (TGA). Berat molekul dan indeks kepoliserakan (PDI) dikaji menggunakan kromatografi penelapan gel (GPC). Kajian mengenai penghidrogenan LENR dikaji berdasarkan beberapa parameter tindak balas seperti sumber diimida, nisbah berat LENR: *p*-toluenasulfonil hidrazida (TSH), suhu, masa dan pelarut tindak balas. Penukaran penghidrogenan yang tertinggi diperolehi apabila tindak balas dijalankan pada suhu 130 °C selama 4 jam, dengan nisbah berat LENR:TSH sebanyak 1:1 serta menggunakan *o*-xilena sebagai pelarut.

**Kata kunci:** penghidrogenan, getah asli cecair, terepoksida, terhidroksil

## Introduction

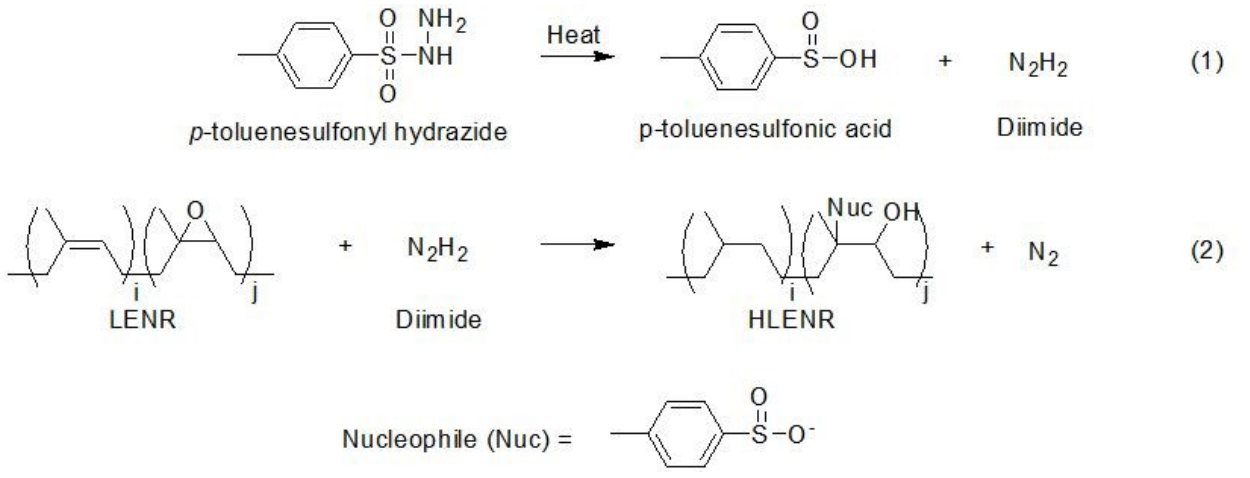
Natural rubber (NR) produced from *Hevea brasiliensis* trees is a crucial raw material for the production of industrial products such as tyres, gloves, adhesives, sealants, medical devices and consumer products [1-3]. NR had been used in various fields of applications due to its high elasticity and flexibility, resilience, abrasion resistance, efficient heat

dispersion, impact resistance and tear strength [4, 5]. However, NR deteriorates against ozone, sunlight, and weathering due to the unsaturated in its polymeric chains [4, 6]. Thus, chemical modifications of NR are very important in order to enhance the chemical, physical and mechanical properties of NR.

Previously, there are many chemical modifications that had been done to NR such as, hydrogenation, epoxidation, halogenation, grafting, metathesis and cyclization [1]. Among these modifications, hydrogenation of NR is significance to improve the properties in terms of its thermal stability, weather resistance and oxidative [7]. There are two types of hydrogenation that had been done to NR, which are catalytic and non-catalytic. Catalytic hydrogenation requires high pressure autoclave and the presence of transition metal catalyst systems such as nickel, titanium, rhodium, ruthenium or palladium [8 – 11]. On the other hand, non-catalytic hydrogenation method is more convenient because it only requires a simple apparatus preparation at atmospheric pressure and employed diimide intermediate from thermal decomposition of arylsulfonyl hydrazide [12]. Mahittikul et al. reported an *in situ* hydrogenated natural rubber latex via thermolysis of *p*-toluenesulfonyl hydrazide (TSH) [13].

Epoxidized natural rubber (ENR) is a chemically modified form of NR, having epoxy functional group and also showed slightly similar drawbacks as NR due to its remaining unsaturated double bonds in polymeric backbones. Hence, hydrogenation of ENR will overcome the drawbacks by saturating the remaining double bonds and ring opened the epoxy groups into hydroxyl groups. Research on the hydrogenation of ENR conducted in latex form requires a deproteinization process to remove the protein in the rubber [11]. Although, chemical reactions conducted in latex form often encountered with problems of latex stability, uneven particle size distribution and contamination due to non-rubber components of natural rubber latex [14]. To overcome the problems encountered by latex, liquid form of ENR is the best solution. The liquid form of ENR which is liquid epoxidized natural rubber (LENR), a partially depolymerized ENR can be produced via mechanical milling, chemical degradation initiated by potassium peroxodisulfate and photooxidation initiated by ultraviolet irradiation [15].

In the present work, we made an attempt to hydrogenate liquid epoxidized natural rubber through the thermal degradation of TSH. The diimide ($N_2H_2$) generated from thermolysis of TSH gives hydrogen molecules ($H_2$) to the C=C and C-O-C of the LENR (Scheme 1) [13, 16, 17]. We also optimize the effect of TSH concentration, temperature, solvent and reaction time. The analysis of the hydrogenated products have been performed using FTIR, $^1$H NMR, TGA and GPC.




Scheme 1. Hydrogenation of LENR using TSH

## Materials and Methods

### Materials

Epoxidized natural rubber-50 (ENR-50) was supplied from Malaysian Rubber Board. Toluene, *o*-xylene, hexane and methanol were supplied by R&M Chemicals. Methylene blue, rose Bengal, *p*-toluenesulfonyl hydrazide (TSH) and 2,4,6-trimethylbenzenesulfonyl hydrazide (MSH) were purchased from Sigma Aldrich.

### Synthesis of LENR

LENR was prepared by photosensitized degradation of ENR-50 [18]. 1 kg of ENR-50 was cut into smaller cube and soaked in 2 L of toluene overnight. Methylene blue (0.10 g) and Rose Bengal (0.15 g) were dissolved in methanol before added into rubber mixture. The mixture was stirred continuously using a mechanical stirrer in the presence of visible light at 70 °C for 10 to 14 days. The mixture was centrifuged to separate the gel formation.

### Hydrogenation of LENR

TSH was used as a diimide source in the hydrogenation reaction. Different amounts of TSH were added to a fixed volume of LENR solution at TSH/LENR weight ratios of 1:1 to 3:1 to determine the effect of TSH concentration on the percentage of hydrogenation. Each mixture was heated to temperature ranging from 90 °C until 150 °C and stirred for 1–5 hours to study the effect of reaction time on the percentage of hydrogenation. The products were filtered and coagulated with hexane to remove the residual TSH. Finally, it was dried in a vacuum oven to remove any remaining solvent. In this work, we also studied the effect of solvent by using *o*-xylene and toluene on the percentage of hydrogenation LENR.

### Characterization

Attenuated total reflectance-Fourier transform infrared (ATR-FTIR) spectroscopy (Perkin Elmer) was used to determine any changes in the functional groups that might have been induced by the hydrogenation reaction. The samples were analysed in the wavenumber range of 4000 – 600 $cm^{-1}$. NMR spectroscopy was used to examine the microstructure of the product. Samples were dissolved in deuterated chloroform ($CDCl_3$) for measurements with the Fourier Transform Nuclear Magnetic Resonance 400MHz Cryoprobe (FT-NMR 400MHz Cryo). Integration of signals from proton NMR ($^1$H NMR) was used to estimate the percentage of conversion of the hydrogenation, content of the epoxy group, content of the residual double bonds and content of the hydroxyl group of HLENR as shown in equation 1 – 4 below:

$$W_{\text{conversion}}\,[\text{mol\%}] = \frac{I_{1.25}/2}{I_{1.25}/2 + I_{2.71} + I_{3.35} + I_{5.14}} \times 100 \quad (1)$$

$$X_{\text{epoxy}}\,[\text{mol\%}] = \frac{I_{2.71}}{I_{1.25}/2 + I_{2.71} + I_{3.35} + I_{5.14}} \times 100 \quad (2)$$

$$Y_{\text{double bond}}\,[\text{mol\%}] = \frac{I_{3.35}}{I_{1.25}/2 + I_{2.71} + I_{3.35} + I_{5.14}} \times 100 \quad (3)$$

$$Z_{\text{hydroxyl}}\,[\text{mol\%}] = \frac{I_{5.14}}{I_{1.25}/2 + I_{2.71} + I_{3.35} + I_{5.14}} \times 100 \quad (4)$$

where *I* is the integration at chemical shifts 1.25, 2.71, 3.35 and 5.14 ppm that correspond to methylene of hydrogenated isoprene units, epoxy methine of epoxidized-*cis*-1,4-isoprene units, hydroxylated methine and olefinic methine of unsaturated *cis*-1,4-isoprene units, respectively, in $^1$H NMR spectrum [11].

Thermogravimetric analysis (TGA) and differential thermal analysis (DTA) were performed on TGA/SDTA 851$^e$, Mettler Toledo. Gel permeation chromatography (GPC) was employed to determine the molecular weight ($M_w$) and polydispersity index (PDI) of LENR and HLENR (Waters 1515 Isocratic HPLC Pump equipped with a Waters 2414 Refractive Index detector, Waters Corporation, USA).

## Results and Discussion

Hydrogenated liquid epoxidized natural rubber (HLENR) was produced via non-catalytic hydrogenation of LENR using diimide intermediate from arylsulfonyl hydrazide such as *p*-toluenesulfonyl hydrazide (TSH) and 2,4,6-trimethylbenzenesulfonyl hydrazide (MSH).

**Microstructure of LENR and HLENR**

Figure 1 depicts the FTIR spectra of LENR and HLENR. The main features of LENR appears at 1251 and 870 $cm^{-1}$ are attributed to the symmetric and asymmetric stretching of the epoxide ring, respectively. The absorption at 1664 and 828 $cm^{-1}$ in LENR spectrum correspond to C=C stretching and olefinic C–H bending, respectively. Both LENR and HLENR spectra show broad absorption bands at 3600-3100 $cm^{-1}$ due to O-H stretching, and the intensities of the absorption bands for HLENR are intense than LENR [19]. The increment of HLENR intensity at 3600-3100 $cm^{-1}$ arised due to the ring opening of epoxy groups into hydroxyl groups.

$^{1}$H NMR spectra of LENR and HLENR were shown in Figure 2. In LENR spectrum, six major signals appeared at 1.30, 1.68, 2.10, 2.20, 2.71 and 5.14 ppm were assigned to methyl of unsaturated *cis*-1,4-isoprene units (*b*), methyl of epoxidized-*cis*-1,4-isoprene units (*e*), methylene of *cis*-1,4-isoprene units (*c*), methylene of epoxidized-*cis*-1,4-isoprene units (*f*), epoxy methine (*d*) and olefinic methine (*a*), respectively. HLENR spectrum showed the appearance of hydrogenated methylene (*a'*) hydroxylated methine (*h*) and hydroxyl proton (*i*) at chemical shifts 1.25, 3.35 and 3.90 ppm, respectively. The signals appeared at 2.30-2.50 ppm on HLENR spectrum correspond to benzylic protons of the remaining TSH and the nucleophile ($CH_3C_6H_5SO_2^-$) [12, 17, 20].

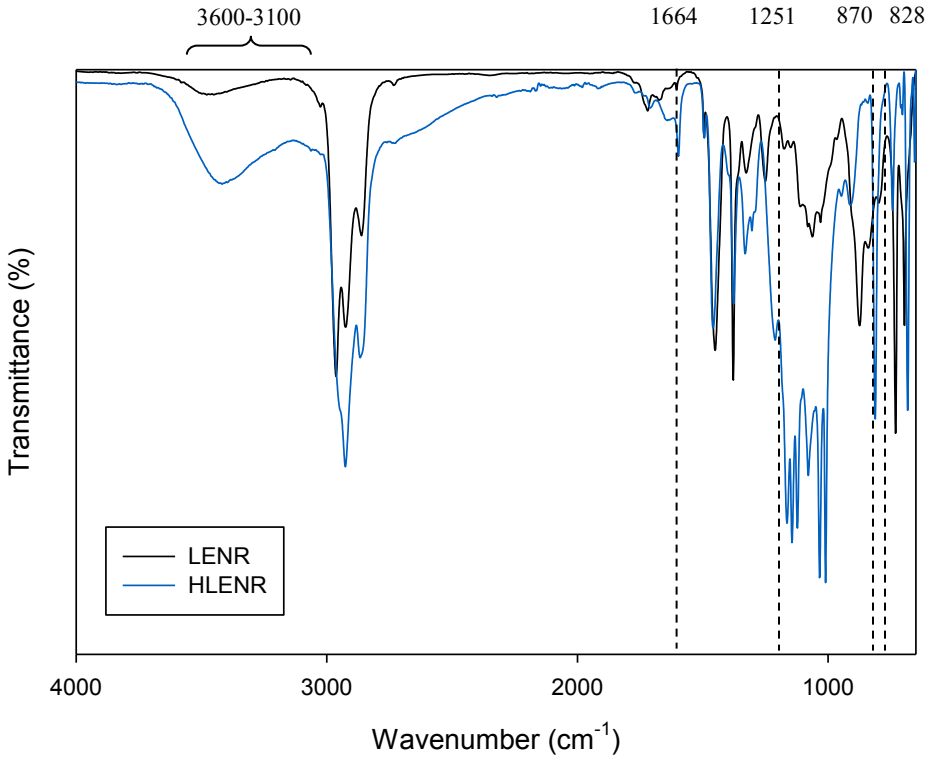



Figure 1. FTIR spectra of LENR and HLENR

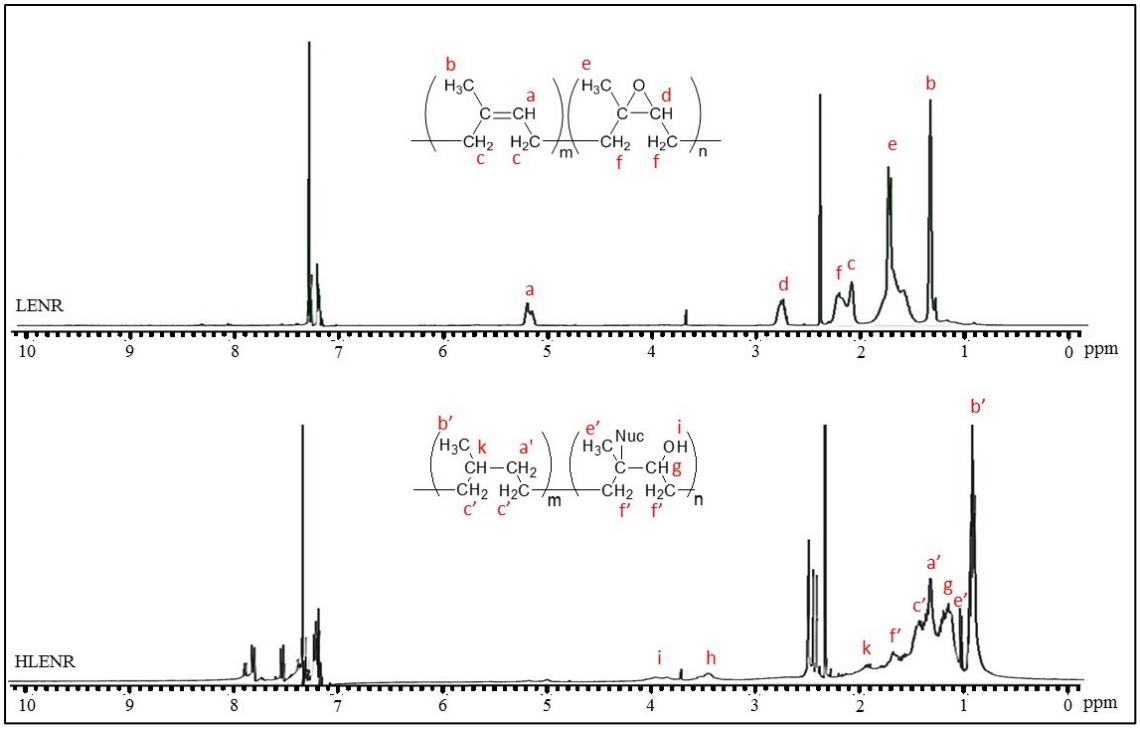



Figure 2. $^{1}$H NMR spectra of LENR and HLENR

**Parameter Studies on Hydrogenation of LENR: Effect of diimide source**

*p*-toluenesulfonyl hydrazide (TSH) and 2,4,6-trimethylbenzenesulfonyl hydrazide (MSH) had been study to produce diimide for the non-catalytic hydrogenation of LENR (Table 1). TSH showed a higher conversion of hydrogenation which is 90.29%. The hydrogenation of LENR using MSH produced more hydroxyl content caused by the stronger nucleophilic attack in the epoxide ring compare to TSH. The content of epoxy group and residual double bonds decreased as the conversion of hydrogenation increased. However, the content of hydroxyl for hydrogenation LENR using MSH was higher compared to TSH because, MSH was quite unstable to undergo hydrogenation.

Table 1. Effect of diimide source on hydrogenation of LENR

| Experiment | Diimide Source | Conversion of Hydrogenation (mol%) | Content of Epoxy Group (mol %) | Content of Residual Double Bonds (mol %) | Content of Hydroxyl Group (mol %) |
|---|---|---|---|---|---|
| 1 | TSH | 90.29 | 0.81 | 0.45 | 8.46 |
| 2 | MSH | 40.80 | 7.94 | 3.80 | 47.47 |

Condition: weight ratio of TSH: LENR = 1:1, temperature = 130 °C, reaction time = 4 hours, solvent = *o*-xylene

**Effect of LENR: TSH weight ratio**

The weight ratio of LENR: TSH was varied for 1:1, 1:2 and 1:3. Table 2 showed the increase in the amount of TSH, resulted to reduce the conversion of hydrogenation of LENR. Higher amount of TSH was expected to undergo side reaction which interrupt the hydrogenation of LENR and reduced the hydroxyl content. The epoxy content increased as the conversion of hydrogenation decreased.

Table 2. Effect of LENR: TSH weight ratio on hydrogenation of LENR

| Experiment | Weight Ratio of LENR:TSH | Conversion of Hydrogenation (mol%) | Content of Epoxy Group (mol%) | Content of Residual Double Bonds (mol%) | Content of Hydroxyl Group (mol%) |
|---|---|---|---|---|---|
| 3 | 1:1 | 90.29 | 0.81 | 0.45 | 8.46 |
| 4 | 1:2 | 56.27 | 40.00 | 0.95 | 2.77 |
| 5 | 1:3 | 56.27 | 42.16 | 0.16 | 1.40 |

Condition: temperature = 130 °C, reaction time = 4 hours, solvent = *o*-xylene

**Effect of temperature**

The effect of temperature was investigated from 90 °C until 150 °C (Table 3). From 90 °C until 130 °C, the conversion of hydrogenation gradually increase to the highest conversion of hydrogenation. TSH solubility with *o*-xylene increased with the increasing temperature because rate decomposition of TSH increased. However, when the temperature was increased to 150 °C, the conversion of hydrogenation slightly dropped due to the occurrence of unduly wasteful side reaction [13]. The content of epoxy group and residual double bonds decreased while content of hydroxyl increased as the conversion of hydrogenation increased.

Table 3. Effect of temperature on hydrogenation of LENR

| Experiment | Temperature (°C) | Conversion of Hydrogenation (mol%) | Content of Epoxy Group (mol%) | Content of Residual Double Bonds (mol%) | Content of Hydroxyl Group (mol%) |
|---|---|---|---|---|---|
| 6 | 90 | 46.78 | 37.27 | 11.42 | 4.53 |
| 7 | 110 | 53.44 | 35.74 | 5.49 | 5.33 |
| 8 | 130 | 90.29 | 0.81 | 0.45 | 8.46 |
| 9 | 150 | 86.6 | 0.18 | 0.77 | 12.45 |

Condition: weight ratio of TSH: LENR = 1:1, reaction time = 4 hours, solvent = *o*-xylene

**Effect of reaction time**

Table 4 showed the increasing trend of reaction time has increased the conversion of hydrogenation. At the reaction of 5 hours, the conversion of hydrogenation almost the same with the conversion of hydrogenation for 4 hours because the reaction already completed at 4 hours reaction time. The content of epoxy group and residual double bonds decreased while content of hydroxyl increased when the conversion of hydrogenation increased.

Table 4. Effect of reaction time on hydrogenation of LENR

| Experiment | Reaction Time (hours) | Conversion of Hydrogenation (mol%) | Content of Epoxy Group (mol%) | Content of Residual Double Bonds (mol%) | Content of Hydroxyl Group (mol%) |
|---|---|---|---|---|---|
| 10 | 1 | 33.71 | 56.78 | 5.87 | 3.64 |
| 11 | 2 | 53.94 | 42.95 | 1.26 | 1.85 |
| 12 | 3 | 78.99 | 15.75 | 2.15 | 8.70 |
| 13 | 4 | 90.29 | 0.81 | 0.45 | 8.46 |
| 14 | 5 | 90.11 | 0.01 | 1.29 | 8.59 |

Condition: weight ratio of TSH: LENR = 1:1, temperature = 130 °C, solvent = *o*-xylene

**Effect of solvent**

There were two types of solvent had been studied on the hydrogenation of LENR. Based from Table 5, *o*-xylene resulted in higher conversion of hydrogenation due to *o*-xylene is more likely to dissolve TSH and easily produced diimide. However, the hydrogenation of LENR using toluene produced a lower conversion of hydrogenation but higher in hydroxyl group.

Table 5. Effect of solvent on hydrogenation of LENR

| Experiment | Solvent | Conversion of Hydrogenation (mol%) | Content of Epoxy Group (mol%) | Content of Residual Double Bonds (mol%) | Content of Hydroxyl Group (mol%) |
|---|---|---|---|---|---|
| 15 | Toluene | 46.45 | ~0 | 2.24 | 51.31 |
| 16 | *o*-xylene | 90.29 | 0.81 | 0.45 | 8.46 |

Condition: weight ratio of TSH: LENR = 1:1, temperature = 130 °C, reaction time = 4 hours

**Thermal analysis of LENR and LNR-OH**

TGA and DTG thermograms of LENR and HLENR were shown on Figure 3 and 4, respectively. LENR and HLENR thermograms showed multi step changes. The first step changes (30 °C – 310 °C) of LENR and HLENR were due to the loss of solvent, moisture and low-molecular-weight oligomers [21]. After 310 °C to 400 °C, the weight loss were due to the unstable intermediates in hydrogenation of LENR. The Figure 4 clearly showed the maximum degradation temperature of LENR and HLENR at 413 °C and 445 °C, respectively. The maximum degradation temperature of HLENR showed a higher temperature compared to LENR because of the hydrogenation reaction had proven to saturate the unsaturated part of LENR.

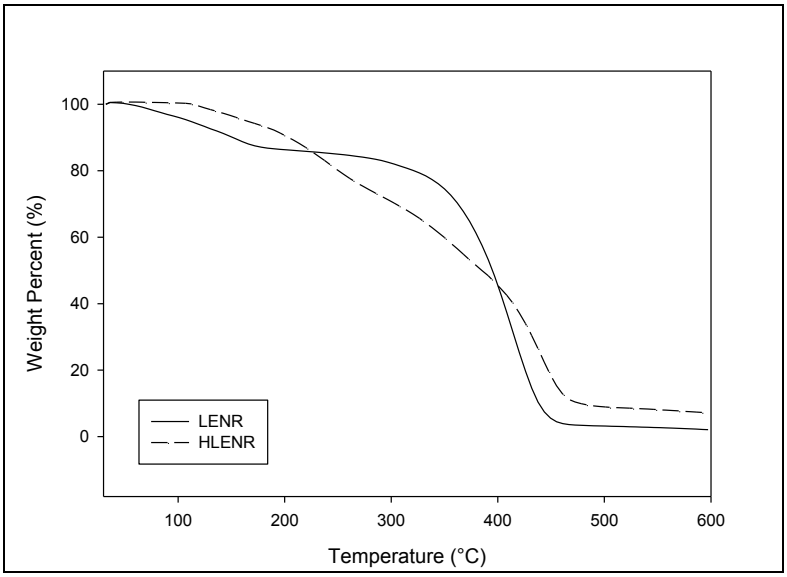



Figure 3. TGA thermograms of LENR and HLENR

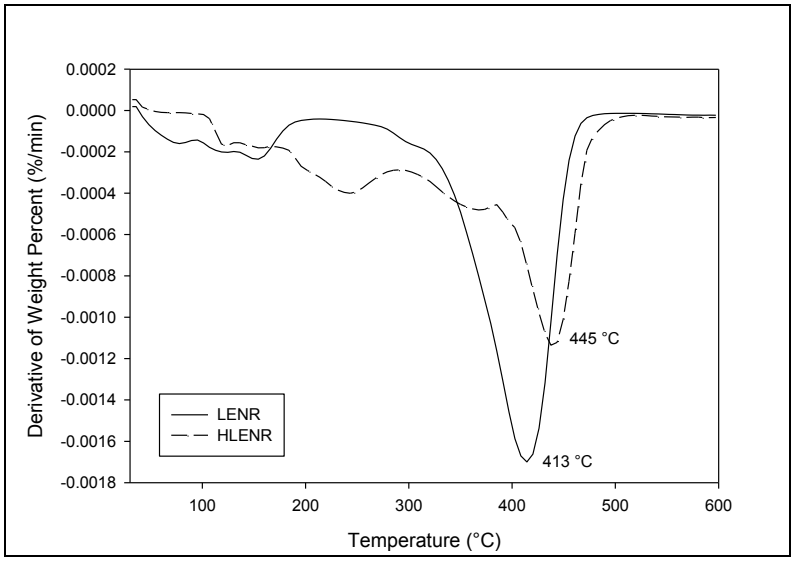



Figure 4. DTG thermograms of LENR and HLENR

**Molecular Weight of LENR and LNR-OH**

Table 6 showed the number average molecular weight ($M_n$), weight average molecular weight ($M_w$) and polydispersity index (PDI) of LENR and HLENR. $M_w$ of LENR and HLENR were reduced from 47900 g/mol to 17000 g/mol due to the high reaction temperature in the hydrogenation of LENR. The high reaction temperature depolymerized the polymeric chains of HLENR.

Table 6. Molecular weight of LENR and HLENR

| Sample | $M_n$ | $M_w$ | PDI |
|---|---|---|---|
| LENR | 18200 | 47900 | 2.63 |
| HLENR | 4600 | 17000 | 3.69 |

## Conclusion

Non-catalytic hydrogenation of LENR using diimide was efficiently conducted to produce hydrogenated rubber containing hydroxyl group. The optimum reaction condition was achieved using TSH as diimide source with 1:1 of LENR: TSH weight ratio at 130 °C for 4 hours of reaction time using *o*-xylene as solvent.

## Acknowledgement

The authors would like to acknowledge Universiti Kebangsaan Malaysia (UKM) for the research grants (GUP-2017-004 and FRGS/1/2016/STG01/UKM/02/4), Ministry of Science, Technology and Innovation (MOSTI), Malaysia for research grant (03-01-02-SF1207) and Centre for Research and Instrumentation (CRIM) at UKM for their facilities.

## References

1. Wongthong, P., Nakason, C., Pan, Q., Rempel, G. L. and Kiatkamjornwong, S. (2013). Modification of deproteinized natural rubber via grafting polymerization with maleic anhydride. *European Polymer Journal*, 49(12): 4035 – 4046.
2. Mooibroek, H. and Cornish, K. (2000). Alternative sources of natural rubber. *Applied Microbiology and Biotechnology*, 53(4): 355 – 365.

3. Hayashi, Y. (2009). Production of natural rubber from Para rubber tree. *Plant Biotechnology*, 26(1): 67 –70.
4. Kongparakul, S., Ng, F. T. T. and Rempel, G. L. (2011). Metathesis hydrogenation of natural rubber latex. *Applied Catalysis A: General*, 405(1-2): 129 – 136.
5. Ayutthaya, W. D. N. and Poompradub, S. (2014). Thermal and mechanical properties of poly(lactic acid)/natural rubber blend using epoxidized natural rubber and poly(methyl methacrylate) as co-compatibilizers. *Macromolecular Research*, 22(7): 686 – 692.
6. Pisuttisap, A., Hinchiranan, N., Rempel, G. L. and Prasassarakich, P. (2013). ABS modified with hydrogenated polystyrene-grafted-natural rubber. *Journal of Applied Polymer Science*, 129(1): 94 – 104.
7. Nghia, P. T., Onoe, H., Yamamoto, Y. and Kawahara, S. (2008). Hydrogenation of natural rubber having epoxy group. *Colloid and Polymer Science*, 286(8-9): 993 – 998.
8. Samran, J., Phinyocheep, P., Daniel, P., Derouet, D. and Buzaré, J. Y. (2004). Raman spectroscopic study of non-catalytic hydrogenation of unsaturated rubbers. *Journal of Raman Spectroscopy*, 35(12): 1073 –1080.
9. Bhattacharjee, S., Bhowmick, A. K. and Avasthi, B. N. (1993). Hydrogenation of epoxidized natural rubber in the presence of palladium acetate catalyst. *Polymer*, 34(24): 5168 – 5173.
10. Sanjoy Roy, S. and Bhattacharjee, B. R. G. (1993). Hydrogenation of epoxidized natural rubber. *Journal of Applied Polymer Science*, 49: 375 – 380.
11. Ha, N. T., Shiobara, K., Yamamoto, Y., Fukuhara, L., Nghia, P. T. and Kawahara, S. (2015). Preparation and characterization of hydrogenated natural rubber with hydroxyl groups. *Polymers for Advanced Technologies*, 26(12): 1504 – 1511.
12. Rasid, H. M., Azhar, N. H. A., Jamaluddin, N. and Yusoff, S. F. M. (2016). Mild approach for non-catalytic hydrogenation of liquid natural rubber using 2,4,6-trimethylbenzenesulfonyl hydrazide as the diimide source. *Bulletin of the Korean Chemical Society*, 37(6): 797 – 801.
13. Mahittikul, A., Prasassarakich, P. and Rempel, G. L. (2007). Noncatalytic hydrogenation of natural rubber latex. *Journal of Applied Polymer Science*, 103(5): 2885 – 2895.
14. Heijden, J. v. d. (2002). Natuurrubber 28 - 4th quarter 2002. *Rubber-Stichting*: pp 1 – 20.
15. Rooshenass, P., Yahya, R. and Gan, S. N. (2016). Comparison of three different degradation methods to produce liquid epoxidized natural rubber. *Rubber Chemistry and Technology*, 89(1): 177 – 198.
16. Hunig, S., Muller, H. R. and Thier, W. (1965). The chemistry of diamine. *Angewandte Chemie International Edition*, 4(4): 271 – 380.
17. Wade, L. G. (2003). Organic chemistry (5th Edition). Prentice Hall, New Jersey.
18. Abdullah, I. (1996). Process for manufacturing liquid natural rubber (LNR). *Malaysian Patent*, MY-108852-A.
19. Jorge, R. M., Lopes, L., Benzi, M. R., Ferreira, M. T., Gomes, A. S. and Nunes, R. C. R. (2010). Thiol addition to epoxidized natural rubber: Effect on the tensile and thermal properties. *International Journal of Polymeric Materials*, 59(5): 330 – 341.
20. Azhar, N. H. A., Jamaluddin, N., Md Rasid, H., Mohd Yusof, M. J. and Yusoff, S. F. M. (2015). Studies on hydrogenation of liquid natural rubber using diimide. *International Journal of Polymer Science*, 2015: 1–6.
21. Mahmood, W. A. K. and Azarian, M. H. (2015). Thermal, surface, nanomechanical and electrical properties of epoxidized natural rubber (ENR-50)/ polyaniline composite films. *Current Applied Physics*, 15(5): 599 – 607.

*Malaysian Journal of Analytical Sciences, Vol 21 No 6 (2017): 1389 - 1398*
*DOI: https://doi.org/10.17576/mjas-2017-2106-21*

MALAYSIAN JOURNAL OF ANALYTICAL SCIENCES
*Published by The Malaysian Analytical Sciences Society*
ISSN 1394 - 2506

# ISOLATION OF TWO BOTRYANES FROM *Hypoxylon rickii* AND IDENTIFICATION OF THE ENCODING GENES

## (Pemencilan Sebatian Botrien dari *Hypoxylon rickii* dan Pengenalpastian Pengekodan Gen)

Afnani Alwi[1], Andi Rifki Rosandy[2], Farah Diba Abu Bakar[1], Rozida Mohd Khalid[2]*

[1]*School of Biology and Biological Sciences, Faculty of Science and Technology*
[2]*School of Chemical Sciences and Food Technology, Faculty of Science and Technology*
*Universiti Kebangsaan Malaysia, 43600 UKM Bangi, Selangor, Malaysia*

**Corresponding author: rozidakhalid@ukm.edu.my*

Received: 28 September 2016; Accepted: 6 March 2017

**Abstract**

10-oxodehydrobotrydial (**1**) and 4β-Acetoxy-9β,10β,15α-trihydroxyprobotrydial (**2**) have been isolated from *Hypoxylon rickii* mycelia extract. Compound **2** is probably an intermediate of botrydial, which is a known sesquiterpene phytotoxin. Cluster Omega and Artemis software analysis suggested that *HRT6,* a possible botrydial-like gene cluster with four genes shows more than 50% similarities compared to *Botrytis cinerea* botrydial gene cluster, *BcBOT*. A comparison between proposed 4β-Acetoxy-9β,10β,15α- trihydroxyprobotrydial (**2**) producing pathway and *BcBOT* proposed pathway shows compatible function of each gene prediction. Further confirmation using RNA gene knock-outs is on-going.

**Keywords**: *Hypoxylon rickii*, botryane, terpene synthase

**Abstrak**

10-oksodehidrobotridial (**1**) dan 4β-Asetoksi-9β,10β,15α-trihidroksiprobotridial (**2**) telah dipencilkan dari ekstrak miselia *Hypoxylon rickii*. Sebatian **2** dijangkakan sebagai sebatian perantara dalam pembentukkan botridial iaitu sejenis fitotoksin sesquiterpena. Penggunaan dua perisian Cluster Omega dan Artemis telah berjaya mengenalpasti gen kelompok yang berkemungkinan dari *H. rickii* sebagai *HRT6* dengan empat gen menunjukkan persamaan lebih daripada 50% berbanding gen kelompok *Botrytis cinerea*, *BcBOT*. Perbandingan antara dengan cadangan laluan biosintesis 4β-Asetoksi-9β,10β,15α-trihidroksiprobotridial (**2**) dengan *BcBOT* menunjukkan persamaan fungsi – fungsi gen. Pengesahan lanjut menggunakan RNA (mendiamkan gen) sedang dijalankan.

**Kata kunci:** *Hypoxylon rickii*, botrien, terpene sintes

## Introduction

Terpene is a diverse class of secondary metabolite (SMs) produced notably by fungi. These compound have a cycloaliphatic basic structure built from isoprene units [1]. Most of the terpenes produced by fungi have various biological functions. Terpene include commercially fascinating compounds due to their properties, such as paxilline an indole diterpene, gibberelic acid, a pentacyclic diterpene plant growth hormone and trichothecenes a sesquiterpene mycotoxin [2, 3].

Botryane are a group of sesquiterpenes produced notably by *Botrytis cinerea* which is a fungus causing gray-rot disease in economically important crops such as grapes, strawberries and many more. They are known as broad spectrum toxins with botrydiol derivatives causing leasions to the leaves [4]. Other bioactivities include fungicide

and cytotoxic activities [5]. Even though sesquiterpenes form the largest group of terpenes and include commercially important compounds, they are difficult to chemically synthesize because of the complex structure that often leads to low yield [6].

*Hypoxylon* sp. was first identified by Ju and Rodgers in 1996 and belong to the Xylariaceae family which has interesting characteristics in producing a variety of secondary metabolites [7]. *Hypoxylon fragiforme* is known to produce frangiformins A and B, cytochalasin H and mitorubin azaphilones [8] while *Hypoxylon rutilum* produces rutilin A and B, entonaemin A, rubiginosin A and B [9].

*Hypoxylon rickii* colonies grown on agar plate, are at first whitish, then becoming fulvous, velvety to felty, azonate, with diffuse margins and a reverse dull green colour can be seen [7]. *Hypoxylon rickii* has a nodulisporium-like conidiogenous structure that differentiates it from other *Hypoxylon* taxa with red to orange red granules in a wild species [7].

The research group of Prof. Marc Stadler in Helmholz Center for Infection Research Institute previously has identified various type of secondary metabolites from *H. rickii* such as Silphiperfolene-type terpenoids, diketopiperzine, botryenanol, α-ramulosin**,** α-eleostearic acid and many more [10]. Recently, they manage to isolate new botryane ((1S)-7-[(2E)-but-2-enoyl]-1,3,3,6-tetramethyl-2,3-dihydro-1H-indene-1 carbaldehyde **3**, (3aS)-6-hydroxy-3a,5,5,8-tetramethyl-3,3a,4,5-tetrahydro-1H-cyclopenta [de] isochromen1-one **4**, (3aS)-7-hydroxy-3a,5,5,8-tetramethyl-3,3a,4,5-tetrahydro-1H- cyclopenta[de]isochromen-1-one **5** with 3 known botryanes (3aS)-3a,5,5,8-tetramethyl-3,3a,4,5-tetrahydro-1H-cy-clopenta[de]isochromen-1-one **6**, (3aS,8R)-3a,5,5,8-tetramethyl-3,3a,4,5,7,8-hexahydro-1H-cy-clopenta[de]isochromen-1-one **7** and botryenanol **8** and many more [11] (Figure 1).

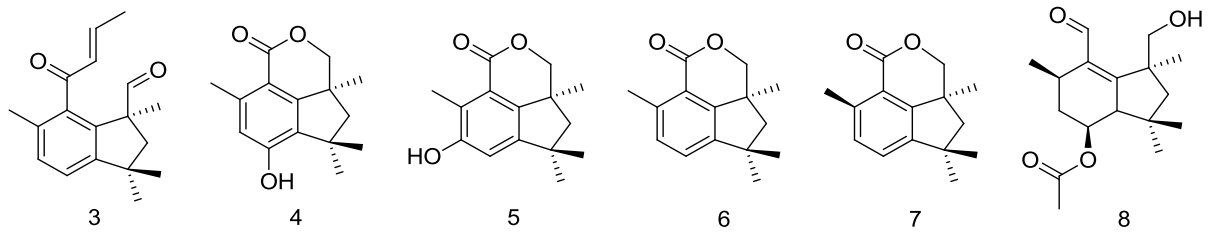



Figure 1. Botryanes isolated from *Hypoxylon rickii*

Genome mining provides information on the gene cluster responsible for producing of respective SMs. Generally, biosynthetic genes for fungal SMs are located in clusters and it can consist of more than 10,000 bases. These clusters contain one or several central biosynthetic genes encoding extremely large multidomains or multimodular enzymes belonging to the polyketide synthases (PKSs), terpene synthases (TSs), non-ribosomal peptide synthases (NRPSs) or a mix of them [12]. Each of the genes in a gene cluster has its own functions corresponding to step of the biosynthesis [13]. This knowledge enables us to manipulate and produce derivatives of the SMs tailored to our needs.

## Materials and Methods

### Material

Strain 53309 from Prof Marc Stadler's group, collected in Martinique, France was used. The sample has been deposited at the public culture collections (MUCL 53309, CBS 129345). It was identified based on comparing the *H. rickii* sample ITS sequence JQ009313 with deposited ITS sequences in the NCBI database under accession number AJ390408 and KC968932.

### Culturing

*Hypoxylon rickii* was grown in the yeast malt glucose (YMG) liquid medium at 25 $^{o}$C with 200 rpm rotation for 3 to 4 days except for isolation of secondary metabolites where 7 to 15 days of cultivation in malt extract medium and tomato medium were required. Each medium was inoculated with a mycelium suspension (100 – 500 µL, 50%

glycerol). For solid medium cultures the plate were inoculated with mycelium from a liquid culture (200 µL) or from an agar plate and incubated at 25 °C.

**Extraction and Isolation**

The production culture was centrifuged (10,000 rpm, 4 $^{o}$C, 25 min). The supernatant was filtered under vacuum to remove any cells that were not pelleted out and its pH adjusted to 4.0. The supernatant was extracted thrice with ethyl acetate. The organic layers were combined and dried over anhydrous magnesium sulphate (Fisher) and filtered under vacuum. Mycelium from previous extraction was extracted thrice with acetone. The organic layers were combined and dried over anhydrous magnesium sulphate (Fisher) and filtered under vacuum.

The supernatant organic extract was evaporated to leave a dark green oil which was dissolved in methanol and analysed by LCMS while the mycelium organic extract was evaporated to leave a dark reddish oil which was dissolved in methanol and analysed by LCMS.

Analytical chromatographic analysis were perform on a Waters Platform 2695 LC system comprising of a Waters 600 pump system, a Waters 2998 diode array detector (detecting between 210 and 400 nm), a Waters 2420 ELS detector, a Waters QuatroMicro Platform LC mass spectrometer (detecting between 150 and 600 *m/z* units $ESI^{+}$) with a Kinetex 2.6 µm $C_{18}$ (Phenomenex, 100 × 4.6 mm) reverse phase column. The mobile phase gradient program was run as follows: 0 – 10 minutes (90% A), 10 – 13 minutes (ramped to 90% B), 13 – 15 minutes (ramped to 90% A). Solvent A: water + 0.05% TFA, solvent B: MeCN + 0.04% TFA. Flow rate: 1 mL/min. Injection volume: 20 µL. Concentration of the sample: 20 mg/mL.

Preparative chromatography was carried out on a Waters Platform 2695 LC system that include diode array detector (detecting between 210 and 400 nm), ELS detector, LC mass spectrometer (detecting between 150 and 600 *m/z* units $ESI^{+}$) with the Kinetex 5 µm $C_{18}$ (New Coloum, 250 × 21.2 mm) reverse phase column. The program was run 0 – 4 minutes (90% A), 4 – 8 minutes (reduced to 70% A), 8 – 17 minutes (ramped to 95% B), 17 – 18 minutes (ramped to 90% A), 18 – 20 minutes (90% A). Solvent A: water + 0.05% TFA, solvent B: MeCN + 0.04% TFA. Flow rate: 20 mL/min. Injection volume: 50 – 200 µL. Concentration of the sample: 20 mg/mL.

NMR spectra recorded on a Bruker 400 MHz Ascend or a Bruker 500 MHz Ultrashield with DRX console and 5 mm TCI 1H-13C/15N (Z-GRD) cryo-probe and BACS sample changer and HR-ESI-MS data were obtained using Micromass GCT.

**Isolation of fungal genomic DNA**

Cells were separated from the liquid medium culture by centrifugation (10,000 rpm, 25 mins, 4 $^{o}$C) and the supernatant removed. The sample then freeze-dried for overnight. The cells (approx. 100 mg) were crushed with a pestle and mortar in liquid nitrogen. The genomic DNA was obtained by following the manufactures instructions of the GenElute Plant Genomic DNA Kit (Sigma) with 100 mg of tissue. gDNA was analysed by gel electrophoresis. Full length genome sequence were obtained using Illumina sequencing service provided by CeBITEC, University of Bielfield, Germany (later transferred to Bioinformatics & Systems Biology Justus-Liebig-University Giessen, Germany).

## Results and Discussion

**Structural elucidation**

Structural elucidation of both compounds was carried out using several spectroscopic techniques including $^{1}$H and $^{13}$C NMR, 2D-COSY, HSQC and HMBC and compare with previous data. The isolated compounds include the following:

***(3aS)-3a,5,5,8-tetramethyl-3,3a,4,5-tetrahydro-1H-cy-clopenta[de]isochromen-1-one (10-oxodehydrobotrydial)*** (**1**):

Colourless oil; Yield 0.8 mg; $^{1}$H NMR (500 MHz) and $^{13}$C NMR (150 MHz) data were consistent with those previously reported [11] are tabulated in Table 1; HRESIMS m/z 231.1392 $[M + H]^{+}$ (calculated for $C_{15}H_{19}O_2$ m/z 231.1380); Rt = 12.2 min; Compound **1** have been previously isolated from *H. rickii* [11]. The structure of

compound **1** was further confirmed using 2D NMR experiments including HMBC. Correlation HMBC showed in Figure 2.

Table 1. NMR Spectroscopic data of 10-Oxodehydrodihydrobotrydial (**1**) in MeOH-$d_4$

| Position | $\delta_C$ (ppm) | | $\delta_H$ (*m*, *J* in Hz, ΣH) | | HMBC |
|---|---|---|---|---|---|
| | 1 | 1* | $\delta_H$ (1) | $\delta_H$ (1*) | |
| 1 | 119.0 | 119.6 | - | - | - |
| 2 | 139.1 | 139.6 | - | - | - |
| 3 | 131.5 | 131.7 | 7.21 (*d*, *J* = 7.7 Hz, 1H) | 7.20 (*d*, *J* = 7.8 Hz, 1H) | C-1, C-2, C-4, C-5 |
| 4 | 127.5 | 127.3 | 7.33 (*d*, *J* = 7.7 Hz, 1H) | 7.14 (*d*, *J* = 7.8 Hz, 1H) | C-2, C-3, C-5 |
| 5 | 151.6 | 151.4 | - | - | - |
| 6 | 40.5 | 40.8 | - | - | - |
| 7 | 51.4 | 52.1 | 2.03 (*d*, *J* = 10.1 Hz, 1H)<br>1.94 (*d*, *J* = 10.1 Hz, 1H) | 1.84 (*d*, *J* = 13.0 Hz, 1H)<br>1.96 (*d*, *J* = 13.0 Hz, 1H) | C-6, C-8, C-14, C-15 |
| 8 | 44.7 | 45.1 | - | - | - |
| 9 | 147.2 | 147.0 | - | - | - |
| 10 | 165.0 | 164.0 | - | - | - |
| 11 | 18.9 | 20.3 | 2.59 (s, 3H) | 2.61 (*s*, 3H) | C-1, C_2, C-3 |
| 12 | 29.6 | 30.7 | 1.35 (s, 3H) | 1.44 (*s*, 3H) | C-5, C-6, C-13 |
| 13 | 29.5 | 30.7 | 1.35 (s, 3H) | 1.31 (*s*, 3H) | C-5, C-6, C-12 |
| 14 | 23.5 | 24.7 | 1.50 (s, 3H) | 1.50 (*s*, 3H) | C-7, C-8, C-9, C-15 |
| 15 | 79.2 | 79.2 | 4.40 (*d*, *J* = 10.1 Hz, 1H)<br>4.17 (*d*, *J* = 10.1 Hz, 1H) | 4.12 (d, *J* = 10.1 Hz, 1H)<br>4.35 (d, *J* = 10.1 Hz, 1H) | C-7, C-8, C-9, C-10, C-14 |

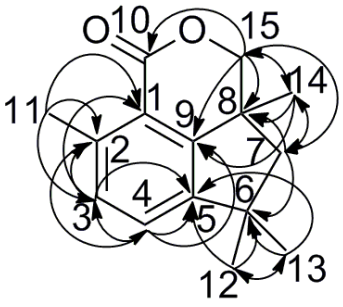



Figure 2. HMBC correlation of 10-Oxodehydrodihydrobotrydial (**1**)

***4β-Acetoxy-9β,10β,15α-trihydroxyprobotrydial*** (**2**)
Yellow oil; Yield 4.3 mg; Compound **2** has not yet isolated from *H. rickii* but similar compound have been isolated from *Botrytis cinera* [12]. $^1$H NMR (500 MHz) and $^{13}$C NMR (150 MHz) are tabulated in Table 2. The structure of compound **2** was further confirmed using 2D NMR experiments including HMBC. Correlation HMBC showed in Figure 3.

Table 2. NMR Spectroscopic data of 4β-Acetoxy-9β,10β,15α trihydroxyprobotrydial (**2**) in Methanol-$d_4$

| **Position** | ***$\delta_C$ (ppm)*** | ***$\delta_H$ (m, J in Hz, ΣH)*** | **HMBC** |
|---|---|---|---|
| | **2** | **2** | |
| 1 | 33.8 | 1.70 (m, 1H) | 21, 4 |
| 2 | 73.1 | 5.11 (td, J = 10.9, 3.9 Hz, 1H) | 1, 4, 11 |
| 3 | 39.5 | 1.19 – 1.14 (m, 1H) | 2, 1 |
| | | 1.83 (dt, J = 12.3, 3.4 Hz, 1H) | 4, 2, 1 |
| 4 | 57.6 | 1.74 (d, J = 10.5 Hz, 1H) | 22, 7, 9, 5, 2 |
| 5 | 94.1 | - | |
| 6 | 59.0 | 1.31 – 1.27 (m, 1H) | 21, 1, 9, 16, 5 |
| 7 | 46.0 | - | |
| 8 | 48.4 | 1.07 (m, 1H ) | 14, 15, 9, 8 |
| | | 2.06 – 2.00 (m, 1H) | 14, 15, 22, 7, 9, 17 |
| 9 | 56.9 | - | |
| 10 | 0 | - | |
| 11 | 171.0 | - | |
| 12 | 19.9 | 1.99 (d, J = 1.7 Hz, 3H) | 11 |
| 13 | 0 | - | |
| 14 | 21.5 | 1.12 (s, 3H) | 8, 9, 17, 5 |
| 15 | 26.7 | 1.13 (s, 3H | 22, 8, 3, 2 |
| 16 | 87.8 | 4.01 (dd, J = 5.7, 3.0 Hz, 1H) | 1, 6, 5, 17 |
| 17 | 82.6 | 4.37 (d, J = 5.6 Hz, 1H) | 14, 8, 9, 16 |
| 18 | 0 | - | |
| 19 | 0 | - | |
| 20 | 0 | - | |
| 21 | 19.9 | 1.01 (d, J = 6.3 Hz, 3H) | 1, 6, 3 |

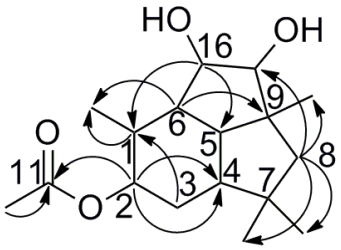
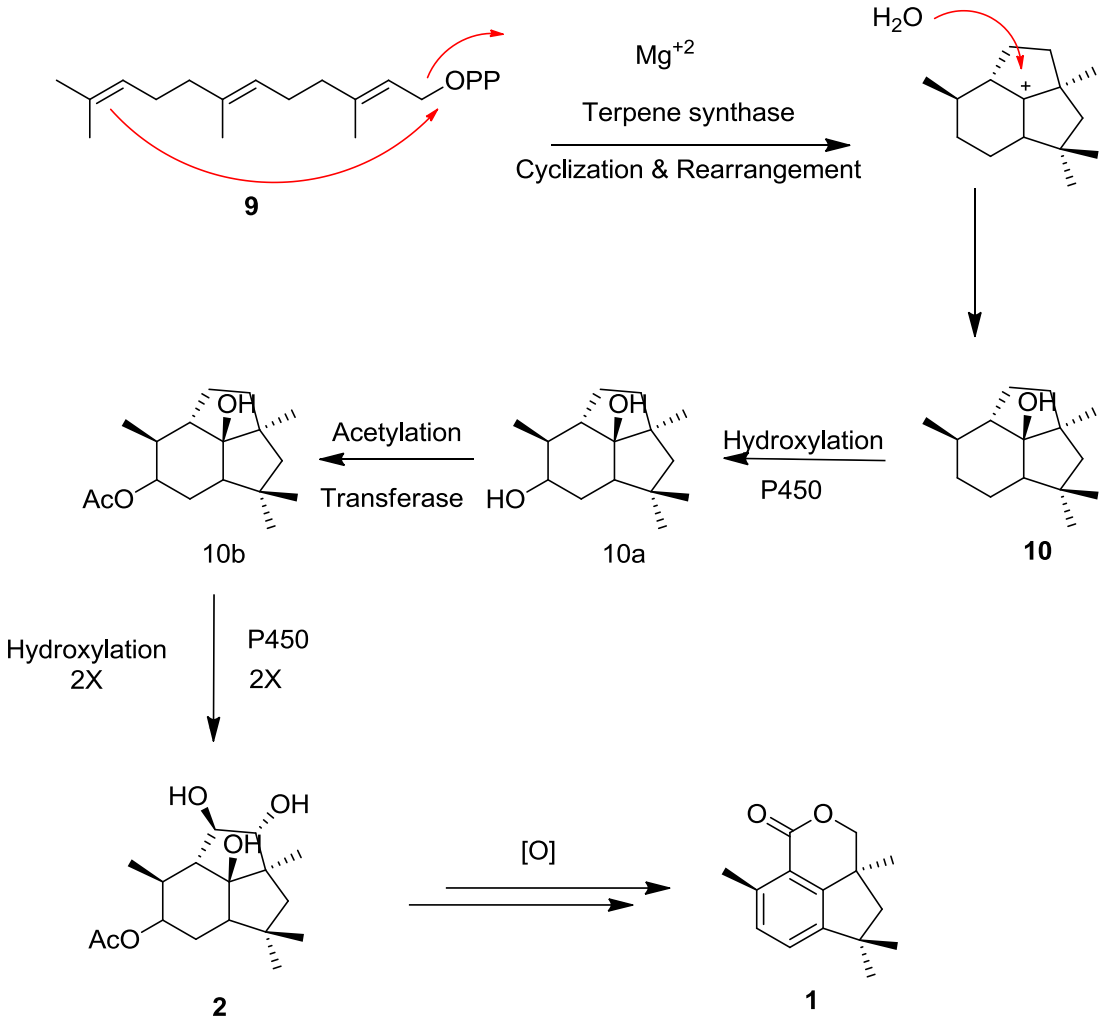



Figure 3. HMBC correlation of 4β-Acetoxy-9β,10β,15α-trihydroxyprobotrydial (**2**)

**Pathway**

It is proposed that both compounds derived from the botryane biosynthetic pathway. The proposed biosynthesis of **2** is shown on Scheme 1. The biosynthesis starts with farnesyl pyrophosphate (FPP) **9**, a sesquiterpene**.** Terpene synthase or sesquiterpene synthase will bind to the pyrophosphate (PP) of FPP via $Mg^{2+}$ and nucleophilic prenyl chain close concurrent to PP cleavage. A few rearrangement and cyclization of the structure produce the intermediate that eventually quenched by $H_2O$ resulting in presilphiperfolan-8β-ol **10**. Hydroxylation at carbon 2 of presilphiperfolan-8β-ol **2** by cytochrome P450, allowed the acetylation of acetate into carbon 2 aided by transferase enzyme. Further hydroxylation via cytochrome P450 at carbon 10 and 15 might produce 4β-Acetoxy-9β,10β,15α-trihydroxyprobotrydial **2** as suggested from previous study using isotope labeling acetate experiment [6].




Farnesyl diphosphate, FPP **9** catalyzed by terpene synthase will undergo multiplestep cyclization to produce tricyclic sesquiterpene alcohol, presilphiperfolan-8β-ol **10**. Trihydroxylbotrydial **1**, is converted to botrydial by the action of cytochrome P450s as well as by an acetyl transferase. As for 10-oxodehydrobotrydial **2**, their oxidative steps are yet to be determined.

Scheme 1. Proposed biosynthetic pathways of botryane

**Gene clustering**

Genome data are stored in the GenDBE system of Bioinformatics & Systems Biology Justus-Liebig-University Giessen, Germany. *Hypoxylon rickii* genes have been annotated to have 59 secondary metabolite producing gene clusters as in Table 3. From this data, the 6th terpene gene cluster out of 12, has been named as *HRT6* gene cluster, consist of terpene cyclase with three cytochrome P450s and two transferases (Figure 4).

Table 3. Number of annotated secondary metabolite gene clusters in *Hypoxylon rickii*

| SM Gene Cluster | No. |
|---|---|
| NRPS-PKS | 4 |
| PKS | 26 |
| NRPS | 5 |
| Terpene | 12 |
| Terpene –PKS | 1 |
| Others | 11 |
| Total | 59 |

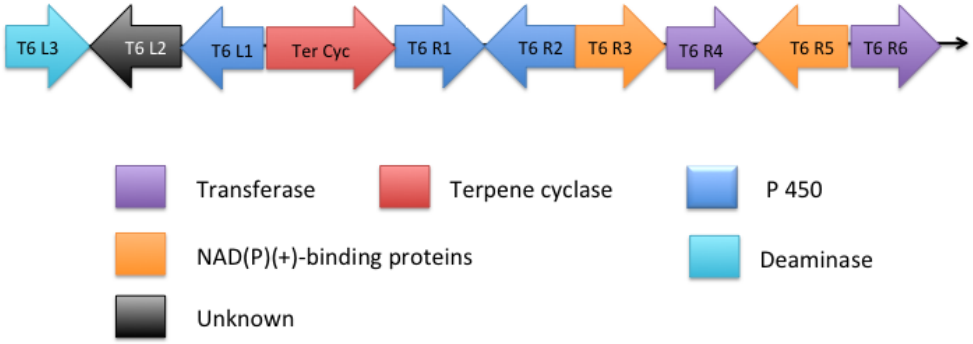
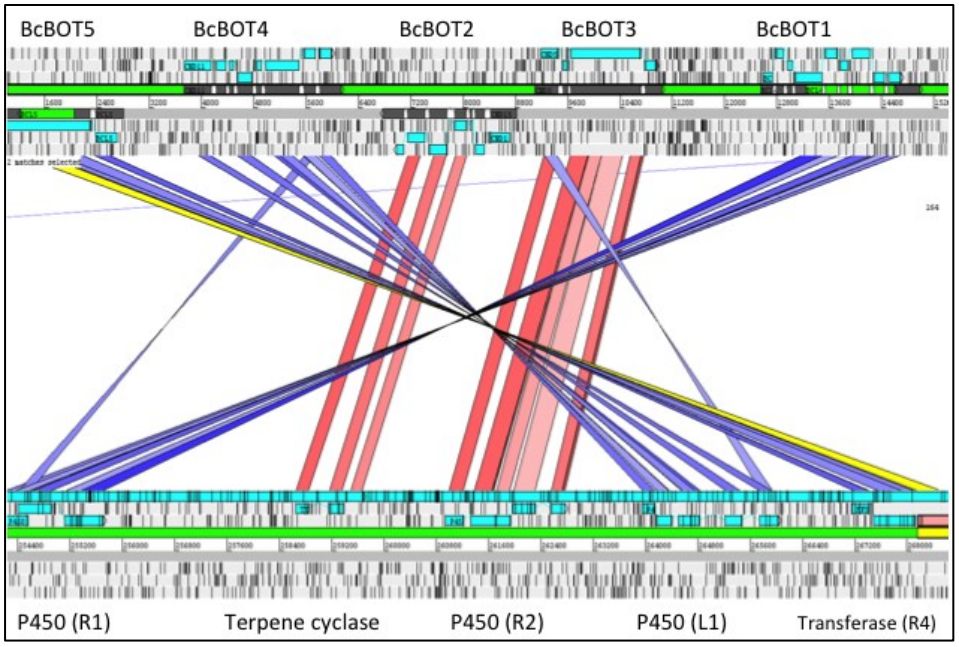



Figure 4. *HRT6* gene cluster of *Hypoxylon rickii*

Comparison of the *HRT6* have been conducted with previously studied *BcBOT* botrydial gene cluster from *Botrytis cinera* using ARTEMIS ACT software and cluster OMEGA. ARTEMIS ACT software allows comparison according to the gene sequences similarities and orientation, while cluster OMEGA allows comparison of the conserved region. Comparison between *BcBOT* and *HRT6* using ARTEMIS ACT shows similarities for five genes, namely three P450s (T6 R1, T6 R2 and T6 L1), one terpence cyclase (Ter Cyc) and one transferase (T6 R4) (Figure 5). All genes showed more than 50% similarities between all conserved regions except for transferases (Table 4).




*Comparison based on ARTEMIS ACT software. Red lines indicate similarities of gene sequence from 5' to 3' and blue lines 3' to 5' respectively

Figure 5. Comparison of gene sequence of *BcBOT* gene cluster with *HRT6* gene cluster

Table 4. Percentage comparison between *BcBOT* gene cluster and *HRT6* gene cluster

| **BcBOT Gene Cluster** | **HRT6 Cluster 6 *H. rickii*** | **% Similarities** |
|---|---|---|
| BcBOT1 P450 | T6 R1 (P450) | 59.17 |
| BcBOT2 (Sesquterpene synthase) | Terpene cyclase | 53.70 |
| BcBOT3 P450 | T6 R2 (P450) | 51.99 |
| BcBOT4 P450 | T6 L1 (P450) | 62.45 |
| BcBOT5 (acetyl Transferase) | T6 R4 (Transferase) | 21.18 |

*Comparison based on Cluster OMEGA program

Study by Pinedo et al. [14] have examined the *BcBOT2* gene as sesquiterpene synthase by knocking it out and the mutant culture did not produce any botryanes. It is presumed that cyclization of FPP **9** to the key probotryane alcohol intermediate presilphiperfolan-8β-ol **10**, thus verifying the biosynthetic pathways of these secondary metabolites. Isotope labeling study also confirmed the backbone arrangement pathway [14].

Recent publication by Moraga et al. [15] have identified successfully the function of all 5 gene in *BcBOT* gene cluster and its as proposed in this *HRT6* gene cluster. *BcBOT4* have catalyzes the first regio- and stereospecific hydroxylation of the probotryane skeleton of presilphiperfolan-8β-ol **10** at C-3, however in *HRT6* gene the first hydroxylation was at carbon 2. For further reaction, *BcBOT1* was responsible for the regiospecific hydroxylation at carbon 16 and *BcBOT3* is involved in the regio- and stereospecific β-hydroxylation at carbon 17 [15] suggesting the same pattern of hydroxylation happen in proposed *HRT6* pathways.

As for the formation of 10-oxodehydrobotrydial **1**, the same study by Moraga et al. [15] have suggest that *BcBOT1* also produce the key intermediate to the structure by cleavage the bond between carbon 16 and 17. *HRT6* gene cluster have an additional transferase (T6 R6) and NAD(P) binding protein that might have mechanism to remove the acetoxyl group at carbon 2 and turned it into benzene ring.

## Conclusion

*Hypoxylon rickii HRT6* gene cluster was annotated to be similar to *BcBOT* botrydial gene cluster isolated from *Botrytis cinera.* Four out of ten genes in the HRT6 gene cluster showed more than 50% similarities to genes from *BcBOT* botrydial gene cluster and similarities in function as well by comparing to the recent study. These findings suggested that *HRT6* highly possible into producing 4β-Acetoxy-9β,10β,15α-trihydroxyprobotrydial and it also might produce 10-oxodehydrobotrydial in right condition. An on-going project is to conduct gene knockout or gene knockdown of the terpene cyclase gene from *HRT6* to support this hypothesis.

## Acknowledgement

We would like to thank Prof. Dr. Marc Stadler of Helmholtze Center for Infection Research, Braunchwig, Germany for the *H. rickii* strain provided. We would also like to thank Prof. Dr. Russell Cox of Leibniz Universität Hannover for assistance in isolation and elucidation of the compounds. Ms Afnani would like to thanks Universiti Sultan Zainal Abidin and Kementerian Pendidikan Tinggi Malaysia for her scholarship.

## References

1. Breitmaier, E. (2006). General Structure: The isoprene rule. In *Terpenes :* Importance, general structure, and biosynthesis. Wiley-VCH Verlag GmbH & Co, Weinheim: pp. 1 – 9.
2. George, D. T., Kuenstner, E. J. and Pronin, S. V. (2015). A concise approach to paxilline indole diterpenes. *Journal of the American Chemical Society*, 137(49): 15410 – 15413.
3. Kuca, K., Dohnal, V., Jezkova, A. and Jun, D. (2008). Metabolic pathways of T-2 toxin. *Current Drug Metabolism*, 9(1): 77 – 82.
4. Colmenares, A. J., Dura, R. M. and Collado, I. G. (2002). Four new lactones from *Botrytis cinerea*,. *Journal of Natural Products*, 65(11): 1724 – 1726.
5. Yuan, Y., Feng, Y., Ren, F., Niu, S., Liu, X. and Che, Y. (2013). A botryane metabolite with a new hexacyclic skeleton from an entomogenous fungus *hypocrea* sp. *Organic Letters*, 15(23): 6050 – 6053.
6. Collado, I. G., Sánchez, A. J. M. and Hanson, J. R. (2007). Fungal terpene metabolites: Biosynthetic relationships and the control of the phytopathogenic fungus Botrytis cinerea. *Natural Product Review*, 24(4): 674 – 686.
7. Ju, Y. M., & Rogers, J. D. (1996). A revision of the genus *Hypoxylon*. *The Mycological Society of America Mycologia Memoir*, 20: 174.
8. Stadler, M., Quang, D. N., Tomita, A., Hashimoto, T. and Asakawa, Y. (2006). Changes in secondary metabolism during stromatal ontogeny of *Hypoxylon fragiforme*. *Mycological Research*, 110(7): 811 –820.
9. Quang, D. N., Hashimoto, T., Stadler, M. and Asakawa Y. (2005). Dimeric azaphilones from the xylariaceous ascomycete *Hypoxylon rutilum. Tetrahedron,* 61(35): 8451 – 8455.
10. Surup, F., Kuhnert, E., Liscinskij, E. and Stadler, M. (2015). Silphiperfolene-type terpenoids and other metabolites from cultures of the tropical ascomycete *Hypoxylon rickii* (Xylariaceae). *Natural Products and Bioprospecting*, 5(3): 167 – 173.
11. Kuhnert, E., Surup, F., Wiebach, V., Bernecker, S. and Stadler, M. 2015. Botryane, noreudesmane and abietane terpenoids from the ascomycete *Hypoxylon rickii. Phytochemistry*, 117: 116 – 122.
12. Brakhage, A. A. (2013). Regulation of fungal secondary metabolism. *Nature Reviews Microbiology*, 11(1): 21 – 32.
13. Smith, D. J., Burnham, M. K., Bull, J. H., Hodgson, J. E., Ward, J. M., Browne, P., Brown, J., Barton, B., Earl, A. J. and Turner, G. (1990). Beta-lactam antibiotic biosynthetic genes have been conserved in clusters in prokaryotes and eukaryotes. *The EMBO Journal*, 9(3): 741 – 747.
14. Pinedo, C., Wang, C. M., Pradier, J. M., Dalmais, B., Choquer, M., Le Pêcheur, P., Morgant, G., Collado, I. G., Cane, D. E. and Viaud, M. (2008). Sesquiterpene synthase from the botrydial biosynthetic gene cluster of the phytopathogen Botrytis cinerea. *ACS Chemical Biology*, 3(12), 791 – 801.

15. Moraga, J., Dalmais, B., Izquierdo-Bueno, I., Aleu, J., Hanson, J. R., Hernández-Galán, R., Viaud, M., and Collado, I. G. (2016). Genetic and molecular basis of botrydial biosynthesis: Connecting cytochrome P450-encoding genes to biosynthetic intermediates. *ACS Chemical Biology*, 11(10): 2838 – 2846.

*Malaysian Journal of Analytical Sciences, Vol 21 No 6 (2017): 1399 - 1408*
*DOI: https://doi.org/10.17576/mjas-2017-2106-22*

MALAYSIAN JOURNAL OF ANALYTICAL SCIENCES
*Published by The Malaysian Analytical Sciences Society*
ISSN 1394 - 2506

# NANOEMULSION BASED PALM OLEIN AS VITAMIN E CARRIER

## (Nanoemulsi Berasaskan Olein Sawit Sebagai Pembawa Vitamin E)

Suria Ramli[1, 2]*, Norhakimah Norhman[1], Norhidayu Zainuddin[1], Safiah Mohamad Ja'afar[1], Irman Abdul Rahman[3]

[1]*School of Chemical Sciences and Food Technology*
[2]*Polymer Research Center*
[3]*School of Applied Physics*
*Faculty of Science and Technology,*
*Universiti Kebangsaan Malaysia, 43600 UKM Bangi, Selangor, Malaysia*

**Corresponding author: su_ramli@ukm.edu.my*

Received: 28 September 2016; Accepted: 6 March 2017

**Abstract**

Aging process makes our skin getting thinner and drier. Antioxidant based on nanoemulsion system is favourable because of its effectiveness. This study was conducted to develop nanoemulsion system based on palm olein as a carrier of vitamin E and the physicochemical behaviours of the system were studied. Palm olein as oil phase, polyoxyethylene (4) lauryl ether (Brij 30) was used as a surfactant and vitamin E as an anti-aging agent. The mixtures of Brij 30 and palm olein at certain ratios were thoroughly mixed and titrated with 5 – 95% wt. of water and homogenized by using homogenizer. The Palm olein/Brij 30/Water mixtures that produced a clear solution and no birefringence after observation under polarized light microscopy are labelled as nanoemulsion. Nanoemulsion region was shown in ternary phase diagram. Based on the ternary diagram, these systems were formed at oil: surfactant (O/S) ratio 4:6, 5:5 and 6:4 and 20 – 50% wt of water. These systems were then characterized for stability test, particle size, electrical conductivity, viscosity and pH. Stability test was done at three temperatures, which were 4, 25 and 40 °C for one month and four cycles of freeze-thaw at storage temperature for 12 hours at each temperature. The systems were stable and no phase separation was observed. Particle size analysis showed that most systems have a particle size within the range of nanoemulsion (20 – 500 nm). Electrical conductivity tests showed that water-in-oil system formed at low water percentage (20 – 30% wt. of water) and bicontinuous at a higher percentage (30 – 50% wt. of water). Viscosity of both systems vitamin E-loaded and unloaded is very low. All systems have a pH value in a range of 6 – 7, which are suitable to be applied to human skin. Based on the physical characteristics of the system, it shows high potential as a vitamin E carrier.

**Keywords**: nanoemulsion, palm olein, vitamin E, ternary phase diagram, anti-aging agent

**Abstrak**

Proses penuaan menyebabkan kulit kita menjadi semakin nipis dan kering. Antioksida yang berasaskan sistem nanoemulsi lebih digemari kerana kesannya yang lebih berkesan. Penyelidikan ini dijalankan untuk membangunkan sistem berasaskan olein sawit sebagai pembawa vitamin E dibangunkan dan sifat fizikokimianya dikaji. Olein sawit sebagai fasa minyak, polioksietilena (4) lauril eter (Brij 30) digunakan sebagai surfaktan dan vitamin E sebagai bahan aktif. Campuran Brij 30 dan olein sawit dikacau sehingga sebati dan seterusnya dititratkan air sebanyak 5 – 95% (berat/berat) dan dihomogenkan menggunakan alat penghomogenan. Campuran Olein Sawit/Brij 30/Air yang menghasilkan larutan jernih dan tiada dwibiasan dilabelkan sebagai nanoemulsi selepas pemerhatian di bawah mikroskop cahaya terkutub. Rantau nanoemulsi ditunjukkan di dalam gambar rajah fasa ternari. Berdasarkan kepada gambar rajah fasa ternari, sistem ini terhasil pada nisbah minyak:surfaktan (M/S) sebanyak 4:6, 5:5 dan 6:4 dengan peratusan air sebanyak 20 – 50% (berat/berat). Seterusnya, sistem tersebut dicirikan melalui ujian kestabilan, saiz partikel, kekonduksian elektrik, kelikatan dan pH. Ujian kestabilan dilakukan pada setiap suhu berbeza iaitu 4 °C, 25 °C dan 40 °C selama sebulan dan empat kitaran pemanasan-penyejukan dengan suhu penyimpanan selama 12 jam pada setiap suhu. Sistem-sistem tersebut adalah stabil dan tidak berlaku perubahan fasa. Ujian pengukuran saiz partikel menunjukkan bahawa

kebanyakan sistem bersaiz di dalam julat saiz nanoemulsi iaitu di antara 20 –500 nm. Melalui ujian kekonduksian elektrik, dijangkakan sistem air-dalam-minyak pada 20% hingga 30% (berat/berat). Kelikatan nanoemulsi tanpa atau dengan bahan aktif pula adalah sangat rendah. Semua sistem mempunyai nilai pH yang berada dalam julat 6 – 7, di mana ianya sesuai diaplikasi pada kulit. Berdasarkan kepada sifat fizikal sistem, ia sesuai diaplikasikan sebagai pembawa vitamin E.

**Kata kunci**: nanoemulsi, olein sawit, vitamin E, rajah fasa ternari, agen anti-penuaan

## Introduction

Aging process is usually associated with changes in skin quality and appearance such as thinning, reduced elasticity and wrinkling of the skin [1]. The term cosmeceuticals was created by Dr. Albert Kligman who identified cosmeceuticals as a hybrid of drugs and cosmetics [2]. Cosmeceuticals are formulated with pharmaceutical-type ingredients that have special ability to treat and enhance the beauty of the skin from inside out [3]. Cosmeceuticals are currently very popular, especially for products that are designed and developed to help in prevention and treatment of aging skin. [4].

In the recent years, nanoemulsion has gain interest as a colloidal delivery system within the food, pharmaceuticals, cosmeceuticals, and other industries to encapsulate, protect and deliver bioactive lipophilic components, such as drugs, vitamins, neutraceuticals and antioxidants [5-7]. Nanoemulsion is defined as emulsion system having particle size ranging from 20 – 500 nm [8, 9]. The size range may vary depending on authors, in which some authors consider 500 nm as the upper limit [10]. Due to small particle size, nanoemulsion possess stability against sedimentation, flocculation or creaming [11]. Nanoemulsion is a non-equilibrium system and cannot be formed spontaneously. Nanoemulsion is only kinetically stable [12], in which it differs from microemulsion, which is also transparent or translucent but thermodynamically stable [13]. The attractions of nanoemulsion in personal care and cosmetics applications are due to the use of low surfactant concentration (3 – 10%) compared to microemulsion (usually 20% or higher) [14], small droplet size for uniform distribution on the skin [15] and efficient drug delivery of active ingredients through the skin [16]. Nowadays, nanoemulsion has been used as nanocarrier to deliver the active component in the product to its targeted cells more effectively due to advancement in nanotechnology [3]. Basically, nanoemulsion can be prepared using two methods: the high energy method that involves the use of mechanical devices (e.g. ultrasonicator, rotor/stator system and high pressure homogenizer) and low energy method in which the chemical potential of the component is used such as phase inversion temperature (PIT), phase inversion composition (PIC) and spontaneous emulsification method [6-7, 10].

Anti-aging agent such as antioxidant has been shown to decrease sunburn cells after UV exposure, neutralize free radicals and act as a humectant when applied on the skin [2]. Vitamin E is the most renowned type of antioxidant [3] and widely used in cosmeceuticals and pharmaceutical industries. It exists in eight different isomers including α, β, γ and δ derivatives of tocopherol and tocotrienol [17]. Among these isomers, α-tocopherol is the form of vitamin E with the highest abundance and biological activity that is important to protect cellular membranes from lipid peroxidation by free radicals [4]. Vitamin E is a lipid soluble antioxidant that scavenges free radicals and protects membrane lipids from peroxidation when taken orally [2]. However, the α-tocopherol form of vitamin E is highly unstable to oxidation due to its chemical degradation [18]. A system that can encapsulate these lipophilic nutraceuticals may able to protect from chemical degradation during storage and increase their bioavailability [19, 20]. For this reason, there has been increasing studies on nanoemulsion-based delivery system as vitamin E carrier [21].

Palm olein is the liquid fraction that is obtained from fractionation of palm oil. It is reported to have a higher content of monounsaturated fatty acid especially oleic acid (C 18:1; 39.8 – 43.9%) [22]. Palm olein has been considered to possess higher antioxidant activity due to presence of natural antioxidants such as α-tocopherol and α-tocotrienol [23, 24]. These natural antioxidants contains in palm olein are physiologically active as vitamin E [25, 26]. There was a research that proved its role as a natural antioxidant supplement that was capable in protecting the brain against oxidative damage [27]. Furthermore, it also possess free radical scavenger properties, which is to protect biological systems against oxidative and carcinogenic stress [28-30], in addition to inhibiting cholesterol biosynthesis and platelet aggregation [31, 32].

In this study, the formulation of nanoemulsions was developed by using palm olein as the oil phase (O), polyoxyethylene (4) lauryl ether (Brij 30) as surfactant (S) and vitamin E as anti-aging agent. This study was conducted to formulate and improve the stability of nanoemulsion system based on palm olein as a carrier of vitamin E and the physicochemical behaviour of the system were studied.

## Materials and Methods

Refined palm olein used in this study was obtained from Delima Oil Products Sdn. Bhd. Vitamin E was purchased from Sigma Aldrich (USA). Nonionic surfactant, polyoxyethylene (4) lauryl ether (Brij 30), $C_{20}H_{42}O_{5;}$ was purchased from ACROS Organics (Singapore). Distilled water was used throughout the experiments. All the chemicals were analytical grade and directly used without further purification.

To determine the concentration range of components that can form nanoemulsions, pseudo-ternary phase diagrams were constructed using water titration method at 25 °C. Brij 30 was mixed with palm olein at oil: surfactant (O/S) ratio of 1:9, 2:8, 3:7, 4:6, 5:5, 6:4, 7:3, 8:2 and 9:1 [33, 34]. The mixtures of oil and surfactant at each specific weight ratios were thoroughly mixed and heated at 50 °C, and then cooled to ambient temperature before titrating with water drop wise from 5 – 95% wt. at 5% wt. of water intervals. The mixtures were then homogenized using homogenizer (IKA® T25 digital ULTRA-TURRAX®) for 3 minutes at 5000 rpm. The mixtures were assessed visually and the regions that formed clear mixtures were mapped on pseudo-ternary phase diagrams. Samples that did not show birefringence under polarized light microscopy were labelled as nanoemulsion. 1% wt. of vitamin E was added to selected nanoemulsion mixtures as shown in Table 1. The vitamin E-loaded and unloaded systems were characterized for stability, particle size, electrical conductivity, viscosity and pH [35, 36].

Table 1. List of the nanoemulsion systems

| System | Details of the System |
|---|---|
| N1 | Palm Olein/Brij 30/Water, ratio O/S=4:6 |
| N2 | Palm Olein/Brij 30/Water, ratio O/S=5:5 |
| N3 | Palm Olein/Brij 30/Water, ratio O/S=6:4 |
| NE1 | N1 with 1% wt. of vitamin E |
| NE2 | N2 with 1% wt. of vitamin E |
| NE3 | N3 with 1% wt. of vitamin E |

The chemical and physical stability of nanoemulsions were studied via clarity and phase separation observation during a period of one month at different storage conditions at 4, 25 and 40 °C. Freeze-thaw cycle test was conducted for four cycles by keeping the nanoemulsion systems at different storage temperature of 12 hours at each temperature. The droplet sizes of nanoemulsions were determined by Particle Size Analyzer Zeta-Sizer (Malvern Instrument, England).

Conductivity measurements were performed at 25 ± 0.2 °C using a conductometer (inoLab cond. Germany). A solution of 0.01 mM sodium chloride (NaCl) was used in the preparation of the nanoemulsion samples instead of distilled water for the electrical conductivity [37]. The viscosity of various nanoemulsions was measured using Anton Paar Rheometer (Physica MCR 301, Austria) at 25 ± 0.2 °C. For pH values determination, the samples were calibrated with pH buffer before the measurements were done. The measurements were carried out triplicate using pH meter (Mettler Toledo MP 200, Switzerland) at 25 °C. All systems were tested and each measurement repeated three experiments.

## Results and Discussion

### Construction of ternary phase diagram

The region of nanoemulsion can be explained with the help of the pseudo-ternary phase diagrams. The phase diagram was constructed based on 'water dilution lines' which demonstrated an increase of water content while

decreasing surfactant content that is represented by the arrow line as shown in Figure 1. The phase diagram of Palm Olein/Brij 30/Water nanoemulsion system which was prepared using homogenizer. Subsequently, the nanoemulsion systems prepared were investigated with a polarizing light microscope. This was to identify the isotropic spherical structure of nanoemulsion (non-birefringent) from a liquid crystalline structures (birefringent) of non-nanoemulsion [33, 34, 38]. The shaded region in Figure 1 represents the nanoemulsion system of Palm Olein/Brij 30/Water with no birefringence under polarized light microscope. A successful pharmaceutical nanoemulsion system should not only have a stable and transparent, but also with a low content of surfactant to avoid skin irritation [14, 39]. Obtained nanoemulsion systems seem to meet these criteria, since it involved a low amount of surfactant as shown by the shaded region that located in the center of phase diagram. Therefore, six formulations N1, N2, N3, NE1, NE2 and NE3 were selected for further investigation (Table 1).

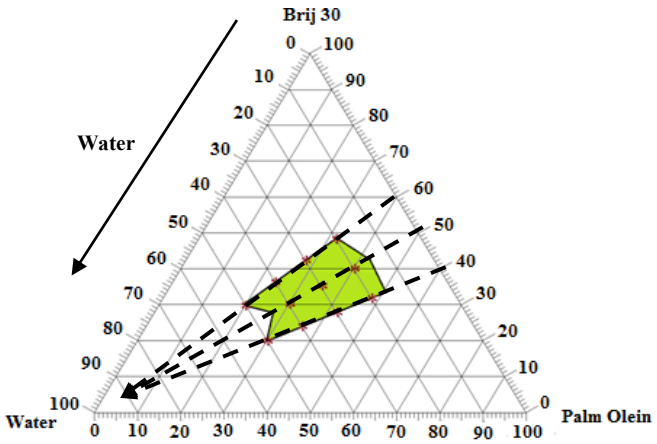



Figure 1. Pseudo-ternary phase diagram of the system Palm olein/Brij 30/Water. The shaded area represents the stable, clear and transparent formulations were produced. Dotted line arrow ( - - → ) shows the water dilution line that representing an increase of water content while decreasing surfactant levels

**Particle size**

The droplet size of the nanoemulsions were measured by assuming a monodispersed phase based on spherical globules. Table 2 show the mean droplet size of nanoemulsion systems. Addition of vitamin E into the system N1 and N2 did not significantly affect the particle size of the nanoemulsion system. However, it seems to significantly affect the particle size of system N3. Both NE1 and NE2 systems with vitamin E-loaded have a particle size in the range of nanoemulsion (20-500 nm). Meanwhile, the NE3 systems resulted on larger particle size (>500 nm). These can be explain that the component's composition may have a considerable effect in the droplet size of system [39]. The larger droplet size (>500 nm) were observed from these formulations might be due to the incompatibility or inhomogeneousity of nanoemulsion's components that caused on particle coagulation [40]. Regarding to the smaller droplet size range as low as <100 nm, the NE1 and NE2 systems should be advantage in dermal and transdermal delivery system of vitamin E [41]. These nano-sized droplets system may have the potential to penetrate to virtually every organ of the body, including lymph nodes and the deep vasculature of solid tumors, yet too small to be readily removed by the liver [42].

Table 2. Particle diameter of Palm olein/Brij 30/Water for system N1, N2, N3, NE1, NE2 and NE3 along the water dilution line

| Water Content (%) | Average Particle Size (nm) | | | | | |
|---|---|---|---|---|---|---|
| | N1 | N2 | N3 | NE1 | NE2 | NE3 |
| 20 | 11.74±0.50 | 10.56±0.66 | 559.95±2.05 | 31.45±0.06 | 28.63±6.97 | 346.10±18.48 |
| 30 | 30.53±1.51 | 546.9±2.69 | 894.05±11.20 | 38.48±8.03 | 27.19±10.66 | 72.99 ± 0.19 |
| 40 | 14.51±0.08 | 42.23±0.06 | 868.15±3.32 | 42.58±24.93 | 47.50±6.84 | 550.70±17.50 |
| 50 | 134.50±2.97 | 625±34.51 | 791. 35±16.41 | 46.50±3.83 | 42.66±7.25 | 560.10±19.56 |

**Stability studies**

Stability studies were imposed on nanoemulsion systems for a month at three different temperatures (4 °C, 25 °C and 40 °C) to observe for any phase separation, sedimentation, flocculation, coalescence or creaming during storage. Based on the observation, all systems are clear and stable at these temperatures with no phase separations as shown in Fig. 2. The samples are also subjected to four freeze-thaw cycle test at 4 °C, 25 °C and 40 °C for 12 hours storage at each temperature. The result shows that nanoemulsion systems with- and without addition of vitamin E are stable during the test cycle. This is due to higher content of oleic acid in palm olein that may have considerable stabilization effect against droplet coalescence [17].

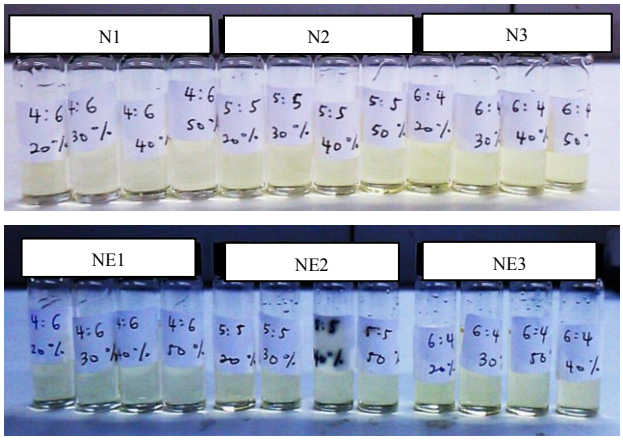



Figure 2. A transparent and stable nanoemulsion systems upon storage after a month

**Conductivity**

Electrical conductivity provide structural information and can be used to differentiate water-in-oil (w/o), bicontinuous (bc) and oil-in-water (o/w) types of nanoemulsion. The conductivity of nanoemulsion system tends to increase with an increase of water content, from (w/o) to (o/w) phase through bicontinuous phase [33-34, 43]. Fig. 3 shows the phase transitions of Palm olein/Brij 30/Water nanoemulsion along water dilution line. All systems shows slow incensement in conductivity from 20 to 30% wt. of water, but start to increase significantly up to 50% wt. of water. The low conductivity region with water content up to 30% wt. represented w/o region of nanoemulsion. At this stage, water droplets were discrete in an oil continuum and possess weak interactions [44, 45]. Subsequently, as the water content is raised up to 50% wt., the conductivity increasing due to increasing interactions between the aqueous domains forming interconnected conductive channels (bc structure). This is due to the attractive interaction between the spherical microdroplets of aqueous phase of w/o nanoemulsion [46, 47] as they changed from w/o structures to the bicontinuous region. Therefore, all systems can be classified as water-in-oil (w/o) at range 20 to 30% wt. of water and bicontinuous (bc) at >40% wt. of water.

The effect of solubilised vitamin E on the microstructure of the nanoemulsions only resulted on small increase in the electrical conductivity of the systems. However, these effect is not significant, especially when water is entrapped in the oil phase (w/o nanoemulsion), but it becomes larger once the continuous phase is water (>40% wt. of water) [48]. In conclusion, this can be considered that there is no major differences between the vitamin E-loaded and unloaded systems at which the phase transition occurs.

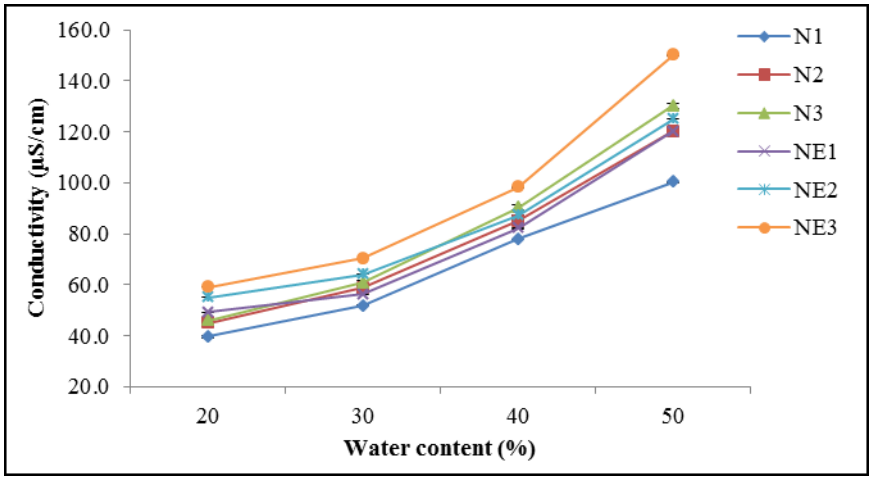



Figure 3. Electrical conductivity of Palm olein/Brij 30/Water nanoemulsion systems

**Viscosity and pH**

The values of pH and viscosity of the nanoemulsion system along water dilution line at 25 ºC as shown in Table 2. Each data point is the mean (± SD) of three experiments. Addition of vitamin E seem not significantly effect the viscosity of the nanoemulsion system. Plus, all systems show a very low viscosity that lies in the range of 0.04 to 0.07 Pa.S. These such low-viscosity colloidal dispersions consisting of micro domains of oil or water stabilized by an interfacial film of surfactant may be a good strategy to enhance the rate of drug delivery [49]. Most likely, the o/w nanoemulsion systems resulted on the lower viscosity compared to w/o nanoemulsion. The o/w nanoemulsion could act as drug reservoirs, where the loaded drug in the dispersed phase is released from the internal phase to the external phase and then improved the rate of drug delivery [50]. As an addition, all systems resulted on the pH values in the range of 6-7. These properties are acceptable in pharmaceutical application, for example, for the use as topical or transdermal drug delivery systems [51].

Table 2. Viscosity and pH of Palm olein/Brij 30/Water nanoemulsion systems

| Formulations | Water Content (% wt.) | Viscosity (Pa.S) | pH |
|---|---|---|---|
| N1 | 20 | 0.0614 ± 0.0024 | 6.10 ± 0.01 |
| | 30 | 0.0702 ± 0.0064 | 6.30 ± 0.01 |
| | 40 | 0.0537 ± 0.0011 | 6.40 ± 0.01 |
| | 50 | 0.0460 ± 0.0000 | 6.40 ± 0.01 |
| N2 | 20 | 0.0625 ± 0.0012 | 6.00 ± 0.01 |
| | 30 | 0.0451 ± 0.0001 | 6.20 ± 0.01 |
| | 40 | 0.0507 ± 0.0002 | 6.50 ± 0.01 |
| | 50 | 0.0447 ± 0.0005 | 6.80 ± 0.01 |

Table 2 (cont'd). Viscosity and pH of Palm olein/Brij 30/Water nanoemulsion systems

| Formulations | Water Content (% wt.) | Viscosity (Pa.S) | pH |
|---|---|---|---|
| N3 | 20 | 0.0510 ± 0.0004 | 6.30 ± 0.01 |
| | 30 | 0.0502 ± 0.0003 | 6.40 ± 0.01 |
| | 40 | 0.0504 ± 0.0001 | 6.50 ± 0.01 |
| | 50 | 0.0496 ± 0.0002 | 6.80 ± 0.01 |
| NE1 | 20 | 0.0453 ± 0.0001 | 6.20 ± 0.01 |
| | 30 | 0.0405 ± 0.0005 | 6.40 ± 0.01 |
| | 40 | 0.0461 ± 0.0009 | 6.50 ± 0.01 |
| | 50 | 0.0463 ± 0.0004 | 6.60 ± 0.01 |
| NE2 | 20 | 0.0500 ± 0.0001 | 6.40 ± 0.01 |
| | 30 | 0.0506 ± 0.0002 | 6.50 ± 0.01 |
| | 40 | 0.0476 ± 0.0004 | 6.60 ± 0.01 |
| | 50 | 0.0488 ± 0.0003 | 6.80 ± 0.01 |
| NE3 | 20 | 0.0525 ± 0.0001 | 6.30 ± 0.01 |
| | 30 | 0.0505 ± 0.0006 | 6.50 ± 0.01 |
| | 40 | 0.0509 ± 0.0006 | 6.70 ± 0.01 |
| | 50 | 0.0493 ± 0.0005 | 6.90 ± 0.01 |

## Conclusion

Nanoemulsion with low content of surfactant were successfully formulated as a carrier of anti-aging agent. The pseudo-ternary phase diagram of nanoemulsion systems were constructed. All systems show high stability in various temperatures (4, 25 and 40 °C). Addition of vitamin E slightly changes the mean droplet size, electrical conductivity, viscosity and pH of system, however, these effects does not alter the microstructure of the system. The electrical conductivity measurement shows the transitions of these microemulsion systems from water-in-oil to bicontinuous phase without undergo phase separation. The antioxidant activity of palm olein together with vitamin E should enhanced the anti-aging activity of these nanoemulsion systems.

## Acknowledgement

The authors would like to thank the Ministry of Higher Education Malaysia and Universiti Kebangsaan Malaysia for supporting this work through the Fundamental Research Grant Scheme (FRGS/1/2013/SG01/UKM/03/1) and Young Researcher Incentive Grant (GGP-2017-087).

## References

1. Sadick, N. S., Karcher. C. And Palminsano, L. (2009). Cosmetic dermatology of the aging face. *Clinics in Dermatology,* 27(3): 3 – 12.
2. Choi, C. M. and Berson, D. S. (2006). Cosmeceuticals. *Seminar in Cutaneous Medicine and Surgery,* 25: 163 – 168.
3. Teo, B. S. X., Basri, M., Zakaria, M. R. S., Salleh, A. B., Raja Abdul Rahman, R., N. Z. and Abdul Rahman, M. B. (2010). A potential tocopherol acetate loaded palm oil ester-in-water nanoemulsion for nanocosmeceuticals. *Journal of Nanobiotechnology,* 8(4): 1 – 11.
4. Manela-Azulay, M. and Bagatin, E. (2009). Cosmeceuticals vitamins. *Clinics in Dermatology,* 27(5): 469 – 474.

5. McCelements, D. J. and Rao, J. (2011). Food-grade nanoemulsions: formulation, fabrication, properties, performance, biological fate and potential toxicity. *Critical Review in Food Science and Nutrition*, 51(4): 285 – 330.
6. Mishra, R. K., Soni, G. C. and Mishra, R. (2014). Nanoemulsion: a novel drug delivery tool. *International Journal of Pharma Research & Review,* 3(7): 32 – 43.
7. Rachmawati, H., Budiputra, D. K., Suhandono, S. and Anggadiredja, K. (2014). Curcumin nanoemulsion for transdermal application: Formulation and evaluation. *Research and Development on Nanotechnology in Indonesia,* 1(1): 5 – 8.
8. Uso'n, N., Garcia, M. J. and Solan, C. (2004). Formation of water-in-oil (w/o) nanoemulsions in a water/mixed non-ionic surfactant/oil system prepared by a low energy emulsification method. *Colloid and Surfaces A: Physicochemical Engineering Aspects,* 250: 415 – 421.
9. Solè, I., Maestro, A., Pey, C. M., Gonzales, C. Solans, C. and Gutierrez, J. M. (2006). Nanoemulsion preparation by low energy methods in an ionic surfactant system. *Colloids and Surfaces A: Physicochemical Engineering Aspects,* 288: 138 – 143.
10. Yukuyama, M. N., Ghilsleni, D. D. M., Pinto, T. J. A. and Bou-Chacra, N. A. (2016). Nanoemulsion: Process selection and application in cosmetics - A review. *International Journal of Cosmetic Science,* 38(1): 13 – 24.
11. Solans, C., Izquerdo, P., Nolla, J., Azemar, N. and Garcia-Celma, M. J. (2005). Nanoemulsion. *Current Opinion in Colloid & Interface Science,* 10: 102 – 110.
12. Gutierrez, J. M., Gonzales, C., Maestro, A., Sole, I., Pey, C. M. and Nolla. J. (2008). Nanoemulsion: New application and optimization of their preparation. *Current Opinion in Colloid & Interface Science,* 13: 245 – 251.
13. Tadros, T. F. (2005). Applied surfactants: Principles and application. Winheim: WILEY-VCH.
14. Bouchemal, K. S., Brianco, E. and Perrier, H. F. (2004). Nanoemulsion formulation using spontaneous emulsification: Solvent, oil and surfactant optimization. *International Journal of Pharmaceutics,* 280(1-2): 241 – 251.
15. Tadros, T., Izqueirdo, P., Esquena, J. and Solans, C. (2004). Formation and stability of nanoemulsions. *Advance in Colloid and Interface Science,* 108-109: 303 – 318.
16. Sonnevile, A. O., Simmonet, J. T. and Alloret, F. L. (2004). Nanoemulsion: A new vehicle for skin products. *Advances in Colloid and Interface Science* 108-09: 145 – 149.
17. Masaki, H. (2010). Role of antioxidants in the skin: anti-aging effects. *Journal of Dermatological Science* 58(2): 85 – 90.
18. Gawrysiak-Witulska, M., Siger, A. and Nogal-Kalucka, M. (2009). Degradation of tocopherols during near-ambient rapeseed drying. *Journal of Food Lipids*, 16(4): 524 – 539.
19. Lesmes, U. and McClements, D. J. (2009). Structure-function relationships to guide rational design and fabrication of particulate food delivery systems. *Trends in Food Science & Technology*, 20(10): 448 –457.
20. McClements, D. J., Decker, E. A., Park, Y. and Weiss, J. (2009). Structural design principles for delivery of bioactive components in nutraceuticals and functional foods. *Criticals Reviews in Food Science and Nutrition*, 49(6): 577 – 606.
21. Yang, Y. and McClements, D. J. (2013). Vitamin E bioaccessibility: Influence of carrier oil type on digestion and release of emulsified α-tocopherol acetate. *Food Chemistry,* 141: 473 – 481.
22. Alzorqi, I., Ketabchi, M. R., Sudheer, S. and Manickam, S. (2016). Optimization of ultrasound induced emulsification on the formulations of palm-olein based nanoemulsion for the incorporation of antioxidant β-D-glucan polysaccharides. *Ultrasonics Sonochemistry,* 31: 71 – 84.
23. Burton, G. W. and Traber, M. G. (1990). Vitamin E: Antioxidant activity biokenetics and bioavailability. *Annual Review of Nutrition,* 10(1): 357 – 382.
24. Gunstone, F. D. (2004). The chemistry of oils and fats: Sources, composition, properties and uses. Blackwell Publisher, USA.
25. Goh, S. H., Choo, Y. M. and Ong, S. H. (1985). Minor carotenoids of palm oil. *Journal of the American Oil Chemists' Society,* 62: 237 – 240.
26. Sundram, K. and Top, A. G. M. (1994). Vitamin E from palm oil. Its extraction and nutritional properties. *Palmas,* 15(1): 77 – 82.
27. Kamat, J. P. and Devasagayam, T. P. A. (1995). Tocotrienols from palm oil as potent inhibitors of lipid peroxidation and protein oxidation in rat brain mitochondria. *Neuroscience Letters,* 195(3): 179 – 182.

28. Krinsky, N. I. (1992). Mechanism of action of biological antioxidants. *Proceedings of the Society for Experimental Biology and Medicine,* 200(2): 248 – 254.
29. Manorama, R., Chinnasamy, N. and Rukmini, C. (1993). Effect of red palm oil on some hepatic drug-metabolizing enzymes in rats. *Food and Chemical Toxicology,* 31(8): 583 – 588.
30. Nesaretnam, K., Devasagayam, T. P., Singh, B. B. and Basiron, Y. (1993). The influence of palm oil or its tocotrienol-rich fraction on the lipid peroxidation potential of rat liver mitochondria and microsomes. *Biochemistry and Molecular Biology International*, 30(1): 159 – 167.
31. Helub, B. J., Sicilia, I. and Mahadevappa, V. G. (1989). Effect of tocotrienol derivatives on collagen and ADP-induced plasma platelet aggregation. Abstracts 1989. *PORIM International Palm Oil Development Conference*, September 5 – 9, Kuala Lumpur, Malaysia.
32. Qureshi, A. A., Qureshi, N., Wright, J. J. K., Shens, S., Kromer, G., Gapor, A., Chong, Y. H., Dewitt, G., Ong, A. S. H., Peterson, D. and Bradlow, B. A. (1991). Lowering of serum cholesterol in hypercholesterolemic humans by tocotrienols (palm vitee). *The American Journal of Clinical Nutrition,* 53: 1021 – 1026.
33. Suria, R., Benjamin, P. R. and Gentle, R. G. I. (2009). Formulation and physical characterization of microemulsions containing isotretinoin. *International Conference on Biomedical and Pharmaceutical Engineering*: pp. 1 – 7.
34. Ramli, S., Ja'afar S. M., Sisak, M. A. A., Zainuddin, N. And Rahman, I. A. (2015). Formulation and physical characterization of microemulsion based carboxymethyl cellulose as vitamin C carrier. *Malaysian Journal of Analytical Sciences*, 19(1): 275 – 283.
35. Ankith, K. R., Subhashis, D. and Niranjan, M. B. (2013). Nanoemulsion a novel approach for lipophilic drugs-a review. *Asian Journal of Pharmaceutical Research,* 3(2): 84 – 92.
36. Subhashis, D., Satayanarayana and Gampa, V. K. (2011). Nanoemulsion – a method to improve the solubility of lipophilic drugs. *An International Journal of Advances in Pharmaceutical Sciences,* 2(2-5): 72 – 83.
37. Chen, C. M. and Warr, G. G. (1992). Rheology of ternary microemulsion. *Journal of Physical Chemistry*, 96: 9492 – 9497.
38. Bagwe, R. P., Kanicky, B. J., Palla, P. K., Patanjail and Shah, D. (2011). Improved drug delivery using microemulsion: Rationale, recent progress and news horizons. *Critical Review in Therapeutic Drug Carrier Systems,* 18: 77 – 140.
39. Kamila, M. M., Mondal, N., Gupta, B. K. and Ghosh, L. K. (2009). Preparation, characterization and in-vitro evaluation of sunflower oil-tween 80-glycerol-based microemulsion formulation of BCS Class-II drug. *Latin American Journal of Pharmacy*, 28(4): 622 – 627.
40. Herrera, J. R., Peralta, R. D., Lopez, R. G., Cesteros, L. C., Mendizabal, E. and Puig, J. E. (2003). Cosurfactant effects on the polymerization of vinyl acetate in anionic microemulsion media. *Polymer* 44(6): 1795 – 1802.
41. Junyaprasert, V. B., Boonme, P., Songkro, S., Krauel, K. and Rades, T. (2007). Transdermal delivery of hydrophobic and hydrophilic local anesthetics from o/w and w/o Brij-97-based microemulsion. *Journal of Pharmacy and Pharmaceutical Sciences,* 10(3): 288 – 298.
42. Garti, N. and Aserin, A. (2006). Microemulsions for solubilization and delivery of nutraceuticals and drugs, in microcapsulation: Methods and industrial applications, Benita, S. (Editor). Taylor & Francis Group: New York: pp. 345 – 428.
43. Sripriya, R., Muthu Raja. K., Santhosh, G., Chandrasekaran, M. and Noel, M. (2007). The effect of structure of oil phase, surfactant and co-surfactant on the physicochemicals and electrochemical properties of bicontinuous microemulsion. *Journal of Colloid and Interface Science,* 314: 712 – 717.
44. Kogan, A., Aserin, A. and Garti, N. (2007). Improved solubilization of carbamazepine and structural transitions in nonionic microemulsions upon aqueous phase dilution. *Journal of Colloid and Interface Science*, 315(2): 637 – 647.
45. Bennet, K. E., Hatfield, J. C., Davis, H. T., Macosko, C. W. and Seriven, L. E. (1982). Microemulsion, Robb, I. D. (Editor). Plenum Press, New York.
46. Djodrjevic, L., Primorac, M., Stupar, M. and Krajisnik, D. (2004). Characterization of caprycaproyl macrogolglycerides based microemulsion drug delivery vehicles for an amphiphilic drug. *International Journal of Pharmacy*, 271: 11 – 19.
47. Moulik, S. P. and Ray, S. (1994). Thermodynamics of clustering of droplets in water/AOT/heptanes microemulsion. *Pure Application of Chemistry*, 66: 521 – 525.

48. Suria, R. (2013). Surfactant protein B-based microemulsion as transdermal carrier for anti-acne agent. Ph.D thesis. The University of Queensland.
49. Austin, C. E. (2000). Drug delivery system. Patents WO2000064528 A1.
50. Peltola, S., Saarinen-Savolainen, P., Kiesvaara, J., Suhonen, T. M. and Urti, A. (2003). Microemulsions for topical delivery of estradiol. *International Journal of Pharmaceutics,* 254(2): 99 – 107.
51. Sinja, M., Jochen, W. and McClements, D. J. (2013). Vitamin E-enrinched nanoemulsions formed by emulsion phase inversion: factors influencing droplet size and stability. *Journal of Colloid and Interface Science,* 402: 122 – 130.

*Malaysian Journal of Analytical Sciences, Vol 21 No 6 (2017): 1409 - 1416*
*DOI: https://doi.org/10.17576/mjas-2017-2106-23*

MALAYSIAN JOURNAL OF ANALYTICAL SCIENCES
*Published by The Malaysian Analytical Sciences Society*
ISSN 1394 - 2506

# STUDY ON THE EFFECT OF OIL PHASE AND CO-SURFACTANT ON MICROEMULSION SYSTEMS

## (Kajian Kesan Fasa Minyak dan Ko-Surfaktan Terhadap Sistem Mikroemulsi)

Muhammad Asri Abd Sisak[1], Rusli Daik[1,2], Suria Ramli[1,2]*

[1]*School of Chemical Sciences and Food Technology*
[2]*Polymer Research Center*
*Faculty of Science and Technology,*
*Universiti Kebangsaan Malaysia, 43600 UKM Bangi, Selangor, Malaysia*

**Corresponding author: su_ramli@ukm.edu.my*

Received: 28 September 2016; Accepted: 6 March 2017

**Abstract**

The purpose of the present study was to investigate the effect of different oil and chain lengths of co-surfactant on microemulsion region. Oleic acid and isopropyl myristate were used as the oil phase, transcutol, polyethylene glycol 400 (PEG 400) and propylene glycol as co-surfactant and Brij 97 as a surfactant. From the ternary phase diagrams, isopropyl myristate based system is more feasible oil phase to formulate microemulsion compared to oleic acid based system. Moreover, transcutol (medium chain length) is the most suitable co-surfactant to blend with a single-chain surfactant, Brij 97 in order to have a high stability and a large area of microemulsion region.

**Keywords:** microemulsion, oleic acid, isopropyl myristate, transcutol, propylene glycol

**Abstrak**

Kajian ini bertujuan untuk mengkaji kesan minyak yang berbeza dan panjang rantai ko-surfaktan terhadap rantau mikroemulsi. Asid oleik dan isopropil miristat telah digunakan sebagai fasa minyak, transcutol, polietilena glikol 400 (PEG 400) dan propilena glikol sebagai ko-surfaktan dan Brij 97 sebagai surfaktan. Berdasarkan rajah fasa tenari, sistem berasaskan isopropil miristat adalah fasa minyak yang lebih sesuai untuk membentuk mikroemulsi berbanding sistem berasaskan asid oleik. Selain itu, transcutol yang berantai sederhana panjang adalah ko-surfaktan yang sesuai untuk diformulasikan bersama surfaktan rantai tunggal, Brij 97 yang memberikan rantau kawasan mikroemulsi yang besar dengan kestabilan yang tinggi.

**Kata kunci**: mikroemulsi, asid oleik, isopropil miristat, transcutol, propilena glikol

## Introduction

Microemulsions are versatile systems and can be used in various applications such as for cutting oils, corrosion inhibitors, biotechnology, fuels, coating and textile finishing, food industries, lubricants, and also in pharmaceuticals [1]. Microemulsions have generated extensive interest over the years as potential drug delivery systems, especially for the delivery of the hydrophilic and lipophilic drug [2]. It is because of its several characteristics such as improved drug solubilization, longer shelf life, ease of preparation and improvement of bioavailability of poorly soluble drugs [3]. It is also can be used to deliver drugs via several routes and making them as a promising dermal delivery of the drug through an efficient route of drug administration [4].

The idea of microemulsion was introduced by Hoar and Schulman as early as the 1940s where they successfully obtained a clear single-phase solution by titrating a milky emulsion with hexanol [5]. That discovery is still used until now even after seven decades had passed. In general, microemulsion is a colloidal dispersion composed of three or four components which are the oil phase, an aqueous phase, surfactant and co-surfactant at applicable ratios. It is a single optically isotropic and thermodynamically or homogeneously stable liquid solution with a nanodroplet diameter [1, 6]. Microemulsion systems formed spontaneously and have low viscosity which behaves as a Newtonian liquid [4]. Microemulsion has been shown to have an ultra low interfacial tension as it can load a large fraction of surfactant/co-surfactant mixture at interface thus thermodynamically stable [7]. Globule size of stable microemulsions is usually within the range of 10 – 100 nm (100 – 1000°A) therefore the whole system is transparent and the globules became invisible to the naked eye due to the fact that dispersed phase droplet does not refract the light [8]. The size of the droplets makes the term of 'microemulsion' is misleading while these systems are actually nano-sized emulsions [1].

Microemulsion is easy to develop and require a low energy contribution during preparation to form a thermodynamic stability, however, it depends on each of the components. This paper will focus on the effect of the oil phase and co-surfactant to the microemulsion system. The oil phase is the most important excipients in the formulation since it governs the selection of the other ingredients for the microemulsion and there are two main factors that need be considered before selecting the appropriate oil phase. The first one is the capability of the oil in solubilizing the active pharmaceutical ingredient (API). Second, the chosen must be such that can result in the large existence area of the microemulsion. Oils with shorter hydrocarbon chains are more facile to form a microemulsion as compared to oils with long hydrocarbon chains. Meanwhile, an oil potentiality to solubilize lipophilic groups is directly proportional to the chain length of the oil [1]. The most common esters used and act as a permeation enhancer in formulations which is isopropyl myristate, IPM ($C_{17}H_{34}O_2$) and also an unsaturated C18 alkyl chain, oleic acid, OA ($C_{18}H_{34}O_2$) are frequently used in microemulsion formulations.

Microemulsions can be formulated using single-chain surfactants or double chain surfactants. Single chain surfactants do not lower the oil-water interfacial tension sufficiently and hence cosurfactants are required [9]. Co-surfactant accumulates substantially at interface layer, increasing the fluidity of interfacial film by penetrating into the surfactant layer. The presence of co-surfactants contributes the interfacial film sufficient flexibility to take up different curvatures required to form a microemulsion over a wide range of composition. If a single surfactant film is desired, the lipophilic chains of the surfactant should be sufficiently short or contain fluidizing groups (e.g. unsaturated bonds). Short to medium chain length alcohols (C3-C8) are commonly added as co-surfactants which further reduce the interfacial tension and increase the fluidity of the interface [1]. The roles of a co-surfactant are to increase the fluidity of the interface, destroy liquid crystalline or gel structure which would prevent the formation of the microemulsion and adjust the HLB value and spontaneous curvature of the interface by changing surfactant partitioning characteristic [4].

In this preliminary study, our aim is to identify the effect of oil and chain lengths of co-surfactant in resulting a large area of the microemulsion region by using oleic acid and IPM as the oil phase, and various co-surfactant, which are transcutol, PEG 400, and propylene glycol.

## Materials and Methods

Oleic acid (OA) was obtained from Bendosen Laboratory Chemical. Isopropyl myristate (IPM) was purchased from Friedemann Schmidt Chemical. Brij 97 (polyoxyethylene-10-oleyl ether), propylene glycol (PG), transcutol (diethylene glycol monoethyl ether), polyethylene glycol 400 (PEG400) were obtained from Sigma-Aldrich Chemical Co. Deionized water was used throughout the experiments. All other chemicals utilize in the experiments were analytical grade.

### Construction of pseudo-ternary phase diagrams

The pseudo-ternary phase diagrams of oil, surfactant, co-surfactant and water were constructed using water titration method to obtain the components and their appropriate ratio which can result to the large existence area of the microemulsion. In brief, the graph was constructed based on water dilution lines, which represent increasing water content and, thus, decreasing a surfactant-cosurfactant concentration. The oils employed in the present study were

oleic acid and IPM. A non-ionic surfactant (Brij 97) was mixed with various co-surfactant (transcutol, propylene glycol, and PEG-400) at a weight ratio of $K_m$ 1:1, $K_m$ 2:1, or $K_m$ 3:1 to obtain surfactant and co-surfactant mixture, S/CoS ($K_m$). Aliquots of each S/CoS were then mixed with oil at room temperature (25 °C). For each phase diagram, the ratio of oil to the S/CoS was varied as 1:9, 2:8, 3:7, 4:6, 5:5, 6:4, 7:3, 8:2, 9:1 (w/w) and the resulting mixtures were subsequently titrated with water under vigorous stirring with a vortex mixer at room temperature. After equilibrium, the samples were visually checked and determined as being clear microemulsions, or emulsions, or gels. The samples were marked as points in the phase diagram. The area covered by these points was considered as the microemulsion region of existence. Quantities of all three phases were taken in % w/w.

**Polarized light microscopy**

Visual inspection was first made after each addition of water to the oil and surfactant and co-surfactant mixture. The samples were identified as microemulsions when they appear as transparent/translucent and easily flowable liquid. The samples were identified as emulsions when they appeared as milky or turbid liquids. The samples were identified as a gel when they did not show a change in the meniscus after tilting to an angle of 90°. Then, the microemulsion samples were verified their isotropic nature under cross-polarizes light microscopy from the image performed. It is expected that the isotropic substance like microemulsion will not reflect the polarized light and the image viewed will remain dark [10].

## Results and Discussion

**Construction of pseudo-ternary phase diagrams**

Pseudo-ternary plot identifies phase boundaries and distinct regions of the ternary mixture (oil, water, surfactant/cosurfactant) where it may exist as biphasic or monophasic, non-isotropic, or liquid crystalline in nature and co-existed in a state of dynamic equilibrium. When four or more components are used pseudo-ternary phase diagrams are used to depict these systems in which each corner represents binary mixtures of two components such as surfactant/co-surfactant, surfactant/water, oil/drug, and water/drug mixtures [1, 11]. Each corner of the ternary phase diagram represents 100% concentrations of a particular component [12].

Three types of system combinations (Brij 97/PEG400/Water, Brij 97/PG/Water, and Brij 97/Transcutol/Water) were developed with specific ratios of S/CoS ($K_m$ = 1:1, 2:1, and 3:1). Two common oil phase used in these systems are oleic acid and isopropyl myristate. Study of the ternary phase diagrams was done to investigate the effect of OA and IPM with the various mixtures of S/CoS on the formation of the stable microemulsion.

**Effect of OA and IPM on the system of Brij 97/PEG 400/Water**

The pseudo-ternary phase diagrams of the Brij 97/PEG 400/Water system using OA and IPM as the oil phase were shown in Figure 1 and 2 where the shaded region represents the microemulsion region. IPM (molecular volume 528.2 g/cm$^3$) based microemulsion system showed a smaller area of microemulsion as compared to a system based on OA (molecular volume 523.9 g/cm$^3$). This result is in accordance with literature reported by [13] that also indicate the smaller area of microemulsion region when used PEG 400 as a co-surfactant, IPM as an oil phase and Brij 30/Brij 35 (HLB ~11.1) as a surfactant. Meanwhile, the result of OA based system is in good agreement with the previous study conducted by [14] that shows stable microemulsion system consisting of oleic acid (oil phase), Tween 20 (surfactant), PEG 400 (co-surfactant), water (aqueous phase). These results might be due to the fact that the lower the molecular volume of oils, the greater the surfactant efficiency [15]. In terms of ratio, $K_m$ 1:1 of oleic acid based system give a larger region compare to $K_m$ 2:1 and $K_m$ 3:1. The further increment of surfactant concentration i.e. S/CoS ratio $K_m$ 2:1 (Figure 1b) and $K_m$ 3:1 (Figure 1c) appeared to have a destabilizing effect on the formation of the microemulsion and led to considerable reduction in microemulsion area. It might be due to insufficient co-surfactant concentration, required to reduce the interfacial tension and provide the flexibility of the interfaces [15]. Both systems show the lower concentration of water except for the phase diagram in Figure 1(a). This might be due to the inversion phase from w/o to o/w system, where a number of liquid crystalline phase are considered as possible intermediates during the process [16]. For those systems that remain clear at higher concentration of water are expected to be the o/w phase with low percentage of oil in the system.

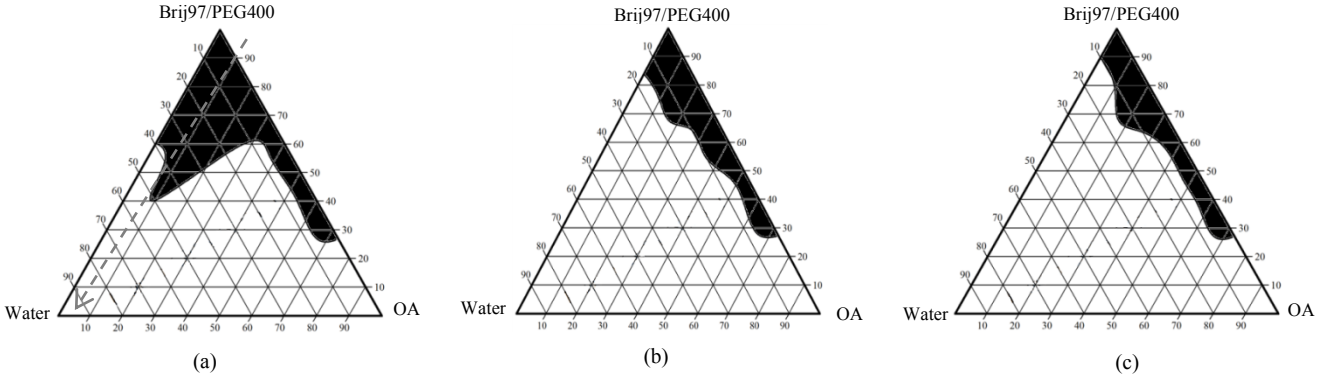



Figure 1. Pseudo-ternary phase diagrams composed of OA/Brij=97/PEG400/water(a)$K_m$ 1:1, (b) $K_m$ 2:1 and (c) $K_m$ 3:1. The shaded region is microemulsion area and ( - - -> ) water dilution line.

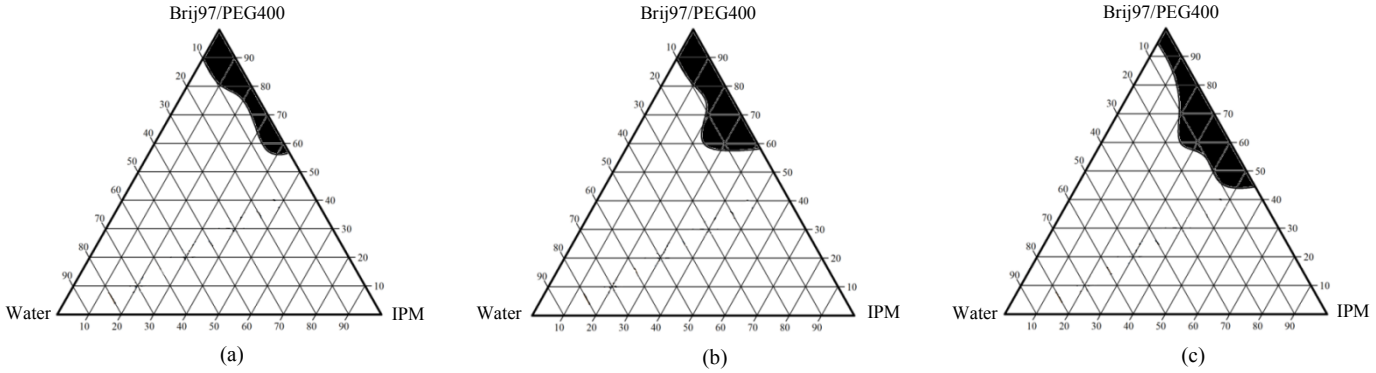



Figure 2. Pseudo-ternary phase diagrams composed of IPM/Brij 97/PEG400/water (a) $K_m$ 1:1, (b) $K_m$ 2:1 and (c) $K_m$ 3:1

**Effect of OA and IPM on the system of Brij 97/PG/Water**

These systems contain PG as a co-surfactant which is a short chain of co-surfactant. The results in Figure 3 and 4 shows that IPM based system give the bigger area of microemulsion region compared to OA based system. This result is similar to the study conducted by Abd-Allah et al. [16] where the clear microemulsion region was from 10 to 30 wt.% of water content in OA based system and when further dilution with the amount of water, resulting in the formation of a gel. This result also ascribed to the large molecular weight, MW of OA (MW = 282.46 g/mol) compared to IPM (MW = 270.45 g/mol) which is not favored to the formation of microemulsion [16]. For IPM based system, $K_m$ 1:1 give the highest concentration of water content (95 wt. %) at a ratio of oil to S/CoS 1:9. However, at $K_m$ 2:1 and $K_m$ 3:1, the region of microemulsion become smaller because of increasing concentration of Brij 97 make the interfacial tension unstable. This is probably due to an inadequate amount of co-surfactant to assist surfactant in lowering the interfacial tension. Furthermore, using propylene glycol in the microemulsion system, increase viscosity and hence gives the high possibility of the gel formation [17].

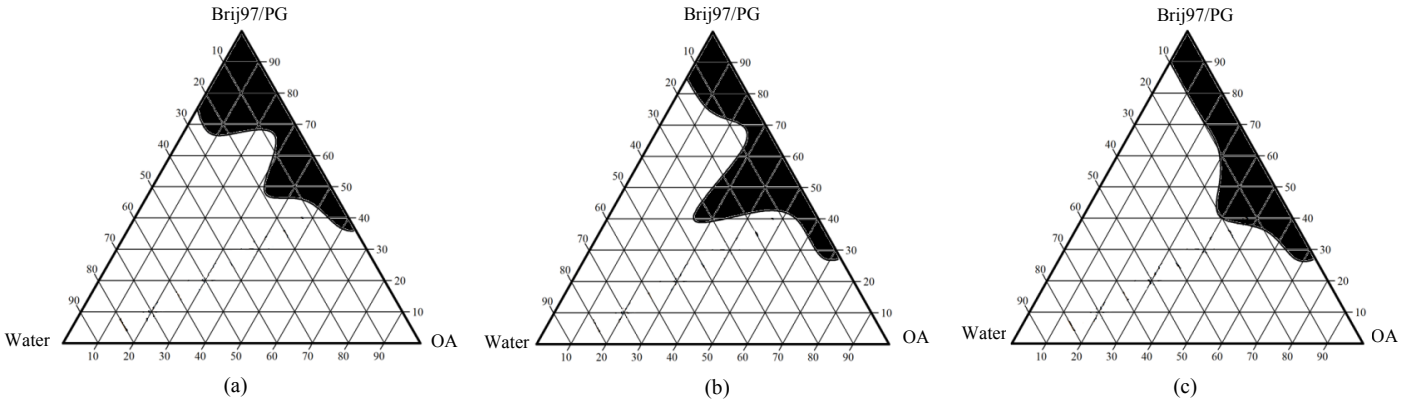



Figure 3. Pseudo-ternary phase diagrams composed of OA/Brij 97/PG/water (a) $K_m$ 1:1, (b) $K_m$ 2:1 and (c) $K_m$ 3:1

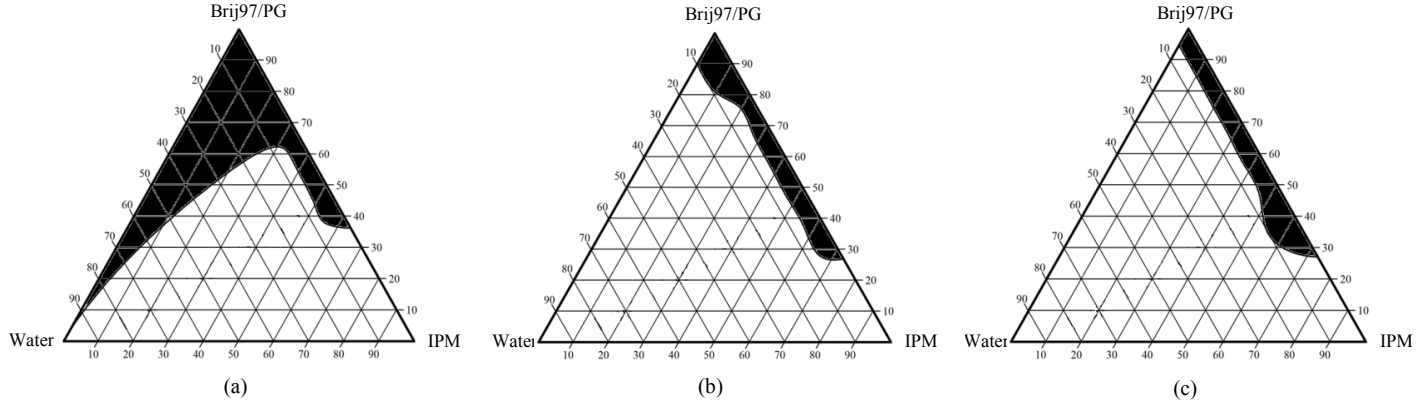



Figure 4. Pseudo-ternary phase diagrams composed of IPM/Brij 97/PG/water (a) $K_m$ 1:1, (b) $K_m$ 2:1 and (c) $K_m$ 3:1

**Effect of OA and IPM on the system of OA/Brij 97/Transcutol/Water**

Transcutol is a medium chain length act as a co-surfactant and frequently proposed as less irritant and alternatives to the medium chain alcohols [18]. The region of microemulsion using transcutol as a co-surfactant form bigger area comparable to PEG 400 and PG for both oleic acid and IPM based formulation as shown in Figure 5 and 6. The best result is still favored to IPM based formulation where both $K_m$ 1:1 and $K_m$ 2:1 give the highest concentration of water (95 wt.%) at ratio oil to S/CoS 1:9. This result attributable to the function of medium chain length alcohols which can increase the flexibility of the hydrocarbon tail and also allow better penetration of the oil into the region of hydrocarbon. In addition, the solubility properties of aqueous and oil phases could also be increased by medium chain length alcohols due to their partitioning behavior between the two phases. [12].

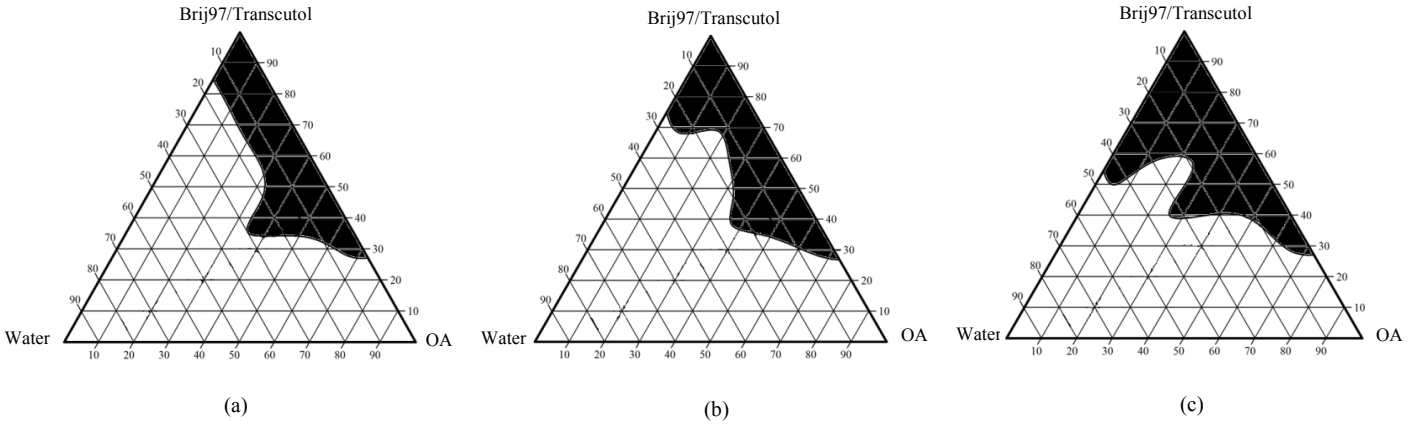



Figure 5. Pseudo-ternary phase diagrams composed of OA/Brij 97/Transcutol/water (a) $K_m$ 1:1, (b) $K_m$ 2:1 and (c) $K_m$ 3:1

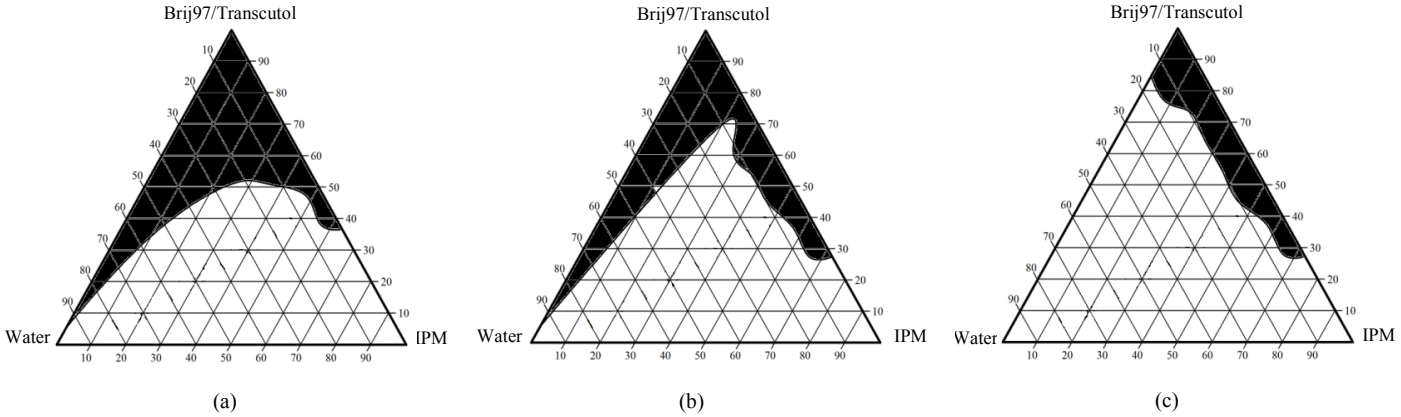



Figure 6. Pseudo-ternary phase diagrams composed of IPM/Brij 97/Transcutol/water (a) $K_m$ 1:1, (b) $K_m$ 2:1 and (c) $K_m$ 3:1

A system which comprises of IPM (oil), Brij 97 (surfactant), transcutol (co-surfactant) and water (aqueous) shows a high stability and a broad microemulsion area (Figure 7) thus, it is potential to utilize in various applications especially in pharmaceutical application due to their safe and pharmaceutical accepted components.

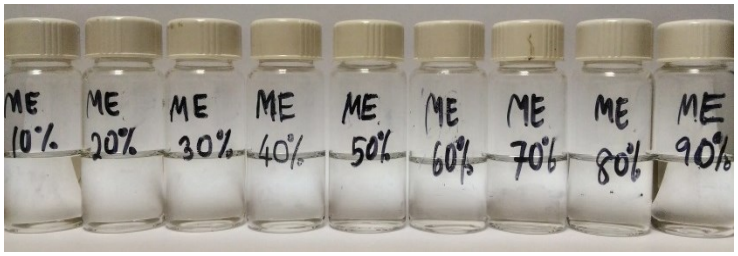



Figure 7. The clear and isotropic of IPM/Brij 97/Transcutol/Water microemulsion system

## Conclusion

A total of 18 phase diagrams were constructed successfully and each formulation gives significant effect on the area of microemulsion region. This study gives two conclusions that could make. First, oleic acid based system (OA/Brij 97/PEG 400/Water, OA/Brij 97/PG/Water, and OA/Brij 97/Transcutol/Water) could not form a large region of microemulsions. Therefore, IPM shows a better choice in order to get a larger area of microemulsion with a higher concentration of water with transition phase from water-in-oil (w/o) to oil-in-water (o/w). Second, the effect of a co-surfactant depends on its chain length, where only appropriate chain lengths are suitable for good microemulsion formation [14]. PEG 400 (long chain), transcutol (medium chain) and propylene glycol (short chain) were used in this study to evaluate the effect of co-surfactants on the formation of microemulsions. In this case, medium chain length is the most suitable co-surfactant in combination with the single-chain surfactant, Brij 97 followed by short and long chain length.

## Acknowledgement

The authors would like to thank Universiti Kebangsaan Malaysia (UKM) and the Malaysian Ministry of Science, Technology, and Innovation (MOSTI) for financial support through the Research University Grant Scheme (GUP-2017-087) and Fundamental Research Grant Scheme (FRGS/1/2013/SG01/UKM/03/1).

## References

1. Sahu, G. K., Sharma, H., Gupta, A. and Kaur, C. D. (2015). Advancements in microemulsion based drug delivery systems for better therapeutic effects. *International Journal of Pharmaceutical Sciences and Developmental Research*, 1: 8 – 15.
2. Ritika, SL, H. & Geeta, A. 2012. Review Article Microemulsion System in Role of Expedient Vehicle for Dermal Application. *Journal of Drug Delivery and Therapeutics*, *2*(4), 23–28.
3. Ghosh, P. and Murthy, R. (2006). Microemulsions: A potential drug delivery system. *Current Drug Delivery*, 3(2): 167 – 180.
4. Muzaffar, F., Singh, U. K. and Chauhan, L. (2013). Review on microemulsion as futuristic drug delivery. *International Journal of Pharmacy and Pharmaceutical Sciences*, 5(3): 39 – 53.
5. Hoar, T. P. and Schulman, J. H. (1943). Transparent water-in-oil dispersions: The oleopathic hydro-micelle. *Nature*, 152: 102 – 103.
6. Talegaonkar, S., Azeem, A., Ahmad, F. J., Khar, R. K., Pathan, S. A. and Khan, Z. I. (2008). Microemulsions: A novel approach to enhanced drug delivery. *Recent Patents on Drug Delivery & Formulation*, 2(3): 238 – 257.
7. Prince, L. M. (1967). A theory of aqueous emulsions I. Negative interfacial tension at the oil/water interface. *Journal of Colloid and Interface Science*, 23(2): 165 – 173.
8. Kumar, A., Kushwaha, V. and Sharma, P. K. (2014). Pharmaceutical microemulsion: Formulation, characterization and drug deliveries across skin. *International Journal of Drug Development and Research*, 6(1): 1 – 21.
9. Grampurohit, N., Ravikumar, P. and Mallya, R. (2011). Microemulsions for topical use- A review. *Indian Journal of Pharmaceutical Education and Research*, 45(1): 100 – 107.
10. Hathout, R. M., Woodman, T. J., Mansour, S., Mortada, N. D., Geneidi, A. S. and Guy, R. H. (2010). Microemulsion formulations for the transdermal delivery of testosterone. *European Journal of Pharmaceutical Sciences*, 40(3): 188 – 196.
11. Ramli, S., Mohd Ja'afar, S., Abd Sisak, M. A., Zainuddin, N. and Rahman, I. A. (2015). Formulation and physical characterization of microemulsions based carboxymethyl cellulose as vitamin C carrier. *Malaysian Journal of Analytical Sciences*, 19(1): 275 – 283.
12. Lawrence, M. J. and Rees, G. D. (2012). Microemulsion-based media as novel drug delivery systems. *Advanced Drug Delivery Reviews*, 64: 175 – 193.
13. Huang, C.-T., Tsai, M.-J., Lin, Y.-H., Fu, Y.-S., Huang, Y.-B., Tsai, Y.-H. and Wu, P.-C. (2013). Effect of microemulsions on transdermal delivery of citalopram: optimization studies using mixture design and response surface methodology. *International Journal of Nanomedicine*, 8: 2295 – 2304.
14. Al Abood, R. M., Talegaonkar, S., Tariq, M. and Ahmad, F. J. (2013). Microemulsion as a tool for the transdermal delivery of ondansetron for the treatment of chemotherapy induced nausea and vomiting. *Colloids*

*and surfaces. B, Biointerfaces*, 101: 143 – 151.

15. Djekic, L. and Primorac, M. (2008). The influence of cosurfactants and oils on the formation of pharmaceutical microemulsions based on PEG-8 caprylic/capric glycerides. *International Journal of Pharmaceutics*, 352(1–2): 231 – 239.
16. Abd-Allah, F. I., Dawaba, H. M. and Ahmed, A. M. S. (2010). Development of a microemulsion-based formulation to improve the availability of poorly water-soluble drug. *Drug Discoveries and Therapeutics*, 4(4): 257 – 266.
17. Yin, Y. M., Cui, F. De, Mu, C. F., Choi, M. K., Kim, J. S., Chung, S. J., Shim, C. K. (2009). Docetaxel microemulsion for enhanced oral bioavailability: Preparation and in vitro and in vivo evaluation. *Journal of Controlled Release*, 140(2): 86 – 94.
18. Santos, P., Watkinson, A. C., Hadgraft, J. and Lane, M. E. (2008). Application of microemulsions in dermal and transdermal drug delivery. *Skin Pharmacology and Physiology*, 21(5): 246 – 259.

*Malaysian Journal of Analytical Sciences, Vol 21 No 6 (2017): 1417 - 1422*
*DOI: https://doi.org/10.17576/mjas-2017-2106-24*

MALAYSIAN JOURNAL OF ANALYTICAL SCIENCES
*Published by The Malaysian Analytical Sciences Society*
ISSN 1394 - 2506

# TENSILE AND THERMAL BEHAVIOURS OF POLY(LACTIC ACID)/ LIQUID NATURAL RUBBER BLEND MATRIX INCORPORATED NICKEL ZINC FERRITE NANOPARTICLES

## (Sifat Regangan dan Terma Matriks Adunan Asid Polilaktik/Cecair Getah Asli Diperkuat Nanozarah Nikel Zink Ferit)

Ruey Shan Chen, Dalila Shahdan, Sahrim Ahmad*

*School of Applied Physics, Faculty of Science and Technology*
*Universiti Kebangsaan Malaysia, 43600 UKM Bangi, Selangor, Malaysia*

**Corresponding author: sahrim@ukm.edu.my*

Received: 28 November 2016; Accepted: 6 March 2017

**Abstract**

Magnetic polymer nanocomposites (MPNCs) based on poly(lactic acid)/liquid natural rubber (PLA/LNR) (90:10) blend and nickel zinc (NiZn) ferrite magnetic nanoparticles were fabricated via melt-blending technique. The effect of NiZn ferrite nanofiller concentration (1 – 5 wt.%) on the tensile and thermal properties of PLA/LNR/NiZn ferrite nanocomposites was investigated. Tensile tests showed that as the tensile strength and modulus increased with the increase of nanofiller concentration until the optimum values of nanofiller concentration was achieved. The thermal behaviour of MPNCs including degradation temperature and its shiftment as well as the remaining residues after complete degradation were determined by thermogravimetric analysis (TGA) measurement. As the NiZn ferrite nanofiller concentration increased, it was noted that the $T_{end}$ of nanocomposites at low amount of nanofillers (1 – 2 wt.%) was higher than neat PLA/LNR and nanocomposites containing high concentration of nanofillers. The current work proves that NiZn ferrite could be served as an excellent reinforcement filer in PLA/LNR matrix. The improved tensile properties and thermal stability of PLA/LNR composites achieved at 2 – 3 wt.% NiZn due to the good dispersion of NiZn ferrite within the PLA/LNR matrix and strong filler-matrix interfacial adhesion, as can be confirmed by the scanning electron microscope (SEM).

**Keywords**: biopolymer, polymer blend, nanocomposite, magnetic particles, melt blending

**Abstrak**

Nanokomposit polimer magnetik (MPNC) berasaskan adunan asid polilaktik/cecair getah asli (PLA/LNR) (90:10) dan nanozarah magnetik nikel zink ferit (NiZn) dihasilkan melalui teknik pengadunan leburan. Kesan kandungan NiZn ferit (1-5 %bt) terhadap sifat regangan dan terma nanokomposit PLA/LNR/NiZn telah dikaji. Ujian regangan menunjukkan bahawa peningkatan kekuatan dan modulus regangan dengan peningkatan kandungan pengisi nano sehingga nilai optimum tercapai. Tingkah laku terma bagi MPNCs termasuk suhu degradasi ($T_{end}$) dan anjakannya serta baki sisa selepas degradasi lengkap telah ditentukan melalui analisis termogravimetri (TGA). Apabila kandungan NiZn ferit pengisi nano meningkat, didapati $T_{end}$ bagi nanokomposit berpengisi nano dalam kandungan kecil (1 – 2 %bt) adalah lebih tinggi daripada PLA/LNR dan nanokomposit terkandung pengisi yang banyak. Hasil kajian ini membuktikan bahawa NiZn ferit boleh bertindak sebagai pengisi pengukuhan yang baik dalam matriks PLA/LNR. Penambahbaikan sifat regangan dan kestabilan terma komposit PLA/LNR tercapai pada 2 – 3 %bt NiZn disebabkan penyebaran NiZn ferit yang baik dalam matriks PLA/LNR dan lekatan antaramuka pengisi-matriks yang kuat, seperti yang disahkan oleh mikroskop elektron imbasan (SEM).

**Kata kunci:** biopolimer, polimer adunan, nanokomposit, zarah magnet, pengadunan leburan

## Introduction

In recent years, the development research works based on the use of biodegradable materials such as poly(lactic acid) (PLA) which served as biopolymer, have been attracted lots of attention from academic and industrial area. Due to the renewability issue and comparable properties with petroleum based polymers, PLA is gaining its popularity [1]. However, as well-established, high brittleness is the main weakness for PLA to be applied in most of the commercial applications [2]. As for that, toughening of PLA by blending with rubber is an applicable method, as a result of the ductility properties imparted by natural rubber (NR). Another advantage could be, NR is derived from renewable sources. Therefore, blending of PLA and NR such as liquid natural rubber (LNR) which is a low molecular weight version of NR, could be a good choice to enhance the toughness of PLA without affecting its biodegradability [1,2]. Somehow, PLA based blending does not provide any high end performance, for examples, electrical, magnetic, conductivity properties and etc. In which these limit its applications in various high performance fields and industries.

Magnetic polymer nanocomposites (MPNCs) are known as materials consisted of an inorganic magnetic component with at least one dimension in the nanometer scale whether in the form of fibers, particles, or lamellae that embedded in an organic polymer [3]. By combining the polymeric matrix materials that are non-magnetic properties with the magnetic nanoparticles as fillers, a new composite material that possesses magnetic properties can be produced and its applications and usefulness can be further expanded. The combination of organic and inorganic materials in magnetic polymer nanocomposites (MPNCs) has produced new properties that could not be obtained by single organic or inorganic material. The applications for MPNCs can be extended from the fields related to the environment [3, 4] until medical field [5]. For instances, technological fields have recently getting more and more attention in the market, especially, in the microwave, electronics and telecommunication industries such as microsensors, magnetic refrigeration, microelectromechanical system, controlling drug delivery and etc. [3, 6].

As well-known, nickel zinc (NiZn) ferrite is soft magnetic material which possesses versatile properties such as high saturation magnetization, electrical resistivity, mechanical hardness, thermal conductivity and chemical stability as well as low coercivity and dielectric losses [7, 8]. In actual sense, not much researchers have studied the use of NiZn ferrite in PLA/LNR matrix [9]. The selection of PLA and LNR to form blend matrix was made because of their biodegradability and cost effectiveness as well as high strength and modulus. Instead of magnetic properties, the objective of this current work is to investigate the effect of NiZn ferrite as nanoparticles on the tensile, thermal and morphological behaviours of nanocomposites based on poly(lactic acid)/liquid natural rubber (LNR) blend.

## Materials and Methods

### Raw materials

The chosen thermoplastic resin, a commercial poly(lactic acid) with the trade name of Natureworks Ingeo Biopolymer 3251D, density of 1.24 g/cm$^3$ and melt flow index of 30 – 40 g/10 min (190 °C/2.16 kg), was obtained from Unic Technology Ltd, China. SMR-L grade natural rubber (NR) which supplied by Malaysian Rubber Board (MRB) was used to synthesize the liquid natural rubber (LNR) via photosensitized chemical oxidation technique. The nanofiller used in this study, nickel zinc (NiZn) ferrite nanoparticles powder with the chemical formula of $Ni_{0.5}Zn_{0.5}Fe_2O_4$, 98.5% purity and 10 – 30 nm particle size was purchased from Nanostructured & Amorphous Materials Inc, USA.

### Preparation of nanocomposites

Prior to mixing, PLA was dried in the oven at 100 °C for 24 hours to eliminate trapped moisture in PLA. PLA/LNR blend and PLA/LNR/NiZn ferrite nanocomposites were melt-blended using an internal mixer machine (Haake Rheomix 600P) at 180 °C, 100 rpm and complete mixing time of 15 minutes. Indirect mixing technique (IDT) was applied to prepare nanocomposites, by pre-mixing the NiZn ferrite powder into LNR before being introduced in the mixer. The ratio of PLA and LNR was mixed at 9:1, whereas the NiZn ferrite nanoparticles was varied from 1 to 5 wt.%. PLA was first introduced into the internal mixer for melting about 3 minutes, then the pre-mixture of LNR and NiZn ferrite was added. The whole mixing process was completed for 15 minutes. In order to produce the composite specimens for characterization, compression molding was carried out via hot/cold pressing process. The temperatures of the upper and lower plates were applied at 180 °C, whereas the pressure was set at 6.9 MPa. The

preheating of 4 minutes, venting of 4 minutes, full pressing of 5 minutes and cold pressing of 3 minutes were applied.

**Characterization**

Tensile testing was conducted using Testomeric tensile machine (Model Testomeric M350-10CT) with load cell of 5 kN and at a crosshead speed of 50 mm/min using 1 mm thickness test specimens in accordance with ASTM 412. At least five replicate specimens were tested for each formulation. Thermogravimetric analysis (TGA) and differential scanning calorimetry (DSC) were carried out using Mettler Toledo TGA/SDTA851$^e$ and DSC 882$^e$, respectively. For TGA, samples were tested at a heating rate of 10 °C/min from 100 °C to 500 °C. The surface morphology of tensile-fractured specimen was analysed using scanning electron microscope (SEM) (Philips XL 30). Energy dispersive X-ray spectroscopy (EDX) was carried out to determine the elemental composition of the nanocomposites containing different NiZn ferrite concentrations.

## Results and Discussion

The effect of NiZn ferrite loadings on the tensile strength and Young's modulus of PLA/LNR nanocomposites is described in Table 1. The tensile results indicates that both tensile strength and Young's modulus exhibited the same trend, that is the increasing concentration of NiZn ferrite increased the tensile properties until an optimum level of nanofillers, and then decreased for higher nanofiller concentrations. Neat PLA/LNR blend possessed 29.93 MPa of tensile strength and 5.29 GPa of Young's modulus. Comparing to that, the highest tensile strength (40.90 MPa) and Young's modulus (7.50 GPa) were achieved at nanocomposite incorporated with 2 wt.% NiZn ferrite, which are increased by 36.65% and 41.78%, respectively. This could be ascribed to the good interfacial interaction between the PLA and NiZn ferrite as a result of the enhanced nanofiller dispersion [2]. When NiZn ferrite nanoparticles added at above 2 wt.%, the tensile strength and Young's modulus decreased gradually from 3 to 5 wt.%. The possible reason is the presence of nanoparticles' agglomerates within the matrix when the content of NiZn ferrite exceeded the optimum level.

Table 1. Tensile strength and Young's modulus of PLA/LNR nanocomposites with various NiZn ferrite loadings

| Sample (wt.% NiZn Ferrite) | Tensile Strength (MPa) | Young's Modulus (GPa) |
|---|---|---|
| PLA/LNR | | |
| 0 | 29.93 ± 0.81 | 5.29 ± 0.04 |
| 1 | 36.70 ± 2.51 | 7.34 ± 0.34 |
| 2 | 40.90 ± 1.61 | 7.50 ± 0.17 |
| 3 | 38.01± 1.50 | 7.14 ± 0.45 |
| 4 | 36.96 ± 1.65 | 6.90 ± 0.04 |
| 5 | 35.45 ± 2.13 | 6.78 ± 0.04 |

Thermogravimetric analysis (TGA) has been carried out to study the mass changes the increase temperature. The mass loss of sample was due to the vaporization process occurred when the temperature increased until a certain high temperature. Figure 1 presents TGA curves of PLA/LNR nanocomposites with various NiZn ferrite loading. Table 2 summarizes the data obtained from TGA testing for all investigated formulations, including temperature of weight loss at 3% ($T_3$) and 50% ($T_{50}$), final degradation temperature ($T_{end}$) as well as residue left after 400 °C. The results of weight loss at 3% ($T_3$) are important to understand the thermal behaviour at initial stage and to determine the thermal stability of nanocomposites. Based on Figure 1, neat PLA/LNR blend and PLA/LNR/NiZn ferrite nanocomposites experienced a dramatic weight loss at around 300 – 350 °C. This represents the degradation of PLA/LNR blend components, as reported by Bijarimi et al. [2]. It was found that PLA/LNR nanocomposites incorporated with 1 and 2 wt.% NiZn ferrite underwent the degradation process at higher temperature.

As compared to neat PLA/LNR blend ($T_3$ = 283.98 °C, $T_{50}$ = 324.75 °C and $T_{end}$ = 396.69 °C), nanocomposite with 1 wt.% NiZn ferrite exhibited $T_3$ = 285.29 °C, $T_{50}$ = 325.44 °C and $T_{end}$ = 412.78 °C while nanocomposite with 2 wt.% NiZn ferrite demonstrated $T_3$ = 285.35 °C, $T_{50}$ = 326.79 °C and $T_{end}$ = 401.91 °C. These phenomenons suggest the improved thermal stability by adding nanofiller in small amount. Similar results were observed for thermoplastic natural rubber (TPNR)/NiZn ferrite nanocomposites [8]. Further increasing the concentration of NiZn ferrite in the PLA/LNR blend matrix, the weight loss curves seemed to be similar (3 and 4 wt.%) and shifted to the left (5 wt.%), as depicted in Figure 1 and Table 2. This might be due to the agglomeration of nanofillers (as shown by 4 wt.% NiZn ferrite in Figure 2(c)) which negatively affects the dispersion and distribution of NiZn ferrite within the PLA/LNR matrix. As the agglomerated NiZn ferrite poorly distributed within the PLA/LNR matrix, the heat transfer from matrix to filler is restricted or delayed in the inhomogenous parts of the composites, and thus, induces the reduced thermal stability of nanocomposites. As the temperature reached to about 400 °C, the change in weight loss as a function of temperature can be considered negligible as a result of the complete degradation of PLA/LNR matrix into carbonaceous products. Therefore, the obtained weight percentages of residues could imply the remaining non-decomposed magnetic nanofillers [8]. As expected, the residues increased with the concentration of NiZn ferrite added from 1 to 5 wt.%.

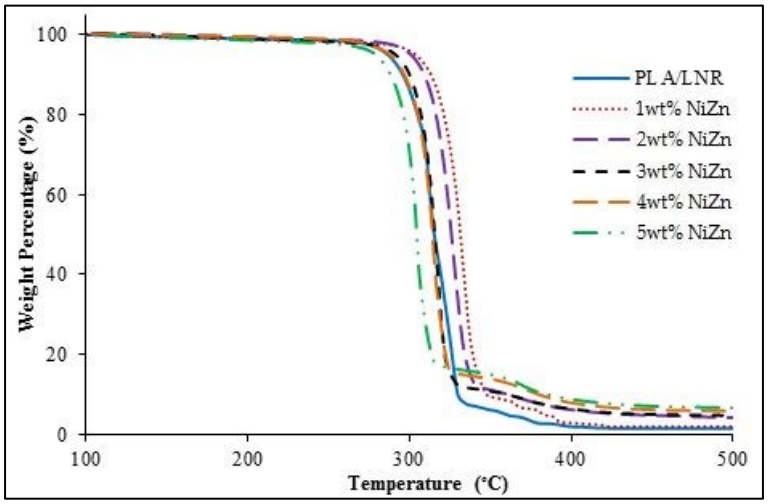



Figure 1. TGA curves of PLA/LNR nanocomposites with various NiZn ferrite loadings

Table 2. TGA data of PLA/LNR nanocomposites with various NiZn ferrite loadings

| Sample (wt.% NiZn ferrite) | $T_3$ (°C) | $T_{50}$ (°C) | $T_{end}$ (°C) | Residue (%) |
|---|---|---|---|---|
| PLA/LNR | | | | |
| 0 | 283.98 | 324.75 | 396.69 | 1.46 |
| 1 | 285.29 | 325.44 | 412.78 | 1.96 |
| 2 | 285.35 | 326.79 | 401.91 | 3.35 |
| 3 | 270.33 | 313.06 | 396.57 | 4.19 |
| 4 | 250.41 | 312.89 | 386.53 | 5.27 |
| 5 | 235.15 | 302.90 | 381.88 | 5.73 |

Figure 2 illustrates the SEM micrograph of PLA/LNR with (a) 0 wt.%, (b) 2 wt.% and (c) 4 wt.% NiZn ferrite nanoparticles. In Figure 2(a), the neat PLA/LNR blend (without NiZn ferrite nanoparticles) showed a one-phase

surface morphology with the existence of holes that indicates rubber particles in the PLA matrix. For Figure 2(b), the presence of holes seemed getting lesser as filled by homogenous dispersion of NiZn ferrite nanoparticles. At higher concentration of NiZn ferrite, for instance at 4 wt.% (Figure 2 (c)), there were many agglomerations of nanoparticles within the matrix, as shown in white circle, and the holes were visible. This observation indicates the poor dispersion of NiZn ferrite nanofillers when the nanofiller concentration exceeds the optimum level, which resulting in the decrease of mechanical and thermal properties. As described in Table 3, the presence of NiZn ferrite in the PLA/LNR matrix was proven by the existence of Ni, Zn and Fe elements in the nanocomposites. It was interesting to observe that the percentage changes in these elements seemed to be inconstant, in which the increase for 3 – 4 wt.% NiZn ferrite was getting larger as compared to low amount (1 to 2 wt.%) and a sudden decrease for 5 wt.% NiZn ferrite. This might be due to (1) the agglomeration of NiZn ferrite within the polymeric matrix, and (2) the EDX analysis had been done in a spot area of morphology.

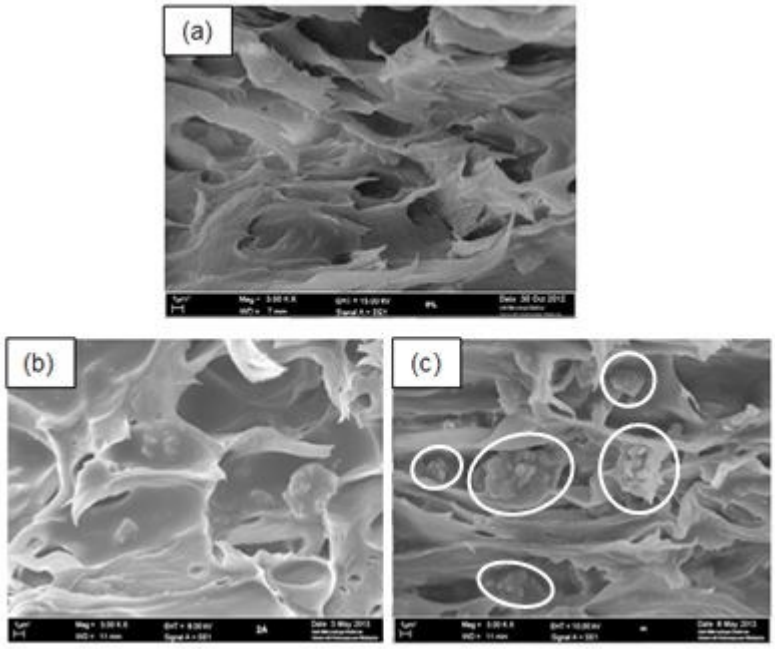



Figure 2. SEM micrograph of PLA/LNR with (a) 0 wt.%, (b) 2 wt.% and (c) 4 wt.% NiZn ferrite

Table 3. Weight and atomic percentage of elements presented in nanocomposites with different concentration of NiZn (obtained from EDX)

| NiZn Ferrite (wt.%) | Weight Percentage of Element (%) | | | | |
|---|---|---|---|---|---|
| | C | O | Ni | Zn | Fe |
| 1 | 54.14 | 44.98 | 0.24 | 0.04 | 0.60 |
| 2 | 53.11 | 44.40 | 0.94 | 0.43 | 1.12 |
| 3 | 50.15 | 41.56 | 1.61 | 0.93 | 5.75 |
| 4 | 47.20 | 35.28 | 4.11 | 1.26 | 12.15 |
| 5 | 47.05 | 43.14 | 2.05 | 0.78 | 6.17 |

## Conclusion

Nanocomposites PLA/LNR embedded with NiZn ferrite at different concentrations were prepared using internal mixer. In overall, the incorporation of NiZn ferrite nanoparticles resulted in positive effect to the mechanical and thermal properties of nanocomposites based on PLA/LNR blend. As the NiZn ferrite nanofiller increased from 0 to 2 wt.%, the tensile strength and modulus of nanocomposites increased up to 36 – 42%. By adding small amount of NiZn ferrite into biodegradable matrix, the thermal stability of nanocomposites enhanced significantly. Once higher NiZn ferrite was introduced, > 2 wt.%, tensile properties and thermal behavior reduced due to the agglomeration of NiZn ferrite, as shown in SEM micrograph. The residues after complete degradation increased accordingly with the filler concentration.

## Acknowledgement

The authors would like to thank the financial support sponsored by UKM under grant No FRGS/1/ 2014/SG06/UKM/01/2, also the Electron Microscopy Unit from UKM for the utilization of SEM machine and cooperation given by the staff.

## References

1. Bijarimi, M., Ahmad, S. and Rasid, R. (2014). Melt blends of poly(lactic acid)/natural rubber and liquid epoxidised natural rubber. *Journal of Rubber Research*, 17 (2): 57 - 68.
2. Bijarimi, M., Ahmad, S. and Rasid, R. (2013). Mechanical, thermal and morphological properties of poly(lactic acid)/natural rubber nanocomposites. *Journal of Reinforced Plastics and Composites*, 32 (21): 1656 - 1667.
3. Zhu, J., Wei, S., Chen, M., Gu, H., Rapole, S. B., Pallavkar, S., Ho, T. C., Hopper, J. and Guo, Z. (2013). Magnetic nanocomposites for environmental remediation. *Advanced Powder Technology*, 24 (2): 459 - 467.
4. Mahmoodi, N. M. (2013). Magnetic ferrite nanoparticle–alginate composite: Synthesis, characterization and binary system dye removal. *Journal of the Taiwan Institute of Chemical Engineers*, 44(2): 322 - 330.
5. Karimi, Z., Karimi, L. and Shokrollahi, H. (2013). Nano-magnetic particles used in biomedicine: Core and coating materials. *Materials Science and Engineering: C*, 33(5): 2465 - 2475.
6. Flaifel, M. H., Ahmad, S., Abdullah, M., Rasid, R., Shaari, A. H., El-Saleh, A. A. and Appadu, S. (2014). Preparation, thermal, magnetic and microwave absorption properties of thermoplastic natural rubber matrix impregnated with NiZn ferrite nanoparticles. *Composites Science and Technology*, 96: 103 - 108.
7. Sarangi, P. P., Vadera, S., Patra, M. and Ghosh, N. (2010). Synthesis and characterization of pure single phase Ni–Zn ferrite nanopowders by oxalate based precursor method. *Powder Technology*, 203(2): 348 -353.
8. Flaifel, M. H., Ahmad, S. H., Abdullah, M. H., Rasid, R., Shaari, A. H., El-Saleh, A. A. and Appadu, S. (2014). Preparation, thermal, magnetic and microwave absorption properties of thermoplastic natural rubber matrix impregnated with NiZn ferrite nanoparticles. *Composites Science and Technology*, 96: 103 - 108.
9. Tarawneh, M. A. A., Shahdan, D. and Ahmad, S. (2013). Investigation on the effect of NiZn ferrite on the mechanical and thermal conductivity of PLA/LNR nanocomposites. *Journal of Nanomaterials*, 2013: 1 - 5.

*Malaysian Journal of Analytical Sciences, Vol 21 No 6 (2017): 1423 - 1431*
*DOI: https://doi.org/10.17576/mjas-2017-2106-25*

MALAYSIAN JOURNAL OF ANALYTICAL SCIENCES
*Published by The Malaysian Analytical Sciences Society*
ISSN 1394 - 2506

# CHEMICAL MODIFICATION OF EPOXIDIZED PALM OIL FOR BIOLUBRICANT APPLICATION

## (Pengubahsuaian Kimia Minyak Sawit Terepoksida Untuk Aplikasi Biopelincir)

Nurazira Mohd Nor, Darfizzi Derawi, Jumat Salimon*

*School of Chemical Sciences and Food Technology,*
*Faculty of Science and Technology,*
*Universiti Kebangsaan Malaysia, 43600 UKM Bangi, Selangor, Malaysia*

**Corresponding author: jumat@ukm.edu.my*

Received: 28 September 2016; Accepted: 6 March 2017

**Abstract**

Refined, bleached and deodorized (RBD) palm oil is one of the interesting renewable resources in biolubricant application. It is due to some advantages such as biodegradable, non-toxic, excellent lubricity and high viscosity index properties. However, direct application of RBD palm oil as biolubricant is restricted due to its poor low temperature property, which limits its use at low operating temperature. This drawback can be overcome by molecule structural redesign through chemical modification process. To produce palm oil based biolubricant with good pour point, epoxidized palm oil (EPO) was chemically modified via ring opening process. EPO was reacted with oleic acid in the presence of *p*-toluenesulfonic acid (PTSA) as catalyst. The molecular structure confirmation of ring opening product which is palm oil hydroxy oleate (POHO) was proven through the oxirane oxygen content (OOC) value, iodin value, hydroxyl value, Fourier transformation infra-red (FTIR), proton and carbon nuclear magnetic resonance ($^{1}$H-NMR and $^{13}$C-NMR) spectroscopy analysis. The physicochemical properties of POHO were determined through its pour point and flash point values. The results showed that the ring opening process for putting bending and branching molecule structures of the oil have improved the pour point (-8.5 $^{o}$C) and increased the flash point of the biolubricant (255 $^{o}$C).

**Keywords**: epoxidized palm oil, oleic acid, ring opening, pour point

**Abstrak**

Minyak sawit tertapis, terluntur dan terbau (RBD) merupakan salah satu sumber boleh diperbaharui yang menarik dalam penghasilan biopelincir. Ini adalah disebabkan oleh kelebihannya seperti boleh dibiodegradasikan, tidak bersifat toksik, mempunyai kebolehpelinciran yang cemerlang dan indeks kelikatan yang tinggi. Walau bagaimanapun, penggunaan secara terus mintak masa RBD sebagai biopelincir adalah terhad disebabkan oleh sifat suhu rendah yang lemah, yang telah mengehadkan penggunaannya dalam operasi bersuhu rendah. Kelemahan ini boleh diatasi dengan melakukan ubahsuai struktur molekul melalui pengubahsuaian kimia. Dalam usaha untuk menghasilkan biopelincir berasaskan minyak sawit dengan nilai takat tuang yang baik, minyak sawit terepoksida telah diubahsuai secara kimia melalui proses pembukaan gelang epoksida. Minyak sawit terepoksida ditindakbalaskan dengan asid oleik dengan kehadiran asid *p*-toluenasulfonik (PTSA) sebagai mangkin. Pengecaman struktur molekul hasil pembukaan gelang epoksida iaitu hidroksi oleate minyak sawit (POHO) dibuktikan melalui nilai kandungan oksigen oksiran, nilai iodin, nilai hidroksil, spektroskopi Infra merah transformasi Fourier (FTIR), proton dan karbon resonans magnetik nuklear ($^{1}$H-NMR dan $^{13}$C-NMR). Sifat fiziko-kimia POHO ditentukan melalui nilai takat tuang dan takat kilat. Hasil kajian menunjukkan proses pembukaan gelang epoksida dengan penambahan struktur molekul bercabang dan bengkok minyak telah memperbaiki nilai takat tuang (-8.5 $^{o}$C) dan meningkatkan nilai takat kilat biopelincir (255 $^{o}$C).

**Kata kunci**: minyak sawit terepoksida, asid oleik, pembukaan gelang, takat tuang

## Introduction

Nowadays, plant oil become one of the interesting renewable resources in biolubricant production in order to replace mineral oil. It is due to some advantages such as biodegradable, non-toxic, excellent lubricity and high viscosity index property [1 – 4]. However, plant oil has some drawback such as poor low temperature properties and it need to be resolved [1]. Poor low-temperature properties include cloudiness, precipitation, poor flowability and solidification at relatively high temperatures [1, 2]. Its poor cold flow property will also limit its use at low operating temperature [5]. The possible way to improve this low temperature properties is molecule structural redesign through chemical modification process. Chemical modifications of the vegetable oils to give more complex structures should improve the low-temperature properties [1]. In general, one of the important modification in plant oils is epoxidation. Refined, bleached and deodorized (RBD) palm oil become one of the potential plant oil for epoxidation to produce biolubricant. RBD palm oil contain high percentage of unsaturated fatty acid (49.4%) which makes it as good starting material for the epoxidation process [6].

The most important modification that can be used to improve poor low temperature properties of plant oil is ring opening reaction. The oxirane ring opening by acidic or alkaline catalyzed reaction with suitable reagent provides interesting polyfunctional compounds [2, 7] whereas reducing structural uniformity of the oil by attaching alkyl side chains would improve the low-temperature performance [2, 8]. The branching group which resulted from ring opening reaction will interfere the formation of macro-crystalline structures during low-temperature applications and provide enhanced fluidity to plant oils [9]. These modified plant oils with chain branching were reported to have superior performance of the physicochemical properties and are promising as biolubricant [9]. Products obtained from ring opening can be used as low-temperature lubricants [10].

Epoxidized RBD palm oil become a promising reactive intermediate, since the epoxy group can be converted to other functional groups through ring-opening reaction due to high reactivity of the oxirane ring [11]. The oxirane ring opening reaction can be carried out through epoxy moiety and takes place through cleavage the carbon oxygen bonds which can be initiated by either electrophiles or nucleophiles, or catalyzed by either acids or bases [12]. The epoxide can react with different nucleophiles to produce alcohols, diols, alkoxyalcohols, hydroxy esters, N-hydroxyalkylamides, mercaptoalcohols, aminoalcohols and so forth [12, 13]. Amongst these classes of products, hydroxy esters find application as biolubricants, polyurethane foams, or casting resins [12]. The physicochemical properties of biolubricants derived from hydroxy esters can be modified using different carboxylic acids [12, 14].

In this paper, we reported the modification of epoxidized palm oil (EPO) molecule structure via ring opening process to produce a base stock oil for lubricant application. Epoxidized palm oil (EPO) was reacted with oleic acid in the presence of *p*-toluenesulfonic acid (PTSA) as catalyst to enhance the lubrication properties. The product of ring opening process which is palm oil hydroxy oleate, (POHO) was screened for low-temperature property through determination of pour point. The pour point of a biolubricant is a good indicator of its low-temperature fluidity. The product also monitored by oxirane oxygen content (OOC) value, iodin value (IV) and hydroxyl value (HV) tests. The physicochemical properties analysis was performed according to the standard methods for pour point and flash point.

## Materials and Methods

### Materials

RBD palm oil was obtained from Sime Darby Jomalina, Teluk Panglima Garang, Selangor, Malaysia. Formic acid (88%) was obtained from Fisher Scientific and hydrogen peroxide 30% from Merck, Germany. Sodium hydrogen carbonate, sodium sulphate, sodium chloride, potassium iodide, Wijs solution, ethyl acetate and *p*-toluenesulfonic acid (PTSA) were purchased from Systerm. Hydrogen bromide 33 wt.% in acetic acid, glacial acetic acid and oleic acid (90%) were obtained from Sigma Aldrich.

### Epoxidation of RBD palm oil

In epoxidation reaction, the mole ratio of RBDPO, formic acid and hydrogen peroxide is 1:5:3. The epoxidation process began by adding RBDPO with formic acid into 250 mL three necks round bottom flask equipped with mechanical stirrer, thermometer and reflux condenser. The mixture of RBDPO and formic acid were heated and

continuously stirred (900 rpm). Hydrogen peroxide was added slowly drop wise. The reaction was carried out for 2.5 hours at 45 $^{o}$C. At the end of reaction, heating was stopped, and product was neutralized with sodium hydrogen carbonate solution (5%), sodium chloride solution (5%) and distilled water. The product which is epoxidized palm oil was kept for overnight by adding anhydrous sodium sulphate to remove water. Then, product was filtered using Whatmann No. 1 filter paper.

**Ring opening of epoxidized palm oil**

In ring opening reaction, the mole ratio of epoxidized palm oil (EPO) and oleic acid is 1: 3. EPO and oleic acid were weighed into a 250 mL three-neck round bottom flask and heated at 70 $^{o}$C to 80 $^{o}$C for 15 minutes. Then, 1% of *p*-toluenesulfonic acid (PTSA) was added to the mixture. The reaction was carried out for 5 hours at 110 $^{o}$C with continuous stirring of 900 rpm using a magnetic stirrer. At the end of reaction, the heating was stopped. The product was neutralized with sodium hydrogen carbonate solution, sodium chloride solution and ethyl acetate. The product which is palm oil hydroxy oleate (POHO) was kept for overnight by adding anhydrous sodium sulphate. The product was filtered by Whatmann No 1 filter paper and the solvent used was isolated by rotary evaporator at 70 $^{o}$C.

**Characterizations**

The formation of palm oil hydroxy oleate (POHO) was confirmed using Fourier Transform Infrared (FTIR) and Nuclear Magnetic Resonance (NMR) spectroscopy. FTIR spectra was recorded on a Perkin Elmer Infrared Spectrophotometer in the range 500 – 4000cm$^{-1}$. NMR spectroscopy was carried out to confirm the molecular structure of the product. $^{1}$H and $^{13}$C NMR were recorded on JEOL-ECP 400 spectrometer (400 MHz $^{1}$H/100.61 MHz$^{13}$C) using $CDCl_3$ as a solvent.

**Determination of oxirane oxygen content**

Oxirane oxygen content (OOC) determines the quantity of oxygen of epoxy groups in percent of mass. Oxygen is directly titrated with hydrobromic acid in acetic acid under defined conditions according to the AOCS Analysis Method Cd 9-57[15]. OOC percentage can be calculated using the following equation 1:

$$\text{Oxirane oxygen content (\%)} = \frac{\text{Volume of hydrobromic acid solution (mL) x N x 1.60}}{\text{Weight of sample (g)}} \quad (1)$$

whereas N is normality of hydrobromic acid solution

**Determination of iodine value**

Iodine value (IV) is a parameter that determines the degree of unsaturation in oils and fats, which are associated with the double bond or triple bond. IV shows the value in grams of iodine absorbed by 100g of fat or oil in the condition specified. Determination of IV generally practiced by Wijs method according to Ainie et al. [16]. IV can be determined by following equation 2:

$$\text{Iodin value (IV)} = \frac{12.69 \text{ x N x } (V_2\text{-}V_1)}{W} \quad (2)$$

whereas N is normality of sodium thiosulphate solution, $V_2$ is volume of sodium thiosulphate solution (mL), required for titration of sample, $V_1$ is volume of sodium thiosulphate solution (mL), required for titration of blank and W is weight of sample (g).

**Determination of hydroxyl value**

The hydroxyl value (HV) is the weight of potassium hydroxide in milligrams (mg) balanced with hydroxyl content of one gram of sample. HV is applied in the determination of oil or its derivatives that have the oxirane ring structure. HV was performed according to the method AOCS Analysis Method Tx 1a-66 [15]. HV can be determined using this following equation 3:

$$\text{Hydroxyl value (HV)} = \frac{B + (WA/C) - S \times N \times 56.1}{W} \quad (3)$$

whereas A is volume of potassium hydroxide solution (mL), required for titration for acidity value and B is volume of potassium hydroxide solution (mL) required for titration of blank test. C is weight of sample (g) used in acid titration, S is volume of potassium hydroxide solution (mL), required for titration in samples that have undergone acetylation process, W is weight of sample (g) used in acetylation and N is normality of potassium hydroxide solution.

**Datermination of flash point value**

Flash point is the lowest temperature at which the vapor sample burns or ignite at a pressure of 101.3 kPa (760 mmHg). Determination of the flash point was carried out by Cleveland open cup method according ASTM D92-05a [17] with modifications.

**Determination of pour point value**

Pour point is the lowest temperature at which the sample begins to flow. Pour point is a good indicator for low temperature fluidity determination. Determination of pour point was conducted according to ASTM D97-98 [17] method with modifications.

## Results and Discussion

Many nucleophilic reagents are known to add to an oxirane ring, resulting in ring opening [13]. The ester branching groups produced from oxirane ring opening based esterification reactions are effective for attaining the desired molecular spacing [13]. Most of the oxirane ring groups were opened and converted into ester bonds in the molecule with hydroxyl group [13]. The modified plant oils with chain branching are reported to have superior performance properties and are promising as biodegradable lubricant [13, 18].

This study reports the oxirane ring opening reaction of epoxidized palm oil (EPO) by the nucleophilic addition of oleic acid (OA) in the presence of homogenous acid catalysts which is *p*-toluenesulfonic acid (PTSA). PTSA was preferred to use in the reactions due to the maximum yield of epoxy ring opening and no evidence of any side reaction occurs during the reaction [9]. The nucleophilic attack by fatty acid molecule which is oleic acid on the oxirane ring of epoxidized palm oil (EPO) in the presence of PTSA as catalyst resulted in the ring opened product which is palm oil hydroxy oleate (POHO).

The results for the ring opening process are shown in Table 1. The average percentage yield of ring opening is 82% (by weight). The ring opening process can be monitored through the OOC value which the value should be as smaller as possible after ring opening process. There is a significant different was observed between the OOC values before and after ring opening process. The initial OOC value of epoxidized palm oil (EPO) before ring opening process is 3.42%. The value of OOC obtained for POHO after ring opening process was significantly low approaching zero (0.04%) with 98% conversion. The reduction of OOC value is proportional to significant number of epoxide ring opening and it prove that the entire epoxide ring was successfully opened during the ring opening reaction with the oleic acid to produce POHO.

The entire epoxide ring has been successfully converted to hydroxyl oleate ester functional groups during the ring opening reaction with oleic acid. This can be evidenced by the increasing of iodine value and hydroxyl value of the product. The addition of the olefin which exist from oleate acyl group has increased the iodine value from initial iodine value of epoxidized palm oil (EPO) which is 0.45 mg/g to 59.9 mg/g after ring opening process.

There is also increasing of hydroxyl value which is from 25 mg/g to 124.8 mg/g after ring opening process. Figure 1 shows the schematic reactions for the modification of RBD palm oil via the epoxidation and ring opening reactions represented by the structure of 1,3-dipalmitoyl-2-oleoyl-gliserol (POP) as the dominant triacylglycerol in RBD palm oil.

Table 1. Analysis tests for ring opening process of epoxidized palm oil

| Compound | EPO | POHO |
|---|---|---|
| Yield (%) | 85 | 82 |
| OOC value (%) | 3.42 | 0.04 |
| Conversion (%) | 98 | 98 |
| Iodine value (mg/g) | 0.45 | 59.9 |
| Hydroxyl value (mg/g) | 25 | 124.8 |

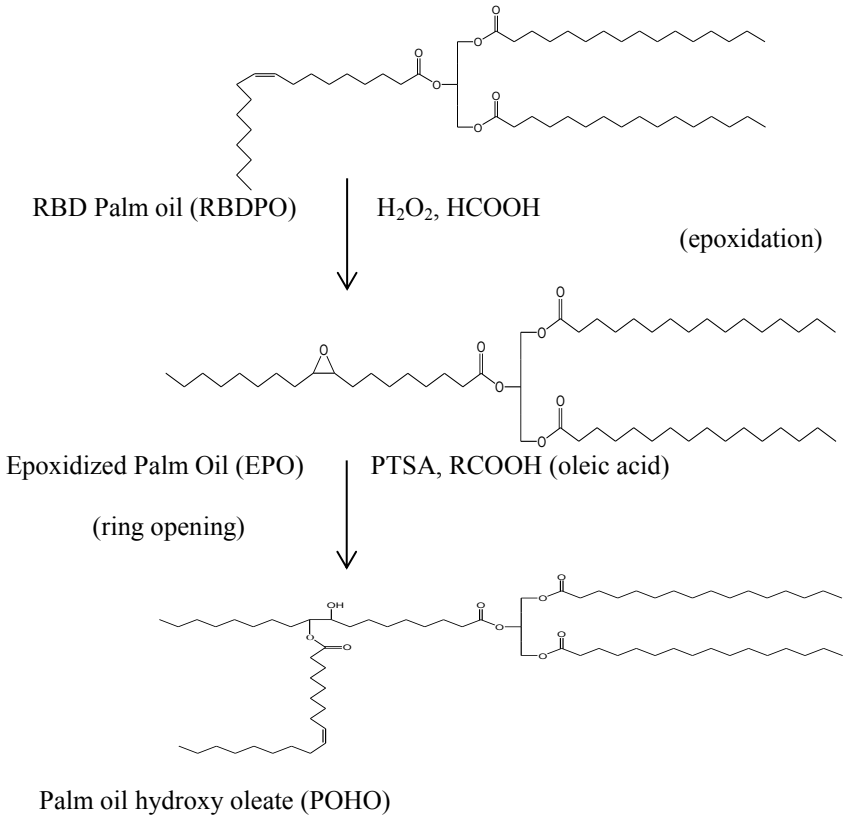



Figure 1. The schematic reactions for the modification of RBD palm oil via epoxidation and ring opening reactions

**FTIR spectra**

The presence of functional groups in the POHO produced were identified by using FTIR spectroscopy. Figure 2 shows comparison of FTIR spectra between RBDPO, EPO and POHO. The disappearance of double bond functional group peak at 3007 $cm^{-1}$ which initially present in RBDPO spectra indicates the conversion of double bond to epoxy group. It can be proved by presence of C-O-C epoxide peak at 826 $cm^{-1}$ in EPO spectra.

The disappearance of the epoxide peak showed that the entire oxirane ring has been successfully converted to hydroxyl oleate ester functional groups in POHO during the ring opening reaction with oleic acid. This is evidenced by the increasing of peaks intensity of the hydroxyl (OH) functional group at 3470 $cm^{-1}$ and C=O stretching at 1741

$cm^{-1}$ in POHO spectra. A significant change in the ring opening process is also can be evidenced by existence of C=C olefin peak of oleate acyl group at 3005 $cm^{-1}$ in POHO spectra.

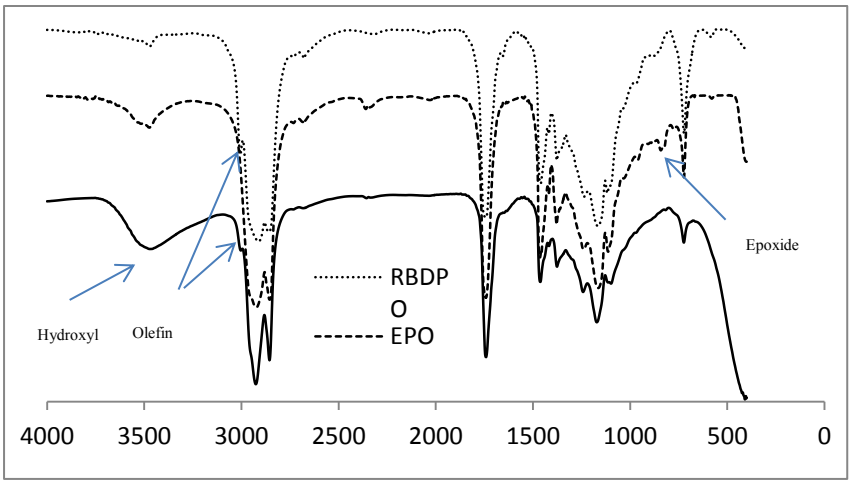



Figure 2. FTIR spectra of RBDPO, EPO and POHO

**NMR spectroscopy**

Table 2 shows the chemical shifts of $^{1}H$ NMR and Table 3 shows chemical shifts of $^{13}C$ NMR spectra for RBDPO, EPO and POHO. In Figure 3(a), the signal at 5.3 ppm is corresponding to vinyl proton (-CH=CH-), while the signal at 2.1 - 2.0 ppm indicate the presence of allylic proton (C=C-C-H), both represent double bond peaks in RBDPO.

Table 2. Chemical shifts of $^{1}H$ NMR spectra for RBDPO, EPO and POHO

| Compound | Chemical shift, ppm | Chemical shift, ppm (Theoretical[19]) | Remarks |
|---|---|---|---|
| RBDPO | 2.1 - 2.0 | 1.6-2.6 | C=C-C-H |
| | 5.3 | 4.5-6.5 | C=C-H |
| EPO | 1.4-1.5 | 1.4-1.5 | $CH_2$-CHOCH-$CH_2$ CHOCH |
| | 2.8 | 2.5-3.5 | |
| POHO | 2.0-1.9 | 1.6-2.6 | C=C-C-H |
| | 4.9 | 0.5-5.0 | C-O-H |
| | 5.3 | 4.5-6.5 | C=C-H |

Table 3. Chemical shifts of $^{13}C$ NMR spectra for RBDPO, EPO and POHO

| Compound | Chemical shift, ppm | Chemical shift, ppm (Theoretical[19]) | Remarks |
|---|---|---|---|
| RBDPO | 130.1- 129.6, 128.0-127.8 | 100-150 | C=C |
| EPO | 57.2-56.6, 54.3-54.1 | 40-80 | C-O-C |
| POHO | 73.5 | 40-80 | HC-OH |
| | 130.2- 129.7 | 100-150 | C=C |

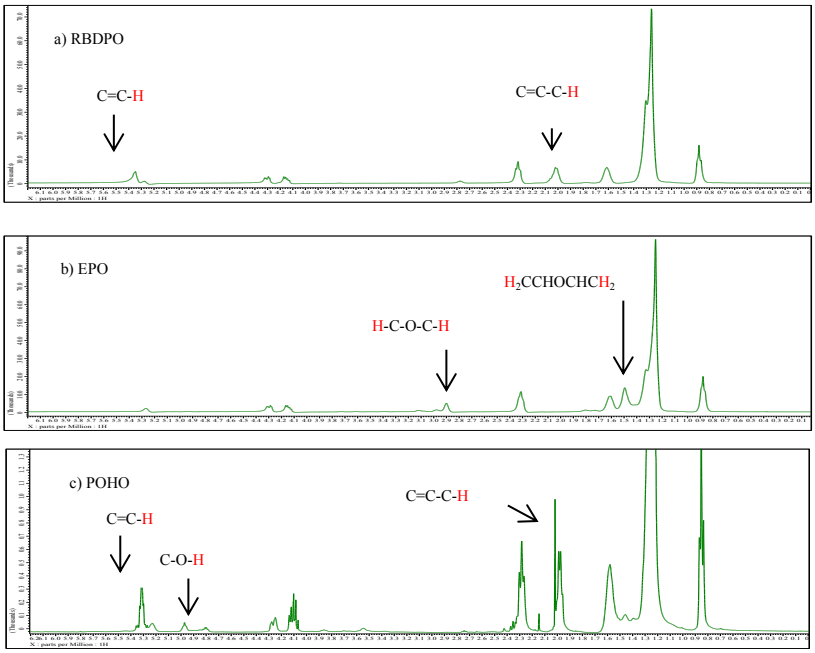



Figure 3. $^{1}$H NMR spectra for a) RBDPO, b) EPO and c) POHO

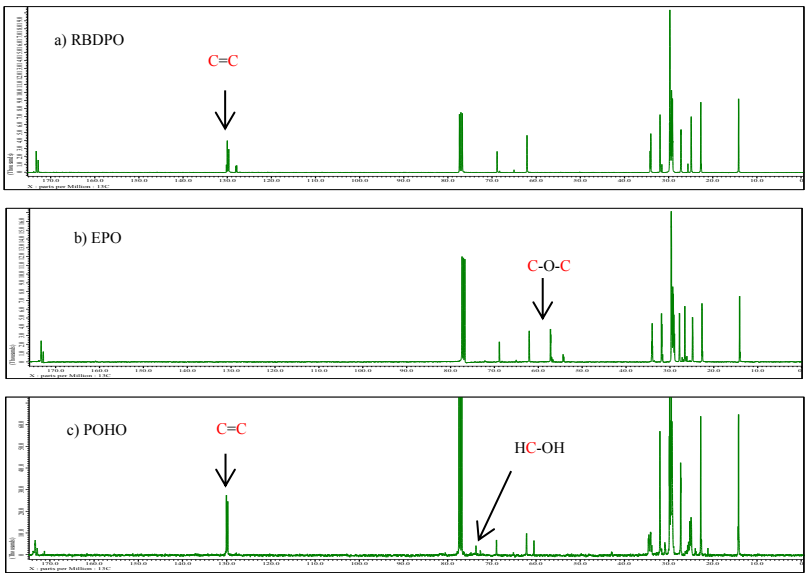



Figure 4. $^{13}$C NMR spectra for a) RBDPO, b) EPO and c) POHO

**Physicochemical properties of palm oil hydroxyl oleate (POHO)**

The physicochemical properties results obtained are shown in Table 4. The ability of a substance to remain liquid at low temperatures is an important attribute for many industrial application materials, such as biolubricants, surfactants and fuels [1, 5]. The cold flow property of plant oils is extremely poor, and this limits their use at low operating temperature especially as automotive and industrial fluids [5]. Plant oils tend to form macrocrystalline

structures at low temperatures through uniform stacking of the 'bend' triacylglycerol (TAG) backbone [5]. Such macrocrystals restrict the easy flow of the system due to loss of kinetic energy of individual molecules during self-stacking [2, 5, 20]. The low temperature properties can be screened by determination of pour point. The pour point of a biolubricant is a good indicator of its low-temperature fluidity. In this study, pour point of RBDPO, EPO and POHO were -3.8 °C, 0.1 °C and -8.5 °C, respectively. After ring opening process, POHO shows a lowest pour point which is -8.5 °C, due to the branching in carbon chain and bent structure. It makes more restrict to self-stacking and more hollows in structure, thus easier to flow which contributed to the lowest pour point. In general, the presence of branching group in the molecule will disrupt this stacking process and create a steric barrier around the individual molecules and inhibits crystallization [11]. This will result in the formation of microcrystalline structures rather than macro structures. At lower temperatures, such microcrystalline structures can easily tumble and glide over one another resulting in better fluidity of the total matrix [5], resulting in lower pour point.

Table 4. The physicochemical properties of RBDPO, EPO and POHO

| Compound | RBDPO | EPO | POHO |
|---|---|---|---|
| Pour point (°C) | -3.8 | 0.1 | -8.5 |
| Flash point (°C) | 240 | 245 | 255 |

Another important factor that determine the efficiency of oil as biolubricant is flash point. The flash point is often used as a descriptive characteristic of fuel oil and it is also used to describe oils that are not used as fuels such as lubricant [5]. Flash point refers to both flammable oils and combustible oils [5]. The oils with a flash point less than 43 $^{o}$C are flammable, while those having a flash point above this temperature are combustible [5]. High flash point is important to ensure that the lubricant is not burned in the engine during its operation. Biolubricant which has a low flash point value is considered to have been contaminated by volatile and usually requires precautions special care when handling this biolubricant [2]. In this study, flash point of RBDPO, EPO and POHO were 240 °C, 245 °C and 255 °C, respectively. After ring opening process, POHO shows the highest flash point which is 255 °C. This is due to an increase in carbon number causes an increasing molecular weight that gives a higher flash point. In addition, POHO also have branched carbon chain molecular structure. The big branched-chain structure requires more energy to burn. This will increase the flash point of POHO.

## Conclusion

The chemically modified epoxidized palm oil (EPO) has improvement in pour point and flash point. The ring opening product which is palm oil hydroxy oleate (POHO) has lowest pour point due to the greater ability of the branching chain esters to disrupt crystalline formation. A bent and branching structure make the molecule less compact, thus improve the lubricity of lubricant. This shows that the cold flow property of biolubricant has improved by reducing the pour point value.

## Acknowledgements

Authors would like to acknowledge the Universiti Kebangsaan Malaysia for the financial support through research grant (FRGS/2/2014/ST01/UKM/01/2) as well as research facilities provided and Ministry of Education for providing scholarship support (MyPHD) for the author.

## References

1. Salimon, J. and Salih, N. (2010). Modification of epoxidized ricinoleic acid for biolubricant base oil with improved flash and pour points. *Asian Journal of Chemistry*, 22(7): 5468 – 5476.
2. Salimon, J. and Salih, N. (2009). Substituted esters of octadecanoic acid as potential biolubricants. *European Journal of Scientific Research*, 31(2): 273 – 227.
3. Salimon, J. and Salih, N. (2009). Oleic acid diesters: Synthesis, characterization and low temperature properties. *European Journal of Scientific Research*, 32(2): 216 – 222.

4. Cerretani, L.A., Bendini, M.T.R., Estrada, E., Vittadini. and Chiavaro, E. (2009). Microwave heating of different commercial categories of olive oil: part I. effect on chemical oxidative stability indices and phenolic compounds. *Food Chemistry*, 115: 1381 – 1388.
5. Salimon, J., Salih, N. and Yousif, E. (2011). Chemically modified biolubricant basestocks from epoxidized oleic acid: Improved low temperature properties and oxidative stability. *Journal of Saudi Chemical Society*, 15: 195 – 201.
6. Njoku, P. C., Egbukole, M. O. and Enenebeaku, C. K. (2010). Physio-chemical characteristics and dietary metal levels of oil from *Elaeis guineensis* species. *Pakistan Journal of Nutrition*, 9(2): 137 – 140.
7. Yunus, R., Razi, A. F., Iyuke T. L. and Idris, A. (2003). Preparation and characterization of trimethylolpropane esters from palm kernel oil methyl esters. *Journal of Oil Palm Research*, 15(2): 42 – 49.
8. Sharma, B. K., Doll, K. M. and Erhan, S. Z. (2008). Ester hydroxy derivatives of methyl oleate: tribological, oxidation and low temperature properties. *Bioresource Technology*, 99: 7333 – 7340.
9. Salimon, J., Abdullah, B. M., Yusop, R. M., Salih, N. and Yousif, E. (2013). Synthesis and optimization ring opening of monoepoxide linoleic acid using *p*-toluenesulfonic acid. *SpringerPlus*, 2: 429.
10. Lathi, P. and Mattiasson, B. (2007). Green approach for the preparation of biodegradable lubricant base stock from epoxidized vegetable oil. *Applied Catalysis B: Environmental*, 69(3-4): 207 – 212.
11. Wang, R. and Schuman, T.P. (2013). Vegetable oil-derived epoxy monomers and polymer blends: A comparative study with review. *Express Polymer Letters*, 7(3): 272 – 292.
12. Salimon, J., Salih, N. and Abdullah, B. M. (2011). Improvement of physicochemical characteristics of monoepoxide linoleic acid ring opening for biolubricant base oil. *Journal of Biomedicine and Biotechnology*, 10: 1155
13. Baumann, H., Buehler, M., Fochem, H., Hirsinger, F., Zoebelein, H. and Falbe, J. (1988). Natural fats and oils – renewable raw materials for the chemical industry. *Angewandte Chemie*, 27(1): 41 – 62.
14. Schuster, H., Rios, L. A., Weckes, P. P. and Hoelderich, W. F. (2008). Heterogeneous catalysts for the production of new lubricants with unique properties. *Applied Catalysis A*, 348(2): 266 – 270.
15. American Oil Chemists Society (1998). Official methods and recommended practices of the American Oil Chemists Society. AOCS Press.
16. Kuntom, A., Lin, S. W., Ai, T. Y., Idris, N. A., Yusof, M., Sue, T. T. and Ibrahim, N. A. (2004). MPOB test methods – a compendium of test on palm oil products, palm kernel products, fatty acids, food related products and others. Bangi: MPOB.
17. American Society for Testing and Materials (2006). Annual Book of ASTM Standards. West Conshohocken. ASTM International.
18. Hwang, H. S. and Erhan, S. Z. (2001). Modification of epoxidized soybean oil for lubricant formulation with improved oxidative stability and low pour point. *Journal of the American Oil Chemist Society*, 78(12): 1179 – 1184.
19. Pavia, D. L., Lampman, G. M., Kriz, G. S. and Vyvyan, J. R. (2001). Introduction of spectroscopy. fourth edition. Nelson Education, Ltd, Canada.
20. Sharma, A., Adhvaryu, A., Liu, Z. and Erhan, S. Z. (2006). Chemical modification of vegetable oils for lubricant applications. *Journal of the American Oil Chemist Society*, 83: 129 – 136.

*Malaysian Journal of Analytical Sciences, Vol 21 No 6 (2017): 1432 - 1437*
*DOI: https://doi.org/10.17576/mjas-2017-2106-26*

MALAYSIAN JOURNAL OF ANALYTICAL SCIENCES
*Published by The Malaysian Analytical Sciences Society*
ISSN 1394 - 2506

# CHARCOAL BASE METALLIC COMPOSITE ELECTRODE FOR WASTEWATER TREATMENT

## (Elektrod Komposit Logam Berasaskan Arang Bagi Rawatan Air Buangan)

Majd Ahmed Jumaah[1]*, Mohamed Rozali Othman[1, 2], Muhammad Rahimi Yusop[1], Jumat Salimon[1], Baydaa Khalaf[1], Wan Mohd Afiq Wan Mohd Khalik[3]

[1]*School of Chemical Sciences and Food Technology*
[2]*Centre for Water Research and Analysis (ALIR)*
*Faculty of Science and Technology,*
*Universiti Kebangsaan Malaysia, 43600 UKM Bangi, Selangor, Malaysia*
[3]*School of Marine and Environmental Sciences,*
*Universiti Malaysia Terengganu, 21030 Kuala Nerus, Terengganu, Malaysia*

**Corresponding author: majd.ahmed88@yahoo.com*

Received: 28 September 2016; Accepted: 6 March 2017

**Abstract**

In this study, a charcoal base metallic composite electrode which is low in cost and effective to treat wastewater from landfill leachate by electrochemical oxidation technique has been fabricated. The charcoal base metallic composite electrode was prepared by mixing together a weighed portion of charcoal, graphite and metals powder in different composition percentage with PVC as a binder in 4 mL THF which act as a solvent. Metals used in the preparation of the electrodes are Ag, Al, Co, Cu and Ni. The results show that the mixture of commercially available charcoal, metals and PVC at a composition of 50:20:30 (w/w), known as C50M20PVC30 electrode give a good stability, low cost and high formation of hypochlorite ion. Hypochlorite ion has been produced linked to the presence of chloride ions, thus having capability to degrade chemical pollutants in wastewater.

**Keywords**: charcoal, electrode, treatment, wastewater

**Abstrak**

Dalam kajian ini, elektrod komposit logam berasaskan arang dengan kos rendah dan efektif dalam merawat air buangan daripada tanah larut resap melalui teknik pengoksidaan elektrokimia telah dibangunkan. Elektrod komposit logam berasaskan arang telah disediakan dengan mencampurkan arang, grafit dan serbuk logam pada peratus komposisi yang berbeza di mana polivinil klorida sebagai pengikat di dalam 4 mL tetrahidrofuran (THF) sebagai pelarut. Logam yang digunakan dalam penyediaan elektrod ialah Ag, Al, Co, Cu dan Ni. Keputusan menunjukkan campuran arang komersial, logam dan PVC pada nisbah 50:20:30 (w/w), yang dikenali sebagai elektrod C50M20PVC30 memberi kestabilan yang baik, berkos rendah dan menghasilkan ion hipoklorit yang tinggi. Semasa pengoksidaan elektrokimia, ion hipoklorit telah dihasilkan disebabkan oleh kehadiran ion klorida yang membawa kepada keupayaan untuk penyingkiran bahan pencemar kimia di dalam air buangan.

**Kata kunci**: arang, elektrod, rawatan, air buangan

## Introduction

Water purification is one of the most pervasive problems affecting people throughout the world [1]. Various methods of wastewater treatment have been reported and this process is divided into three, namely chemical, physical and biological [2]. Up to now, electrochemical oxidation process has been proved to be promising for

wastewater treatment mainly due to its high effectiveness, easy to operate and more economic [3, 4]. In the case of landfill leachate, it was known having high concentration chloride ions and good conductivity. Many researchers have investigated the effectiveness of electrochemical oxidation process toward various types of wastewater including leachate wastewater [5, 6]. Leachate also known having high chemical oxygen demand (COD), high levels of ammonia and phosphorus as well as total dissolved solid content (TDS) [7]. To reach environmental friendly criteria for landfill leachate, chemical pollution should be minimized to an acceptable discharge limit [8].

Therefore, the aim of this study is to evaluate the effectiveness of charcoal base metallic composite electrode for color removal during electrochemical oxidation process. Characterization of prepared charcoal base metallic composite electrodes also has been studied.

## Materials and Methods

### Preparation of electrodes

Composite electrodes based on ratio composition of charcoal-metals-PVC were prepared. A weighed portion of charcoal powder, metals with PVC in 4 mL tetrahydrofuran (THF) solvent was mixed together and swirled flatly to homogeneous, followed by drying in an oven at temperature set 100˚ C for 3 hours. The mixture was then placed in 1 cm diameter stainless steel mould and pressed at 10 ton/cm [9]. The pellets were connected to silver wire with epoxy gum and coated silver conducting paint.

### Experimental procedures

All experiments were carried out at ambient temperature. The lab scale electrochemical cell was designed by using DC set power supply, glass reactor and magnetic stirrer. Leachate sample (50 mL) was then added into cell with known concentration supporting electrolyte. Sample in the electrochemical cell was kept stirred at 300 rpm for homogenise condition. The effect of pH was studied by adjusting leachate sample using HCl or NaOH solution. The effect of sodium chloride concentration as the supporting electrolyte also was carried out. Electrochemical reaction was started once the specified voltage was introduced into the system. Leachate samples were treated at different time and different operating parameters. The removal efficiency (% R) of color sample during electrochemical oxidation process was calculated using following equation 1 [10].

$$\% \, R = \frac{[100 \, (R_0 - R_t)]}{R_0} \tag{1}$$

where % R is the removal percentage for color, $R_0$ is initial value of color, $R_t$ is the value color at time t.

### Sampling

Leachate samples were collected from Jeram Sanitary Landfill, situated in oil palm plantation near Mukim Jeram, Kuala Selangor. Leachate samples were transported to chemical laboratory and stored in a refrigerator at 4˚C prior analysis.

## Results and Discussion

### The stability of electrode

Different compositions of commercially available charcoal powder base metallic composite electrode with PVC were prepared. Different types of metals such as silver, aluminum, cobalt, copper and nickel were used as metal based. All electrodes hardness was tested to determine whether composition of charcoal and metal powders having high stability to use it during electrochemical treatment process. Table 1 depicted the stability of charcoal base metallic composite electrode.

Finding study shows ten composition of electrodes having good stability which can be used in electrochemical treatment process. The stability of composite electrode was improved once the percentage of PVC was increased. The characterization explains that PVC acts as a binder, filled the porosity of charcoal and increase resistivity of electrode [10, 11]. Nonetheless, the amount of PVC was kept as low as possible, to avoid reducing surface area or conductivity of composite electrode during this study.

Table 1. The stability of commercially available charcoal powder base metallic composite electrode

| Percentage % (w/w) | | | Electrode Stability |
|---|---|---|---|
| Charcoal | PVC | Metal Powder | |
| 10 | 10 | 80 | Hard |
| 20 | 10 | 70 | Hard |
| 30 | 15 | 60 | Hard |
| 40 | 15 | 45 | Hard |
| 50 | 20 | 30 | Hard |
| 60 | 30 | 10 | Hard |
| 70 | 20 | 10 | Hard |
| 80 | 10 | 10 | Crumble |
| 85 | 10 | 5 | Crumble |
| 90 | 5 | 5 | Crumble |
| 95 | 5 | - | Crumble |
| 90 | 10 | - | Crumble |
| 85 | 15 | - | Breakable |
| 80 | 20 | - | Breakable |
| 75 | 25 | - | Breakable |
| 70 | 30 | - | Hard |
| 60 | 40 | - | Hard |
| 50 | 50 | - | Hard |

Note: stability of electrode = The hardness of pellet after preparation

**Optimization of anode material composition**

Electrode based materials was known having influence toward the efficiency of electrochemical process include for wastewater treatment [12, 13]. Good composite electrode was evaluated based on the efficiency of color removal in leachate samples. The operating condition: applied voltage (10 V) and NaCl concentration (1.5% w/v) was remain constant during treatment process. Expenses costs of all composite electrodes used in this study were calculated based on manufacturer prices (Sigma-Aldrich, USA). The results obtained is summarised as in Table 2.

Table 2. Electrochemical oxidation of landfill leachate under different operating condition

| Electrode | Electrolysis Time (min) | Color Removal (%) | Observation | | Cost USD | $ClO^-$ Production (Abs) |
|---|---|---|---|---|---|---|
| | | | Electrolysis Product | Anode | | |
| C50Ag20PVC30 | 360 | 61 | Yellowish Solution | Slightly corroded | 1.13 | 3.9 |
| C50Co20PVC30 | 120 | 58 | Yellowish Solution | Unchanged | 0.30 | 1.2 |
| C50Cu20PVC30 | 180 | 44 | Yellowish Solution | Completely corroded | 1 | - |
| C50Al20PVC30 | 300 | 23 | Yellowish Solution | Unchanged | 0.15 | 0.3 |

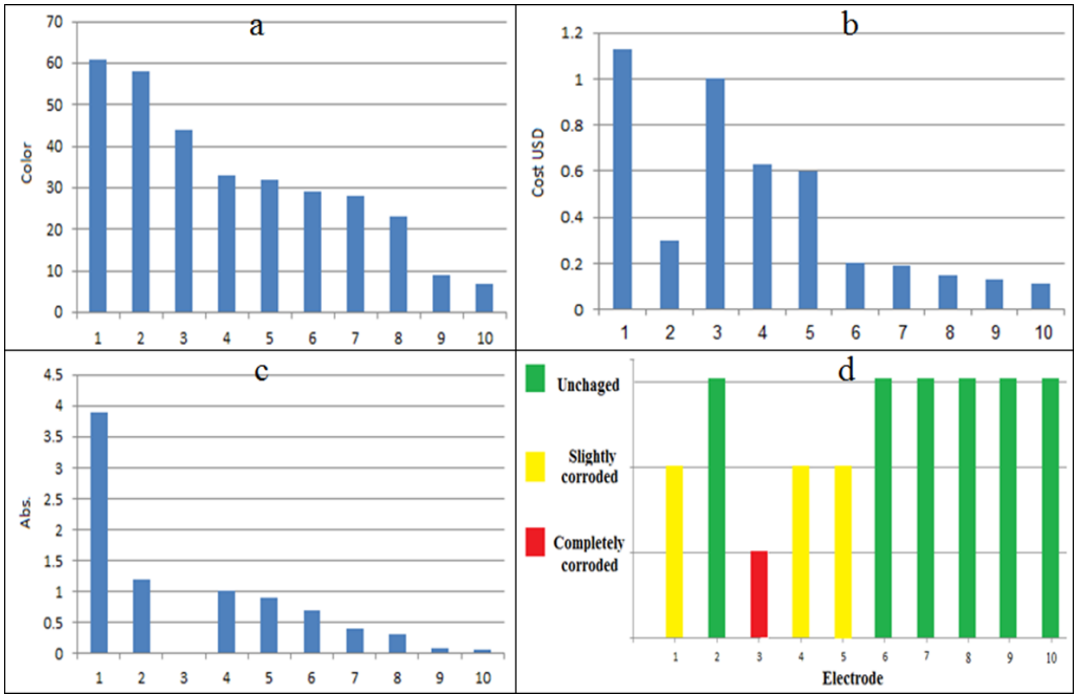
Table 2 (cont'd). Electrochemical oxidation of landfill leachate under different operating condition

| Electrode | Electrolysis Time (min) | Color Removal (%) | Observation | | Cost USD | $ClO^-$ Production (Abs) |
|---|---|---|---|---|---|---|
| | | | Electrolysis Product | Anode | | |
| C50Ni20PVC30 | 360 | 4 | Color unchanged | Completely corroded | 0.97 | - |
| C60Ag10PVC30 | 180 | 33 | Yellowish Solution | Slightly corroded | 0.63 | 1 |
| C60Co10PVC30 | 120 | 29 | Yellowish Solution | Unchanged | 0.20 | 0.7 |
| C60Cu10PVC30 | 180 | 22 | Yellowish Solution | Completely corroded | 0.86 | - |
| C60Al10PVC30 | 180 | 7 | Color unchanged | Unchanged | 0.13 | 0.08 |
| C60Ni10PVC30 | 180 | 5 | Color unchanged | Completely corroded | 0.71 | - |
| C70Ag10PVC20 | 180 | 32 | Yellowish Solution | Slightly corroded | 0.60 | 0.9 |
| C70Co10PVC20 | 240 | 32 | Yellowish Solution | Unchanged | 0.19 | 0.4 |
| C70Cu10PVC20 | 180 | 28 | Yellowish Solution | Completely corroded | 0.81 | - |
| C70Al10PVC20 | 180 | 9 | Color unchanged | Unchanged | 0.11 | 0.05 |
| C70Ni10PVC20 | 240 | 6 | Color unchanged | Completely corroded | 0.67 | - |

Note: $OCl^-$ = the formation of hypochlorite ion in 50 mL deionized water, 1.5% (w/v) NaCl and 30 minutes electrolysis time for only the stable electrodes.

Finding study shown that the best composite electrode (C50Co20PVC30) gave 58% of color removal without any changes on physical properties. Although C50Ag20PVC30 composite electrode record color removal till 61% but the stability of electrode is low and the cost to fabricate the electrode was higher. As the main criteria electrode used in any electrochemical process should be stable chemically and physically [14, 15]. Therefore, the selection of good composite electrode is not only based on the ability to remove the color, but chemical stability as well. The composition of C50Co20PVC30 was identified as best composite, then it was used in the next experiment.

In further experiment, formation of hypochlorite ion has been investigated by adding 1.5% (w/v) NaCl solution to 50 mL of deionized water in electrochemical cell. During treatment process, hypochlorite ions production was linked to presence of chloride ions. It was believed that the presence of hypochlorite ions able to degrade chemical pollutants in leachate samples [16]. The formation of hypochlorite ion in aqueous solution was determined using UV-visible spectrophotometer. Comparison of four characteristics (color, cost, hypochlorite ion formation and electrode stability) to determine the best composite electrode is shown in Figure 1.




Note: 1. C50Ag20PVC30, 2. C50Co20PVC30, 3. C60Ag10PVC30, 4. C70Ag10PVC30, 5. C70Ag10PVC20, 6. C60Co10PVC30, 7. C70Co10PVC30, 8. C50Al20PVC30, 9. C60Al10PVC30 and 10. C70Al10PVC20

Figure 1. Comparison of different composite electrode in term of a) color removal, b) electrode cost in USD, c) hypochlorite ion formation in deionize water and d) electrode stability

## Conclusion

The present study successfully proves the most suitable charcoal base metallic composite electrode is C50Co20PVC30 as anode in electrochemical oxidation process for the treatment of landfill leachate. It was successfully performed for color removal and good stability. The color removal efficiency (58%) linked to increase the presence of hypochlorite ion, then lead the degradation of organics present in the effluent.

## Acknowledgement

This work was supported by the National University of Malaysia and Ministry of Higher Education, Malaysia through grants number FRGS/2/2013/SG01/UKM/01/1 are gratefully acknowledged.

## References

1. Noruzman, H. A., Ismail, M. B. and Abdul-Majid, Z. (2012). Characteristics of treated effluents and their potential applications for producing concrete. *Journal of Environmental Management*, 15: 27 – 32.
2. Jumaah, M. A., Othman, M. R. and Yusop, M. R. (2016). Batch method treatment of landfill leachate using charcoal composite. *International Journal of Chem Tech Research*, 9: 583 – 586.
3. Pérez-González, A., Urtiaga, A. M., Ibáñez, R. and Ortiz, I. (2012). State of the art and review on the treatment technologies of water reverse osmosis concentrates. *Water Research*, 46(2): 267 – 283.
4. Martinez-Huitle, C. A. and Ferro, S. (2006). Electrochemical oxidation of organic pollutants for the wastewater treatment: Direct and indirect processes. *Chemical Society Reviews* 35: 1324 – 1340.
5. Deng, Y. and James, D. E. (2007). Electrochemical oxidation for landfill leachate treatment. *Waste Management,* 27: 380 – 388.

6. Mook, W. T., Chakrabarti, M. H., Aroua, M. K., Khan, G. M. A., Ali, B. S., Islam, M. S. and Hassan, M. A. (2012). Removal of total ammonia nitrogen (TAN), nitrate and total organic carbon (TOC) from aquaculture wastewater using electrochemical technology: A review. *Desalination*, 285: 1 – 13.
7. Jumaah, M. A., Othman, M. R. and Yusop, M. R. (2016). Characterization of leachate from Jeram Sanitary Landfill-Malaysia. *International Journal of ChemTech Research,* 9: 571 – 574.
8. MoayeriKashani, M., Soltani, S. M. and Sobri, S. (2012). Treatment of a Malaysian leachate sample using electrocoagulation. *International Journal of Chemical Engineering and Applications*, 3(1): 63 – 66.
9. Zakaria, Z., Nordin, N., Hasan, S. Z., Baharuddin, N. F., Jumaah, M. A. and Othman, M. R. (2015). Decolorization of reactive orange 16 dye using fabricated charcoal base metallic composite electrode. *Malaysian Journal of Analytical Sciences,* 19: 493 – 502.
10. Jumaah, M. A., Othman, M. R. and Zakaria, Z. (2015). Fabrication of selected metal powder composite electrode for landfill leachate treatment using electrochemical method. *International Journal of Chemical Sciences* 13: 943 – 954.
11. Ruiz, V., Blanco, C., Granda, M., Menéndez, R. and Santamaría, R. (2007). Influence of electrode preparation on the electrochemical behaviour of carbon-based supercapacitors. *Journal of Applied Electrochemistry,* 6: 717 – 721.
12. Jumaah, M. A. and Othman, M. R. (2015). Study the efficiency of various metal powder composition electrodes based on landfill leachate treatment. *International Journal of ChemTech Research,* 8: 559 –563.
13. Jumaah, M. A. and Othman, M. R. (2015). Optimization of operating conditions for landfill leachate treatment using electrochemical oxidation technique. *International Journal of ChemTech Research* 8: 783 – 787.
14. Jumaah, M. A. and Othman, M. R. (2015). COD removal from landfill leachate by electrochemical method using charcoal-PVC electrode. *International Journal of ChemTech Research* 8: 604 – 609.
15. Nordin, N., Amir, S. F. M., Yusop, M. R. and Othman, M. R. (2015). Decolorization of CI reactive orange 4 and textile effluents by electrochemical oxidation technique using silver-carbon composite electrode. *Acta Chimica Slovenica*, 62: 642 – 651.
16. Jumaah, M. A. and Othman, M. R. (2015). Optimization of electrochemical parameters for landfill leachate treatment using charcoal base metallic composite electrode. *Malaysian Journal of Analytical Sciences*, 19: 531 – 540.
17. Othman, M. R. and Riyanto (2012). Electrochemical stability of Cu, Ni, Co, Pt and Ir metals sheet and their composite electrodes in potassium hydrox de solution. *International Journal of Electrochemical Science*, 7: 8408 – 8419.
18. Jumaah, M. A., Othman, M. R. and Yusop, M. R. (2016). Electrochemical treatment of landfill leachate: Optimization of COD removal using charcoal- graphite- cobalt- polyvinyl chloride electrode. *Research Journal of Pharmaceutical, Biological and Chemical Science,* 7: 2812 – 2816.